CONSULTANT REPORT

PIER
Public Interest Energy Research
CALIFORNIA ENERGY COMMISSION

Strategic Energy Research

ELECTRIC SYSTEM SEISMIC SAFETY AND RELIABILITY

Gray Davis, *Governor*

JUNE 2000

CALIFORNIA ENERGY COMMISSION

RESOURCES AGENCY

P600-00-031

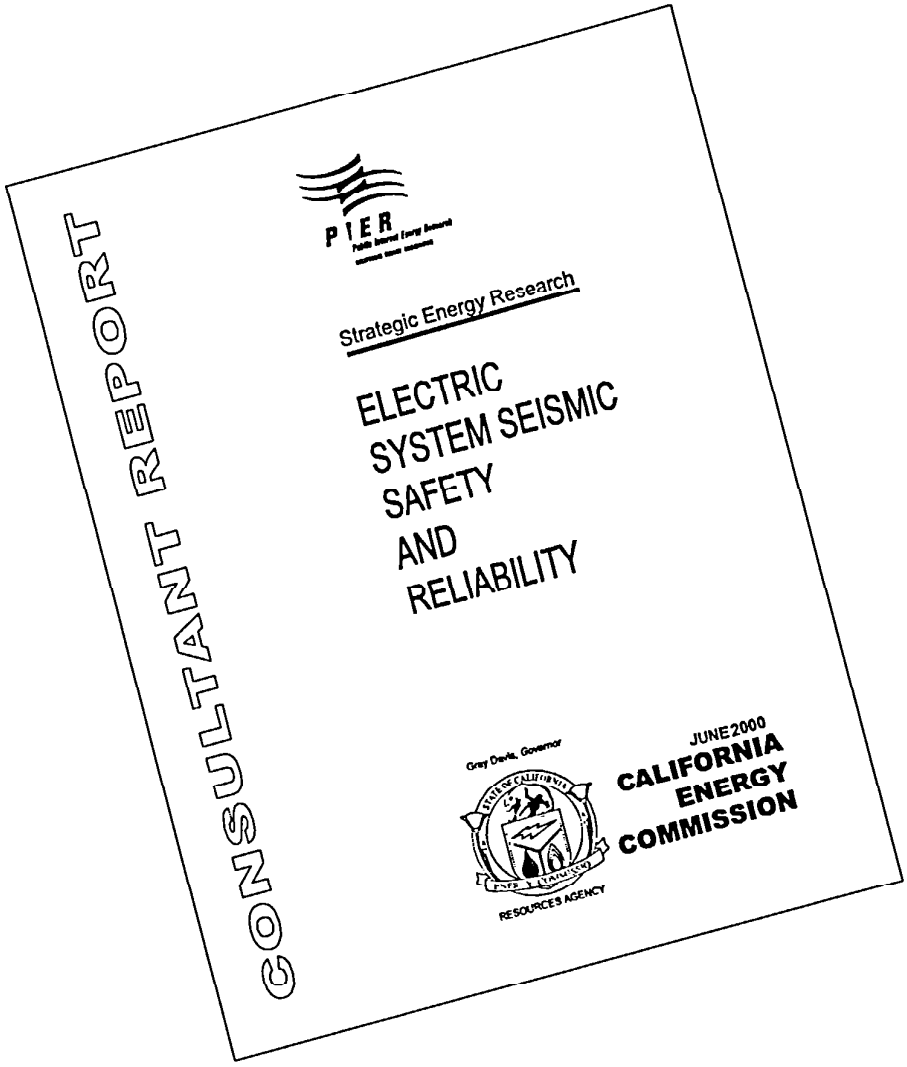

CALIFORNIA ENERGY COMMISSION

Prepared for:
CALIFORNIA ENERGY COMMISSION

Prepared by:
William Savage
PACIFIC GAS AND ELECTRIC COMPANY

San Francisco, CA

Contract No. 500-97-010
Project No. 09

Contract Amount: $1,000,000

Robert Anderson, *Project Manager*
ENGINEERING OFFICE

Robert Therkelsen, *Deputy Director*
ENERGY FACILITIES SITING & ENVIRONMENTAL PROTECTION DIVISION

Gary Klein, *Contract Manager*
ENERGY TECHNOLOGY DEVELOPMENT DIVISION

Legal Notice

This report was prepared as a result of work sponsored by the California Energy Commission (Commission). It does not necessarily represent the views of the Commission, its employees, or the State of California. The Commission, the State of California, its employees, contractors, and subcontractors make no warranty, express or implied, and assume no legal liability for the information in this report; nor does any party represent that the use of this information will not infringe upon privately owned rights. This report has not been approved or disapproved by the Commission nor has the Commission passed upon the accuracy or adequacy of this information in this report.

Pacific Gas and Electric Company prepared this report. Neither Pacific Gas and Electric Company nor any of its employees and agents:

Make any written or oral warranty, expressed or implied, including, but not limited to those concerning merchantability or fitness for a particular purpose.

Assume any legal liability or responsibility for the accuracy, completeness, or usefulness of any information, apparatus, product, process, method, or policy contained herein.

Represent that its use would not infringe any privately owned rights, including, but not limited to, patents, trademarks, or copyrights.

Acknowledgments

The success of a research program of this size and complexity depends on the efforts of many individuals. The project's success was also the product of the alignment of interests and administrative support of the participating institutions: the General Services, Distribution and Customer Service, and Generation, Transmission, and Supply Business Units of Pacific Gas and Electric Company (PG&E); the Pacific Earthquake Engineering Research Center (PEER) administered by the University of California at Berkeley (UC Berkeley); and the Public Interest Energy Research (PIER) Program at the California Energy Commission (Commission). This work was supported in part by PEER through the Earthquake Engineering Research Centers program of the National Science Foundation under Award Number EEC-9701568. Common interest components of this program were cost-shared by the California Department of Transportation (Caltrans) under the Program of Earthquake Applied Research for Lifelines (PEARL).

The participation of the following individuals is recognized and acknowledged:

Project Management:

Dr. William Savage, Dr. Norman Abrahamson, and Mr. Lloyd Cluff, PG&E
Professors Gregory Fenves and Jack Moehle, PEER
Mr. Bob Anderson, Ms. Judy Grau, and Mr. Gary Klein, Commission

Joint Management Committee (JMC)

PG&E Members:

Dr. Norman Abrahamson, Senior Engineering Seismologist
Mr. Lloyd Cluff, Seismic Geologist and Manager, Geosciences Dept.
Mr. Kent Ferre, Senior Structural Engineer
Mr. Eric Fujisaki, Senior Civil Engineer
Mr. Edward Matsuda, Grid Engineering Supervisor
Dr. William Savage, Senior Seismologist

PEER Members:

Prof. Jonathan Bray, UC Berkeley
Prof. Gregory Fenves, UC Berkeley, Chair of the JMC
Prof. Wilfred Iwan, California Institute of Technology
Prof. Anne Kiremidjian, Stanford University
Prof. Jack Moehle, UC Berkeley

Caltrans Member:

Dr. Clifford Roblee, Chief, Geotechnical Research

Of the many others who assisted in the conduct of the research program, the following are particularly recognized:

PG&E: Tammie Candelario, Tom Walsh, Roger Gray, Nancy Stamm, Maria Poppas, Katherine Lee, Henry Ho, and Joyce Chan
PEER and UC Berkeley: Joanne Cortez, Linda Rutkowski, Janet Cooks, and Betty Marton
Commission: Judy Efhan, Thomas Tanton, and Commissioner David Rohy

The research included individuals from other West Coast utilities. The participation and expertise of James Kennedy (Southern California Edison), Alan King (BC Hydro), Leon Kempner (Bonneville Power Administration), and Anshel Schiff (Consultant) are acknowledged.

Table of Contents

Section **Page**

PREFACE ..... **VIII**

EXECUTIVE SUMMARY **2**

ABSTRACT **12**

1.0 INTRODUCTION **14**

1.1 Purpose of Research 14
1.2 Background 15
1.3 Transition Funding for Strategic Energy Research 16
1.3.1 Research Topics 16
1.3.2 Project Selection 17

2.0 RESEARCH RESULTS **20**

2.1 Topic 1: Ground Motion and Site Response 20
2.1.1 Objectives 20
2.1.2 Evaluation of Three Numerical Procedures for Simulating Near-fault Long-period Ground Motions. 20
2.1.3 Surface Geology-Based Strong-Motion Amplification Factors for San Francisco and Los Angeles Areas 23
2.1.4 Evaluation of Uncertainties in Ground-Motion Estimates for Soil Sites 25
2.1.5 Ground Motions for Site Response Estimates—Two Applications 27
2.1.6 Resolution of Site Response Issues for the Northridge Earthquake (ROSRINE IV-A) 28
2.1.7 Conclusions and Recommendations 29
2.2 Topic 2: Ground Motion Estimates for Emergency Response 30
2.2.1 Objective 30
2.2.2 Rapid Estimation of Ground Shaking for Emergency Response 30
2.2.3 Conclusions and Recommendations 31
2.3 Topic 3: Ground Deformation Database 32
2.3.1 Objective 32
2.3.2 Enhanced Ground Deformation Database 32
2.3.3 Conclusions and Recommendations 33
2.4 Topic 4: Electrical Substation Equipment Performance 34
2.4.1 Objectives 34
2.4.2 Seismic Evaluation of 550 kV Porcelain Transformer Bushings 34
2.4.3 Performance of 230 kV and 500 kV Bushings 36
2.4.4 Analytic Studies of Substation Equipment Interaction 38
2.4.5 Experimental Studies of Substation Equipment Interaction 41
2.4.6 Amplification of Ground Motions at the Base of Transformer Bushings 43
2.4.7 Rocking Response and Overturning of Equipment 45
2.4.8 Field Investigation of Effects of the Kocaeli, Turkey, Earthquake 47
2.4.9 Conclusions and Recommendations 49
2.5 Topic 5: Earthquake Fire Safety Associated with Gas and Electric Systems 51

2.5.1 Objective 51
2.5.2 Ignition of Fires Following Earthquakes Associated with Natural Gas and Electric Distribution Systems 51
2.5.3 Conclusions and Recommendations 54

3.0 PROJECT ADMINISTRATION 56

4.0 CONCLUSIONS AND RECOMMENDATIONS 58

4.1 Conclusions 58
4.2 Benefits to California 59
4.3 Recommendations 60

Appendices

Appendix I Phase I Research Projects

Appendix II Request For Proposals

Appendix III Final Reports of Research Projects

Evaluation of Numerical Procedures for Simulating Near-fault Long-period Ground Motions Using Graves Method; P. Somerville, Woodward-Clyde Federal Services

Evaluation of Numerical Procedures for Simulating Near-fault Long-period Ground Motions Using Zeng Method; Y. Zeng and J. Anderson, University of Nevada, Reno

Evaluation of Numerical Procedures for Simulating Near-fault Long-period Ground Motions Using Silva Method; W. Silva, Pacific Engineering and Analysis

Surface Geology-based Strong-motion Amplification Factors for San Francisco and Los Angeles Areas; W. Silva, Pacific Engineering and Analysis

Evaluation of Uncertainties in Ground Motion Estimates for Soil Sites; J. Stewart, UCLA

Ground Motions for Site Response Estimates—1906 Earthquake; P. Somerville, Woodward-Clyde Federal Services

Ground Motions for Site Response Estimates—Permanent Ground Deformation Models; W. Silva, Pacific Engineering and Analysis

ROSRINE IV-A; T. Henyey, University of Southern California

Rapid Estimation of Ground Shaking for Emergency Response; D. Dreger, UC Berkeley

Enhanced Ground Deformation Database, J. P. Bardet, UC Santa Barbara

Seismic Evaluation of 550 kV Porcelain Transformer Bushings, G. Fenves and A. Whittaker, UC Berkeley

Performance of 230 kV and 500 kV Bushings; G. Fenves and A. Whittaker, UC Berkeley

Analytical Studies of Substation Equipment Interaction; A. Der Kiureghian, UC Berkeley

Experimental Studies of Substation Equipment Interaction; A. Filiatrault, UC San Diego

Amplification of Ground Motions at the Base of Transformer Bushings; R. Villaverde and G. Pardoen, UC Irvine

Rocking Response and Overturning of Equipment; N. Makris, UC Berkeley

Field Investigation of Effects of the Kocaeli, Turkey, Earthquake; R. Anderson, CA Energy Commission, W. Savage, Pacific Gas and Electric Company, and F. Erdogan, Turkish Electric Generation and Transmission Company

Ignition of Fires Following Earthquakes Associated with Natural Gas and Electric Distribution Systems; R. B. Williamson, UC Berkeley

List of Tables

Table	Page
Table 1. Funded Research Projects 1998-2000	18
Table 2. Site Categories Based on Surface Geology	24
Table 3. ROSRINE Program Sites	29
Table 4. Kocaeli Earthquake Investigation Team and Collaborators	47

Preface

The Public Interest Energy Research (PIER) Program supports public interest energy research and development that will help improve the quality of life in California by bringing environmentally safe, affordable, and reliable energy services and products to the marketplace.

The PIER Program, managed by the California Energy Commission (Commission), annually awards up to $62 million through the Year 2001 to conduct the most promising public interest energy research by partnering with Research, Development, and Demonstration (RD&D) organizations, including individuals, businesses, utilities, and public or private research institutions.

PIER funding efforts are focused on the following six RD&D program areas:

- Buildings End-Use Energy Efficiency
- Industrial/Agricultural/Water End-Use Energy Efficiency
- Renewable Energy
- Environmentally-Preferred Advanced Generation
- Energy-Related Environmental Research
- Strategic Energy Research.

In 1998, the Commission awarded approximately $17 million to 39 separate transition RD&D projects covering the five PIER subject areas. These projects were selected to preserve the benefits of the most promising ongoing public interest RD&D efforts conducted by investor-owned utilities prior to the onset of electricity restructuring.

What follows is the final report for the Electric System Seismic Safety and Reliability project, one of nine projects conducted by the Pacific Gas and Electric Company. This project contributes to the Strategic Energy Research program.

For more information on the PIER Program, please visit the Commission's Web site at: http://www.energy.ca.gov/research/index.html or contact the Commission's Publications Unit at 916-654-5200.

Executive Summary

The safety and reliability of electric power is given high priority by almost all sectors of society in California. Electricity is the fundamental fuel for the economic engine of technology, manufacturing, and commerce. Even brief power outages can be costly and disruptive to the current fast pace of business and everyday life. The earthquakes in California in 1989 and 1994 are a warning of the potential of even larger and more severe earthquakes to affect the state. Thus, evaluating and improving the post-earthquake functioning of electric power service is an important priority both for providers of that service and for their customers. This report describes the results of applied research being conducted under the direction of Pacific Gas and Electric Company (PG&E) through support of the California Energy Commission (Commission), with the objective of systematically reducing earthquake risks to electric power in California.

Background

In 1996, PG&E initiated a rate-payer funded, utility-directed research program to develop new and improved data sets, models, and methods that could be rapidly incorporated into the company's Earthquake Risk Management Program. This program had been initiated in 1987 and was expanded and accelerated with the experience and lessons of the 1989 Loma Prieta and 1994 Northridge earthquakes. The goal of the applied research program was to allow the utility to better understand the earthquake performance of gas and electric systems, and to develop ways and means, beyond those already known and applied, to improve the systems' safety and reliability, thereby significantly reducing earthquake risks.

A partnership was established with the Pacific Engineering Research Center (PEER), based at the University of California, Berkeley (UC Berkeley), to conduct the research. This collaboration quickly became effective, producing practical results that built on the involvement of talented researchers and excellent facilities in the PEER consortium of universities.

Objective

The objective of this project is to provide data, models, and methods needed to reduce the earthquake vulnerability and to improve the system reliability and safety of electric transmission and distribution systems. Once implemented, these research results would enable faster post-earthquake restoration of customer service by reducing the amount of damage and disruption of electric transmission and distribution service caused by earthquakes, and by providing more accurate and rapidly available post-earthquake information about the state of damage produced by earthquakes. The research results could also be used, as appropriate, by businesses, industry, regulatory agencies, and the general public to reduce earthquake vulnerabilities and respond more effectively to earthquake affects in California and elsewhere.

Topics

PG&E scientists, engineers, and operations specialists identified seven topics of needed research based on the current state of knowledge about earthquake hazards and vulnerabilities of the electric transmission and distribution systems. These topics, incorporating the results of previous research conducted by PG&E and PEER, are described below.

- **Topic 1**: Ground Motion and Site Response -- The site-specific assessments of near-fault ground shaking, and of ground motions at soil sites, need to be improved for more accurate performance assessments of facilities exposed to large earthquakes.
- **Topic 2**: Ground Motion Estimates for Emergency Response -- Accurate and quickly available post-earthquake information about the location of potentially damaging strong ground motions is needed to improve emergency response by utilities for more rapid restoration of utility service.
- **Topic 3**: Ground Deformation Database -- The empirical basis for estimating potential earthquake-related ground deformation needs to be more reliable and accurate for the design of substations and other critical components in the transmission and distribution system.
- **Topic 4**: Electrical Substation Equipment Performance -- Experimental studies and related analyses of different designs and retrofits of high-voltage transformer and interconnected equipment are needed to assure the adequate performance of the electric transmission grid in earthquakes.
- **Topic 5**: Earthquake Fire Safety Associated with Gas and Electric Systems -- A basis is needed for choosing optimal ways to reduce the threat of post-earthquake fires due to natural gas and electric power.
- **Topic 6**: Building Vulnerability -- The protection of utility employees and the general public, and the ability to rapidly restore utility services, are both dependent on assuring the appropriate level of earthquake performance of utility office building, warehouses, service centers, and control buildings. The ability to make accurate assessments of building performance when exposed to various levels of earthquake shaking needs to be improved.
- **Topic 7**: Seismic Vulnerability of Underground Cables -- Because underground high-voltage and low-voltage electric cables are potentially exposed to damaging permanent ground deformation in earthquakes, the vulnerability of existing cables needs to be quantitatively assessed.

The research topics listed above are broad, and it was not immediately obvious what specific research steps were optimal to address the identified needs. PG&E and PEER developed an innovative and effective means to develop specific research projects that would involve the most knowledgeable academic personnel and would provide practical results at the end of each project. PG&E and PEER formed a Joint Management Committee (JMC) composed of five or six representatives from each organization. The JMC provided a forum for identifying the scopes of work of well-focused research projects, selecting highly qualified investigators to conduct the projects, and monitoring the work so that utility user needs would be met. The JMC made coordination with other research activities outside of the Commission-funded project more effective. A representative of the California Department of Transportation joined the JMC during the course of the program to provide input and coordination with their ongoing research.

The JMC approved a detailed Request for Proposals to address the seven topics. Based on the responses received, the JMC decided to eliminate Topics 6 and 7 and to concentrate on the first five topics in this program, deferring research on the other two topics to the future. This

program funded a total of 18 research projects. The following discussions, organized around the five topics, summarize the results of these research projects.

Topic 1: Ground Motion and Site Response

Objective

In this topic, eight interrelated projects were carried out to improve and verify the data, models, and methods used to predict earthquake ground motions at utility structures and equipment sites, thus improving inputs to earthquake performance assessments of those facilities. Accurately estimating the ground-shaking effects of future earthquakes is complex and depends on (1) accurate observations of ground motions and the sites on which they are located, and (2) unbiased models and methods for predicting ground motions at any location. The projects described below comprehensively address these needs.

While the strong shaking expected near faults in large (magnitude 7 or greater) earthquakes is very important for facility design and performance evaluation, to date there is only one very well recorded earthquake—the Chi-Chi, Taiwan event of September 21, 1999. In the absence of a robust statistical database, numerical procedures for the reliable simulation of near-fault ground motions are needed for engineering purposes.

Outcomes

In three parallel projects, the ability for three widely used simulation methods to predict the near-fault (within 15 km) recorded ground motions from five pre-1999 earthquakes was evaluated. The evaluation showed that all three methods were successful in replicating the main effects of rupture directivity on ground motions greater than one second in period. With this level of confidence, the models will next be tested against the 1999 data from Taiwan and Turkey. When those data are correctly replicated, the numerical procedures can be used to develop simple parametric models for near-fault ground motions for use in seismic hazard analysis.

In the interim, before the simulation methods can be fully tested, two additional projects exercised the best available techniques to provide estimated ground motions to be used by other projects in this program in cases in which no recorded ground motions were available. The simulated motions were used in the ground response and ground deformation database projects.

The collaborative project called Resolution of Site Response Issues for the Northridge Earthquake (ROSRINE) has been of great value in improving engineering models for estimating site response, and has collected data for more than 40 sites. This PG&E-PEER project supported the collection of site characterization data using boreholes and surface measurements for six additional sites. As shown in the next project summary, the aggregate site characterization database enables the development of improved analysis tools for ground motion response for design and performance assessments.

It is widely observed that ground motions on soil are different from, and typically more severe than, those observed on nearby rock outcrops. In two companion projects, the existing data base of ground motions was analyzed to determine site response factors that quantify the differences in ground motions for difference types of soil, and the benefit of using such site

response factors was quantitatively assessed. The site response analysis using surface geology classifications was calibrated using the high-quality site soil characteristics determined in the ROSRINE project. The study showed the site-specific analysis provides significantly improved accuracy in estimating the response of an individual site compared to using generic soil models. Uncertainties in site response estimation are relatively high for soft clay sites, but can be estimated from broad site categories for stiffer sites. These results are immediately useful in utility ground motion evaluations, both probabilistic and deterministic.

Summary

The results of the projects under this topic have immediate application to refined ground motion assessments at sites of both utility and customer facilities. These more accurate assessments can be used for design of new facilities to resist earthquake effects, as well as for the identification of facilities whose future performance in earthquakes is not adequate and needs improvement. In both cases, the implementation of these results leads to greater service reliability and improved safety for utility customers.

Topic 2: Ground Motion Estimates for Emergency Response

Objective

The objective of the project carried out for this topic was to make significant progress in improving the immediate post-earthquake location of areas of strong earthquake shaking, and thus of potential building damage, to enable utility and other emergency responses to be more accurately deployed. In some portions of Southern California there are now sufficient closely spaced strong-motion instruments to enable such information to be compiled into what is called a ShakeMap. However, in other parts of the state, more widely distributed instrumentation exists, including both strong motion and broadband instruments.

Outcomes

This project focused on developing a procedure to rapidly analyze broadband seismic data to estimate the pattern of strong ground motions following a potentially damaging earthquake. The method has been calibrated using the records from the 1992 Landers and 1994 Northridge earthquakes and can provide results in about 20 minutes for any area in the state.

Summary

Future plans for this method are to improve it to better handle earthquakes with large fault ruptures, and to integrate it into the rapid earthquake analysis systems being operated by United States Geological Survey (USGS), California Institute of Technology (Caltech), and UC Berkeley. When these results are implemented, PG&E's emergency response personnel and customers and other Californians in earthquake-affected areas can benefit by emergency response that is more rapidly and more accurately directed to the areas with severe building damage and utility and transportation system disruption. This improved emergency response will save lives and promote faster restoration of utility services and recovery of normal living conditions following the earthquake.

Topic 3: Ground Deformation Database

Objective

The objective of the project carried out under this topic was to improve the existing database of ground deformations observed in past earthquakes.

Outcomes

Extensive data on amounts of ground deformation due to liquefaction from the 1995 Kobe, Japan earthquake were quality checked and incorporated into the existing statistical database. Pre-1995 data in the database were systematically reviewed and checked using original sources. Particular attention was paid to smaller deformations, in the range of 0.1 to 2 meters, which are significant for underground utilities, but have received little attention from the research community.

Summary

The database produced by this project will be the basis for developing a simplified model for preparing probabilistic maps of potential ground deformation following earthquakes. With the application of these products, electric power customers will benefit from reduced outages due to new facilities being better designed to avoid or resist earthquake-related ground deformation. As a byproduct of these results, other critical utilities, such as water and natural gas distribution and wastewater collection, can take advantage of the improved knowledge of ground deformation hazards to reduce future earthquake losses and improve the reliability of post-earthquake functionality.

Topic 4: Electrical Substation Equipment Performance

Objectives

The vulnerability of high-voltage substation equipment, particularly transformers, has been the primary reason that power grids have failed in past earthquakes. The objectives of the seven projects carried out under this topic were to improve the understanding of the vulnerability of transformers and interconnected substation equipment, and to identify specific actions that can be taken to reduce significant vulnerabilities.

Outcomes

Two projects focused on the porcelain insulators used in power transformers to insulate the conductors that pass through the body of the transformer to connect to the internal windings. Shaking-table tests were performed on several different transformer insulators, called bushings, in two voltage classes, 196,000 volts (196 kV) and 550 kV. Testing was done in accordance with the shaking levels used in the industry qualification standard for substation equipment, Institute of Electrical and Electronics Engineers (IEEE) Std 693-1997. Data collected during the tests identified factors that lead to improved bushing ruggedness, including higher clamping forces holding the bushing on the transformer, and using a modified retrofitted retaining ring at the base of the bushing. Important modifications needed in the IEEE Std 693-1997 testing and analysis procedures were also identified.

In a related study, experimental data on the vibratory response of large transformers were collected to measure the effect that the transformer body has on the level of shaking transmitted to the bushing in an earthquake. These tests revealed that the sources of flexibility of a

transformer need to be better understood, since there was a significant reduction in the vibration frequency of bushings mounted on a transformer versus the same bushing tested on a shaking table support. The tests also indicated that the simple model used in IEEE Std 693-1997 is not adequate to account for the complex behavior of the bushing and support system of a large transformer.

Conductors that are used to electrically interconnect substation components can also damage those components if the relative motions of the components exceed the conductor slack. Shaking table testing and analytical modeling of flexible strap and cable connectors of configurations currently in use by PG&E and other utilities were carried out in two projects. The analytical studies developed a simple concept of Response Ratios that relates the unconnected performance of the equipment to its performance when connected. A method was also developed to estimate the conductor slack required to prevent the effects of interaction during strong shaking. A coordinated set of shaking table tests on bus connectors produced a good test data set that confirmed the analytical studies and demonstrated that significant energy dissipation occurs when shaken equipment is connected.

In past earthquakes, rocking and toppling of substation equipment, particularly transformers, has been observed. Analytical studies were extended to investigate such factors as the influence of anchorage strength, the role of vertical seismic motions, and the impact loading associated with rocking. The results showed that conventional engineering methods using static coefficient analysis provide a safe design in most cases. Although vertical motions were found to be insignificant, there are certain frequencies of rocking that have a heightened potential for overturning. These results can be readily formed into practical engineering design guidelines.

A special project was instituted late in the research program to help deploy a post-earthquake investigation team from PG&E and the Commission to assess the impacts of the Kocaeli, Turkey earthquake of August 17, 1999 on the Turkish electric transmission and distribution system. The team found that the types of damage that occurred were typical of past earthquakes, but that the designed redundancy of the transmission system coupled with an aggressive emergency response effort enabled power to be restored within less than one day to all but the most heavily damaged cities. The lessons from this earthquake affirmed the scope and purpose of the PG&E-PEER-Commission research program.

Summary

These results provided both immediately useable performance information about currently installed equipment, and guidance for additional studies to specify practical mitigations of significant earthquake vulnerabilities in substation equipment. The application of these results could lead to improved designs and procedures for substation equipment purchase and installation, directly providing reduced outage times for the electric grid following earthquakes, both benefiting customers and optimizing equipment expenditures by the utility.

Topic 5: Earthquake Fire Safety Associated with Gas and Electric Systems

Objectives

The ignition and fueling of fires following earthquakes has long been a concern in earthquake-prone regions. This study focused on life-safety issues. It used a logical methodology to

examine the factors affecting sources of fuel and ignition, and the potential for structural damage that could trap occupants.

Outcomes

In this project, the scenarios that have led to fire ignitions in past earthquakes were derived from review of post-earthquake fire data for the 20th century. The primary factor involved in fire ignitions is structural and non-structural building damage. Alternate means to reduce fire risks were analyzed for residential structures. The study resulted in identifying older, seismically vulnerable multi-family residential buildings (R-1 occupancies) as presenting the most likely setting for people to be trapped inside and exposed to life-safety threats from fire.

Summary

Improvement of structural performance would significantly improve fire safety in these structures; however, the installation of appropriate gas flow interruption devices could provide some protection to the occupants in the absence of structural improvements. One- or two-family residences (R-3 occupancies) typically have multiple means of egress and pose a significantly lower life-safety threat. For R-3 structures, the primary fire-safety improvements are to anchor water heaters and other appliances, and install flexible connectors to reduce the potential for gas leaks. This study provided information and analyses that are useful contributions towards the process of improving earthquake-related fire safety and promotes the wider distribution of accurate information on alternative safety improvement actions.

Conclusions and Recommendations

Conclusions

The goal of this applied research program was to improve the earthquake safety and reliability of electric power transmission and distribution in California. The research program was organized by the JMC to assure that the research results would directly address electric utility needs in preparing for future earthquake occurrences, and that the results could be quickly implemented by utility personnel or their consultants.

As described in the previous sections of this report, the 18 projects have provided useful results that meet utility needs in the five topic areas. However, it is important to also note the integration of the projects to meet the goal of the program, namely to improve utility earthquake performance. The following bullets summarize, in narrative form, the cumulative connections between the topics that address the goal.

- **Topic 1** results (improved ground motion and site response models and methods) are used as input to **Topic 2** (rapid estimation of ground shaking for emergency response)
- Topic 1 results are used as input to **Topic 3** (ground motion database) to improve the assessment of locations and amounts of post-earthquake permanent ground deformation caused by ground shaking.
- Topic 1 results, along with Topic 3 results, are used as input to **Topic 4** (assessing the vulnerability of pieces of substation equipment and the vulnerability of interconnected equipment). Severe ground shaking and ground failure are the direct causes of substation damage that can disrupt power transmission to customers.

- Topic 1 and 3 results improve the assessment of building damage (damaged buildings are the structures within which most earthquake-caused fires start), and thus underlie and are input to **Topic 5** (earthquake fire safety associated with gas and electric systems). Levels of ground shaking can be used to control utility service shutoff valves and to quickly identify likely locations of damaged buildings where fires could start and people could be trapped.

Although the connections among the individual projects are multi-faceted, a broad picture can be seen of the research results linking up to enable utility personnel (and their regulatory counterparts) to have significantly improved information for taking actions regarding earthquake risks. These actions often include retrofitting a vulnerable building that houses office workers, upgrading equipment and improving anchorages in substation yards, and modifying emergency response procedures to take advantage of new information. The customer benefits from these actions following an earthquake in terms of greater electric power reliability, and faster and less expensive recovery of the overall functioning of society. Of course, there will always be some utility system damage due to random failures of components or facilities. However, the redundant electric system design and the operation skill of utility personnel can make the extent and duration of outages no worse than those of a winter storm.

Benefits to California

The measure of the success of this user-driven, applied research program is the extent to which the results are being put to use to directly benefit the California electric power ratepayers and others in the state. Even before the reports were prepared, some of the results, such as the substation equipment seismic performance data and analyses, were being implemented in managing the equipment inventory at several utilities and in preparing to modify the national seismic qualification procedures for substation equipment. Significant progress has been made in the ultimate goal of the project, to improve electric system safety and reliability in earthquakes. Clear directions for further applied research were also identified, and provide the basis for planning the next phase of work.

When the results have been implemented in the utility system, then the ratepayers (who have funded this research) and other members of society will benefit from the research by (1) receiving more rapid restoration of service following an earthquake due to less utility damage and improved emergency response capability, (2) avoiding possible utility rate increases because there is less direct damage to equipment and facilities, and (3) experiencing more rapid overall recovery of societal functioning following the earthquake due to rapid power restoration and use of the research results by other organizations to recover their functionality more quickly.

This research program provides several additional benefits to utilities and to the State of California. Although they are secondary to the goal of this program, these benefits have substantial long-term value.

- Enhanced academic expertise: This research program has created an expanded group of university faculty who have gained extensive knowledge about electric utility systems and who have demonstrated interest and talent in addressing utility research needs and problems. In the future, they will have opportunities to continue research in these areas,

and to guide their students into graduate work involving utility systems and earthquakes. This reservoir of academic experience will provide ongoing benefits to the utility industry and the State.

- The establishment of the PG&E-PEER-Commission research program has attracted great interest nationally. Other organizations, both public and private at the local to national level, have observed the success of the program, and are influenced by its research goals and project topics. Thus, by providing strong technical leadership, well-defined research project scopes, and results that have clear value and applicability, the PG&E-PEER-Commission program is helping to shape the direction and topics of other research activities. Over the next several years, there will be more coordination of research among the funding agencies, if not among the individual researchers. This coordination will significantly leverage the results of the studies reported herein.

- The PG&E-PEER-Commission program has also attracted highly motivated research partners who are willing to co-fund this program's future work or to perform separately funded but closely coordinated studies that fit together nearly seamlessly. The California Department of Transportation (Caltrans) is the first such partner. It is likely that in the next several years a number of others will join.

Recommendations

Although the results of the individual research projects reported herein have successfully met their objectives, it is clear that there are additional research activities whose results would provide further improvements in the earthquake performance of utility systems. Many of these opportunities for further study and implementation have been identified in previous sections. They include the following major research areas:

- Ground Motion and Site Response: More accurate ground-motion assessments for utility sites are critical to evaluate the seismic hazard at those sites and to make good risk management decisions. Data and models to reduce uncertainties in ground motions are needed, particularly for locations near large-magnitude seismic events. Because current databases and models for predicting site response have limitations and uncertainties, improved and reliable methods for assessing site response are needed for assessing site-specific ground motions.
- Ground Deformation Database: Expanded empirical databases and new analysis tools need to be developed to better model the probability of permanent ground deformation as a function of geologic and geotechnical data and level of strong ground shaking, so that potential extensive damage to underground as well as above-ground utility structures can be reduced or avoided.
- Electrical Substation Equipment Performance: Further efforts are needed to accurately understand the seismic performance of existing high-voltage equipment to be able to either use elsewhere or replace equipment that is unacceptably vulnerable in its current locations. Seismic performance data obtained from shaking table tests and analytical models of substation equipment, their interconnections, and their system functionality under various earthquake scenarios would be important products of this research.

- Ground Motion Estimates for Emergency Response: Advanced instrumentation capabilities and methods for using them are needed so that strong-motion data and other data can be used to make rapid estimates of damage and functionality prior to getting input from experienced field operations personnel.
- Building Vulnerability: Additional data and models are needed to better assess expected earthquake performance of older substation buildings and service buildings to enable better decision-making by utilities regarding seismic retrofits or other mitigation measures for these buildings.
- Seismic Risk Analysis: A flexible and powerful capability to evaluate the likely functionality of customer services following earthquakes is needed. This capability could be used to evaluate alternative earthquake mitigation actions, and to evaluate the current state of earthquake preparedness of the utility system from the perspective of the utility, customer and regulator.

It is recommended that this successful earthquake research program be continued to address these and other topics.

The scope of further research projects needs to be viewed from a broad and integrated perspective to ensure that other related opportunities are not being missed. It is recommended that the continuation of this program should incorporate a comprehensive planning effort by the JMC.

It is also recommended that the next phase of the program be structured to provide for and to optimize the involvement of multiple co-funding organizations, particularly Caltrans. The JMC member organizations (PG&E, PEER, and Commission) should identify prospective additional partners and enlist their participation. Such efforts will enable significant leveraging of the available funding and make possible rapid gains in knowledge and applications to profoundly reduce earthquake risk in California.

Abstract

Pacific Gas and Electric Company (PG&E) under California Energy Commission contract number 500-97-010 has conducted a one-year user-driven applied research program in partnership with the Pacific Earthquake Engineering Research Center (PEER) based at the University of California, Berkeley. The goal of the program was to collect data, prepare models, and develop methods that could be rapidly and systematically applied to reduce earthquake vulnerability and improve earthquake safety and reliability of electric power for the benefit of utility customers and others in California. Once implemented, these research results would enable faster post-earthquake restoration of customer service through reducing the amount of damage and disruption of electric transmission and distribution service caused by earthquakes, and through providing more accurate and rapidly available post-earthquake information about the state of damage produced by earthquakes.

Five topics involving 18 research projects were addressed based on utility-identified needs for improving knowledge about earthquake hazards and vulnerabilities of electric transmission and distribution systems. PEER management and PG&E technical specialists monitored the projects, individually and collectively, to assure that practical, useful results were obtained.

1. Ground Motion and Site Response: Three numerical procedures for estimating near-fault ground motions were tested against data from recent earthquakes. After further calibration, these methods can be used for predicting ground motions near large-magnitude earthquakes. As part of the collaborative Resolution of Site Response Issues for the Northridge Earthquake (ROSRINE) project, six additional sites where strong ground motions were recorded in the Northridge earthquake were characterized using boreholes and geophysical measurements. These data will be used in future site response studies. Additional studies quantified site response effects, using the ROSRINE data for calibration of soil conditions.

2. Ground Motion Estimates for Emergency Response: A method was developed to estimate rapidly the distribution of strong ground motions from a large earthquake in California using a small number of broadband recordings of the event. This method supplements the use of strong-motion recordings in urban areas and provides maps of shaking severity anywhere in the State, for utilities and emergency response agencies.

3. Ground Deformation Database: Improvements were made in the accuracy and completeness of compiled observations of past earthquake-caused permanent ground deformation, particularly involving liquefaction and lateral spreading. This database will lead to improved probabilistic models for ground deformation, which can be used by utilities to design for or avoid areas of potentially damaging ground failure when installing facilities.

4. Electric Substation Equipment Performance: Shaking table testing and related analysis of high-voltage transformers and bushings led to improved fragility models for these critical substation components, and identified areas for improved design or retrofit practices. The potential for overturning of massive equipment and the effect of interconnection of pieces of equipment were also analyzed. The results are leading to

changes in industry practices and design of new equipment that will provide increased power reliability after a major earthquake.

5. Earthquake Fire Safety Associated with Gas and Electric Systems: Fire-safety factors were identified and logically modeled through assessment of past earthquake-caused fires,. Fires occur in proportion to building damage. Older, seismically vulnerable multi-family residential buildings are a particular concern for life safety. Alternate means of improving fire safety were reviewed, including building strengthening, water heater anchorage, gas shutoff devices, and coordination of power restoration where significant building damage occurs.

1.0 Introduction

1.1 Purpose of Research

The greatest single natural-hazard threat to the reliability of the electric power system in California is the likely occurrence of a major urban earthquake. The 1989 Loma Prieta and 1994 Northridge earthquakes, although deadly and destructive events, were only a portent of potential future earthquake affects. They serve as a warning to all sectors of society to increase the state of earthquake readiness. Emergency responders and society in general view post-earthquake functioning of utility systems, in particular electric power service, as absolutely vital for rapid response and recovery from a major urban earthquake.

In typical academic-based research, there is a time interval of as long as 10 to 20 years between the start of the research and the results being in a form useable for engineering applications. Preparing for earthquakes in California is too urgent to wait for a decade or more for implementation of research findings. The results are needed in the short term, not in the long term. The goal of this user-driven research program was to shorten the time between initiating research and practical application to less than two or three years.

Because of this accelerated schedule for getting the research into use, a framework has been developed to organize the types of research. We developed three classifications for the research conducted under this program: data, models, and methods.

- Research projects classified as **data** produce the scientific or engineering data sets that are necessary for subsequent studies. The data can be either empirical observations or data generated as part of numerical or experimental studies. In general, data are not the useable result, but rather are the input for the development of models or methods as discussed below. An example of a data project is the development of a database of ground deformations and the associated site information.
- Research projects classified as **models** produce simplified descriptions of data. Models can be either parametric descriptions of data (such as equations) or maps. An example of a model project is deriving an algorithm for the amount of amplification of the ground motion expected for a given site condition.
- Research projects classified as **methods** develop new procedures or evaluate existing ones for using models or data to compute a desired parameter. An example of a method project is the evaluation of the relative accuracy of different procedures for predicting site response.

The purpose of this research program was to provide data, models, and methods needed to reduce the earthquake vulnerability and improve the system reliability and safety of electric transmission and distribution systems. Once implemented, these research results will enable faster post-earthquake restoration of customer service by reducing the amount of damage and disruption of electric transmission and distribution service caused by earthquakes, and by providing more accurate and rapidly available post-earthquake information about the state of damage produced by earthquakes. The research results can also be used, as appropriate, by businesses, industry, regulatory agencies, and the general public to reduce earthquake vulnerabilities and respond more effectively to earthquake effects in California and elsewhere.

1.2 Background

This program continues utility-directed seismic safety and reliability research that Pacific Gas and Electric Company (PG&E) initiated at the end of 1996 using funding provided by the ratepayer-financed investor-owned utility research and development (R&D) program. The applied research needs were identified as vital to optimize PG&E's Seismic Risk Management Program, which was initiated prior to the 1989 Loma Prieta earthquake. The objective of the applied research was to allow the utility to better understand the earthquake performance of gas and electric systems, and to develop ways and means of improving the systems' reliability and safety, thereby significantly reducing earthquake risks.

A partnership was established with the Pacific Earthquake Engineering Research Center (PEER), based at the University of California, Berkeley (UC Berkeley), to involve talented academic engineers and scientists and their students in the research. PEER is a consortium of 18 universities whose mission is to reduce the risk of constructed facilities through research and implementation of performance-based design methodologies. PG&E's investment in PEER as a Founding Partner in the Utility Component of the PEER Business and Industry Partnership helped to secure National Science Foundation funding for PEER. PG&E's support and involvement in PEER helped to focus the research on California utility infrastructure, important because of the life-safety issues and economic consequences that significant seismic events cause to this infrastructure.

To develop and manage this user-directed program, PG&E and PEER established the Joint Management Committee (JMC). Collaborative management through the JMC has become a highly effective approach to identify specific research studies and to assure that they are focused on utility needs and provide results that can be directly used by the utility. In the JMC, a small group of PEER and PG&E representatives agreed upon specific research scopes that would meet PG&E's needs. They selected Principal Investigators (PIs) to carry out the desired studies according to planned schedules and budgets, and guided the PIs to provide results in formats that utility personnel could quickly implement. The JMC was successful in engaging academic PIs from within the PEER member institutions and consulting PIs in private practice, who were enthusiastic about the applied research topics and were diligent about meeting the research commitments. The JMC also provided coordination between the PG&E/PEER research activities and complementary applied research in the earth sciences that PG&E supported at the U. S. Geological Survey (USGS) in Menlo Park, CA, through a Cooperative Research and Development Agreement. A representative of the California Department of Transportation joined the JMC during the course of the program to provide input and coordination with their ongoing research.

The research needs identified by PG&E consisted of a set of topics that addressed the board needs of earthquake hazard assessment and earthquake risk reduction, and that were intended to set the framework for a multiyear, comprehensive, utility-focused applied research program.

A total of 25 individual research projects were carried out in this initial program. Appendix I identifies the specific projects by topic and provides the Principal Investigator, the institution, and a brief description for each project.

PG&E and PEER JMC representatives, technical and administrative personnel in the two organizations, and individual researchers were very satisfied with the results achieved by the

initial projects. The experience provided some suggestions for improving the administrative process, but the quality of the research effort and the value of the result were both quite high.

1.3 Transition Funding for Strategic Energy Research

As part of the implementation of Legislative Act AB 1890, the California Energy Commission (Commission) established a Public Interest Energy Research (PIER) program, which coincided with the termination of most investor-owned utility ratepayer funded R&D. To preserve the benefits of promising public interest R&D projects, such as the PG&E utility-directed seismic safety and reliability research, the Commission funded the continuation of the earthquake studies under the PIER Transition Research Program.

During the first four months of 1998, the JMC selected topics for possible research, prepared a request for proposals (RFP) on the topics, and selected the projects to be carried out.

1.3.1 Research Topics

The topics from the initial PG&E/PEER research were reviewed and the following were chosen as a focus for the preparation of the RFP. The following list gives a brief description of the needed studies for each topic.

- Topic 1. Ground Motion and Site Response
  - A number of studies under this topic are needed to improve the site-specific assessments of near-fault ground shaking and ground motions at soil sites.
- Topic 2. Ground Motion Estimates for Emergency Response
  - Emergency response by utilities requires rapid information about the location of potentially damaging strong ground motions.
- Topic 3. Ground Deformation Database
  - Further work beyond the initial PG&E/PEER study is needed to improve the quality of the empirical ground-deformation database.
- Topic 4. Electrical Substation Equipment Performance
  - Shaking-table studies of different designs and retrofits of high-voltage transformer bushings are needed to extend the results of the initial PG&E/PEER studies.
- Topic 5. Earthquake Fire Safety Associated with Gas and Electric Systems
  - The previous study of the role of natural gas in post-earthquake fires is extended by incorporating consideration of the role of electric power.
- Topic 6. Building Vulnerability
  - Improved techniques to analyze building performance in earthquakes are needed to extend the initial PG&E/PEER studies.
- Topic 7. Seismic Vulnerability of Underground Cables
  - This new topic addresses the need to investigate the deformation capacity of older underground electric cables.

1.3.2 Project Selection

The JMC prepared and issued a RFP that addressed these topics and described in detail the desired research (Appendix II). The JMC received and reviewed more than 32 proposals. Because the total requested amount was much greater than the available funding, the JMC had to both evaluate and rate the proposals and then prioritize the projects that would be funded. The decision was made to give lower priority to Topics 6 and 7. As other organizations were analyzing the earthquake performance of typical utility buildings, it was judged that the consequences of not funding Topic 6 were relatively small. There was limited response to Topic 7, and it was decided to not fund work in this area until a more refined research need could be prepared and another solicitation issued. This process resulted in the selection of 17 projects and established contracts with the host institutions (Table 1). The actual expenditures for these projects are also listed in the table.

An additional special project was created late in the research period to partially support travel by PG&E and Commission personnel to the site of the August 17, 1999 Kocaeli, Turkey earthquake to investigate the consequences of the event on the Turkish electric power system.

Section 2 of this report summarizes the need, project description, results, and applications of the research program. The goal of this summary is to concisely convey (1) the importance of the applied research in addressing real utility needs in providing safe and reliable services in the face of significant earthquake hazards and significant earthquake vulnerabilities of system components or significant consequences in the event of utility service disruption or damage; and (2) the direct and immediate applicability of the research results to satisfy these needs. Appendix III contains the complete final reports for each project.

Table 1. Funded Research Projects 1998-2000

Project Title and Number*	PI and Institution	Amount
Topic 1: Ground Motion and Site Response		
Evaluation of Numerical Procedures for Simulating Near-fault Long-period Ground Motions Using Graves Method (5A)	P. Somerville, Woodward-Clyde Federal Services	$45,642
Evaluation of Numerical Procedures for Simulating Near-fault Long-period Ground Motions Using Zeng Method (5.A)	Y. Zeng and J. Anderson, University of Nevada, Reno	$49,269
Evaluation of Numerical Procedures for Simulating Near-fault Long-period Ground Motions Using Silva Method (5.A)	W. Silva, Pacific Engineering and Analysis	$33,732
Surface Geology-based Strong-motion Amplification Factors for San Francisco and Los Angeles Areas (5.B)	W. Silva, Pacific Engineering and Analysis	$41,007
Evaluation of Uncertainties in Ground Motion Estimates for Soil Sites (5.B)	J. Stewart, UCLA	$50,000
Ground Motions for Site Response Estimates—1906 Earthquake (5.C)	P. Somerville, Woodward-Clyde Federal Services	$15,000
Ground Motions for Site Response Estimates—Permanent Ground Deformation Models (5.C)	W. Silva, Pacific Engineering and Analysis	$4,000
ROSRINE IV-A (5.C)	T. Henyey, University of Southern California	$99,990
Topic 2: Ground Motion Estimates for Emergency Response		
Rapid Estimation of Ground Shaking for Emergency Response (7)	D. Dreger, UC Berkeley	$50,000
Topic 3: Ground Deformation Database		
Enhanced Ground Deformation Database (4)	J. P. Bardet, UC Santa Barbara	$63,633
Topic 4: Electrical Substation Equipment Performance		
Seismic Evaluation of 550 kV Porcelain Transformer Bushings (2.A)	G. Fenves and A. Whittaker, UC Berkeley	$79,807
Performance of 230 kV and 500 kV Bushings (2.B)	G. Fenves and A. Whittaker, UC Berkeley	$92,051 + $65,000 cofunding
Analytical Studies of Substation Equipment Interaction (2.C)	A. Der Kiureghian, UC Berkeley	$49,614
Experimental Studies of Substation Equipment Interaction (2.C)	A. Filiatrault, UC San Diego	$118,651
Amplification of Ground Motions at the Base of Transformer Bushings (2.D)	R. Villaverde and G. Pardoen, UC Irvine	$50,000
Rocking Response and Overturning of Equipment (2.D)	N. Makris, UC Berkeley	$49,981

Project Title and Number*	PI and Institution	Amount
Field Investigation of Effects of the Kocaeli, Turkey, Earthquake	G. Fenves, UC Berkeley	$7,627 + >$20,000 cofunding
Topic 5: Earthquake Fire Safety Associated with Gas and Electric Systems		
Ignition of Fires Following Earthquakes Associated with Natural Gas and Electric Distribution Systems (6)	R. B. Williamson, UC Berkeley	$47,308
Project Administration	G. Fenves, UC Berkeley	$48,607
TOTAL for 18 Projects and Program Administration by PEER		**$995,919**

*The project numbers shown in parenthesis were used during administration of the research program and are provided only because they are used in the technical reports in Appendix III.

2.0 Research Results

2.1 Topic 1: Ground Motion and Site Response

2.1.1 Objectives

This topic addressed a number of requirements for improving the estimates of earthquake ground motion and response at specific sites. The objectives were to:

- Improve methods to predict near-fault ground motions from large earthquakes.
- Improve accuracy and reduce uncertainties in predicting the effects of soil on site response estimates.
- Provide additional site characterization data for sites that have recorded strong ground motions.

The outcomes of the specific projects that address these objectives are described in Sections 2.1.2 through 2.1.6.

This topic is at the core of addressing earthquake hazards, since the level of shaking at an individual site is the primary earthquake hazard that affects soils, foundations, and structures. The seven projects that addressed the objectives listed above focused on particularly important needs for utility facilities constructed in areas exposed to very strong levels of ground motion. Uncertainties in the input ground motion for design or for performance evaluation can lead to large unnecessary cost if the ground motions are overestimated, or to significant damage if they are underestimated. There is great benefit, then, to utilities as well as owners of other facilities, to use accurate ground motion assessments that fully consider site response.

2.1.2 Evaluation of Three Numerical Procedures for Simulating Near-fault Long-period Ground Motions

Background and User Needs

The ground shaking close to large earthquakes can have special characteristics with very different impacts on structures than typical ground shaking observed in past earthquakes. These near-fault effects on ground motions are strongest at low frequencies (< 1 Hz). To date, there are only a small number of instrumental recordings of ground shaking close to a few large earthquakes (i. e., within about 15 km of the fault rupture). As a result, we are not sure that the available empirical data set of ground motions provides a reliable statistical sample of the characteristics of ground motions close to large earthquakes.

One way to augment the sparse data set of recorded ground motions is to use computer models to artificially generate ground motions close to the fault. There are several computer models that have been developed to simulate earthquake ground motions. However, the calibration of these computer models has not addressed important features of ground motions close to the fault: the dependence on whether the rupture is toward the site or away from the site (directivity effect); and the differences between the ground motion on the two horizontal components oriented parallel and perpendicular to the fault strike (orientation effect). Before engineers should rely on the computer models to predict ground motions close large earthquakes, the models have to be checked for their ability to simulate the key features of

observed near fault ground motions from past large earthquakes, including directivity and orientation effects.

Project Approach

This project tested the ability of three widely used ground-motion simulation procedures to simulate the key features of near fault ground motions. In previous work for the PG&E-PEER program, these three simulation methods were applied in a forward prediction of the near-fault ground motion for a specified hypothetical earthquake. They produced very different results. The current evaluation of the three methods was intended to help understand what caused the differences between the three methods and, if possible, to calibrate the methods.

The objective of this project was to evaluate the ability of the three ground motion simulation computer programs to predict the recorded near-fault ground motions from the following five large earthquakes:

- 1979 Imperial Valley M=6.4 29 recordings
- 1989 Loma Prieta M=6.9 34 recordings
- 1992 Landers M=7.2 13 recordings
- 1994 Northridge M=6.7 34 recordings
- 1995 Kobe M=6.9 18 recordings

These earthquakes were selected because they have a relatively large number of near-fault ground motions (the number of strong motion recordings within 30 km for each earthquake is also listed). We evaluated the ability of the model to predict directivity effects on the low frequency ground motion and any systematic differences in the ground motion on the two horizontal components of shaking oriented parallel and perpendicular to the strike of the fault. The evaluation considered all sites within 30 km of the fault, and addressed low frequency ground motions (0.125 to 1.43 Hz).

The evaluation was carried out in three parallel efforts under the direction of three PIs and their colleagues who developed and improved the three alternative ground motion simulation computer programs:

- Graves, Pitarka, Collins, and Somerville of Woodward-Clyde Federal Services (referred to as the Graves method)
- Zeng and Anderson of the University of Nevada, Reno (referred to as the Zeng method)
- Silva, Gregor, and Darragh of Pacific Engineering and Analysis (referred to as the Silva method)

Norm Abrahamson was the PG&E Technical Contact.

All three simulations are finite-fault methods in that they break the fault into a subset of small sub-events, propagate the ground motion from each sub-event to the site, and then sum up the ground motions from each sub-event to estimate the total ground motion during the earthquake. These models make different assumptions about the seismic source, wave propagation, and site response that affect the prediction of ground motions. The most important differences in the methods are as follows: (1) the Silva method is the only one that fully treats non-linear site response, while the other models only treat gross soil-versus-rock

site categories; and (2) the Graves and Zeng methods generate three components of motion, whereas the Silva method generates an average horizontal component.

Outcomes

Each of the three alternative methods were used to predict the ground motions at locations that recorded the five large earthquakes listed above. To evaluate the ability of a method to predict directivity effects, the differences in the response spectra for the simulated and observed ground motions (residuals) were computed for response spectral periods of 0.125 Hz to 1.4 Hz. If the simulations were properly modeling the directivity effects, then the residuals would be randomly scattered about zero as a function of the rupture direction. On the other hand, if, on average, the residuals are positive for forward rupture and negative for backward rupture, that would indicate that the model is not predicting near-fault rupture directivity effects.

- Graves, Pitarka, Collins, and Somerville. In general, the residuals based on the Graves simulation method do not show a trend as a function of rupture direction, indicting that the simulation is capturing the main effects of directivity on the ground motion. This indicates that the computer simulation is picking up directivity effects that the empirical attenuation relation has not picked up. This indicates some of the potential improvements that can be made in ground motion models by using numerical simulations.
- Zeng and Anderson. In general, the residuals based on the Zeng method also do not show a trend as a function of rupture direction, indicting that the simulation is capturing the main effects of the directivity on the ground motion.
- Silva, Gregor, and Darragh. The Silva method found a trend in the residuals as a function of the rupture direction. It found that inclusion of site response effects significantly affects the predicted ground motions. Since the models of the slip on the fault were determined from previous studies that did not include site response effects, these slip models may incorporate site-response effects into the slip models. This result indicates that the site response needs to be incorporated into the slip model inversions.

The comparison of these three methods identified an important potential shortcoming of the current standard for predicting ground motions. Site effects need to be added to the method that generates the slip model on the fault. If that is not done, then the site-specific site effects cannot be added to simulations since they are to some extent incorporated in the slip model.

Application and implementation

These results are one step in the development of a methodology for generating artificial ground motions close to large earthquakes. This methodology is not complete with the results of this project. With the occurrence of the 1999 Turkey and 1999 Taiwan earthquakes, there has been a tremendous increase in the number of ground-motion recordings that are available close to large earthquakes. These important recordings are included in the planned evaluation of the simulation procedures to be conducted in the next phase of applied research work.

Once this additional evaluation is complete and the models modified, if needed, they can then be used to generate artificial ground motions for a suite of possible future earthquakes on the major faults in northern California. This simulated data set will then be used to develop

simplified parametric models of the behavior of near-fault ground motions for use in seismic hazard analyses.

2.1.3 Surface Geology-Based Strong-Motion Amplification Factors for San Francisco and Los Angeles Areas

Background and User Needs

The primary tool used for predicting ground motions for engineering applications have been empirical attenuation relations. Most empirical attenuation relations have used very simple site classifications of soil and rock. It has long been known that local site conditions can have a significant effect on ground motions and that there can be large differences in the site response effects for different types of soils.

Recently, the 1997 Uniform Building Code used the average shear wave velocity in the top 30 m as the site parameter to distinguish between the site response effects for different types of soils. This approach provides a clear definition of the site category; however, for most projects, measurements of the shear-wave velocity are not available.

There is a need for attenuation relations that incorporate the site effects better than just simple soil versus rock categories, yet use readily available site classification information.

Project Approach

Surface geology maps provide a readily available means of classifying sites into sub-categories for different soil conditions. The objective of this project was to develop site response factors that quantify the differences in the ground motions for different site categories based on the surface geology.

Ideally, site response factors could be developed based entirely on observations of strong motion data. But the limited number of strong motion recordings does not provide enough observations on each geology class for a range of earthquakes magnitudes and distances. In particular, the different geologic categories are not well sampled for very high levels of shaking. Because of this limitation of the empirical data, 1-D numerical simulations are used to develop a comprehensive site response data set.

Measurements of the shear-wave velocity at strong motion sites from the ROSRINE and other site characterization studies were grouped according to the surface geology for each borehole site. With this grouping, the median and variability of the velocity profile was estimated for each geologic category. This allows the input soil profile for the analytical models to be tied back to a general surface geology category.

In addition to the velocity profile, non-linear soil properties must also be defined for each geologic category. Again, the ROSRINE database and other site response studies are used to correlate the non-linear soil properties with the surface geology. Separate non-linear properties (G/Gmax and hysteretic damping curves) are used for San Francisco Bay Area and Los Angeles area cohesionless soils to reflect the different degrees of non-linear response of the soil in these two regions.

The amplification factors are then computed relative to rock site geology conditions in the San Francisco Bay area (Franciscan) and Los Angeles area (granite). This allows the standard

attenuation relations to be used to develop the reference ground motion. Then the amplification factors can be used to scale the median ground motion from the rock attenuation relations to define the median ground motion on different soil categories.

W. Silva of Pacific Engineering and Analysis, located in Berkeley, CA, carried out this project. S. Li, R. Darragh and N. Gregor assisted him. Norm Abrahamson was the PG&E Technical Contact.

Results

Analytical site response calculations were made for 11 geologic categories (Table 2). In addition to varying the geologic category, the thickness of the soil deposit was also included as a site parameter (soil thickness varied from 30 m to 1500 m). To account for on-linear site response effects, the amplification factors are functions of the input rock peak acceleration (0.05g, 0.1g, 0.2g, 0.4g, 0.75g, 1.0g, and 1.25g). In all, several thousand site-response calculations were run to cover all of the combinations of soil properties and ground motion levels.

Table 2. Site Categories Based on Surface Geology

Northern California	Southern California
Kjf (Franciscan)	Mxb (Granite)
TMzs (Tertiary Bedrock)	Ts (Saugus)
QTs (Quaternary/Tertiary)	Ts (Tertiary)
Qoa (older alluvium)	Qo (older alluvium)
Qal (Quaternary alluvium)	Qy (Quaternary alluvium)
Qm (Bay mud)	Qm (Holocene alluvium)

The large set of calculated amplification factors were then parameterized into simplified probabilistic models of the site amplification factors (e.g., median and standard deviation) for each of the surface geology site categories.

The amplification factors computed in this project were compared to the current National Earthquake Hazards Reduction Program (NEHRP) factors and to empirical amplification factors for both regions. Comparisons with the NEHRP amplification factors showed reasonable agreement for the San Francisco Bay area except for Bay mud. For the Los Angeles area, good agreement was seen with the NEHRP amplification factors at low ground motion levels (<0.1g) but the computed amplification factors were much lower than the NEHRP factors at high levels of shaking.

Application and Implementation

The site amplification models developed in this project will be used together with rock attenuation relations to define a model for the attenuation relations for the different surface geology classifications. Since surface geology information is available in map form, these new attenuation models can be immediately incorporated into ground motion evaluations. In addition, since the amplification factors are described probabilistically, these models can be used in both probabilistic and deterministic ground motion evaluations.

2.1.4 Evaluation of Uncertainties in Ground-Motion Estimates for Soil Sites

Background and User Needs

As discussed in Section 2.1.3, the primary tool used for predicting ground motions for engineering applications have been empirical attenuation relations, which have used very simple site classifications of soil and rock. Local site conditions can have a significant effect on ground motions and there can be large differences in the site response effects for different types of soils.

In the preceding project (Section 2.1.3), the generic soil site classification was subdivided into several categories based on surface geology as a way to improve the prediction of the site response. As an alternative to site categories, site-specific site response calculations can be made using analytical models of the site response that distinguish between different sites within a site category by having models of the site parameters for each individual site. Such site-specific site response calculations are commonly carried out for critical facilities, but they are typically not used for most facilities because of the cost of collecting the site information (e.g. shear-wave velocity profile).

Geotechnical engineers have long thought that the variability (standard deviation) of attenuation relations could be greatly reduced if the site-specific shallow site properties were taken into account (e.g. the 1-D shallow velocity structure and non-linear soil properties). There is a need to determine how much ground motion estimates can be improved if site-specific site response calculations are performed, rather than relying on attenuation relations for broad site categories. Are costly site exploration work and site-response analyses justified in terms of the reduction in the uncertainty of the estimated ground motion?

Project Approach

The objective of this project was to evaluate the benefit of site-specific site response analyses as compared to the use of generic soil attenuation relations.

The site response modeling was performed using the program SHAKE91, which represents the state-of-the-practice for site response calculations. The predicted ground motions were then compared to the observed ground motions to estimate the uncertainty of site-specific site response procedures. Standard empirical attenuation relations were also used to predict the ground motions at each site.

The predictive ability of the site-specific site-response analysis is compared to that of the empirical attenuation model by comparing the standard deviation of the residuals (the difference between the observed ground motion and the predicted ground motion) for subsets of soil categories. If the site-specific analysis leads to a significant reduction in the standard deviation, that would indicate that site-specific analyses can explain much of the variability of the ground motion within a soil category.

The project Principal Investigator is Professor J. Stewart of the Civil engineering Department at the University of California at Los Angeles. M. Baturay assisted him. The PG&E Technical Contact was Norm Abrahamson.

Results

Site-specific site response analyses were performed for 36 sites with widely varying geologic conditions that have recorded strong ground motions and that have site-specific information available (e.g. measured shear wave velocity profile). The sites were divided into four soil categories based on the geotechnical properties of the sites. (Note that these are different soil categories than were developed in Section 2.1.3) The soil categories are listed below:

C2 Shallow stiff soil over rock (soil thickness less than 30m)

C3 Moderate thickness stiff soil (soil thickness 45 to 90m)

D Deep stiff soil (soil depth greater than 120 m)

E Soft soil (Vs (Shear Wave Velocity) less than 150 m/s, soft soil thickness greater than 3 m)

A key issue for site-specific site response calculations for past earthquakes is the estimation of the ground motion that is input into the soil profile (input rock motion). In most cases, nearby rock ground motions are not available to be used as input motions. In this study, careful efforts were made to define a suite of input motions. Empirical ground motion recordings at rock sites for the appropriate magnitude and distance range were selected and then scaled to the median ground motion as predicted by empirical attenuation relations. These scaled motions were then modified to account for event-specific attenuation (this accounts for some earthquakes producing larger-than-average ground motions, and some earthquakes producing lower-than-average ground motions), site-specific rupture directivity effects for each event, and near-surface amplification effects at weathered rock sites.

Ten sets of input ground motions were developed for each of the 36 sites. The site response analysis was performed for each input ground motion and the resulting ground motions were compared to the observed ground motions at each site. The results of this suite of site response studies were grouped into the four site categories listed above and they were parameterized in terms of the median residual and the standard deviation of the residuals for each site class. As a base case, the median residual and standard deviation were also computed using empirical attenuation relations (without site-specific effects).

The evaluation found that there was a significant bias in the ground motion prediction for each soil category based on the generic soil attenuation relation; the bias was greatly reduced when the site-specific response was used. This supports using more refined soil categories (rather than just generic soil), which is consistent with the study by Silva et al. (Section 2.1.3)

The site-specific analysis led to a large reduction in the standard deviation for soft clay sites compared to generic soil attenuation models. At periods less than 1 second, the reduction in the standard deviation is from 0.68 to 0.28 natural log units. At long periods (T>1 second), the reduction is less (0.49 to 0.41).

For other site categories, the standard deviations are similar for the site-specific analysis and the generic attenuation relation, indicating that factors other than 1-D site response are randomly varying the ground motion from site-to-site. These other factors may include effects of the seismic source and the regional wave-propagation.

Application and Implementation

Based on this evaluation of a site response methodology, site-specific response methods need to be used for soft clay sites. Attenuation relations for broad categories are adequate for other soil sites, but these categories should be more refined than just generic soil.

2.1.5 Ground Motions for Site Response Estimates—Two Applications

Background and User Needs

In many instances, there are not relevant recorded ground motions near sites that are being studied for site response, liquefaction, or ground deformation. For example, often a site with liquefaction does not have a nearby ground motion recording that can be used as an estimate of the input motion into the soil column. To enable these data to be used in building models or ground-failure assessments, ground motions need to be estimated for these sites.

Project Approach

The objective of this project was to provide expertise for making estimates of the ground motions at sites being studied as part of the PG&E-PEER-Commission and PG&E-USGS seismic research programs. Numerical simulation methods are used to estimate the ground motion. Two of the better-validated methods that have extensive engineering application are the finite-fault stochastic model by Silva and the broadband empirical source function method by Somerville. These two methods are used to predict ground motions at sites as needed for the other projects.

Dr. Walt Silva of Pacific Engineering and Analysis, Berkeley and Dr. Paul Somerville of Woodward-Clyde Federal Services performed specific ground-motion calculations. Norm Abrahamson was the PG&E Technical Contact.

Results

Liquefaction was observed during the 1906 earthquake, but there were not strong motion instruments at that time. To estimate the input ground motions for these sites, Somerville applied his numerical simulation method to estimate the ground motion during the 1906 earthquake at the liquefaction site locations.

Silva generated representative ground motions for large earthquakes that could be used as input motions for analytical calculations of ground deformation. These ground motions are used to augment the sparse empirical database. Ground motions were generated for fault distances of 7.5 km and 37.5 km for magnitude 7.0 and 8.0 earthquakes. Both soft rock and deep firm soil conditions were modeled. Thirty sets of ground motions were generated to reflect the variability in the slip on the fault, in the location of the hypocenter on the fault plane, and in non-linear properties of the soil.

Application and Implementation

The simulated ground motion data from these projects are used as inputs for other evaluations of site response and ground deformation. These ground motions can also be used to define time histories from large earthquakes for structural engineering analyses.

2.1.6 Resolution of Site Response Issues for the Northridge Earthquake (ROSRINE IV-A)

Background and User Needs

It has long been known that local site conditions can have a significant effect on ground motions. However, for most sites that have recorded strong ground motions, the subsurface site information has not been collected due to the high cost of collecting the data. This lack of basic site characterization data has hindered the improvement and calibration of site response methods.

ROSRINE is a collaborative research project focused on improving engineering models for estimating site response effects. The central component of this project is the collection, synthesis, and dissemination of high-quality site characterization data from strong-motion instrument sites that recorded the 1994 Northridge Earthquake. Previous funding for this program has come from the National Science Foundation, Caltrans, Electric Power Research Institute, and PEER/PG&E. Other collaborations have been made by the U.S. Geological Survey, LADWP, LAWRD, and SCEC. This project represents Phase IV-A of the on-going ROSRINE program.

The user need is basic site characterization information that can be used to help in the interpretation of recorded ground motions and to improve empirical and analytical models of site response.

Project Approach

The objective of this project was to collect additional site characterization data for strong-motion sites that recorded the 1994 Northridge earthquake.

The site characterization includes measurement of the shear-wave velocity profile and some sampling of the soils that can be used to in laboratory evaluations to determine the non-linear properties of the soil.

The ROSRINE project has been administered through the Southern California Earthquake Center (SCEC). The PI for this project is T. Henyey, who is the SCEC representative, and R. Nigbor oversaw this part of the ROSRINE program. Norm Abrahamson was the PG&E Technical Contact.

Results

In this phase of the ROSRINE program, the standard site characterization data were collected at six sites (Table 3). In addition, index property testing of selected soil samples was performed and the data are disseminated through the ROSRINE website.

Table 3. ROSRINE Program Sites

Site	Work Performed
Saturn School	Drilling, sampling, logging
Dayton Heights School	Drilling, sampling, logging
Brentwood VA Hospital	Logging
LADWP Receiving Station East	Logging
ETEC RD-7	Logging
ETEC RD-20	Logging

Application and Implementation

The results of this study provide site characterization data that will be used in future projects that address site response.

2.1.7 Conclusions and Recommendations

The three objectives identified in Section 2.1.1 called for progress in addressing three needs related to predicting ground shaking at sites of utility interest.

- Improve methods to predict near-fault ground motions from large earthquakes incorporating site conditions.
- Improve accuracy and reduce uncertainties in predicting the effects of soil on site response estimates.
- Provide additional site characterization data for sites that have recorded strong ground motions.

The projects carried out to address these needs made significant progress. The results described in Sections 2.1.2 through 2.1.6 met these objectives in that:

- Numerical methods were calibrated with data from near-fault recordings of large earthquakes.
- Models were improved to refine the accuracy and reduce the uncertainty in estimates soil site response.
- Six sites of strong ground recordings in the 1994 Northridge earthquake were characterized according to the procedures used in the on-going ROSRINE project.

The results also provided clear direction for further studies on ground motions and site response.

2.2 Topic 2: Ground Motion Estimates for Emergency Response

2.2.1 Objective

The objective of this topic was the development and implementation of methods for rapidly estimating the pattern of strong ground shaking for a significant earthquake occurring anywhere in the state of California. This project brings highly valued benefits to portions of California that currently do not have dense networks of strong-motion instruments with which to measure potentially damaging ground shaking in earthquakes. Utilities, other emergency responders, and utility customers are eager to learn as quickly as they can where earthquake shaking effects are most severe, so they can take more effective and more rapid actions that can save lives and begin to recover from the earthquake.

2.2.2 Rapid Estimation of Ground Shaking for Emergency Response

Background and User Needs

Following a major earthquake, one of the important needs for emergency response is a rapid estimate of the extent of the damage. Currently, the magnitude and location of the epicenter are available quickly after an earthquake. While this information provides a general estimate of what happened, it does not provide enough detailed information on the locations that may have the greatest damage.

Maps of the strength of the ground motion over a region are called ShakeMaps. With estimates of the level of the shaking, preliminary estimates of the damage to the electric system and customer facilities can be made. In the Los Angeles region, rapid estimates of earthquake shaking are produced as part of the TRINET program. This program relies on a dense network of strong motion instruments to provide input to a ShakeMap.

In many parts of California, including the San Francisco Bay Area, there is not a sufficiently dense distribution of strong motion instruments for developing a ShakeMap from only strong motion data. Until adequate strong motion instrumentation is installed, the data need to be supplemented with predictions of the ground motion based on other information.

One source of information that is available throughout the state is regional broadband instruments. These are seismometers that provide high quality measurements of the ground motion from both weak and strong motions. The users need a method for computing ShakeMaps based on data recorded by the currently available regional seismic instrumentation.

Project Approach

The approach in this project was to develop a procedure for rapidly estimating the ground motions following a large earthquake using seismic data from broadband stations recorded at regional distances (e.g. 50 to 200 km) to infer the properties of the seismic source. The key source properties are rupture dimension, location, directivity, and velocity, and slip model. These source properties are then used to predict the ground motion using either empirical attenuation relations or numerical simulations.

This project developed a robust method to rapidly invert the regional seismic data to estimate the source properties. The key was to get a stable process that can be automated. In the past, this type of source inversion required hands-on analysis by a seismologist.

Given the source properties, the next step was to estimate the ground motions at a grid of locations that can be contoured to form a ShakeMap. For this purpose, a numerical simulation method that used the source characterization developed from the source inversion was refined from previously developed numerical simulation models. Again, the key was to automate the process so that the ShakeMap can be created in a timely manner.

Dr. Doug Dreger of the UC Berkeley Seismological Laboratory, with assistance from graduate student A. Kaverina, carried out the project. Norm Abrahamson was the PG&E Technical Contact.

Results

The essential source information needed for ground motions and ShakeMap estimation can be developed in 4 to 20 minutes following an earthquake. First, the estimates of the rupture dimension and rupture location are calculated in approximately four minutes following an earthquake. Knowing the rupture location (length, width, and dip), the earthquake magnitude, and the hypocenter location on the rupture plane, the ground motions are estimated using standard ground motion attenuation relations. From these estimates, a preliminary ShakeMap can be developed. Following this initial result, the estimate of the slip distribution on the fault plane is calculated in approximately 20 minutes following an earthquake. This slip distribution is then used as input to the numerical simulation program to compute revised ground motions. These numerical simulations provide an improved estimate of the ground motion that accounts for the variations in the slip on the fault (the empirical attenuation model just uses the distance from the site to the fault rupture). These simulated data are then used to produce an updated ShakeMap.

This method has been calibrated using regional and strong motion data from the 1992 Landers and 1994 Northridge earthquakes. The ground motion as estimated using only the regional data and the predictions were compared to the observed ground motions. The predictions using the regional data were generally only within 50 percent of the observed ground motions over distances up to 50 km from the fault. When the data were smoothed (spatially) to form a ShakeMap, the agreement between the simulations based on regional data and the observations is improved to within about 30 percent of the observations. This result indicated that this method makes it is possible to calculate robust ShakeMaps even in areas with sparse coverage of strong motion instruments.

2.2.3 Conclusions and Recommendations

The methodology for rapidly predicting ground motions based on regional seismic data provides a key tool for making ground-motion maps following an earthquake, and is successfully addressing the objective of the topic. For the results to be useable, this methodology next needs to automated and integrated into the routine provision of rapid earthquake information.

2.3 Topic 3: Ground Deformation Database

2.3.1 Objective

The objective of this topic was to develop a greatly improved empirical database of ground deformations in past earthquakes that can be used to calibrate statistical and numerical predictions of permanent ground deformation for future earthquakes. In past earthquakes, utilities and transportation systems with underground components have experienced minor to extensive damage due to earthquake-caused permanent ground deformation. The empirical database developed during this project will enable the development of improved predictive tools to better identify the locations of potential ground failure and to more accurately predict the expected amounts of ground deformation. These results will enable power customers, other utility customers, and the state in general to benefit from reduced outages due to improved utility designs that successfully avoid or resist earthquake-related ground deformation.

2.3.2 Enhanced Ground Deformation Database

Background and User Needs

Permanent ground deformations are the primary cause of the earthquake failure of pipelines and buried electric conduits. In addition, they can damage or deform the foundations of utility facilities. Therefore, parametric models of the amount of ground deformation as a function of magnitude, distance and site condition are needed for the evaluation of underground system damage.

In the past, empirically based models of liquefaction induced ground deformation have been developed, but they have focused on the largest deformations (greater than two meters). If such large deformations occur, then the underground facilities will very likely be damaged. If the deformations are less than 0.1 m, then it is very unlikely that modern buried pipe or modern foundations will fail. The key range of deformations for which improved models are needed is in the range of 0.1 to 2 m.

Much of the existing ground deformation data in this 0.1 to 2 m range also has errors in the standard reference database. In addition, the parametric models did not fit the data at small deformations well.

The user need is for a simplified parametric model of the liquefaction-induced ground deformation as a function of the earthquake magnitude, distance from the site to the fault, and geotechnical site conditions. Before such a model can be developed, a comprehensive database of ground deformation has to be developed.

Project Approach

The objective of this project was to develop a reliable database of liquefaction-induced ground deformations, including a characterization of the site conditions and input ground motions. This will then serve as input for subsequent model development tasks.

To deal with errors in ground deformation databases used in previous studies, the ground motion deformations data from pre-1995 earthquakes were re-evaluated using the original

sources of data. To bring the database up to date, data from the 1994 Northridge and 1995 Kobe earthquakes were identified, collected, organized, and digitized.

Professor J. P. Bardet of the University of Southern California conducted this project. Norm Abrahamson was the PG&E Technical Contact.

Results

A relational database framework was developed for storing and structuring the large amount of data on liquefaction-induced ground deformations. These include data sets on the displacement vectors and soil properties including SPT and CPT. The database contains 16,000 displacement vectors, 902 SPT measurements, and 229 CPT soundings.

2.3.3 Conclusions and Recommendations

The database produced by this project will serve as the key input data for developing simplified parametric models of ground deformation as a function of magnitude, distance, and site condition that can be used to develop probabilistic maps of ground deformation due to liquefaction. Further data need to be added to the database, particularly those from the recent Taiwan and Turkey earthquakes in 1999. The database also needs to be provided to the research community so that workers can use this new resource to improve predictive models and methods for assessing the potential for permanent ground deformation in earthquakes.

2.4 Topic 4: Electrical Substation Equipment Performance

2.4.1 Objectives

The objective of this topic was to develop data and methods for accurately evaluating the expected earthquake performance of high-voltage substation equipment currently in use by major California utilities. The primary focus of the objective is on transformers, the most critical elements in a substation for restoring power after a major earthquake. The occurrence of a major earthquake in Turkey near the end of the research work provided an opportunity to verify the proper focus of this topic.

The projects in this topic improved the design of critical substation components to reduce earthquake damage and our understanding of the seismic capacity of existing components. Both aspects allow utilities to be able to reduce earthquake damages in substations, historically the leading cause of extensive power outages.

2.4.2 Seismic Evaluation of 550 kV Porcelain Transformer Bushings

Background and User Needs

A transformer typically consists of a closed steel tank, filled with oil, housing a massive core and coils. The bushings, mounted on top of the transformer tank, are used to house and insulate electrical conductors leading from overhead conductors to the inside of the tank. The insulating sections of bushings are almost exclusively made of porcelain, although in recent years some manufacturers have introduced composite polymer models.

Transformers provide the means for connecting power systems of different voltage levels and are one of the most vital components of an electrical substation. Following a significant earthquake, some types of damaged substation equipment might be temporarily bypassed to quickly restore electric service. This is not the case with transformers.

Past earthquake experience in California and other seismically active areas has shown that porcelain bushings are frequently the most vulnerable components of a transformer. Even at relatively low levels of shaking (about 0.3 g peak ground acceleration [pga]), shifting of the porcelain relative to the flange and oil leakage occurred on several 500 kV bushings during the 1983 Coalinga and 1989 Loma Prieta earthquakes, caused the transformers to be taken out of service for several weeks. Numerous failures occurred in 500 kV and 230 kV transformer bushings of Southern California utilities during the 1971 San Fernando, 1986 North Palm Springs, 1992 Landers, and 1994 Northridge earthquakes. During the 1978 Off-Miyagi Earthquake, Japanese utilities reported several porcelain bushing failures. Although utility practices may vary, a transformer will often be removed from service in the event of excessive bushing oil leaks or porcelain slippage because of the risk that internal damage to the bushing could result in fire or explosion.

Several alternative modifications have been proposed to improve the earthquake performance of transformer bushings. There is a need to collect data on the seismic performance of these alternatives. Two projects were carried out to collect data on how well the bushings perform as independent units with and without modifications:

- Seismic Evaluation of 550 kV Porcelain Transformer Bushings
- Performance of 230 kV and 500 kV Bushings

A second issue that affects seismic performance is the effect of equipment interactions. This issue is addressed by projects discussed in Sections 2.4.4 and 2.4.5.

Project Approach

The first of these projects addressed a class of large bushings that have evidenced vulnerability to even low levels of ground motion. The objectives of this project were to obtain information on the seismic capacity (called fragility) of 550 kV bushings through earthquake simulator testing and to assess the effectiveness of relatively simple design improvements on new bushings.

A previous PEER project investigated the seismic capability of 196 kV porcelain bushings (used on 230 kV transformers) through earthquake simulator tests conducted at the Richmond Field Station of the UC Berkeley. The present project investigates the performance of 550 kV bushings (used on 500 kV transformers). The methodology was very similar to that used in the previous study of 196 kV bushings.

Porcelain bushings generally consist of a metal flange assembly, core tube, and porcelain sections that are stacked in series. Insulating oil fills the annular space between the core tube and the inner surface of the porcelain sections. Gaskets are placed at the joints to contain the oil. During assembly, the bushing's core tube is pre-loaded to deliver a clamping force that holds the bushing together. It is from this clamping force that the bushing derives its strength against lateral loading caused by earthquake shaking.

Three 550 kV porcelain bushings were furnished by ABB Power T&D Company for use in testing. These bushings had the following key characteristics:

- Bushing 1: standard design
- Bushing 2: modified design, with higher core clamping force, and stiffer gaskets than standard design.
- Bushing 3: same modified design as Bushing 2, except electrically fully functional.

Tests on Bushing 1 were intended to provide a set of baseline data from which the performance of the modified bushings could be gauged. Higher clamping forces and stiffer gaskets were expected to improve performance of the Bushings 2 and 3 by increasing the friction forces at the gasketed joints and resistance to leakage. It was hoped that the relatively simple and inexpensive improvements made in Bushings 2 and 3 would be sufficient to achieve qualification at the IEEE Std 693-1997 Moderate level of ground motion. Because electrical functionality must typically be verified following shaking table tests, Bushing 3 was prepared for this purpose.

The Principal Investigator for this project was Professor Gregory Fenves of the University of California, Berkeley. Co-investigators were Andrew Whittaker and Amir Gilani. The same team performed shaking table tests on 196 kV porcelain bushings in the previous PEER project. Eric Fujisaki was the PG&E Technical Contact.

Results

Tests on Bushing 1 (standard design, unmodified) confirmed the vulnerability of this class of bushing. It failed because of oil leakage at a pga of about 0.5g. Bushings 2 and 3, which had an increased clamping force and improved gasket configuration, demonstrated a significant improvement in performance, and failed at close to 1.0g. Unfortunately, the modified bushings did not pass the IEEE Std 693-1997 Moderate level of qualification (1.0g, pga).

Application and Implementation

The testing of 550 kV bushings demonstrated the beneficial effect of increased clamping forces on the seismic performance of a bushing. These data will serve as critical benchmarks in the future development of analytical models for predicting the performance of these components. Data collected during the tests on the dynamic behavior of the bushings will also greatly contribute to the validation of analytical methods. The outcome of shaking table tests also points the way to the types of new designs improvements needed to achieve adequate performance in areas of high seismic hazard. The improvement in performance observed in these tests, although significant, does not appear to be sufficient for IEEE Std 693-1997 Moderate seismic level qualification and beyond. This outcome suggests that more drastic design changes should be pursued.

2.4.3 Performance of 230 kV and 500 kV Bushings

Background and User Needs

The background for this project is the same as that for the project described in Section 2.4.2.

Project Approach

This project investigated the effectiveness of simple field retrofits to improve the seismic capacity of bushings in utilities' installed inventories. We selected a bushing type that was observed to have failed in past earthquakes for testing with and without the strengthening retrofit. In addition, this project was intended to yield an improved understanding of the behavior of transformer bushings under lateral load.

Utilities maintain a large inventory of porcelain transformer bushings, many of which appear to be vulnerable to strong earthquake motions. Although more seismically rugged bushings have now become available, the wholesale replacement of vulnerable bushings with these models is cost-prohibitive. As a result, an inexpensive retrofit that could be applied in the field to improve the seismic capacity of installed bushings would be very attractive. This project arose as a way to meet these needs.

In addition to PG&E, Bonneville Power Adminstration (BPA), Southern California Edison (SCE), and BC Hydro supported this project. In addition to funding contributions, the utility partners provided the technical assistance of their engineering staffs, bushing specimens for use in testing, and retrofit devices. Bushing manufacturers also participated in the project by providing specification data on test specimens, and reviewing and commenting on the approaches considered in the project.

This project included the following major activities:

- Identify vulnerable types of bushings, and obtain test specimens.
- Perform shaking table test on unmodified bushings.
- Perform static/cyclic tests on unmodified bushings.
- Develop retrofit scheme, and install on bushing.
- Perform static/cyclic tests on modified bushing.
- Perform shaking table tests on modified bushing to prove concept.

Based upon the observed performance of porcelain transformer bushings in past earthquakes, a vulnerable model of bushing was identified. Several identical specimens of a 196 kV bushing model were provided by BPA. SCE provided one model of a 550 kV bushing. Because of the relative ease of handling a 196 kV bushing compared to the much larger 550 kV model, the 196 kV model was chosen for testing.

Shaking table tests were first performed on unmodified bushings to obtain a set of baseline data for comparison purposes. Since the key objective of the project was to develop an effective retrofit, it was necessary to achieve a better understanding of the behavior of bushing when subjected to earthquake motions. Unlike previous tests on bushings, this project included a set of static/cyclic tests that were intended to study the behavior of the bushing when subjected to controlled lateral loads. In the static/cyclic tests, the bushing specimen was mounted on a stiff stand and subjected to forces applied by hydraulic actuators. Static/cyclic tests permit controlled rates of loading or displacements in order to gain an improved understanding of mechanical behavior. A retrofit ring similar to a pipe clamp, with the annular space filled with an epoxy grout, was developed and applied to the bushing. Static/cyclic and shaking table tests were conducted with the ring in place.

The Principal Investigator for this project was Professor Gregory Fenves of the University of California, Berkeley. Co-investigators were Andrew Whittaker and Amir Gilani. The same team performed shaking table tests on 196 kV porcelain bushings in the previous PEER project. BPA ($25,000), SCE ($20,000), and BC Hydro ($20,000) cofunded the project. Key industry participants were Dr. Anshel Schiff (consultant to SCE), Dr. Leon Kempner, Jr. (BPA), Mr. James T. Kennedy (SCE), and Mr. Alan J. King (BC Hydro). Eric Fujisaki was the PG&E Technical Contact.

Results

Shaking table tests of unmodified 196 kV bushings were unable to cause failure. The performance of the specimen tested exceeded the expectations of utility participants and the investigators. Consequently, it was necessary to use the static/cyclic tests to assess the effectiveness of the retrofit. Static/cyclic tests also demonstrated the high lateral load capacity of these bushings. However, the improvement in performance of the retrofitted bushing was found to be marginal.

A modified retrofit ring, using better attachment clamps to the bushing flange and a smaller gap to the porcelain, was applied to a 196 kV bushing that was then subjected to shaking table tests. In these latter tests, a flexible mounting plate was used to support the bushing as opposed to the rigid support previously used. The flexible support was intended to better simulate

actual bushing support conditions. The modified ring resulted in a capacity of 2.0g pga before major slip, compared to 1.4g pga without the ring.

Application and Implementation

The retrofit for 230 kV and 500 kV bushings developed in the second of these projects achieved limited success. The modified retaining ring resulted in a significant improvement in bushing fragility for the porcelain slip failure mode. However, its capacity even without the ring was somewhat higher than a prediction based upon earthquake experience data. Significant differences in the dynamic behavior of bushings were observed compared to expected behavior based on current knowledge. This implies that the interactions of the mechanical parts of a bushing, and with its supports and attachments, are complex and still not well understood. The favorable performance of 196 kV bushings in tests compared to poor performance in past earthquakes highlights the need for improvements in the qualification procedures of IEEE 693-1997. As a direct result of this project, the committee responsible for the standard is currently considering such changes. In particular, the use of more realistic support conditions during testing (i.e., flexible versus rigid stand) and improved methods to account for the effects of interaction with adjacent equipment are needed. The dynamic characteristics of bushings investigated in this project also have a direct bearing on the effects of equipment interaction, which are discussed in Sections 2.4.4 and 2.4.5.

2.4.4 Analytic Studies of Substation Equipment Interaction

Background and User Needs

Electrical substation equipment is connected by different types of electrical conductors. In broad terms, these conductors may be categorized as rigid and flexible buses. Rigid buses usually consist of aluminum pipes that are attached to equipment and other sections of the bus by various types of connectors. Flexible buses are usually made up of cables composed of a number of aluminum wires with end fittings used for making the connection to equipment terminals.

Rigid buses find wide use among utilities because they maintain a fixed shape and provide better control of clearances to adjacent equipment, buses, or the ground necessary for safety and operability. Maintaining control over clearances is particularly important when limited space is available, such as when a substation of a fixed size requires additional equipment to accommodate load growth. Flexible connector fittings are employed to relieve stresses induced by thermal expansion and contraction of a rigid bus system, but these connectors also influence the behavior of the system during earthquakes. Rigid bus systems provide a stiff mechanical link between adjacent equipment, which raises concerns about how connected equipment might interact with one another.

To mitigate interaction effects, utilities have often installed flexible bus systems. If sufficient slack in the cables is provided, flexible buses should have a minimal effect on the behavior of the connected equipment, effectively making them behave as if they were not connected. The disadvantage of flexible bus systems is that by their very nature, they allow more movement. Consequently, their design involves issues such as maintaining electrical clearances and transverse stability under wind and other loads.

One obvious way for connected equipment to interact during an earthquake is for one to collapse, pulling down connected equipment. Perhaps less apparent but equally important is the fact that the connected equipment, including the conductors, form a mechanical system that does not behave in the same manner as when the equipment is unconnected. In past earthquakes, interaction between adjacent connected equipment has been suspected of contributing to equipment damage. Unfortunately, damage assessments by trained observers are done after the fact, making it difficult, if not impossible to reach a firm conclusion about the importance of interaction effects. IEEE Std 693-1997, the new national standard for the seismic qualification of substation equipment, recognizes the importance of interaction effects, but only provides qualitative design guidance. Furthermore, equipment seismic qualification tests or analyses have always been done with the equipment in an unconnected condition. Clearly, this topic is one of great interest and importance to utilities in high seismic areas.

Project Approach

The objective of the analytical studies was to develop mathematical models to predict interaction effects on two pieces of equipment connected by a specified type of bus/connector system. This project was an extension of previous work on the same topical area, but focused on specific connector types and properties.

A previous PEER project developed the basic framework for interconnected equipment. Models and critical parameters were identified generically for equipment and rigid and flexible conductors. Rigid bus systems were limited to linear elastic elements. Models for flexible bus systems did not consider the bending stiffnesses of cables. This project continued the development of analytical models to predict the response of equipment connected by conductors, focusing on two specific types:

- Spring connectors (called flexible strap connectors or) with rigid bus, including nonlinear behavior of connector
- Cable conductors, including bending stiffness properties.

The spring connector is frequently used in rigid bus installations by several utilities. Several different styles of this connector are used, but all consist of several copper current-carrying straps formed into a ‘U’ shape to provide some flexibility and bolted to terminal pads at each end. Since these connectors were tested in the experimental studies portion of this topic (Section 2.4.5), some of the basic mechanical properties were available for use in the analytical studies. These basic properties were used to develop detailed mathematical models of the connector, which were then converted to a simpler representation for use in the analysis of the bus system. Because of the large displacement demands that might be imposed on such a spring connector during a major earthquake, a great deal of nonlinear behavior would be expected, which would be expected to affect the response of the connected system. This nonlinear behavior was included in the bus system analyses.

Models for cable conductors including bending stiffness properties were also considered in the analytical studies. The bending stiffness of cables would be expected to have a more important effect on the behavior of shorter cables. Cable conductors have been used by a number of utilities to provide more flexible connections between equipment. IEEE Std 693-1997 suggests several shapes of short jumper cables for this purpose. During previous developments, however, design guidance has been limited to qualitative suggestions. One of the reasons for

the scarcity of specific design guidance is the complexity and nonlinearities characteristic of the problem. Available information on the properties and behavior of cables was gathered and used in the development of analytical models. The results of experiments on cables previously conducted by Dastous and Pierre of Hydro Quebec were also investigated for comparison with the analysis results. Detailed analytical models were developed and analyzed with several ground motion inputs and varied slack.

The Principal Investigator for the analytical project was Professor Armen Der Kiureghian of the University of California, Berkeley, assisted by Professor (Emeritus) Jerome Sackman of the University of California, Berkeley. K-J Hong was a co-investigator. This same team developed the basic framework for analytical methods in a previous PEER project. Eric Fujisaki was the PG&E Technical Contact.

Results

The analytical studies demonstrated a method for modeling a spring type bus connector, including nonlinear effects. A detailed finite element model for each of three connectors was developed. A sample analysis of one of the spring connectors indicates that a de-amplification (i.e., reduction in response of the connected equipment compared to the unconnected equipment) occurs for both equipment items, due to the flexibility of the spring connector and the energy dissipated by yielding of the spring connector. The results of analyses are reported in terms of non-dimensional Response Ratios.

For the analysis of flexible bus systems, good qualitative agreement was obtained from the analytical model compared to experimental results reported by Dastous and Pierre. Parametric studies were performed to assess the importance of flexural stiffness and damping of the cable, and ground motion variability. Non-dimensional Response Ratios were calculated and reported as a function of an interaction parameter that describes the amount of slack provided in a flexible bus system.

Application and Implementation

One of the most important contributions of the analytical studies was the structuring of the interaction problem and the development of the concept of Response Ratios to quantify the effects of interaction. Because the Response Ratio for given equipment is defined as the maximum displacement of the equipment in the connected condition compared to that in the unconnected condition, this quantity represents the total load demand on the equipment. As discussed earlier in this section, equipment is seismically qualified in the unconnected condition. Consequently, Response Ratios provide a convenient means of relating equipment qualification levels to the expected performance of the equipment in a connected condition. The suitability and simplicity of this description of interaction make it an attractive measure for use in the specification, analysis, and testing of connected equipment. Similarly, the development of the interaction parameter for flexible cables in terms of readily available design quantities represents a major step forward in designing for the effects of interaction.

The development of analytical models of one type of rigid bus connector suggests that it is even feasible to perform such analyses with computer codes commercially available in the industry. The analytical studies also resulted in a method for estimating the slack required in a cable to prevent the effects of interaction, considering bending and axial stiffness properties, and

several different earthquake ground motions. With an appropriate amount of parametric variation, these values can provide valuable design guidance for flexible bus systems in substations.

2.4.5 Experimental Studies of Substation Equipment Interaction

Background and User Needs

The background and user needs for this project are the same as that for the project described in Section 2.4.4.

Project Approach

The experimental studies were intended to complement the analytical studies described in Section 2.4.4, and to obtain basic mechanical properties of connectors, provide data to validate analytical methods developed previously as well as in the concurrent project, and investigate the effectiveness of different types of rigid bus connectors. In addition, similar experiments on flexible cable jumpers were planned. Rigid and flexible bus assemblies and connectors were fabricated by PG&E and provided for testing. A flexible connector that BPA has installed with rigid buses in some of their substations was also provided for testing.

The experimental portion of this project included static/cyclic or shaking table tests of the following bus/connector assemblies:

- Spring connector with rigid bus (3 types)
- Expansion slider with rigid bus
- BPA flexible connector with rigid bus
- Three types of flexible cable assemblies.

The spring connectors are the same components that were evaluated in the analytical portion of the project. The expansion slider consists of a plunger that slides inside of the bus tube to maintain alignment and aluminum cable jumpers that carry electrical current. The cables also act as springs to restore the connector to its original position. The BPA flexible connector is constructed of three vertical aluminum cables that are welded to two horizontal terminal pads. The bending stiffness of this connector is large enough to support the weight of the bus assembly connected to it and maintain stability against lateral loading, but small enough to keep forces between the equipment low during earthquake motions. Single and bundled (two cables side-by-side tied by clamping bars) cable jumper specimens of two lengths (15 feet and 25 feet) were prepared for the tests.

Static/cyclic tests were conducted using all of the listed connectors and the flexible cable assemblies. These tests gathered force versus displacement data on each connector type to use as inputs to analytical models. Material tests were conducted to obtain basic data, also for use in analytical studies, on the spring connector.

Shaking table tests were conducted on one type of spring connector, the expansion slider, and the BPA connector. The rigid bus assemblies were approximately 10 feet long, with the connector attached at one end. To study the interaction behavior of equipment connected by these bus assemblies, cantilever posts with provisions for adjusting the mass at their tops were constructed to simulate the equipment. A range of frequencies and masses for each piece of

simulated equipment were developed for use in testing. Five different equipment pairs were selected for testing. The simulated equipment and buses were subjected to different intensities of motion from two different earthquakes. Stand-alone equipment tests were also conducted to establish the responses of the unconnected equipment. About 160 different shaking table tests were performed for different combinations of equipment pair, bus connector type, ground motion, and intensity of motion. Flexible cable assemblies of the lengths chosen were found to have such low bending stiffness that shaking table tests were not performed.

The Principal Investigator for the experimental project was Professor Andre Filiatrault of the University of California, San Diego (UCSD). Spyridon Kremmidas, Ahmed Elgamal, and Frieder Sieble were co-investigators. Eric Fujisaki was the PG&E Technical Contact.

Results

The spring type rigid bus connectors exhibited good energy dissipation characteristics during static/cyclic tests. Their displacement capacity was shown to be from six to eight inches in each direction, depending on the style of spring connector. The expansion slider connector demonstrated the characteristics of a friction-damper type device in static/cyclic tests. Its behavior is characterized by low stiffness (due to the flexibility of the cables) and good energy dissipation (resulting from friction forces generated at the plunger/pipe interface). Static/cyclic tests on the flexible cable assemblies showed that for the lengths chosen, the bending stiffness of the cables was insignificant. No other tests were performed with the cable assemblies.

In shaking table tests, the expansion slider consistently exhibited the most favorable behavior of the three connectors tested. Response Ratios (discussed earlier in this section), determined from quantities measured during the tests, showed that the seismic responses of both equipment items were de-amplified during virtually every test. This means that the responses of the equipment when connected are lower than the unconnected equipment. The de-amplification of responses is attributed to the energy dissipated by frictional forces in the connector, which are generated even at low levels of motion. At the highest intensities of ground motion, however, the displacement capacity of the slider was exceeded, causing the plunger to come out of the tube.

At lower levels of shaking, the BPA flexible connector seemed to perform reasonably well to mechanically isolate the connected components. In general, both the spring connector and the BPA flexible connector caused amplification in the higher frequency equipment, while de-amplifying the response of the lower frequency equipment. This behavior is in agreement with one of the general trends identified in previous analytical studies and occurred even though significant levels of inelastic behavior occurred in the spring connector.

Application and Implementation

Experiments validated previous analytical studies, which suggested that a flexible connector with significant energy dissipation would be effective in reducing the responses of the connected equipment. The expansion slider was shown in experiments to be consistently effective in de-amplifying the responses of both pieces of equipment. This type of behavior was not observed in the other two connectors tested. Such a result suggests that more attention should be focused on the use of such a connector. PG&E has discussed increasing the displacement capacity of the expansion slider with one of its suppliers for future validation

tests. Experimental results for the spring connector and the BPA flexible connector were not as favorable as the expansion slider. Response Ratios determined from tests will provide valuable data for benchmarking analytical methods, and guiding future actions on connector selection for use with rigid buses. Tests involving the BPA connector showed that amplification still occurred in at least one equipment item, particularly at high intensities of shaking. This result raises some question about the effectiveness of flexible connectors with low damping, which traditionally has been the preferred approach in connection design to prevent interaction. Previous analytical work taken together with these experimental results provides an indication of the magnitude of stiffness required for these connectors to prevent or minimize the effects of interaction.

2.4.6 Amplification of Ground Motions at the Base of Transformer Bushings

Background and User Needs

As discussed in Section 2.4.2, transformers are one of the most vital types of equipment in a substation, and porcelain bushings have been shown to be a weak link in past earthquakes. Seismic qualification requirements for bushings given in IEEE 693-1997 specify shaking table tests for bushings to simulate earthquake ground motions. Because the structures that support a transformer bushing (the transformer tank, turret, or other support structure) are not rigid, earthquake motions applied at the base of a transformer are amplified at the bushing support point. Physical limitations and the expense of shaking table tests preclude testing a transformer with the bushing mounted on it. Consequently, test standards require that the bushing be mounted on a rigid test stand and subjected to motions amplified by a factor of two.

Very little experimental or analytical data exists on the adequacy or appropriateness of the amplification factor of two for bushing qualification. Different manufacturers of transformers configure the tank and bushing support structures differently, resulting in a variety of bushing support conditions. In the past, little attention has been paid to the structural design of the bushing support structures. Research efforts to estimate the magnitude of the amplification factor and the reasonableness of the value given in specifications were considered to be of great value.

Project Approach

The objective of this project was to obtain experimental data from field measurements, to better define the dynamic characteristics of large transformers, develop simple mathematical models to predict the transformer and bushing responses, and estimate the amplification factors appropriate for different transformers. The following major activities occurred in this project:

- Select transformers (spares or new equipment that is de-energized) for investigation.
- Install instrumentation and shake the equipment by impact hammer or portable shaker and record responses.
- Develop simple analytical models and benchmark against experimental data.
- Estimate amplification factors and assess reasonableness of factor of two.

Four transformers located in PG&E substations were selected for testing. We selected transformers with high-side voltages of 230 kV and 500 kV because, based on past experience, bushings of this class are the most vulnerable to earthquakes. Different styles of transformers

and bushing supports were chosen for testing. Two 500 kV single-phase units, one 230 kV single-phase unit, and one 230 kV three-phase unit were tested. Two of the transformers were older spare units located in substations, and two were new units just about to enter service. In all cases, the transformers were not connected to the station buses while testing was performed. For each transformer, instrumentation was installed. A 160-pound electromagnetic shaker mounted on the transformer tank and controlled by a PC-based signal analyzer applied low-level input.

Based upon outline and limited structural drawings of the equipment, simple mathematical models for two of the four transformers were developed. These models were benchmarked against experimental data gathered through field tests, and adjustments made to achieve similar behavior. These mathematical models were then used to study the dynamic behavior of the transformer and bushing system and to estimate amplification factors at the bushing support points.

The Principal Investigators for this project were Professors Roberto Villaverde and Gerald Pardoen of the University of California, Irvine. Eric Fujisaki was the PG&E Technical Contact.

Results

Experimental data on the important frequencies of vibration for the four transformers were gathered during testing. Simple lumped mass and stick analytical models were developed for the two 500 kV transformers. Frequencies ranged from about 3 to 4 Hz for the 500 kV bushings and about 4.5 to 6 Hz for the 230 kV bushings. Measurements made at low levels of shaking indicate damping ratios of about 1.5 percent to 4 percent of critical. Analytical models for the two 230 kV transformers were not developed; however, it appears that the frequencies of vibration of the 230 kV bushings would be in a similar range to that described above.

The simple mathematical models of the two transformers were adjusted to achieve a reasonable match with the results of measured field responses. Amplification factors for the responses of the bushings were computed from these models and reported as approximately two for the 500 kV bushings and about four for the 230 kV bushings. However, due to the unavailability of detailed data on transformer structures and components, and a lack of understanding of the basic properties of bushings (such as those discussed in the projects on high voltage transformer bushings described in Sections 2.4.2 and 2.4.3), there is significant uncertainty in accuracy of these calculated values. It was also suspected that the small magnitude of forces imparted by the shaker might not have adequately excited some parts or components of the transformer, introducing further uncertainty into the results.

Application and Implementation

This project resulted in two important and useful outcomes. First, the frequencies of vibration measured in field tests were substantially lower than those measured for similar bushings in seismic qualification tests. For example, 500 kV bushings in field tests had frequencies of vibration of 3 to 4 Hz compared to about 8 Hz in shaking table tests; 196 kV bushings had frequencies in field tests of 4.5 to 6 Hz compared to 14 to 20 Hz in shaking table tests. Although a reduction in frequencies of vibration was expected due to the different support conditions when these measurements were made, the magnitude of the reduction is significant. This

suggests that other sources of flexibility, such as several rubber gaskets at cover plates and flanges, need to be considered in the analysis and design of the bushing support structure.

The second important outcome of this project deals with the basic approach specified in IEEE Std 693-1997 to account for the bushing support amplification. Although the amplification factor method prescribed by the standard is simple to apply for bushing qualification tests, it may be inadequate for dealing with the wide variation in bushing support responses and the complex behavior of the bushing/support system. The difficulties and uncertainties encountered in this project highlight the need for a more integrated design of the bushing and its support and for more definitive guidance in the design of the bushing support structure in IEEE Std 693-1997.

2.4.7 Rocking Response and Overturning of Equipment

Background and User Needs

California utilities maintain a large number of substations in high seismic hazard areas. Within these substations is a significant amount of equipment that is poorly anchored, and in some cases, unanchored. At PG&E and other utilities, equipment anchorage strengthening efforts have focused on transformers because of their importance to substation operation. Equipment anchorages are designed to restrain the equipment from sliding and overturning, the latter generally producing more damage.

Rocking or toppling of equipment or the equipment and its foundation has been observed in past earthquakes. Analytical studies performed by others have suggested that objects have a much higher capacity against toppling during earthquakes than assumed in conventional engineering design because of the limited amount of energy supplied by the earthquake. While previous studies and methods of assessing vulnerability to overturning have been limited to actual toppling, rocking is also of interest to the utility since equipment would likely be severely damaged by equipment impact with the ground even before toppling occurs. A better understanding of the rocking phenomenon and identification of factors that contribute to the vulnerability to rocking and toppling would help to prioritize future anchorage strengthening efforts.

Project Approach

Previous analytical studies investigated the rocking response of freestanding rigid blocks and their response to pulse-type motions. The current project continued this work and investigated the following major issues:

- Influence of anchorages of varying strength
- Effect of variation in coefficient of restitution on rocking response
- Contribution of vertical seismic input to overturning
- Characterization of rocking response (uplift or angular velocity).

The investigations conducted in this project were intended to address several practical aspects of the overturning problem. Because actual substation equipment are connected to foundation slabs on soil, an important consideration in the rocking problem are the effects of inelastic collision with the ground (influence of coefficient of restitution) and anchorages of varying

strength. Previous analytical work considered only horizontal input motions; vertical input motions generally have been considered to be detrimental to rocking response, since upward motion tends to reduce the restoring forces that would return the object to its initial stable position. Finally, as discussed previously, rocking as opposed to actual toppling is of interest in order to ensure that the equipment does not sustain severe damage from impact loading.

The Principal Investigator for this project was Professor Nicos Makris of the University of California, Berkeley. Jian Zhang was Co-Investigator. Professor Makris was the Principal Investigator in a previous PEER project on equipment overturning. Eric Fujisaki was the PG&E Technical Contact.

Results

Analytical models were developed to investigate the rocking behavior of various blocks with anchorages of varying strength. In a manner similar to previous studies, an impulsive motion was used as an input, and rocking spectra were computed. These spectra related the pulse frequency/block size to the amplitude of the pulse acceleration required to cause toppling to occur. These spectra indicated that there is high capacity against overturning for small blocks, or at high pulse frequency. For large blocks or low pulse frequencies, overturning capacities are lower. These spectra also indicated that for some frequency ranges, the conventional engineering evaluation would tend to predict a higher capacity for resisting overturning than suggested by this study. Some limited investigations were performed on the influence of the coefficient of restitution. These show that although the magnitude of the uplift decreases with more inelastic collisions (which is expected), the impact velocities are sometimes higher. Vertical seismic input was found to have an insignificant influence on rocking response.

Application and Implementation

This project demonstrated that conventional engineering methods using static coefficient analysis provide, in most cases, a safe design. However, rocking spectra also identified a frequency range where the conventional approach underestimates the potential for overturning. Because vertical input motions were shown to have an insignificant effect on overturning, they can be safely ignored in engineering evaluations. These results can be incorporated into engineering design criteria.

Rotation and angular velocity spectra for blocks of different slenderness parameters were calculated and plotted for two sample earthquakes and different values of the coefficient of restitution. These results give an indication of the importance of the coefficient of restitution on rocking response. These results also directly provide uplift displacements and impact velocities, which can be compared to values established by equipment manufacturers. An extension of these calculations to include the effects of foundation slabs would result in data on the uplift and impact velocities for the equipment/foundation system. Results from both of these cases (equipment uplift and equipment/foundation uplift) can be used to establish the vulnerability of equipment to rocking, given input motion records appropriate for the site.

For a given site near a fault zone, predictions of pulse frequency and amplitude, and equipment size parameters can be coupled with the calculated overturning spectra to provide an indication of the vulnerability of equipment. Prior to use, however, these spectra should be recast to

define failure as rocking uplift or impact velocity of a specified magnitude. This information can then be used to prioritize strengthening modifications for equipment anchorage.

2.4.8 Field Investigation of Effects of the Kocaeli, Turkey, Earthquake

Background and User Needs

On August 17, 1999, at 3:01 AM, a magnitude 7.4 earthquake hit the industrial heart of the country of Turkey (the Izmit Bay area). The earthquake was accompanied by severe ground shaking, more than 100 km of surface fault rupture of several meters, and shaking-induced ground failure in urbanized areas. In the days following the earthquake, as televised reports and information on the Internet flowed out of the densely urbanized Kocaeli Province and adjacent provinces in western Turkey, it became clear that significant information on the performance of the Turkish electric power system could be gained by studying this earthquake. This information would bring increased relevance to the Commission-supported research program.

Project Approach

PG&E organized a reconnaissance team to travel to Turkey and gather critical, time-sensitive data and information regarding the earthquake and its effects on electric power reliability and on the electric utility customers. The team was in Turkey from September 2 to September 13. Table 4 lists members of the team. The team included very knowledgeable collaborators from Turkey, who greatly added to the effectiveness of the PG&E-Commission team in the field.

Table 4. Kocaeli Earthquake Investigation Team and Collaborators

Name	Primary Topics of Investigation	Organization
Lloyd Cluff, Team Leader	Seismic Geology, Damage Assessment and Structural performance	PG&E, Manager, Geosciences Dept.
Norman Abrahamson	Engineering Seismology	PG&E, Geosciences Dept.
Robert Panero	Utility risk management	PG&E, Insurance Dept.
William Savage	Seismic Hazards, Electric Power Systems	PG&E, Geosciences Dept.
Robert Anderson	Engineering Geology, Power Systems	CEC, Energy Facilities Siting & Environmental Protection Division
Aykut Barka	Seismic Geology	Istanbul Technical University, Geology Dept.
Fakir Erdogan	Electric Power Systems	TEAS, Nuclear Engineering Dept.
Muzaffer Genc	Geology	TEAS, Nuclear Engineering Dept.

The team visited the Turkish Electric Generation and Transmission Company (TEAS) in Ankara to receive detailed briefings on the performance of the utility systems in the earthquake. Several field tours allowed the team to inspect many features of the surface fault rupture and its effect

on structures and utility and transportation systems. In particular, the Adapazari substation near the epicenter of the earthquake was inspected, and valuable information about damage to substation components was obtained. Travel through some of the heavily damaged areas permitted a close look at the interaction between building damage and electric utility damage. Inspection of the surface fault features at selected locations illustrated many examples of poor and good performance of buildings, pipelines, and transportation corridors. The trip ended with a four-hour helicopter overflight of much of the entire length of the fault rupture, permitting close visual inspection and photography of geologic and man-made features associated with the earthquake.

Results

In spite of the severe earthquake conditions, the Turkish electric power transmission system was quickly restored on the day of the earthquake, promoting the timely restoration of customer service in all but the most severely damaged urban areas. The team made several important observations:

- The extensive damage to several 380 kV substations was not a major factor in transmission power restoration due to the existence of 380 kV transmission lines that bypassed the damaged stations. Power could then be rerouted to the distribution system via the 154 kV transmission system, whose substations were much less damaged. The redundant system design used by TEAS performed successfully in this earthquake, even though explicit planning for such earthquakes had not been done.
- The power generation and transmission personnel were responsive and organized in their efforts to stabilize the post-earthquake situation, rapidly assess critical damage, and restore system operations. In general, the crisis management actions taken by TEAS were effective.
- The distribution company actions were also responsive and effective. Of particular importance was the coordination between local government representatives and the local distribution companies to safely restore power. This avoided the danger of restoring power into damaged or collapsed buildings.

The physical damage to generation, transmission, and distribution equipment was consistent with the experiences of past earthquakes in California, Japan, and elsewhere and included the following typical observations:

- Generating plants are usually resistant to significant damage in earthquakes, provided their foundations do not undergo large deformations.
- Transmission towers and lines are highly resistant to earthquake damage even when displaced by surface fault rupture.
- Porcelain insulators used in high-voltage substation equipment are generally vulnerable to strong earthquake shaking and loading caused by interconnection with other equipment, unless high-strength insulators and appropriate seismic designs are used.
- Unanchored equipment is seismically vulnerable, particularly transformers sitting on rails or inadequately attached pole-mounted transformers. Transformer damage can significantly delay customer service restoration.

- Distribution power poles and towers are vulnerable to damage due to liquefaction and other ground failures, particularly in urban areas where buildings are likely to be damaged as well and can fall into the poles and towers.
- Pole-mounted transformers fail if shaking causes the poles to break, or if they are not adequately anchored to the poles.
- Underground cables are prone to damage where they connect to surface electrical supplies or buildings because of subsequent degradation in cable insulation due to physical or electrical effects. Such damage can lead to long delays in power restoration because of the relative difficulty in repairing underground cables compared to overhead lines.

Application and Implementation

The observations made of earthquake damage and its impact on restoration of customer service in the electric and natural gas systems in the Izmit region of Turkey were quite consistent with the types of damage and service disruptions observed in past earthquakes in California. The damage to high-voltage substation equipment confirmed the wisdom of the diverse testing and analysis program that is being carried out in the PG&E-Commission program. In past earthquakes in California there has not been extensive damage to underground electric cables, nor has there been the need for rapidly constructed utility services to refugee camps. However, these issues could arise in future earthquakes in selected localities, and their implications will be incorporated in future research planning. The immediate post-earthquake response of TEAS to the earthquake damage provided important lessons for emergency response and system risk analysis. It took many hours to gather information on what the level of damage was at individual utility facilities, and to begin to comprehend the huge societal impact of the damage. Research efforts to accelerate this information-gathering using ground motions and vulnerability curves is properly directed. Similarly, the benefit of pre-earthquake understanding of the role of redundant transmission paths and operational alternatives given various states of equipment damage is incorporated in the topics for future research that address modeling seismic risk.

In addition, the personal experiences gained by the investigation team have had a large impact in their convictions about the importance of the PG&E-Commission research program, and has reinforced their resolve to continue to focus on the critical issues that affect safety and reliability of electric power in California. Along with the detailed observations and data collected, the lessons they learned during and following the field investigation are being incorporated into planning ongoing and future research activities covering all program topics.

2.4.9 Conclusions and Recommendations

A well-integrated range of projects provided results that address the Electrical Substation Equipment Performance topic, and incorporated field experiments, laboratory testing on shake tables, and sophisticated analysis and modeling. The extensive observations made following the Kocaeli earthquake helped confirm the appropriateness of the projects and emphasized the benefits and urgency of the work. As noted in the discussion of each of the project results, there were numerous specific data sets and analysis results that can in some cases be used immediately. These results also point to additional studies necessary to fulfill the topic objective of understanding the seismic vulnerabilities of substation equipment so that

appropriate improvement in existing equipment and installation of well-performing new equipment can lead to predictable and acceptable electric system performance in future earthquakes.

2.5 Topic 5: Earthquake Fire Safety Associated with Gas and Electric Systems

2.5.1 Objective

The objective of this topic is to systematically identify the bases for assessing fire safety issues related to natural gas and electric power systems, considering both utility-owned facilities (pipes, wires, and meters) and customer-owned facilities (residences and businesses). Although fires have not typically been a severe consequence of earthquakes in modern Californian cities, the threat of fire, including conflagration, is a prominent factor in planning for earthquake safety. This study provided an overview of this complex and variable hazard in earthquakes, and then focused on key issues dealing with residential structures and life safety. These results are a beneficial step toward informing the various parties responsible for fire safety, including building owners and occupants, about the causes of earthquake-related fires and alternative safety improvement actions.

2.5.2 Ignition of Fires Following Earthquakes Associated with Natural Gas and Electric Distribution Systems

Background and User Needs

Utility providers of natural gas and electric power work diligently to provide safe and reliable services. Nonetheless, concerns about potential safety threats accompanying the occurrence of earthquakes have been raised regarding both gas and electric power. The ignition of gas leaks inside buildings resulting from damage to customer-owned piping and appliances, or ignition of natural gas escaping from damaged pipelines in streets or near buildings, could lead to property damage and threaten the life safety of individuals. These occurrences have led to suggestions for reducing fire risk by reducing the occurrence of leaks through numerous measures, including strengthening buildings, anchoring appliances and other gas-burning devices, and installing gas shutoff valves that respond to earthquake shaking, excessive gas flow, or the presence of leaked gas. However, each of these alternatives has various adverse consequences, including high installation costs, long implementation time, prolonged service outage durations, and potentially dangerous customer behaviors that may negatively effect gas safety or reliability if actually implemented.

Statistics from earthquakes in the past decade indicate that electric power can be as significant as natural gas in causing post-earthquake fires. The source of ignition may be due to electric appliance and wiring failures causing a spark in a damaged building or downed, energized overhead distribution lines. Recent and ongoing improvements in the post-earthquake reliability of high-voltage electric transmission systems have increased the potential for electric distribution service to continue to be provided to areas containing seismically damaged buildings or contents.

Utilities, their customers, government agencies, and regulators need to understand and consider the issues and implications associated with various alternatives to reduce earthquake risk due to natural gas and electric power when preparing for future emergencies.

Project Approach

During the initial PG&E-PEER research program, a project to study these topics, focused on natural gas, was conducted. A second phase of this research was carried out to incorporate electric power issues, since work during the first phase indicted that electric power was also a primary ignition source for fires following earthquakes. The two studies have been integrated herein and are reported together.

The scope of the project involved reviewing the causes of fires in earthquakes beginning with the Great San Francisco earthquake of 1906 and concluding with the Kobe, Japan event in 1995. The review includes consideration of facilities and structural performance, human factors, and organizational factors. The project created an inventory of fire ignition scenarios. These scenarios were used to identify and consider alternative means to reduce the safety threats posed by fires, including appliance anchorage and flexible gas connections, gas and electric shutoff devices for residences and businesses, and gas and electric distribution shutdowns. Public education and service restoration coordination in the aftermath of a major earthquake were also considered.

The project was conducted by Dr. R. Brady Williamson, professor of Engineering Science in the Fire Safety Engineering Science Program, a part of the Department of Civil and Environmental Engineering at the University of California, Berkeley. Dr. Norman Groner assisted Dr. Williamson. William Savage was the PG&E Technical Contact.

Results

The causes of fires in eleven twentieth-century earthquakes were reviewed. From this review, the degree of structural damage was found to be a direct indicator of the potential incidence of fires following an earthquake. Using the earthquake fire history and other information, a list of fire ignition scenarios was developed involving gas and electric service. The scenarios incorporate the necessary presence of a fuel source and a source of ignition.

- A gas pipe in a building is broken, **and** an electric spark from damaged electrical wiring is present near the released gas to cause ignition.
- Bottles or open cans of flammable liquids are thrown to the floor by the earthquake, **and** an open gas flame or an electric spark is present to ignite the vapors from the spilled liquid.
- A water heater is overturned by the earthquake, **and** the customer's house gas piping is ruptured, **and** released gas is ignited by a flame or spark.
- A gas pipe in a building is broken due to building structural damage, **and** the delayed ignition of the released gas occurs when an ignitable mixture of gas and air is reached in the presence of a source of ignition.
- Cooking oils and other kitchen fuels are spilled during the earthquake, **and** either electrical- or gas-based cooking equipment ignites these fuels.
- Electrical service to a structure is interrupted by the earthquake, **and** an electric-powered device is displaced or damaged by the earthquake **and** comes into contact with a quantity of fuel that is in a flammable state, **and** when the electric power is restored to

the building, this device causes the ignition of the flammable fuel. (An example of such a scenario might be a high-intensity light falling onto a polyurethane mattress or couch.)

- A person ignites a fire by means such as arson or turning on light switches in the presence of a gaseous fuel.

The study focused on the life-safety implications of these fire scenarios for residential structures, specifically R-1 (three or more dwelling units) and R-3 (one or two dwelling units). From the standpoint of fire threatening people trapped inside a structure following an earthquake, R-1 occupancies are considered to be the more serious concern due to the greater number of occupants with a smaller number of exits. This is particularly true for buildings of more than two stories than for single-family or duplex residences. Schematic goal decomposition models and influence diagrams for gas and electric utility-related earthquake fires were developed to aid in understanding the logical relations among factors affecting gas and other sources of fuel; gas flames, electric sparks or heating elements, and other ignition sources; and life-safety issues such as injuries or egress blockage due to building damage.

Finally, alternative means to reduce fire risks following earthquakes were analyzed. The interrelated performance in an earthquake is very complex among residential structures, customer and utility gas lines, electric distribution and residence wiring, electric safety systems, gas and electric appliances, gas and electric shutoff devices in the building, and people affected by or responding to the earthquake. While this study does not reach conclusions about all these relationships, it does provide a logical framework to analyze them. For some situations involving life-safety issues, there were several conclusions reached regarding the most effective measures to reduce life-safety threats due to post-earthquake fires.

- Older multifamily residential buildings (R-1 occupancies) that are susceptible to structural damage and potential collapse appear to represent the most likely setting for people to be trapped and exposed to life-safety threats from fire. Improvement of structural performance of these structures could significantly improve fire safety. Gas flow interruption devices, such as seismically activated valves or excess flow valves, can also make improvements in safety, provided that they have appropriate performance characteristics for the seismic hazard exposure and for the level of seismic vulnerability of each structure and its contents.
- For one- or two-family residences (R-3 occupancies) of good, earthquake-resistant design and construction, life-safety is provided by such current practices as water-heater and other appliance anchorage, strong attachment of the structure to its foundation, and multiple means of egress. For older R-3 occupancies, important first steps to improve safety are to anchor water heaters and other gas appliances, and install flexible connectors.
- The report discusses alternative means to shut off gas to a structurally damaged residential building to stop gas leaks that could lead to fires. The first alternative is to manually shut off the building gas valve, which building occupants are recommended to do if they smell gas. This has proven effective in past earthquakes. The second alternative is to install automatic gas shutoff devices either activated by earthquake shaking above a set level or by gas flow rate above a set level. Performance characteristics of the two types of devices were reviewed, and their respective

advantages and disadvantages summarized. It was noted that a new standard for the activation of seismic shutoff valves, ASCE 25-97, has been developed for R-3 occupancies, but it does not apply to R-1 occupancies. Adoption of current standards for seismically activated shutoff valves and excess flow valves is pending in California.

- Electric power service will most likely be interrupted to the earthquake-affected area. To prevent power from being restored into areas with gas leaks or other damage that could lead to fire ignitions, there should be an exchange of information between emergency responders (fire protection, police, and utility field personnel) and the utility emergency control center.

Application and Implementation

This report provides a logical framework for identifying and analyzing earthquake-related fire safety issues involving gas and electric utilities. It is clear that these issues are multi-disciplinary and multi-jurisdictional, involving utilities, regulators, public officials, fire departments, building owners, and manufacturers of gas and electric safety devices, appliances, and building and utility components. Improvements in fire safety involve a complex process of risk identification, evaluation of safety alternatives under various scenarios, and implementation of effective choices. This study represents progress in this process and is a useful review of current knowledge about earthquake fire safety.

The study is restricted in scope to consideration of residential life safety issues, and has identified two focus areas for the application of the findings of the study.

- The study notes that earthquake fire safety is strongly dependent on the structural integrity of buildings and their contents, and that older multi-family residential units are likely the highest life-safety risk structures. Using its experience and expertise, PG&E is assisting in the preparation of gas and electric safety information to be made available to local governments and building owners and occupants to assist them in making informed decisions about the best actions to take to reduce earthquake-related fire safety risks.
- PG&E recognizes the importance of coordinating electric power restoration with gas safety checks. This was demonstrated during the power restoration of San Francisco and other localities following the Loma Prieta earthquake. In addition, PG&E is working with the local and national offices of the Federal Emergency Management Agency (FEMA) and California's Office of Emergency Services (OES) and Division of Mines and Geology to enhance the application of FEMA's HAZUS software within a few hours following an earthquake to identify areas of severe building damage in the greater San Francisco Bay area. As currently envisioned, this information would be distributed by OES and could augment initial field reports to improve the safety of power restoration and other post-earthquake responses.

2.5.3 Conclusions and Recommendations

The report for this project contains a useful framework for further analysis of fire safety. However, at the present time, this framework and the scope of possible additional studies need further consideration in the context of the large amount of information available before further work is pursued.

3.0 Project Administration

PG&E and PEER carried out the administration of the project. The two organizations maintained close and effective coordination in preparing contracts, subcontracts, and subawards through their respective project managers, Dr. William U. Savage and Professor Gregory L. Fenves. The following paragraphs describe the administrative functions of the program of research.

Pacific Gas and Electric Company

As the prime contractor with the Commission for this project, PG&E provided project management and financial services for the project. Dr. Savage was the principal contact with Ms. Judy Grau and her successor Mr. Robert Anderson, Commission Project Manager, and with others at the Commission. He prepared contractual Quarterly Progress Reports and Quarterly Status Reports and forwarded them to the Commission Project Manager, approved invoices before their submission to the Commission, and provided other information and attended meetings as requested by the Commission.

PG&E subcontracted with PEER to perform the research activities as approved by the JMC. Dr. Savage also maintained primary project management relations with Dr. Fenves and others at PEER, in support of their subcontract to PG&E to conduct the research projects. PEER personnel were very responsive in providing information as needed during the course of the program. Their administrative activities are described in the next section.

Key PG&E personnel participated in the JMC, including Mr. Lloyd Cluff, Seismic Geologist and Manager of PG&E's Geosciences Department; Dr. Norman Abrahamson, Senior Engineering Seismologist; Mr. Edward Matsuda, Supervising Civil/Structural Engineer; Mr. Eric Fujisaki, Civil/Structural Engineer; Mr. Kent Ferre, Civil/Structural Engineer; and Mr. Robert White, Geotechnical Engineer. These individuals also served as Technical Contacts for the individual PEER research projects, providing technical information, guidance, and advice as needed to help the Principal Investigators and projects to be successful.

The costs of the PG&E administrative and technical management, amounting to more than three man-years, have been borne by PG&E. This funding was provided in the expectation that the results of the research would be quickly incorporated into ongoing utility activities and result in safer and more reliable electric power provided to customers. Earthquake specialists in other utilities in the state have been either directly involved in research projects or have been kept informed of results that they can apply to their own systems.

Pacific Earthquake Engineering Research Center

Based at the University of California, Berkeley, PEER was responsible for managing the user-directed research program under a contract with the Pacific Gas & Electric Company. As described previously, the JMC established policies and made the major decisions affecting the program. Professor Gregory L. Fenves, assistant director at PEER, chaired the JMC and served as program manager for PEER. As chair of the JMC, Dr. Fenves organized the meetings and their agendas, in consultation with the staff of PG&E, Commission, and the other utilities

involved in the research program. Dr. Fenves kept in close contact with Dr. Savage at PG&E to assure smooth operation of the program.

After the JMC approved the 18 projects, PEER administered them. Working under the supervision of Dr. Fenves, Administrative Assistant Joanne Cortez prepared the subaward contracts from UC Berkeley to the project investigators. After signed approval of the subaward by voting members of the JMC, UC Berkeley issued the subaward. Generally this process went smoothly. With projects underway, the major administrative task was to monitor progress of the projects and review and approve invoices for payment. The following payment process was established. A subaward organization sent an invoice to UC Berkeley. Ms. Cortez prepared a summary table showing expenditures to date and receipt of quarterly reports. Dr. Fenves reviewed the request for payment, the quarterly report, and presentations at quarterly coordination meetings. If progress was adequate, Dr. Fenves approved invoice payment. If there were questions, Dr. Fenves spoke with the technical contact for the project and investigator. Once Dr. Fenves approved the invoices, they were sent to UC Berkeley Accounting for payment. Invoices to PG&E were issued by Accounting based on payments to subawardees.

During the course of the project, PG&E identified a significant problem in the low amount of invoices, well below the projected cash flow, from UC Berkeley. After investigation with UC Berkeley Accounting, Dr. Fenves discovered that Accounting did not prepare invoices to PG&E in a timely manner because of the manual business systems. Although discovered late in the process, PEER has received assurance from UC Berkeley Accounting that they will prepare and send invoices to PG&E in a more timely manner.

As the individual projects reached their end, PEER withheld 10 percent of the total payment until the investigators submitted the final report and it had been accepted. The technical contact and one or two other reviewers reviewed all final reports. Based on those comments, Dr. Fenves determined whether a report was acceptable or required modification. After the final report was approved, the withheld sum from the contract was paid to the subawardee. Summaries of the reports were provided to the JMC in addition to copies of the reports requested by JMC members.

4.0 Conclusions and Recommendations

4.1 Conclusions

The goal of this applied research program was to improve the earthquake safety and reliability of electric power transmission and distribution in California. The research program was organized by the JMC to assure that the research results would directly address electric utility needs in preparing for future earthquake occurrences, and that utility personnel or their consultants could quickly implement the results.

As described in the previous sections of this report, the 18 projects have provided useful results that meet utility needs in the five topic areas. However, it is important to also note the integration of the projects to meet the goal of the program, namely to improve utility earthquake performance. The following bullets summarize, in narrative form, the cumulative connections between the topics that address the goal.

- **Topic 1** results (improved ground motion and site response models and methods) are used as input to **Topic 2** (ground motion estimates for emergency response)
- Topic 1 results are used as input to **Topic 3** (ground motion database) to improve the assessment of locations and amounts of post-earthquake permanent ground deformation caused by ground shaking.
- Topic 1 results, along with Topic 3 results, are used as input to **Topic 4** projects (assessing the vulnerability of pieces of substation equipment and the vulnerability of interconnected equipment). Severe ground shaking and ground failure are the direct causes of substation damage that can disrupt power transmission to customers.
- Topic 1 and 3 results improve the assessment of building damage (damaged buildings are the structures within which most earthquake-caused fires start), and thus underlie and are input to **Topic 5** (earthquake fire safety of gas and electricity). Levels of ground shaking can be used to control utility service shutoff valves and to quickly identify likely locations of damaged buildings where fires could start and people could be trapped.

Although the connections among the individual projects are multi-faceted, a broad picture can be seen of the research results linking up to enable utility personnel (and their regulatory counterparts) to have significantly improved information for taking actions regarding earthquake risks. These actions often include retrofitting a vulnerable building that houses office workers, upgrading equipment and improving anchorages in substation yards, and modifying emergency response procedures to take advantage of new information. The customer benefits from these actions following an earthquake in terms of greater electric power reliability, and faster and less expensive recovery of the overall functioning of society. Of course, there will always be some utility system damage due to random failures of components or facilities. However, the redundant electric system design and the operation skill of utility personnel can make the extent and duration of outages no worse than those of a winter storm.

4.2 Benefits to California

The measure of the success of this user-driven, applied research program is the extent to which the results are being put to use to directly benefit the California electric power ratepayers and others in the state. Even before the reports were prepared, some of the results, such as the substation equipment seismic performance data and analyses, were being implemented in managing the equipment inventory at several utilities and in preparing to modify the national seismic qualification procedures for substation equipment. Significant progress has been made in the ultimate goal of the project, to improve electric system safety and reliability in earthquakes. Clear directions for further applied research were also identified, and provide the basis for planning the next phase of work.

When the results have been implemented in the utility system, then the ratepayers (who have funded this research) and other members of society will benefit from the research by (1) receiving more rapid restoration of service following an earthquake due to less utility damage and improved emergency response capability, (2) avoiding possible utility rate increases because there is less direct damage to equipment and facilities, and (3) experiencing more rapid overall recovery of societal functioning following the earthquake due to rapid power restoration and use of the research results by other organizations to recover their functionality more quickly.

This research program provides several additional benefits to utilities and to the State of California. Although they are secondary to the goal of this program, these benefits have substantial long-term value.

- Enhanced academic expertise: This research program has created an expanded group of university faculty who have gained extensive knowledge about electric utility systems and who have demonstrated interest and talent in addressing utility research needs and problems. In the future, they will have opportunities to continue research in these areas, and to guide their students into graduate work involving utility systems and earthquakes. This reservoir of academic experience will provide ongoing benefits to the utility industry and the State.

- The establishment of the PG&E-PEER-Commission research program has attracted great interest nationally. Other organizations, both public and private at the local to national level, have observed the success of the program, and are influenced by its research goals and project topics. Thus, by providing strong technical leadership, well-defined research project scopes, and results that have clear value and applicability, the PG&E-PEER-Commission program is helping to shape the direction and topics of other research activities. Over the next several years, there will be more coordination of research among the funding agencies, if not among the individual researchers. This coordination will significantly leverage the results of the studies reported herein.

- The PG&E-PEER-Commission program has also attracted highly motivated research partners who are willing to co-fund this program's future work or to perform separately funded but closely coordinated studies that fit together nearly seamlessly. The California Department of Transportation (Caltrans) is the first such partner. It is likely that in the next several years a number of others will join.

4.3 Recommendations

Although the results of the individual research projects reported herein have successfully met their objectives, it is clear that there are additional research activities whose results would provide further improvements in the earthquake performance of utility systems. Many of these opportunities for further study and implementation have been identified in previous sections. They include the following major research areas:

- Ground Motion and Site Response: More accurate ground-motion assessments for utility sites are critical to evaluate the seismic hazard at those sites and to make good risk management decisions. Data and models to reduce uncertainties in ground motions are needed, particularly for locations near large-magnitude seismic events. Because current databases and models for predicting site response have limitations and uncertainties, improved and reliable methods for assessing site response are needed for assessing site-specific ground motions.
- Ground Deformation Database: Expanded empirical databases and new analysis tools need to be developed to better model the probability of permanent ground deformation as a function of geologic and geotechnical data and level of strong ground shaking, so that potential extensive damage to underground as well as above-ground utility structures can be reduced or avoided.
- Electrical Substation Equipment Performance: Further efforts are needed to accurately understand the seismic performance of existing high-voltage equipment to be able to either use elsewhere or replace equipment that is unacceptably vulnerable in its current locations. Seismic performance data obtained from shaking table tests and analytical models of substation equipment, their interconnections, and their system functionality under various earthquake scenarios would be important products of this research.
- Ground Motion Estimates for Emergency Response: Advanced instrumentation capabilities and methods for using them are needed so that strong-motion data and other data can be used to make rapid estimates of damage and functionality prior to getting input from experienced field operations personnel.
- Building Vulnerability: Additional data and models are needed to better assess expected earthquake performance of older substation buildings and service buildings to enable better decision-making by utilities regarding seismic retrofits or other mitigation measures for these buildings.
- Seismic Risk Analysis: A flexible and powerful capability to evaluate the likely functionality of customer services following earthquakes is needed. This capability could be used to evaluate alternative earthquake mitigation actions, and to evaluate the current state of earthquake preparedness of the utility system from the perspective of the utility, customer and regulator.

It is recommended that this successful earthquake research program be continued to address these and other topics.

The scope of further research projects needs to be viewed from a broad and integrated perspective to ensure that other related opportunities are not being missed. It is recommended that the continuation of this program should incorporate a comprehensive planning effort by the JMC.

It is also recommended that the next phase of the program be structured to provide for and to optimize the involvement of multiple co-funding organizations, particularly Caltrans. The JMC member organizations (PG&E, PEER, and Commission) should identify prospective additional partners and enlist their participation. Such efforts will enable significant leveraging of the available funding and make possible rapid gains in knowledge and applications to profoundly reduce earthquake risk in California.

Appendix I
Phase I Research Projects

Appendix II
Request For Proposals

Appendix III
Final Reports of Research Projects

Appendix I
Phase I Research Projects

The following 25 research projects were carried out during the initial phase of the PG&E/PEER Research Program in 1997 and 1998. The projects are listed by topic. Topic numbers and headings in the main report now follow the new naming and numbering format listed in Table 1.

Principal Investigator	Project Description
TOPIC 1: BUILDING VULNERABILITY	
W. Iwan, California Institute of Technology	Examine methods for estimating maximum displacement with an emphasis on high-velocity pulses from near source ground motions. Provided recommendations for estimating maximum displacement during an earthquake.
C.W. Roeder, University of Washington	Develop a simplified model for out-of-plane behavior of concrete infill panels on substation buildings; examine performance of mill-type buildings to near source ground motions. Provide a simplified model that can be used in retrofit design.
J. Wallace, UC Los Angeles	Study mill-type substation buildings, focusing on three-dimensional behavior and soil structure interaction. Provide recommendations on modeling for retrofit and guidance on effects of soil-structure interaction for short-period buildings.
J. Hall, California Institute of Technology	Conduct detailed nonlinear analysis of tilt-up buildings with flexible timber roof diaphragms. Assess the deformation demands on the diaphragm and anchorages.
G. Pardoen, UC San Diego	Perform laboratory testing of timber diaphragm roof components. Develop database of cyclic force versus deformation relationship for retrofit design.
TOPIC 2: SUBSTATION VULNERABILITY	
P. Somerville, Woodward-Clyde Federal Services	Develop ground motion estimates at substation locations for historical earthquakes. Information used for developing equipment fragility relationships.
T. Anagnos, San Jose State University	Develop equipment fragility relationships from historical data on damage and ground motion estimates using statistical techniques.
A. Der Kiureghian, UC Berkeley	Improve methodology for equipment fragility based on Bayesian statistics. Used to integrate observed and model data in fragility models.
A. Der Kiureghian, UC Berkeley	Develop new methodology for accounting for dynamic interaction between interconnected substation equipment. Provide design guidance on amplification factors due to interaction.
N. Makris, UC Berkeley	Identify overturning potential of large electrical equipment due to large velocity pulse near-source ground motion.
G. Fenves, UC Berkeley	Perform shaking table testing of porcelain transformer bushing to determine qualification and fragility. Model identified major modes of deformation and failure.
G. Fenves, UC Berkeley	Perform shaking table testing of disconnect switches to determine qualification and fragility. Model identified major modes of deformation and failure.

Principal Investigator	Project Description
TOPIC 3: CHARACTERIZATION OF SITE RESPONSE	
J. Bray, UC Berkeley	Improve site classification scheme based on engineering properties of soil to represent site response effects.
Y. Zeng, University of Nevada, Reno	Develop simplified categories for basin effects using ray-tracing procedures.
I.M. Idriss, UC Davis	Develop alternative classification scheme for geotechnical classification of soils for site response.
S. Chang, University Washington	Analyze whether variability of ground motion is due to site response or source mechanisms.
S. Glaser, UC Berkeley	Evaluate use of downhole arrays to characterize site response effects.
TOPIC 4: EARTHQUAKE-INDUCED GROUND DEFORMATION AND FAILURE	
R. Seed, UC Berkeley	Develop probabilistic procedure for predicting onset of liquefaction.
J-P Bardet, University of Southern California	Create GIS database of liquefaction and ground deformation measurements from past earthquakes.
N. Sitar, UC Berkeley	Develop new methods for probabilistic assessment of landslide potential in natural slopes.
J. Stewart, UC Los Angeles	Develop ground deformation estimates at boundary between fills and natural soil based on measurements in past earthquakes.
TOPIC 5: GAS AND ELECTRIC FIRES FOLLOWING EARTHQUAKES	
R. Williamson, UC Berkeley	Identify ignition sources for fires after earthquakes and examine role of natural gas service as a cause.
TOPIC 6: STRONG GROUND MOTION DATA SET	
W. Silva, Pacific Engineering and Analysis	Develop database of strong ground motion records using consistent processing procedures.
Y. Zeng, University of Nevada, Reno	Recover strong motion data from reverse fault earthquake in China.
TOPIC 7: COOPERATIVE EARTHQUAKE RESEARCH AT SOUTHERN CALIFORNIA EARTHQUAKE CENTER	
T. Henyey, University of Southern California	Develop improved simulation models for strong ground motion; improve hazard estimate of San Andreas fault and faults in Eastern California Shear Zone; expand ROSRINE program for characterizing recording sites of Northridge earthquake strong motions
MANAGEMENT	
J. Moehle & G. Fenves, UC Berkeley	Manage PEER contract for research program through the JMC, coordination meetings, workshops, and project administration.

Appendix II
Request for Proposals

Introduction

This Appendix presents the specific research needs prepared by PG&E and PEER and approved by the JMC for purposes of seeking proposals to satisfy the specified needs. As noted in Section 1.2.2, not all of these requests led to contracts to perform the desired work. In some cases, several investigators were chosen to carry out parallel studies in the same project. The selection of the seven topics is described in Section 1.2.1.

TOPIC 1 – BUILDING VULNERABILITY

Background information

Utilities are in the process of conducting seismic performance studies on a large number of existing buildings with a view toward determining whether seismic upgrading is necessary. In Phase I of the PEER-PG&E program, several projects are examining the state of the practice of performance-based earthquake engineering. The objectives of the current projects are to improve the understanding of the effects of near-source ground motions on the seismic response of buildings, and evaluate assessment methodologies ranging from simple to complex methods.

Phase II of the building vulnerability topic addresses other important aspects of building performance for the purpose deciding on seismic upgrade. The first project is to investigate current methodologies for developing building specific fragility curves. The second project is to investigate improved analysis methods for evaluating seismic performance. Both projects are closely related to projects in the PEER core research program, and they offer an opportunity to apply methodologies developed in PEER for performance based earthquake engineering.

Project 1.A – Evaluation of Building-Specific Fragility Curve Methodologies

The primary objective of this project is to evaluate existing methods for determining fragility curves for typical substation buildings. Fragility curves for a specific building should be consistent for loss estimation and for use in making decisions on retrofit. Previous work has been done for the FEMA / NIBS earthquake loss estimation methodology (Kircher et al., *Earthquake Spectra*, Nov. 1997). This project would include review of current methodologies for fragility curves, determination of appropriateness for typical substation buildings, and identification of improvements. Techniques for developing building specific fragility curves may include use of capacity curves and spectral evaluation of demands. The study should investigate how potential retrofits are reflected in the fragility curves. Specific buildings will be selected in conjunction with PG&E technical staff. Approximately 10 buildings should be considered, ranging from new to old, and low rise to high rise.

Project 1.B – Development of Improved Analysis Methodology for Substation Buildings

The objective for this project is to develop improved practical methods for evaluating the seismic performance of older concrete shear wall and steel frame substation buildings. These types of buildings have historically performed well in moderate earthquakes. However, current analysis techniques and element type testing have been unable to demonstrate this good performance. These substation buildings are typically

unmanned and in some cases have minimal equipment other than controls for the substation. The performance goals for major earthquakes are no collapse and access to critical areas within the building.

The investigation is likely to examine the efficacy of improved analysis methods on buildings that have demonstrated good performance in past earthquakes but do not satisfy a code type evaluation. Detailed case studies of typical older substation buildings should be conducted to examine the results using various analysis methods. The final product should be an analysis methodology that: 1) predicts the behavior of older concrete wall/steel frame substation building behavior, and 2) would be usable in a structural engineering office.

TOPIC 2 – ELECTRICAL SUBSTATION EQUIPMENT VULNERABILITY

Background

Phase I of the PEER-PG&E program investigated the seismic performance of a particular model of 196kV, 800A transformer bushing by shaking table testing. Although this model performed well, other designs may not have as high capacity. Other designs of 230kV bushings, and those with higher voltage ratings, which are significantly larger, have failed by oil leakage or porcelain fracture in past earthquakes. The objective of Phase II of this project is to investigate the seismic performance of different designs of 500kV and 230kV transformer bushings, and assess the performance of various retrofit schemes. The project will be organized in two parts, Project 2.A on 500kV porcelain bushing and retrofit, and Project 2.B on other designs of 230kV and 500kV bushings. Project 2.C will investigate the important problem of earthquake dynamics of interconnected equipment.

The first phase of the PEER-PG&E program is also developing new information about the seismic performance of electrical substation equipment including overturning effects and fragility characterization. Phase II includes two related projects on additional aspects of the earthquake performance of electrical substation equipment.

Project 2.A – Seismic Performance of 500kV Porcelain Bushing and Retrofit

The objective of this project is to investigate the seismic performance of ABB 500kV transformer bushing and at least one retrofit scheme. The bushings are to be provided by ABB (tentative). Input motions matching the target spectrum (or portions of the target spectrum) defined by the Moderate Level of IEEE 693-1998 should be used. If the bushing is undamaged structurally during this test, it will undergo electrical and functional tests by the vendor to determine if qualification requirements are met. A second retrofitted bushing will then be tested in a similar fashion, except that the input motions will be increased in increments up to its failure. Instrumentation and procedures similar to those used in Phase I of the bushing testing should be used.

The project should encompass the following components:

- Development of representative input motions, in consultation with PG&E technical staff.

- Design and fabricate any additional hardware needed for testing. Receive and prepare specimen(s) for testing. Perform shake table testing for original bushing.
- Identify retrofit measures. Depending on the retrofitting, it may be done by the proposer or the manufacturer, subject to agreement by PG&E.
- Develop an analytical model that represents the fundamental earthquake behavior of the original and retrofitted bushing.

Project 2.B – Seismic Performance of 230kV and 500kV Bushings of Various Design and Retrofits

This phase of testing includes the investigation of seismic performance of various 230kV and 500kV porcelain transformer bushings produced by different manufacturers. The project will be conducted in conjunction with other West Coast utilities (BC Hydro, Bonneville Power Administration, and Southern California Edison). Transformer bushings of these ratings represent a very vulnerable class of equipment for utilities. While some utilities have chosen to procure composite bushings for new installations and to replace failed equipment, a large inventory of porcelain bushings remains. The review will be limited to the types of bushings still in use by the participating utilities. Project 2.B work therefore involves investigation of the failure modes of various bushing designs used by the participating utilities, developing analytical models, and development and testing of simple retrofit schemes to improve seismic performance. Participating utilities should form a technical committee to work with project investigators.

Preliminary work by participating utilities is needed to assess the types of bushings in their inventories and identify the candidate bushings. The candidate bushings, presumably from different manufacturers, will then be grouped by basic design characteristics, such as structural configuration or gasket type. Available information on failures (or good performances) during past earthquakes will also be gathered from the participating utilities. It is anticipated that specimens for testing will be provided by participating utilities or equipment manufacturers at no cost to this project.

The project should encompass the following aspects:

- Develop possible retrofit schemes for testing that fit the design type of a particular group of candidate bushings. Retrofits must satisfy electrical functionality requirements and be economical to perform in the field. Discussion with utilities and manufacturers will be needed in designing and selecting retrofit alternatives.
- Perform shaking table testing of retrofit schemes. Assess effectiveness of retrofit schemes. Develop analytical models that show the fundamental behavior of the different types of bushings.
- The project funding includes augmentation from other participating utilities.

Project 2.C – Substation Equipment Interaction—Rigid and Flexible Conductor Studies

Substation equipment is connected by both rigid and flexible conductors. During earthquakes, significant interactions and equipment damage due to forces transferred

through the connectors have been observed. Flexible buses (“cables”) provide relatively little force, provided that they remain slack. Rigid bus (typically aluminum cables) may utilize connectors with small gaps for thermal displacement, thus accommodating some seismic displacement before transferring forces between the connected equipment. Some utilities have implemented slack or loops in flexible and rigid bus to provide flexibility between interconnected equipment. In a current PEER-PG&E project, analytical methods are being used to study the case with equipment connected by flexible bus.

The objective of this project is to investigate by testing the interactions between substation equipment connected by both flexible and rigid bus. It is expected that the results of these investigations would be used to provide guidance in the design of conductor slack and flexibility loops. Scale model testing may be considered if appropriate.

Rigid and flexible bus with connections typically used in the filed should be included in the tests. Flexible bus with various loop shapes and slack lengths should be studied. Rigid bus should be tested with various flexibility loops. The configuration of all specimens must be coordinated closely with PG&E prior to testing to ensure electrical functionality and feasibility. The conductors should be supported at their ends by structures simulating the dynamic response of various types of substation equipment. The support structures should be designed such that their frequencies can be varied as part of the test procedure. Investigators should consider the need for and importance of multiple (more than two) supports.

Earthquake records should be developed in conjunction with PG&E. Records should be modified to match a target spectral shape (or portions of a target spectral shape) agreed upon by the investigators and PG&E.

A detailed work plan will be developed in the first quarter of the project. The work plan should include identifying the types of equipment and their dynamic characteristics, types of conductors and connectors used, selection of earthquake records and criteria for modification, and a test plan. Equipment types to be considered and earthquake records will be chosen in conjunction with PG&E.

The proposal and budget should include design and fabrication of hardware for use in testing, including simulated conductor support structures, conductors, and connecting hardware.

Using the shaking table results, a preliminary examination of analytical methods for interacting equipment should be evaluated.

Project 2.D – Transformer Structure and Turret Amplification Studies

IEEE 693 (Recommended Practices for the Seismic Design of Substations) specifies that a scale factor of 2 be applied to input motions for transformer bushing seismic qualification. This factor is intended to account for amplification of ground motions due to the flexibility of the transformer tank and bushing support structure. Only a limited amount of information is available on the magnitude of the amplification factor.

Transformer bushings are mounted in a variety of ways that differ between manufacturers and models of transformer. Some models mount the bushing(s) on a flat panel on top of the transformer tank. Others may use a turret consisting of a cylindrical shell protruding from the tank, with a cover plate serving as the mounting surface for the bushing. In addition to the flexibility provided by the turret and tank, a significant rotational flexibility may result from bending of mounting plate where the bushing flange is attached. Quantifying the range of this factor has important implications for seismic qualification and fragility of both composite and porcelain transformer bushings.

The objective of this project is to quantify the amplification factor and its variation for different types of transformer structures. Analysis or simple tests, if required, should be used to determine the amplification factor associated with the various equipment types. Recommended improvements, guidelines, or cautions to engineers and designers involved with the design of such structures should be made.

The study should survey most common types of transformer structures and turrets. Similar configurations should be grouped together, if possible, for use by engineers and for fragility analysis. Mountings for 230kV and higher rated bushings should be considered.

In the analysis of dynamic responses of equipment, a range of typical configurations should be examined. The effect of variations of relevant parameters will give insight into the factors affecting amplification of ground motion input into the bushing. The importance of interaction between the bushing and equipment should be investigated. The study is expected to provide response factors and corresponding uncertainties for use in fragility analysis.

The final result of the project should be recommendations in a form suitable for use by engineers and designers of transformer structures to minimize the amplification of motions at the bushing flange.

Previous work also has found that the rocking response and overturning of freestanding electrical equipment due to ground shaking can be quite ordered and predictable. However, three topics of further investigation were identified: (1) the effect of typical anchorages used to prevent toppling, (2) the effect of the vertical component of ground motion, and (3) the effect of inelastic impact. Additional study should be carried out on these topics. The final result should be a practical understanding of the significance of rocking and overturning failure mechanisms, and recommendations for utility procedures to address the significance.

Project 2.E – Protocol for Pre- and Post- Earthquake Data Collections for Substations

The existing utility database containing statistics on substation equipment damaged during earthquake has evolved over time from a relatively ad hoc effort, but still suffers from inconsistencies in the collection strategy, including lack of data on undamaged equipment. In addition, there may be some as yet unrealized benefit to collecting certain equipment data such as conductor slack, prior to earthquake damage. This project

would develop recommendations for a protocol to gather substation equipment data both prior to and following an earthquake.

The objective of this project is to develop guidelines that may be employed by utility engineers to gather data at substations prior to and following a significant earthquake. Investigators should focus on data that can be gathered most easily, with the equipment energized. Equipment that is most likely to sustain damage should be emphasized.

Available data on substation equipment fragility should be reviewed. Results on the Phase I fragility projects should be reviewed. The investigation should identify parameters for data collection, and missing data from previous post-earthquake walkdowns. Both pre- and post-earthquake data collection guidelines should be developed. In conjunction with PG&E staff, substations should be selected for testing the guidelines.

TOPIC 3 – SEISMIC VULNERABILITY OF UNDERGROUND CABLE

Background

PG&E and other electric utilities maintain extensive networks of high voltage underground cables (HVUC). These cables are of various vintages (some over 50 years old), and may be vulnerable to ground displacement developed during earthquakes. The project addresses the need for a fundamental examination of the deformation capacity of older underground cables. A Phase I PEER-PG&E project investigated earthquake-induced ground deformation and failure, which is directly relevant to the project.

Project Description

The first objective of the HVUC Seismic Vulnerability project is to identify the type of locations where HVUC is vulnerable to damage from large ground deformations, such as due to fault crossings, landslides, and liquefaction zones. The second objective is to develop methods for estimating deformation capacity of underground cables by testing, analysis, or a combination of the two. Finally, the project should examine the behavior of HVUC to determine what mitigation measures are necessary to prevent cable failures. Coordination with other PEER-PG&E projects that are developing ground deformation is expected, as is coordination with ongoing PG&E testing of HVUC.

The proposal is expected to include the following elements:

- Identify Vulnerable Areas—Identify the types of locations in which HVUC are vulnerable. Methods for determining the vulnerability in terms of ground deformation should be developed.
- Deformation Capacity—Testing and analysis procedures for deterring the deformation capacity of HVUC are expected. It is important to recognize the effect of aged and degraded material in the cables. Functional tests and acceptance criteria should be developed in concert with PG&E.
- Mitigation Measures—Measures to mitigate the effects of ground deformation on HVUC performance should be developed.

TOPIC 4 – GROUND DEFORMATION DATABASE

Background

In the ongoing work of Phase I, updated models for ground deformation are being developed. This work has highlighted some of the shortcomings of the ground deformation database. There is an important need to go back and develop a high quality database before trying to improve the models for ground deformations. A new high quality database will be used in later phases for improving empirical models and for validating analytical models and numerical simulations of ground deformation.

Project Description

In this project, the existing data for ground deformation is being reevaluated. Questionable data are to be removed from the database. Sites for which additional geotechnical parameters are needed are to be identified. (Where feasible, this information will be collected as part of other projects in this overall program.) The emphasis needs to be on the 0.1 to 0.2 m deformations. Ground deformations from the 1995 Kobe earthquake should be included in this database.

TOPIC 5 – GROUND MOTION AND SITE RESPONSE

Background

This topic contains a number of projects related to improving the estimates of earthquake ground motion and response at specific sites.

Project 5.A – Near-fault Ground Motions

To date, attenuation relations have been developed without consideration or near-fault effects such as directivity. The near-fault effects have been parameterized in terms of adjustment factors (such as by Somerville), but have not been incorporated directly into the development of attenuation relations.

In this project, near-fault ground motions should be parameterized in terms of attenuation relations that incorporate near-fault effects including directivity. In addition, site response effects should be evaluated as part of the attenuation relations. That is, the correlation of near-fault effects and site response effects, which have been treated as independent factors in the past, should be considered simultaneously to address possible nonlinear site effects due to near-fault effects.

Project 5.B – Consistent Site Response Estimates

In practice, there is a large variation in the amount of site-specific information that is available for estimating ground motion at a site. In some cases, all that is known is the gross category based on a geologic map. In other cases, some geotechnical site descriptions may be available, and in other cases, detailed site information such as shear-wave velocity, or modulus and damping curves may be available. The current procedures used to estimate the site responses for these different situations are not always consistent. The uncertainty in site response for the cases in which little site information is known should be larger than the uncertainty for the case in which site-specific measurements are available.

In this project, a consistent procedure for estimating site response for various levels of site information is to be developed. This procedure should include appropriate uncertainties.

Project 5.C – Site Characterization of Strong-motion Sites

Many of the sites that have recorded strong ground motions still do not have geotechnical site parameters measured. To improve the models of site response, geotechnical data needs to be collected at these sites. This project will continue the ROSRINE project to drill additional sites. The focus of this phase of the site characterization will be focused on rock sites.

Project 5.D – 3-D Basin Response

Ongoing work in Phase I is addressing using simplified models to predict basin response. Parameter studies are being used to identify the important factor affecting basin response.

In this project, this evaluation needs to produce basin site response factors that can be applied to long period attenuation relations. This project should consider both empirical data and numerical simulations in the development of the model. The model needs to be a probabilistic description including the probability distribution of the data.

TOPIC 6 – FIRE SAFETY AND ELECTRIC POWER

Background

In past earthquakes in California and Japan, electricity has been a significant cause of post-earthquake fires. Although some fires have been electrically ignited immediately after an earthquake, the proportion of electrical causes typically increases with time as power is restored. These later fires are probably due to the reintroduction of power to damaged buildings.

Project Description

In this project, data on fires in past earthquakes will be reviewed to characterize the cases of electrical ignitions. An inventory of fire ignition scenarios will be developed for electrical causes. Using the historical data and the electrical ignition scenarios, the specific conditions that lead to ignitions will be identified, and their relative likelihood in relation to damages caused by earthquakes will be assessed.

Possible mitigation strategies for electrical systems will be identified and evaluated. In particular, the possible use of “Seismic Shut-Off Circuit Breakers” will be considered. The effectiveness of alternative strategies will be evaluated in reducing human safety risks and property damage in earthquakes versus the cost of the strategies.

TOPIC 7 – GROUND MOTION ESTIMATES FOR EMERGENCY RESPONSE

Background

Electrical utility response personnel need information on the levels of damage at facilities as soon as possible following an earthquake. To that end, PG&E has installed 40 strong-motion instruments at the sites of key facilities, and has prepared fragility curves for those facilities and for key equipment. Strong-motion records following an

earthquake will be compared to the fragility curves to assess damage within about 10 minutes.

Project Description

The objective of this project is to develop a procedure for rapid estimates of ground shaking following an earthquake. The ground motion estimates should use both recorded ground motions and numerical simulations. The recorded ground motions will include the PG&E strong-motion network and any other strong motion data (from public or private arrays) that can be readily accessed. The numerical simulations should be broadband (e.g. 0.2 to 0.25 Hz) and should be based on source parameters that are rapidly determined. Since the main interest is in large events, the numerical simulations need to account for source dimension. The numerical simulation should be used to produce stable estimates of the ground motion for sites that are not near a strong-motion recording. A procedure for combining the empirical data and the numerical simulations to form a single ground motion map (including gross site conditions) needs to be developed.

PG&E – PEER Directed Studies Program, Phase II

GOODNESS OF FIT IN SIMULATED NEAR-FAULT LONG PERIOD GROUND MOTIONS

FINAL REPORT

by

Robert Graves, Arben Pitarka, Nancy Collins, Paul Somerville
URS Greiner Woodward Clyde, Pasadena, CA

August 31, 1999

PG&E - PEER DIRECTED STUDIES PROGRAM, Phase II

GOODNESS OF FIT IN SIMULATED NEAR-FAULT LONG PERIOD GROUND MOTIONS

FINAL REPORT

August 31, 1999

Robert Graves, Arben Pitarka, Nancy Collins, Paul Somerville
URS Greiner Woodward Clyde, Pasadena, CA

INTRODUCTION

The objective of this project is to validate procedures for generating near-fault ground motions by simulating the ground motions of past earthquakes and comparing the results with the recorded ground motions. The period range of interest in this project is specified to be 0.125 Hz to 1.43 Hz (8 seconds to 0.7 seconds period). In this project, we have validated our simulation procedures against recordings of the five earthquakes listed in Table 1, which all have important near-fault recordings.

Near-fault ground motions have special characteristics (Somerville et al., 1997) which need to be considered in selecting procedures for quantifying the goodness of fit. First, the fault-normal component is systematically larger than the fault parallel component at periods longer than about 0.5 seconds. In characterizing near-fault ground motions for design, it is often appropriate to specify the fault normal and fault components separately. Accordingly, in validating a near-fault ground motion simulation procedure, it is appropriate to generate separate fault normal and fault parallel components and validate them against the corresponding recorded components. Second, the fault-normal component is often characterized by a coherent pulse of long-period motion. Unlike the case with most strong motion recordings which are predominantly stochastic, the waveform of this long-period is pulse is predominantly deterministic and is amenable to waveform modeling.

METHODS OF QUANTIFYING GOODNESS OF FIT

Based on the characteristics of near-fault ground motions described above, the methods that were selected to measure the goodness of fit between the recorded and simulated ground motions are as follows:

1. Response spectral ratio at 5% damping, measured by the natural logarithm of the difference between the recorded and simulated ground motions (Abrahamson et al., 1990). This is the conventional means of specifying design ground motions. It is sensitive to both the amplitude and the phasing of the ground motions, and is sensitive to a range of periods surrounding the specified ground motion period. Its value is 0 for a perfect fit, positive for underprediction, and negative for overprediction.

2. Fourier amplitude spectral ratio, measured by the natural logarithm of the difference between the recorded and simulated ground motions. This is the conventional means of quantifying spectral amplitudes in seismology. It is sensitive to absolute amplitude but insensitive to phase. Smoothing of the Fourier spectrum is required to give a meaningful estimate. Its value is 0 for a perfect fit, positive for underprediction, and negative for overprediction.

3. Cross correlation between the simulated and recorded ground motions. This provides a measure of the waveform fit, and is sensitive to phasing - the distribution of energy with time - but is insensitive to absolute amplitude. Its value lies in the range of 1 (perfect fit) to -1 (perfect anticorrelation). We use a window length of 15 seconds for the cross correlation.

4. Least squares fit, as measured by the equation

$$r^2 = (SRSS_{data} - SRSS_{residual}) / SRSS_{data}$$

where SRSS = square root of sum of squares, summed over the time series. We use a window length of 15 seconds for the cross correlation. The time series is the recorded time history for *data* and the difference between the recorded and simulated time histories for *residual*. This measure is sensitive to both absolute amplitude and phase. Its maximum value (for a perfect fit) is 1. For a null simulation, its value is zero, and it can have an unbounded negative value if the wave forms have negative correlation and very large differences in amplitude.

SIMULATION PROCEDURE

To simulate broadband time histories, the ground motions are computed separately in the short period and long period ranges, and then combined into a single broadband time history (Somerville et al., 1995; 1996). The use of different methods in these two period ranges is necessitated by the observation that ground motions have fundamentally different characteristics in these two period ranges. At long periods (longer than about 1 second), strong ground motions are deterministic in the sense that seismological models are capable of matching not only the spectral amplitudes but also the waveforms of recorded long period ground motions, once the rupture model of the earthquake and the seismic velocity structure of the region surrounding the earthquake are known. At short periods (shorter than about 1 second), strong ground motions become increasingly stochastic in nature. Seismological models are generally capable of matching the spectral amplitudes of the short period ground motions, but are generally not capable of matching the recorded waveforms. The transition from deterministic to stochastic behavior appears to be due to a transition from coherent source radiation and wave propagation conditions at long periods (over long dimensions) to incoherent source radiation and wave propagation conditions at short periods (over short dimensions). The two simulations are combined using matched filters at 1 Hz. For this study, we have used just the long period component of the broadband simulation procedure, because it almost spans the frequency range of interest in this study, which is 0.125 Hz to 1.43 Hz.

The Green's function method that we use to calculate the long period ground motions has a rigorous basis in theoretical and computational seismology (Helmberger, 1983). The earthquake source is represented as a shear dislocation on an extended fault plane, whose radiation pattern is accurately represented. Wave propagation is represented rigorously by Green's functions

computed for the seismic velocity structure which contains the fault and the site. These Green's functions contain both body waves and surface waves. The ground motion time history is calculated in the time domain using the elastodynamic representation theorem. This involves integration over the fault surface of the convolution of the slip time function on the fault with the Green's function for the appropriate depth and distance.

The near-fault strong motion recordings of the 1995 Kobe earthquake were strongly influenced by the basin edge effect due to the interaction of direct and diffracted waves at the edge of the Osaka basin (Pitarka et al., 1999). For this earthquake, at some stations it was necessary to use Green's functions calculated for a 3D velocity model using finite difference methods (e.g. Graves, 1996). For the other four earthquakes, the near-fault ground motions were not so strongly influenced by 3D velocity structure. In the 1994 Northridge earthquake, the deep structure of the Los Angeles basin had a strong influence on the ground motions recorded in the Los Angeles basin (Graves et al., 1999). These recordings do not contain forward rupture directivity effects, and so they were excluded from this study.

EARTHQUAKE RUPTURE MODELS AND CRUSTAL VELOCITY MODELS

In this study, we used earthquake rupture models derived by other investigators from the inversion of strong motion and other data. These rupture models are listed in Table 1 and analyzed in Somerville et al. (1999). The inversion process involves the calculation of Green's functions that represent the propagation of seismic waves between the source and the site. The degree to which we can accurately represent site effects in our simulations depends on the appropriateness of the shallow seismic velocity structures that were used in the rupture model inversions. The velocity models used in the simulations of the five events are listed in Tables 2 through 6.

For two of the five events analyzed, we consider that the velocity models used were quite realistic. In the 1979 Imperial Valley earthquake, all of the recording sites are on alluvium, and the Green's functions were calculated using a single seismic velocity model representing these uniform site conditions. We used this seismic velocity model to calculate the Green's functions used in our simulations. For the 1995 Kobe earthquake, the simulations at soil and rock sites were done using separate velocity models. In addition, Green's functions for a 3D basin velocity model were used to calculate the ground motions at sites located on the Osaka basin.

For the other three events analyzed, the velocity models used in the rupture model inversion may be less realistic. For the 1989 Loma Prieta earthquake, the inversion was based on a single seismic velocity model that is representative of rock site conditions. We used this seismic velocity model to simulate the ground motions on both rock and soil sites. In the 1994 Northridge earthquake, separate Green's functions for rock and soil sites were used in the inversion of the rupture model. We used the velocity model for rock sites to calculate the Green's functions for simulations on both rock and soil sites. It would have been preferable to use Green's functions calculated for separate rock and soil velocity models in simulations for the respective site categories. The rupture model of the 1992 Landers earthquake was generated using a seismic velocity having quite high surface velocity. We used separate velocity models for soil and rock conditions in our simulations for this earthquake. The only rock site that we modeled was the Lucerne recording.

RESULTS

The results of the validation studies are presented as sets of tables and figures for each earthquake. The table contains a summary of the goodness of fit measurements. These measurements are provided for individual stations, listed on the left hand column of the table. The median, standard deviation, and standard error of the mean of the stations are given at the bottom of the table. The first two columns show the maximum cross correlation between the recorded and simulated velocity time history, where each has been bandpass filtered with a 3 pole Butterworth filter in the frequency range of 0.125 Hz to 1.43 Hz. The first column shows the peak cross correlation for the fault normal component, and the second column shows the peak cross correlation for the fault parallel component in cases where the time lag for maximum cross correlation for the fault normal and fault parallel components are within 0.25 seconds of each other. We assume that the cross correlation lag of the dominant fault normal component is correct, and do not use the peak cross correlation of the fault parallel component if its lag is too different from that of the fault normal component. In most cases, only those recordings with strong forward rupture directivity effects and simple velocity waveforms have coincident peak cross correlations.

The third column show the minimum least squares fit for the fault normal component, and the fourth column shows the minimum least squares fit to the fault parallel component in cases where the time lag for minimum least squares for the fault normal and fault parallel components are within 0.25 seconds of each other. The least squares fit can be low even where the cross correlation is high if there are large differences in the amplitudes of the recorded and simulated waveforms. This is because the cross correlation is not sensitive to amplitude but the least squares measure is. In most cases, only those recordings with strong forward rupture directivity effects and simple velocity waveforms have coincident minimum least squares. In some cases, the least squares measure is less than zero, indicating a fit that is worse than a null simulation. These negative values arise from large discrepancies in amplitude and phase between the recorded and simulated ground motions. We do not find these results intuitively meaningful, because the simulations appear to be much better fits to the data than a null simulation, and have fairly high cross correlations.

The fifth and sixth columns show the natural logarithm of the difference between the recorded and simulated response spectrum, and the seventh and eighth columns show the natural logarithm of the difference between the recorded and simulated Fourier amplitude spectrum, averaged over the frequency range of 0.125 to 1.43 Hz. We used frequencies that were approximately evenly spaced in log frequency to give more weight to the longer periods. These values are shown separately for the fault normal and fault parallel components.

Following the table, the recorded and simulated velocity waveforms, bandpass filtered with a 3 pole Butterworth filter in the frequency range of 0.125 Hz to 1.43 Hz, are compared for each recording of the event. The comparisons for fault normal and fault parallel components are shown on separate pages. The recorded and simulated waveforms are aligned at the time lag that gives the maximum cross correlation for the fault normal component. The cross correlation and least squares values are given in the table described above.

The time history plots are followed by plots comparing the velocity response spectra and the Fourier amplitude spectra of the recorded and simulated velocity time histories, with one figure for each recording. Summary station by station plots of all recordings analyzed are first

presented, together with goodness of fit plots (showing bais and standard error) for the set of stations. These are followed by detailed plots of Fourier amplitude velocity spectra for each recording station. The figures on the left show the two spectra, and the figures on the right show the ratio of recorded to simulated motions. The top two plots show these comparisons separately for the fault normal and fault parallel components on a log-log scale. The bottom two plots show the same comparisons on a linear-linear scale.

TEST FOR DIRECTIVITY EFFECTS IN DATA AND SIMULATIONS

To evaluate the efficacy of the simulation procedure in predicting near-fault rupture directivity effects, we can examine whether the residuals between recorded and simulated ground motions have a trend that is related to rupture directivity. If a ground motion model (such as a conventional empirical attenuation relation) does not address rupture directivity effects, then this trend should be present in the residuals. If the simulation is effective in representing directivity effects, then this trend should not be present in the residuals.

We parameterize the rupture directivity effect by the directivity function X cos θ (for the strike-slip component of faulting) and Y cos ϕ (for the dip slip component of faulting), as shown in Figure 1, following Somerville et al. (1997). The angles θ and ϕ represent the angle between the fault plane and the line connecting the hypocenter to the site (θ is measured in the horizontal plane for strike-slip faulting and ϕ is measured in the vertical plane for dip-slip faulting). X and Y represent the fraction of the fault rupture that lies between the hypocenter and the site (X is measured along strike for strike-slip faulting and Y is measured up dip for dip-slip faulting). The form X cos θ and Y cos ϕ used in the directivity function is based on the assumption that directivity effects are influenced by two geometrical parameters. First, the smaller the angle between the direction of rupture propagation and the direction of waves travelling to the site, the larger the amplitude of the ground motion. Second, the larger the fraction of the fault rupture surface that lies between the hypocenter and the site, the larger the amplitude. This model was subsequently revised by Abrahamson (report to Caltrans, 1999) such that the directivity effect saturates for X and Y values larger than 0.4.

Of the four parameters we have used to measured goodness of fit in this study, only one (response spectral acceleration) is addressed in the rupture directivity model of Somerville et al. (1997) and in standard ground motion models. Accordingly, we have used response spectral acceleration at a fixed response spectral period as the parameter with which to analyze the effectiveness of the simulation procedure.

The figures show the results for the strike slip component of rupture directivity (X cos θ) on the left side, and the dip slip component of rupture directivity (Y cos ϕ) on the right side for a specified ground motion period. The top part of each figure shows the residuals between the recorded data and the empirical ground motion model of Abrahamson and Silva (1997). This model does not include the directivity function as a parameter. For all earthquakes, the residuals between the data and the Abrahamson and Silva (1997) model show a trend of increasing residual with increasing directivity function at some periods. This demonstrates that there are directivity effects in the data and that these effects have the trend expected from the model of directivity effects represented by the directivity function. The lower part of each figure shows the residuals between the data and our simulation results. These residuals do not have the trend that is present in the upper figure, indicating that the simulations are effective in modeling the directivity effects

that are present in the data.

REFERENCES

Abrahamson, N.A. and W.J. Silva (1997). Empirical response spectral attenuation relations for shallow crustal earthquakes, *Seismological Research Letters* 68, 94-127.

Abrahamson, N.A., P.G. Somerville, and C. Allin Cornell (1990). Uncertainty in numerical strong motion predictions, *Proc. 4th U.S. National Conference on Earthquake Engineering,* **1**, 407-416.

Graves, R. W., A. Pitarka, and P. G. Somerville (1998). Ground motion amplification in the Santa Monica area: effects of shallow basin edge structure, *Bull. Seism. Soc. Am.*, 88, 1224-1242.

Graves, R. W. (1966). Simulating seismic wave propagation in 3D elastic media using staggered-grid finite-differences, *Bull. Seism. Soc. Am.*, 86, 1091-1106.

Hartzell, S. H. and T. H. Heaton (1983). Inversion of strong ground motion and teleseismic waveform data for the fault rupture history of the 1979 Imperial Valley, California, earthquake, *Bull. Seism. Soc. Am.*, **73**, 1553-1583.

Helmberger, D.V. (1983). Theory and application of synthetic seismograms, in Earthquakes: Observation, Theory and Interpretation, Proc. Int. Sch. Phys. "Enrico Fermi" Course LXXXV, pp. 174-221, eds. Kanamori, H. and E. Boschi, North-Holland, Amsterdam.

Kamae, K., K. Irikura and A. Pitarka (1998). A technique for simulating strong ground motion using hybrid Green's functions, *Bull. Seism. Soc. Am.*, 88, 357-367.

Pitarka, A., P. Somerville, Y. Fukushima, T. Uetake, and K. Irikura (1999). Simulation of near-fault ground motion using hybrid Green's functions, submitted to BSSA.

Pitarka, A., K. Irikura, T. Iwata and H. Sekiguchi (1998). Three-dimensional simulation of the near-fault ground motion for the 1995 Hyogo-ken Nanbu (Kobe), Japan, earthquake. *Bull. Seism. Soc. Am.* 88, 428-440.

Somerville, P.G., K. Irikura, R. Graves, S. Sawada, D. Wald, N. Abrahamson, Y. Iwasaki, T. Kagawa, N. Smith and A. Kowada (1999). Characterizing earthquake slip models for the prediction of strong ground motion. *Seismological Research Letters* 70, 59-80.

Somerville, P.G., N.F. Smith, R.W. Graves, and N.A. Abrahamson (1997). Modification of empirical strong ground motion attenuation relations to include the amplitude and duration effects of rupture directivity, *Seismological Research Letters* 68, 199-222.

Somerville, P., C.K. Saikia, D. Wald, and R. Graves (1996). Implications of the Northridge earthquake for strong ground motions from thrust faults, *Bull. Seism. Soc. Am.*, 86, S115-S125.

Somerville, P.G., R.W. Graves, and C.K. Saikia (1995). Characterization of Ground Motions during the Northridge Earthquake of January 17, 1994. *Program to Reduce the Earthquake Hazards of Steel Moment Frame Buildings,* SAC Report 95-03.

Somerville, P.G., D.J. Wald, and N.F. Smith (1993). Prediction of the near-source ground accelerations of the Loma Prieta earthquake using a heterogeneous slip model. Unpublished manuscript.

Wald, D. J., D. V. Helmberger and T. H. Heaton (1991). Rupture model of the 1989 Loma Prieta earthquake from the inversion of strong motion and broadband teleseismic data, *Bull. Seism. Soc. Am.* **81**, 1540-1572.

Wald, D.J., and T.H. Heaton (1994). Spatial and temporal distribution of slip of the 1992 Landers, California earthquake, *Bull. Seism. Soc. Am.* **84**, 668-691.

Wald, D.J., T.H. Heaton, and K.W. Hudnut (1996). The slip history of the 1994 Northridge, California earthquake determined from strong motion, teleseismic, GPS and leveling data. *Bull. Seism. Soc. Am.* **86**, S49-S7

Table 1. Source Parameters of Earthquakes

Earthquake, Location	Date	Mech.	Mo x 10^{25} dyne-cm	Mw	Slip Model Reference
Imperial Valley, Ca.	1979.10.15	SS	5	6.43	Hartzell & Heaton, 1983
Loma Prieta, Ca.	1989.10.17	OB	30	6.95	Somerville et al., 1993; Wald et al., 1991
Landers, Ca.	1992.6.28	SS	75	7.22	Wald et al., 1994
Northridge, Ca.	1994.1.17	RV	11	6.66	Wald et al., 1996
Kobe, Japan	1995.1.17	SS	24	6.9	Pitarka et al.,1999 Kamae et al., 1998

Table 2

Imperial Valley: One-Dimensional Soil Velocity Model

Thickness (km)	Vp (km/s)	Vs (km/s)	Density (g/cm^3)	Qp	Qs
0.50	1.70	0.50	1.80	200	50
0.50	2.10	0.77	1.88	250	80
0.50	2.50	1.05	1.97	500	150
0.50	2.90	1.33	2.05	800	200
0.50	3.40	1.61	2.13	900	250
0.50	3.80	1.89	2.21	1000	300
0.50	4.20	2.16	2.30	1200	350
0.50	4.70	2.44	2.38	1500	500
0.50	5.10	2.72	2.46	1700	700
0.50	5.50	3.00	2.55	2000	800
3.0	5.60	3.14	2.70	2000	800
3.0	5.60	3.14	2.70	2000	800
0.5	7.20	4.16	2.80	2000	800
0.0	7.20	4.16	2.80	2000	800

Table 3

Loma Prieta Velocity Model

Vp (km/sec)	Vs (km/sec)	Density (g/cm^3)	Depth (km)
1.730	1.00	1.50	0.10
3.380	1.95	1.55	0.50
4.290	2.48	1.85	1.00
4.790	2.77	2.05	3.00
5.365	3.10	2.26	5.00
5.740	3.31	2.45	7.00
6.150	3.55	2.58	9.00
6.245	3.61	2.62	13.00
6.270	3.62	2.63	18.00
6.665	3.85	2.77	25.00
8.000	4.62	3.28	

Table 4

Landers: One-Dimensional Soil Velocity Model

Thickness (km)	Vp (km/s)	Vs (km/s)	Density (g/cm^3)	Qp	Qs
0.02	1.40	0.50	1:70	100	30
0.03	1.50	0.75	1.90	100	30
0.05	1.80	1.06	2.00	100	30
0.40	2.30	1.33	2.10	200	100
0.50	2.80	1.66	2.20	600	300
0.50	3.80	1.98	2.30	600	300
2.50	5.50	3.15	2.60	600	300
6.00	6.20	3.52	2.70	600	300
16.00	6.20	3.52	2.70	600	300
6.00	6.80	3.83	2.87	600	300
0.00	8.00	4.64	3.50	600	300

Landers: One-Dimensional Rock Velocity Model

Thickness (km)	Vp (km/s)	Vs (km/s)	Density (g/cm^3)	Qp	Qs
1.50	3.80	1.98	2.30	100	30
2.50	5.50	3.15	2.60	600	300
6.00	6.20	3.52	2.70	600	300
16.00	6.20	3.52	2.70	600	300
6.00	6.80	3.83	2.87	600	300
0.00	8.00	4.64	3.50	600	300

Table 5

Northridge Regional Velocity Structure

A. Rock Stations

Vp (km/sec)	Vs (km/sec)	Density (g/cm)	Thickness (km)	Depth (km)
1.9	1.0	2.1	0.5	0.0
4.0	2.0	2.4	1.0	0.5
5.5	3.2	2.7	2.5	1.5
6.3	3.6	2.8	23.0	4.0
6.8	3.9	2.9	13.0	27.0
7.8	4.5	3.3		40.0

B. Soil Stations

Vp (km/sec)	Vs (km/sec)	Density (g/cm)	Thickness (km)	Depth (km)
0.8	0.3	1.7	0.1	0.0
1.2	0.5	1.8	0.2	0.1
1.9	1.0	2.1	0.2	0.3
4.0	2.0	2.4	1.0	0.5
5.5	3.2	2.7	2.5	1.5
6.3	3.6	2.8	23.0	4.0
6.8	3.9	2.9	13.0	27.0
7.8	4.5	3.3		40.0

Table 6a

Kobe One-Dimensional Velocity Models

Site: KBU					
Depth (km)	Vp (km/s)	Vs (km/s)	Density (g/cm^3)	Qp	Qs
0.5	3.2	1.8	2.0	500	300
5.0	5.7	3.2	2.4	1000	400
>5.0	6.0	3.46	2.7	1000	500

Site: KOB					
Depth (km)	Vp (km/s)	Vs (km/s)	Density (g/cm^3)	Qp	Qs
0.06	1.5	0.45	1.9	150	80
0.2	1.7	0.55	2.0	150	80
0.4	1.8	0.65	2.0	150	80
0.6	1.9	1.1	2.2	300	170
5.0	5.7	3.2	2.4	1000	400
>5.0	6.0	3.46	2.7	1000	500

Site: MOT					
Depth (km)	Vp (km/s)	Vs (km/s)	Density (g/cm^3)	Qp	Qs
0.035	1.5	0.3	1.9	130	50
0.05	1.7	0.45	1.9	150	80
0.15	1.8	0.50	2.0	150	80
0.30	1.8	0.65	2.0	150	80
0.6	1.9	1.1	2.2	300	170
5.0	5.7	3.2	2.4	1000	400
>5.0	6.0	3.46	2.7	1000	500

Table 6b

Kobe Site: Takatori; 1D slice through3D velocity model

Vp (km/sec)	Vs (km/sec)	Density (g/cm^3)	Depth (km)
1.4	0.15	1.8	0.0
1.5	0.30	1.8	0.01
1.5	0.40	1.8	0.02
1.5	0.45	1.8	0.03
1.6	0.50	1.85	0.04
1.6	0.55	1.85	0.1
1.6	0.60	1.85	0.2
1.7	0.70	1.9	0.3
1.8	0.75	1.9	0.4
1.9	0.85	1.95	0.5
2.0	0.92	2.0	0.6
2.1	1.1	2.0	0.8
5.4	3.2	2.6	>1.0

Kobe, Landers, Loma Prieta, Northridge - Fault Normal

Spectral Acceleration at 5.0 sec

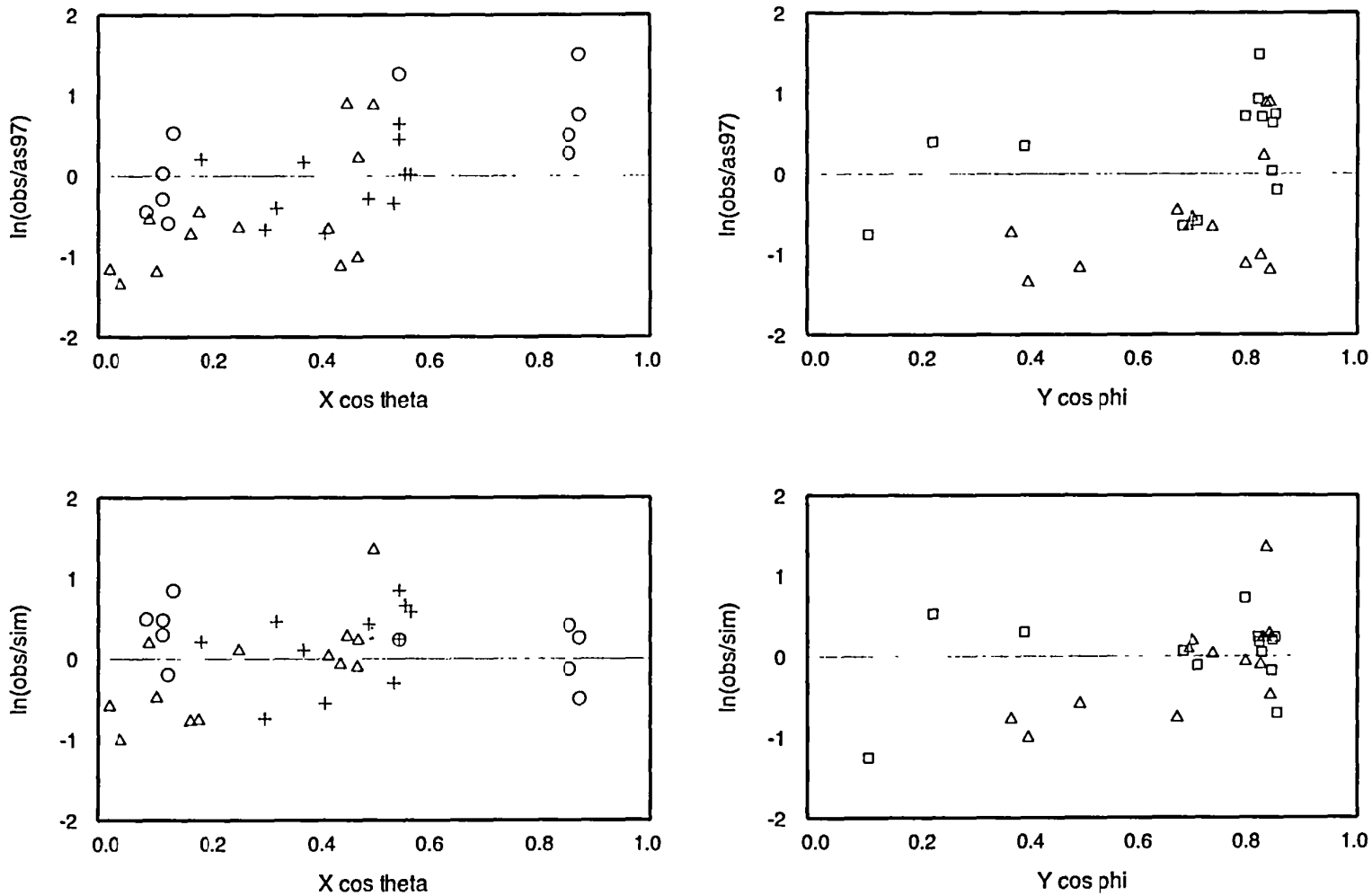

+ Kobe
○ Landers
△ Loma Prieta
□ Northridge

GMT Aug 25 11:16:45 1999 /u1/nancy/PEER-5/Comparisons

Kobe, Landers, Loma Prieta, Northridge - Fault Parallel

Spectral Acceleration at 5.0 sec

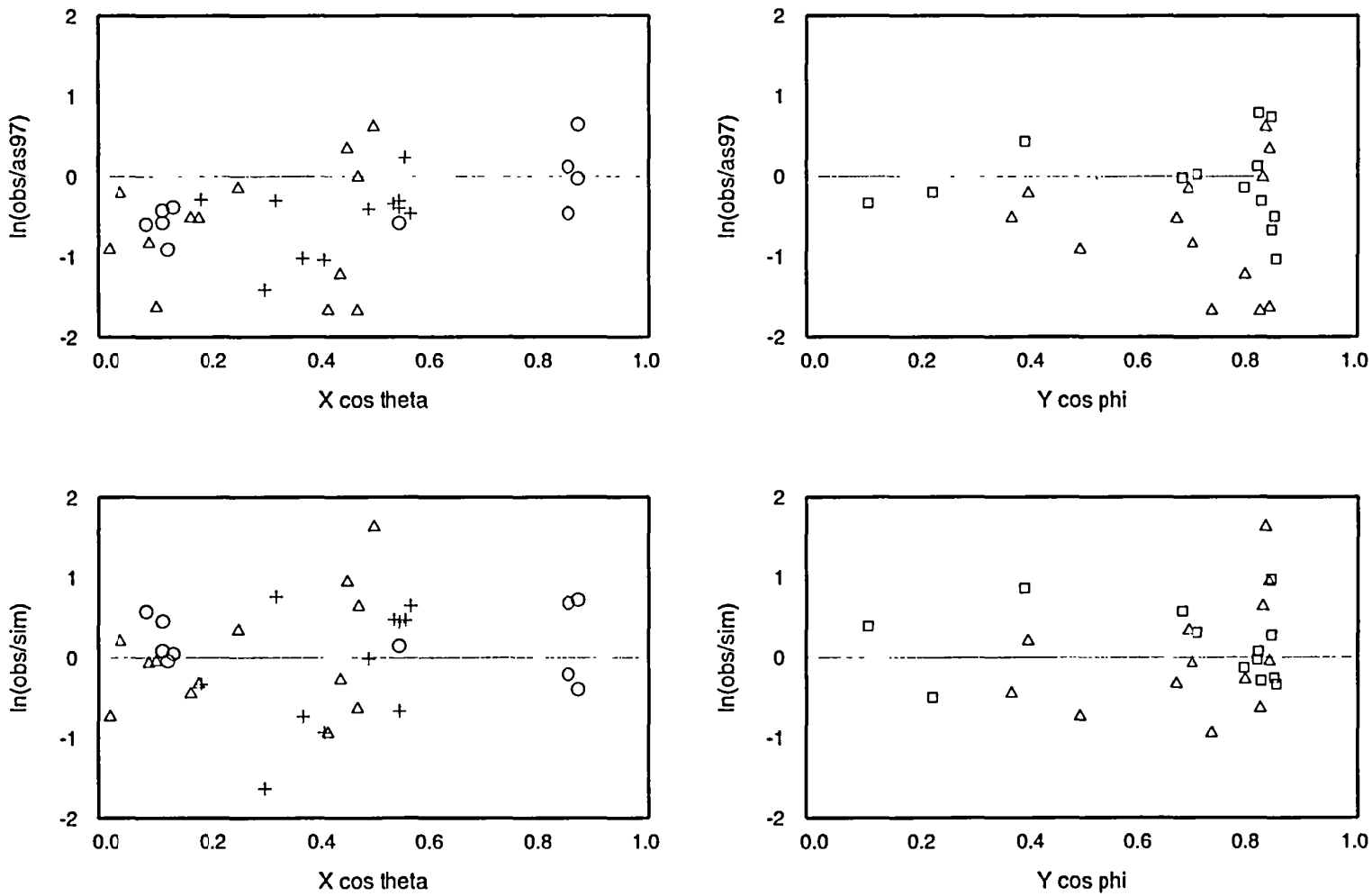

Kobe
Landers
Loma Prieta
Northridge

GMT Aug 25 11:16:57 1999 /u1/nancy/PEER-5/Comparisons

Kobe, Landers, Loma Prieta, Northridge - Fault Normal

Spectral Acceleration at 4.0 sec

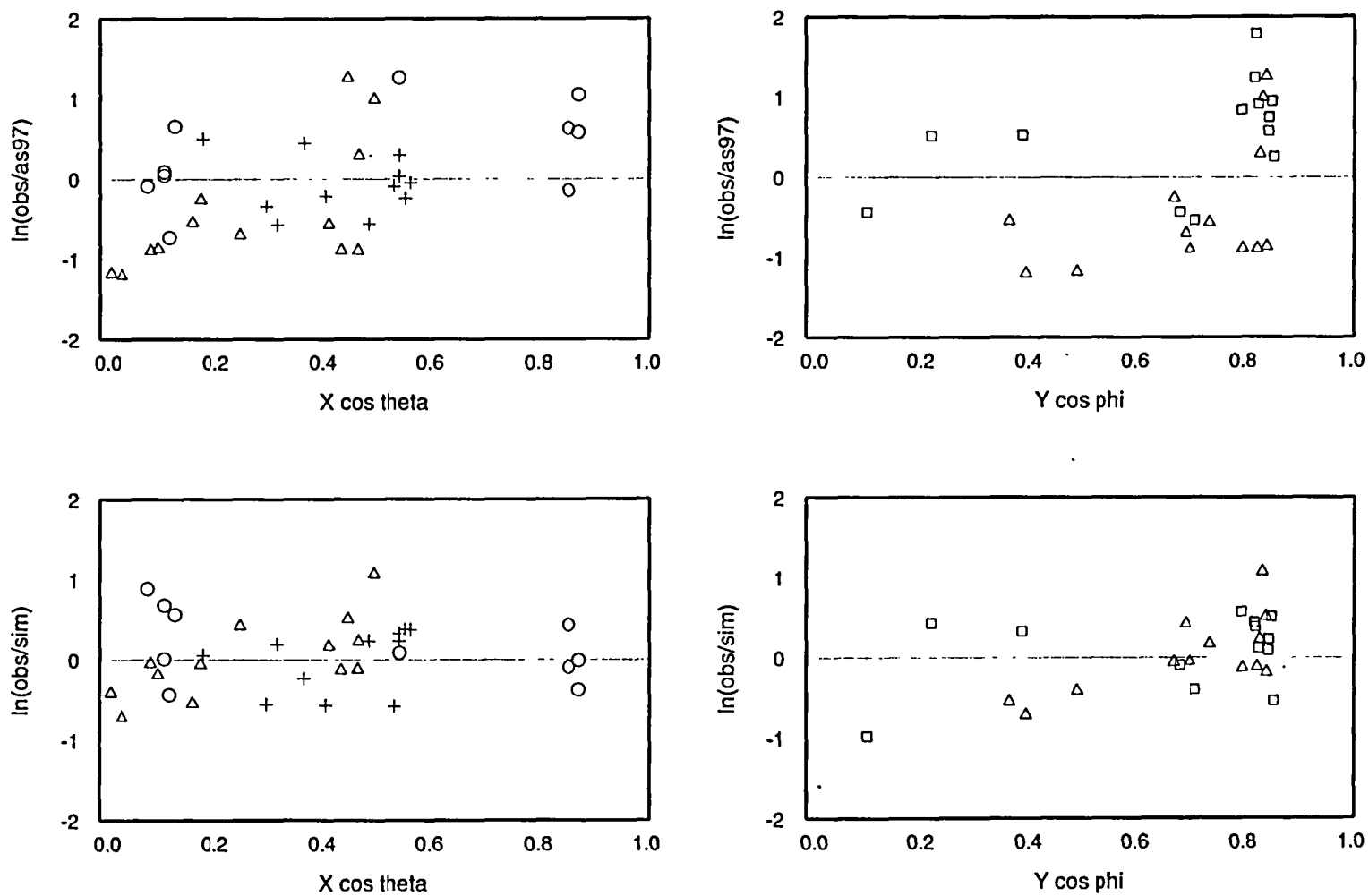

+ Kobe
○ Landers
△ Loma Prieta
□ Northridge

GMT Aug 25 11:17:11 1999 /u1/nancy/PEER-5/Comparisons

Kobe, Landers, Loma Prieta, Northridge - Fault Parallel

Spectral Acceleration at 4.0 sec

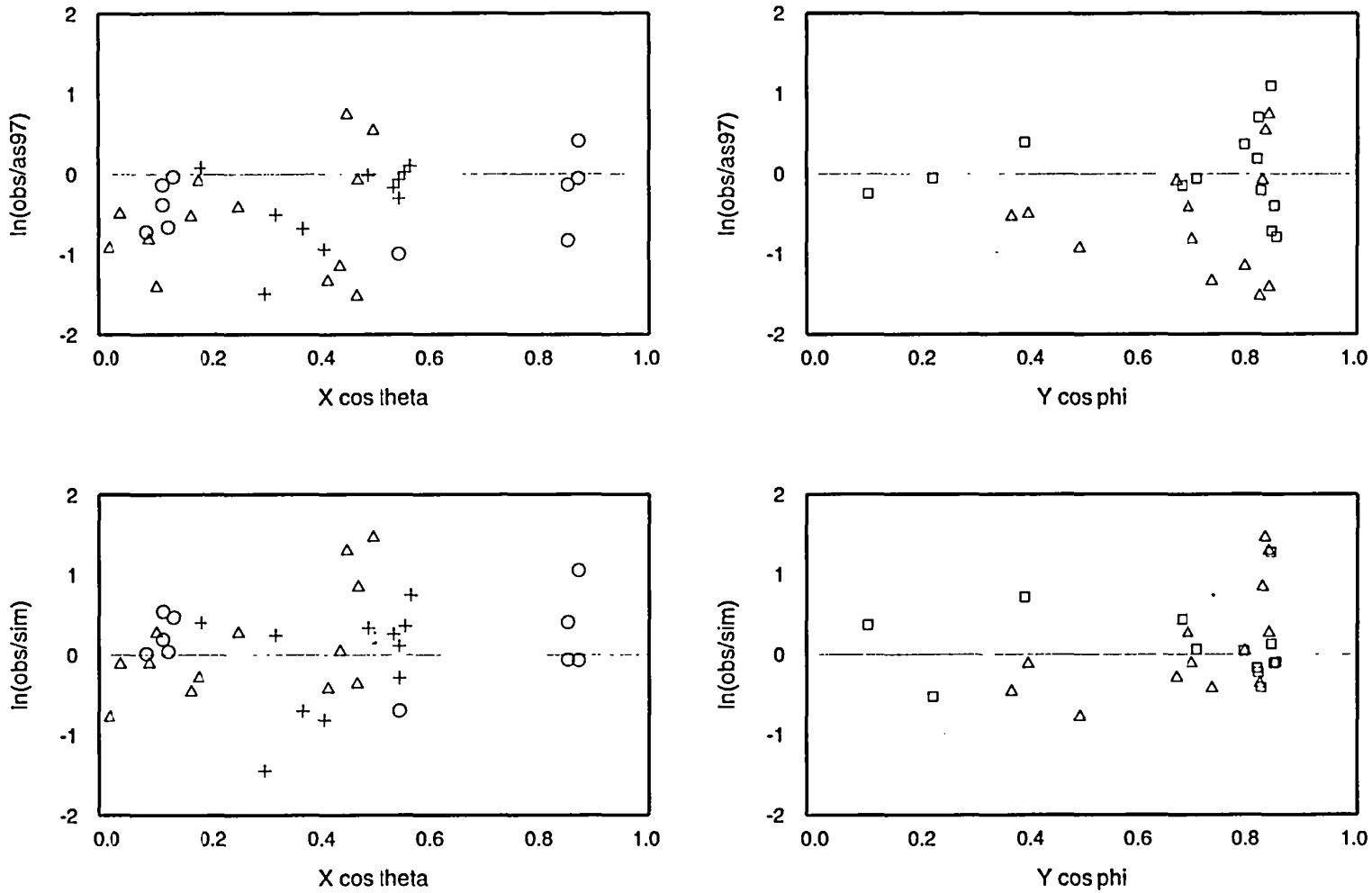

+ Kobe
○ Landers
△ Loma Prieta
□ Northridge

GMT Aug 25 11:17:24 1999 /u1/nancy/PEER-5/Comparisons

Kobe, Landers, Loma Prieta, Northridge - Fault Normal

Spectral Acceleration at 3.0 sec

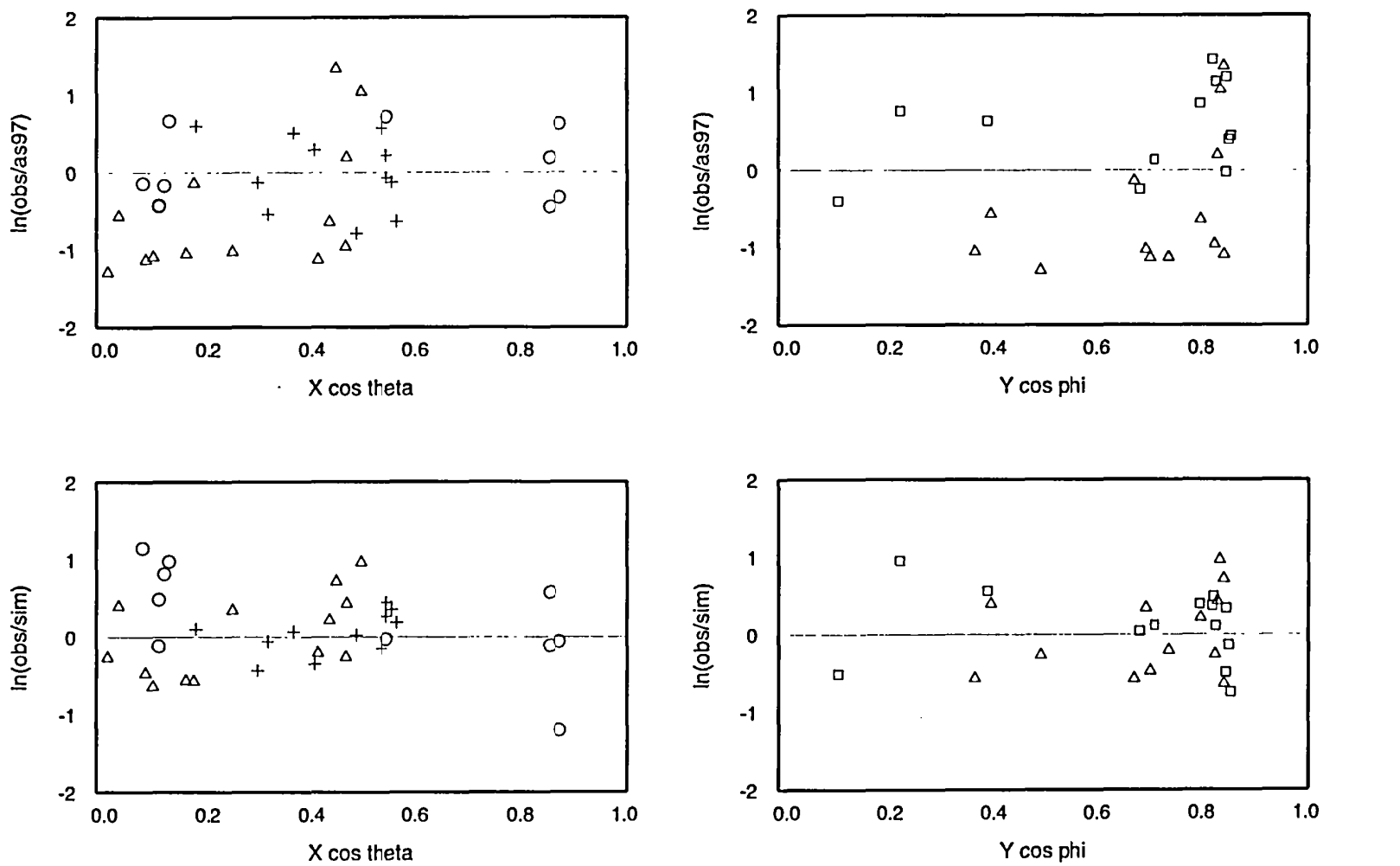

GMT Aug 25 11:17:37 1999 /u1/nancy/PEER-5/Comparisons

Kobe, Landers, Loma Prieta, Northridge - Fault Parallel

Spectral Acceleration at 3.0 sec

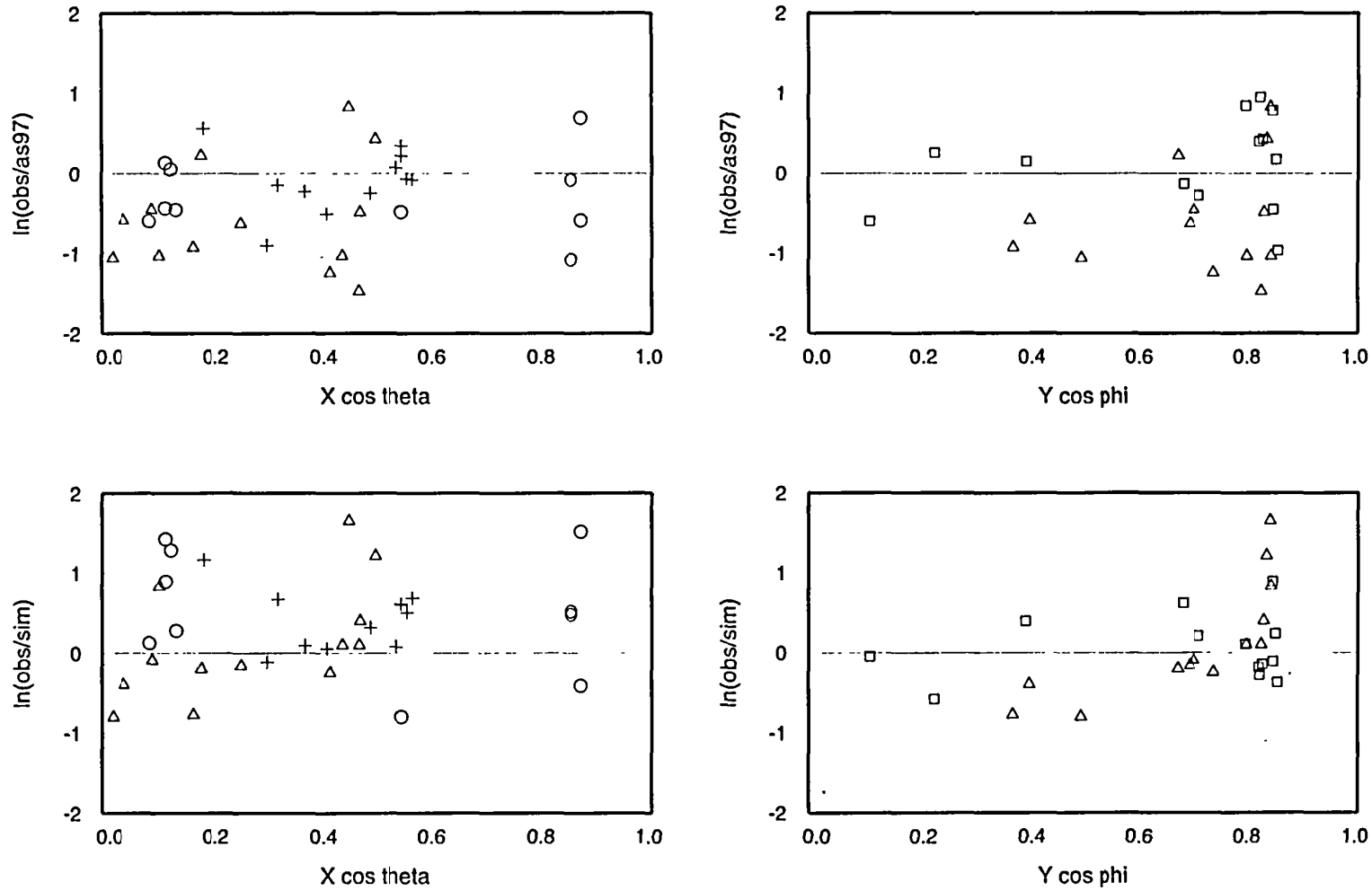

+ Kobe
○ Landers
△ Loma Prieta
□ Northridge

GMT Aug 25 11:17:50 1999 /u1/nancy/PEER-5/Comparisons

Kobe, Landers, Loma Prieta, Northridge - Fault Normal

Spectral Acceleration at 2.0 sec

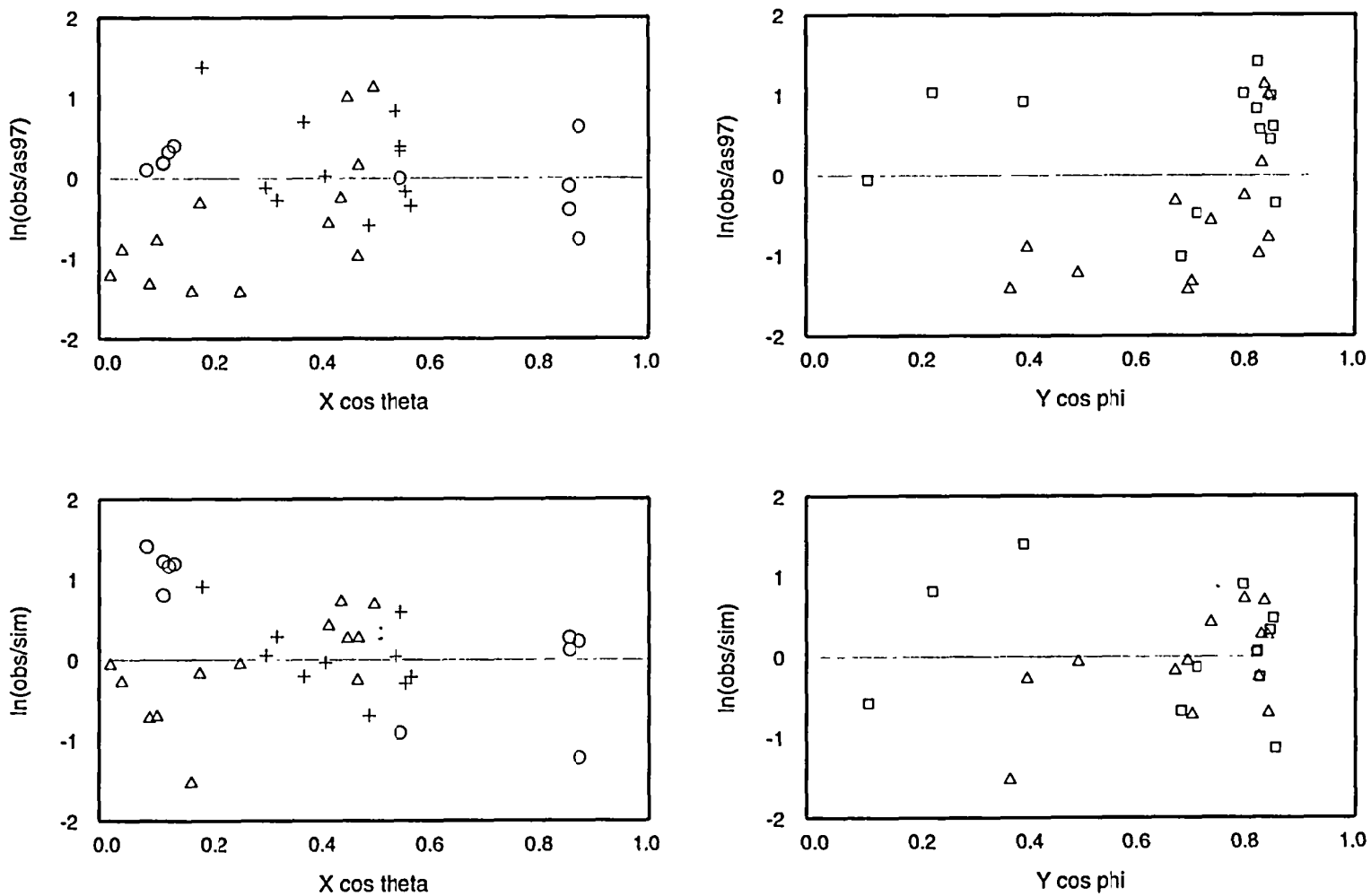

+ Kobe
O Landers
Δ Loma Prieta
□ Northridge

GMT Aug 25 11:18 04 1999 /u1/nancy/PEER-5/Comparisons

Kobe, Landers, Loma Prieta, Northridge - Fault Parallel

Spectral Acceleration at 2.0 sec

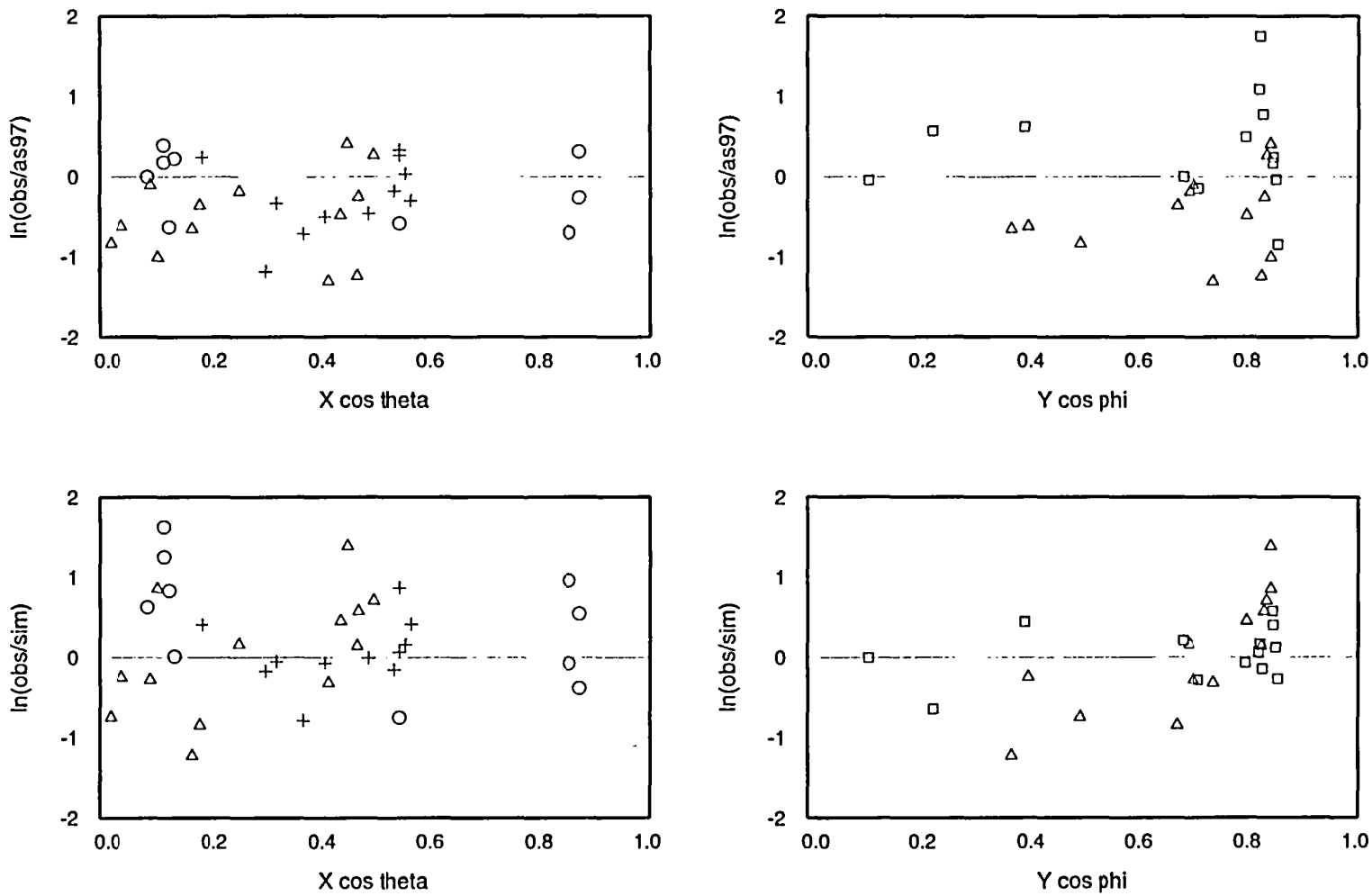

+ Kobe
○ Landers
△ Loma Prieta
□ Northridge

GMT Aug 25 11:18:18 1999 /u1/nancy/PEER-5/Comparisons

Kobe, Landers, Loma Prieta, Northridge - Fault Normal

Spectral Acceleration at 1.5 sec

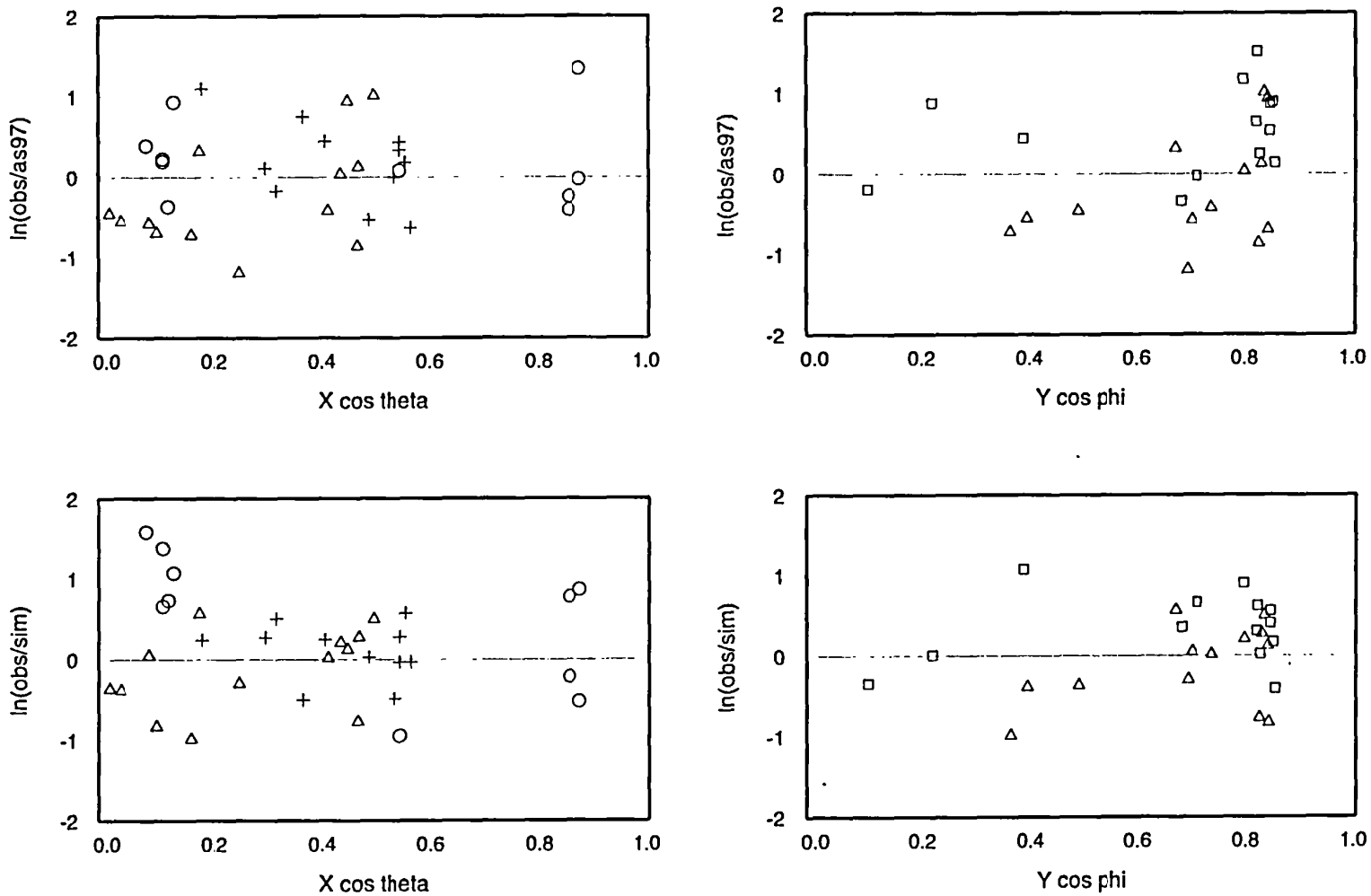

+ Kobe
○ Landers
△ Loma Prieta
□ Northridge

GMT Aug 25 11:18:31 1999 /u1/nancy/PEER-5/Comparisons

Kobe, Landers, Loma Prieta, Northridge - Fault Parallel

Spectral Acceleration at 1.5 sec

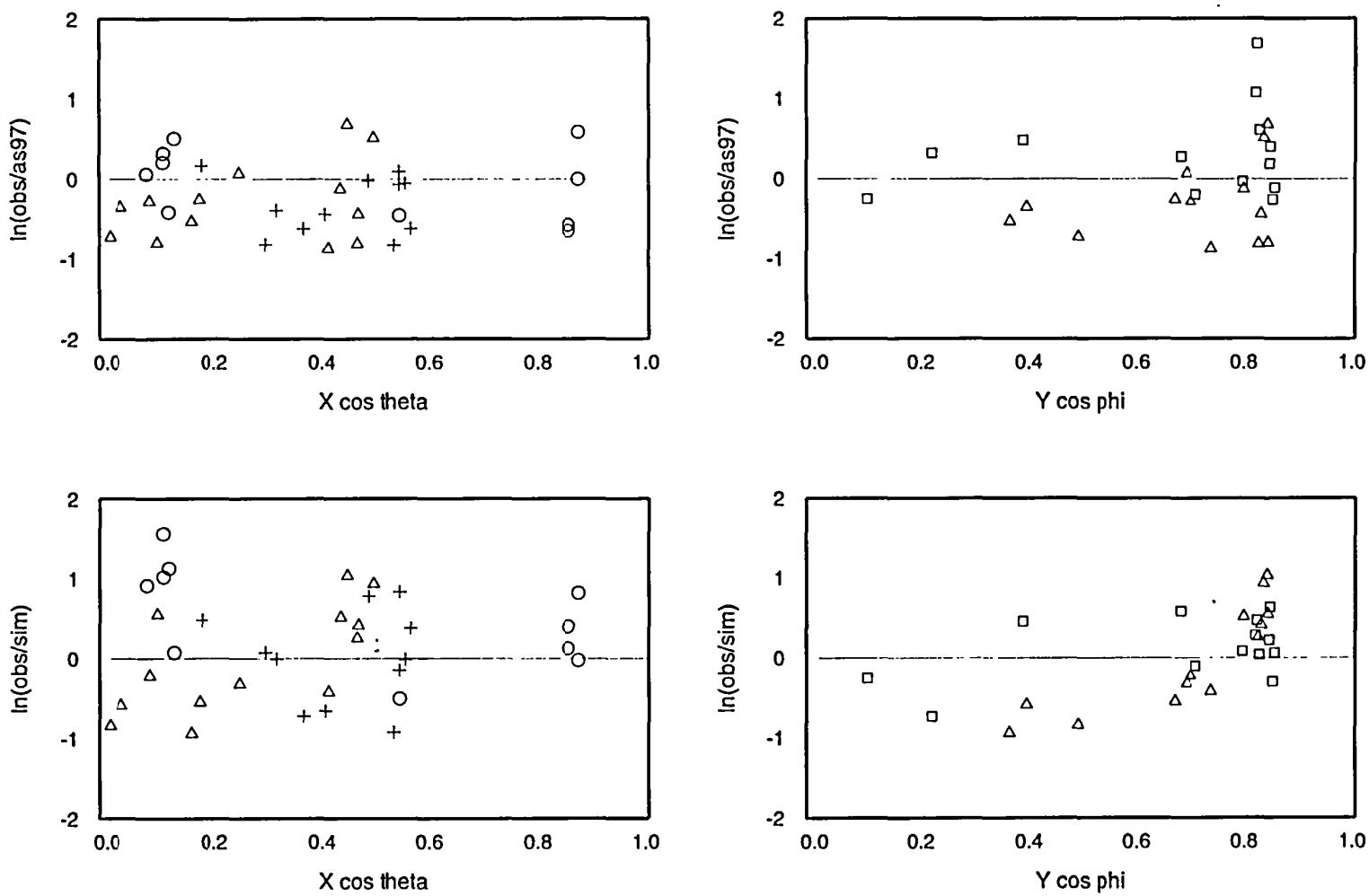

+ Kobe
○ Landers
△ Loma Prieta
□ Northridge

GMT Aug 25 11:18:44 1999 /u1/nancy/PEER-5/Comparisons

Kobe, Landers, Loma Prieta, Northridge - Fault Normal

Spectral Acceleration at 1.0 sec

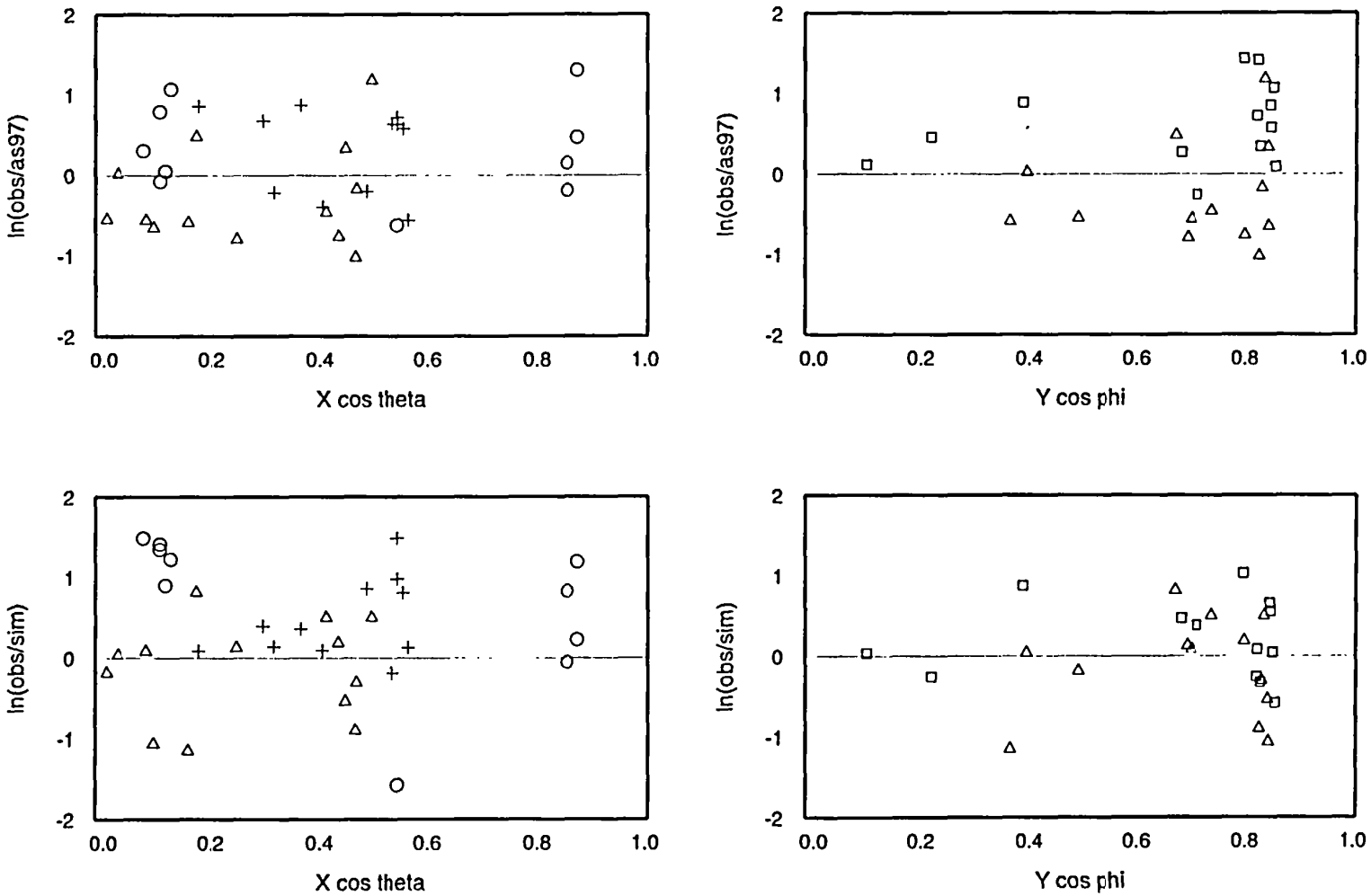

+ Kobe
○ Landers
△ Loma Prieta
□ Northridge

GMT Aug 25 11:18:57 1999 /u1/nancy/PEER-5/Comparisons

Kobe, Landers, Loma Prieta, Northridge - Fault Parallel

Spectral Acceleration at 1.0 sec

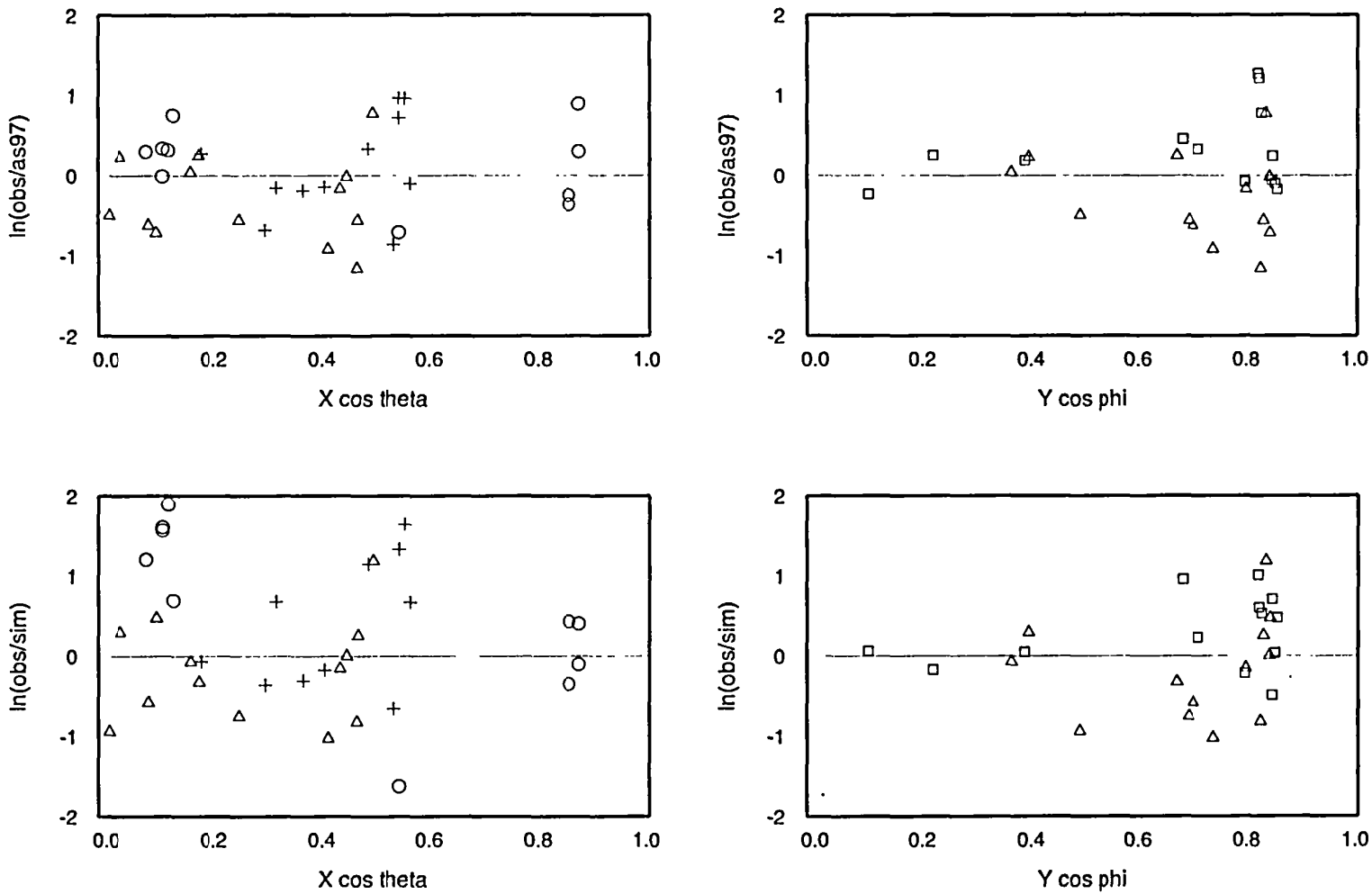

+ Kobe
○ Landers
△ Loma Prieta
□ Northridge

GMT Aug 25 11:19:10 1999 /u1/nancy/PEER-5/Comparisons

/u1/nancy/PEER-5/Loma/Comparisons/Tabulate
tableout

Station	Correlation FN	Correlation FP	Least Squares FN	Least Squares FP	Response Spectra FN	Response Spectra FP	Fourier Spectra FN	Fourier Spectra FP
andd	0.420		-0.044		0.043	-0.353	0.129	-0.206
bran	0.382		-0.018		0.428	-0.337	0.338	-0.307
capi	0.509		0.130		-0.266	-0.899	0.353	0.027
cldd	0.478		-0.027		-0.140	-0.323	-0.037	-0.189
cor	0.423		-0.682		-0.729	0.427	-0.395	0.638
gav	0.498		-0.475		-0.631	-0.298	-0.410	-0.224
gil6	0.615		0.173		0.207	-0.632	0.204	-0.497
gilb	0.680		0.261		0.047	0.041	-0.097	-0.120
hol	0.722		0.265		0.542	1.101	0.651	1.229
lgpc	0.705		0.290		0.009	0.638	-0.031	0.721
srtg	0.784	0.691	0.378	0.267	0.078	0.452	0.270	0.481
ucsc	0.461	0.323	-1.344	-0.779	-1.093	-0.612	-0.929	-0.737
waho	0.513		-0.007		-0.116	-0.049	-0.109	-0.024
Average	0.553	0.507	-0.085	-0.256	-0.125	-0.065	-0.005	0.061
Sigma	0.132		0.485		0.496	0.797	0.828	1.251
Sigma Mean	0.037		0.134		0.137	0.221	0.230	0.347

Loma Prieta - Fault Normal

Simulations and Data Band Pass Filtered 0.125-1.43 Hz

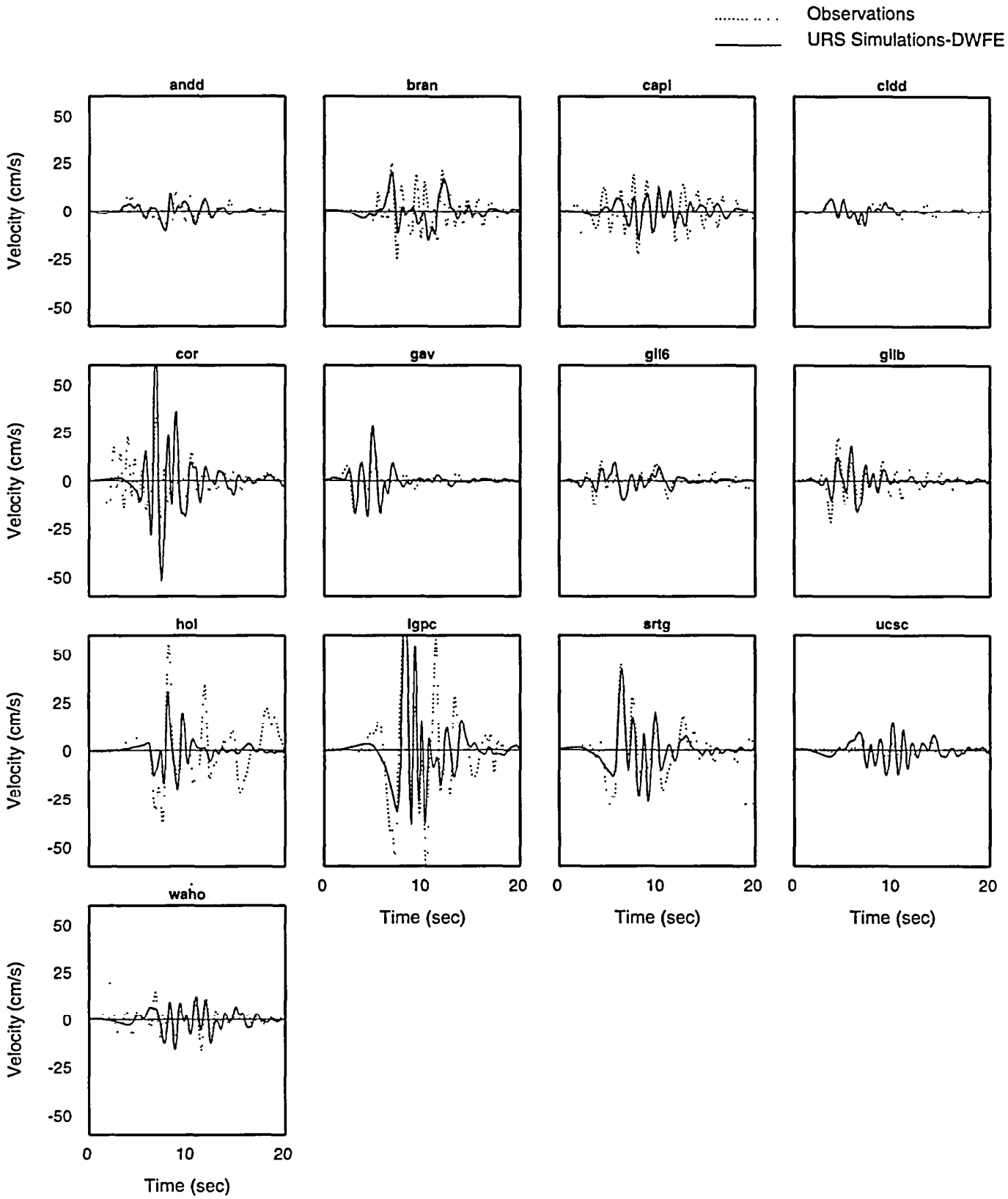

GMT Aug 31 10:46:37 1999 /u2/nancy/PEER-5/Loma/Comparisons

Loma Prieta - Fault Parallel

Simulations and Data Band Pass Filtered 0.125-1.43 Hz

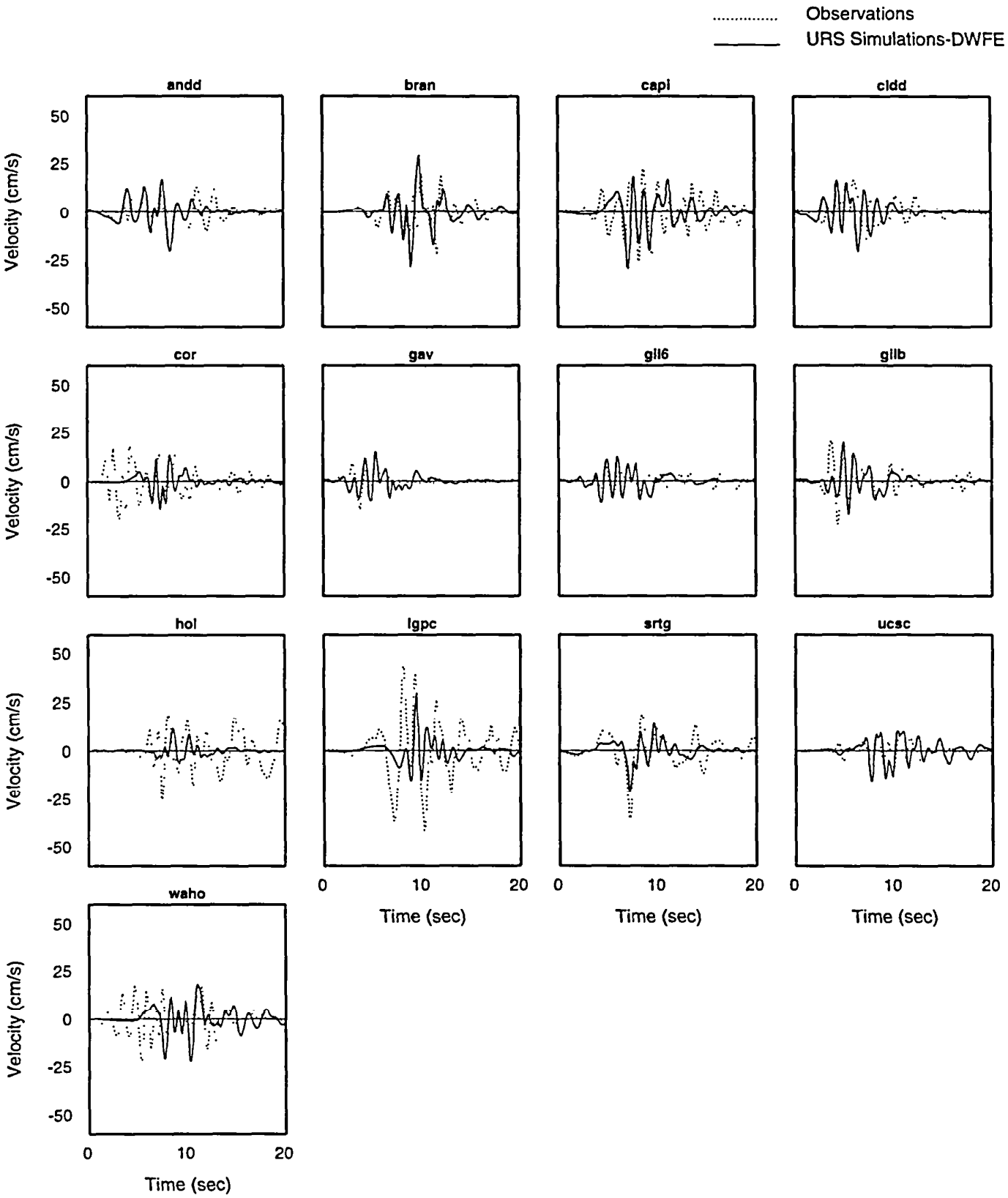

GMT Aug 31 10:47:11 1999 /u2/nancy/PEER-5/Loma/Comparisons

Loma Prieta - Fault Normal

Simulations and Data

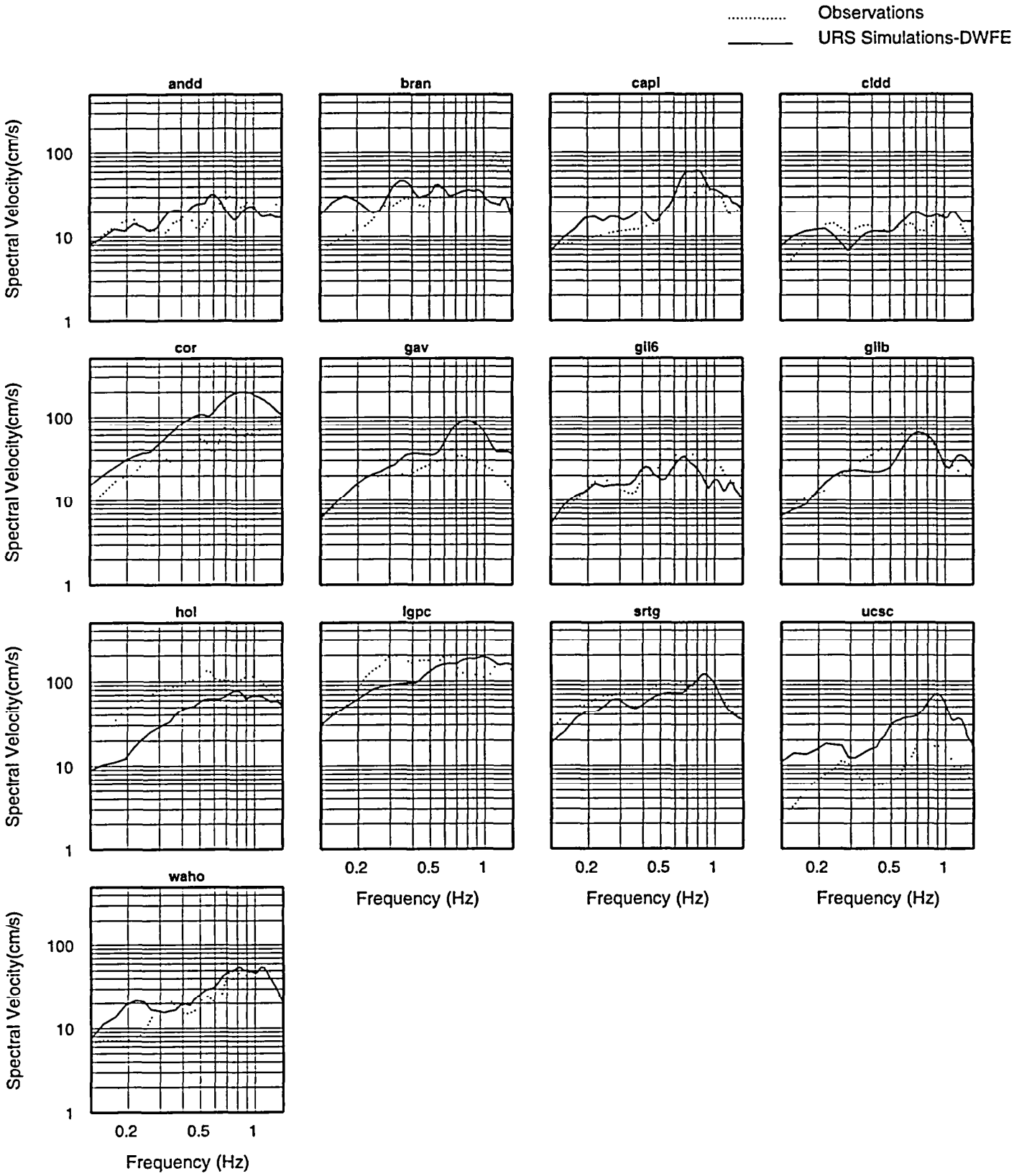

GMT Aug 31 15:19:01 1999 /u2/nancy/PEER-5/Loma/Comparisons

Loma Prieta - Fault Parallel

Simulations and Data

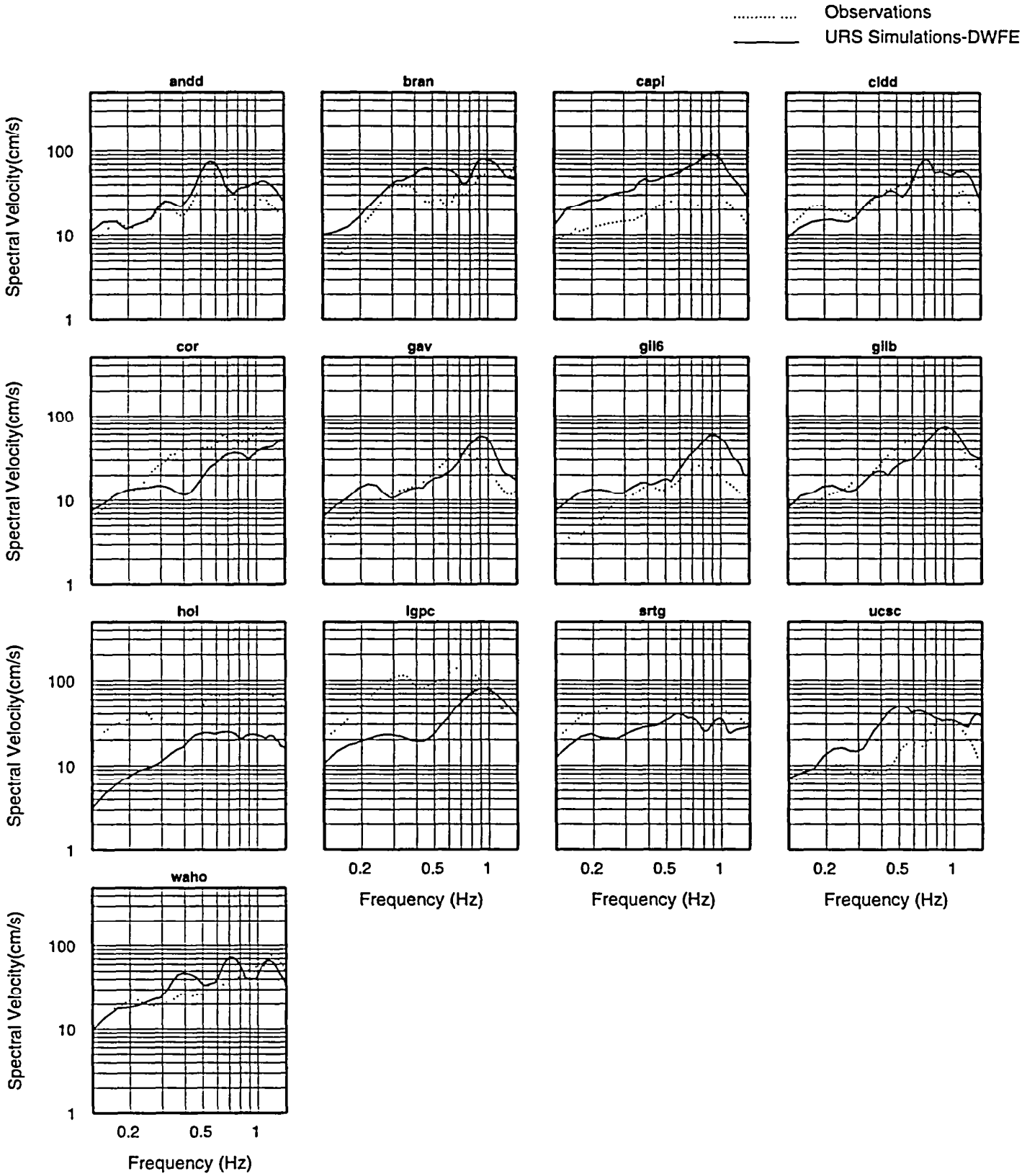

GMT Aug 31 15:19:17 1999 /u2/nancy/PEER-5/Loma/Comparisons

Loma Prieta - Fault Normal

Simulations and Data Band Pass Filtered 0.125-1.43 sec

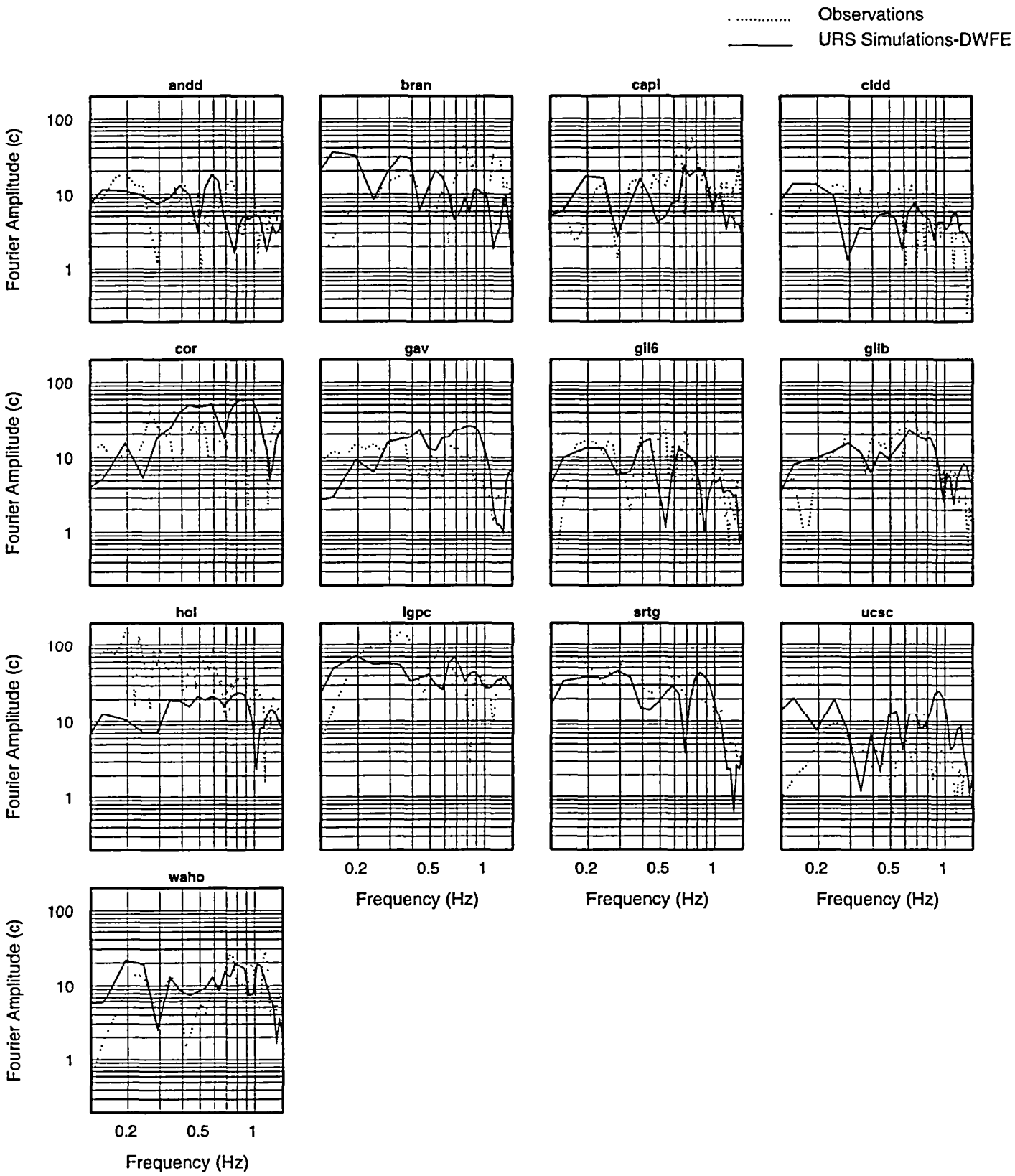

GMT Aug 31 15:23.42 1999 /u2/nancy/PEER-5/Loma/Comparisons

Loma Prieta - Fault Parallel

Simulations and Data Band Pass Filtered 0.125-1.43 sec

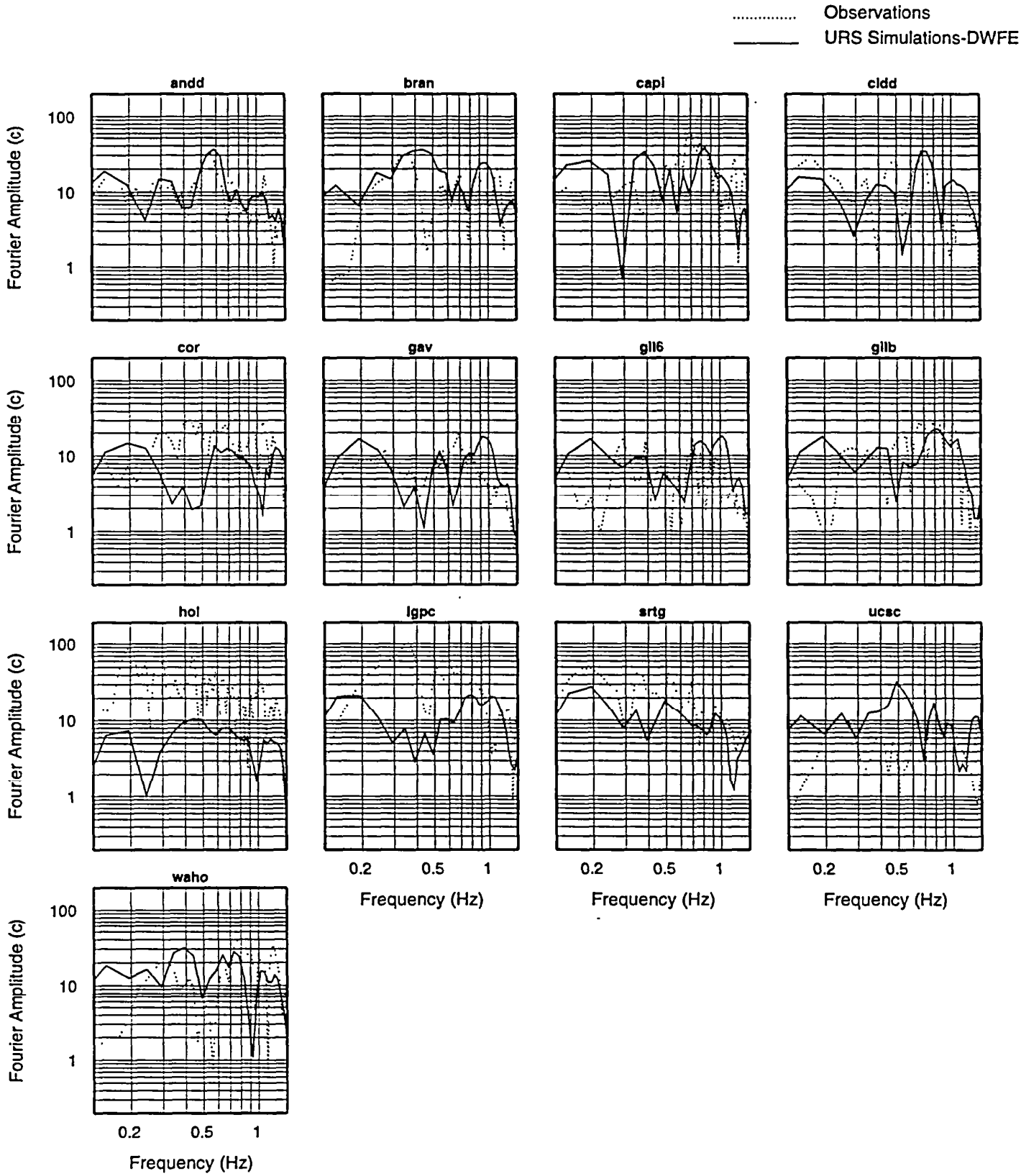

GMT Aug 31 15:23.59 1999 /u2/nancy/PEER-5/Loma/Comparisons

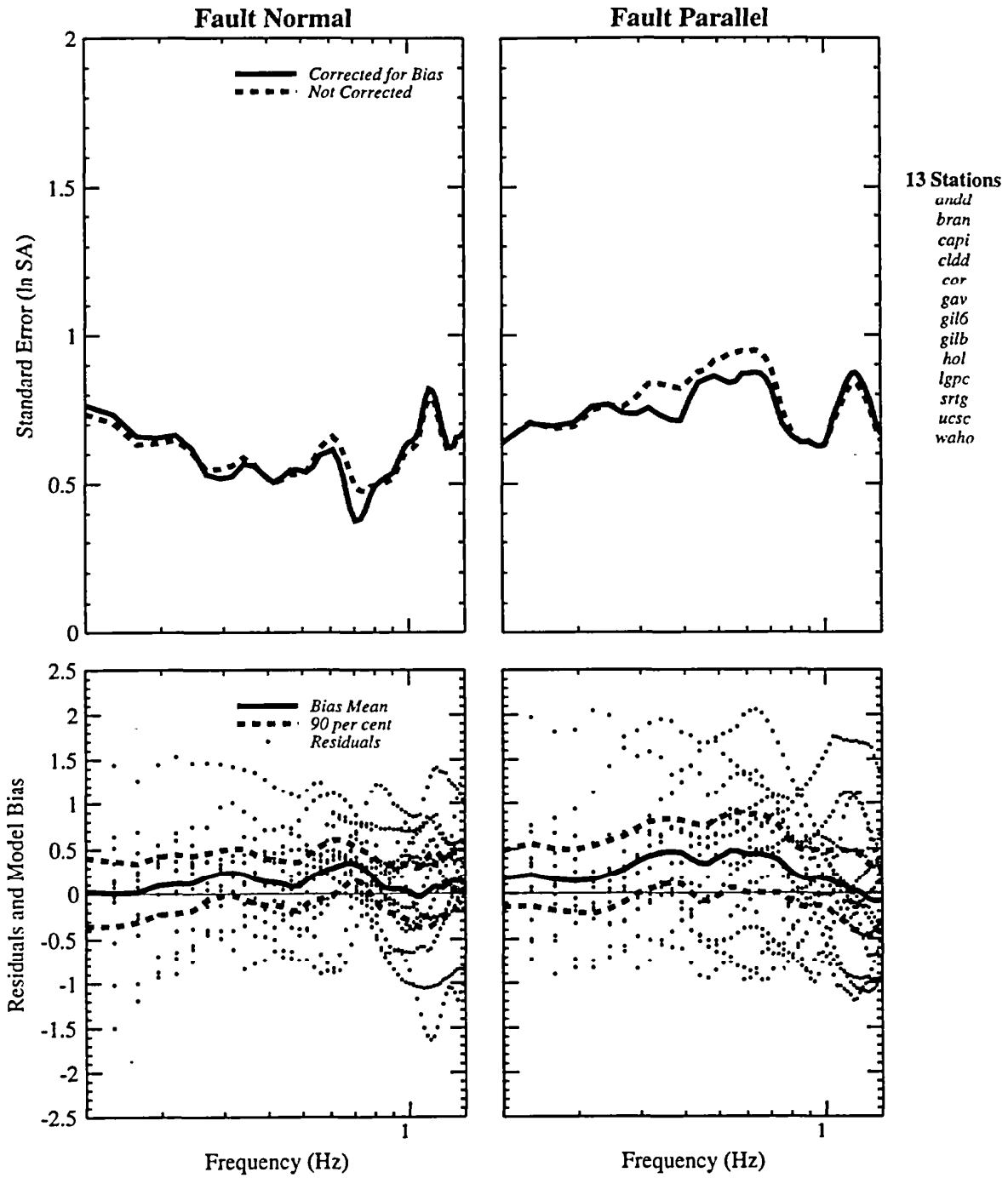

Loma Prieta Spectral Acceleration Goodness of Fit
Observed minus Synthetic (obs - sim)

nfsmith0 Tue Aug 31 13 39 26 PDT 1999
/u2/nancy/PEER-5/Loma/GoodFit/mplot_goodfit csh

Loma Prieta 10/17/89 - andd

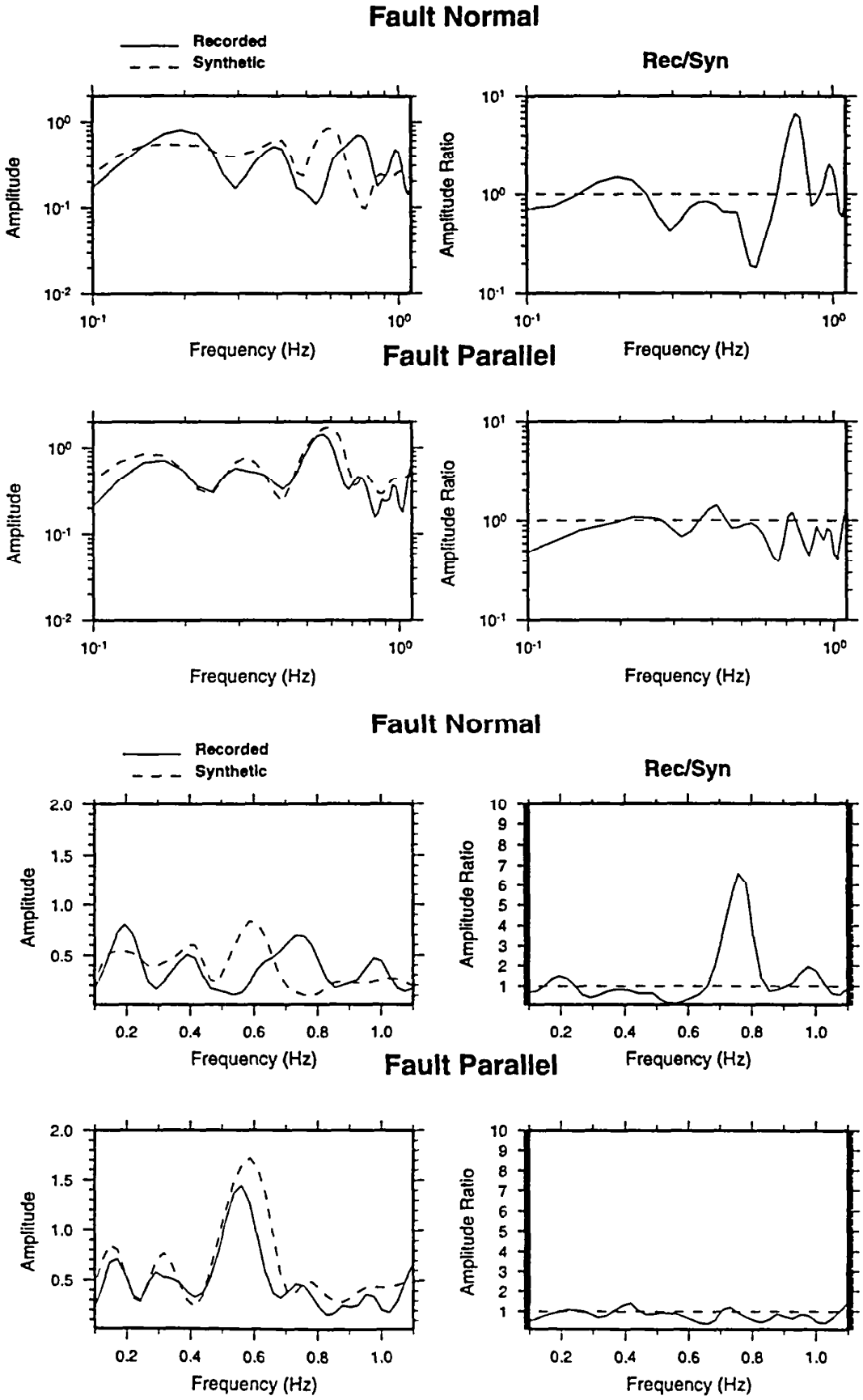

Loma Prieta 10/17/89 - bran

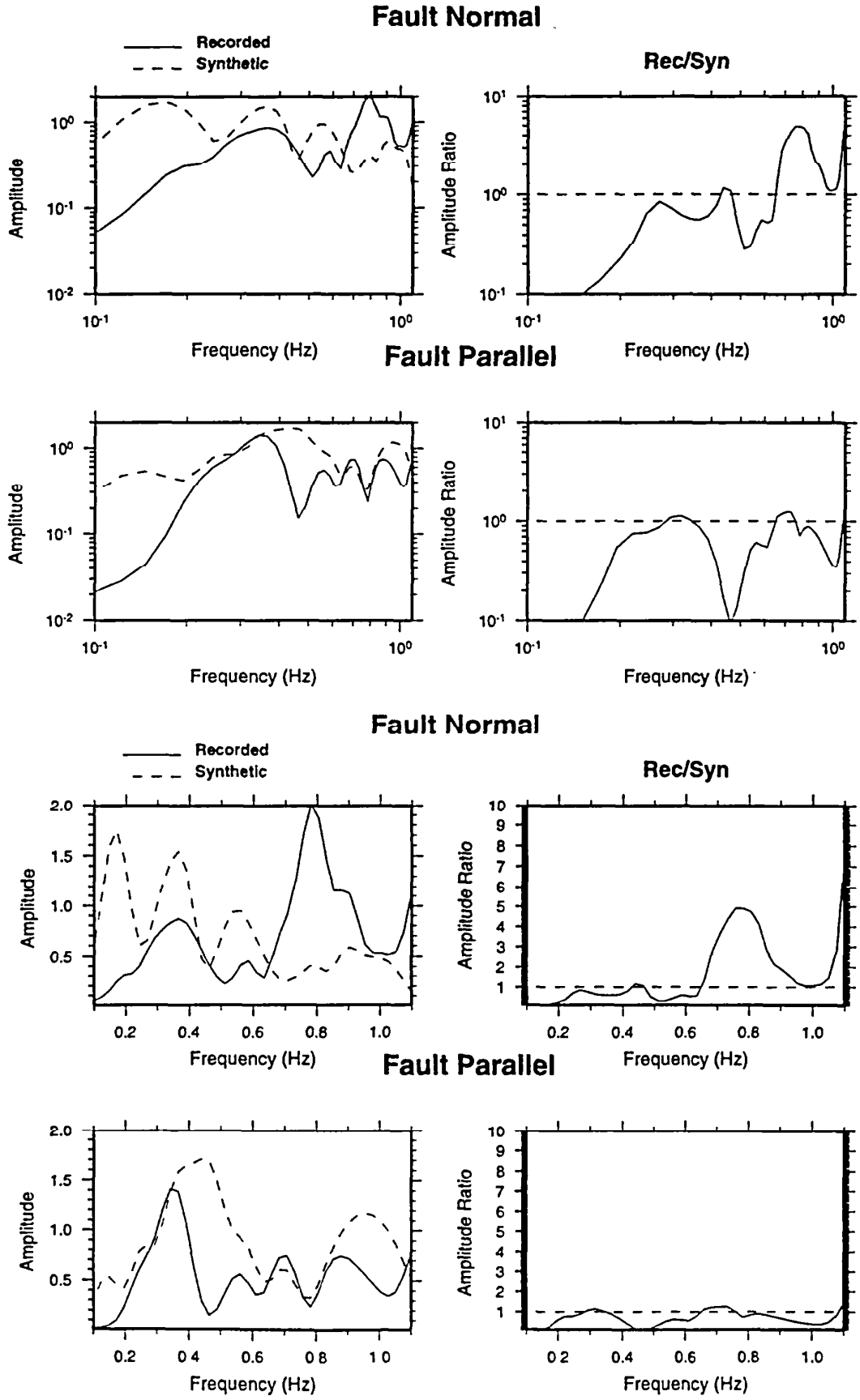

Loma Prieta 10/17/89 - capi

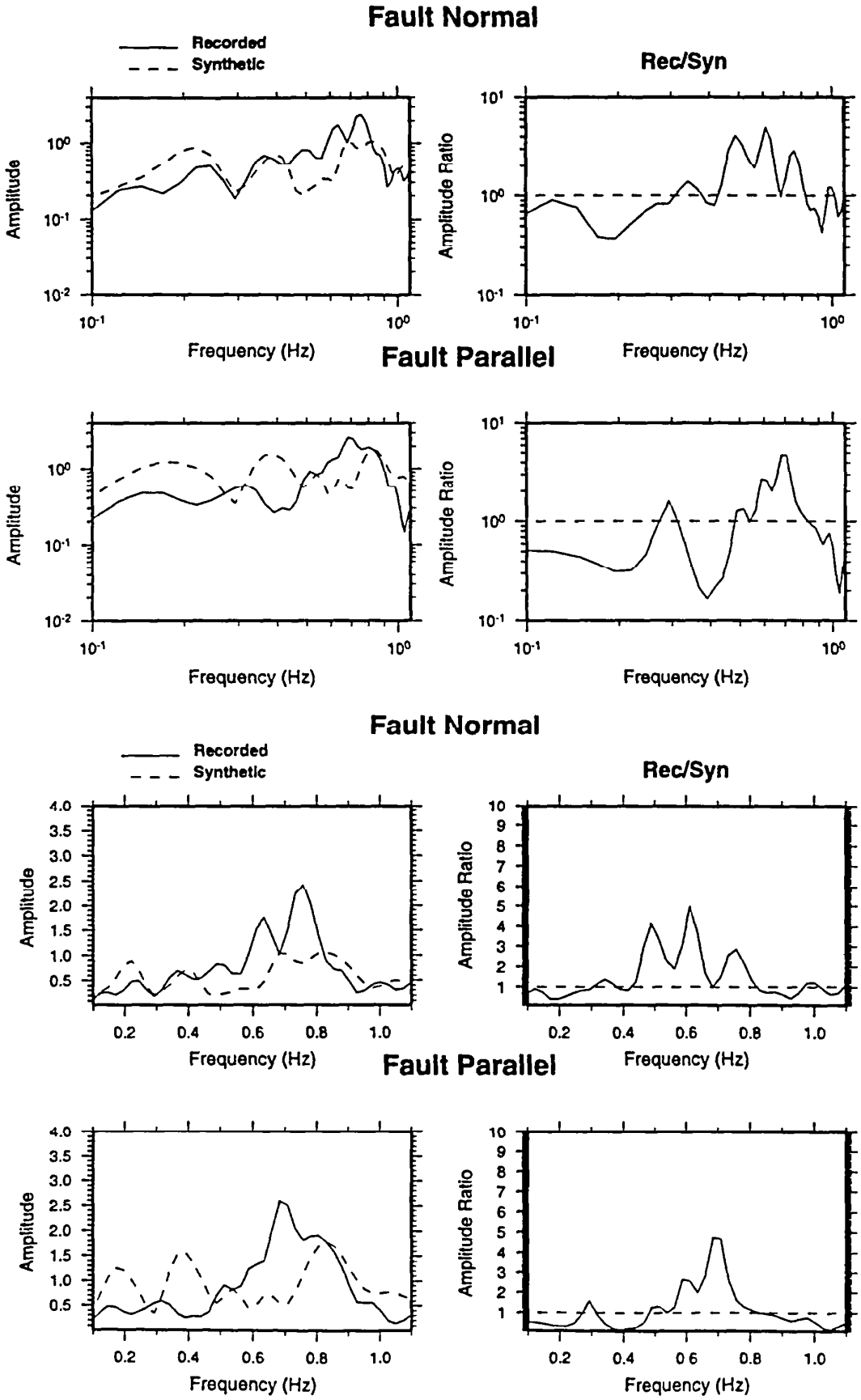

Loma Prieta 10/17/89 - cldd

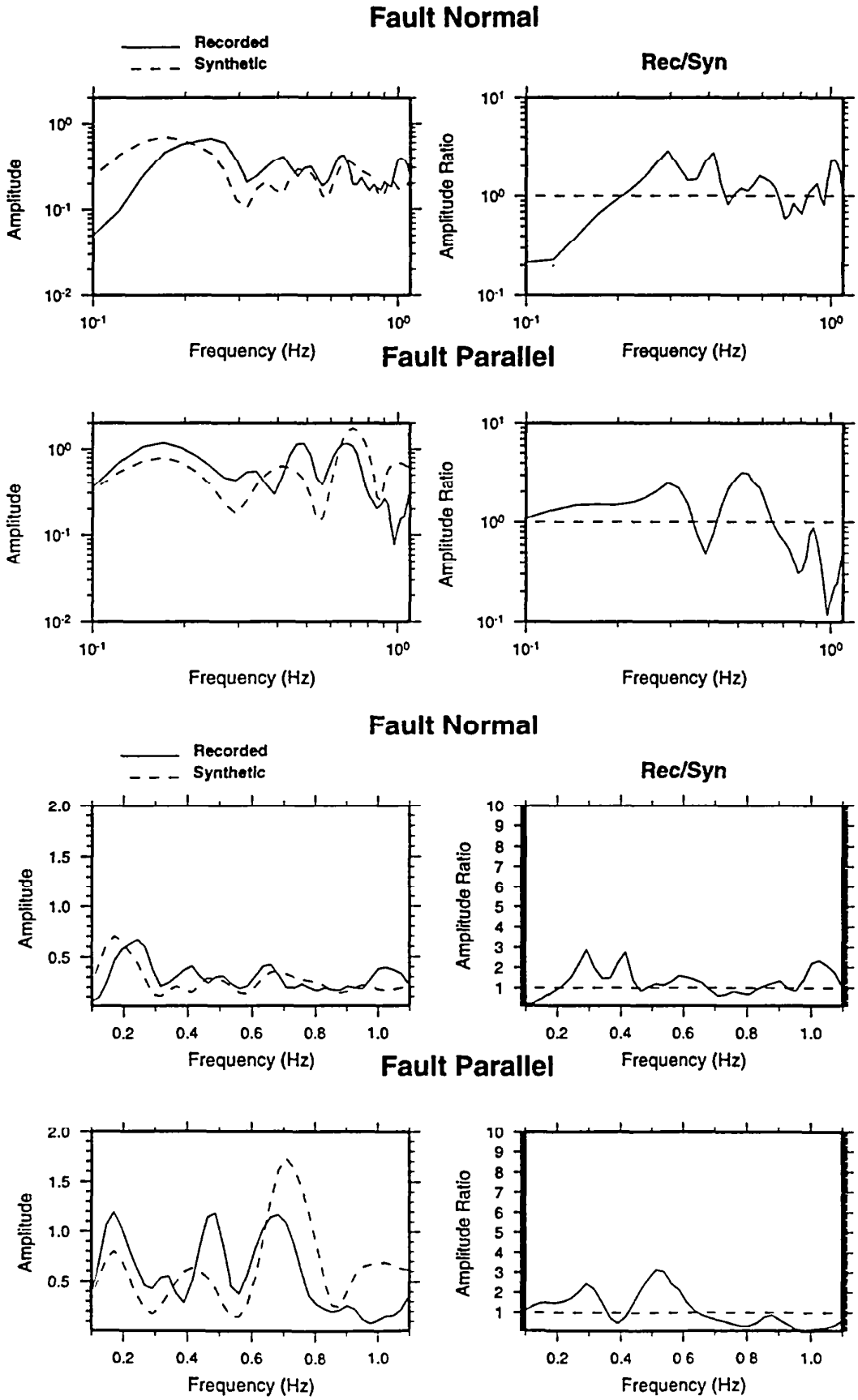

Loma Prieta 10/17/89 - cor

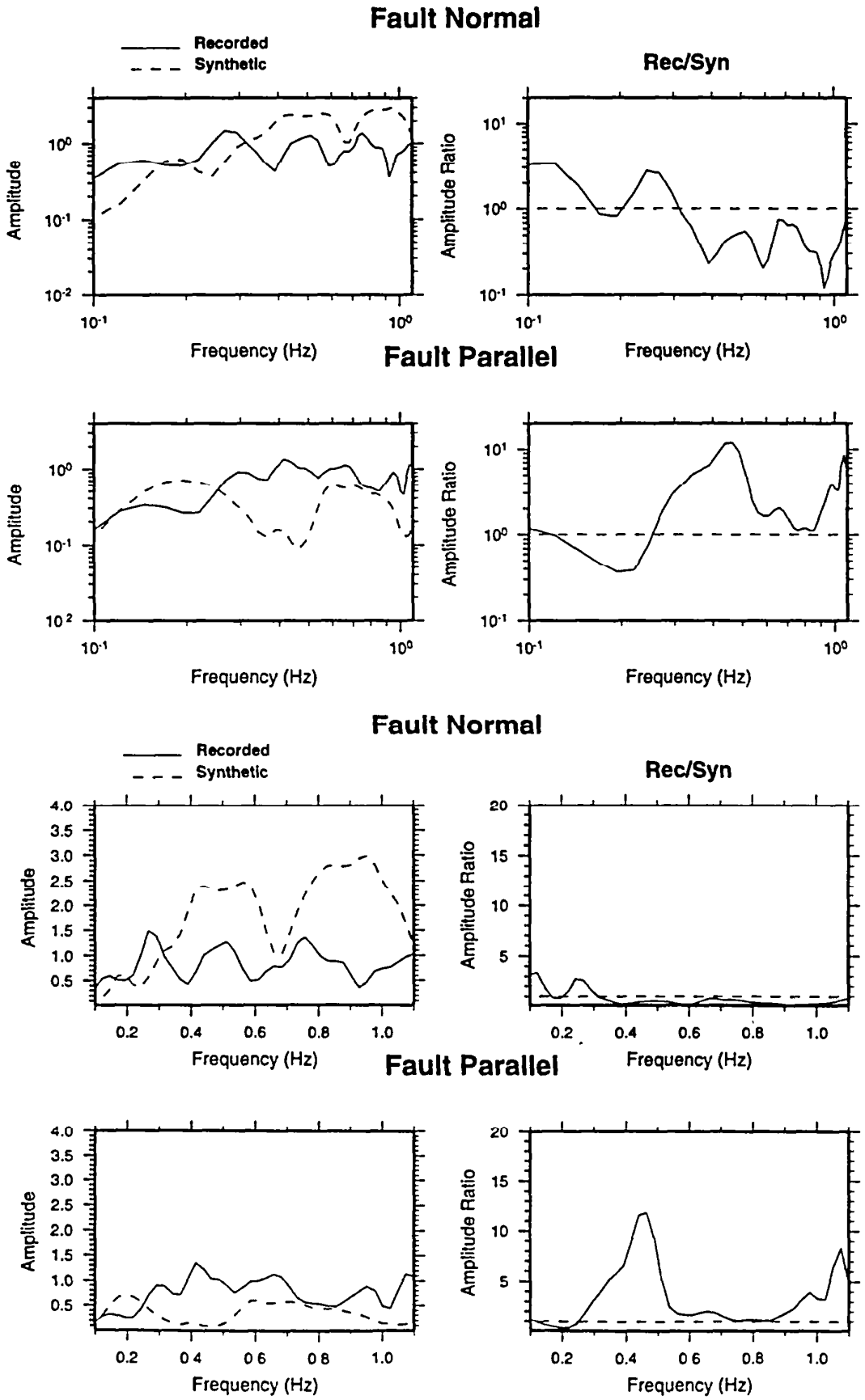

Loma Prieta 10/17/89 - gav

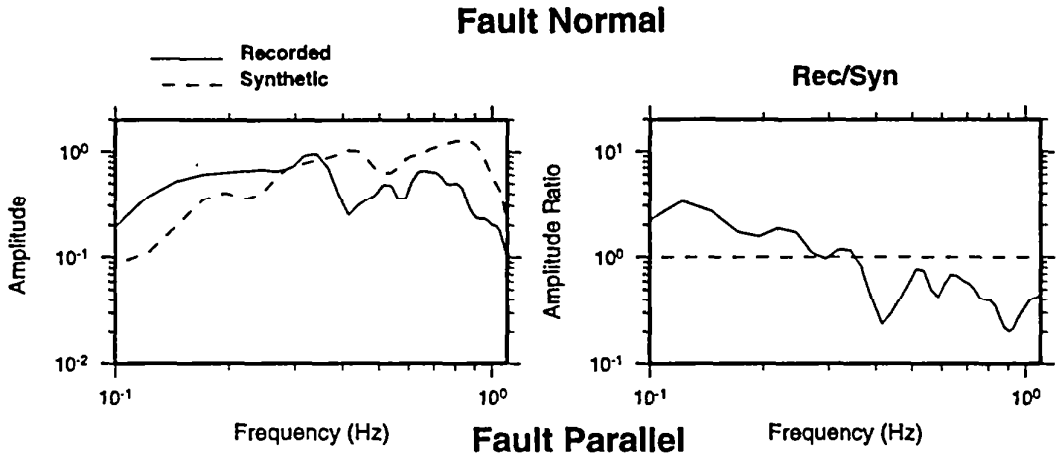

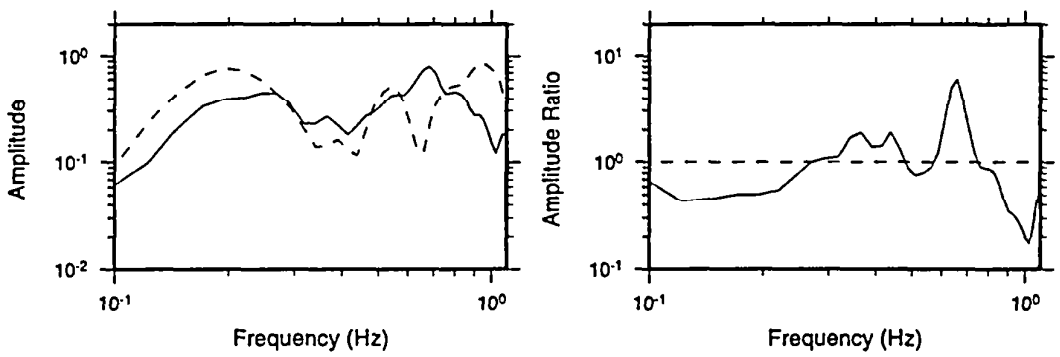

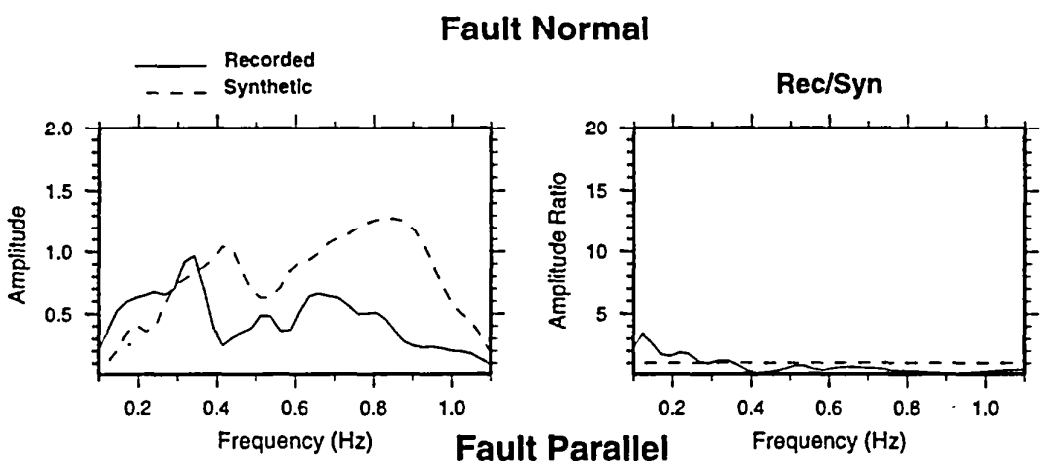

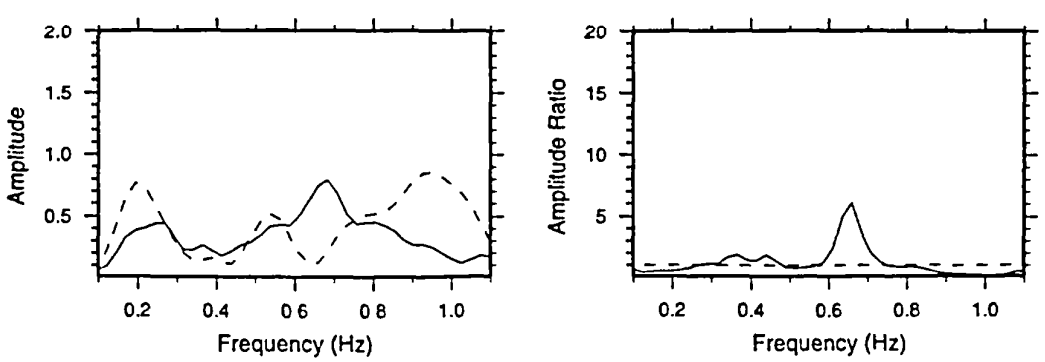

Loma Prieta 10/17/89 - gil6

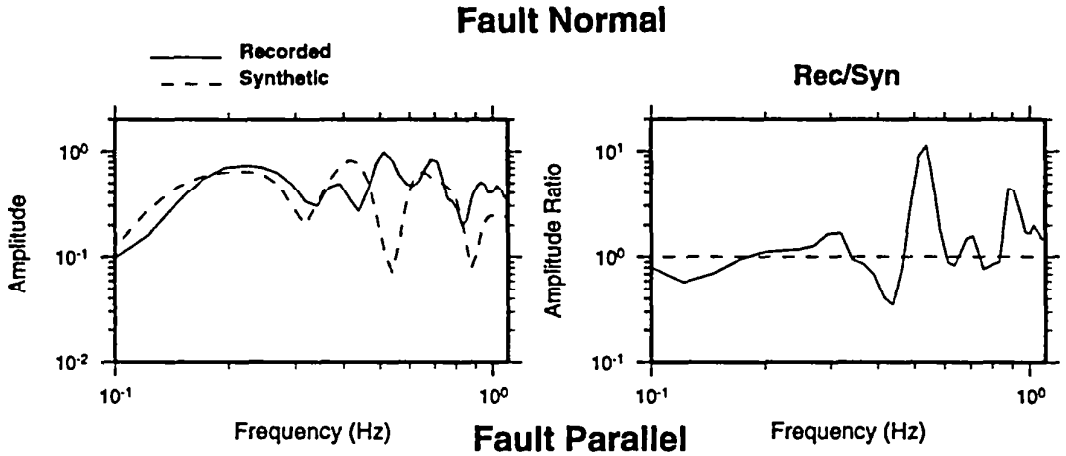

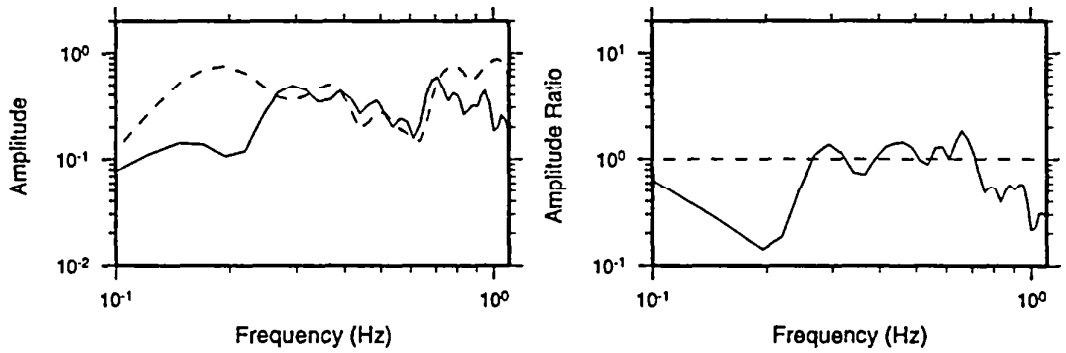

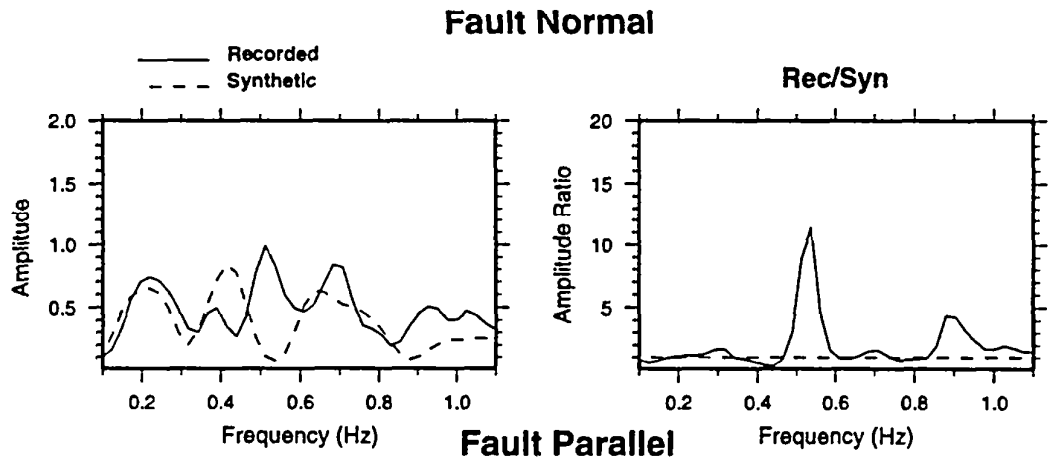

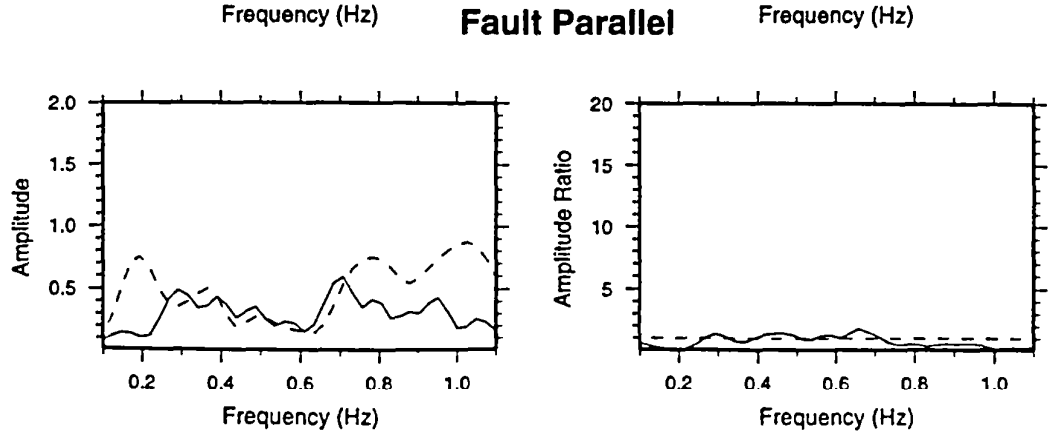

Loma Prieta 10/17/89 - gilb

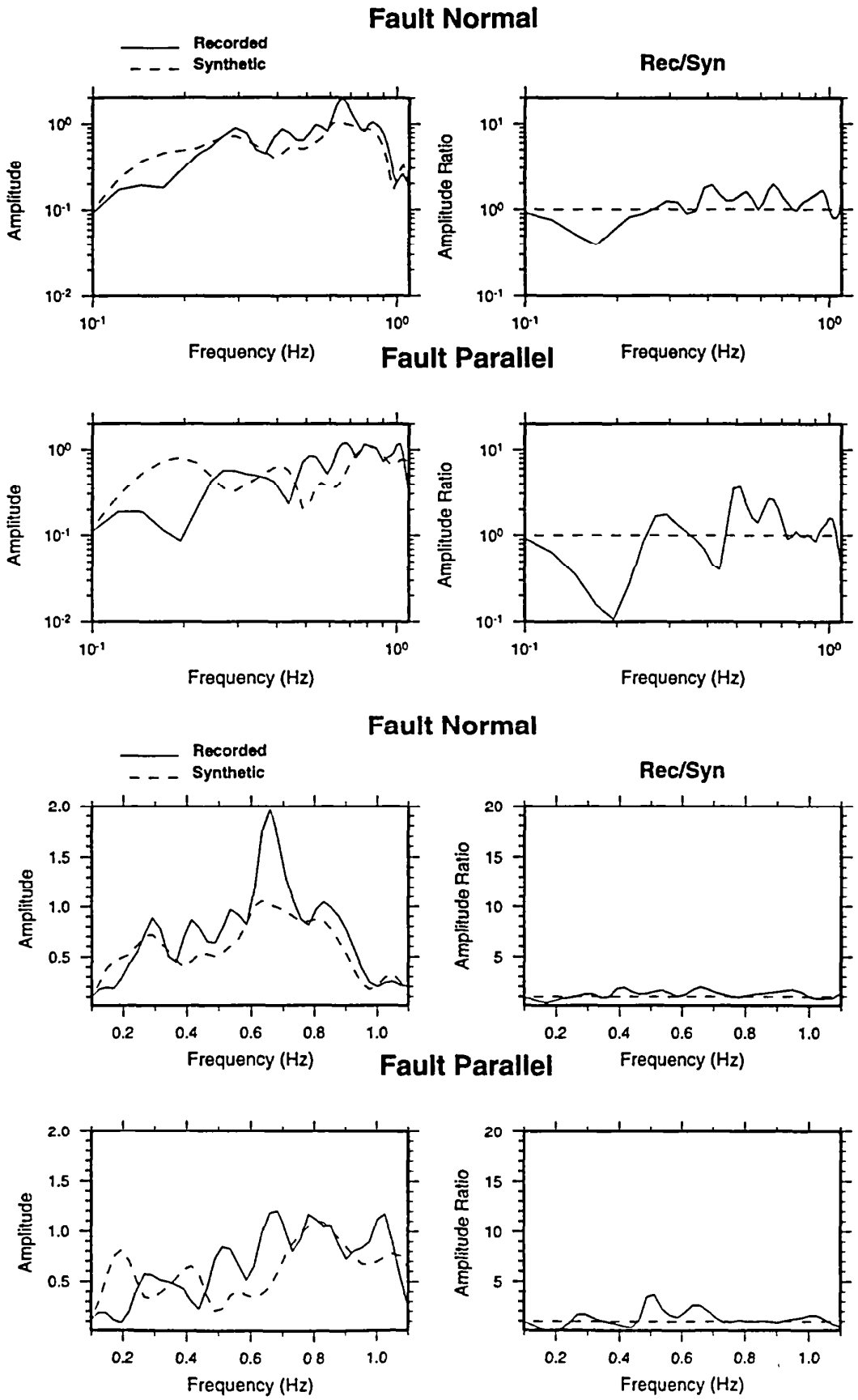

Loma Prieta 10/17/89 - hol

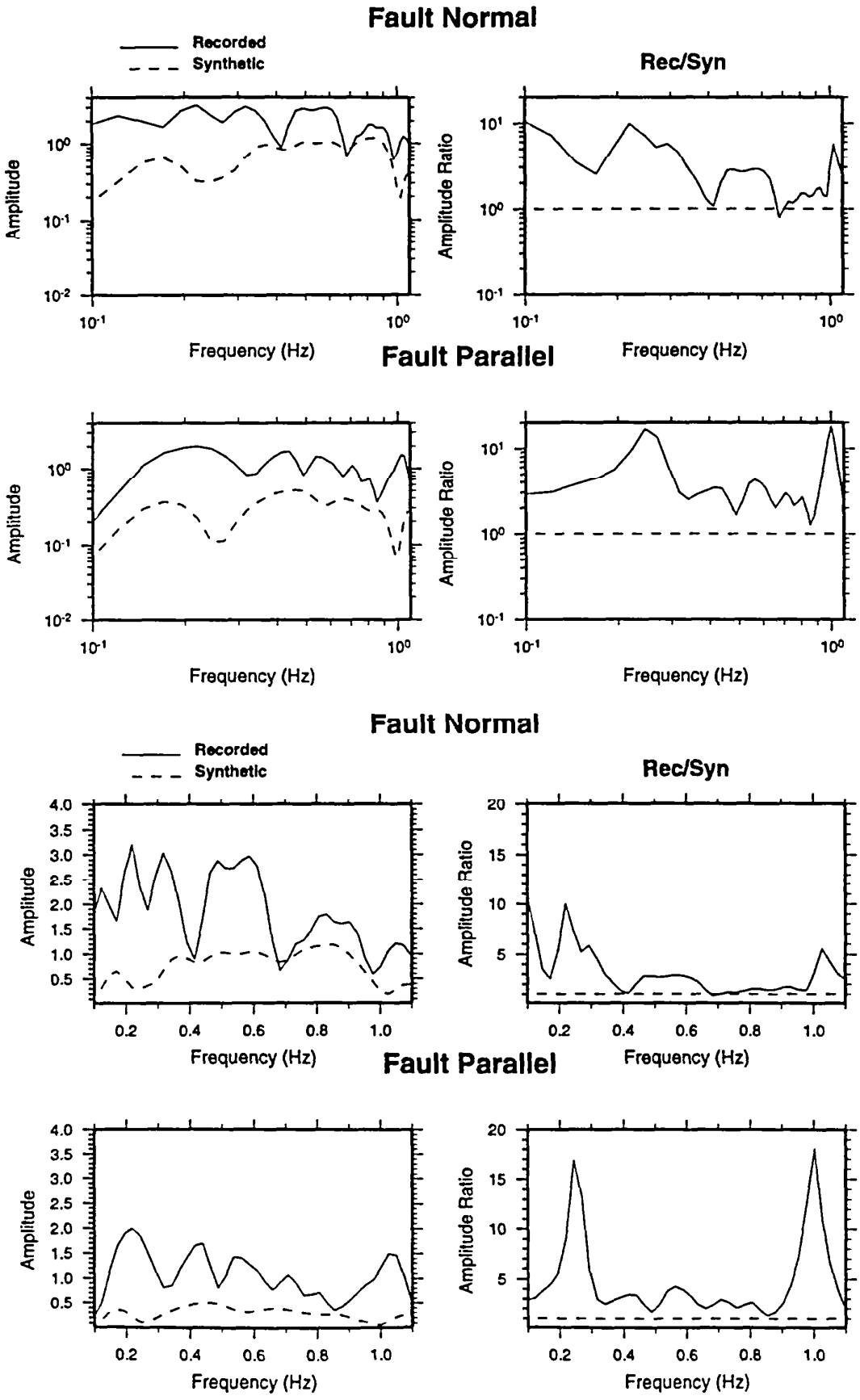

Loma Prieta 10/17/89 - lgpc

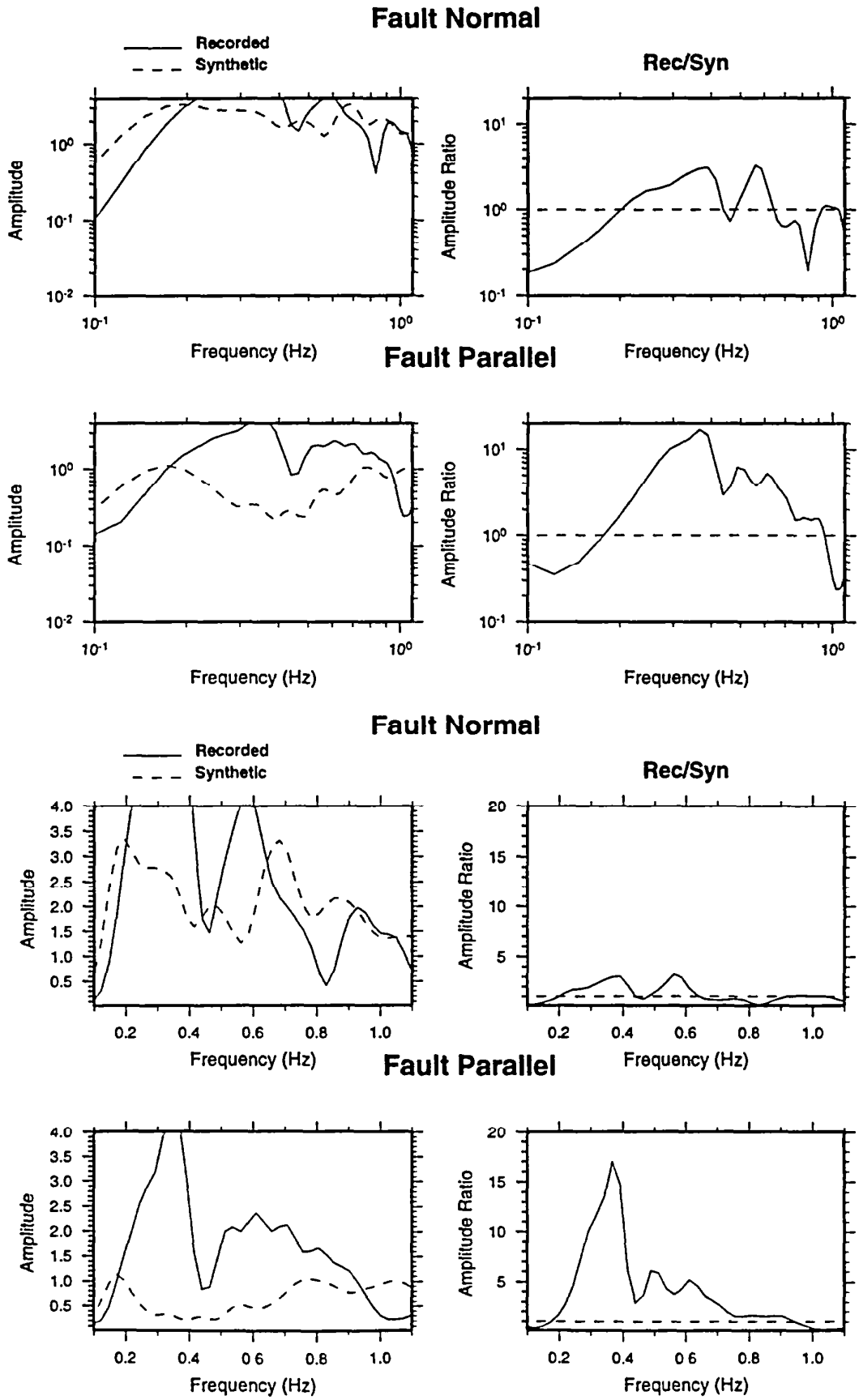

Loma Prieta 10/17/89 - srtg

Fault Normal

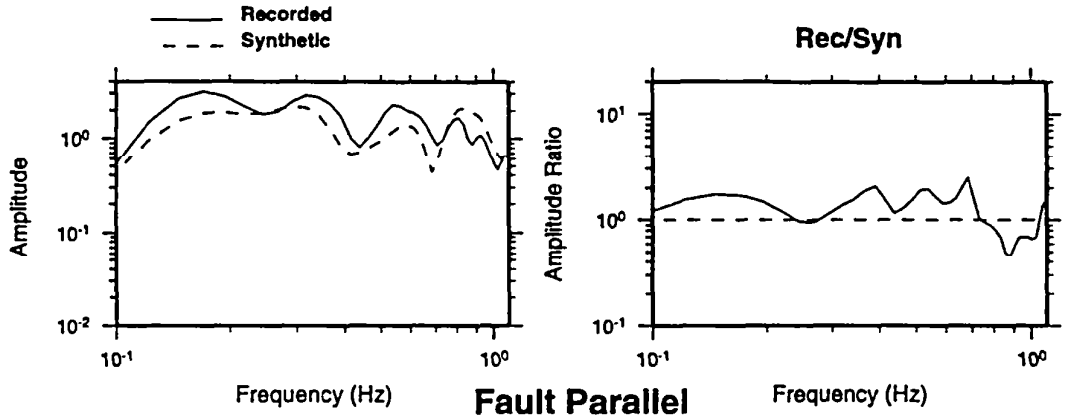

Fault Parallel

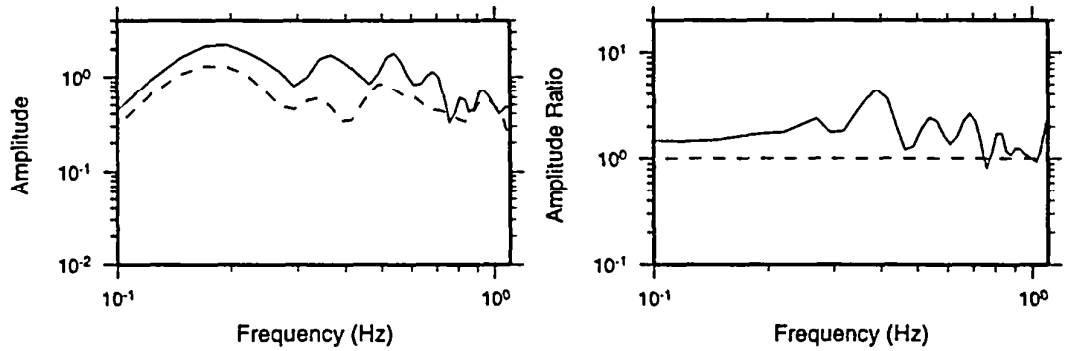

Fault Normal

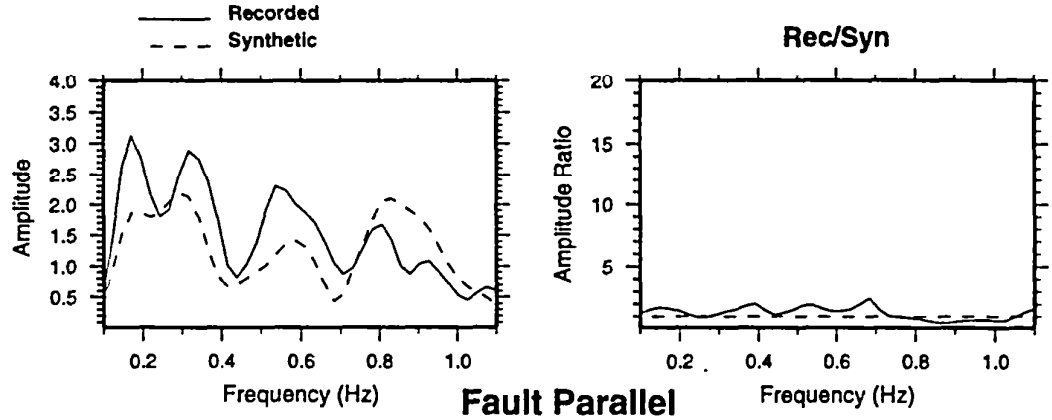

Fault Parallel

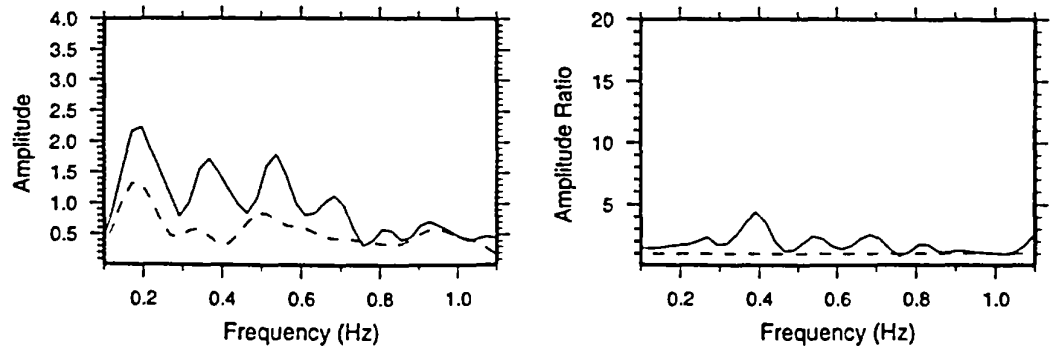

Loma Prieta 10/17/89 - ucsc

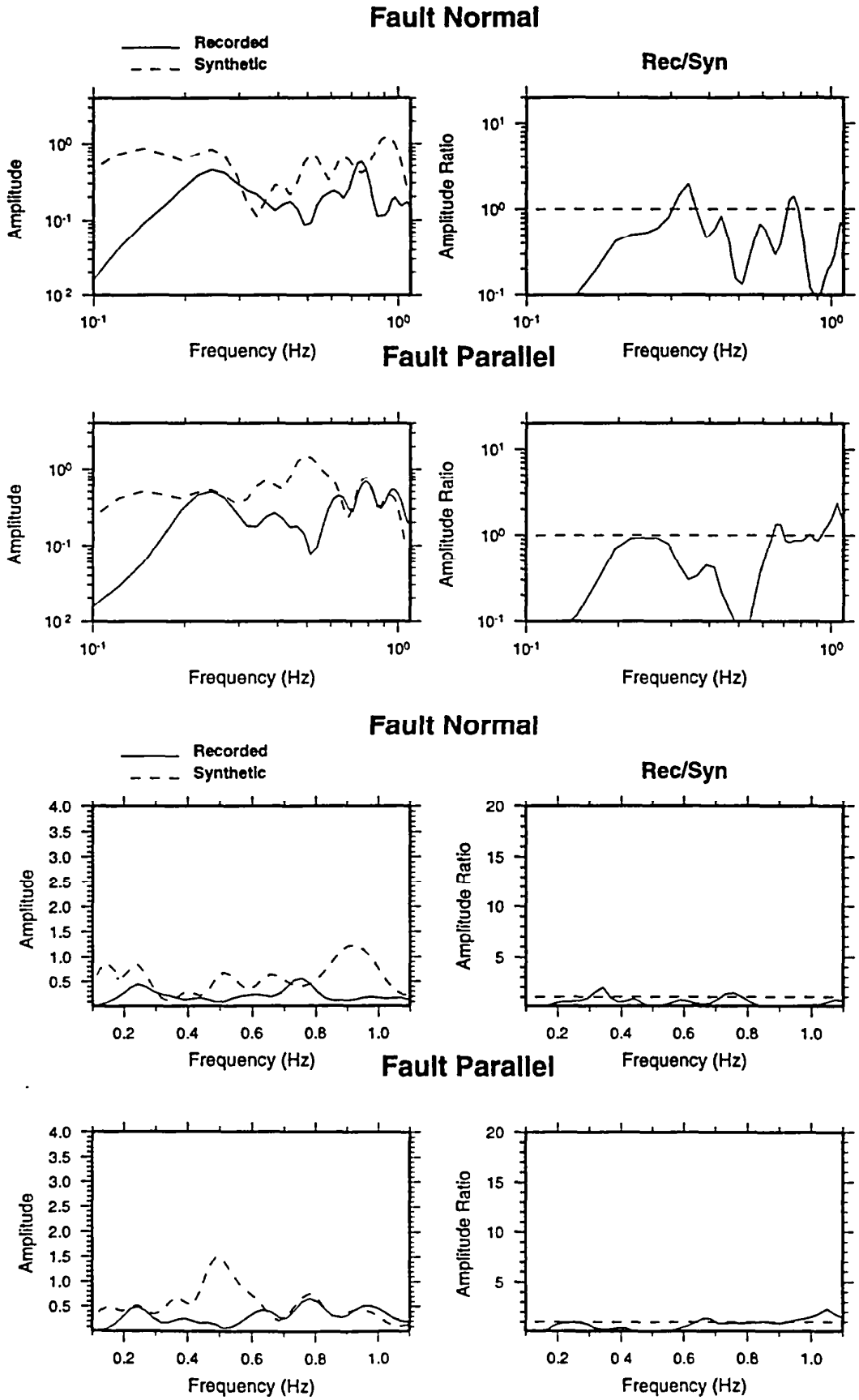

Loma Prieta 10/17/89 - waho

Fault Normal

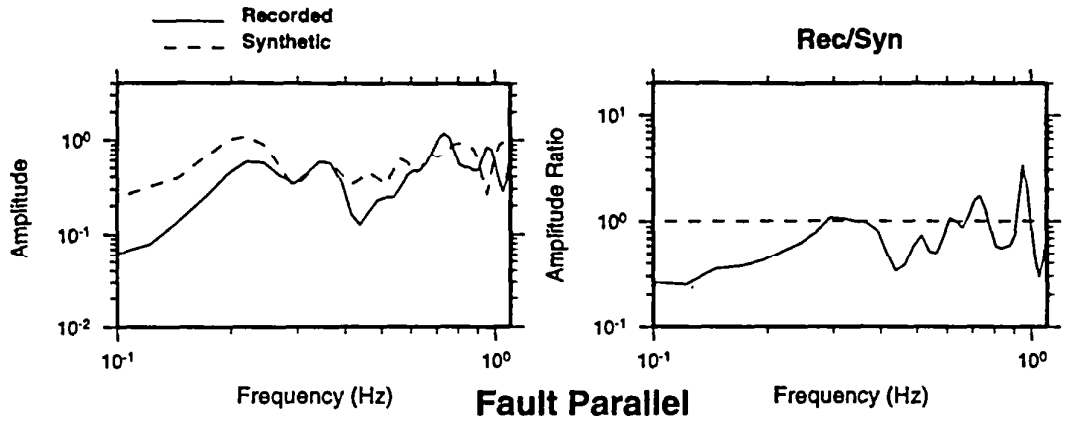

Fault Parallel

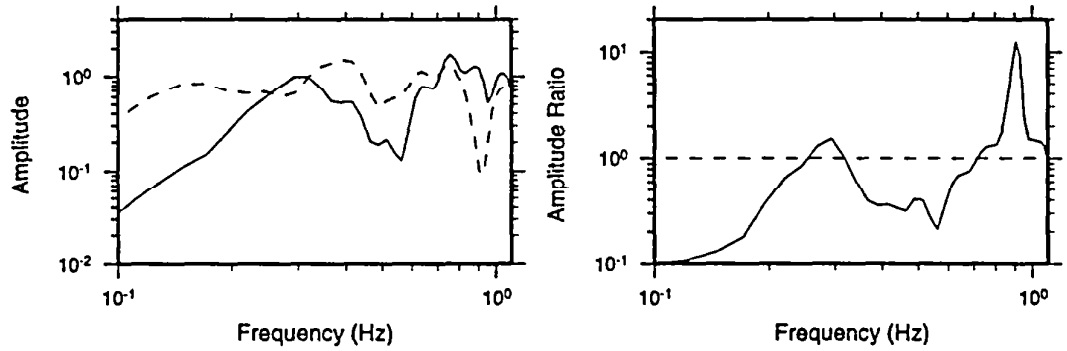

Fault Normal

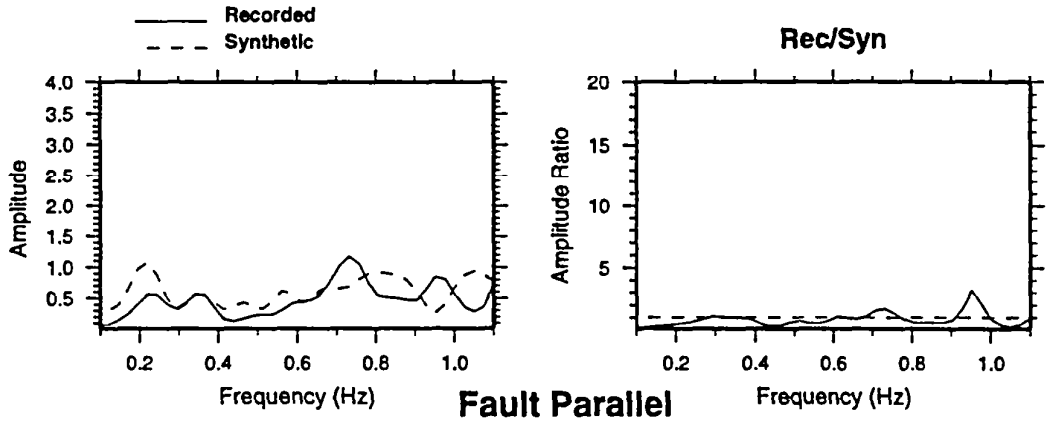

Fault Parallel

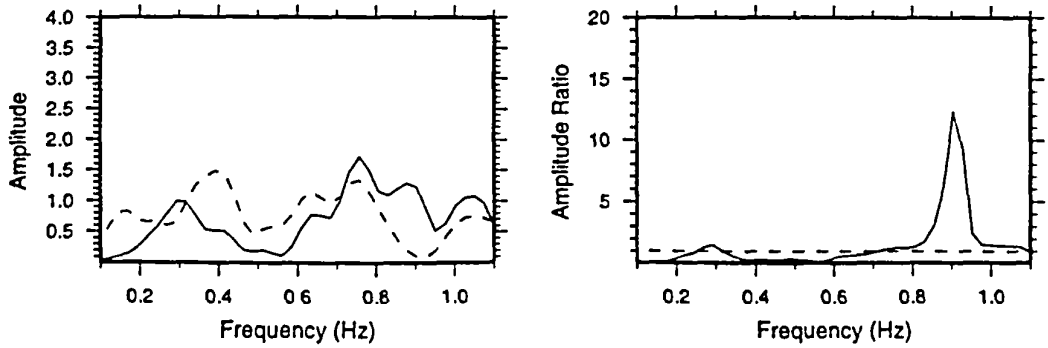

Loma Prieta - Fault Normal

SA at 7.0 sec

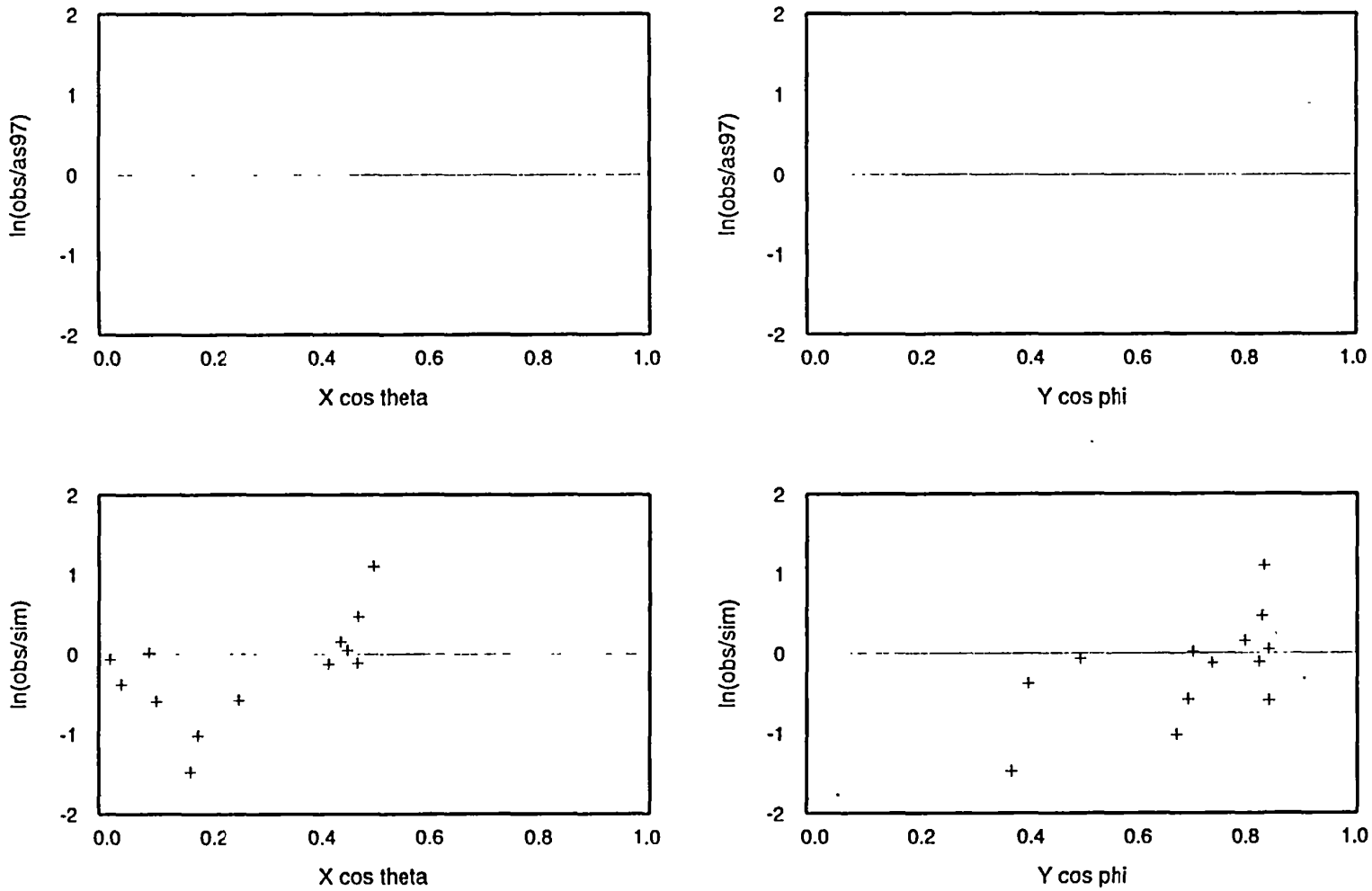

Loma Prieta - Fault Parallel

SA at 7.0 sec

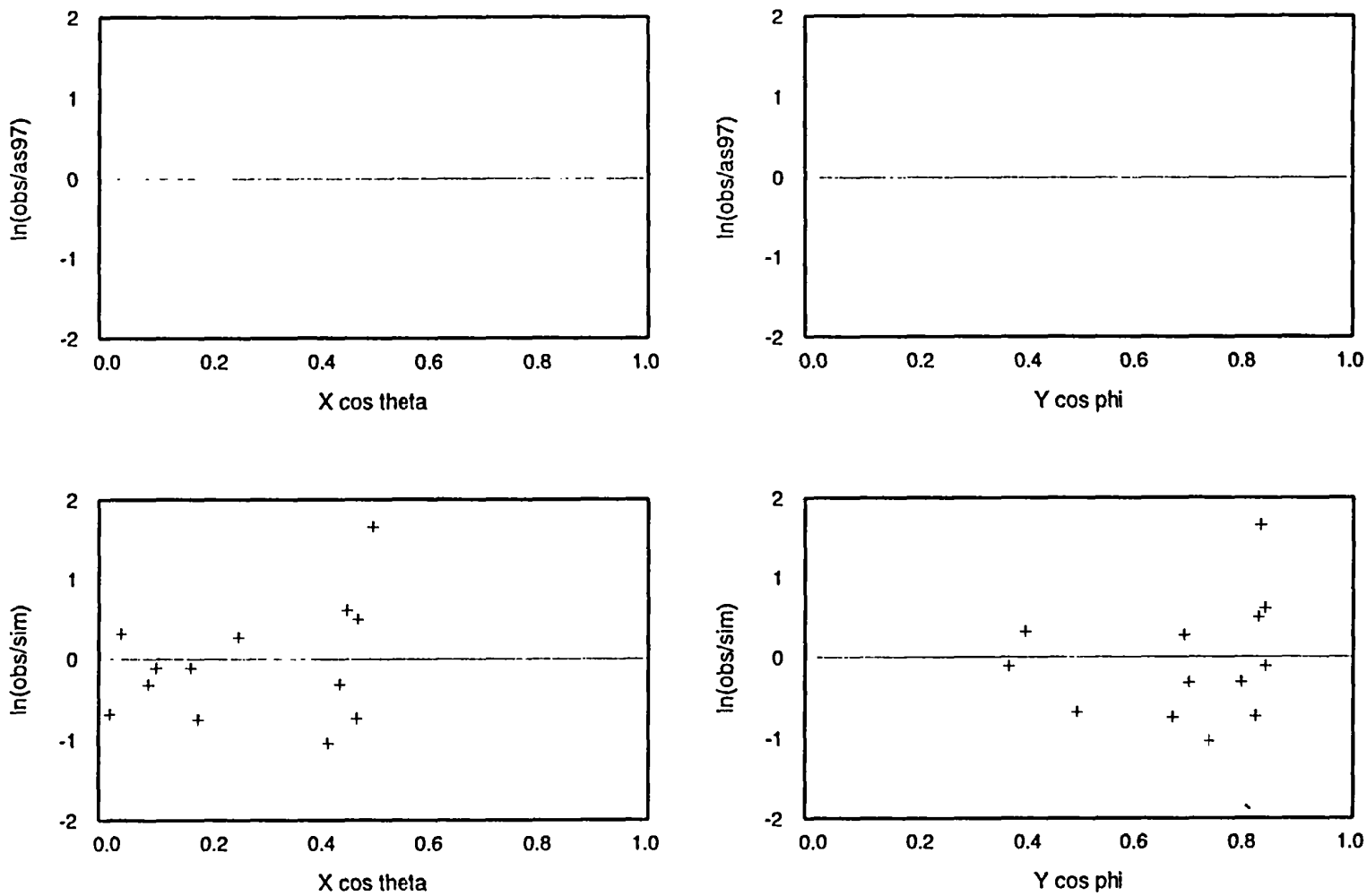

GMT Aug 24 14:54:07 1999 /u1/nancy/PEER-5/Loma/Comparisons/Resid_plots

Loma Prieta - Fault Normal

SA at 6.0 sec

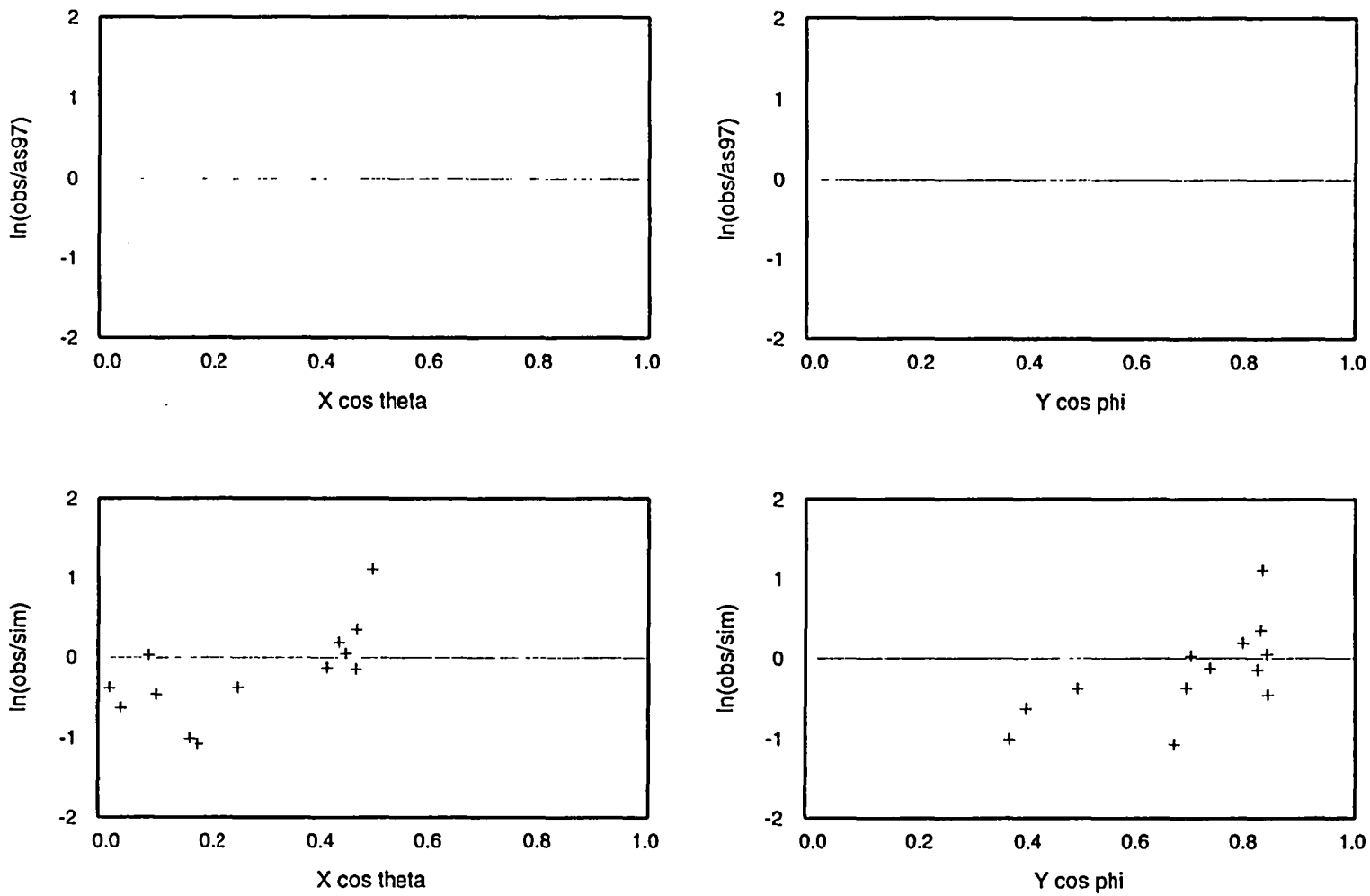

GMT Aug 24 14:54:21 1999 /u1/nancy/PEER-5/Loma/Comparisons/Resid_plots

Loma Prieta - Fault Parallel

SA at 6.0 sec

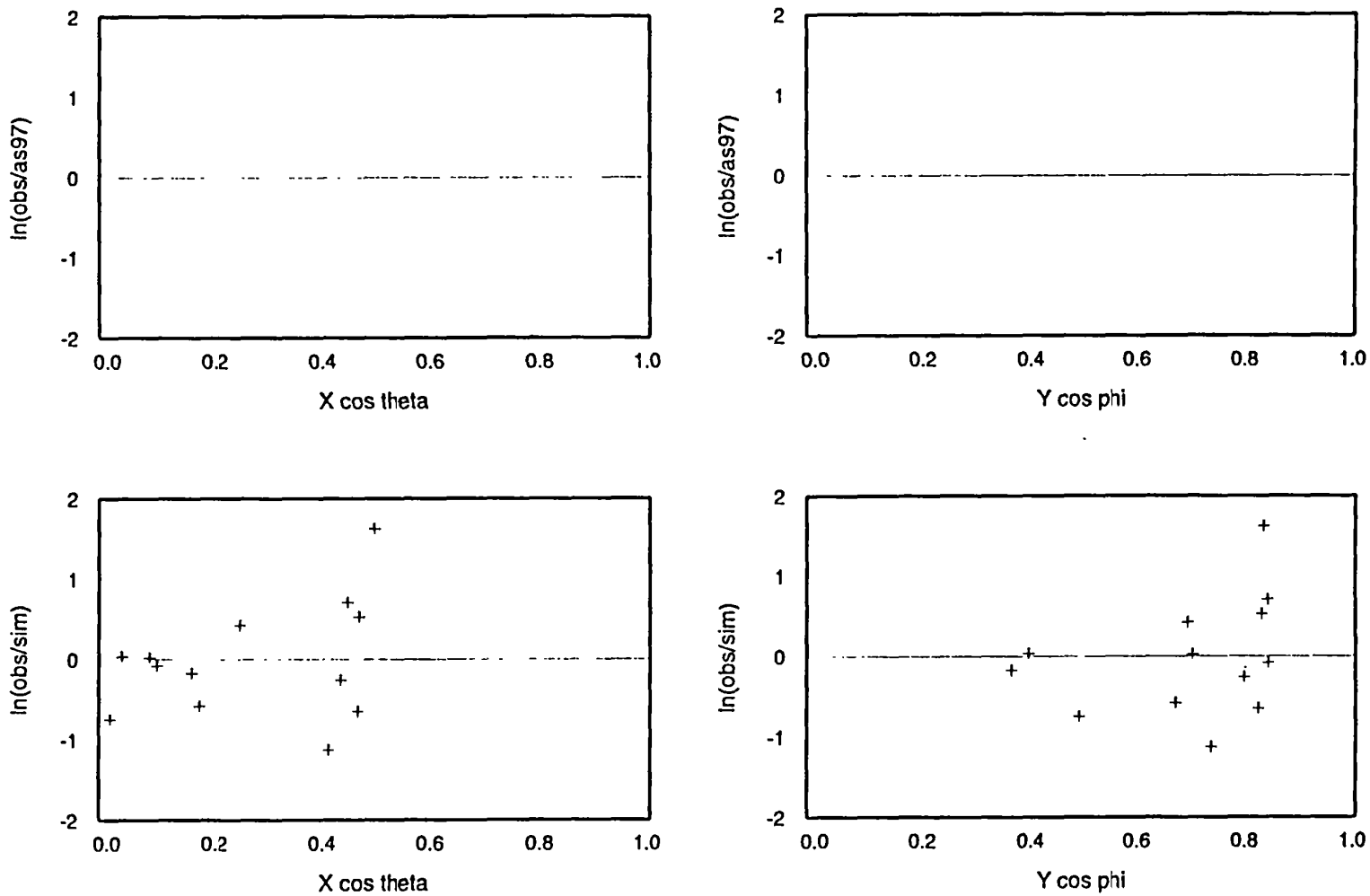

GMT Aug 24 14:54:34 1999 /u1/nancy/PEER-5/Loma/Comparisons/Resid_plots

Loma Prieta - Fault Normal

SA at 5.0 sec

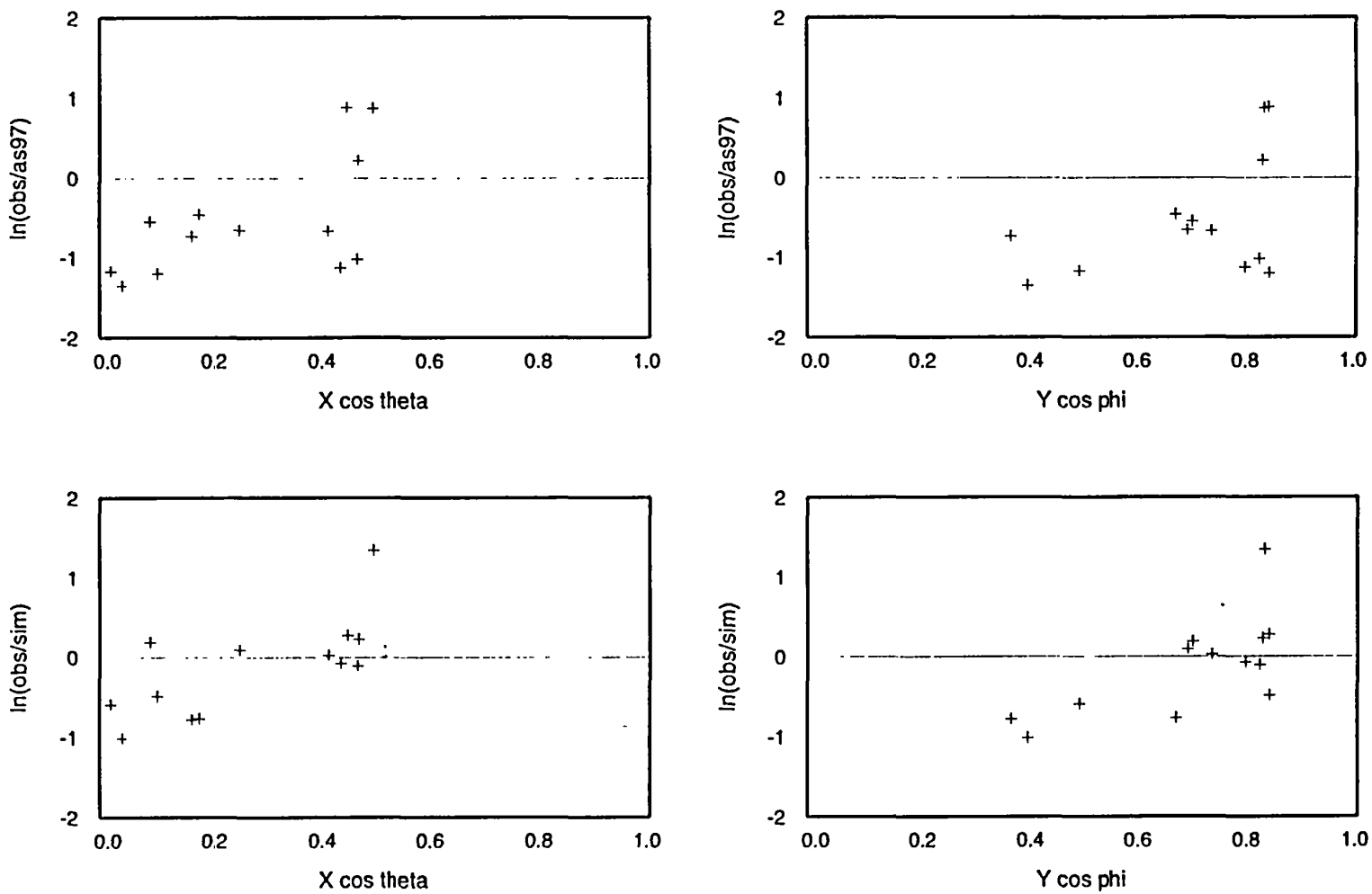

GMT Aug 24 14:54:49 1999 /u1/nancy/PEER-5/Loma/Comparisons/Resid_plots

Loma Prieta - Fault Parallel

SA at 5.0 sec

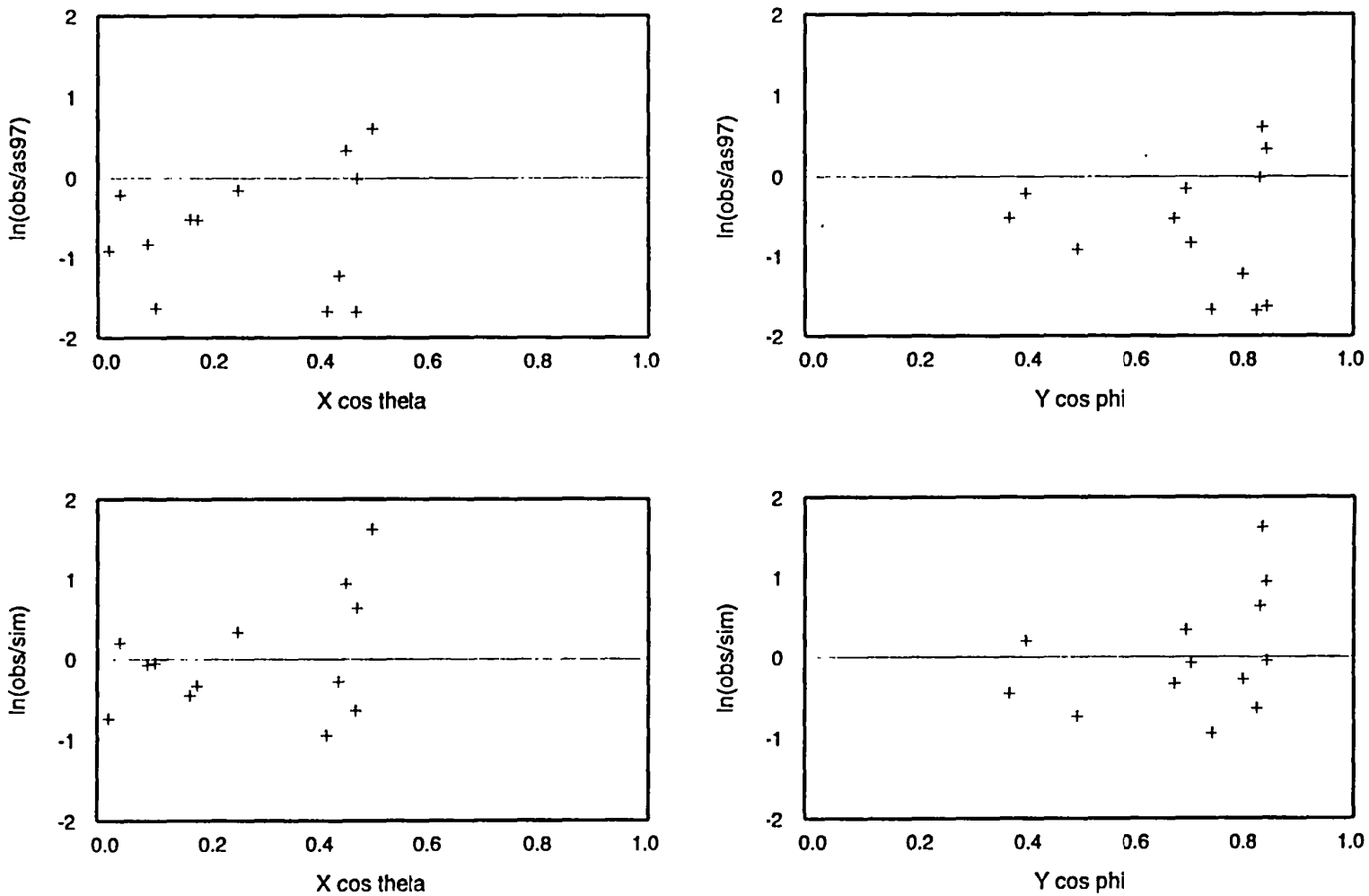

GMT Aug 24 14:55:02 1999 /u1/nancy/PEER-5/Loma/Comparisons/Resid_plots

Loma Prieta - Fault Normal

SA at 4.0 sec

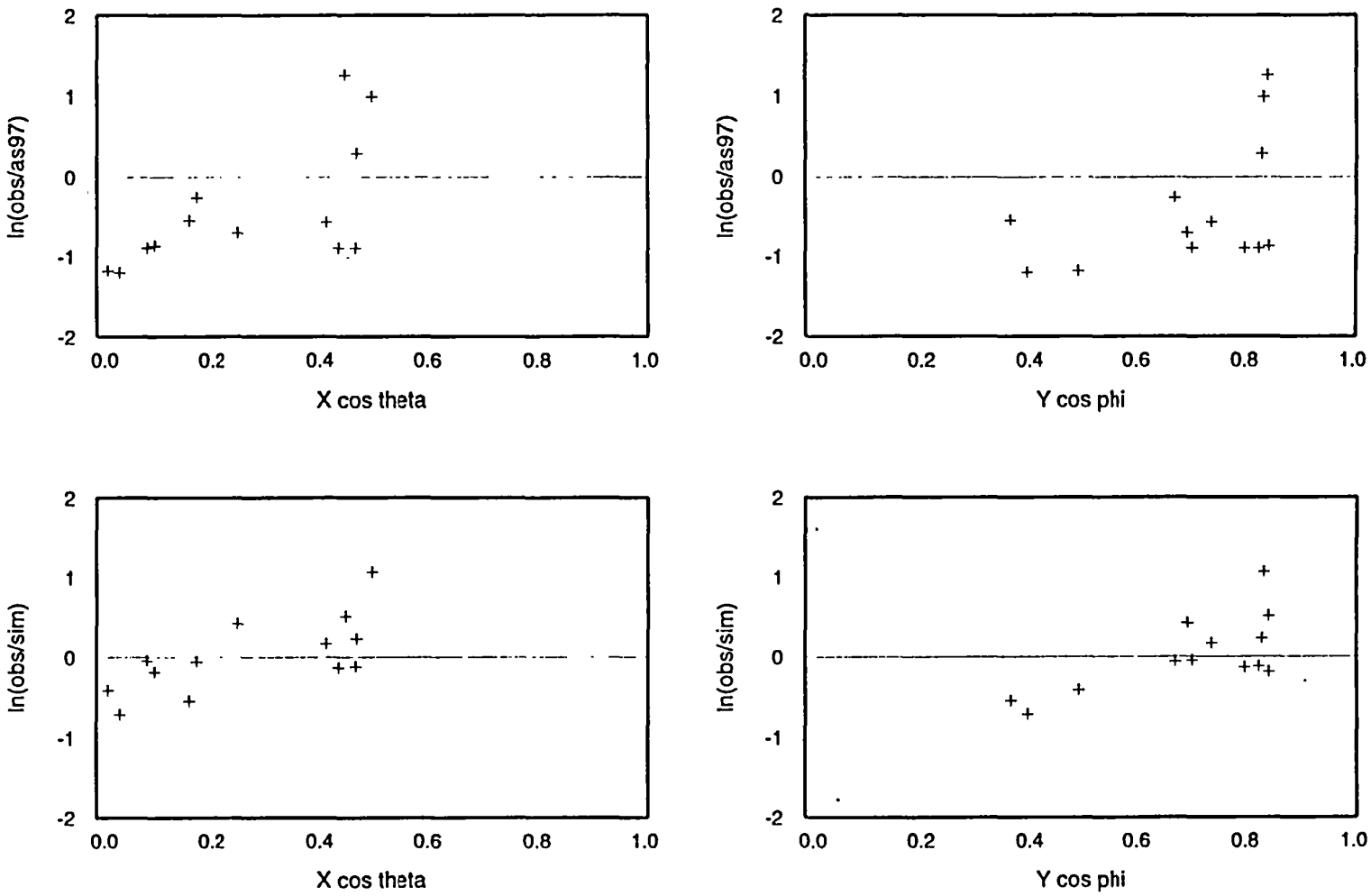

GMT Aug 24 14:55:17 1999 /u1/nancy/PEER-5/Loma/Comparisons/Resid_plots

Loma Prieta - Fault Parallel

SA at 4.0 sec

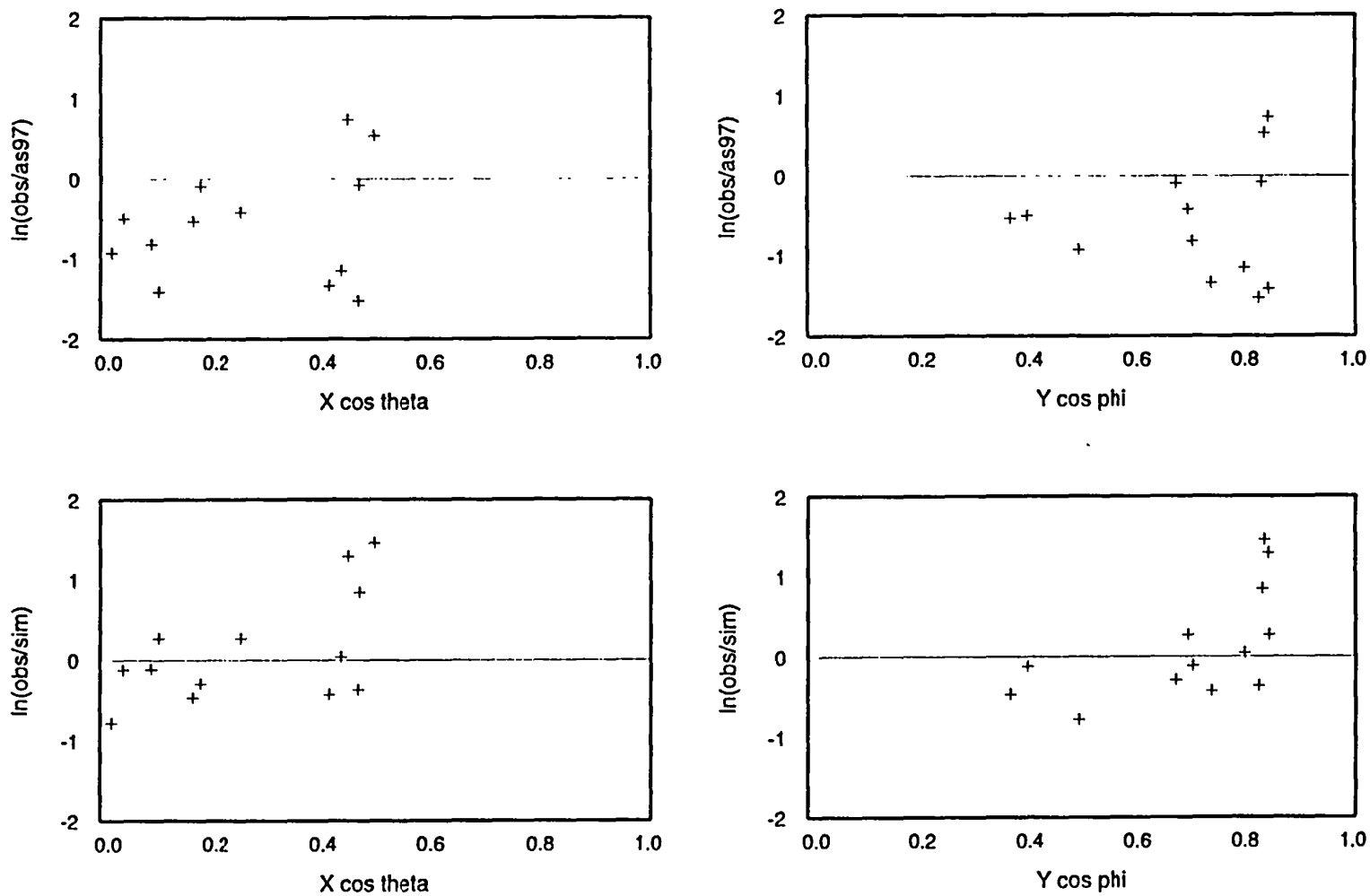

GMT Aug 24 14:55:30 1999 /u1/nancy/PEER-5/Loma/Comparisons/Resid_plots

Loma Prieta - Fault Normal

SA at 3.0 sec

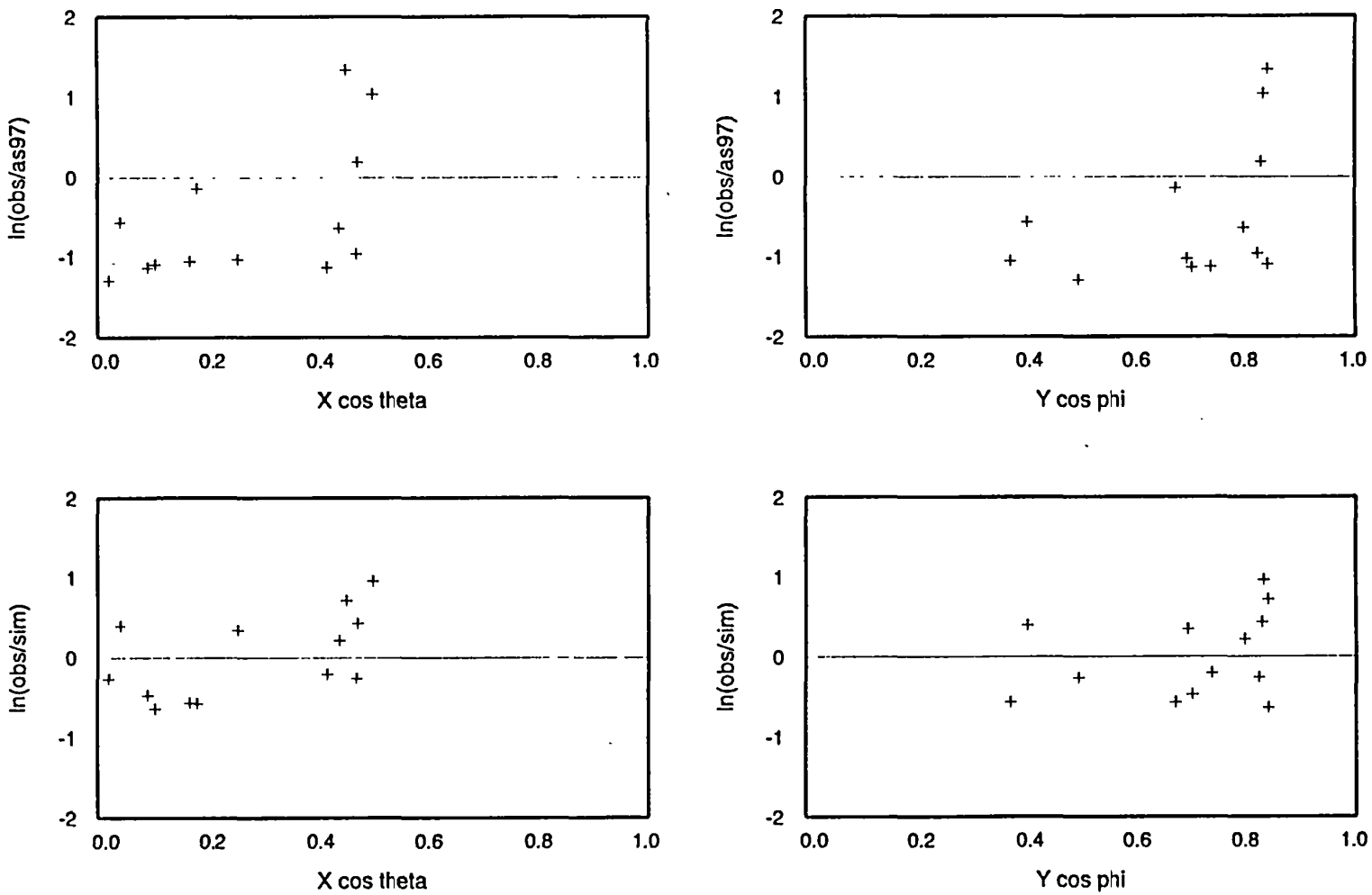

GMT Aug 24 14:55:43 1999 /u1/nancy/PEER-5/Loma/Comparisons/Resid_plots

Loma Prieta - Fault Parallel

SA at 3.0 sec

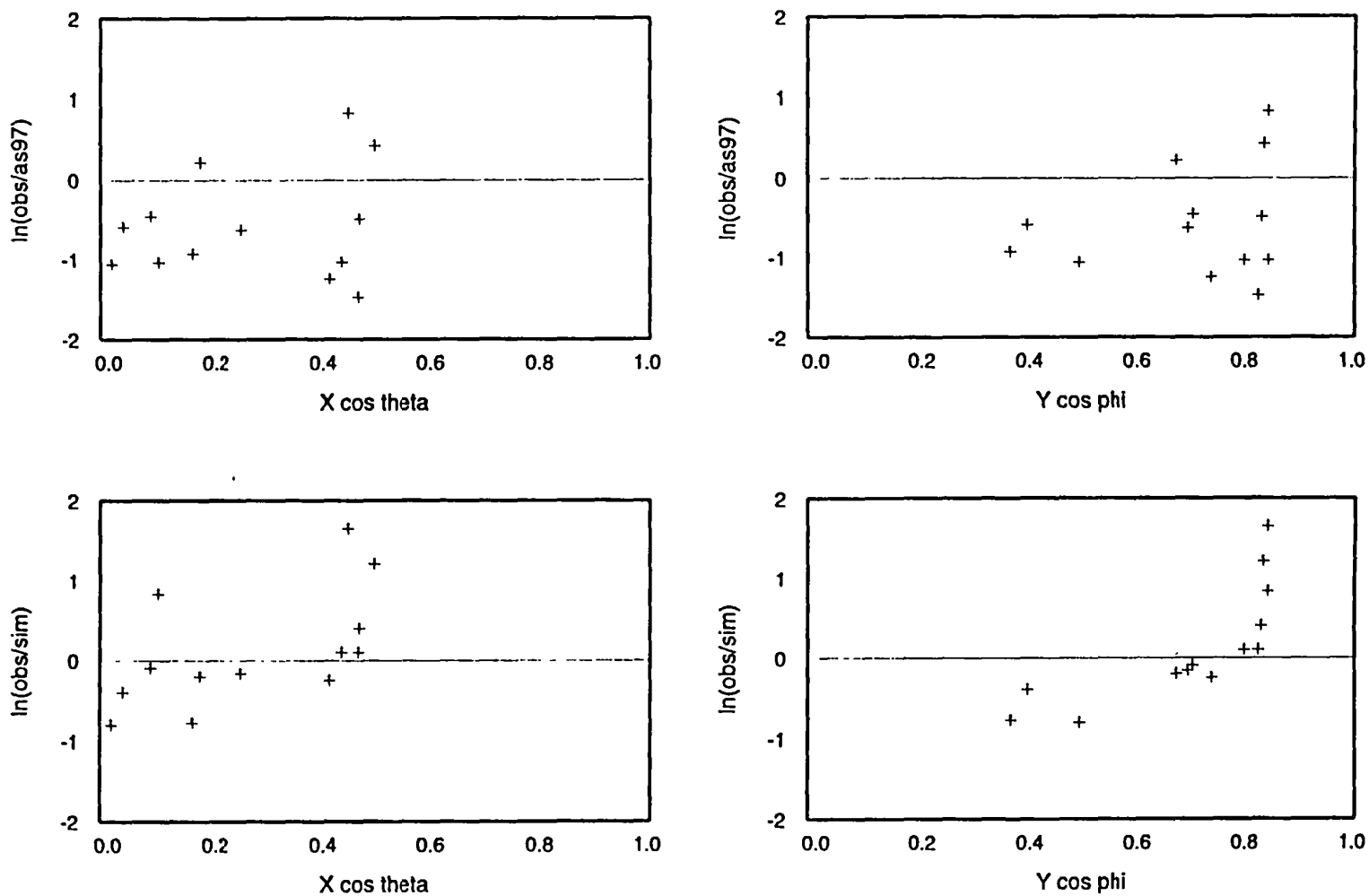

Loma Prieta - Fault Normal

SA at 2.0 sec

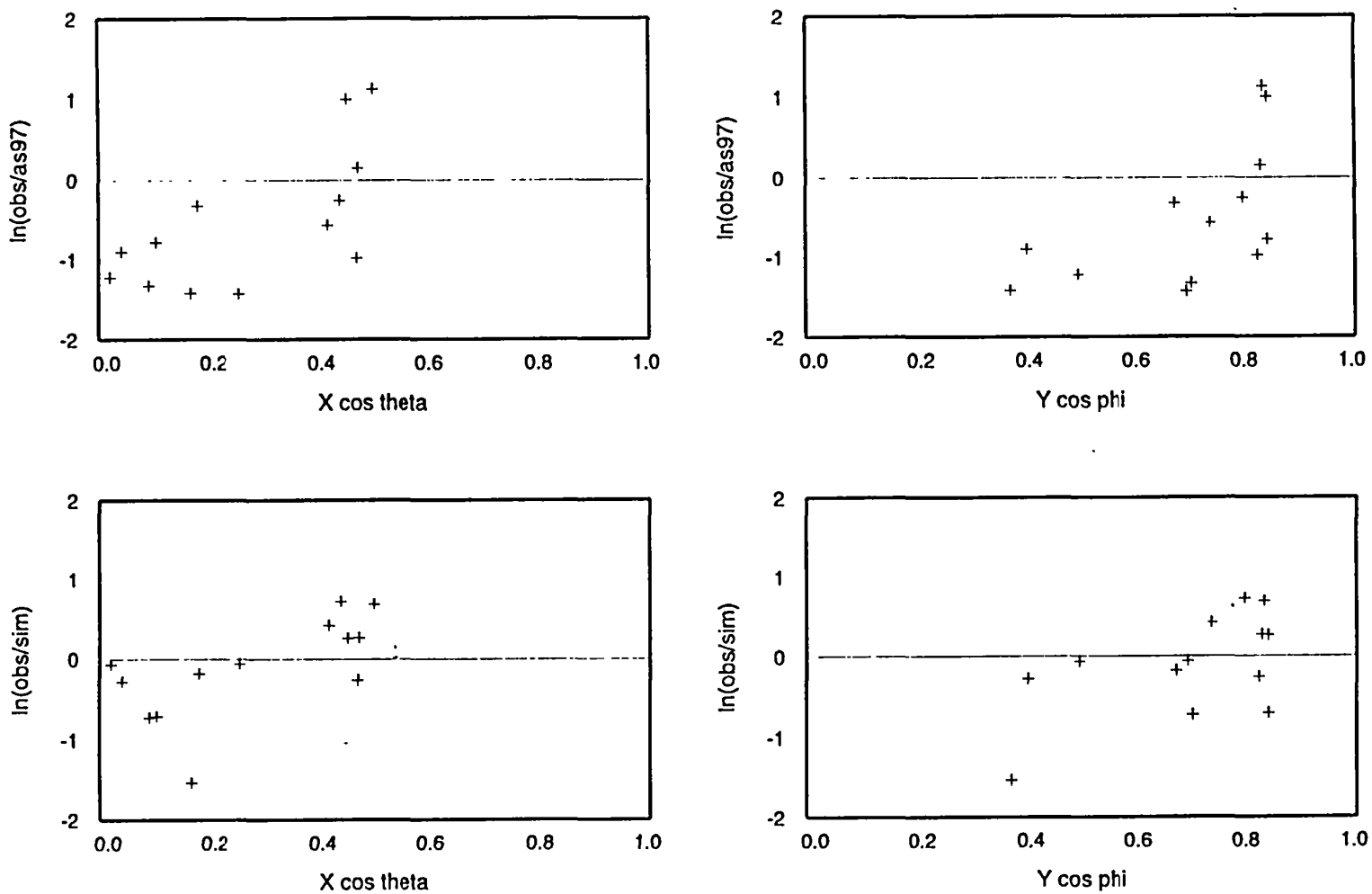

GMT Aug 24 14:57:46 1999 /u1/nancy/PEER-5/Loma/Comparisons/Resid_plots

Loma Prieta - Fault Parallel

SA at 2.0 sec

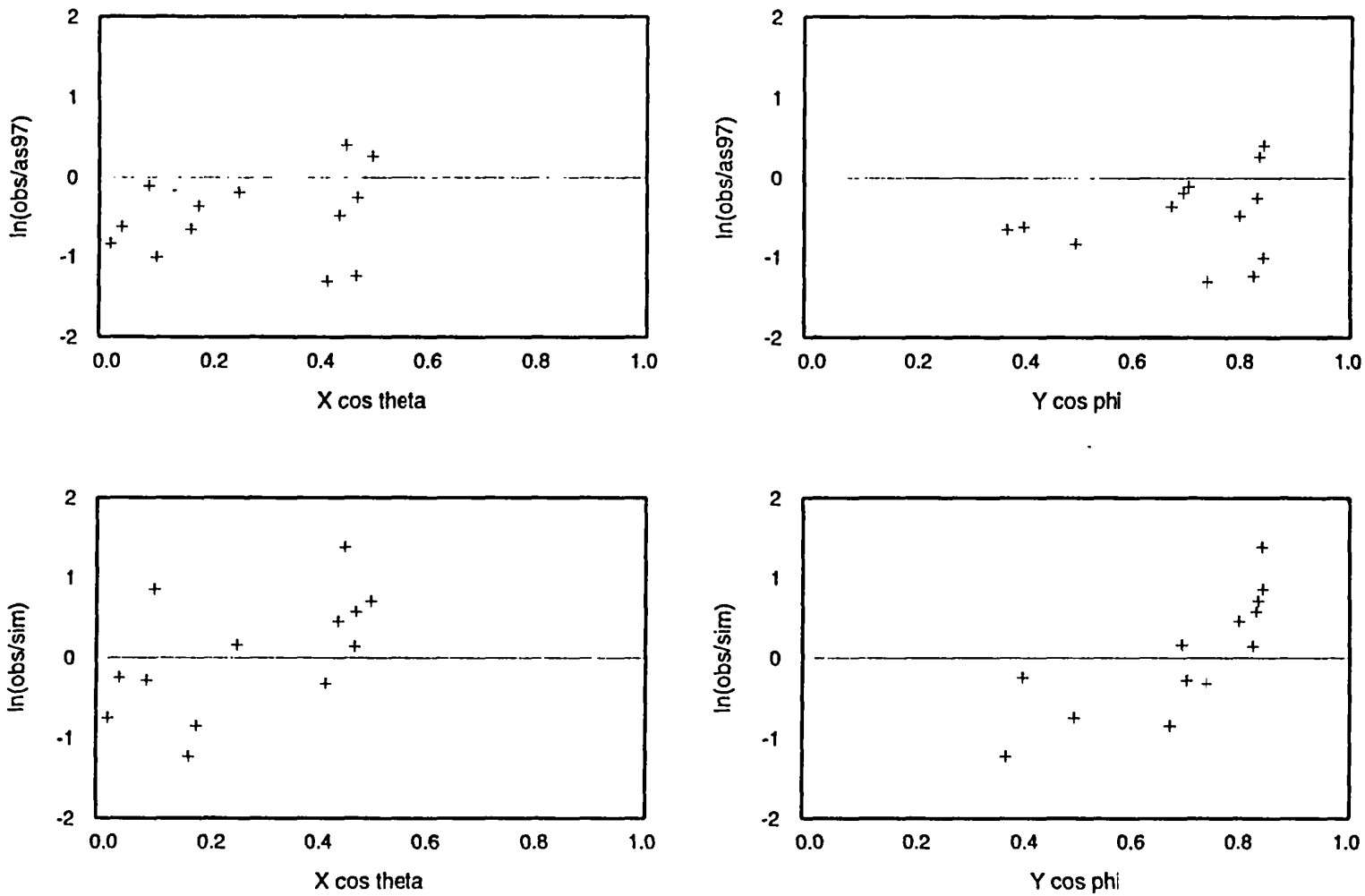

GMT Aug 24 14:57:58 1999 /u1/nancy/PEER-5/Loma/Comparisons/Resid_plots

Loma Prieta - Fault Normal

SA at 1.5 sec

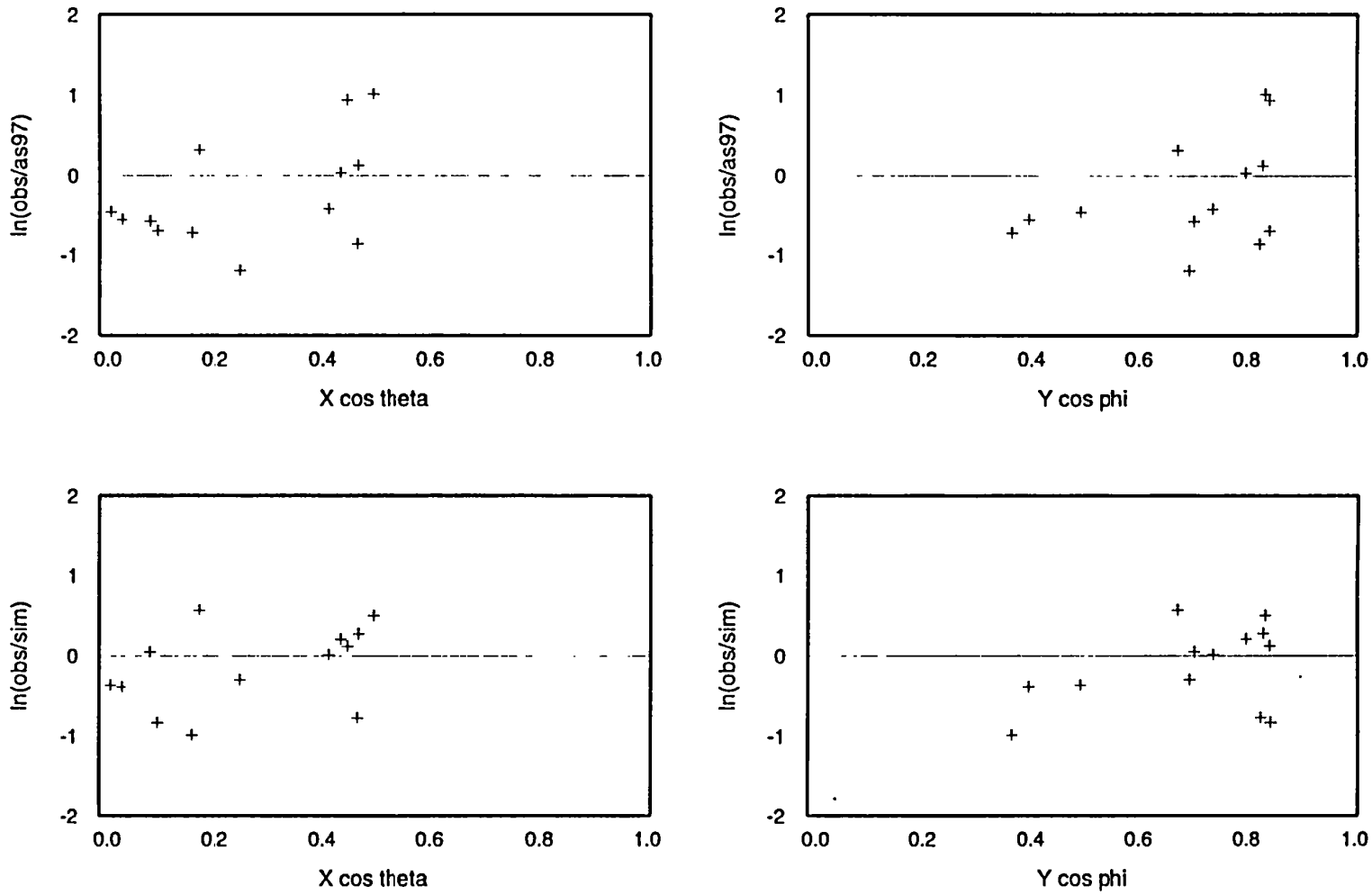

GMT Aug 24 14:58:10 1999 /u1/nancy/PEER-5/Loma/Comparisons/Resid_plots

Loma Prieta - Fault Parallel

SA at 1.5 sec

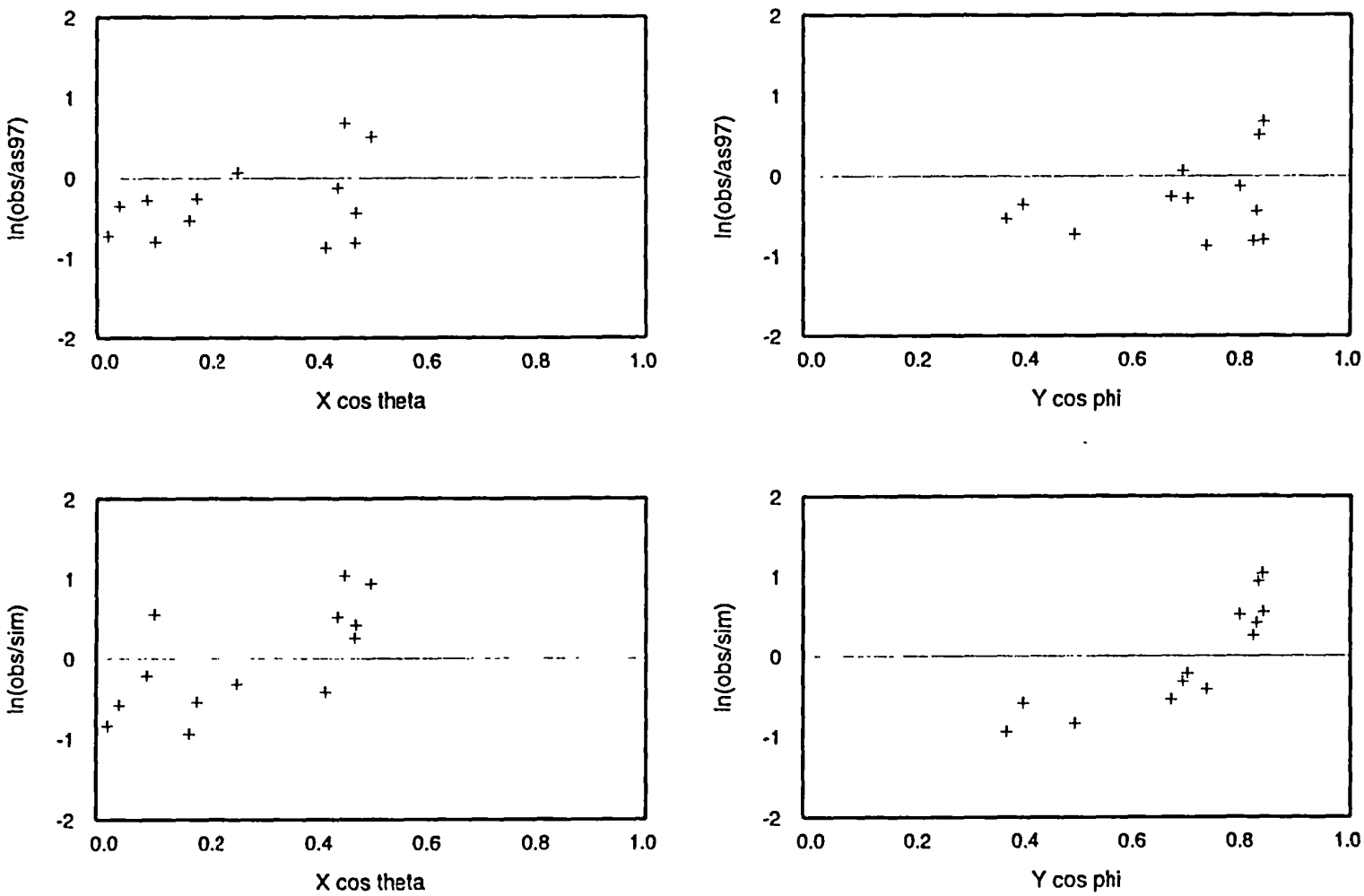

GMT Aug 24 14:58:22 1999 /u1/nancy/PEER-5/Loma/Comparisons/Resid_plots

Loma Prieta - Fault Normal

SA at 1.0 sec

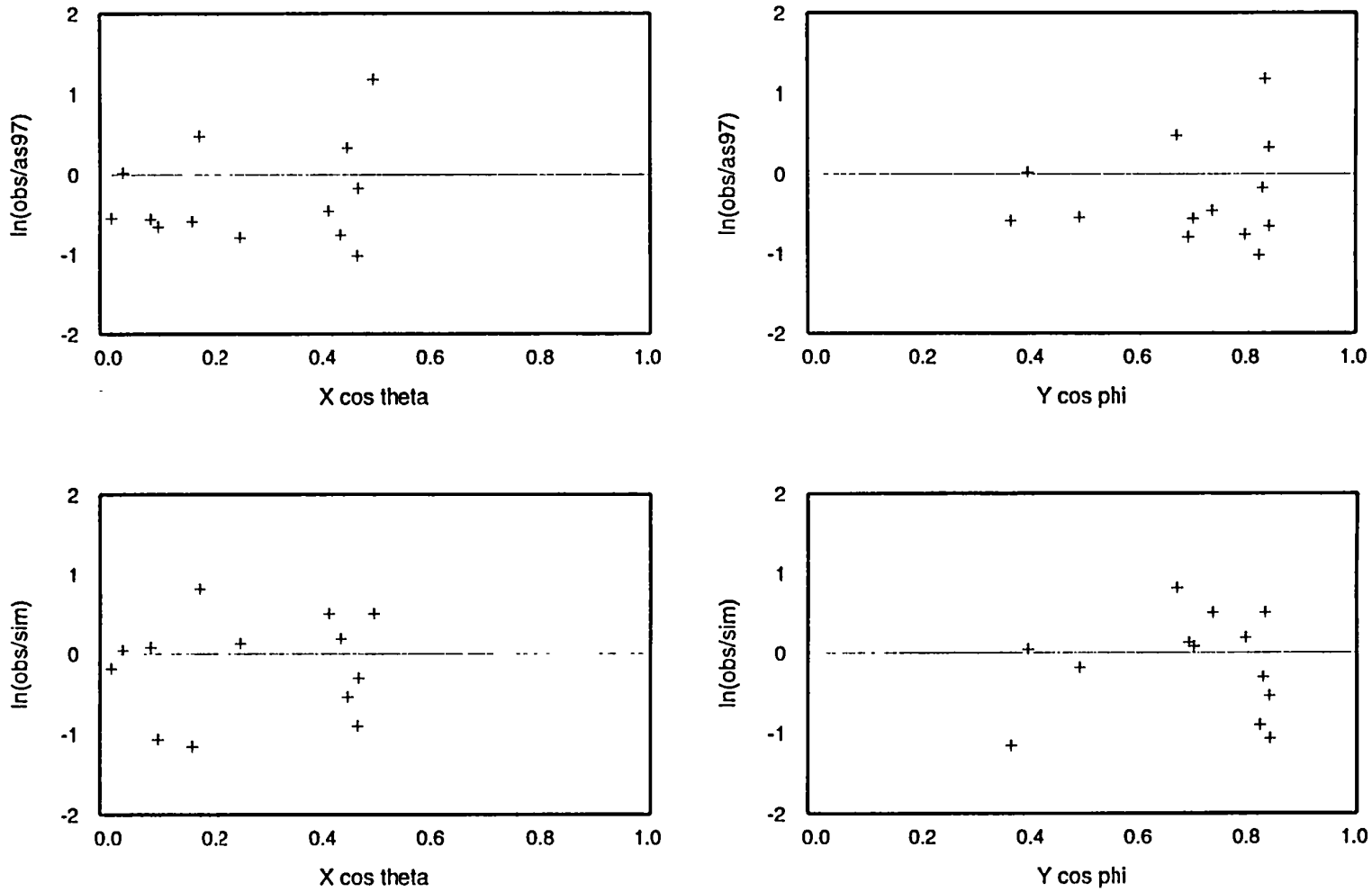

GMT Aug 24 14:58:35 1999 /u1/nancy/PEER-5/Loma/Comparisons/Resid_plots

Loma Prieta - Fault Parallel

SA at 1.0 sec

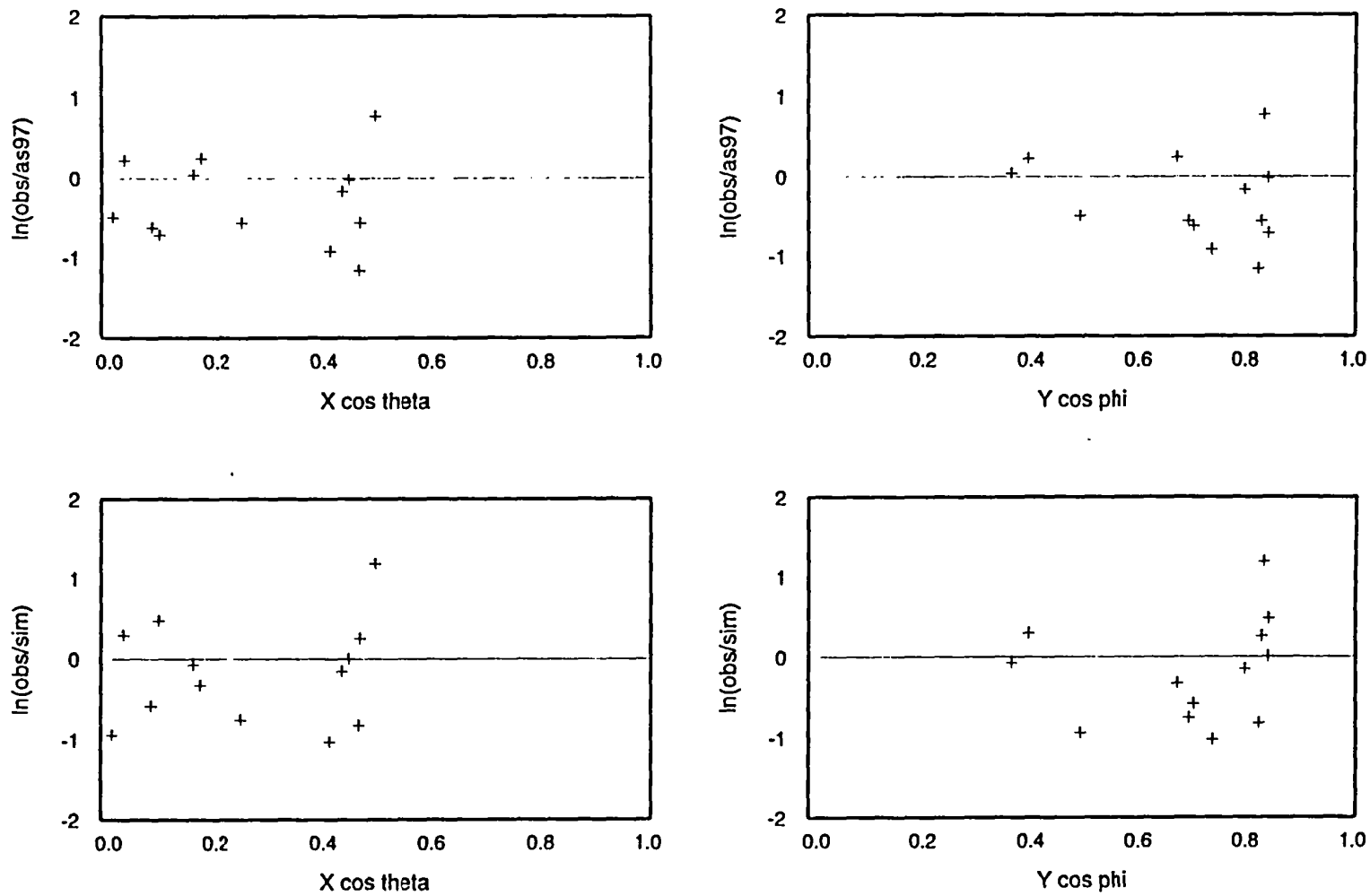

Station	Correlation FN	Correlation FP	Least Squares FN	Least Squares FP	Response Spectra FN	Response Spectra FP	Fourier Spectra FN	Fourier Spectra FP
bars	0.752		0.329		0.427	-0.044	0.377	0.153
cool	0.618		-0.155		-0.698	-0.224	-0.595	-0.253
dhsp	0.359		0.054		0.533	0.951	0.623	1.080
frti	0.618		0.181		0.073	0.705	-0.128	0.703
josh	0.311		0.029		1.032	0.336	0.994	0.423
lcss	0.622		-0.013		-0.475	-0.559	-0.679	-0.455
mvfs	0.273		0.038		1.080	0.780	1.041	0.929
nplm	0.374		0.055		0.962	1.132	0.965	1.179
plma	0.584		0.184		0.553	0.873	0.708	0.981
yerm	0.633		0.011		0.439	0.707	0.352	0.653
Average	0.514		0.071		0.393	0.466	0.366	0.539
Sigma	0.167		0.132		0.612	0.838	0.620	1.132
Sigma Mean	0.053		0.042		0.193	0.265	0.196	0.358

Landers - Fault Normal

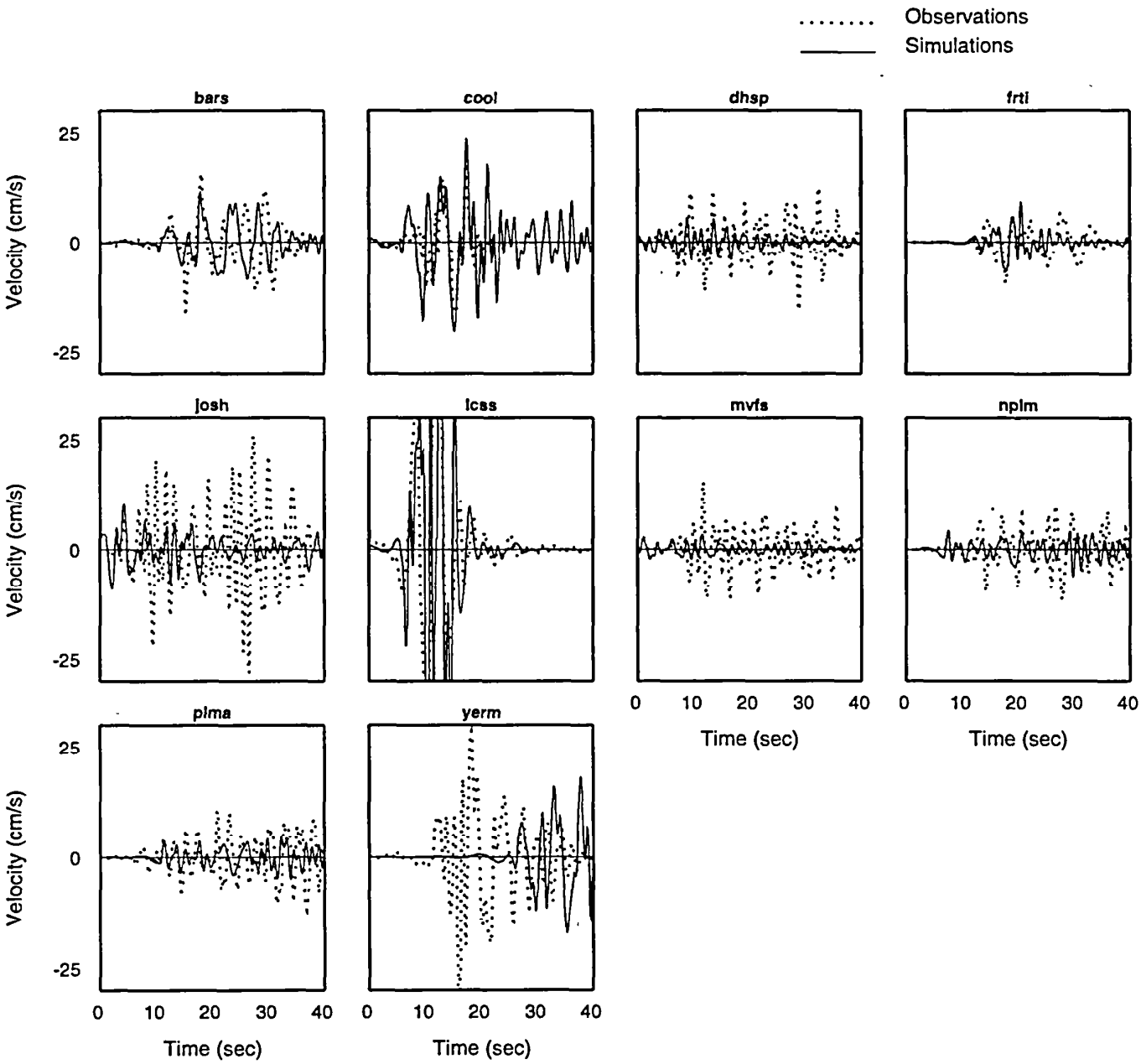

Landers - Fault Parallel

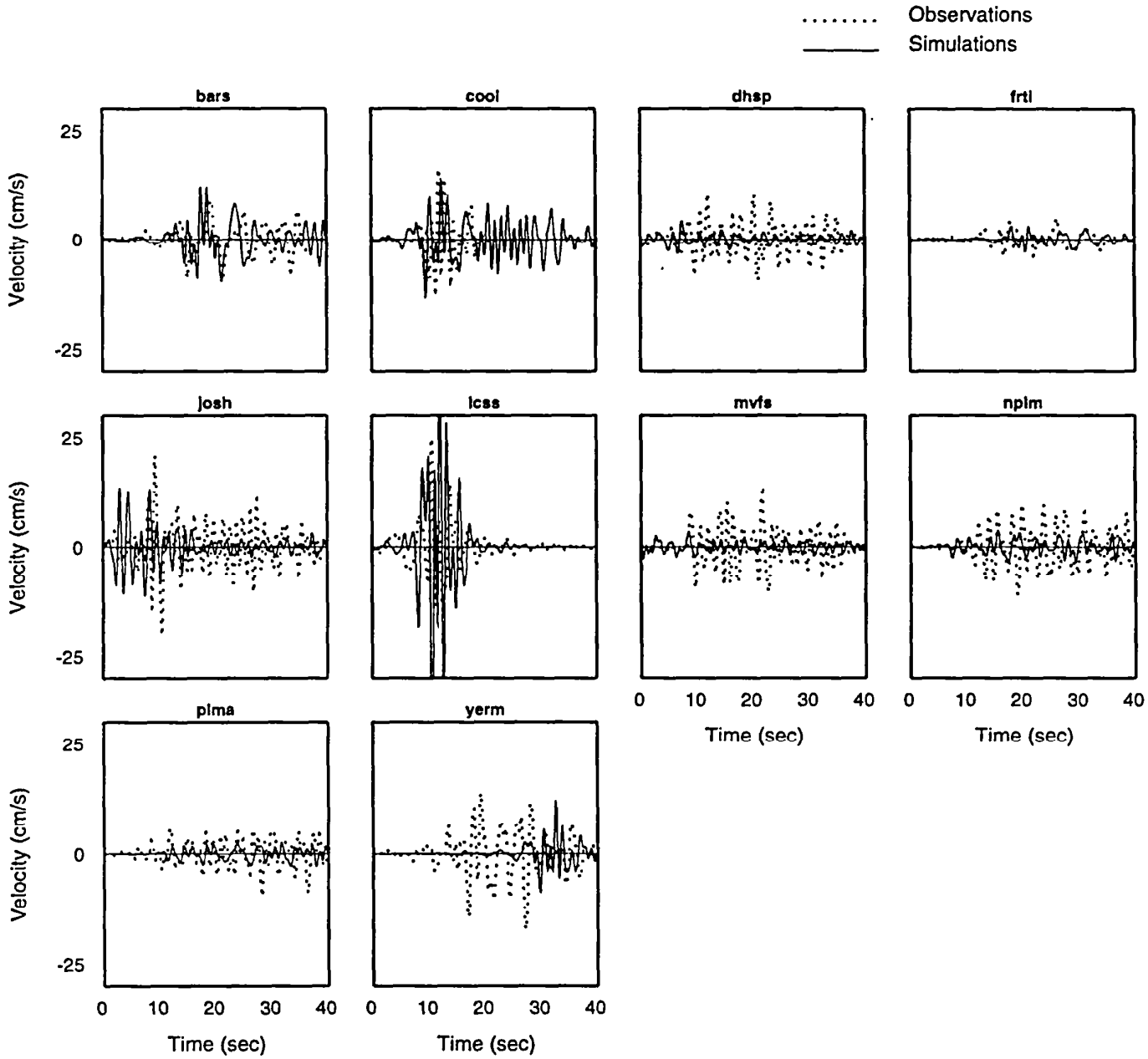

Landers - Fault Normal

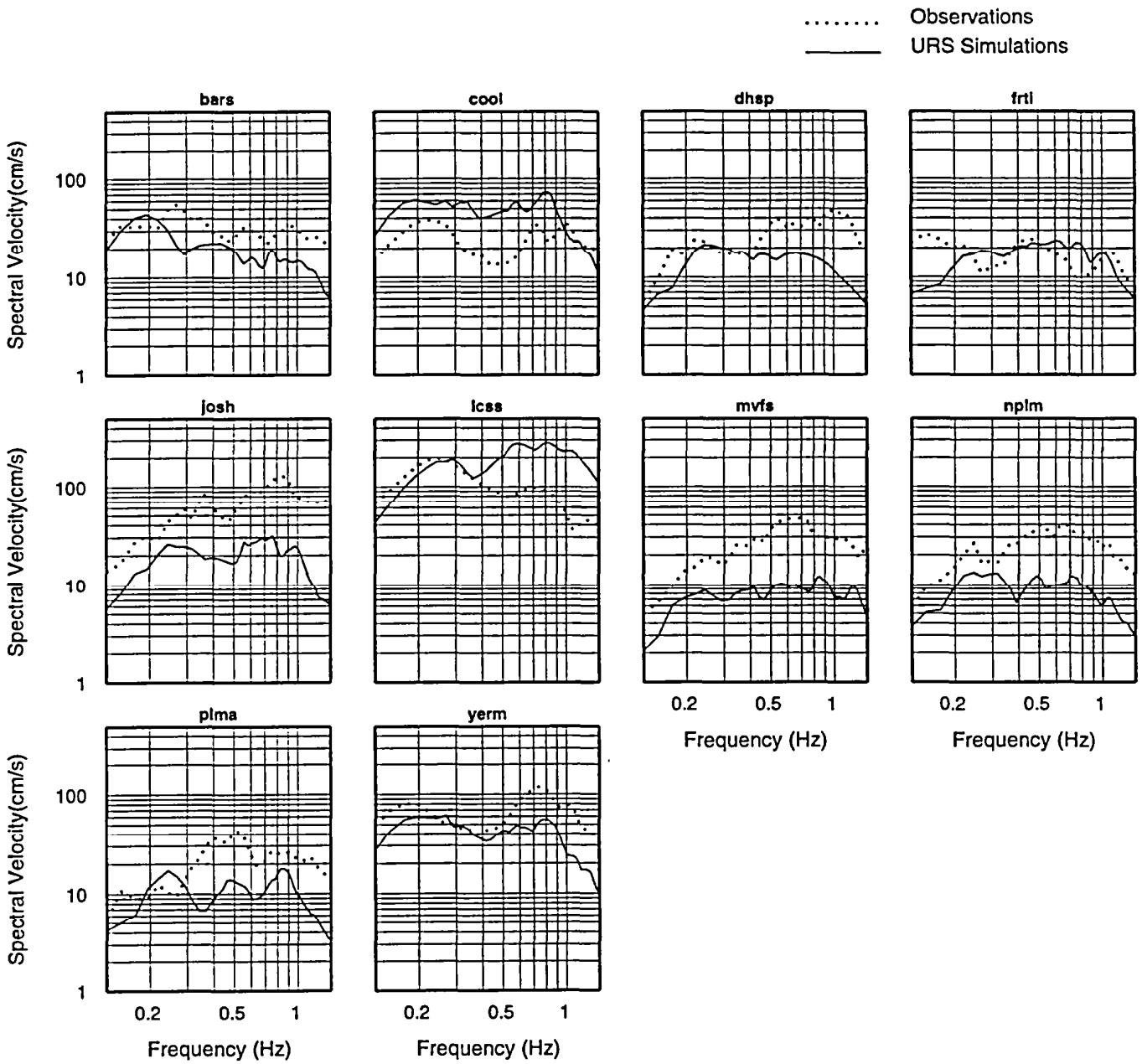

Landers - Fault Parallel

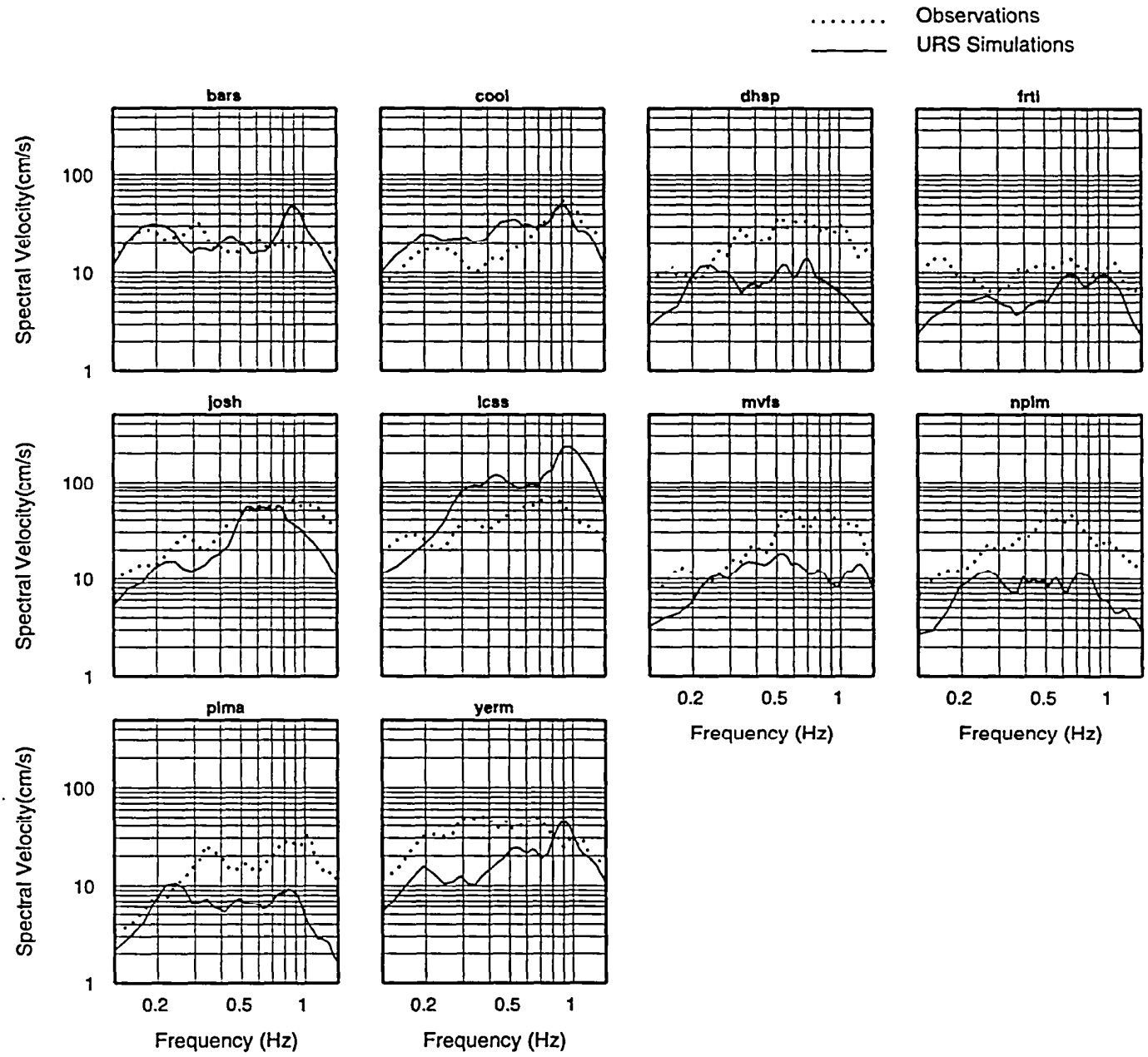

Landers - Fault Normal

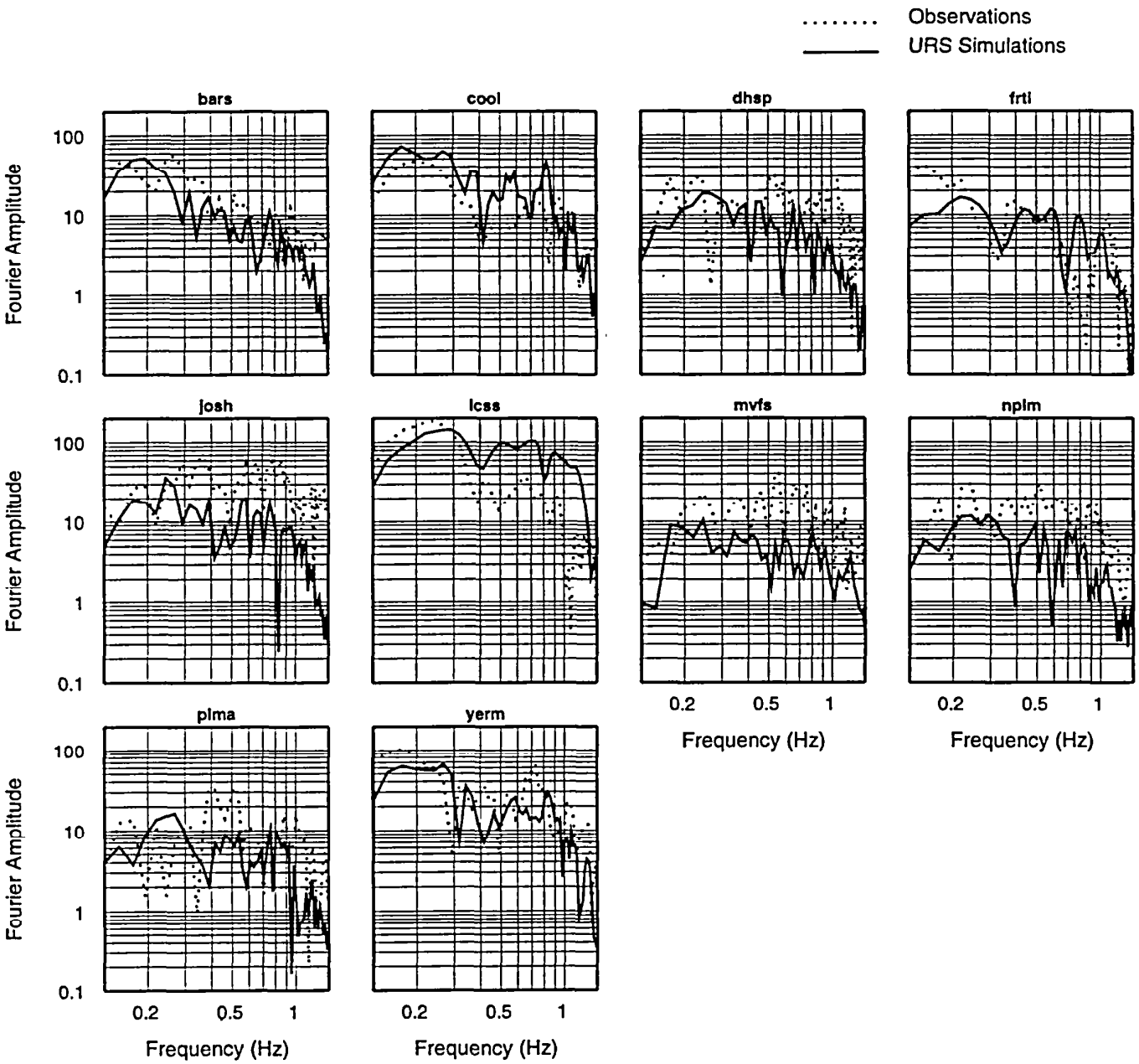

Landers - Fault Parallel

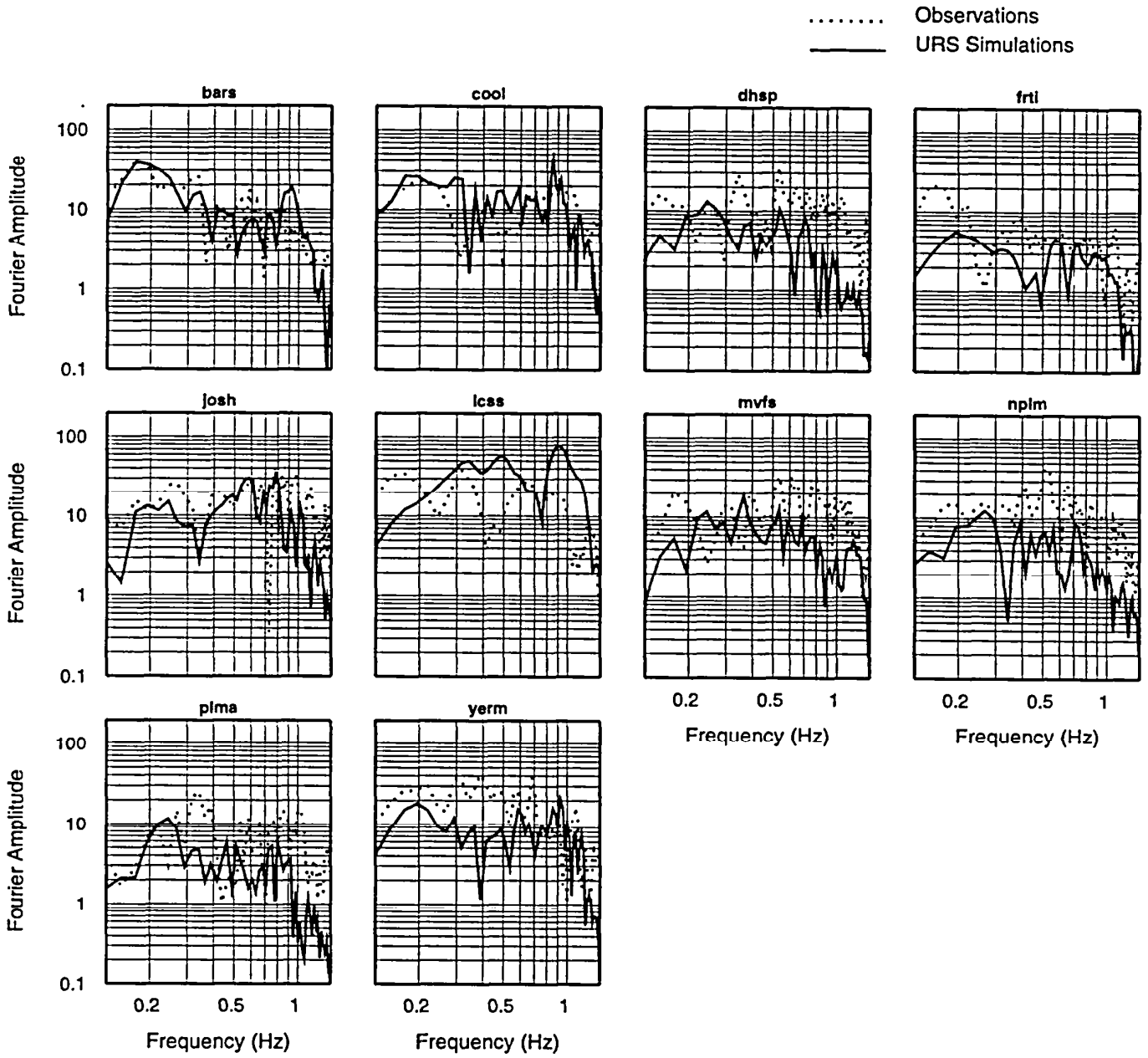

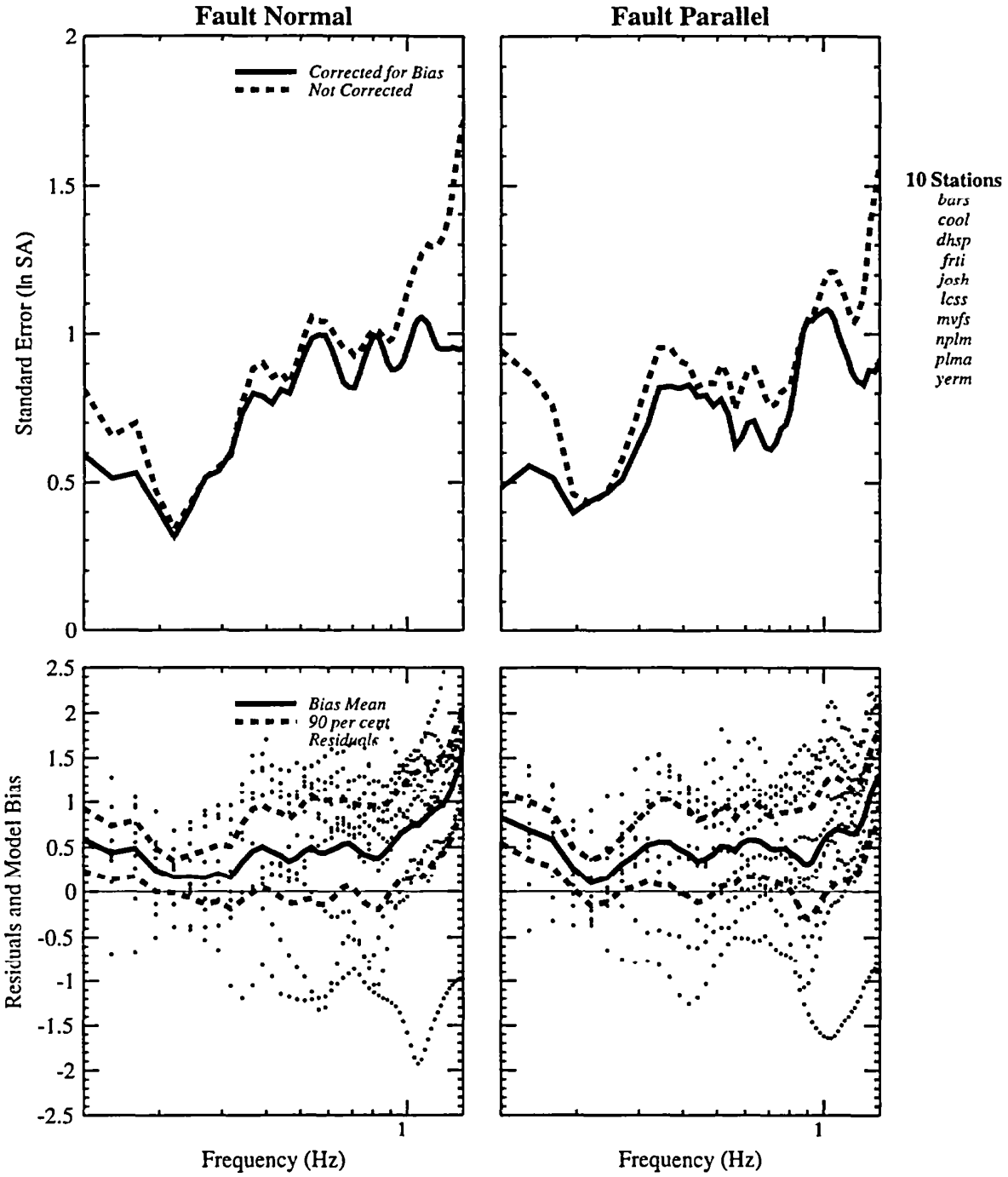

Landers Spectral Acceleration Goodness of Fit
Observed minus Synthetic (obs - sim)

n/smth0 Tue Aug 31 14:16:48 PDT 1999
/u2/mavy/PEER-5/Landers/GoodFit/mplot_goodfit.csh

Landers - Filter 0.125-1.43 Hz, Norma BB Sims - josh

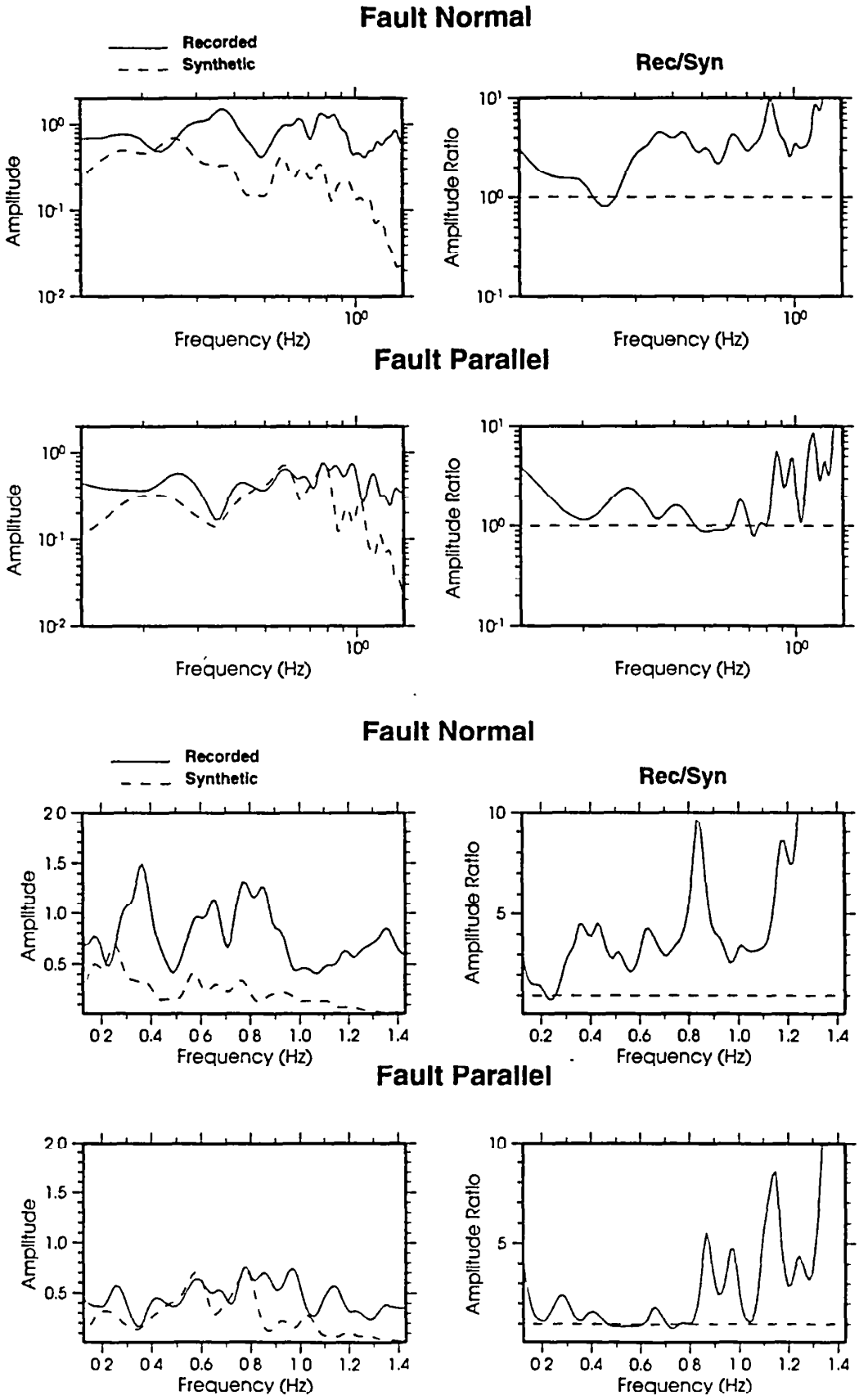

GMT Aug 24 15 26:24 1999 /net/coda/u2/arben/landers/shells

Landers - Filter 0.125-1.43 Hz, Norma BB Sims - frti

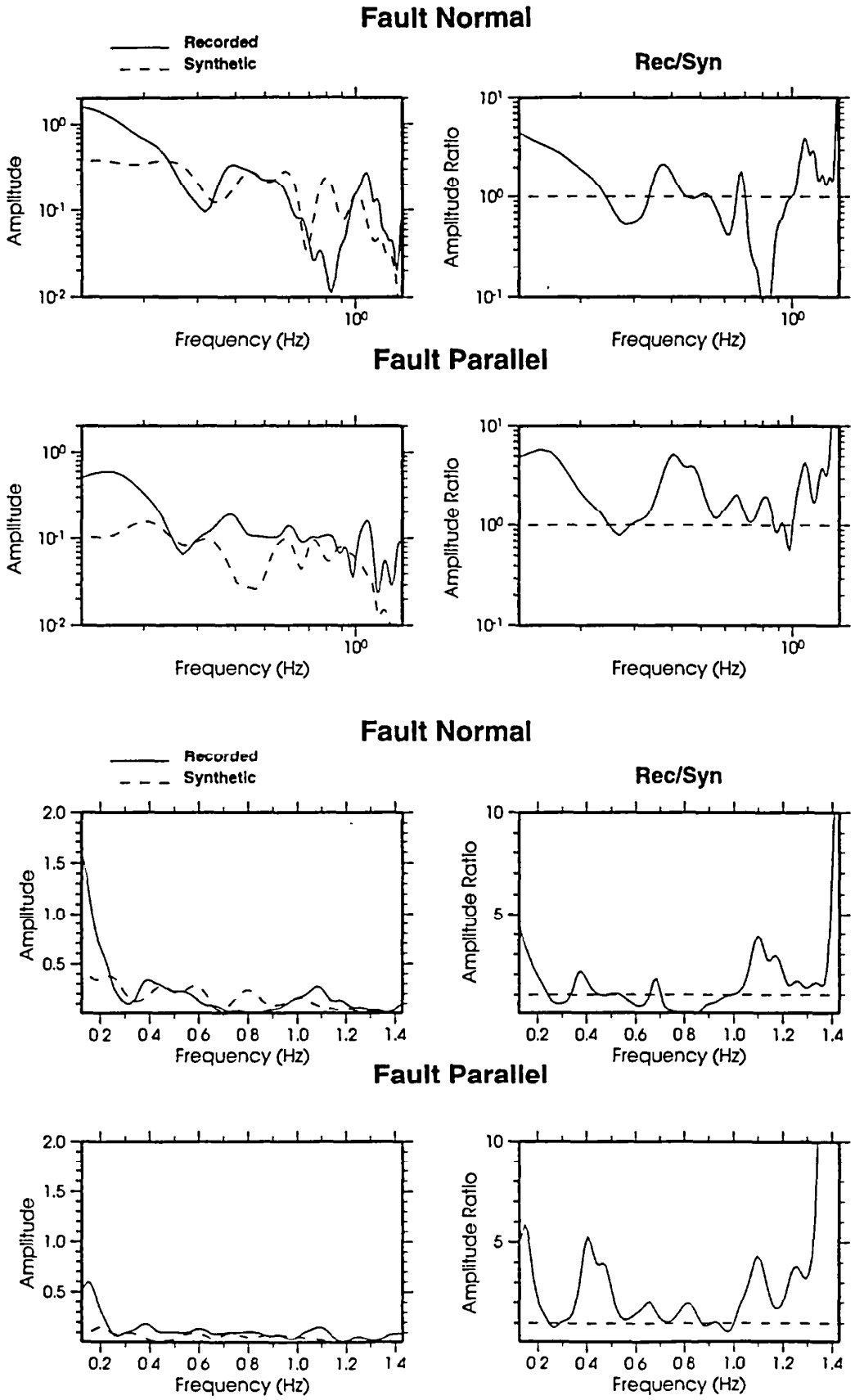

GMT Aug 24 15:25.58 1999 /net/coda/u2/arben/landers/shells

Landers - Filter 0.125-1.43 Hz, Norma BB Sims - cool

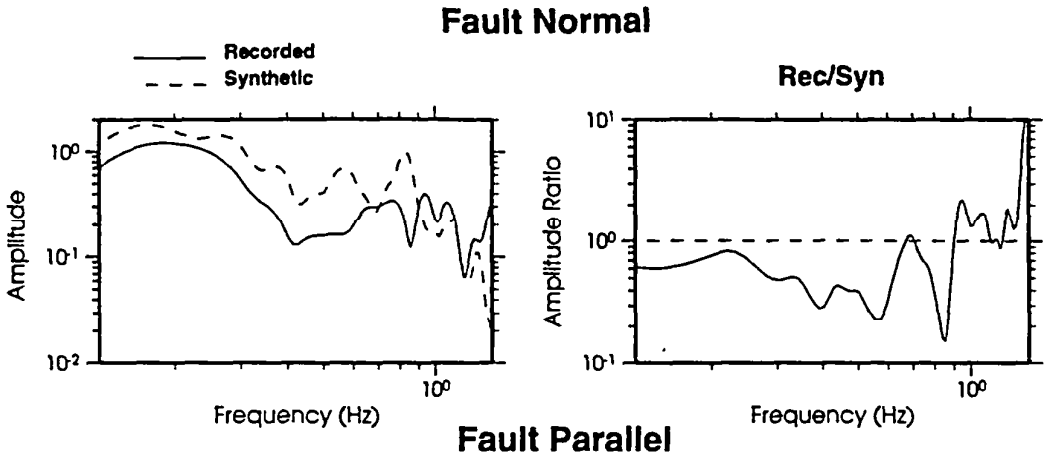

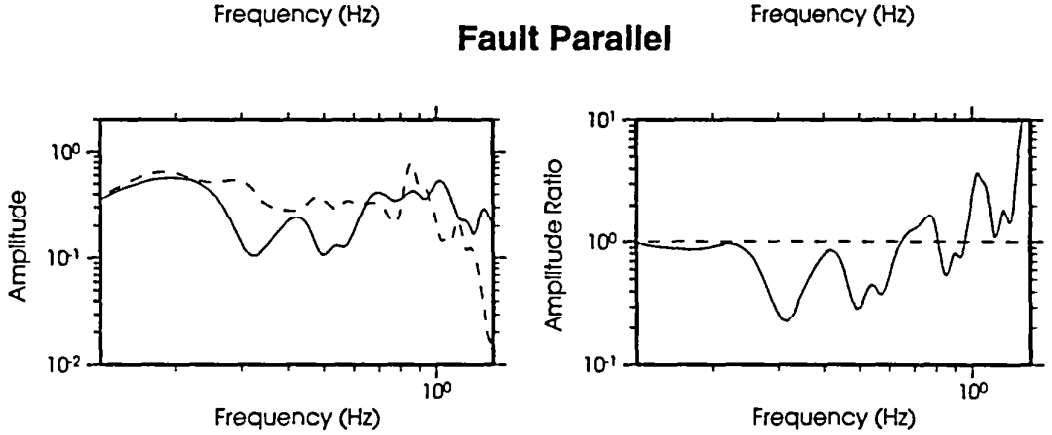

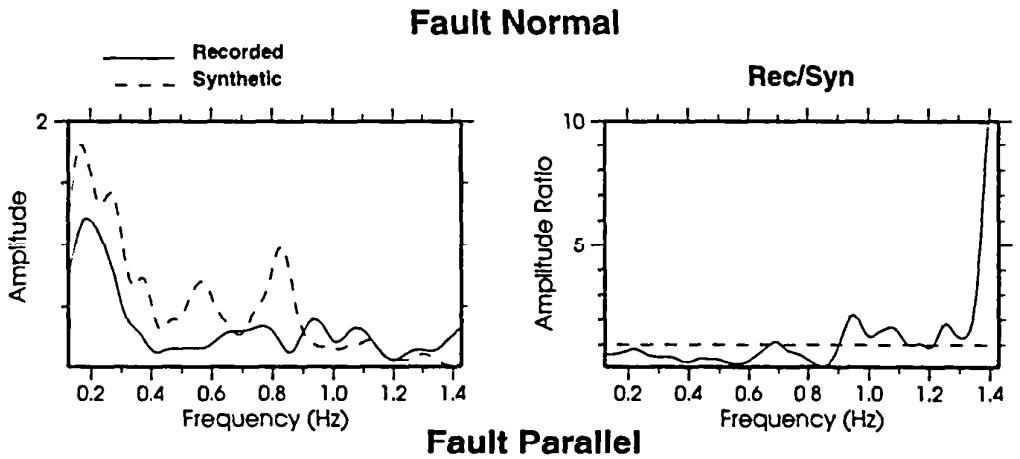

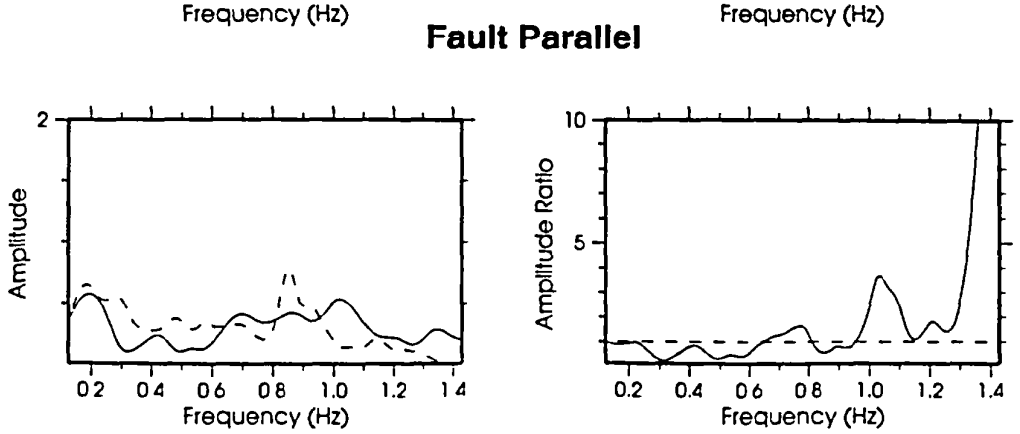

GMT Aug 24 15:25:04 1999 /net/coda/u2/arben/landers/shells

Landers - Filter 0.125-1.43 Hz, Norma BB Sims - bars

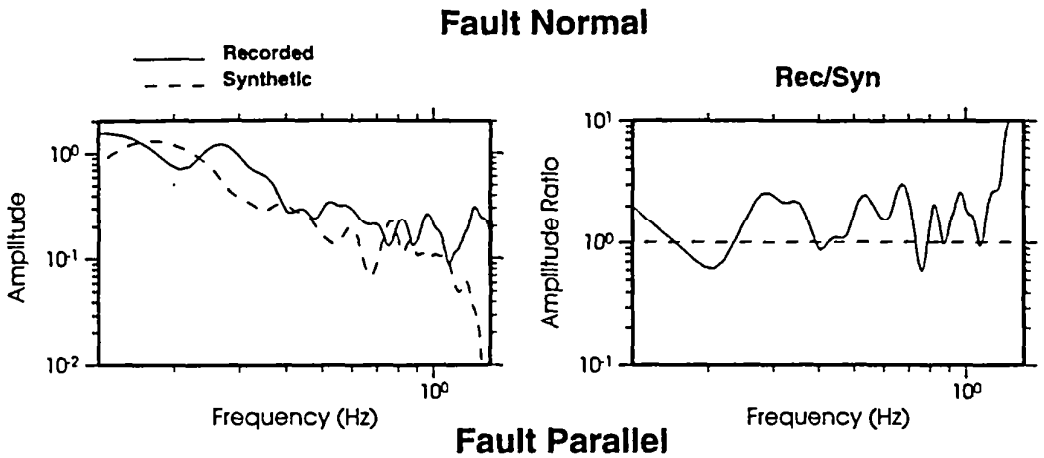

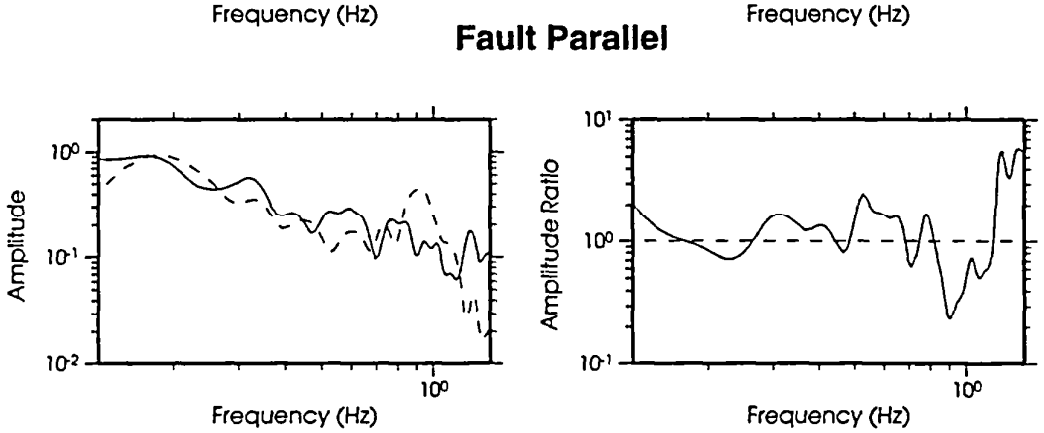

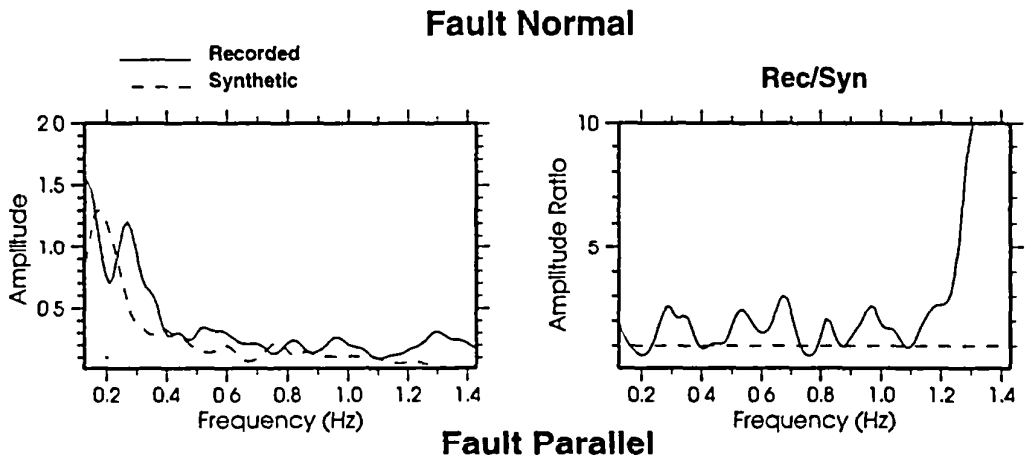

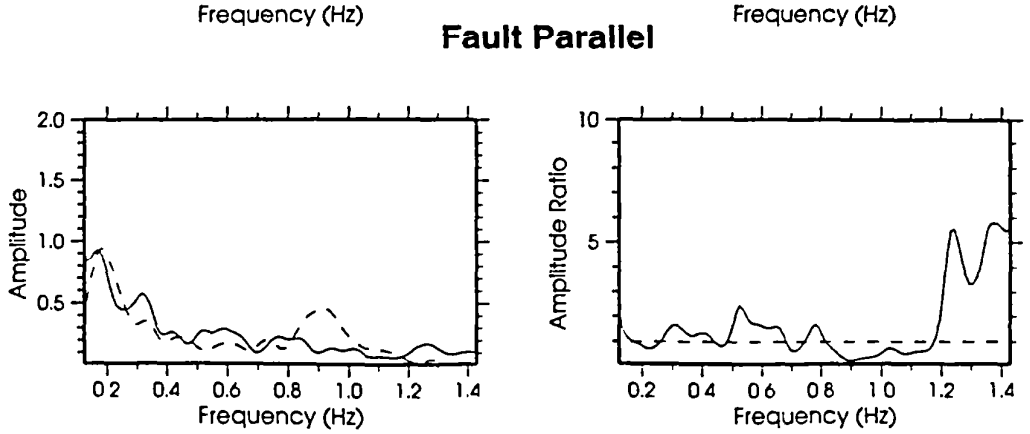

GMT Aug 24 15:24 38 1999 /net/coda/u2/arben/landers/shells

Landers - Filter 0.125-1.43 Hz, Norma BB Sims - yerm

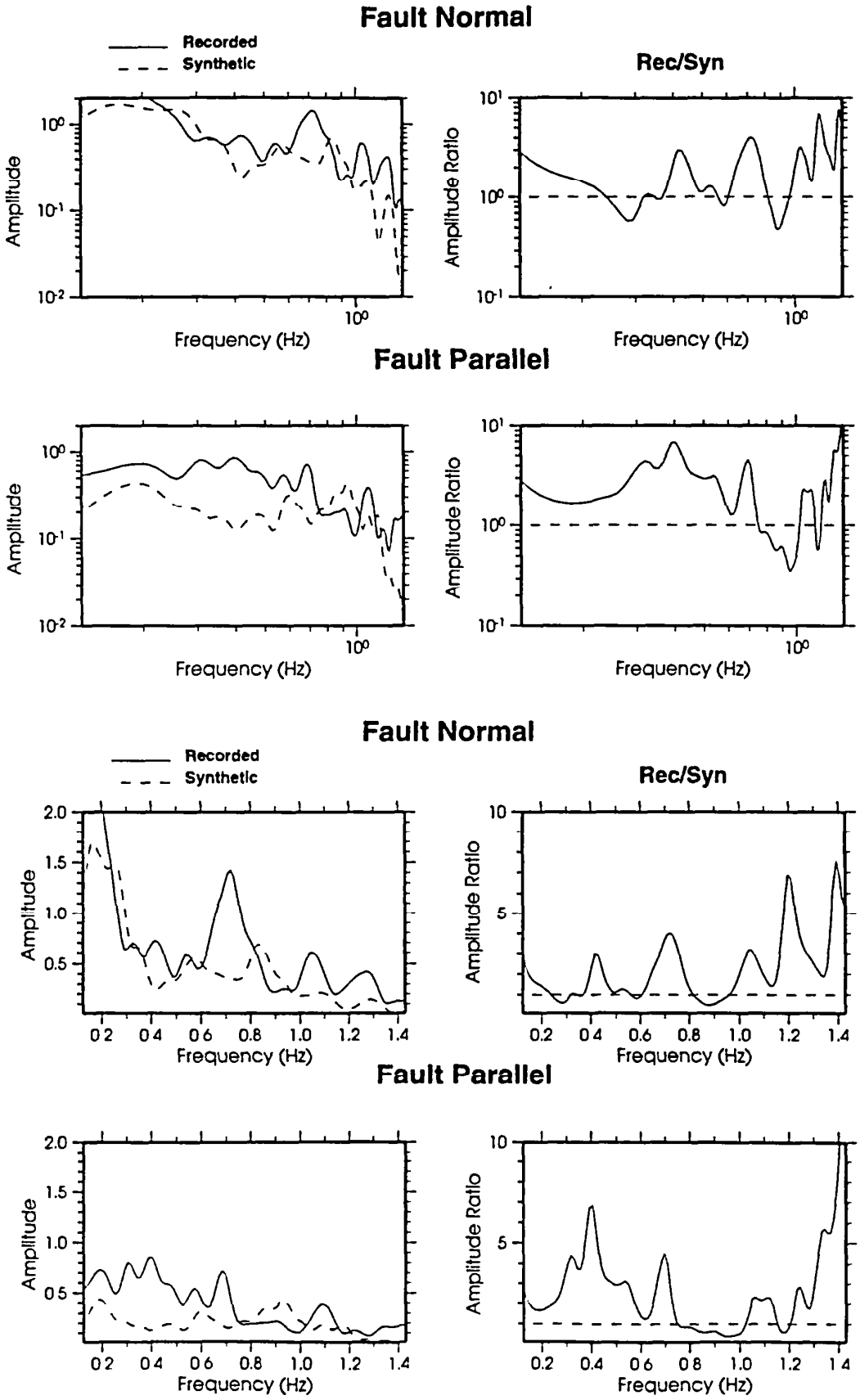

GMT Aug 24 15 28 18 1999 /net/coda/u2/arben/landers/shells

Landers - Filter 0.125-1.43 Hz, Norma BB Sims - lcss

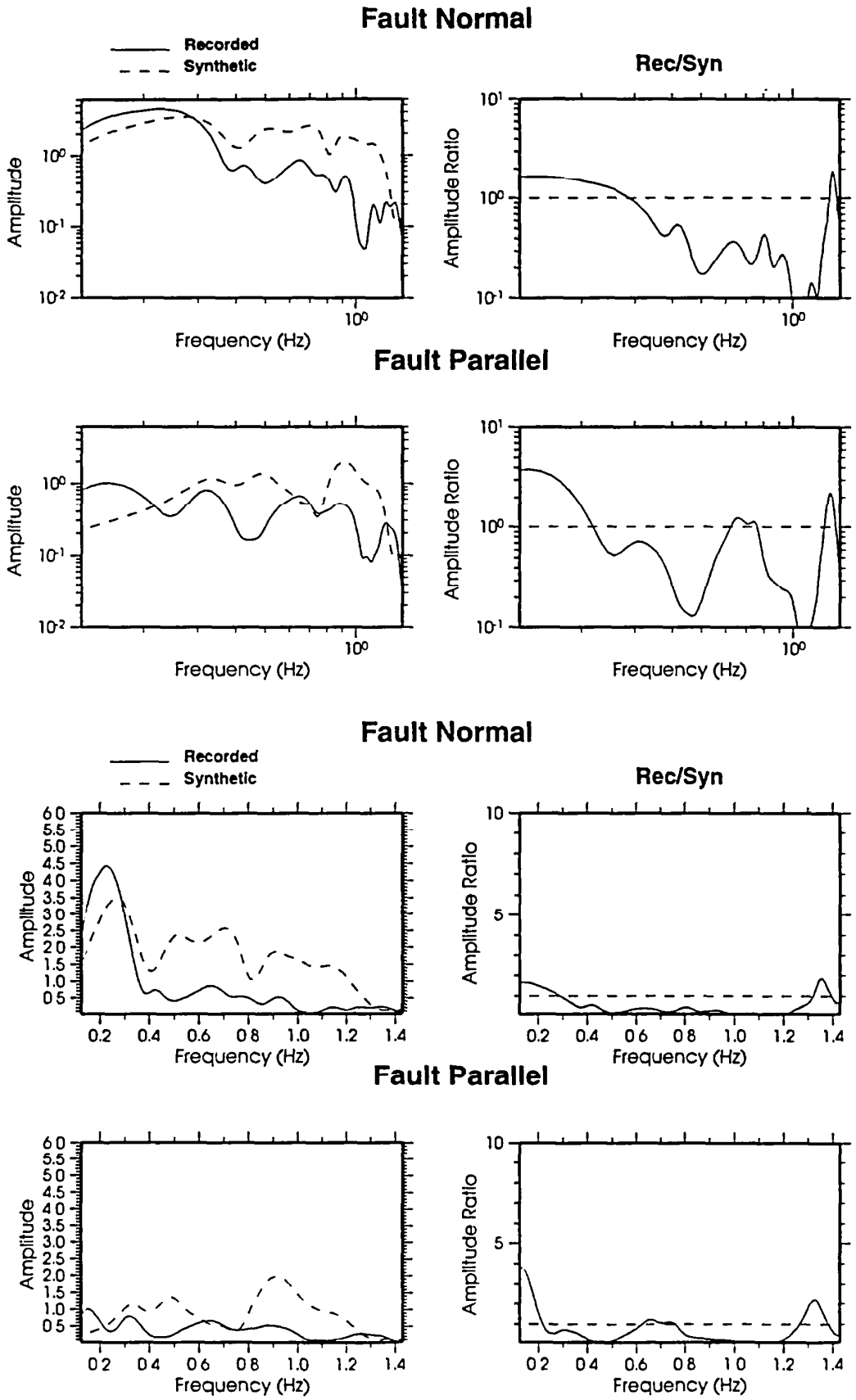

GMT Aug 24 15 23 47 1999 /net/coda/u2/arben/landers/shells

Landers - Filter 0.125-1.43 Hz, Norma BB Sims - dhsp

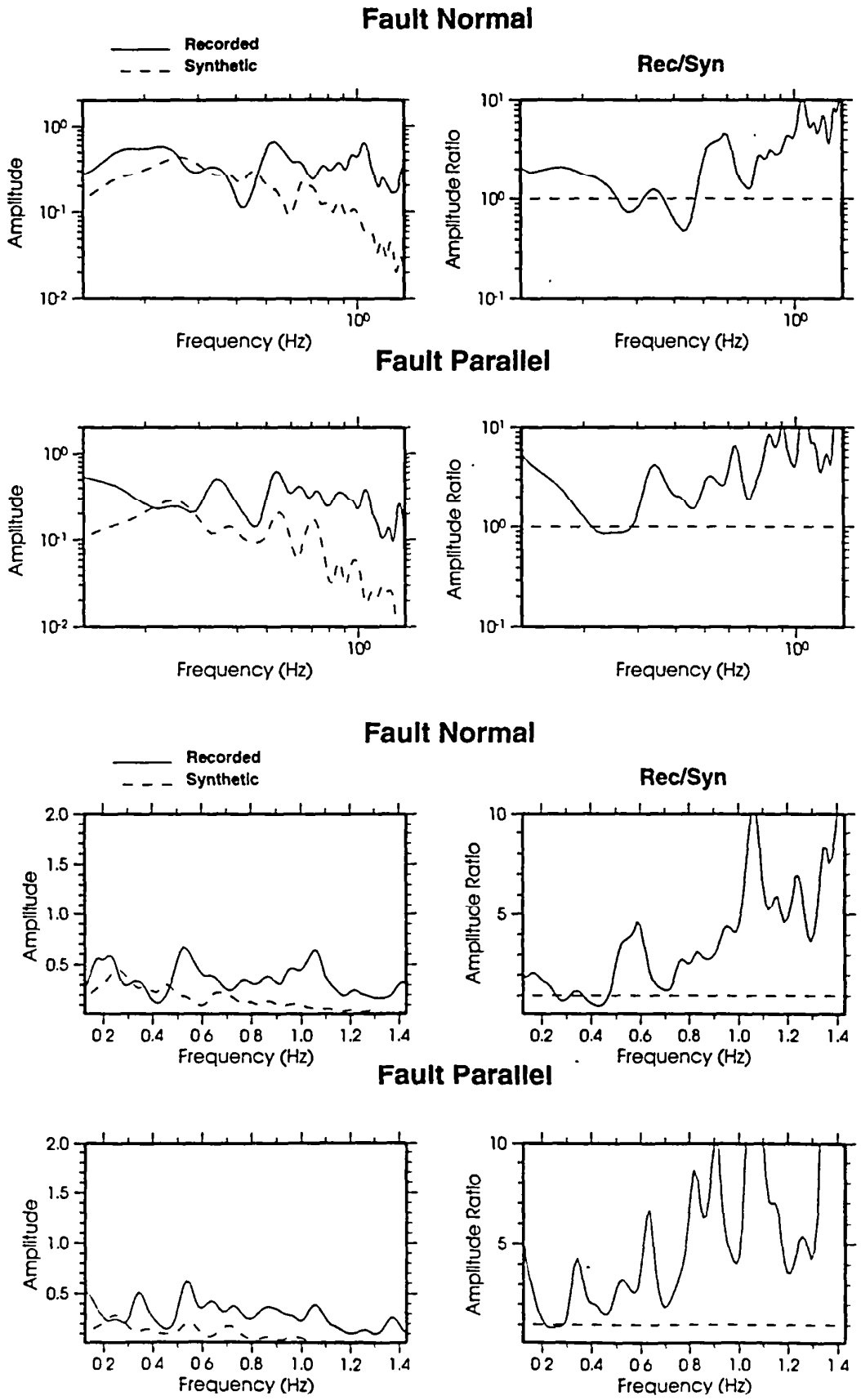

GMT Aug 24 15 25.30 1999 /net/coda/u2/arben/landers/shells

Landers - Filter 0.125-1.43 Hz, Norma BB Sims - plma

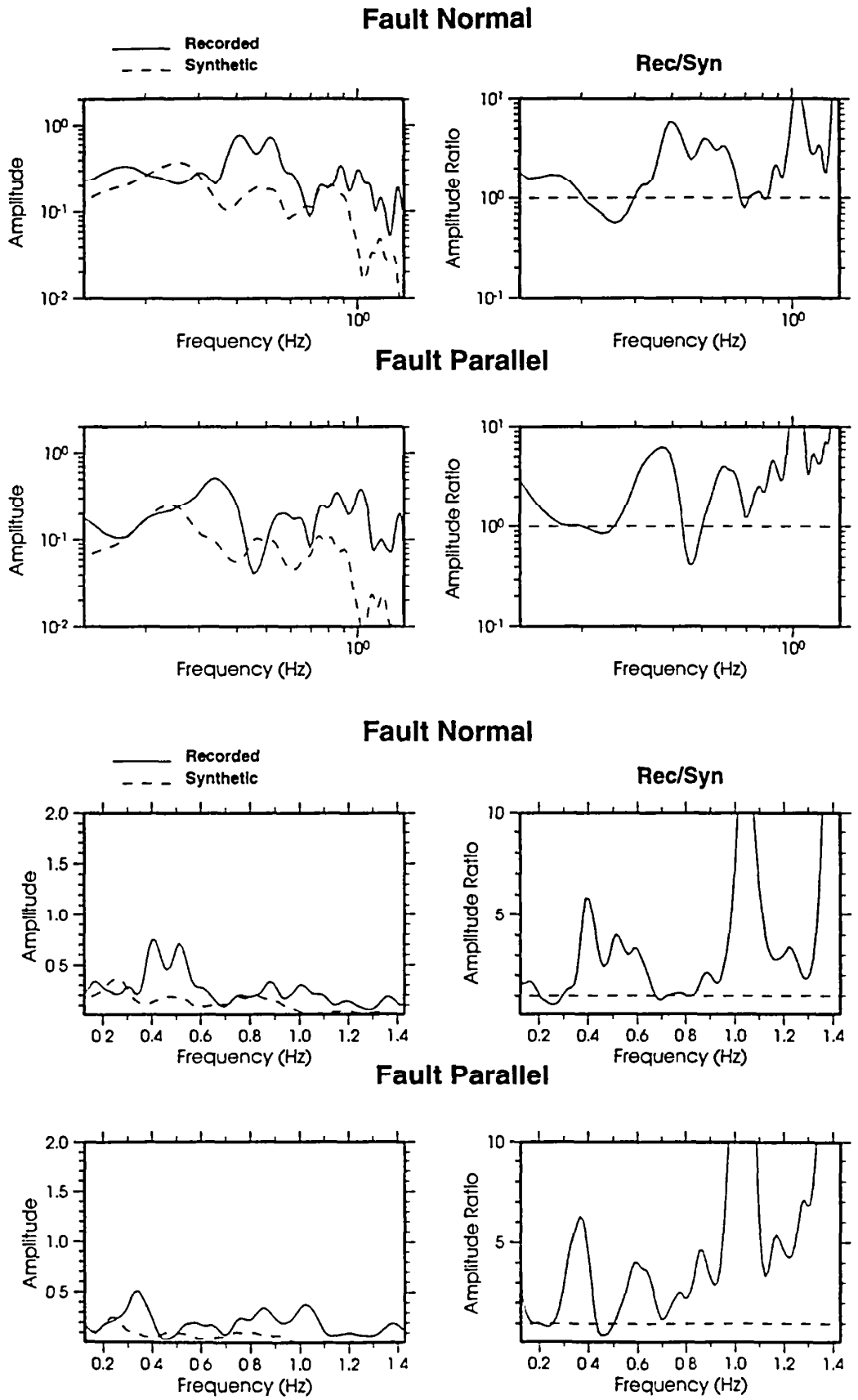

GMT Aug 24 15:27.48 1999 /net/coda/u2/arben/landers/shells

Landers - Filter 0.125-1.43 Hz, Norma BB Sims - nplm

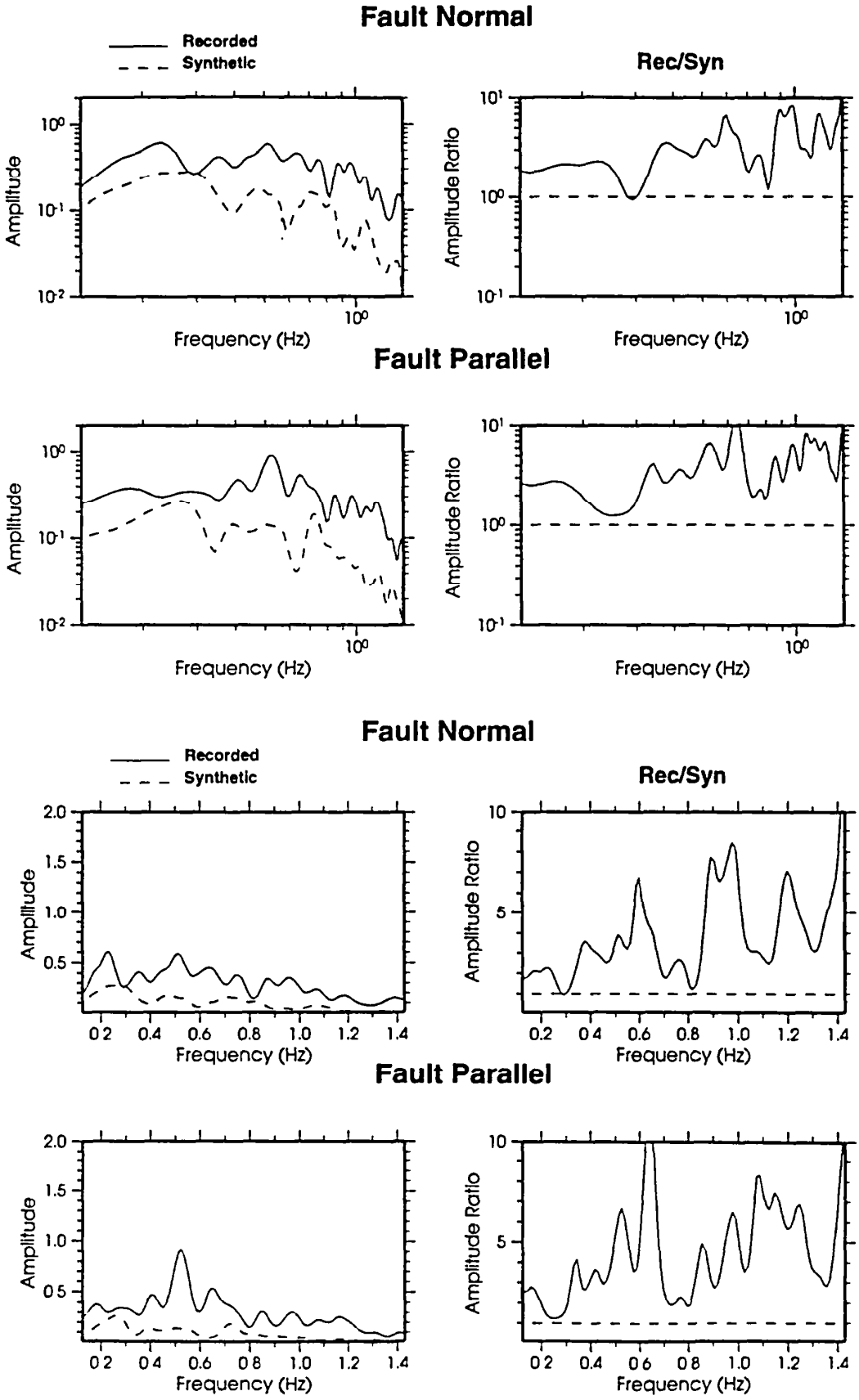

GMT Aug 24 15:27:19 1999 /net/coda/u2/arben/landers/shells

Landers - Filter 0.125-1.43 Hz, Norma BB Sims - mvfs

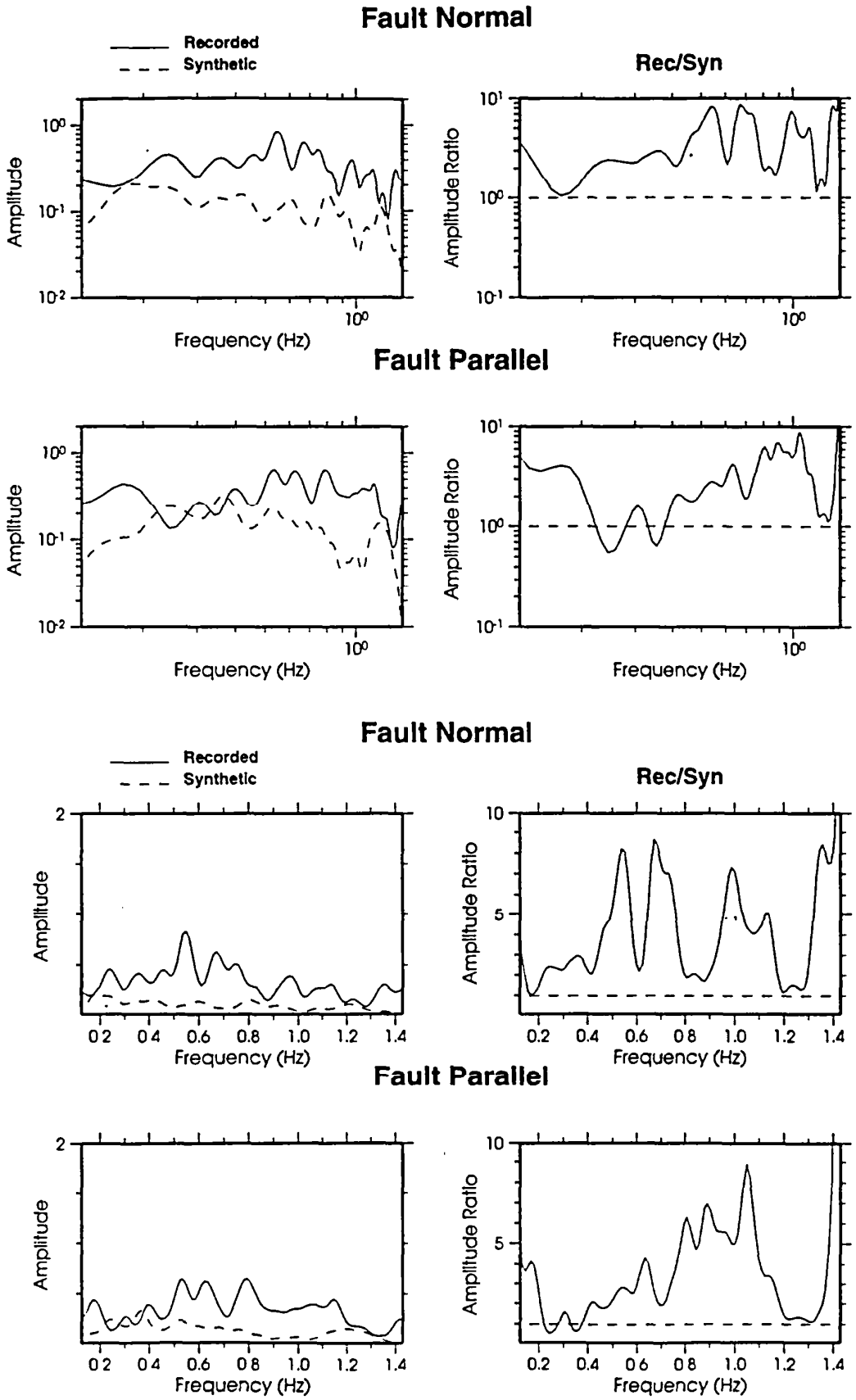

GMT Aug 24 15 26:51 1999 /net/coda/u2/arben/landers/shells

Landers Earthquake - Fault Normal

SA at 5.0 sec

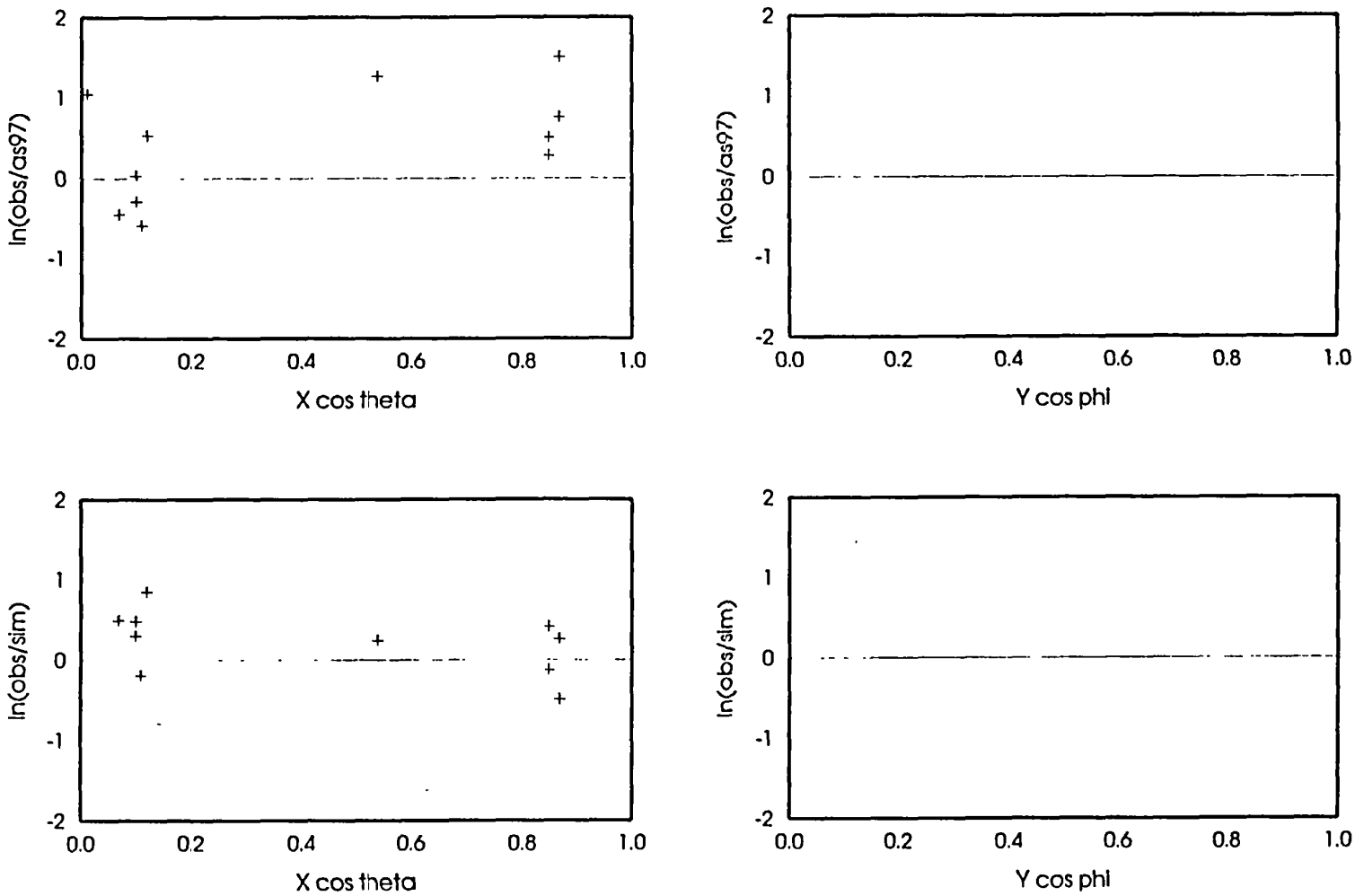

GMT Aug 24 15:26:32 1999 /net/coda/u2/arben/landers/Comparisons/Resid_plots

Landers Earthquake - Fault Parallel

SA at 5.0 sec

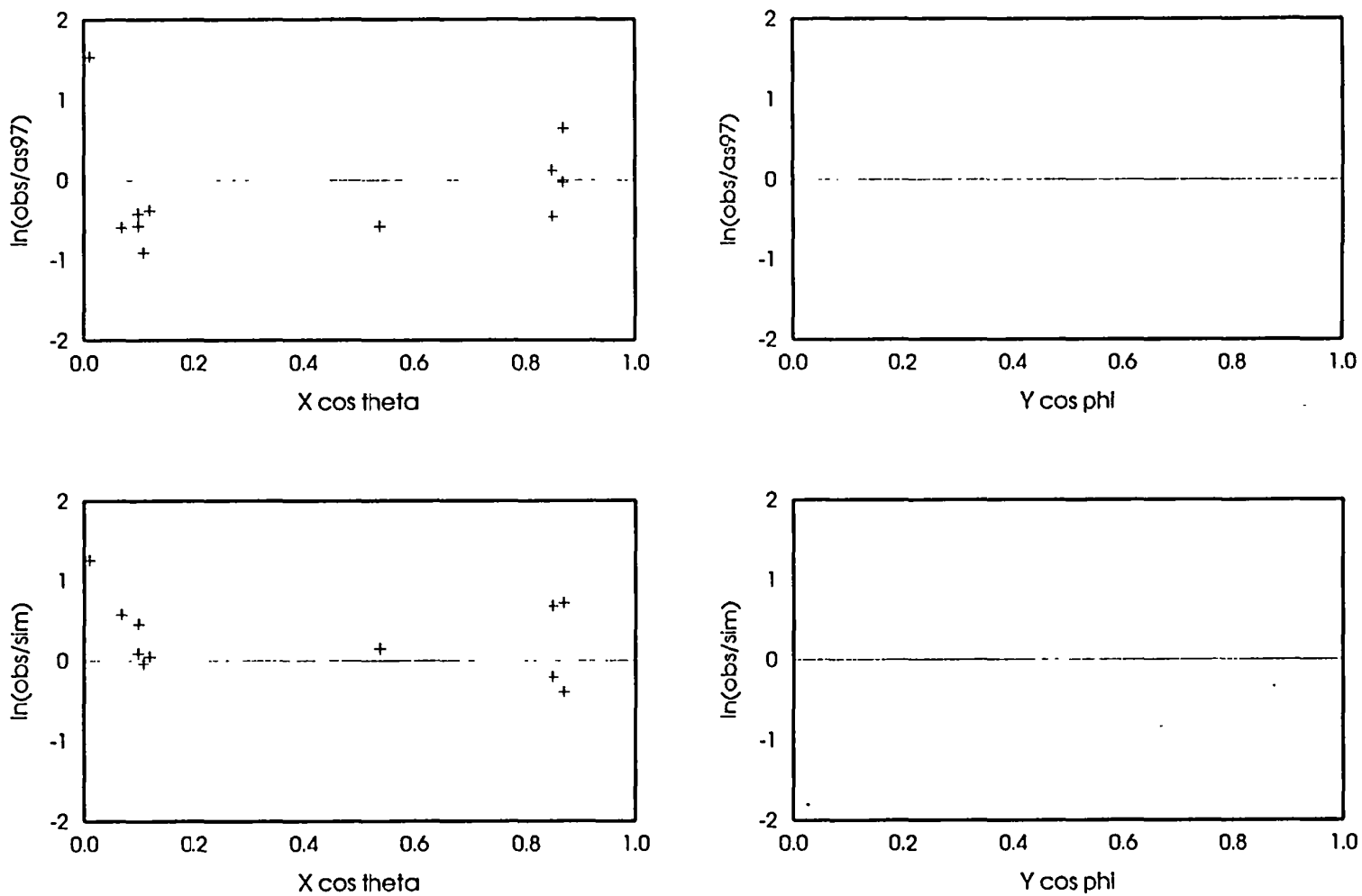

GMT Aug 24 15:26:34 1999 /net/coda/u2/arben/landers/Comparisons/Resid_plots

Landers Earthquake - Fault Normal

SA at 4.0 sec

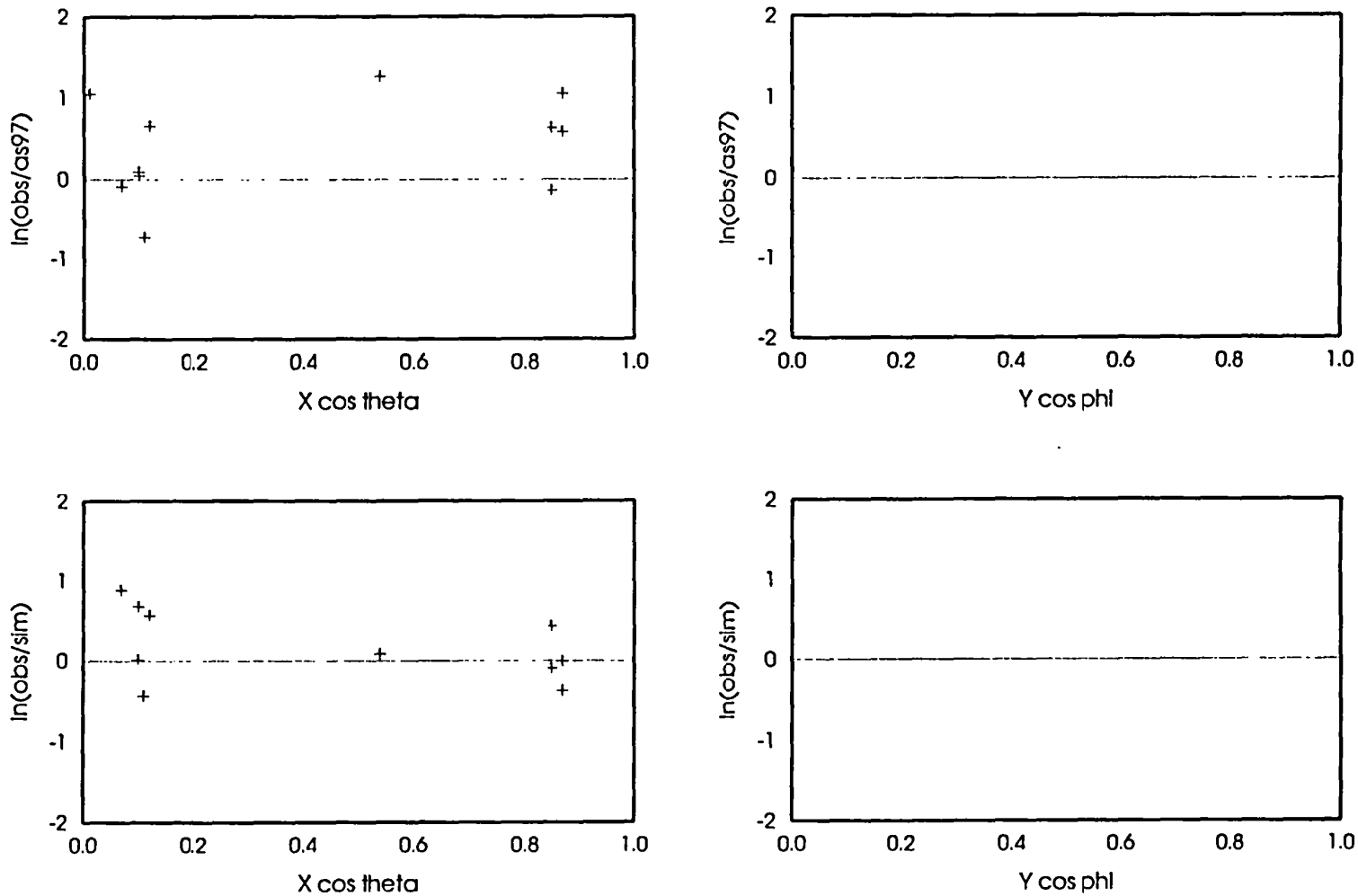

GMT Aug 24 15:26:37 1999 /net/coda/u2/arben/landers/Comparisons/Resid_plots

Landers Earthquake - Fault Parallel

SA at 4.0 sec

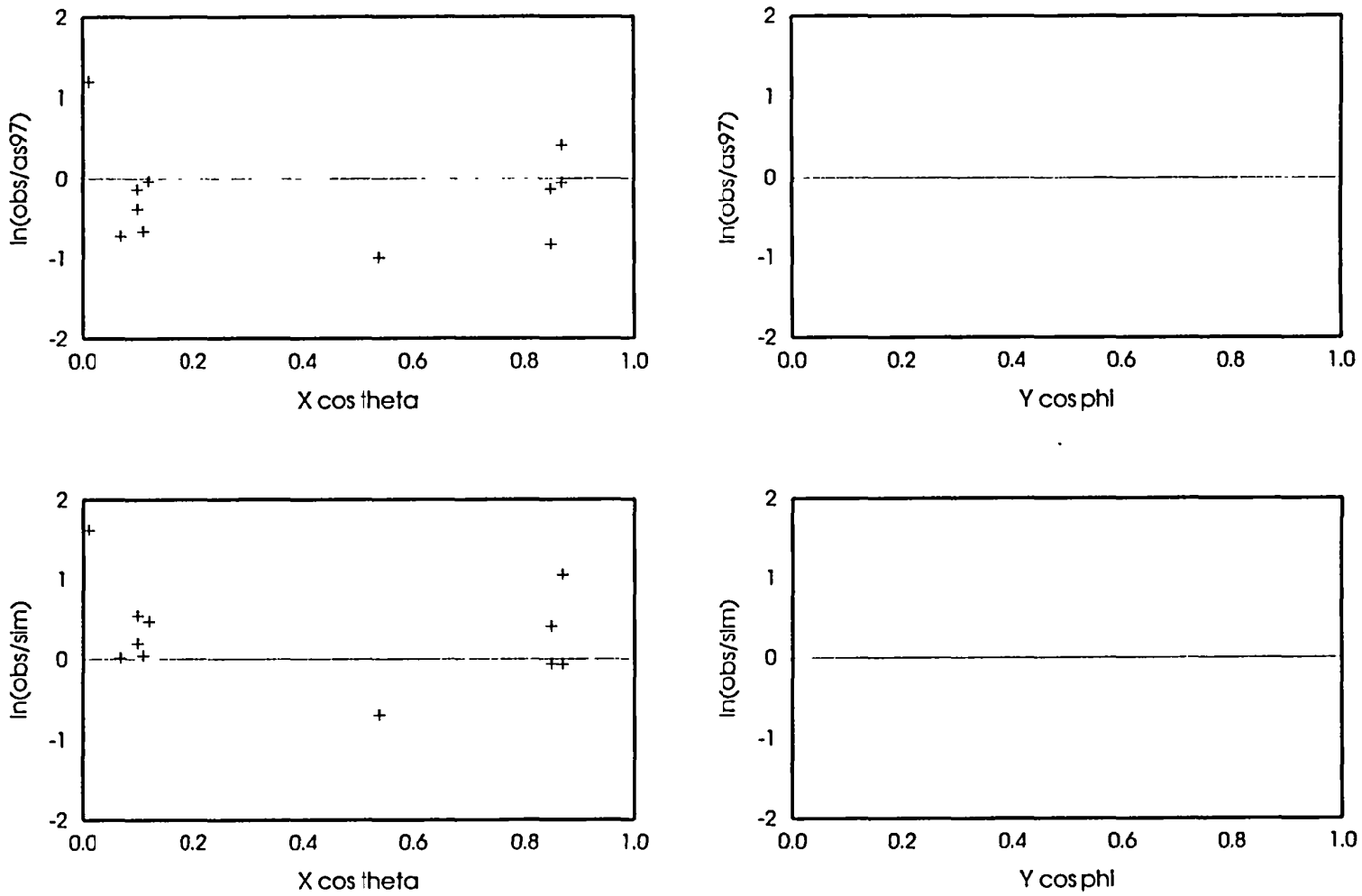

GMT Aug 24 15:26:39 1999 /nel/coda/u2/arben/landers/Comparisons/Resid_plots

Landers Earthquake - Fault Normal

SA at 3.0 sec

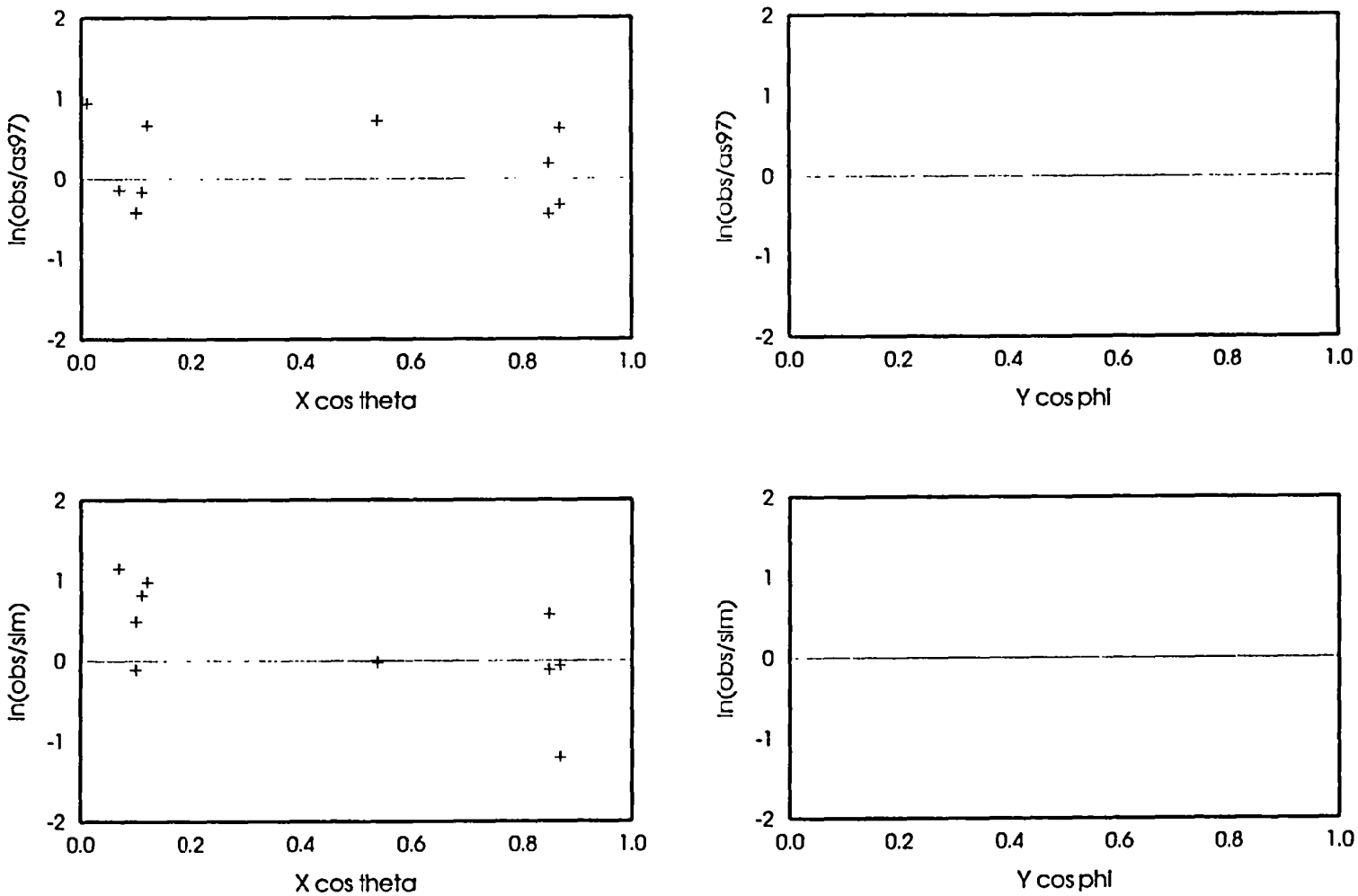

GMT Aug 24 15:26:41 1999 /net/coda/u2/arben/landers/Comparisons/Resid_plots

Landers Earthquake - Fault Parallel

SA at 3.0 sec

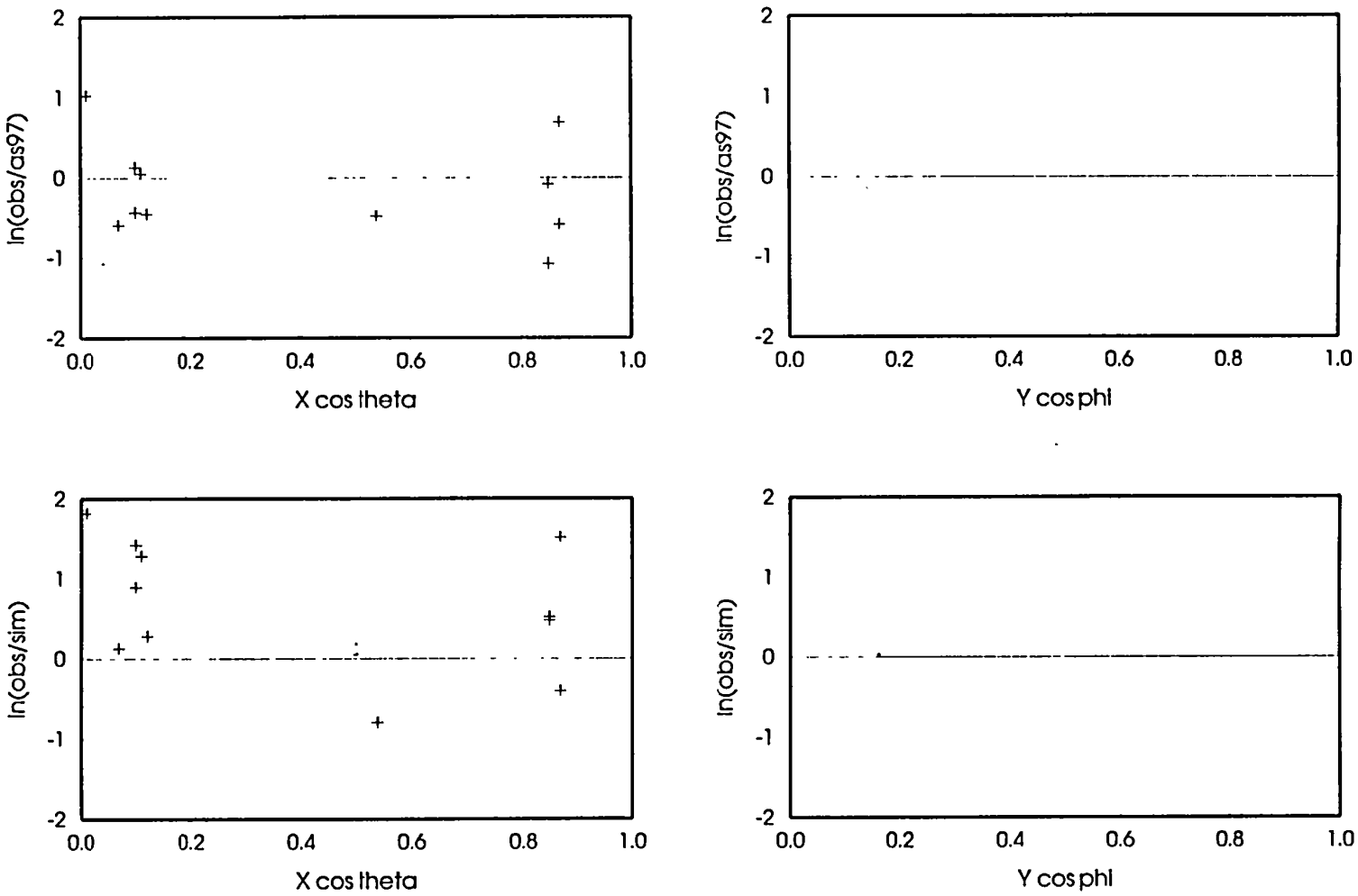

GMT Aug 24 15:26:44 1999 /net/coda/u2/arben/landers/Comparisons/Resid_plots

Landers Earthquake - Fault Normal

SA at 2.0 sec

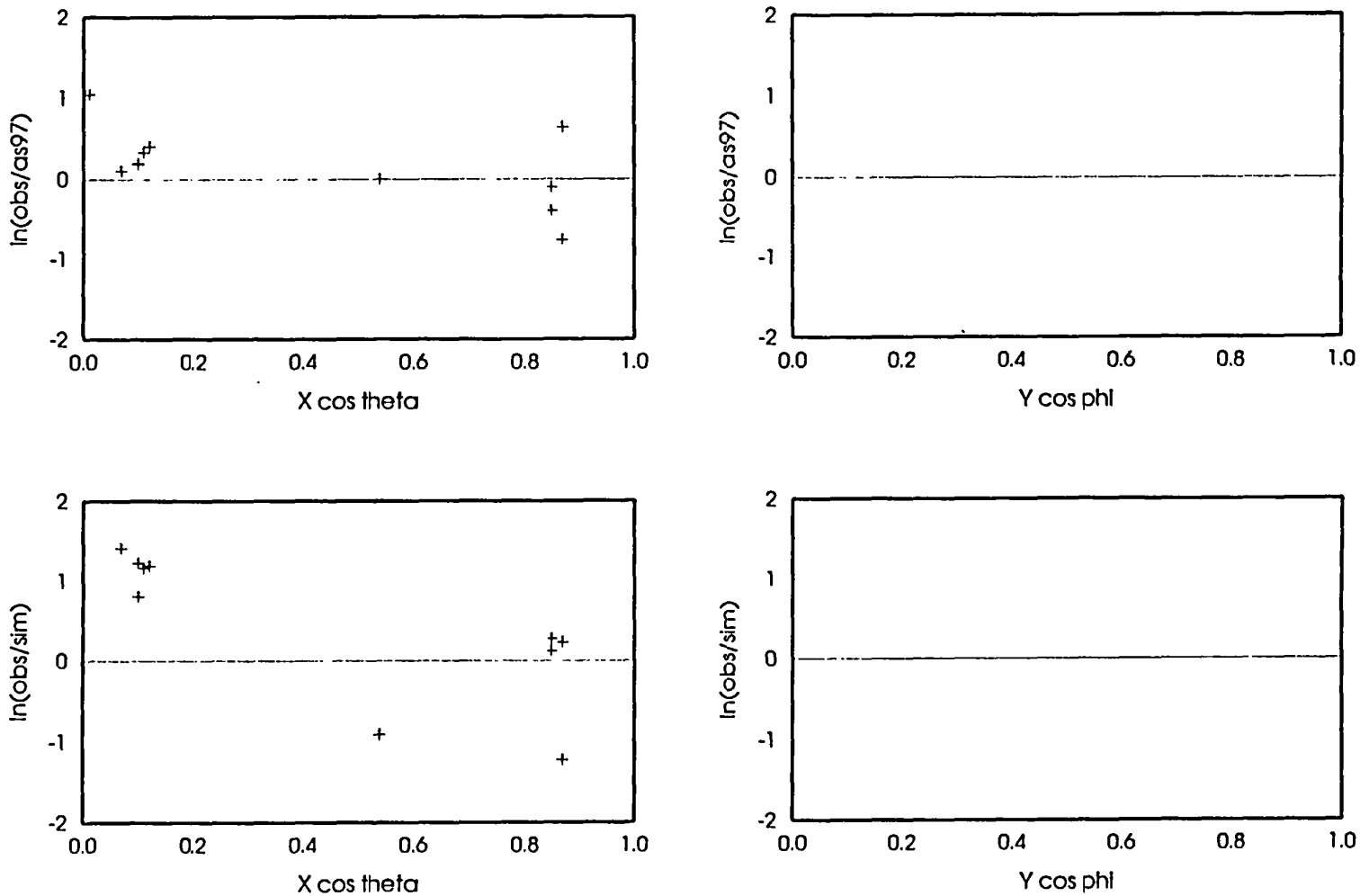

GMT Aug 24 15:26:46 1999 /net/coda/u2/arben/landers/Comparisons/Resid_plots

Landers Earthquake - Fault Parallel

SA at 2.0 sec

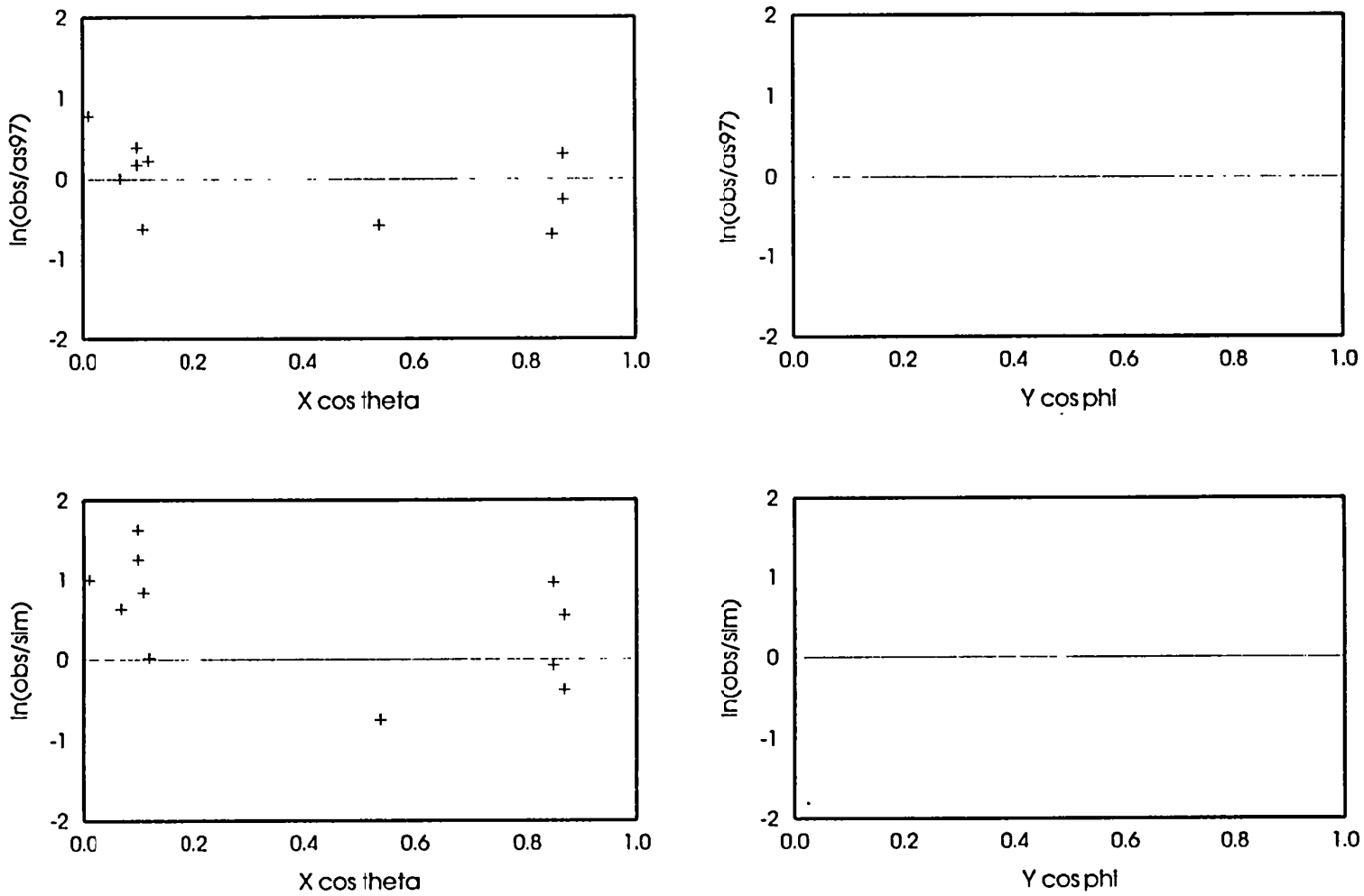

GMT Aug 24 15:26:48 1999 /net/coda/u2/arben/landers/Comparisons/Resid_plots

Landers Earthquake - Fault Normal

SA at 1.5 sec

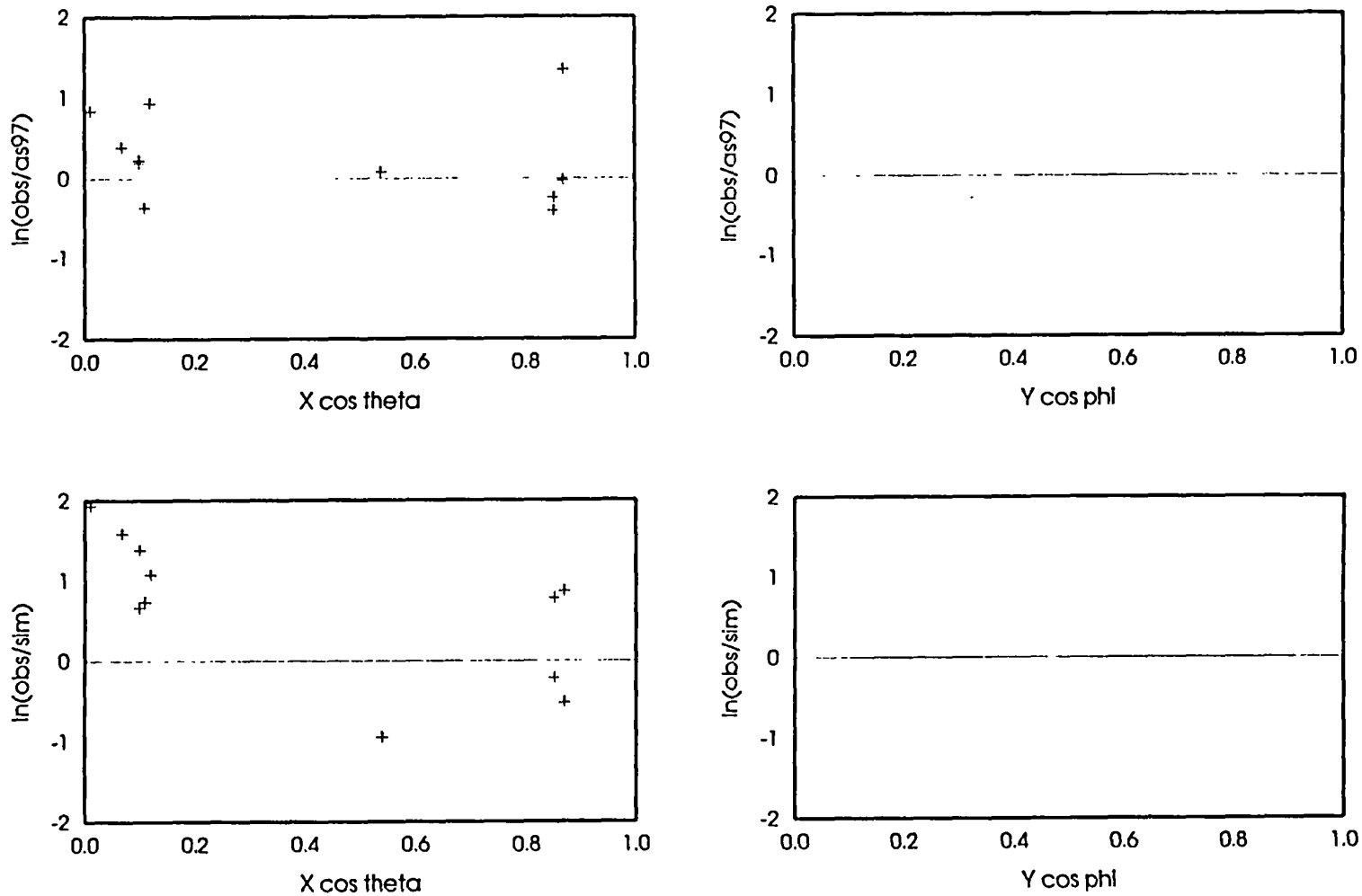

GMT Aug 24 15:26:51 1999 /net/coda/u2/arben/landers/Comparisons/Resid_plots

Landers Earthquake - Fault Parallel

SA at 1.5 sec

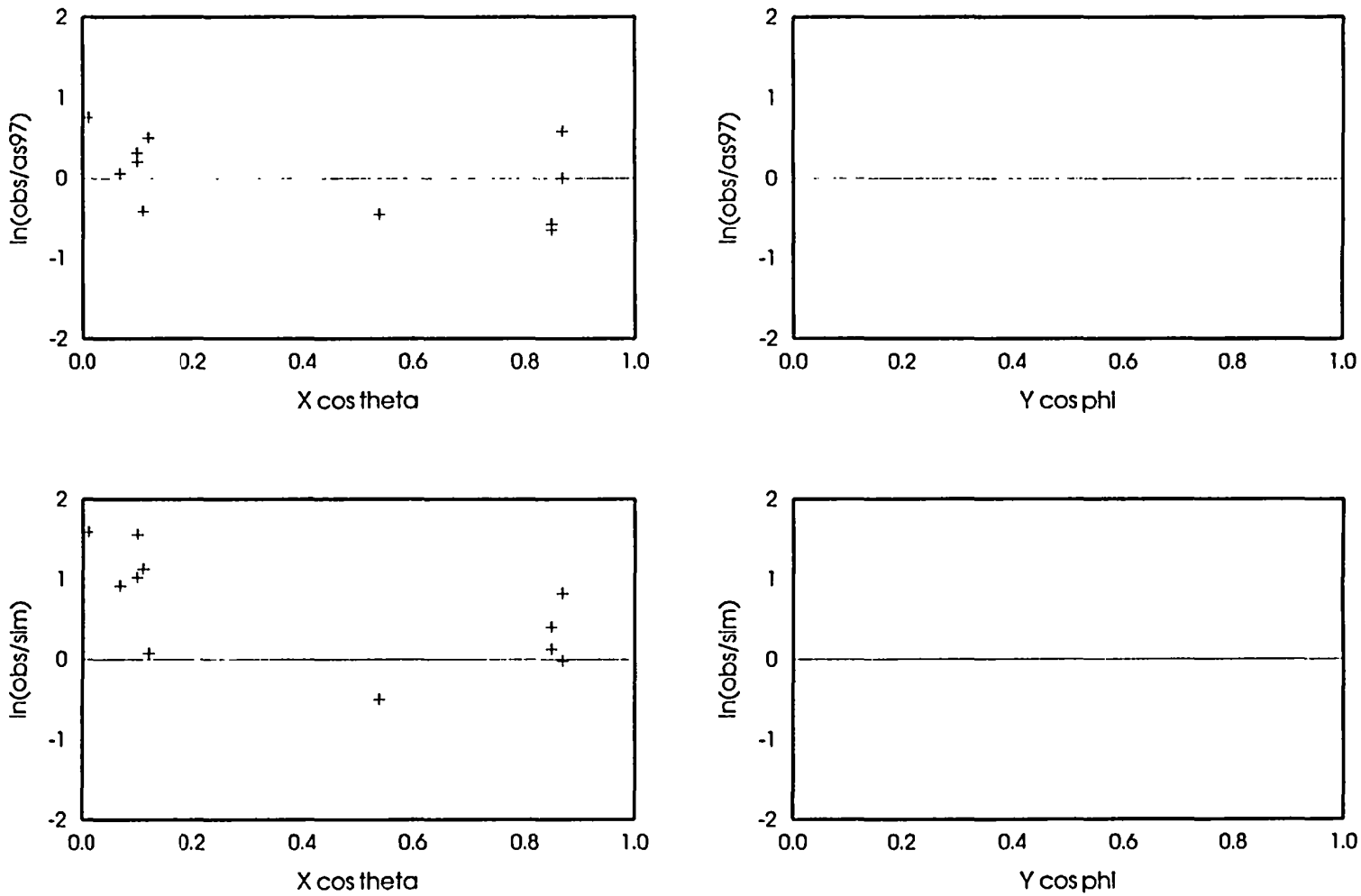

GMT Aug 24 15:26:55 1999 /net/coda/u2/arben/landers/Comparisons/Resid_plots

Landers Earthquake - Fault Normal

SA at 1.0 sec

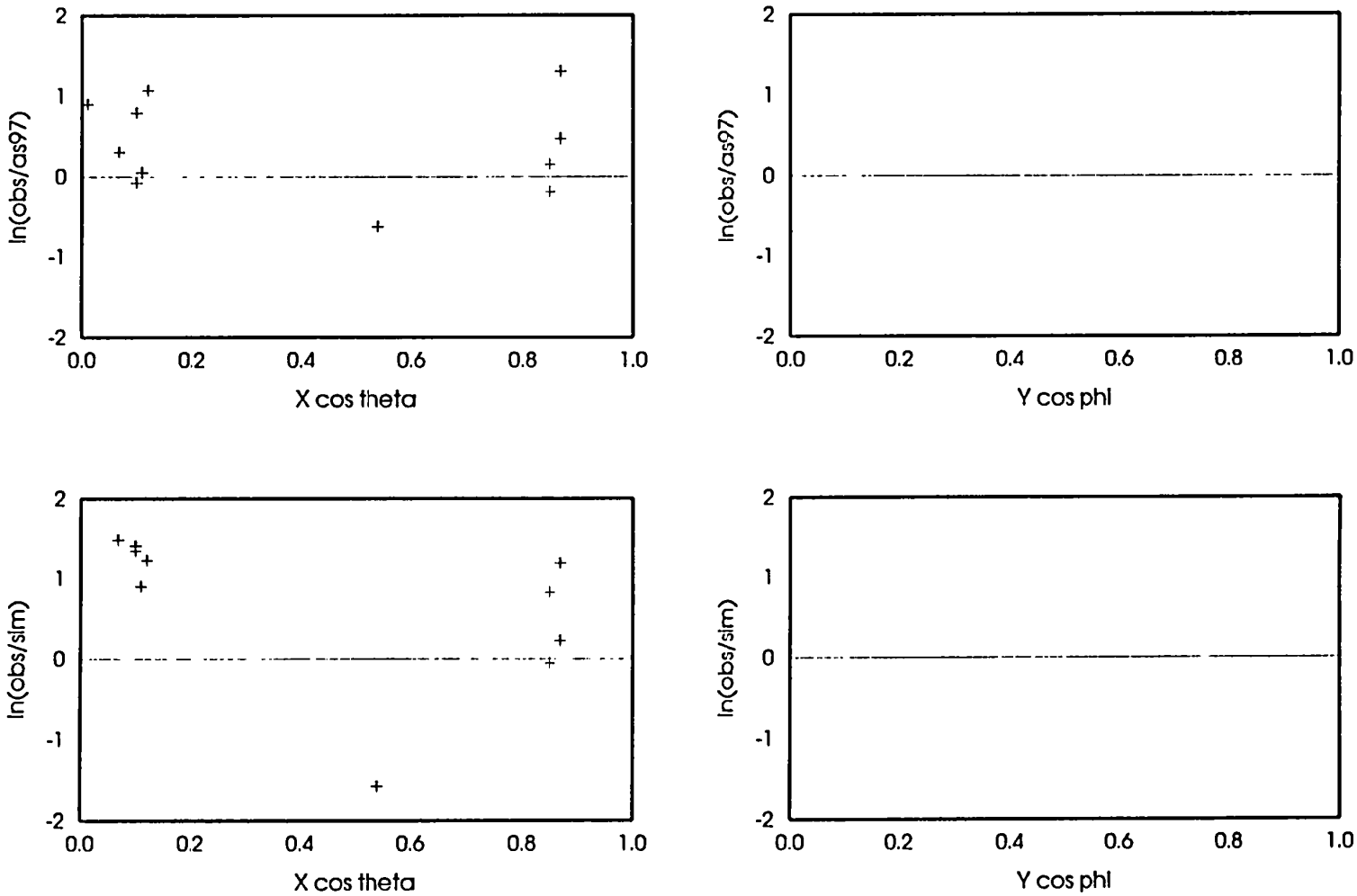

GMT Aug 24 15:26:59 1999 /net/coda/u2/arben/landers/Comparisons/Resid_plots

Landers Earthquake - Fault Parallel

SA at 1.0 sec

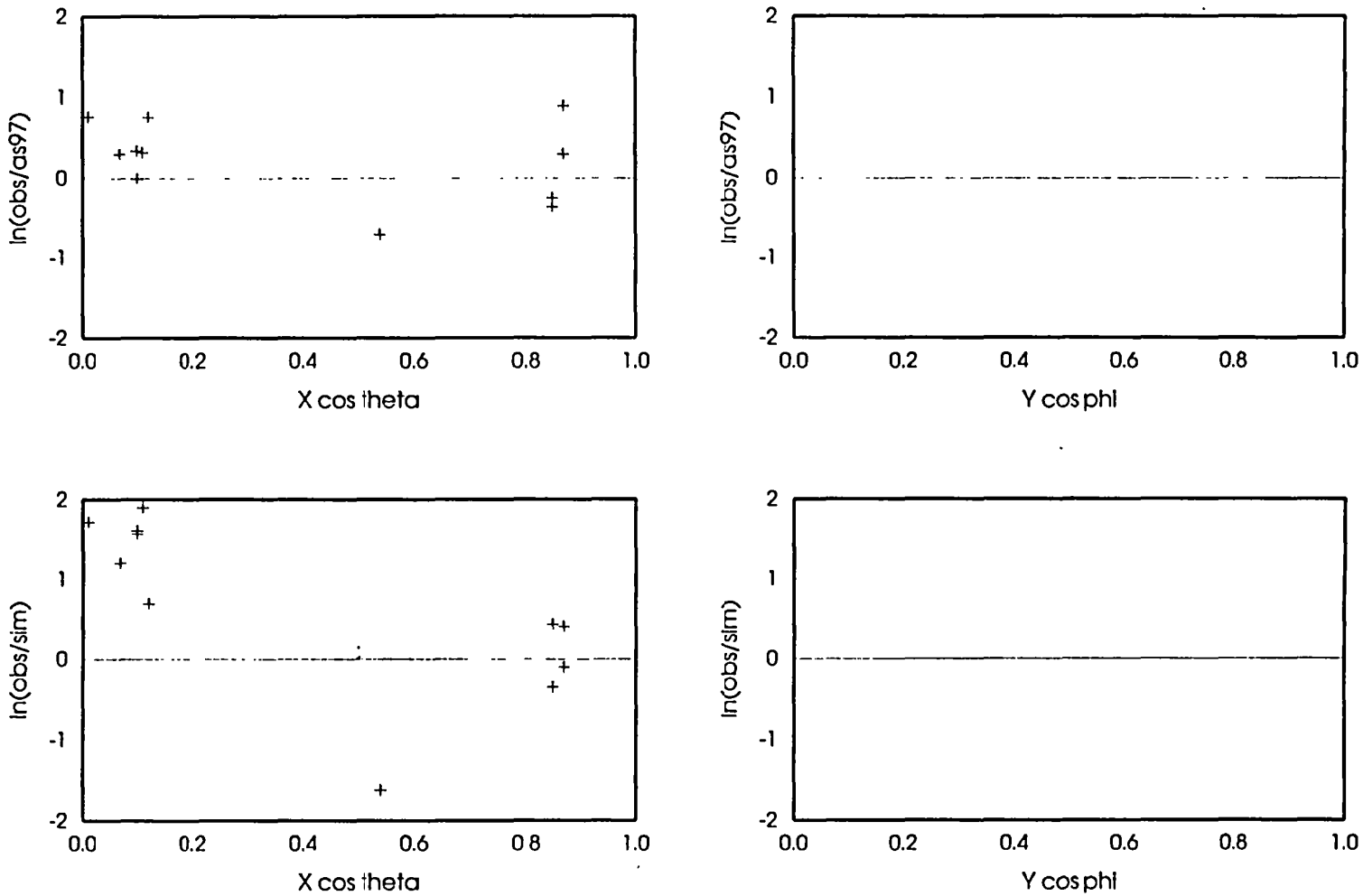

GMT Aug 24 15:27:01 1999 /net/coda/u2/arben/landers/Comparisons/Resid_plots

/u1/nancy/PEER-5/Northridge/Comparisons.990823/Tabulate
tableout

Station	Correlation FN	Correlation FP	Least Squares FN	Least Squares FP	Response Spectra FN	Response Spectra FP	Fourier Spectra FN	Fourier Spectra FP
cnpk	0.402		0.053		0.355	-0.610	0.583	-0.094
jeng	0.594	0.593	0.169	0.183	0.195	0.185	0.536	0.049
kagc	0.483		0.104		0.122	0.631	0.381	0.649
newh	0.760		0.348		0.172	-0.035	0.161	0.284
nord	0.493	0.764	0.058	0.338	0.010	0.069	-0.015	0.237
pacd	0.796		-0.393		-0.736	-0.205	-0.569	-0.057
rosc	0.476		0.052		0.117	0.553	0.153	0.633
rrs	0.717	0.819	0.255	0.424	0.736	0.061	0.683	0.143
sati	0.431	0.519	0.096	0.143	0.820	0.500	0.733	0.737
scs	0.668		0.254		0.344	0.233	0.571	0.370
scse	0.696	0.857	0.230	0.462	-0.011	0.040	0.108	0.003
ssus	0.391		-0.583		-0.628	0.078	-0.611	0.222
sylm	0.818	0.586	0.408	0.189	0.364	0.310	0.323	0.096
Average	0.594	0.690	0.081	0.290	0.143	0.139	0.234	0.252
Sigma	0.156	0.243	0.279	0.357	0.424	0.380	0.602	0.498
Sigma Mean	0.043	0.099	0.077	0.146	0.118	0.105	0.167	0.138

Northridge - Fault Normal

Simulations and Data Band Pass Filtered 0.125-1.43 Hz

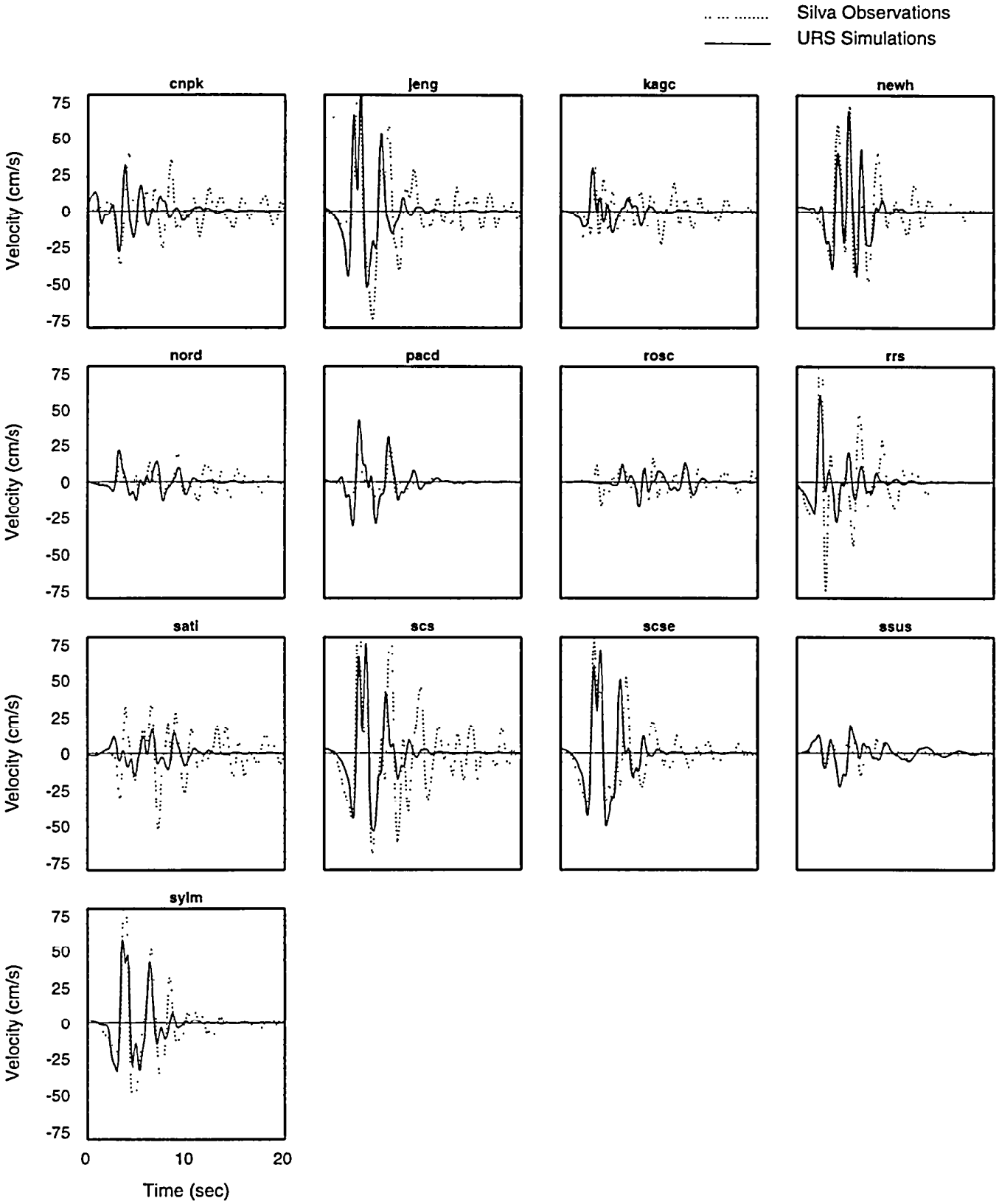

GMT Aug 31 11:04:15 1999 /u1/nancy/PEER-5/Northridge/Comparisons.990823/ExtraPlots

Northridge - Fault Parallel

Simulations and Data Band Pass Filtered 0.125-1.43 Hz

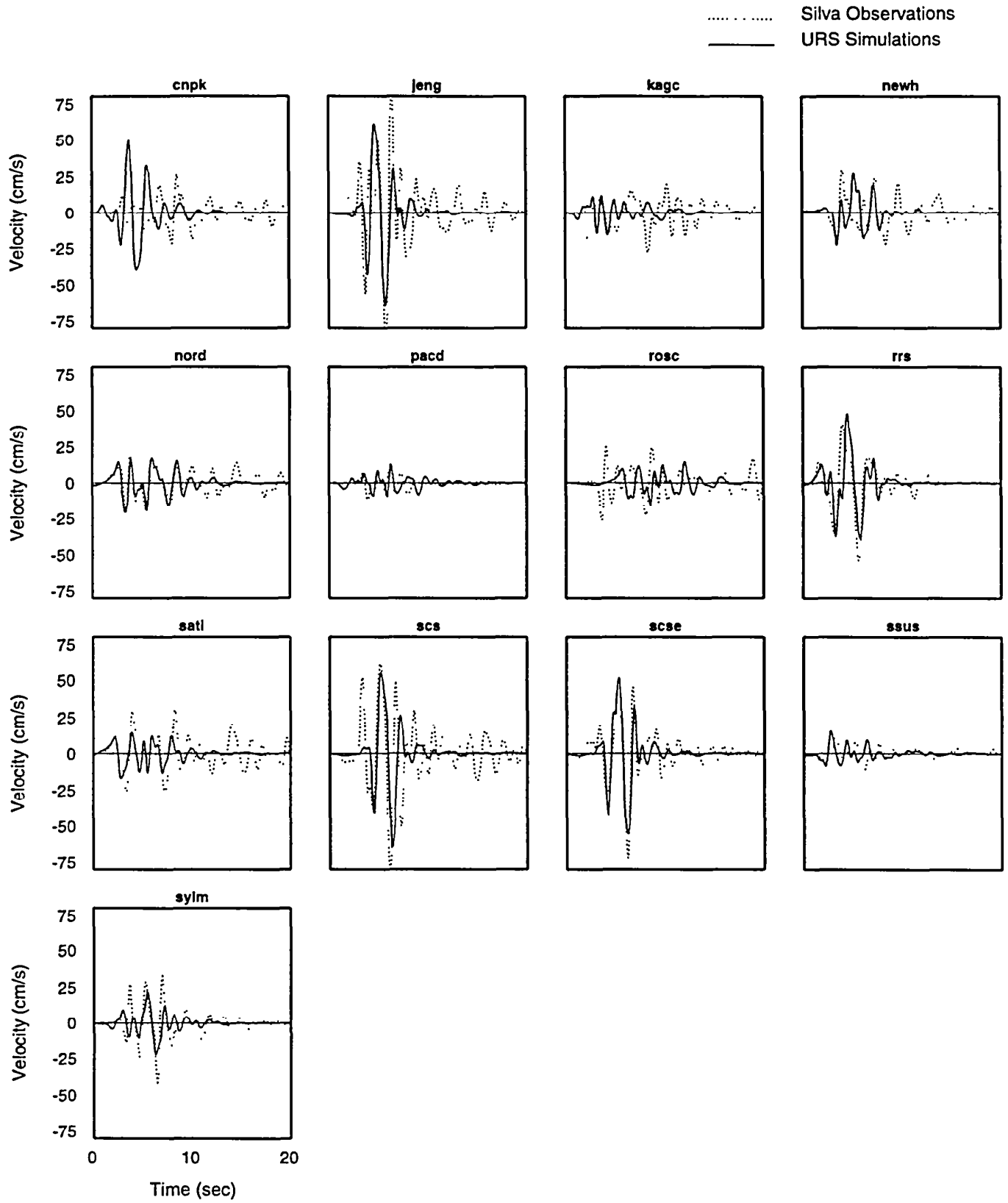

GMT Aug 31 11:04:40 1999 /u1/nancy/PEER-5/Northridge/Comparisons.990823/ExtraPlots

Northridge - Fault Normal

Simulations and Data

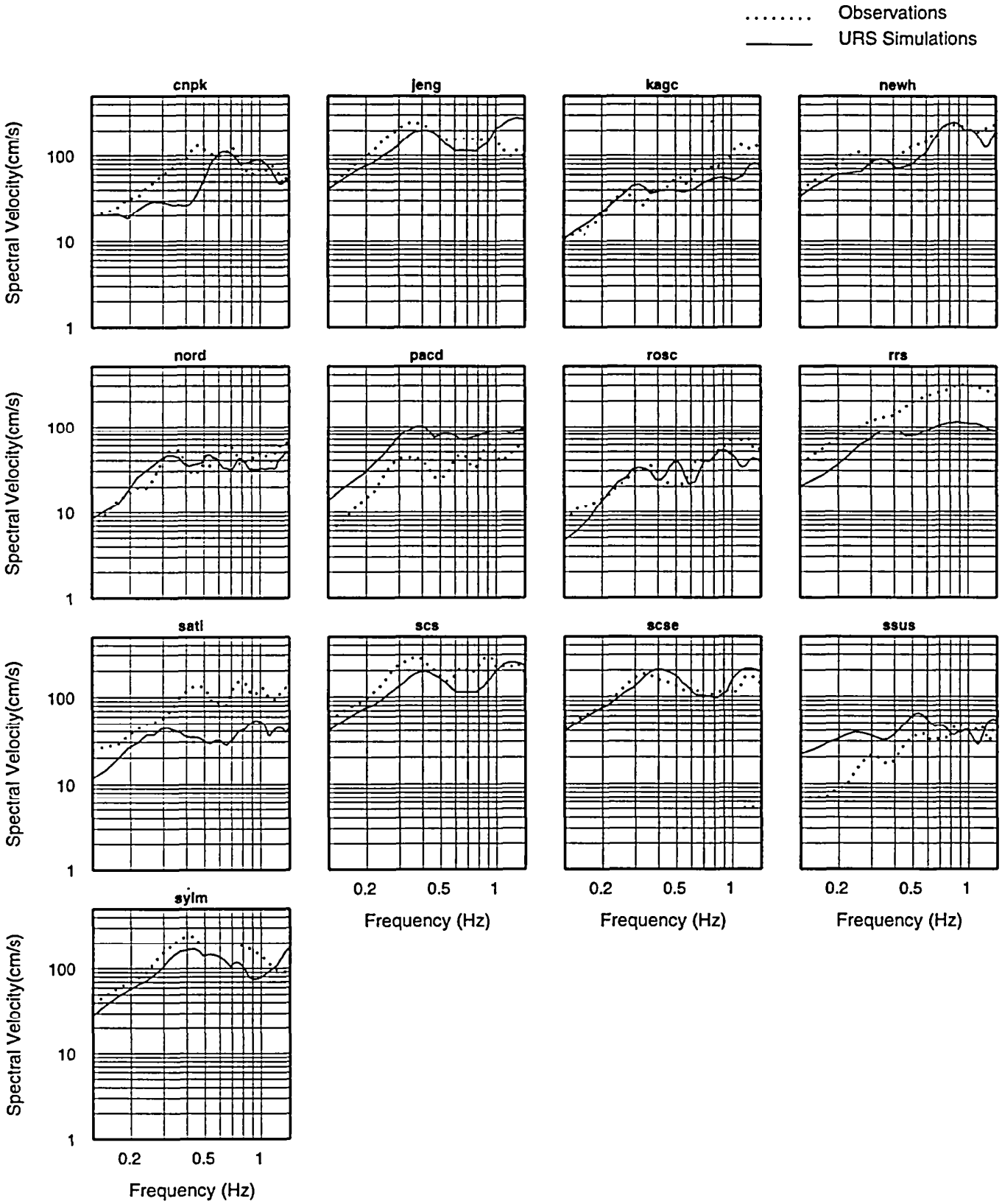

GMT Aug 31 15:56:15 1999 /u1/nancy/PEER-5/Northridge/Comparisons.990823/ExtraPlots

Northridge - Fault Parallel

Simulations and Data

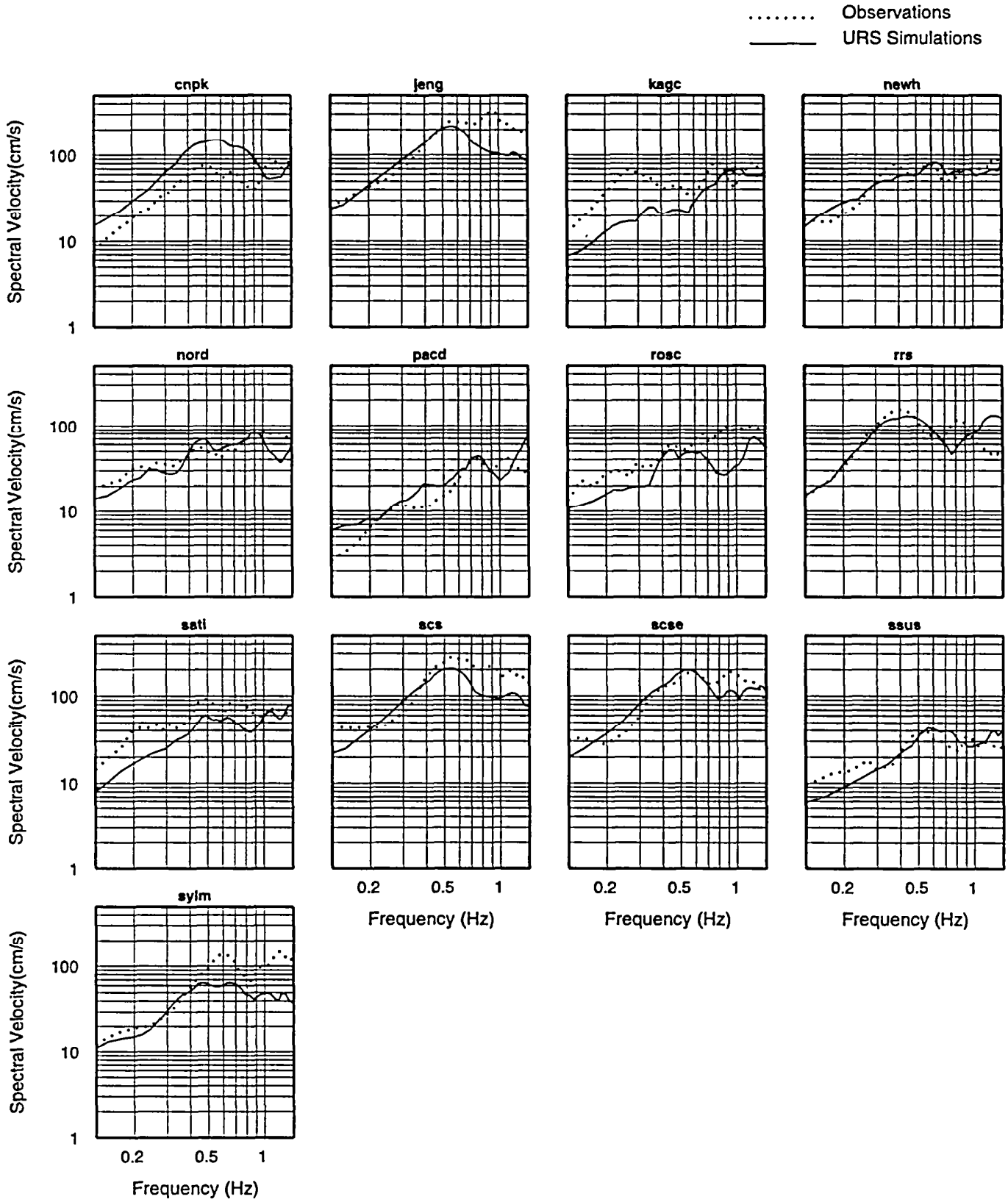

GMT Aug 31 15:56:49 1999 /u1/nancy/PEER-5/Northridge/Comparisons.990823/ExtraPlots

Northridge - Fault Normal

Simulations and Data Band Pass Filtered 0.125-1.43 Hz

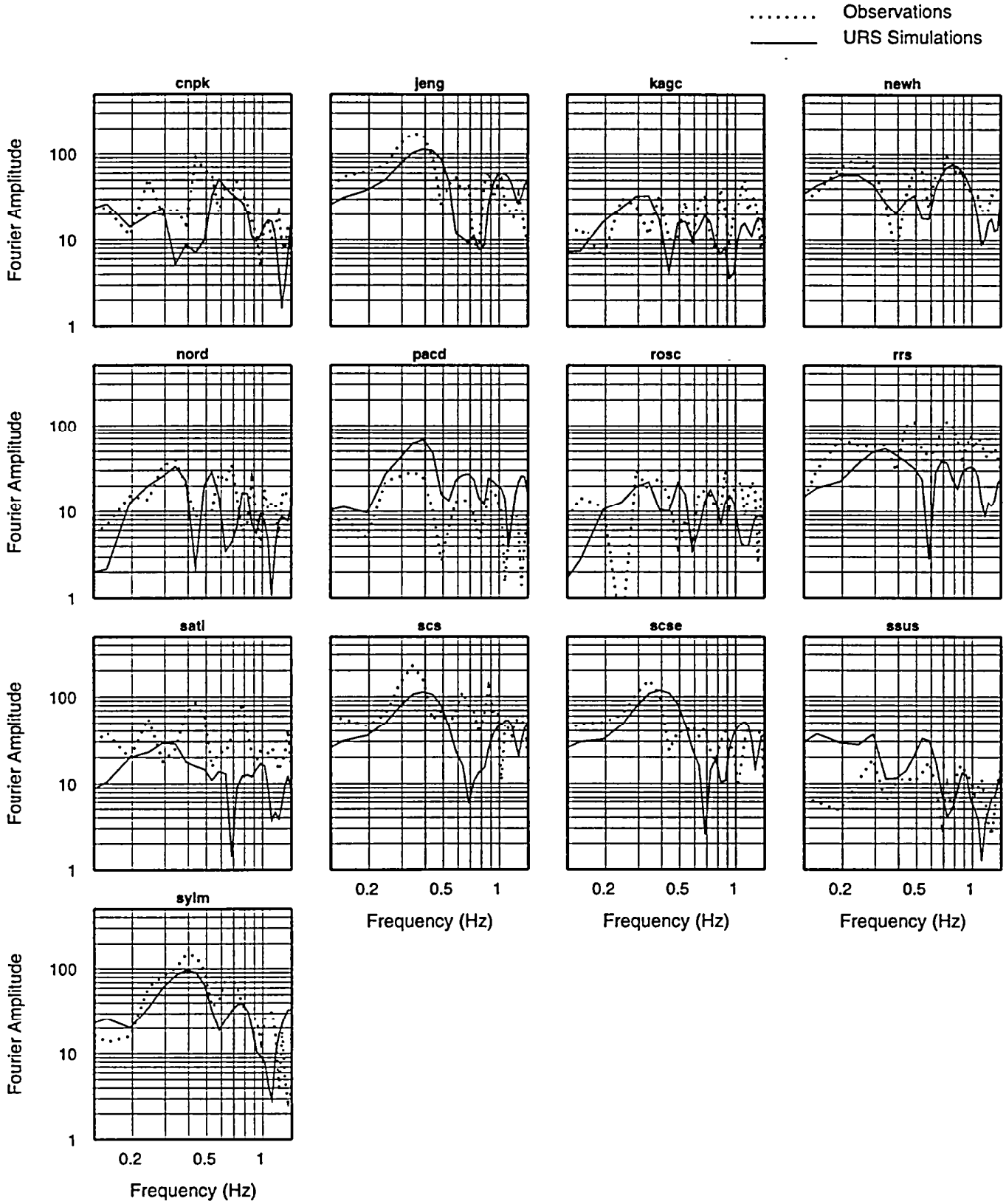

GMT Aug 31 15:49:28 1999 /u1/nancy/PEER-5/Northridge/Comparisons.990823/ExtraPlots

Northridge - Fault Parallel

Simulations and Data Band Pass Filtered 0.125-1.43 Hz

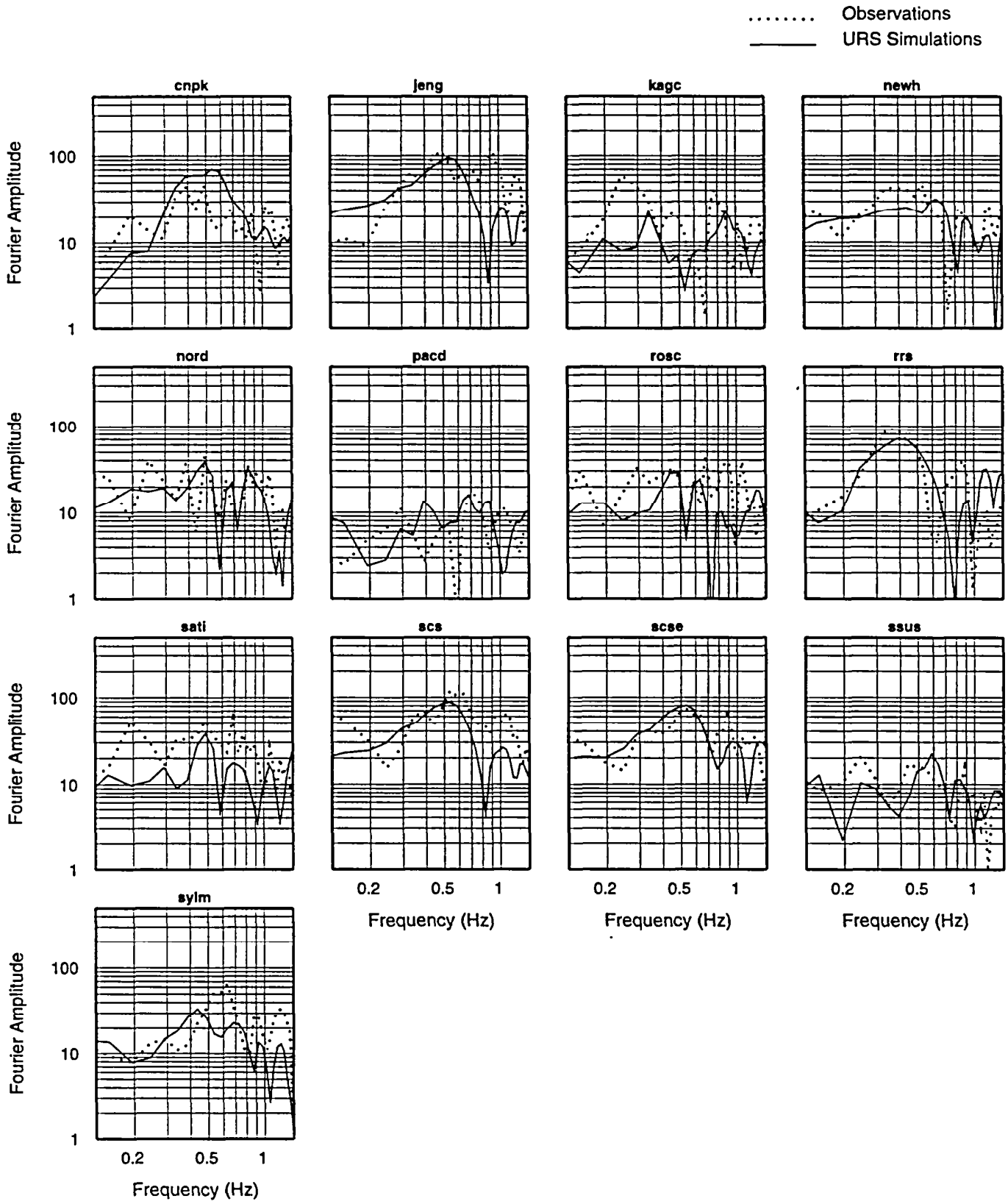

GMT Aug 31 15:50:23 1999 /u1/nancy/PEER-5/Northridge/Comparisons.990823/ExtraPlots

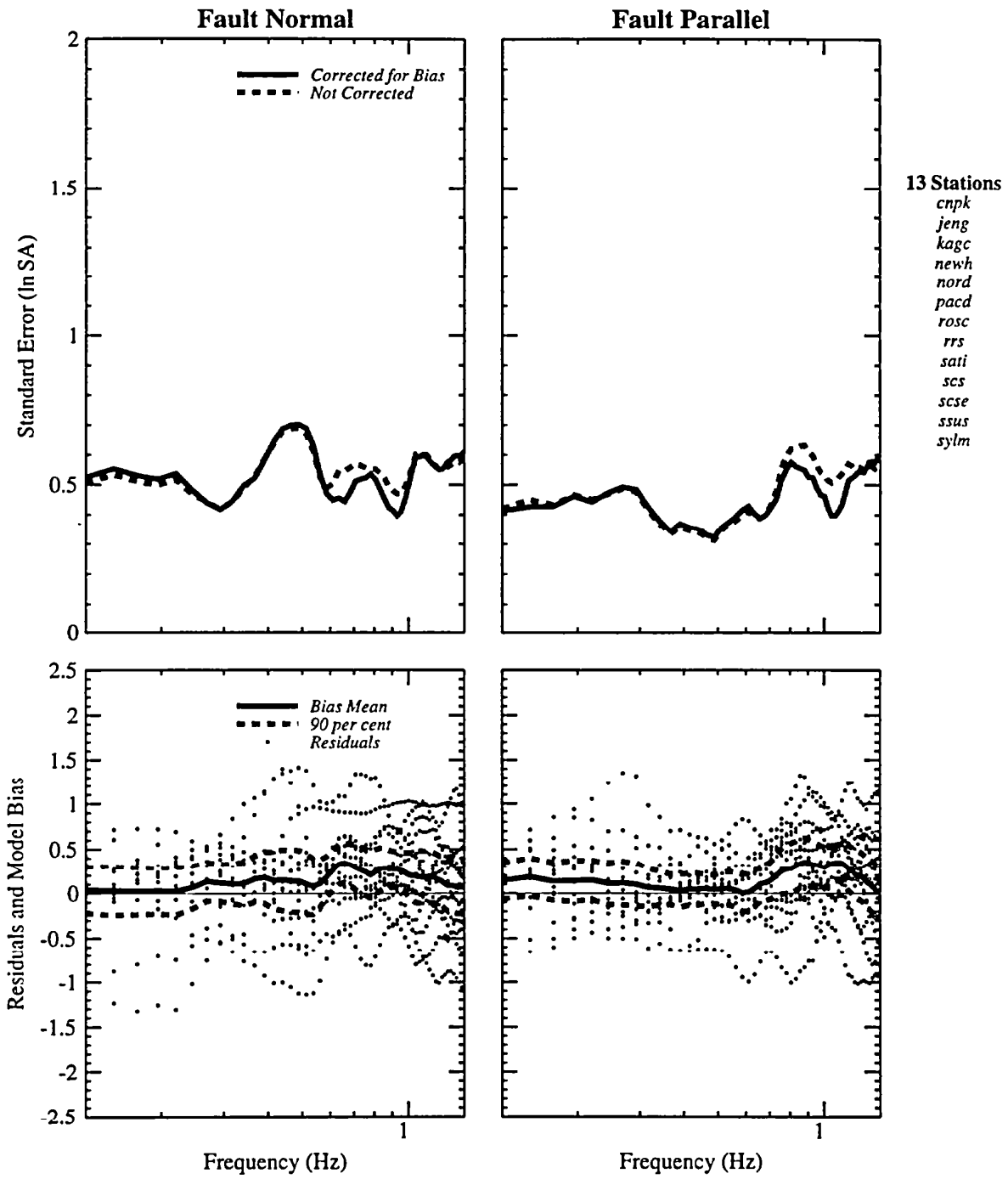

Northridge Spectral Acceleration Goodness of Fit
Observed minus Synthetic (obs - sim)

nfsmith0 Tue Aug 31 14:04:10 PDT 1999
/u1/nancy/PEER-5/Northridge/GoodFit/mplot_goodfit.csh

Northridge - Filter 0.125-1.43 Hz, Pas 94 BB Sims - cnpk

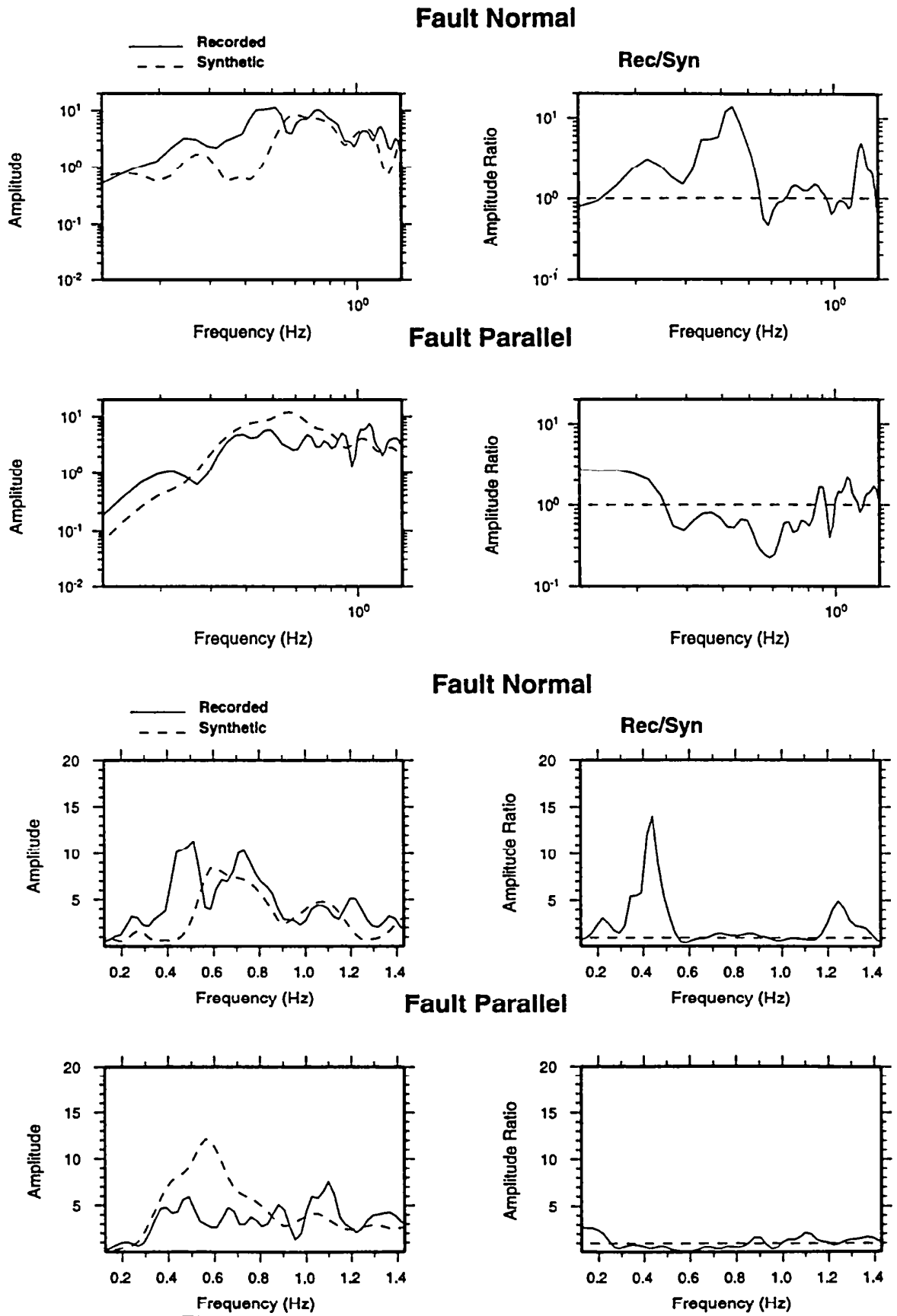

GMT Aug 23 13:57:01 1999 /u1/nancy/PEER-5/Northridge/Comparisons.990823/AP_fspec

Northridge - Filter 0.125-1.43 Hz, Pas 94 BB Sims - jeng

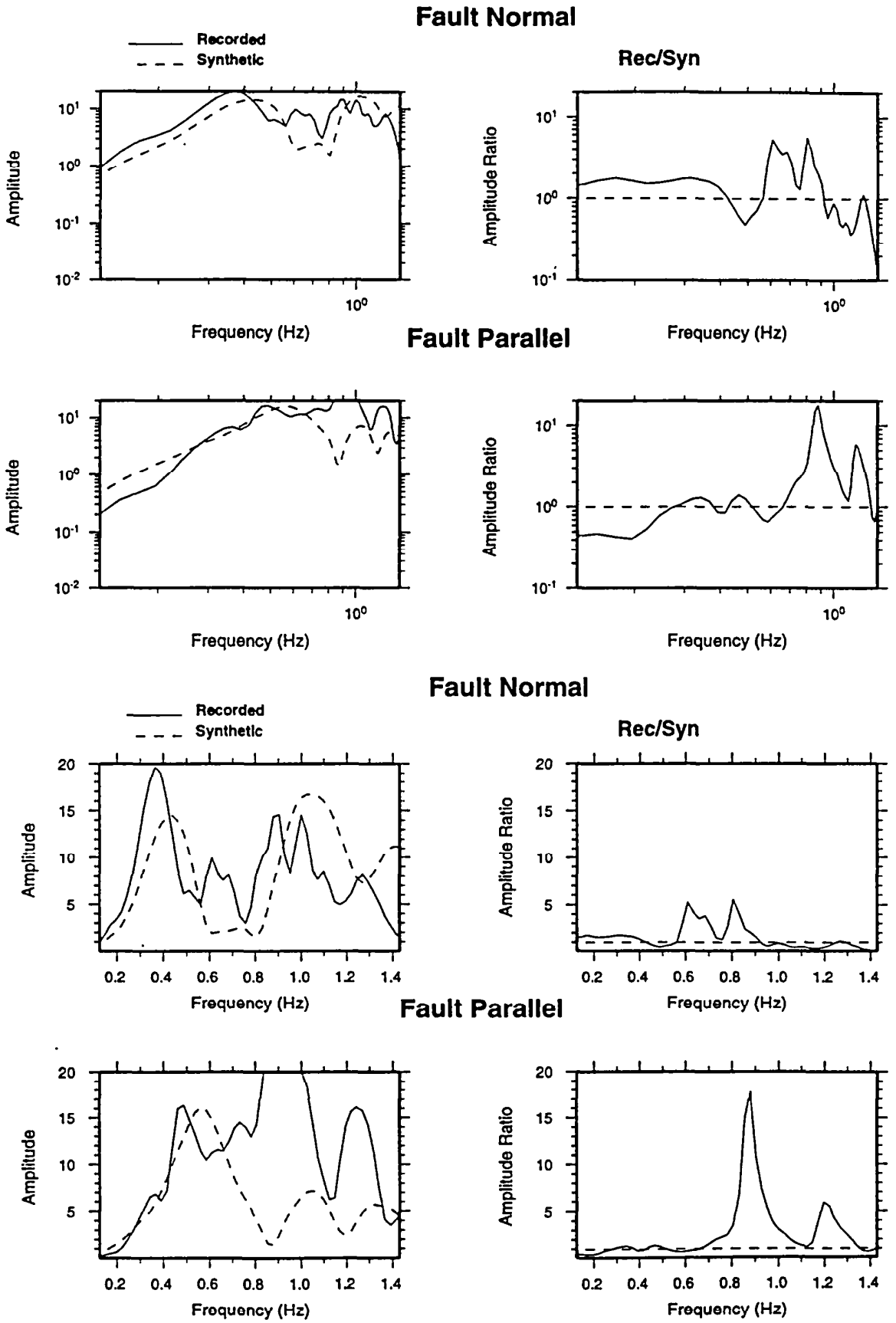

GMT Aug 23 13:57:21 1999 /u1/nancy/PEER-5/Northridge/Comparisons.990823/AP_fspec

Northridge - Filter 0.125-1.43 Hz, Pas 94 BB Sims - kagc

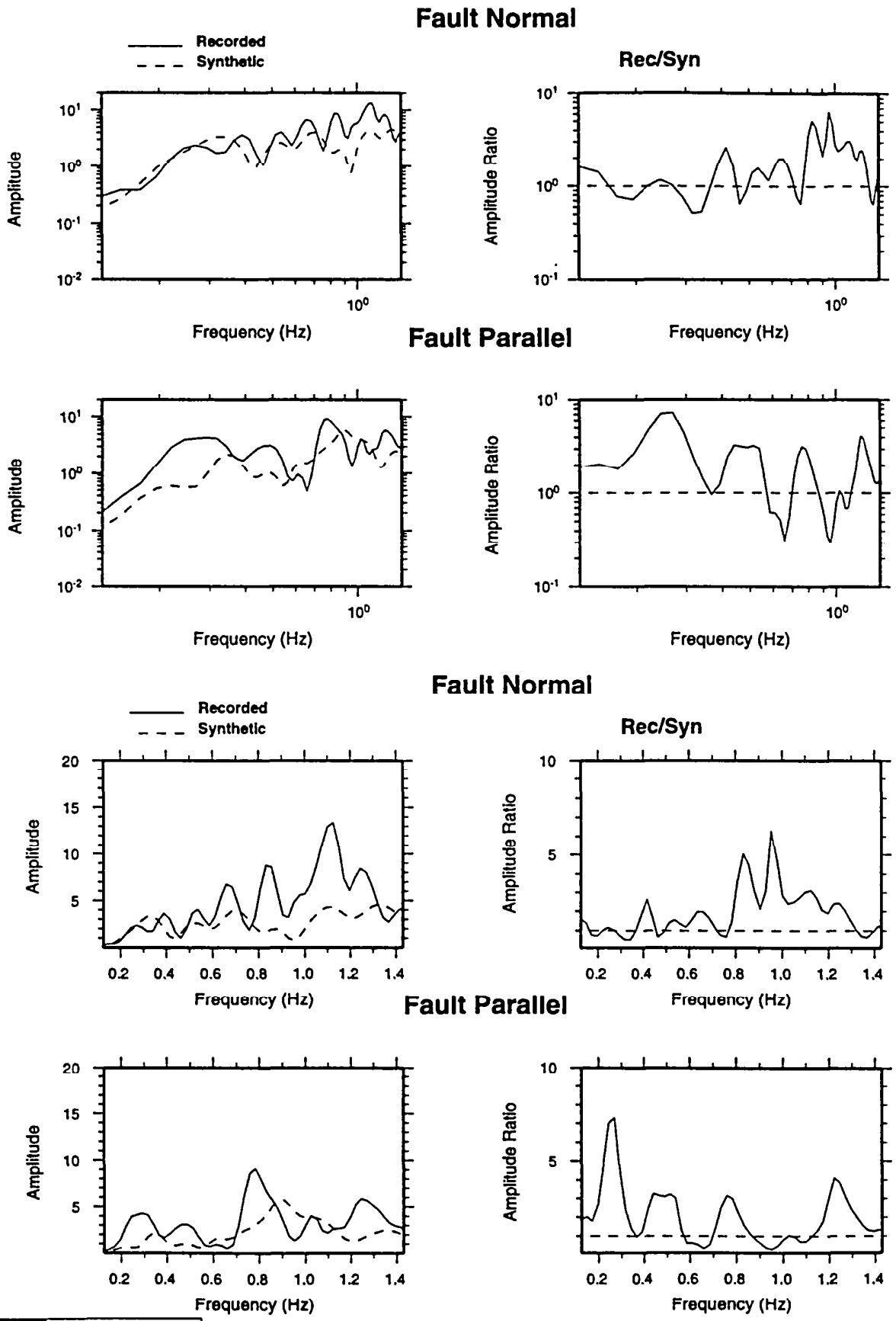

Northridge - Filter 0.125-1.43 Hz, Pas 94 BB Sims - newh

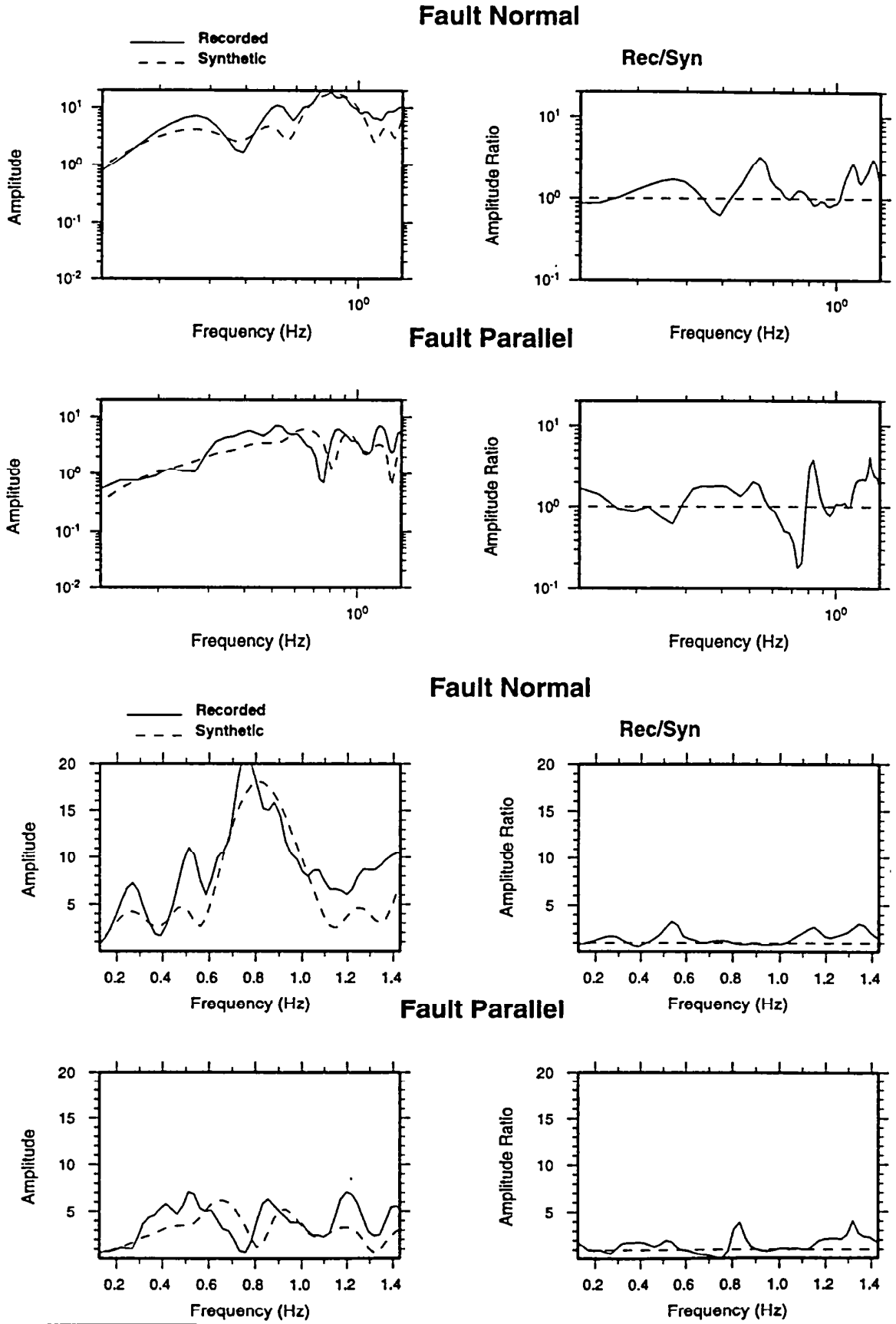

GMT Aug 23 13:58:01 1999 /u1/nancy/PEER-5/Northridge/Comparisons.990823/AP_fspec

Northridge - Filter 0.125-1.43 Hz, Pas 94 BB Sims - nord

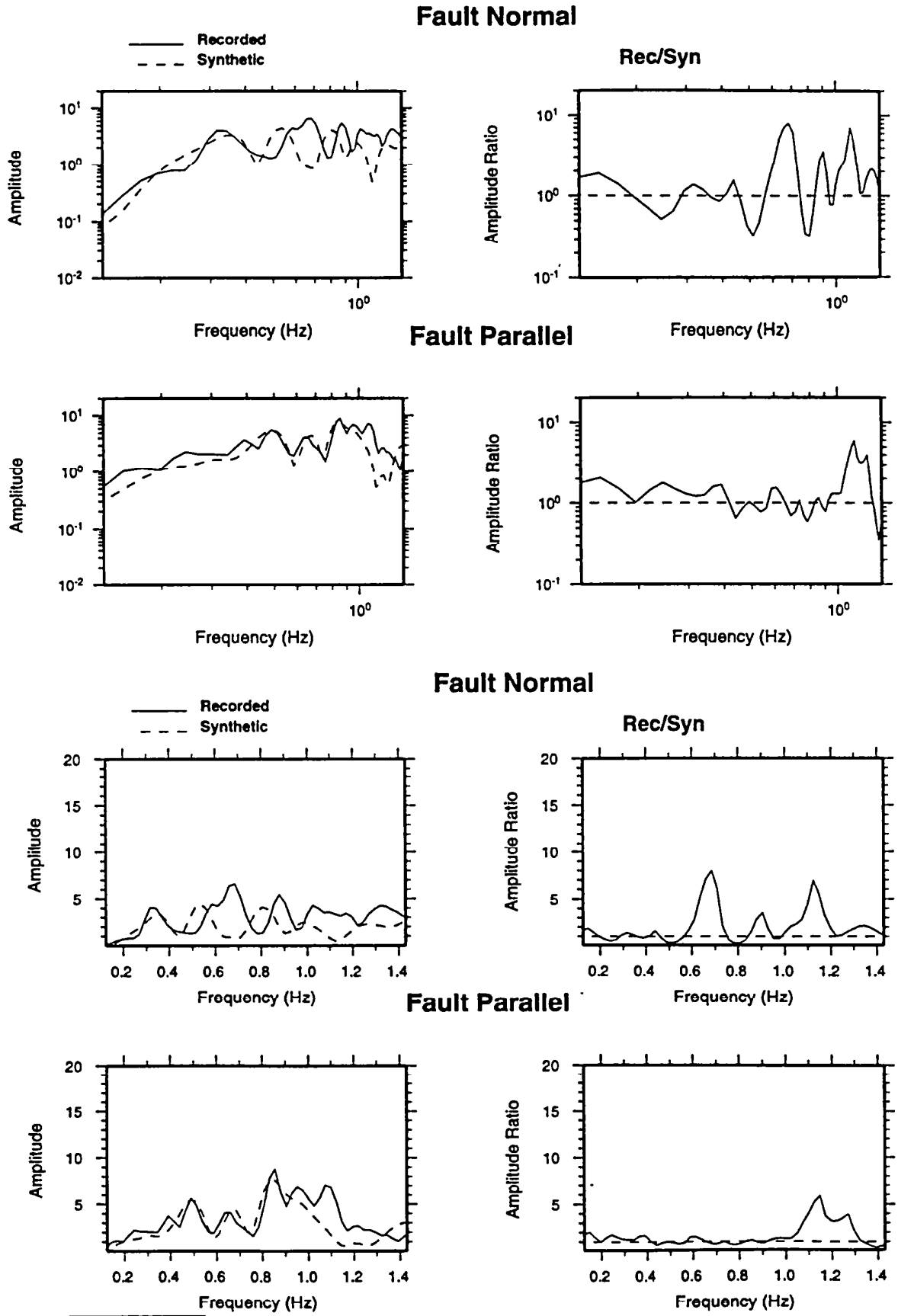

GMT Aug 23 13:58:21 1999 /u1/nancy/PEER-5/Northridge/Comparisons.990823/AP_fspec

Northridge - Filter 0.125-1.43 Hz, Pas 94 BB Sims - pacd

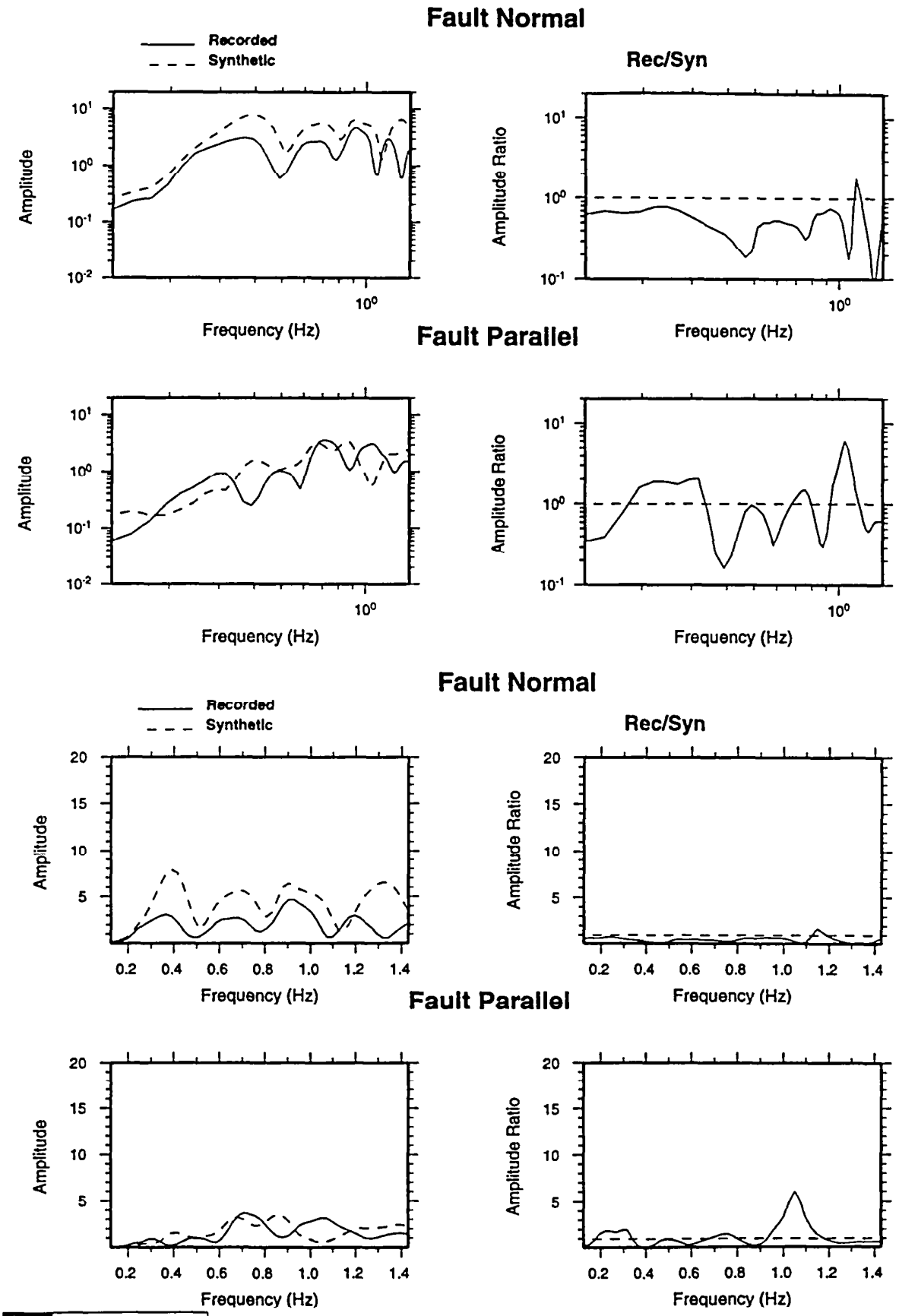

GMT Aug 23 13:58:41 1999 /u1/nancy/PEER-5/Northridge/Comparisons.990823/AP_fspec

Northridge - Filter 0.125-1.43 Hz, Pas 94 BB Sims - rosc

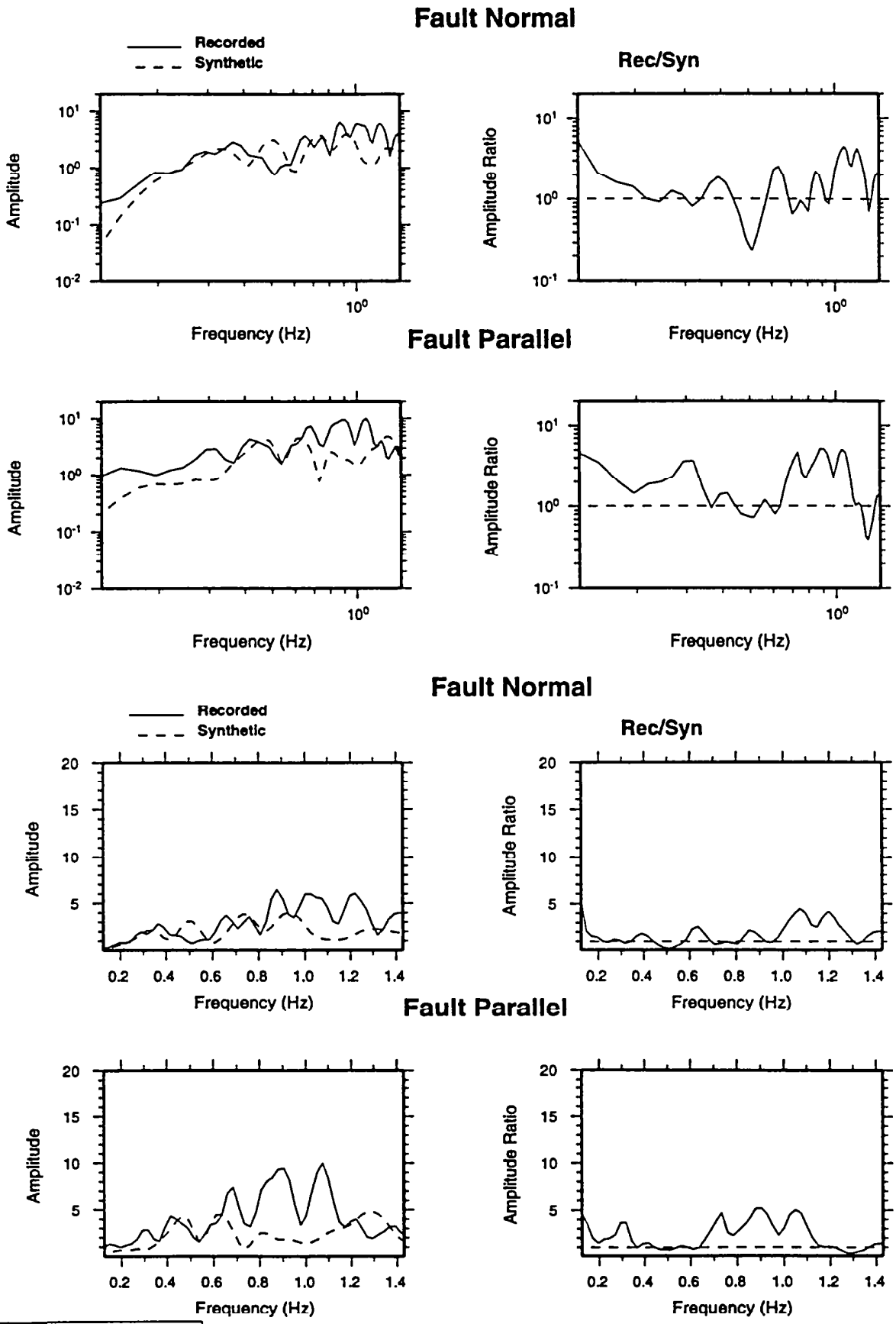

GMT Aug 23 14:00:08 1999 /u1/nancy/PEER-5/Northridge/Comparisons.990823/AP_fspec

Northridge - Filter 0.125-1.43 Hz, Pas 94 BB Sims - rrs

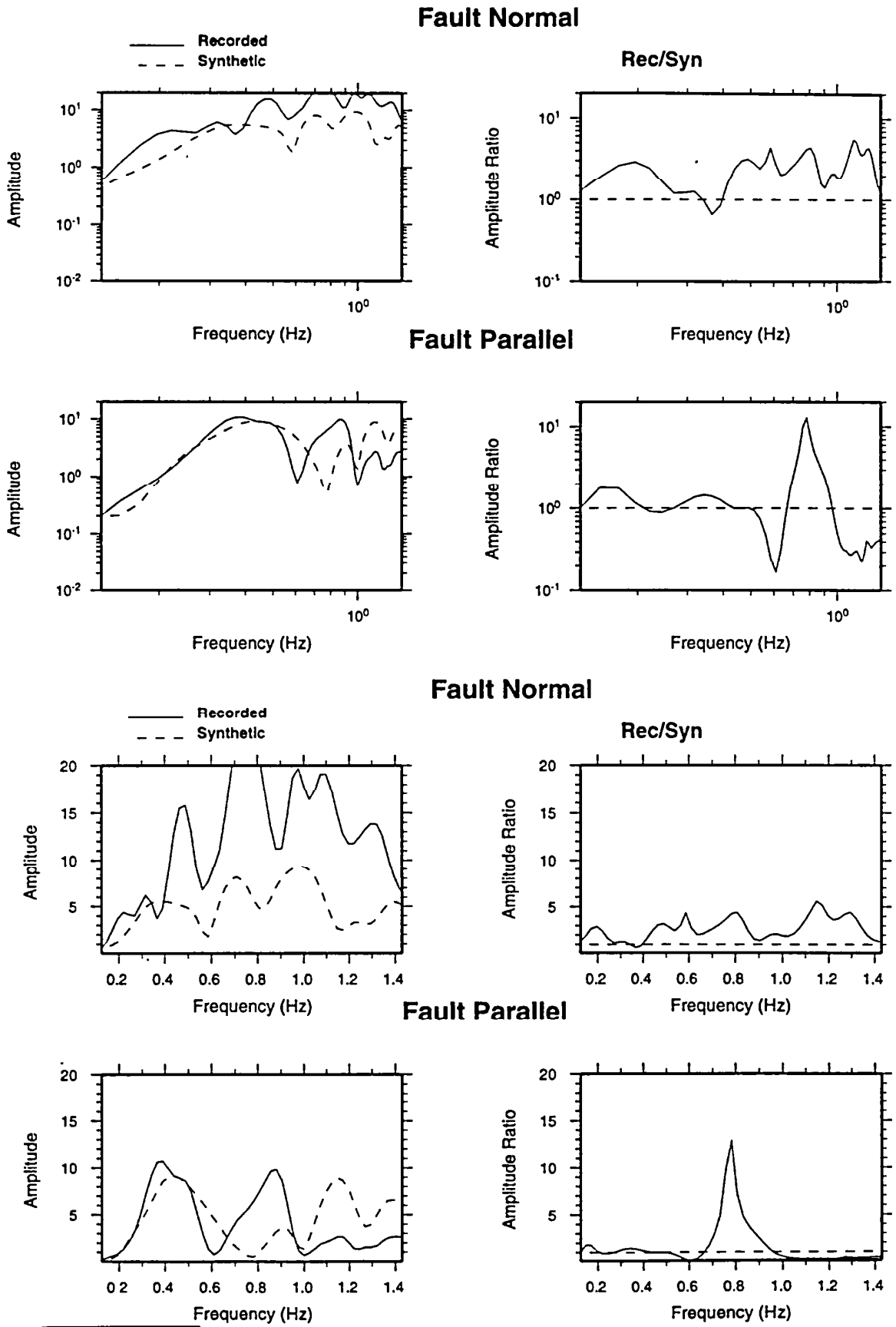

GMT Aug 24 10:56:58 1999 /u1/nancy/PEER-5/Northridge/Comparisons.990823/AP_fspec

Northridge - Filter 0.125-1.43 Hz, Pas 94 BB Sims - sati

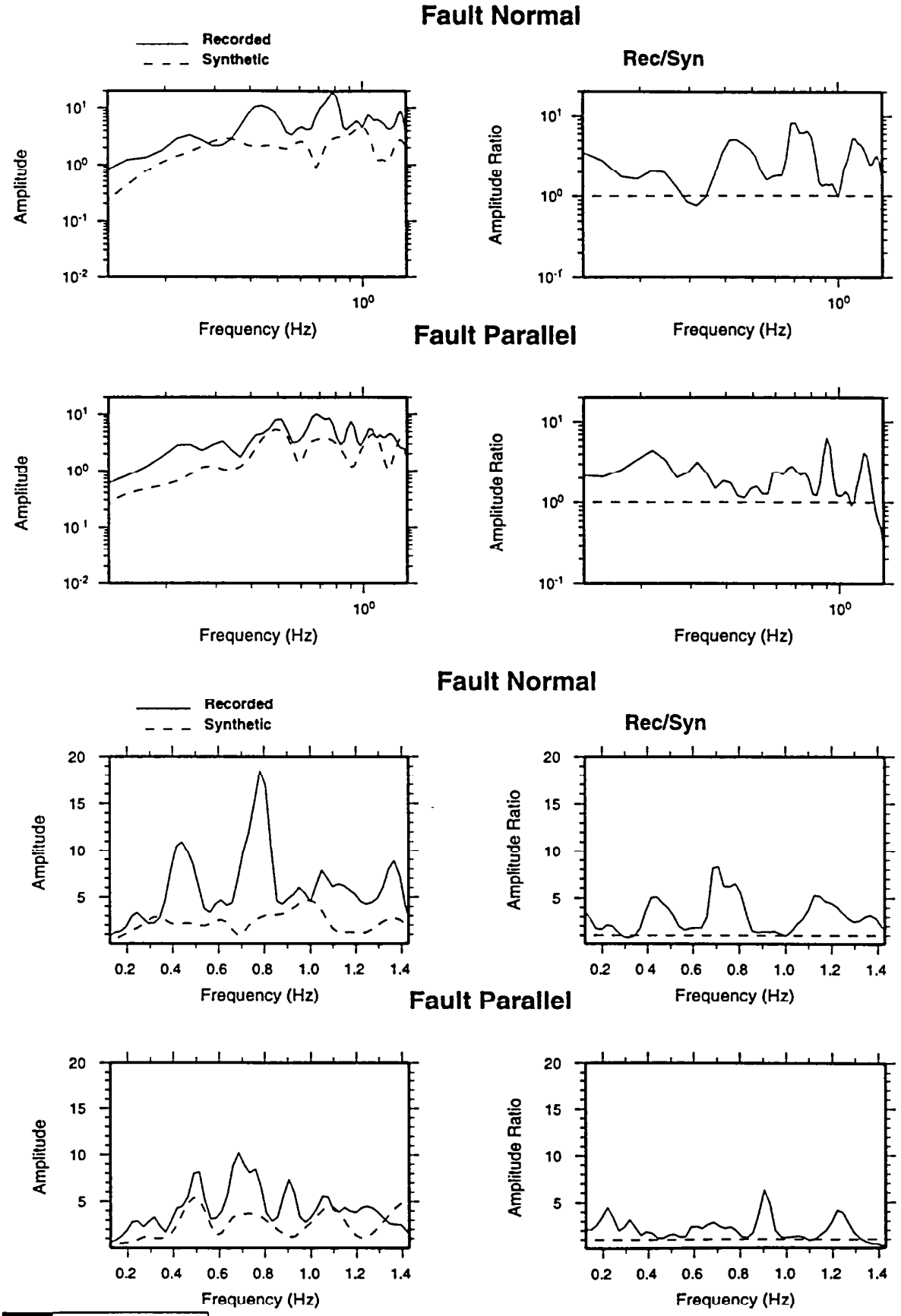

GMT Aug 24 10:57:31 1999 /u1/nancy/PEER-5/Northridge/Comparisons.990823/AP_fspec

Northridge - Filter 0.125-1.43 Hz, Pas 94 BB Sims - scs

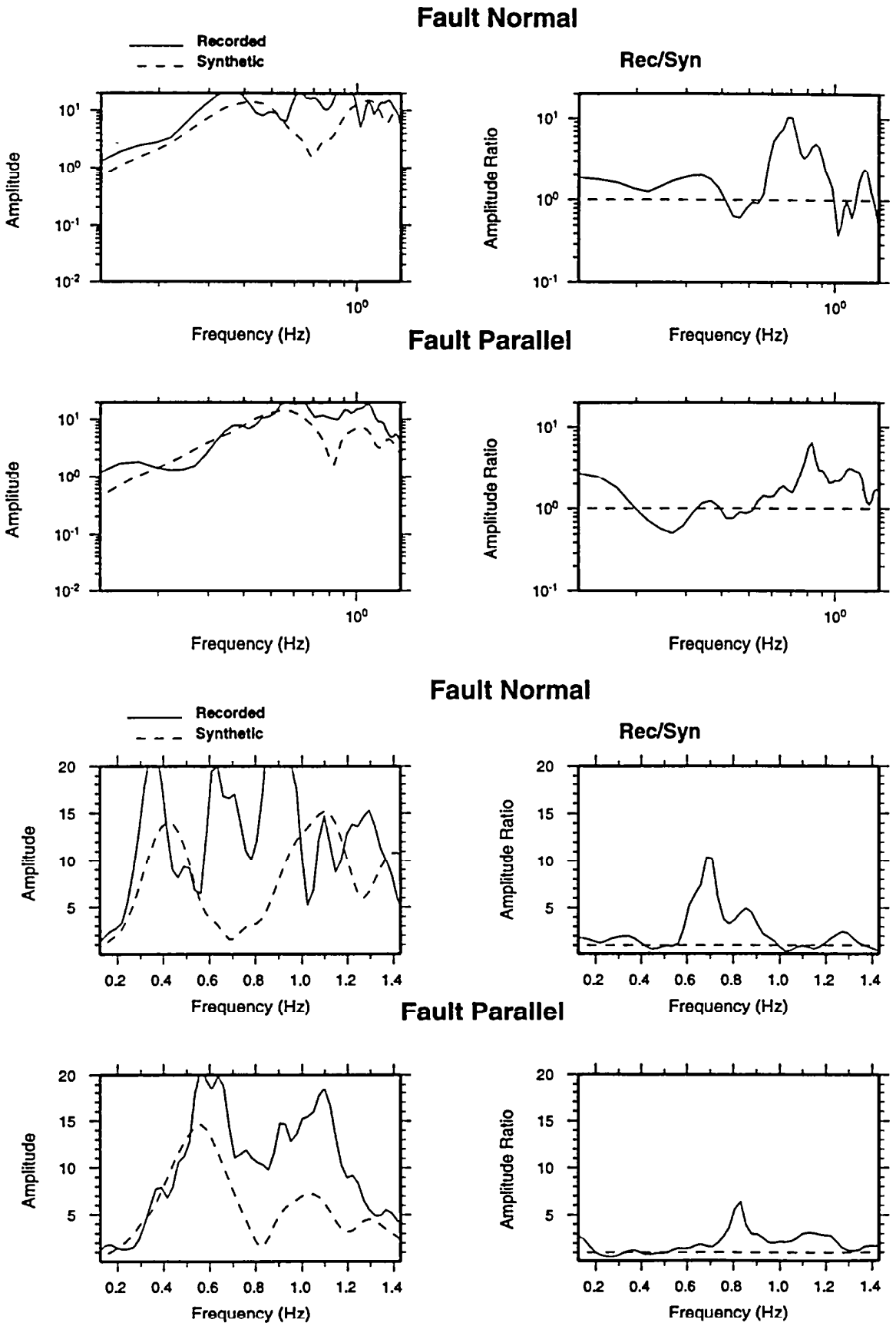

GMT Aug 23 14:01:09 1999 /u1/nancy/PEER-5/Northridge/Comparisons.990823/AP_fspec

Northridge - Filter 0.125-1.43 Hz, Pas 94 BB Sims - scse

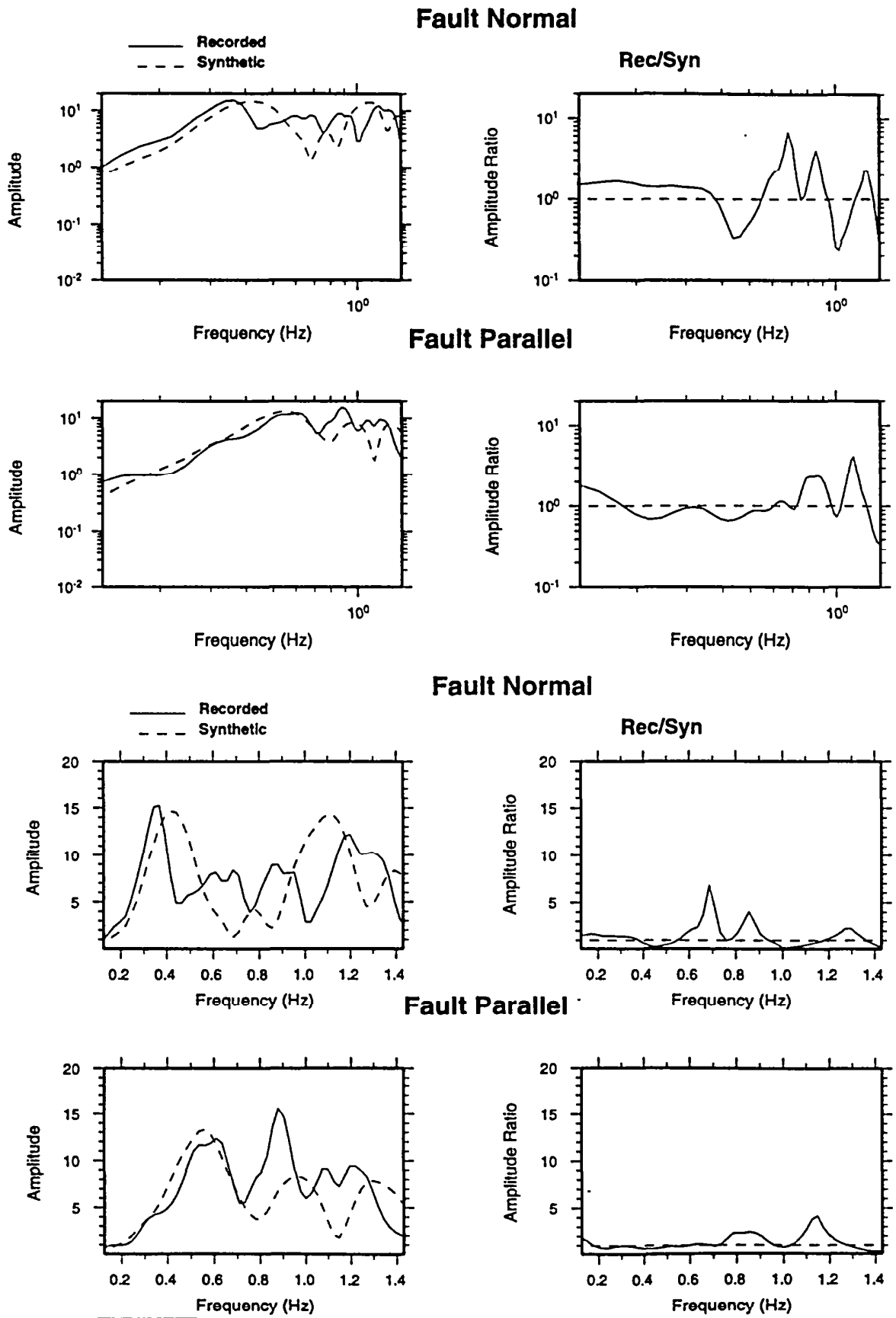

GMT Aug 23 14:01:29 1999 /u1/nancy/PEER-5/Northridge/Comparisons.990823/AP_fspec

Northridge - Filter 0.125-1.43 Hz, Pas 94 BB Sims - ssus

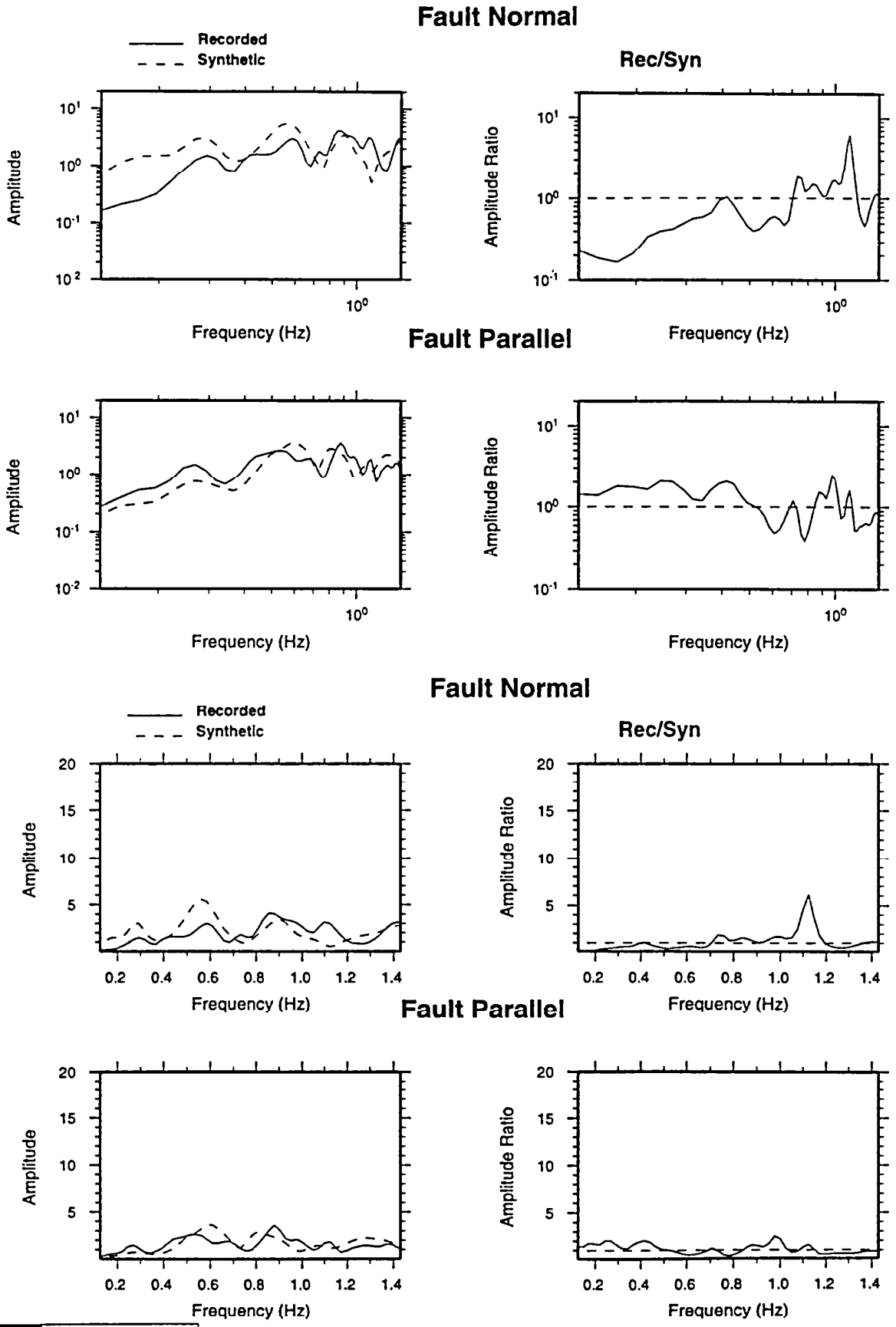

GMT Aug 24 10.58.40 1999 /u1/nancy/PEER-5/Northridge/Comparisons.990823/AP_fspec

Northridge - Filter 0.125-1.43 Hz, Pas 94 BB Sims - sylm

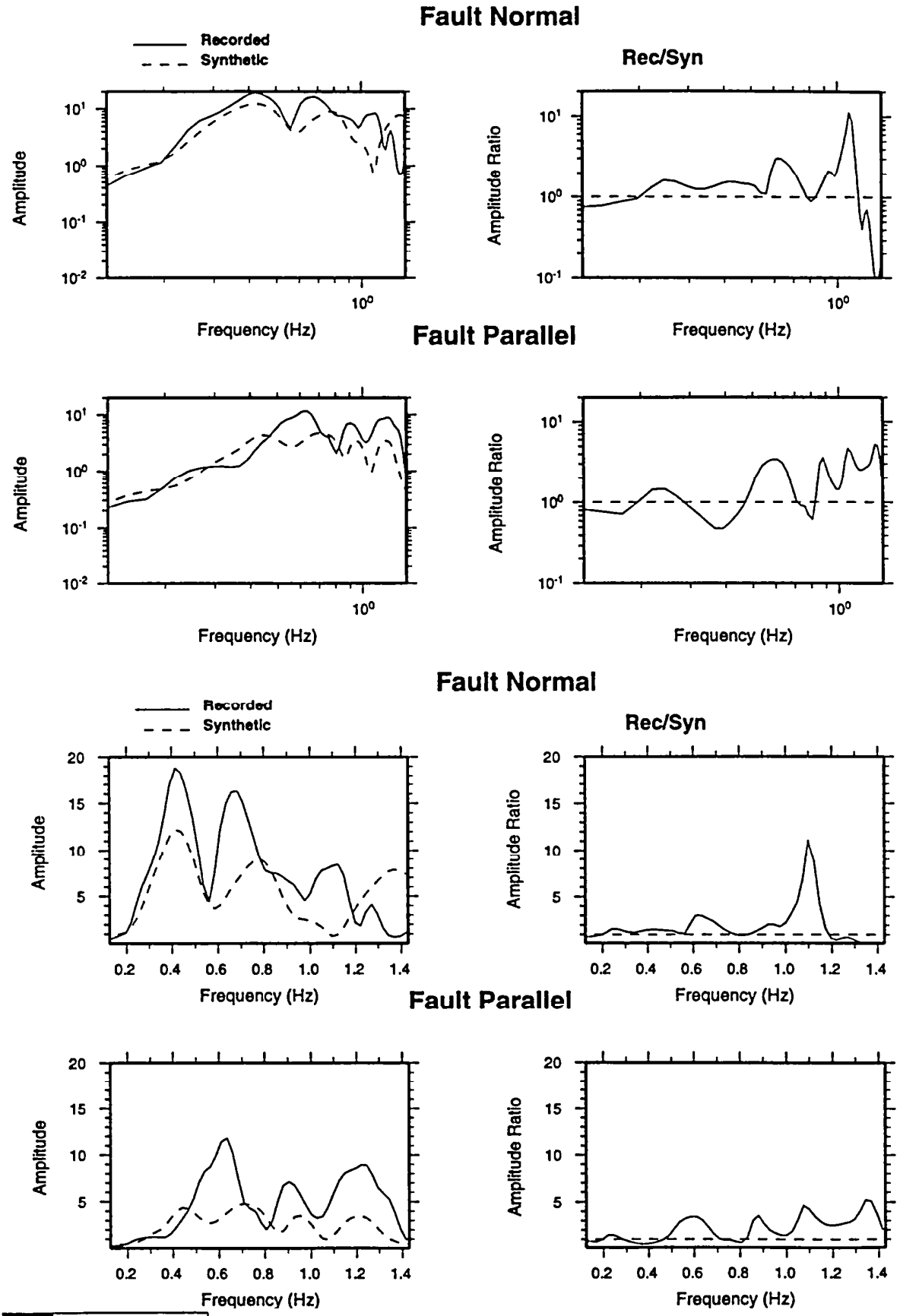

GMT Aug 23 14:02:09 1999 /u1/nancy/PEER-5/Northridge/Comparisons.990823/AP_fspec

Northridge - Fault Normal

SA at 7.0 sec

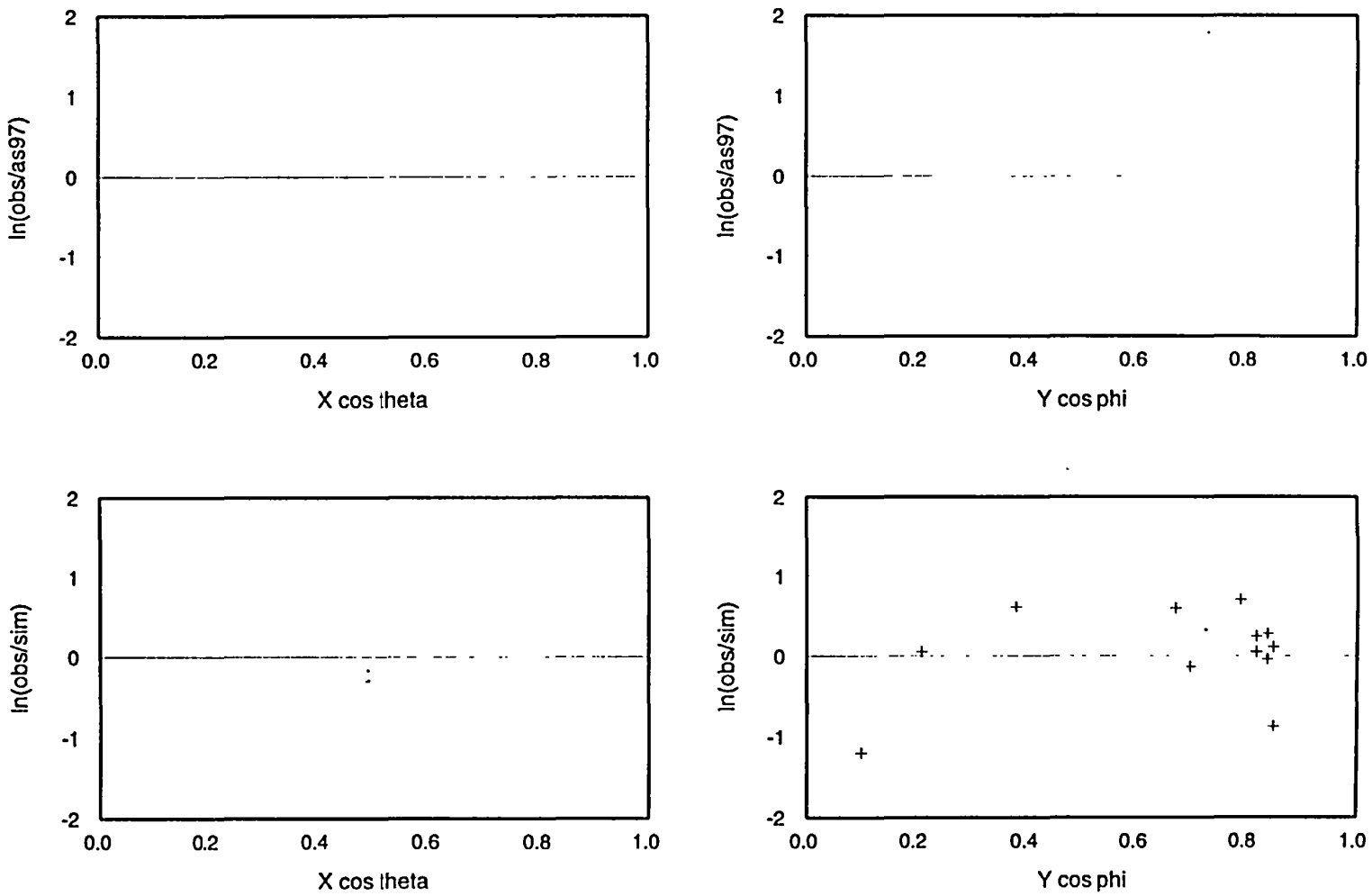

GMT Aug 24 11:15:05 1999 /u1/nancy/PEER-5/Northridge/Comparisons.990823/Resid_plots

Northridge - Fault Parallel

SA at 7.0 sec

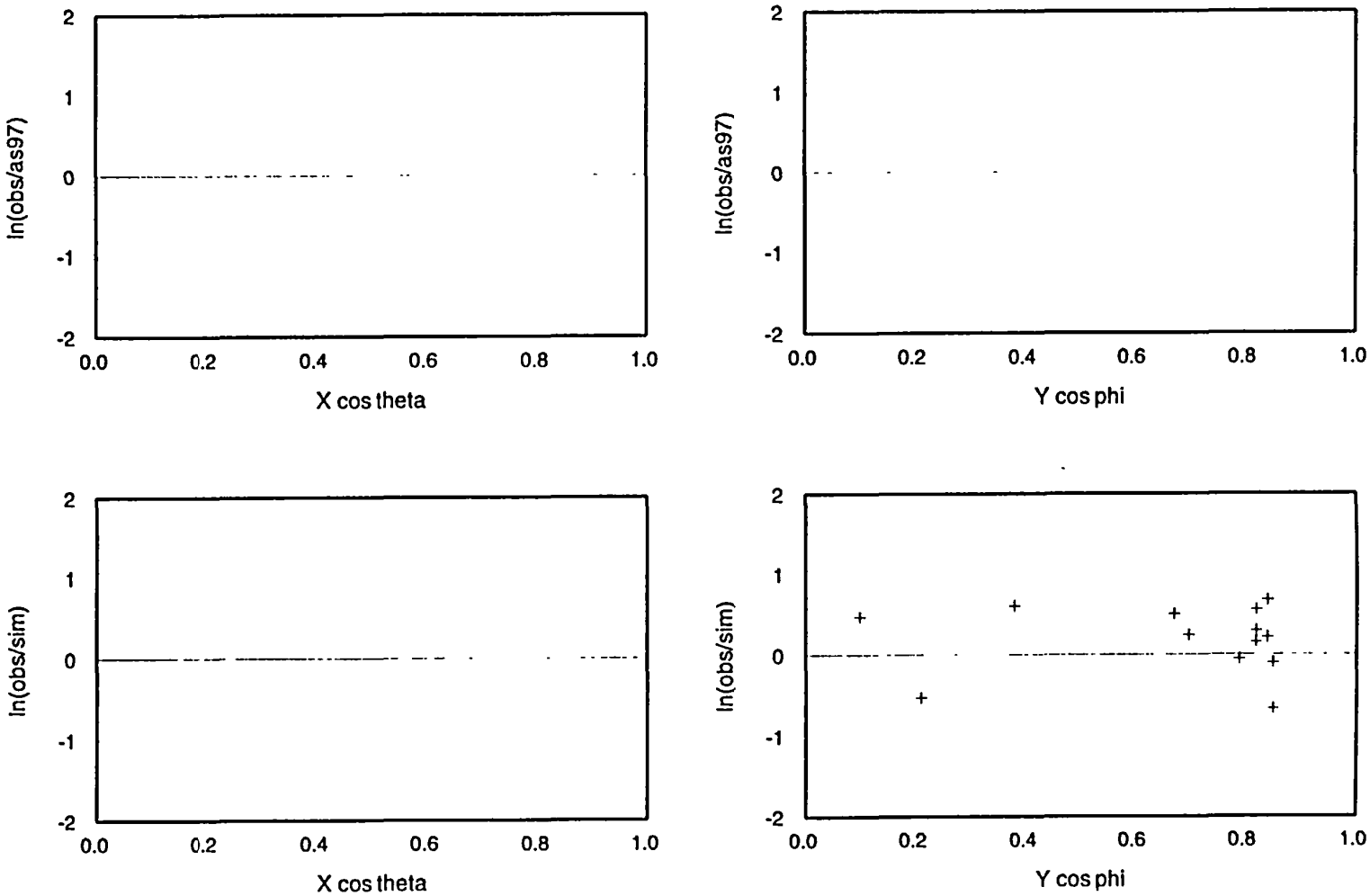

GMT Aug 24 11:15:30 1999 /u1/nancy/PEER-5/Northridge/Comparisons.990823/Resid_plots

Northridge - Fault Normal

SA at 6.0 sec

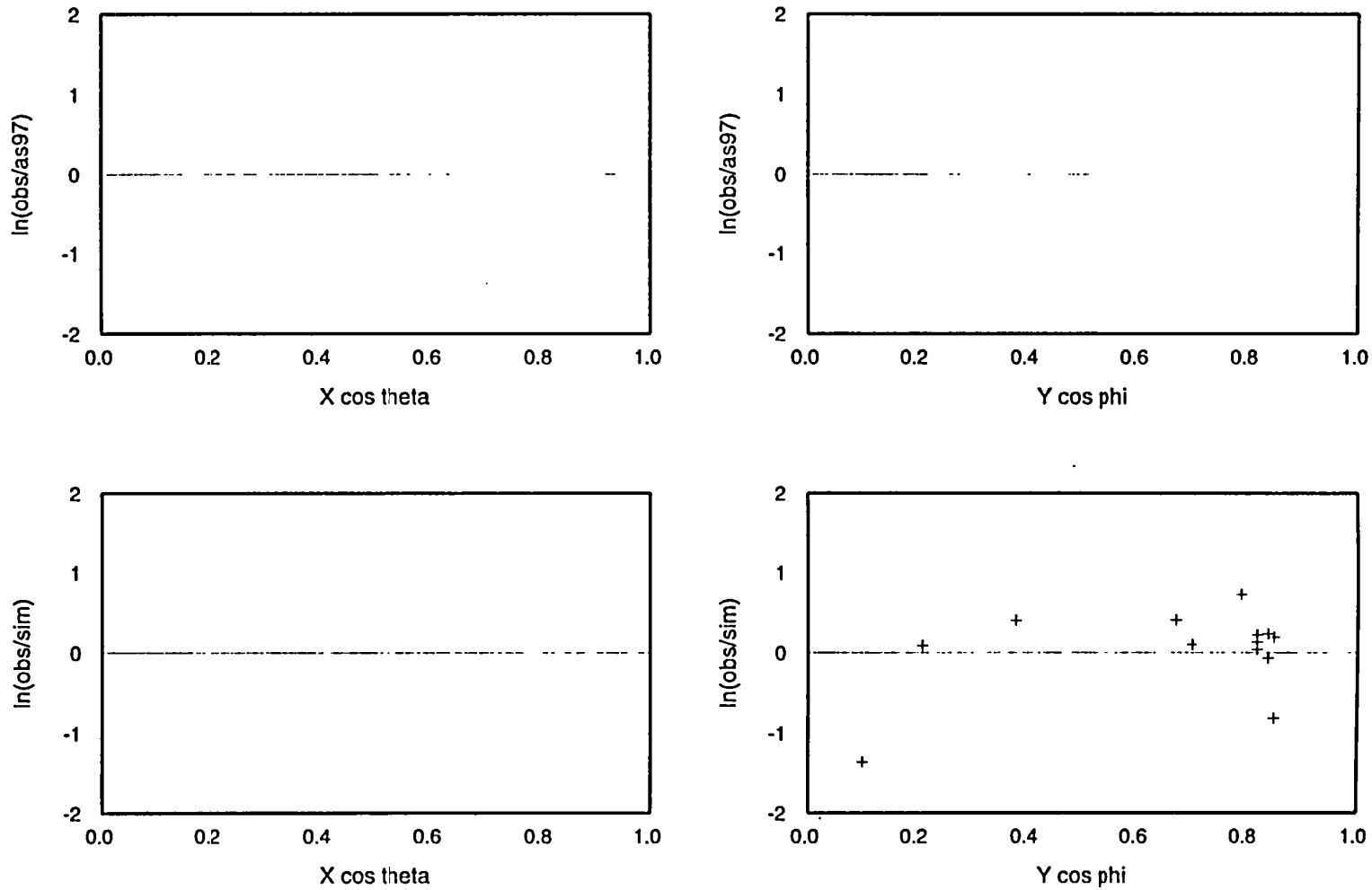

GMT Aug 24 11:15:56 1999 /u1/nancy/PEER-5/Northridge/Comparisons.990823/Resid_plots

Northridge - Fault Parallel

SA at 6.0 sec

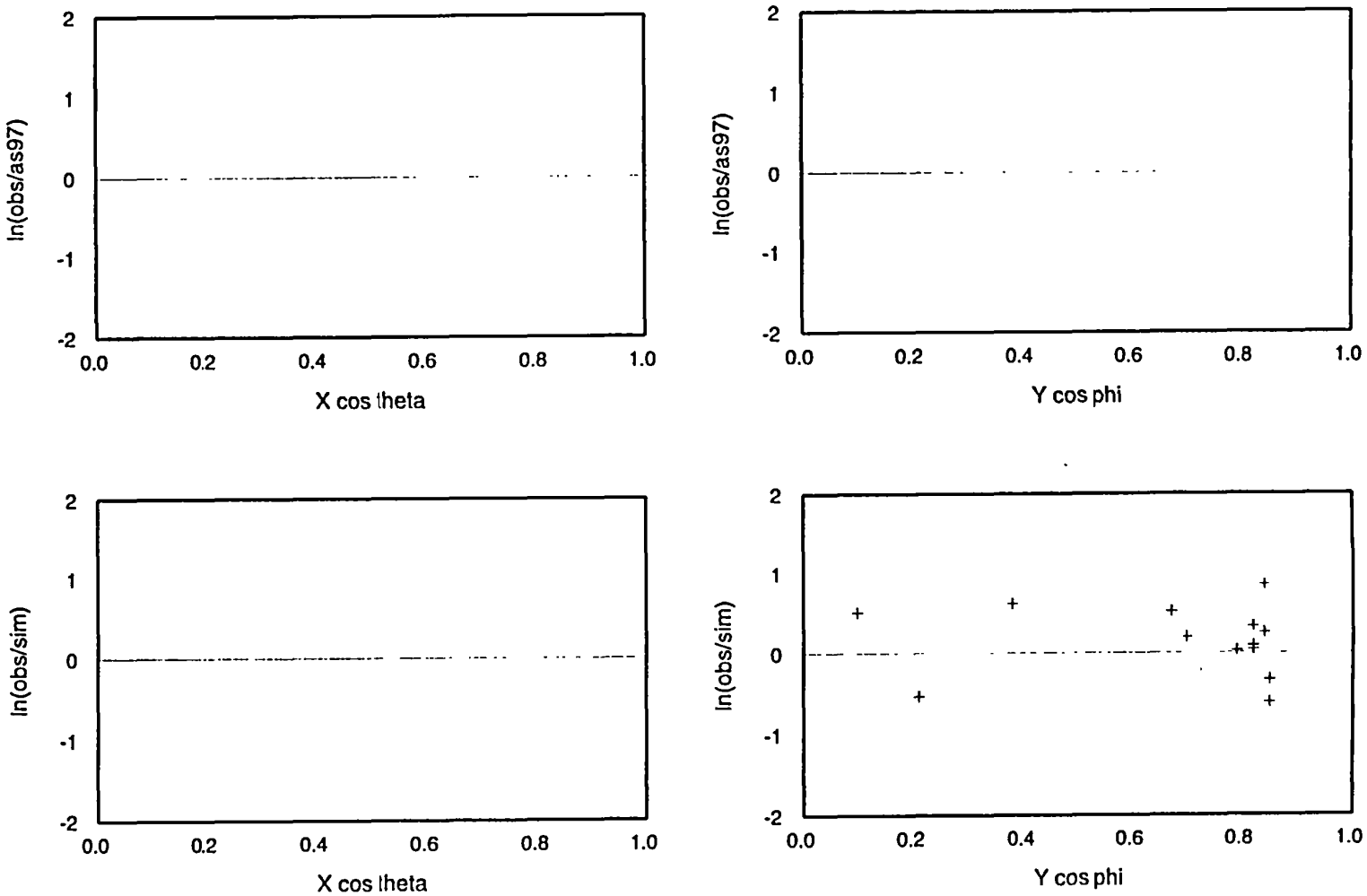

GMT Aug 24 11:16:09 1999 /u1/nancy/PEER-5/Northridge/Comparisons.990823/Resid_plots

Northridge - Fault Normal

SA at 5.0 sec

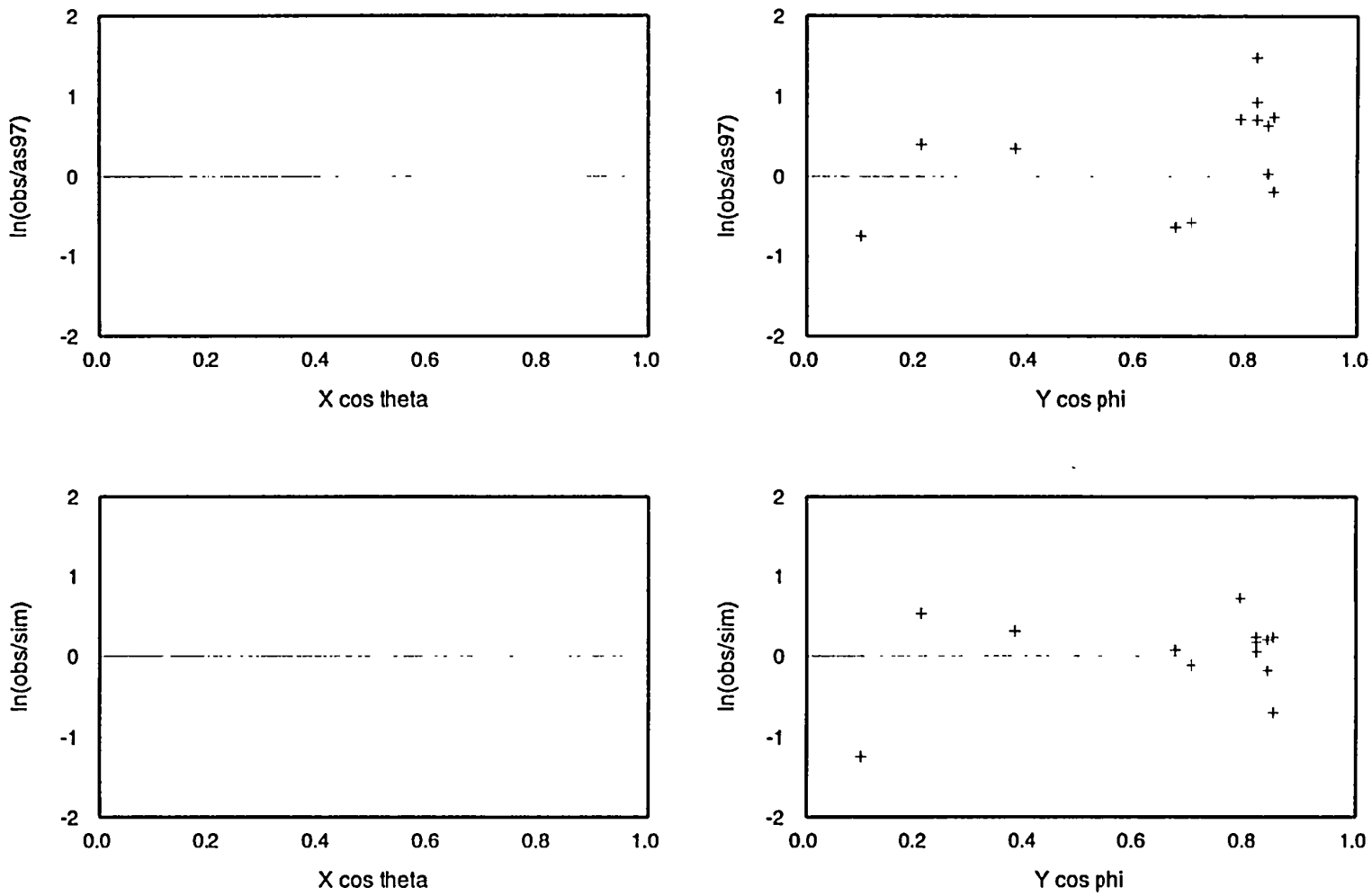

GMT Aug 24 11:16:19 1999 /u1/nancy/PEER-5/Northridge/Comparisons.990823/Resid_plots

Northridge - Fault Parallel

SA at 5.0 sec

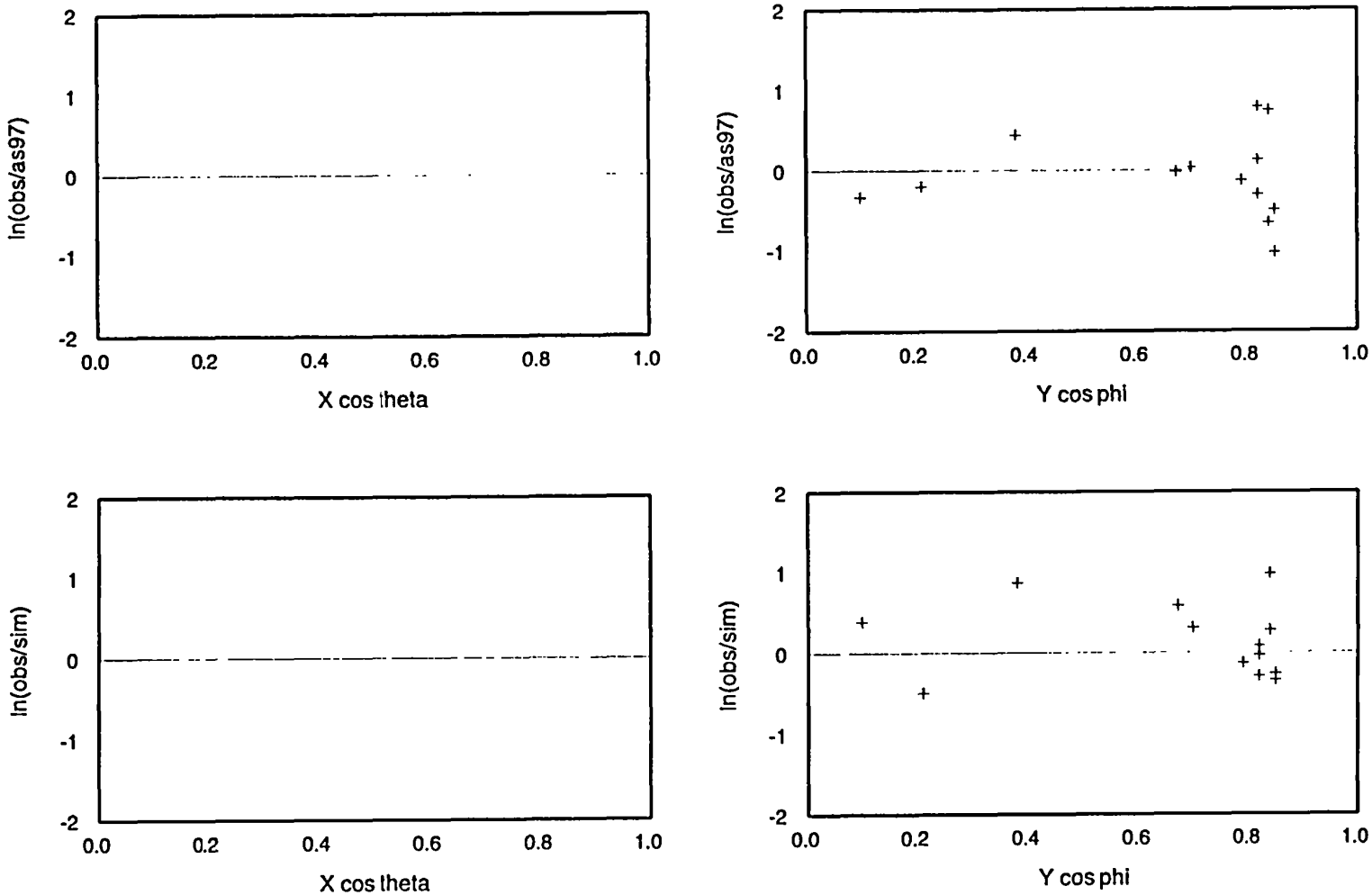

GMT Aug 24 11:16:35 1999 /u1/nancy/PEER-5/Northridge/Comparisons.990823/Resid_plots

Northridge - Fault Normal

SA at 4.0 sec

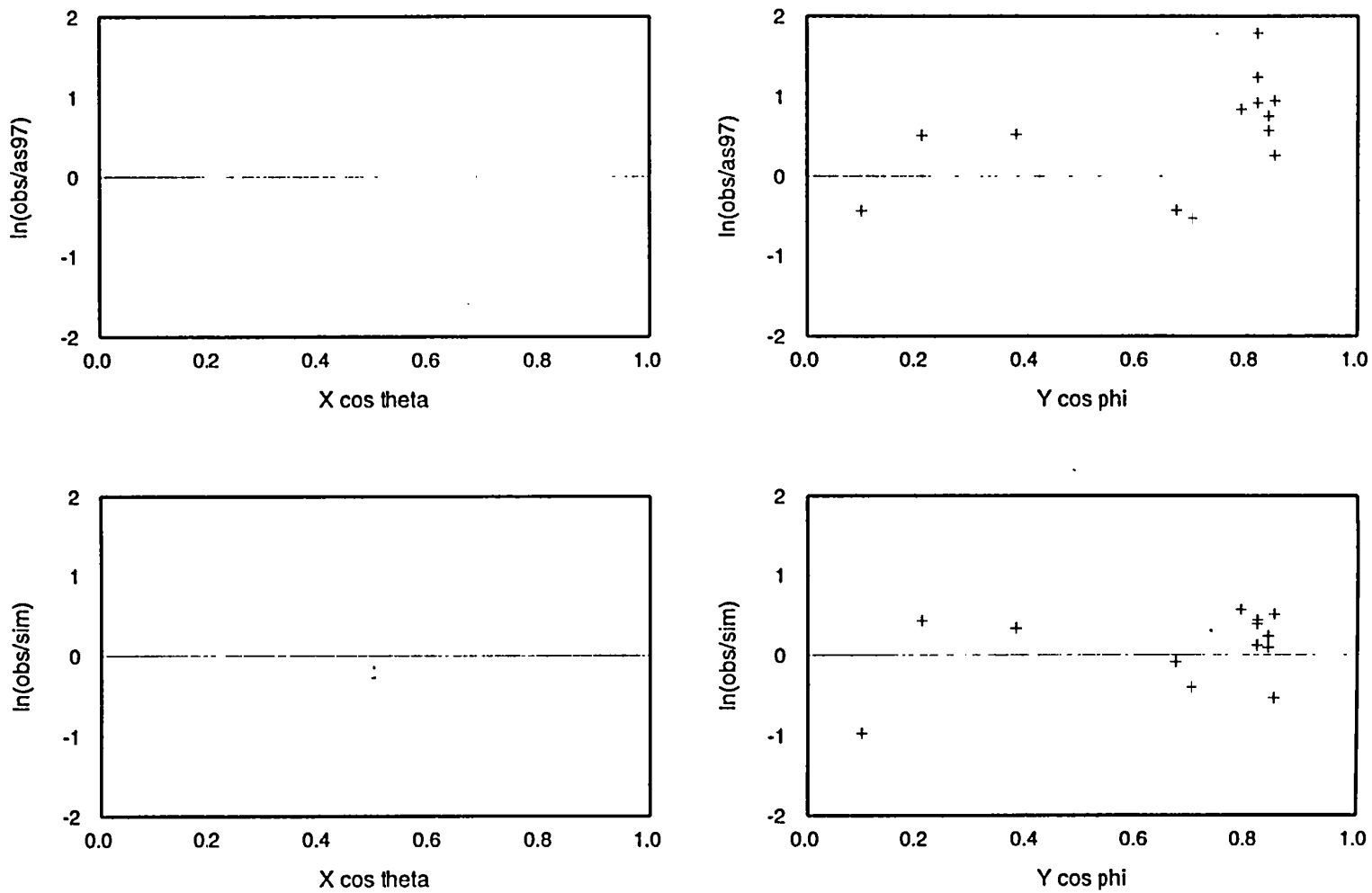

GMT Aug 24 11:16:46 1999 /u1/nancy/PEER-5/Northridge/Comparisons.990823/Resld_plots

Northridge - Fault Parallel

SA at 4.0 sec

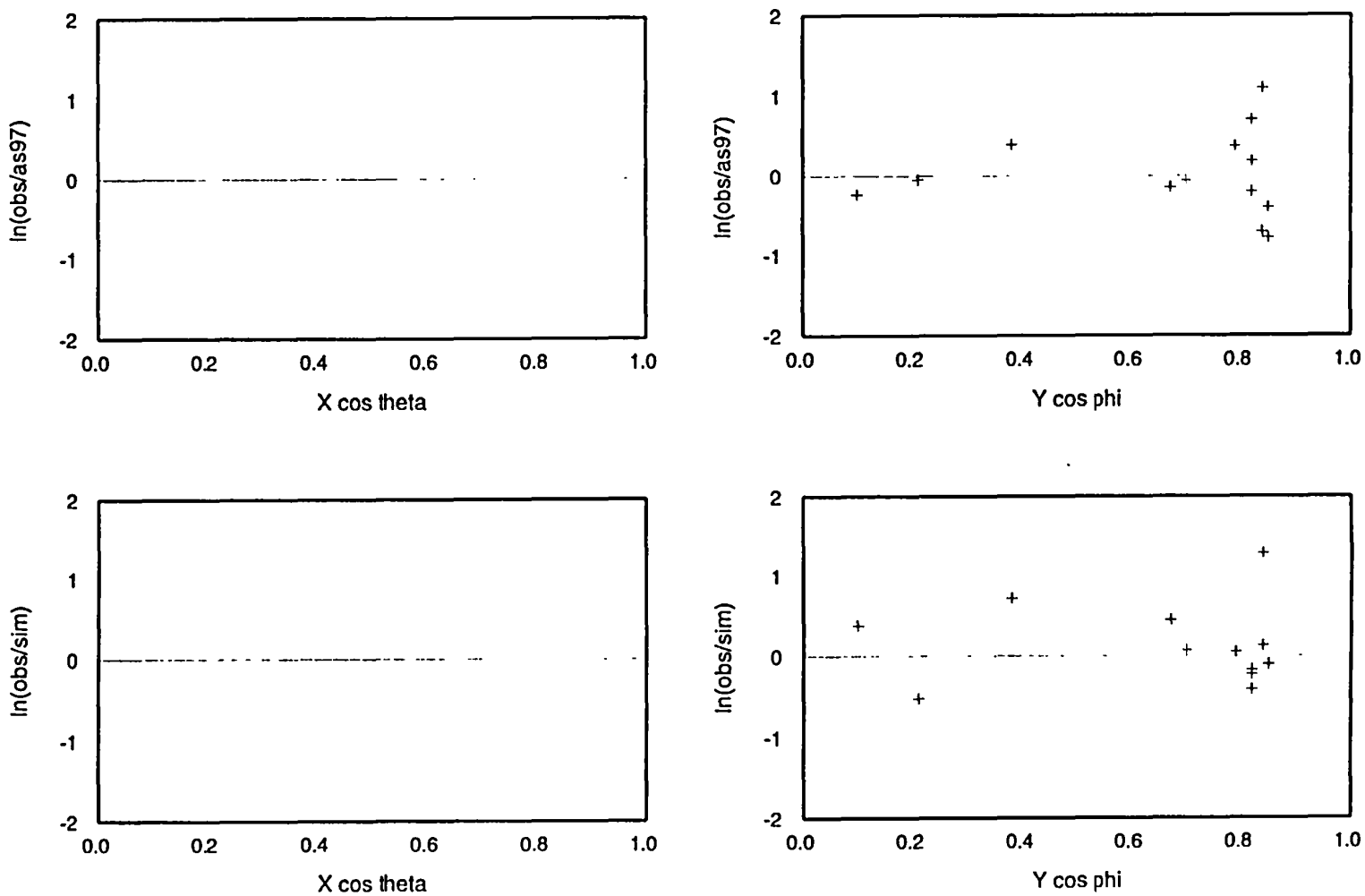

GMT Aug 24 11:18:05 1999 /u1/nancy/PEER-5/Northridge/Comparisons.990823/Resid_plots

Northridge - Fault Normal

SA at 3.0 sec

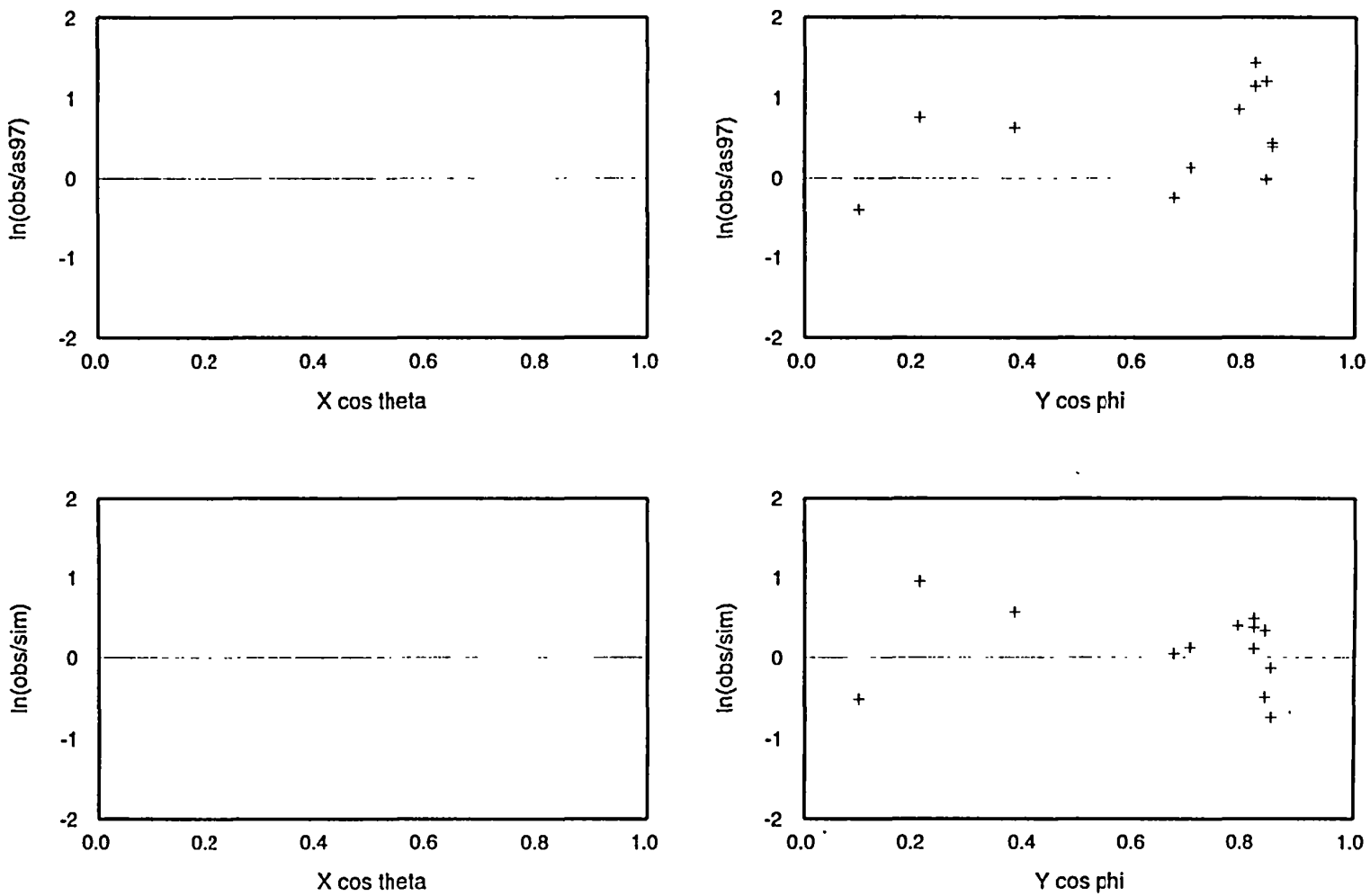

GMT Aug 24 11:18:18 1999 /u1/nancy/PEER-5/Northridge/Comparisons.990823/Resid_plots

Northridge - Fault Parallel

SA at 3.0 sec

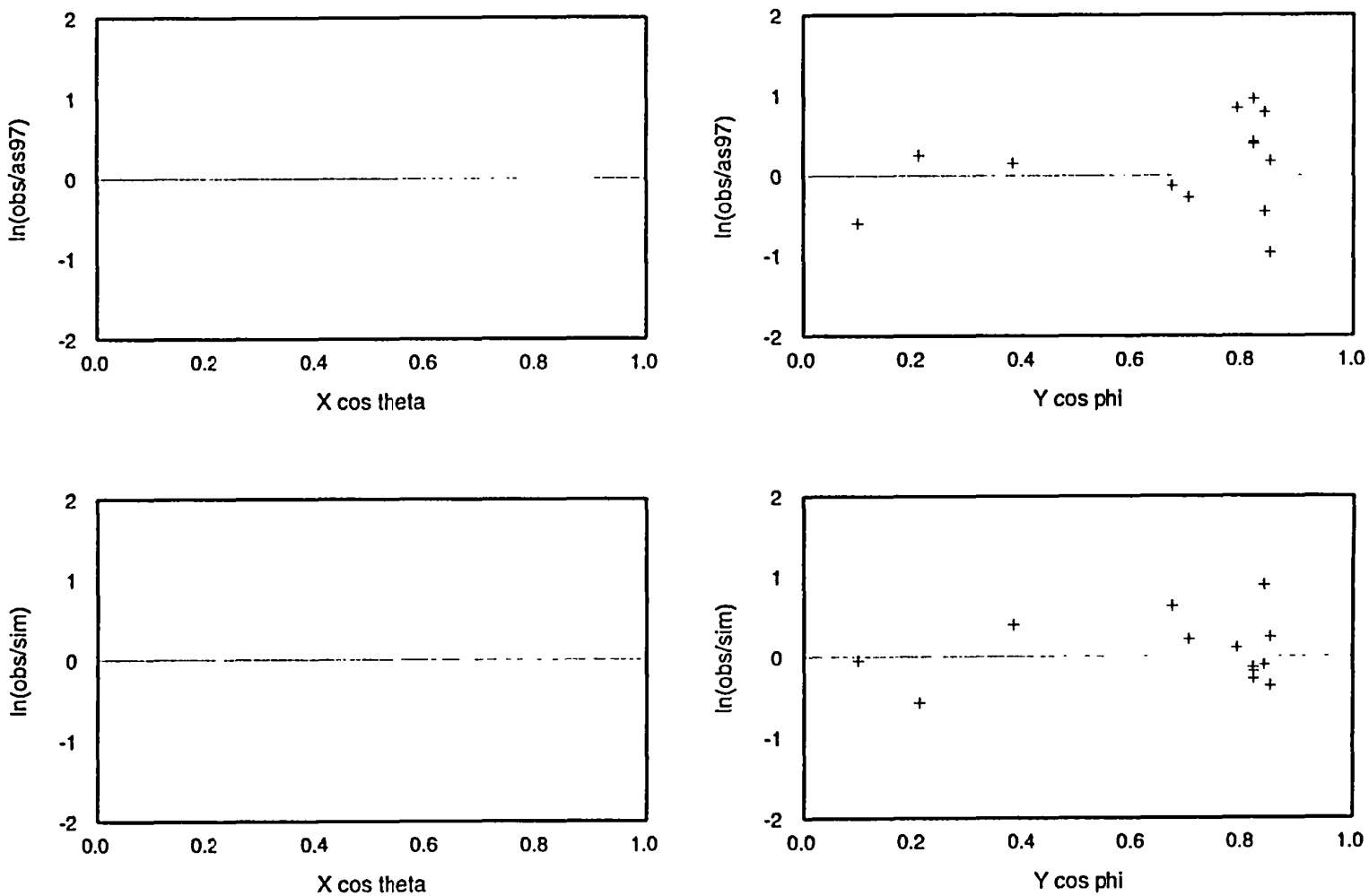

GMT Aug 24 11:19:27 1999 /u1/nancy/PEER-5/Northridge/Comparisons.990823/Resid_plots

Northridge - Fault Normal

SA at 2.0 sec

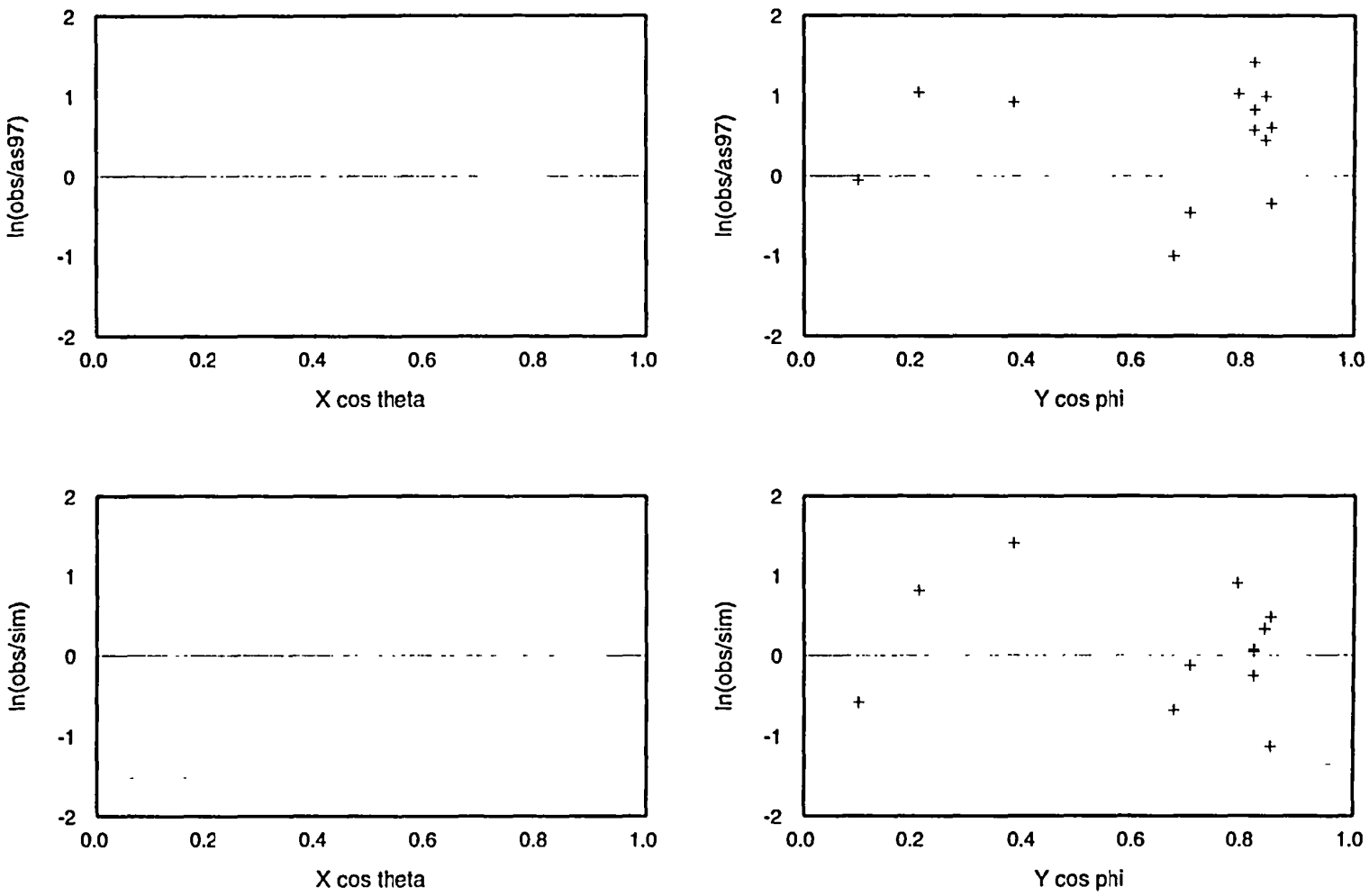

GMT Aug 24 11:19:50 1999 /u1/nancy/PEER-5/Northridge/Comparisons.990823/Resid_plots

Northridge - Fault Normal

SA at 1.5 sec

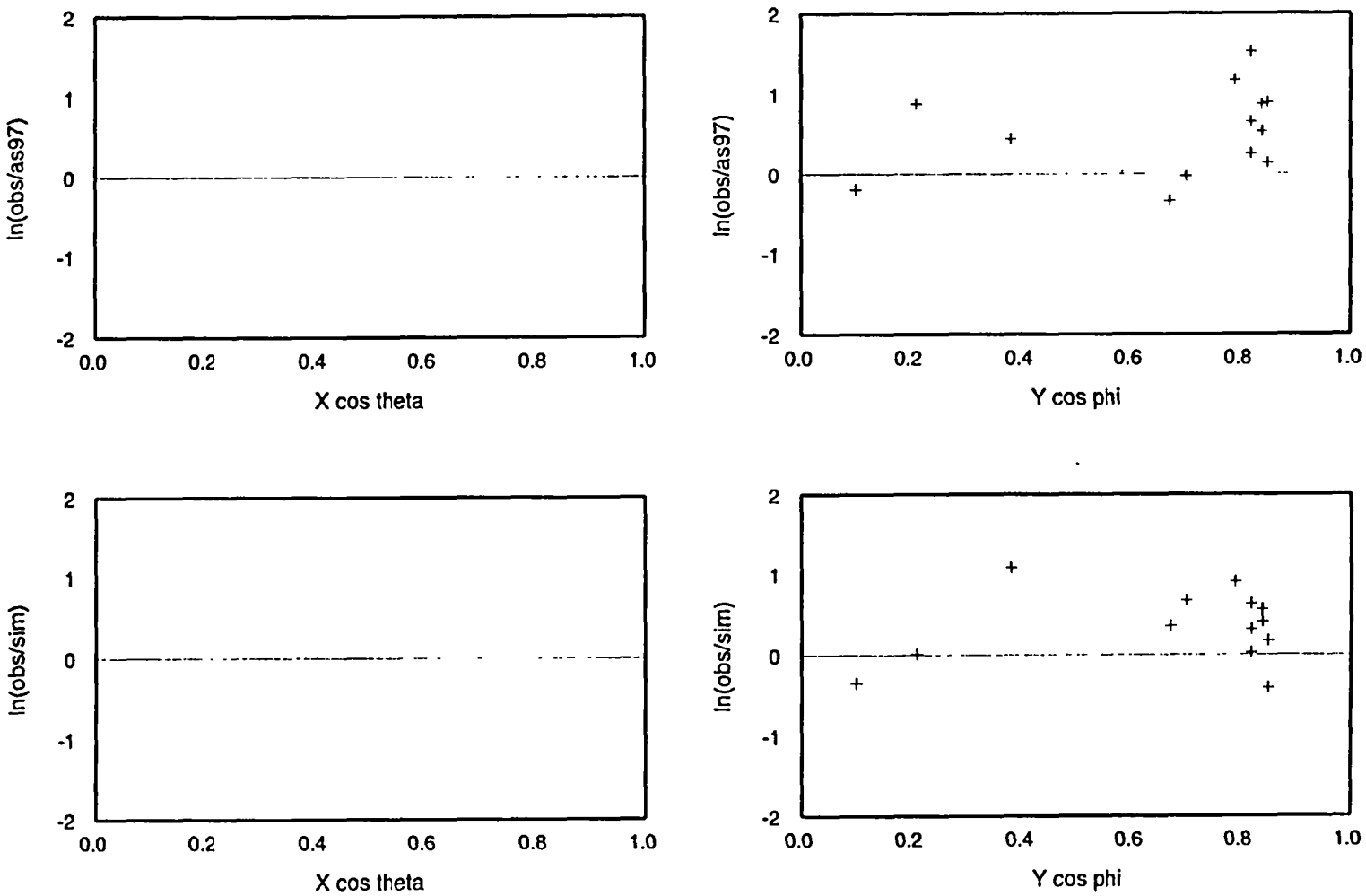

GMT Aug 24 11:21:53 1999 /u1/nancy/PEER-5/Northridge/Comparisons.990823/Resid_plots

Northridge - Fault Parallel

SA at 1.5 sec

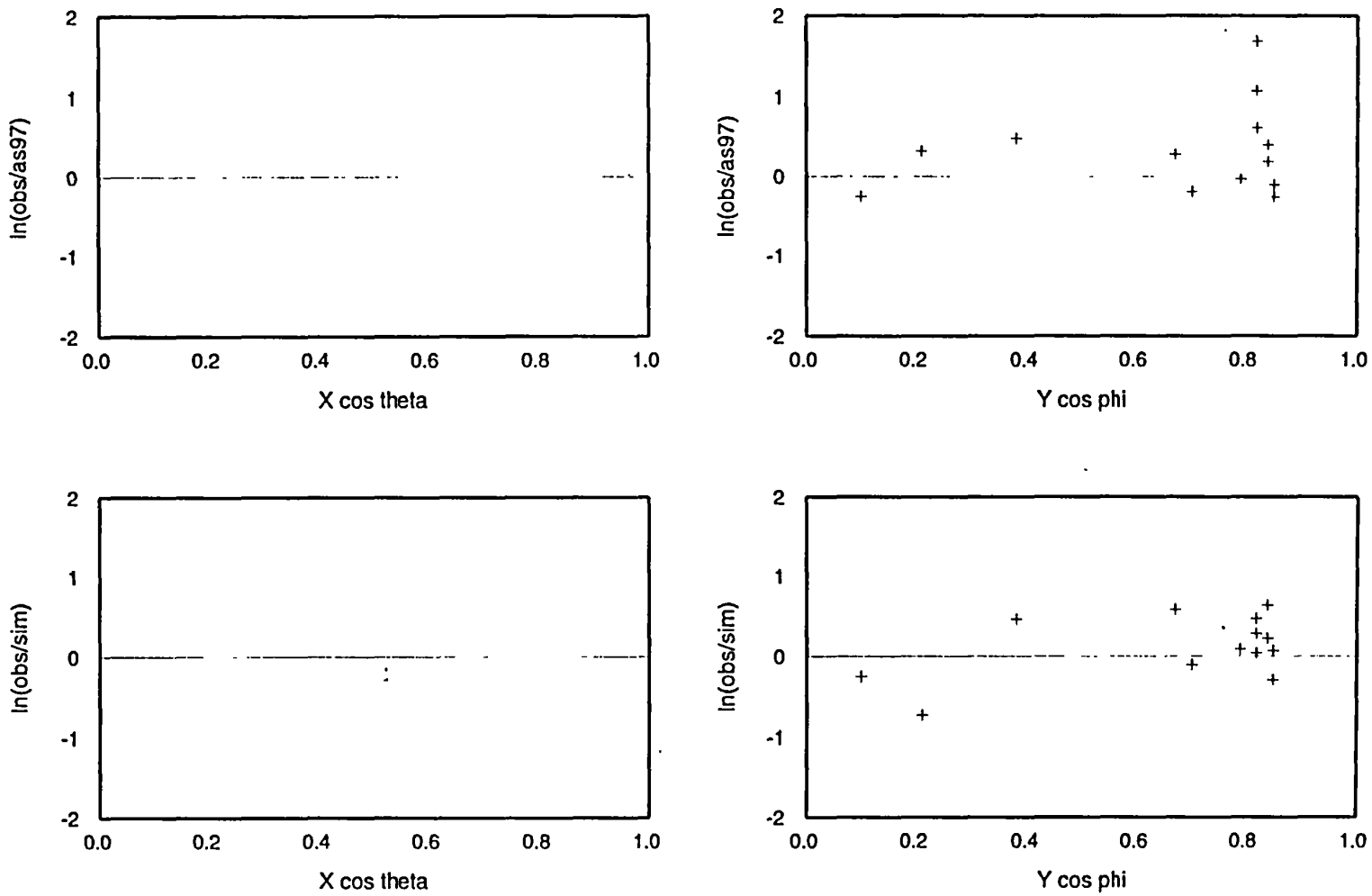

GMT Aug 24 11:22:02 1999 /u1/nancy/PEER-5/Northridge/Comparisons.990823/Resid_plots

Northridge - Fault Normal

SA at 1.0 sec

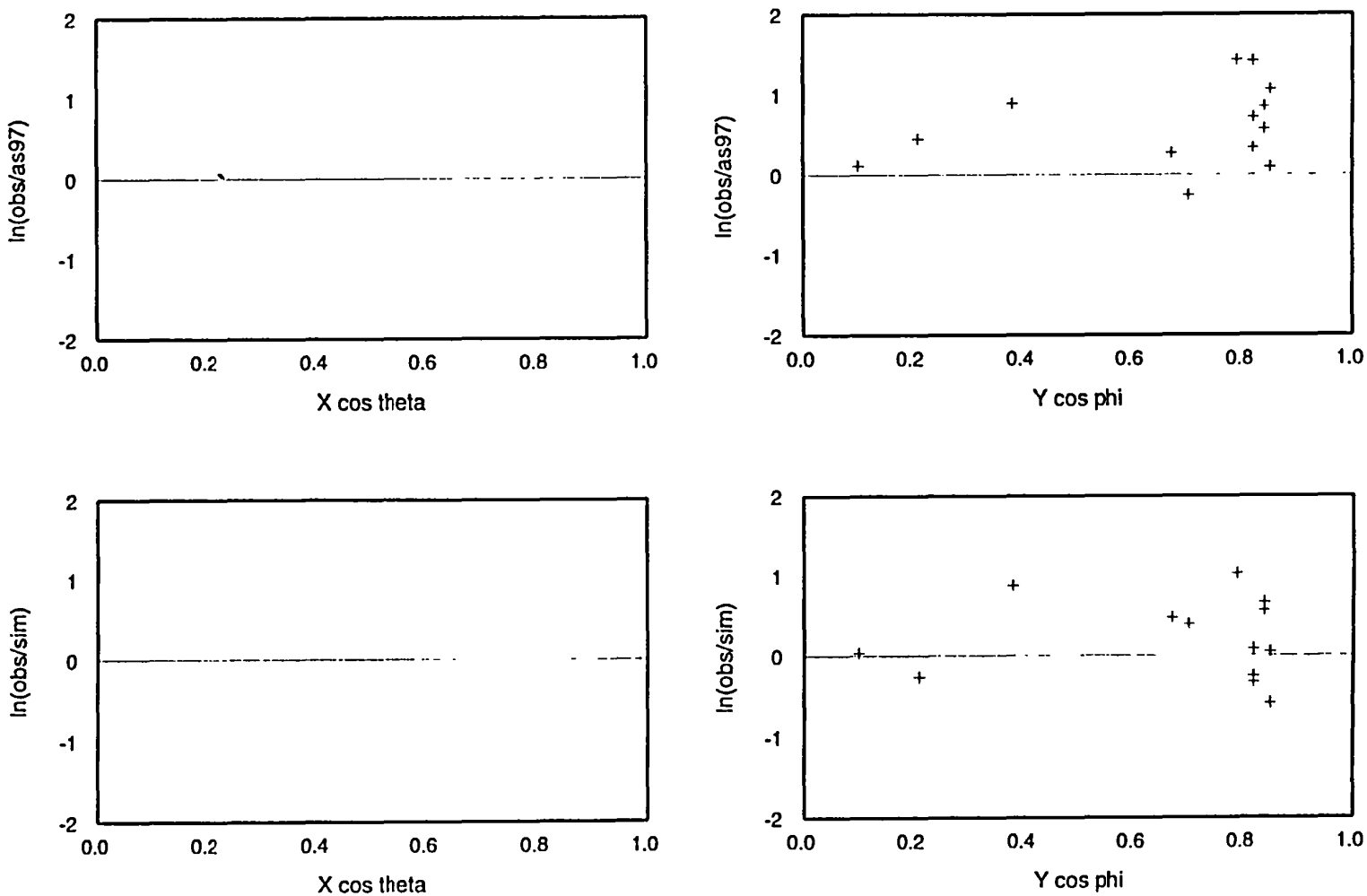

GMT Aug 24 11:22:12 1999 /u1/nancy/PEER-5/Northridge/Comparisons.990823/Resid_plots

Northridge - Fault Parallel

SA at 1.0 sec

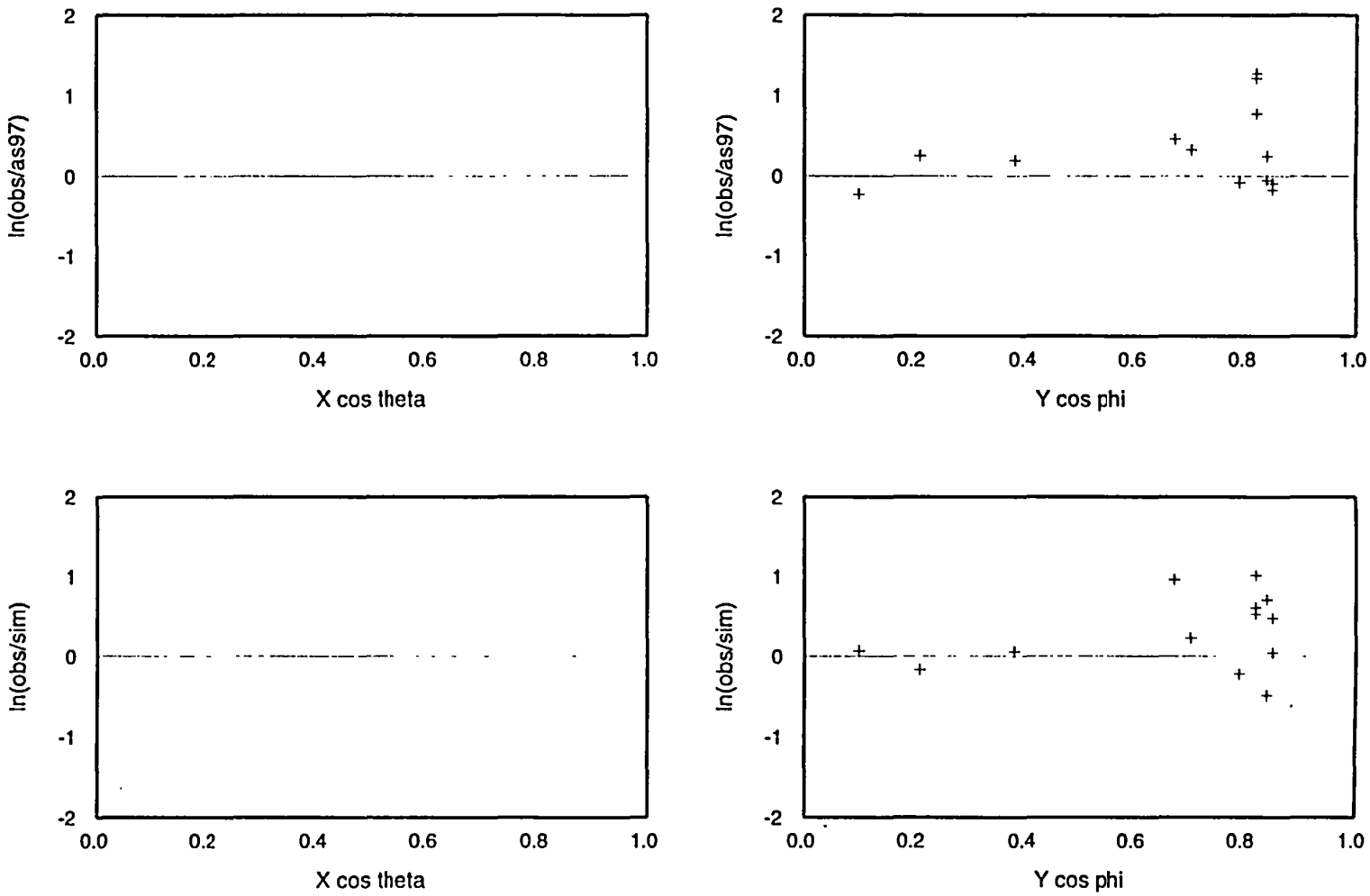

GMT Aug 24 11:22:24 1999 /u1/nancy/PEER-5/Northridge/Comparisons.990823/Resid_plots

/u1/nancy/PEER-5/Kobe/Comparisons/Tabulate
tableout

Station	Correlation FN	Correlation FP	Least Squares FN	Least Squares FP	Response Spectra FN	Response Spectra FP	Fourier Spectra FN	Fourier Spectra FP
abn	0.617		-1.297		0.069	0.473	-0.139	0.398
ama	0.403		0.084		0.568	0.213	0.535	0.346
fka2	0.688		0.107		-0.072	-0.476	-0.336	-0.561
fks	0.387		0.078		0.692	0.835	0.422	0.681
kbu2	0.836		0.383		-0.177	-0.402	-0.020	-0.592
kob2	0.565		-0.011		-0.234	-0.541	-0.456	-0.766
mot2	0.828		0.340		-0.229	-0.174	-0.042	-0.106
mrg	0.455		0.103		0.413	0.447	0.212	-0.040
osa	0.483		0.078		0.229	0.401	-0.302	-0.160
ski	0.675		0.153		0.171	0.529	0.231	0.345
tkt2	0.300		0.017		0.391	0.372	0.097	0.152
Average	0.567		0.003		0.166	0.152	0.018	-0.028
Sigma	0.179		0.448		0.582	0.786	1.028	1.199
Sigma Mean	0.054		0.135		0.176	0.237	0.310	0.362

Kobe - Fault Normal

Simulations and Data Band Pass Filtered 0.125-1.43 Hz

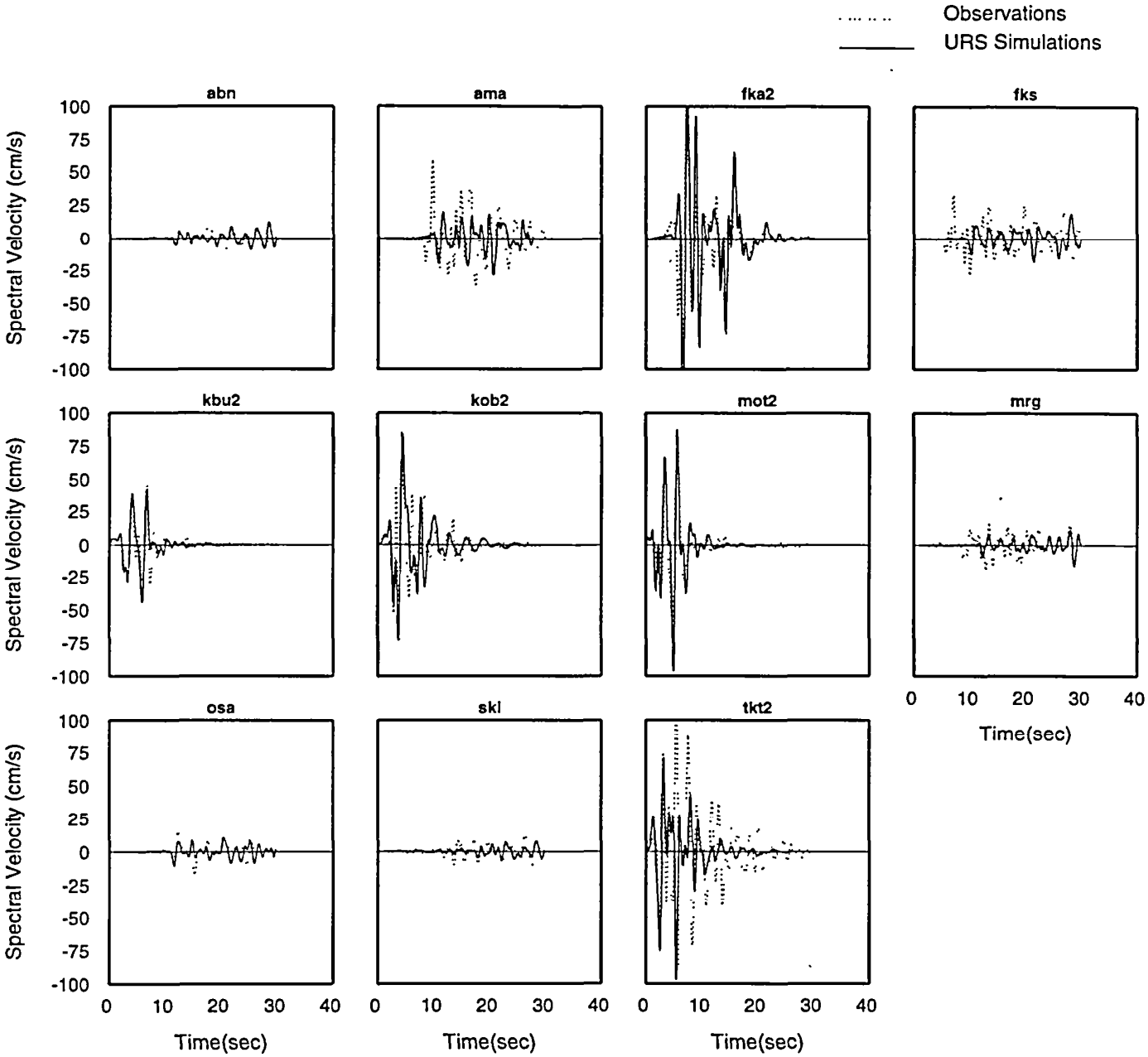

Kobe - Fault Parallel

Simulations and Data Band Pass Filtered 0.125-1.43 Hz

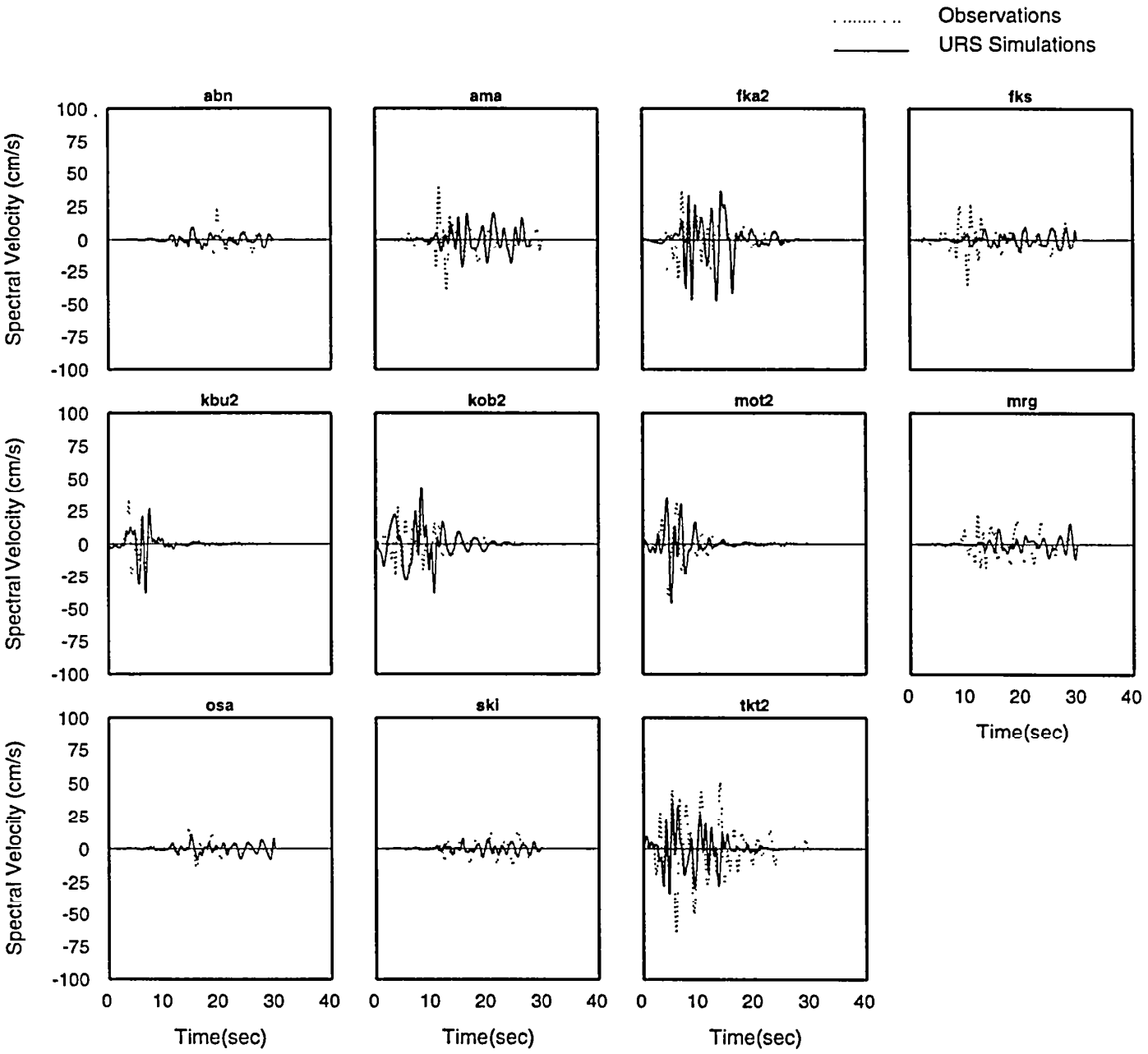

GMT Aug 31 12.26:06 1999 /u1/nancy/PEER-5/Kobe/Comparisons/Extra_plots

Kobe - Fault Normal

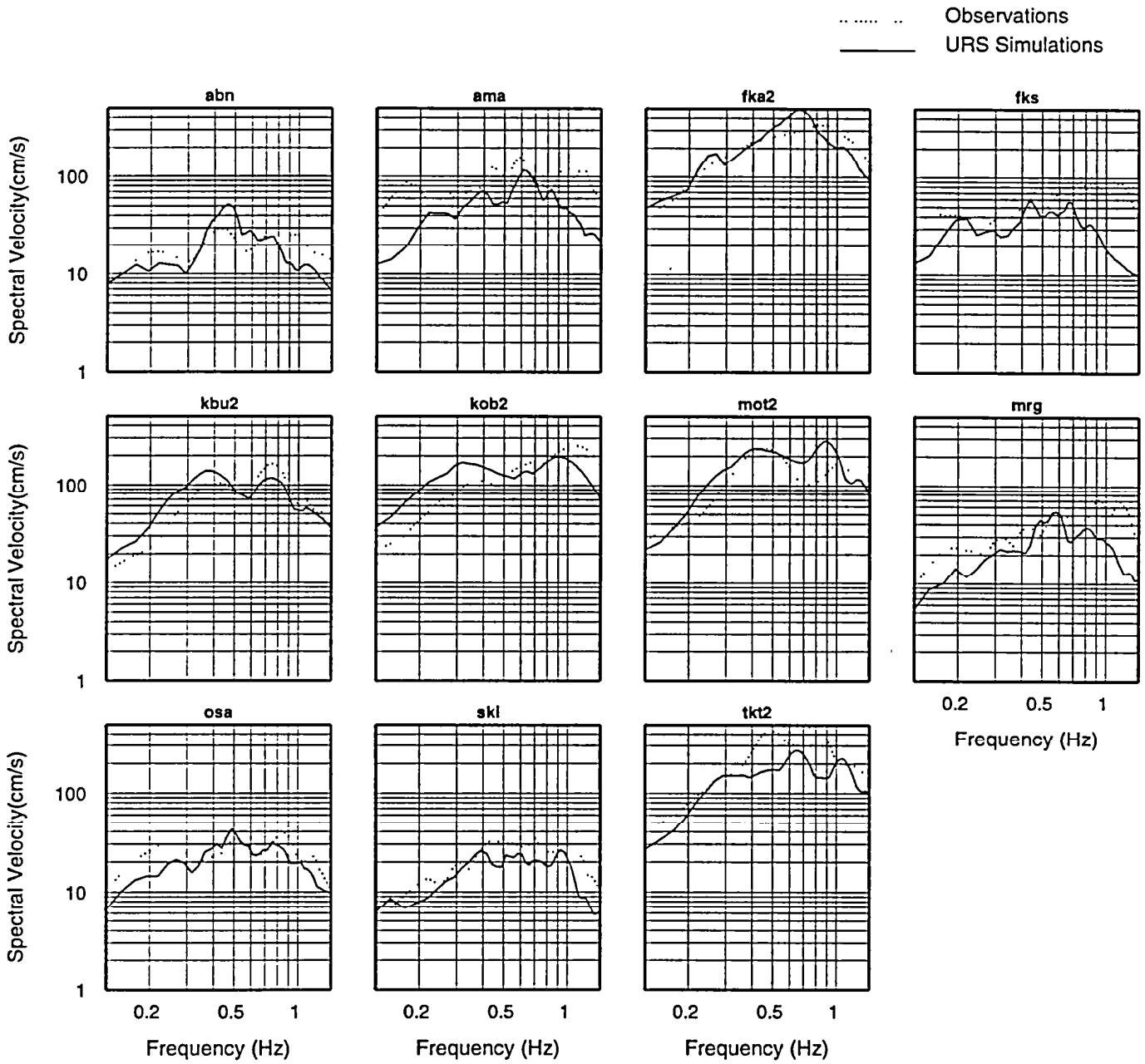

Kobe - Fault Parallel

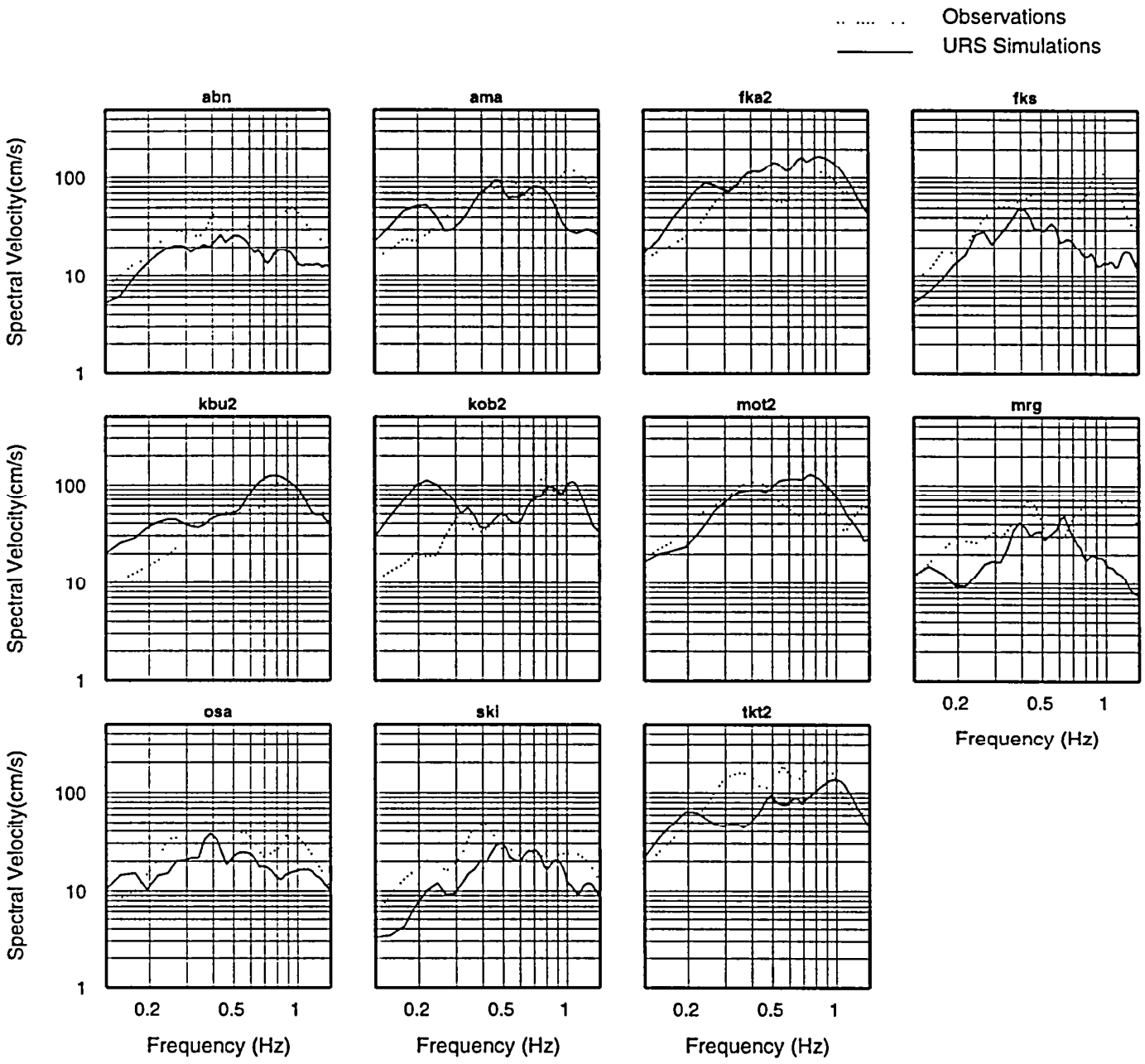

Kobe - Fault Normal

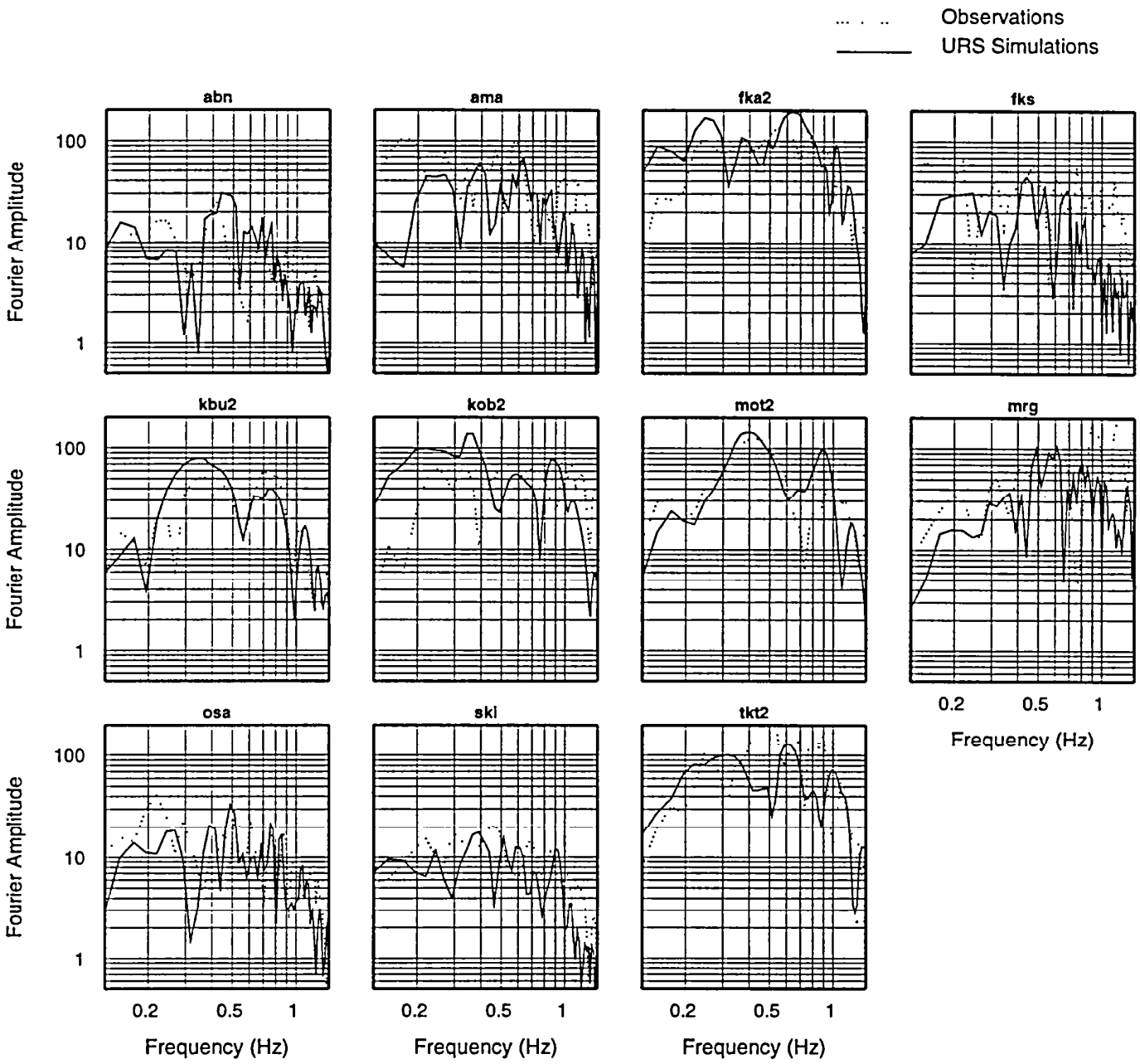

Kobe - Fault Parallel

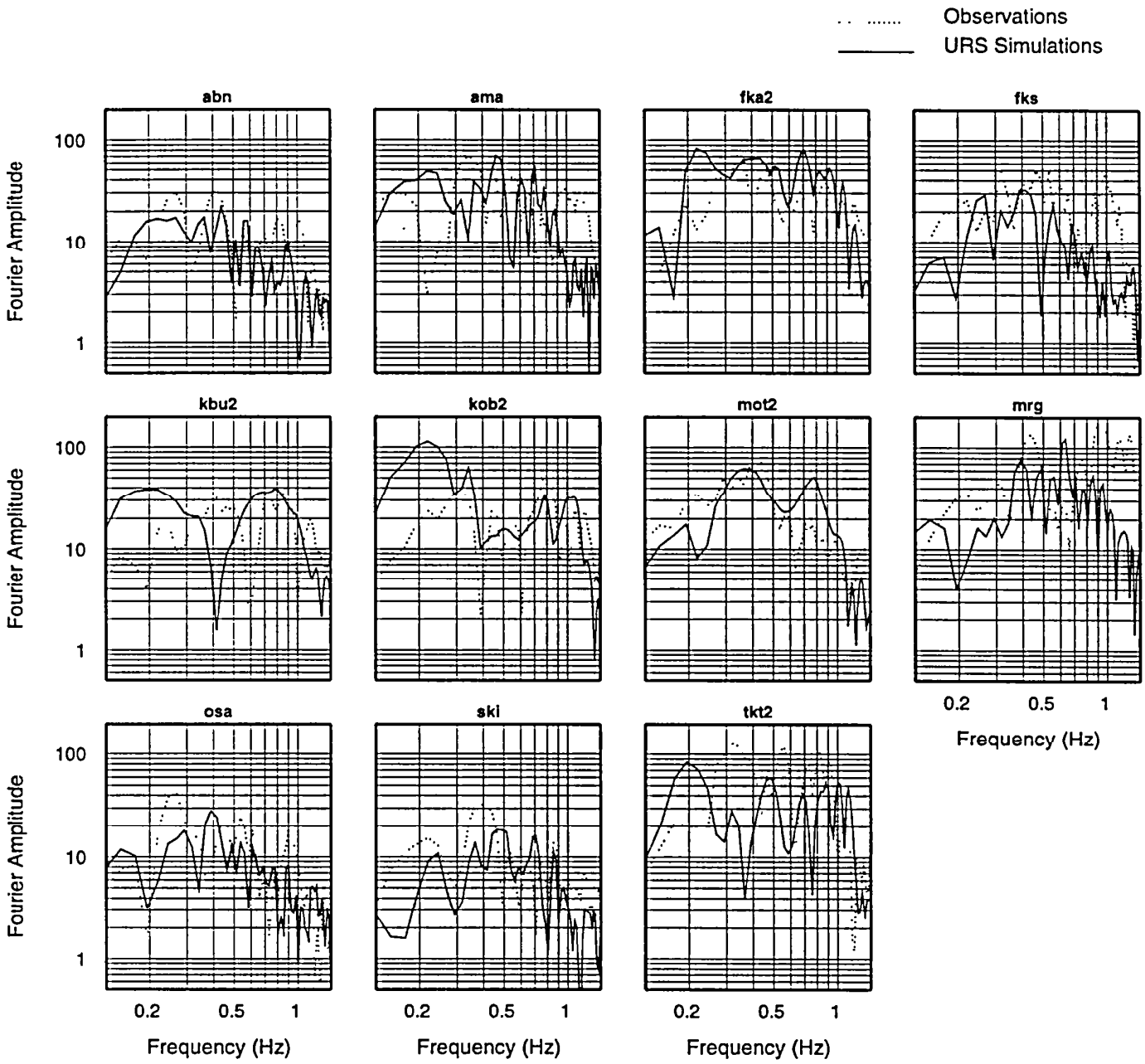

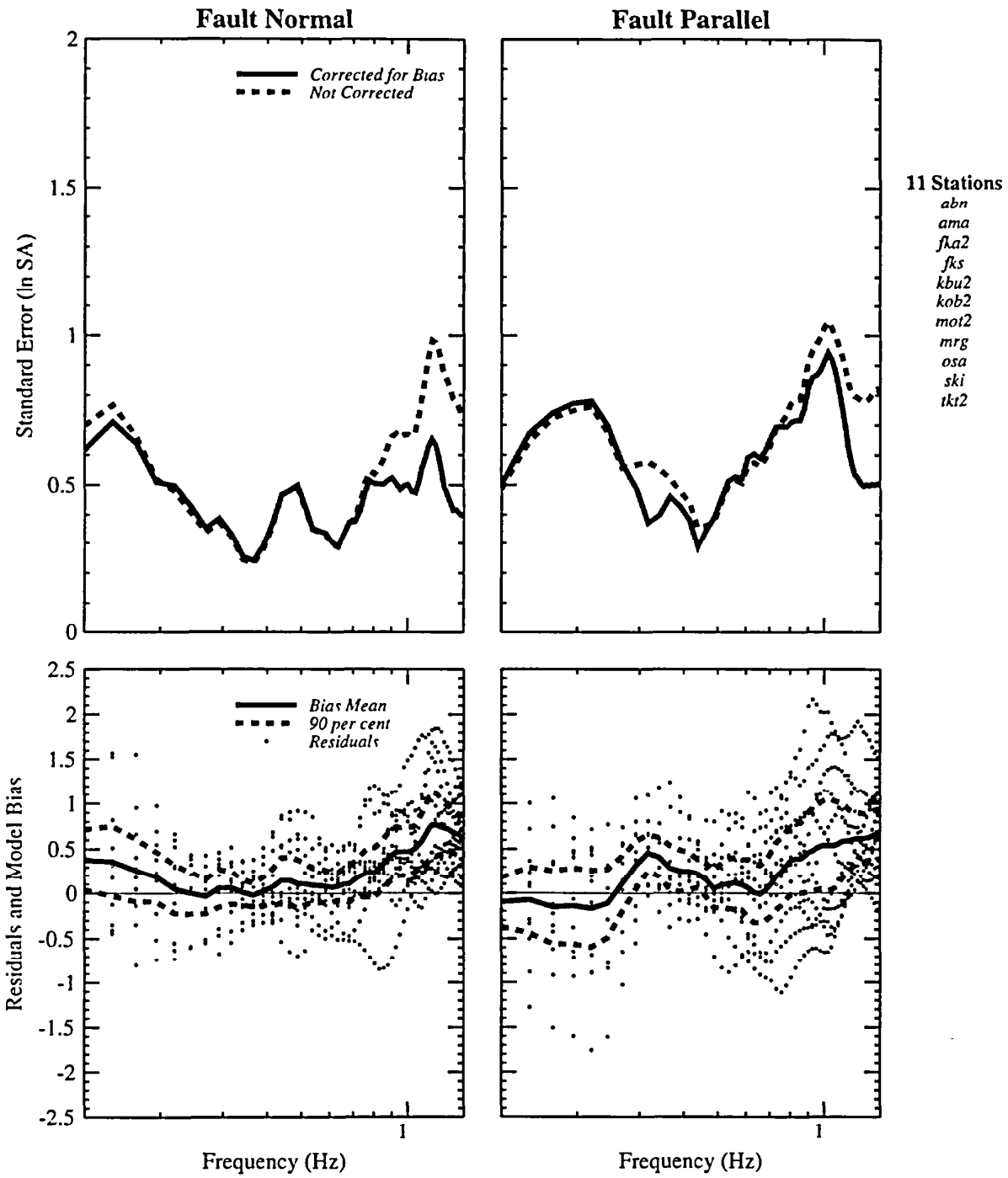

Kobe Spectral Acceleration Goodness of Fit
Observed minus Synthetic (obs - sim)

Kobe - Filter 0.125-1.43 Hz, HYBRID BB Sims - fka

Fault Normal

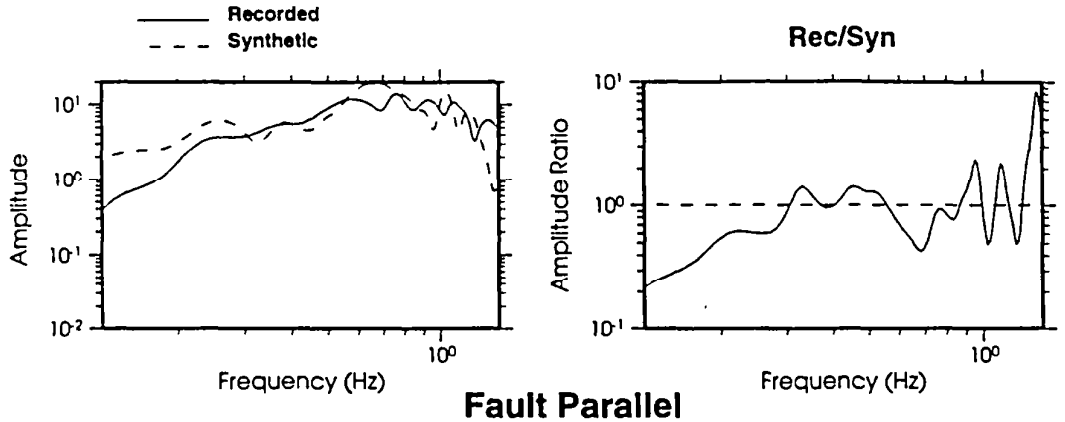

Fault Parallel

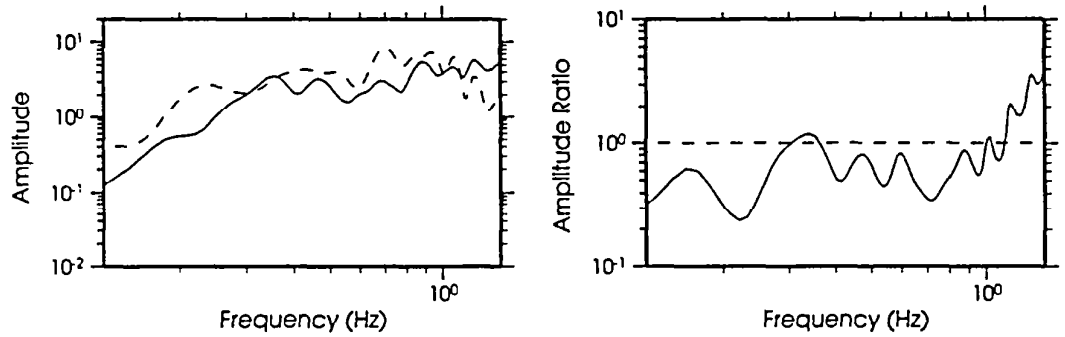

Fault Normal

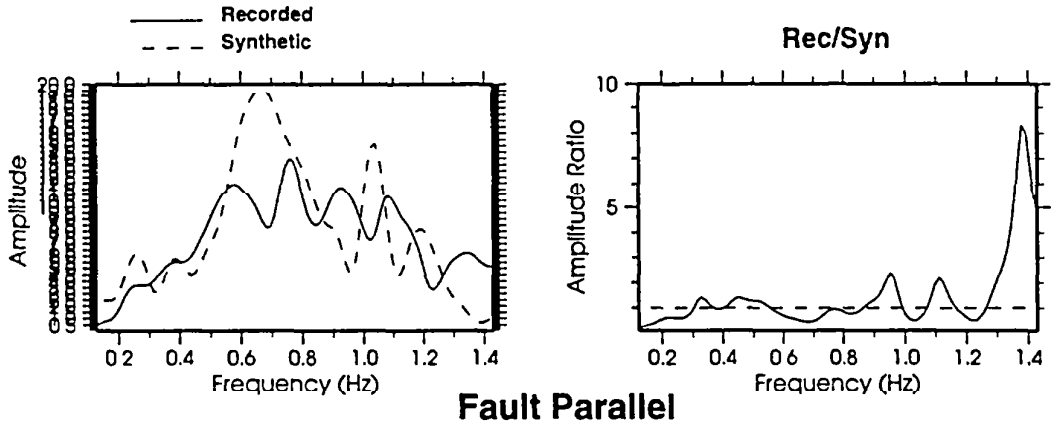

Fault Parallel

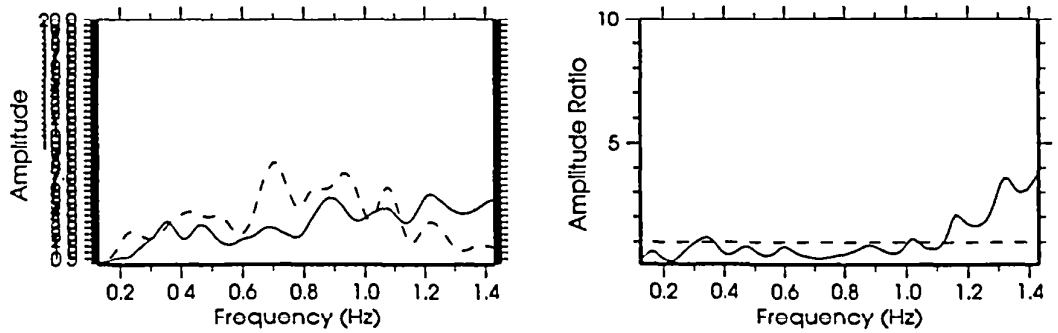

GMT Aug 24 16:23 57 1999 /net/coda/u2/arben/Kobe/shells

Kobe - Filter 0.125-1.43 Hz, HYBRID BB Sims - kbu

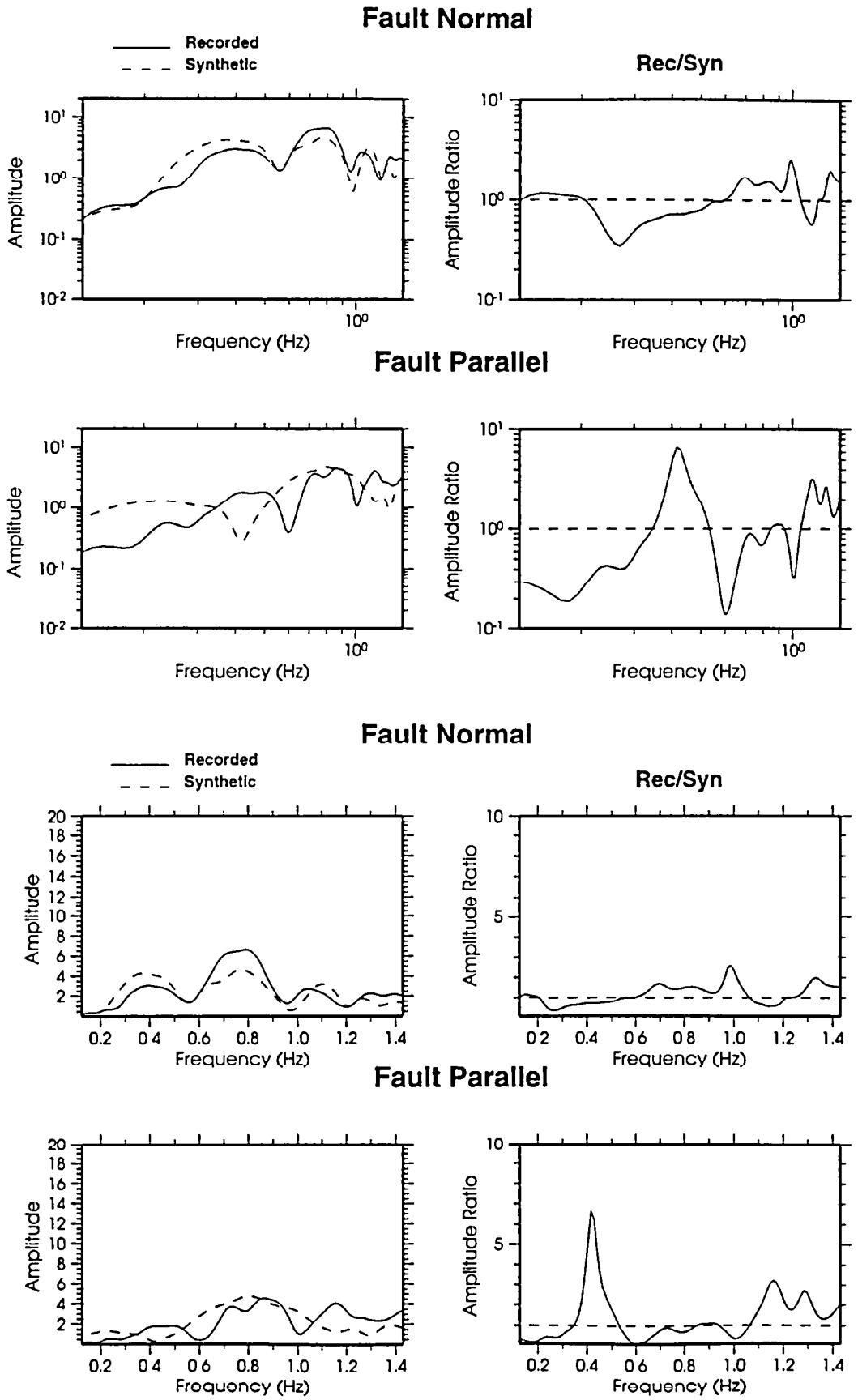

GMT Aug 24 16.24:23 1999 /net/coda/u2/arben/Kobe/shells

Kobe - Filter 0.125-1.43 Hz, HYBRID BB Sims - kob

Fault Normal

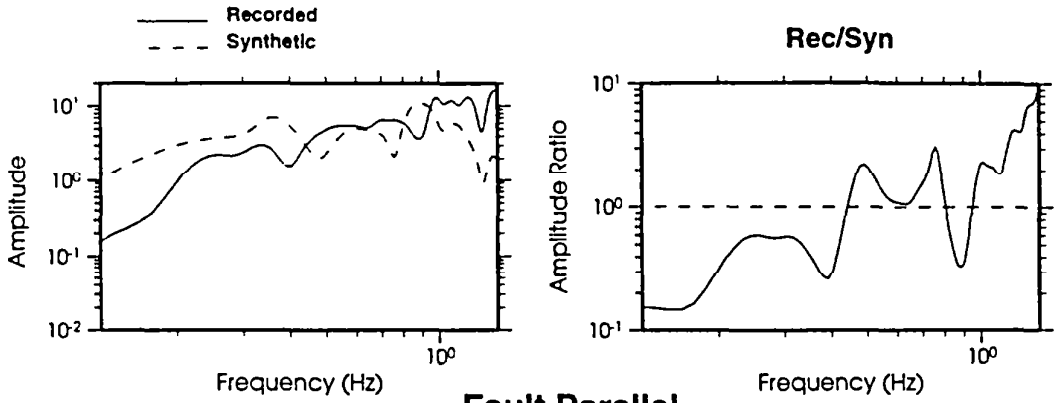

Fault Parallel

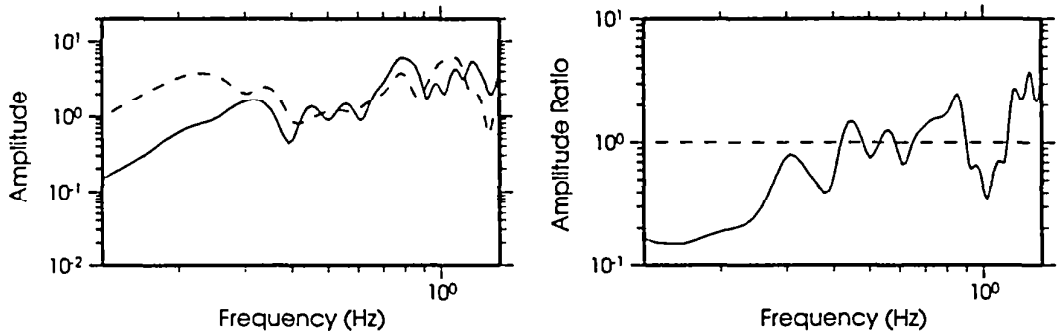

Fault Normal

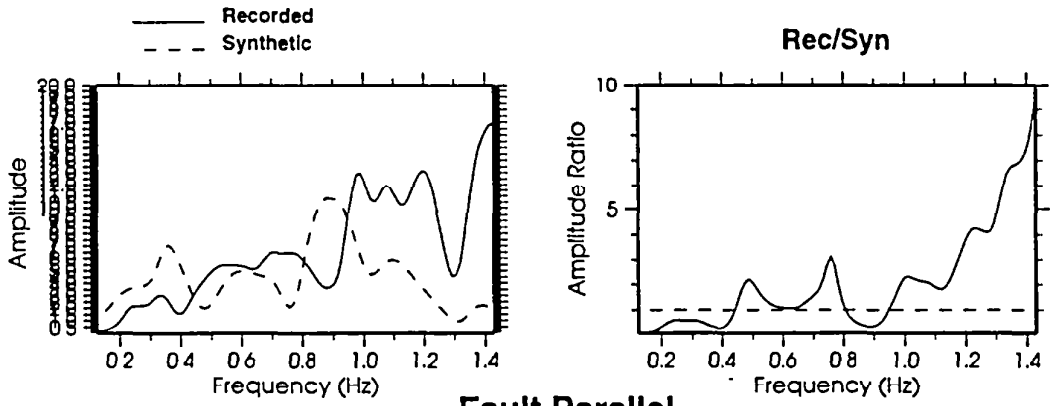

Fault Parallel

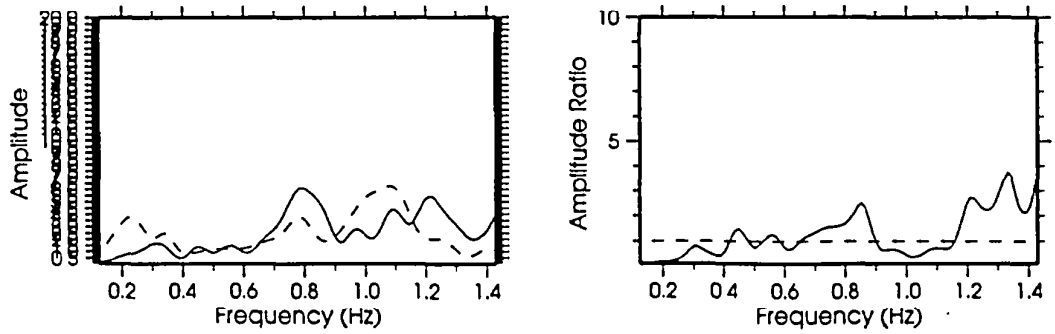

Kobe - Filter 0.125-1.43 Hz, HYBRID BB Sims - mot

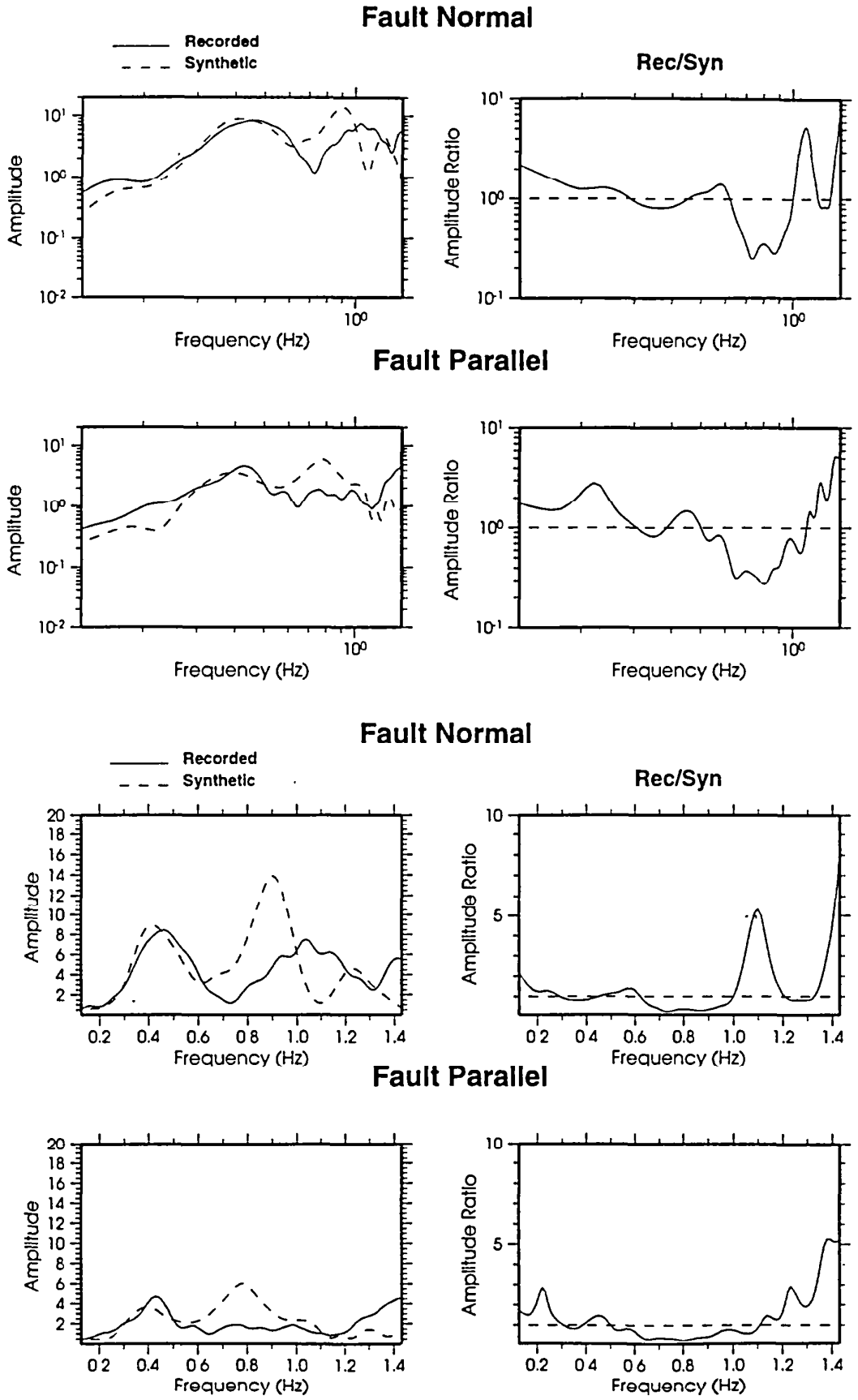

GMT Aug 24 16 25:14 1999 /net/coda/u2/arben/Kobe/shells

Kobe - Filter 0.125-1.43 Hz, HYBRID BB Sims - tkt

Fault Normal

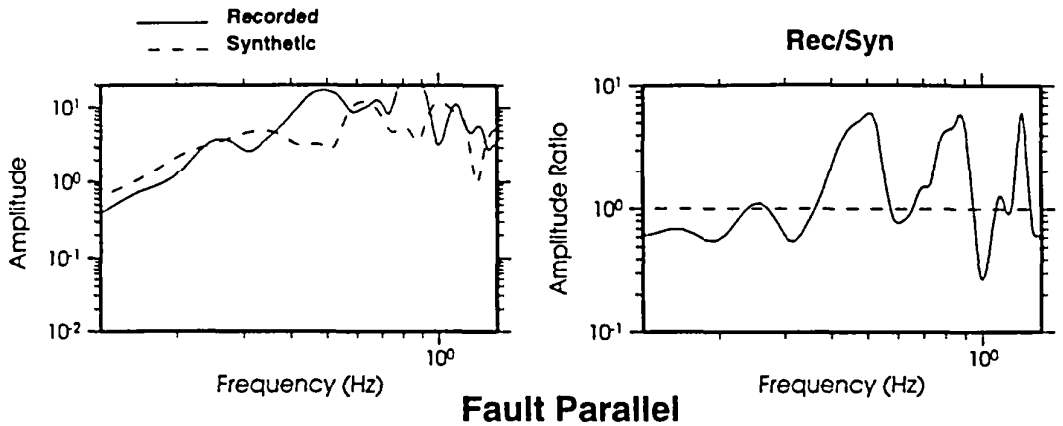

Fault Parallel

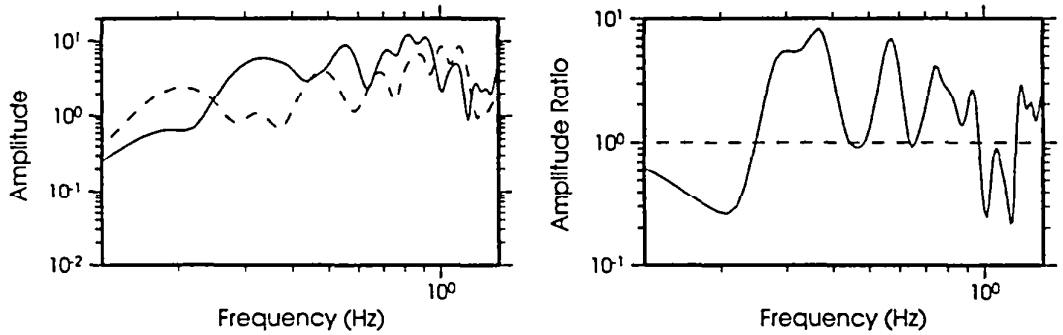

Fault Normal

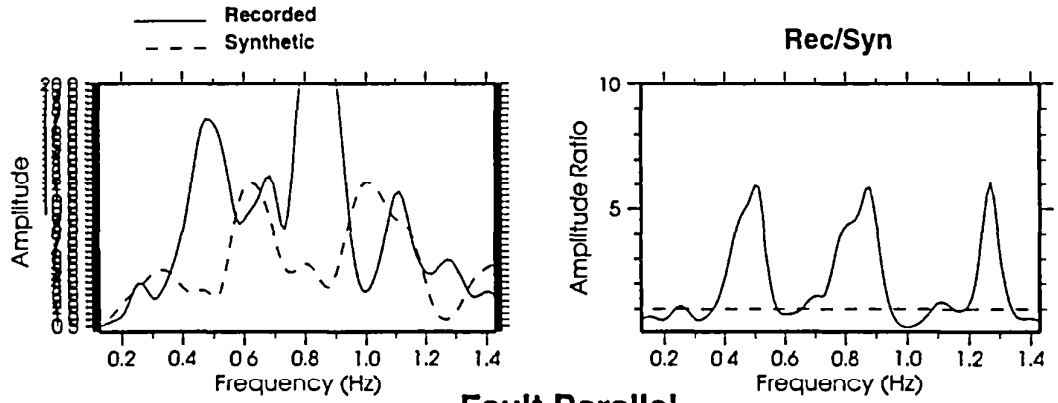

Fault Parallel

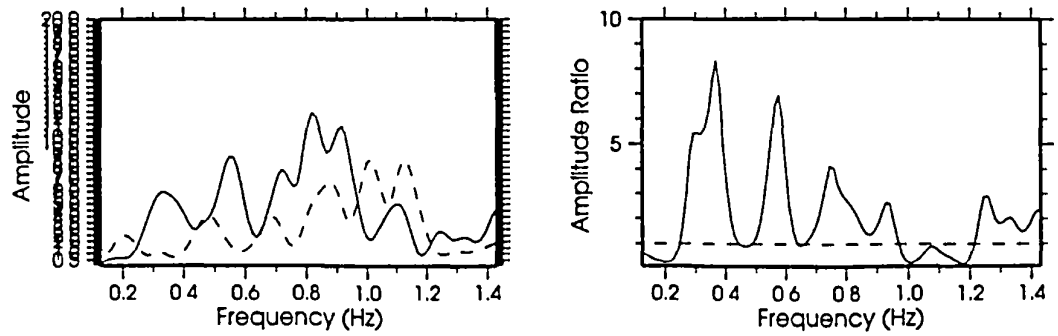

GMT Aug 24 16:25:40 1999 /net/coda/u2/arben/Kobe/shells

Kobe - Filter 0.125-1.43 Hz, Norma BB Sims - ski

Fault Normal

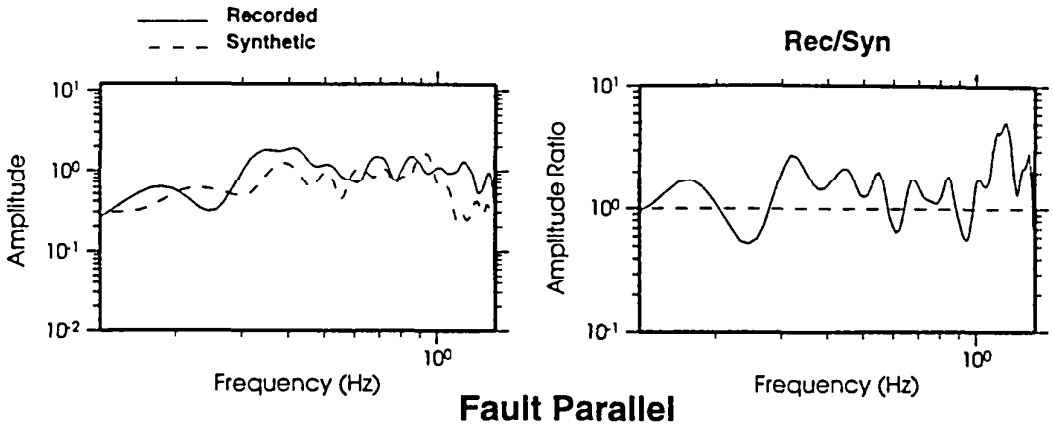

Fault Parallel

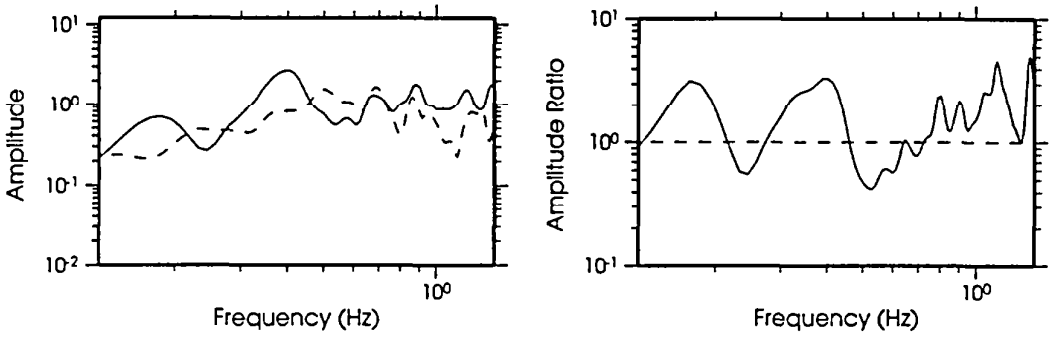

Fault Normal

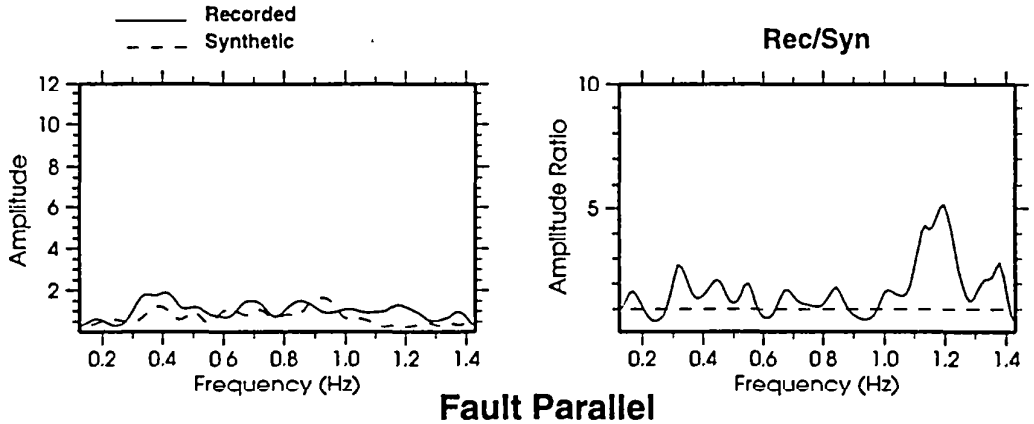

Fault Parallel

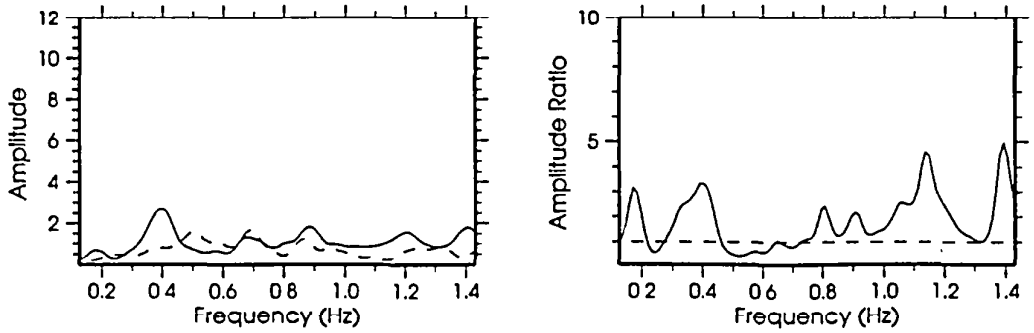

Kobe - Filter 0.125-1.43 Hz, Norma BB Sims - osa

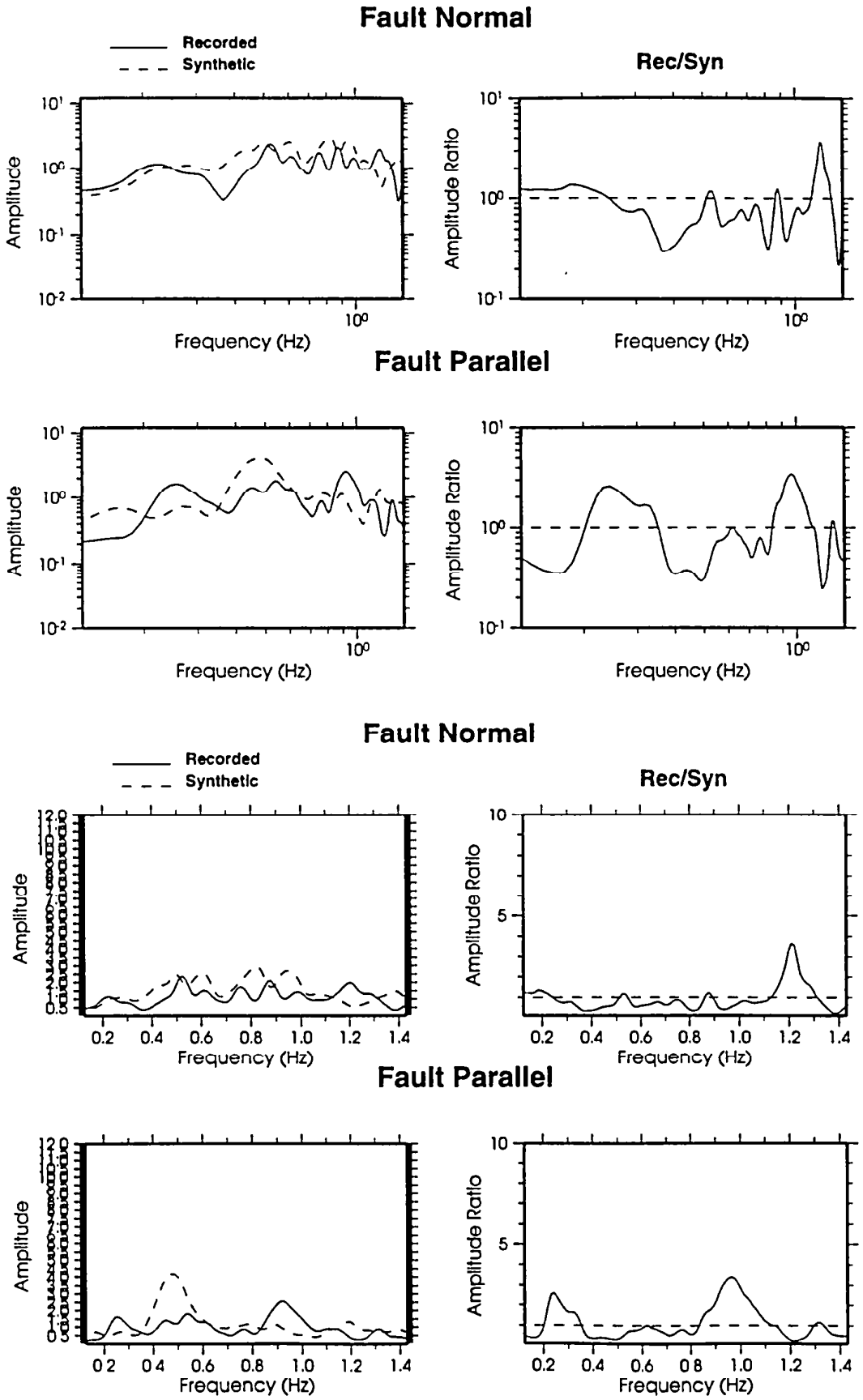

GMT Aug 24 18:14:19 1999 /net/coda/u2/arben/Kobe/shells

Kobe - Filter 0.125-1.43 Hz, Norma BB Sims - mrg

Fault Normal

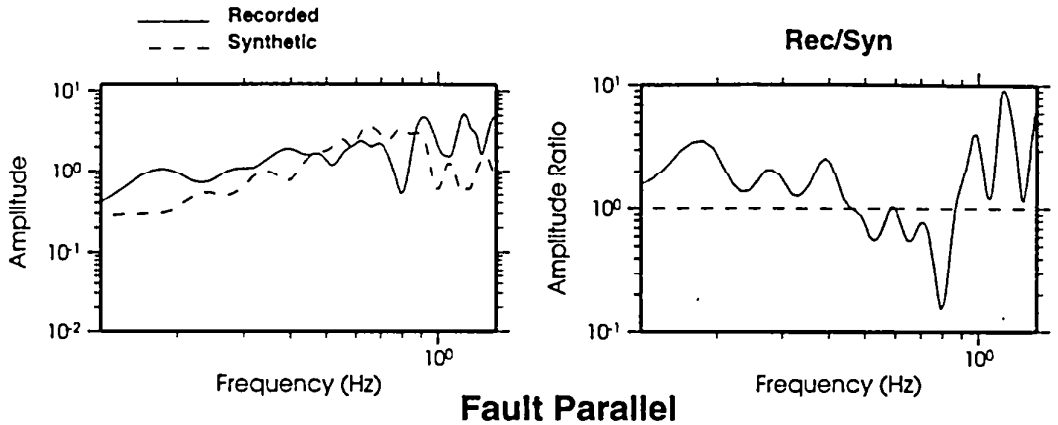

Fault Parallel

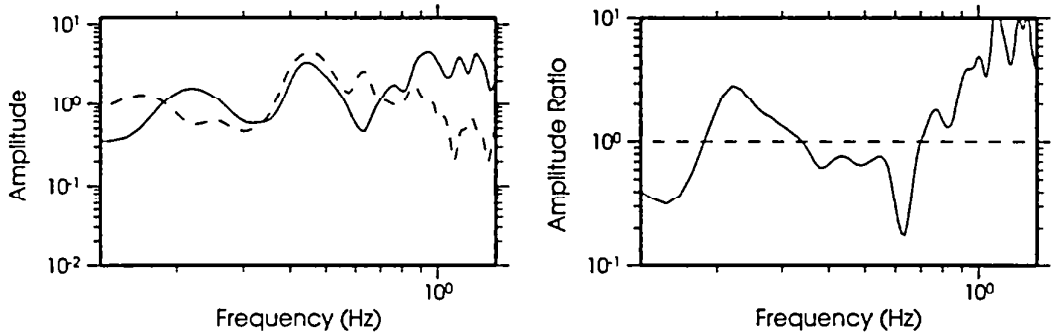

Fault Normal

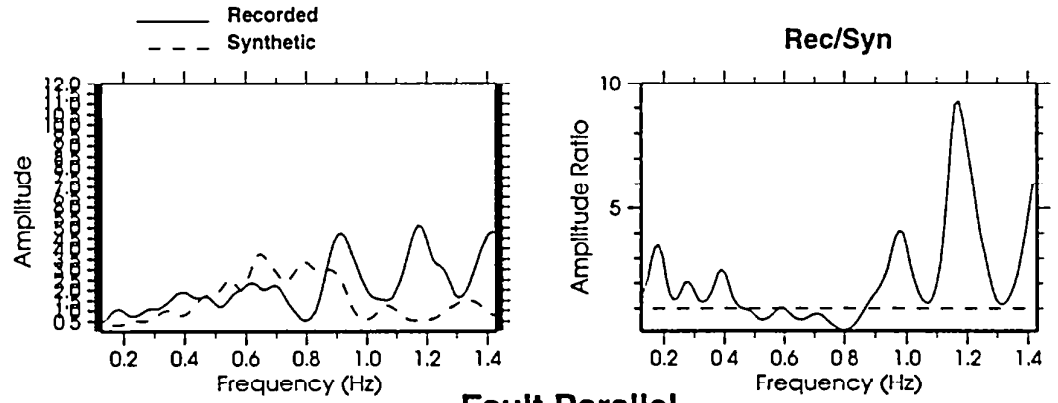

Fault Parallel

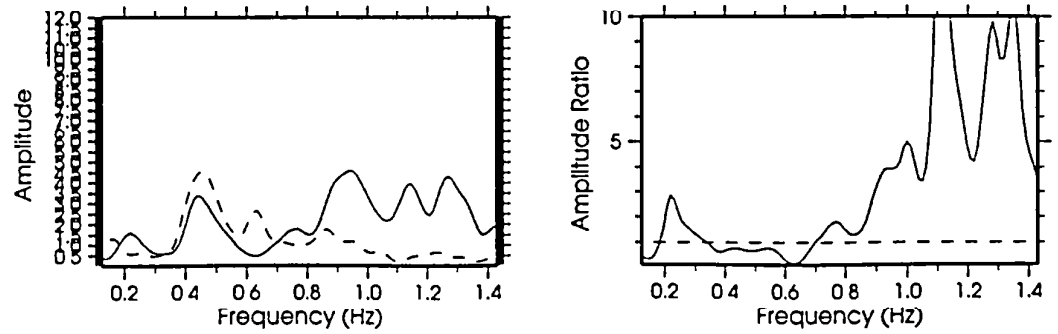

Kobe - Filter 0.125-1.43 Hz, Norma BB Sims - fks

Fault Normal

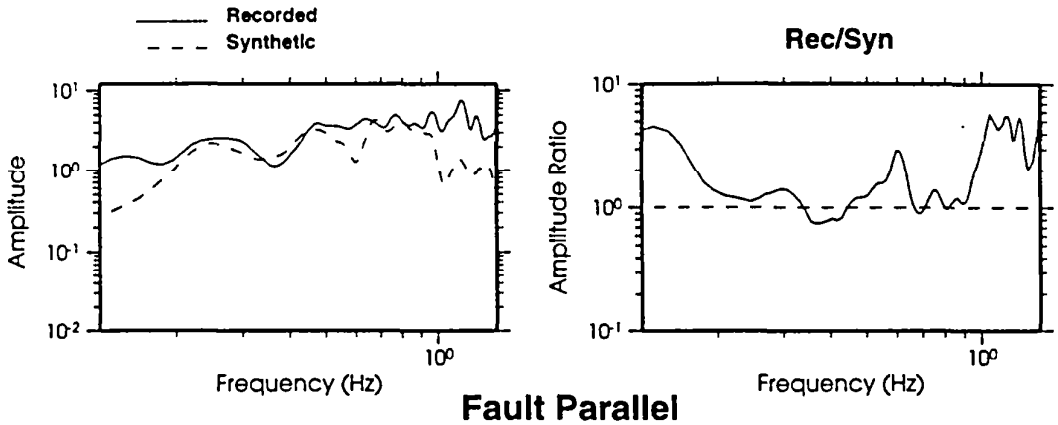

Fault Parallel

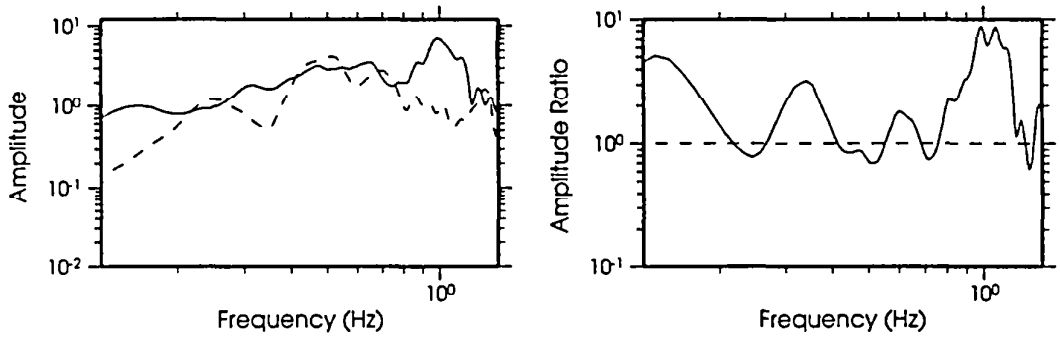

Fault Normal

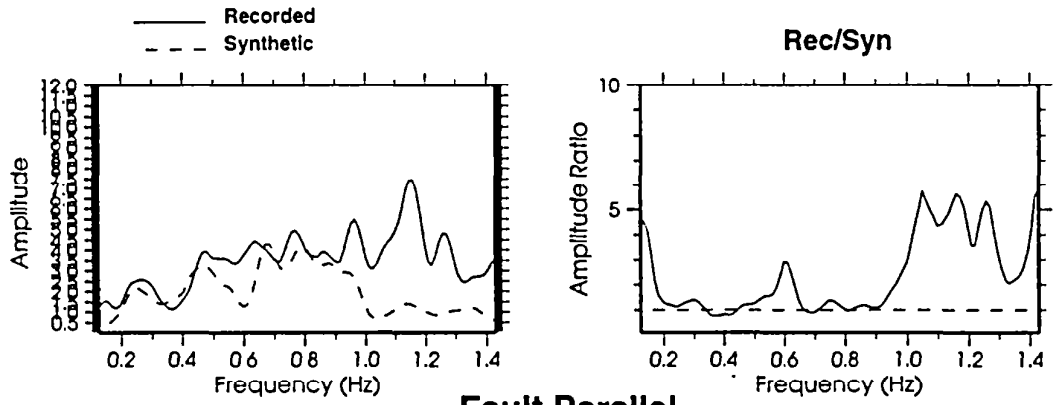

Fault Parallel

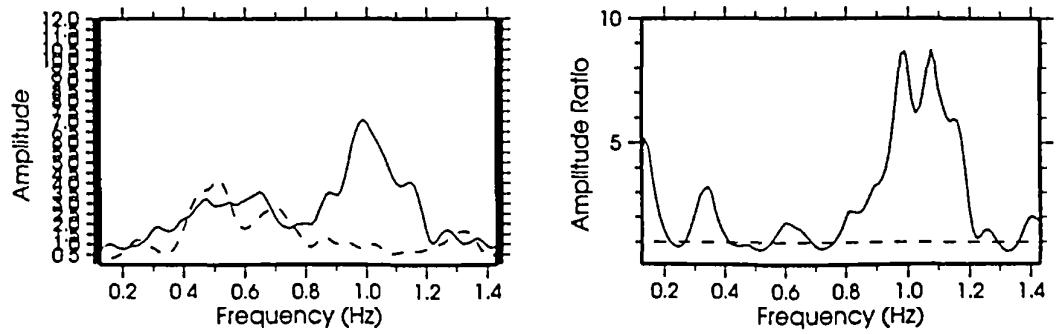

GMT Aug 24 18:13.55 1999 /net/coda/u2/arben/Kobe/shells

Kobe - Filter 0.125-1.43 Hz, Norma BB Sims - ama

Fault Normal

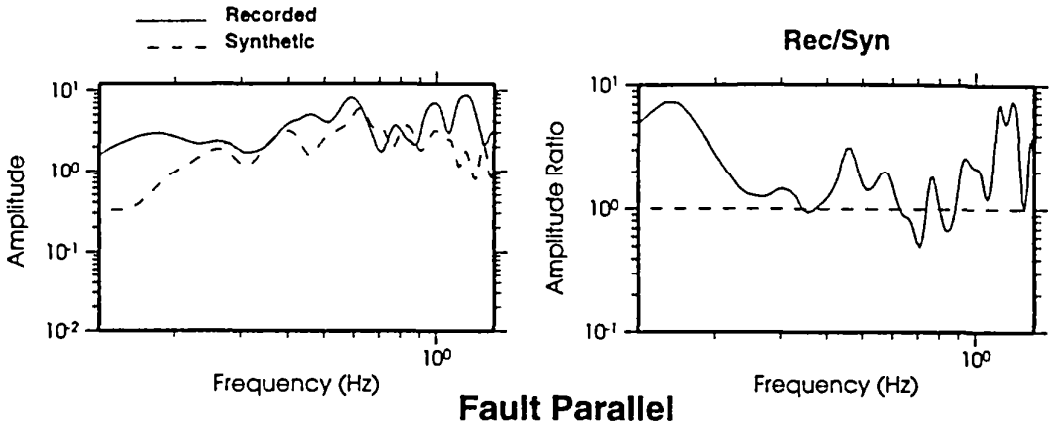

Fault Parallel

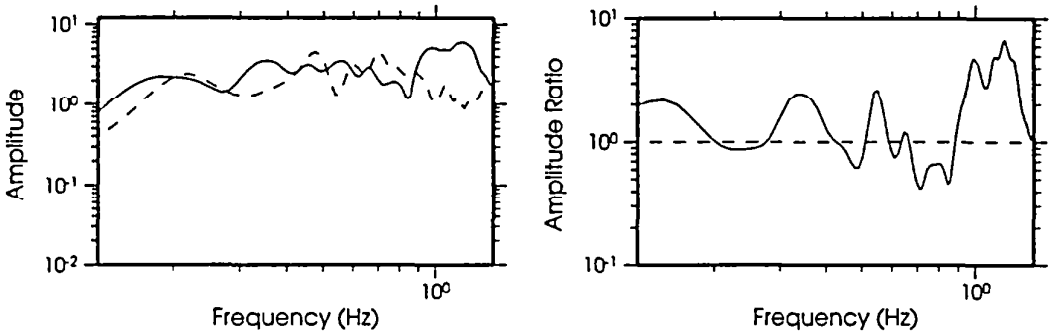

Fault Normal

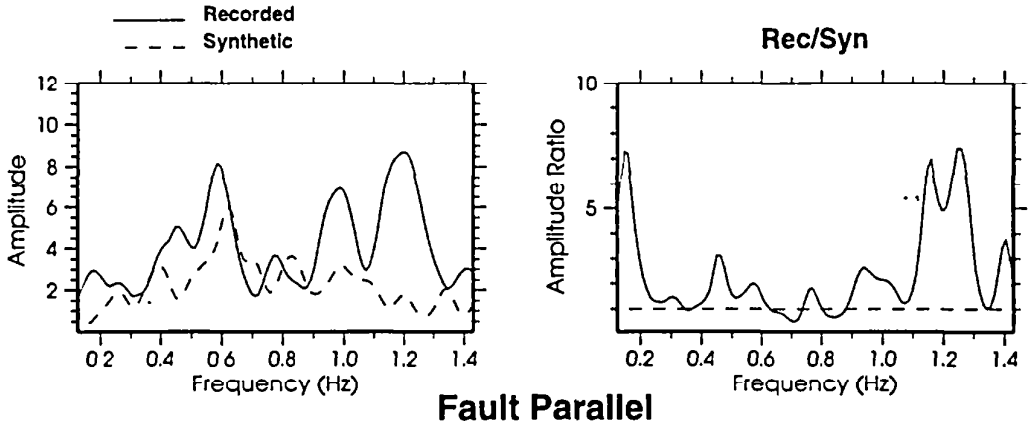

Fault Parallel

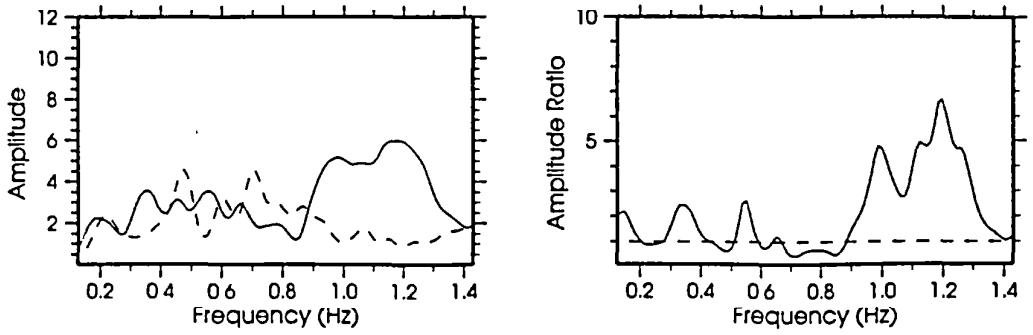

Kobe - Filter 0.125-1.43 Hz, Norma BB Sims - abn

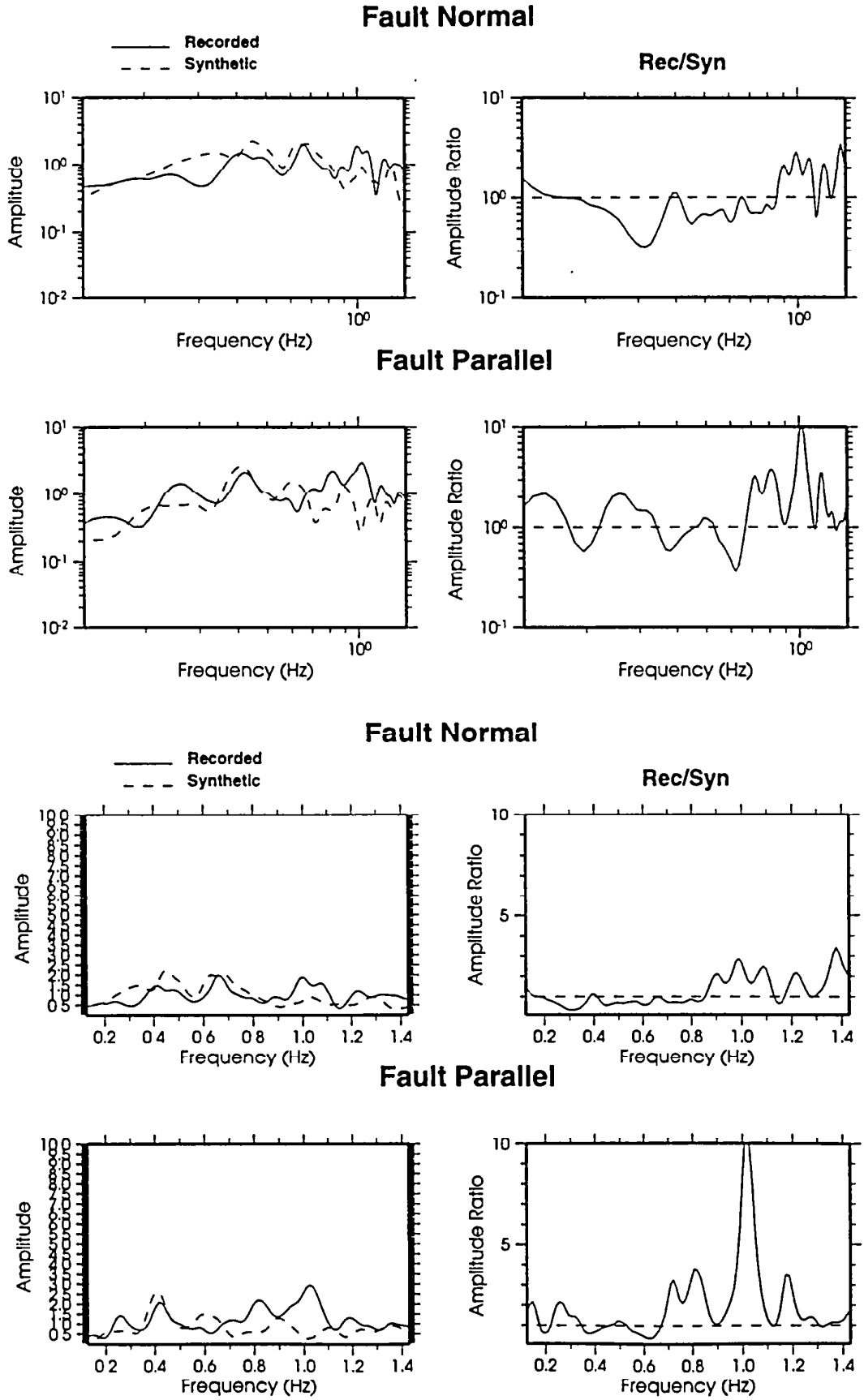

GMT Aug 24 18:13:44 1999 /net/coda/u2/arben/Kobe/shells

Kobe - Fault Normal

SA at 5.0 sec

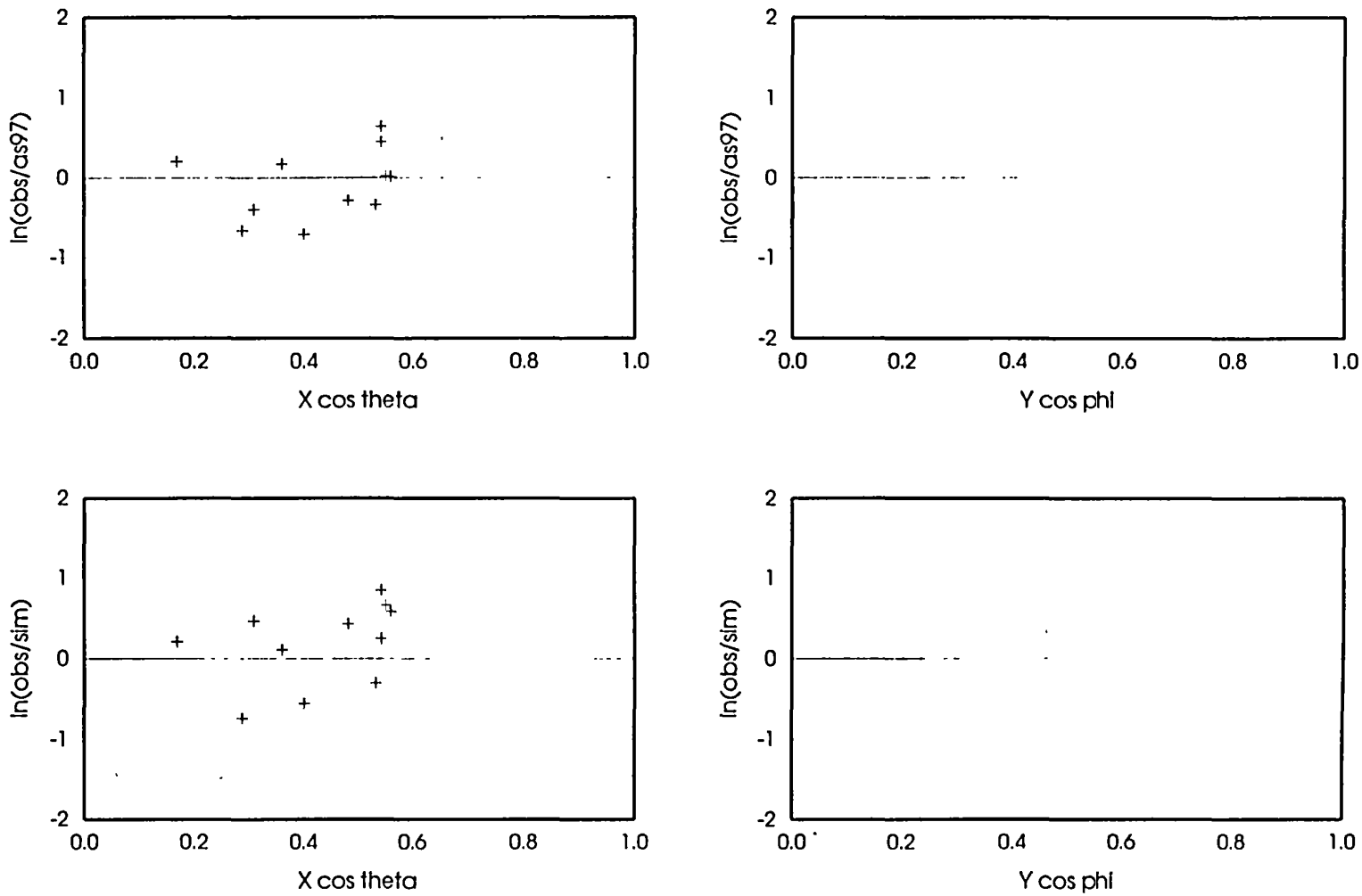

GMT Aug 24 17:56:17 1999 /net/coda/u2/arben/Kobe/Comparisons/Resid_plots

Kobe - Fault Parallel

SA at 5.0 sec

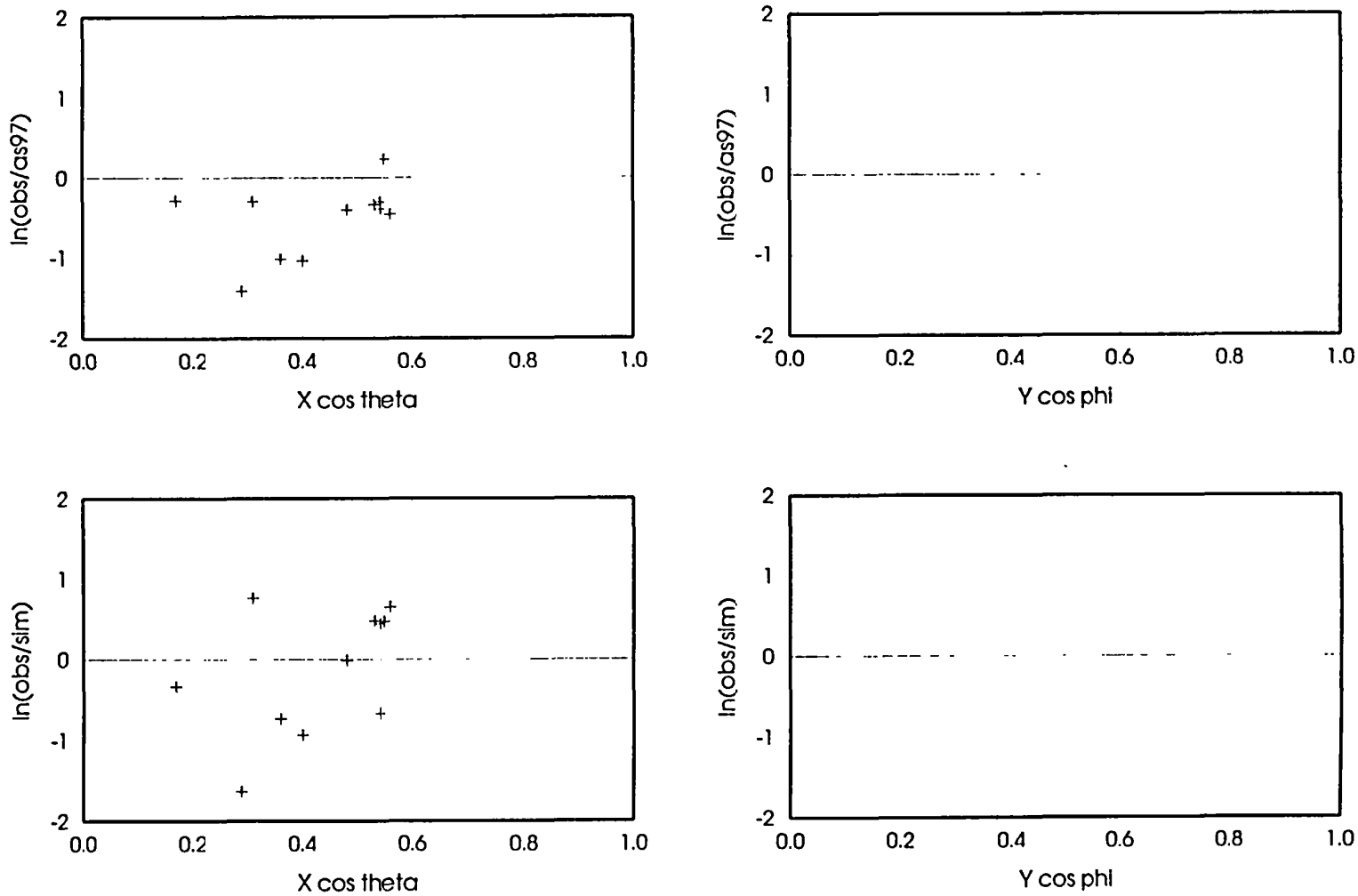

GMT Aug 24 17:56:19 1999 /net/coda/u2/arben/Kobe/Comparisons/Resid_plots

Kobe - Fault Normal

SA at 4.0 sec

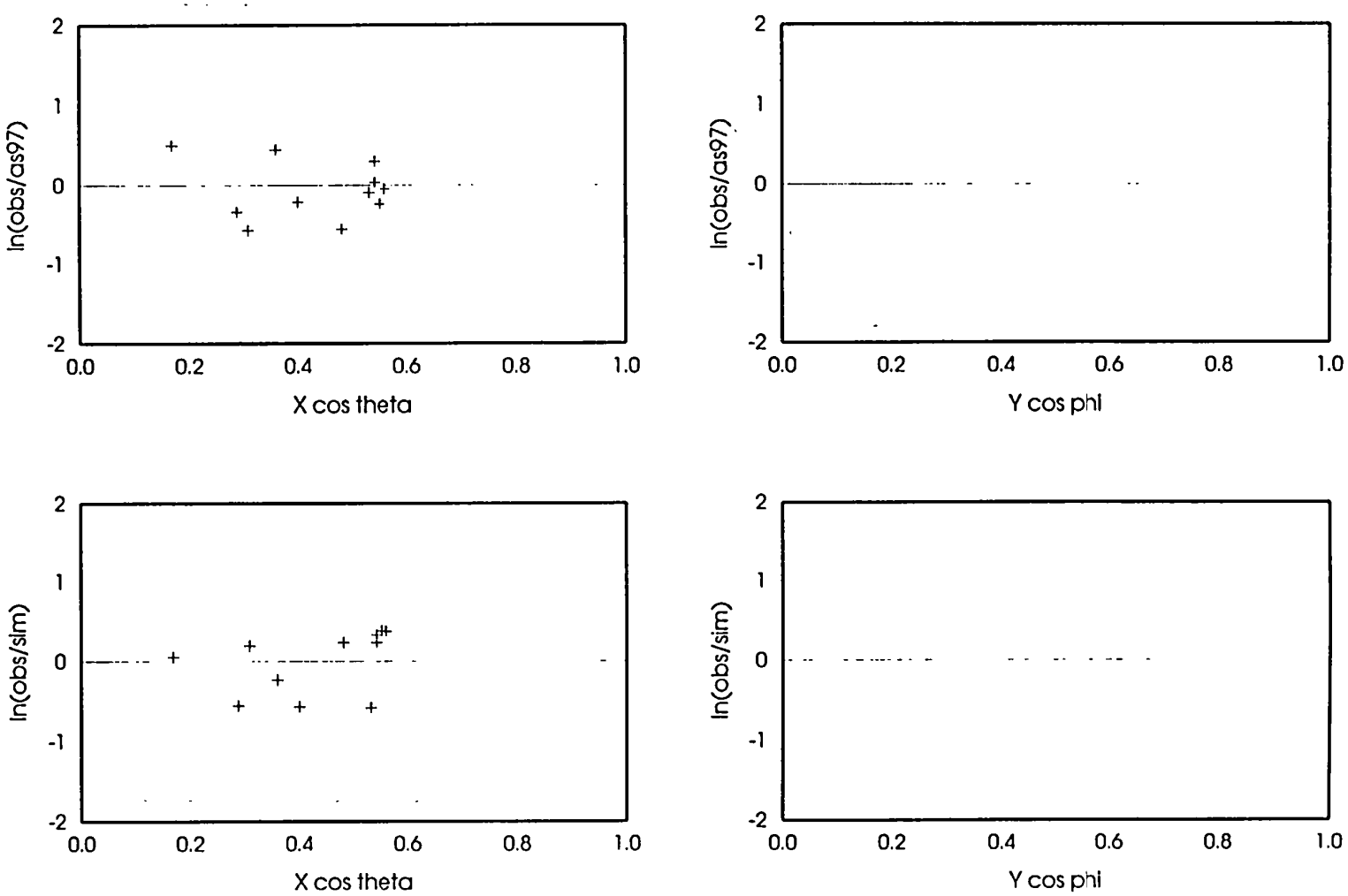

GMT Aug 24 17:56:21 1999 /net/coda/u2/arben/Kobe/Comparisons/Resid_plots

Kobe - Fault Parallel

SA at 4.0 sec

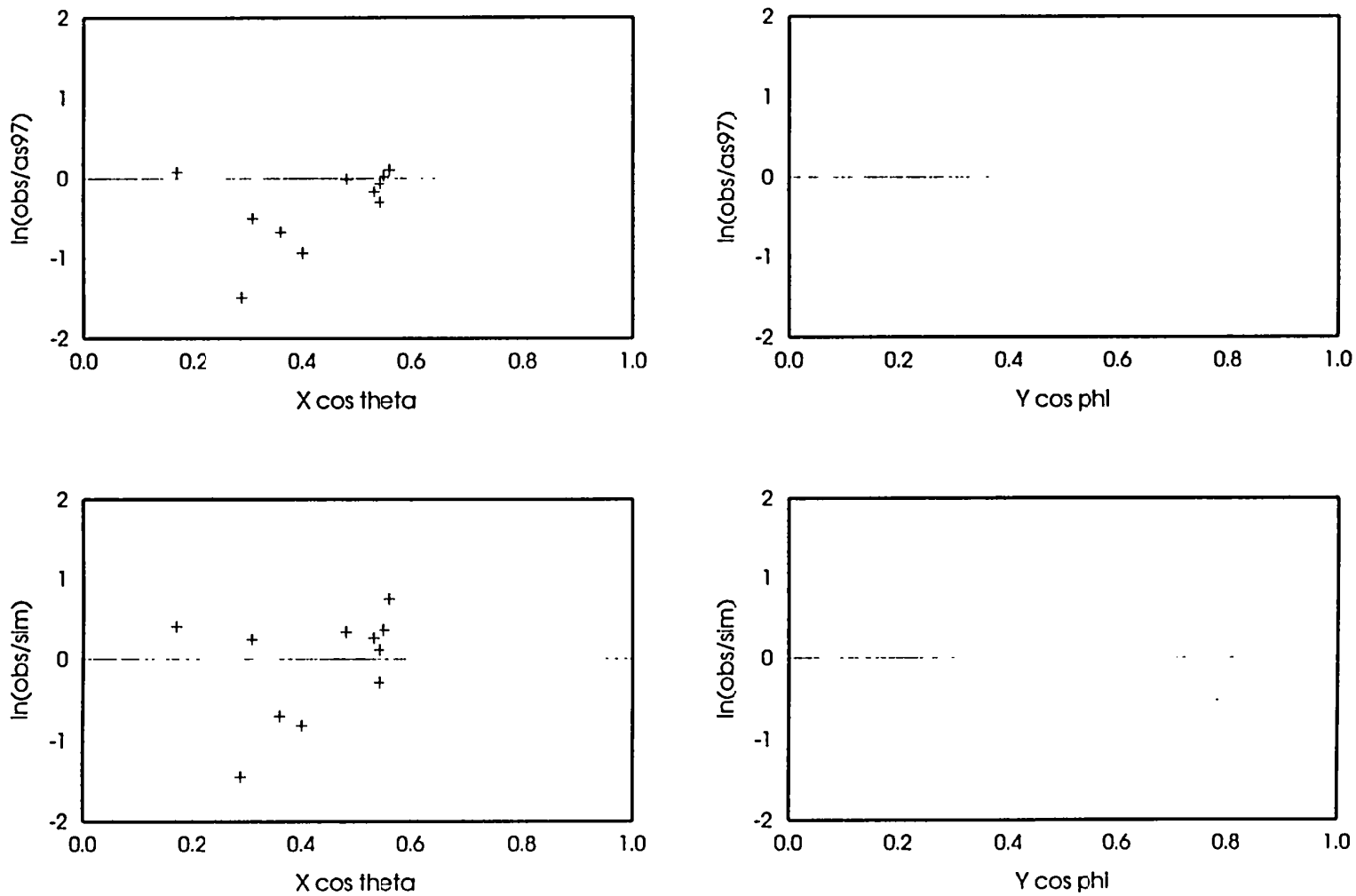

GMT Aug 24 17:56:23 1999 /net/coda/u2/arben/Kobe/Comparisons/Resid_plots

Kobe - Fault Normal

SA at 3.0 sec

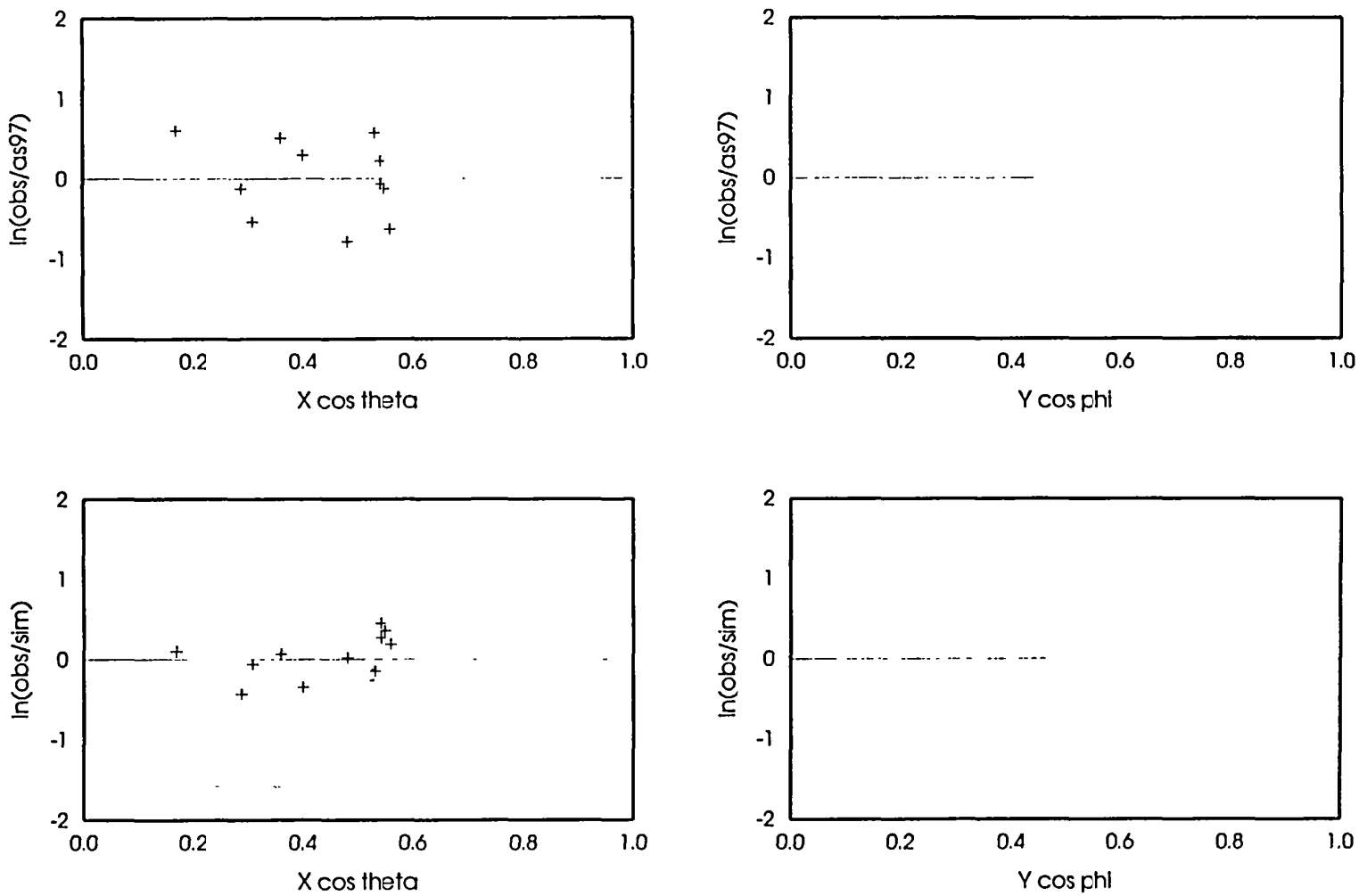

GMT Aug 24 17:56:26 1999 /net/coda/u2/arben/Kobe/Comparisons/Resid_plots

Kobe - Fault Parallel

SA at 3.0 sec

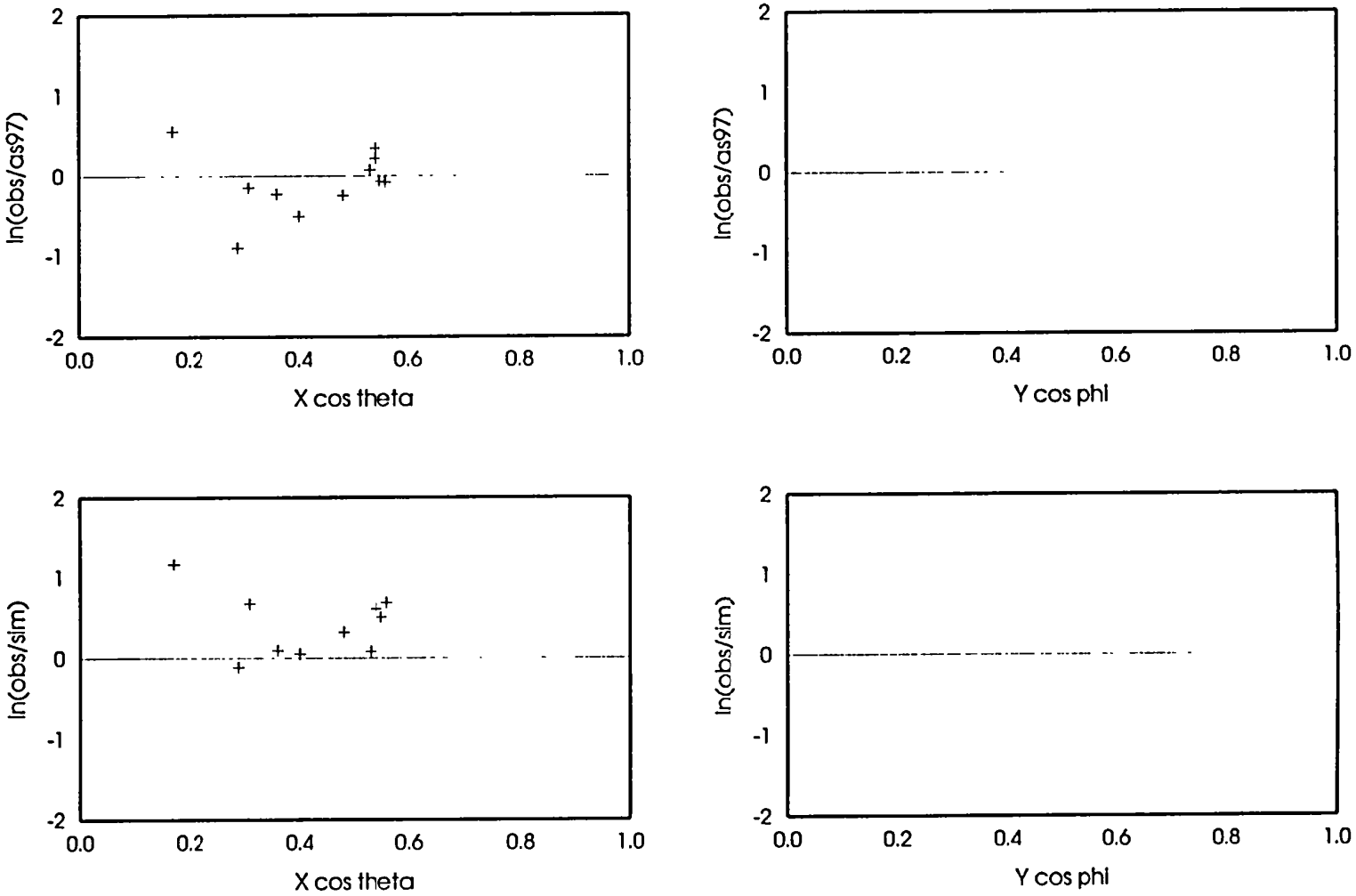

GMT Aug 24 17:56:28 1999 /net/coda/u2/arben/Kobe/Comparisons/Resid_plots

Kobe - Fault Normal

SA at 2.0 sec

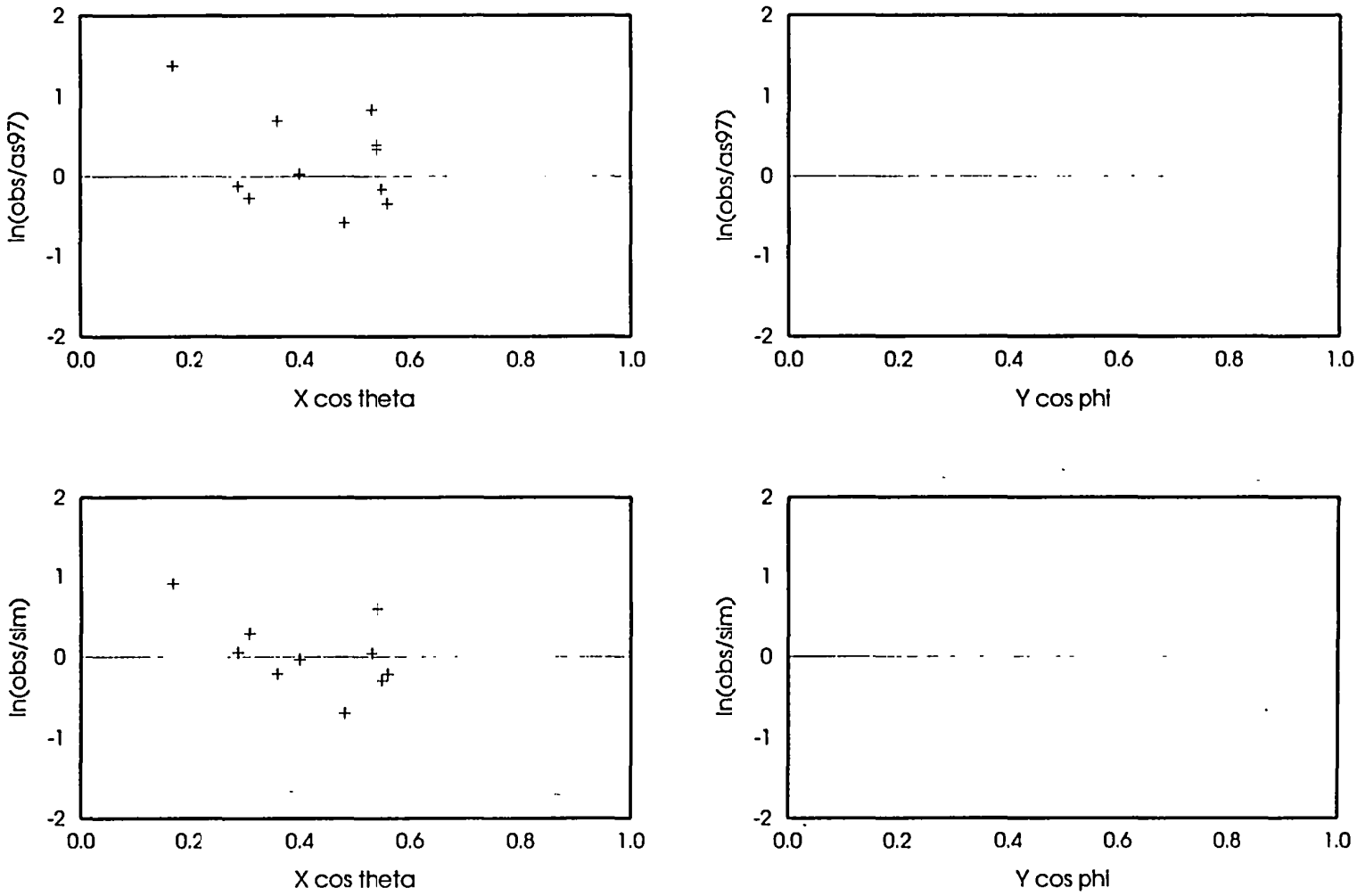

GMT Aug 24 17:56:30 1999 /net/coda/u2/arben/Kobe/Comparisons/Resid_plots

Kobe - Fault Parallel

SA at 2.0 sec

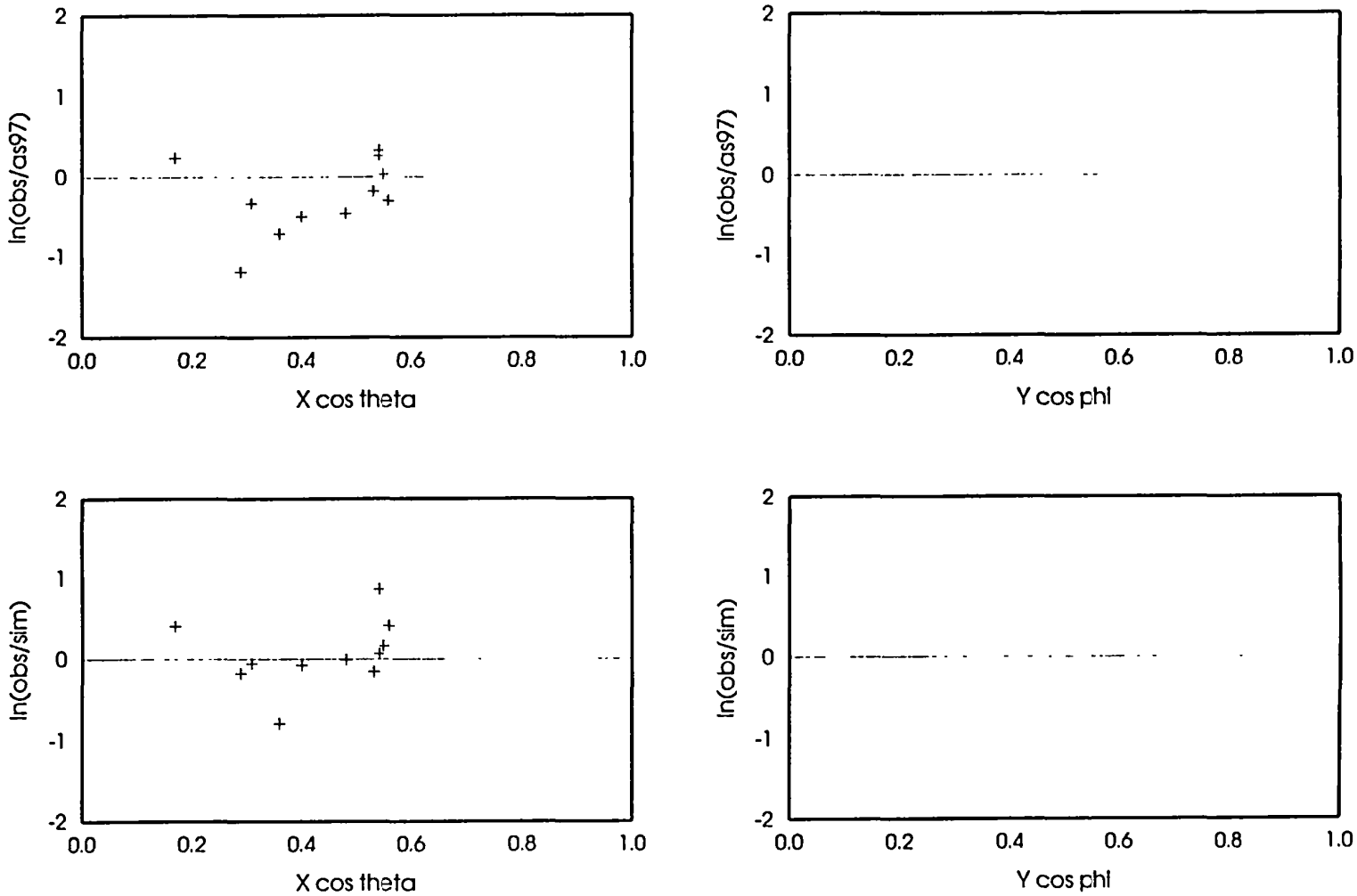

GMT Aug 24 17:56:32 1999 /net/coda/u2/arben/Kobe/Comparisons/Resid_plots

Kobe - Fault Normal

SA at 1.5 sec

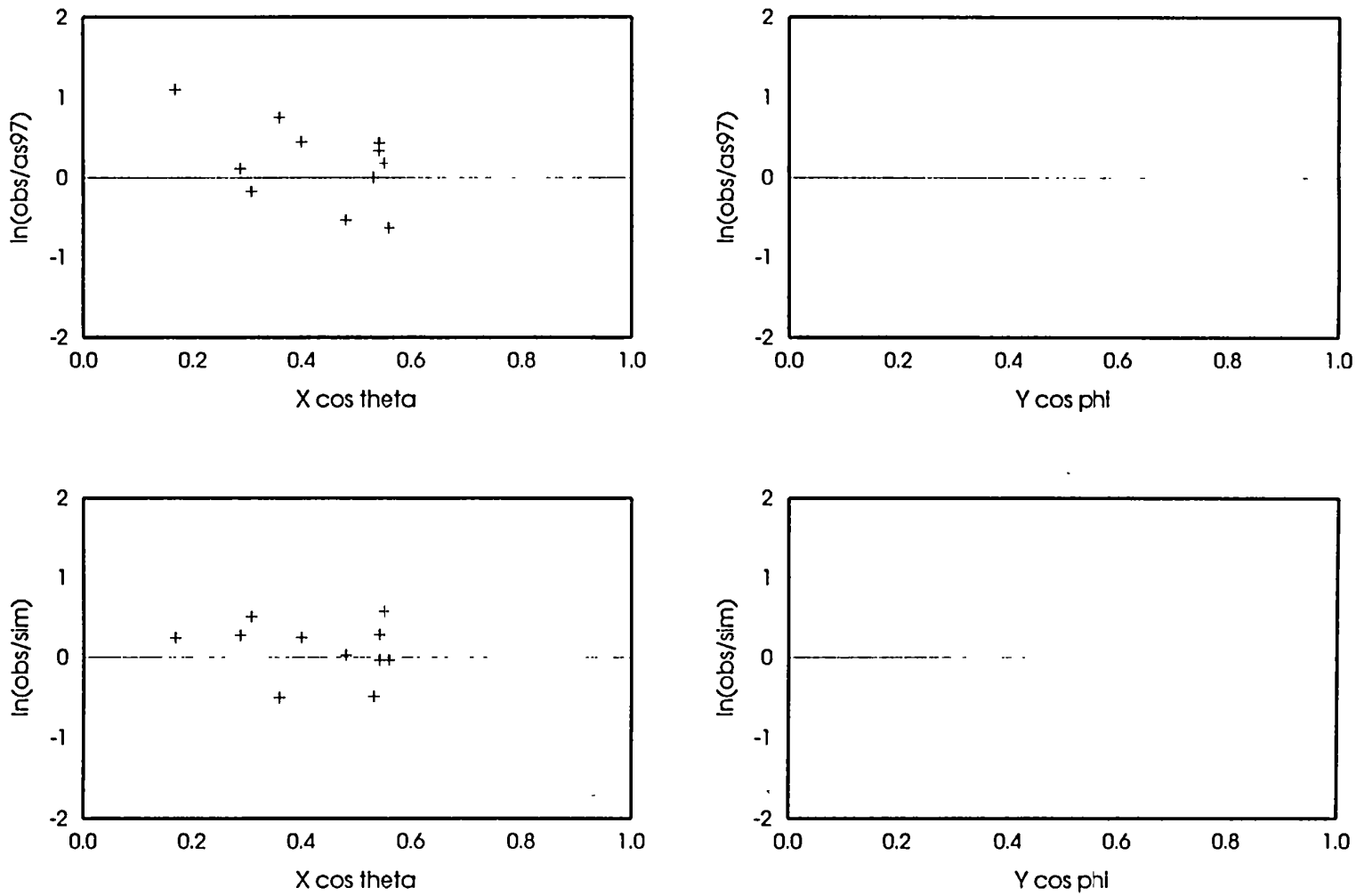

GMT Aug 24 17:56:34 1999 /net/coda/u2/arben/Kobe/Comparisons/Resid_plots

Kobe - Fault Parallel

SA at 1.5 sec

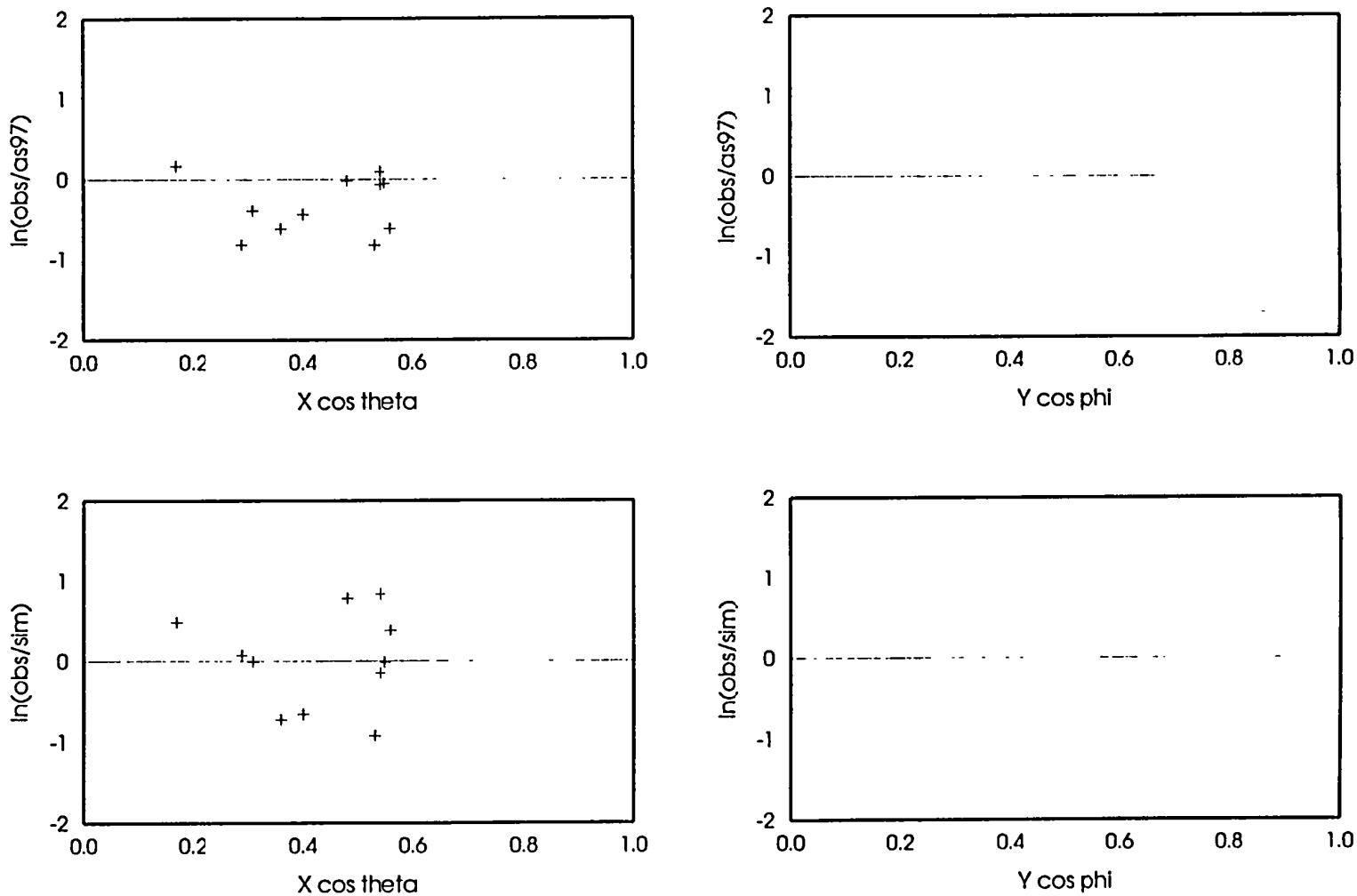

GMT Aug 24 17:56:36 1999 /net/coda/u2/arben/Kobe/Comparisons/Resid_plots

Kobe - Fault Normal

SA at 1.0 sec

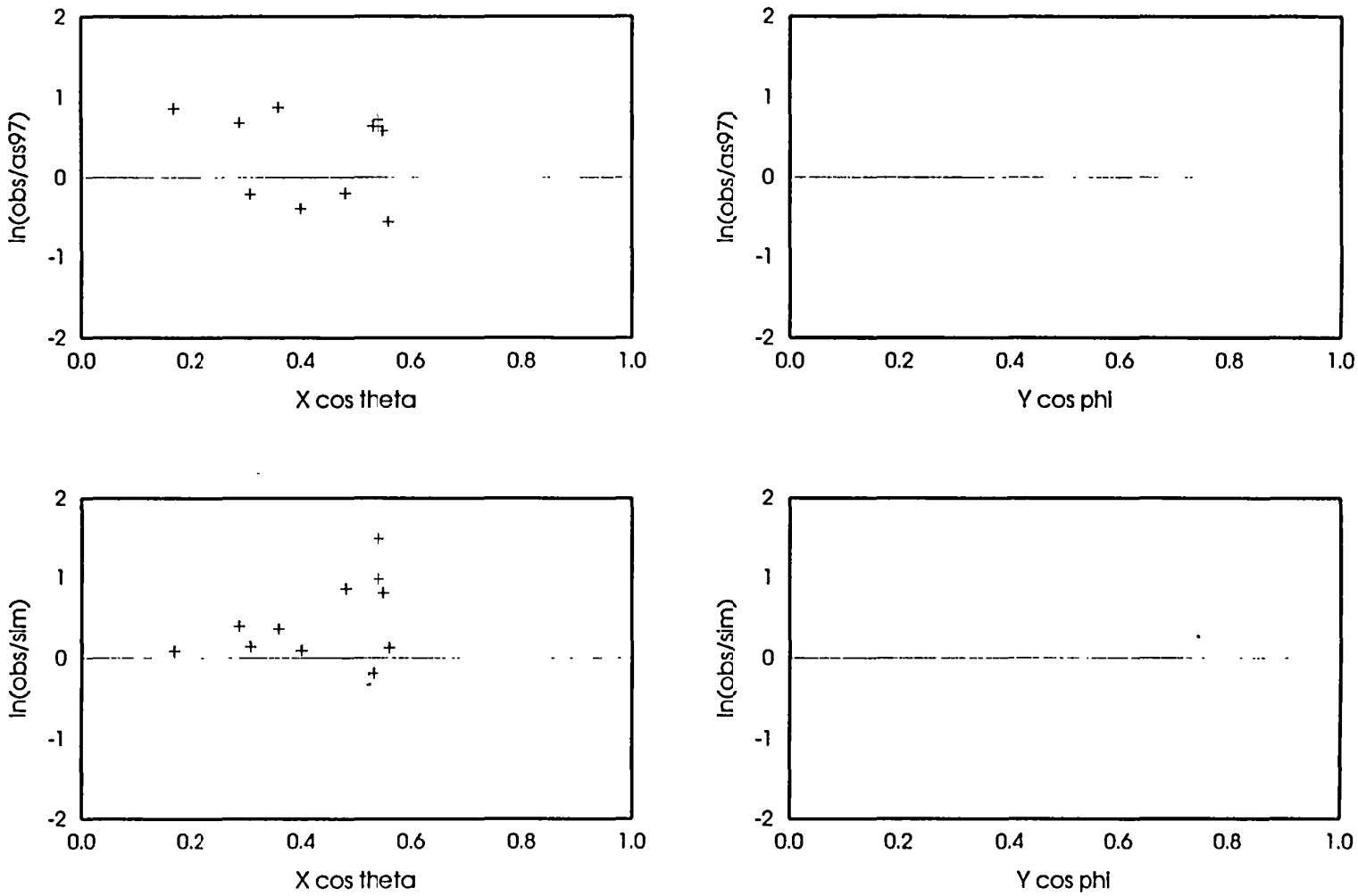

GMT Aug 24 17:56:38 1999 /net/coda/u2/arben/Kobe/Comparisons/Resid_plots

Kobe - Fault Parallel

SA at 1.0 sec

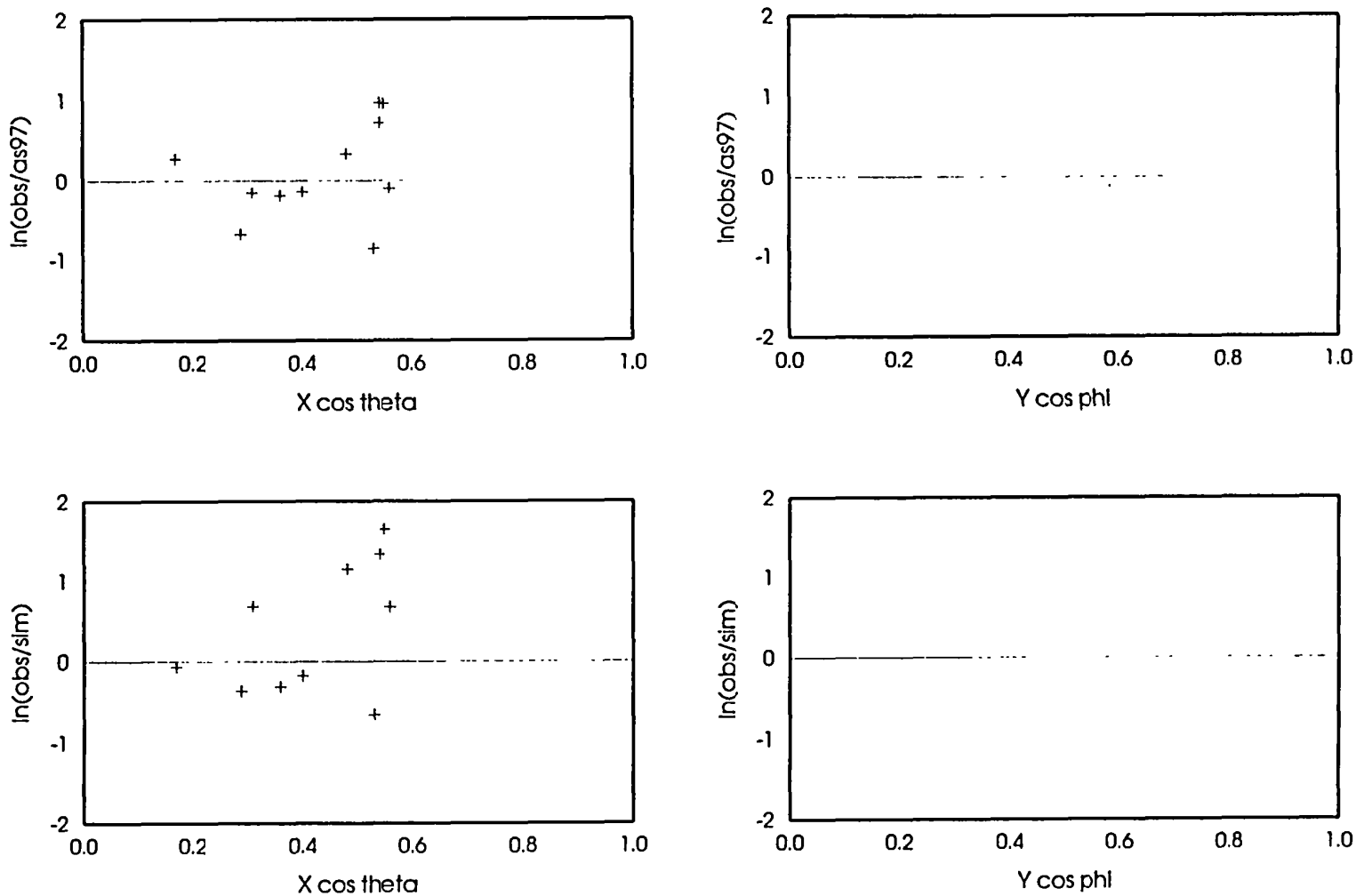

GMT Aug 24 17:56:40 1999 /net/ccda/u2/arben/Kobe/Comparisons/Resid_plots

PACIFIC EARTHQUAKE ENGINEERING RESEARCH CENTER

Evaluation of Numerical Procedures for Simulating Near-Fault Long-Period Ground Motions Using Zeng Method

Yuehua Zeng

John Anderson
University of Nevada, Reno

A report to the PEER Program of Applied Earthquake Engineering Research on Lifeline Systems

The financial support of the sponsor organizations including the Pacific Gas & Electric Company (PG&E), the California Energy Commission (CEC), and the California Department of Transportation (Caltrans) is acknowledged.

PEER UTILITIES PROGRAM
REPORT NO. 2000/01

Final Technical Report on Near Fault Ground Motions

Phase II, Task 5: Near-fault ground motions

Yuehua Zeng and John Anderson
Seismological Lab, University of Nevada - Reno

Introduction

Over the past several years, we have developed theories and methods for modeling synthetic strong ground motion using a composite source model (Zeng et al., 1994). The method has been successful in generating realistic strong motion seismograms. The realism is demonstrated by comparing synthetic strong motions with observations from the recent California earthquakes at Landers, Loma Prieta (Su et al., 1994a,b) and Northridge (Zeng and Anderson, 1996; Anderson and Yu, 1996; Su et al., 1998), earthquakes in the eastern US (Ni et al., 1999) and earthquakes in Guerrero, Mexico (Yu, 1994; Johnson, 1999), Turkey (Anderson et al., 1997) and India (Khattri et al, 1994; Zeng et al, 1995). We have also successfully applied the method for earthquake engineering applications to compute the ground motion of scenario earthquakes. During the process of continuing development, we have included scattering waves from small scale heterogeneity structure of the earth, site specific ground motion prediction using weak motion site amplification, and nonlinear soil response using the geotechnical engineering model.

In this report, we investigate the effect of rupture directivity from large damaging earthquakes. First we will find the earthquake source models that best describe the ground motion waveform recorded at the strong motion stations. Then we will use those earthquake source models to simulate near fault ground motion and compared them with the recorded strong motion seismograms. Finally, we will use the near-fault directivity model of Somerville et al. (1997) to test the synthetic prediction of the rupture directivity effect from those earthquake ground motions in term fault normal and fault parallel components.

Method

Composite Source Model

We have developed a composite source model (Zeng et al., 1994) for realistic synthetic strong ground motion seismograms computation. This method uses synthetic Green's functions, which characterize wave propagation in a flat-layered medium, convolved with the composite source time functions. The source is a superposition of circular subevents with constant stress drop. The number of subevents and their radius follows a power law given by

$$\frac{dN}{d(\ln R)} = pR^{D}$$

where D is the fractal dimension that equals twice the b-value, N is the number of subevents, and p is a constant of proportionality. The random nature of the heterogeneities on a complex fault is simulated by distributing the subevents randomly on the fault plane. Rupture propagates from the hypocenter at a constant velocity, and each subevent initiates the radiation of a displacement pulse of a crack model. The heterogeneous nature of the composite earthquake faulting is apparently characterized by the maximum subevents size and the subevents stress drop, which can be constrained by other independent geophysical data.

The synthetic Green's function has been modified to consider the effect of the random lateral heterogeneity of the earth by adding scattered waves into the Green's function (Zeng, 1995). The solution is then convolved with a plane wave propagation function through a near surface 1-D velocity layering as complex as that suggested by sonic well logs. Thus the complex high-frequency waveform of our simulation is generated from a combination of a heterogeneous source (Figure 1), wave reverberation in a stratified crustal structure (Figure 2) and scattering from lateral inhomogeneity of the earth (Figure 3).

Earthquake source Imaging Using Genetic Algorithm

Zeng and Anderson (1996) used a Genetic Algorithm to find a specific composite source model that best fit the observed waveform data for the Northridge earthquake. The Genetic Algorithm works by mimicking the process of natural selection principle of survival of the fittest. By analogy with the natural behavior, it starts with an initial "population" of "individuals" (e.g., models of the subevent locations), each representing a possible solution. A fitness score is assigned to each individual. Individuals with higher fitness are given better opportunities to "crossbreed" with others in the population to produce "offspring" that form a new population the same size as the original. The algorithm iterates by taking those offspring as a new generation and repeats the process until a satisfactory solution is obtained.

The fitness function in our waveform inversion is defined as

$$F(m^i) = \underset{\substack{stations and \\ components}}{} \frac{\min(u^o_{\max}, u^s_{\max})}{\max(u^o_{\max}, u^s_{\max})} \left(\frac{\sum_l u^o_l u^s_l}{\sqrt{\sum_l u^o_l u^o_l}\sqrt{\sum_l u^s_l u^s_l}} \right)$$

where m^i is the *i*th individual; u^o_l is the observed seismogram; u^s_l is the corresponding synthetic seismogram; and $u^o_{\max}$ and $u^o_{\max}$ are the corresponding peak values of the observed and synthetic seismograms, respectively. The representation in the parentheses gives the cross-correlation coefficient of the synthetic with the data. The weights given to the correlation coefficients penalize seismograms with similar waveforms but different amplitudes. Each individual is assigned a fitness value based on the above equation.

Next, we pick two individuals as "parents" for a reproduction event using the so-called roulette wheel selection scheme. The two parents are used to generate two offspring by recombining their "chromosomes" using the mechanisms of cross-over and mutation. The chromosomes in our case are the subevent locations on the rupture plane. The subevents of both models are divided randomly into 10 groups exactly, and their positions are copied into their offspring according to a randomly generated "cross-over mask." Mutation is applied to each offspring individually after cross-over. It is done by randomly altering the location of each subevent with a probability of 0.01.

Modified Source Radiation

Motivated by the fact that we do not observe any distinct radiation pattern and wave polarization at high frequency, we introduced an effective high frequency source radiation term. This source radiation consists of energy contributions from an angular cross section centered at the direction from the source to receiver in order to simulate high frequency wave reflection and scattering at the fault zone. The total source radiation then equals

*effective-source-radiation + (1-)*double-couple-source-radiation,

where is a continuo function of frequency. It equals 1 above a high frequency threshold and tapers to 0 at low frequency since this reflection and scattering at the source zone has less an effect at lower frequencies (Figure 4). The results were validated with the Northridge strong motion observations. We have compared the results with the observed and regression prediction (Abrahamson and Silva, 1997) of the PGA and SA at 3 second. The synthetic simulations clearly predict the trends of the observed ground motion parameters better than the regression. The scatter in the data is presumably caused by local site and basin response effects.

Data and Analysis

We selected several important earthquakes for the validation study of the composite source model. These events are selected through PEER and PG&E project coordination meeting. A list of those events is given in Table 1.

Table 1. Earthquakes used for the model validation

Event year	Event name	Epicenter Latitude	Epicenter Longitude	Hypocenter Depth

1979	Imperial Valley earthquake, CA	32.6435	115.3088	8.0
1989	Loma Prieta earthquake, CA	37.0407	121.8829	17.6
1992	Landers earthquake, CA	34.2000	116.4300	7.0
1994	Northridge earthquake, CA	34.215	118.538	17.5
1995	Kobe earthquake, Japan	34.5948	135.0121	16.9

Near field strong motion seismograms from those events within about 40 km of the fault planes were selected. Table 2a, 2b, 2c, 2d and 2e list the station names, locations for the strong motion data analysis of the 5 earthquakes listed in Table 1, respectively. The total number of strong motion stations selected for Imperial Valley, Loma Prieta, Landers, Northridge, and Kobe earthquakes are 28, 34, 13, 33 and 15, respectively.

Table 2a

Station names and locations for the Imperial Valley earthquake

Name	Latitude	Longitude	Description
AEPI	32.6510	-115.3320	Aeropuerto Mexicali
AGRI	32.6210	-115.3010	Agrarias
BCRI	32.6930	-115.3380	Bonds Corner
BRAI	32.9910	-115.5120	Brawley Airport
CXOI	32.6690	-115.4920	Calexico Fire Station
CALI	33.1300	-115.5200	Calipatria Fire Station
CPEI	32.4200	-115.3010	Cerro Prieto
CHII	32.4840	-115.2400	Chihuahua
ECCI	32.7930	-115.5620	El Centro - Imp County Center FF
EMOI	32.7730	-115.4470	El Centro - Meloland Overpass FF
E01I	32.9600	-115.3190	El Centro #1
E03I	32.8940	-115.3800	El Centro #3
E04I	32.8640	-115.4320	El Centro #4
E05I	32.8550	-115.4660	El Centro #5
E06I	32.8390	-115.4870	El Centro #6
E07I	32.8290	-115.5040	El Centro #7
E08I	32.8110	-115.5320	El Centro #8
E10I	32.7800	-115.5670	El Centro #10
E11I	32.7520	-115.5940	El Centro #11
E12I	32.7180	-115.6370	El Centro #12
E13I	32.7090	-115.6830	El Centro #13
EDAI	32.7960	-115.5350	El Centro Diff Array #1
HVPI	32.8120	-115.3770	Holtville Post Office
PTSI	32.9290	-115.6990	Parachute Test Site
PLSI	32.7900	-115.8600	Plaster City
SHPI	32.6180	-115.4280	SAHOP Casa Flores
SUPI	32.9550	-115.8230	Superstition Mountain
WSMI	33.0370	-115.6230	Westmorland

Table 2b

Station names and locations for the Loma Prieta earthquake

Name	Latitude	Longitude	Description
AGWI	37.3970	-121.9520	Agnews State Hospital
ANDI	37.1650	-121.6310	Anderson Dam (downstream)
ADLI	37.1650	-121.6320	Anderson Dam, L Abut
A07I	37.4900	-122.3100	APEEL 7 - Pulgas
A09I	37.4700	-122.3200	APEEL 9 - Crystal Springs Res

A10I	37.4650	-122.3430	APEEL 10 - Skyline
BESI	37.5120	-122.3080	Belmont - Envirotech
BRNI	37.0470	-121.9850	BRAN
CAPI	36.9740	-121.9520	Capitola
CLSI	37.0460	-121.8030	Corralitos
CLDI	37.1240	-121.5510	Coyote Lake Dam (Downstr)
CYCI	37.1180	-121.5500	Coyote Lake Dam (SW Abut)
GILI	36.9730	-121.5680	Gilroy Gavilan College
GOFI	37.0090	-121.5690	Gilroy, Historic Bldg
G01I	36.9730	-121.5720	Gilroy #1
G02I	36.9820	-121.5560	Gilroy #2
G03I	36.9870	-121.5360	Gilroy #3
G04I	37.0050	-121.5220	Gilroy #4
G06I	37.0260	-121.4840	Gilroy #6
GMRI	37.0330	-121.4340	Gilroy #7
HCHI	36.8510	-121.4020	Hollister City Hall
HDAI	36.8880	-121.4130	Hollister Differential Array
HSPI	36.8480	-121.3970	Hollister-South & Pine
LGPI	37.1720	-122.0100	LGPC
PAEI	37.4530	-122.1120	Palo Alto - 1900 Embarcadero
SLCI	37.4190	-122.2050	Palo Alto - SLAC
SJWI	36.6710	-121.6420	Salinas
STGI	37.2550	-122.0310	Saratoga-Aloha
WVCI	37.2620	-122.0090	Saratoga WVC
SVLI	37.4020	-122.0240	Sunnyvale - Colton Ave
UC2I	37.0000	-122.0620	UCSC
LOBI	37.0370	-121.8830	Santa Cruz UCSC/Lick
WAHI	36.9720	-121.9950	UCSC WAHO
WDSI	37.4290	-122.2580	Woodside

Table 2c

Station names and locations for the Landers earthquake

Name	Latitude	Longitude	Description
BRSL	34.8870	-117.0470	BARSTOW
DSPL	33.9620	-116.5090	DESERT HOT SPRINGS
INDL	33.7170	-116.1560	INDIO - COACHELLA CANAL
JOSL	34.1310	-116.3140	JOSHUA TREE
LCNL	34.5680	-116.6120	LUCERNE
MCFL	34.9050	-116.4190	MISSION CREEK FAULT
MVHL	34.0480	-116.5770	MORONGO VALLEY
NPSL	33.9240	-116.5430	NORTH PALM SPRINGS
PSAL	33.8290	-116.5010	PALM SPRINGS AIRPORT
SILL	33.8510	-116.8520	SILENT VALLEY - POPPET FLAT
29PL	34.0210	-116.0090	TWENTY NINE PALMS
YERL	34.9030	-116.8230	YERMO FIRE STATION
CLWL	34.8520	-116.8580	COOLWATER

Table 2d

Station names and locations for the Northridge earthquake

Name	Latitude	Longitude	Description
ARLN	34.236	-118.439	ARLETA - SAN FERNANDO
TUJN	34.286	-118.225	BIG TUJUNGA STATION USC #61
BVAN	34.063	-118.463	BRENTWOOD VA HOSP BLDG 259

HOWN	34.204	-118.302	BURBANK 1250 HOWARD RD
CNPN	34.212	-118.605	CANOGA PARK 7769 TOPANGA CANYON BLVD
LOSN	34.419	-118.426	CANYON COUNTRY 16628 W LOST CANYON RD
ORRN	34.564	-118.642	CASTAIC - OLD RIDGE ROUTE
GLPN	34.2	-118.231	GLENDALE 3320 LAS PALMAS AVE
JENN	34.312	-118.496	JENSEN FILTRATION PLANT ADMIN. BLDG
LDMN	34.295	-118.479	LA DAM FOUNDATION
WONN	34.114	-118.38	LOS ANGELES 8510 WONDERLAND AVE
NYAN	34.238	-118.253	LA CRESCENTA 4747 NEW YORK AVE
L09N	34.608	-118.558	LAKE HUGHES #9
H12N	34.57	-118.56	LAKE HUGHES ARRAY #12
MRPN	34.288	-118.881	MOORPARK
CWCN	34.194	-118.411	NORTH HOLLYWOOD 6850 COLDWATER CANYON
NWHN	34.387	-118.530	NEWHALL - LA COUNTY FIRE STATION
WPIN	34.391	-118.621	NEWHALL W PICO CANYON BLVD
STCN	34.209	-118.517	NORTHRIDGE 17645 SATICOY ST
PACN	34.334	-118.396	PACOIMA DAM - DOWN STREAM
PKCN	34.288	-118.375	PACOIMA - KAGEL CANYON
RRSN	34.281	-118.478	RINALDI RECEIVING STATION
SSUN	34.231	-118.713	SANTA SUSANA ETEC LIQUID METAL ENG CTR
SPVN	34.249	-118.478	SEPULVEDA VA HOSP
KATN	34.264	-118.666	SIMI VALLEY 6334 KATHERINE RD
SCRN	34.106	-118.454	STONE CANYON RES DAM
RO3N	34.221	-118.421	SUN VALLEY 13248 ROSCOE BLVD
GLEN	34.269	-118.303	SUNLAND 10965 MT GLEASON AVE
SCSN	34.311	-118.49	SYLMAR CONVERTER STATION
SCEN	34.312	-118.481	SYLMAR CONVERTER STATION EAST
SYLN	34.326	-118.444	SYLMAR OLIVE VIEW MEDICAL CENTER
TPFN	34.084	-118.599	TOPANGA FIRE STATION
VASN	34.492	-118.327	VASQUEZ ROCKS PARK
PARN	34.44	-118.58	Pardee - SCE

Table 2e

Station names and locations for the Kobe earthquake

Name	Latitude	Longitude	Description
ABNK	34.636	135.519	ABENO (ABN)
AMAK	34.718	135.408	AMAGASAKI (AMA)
FKSK	34.687	135.474	FUKUSHIMA (FKS)
KAKK	34.725	134.843	KAKOGAWA (KAK)
KBUK	34.725	135.240	KOBE UNIVERSITY (KBU)
KJMK	34.688	135.180	KJMA (KJM)
MRGK	34.680	135.572	MORIGAWACHI (MRG)
NISK	34.664	134.964	NISHI-AKASHI (NIS)
OSAK	34.678	135.520	OSAJ (OSA)
SKIK	34.564	135.469	SAKAI (SKI)
SHIK	34.737	135.516	SHIN-OSAKA (SHI)
TDOK	34.480	135.408	TADOKA (TDO)
TAZK	34.809	135.344	TAKARAZUKA (TAZ)
TAKK	34.649	135.139	TAKATORI (TAK)
YAEK	34.680	135.612	YAE
CHYK	34.439	135.659	CHICAYA (CHY)
PRIK	34.670	135.201	PORT ISLAND (0 M) (PRI)
KP2K	34.670	135.201	PORT ISLAND (16 M) (KP2)
KP3K	34.670	135.201	PORT ISLAND (32 M) (KP3)
KP4K	34.670	135.201	PORT ISLAND (83 M) (KP4)
TOTK	34.240	134.240	TOT

We filtered all the seismograms using a 4th order non-causal Butterworth filter with a pass band specified between 8 to 0.7 second period range. The S-wave arrival times of the strong motion records were picked and matched with the theoretical calculations based on a flat-layered crustal velocity model of the region. The crustal velocity model for the Imperial Valley, Landers and Northridge earthquakes are modified from Wald et al. (1996). The crustal velocity model for the Loma Prieta earthquake is modified from Somerville and Yoshimura (1990). The velocity model for the Kobe, Japan, earthquake is modified from Wald (1996). The modification is to add a 30 meters low velocity layer and a 100 meters transition layer on top of those regional velocity models to accommodate the site condition at each station. The site classifications for all strong motion stations are provided by Walt (1999, personal communication). The average shear wave velocity of the top 30 meter surface layer is assigned according to the USGS published site classification using shear wave velocities. These results are then used to calculated source inversion to determine the source rupture process of those earthquake events.

Earthquake Models

Using the Genetic Algorithm inversion, we inverted the strong motion data to obtain the earthquake source rupture processes of the earthquake events listed in Table 1.

We first studied the Imperial Valley earthquake source rupture process using the composite source model. This earthquake occurred on October 15, 1979 and has generated a large amount of strong motion records. A total of 28 stations were selected for the source inversion. Figure 5a shows a map view of the station and fault geometry distribution. We used the same fault geometry and seismic moment for the event as that of Hartzell and Heaton (1983). Figure 5b shows the slip distribution of this earthquake ploted in both slip vector and amplitude intensity scale. We found one large slip zone in the center on the fault. This result is consistent with the solution obtained by Hartzell and Heaton for the Imperial Valley earthquake source rupture process using teleseismic and strong motion inversion. From the slip vector distribution, we can see that this earthquake is almost a pure strike slip event. There is little or event no slip near the hypocenter area. Hartzell and Heaton have suggested that rupture has been accelerated from the hypocenter northward. The large slip in the middle of the fault could be a triggered event by a smaller rupture event near the hypocenter.

The Loma Prieta earthquake struck the San Francisco Bay area on October 17, 1989 and ruptured a 40 km segment of the San Andreas fault in the southern Santa Cruz area. Figure 6a is a map view of the fault geometry and the distribution of the strong motion stations used for the waveform inversion. There are total 34 station were selected for the waveform inversion to find a specific composite source model of the Loma Prieta earthquake. The seismic moment of this earthquake is estimated at 2.9×10^{26} dyne-cm. Figure 6b plots the slip distribution in vector and amplitude intensity scale. The result shows a large slip source located on the southeast side of the fault and another large slip source on the northwest side of the fault. Slip orientation changes from pure strike slip on the southeast side of the fault to oblique slip on the northwest side of the rupture plane. This solution agrees very well with Wald et al. (1991) and other studies of the Loma Prieta earthquake using different techniques. Strong nonlinear soil responses have been observed at site of strong motion station (Chin and Aki, 1992). The effect of the nonlinearity is not considered in the present investigation.

The 28 June 1992 Landers earthquake (Mw 7.2) ruptured through the fault of 70 km long with a long duration of around 24 second. A map view of the fault geometry and strong motion stations used for this source inversion is shown in Figure 7a. A total of 13 stations were used for the study. The seismic moment of this event is estimated to be 7.7×10^{26} dyn-cm. Figure 7b plots the distribution of slip vector and amplitude over the fault plane. Our inversion solution differs from Wald et al. (1994) and shows large slip zones near the centers of the three fault segments. Location of minimum fault slips coincide well with the ends or stepping sections of the fault, suggesting that fault stepovers act like barriers to the source dynamic rupture.

The 17 January 1994 Northridge earthquake (Mw 6.7) occurred on a buried thrust fault in the northwest Los Angeles metropolitan area. Zeng and Anderson (1996) studied this earthquake rupture process using the Genetic Algorithm and the composite source model. This study differs from the previous investigation by using a variable rake for the fault slip and a total of 33 strong motion records instead of 10 seismograms (Figure 8a). We used the same fault geometry as that of Wald et al. (1996). The seismic moment of this earthquake is estimated to be 1.4×10^{26} dyne-cm. Figure 4a shows a map view of the station and fault geometry distribution. Figure 8b plots the earthquake slip distribution of the composite source model and the slip vector distribution over the fault plane.

The result indicates a complex earthquake rupture process with three large slip zones: one above the hypocenter, and two others located to the west of the hypocenter. This result is essentially the same as our previous study.

Near fault strong motion records of the January 17, 1995 Kobe, Japan earthquake were also used to study the rupture process of the source. Figure 9a shows a map view of the station distribution and fault geometry. A total of 15 strong motion seismograms within about 30 km of the fault were selected. We applied Genetic Algorithm to find the specific composite source model that best fit the observed strong motion waveforms. We used the same fault geometry of Wald (1996). The moment of the earthquake is estimated about 2.4×10^{24} dyne-cm. Figure 9b shows the resulting slip and rake distribution of the composite source model determined from the waveform inversion. The plot suggests that much of the earthquake moment was released at shallow depths of the first fault segment. However, the smaller slip sources from the second fault segment actually causes more damage to the surface structures.

Rupture directivity

With the earthquake source model derived above, we then test the effect of rupture directivity of the composite source model comparing with the observation. Such an effect will be examined using different fitness functions. However, the effect of predicted directivity is not measured by the absolute value of those fitness parameters. Instead, we are looking for the trend of those values related to the directivity model parameter.

Somerville et al. (1997) have parameterized the rupture directivity as a function of X*cos( ) for strike slip fault and Y*cos( ) for dip slip fault, where X and Y represent the fraction of the rupture between the hypocenter and the station, represents the angle between the fault strike and the line connecting the epicenter to the station, and represents the angle between the dip direction of the fault to the line connecting the hypocenter to the station. Figure 10 is reproduced from Somerville et al. (1997) to illustrate the meaning of those variables for the directivity model. Thus the smaller the angle between rupture propagation and wave propagation, the larger the rupture directivity effect. Also the large the fraction of the fault lies between the hypocenter and station, the large the rupture directivity.

For the fitness parameter, we will use the weighted cross-correlation. This parameter provides good measure of the match in phase between synthetic prediction and the observation. However, a large difference in amplitude between synthetics and observation may result in the same cross-correlation. This is remedied by introducing a weighting parameter we have discussed earlier in the method section. We will also use the ratio of the synthetic and the observed response spectrum at different periods to test the rupture directivity.

Figure 11 plots the weighted cross-correlations versus the directivity parameter defined by Somerville et al. (1997). Symbols in different colors represent values computed for different earthquakes. The solid line represents a moving average for all parameters. The dotted lines are $\pm$ two mean-standard-eror from the average cross-correlation. The top panel of the plot is for fault parallel and the lower panel of the plot is for fault normal. Figure 12, 13 and 14 are the same figure but for spectral ratio of the observation and the synthetics at 1, 3, and 5 seconds. There are slight over prediction at the zero fault directivity, especially for the normal component. Overall, by carefully examine the trend of those ratio versus directivity parameter for all stations, we did not find any significant bias or trends in the results. This suggests that the composite source model predicts the observed directivity very well.

Conclusion

1. We have used Genetic Algorithm to find a specific composite source model for each large earthquake used for the near field ground motion analysis. The models give best fit to the ground motion waveform in terms of the weighted cross-correlation between synthetics and observations.

2. Our composite source slip models agree with results from other studies using different earthquake source modeling methods for Loma Prieta, Imperial Valley, Northridge and Kobe events. For Landers event, Our model shows large slip occurred near the centers of the fault segments. Locations of minimum slips on the fault coincide with the segment boundaries, suggesting fault stepovers act as barriers to earthquake rupture.

3. In terms of near fault rupture directivity, our error analysis shows the composite source model simulations are consistent with the observed directivity effects. We did not find any significant bias trends in terms of the weighted cross-correlation and response spectrum ratios between synthetics and observations.

Reference

Abrahamson, N. A. and W. J. Silva (1997). Equations for estimating horizontal response spectra and peak acceleration from western North American earthquakes: a summary of recent work, Seism. Res. Lett., 68, 94-127.

Anderson , J. G. and G. Yu (1996). Predictability of strong motions from the Northridge, California, earthquake, Bull. Seism. Soc. Am. No. 86, 1B, S100-S114.

Anderson, J. G., Y. Zeng, H. Sucuoglu (1997). Analysis accelerations from the Dinar, Turkey earthquake, presented at the Eighth International Conference on Soil Dynamics and Earthquake Engineering at Istanbul, Turkey.

Chin, B. H. and K. Aki (1991). Simultaneous study of the source, path and site effects on strong ground motion during the 1989 Loma Prieta earthquake: A preliminary result on pervasive nonlinear site effects, Bull. Seism. Soc. Am. No. 81, 1859-1884.

Hartzell, S. H. and T. H. Heaton (1983). Inversion of strong ground motion and teleseismic waveform data for the fault rupture history of the 1979 Imperial Valley, California, earthquake, Bull. Seism. Soc. Am. No. 73, 6, 1553-1583.

Johnson, M. (1999). Composite source model parameters for large earthquakes (M>5.0) in the Mexican subduction zone, M. S. thesis, University of Nevada, Reno.

Khattri, K. N., Y. Guang, J. G. Anderson, J. N. Brune and Y. Zeng (1994). Seismic hazard estimation using modelling of earthquake strong ground motions: A brief analysis of 1991 Uttarkashi earthquake, Himalaya and prognostication for a great earthquake in the region, *Current Science*, 67, 343-353

Ni., S.-D., J. G. Anderson, Y. Zeng (1999). Comparison of strong ground motions from the 1988 Seguenay earthquake with the synthetic simulations using the composite source model, in preparation.

Somerville, P. G. and J. Yoshimura (1990). The influence of critical Moho reflections on strong ground motions recorded in San Francisco and Oakland during the 1989 Loma Prieta earthquake, Geophy. Res. Lett., 17, 1203-1206.

Somerville, P. G., N. F. Smith, R. W. Graves, and N. A. Abrahamson (1997). Modefication of empirical strong ground motion attenuation relations to include the amplitude and duration effects of rupture Directivity, Seism. Res. Lett., 68, 199-222.

Su, Feng, Y. Zeng and J. G. Anderson (1994a). Simulation of the Loma Prieta earthquake strong ground motion using a composite source model, EOS, Trans. A.G.U., **75**, 44, p448.

Su, F., Y. Zeng and J. G. Anderson (1994b). Simulation of Landers earthquake strong ground motion using a composite source model, Seism. Res. Lett., **65**, p52.

Su, F., J. G. Anderson and Y. Zeng (1998). Study of weak and strong motion including nonlinearity in the Northridge, California, earthquake sequence, submitted to *Bull. Seis. Soc. Am*. **88**, 1411-1425.

Wald, D. J., T. H. Heaton, and D. V. Helmberger, (1991), Rupture model of the 1989 Loma Prieta earthquake from the inversion of strong motion and broadband teleseismic data, Bull. Seism. Soc. Am, 81, 1540-1572, 1991.

Wald, D. J., and T. H. Heaton (1994), Spatial and temporal distribution of slip for the 1992 Landers, California, earthquake, Bull. Seism. Soc. Am, 84, 668-691, 1994.

Wald, D. J., T. H. Heaton, and K. W. Hudnut (1996). The slip history of the 1994 Northridge, California, earthquake determined from strong-motion, teleseismic, GPS, and Leveling data, BSSA, 86, S49-S70.

Wald, D. J. (1996). Slip history of the 1995 Kobe, Japan, earthquake determined from strong ground motions, teleseismic, geodetic data, J. Physics of the Earth, 44, 489-504.

Yu, G., 1994. Some aspects of earthquake seismology: slip partitioning along major convergent plate boundaries; composite source model for estimation of strong motion; and nonlinear soil response modeling, PH.D Thesis, *University of Nevada*, Reno, Nevada.

Zeng, Y., J. G. Anderson and G. Yu (1994). A composite source model for computing realistic synthetic strong ground motions, *J. Res. Lett.*, **21**, 725-728.

Zeng, Y., J. G. Anderson and Feng Su (1995). Subevent rake and scattering effects in realistic strong ground motion simulation, *Geophy. Res. Lett*, **22**, 17-20.

Zeng, Y. (1995). A realistic synthetic Green's function calculation using a combined deterministic and stochastic modeling approach, *EOS, Trans. A.G.U.*, **76**, F357.

Zeng, Y. and J. G. Anderson (1996). A composite source modeling of the 1994 North-ridge earthquake using Genetic Algorithm,Bull. Seism. Soc. Am. 86, No. 1B, 71-83.

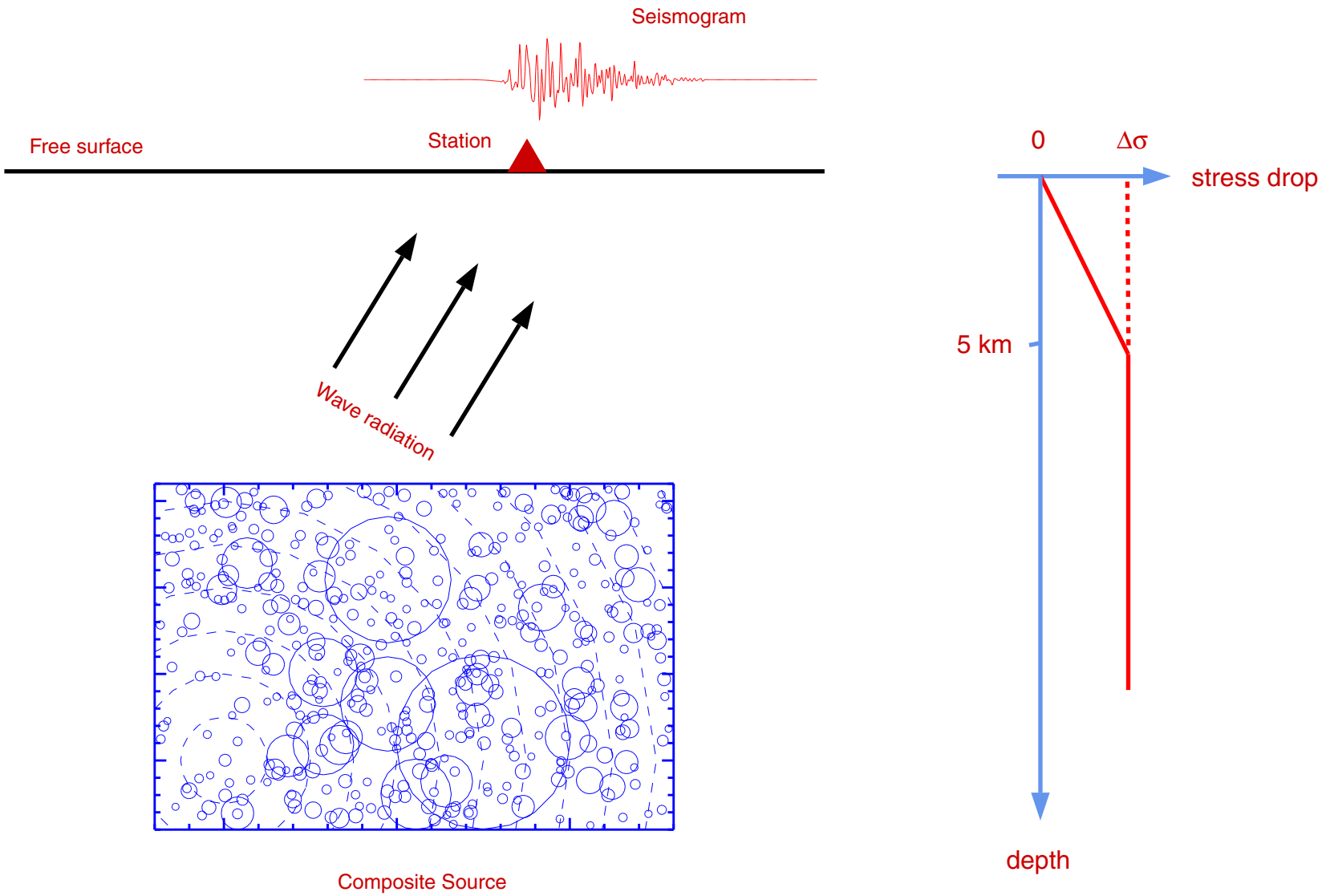

Figure 1. Schematic plot of the complexity in wave field caused by composite source of earthquake.

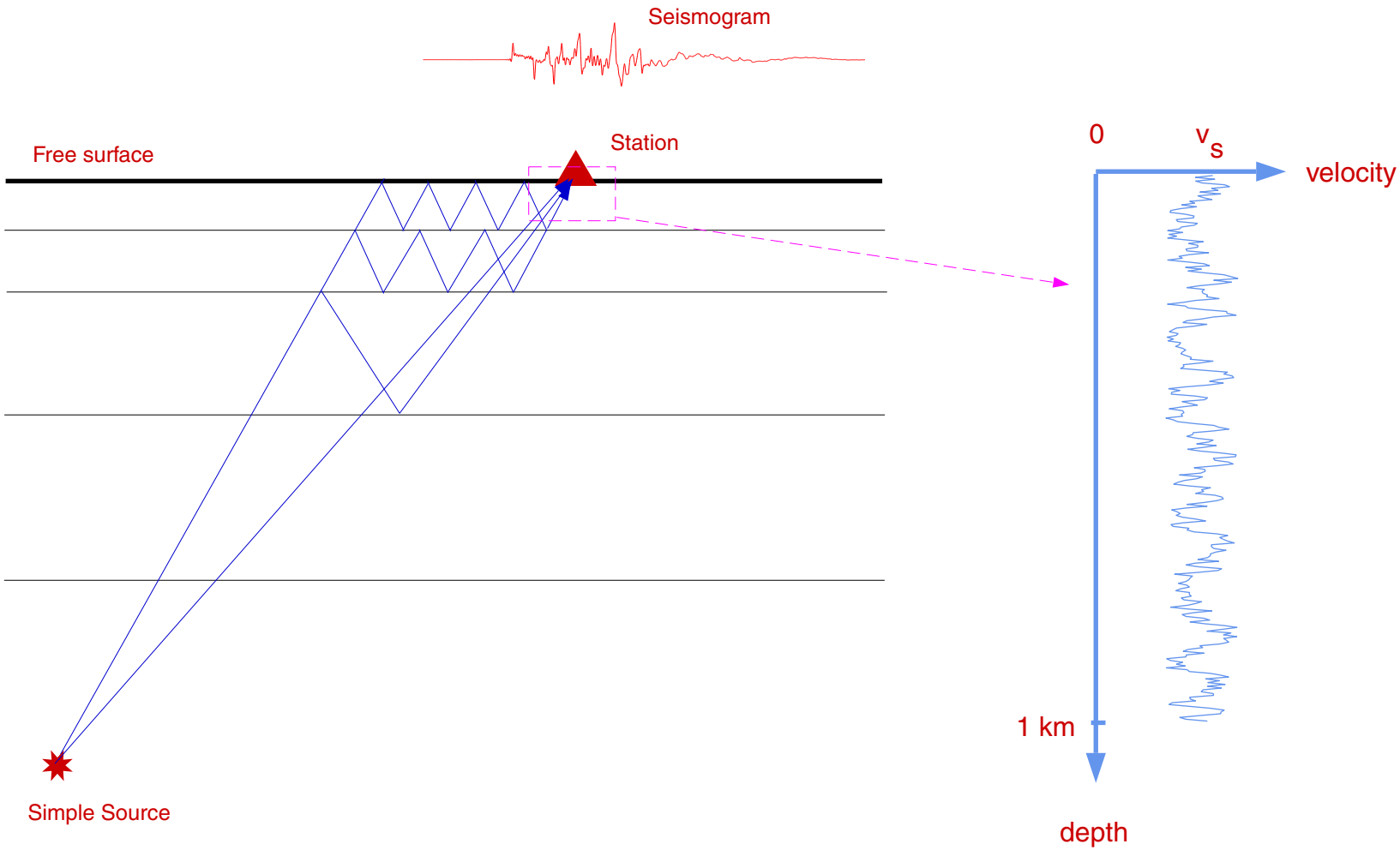

Figure 2. Schematic plot of the complexity in wave field caused by reverbration of waves in a vertically inhomogeneous structure of the earth.

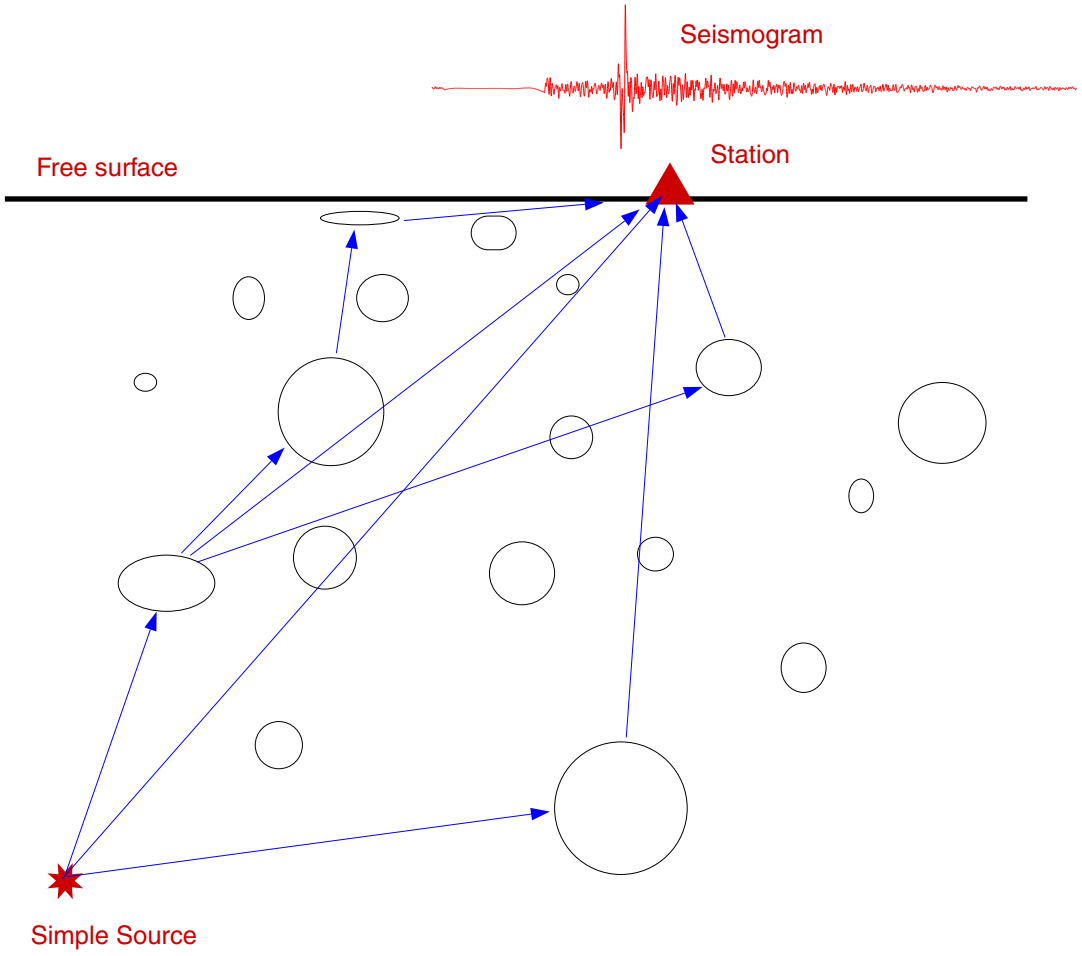

Figure 3. Schematic plot of the complexity in wave field caused by scattering waves from a laterally inhomogeneous structure of the earth.

Source Radiation:

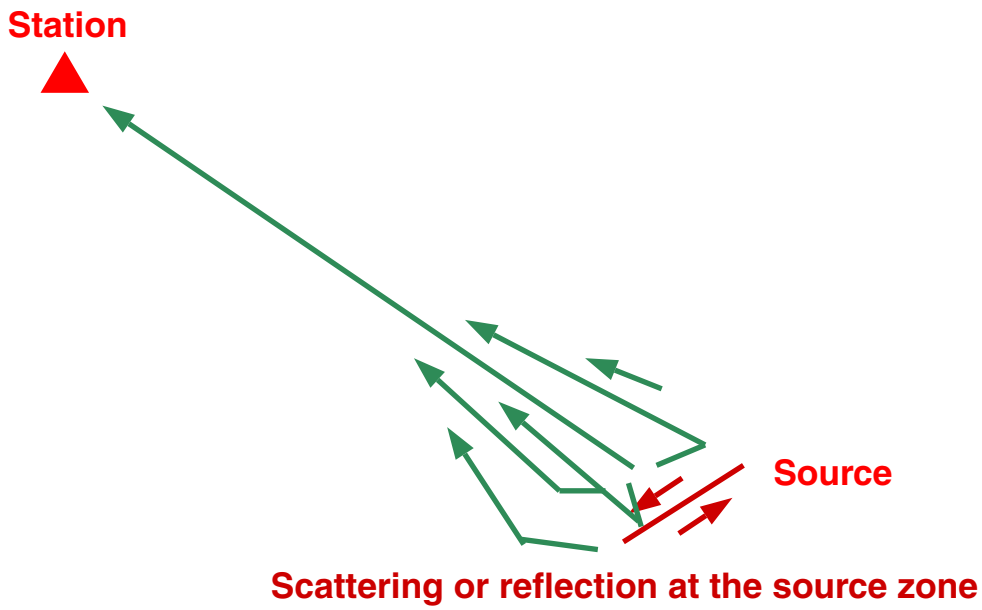

Total source radiation =

α x Effective-source-radiation + (1 + α) x double-couple-source

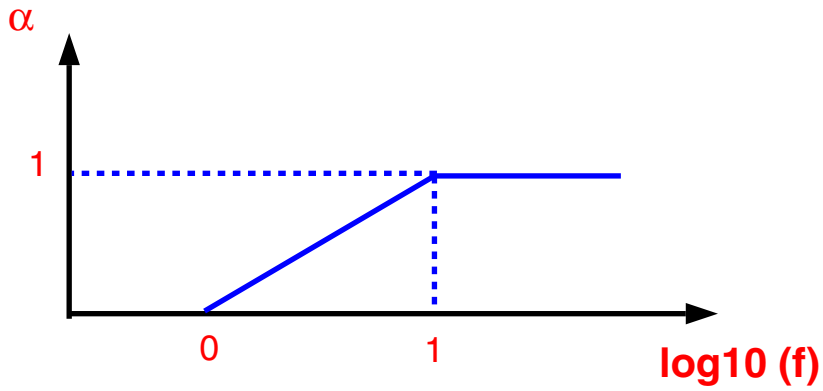

Figure 4. Schematic plot of the effective source radiation.

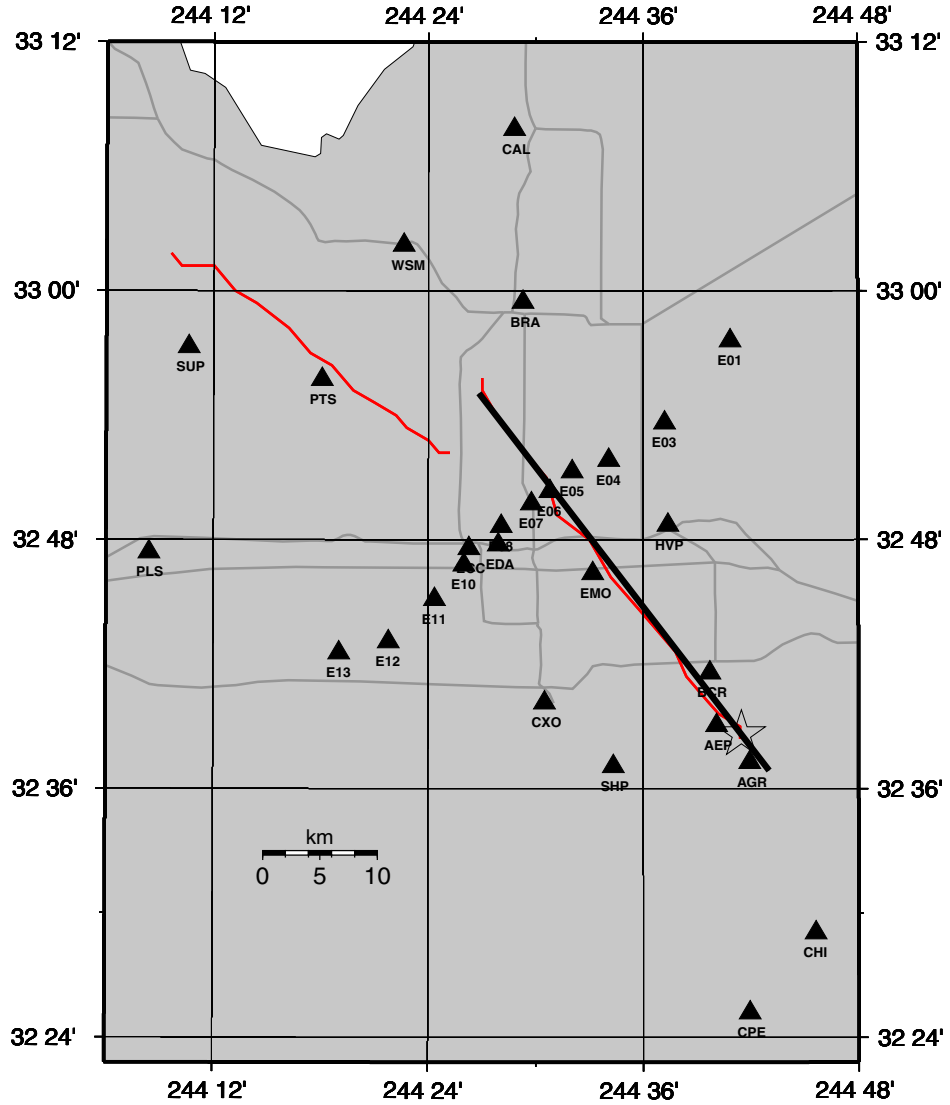

(a)

Slip Amplitude Distribution of the Imperial Valley Earthquake

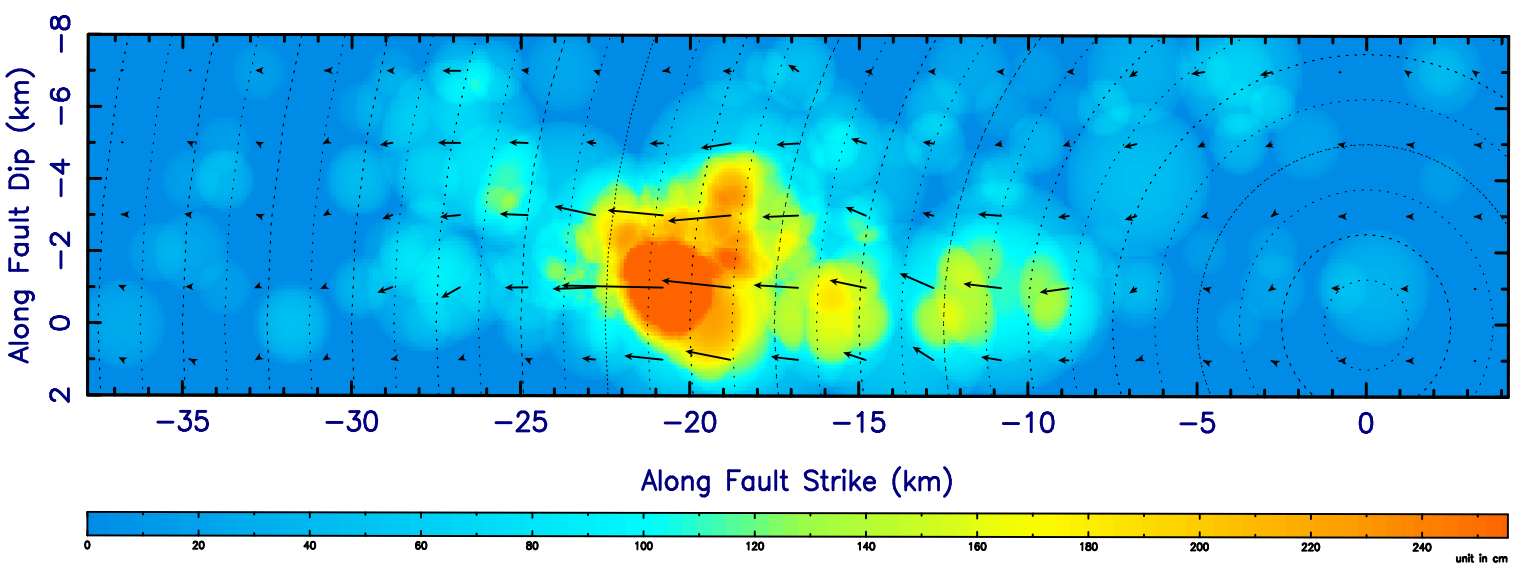

(b)

Figure 5. (a) Fault geometry and stations distribution. (b) Slip distribution of the composite source model.

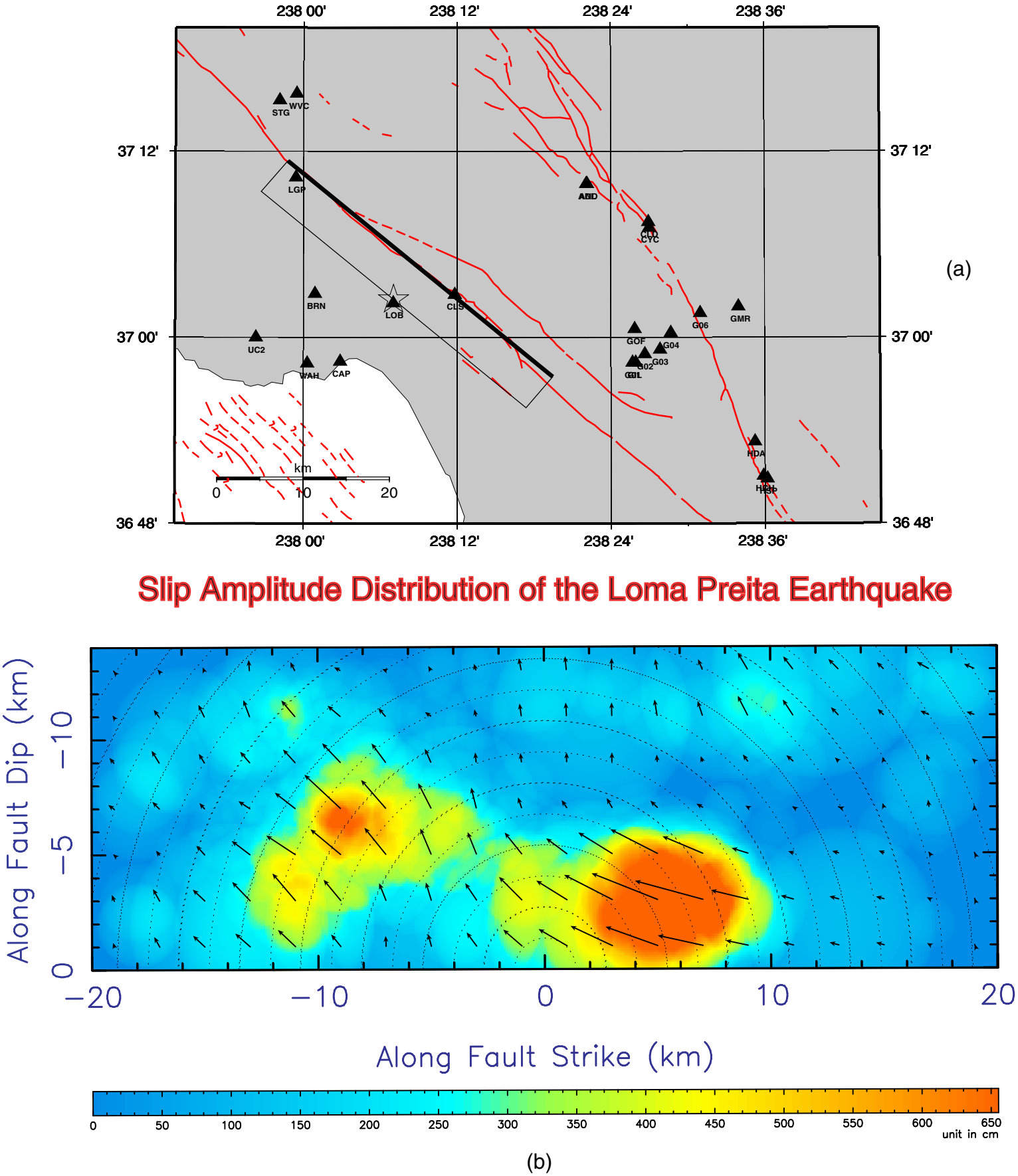

Figure 6. (a) Fault geometry and stations distribution. (b) Slip distribution of the composite source model.

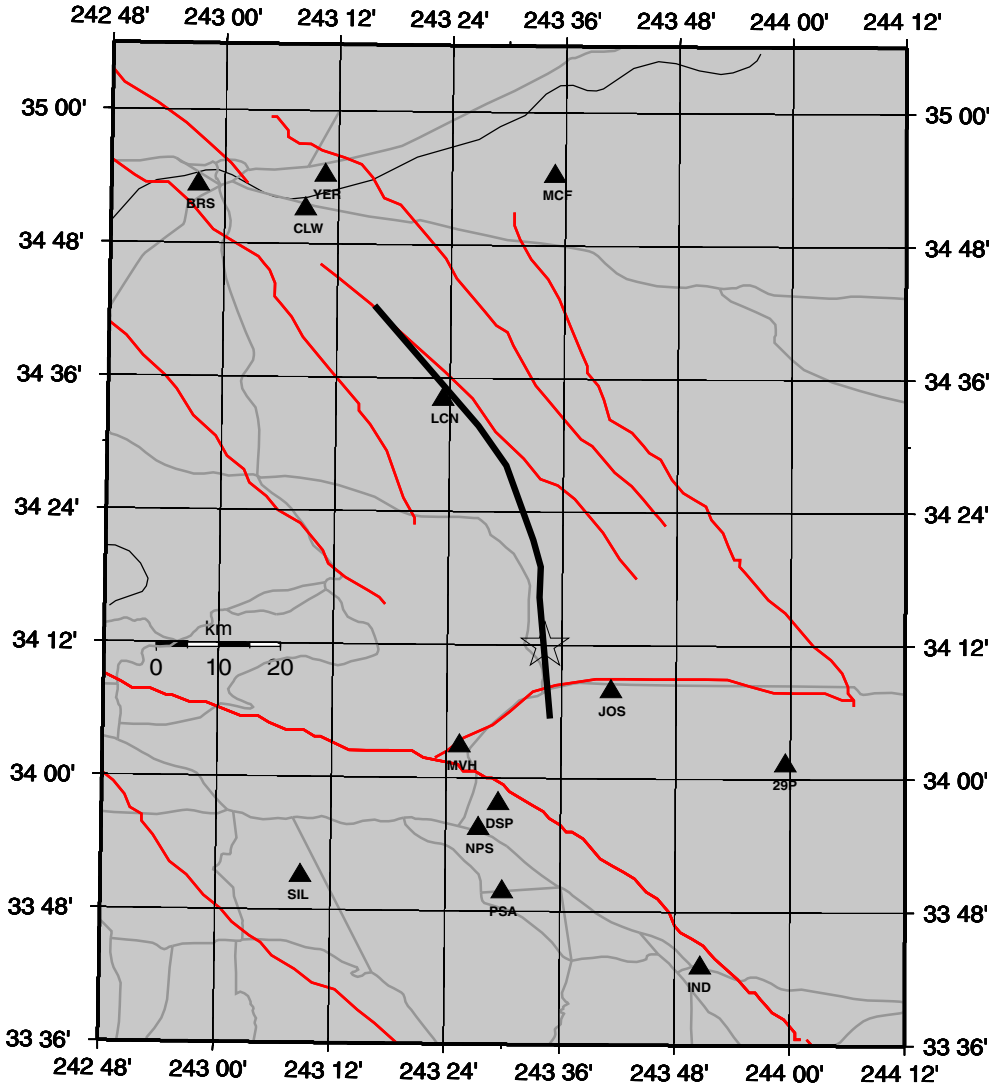

(a)

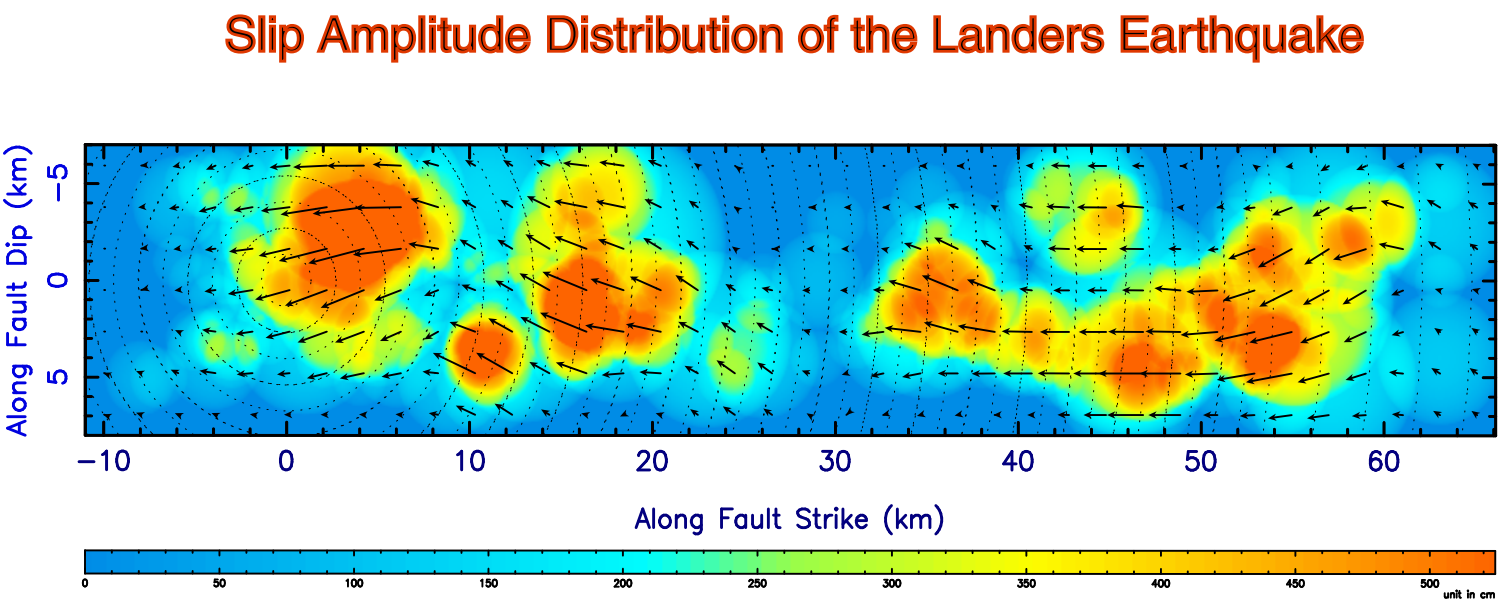

(b)

Figure 7. (a) Fault geometry and stations distribution. (b) Slip distribution of the composite source model.

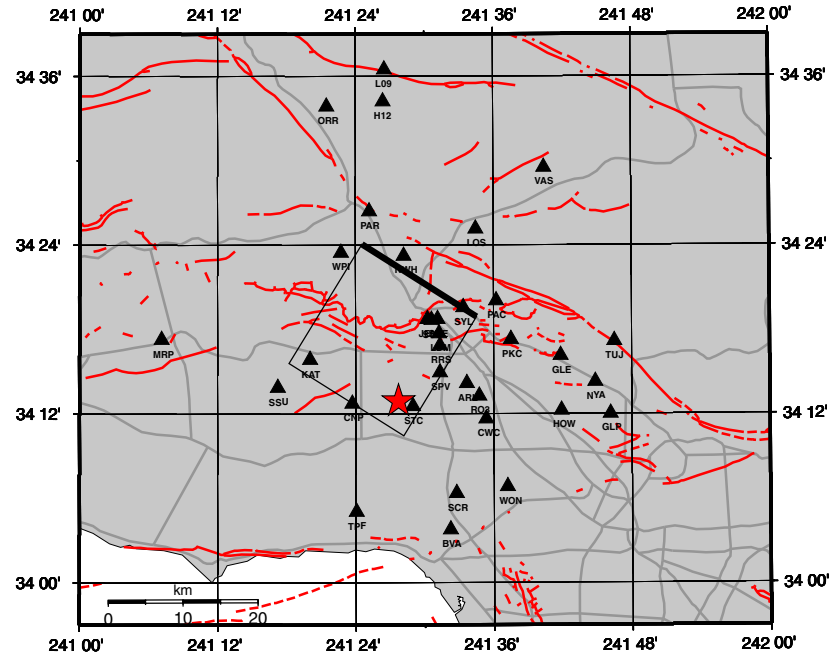

(a)

Slip amplitude distribution for the Northridge earthquake

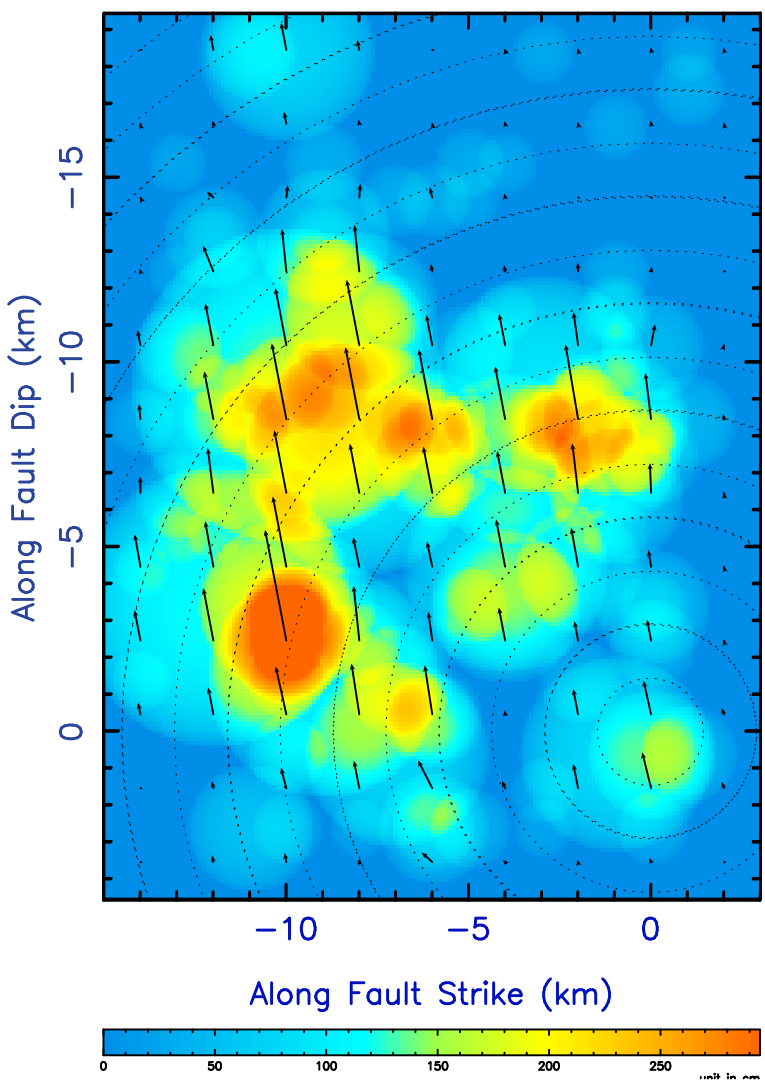

(b)

Figure 8. (a) Fault geometry and stations distribution. (b) Slip distribution of the composite source model.

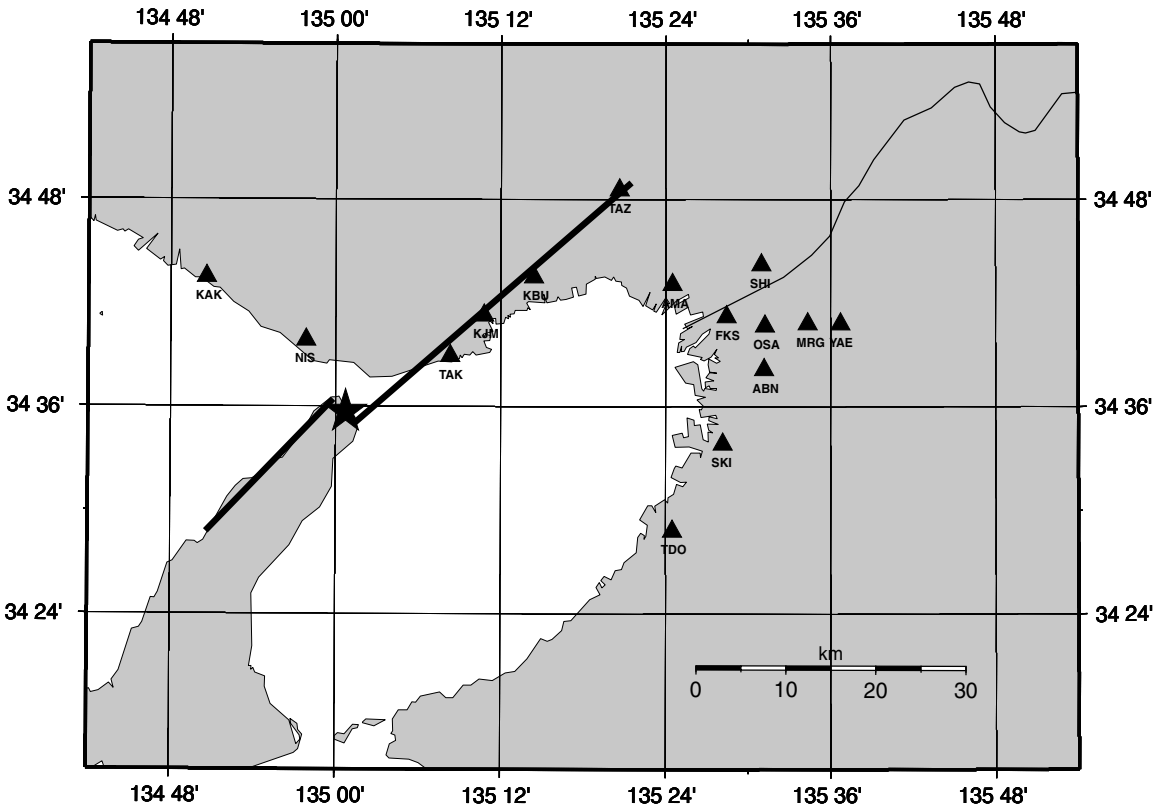

(a)

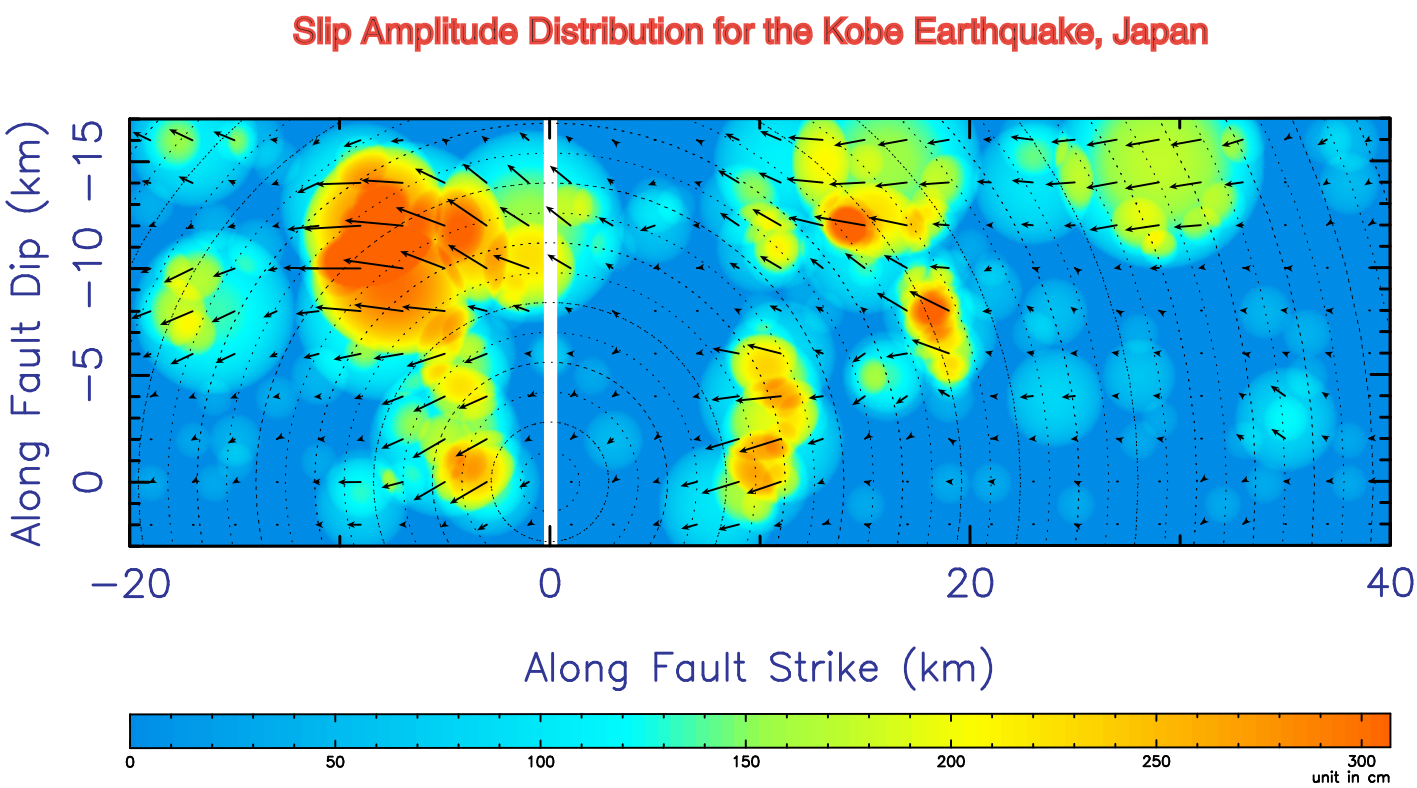

(b)

Figure 9. (a) Map view of the Kobe earthquake fault geometry and strong motion station distribution. (b) Slip distribution of the composite source model for the Kobe earthquake obtained from waveform fitting between the observed and synthetic strong motion seismograms.

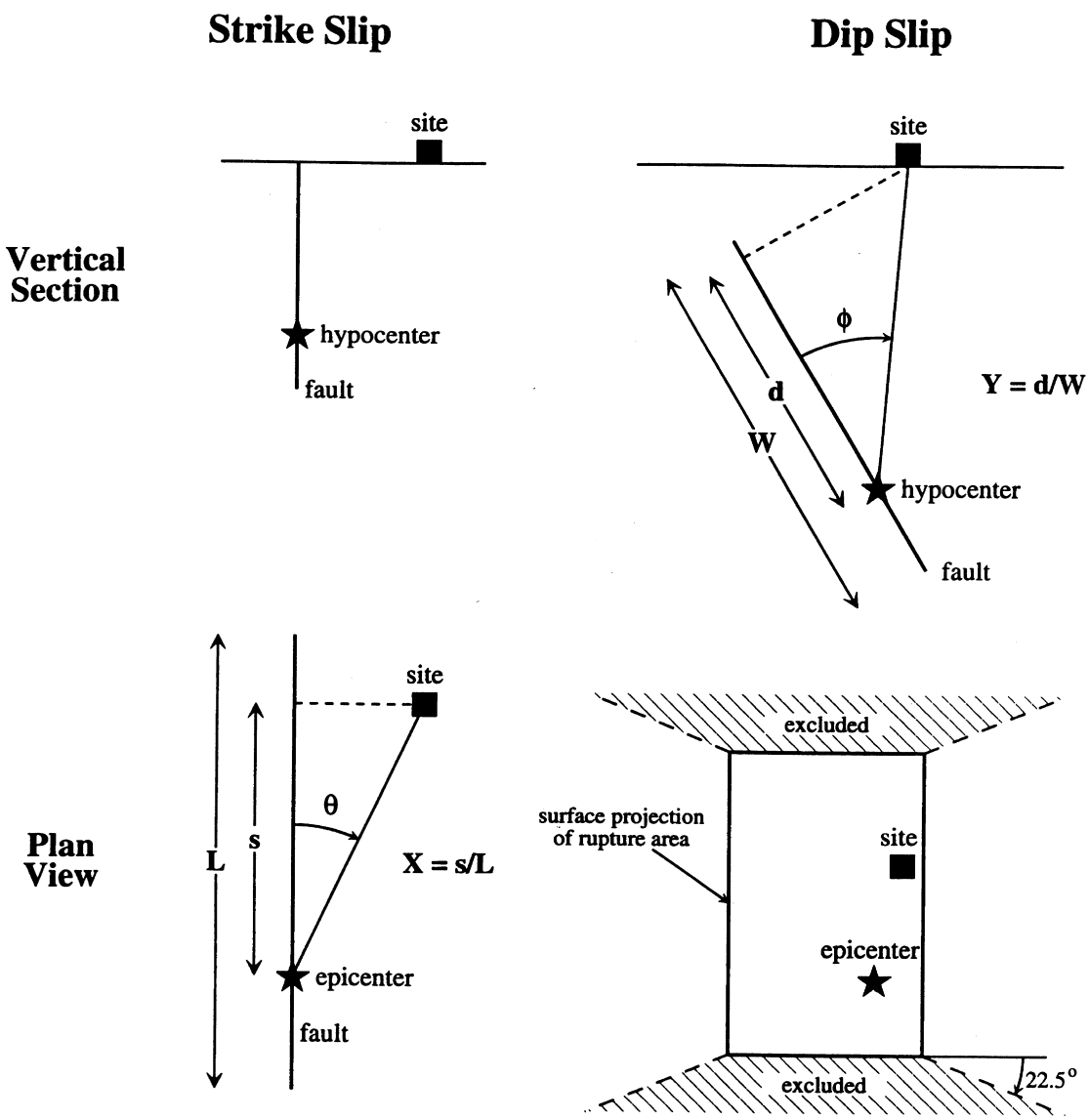

Figure 10. Geomatrical configuration for fault directivity parameters from Sommervile et al. (1997).

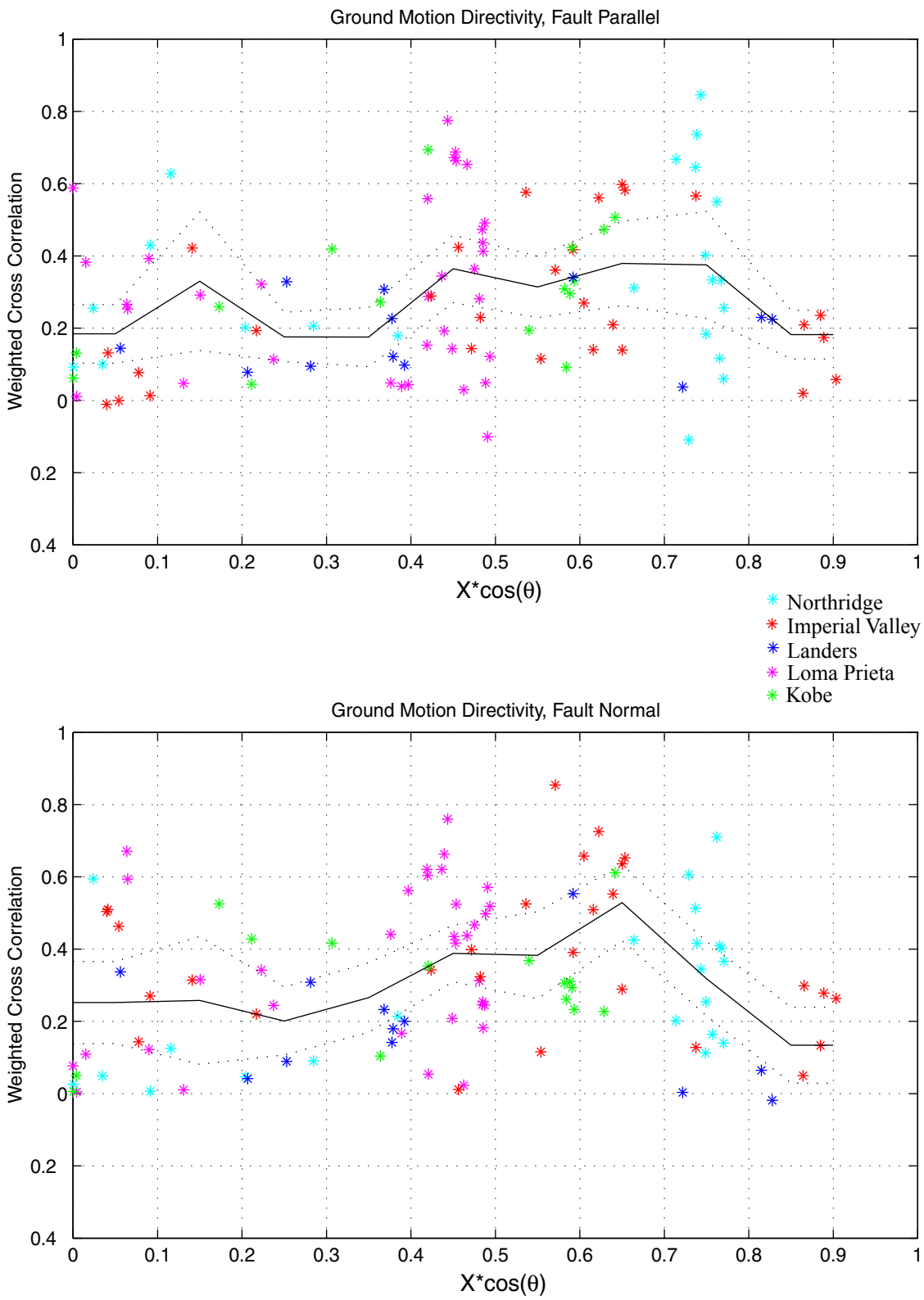

Figure 11. Effect of directivity.

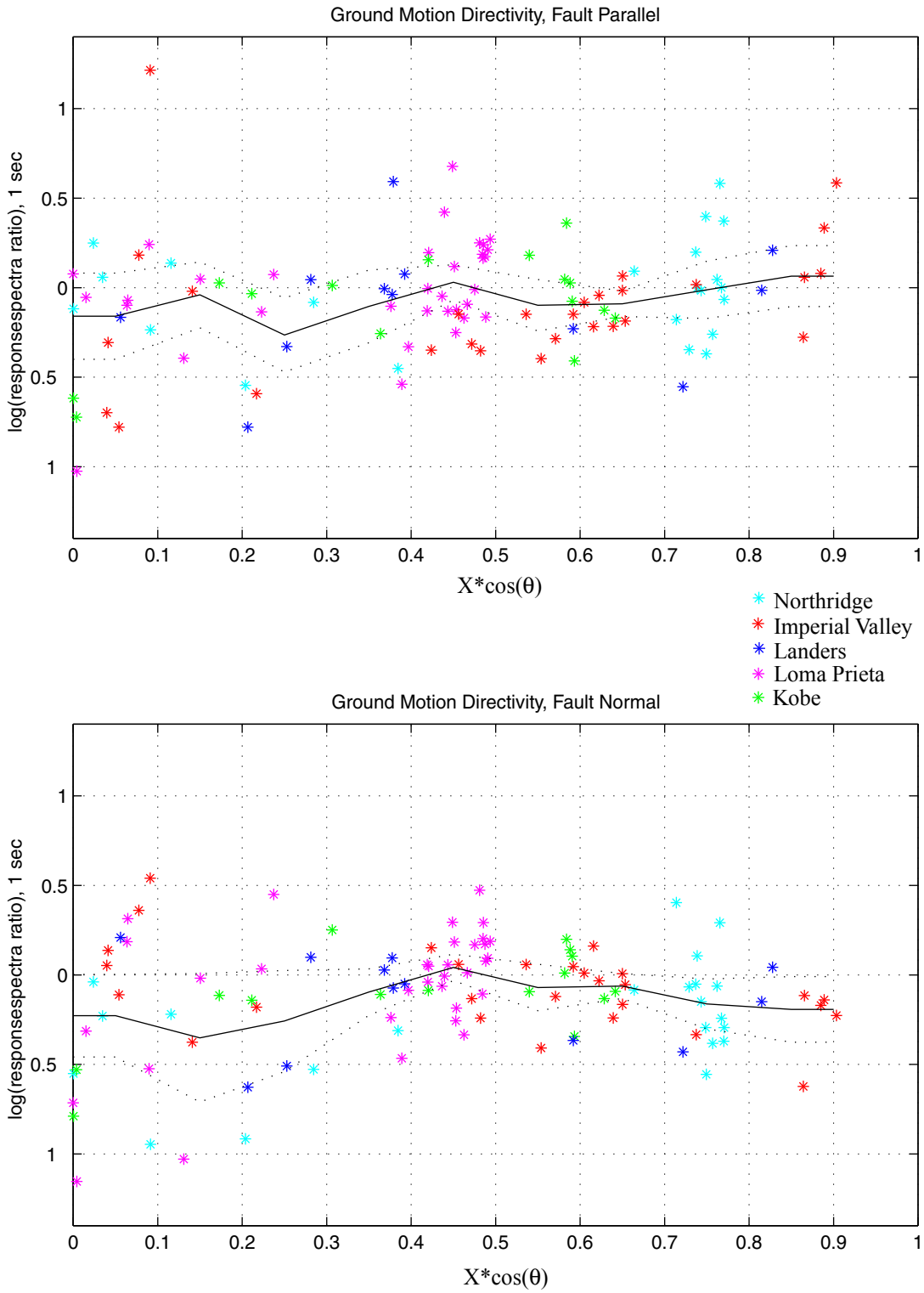

Figure 12. Effect of source directivity.

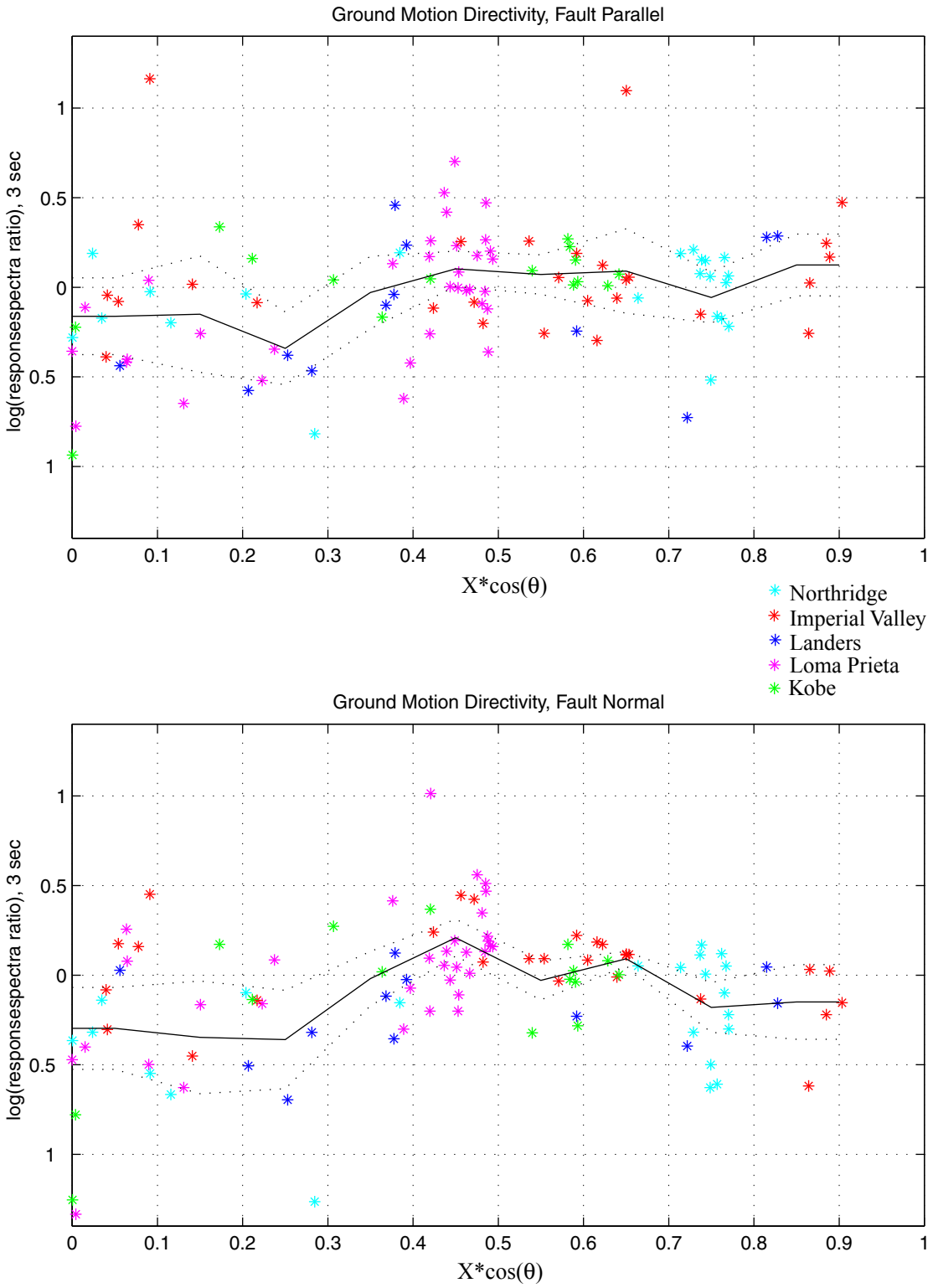

Figure 13. Effect of source directivity.

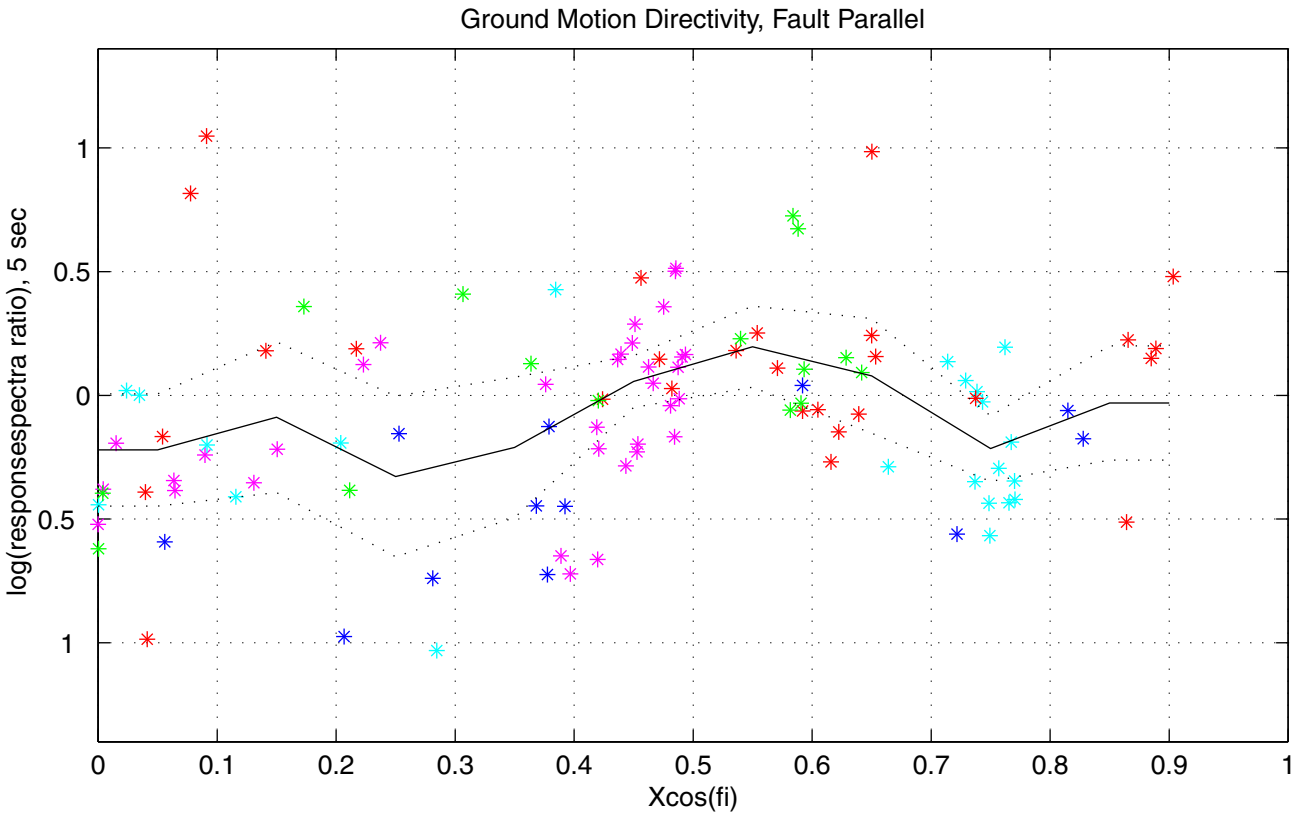

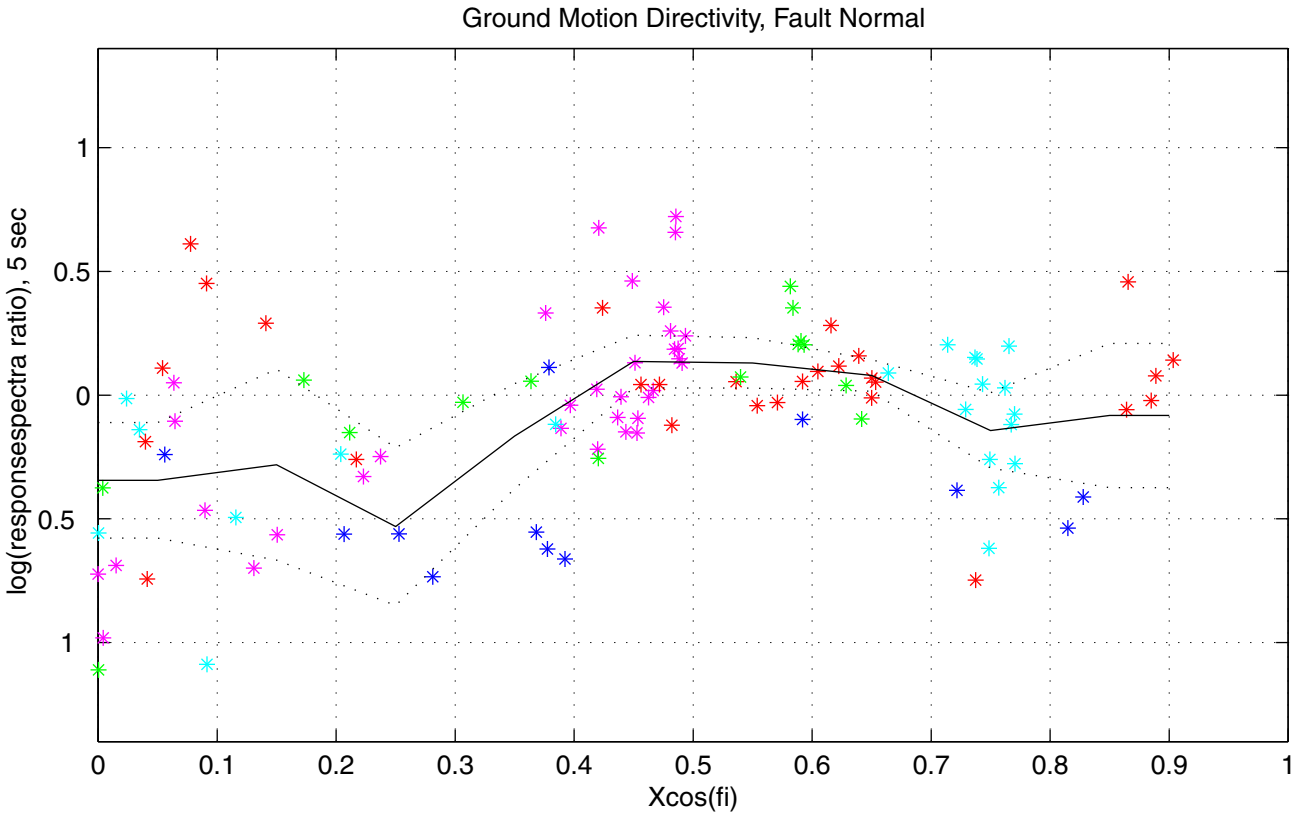

Figure 14. Effect of source directivity.

Acknowledgments

The work described in this report was funded by the Pacific Earthquake Engineering Research (PEER) Center under the Pacific Gas & Electric Company Contract No. 09566. This financial support is gratefully acknowledged.

This work made use of Pacific Earthquake Engineering Research Center Shared Facilities supported by the Earthquake Engineering Research Center Program of the National Science Foundation under Award Number EEC-9701568.

The financial support of the PEARL sponsor organizations including the Pacific Gas & Electric Company (PG&E), the California Energy Commission (CEC), and the California Department of Transportation (Caltrans) is acknowledged.

September 15, 1999
FINAL REPORT

NEAR FAULT GROUND MOTIONS

Prepared for

PG&E PEER - TASK 5.A

by

Walter Silva
Nick Gregor
Bob Darragh

of

Pacific Engineering and Analysis
311 Pomona Avenue
El Cerrito, CA 94530

CONTENTS

Section		Page
1.0	Introduction	1
2.0	Stochastic Finite Fault Model	2
3.0	Earthquakes, Sites, Profiles, and Slip Models	3
4.0	Results of Analyses	4
4.1	Landers Earthquake	4
4.2	Loma Prieta Earthquake	4
4.3	Northridge Earthquake	5
4.4	Imperial Valley Earthquake	5
4.5	Kobe Earthquake	5
5.0	Summary	6
	References	7
Appendix A:	Stochastic Ground Motion Model Description	A-1
	References	A-16
Appendix B:	Site Response Analysis Method	B-1
	References	B-5

LIST OF TABLES

Table Number		Page
1	Earthquakes and Sites	8
2	Landers Crustal Model (from Wald and Heaton, 1994)	14
3	Loma Prieta Crustal Model (from Wald et al., 1991)	15
4	Northridge Crustal Model (from Wald et al., 1996)	16
5	Imperial Valley Crustal Model (from Hartzell and Helmberger, 1982)	17
6	Kobe Regional Velocity Model (from Wald, 1996)	18

LIST OF FIGURES

Figure Number		Page
1	Schematic of Ground Motion Model	19
2	Shallow shear-wave velocity profiles used in modeling the Landers earthquake	20
3	Shallow shear-wave velocity profiles used in modeling the Loma Prieta earthquake	21
4	Shallow shear-wave velocity profiles used in modeling the Northridge earthquake	22
5	Slip model for the Northridge earthquake determined using a single shallow shear-wave velocity profile	23
6	Slip model for the Northridge earthquake determined using rock and soil shallow shear-wave velocity profiles	24
7	Shallow shear-wave velocity profiles used in modeling the Imperial Valley earthquake	25
8	Shallow shear-wave velocity profiles used in modeling the Kobe earthquake	26
9	Median and $\pm$ 1 σ amplification factors for 5% damped response spectra computed for generic rock	27
10	Ratio (data/model prediction) of 5% damped response spectra for an average horizontal component at a period of 3 sec versus directivity parameter X cos θ. Landers earthquake	29
11	Ratio (data/model prediction) of 5% damped response spectra for an average horizontal component at a period of 5 sec versus directivity parameter X cos θ. Landers earthquake	30

LIST OF FIGURES

Figure Number		Page
12	Ratio (data/model prediction) of 5% damped response spectra for an average horizontal component at a period of 3 sec versus directivity parameter X cos θ. Loma Prieta earthquake, rise time of 1.5 sec	31
13	Ratio (data/model prediction) of 5% damped response spectra for an average horizontal component at a period of 5 sec versus directivity parameter X cos θ. Loma Prieta earthquake, rise time of 1.5 sec	32
14	Ratio (data/model prediction) of 5% damped response spectra for an average horizontal component at a period of 3 sec versus directivity parameter X cos θ. Loma Prieta earthquake, rise time of 0.5 sec	33
15	Ratio (data/model prediction) of 5% damped response spectra for an average horizontal component at a period of 5 sec versus directivity parameter X cos θ. Loma Prieta earthquake, rise time of 0.5 sec.	34
16	Ratio (data/model prediction) of 5% damped response spectra for an average horizontal component at a period of 3 sec versus directivity parameter Y cos ϕ. Northridge earthquake, rise time of 1.4 sec	35
17	Ratio (data/model prediction) of 5% damped response spectra for an average horizontal component at a period of 5 sec versus directivity parameter Y cos ϕ. Northridge earthquake, rise time of 1.4 sec	36
18	Ratio (data/model prediction) of 5% damped response spectra for an average horizontal component at a period of 3 sec versus directivity parameter Y cos ϕ. Northridge earthquake, rise time of 1.0 sec	37

LIST OF FIGURES

Figure Number		Page
19	Ratio (data/model prediction) of 5% damped response spectra for an average horizontal component at a period of 5 sec versus directivity parameter Y cos ϕ. Northridge earthquake, rise time of 1.0 sec	38
20	Ratio (data/model prediction) of 5% damped response spectra for an average horizontal component at a period of 3 sec versus directivity parameter Y cos ϕ. Northridge earthquake, rise time of 1.4 sec, slip model derived using shallow rock and soil profiles	39
21	Ratio (data/model prediction) of 5% damped response spectra for an average horizontal component at a period of 5 sec versus directivity parameter Y cos ϕ. Northridge earthquake, rise time of 1.4 sec, slip model derived using shallow rock and soil profiles	40
22	Ratio (data/model prediction) of 5% damped response spectra for an average horizontal component at a period of 3 sec versus directivity parameter Y cos ϕ. Imperial Valley earthquake	41
23	Ratio (data/model prediction) of 5% damped response spectra for an average horizontal component at a period of 5 sec versus directivity parameter X cos θ. Imperial Valley earthquake	42
24	Ratio (data/model prediction) of 5% damped response spectra for an average horizontal component at a period of 3 sec versus directivity parameter X cos θ. Kobe earthquake	43
25	Ratio (data/model prediction) of 5% damped response spectra for an average horizontal component at a period of 5 sec versus directivity parameter X cos θ. Kobe earthquake	44

EXECUTIVE SUMMARY

NEAR FAULT GROUND MOTIONS

Pacific Engineering and Analysis

The stochastic finite-fault ground motion model was implemented to validate the ability of the model to predict the effects of rupture directivity on low frequency (< 1 Hz) near source strong ground motions. Validation exercises consisted of examining the ratio (data/model) of average horizontal component 5% damped response spectra versus directivity parameters (Somerville et al., 1997) for oscillator periods of 3 sec and 5 sec. Analyses were performed for five large and well recorded earthquakes: Landers, Loma Prieta, Northridge, Imperial Valley (1979), and Kobe.

Due to constraints in both time and scope, published slip models were used that were largely determined with site (rock or soil) independent shear-wave velocity profiles. These profiles generally have shallow shear-wave velocities that exceed nominal values by factors of 2 and greater, resulting in too little amplification. Using these slip models with realistic shallow generic rock and soil profiles resulted in a large overprediction of motions, even at an oscillator period of 5 sec. Increasing the rise time to produce unbiased motions resulted in unmodeled effects of rupture directivity, that is, poor site specific model performance versus parameters X cos θ and Y cos ϕ, but good average model performance (zero bias). Using slip model consistent rise times significantly improved model site specific performance (with respect to rupture directivity) but increased model bias significantly. For one earthquake, Northridge, two slip models are available, one based on site independent shallow velocities and one based on site (rock and soil) dependent shallow velocities. Results using the slip model based on site dependent shallow profiles along with a rise time that resulted in zero bias produced a good overall prediction of rupture directivity. These validation exercises suggest that shallow geotechnical profiles may affect the determination of slip models from low frequency ($\leq$ 1 Hz) strong ground motions. Additionally, strong coupling likely exists between source parameters

such as rise time, slip distribution, and rupture velocity along with shallow shear-wave velocities. Rupture directivity effects may be sensitive to these interactions. There results indicate that in order to preserve a strong physical interpretation of source parameters such rise time, slip distribution, and rupture velocity, appropriately realistic shallow generic rock and soil profiles should be incorporated into source inversions. Additionally, validations and simulations for applications to engineering design practice should include model consistent parameters, accommodating generic site effects that realistically distinguish between rock and soil (shallow geotechnical) site conditions.

NEAR FAULT GROUND MOTIONS

1.0 INTRODUCTION

The original proposal funded under this task was to quantify the effects of near-source ground motions on nonlinear site response and to develop a site response analysis procedure that accommodates differences in fault-normal and fault-parallel low frequency control motions in a manner consistent with observations. This remains an important issue as a potential contradiction exists in having significantly different fault-normal and fault-parallel low-frequency (< 1 Hz) motions and similar high-frequency motions at both rock and soil sites. Typical site response analyses would not preserve these trends at deep soil sites provided they were present in the rock or control motions.

As a result of the recent development of design motions for the San Francisco-Oakland Bay Bridge, issues arose concerning the appropriateness of empirical spectral adjustment factors (Somerville et al., 1997) to accommodate the near-fault effects of rupture directivity. Since the empirical adjustment factors are not well constrained due to the paucity of data for cases where most of the rupture is toward the site in large earthquakes (M > 7), numerical modeling provides the only means of assessing their appropriateness. As a result, this project was redirected to validate the stochastic finite-fault ground motion model (Silva et al., 1997), along with two other methodologies, with recordings that display near-source directivity features: an increase (decrease) in low frequency (< 1 Hz) spectral levels for sites with rupture toward the (away from) site relative to average spectral levels over all near-source sites. These trends exist in average horizontal component spectra as well as in fault-normal and fault-parallel component spectra.

Accompanying features in the low frequency time domain that are characteristic for fault-normal and fault-parallel motions include pulse-like motions for rupture toward the site with lower and more oscillatory motions at sites with rupture predominately away from the site. Theoretically, and (in some cases observed), fault normal displacements are expected to be one sided (most of the motion in a single direction) while fault parallel displacements are two (multiple) sided. These time domain features, as well as near-fault response spectral features are also expected to be modulated by relative positions of rupture nucleation, asperity (high slip) locations, and site locations as well as additional geologic noise such as crustal structure variability, non planar faults (e.g., Landers rupture surface), chaotic fault rupture dynamics (variable rise time and rupture velocity), and site effects (1, 2, and 3-D, e.g., Kobe).

As a result of these possible (likely) effects, development of empirical models with few earthquakes and few near-source recordings may be subject to potential bias. Model simulations, with well validated and unbiased models, when averaged over multiple realizations of source, path, and site properties, should provide reliable estimates of the stable features of rupture directivity. If models provide unbiased estimates of currently available near-source records which display directivity features, confidence is gained in exercising the models for ranges in

conditions (source size and site location) not reflected in the current strong motion data set which impacts engineering design practice.

The validation exercise is intended to evaluate the model's capability to match the response spectral and time domain trends displayed in near-fault recorded motions using a suite of "goodness of fit" parameters.

In our implementation of the stochastic finite-fault model, near surface (top 100-1,000 ft) materials are considered in detail through an equivalent-linear formulation (Appendix B). These shallow profiles are generally neglected in seismological determinations of slip models using recordings of strong ground motion. Since we were unable to develop slip models that incorporate the effects of shallow materials due to insufficient time and scope, we relied on published slip distributions. The anticipated effect was obvious, a general large overprediction of motions. As a result, our validation did not include fault-normal and fault-parallel response spectral and time domain analyses.

Due to the implied importance of near-surface materials (site response) in low frequency strong ground motions, slip models should be determined that are consistent with the shallow rock and soil site conditions that exist at recording sites. Additionally, the coupling that exists between source parameters such as slip distribution, rise time, and rupture velocity further emphasize the importance of determining consistent model parameters for use in modeling cases for which no data exist: very large earthquakes at close site distances. That is, even when very rigorous seismological models are used to infer source parameters, neglecting important amplification effects in the recorded motions due to site response compromises the physical interpretation of source parameters such as rise time, slip distribution, and rupture velocity. This can result in considerable ambiguity in applications to future earthquakes as the unmodeled site effects have likely been incorporated into source parameters. Additionally, for simulation methodologies that do not accommodate rock and soil site effects in validations, a similar ambiguity exists in how the simulated motions are to be treated in design practice: do they represent rock or soil site motions and should they be used in site response analyses for applications to soil sites.

2.0 STOCHASTIC FINITE-FAULT MODEL

The stochastic finite-fault model implemented here is quite simple in concept, using a single-corner-frequency omega-square source spectrum (M = 5.0) for each subfault. Large earthquakes are simulated by simply delaying and summing contributions from the M 5 subfaults. The process is depicted schematically in Figure 1 and discussed in detail in Appendix A. The model is simple, includes a frequency domain random vibration theory equivalent-linear site response (Appendix B) implemented for both rock and soil sites (Silva et al., 1997). The model, including site effects, has recently been validated at about 500 sites for 15 earthquakes (M 5.2 to 7.4) over fault distances ranging from 1 km to 470 km (Silva et al., 1997) and for subduction zone earthquakes for M up to 8.1. In general, the model is unbiased over the frequency range of recorded motions (spectral acceleration averaging from about 0.3 to 100 Hz).

3.0 EARTHQUAKES, SITES, PROFILES, AND SLIP MODELS

Five large and well recorded earthquakes were modeled in this exercise: 1992 M 7.3 Landers, 1989 M 6.9 Loma Prieta, 1994 M 6.7 Northridge, 1979 M 6.5 Imperial Valley, and the 1995 M 6.9 Kobe. The recording sites are those within about 30 km of the rupture surface and are listed in Table 1 along with their directivity parameters (Somerville et al., 1997). To illustrate the differences in the shallow shear-wave velocity profiles, Figures 2-4 and 7-8 show the generic rock and soil profiles used in the current modeling exercises along with those used to determine the slip models.

For the Landers earthquake, the slip model of Wald and Heaton (1994) was used and Figure 2 shows the large difference in shallow shear-wave velocities between generic rock and soil profiles and the site independent shear-wave velocity used in determining the slip model. The difference in amplification between the two is large, about a factor of three, resulting in a large overprediction in ground motions (next Section).

The Loma Prieta profiles are shown in Figure 3 and the slip model used is from Wald et al., 1991. In this case, the shallow shear-wave velocity used in determining the slip model is lower than at Landers (1 km/sec compared to 1.8 km/sec, see Tables 2 and 3). The difference in amplification is still large however, about a factor of 2.

For the Northridge earthquake, two slip models are available, one using a single profile for rock and soil sites (Wald and Heaton, 1994) and one determined using separate rock and soil site profiles (Wald et al., 1996) (Figure 4). The two slip models are shown in Figures 5 and 6 respectively. Although the pattern in overall slip is similar between the two inversions, the two zones of high slip (large asperities) have different amplitudes and have moved both absolutely as well as relative to each other. Additionally, resulting rise times are somewhat different as expected (Wald et al., 1996). The different slip models result in different directivity effects (next Section), suggesting the importance of incorporating more realistic shallow velocities in source inversions.

The Imperial Valley earthquake profiles are shown in Figure 7 and the slip model is from Hartzell and Helmberger (1982). In this case only soil sites were used in the source inversion and the shallow profile is at 700 m/sec (top 105m) which is much greater than the measured values across the El Centro Array from which the generic profile was developed (Figure 7).

In the final earthquake, Kobe, three soil profiles and one rock profile were used (Figure 8) in the modeling. A slip model developed by Wald et al. (1996), using separate rock and soil profiles (Figure 8), resulted is a large broad-band underprediction at all sites. Significantly better results were found using a more compact slip model which was based on empirical (aftershock) Green functions (Kamae and Irikura, 1998). Any 2D and 3D effects due to the basin edge on the recorded motions for both the main shock and empirical Green functions should be appropriately accommodated. Since we do not include these effects in our 1D profiles, an apparent contradiction may exist (providing the basin edge effects are significant at the recording stations used in determining the slip model). This further emphasized the importance of using model consistent parameters and should be evaluated by determining slip

models with both 1D and 3D structures.

To illustrate the potential differences in amplification between the generic shallow rock and soil profiles used here and the site independent profiles used in developing the slip models, Figure 9 shows median and $\pm$ 1 σ amplification factors for 5% damped response spectra. These amplification factors are computed for the Los Angeles area (Northridge earthquake) and are given relative to the site independent profile (Figure 4, 1 km/sec). They are keyed to the expected rock outcrop (1 km/sec) PGA values to accommodate nonlinear response effects. At low frequency (< 1 Hz) the generic rock amplification shows a deamplification (0.7 to 0.9) while the deep generic soil show an amplification of about 50%. These differences may then be projected into the source parameters if a single high velocity (1 km/sec) profile is used in the source inversions.

4.0 RESULTS OF ANALYSES

Analyses consisted of examining the ratio (data to model) of average (log) horizontal component 5% damped response spectra plotted as functions of directivity parameters X cos θ and Y sin ϕ in (Somerville et al., 1997) Table 1. Oscillator periods of both 3 sec and 5 sec are analyzed.

4.1 Landers Earthquake

Figure 10 shows the Sa (data)/Sa (model) at an oscillator period of 3 sec versus X cos θ. If there are no trends in the data with the directivity parameter and the ratios are near 1, the model is capturing the observed features of directivity and is unbiased. In general the trend is reasonably flat but in the range of 0.1 to 0.3, indicating that the model captures directivity effects but is dramatically overpredicting the recorded motions. The difference in the shallow profiles between the generic rock and soil used in the validation exercise and the very stiff (1.8 km/sec, Figure 2) profile used in determining the slip model is likely causing the difference.

For a period of 5 sec, Figure 11 shows the corresponding results. The trend is similar and nearly flat except for 1 site at X cos θ near 0.9.

4.2 Loma Prieta Earthquake

Figures 12 and 13 shows the 3 sec and 5 sec oscillator results respectively for the Loma Prieta earthquake. In this case the trends (slope) in the ratios indicate that the model is not capturing directivity effects. The average levels indicate that the model is underpredicting as well (particularly at 5 sec). In this case a rise time of 1.5 sec was used which gave largely unbiased predictions over all sites, near-source and distant (out to about 80 km), and over a wide frequency range (0.3 to 100 Hz). Reducing the source rise time to 0.5 sec to be consistent with that obtained in the slip model inversion gave the results shown in Figures 14 and 15. With the

reduced rise time, the trend (slope) is significantly reduced accompanied with a marked overprediction. Interestingly these results imply that rise time is important not only in overall spectral levels but in directivity effects as well. Since source rise times are poorly resolved and highly variable, these results indicate that directivity effects may be highly variable as well. Rise times, directivity effects, and shallow geotechnical properties are likely strongly coupled parameters.

4.3 Northridge Earthquake

For the Northridge earthquake, due to its shallow dip, analyses were done only for the Y cos ϕ directivity parameter. For the rise time that results in unbiased motions (1.4 sec), Figures 16 and 17 show the ratios of data to model predictions for 3 sec and 5 sec respectively using the slip model determined with the site independent shallow velocity profile (figure 5). The results show a trend, particularly for Y cos ϕ values above 0.75. As with the Loma Prieta earthquake, reducing the rise time to a value more consistent with that obtained in the inversions to obtain the slip model (1.0 sec) shows a significant reduction in slope with the accompanying overprediction (Figures 18 and 19).

If a slip model is used that results from different shallow rock and soil site profiles (Figure 6) along with the rise time that results in zero bias (1.4 sec), the trends in Y cos ϕ are largely absent (Figures 20 and 21). As with the Loma Prieta earthquake, these results suggest the importance of the shallow profiles along with coupling between rise time, slip model, and site dynamic material properties.

4.4 Imperial Valley Earthquake

Figures 22 and 23 show the 3 sec and 5 sec results for the Imperial Valley earthquake using the generic El Centro Array profile (Figure 7). The expected overprediction is seen (on average) with little overall trend as Y cos θ increases. In general the model is capturing most of the directivity variations.

4.5 Kobe Earthquake

For the Kobe earthquake, the directivity results are shown in Figures 24 and 25 for 3 sec and 5 sec respectively. In this case, using the slip model based on empirical Green functions and a rise time that results in unbiased motions, a general trend is seen in both Figures but only for soil sites. The model is not completely accommodating directivity effects for soil sites but appears to perform reasonably well for rock sites, although the number of rock sites is small. This may be related to basin edge effects incorporated in determining the slip model but neglected in the use of 1D site profiles. This would not be expected to affect rock sites.

5.0 SUMMARY

The stochastic finite-fault ground motion model was implemented to validate the ability of the model to predict the effects of rupture directivity on low frequency (< 1 Hz) near source strong ground motions. Validation exercises consisted of examining the ratio (data/model) of average horizontal component 5% damped response spectra versus directivity parameters (Somerville et al., 1997) for oscillator periods of 3 sec and 5 sec. Analyses were performed for five large and well recorded earthquakes: Landers, Loma Prieta, Northridge, Imperial Valley (1979), and Kobe.

Due to constraints in both time and scope, published slip models were used that were largely determined with site (rock or soil) independent shear-wave velocity profiles. These profiles generally have shallow shear-wave velocities that exceed nominal values by factors of 2 and greater, resulting in too little amplification. Using these slip models with realistic shallow generic rock and soil profiles resulted in a large overprediction of motions, even at an oscillator period of 5 sec. Increasing the rise time to produce unbiased motions resulted in unmodeled effects of rupture directivity, that is, poor site specific model performance versus parameters X cos θ and Y cos ϕ, but good average model performance (zero bias). Using slip model consistent rise times significantly improved model site specific performance (with respect to rupture directivity) but increased model bias significantly. For one earthquake, Northridge, two slip models are available, one based on site independent shallow velocities and one based on site (rock and soil) dependent shallow velocities. Results using the slip model based on site dependent shallow profiles along with a rise time that resulted in zero bias produced a good overall prediction of rupture directivity. These validation exercises suggest that shallow geotechnical profiles may affect the determination of slip models from low frequency ($\leq$ 1 Hz) strong ground motions. Additionally, strong coupling likely exists between source parameters such as rise time, slip distribution, and rupture velocity along with shallow shear-wave velocities. Rupture directivity effects may be sensitive to these interactions. There results indicate that in order to preserve a strong physical interpretation of source parameters such rise time, slip distribution, and rupture velocity, appropriately realistic shallow generic rock and soil profiles should be incorporated into source inversions. Additionally, validations and simulations for applications to engineering design practice should include model consistent parameters, accommodating generic site effects that realistically distinguish between rock and soil (shallow geotechnical) site conditions.

REFERENCES

Hartzell, S.H., and Helmberger, D.V. (1982). "Strong-motion modeling of the Imperial Valley earthquake of 1979." *Bull. Seism. Soc. Am.*, 72(2), 571-596.

Kamae, K. and K. Irikura (1998). "Source model of the 1995 Hyogo-ken Nanbu earthquake and simulation of near-source ground motion." *Bull. Seism. Soc. Am.*, 88(2), 400-412.

Liu, H-L, and Helmberger, D.V. (1985). "The 23:19 aftershock of the 15 October 1979 Imperial Valley Earthquake: More evidence for an asperity." *Bull. Seism. Soc. Am.*, 75(3), 689-708.

Silva, W.J., N. Abrahamson, G. Toro, C. Costantino (1997). "Description and validation of the stochastic ground motion model." Submitted to Brookhaven National Laboratory, Associated Universities, Inc. Upton, New York.

Somerville, P.G., Smith, N.F., Graves, R.W. and Abrahamson, N.A. (1997). "Modification of empirical strong ground motion attenuation relations to include the amplitude and duration effects of rupture directivity." *Seism. Resear. Lett.*, 68(1), 199-222.

Wald, D.J. (1996). "Slip history of the 1995 Kobe, Japan, earthquake determined from strong motion, teleseismic, and geodetic data.". *J. of Physics of the Earth*, in press.

Wald, D.J., T.H. Heaton and K.W. Hudnut (1996). "The slip history of the 1994 Northridge, California, earthquake determined from strong-motion, teleseismic, GPS, and leveling data." *Bull. Seism. Soc. Am.*, 86(1B), S49-S70.

Wald, D.J., Heaton, T.H. (1994). "Spatial and temporal distribution of slip for the 1992 Landers, California, earthquake." *Bull. Seism. Soc. Amer.*, 84(3), 668-691.

Wald, D.J., D.V. Helmberger, and T.R. Heaton (1991). "Rupture model of the 1989 Loma Prieta Earthquake from the inversion of strong motion and broadband teleseismic data." *Bull. Seism. Soc. Amer.*, 81(5), 1540-1572.

Table 1 EARTHQUAKES AND SITES						
Earthquake	Mag	Station Name	Condition	Closest to Rupture (km)	X*cos(theta)	Y*cos(phi)
Landers 06/28/92	7.3	Barstow	rock	35.41*	0.79194	0.09113
		Coolwater	rock	19.15*	0.85274	0.16137
		Desert Hot Springs	rock	22.77	0.06559	0.13812
		Fort Irwin	rock			
		Joshua Tree	rock	10.60	0.04554	0.25900
		Lucerne	rock	4.67*	0.58240	0.39102
		Morongo Valley	rock	18.37	0.05051	0.16736
		North Palm Springs	rock	27.85	0.06404	0.11458
		Palm Springs Airport	soil	36.84	0.06790	0.08775
		Yermo Fire Station	soil	21.80*	0.87491	0.14368
Loma Prieta 10/18/89	6.9	Agnews State Hospital	soil	24.52	0.36454	0.77064
		Anderson Dam (Downstream)	rock	20.05	0.08010	0.79733
		Anderson Dam, L Abut	rock	19.99	0.07972	0.79749
		APEEL #2 Redwood City	soil	43.86	0.45984	0.56298
		APEEL 7 - Pulgas	rock	42.19	0.48348	0.49742
		APEEL 9 - Crystal Springs Res	rock	41.00	0.48746	0.48587
		APEEL 10 - Skyline	rock	41.92	0.49068	0.46257
		Belmont - Envirotech	rock	44.06	0.48010	0.50078
		BRAN	rock	10.72	0.15820	0.70134
		Capitola	soil	15.02	0.00029	0.48239
		Corralitos	rock	3.85	0.09555	0.82318
		Coyote Lake Dam (Downstr)	rock	20.83	0.24998	0.79516

Table 1 (cont.) EARTHQUAKES AND SITES						
Earthquake	Mag	Station Name	Condition	Closest to Rupture (km)	X*cos(theta)	Y*cos(phi)
		Coyote Lake Dam (SW Abut)	rock	20.37	0.26355	0.79643
		Gilroy Gavilan College	rock	10.02	0.46029	0.80453
		Gilroy, Historic Bldg	soil	11.02	0.42944	0.81560
		Gilroy #1	rock	9.69	0.46093	0.80639
		Gilroy #2	soil	11.13	0.45178	0.80294
		Gilroy #3	soil	12.88	0.44523	0.79528
		Gilroy #4	soil	14.52	0.42876	0.79495
		Gilroy #6	rock	18.38	0.40777	0.78297
		Gilroy #7	soil	22.73	0.40052	0.76185
		Hollister City Hall	soil	27.42	0.48940	0.57927
		Hollister Differential Array	soil	24.86	0.48075	0.63516
		Hollister-South & Pine	soil	27.96	0.48961	0.57322
		LGPC	rock	3.87	0.43623	0.82200
		Palo Alto - 1900 Embarcadero	soil	30.74	0.44127	0.67208
		Palo Alto - SLAC	soil	30.50	0.47620	0.60166
		Salinas - John & Work	soil	32.65	0.45549	0.05056
		Saratoga-Aloha	rock	8.49	0.46008	0.81511
		Saratoga WVC	rock	9.30	0.44359	0.81911
		Sunnyvale - Colton Ave	soil	24.18	0.41127	0.74575
		UCSC	rock	18.54	0.14161	0.29339
		Santa Cruz UCSC/Lick Observator	rock	6.55	0.00605	0.78483
		UCSC WAHO	soil	17.39	0.02015	0.35127

Table 1 (cont.) EARTHQUAKES AND SITES						
Earthquake	Mag	Station Name	Condition	Closest to Rupture (km)	X*cos(theta)	Y*cos(phi)
		Woodside	rock	34.06	0.48446	0.54606
Northridge 01/17/94	6.7	Arleta - Nordhoff Fire Sta	rock	8.63	0.14256	0.68047
		Big Tujunga, Angeles Nat F	rock	19.75	0.14586	0.72062
		Brentwood V.A. Hospital	rock	22.42	0.19035	0.02212
		Burbank - Howard Rd.	rock	16.92	0.18772	0.65704
		Canoga Park - Topanga Can	soil	14.66	0.22876	0.22832
		Canyon Country - W Lost Cany	soil	12.45	0.01461	0.80876
		Castaic - Old Ridge Route	rock	20.66	0.53711	0.75816
		Glendale - Las Palmas	soil	22.22	0.18901	0.61886
		Jensen Filter Plant	soil	5.42	0.01333	0.79083
		LA Dam	rock	5.66	0.00447	0.78775
		LA - Wonderland Ave	rock	20.22	0.22000	0.23429
		La Crescenta - New York	soil	18.56	0.17017	0.68383
		Lake Hughes 9	rock	25.29	0.41886	0.77920
		Lake Hughes 12A	rock	21.30	0.42242	0.78801
		N. Hollywood - Coldwater Can	rock	12.46	0.19699	0.53825
		Newhall - Fire Sta	soil	6.16	0.21809	0.80753
		Newhall - W. Pico Canyon Rd.	rock	6.00	0.21296	0.80714
		Northridge - 17645 Saticoy St	soil	12.05	0.11798	0.40767
		Pacoima Dam (downstr)	rock	7.03	0.05181	0.80852

Table 1 (cont.) EARTHQUAKES AND SITES						
Earthquake	Mag	Station Name	Condition	Closest to Rupture (km)	X*cos(theta)	Y*cos(phi)
		Pacoima Kagel Canyon	rock	7.40	0.10673	0.78953
		Pardee - SCE Substation	soil	7.45	0.47818	0.80811
		Rinaldi Receiving Sta	soil	6.51	0.01053	0.77803
		Santa Susana Ground	rock	16.87	0.71808	0.10619
		Sepulveda VA	soil	8.41	0.07582	0.66128
		Simi Valley - Katherine Rd	soil	13.44	0.68000	0.30903
		Stone Canyon	rock	19.01	0.20898	0.11400
		Sun Valley - Roscoe Blvd	soil	9.98	0.16823	0.64198
		Sunland - Mt Gleason Ave	rock	13.38	0.14468	0.74483
		Sylmar - Converter Sta South	soil	5.18	0.00163	0.79427
		Sylmar - Converter Sta East	soil	5.34	0.00642	0.79180
		Sylmar - Olive View Med FF	soil	5.30	0.00813	0.80432
		Topanga - Fire Sta	rock	22.21	0.05014	-0.00260
		Vasquez Rocks Park	rock	23.61	0.00115	0.79679
Imperial Val. 10/15/79	6.5	Aeropuerto Mexicali	soil	1.24	0.04236	0.99235
		Agrarias	soil	1.02	0.04678	0.99479
		Bonds Corner	soil	1.11	0.15733	0.99383
		Brawley Airport	soil	10.13	0.93342	0.70103
		Calexico Fire Sta.	soil	12.01	0.23874	0.63837
		Calipatria Fire Sta.	soil	25.27	0.90907	0.36666

Table 1 (cont.) EARTHQUAKES AND SITES						
Earthquake	Mag	Station Name	Condition	Closest to Rupture (km)	X*cos(theta)	Y*cos(phi)
		Cerro Prieto	rock	23.20	0.04080	0.39442
		Chihuahua	soil	16.94	0.04783	0.50679
		Cucupah	soil			
		El Centro - Imp County Center	soil	8.97	0.68449	0.74303
		El Centro - Meloland Overpass	soil	1.71	0.50801	0.98564
		El Centro #1	soil	20.33	0.61104	0.43994
		El Centro #2	soil	13.88	0.64187	0.58283
		El Centro #3	soil	11.37	0.63277	0.65882
		El Centro #4	soil	5.48	0.68538	0.87597
		El Centro #5	soil	2.34	0.72736	0.97342
		El Centro #6	soil	0.29	0.71996	0.99957
		El Centro #7	soil	2.23	0.71763	0.97580
		El Centro #8	soil	5.53	0.70580	0.87445
		El Centro #10	soil	10.21	0.65359	0.69817
		El Centro #11	soil	14.10	0.59600	0.57700
		El Centro #12	soil	19.59	0.52023	0.45321
		El Centro #13	soil	23.63	0.53332	0.38848
		El Centro Diff Array, Dogwood	soil	6.75	0.66823	0.82777
		Holtville Post Office	soil	6.13	0.46573	0.85173
		Parachute Test Site	rock	15.16	0.92889	0.54917
		Plaster City	soil	32.46	0.77293	0.29337
		SAHOP Casa Flores	soil	10.62	0.04652	0.68404
		Superstition Mountain	rock	27.10	0.90678	0.34497
		Westmorland	soil	16.79	0.94868	0.51024

Table 1 (cont.) EARTHQUAKES AND SITES						
Earthquake	Mag	Station Name	Condition	Closest to Rupture (km)	X*cos(theta)	Y*cos(phi)
Kobe 01/16/95	6.9	Abeno	soil	24.81	0.52820	0.82467
		AmagasakI	soil	11.31	0.57551	0.86624
		Chihaya	rock	49.81	0.31692	0.77030
		Fukushima	soil	17.82	0.58211	0.84552
		Kakogawa	soil	19.27*	0.00489	0.34163
		Kobe University	rock	0.85	0.41818	0.88987
		KJMA	rock	0.45	0.30828	0.88999
		Morigawachi	soil	24.78	0.58273	0.82076
		Nishi-Akashi	soil	7.04*	0.00527	0.77627
		OSAJ	soil	21.33	0.58741	0.83434
		Port Island (0m)	soil	3.21	0.30042	0.88738
		Port Island (16m)		3.21	0.30042	0.88738
		Port Island (32m)	soil	3.21	0.30042	0.88738
		Port Island (83m)	soil	3.21	0.30042	0.88738
		Sakai	soil	27.99	0.35565	0.81606
		Shin-Osaka	soil	16.96	0.62491	0.84247
		Tadoka	soil	31.53	0.16843	0.80701
		Takarazuka	soil	0.28	0.63961	0.88994
		Takatori	soil	1.35	0.20488	0.88958
		Yae	soil	27.77	0.57877	0.80818

NOTES:

For the San Fernando earthquake all the distances are to the closest idealized rupture plane. The distances with a * are to the San Fernando rupture plane. The distances without a * are to the Sierra Madre rupture plane.

For the Landers earthquake all the distances are to the closest idealized rupture plane. The distances with a * are to the Camp Rock rupture plane. The distances without a * are to the Johnson Valley rupture plane.

For the Kobe earthquake all the distances are to the closest idealized rupture plane. The distances with a * are to the Nojima rupture plane. The distances without a * are to the Suma/Suwayama rupture plane.

Table 2 LANDERS CRUSTAL MODEL (from Wald and Heaton, 1994)		
Thickness (km)	V_s (km/sec)	Density (cgs)
1.5	1.98	2.30
2.5	3.15	2.60
22.0	3.52	2.70
5.0	3.83	2.87
	4.50	3.10

Table 3 LOMA PRIETA CRUSTAL MODEL (from Wald et al., 1991)		
Thickness (km)	V_s (km/sec)	Density (cgs)
0.1	1.00	2.00
0.4	1.95	2.30
0.5	2.48	2.35
2.0	2.77	2.35
2.0	3.10	2.35
2.0	3.31	2.45
2.0	3.55	2.58
4.0	3.61	2.62
5.0	3.62	2.63
7.0	3.85	2.77
	4.62	3.28

Table 4 NORTHRIDGE CRUSTAL MODEL (from Wald et al., 1996)		
Rock Sites		
Thickness (km)	V_s (km/sec)	Density (cgs)
0.5	1.0	2.1
1.5	2.0	2.3
2.5	3.2	2.5
23.0	3.6	2.6
13.0	3.9	2.9
----	4.5	3.0
Soil Sites		
Thickness (km)	V_s (km/sec)	Density (cgs)
0.1	0.3	1.7
0.2	0.5	1.8
0.2	1.0	2.1
1.0	2.0	2.4
2.5	3.2	2.7
23.0	3.6	2.8
13.0	3.9	2.9
----	4.5	3.3

Table 5 IMPERIAL VALLEY CRUSTAL MODEL (from Hartzell and Helmberger, 1982)		
Thickness (m)	V_s (m/sec)	Density (cgs)
105.00	700.00	1.74
105.00	800.00	1.85
105.00	900.00	1.89
105.00	1000.00	1.94
105.00	1150.00	2.03
105.00	1300.00	2.15
339.00	1500.00	2.26
480.00	1640.00	2.36
160.00	1740.00	2.39
160.00	1910.00	2.44
160.00	2080.00	2.48
160.00	2150.00	2.50
640.00	2220.00	2.52
160.00	2300.00	2.55
160.00	2500.00	2.60
160.00	2710.00	2.63
2271.00	2750.00	2.65
5000.00	3180.00	2.75
10000.00	4100.00	2.80
0.00	4500.00	3.20

Table 6 KOBE REGIONAL VELOCITY MODEL (from Wald, 1996)		
Rock Sites		
Thickness (km)	V_s (km/sec)	Density (cgs)
0.10	1.00	2.10
0.40	1.80	2.10
4.50	3.20	2.60
22.00	3.46	2.70
5.00	3.83	2.87
	4.50	3.50
Soil Sites		
Thickness (km)	V_s (km/s)	Density (g/cm^3)
0.10	0.30	1.70
0.10	0.50	1.82
1.00	1.00	2.10
0.40	1.80	2.10
4.50	3.20	2.60
20.90	3.46	2.70
5.00	3.83	2.87
	4.50	3.50

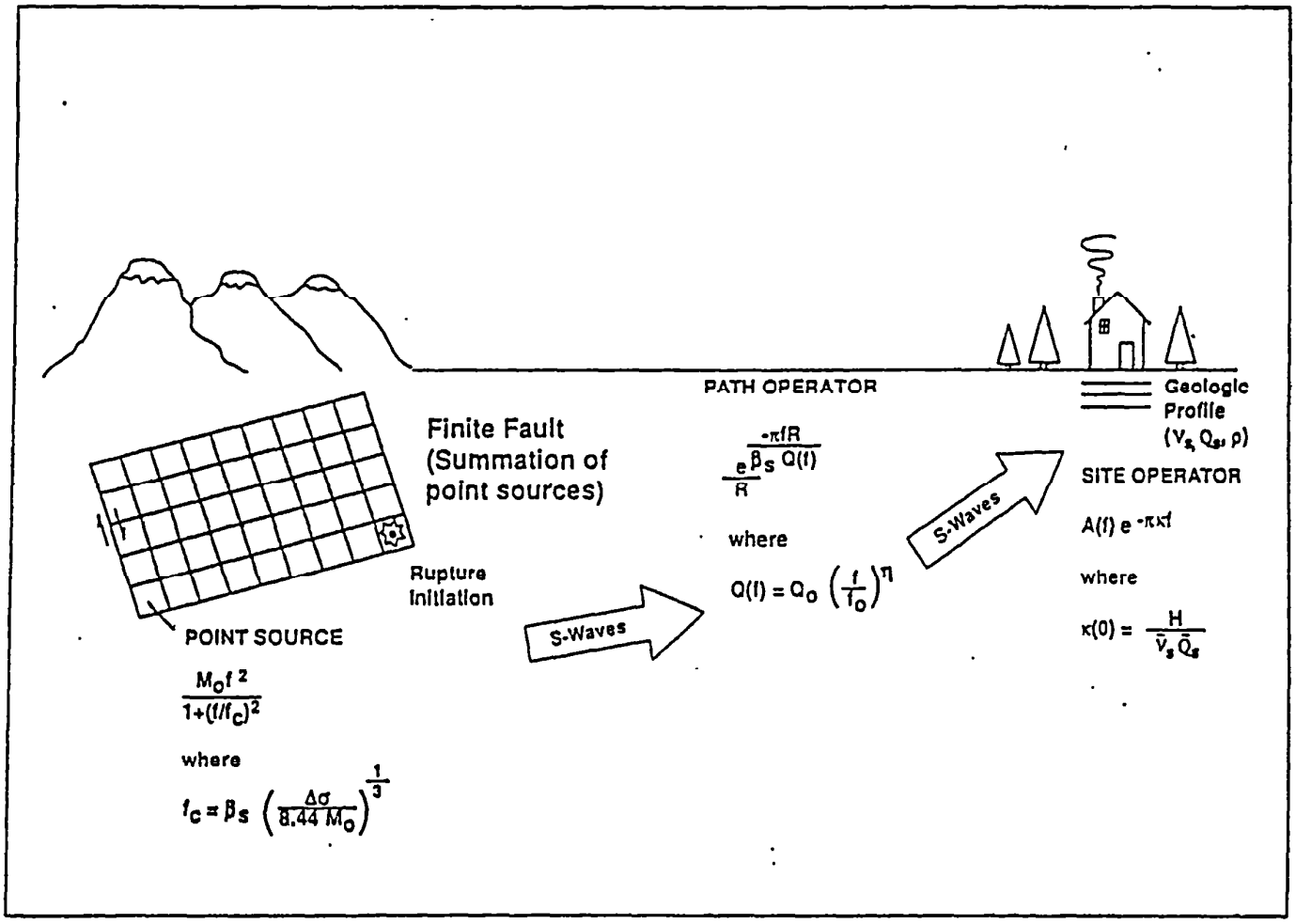

Figure 1. Schematic of ground motion model.

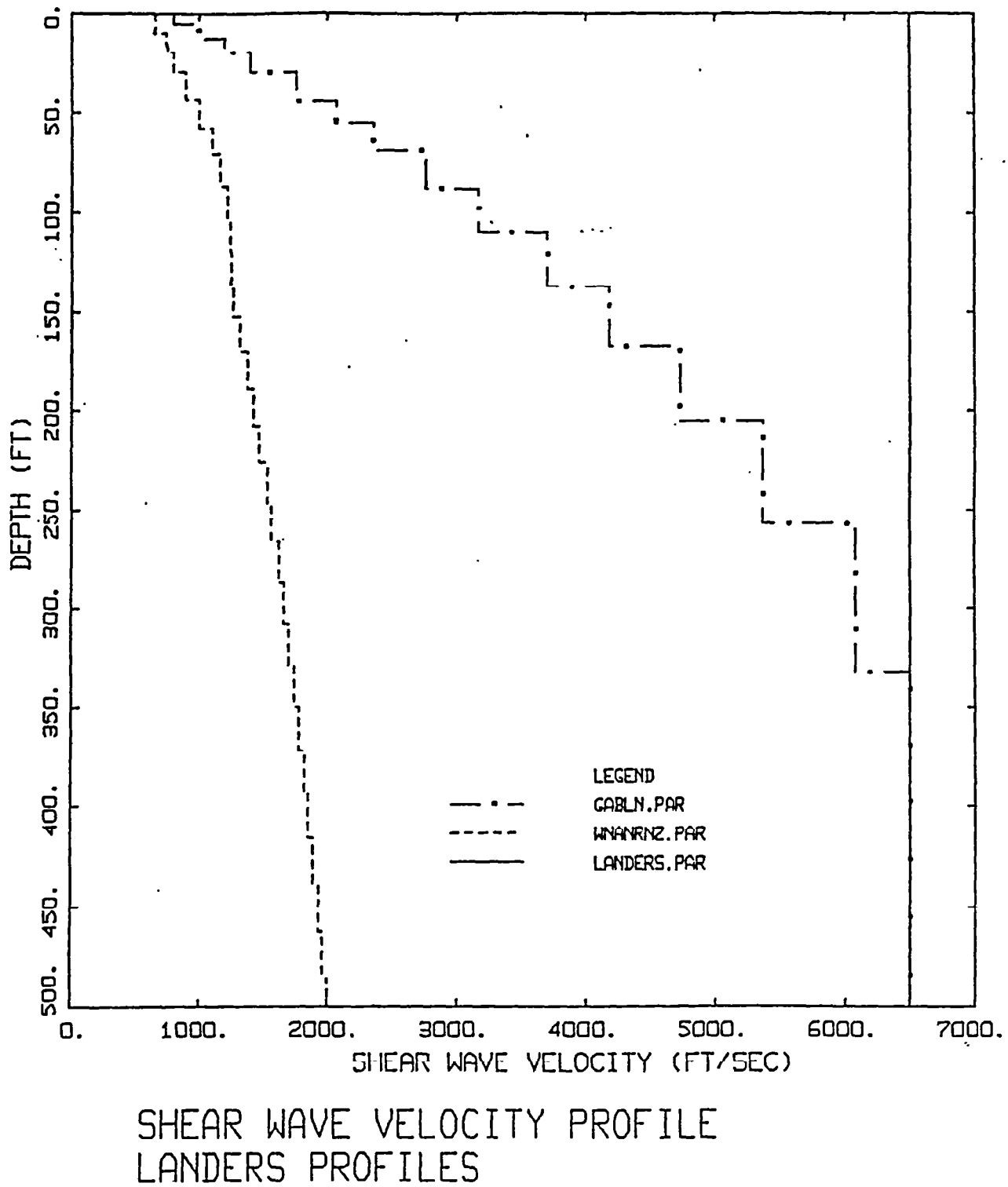

Figure 2. Shallow shear-wave velocity profiles used in modeling the Landers earthquake (rock, dash dotted; soil, dashed) and in determining the slip model (rock and soil, solid) (Table 2).

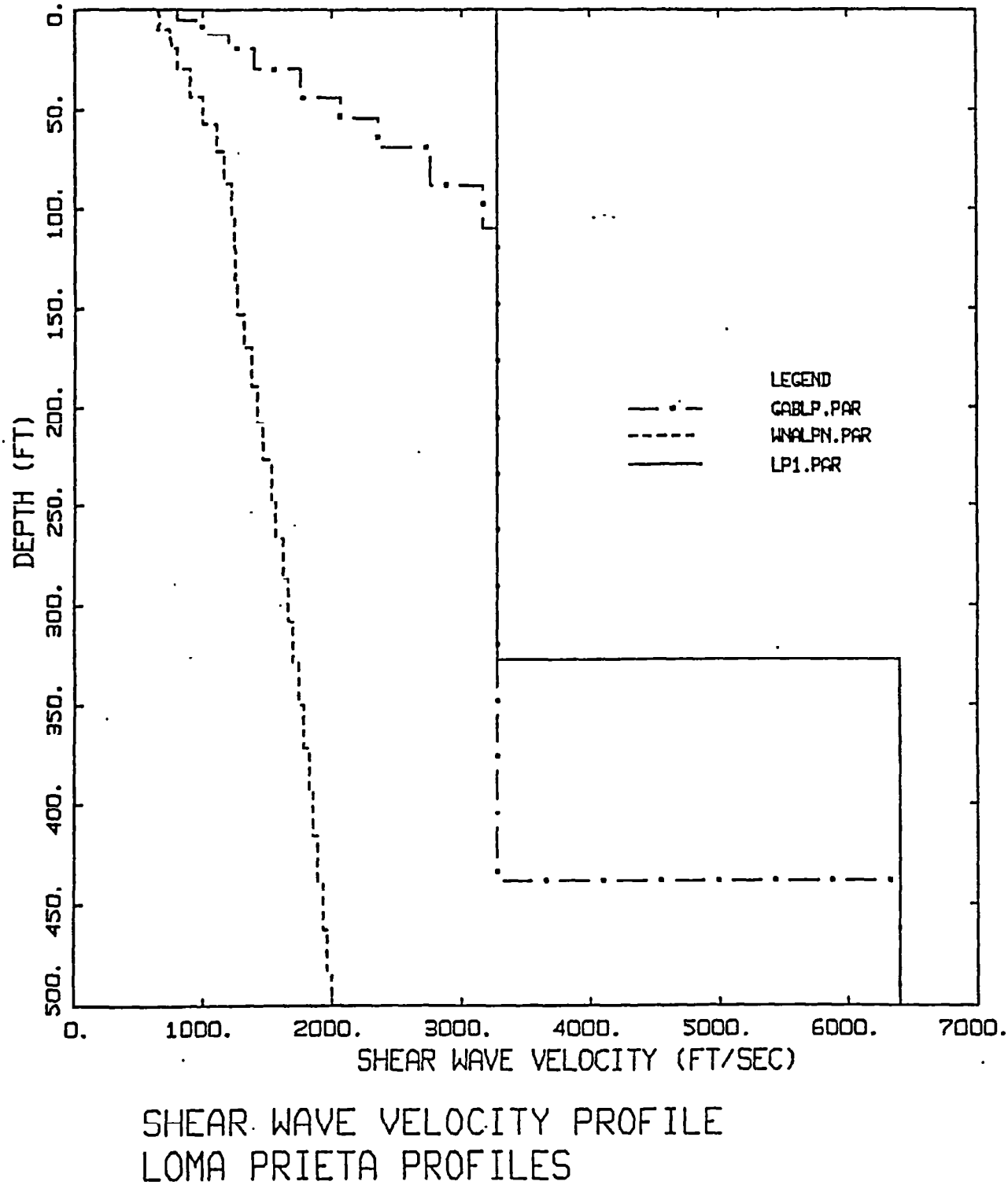

Figure 3. Shallow shear-wave velocity profiles used in modeling the Loma Prieta earthquake (rock, dash dotted; soil, dashed) and in determining the slip model (rock and soil, solid) (Table 3).

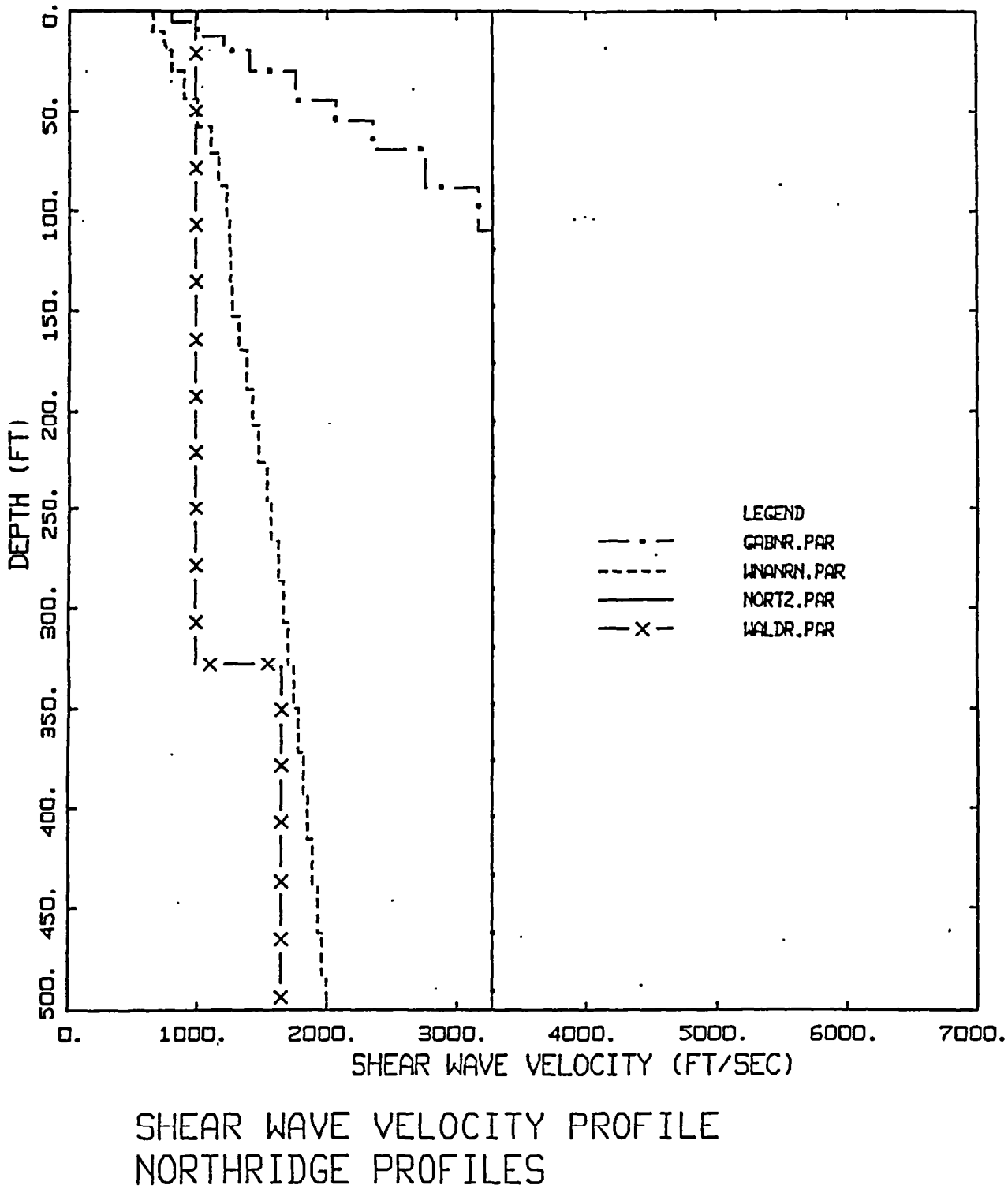

Figure 4. Shallow shear-wave velocity profiles used in modeling the Northridge earthquake (rock, dash dotted; soil, dashed) and in determining the slip model (rock, solid; dash crosses, soil) (Table 4).

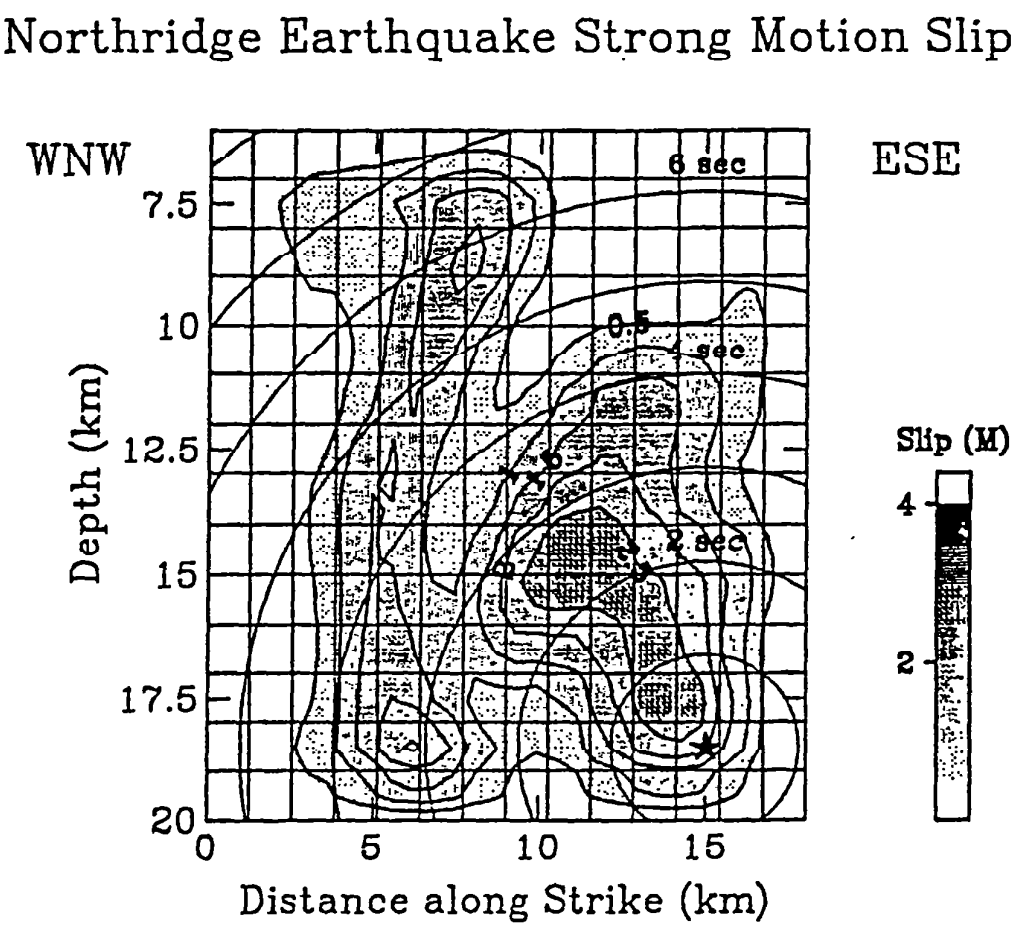

Figure 5. Slip model for the Northridge earthquake determined using a single shallow shear-wave velocity profile (1 km/sec, Figure 4). Source, Wald and Heaton, 1994.

Northridge Earthquake Strong Motion Slip

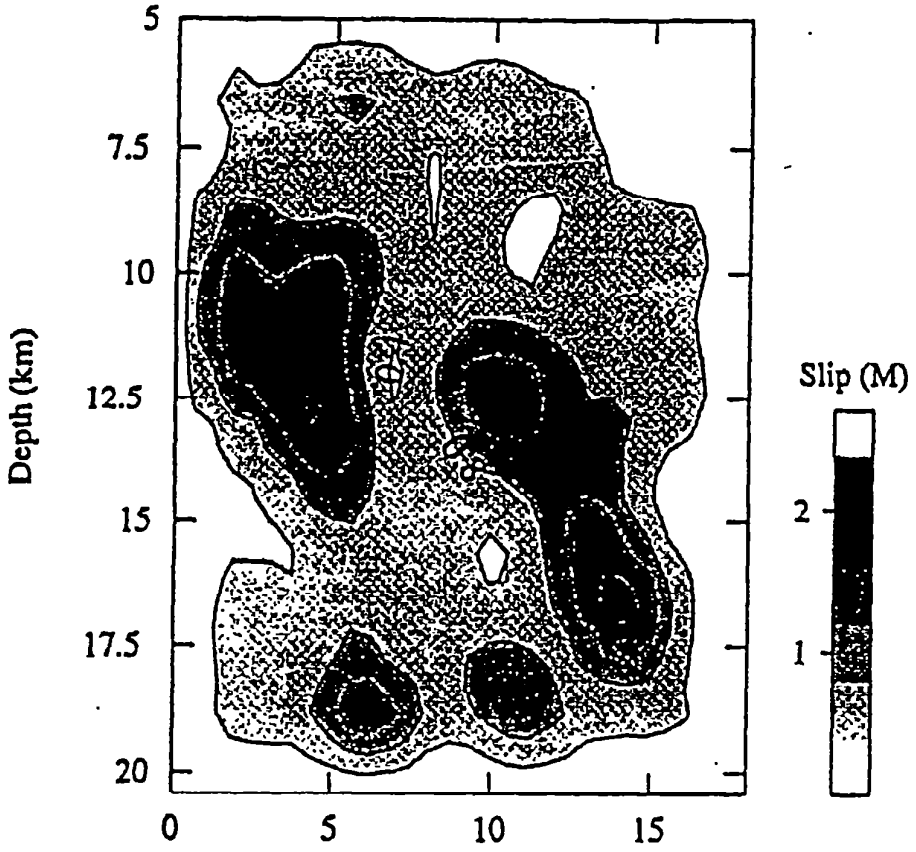

Figure 6. Slip model for the Northridge earthquake determined using rock and soil shallow shear-wave velocity profiles (Figure 4). Source, Wald et al., 1996.

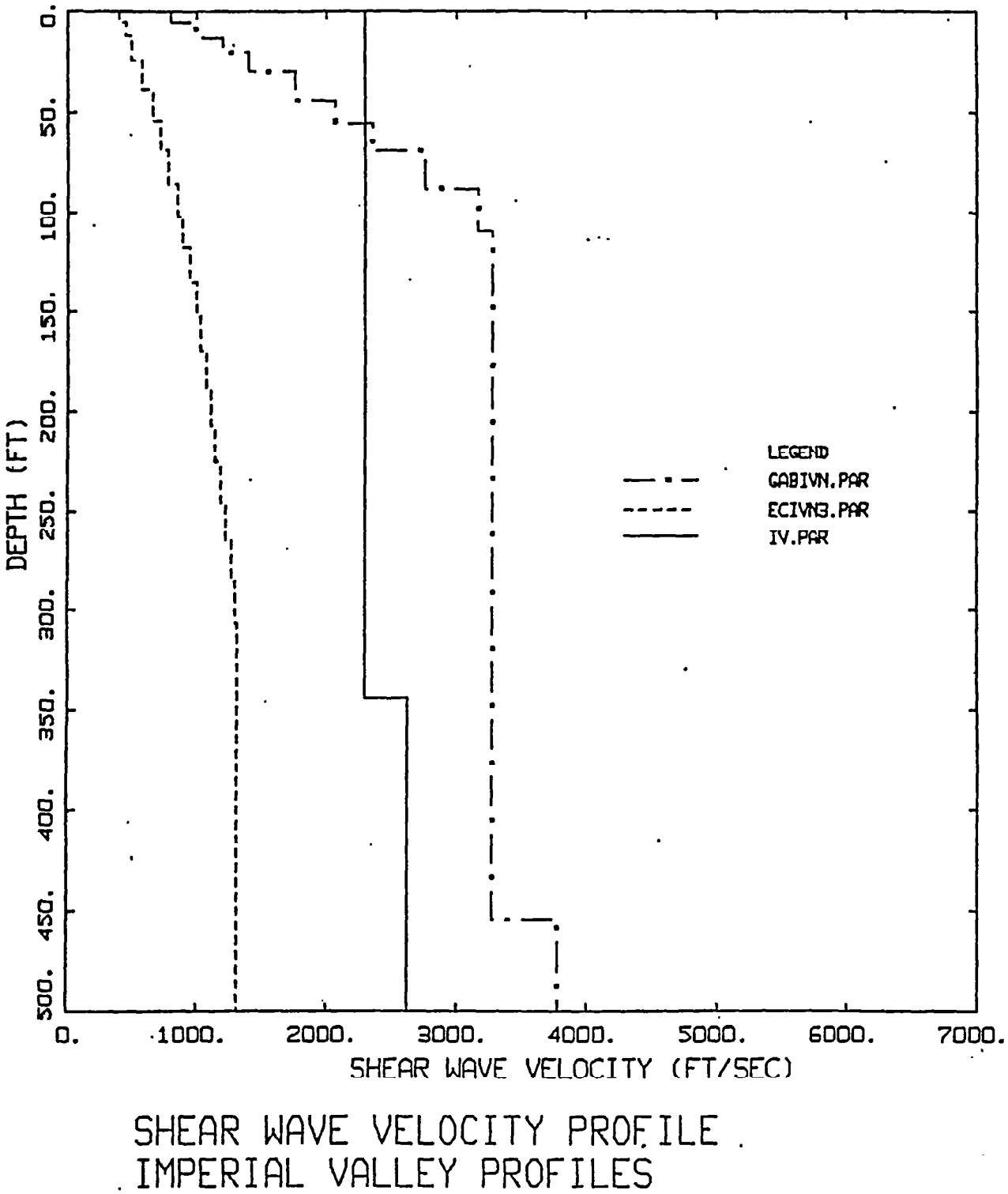

Figure 7. Shallow shear-wave velocity profiles used in modeling the Imperial Valley earthquake (rock, dash dotted; soil, dashed) and in determining the slip model (soil, solid) (Table 5).

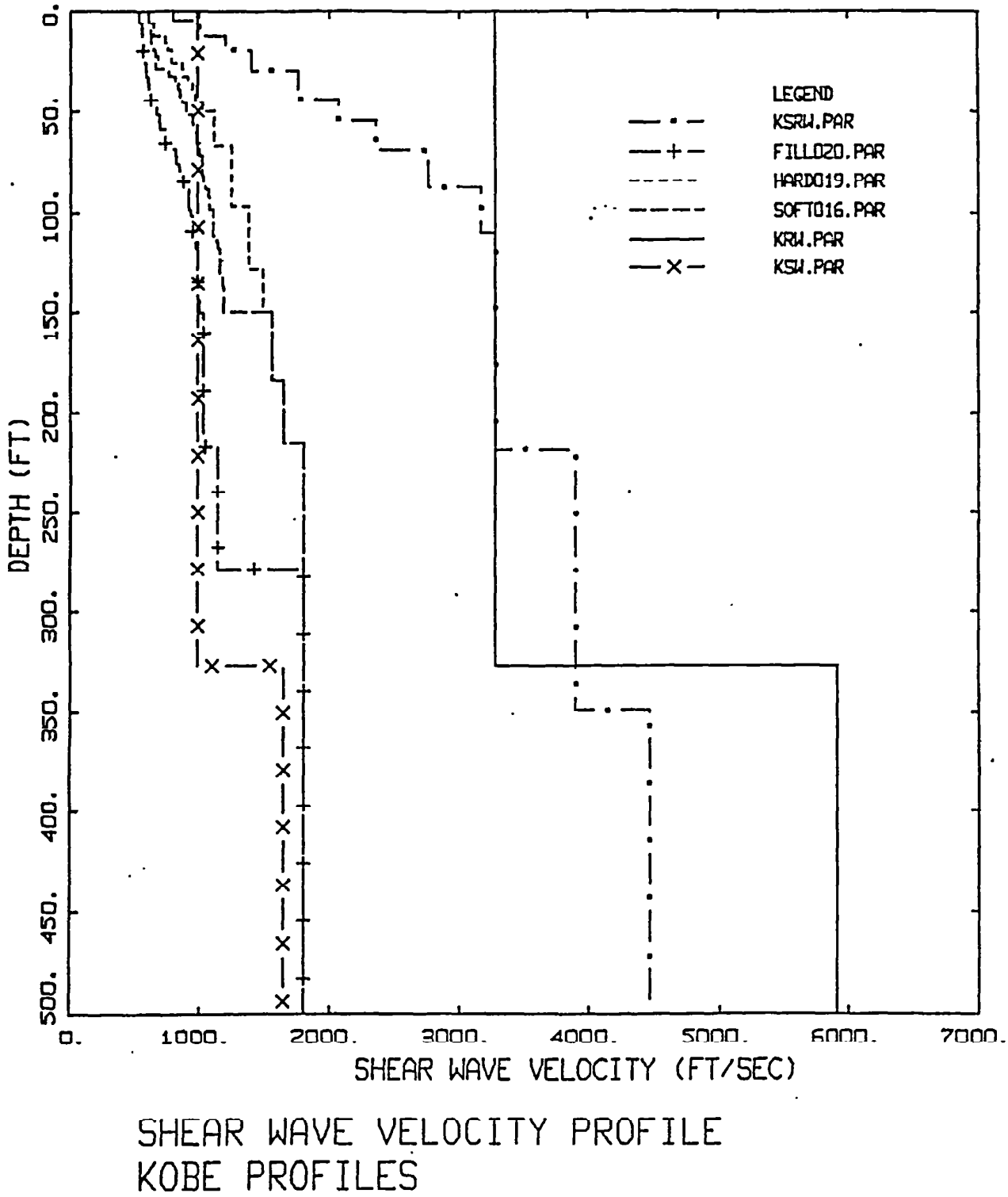

Figure 8. Shallow shear-wave velocity profiles used in modeling the Kobe earthquake. Rock is the dash-dotted profile and generic soil profiles were developed for alluvium (soft soil, dashed), diluvium (hard soil, short dashed) and fill (dash plus) soils. Rock (solid), and soil (dash crosses) profiles were used in developing the slip models (Table 6).

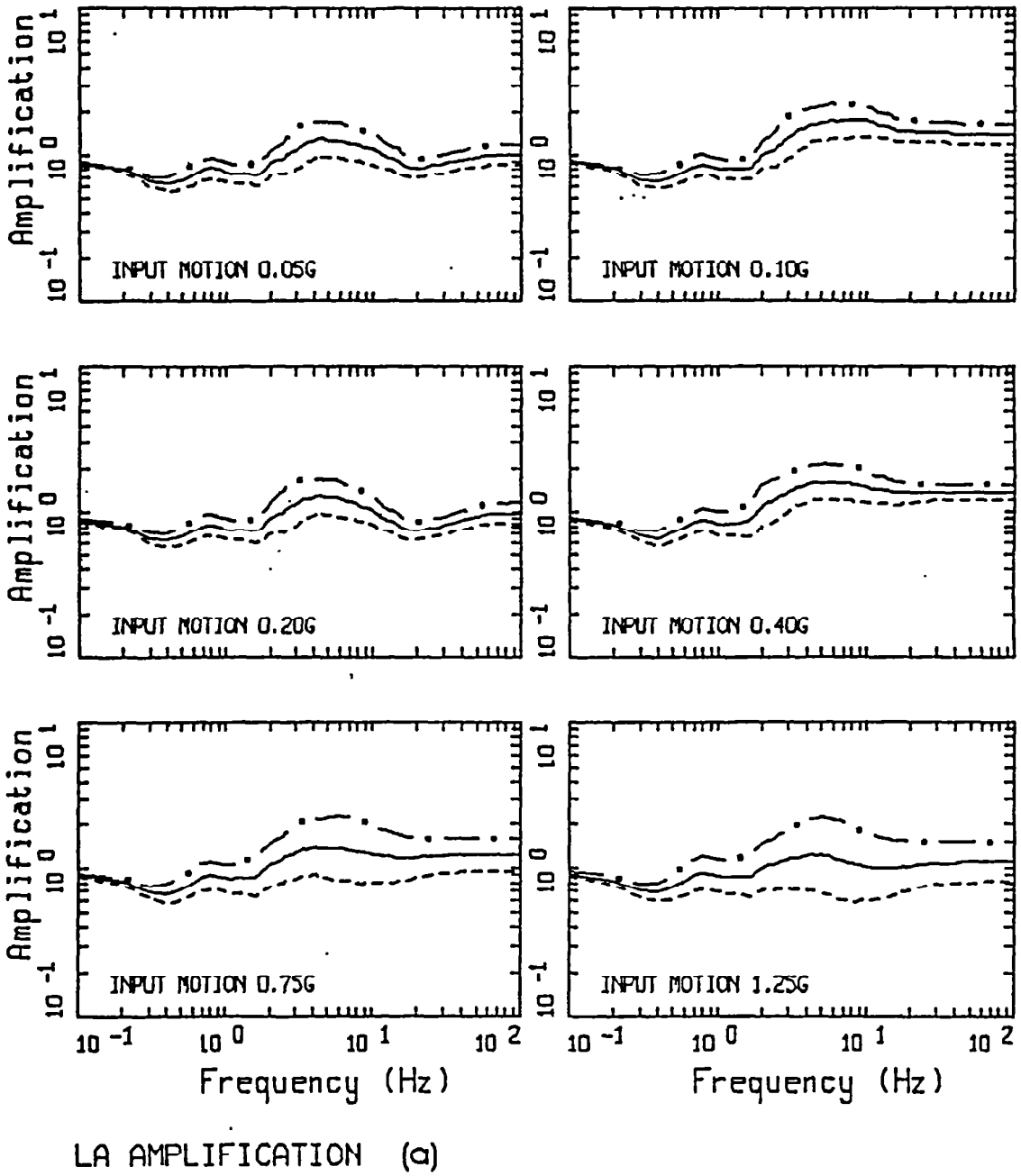

Figure 9. Median and ± 1 σ amplification factors for 5% damped response spectra computed for generic rock (a) and generic deep soil (b) relative to the profile used in determining the site independent slip model for the Northridge earthquake.

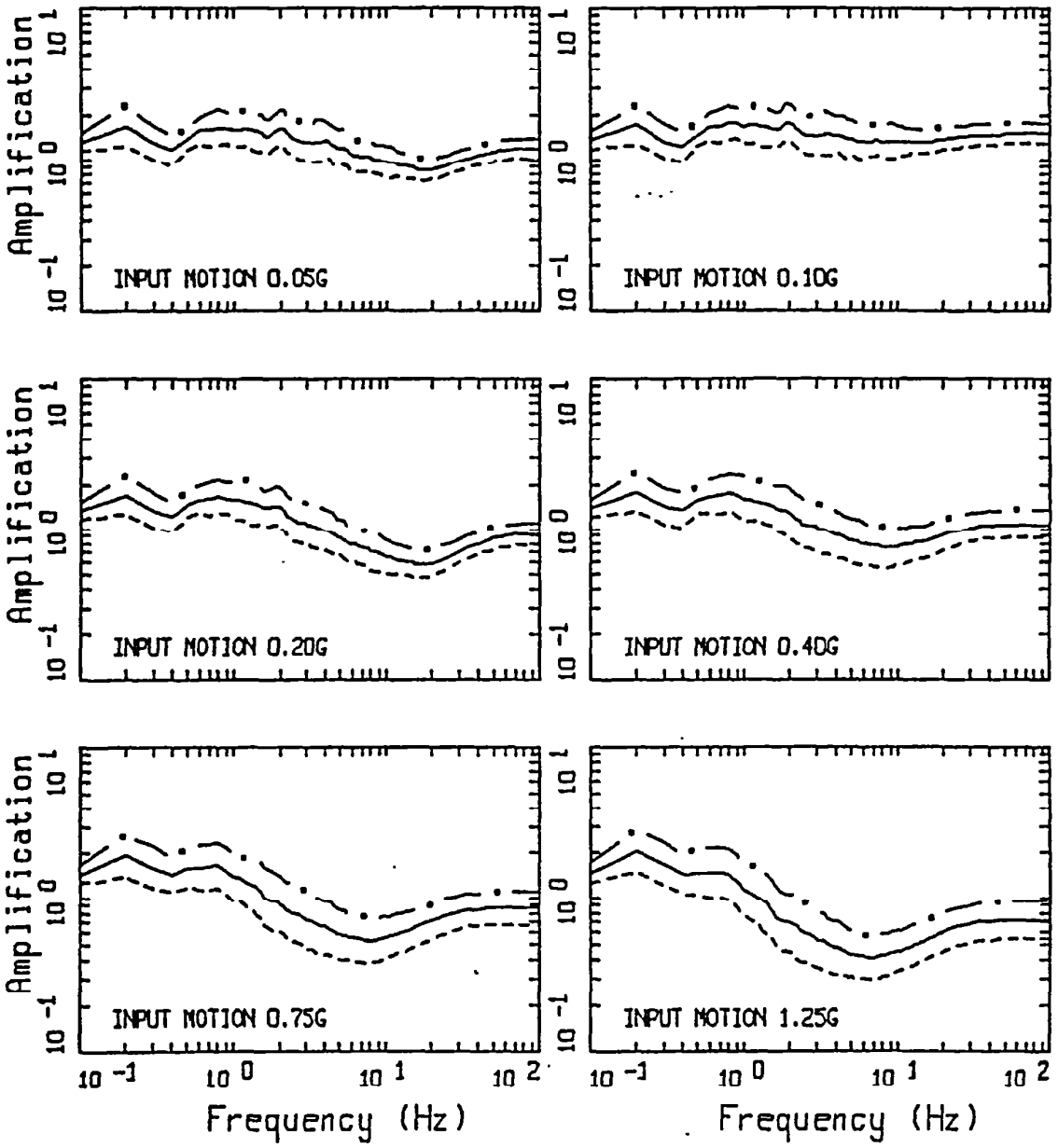

LA AMPLIFICATION (b)

Qy (500 - 1500 FT) over Wald

Figure 9. (Cont.)

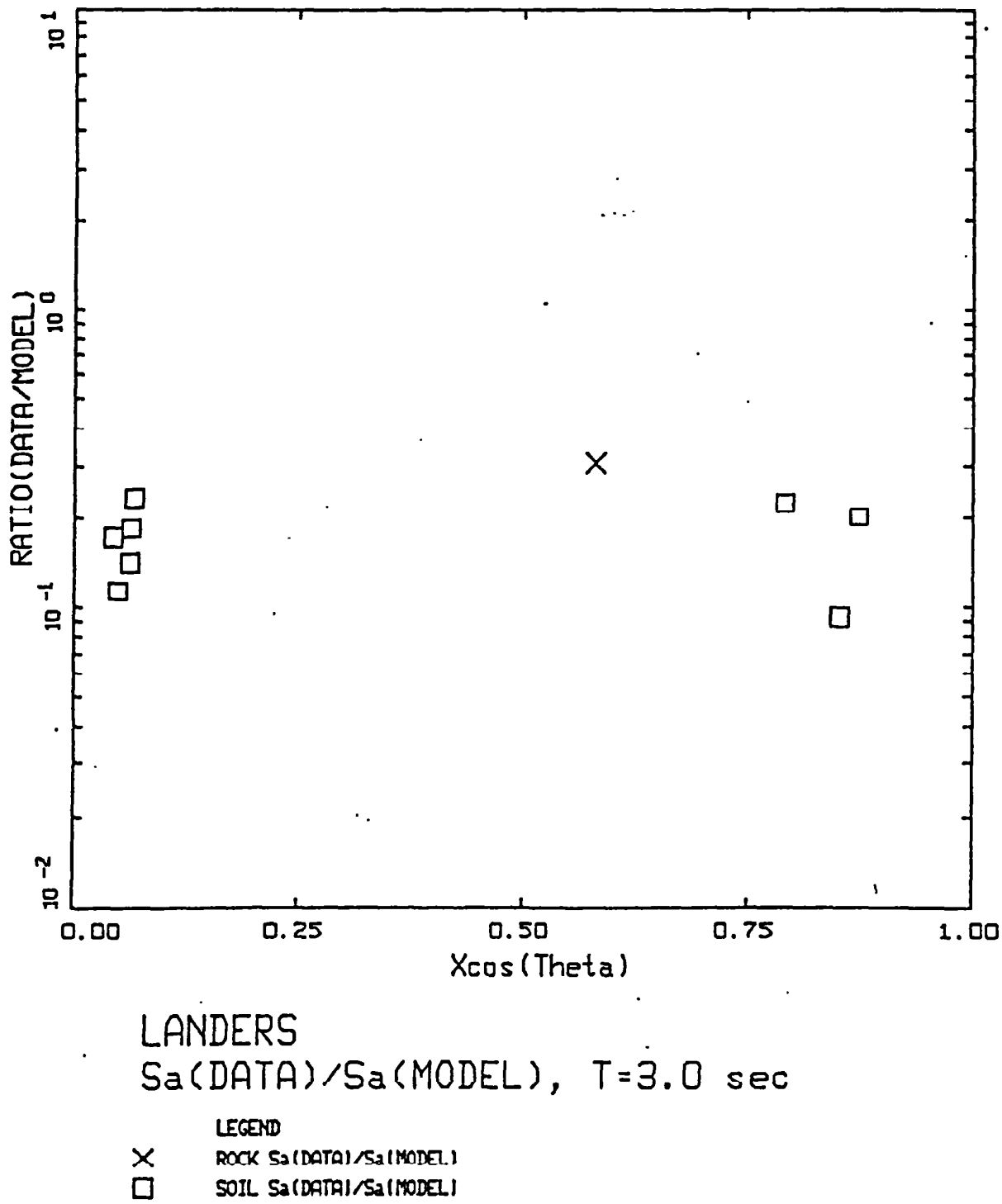

Figure 10. Ratio (data/model prediction) of 5% damped response spectra for an average horizontal component at a period of 3 sec versus directivity parameter $X \cos \theta$. Landers earthquake.

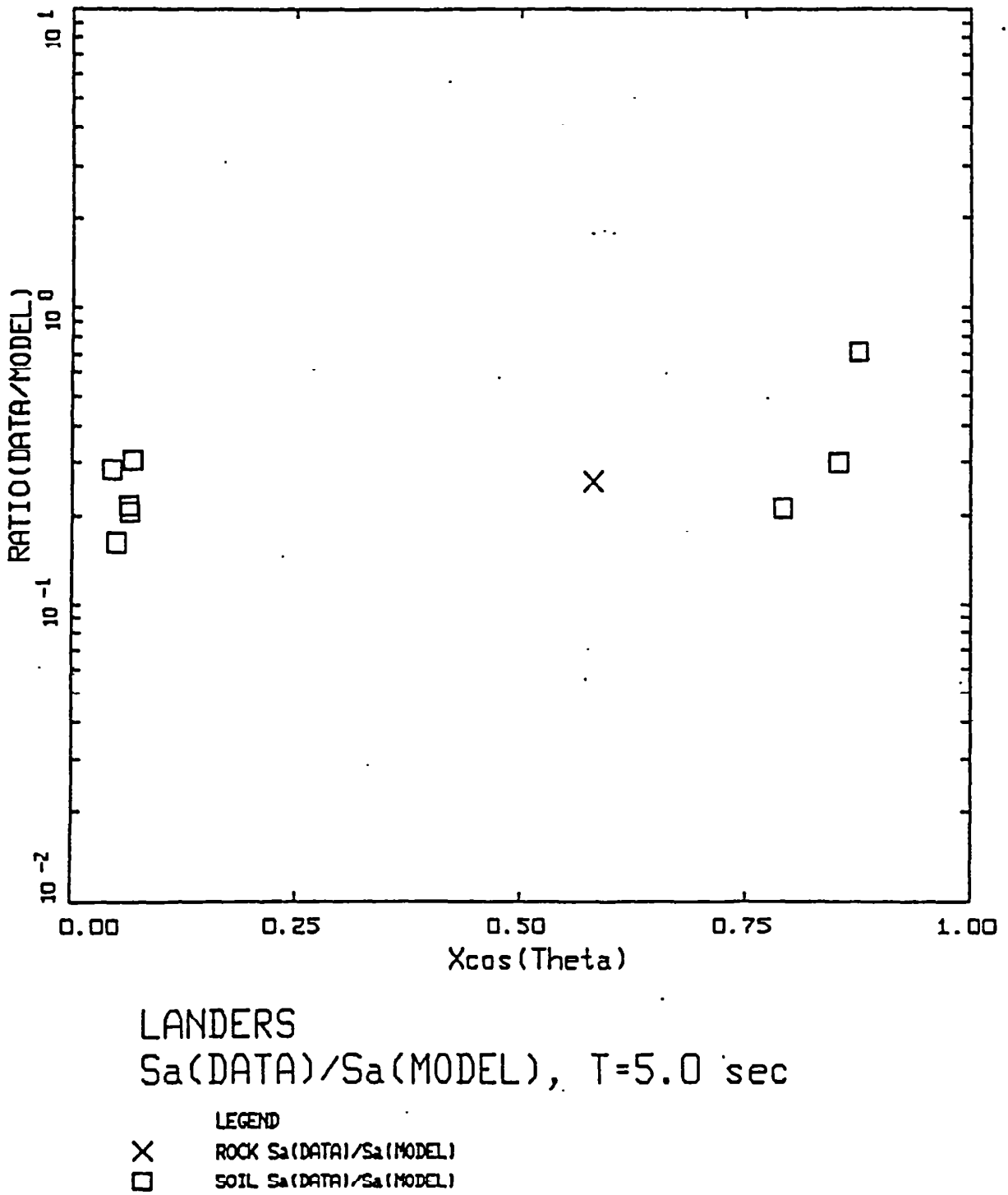

Figure 11. Ratio (data/model prediction) of 5% damped response spectra for an average horizontal component at a period of 5 sec versus directivity parameter X cos θ. Landers earthquake.

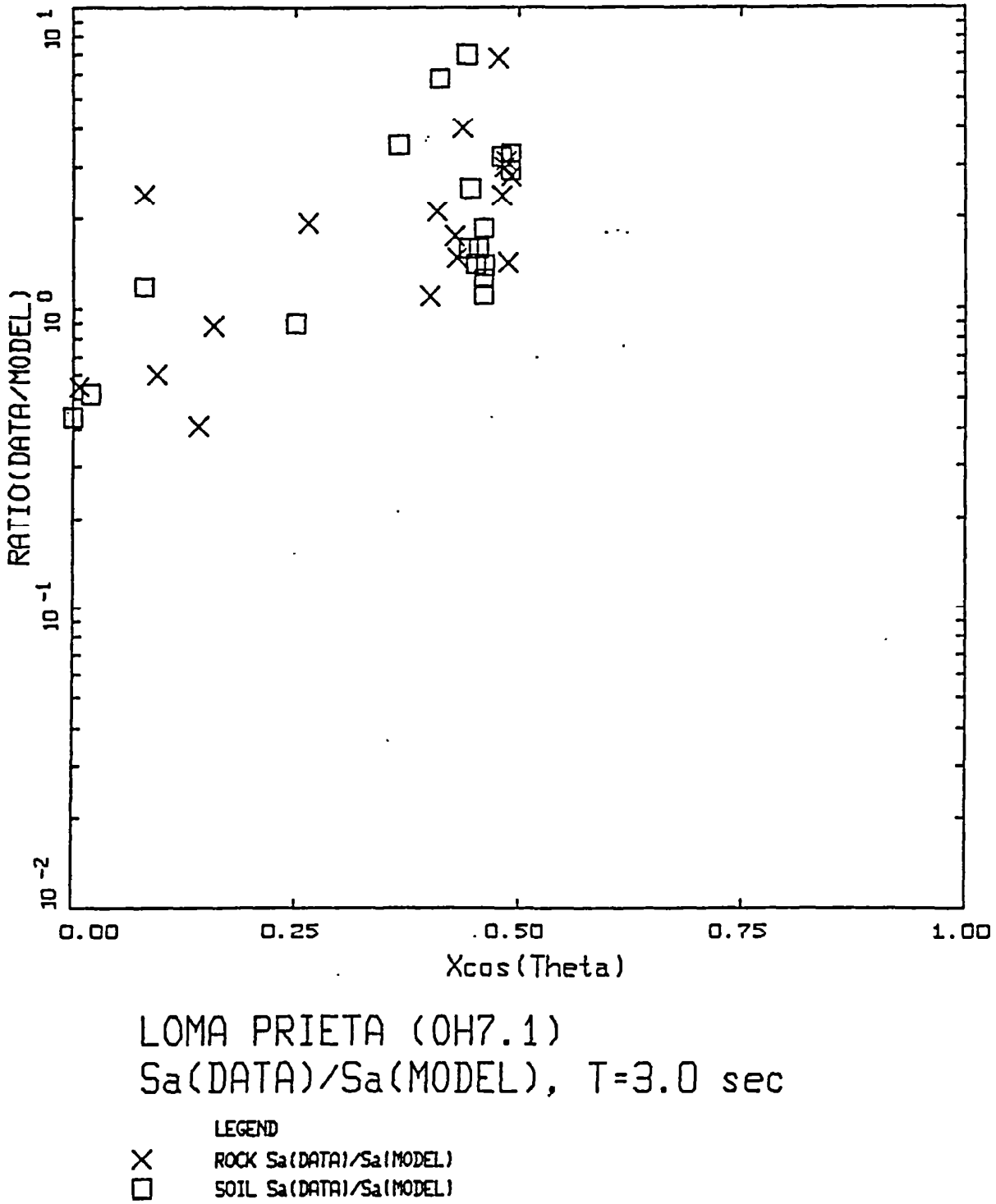

Figure 12. Ratio (data/model prediction) of 5% damped response spectra for an average horizontal component at a period of 3 sec versus directivity parameter X cos θ. Loma Prieta earthquake, rise time of 1.5 sec.

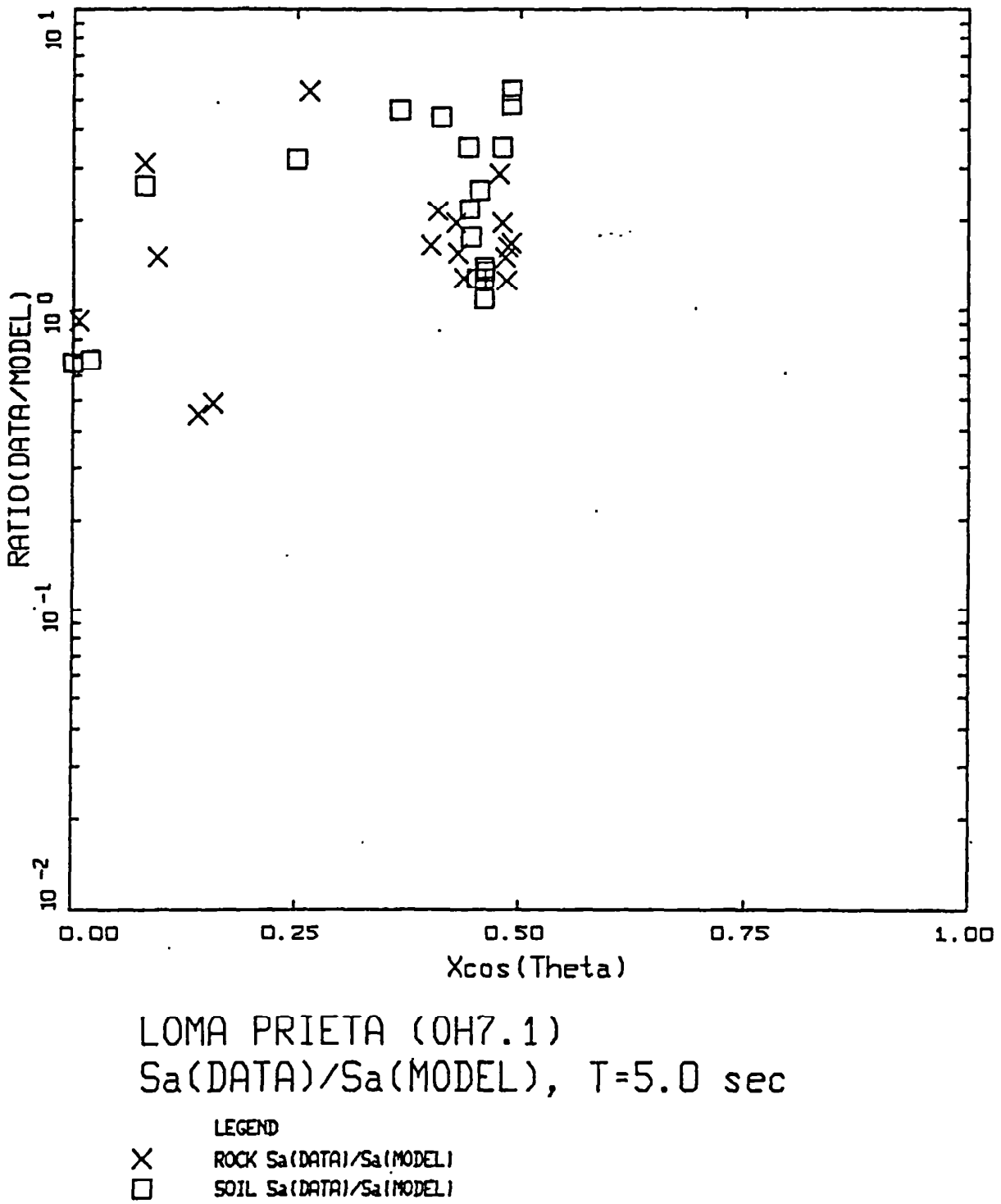

Figure 13. Ratio (data/model prediction) of 5% damped response spectra for an average horizontal component at a period of 5 sec versus directivity parameter X cos θ. Loma Prieta earthquake, rise time of 1.5 sec.

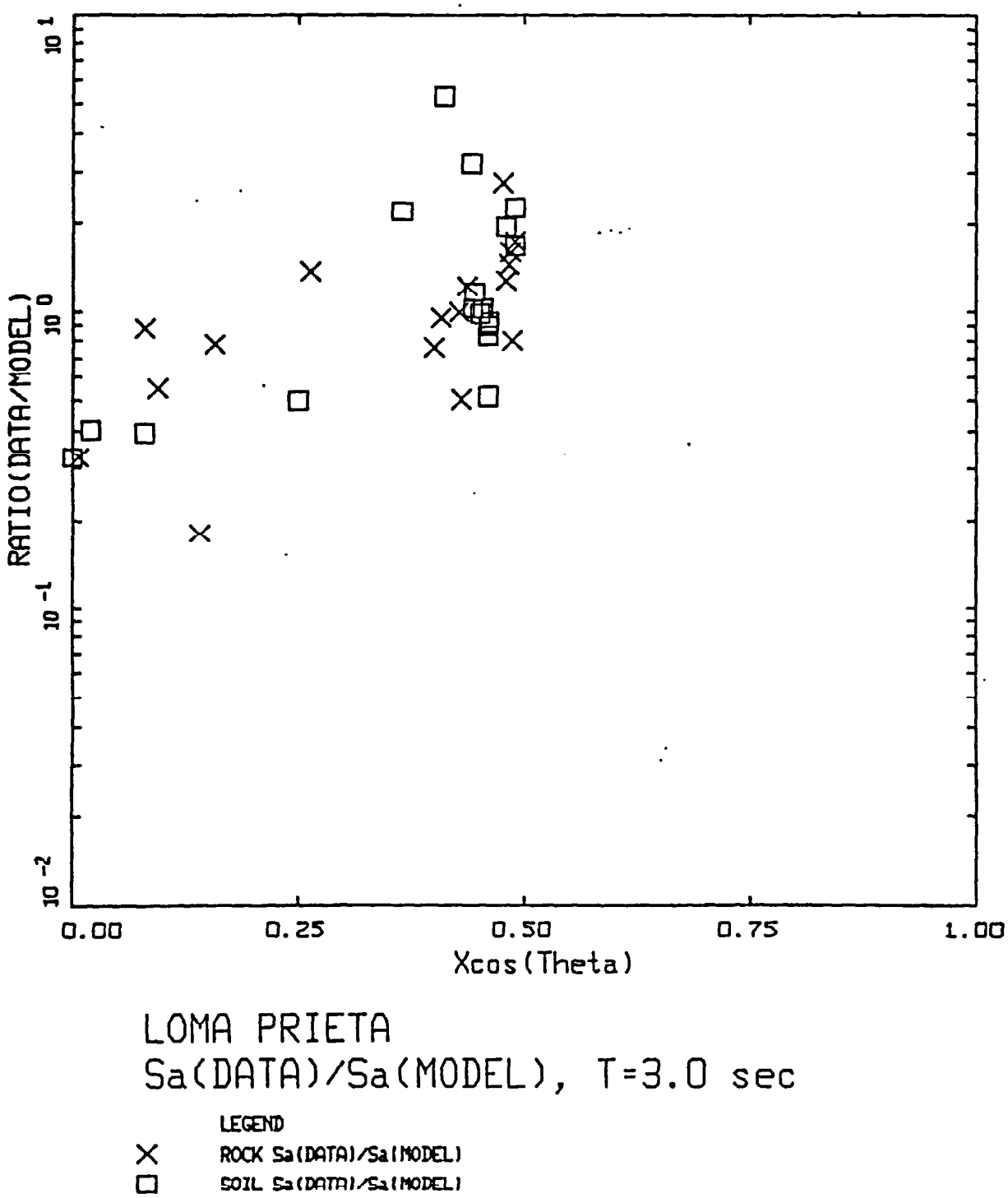

Figure 14. Ratio (data/model prediction) of 5% damped response spectra for an average horizontal component at a period of 3 sec versus directivity parameter X cos θ. Loma Prieta earthquake, rise time of 0.5 sec.

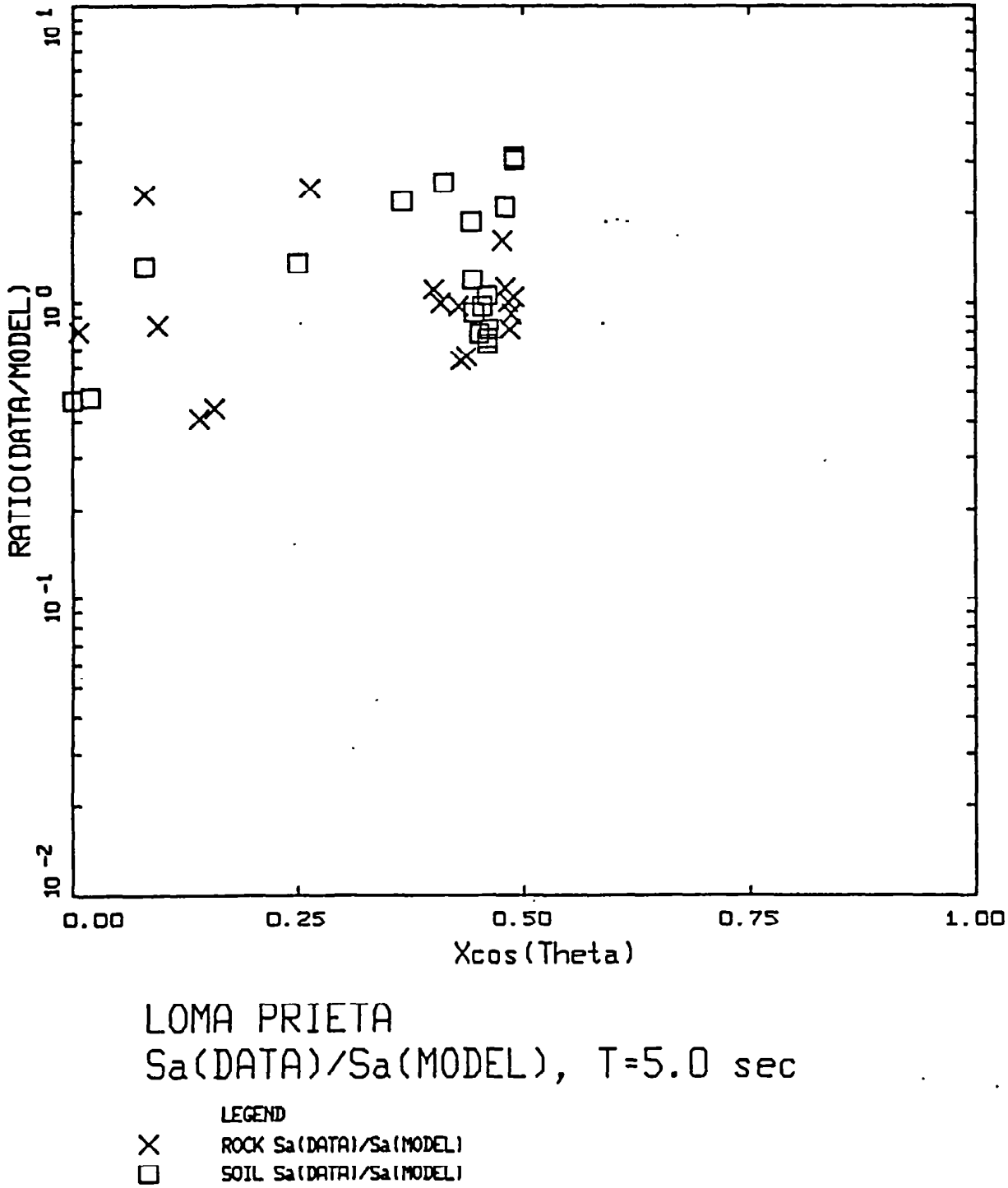

Figure 15. Ratio (data/model prediction) of 5% damped response spectra for an average horizontal component at a period of 5 sec versus directivity parameter X cos θ. Loma Prieta earthquake, rise time of 0.5 sec.

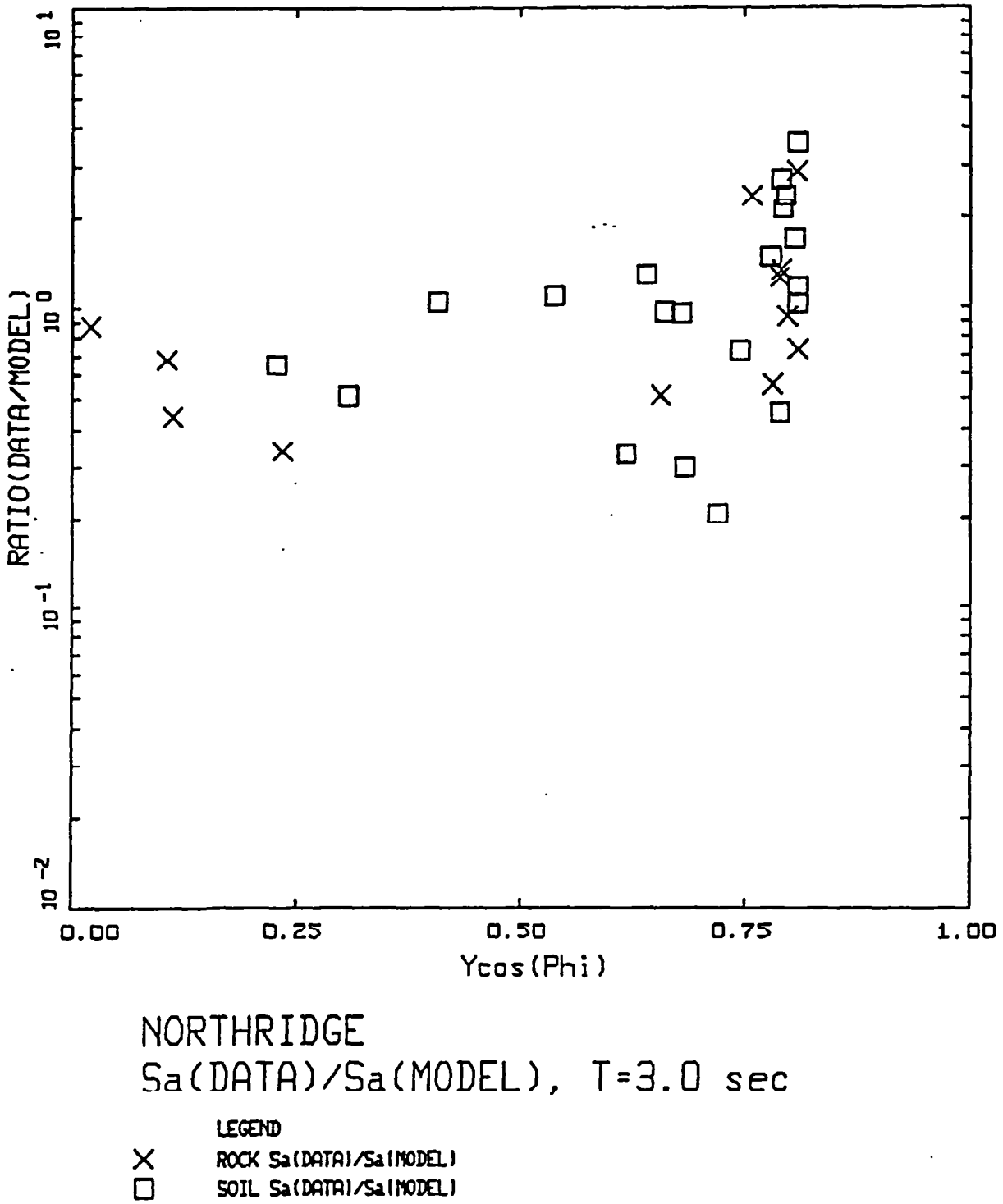

Figure 16. Ratio (data/model prediction) of 5% damped response spectra for an average horizontal component at a period of 3 sec versus directivity parameter Y cos ϕ. Northridge earthquake, rise time of 1.4 sec.

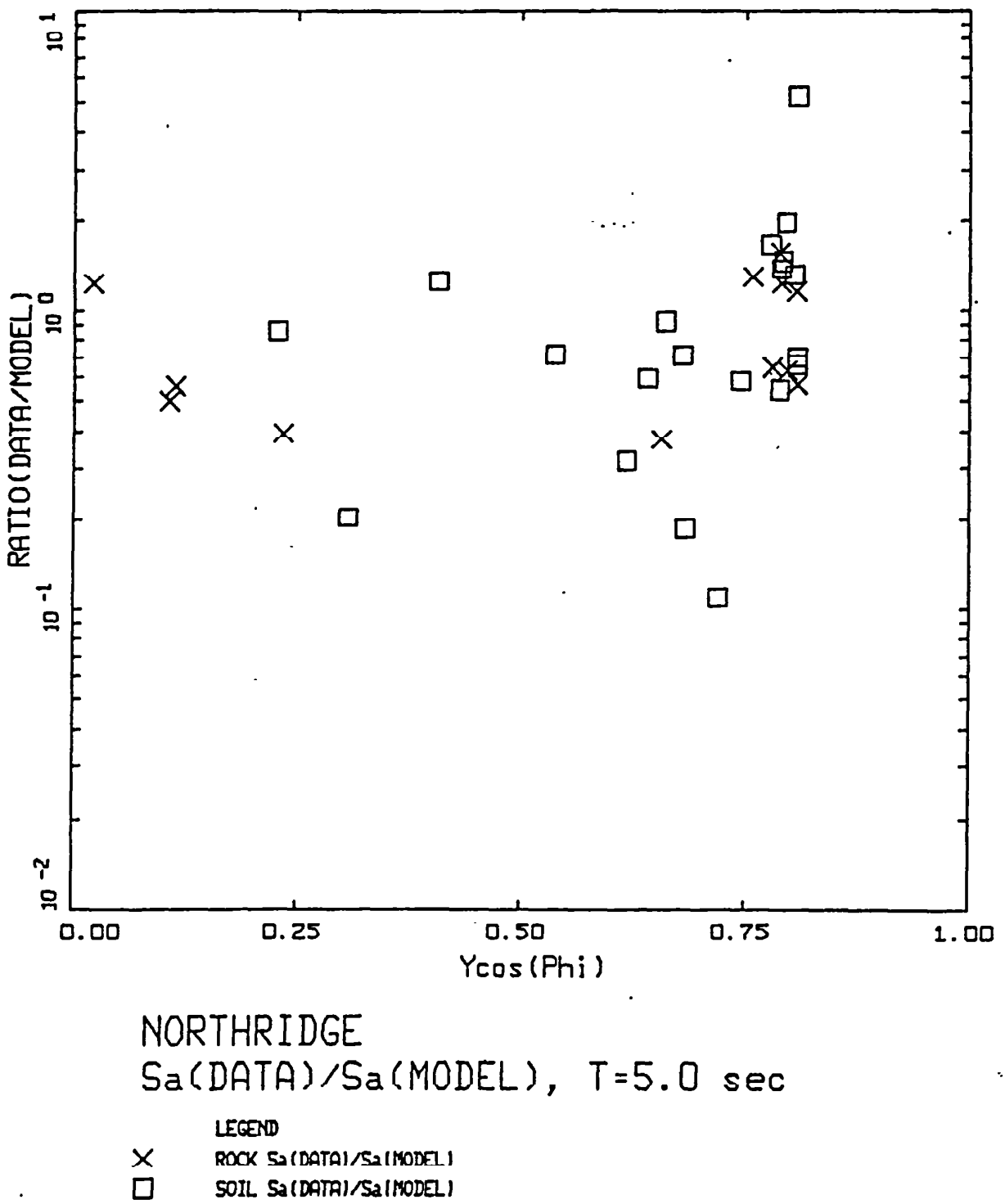

Figure 17. Ratio (data/model prediction) of 5% damped response spectra for an average horizontal component at a period of 5 sec versus directivity parameter Y cos ϕ. Northridge earthquake, rise time of 1.4 sec.

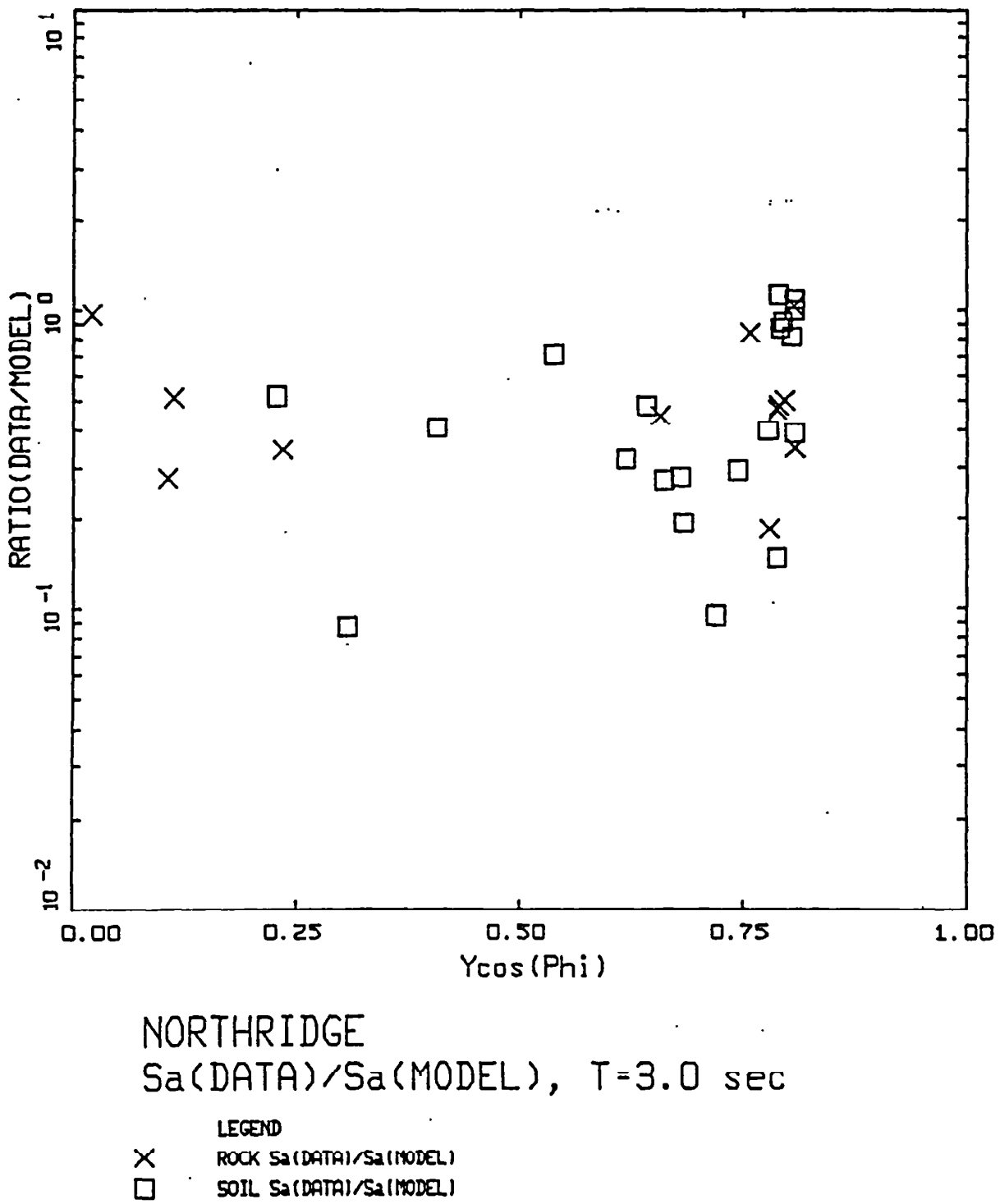

Figure 18. Ratio (data/model prediction) of 5% damped response spectra for an average horizontal component at a period of 3 sec versus directivity parameter Y cos ϕ. Northridge earthquake, rise time of 1.0 sec.

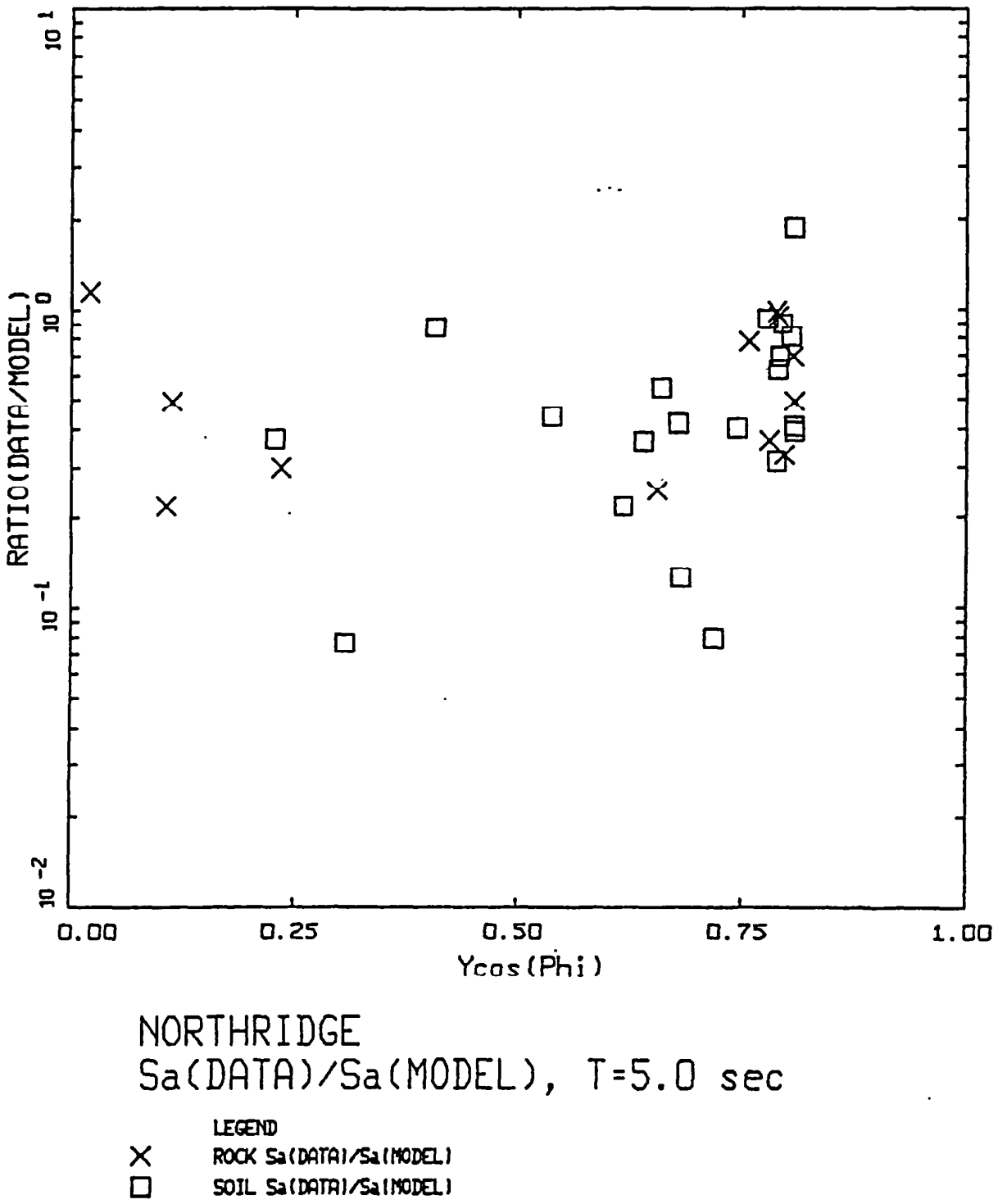

Figure 19. Ratio (data/model prediction) of 5% damped response spectra for an average horizontal component at a period of 5 sec versus directivity parameter Y cos ϕ. Northridge earthquake, rise time of 1.0 sec.

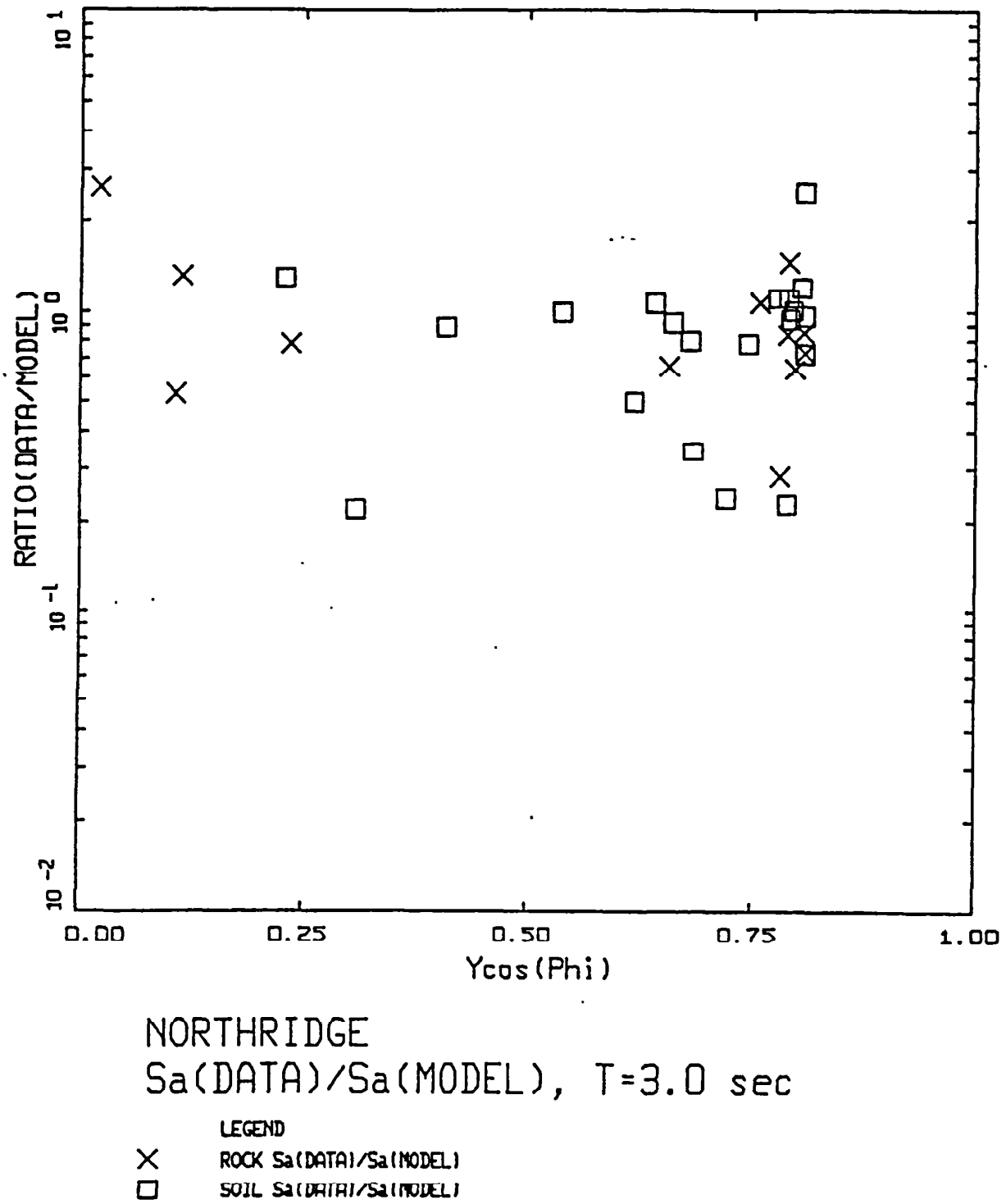

Figure 20. Ratio (data/model prediction) of 5% damped response spectra for an average horizontal component at a period of 3 sec versus directivity parameter Y cos ϕ. Northridge earthquake, rise time of 1.4 sec, slip model derived using shallow rock and soil profiles (Figure 6).

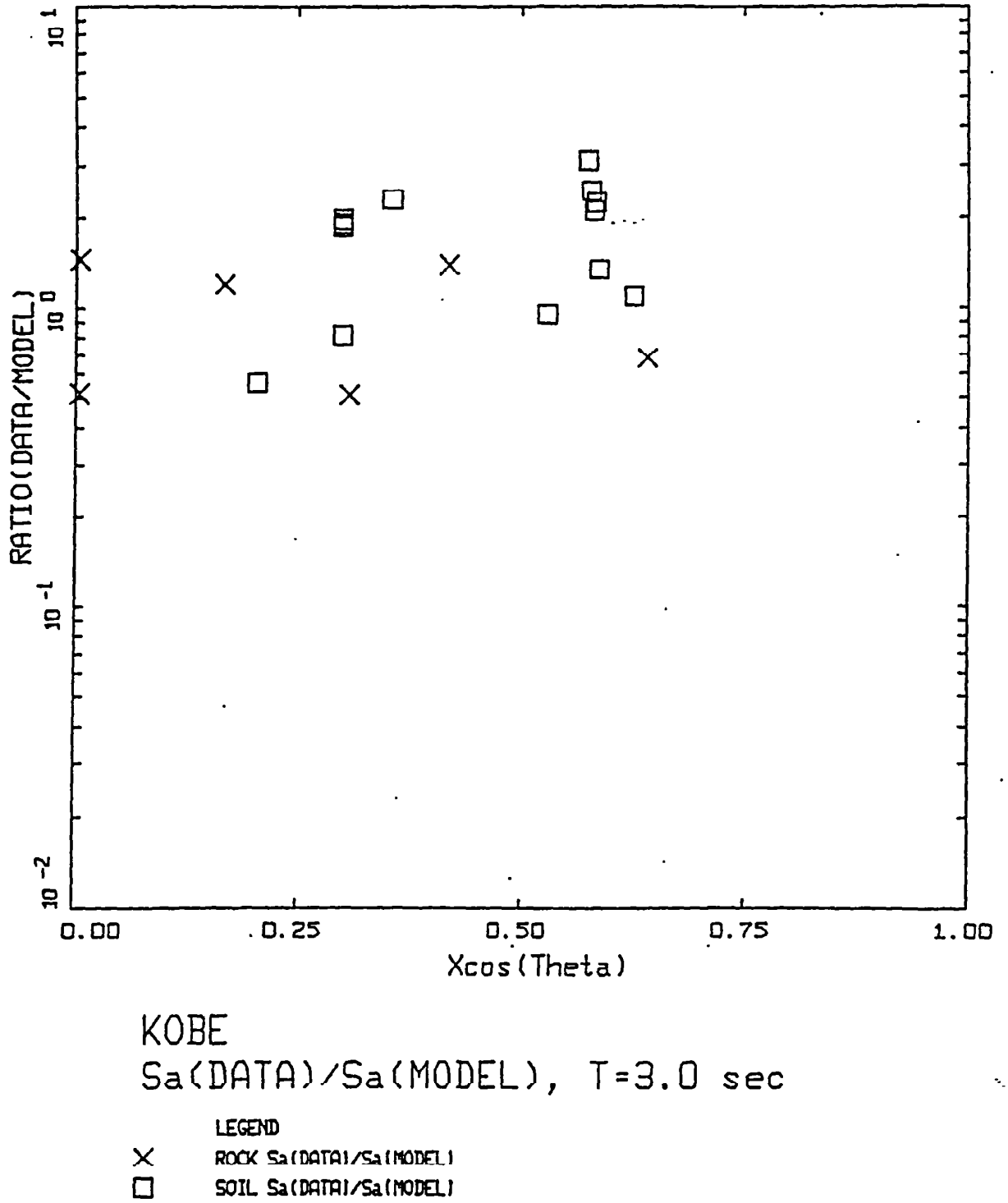

Figure 24. Ratio (data/model prediction) of 5% damped response spectra for an average horizontal component at a period of 3 sec versus directivity parameter $X \cos \theta$. Kobe earthquake.

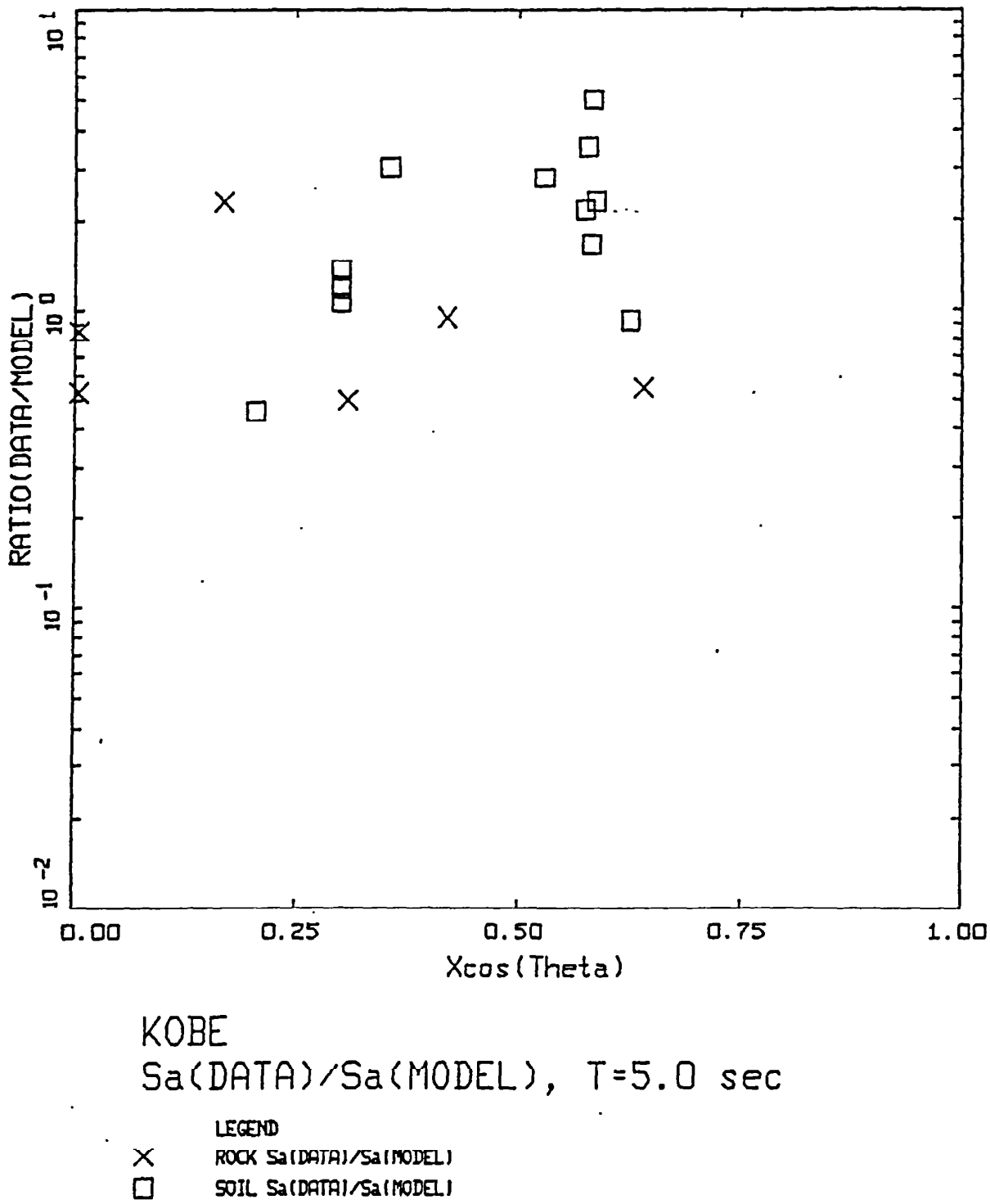

Figure 25. Ratio (data/model prediction) of 5% damped response spectra for an average horizontal component at a period of 5 sec versus directivity parameter $X \cos \theta$. Kobe earthquake.

APPENDIX A

STOCHASTIC GROUND MOTION MODEL DESCRIPTION

BACKGROUND

In the context of strong ground motion, the term "stochastic" can be a fearful concept to some and may be interpreted to represent a fundamentally incorrect or inappropriate model (albeit the many examples demonstrating that it works well; Boore, 1983, 1986). To allay any initial misgivings, a brief discussion seems prudent to explain the term stochastic in the stochastic ground motion model.

The stochastic point-source model may be termed a spectral model in that it fundamentally describes the Fourier amplitude spectral density at the surface of a half-space (Hanks and McGuire, 1981). The model uses a Brune (1970, 1971) omega-square description of the earthquake source Fourier amplitude spectral density. This model is easily the most widely used and qualitatively validated source description available. Seismic sources ranging from M = -6 (hydrofracture) to M = 8 have been interpreted in terms of the Brune omega-square model in dozens of papers over the last 30 years. The general conclusion is that it provides a reasonable and consistent representation of crustal sources, particularly for tectonically active regions such as plate margins. A unique phase spectrum can be associated with the Brune source amplitude spectrum to produce a complex spectrum which can be propagated using either exact or approximate (1-2- or 3-D) wave propagation algorithms to produce single or multiple component time histories. In this context the model is not stochastic, it is decidedly deterministic and as exact and rigorous as one chooses. A two-dimensional array of such point-sources may be appropriately located on a fault surface (area) and fired with suitable delays to simulate rupture propagation on an extended rupture plane (Section 2.2). As with the single point-source, any degree of rigor may be used in the wave propagation algorithm to produce multiple component or average horizontal component time histories. The result is a kinematic[1] finite-source model which has as its basis a source time history defined as a Brune pulse whose Fourier amplitude spectrum follows an omega-square model. This finite-fault model would be very similar to that used in published inversions for slip models (Chapter 4) if the 1-D propagation were treated using a reflectivity algorithm (Aki and Richards, 1980). This algorithm is a complete solution to the wave equation from static offsets (near-field terms) to an arbitrarily selected high frequency cutoff (generally 1-2 Hz).

Alternatively, to model the wave propagation more accurately, recordings of small earthquakes at the site of interest and with source locations distributed along the fault of interest may be used as empirical Green functions (Hartzell, 1978). To model the design earthquake,

---

[1]Kinematic source model is one whose slip (displacement) is defined (imposed) while in a dynamic source model forces (stress) are defined (see Aki and Richards 1980 for a complete description).

the empirical Green functions are delayed and summed in a manner to simulate rupture propagation (Hartzell, 1978). Provided a sufficient number of small earthquakes are recorded at the site of interest, the source locations adequately cover the expected rupture surface, and sufficient low frequency energy is present in the Green functions, this would be the most appropriate procedure to use if nonlinear site response is not an issue. With this approach the wave propagation is, in principle, exactly represented from each Green function source to the site. However, nonlinear site response is not treated unless Green function motions are recorded at a nearby rock outcrop with dynamic material properties similar to the rock underlying the soils at the site or recordings are made at depth within the site soil column. These motions may then be used as input to either total or effective stress site response codes to model nonlinear effects. Important issues associated with this approach include the availability of an appropriate nearby (1 to 2 km) rock outcrop and, for the downhole recordings, the necessity to remove all downgoing energy from the at-depth soil recordings. The downgoing energy must be removed from the downhole Green functions (recordings) prior to generating the control motions (summing) as only the upgoing wavefields are used as input to the nonlinear site response analyses. Removal of the downgoing energy from each recording requires multiple site response analyses which introduce uncertainty into the Green functions due to uncertainty in dynamic material properties and the numerical site response model used to separate the upgoing and downgoing wavefields.

To alleviate these difficulties one can use recordings well distributed in azimuth at close distances to a small earthquake and correct the recordings back to the source by removing wave propagation effects using a simple approximation (say 1/R plus a constant for crustal amplification and radiation pattern), to obtain an empirical source function. This source function can be used to replace the Brune pulse to introduce some natural (although source, path, and site specific) variation into the dislocation time history. If this is coupled to an approximate wave propagation algorithm (asymptotic ray theory) which includes the direct rays and those which have undergone a single reflection, the result is the empirical source function method (EPRI, 1993). Combining the reflectivity propagation (which is generally limited to frequencies $\leq$ 1-2 Hz due to computational demands) with the empirical source function approach (appropriate for frequencies $\geq$ 1 Hz; EPRI, 1993) results in a broad band simulation procedure which is strictly deterministic at low frequencies (where an analytical source function is used) and incorporates some natural variation at high frequencies through the use of an empirical source function (Sommerville et al., 1995).

All of these techniques are fundamentally similar, well founded in seismic source and wave propagation physics, and importantly, they are <u>all</u> approximate. Simply put, all models are wrong (approximate) and the single essential element in selecting a model is to incorporate the appropriate degree of rigor, commensurate with uncertainties and variabilities in crustal structure and site effects, through extensive validation exercises. It is generally felt that more complicated models produce more accurate results, however, the implications of more sophisticated models with the increased number of parameters which must be specified is often overlooked. This is not too serious a consequence in modeling past earthquakes since a reasonable range in parameter space can be explored to give the "best" results. However for future predictions, this increased rigor may carry undesirable baggage in increased parametric variability (Roblee et al., 1996). The effects of lack of knowledge (epistemic uncertainty; EPRI,

1993) regarding parameter values for future occurrences results in uncertainty or variability in ground motion predictions. It may easily be the case that a very simple model, such as the point-source model can have comparable, or even smaller, total variability (modeling plus parametric) than a much more rigorous model with an increased number of parameters (EPRI, 1993). What is desired in a model is sufficient sophistication such that it captures the dominant and stable features of source, distance, and site dependencies observed in strong ground motions. It is these considerations which led to the development of the stochastic point- and finite-source models and, in part, leads to the stochastic element of the models.

The stochastic nature of the point- and finite-source RVT models is simply the assumption made about the character of ground motion time histories that permits stable estimates of peak parameters (e.g. acceleration, velocity, strain, stress, oscillator response) to be made without computing detailed time histories (Hanks and McGuire, 1981; Boore, 1983). This process uses random vibration theory to relate a time domain peak value to the time history root-mean-square (RMS) value (Boore, 1983). The assumption of the character of the time history for this process to strictly apply is that it be normally distributed random noise and stationary (its statistics do not change with time) over its duration. A visual examination of any time history quickly reveals that this is clearly not the case: time histories (acceleration, velocity, stress, strain, oscillator) start, build up, and then diminish with time. However poor the assumption of stationary Gaussian noise may appear, the net result is that the assumption is weak enough to permit the approach to work surprisingly well, as numerous comparisons with recorded motions and both qualitative and quantative validations have shown (Hanks and McGuire, 1981; Boore, 1983, 1986; McGuire et al., 1984; Boore and Atkinson, 1987; Silva and Lee, 1987; Toro and McGuire, 1987; Silva et al., 1990; EPRI, 1993; Schneider et al., 1993; Silva and Darragh, 1995; Silva et al., 1997). Corrections to RVT are available to accommodate different distributions as well as non-stationarity and are usually applied to the estimation of peak oscillator response in the calculated response spectra (Boore and Joyner, 1984; Toro, 1985).

Point-source Model

The conventional stochastic ground motion model uses an ω-square source model (Brune, 1970, 1971) with a single corner frequency and a constant stress drop (Boore, 1983; Atkinson, 1984). Random vibration theory is used to relate RMS (root-mean-square) values to peak values of acceleration (Boore, 1983), and oscillator response (Boore and Joyner, 1984; Toro, 1985; Silva and Lee, 1987) computed from the power spectra to expected peak time domain values (Boore, 1983).

The shape of the acceleration spectral density, a(f), is given by

$$a(f) = C \frac{f^2}{1+(\frac{f}{f_0})^2} \frac{M_0}{R} P(f)\, A(f)\, e^{-\frac{\pi f R}{\beta_0 Q(f)}} \qquad \text{(A-1)}$$

where

$$C = \left(\frac{1}{\rho_0 \beta_0^3}\right) \cdot (2) \cdot (0.55) \cdot \left(\frac{1}{\sqrt{2}}\right) \cdot \pi.$$

M_0 = seismic moment,
R = hypocentral distance,
β_0 = shear-wave velocity at the source,
ρ_0 = density at the source
$Q(f)$ = frequency dependent quality factor (crustal damping),
$A(f)$ = crustal amplification,
$P(f)$ = high-frequency truncation filter,
f_0 = source corner frequency.

C is a constant which contains source region density (ρ_0) and shear-wave velocity terms and accounts for the free-surface effect (factor of 2), the source radiation pattern averaged over a sphere (0.55) (Boore, 1986), and the partition of energy into two horizontal components ($1/\sqrt{2}$).

Source scaling is provided by specifying two independent parameters, the seismic moment (M_0) and the high-frequency stress parameter or stress drop ($\Delta\sigma$). The seismic moment is related to magnitude through the definition of moment magnitude M by the relation

$$\log M_0 = 1.5\,M + 16.05 \qquad \text{(Hanks and Kanamori, 1979)} \qquad \text{(C-2).}$$

The stress drop ($\Delta\sigma$) relates the corner frequency f_0 to M_0 through the relation

$$f_0 = \beta_0\,(\Delta\sigma/8.44\,M_0)^{1/3} \qquad \text{(Brune; 1970, 1971)} \qquad \text{(C-3).}$$

The stress drop is sometimes referred to as the high frequency stress parameter (Boore, 1983) (or simply the stress parameter) since it directly scales the Fourier amplitude spectrum for frequencies above the corner frequency (Silva, 1991; Silva and Darragh 1995). High (> 1 Hz) frequency model predictions are then very sensitive to this parameter (Silva, 1991; EPRI, 1993) and the interpretation of it being a stress drop or simply a scaling parameter depends upon how well real earthquake sources (on average) obey the omega-square scaling (Equation A-3) and how well they are fit by the single-corner-frequency model. If earthquakes truly have single-corner-frequency omega-square sources, the stress drop in Equation A-3 is a physical parameter and its values have a physical interpretation of the forces (stresses) accelerating the relative slip across the rupture surface. High stress drop sources are due to a smaller source (fault) area (for the same M) than low stress drop sources (Brune, 1970). Otherwise, it simply a high frequency scaling or fitting parameter.

The spectral shape of the single-corner-frequency ω-square source model is then described by the two free parameters M_0 and $\Delta\sigma$. The corner frequency increases with the shear-wave velocity and with increasing stress drop, both of which may be region dependent.

The crustal amplification accounts for the increase in wave amplitude as seismic energy travels through lower- velocity crustal materials from the source to the surface. The amplification depends on average crustal and near surface shear-wave velocity and density (Boore, 1986).

The P(f) filter is used in an attempt to model the observation that acceleration spectral density appears to fall off rapidly beyond some region- or site-dependent maximum frequency (Hanks, 1982; Silva and Darragh, 1995). This observed phenomenon truncates the high frequency portion of the spectrum and is responsible for the band-limited nature of the stochastic model. The band limits are the source corner frequency at low frequency and the high frequency spectral attenuation. This spectral fall-off at high frequency has been attributed to near-site attenuation (Hanks, 1982; Anderson and Hough, 1984) or to source processes (Papageorgiou and Aki, 1983) or perhaps to both effects. In the Anderson and Hough (1984) attenuation model, adopted here, the form of the P(f) filter is taken as

$$P(f, r) = e^{-\pi\kappa(r)f} \qquad \text{(A-4).}$$

Kappa (r) (κ(r) in Equation C-4) is a site and distance dependent parameter that represents the effect of intrinsic attenuation upon the wavefield as it propagates through the crust from source to receiver. Kappa (r) depends on epicentral distance (r) and on both the shear-wave velocity (β) and quality factor (Q_s) averaged over a depth of H beneath the site (Hough et al., 1988). At zero epicentral distance kappa (κ) is given by

$$\kappa(0) = \frac{H}{\bar{\beta}\,\overline{Q_s}} \qquad \text{(A-5),}$$

and is referred to as κ.

The bar in Equation C-5 represents an average of these quantities over a depth H. The value of kappa at zero epicentral distance is attributed to attenuation in the very shallow crust directly below the site (Hough and Anderson, 1988; Silva and Darragh, 1995). The intrinsic attenuation along this part of the path is not thought to be frequency dependent and is modeled as a frequency independent, but site and crustal region dependent, constant value of kappa (Hough et al., 1988; Rovelli et al., 1988). This zero epicentral distance kappa is the model implemented in this study.

The crustal path attenuation from the source to just below the site is modeled with the frequency- dependent quality factor Q(f). Thus the distance component of the original κ(r) (Equation A-4) is accommodated by Q(f) and R in the last term of Equation A-1:

$$\kappa(r) = \frac{H}{\bar{\beta}\,\bar{Q}_S} + \frac{R}{\beta_0\,Q(f)} \qquad \text{(A-6).}$$

The Fourier amplitude spectrum, a(f), given by Equation C-1 represents the stochastic ground motion model employing a Brune source spectrum that is characterized by a single corner frequency. It is a point source and models direct shear-waves in a homogeneous half-space (with effects of a velocity gradient captured by the A(f) filter, Equation A-1). For horizontal motions, vertically propagating shear-waves are assumed. Validations using incident inclined SH-waves accompanied with raytracing to find appropriate incidence angles leaving the source showed little reduction in uncertainty compared to results using vertically propagating shear-waves. For vertical motions, P/SV propagators are used coupled with raytracing to model incident inclined plane waves (EPRI, 1993). This approach has been validated with recordings from the 1989 M 6.9 Loma Prieta earthquake (EPRI, 1993).

Equation C-1 represents an elegant ground motion model that accommodates source and wave propagation physics as well as propagation path and site effects with an attractive simplicity. The model is appropriate for an engineering characterization of ground motion since it captures the general features of strong ground motion in terms of peak acceleration and spectral composition with a minimum of free parameters (Boore, 1983; McGuire et al., 1984; Boore, 1986; Silva and Green, 1988; Silva et al., 1988; Schneider et al., 1993; Silva and Darragh, 1995). An additional important aspect of the stochastic model employing a simple source description is that the region-dependent parameters may be evaluated by observations of small local or regional earthquakes. Region-specific seismic hazard evaluations can then be made for areas with sparse strong motion data with relatively simple spectral analyses of weak motion (Silva, 1992).

In order to compute peak time-domain values, i.e. peak acceleration and oscillator response, RVT is used to relate RMS computations to peak value estimates. Boore (1983) and Boore and Joyner (1984) present an excellent development of the RVT methodology as applied to the stochastic ground motion model. The procedure involves computing the RMS value by integrating the power spectrum from zero frequency to the Nyquist frequency and applying Parsevall's relation. Extreme value theory is then used to estimate the expected ratio of the peak value to the RMS value of a specified duration of the stochastic time history. The duration is taken as the inverse of the source corner frequency (Boore, 1983).

Factors that affect strong ground motions such as surface topography, finite and propagating seismic sources, laterally varying near-surface velocity and Q gradients, and random inhomogeneities along the propagation path are not included in the model. While some or all of these factors are generally present in any observation of ground motion and may exert controlling influences in some cases, the simple stochastic point-source model appears to be robust in predicting median or average properties of ground motion (Boore 1983, 1986; Schneider et al., 1993; Silva and Stark, 1993). For this reason it represents a powerful predictive and interpretative tool for engineering characterization of strong ground motion.

Finite-source Model Ground Motion Model

In the near-source region of large earthquakes, aspects of a finite-source including rupture propagation, directivity, and source-receiver geometry can be significant and may be incorporated into strong ground motion predictions. To accommodate these effects, a methodology that combines the aspects of finite-earthquake-source modeling techniques (Hartzell, 1978; Irikura 1983) with the stochastic point-source ground motion model has been developed to produce response spectra as well as time histories appropriate for engineering design (Silva et al., 1990; Silva and Stark, 1993; Schneider et al., 1993). The approach is very similar to the empirical Green function methodology introduced by Hartzell (1978) and Irikura (1983). In this case however, the stochastic point-source is substituted for the empirical Green function and peak amplitudes; PGA, PGV, and response spectra (when time histories are not produced) are estimated using random process theory.

Use of the stochastic point-source as a Green function is motivated by its demonstrated success in modeling ground motions in general and strong ground motions in particular (Boore, 1983, 1986; Silva and Stark, 1993; Schneider et al., 1993; Silva and Darragh, 1995) and the desire to have a model that is truly site- and region-specific. The model can accommodate a region specific Q(f), Green function sources of arbitrary moment or stress drop, and site specific kappa values. The necessity for having available regional and site specific recordings or modifying possibly inappropriate empirical Green functions is eliminated.

For the finite-source characterization, a rectangular fault is discretized into NS subfaults of moment M_0^s. The empirical relationship

$$\log(A) = M - 4.0, \quad A \text{ in km}^2 \qquad \text{(A-7).}$$

is used to assign areas to both the target earthquake (if its rupture surface is not fixed) as well as to the subfaults. This relation results from regressing log area on M using the data of Wells and Coppersmith (1994). In the regression, the coefficient on M is set to unity which implies a constant static stress drop of about 30 bars (Equation A-9). This is consistent with the general observation of a constant static stress drop for earthquakes based on aftershock locations (Wells and Coppersmith 1994). The static stress drop, defined by Equation A-10, is related to the average slip over the rupture surface as well as rupture area. It is theoretically identical to the stress drop in Equation A-3 which defines the omega-square source corner frequency assuming the rupture surface is a circular crack model (Brune, 1970; 1971). The stress drop determined by the source corner frequency (or source duration) is usually estimated through the Fourier amplitude spectral density while the static stress drop uses the moment magnitude and an estimate of the rupture area. The two estimates for the same earthquake seldom yield the same values with the static generally being the smaller. In a recent study (Silva et al., 1997), the average stress drop based on Fourier amplitude spectra determined from an empirical attenuation relation (Abrahamson and Silva, 1997) is about 70 bars while the average static stress drop for the crustal earthquakes studied by Wells and Coppersmith (1994) is about 30 bars. These results reflect a general factor of about 2 on average between the two values. These large differences

may simply be the result of using an inappropriate estimate of rupture area as the zone of actual slip is difficult to determine unambiguously. In general however, even for individual earthquakes, the two stress drops scale similarly with high static stress drops (> 30 bars) resulting in large high frequency (> 1 Hz for M ≥ 5) ground motions which translates to high corner frequencies (Equation A-3).

The subevent magnitude M_s is generally taken in the range of 5.0-6.5 depending upon the size of the target event. M_s 5.0 is used for crustal earthquakes with M in the range of 5.5 to 8.0 and M_s 6.4 is used for large subduction earthquakes with M > 7.5. The value of NS is determined as the ratio of the target event area to the subfault area. To constrain the proper moment, the total number of events summed (N) is given by the ratio of the target event moment to the subevent moment. The subevent and target event rise times (duration of slip at a point) are determined by the equation

$$\log \tau = 0.33 \log M_0 - 8.54 \qquad \text{(A-8)}$$

which results from a fit to the rise times used in the finite-fault modeling exercises, (Silva et al., 1997). Slip on each subfault is assumed to continue for a time τ. The ratio of target-to-subevent rise times is given by

$$\frac{\tau}{\tau^s} = 10^{0.5\,(M - M^s)} \qquad \text{(A-9)}$$

and determines the number of subevents to sum in each subfault. This approach is generally referred to as the constant-rise-time model and results in variable slip velocity for nonuniform slip distributions. Alternatively, one can assume a constant slip velocity resulting in a variable-rise-time model for heterogenous slip distributions.

Recent modeling of the Landers (Wald and Heaton, 1994), Kobe (Wald, 1996) and Northridge (Hartzell et al. 1996) earthquakes suggests that a mixture of both constant rise time and constant slip velocity may be present. Longer rise times seem to be associated with areas of larger slip with the ratio of slip-to-rise time (slip velocity) being depth dependent. Lower slip velocities (longer rise times) are associated with shallow slip resulting in relatively less short period seismic radiation. This result may explain the general observation that shallow slip is largely aseismic. The significant contributions to strong ground motions appear to originate at depths exceeding about 4 km (Campbell, 1993; Boore et al., 1994) as the fictitious depth term in empirical attenuation relation (Abrahamson and Silva, 1997; Boore et al., 1997). Finite-fault models generally predict unrealistically large strong ground motions for large shallow (near surface) slip using rise times or slip velocities associated with deeper (> 4 km) zones of slip. This is an important and unresolved issue in finite-fault modeling and the general approach is constrain the slip to relatively small values in the top 2 to 4 km. A more thorough analysis is necessary, ideally using several well validated models, before this issue can be satisfactorily

resolved.

To introduce heterogeneity of the earthquake source process into the stochastic finite-fault model, the location of the sub-events within each subfault (Hartzell, 1978) are randomized as well as the subevent rise time. The stress drop of the stochastic point-source Green function is taken as 30 bars, consistent with the static value based on the M 5.0 subevent area using the equation

$$\Delta\sigma = \frac{7}{16}\left(\frac{M_e}{R_e^3}\right) \qquad \text{(Brune, 1970, 1971)} \qquad \text{(A-10)}$$

where R_e is the equivalent circular radius of the rectangular sub-event.

Different values of slip are assigned to each subfault as relative weights so that asperities or non-uniform slip can be incorporated into the methodology. For validation exercises, slip models are taken from the literature and are based on inversions of strong motion as well as regional or teleseismic recordings. To produce slip distributions for future earthquakes, random slip models are generated based on a statistical asperity model with parameters calibrated to the published slip distributions. This approach has been validated by comparing the modeling uncertainty and bias estimates for the Loma Prieta and Whittier Narrows earthquakes using motion at each site averaged over several (30) random slip models to the bias and uncertainty estimates using the published slip model. The results show nearly identical bias and uncertainty estimates suggesting that averaging the motions over random slip models produces as accurate a prediction at a site as a single motion computed using the "true" slip model which is determined from inverting actual recordings.

The rupture velocity is taken as depth independent at a value of 0.8 times the shear-wave velocity, generally at the depth of the dominant slip. This value is based on a number of studies of source rupture processes which also suggest that rupture velocity is non-uniform. To capture the effects of non-uniform rupture velocity, a random component (20%) is added. The radiation pattern is computed for each subfault, a random component added, and the RMS applied to the motions computed at the site.

The ground-motion time history at the receiver is computed by summing the contributions from each subfault associated with the closest Green function, transforming to the frequency domain, and convolving with the Green function spectrum (Equation A-1). The locations of the Green functions are generally taken at center of each subfault for small subfaults or at a maximum separation of about 5 to 10 km for large subfaults. As a final step, the individual contributions associated with each Green function are summed in the frequency domain, multiplied by the RMS radiation pattern, and the resultant power spectrum at the site is computed. The appropriate duration used in the RVT computations for PGA, PGV, and oscillator response is computed by transforming the summed Fourier spectrum into the time domain and computing the 5 to 75% Arias intensity (Ou and Herrmann, 1990).

As with the point-source model, crustal response effects are accommodated through the

amplification factor (A(f)) or by using vertically propagating shear waves through a vertically heterogenous crustal structure. Propagation path damping, through the Q(f) model, is incorporated from each fault element to the site. Near-surface crustal damping is incorporated through the kappa operator (Equation A-1). To model crustal propagation path effects, the raytracing method of Ou and Herrmann (1990) is applied from each subfault to the site.

Time histories may be computed in the process as well by simply adding a phase spectrum appropriate to the subevent earthquake. The phase spectrum can be extracted from a recording made at close distance to an earthquake of a size comparable to that of the subevent (generally M 5.0 to 6.5). Interestingly, the phase spectrum need not be from a recording in the region of interest (Silva et al., 1989). A recording in WNA (Western North America) can effectively be used to simulate motions appropriate to ENA (Eastern North America). Transforming the Fourier spectrum computed at the site into the time domain results in a computed time history which then includes all of the aspects of rupture propagation and source finiteness, as well as region specific propagation path and site effects.

For fixed fault size, mechanism, and moment, the specific source parameters for the finite-fault are slip distribution, location of nucleation point, and site azimuth. The propagation path and site parameters remain identical for both the point- and finite-source models.

Partition and assessment of ground motion variability

An essential requirement of any numerical modeling approach, particularly one which is implemented in the process of defining design ground motions, is a quantative assessment of prediction accuracy. A desirable approach to achieving this goal is in a manner which lends itself to characterizing the variability associated with model predictions. For a ground motion model, prediction variability is comprised of two components: modeling variability and parametric variability. Modeling variability is a measure of how well the model works (how accurately it predicts ground motions) when specific parameter values are known. Modeling variability is measured by misfits of model predictions to recorded motions through validation exercises and is due to unaccounted for components in the source, path, and site models (i.e. a point-source cannot model the effects of directivity and linear site response cannot accommodate nonlinear effects). Results from a viable range of values for model parameters (i.e., slip distribution, soil profile, G/G_{max} and hysteretic damping curves, etc). Parametric variability is the sensitivity of a model to a viable range of values for model parameters. The total variability, modeling plus parametric, represents the variance associated with the ground motion prediction and, because it is a necessary component in estimating fractile levels, may be regarded as important as median predictions.

Both the modeling and parametric variabilities may have components of randomness and uncertainty. Table A.1 summarizes the four components of total variability in the context of ground motion predictions. Uncertainty is that portion of both modeling and parametric variability which, in principle, can be reduced as additional information becomes available, whereas randomness represents the intrinsic or irreducible component of variability for a given model or parameter. Randomness is that component of variability which is intrinsic or irreducible <u>for a given model.</u> The uncertainty component reflects a lack of knowledge and may

be reduced as more data are analyzed. For example, in the point-source model, stress drop is generally taken to be independent of source mechanism as well as tectonic region and is found to have a standard error of about 0.7 (natural log) for the CEUS (EPRI, 1993). This variation or uncertainty plus randomness in $\Delta\sigma$ results in a variability in ground motion predictions for future earthquakes. If, for example, it is found that normal faulting earthquakes have generally lower stress drops than strike-slip which are, in turn, lower than reverse mechanism earthquakes, perhaps much of the variability in $\Delta\sigma$ may be reduced. In extensional regimes, where normal faulting earthquakes are most likely to occur, this new information may provide a reduction in variability (uncertainty component) for stress drop, say to 0.3 or 0.4 resulting in less ground motion variation due to a lack of knowledge of the mean or median stress drop. There is, however, a component of this stress drop variability which can never be reduced in the context of the Brune model. This is simply due to the heterogeneity of the earthquake dynamics which is not accounted for in the model and results in the randomness component of parametric variability in stress drop. A more sophisticated model may be able to accommodate or model more accurately source dynamics but, perhaps, at the expense of a larger number of parameters and increased parametric uncertainty (i.e. the finite-fault with slip model and nucleation point as unknown parameters for future earthquakes). That is, more complex models typically seek to reduce modeling randomness by more closely modeling physical phenomena. However, such models often require more comprehensive sets of observed data to constrain additional model parameters, which generally leads to increased parametric variability. If the increased parametric variability is primarily in the form of uncertainty, it is possible to reduce total variability, but only at the additional expense of constraining the additional parameters. Therefore, existing knowledge and/or available resources may limit the ability of more complex models to reduce total variability.

The distinction of randomness and uncertainty is model driven and somewhat arbitrary. The allocation is only important in the context of probabilistic seismic hazard analyses as uncertainty is treated as alternative hypotheses in logic trees while randomness is integrated over in the hazard calculation (Cornell, 1968). For example, the uncertainty component in stress drop may be treated by using an N-point approximation to the stress drop distribution and assigning a branch in a logic tree for each stress drop and associated weight. A reasonable three point approximation to a normal distribution is given by weights of 0.2, 0.6, 0.2 for expected 5%, mean, and 95% values of stress drop respectively. If the distribution of uncertainty in stress drop was such that the 5%, mean, and 95% values were 50, 100, and 200 bars respectively, the stress drop branch on a logic tree would have 50, and 200 bars with weights of 0.2 and 100 bars with a weight of 0.6. The randomness component in stress drop variability would then be formally integrated over in the hazard calculation.

Assessment of Modeling Variability

Modeling variability (uncertainty plus randomness) is usually evaluated by comparing response spectra computed from recordings to predicted spectra and is a direct assessment of model accuracy. The modeling variability is defined as the standard error of the residuals of the log of the average horizontal component (or vertical component) response spectra. The residual is defined as the difference of the logarithms of the observed average 5% damped acceleration response spectra and the predicted response spectra. At each period, the residuals

are squared, and summed over the total number of sites for one or all earthquakes modeled. Dividing the resultant sum by the number of sites results in an estimate of the model variance. Any model bias (average offset) that exists may be estimated in the process (Abrahamson et al., 1990; EPRI, 1993) and used to correct (lower) the variance (and to adjust the median as well). In this approach, the modeling variability can be separated into randomness and uncertainty where the bias corrected variability represents randomness and the total variability represents randomness plus uncertainty. The uncertainty is captured in the model bias as this may be reduced in the future by refining the model. The remaining variability (randomness) remains irreducible for this model. In computing the variance and bias estimates only the frequency range between processing filters at each site (minimum of the 2 components) should be used.

Assessment of Parametric Variability

Parametric variability, or the variation in ground motion predictions due to uncertainty and randomness in model parameters is difficult to assess. Formally, it is straight-forward in that a Monte Carlo approach may be used with each parameter randomly sampled about its mean (median) value either individually for sensitivity analyses (Silva, 1992; Roblee et al., 1996) or in combination to estimate the total parametric variability (Silva, 1992; EPRI, 1993). In reality, however, there are two complicating factors.

The first factor involves the specific parameters kept fixed with all earthquakes, paths, and sites when computing the modeling variability. These parameters are then implicitly included in modeling variability provided the data sample a sufficiently wide range in source, path, and site conditions. The parameters which are varied during the assessment of modeling variation should have a degree of uncertainty and randomness associated with them for the next earthquake. Any ground motion prediction should then have a variation reflecting this lack of knowledge and randomness in the free parameters.

An important adjunct to fixed and free parameters is the issue of parameters which may vary but by fixed rules. For example, source rise time (Equation A-8) is magnitude dependent and in the stochastic finite-source model is specified by an empirical relation. In evaluating the modeling variability with different magnitude earthquakes, rise time is varied, but because it follows a strict rule, any variability associated with rise time variation is counted in modeling variability. This is strictly true only if the sample of earthquakes has adequately spanned the space of magnitude, source mechanism, and other factors which may affect rise time. Also, the earthquake to be modeled must be within that validation space. As a result, the validation or assessment of model variation should be done on as large a number of earthquakes of varying sizes and mechanisms as possible.

The second, more obvious factor in assessing parametric variability is a knowledge of the appropriate distributions for the parameters (assuming correct values for median or mean estimates are known). In general, for the stochastic models, median parameter values and uncertainties are based, to the extent possible, on evaluating the parameters derived from previous earthquakes (Silva, 1992; EPRI, 1993).

The parametric variability is site, path, and source dependent and must be evaluated for

each modeling application (Roblee et al., 1996). For example, at large source-to-site distances, crustal path damping may control short-period motions. At close distances to a large fault, both the site and finite-source (asperity location and nucleation point) may dominate, and, depending upon site characteristics, the source or site may control different frequency ranges (Silva, 1992; Roblee et al., 1996). Additionally, level of control motion may affect the relative importance of G/G_{max} and hysteretic damping curves.

In combining modeling and parametric variations, independence is assumed (covariance is zero) and the variances are simply added to give the total variability.

$$_{ln}\sigma^2_T = {}_{ln}\sigma^2_M + {}_{ln}\sigma^2_P{}^2 \qquad \text{(A-11)},$$

where

$_{ln}\sigma^2_M$ = modeling variation,

$_{ln}\sigma^2_P$ = parametric variation.

Validation Of The Point- and Finite-Source Models

In a recent Department of Energy sponsored project (Silva et al., 1997), both the point- and finite-source stochastic models were validated in a systematic and comprehensive manner. In this project, 16 well recorded earthquakes were modeled at about 500 sites. Magnitudes ranged from M 5.3 to M 7.4 with fault distances from about 1 km out to 218 km for WUS earthquakes and 460 km for CEUS earthquakes. This range in magnitude and distance as well as number of earthquakes and sites results in the most comprehensively validated model currently available to simulate strong ground motions.

A unique aspect of this validation is that rock and soil sites were modeled using generic rock and soil profiles and equivalent-linear site response. Validations done with other simulation procedures typically neglect site conditions as well as nonlinearity resulting in ambiguity in interpretation of the simulated motions.

Point-Source Model

Final model bias and variability estimates for the point-source model are shown in Figure A1. Over all the sites (Figure A1) the bias is slightly positive for frequencies greater than about 10 Hz and is near zero from about 10 Hz to 1 Hz. Below 1 Hz, a stable point-source

---

[2]Strong ground motions are generally considered to be log normally distributed.

overprediction is reflected in the negative bias. The analyses are considered reliable down to about 0.3 Hz (3.3 sec) where the point-source shows about a 40% overprediction.

The model variability is low, about 0.5 above about 3 to 4 Hz and increases with decreasing frequency to near 1 at 0.3 Hz. Above 1 Hz, there is little difference between the total variability (uncertainty plus randomness) and randomness (bias corrected variability) reflecting the near zero bias estimates. Below 1 Hz there is considerable uncertainty contributing to the total variability suggesting that the model can be measurably improved as its predictions tend to be consistently high at very low frequencies ($\leq$ 1 Hz). This stable misfit may be interpreted as the presence of a second corner frequency for WNA sources (Atkinson and Silva, 1997).

Finite-Source Model

For the finite-fault, Figure A2 shows the corresponding bias and variability estimates. For all the sites, the finite-source model provides slightly smaller bias estimates and, surprisingly, slightly higher variability for frequencies exceeding about 5 Hz. The low frequency ($\leq$ 1 Hz) point-source overprediction is not present in the finite-source results, indicating that it is giving more accurate predictions than the point-source model over a broad frequency range, from about 0.3 Hz (the lowest frequency of reliable analyses) to the highest frequency of the analyses.

In general, for frequencies of about 1 Hz and above the point-source and finite-source give comparable results: the bias estimates are small (near zero) and the variabilities range from about 0.5 to 0.6. These estimates are low considering the analyses are based on a data set comprised of earthquakes with M less than M 6.5 (288 of 513 sites) and high frequency ground motion variance decreases with increasing magnitude, particularly above M 6.5 (Youngs et al., 1995) Additionally, for the vast majority of sites, generic site conditions were used (inversion kappa values were used for only the Saguenay and Nahanni earthquake analyses, 25 rock sites). As a result, the model variability (mean = 0) contains the total uncertainty and randomness contribution for the site. The parametric variability due to uncertainty and randomness in site parameters: shear-wave velocity, profile depth, G/G_{max} and hysteretic damping curves need not be added to the model variability estimates. It is useful to perform parametric variations to assess site parameter sensitivities on the ground motions, but only source and path damping Q(f) parametric variabilities require assessment on a site specific basis and added to the model variability. The source uncertainty and randomness components include point-source stress drop and finite-source slip model and nucleation point variations (Silva, 1992).

Empirical Attenuation Model

As an additional assessment of the stochastic models, bias and variability estimates were made over the same earthquakes (except Saguenay since it was not used in the regressions) and sites using a recently develop empirical attenuation relation (Abrahamson and Silva, 1997). For all the sites, the estimates are shown in Figure A3. Interestingly, the point-source overprediction below about 1 Hz is present in the empirical relation perhaps suggesting that this suite of earthquakes possess lower than expected motions in this frequency range as the empirical model

REFERENCES

Abrahamson, N.A. and W.J. Silva (1997). "Empirical response spectral attenuation relations for shallow crustal earthquakes." *Seismological Research Let.*, 68(1), 94-127.

Abrahamson, N.A., P.G. Somerville, and C.A. Cornell (1990). "Uncertainty in numerical strong motion predictions" *Proc. Fourth U.S. Nat. Conf. Earth. Engin.*, Palm Springs, CA., 1, 407-416.

Aki, K. and P.G. Richards. (1980). *"Quantitative siesmology."* W. H. Freeman and Co., San Francisco, California.

Atkinson, G.M and W.J. Silva (1997). "An empirical study of earthquake source spectra for California earthquakes." *Bull. Seism. Soc. Am.* 87(1), 97-113.

Anderson, J.G. and S.E. Hough (1984). "A Model for the Shape of the Fourier Amplitude Spectrum of Acceleration at High Frequencies." *Bulletin of the Seismological Society of America,* 74(5), 1969-1993.

Atkinson, G.M. (1984). "Attenuation of strong ground motion in Canada from a random vibrations approach." *Bull. Seism. Soc. Am.*, 74(5), 2629-2653.

Boore, D.M., W.B. Joyner, and T.E. Fumal (1997). "Equations for estimating horizontal response spectra and peak acceleration from Western North American earthquakes: A summary of recent work." *Seism. Res. Lett.* 68(1), 128-153.

Boore, D.M., W.B. Joyner, and T.E. Fumal (1994). "Estimation of response spectra and peak accelerations from western North American earthquakes: and interim report. Part 2. *U.S. Geological Survey Open-File Rept.* 94-127.

Boore, D.M., and G.M. Atkinson (1987). "Stochastic prediction of ground motion and spectral response parameters at hard-rock sites in eastern North America." *Bull. Seism. Soc. Am.*, 77(2), 440-467.

Boore, D.M. (1986). "Short-period P- and S-wave radiation from large earthquakes: implications for spectral scaling relations." *Bull. Seism. Soc. Am.*, 76(1) 43-64.

Boore, D.M. and W.B. Joyner (1984). "A note on the use of random vibration theory to predict peak amplitudes of transient signals." *Bull. Seism. Soc. Am.*, 74, 2035-2039.

Boore, D.M. (1983). "Stochastic simulation of high-frequency ground motions based on seismological models of the radiated spectra." *Bull. Seism. Soc. Am.*, 73(6), 1865-1894.

Brune, J.N. (1971). "Correction." *J. Geophys. Res.* 76, 5002.

Brune, J.N. (1970). "Tectonic stress and the spectra of seismic shear waves from earthquakes." *J. Geophys. Res.* 75, 4997-5009.

Campbell, K.W. (1993) "Empirical prediction of near-source ground motion from large earthquakes." in V.K. Gaur, ed., *Proceedings, Intern'l Workshop on Earthquake Hazard and Large Dams in the Himalya.* INTACH, New Delhi, p. 93-103.

Cornell, C.A. (1968). "Engineering seismic risk analysis." *Bull. Seism. Soc. Am.*, 58, 1583-1606.

Electric Power Research Institute (1993). "Guidelines for determining design basis ground motions." Palo Alto, Calif: Electric Power Research Institute, vol. 1-5, EPRI TR-102293.
vol. 1: Methodology and guidelines for estimating earthquake ground motion in eastern North America.
vol. 2: Appendices for ground motion estimation.
vol. 3: Appendices for field investigations.
vol. 4: Appendices for laboratory investigations.
vol. 5: Quantification of seismic source effects.

Hanks, T.C. (1982). "f_{max}." *Bull. Seism. Soc. Am.*, 72, 1867-1879.

Hanks, T.C. and R.K. McGuire (1981). "The character of high-frequency strong ground motion." *Bull. Seism. Soc. Am.*, 71(6), 2071-2095.

Hanks, T.C. and H. Kanamori (1979). "A moment magnitude scale." *J. Geophys. Res.*, 84, 2348-2350.

Hartzell, S., A. Leeds, A. Frankel, and J. Michael (1996). "Site response for urban Los Angeles using aftershocks of the Northridge earthquake." *Bull. Seism. Soc. Am.*, 86(1B), S168-S192.

Hartzell, S.H. (1978). "Earthquake aftershocks as Green's functions." *Geophys. Res. Letters*, 5, 1-4.

Hough, S.E., J.G. Anderson, J. Brune, F. Vernon III, J. Berger, J. Fletcher, L. Haar, T. Hanks, and L. Baker (1988). "Attenuation near Anza, California." *Bull. Seism. Soc. Am.*, 78(2), 672-691.

Hough, S.E. and J.G. Anderson (1988). "High-Frequency Spectra Observed at Anza, California: Implications for Q Structure." *Bull. Seism. Soc. Am.*, 78(2), 692-707.

Irikura, K. (1983). "Semi-empirical estimation of strong ground motions during large earthquakes." *Bull. Disaster Prevention Res. Inst.*, Kyoto Univ., 33, 63-104.

McGuire, R. K., A.M. Becker, and N.C. Donovan (1984). "Spectral Estimates of Seismic Shear Waves." *Bull. Seism. Soc. Am.*, 74(4), 1427-1440.

Ou, G.B. and R.B. Herrmann (1990). "Estimation theory for strong ground motion." *Seism. Res. Letters.* 61.

Papageorgiou, A.S. and K. Aki (1983). "A specific barrier model for the quantitative description of inhomogeneous faulting and the prediction of strong ground motion, part I, Description of the model." *Bull. Seism. Soc. Am.*, 73(4), 693-722.

Roblee, C.J., W.J. Silva, G.R. Toro and N. Abrahamson (1996). "Variability in site-specific seismic ground-motion design predictions." in press.

Rovelli, A., O. Bonamassa, M. Cocco, M. Di Bona, and S. Mazza (1988). "Scaling laws and spectral parameters of the ground motion in active extensional areas in Italy." *Bull. Seism. Soc. Am.*, 78(2), 530-560.

Schneider, J.F., W.J. Silva, and C.L. Stark (1993). "Ground motion model for the 1989 M 6.9 Loma Prieta earthquake including effects of source, path and site." *Earthquake Spectra*, 9(2), 251-287.

Silva, W.J., N. Abrahamson, G. Toro, and C. Costantino (1997). "Description and validation of the stochastic ground motion model." Submitted to Brookhaven National Laboratory, Associated Universities, Inc. Upton, New York.

Silva, W.J. and R. Darragh (1995). "Engineering characterization of earthquake strong ground motion recorded at rock sites." Palo Alto, Calif:Electric Power Research Institute, TR-102261.

Silva, W.J. and C.L. Stark (1993) "Source, path, and site ground motion model for the 1989 M 6.9 Loma Prieta earthquake." CDMG draft final report.

Silva, W.J. (1992). "Factors controlling strong ground motions and their associated uncertainties." *Dynamic Analysis and Design Considerations for High Level Nuclear Waste Repositories, ASCE* 132-161.

Silva, W.J. (1991). "Global characteristics and site geometry." Chapter 6 in *Proceedings: NSF/EPRI Workshop on Dynamic Soil Properties and Site Characterization.* Palo Alto, Calif.: Electric Power Research Institute, NP-7337.

Silva, W. J., R. Darragh, C. Stark, I. Wong, J. C. Stepp, J. Schneider, and S-J. Chiou (1990). "A Methodology to Estimate Design Response Spectra in the Near-Source Region of Large Earthquakes Using the Band-Limited-White-Noise Ground Motion Model". *Procee. of the Fourth U.S. Conf. on Earthquake Engineering,* Palm Springs, California. 1, 487-494.

Silva, W.J., R.B. Darragh, R.K. Green and F.T. Turcotte (1989). *Estimated Ground Motions for a new madrid Event.* U.S. Army Engineer Waterways Experiment Station, Wash., DC, Misc. Paper GL-89-17.

Silva, W. J. and R. K. Green (1988). "Magnitude and Distance Scaling of Response Spectral Shapes for Rock Sites with Applications to North American Environments." In *Proceedings: Workshop on Estimation of Ground Motion in the Eastern United States*, EPRI NP-5875, Electric Power Research Institute.

Silva, W. J., T. Turcotte, and Y. Moriwaki (1988). "Soil Response to Earthquake Ground Motion," Electric Power Research Institute, Walnut Creek, California, Report No. NP-5747.

Silva, W.J. and K. Lee (1987). "*WES RASCAL code for synthesizing earthquake ground motions.*" State-of-the-Art for Assessing Earthquake Hazards in the United States, Report 24, U.S. Army Engineers Waterways Experiment Station, Miscellaneous Paper S-73-1.

Somerville, P.G., R. Graves and C. Saikia (1995). "TECHNICAL REPORT: Characterization of ground motions during the Northridge earthquake of January 17, 1994." *Structural Engineers Association of California (SEAOC).* Report No. SAC-95-03.

Toro, G. R. and R. K. McGuire (1987). "An Investigation into Earthquake Ground Motion Characteristics in Eastern North America." *Bull. Seism. Soc. Am.*, 77(2), 468-489.

Toro, G. R. (1985). "Stochastic Model Estimates of Strong Ground Motion." In *Seismic Hazard Methodology for Nuclear Facilities in the Eastern United States*, Appendix B, R. K. McGuire, ed., Electric Power Research Institute, Project P101-29.

Wald, D.J. (1996). "Slip history of the 1995 Kobe, Japan, earthquake determined from strong motion, teleseismic, and geodetic data." *J. of Physics of the Earth,* in press.

Wald, D.J. and T.H. Heaton (1994). "Spatial and temporal distribution of slip for the 1992 Landers, California, earthquake." *Bull. Seism. Soc. Amer.*, 84(3), 668-691.

Wells, D.L. and K.J. Coppersmith (1994). "New empirical relationships among magnitude, rupture length, rupture width, rupture area, and surface displacement." *Bull. Seism. Soc. Am.* 84(4), 974-1002.

Youngs, R.R., N.A. Abrahamson, F. Makdisi, and K. Sadigh (1995). "Magnitude dependent dispersion in peak ground acceleration." *Bull. Seism. Soc. Amer.*, 85(1), 161-1, 176.

Table A.1

CONTRIBUTIONS TO TOTAL VARIABILITY
IN GROUND MOTION MODELS

	Modeling Variability	Parametric Variability
Uncertainty *(also Epistemic Uncertainty)*	Modeling Uncertainty: Variability in predicted motions resulting from particular model assumptions, simplifications and/or fixed parameter values. *Can be reduced by adjusting or "calibrating" model to better fit observed earthquake response.*	Parametric Uncertainty: Variability in predicted motions resulting from incomplete data needed to characterize parameters. *Can be reduced by collection of additional information which better constrains parameters*
Randomness *(also Aleatory Uncertainty)*	Modeling Randomness: Variability in predicted motions resulting from discrepancies between model and actual complex physical processes. *Cannot be reduced for a given model form.*	Parametric Randomness: Variability in predicted motions resulting from inherent randomness of parameter values. *Cannot be reduced a priori*** by collection of additional information.*

***Some parameters (e.g. source characteristics) may be well defined after an earthquakes.

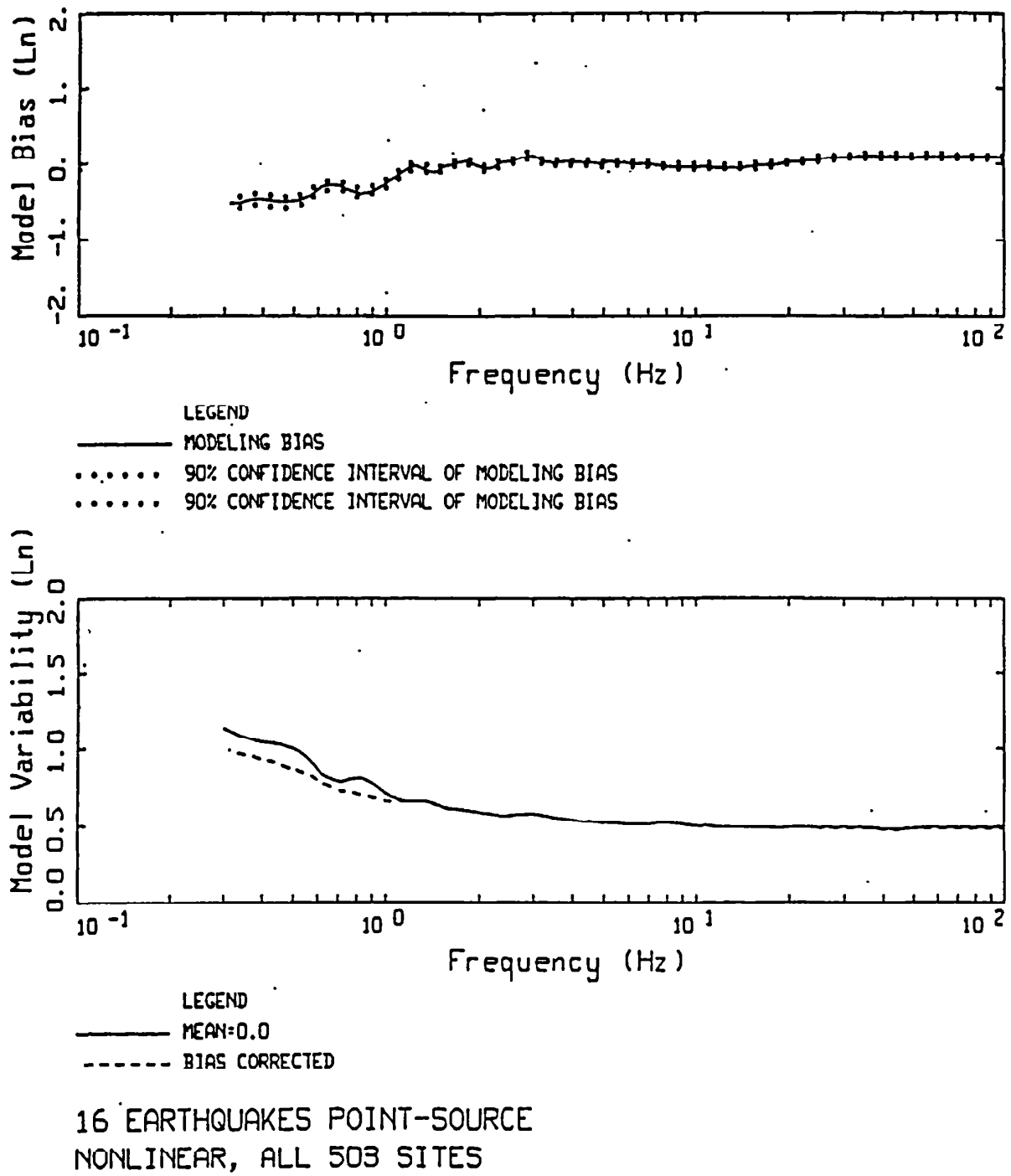

Figure A1. Model bias and variability estimates for all earthquakes computed over all 503 sites for the point-source model.

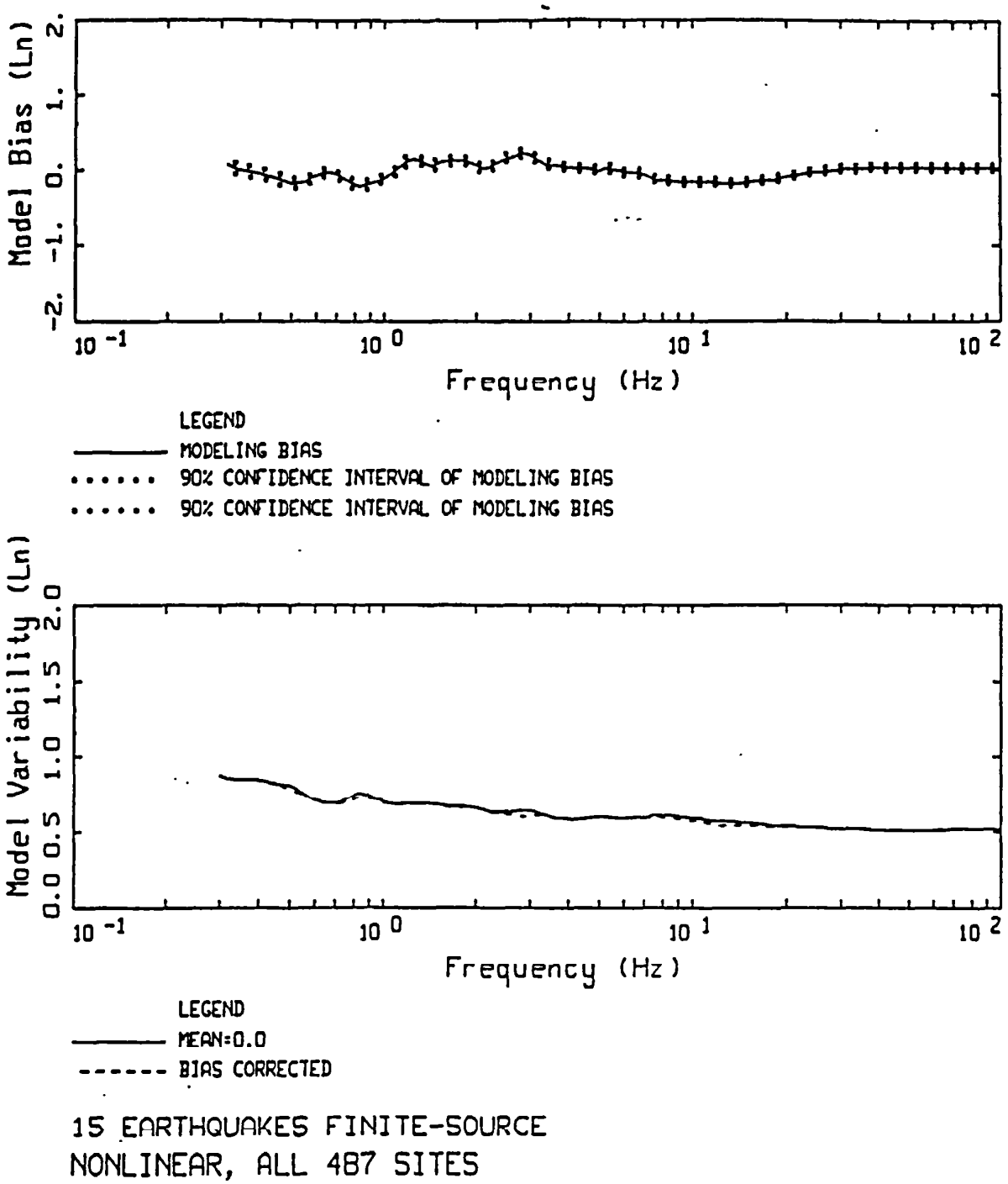

Figure A2. Model bias and variability estimates for all earthquakes computed over all 487 sites for the finite-source model.

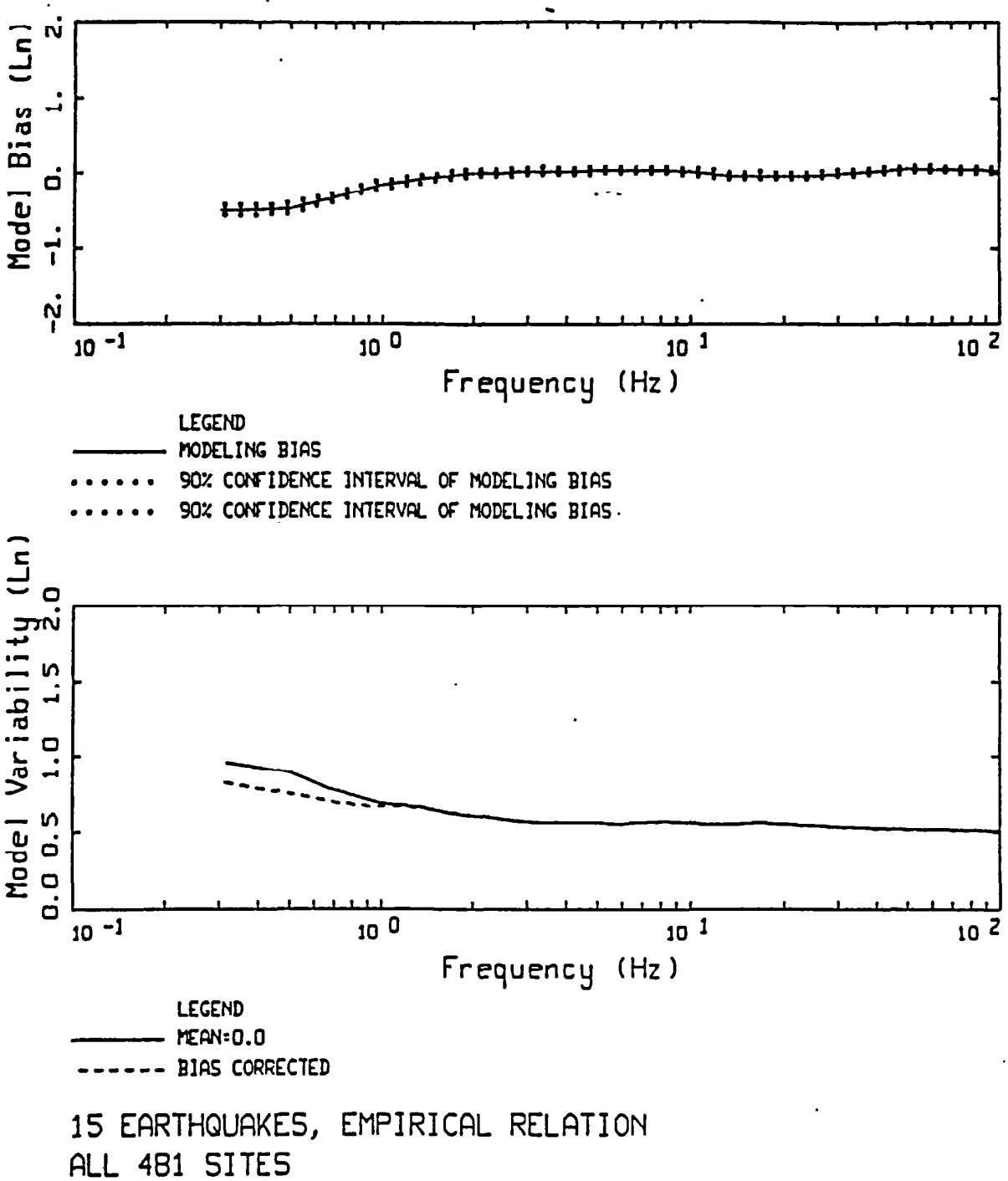

Figure A3. Model bias and variability estimates for all earthquakes computed over all 481 sites for the empirical model.

APPENDIX B

SITE RESPONSE ANALYSIS METHOD

Development of Site Specific Soil Motions

The conventional approach to estimating the effects of site specific site conditions on strong ground motions involves development of a set (1, 2, or 3 component) of time histories compatible with the specified outcrop response spectra to serve as control (or input) motions. The control motions are then used to drive a nonlinear computational formulation to transmit the motions through the profile. Simplified analyses generally assume vertically propagating shear-waves for horizontal components and vertically propagating compression-waves for vertical motions. These are termed one-dimensional site response analyses.

Equivalent-Linear Computational Scheme

The computational scheme which has been most widely employed to evaluate one-dimensional site response assumes vertically-propagating plane shear-waves. Departures of soil response from a linear constitutive relation are treated in an approximate manner through the use of the equivalent-linear approach.

The equivalent-linear approach, in its present form, was introduced by Seed and Idriss (1970). This scheme is a particular application of the general equivalent-linear theory developed by Iwan (1967). Basically, the approach is to approximate a second order nonlinear equation, over a limited range of its variables, by a linear equation. Formally this is done in such a way that the average of the difference between the two systems is minimized. This was done in an ad-hoc manner for ground response modeling by defining an effective strain which is assumed to exist for the duration of the excitation. This value is usually taken as 65% of the peak time-domain strain calculated at the midpoint of each layer, using a linear analysis. Modulus reduction and hysteretic damping curves are then used to define new parameters for each layer based on the effective strain computations. The linear response calculation is repeated, new effective strains evaluated, and iterations performed until the changes in parameters are below some tolerance level. Generally a few iterations are sufficient to achieve a strain-compatible linear solution.

This stepwise analysis procedure was formalized into a one-dimensional, vertically propagating shear-wave code called SHAKE (Schnabel et al., 1972). Subsequently, this code has easily become the most widely used analysis package for one-dimensional site response calculations.

The advantages of the equivalent-linear approach are that parameterization of complex nonlinear soil models is avoided and the mathematical simplicity of a linear analysis is preserved. A truly nonlinear approach requires the specification of the shapes of hysteresis curves and their cyclic dependencies through an increased number of material parameters. In

the equivalent-linear methodology the soil data are utilized directly and, because at each iteration the problem is linear and the material properties are frequency independent, the damping is rate independent and hysteresis loops close.

Careful validation exercises between equivalent-linear and fully nonlinear formulations using recorded motions from 0.05 to 0.50g showed little difference in results (EPRI, 1993). Both formulations compared very favorably to recorded motions suggesting both the adequacy of the vertically propagating shear-wave model and the approximate equivalent-linear formulation. While the assumptions of vertically propagating shear-waves and equivalent-linear soil response certainly represent approximations to actual conditions, their combination has achieved demonstrated success in modeling observations of site effects and represent a stable, mature, and reliable means of estimating the effects of site conditions on strong ground motions (Schnabel et al., 1972; Silva et al., 1988; Schneider et al., 1993; EPRI, 1993).

To accommodate both uncertainty and randomness in dynamic material properties, analyses are typically done for the best estimate shear-wave velocity profile as well as upper- and lower-range profiles. The upper- and lower-ranges are usually specified as twice and one-half the best estimate shear-wave moduli. Depending upon the nature of the structure, the final design spectrum is then based upon an envelope or average of the three spectra.

For vertical motions, the SHAKE code is also used with compression-wave velocities and damping substituted for the shear-wave values. To accommodate possible nonlinear response on the vertical component, since modulus reduction and hysteretic damping curves are not generally available for the constrained modulus, the low-strain Poisson's ratio is usually fixed and strain compatible compression-wave velocities calculated using the strain compatible shear moduli from the horizontal component analyses combined with the low-strain Poisson's ratios. In a similar manner, strain compatible compression-wave damping values are estimated by combining the strain compatible shear-wave damping values with the low-strain damping in bulk or pure volume change. This process assumes the loss in bulk (volume change) is constant or strain independent. Alternatively, zero loss in bulk is assumed and the equation relating shear- and compression-wave damping (η_S and η_P) and velocities (V_S and V_P)

$$\eta_P \approx \frac{4}{3} \frac{V_S}{V_P} \eta_S \,, \qquad \text{(B-1)}$$

is used.

RVT Based Computational Scheme

The computational scheme employed to compute the site response for this project uses an alternative approach employing random vibration theory (RVT). In this approach the control motion power spectrum is propagated through the one-dimensional soil profile using the plane-

wave propagators of Silva (1976). In this formulation only SH waves are considered. Arbitrary angles of incidence may be specified but normal incidence is used throughout the present analyses.

In order to treat possible material nonlinearities, an RVT based equivalent-linear formulation is employed. Random process theory is used to predict peak time domain values of shear-strain based upon the shear-strain power spectrum. In this sense the procedure is analogous to the program SHAKE except that peak shear-strains in SHAKE are measured in the time domain. The purely frequency domain approach obviates a time domain control motion and, perhaps just as significant, eliminates the need for a suite of analyses based on different input motions. This arises because each time domain analysis may be viewed as one realization of a random process. Different control motion time histories reflecting different time domain characteristics but with nearly identical response spectra can result in different nonlinear and equivalent-linear response.

In this case, several realizations of the random process must be sampled to have a statistically stable estimate of site response. The realizations are usually performed by employing different control motions with approximately the same level of peak accelerations and response spectra.

In the case of the frequency domain approach, the estimates of peak shear-strain as well as oscillator response are, as a result of the random process theory, fundamentally probabilistic in nature. For fixed material properties, stable estimates of site response can then be obtained with a single run.

In the context of the RVT equivalent-linear approach, a more robust method of incorporating uncertainty and randomness of dynamic material properties into the computed response has been developed. Because analyses with multiple time histories are not required, parametric variability can be accurately assessed through a Monte Carlo approach by randomly varying dynamic material properties. This results in median as well as other fractile levels (e.g. 16th, mean, 84th) of smooth response spectra at the surface of the site. The availability of fractile levels reflecting randomness and uncertainty in dynamic material properties then permits a more rational basis for selecting levels of risk.

In order to randomly vary the shear-wave velocity profile, a profile randomization scheme has been developed which varies both layer velocity and thickness. The randomization is based on a correlation model developed from an analysis of variance on about 500 measured shear-wave velocity profiles (EPRI, 1993; Silva et al., 1997). Profile depth (depth to competent material) is also varied on a site specific basis using a uniform distribution. The depth range is generally selected to reflect expected variability over the structural foundation as well as uncertainty in the estimation of depth to competent material.

To model parametric variability for compression-waves, the base-case Poisson's ratio is generally fixed. Suites of compatible random compression- and shear-wave velocities are then generated based on the random shear-wave velocities profiles.

To accommodate variability in modulus reduction and hysteretic damping curves on a generic basis, the curves are independently randomized about the base case values. A log normal distribution is assumed with a σ_{ln} of 0.35 at a cyclic shear strain of 3 x 10^{-2}%. These values are based on an analysis of variance on a suite of laboratory test results. An upper and lower bound truncation of 2σ is used to prevent modulus reduction or damping models that are not physically possible. The random curves are generated by sampling the transformed normal distribution with a σ_{ln} of 0.35, computing the change in normalized modulus reduction or percent damping at 3 x 10^{-2}% shear strain, and applying this factor at all strains. The random perturbation factor is reduced or tapered near the ends of the strain range to preserve the general shape of the median curves (Silva, 1992).

To model vertical motions, incident inclined compression- and shear (SV)-waves and assumed. Raytracing is done from the source location to the site to obtain appropriate angles of incidence. In the P-SV site response analyses, linear response is assumed in both compression and shear with the low-strain shear-wave damping used for the compression-wave damping (Johnson and Silva, 1981). The vertical and horizontal motions are treated independently in separate analyses. Validation exercises with a fully 3-D soil model using recorded motions up to 0.50%g showed these approximations to be validate (EPRI, 1993).

In addition, the site response model for the vertical motions has been validated at over 100 rock and soil sites for three large earthquakes: 1989 M 6.9 Loma Prieta, 1992 M 7.2 Landers, and the 1994 Northridge earthquakes. In general, the model performs well and captures the site and distance dependency of vertical motions over the frequency range of about 0.3 to 50.0 Hz and the fault distance range of about 1 to 100 km.

REFERENCES

Electric Power Research Institute (1993). "Guidelines for determining design basis ground motions." Palo Alto, Calif: Electric Power Research Institute, vol. 1-5, EPRI TR-102293.

vol. 1: Methodology and guidelines for estimating earthquake ground motion in eastern North America.
vol. 2: Appendices for ground motion estimation.
vol. 3: Appendices for field investigations.
vol. 4: Appendices for laboratory investigations.
vol. 5: Quantification of seismic source effects.

Iwan, W.D. (1967). "On a class of models for the yielding behavior of continuous and composite systems." *J. Appl. Mech.*, 34, 612-617.

Johnson, L.R. and W.J. Silva (1981). "The effects of unconsolidated sediments upon the ground motion during local earthquakes." *Bull. Seism. Soc. Am.*, 71, 127-142.

Schnabel, P.B., J. Lysmer, and H.B. Seed (1972). *SHAKE: a Computer Program for Earthquake Response Analysis of Horizontally Layered Sites.* Earthq. Engin. Res. Center, Univ. of Calif. at Berkeley, EERC 72-12.

Schneider, J.F., W.J. Silva, and C.L. Stark (1993). Ground motion model for the 1989 M 6.9 Loma Prieta earthquake including effects of source, path and site. *Earthquake Spectra,* 9(2), 251-287.

Seed, H.B. and I.M. Idriss (1970). "*Soil Moduli and Damping Factors for Dynamic Response Analyses,*" Earthq. Eng. Res. Center, Univ. of Calif. at Berkeley, Report No. UCB/EERC-70/10.

Silva, W.J., N. Abrahamson, G. Toro, and C. Costantino (1997). "Description and validation of the stochastic ground motion model." Submitted to Brookhaven National Laboratory, Associated Universities, Inc. Upton, New York.

Silva, W.J. (1992). "Factors controlling strong ground motions and their associated uncertainties." *Dynamic Analysis and Design Considerations for High Level Nuclear Waste Repositories, ASCE* 132-161.

Silva, W. J., T. Turcotte, and Y. Moriwaki, (1988). "Soil Response to Earthquake Ground Motion," Electric Power Research Institute, Walnut Creek, California, Report No. NP-5747.

Silva, W.J. (1976). "Body Waves in a Layered Anelastic soilid." *Bull. Seis. Soc. Am.*, vol. 66(5), 1539-1554.

September 27, 1999
FINAL REPORT

SURFACE GEOLOGY BASED STRONG MOTION AMPLIFICATION FACTORS FOR THE SAN FRANCISCO BAY AND LOS ANGELES AREAS

Prepared for

PG&E PEER - TASK 5.B

by

Walter Silva
Syliva Li
Bob Darragh
Nick Gregor

of

Pacific Engineering and Analysis
311 Pomona Avenue
El Cerrito, CA 94530

EXECUTIVE SUMMARY

SURFACE GEOLOGY BASED STRONG MOTION AMPLIFICATION FACTORS FOR THE SAN FRANCISCO BAY AND LOS ANGELES AREAS

Pacific Engineering and Analysis

For both the San Francisco Bay and Los Angeles areas, surface geology based amplification factors have been developed for 5% damped response spectra. The factors are computed relative to reference rock site geology, K_{jf} (Franciscan) for the San Francisco Bay area and M_{xb} (Granite) for the Los Angeles area. The factors are functions of profile depth (or depth range) as well as expected reference rock peak acceleration values ranging from 0.05g to 1.25g.

The amplification factors are computed using average measured shear-wave velocity profiles at sites located within the surficial geologic units with an RVT (Random Vibration Theory) based equivalent-linear site response approach. Separate G/Gmax and hysteretic damping curves are used for San Francisco (North Coast) and Los Angeles (Peninsular Range) cohesionless soils reflecting different degrees of nonlinear response in both regions. These curves, along with G/Gmax and hysteretic damping for rock site conditions which are the same for both regions, were validated by modeling recorded motions in both regions.

The analytical amplifications factors are compared to published empirical as well as current NEHRP factors for both regions. Comparisons with the empirical factors show good agreement for empirical factors computed for 5% damped response spectra and reasonable agreement for empirical factors for Fourier amplitude spectra. The analytical factors were generally below the empirical for Fourier amplitude spectra but agreed in shape and general trends: soft alluvium higher than stiff alluvium at low frequency but crossing over at high frequency. Comparisons with the NEHRP provisions showed reasonable agreement for the San Francisco Bay area, except for the Bay Muds (Q_m) being classified as NEHRP D (based on actual average shear-wave velocity over the top 100 ft). For the Los Angeles area, good

agreement was seen with the NEHRP amplification factors at low levels of loading (up to about 0.10g). At higher loading levels the low frequency NEHRP factors wee significantly exceeded while the high frequency NEHRP factors appear to reflect considerable conservatism at very high loading levels.

The amplification factors developed in this project extend to 1,000 ft for the San Francisco Bay area and 1,500 ft for the Los Angeles area. They may be used to approximately accommodate the effects of near surface geology for seismic hazard evaluations.

CONTENTS

Section		Page
1.0	Introduction	1
2.0	Geology Based Profiles	2
2.1	San Francisco Bay Area Profiles	3
2.2	Los Angeles Area Profiles	4
2.3	Comparison of San Francisco and Los Angeles Profiles	4
2.4	Development of Smooth Profiles For Site Response Analyses	5
3.0	Geology Based Amplification Factors	5
3.1	Methodology	6
3.1.1	Equivalent-Linear Computational Scheme	6
3.1.2	RVT Based Computational Scheme	7
3.2	G/Gmax and Hysteretic Damping Curves	7
3.3	Specification of Control Motions	8
3.4	Development of Site Amplification Factors	10
3.4.1	Amplification Factors for the San Francisco Bay Area	11
3.4.2	Amplification Factors For The Los Angeles Area	13
3.5	Adjustment Factors For Soft Rock Conditions	16
4.0	Summary	16
	References	18
Appendix A:		A-1
Appendix B:		B-1

LIST OF TABLES

Table Number		Page
1	Surface Geology Based Profiles, Site Classes, and Dynamic Material Properties	22
2	Site Classifications	23
3	Loma Prieta Crustal Model (from Wald et Al., 1991)	24
4	Franciscan Reference Site Ground Motion Parameters San Francisco Bay Area	25
5	Depth Categories and Depth Ranges	26

LIST OF FIGURES

Figure Number		Page
1	Effects of near surface soil conditions on 5% damped response spectral shapes (source: Seed, Ugas, and Lysmor, 1976)	27
2	Effects of hard and soft rock site conditions and magnitude	28
3	Mapped surface geology for the San Francisco Bay Area	29
4	Surface geology based shear-wave velocity profiles for the San Francisco Bay area	30
5	Surface geology based shear-wave velocity profiles for the Los Angeles area	31
6	Comparison of median baserock shear-wave velocity profiles for San Francisco and Los Angeles areas	32
7	Comparison of median Tertiary shear-wave velocity profiles for San Francisco and Los Angeles areas	33
8	Comparison of median Alluvium shear-wave velocity profiles for San Francisco and Los Angeles areas	34
9	Median and $\pm$ 1 σ shear-wave velocity profiles for the San Francisco Bay area surface geologic unit K_{jf}, Franciscan	3[illegible]
10	Median and $\pm$ 1 σ shear-wave velocity profiles for the San Francisco Bay area surface geologic unit TM_{zs}, Tertiary Bedrock	25
11	Median and $\pm$ 1 σ shear-wave velocity profiles for the San Francisco Bay area surface geologic unit QT_s, Quaternary/Tertiary	
12	Median and $\pm$ 1 σ shear-wave velocity profiles for the San Francis Bay area surface geologic unit Q_{oa}, Older Alluvium	26
13	Median and $\pm$ 1 σ shear-wave velocity profiles for the San Fran Bay area surface geologic unit Q_{al}, Quaternary Alluvium	
14	Median and $\pm$ 1 σ shear-wave velocity profiles for the San Francisco Bay area surface geologic unit Q_m, Bay Mud	

LIST OF FIGURES

Figure Number		Page
15	Median and $\pm$ 1 σ shear-wave velocity profiles for the Los Angeles area surface geologic unit M_{xb}, Granite	41
16	Median and $\pm$ 1 σ shear-wave velocity profiles for the Los Angeles area surface geologic unit T_s, Tertiary	42
17	Median and $\pm$ 1 σ shear-wave velocity profiles for the San Francisco Bay area surface geologic unit T_s, Saugus	43
18	Median and $\pm$ 1 σ shear-wave velocity profiles for the Los Angeles area surface geologic unit Q_{oa}, Older Alluvium	44
19	Median and $\pm$ 1 σ shear-wave velocity profiles for the Los Angeles area surface geologic unit Q_y, Younger Alluvium	45
20	Generic G/Gmax and hysteretic damping curves for rock site conditions	46
21	Generic G/Gmax and hysteretic damping curves for North Coast cohesionless soil site conditions (EPRI, 1993).	47
22	Generic G/Gmax and hysteretic damping curves for cohesive soil site conditions (Vucetic and Dobry, 1991)	48
23	Generic G/Gmax and hysteretic damping curves for Peninsular Range cohesionless soil site conditions (Silva et al., 1997).	49
24	Median and $\pm$ 1 σ 5% damped baserock (Franciscan) motions for 5%g (Table 4): M = 6.5, stress drop = 60 bars. Parametric variation includes top 250 ft of the profile (Figure 15) and nonlinear properties	50
25	Comparison of median 5% damped response spectra computed for San Francisco (solid) and Los Angeles (dashed) area baserock site conditions for suite of outcrop peak acceleration values (Table 4): M = 6.5, stress drop: 60 bars	51
26	Comparison of median and $\pm$ 1 σ amplification factors (5% damped response spectra) for San Francisco area Quaternary Alluvium (Q_{al}) depth category 4 (30 to 1,000 ft) for reference Franciscan rock outcrop median peak acceleration values of 0.05g and 0.40g	52

LIST OF FIGURES

Figure Number		Page
27	Comparison of median amplification factors (5% damped response spectra) computed for reference Franciscan outcrop peak acceleration of 0.05g with empirical factors (smoothed Fourier amplitude spectra; Borcherdt and Glassmoyer, 1992). Empirical factors were computed using low levels of loading (generally $\leq$ 0.10g)	53
28	Comparison of median amplification factors (5% damped response spectra) computed for reference Franciscan outcrop peak acceleration of 0.40g with empirical factors (smoothed Fourier amplitude spectra; Borcherdt and Glassmoyer, 1992). Empirical factors were computed using low levels of loading (generally $\leq$ 0.10g)	54
29	Median amplification factors computed for QT_s, Q_{al}, Q_m, for different depth categories: 30 to 150 ft, dash dots; 150 to 350, solid; 350 to 650, dashes	55
30	Comparison of median amplification factors with NEHRP provisions	56
31	Median and $\pm$ 1 σ amplification factors computed for San Francisco area surficial geologic unit TM_{zs}	57
32	Median and $\pm$ 1 σ amplification factors computed for San Francisco area surficial geologic unit QT_s	58
33	Median and $\pm$ 1 σ amplification factors computed for San Francisco area surficial geologic unit Q_{ca}	59
34	Median and $\pm$ 1 σ amplification factors computed for San Francisco area surficial geologic unit Q_{al}	60
35	Median and $\pm$ 1 σ amplification factors computed for San Francisco area surficial geologic unit Q_m	61
36	Comparison of median amplification factors computed for units Q_y, Q_o, Saugus (T_s), T_s, and Q_o + T_s (Table 1) for the depth categories with the widest depth ranges	62

LIST OF FIGURES

Figure Number		Page
37	Comparison of median amplification factors (5% damped response spectra) computed for reference Granite outcrop peak acceleration of 0.05g with empirical factors (smoothed Fourier amplitude spectra; Bonilla et al., 1997). Empirical factors are based on small earthquakes	63
38	Deep firm to stiff soil (Geomatrix C + D, Table 2) amplification of 5% damped response spectra relative to soft rock (Geomatrix A + B) from an empirical attenuation relation (Abrahamson and Silva, 1997)	64
39	Comparison of median amplification factors (5% damped response spectra) computed for reference Granite outcrop peak acceleration of 0.10g with empirical factors (5% damped response spectra; Borcherdt, 1996) Empirical factors are based on recordings of the 1994 M 6.7 Northridge	65
40	Comparison of median amplification factors (5% damped response spectra) computed for reference Granite outcrop peak acceleration of 0.10g with empirical factors (smoothed Fourier amplitude spectra; Harmsen, 1997). Empirical factors are based on the 1971 San Fernando, 1987 Whittier Narrows, 1991 Sierra Madre, and 1994 Northridge earthquakes	66
41	Comparison of median amplification factors with NEHRP provisions	67
42	Amplification factors computed for Geomatrix site categories A and B (Figure 6, Table 2) relative to San Francisco area reference rock outcrop Franciscan	68
43	Amplification factors computed for Geomatrix site categories A and B (Figure 6, Table 2) relative to Los Angeles area reference rock outcrop Granite	69

SURFACE GEOLOGY BASED STRONG MOTION AMPLIFICATION FACTORS FOR THE SAN FRANCISCO BAY AND LOS ANGELES AREAS

1.0 INTRODUCTION

Observations of the effects of the ground on shaking during earthquakes have a long history. Del Barrio, in the 1855 Proceedings of the University of Chile states*"...a movement.... must be modified while passing through media of different constitutions. Therefore, the earthquake effects will arrive to the surface with higher or lesser violence according to the state of aggregation of the terrain which conducted the movement. This seems to be, in fact, what we have observed in the Colchagua Province (of Chile) as well as in many other cases" (Del Barrio, 1855). In 1862, Mallet (1862) noted the effect of geology upon earthquake damage. Milne (1908) observed that in soft "damp" ground it was easy to produce vibrations of large amplitudes and long duration, while in rock it was difficult to produce vibrations of sufficient amplitude to be recorded.

Wood (1908) and Reid (1910), using apparent intensity of shaking and distribution of damage in the San Francisco Bay area during the 1906 earthquake, gave evidence that the severity of shaking can be substantially affected by the local geology and soil conditions. Gutenberg (1927, 1957) developed amplification factors representing different site geology by examining recordings of microseisms and earthquakes from instruments located on various types of ground. Figure 1 shows average spectral shapes (response spectral acceleration divided by peak acceleration) computed from recordings made on rock and soil sites at close distances to earthquakes in the magnitude range of about M 6 to 7. The differences in spectral shapes are significant and depend strongly upon the general site classifications. These variations in spectral content represent average site dependent ground motion characteristics and result from vertical variations in soil material properties (Hayashi et al., 1971; Mohraz, 1976; Seed et al., 1976). Due primarily to the limited number of records from earthquakes of different magnitudes, spectral content in terms of response spectral shapes was for some time interpreted not to depend upon magnitude nor distance, but primarily on the stiffness and depth of the local soil profile. However, with an increase in the strong motion database, it has become apparent that spectral shapes depend strongly upon magnitude as well as site conditions (Joyner and Boore, 1982, Idriss, 1985; Silva and Green, 1989), and distance (Silva and Green, 1989), and that site effects extend to rock sites as well (Boatwright and Astrue, 1983; Campbell 1981, 1985, 1988; Cranswick et al., 1985; Silva and Darragh, 1995).

Examples of differences in spectral content largely attributable to one-dimensional site effects at rock sites can be seen in comparisons of response spectral shapes computed from motions recorded in both active and stable tectonic regions (Silva and Darragh, 1995). Figure 2 shows average spectral shapes (Sa/amax) computed from recordings made on rock at close

---

*Translated from the old Spanish by Professor Ricardo Dobry.

distances to large and small earthquakes. For both magnitudes (moment magnitude M 6.4 and 4.0), the motions recorded in Eastern North America (ENA), a stable tectonic region, show a dramatic shift in the maximum spectral amplification toward higher frequencies compared to the Western North American (WNA) motions. These differences in spectral content are significant and are interpreted as primarily resulting from differences in the shear-wave velocity and damping in the rocks directly beneath the site (Boore and Atkinson, 1987; Toro and McGuire, 1987; Silva and Green, 1989; Silva and Darragh, 1995). Also evident in Figure 2 is the strong magnitude dependency of the response spectral shapes. The smaller earthquakes show a much narrower bandwidth. This is a consequence of higher corner frequencies for smaller magnitude earthquakes (Boore, 1983; Silva and Green, 1989; Silva and Darragh, 1995).

The difference in spectral content due to soil site effects, as shown in Figure 1, and due to rock site effects, as shown in Figure 2, are dramatic and illustrate the degree to which one-dimensional site conditions (vertical variations in dynamic material properties) control strong ground motions.

In order to capture these geologically controlled differences in ground motions, site amplification factors are developed in a manner that is appropriate for San Francisco Bay area and Los Angeles area soil and rock-sites. For wide applicability, both the rock and soil conditions are based upon mapped surface geology with appropriate shear-wave velocity profiles developed for each geology type. The amplification factors are developed for 5% damped response spectra (values at 100 Hz apply to peak acceleration) and are relative to a generic Franciscan rock site for the San Francisco Bay area and a generic granitic rock site for the Los Angeles region. The factors accommodate nonlinear soil/rock response and are produced as a function of expected Franciscan or granitic rock peak acceleration values. Because of this, they may be applied to any size earthquake at any distance with knowledge only of the expected rock peak acceleration. The factors are considered appropriate for rock outcrop peak accelerations up to 1.25g and over the frequency range of 0.1 to 100.0 Hz. At long periods, due to possible basin effects, care should be exercised in applying the factors to deep soil sites at frequencies less than about 0.5 Hz for distant (> 50 km) earthquakes.

2.0 GEOLOGY BASED PROFILES

The development of shear-wave velocity profiles appropriate for the mapped surface geology of the San Francisco Bay and Los Angeles areas was a cooperative effort between Pacific Engineering and Analysis (PE&A) and Chris Wills of the California Division of Mines and Geology (CDMG). As part of the CDMG effort in developing state-wide probabalistic seismic shaking maps, Mr. Wills was tasked with associating site categories based on average velocity over the top 30m with surface geology. To accomplish this task, he was planning on developing a shear-wave velocity profile database to correlate the profile averages with the mapped geology at the profile locations. Since PE&A already possessed a large proprietary database, an agreement was reached such that the CDMG could use the database provided any augmentation was shared with PE&A. As a result, Mr. Wills added many profiles along with missing profile coordinates, merged the database with a GIS system, and plotted the profiles on a basemap map of surface geology (Figure 3). The result is a tabulation of profiles for each

geology type. Rock units consist of Franciscan, Quaternary-Tertiary, and Tertiary for the San Francisco area and Granite, Tertiary, and Saugus (Tertiary) for the Los Angeles area. Soil units consist of Quaternary and Older Alluvium, and Bay Mud for the San Francisco Bay area and Quaternary and Older Alluvium for the Los Angeles area. Table 1 lists the geology types, average shear-wave velocity to 30m, the corresponding USGS and NEHRP site categories (Table 2), and number of shear-wave velocity profiles currently in each category.

To develop profiles appropriate for the different geology types, median and $\pm 1\sigma$ (lognormal) profiles were computed for the profiles in each geology group. Figures 4 and 5 show median profiles for the San Francisco and Los Angeles areas respectively. For the San Francisco area, the geologic units generally show distinct median profiles with the exception of Quaternary Alluvium (Q_{al}) and Older Alluvium (Q_{oa}). Distinct NEHRP categories include Franciscan (K_{jf}, NEHRP B), Tertiary Bedrock (TM_{ZS}, C) and Quaternary/Tertiary Rock (QT_S, C) and the stiff to firm soils (all NEHRP category D). Unfortunately, the median Bay Mud profile (Q_m), with its 30m average shear-wave velocity of about 188m/sec, is placed in NEHRP Category C, with the firm to stiff soils (Table 2).

2.1 San Francisco Bay Area Profiles

The profile figures show several features of interest. For the rock classes, Franciscan and Tertiary, a significant difference exists with the Tertiary profile being much softer (NEHRP site class C) than the Franciscan and resembling a stiff soil (Older Alluvium) at shallow depths. The Franciscan is considered soft rock but is stiff enough (NEHRP site class B) to form the basis for the San Francisco area amplification factors. That is, the site amplification factors will be computed relative to Franciscan rock outcropping as defined by the Franciscan profile in Figure 4.

For the alluvium, little difference in stiffness is seen between the Older and Quaternary Alluvium profiles. This suggests that, in view of uncertainty in the median profiles, there may be no statistically significant differences in the amplification factors. This is examined in Section 3 resulting in the combining of the two sets of amplification factors into one set, reflecting the broader class of alluvium.

The Bay Mud profile shows a shallow low velocity zone with higher shear-wave velocities at the surface than at a depth of about 20 ft. This velocity reversal is likely due to the presence of fill material which is a common occurrence in the built environment near San Francisco Bay. This profile is not unexpected since velocity measurements (boreholes) are generally associated with structures of some kind. Because such features can have a strong effect on ground motions at high levels of loading, they are most appropriately addressed on a site-specific basis. The base case profile was smoothed through this feature. The amplification factors for Bay Mud surface geology should then be considered to have higher uncertainty at higher loading levels (expected Franciscan PGA $\geq$ 40%g) and at short periods ($\leq$ 0.2 sec).

2.2 Los Angeles Area Profiles

For the Los Angeles area, Figure 5 compares the median surface geology based profiles and shows several features of interest as well. For the alluvium, the Older Alluvium (Q_o) profile is significantly stiffer than the Quaternary Alluvium (Q_y) profile, unlike the corresponding profiles for the San Francisco Bay area (Figure 4).

The three rock classes (Table 1): Granite, Tertiary, and Saugus show significant differences in shear-wave velocities since both the Tertiary and Saugus (NEHRP site class C) are much softer than the Granite (NEHRP site class B). The shallow portion of the Tertiary resembles a firm soil (Older Alluvium). Interestingly, in the top 50 to 100 feet, the Saugus profile is stiffer than either Tertiary or Older Alluvium. This suggests that, in view of the uncertainty and variability in the shear-wave velocity profiles, there may be no statistically significant differences in the amplification factors. This is examined in Section 3 resulting in a combining of the three sets of amplification factors into one, reflecting a broader classification.

2.3 Comparison of San Francisco and Los Angeles Profiles

To compare median profiles for the two regions, Figures 6 to 8 show profiles for the corresponding surface geology. Figure 6 compares the two hard (California) rock profiles, Franciscan and Granite. For the depth range of overlap, the two profiles are similar suggesting similar strong ground motion response, all else being comparable. Unfortunately, only 8 Granite profiles are available (Table 1) compared to 30 for the Franciscan surficial geology, as a result a bias may exist for the Los Angeles area Granite profile. For the available data, these profiles may suggest very similar dynamic material properties for the Franciscan and Granite site geologies for the two regions. Since these profiles represent the stiffest materials, they are taken as the reference rock site conditions, consistent with regional empirical site response studies (Borcherdt and Glassmoyer, 1992; Harmsen, 1997; Bonilla et al., 1997).

It is important to point out that this rock category (Franciscan and Granite) is likely significantly stiffer than "rock" site conditions which characterize most empirical attenuation relation for tectonically active regions (Abrahamson and Shellock, 1997). As a result, the "soil" amplification factors may not be strictly appropriate for application to rock motions estimated using generic rock attenuation relations.

To illustrate the differences in shallow shear-wave velocities between the Franciscan and Granite baserock geologies and those implied in WNA rock empirical attenuation relations, the median profile for Geomatrix site category A and B was added to Figure 6. The Geomatrix A and B profile reflects rock and very shallow soil (< 10m) which are traditionally interpreted as "rock" site conditions in the development of empirical attenuation relations. In general, both the Franciscan and Granite baserock profiles are stiffer than the Geomatrix A and B category suggesting a possible difference in site response. As a result, amplification factors are developed for a Geomatrix A and B site category (Section 3.5) to provide an assessment of potential differences in response. The amplification factors may be used to "adjust" the soil factors as well.

Figure 7 shows corresponding median Tertiary profiles for the two regions. Apart from the Saugus profile, the T_s profile for the Los Angeles Area is intermediate between the San Francisco TM_{Zs}, and QT_s profiles. Although the three profiles are similar for depths less than about 100 ft, the differences shown by the velocity trends at greater depths result in significant differences in mean response (amplification).

Figure 8 shows median alluvial profiles for both regions. The Q_y, Q_{al}, and Q_{oa} (below about 100 ft) are very similar with Q_o (Older Alluvium for Los Angeles) showing significantly higher velocities. Conversely, the Bay Muds (Q_m) show very low velocities throughout the entire depth range. While profiles of similar very soft soils for the Los Angeles Area (e.g. Los Angeles Harbor area) were not available, amplification factors computed for Bay Mud would be more appropriate than those computed for either Q_y or Q_o for these very soft soils in the Los Angeles Area.

2.4 Development of Smooth Profiles For Site Response Analyses

Smooth profiles were drawn through the median values and, where necessary, extrapolated to deeper depths to develop profiles for computing strong ground motions (PGA, PGV, PGD, and 5% damped response spectra). Both median and $\pm$ 1 σ surface geology based profiles as well as smooth and extrapolated versions for site response calculations are shown in Figures 9 to 14 for the San Francisco Bay region and Figures 15 to 19 for the Los Angeles area. For source-to-site modeling in the San Francisco area, the shallow profiles are merged with the Wald et al. (1991) Loma Prieta crustal model (Table 3). For the Franciscan unit, the profile is merged with the second layer of the Wald et al. (1991) crust (Figure 9). The remaining geologic unit profiles are simply placed on top of the Wald crust which has a shear-wave velocity of 3,281 ft/sec in the top layer (Table 3).

For the Los Angeles area, the Granitic unit profile is considered the same as the Franciscan (Figure 6), replacing the properties of the top layer of the Wald et al. (1996) crust (Table 3, Figure 15). As with the San Francisco area profile, the remaining geologic unit profiles are simply placed on top of the Wald et al. (1996) crust that again has a shear-wave velocity of 3,281 ft/sec (1.0 km/sec) in the top layer (Table 3).

3.0 GEOLOGY BASED AMPLIFICATION FACTORS

Certainly the most satisfying approach to account for the effects of surficial materials on strong ground motion is empirical. Ideally, amplification factors could be developed based entirely upon observation of strong ground motion. Studies using data recorded on rock and on different classes of soil profiles, such as stiff soils and deep cohesionless soils, have demonstrated large differences in spectral amplification (Sa/amax) and in spectral velocity due to the presence of the soils (Seed et al., 1976; Mohraz, 1976; Joyner and Fumal, 1984; Abrahamson and Silva, 1997). Empirical studies of geologically based amplification factors for the San Francisco Bay area have shown large and stable differences in weak motion Fourier amplitude spectra (Borcherdt, 1970, Borcherdt and Glassmoyer, 1992). While these studies are

extremely useful in a general sense, the limited number and size of earthquakes and different types of profiles as well as poorly known recording site conditions preclude relying directly upon empirical results. In particular, few data are available for very high levels of shaking and for a variety of site conditions. Also, few ground motion recording sites have detailed soil/rock profiles for which reliable soil/rock properties are available. Because of these limitations, some form of computational analysis is desirable and direct observations of soil response can then be used as calibrations and to provide a basis for assessing the reasonableness of the results of analytical computations.

3.1 Methodology

The conventional computational approach in developing spectral amplification factors appropriate for specific profiles would involve selection of suitable time histories to serve as control or rock outcrop motions and a suitable nonlinear computational formulation to transmit the motion through the profile.

3.1.1 Equivalent-Linear Computational Scheme

The computational scheme which has been most widely employed to evaluate one-dimensional site response assumes vertically-propagating plane shear waves. Departures of soil response from a linear constitutive relation are treated in an approximate manner through the use of the equivalent-linear approach.

The equivalent-linear approach, in its present form, was introduced by Seed and Idriss (1970). This scheme is a particular application of the general equivalent linear theory introduced by Iwan (1967). Basically, the approach is to approximate a second order nonlinear equation, over a limited range of its variables, by a linear equation. Formally this is done in such a way that an average of the difference between the two systems is minimized. This was done in an ad-hoc manner for ground response modeling by defining an effective strain which is assumed to exist for the duration of the excitation. This value is usually taken as 65% of the peak time-domain strain calculated at the midpoint of each layer, using a linear analysis. Modulus and damping curves are then used to define new parameters for each layer based on the effective strain computations. The linear response calculation is repeated, new effective strains evaluated, and iterations performed until the changes in parameters are below some tolerance level. Generally a few iterations are sufficient to achieve a strain-compatible linear solution.

This stepwise analysis procedure was formalized into a one-dimensional, vertically propagating shear-wave code called SHAKE (Schnabel et al., 1972). Subsequently, this code has easily become the most widely used analysis package for one-dimensional site response calculations.

The advantages of the equivalent-linear approach are that parameterization of complex nonlinear soil models is avoided and the mathematical simplicity of linear analysis is preserved. A truly nonlinear approach requires the specification of the shapes of hysteresis curves and their

cyclic dependencies. In the equivalent-linear methodology the soil data are utilized directly and, because at each iteration the problem is linear and the material properties are frequency independent, the damping is rate independent and hysteresis loops close.

While the assumptions of vertically propagating shear waves and equivalent-linear soil response certainly represent approximations to actual conditions, their combination has achieved demonstrated success in modeling observations of site effects (Schnabel et al., 1972; Silva et al., 1988; Schneider et al., 1993; EPRI, 1993).

3.1.2 RVT Based Computational Scheme

The computational scheme employed to compute the site response uses the stochastic model to generate the power spectral density and spectral acceleration of the rock or control motion. This motion or power spectrum is then propagated through the one-dimensional soil profile using the plane-wave propagators of Silva (1976). In this formulation only SH waves are considered. Arbitrary angles of incidence may be specified but normal incidence is used throughout the present analyses.

In order to treat possible material nonlinearities, an RVT (Random Vibration Theory) based equivalent-linear formulation is employed. Random process theory is used to predict peak time domain values of shear strain based upon the shear strain power spectrum. In this sense the procedure is analogous to the program SHAKE except that peak shear strains in SHAKE are measured in the time domain. The purely frequency domain approach obviates a time domain control motion and, perhaps just as significant, eliminates the need for a suite of analyses based on different input motions. This arises because each time domain analysis may be viewed as one realization of a random process. In this case, several realizations of the random process must be sampled to have a statistically stable estimate of site response. The realizations are usually performed by employing different control motions with approximately the same level of peak acceleration and response spectrum.

In the case of the frequency domain approach the estimates of peak shear strain as well as oscillator response are, as a result of the random process theory, fundamentally probabilistic in nature. Stable estimates of site response can then be computed by forming the ratio of spectral acceleration predicted at the surface of a soil profile to the spectral acceleration predicted for the control motion.

The procedure of generating the point-source stochastic power spectrum computing the equivalent-linear layered-soil response, and estimating peak time domain values has been incorporated into a single code termed RASCALS (Schneider et al., 1993).

3.2 G/Gmax and Hysteretic Damping Curves

Four sets of G/Gmax and hysteretic damping curves are used: generic rock (K_{jf}, TM_{ZS}, M_{xb} and T_S), cohesionless soils (QT_s, Q_{al}, Q_o, Q_y, QT_s, T_S (Saugus)), and cohesive soils (Q_m)

(Table 1). The rock curves (Figure 20) are based on point-source modeling of the rock site empirical attenuation relation of Abrahamson and Silva (1997) for a range in magnitudes and distances using a generic rock profile (Geomatrix A and B, Figure 6) (Silva et al., 1997).

For the geologic units which are considered cohesionless soils in the San Francisco Bay area (gravels, sands, and low PI clays) in terms of high-strain dynamic material properties (QTs, Qal), the recent EPRI (1993) G/Gmax and hysteretic damping curves are used (Figure 21). These curves were developed for generic applications to cohesionless soils in the general range of gravelly sands to low plasticity silts or sandy clays. For application to Quaternary/Tertiary rocks (QT_s), the implied assumption is that these sites behave more like a stiff soil (gravely sand) than rock. A not unreasonable assumption considering a surface velocity of about 800 ft/sec (Figure 4) and a NEHRP site class C (Table 1). The EPRI (1993) curves have recently been validated at 48 San Francisco Bay area cohesionless soil sites (Geomatrix site class C or D, Table 2) through modeling strong ground motions from the Coyote Lake, Morgan Hill, and Loma Prieta earthquakes (Silva et al., 1997).

For the Bay Mud (Q_m) categories, generic sections of Fill (15 ft), young Bay Mud (50 ft) and old Bay Clay (30 ft) over Quaternary Alluvium (Q_{al}) are assumed. These generic zones are based on an examination of several CALTRANS boreholes located near highway bridges (Cliff Roblee, personal communication) and are used only to assign G/Gmax and hysteretic damping curves. For the Fill material and the Alluvium, EPRI (1993) curves are used. For the young Bay Muds and Old Bay Clay, the Vucetic and Dobry (1991) cohesive soil curves for a PI of 40%, an average value for these cohesive soils, are used (Figure 22).

For the geologic units which are considered cohesionless soils in the Los Angeles area (QT_s, Q_o, Q_y, Saugus), recent strong ground motion analyses for about 80 sites which recorded the 1994 Northridge earthquake found the EPRI G/Gmax and hysteretic damping curves showed too much nonlinearity (Silva et al., 1997). As a result, a revised set of G/Gmax and hysteretic damping curves were developed for Peninsular Range cohesionless soils and are shown in Figure 23.

3.3 Specification of Control Motions

The Franciscan K_{jf} and Granite (M_{xb}) profiles (Figures 9 and 15) represent the stiffest of the suite of geologically based profiles, and are taken as the reference site geology (Table 1). The Franciscan unit was also used as a reference site condition by Borcherdt and Glasssmoyer (1992) and the Granite unit by Harmsen (1997) and Bonilla et al. (1997). The common reference permits a comparison of analytical to empirical amplification factors developed from either recordings of the M 6.9 1989 Loma Prieta or several Los Angeles area earthquakes using generally low levels of reference rock motions.

Since time histories are not required for the RVT based equivalent-linear site response analyses, the stochastic point-source model is used to compute the motions at the surface of the baserock or reference rock as well as the other profiles. Both qualitative assessments and quantative validations of the stochastic point-source model (Hanks and McGuire, 1981; Boore,

1983, 1986; McGuire et al., 1984; Boore and Atkinson, 1987; Silva and Lee, 1987; Toro and McGuire, 1987; Silva et al., 1990; EPRI, 1993; Schneider et al., 1993; Silva and Darragh, 1995; Silva et al., 1997) have demonstrated that it provides accurate ground motion estimates, making it an appropriate choice to produce ground motions representative of the geologic based profiles.

To generate the motions, a M 6.5 earthquake is used with the distance (epicentral) varied to produce a suite of distinct peak acceleration values at the surface of the reference rock unit (Table 4). The same source and path parameters are then used for the other unit profiles resulting in a suite of amplification factors as a function of reference rock outcrop peak acceleration values (EPRI, 1993; Toro et al., 1992). For the point-source, a stress drop of 60 bars (Silva and Darragh, 1995) and a small strain total kappa value of 0.04 sec are used for all the profiles. The total kappa value includes the small strain damping in the nonlinear zone. These values were determined in an inversion of the Abrahamson and Silva (1997) empirical attenuation relation (Silva et al., 1997). The rock profiles (Franciscan, Tertiary, and Granite) are permitted to exhibit material nonlinearity to depths where the velocities exceed about 3,400 ft/sec (Figures 9, 10, 15, and 16). This occurs at about 70 ft for the Franciscan and Granite profiles and at about 250 ft for the Tertiary profiles. The soil sites are treated as potentially nonlinear to the top of the Wald et al. (1991, 1996) crusts (Table 3) provided this depth is $\leq$ 500 ft. The depth to this assumed basement material varies from 30 to 1,500 ft, depending upon category depth (Table 5). All soils are constrained to be linear in response below 500 ft.

The Q(f) model is 176 $f^{0.6}$ for the San Francisco Bay area and 275 $f^{0.6}$ for the Los Angeles area. These values were determined from inversions of northern California earthquakes Loma Prieta, Coyote Lake, and Morgan Hill recorded at about 90 sites over the fault distance range of about 12 to 90 km and Peninsular Range earthquakes Northridge, San Fernando, and Whittier Narrows at 180 sites over the fault distance range of about 10 to 200 km (Silva et al., 1997).

To generate motions which cover the range from linear response to the potentially largest horizontal motions to be expected, six distances are run with reference rock outcrop peak accelerations ranging from 0.05g to 1.25g (Table 4). The magnitude and stress drop is fixed at M 6.5 and 60 bars respectively with the assumption that the amplification factors (ratios) are not highly sensitive to either magnitude or stress drop (EPRI, 1993). Since the profiles are randomized in velocity and layer thickness, the median peak acceleration does not exactly correspond to the target peak acceleration (Table 4). In general, the median values are very close, within about 10% of the target which is considered acceptable since the amplifications vary little for a 10% change in input motions.

The profile randomization scheme, which varies both layer velocity and thickness, is based on a correlation model developed from an analysis of variance on about 500 measured shear-wave velocity profiles (EPRI, 1993; Silva et al., 1997). Figure 24 shows the Franciscan outcrop 5% damped pseudo acceleration spectra (median and $\pm$ 1 σ for the lowest level of motion, 0.05g. The profile is varied to the top layer of the Wald et al., (1991) Loma Prieta crust, a depth of about 250 ft. The parametric variation, reflected in the sigma (σ_{ln} = 0.15 for PGA), includes profile velocity and layer thickness variation in addition to variability in the

G/Gmax and hysteretic damping curves.

To accommodate variability in the modulus reduction and damping curves on a generic basis, the curves were independently randomized about the base case values. A log normal distribution was assumed with a σ_{ln} of 0.35 at a cyclic shear strain of 3 x 10^{-2}% with upper and lower bounds of 2σ. The truncation was necessary to prevent modulus reduction or damping models that are not physically possible. The random curves are generated by sampling the transformed normal distribution with a σ_{ln} of 0.35, computing the change in normalized modulus reduction or percent damping at 3 x 10^{-2}% shear strain, and applying this factor at all strains. The random perturbation factor is reduced or tapered near the ends of the strain range to preserve the general shape of the median curves (Silva, 1992). The parametric variability shown in Figure 24 then represents the contribution to the uncertainty in strong ground motions due to the top 200 to 300 ft at hard California rock (Franciscan) sites in the San Francisco Bay (and Los Angeles) area.

The remaining reference rock outcrop median spectra are shown in Figure 25. These median spectra then represent the denominator or reference geologic unit in the amplification factors. Since the shallow profile is taken as the same for both Franciscan and Granite reference rock conditions, the differences in median motions are due only to differences in the deep crust (Table 3).

3.4 Development of Site Amplification Factors

Site amplification factors are computed as the ratio of 5% damping response spectral acceleration (Sa) computed at the surface of each site for each randomized profile to the median 5% damping response spectral acceleration (Sa) computed for the reference rock outcrop motion (Figure 25). In addition, peak acceleration, peak particle velocity, and peak particle displacement were computed for the site and reference outcrop as well. Levels of reference rock outcrop peak acceleration values of 0.05, 0.1, 0.2, 0.4, 0.75, 1.0, and 1.25g were used to accommodate the effects of material nonlinearity upon site response. Table 4 shows the magnitude (M), distance (R), peak acceleration, peak particle velocity, and peak particle displacement computed for the outcrop motions.

To accommodate likely profile depth ranges appropriate for the two areas, categories based upon depth to basement (taken here as top of Wald et al., 1991, 1996 crusts; Table 3) were developed. The categories reflect a mean depth and a range over which the amplification factors are considered applicable. Table 5 lists the categories, depth ranges, and the corresponding geologic units which are considered to have underlying basement material. The range in depth to basement material over which the amplification factors for each depth category are considered applicable are based on the randomization (uniform distribution) depth range. While the depth randomization is intended to capture the profile depth range over which the amplification factors may be applied, the factors are strictly only applicable for a reduced range about the mean depth. That is, averaging amplifications computed for deep profiles with those computed for shallow profiles broadens the amplification but tends to lower the values at frequencies above and below the fundamental frequency of the mean profile depth. This effect

becomes more pronounced as the depth range is increased. An enveloping scheme needs to be developed over amplification factors developed using overlapping depth ranges to produce factors strictly appropriate for applications to wide depth ranges. As a result, case must be exercised in implementing the factors for depths exceeding about $\pm$ 50% of the mean category depths (Table 5). This averaging artifact partially motivated the approximately $\pm$ 50% ranges in depth categories 1 to 3 (and 5 for Los Angeles, Table 5) and is not considered a significant issue for these cases. For the wide depth bins however, one should use conservative factors based on estimated profile depth and an examination of the suite of factors plotted in Appendices A and B.

For the soils, the existence of basement material is clear. However for the QT_s (Quaternary/Tertiary) rock unit in the San Francisco Bay area, which consists of conglomerates, lesser sandstones, siltstones, and claystones of the Santa Clara, Ukiah, and Paso Robles formations and for the T_s and combined Q_o and T_s in the Los Angeles area, the existence of a basement complex is doubtful. It should be pointed out however, that we are defining basement in terms of a steep shear-wave velocity gradient (approximated as a step) which, for shallow depths (category 1) may represent weathering. For the deeper categories, the rapid increase in shear-wave velocity may be interpreted as a transition to much more competent QT_s over a fairly narrow depth zone. Sufficient deep borehole data are simply not currently available to resolve this issue.

3.4.1 Amplification Factors For The San Francisco Bay Area

The amplification factors, 5% damped Sa/Sa (reference rock), were computed at approximately 90 frequencies from approximately 0.10 Hz to 100 Hz.

As an example of the general shape of the amplification factors, Figure 26 shows the median factors and $\pm$ 1 σ sigma values computed for Quaternary Alluvium Category 4 (30 to 1,000 ft, Table 5) for Franciscan outcrop peak acceleration values of 0.05 and 0.40g (solid and dashed lines respectively). Due to the randomizing over depth, only a minor contribution of the fundamental resonance is present. The variability reflects parametric uncertainty in the profile, and includes profile layer thickness, shear-wave velocity, profile depth (30 to 1,000 ft), and G/Gmax and hysteretic damping curves. The first layer of the Wald et al. (1991) crust (base of the profiles) is also randomly varied assuming a lognormal distribution with a σ_{ln} of 0.3 (EPRI, 1993). The depth variation assumes a uniform distribution resulting in a mean profile depth (depth to first layer of the Wald crust) of 515 ft (Table 5).

The effects of nonlinearity are seen in the reduction of amplification at high frequency and the shifting of amplification to lower frequency for the 40%g Franciscan outcrop motions. The increase in variability apparent in the higher motions is likely due to the effects of variability in the G/Gmax and hysteretic damping curves.

To assess the actual number of potentially distinct geologic units in terms of site response for the San Francisco Bay area, Figures 27 and 28 show median amplification factors computed for Bay Mud, Quaternary Alluvium, Older Alluvium, and Quaternary/Tertiary units for

outcropping Franciscan of 0.05g and 0.40g respectively. Also shown in the Figures are the empirical amplification factors computed for Fourier amplitude spectra by Borcherdt and Glassmoyer (1992). These factors were estimated from low level recordings of the M 6.9 1989 Loma Prieta earthquake at sites located in the same geologic units. For both the low- and high-strain analytical factors (Figures 27 and 28), little difference is seen between the Older Alluvium (Q_{oa}) and Quaternary Alluvium (Q_{al}). As a result, the factors are combined into one Q_{al} unit (Table 1). For the low-strain factors shown in Figure 27, the comparison between the analytical and empirical results is surprisingly good. Since the analytical factors are computed for 5% damped response spectra, to allow direct use in hazard assessment, and the empirical factors were computed for Fourier amplitude spectra which results in an amplitude dependence upon degree of smoothing, the close agreement is particularly encouraging.

The effects of nonlinear response are evident in the higher-motion analytical factors computed for Franciscan outcrop motions of 40%g. Figure 28 shows a significant reduction in motions, mostly at high frequency ($\geq$ 3 Hz), for the Bay Mud and Alluvial soils and for the Quaternary/Tertiary rock units. The Tertiary unit, being quite stiff, remain largely linear in response (relative to Franciscan). The accompanying shift in dominate frequency is also apparent, moving from about 1 to 2 Hz to below 1 Hz as the Franciscan outcrop peak acceleration increases from 0.05g to 0.40g. These trends are not apparent in the empirical factors, being based on generally low levels of input (Franciscan) motions.

To illustrate the important effects of depth to bedrock or basement material, Figure 29 shows QT_s, Q_{al}, and Q_m median amplification factors computed for Franciscan outcrop peak acceleration of 0.20g and 0.40g for depth Categories 1, 2, and 3 (Table 5). The mean category depths are 90, 250, and 500 feet, respectively. Figure 29 shows the broadening and shifting of peak amplification to lower frequencies as depth to basement increases. There is also an accompanying decrease in high frequency amplification due to material damping. These results show that depth to basement material is a first order effect in amplification factors and should be accommodated in their development as well as implementation.

To illustrate the differences between the current NEHRP amplification factors and those based on surface geology, Figure 30 shows median factors computed for the broadest depth categories along with corresponding NEHRP recommendations. Except for the Q_m category, which classifies as NEHRP category D based on velocity (but should be NEHRP category E based on surface geology and response), favorable agreement is seen for reference Franciscan (NEHRP category B, Table 1) and for peak acceleration values up to about 0.20g. At higher loading levels, however, Figure 30* shows departures which are both conservative and unconservative. The high frequency NEHRP factors (2.0 Hz to 10.0 Hz) are conservative for NEHRP profile D but appear to be low for profile NEHRP profile C. For the low frequency NEHRP factors (0.5 Hz to 2.5 Hz), profile D appears low compared to Q_{al} (combined Q_o and Q_{al}, Table 5).

---

*For reference rock peak accelerations exceeding 0.4g, NEHRP recommends site specific evaluations for category E.

The final set of median amplification factors covering the complete range in Franciscan outcrop peak accelerations (0.05 to 1.25g) are shown in Figures 31 to 35 for the categories reflecting the widest depth ranges (Table 5). Each Figure shows median and $\pm$ 1 σ amplification factors (5% damped response spectra) computed for the Bay Mud, Older Alluvium, Quaternary Alluvium, Quaternary/Tertiary, and Tertiary surface geologic units. Interestingly, for the widest depth ranges, there is a distinction between Older Alluvium and Quaternary Alluvium (Figures 33 and 34 respectively). As a result, the categories are retained. The units may be combined by averaging the separate amplification factors for applications where the distinction is small (e.g. 350 to 650 ft depth range, Figures 27 and 28).

The amplification of peak acceleration (100 Hz on the plots) is large, about a factor of 2 for the soil profiles at low levels of motions (Figures 33 to 35). At around 0.20 to 0.40g, the effects of nonlinearity become significant, reducing high frequency motions ($f \geq 10$ Hz) and increasing low frequency ($f \leq 1$ Hz) motions. These trends are, as expected, more pronounced as profile stiffness decreases and are reflected in a change in shape of soil spectra with increasing loading levels. For the highest levels of motions (0.075g and 1.25g for outcropping Franciscan) the Quaternary Alluvium and Bay Mud profiles show extreme nonlinearity. These results must be viewed in the context of the equivalent-linear approximation and may be overdamped compared to appropriate equivalent fully nonlinear analyses. These levels of motions are beyond the current sampling in the empirical strong motion database and a reasonable lower limit of amplification for these generic results is about 0.5 to 0.6, a value supported empirically for generic deep soil (Abrahamson and Silva, 1997).

The complete suite of amplification factors is included in Appendix A. These amplification factors are designed to serve as a means of approximately accounting for the effects of surficial geology and depth to basement for seismic hazard estimation. Although detailed site specific results could produce results different from those predicted for these generalized categories, we believe that the results presented are appropriate and represent a useful tool for use in seismic hazard estimation for applications to the San Francisco Bay area. Linear interpolation may be used to provide amplifications between frequency and reference rock peak acceleration values.

3.4.2 Amplification Factors For The Los Angeles Area

Although median shear-wave velocity profiles for baserock conditions are quite similar for the San Francisco Bay (K_{jf}) and Los Angeles (M_{xb}) areas (Figure 6) resulting in similar rock motions (Figure 25), differences in both the soil profiles and nonlinear properties between the regions suggest that important differences in response will occur. As a result, separate amplification factors are developed for Los Angeles area soils and soft rock. Since profiles were not available for very soft Los Angeles area materials (e.g., Los Angeles Harbor area), the use of San Francisco Bay area amplification factors computed for Bay Mud (Q_m) site conditions are recommended.

To assess the actual number of distinct geologic units in terms of site response, Figure 36 shows median amplification factors computed for Quaternary Alluvium, Older Alluvium,

Quaternary + Tertiary, Saugus, and Tertiary units for outcropping Granite in the range of 0.05g to 1.25g.

The depth range is 30 to 1,000 ft (average depth 515 ft), except for Tertiary as it reaches about 3,000 ft/sec at a depth of 200 ft (Figure 16). The Saugus (Tertiary rock) category is retained as a distinct category for comparison but is also included in the combined QT_s category. From a visual qualitative analysis, it appears that Q_y (solid lines) and T_s (solid dotted) are distinct categories along with the Saugus (crosses). There is also an indication of differentiation of these categories and the combined QT_s category (dots). Larger depth ranges generally result in fewer distinct (resolvable) categories due to the inherent smoothing or averaging, so care is warranted in such qualitative assessments. Over most of the frequency range and loading levels up to about 0.40g, Quaternary Alluvium (Q_y) provides a reasonable suite of factors for general applicability for sites with depths not exceeding around 700 ft (depths not exceeding about 50% of the mean depth). For applications to profiles of greater depths, a deeper depth category should be used. At higher loading levels, due to nonlinearity the stiffer Tertiary (T_s) profile is significantly above the Q_y amplification for frequencies above about 1 Hz.

While a statistically quantative measure of distinct categories is desirable, with analytical factors such an assessment remains an elusive objective. Statistically significant differences in mean amplification must ultimately be assessed with ground motion (recordings) of sufficient quantity and quality (range in loading levels, and accurate site categorizations). Probably the most complete set of data in this respect is in southern California and several empirical site response analyses have been performed using similar surficial geologic units (Bonilla et al., 1997; Borcherdt, 1996; and Harmsen, 1997). Figure 37 compares empirical amplification factors (Bonilla et al., 1997) computed for Fourier amplitude spectra to the analytical factors for surficial geologic units Q_y (Quaternary Alluvium) and the combined $Q_o + T_s$ (Older Alluvium plus Tertiary "rock"). The empirical factors are relative to Granite (M_{xb}) and are based upon aftershocks of the 1994 M 6.7 Northridge earthquake, generally reflecting low levels of motion. The two geologic units (Q_y and $Q_o + T_s$) were found by Bonilla et al. (1997) to have significantly different response, based up analyses of multiple earthquakes and multiple sites. The analytical factors are for deep soil conditions (average depth of 500 ft) as most of the stations are assumed to reflect deep basement conditions. Both the trends and relative levels between the Q_y and $Q_o + T_s$ amplifications are reflected in the analytical factors. Both empirical factors exceed the analytical, possibly due to the mixture of Fourier and response spectra. Additionally, few rock sites (M_{xb}) were available for the empirical analyses which may result in a bias in the baserock motions. Stable levels of amplification of 5% damped response spectra of strong ground motion at firm to stiff soil sites relative to soft rock sites generally do not exceed factors of about 2 to 2½ (at low frequency). This is supported by Figure 38 which shows soil site amplification (Geomatrix C + D, Table 2) relative to soft rock (Geomatrix A + B) from the empirical attenuation relation of Abrahamson and Silva (1997). The maximum amplification occurs at low frequency and is near 2. For low levels of expected rock peak acceleration, the shape of the empirical amplification factors for generic firm soil, based solely on strong ground motions (Figure 38), is similar to the analytical factors (Figure 37) and of comparable levels.

For the same surficial geologic units, Borcherdt (1996) developed amplification factors (for 5% damped response spectra) from strong ground motion recording of the 1994 M 6.7 Northridge earthquake. The comparison of the analytical factors to the empirical factors of Borcherdt (1996) are shown in Figure 39. For this comparison a reference rock peak acceleration of 0.10g is used to reflect average levels for the recordings. As with the previous comparison, analytical factors were computed for a depth range of 30 to 1,000 ft (average depth of 515 ft) and are most appropriate for profiles with depth less than about 700 ft. In this comparison, the agreement is more favorable. The underprediction at low frequency (0.20 to 0.67 Hz) would largely be eliminated using the 500 to 1,500 ft suite of factors (Appendix B). Interestingly, the high frequency crossover seen in the empirical factors is reflected in the analytical factors as well.

A final comparison with empirical factors is shown in Figure 40. These empirical amplification factors were estimated by Harmsen (1997) from acceleragraph recordings of the 1971 San Fernando, 1987 Whittier Narrows, 1991 Sierra Madre, and 1994 Northridge earthquakes. The factors are relative to granite outcropping (M_{xb}) and were computed for Fourier amplitude spectra. In this case Older Alluvium was considered distinct from Tertiary (T_s) in mean amplification. This distinction in amplification based on surface geology is not resolved by categories based on average shear-wave velocity over the top 100 ft as Q_o and T_s (along with Saugus) are NEHRP category C (Table 1, Figure 40).

As with the other comparison with Fourier amplitude amplification (Figure 37), the general trends are captured (along with the high frequency crossover) but with a low frequency underprediction. A similar consistent difference is also seen between the empirical Fourier amplitude and empirical 5% damped response spectra amplification factors.

To examine the comparison of the NEHRP amplification factors, Figure 41 shows the Q_y (NEHRP D) and $Q_o + T_s$ (NEHRP C) for the depth range of 30 to 1,000 ft (mean depth of 515 ft) along with the recommended provisions. Close agreement is seen at low loading levels (0.05 and 0.10g) but the low-frequency factors (0.50 to 2.5 Hz) appear to reflect too much nonlinearity at the higher levels.

This trend was also found by both Silva and Toro (1998) and Crouse and McGuire (1996) who also concluded that the NEHRP factors probably reflected too much nonlinear response. Interestingly, the high-frequency NEHRP provisions for loading levels of 0.75g and above appear conservative, showing less nonlinear response than the factors computed here, particularly for frequencies exceeding about 5 Hz.

The complete suite of amplification factors is included in Appendix A. These amplification factors are designed to serve as a means of approximately accounting for the effects of surficial geology and depth to basement for seismic hazard estimation. Although detailed site specific results could produce results different from those predicted for these generalized categories, we believe that the results presented are appropriate and represent a useful tool for use in seismic hazard estimation for applications to the Los Angeles area. Linear interpolation may be used to provide amplifications between frequency and reference rock peak acceleration values.

3.5 Adjustment Factors For Soft Rock Conditions

As previously mentioned, reference rock site conditions for both the San Francisco (K_{jf}) and Los Angeles (M_{xb}) areas reflect somewhat stiffer shallow site conditions than typical rock site conditions implicit in WNA empirical attenuation relations (assumed Geomatrix Category A + B, Figure 6). Since the amplification factors (Appendices A and B) are computed relative to the baserock surface geology (to compare with site response studies), another suite of factors has been computed as Geomatrix site Category A + B relative to K_{jf} (San Francisco area) and M_{xb} (Los Angeles area). Figures 42 and 43 show the soft rock to reference rock amplification factors for the San Francisco and Los Angeles areas respectively. The factors are nearly identical for the two regions since the same shallow reference rock profiles are used to generate the outcrop motions. These factors show a slight amplification near 3 Hz at all loading levels and deamplification near 10 Hz at high levels of loading. These effects are attributed to the softer Geomatrix A + B profiles compared to K_{jf} and M_{xb} profile. Since peak acceleration is affected very little, hazard results from empirical rock site attenuation relations may be used to select appropriate amplification factors. These adjustment factors may then be used to condition the amplification factors to soft rock conditions by division prior to applying the empirical rock spectrum.

4.0 SUMMARY

For both the San Francisco Bay and Los Angeles areas, surface geology based amplification factors have been developed for 5% damped response spectra. The factors are computed relative to reference rock site geology, K_{jf} (Franciscan) for the San Francisco Bay area and M_{xb} (Granite) for the Los Angeles area. The factors are functions of profile depth (or depth range) as well as expected reference rock peak acceleration values ranging from 0.05g to 1.25g.

The amplification factors are computed using average measured shear-wave velocity profiles at sites located within the surficial geologic units with an RVT (Random Vibration Theory) based equivalent-linear site response approach. Separate G/Gmax and hysteretic damping curves are used for San Francisco (North Coast) and Los Angeles (Peninsular Range) cohesionless soils reflecting different degrees of nonlinear response in both regions. These curves, along with G/Gmax and hysteretic damping for rock site conditions which are the same for both regions, were validated by modeling recorded motions in both regions.

The analytical amplifications factors are compared to published empirical as well as current NEHRP factors for both regions. Comparisons with the empirical factors show good agreement for empirical factors computed for 5% damped response spectra and reasonable agreement for empirical factors for Fourier amplitude spectra. The analytical factors were generally below the empirical for Fourier amplitude spectra but agreed in shape and general trends: soft alluvium higher than stiff alluvium at low frequency but crossing over at high frequency. Comparisons with the NEHRP provisions showed reasonable agreement for the San Francisco Bay area, except for the Bay Muds (Q_m) being classified as NEHRP D (based on actual average shear-wave velocity over the top 100 ft). For the Los Angeles area, good agreement was seen with the NEHRP amplification factors at low levels of loading (up to about

0.10g). At higher loading levels the low frequency NEHRP factors wee significantly exceeded while the high frequency NEHRP factors appear to reflect considerable conservatism at very high loading levels.

The amplification factors developed in this project extend to 1,000 ft for the San Francisco Bay area and 1,500 ft for the Los Angeles area. They may be used to approximately accommodate the effects of near surface geology for seismic hazard evaluations.

REFERENCES

Abrahamson, N.A and K.M. Shedlock (1997). "Overview." *Seis. Research Lett.*, 68(1), 9-23.

Abrahamson and Silva (1997). "Empirical response spectral attenuation relations." to appear in Seismological Research Letters.

Boatwright, J., and Astrue, M. (1983). "Analysis of the aftershocks of the New Brunswick earthquake." *Workshop on Site-Specific Effects of Soil and Rock on Ground Motion and the Implications for Earthquake-Resistant Design.* USGS Open-File Rept. 83-245.

Bonilla, L.F., J.H. Steidl, G.T., Lindley, A.G Tumarkin and R.J. Archuleta (1997). "Site amplification in the San Fernando Valley, California: Variability of Site-effect estimation using the S-wave, coda, and H/V methods. *Bull. Seism. Soc. Am.*, 87(3), 710-730.

Boore, D.M., and Atkinson, G.M. (1987). "Stochastic prediction of ground motion and spectral response parameters at hard-rock sites in eastern North America." *Bull. Seism. Soc. Am.*, 77(2), 440-467.

Boore, D.M. (1986). "Short-period P- and S-wave radiation from large earthquakes: implications for spectral scaling relations." *Bull. Seism. Soc. Am.*, 76(1) 43-64.

Boore, D.M. (1983). "Stochastic simulation of high-frequency ground motions based on seismological models of the radiated spectra." *Bull. Seism. Soc. Am.*, 73, 1865-1894.

Borcherdt, R. D. (1996). "Preliminary amplification estimates inferred from strong ground-motion recordings of the Northridge earthquake of January 17, 1994." *Proceedings of the Internatonal Workshop on Site Response Subjected to Strong Earthquake Motions.* Yokosuka Japan, 1-26.

Borcherdt, R. D. and Glassmoyer, G. (1992). "On the Characteristics of Local Geology and Their Influence on Ground Motions Generated by the Loma Prieta Earthquake in the San Francisco Bay region, California." *Bull. Seism. Soc. Am.*, 82(2), 603-641.

Borcherdt, R.D. (1970). "Effects of local geology on ground motion near San Francisco Bay." *Bull. Seism. Soc. Am.*, 60:29-61.

Campbell, K.W. (1988). "Predicting strong ground motion in Utah." *Evaluation of Regional and Urban Earthquake Hazards and Risk in Utah,* edited by W.W. Hays and P.L. Gori, USGS Prof. Paper.

Campbell, K.W. (1985). "Near-source estimation of strong ground motion for the Eastern United States: second quarter progress report - FY 1985." Submitted to *Nuclear Regulatory Commission,* 14 pages.

Campbell, K.W. (1981). "Near-source attenuation of peak horizontal acceleration." *Bull. Seism. Soc. Am.*, 71(6), 2039-2070.

Cranswick, E., Wetmiller, R., and Boatwright, J. (1985). "High-frequency observations and source parameters of microearthquakes recorded at hard-rock sites." *Bull. Seism. Soc. Am.*, 75(6), 1535-1567.

Crouse, C. B. and McGuire, J.W. (1996). "Site response studies for purpose of revising NEHRP seismic provisions." *Earthquake Spectra,* 12(3), 407-439.

Electric Power Research Institute (1993). "Guidelines for determining design basis ground motions." Palo Alto, Calif: Electric Power Research Institute, vol. 1-5, EPRI TR-102293.
vol. 1: Methodology and guidelines for estimating earthquake ground motion in eastern North America.
vol. 2: Appendices for ground motion estimation.
vol. 3: Appendices for field investigations.
vol. 4: Appendices for laboratory investigations.
vol. 5: Quantification of seismic source effects.

Gutenberg, B. (1927). *Grundlagen der Erdlebenkunde.* Berlin.

Gutenberg, B. (1957). "Effects of ground on earthquake motion." *Bull. Seism. Soc. Am.*, 47(1), 221-250.

Hanks, T.C., and McGuire, R.K. (1981). "The character of high-frequency strong ground motion." *Bull. Seism. Soc. Am.*, 71, 2071-2095.

Harmsen, S.C. (1997). "Determination of site amplification in the Los Angeles urban area from inversion of strong-motion records." *Bull. Seism. Soc. Am.,* 87(4), 866-887.

Hayashi, S., H. Tsuchida, and E. Kurata (1971). "Average response spectra for various subsoil conditions." *Third Joint Meeting, US-Japan Panel on Wind and Seismic Effects,* UJNR, Tokyo.

Idriss, I.M. (1985). "Evaluating seismic risk in engineering practice." *Proc. Eleventh Internat. Conf. on Soil Mech. and Foundation Eng.*, San Francisco, edited by A.A. Balkema, Rotterdam, 1, 255-320.

Iwan, W.D. (1967). "On a class of models for the yielding behavior of continuous and composite systems." *J. Appl. Mech.*, 34, 612-617.

Joyner, W.B., and Fumal, T.E. (1984). "Use of measured shear-wave velocity for predicting geologic site effects on strong ground motion." *Proc. Eighth World Conf. on Earthq. Engin.*, San Francisco, 2, 777-783.

Joyner, H.B. and D.M. Boore (1982) "Prediction of earthquake response spectra." *USGS,* Open-File Rept. 82-977.

Mallet, R. (1862). *"Great Neopolitan earthquake of 1857, London."* 2 vols.

Milne, J. (1908). "*Seismology, London.*" 2nd edition.

McGuire, R.K., A.M. Becker, and N.C. Donovan (1984). "Spectral estimates of seismic shear waves." *Bull. Seism. Soc. Am.*, 74(4), 1427-1440.

Mohraz, B. (1976). "A study of earthquake response spectra for different geological conditions." *Bull. Seism. Soc. Am.*, 66(3) 915-935.

Reid, H.F. (1910). "*The California earthquake of April 18, 1907.*" The Mechanics of the Earthquake, Carnegie Inst. of Washington, Publ. 87, 21.

Schnabel, P.B., Lysmer, J., and Seed, H.B. (1972). *SHAKE: a Computer Program for Earthquake Response Analysis of Horizontally Layered Sites.* Earthq. Engin. Res. Center, Univ. of Calif. at Berkeley, EERC 72-12.

Schneider, J.F., W.J. Silva, and C.L. Stark (1993). Ground motion model for the 1989 M 6.9 Loma Prieta earthquake including effects of source, path and site. *Earthquake Spectra,* 9(2), 251-287.

Seed, H.B., C. Ugas and J. Lysmer. (1976). "Site-dependent spectra for earthquake resistant design." *Bull. Seism. Soc. Am.*, 66(1), 221-243.

Seed, H.B. and I.M. Idriss (1970). "*Soil moduli and damping factors for dynamic response analyses.*" Earthq. Eng. Res. Center, Univ. of Calif. at Berkeley, Report No. UCB/EERC-70/10.

Silva, W.J. and G. Toro (1998) "Verification of response spectral shapes and anchor points for different site categories for building design codes." California Department of Conservation, Division of Mines and Geology, Report CSMIP/97-08.

Silva, W.J., N. Abrahamson, G. Toro and C. Costantino. (1997). "Description and validation of the stochastic ground motion model." Report Submitted to Brookhaven National Laboratory, Associated Universities, Inc. Upton, New York 11973, Contract No. 770573

Silva, W.J. and R. Darragh (1995). "Engineering characterization of earthquake strong ground motion recorded at rock sites." Palo Alto, Calif:Electric Power Research Institute, TR-102261.

Silva, W.J. (1992). "Factors controlling strong ground motions and their associated uncertainties." *Dynamic Analysis and Design Considerations for High Level Nuclear Waste Repositories, ASCE* 132-161.

Silva, W.J., Darragh, R.B., and Wong, I.G. (1990). "Engineering characterization of earthquake strong ground motions with applications to the Pacific Northwest." in Hays, W.W., ed., *Proceedings of the Third NEHRP Workshop on earthquake Hazards in the Puget sound/Portland region*, U.S. geological Survey Open-File report (in press).

Silva, W.J., and Green, R.K. (1989). "Magnitude and distance scaling of response spectral shapes for rock sites with applications to North American tectonic environment." *Earthquake Spectra,* 5(3), 591-624.

Silva, W. J.; Turcotte, T.; Moriwaki, Y. (1988). "Soil Response to Earthquake Ground Motion," Electric Power Research Institute, Walnut Creek, California, Report No. NP-5747.

Silva, W.J., and Lee, K. (1987). "*WES RASCAL code for synthesizing earthquake ground motions.*" State-of-the-Art for Assessing Earthquake Hazards in the United States, Report 24, U.S. Army Engineers Waterways Experiment Station, Misc. Paper S-73-1.

Silva, W.J. (1976). "Body Waves in a Layered Anelastic soilid." *Bull. Seis. Soc. Am.*, vol. 66(5), 1539-1554.

Toro, G.R., Silva, W.J., McGuire, R.K., and Herrmann, R.B. (1992). "Probabilistic seismic hazard mapping of the Mississippi embayment." *Seism. Res. Letters,* 63(3), 449-??.

Toro, G.R., and McGuire, R.K. (1987). "An investigation into earthquake ground motion characteristics in eastern North America." *Bull. Seism. Soc. Am.*, 77, 468-489.

Vucetic, M.; Dobry, R. (1991). "Effects of Soil Plasticity on Cyclic Response," *Journal of Geotechnical Engineering, ASCE,* 117(1), 89-107.

Wald, D.J., T.H. Heaton and K.W. Hudnut (1996). "The slip history of the 1994 Northridge, California, earthquake determined from strong-motion, teleseismic, GPS, and leveling data." *Bull. Seism. Soc. Am.*, 86(1B), S49-S70.

Wald, D.J., D.V. Helmberger, and T.R. Heaton (1991). "Rupture model of the 1989 Loma Prieta Earthquake from the inversion of strong motion and broadband teleseismic data." *Bull. Seism. Soc. Amer.*, 81(5), 1540-1572.

Wood, H.O. (1908). "Distribution of apparent intensity in San Francisco, in the California earthquake of April 18, 1906." *Report of the State Earthquake Investigation Commission*, Wash., D.C.: Carnegie Institute, 1, 220-245.

September 27, 1999
FINAL REPORT

SURFACE GEOLOGY BASED STRONG MOTION AMPLIFICATION FACTORS FOR THE SAN FRANCISCO BAY AND LOS ANGELES AREAS

Prepared for

PG&E PEER - TASK 5.B

by

Walter Silva
Syliva Li
Bob Darragh
Nick Gregor

of

Pacific Engineering and Analysis
311 Pomona Avenue
El Cerrito, CA 94530

Table 1

SURFACE GEOLOGY BASED PROFILES, SITE CLASSES, AND DYNAMIC MATERIAL PROPERTIES

SAN FRANCISCO BAY AREA

Geology	Average Velocity over 30m	Site Classes		Number of Profiles	G/Gmax and Hysteretic Damping
		USGS	NEHRP		
K_{jf}(Franciscan)	771.44 m/s	A	B	30	Generic rock
TM_{zs}(Tertiary Bedrock)	506.13 m/s	B	C	18	Generic rock
QT_s(Quaternary/Tertiary)	466.12 m/s	B	C	9	EPRI
Q_{oa}(older alluvium)	353.44 m/s	C	D	16	EPRI
Q_{al}(Quaternary alluvium)	296.49 m/s	C	D	37	EPRI
Q_{oa} + Q_{al}	312.15 m/s	C	D	53	EPRI
Q_m(Bay mud)	187.87 m/s	C	D	60	Vucetic/Doby, EPRI
				170	

LOS ANGELES AREA

Geology	Average Velocity over 30m	Site Classes		Number of Profiles	G/Gmax and Hysteretic Damping
		USGS	NEHRP		
M_{xb} (Granite)	843.78 m/s	A	B	8	Generic rock
T_S (Saugus)	576.81 m/s	B	C	4	Peninsular Range
T_S (Tertiary)	436.39 m/s	B	C	43	Generic rock
Q_o(Older alluvium)	391.24 m/s	B	C	124	Peninsular Range
QT_S (Q_o + T_S)	508.61 m/s	B	C	171	Peninsular Range
Q_y(Quaternary alluvium)	317.68 m/s	C	D	219	Peninsular Range
				398	

Table 2

SITE CLASSIFICATIONS

Average shear-wave velocity to a depth of 30m is:

USGS Site Classification (Boore et al., 1994)	NEHRP 1994	UBC 1997
A = > 750 m/s	A = > 1,500 m/s	> 5,000 ft/sec
B = 360 - 750	B = 760 - 1,500	2,500 - 5,000
C = 180 - 360	C = 360 - 760	1,200 - 2,500
D = < 180 m/s	D = 180 - 360	600 - 1,200
	E = < 180	< 600 ft/sec

GEOMATRIX Site Classification

Geotechnical subsurface characteristics (Robert Youngs, personal communications)

A = Rock. Instrument on rock (V_s > 600 mps or < 5m of soil over rock.

B = Shallow (stiff) soil. Instrument on/in soil profile up to 20m thick overlying rock.

C = Deep narrow soil. Instrument on/in soil profile at least 20m thick overlying rock, in a narrow canyon or valley no more than several km wide.

D = Deep broad soil. Instrument on/in a soil profile at least 20m thick overlying rock, in a broad valley.

E = Soft deep soil. Instrument on/in deep soil profile with average V_s < 150 mps.

Relations To Building Code Classifications

UBC	USGS	NEHRP	GEOMATRIX
S1	A + B	B + C	A + B
S2	B + C	C + D	C + D
S3	D	E	E
S4	E		

Table 3 LOMA PRIETA CRUSTAL MODEL (from Wald et al., 1991)		
Thickness (km)	V_s (km/sec)	Density (cgs)
0.1	1.00	2.00
0.4	1.95	2.30
0.5	2.48	2.35
2.0	2.77	2.35
2.0	3.10	2.35
2.0	3.31	2.45
2.0	3.55	2.58
4.0	3.61	2.62
5.0	3.62	2.63
7.0	3.85	2.77
	4.62	3.28
NORTHRIDGE CRUSTAL MODEL (from Wald et al., 1996)		
Thickness (km)	V_s (km/sec)	Density (cgs)
0.5	1.00	2.10
1.5	2.00	2.30
2.5	3.20	2.50
23.0	3.60	2.60
5.0	3.90	2.90
	4.50	3.00

Table 4

FRANCISCAN REFERENCE SITE GROUND MOTION PARAMETERS
SAN FRANCISCO BAY AREA

Target Outcrop* PGA(g)	Median Outcrop* PGA(g)	Median Outcrop* PGV(cm/sec)	Median Outcrop* PGD(cm)	Median Outcrop* V/A (cm/sec/g)	Median Outcrop* AD/V² (gcm/cm² /sec²)	Dist. (km)	Depth (km)	M	Δσ (bars)
0.05	0.05	5.08	2.30	101.63	4.35	42.00	8.00	6.5	60
0.10	0.11	10.16	4.45	92.42	4.63	22.00	8.00	6.5	60
0.20	0.20	17.46	7.51	88.14	4.76	11.80	8.00	6.5	60
0.40	0.39	33.03	14.00	84.96	4.87	0.00	7.80	6.5	60
0.75	0.74	65.22	28.80	87.82	4.94	0.00	4.50	6.5	60
1.25	1.30	122.25	52.93	94.12	5.01	0.00	2.54	6.5	60

Q(f) = 176 $f^{0.6}$ (San Francisco; based on regional inversions, Silva et al., 1997)

GRANITE REFERENCE SITE GROUND MOTION PARAMETERS
LOS ANGELES AREA

Target Outcrop** PGA(g)	Median Outcrop** PGA(g)	Median Outcrop** PGV(cm/sec)	Median Outcrop** PGD(cm)	Median Outcrop** V/A (cm/sec/g)	Median Outcrop** AD/V² (gcm/cm² /sec²)	Dist. (km)	Depth (km)	M	Δσ (bars)
0.05	0.05	4.84	2.15	95.34	4.56	46.00	8.00	6.5	60
0.10	0.10	9.16	3.97	89.29	4.75	25.00	8.00	6.5	60
0.20	0.20	17.29	7.39	85.89	4.87	12.00	8.00	6.5	60
0.40	0.40	33.57	14.22	83.95	4.95	0.00	7.60	6.5	60
0.75	0.77	67.34	26.30	87.47	4.96	0.00	4.49	6.5	60
1.25	1.26	110.55	48.76	87.44	5.01	0.00	2.77	6.5	60

Q(f) = 275 $f^{0.6}$ (Los Angeles; based on regional inversions, Silva et al., 1997)
Kappa = 0.04 sec, low strain

*Top of Franciscan Profile
**Top of Granitic Profile

Table 5 DEPTH CATEGORIES AND DEPTH RANGES		
SAN FRANCISCO BAY AREA		
Category	Mean Depth (ft)	Range* (ft)
1	90	30 - 150
2	250	150 - 350
3	500	350 - 650
4	515	30 - 1,000
5	250	30 - 450
6	340	30 - 650
Geologic Units and Depth Categories		
Geologic Unit		Depth Categories
Quaternary/Tertiary (QT_S)		1, 2, 3, 6
Older Alluvium (Q_{oa})		1, 2, 3, 4, 5
Quaternary Alluvium (Q_{AL})		1, 2, 3, 4, 5
Bay Mud (Q_m)		1, 2, 3, 6
LOS ANGELES AREA		
Category	Mean Depth (ft)	Range* (ft)
1	90	30 - 150
2	250	150 - 350
3	500	350 - 650
4	515	30 - 1000
5	1,000	500 - 1,500
Geologic Units and Depth Categories		
Geologic Unit		Depth Categories
Saugus (T_S)		1, 2, 3, 4
Old Alluvium + Tertiary (Q_o + T_S)		1, 2, 3, 4, 5
Old Alluvium (Q_o)		1, 2, 3, 4
Quaternary Alluvium (Q_y)		1, 2, 3, 4, 5

*Range of profile depth over which category applies as well as range of depth randomization for each category. Profile depth is defined as depth to basement material: top of Wald et al. (1991; 1996) crusts (Table 3).

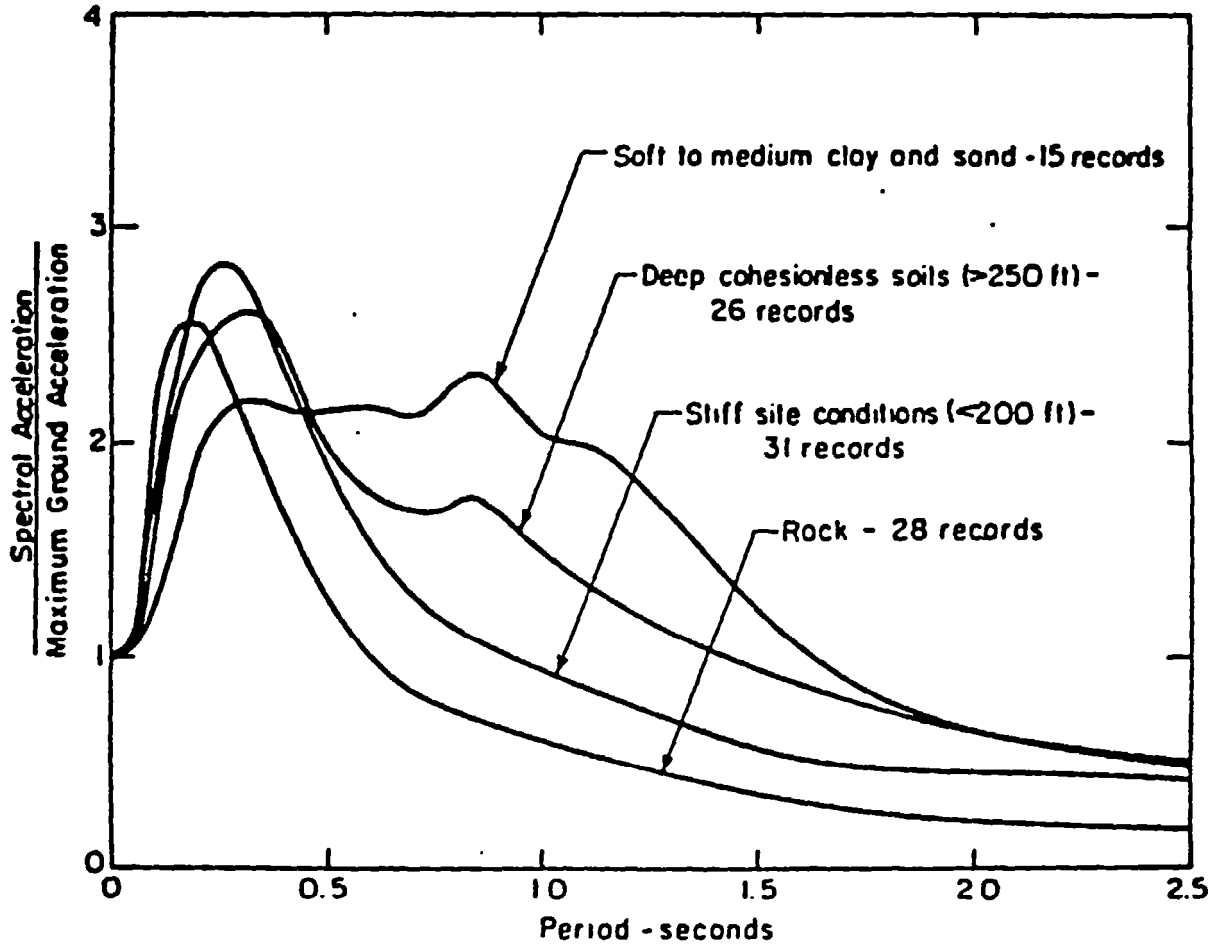

Figure 1. Effects of near surface soil conditions on 5% damped response spectral shapes (source: Seed, Ugas, and Lysmor, 1976).

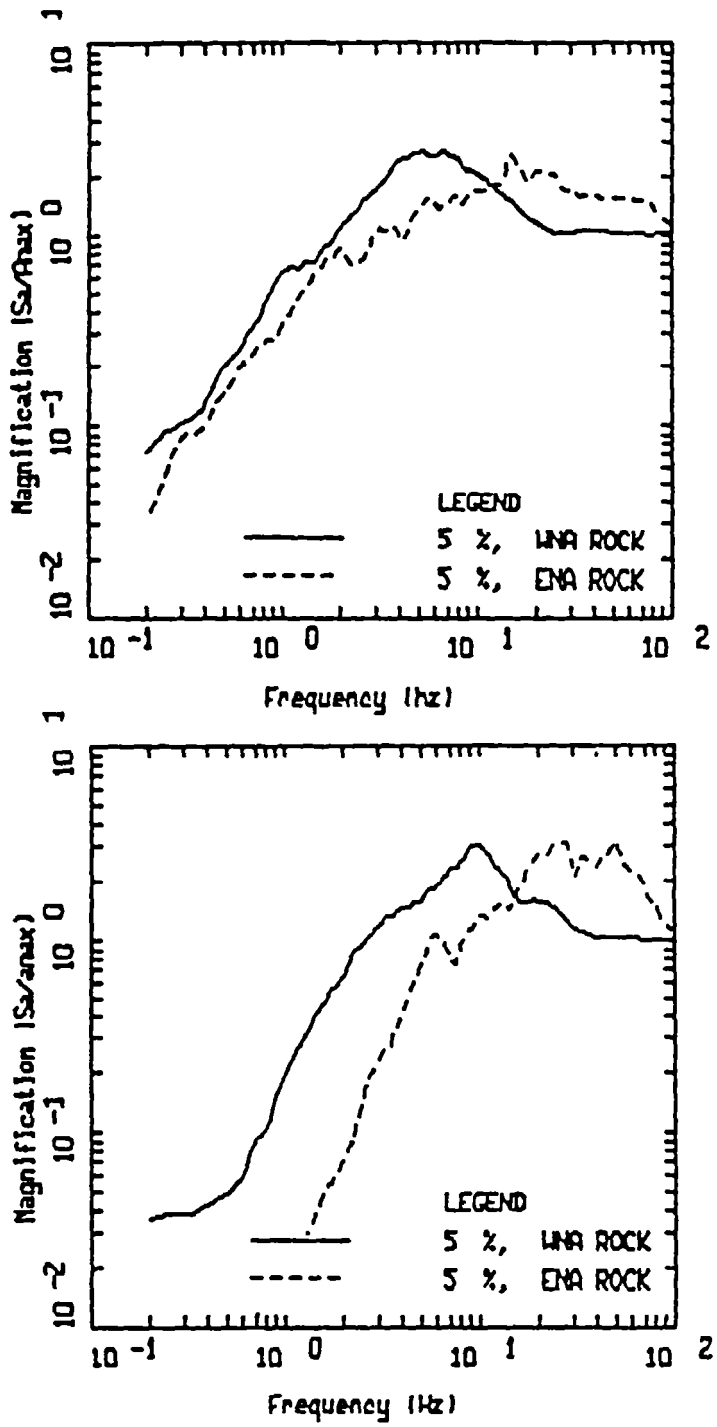

Figure 2. Effects of hard and soft rock site conditions and magnitude on 5% damped response spectral shapes for earthquakes with M ≈ 6.5 (upper) and M ≈ 4.5 (lower) (source: Silva and Darragh, 1995).

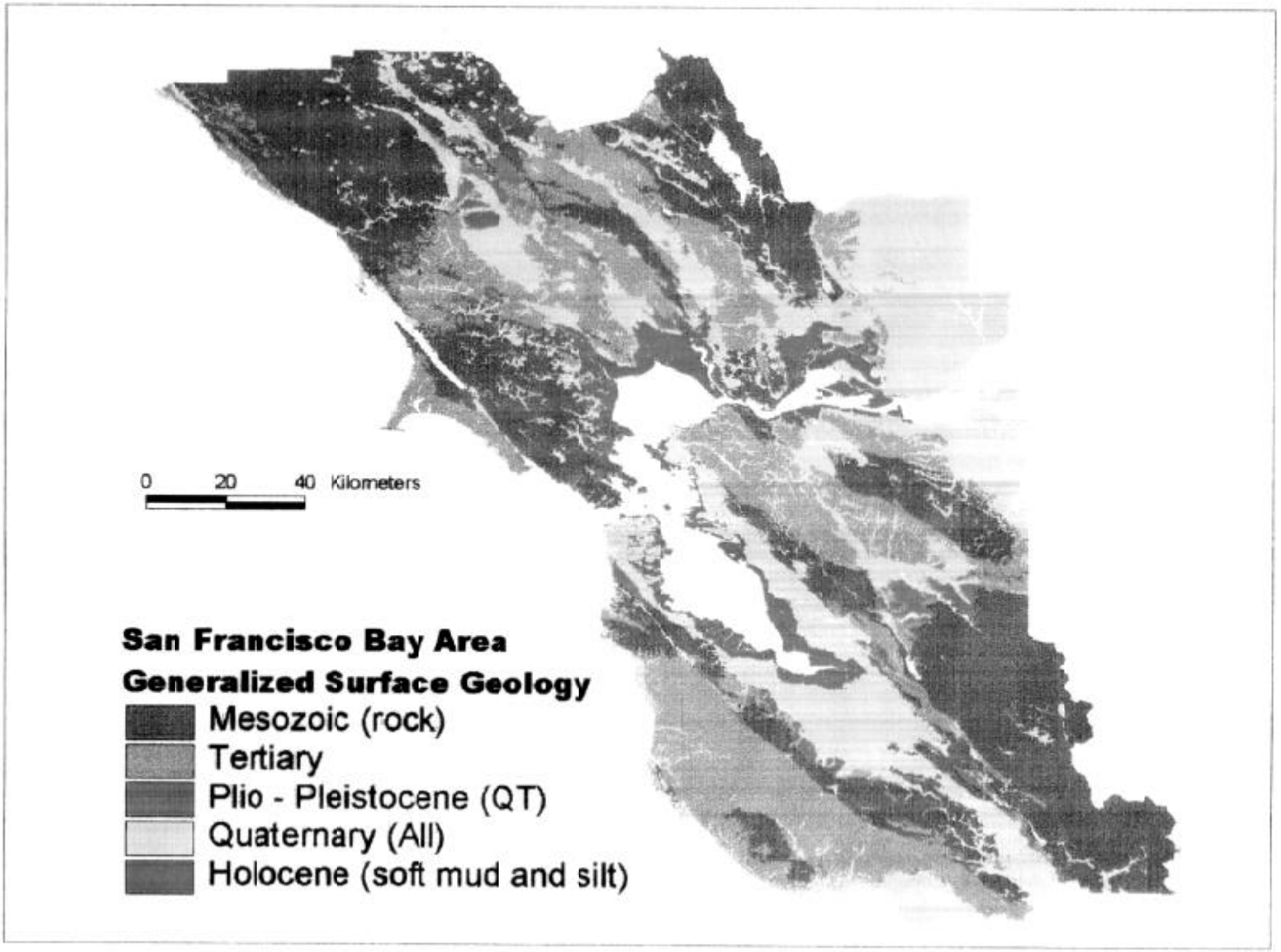

Figure 3. Mapped surface geology for the San Francisco Bay Area showing categories Bay Mud (Q_m) Quaternary Alluvium (Q_a + Q_{oa}), Quaternary/Tertiary (Q_{TS}), Tertiary Bedrock (T_S), and Franciscan (K_{jf}) (source: Wentworth (1997)).

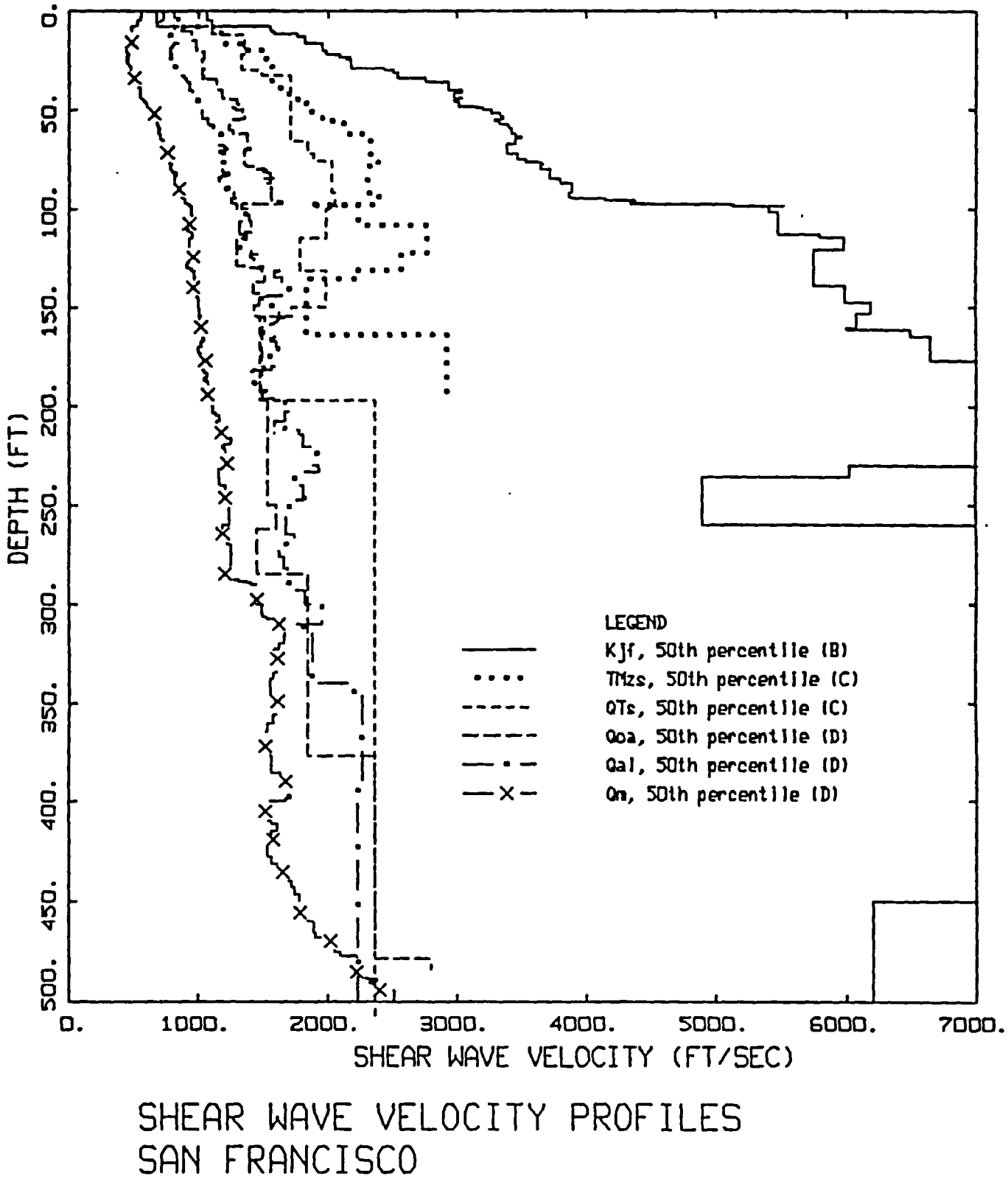

Figure 4. Surface geology based shear-wave velocity profiles for the San Francisco Bay area. Profiles are median estimates based on borehole measurements. Corresponding NEHRP categories are shown (Table 1).

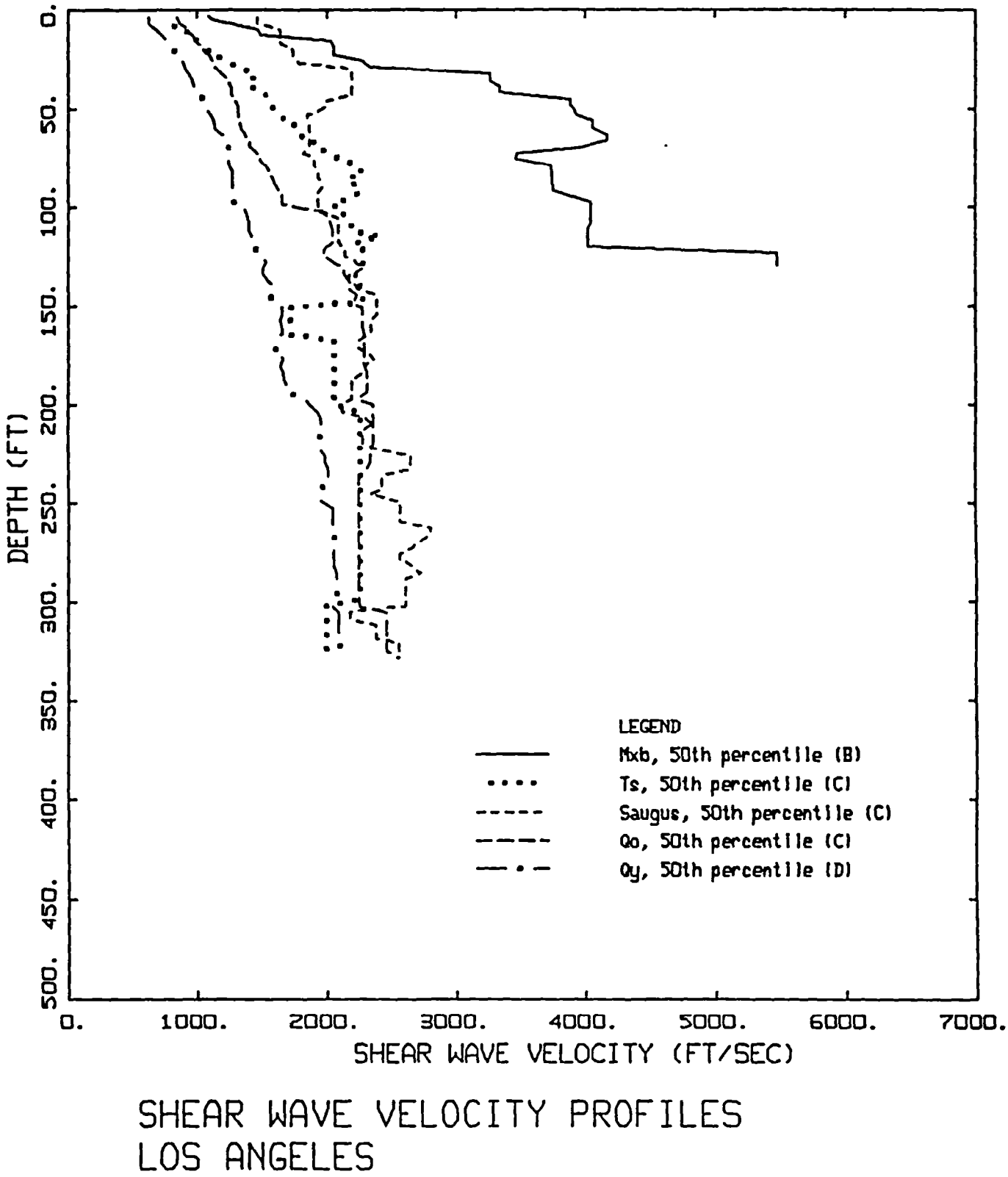

Figure 5. Surface geology based shear-wave velocity profiles for the Los Angeles area. Profiles are median estimates based on borehole measurements. Corresponding NEHRP categories are shown (Table 1).

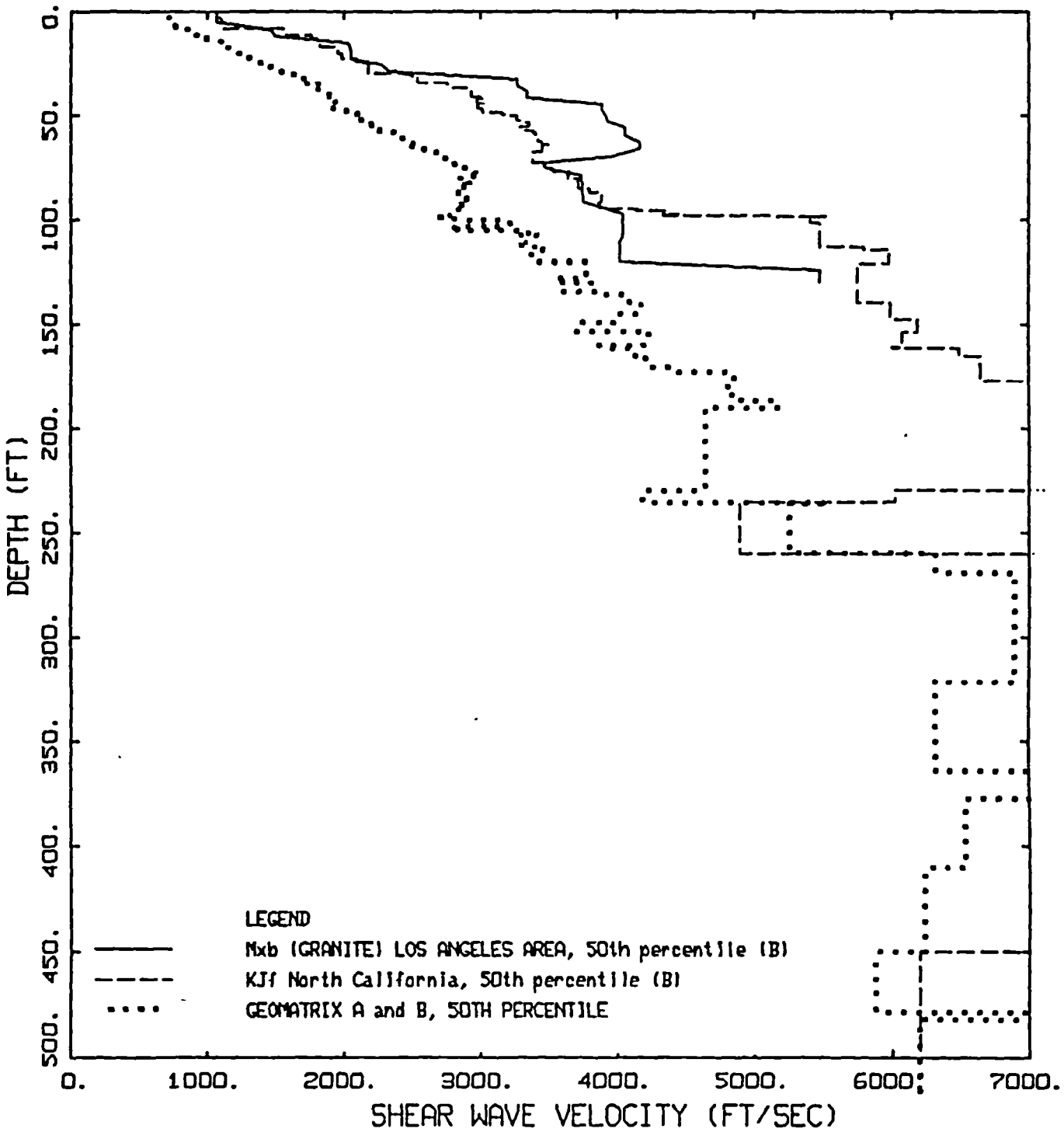

SHEAR WAVE VELOCITY PROFILES
SF, LA BASE ROCK COMPARISON

Figure 6. Comparison of median baserock shear-wave velocity profiles for San Francisco (Figure 4) and Los Angeles (Figure 5) areas. Dotted line is median profile for Geomatrix Category A and B, generally reflecting soft rock site conditions for California based empirical attenuation relations (Silva et al., 1997).

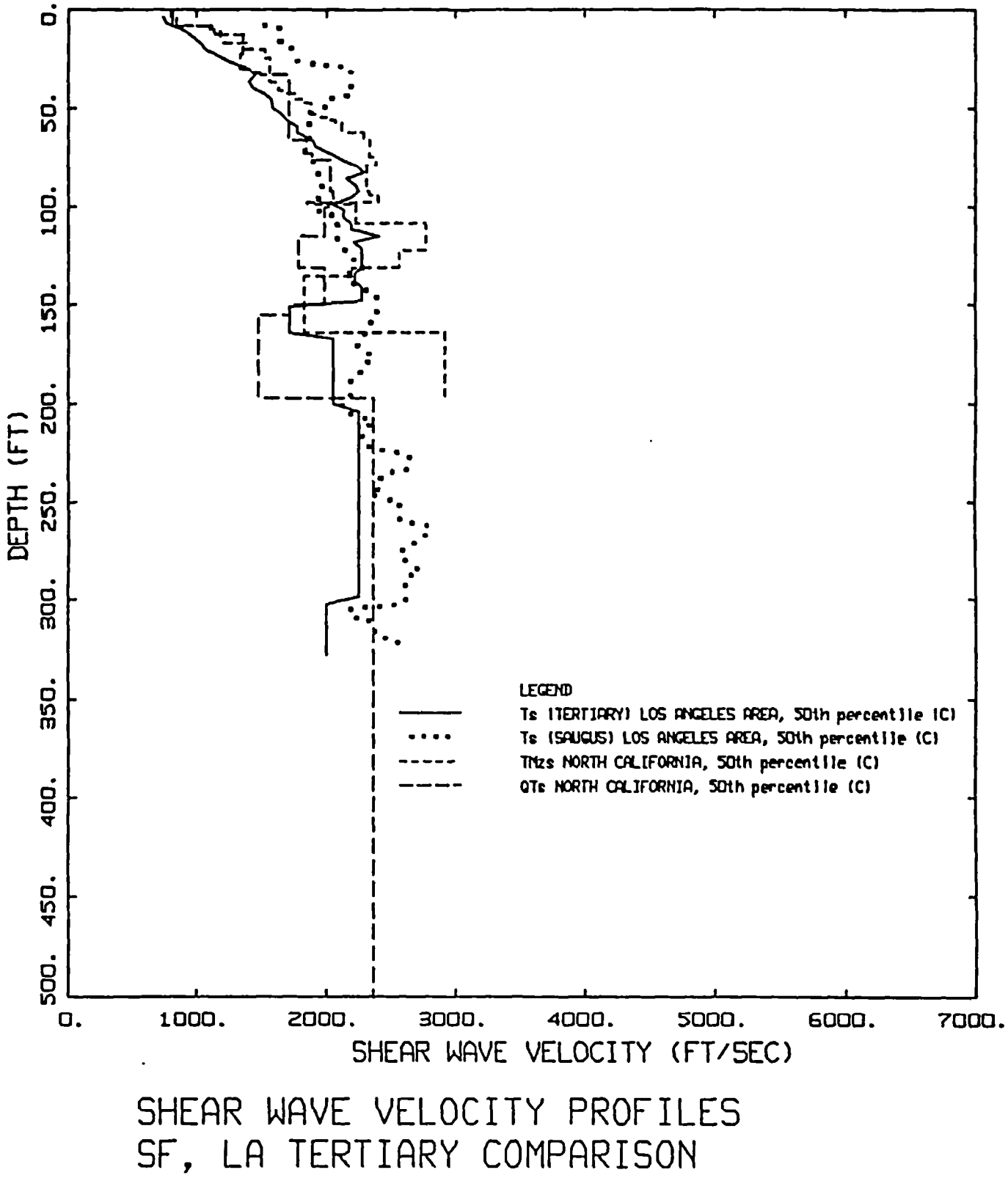

Figure 7. Comparison of median Tertiary shear-wave velocity profiles for San Francisco (Figure 4) and Los Angeles (Figure 5) areas.

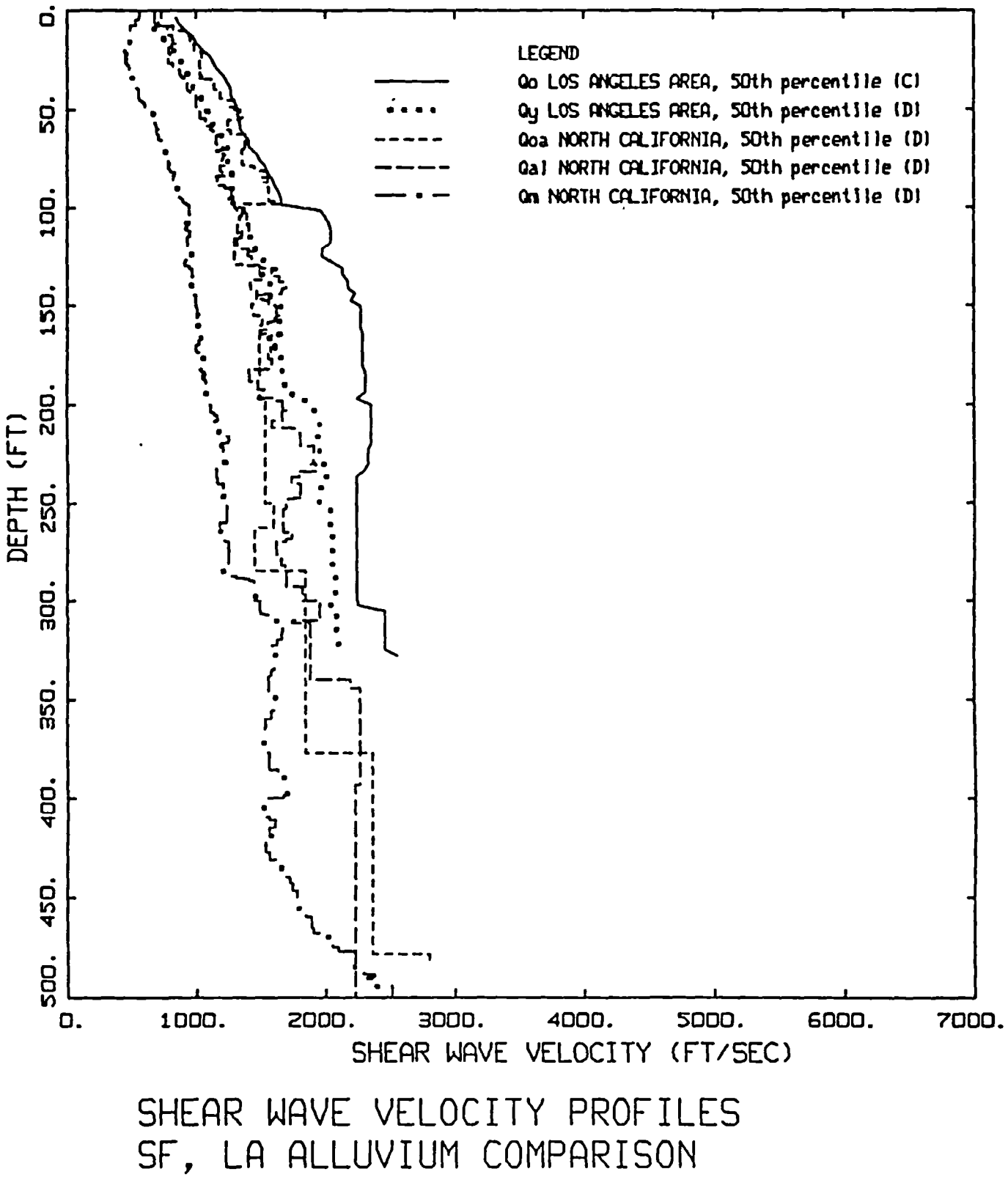

SHEAR WAVE VELOCITY PROFILES
SF, LA ALLUVIUM COMPARISON

Figure 8. Comparison of median Alluvium shear-wave velocity profiles for San Francisco (Figure 4) and Los Angeles (Figure 5) areas.

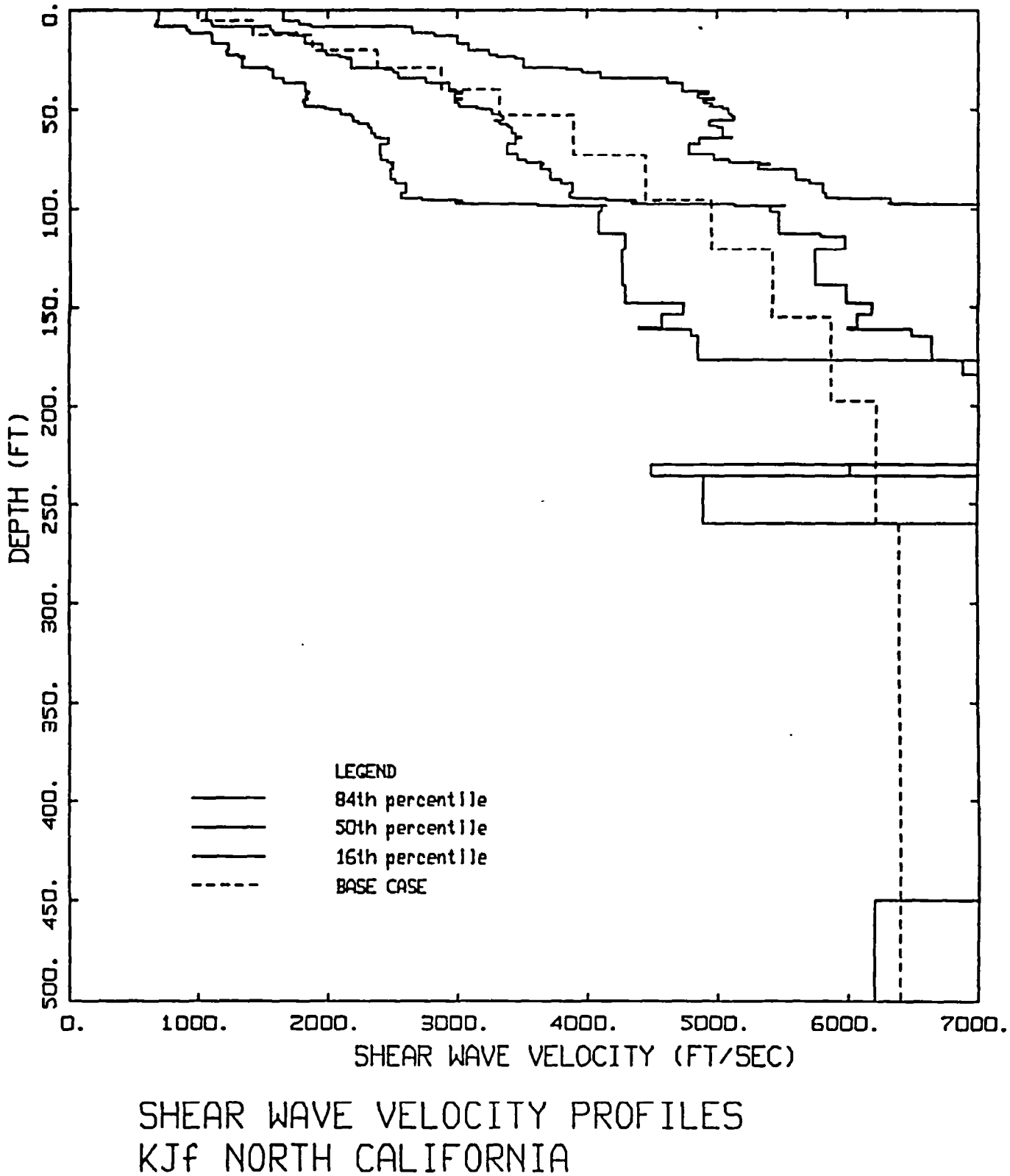

Figure 9. Median and ± 1 σ shear-wave velocity profiles for the San Francisco Bay area surface geologic unit K_{jf}, Franciscan (Table 1).

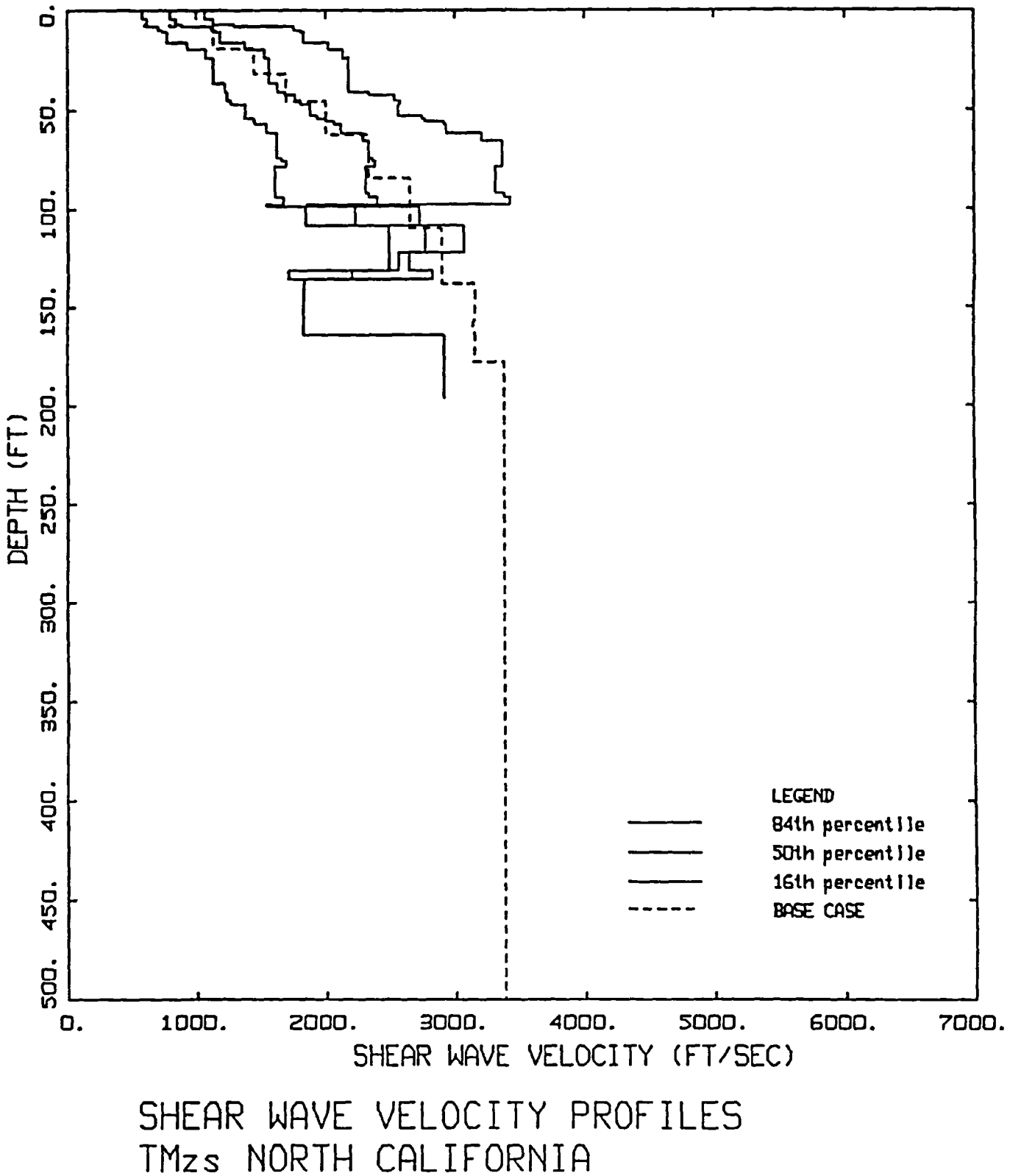

Figure 10. Median and ± 1 σ shear-wave velocity profiles for the San Francisco Bay area surface geologic unit TM_{zs}, Tertiary Bedrock (Table 1).

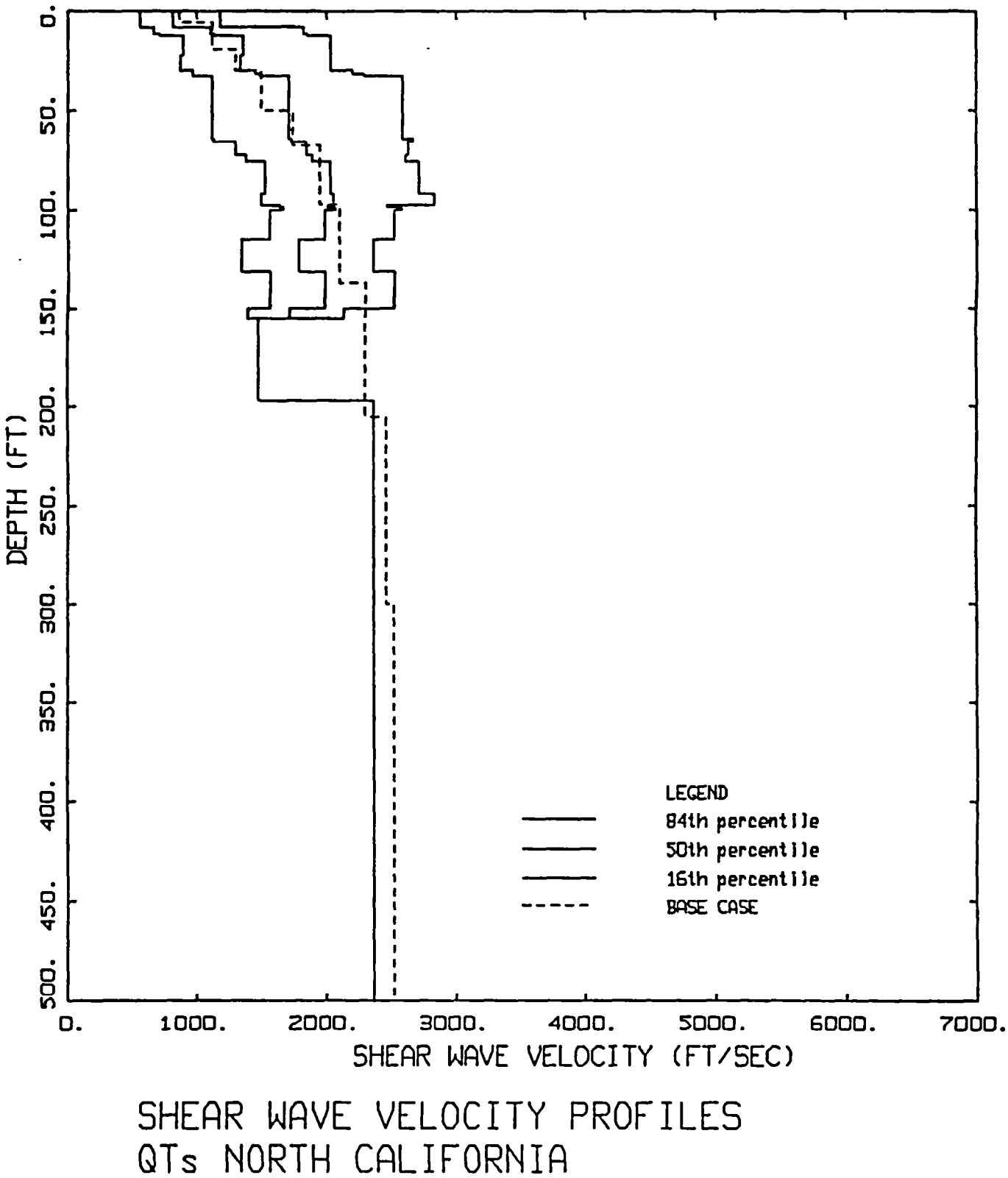

Figure 11. Median and ± 1 σ shear-wave velocity profiles for the San Francisco Bay area surface geologic unit QT_s, Quaternary/Tertiary (Table 1).

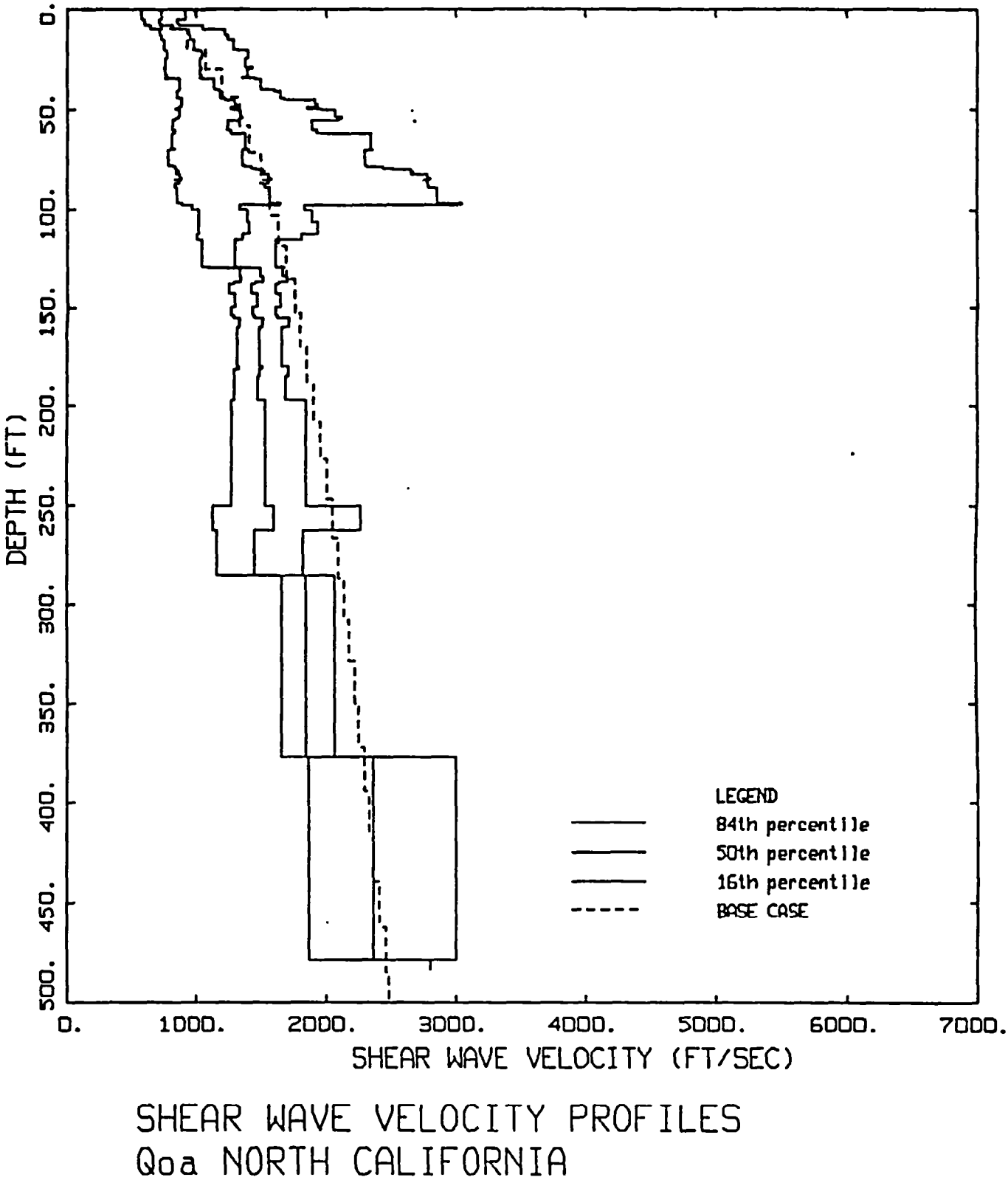

Figure 12. Median and ± 1 σ shear-wave velocity profiles for the San Francisco Bay area surface geologic unit Q_{oa}, Older Alluvium (Table 1).

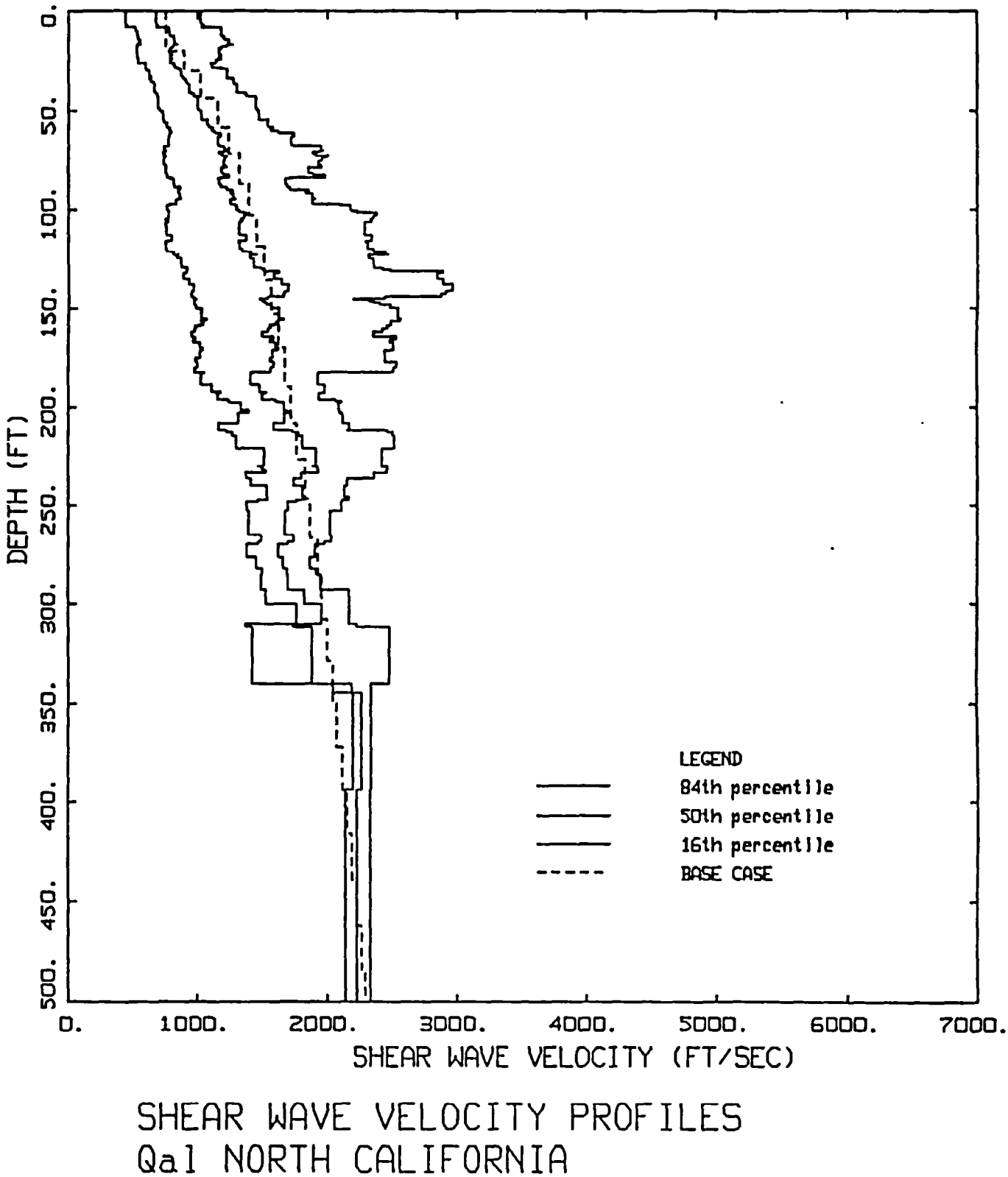

Figure 13. Median and ± 1 σ shear-wave velocity profiles for the San Francisco Bay area surface geologic unit Q_{al}, Quaternary Alluvium (Table 1).

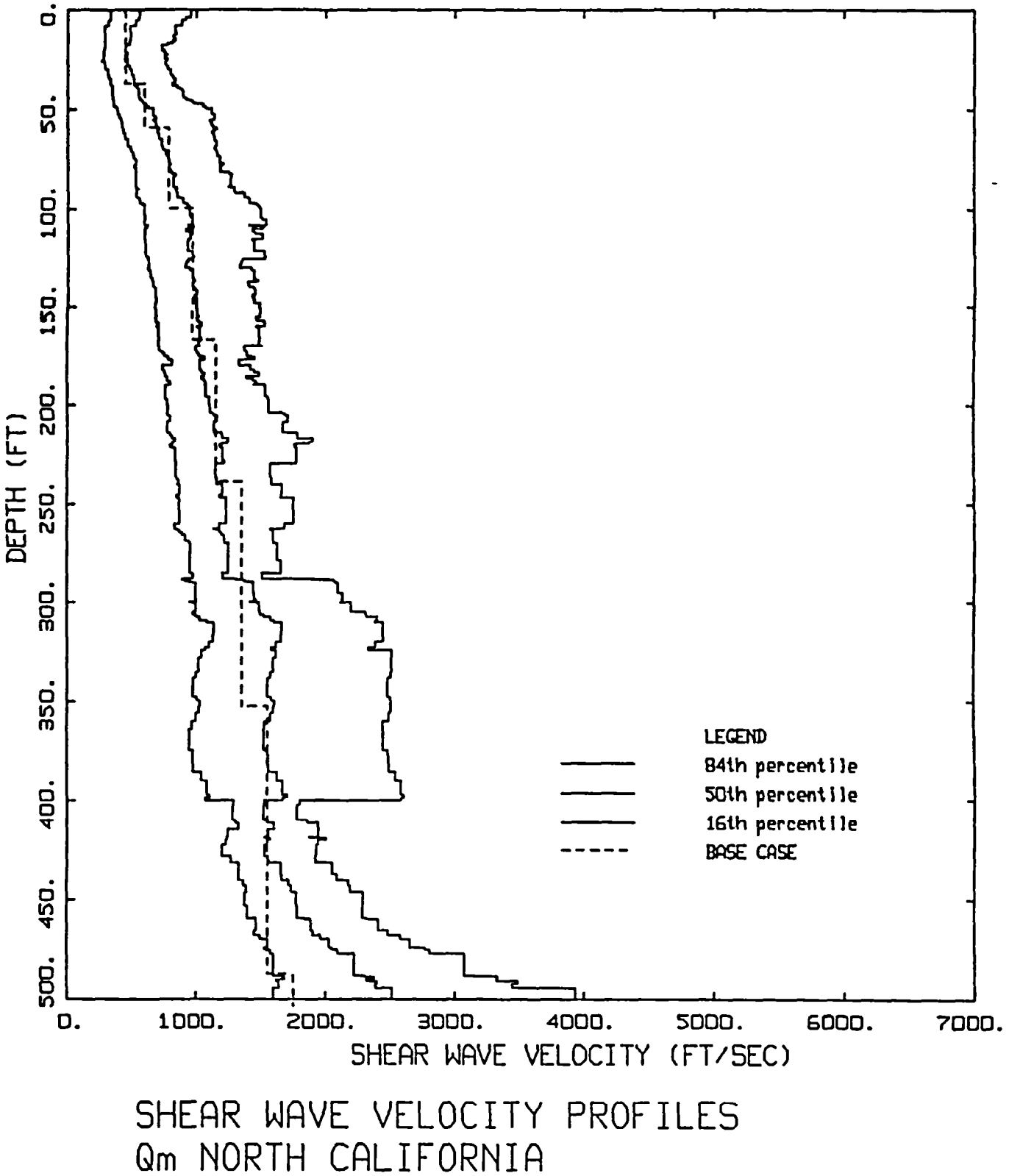

Figure 14. Median and ± 1 σ shear-wave velocity profiles for the San Francisco Bay area surface geologic unit Q_m, Bay Mud (Table 1).

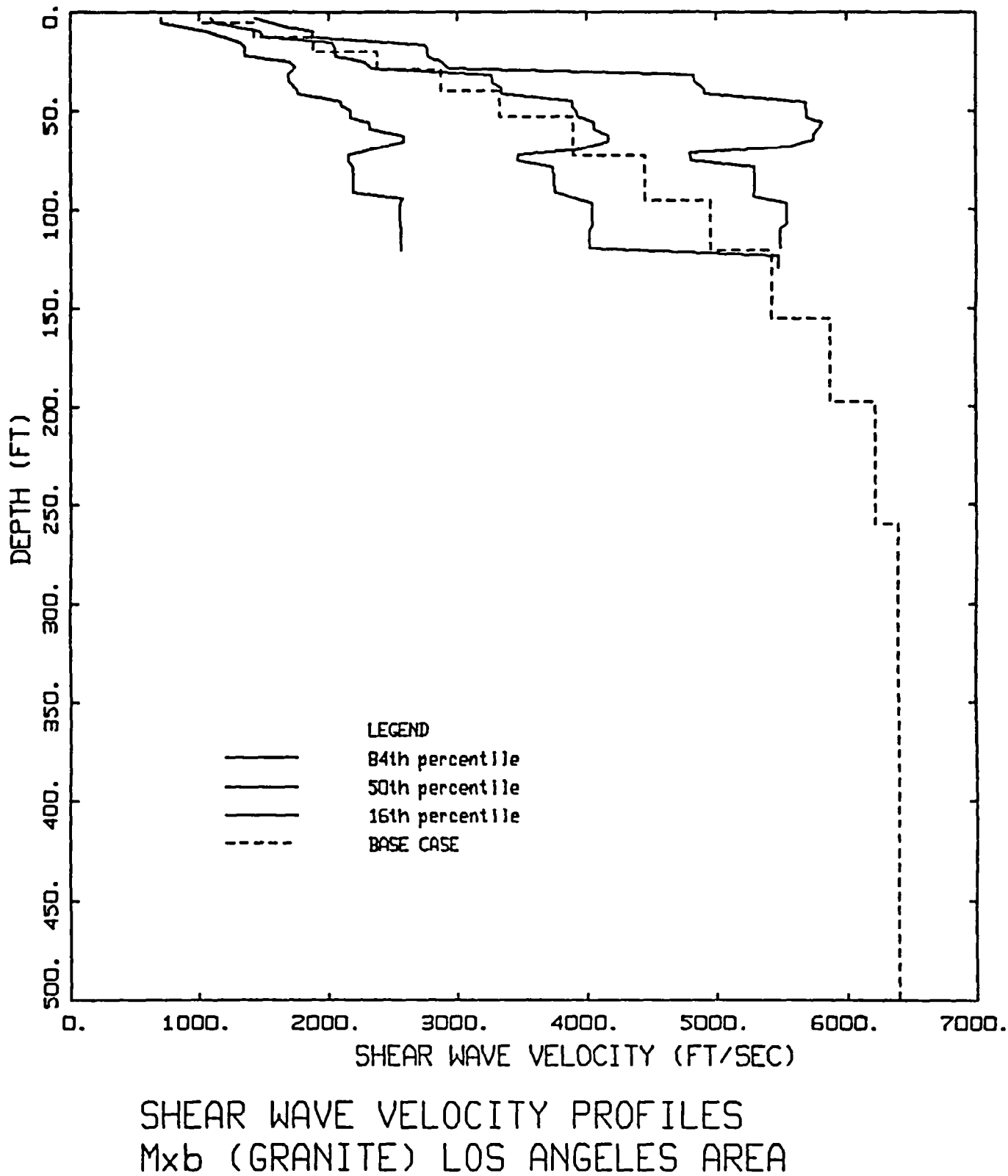

Figure 15. Median and ± 1 σ shear-wave velocity profiles for the Los Angeles area surface geologic unit M_{xb}, Granite (Table 1).

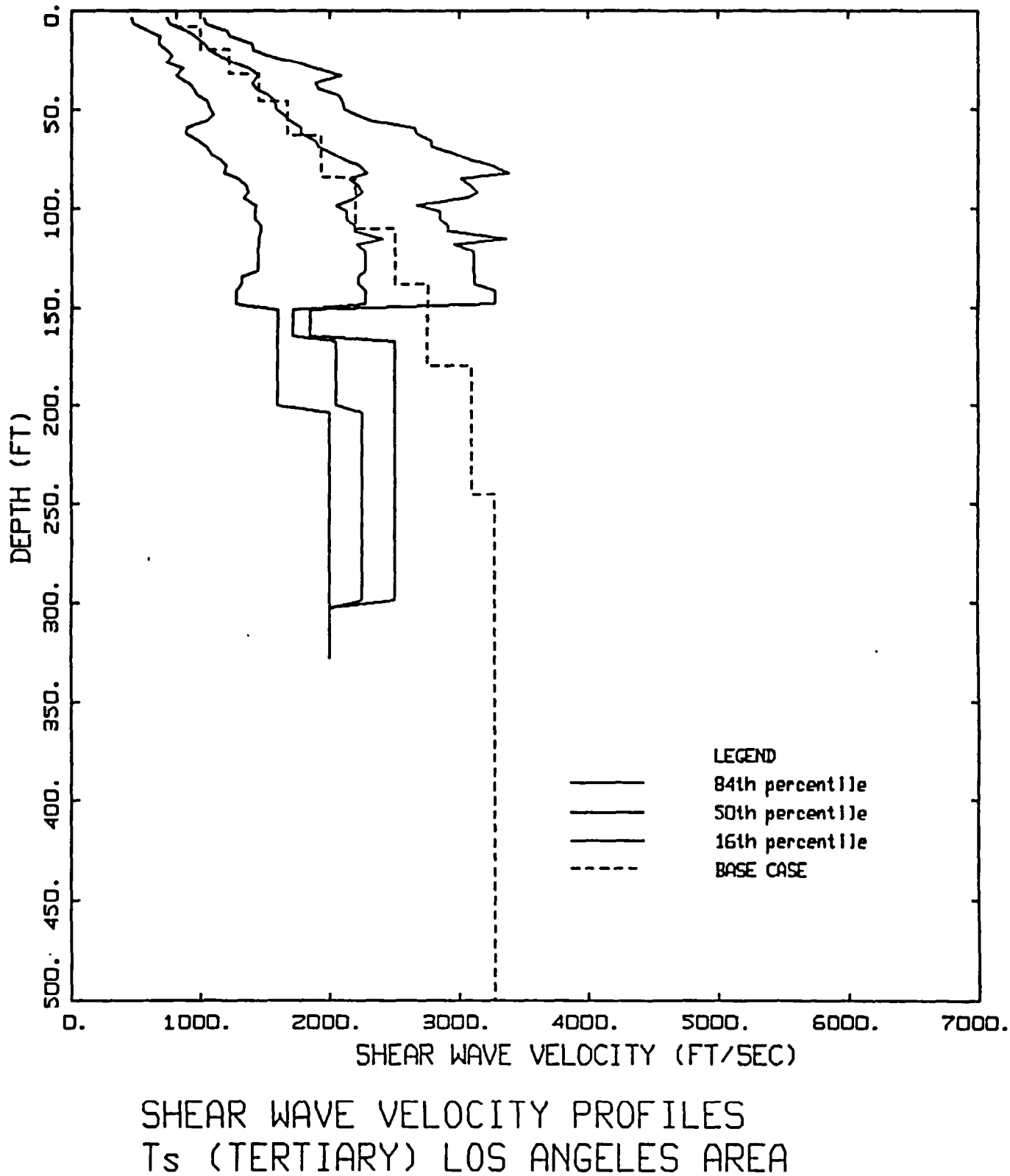

Figure 16. Median and ± 1 σ shear-wave velocity profiles for the Los Angeles area surface geologic unit T_s, Tertiary (Table 1).

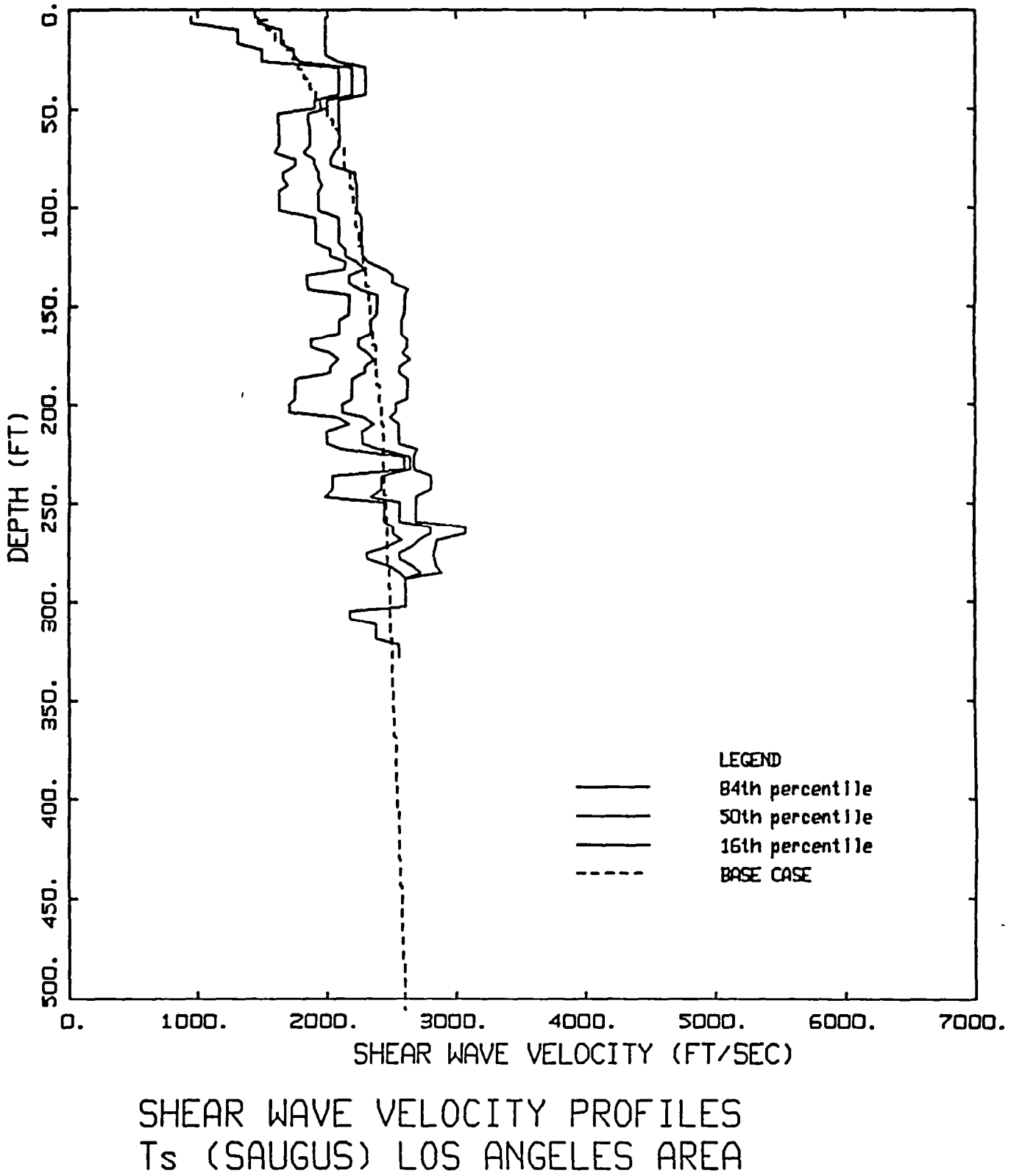

Figure 17. Median and ± 1 σ shear-wave velocity profiles for the San Francisco Bay area surface geologic unit T_s, Saugus (Table 1).

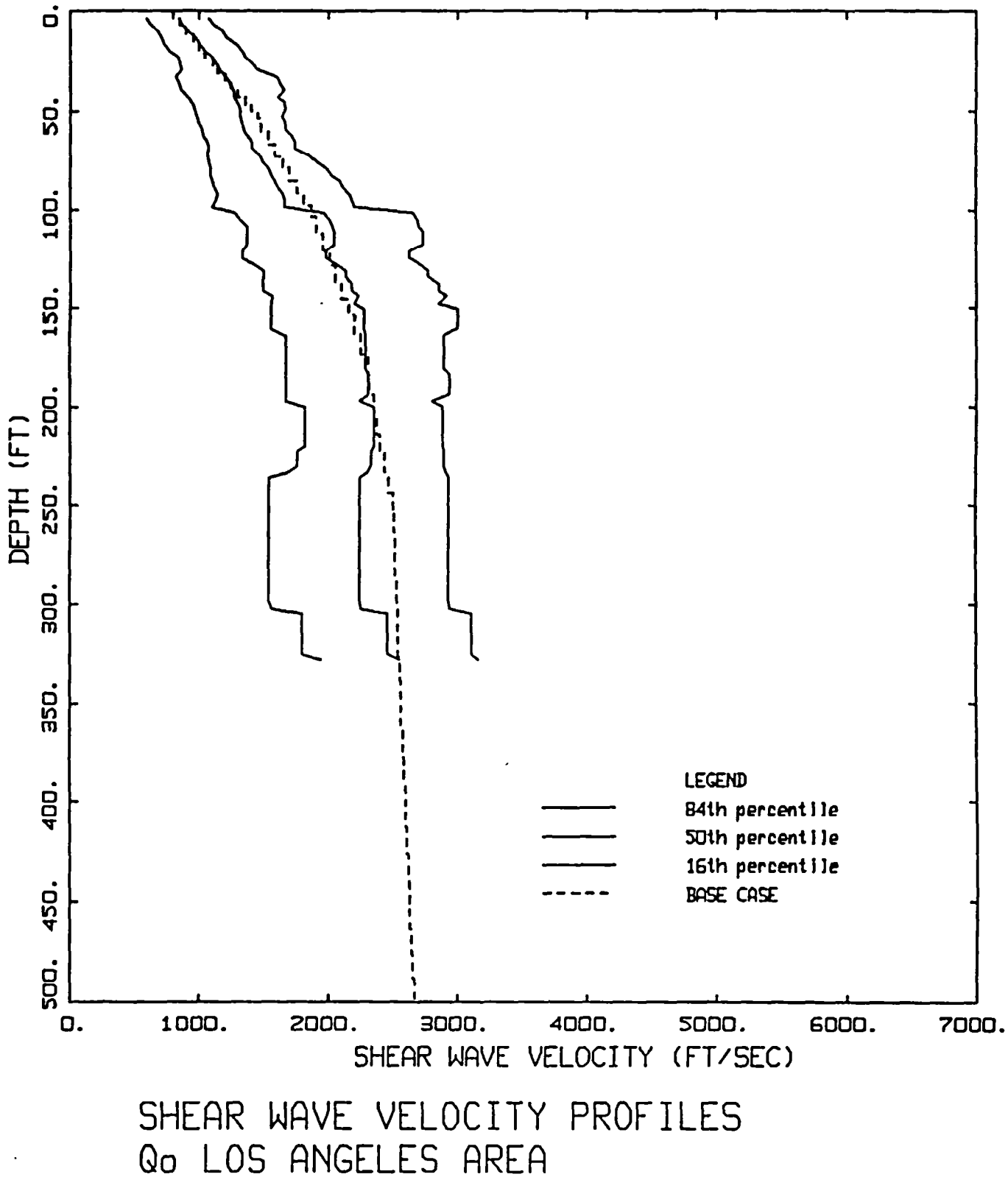

Figure 18. Median and ± 1 σ shear-wave velocity profiles for the Los Angeles area surface geologic unit Q_{oa}, Older Alluvium (Table 1).

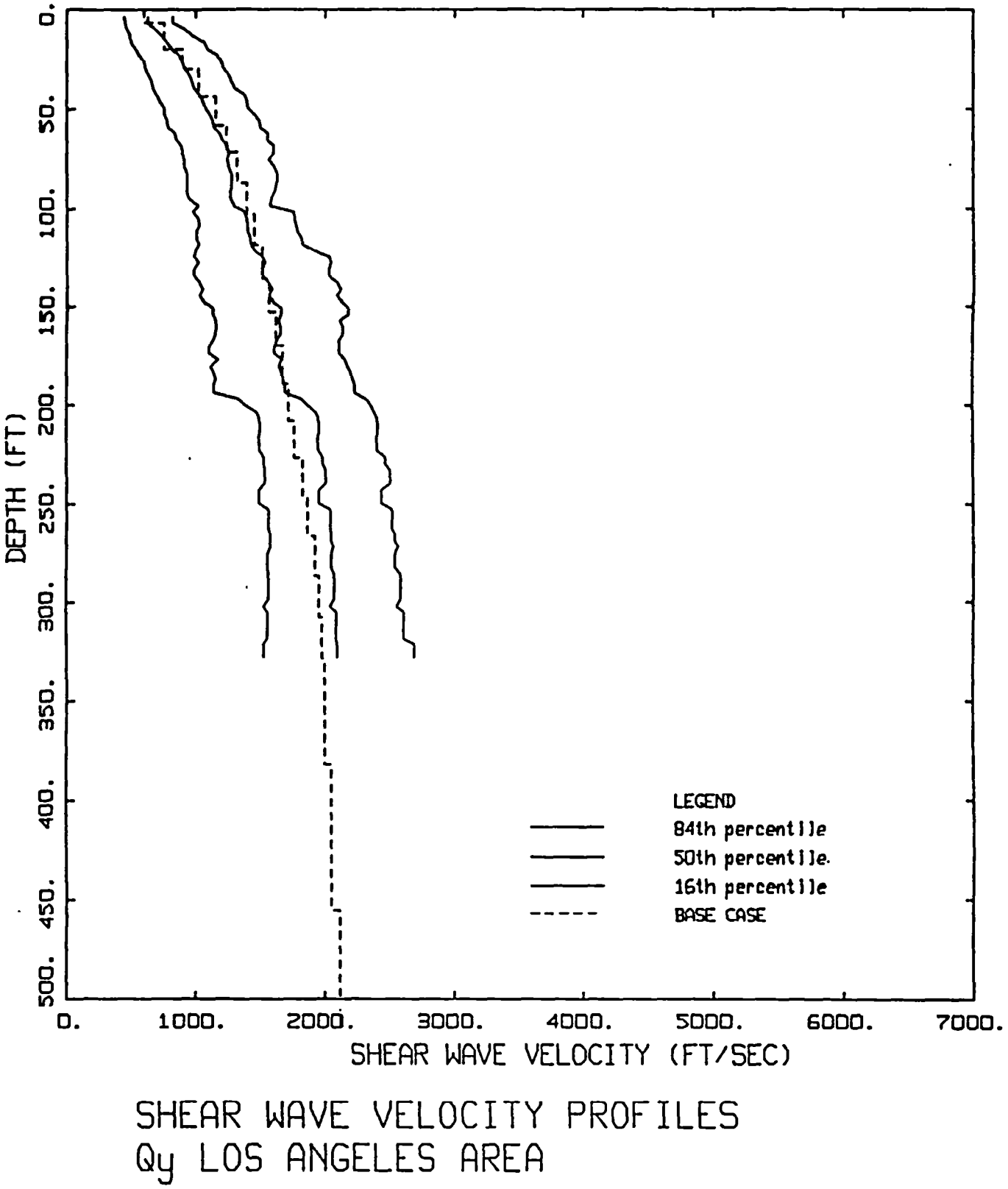

Figure 19. Median and ± 1 σ shear-wave velocity profiles for the Los Angeles area surface geologic unit Q_y, Younger Alluvium (Table 1).

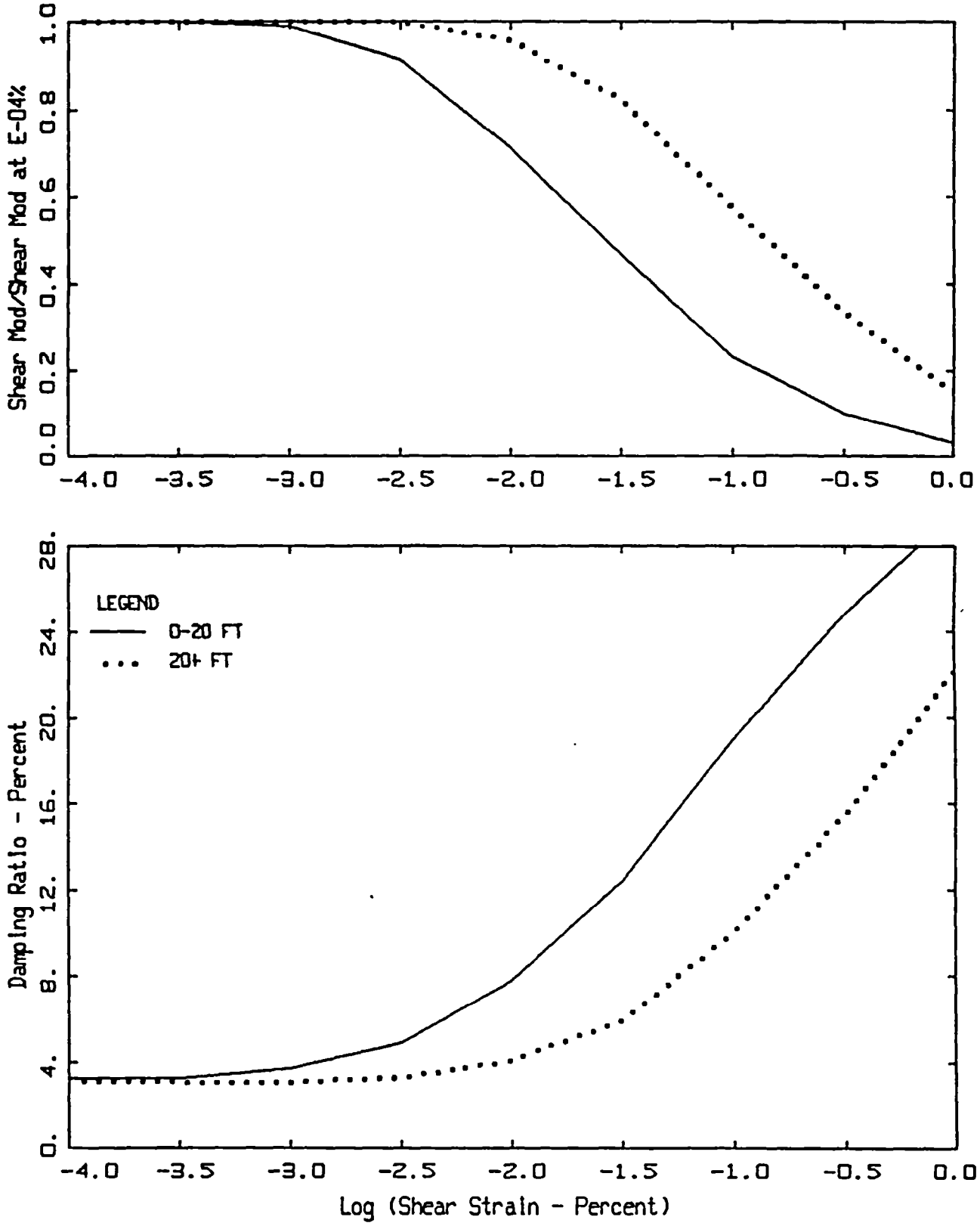

MODULUS REDUCTION AND DAMPING CURVES FOR ROCK

Figure 20. Generic G/Gmax and hysteretic damping curves for rock site conditions.

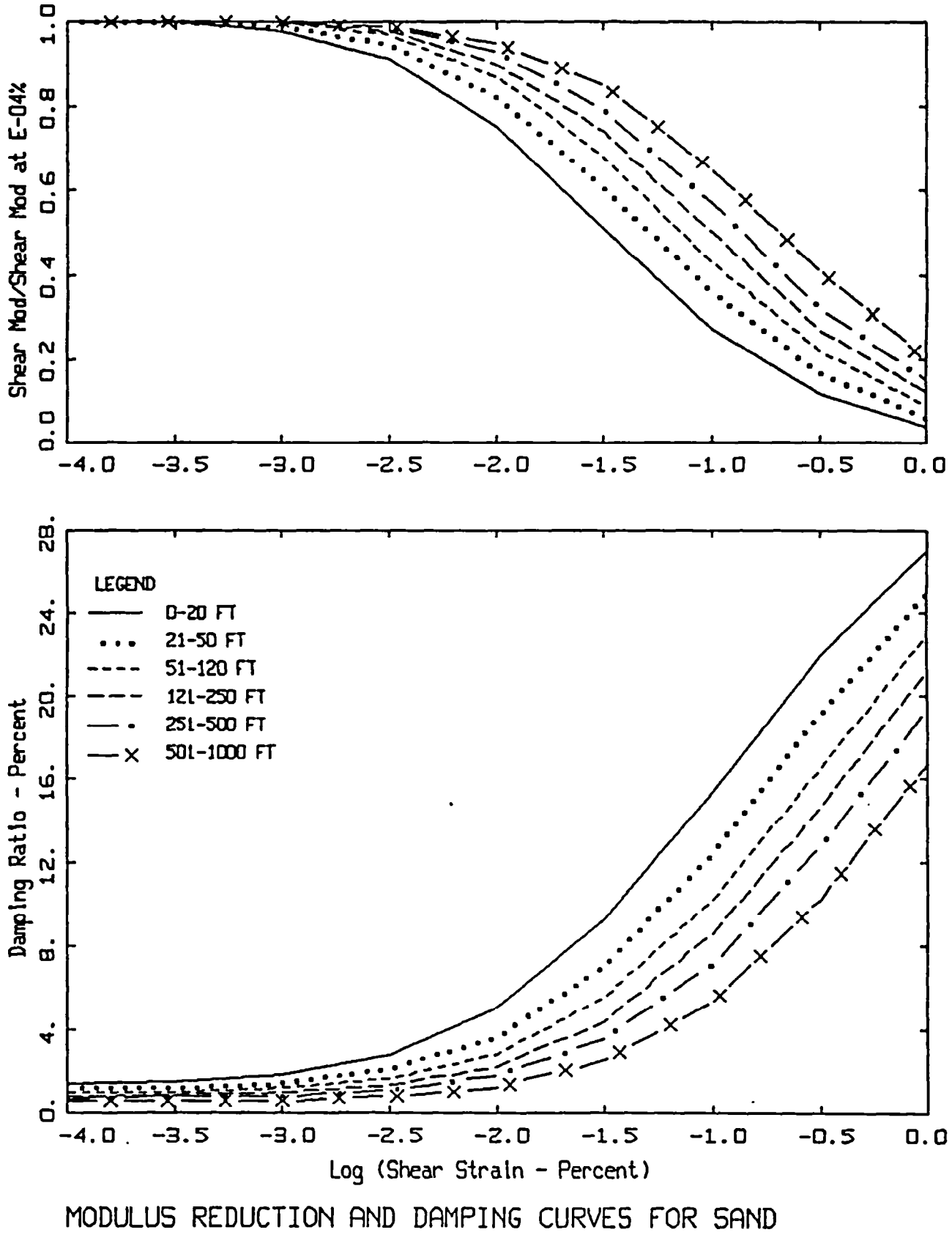

Figure 21. Generic G/Gmax and hysteretic damping curves for North Coast cohesionless soil site conditions (EPRI, 1993).

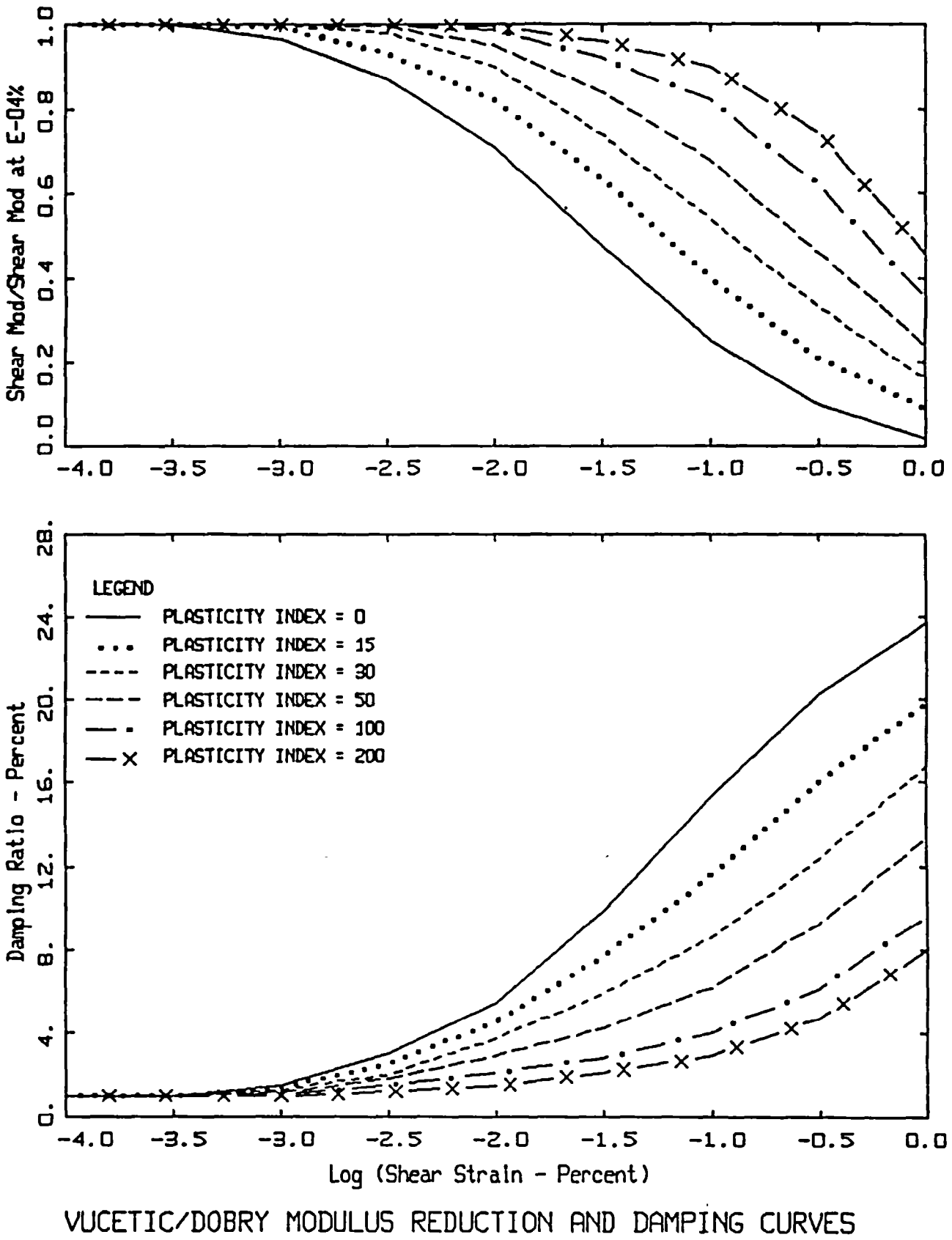

Figure 22. Generic G/Gmax and hysteretic damping curves for cohesive soil site conditions (Vucetic and Dobry, 1991).

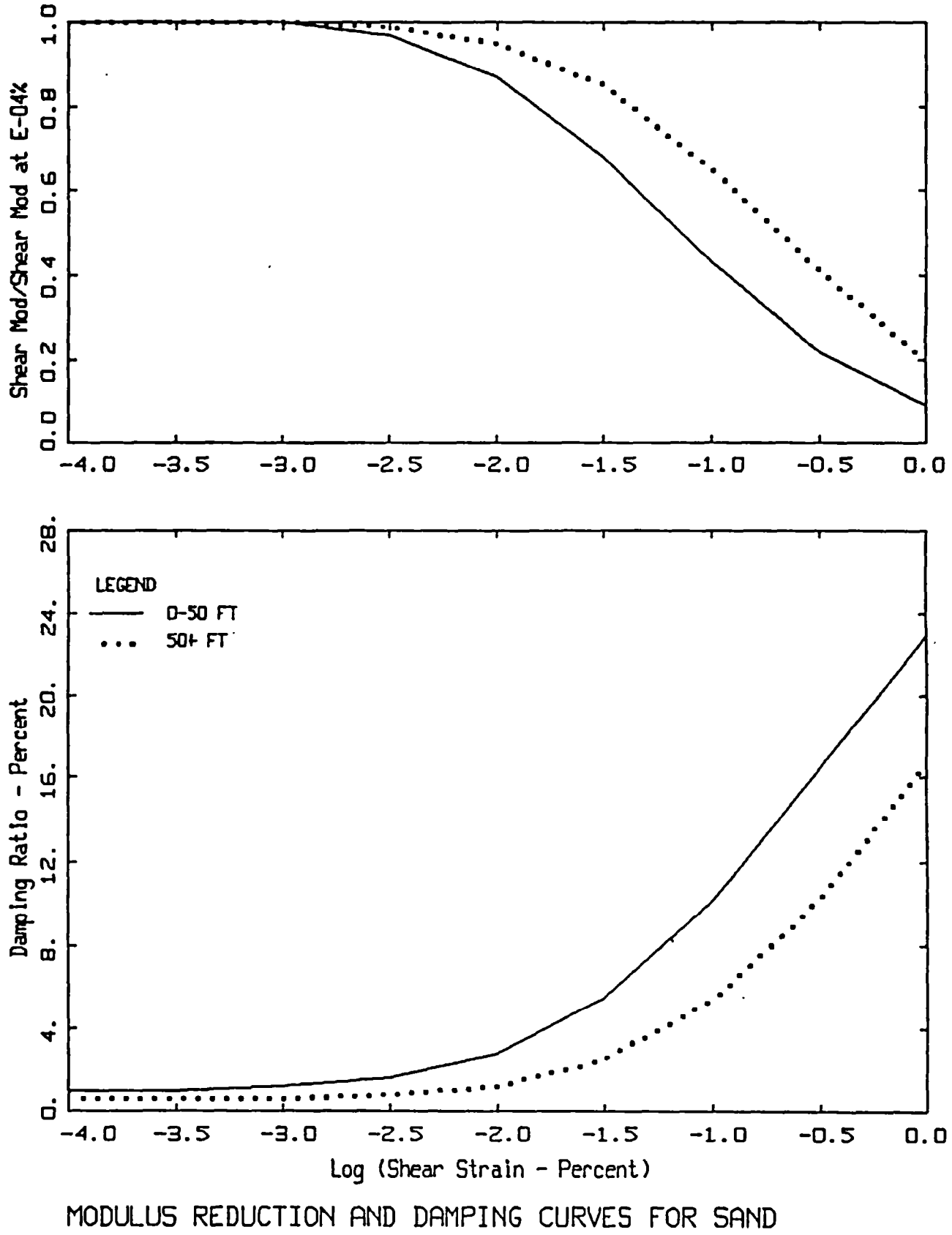

Figure 23. Generic G/Gmax and hysteretic damping curves for Peninsular Range cohesionless soil site conditions (Silva et al., 1997).

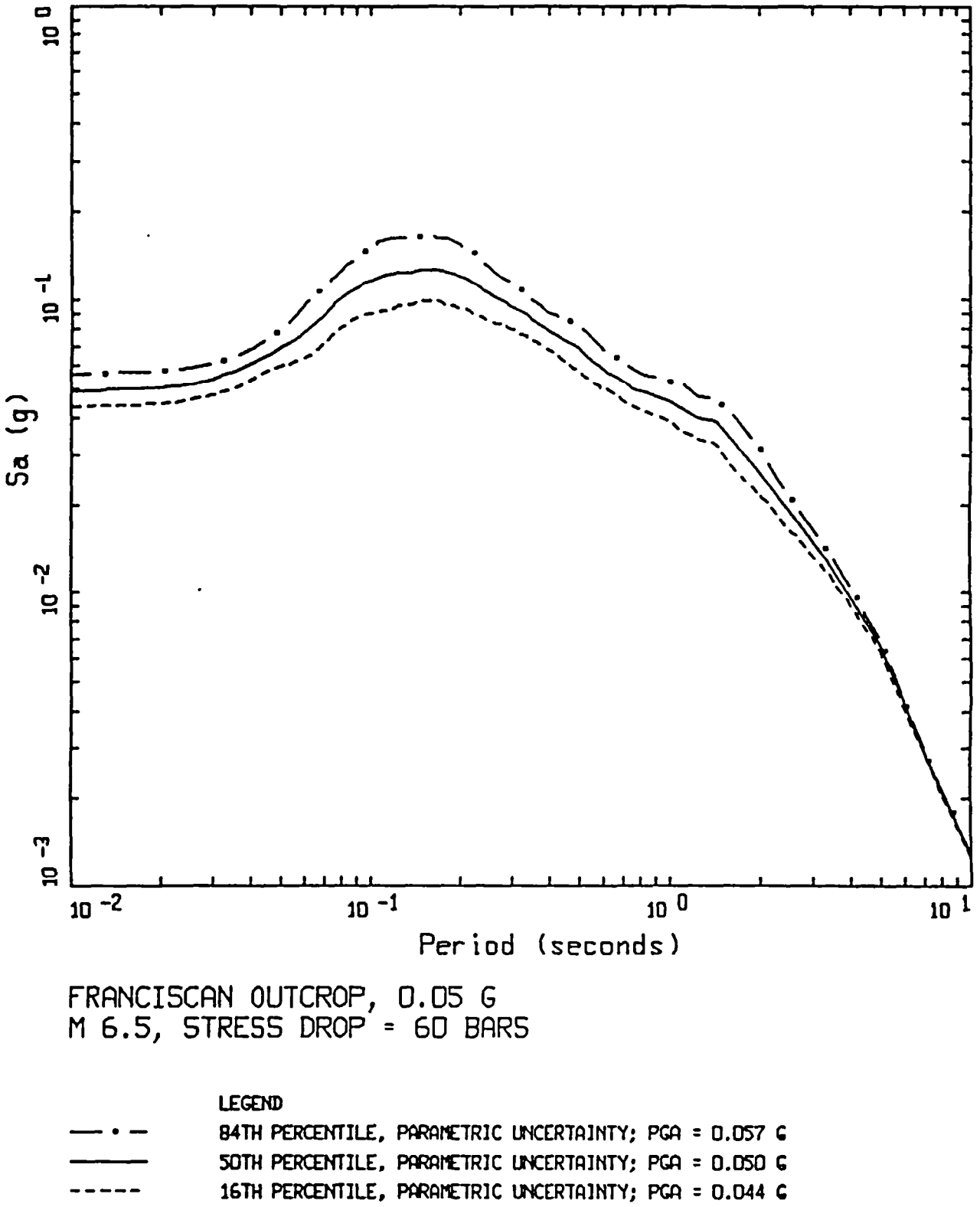

Figure 24. Median and ± 1 σ 5% damped baserock (Franciscan) motions for 5%g (Table 4): M = 6.5, stress drop = 60 bars. Parametric variation includes top 250 ft of the profile (Figure 15) and nonlinear properties (Figure 20).

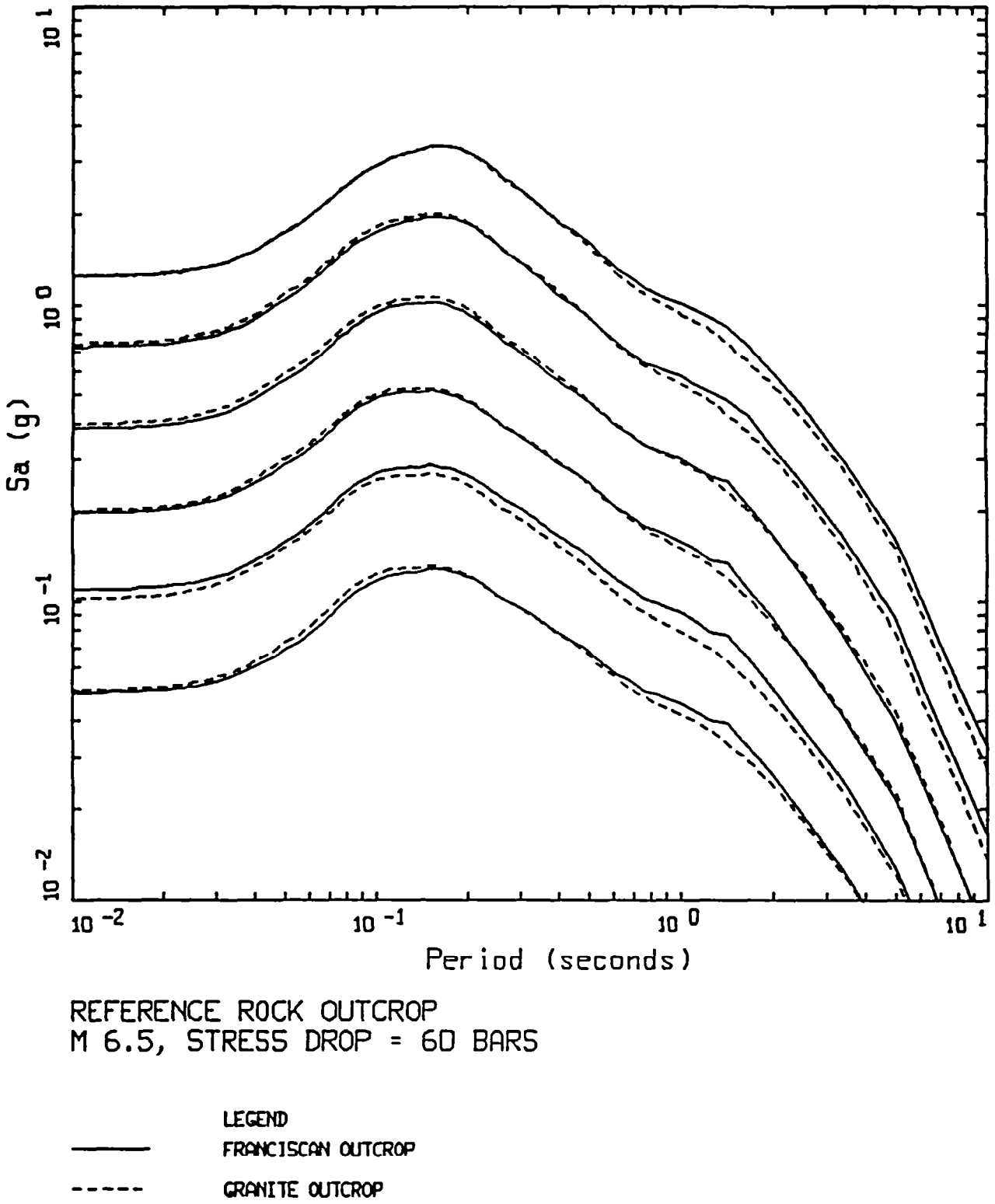

Figure 25. Comparison of median 5% damped response spectra computed for San Francisco (solid) and Los Angeles (dashed) area baserock site conditions for suite of outcrop peak acceleration values (Table 4): M = 6.5, stress drop: 60 bars.

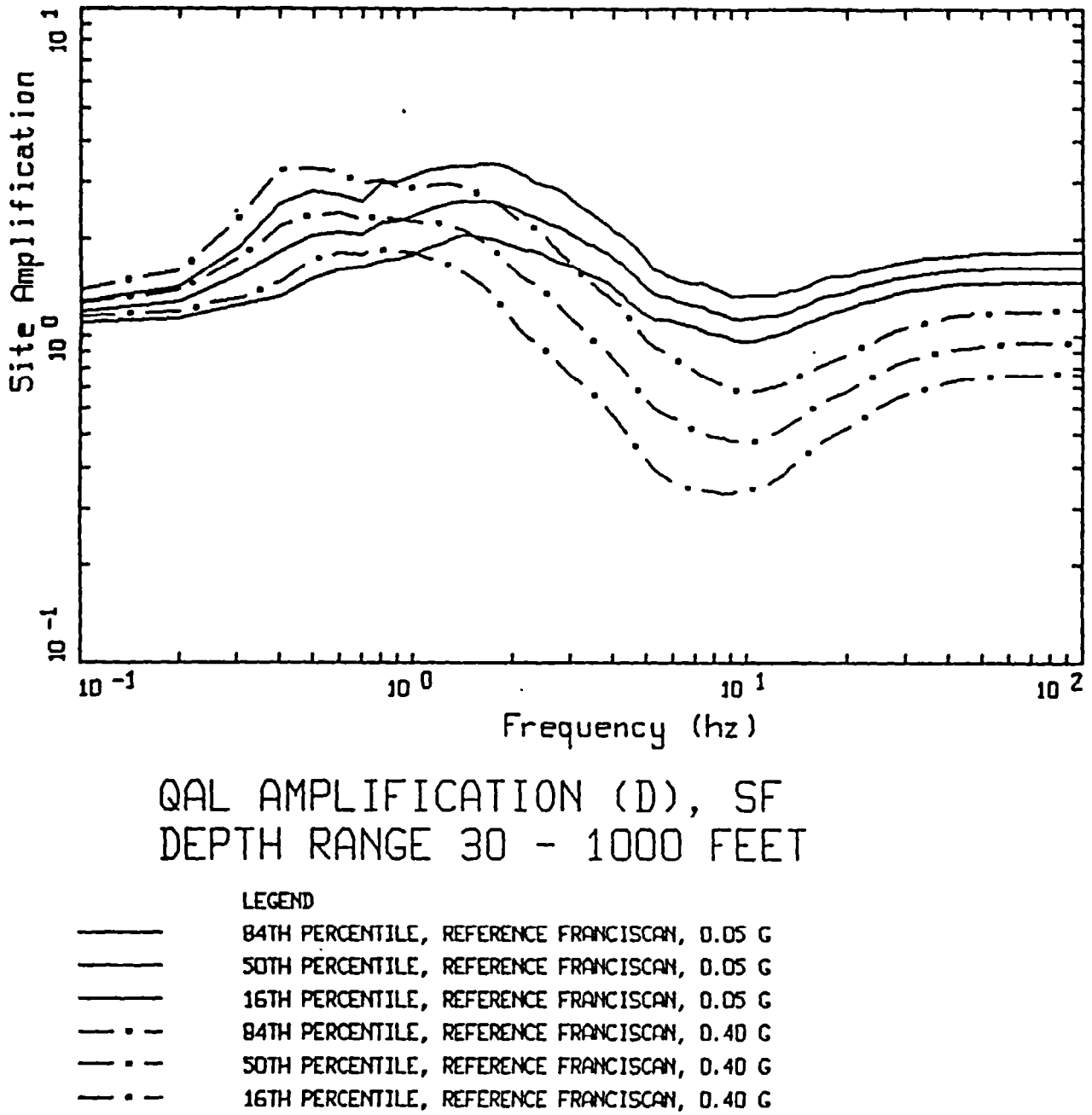

Figure 26. Comparison of median and ± 1 σ amplification factors (5% damped response spectra) for San Francisco area Quaternary Alluvium (Q_a) depth category 4 (30 to 1,000 ft) for reference Franciscan rock outcrop median peak acceleration values of 0.05g and 0.40g.

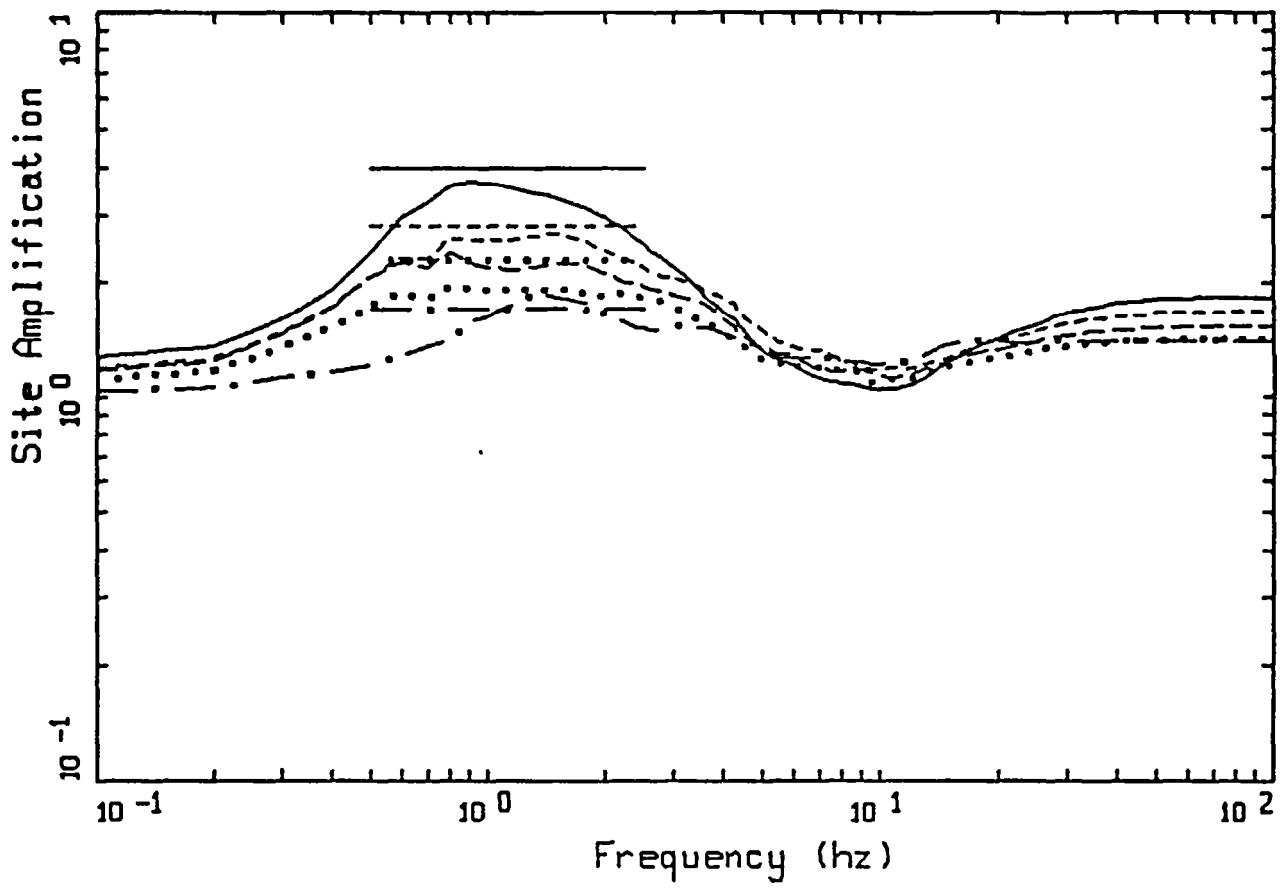

AMPLIFICATION: 5% DAMPED RESPONSE SPECTRA
REFERENCE FRANCISCAN 0.05 G

LEGEND

———	BAY MUD, 150-350ft (5% Damped Response Spectra, median)
- - - - -	QAL, 350-650ft (5% Damped Response Spectra, median)
— — — —	QOA, 350-650ft (5% Damped Response Spectra, median)
• • • •	QUATERNARY/TERTIARY, 350-650ft (5% Damped Response Spectra, median)
— • —	TERTIARY (5% Damped Response Spectra, median)
———	BAY MUD (Borcherdt (1992) Empirical Fourier Amplitude Spectra, average)
- - - - -	QAL (Borcherdt (1992) Empirical Fourier Amplitude Spectra, average)
• • • •	QUATERNARY/TERTIARY (Borcherdt (1992) Empirical Fourier Amplitude Spectra, average)
— • —	TERTIARY (Borcherdt (1992) Empirical Fourier Amplitude Spectra, average)

Figure 27. Comparison of median amplification factors (5% damped response spectra) computed for reference Franciscan outcrop peak acceleration of 0.05g with empirical factors (smoothed Fourier amplitude spectra; Borcherdt and Glassmoyer, 1992). Empirical factors were computed using low levels of loading (generally ≤ 0.10g).

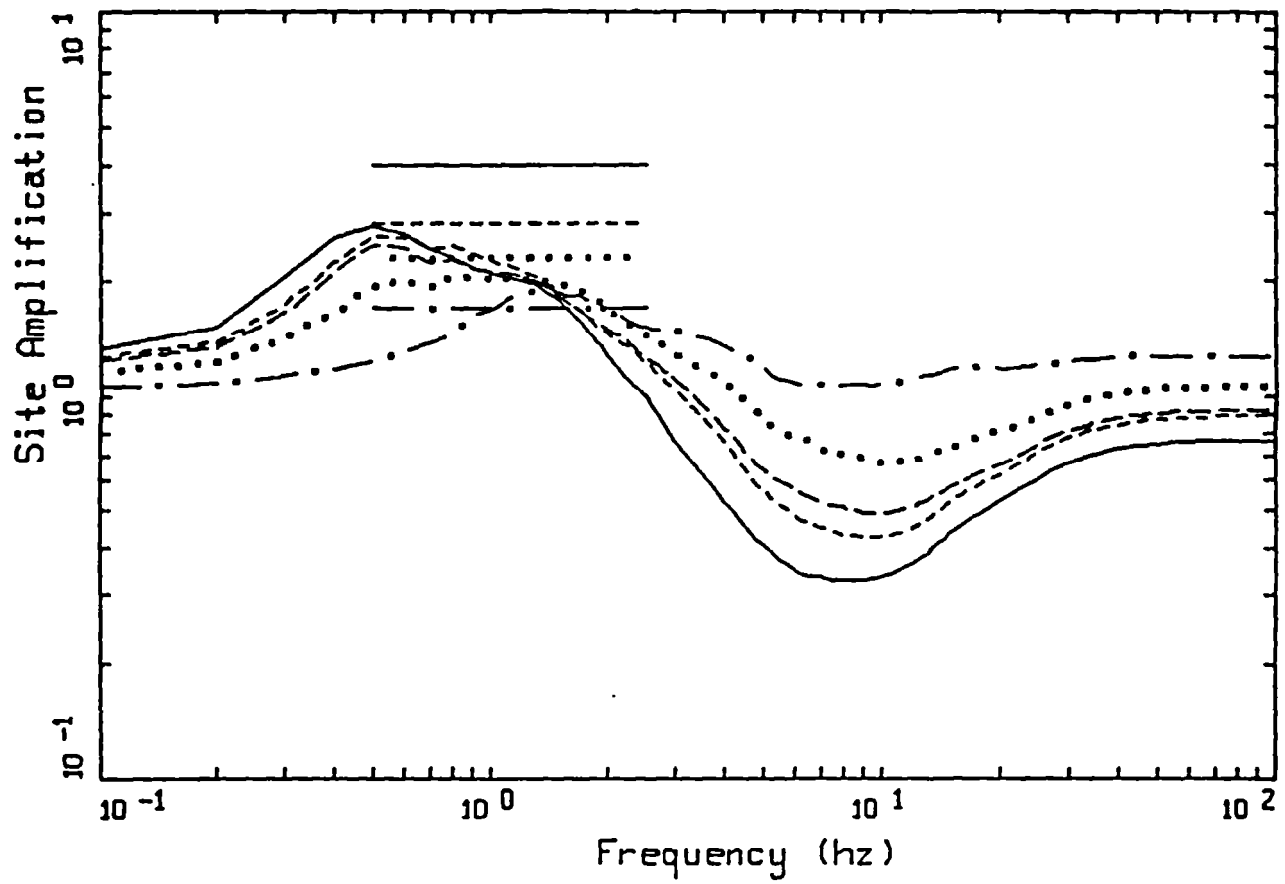

AMPLIFICATION: 5% DAMPED RESPONSE SPECTRA
REFERENCE FRANCISCAN 0.40 G

LEGEND

———	BAY MUD, 150-350ft (5% Damped Response Spectra, median)
- - - - -	QAL, 350-650ft (5% Damped Response Spectra, median)
— — — —	QOA, 350-650ft (5% Damped Response Spectra, median)
• • • •	QUATERNARY/TERTIARY, 350-650ft (5% Damped Response Spectra, median)
— • —	TERTIARY (5% Damped Response Spectra, median)
———	BAY MUD (Empirical Fourier Amplitude Spectra, average)
- - - - -	QAL (Empirical Fourier Amplitude Spectra, average)
• • • •	QUATERNARY/TERTIARY (Empirical Fourier Amplitude Spectra, average)
— • —	TERTIARY (Empirical Fourier Amplitude Spectra, average)

Figure 28. Comparison of median amplification factors (5% damped response spectra) computed for reference Franciscan outcrop peak acceleration of 0.40g with empirical factors (smoothed Fourier amplitude spectra; Borcherdt and Glassmoyer, 1992). Empirical factors were computed using low levels of loading (generally ≤ 0.10g).

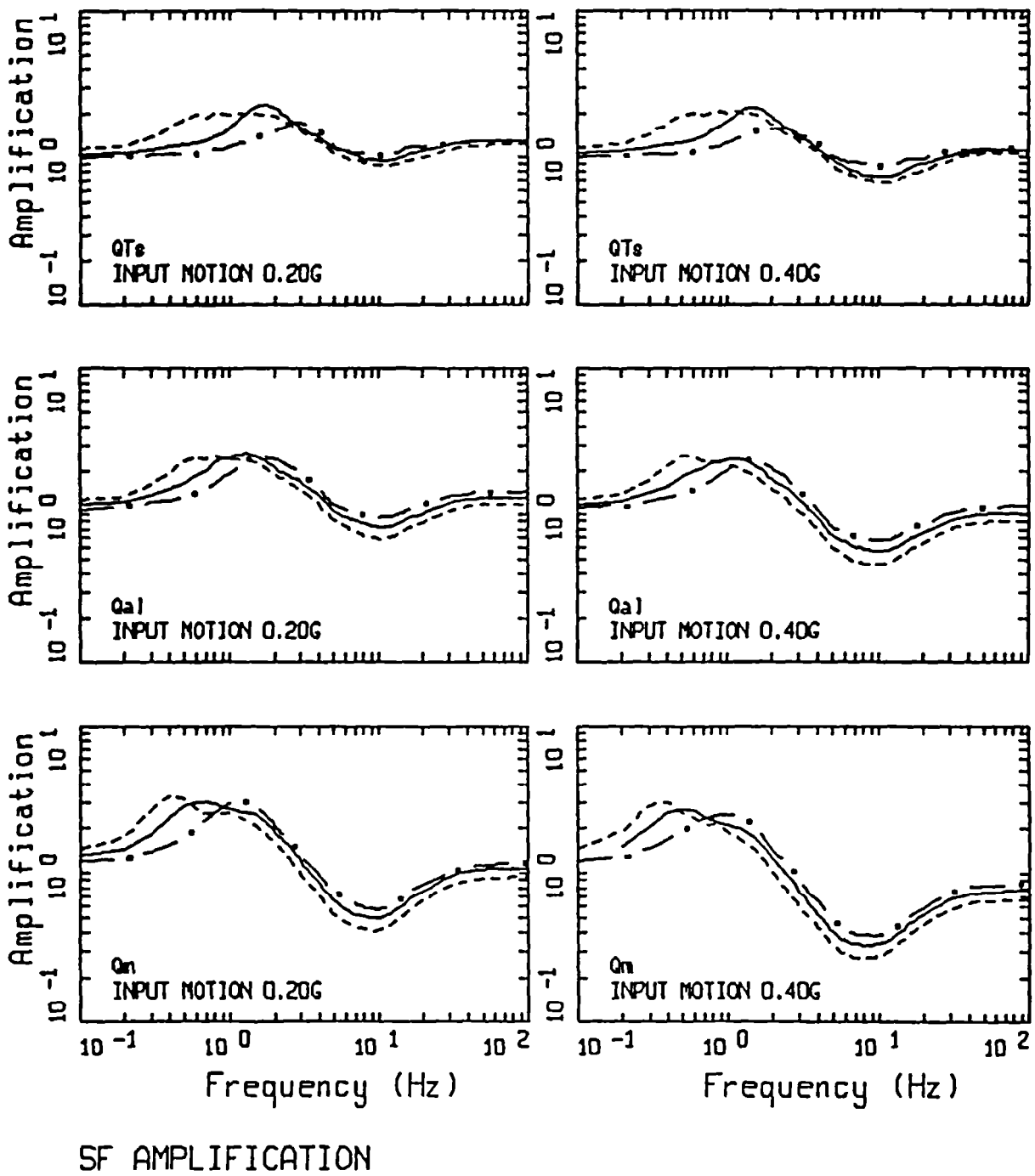

Figure 29. Median amplification factors computed for QT_s, Q_{al}, Q_m, for different depth categories: 30 ft to 150 ft, dash dots; 150 ft to 350 ft, solid; 350 ft to 650 ft, dashes.

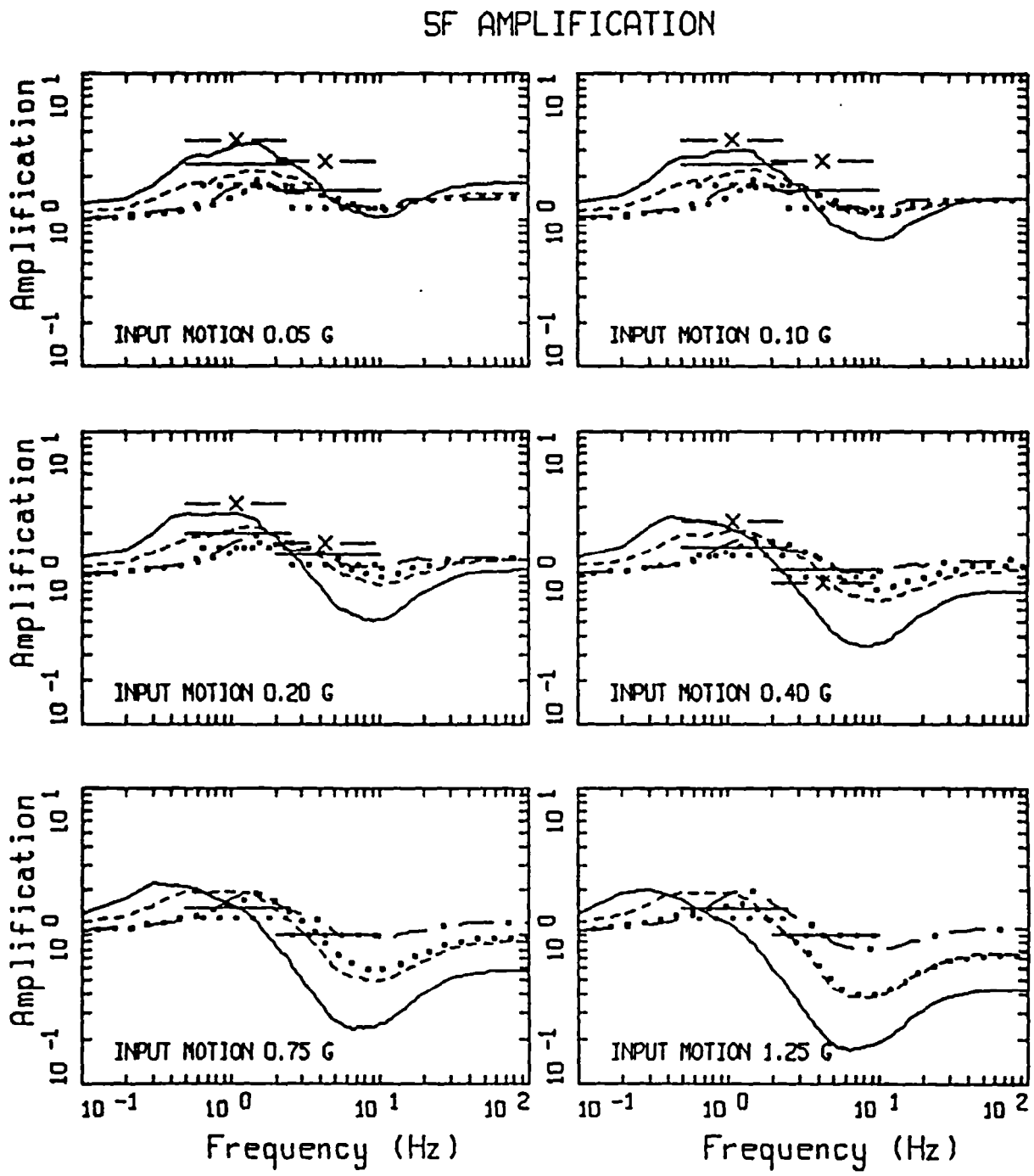

LEGEND

———	BAY MUD (D), CATEGORY 6 (30-650ft)
- - - - -	ALLUVIUM (D), CATEGORY 4 (30-1000ft)
• • • •	QUATERNARY/TERTIARY (C), CATEGORY 5 (30-450ft)
— • —	TERTIARY (C)
—X—	E: 0.50-2.5 Hz, 2.0-10.00 Hz (NEHRP, 1994)
———	D(Qal + Qoa + Qm): 0.50-2.5 Hz, 2.0-10.00 Hz (NEHRP, 1994)
• • • •	C(TMzs + QTs): 0.50-2.5 Hz, 2.0-10.00 Hz (NEHRP, 1994)

Figure 30. Comparison of median amplification factors with NEHRP provisions.

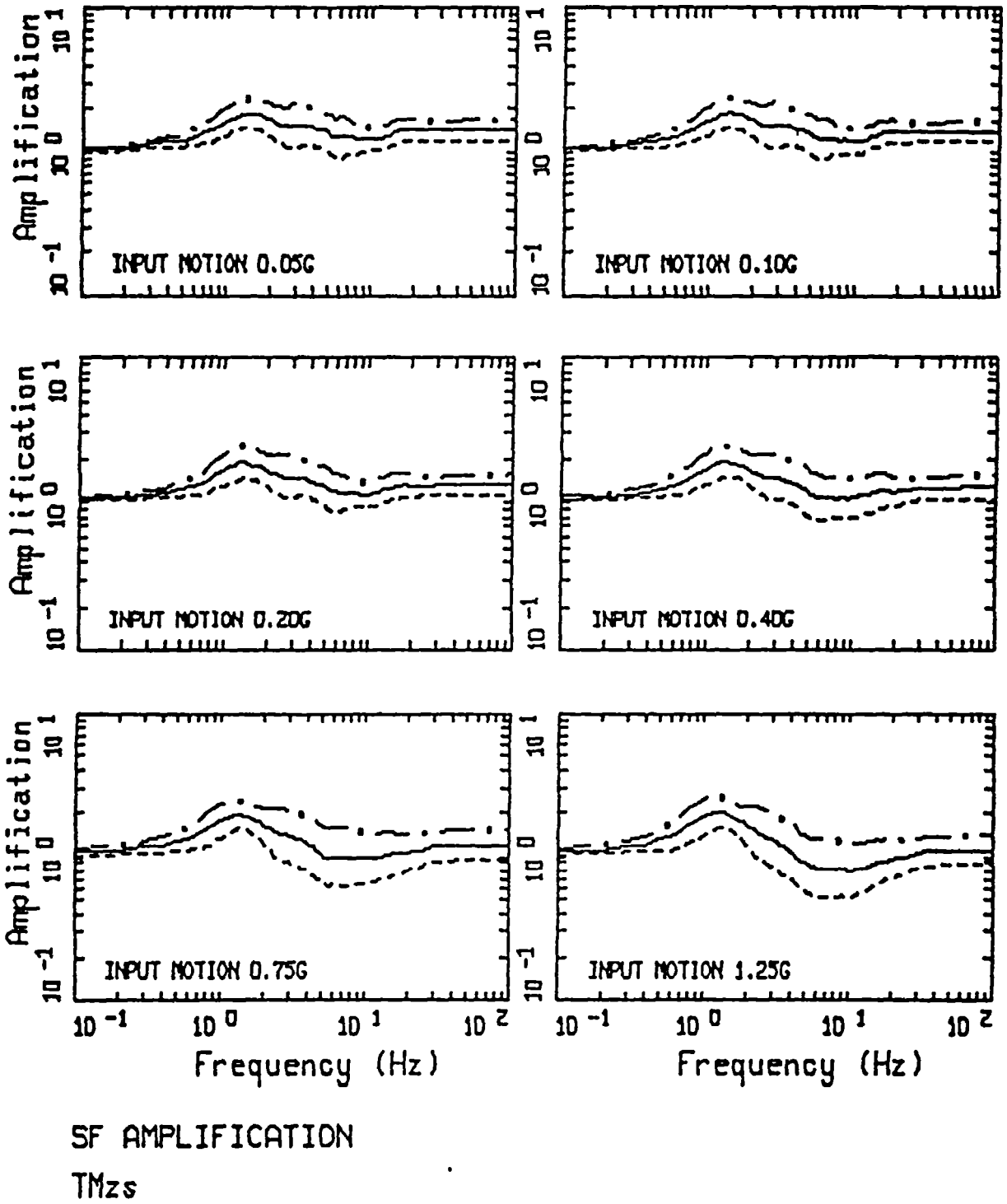

Figure 31. Median and ± 1 σ amplification factors computed for San Francisco area surficial geologic unit TM_{zs} (Table 1).

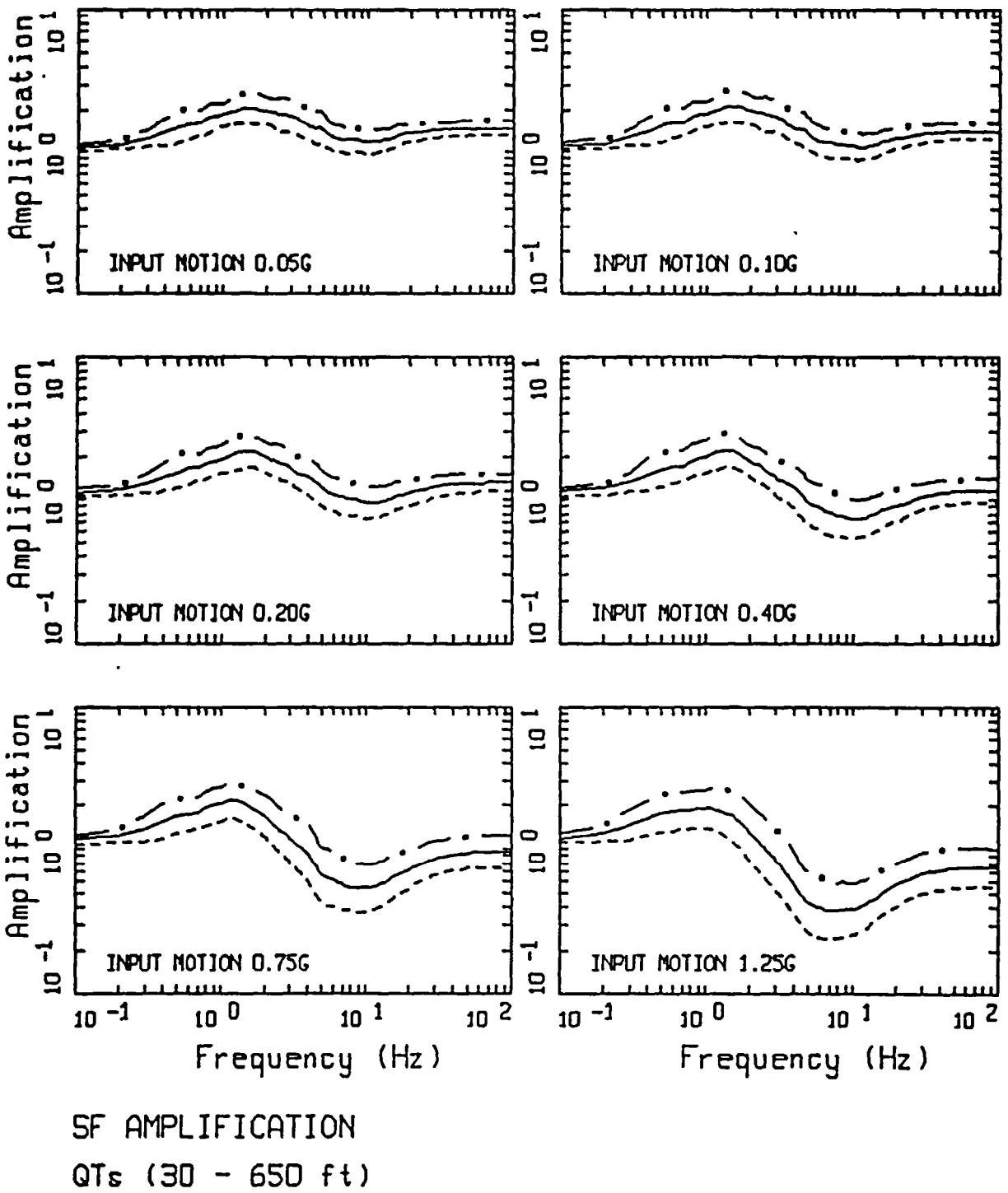

Figure 32. Median and ± 1 σ amplification factors computed for San Francisco area surficial geologic unit QT_s (Table 1).

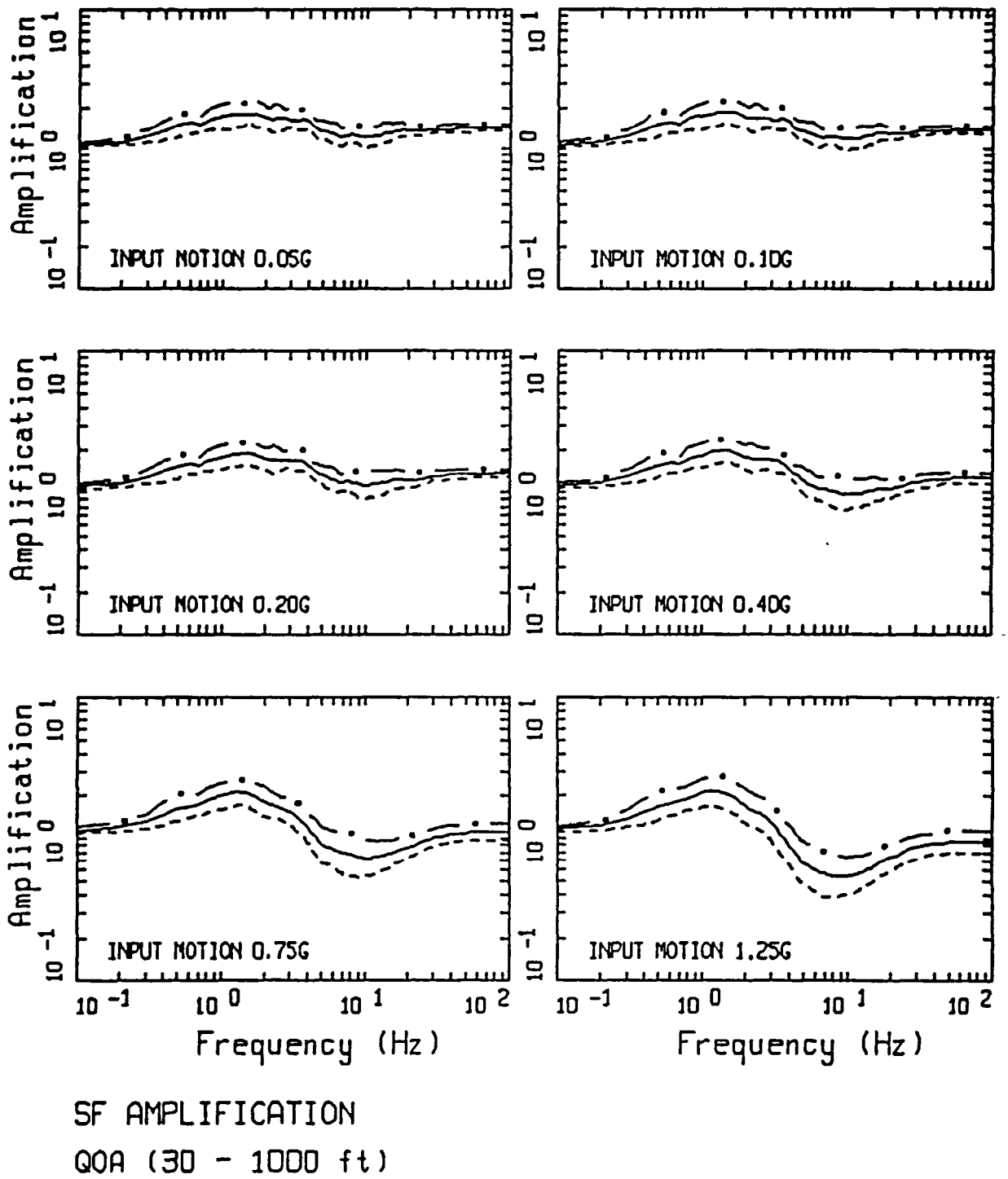

Figure 33. Median and ± 1 σ amplification factors computed for San Francisco area surficial geologic unit Q_{oa} (Table 1).

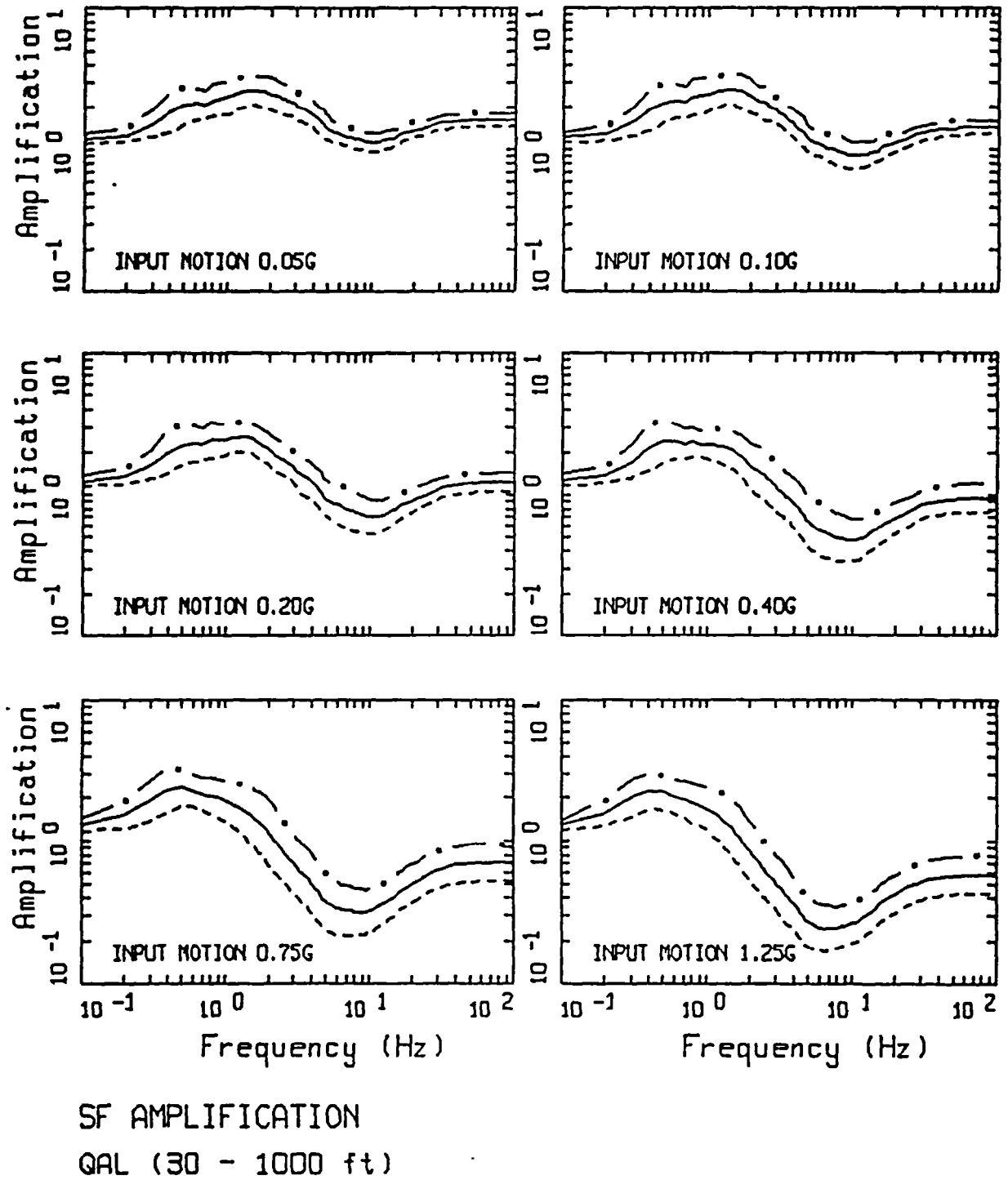

Figure 34. Median and ± 1 σ amplification factors computed for San Francisco area surficial geologic unit Q_a (Table 1).

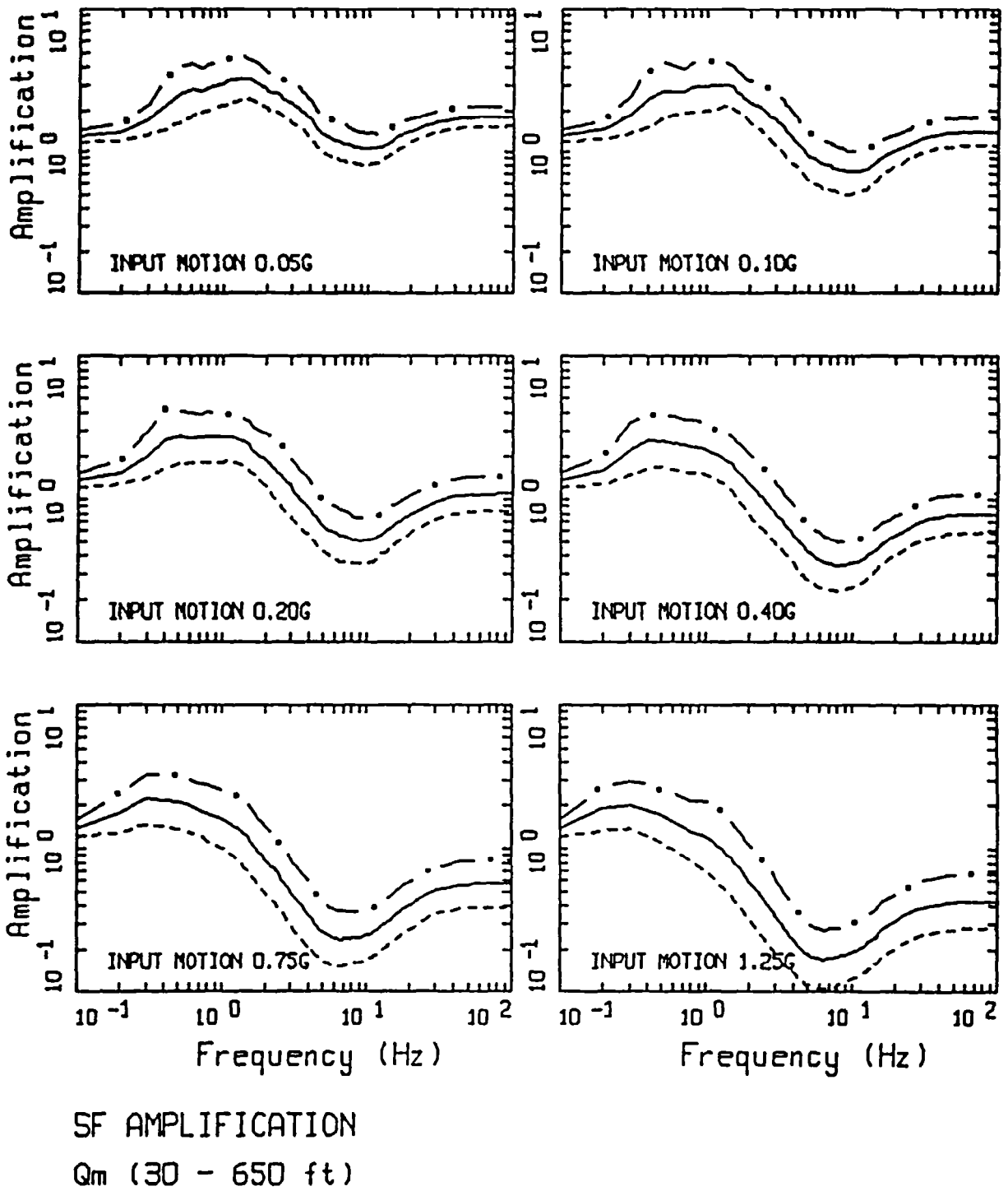

Figure 35. Median and ± 1 σ amplification factors computed for San Francisco area surficial geologic unit Q_m (Table 1).

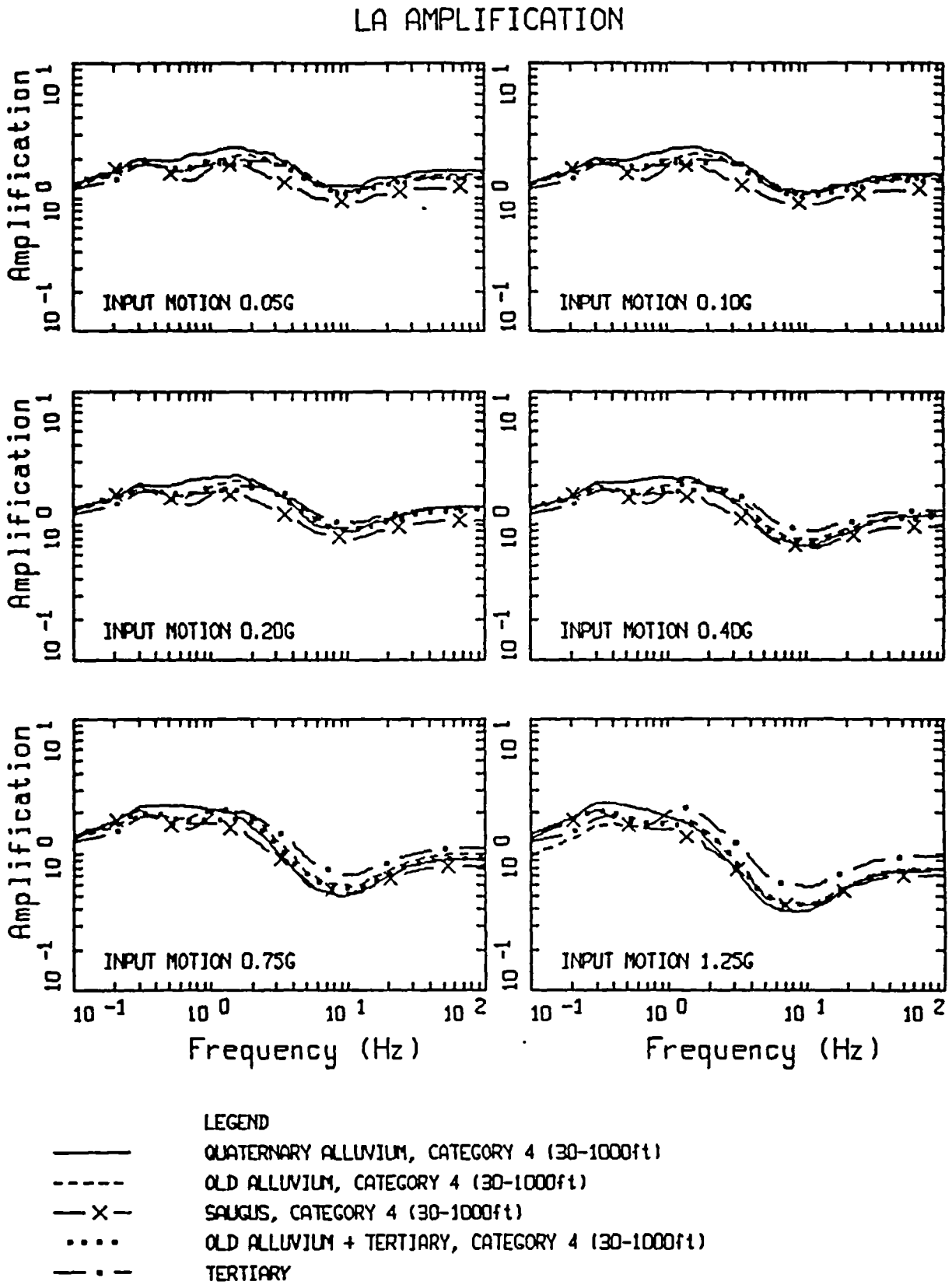

Figure 36. Comparison of median amplification factors computed for units Q_y, Q_o, Saugus (T_s), T_s, and $Q_o + T_s$ (Table 1) for the depth categories with the widest depth ranges (Table 5).

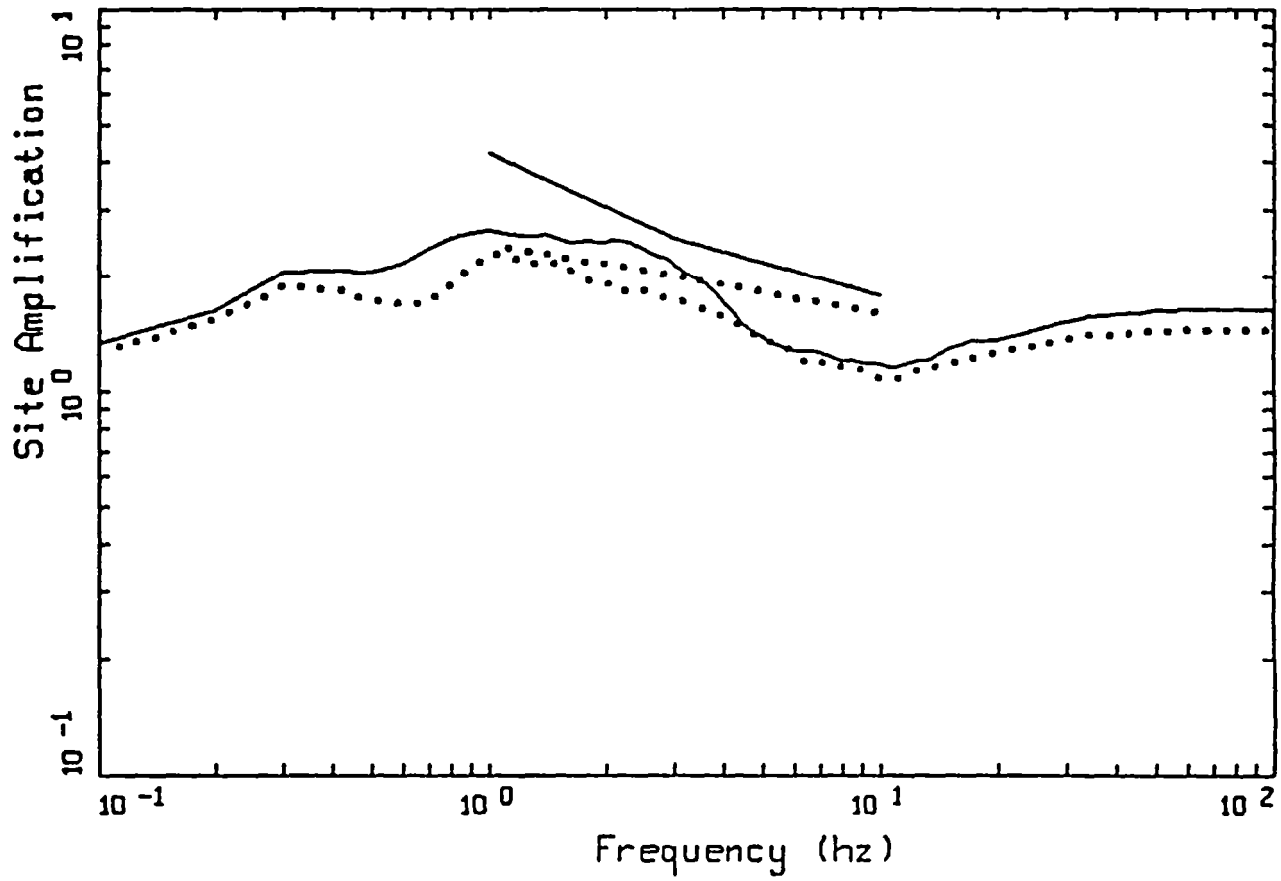

AMPLIFICATION: 5% DAMPED RESPONSE SPECTRA
REFERENCE GRANITE 0.05 G

LEGEND

——— Qy, 350-650ft (5% Damped Response Spectra, median)

• • • • QUATERNARY(Qo)+TERTIARY(Ts) 350-650ft (5% Damped Response Spectra, median)

——— Qy(D) (Bonilla et al (1997) Empirical Fourier Amplitude Spectra, average)

• • • • Qo+Ts(C) (Bonilla et al (1997) Empirical Fourier Amplitude Spectra, average)

Figure 37. Comparison of median amplification factors (5% damped response spectra) computed for reference Granite outcrop peak acceleration of 0.05g with empirical factors (smoothed Fourier amplitude spectra; Bonilla et al., 1997). Empirical factors are based on small earthquakes.

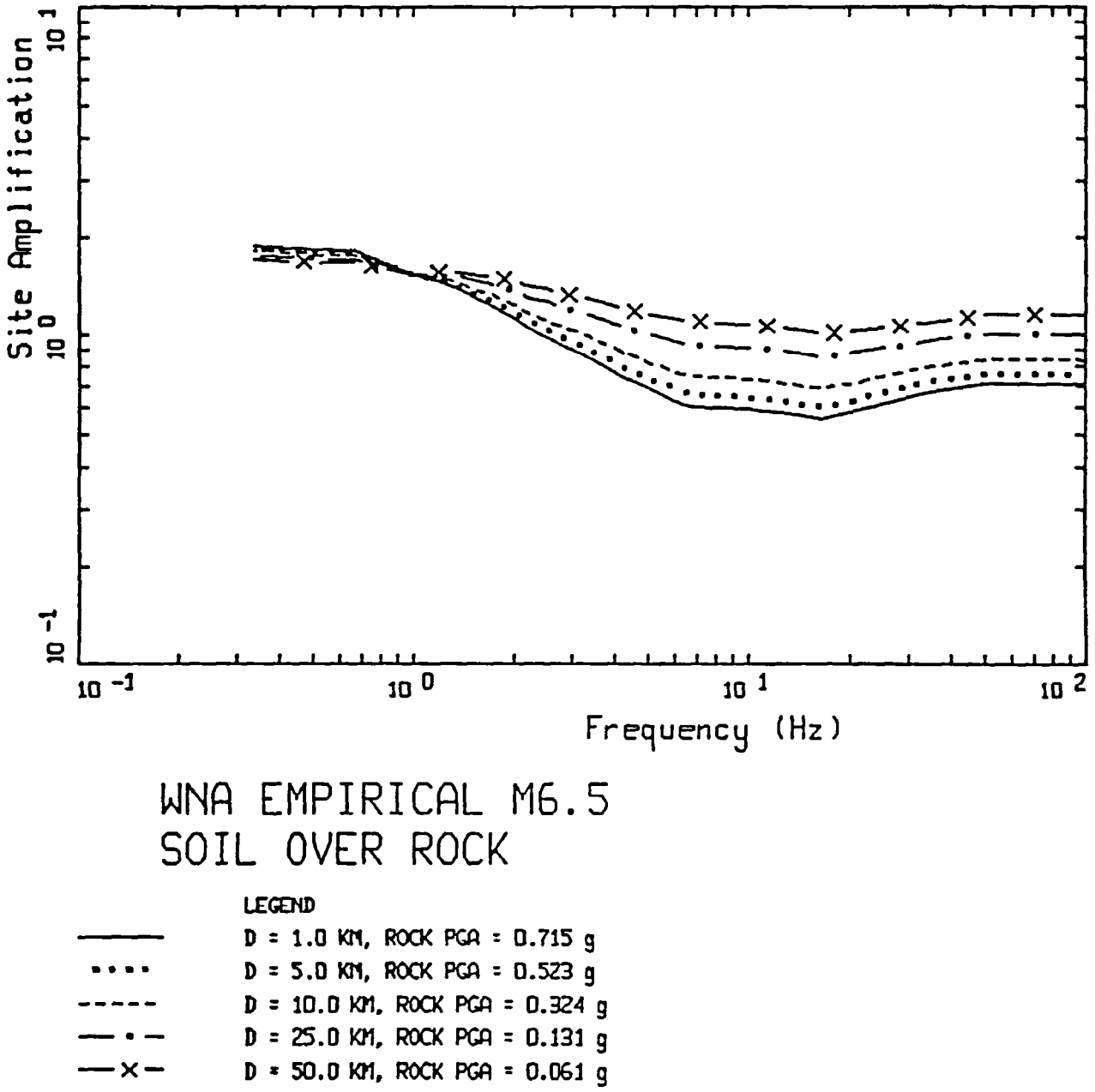

Figure 38. Deep firm to stiff soil (Geomatrix C + D, Table 2) amplification of 5% damped response spectra relative to soft rock (Geomatrix A + B) from an empirical attenuation relation (Abrahamson and Silva, 1997).

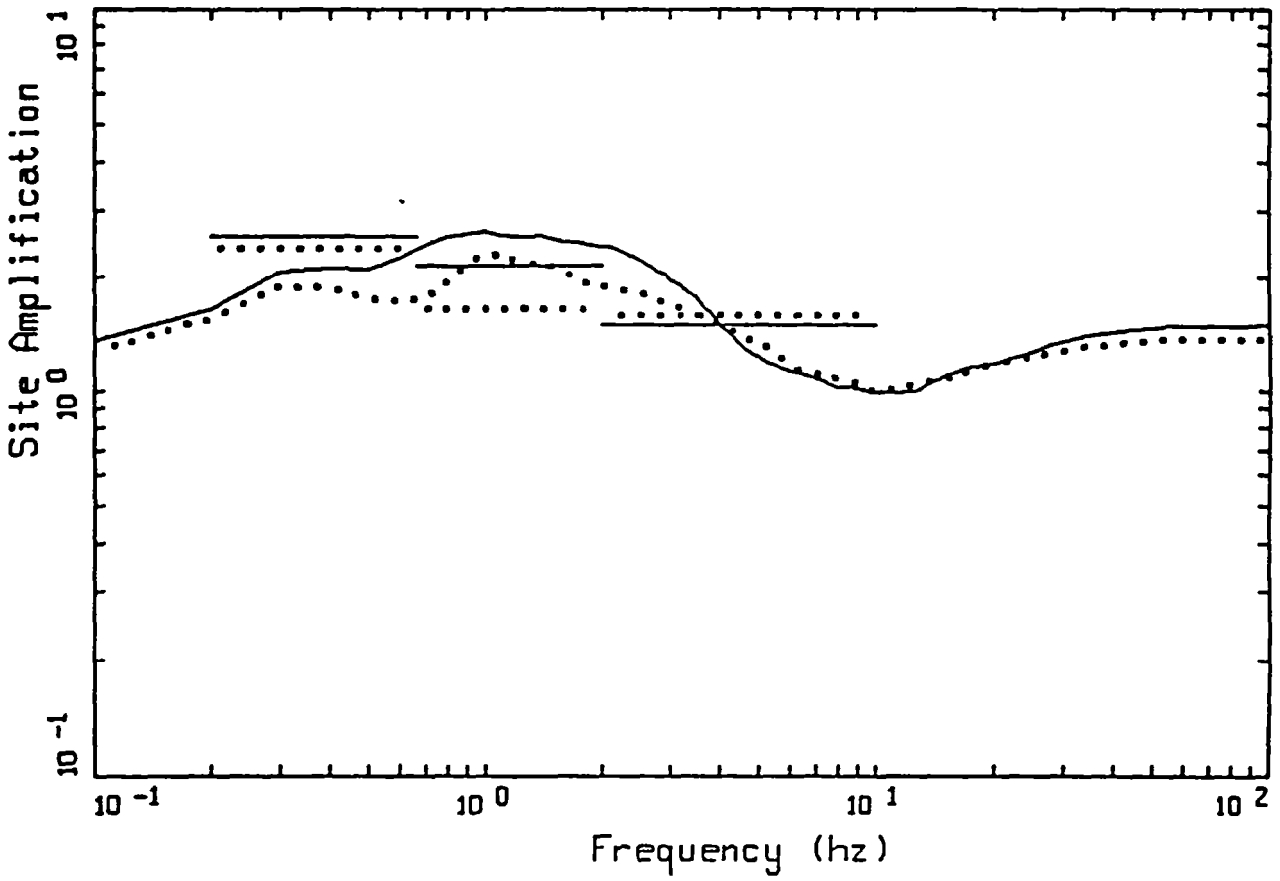

AMPLIFICATION: 5% DAMPED RESPONSE SPECTRA
REFERENCE GRANITE 0.10 G

LEGEND

———	Qy, Category 3 (350-650 ft)
• • • •	QUATERNARY (Qo) + TERTIARY (Ts), Category 3 (350-650 ft)
———	Qy(D): 2-10 Hz (Borcherdt (1996) Empirical 5% Damped Response Spectra, average)
———	Qy(D): 0.67-2.0 Hz
———	Qy(D): 0.2-0.67 Hz
• • • •	Qo+Ts(C): 2.0-10.0 Hz
• • • •	Qo+Ts(C): 0.67-2.0 Hz
• • • •	Qo+Ts(C): 0.2-0.67 Hz

Figure 39. Comparison of median amplification factors (5% damped response spectra) computed for reference Granite outcrop peak acceleration of 0.10g with empirical factors (5% damped response spectra; Borcherdt, 1996). Empirical factors are based on recordings of the 1994 M 6.7 Northridge.

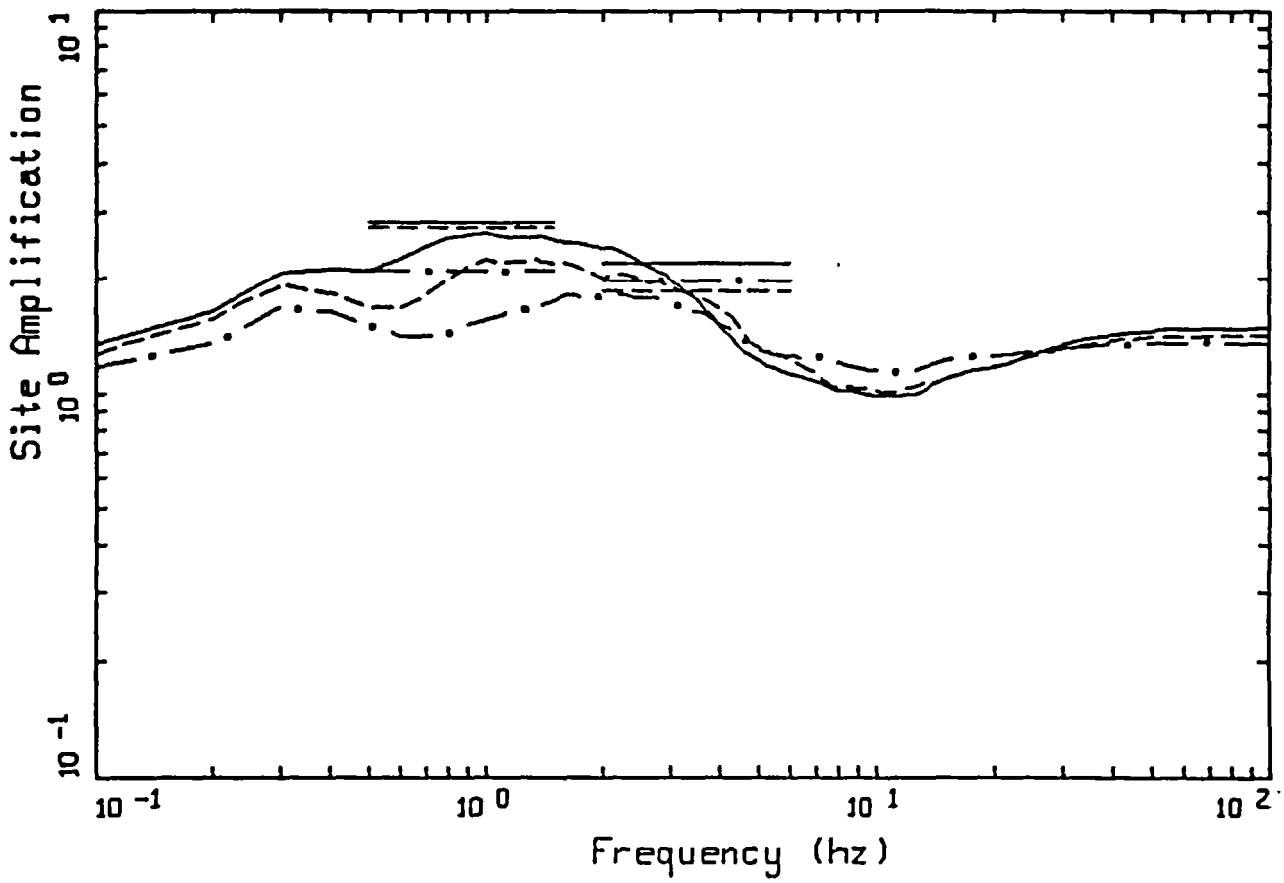

AMPLIFICATION: 5% DAMPED RESPONSE SPECTRA
REFERENCE GRANITE 0.10 G

LEGEND

———	Qy, Category 3 (350-650ft) (5% Damped Response Spectra, median)
- - - -	Qo, Category 3 (350-650ft) (5% Damped Response Spectra, median)
— • —	Ts (5% Damped Response Spectra, median)
———	Qy(D): 0.5-1.5 Hz (Harmsen (1997): Empirical Fourier Amplitude Spectra, average)
- - - -	Qo(C): 0.5-1.5 Hz
— • —	Ts(C): 0.5 - 1.5 Hz
———	Qy(D): 2.0-6.0 Hz (Harmsen (1997): Empirical Fourier Amplitude Spectra, average)
- - - -	Qo(C): 2.0-6.0 Hz
— • —	Ts(C): 2.0-6.0 Hz

Figure 40. Comparison of median amplification factors (5% damped response spectra) computed for reference Granite outcrop peak acceleration of 0.10g with empirical factors (smoothed Fourier amplitude spectra; Harmsen, 1997). Empirical factors are based on the 1971 San Fernando, 1987 Whittier Narrows, 1991 Sierra Madre, and 1994 Northridge earthquakes.

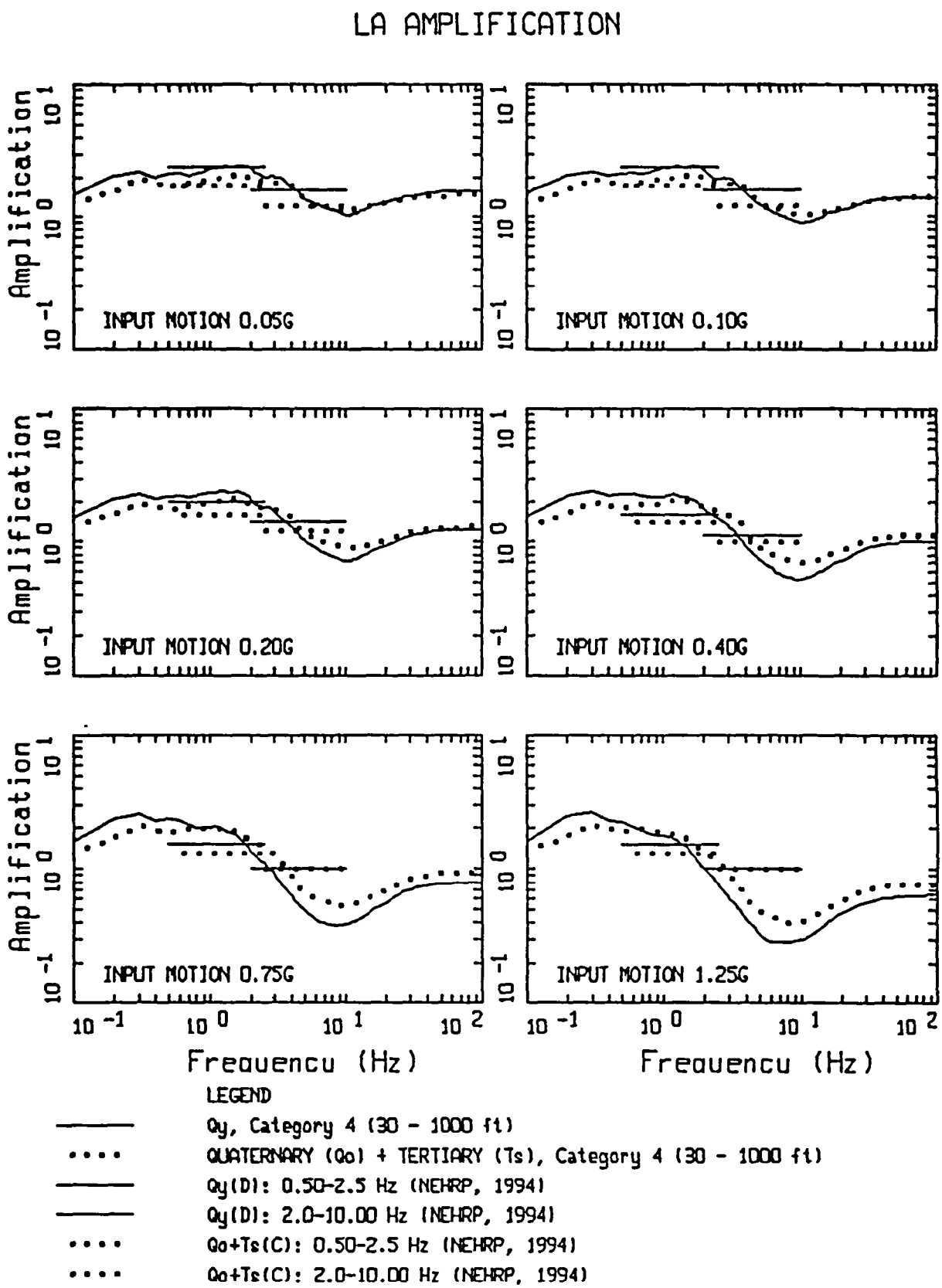

Figure 41. Comparison of median amplification factors with NEHRP provisions.

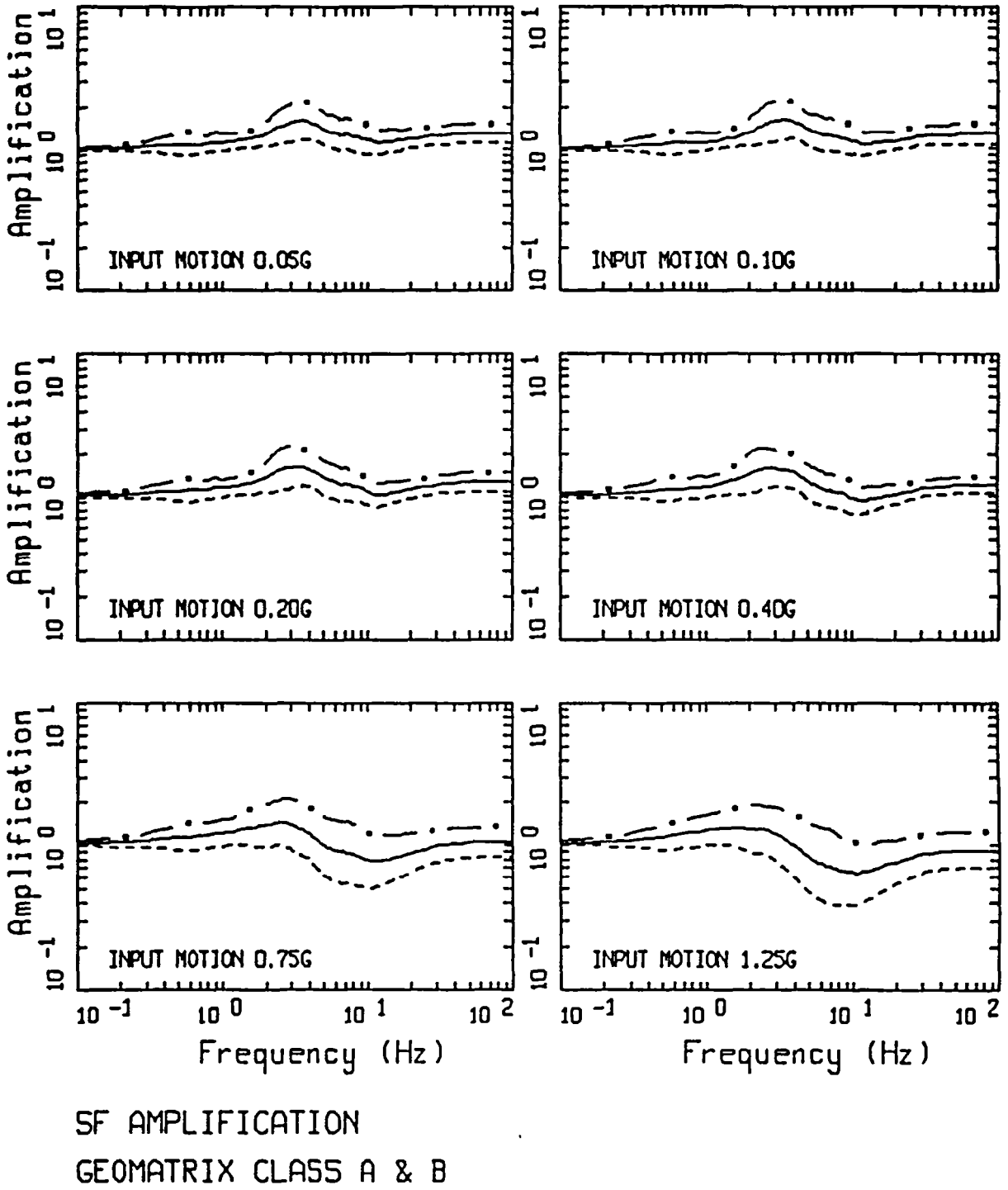

Figure 42. Amplification factors computed for Geomatrix site categories A and B (Figure 6, Table 2) relative to San Francisco area reference rock outcrop Franciscan.

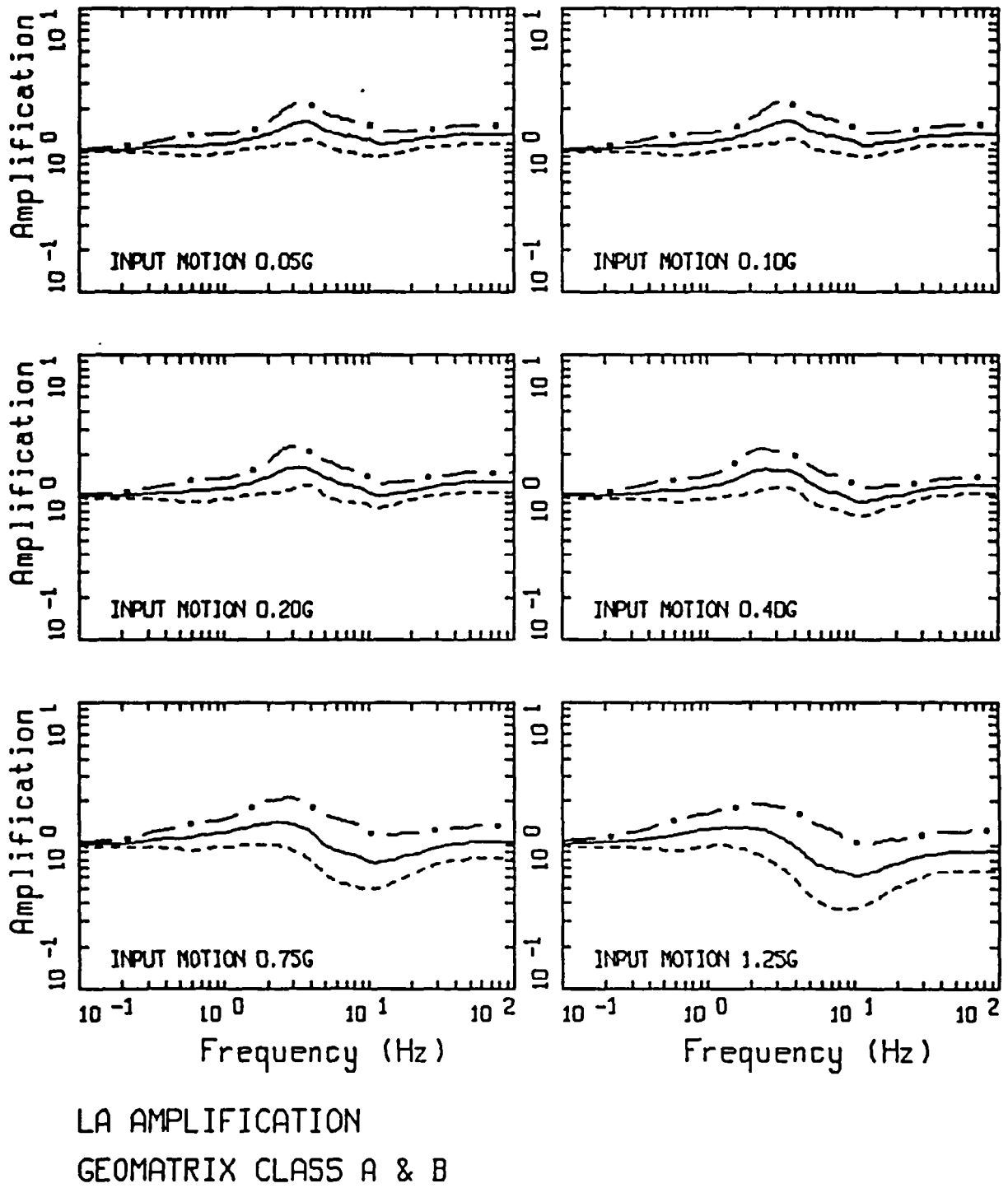

Figure 43. Amplification factors computed for Geomatrix site categories A and B (Figure 6, Table 2) relative to Los Angeles area reference rock outcrop Granite.

APPENDIX A

Amplification Factors (5% damped response spectra) For The San Francisco Bay Area Based on Surface Geology: TM_{ZS}, QT_S, Q_{oa}, Q_{al}, and Q_m (Table 1).

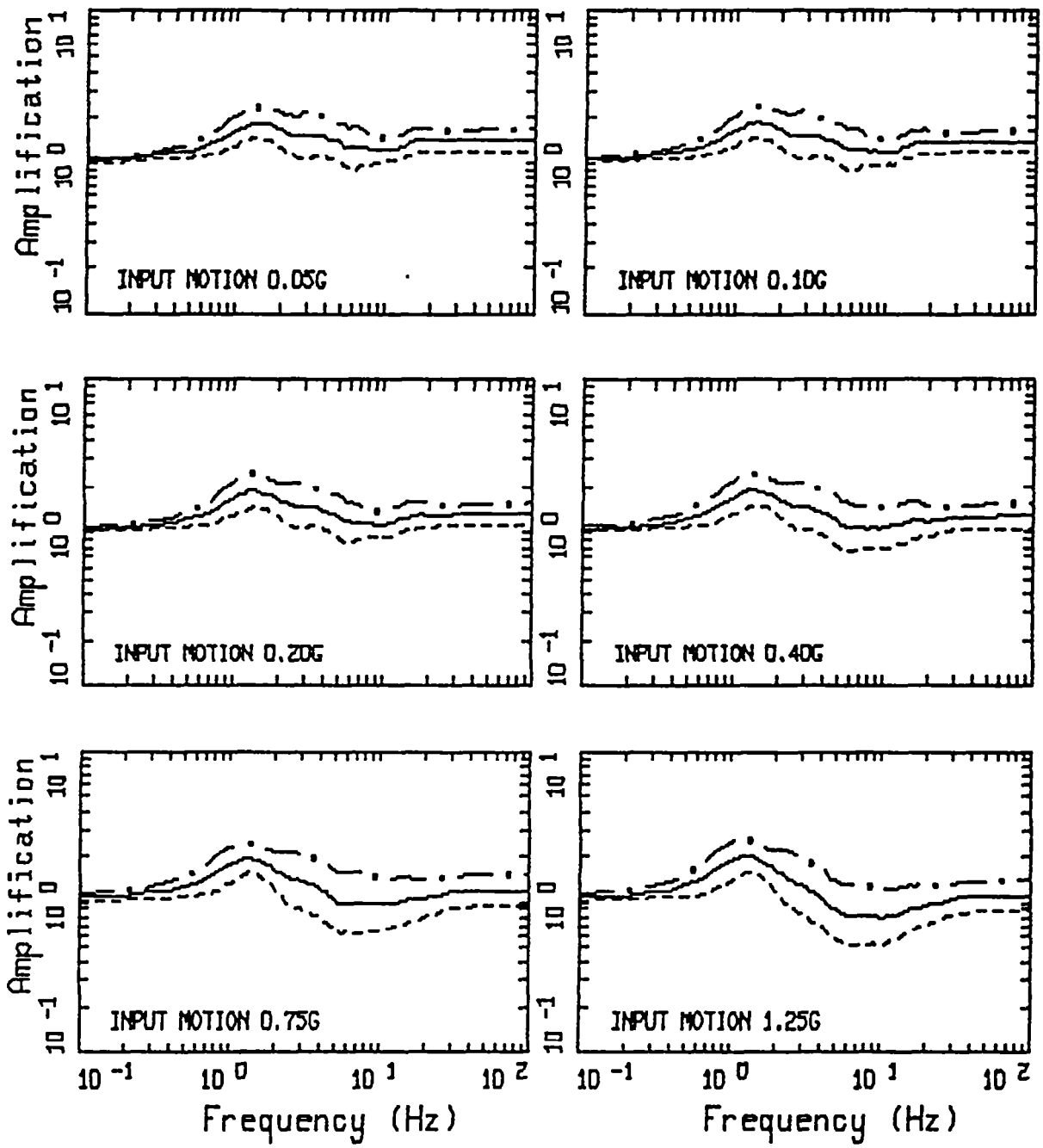

SF AMPLIFICATION

TMzs

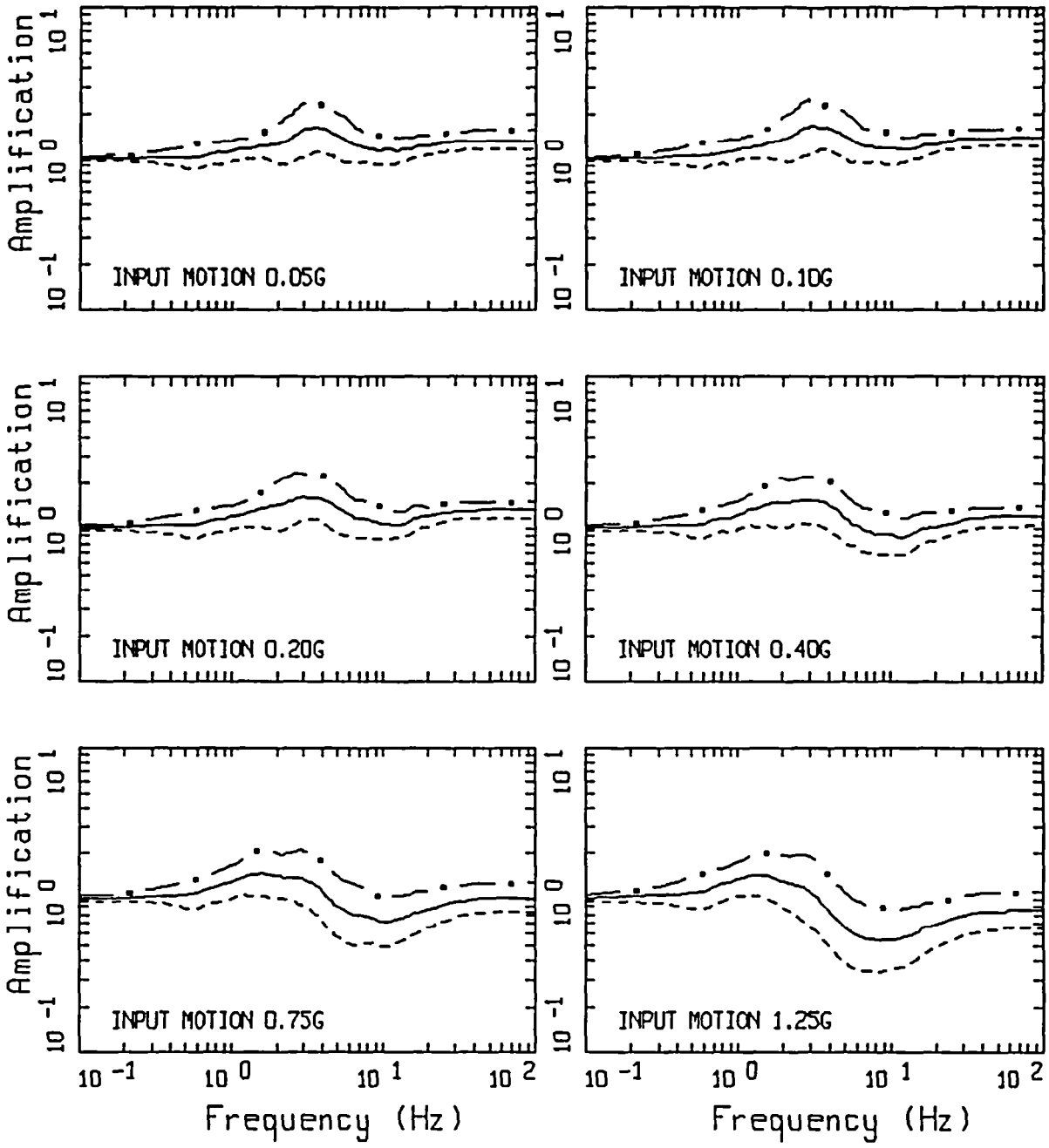

SF AMPLIFICATION

QTs (30 - 150 ft)

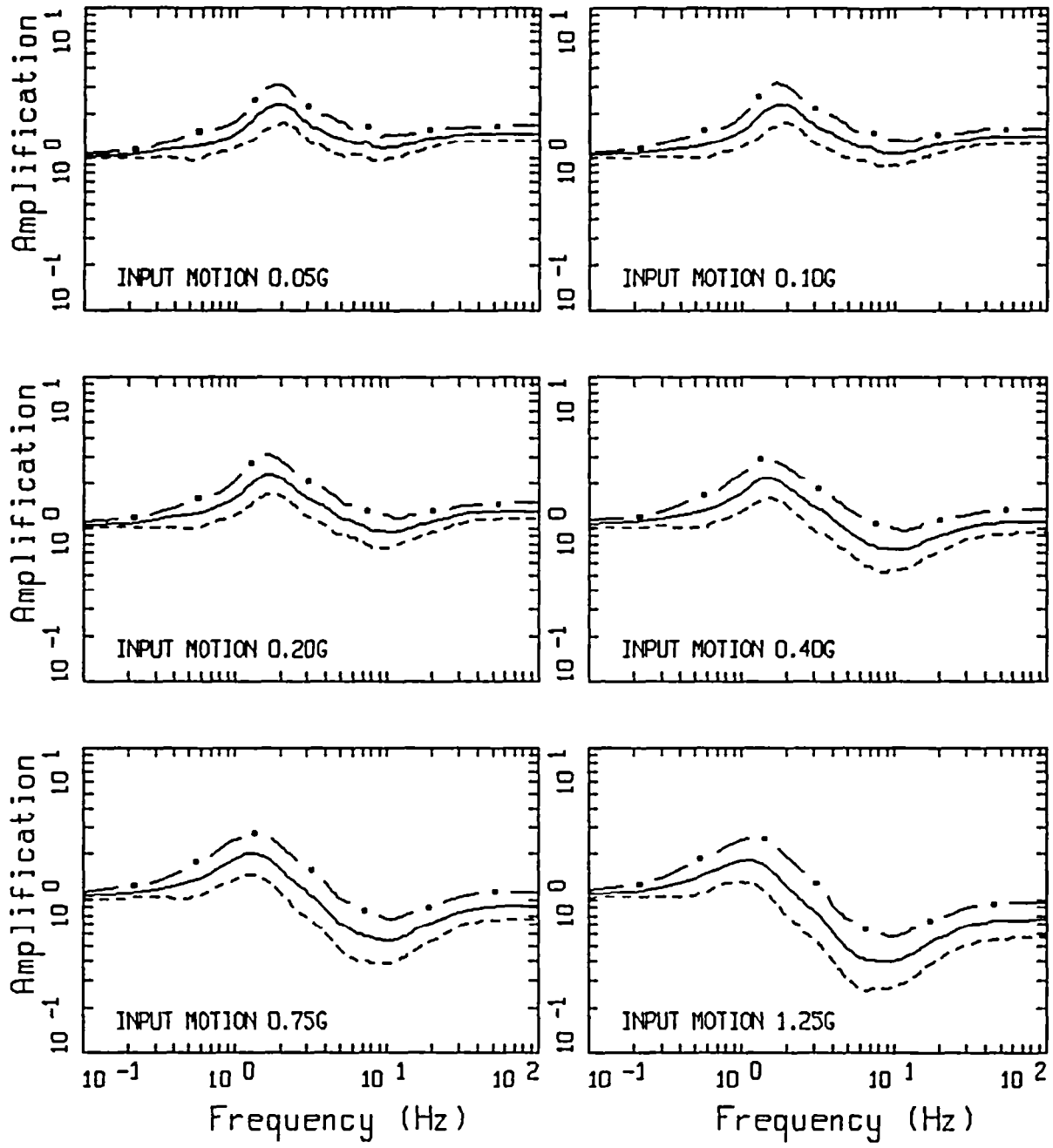

SF AMPLIFICATION

QTs (150 - 350 ft)

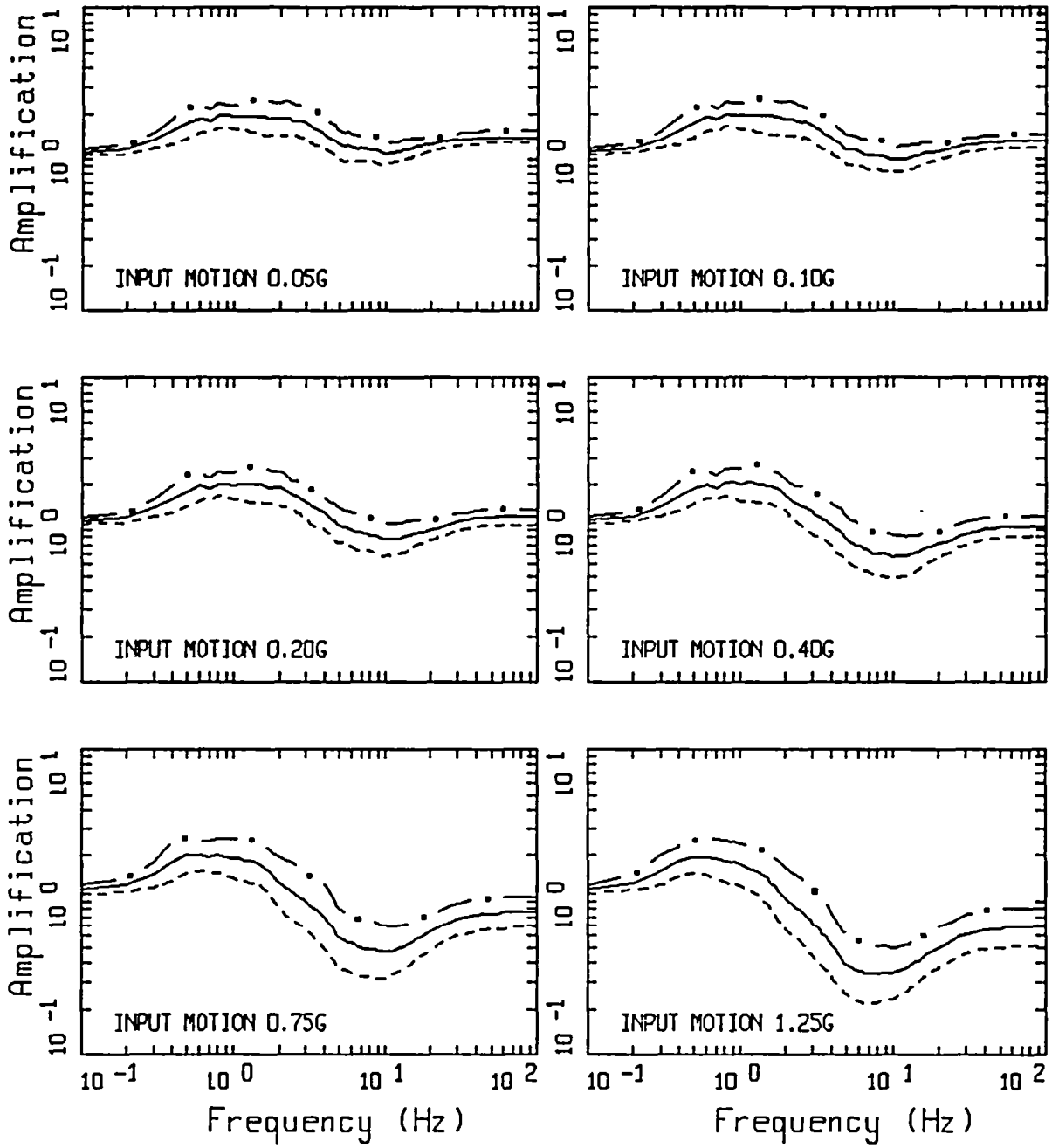

SF AMPLIFICATION

QTs (350 - 650 ft)

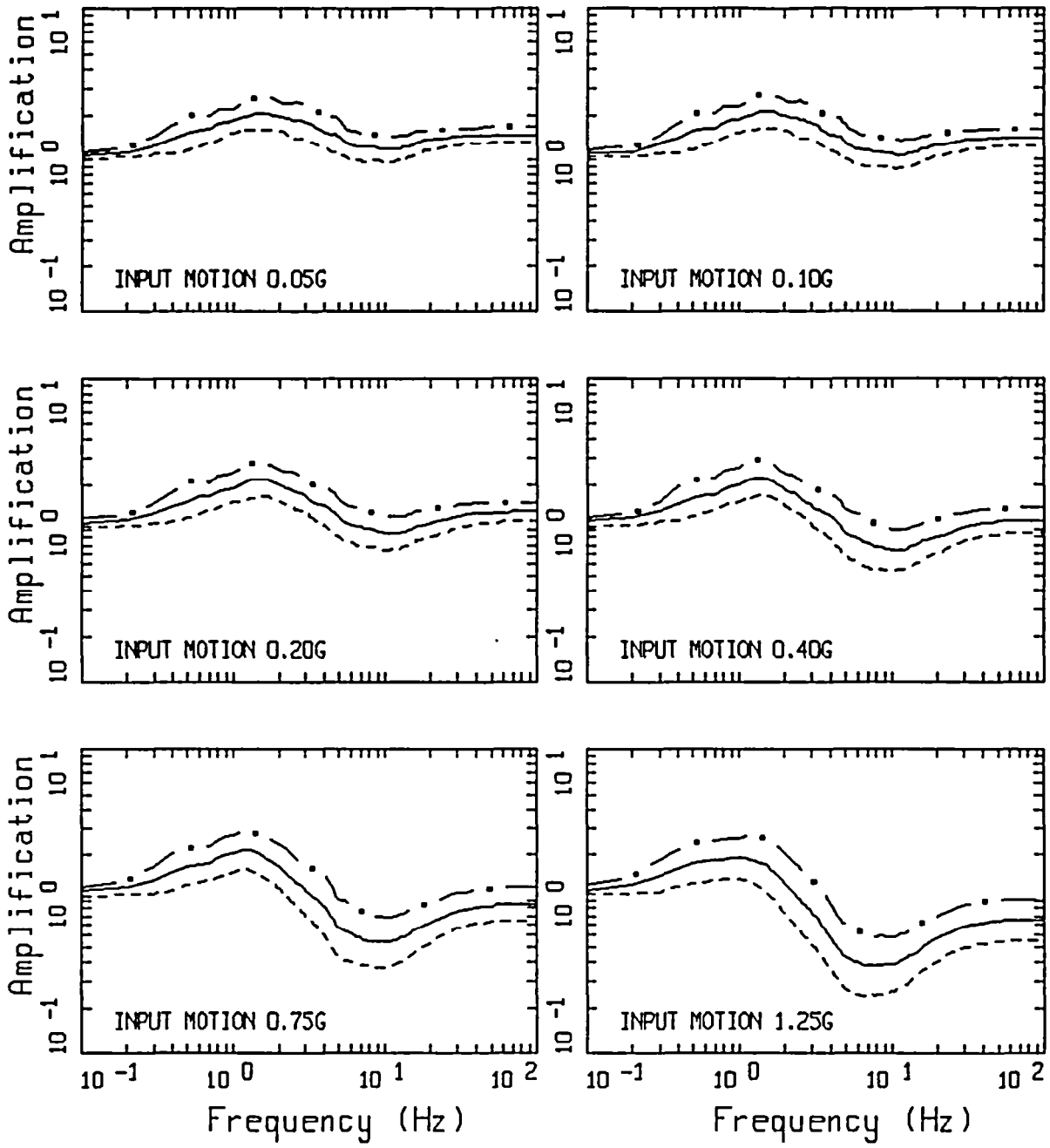

SF AMPLIFICATION

QTs (30 - 650 ft)

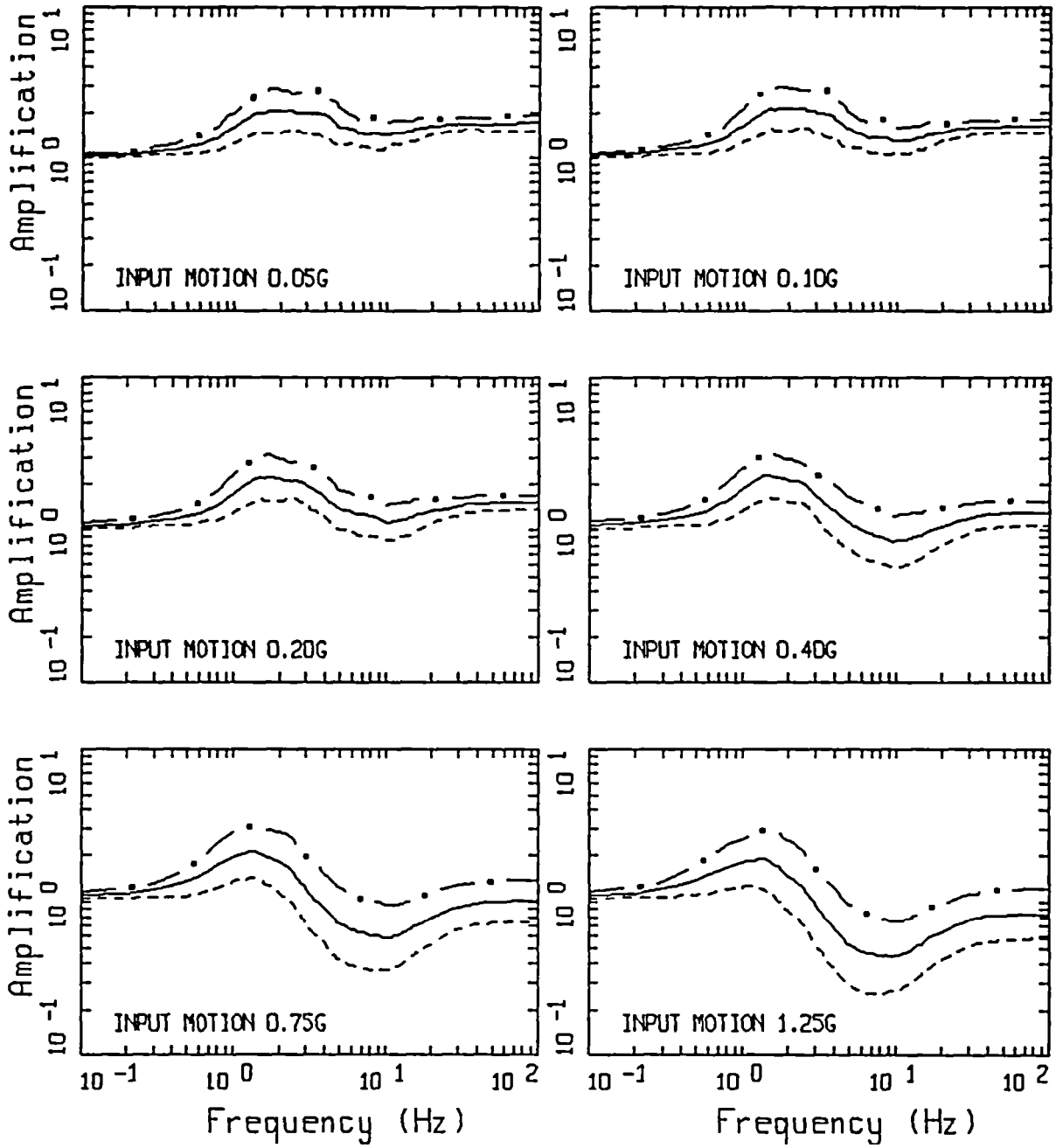

SF AMPLIFICATION

QOA (30 - 150 ft)

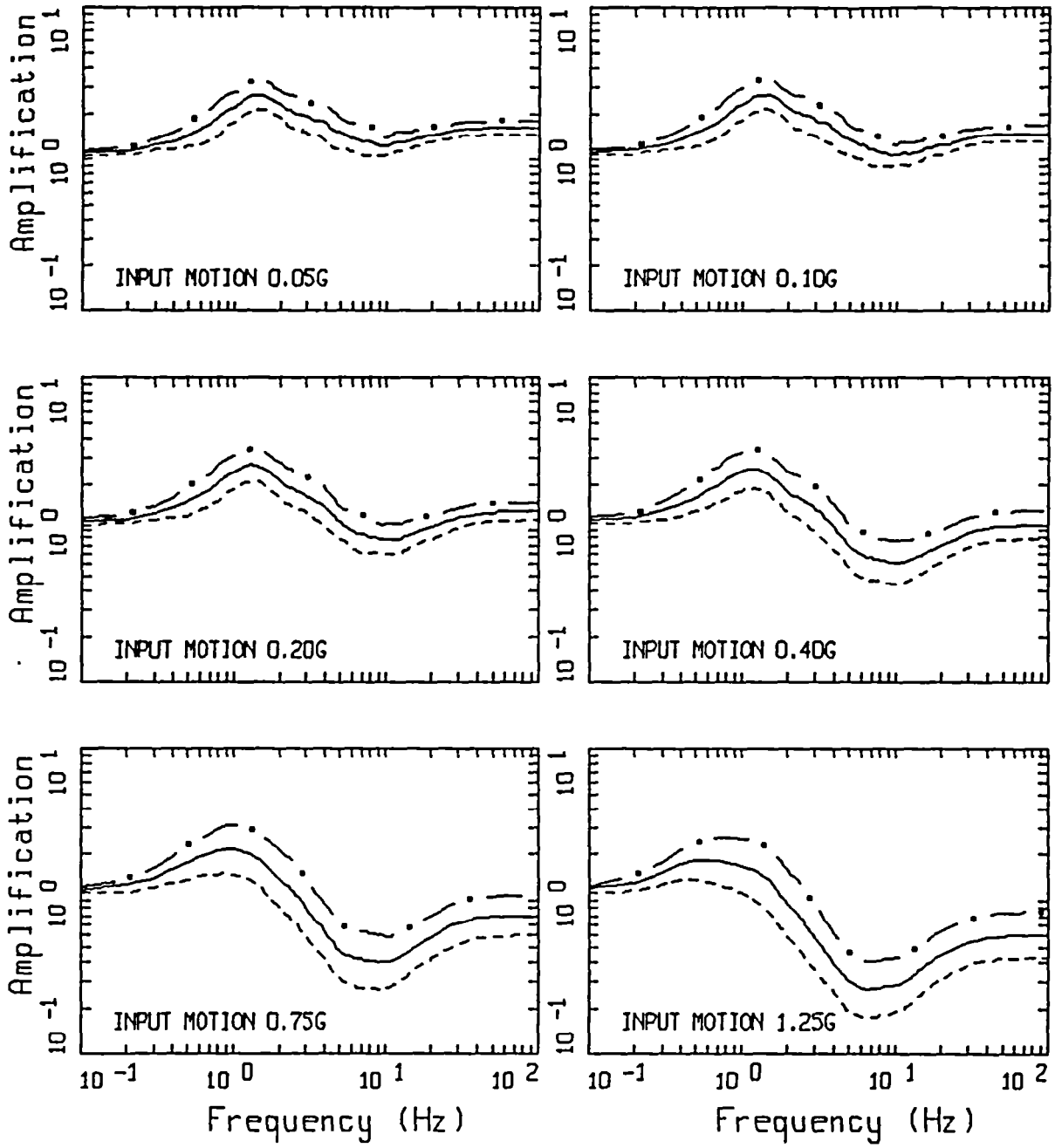

SF AMPLIFICATION

QOA (150 - 350 ft)

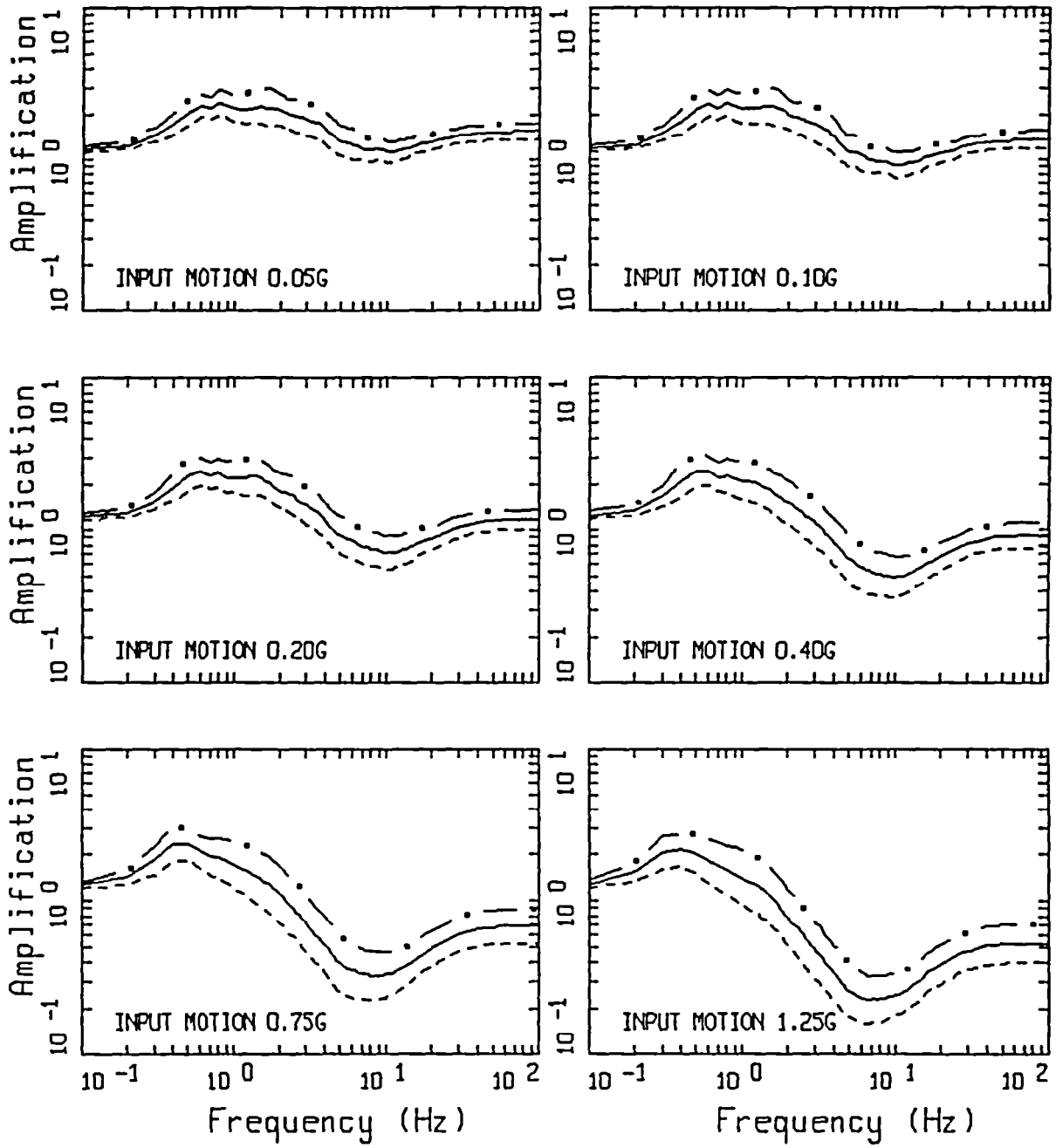

SF AMPLIFICATION

QOA (350 - 650 ft)

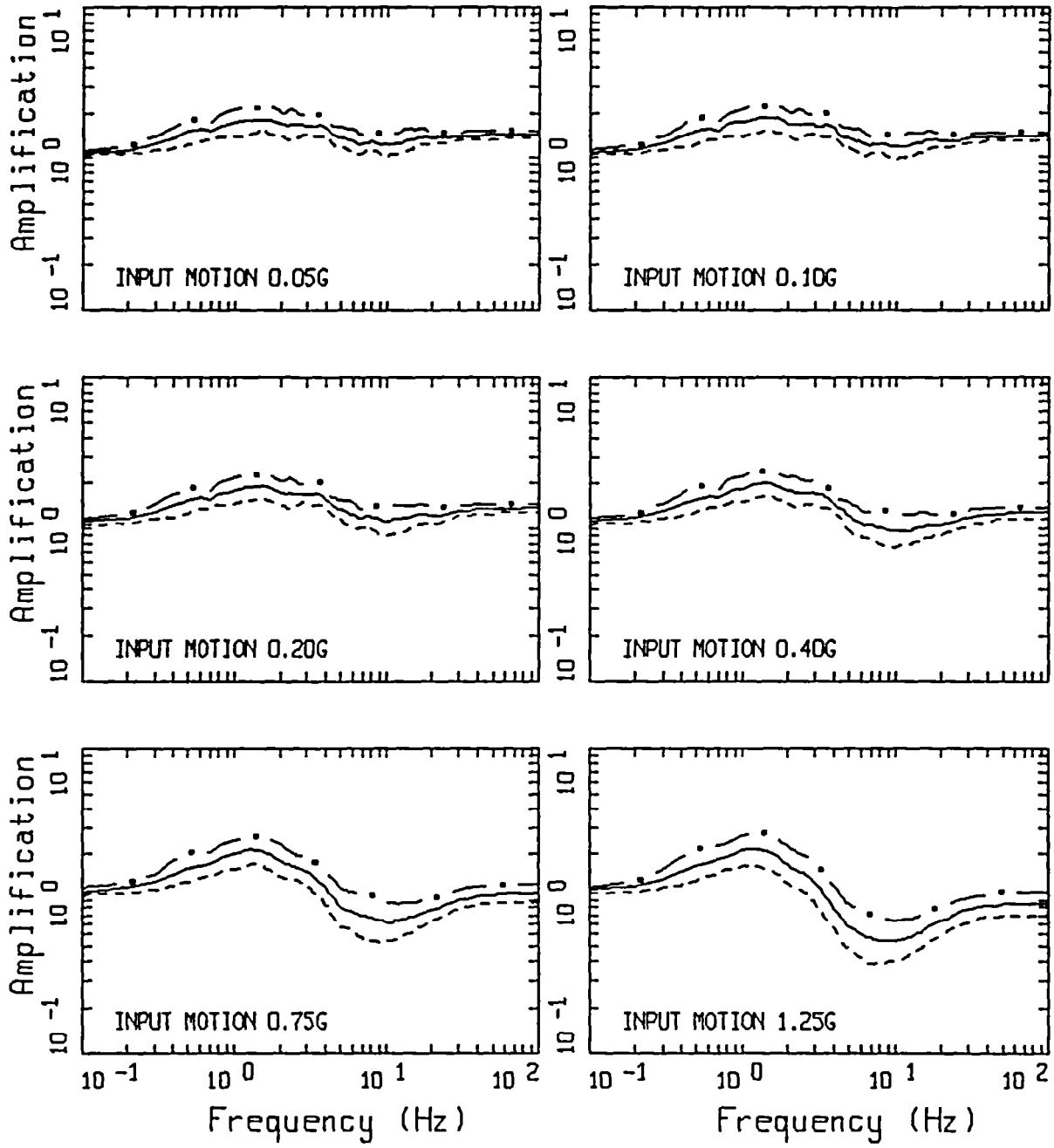

SF AMPLIFICATION

QOA (30 - 1000 ft)

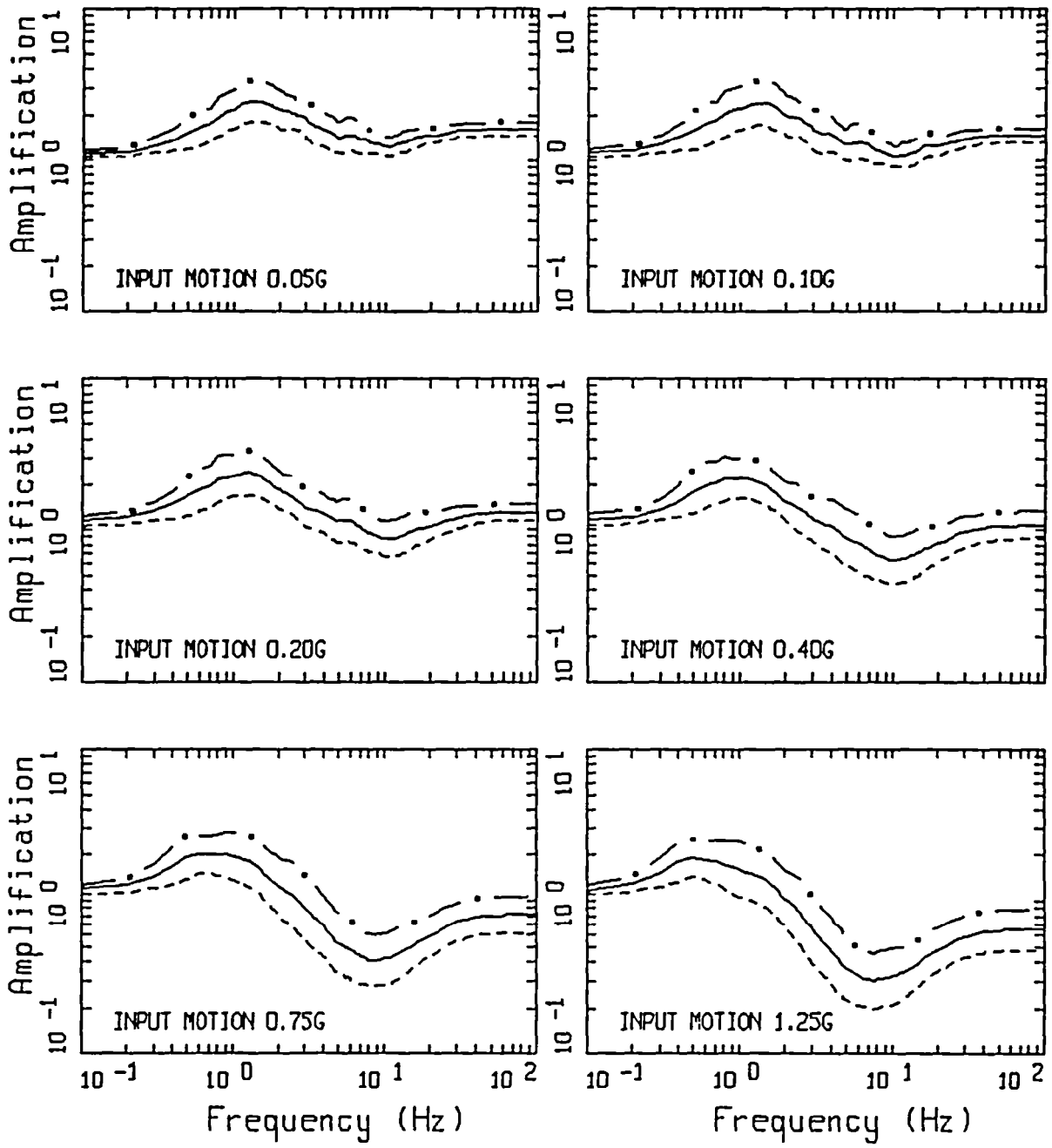

SF AMPLIFICATION

QOA (30 - 450 ft)

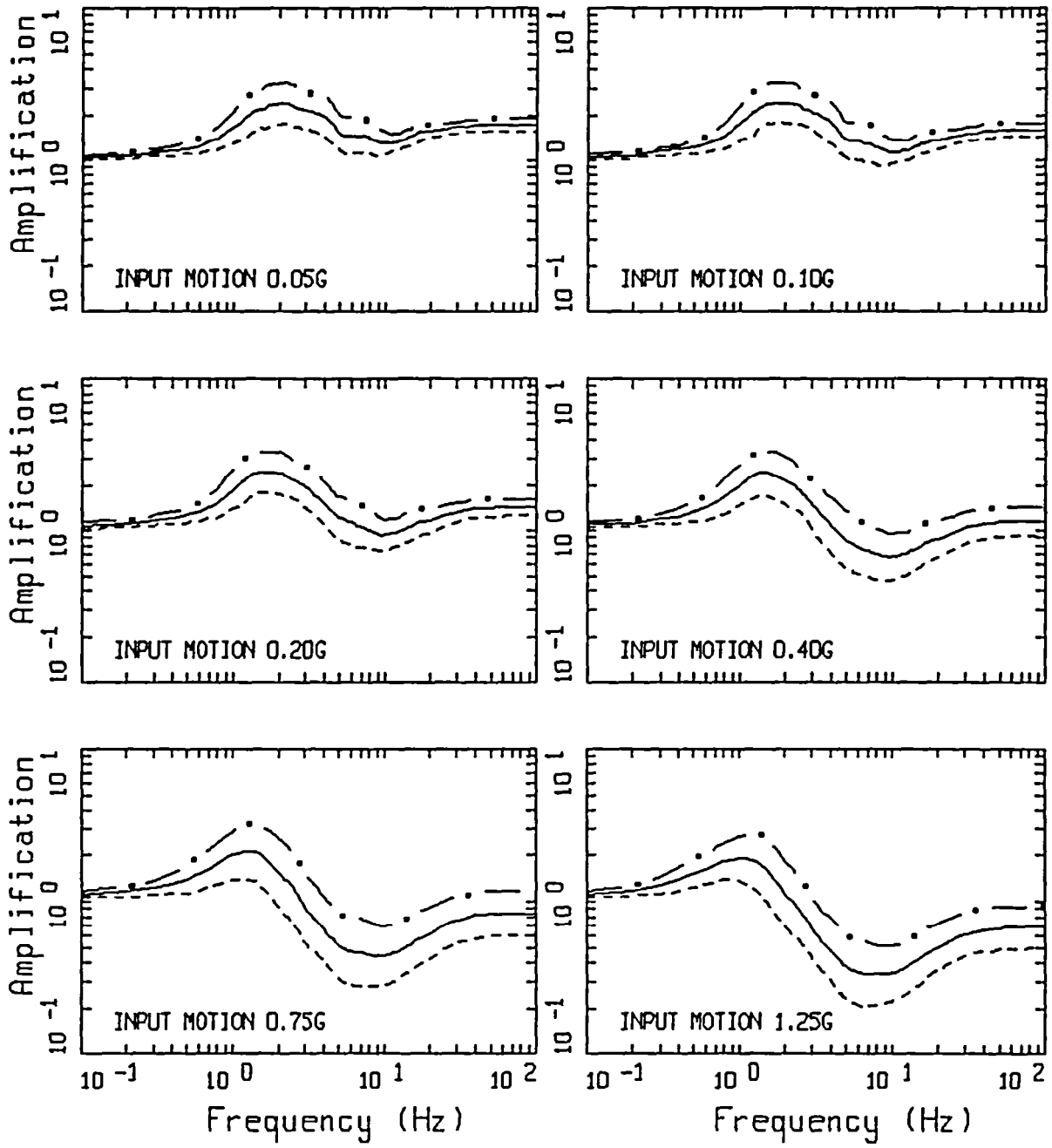

SF AMPLIFICATION

QAL (30 - 150 ft)

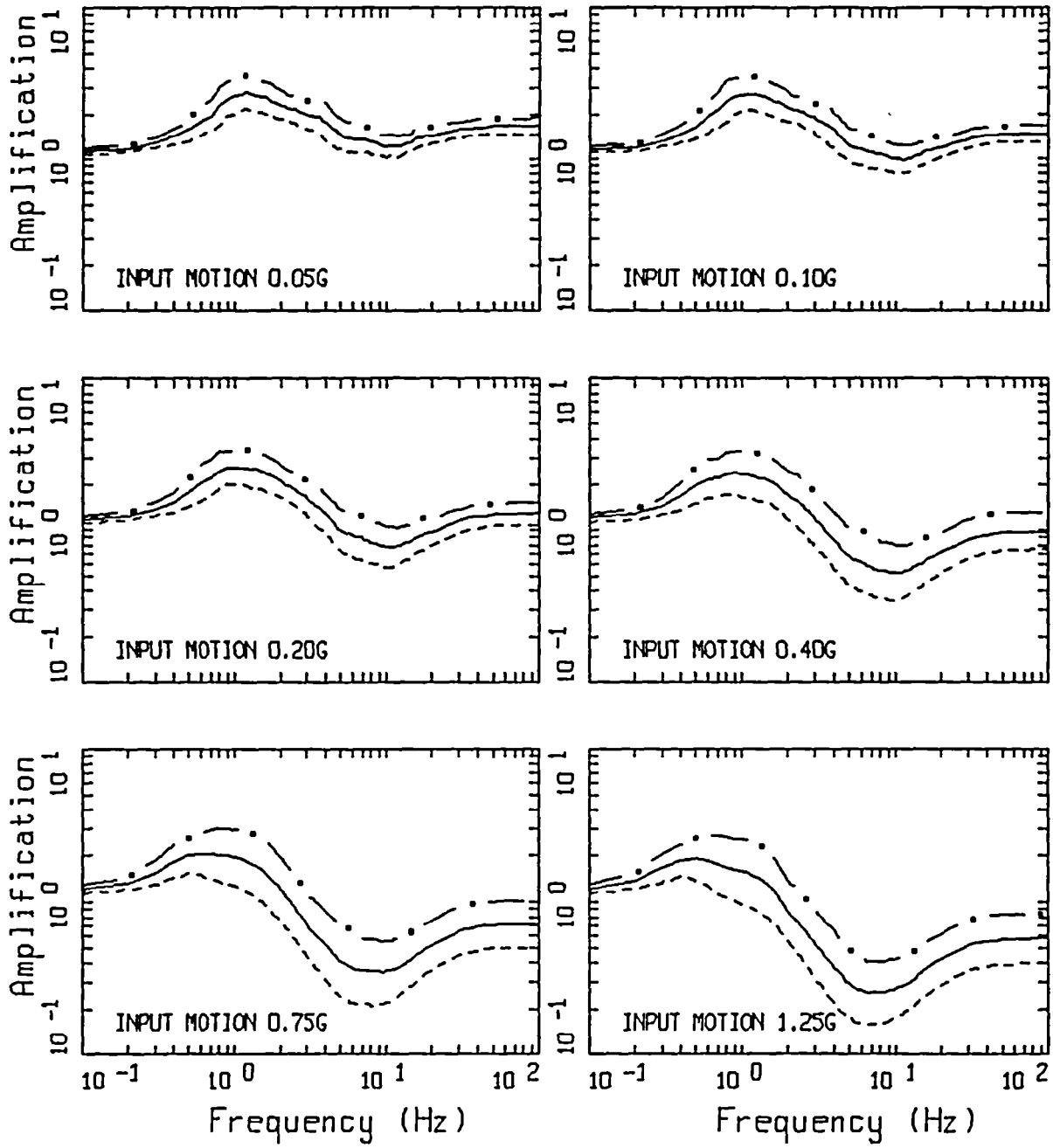

SF AMPLIFICATION

QAL (150 - 350 ft)

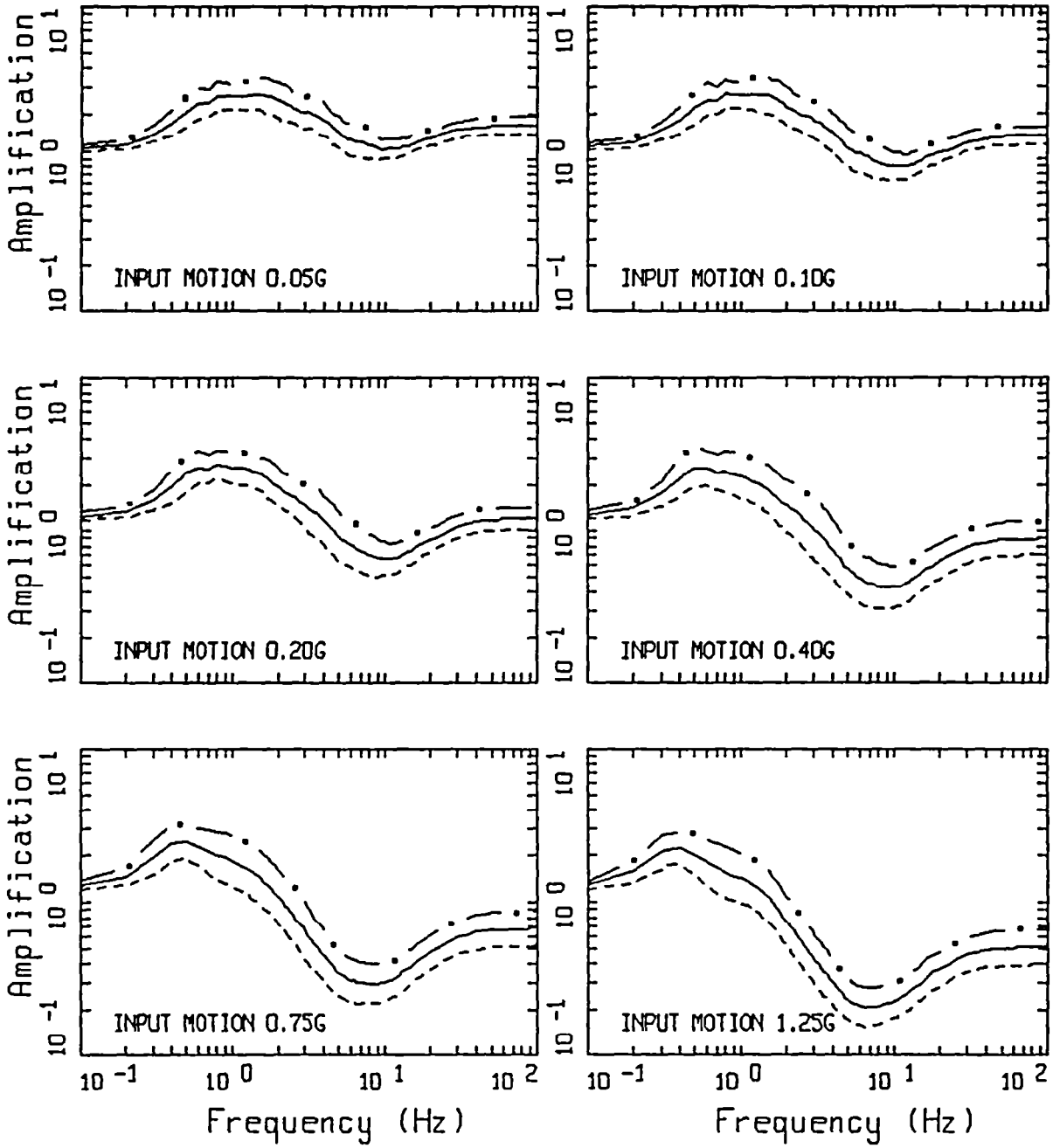

SF AMPLIFICATION

QAL (350 - 650 ft)

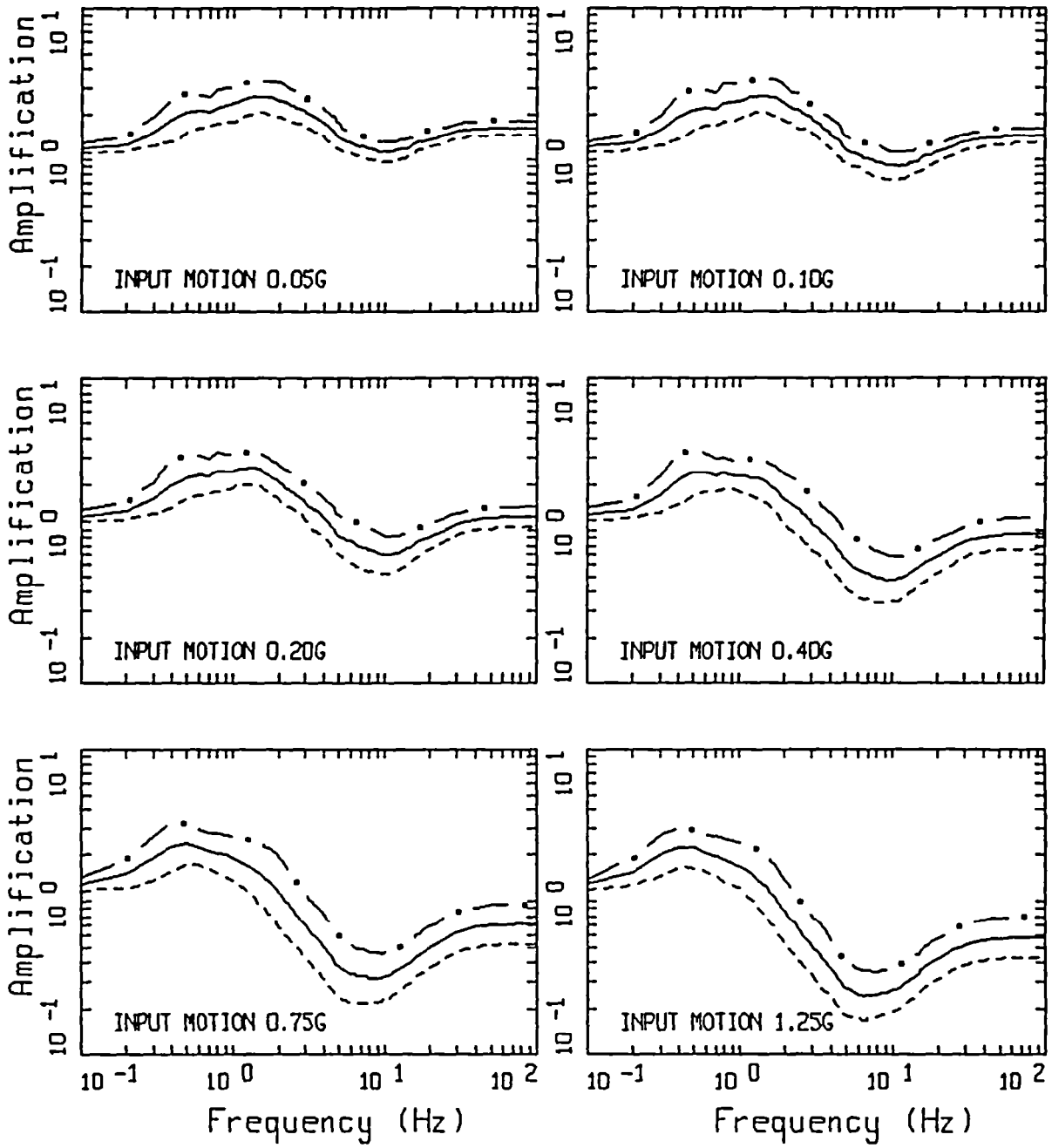

SF AMPLIFICATION

QAL (30 - 1000 ft)

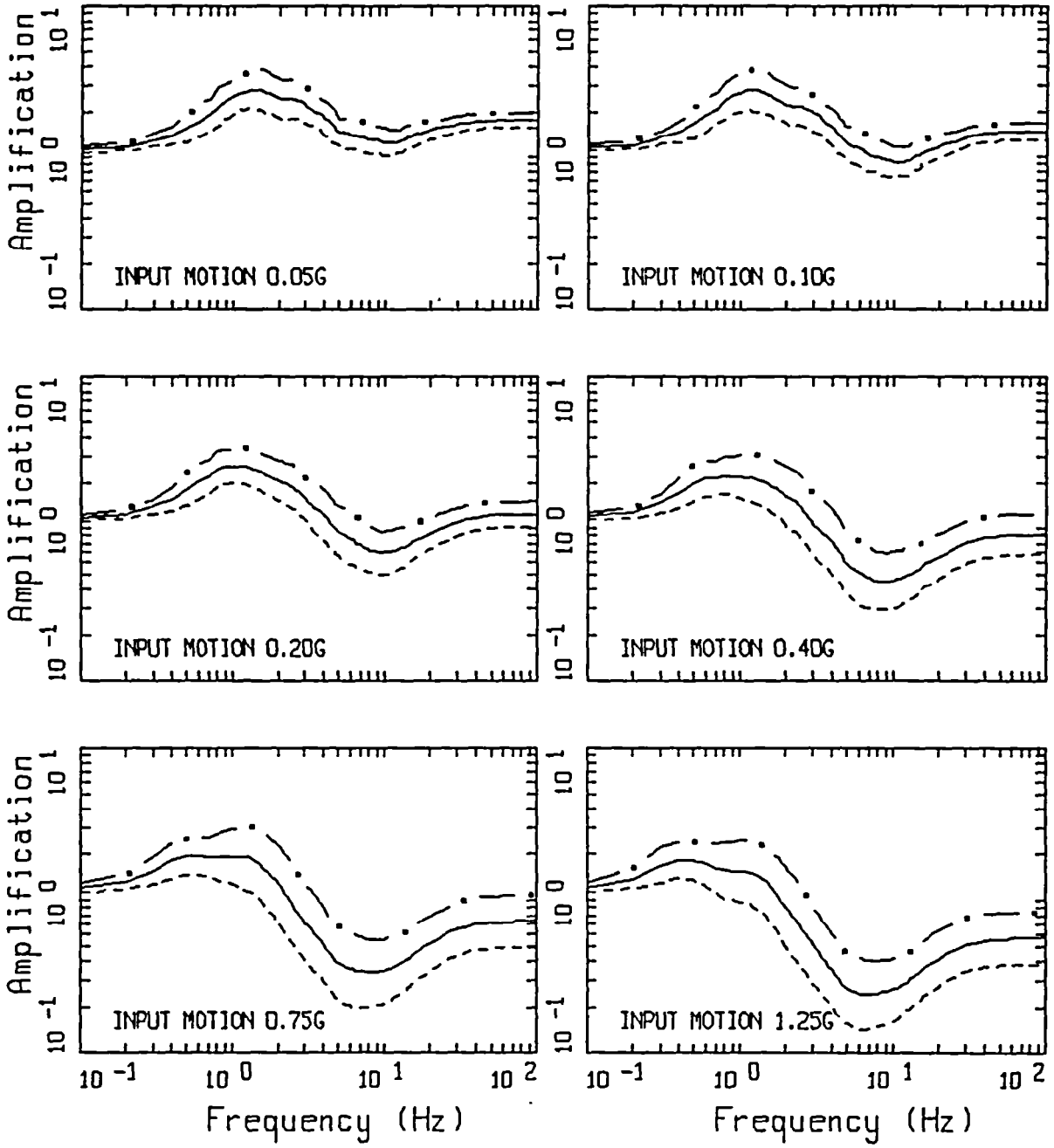

SF AMPLIFICATION

QAL (30 - 450 ft)

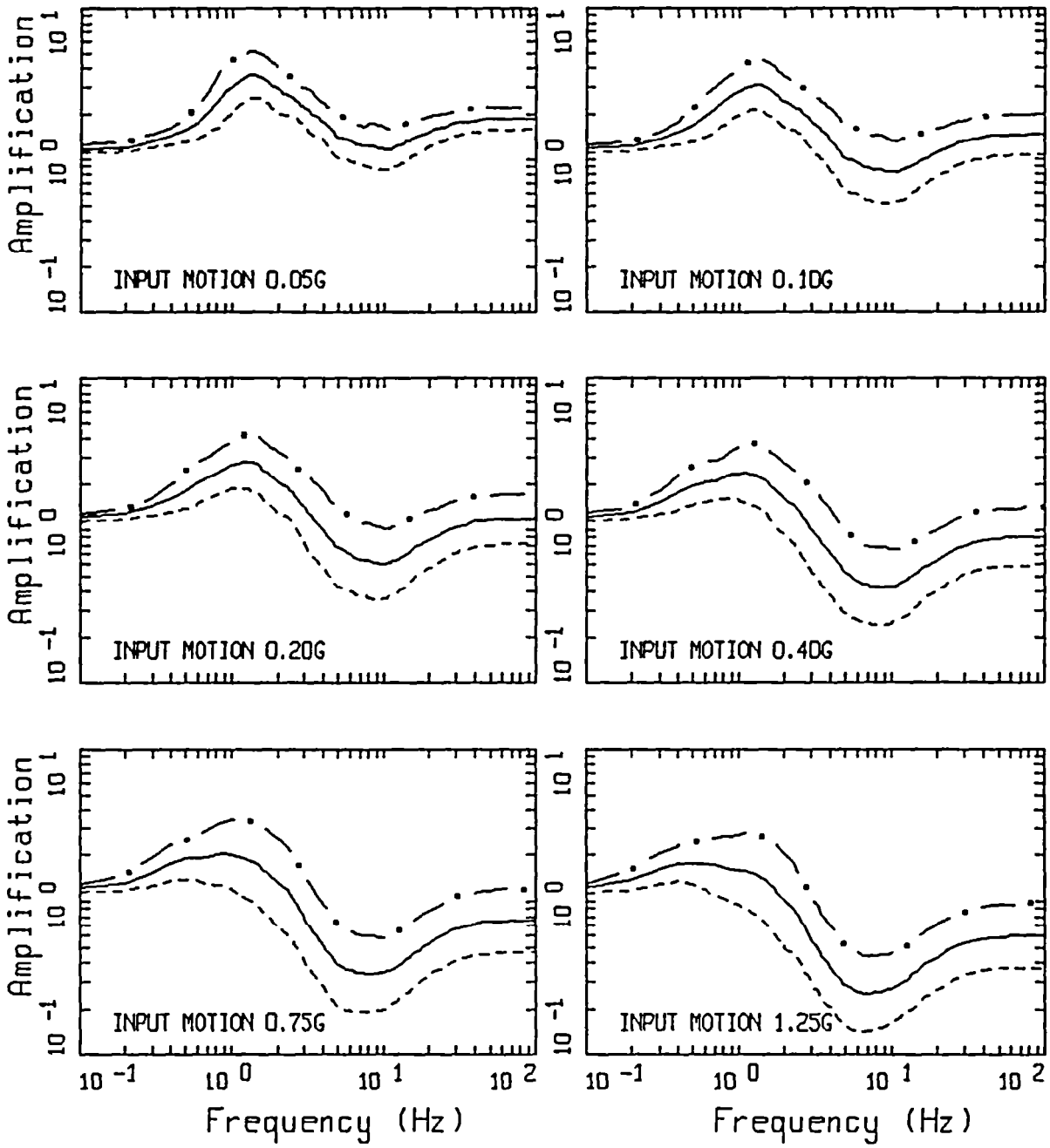

SF AMPLIFICATION

Qm (30 - 150 ft)

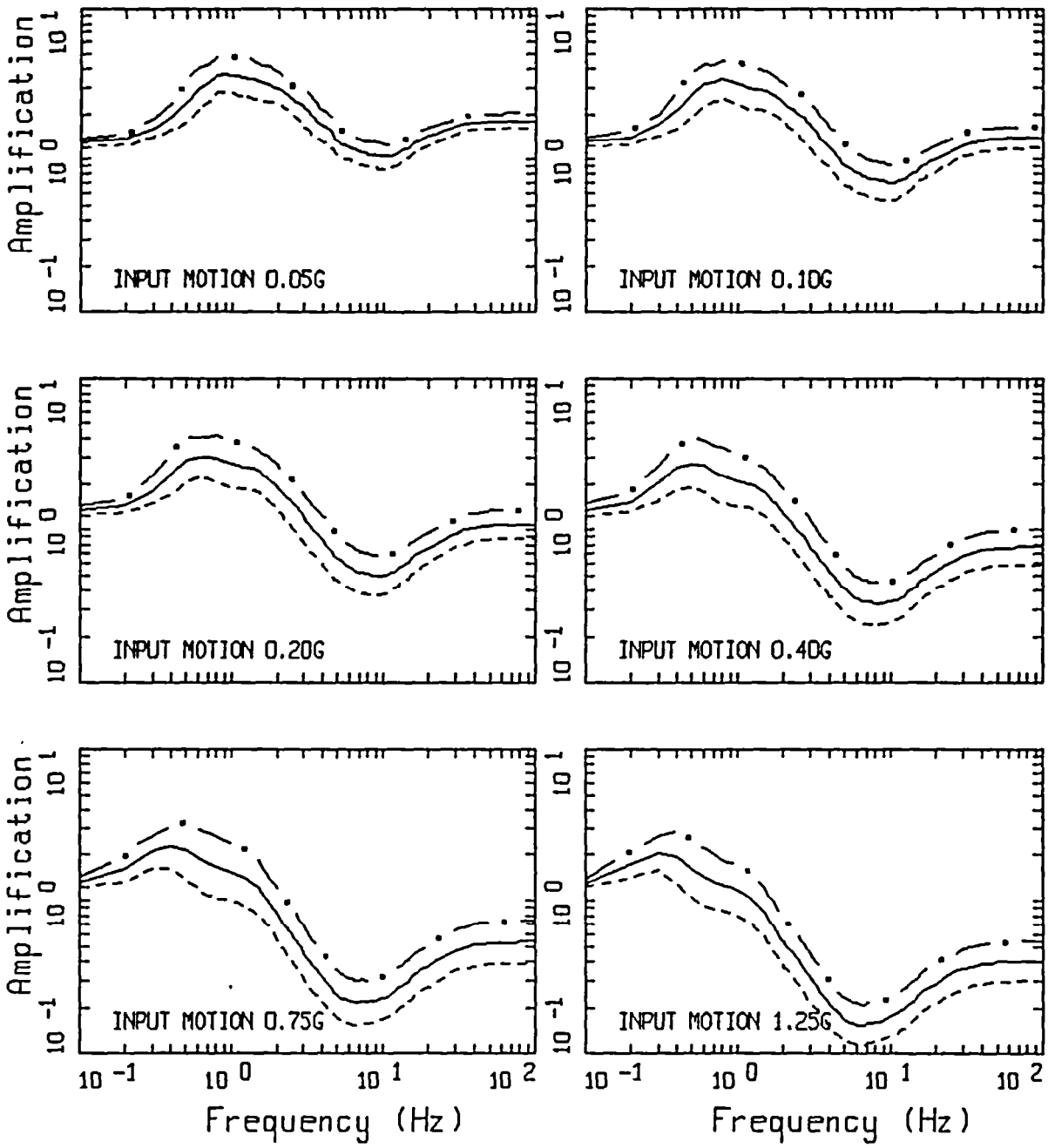

SF AMPLIFICATION

Qm (150 - 350 ft)

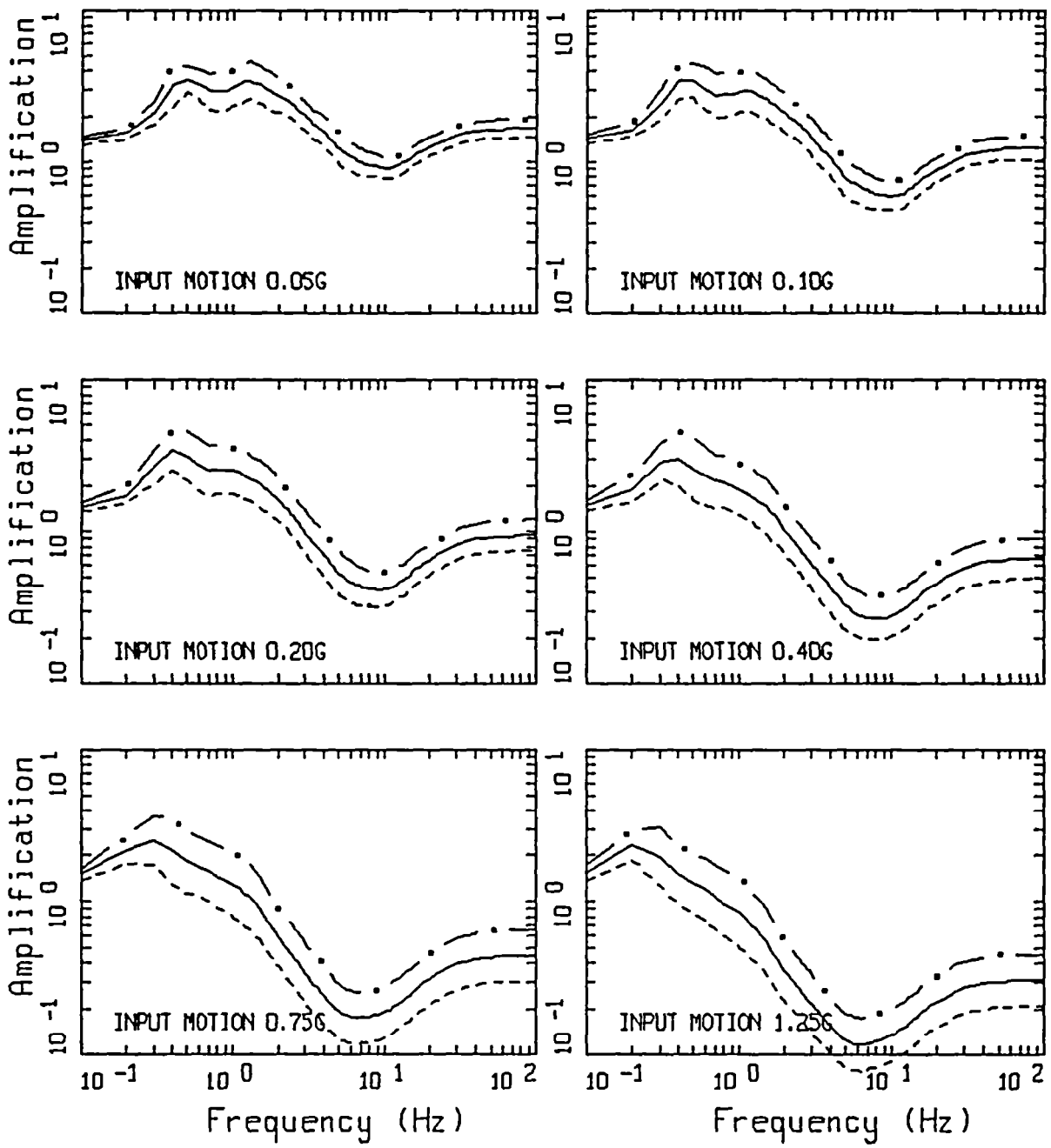

SF AMPLIFICATION

Qm (350 - 650 ft)

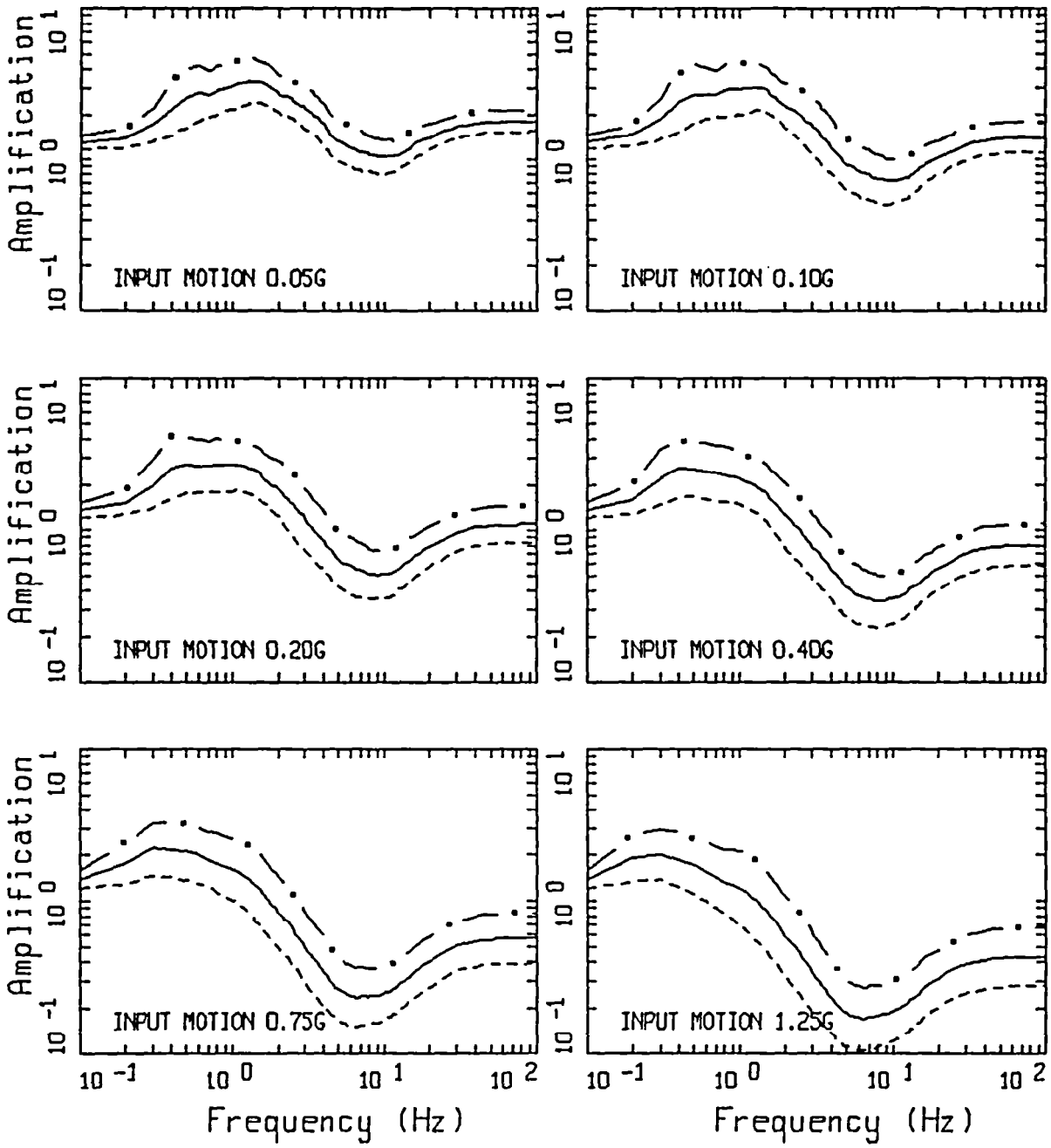

SF AMPLIFICATION

Qm (30 - 650 ft)

APPENDIX B

Amplification Factors (5% damped response spectra) For The Los Angeles Area Based on Surface Geology: TM_{ZS}, QT_S, Q_{oa}, Q_{al}, and Q_m (Table 1).

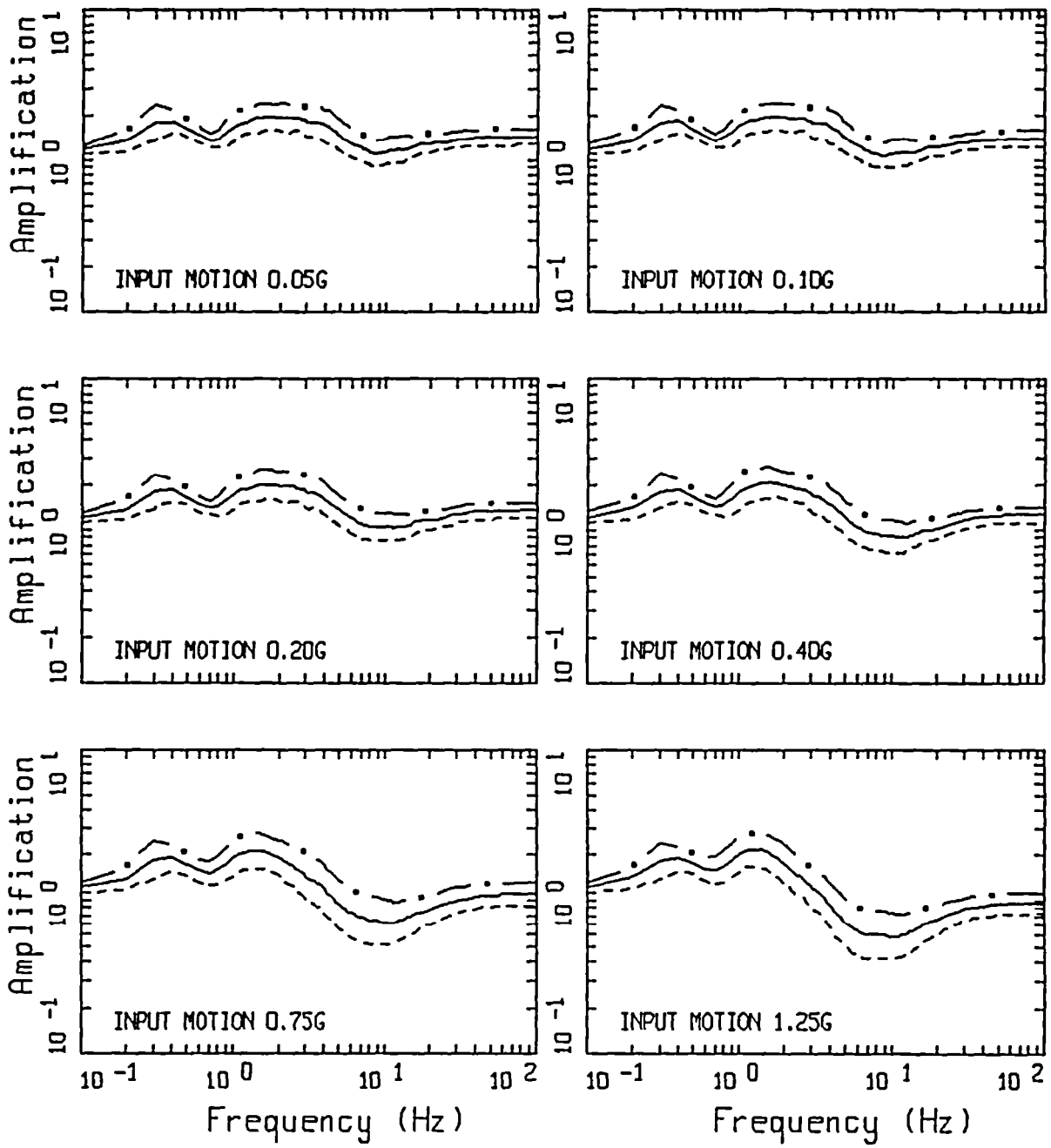

LA AMPLIFICATION

Ts

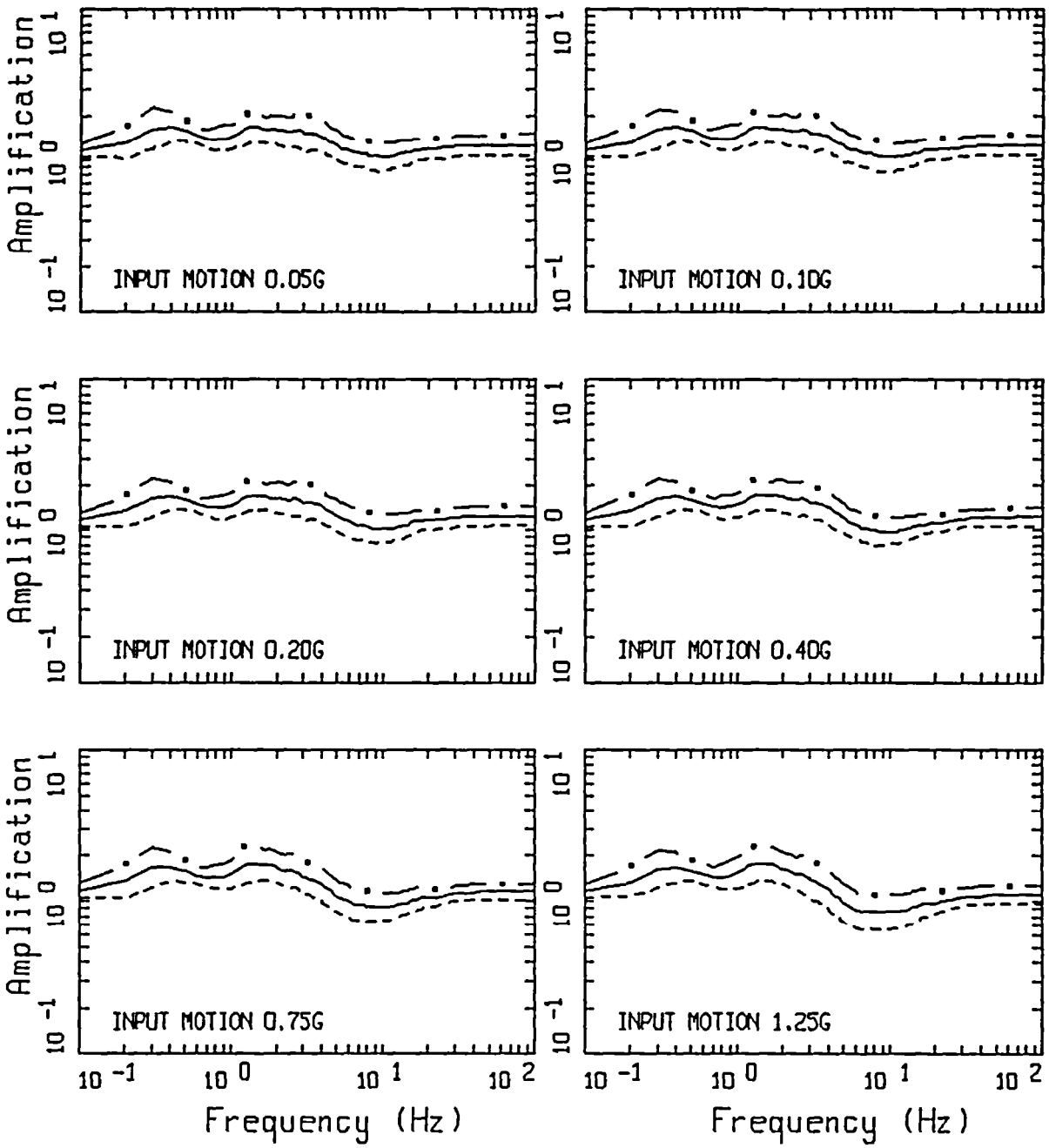

LA AMPLIFICATION

Saugus (Ts) (30 - 150 ft)

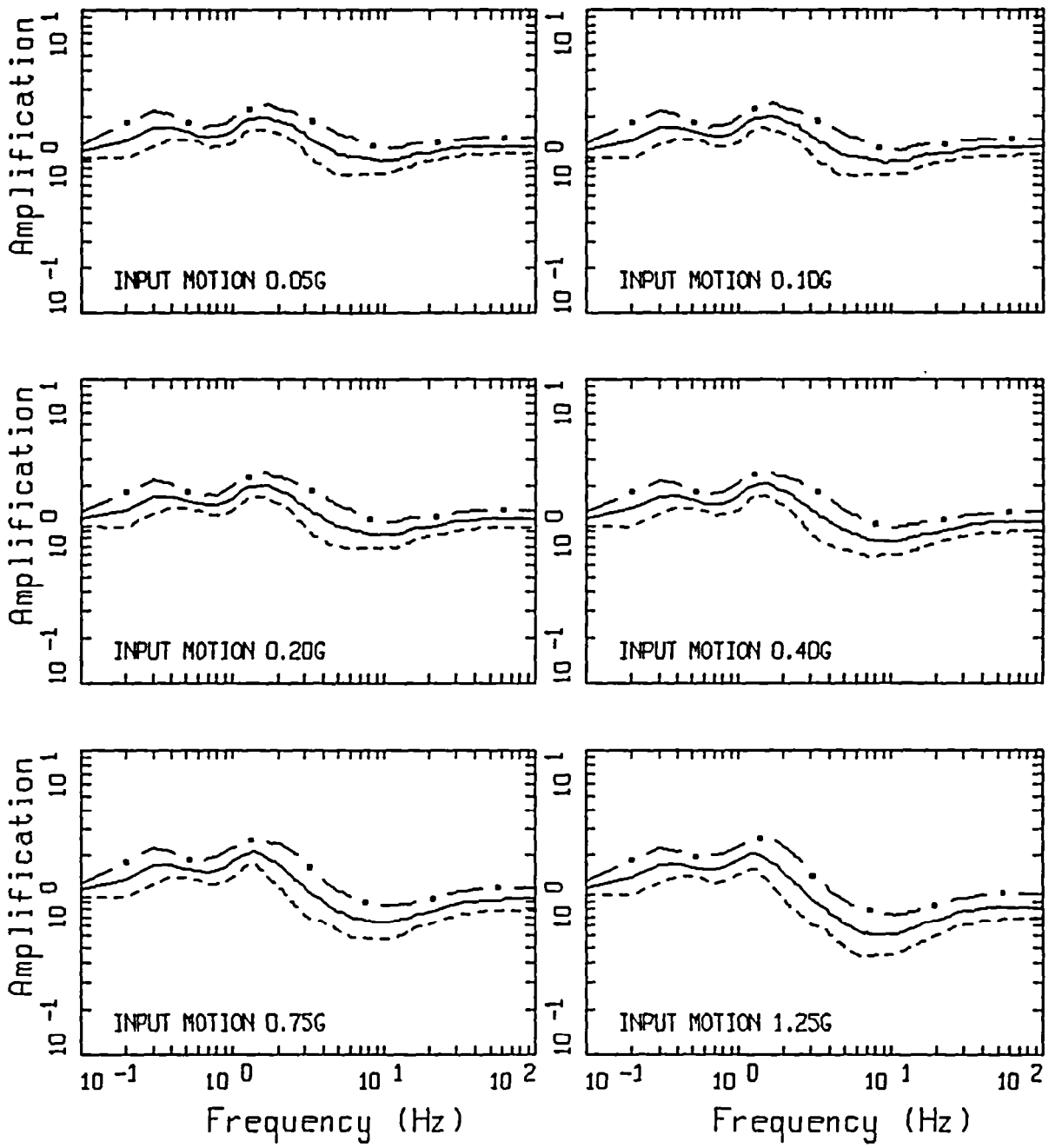

LA AMPLIFICATION

Saugus (Ts) (150 - 350 ft)

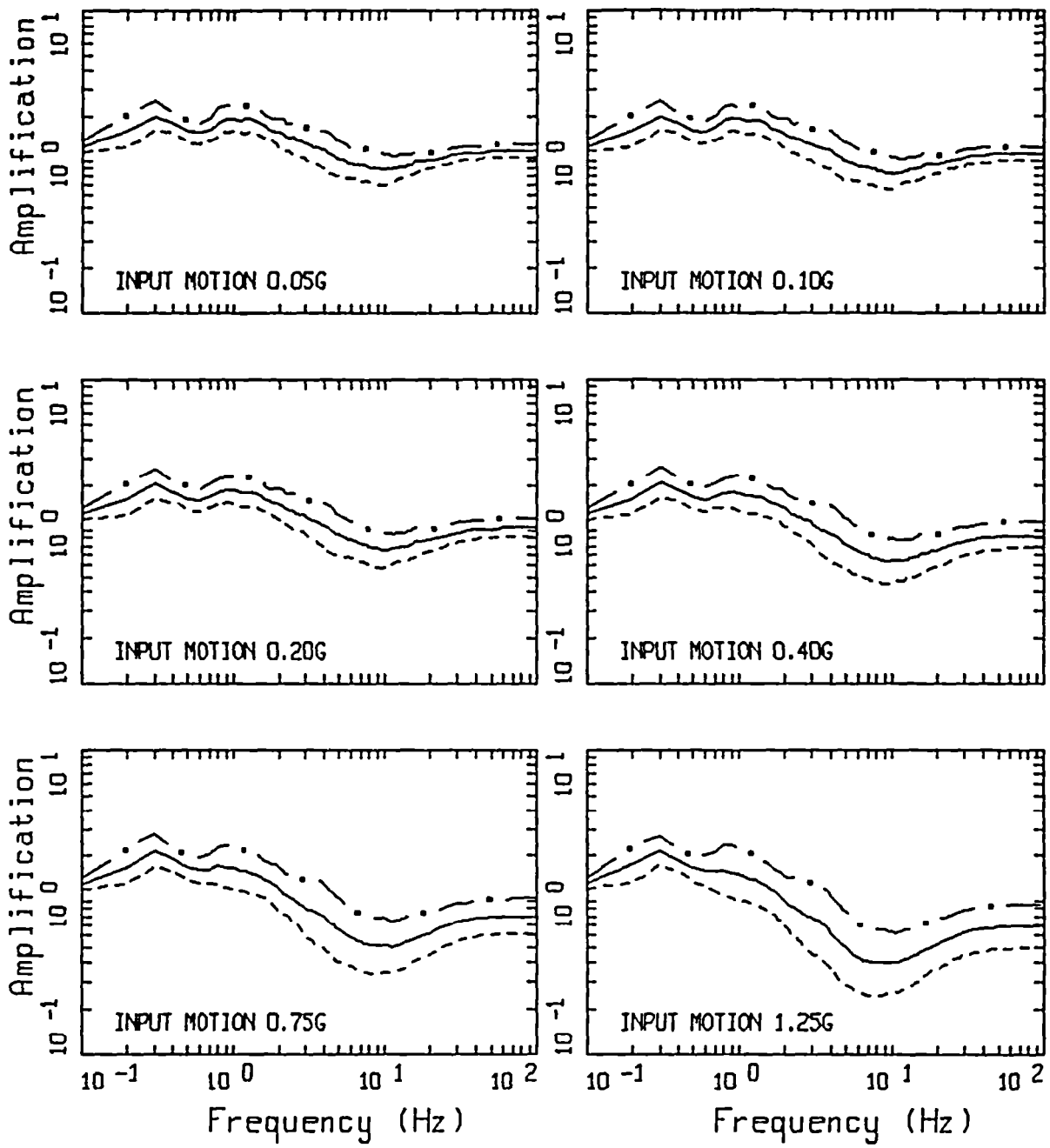

LA AMPLIFICATION

Saugus (Ts) (350 - 650 ft)

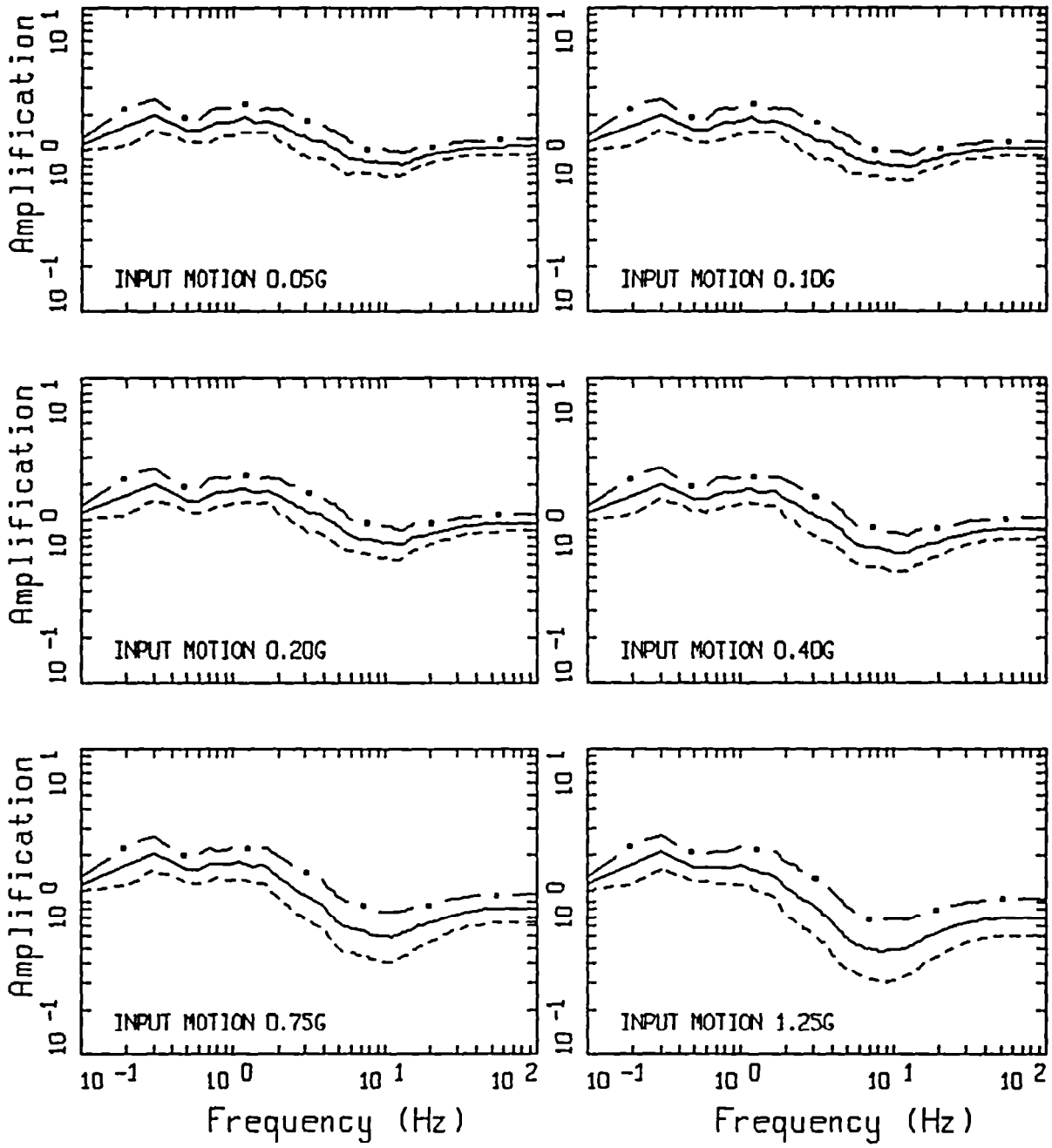

LA AMPLIFICATION

Saugus (Ts) (30 - 1000 ft)

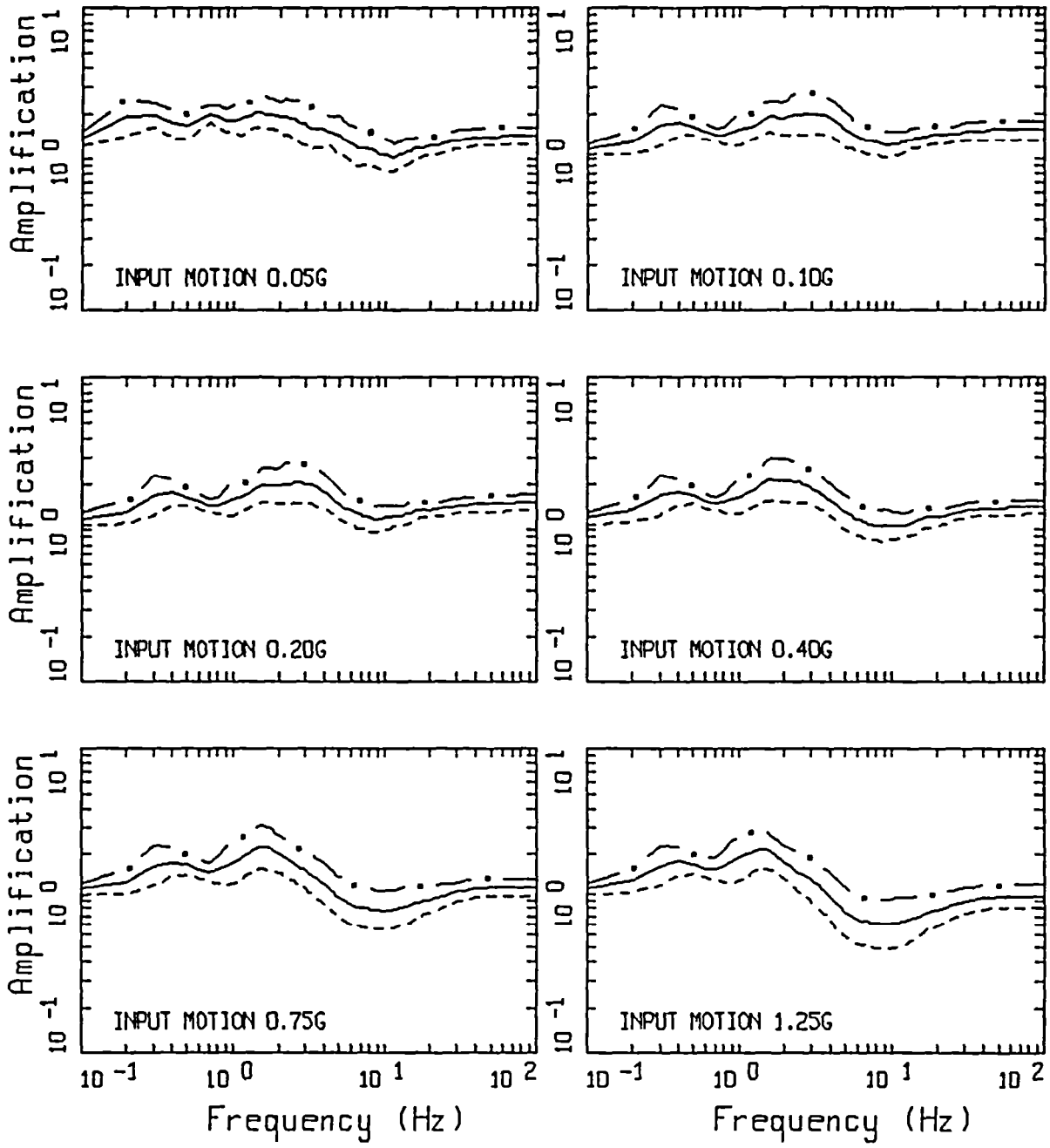

LA AMPLIFICATION

Qo + Ts (30 - 150 ft)

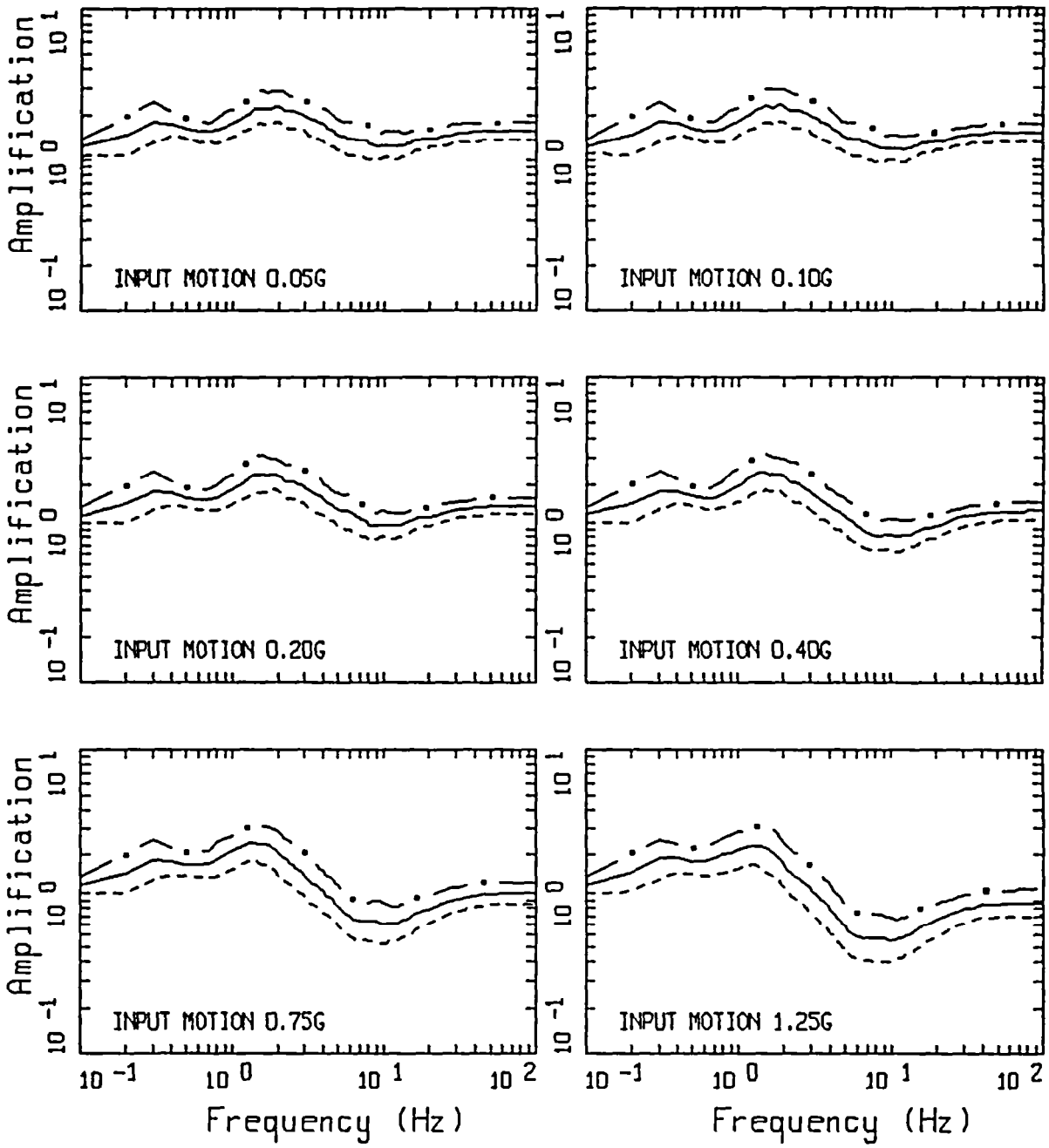

LA AMPLIFICATION

Qo + Ts (150 - 350 ft)

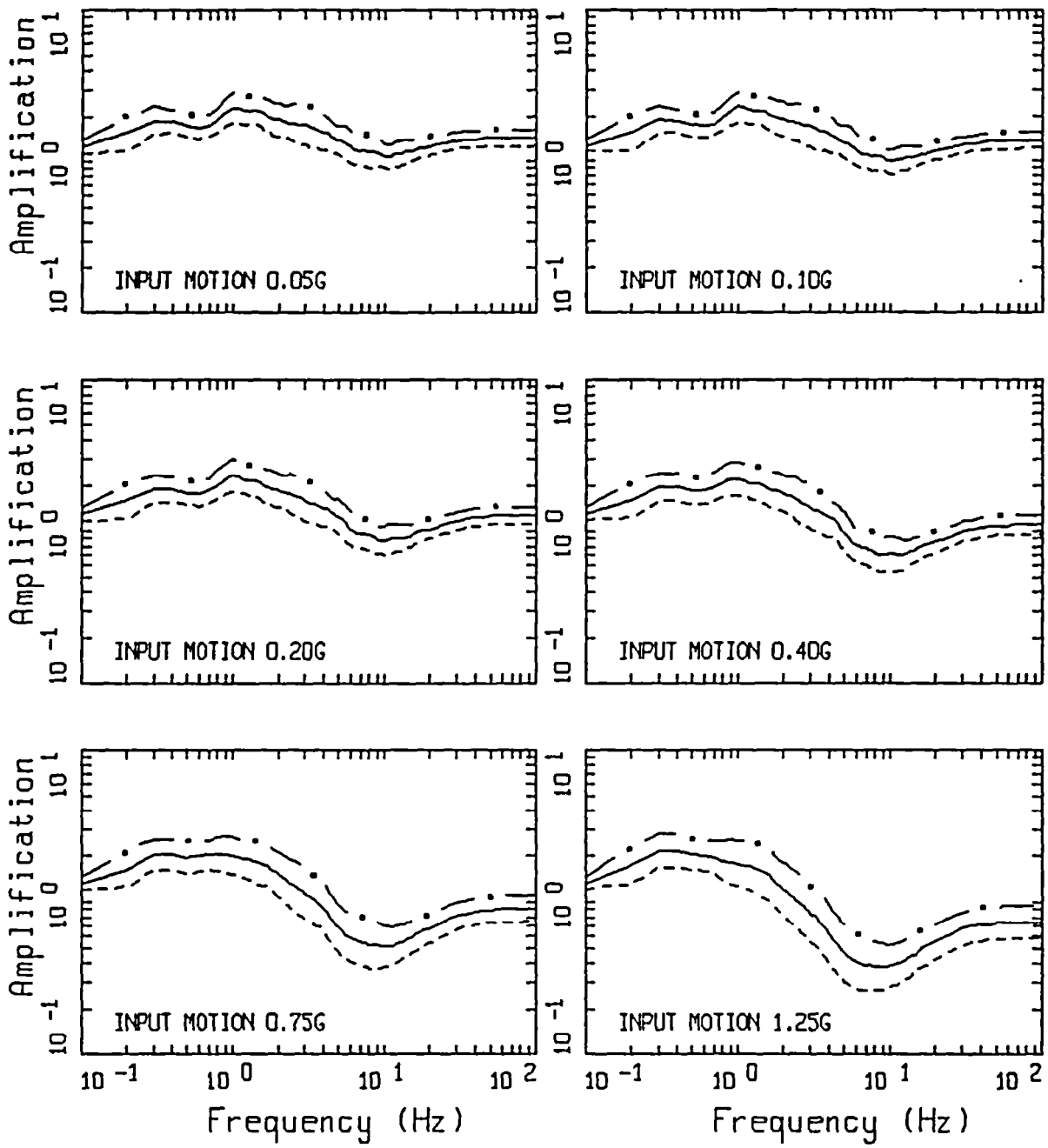

LA AMPLIFICATION

Qo + Ts (350 - 650 ft)

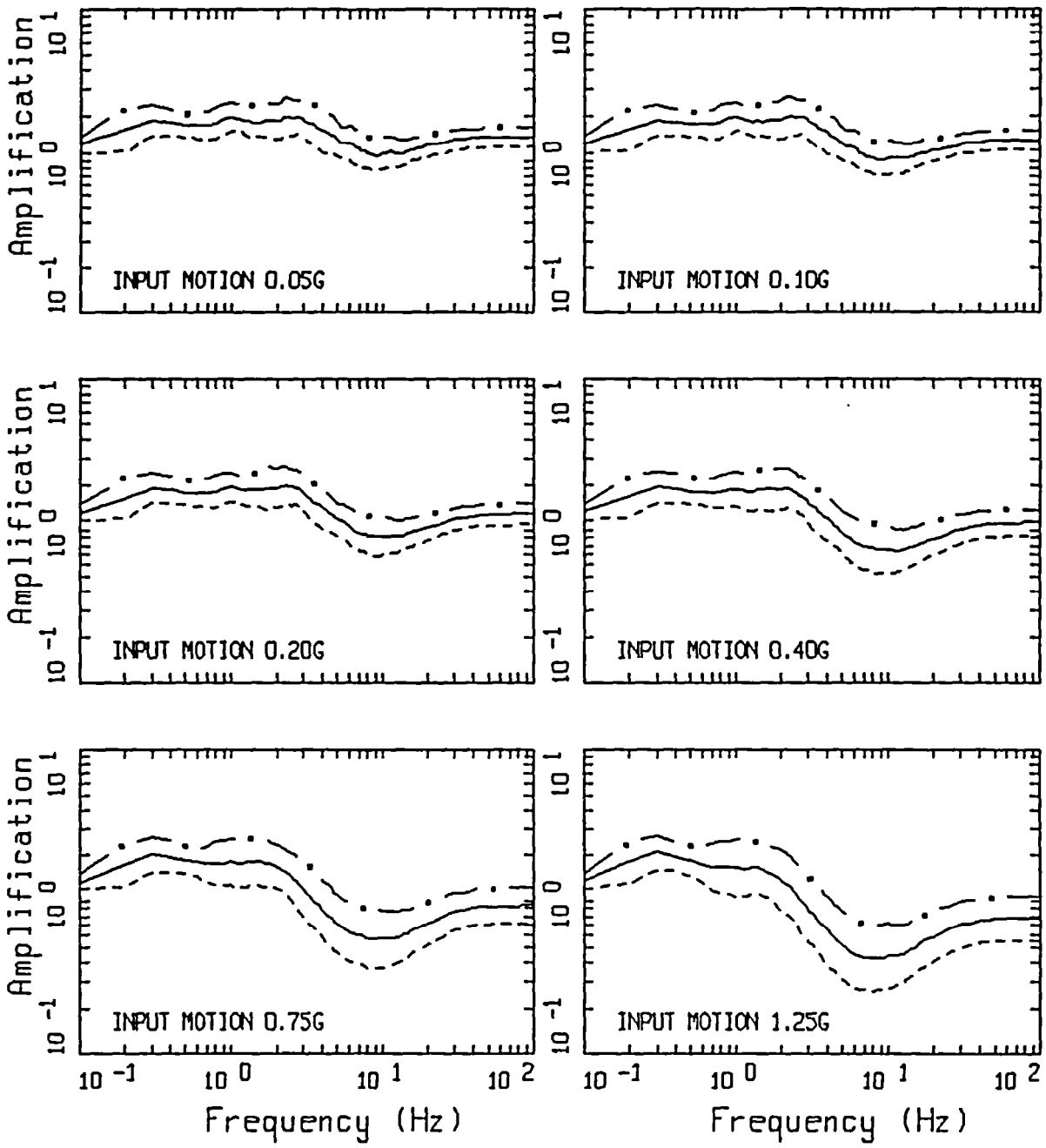

LA AMPLIFICATION

Qo + Ts (30 - 1000 ft)

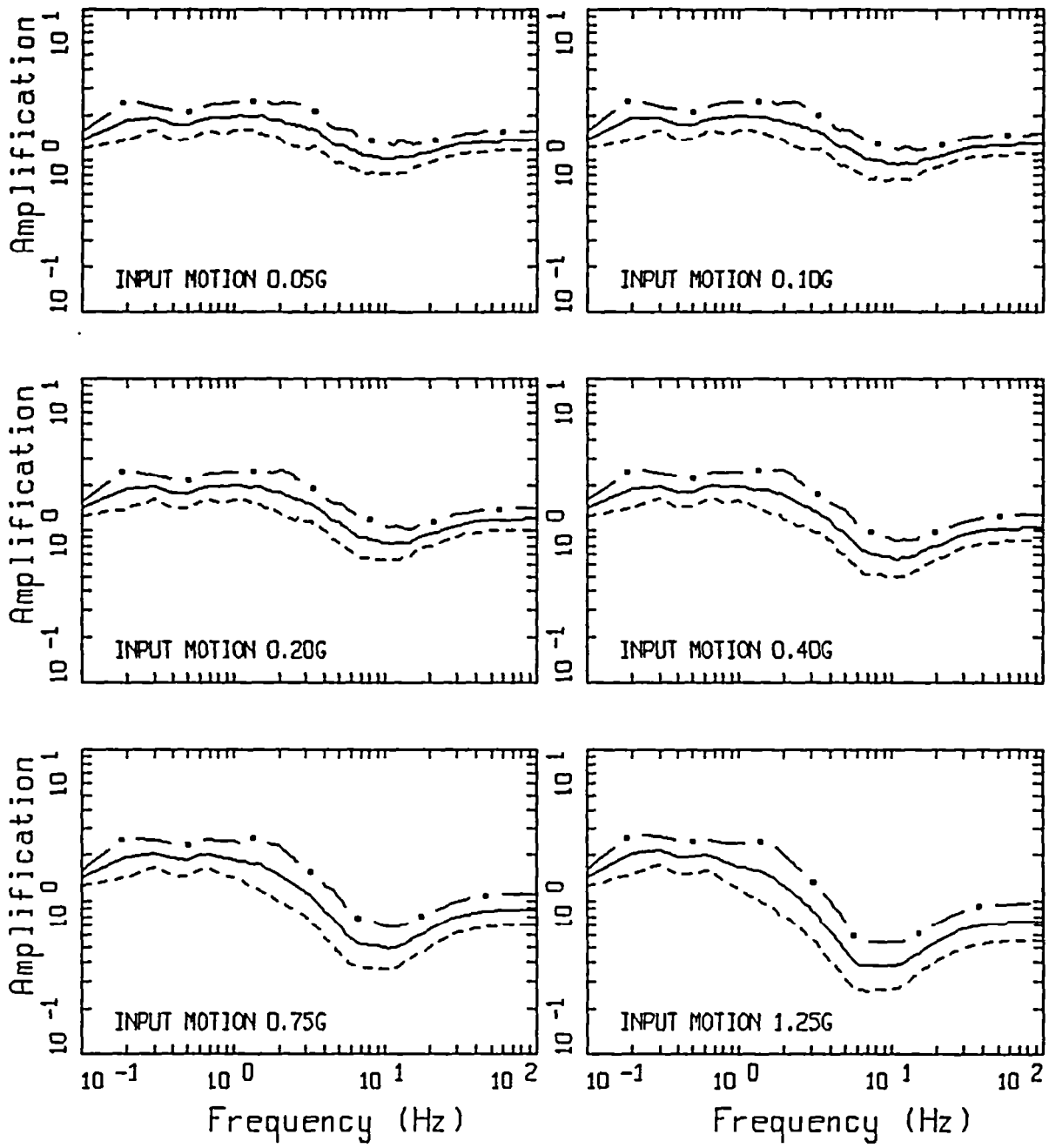

LA AMPLIFICATION

Qo + Ts (500 - 1500 ft)

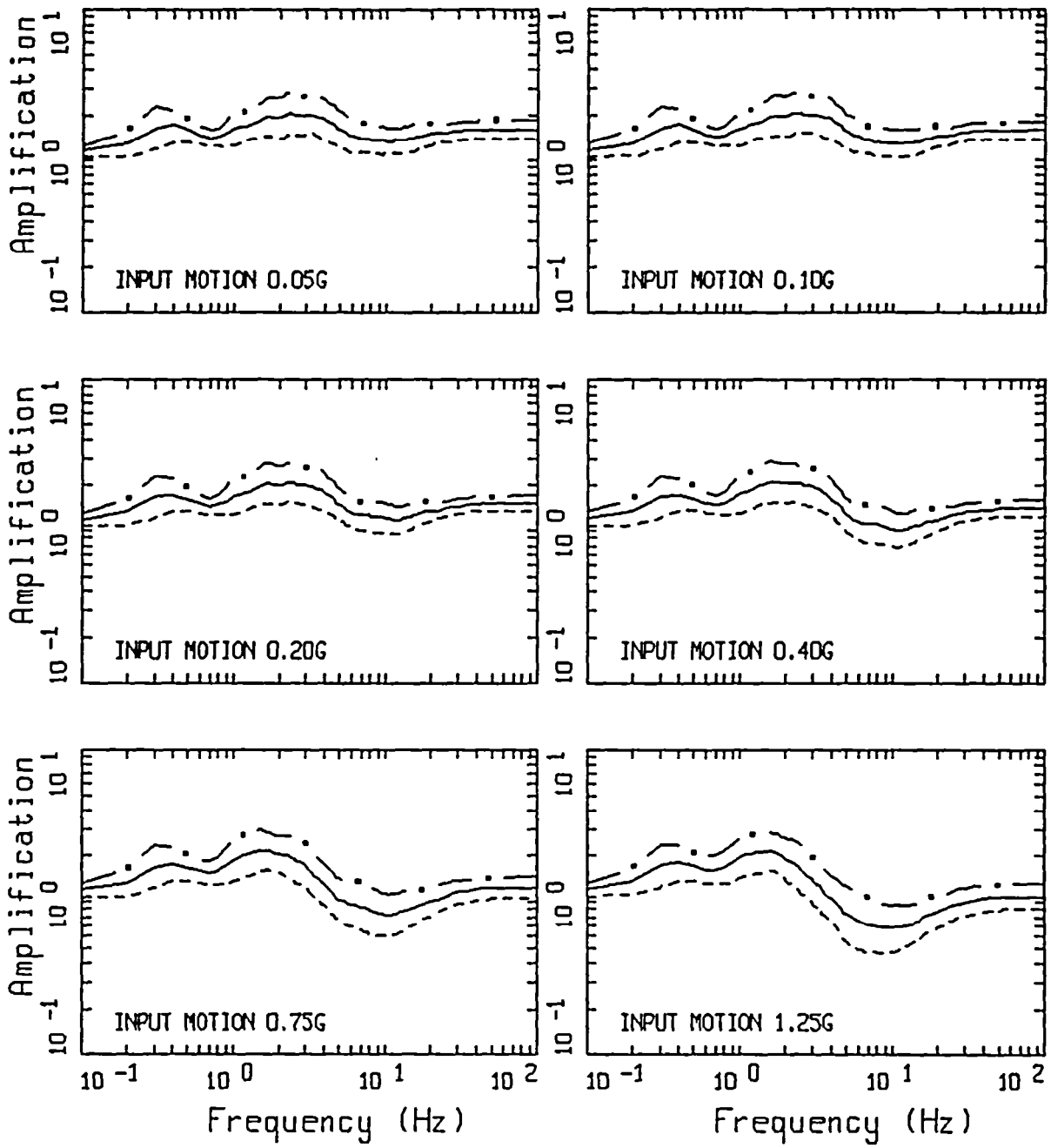

LA AMPLIFICATION

Qo (30 - 150 ft)

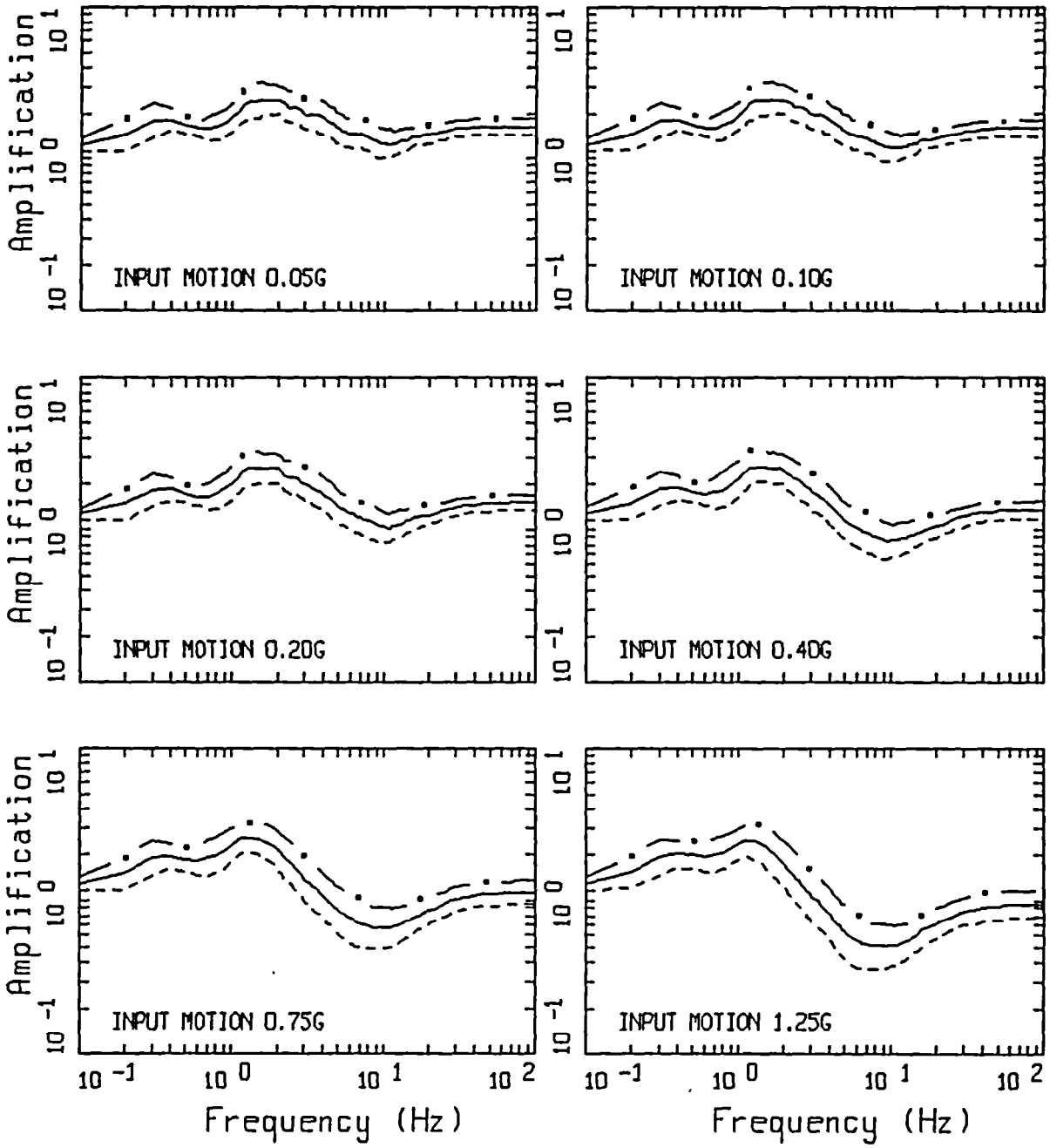

LA AMPLIFICATION

Qo (150 - 350 ft)

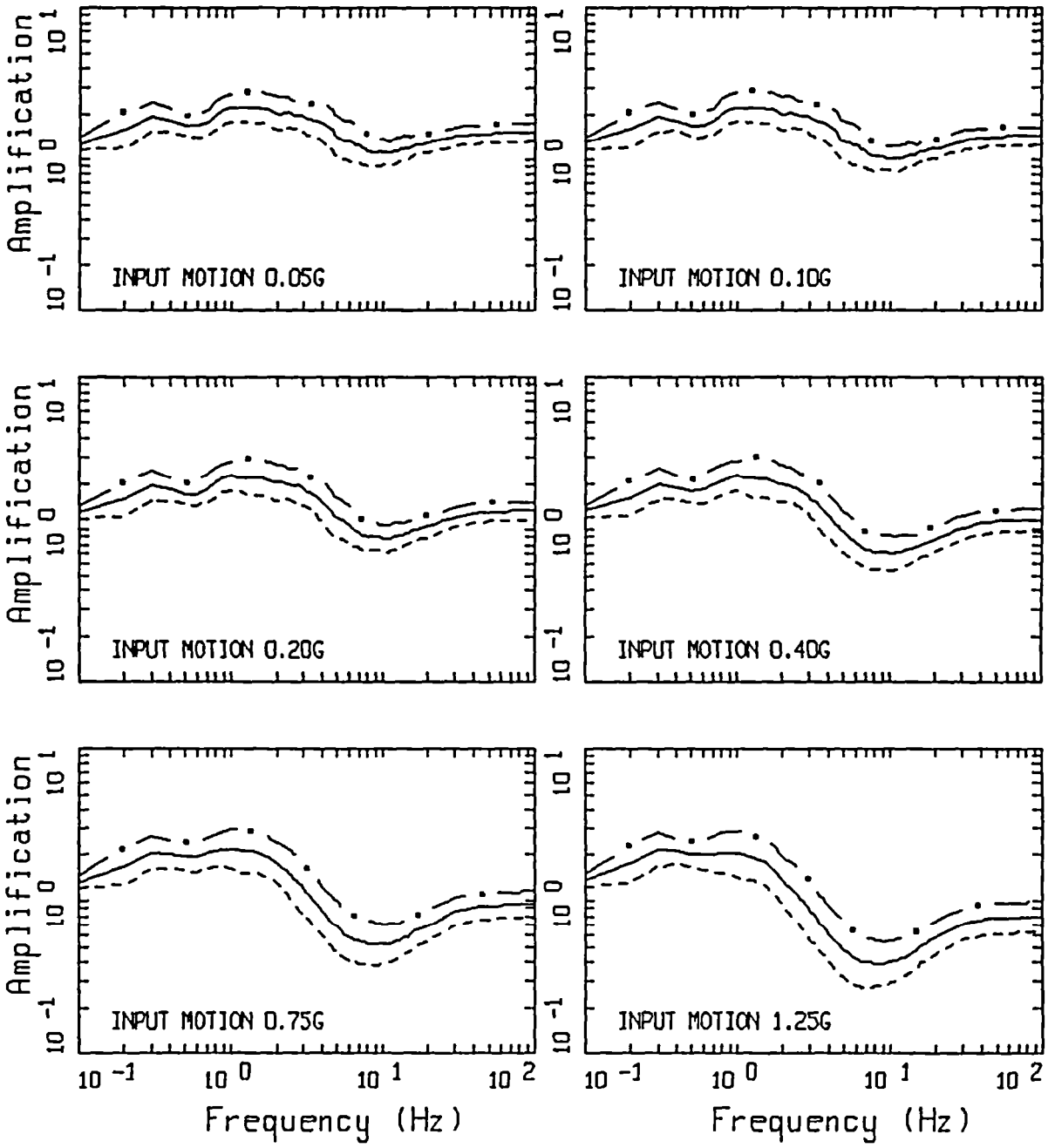

LA AMPLIFICATION

Qo (350 - 650 ft)

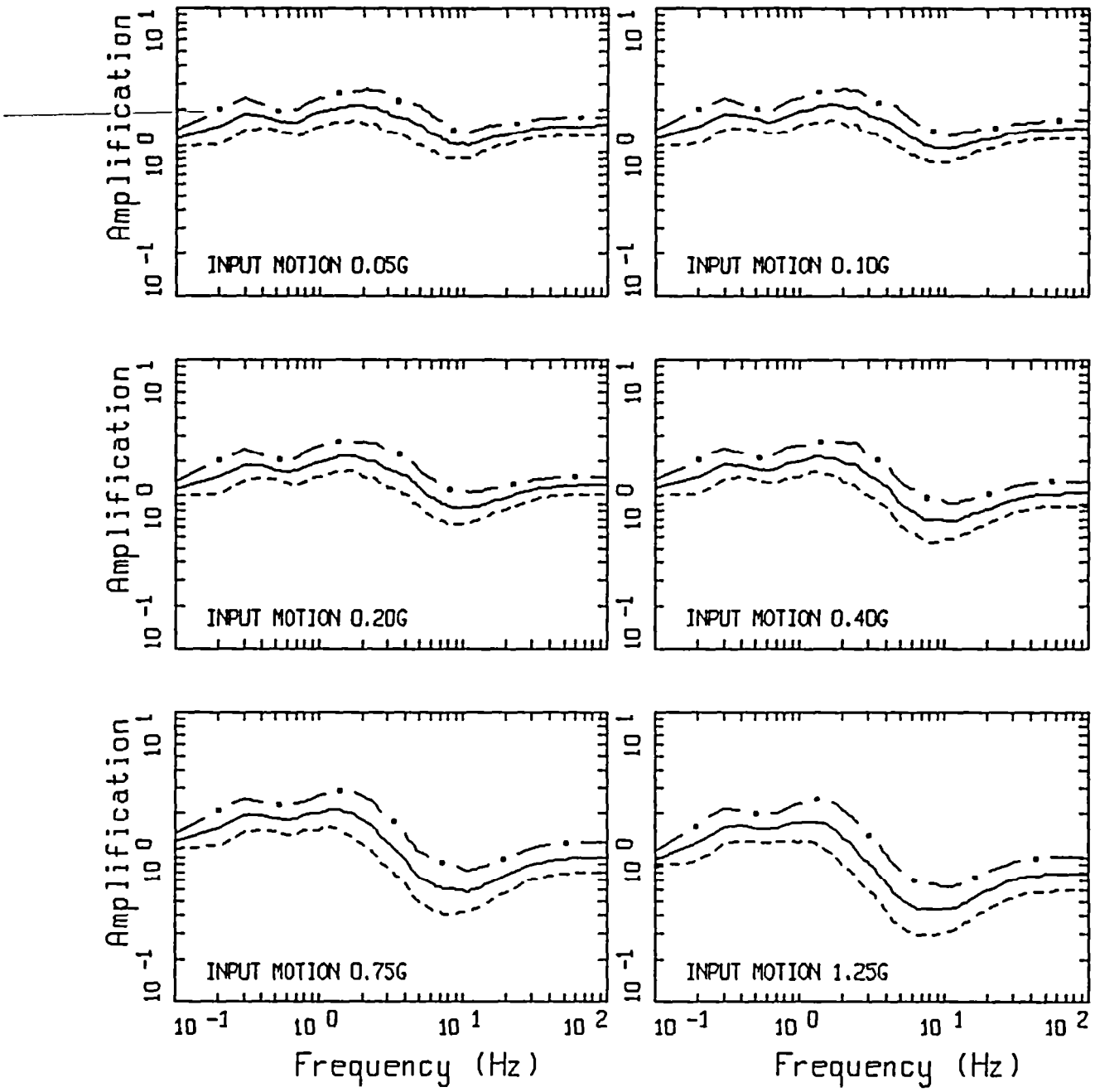

LA AMPLIFICATION

Qo (30 - 1000 ft)

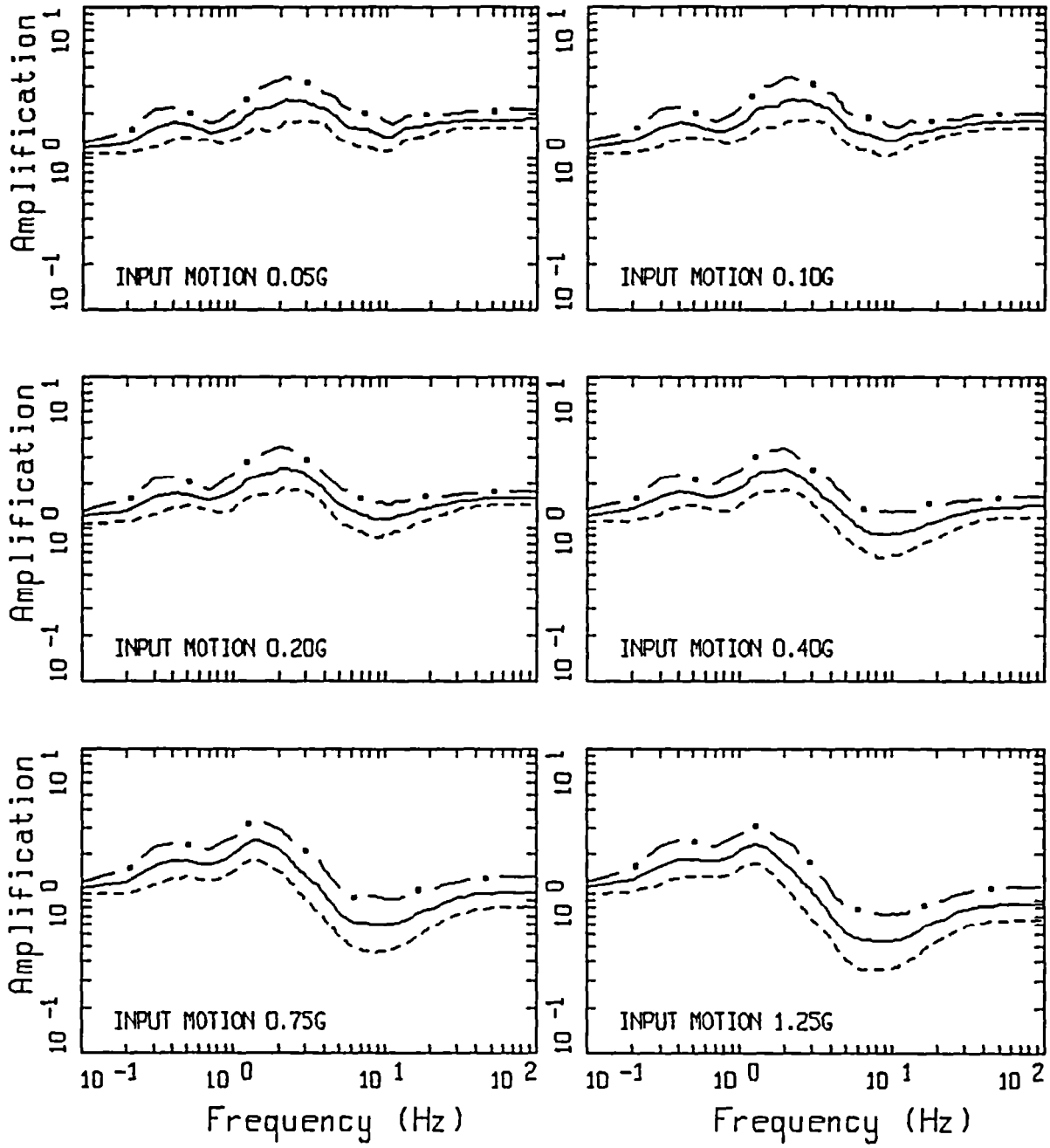

LA AMPLIFICATION

Qy (30 - 150 ft)

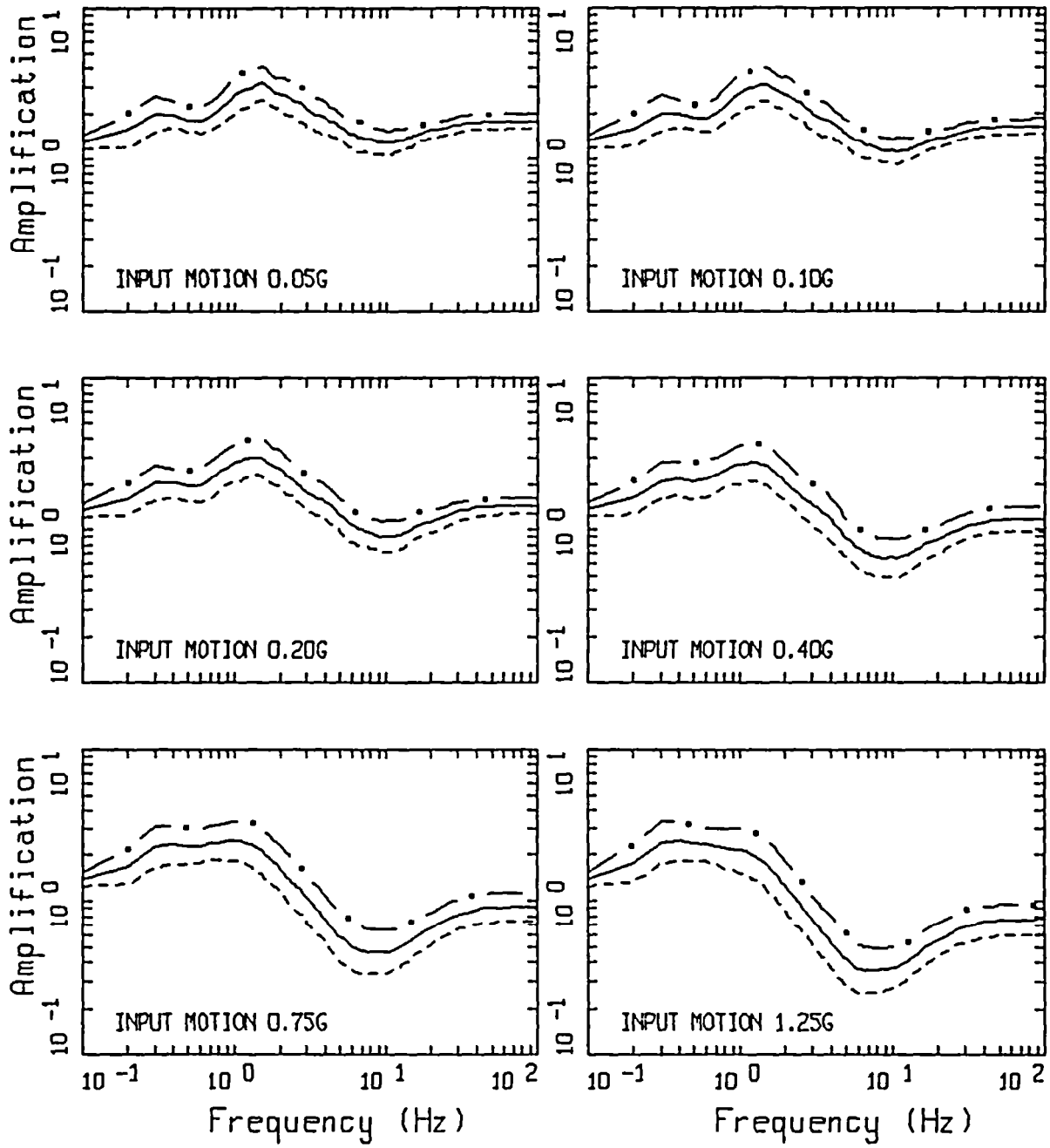

LA AMPLIFICATION

Qy (150 - 350 ft)

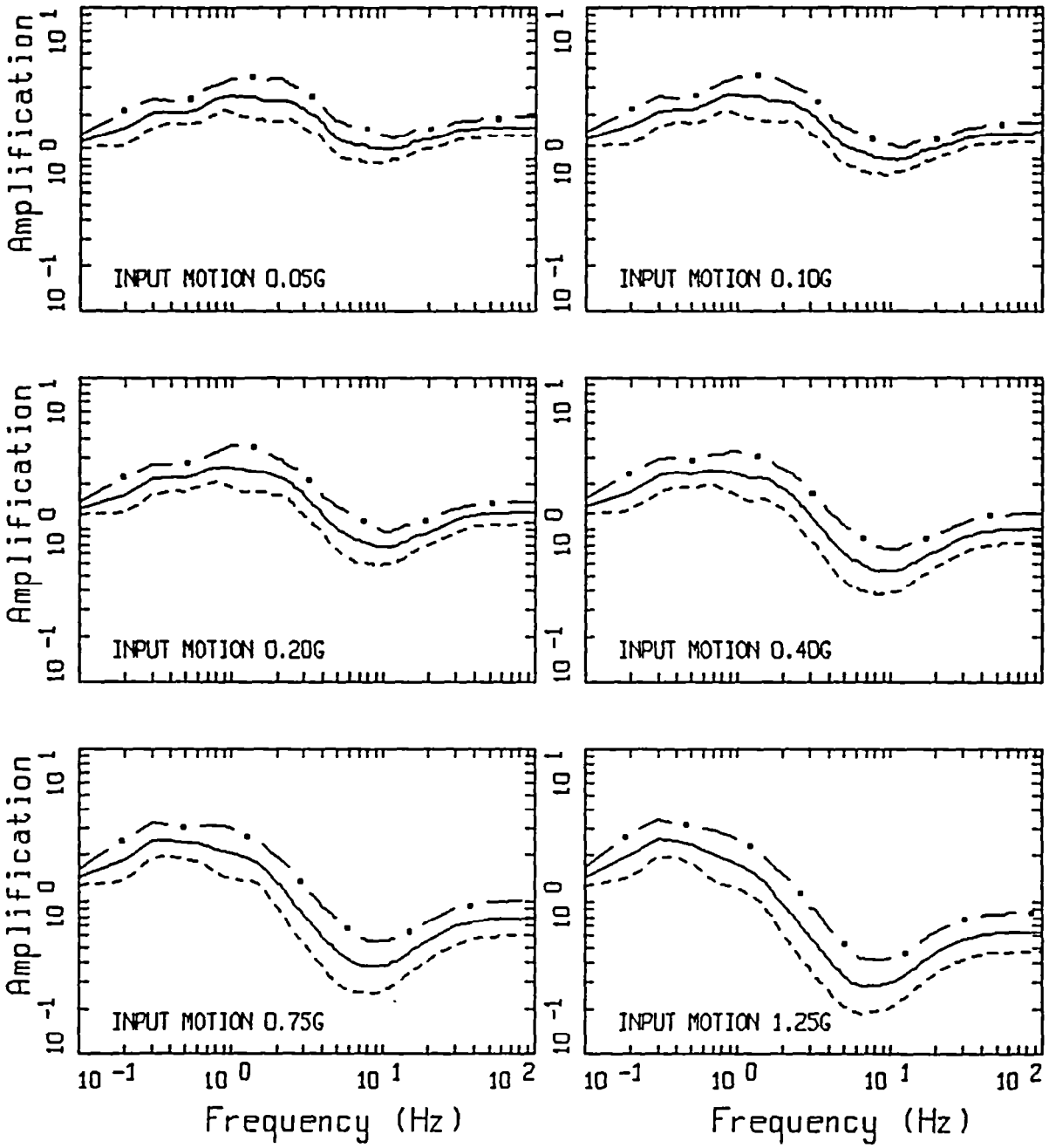

LA AMPLIFICATION

Qy (350 - 650 ft)

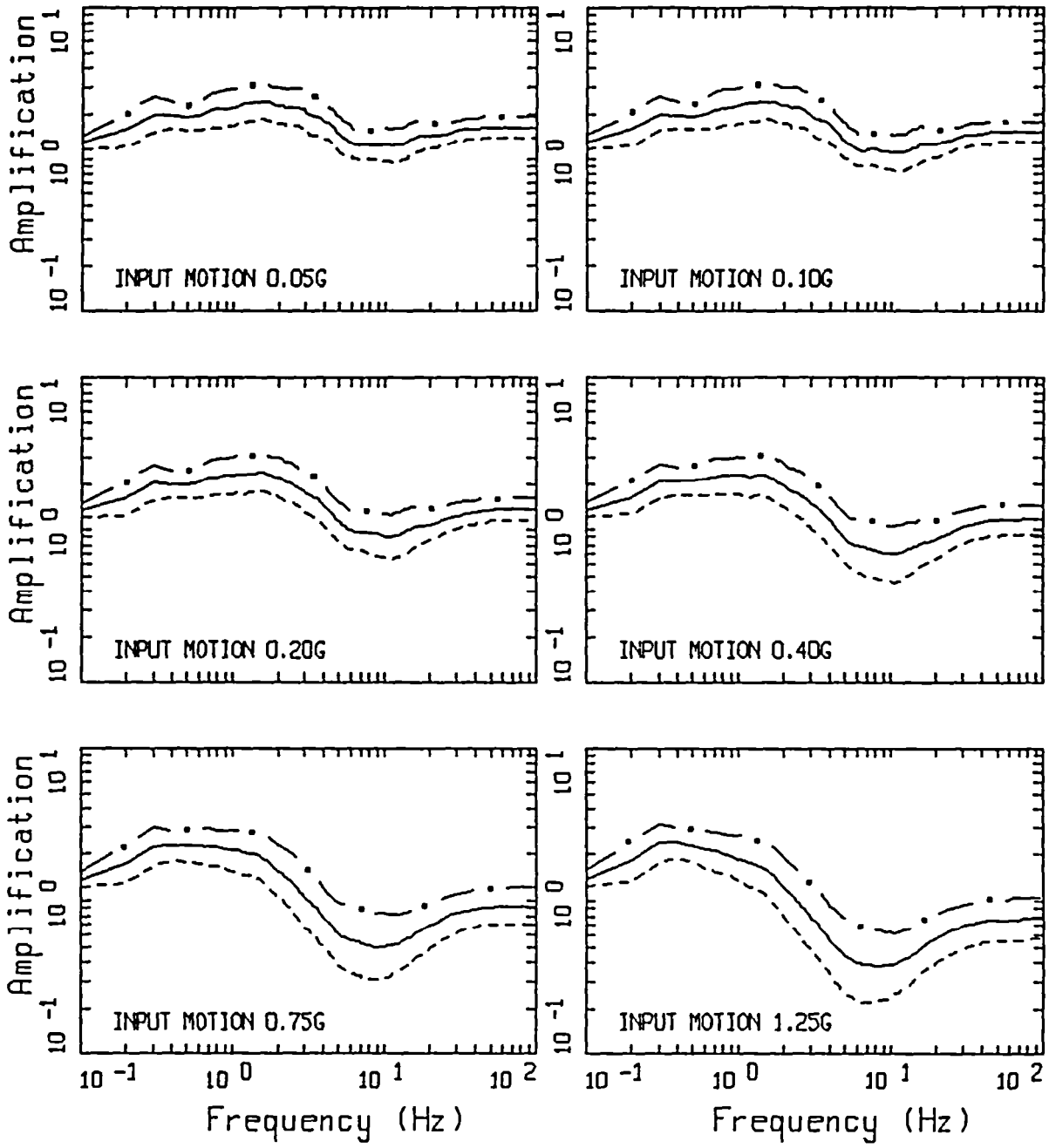

LA AMPLIFICATION

Qy (30 - 1000 ft)

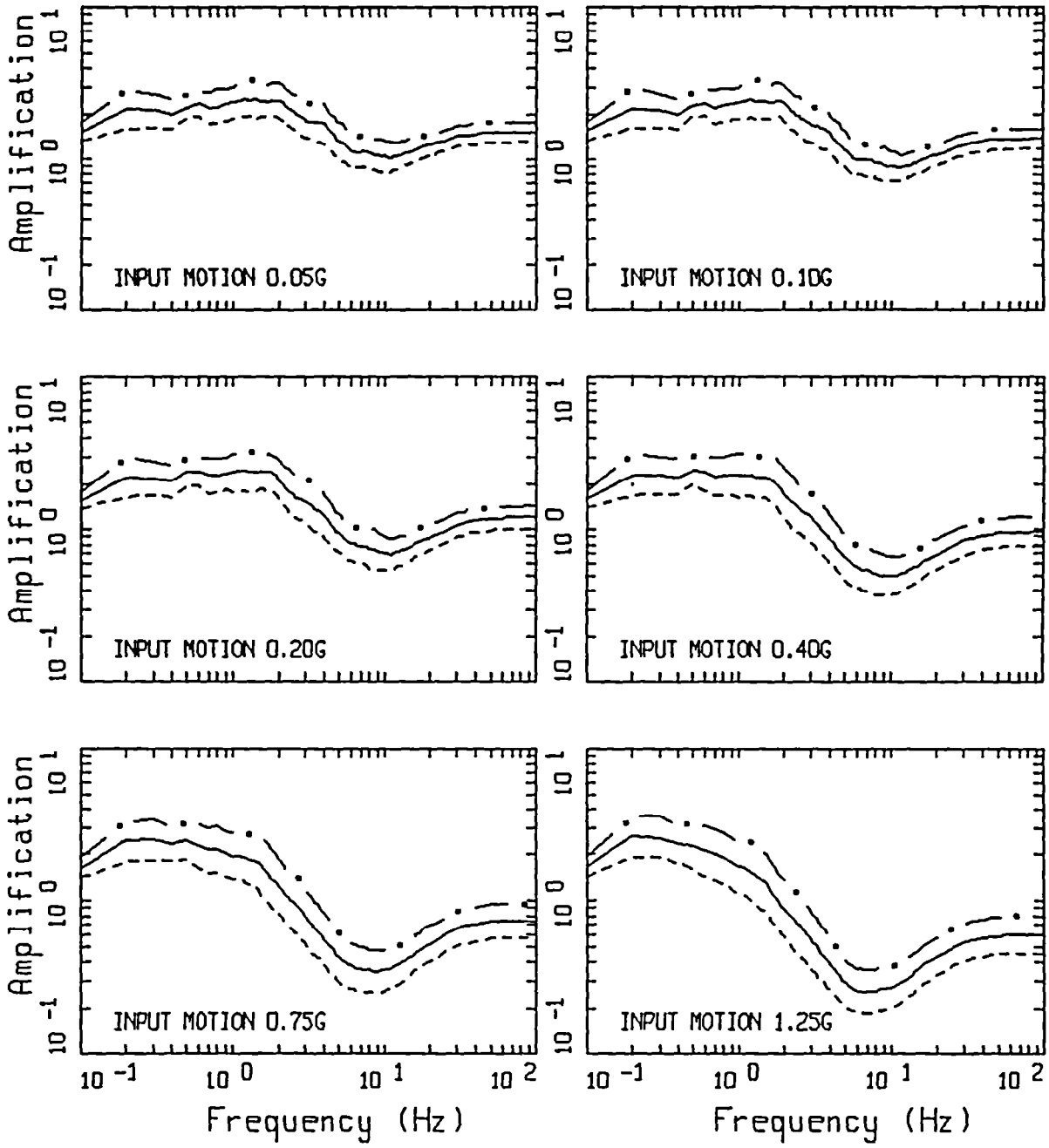

LA AMPLIFICATION

Qy (500 - 1500 ft)

PACIFIC EARTHQUAKE ENGINEERING RESEARCH CENTER

Evaluation of Uncertainties in Ground Motion Estimates for Soil Sites

Jonathan P. Stewart

Mehmet B. Baturay

University of California, Los Angeles

A report to the PEER Program of Applied Earthquake Engineering Research on Lifeline Systems

The financial support of the sponsor organizations including the Pacific Gas & Electric Company (PG&E), the California Energy Commission (CEC), and the California Department of Transportation (Caltrans) is acknowledged.

PEER UTILITIES PROGRAM
REPORT NO. 2000/04

TASK 5

EVALUATION OF UNCERTAINTIES IN GROUND MOTION ESTIMATES AT SOIL SITES

by

Jonathan P. Stewart and Mehmet B. Baturay

Research supported by the PEARL sponsor organizations including the Pacific Gas & Electric Company, the California Energy Commission, and the California Department of Transportation under Award Number 09566.

Report No. UCLA/CEE-2000/01

Department of Civil & Environmental Engineering
University of California
Los Angeles, California

January 2000

Abstract

For a given seismic source, ground motions at soil sites can be estimated using either soil attenuation relationships, or ground response analyses with input motions scaled to match specified spectral ordinates from rock attenuation relationships. When engineers perform ground response analyses, it is with the expectation that accounting for nonlinear sediment response will improve the accuracy and reduce the uncertainty in estimated ground motions. This study investigates such benefits of ground response analyses as a function of site condition. A total of 36 strong motion sites are investigated, with roughly equal representation in the site categories of: (1) shallow stiff soil, (2) moderate-depth stiff soil, (3) deep stiff soil, and (4) soft clay.

Procedures were developed for selecting and scaling suites of input motions for ground response analyses that incorporate key source and path information such as magnitude, distance, and rupture directivity. The median of the input suite is scaled to match a "best estimate" target spectrum established from a rock attenuation relationship modified to incorporate an event term, rupture directivity effects (if applicable), and weathered rock correction factors. Since only the median of the suite is scaled to match the target, the aleatory uncertainty of source/path is retained. The results of ground response analyses using these input motions are expressed statistically in the form of medians and standard error terms. These statistical quantities are the ground response counterparts to the median and standard error of spectral ordinates from a soil attenuation relationship.

Residuals between recorded and estimated motion were calculated to elucidate trends in the results of each ground motion estimation procedure across geotechnical site categories. For $T < 1$ s, ground response analyses are found to improve the accuracy of ground motion predictions relative to attenuation in all site categories. However a positive bias in median ground response

estimates is found for most site categories, indicating a systematic underprediction of ground motion that is not yet fully understood. In addition, the uncertainty in the residual of the estimated ground motions is large for stiff soil sites, indicating that source/path effects are "randomly" and significantly varying the motions from site-to-site. Conversely, for soft clay sites, the standard error of ground response estimates is small, indicating a strong and systematic influence of ground response that is reasonably well captured by the analysis. For $T > 1$ s, substantial positive bias is observed in results for moderate to deep stiff soil sites, which may be a basin effect. In light of the observed biases, recommendations on the interpretation of ground response results are provided.

Table of Contents

Abstract ii

Table of Contents iv

List of Tables and Figures vi

Acknowledgments vii

1.0 INTRODUCTION 1

2.0 SITE SELECTION 3

3.0 DEVELOPMENT OF INPUT MOTIONS 7

3.1 Strong Motion Database 7

3.2 Time History Selection Criteria 8

3.3 Scaling of Input 10

4.0 GROUND RESPONSE MODELLING 12

4.1 Dynamic Soil Properties 12

4.2 Location of Control (Input) Motion 14

4.3 Analysis of Strain-Dependent Soil Properties 15

5.0 STATISTICAL ANALYSIS OF RESULTS 16

5.1 Analysis 16

5.2 Results 18

6.0 SENSITIVITY OF GROUND RESPONSE TO INPUT SCALING PROCEDURES 26

6.1 Importance of Rock Correction Factors 26

6.2 Use of Spectrum Compatible Input Motions to Evaluate Median Ground Response 29

7.0 SUMMARY AND CONCLUSIONS 31

REFERENCES 32

APPENDIX A: Soil Sites with Well Characterized Geotechnical Conditions and Strong Motion Recordings in California, pgs. A-1 to A-4

APPENDIX B: Site Specific Data and Analysis Results, pgs. B-1 to B-184

List of Tables

Table 1: Geotechnical site classification scheme proposed by Rodriguez-Marek et al. (1999).....4

Table 2: Sites/earthquakes used in this study.....6

Table 3: Criteria for selection of modulus reduction and damping curves 13

Table 4a: Average category residuals and standard errors of median (m) ground motion estimates.....19

Table 4b: Average category residuals and standard errors of $m+s$ ground motion estimates 19

List of Figures

Figure 1: Rupture directivity parameters for strike-slip faults (X,) and dip-slip faults (Y,) defined by Somerville et al. (1997).....8

Figure 2a: Category median residuals and standard error terms, Type I sites (C2, soil depth < 30 m) 20

Figure 2b: Category median residuals and standard error terms, Type II sites (C3 & shallow D1/D2, soil depth = 45-90 m) 21

Figure 2c: Category median residuals and standard error terms, Type III sites (Deep D, soil depth > 120 m).....22

Figure 2d: Category median residuals and standard error terms, Type IV sites (E, soft soil depth > 3 m) 23

Figure 3: Response spectral scale factor to correct rock attenuation relations (after Idriss, 1999).....27

Figure 4a: Spectra and residuals with and without rock correction to input, Palo Alto VA 28

Figure 4b: Spectra and residuals with and without rock correction to input, Castaic Dam 28

Figure 4c: Comparison of rock correction effect on residuals 28

Figure 5: Comparison of scaled and spectrum compatible median spectral accelerations 30

Acknowledgements

We would like to thank Nancy Smith and Paul Somerville URS Greiner Woodward Clyde, Pasadena Office, for providing rupture directivity parameters for strong motion stations. Thanks are also extended to Walt Silva of Pacific Engineering and Analysis and Norm Abrahamson of PG&E for helpful comments made in numerous discussions about this topic. We appreciate the efforts of Andrew Liu of UCLA, who helped prepare input files for ground response studies. The financial support of the PEARL sponsor organizations including the Pacific Gas and Electric Company (PG&E), the California Energy Commission (CEC), and the California Department of Transportation (Caltrans) is acknowledged.

1.0 INTRODUCTION

For a given seismic source, ground motions at soil sites are generally estimated using either soil attenuation relationships, or ground response analyses with input motions scaled to match specified spectral ordinates from rock attenuation relationships. In either case the attenuation relationships are relied upon to capture source and path effects on ground motion. Site response analyses are performed to account for the nonlinear response of shallow sediments, and hopefully reduce the uncertainty in the estimated ground motions on soil.

The relative influence of source/path and site response effects on residuals between recorded and estimated soil site ground motions have been investigated by numerous researchers. Lee (1996) examined the southern California strong motion inventory for soil and rock sites compiled by SCEC. He found that residuals from the Abrahamson and Silva (1997) attenuation relationship at short and intermediate periods are not systematically high or low for soil sites with multiple ground motion recordings, implying that "random" source/path variability is far more pronounced than the site response effect (which should produce a fairly consistent residual across multiple events). Other researchers have found consistent and pronounced site response effects through comparisons of strong motions from a particular event recorded at similar site-source distances and azimuths, but different site conditions (Seed et al., 1987; Idriss, 1990; Seed and Dickenson, 1996; Chang, 1996; Darragh and Idriss, 1997; Woodworth et al., 1998). Site effects during specific events have also been identified from statistical studies of the regional variations in spectral ordinates across different geologic conditions (Borcherdt and Gibbs, 1976; Borcherdt, 1994; Rodriguez-Marek et al., 1999). Analytical studies by Roblee et al. (1996) invoking a stochastic finite source model and an equivalent-linear formulation for site effects

have shown that variability in site effects arising from uncertainty in soil properties can overwhelm the variability in source and path effects. The relative significance of site response variability as compared to source/path variability increased with decreasing site-source distance, and increasing site period.

The disconnect between the findings from Lee's interpretation of southern California data and the significant site effects found from other empirical and analytical studies indicates a clear need to identify the geologic conditions where site effects cause ground motions on soil to significantly and consistently differ from the predictions of soil attenuation relations. Accordingly, this study evaluates the "benefit" gained from ground response studies as compared to the simple use of soil attenuation relations as a function of the general geologic conditions underlying a site. Specifically, we compare the ability of soil attenuation relations and carefully performed ground response studies to capture the 5%-damped spectral accelerations for 36 sites with widely varying geologic conditions that have recorded strong ground motion. The intent is to provide to earthquake engineers a rational basis for deciding when costly site exploration work and ground response analyses are justified from the standpoint of their ability to reduce the residuals and the uncertainty in ground motion estimates on soil.

The report begins in Section 2.0 by describing the geotechnical site classification scheme and site selection procedures used in this study. Sections 3.0 and 4.0 describe procedures for input motion selection and scaling, and performing ground response analyses, respectively. Section 5.0 presents statistical analyses of residuals between recorded and prediction ground motions for sites in various geotechnical categories. Section 6.0 presents results of sensitivity analyses investigating the significance of scaling procedures for input motions used in ground response analyses. Site data and site-specific analysis results are presented in Appendix B.

2.0 SITE SELECTION

The principal criteria used for site selection were: (1) at least one strong motion recording must be available at the site, (2) soil conditions at the site must be well characterized, including in situ measurements of shear wave velocity, and (3) the distribution of soil conditions across the locus of sites must include roughly equal numbers of shallow stiff soil sites, moderately deep stiff soil sites, deep stiff soil sites, and soft soil sites.

The grouping of sites according to soil conditions was made using a geotechnical site classification scheme that was introduced by Seed and Dickenson (1996) and modified by Rodriguez-Marek, et al. (1999). This classification scheme is presented in Table 1. Rodriguez-Marek, et al. (1999) performed event-specific regressions for the 1989 Loma Prieta and 1994 Northridge earthquakes, and found reasonably consistent trends in the attenuation for Category D sites (deep stiff soil), as demonstrated by error terms ( ) that were smaller than those obtained by grouping all soil sites together. In contrast, error terms for the C category (shallow stiff soil) were larger than those for the aggregate of soil sites. Based on these results, Rodriguez-Marek et al. suggested further subdivision of the C category may be appropriate, possibly based on 30 m shear wave velocity. They also noted that the data was too sparse to justify subdivision of the D category, but that soil depth, age, and soil type are likely significant. Idriss (1990) found fairly consistent trends in the Maximum Horizontal Accelerations (MHA) at E sites (soft clay) relative to nearby rock sites during the 1989 Loma Prieta earthquake. These results generally support the use of the classification scheme in Table 1, although the scatter within category C is of concern.

Table 1: Geotechnical site classification scheme proposed by Rodriguez-Marek et al. (1999)

Site	Description	Approx. Site Period (s)	Comments
A	Hard Rock	0.1	Crystalline Bedrock; V_s 5000 fps
B	Competent Bedrock	0.2	V_s 2000 fps or < 30 ft. (10 m) of soil. Most "unweathered" California Rock cases
C1	Weathered Rock	0.4	V_s 1000 fps increasing to > 2000 fps, weathering zone > 30 ft. and < 100 ft.
C2	Shallow Stiff Soil	0.5	Soil depth > 30 ft. and < 100 ft.
C3	Intermediate Depth Stiff Soil	0.8	Soil depth > 100 ft. and < 200 ft.
D1	Deep Stiff Holocene Soil, either **C** (Cohesive) or **S** (Cohesionless)	1.4	Depth > 200 ft. and < 700 ft. Cohesive loosely interpreted. Tentatively use PI > 5% for the fines fraction. Cohesionless soils are those either with low fines content (i.e. < 15%) or with non-plastic fines (PI < 5%)
D2	Deep Stiff Pleistocene Soil, either **C** (Cohesive) or **S** (Cohesionless)	1.4	Depth > 200 ft. and < 700 ft. Division between S and C probably not required
D3	Very Deep Stiff Soil	2.0	Depth > 700 ft.
E1	Medium Thickness Soft Clay	0.7	Thickness of soft clay layer 10 ft. to 40 ft.
E2	Deep Soft Clay	1.4	Thickness of soft clay layer > 40 ft.
F	Potentially Liquefiable Sand	1.0	Holocene loose sand with high water table (z_w 20ft.)

The literature of published soil site data was reviewed to identify sites where the amount of subsurface exploration was sufficient for the purposes of both reliably classifying the site (per Table 1) and for performing ground response studies. This effort resulted in the classification of 105 soil sites in California. These sites are listed in Appendix A along with: (1) the sources of the geotechnical data, (2) the classification from this study, (3) the classification by Rodriguez-Marek et al. (where available), (4) the depth to bedrock, as defined on the geologic log, (4) the depth to a shear wave velocity of 600 m/s, and (5) the earthquakes recorded at the site along with the corresponding MHAs. From the list in Appendix A, we sought approximately 9-10 sites having each of the following general characteristics:

I. Shallow stiff soil over rock (soil depth < 30 m): Category C2 in Table 1

II. Moderate depth stiff soil (soil depth = 45-90 m): Category C3 and shallow D1/D2

III. Deep stiff soil (soil depth > 120 m): Category D1, D2 or D3

IV. Soft soil (soft implies Vs 150 m/s; soft soil depth > 3 m): Category E

This delineation generally parallels the groupings in Table 1 by using soil depth as a principal factor thought to control site response (with the exception of E). Note that the above is not a proposed new classification scheme, but rather is a convenient grouping of sites for the purpose of this study. The sites and earthquakes selected for analysis are listed in Table 2, along with the range of soil depths actually represented within each group. Seventeen of the recordings are from the 1989 Loma Prieta earthquake, 11 from the 1994 Northridge earthquake, and 8 from other earthquakes.

Table 2: Sites/earthquakes used in this study

I. <u>Shallow Stiff Soil, C2 (soil depth < 30 m)</u>

Capitola (89LP)	Gilroy #7 (89LP)	Petrolia Gen. Store (92CM)
Castaic Dam (94NR)	Halls Valley (89LP)	Potrero Canyon (94NR)
Gilroy Phy. Sci. Bldg. (89LP)	Newhall (94NR)	Simi Valley, Knolls (94NR)

Range of soil depth is 12 to 28 m

II. <u>Moderate Depth Stiff Soil, C3 & Shallow D1/D2 (soil depth = 45-90m)</u>

Arleta F.S. (94NR)	LA, Wadsworth No. (94NR)	Taft, Lincoln School (52KC)
LA, Epiphany Church (94NR)	LA, White Oak (94NR)	
LA, Hollywood Sto. (71SF)	Sylmar, Hospital (94NR)	

Range of soil depths is 49 to 91 m

III. <u>Deep Stiff Soil, Bray D (soil depth > 120m)</u>

El Centro Array #9 (40IV)	LA, Sepulveda VA (94NR)	Palo Alto VA (89LP)
Eureka Apts. FF (92CM)	LA, Wadsworth So. (94NR)	Santa Barbara Court. (78SB)
Gilroy #2 (89LP)	Oakland Outer Harbor (89LP)	Sunnyvale Colton (89LP)
Hollister City Hall (89LP)	Oakland 2-Story (89LP)	

Range of soil depth is 130 to > 244 m

IV. <u>Soft Soil, Bray E (soft soil depth > 3m)</u>

Alameda NAS (89LP)	El Centro #6 (79IV)	Larkspur Ferry (89LP)
Apeel #1 (89LP)	Emeryville (89LP)	Meloland O/C FF (79IV)
Apeel #2 (89LP)	Foster City Menhaden (89LP)	San Francisco Airport (89LP)

Range of soft clay depths (Vs < 150 m/s) is 3 to 27 m

3.0 DEVELOPMENT OF INPUT MOTIONS

This section reviews the means by which input motions were selected for use in ground response analyses for each of the sites/earthquakes listed in Table 2.

3.1 Strong Motion Database

Database development began with the strong motion database for shallow crustal earthquakes in active tectonic regions by Pacific Engineering and Analysis (W. Silva, *personal communication*). The database was augmented with (1) selected free-field motions, and (2) selected recordings from the ground level of building structures. We have not attempted to incorporate all potentially useful structural recordings into the database, this is the focus of a continuing effort by the authors.

For each motion in the augmented database, we attempted to assess the possible influence of near-fault rupture directivity effects. Rupture directivity effects were assumed to be negligible for moment magnitudes, M_W 6.0, and site-source distances, $r > 60$ km (N. Abrahamson, 1999, *personal communication*). For motions with $M_W > 6.0$ and $r < 60$ km, the geometric rupture directivity parameters defined in Fig. 1 were obtained from a previous compilation (N. Smith, 1999, *personal communication*), and for sites missing in this compilation, were measured based on published fault rupture models. As shown in Fig. 1, recordings triggered by dip-slip earthquakes but made at sites located off the ends of the fault were assumed to have no rupture directivity effect. Based on the above data, the rupture directivity model for spectral acceleration by Somerville et al. (1997) and modified by Abrahamson (1999, *personal communication*) was invoked to evaluate the expected rupture directivity effect for each site in the database. These

effects were expressed using a Rupture Directivity Index (RDI), defined as the amplification/de-amplification of the geometric mean of $T = 3$ s spectral acceleration due to rupture directivity effects as computed by the Somerville/Abrahamson model. A site experiencing no rupture directivity effect has RDI=1.0. For strike-slip faults, RDI varies from 1.48 (forward directivity), to 0.55 (backward directivity). The range for dip slip faults is 1.16 to 0.72.

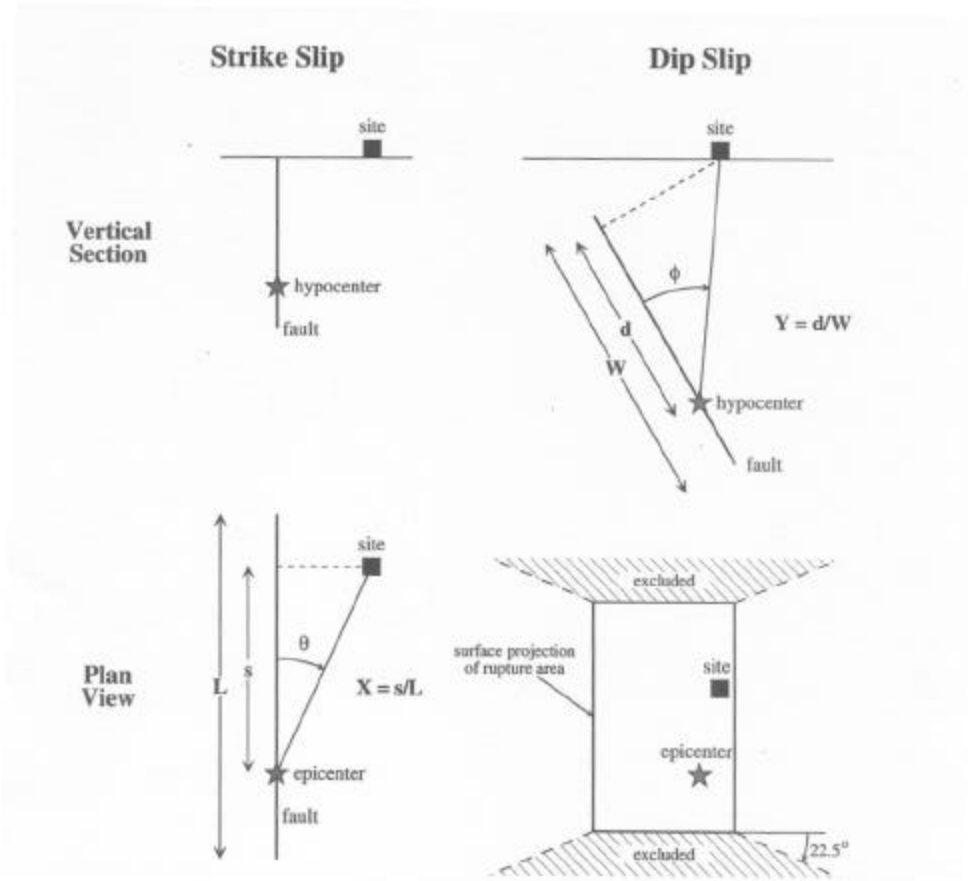

Fig. 1: Rupture directivity parameters for strike-slip faults (X,) and dip-slip faults (Y,) defined by Somerville et al. (1997)

3.2 Time History Selection Criteria

The database described in Section 3.1 was used to select specific time histories representing possible realizations of the motion that would have been expected at the site had the geologic

condition been rock. After appropriate scaling described in Section 3.3, these time histories comprised the input for ground response analyses for the sites listed in Table 2.

The seismological criteria by which these rock time histories were selected are listed below, where the term "target" refers to a characteristic of the causative earthquake for the subject site.

Magnitude: Selected recordings must have been triggered by an event with a magnitude within ± 0.5 of the target.

Amplitude: Time histories were sought that had an MHA within a factor of two to four of the target MHA on rock (evaluation of target MHA on rock is described in Section 3.3).

Site Condition: For relatively deep soil sites, (Types II to IV), time histories were selected from rock sites or C sites with < 20 m of soil (Geomatrix A and B sites). For Type I sites, time histories were selected from only rock sites (Geomatrix A).

Rupture Directivity: Time histories should have RDI's that are similar to the target RDI. Target RDI is based on site location relative to the fault plane, not deviations of the recorded motion from an attenuation model.

Orientations of time histories that were used in analysis were selected as follows:

For sites with RDI=1.0 because M_W 6.0 or r > 60 km, a single random horizontal component of each time history was selected. The ensemble of these random components is intended to represent the geometric mean.

For sites with RDI 1.0 and angle (strike-slip) or (dip-slip) < 45 degrees, the model of Somerville et al. (1997) suggests that there is a motion orientation effect associated with the

near-fault wave pattern. Accordingly, time histories are rotated into fault normal and fault parallel components for separate ground response analyses for these two orientations.

For sites with RDI 1.0, and angle (strike-slip) or (dip-slip) > 45 degrees, the Somerville et al. model suggests no significant motion orientation effect. Since many selected time histories for such sites have or < 45 degrees, we eliminate the orientation effect by using the geometric mean. This is accomplished by retaining both components of an input time history during the ground response analysis, but taking the geometric mean of the computed response as the result.

For sites with RDI=1.0 because the site is located off the end wall, the Somerville model suggests that motion orientation effects can be present (provided , < 45 degrees) despite the absence of rupture directivity effects. Hence, time histories are rotated into separate fault normal and fault parallel components.

We did not consider rupture mechanism or hanging wall effects in time history selection. The specific selection criteria and motions for each site are listed in Appendix B.

3.3 Scaling of Input

The time histories selected according to the criteria in Section 3.2 were scaled prior their use in ground response analyses. The intent of the scaling was to provide an ensemble of time histories with median spectral ordinates matching the "best estimate" soft rock spectrum for the subject event and site, while retaining the inherent variability in the estimated rock motion.

The best estimate spectrum is taken as median 5% damped spectral ordinates from the Abrahamson and Silva (1997) rock site attenuation relation, with the following modifications:

Period dependent event terms provided by Abrahamson (1999, *personal communication*) which quantify event-specific deviations from the general attenuation model.

Median rupture directivity effects and motion orientation effects as computed by the models in Somerville et al. (1997) and modified by Abrahamson (1999, *personal communication*).

Removal of near-surface amplification effects at weathered California rock sites. This is accomplished using period-dependent reductions of outcropping rock motion by Idriss (1999) to more adequately represent the motions anticipated on less weathered rock profiles such as occur at depth (i.e. underlying a soil profile).

This best estimate spectrum obtained by these procedures represents the median ground motion that would have been expected at the site had the geologic condition been soft rock. At a particular period, T, this median spectral acceleration is denoted $m_{be}(T)$. The objective of the time history scaling is for the median of the ensemble of time histories, $m_{th}(T)$, to match $m_{be}(T)$.

The scaling of the time histories is performed in two stages. First, individual time history i is scaled up or down by factor $(F_1)_i$ so that its response spectrum, $S_i(T)$, matches $m_{be}(T)$ in an average sense over the range T=0-1 s. Denoting the median spectra of the scaled time histories as $m_{sth}(T)$ [i.e., $m_{sth}(T)$ is the median of $S_i(T) \times (F_1)_i$ across all i], a set of period-dependent scaling factors are defined as:

$$F_2(T) = \frac{m_{be}(T)}{m_{sth}(T)} \tag{1}$$

The second scaling consists of time domain response spectral matching of each individual time history i to a target spectrum that is $S_i(T) \times (F_1)_i \times F_2(T)$. The time domain response spectral matching is performed with the program RSPMATCH (Abrahamson, 1998).

The above procedure ensures that the median spectral ordinates of the twice scaled time histories match the best estimate spectrum, $m_{be}(T)$. Further, the inherent variability across the time histories is preserved. Shown in Appendix B for each site/earthquake in Table 2 are the best estimate spectrum (from modified attenuation) along with the median and median ± one standard error of the twice scaled input rock motions (assuming log-normal distribution). For every site, the match between the median rock time histories and best estimate spectrum is excellent.

4.0 GROUND RESPONSE MODELING

Ground response modeling was performed using an equivalent-linear characterization of dynamic soil properties as implemented in the program SHAKE91 (Idriss and Sun, 1992) which is a modified edition of the original SHAKE program (Schnabel et al., 1972). The program computes the response of a horizontally layered soil deposit over a uniform half-space subjected to vertically propagating shear waves. This modeling only accounts for one-dimensional ground response effects. Two-and three-dimensional factors such as basin response, topographic amplification, and surface waves are not considered. The following sections review several important details of the SHAKE91 analyses.

4.1 Dynamic Soil Properties

The characterization of soil conditions for each site consists of specifying: (1) a profile of small strain shear wave velocity (V_S), and (2) relationships for the variation of normalized shear modulus (G/G_{max}) and hysteretic soil damping (b) with shear strain (g) within the soil. For each of the sites selected for this study, V_S profiles were obtained from in situ measurements by either

downhole or suspension logging techniques. Specific sources of V_S data for each site are listed in Appendix B. Modulus reduction and damping curves were specified on the basis of soil type as indicated in Table 3. The specific curves selected for materials at each site are indicated on the geologic logs in Appendix B.

Table 3: Criteria for selection of modulus reduction and damping curves.

Soil Type	Condition[1]	Reference
Sand and silty sand	Z < 100 m	Seed et al. (1984), upper bound sand G/G_{max}, lower bound b
	Z > 100 m	EPRI (1993): Z=251-500 ft.
Clays, silty clays, loams	PI = 15 & Z < 100m	Vucetic and Dobry (1991), PI=15[2]
	PI = 15 & Z > 100 m	Stokoe (1999), CL curve, Z = 100-250 m
	PI 30	Vucetic and Dobry (1991)
	Bay Mud	Sun et al. (1988)
	Old Bay Clay	Vucetic and Dobry (1991), PI=30[3]
Bedrock	V_S < 900 m/s	Use soil curves for appropriate material type, depth, and PI
	V_S > 900 m/s	Schnabel (1973)

[1] Z=depth, PI = plasticity index

[2] Consistent with Stokoe (1999), CL curve, Z < 100 m

[3] Consistent with Guha et al. (1993) material testing

It should be noted that the dynamic soil properties at the subject sites were fixed at the values indicated in Appendix B, and no variability in soil properties was considered. The effect of soil property variability on uncertainty in soil site ground motions has been investigated by

others (Roblee et al., 1996; EPRI, 1993). The effects are most pronounced at $T < 1$ s, and obviously increase in significance with the level of uncertainty in soil properties (i.e., these effects are less significant for well characterized sites, such as the sites considered in this study). These effects are being investigated in a parallel study by Silva (1999) in the FY 1998-99 PEER-PG&E research program, and hence were not a focus of this study.

4.2 Location of Control (Input) Motion

As described in Section 3.2, we selected time histories from rock sites for use as input in ground response analyses. Accordingly, control motions were input at or slightly below soil-bedrock interface for sites where this depth is known or could be estimated. However, for several sites in the San Fernando, Imperial, and Santa Clara basins, bedrock occurs at depths beyond the practical limits of geotechnical subsurface exploration, and hence little data exists from which to estimate dynamic soil properties at depth. These sites are Arleta, Eureka, El Centro Array #6 and #9, Hollister, Meloland, Santa Barbara, Sepulveda VA, and Sunnyvale. For these sites, the base of the ground response model is in soil, calling into question the appropriateness of using rock time histories as input.

The other option, of course, is to use input time histories recorded at soil sites. Attenuation relationships indicate that ground motions on soil are richer in long period energy than ground motions on rock (e.g. Abrahamson and Silva, 1997). Recent studies have suggested that much of the ground response effect (which creates the difference between rock and soil motions) is controlled by the upper 30 m of soil (Borcherdt, 1994). While this finding remains controversial (e.g. Anderson et al., 1996), it seems reasonable to postulate that near-surface soils (tens to 100 m depth) with relatively low shear wave velocities ($V_S <$ 600 m/s) exert a stronger influence on

one-dimensional site amplification than the deeper, stiffer basin structure. Accordingly, the use of soil site recordings as input motions for ground response analyses would be expected to overestimate the long period components of ground motion on soil.

Based on this reasoning, we elected to use time histories recorded at rock sites for input motions in ground response models that terminate in soil. In each such case, the soil profile was extended to depths where increases in V_S with depth are relatively gradual. Shear wave velocities in soil at the base of each such profile were greater than about 600 m/s, with the exception of the El Centro Array sites where V_S 450 m/s.

4.3 Analysis of Strain-Dependent Soil Properties

SHAKE91 analyses are performed for one direction of shaking, hence consideration must be given to which ground motion component is used to calculate the equivalent linear soil properties. Some of the sites considered in study are subject to near-fault directivity effects in which fault normal motions exceed fault parallel motions at long periods (spectral ordinates for $T < 0.6$ s are identical for both horizontal directions). For these sites, dynamic soil properties are estimated based on the ground response analysis for the fault normal direction, and these properties are applied for the calculation of fault parallel ground response (for which the calculated shear strains would otherwise be smaller).

For sites subject to near-fault effects but for which the fault normal/fault parallel ratio is expected to be unity based on the Somerville et al. (1997) model, the geometric mean of the calculated response from the two horizontal components is used. In these cases, dynamic soil properties are separately evaluated for the two horizontal directions. For non near-fault sites, only one randomly oriented horizontal component of input motions is used.

5.0 STATISTICAL ANALYSIS OF RESULTS

5.1 Analysis

In this section, we compare 5% damped spectral accelerations of recorded time histories on soil to estimated spectra from: (1) a modified soil attenuation relationship and (2) ground response analyses. Estimated spectra by both methods are represented in terms of their median value and their standard error term in natural log units.

The first estimate of soil spectra is taken using the Abrahamson and Silva (1997) soil attenuation relation, with modifications for event terms and near-fault effects as described previously for rock sites in Section 3.3. For soil site j in site category i, the natural logs of the median spectral ordinates obtained by the modified attenuation relation are denoted $A_{ij}(T)$, and the standard error term is denoted $[s_a(T)])_{ij}$. Since all the median and standard error terms considered here have a functional dependence on period, this will be dropped in subsequent nomenclature. The second estimate of soil spectra is from ground response analysis. Again considering soil site j in site category i, the natural log of the calculated spectra using input motion k is denoted $(G_{ij})_k$. Taking N_j as the number of input time histories used in ground response analyses for site j, the median and standard error of $(G_{ij})_k$ for k=1..N_j are denoted G_{ij} and $(s_g)_{ij}$, respectively. Hence, for soil site j in site category i, the two statistical estimates of computed soil spectra are denoted:

	Attenuation	Ground Response Analysis
Median	A_{ij}	G_{ij}
Standard Error	$(s_a)_{ij}$	$(s_g)_{ij}$

In Appendix B are plots for each site of the exponent of A_{ij} & $A_{ij}\pm(s_a)_{ij}$ and G_{ij} & $G_{ij}\pm(s_g)_{ij}$ vs. period.

Denoting the natural log of the recorded, or "observed," ground motion as O_{ij}, residuals between the estimated median spectra (i.e., "*m*" spectra) and observed spectra for soil site j in site category i are taken as:

$$\left(r_{g1}\right)_{ij} = O_{ij} \quad G_{ij}: \qquad \text{residual, } m \text{ estimate, ground response}$$

$$\left(r_{a1}\right)_{ij} = O_{ij} \quad A_{ij}: \qquad \text{residual, } m \text{ estimate, modified soil attenuation} \tag{1}$$

We also consider a separate, median plus one standard error estimate of ground motion (i.e. the "$m+s$" spectra). Residuals of these ground motion estimates are taken as:

$$\left(r_{g2}\right)_{ij} = O_{ij} \quad \left(G_{ij} + \left(s_{\ g}\right)_{ij}\right): \text{ residual, } m+s \text{ estimate, ground response}$$

$$\left(r_{a2}\right)_{ij} = O_{ij} \quad \left(A_{ij} + \left(s_{\ a}\right)_{ij}\right): \text{ residual, } m+s \text{ estimate, modified soil attenuation} \tag{2}$$

Median minus one standard error ground motion estimates were also considered, but were found to be poor predictors of observed ground motion at all periods, and hence are not carried forward. In Appendix B are plots for each site of $(r_{a1})_{ij}$ & $(r_{a2})_{ij}$ and $(r_{g1})_{ij}$ & $(r_{g2})_{ij}$.

The medians and standard errors of residuals within category i are taken across the j=1..M_i sites (assuming category i to have M_i sites). These statistical quantities are denoted as follows:

$$(R_{g1})_i,\ (s_{g1})_i = \text{median, standard error of } (r_{g1})_{ij}$$

$$(R_{a1})_i,\ (s_{a1})_i = \text{median, standard error of } (r_{a1})_{ij} \tag{3}$$

Similar definitions apply for the median plus one standard error ground motion estimates, with "2" replacing "1" in the subscripts in Eq. 3. Since the number of sites in each category (M_i) is fairly small (7-11), the uncertainty in the estimates of median quantities $(R_{g1})_i$ & $(R_{g2})_i$ and $(R_{a1})_i$

& $(R_{a1})_i$ should be considered. Statistical theory indicates this uncertainty in these medians can be estimated as (Ang and Tang, 1975),

$$\left(\bar{s}_{g1}\right)_i^2 = \left(s_{g1}\right)_i^2 / M_i \tag{4}$$

where $\left(\bar{s}_{g1}\right)_i$ denotes the standard error of the estimate of $(R_{g1})_i$. Similar definitions apply for the other median quantities considered.

Figures 2 (a)-(d) present the variation of category median residuals ($R_{g1\text{-}2} \pm \bar{s}_{g1}$ and $R_{a1\text{-}2} \pm \bar{s}_{a1}$) and category standard errors ($s_{g1\text{-}2}$ and $s_{a1\text{-}2}$) with period, T. Table 4 summarizes average residuals of m and $m+s$ ground motion estimates across period ranges T 1.0 s and $T > 1.0$ s.

5.2 Interpretation

We begin our interpretation of the results by focusing on E sites, for which the trends are most clearly defined. Referring to Fig. 2(d) and Table 4, two principal findings emerge from the category statistics:

1. *Benefit of ground response analysis*: The benefit of performing ground response analysis is measured by comparing category residuals and standard errors for the m ground response and soil attenuation ground motion estimates. Both category residuals and standard errors are smaller for the ground response estimates for $T <$ 1-2 s. The smaller residual means that ground response analyses more accurately predict ground motions, and the smaller standard error means that the residuals are more consistent across sites in the category. Of the two benefits, the reduction in standard error is most pronounced.

Table 4a: Average category residuals and standard errors of median (m) ground motion estimates

Site Category	Average Category Residual[1] (T 1.0 s)		Average Category Residual[1] (T > 1.0 s)		Average Category Standard Error (T 1.0 s)		Average Category Standard Error (T > 1.0 s)	
	R_{g1}	R_{a1}	R_{g1}	R_{a1}	s_{g1}	s_{a1}	s_{g1}	s_{a1}
I (C2)*	0.03 ± 0.17	0.22 ± 0.16	0.30 ± 0.25	-0.08 ± 0.20	0.47	0.44	0.71	0.55
II (C3, shallow D1/D2)	0.15 ± 0.19	0.28 ± 0.12	0.75 ± 0.17	0.38 ± 0.17	0.49	0.32	0.44	0.46
III (deep D)	0.29 ± 0.14	0.34 ± 0.15	0.58 ± 0.17	0.19 ± 0.17	0.45	0.48	0.57	0.57
IV (E)	0.39 ± 0.09	0.54 ± 0.23	0.25 ± 0.14	0.11 ± 0.16	0.28	0.68	0.41	0.49

Table 4b: Average category residuals and standard errors of $m+s$ ground motion estimates

Site Category	Average Category Residual[1] (T 1.0 s)		Average Category Residual[1] (T > 1.0 s)		Average Category Standard Error (T 1.0 s)		Average Category Standard Error (T > 1.0 s)	
	R_{g2}	R_{a2}	R_{g2}	R_{a2}	s_{g2}	s_{a2}	s_{g2}	s_{a2}
I (C2)*	-0.30 ± 0.17	-0.26 ± 0.16	-0.37 ± 0.25	-0.69 ± 0.20	0.48	0.44	0.75	0.56
II (C3, shallow D1/D2)	-0.16 ± 0.20	-0.22 ± 0.12	0.15 ± 0.20	-0.24 ± 0.18	0.53	0.32	0.53	0.47
III (deep D)	0.00± 0.14	-0.17± 0.15	-0.16± 0.18	-0.43 0.18	0.45	0.51	0.60	0.58
IV (E)	0.07± 0.09	0.03± 0.24	-0.46± 0.13	-0.53 0.16	0.27	0.72	0.40	0.49

[1]Error terms are standard errors of the median (Eq. 4)

*omitting Potrero Canyon

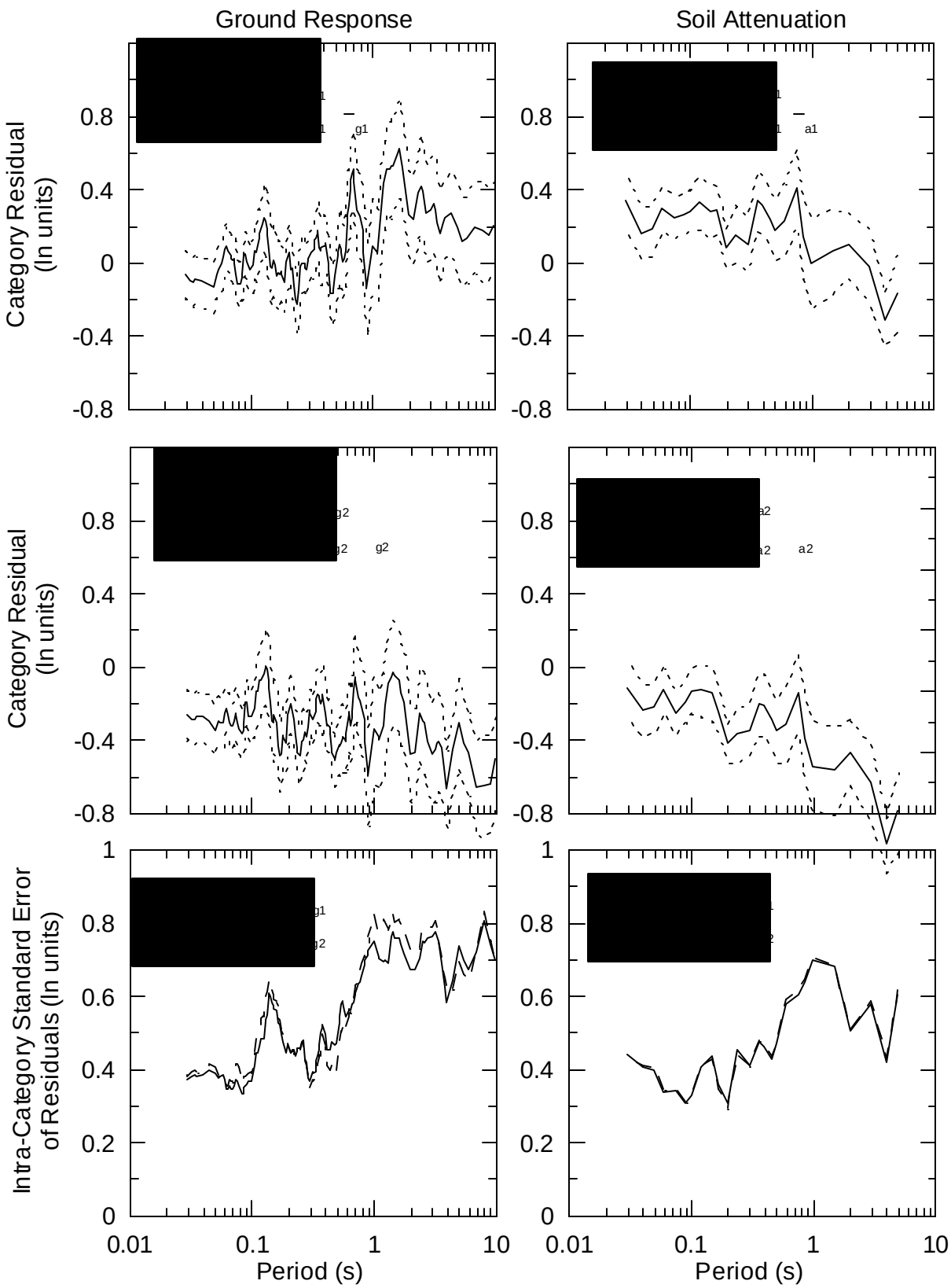

Fig. 2(a): Category median residuals and standard error terms, Type I sites (C2, Soil Depth < 30 m)

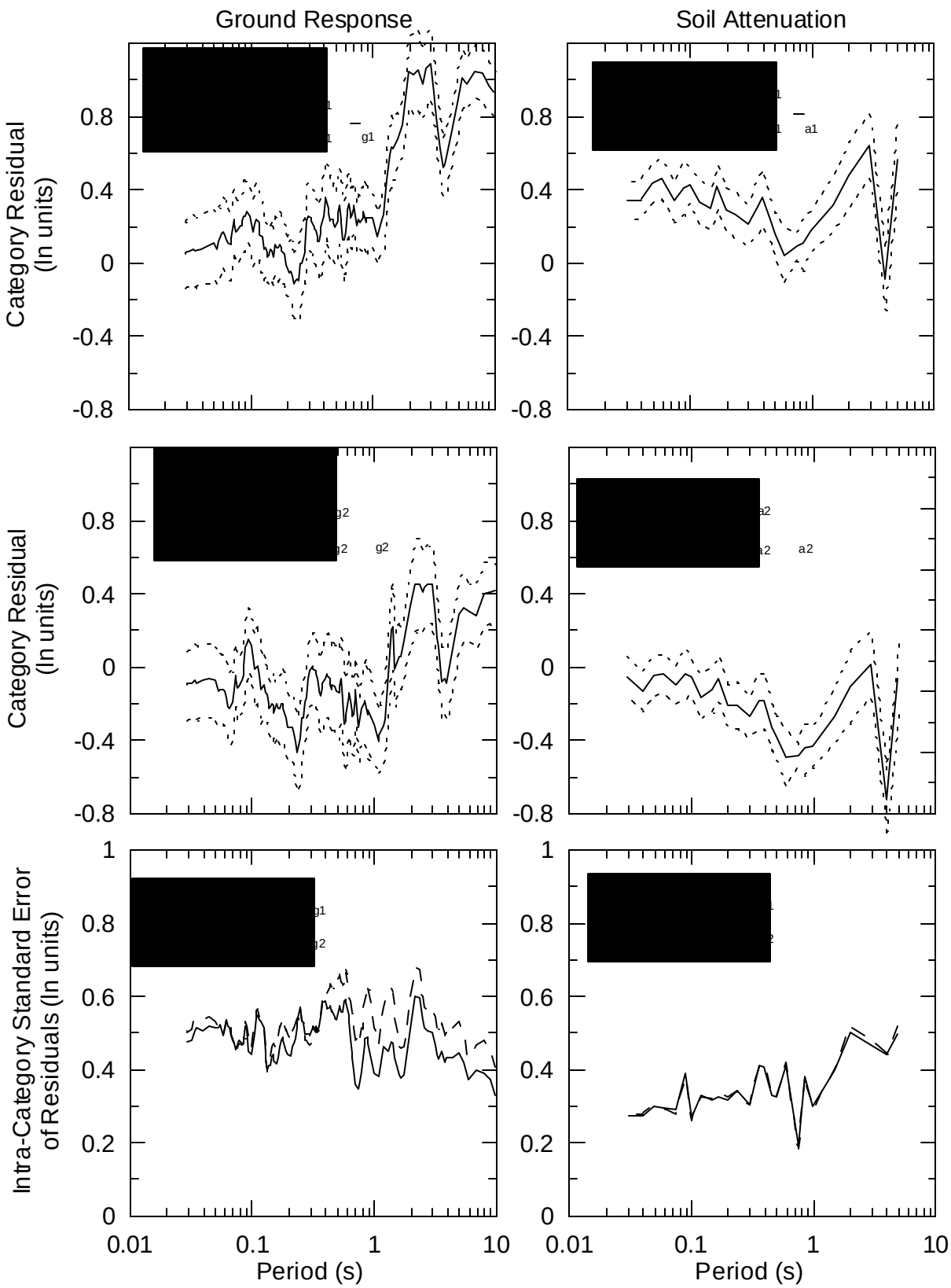

Fig. 2(b): Category median residuals and standard error terms, Type II sites (C3 & shallow D1/D2, Soil Depth = 45-90 m)

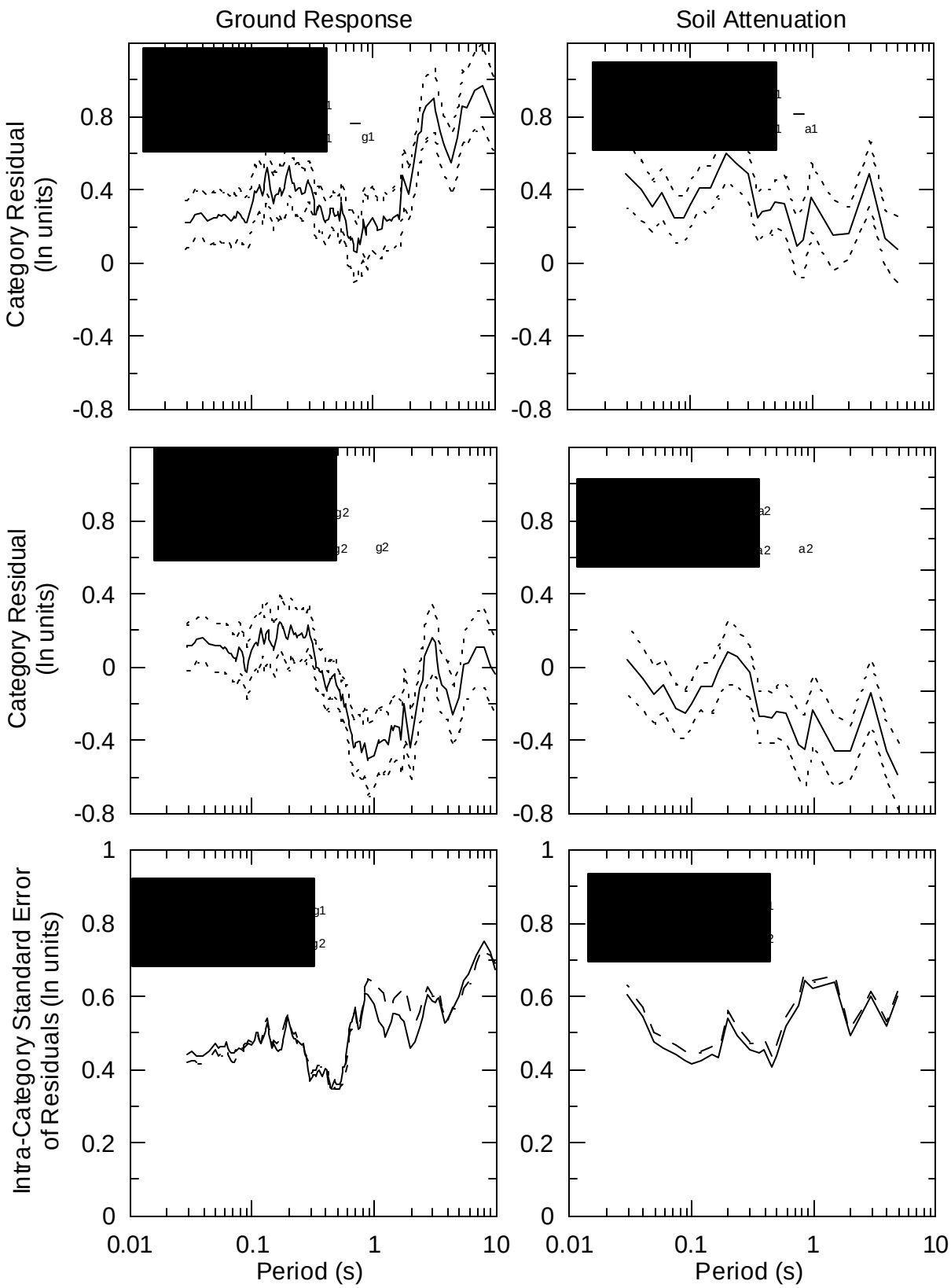

Fig. 2(c): Category median residuals and standard error terms, Type III sites (Deep D, Soil Depth > 120 m)

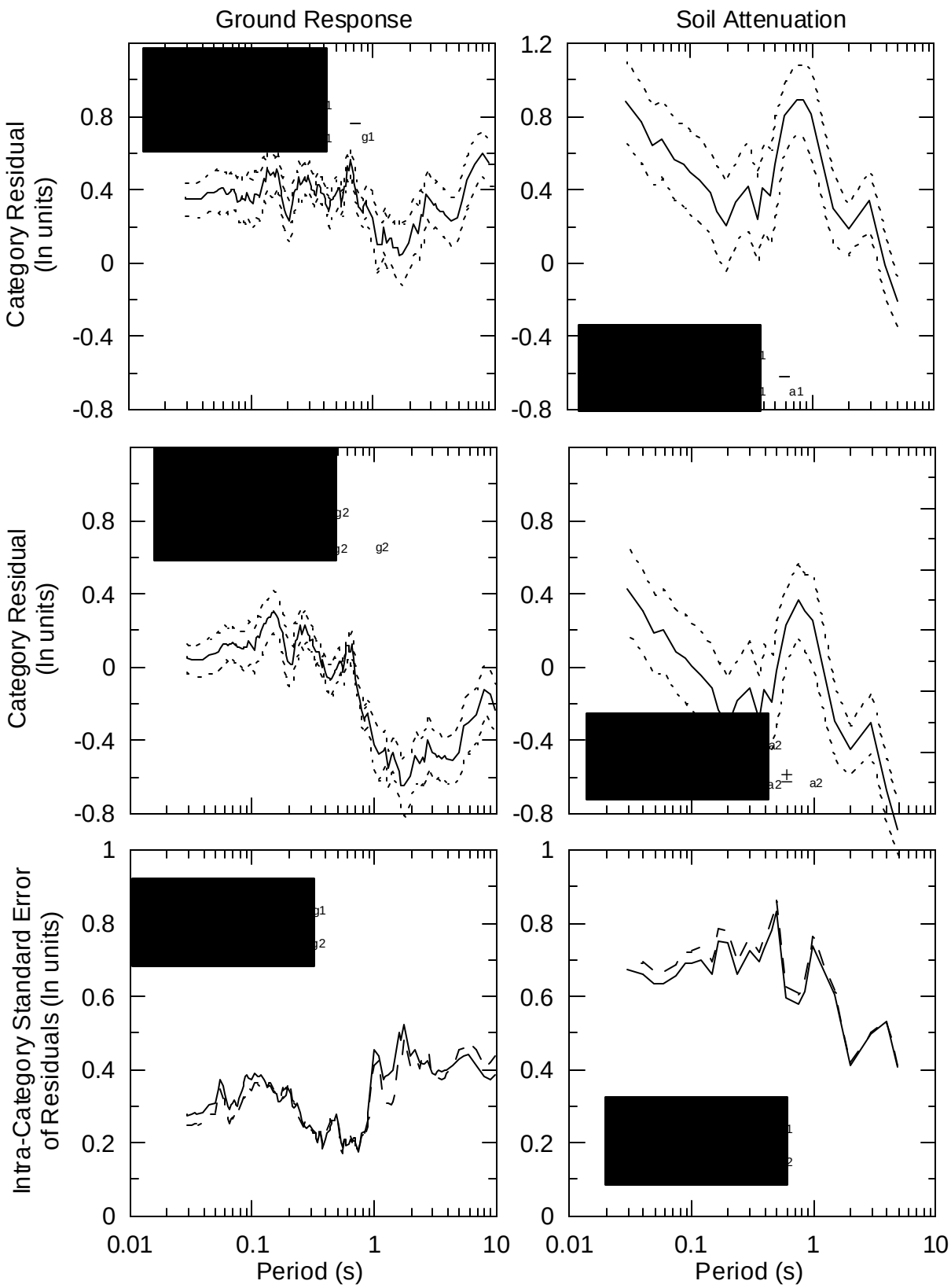

Fig. 2(d): Category median residuals and standard error terms, Type IV sites (E, Soft Soil Depth > 3 m)

2. *Bias in ground response results*: The category residuals for the m ground response estimates are non-zero with a high level of confidence for $T <$ 1 s. Across this period range, the $m+s$ estimate has much smaller residuals (average of 0.06 as compared to 0.36 for m). At longer periods, the results are less consistent, although the m estimate preliminarily appears to be reasonable.

With respect to the first comment above (benefit of ground response), site categories other than E exhibit mixed trends. For T 1 s, m ground response estimates have smaller residuals than m soil attenuation estimates in all site categories. The residual reduction for m ground response estimates at T 1 s is modest for deep D and C3/shallow D, but is relatively pronounced for C sites. The significant uncertainty reduction observed in ground response results for E sites is not observed for other site categories. Comparing averaged s_{g1} and s_{a1} values in Table 4a, ground response is seen to provide lower uncertainty for deep D sites, but s_{g1} is actually larger than s_{a1} for C3/shallow D and C2 sites. These results indicate that while ground response generally provides more accurate spectra for these site classes (i.e., $R_{g1} < R_{a1}$), there is a relatively high level of uncertainty in the amount of bias in computed spectra. This means that the ground response procedures are modeling ground motion variations between sites relatively poorly, implying that other factors are significantly affecting these variations (e.g., source and path effects).

The bias observed at E sites in the m ground motion estimates for $T <$ 1 s is also present at deep D and C3/shallow D sites. No significant bias is observed for T 1 s at C2 sites. Median attenuation estimates are also biased for T 1 s in all site categories, indicating that motions in each category exceed the median values for soil sites. Nonetheless, based on the results presently

available, the following usage of ground response analysis results appears to provide the smallest residuals for T 1 s:

C2:	m estimate
C3/shallow D1/D2:	$m+0.5s$ estimate
Deep D:	$m+s$ estimate
E:	$m+s$ estimate

The cause of the bias for the last three site categories is not well understood. However, since m residuals for soil attenuation estimates are also positive, some of the bias may be attributable to underestimates of the input (rock) ground motion amplitudes (i.e., median rock attenuation ordinates from which the "best estimate" target spectrum is derived may be low). The bias may also be partially attributable to errors associated with the use of the equivalent linear method of ground response computation, or errors in the selection of dynamic soil properties. It is noted that ground motion estimates at small periods (where the bias is most consistently observed) are especially sensitive to soil hysteretic damping ratio, b. Overestimation of b would cause an underestimation of ground response that would increase with soil thickness (because for a given frequency more wavelengths subject to soil damping will be present in thicker soil deposits). This trend is observed in the data, i.e. R_g increases with increasing depth of soil.

For $T > 1$ s, the m ground response estimate provides large residuals for deep D and C3/shallow D sites, implying that the ground response models are not capturing the long-period components of the ground motions. This is not surprising, as many of the sites in these categories are near basin edges where basin edge effects can be significant at large periods. The bias in this period range for m soil attenuation is smaller, implying that basin effects are to some degree represented in the empirical database for soil sites. Further, no significant long period bias is

observed in m ground response estimates at C2 sites, where basin edge effects would generally not be expected.

The observed significance of site response effects for E sites, and to some extent deep D sites, is consistent with many previous studies that have focused on sites within these categories (e.g., Seed and Dickenson, 1996; Chang, 1996; Idriss, 1990; Darragh and Idriss, 1997*)*. In addition, the large s_g values for the deep D and C3/shallow D categories appear to be consistent with Lee's (1996) finding that ground response effects are generally small relative to source/path effects at soil sites in southern California.

Finally, it should be noted that the results summarized in Fig. 2 and Table 4 are for a limited number of sites within each category. Many more sites should be added within each category to enable more stable and robust estimates of the category residuals and standard errors terms. Such work could change somewhat the findings reported above.

6.0 SENSITIVITY OF GROUND RESPONSE TO INPUT SCALING PROCEDURES

6.1 Importance of Rock Correction Factors

As noted in Section 3.3, the target response spectrum for the median of the scaled time histories includes a correction to account for amplification in the near-surface weathered zones of outcropping rock sites. As shown in Fig. 3, the correction reduces the amplitude of the target spectrum at low periods. Fig. 4 shows the impact of this correction on the computed response of a deep stiff soil site (Palo Alto VA Building) and shallow stiff soil site (Castaic Dam Toe).

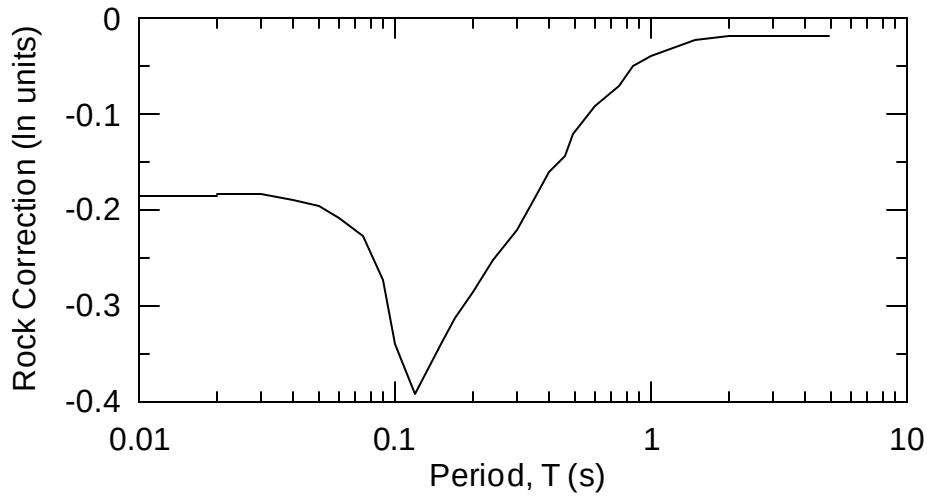

Fig. 3: Response spectral scale factor to correct rock attenuation relations (after Idriss, 1999)

Shown in Figs. 4(a)-(b) are median computed responses (i.e., exponent of G_{ij}) from the ensemble of time histories for these sites, with and without corrections to the input target rock spectra, along with the spectra of the recorded motions (which happen to be fault normal components). Also shown in Figs. 4(a)-(b) are residuals of the computed spectral accelerations evaluated as per Eq. 1 (i.e., $(r_{g1})_{ij}$). Fig. 4(c) shows the difference between the residuals with and without the rock outcrop correction for the two sites. Despite the large difference in the soil conditions and ground responses at these two sites, the effects of the rock correction on the computed motions for both sites are similar. This residual difference is about 0.2 for $T <$ 0.2 s, and decreases to essentially null at about $T = 1 - 2$ s. This difference could explain much of the bias noted in Section 5.2 for the C3/shallow D and deep D site categories. However, other considerations could also explain the bias, and no firm conclusions can be drawn at present.

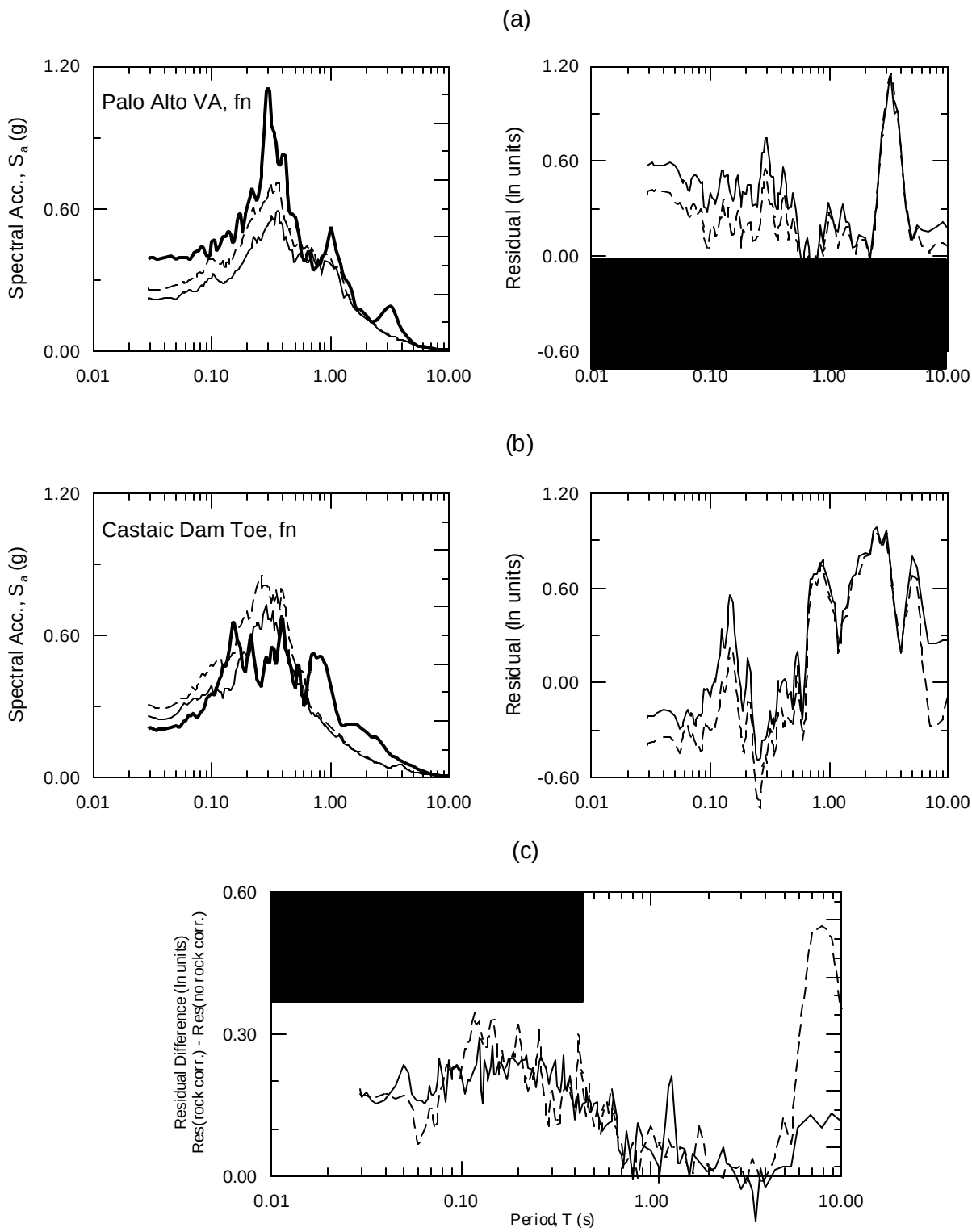

Fig. 4: (a) Spectra and residuals with and without rock correction to input, Palo Alto VA
(b) Spectra and residuals with and without rock correction to input, Castaic Dam
(c) Comparison of rock correction effect on residuals

6.2 Use of Spectrum Compatible Input Motions to Evaluate Median Ground Response

Scaling procedures for input time histories used in this study were described in Section 3.3. The intent of the scaling was to provide an ensemble of time histories with a median spectral response matching the "best estimate" soft rock spectrum for the subject event and site, while retaining the inherent variability in the estimated rock motion. Here we investigate an alternative time history scaling procedure, which consists of modifying each time history in the time domain such that its response spectrum fully matches the target (Abrahamson, 1998). Using the site-specific target spectrum and input time histories developed according to the procedures described previously, a comparison is made as follows. The time histories are scaled once according to the criteria set forth in Section 3.3 (Suite 1, denoted as "scaled"), and again using time-domain response spectral matching procedures to fully match each time history to the target spectrum (Suite 2, denoted as "spectrum compatible"). Ground response analyses are performed using both suites of scaled motions. The natural log is taken of spectral ordinates near the site period, and for each period the median spectral ordinate from n of the time histories is calculated. Plotted in Fig. 5 is the average of the median spectral ordinates across the period range indicated as a function of n, which is varied from 3 to N_j. This exercise is carried out for the following sites (one site per category): Castaic, Sylmar, Palo Alto VA, and Larkspur.

The results indicate that ground response analyses using spectrum compatible time histories converge to a stable median with as few as 3 time histories, whereas results from the "scaled" suite require on the order of 10-15 time histories to converge. Not surprisingly, the standard error of the median is relatively low with the spectrum compatible results. The Larkspur and Palo Alto sites indicate a positive bias in spectrum compatible results, but this effect is not observed at Castaic and Sylmar, and no firm conclusions about a bias can be drawn at present.

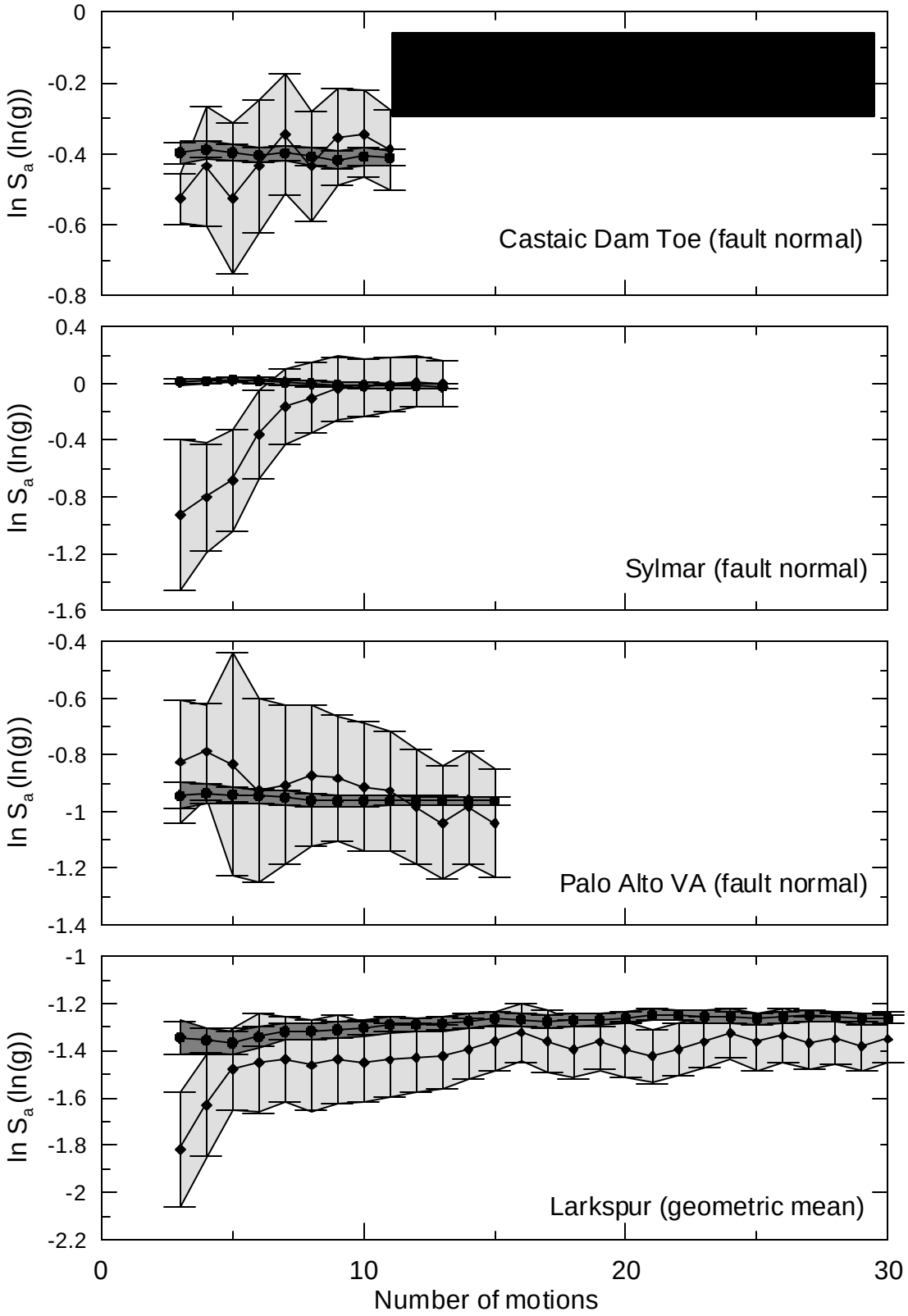

Fig. 5: Comparison of scaled and spectrum compatible median spectral accelerations

7.0 SUMMARY AND CONCLUSIONS

In this study we have estimated ground motions for accelerograph stations on soil using ground response analyses and a modified version of the soil attenuation relationship by Abrahamson and Silva (1997). Residuals between recorded and estimated motion were calculated to elucidate trends in the results of each ground motion estimation procedures across geotechnical site categories. For $T < 1$ s, we find that ground response analyses improve the accuracy of ground motion predictions relative to attenuation in all site categories. However, the uncertainty in the residual of the estimated ground motions is large for C and D sites, indicating that factors other than site response are "randomly" varying the motions from site-to-site. We interpret this as evidence for a strong influence of source and path effects on soil site ground motions. Conversely, for E sites, the standard error of ground response estimates is small, indicating a strong and systematic influence of ground response that is reasonably well captured by the analysis.

For $T > 1$ s, substantial positive bias is observed in median ground response results for D sites, which may be a basin effect. Ground motion estimates from soil attenuation relations are more accurate within this period range for D sites. A somewhat surprising result from this study is a consistent bias for $T < 1$ s in ground response results for site categories other than C2. Given this bias, our recommendation for the interpretation of ground response results is that median plus one standard error ground motions be used for E and deep D sites if the input is scaled to the median rock motion. For C3/shallow D and C2 sites, median plus half-standard error and median ground motions should be used, respectively.

REFERENCES

Abrahamson, N.A. (1998). "Non-stationary spectral matching program RSPMATCH," PG&E Internal Report, February.

Abrahamson, N.A. and Silva, W.J. (1997). "Empirical response spectral attenuation relations for shallow crustal earthquakes," *Seism. Research Letters*, 68(1), 94-127.

Anderson, J.G., Lee, Y., Zeng, Y., and Day, S. (1996). "Control of strong motion by the upper 30 meters," *Bull. Seism. Soc. Am*., 86(6), 1749-1759.

Ang, A. H-S. and Tang, W.H. (1975). *Probability concepts in engineering planning and design: Volume I – Basic principles*, John Wiley & Sons, New York, NY.

Borcherdt, R. D. and Gibbs, J. F. (1976). "Effects of local geological conditions in the San Francisco Bay region on ground motions and the intensities of the 1906 earthquake," *Bull. Seism. Soc. Am*., 66 (2), 467-500.

Borcherdt, R.D. (1994). "Estimates of site dependent response spectra for design (methodology and justification)," *Earthquake Spectra*, EERI, 10(4), 617-653.

Chang, S.W. (1996). "Seismic response of deep stiff soil deposits," *Ph.D. Dissertation*, Univ. of California, Berkeley.

Darragh, R.B. and Idriss, I.M. (1997). "A tale of two sites: Gilroy #2 and Treasure Island – Site response using and equivalent linear technique," NEHRP Professional Fellowship Report, EERI, Oakland, CA.

Dickenson, S.E. (1994). "The dynamic response of soft and deep cohesive soils during the Loma Prieta earthquake of October 17, 1989," *Ph.D. Dissertation*, Univ. of California, Berkeley.

Dickenson, S.E. and Seed, R.B. (1996). "Nonlinear dynamic response of soft and deep cohesive soil deposits," Proceedings of the International Workshop on Site Response Subjected to Strong Earthquake Motions: Yokosuka, Japan, January 16-17, 1996, Japan Port and Harbour Research Inst., Yokosuka, Japan, Vol. 2, 1996, pages 67-81.

Electrical Power Research Institute, EPRI (1993). "Guidelines for determining design basis ground motions. Volume 1: Method and guidelines for estimating earthquake ground motion in eastern North America," *Rpt. No. EPRI TR-102293*, Palo Alto, CA.

Frankel, A.and Vidale, J. (1992). "A three-dimensional simulation of seismic waves in the Santa Clara Valley, California, from a Loma Prieta aftershock," *Bull. Seism. Soc. Am*., 82 (5), 2045-2074.

Fumal, T.E., Gibbs, J.F., and Roth, E.F. (1982). "In-situ measurements of seismic velocity at 22 locations in the Los Angeles, CA region," *OFR 82-833*, U.S. Geological Survey, Menlo Park, CA.

Gibbs, J.F., Fumal, T.E., Boore, D.M., and Powers, T.J. (1992). "Seismic velocities and geologic logs from borehole measurements at seven strong motion stations that recorded the 1989 Loma Prieta, California, earthquake," *OFR 92-287*, U.S. Geological Survey, Menlo Park, CA.

Gibbs, J.F., Fumal, T.E., and Powers, T.J. (1993). "Seismic velocities and geologic logs from borehole measurements at eight strong motion stations that recorded the 1989 Loma Prieta, California, earthquake," *OFR 93-376*, U.S. Geological Survey, Menlo Park, CA.

Gibbs, J.F., Fumal, T.E., and Powers, T.J. (1994). "Seismic velocities and geologic logs from borehole measurements at eight strong motion stations that recorded the 1989 Loma Prieta, California, earthquake," *OFR 94-222*, U.S. Geological Survey, Menlo Park, CA.

Gibbs, J.F., Tinsley, J.C., and Joyner, W.B. (1996). "Seismic velocities and geologic conditions at twelve sites subjected to strong ground motion in the 1994 Northridge, California, earthquake," *OFR 96-740*, U.S. Geological Survey, Menlo Park, CA.

Guha, S., Bray, J.D. and Drnevich, V.P. (1993). "Characteristics of the deep old bay clay deposits in the east San Francisco bay area," *Rpt. No. UCB/GT/93-09*, Univ. of California, Berkeley.

Idriss, I.M. (1990). "Response of soft soil sites during earthquakes," *Proc. H. Bolton Seed Memorial Symposium*, J.M. Duncan (ed.), Vol. 2, 273-290.

Idriss, I.M. (1999). "Quantitative geotechnical site characterization," PG&E/PEER Task 3.E Internal Report.

Idriss, I.M. and Sun, J.I. (1992). "SHAKE91: A computer program for conducting equivalent linear seismic response analyses of horizontally layered soil deposits," Center for Geotech. Modeling, Univ. of California, Davis.

Lee, Y. (1996). "Evaluation of attenuation relations in the Southern California region," M.S. Dissertation, Geophysics Department, Univ. of Nevada, Reno.

Nibor, R.L. and Steller, R.A. (1993). "Borehole geophysical measurements at 24 rock and soil sites," Report to EPRI, Agbabian Assoc., March.

Porcella, R.L. (1984). "Geotechnical investigations at strong-motion stations in the Imperial Valley, California," *OFR 84-562*, U.S. Geological Survey, Menlo Park, CA.

Powers, T.J. and Fumal, T.E. (1993). "Geologic logs from 25 boreholes near strong motion accelerographs that recorded the 1989 Loma Prieta, California, earthquake," *OFR 93-502*, U.S. Geological Survey, Menlo Park, CA.

Roblee, C.J., Silva, W.J., Toro, G.R., and Abrahamson, N.A. (1996). "Variability in site-specific seismic ground motion design predictions," *ASCE Geotech. Special Publication No. 58*, Uncertainty in the Geologic Environment: From Theory to Practice, C.D. Shakelford, P.P. Nelson (eds.), Vol. 2, 1113-1133.

Rodriguez-Marek, A., Bray, J.D., and Abrahamson, N.A. (1999). "Task 3: Characterization of site response, general site categories," *Rpt. No. PEER 1999/03*, Pacific Earthquake Engineering Research Center, Richmond, CA.

Rogers, J.D. and Figuers, S.H. (1991). "Engineering geologic site characterization of the greater Oakland-Alameda area, Alameda and San Francisco Counties, California," Final Report to National Science Foundation, Rogers/Pacific, Inc., Pleasant Hill, CA.

ROSRINE, Resolution of Site Response Issues from the Northridge Earthquake, data dissemination via world-wide web.

Schnabel, P.B., Lysmer, J. and Seed, H.B. (1972). "SHAKE: A computer program for earthquake response analysis of horizontally layered sites," *Rpt. No. EERC 72/12*, Earthquake Engineering Research Center, Univ. of California, Berkeley.

Schnabel, P.B. (1973). "Effects of local geology and distance from source on earthquake ground motions," Ph.D. Dissertation, Civil Engineering Dept., Univ. of California, Berkeley.

Seed, H.B., Wong, R.T., Idriss, I.M., and Tokimatsu, K. (1984). "Moduli and damping factors for dynamic analyses of cohesionless soils," *Rpt. No. UCB/EERC-84/14*, Earthquake Engineering Research Center, Univ. of California, Berkeley.

Seed, H.B., Romo, M.P., Sun, J.I., Jaime, A., and Lysmer, J. (1987). "Relationships between soil conditions and earthquake ground motions in Mexico City in the earthquake of September 19, 1985," *Rpt. No. UCB/EERC-87/15*, Earthquake Engineering Research Center, Univ. of California, Berkeley.

Shannon & Wilson/Agbabian Associates, SW/AA (1980). "Geotechnical data from accelerograph stations investigated during the period 1975-1979, summary report," Report to U.S. Nuclear Regulatory Commission, Washington, D.C.

Silva, W.J. (1999). "Consistent site response estimates," PG&E/PEER Task 5.B Internal Report.

Somerville, P.G., Smith, N.F., Graves, R.W., and Abrahamson, N.A. (1997). "Modification of empirical strong motion attenuation relations to include the amplitude and duration effects of rupture directivity," *Seism. Research Letters*, 68(1), 94-127.

Stewart, J.P. and Stewart, A.F. (1997). "Analysis of soil-structure interaction effects on building response from earthquake strong motion recordings at 58 sites," *Rpt. No. UCB/EERC-97/01*, Earthquake Engineering Research Center, Univ. of California, Berkeley.

Stokoe, K.H. Darendeli, M.B., Andrus, R.D., and Brown, L.T. (1999). "Dynamic soil properties: Laboratory, field and correlation studies," *Earthquake Geotechnical Engineering*, S. Pinto (ed.), Balkema, Rotterdam, Vol. 3, 811-845.

Sun, J.I., Golesorkhi, R., and Seed, H.B. (1988). "Dynamic moduli and damping ratios for cohesive soils," *Rpt. No. UCB/EERC-88/15*, Earthquake Engineering Research Center, Univ. of California, Berkeley.

Thiel, C.C. and Schneider, J.F. (1993). "Investigations of thirty-three Loma Prieta earthquake strong motion recording sites," Report to Building Contractors Society of Japan and Electical Power Research Institute, California Universities for Research in Earthquake Engineering, Stanford, CA.

Vucetic, M. and Dobry, R. (1991). "Effect of soil plasticity on cyclic response," *J. Geotech. Engrg.*, ASCE, 117(1), 89-107.

Woodworth, M.G., Chang, S.W., Stewart, J.P., and Baturay, M.B. (1998). "Repeatability and uncertainty of seismic site response," Report to PG&E/PEER, Task 3.F.

APPENDIX A

SOIL SITES WITH WELL CHARACTERIZED GEOTECHNICAL CONDITIONS

AND STRONG MOTION RECORDINGS IN CALIFORNIA

Acknowledgements

The work described in this report was funded by the Pacific Earthquake Engineering Research (PEER) Center under the Pacific Gas & Electric Company Contract No. 09566. This financial support is gratefully acknowledged.

This work made use of Pacific Earthquake Engineering Research Center Shared Facilities supported by the Earthquake Engineering Research Center Program of the National Science Foundation under Award Number EEC-9701568.

The financial support of the PEARL sponsor organizations including the Pacific Gas & Electric Company (PG&E), the California Energy Commission (CEC), and the California Department of Transportation (Caltrans) is acknowledged.

We would like to thank Nancy Smith and Paul Somerville URS Greiner Woodward Clyde, Pasadena Office, for providing rupture directivity parameters for strong motion stations. Thanks are also extended to Walt Silva of Pacific Engineering and Analysis and Norm Abrahamson of PG&E for helpful comments made in numerous discussions about this topic. We appreciate the efforts of Andrew Liu of UCLA, who helped prepare input files for ground response studies.

PACIFIC EARTHQUAKE ENGINEERING RESEARCH CENTER

Ground Motions for Site Response Estimates —1906 Earthquake

Paul Somerville

Robert Graves

Nancy Collins
URS Greiner Woodward Clyde
Pasadena, California

A report to the PEER Program of Applied Earthquake Engineering Research on Lifeline Systems

The financial support of the sponsor organizations including the Pacific Gas & Electric Company (PG&E), the California Energy Commission (CEC), and the California Department of Transportation (Caltrans) is acknowledged.

PEER UTILITIES PROGRAM
REPORT NO. 2000/05

PG&E-PEER DIRECTED STUDIES PROGRAM, PHASE II

SIMULATED TIME HISTORY OF THE 1906 SAN FRANCISCO EARTHQUAKE AT COYOTE CREEK, SAN JOSE

TASK 5C FINAL REPORT

JUNE 6, 2000

Paul Somerville, Robert Graves, Nancy Collins

URS Corporation, Pasadena, CA.

INTRODUCTION

This report describes the generation of a ground motion time history of the 1906 earthquake that represents the ground motions experienced at Coyote Creek, San Jose. The time history was generated using a broadband simulation procedure that is summarized in the following section and described in detail in the Appendix. The simulated ground motions are representative of stiff alluvial site conditions. The source rupture model of the 1906 San Francisco earthquake used in the simulation was derived from the model of Wald et al. (1993). The Coyote Creek site is located at Lat. 37 degrees 25.609 minutes north, 121 degrees 55.643 minutes west, North American datum 1927. The site is about 20.9 km northeast of the San Andreas fault, between the epicenter and the southern termination of rupture at San Juan Bautista, as shown in Figure 1.

The ground motions at the Coyote Creek site have moderate amplitudes because the site is located near a part of the fault that had low slip, and because it is located relatively close to the epicenter of the earthquake, and thus has moderate rupture directivity effects. For these reasons, the ground motions that were simulated at the Coyote Creek site are not representative of the ground motions of the 1906 earthquake at a distance of 20.9 km from the fault, especially in the region north of the San Francisco Bay.

SOURCE MODEL OF THE 1906 SAN FRANCISCO EARTHQUAKE

A rupture model of the 1906 San Francisco earthquake derived from teleseismic data by Wald et al. (1993) is shown in Figure 2. This figure also shows a comparison of the fault slip inferred from the teleseismic data with the geologically and geodetically measured fault slip. The overall rupture length of the earthquake was 340 km. The hypocenter of the earthquake was assumed to be in Daly City, based on Bolt (1968) and Boore (1977). The largest concentration of slip occurred well north of the epicenter, between Point Reyes and Fort Ross. A smaller concentration of slip occurred immediately south of the epicenter in Daly City.

Experience in the analysis of ground motions from well recorded strike-slip earthquakes, such as the 1989 Loma Prieta and 1995 Kobe earthquakes (Wald et al.,

1991, Figure 11; Wald, 1996, Figure 11), shows that the strong motions experienced at a site are dominated by the part of the rupture that lies between the epicenter and the site. This is especially true of rupture directivity effects, which influence the ground motions at periods longer than about 0.5 seconds. Our simulations confirm our expectation that the only part of the 1906 fault rupture that produced significant ground motion levels at the Coyote Creek site is the segment that lies between the epicenter and San Juan Bautista. According to the Wald et al. (1993) rupture model, the slip on the San Andreas fault was about 6.5 meters at the epicenter of the 1906 earthquake, and decreased steadily to zero about 70 km southeast of the epicenter. At the closest point on the fault to the Coyote Creek site, the slip was less than 2 meters. The region of large slip between Point Reyes and Fort Ross, characterized by fault slip of as much as 10 meters, is located more than 150 km from the site.

The fault parameters used in the simulation are summarized in Table 2. We modeled a 260 km long segment of the rupture that contains almost all of the seismic moment of the earthquake. The 80 km segment at the northwestern part of the fault, which was not included in the rupture model used in the ground motion simulations, would have a negligible effect on the ground motions at Coyote Creek. We used the scaling relations for crustal earthquakes developed by Somerville et al. (1999) to estimate a rise time of 3.2 seconds. The sensitivity of simulated ground motions to the source parameters of large San Andreas earthquakes has been investigated by Graves (1998).

Table 1. Source Parameters for the 1906 San Francisco Earthquake Simulation

PARAMETER	VALUE
Seismic Moment	3.3×10^{27} dyne cm
Mw	7.65
Length	260 km
Width	12 km
Depth to Top	1.5 km
Strike	141
Dip	90
Rake	180
Hypocenter	37.67N, 122.46 E, 8 km depth
Length northwest of epicenter	165 km
Length southwest of epicenter	95 km
Rupture velocity	2.7 km/sec
Rise Time	3.22 sec
Slip Model, Crustal Velocity Model	Wald et al., 1991

BROADBAND SIMULATION METHOD

The broadband ground motion simulation procedure is a hybrid procedure that computes the low frequency and high frequency ranges separately and then combines the two to produce a single time history. At frequencies below 1 Hz, it contains a theoretically rigorous representation of radiation pattern, rupture directivity and wave propagation effects, and reproduces recorded ground motion waveforms and amplitudes.

At frequencies above 1 Hz, it uses a theoretically rigorous representation of wave propagation effects which is combined with theoretically-based semi-empirical representations of stochastic processes including source radiation pattern and scattering in the path and site. The simulation procedure has been calibrated against the recorded strong motions from numerous earthquakes.

The synthetic seismogram procedure that we use to generate the low frequency part of the broadband seismogram is described by Hartzell and Heaton (1983). It is implemented using frequency-wavenumber integration to compute Green's functions which are convolved with the slip function on the fault. The high frequency ground motion simulation procedure that we use is described by Wald et al. (1988) and Somerville (1993). It is implemented using a generalized ray method to calculate simplified Green's functions, which are convolved with empirical source functions derived from near-fault strong motion recordings of small earthquakes. The low frequency and high frequency parts of the simulation are combined using matched filters, as described by Somerville et al. (1995a,b). An outline of the procedure is given in the following paragraphs.

The fault model is specified as a finite rectangular fault surface that is divided into discrete sub-fault elements, and the motions from these elements are summed and lagged to simulate the propagation of rupture over the fault surface. The parameters required for specifying the source are seismic moment, fault length, fault width, strike, dip, rake, depth of top of fault, hypocenter, rupture velocity, and slip distribution (which may include spatially variable rake and time function of slip). Radiation pattern and fault subevents are treated differently in two different frequency ranges. At low frequencies (<1 Hz), the fault is discretized finely enough to produce a continuous slip function for frequencies below one second, and the theoretical radiation pattern is used. At high frequencies (>1 Hz), the fault is discretized into sub-fault elements having dimensions of several km. The radiation of seismic waves from these sub-fault elements is represented by empirical source functions, which are recorded accelerograms of events having the dimensions of the fault elements (magnitude ~5 earthquakes) that have been corrected back to the source. The radiation pattern is represented empirically by selecting source functions having the required theoretical radiation pattern value for each sub-fault element. We have used empirical source functions derived from an aftershock of the 1979 Imperial Valley earthquake.

The modeling of wave propagation effects requires the specification of seismic velocities, density, and Q of a flat layered crustal model. We have used the velocity model used by Wald et al. (1991) in modeling the 1989 Loma Prieta earthquake. Path effects are treated differently in these two different frequency ranges. At low frequencies (<1 Hz), path effects are represented by Green's functions calculated using an efficient frequency-wavenumber integration scheme (Saikia, 1994). These Green's functions contain the complete response of the anelastic layered medium (all body wave and surface wave phases) for frequencies below a given value (typically chosen to be 5 Hz). They also contain the near-field term in addition to the far-field term, and include the static displacement field of the earthquake. At high frequencies (>1 Hz), path effects are represented by simplified Green's functions calculated using generalized ray theory (Helmberger and Harkrider, 1978). These Green's functions are accurate up to indefinitely high frequencies (typically 50 Hz), and contain all of the significant rays.

They are simplified in the sense that they do not include the radiation pattern and the receiver function. The simplified Green's functions are used to transfer the empirical source functions from the depth, horizontal range and velocity structure in which they were recorded to the depth, horizontal range and velocity structure in which they are to be used for ground motion simulation. Scattering effects in the path are represented empirically by wave propagation effects contained in the recorded source functions.

At low frequencies, site effects are incorporated by calculating Green's functions using surface velocity, density and Q appropriate for the site. For the high frequency part of the simulation, the receiver function is included empirically in the recorded source functions; the partitioning of energy among components is treated in a site-specific manner by applying a receiver function correction to the empirical source functions which rotates the recorded wave field into the appropriate partitioning for the velocity structure at the site. Scattering effects near the site are represented by wave propagation effects contained in the empirical source functions that are not modeled by the simplified Green's functions. The site attenuation contained in the empirical source functions is adjusted to provide the value that is appropriate at the site.

The ground motion model has no free parameters when used to model the recorded ground motions of an earthquake. The method has been validated against the recorded strong ground motions of numerous earthquakes, including the 1989 Loma Prieta earthquake (Somerville et al., 1994a,b). Based on this validation experience, we have documented that the ground motion simulation procedure is applicable for magnitudes in the range of 5 to 8; distances from 0 to 200 km, and frequencies between 0.2 and 35 Hz.

GROUND MOTION TIME HISTORY AT COYOTE CREEK

The north, east and vertical components of acceleration, velocity and displacement for simulated ground motion time history are shown in Figure 3. The separate contributions of the two main concentrations of slip on the fault are evident in these time histories. The asperity immediately south of the epicenter produces about 10 seconds of horizontal component acceleration with peaks of about 0.1g, a long period velocity pulse with a peak velocity of 16.5 and 12 cm/sec on the north and east components respectively, and a corresponding displacement pulse with peak displacements of about 20 and 40 cm on these two components. The asperity between Point Reyes and Fort Ross produces much smaller ground motions that arrive about one minute later. At long periods, the ground motions are much smaller because of backward

Boore (1977) described an analysis of strong motion recordings of the 1906 earthquake. The recordings were made on primitive seismographs that were all driven off scale. The clearest recording was made on a three-component Ewing instrument at Mount Hamilton (Boore, 1997, Figure 3). This recording, normalized by the static magnification of the instrument, shows clipping at about 3 cm of displacement soon after the inferred onset of the S wave. Modeling of this record is beyond the scope of the present study, but the simulations described in this report are considered to be not inconsistent with the Mount Hamilton record. The ground displacement calculations at Mount Hamilton shown by Boore (1977) in Figure 7 are quite compatible with those in

Figure 3 of this report, both in polarity and amplitude, although the calculations in this report are somewhat larger because their body waves were calculated for a layered crustal model.

The response spectra of the simulated ground motions are shown in Figure 4. These response spectra show the separate contributions of the low frequency and high frequency simulations, in addition to the response spectra of the combined broadband time histories. The simulated response spectra are compared with the prediction of the empirical model of Abrahamson and Silva (1997) for soil sites. The simulated spectra are lower than the empirical spectra at all periods. This difference may be attributable to the following factors.

The largest concentration of slip in the 1906 earthquake occurred well north of the epicenter, between Point Reyes and Fort Ross. This main asperity of the 1906 earthquake produced insignificant ground motion levels at the Coyote Creek site, because of its distance from the site (about 160 km) and because rupture of this segment propagated away from the Coyote Creek site. A smaller concentration of slip occurred immediately south of the epicenter in Daly City. The ground motions at the Coyote Creek site have moderate amplitudes because the site is located near a part of the fault that had low slip, and because it is located relatively close to the epicenter of the earthquake, and thus has moderate rupture directivity effects. For these reasons, the ground motions that were simulated at the Coyote Creek site are not representative of the ground motions of the 1906 earthquake at a distance of 20.9 km from the fault, especially in the region north of the San Francisco Bay.

There is no strong motion recording of the 1989 Loma Prieta earthquake at Coyote Creek. The closest recording site is the Milpitas site (CSMIP #57502), about 3 km east of Coyote Creek, where the instrument is located on the floor beside the wall of a two story building. The north, east and vertical components of acceleration, velocity and displacement recorded at the Milpitas site during the 1989 Loma Prieta earthquake are shown in Figure 5. The duration of the Milpitas acceleration time history is similar to that of the 1906 Coyote Creek simulation.

The response spectrum of the Milpitas recording of the 1989 Loma Prieta earthquake is compared with the response spectrum of the 1906 earthquake simulation at Coyote Creek in Figure 6. The response spectra are similar at short periods, but the Loma Prieta earthquake is larger at periods longer than about 2 seconds. This may reflect the fact that the 1989 Loma Prieta earthquake is closer to Coyote Creek than the Daly City asperity of the 1906 earthquake, although it has a smaller seismic moment (M_w 6.95 for Loma Prieta compared to M_w 7.15 for the Daly City asperity of the 1906 earthquake).

Our simulations of the 1906 earthquake at Coyote Creek are for stiff alluvial site conditions, and have not taken site specific ground conditions at Coyote Creek into account. These conditions may include the effects of the response of the Santa Clara basin, which may be significant in the Milpitas recording of the 1989 Loma Prieta earthquake. The development of reliable 3D velocity models of the Santa Clara basin may provide the means to test the modeling of Santa Clara basin effects using the Loma Prieta recordings, and the application of basin modeling to incorporate basin effects in the simulation of ground motions from the 1906 earthquake.

REFERENCES

Abrahamson, N.A. and W.J. Silva (1997). Empirical response spectral attenuation relations for shallow crustal earthquakes. Seismological Research Letters 68, 94-127.

Abrahamson, N.A., P.G. Somerville, and C. Allin Cornell (1990). Uncertainty in numerical strong motion predictions, *Proc. 4th U.S. National Conference on Earthquake Engineering,,* **1**, 407-416.

Bolt, B.A. (1968). The focus of the 1906 California earthquake. Bull. Seism. Soc. Am. 58, 457-471.

Boore, D.M. (1977). Strong motion recordings of the California earthquake of April 18, 1906. Bull. Seism. Soc. Am. 67, 561-577.

Graves, R. (1998). Three-dimensional finite-difference modeling of the San Andreas fault: source parameterization and ground-motion levels. Bull. Seism. Soc. Am. 88, 881-897.

Hartzell, S.H. and T.H. Heaton (1983). Inversion of strong ground motion and teleseismic waveform data for the fault rupture of the 1979 Imperial Valley, California earthquake, *Bull. Seism. Soc. Am.* 83, 780-810.

Helmberger, D.V. (1983). Theory and application of synthetic seismograms. in Earthquakes:Observation, Theory and Interpretation, Proc. Int. Sch. Phys. "Enrico Fermi" Course LXXXV, pp. 174-221, eds. Kanamori, H. and E. Boschi, North- Holland, Amsterdam.

Saikia, C.K. (1994a). Modified frequency-wavenumber algorithm for regional seismograms using Filon's quadrature: modeling of Lg waves in eastern North America. *Geophys. J. Int.* 118, 142-158.

Somerville, P.G., K. Irikura, R, Graves, S. Sawada, D. Wald, N. Abrahamson, Y. Iwasaki, T. Kagawa, N. Smith and A. Kowada (1999). Characterizing crustal earthquake slip models for the prediction of strong ground motion. Seism. Res. Lett. 70, 59-80.

Somerville, P.G., R.W. Graves, and C.K. Saikia (1995). Characterization of Ground Motions during the Northridge Earthquake of January 17, 1994, SAC Steel Project Report SAC 95-03.

Somerville, P.G., N.F. Smith and R.W. Graves (1994a). The effect of critical Moho reflections on the attenuation of strong motion from the 1989 Loma Prieta, in *"The Loma Prieta, California, Earthquake of October 17, 1989 - Strong Ground Motion,"* U.S.G.S. Professional Paper 1551-A, A67-A75.

Somerville, P.G., D.J. Wald, and N.F. Smith (1994b). Prediction of the near-source ground accelerations of the Loma Prieta earthquake using a heterogeneous slip model, unpublished manuscript.

Somerville, P., C. Saikia, D. Wald, and R. Graves (1995b). Implications of the Northridge earthquake for strong ground motions from thrust faults, Bull. Seism. Soc. Am. 86, Part 1, S115-S125.

Wald, D.J. (1996). Slip history of the 1995 Kobe, Japan earthquake determined from strong motion, teleseismic, and geodetic data. J. Phys. Earth 44, 489-503.

Somerville, P.G. (1993). Engineering applications of strong motion simulation, *Tectonophysics*, 218, 195-219.

Wald, D.J., H. Kanamori, D. Helmberger, and T.H. Heaton (1993). Source study of the 1906 San Francisco earthquake. Bull. Seism. Soc. Am. 83, 981-1019.

Wald, D.J., D. Helmberger, and T.H. Heaton (1991). Rupture model of the 1989 Loma Prieta earthquake from the inversion of strong-motion and broadband teleseismic data. Bull. Seism. Soc. Am. 81, 1540-1572.

Wald, D.J., L.J. Burdick and P.G. Somerville (1988). Simulation of acceleration time histories close to large earthquakes. *Earthquake Engineering and Soil Dynamics II - Recent Advances in Ground Motion Evaluation*, Geotechnical Special Publication 20, J. Lawrence Von Thun, ed., 430-444.

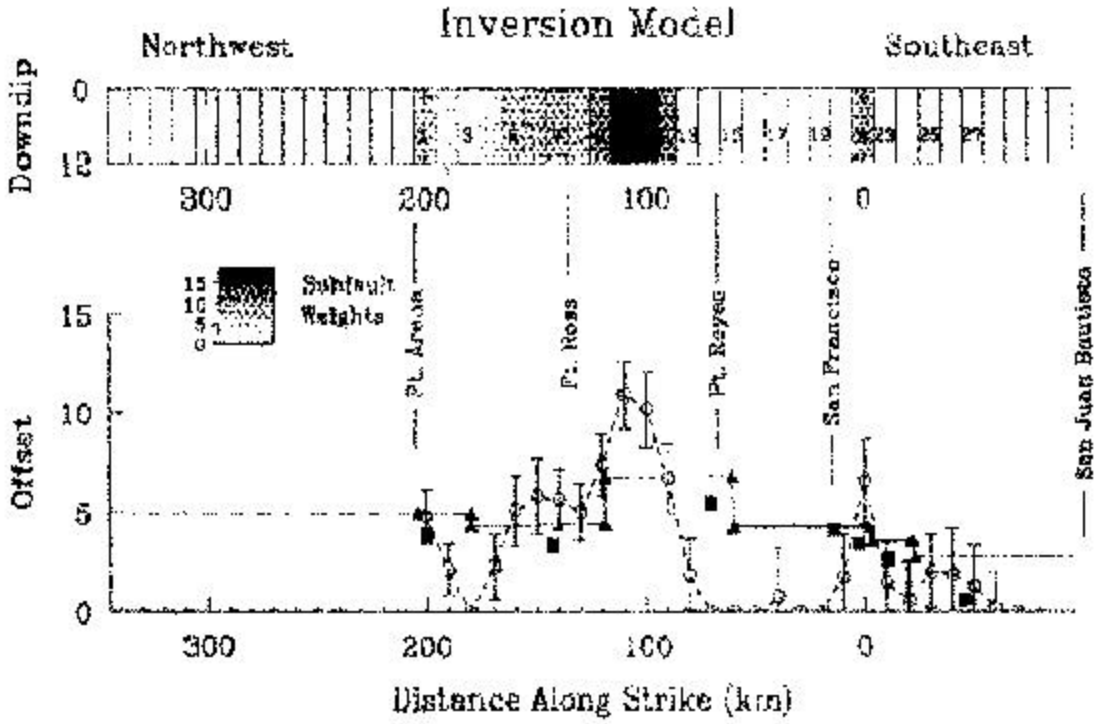

Figure 2. Rupture model of the 1906 San Francisco earthquake (top) and comparison of its slip distribution (circles with uncertainty bars connected by a dashed line) with geodetic data (solid triangles connected by lines and geological data (solid squares) from Thatcher, 1975. Source: Wald et al., 1993.

APPENDIX 1.
BROADBAND GROUND MOTION SIMULATION METHOD

Introduction

The broadband strong motion simulation method is a hybrid method that computes the ground motions separately in the short period and long period ranges and then combines them. We used a transition period of 1 seconds between the short period and long period ranges in the simulations described in this report; Figure A1-1 schematically shows the matched filters for a period of 3 seconds. The method used for short periods is based on the summation of strong motion recordings from smaller earthquakes. The method used for long periods is a standard method for calculating synthetic seismograms based on theoretical Green's functions. This standard method has been used extensively to successfully model the waveforms of long period strong ground motions recorded from many recent earthquakes, and is the basis for the rupture models of earthquakes that are inverted from strong motion recordings.

The fault model is specified as a finite rectangular fault surface that is divided into discrete sub-fault elements, and the motions from these elements are summed and lagged to simulate the propagation of rupture over the fault surface. The parameters required for specifying the source are seismic moment, fault length, fault width, strike, dip, rake, depth of top of fault, hypocenter, rupture velocity, and slip distribution (which may include spatially variable rake and time function of slip). Radiation pattern and fault subevents are treated differently in two different period ranges. For the long period simulation, the fault is discretized finely enough to produce a continuous slip function for periods longer than the transition period, and the theoretical radiation pattern is used.

For the short period simulation, the fault is discretized into sub-fault elements whose dimensions are chosen so as to maintain self-similarity in the spectral shape between the subevent on the fault element and the large event based on an omega-squared scaling relation (Joyner and Boore, 1986), as described by Somerville et al. (1991). The radiation of seismic waves from these sub-fault elements is represented by empirical source functions, which are recorded accelerograms of events having the dimensions of the fault elements and that have been corrected back to the source.

The modeling of wave propagation effects requires the specification of seismic velocities, density, and Q of a flat layered crustal model. Path effects are treated differently in these two different period ranges. At long periods, path effects are represented by Green's functions calculated using an efficient frequency-wavenumber integration scheme (Saikia, 1994). These Green's functions contain the complete response of the anelastic layered medium (all body wave and surface wave phases) for frequencies below a given value (typically chosen to be 5 Hz). They also contain the near-field term in addition to the far-field term, and include the static displacement field of the earthquake. At short periods, path effects are represented by simplified Green's functions calculated using generalized ray theory (Helmberger, 1983). These Green's functions are accurate up to indefinitely high frequencies (typically 50 Hz), and contain

all of the significant rays. They are simplified in the sense that they do not include the radiation pattern and the receiver function. The simplified Green's functions are used to transfer the empirical source functions from the depth, horizontal range and velocity structure in which they were recorded to the depth, horizontal range and velocity structure in which they are to be used for ground motion simulation. Scattering effects in the path are represented empirically by wave propagation effects contained in the recorded source functions.

At long periods, site effects are incorporated by calculating Green's functions using surface velocity, density and Q appropriate for the site. For the short period part of the simulation, the receiver function is included empirically in the recorded source functions; the partitioning of energy among components is treated in a site-specific manner by applying a receiver function correction to the empirical source functions which rotates the recorded wave field into the appropriate partitioning for the velocity structure at the site. Scattering effects near the site are represented by wave propagation effects contained in the empirical source functions that are not modeled by the simplified Green's functions. The site attenuation contained in the empirical source functions is adjusted to provide the value that is appropriate at the site.

In the following sections, we provide more detail about specific aspects of the broadband strong motion simulation procedure. This description addresses the earthquake source, the propagation path, and the site, and summarizes the parameters requiring specification. It also describes important features of the procedure and the validation of the procedure against recorded strong ground motions.

Source

A finite source is used. For the simulation of ground motions from an earthquake for which a rupture model has been inverted, the parameters derived from the inversion provide all of the information needed to characterize the source. For the simulation of ground motion for a future earthquake, the slip distribution is generated from a frequency-wavenumber model of slip distribution whose parameters are constrained by the slip models of past earthquakes (Somerville and Abrahamson, 1991). The slip direction on the fault (rake angle) can vary spatially over the fault, and can also vary in time at a given point on the fault. The rise time (slip velocity) is based on an empirical relation derived from the same ten events. The rupture velocity is assumed to be 0.85 times the shear wave velocity. Radiation pattern and fault subevents are treated differently in two different period ranges.

Long Period: The fault is discretized finely enough to produce a continuous plane for frequencies below one second. The theoretical radiation pattern is used.

Short Period: The fault is discretized into fault elements. The size of the fault elements is chosen so as to maintain self-similarity in the spectral shape between the subevent on the fault element and the large event based on an omega-squared scaling relation (Joyner and Boore, 1986), as described by Somerville et al. (1991). The condition is that the total number of

subevents added be the four-thirds power of the moment ratio of the large event to the subevent.

The radiation of seismic waves from these fault elements is represented by empirical source functions, which are accelerograms of events having the dimensions of the fault elements that were recorded near the source and have been corrected back to the source. Where multiple empirical source functions are available, the radiation pattern is represented empirically using these source functions, by selecting recordings having the required theoretical radiation pattern value for each fault element.

Path

For 1D models of crustal structure, path effects are treated differently in two different period ranges.

Long Period: Path effects are represented by Green's functions calculated using an efficient frequency-wavenumber integration scheme (Saikia, 1994). In the frequency-wavenumber integration method, the solutions due to a point source are expressed in terms of a double integral transformation over horizontal wavenumber and frequency by taking temporal and spatial Fourier transforms. For a stack of homogeneous plane layers, the kernel of the integrand is expressed by the propagator matrix. The integral of the kernel over the horizontal wavenumber is carried out numerically at a sequence of different frequencies. Time domain solutions are obtained by an inverse Fourier transform. These Green's functions contain the complete response of the layered medium (all body wave and surface wave phases) for frequencies below a given value (typically chosen to be 5 Hz). They also contain the near-field term in addition to the far-field term, and include the static displacement field of the earthquake. The Green's functions include the effects of a layered Q model.

Short Period: Path effects are represented by simplified Green's functions calculated using generalized ray theory (Helmberger, 1983). These Green's functions are accurate up to indefinitely high frequencies (typically 50 Hz), and contain all of the significant rays. They are simplified in the sense that they do not include the radiation pattern and the receiver function; these are excluded because they are represented empirically in the empirical source functions. The simplified Green's functions are used to transfer the empirical source functions from the depth, horizontal range and velocity structure in which they were recorded to the depth, horizontal range and velocity structure in which they are to be used for ground motion simulation. Scattering effects in the path are represented empirically by wave propagation effects contained in the source functions that are not modeled by the simplified Green's functions used in their correction.

Geometrical ray theory breaks down when there are strong velocity gradients. For calculating the propagation of seismic waves in a layered crust, we need to use generalized ray theory which includes refracted arrivals (head waves) as well as reflected arrivals. In the generalized ray method, the kernel of a double integral transformation is obtained by taking a

Laplace transform over time and a spatial Fourier transform over horizontal coordinate. Then, by introducing ray parameter and a relationship between the ray parameter and travel time (Cagniard path), the integral of the kernel which corresponds to an inverse Laplace transform is analytically carried out in order to obtain a time domain solution. The method of generalized rays allows separation of the wavefield into energy that radiates downward and energy that travels upward. To illustrate generalized rays, we describe the decomposition of the wavefield into the following three travel paths:

(1) direct arrival plus surface layer multiples (shallow Love waves);
(2) downgoing (diving) energy paths (lower crustal triplications); and
(3) surface reflected paths which are reflected again below the source (*sS*).

A smooth velocity model composed of approximately 50 layers is shown in Figure A1-2. This figure also displays two generalized ray sets used in constructing the wavefield: the downgoing ray set and the upgoing ray set (excluding the direct arrival). The upper portion of Figure A1-3 displays the various contributions of these three ray sets to the total potential field. These three contributions are the direct ray, a large set of downgoing rays that are reflected back to the surface, and a large set of upgoing rays that are reflected at the surface and are reflected or refracted back to the surface. These responses were produced by applying the Cagniard-de Hoop technique to the generalized rays (Helmberger, Engen & Grand 1985). These three contributions dominate the wavefield, as can be demonstrated by generating complete synthetic seismorgams by the reflectivity method (Saikia, 1994). The upper row shows the decrease in short-period energy with increasing distance as the waves becomes diffracted. The downgoing rays (or diving rays) contribute significantly to the short period content. The Moho reflection SmS and the Moho refracted wave Sn (head wave) produce further complexity, especially due to contributions from *sS*.

Path effects are treated in one of two different methods in 2D crustal models. One method uses generalized rays (Helmberger et al., 1995), and is accurate up to indefinitely high frequencies (typically to 50 Hz). The other method uses finite difference (Helmberger and Vidale, 1988), and contains all body wave and surface wave arrivals for periods longer than a specified cutoff period. This method can also be used for 3-D crustal models.

Site

Site effects are incorporated by calculating Green's functions using the velocity model appropriate for the site. For the short period part of the simulation, the receiver function is included empirically in the empirical source functions; the partitioning of energy among components is treated in a site-specific manner by applying a receiver function correction to the empirical source functions which rotates the recorded partition into that appropriate to the velocity structure at the site. Scattering effects near the site are represented empirically by wave propagation effects contained in the empirical source functions that are not modeled by the simplified Green's functions used in their correction. The site attenuation (kappa) contained in the empirical source functions is adjusted to provide the value that is appropriate at the site.

Non-linear effects can be included in an approximate way by using a 1-D equivalent linear approach.

Parameters Requiring Specification

Source: Seismic moment, fault length, fault width, strike, dip, rake, depth of top of fault, hypocenter, rupture velocity, the time function of slip at each point on the fault, and the direction of slip on the fault.

Path: Seismic velocities, density, and Q (material damping factor) of a crustal model that may be plane layered (1D), 2D or 3D. The most sensitive parameters are velocity gradients in the shallow and deep parts of the crust.

Site: Surface seismic velocities, density, and Q (material damping factor). If nonlinear soil response is to be included, we need shear modulus and damping as a function of strain level.

Important Features of the Broadband Ground Motion Simulation Method

As determined from validation against recorded data documented below, the ground motion method is broadband (zero frequency to 50 Hz); is applicable for magnitudes in the range of 5 to 8; and is applicable to distances from 0km to 200km or more. It has no free parameters when used to model the recorded ground motions of an earthquake, and hence no calibration of the model is required. The model has been extensively validated against the recorded strong ground motions of crustal earthquakes using flat layered (1-D) crustal models and more complex (2-D and 3-D) models. At long periods, it contains a theoretically rigorous representation of radiation pattern, rupture directivity and wave propagation effects, and reproduces the recorded ground motion waveforms. At short periods, it uses a theoretically rigorous representation of wave propagation effects which is combined with theoretically-based semi-empirical representations of stochastic processes including source radiation pattern and scattering in the path and site.

The broadband simulation method is based on standard time-domain methods for estimating earthquake source parameters and analyzing seismic wave propagation, and can therefore be readily applied using standard parameterizations of the earthquake source and crustal structure. It has been extensively validated against recorded strong ground motions from both tectonically active regions and tectonically stable regions. It has no free parameters when used to model the recorded ground motions of an earthquake, and hence no calibration of the model is required. The ground motion attenuation function is determined by the crustal structure and the source depth, and thus has predictive power in locations where crustal structure and source depth are available but few strong motion recordings exist. The method can include Green's functions calculated using 2-D or 3-D models of crust structure.

Validation of the Broadband Strong Motion Simulation Method Against Recorded Data

The ground motion model has no free parameters when used to model the recorded ground motions of an earthquake, and hence no calibration of the model is required. The 1-D ground motion model has been validated against the recorded strong ground motions of the following earthquakes: 1978 Tabas (Saikia, 1994); 1979 Imperial Valley (Wald et al., 1988a); 1985 Michoacan, Mexico and Valparaiso, Chile (Somerville et al., 1991); 1987 Whittier Narrows (Wald et al., 1998b; Saikia, 1992); 1988 Saguenay (Somerville et al., 1990; Atkinson and Somerville, 1994); 1988 Nahanni (PG&E, 1988); 1989 Loma Prieta (Somerville et al., 1994a,b); 1994 Northridge (Somerville et al., 1995). The 2-D and 3-D modeling approach, which to date has been applied at periods of 1 sec and longer, has been applied to the ground motions of a Loma Prieta aftershock recorded in the Marina District basin in San Francisco (Graves, 1993); to the ground motions of the 1992 Cape Mendocino earthquake recorded in the Eel River Valley (Graves, 1994a); to the ground motions of the 1994 Northridge earthquake recorded in the northwestern Los Angeles basin (Graves, 1994b); and to the ground motions of the 1995 Kobe earthquake recorded in the Kinki district (Somerville and Graves, 1996).

Uncertainty in Ground Motions Generated using the Broadband Procedure

The uncertainty in ground motions predicted by the model is characterized by the procedure described by Abrahamson et al. (1990). There are two kinds of uncertainty in modeling ground motion, and each contributes about equally to the overall uncertainty. One is variability due to modeling uncertainty associated with the modeling procedure. The other source of uncertainty is that associated with uncertainty in the parameters of future earthquakes. These parameters include the slip distribution, the location of the hypocenter, the slip velocity and the rupture velocity.

The modeling uncertainty is estimated from comparison between recorded and simulated ground motions of earthquakes for which estimates of all of the parameters required by the model are available. The goodness of fit measurement is described by two parameters: the bias and the standard error. In this formulation, the bias measures the difference between recorded and simulated motions averaged over all stations, and provides an indication of whether, on average, the simulation procedure is overpredicting, underpredicting, or evenpredicting the recorded motions. The standard error measures the average difference between the simulated and recorded motions for a single observation, and provides an indication of the uncertainty involved in predicting a single value. The average of all these errors, which include both overprediction and underprediction, is the bias. The standard error in the prediction of a single observation (response spectral velocity at 5% damping) is about a factor of 1.4 (natural logarithm of standard error = 0.35) in the period range of 0.05 to 10 seconds. .

References

Abrahamson, N.A., P.G. Somerville, and C.A. Cornell (1990). Uncertainty in numerical strong motion predictions. Proc. *Fourth U.S. Nat. Conf. Earthq. Eng., Palm Springs, CA,*1, 407-416.

Atkinson, G.M. and P.G. Somerville (1994). Calibration of time history simulation methods, *Bull. Seism. Soc. Am*. 84, 400-414.

Graves, R.W. and P.G. Somerville (1995). Characterization of long period (1-10 sec) ground motions for base isolated structures located in sedimentary basins. Seismic, Shock and Vibration Isolation, PVP-Vol. 319, Proceedings of the 1995 Joint ASME/JSME Pressure Vessels and Piping Conference, Honolulu, Hawaii, July 23-27, 1995.

Graves, R.W. (1993). Modeling three-dimensional site response effects in the Marina District basin, San Francisco, California.

Graves, R.W. (1994a). Simulating the 3D basin response in the Portland and Puget Sound regions from large subduction zone earthquakes, Annual Technical Report to USGS, Award 1434-93-G-2327.

Graves, R.W. (1994b). Preliminary analysis of long-period basin response in the Los Angeles region from the 1994 Northridge earthquake, *Geophys. Res. Lett.,* 22, 101-104.

Helmberger, D.V., G. Engen and S. Grand (1985). Notes on wave propagation in laterally varying structure, J. Geophys. Res. 58, 82-91.

Helmberger, D.V. (1983). Theory and application of synthetic seismograms. in Earthquakes: Observation, Theory and Interpretation, Proc. Int. Sch. Phys. "Enrico Fermi" Course LXXXV, pp. 174-221, eds. Kanamori, H. and E. Boschi, North- Holland, Amsterdam.

Helmberger, D.V., R. Stead, P. Ho-Liu, and D. Dreger (1992). Broadband modeling of regional seismograms: Imperial Valley to Pasadena, Geophys. J. Int. 110, 42-54.

Helmberger, D.V. and J.E. Vidale (1988). Modeling strong motions with two-dimensional numerical codes, *Bull. Seism. Soc. Am*. 78, 109-121.

Helmberger, D.V., L.-S. Zhao, and E. Garnero (1995). Construction of synthetic seismograms for 2D structures: core phases, in *Earthquakes,: Observation, Theory and Interpretation,* n. LXXV, Corso, Italiana di Fisica - Bologna, Italy, in press.

Joyner, W.B. and D.M. Boore (1986). On simulating large earthquakes by Green's function addition of smaller earthquakes, in *Earthquake Source Mechanics*, D. Das, J. Boatwright, and C.H. Scholz

Pacific Gas & Electric Company (1988). Final Report of the Diablo Canyon Long Term Seismic Program for the Diablo Canyon Power Plant, Report to the U.S.N.R.C.

Saikia, C.K. (1993). Estimated ground motions in Los Angeles due to a M=7 earthquake on the Elysian thrust fault, *Bull. Seism. Soc. Am*. 83, 780-810.

Saikia, C.K. (1994). Modeling of strong ground motions from the 16 September 1978 Tabas, Iran, Earthquake, *Bull. Seism. Soc. Am*. 84, 31-46.

Saikia, C.K. (1994). Modified frequency-wavenumber algorithm for regional seismograms using Filon's quadrature: modeling of Lg waves in eastern North America. *Geophys. J. Int.* 118, 142-158.

Somerville, P.G. (1992). Engineering applications of strong motion simulation,*Tectono-physics*, 218, 195-219.

Somerville, P.G., J.P. McLaren, L.V. LeFevre, R.W. Burger, and D.V. Helmberger (1987). Comparison of source scaling relations of eastern and western North American earthquakes, *Bull. Seism. Soc. Am*. 77, 322-346.

Somerville, P.G., J.P. McLaren, C.K. Saikia, and D.V. Helmberger (1990). The 25 November, 1988 Saguenay, Quebec earthquake: source parameters and the attenuation of strong ground motion, *Bull. Seism. Soc. Am*. 80, 1118-1143.

Somerville, P.G., M.K. Sen and B.P. Cohee (1991). Simulation of strong ground motions recorded during the 1985 Michoacan, Mexico and Valaparaiso, Chile earthquakes, *Bull. Seism. Soc. Am*. 81, 1-27.

Somerville, P.G. and N.A. Abrahamson (1991). Characterizing earthquake slip models for the prediction of strong ground motions, EOS 72, 341. (abstract).

Somerville, P.G., K. Irikura, S. Sawada, Y. Iwasaki, M. Tai and M. Fushimi (1993). Character izing earthquake slip models for the prediction of strong ground motion. Proceedings of the 22nd JSCE Earthquake Engineering Symposium - 1993, Japan Society of Civil Engineers, p. 291-294.

Somerville, P.G., D.J. Wald, and N.F. Smith (1994a). Prediction of near fault ground motions of the 1989 Loma Prieta earthquake using a heterogeneous slip model, unpublished manuscript.

Somerville, P.G., N.F. Smith and R.W. Graves (1994b). The effect of critical Moho reflections on the attenuation of strong motion from the 1989 Loma Prieta, in *"The Loma Prieta, California, Earthquake of October 17, 1989 - Strong Ground Motion,"* U.S.G.S. Professional Paper 1551-A, A67-A75.

Somerville, P.G., R.W. Graves, and C.K. Saikia (1995). Characterization of Ground Motions during the Northridge Earthquake of January 17, 1994. Program to Reduce the Earthquake Hazards of Steel Moment Frame Buildings, SAC Report 95-03.

Somerville, P., C. Saikia, D. Wald, and R. Graves (1996). Implications of the Northridge earthquake for strong ground motions from thrust faults, Bull. Seism. Soc. Am. 86, S115-S125.

Somerville, P.G. and R.W. Graves (1996). Strong ground motions of the Kobe, Japan earthquake of Jan. 17, 1995, and development of a model of forward rupture directivity applicable in California. Proceedings of the Western Regional Technical Seminar on Earthquake Engineering for Dams, Association of State Dam Safety Officials, Sacramento, California, April 11-12, 1996.

Wald, D.J., L.J. Burdick and P.G. Somerville (1988a). Simulation of acceleration time histories close to large earthquakes. *Earthquake Engineering and Soil Dynamics II - Recent Advances in Ground Motion Evaluation,* Geotechnical Special Publication 20, J. Lawrence Von Thun, ed., 430-444.

Wald, D.J., P.G. Somerville and L.J. Burdick (1988b). Simulation of recorded acceler- ations of the 1987 Whittier Narrows earthquake, *Earthquake Spectra* 4, 139-156.

Wald, D.J. and T.H. Heaton (1994). Spatial and temporal distribution of slip for the 1992 Landers, California earthquake. Bull. Seism. Soc. Am 84, 668-691.

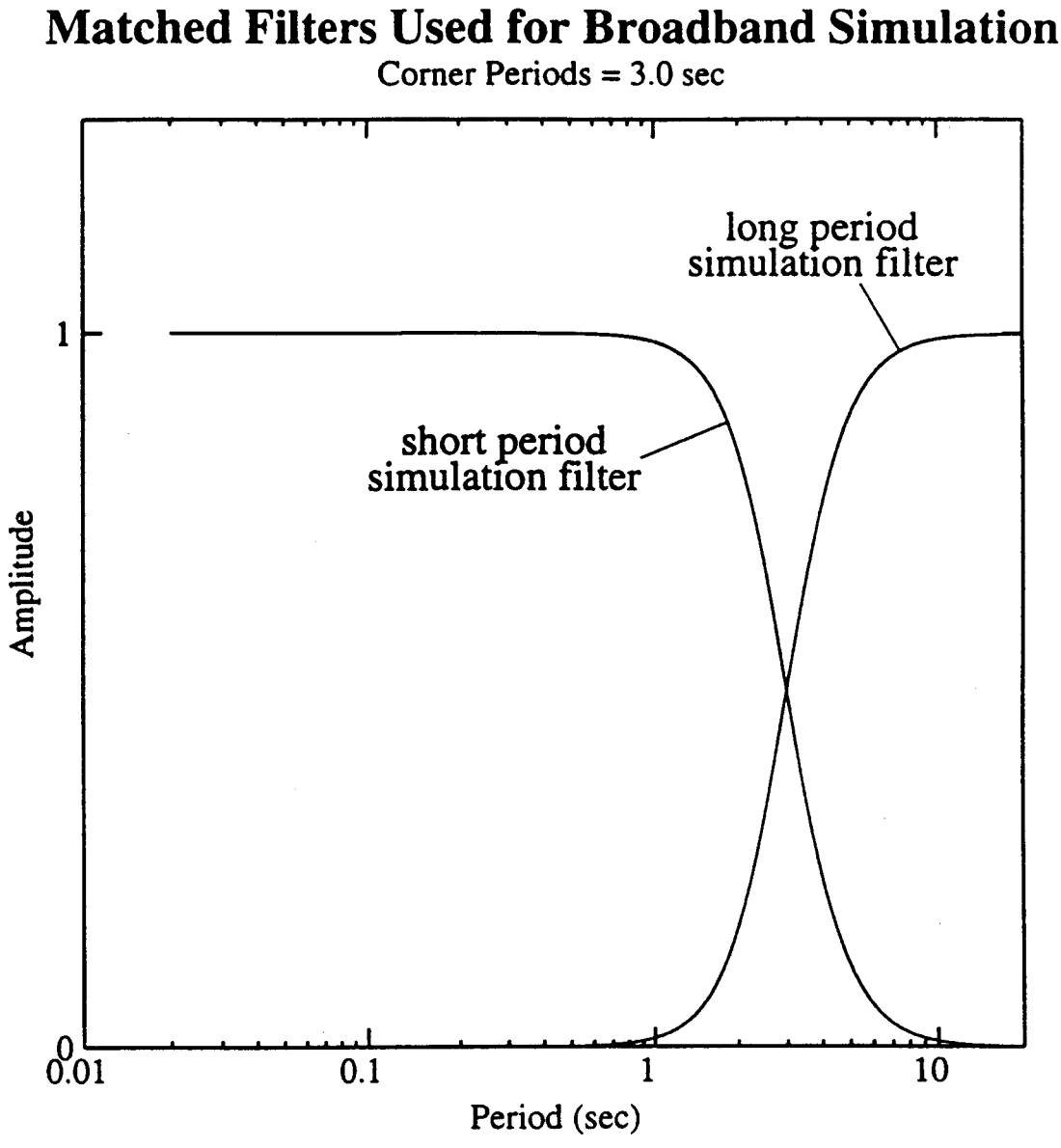

Figure A1-1. Schematic diagram showing the matched filters used to combine the short period and long period simulations. The sum of the matched filters is unity at all periods.

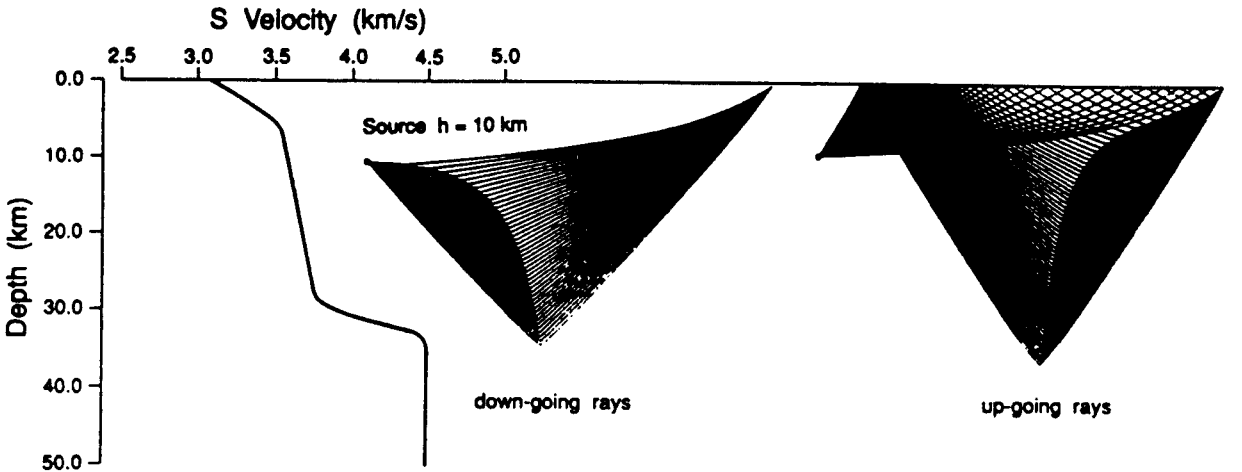

Figure A1-2. A smooth velocity-depth function and generalized ray paths used to construct the synthetic seismograms shown in Figure A1-3. Source: Helmberger et al. (1992).

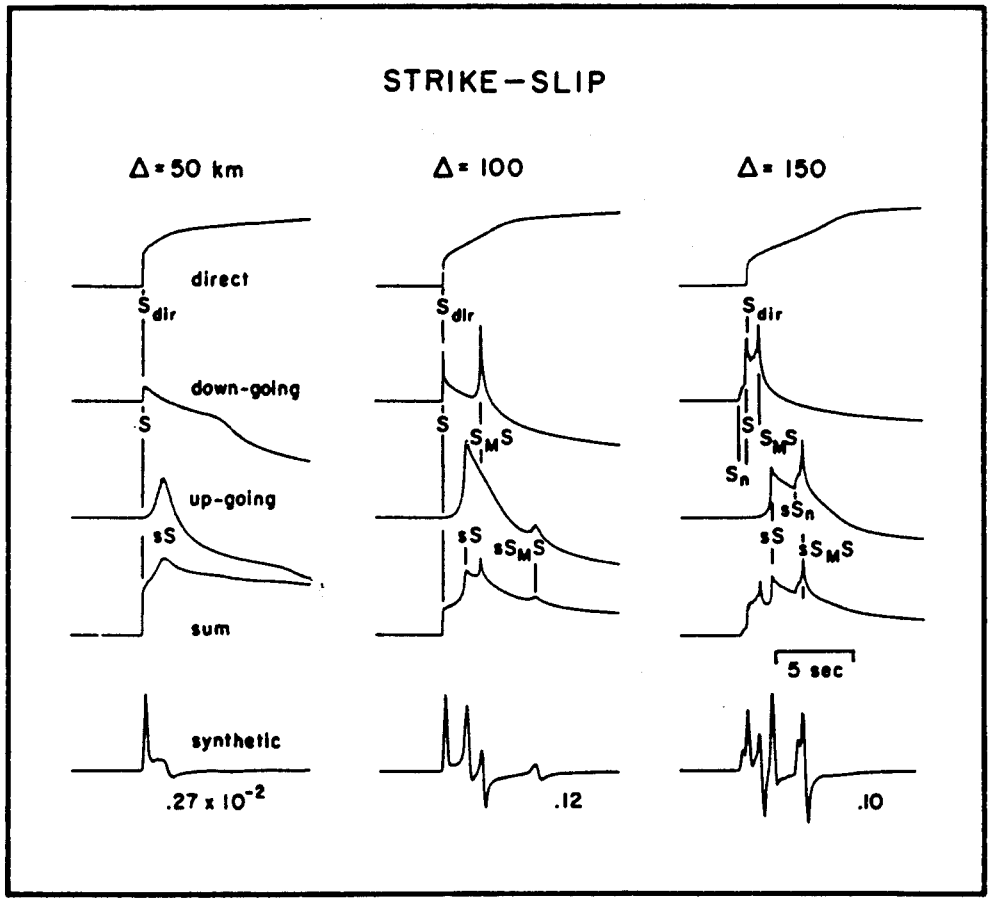

Figure A1-3. Wavefield decomposition showing the response of the direct arrival at the top followed by the contribution from downgoing paths (S) and upgoing paths (sS). The bottom row shows synthetic seismograms computed using a (0.2, 0.2, 0.2) second trapezoidal source. Source: Helmberger et al. (1992).

ACKNOWLEDGEMENTS

The work described in this report was funded by the Pacific Earthquake Engineering Research (PEER) Center under the Pacific Gas & Electric Company Contract No. 09566. This financial support is gratefully acknowledged.

The financial support of the PEARL sponsor organizations including the Pacific Gas & Electric Company (PG&E), the California Energy Commission (CEC), and the California Department of Transportation (Caltrans) is acknowledged.

University of California, Berkeley
Seismological Laboratory

Development of Procedures for the Rapid Estimation of Ground Shaking
Task 7: Ground Motion Estimates for Emergency Response

By

Douglas Dreger and Anastasia Kaverina

A Report to PEER/PG&E

August 31, 1999

Development of Procedures for the Rapid Estimation of Ground Shaking
Task 7: Ground Motion Estimates for Emergency Response
Final Report

Douglas Dreger and Anastasia Kaverina
University of California, Berkeley, Seismological Laboratory

Executive Summary

This project focused on the development of methodology for the near-real-time estimation of earthquake strong ground motion with the objective of providing this information on a regional (statewide) scale. A critical objective of our development was to provide seamless implementation and uniform performance in varied network coverage. To accomplish this goal we: 1) refined a finite fault inverse method to determine fault slip using regional distance stations; 2) developed a strong motion simulation procedure that uses finite source information as input; 3) investigated the incorporation of site type correction factors, 4) and investigated alternative methods to improve the simulation of high frequency strong ground motions. We have successfully completed these tasks and have developed software that calculates model-based estimates of strong shaking that include the focussing effects due to source directivity. The method we have developed estimates PGA, PGV and spectral acceleration at periods of 0.3, 1.0 and 3.0 seconds. These model predictions may be used to interpolate actual strong motion observations (when available) in the same manner as the southern California TriNet ShakeMap (Wald et al. 1999), and we provide examples of data/model shakemaps for the Landers and Northridge earthquakes. These examples show that it is possible to calculate robust shakemaps even in extremely sparse coverage. In the following the results of each component of the project are summarized.

Under task 1, the refinement of the finite source inverse code largely involved testing and program error fixes to produce stable maps of fault slip using broadband stations located at regional distances. We extensively tested the algorithms with data recorded for the 1992 Landers and 1994 Northridge earthquakes, and compared our regionally derived fault slip maps with those obtained using local strong motion recordings. Favorable comparisons indicate that our methodology is capable of uniquely determining the causative fault plane of the earthquake, the slip dimension (both along strike and down dip), the earthquake rupture velocity, and a reasonable characterization of the gross slip distribution, suggesting that the derived source parameters may be used to simulate near-source strong ground motions. As part of a complementary project we modified the code to facilitate its integration into the Rapid Earthquake Data Integration (REDI) system (Gee et al., 1996) operated by the Berkeley Seismological Laboratory. The codes must still be integrated and tested within the REDI operating environment and we expect that this work will be accomplished in the coming year. Our preliminary testing indicates that the essential source information may be obtained within 4 to 20 minutes following the determination of a seismic moment tensor solution depending upon the level of approximation required.

The focus of task 2 was to use the regionally derived fault slip maps to simulate the distribution of near-source strong ground motion, and to compare the model predictions with observations to calibrate the methodology. Additionally, task 4 involved the testing of hybrid Green" function (Pitarka et al., 1999) and the composite source (Zeng et al., 1994) methods to attempt to better simulate higher frequency ground motions. At the request of the program management committee we also investigated the use of an empirical attenuation relationship that incorporates source specific directivity information (Somerville et al., 1997). For each of the methods we compared predicted values of PGA, PGV and Sa (0.3, 1.0 & 3.0 seconds) against the observations, with the exception of the empirical method because a PGV relationship is not yet available. Our basic method of ground motion simulation is one we developed in which fault slip is deterministically integrated using appropriate local Green's functions. We found that this deterministic approach performed reasonably well in the comparisons of PGV, however the Sa comparisons had mixed results. The PGA, PGV and Sa maps were all found to be successful in outlining the area of observed large ground motions, however there were varying degrees of misfit of the location of predicted and observed maximal values. The methods of Pitarka et al., (1999) and Zeng et al., (1994) improved the results somewhat but not to a degree that offsets their higher computational expense. The glowing success in this project involved the incorporation of the empirical attenuation relationship. PGA and Sa (0.3, 1.0 and 3.0 seconds) were well modeled using the approach of Somerville et al. (1997), which utilized the regionally derived finite source information as input. The empirical approach is also extremely fast and requires information available after the initial fault plane and rupture velocity inversion, which is also relatively fast. The best shakemaps for the two study events were obtained by taking the larger of the two values from the deterministic and the empirical maps. We call this map our 'conservative shakemap'. The empirical component of the conservative shakemap is found to explain the mean attenuation of the observed strong motions very well and the deterministic component provides a better estimate of the large near-fault ground motions.

Under task 3 we explored ways to improve the predicted strong motion parameters by applying site corrections to the synthetic ground motions. To facilitate this comparison we utilized the methodology implemented by Wald et al. (1999) for the southern California TriNet ShakeMap. In this case the site geology is classified as quaternary, tertiary and Mesozoic (QTM), and site corrections after Borcherdt (1994) are applied. We found that the QTM corrections improved the agreement with the observations but not enough to offset a systematic under prediction at LA basin sites. A second method used two 1D velocity models to characterize rock and soil sites. The application of site specific Green's functions provided a noticeable improvement in the predicted shakemap. However we note that stations located within the LA Basin remain under predicted. The results show that empirically derived site corrections applied to synthesized time histories is not enough to offset the effects due to large scale 3D structures such as the LA basin. It may be possible to determine site adjustments for specific 1D velocity models numerically using finite difference methods and appropriately calibrated 3D structure models to develop a table of 3D-to-1D site adjustments. This can presently be accomplished in southern California and the San Francisco bay area, however in large regions of central and northern California such a calibration would require a very considerable effort to compile and verify a suitable 3D structure model.

Through the course of this research we have developed a multi-staged algorithm to generate a shakemap. First, line source or course planar inversions are performed to determine the rupture velocity, causative fault plane and slip dimension of an earthquake. This information may then be used to generate a shakemap using a directivity sensitive attenuation relationship (e.g. Somerville et al. 1997). Site adjustments are applied to the empirical rock ground motions. This stage of processing may only consume 4 to 15 minutes of CPU time depending upon the level of approximation. Strong ground motion parameters that may be estimated at this stage include PGA and spectral acceleration at 0.3, 1.0 and 3.0 seconds period. It will be necessary to develop a directivity sensitive PGV attenuation relationship to provide a seamless methodology. If local strong motion data is available it may be integrated with the empirical values to develop a data/model shakemap. With relatively dense coverage the map would be data driven with model predictions contributing only in the regions where there are gaps in coverage. Following the determination of the causative fault plane and rupture velocity, processing may be continued to determine a higher resolution picture of the distribution of fault slip. This additional processing step consumes an additional 18 minutes for both of the earthquakes we studied. The higher resolution slip map is then used to simulate near-source synthetic time histories from which values of PGA, PGV and spectral acceleration may be measured. We then combine the larger of the simulated and the empirical ground motions to produce a 'conservative shakemap'. As in the first stage of processing available data may be integrated into the shakemap, where model predictions are used to interpolate only in areas where there are no observations. Using the attenuation relationship as an integral component of the methodology allows various levels of approximation such as the use of a strong motion centroid with point-source attenuation (e.g. Wald et al., 1999), source directivity specific empirical attenuation, and finally the source directivity specific 'conservative shakemap' developed in this study. A common multi-parametric attenuation relationship provides seamless transition from one level of approximation to another as more data and model information becomes available. We conclude this report with examples of the evolution of a shakemap for the Northridge and Landers earthquakes in very sparse network coverage as may be anticipated in large areas of California and the western United States.

Introduction

Earthquake information available soon after a damaging earthquake begins with estimates of the time of occurrence, the epicenter and hypocenter, an estimate of the magnitude, and fairly recently a seismic moment tensor solution providing a more robust estimate of earthquake size and the radiation pattern (e.g. Pasyanos et al. 1996). While such basic information is essential in the rapid characterization of the likely damage due to strong ground motions from the earthquake it is a rather limited characterization. Ideally city and state emergency response providers, public utilities and earthquake engineers would like to know where the strongest shaking occurred, which in a large extended earthquake is very likely not co-located with the epicenter.

In southern California this problem has been addressed with the development of the TriNet network of broadband and strong motion instruments that provide digital data in near real-time. The TriNet calls for the installation of 600 digitally recorded accelerometers to monitor strong ground motions throughout southern California, with the greatest density of coverage in the urban area. Figure 1 shows the locations of TriNet stations that are in the ground and compares the monitoring regions of both southern and northern California. These stations are currently being used to rapidly contour the regional extent of strong ground shaking (Wald et al., 1999). Parameters relevant to emergency response providers, utilities and engineers such as peak ground acceleration (PGA), peak ground velocity (PGV) and, spectral acceleration at periods of 0.3-1.0-3.0 s, and instrumental intensity are automatically determined and posted to the WWW. Additionally, seismological information such as first-motion focal mechanisms and seismic moment tensors are also provided. Figure 2 compares TriNet PGV shakemaps for the Northridge and Landers earthquakes. In the case of the Northridge earthquake (Figure 2b) the station coverage is quite good and there is considerable definition of the shakemap contours. The region of elevated PGV north of the epicenter is due to directivity focusing and the region northeast of the epicenter is due to both directivity and basin amplification. In contrast the station coverage for the 1992 Landers earthquake is sparse and the fortuitous location of the Lucerne Valley station is controlling the mapping of PGV near the fault.

In northern California there are plans to develop a TriNet like system, however because the monitoring area in northern California is considerably larger and a northern California TriNet is only in its conceptual phase, interim methods and methods suitable for sparse networks need to be developed. The distributed nature of at risk facilities is demonstrated by the locations of the dense urban areas of the San Francisco Bay and Sacramento, hydroelectric power generation facilities, rail transportation, state and national public highways, and the state aqueduct system. Thus a shakemap system for central and northern California needs to provide rapid estimates of strong shaking in the urban areas as

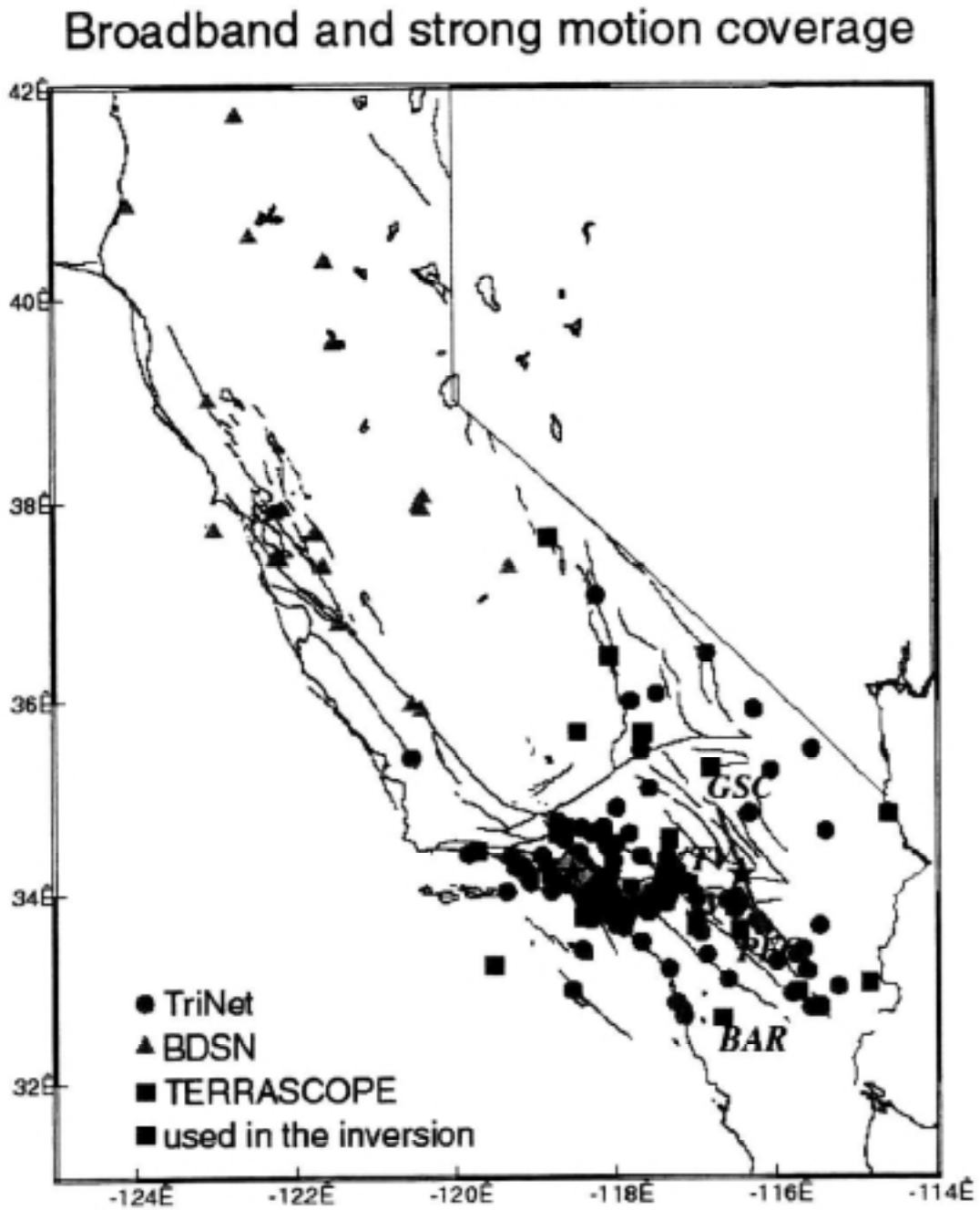

Figure 1. Map showing broadband and strong motion coverage in southern California. The red circles show strong motion stations of the TriNet, and the blue squares show broadband TERRAscope stations. The broadband Berkeley Digital Seismic Network (green triangles) compares the broadband coverage in central and northern California. Stations that were used in our analysis are identified by name.

well as the surrounding rural areas where most of the supporting infrastructure is located. The focus of this research project is to develop such as system that simulates near-source strong ground motions using event specific source information derived from the regional Berkeley Digital Seismic Network (BDSN, Figure 1). The BDSN is a continuously recording and digitally telemetered network with co-sited weak and strong motion sensors. The data latency of this system is minimal and data from this system is used to locate, estimate magnitude, and provide strong motion values for earthquakes in near-real-time (Gee et al., 1996). The data from this network is further used to determine the seismic moment tensor of M>3.5 earthquakes throughout central and northern California in near-real-time (Pasyanos et al., 1996). The software and methodology we have developed under this contract naturally builds on the automatic processing that has already been implemented. In this study we test the new methods using regional and broadband data sets collected for the June 28, 1992 Landers (M_W7.1) and the January 16, 1994 Northridge (M_W6.7) earthquakes.

Landers Trinet ShakeMap, PGV

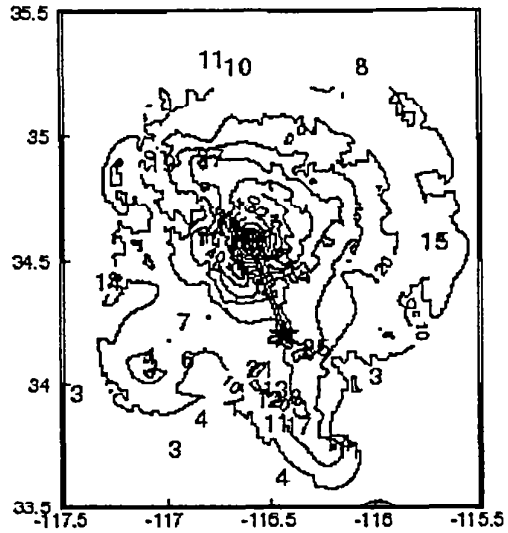

Northridge Trinet ShakeMap, PGV

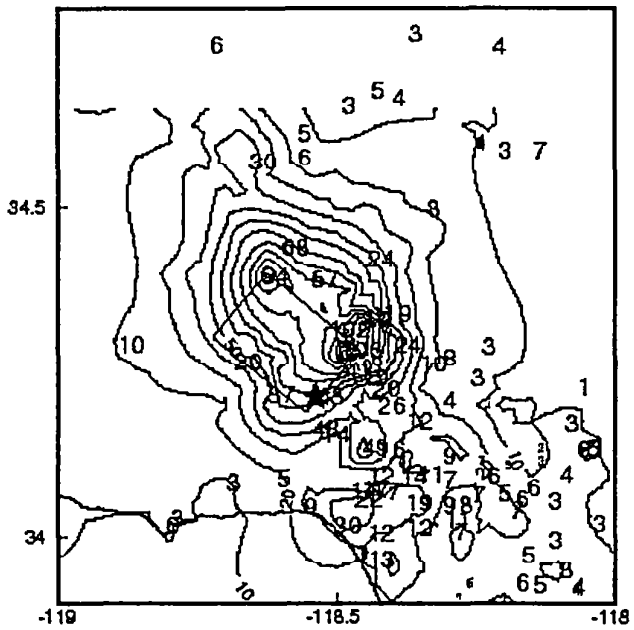

Figure 2. TriNet PGV shakemaps are compared for the 1992 Landers (a) and the 1994 Northridge (b) earthquakes. The contours show TriNet shakemap values and the red numbers show the observed PGV at individual recording stations. Both are in units of cm/s Note that only the stations shown were used in the determination of the shakemap contours, however an attenuation model scaled from the observed strong motion centroid was used to help interpolate the map were data does not exist (e.g. Wald et al., 1999). The stars identify the epicenters.

Section I: Regional Distance Finite Fault Determination

Following the occurrence of an earthquake in central and northern California there is a hierarchy of information that is determined by the UCB/USGS Joint Notification System. Earthquake locations are obtained within several minutes. Broadband waveform data recorded by the BDSN is used to estimate a local magnitude (M_L) and if the M_L is greater than 3.5 a seismic moment tensor is determined. Typically the seismic moment tensor is obtained within 6-9 minutes after the occurrence of an earthquake. The seismic moment tensor inversion provides estimates of the scalar seismic moment, a centroid depth and the orientations of two possible fault planes. The point-source representation used in the seismic moment tensor method results in a fault plane ambiguity. The ability to rapidly determine the causative fault plane is of value in itself to understand the possible extent of damage following an earthquake. We have modified a method to determine earthquake finite source parameters (fault slip, dislocation rise time and rupture velocity) to use regionally recorded broadband waveforms. In this method, given a hypocenter location and a source mechanism of an earthquake, we use a non-negative least squares solver to determine the distribution of fault slip from regionally recorded broadband data. This method is similar to those used to invert local strong motion data for earthquake source parameters (e.g. Cohee and Beroza, 1994; Wald and Heaton, 1994). In the source model, the rupture propagates with constant velocity over a grid of point sources each with constant dislocation rise time, and the Green's functions are shifted in time to account for relative hypocenter-subfault-station distances and the time for the passage of a circular rupture front. We use a precompiled catalog of Green's functions for point source responses. The Green's functions are computed using a frequency-wavenumber approach developed by Saikia (1994) and must be computed in advance since this preparatory step is very time consuming. The velocity model we use to estimate the source parameters is SoCal (Dreger and Helmberger, 1993), which has been found to be an appropriate representation of average crustal properties throughout southern California. The implementation of the procedures described in this report in central and northern California will require a different set of Green's functions. The central and northern California region may be approximated by both the SoCal and the GIL7 velocity models (Dreger and Romanowicz, 1994; Pasyanos et al., 1996). Because of the regional nature of the inverse problem we are solving we simplify the problem by considering only constant values of dislocation rise time and rupture velocity. In addition we assume that the rake angle of individual subfaults is constant and equal to average value obtained from automatic moment tensor analysis.

The code we have developed solves the following system of linear equations subject to non-negativity in slip, slip smoothing, fault edge damping.

$$\begin{bmatrix} A \\ \hline \frac{\lambda \cdot S}{E} \end{bmatrix} \bullet [U] = \begin{bmatrix} d \\ \hline 0 \\ \hline 0 \end{bmatrix}$$

A is a matrix of Green's functions, S is a smoothing matrix with relative weight, λ; E is a matrix defining the edges of the distributed fault plane. U is the slip that is solved for and d is the input broadband waveform data. The smoothing (S) and fault edge (E) parameters are included to damp the inversion minimizing slip roughness and edge slip, respectively.

The inverse procedure begins by testing the two possible fault planes determined from the seismic moment tensor analysis. In order to do this it is necessary to scale the inverse problem to the size appropriate for the reported scalar seismic moment. This is accomplished by using the empirical relationships of Wells and Coppersmith (1994) for fault dimension, doubling them to allow for bilateral rupture and increasing them by 20% to be safe. To determine the appropriate dislocation rise time to use we assume that the rupture velocity is 80% of the local shear wave velocity and that the total duration of the earthquake is equal to the fault dimension divided by the rupture velocity. The dislocation rise time is assumed to be 10% of the approximate total duration after Heaton (1990). For the Landers and Northridge earthquake values of 3.7s and 1.4s are obtained by this method and are found to be reasonable in view of reported values for these respective earthquakes. Given the overall dimension of the distributed fault and the assumed dislocation rise time the two possible fault planes are tested by performing separate inversions over a range of rupture velocity. To speed up this process and to minimize computer load the code has the option of using either a line source representation of the source or a planar fault with relatively large subfaults. The best solution is the one that maximizes the variance reduction,

$$VR = \left(1.0 - \frac{\Sigma (d_i - s_i)^2}{\Sigma d_i^2} \right) \bullet 100,$$

where d and s are the observed and synthetic waveform, respectively, and i is a time index. Once the causal fault plane and rupture velocity are found the inversion is performed once more with a higher resolution to better characterize the fault slip.

We have found that it is possible to determine finite source parameters that compare quite well with those obtained using local strong motion records. Figure 3 compares slip maps for the January 16, 1994 Northridge earthquake obtained using strong motion records (Wald et al., 1996 and Zeng and Anderson, 1996) with those obtained at regional distances using an empirical Green's function method (Dreger, 1994, 1996) and using theoretical Green's functions (this study). It is clear that the slip maps are very similar suggesting that the regionally derived maps may be used to estimate the level of shaking in the near-source region. We obtain an equally impressive comparison for the Landers earthquake.

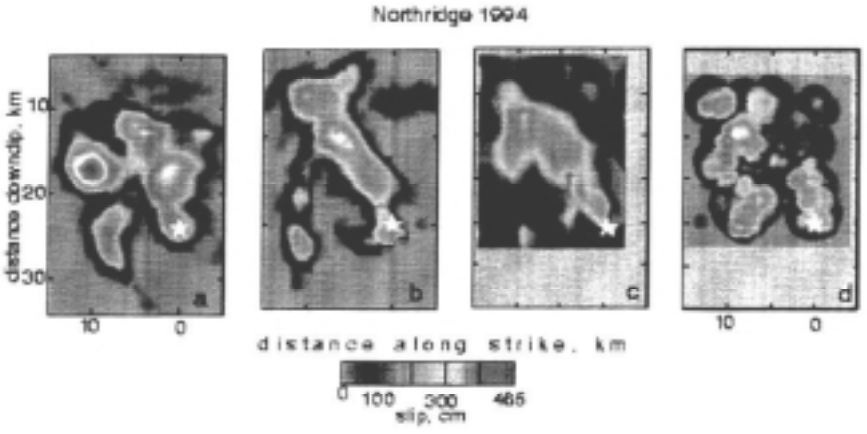

Figure 3. Fault slip maps for the 1994 Northridge earthquake are compared. (a) The slip map obtained in this study by inverting regional distance broadband data. (b) The slip map obtained by inverting seismic moment rate functions derived from empirical Green's function deconvolution (Dreger, 1994; Dreger, 1997). These maps compare well with those obtained by inverting local strong ground motions. (c) compares the map of Wald et al. (1996) obtained from local strong motion, teleseismic waveform data, and geodetic and leveling data. (d) Zeng and Anderson (1996) inverted only strong motion data using a different methodology. Each map has the same scaling and the white star identifies the hypocenter.

Landers Earthquake Application

Four TERRAscope stations, GSC, PAS, PFO and SVD (Figure 1) were used to determine the slip for the Landers earthquake. Figure 4a shows the best line source inversion results and the variance reduction plotted as a function of rupture velocity. In this case the northwest striking nodal plane is found to fit the data much better than the east west striking nodal plane that results in a flat variance reduction curve. The line source results show that slip is unilateral to the north-northwest. The total calculation time for all 18 rupture velocities tested was 3.5 minutes. This line source run is quite rapid and derives the necessary information for the implementation of a shakemap based on directivity sensitive empirical attenuation relationships (e.g. Somerville et al., 1997). Such an implementation will be discussed in a later section of the report. Figure 4b shows the high-resolution inversion results. In this case the model is found to be unilateral with the bulk of slip being located approximately 50-km north-northwest of the hypocenter. Furthermore, the slip is found to be relatively shallow, although the inversion was allowed to place slip as deep as 25 km if required by the data. The total processing time for the high resolution run was 18.5 minutes.

The source models shown in Figure 4 do not include a 2.5 s delay in the start of significant rupture reported by several researchers (Abercrombie, 1994; Cohee and Beroza, 1994; Dreger, 1994b; Wald et al., 1994). Furthermore the Landers earthquake also involved rupture of multiple segments with a 35-degree variation in fault strike (Wald et al., 1994). With automatic processing it will not be possible to take this level of complexity into account. Nevertheless the slip distribution we obtain with a single fault plane compares well with the multi-planar results of Wald et al. (1994) when their slip is projected onto our fault plane, and

we consider the 2.5s delay in our inversion for fault slip. In a later section of the report we demonstrate that although we have significantly simplified the source model of Landers it is still possible to obtain a shakemap with good agreement to the data, and excellent results when both data and model predictions are combined.

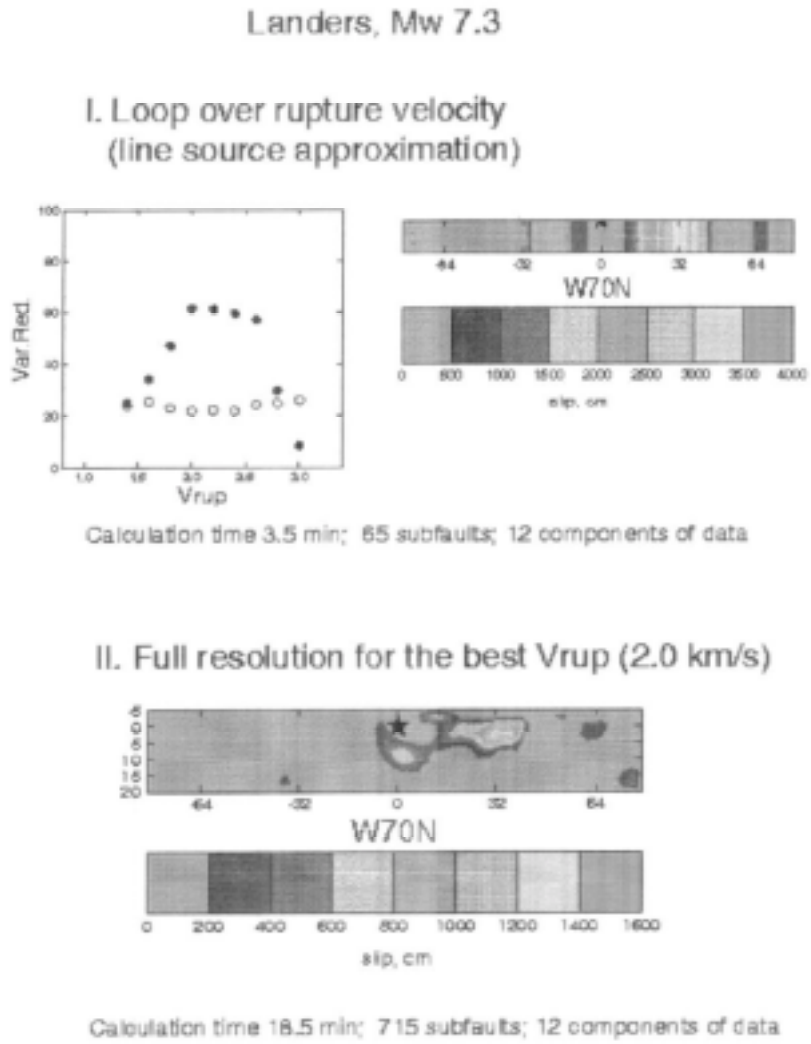

Figure 4. (I) The variance reduction verses rupture velocity is plotted for both possible nodal planes for the Landers earthquake using a line source model parameterization. The solid circles show variance reduction values for the north-northwest striking plane and the open circles show values for the conjugate east-west striking plane. This example clearly shows that the north-northwest plane provides a superior fit to the data. The best line source slip distribution is shown to the right and results in unilateral rupture to the north-northwest. (II) The full resolution inversion results are compared to the line source result.

Northridge Earthquake Application

Five TERRAscope stations, BAR, GSC, PFO, SVD, and VTV (Figure 1) were used to determine the slip for the Northridge earthquake. Figure 5 compares a low-resolution planar fault inversion with a high-resolution inversion for the Northridge earthquake. As the variance reduction vs. rupture velocity plot shows there is not as much separation between the two possible fault planes as was found for Landers. This is function of the relative size and the type of earthquake. The Landers earthquake being larger and strike-slip produces a stronger horizontal directivity function than the smaller reverse-slip Northridge earthquake. Nevertheless, as the variance reduction plot shows the south dipping fault plane is correctly identified for Northridge. The total calculation time for the 18 rupture velocities tested was 15 minutes. The high-resolution run produces additional complexity in the slip distribution. The total processing time for the high resolution run was 17 minutes. Figure 3 shows that the results are very similar to those obtained using local strong motions.

Section I: Conclusions and Recommendations

Our application of a regional distance finite fault inverse methodology to TERRAscope broadband data for the Landers and Northridge earthquakes reveals that the obtained slip models compare well with those obtained by inversion of local strong motion waveforms. The comparisons indicate that the regional estimates of fault dimension, gross slip distribution and directivity are reasonably well determined for these earthquakes. In the next section we demonstrate that near-source strong shaking determined from these slip maps models the observed strong shaking fairly well.

The calculations we have performed under this contract were carried out on a SUN Enterprise server with 400MHz CPUs. These systems are relatively standard and faster workstations are now becoming available indicating that the process times of the various steps that we have outlined are likely to be significantly reduced in the future.

At the time of the Landers earthquake six TERRAscope stations were available. The four that we used are located in vaults on relatively competent material. The ISA station was not used because of non-standard orientation of the horizontal components. The SBC station was not used because the path from Landers to San Barbara crosses significant basin structures and the 1D models that we employ are not adequate to explain the complex seismograms (Dreger and Helmberger, 1991). It is noted however that for the Northridge earthquake a number of the stations that we use do traverse the Los Angeles basin and the 1D structure appears to perform well. The implementation of this stage of processing will certainly require the careful calibration and verification that the 1D-velocity models employed are reasonable estimates of average path structure, and some regional stations with substantial site effects should be removed from processing to minimize possible bias due to unmodeled Earth structure.

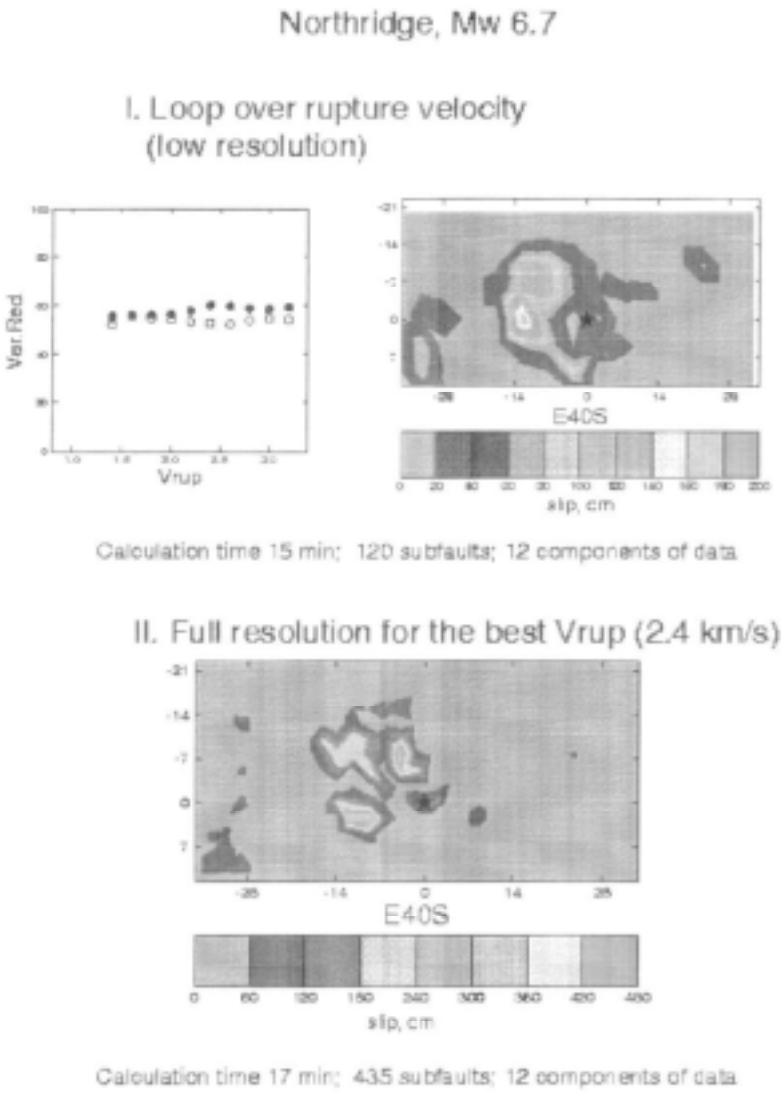

Figure 5. (I) The variance reduction verses rupture velocity is plotted for both possible nodal planes for the Northridge earthquake using a low resolution planar model. The solid circles show variance reduction values for the best fitting south dipping plane and the open circles show values for the conjugate north-dipping plane. The best low-resolution plane slip distribution is shown to the right, and shows northward updip directivity. (II) The full resolution inversion results are compared to the low-resolution result.

Section II. Near-Source Shakemap Simulation

Given a representation of the earthquake specific slip distribution it becomes possible to integrate the slip both spatially and temporally for stations located above the source to generate a suite of near-source time histories from which to determine strong motion parameters such as PGA, PGV and spectral acceleration. We keep the parameterization in the forward problem simple by assuming that the rupture velocity and the dislocation rise time are

constant throughout the rupture. The rupture velocity obtained from the source inversion is used and the dislocation rise time is determined from the derived slip, rupture velocity and the observations of Heaton (1990). The values of dislocation rise time used in this step are 2.4s and 0.9s for the Landers and Northridge earthquakes, respectively. These values are consistent with those previously reported for these earthquakes. In the following we compare our predicted PGV and spectral acceleration maps with observations from both the Landers and Northridge earthquakes. Our predicted shakemaps utilize site specific Green's functions calculated from two velocity models, one for hard rock and the other for soft rock. These velocity models are shown in Table 1 and were used by Wald et al. (1996) to invert for Northridge fault slip. In a later section we illustrate the benefit of using the two 1D models to account for site variability.

Table 1a: Hard Rock Velocity Model

V_P (km/s)	V_S (km/s)	Density (g/cm^3)	Depth (km)
1.9	1.0	2.1	0.0
4.0	2.0	2.4	0.5
5.5	3.2	2.7	1.5
6.3	3.6	2.8	4.0
6.8	3.9	2.9	27.0
7.8	4.5	3.3	40.0

Table 1b: Soil Velocity Model

V_P (km/s)	V_S (km/s)	Density (g/cm^3)	Depth (km)
0.8	0.3	1.7	0.0
1.2	0.5	1.8	0.1
1.9	1.0	2.1	0.3
4.0	2.0	2.4	0.5
5.5	3.2	2.7	1.5
6.3	3.6	2.8	4.0
6.8	3.9	2.9	27.0
7.8	4.5	3.3	40.0

Deterministic Peak Ground Velocity (PGV) Maps

Predicted and observed PGV for the Landers earthquake are compared in Figure 6. The predicted values were computed with site specific Green's functions in the 0.1 to 1.0 Hz pass band. In Figure 6a contouring was done for predicted values at the same locations as the observations, and the shape of the contours is an artifact of the station geometry. This PGV map compares well with the one obtained by the TriNet ShakeMap system (Figure 2a). Figure 6b compares the contours for a dense grid of stations, and shows an elongate region of high PGV close to the fault as would be expected for an extended fault rupture such as Landers. The site specific calculation shows our best results for Landers and it is evident that we are over predicting the PGV at the Lucerne station (LUC) by a factor of two. In contrast the hard rock prediction (Figure 6b) is much better at LUC. Other stations relatively close to the fault are well modeled however. There could be a number of factors such as inappropriate site

classification, problems with the Green's functions, and most likely the artificial closeness of the fault that could be causing the over prediction at LUC. The fault from our single plane model passes within 0.3 km of LUC while the closest mapped trace is approximately 3 km away. In fact a calculation that takes the curvature of the Landers fault into account results in much better estimates at LUC. Unfortunately this level of complexity can not be done automatically. Figure 6c shows the comparison of PGV as a function of distance. The predicted values span the range observed in the data and describe the attenuation of PGV with distance quite well. The cluster of large amplitude observations at a distance of approximately 150-km is from stations located in the Los Angeles basin.

Predicted and observed PGV for the Northridge earthquake are compared in Figure 7. The predicted values were computed with site specific Green's functions in the 0.1 to 1.0 Hz pass band. The observed PGV were computed by integrating the accelerograms and band pass filtering the derived velocity seismograms in the 0.1 to 1.0 Hz pass band, and picking the maximum value. The PGV map (Figure 7a) is successful in the characterization of the region that experienced the largest ground motions (PGV>10 cm/s). The map further shows that elevated PGV are predicted north of the epicenter due to updip rupture directivity, which is consistent with observation. Both over and under prediction is observed in the forward directivity region, and these discrepancies are likely to be due to a combination of the simplified source model obtained from regional distance data, site variability in observed PGV, and the use of simplified 1D velocity models. Figure 7b shows that the predicted values describe the attenuation very well, however there is a systematic under prediction of PGV at sites located in the Los Angeles basin (distance range of 30 to 150 km in Figure 7b).

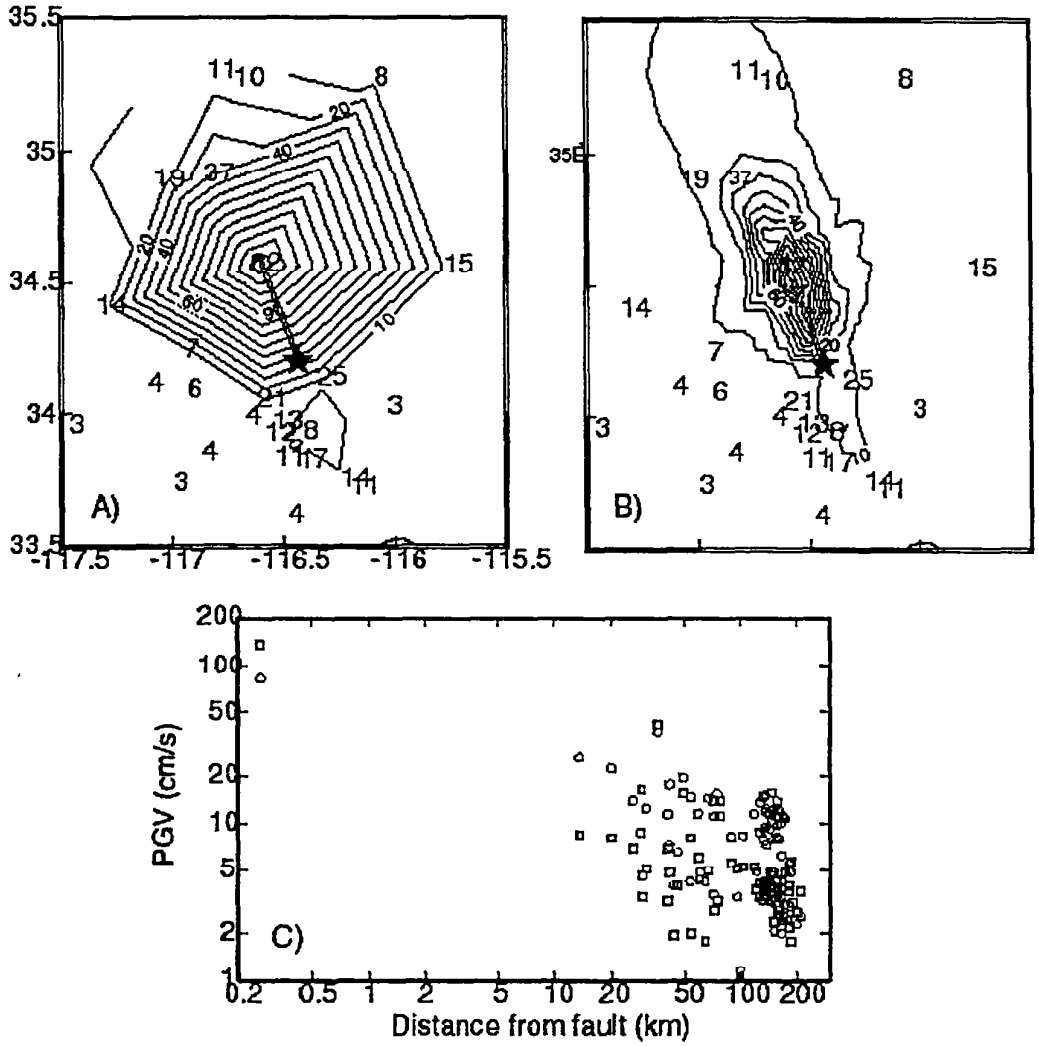

Figure 6. (a) Comparison of predicted (contours) and observed (red numbers in cm/s) PGV for the Landers earthquake. Both the predicted and observed PGV were determined from the 0.1 to 1.0 Hz pass band. The predicted PGV were measured from synthetic time histories generated using site specific Green's functions (see Table 1). (b) PGV contoured from a dense distribution of stations using hard rock Green's functions. (c) Log-log plot comparing observed PGV (red circles) and predicted values (black squares). The predicted values are for the site specific calculation shown in (a). The cluster of elevated observed ground motions at a distance of 150 km are from sites located in the Los Angeles basin southwest of the area shown in (a).

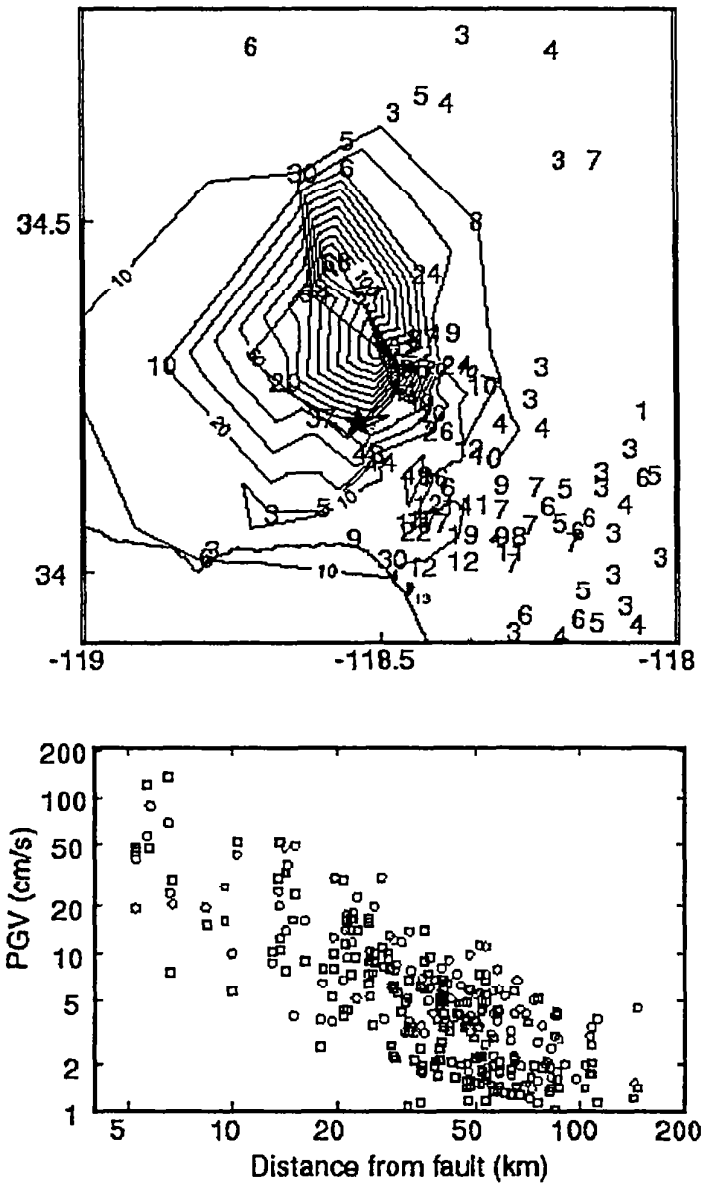

Figure 7 (a) Comparison of predicted (contours) and observed (red numbers in cm/s) PGV for the Northridge earthquake. Both the predicted and observed PGV were determined from the 0.1 to 1.0 Hz pass band. The predicted PGV were measured from synthetic time histories generated using site specific Green's functions (see Table 1). (b) Log-log plot comparing observed PGV (red circles) and predicted values (black squares). The predicted values are for the site specific calculation shown in (a). PGV is under predicted at LA Basin sites in the 30 to 150 km distance range.

Deterministic Spectral Acceleration Maps

Spectral acceleration (Sa) at 0.3, 1.0 and 3.0 seconds period was determined from the simulated time histories for both earthquakes. Figure 8 compares the predicted and observed Sa for the Northridge earthquake for the three specific periods. In this comparison the site specific Green's functions were used. The map view comparison is fairly good in that elevated regions of Sa are distinguished from areas with low relative Sa. For example in the 0.3 second plot the maximum observed Sa of 2.1 g correlates well with the predicted maximum although the predicted value of 2.8g is too large. In contrast stations to the southeast in the LA basin have relatively lower Sa. In the 1.0 second Sa plot the 0.1g contour separates the regions of higher and lower observations. The best agreement is for the 3.0 second Sa map. Figure 8b compares observed and predicted Sa as a function of distance, where the scatter in the data and the attenuation of Sa are well modeled. The 1.0 and 0.3 second distance plots (Figure 8b) tend to show that the model under predicts Sa in the 30-150 km distance range primarily for LA basin sites.

As was the case for Northridge the predicted Sa for Landers defines the region of strongest shaking, however there is a general under prediction. 3.0 second period Sa at LUC is significantly over predicted while the 1.0 second and 0.3 second period Sa are significantly under predicted. Part of the misfit is likely to be due to the artificial closeness of LUC to the model fault. The fact that some periods are over predicted and others under predicted and the general under prediction of Sa for all distances suggests that there is a problem in the spectral content of the simulated time histories. It is curious however that the PGA and PGV maps for Landers compare with the observations fairly well. Further study is needed to explore the sensitivity of the simulated time histories and estimated PGA, PGV and Sa to slip model, Green's function, site response, and rupture velocity and dislocation rise time uncertainty as well as simulation methodology. We tested the methods of Pitarka et al. (1999) and Zeng et al. (1994) and found minimal improvement for Northridge. It may be worthwhile to test their methods in simulating Sa for Landers. It is noted however that the empirical attenuation relationship described in the next section significantly improves the predicted Sa at all three periods.

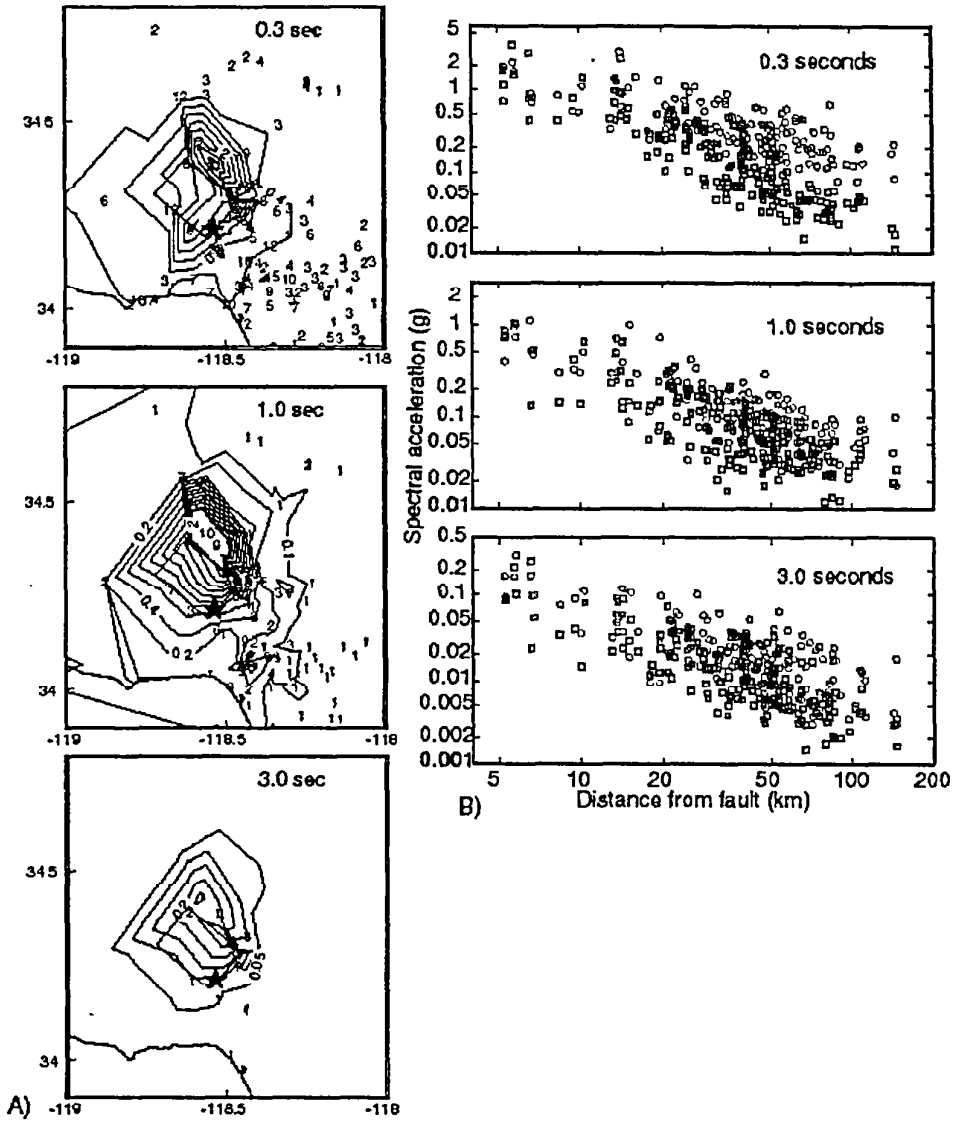

Figure 8. (a) Spectral acceleration at 0.3, 1.0 and 3.0 seconds period is compared for the Northridge earthquake. Contoured values were obtained by simulation using the Northridge slip model (Figure 3a) and site-specific Green's functions (Table 1). Contours are in 0.4, 0.2 and 0.05g intervals for the respective periods, and were constructed from predicted values only at the locations of the recording stations that are shown. The observed values (red numbers) are given in tenths of a g. Only observed values above 0.1g are plotted. (b) The predicted (black squares) and observed (red circles) spectral acceleration is compared as a function of distance for the three periods.

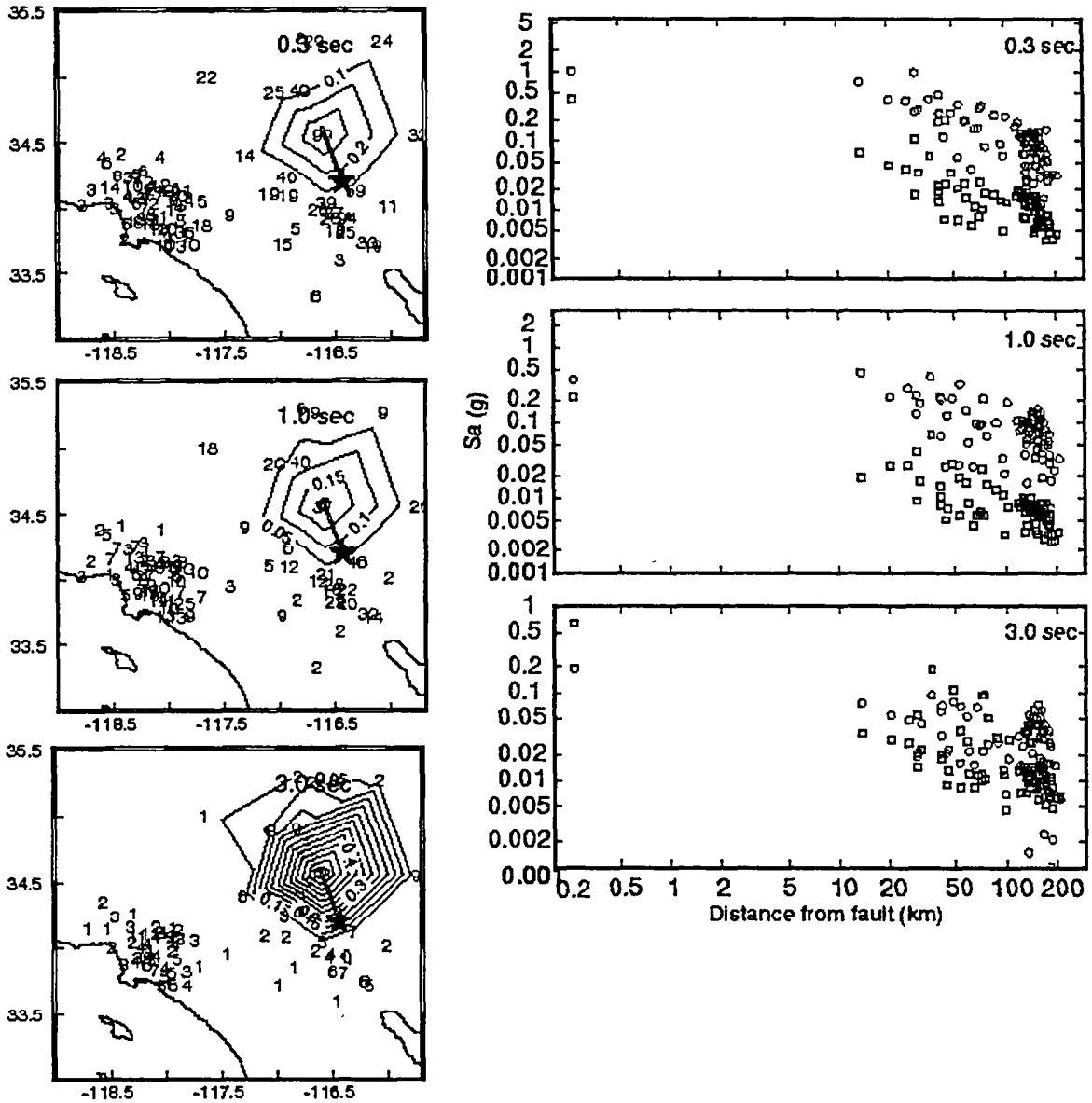

Figure 9. (a) Spectral acceleration at 0.3, 1.0 and 3.0 seconds period is compared for the Landers earthquake. Contoured values were obtained by simulation using the Landers slip model (Figure 4II) and site specific Green's functions. Contours are in 0.4, 0.2 and 0.05g intervals for the respective periods. The observed values (red numbers) are given in hundredths of a g. Only observed values above 0.01g are plotted. (b) The predicted (black squares) and observed (red circles) spectral acceleration is compared as a function of distance for the three periods.

Empirical Spectral Acceleration Maps

A recently developed directivity sensitive attenuation model (Somerville et al., 1997) was used to simulate PGA and Sa at 0.3, 1.0 and 3.0 seconds period. This model takes the scalar

seismic moment, fault orientation, and slip distribution that we obtain by our source inversion as input. The empirical model describes the mean attenuation observed for the Landers earthquake (compare figures 10a to 9b), and is a significant improvement over the deterministic Sa shown in Figure 9. For the Northridge earthquake the empirical relationship also describes the observed mean attenuation, although at near-distances it under predicts the Sa.

If one integrates the maximum predicted values from the deterministic and empirical models a conservative map is obtained (Figure 11). This map is found to provide the best agreement to the data. The empirical model provides a mean value estimate for stations at all distance ranges and the deterministic calculation contributes mostly in the very near source distance range where source specific information is important.

In the case of Landers the conservative 0.3 and 1.0 second Sa shakemaps are a big improvement and stations close to the fault have values close to those indicated by the contours. LUC is now slightly over predicted which is likely to be due to the artificial closeness of the station to the model fault. The 3.0 second map is not changed very much. For Northridge there is some improvement particularly in the 0.4, 0.1 and 0.05g contours for the 0.3, 1.0 and 3.0 second Sa maps, respectively.

Section II: Conclusions & Recommendations

In this section we have demonstrated that a conservative shakemap that takes the larger of two values, one calculated by deterministic integration of fault slip, and the other by a directivity sensitive attenuation relationship provides reasonable agreement with observed PGA and Sa. The attenuation model we used (Somerville et al., 1997) does not presently have regression formulas for PGV. It is recommended that a PGV relationship be constructed from the same data set used for the PGA and Sa relationships to provide a seamless 'conservative shakemap' for all of the strong motion parameters of interest.

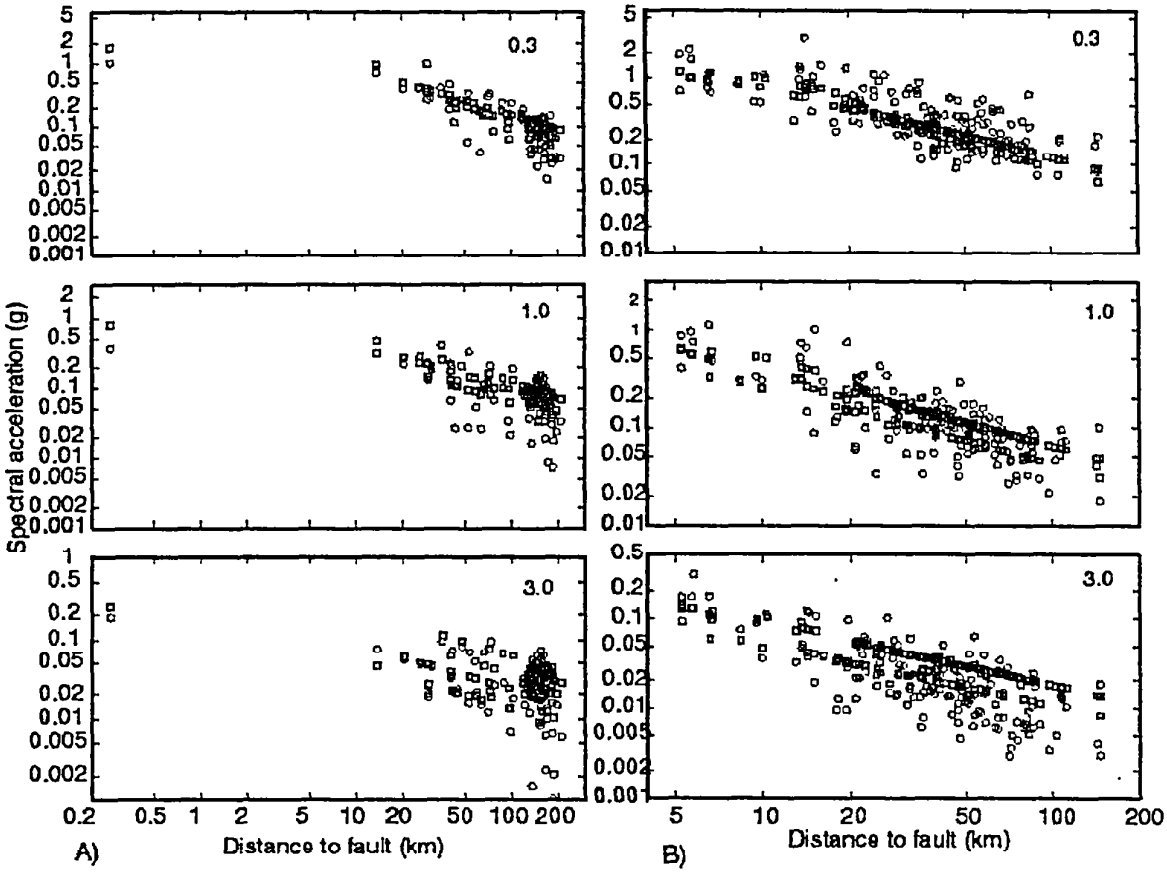

Figure 10. (a) Predicted (black squares) and observed (red circles) Sa at periods of 0.3, 1.0 and 3.0 seconds are compared for the Landers earthquake. The predicted values were obtained using the relationships of Somerville et al., (1997) and the fault orientation, scalar seismic moment and slip dimension determined in our finite source inversion. (b) Same as (a) for the Northridge earthquake.

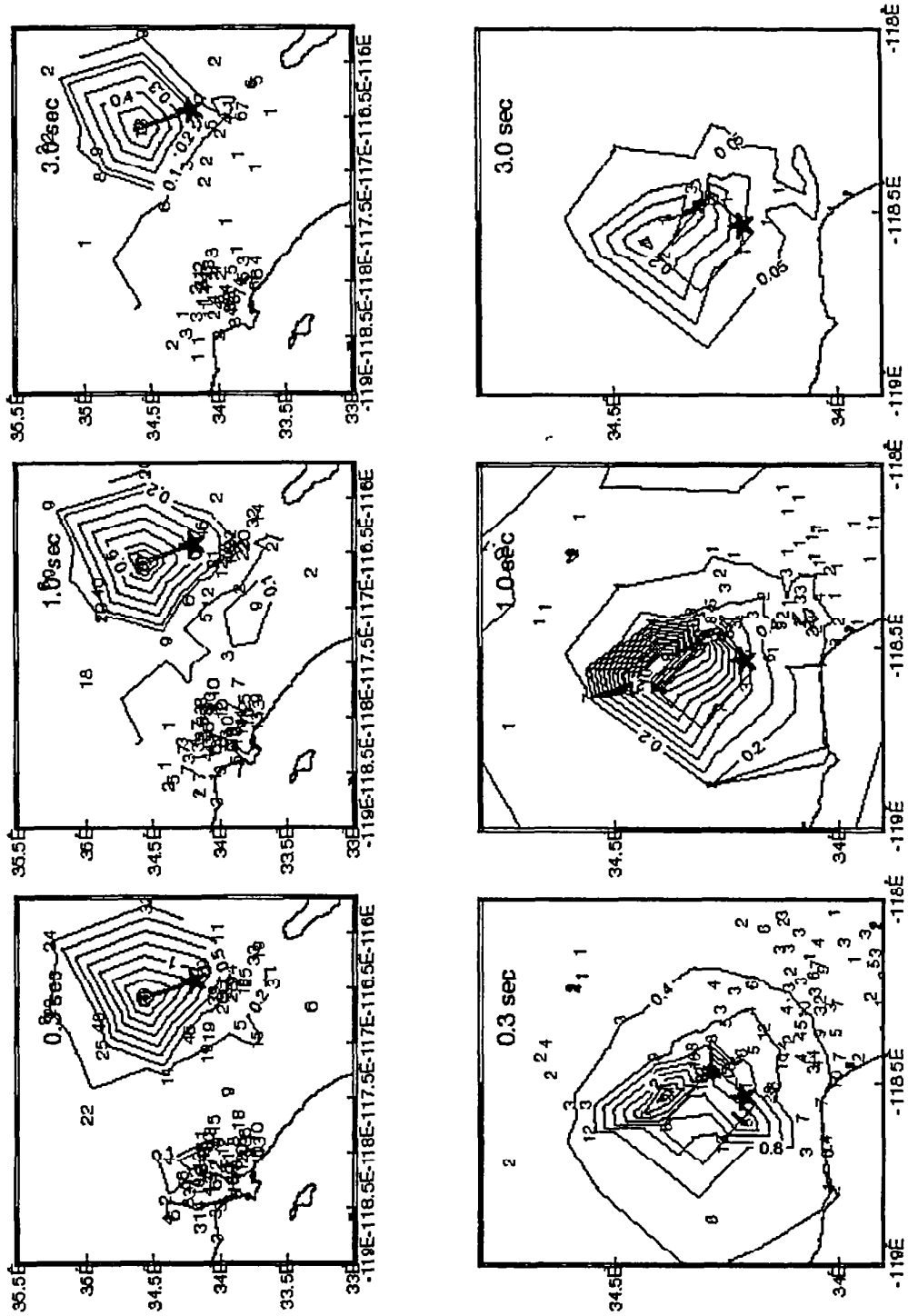

Figure 11. (a) Conservative Sa shakemaps (contours in units of g) are compared to observations (red numbers in hundredths of a g) for the Landers earthquake. Contour intervals are 0.2, 0.1 and 0.1 g for periods of 0.3, 1.0 and 3.0 seconds, respectively. (b) Conservative Sa shakemaps (contours in units of

g) are compared to observations (red numbers in tenths of a g) for the Northridge earthquake. Contour intervals are 0.4, 0.2 and 0.05 g for periods of 0.3, 1.0 and 3.0 seconds, respectively.

Section III. Site Response Effects in Simulated Shakemaps

In this section we demonstrate the effectiveness of two different approaches of correcting for site variability. One approach involves using site classification and empirically derived adjustment factors. In this comparison we use the regional quaternary/tertiary/Mesozoic (QTM) classification developed by Park and Elrick (1998) for southern California and used in the TriNet ShakeMap (Wald et al., 1999). A regional map of QTM is used to determine site type and frequency dependent site corrections derived from Borchardt (1994) are applied to the simulated time histories. The other method involves the use of different velocity structures to develop Green's functions for varied site type. This method performed better and was used in our deterministic shakemaps presented in section II.

It is important to note that in the TriNet application the site corrections are applied to an empirically derived hard rock attenuation relationship (Joyner and Boore, 1981) and therefore the mapping from the mean hardrock response to site specific response is straightforward. The application of QTM corrections to our hard rock synthetics improves the predictions but not as much as desired.

Figure 12a illustrates the misfit between our predicted hard rock PGV and observations for the Northridge earthquake in map view. Circles show soil sites and squares show rock sites. Open circles and squares indicate that the model under predicts the observations and the filled symbols indicate the model over predicts the observations. Near the source, the predicted values are relatively good however at distance from the source we find that generally the ground motions are under predicted by as much as a factor of three at some stations. Both soil and rock sites are under predicted although the greatest misfit is for LA basin stations. Figure 12b compares the predicted-to-observed PGV ratios for the case in which the hard rock PGV were adjusted using published QTM corrections (Table 2). There is marked improvement at a number of soil sites classified mostly as quaternary or tertiary. However as the symbols in Figure 12b show the amount of under prediction remains rather high. Figure 13a compares the $\log_{10}$ of the predicted-to-observed ratio for QTM corrected PGV. The bins show a tendency toward negative values. The red bars in Figure 13 indicate that most of the under prediction is for sites located within the LA basin. The mean $\log_{10}$ value for LA basin sites is –0.48. Quaternary sites outside the LA basin have a mean value of –0.22, and tertiary and Mesozoic sites have mean values of –0.10 and –0.14 respectively. While there is substantial improvement by applying the QTM corrections to our simulated PGV there remains a systematic under prediction in the LA basin and relatively large uncertainty. It is very important to note however that this comparison does not distinguish between the relative amplitude of the PGV. It is observed that the overall misfit in the San Fernando and Northridge region, that experienced the largest ground motions, is relatively small.

Figure 12c compares the predicted-to-observed PGV ratios for the site specific Green's function simulation. This simulation is found to be significantly better than both the raw hard

rock and the QTM corrected hard rock simulations. Figure 13b compares the site specific PGV $\log_{10}$ ratios binned according to Geomatrix site classification. This figure shows that LA basin sites remain under predicted however the distribution is skewed toward values closer to 0.0. The Geomatrix soil classifications B, C and D for sites located outside the LA basin have $\log_{10}$ values of –0.02, -0.12 and –0.02, respectively, indicating the predictions agree well with the observations. It is curious that rock sites around the fringes of the LA basin are significantly under predicted. This may be due to improper site classification or possibly regional amplification due to the LA basin 3D structure (e.g. Olsen et al., 1995). It may be necessary to numerically develop a suite of synthetic 1D-to-3D site corrections for large-scale structures such as the LA basin.

Table 2: QTM Site Corrections

Site Type (V_S, m/s)*	Corrections for Specified Input PGA			
	< 15%g	15-25%g	25-35%g	>35%g
Mesozoic (589 m/s)				
0.1-0.5 sec. period	1.0	1.0	1.0	1.0
0.5-2.0 sec. period	1.0	1.0	1.0	1.0
Tertiary (406 m/s)				
0.1-0.5 sec. period	1.14	1.10	1.04	0.98
0.5-2.0 sec. period	1.27	1.25	1.22	1.18
Quaternary (333 m/s)				
0.1-0.5 sec. period	1.22	1.15	1.06	0.97
0.5-2.0 sec. period	1.45	1.41	1.35	1.29

* This is a simplified table for average 30m depth site velocities by type. In the map of Park and Elrick (1998) surface velocity is mapped for the southern California region and it is possible to use more specific site velocity either know or inferred to produce period specific amplitude corrections following Borcherdt (1994).

Section III Conclusions

It is clear from the preceding comparisons that applying site specific corrections derived empirically improve results but not to the degree hoped, nor to a degree better than what is achieved when we use two 1D velocity models to represent rock and non-rock sites. There is a systematic bias toward under prediction of PGV, particularly at LA basin sites. Even rock sites along the fringes of LA basin are under predicted. This suggests that at these sites the rock velocity model (Table 1) used to compute the Green's functions is not appropriate and that 3D basin effects may be important. In fact, the work of Olsen et al. (1995) shows substantial amplification effects due to the LA basin in their finite difference simulations. Stidham et al. (1999) in their study of three dimensional wave propagation in the San Francisco bay area discovered basin amplification of as much as 3-4 over reference 1D ground motions within the tertiary basins, and more importantly that the basin amplification effects can extend beyond the boundaries of the mapped basins. Because we are using synthetic seismograms in our deterministic shakemaps it seems reasonable that we need to apply correction factors that are relative to the specific 1D model used. This can be accomplished by simulating ground motions using finite difference methods for a reference 1D velocity model and best estimate 3D structure in the Los Angeles and SF Bay Area

regions. A regional table of 1D-to-3D site corrections may be developed by considering an ensemble average of calculations for sources distributed around the region.

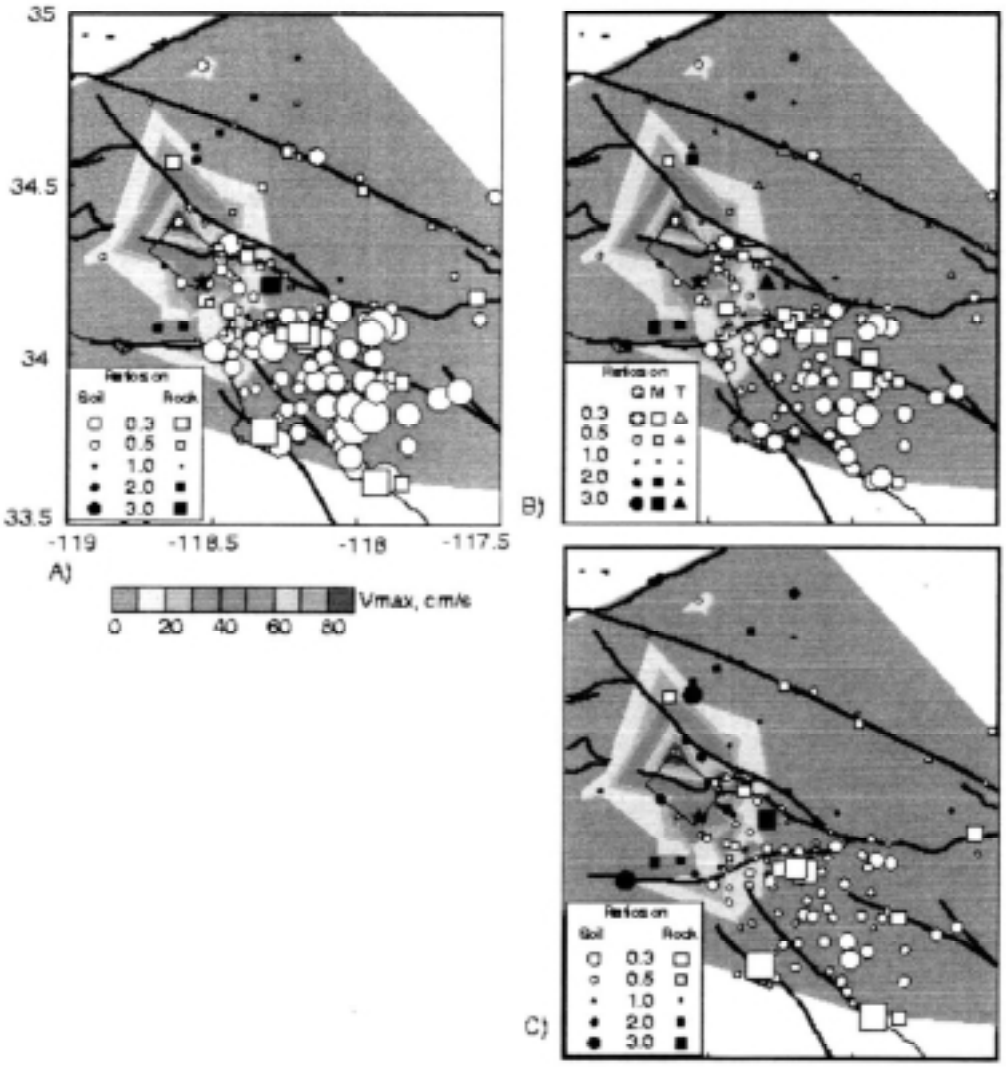

Figure 12. Predicted to observed PGV amplitude ratios for soil sites (circles) and rock sites (squares) are plotted in map view. (a) The predicted PGV were computed using the hard rock model (Table 1) and the Northridge slip (Figure 3a). (b) The predicted PGV were computed with the hard rock model (Table 1) with applied QTM corrections (Table 2). Quaternary, tertiary and Mesozoic sites are indicated by circles, squares and triangles, respectively. (c) The predicted site specific PGV were computed using both the hard rock and soil models (Table 1) and the Northridge slip (Figure 3a). In each example the size of the symbol is proportional to the predicted-to-observed ratio, and open symbols indicate under prediction and filled symbols indicate over prediction

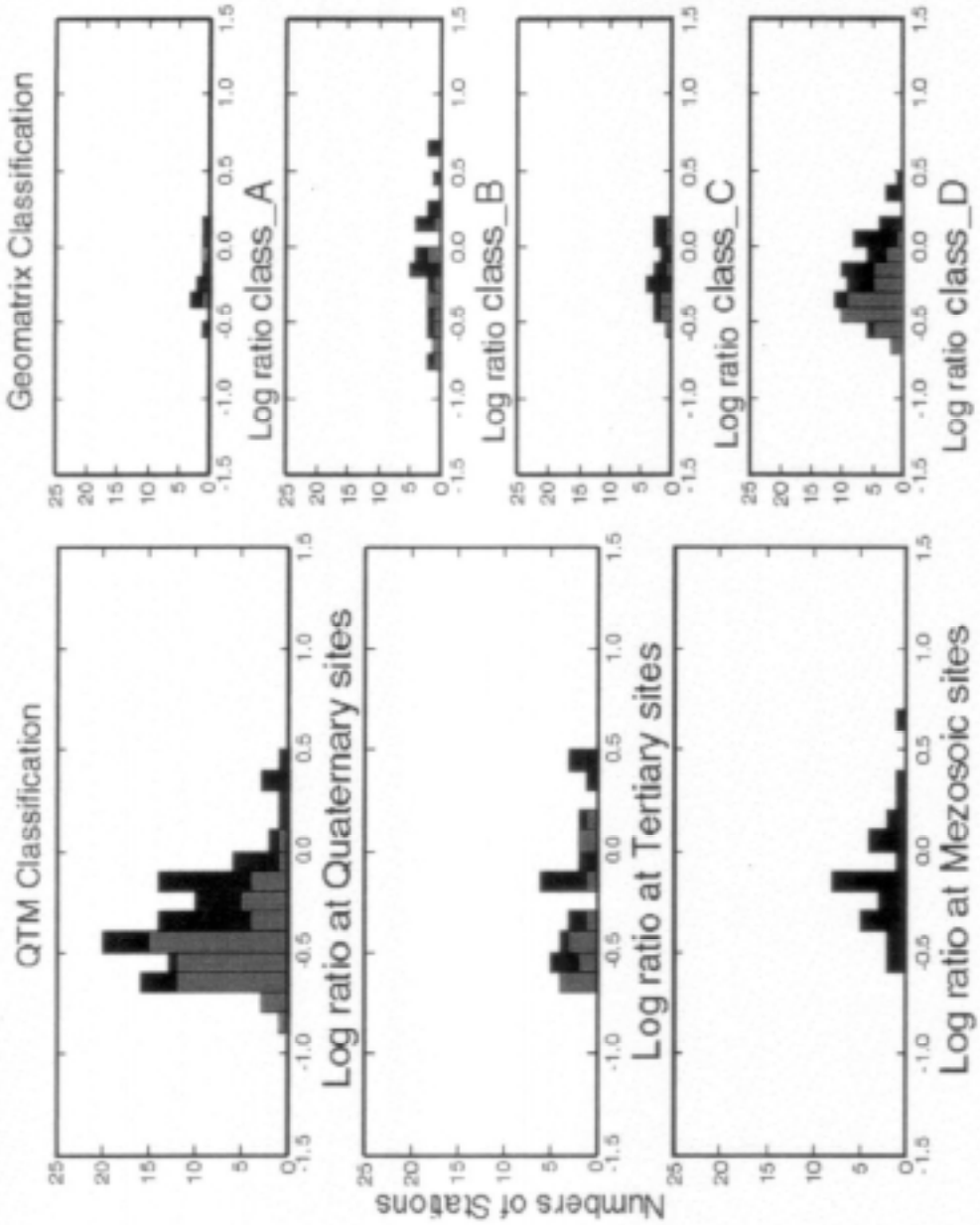

Figure 13. The $\log_{10}$ of the predicted-to-observed PGV amplitude ratio for Northridge is compared for the case where hard rock synthetic PGV have QTM corrections (Table 2) applied (a), and the site specific PGV classified according to the Geomatrix scheme. The black bars show all stations and the red bars show stations located in the Los Angeles basin. A value of 0.0 indicates a predicted-to-observed ratio of 1.

Section IV: Application of Data/Model Shakemaps

This report is concluded by demonstrating how our 'conservative shakemap' may be integrated with actual observations to produce a data/model shakemap. At the outset of this study we have been concerned with developing methodology that will perform in very sparse station coverage situations. Sparse coverage is a function of population density and there are vast areas of California with relatively sparse coverage. Recent earthquakes in southern Oregon (1993 Klamath Falls M6) and near Lake Tahoe (1994 Double Springs Flat M6) are cases in which the closest strong motion stations were located 60-80 km away. Figure 14 compares data only PGA shakemaps obtained by direct contouring of observations for the Northridge earthquake. Figure 14a shows the shakemap obtained by using only the 13 TriNet stations located in the region. This figure identifies the region of strong shaking by the 0.4g contour and compares well with the results obtained for PGV with many more stations (Figure 2b). In Figure 14b we consider a case in which strong motion station spacing is approximately 30 km with one station located in the forward directivity region. This map is successful in identifying the region of strongest shaking but the 0.4g contour is not closed. If the forward directivity station is removed it is not possible to obtain a useable PGA shakemap by contouring only data. Determination of a strong motion centroid and application of point-source attenuation models to interpolate the map improves a sparse station shakemap (e.g. Wald et al., 1999). In very sparse coverage it may be difficult to obtain a strong motion centroid that correlates with where the strongest shaking occurred.

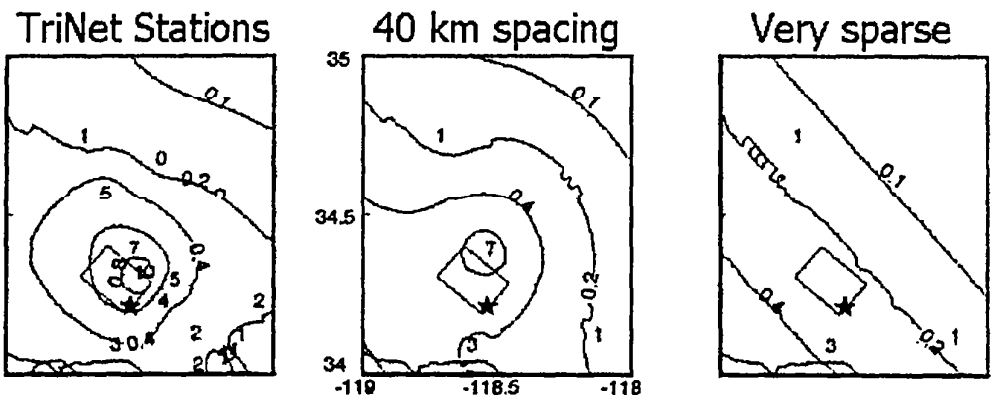

Figure 14. PGA shakemaps obtained by contouring only data values for the Northridge earthquake are compared for cases with (a) 13 nearby TriNet stations, (b) 30 km station spacing with one station located in the forward directivity region, and (c) 30 km station spacing as might be anticipated in sparsely instrumented regions or regions with few digitally telemetered strong motion stations. The contours show PGA in g and the red numbers show the observed PGA in tenths of a g that were used to develop the shakemap contours.

Figure 15 compares a combined model/data shakemap obtained using QTM adjusted hard rock simulations and the directivity sensitive attenuation model (Somerville et al., 1997). The red circles show where model predictions were incorporated in shakemap contouring. In these maps the model predictions are introduced at regular intervals only in regions where there is no observing station located within 22 km. The course grid of model predictions and data is then finely interpolated onto a mesh 1/10th of the spacing shown and contoured. At this final interpolation and contouring stage QTM corrections are applied. Observed data values are uncorrected. This is essentially the same approach outlined by Wald et al. (1999) and used in the TriNet shakemap. Figure 15a illustrates that such a map with many direct observations is controlled by the data (i.e. Figure 14a and 15a are very similar). Figures 15b and 15c show that the model contributes significantly in sparse station coverage by producing shakemaps that accurately describe the forward directivity amplification of ground motion. It is interesting that the 0.7g observation in Figure 15b pins the map at this level and therefore results in an under prediction where the 1 g PGA was observed in Figure 15a. Figure 15c, with the 0.7g observation removed actually performs better because a maximal PGA of 1 g is obtained indicating the severity of the earthquake and the resulting 0.8g contour lies near the location of the 1g observation.

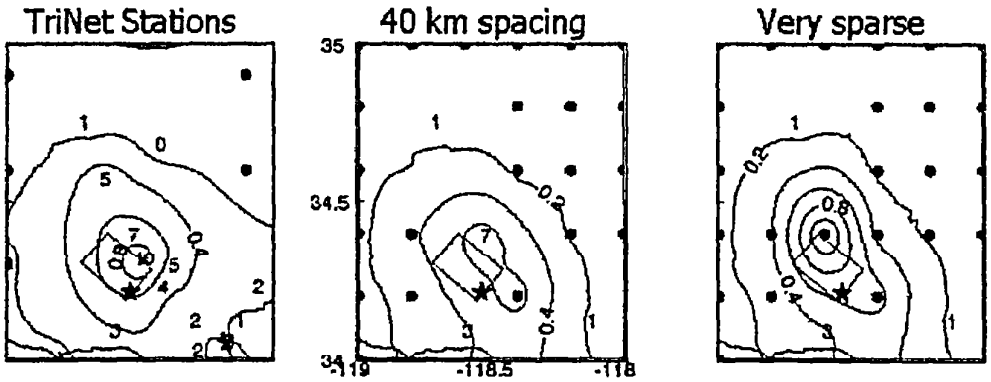

Figure 15. PGA shakemaps obtained by contouring data and model values for the Northridge earthquake are compared for cases with (a) 13 nearby TriNet stations, (b) 30 km station spacing with one station located in the forward directivity region, and (c) 30 km station spacing. The contours show PGA in g, the red numbers show the observed PGA in tenths of a g and the red circles show the locations of where model predictions were added to develop the shakemap contours.

The extended nature of the Landers earthquake is illustrated in the last example. Figure 16a and 16b compare data only PGA shakemaps with and without the near-fault LUC station. The near-fault ground motions in Figure 16a is controlled by the LUC station. When LUC is removed the near-fault ground motion is significantly under predicted when only data is contoured. Again by considering the location of a strong motion centroid and model predictions using point-source attenuation (e.g. Wald et al., 1999) the near fault predictions without LUC would be expected to be better, however the pattern would likely be similar to that in Figure 16a or Figure 2a with a central point of high ground motion. Figures 16c and 16d compare data/model PGA shakemaps for the cases with and without the LUC station. With LUC the overall map is very similar to that in Figure 16a however near the fault the

model produces an elongate region of elevated ground motions that would be expected for an extended rupture of the size experienced in the Landers earthquake. If LUC is removed (Figure 16d) the resulting map retains the elongate near-fault pattern of large PGA, and in fact the LUC site lies between the 0.5 and 0.6g contours of the map, which is a fairly good estimate of the observed 0.76g acceleration. Probably the most important lesson from Figure 16 is that it is not enough to have a single near-fault observation to characterize ground motions for a large extended rupture. A better scenario would have an array of observing stations along the length of the fault. This may be possible in densely instrumented regions, but is not practical in many areas of California. For earthquakes such as Landers, where instrumentation is relatively sparse, considering a source specific directivity model to fill in the holes in observations may result in better estimates of near fault ground motions. Unfortunately along most of the length of Landers we don't know what the actual ground motion levels were, however based on the slip models that have been published it is likely that ground motions close to that observed at LUC occurred along the whole length of the fault.

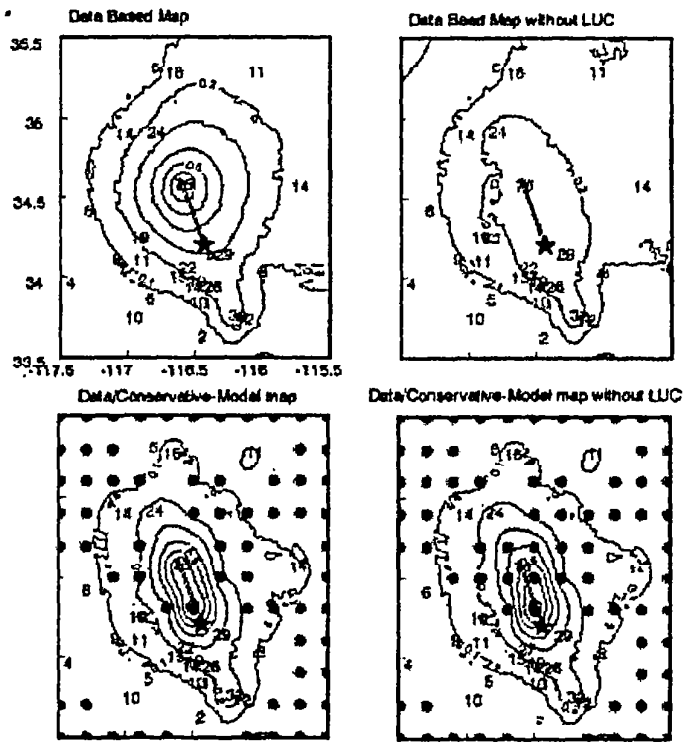

Figure 16. Data only PGA shakemaps for the Landers earthquake are compared for cases with (a) and without (b) the near-fault LUC station. These maps were obtained by direct contouring of the data shown in red (numbers in units of hundredths of a g). The contours are in units of g. The data/model shakemaps are compared for the same cases with (c) and without (d) the LUC station. The red circles show where model predictions were incorporated into the contouring process

In summary, the objectives of this study have been met and software for the determination of combined model/data shakemaps that incorporate source specific directivity effects has been

developed. Comparisons of shakemaps for Landers and Northridge indicate the procedure performs well. In the coming year this method will be integrated into the offline REDI system to being testing under operational conditions.

References

Abercrombie, R. E. Local observations of the onset of a large earthquake; 28 June 1992 Landers, California, Bull. Seism. Soc. Am., 84, 725-734.

Borcherdt, R. D. (1994) Estimates of site-dependent response spectra for design (methodology and justification), Earthquake Spectra, 10, 617-653.

Cohee, B. P., and G. C. Beroza (1994). A comparison of two methods for earthquake source inversion using strong motion seismograms, *Annali Di Geophysica,* **37**, 1515-1538.

Dreger, D. S., and D. V. Helmberger (1991). Source Parameters of the Sierra Madre Earthquake from Regional and Local Body Waves, Geophys. Res. Let., 18 2015-2018.

Dreger, D. S., and D. V. Helmberger (1993), Determination of Source Parameters at Regional Distances with Single Station or Sparse Network Data, Journ. Geophys. Res., 98, 8107-8125.

Dreger, D. and B. Romanowicz (1994). Source Characteristics of Events in the San Francisco Bay Region, *USGS Open-file report*, 94-176, 301-309.

Dreger, D. (1994a). Empirical Green's function study of the January 17, 1994 Northridge mainshock (M_w6.7), *Geophys. Res. Lett.*, **21**, 2633-2636.

Dreger, D. S. (1994b), Investigation of the Rupture Process of the 28 June 1992 Landers Earthquake Utilizing TERRAscope, Bull. Seism. Soc. Am., 84, 713-724.

Dreger, D. (1997), The Large Aftershocks of the Northridge Earthquake and their Relationship to Mainshock Slip and Fault Zone Complexity, Bull. Seism. Soc. Am., 87, 1259-1266.

Gee, L. S., D. S. Neuhauser, D. S. Dreger, M. Pasyanos, R. A. Uhrhammer, and B. Romanowicz (1996), Real-Time Seismology at UC Berkeley: The Rapid Earthquake Data Integration Project, Bull. Seism. Soc. Am., 86, 936-945.

Heaton, T. H. (1990) Evidence for and implications of self-healing pulses of slip in earthquake rupture, Phys. Earth and Planet. Int., 64, 1-20.

Joyner, B. and D. Boore (1981) Peak horizontal accelerations and velocity from strong-motion records including records from the 1979 Imperial Valley, California, earthquake, Bull. Seism. Soc. Am., 71, 2011-2038.

Olsen, K. B., R. J. Archuleta, and J. R. Matarese (1995) Three-dimensional simulation of a magnitude 7.75 earthquake on the San Andreas Fault, Science, 270, 1628-1632.

Park, S., and S. Elrick (1998) Predictions of shear-wave velocities in southern California using surface geology, Bull. Seism. Soc. Am., 88, 677-685.

Pasyanos, M. E., D. S. Dreger, and B. Romanowicz (1996), Towards Real-Time Determination of Regional Moment Tensors, Bull. Seism. Soc. Am., 86, 1255-1269.

Pitarka, A., P. Somerville, Y. Fukushima, T, Uetake, K. Irikura (1999) Simulation of near-fault strong ground motion using hybrid Green's functions, submitted to Bull. Seism. Soc. Am.

Saikia, C. (1994) Modified frequency-wavenumber algorithm for regional seismograms using Filon's quadrature; modeling of L_g waves in eastern North America, Geophys. Journ. Int., 118, 142-158.

Somerville, P. G., N. F. Smith, R. W. Graves, and N. A. Abrahamson (1997) Modification of empirical strong ground motion attenuation relations to include the amplitude and duration effects of rupture directivity, Seism. Res. Lett., 68, 199-222.

Stidham, C., M. Antolik, D. Dreger, S. Larsen and B. Romanowicz (1999) Three-dimensional structure influences on the strong motion wavefield of the 1989 Loma Prieta earthquake, in press Bull. Seism. Soc. Am.

Wald, D. J., V. Quitoriano, T. H. Heaton, H. Kanamori, C. W. Scrivner, and C. B. Worden (1999) TriNet ``ShakeMaps": Rapid Generation of Instrumental Ground Motion and Intensity Maps for Earthquakes in Southern California, in press Earthquake Spectra.

Wald, D. J., and T. H. Heaton (1994). Spatial and temporal distribution of slip for the 1992 Landers, California, earthquake, *Bull. Seism. Soc. Am.*, **84**, 668-691.

Wald, D. J., T. H. Heaton, and K. W. Hudnut (1996). The slip history of the 1994 Northridge, California, earthquake determined from strong-motion, teleseismic, GPS, and leveling data, *Bull. Seism. Soc. Am.*, **86**, s49-s70.

Wells, D. L., and K. J. Coppersmith (1994) New empirical relationships among magnitude, rupture length, rupture width, rupture area, and surface displacement, Bull. Seism. Soc. Am., 84, 974-1002.

Zeng, Y., J. G. Anderson, and G. Yu (1994) A composite source model for computing realistic synthetic strong ground motions, Geophys. Res. Lett., 21, 725-728.

Zeng, Y., and J. G. Anderson (1996). A composite source model of the 1994 Northridge earthquake using genetic algorithms, *Bull. Seism. Soc. Am.*, 86, s71-s83.

PACIFIC EARTHQUAKE ENGINEERING RESEARCH CENTER

Ground Motion Estimates for Emergency Response

Thomas L. Henyey
SCEC
University of Southern California

Agbabian Associates
Padadena, California

A report to the PEER Program of Applied Earthquake Engineering Research on Lifeline Systems

The financial support of the sponsor organizations including the Pacific Gas & Electric Company (PG&E), the California Energy Commission (CEC), and the California Department of Transportation (Caltrans) is acknowledged.

PEER UTILITIES PROGRAM
REPORT NO. 2000/06

AGBABIAN ASSOCIATES
engineers and consultants

ROSRINE 4A

FINAL REPORT

August 18, 1999

ROSRINE 4A
Final Report

by

Agbabian Associates
1111 So. Arroyo Pkwy, Suite 470
Pasadena, California 91105

Report No. R-9818-6695
August 18, 1999

Final Progress Report

TABLE OF CONTENTS

Final Progress Report i

TABLE OF CONTENTS ii

1.0 INTRODUCTION 1

2.0 Brentwood VA Hospital 4

3.0 Dayton Heights School 8

4.0 ETEC RD-7 18

5.0 ETEC RD-20 22

6.0 LADWP Receiving Station East 26

7.0 Saturn Street School 30

1.0 INTRODUCTION

OVERVIEW: ROSRINE is a collaborative research project ultimately focused on improving engineering models for estimation of earthquake ground motions. The central component of this project is the collection, synthesis, and dissemination to both the research and design communities of high quality subsurface data obtained primarily from instrument sites that recorded strong shaking during the 1994 Northridge earthquake. Project funding initially came from NSF (this grant), Caltrans, and the Electric Power Research Institute. Additional follow-on funding has come from CEC/PEER/PG&E through the current grant. Support by CEC, PEER, and PG&E of our ongoing efforts is gratefully acknowledged.

Cost sharing has been contributed by all of the investigating organizations, and in-kind contributions have been made by the USGS, LADWP, LAWRD, SCEC, and other organizations.

ROSRINE-related strong motion site characterization is being accomplished by geologists, geotechnical engineers and geophysicists from a variety of public and private organizations. Typical field data includes geologic and geophysical logs to depths of 100 meters or more. To date, approximately 45 strong-motion recording sites have been characterized. A web site (**http://rccg03.usc.edu/rosrine/**) has been established for data dissemination, and geophysical information have been presented and published. Results show that many strong motion sites had been previously misclassified.

SUMMARY OF EFFORTS:
Under Contract No. 500-97-010 between Pacific Gas & Electric and University of California Berkeley, UCB Subaward SA2121-59652 to University of Southern California, and Purchase Order No. 036709 between Agbabian Associates, Inc. and University of Southern California, the following work was performed:

1. Site Characterization (drilling, sampling, logging) at the following ROSRINE sites:
   Saturn School
   Dayton Heights School
2. Collaborative site characterization (logging only) at the following USGS sites:
   Brentwood VA Hospital
   LADWP Receiving Station East
   ETEC RD-7
   ETEC RD-20
3. Index property testing of selected soil samples at a commercial soil laboratory (Hydrologue).
4. Preparation and transmittal to UCLA Soils Lab of selected soil samples.
5. Preparation for data workshop.
6. Participation in ROSRINE Data Dissemination Workshop at USC on December 15-16, 1998.
7. Attempt logging in existing borehole at Caltech/Kresge lab.
8. Data dissemination through the project website (rccg03.usc.edu/rosrine).

DATA/INFORMATION DISSEMINATION:

The project's Web page is designed to be the main vehicle for data and information dissemination from the ROSRINE project. The address is *rccg03.usc.edu/Rosrine*.

Members of the ROSRINE project have presented papers at various conferences and workshops.

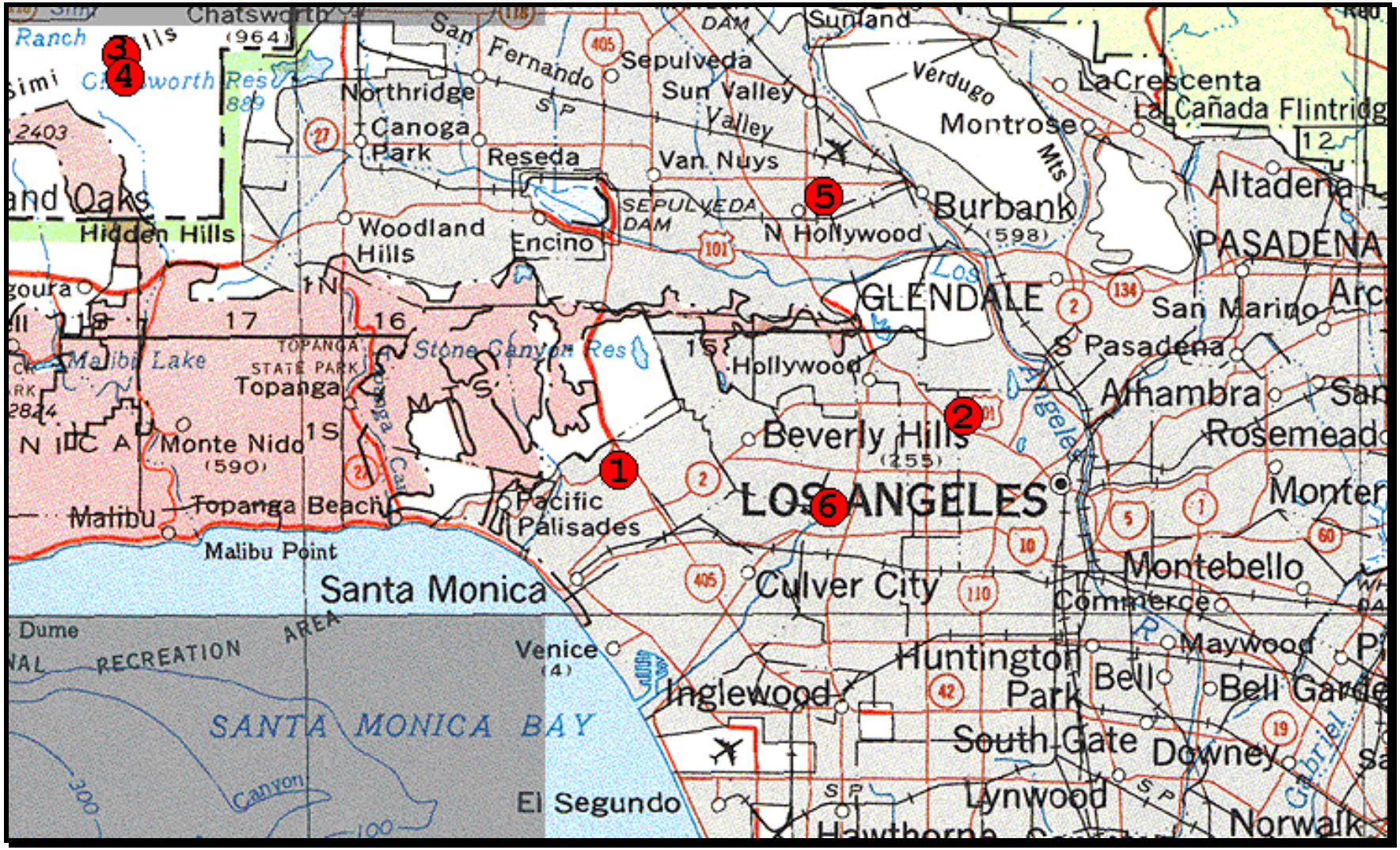

Fig. 1-1 Site Map

2.0 Brentwood VA Hospital

Site Description

Located in Brentwood, CA
Latitude = 34.063, Longitude = -118.463

Work Performed

P- & S-Wave Velocity Measurements Using Suspension Logging

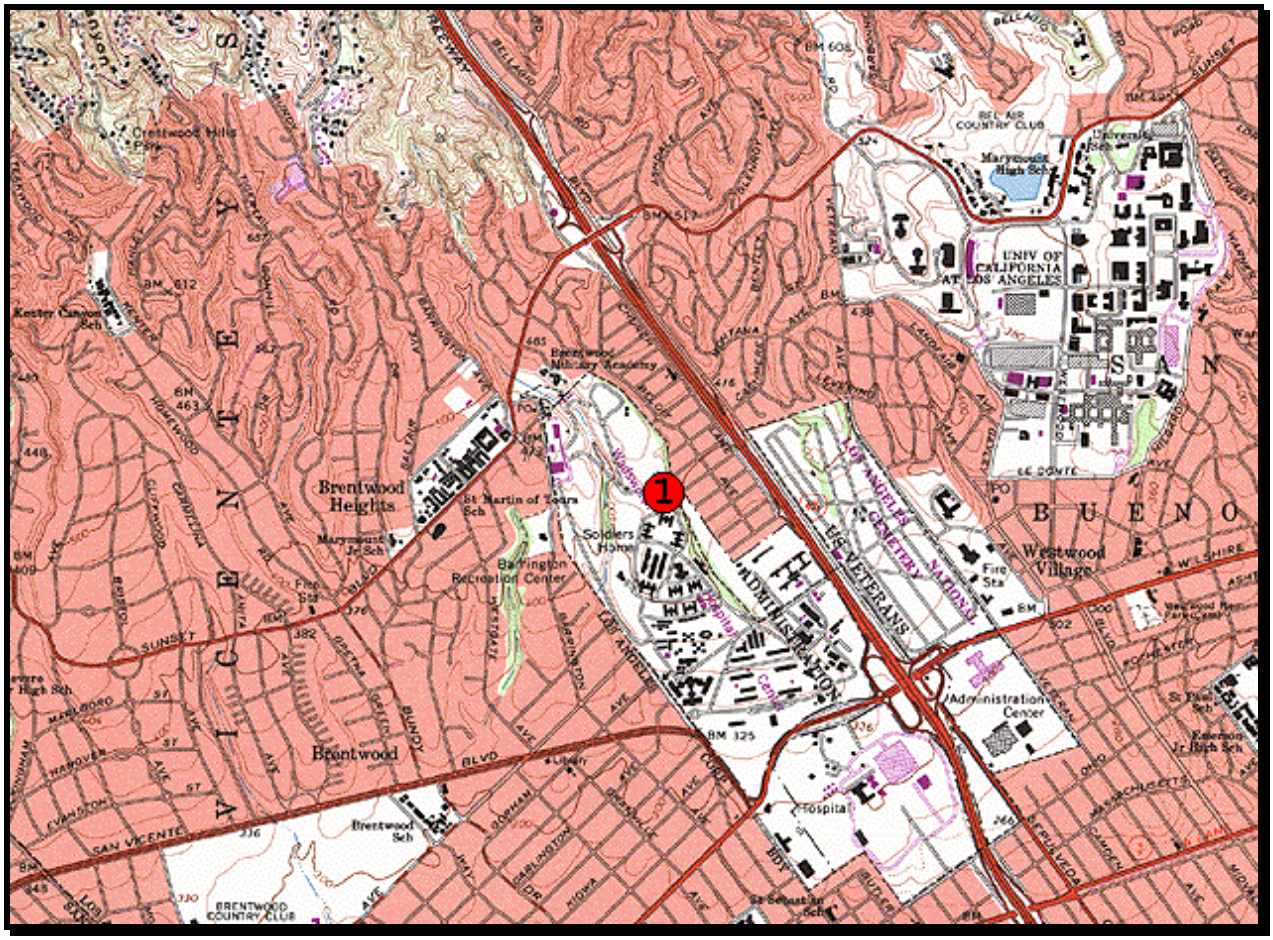

Fig. 2-1 Local Site Map of Brentwood Hospital Location

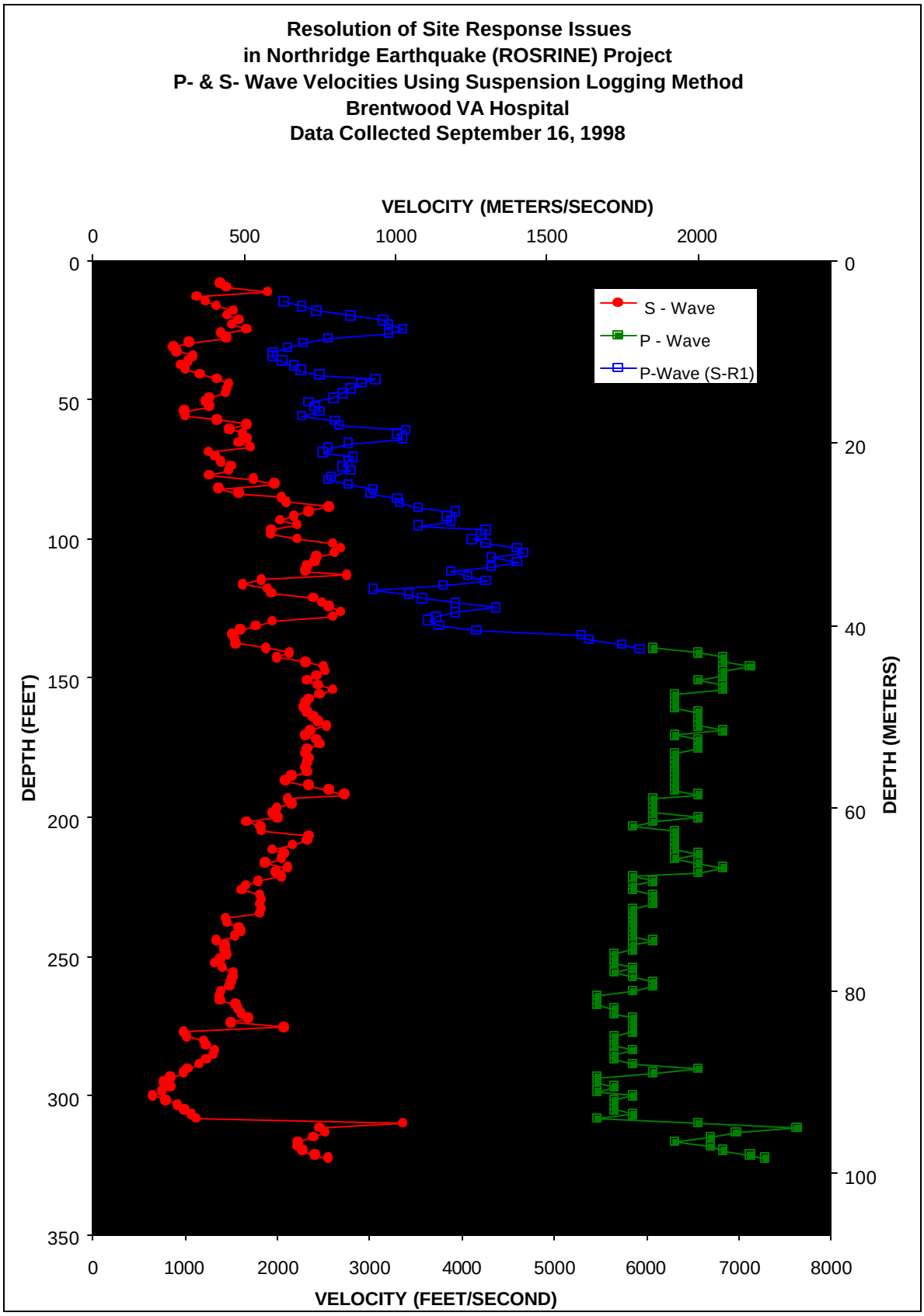

Fig. 2-2 Brentwood VA Hospital Suspension Logging

Depth (feet)	V_s (ft/s)	V_p (ft/s)	Avg. Depth (feet)	V_p (S-R1) (ft/s)
5.3			15.0	2071
6.6			16.6	2273
8.2	1384		18.3	2431
9.8	1452		19.9	2800
11.5	1896		21.5	3153
13.1	1131		23.2	3211
14.8	1229		24.8	3365
16.4	1345		26.5	3211
18.0	1526		28.1	2555
19.7	1465		29.8	2288
21.3	1585		31.4	2121
23.0	1512		33.0	1955
24.6	1674		34.7	1955
26.3	1396		36.3	2059
27.9	1452		38.0	2188
29.5	1052		39.6	2258
31.2	882		41.2	2465
32.8	914		42.9	3070
34.5	1086		44.2	2917
36.1	1042		46.2	2800
37.7	968		47.8	2713
39.0	1006		49.4	2612
41.0	1172		51.1	2349
42.7	1350		52.7	2414
44.3	1478		54.4	2465
45.9	1465		56.0	2273
47.6	1445		57.6	2632
49.2	1272		59.3	2672
50.9	1224		60.9	3398
52.5	1272		62.6	3302
54.1	1000		64.2	3365
55.8	1003		65.8	2778
57.4	1350		67.5	2555
59.1	1674		69.1	2500
60.7	1491		70.8	2823
62.3	1632		72.4	2778
64.0	1674		74.0	2713
65.6	1585		75.7	2800
67.3	1718		77.7	2593
68.9	1257		79.0	2555
70.5	1334		80.6	2778
72.5	1390		82.2	3043
73.8	1505		83.9	3017
75.5	1478		85.5	3302
77.1	1267		87.2	3333
78.7	1745		88.8	3535
80.4	1976		90.4	3933
82.0	1373		92.1	3846
83.7	1585		93.7	3889
85.3	2051		95.4	3535
86.9	2103		97.0	4268
88.6	2563		98.6	4217
90.2	2343		100.3	4118
91.9	2187		101.9	4268
93.5	2038		103.6	4605
95.1	2217		105.2	4667
96.8	1941		106.9	4321
98.4	1930		108.5	4605
100.1	2217		110.1	4321
101.7	2604		111.8	3889
103.4	2689		113.4	4070
105.0	2625		115.1	4268
106.6	2430		116.7	3804
108.3	2412		118.3	3043
109.9	2327		120.0	3431

Depth (feet)	V_s (ft/s)	V_p (ft/s)	Avg. Depth (feet)	V_p (S-R1) (ft/s)
111.6	2310		121.6	3571
113.2	2757		123.3	3933
114.8	1833		124.9	4375
116.5	1632		126.5	3933
118.1	1896		128.2	3723
119.8	1941		129.5	3646
121.4	2395		131.5	3763
123.0	2485		133.1	4167
124.3	2563		134.7	5303
126.3	2689		136.4	5385
128.0	2604		138.0	5738
129.6	1953		139.7	5932
131.2	1773		141.3	6364
132.9	1600			
134.5	1519			
136.2	1548			
137.8	1555			
139.4	1886	6076		
141.1	2130	6562		
142.7	2001	6835		
144.4	2310	6835		
146.0	2504	7132		
147.6	2524	6835		
149.3	2430	6835		
150.9	2327	6562		
152.6	2448	6835		
154.2	2604	6835		
155.8	2467	6309		
157.5	2343	6309		
159.1	2310	6309		
160.8	2294	6309		
162.4	2327	6562		
164.0	2395	6562		
165.7	2448	6562		
167.3	2543	6562		
169.0	2360	6835		
170.6	2310	6309		
172.2	2430	6562		
173.9	2467	6562		
175.5	2327	6562		
177.2	2310	6309		
178.8	2343	6309		
180.5	2327	6309		
182.1	2310	6309		
183.7	2327	6309		
185.4	2158	6309		
187.0	2090	6309		
188.7	2343	6309		
190.3	2563	6309		
191.9	2734	6562		
193.6	2117	6076		
195.2	2158	6076		
196.9	2001	6076		
198.5	1953	6076		
200.1	2013	6562		
201.8	1674	6076		
203.4	1823	5859		
205.1	1833	6309		
206.7	2343	6309		
208.3	2327	6309		
210.0	2173	6309		
211.6	1953	6309		
213.3	2076	6562		
214.9	2051	6309		
216.5	1875	6562		

Depth (feet)	V_s (ft/s)	V_p (ft/s)
218.2	2117	6835
219.8	1988	6562
221.5	2051	5859
223.1	1803	6076
224.7	1665	5859
226.4	1624	5859
228.0	1813	6076
229.7	1833	6076
231.3	1813	6076
232.9	1833	5859
234.6	1813	5859
236.2	1445	5859
237.9	1465	5859
239.5	1593	5859
241.1	1608	5859
242.8	1548	5859
244.4	1345	6076
246.1	1439	5859
247.7	1439	5859
249.3	1458	5657
251.0	1384	5657
252.6	1328	5657
254.3	1414	5859
255.9	1533	5657
257.6	1519	5859
259.2	1505	6076
260.8	1491	6076
262.5	1390	5859
264.1	1379	5468
265.8	1384	5468
267.4	1555	5468
269.0	1577	5657
270.7	1616	5657
272.3	1691	5859
274.0	1505	5859
275.6	2076	5859
277.2	988	5859
278.9	1019	5657
280.5	1211	5657
282.2	1233	5657
283.8	1328	5859
285.4	1312	5657
287.1	1233	5657
288.7	1159	5859
290.4	1032	6562
292.0	991	6076
293.6	846	5468
295.3	774	5468
296.9	850	5657
298.6	756	5468
300.2	655	5859
301.8	800	5657
303.5	919	5657
305.1	997	5657
306.8	1076	5859
308.4	1124	5468
310.0	3365	6562
311.7	2467	7630
313.3	2524	6981
315.0	2395	6696
316.6	2224	6309
318.2	2232	6696
319.9	2278	6835
321.5	2412	7132
322.5	2553	7291

Fig. 2-3 Brentwood VA Hospital Suspension Data

3.0 Dayton Heights School

Site Description

Located in Los Angeles, CA off Westmoreland Avenue
Latitude = 34.082, Longitude = -118.286

Work Performed

P- & S-Wave Velocity Measurements Using Suspension Logging
Geologic Logging

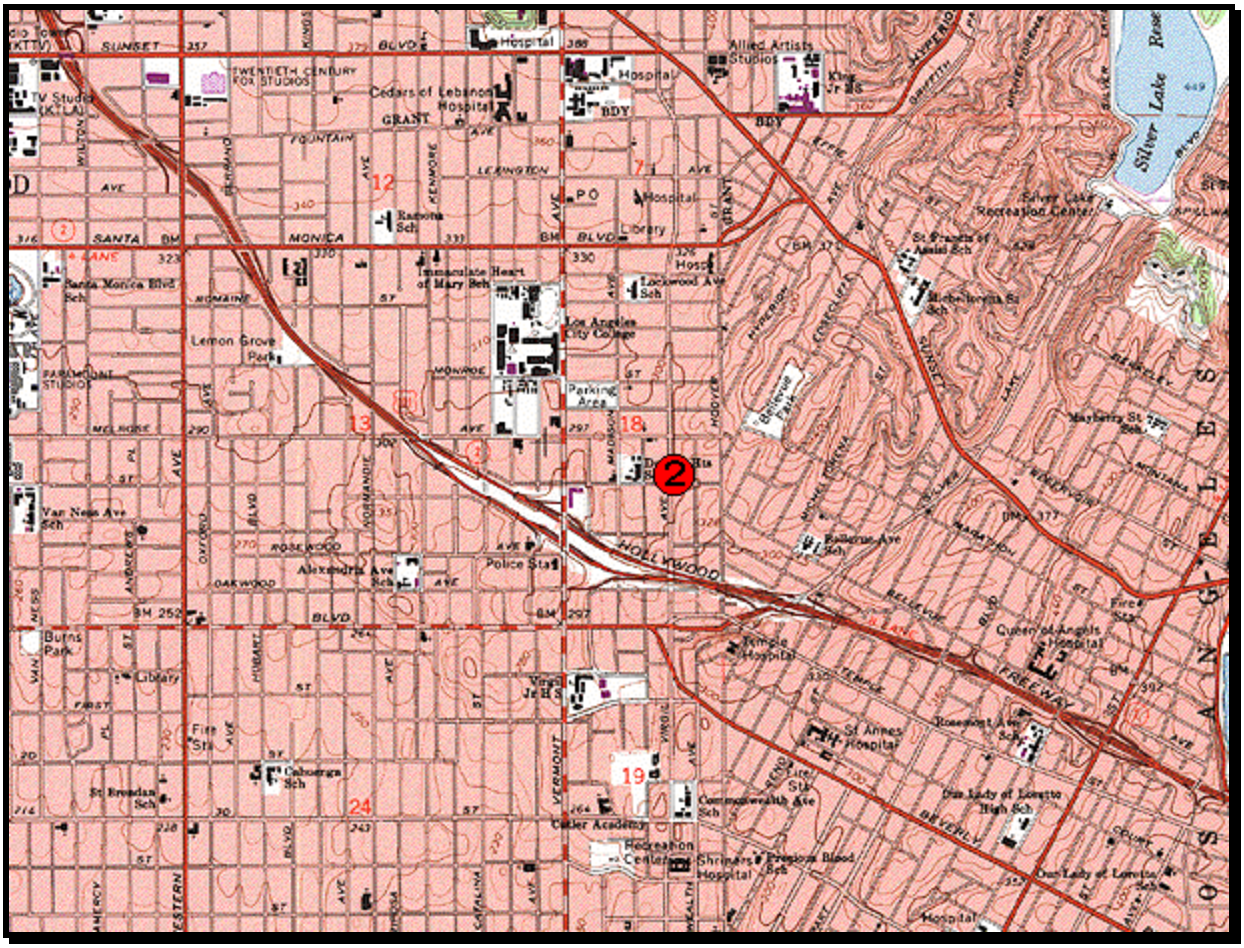

Fig. 3-1 Local Site Map of Dayton Heights Location

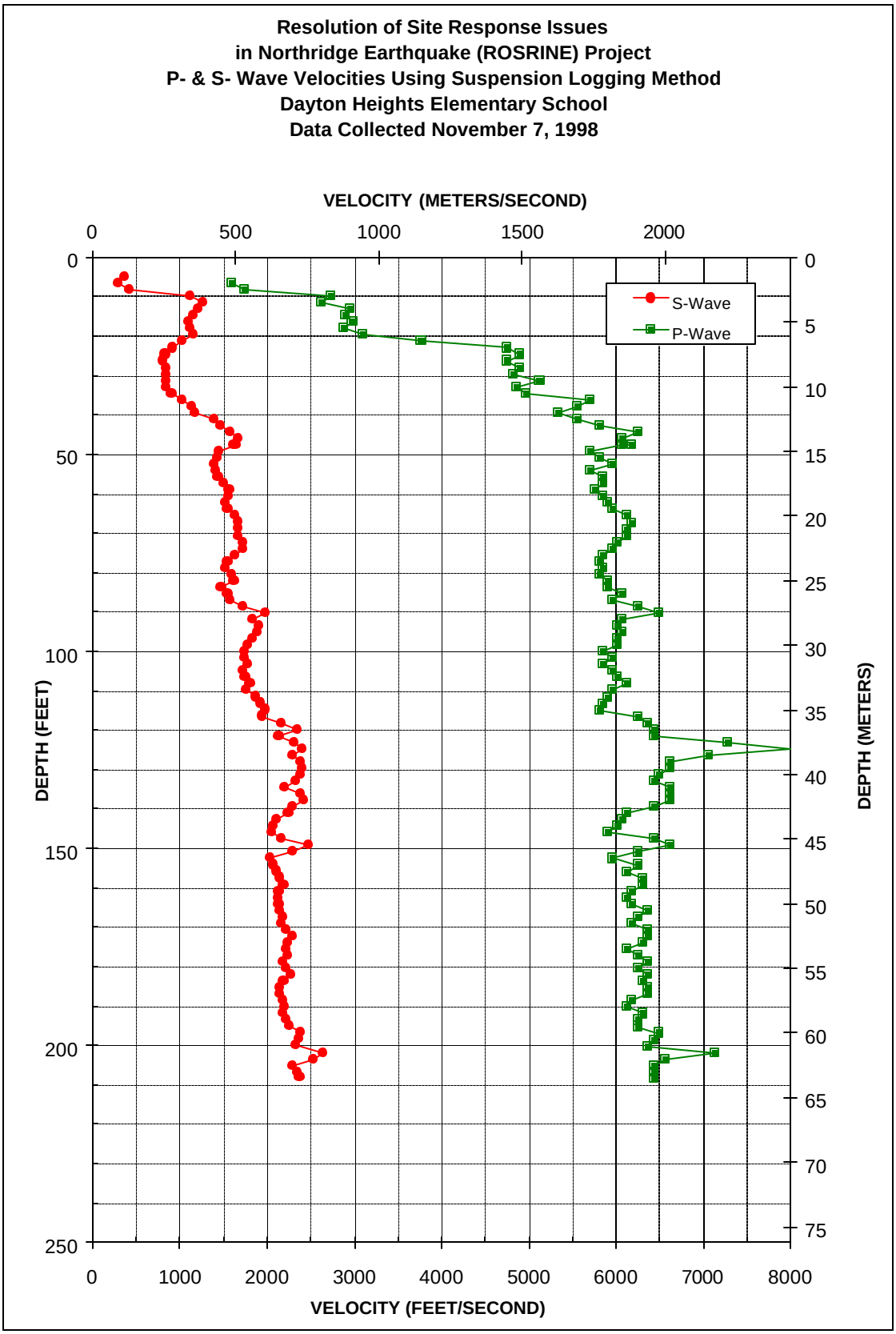

Fig. 3-2 Dayton Heights School Suspension Logging

Depth (feet)	Vs (feet/s)	Vp (feet/s)
4.9	365	
6.6	299	1593
8.2	421	1745
9.8	1116	2734
11.5	1267	2625
13.1	1206	2956
14.8	1151	2903
16.4	1101	2983
18.1	1124	2878
19.7	1151	3095
21.3	1025	3771
23.0	924	4755
24.6	835	4897
26.3	812	4755
27.9	850	4897
29.5	850	4825
31.2	841	5126
32.8	851	4861
34.5	909	4971
36.1	1022	5706
37.7	1143	5561
39.4	1180	5335
41.0	1387	5561
42.7	1475	5807
44.3	1574	6249
45.9	1678	6076
47.6	1620	6190
47.6	1645	6076
49.2	1455	5706
50.9	1436	5807
52.5	1387	5965
54.1	1414	5706
55.8	1442	5859
57.4	1512	5859
59.1	1570	5756
60.7	1555	5859
62.3	1522	5911
64.0	1551	5965
65.6	1632	6132
67.3	1670	6190
68.9	1665	6132
70.5	1665	6132

Depth (feet)	Vs (feet/s)	Vp (feet/s)
72.2	1722	6020
73.8	1718	5965
75.5	1632	5859
77.1	1551	5807
78.7	1519	5859
80.4	1600	5807
82.0	1624	5911
83.7	1478	5911
85.3	1551	6076
86.9	1581	5965
88.6	1727	6249
90.2	1988	6497
91.9	1838	6076
93.5	1913	6020
95.2	1891	6076
96.8	1833	6020
98.4	1788	6020
100.1	1740	5859
101.7	1750	5965
103.4	1783	5859
105.0	1727	5965
106.6	1754	6020
108.3	1808	6132
109.9	1769	5965
111.6	1875	5911
113.2	1930	5859
114.8	1982	5807
116.5	1947	6249
118.1	2166	6371
119.8	2352	6433
121.4	2137	6433
123.0	2319	7291
124.7	2404	8002
126.3	2302	7056
128.0	2377	6628
129.6	2412	6628
131.2	2386	6497
132.9	2327	6433
134.5	2209	6628
136.2	2377	6628
137.8	2421	6628
139.4	2294	6433

Depth (feet)	Vs (feet/s)	Vp (feet/s)
141.1	2247	6132
142.7	2110	6076
144.4	2070	6020
146.0	2057	5911
147.6	2166	6433
149.3	2476	6628
150.9	2286	6249
152.6	2038	5965
154.2	2070	6249
155.8	2110	6132
157.5	2151	6309
159.1	2195	6309
160.8	2137	6190
162.4	2124	6132
164.0	2137	6190
165.7	2151	6371
167.3	2180	6249
169.0	2173	6190
170.6	2217	6371
172.2	2302	6371
173.9	2239	6309
175.5	2224	6132
177.2	2239	6249
178.8	2187	6371
180.5	2224	6249
182.1	2278	6371
183.7	2195	6309
185.4	2151	6371
187.0	2151	6371
188.7	2180	6190
190.3	2202	6132
191.9	2187	6309
193.6	2217	6249
195.2	2255	6249
196.9	2386	6497
198.5	2360	6433
200.1	2335	6371
201.8	2646	7132
203.4	2533	6562
205.1	2286	6433
206.7	2352	6433
208.2	2377	6433

Fig. 3-3 Dayton Heights School Suspension Logging

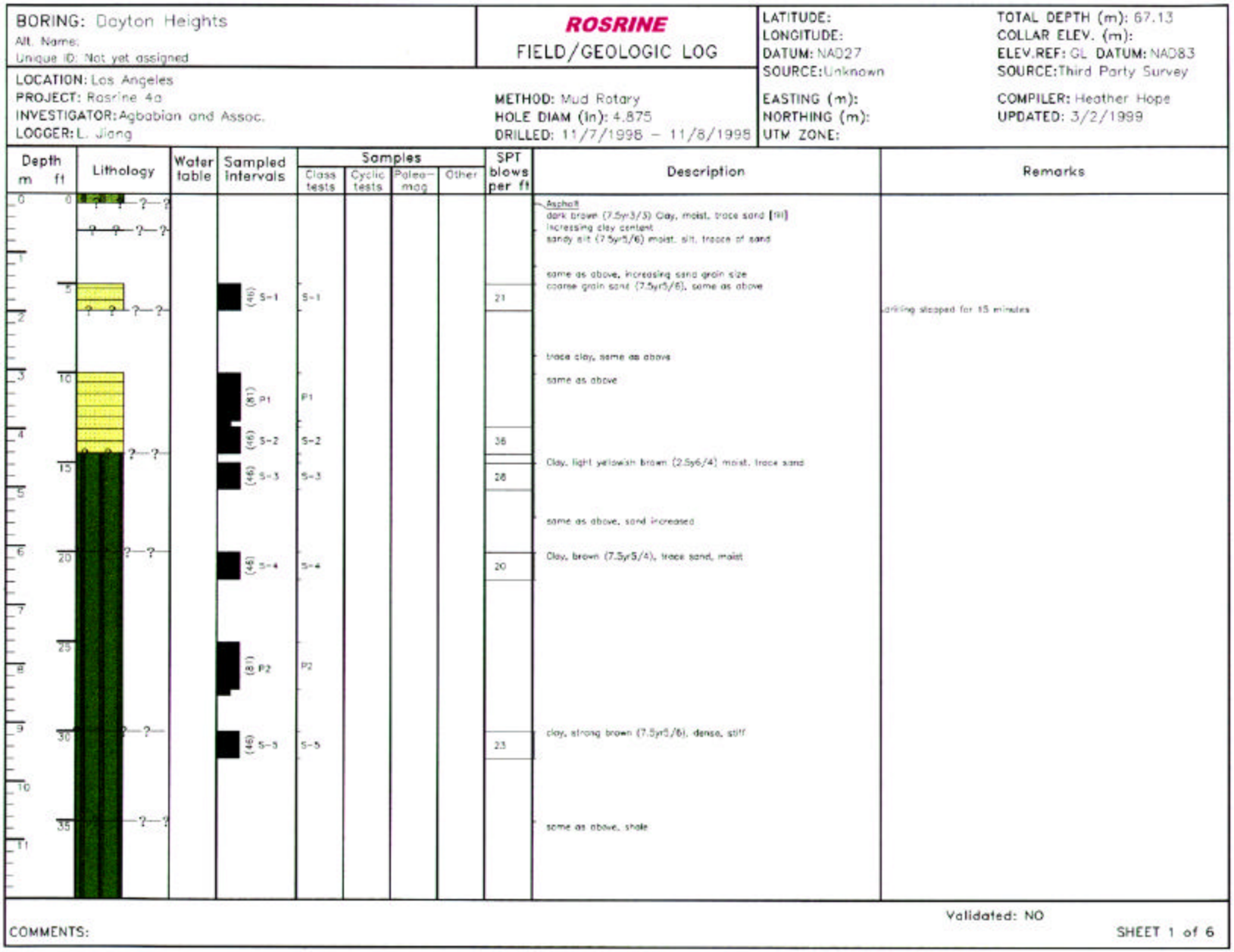

Fig 3-4 Dayton Heights School Geologic Log

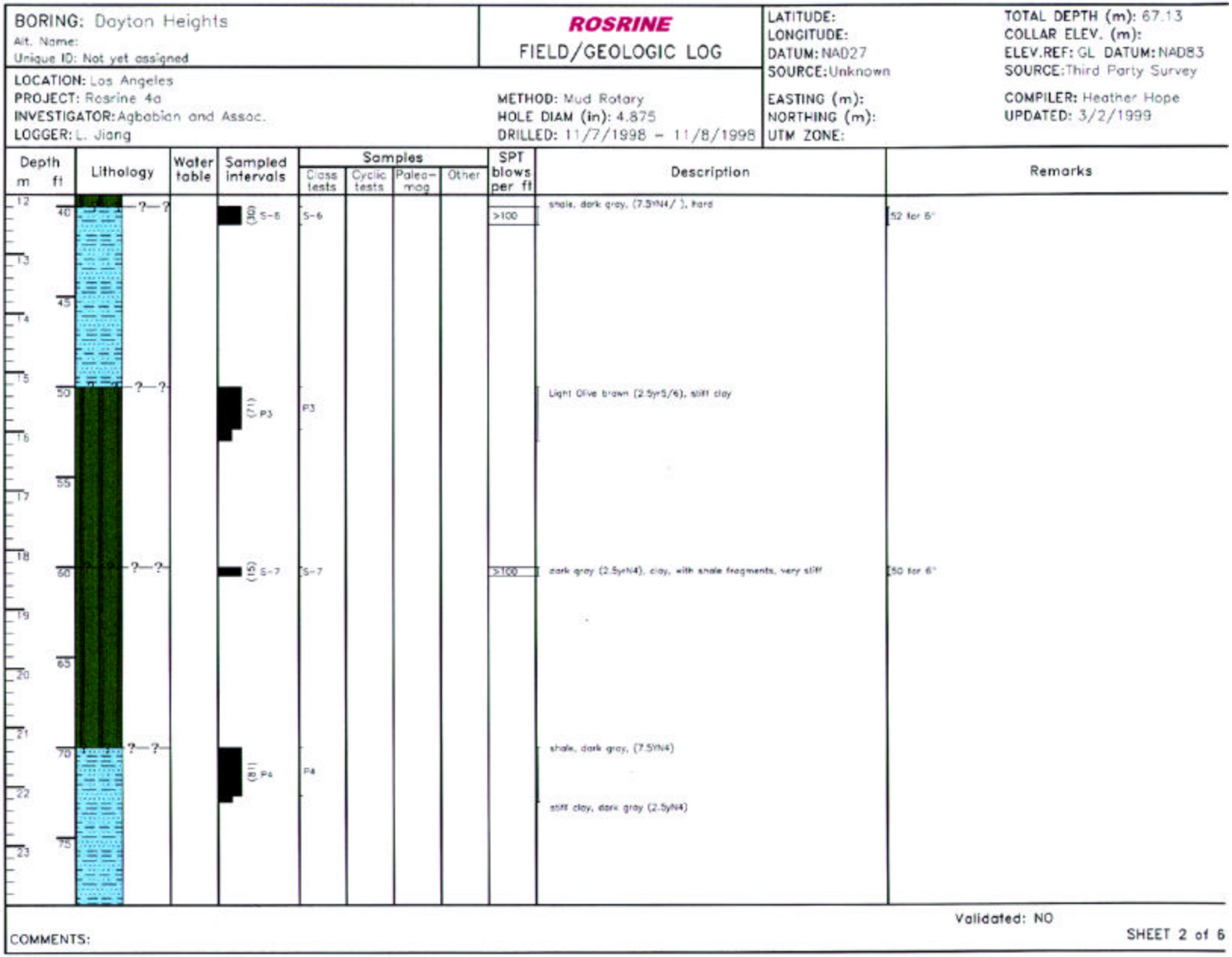

Fig 3-4 (Continued) Dayton Heights School Geologic Log

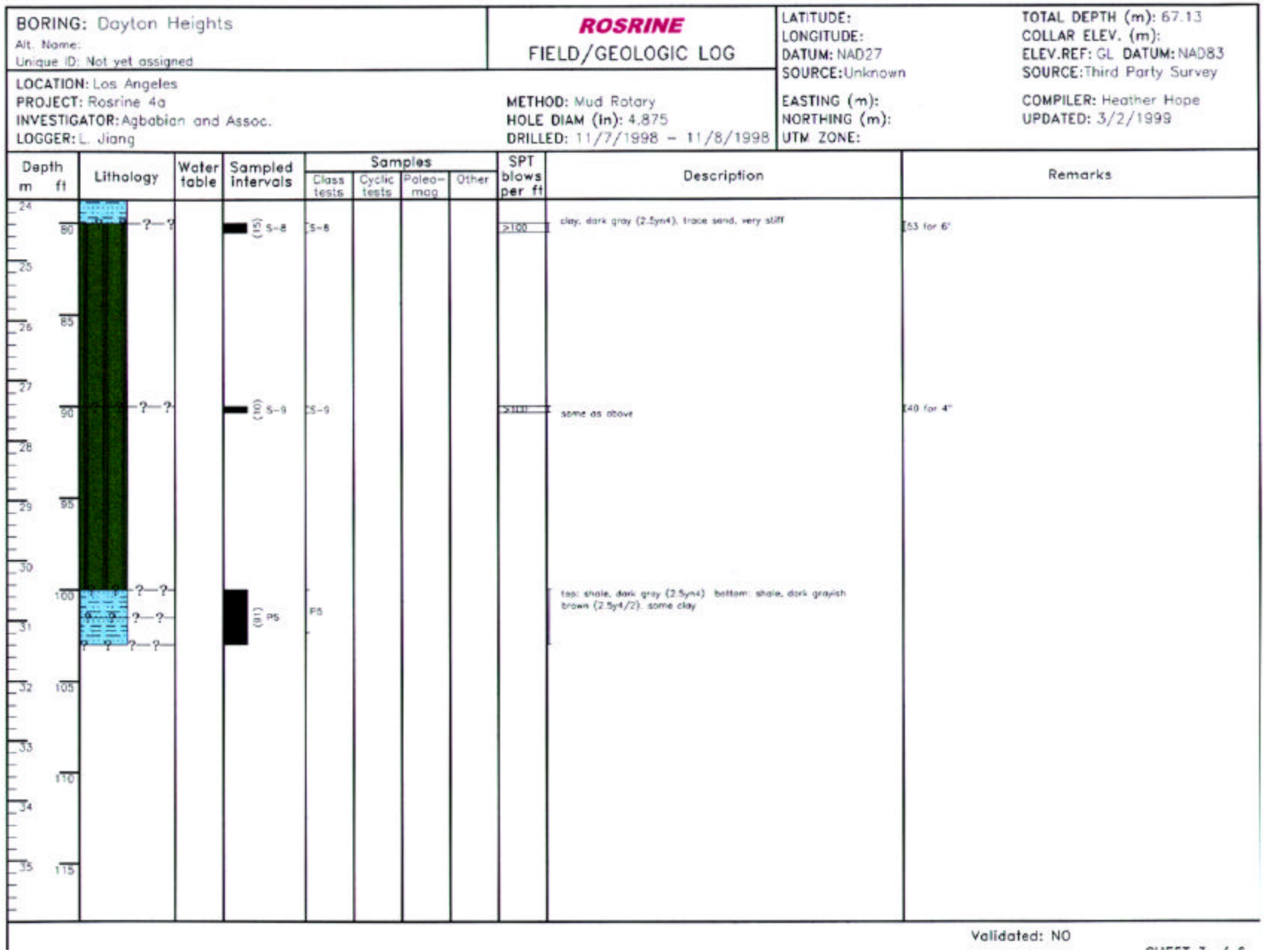

Fig 3-4 (Continued) Dayton Heights School Geologic Log

BORING: Dayton Heights
Alt. Name:
Unique ID: Not yet assigned

ROSRINE
FIELD/GEOLOGIC LOG

LATITUDE:
LONGITUDE:
DATUM: NAD27
SOURCE: Unknown
EASTING (m):
NORTHING (m):
UTM ZONE:

TOTAL DEPTH (m): 67.13
COLLAR ELEV. (m):
ELEV.REF: GL DATUM: NAD83
SOURCE: Third Party Survey
COMPILER: Heather Hope
UPDATED: 3/2/1999

LOCATION: Los Angeles
PROJECT: Rosrine 4a
INVESTIGATOR: Agbabian and Assoc.
LOGGER: L. Jiang

METHOD: Mud Rotary
HOLE DIAM (in): 4.875
DRILLED: 11/7/1998 – 11/8/1998

Depth m	Depth ft	Lithology	Water table	Sampled intervals	Samples: Class tests	Samples: Cyclic tests	Samples: Paleo-mag	Samples: Other	SPT blows per ft	Description	Remarks
36	120										
37											
38	125										
39											
	130										
40											
41	135										
42											
	140										
43		? ?		(13) 5-10	5-10				>100	clay, dark gray (2.5y4).very stiff, oil	54 for 6"
44	145										
45											
	150										
46										shale, cemented, hard, about 1' thick, concretion	
47	155										

COMMENTS:

Validated: NO

SHEET 4 of 6

Fig 3-4 (Continued) Dayton Heights School Geologic Log

BORING: Dayton Heights
Alt. Name:
Unique ID: Not yet assigned

ROSRINE
FIELD/GEOLOGIC LOG

LATITUDE:
LONGITUDE:
DATUM: NAD27
SOURCE: Unknown
EASTING (m):
NORTHING (m):
UTM ZONE:

TOTAL DEPTH (m): 67.13
COLLAR ELEV. (m):
ELEV.REF: GL DATUM: NAD83
SOURCE: Third Party Survey
COMPILER: Heather Hope
UPDATED: 3/2/1999

LOCATION: Los Angeles
PROJECT: Rosrine 4a
INVESTIGATOR: Agbabian and Assoc.
LOGGER: L. Jiang

METHOD: Mud Rotary
HOLE DIAM (in): 4.875
DRILLED: 11/7/1998 – 11/8/1998

Depth m	Depth ft	Lithology	Water table	Sampled intervals	Samples: Class tests	Samples: Cyclic tests	Samples: Paleo-mag	Samples: Other	SPT blows per ft	Description	Remarks
48											
	160										
49											
50											
	165										
51											
52	170									hard layer, same as above, 6" thick, cemented concretion	
53											
	175										
54											
55	180	?—?		S-11	S-11				>100	Clay, dark gray (2.5YN3), stiff	57 for 6"
56											
	185										
57											
58	190										
59											
	195									enter hard layer, same as above, 1' thick	

Validated: NO

COMMENTS:

SHEET 5 of 6

Fig 3-4 (Continued) Dayton Heights School Geologic Log

BORING: Dayton Heights
Alt. Name:
Unique ID: Not yet assigned

ROSRINE
FIELD/GEOLOGIC LOG

LATITUDE:
LONGITUDE:
DATUM: NAD27
SOURCE: Unknown
EASTING (m):
NORTHING (m):
UTM ZONE:

TOTAL DEPTH (m): 67.13
COLLAR ELEV. (m):
ELEV.REF: GL DATUM: NAD83
SOURCE: Third Party Survey
COMPILER: Heather Hope
UPDATED: 3/2/1999

LOCATION: Los Angeles
PROJECT: Rosrine 4a
INVESTIGATOR: Agbabian and Assoc.
LOGGER: L. Jiang

METHOD: Mud Rotary
HOLE DIAM (in): 4.875
DRILLED: 11/7/1998 – 11/8/1998

Depth m	Depth ft	Lithology	Water table	Sampled intervals	Samples: Class tests	Samples: Cyclic tests	Samples: Paleo-mag	Samples: Other	SPT blows per ft	Description	Remarks
60											
61	200										
62	205									hard layer, same as above, 3" – 6" thick, cemented concretion	
63											
64	210										
65	215										
66											
67	220										

E.O.H 67.13 m

COMMENTS:

Validated: NO

SHEET 6 of 6

Fig 3-4 (Continued) Dayton Heights School Geologic Log

4.0 ETEC RD-7

Site Description

Located at ETEC Santa Susana Field Laboratory
Latitude = 34.231, Longitude = -118.715

Work Performed

P- & S-Wave Velocity Measurements Using Suspension Logging

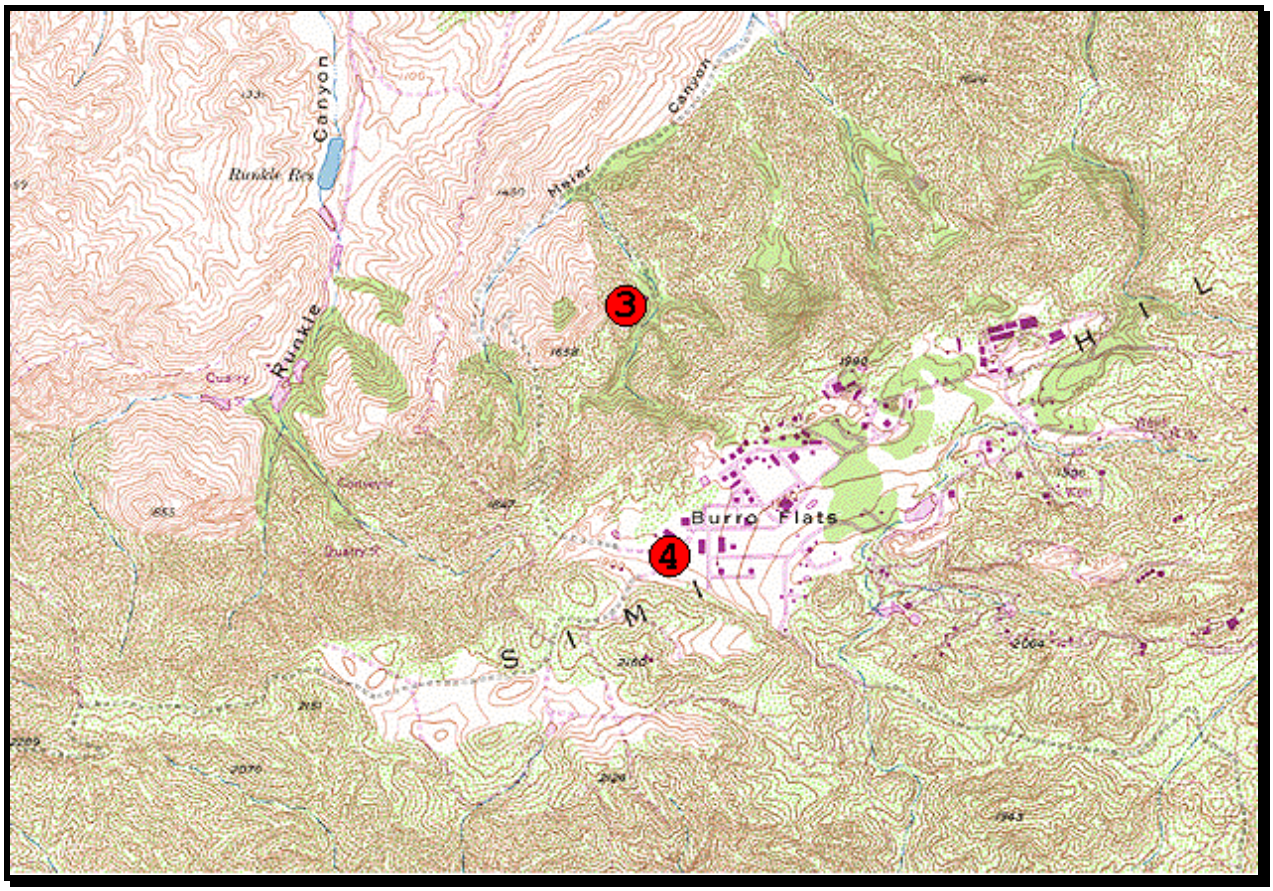

Fig. 4-1 Local Site Map of ETEC RD-7 Location

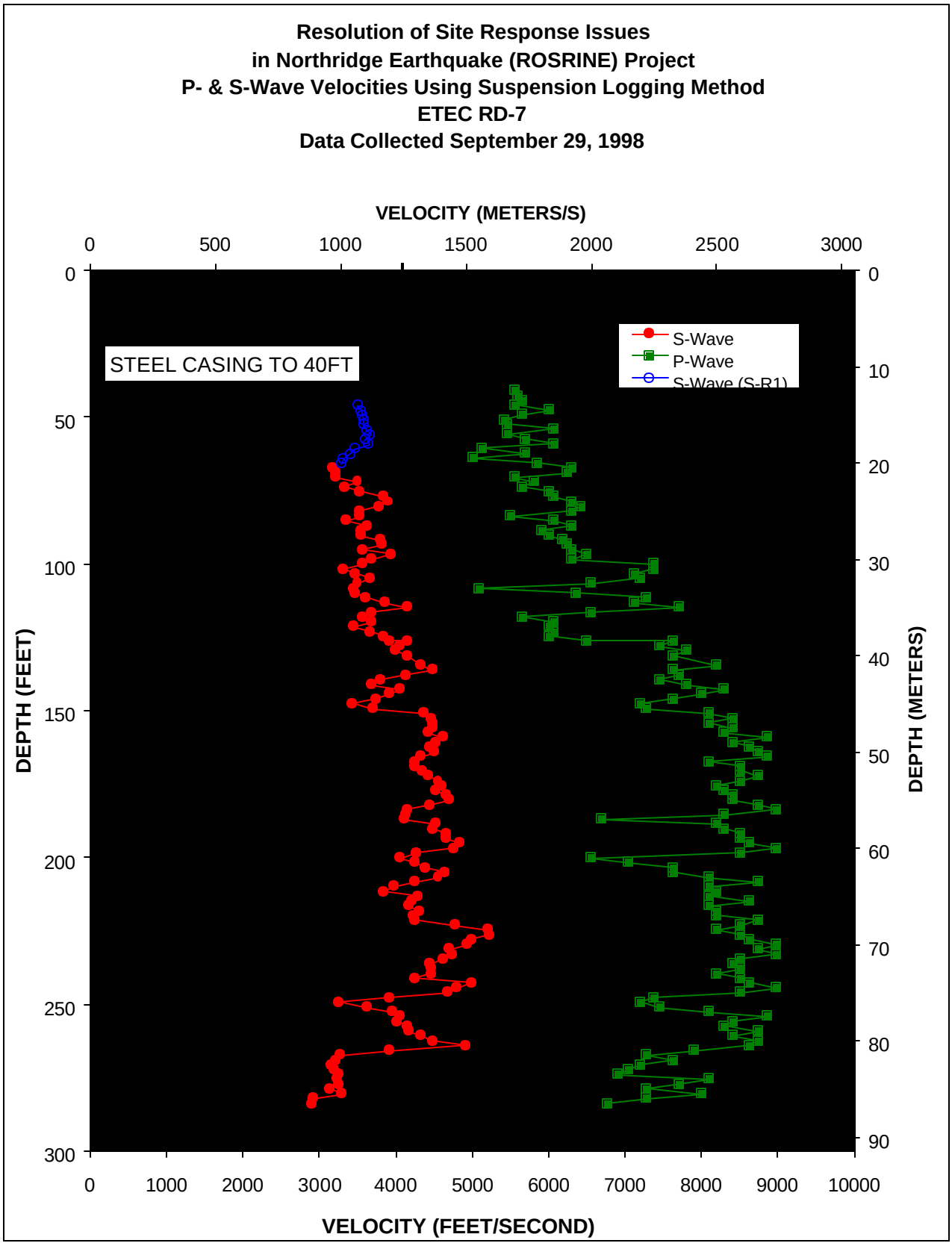

Fig. 4-2 ETEC RD-07 Suspension Logging

Depth (feet)	V_s (ft/s)	V_p (ft/s)
41.0		5561
42.7		5608
44.3		5657
45.9		5561
47.6		6020
49.2		5657
50.9		5423
52.5		5468
54.1		6076
55.8		5468
57.4		5706
59.1		6076
60.7		5126
62.3		5706
64.0		5009
65.6		5859
67.3	3178	6309
68.9	3209	6249
70.5	3224	5561
72.2	3500	5807
73.8	3331	5657
75.5	3537	6020
77.1	3848	6076
79	3906	6309
80.4	3782	6433
82.0	3537	6309
83.7	3537	5514
85.3	3356	6076
86.9	3625	6309
88.6	3556	5911
90.2	3547	6020
91.9	3804	6190
93.5	3826	6249
95.1	3566	6309
96.8	3941	6497
98.4	3686	6309
100.1	3576	7373
101.7	3314	7373
103.4	3463	7132
105.0	3666	7211
106.6	3500	6562
108.3	3454	5087
109.9	3463	6371
111.6	3615	7291
113.2	3860	7132
114.8	4153	7720
116.5	3676	6562
118.1	3566	5657
119.8	3676	6076
121.4	3444	6020

Avg. Depth (feet)	V_s (S-R1) (ft/s)
46.2	3509
47.8	3553
49.4	3567
51.1	3585
52.7	3581
54.4	3622
56.0	3675
57.6	3608
59.3	3655
60.9	3461
62.6	3410
64.2	3318
65.8	3290

Depth (feet)	V_s (ft/s)	V_p (ft/s)
123.0	3666	6076
124.7	3848	6020
126.3	3929	6497
126.3	4153	7630
128.0	4050	7456
129.6	4001	7812
131.2	4153	7630
134.5	4331	8202
136.2	4479	7630
137.8	4127	7720
139.4	3804	7456
141.1	3676	7812
142.7	4063	8306
144.4	3917	8002
146.0	3739	7630
147.6	3435	7211
149.3	3697	7291
150.9	4374	8101
152.6	4464	8412
154.2	4479	8101
155.8	4479	8412
157.5	4419	8306
159.1	4621	8867
160.8	4525	8412
162.4	4449	8634
164.0	4510	8749
165.7	4331	8867
167.3	4261	8101
169.0	4261	8522
170.6	4345	8522
172.2	4434	8749
173.9	4557	8522
175.5	4605	8202
177.2	4525	8306
178.8	4654	8412
180.5	4704	8412
182.1	4449	8749
183.7	4153	8989
185.4	4127	8306
187.0	4114	6696
188.7	4525	8202
190.3	4479	8306
191.9	4654	8522
193.6	4670	8522
195.2	4843	8634
196.9	4755	8989
198.5	4275	8522
200.1	4063	6562
201.8	4261	7056
203.4	4389	7630

Depth (feet)	V_s (ft/s)	V_p (ft/s)
205.1	4637	7630
206.7	4557	8101
208.3	4247	8749
210.0	3977	8101
211.6	3848	8202
213.3	4289	8101
214.9	4206	8634
216.5	4166	8101
218.2	4303	8202
219.8	4233	8202
221.5	4247	8749
223.1	4772	8522
224.7	5208	8202
226.4	5228	8522
228.0	4990	8634
229.7	4934	8989
231.3	4704	8749
232.9	4738	8989
234.6	4621	8522
236.2	4449	8412
236.2	4449	8412
237.9	4464	8522
239.5	4464	8202
241.1	4247	8522
242.8	4990	8634
244.4	4807	8989
246.1	4687	8522
247.7	3929	7373
249.3	3256	7211
251.0	3625	7456
252.6	3953	8101
254.3	4050	8867
255.9	4026	8412
257.6	4153	8306
259.2	4166	8749
260.8	4331	8412
262.5	4479	8749
264.1	4915	8634
265.8	3917	7906
267.4	3281	7291
269.0	3217	7630
270.7	3162	7211
272.3	3201	7056
274.0	3256	6907
275.6	3232	8101
277.2	3256	7720
278.9	3140	7291
280.5	3297	8002
282.2	2923	7291
283.8	2897	6765

Fig. 4-3 ETEC RD-07 Suspension Logging

5.0 ETEC RD-20

Site Description

Located at ETEC Santa Susana Field Laboratory
Latitude = 34.239, Longitude = -118.719

Work Performed

P- & S-Wave Velocity Measurements Using Suspension Logging

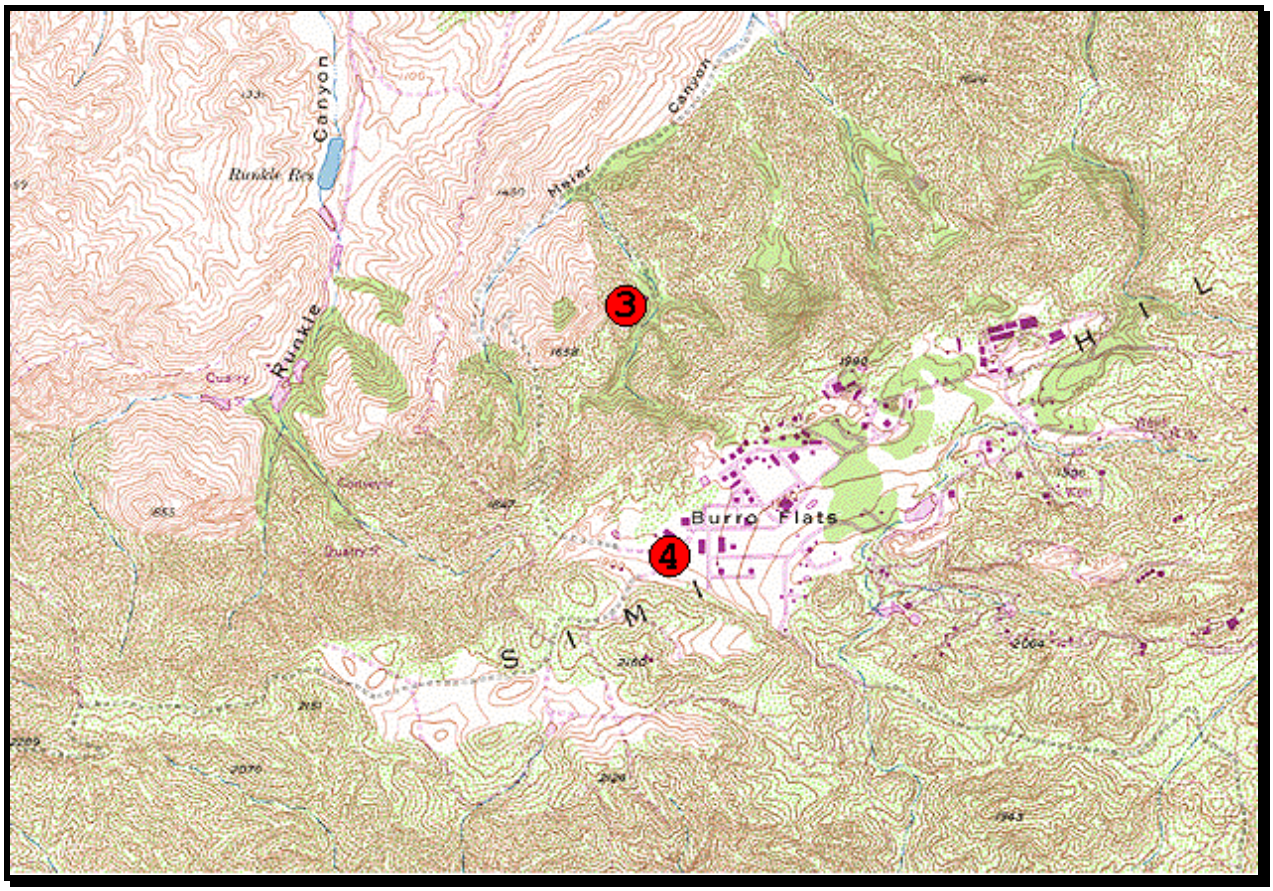

Fig. 5-1 Site Map of ETEC RD-20 Location

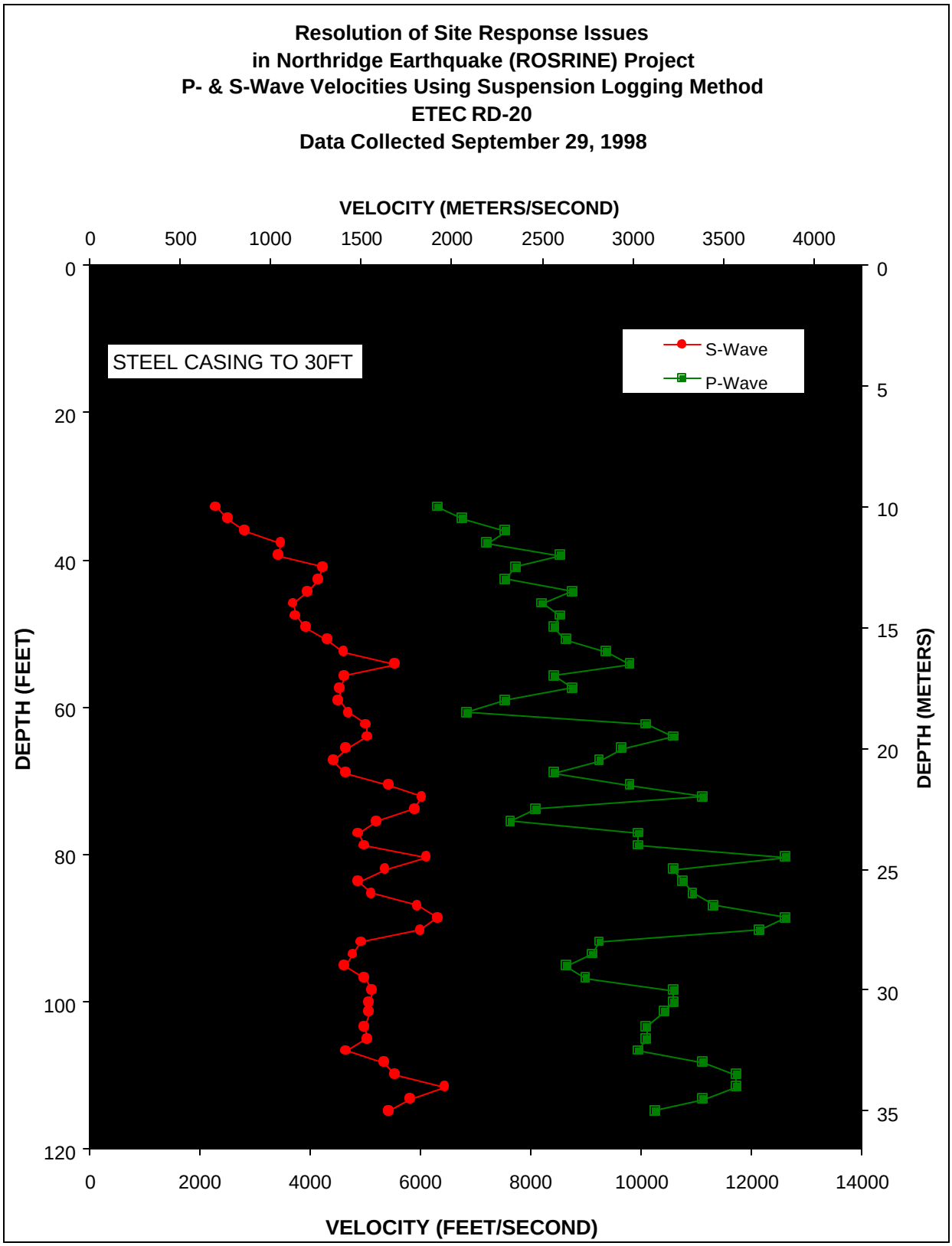

Fig. 5-2 ETEC RD-20 Suspension Logging

Depth (feet)	V_s (feet/s)	V_p (feet/s)
32.8	2286	6309
34.5	2504	6765
36.1	2822	7542
37.7	3463	7211
39.4	3418	8522
41.0	4220	7720
42.7	4153	7542
44.3	3953	8749
45.9	3686	8202
47.6	3739	8522
49.2	3917	8412
50.9	4303	8634
52.5	4605	9374
54.1	5537	9794
55.8	4621	8412
57.4	4541	8749
59.1	4510	7542
60.7	4687	6835
62.3	5009	10095
64.0	5028	10583
65.6	4654	9650
67.3	4419	9242
68.9	4637	8412
70.5	5423	9794
72.2	6020	11122

Depth (feet)	V_s (feet/s)	V_p (feet/s)
75.5	5208	7630
77.1	4879	9942
78.7	4971	9942
80.4	6104	12619
82.0	5356	10583
83.7	4879	10757
85.3	5106	10936
86.9	5938	11313
88.6	6309	12619
90.2	5992	12151
91.9	4915	9242
93.5	4772	9113
95.1	4621	8634
96.8	4990	8989
98.4	5126	10583
100.1	5067	10583
101.4	5067	10415
103.4	4990	10095
105.0	5028	10095
106.6	4654	9942
108.3	5335	11121
109.9	5537	11717
111.6	6433	11717
113.2	5807	11121
114.8	5423	10253

Fig. 5-3 ETEC RD-20 Suspension Logging

6.0 LADWP Receiving Station East

Site Description

Located in North Hollywood, CA
Latitude = 34.177, Longitude = -118.359

Work Performed

P- & S-Wave Velocity Measurements Using Suspension Logging

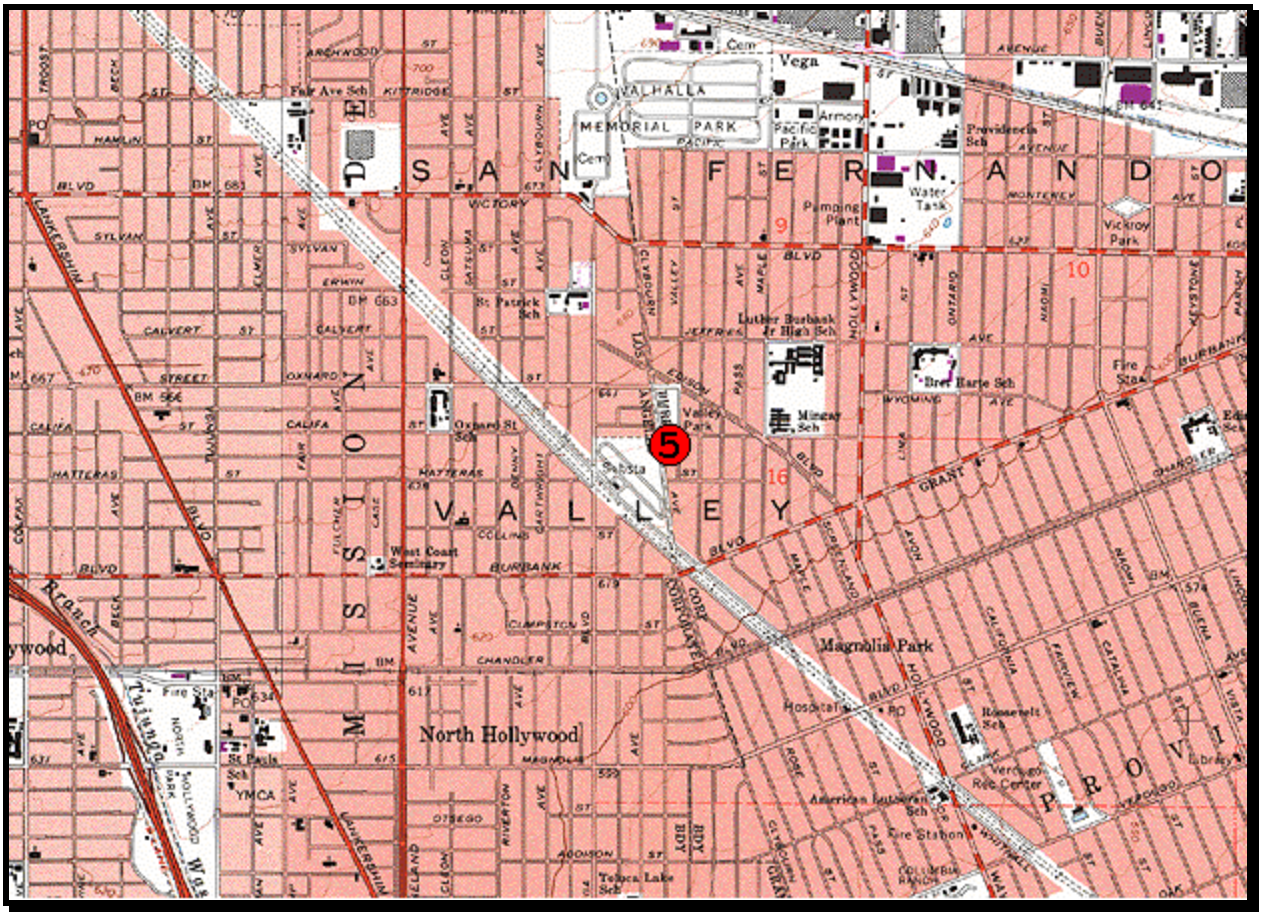

Fig. 6-1 Site Map of LADWP Receiving Station East Location

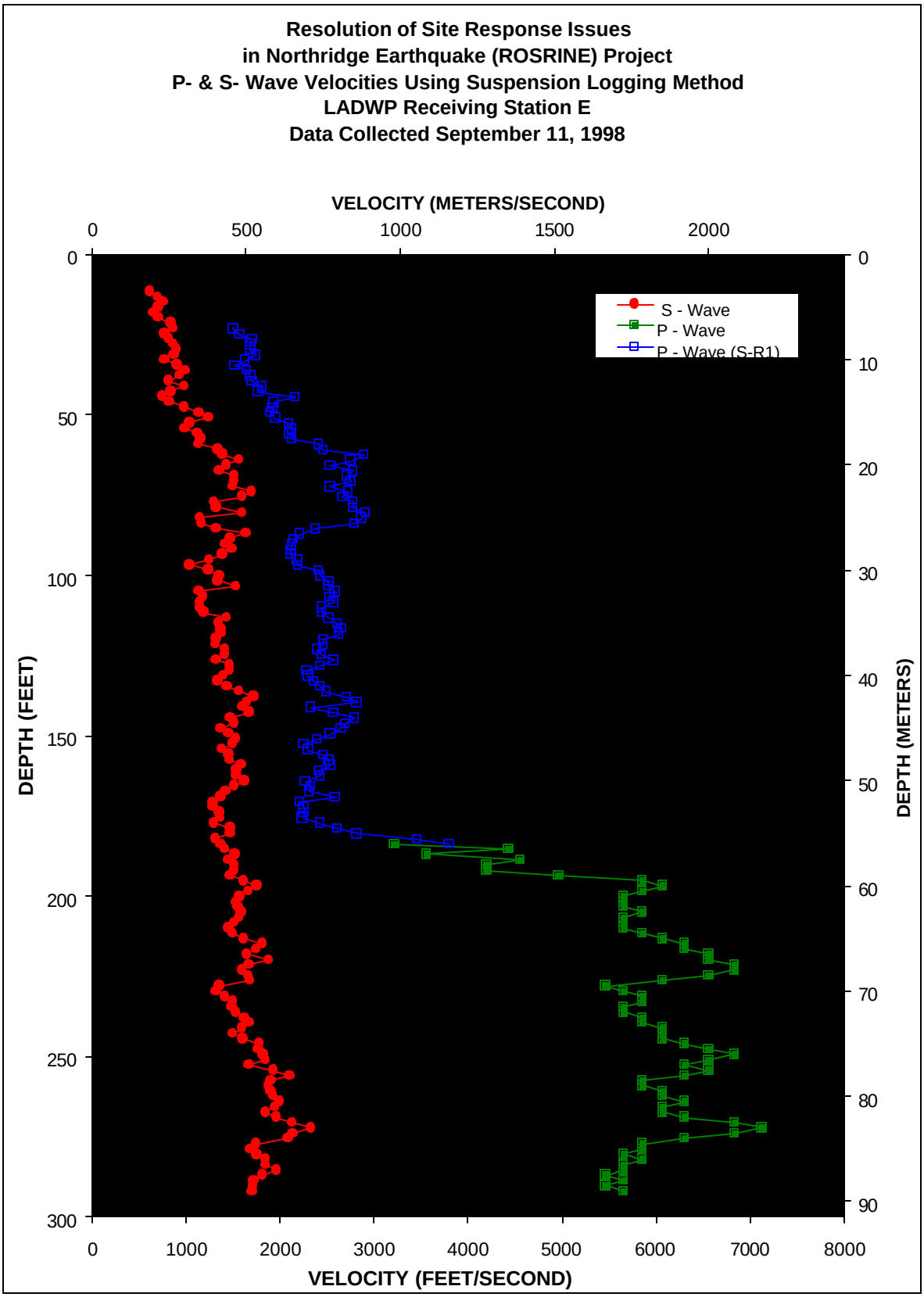

Fig. 6-2 LADWP Receiving Station East Suspension Logging

Depth (feet)	V_s (ft/s)	V_p (ft/s)	Depth (feet)	V_p (S-R1) (ft/s)
11.5	619		23.2	1505
13.1	706		24.8	1573
14.8	763		26.5	1707
16.4	713		28.1	1687
18.0	650		29.8	1687
19.7	709		31.4	1750
21.3	841		33.0	1628
23.0	863		34.7	1522
24.6	777		36.3	1647
26.3	820		38.0	1687
27.9	869		39.6	1707
29.5	905		41.2	1818
31.2	875		42.9	1772
32.8	777		44.5	2160
34.5	911		46.2	1944
36.1	994		47.8	1923
37.7	937		49.4	1902
39.4	814		51.1	1955
41.0	979		52.7	2096
42.7	841		54.4	2134
44.3	752		56.0	2108
45.9	828		57.6	2134
47.6	979		59.3	2414
49.2	1139		60.9	2465
50.9	1238		62.6	2893
52.5	1045		64.2	2756
54.1	991		65.8	2536
55.8	1127		67.5	2778
57.4	1159		69.1	2713
59.1	1131		70.8	2756
60.7	1345		72.4	2536
62.3	1390		74.0	2734
64.0	1562		75.7	2672
65.6	1433		77.3	2778
67.3	1356		79.0	2778
68.9	1512		80.6	2917
70.5	1512		82.2	2869
72.2	1505		83.9	2800
73.8	1700		85.5	2381
75.5	1600		87.2	2215
77.1	1302		88.8	2147
78.7	1323		90.4	2134
80.4	1600		92.1	2121
82.0	1151		93.7	2121
83.7	1163		95.4	2188
85.3	1328		97.0	2201
86.9	1640		98.6	2414
88.6	1471		100.3	2431
90.2	1426		101.9	2518
91.9	1491		103.6	2518
93.5	1390		105.2	2593
95.1	1247		106.9	2536
96.8	1045		108.5	2574
98.4	1243		110.1	2448
100.1	1356		111.8	2448
101.7	1345		113.4	2518
103.4	1533		115.1	2612
105.0	1143		116.7	2652

Depth (feet)	V_s (ft/s)	V_p (ft/s)	Depth (feet)	V_p (S-R1) (ft/s)
106.6	1180		118.3	2632
108.3	1151		120.0	2465
109.9	1151		121.6	2465
111.6	1189		123.3	2397
113.2	1433		124.9	2448
114.8	1350		126.5	2574
116.5	1373		128.2	2431
118.1	1379		129.8	2288
119.8	1328		131.5	2303
121.4	1318		133.1	2365
123.0	1414		134.7	2431
124.7	1414		136.4	2500
126.3	1328		138.0	2713
128.0	1465		139.7	2823
129.6	1465		141.3	2333
131.2	1396		142.9	2574
132.9	1345		144.6	2800
134.5	1439		146.2	2692
136.2	1562		147.9	2652
137.8	1727		149.5	2536
139.4	1649		151.1	2397
141.1	1608		152.8	2258
142.7	1674		154.4	2303
144.4	1478		156.1	2465
146.0	1512		157.7	2518
147.6	1379		159.3	2536
149.3	1458		161.0	2414
150.9	1533		162.6	2431
152.6	1498		164.3	2273
154.2	1384		165.9	2333
155.8	1458		167.5	2318
157.5	1465		169.2	2593
159.1	1593		170.8	2215
160.8	1540		172.5	2258
162.4	1540		174.1	2258
164.0	1624		175.7	2244
165.7	1512		177.4	2431
167.3	1426		179.0	2612
169.0	1379		180.7	2823
170.6	1292		182.3	3465
172.2	1292		184.0	3804
173.9	1361			
175.5	1367			
177.2	1297			
178.8	1471			
180.5	1478			
182.1	1318			
183.7	1373	3217		
185.4	1420	4434		
187.0	1526	3566		
188.7	1458	4557		
190.3	1519	4206		
191.9	1519	4206		
193.6	1478	4971		
195.2	1616	5859		
196.9	1754	6076		
198.5	1665	5859		
200.1	1577	5657		

Depth (feet)	V_s (feet/s)	V_p (feet/s)
201.8	1533	5657
203.4	1555	5657
205.1	1593	5859
206.7	1562	5657
208.3	1519	5657
210.0	1458	5657
211.6	1498	5859
213.3	1616	6076
214.9	1813	6309
216.5	1745	6309
218.2	1649	6562
219.8	1886	6562
221.5	1674	6835
223.1	1600	6835
224.7	1665	6562
226.4	1682	6076
228.0	1356	5468
229.7	1328	5657
231.3	1414	5859
232.9	1505	5859
234.6	1491	5657
236.2	1533	5657
237.9	1624	5859
239.5	1674	5859
241.1	1600	6076
242.8	1505	6076
244.4	1608	6076
246.1	1783	6309
247.7	1773	6562
249.3	1823	6835
251.0	1854	6562
252.6	1674	6309
254.3	1930	6562
255.9	2103	6309
257.6	1907	5859
259.2	1886	5859
260.8	1907	6076
262.5	1930	6076
264.1	2001	6309
265.8	1953	6076
267.4	1854	6076
269.0	1965	6309
270.7	2130	6835
272.3	2327	7132
274.0	2144	6835
275.6	2090	6309
277.2	1745	5859
278.9	1691	5859
280.5	1754	5657
282.2	1854	5859
283.8	1854	5657
285.4	1965	5657
287.1	1813	5468
288.7	1727	5657
290.4	1718	5468
292.0	1709	5657

Fig. 6-3 LADWP Receiving Station East Suspension Logging

7.0 Saturn Street School

Site Description

Located in Los Angeles, CA off Saturn Street
Latitude = 34.046, Longitude = -118.356

Work Performed

P- & S-Wave Velocity Measurements Using Suspension Logging
Geologic Logging

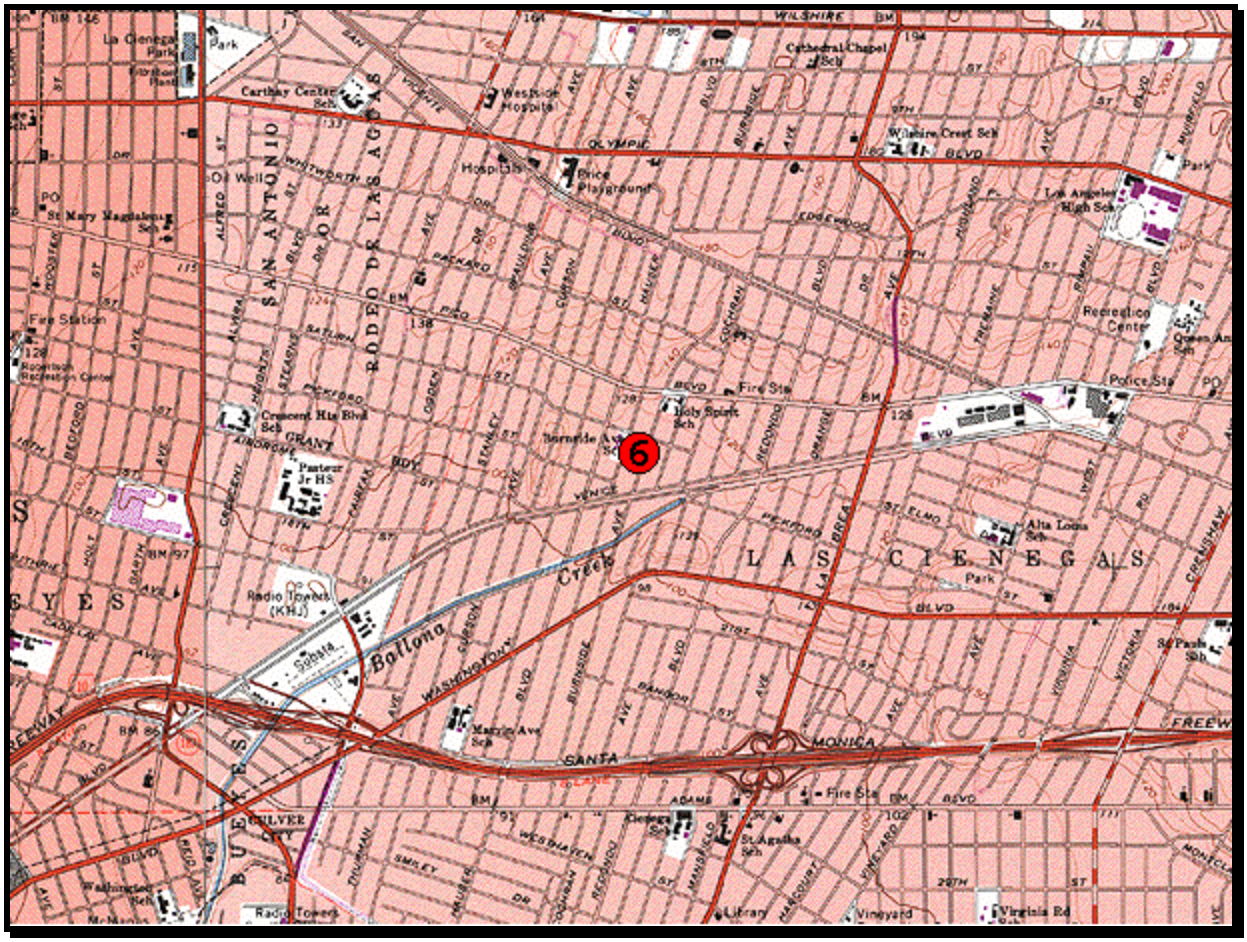

Fig. 7-1 Site Map of Saturn Street School Location

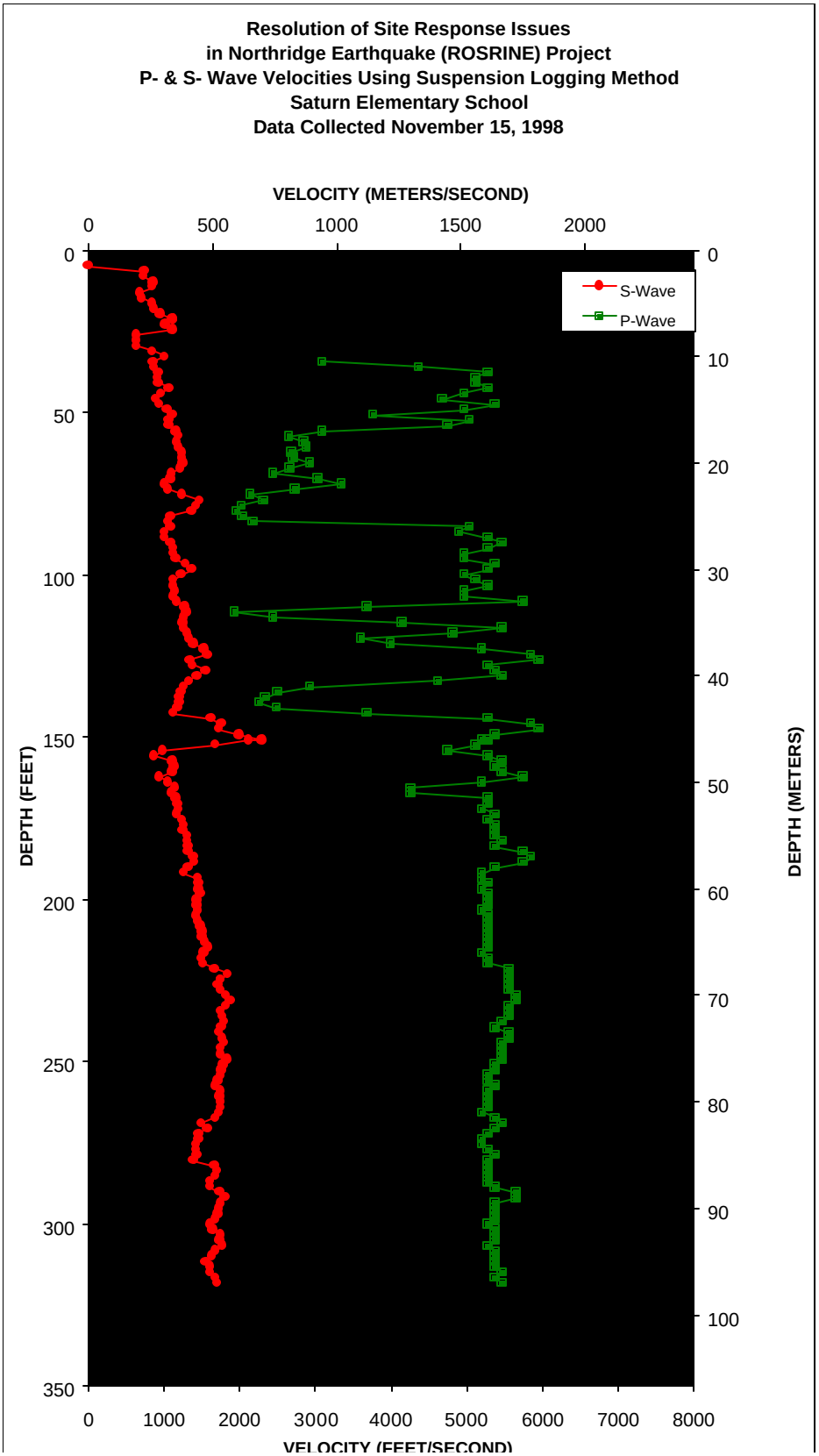

Fig. 7-2 PS Log Chart

Depth (feet)	Vs (feet/s)	Vp (feet/s)
4.9	0	
6.6	743	
8.2	727	
9.8	852	
11.5	846	
13.1	674	
14.8	704	
16.4	848	
18.0	863	
19.7	943	
21.3	1112	
21.3	1120	
23.0	1017	
24.6	1112	
26.3	631	
27.9	629	1131
29.5	630	1101
31.2	848	1793
32.8	1009	1965
34.5	852	3095
36.1	863	4374
37.7	929	5292
39.4	919	5126
41.0	929	5126
42.7	1062	5292
44.3	959	4971
45.9	892	4687
47.6	937	5378
49.2	1042	4971
50.9	1108	3771
52.5	1062	5047
54.1	1069	4755
55.8	1155	3095
57.4	1193	2646
59.1	1163	2853
60.7	1189	2878
62.3	1243	2689
64.0	1238	2711
65.6	1252	2929
67.3	1211	2667
68.9	1097	2448
70.5	1086	3038
72.2	1009	3348
73.8	1058	2734
75.5	1243	2144
77.1	1465	2310
78.7	1420	2025
80.4	1367	1953
82.0	1086	2038
83.7	1058	2173
85.3	1090	5047
86.9	1000	4897
88.6	1003	5292
90.2	1090	5468
91.9	1120	5292
93.5	1124	4971
95.1	1159	4971
96.8	1287	5378
98.4	1361	5292
100.1	1229	4971
101.7	1116	5126
103.4	1120	5292
105.0	1147	4971
106.6	1120	4971
108.3	1163	5756

Depth (feet)	Vs (feet/s)	Vp (feet/s)
109.9	1277	3686
111.6	1297	1930
113.2	1262	2448
114.8	1247	4153
116.5	1262	5468
118.1	1302	4825
119.8	1334	3605
121.4	1390	4001
123.0	1533	5208
124.7	1570	5859
126.3	1345	5965
128.0	1379	5292
129.6	1555	5378
131.2	1439	5468
132.9	1328	4621
134.5	1262	2929
136.2	1229	2504
137.8	1202	2343
139.4	1206	2263
141.1	1176	2485
142.7	1116	3686
144.4	1624	5292
146.0	1764	5859
147.6	1718	5965
149.3	1988	5378
150.9	2294	5208
150.9	2117	5292
152.6	1674	5126
154.2	976	4755
155.8	868	5292
157.5	1105	5468
159.1	1135	5378
160.8	1108	5468
162.4	940	5756
164.0	1052	5208
165.7	1139	4261
167.3	1094	4261
169.0	1159	5292
170.6	1180	5292
172.2	1189	5208
173.9	1172	5378
175.5	1233	5292
177.2	1262	5378
178.8	1252	5378
180.5	1302	5378
182.1	1312	5468
183.7	1318	5378
185.4	1318	5756
187.0	1384	5859
188.7	1402	5756
190.3	1318	5378
191.9	1257	5208
193.6	1445	5208
195.2	1458	5292
196.9	1458	5208
198.5	1478	5292
200.1	1433	5292
201.8	1439	5292
203.4	1452	5208
205.1	1426	5292
206.7	1445	5292
208.3	1485	5292
210.0	1505	5292
211.6	1505	5292
213.3	1540	5292

Depth (feet)	Vs (feet/s)	Vp (feet/s)
214.9	1585	5292
216.5	1533	5208
218.2	1498	5292
219.8	1512	5292
221.5	1665	5561
223.1	1843	5561
224.7	1754	5561
224.7	1754	5561
226.4	1709	5561
228.0	1745	5561
229.7	1823	5657
231.3	1875	5657
232.9	1823	5561
234.6	1745	5561
236.2	1773	5561
237.9	1793	5468
239.5	1764	5378
241.1	1727	5561
242.8	1773	5561
244.4	1793	5468
246.1	1754	5468
247.7	1754	5468
249.3	1833	5468
251.0	1783	5378
252.6	1764	5378
254.3	1745	5292
255.9	1709	5292
257.6	1682	5378
259.2	1745	5292
260.8	1736	5292
262.5	1745	5292
264.1	1745	5292
265.8	1718	5208
267.4	1674	5378
269.0	1498	5468
270.7	1570	5378
272.3	1458	5292
274.0	1458	5208
275.6	1420	5208
277.2	1426	5292
278.9	1433	5378
280.5	1384	5292
282.2	1665	5292
283.8	1700	5292
285.4	1674	5292
287.1	1616	5292
288.7	1608	5378
290.4	1736	5657
292.0	1803	5657
293.6	1745	5378
295.3	1727	5378
296.9	1709	5378
298.6	1674	5378
300.2	1616	5292
301.8	1640	5378
303.5	1745	5378
305.1	1736	5378
306.8	1773	5292
308.4	1682	5378
310.0	1632	5378
311.7	1548	5378
313.3	1608	5378
315.0	1616	5468
316.6	1674	5378
318.2	1700	5468

Fig. 7-3 Saturn Elementary School Suspension Logging

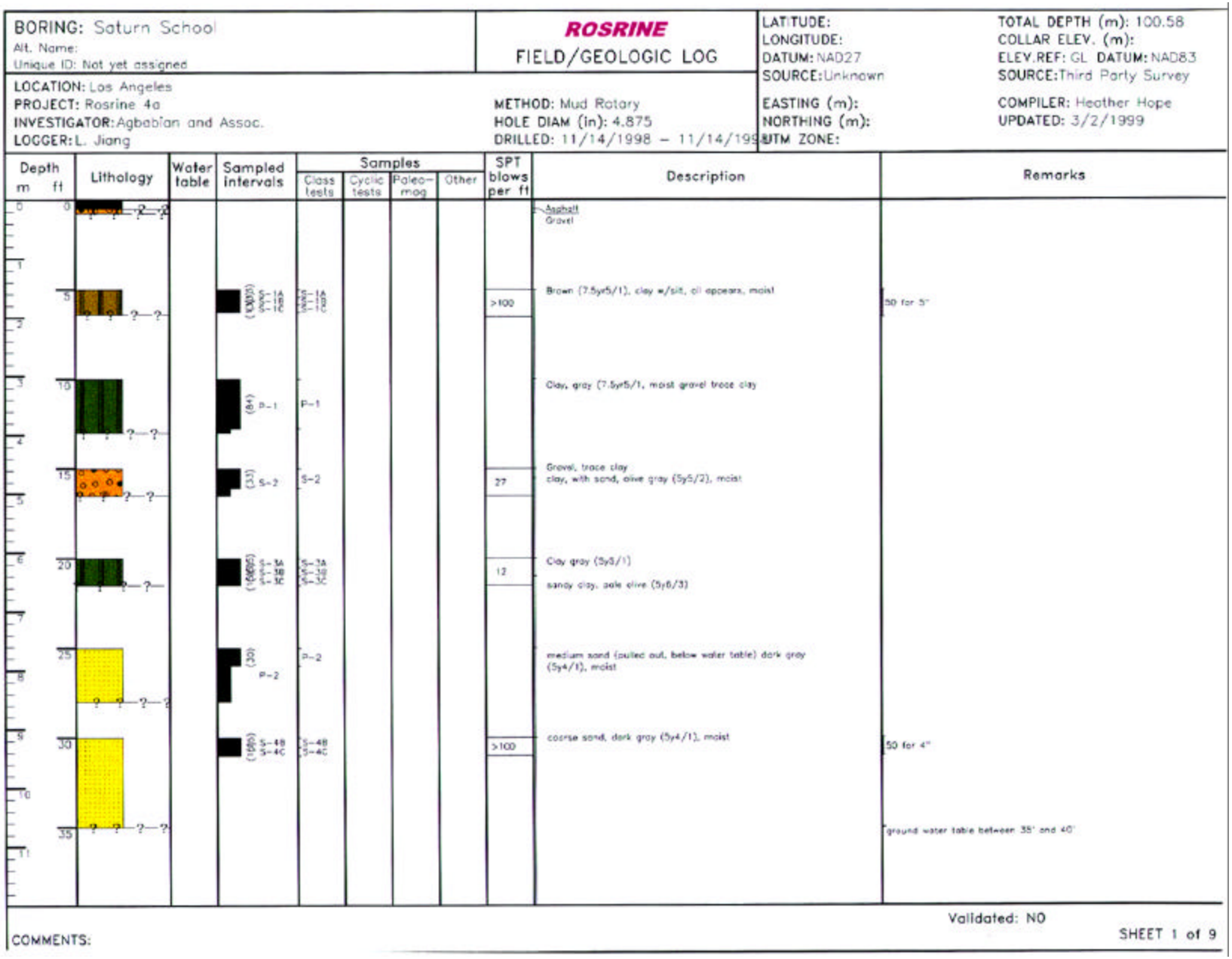

Fig. 7-4 Saturn Elementary School Geologic Logs

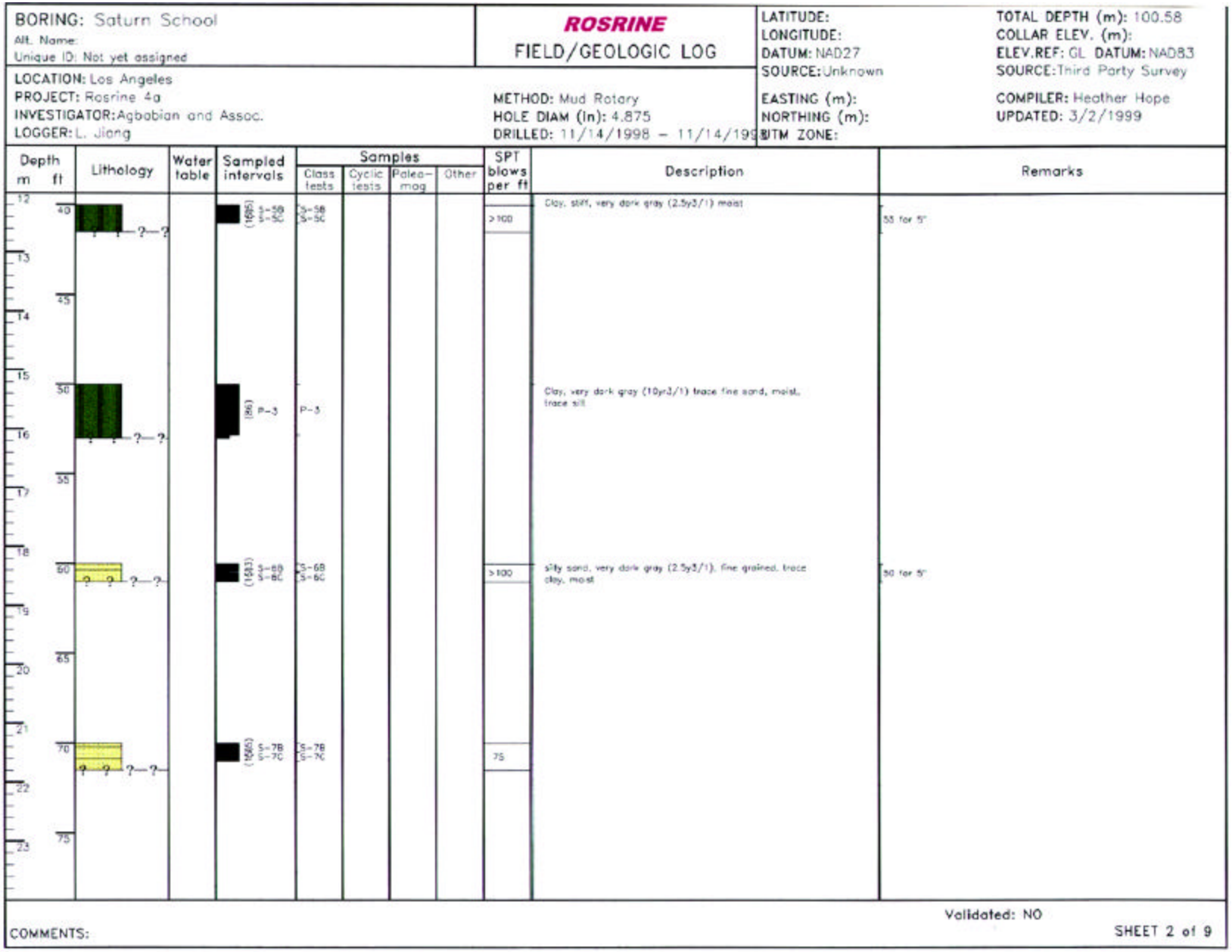

Fig. 7-4 (Continued) Saturn Elementary School Geologic Logs

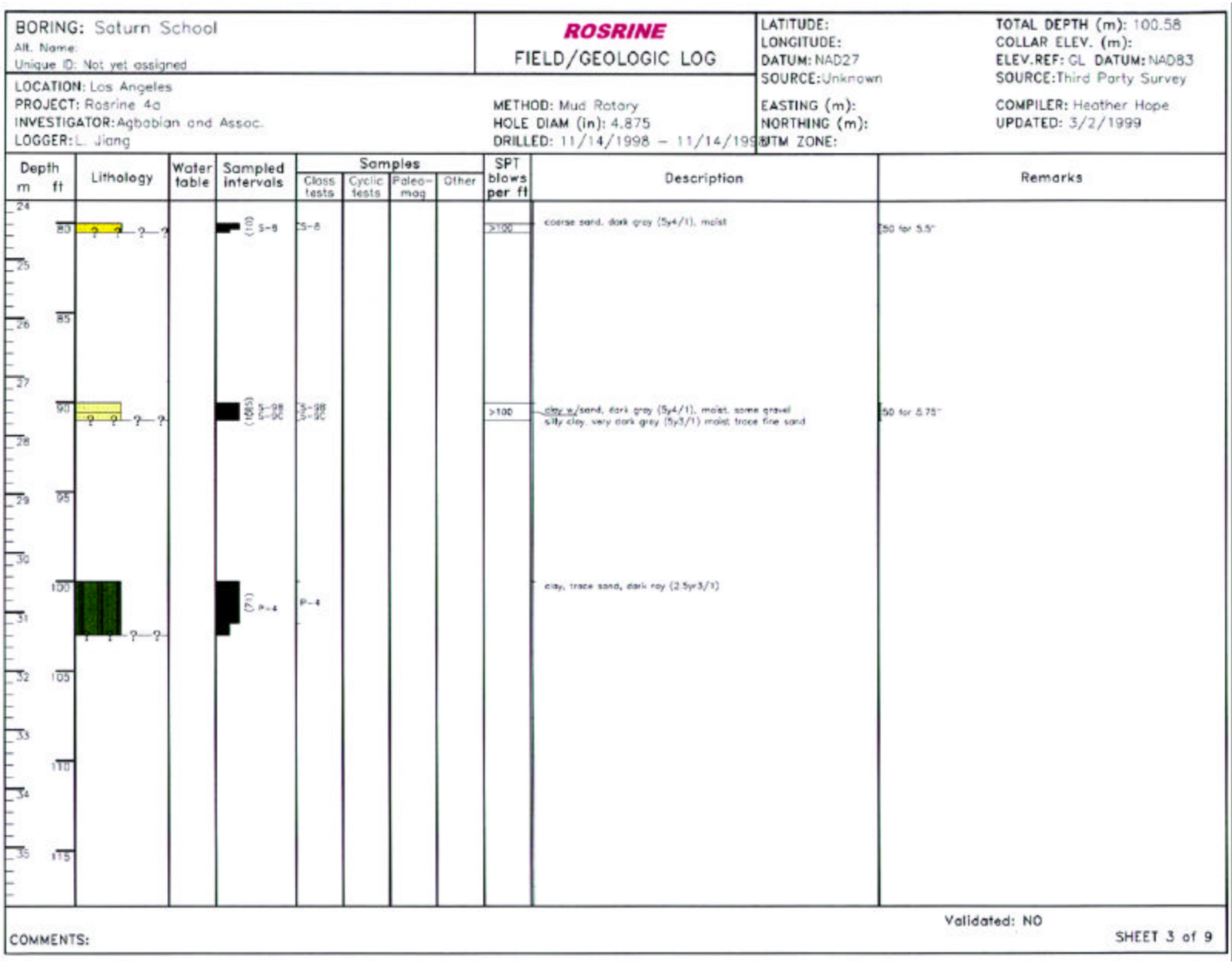

Fig. 7-4 (Continued) Saturn Elementary School Geologic Logs

BORING: Saturn School
Alt. Name:
Unique ID: Not yet assigned

ROSRINE
FIELD/GEOLOGIC LOG

LATITUDE:
LONGITUDE:
DATUM: NAD27
SOURCE: Unknown
EASTING (m):
NORTHING (m):
UTM ZONE:

TOTAL DEPTH (m): 100.58
COLLAR ELEV. (m):
ELEV.REF: GL DATUM: NAD83
SOURCE: Third Party Survey
COMPILER: Heather Hope
UPDATED: 3/2/1999

LOCATION: Los Angeles
PROJECT: Rosrine 4a
INVESTIGATOR: Agbabian and Assoc.
LOGGER: L. Jiang

METHOD: Mud Rotary
HOLE DIAM (in): 4.875
DRILLED: 11/14/1998 – 11/14/199

Depth m	Depth ft	Lithology	Water table	Sampled intervals	Samples: Class tests	Samples: Cyclic tests	Samples: Paleo-mag	Samples: Other	SPT blows per ft	Description	Remarks
36											
	120										driving through boulder, switch to rock bit, 6" – 8" boulders
37											
38	125										
39											
	130										
40											
41	135										
42											
	140	? ? ? ?		5–10	5–10				>100	silt, gray (7.5yr5/1) moist, trace sand	50 for 2"
43											
44	145										
45											
	150										
46											
47	155										

Validated: NO

COMMENTS:

SHEET 4 of 9

Fig. 7-4 (Continued) Saturn Elementary School Geologic Logs

BORING: Saturn School
Alt. Name:
Unique ID: Not yet assigned

ROSRINE
FIELD/GEOLOGIC LOG

LATITUDE:
LONGITUDE:
DATUM: NAD27
SOURCE: Unknown

TOTAL DEPTH (m): 100.58
COLLAR ELEV. (m):
ELEV.REF: GL DATUM: NAD83
SOURCE: Third Party Survey

LOCATION: Los Angeles
PROJECT: Rosrine 4a
INVESTIGATOR: Agbabian and Assoc.
LOGGER: L. Jiang

METHOD: Mud Rotary
HOLE DIAM (in): 4.875
DRILLED: 11/14/1998 – 11/14/199

EASTING (m):
NORTHING (m):
UTM ZONE:

COMPILER: Heather Hope
UPDATED: 3/2/1999

Depth m	Depth ft	Lithology	Water table	Sampled intervals	Samples: Class tests	Samples: Cyclic tests	Samples: Paleo-mag	Samples: Other	SPT blows per ft	Description	Remarks
48											
	160										
49											
50											
	165										
51											
	170										
52											
53											
	175										
54											
55	180	? ? ? ?		S-11	S-11				>100	sand (medium) dark gray (5Y4/1)	100 for 5"
56											
	185										
57											
58	190										
59											
	195										

COMMENTS:

Validated: NO

SHEET 5 of 9

Fig. 7-4 (Continued) Saturn Elementary School Geologic Logs

BORING: Saturn School
Alt. Name:
Unique ID: Not yet assigned

ROSRINE
FIELD/GEOLOGIC LOG

LATITUDE:
LONGITUDE:
DATUM: NAD27
SOURCE: Unknown
EASTING (m):
NORTHING (m):
UTM ZONE:

TOTAL DEPTH (m): 100.58
COLLAR ELEV. (m):
ELEV.REF: GL DATUM: NAD83
SOURCE: Third Party Survey
COMPILER: Heather Hope
UPDATED: 3/2/1999

LOCATION: Los Angeles
PROJECT: Rosrine 4a
INVESTIGATOR: Agbabian and Assoc.
LOGGER: L. Jiang

METHOD: Mud Rotary
HOLE DIAM (in): 4.875
DRILLED: 11/14/1998 – 11/14/199

Depth m	Depth ft	Lithology	Water table	Sampled intervals	Samples: Class tests	Samples: Cyclic tests	Samples: Paleo-mag	Samples: Other	SPT blows per ft	Description	Remarks
60											
61	200										
62	205										
63											
64	210										
65	215										
66											
67	220			S-12	S-12				>100	silt, dark gray (7.5y4/1, moist shell fragment s in silt, some sand	50 for 4" rig rattles – 8' thick gravel layer
68	225										
69											
70	230										
71	235								>100		50 for 2.5"

Validated: NO

COMMENTS:

SHEET 6 of 9

Fig. 7-4 (Continued) Saturn Elementary School Geologic Logs

BORING: Saturn School
Alt. Name:
Unique ID: Not yet assigned

ROSRINE
FIELD/GEOLOGIC LOG

LATITUDE:
LONGITUDE:
DATUM: NAD27
SOURCE: Unknown
EASTING (m):
NORTHING (m):
UTM ZONE:

TOTAL DEPTH (m): 100.58
COLLAR ELEV. (m):
ELEV.REF: GL DATUM: NAD83
SOURCE: Third Party Survey
COMPILER: Heather Hope
UPDATED: 3/2/1999

LOCATION: Los Angeles
PROJECT: Rosrine 4a
INVESTIGATOR: Agbabian and Assoc.
LOGGER: L. Jiang

METHOD: Mud Rotary
HOLE DIAM (in): 4.875
DRILLED: 11/14/1998 – 11/14/199

Depth m	Depth ft	Lithology	Water table	Sampled intervals	Samples: Class tests	Samples: Cyclic tests	Samples: Palea-mag	Samples: Other	SPT blows per ft	Description	Remarks
72											
73	240										
74	245										
75											
76	250	@									
77											
78	255								>100		50 for 2.5"
79	260										
80											
81	265										
82	270										
83											
	275										

COMMENTS:

Validated: NO

SHEET 7 of 9

Fig. 7-4 (Continued) Saturn Elementary School Geologic Logs

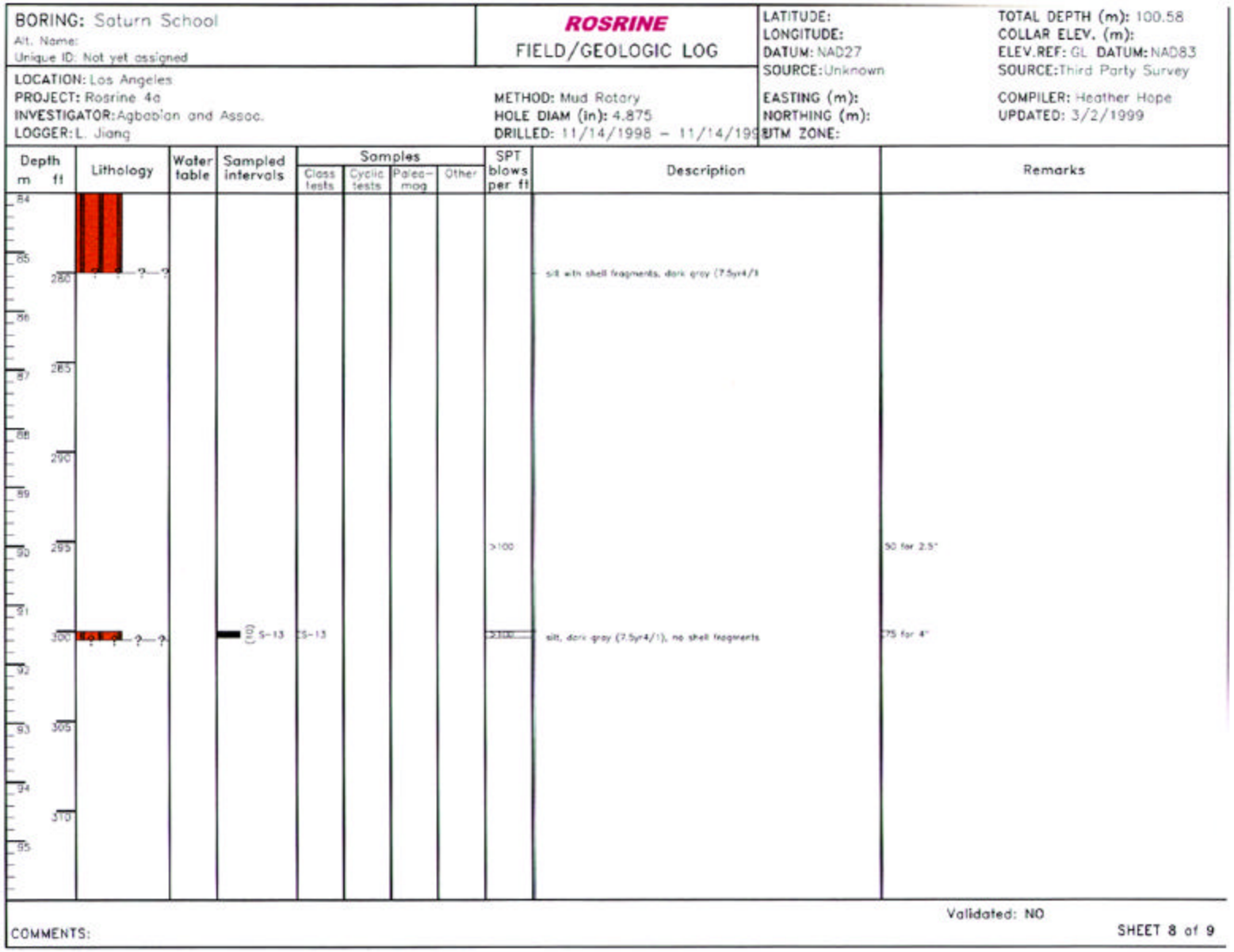

Fig. 7-4 (Continued) Saturn Elementary School Geologic Logs

BORING: Saturn School
Alt. Name:
Unique ID: Not yet assigned

ROSRINE
FIELD/GEOLOGIC LOG

LATITUDE:
LONGITUDE:
DATUM: NAD27
SOURCE: Unknown
EASTING (m):
NORTHING (m):
UTM ZONE:

TOTAL DEPTH (m): 100.58
COLLAR ELEV. (m):
ELEV.REF: GL DATUM: NAD83
SOURCE: Third Party Survey
COMPILER: Heather Hope
UPDATED: 3/2/1999

LOCATION: Los Angeles
PROJECT: Rosrine 4a
INVESTIGATOR: Agbabian and Assoc.
LOGGER: L. Jiang

METHOD: Mud Rotary
HOLE DIAM (in): 4.875
DRILLED: 11/14/1998 – 11/14/199

Depth m	Depth ft	Lithology	Water table	Sampled intervals	Samples: Class tests	Samples: Cyclic tests	Samples: Paleo-mag	Samples: Other	SPT blows per ft	Description	Remarks
96	315										
97											
	320										
98									>100		50 for 2.5"
99	325										
100											

E.O.H 100.58 m

COMMENTS:

Validated: NO

SHEET 9 of 9

Fig. 7-4 (Continued) Saturn Elementary School Geologic Logs

Acknowledgments

The work described in this report was funded by the Pacific Earthquake Engineering Research (PEER) Center under the Pacific Gas & Electric Company Contract No. 09566. This financial support is gratefully acknowledged.

This work made use of Pacific Earthquake Engineering Research Center Shared Facilities supported by the Earthquake Engineering Research Center Program of the National Science Foundation under Award Number EEC-9701568.

The financial support of the PEARL sponsor organizations including the Pacific Gas & Electric Company (PG&E), the California Energy Commission (CEC), and the California Department of Transportation (Caltrans) is acknowledged.

ACKNOWLEDGMENTS

The work described in this report was funded by the Pacific Earthquake Engineering Research (PEER) Center under the Pacific Gas & Electric Company Contract No. 09566. This financial support is gratefully acknowledged.

This work made use of Pacific Earthquake Engineering Research Center Shared Facilities supported by the Earthquake Engineering Research Center Program of the National Science Foundation under Award Number EEC-9701568.

The financial support of the PEARL sponsor organizations including the Pacific Gas & Electric Company (PG&E), the California Energy Commission (CEC), and the California Department of Transportation (Caltrans) is acknowledged.

PACIFIC EARTHQUAKE ENGINEERING RESEARCH CENTER

Rapid Estimation of Ground Shaking for Emergency Response

Douglas Dreger

Anastasia Kaverina
University of California, Berkeley

A report to the PEER Program of Applied Earthquake Engineering Research on Lifeline Systems

The financial support of the sponsor organizations including the Pacific Gas & Electric Company (PG&E), the California Energy Commission (CEC), and the California Department of Transportation (Caltrans) is acknowledged.

PEER UTILITIES PROGRAM
REPORT NO. 2000/07

Development of Procedures for the Rapid Estimation of Ground Shaking
Task 7: Ground Motion Estimates for Emergency Response
Final Report

Douglas Dreger and Anastasia Kaverina
University of California, Berkeley, Seismological Laboratory

Executive Summary

This project focused on the development of methodology for the near-real-time estimation of earthquake strong ground motion with the objective of providing this information on a regional (statewide) scale. A critical objective of our development was to provide seamless implementation and uniform performance in varied network coverage. To accomplish this goal we: 1) refined a finite fault inverse method to determine fault slip using regional distance stations; 2) developed a strong motion simulation procedure that uses finite source information as input; 3) investigated the incorporation of site type correction factors, 4) and investigated alternative methods to improve the simulation of high frequency strong ground motions. We have successfully completed these tasks and have developed software that calculates model-based estimates of strong shaking that include the focussing effects due to source directivity. The method we have developed estimates PGA, PGV and spectral acceleration at periods of 0.3, 1.0 and 3.0 seconds. These model predictions may be used to interpolate actual strong motion observations (when available) in the same manner as the southern California TriNet ShakeMap (Wald et al. 1999), and we provide examples of data/model shakemaps for the Landers and Northridge earthquakes. These examples show that it is possible to calculate robust shakemaps even in extremely sparse coverage. In the following the results of each component of the project are summarized.

Under task 1, the refinement of the finite source inverse code largely involved testing and program error fixes to produce stable maps of fault slip using broadband stations located at regional distances. We extensively tested the algorithms with data recorded for the 1992 Landers and 1994 Northridge earthquakes, and compared our regionally derived fault slip maps with those obtained using local strong motion recordings. Favorable comparisons indicate that our methodology is capable of uniquely determining the causative fault plane of the earthquake, the slip dimension (both along strike and down dip), the earthquake rupture velocity, and a reasonable characterization of the gross slip distribution, suggesting that the derived source parameters may be used to simulate near-source strong ground motions. As part of a complementary project we modified the code to facilitate its integration into the Rapid Earthquake Data Integration (REDI) system (Gee et al., 1996) operated by the Berkeley Seismological Laboratory. The codes must still be integrated and tested within the REDI operating environment and we expect that this work will be accomplished in the coming year. Our preliminary testing indicates that the essential source information may be obtained within 4 to 20 minutes following the determination of a seismic moment tensor solution depending upon the level of approximation required.

The focus of task 2 was to use the regionally derived fault slip maps to simulate the distribution of near-source strong ground motion, and to compare the model predictions with observations to calibrate the methodology. Additionally, task 4 involved the testing of hybrid Green'' function (Pitarka et al., 1999) and the composite source (Zeng et al., 1994) methods to attempt to better simulate higher frequency ground motions. At the request of the program management committee we also investigated the use of an empirical attenuation relationship that incorporates source specific directivity information (Somerville et al., 1997). For each of the methods we compared predicted values of PGA, PGV and Sa (0.3, 1.0 & 3.0 seconds) against the observations, with the exception of the empirical method because a PGV relationship is not yet available. Our basic method of ground motion simulation is one we developed in which fault slip is deterministically integrated using appropriate local Green's functions. We found that this deterministic approach performed reasonably well in the comparisons of PGV, however the Sa comparisons had mixed results. The PGA, PGV and Sa maps were all found to be successful in outlining the area of observed large ground motions, however there were varying degrees of misfit of the location of predicted and observed maximal values. The methods of Pitarka et al., (1999) and Zeng et al., (1994) improved the results somewhat but not to a degree that offsets their higher computational expense. The glowing success in this project involved the incorporation of the empirical attenuation relationship. PGA and Sa (0.3, 1.0 and 3.0 seconds) were well modeled using the approach of Somerville et al. (1997), which utilized the regionally derived finite source information as input. The empirical approach is also extremely fast and requires information available after the initial fault plane and rupture velocity inversion, which is also relatively fast. The best shakemaps for the two study events were obtained by taking the larger of the two values from the deterministic and the empirical maps. We call this map our 'conservative shakemap'. The empirical component of the conservative shakemap is found to explain the mean attenuation of the observed strong motions very well and the deterministic component provides a better estimate of the large near-fault ground motions.

Under task 3 we explored ways to improve the predicted strong motion parameters by applying site corrections to the synthetic ground motions. To facilitate this comparison we utilized the methodology implemented by Wald et al. (1999) for the southern California TriNet ShakeMap. In this case the site geology is classified as quaternary, tertiary and Mesozoic (QTM), and site corrections after Borcherdt (1994) are applied. We found that the QTM corrections improved the agreement with the observations but not enough to offset a systematic under prediction at LA basin sites. A second method used two 1D velocity models to characterize rock and soil sites. The application of site specific Green's functions provided a noticeable improvement in the predicted shakemap. However we note that stations located within the LA Basin remain under predicted. The results show that empirically derived site corrections applied to synthesized time histories is not enough to offset the effects due to large scale 3D structures such as the LA basin. It may be possible to determine site adjustments for specific 1D velocity models numerically using finite difference methods and appropriately calibrated 3D structure models to develop a table of 3D-to-1D site adjustments. This can presently be accomplished in southern California and the San Francisco bay area, however in large regions of central and northern California such a calibration would require a very considerable effort to compile and verify a suitable 3D structure model.

Through the course of this research we have developed a multi-staged algorithm to generate a shakemap. First, line source or course planar inversions are performed to determine the rupture velocity, causative fault plane and slip dimension of an earthquake. This information may then be used to generate a shakemap using a directivity sensitive attenuation relationship (e.g. Somerville et al. 1997). Site adjustments are applied to the empirical rock ground motions. This stage of processing may only consume 4 to 15 minutes of CPU time depending upon the level of approximation. Strong ground motion parameters that may be estimated at this stage include PGA and spectral acceleration at 0.3, 1.0 and 3.0 seconds period. It will be necessary to develop a directivity sensitive PGV attenuation relationship to provide a seamless methodology. If local strong motion data is available it may be integrated with the empirical values to develop a data/model shakemap. With relatively dense coverage the map would be data driven with model predictions contributing only in the regions where there are gaps in coverage. Following the determination of the causative fault plane and rupture velocity, processing may be continued to determine a higher resolution picture of the distribution of fault slip. This additional processing step consumes an additional 18 minutes for both of the earthquakes we studied. The higher resolution slip map is then used to simulate near-source synthetic time histories from which values of PGA, PGV and spectral acceleration may be measured. We then combine the larger of the simulated and the empirical ground motions to produce a 'conservative shakemap'. As in the first stage of processing available data may be integrated into the shakemap, where model predictions are used to interpolate only in areas where there are no observations. Using the attenuation relationship as an integral component of the methodology allows various levels of approximation such as the use of a strong motion centroid with point-source attenuation (e.g. Wald et al., 1999), source directivity specific empirical attenuation, and finally the source directivity specific 'conservative shakemap' developed in this study. A common multi-parametric attenuation relationship provides seamless transition from one level of approximation to another as more data and model information becomes available. We conclude this report with examples of the evolution of a shakemap for the Northridge and Landers earthquakes in very sparse network coverage as may be anticipated in large areas of California and the western United States.

Introduction

Earthquake information available soon after a damaging earthquake begins with estimates of the time of occurrence, the epicenter and hypocenter, an estimate of the magnitude, and fairly recently a seismic moment tensor solution providing a more robust estimate of earthquake size and the radiation pattern (e.g. Pasyanos et al. 1996). While such basic information is essential in the rapid characterization of the likely damage due to strong ground motions from the earthquake it is a rather limited characterization. Ideally city and state emergency response providers, public utilities and earthquake engineers would like to know where the strongest shaking occurred, which in a large extended earthquake is very likely not co-located with the epicenter.

In southern California this problem has been addressed with the development of the TriNet network of broadband and strong motion instruments that provide digital data in near real-time. The TriNet calls for the installation of 600 digitally recorded accelerometers to monitor strong ground motions throughout southern California, with the greatest density of coverage in the urban area. Figure 1 shows the locations of TriNet stations that are in the ground and compares the monitoring regions of both southern and northern California. These stations are currently being used to rapidly contour the regional extent of strong ground shaking (Wald et al., 1999). Parameters relevant to emergency response providers, utilities and engineers such as peak ground acceleration (PGA), peak ground velocity (PGV) and, spectral acceleration at periods of 0.3-1.0-3.0 s, and instrumental intensity are automatically determined and posted to the WWW. Additionally, seismological information such as first-motion focal mechanisms and seismic moment tensors are also provided. Figure 2 compares TriNet PGV shakemaps for the Northridge and Landers earthquakes. In the case of the Northridge earthquake (Figure 2b) the station coverage is quite good and there is considerable definition of the shakemap contours. The region of elevated PGV north of the epicenter is due to directivity focusing and the region northeast of the epicenter is due to both directivity and basin amplification. In contrast the station coverage for the 1992 Landers earthquake is sparse and the fortuitous location of the Lucerne Valley station is controlling the mapping of PGV near the fault.

In northern California there are plans to develop a TriNet like system, however because the monitoring area in northern California is considerably larger and a northern California TriNet is only in its conceptual phase, interim methods and methods suitable for sparse networks need to be developed. The distributed nature of at risk facilities is demonstrated by the locations of the dense urban areas of the San Francisco Bay and Sacramento, hydroelectric power generation facilities, rail transportation, state and national public highways, and the state aqueduct system. Thus a shakemap system for central and northern California needs to provide rapid estimates of strong shaking in the urban areas as

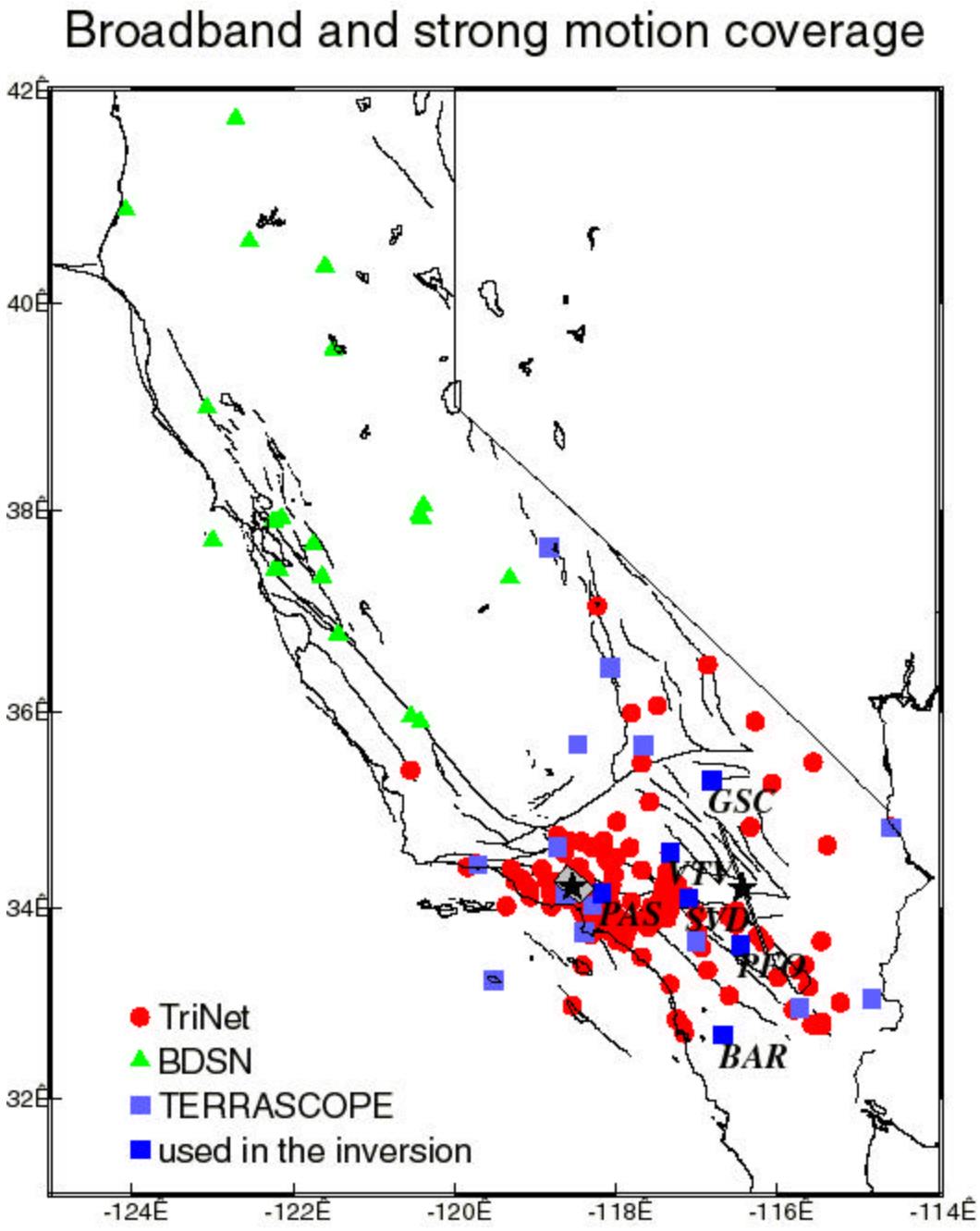

Figure 1. Map showing broadband and strong motion coverage in southern California. The red circles show strong motion stations of the TriNet, and the blue squares show broadband TERRAscope stations. The broadband Berkeley Digital Seismic Network (green triangles) compares the broadband coverage in central and northern California. Stations that were used in our analysis are identified by name.

well as the surrounding rural areas where most of the supporting infrastructure is located. The focus of this research project is to develop such as system that simulates near-source strong ground motions using event specific source information derived from the regional Berkeley Digital Seismic Network (BDSN, Figure 1). The BDSN is a continuously recording and digitally telemetered network with co-sited weak and strong motion sensors. The data latency of this system is minimal and data from this system is used to locate, estimate magnitude, and provide strong motion values for earthquakes in near-real-time (Gee et al., 1996). The data from this network is further used to determine the seismic moment tensor of M>3.5 earthquakes throughout central and northern California in near-real-time (Pasyanos et al., 1996). The software and methodology we have developed under this contract naturally builds on the automatic processing that has already been implemented. In this study we test the new methods using regional and broadband data sets collected for the June 28, 1992 Landers (M_W7.1) and the January 16, 1994 Northridge (M_W6.7) earthquakes.

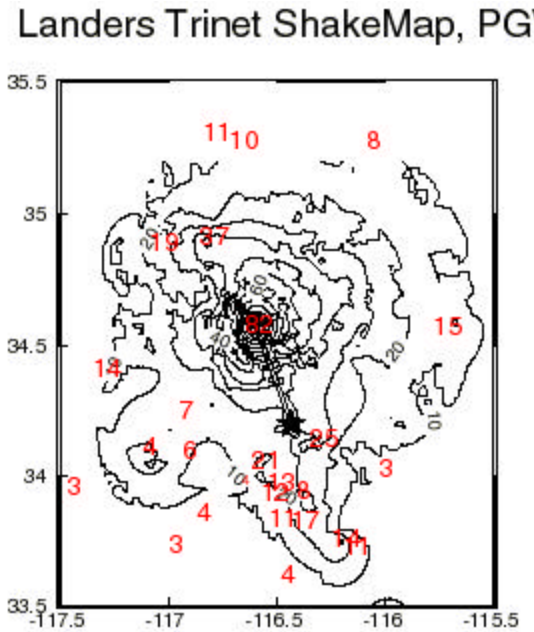

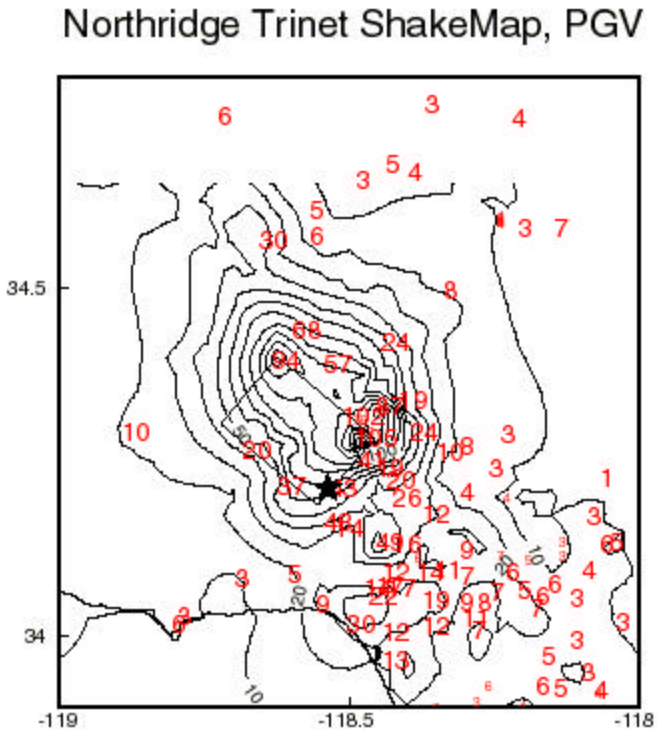

Figure 2. TriNet PGV shakemaps are compared for the 1992 Landers (a) and the 1994 Northridge (b) earthquakes. The contours show TriNet shakemap values and the red numbers show the observed PGV at individual recording stations. Both are in units of cm/s Note that only the stations shown were used in the determination of the shakemap contours, however an attenuation model scaled from the observed strong motion centroid was used to help interpolate the map were data does not exist (e.g. Wald et al., 1999). The stars identify the epicenters.

Section I: Regional Distance Finite Fault Determination

Following the occurrence of an earthquake in central and northern California there is a hierarchy of information that is determined by the UCB/USGS Joint Notification System. Earthquake locations are obtained within several minutes. Broadband waveform data recorded by the BDSN is used to estimate a local magnitude (M_L) and if the M_L is greater than 3.5 a seismic moment tensor is determined. Typically the seismic moment tensor is obtained within 6-9 minutes after the occurrence of an earthquake. The seismic moment tensor inversion provides estimates of the scalar seismic moment, a centroid depth and the orientations of two possible fault planes. The point-source representation used in the seismic moment tensor method results in a fault plane ambiguity. The ability to rapidly determine the causative fault plane is of value in itself to understand the possible extent of damage following an earthquake. We have modified a method to determine earthquake finite source parameters (fault slip, dislocation rise time and rupture velocity) to use regionally recorded broadband waveforms. In this method, given a hypocenter location and a source mechanism of an earthquake, we use a non-negative least squares solver to determine the distribution of fault slip from regionally recorded broadband data. This method is similar to those used to invert local strong motion data for earthquake source parameters (e.g. Cohee and Beroza, 1994; Wald and Heaton, 1994). In the source model, the rupture propagates with constant velocity over a grid of point sources each with constant dislocation rise time, and the Green's functions are shifted in time to account for relative hypocenter-subfault-station distances and the time for the passage of a circular rupture front. We use a precompiled catalog of Green's functions for point source responses. The Green's functions are computed using a frequency-wavenumber approach developed by Saikia (1994) and must be computed in advance since this preparatory step is very time consuming. The velocity model we use to estimate the source parameters is SoCal (Dreger and Helmberger, 1993), which has been found to be an appropriate representation of average crustal properties throughout southern California. The implementation of the procedures described in this report in central and northern California will require a different set of Green's functions. The central and northern California region may be approximated by both the SoCal and the GIL7 velocity models (Dreger and Romanowicz, 1994; Pasyanos et al., 1996). Because of the regional nature of the inverse problem we are solving we simplify the problem by considering only constant values of dislocation rise time and rupture velocity. In addition we assume that the rake angle of individual subfaults is constant and equal to average value obtained from automatic moment tensor analysis.

The code we have developed solves the following system of linear equations subject to non-negativity in slip, slip smoothing, fault edge damping.

$$\begin{matrix} A \\ \hline l \times S \\ \hline E \end{matrix} \quad [U] = \begin{matrix} d \\ \hline 0 \\ \hline 0 \end{matrix}$$

A is a matrix of Green's functions, S is a smoothing matrix with relative weight, l; E is a matrix defining the edges of the distributed fault plane. U is the slip that is solved for and d is the input broadband waveform data. The smoothing (S) and fault edge (E) parameters are included to damp the inversion minimizing slip roughness and edge slip, respectively.

The inverse procedure begins by testing the two possible fault planes determined from the seismic moment tensor analysis. In order to do this it is necessary to scale the inverse problem to the size appropriate for the reported scalar seismic moment. This is accomplished by using the empirical relationships of Wells and Coppersmith (1994) for fault dimension, doubling them to allow for bilateral rupture and increasing them by 20% to be safe. To determine the appropriate dislocation rise time to use we assume that the rupture velocity is 80% of the local shear wave velocity and that the total duration of the earthquake is equal to the fault dimension divided by the rupture velocity. The dislocation rise time is assumed to be 10% of the approximate total duration after Heaton (1990). For the Landers and Northridge earthquake values of 3.7s and 1.4s are obtained by this method and are found to be reasonable in view of reported values for these respective earthquakes. Given the overall dimension of the distributed fault and the assumed dislocation rise time the two possible fault planes are tested by performing separate inversions over a range of rupture velocity. To speed up this process and to minimize computer load the code has the option of using either a line source representation of the source or a planar fault with relatively large subfaults. The best solution is the one that maximizes the variance reduction,

$$VR = 1.0 \quad \frac{\left(d_i \quad s_i\right)^2}{d_i^2} \div \quad 100,$$

where d and s are the observed and synthetic waveform, respectively, and i is a time index. Once the causal fault plane and rupture velocity are found the inversion is performed once more with a higher resolution to better characterize the fault slip.

We have found that it is possible to determine finite source parameters that compare quite well with those obtained using local strong motion records. Figure 3 compares slip maps for the January 16, 1994 Northridge earthquake obtained using strong motion records (Wald et al., 1996 and Zeng and Anderson, 1996) with those obtained at regional distances using an empirical Green's function method (Dreger, 1994, 1996) and using theoretical Green's functions (this study). It is clear that the slip maps are very similar suggesting that the regionally derived maps may be used to estimate the level of shaking in the near-source region. We obtain an equally impressive comparison for the Landers earthquake.

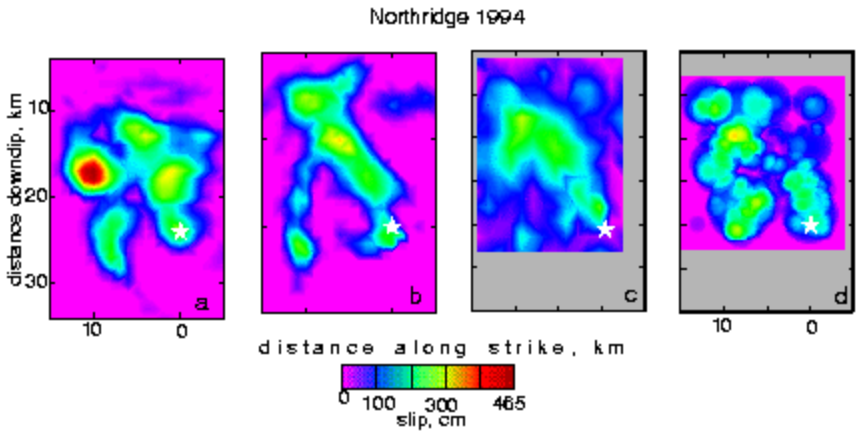

Figure 3. Fault slip maps for the 1994 Northridge earthquake are compared. (a) The slip map obtained in this study by inverting regional distance broadband data. (b) The slip map obtained by inverting seismic moment rate functions derived from empirical Green's function deconvolution (Dreger, 1994; Dreger, 1997). These maps compare well with those obtained by inverting local strong ground motions. (c) compares the map of Wald et al. (1996) obtained from local strong motion, teleseismic waveform data, and geodetic and leveling data. (d) Zeng and Anderson (1996) inverted only strong motion data using a different methodology. Each map has the same scaling and the white star identifies the hypocenter.

Landers Earthquake Application

Four TERRAscope stations, GSC, PAS, PFO and SVD (Figure 1) were used to determine the slip for the Landers earthquake. Figure 4a shows the best line source inversion results and the variance reduction plotted as a function of rupture velocity. In this case the northwest striking nodal plane is found to fit the data much better than the east west striking nodal plane that results in a flat variance reduction curve. The line source results show that slip is unilateral to the north-northwest. The total calculation time for all 18 rupture velocities tested was 3.5 minutes. This line source run is quite rapid and derives the necessary information for the implementation of a shakemap based on directivity sensitive empirical attenuation relationships (e.g. Somerville et al., 1997). Such an implementation will be discussed in a later section of the report. Figure 4b shows the high-resolution inversion results. In this case the model is found to be unilateral with the bulk of slip being located approximately 50-km north-northwest of the hypocenter. Furthermore, the slip is found to be relatively shallow, although the inversion was allowed to place slip as deep as 25 km if required by the data. The total processing time for the high resolution run was 18.5 minutes.

The source models shown in Figure 4 do not include a 2.5 s delay in the start of significant rupture reported by several researchers (Abercrombie, 1994; Cohee and Beroza, 1994; Dreger, 1994b; Wald et al., 1994). Furthermore the Landers earthquake also involved rupture of multiple segments with a 35-degree variation in fault strike (Wald et al., 1994). With automatic processing it will not be possible to take this level of complexity into account. Nevertheless the slip distribution we obtain with a single fault plane compares well with the multi-planar results of Wald et al. (1994) when their slip is projected onto our fault plane, and

we consider the 2.5s delay in our inversion for fault slip. In a later section of the report we demonstrate that although we have significantly simplified the source model of Landers it is still possible to obtain a shakemap with good agreement to the data, and excellent results when both data and model predictions are combined.

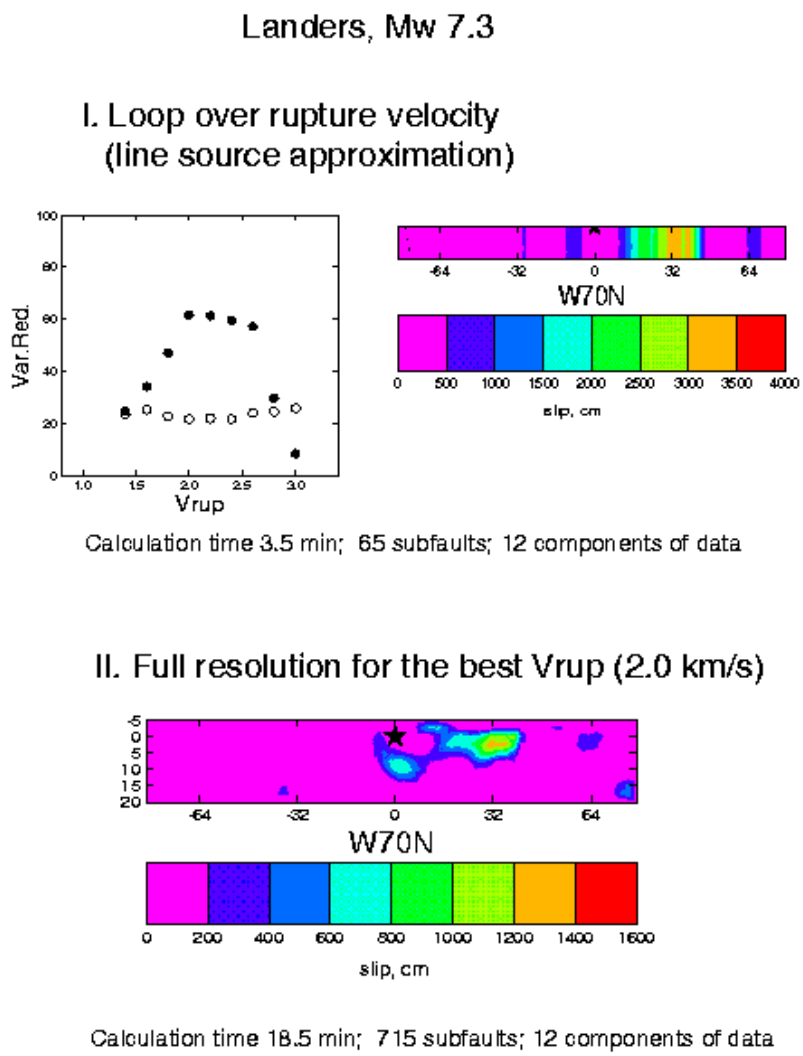

Figure 4. (I) The variance reduction verses rupture velocity is plotted for both possible nodal planes for the Landers earthquake using a line source model parameterization. The solid circles show variance reduction values for the north-northwest striking plane and the open circles show values for the conjugate east-west striking plane. This example clearly shows that the north-northwest plane provides a superior fit to the data. The best line source slip distribution is shown to the right and results in unilateral rupture to the north-northwest. (II) The full resolution inversion results are compared to the line source result.

Northridge Earthquake Application

Five TERRAscope stations, BAR, GSC, PFO, SVD, and VTV (Figure 1) were used to determine the slip for the Northridge earthquake. Figure 5 compares a low-resolution planar fault inversion with a high-resolution inversion for the Northridge earthquake. As the variance reduction vs. rupture velocity plot shows there is not as much separation between the two possible fault planes as was found for Landers. This is function of the relative size and the type of earthquake. The Landers earthquake being larger and strike-slip produces a stronger horizontal directivity function than the smaller reverse-slip Northridge earthquake. Nevertheless, as the variance reduction plot shows the south dipping fault plane is correctly identified for Northridge. The total calculation time for the 18 rupture velocities tested was 15 minutes. The high-resolution run produces additional complexity in the slip distribution. The total processing time for the high resolution run was 17 minutes. Figure 3 shows that the results are very similar to those obtained using local strong motions.

Section I: Conclusions and Recommendations

Our application of a regional distance finite fault inverse methodology to TERRAscope broadband data for the Landers and Northridge earthquakes reveals that the obtained slip models compare well with those obtained by inversion of local strong motion waveforms. The comparisons indicate that the regional estimates of fault dimension, gross slip distribution and directivity are reasonably well determined for these earthquakes. In the next section we demonstrate that near-source strong shaking determined from these slip maps models the observed strong shaking fairly well.

The calculations we have performed under this contract were carried out on a SUN Enterprise server with 400MHz CPUs. These systems are relatively standard and faster workstations are now becoming available indicating that the process times of the various steps that we have outlined are likely to be significantly reduced in the future.

At the time of the Landers earthquake six TERRAscope stations were available. The four that we used are located in vaults on relatively competent material. The ISA station was not used because of non-standard orientation of the horizontal components. The SBC station was not used because the path from Landers to San Barbara crosses significant basin structures and the 1D models that we employ are not adequate to explain the complex seismograms (Dreger and Helmberger, 1991). It is noted however that for the Northridge earthquake a number of the stations that we use do traverse the Los Angeles basin and the 1D structure appears to perform well. The implementation of this stage of processing will certainly require the careful calibration and verification that the 1D-velocity models employed are reasonable estimates of average path structure, and some regional stations with substantial site effects should be removed from processing to minimize possible bias due to unmodeled Earth structure.

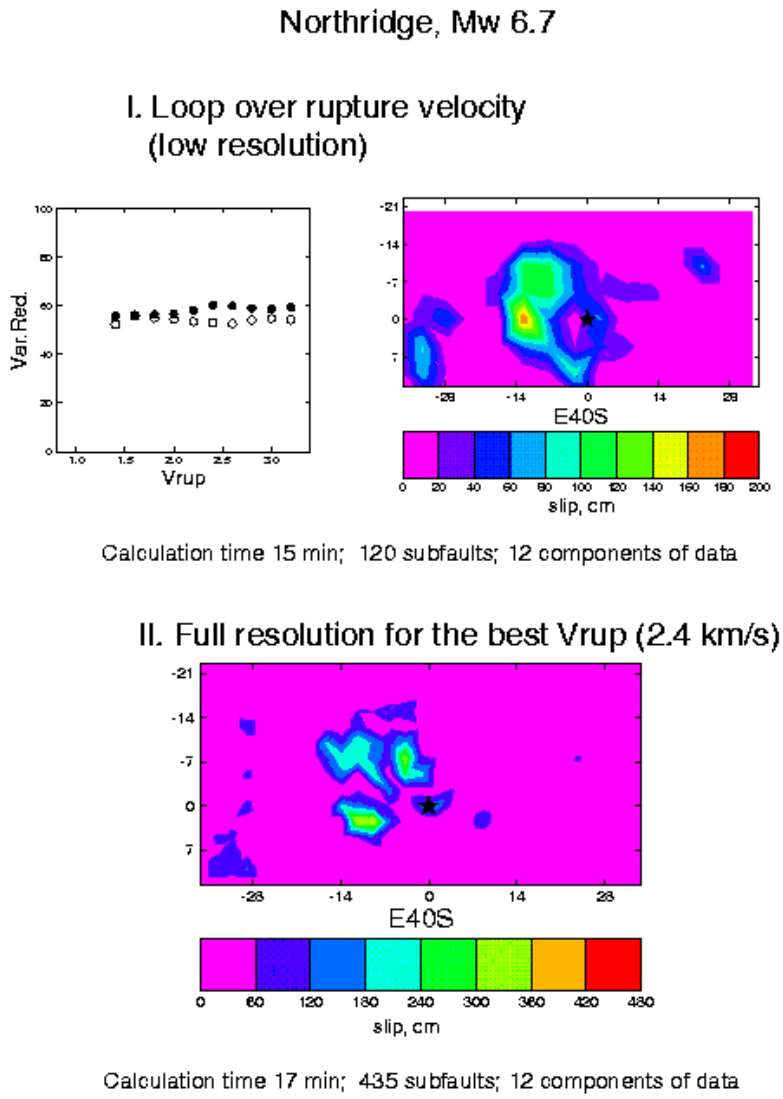

Figure 5. (I) The variance reduction verses rupture velocity is plotted for both possible nodal planes for the Northridge earthquake using a low resolution planar model. The solid circles show variance reduction values for the best fitting south dipping plane and the open circles show values for the conjugate north-dipping plane. The best low-resolution plane slip distribution is shown to the right, and shows northward updip directivity. (II) The full resolution inversion results are compared to the low-resolution result.

Section II. Near-Source Shakemap Simulation

Given a representation of the earthquake specific slip distribution it becomes possible to integrate the slip both spatially and temporally for stations located above the source to generate a suite of near-source time histories from which to determine strong motion parameters such as PGA, PGV and spectral acceleration. We keep the parameterization in the forward problem simple by assuming that the rupture velocity and the dislocation rise time are

constant throughout the rupture. The rupture velocity obtained from the source inversion is used and the dislocation rise time is determined from the derived slip, rupture velocity and the observations of Heaton (1990). The values of dislocation rise time used in this step are 2.4s and 0.9s for the Landers and Northridge earthquakes, respectively. These values are consistent with those previously reported for these earthquakes. In the following we compare our predicted PGV and spectral acceleration maps with observations from both the Landers and Northridge earthquakes. Our predicted shakemaps utilize site specific Green's functions calculated from two velocity models, one for hard rock and the other for soft rock. These velocity models are shown in Table 1 and were used by Wald et al. (1996) to invert for Northridge fault slip. In a later section we illustrate the benefit of using the two 1D models to account for site variability.

Table 1a: Hard Rock Velocity Model

V_P (km/s)	V_S (km/s)	Density (g/cm^3)	Depth (km)
1.9	1.0	2.1	0.0
4.0	2.0	2.4	0.5
5.5	3.2	2.7	1.5
6.3	3.6	2.8	4.0
6.8	3.9	2.9	27.0
7.8	4.5	3.3	40.0

Table 1b: Soil Velocity Model

V_P (km/s)	V_S (km/s)	Density (g/cm^3)	Depth (km)
0.8	0.3	1.7	0.0
1.2	0.5	1.8	0.1
1.9	1.0	2.1	0.3
4.0	2.0	2.4	0.5
5.5	3.2	2.7	1.5
6.3	3.6	2.8	4.0
6.8	3.9	2.9	27.0
7.8	4.5	3.3	40.0

Deterministic Peak Ground Velocity (PGV) Maps

Predicted and observed PGV for the Landers earthquake are compared in Figure 6. The predicted values were computed with site specific Green's functions in the 0.1 to 1.0 Hz pass band. In Figure 6a contouring was done for predicted values at the same locations as the observations, and the shape of the contours is an artifact of the station geometry. This PGV map compares well with the one obtained by the TriNet ShakeMap system (Figure 2a). Figure 6b compares the contours for a dense grid of stations, and shows an elongate region of high PGV close to the fault as would be expected for an extended fault rupture such as Landers. The site specific calculation shows our best results for Landers and it is evident that we are over predicting the PGV at the Lucerne station (LUC) by a factor of two. In contrast the hard rock prediction (Figure 6b) is much better at LUC. Other stations relatively close to the fault are well modeled however. There could be a number of factors such as inappropriate site

classification, problems with the Green's functions, and most likely the artificial closeness of the fault that could be causing the over prediction at LUC. The fault from our single plane model passes within 0.3 km of LUC while the closest mapped trace is approximately 3 km away. In fact a calculation that takes the curvature of the Landers fault into account results in much better estimates at LUC. Unfortunately this level of complexity can not be done automatically. Figure 6c shows the comparison of PGV as a function of distance. The predicted values span the range observed in the data and describe the attenuation of PGV with distance quite well. The cluster of large amplitude observations at a distance of approximately 150-km is from stations located in the Los Angeles basin.

Predicted and observed PGV for the Northridge earthquake are compared in Figure 7. The predicted values were computed with site specific Green's functions in the 0.1 to 1.0 Hz pass band. The observed PGV were computed by integrating the accelerograms and band pass filtering the derived velocity seismograms in the 0.1 to 1.0 Hz pass band, and picking the maximum value. The PGV map (Figure 7a) is successful in the characterization of the region that experienced the largest ground motions (PGV>10 cm/s). The map further shows that elevated PGV are predicted north of the epicenter due to updip rupture directivity, which is consistent with observation. Both over and under prediction is observed in the forward directivity region, and these discrepancies are likely to be due to a combination of the simplified source model obtained from regional distance data, site variability in observed PGV, and the use of simplified 1D velocity models. Figure 7b shows that the predicted values describe the attenuation very well, however there is a systematic under prediction of PGV at sites located in the Los Angeles basin (distance range of 30 to 150 km in Figure 7b).

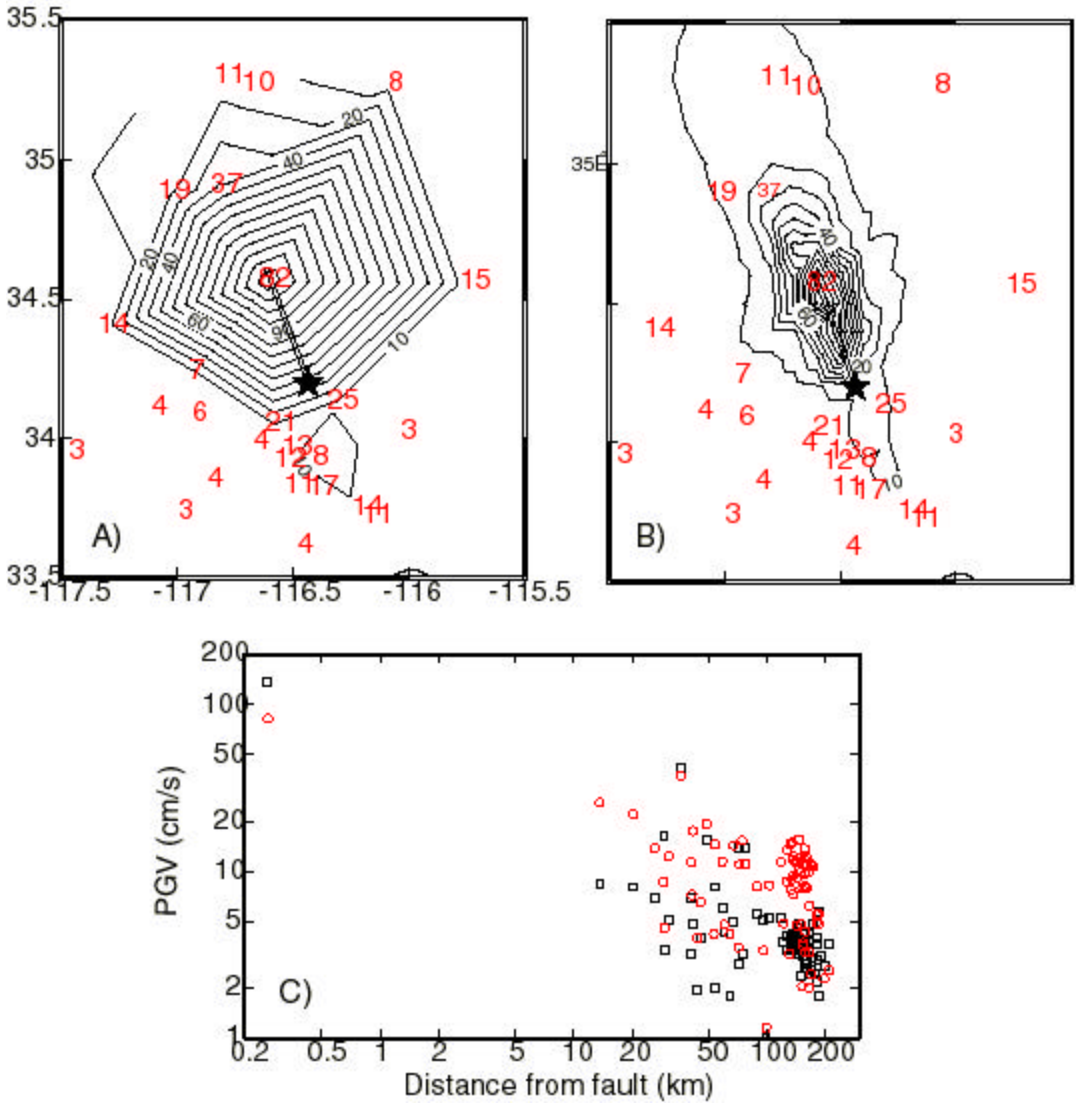

Figure 6. (a) Comparison of predicted (contours) and observed (red numbers in cm/s) PGV for the Landers earthquake. Both the predicted and observed PGV were determined from the 0.1 to 1.0 Hz pass band. The predicted PGV were measured from synthetic time histories generated using site specific Green's functions (see Table 1). (b) PGV contoured from a dense distribution of stations using hard rock Green's functions. (c) Log-log plot comparing observed PGV (red circles) and predicted values (black squares). The predicted values are for the site specific calculation shown in (a). The cluster of elevated observed ground motions at a distance of 150 km are from sites located in the Los Angeles basin southwest of the area shown in (a).

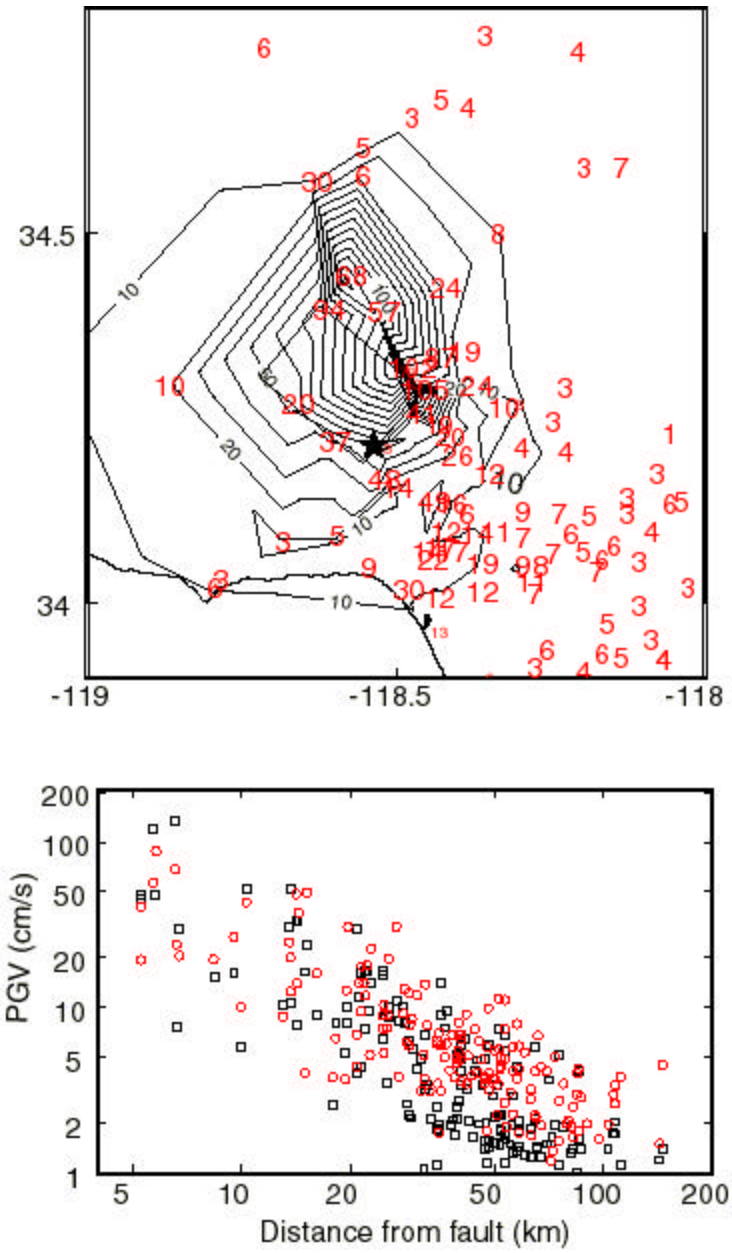

Figure 7 (a) Comparison of predicted (contours) and observed (red numbers in cm/s) PGV for the Northridge earthquake. Both the predicted and observed PGV were determined from the 0.1 to 1.0 Hz pass band. The predicted PGV were measured from synthetic time histories generated using site specific Green's functions (see Table 1). (b) Log-log plot comparing observed PGV (red circles) and predicted values (black squares). The predicted values are for the site specific calculation shown in (a). PGV is under predicted at LA Basin sites in the 30 to 150 km distance range.

Deterministic Spectral Acceleration Maps

Spectral acceleration (Sa) at 0.3, 1.0 and 3.0 seconds period was determined from the simulated time histories for both earthquakes. Figure 8 compares the predicted and observed Sa for the Northridge earthquake for the three specific periods. In this comparison the site specific Green's functions were used. The map view comparison is fairly good in that elevated regions of Sa are distinguished from areas with low relative Sa. For example in the 0.3 second plot the maximum observed Sa of 2.1 g correlates well with the predicted maximum although the predicted value of 2.8g is too large. In contrast stations to the southeast in the LA basin have relatively lower Sa. In the 1.0 second Sa plot the 0.1g contour separates the regions of higher and lower observations. The best agreement is for the 3.0 second Sa map. Figure 8b compares observed and predicted Sa as a function of distance, where the scatter in the data and the attenuation of Sa are well modeled. The 1.0 and 0.3 second distance plots (Figure 8b) tend to show that the model under predicts Sa in the 30-150 km distance range primarily for LA basin sites.

As was the case for Northridge the predicted Sa for Landers defines the region of strongest shaking, however there is a general under prediction. 3.0 second period Sa at LUC is significantly over predicted while the 1.0 second and 0.3 second period Sa are significantly under predicted. Part of the misfit is likely to be due to the artificial closeness of LUC to the model fault. The fact that some periods are over predicted and others under predicted and the general under prediction of Sa for all distances suggests that there is a problem in the spectral content of the simulated time histories. It is curious however that the PGA and PGV maps for Landers compare with the observations fairly well. Further study is needed to explore the sensitivity of the simulated time histories and estimated PGA, PGV and Sa to slip model, Green's function, site response, and rupture velocity and dislocation rise time uncertainty as well as simulation methodology. We tested the methods of Pitarka et al. (1999) and Zeng et al. (1994) and found minimal improvement for Northridge. It may be worthwhile to test their methods in simulating Sa for Landers. It is noted however that the empirical attenuation relationship described in the next section significantly improves the predicted Sa at all three periods.

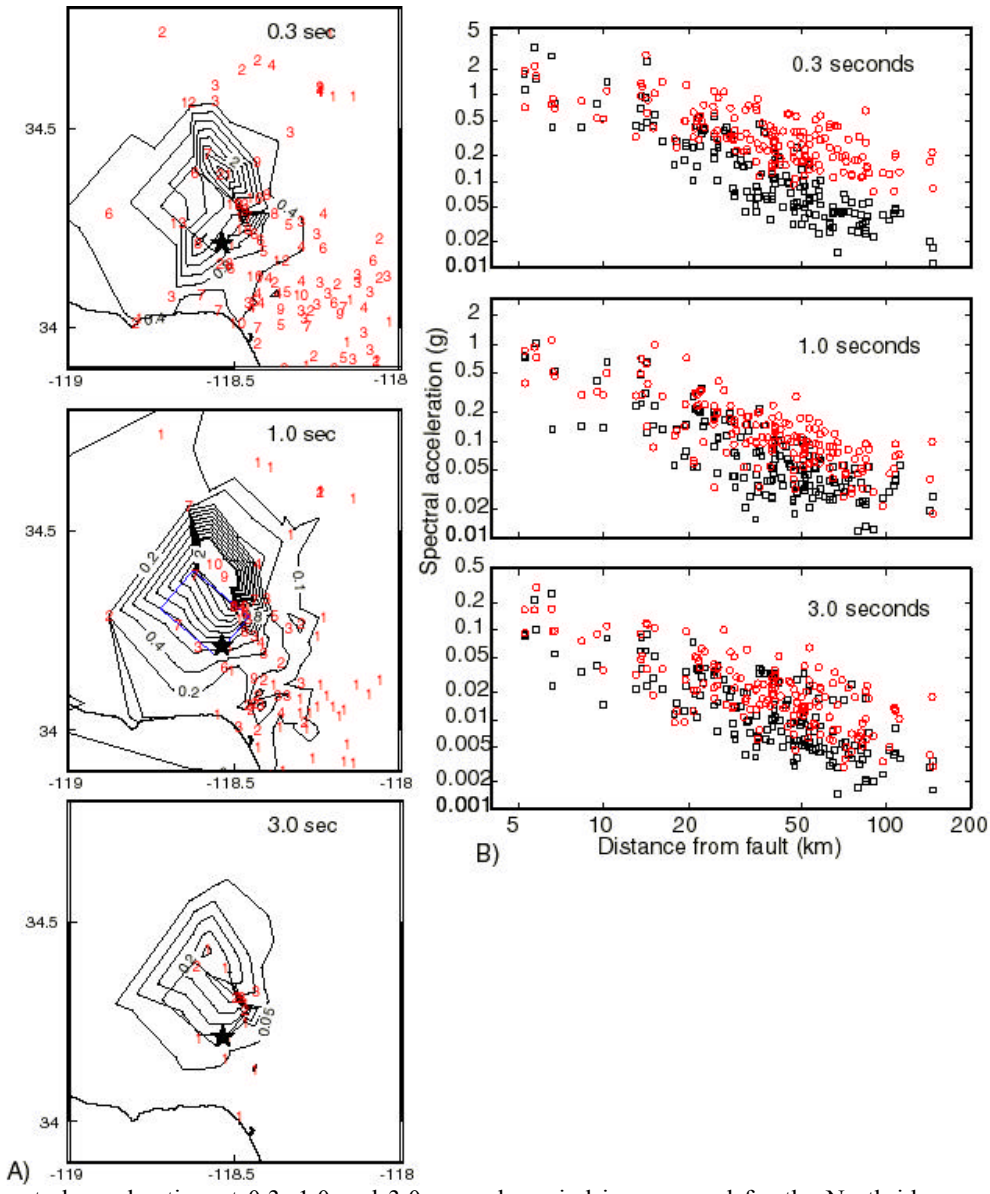

Figure 8. (a) Spectral acceleration at 0.3, 1.0 and 3.0 seconds period is compared for the Northridge earthquake. Contoured values were obtained by simulation using the Northridge slip model (Figure 3a) and site-specific Green's functions (Table 1). Contours are in 0.4, 0.2 and 0.05g intervals for the respective periods, and were constructed from predicted values only at the locations of the recording stations that are shown. The observed values (red numbers) are given in tenths of a g. Only observed values above 0.1g are plotted. (b) The predicted (black squares) and observed (red circles) spectral acceleration is compared as a function of distance for the three periods.

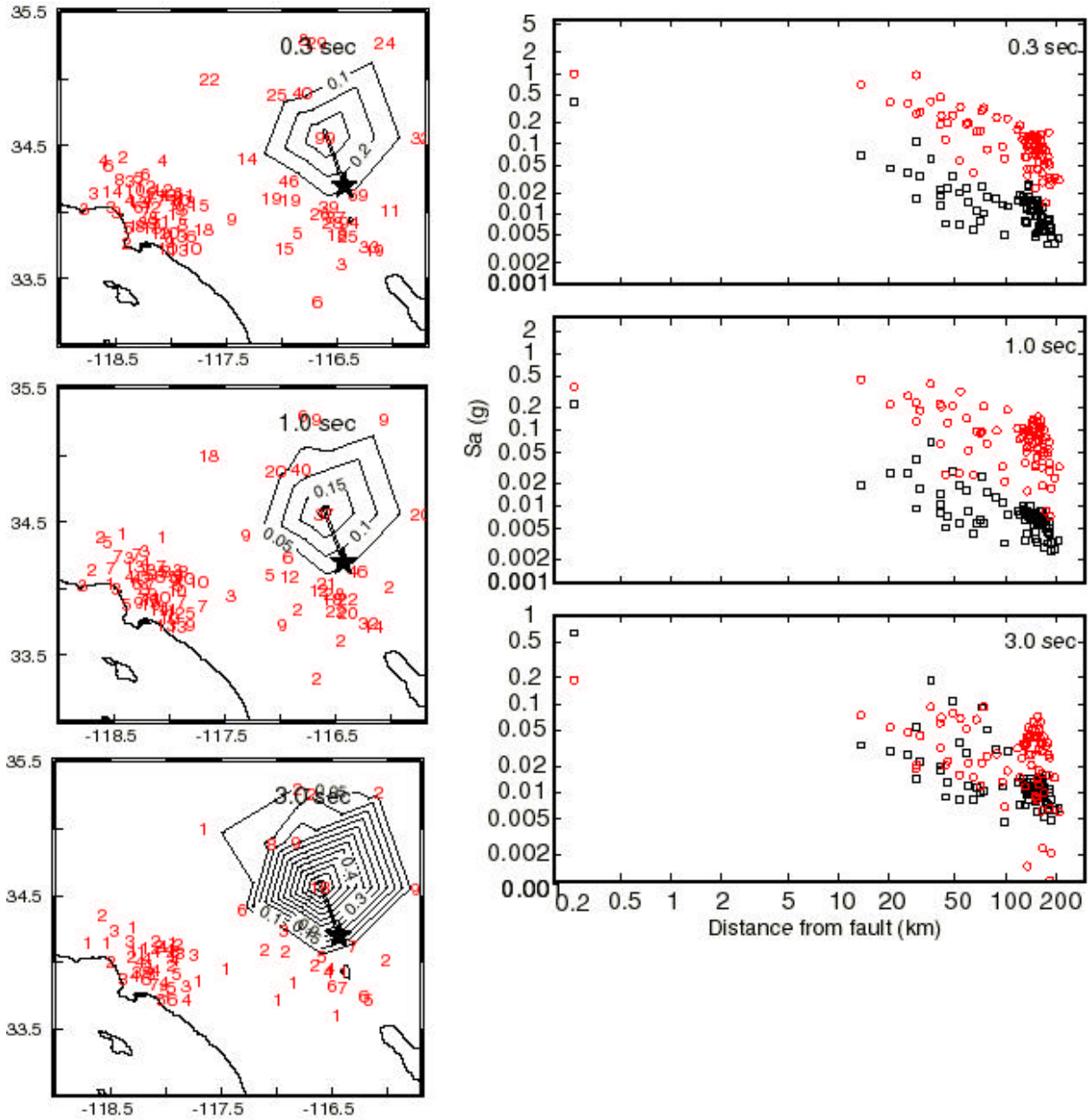

Figure 9. (a) Spectral acceleration at 0.3, 1.0 and 3.0 seconds period is compared for the Landers earthquake. Contoured values were obtained by simulation using the Landers slip model (Figure 4II) and site specific Green's functions. Contours are in 0.4, 0.2 and 0.05g intervals for the respective periods. The observed values (red numbers) are given in hundredths of a g. Only observed values above 0.01g are plotted. (b) The predicted (black squares) and observed (red circles) spectral acceleration is compared as a function of distance for the three periods.

Empirical Spectral Acceleration Maps

A recently developed directivity sensitive attenuation model (Somerville et al., 1997) was used to simulate PGA and Sa at 0.3, 1.0 and 3.0 seconds period. This model takes the scalar seismic moment, fault orientation, and slip distribution that we obtain by our source inversion as input. The empirical model describes the mean attenuation observed for the Landers earthquake (compare figures 10a to 9b), and is a significant improvement over the deterministic Sa shown in Figure 9. For the Northridge earthquake the empirical relationship also describes the observed mean attenuation, although at near-distances it under predicts the Sa.

If one integrates the maximum predicted values from the deterministic and empirical models a conservative map is obtained (Figure 11). This map is found to provide the best agreement to the data. The empirical model provides a mean value estimate for stations at all distance ranges and the deterministic calculation contributes mostly in the very near source distance range where source specific information is important.

In the case of Landers the conservative 0.3 and 1.0 second Sa shakemaps are a big improvement and stations close to the fault have values close to those indicated by the contours. LUC is now slightly over predicted which is likely to be due to the artificial closeness of the station to the model fault. The 3.0 second map is not changed very much. For Northridge there is some improvement particularly in the 0.4, 0.1 and 0.05g contours for the 0.3, 1.0 and 3.0 second Sa maps, respectively.

Section II: Conclusions & Recommendations

In this section we have demonstrated that a conservative shakemap that takes the larger of two values, one calculated by deterministic integration of fault slip, and the other by a directivity sensitive attenuation relationship provides reasonable agreement with observed PGA and Sa. The attenuation model we used (Somerville et al., 1997) does not presently have regression formulas for PGV. It is recommended that a PGV relationship be constructed from the same data set used for the PGA and Sa relationships to provide a seamless 'conservative shakemap' for all of the strong motion parameters of interest.

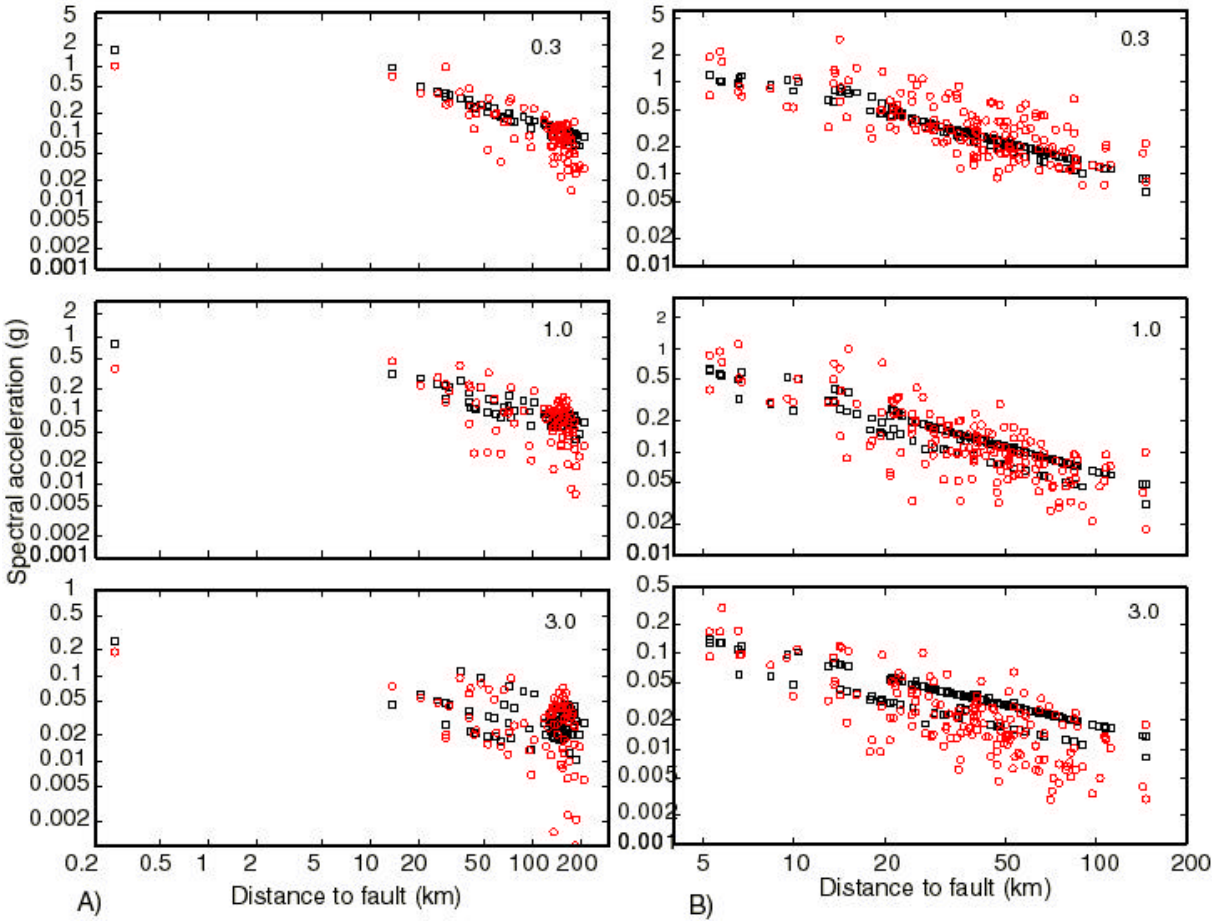

Figure 10. (a) Predicted (black squares) and observed (red circles) Sa at periods of 0.3, 1.0 and 3.0 seconds are compared for the Landers earthquake. The predicted values were obtained using the relationships of Somerville et al., (1997) and the fault orientation, scalar seismic moment and slip dimension determined in our finite source inversion. (b) Same as (a) for the Northridge earthquake.

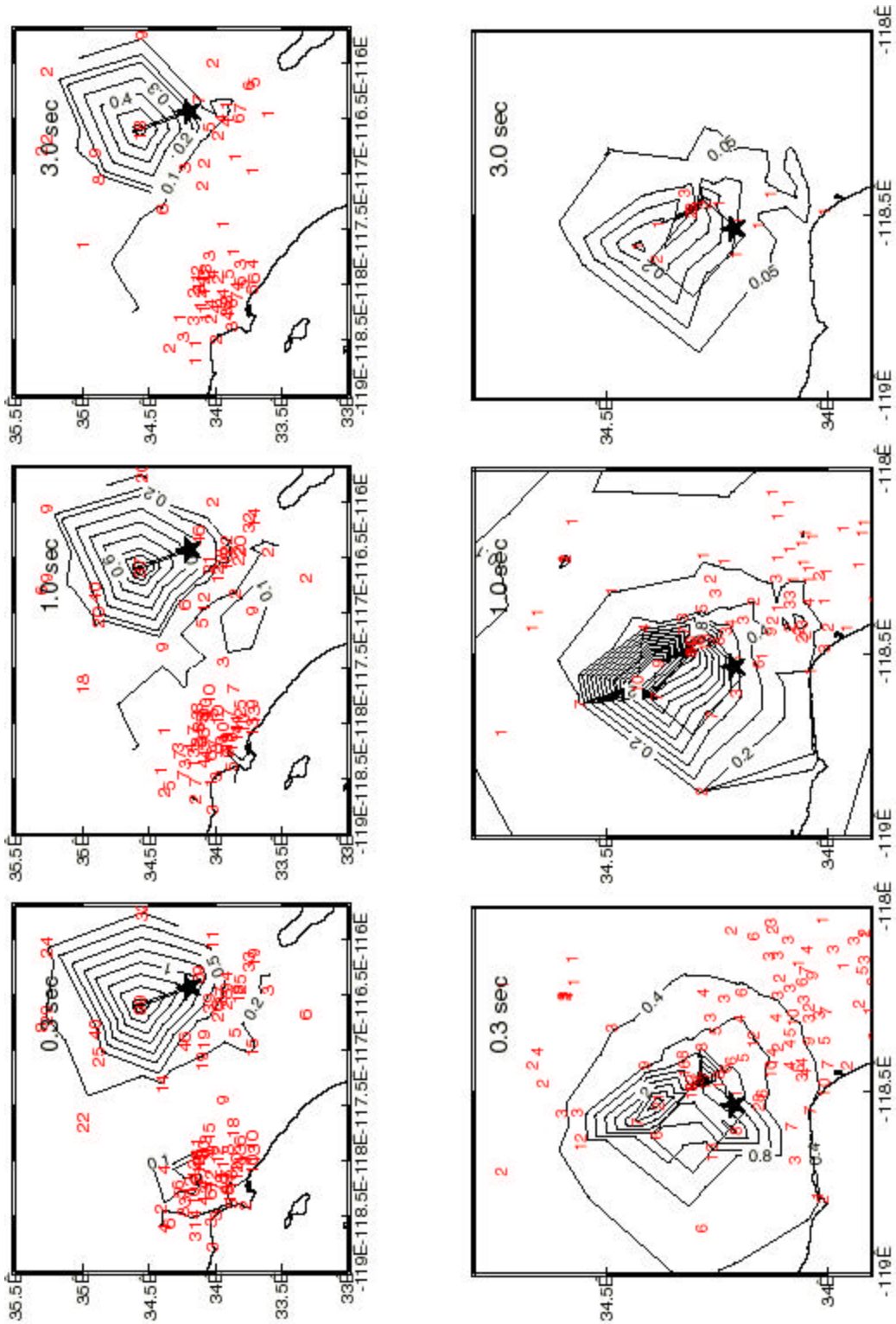

Figure 11. (a) Conservative Sa shakemaps (contours in units of g) are compared to observations (red numbers in hundredths of a g) for the Landers earthquake. Contour intervals are 0.2, 0.1 and 0.1 g for periods of 0.3, 1.0 and 3.0 seconds, respectively. (b) Conservative Sa shakemaps (contours in units of

g) are compared to observations (red numbers in tenths of a g) for the Northridge earthquake. Contour intervals are 0.4, 0.2 and 0.05 g for periods of 0.3, 1.0 and 3.0 seconds, respectively.

Section III. Site Response Effects in Simulated Shakemaps

In this section we demonstrate the effectiveness of two different approaches of correcting for site variability. One approach involves using site classification and empirically derived adjustment factors. In this comparison we use the regional quaternary/tertiary/Mesozoic (QTM) classification developed by Park and Elrick (1998) for southern California and used in the TriNet ShakeMap (Wald et al., 1999). A regional map of QTM is used to determine site type and frequency dependent site corrections derived from Borchardt (1994) are applied to the simulated time histories. The other method involves the use of different velocity structures to develop Green's functions for varied site type. This method performed better and was used in our deterministic shakemaps presented in section II.

It is important to note that in the TriNet application the site corrections are applied to an empirically derived hard rock attenuation relationship (Joyner and Boore, 1981) and therefore the mapping from the mean hardrock response to site specific response is straightforward. The application of QTM corrections to our hard rock synthetics improves the predictions but not as much as desired.

Figure 12a illustrates the misfit between our predicted hard rock PGV and observations for the Northridge earthquake in map view. Circles show soil sites and squares show rock sites. Open circles and squares indicate that the model under predicts the observations and the filled symbols indicate the model over predicts the observations. Near the source, the predicted values are relatively good however at distance from the source we find that generally the ground motions are under predicted by as much as a factor of three at some stations. Both soil and rock sites are under predicted although the greatest misfit is for LA basin stations. Figure 12b compares the predicted-to-observed PGV ratios for the case in which the hard rock PGV were adjusted using published QTM corrections (Table 2). There is marked improvement at a number of soil sites classified mostly as quaternary or tertiary. However as the symbols in Figure 12b show the amount of under prediction remains rather high. Figure 13a compares the $\log_{10}$ of the predicted-to-observed ratio for QTM corrected PGV. The bins show a tendency toward negative values. The red bars in Figure 13 indicate that most of the under prediction is for sites located within the LA basin. The mean $\log_{10}$ value for LA basin sites is –0.48. Quaternary sites outside the LA basin have a mean value of –0.22, and tertiary and Mesozoic sites have mean values of –0.10 and –0.14 respectively. While there is substantial improvement by applying the QTM corrections to our simulated PGV there remains a systematic under prediction in the LA basin and relatively large uncertainty. It is very important to note however that this comparison does not distinguish between the relative amplitude of the PGV. It is observed that the overall misfit in the San Fernando and Northridge region, that experienced the largest ground motions, is relatively small.

Figure 12c compares the predicted-to-observed PGV ratios for the site specific Green's function simulation. This simulation is found to be significantly better than both the raw hard

rock and the QTM corrected hard rock simulations. Figure 13b compares the site specific PGV $\log_{10}$ ratios binned according to Geomatrix site classification. This figure shows that LA basin sites remain under predicted however the distribution is skewed toward values closer to 0.0. The Geomatrix soil classifications B, C and D for sites located outside the LA basin have $\log_{10}$ values of –0.02, -0.12 and –0.02, respectively, indicating the predictions agree well with the observations. It is curious that rock sites around the fringes of the LA basin are significantly under predicted. This may be due to improper site classification or possibly regional amplification due to the LA basin 3D structure (e.g. Olsen et al., 1995). It may be necessary to numerically develop a suite of synthetic 1D-to-3D site corrections for large-scale structures such as the LA basin.

Table 2: QTM Site Corrections

Site Type (V_S, m/s)*	Corrections for Specified Input PGA			
	< 15%g	15-25%g	25-35%g	>35%g
Mesozoic (589 m/s)				
0.1-0.5 sec. period	1.0	1.0	1.0	1.0
0.5-2.0 sec. period	1.0	1.0	1.0	1.0
Tertiary (406 m/s)				
0.1-0.5 sec. period	1.14	1.10	1.04	0.98
0.5-2.0 sec. period	1.27	1.25	1.22	1.18
Quaternary (333 m/s)				
0.1-0.5 sec. period	1.22	1.15	1.06	0.97
0.5-2.0 sec. period	1.45	1.41	1.35	1.29

* This is a simplified table for average 30m depth site velocities by type. In the map of Park and Elrick (1998) surface velocity is mapped for the southern California region and it is possible to use more specific site velocity either know or inferred to produce period specific amplitude corrections following Borcherdt (1994).

Section III Conclusions

It is clear from the preceding comparisons that applying site specific corrections derived empirically improve results but not to the degree hoped, nor to a degree better than what is achieved when we use two 1D velocity models to represent rock and non-rock sites. There is a systematic bias toward under prediction of PGV, particularly at LA basin sites. Even rock sites along the fringes of LA basin are under predicted. This suggests that at these sites the rock velocity model (Table 1) used to compute the Green's functions is not appropriate and that 3D basin effects may be important. In fact, the work of Olsen et al. (1995) shows substantial amplification effects due to the LA basin in their finite difference simulations. Stidham et al. (1999) in their study of three dimensional wave propagation in the San Francisco bay area discovered basin amplification of as much as 3-4 over reference 1D ground motions within the tertiary basins, and more importantly that the basin amplification effects can extend beyond the boundaries of the mapped basins. Because we are using synthetic seismograms in our deterministic shakemaps it seems reasonable that we need to apply correction factors that are relative to the specific 1D model used. This can be accomplished by simulating ground motions using finite difference methods for a reference 1D velocity model and best estimate 3D structure in the Los Angeles and SF Bay Area

regions. A regional table of 1D-to-3D site corrections may be developed by considering an ensemble average of calculations for sources distributed around the region.

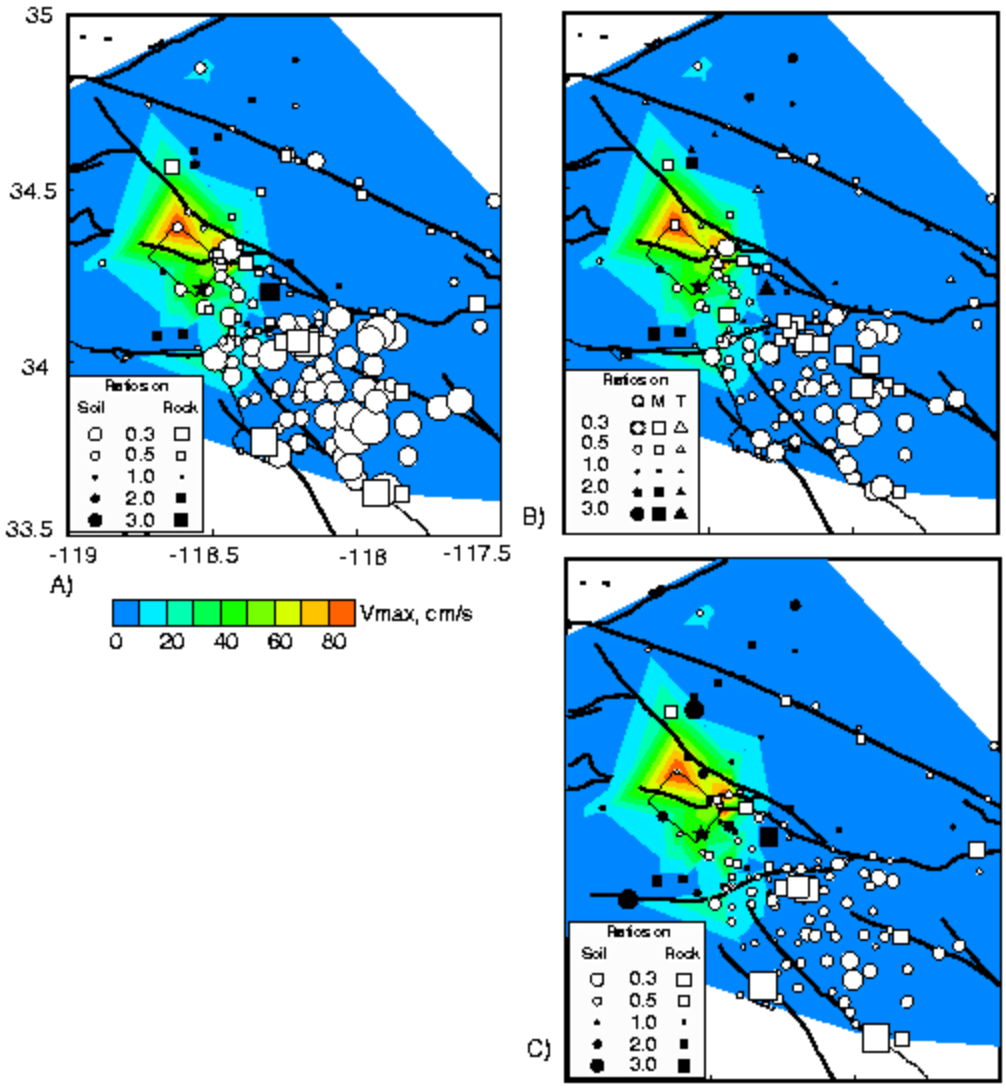

Figure 12. Predicted to observed PGV amplitude ratios for soil sites (circles) and rock sites (squares) are plotted in map view. (a) The predicted PGV were computed using the hard rock model (Table 1) and the Northridge slip (Figure 3a). (b) The predicted PGV were computed with the hard rock model (Table 1) with applied QTM corrections (Table 2). Quaternary, tertiary and Mesozoic sites are indicated by circles, squares and triangles, respectively. (c) The predicted site specific PGV were computed using both the hard rock and soil models (Table 1) and the Northridge slip (Figure 3a). In each example the size of the symbol is proportional to the predicted-to-observed ratio, and open symbols indicate under prediction and filled symbols indicate over prediction

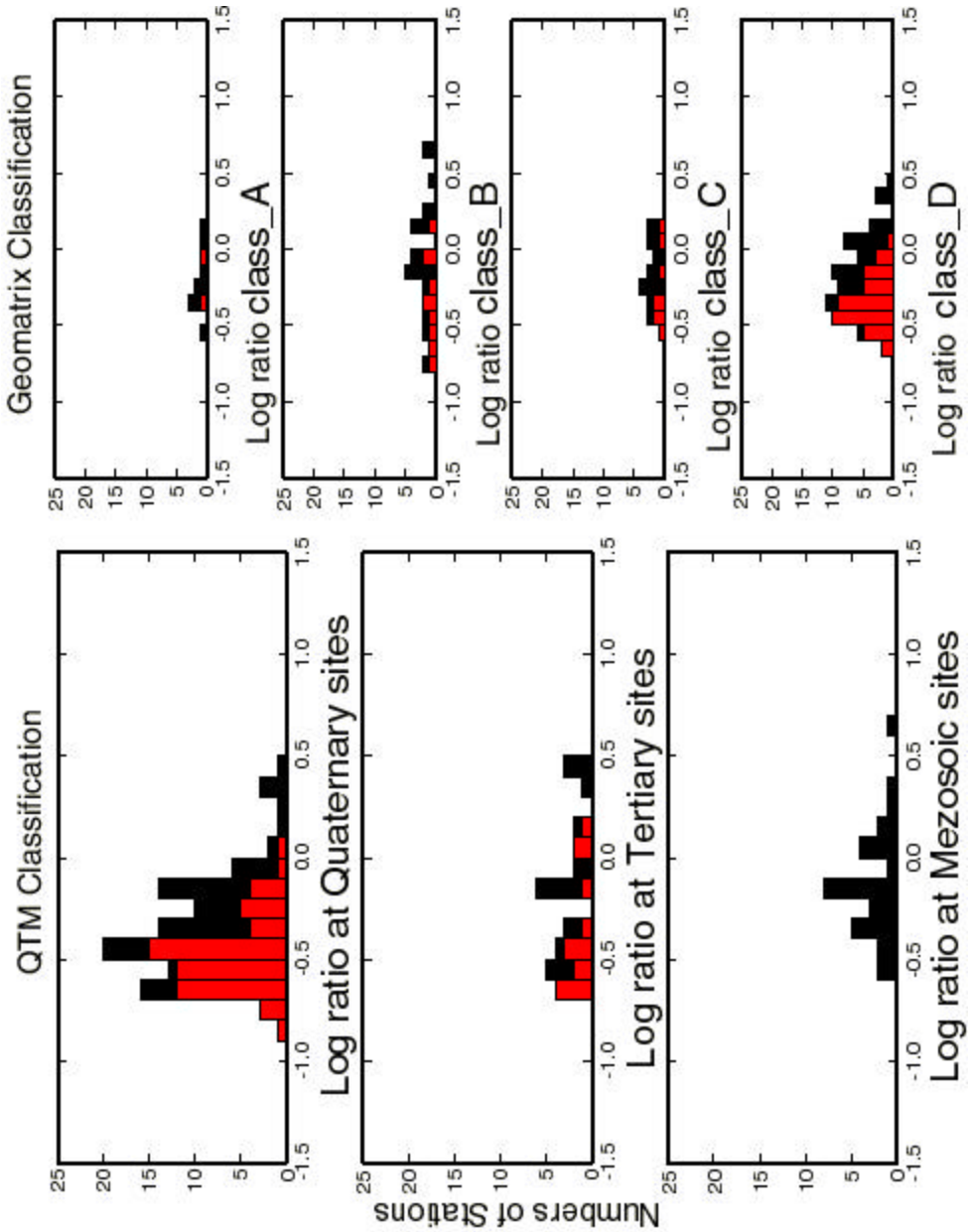

Figure 13. The $\log_{10}$ of the predicted-to-observed PGV amplitude ratio for Northridge is compared for the case where hard rock synthetic PGV have QTM corrections (Table 2) applied (a), and the site specific PGV classified according to the Geomatrix scheme. The black bars show all stations and the red bars show stations located in the Los Angeles basin. A value of 0.0 indicates a predicted-to-observed ratio of 1.

Section IV: Application of Data/Model Shakemaps

This report is concluded by demonstrating how our 'conservative shakemap' may be integrated with actual observations to produce a data/model shakemap. At the outset of this study we have been concerned with developing methodology that will perform in very sparse station coverage situations. Sparse coverage is a function of population density and there are vast areas of California with relatively sparse coverage. Recent earthquakes in southern Oregon (1993 Klamath Falls M6) and near Lake Tahoe (1994 Double Springs Flat M6) are cases in which the closest strong motion stations were located 60-80 km away. Figure 14 compares data only PGA shakemaps obtained by direct contouring of observations for the Northridge earthquake. Figure 14a shows the shakemap obtained by using only the 13 TriNet stations located in the region. This figure identifies the region of strong shaking by the 0.4g contour and compares well with the results obtained for PGV with many more stations (Figure 2b). In Figure 14b we consider a case in which strong motion station spacing is approximately 30 km with one station located in the forward directivity region. This map is successful in identifying the region of strongest shaking but the 0.4g contour is not closed. If the forward directivity station is removed it is not possible to obtain a useable PGA shakemap by contouring only data. Determination of a strong motion centroid and application of point-source attenuation models to interpolate the map improves a sparse station shakemap (e.g. Wald et al., 1999). In very sparse coverage it may be difficult to obtain a strong motion centroid that correlates with where the strongest shaking occurred.

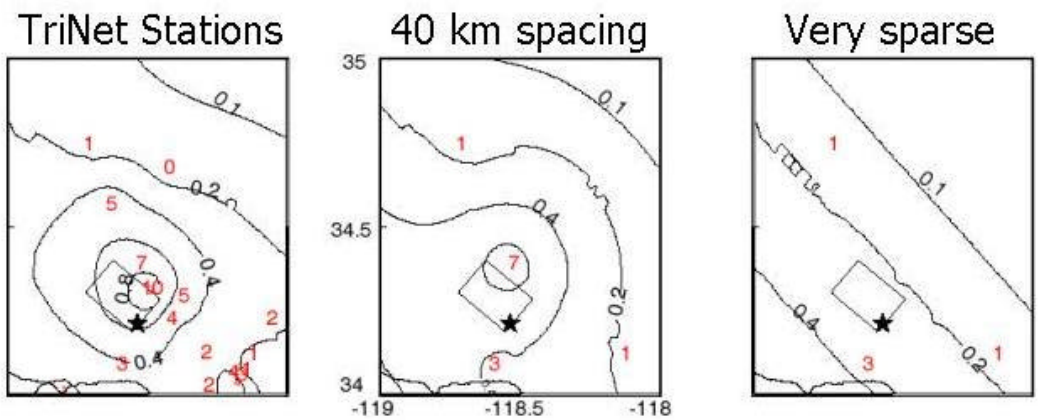

Figure 14. PGA shakemaps obtained by contouring only data values for the Northridge earthquake are compared for cases with (a) 13 nearby TriNet stations, (b) 30 km station spacing with one station located in the forward directivity region, and (c) 30 km station spacing as might be anticipated in sparsely instrumented regions or regions with few digitally telemetered strong motion stations. The contours show PGA in g and the red numbers show the observed PGA in tenths of a g that were used to develop the shakemap contours.

Figure 15 compares a combined model/data shakemap obtained using QTM adjusted hard rock simulations and the directivity sensitive attenuation model (Somerville et al., 1997). The red circles show where model predictions were incorporated in shakemap contouring. In these maps the model predictions are introduced at regular intervals only in regions where there is no observing station located within 22 km. The course grid of model predictions and data is then finely interpolated onto a mesh 1/10th of the spacing shown and contoured. At this final interpolation and contouring stage QTM corrections are applied. Observed data values are uncorrected. This is essentially the same approach outlined by Wald et al. (1999) and used in the TriNet shakemap. Figure 15a illustrates that such a map with many direct observations is controlled by the data (i.e. Figure 14a and 15a are very similar). Figures 15b and 15c show that the model contributes significantly in sparse station coverage by producing shakemaps that accurately describe the forward directivity amplification of ground motion. It is interesting that the 0.7g observation in Figure 15b pins the map at this level and therefore results in an under prediction where the 1 g PGA was observed in Figure 15a. Figure 15c, with the 0.7g observation removed actually performs better because a maximal PGA of 1 g is obtained indicating the severity of the earthquake and the resulting 0.8g contour lies near the location of the 1g observation.

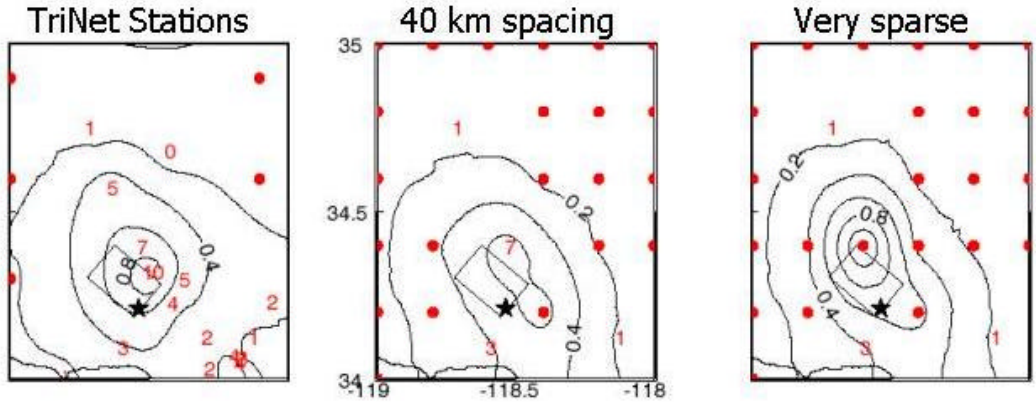

Figure 15. PGA shakemaps obtained by contouring data and model values for the Northridge earthquake are compared for cases with (a) 13 nearby TriNet stations, (b) 30 km station spacing with one station located in the forward directivity region, and (c) 30 km station spacing. The contours show PGA in g, the red numbers show the observed PGA in tenths of a g and the red circles show the locations of where model predictions were added to develop the shakemap contours.

The extended nature of the Landers earthquake is illustrated in the last example. Figure 16a and 16b compare data only PGA shakemaps with and without the near-fault LUC station. The near-fault ground motions in Figure 16a is controlled by the LUC station. When LUC is removed the near-fault ground motion is significantly under predicted when only data is contoured. Again by considering the location of a strong motion centroid and model predictions using point-source attenuation (e.g. Wald et al., 1999) the near fault predictions without LUC would be expected to be better, however the pattern would likely be similar to that in Figure 16a or Figure 2a with a central point of high ground motion. Figures 16c and 16d compare data/model PGA shakemaps for the cases with and without the LUC station. With LUC the overall map is very similar to that in Figure 16a however near the fault the

model produces an elongate region of elevated ground motions that would be expected for an extended rupture of the size experienced in the Landers earthquake. If LUC is removed (Figure 16d) the resulting map retains the elongate near-fault pattern of large PGA, and in fact the LUC site lies between the 0.5 and 0.6g contours of the map, which is a fairly good estimate of the observed 0.76g acceleration. Probably the most important lesson from Figure 16 is that it is not enough to have a single near-fault observation to characterize ground motions for a large extended rupture. A better scenario would have an array of observing stations along the length of the fault. This may be possible in densely instrumented regions, but is not practical in many areas of California. For earthquakes such as Landers, where instrumentation is relatively sparse, considering a source specific directivity model to fill in the holes in observations may result in better estimates of near fault ground motions. Unfortunately along most of the length of Landers we don't know what the actual ground motion levels were, however based on the slip models that have been published it is likely that ground motions close to that observed at LUC occurred along the whole length of the fault.

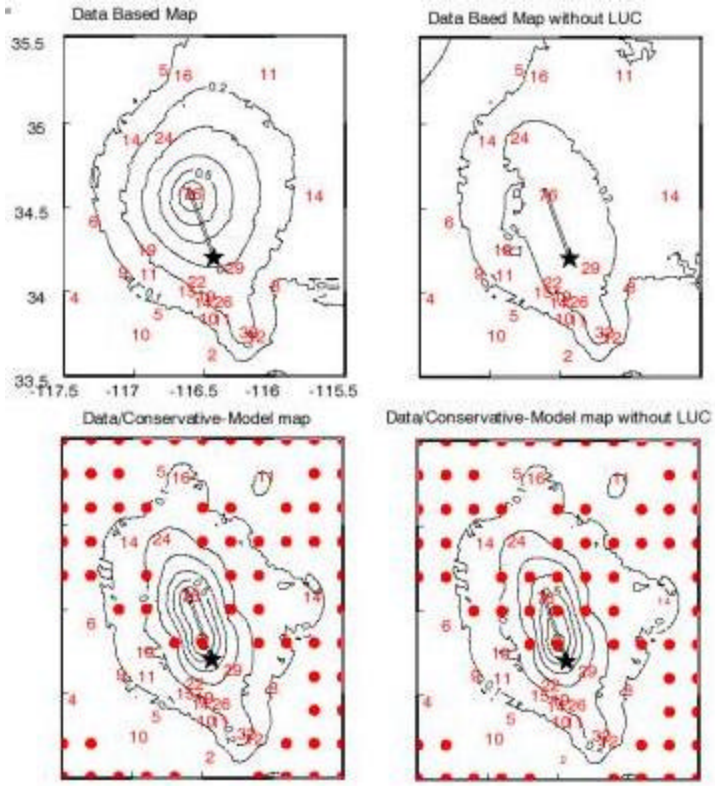

Figure 16. Data only PGA shakemaps for the Landers earthquake are compared for cases with (a) and without (b) the near-fault LUC station. These maps were obtained by direct contouring of the data shown in red (numbers in units of hundredths of a g). The contours are in units of g. The data/model shakemaps are compared for the same cases with (c) and without (d) the LUC station. The red circles show where model predictions were incorporated into the contouring process

In summary, the objectives of this study have been met and software for the determination of combined model/data shakemaps that incorporate source specific directivity effects has been developed. Comparisons of shakemaps for Landers and Northridge indicate the procedure performs well. In the coming year this method will be integrated into the offline REDI system to being testing under operational conditions.

References

Abercrombie, R. E. Local observations of the onset of a large earthquake; 28 June 1992 Landers, California, Bull. Seism. Soc. Am., 84, 725-734.

Borcherdt, R. D. (1994) Estimates of site-dependent response spectra for design (methodology and justification), Earthquake Spectra, 10, 617-653.

Cohee, B. P., and G. C. Beroza (1994). A comparison of two methods for earthquake source inversion using strong motion seismograms, *Annali Di Geophysica,* **37**, 1515-1538.

Dreger, D. S., and D. V. Helmberger (1991). Source Parameters of the Sierra Madre Earthquake from Regional and Local Body Waves, Geophys. Res. Let., 18 2015-2018.

Dreger, D. S., and D. V. Helmberger (1993), Determination of Source Parameters at Regional Distances with Single Station or Sparse Network Data, Journ. Geophys. Res., 98, 8107-8125.

Dreger, D. and B. Romanowicz (1994). Source Characteristics of Events in the San Francisco Bay Region, *USGS Open-file report*, 94-176, 301-309.

Dreger, D. (1994a). Empirical Green's function study of the January 17, 1994 Northridge mainshock (M_w6.7), *Geophys. Res. Lett.,* **21**, 2633-2636.

Dreger, D. S. (1994b), Investigation of the Rupture Process of the 28 June 1992 Landers Earthquake Utilizing TERRAscope, Bull. Seism. Soc. Am., 84, 713-724.

Dreger, D. (1997), The Large Aftershocks of the Northridge Earthquake and their Relationship to Mainshock Slip and Fault Zone Complexity, Bull. Seism. Soc. Am., 87, 1259-1266.

Gee, L. S., D. S. Neuhauser, D. S. Dreger, M. Pasyanos, R. A. Uhrhammer, and B. Romanowicz (1996), Real-Time Seismology at UC Berkeley: The Rapid Earthquake Data Integration Project, Bull. Seism. Soc. Am., 86, 936-945.

Heaton, T. H. (1990) Evidence for and implications of self-healing pulses of slip in earthquake rupture, Phys. Earth and Planet. Int., 64, 1-20.

Joyner, B. and D. Boore (1981) Peak horizontal accelerations and velocity from strong-motion records including records from the 1979 Imperial Valley, California, earthquake, Bull. Seism. Soc. Am., 71, 2011-2038.

Olsen, K. B., R. J. Archuleta, and J. R. Matarese (1995) Three-dimensional simulation of a magnitude 7.75 earthquake on the San Andreas Fault, Science, 270, 1628-1632.

Park, S., and S. Elrick (1998) Predictions of shear-wave velocities in southern California using surface geology, Bull. Seism. Soc. Am., 88, 677-685.

Pasyanos, M. E., D. S. Dreger, and B. Romanowicz (1996), Towards Real-Time Determination of Regional Moment Tensors, Bull. Seism. Soc. Am., 86, 1255-1269.

Pitarka, A., P. Somerville, Y. Fukushima, T, Uetake, K. Irikura (1999) Simulation of near-fault strong ground motion using hybrid Green's functions, submitted to Bull. Seism. Soc. Am.

Saikia, C. (1994) Modified frequency-wavenumber algorithm for regional seismograms using Filon's quadrature; modeling of L_g waves in eastern North America, Geophys. Journ. Int., 118, 142-158.

Somerville, P. G., N. F. Smith, R. W. Graves, and N. A. Abrahamson (1997) Modification of empirical strong ground motion attenuation relations to include the amplitude and duration effects of rupture directivity, Seism. Res. Lett., 68, 199-222.

Stidham, C., M. Antolik, D. Dreger, S. Larsen and B. Romanowicz (1999) Three-dimensional structure influences on the strong motion wavefield of the 1989 Loma Prieta earthquake, in press Bull. Seism. Soc. Am.

Wald, D. J., V. Quitoriano, T. H. Heaton, H. Kanamori, C. W. Scrivner, and C. B. Worden (1999) TriNet ``ShakeMaps": Rapid Generation of Instrumental Ground Motion and Intensity Maps for Earthquakes in Southern California, in press Earthquake Spectra.

Wald, D. J., and T. H. Heaton (1994). Spatial and temporal distribution of slip for the 1992 Landers, California, earthquake, *Bull. Seism. Soc. Am.,* **84**, 668-691.

Wald, D. J., T. H. Heaton, and K. W. Hudnut (1996). The slip history of the 1994 Northridge, California, earthquake determined from strong-motion, teleseismic, GPS, and leveling data, *Bull. Seism. Soc. Am.,* **86**, s49-s70.

Wells, D. L., and K. J. Coppersmith (1994) New empirical relationships among magnitude, rupture length, rupture width, rupture area, and surface displacement, Bull. Seism. Soc. Am., 84, 974-1002.

Zeng, Y., J. G. Anderson, and G. Yu (1994) A composite source model for computing realistic synthetic strong ground motions, Geophys. Res. Lett., 21, 725-728.

Zeng, Y., and J. G. Anderson (1996). A composite source model of the 1994 Northridge earthquake using genetic algorithms, *Bull. Seism. Soc. Am.,* 86, s71-s83.

Acknowledgements

The work described in this report was funded by the Pacific Earthquake Engineering Research (PEER) Center under the Pacific Gas & Electric Company Contract No. 09566. This financial support is gratefully acknowledged.

The financial support of the PEARL sponsor organizations including the Pacific Gas & Electric Company (PG&E), the California Energy Commission (CEC), and the California Department of Transportation (Caltrans) is acknowledged.

This work was supported in part by the Pacific Earthquake Engineering Research Center through the Earthquake Engineering Research Centers Program of the National Science Foundation under Award number EEC-9701568.

ACKNOWLEDGEMENTS

The work described in this report was funded by the Pacific Earthquake Engineering Research (PEER) Center under the Pacific Gas & Electric Company Contract No. 09566. This financial support is gratefully acknowledged.

The financial support of the PEARL sponsor organizations including the Pacific Gas & Electric Company (PG&E), the California Energy Commission (CEC), and the California Department of Transportation (Caltrans) is acknowledged.

This work was supported in part by the Pacific Earthquake Engineering Research Center through the Earthquake Engineering Research Centers Program of the National Science Foundation under Award number EEC-9701568.

UNIVERSITY OF
SOUTHERN CALIFORNIA

Department of Civil Engineering

Liquefaction-induced Ground Deformation and Failure

by

Jean-Pierre Bardet, Nicholas Mace and Tetsuo Tobita

A Report to PEER/PG&E

Task 4A - Phase 1

May 4, 1999

Table of contents

Abstract iii
Acknowledgements iv
1. Introduction 5
1.1 Liquefaction-induced lateral spreads 5
1.2 Field measurement of lateral ground deformation 8
2. Mechanisms of lateral ground deformation 11
2.1 Laboratory approach 11
2.1.1 Pre-liquefaction behavior 11
2.1.2 Post-liquefaction volumetric deformation 11
2.1.3 Post-liquefaction shear deformation 14
2.1.4 Example of calculation of lateral spread displacement based on laboratory tests 15
2.2 Centrifuge modeling of liquefaction induced ground displacement 17
2.3 Shaking Table Experiments 23
2.4 Summary of observations from laboratory, shaking table, and centrifuge experiments 25
2.5 Analytical Modeling of liquefaction-induced deformation 26
2.5.1 Newmark sliding block model 26
2.5.2 Model with shear strength loss and strain rehardening 28
2.5.3 Minimum potential energy model 29
2.5.4 Viscous models 30
2.5.5 Constitutive modeling and numerical analysis 31
3. Databases of liquefaction case histories 33
3.1 Liquefaction occurrence database (Harder, 1991) and liquefaction analysis (Youd and Idriss, 1998) 33
3.2 Liquefaction-Induced ground deformation database (Bartlett and Youd, 1992) 35
3.2.1 Seismic data 35
3.2.2 Ground displacement amplitude data 35
3.2.3 Slope and free face data 36
3.2.4 Borehole data 37
3.2.5 Determination of average soil properties at vector location 38
3.2.6 Comparison of Harder (1991) and Bartlett and Youd (1992) databases 40
3.2.7 Parameters controlling ground deformation 41
3.3 Liquefaction-Induced lateral spread database (Rauch, 1997) 43
4. Review of empirical models 46
4.1 Youd and Perkins (1987) LSI model 46
4.2 Hamada et al. (1986) 47
4.3 Bartlett and Youd (1992) MLR model 48
4.4 Rauch (1997) models 49
4.5 Comparison of existing models 51
4.5.1 Seismological parameters 51
4.5.2 Topographical parameters 52
4.5.3 Geotechnical parameters 53

5. MLR Models for liquefaction-induced ground deformation 54
5.1 Selection of database 54
5.2 Selection of variables and models 55
5.3 Six-parameter MLR models 59
5.4 Four-parameter MLR model 66
5.5 Comparison of MLR models and recommendations 71
5.6 Suggestion for future work 74
5.7 Mapping of liquefaction-induced ground deformation 74
6. Probabilistic model of liquefaction-induced ground deformation 79
6.1 Mean and variance of ground deformation 79
6.2 Confidence limits 81
6.3 Probabilistic model 82
6.4 Confidence intervals for liquefaction-induced ground deformation 84
6.5 Probability calculation 90
6.6 Future work 92
7. Conclusion 93
8. References 94
Appendix A: Liquefaction databases 102
Appendix B: Coefficients for MLR and probalistic models 103
Appendix C: Outputs of Minitab Regression analyses 109
Minitab regression analysis from the original database by Bartlett and Youd (1992) 109
Minitab regression analysis for FFGS6-A model 111
Minitab regression analysis for model FF6-A 113
Minitab regression analysis for model GS6-A 114
Minitab regression analysis for model FFGS6-B 115
Minitab regression analysis for model FF6-B 117
Minitab regression analysis for model GS6-B 118
Minitab regression analysis for model FFGS4-A 119
Minitab regression analysis for model FF4-A 121
Minitab regression analysis for model GS4-A 122
Minitab regression analysis for model FFGS4-B 123
Minitab regression analysis for model FF4-B 124
Minitab regression analysis for model GS4-B 125

ABSTRACT

Liquefaction-induced ground deformation is a potential source of major damage to gas distribution networks during earthquakes. This type of permanent ground displacement, which has amplitudes ranging from a few centimeters to 10 meters and more, caused substantial damage to lifelines and pile-foundations of buildings and bridge piers along the Kobe shoreline during the 1995 Hyogoken Nanbu, Japan, earthquake. The overall research objective is to develop probabilistic models of liquefaction-induced ground displacement useful for estimating the cost of damage and repair to gas distribution networks during future earthquakes. This report summarizes the findings of the first phase of a long-term research program. It provides some preliminary results and recommendations for estimating (1) the amplitude of liquefaction-induced ground displacement and (2) the probability for these displacements to exceed some threshold amplitude. The amplitude and probabilistic models of liquefaction-induced ground deformation are based on measured displacement data, topographical data, soil borehole information, and earthquake data prior to the 1994 Northridge earthquake and 1995 Hyogoken Nanbu earthquake. In this report, the present state of understanding of the mechanisms of liquefaction-induced ground deformation has been reviewed based on past work in the field, laboratory, shaking table tests, centrifuge experiments, and empirical and analytical modeling. Among all these various approaches, the empirical multi-regression modeling of case histories emerge as the most relevant, practical and feasible approach for predicting liquefaction-induced deformation over the large areas covered by gas distribution networks. Twelve Multiple Linear Regression (MLR) models have been calibrated for modeling liquefaction-induced ground deformations. These MLR models have six and four parameters, respectively, and cover ground-slope and free-face conditions. They were calibrated from two data sets: one for displacements of all magnitudes, and the other for displacements smaller than 2 meters. In parallel to these MLR models, twelve statistical models have been proposed for assessing the confidence interval for predicting liquefaction-induced ground deformation and the probability of exceeding some ground deformation levels. The four-parameter models are more approximate than the six-parameter models and are recommended when there is limited borehole data. Both MLR and probabilistic models are preliminary because they are only based on data from earthquakes prior to 1994. The next phase of the research is presently focusing on the data collection of high-quality case histories of liquefaction-induced ground deformation in the 1994 Northridge and 1995 Hyogoken Nanbu earthquakes. Following the completion of the new database on liquefaction-induced ground deformation, new generations of probabilistic models will be proposed.

ACKNOWLEDGEMENTS

The financial support of the Pacific Earthquake Engineering Research center (PEER)-and the Pacific Gas and Electric Company (PG&E) is acknowledged. The authors thank Norm Abrahamson of PG&E for his help and advice during the conduct of the research project. The authors thank Prof. L. Youd of Brigham Young University, and Dr. S. Bartlett of the Utah Department of Transportation, for sharing their databases.

1. INTRODUCTION

Liquefaction-induced ground deformations have been identified as a potential source of major damage to pipeline networks during earthquakes. These permanent displacements have amplitude ranging from few centimeters to 10 meters and more. They were numerous during the 1995 Hyogoken-Nanbu earthquake (Hamada et al., 1996a and 1996b) and caused substantial damage to lifelines and pile-foundations of building and bridge piers along the Kobe shoreline (Hamada et al, 1996a; Karube and Kimura, 1996; Matsui and Oda, 1996; and Tokimatsu et al., 1996).

The overall research objective is to develop and improve methods for assessing and quantifying the liquefaction potential of ground deformation utilizing regional geologic data and detailed borehole data. Ultimately, this research is to produce probabilistic models of liquefaction-induced ground displacement useful for estimating the cost of damage and repair to gas distribution network during future earthquakes.

The specific objectives of the first research phase are:

(1) Review the present state of understanding of the mechanisms of liquefaction-induced deformation,

(2) Review and examine the case histories of liquefaction occurrences and liquefaction-induced ground deformation, and the models for liquefaction-induced lateral deformation, and

(3) Develop empirical and probabilistic models for liquefaction-induced lateral deformation applicable to deformations smaller than 2 meters.

This report summarizes the research results obtained during the first research phase, and gives some preliminary results and recommendations for estimating the amplitude and probability of liquefaction-induced ground displacement.

This report has six sections. The first section describes the phenomenon of liquefaction-induced deformation observed during earthquakes. The second section reviews the explanations for the mechanisms of liquefaction-induced ground displacement based on laboratory observations, shaking table tests, and centrifuge experiments, and surveys the analytical models for describing liquefaction-induced deformation. The third section examines the existing databases on liquefaction-induced deformation. The fourth section describes the empirical models calibrated from these databases. The fifth section presents the newly developed multiple-linear-regression models for assessing liquefaction-induced deformation. The last section presents the probabilistic models generated from the MLR models for assessing the confidence intervals for liquefaction-induced ground deformation and the probability for liquefaction-induced deformation to exceed some amplitude level.

1.1 Liquefaction-induced lateral spreads

During past earthquakes, large areas of ground were observed to shift laterally due to soil liquefaction. These liquefaction-induced lateral ground deformation have amplitudes ranging from

small (1 cm) to very large (>10 m) in the case of flow slides. They can take place for gently sloping ground conditions (0.1% to 6%). Examples of liquefaction-induced ground deformation during the 1994 Northridge earthquake were observed at the Power Plant Tailrace (>1 m) in the Van Norman Complex, and the Lower San Fernando Dam (0.3 m) (Bardet and Davis, 1996). As illustrated in Fig.1, liquefaction-induced ground deformations are generally observed close to open faces, or in gently sloping ground. These deformations are usually driven by a combination of transient and static shear stresses and attributed to the loss of shear strength of underlying saturated soils. As illustrated in Fig. 2, the permanent ground deformations, which have complicated patterns, may extend beyond liquefied areas.

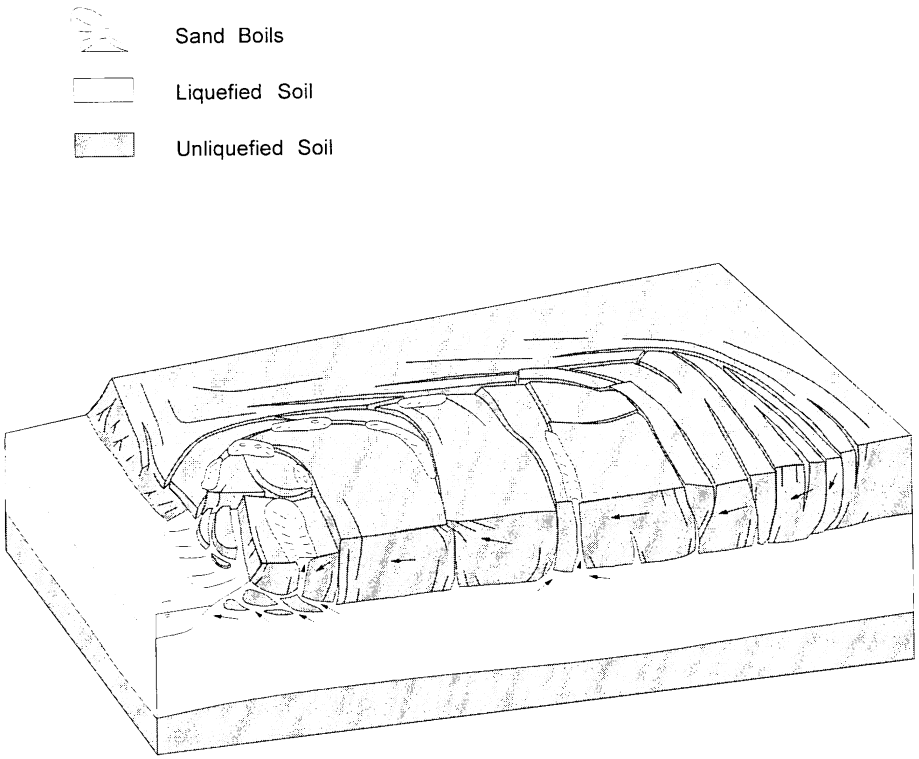

Figure 1-1. Schematic description of a lateral spread resulting from soil liquefaction during an earthquake (Rauch, 1997).

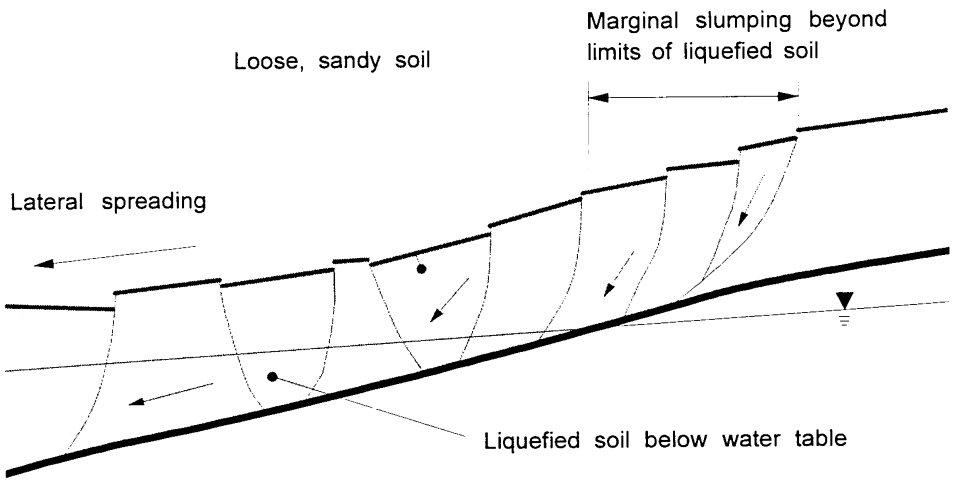

Figure 1-2. Extent of lateral spread beyond liquefaction areas (Rauch, 1997).

During the 1995 Hyogoken-Nanbu earthquake, liquefaction induced lateral ground deformation was one of the major causes of damage to lifelines and pile-foundations of building and bridge piers along the Kobe shoreline (Hamada et al, 1996; Karube and Kimura, 1996; Matsui and Oda, 1996; and Tokimatsu et al., 1996). As shown in Figs. 3 and 4, lateral ground deformations can cause bending and axial compression in buried pipes, which may damage pipes during earthquakes.

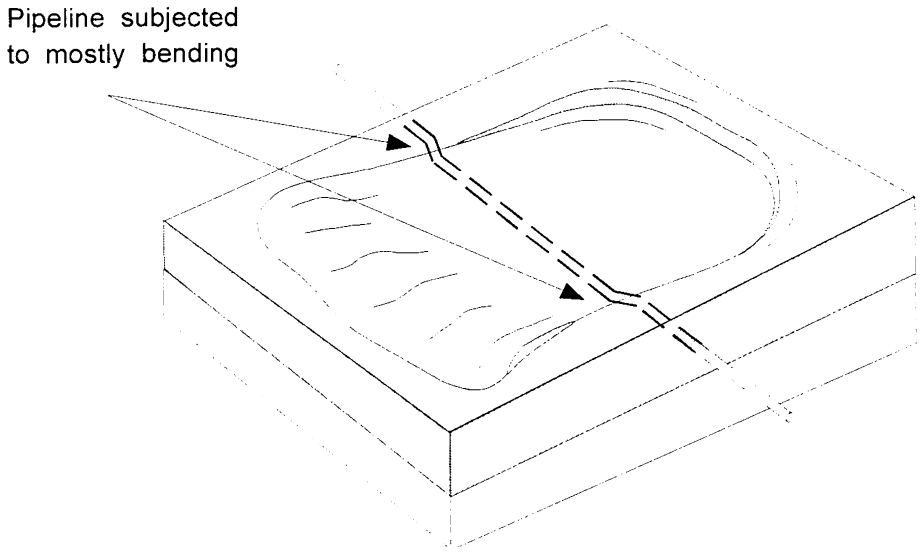

Figure 1-3. Illustration of damage to pipeline subjected to liquefaction-induced lateral spread after an earthquake (Rauch, 1997).

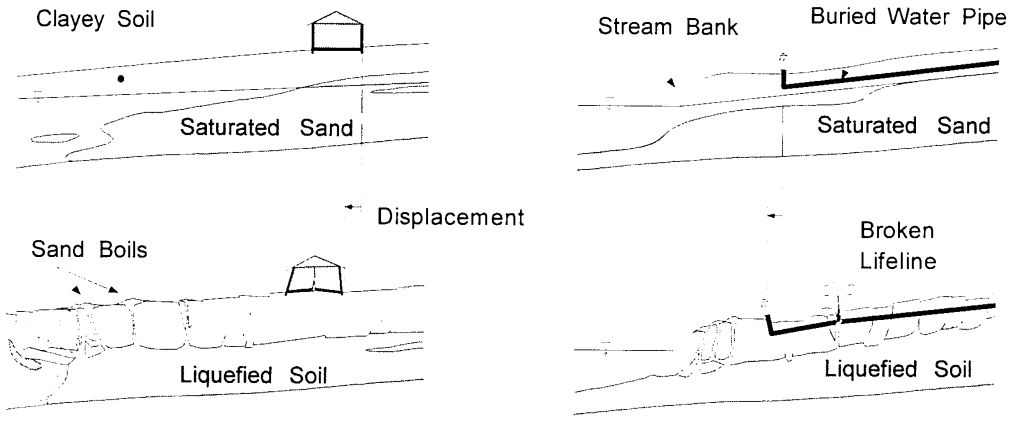

Figure 1-4. Illustration of liquefaction-induced ground deformation and associated damage to buried pipelines for ground-slope and free-face cases (Rauch, 1997).

1.2 Field measurement of lateral ground deformation

A large number of case histories of liquefaction-induced lateral spreads have been compiled in the two volumes edited by Hamada and O'Rourke (1992). Some examples of case histories are:

- 1964 Niigata earthquake (Youd and Kiehl, 1996)
- 1971 San Fernando earthquake, Van Norman Complex areas
- 1983 Ninhonkai-Chubu
- 1983 Borah peak, Idaho, earthquake (Youd et al., 1985)
- 1987 Superstition Hills, California, Earthquake (Wildlife Site, Youd and Holtzer, 1994; and Scott and Hushmand, 1995)
- 1989 Loma Prieta earthquake, Watsonville (Holtzer et al., 1994)
- 1993 Hokkaido Nansei-oki Earthquake (Isoyama, 1994)
- 1994 Northridge earthquake, Balboa Blvd (Holzer et al., 1996) and Van Norman Complex (Bardet and Davis, 1996; Davis and Bardet, 1996)
- 1995 Hyogoken-Nanbu earthquake (Hamada et al., 1996, Ishihara et al., 1996)

There are two main techniques for measuring permanent lateral ground deformation: ground surveying and processing of aerial photographs.

Ground surveys are commonly used in assessing the damage to constructed facilities. They are based on well-established optical measurements, and are sometimes tied up with satellite global positioning system (GPS) techniques. Ground surveying is extremely accurate (<5 mm) but unfortunately limited to areas that have been equipped with survey monuments prior to earthquakes. Examples of accurate ground surveying can be found in Bardet and Davis (1996). In

the studies of permanent ground deformation, the main drawback of ground survey is that their results are confined to areas of limited extent, and may be missing the global modes of deformation of larger areas.

Aerial photographs have been used to display comprehensive fields of permanent displacement after earthquakes (e.g., Hamada et al., 1996). Figure 5 shows an example of such field of ground displacement obtained using aerial photographs in Kawagachi-cho, Niigata, Japan, after the 1964 Niigata, Japan, earthquake (Hamada et al., 1993).

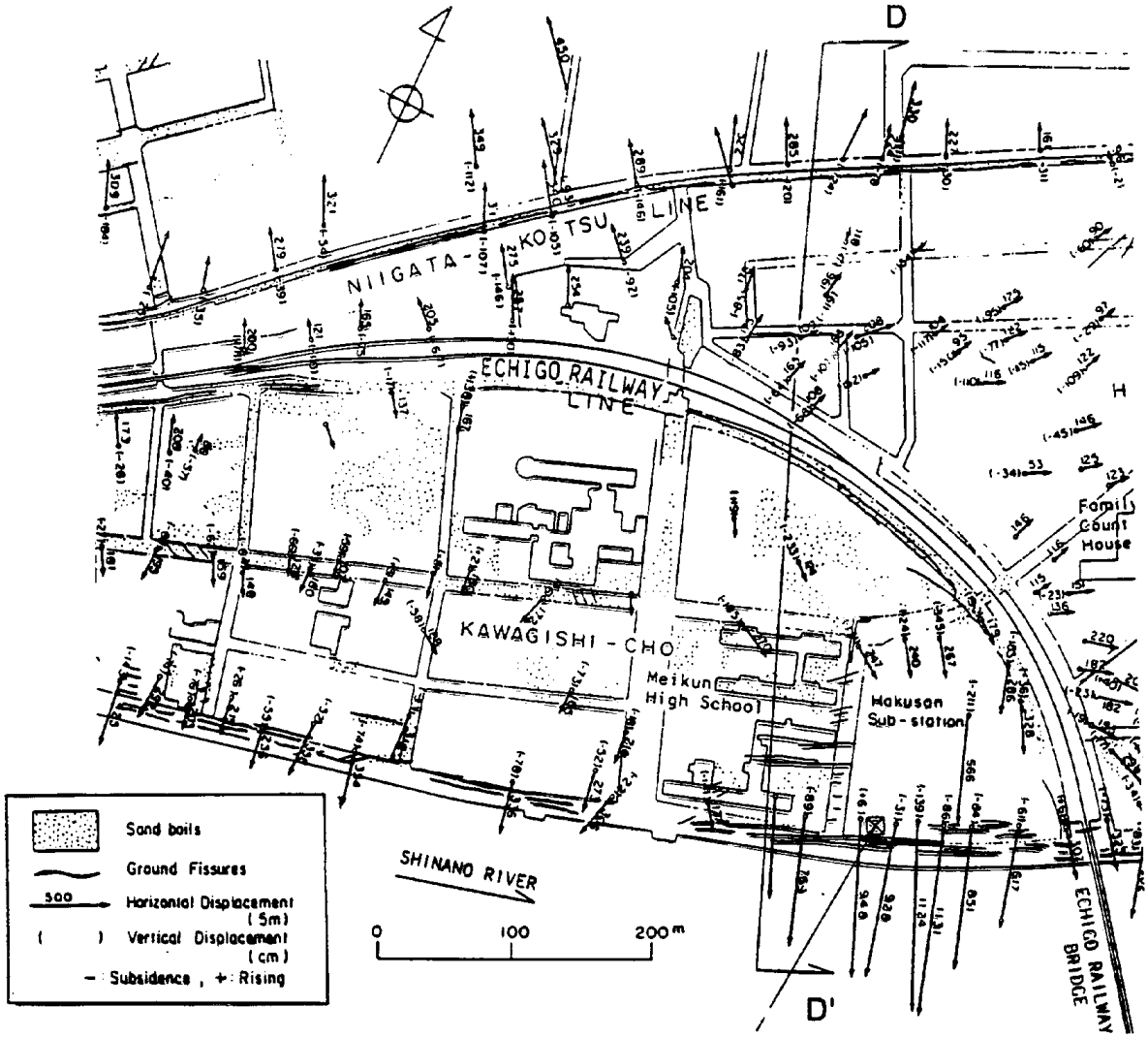

Figure 1-5. Examples of ground displacement vectors obtained in Kawagachi-cho, Niigata, Japan, after the 1964 Niigata, Japan, earthquake using aerial photographs (Hamada et al., 1993).

The determination of ground displacement requires aerial photographs taken before and after the earthquake. The accuracy of the measured amplitude of ground displacements depends on the scale and timing of the aerial photographs. The best measurements correspond to low-altitude

photographs taken just before and after the earthquake. In general, low-altitude photographs are much more difficult to find before rather than after the earthquake, which mostly limits the accuracy of past analyses. In the 1994 Northridge earthquake, the aerial photographs faced a new problem posed by the tectonic deformation, which had amplitudes comparable to that of permanent surficial ground deformation (Bardet and Davis, 1996).

2. MECHANISMS OF LATERAL GROUND DEFORMATION

The physical mechanisms causing liquefaction-induced ground deformation have been investigated by the means of laboratory tests, shaking table tests, and centrifuge experiments.

2.1 Laboratory approach

Laboratory experiments are useful to investigate under controlled conditions the aspects of soil behavior related to liquefaction-induced deformation. Laboratory experiments attempt to simulate the field conditions of the saturated soils during and after the cyclic loads applied by earthquakes.

2.1.1 Pre-liquefaction behavior

The behavior of saturated sands leading to liquefaction has been extensively studied in the laboratory under undrained conditions (e.g., Ishihara, 1993 and 1996). Figure 1 illustrates the typical response of saturated sand observed in cyclic undrained triaxial tests. During the axial loading cycles, the porepressure gradually increases (Fig. 1c) and the effective mean pressure decreases until it reaches a zero value (Fig. 1f). As the mean effective pressure approaches zero, large shear strains are developed in the soil sample. The magnitudes of these shear strains are limited by the effects of stress-dilatancy, which increases the mean effective pressure and therefore the shear strength of sands. Based on the typical results shown in Fig. 1, it is concluded that shear deformations in the field may accumulate due to shear stress cycles during the earthquake shakings. This cyclic accumulation of permanent shear strain (or rachetting) is certainly a plausible interpretation of the physical mechanisms of liquefaction-induced deformation in the field.

2.1.2 Post-liquefaction volumetric deformation

There is another aspect of soil behavior in the laboratory, besides the undrained response shown in Fig. 1, which is relevant to liquefaction-induced ground deformation. This particular behavior, which follows the reduction of mean effective pressure caused by cyclic loadings, is referred to as post-liquefaction behavior. As shown in Fig. 2, the amount of post-liquefaction volumetric deformation depends on not only the initial relative density D_r, but also the maximum amplitude of cyclic strain applied to soils. Ishihara (1993 and 1996) defines the onset of initial liquefaction when the soil sample undergoes cyclic shear strain in excess of 3.5%. As shown in Fig. 3, this maximum shear strain applied to the liquefied soil can also be expressed in terms of the factor of safety against liquefaction, F_l:

$$F_l = (\tau_{av,l}/\sigma'_v)/(\tau_{av}/\sigma'_v)$$

where $\tau_{av,l}/\sigma'_v$ is the ratio of shear stress amplitude $\tau_{av,l}$ to effective vertical stress σ'_v required for liquefaction, and the applied ratio of shear stress amplitude τ_{av} to effective vertical stress. As shown in Fig. 4, the amount of volumetric strain can therefore be related to F_l. The post-liquefaction volumetric strain of soils therefore depends on their initial density and the safety factor against liquefaction. Figure 4 also shows some approximate correlations between relative density, normalized standard penetration test (SPT) blow count, and normalized cone penetration test (CPT) resistance.

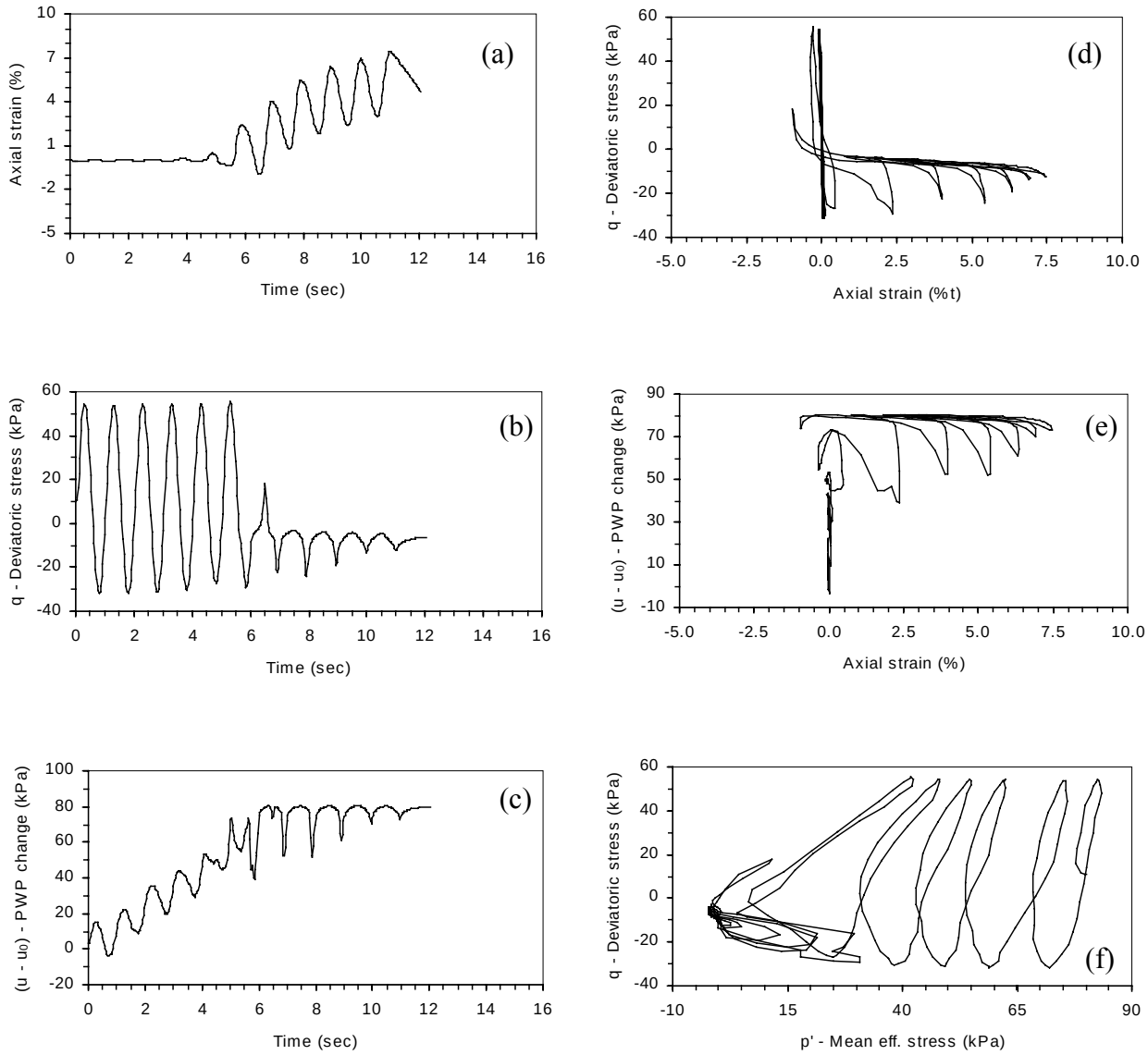

Figure 2-1. Cyclic triaxial undrained test at 80 kPa confining pressure on 60% relative density Nevada Sand. Time histories of (a) axial strain; (b) deviator stress; and (c) porepressure change; (d) stress-strain response, (e) porepressure-strain response, and (f) effective stress path (Arulmoli et al., 1992).

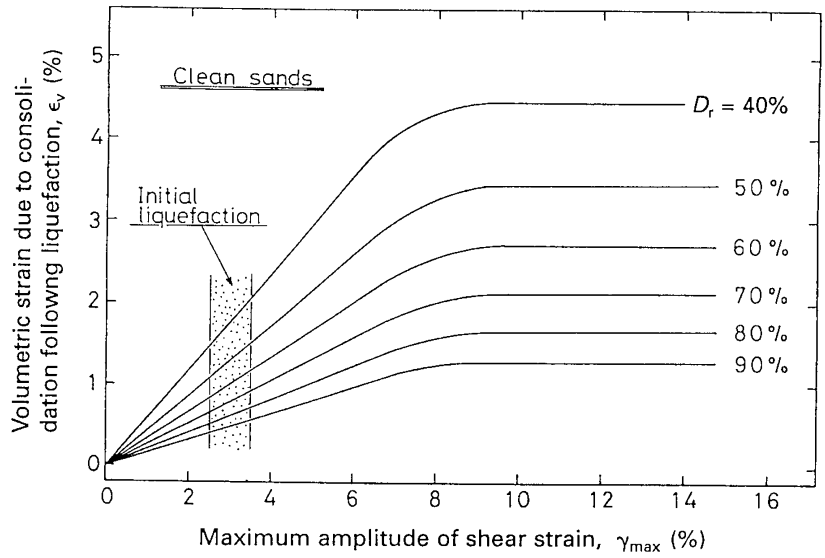

Figure 2-2. Post-liquefaction volumetric strain of clean sands plotted against maximum shear strain (Ishihara, 1996).

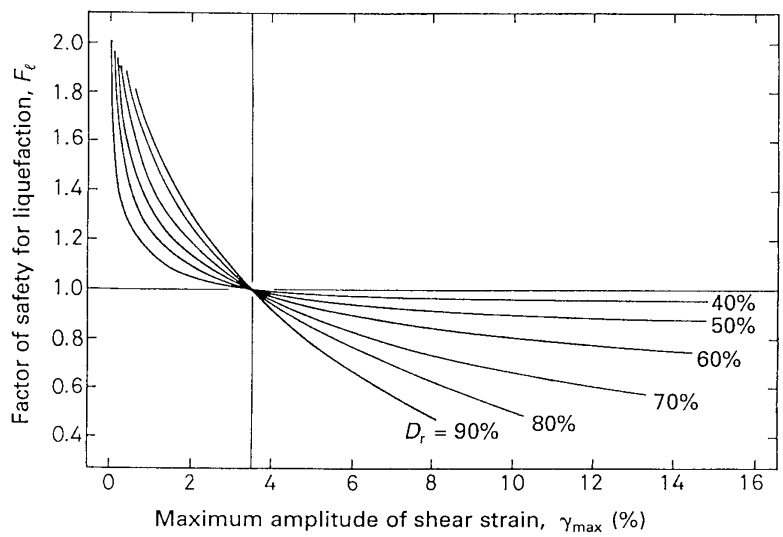

Figure 2-3. Relation between factor of safety F_l and maximum shear strain for clean sands (Ishihara, 1996).

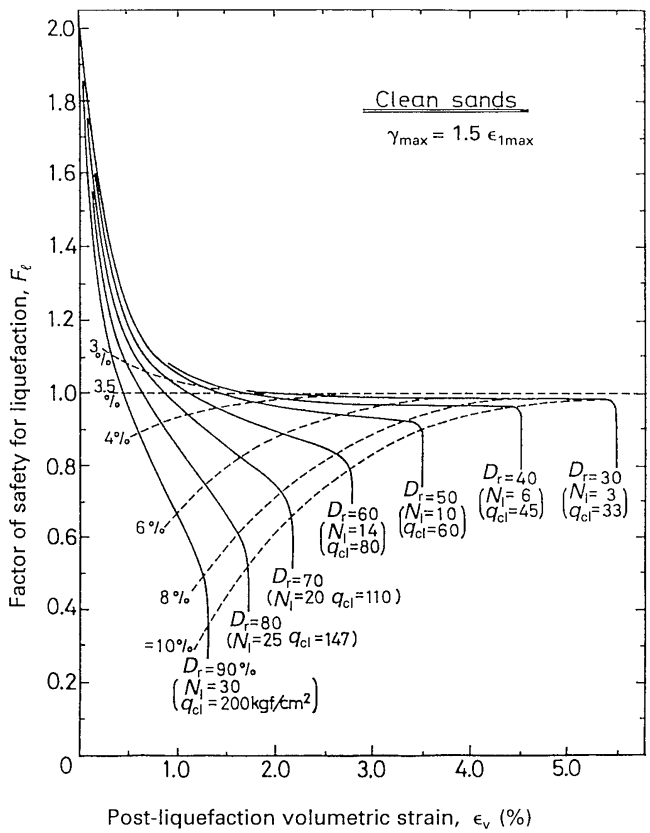

Figure 2-4. Chart for determination of post-liquefaction volumetric strain of clean sands as a function of factor of safety (Ishihara, 1996).

2.1.3 Post-liquefaction shear deformation

The mechanism of post-liquefaction shear deformation in saturated sands were experimentally investigated by using torsional test (e.g., Yasuda et al., 1994; and Shamoto et al., 1997) and triaxial tests (e.g., Nakase et al., 1997). Both undrained torsional tests (Yasuda et al., 1994; and Shamoto et al., 1997) and undrained triaxial tests (Nakase et al., 1997) indicate that liquefied soils regain shear-strength beyond some shear strain threshold γ_L. Figure 5 shows an example of such a re-hardening during a monotonic undrained torsional shear test following cyclic liquefaction (Peiris and Yoshida, 1996). As shown in Fig. 5, the liquefied sand gradually regains shear strength when it is sheared beyond some threshold shear strain γ_L. The value of γ_L depends on the relative density D_r and the amount cyclic shear strain prior to liquefaction, or the factor of safety against liquefaction. As shown in Figs. 5 and 6, Yoshida (1996) proposed a stress-dilatancy model, which describes well the stress-strain curves in the post-liquefaction range. This strain-dependent type of stress-dilatancy is a new in constitutive modeling, and deserves further investigation. The strain threshold γ_L is related to the maximum displacement of lateral spreads, and is useful for predicting the upper-bound of liquefaction-induced lateral displacements.

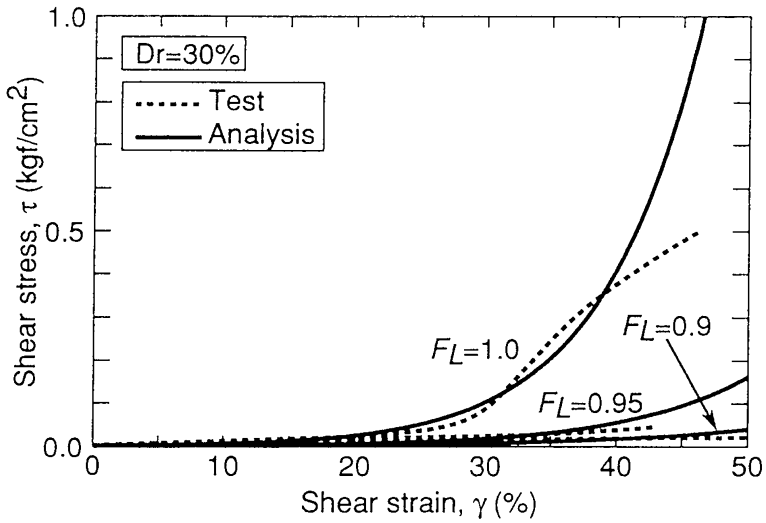

Figure 2-5. Stress-strain response of Toyoura sand at 30% relative density in the post-liquefaction range during undrained torsional tests (data after Yasuda et al., 1994; model after Yoshida, 1996).

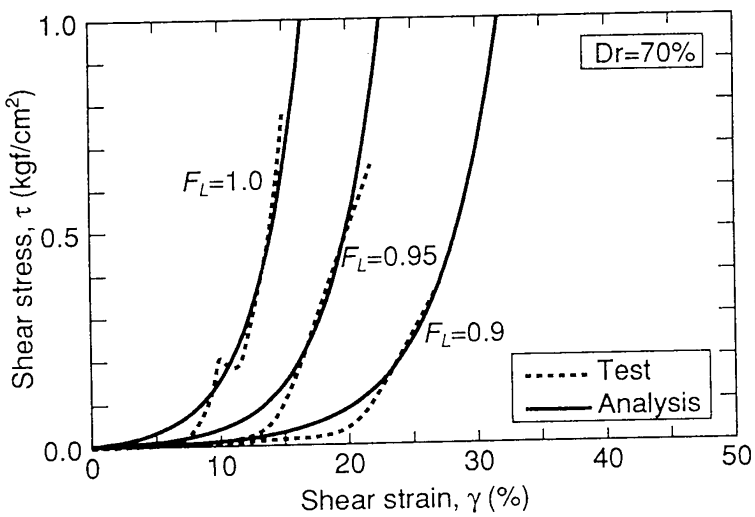

Figure 2-6. Stress-strain response of Toyoura sand at 70% relative density in the post-liquefaction range during undrained torsional tests data after Yasuda et al., 1994; model after Yoshida, 1996).

2.1.4 Example of calculation of lateral spread displacement based on laboratory tests

The results of laboratory tests on post-liquefaction shear deformation can be used to estimate the maximum amount of lateral displacement in a saturated soil layer. An example of calculation is shown in Table 1 and Figure 7. The 10-m thick layer is gently sloping. It is made of clean sand

with a 30% relative density and a saturated unit weight of 18.62 kN/m^3. The water table is assumed to be at the ground surface. The sand is assumed to have liquefied during the earthquake, and the liquefaction severity is estimated by using F_L, the factor of safety against liquefaction. In this example, $F_L = 0.95$. As shown in Table 1, the laboratory test results give the limiting strain γ_L for three different values of initial effective stress σ'_v. The experimental results indicate that γ_L increases with σ'_v, e.g., γ_L increases from 28% to 47 % when σ'_v varies from 24.5 kPa to 98 kPa. Based on these laboratory results, the limiting strain is calculated from the vertical effective stress at three different depths in the layer, and the resulting displacement is calculated in each layer. The maximum total displacement, which is the sum of the displacements of each layer, is found to be 3.5 m. This displacement corresponds to an average shear strain in the complete layer equal to 35%. The displacement calculated above corresponds to very large strain. It is an upper bound of the possible strain that may develop in this particular slope. According to these calculations, the upper bound does not depend on the slope angle and inertial effects.

Table 2-1. Calculation of the maximum amplitude of lateral spread based on laboratory test results.

			σ'_v (kPa)	γ_L (%)
γ_{sat} =	18.62 kN/m^3			
D_r =	30%		24.5	28
F_l =	0.95		49.0	42
			98.0	47
Depth (m)	σ'_v (kPa)	Thickness (m)	γ_L (%)	Displacement (m)
1.7	14.7	3.3	22.4	0.7
5.0	44.1	3.3	39.2	1.3
8.3	73.5	3.3	44.5	1.5
		Total displacement =		3.5 m

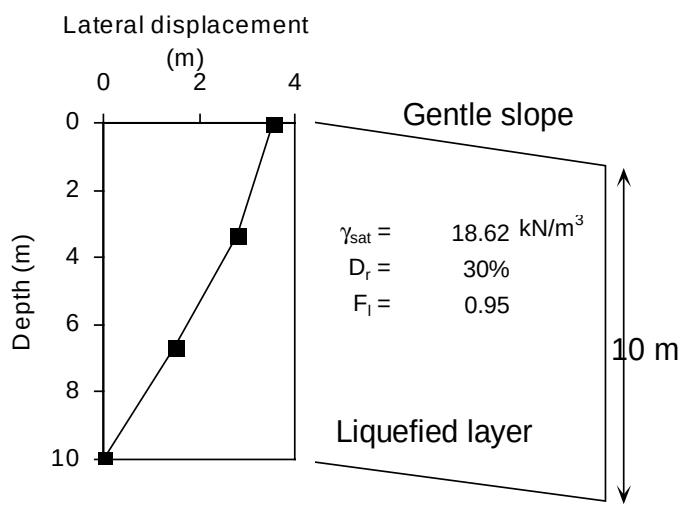

Figure 2-7. Example of calculation of maximum lateral displacement based on laboratory tests (after Yasuda et al., 1994).

2.2 Centrifuge modeling of liquefaction induced ground displacement

The principles of centrifuge modeling are well described in several technical papers (e.g., Ko, 1988). In centrifuge modeling, reduced-scale models are constructed to represent larger prototypes and subjected to a centrifugal acceleration *n* generated by the rotation of the centrifuge arm. In the case of centrifuge modeling of soil deposits shaken by earthquakes, the model is enclosed in a laminar box, and is shaken in flight by an hydraulic shaker through its base (Figs. 8, 9, and 10).

As shown in Table 2, all physical quantities in the centrifuge models are scaled to determine the prototype responses. In these scaling relations, the stresses and strains have identical scaling in the model and prototype, which preserve the nonlinear stress-strain relationships of soils. Lengths are scaled with n. Time in dynamic processes is scaled with $1/n$, whereas time in diffusion processes is scaled with $1/n^2$. Consequently, the prototypes involving simultaneously dynamic and diffusion processes cannot be modeled exactly in the centrifuge by simply reducing the model size. This is the case of liquefaction-induced lateral displacements, which involve nonlinear transient soil behaviors coupled to the diffusion of interstitial water (i.e., consolidation). The modeling of such phenomena requires the introduction of viscous additives into the interstitial water to scale the consolidation time (e.g., Ko, 1988).

The interpretation of lateral spread with centrifuge experiments is described Dobry et al. (1995). In a particular experiment, Dobry simulated lateral spreads in inclined laminar boxes (Fig. 11) using a 10-m thick clean Nevada sand deposit, which has a gentle slope inclination of 2%. Three different relative densities were used: 40%, 65% and 80%. The sand was saturated by using interstitial water without viscous additives. The laminar box was shaken by a sine-like input ground motion at its base. The pore pressure, acceleration, and lateral displacement were recorded at various depths. As shown in Figs. 12 to 15, the centrifuge results indicate that (1) the lateral ground deformation is associated with unsymmetric spikes of ground acceleration in the downhill direction, (2) there are negative pore pressure spikes which increase the effective stress and stop the downhill ground deformation, (3) the lateral ground deformation does not continue after the shaking, and (4) the lateral displacement and the thickness of the liquefied layer decreases with relative density.

The centrifuge test results indicate that permanent lateral ground deformation is a rachetting phenomenon, the amplitude of which is controlled by stress-dilatancy. They also show that the magnitude of permanent ground displacement is related to relative density and thickness of liquefied layer. However, the timing of lateral spreading observed in centrifuge experiments does not agree with the delayed ground deformations and failures observed after the 1964 Niigata earthquake. In future work, there is a need for increasing the interstitial fluid viscosity and for examining the effects of properly-scaled diffusion on lateral spreading. In spite of some limitations, the centrifuge remains a useful tool for comprehending the mechanism of lateral ground deformation.

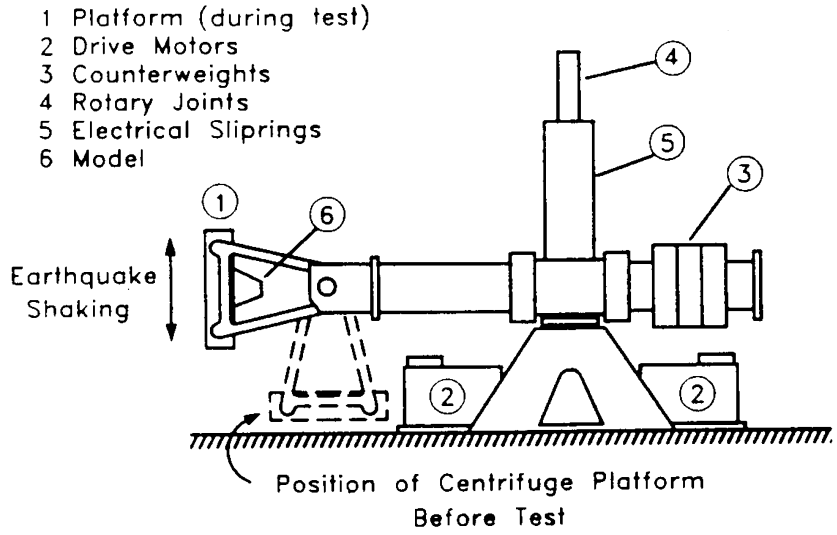

Figure 2-8. Sketch of RPI geotechnical centrifuge (Dobry et al., 1995).

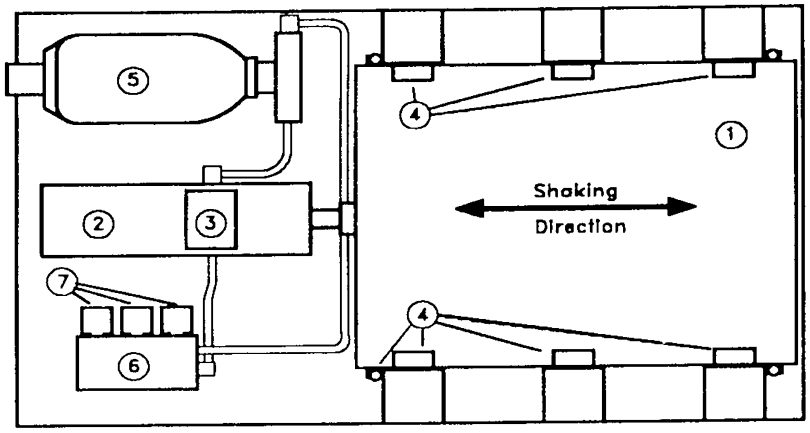

Figure 2-9. Schematic view of in-flight shaker at RPI (Dobry et al., 1995).

Table 2-2. Scaling relations used for centrifuge modeling (Dobry et al., 1995).

Parameter	Model units	Prototype units
Length	1/n	1
Velocity	1	1
Acceleration	n	1
Stress	1	1
Strain	1	1
Time:		
Dynamic	1/n	1
Diffusion	$1/n^2$	1
Frequency	n	1

(n = centrifuge acceleration in g)

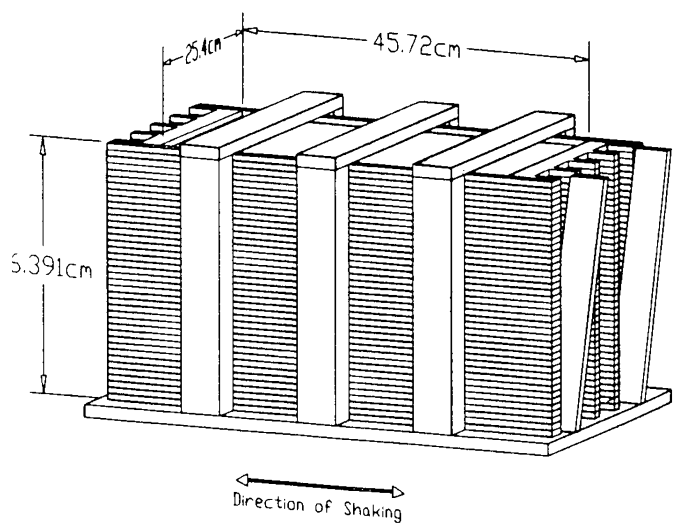

Figure 2-10. Schematic view of the RPI laminar box (Dobry et al., 1995).

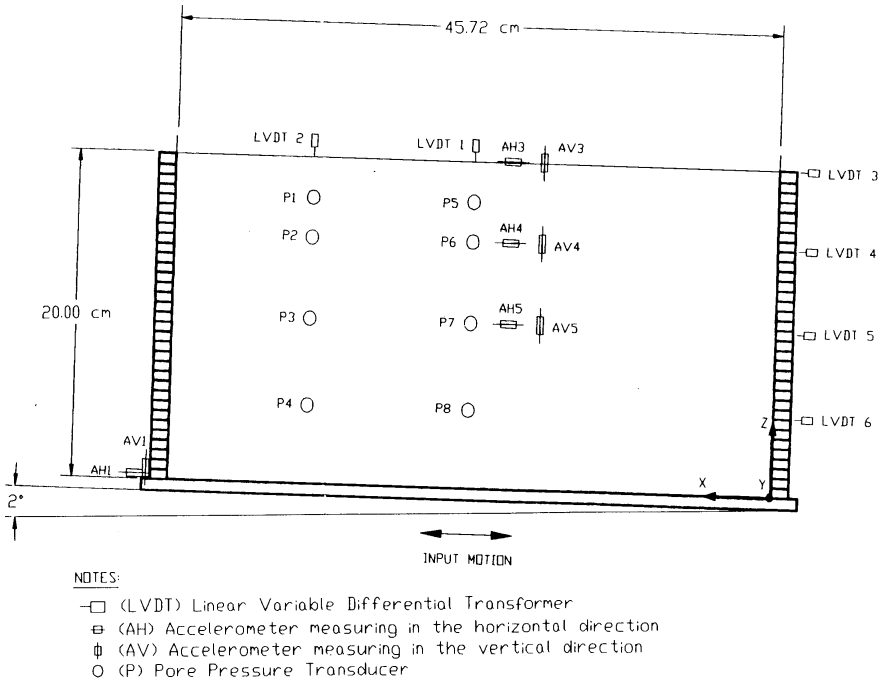

Figure 2-11. RPI laminar box and Model No.2 (Dobry et al., 1995).

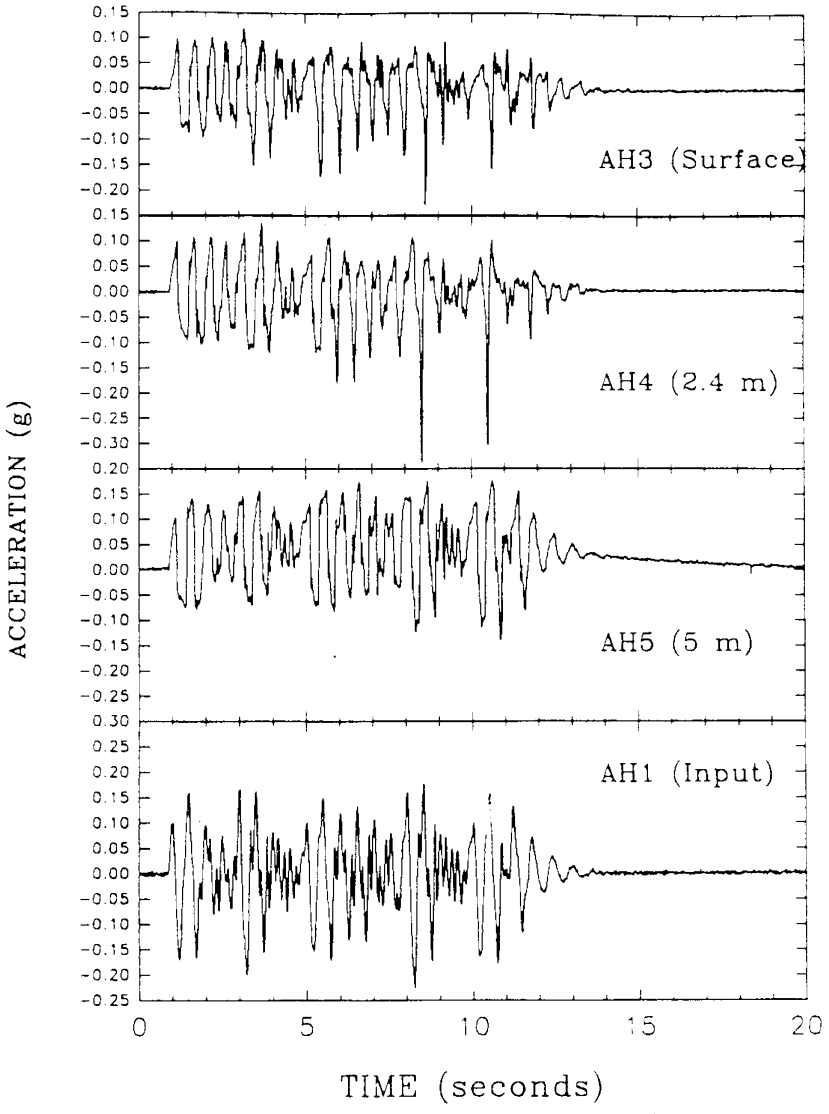

Figure 2-12. Lateral acceleration time histories for Model No. 2 (Dobry et al., 1995).

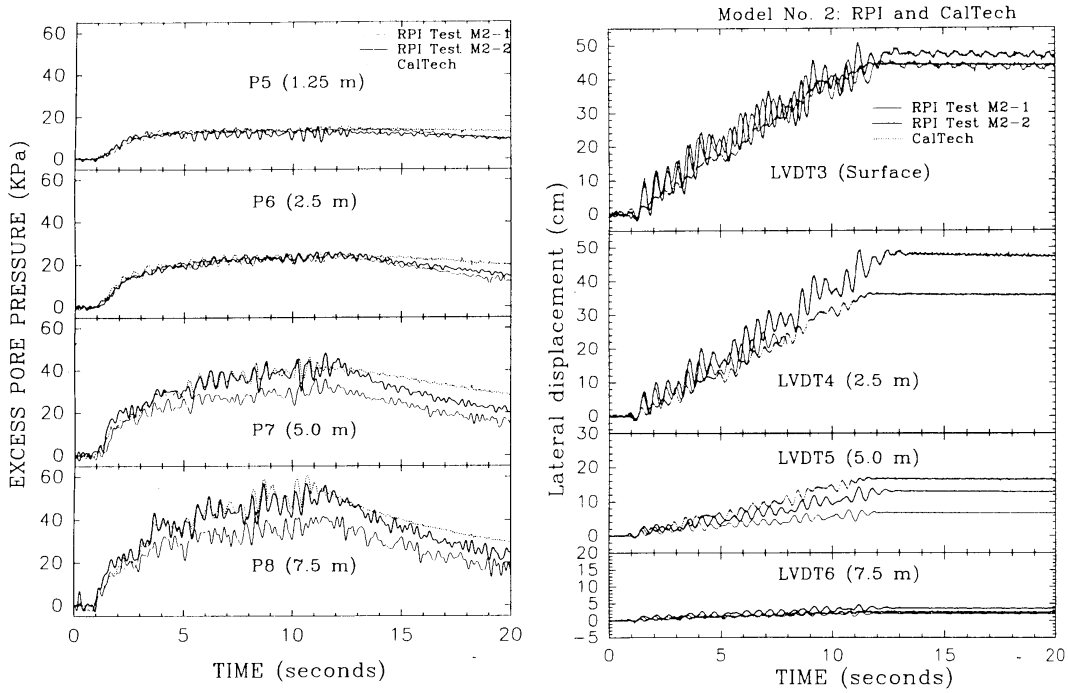

Figure 2-13. Time histories of excess pore pressure and lateral displacement recorded at Caltech and RPI for Model No. 2 (Dobry et al., 1995).

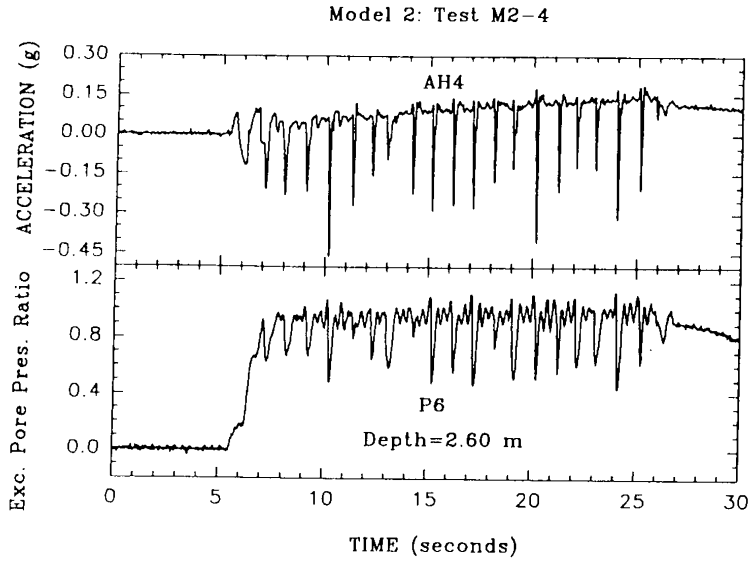

Figure 2-14. Time histories of acceleration and excess pore pressure recorded at RPI for Model No. 2-4 (Dobry et al., 1995).

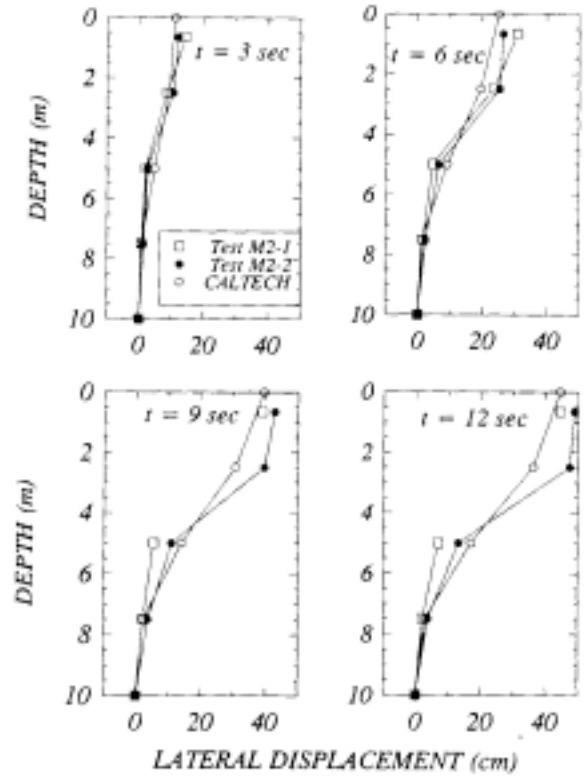

Figure 2-15. Lateral displacement profiles at various times during shaking for tests at Caltech and RPI, Model No. 2 (Dobry et al., 1995).

2.3 Shaking Table Experiments

Liquefaction-induced lateral spreads have extensively been investigated using shaking tables (e.g., Towhata et al., 1996). In these types of experiments, a reduced-scale model of soil deposits is subjected to short pulses or continuous time history of acceleration simulating the earthquake ground motion. Figure 16 shows typical results of ground deformation obtained in shaking table tests. The acceleration, pore pressure, and displacement are measured at various locations in the reduced-scale model, which is 2 m long and 50 cm high. In the impact test (Fig. 16a), the model is subjected to a very short acceleration pulse. The pore pressure rises very quickly, and the deformation takes place over an extended period of time. In the shaking test (Fig. 16b), the model is subjected to a sine-like base acceleration. The porepressure gradually builds up until the soil liquefies. The ground deformations are progressive, and stop with the base acceleration. This observation is in agreement with those of centrifuge experiments without viscous additives. However, the observations for the impact test in shaking table test do not agree with the centrifuge observations.

Figure 17 summarizes possible explanations proposed by Towhata et al. (1996) for ground deformation simultaneous to ground shaking, or delayed after the ground shaking. Due to the

seismic shaking, the pore pressure raises until the soil liquefies. The onset of liquefaction is generally reached during the earthquake shaking. The state of liquefaction is sustained during some time interval, then pore pressure decreases depending on drainage conditions. The timing of the liquefaction-induced deformation depends on the time history of driving stress and shear strength. The deformation starts when the shear strength is smaller than the driving shear stress, and stops when the shear strength is larger than the driving shear stress. In the case of rapid drainage, the shear strength is likely to be regained after the shaking stops, and the deformation will stop with the shaking. In the case of slower drainage, the shear strength may be regained much more slowly, and the deformation may extend after the shaking.

In shaking table tests, Kokusho et al. (1998) reported that a water film formed beneath a thin layer of silt sandwiched between sand layers. They observed that, when such a film appeared, the soil mass above the silt layer glided in the downward direction not only during but after the shaking. When the film did not form, the lateral flow took place mainly during the shaking. This shaking table test experiment clearly demonstrates liquefaction-induced deformations are influenced by drainage conditions.

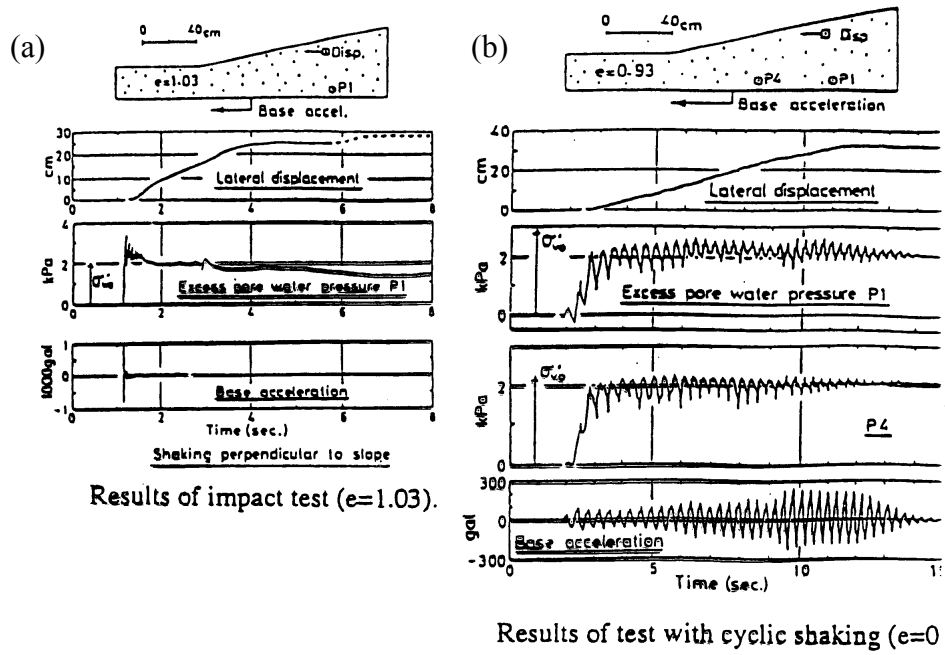

Figure 2-16. Time history of acceleration, porepressure, and lateral displacement observed in shaking table test: (a) impact test; and (b) cyclic shaking (Towhata et al., 1996).

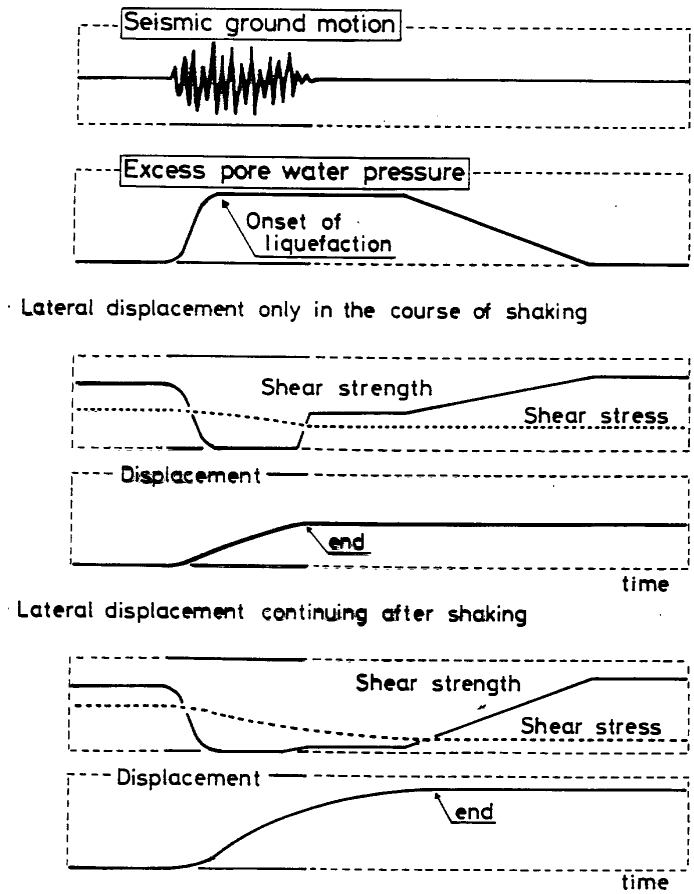

Figure 2-17. Possible explanations for the continuation and cessation of liquefaction-induced ground deformation after the earthquake shaking (after Towhata et al., 1997).

2.4 Summary of observations from laboratory, shaking table, and centrifuge experiments

The results of laboratory, shaking table and centrifuge experiments are useful to understand the physical mechanisms of liquefaction-induced deformation generated by earthquakes. The laboratory tests indicate that liquefied soils may deform during and after transient earthquake loadings. The lower range of liquefaction-induced deformation correspond mainly to cyclic ratchetting during transient earthquake loading, and is controlled by transient shear stress, number of loading cycles, relative density and stress-dilatancy. The upper range of liquefaction-induced deformation corresponds to post-liquefaction behavior with a regain of shear strength, which is also induced by stress-dilatancy. This regain of shear strength is observed for a threshold shear strain γ_L, which depends on the initial relative density and the maximum amplitude of cyclic shear strain. The inclusion of post-liquefaction re-hardening effects into constitutive modeling offers a promising approach for predicting the maximum magnitude of lateral spread. The centrifuge and shaking table experiments indicate that the slope of the ground surface affects significantly the permanent displacement in ground-slope cases. There are still some disagreements about the timing of liquefaction-induced ground deformation between the field observations and the experiments in shaking table, centrifuge and laboratory. There is not yet a rational explanation for the occurrence of lateral ground deformation after the earthquake shaking. Such delayed ground

deformations need to be investigated and understood for modeling accurately lateral ground deformation in simplified engineering analyses and advanced analytical procedures.

2.5 Analytical Modeling of liquefaction-induced deformation

Several analytical models have been proposed to simulate the amplitude of liquefaction-induced ground deformation. These models are based on different types of approaches, and fall in the following categories:

- Newmark sliding block model
- Minimum potential energy model
- Model with shear strength loss and strain rehardening
- Viscous model
- Effective stress model

2.5.1 Newmark sliding block model

Several models have been proposed based on the concept that Newmark (1965) developed for calculating the deformation of earth dams during earthquakes.

Yegian et al. (1991) proposed that the amplitude D of permanent displacement is:

$$D = N_{eq}\, T^2\, a_p\, f(a_y/a_p) \tag{2.1}$$

where N_{eq} is the number of cycles equivalent uniform base motion, T the period (s), a_y the yield acceleration, a_p the peak acceleration (g), and f the dimensionless function depending on base motion.

Baziar et al. (1992) proposed that D depends on peak velocity:

$$D = N_{eq}\, v^2_{max}/a_{max} \,/\, f(a_y/a_{max}) \tag{2.2}$$

where a_{max} is the peak acceleration, and v_{max} the peak velocity.

Jibson (1993) proposed that D (cm) depends on the Aria intensity:

$$Log\ D = 1.46 \log I_a - 6.642\, a_y + 1.546 \tag{2.3}$$

where I_a the Aria intensity (m/s), and a_y the yield acceleration (g).

The models based on Newmark sliding blocks assume that the deformation takes place on a well-defined failure surface, the yield acceleration remains constant during shaking, and the soil is perfectly plastic. However, these assumptions do not hold in the case of liquefied soils and lateral spreads, because (1) the shear strain in liquefied soil does not concentrate within a well defined surface, (2) the shear strength (and yield acceleration) of saturated soils varies during cyclic loading as pore pressure varies, and (3) soils are generally not perfectly plastic materials, but commonly harden and/or soften.

Byrne (1991) extended the concepts of Newmark sliding block by introducing a resisting force varying with displacement. As shown in Fig. 18, the mass M with an initial velocity V is subjected to a driving force D due to the gravity and slope inclination α, and a resisting force R. The mass stops when the initial kinetic energy (i.e., $MV^2/2$) is dissipated by the resisting force R. As shown in Fig. 18, the final displacement can be much greater when the resisting force vary linearly with displacement. Byrne (1991) claimed that the total displacement may well be 2 or 3 times the standard Newmark estimate. Byrne's method requires the selection of a final residual shear strength S_R and limiting strain γ_R. Typical values of S_R and γ_R are listed in Table 4.

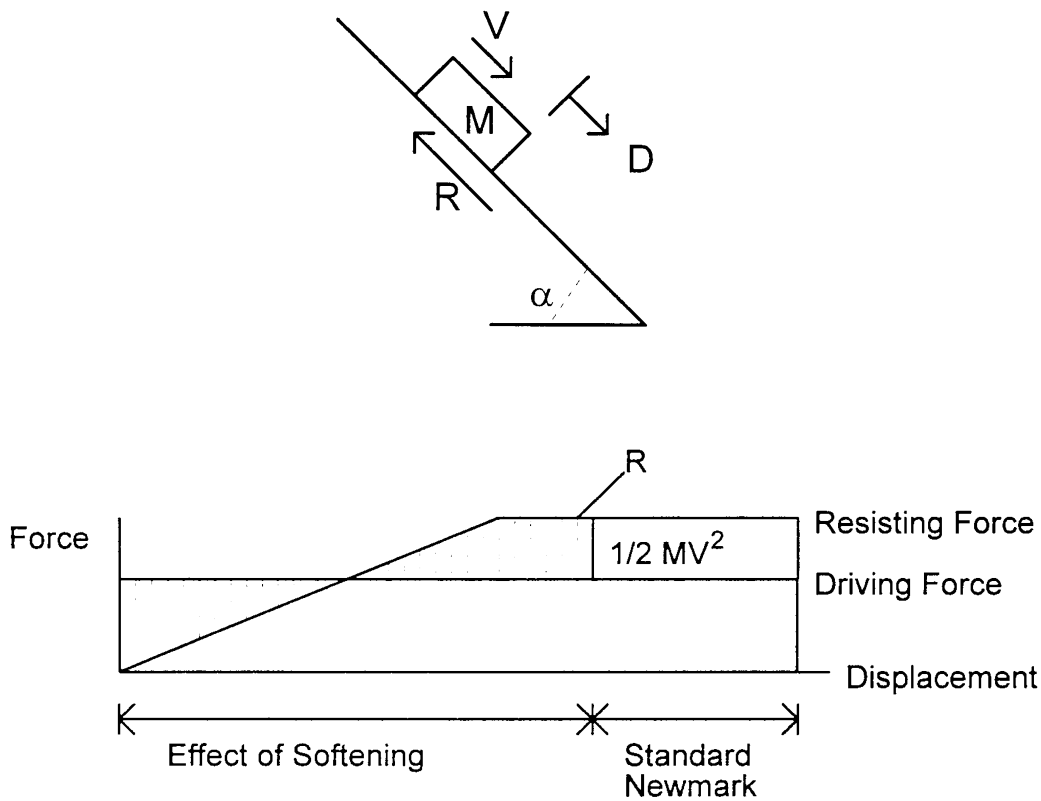

Figure 2-18. Extended Newmark sliding block concept for calculation of liquefaction-induced lateral spread (Byrne, 1991).

Table 2-4. Estimated values of shear strain and residual shear strength for extended Newmark sliding block analysis (Byrne, 1991).

$(N_1)_{60}$	s_u/p	γ_F (%)	
		$F_{TRIG} \approx 1.0$	$F_{TRIG} = 0.5$
0 - 4	0.05 - 0.10	25 - 50	>100
4 - 10	0.10 - 0.20	10 - 25	30 - >100
10 - 15	0.15 - 0.4	8 - 15	20 - 35
15 - 20	0.3 - 0.5	5 - 10	15 - 25
>20	> 0.5	< 5	< 15

2.5.2 Model with shear strength loss and strain rehardening

Byrne (1997) proposed to calculate the final position of a slope that liquefies by using the finite difference program FLAC (1995). In the zone of liquefaction, the liquefied material is assumed to be initially free of shear, and to undergo isotropic pressure. Following this instantaneous melting of the liquefied soil, the shear stress τ is assumed to increase with shear strain until it reaches some residual shear strength τ_{ST} (Fig. 19). While the liquefied soil regains shear strength, the shear modulus is assumed to take a constant value G_{LIQ}. The final position of the slope is calculated by using the dynamic equation of motion.

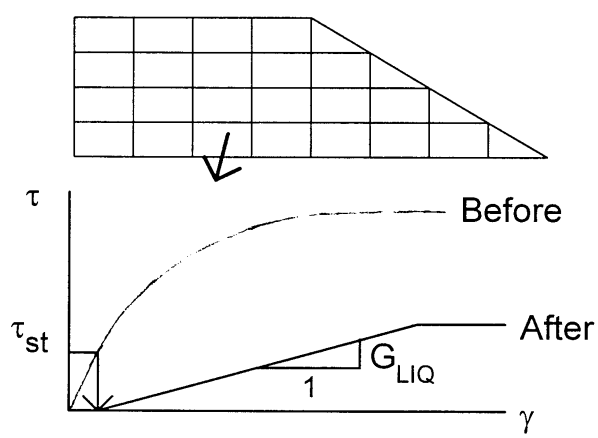

Figure 2-19. Illustration of principle in the dynamic method of Byrne (1997).

2.5.3 Minimum potential energy model

Towhata et al. (1997) developed a minimum potential energy model, the principles of which are schematized in Fig. 20. Soil layers of irregular shape are divided into vertical slices in which the lateral displacement is assumed to vary as a sine function with depth. The model determines the final position of the soil layers that liquefy by invoking the principle of minimum potential energy. The model also predicts the variation of displacement with time by using Lagrangian equations of motion. As shown in Fig. 21, the model was successfully applied to model various shaking table test results. The model was extended to three-dimensions (Orense and Towhata, 1996), and applied to simulate case histories of liquefaction-induced lateral ground deformation during the Niigata, 1964, earthquake.

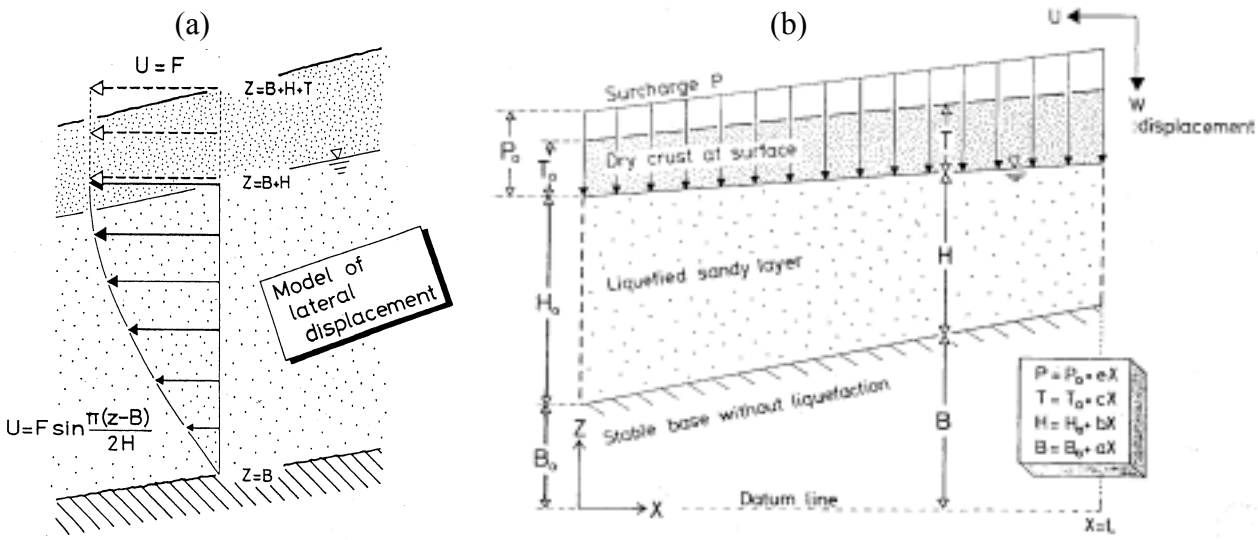

Figure 2-20. Towhata et al. (1997) minimum potential energy model: (a) Sinusoidal variation of lateral displacement along vertical axis; and (b) Simplified model of liquefied slope..

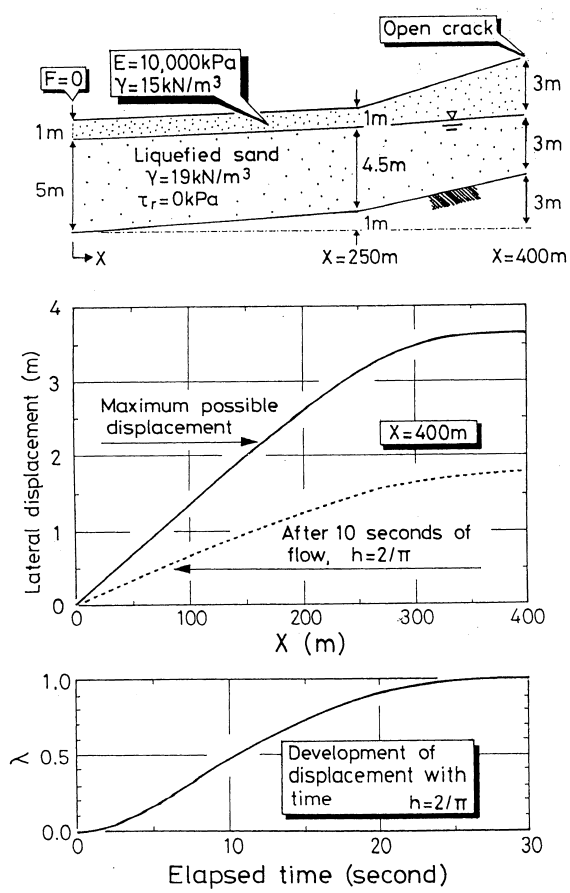

Figure 2-21. Analysis of lateral displacement of gentle slope with the minimum potential energy model of Towhata et al. (1997).

2.5.4 Viscous models

Hamada et al. (1994) proposed the use of viscous models to simulate the liquefaction-induced deformation of soils and the forces applied to buried structures such as piles. The apparent viscosity of liquefied soils was determined in the laboratory by measuring the drag force applied to a sphere immersed in liquefied soils.

Yashima et al. (1997) used a viscous model and the finite difference method for simulating the displacement of a liquefied embankment. As shown in Fig. 22, the liquefied material of the compacted fill is assumed to become instantaneously a viscous fluid, and the displacement of the viscous fluid is calculated at various time intervals. This numerical approach allows the calculation to proceed for very large shear strains.

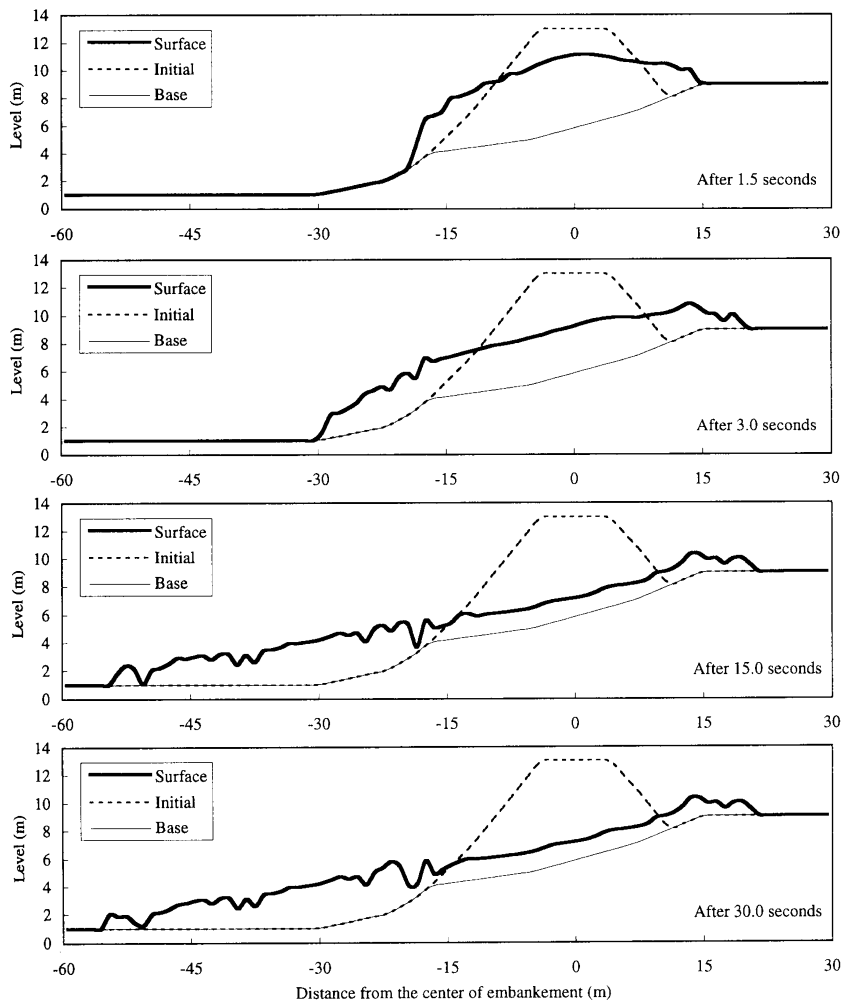

Figure 2-22. Simulated progressive failure configurations of embankment at various times after the initial liquefaction (Yashima et al., 1997).

2.5.5 Constitutive modeling and numerical analysis

Many effective stress models (e.g., Dafalias and Herman, 1982; Pastor et al., 1985; Bardet, 1986, 1990, and 1995; Adachi and Oka, 1982; and Taguchi et al., 1995) have been proposed to calculate liquefaction-induced lateral deformations. There are too many constitutive models applicable to liquefied soils to reference them all. Some models are described in the VELACS project (Arulanandan and Scott, 1993-1994; Bardet et al., 1993; and Smith, 1994). These models are usually based on a constitutive model formulated in terms of effective stress, the Biot dynamic consolidation theory, and a finite element or finite difference computer program with step-by-step time integration (e.g., Zienkiewicz et al., 1984 and 1990). Several of these models were used in the VELACS project (Arulanadan and Scott, 1993, 1994), especially for Model No.3 of VELACS which simulates a gentle slope made of liquefiable Nevada Sand.

However, several important aspects of soil behavior are not yet incorporated into these constitutive models – especially post-liquefaction behavior and low-mean effective pressure behavior of soils.

Most models (e.g., Parra-Colmenares, 1996) are only applicable to model cyclic strain, and cannot describe the post-liquefaction re-hardening, because they were not designed for this purpose. Peiris and Yoshida (1995, 1996) developed new one-dimensional constitutive models, capable of describing the post-liquefied stress-strain response of saturated sands. However, their models remain to be generalized to three-dimensions and used in finite element analysis.

3. DATABASES OF LIQUEFACTION CASE HISTORIES

The past section reviewed several analytical approaches, which have been proposed to model liquefaction-induced ground deformation. These analytical models are capable of explaining successfully a few, but not all, aspects of liquefaction-induced deformations. Most of the analytical models require the calibration of numerous parameters for predicting liquefaction-induced deformation, and are therefore impractical to apply over the large areas covered by gas distribution networks. The empirical methods based on case histories of liquefaction-induced deformation are alternate approaches readily applicable for assessing damage to gas distribution networks after earthquakes. This section reviews the databases of case histories of liquefaction-induced deformation, and the next section the empirical models based on these databases.

The case histories of liquefaction occurrence and liquefaction-induced ground deformation during past earthquakes are essential for understanding and characterizing the effects of liquefaction, and for developing physical and empirical models to predict liquefaction damage. In this project, the following liquefaction databases have been examined:

- Liquefaction occurrence database (Harder, 1991)
- Liquefaction-induced ground deformation databases (Bartlett and Youd, 1992; Rauch, 1997; Bartlett, 1998)

These databases have been organized into Excel workbooks, and are listed in Appendix A.

3.1 Liquefaction occurrence database (Harder, 1991) and liquefaction analysis (Youd and Idriss, 1998)

Harder (1991) reported a database for case histories of liquefaction occurrence. This database includes case histories for which there was either evidence of liquefaction or no evidence for liquefaction. Such a database is the basis of most liquefaction analysis procedures, as recently described by Youd and Idriss (1998). Since 1991, new databases of liquefaction occurrence have been developed based on shear wave velocity (Stokoe et al., 1988) and cone penetration test (CPT) data (Robertson and Campanella, 1985). However, these databases have not been considered in the present study.

As shown in Figs. 1 and 2, the liquefaction occurrence database has 125 entries from 17 earthquakes. The soil properties are characterized by standard penetration tests (SPT) and normalized blow counts $N1_{60}$. The blow count N, which is measured in the field, is normalized by using a procedure accounting for the diversity of SPT equipment and depth of testing (Youd and Idriss, 1998). The earthquake intensity at the site is characterized by the peak ground acceleration and magnitude, and the loading on the soil at a particular depth is defined by the cyclic stress ratio $\Delta\tau/\sigma'_0$ where $\Delta\tau$ is the equivalent cyclic stress amplitude and σ'_0 is the initial vertical effective stress.

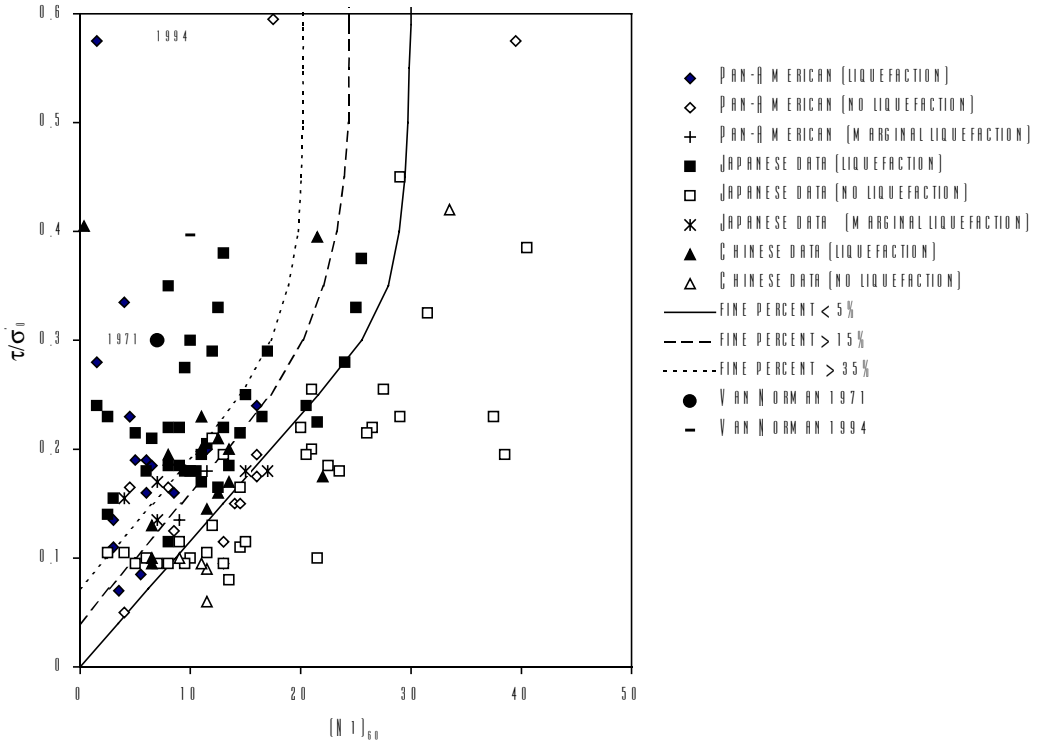

Figure 3-1. Cyclic stress ratio and normalized blow count for case histories in liquefaction occurrence database (Harder, 1991).

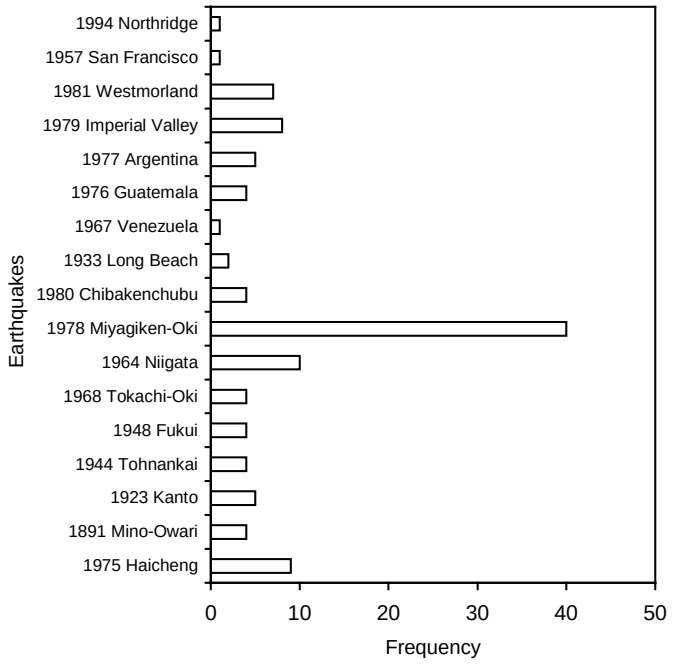

Figure 3-2. Distribution of earthquakes in liquefaction occurrence database (Harder, 1991).

3.2 Liquefaction-Induced ground deformation database (Bartlett and Youd, 1992)

In the database of liquefaction-induced ground deformation compiled by Bartlett and Youd (1992), there are 448 entries from 7 earthquakes:

- 1906 San Francisco, California
- 1964 Anchorage, Alaska
- 1964 Niigata, Japan
- 1971 San Fernando, California
- 1979 Imperial Valley, California
- 1983 Nihonkai-Chubu, Japan
- 1987 Superstition Hills, California

The data in the Bartlett and Youd (1992) database can be divided into four main categories:

- Ground displacement amplitude data
- Borehole data
- Ground-slope and free-face topographical data
- Seismic data

3.2.1 Seismic data

Table 1 summarizes the seismic parameters on the seven earthquakes in the database. There are minor variations in site specific parameters, i.e., epicentral distance (distance between the epicenter and location at which ground displacements are measured), and peak ground acceleration (PGA). During the earthquakes prior to 1979, the transient ground motion was poorly recorded, mainly because there were very few strong motion instruments deployed before 1979.

Table 3-1. Seismic parameters for earthquakes in Bartlett and Youd (1992) database.

Earthquake Name	Magnitude	PGA (g)	Epicentral distance (km)
1906 San Francisco Earthquake	7.9	0.28-0.26	13-27
1964 Alaska Earthquake	9.2	0.21-0.39	35-100
1964 Niigata, Japan Earthquake	7.5	0.19	21
1971 San Fernando Earthquake	6.4	0.55	1
1979 Imperial Valley Earthquake	6.5-6.6	0.21-0.51	2-6
1983 Nihonkai-Chubu, Japan Earthquake	7.7	0.25	27
1987 Superstition Hills Earthquake	6.6	0.21	23

3.2.2 Ground displacement amplitude data

Table 2 summarizes the number of data on ground displacement amplitudes per earthquake and site. For Bartlett and Youd (1992), a site is an area in which the measured displacement vectors can be regrouped to delineate a consistent slide. The vectors inside slide area are included in the database, while the vectors which are isolated or too distant from geotechnical boreholes, are excluded. The delineation of liquefaction-induced slides from aerial maps is not straightforward in

all cases, and requires some engineering judgement. It becomes difficult when there are a few displacement vectors and small displacement amplitudes. Figure 3 shows the distribution of displacement amplitude. In most instances, the amplitude of permanent ground deformation was measured directly from vector maps. The position coordinates and vector coordinates corresponding to each amplitude were however not defined, which make it difficult to verify the amplitude data from the original maps with a large number of vectors (e.g., data from Niigata and Noshiro).

Table 3-2. Distribution of ground deformation data in Bartlett and Youd (1992) database.

Earthquake Name	Number of Site	Number of vector
1906 San Francisco Earthquake	4	4
1964 Alaska Earthquake	5	7
1964 Niigata, Japan Earthquake	14	299
1971 San Fernando Earthquake	2	28
1979 Imperial Valley Earthquake	2	32
1983 Nihonkai-Chubu, Japan Earthquake	1	72
1987 Superstition Hills Earthquake	1	6

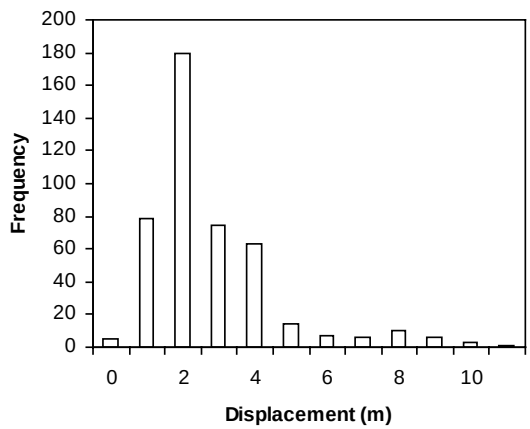

Figure 3-3. Distribution of vectors with amplitude in liquefaction-induced ground deformation database.

3.2.3 Slope and free face data

The ground slope and free-face data characterizes the geometry of ground surface at the location of the displacement vectors. This topographical data is related to the static shear loads that drive liquefaction-induced displacements. As shown in Fig. 4, the ground slope *S* is the inclination of the ground surface at the location of the displacement vector. As shown in Fig. 4, the free-face data is characterized by the free face ratio *H/L*, where *H* is the height of the free face (i.e., difference between crest elevation and toe elevation) and *L* the horizontal distance from the toe of free face to the displacement vector.

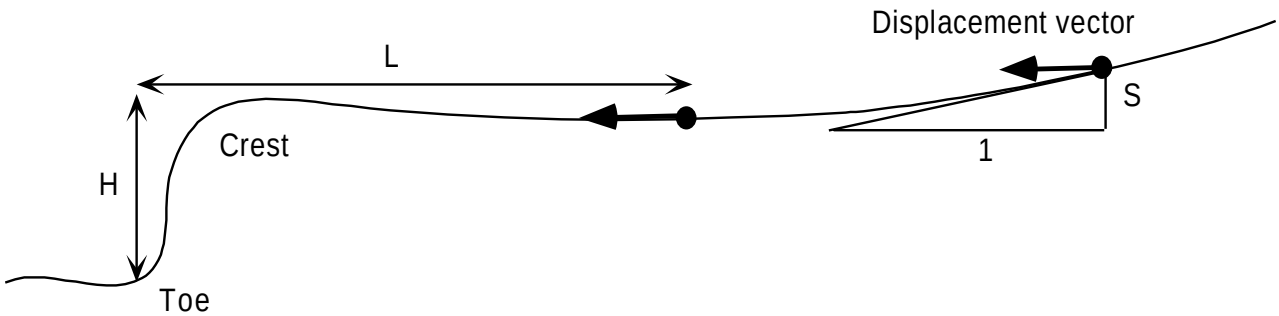

Figure 3-4. Definition of free-face ratio *H/L* and ground slope *S* in Bartlett and Youd (1992) database.

The distributions of ground-slope *S* and free-face ratio *H/L* are shown in Fig. 5. In most instances, this data has been obtained by measuring slopes on topographical maps by hand. The ground slope is measured from the elevation contours, and some control points whenever present. The free-face height and the distance to the free-face is also measured or estimated from topographical maps.

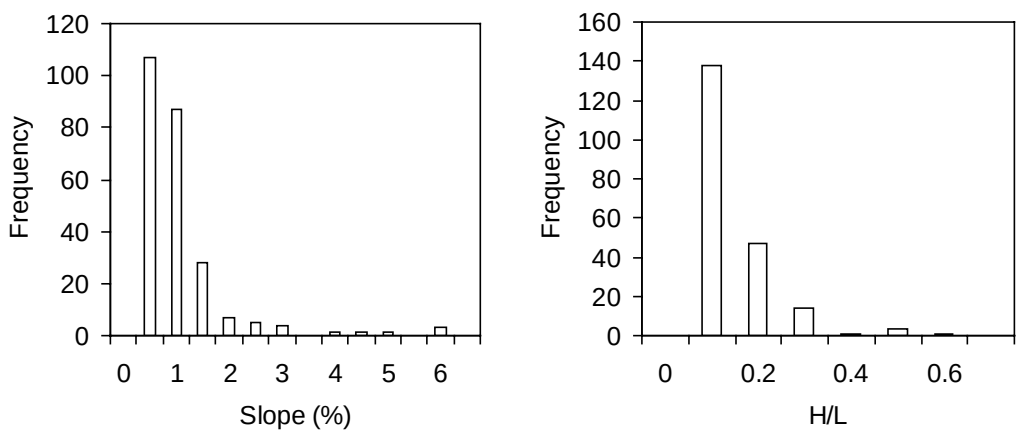

Figure 3-5. Distribution of ground slope *S* and free-face ratio *H/L* in Bartlett and Youd (1992) database.

3.2.4 Borehole data

The borehole data characterizes the geometry of soil profile and soil properties at the borehole location and its immediate vicinity. Table 3 summarizes the various types of borehole data and their number.

Table 3-3. Type and number of borehole data in Bartlett and Youd (1992) database.

Earthquake	Type of Samplar	Penetration	Number used	Reference
1906, San Francisco	2 Inch Sampler Assumed	SPT	1	*Youd and Hoose, 1978*
	Non Standard Sampler	SPT	2	*O'Rourke et al., 1991*
	2 Inch Standard Sampler	SPT	1	*Youd and Bennett, 1981*
1964, Alaska	2 Inch Standard Sampler	SPT	16	*Utermohle, 1963*
	Cpt Data Converted To Spt Data	CPT	2	*Bartlett and Youd, 1992*
	2 1/2 In. Penetrometer	NON STANDARD SPT	3	*Mcculloch and Bonilla, 1970*
	2 Inch Standard Sampler	SPT	6	*Mcculloch and Bonilla, 1970*
	1.4 Inch Sampler	SPT	1	*Mcculloch and Bonilla, 1970*
	2 Inch Sampler Assumed	SPT	3	*Bartlett and Youd, 1992*
1964, Niigata	2 Inch Sampler Assumed	SPT	119	*Unpublished Logs From Hamada*
1971, San Fernando	Ado Sampler	SPT	6	*Bennett, 1989*
	2 Inch Sampler Assumed	SPT	17	*O'Rourke et al., 1990*
1979, Imperial Valley	Cpt Data Converted To Spt	CPT	8	*Bennett et al., 1981*
	2 Inch Standard Sampler	SPT	7	*Bennett et al., 1981*
1983, Borah Peak, Id.	2 Inch Sampler Assumed	SPT	1	*Andrus et. al., 1991*
	2 Inch Standard Sampler	SPT	3	*Andrus and Youd, 1987*
1983, Nihonkai-Chubu	2 Inch Sampler Assumed	SPT	33	*Hamada et al., 1986*
1987, Superstition Hills	2 Inch Standard Sampler	SPT	5	*Bennett et al., 1984*
	Cpt Data Converted To Spt	CPT	5	*Bennett et al., 1984*

The parameters which characterizes borehole data are:

- N, the standard penetration blow count
- D_{50}, the mean grain diameter, and
- F, fines contents (percent by weight smaller than 75 μm)
- Visual soil classification and/or soil classification (e.g., USCS)

In geotechnical engineering, the blow count *N* is measured by counting the number of blows required to push a spilt barrel sampler 30 centimeters in the ground. The vertical resolution of the SPT data is therefore larger than 30 cm. However, Bartlett and Youd (1992) calculated the SPT blow counts at 10 cm interval by using linear interpolation, and introduced additional layers at the interfaces between two different soil layers to account for the sudden jump of blow count at interfaces.

In some instances, the blow counts *N* were not directly measured in the field but calculated from CPT data using correlations (e.g., Seed and DeAlba, 1986). The variations of fine contents and mean grain size with depth were obtained based on grain size distribution analysis, and engineering judgement. Based on our experience, the data on fine contents and grain size distribution is the most difficult data to reconstitute from the original soil reports. In some instances (e.g., samples lost during SPT sampling), this data had to be assumed in order to complete the analysis.

3.2.5 Determination of average soil properties at vector location

Bartlett and Youd (1992) define three average soil properties at the location of the displacement vectors: T_{15}, the cumulated thickness of saturated cohesionless soils having a blow count $N1_{60}$ smaller than or equal to 15; F_{15}, the average fine contents in the layer(s) of thickness T_{15}; and $D50_{15}$, the mean grain size in the layer(s) of thickness T_{15}). The values of T_{15}, F_{15} and $D50_{15}$ are first determined at the borehole location. The values of SPT blow count $N1_{60}$, fine contents *F* and

mean grain size *D50* are calculated for every 10 cm depth increment by interpolating the discrete borehole data. At each depth, a liquefaction analysis is performed to check whether $N1_{60}$ is smaller or equal to 15, and whether liquefaction occurs. When these two conditions are met, the average thickness T_{15} of liquefiable layers is incremented by 10 cm, and the values of *F* and *D50* are included to the average values F_{15} and $D50_{15}$.

Since boreholes and displacement vectors have usually different locations, Bartlett and Youd (1992) had to devise an interpolation scheme to determine the average soil properties at the location of the displacement vectors. As shown in Fig. 6, the average soil properties $\overline{X}$ at the location of the displacement vectors are calculated from the average soil properties X_i surrounding the displacement vector through the following weighted average:

$$\overline{X} = \sum_{i=1}^{n} \frac{X_i}{d_i \sum_{j=1}^{n} \left(\frac{1}{d_j} \right)} \tag{3.1}$$

where *n* is the number of boreholes used for averaging (the maximum value of *n* is 4), and d_i is the distance between the ith borehole and the displacement vector.

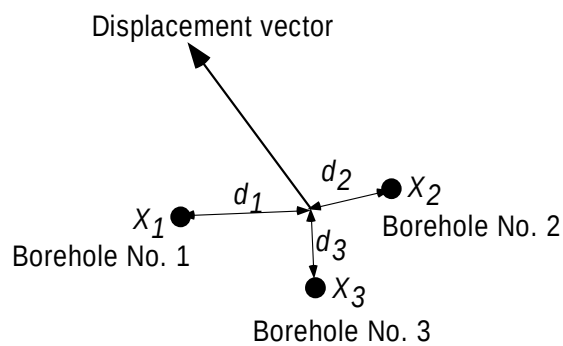

Figure 3-6. Relation of displacement vectors and boreholes (after Bartlett and Youd, 1992).

The displacement vectors obtained from field surveys and/or aerial photographs were selected from existing maps based on their significance and proximity to boreholes. Figure 7 shows the distribution of the minimum distance between the locations of displacement vectors and borehole data. In some cases, the minimum distance exceeds 400 m, which raises legitimate questions on the correlation between geotechnical and displacement data.

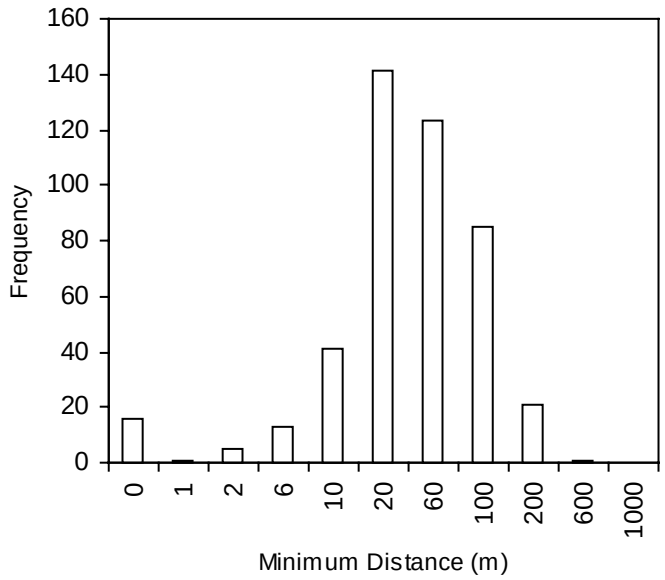

Figure 3-7. Minimum distance between location of boreholes and displacement vectors in Bartlett and Youd (1992).

3.2.6 Comparison of Harder (1991) and Bartlett and Youd (1992) databases

Figure 8 compares the databases of Harder (1991) and Bartlett and Youd (1992). Almost all cases of lateral spreading fall within the boundaries of liquefaction occurrence. The rare cases, for which lateral spreads occurred outside the accepted boundaries of liquefaction occurrence, deserve to be studied in detail. In default of detailed information on these particular cases, it is speculated that these lateral deformations were generated by the deformation of nearby liquefied soils. This explanation is consistent with the mechanism of ground deformation shown in Fig. 1-2.

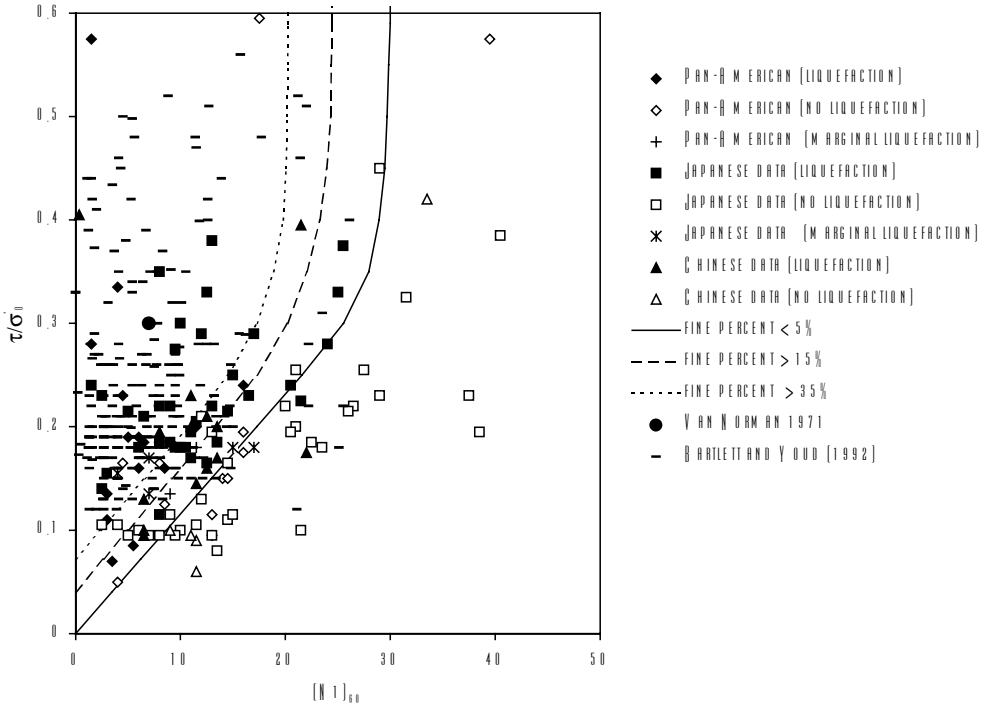

Figure 3-8. Comparison of databases of Harder (1991) and Bartlett and Youd (1998).

3.2.7 Parameters controlling ground deformation

Based on the examination of various parameters through statistical means, Bartlett and Youd (1992) identified the following parameters as controlling parameters of liquefaction induced ground deformation:

D	horizontal displacement (m)
M_w	moment magnitude
R	nearest horizontal distance (km) to seismic energy source or fault rupture
S	slope (%) of ground surface
W	free face ratio (%)
T_{15}	thickness (m) of saturated cohesionless soils (excluding depth >20 and >15% clay content) with $N1_{60}$<15
F_{15}	average fine content (% finer than 75 μm)
$D50_{15}$	average D_{50} grain size (mm) in T_{15}

Figure 9 shows the statistical distribution the parameters listed above in the Bartlett and Youd (1992) database. As shown in Fig. 9, some of these parameters (e.g., M_w, A_{max}, F_{15}, and $D50_{15}$) have a narrow value range, which introduces bias in the database.

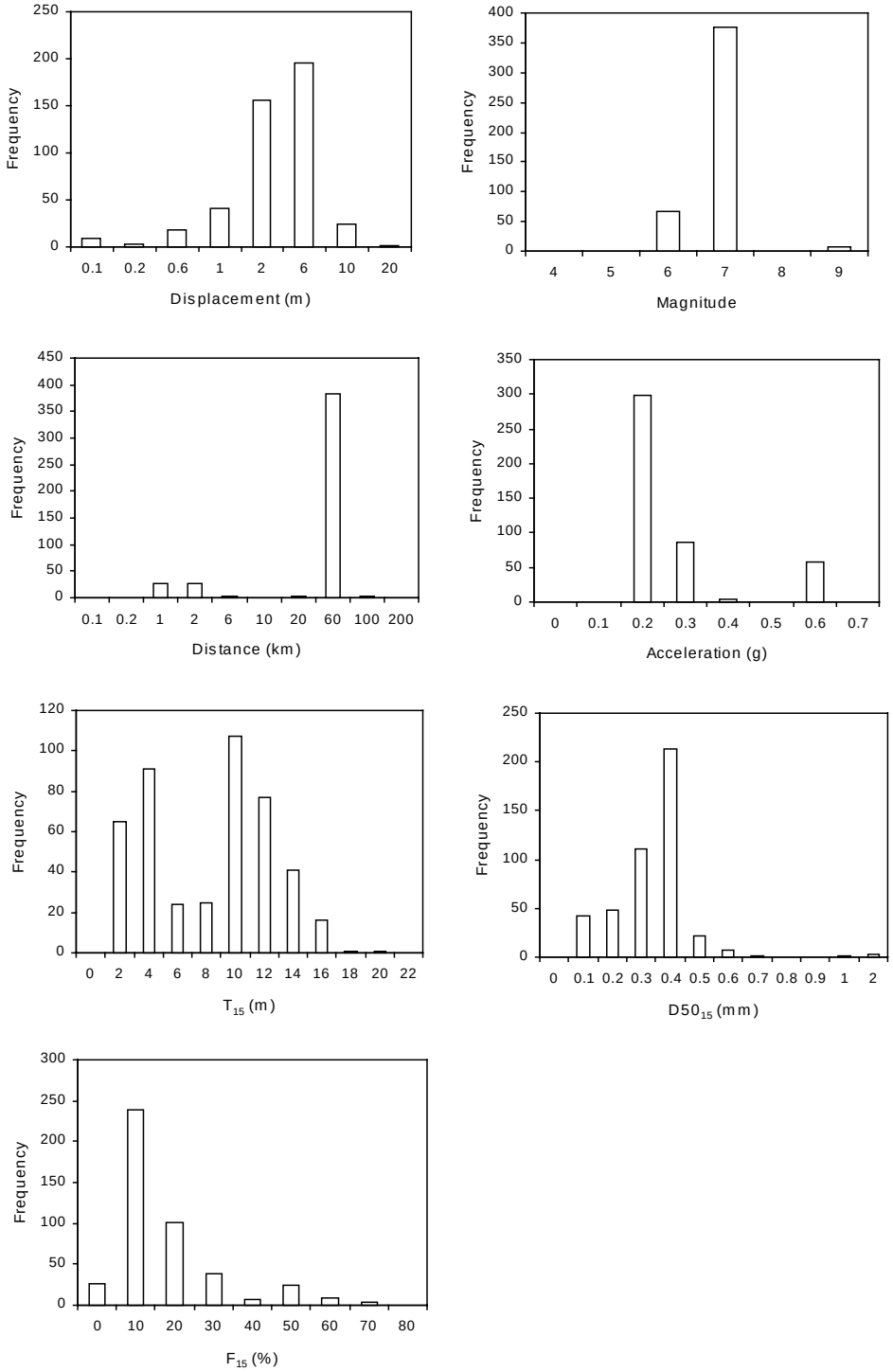

Figure 3-9. Bartlett and Youd (1992) database of liquefaction-induced lateral displacement: Distribution of main parameters including amplitude of displacement, earthquake magnitude, distance, peak ground acceleration, T_{15} thickness of soil zones with $N1_{60}$ <15, $D50_{15}$ average mean grain size in T_{15}, and F_{15} percent of fines in T_{15}.

3.3 Liquefaction-Induced lateral spread database (Rauch, 1997)

Rauch (1997) extended the Bartlett and Youd (1992) database, and added data from the following earthquakes:

- 1923 Kanto, Japan
- 1989 Loma Prieta, California
- 1990 Luzon, Philipipines
- 1991 Telire-limon, Costa Rica
- 1993 Hokkaido Nansei-oki, Japan
- 1994 Northridge, California

Like Bartlett and Youd (1992), Rauch (1997) delineates liquefaction-induced slides from the map of displacement vectors, and annotations on ground cracking. As shown in Fig. 10, the individual displacement vectors are regrouped to delineate slides. As previously mentioned, the delineation of slides from aerial maps becomes difficult and subjective when the displacement vectors are scarce and have small amplitudes. Figure 11 show the histograms of the slide area, slide length, number of vectors per slide, and number of boreholes per slide in Rauch (1997) database. The slide areas vary from 0.08 to 0.864 km^2, while the slide lengths vary from 20 to 1360 m. As shown in Table 4, there is a total of 78 slides, and 1385 vectors.

Whereas Bartlett and Youd (1992) delineate slides only for including or excluding displacement vectors in their database, Rauch (1997) define for each slide the average and standard deviation of displacement vectors, and average borehole properties. In some instances, there are unfortunately not enough vectors and borehole data for a specific slide, and the statistical quantities become meaningless. The databases of Bartlett and Youd (1992) and Rauch (1997) are based on almost the same field measurements, i.e., use the same displacement vectors, borehole data, seismic parameters, and topographic information. However, they use different variables to characterize liquefaction-induced ground deformation. Bartlett and Youd (1992) consider individual displacement vectors and average soil properties at the vector locations, while Rauch (1997) considers average deformation of liquefaction-induced slides and averages soil properties within these slides.

Table 3-4. Number of field measurements and data points in Bartlett and Youd (1992) and Rauch (1997) databases.

Quantity	Bartlettand Youd (1992)	Rauch (1997)
Data points	448	78
Boreholes	267	248
Displacement vectors	448	1385

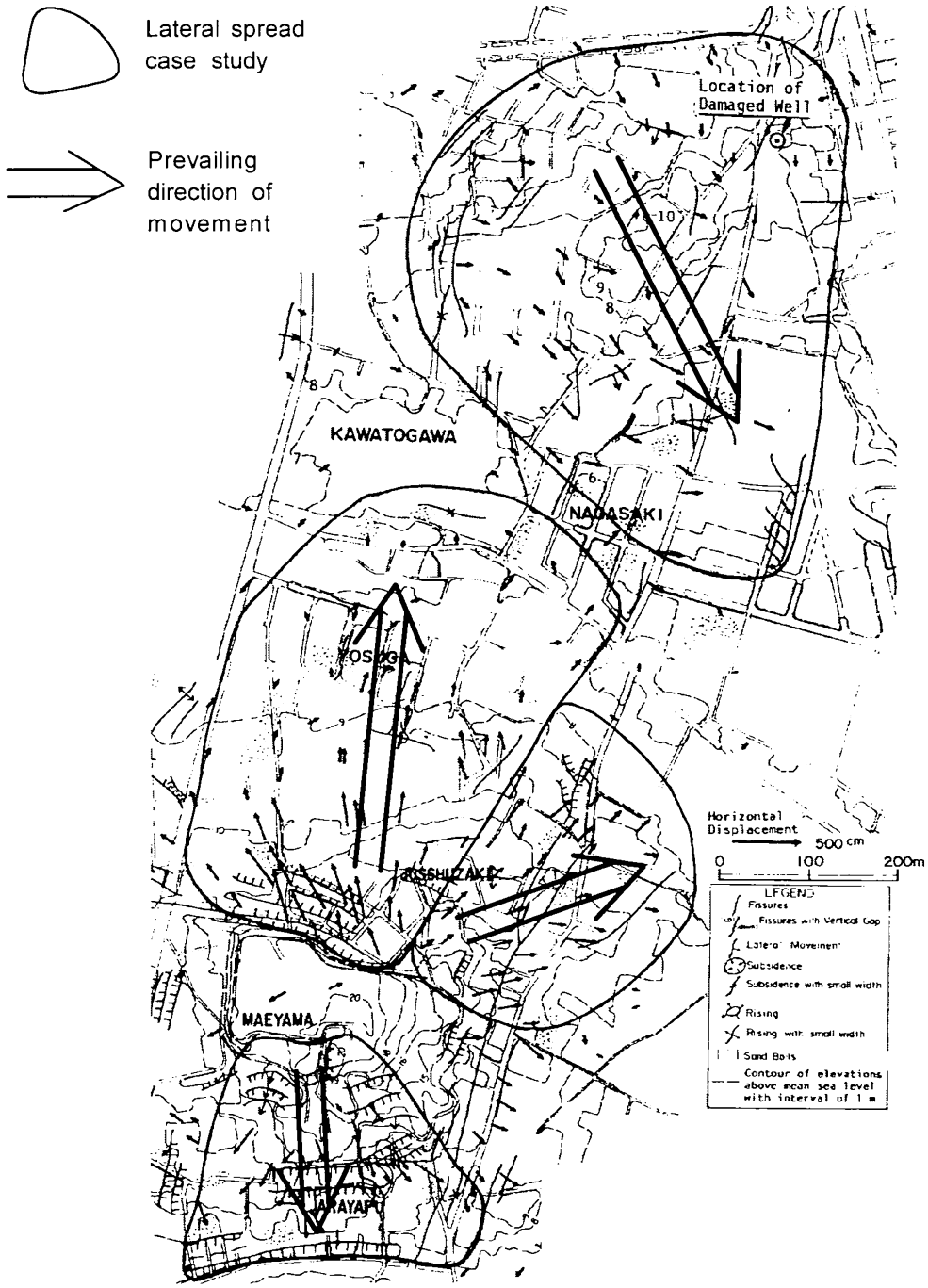

Figure 3-10. Delineation of four lateral spreads in Noshiro, Japan, in Rauch (1997) database.

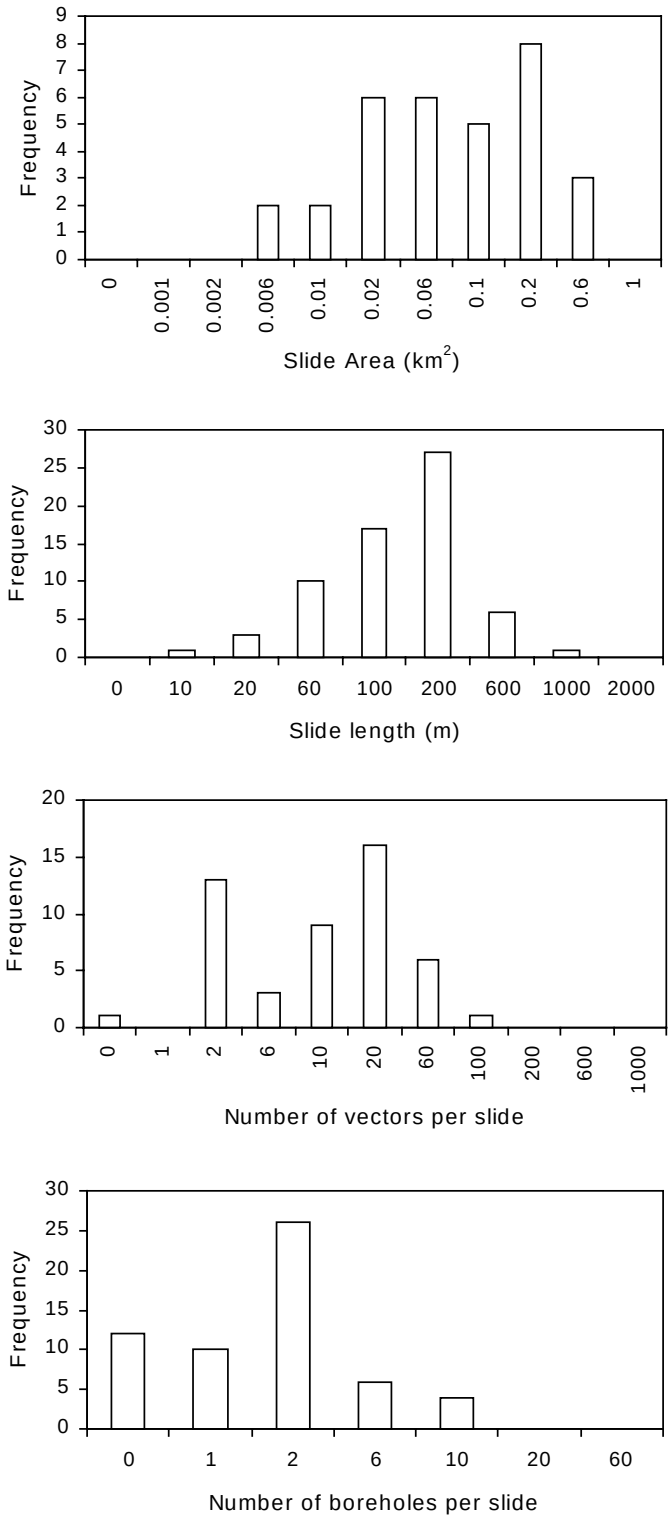

Figure 3-11. Rauch (1997) database of liquefaction-induced lateral displacement: Distributions of slide area, slide length, number of displacement vectors per slide and number of boreholes per slide.

4. REVIEW OF EMPIRICAL MODELS

In geotechnical earthquake engineering practice, liquefaction-induced ground deformations are usually estimated using three different types of empirical models which predict separately (1) the occurrence of liquefaction (e.g., Seed et al., 1985), (2) the ground settlement (e.g., Ishihara, 1996), and (3) the lateral ground deformation (e.g., Hamada et al., 1986; Pease and O'Rourke, 1993; Youd and Perkins, 1987; and Barlett and Youd, 1995). There are four basic models for assessing liquefaction-induced lateral displacements:

- Youd and Perkins (1987) LSI model
- Hamada (1986)
- Bartlett and Youd (1992) model
- Rauch (1997) model

4.1 Youd and Perkins (1987) LSI model

The LSI model has similarities to attenuation curves for peak ground acceleration. It relates the amplitude of horizontal ground deformation to distance from seismic energy source and moment magnitude as follows:

$$\log LSI = -3.49 - 1.86 \log R + 0.98 M_w \tag{4.1}$$

where LSI is the general maximum amplitude of ground failure displacement (inch), R is the horizontal distance (km) to seismic energy source, and M_w is the earthquake moment magnitude.

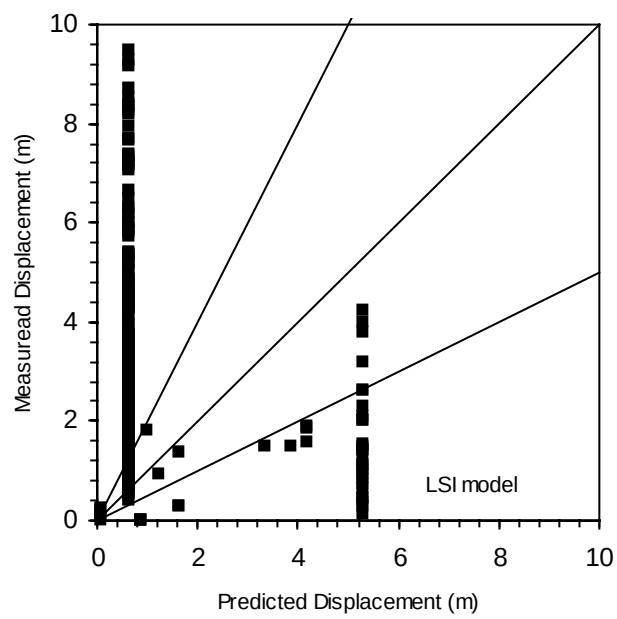

Figure 4-1. LSI model (Youd and Perkins, 1987): measured versus predicted liquefaction-induced lateral displacement (data points from Bartlett and Youd (1992) database).

Figure 1 shows the comparison between the measured displacements and those calculated using Eq. 1 for all the entries in the Bartlett and Youd (1992) database. The points should fall on the line with a 1:1 slope for a perfect prediction, and on the lines with 1:0.5 and 1:2 slope when the prediction is half or twice the measured value, respectively. As shown in Fig. 1, there is a poor agreement between measured and calculated displacements, which implies that distance R and magnitude M_w are not sufficient for predicting liquefaction-induced displacement.

4.2 Hamada et al. (1986)

Hamada et al (1986) predict the amplitude of horizontal ground deformation only in terms of slope and thickness of liquefied layer:

$$D = 0.75\, H^{0.5}\, \theta^{0.33} \tag{4.2}$$

where D is the horizontal displacement (m), θ is the slope (%) of ground surface or base of liquefied soil, and H is the thickness (m) of liquefied soil

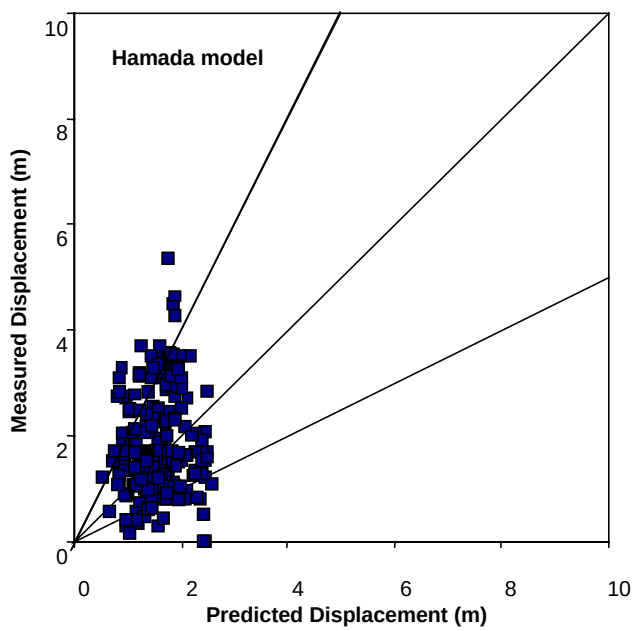

Figure 4-2. Hamada model (Hamada et al., 1986) for ground slope: measured versus predicted liquefaction-induced lateral displacement (data points from Bartlett and Youd (1992) database).

The Hamada model is only based on topographic and geotechnical parameters (i.e., S and H), and no seismic parameters (e.g., R and M_w). Figure 2 shows the comparison of measured displacement with those calculated using Eq. 2 for the ground-slope entries in the Bartlett and Youd (1992) database. In this comparison, the liquefied thickness H was assumed to be equal to T_{15}, the cumulated thickness of zones with $N1_{60}$ smaller than 15.

4.3 Bartlett and Youd (1992) MLR model

Bartlett and Youd devised two separate models: one for ground slope of infinite extent, and the other for free face:
Ground slope

$$\log(D+0.01) = -15.787+1.178\,M_w-0.927\log R-0.013\,R+0.429\log S + 0.348\log T_{15}+4.527\log(100-F_{15})-0.922\,D50_{15} \quad (4.3)$$

Free face

$$\log(D+0.01) = -16.366+1.178\,M_w-0.927\log R-0.013\,R+0.657\log W + 0.348\log T_{15}+4.527\log(100-F_{15})-0.922\,D50_{15} \quad (4.4)$$

where

D	horizontal displacement (m)
M_w	moment magnitude
R	nearest horizontal distance (km) to seismic energy source or fault rupture
S	slope (%) of ground surface
W	free face ratio (%)
T_{15}	thickness (m) of saturated cohesionless soils (excluding depth >20 and >15% clay content) with $N1_{60}<15$
F_{15}	average fine content (% finer than 75 μm)
$D50_{15}$	average D_{50} grain size (mm) in T_{15}

As shown in Fig. 3, most of the model predictions are scattered within the lines with 1:0.5 and 1:2 slope, while they should fall close to the line with a 1:1 slope for a perfect prediction.

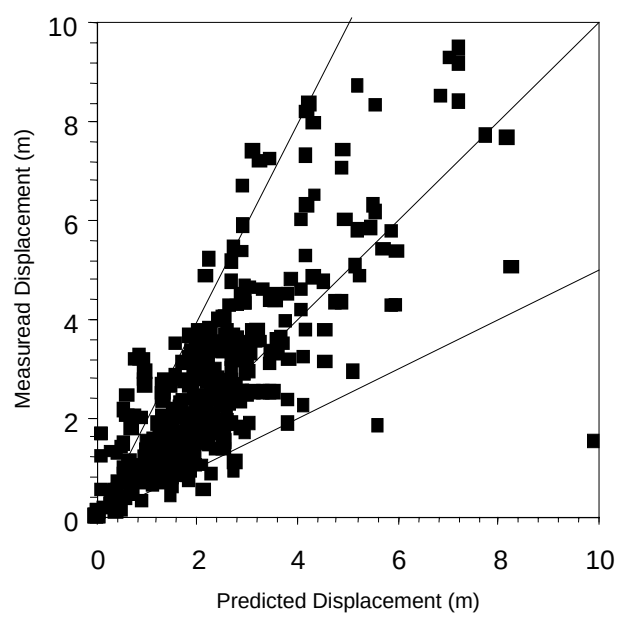

Figure 4-3. Bartlett and Youd (1992) model: measured versus predicted liquefaction-induced lateral displacement (data points from the database of Bartlett and Youd, 1992).

4.4 Rauch (1997) models

Rauch (1997) considered liquefaction-induced ground deformation as slides of finite area, instead of individual displacement vectors. He applied multiple-linear-regression methods to these liquefaction-induced slides. Rauch proposed three different models for the average lateral ground displacement, which are referred to as regional, site and geotechnical:

Regional average

$$D = (D_R - 2.21)^2 + 0.149 \tag{4.5a}$$

$$D_R = (613\ M_w - 13.9\ R_f - 2420\ A_{max} - 11.4\ T_d\ )/1000 \tag{4.5b}$$

D average horizontal displacement (m)
R_f shortest horizontal distance (km) to fault rupture
M_w moment magnitude
A_{max} peak horizontal acceleration (g) at ground surface
T_d duration (s) of strong earthquake motions (>0.05g)

Site average

$$D = (D_R + D_S - 2.44)^2 + 0.111 \tag{4.6a}$$

$$D_S = (0.523\ L_{slide} + 42.3\ S_{top} + 31.3\ H_{face})/1000 \tag{4.6b}$$

L_{slide} length (m) of slide area from head to toe
S_{top} average slope (%) across the surface of lateral spread
H_{face} height of free face (m) measure vertically from toe to crest

Geotechnical average

$$D = (D_R + D_S + D_G - 2.49)^2 + 0.124 \tag{4.7a}$$

$$D_S = (50.6\ Z_{FSmin} - 86.1\ Z_{liq})/1000 \tag{4.7b}$$

Z_{FSmin} average depth (m) corresponding to minimum factor of safety
Z_{liq} average depth (m) to top of liquefied layer

Figure 4 shows the comparison of measured versus calculated average displacements, using the entries of Rauch (1997) database. As shown in Fig. 4, there are less data points in Rauch's database than in Bartlett and Youd's database, because the data on average slide displacement is less abundant than data on individual displacement vectors. As shown in Fig. 4, there is a poor agreement between measurement and prediction.

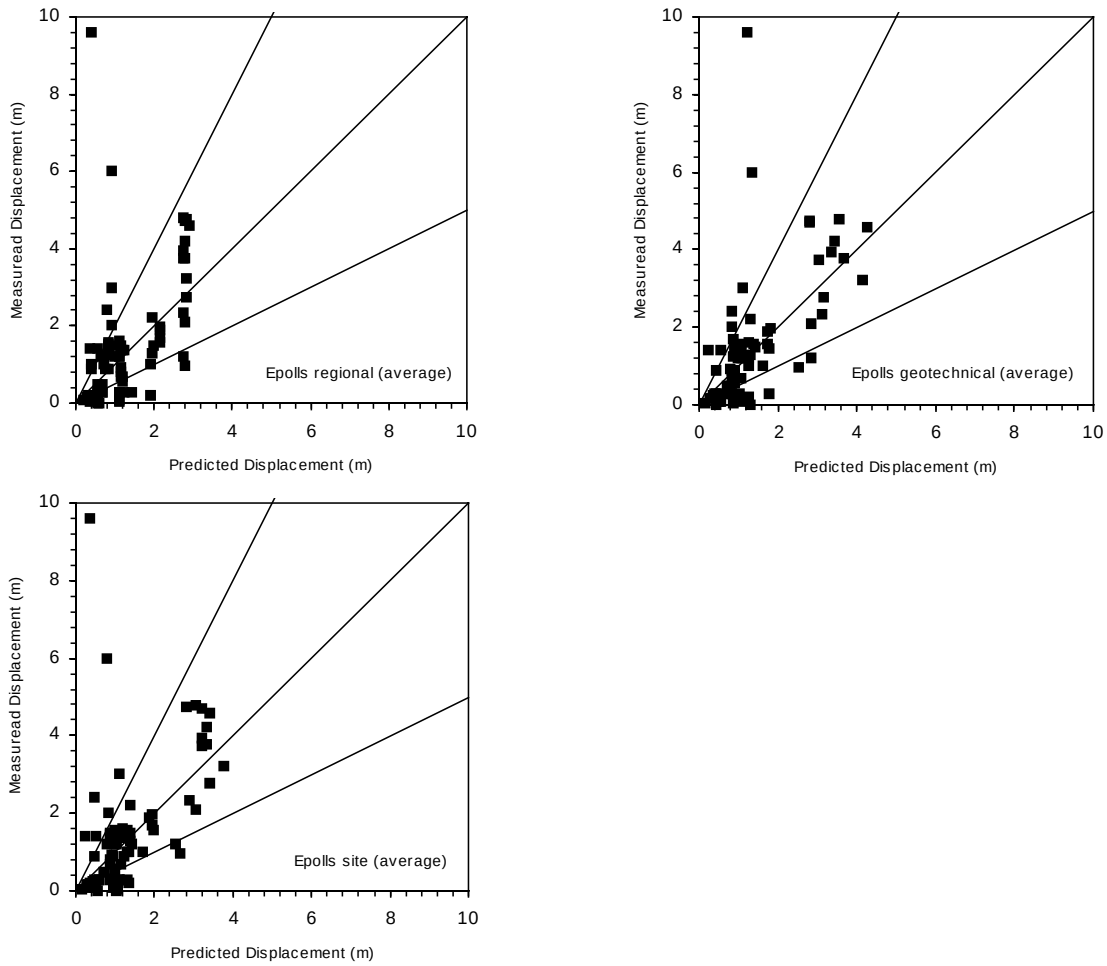

Figure 4-4. Regional, site and geotechnical models (Rauch, 1997): measured versus calculated average displacements (data points form Rauch (1997) database).

Rauch (1997) also proposed the following three models for characterizing the standard deviation from the average predictions of displacement:

$\sigma_D = 0.589\ D$ Regional standard deviation (4.11)

$\sigma_D = 0.560\ D$ Site standard deviation (4.12)

$\sigma_D = 0.542\ D$ Geotechnical standard deviation (4.13)

These standard deviations describe the variation of displacement amplitude about the average displacement of a slide.

4.5 Comparison of existing models

The empirical models of liquefaction-induced lateral spreads relate selected physical parameters by fitting data points with a multiple linear regression. Their parameters are of seismological, topographical or geotechnical origins.

4.5.1 Seismological parameters

Youd and Perkins (1987) and Bartlett and Youd (1992) characterize the ground motion at a given site by using two parameters:

- R horizontal distance (km) to seismic energy source, and
- M_w moment magnitude of earthquake.

whereas Rauch (1997) requires four seismic parameters

- R_f shortest horizontal distance (km) to fault rupture
- M_w moment magnitude
- A_{max} peak horizontal acceleration (g) at ground surface
- T_d duration (s) of strong earthquake motions (>0.05g)

In the models of liquefaction occurrence (e. g., Idriss and Youd, 1998), the ground motion is characterized by only two parameters:

- M_w moment magnitude
- A_{max} peak horizontal acceleration (g) at ground surface

The cyclic stress ratio τ/σ'_0 is proportional to A_{max}, and increases with M_w (Youd and Idriss, 1998). Therefore the potential for occurrence of liquefaction increases with A_{max} and M_w.

In the Rauch regional model (Eq. 5), the amplitude of lateral spread D decreases unrealistically with A_{max}, which may result from the dependence on M_w, A_{max} and T_d. The Rauch model is therefore applicable within a particular range of seismic parameters, and may give unrealistic predictions outside this range. For instance, Table 1 gives examples for which Rauch overestimates D in cases of unlikely liquefaction. In these cases, LSI model gave reasonable predictions.

Table 4.1. Examples of unrealistic predictions by Rauch (1997) model.

				Rauch(1997)	LSI
M_w	A_{max} (g)	R_f (km)	T_d (sec)	D (m)	
4	0.01	1	0.1	0.19	0.07
5	0.01	10	1	0.61	0.01
5	0.05	10	1	0.49	0.01

It would be logical to use the same seismic parameters for models of liquefaction occurrence and liquefaction-induced deformation, i.e., M_w and A_{max}. However, there is a definite bias in the database, which is demonstrated in Fig. 5 by the decrease of displacement D with increasing peak ground acceleration A_{max}. Bartlett and Youd (1992) avoided this problem by using R instead of A_{max} in their model.

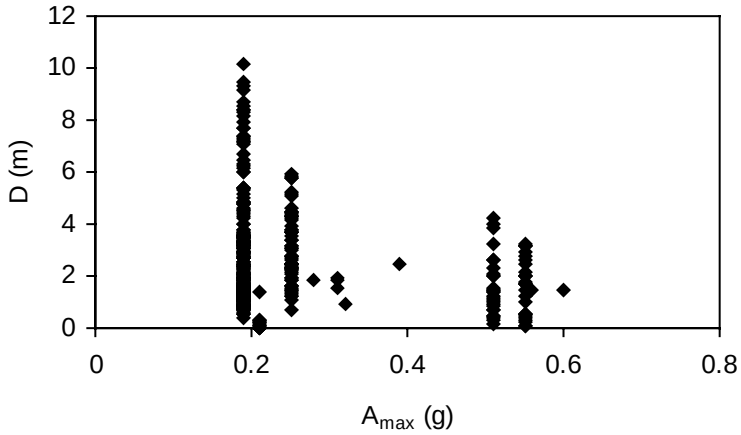

Figure 4-5. Variation of peak ground acceleration with lateral ground deformation in Youd and Bartlett (1992) database.

4.5.2 Topographical parameters

The topographical parameters used by Bartlett and Youd (1992) are:

S	slope (%) of ground surface
W	free face ratio (%)

while those of Rauch (1997) are:

L_{slide}	length (m) of slide area from head to toe,
S_{top}	average slope (%) across the surface of lateral spread, and
H_{face}	height of free face (m) measure vertically from toe to crest

Rauch (1997) use non symmetric distribution for modeling the systematic decrease in displacement amplitude with distance away from free-faces, which has been well-documented after the 1995 Hyogoken-Nanbu earthquake (e.g., Fig. 6).

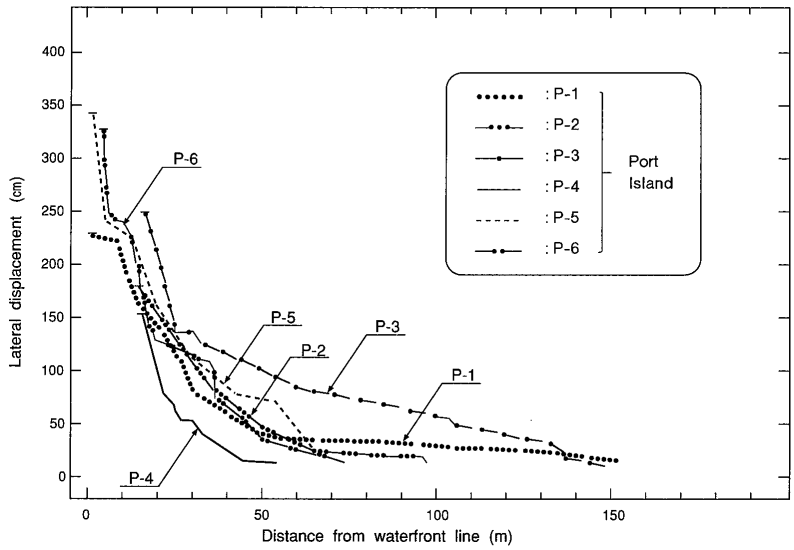

Figure 4-6. Typical variation of liquefaction-induced displacement behind quaywalls in Port Island after the 1995 Hyogoken-Nanbu earthquake (Ishihara et al., 1996, 1997).

4.5.3 Geotechnical parameters

The geotechnical parameters used by Bartlett and Youd (1992) are:

- T_{15} thickness (m) of saturated cohesionless soils (excluding depth > 20 m and clay content >15%) with $N1_{60}$<15
- F_{15} average fine content (% finer than 75 μm)
- $D50_{15}$ average D_{50} grain size (mm) in T_{15}

while those of Rauch (1997) are:

- Z_{FSmin} average depth (m) corresponding to minimum factor of safety
- Z_{liq} average depth (m) to top of liquefied layer

Rauch's parameters are derived from liquefaction analyses, whereas those of Bartlett and Youd are directly obtained from borehole measurements.

5. MLR MODELS FOR LIQUEFACTION-INDUCED GROUND DEFORMATION

Based on the review and comparison of empirical existing models and databases, it was decided to model liquefaction-induced ground displacement using a MLR approach similar to that of Bartlett and Youd (1992), and to use the most recent database of liquefaction-induced ground deformation (Bartlett, 1998).

5.1 Selection of database

The new database (Bartlett, 1998) was corrected for some digitizing errors on displacement vectors in the original database (Bartlett and Youd, 1992). As shown in Fig. 1, the difference between the new and old databases is significant enough to be detectable from the histograms of displacement amplitude. As shown later, the difference in data will lead to MLR models slightly different from that of Bartlett and Youd (1992).

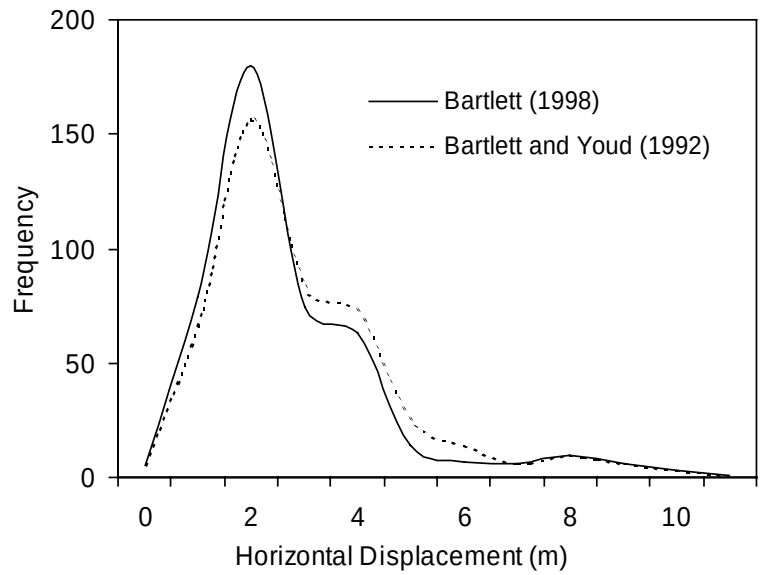

Figure 5-1. Comparison of histograms of displacement amplitude for original database (Bartlett and Youd, 1992) and corrected database (Bartlett, 1998) on liquefaction-induced lateral displacement.

The data in the new database was divided in two data sets: (a) complete data for all ranges of displacement amplitude; and (b) data limited to displacement amplitudes smaller than 2 meters. The former data set will be referred to as A, and the latter as B. The latter data set, in which displacement amplitudes in excess of 2 m were excluded, was intended to be more relevant to engineering design. Amplitudes in excess of 2 m were assumed to be too large for accurate measurement, and to cause excessive ground damage impractical to mitigate. Table 1 gives the number of entries in data sets A and B, with their respective partition in free-face and ground slope cases.

Table 5-1. Data sets used in MLR models

Notation	Definition	Number of data points
A	All data	467
	All free-face (FF) data	213
	All ground slope (GS) data	254
B	All data with displacement smaller than 2 m	283
	Free-face (FF) data with displacement smaller than 2 m	118
	Ground slope (GS) data with displacement smaller than 2 m	165

5.2 Selection of variables and models

The identification of controlling variables is a critical step in MLR analysis. The controlling parameters in the MLR analysis were identified as those of Bartlett and Youd (1992) after careful consideration of other combinations of variables. One of the main criteria for selecting variables was their direct relation to measured data, with as little influence as possible from analysis. For instance, the thickness T_{15} can be directly obtained from SPT profiles. In contrast, the average depth corresponding to minimum factor of safety Z_{Fsmin}, which is used by Rauch (1997), depends on liquefaction analysis. Given the limitations of the seismic and geotechnical data in the existing database, combinations of variables other than those used by Bartlett and Youd (1992) did not seem promising. However, future MLR studies will need to examine other combinations of variables as other types of entries (e.g., CPT data) are made to the database.

Table 2 lists all the variables used in the MLR modeling. There is a total of 6 independent variables. The free-face ratio *W* and ground slope *S* are independent variables, which are not used simultaneously. The present MLR modeling assumes that liquefaction-induced deformation depends on the distance *L* to the free face divided by the free-face height *H* in close proximity of the free face, and not on ground slope. The distinction between free-face and ground slope conditions may not always be obvious in all circumstances. It is still unclear how far the free-face effects can extend from free faces, and how they combine with ground slope effects.

Table 5-2. List of controlling variables for MLR analysis.

Notation	Definition
D_H (m)	Amplitude of ground deformation (Output)
M	Earthquake moment magnitude
R (km)	Closest distance to source
W	Free face ratio $W = 100H/L$ L: Distance to the free face from the point of displacement in m H: Height of free face in m)
S (%)	Ground slope
T_{15} (m)	Thickness of saturated cohesionless soils with $(N1)_{60}<15$
F_{15} (%)	Average fines content (<75 μm) in layer of thickness T_{15}
$D50_{15}$ (mm)	Average mean grain size D_{50} in layer of thickness T_{15}

Table 3 shows the range of values for the MLR variables in the data sets A and B, and their corresponding free-face and ground-slope data subsets. The data set are referred to as *FF, GS* and *FFGS*, which stands for Free-Face, Ground-Slope, and Free-Face & Ground-Slope, respectively. In data set A, the maximum ground-slope displacement (i.e., 5.35 m) is half the maximum free-face displacement. In data set B, both maxima are set equal to 2 m. The range of variables *M, R, W, S,* T_{15}, F_{15} and $D50_{15}$ are almost identical for data sets A and B, and their free-face and ground-slope subsets. Table 3 is useful to define the domain of applicability of MLR models. It is not recommended to use MLR models for variable values that fall outside the ranges of Table 3.

Table 5-3. Range of values for MLR variables in data sets A and B, and their free-face and ground-slope subsets.

	Data Set A			Data Set B		
Variables	Complete FFGS-A	Free-Field FF-A	Ground-Slope GS-A	Complete FFGS-B	Free-Field FF-B	Ground-Slope GS-B
DH (m)	0 - 10.15	0 - 10.15	0 - 5.35	0-1.99	0-1.98	0-1.99
M	6.4 - 9.2	6.4 - 9.2	6.4 - 9.2	6.4 - 9.2	6.4 - 9.2	6.4 - 9.2
R (km)	0.2 - 100	0.5 - 100	0.2 - 100	0.2 - 100	0.5 - 100	0.2 - 100
W_{ff}	1.64 - 55.68	1.64 - 55.68	-	1.64 - 48.98	1.64 - 48.98	-
S (%)	0.05 - 5.90	-	0.05 - 5.90	0.05 - 2.5	-	0.05 - 2.5
T_{15} *(m)*	0.2 - 19.7	0.2 - 16.7	0.7 - 19.7	0.2 - 19.7	0.2 - 13.6	0.7 - 19.7
F_{15} *(%)*	0 - 70	2 - 70	0 - 68	0 - 70	3 - 70	0 - 68
$D50_{15}$ *(mm)*	0.04 - 1.47	0.04 - 1.47	0.06 - 1.19	0.04 - 1.47	0.04 - 1.47	0.06 - 1.19

Figures 2 to 9 show the distribution of variable values over their respective ranges. As shown in Fig. 2, ground displacements are much larger in the case of free-face than in the case of ground slope.

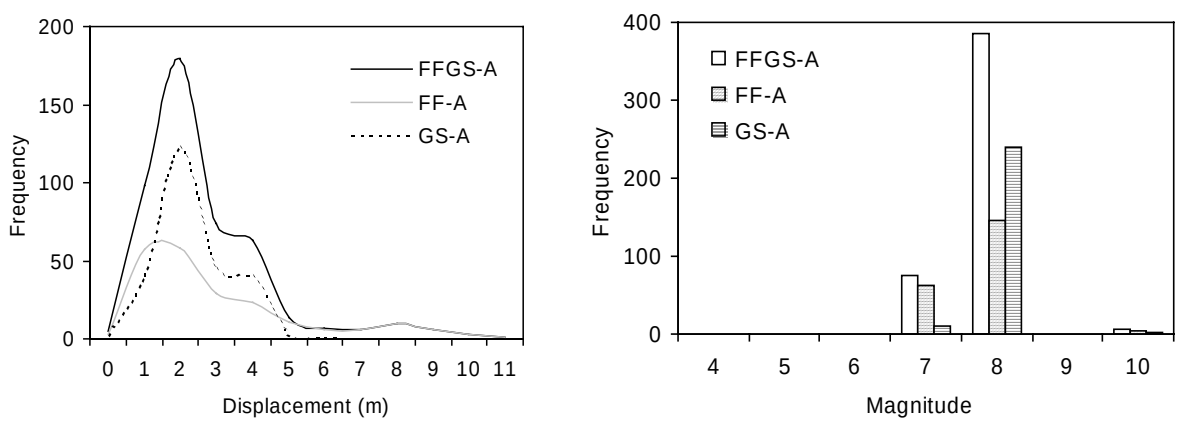

Figure 5-2. Histograms of displacement-amplitudes and earthquake-magnitudes in data sets FFGS-A, FF-A and GS-A.

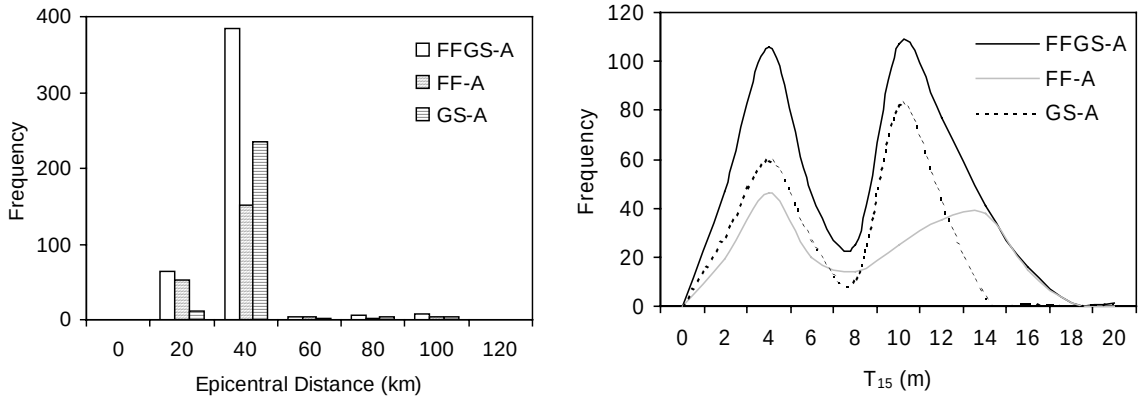

Figure 5-3. Histograms of epicentral distance and thickness T_{15} in data sets FFGS-A, FF-A and GS-A.

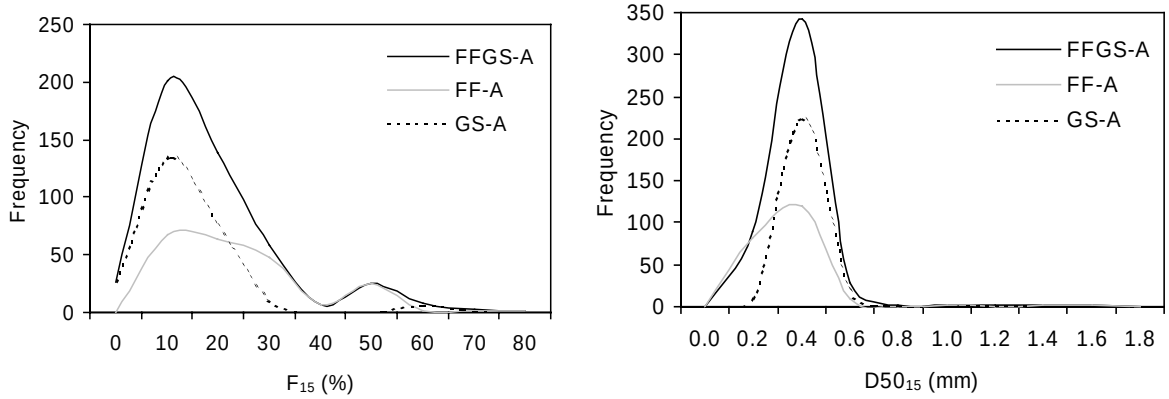

Figure 5-4. Histograms of fine contents F_{15} and mean grain size $D50_{15}$ in data sets FFGS-A, FF-A and GS-A.

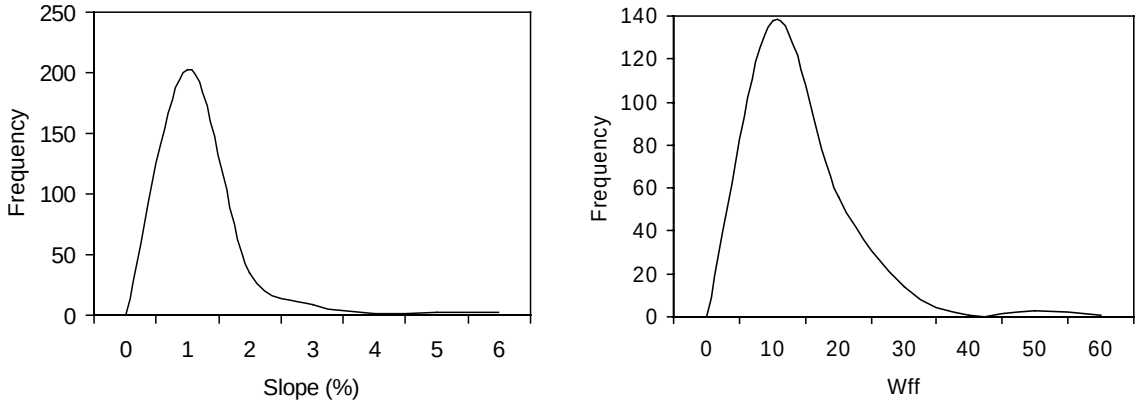

Figure 5-5. Histograms of ground-slope and free-face ratio in data set A.

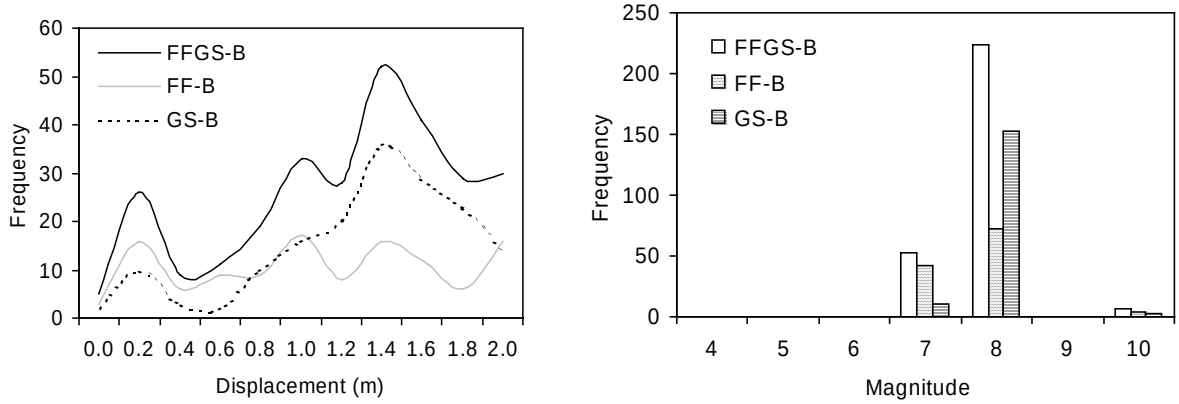

Figure 5-6. Histograms of displacement-amplitude and earthquake magnitude in data sets FFGS-B, FF-B and GS-B.

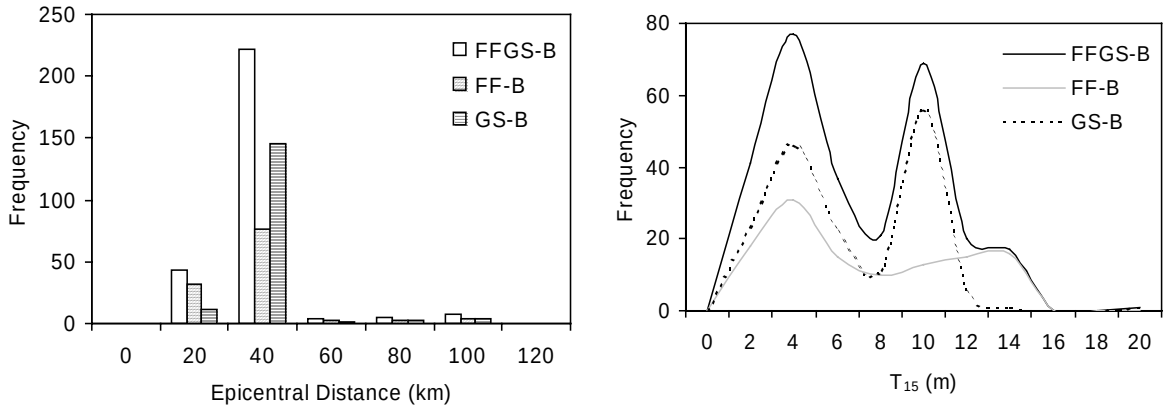

Figure 5-7. Histograms of epicentral distance and thickness T_{15} in data sets FFGS-B, FF-B and GS-B.

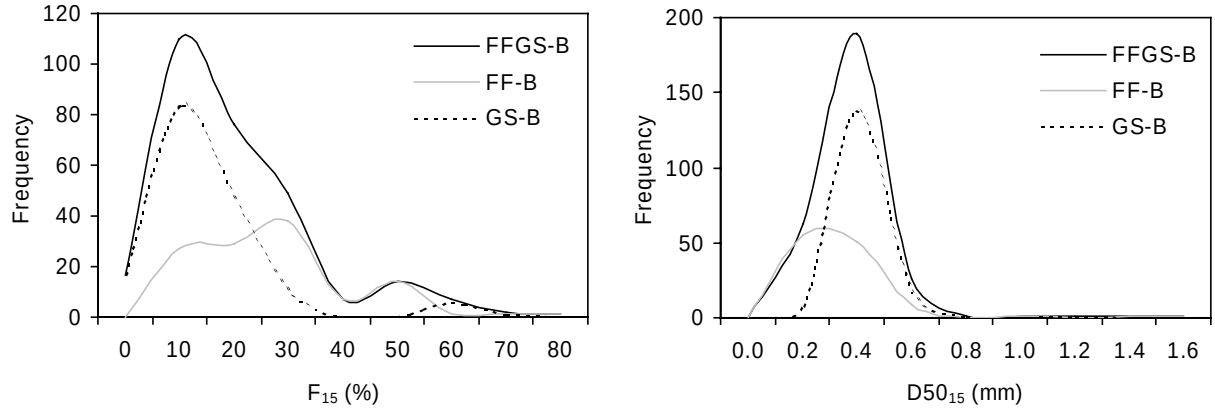

Figure 5-8. Histograms of fine contents F_{15} and mean grain size $D50_{15}$ in data sets FFGS-B, FF-B and GS-B.

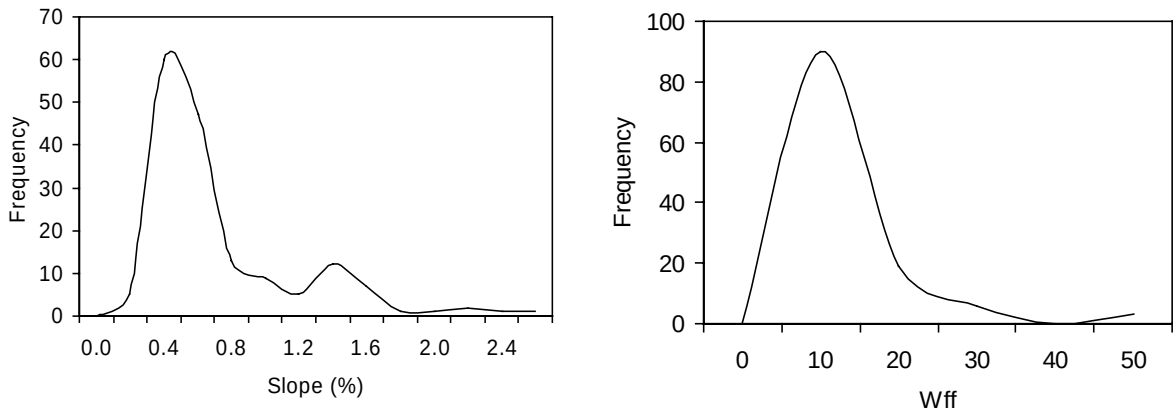

Figure 5-9. Histograms of ground-slope and free-face ratio in data set B.

As shown in Table 4, the variables were combined to form six different MLR models, which are designated *FFGS4, FF6, GS6, FFGS4, FF4*, and *GS4*. As previously defined, *FF, GS* and *FFGS* stand for Free-Face, Ground-Slope, and Free-Face & Ground-Slope, respectively. The variables related to mean grain size and fine contents (i.e., $D50_{15}$ and F_{15}) are average geotechnical parameters, which are rather difficult to determine precisely over large areas. For this reason, simpler MLR models with only 4 variables are proposed. These six models will be calibrated using the data sets A and B, therefore producing a total of 12 different MLR models.

Table 5-4. List of MLR models developed in present study.

Notation	Definition	Number of variables	Variables
FFGS6	Combined Free-Face and Ground-Slope MLR model	6	*M, R, W (*or *S)* T_{15}, F_{15}, and $D50_{15}$
FF6	Free-Face MLR model	6	*M, R, W,* T_{15}, F_{15}, and $D50_{15}$
GS6	Ground-Slope MLR model	6	*M, R, S,* T_{15}, F_{15}, and $D50_{15}$
FFGS4	Combined Free-Face and Ground-Slope MLR model	4	*M, R, W (*or *S),* T_{15}
FF4	Free-Face MLR model	4	*M, R, W,* T_{15}
GS4	Ground-Slope MLR model	4	*M, R, S,* T_{15}

5.3 Six-parameter MLR models

The amplitude D_H of ground deformation will be estimated by using the same generic MLR relations as Barlett and Youd (1992):

$$Log(D_H + 0.01) = b_0 + b_{off} + b_1 M + b_2 Log(R) + b_3 R + b_4 Log(W_{ff}) + b_5 Log(S_{gs}) + b_6 Log(T_{15}) + b_7 Log(100 - F_{15}) + b_8 D50_{15} \quad (5.1)$$

where the variables *M, R, W, S,* T_{15}, $D50_{15}$, and F_{15} are defined in Table 2, and the values of the ten constant coefficients - b_0, b_{off}, and b_1 to b_8 - are given in Table 5. The relation in Eq. 5.1 corresponds to Eq. 4.1.9 in Bartlett and Youd (1992). It is general enough to apply to all types of ground deformation, including free-face and ground-slope cases. In the free-face cases, the term *Log(S)* is set equal to zero. In the ground slope cases, the term *Log(W)* is set equal to zero. The coefficient b_{off} only applies to the free-face cases, and is set equal to zero in the ground slope cases. In order to differentiate the free-field and ground-slope cases in the MLR analysis, the additional discrete variable *X* is introduced. The value of X is set equal to 1 for free-field case (i.e., *Log(S)* = 0) and 0 for ground-slope cases (i.e., *Log(W)* = 0).

The values of the *b*-coefficients were obtained by performing a regression analysis with the regression program Minitab (1989) and the "Data Analysis" tool package of Microsoft Excel (1994). Both methods of analysis gave identical results. The Minitab results of all the analyses are given in Appendix C. As shown in Table 5, the values of the coefficients for FFGS6 model are slightly different from those of Bartlett and Youd (1992) due to the difference of data in the new database and that used by Bartlett and Youd (1992). The coefficient values were found to be exactly identical to those of Bartlett and Youd (1992) when the old database was used.

In the FFGS6 models, the coefficients b_1, b_2, and b_3, which control the magnitude-dependent attenuation of liquefaction-induced displacements with distance, are the same for free-face and ground-slope cases. The attenuation relation for large distance is largely controlled by the additional data points from Ambraseys (1988). The model FFGS6 was calibrated for data sets A and B, therefore producing model FFGS6-A and FFGS6-B. As shown in Table 5, the coefficient values of these two models are similar, and their adjusted R^2 values are 80.6% and 81.1%, respectively. The R^2 coefficient, which measures the accuracy of the multiple linear regression, is adjusted to account for the difference in the number of data points in data sets A and B. Based on the results of Table 5, it is concluded that models FFGS6-A and -B fit data sets A and B with similar accuracy.

Two other MLR models - FF6 and GS6 - were calibrated to examine the free-field and ground-slope cases. The formula for the free-face MLR model (FF6) is:

$$Log(D_H + 0.01) = b_0 + b_1 M + b_2 Log(R) + b_3 R + b_4 Log(W) + b_6 Log(T_{15}) + b_7 Log(100 - F_{15}) + b_8 D50_{15} \quad (5.2)$$

and that of the ground-slope MLR model (GS6) is:

$$Log(D_H + 0.01) = b_0 + b_1 M + b_2 Log(R) + b_3 R + b_5 Log(S) + b_6 Log(T_{15}) + b_7 Log(100 - F_{15}) + b_8 D50_{15} \quad (5.3)$$

The coefficients of each model were obtained by subdividing data set A and B into free-field and ground slope cases. As shown in Table 5, the models FF6-A and GS6-A have slightly different

coefficients, and fit data set A only slightly better than FFGS6-A. The adjusted R^2 values are 82.1% and 82.4%, for models FF6-A and GS6-A, respectively, in comparison to 80.6% for model FFGS6-A. In contrast to models FF6-A and GS6-A, models FF6-B and GS6-B fit the B-data set with different accuracy. The adjusted R^2 values of models FF6-B and GS6-B are 80.2% and 87.9%, respectively. Model GS6-B is much more accurate than model FF6-B. The attenuation curves of these models are also different. From this comparison, it is concluded that model GS6-B predicts reasonably liquefaction-induced displacement in ground-slope cases, and that model FF6-B does not work as well as GS6-A. This implies that there may be alternate sets of controlling variables, which could describe free-face cases better.

Table 5-5. Coefficients of Multiple Linear Regression (MLR) and adjusted R^2 values for models FFGS6, FF6 and GS6.

	Old data	Data set A (all displacements)			Data set B (displacements < 2m)		
Number of data points	467	467	213	254	283	118	165
Model coefficients	Bartlett-Youd (1992)	FFGS6-A	FF6-A	GS6-A	FFGS6-B	FF6-B	GS6-B
b_0	-15.787	-14.551	-17.372	-14.152	-13.261	-15.067	-14.212
b_{off}	-0.579	-0.483	-	-	-0.261	-	-
b_1	1.178	1.096	1.248	0.988	1.050	1.130	0.800
b_2	-0.927	-0.873	-0.923	-1.049	-0.778	-0.738	-1.198
b_3	-0.013	-0.014	-0.014	-0.011	-0.013	-0.012	-0.006
b_4	0.657	0.634	0.685	-	0.370	0.396	-
b_5	0.429	0.275	-	0.318	0.106	-	0.071
b_6	0.348	0.494	0.300	0.619	0.270	0.135	0.373
b_7	4.527	4.053	4.826	4.287	3.481	4.032	5.090
b_8	-0.922	-0.814	-1.091	-0.705	-0.715	-0.908	-0.704
R^2 adjusted	82.60%	80.61%	82.10%	82.41%	81.08%	80.24%	87.88%

Figures 10-12 show the measured displacements plotted against those predicted by models FF6, GS6, and FFGS6 for data sets A and B. These figures also show the lines of slopes 0.5, 1 and 2. The data points should fall on the 1:1 line for an ideal result. The lines of slopes 0.5 and 2 correspond to predicted displacement twice and half their measured values, respectively. As shown in Fig. 10, the points are scattered about the 1:1 line in the case of models FF6-A and -B. As shown in Figs. 11 and 12, with the exception of a few particular points, the GS6 models predict ground-slope displacements more accurately than the FF6-models predict free-face ground displacements. This result was previously established by comparing the adjusted R^2 values of models FF6 and GS6 in Table 5.

Figures 13 and 14 compare the measured displacements in data sets A and B to those predicted by models FF6, GS6, and FFGS6 in a way different from that in Figs. 10-12. The observed and predicted values of displacement are plotted as a function of the entry number in the data sets. This alternate representation indicates that models FFGS6, FF6 and GS6 are capable of modeling the ground displacement over a wide range of displacement amplitude.

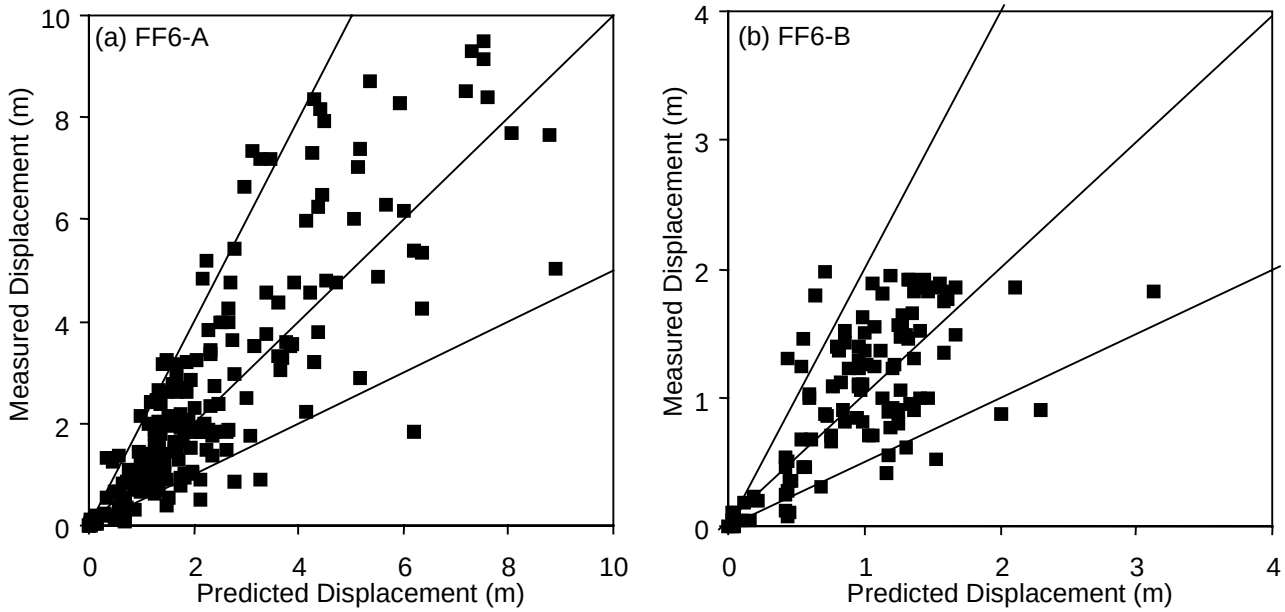

Figure 5-10. Measured versus predicted displacements for six-parameters free-face models (FF6) calibrated from (a) data set A, and (b) data set B.

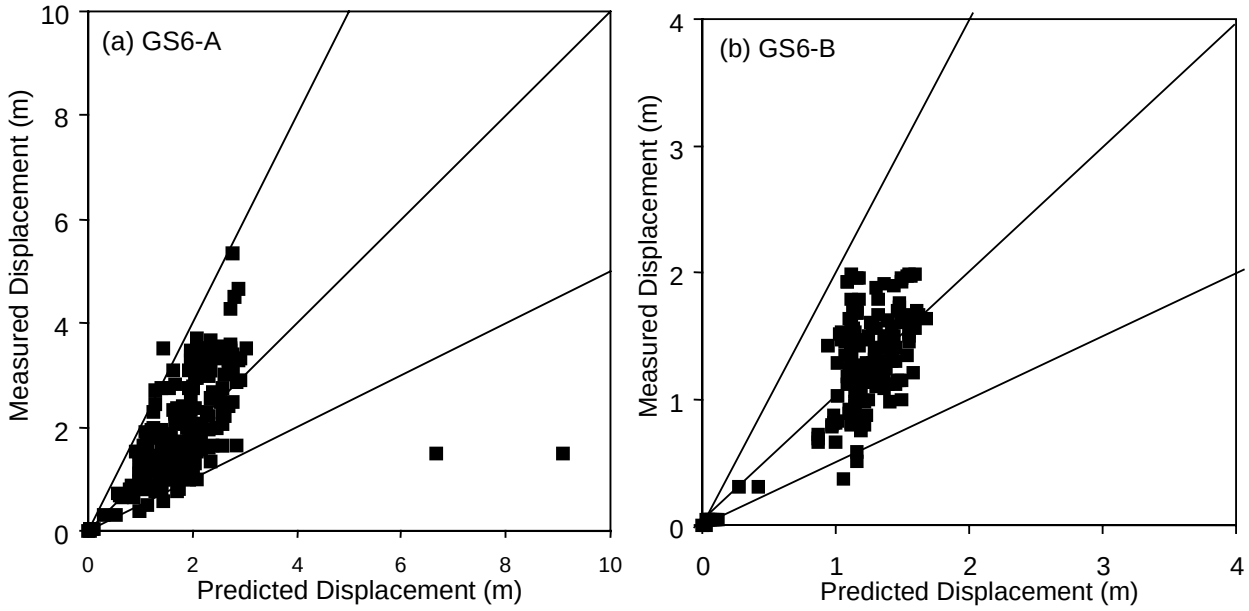

Figure 5-11. Measured versus predicted displacements for six-parameter ground-slope model (GS6) calibrated from (a) data set A, and (b) data set B.

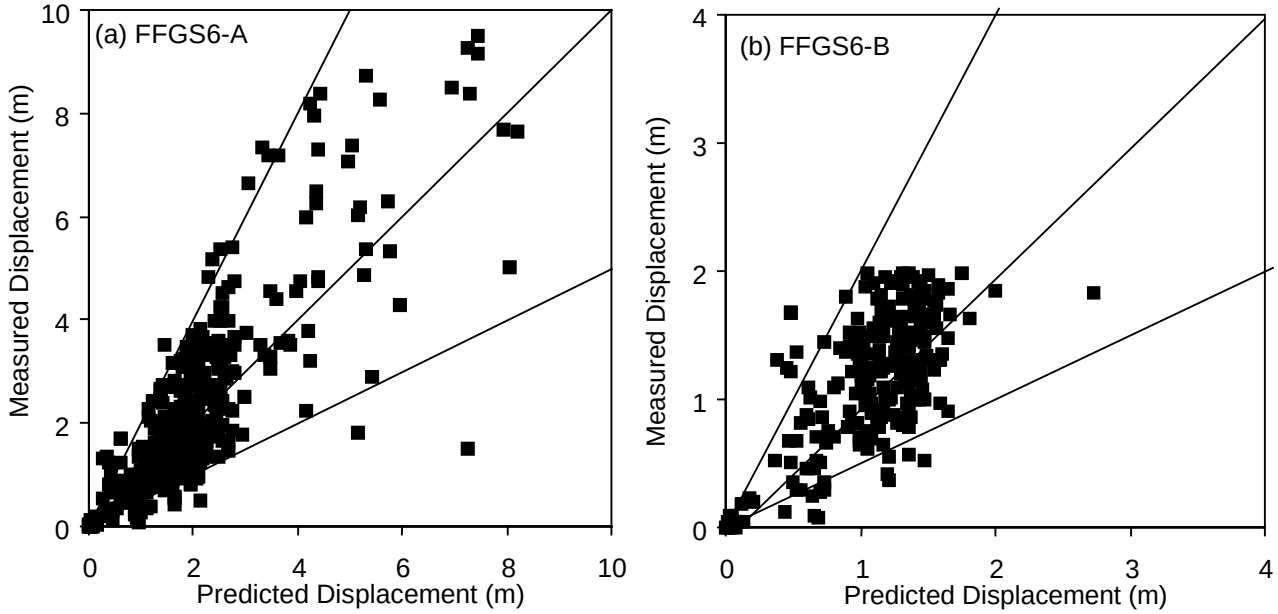

Figure 5-12. Measured versus predicted displacements for six-parameter model (FFGS6) calibrated from (a) data set A, and (b) data set B.

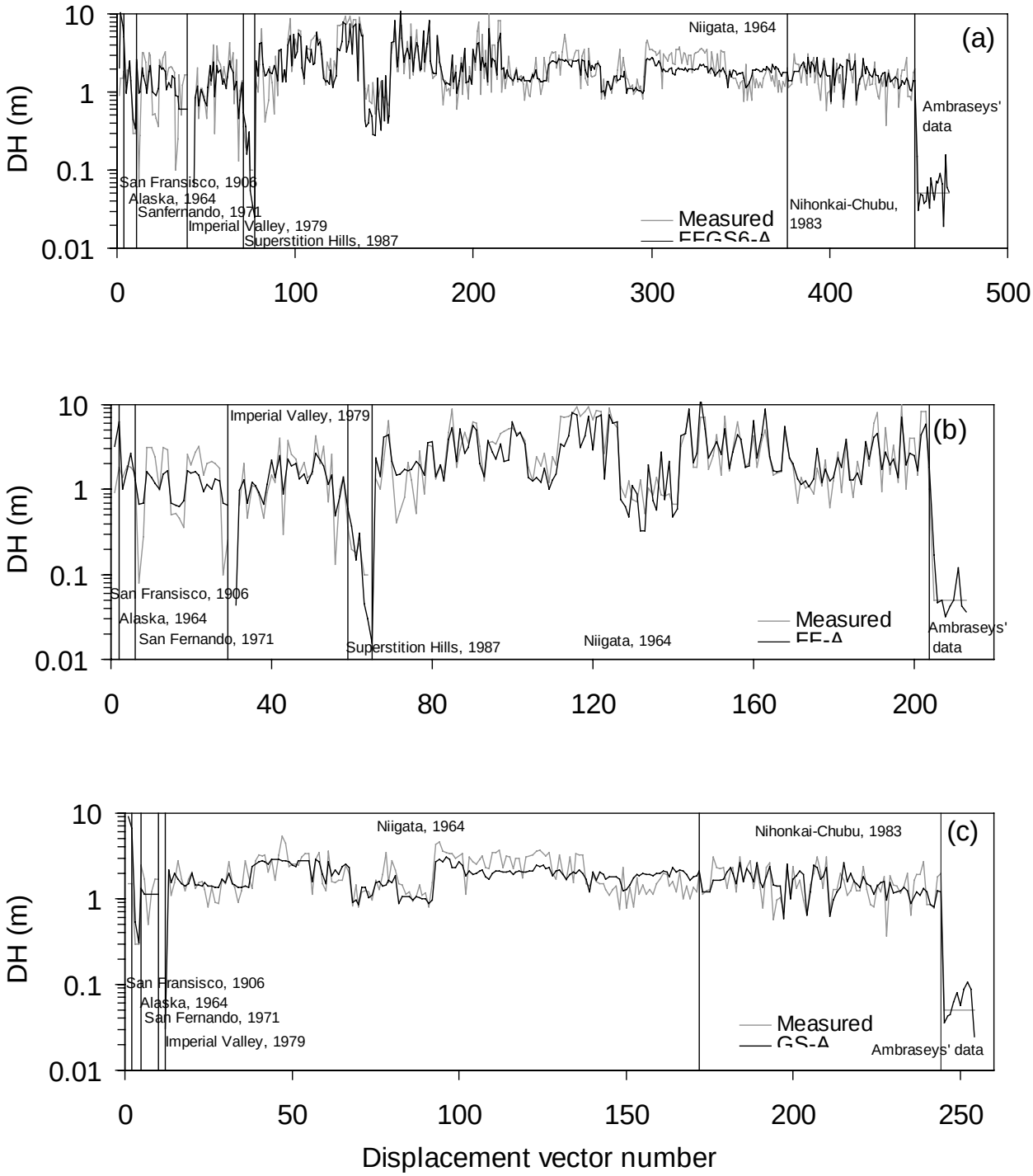

Figure 5-13. Comparison of the amplitudes of liquefaction-induced lateral displacements measured and predicted for data set A (entire database) by 6-parameter models: (a) FFGS6-A, (b) FF6-A, and (c) GS6-A.

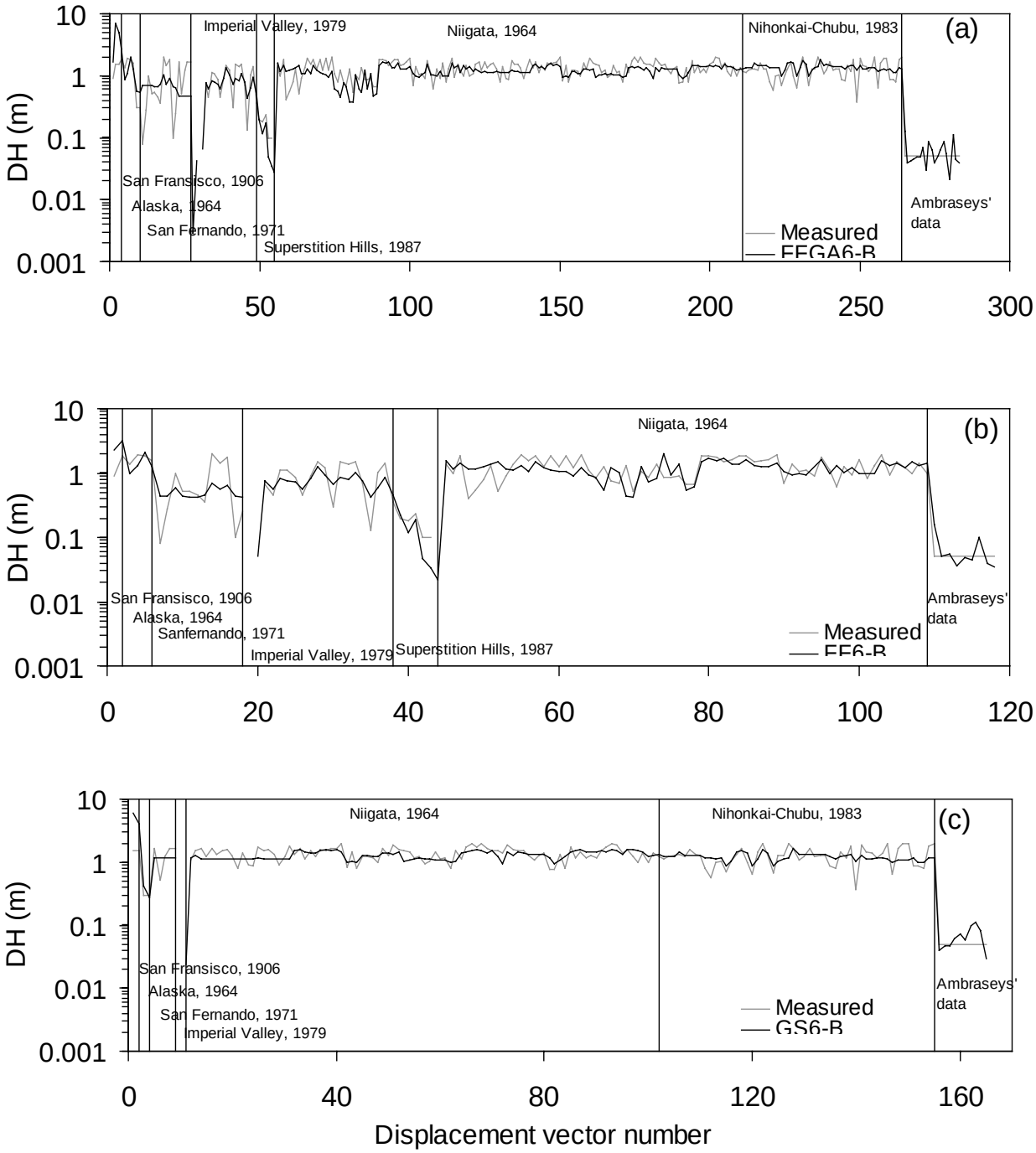

Figure 5-14. Comparison of the amplitudes of liquefaction-induced lateral displacements measured and predicted for data set B (displacement amplitude smaller than 2m) by 6-parameter models: (a) FFGS6-B, (b) FF6-B, and (c) GS6-B.

5.4 Four-parameter MLR model

The parameters F_{15} and $D50_{15}$ of the six-parameter models GS6, FF6 and FFGS6 are rather difficult to obtain from borehole data. They require taking soil sampling from the boreholes, performing grain-size analysis in the laboratory, and computing averages in the layers with a SPT blow count smaller than 15. It is obvious that this task can be formidable, and even impractical when the areas under investigation are large. In the present database (Bartlett, 1998), it is unclear how many values of F_{15} and $D50_{15}$ were actually measured, interpolated, extrapolated, or assumed. The uncertainties on variables F_{15} and $D50_{15}$ are certainly larger than on any other MLR variables.

The four-parameter MLR model was developed to provide a first-order approximation of liquefaction-induced displacement, and to eliminate the errors related to the determination of F_{15} and $D50_{15}$. The model FFGS4 has the following generic equation:

$$\begin{aligned} Log(D_H + 0.01) = b_0 + b_{off} + b_1 M + b_2 Log(R) + b_3 R \\ + b_4 Log(W_{ff}) + b_5 Log(S_{gs}) + b_6 Log(T_{15}) \end{aligned} \tag{5.4}$$

where the variables M, R, W, S, and T_{15} are defined in Table 2, and the values of the ten constant coefficients - b_0, b_{off}, and b_1 to b_8 - are given in Table 6. As for the six-parameter models, the free-face and ground-slope case were modeled separately by introducing the four-parameter models FF4 and GS4 and calibrating them from the data sets A and B. The expression of model FF4 is:

$$Log(D_H + 0.01) = b_0 + b_1 M + b_2 Log(R) + b_3 R + b_4 Log(W) + b_6 Log(T_{15}) \tag{5.5}$$

and that of model GS4 is:

$$Log(D_H + 0.01) = b_0 + b_1 M + b_2 Log(R) + b_3 R + b_5 Log(S) + b_6 Log(T_{15}) \tag{5.6}$$

The coefficients of the four-parameter models were calibrated from data sets A and B by using the same regression analysis techniques as for the six-parameter models. The values of the coefficients and adjusted R^2- values for models FFGS4, FF4 and GS4 are listed in Table 6. As shown in Table 6, the adjusted R^2-values are 64.3%, 62.2% and 68.5% for models FFGS4-A, FF4-A, and GS4-A, respectively, and 64.3%, 57.7% and 71.4% for models FFGS4-B, FF4-B, and GS4-B, respectively. Overall, the adjusted R^2-values of the four-parameter models are lower than those of the six-parameters models. As expected, the four-parameter models do not predict measured ground displacement as accurately as the six-parameter models. The adjusted R^2-value is the best (i.e., 71.4%) in the case of model GS4-B, which is remarkable in view of the model simplicity. The four-parameter model predicts the free-face displacements less accurately than ground-slope displacements for both data sets A and B, as was the case for the six-parameters models.

Figures 15 - 17 show the measured displacements plotted against those predicted by models FF4, GS4, and FFGS4 for data sets A and B, as was previously done for models FFGS6, FF6, and GS6. The results of Figs. 15-17 and 10-12 are similar. The points are however more scattered about the 1:1 line than in Figs. 10-12, which corresponds to lower values of adjusted R^2 coefficients.

Figures 18 and 19 compare the measured displacements in data sets A and B to those predicted by models FF4, GS4, and FFGS4 as in Figs. 13 and 14. Overall, this representation indicates that models FFGS4, FF4 and GS4 do not follow the observed displacement amplitude as well as models FF6, GS6, and FFGS6 over a wide range of displacement amplitude.

Table 5-6. Coefficients of Multiple Linear Regression (MLR) model with 4 parameters.

	Data set A (all displacements)			Data set B (displacements < 2m)		
Number of data points	467	213	254	283	118	165
Model coefficients	FFGS4-A	FF4-A	GS4-A	FFGS4-B	FF4-B	GS4-B
b_0	-6.815	-6.968	-7.586	-6.747	-6.034	-8.410
b_{off}	-0.465	-	-	-0.162	-	-
b_1	1.017	0.972	1.109	1.001	0.880	1.239
b_2	-0.278	-0.271	-0.233	-0.289	-0.271	-0.358
b_3	-0.026	-0.027	-0.025	-0.021	-0.018	-0.024
b_4	0.497	0.497	-	0.090	0.013	-
b_5	0.454	-	0.477	0.203	-	0.266
b_6	0.558	0.584	0.579	0.289	0.257	0.373
R^2 adjusted	64.25%	62.22%	68.48%	64.27%	57.71%	71.42%

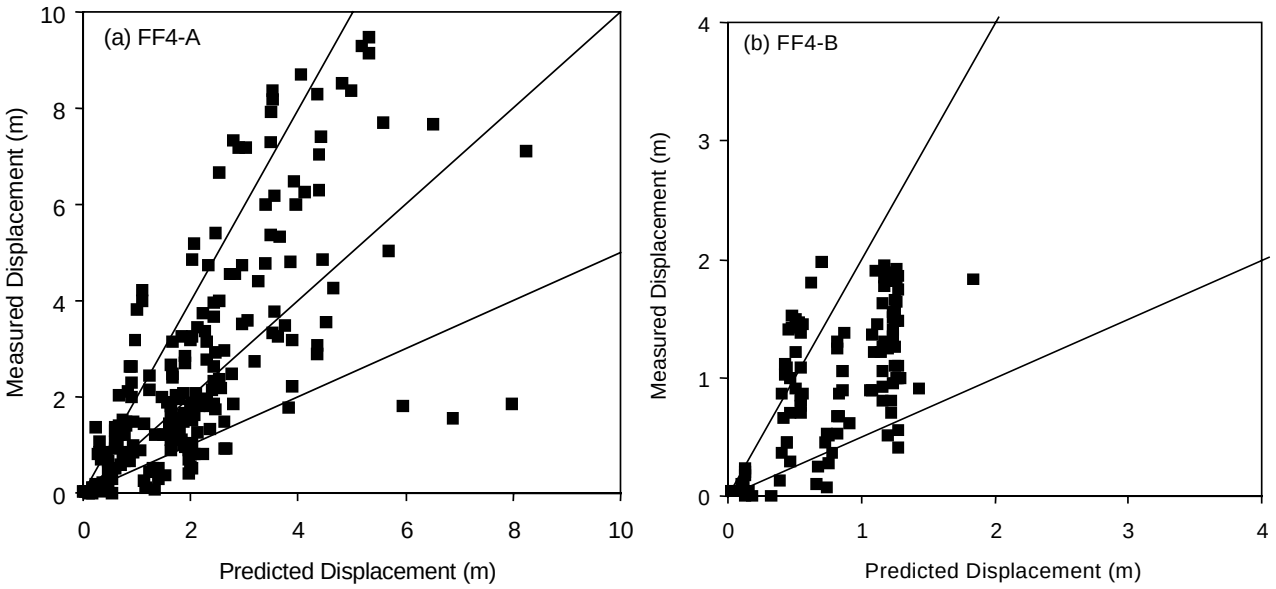

Figure 5-15. Measured versus predicted displacements for four-parameter model FF4 calibrated from (a) data set A, and (b) data set B.

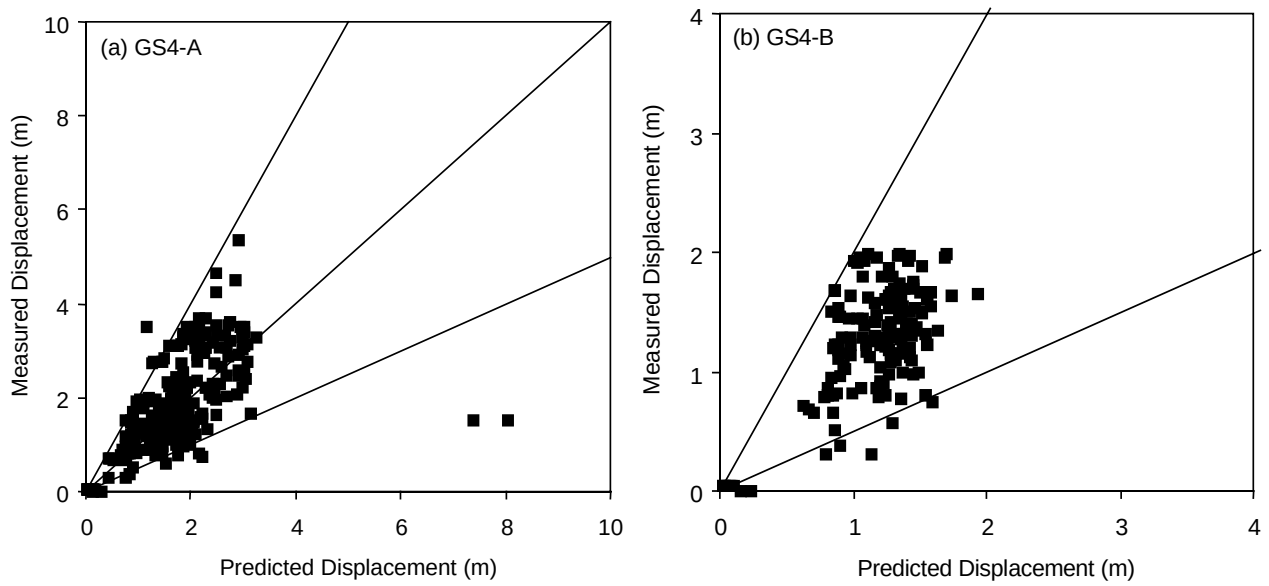

Figure 5-16. Measured versus predicted displacements for four-parameter model FFGS4 calibrated from (a) data set A, and (b) data set B.

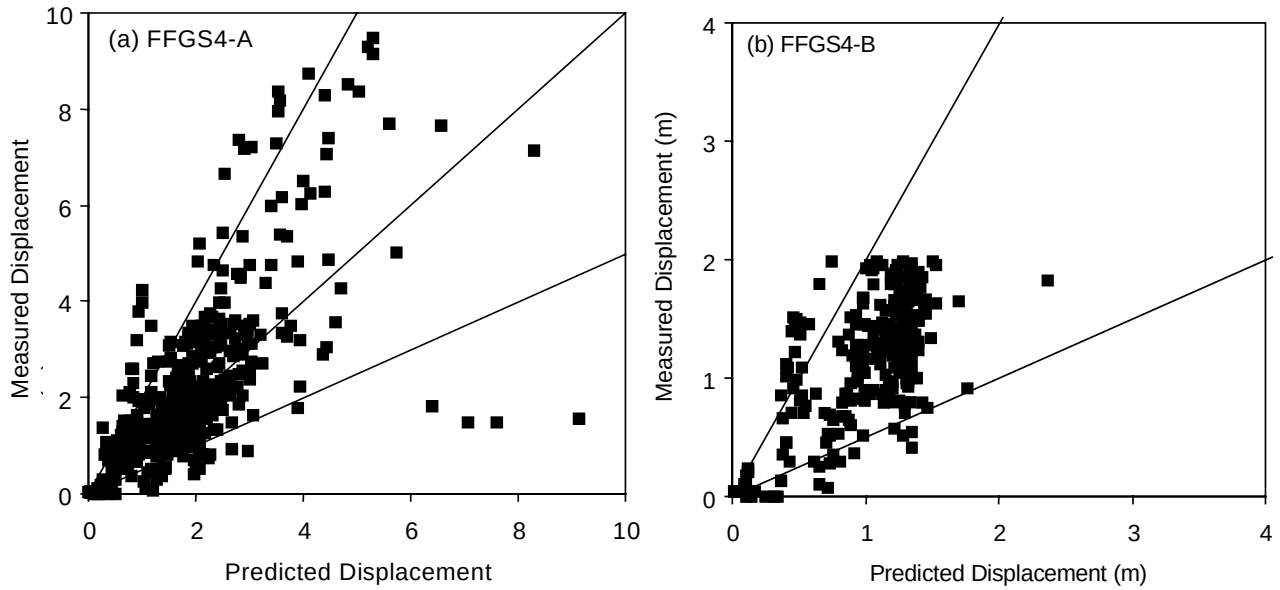

Figure 5-17. Measured versus predicted displacements for four-parameter model FFGS4 calibrated from (a) data set A, and (b) data set B.

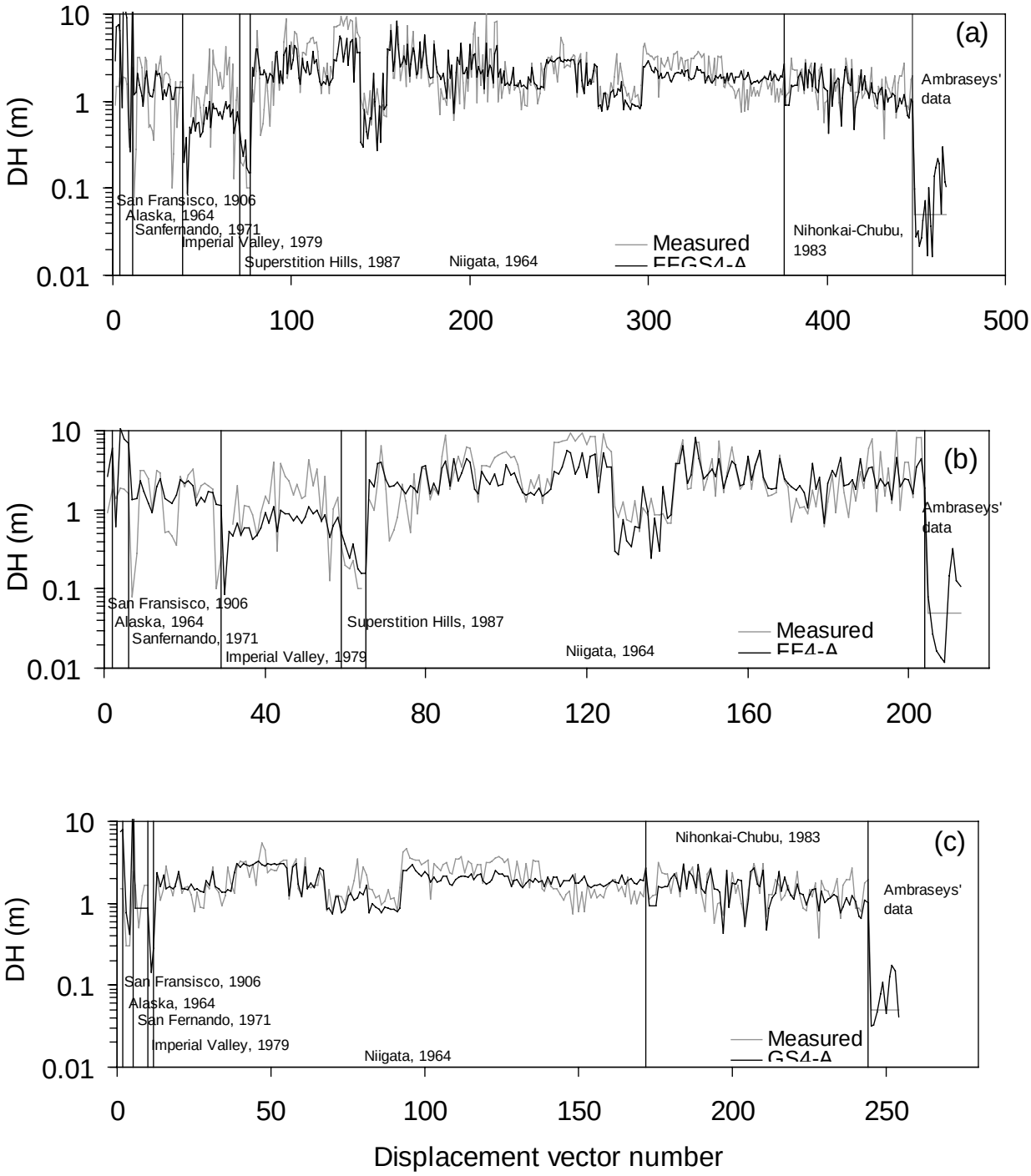

Figure 5-18. Comparison of amplitudes of liquefaction-induced lateral displacements measured and predicted for data set A by 4-parameter models: (a) FFGS4-A, (b) FF4-A, and (c) GS4-A.

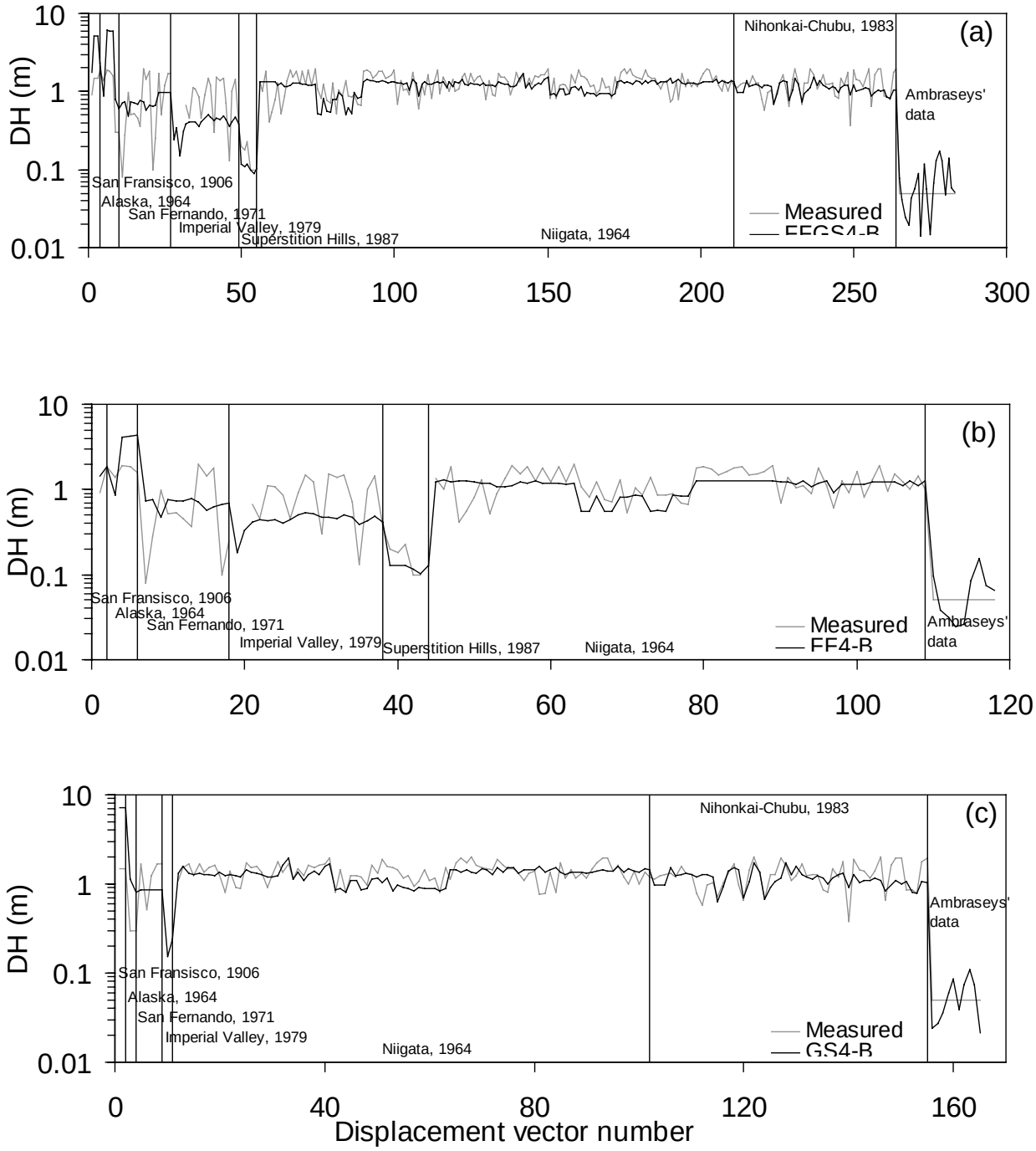

Figure 5-19. Comparison of amplitudes of liquefaction-induced lateral displacements measured and predicted for data set B by 4-parameter models: (a) FFGS4-B, (b) FF4-B, and (c) GS4-B.

5.5 Comparison of MLR models and recommendations

A total of twelve MLR models have been calibrated in this study. Table 7 summarizes the adjusted R^2 coefficients for all these models. It is clear that six-parameter models are systematically more accurate than four-parameter models.

Table 5-7. Comparison of adjusted R^2 for all MLR models

Models	Data set A	Data set B
FFGS4	64.3%	64.3%
FF4	62.2%	57.7%
GS4	68.5%	71.4%
FFGS6	80.6%	81.1%
FF6	82.1%	80.2%
GS6	82.4%	87.9%

These twelve models are compared in Figs. 20 and 21 by plotting the relative error between the measured and predicted displacements. The relative error is defined as follows:

$$\varepsilon = 100\ |DH_m - DH_p|/DH_m\ (\%) \tag{7}$$

where DH_m is the measured displacement amplitude, and DH_p is the predicted displacement amplitude. As shown in Figs. 20 and 21, the six-parameter models are more accurate than the 4-parameter models.

Based on the preceding analysis, some preliminary recommendations can be made regarding the selection of MLR models for predicting liquefaction-induced ground displacement. The choice of a particular model depends on (1) the site conditions (free face or ground slope) and (2) the availability of geotechnical data. For engineering design requiring an estimate of ground displacements, the models calibrated from the data set B are recommended compared to those calibrated from data set A.

When there is information available on the grain-size distribution of soils, the *FFGS6-B* model is recommended in the free-face and ground-slope conditions. The model GS6-B is especially recommended for ground slope conditions.

When there is little information on the soil grain-size distribution, the model FFGS4-B is recommended for free-face and ground-slope conditions, and the model GS4-B for ground-slope conditions.

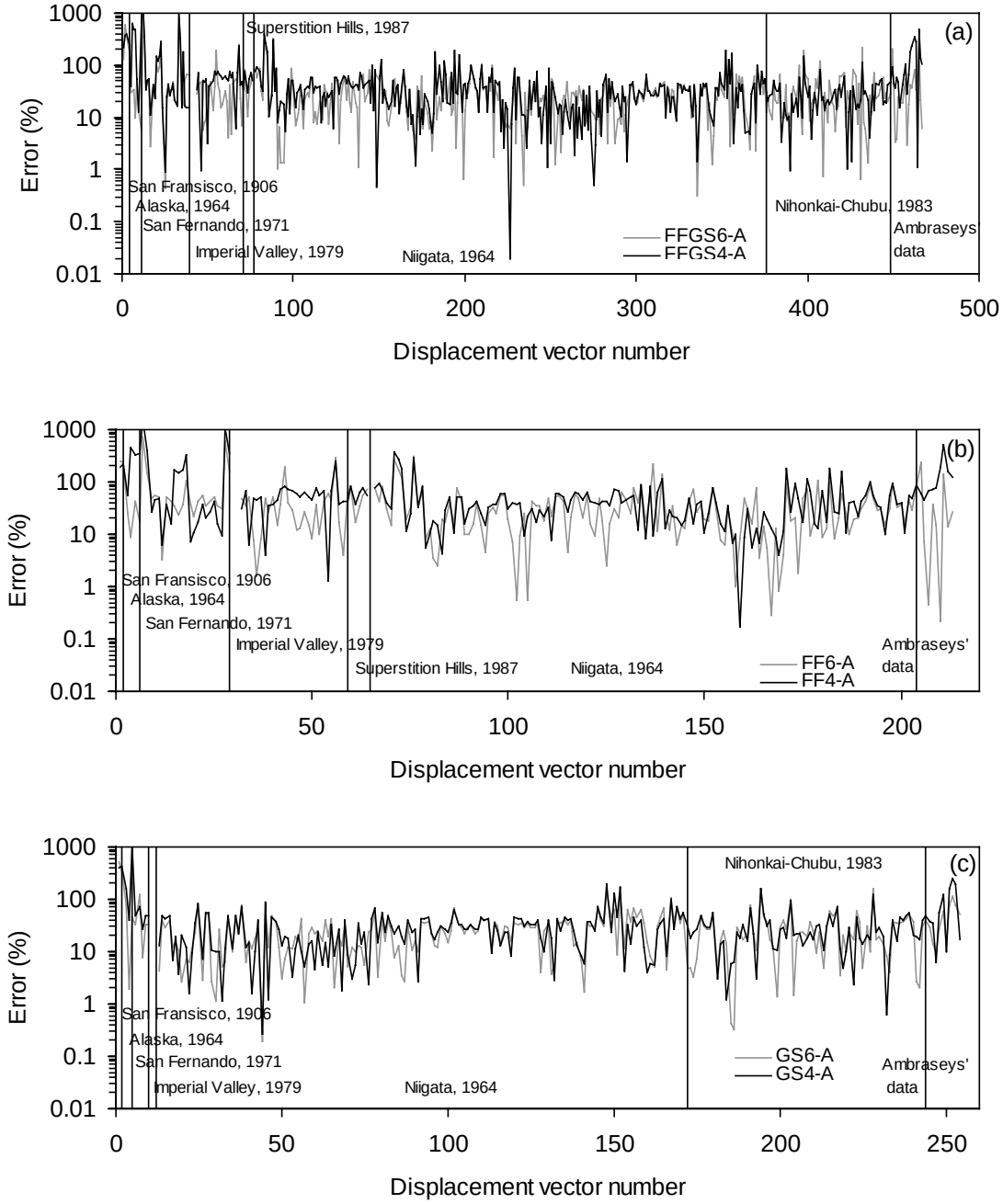

Figure 5-20. Comparison of relative errors between measured displacement and displacement predicted by 6 and 4 parameter models for data set A (all ranges of displacement amplitude): (a) FFGS6-A and FFGS4-A; (b) FF6-A and FF4-A; and (c) GS6-A and GS4-A.

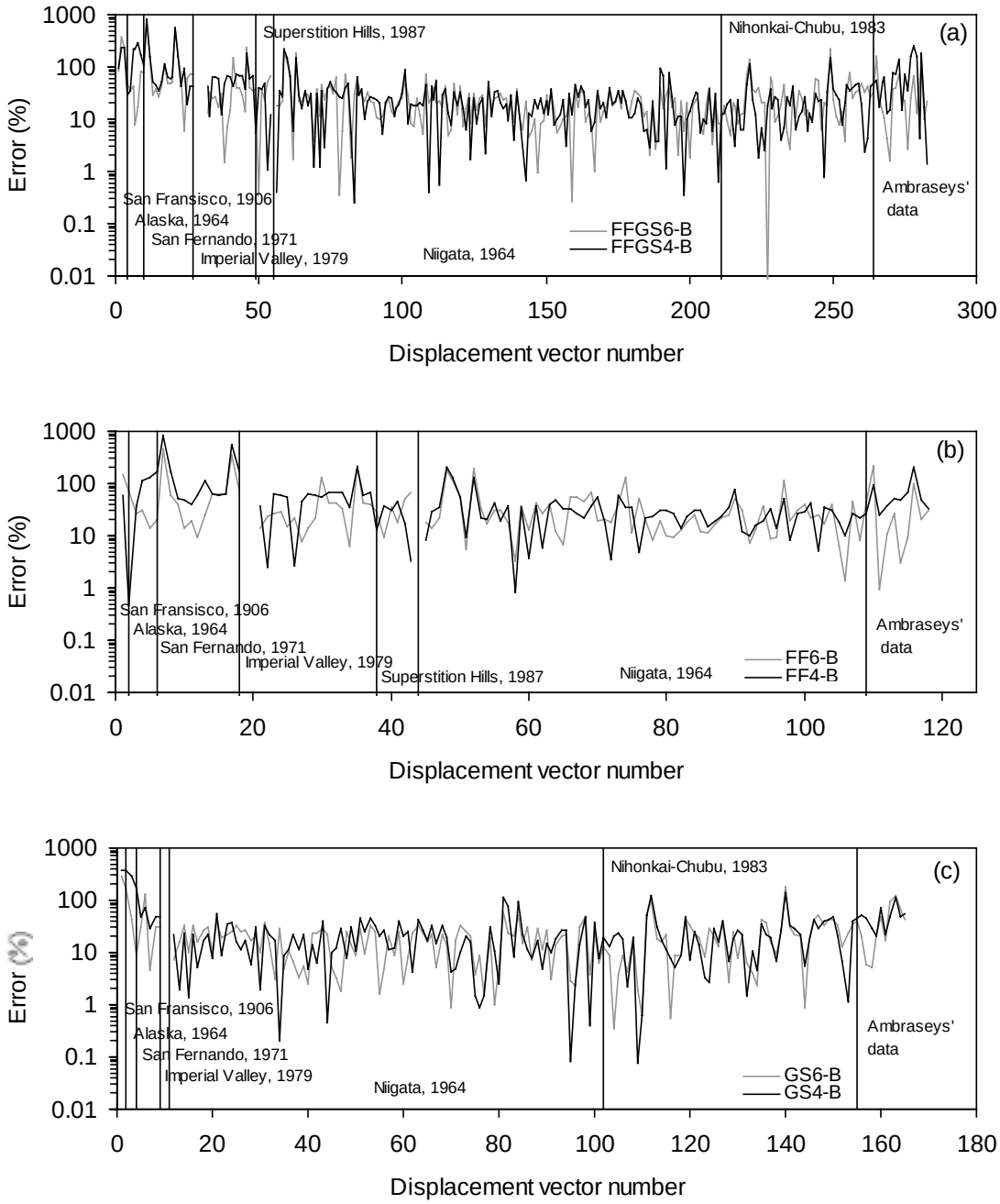

Figure 5-21. Comparison of relative error between measured displacement and displacement predicted by 6 and 4 parameter models in the case of data set B (displacement smaller than 2 m): (a) FFGS6-B and FFGS4-B; (b) FF6-B and FF4-B; and (c) GS6-B and GS4-B.

5.6 Suggestion for future work

There are statistical methods in seismology which could be used for constructing the empirical models of liquefaction-induced ground displacement instead of the multi-linear regression techniques (Abrahamson, private communication, 1998). These methods, which have successfully been used to develop attenuation curves in seismology, have the capabilities of dealing with bias in data. These methods will be applied to deriving new empirical models once the recent data from the 1994 Northridge and 1995 Hyogoken-Nanbu earthquakes has been added to the database of liquefaction-induced displacements.

5.7 Mapping of liquefaction-induced ground deformation

In the previous section, the amplitudes of liquefaction-induced displacements predicted by MLR models were compared to the observed values as individual data points, independently from their spatial distributions over the slide areas. The present section introduces the concepts of spatial distribution and direction of liquefaction-induced displacements, and briefly investigates the ability of MLR models to predict the spatial distribution of liquefaction-induced displacement vectors in two examples of free-face and ground-slope cases. Additional assumptions are required to predict the direction of liquefaction-induced lateral displacement. In the free-face cases, the horizontal displacements are assumed to be perpendicular to the free-face. In the ground slope cases, the horizontal displacements are assumed to be collinear to the average slope gradient direction.

Figure 22 shows the surface elevation and the contours of measured displacement amplitudes for the slide G-10 FF' at Niigata, Japan, during the 1964 Niigata earthquake. The measured displacement amplitudes are the largest on the free face (i.e., the Shinano River), and decrease with the distance from the free face. As shown in Fig. 23, the displacement vectors are oriented perpendicular to the free face, and in the opposite direction to the ground slope gradient. The slide G-10 FF' at Niigata is a clear case of free-face liquefaction-induced slide. As shown in Fig. 24, kriging techniques (Surfer, 1998) are used to predict a continuous spatial distribution of the liquefaction-induced displacements predicted by model FFGS6-A for the slide G-10 FF' at Niigata, Japan, during the 1964 Niigata earthquake. This predicted spatial distribution is obtained from the discrete displacements predicted at the locations of measured displacements. As shown in Figs. 23 and 24, the FFGS6-A model predicts reasonably the amplitude and spatial distribution of liquefaction-induced displacements over the slide area.

In theory, the model FFGS6-A variables could be extrapolated beyond the slide areas to obtain the spatial distributions of predicted displacements over large areas. Figure 24 also shows the continuous spatial distributions of the geotechnical properties, T_{15}, F_{15}, and $D50_{15}$ over the area encompassing slide G-10 FF'. A kriging technique (Surfer, 1998) is used to compute the values of T_{15}, F_{15}, and $D50_1$ in the slide vicinity. Theses values are interpolated or extrapolated at evenly spaced grid nodes (49 x 43) from the variable values at the borehole locations represented as numbered pins in Fig. 24. There are definite uncertainties in extrapolating spatially the averages from borehole data (i.e., T_{15}, F_{15} and $D50_{15}$). This extrapolation was found to overestimate the extent of liquefaction-induced slides. There is a need to collect data outside slide areas for assessing more accurately the spatial extent of liquefaction-induced displacements.

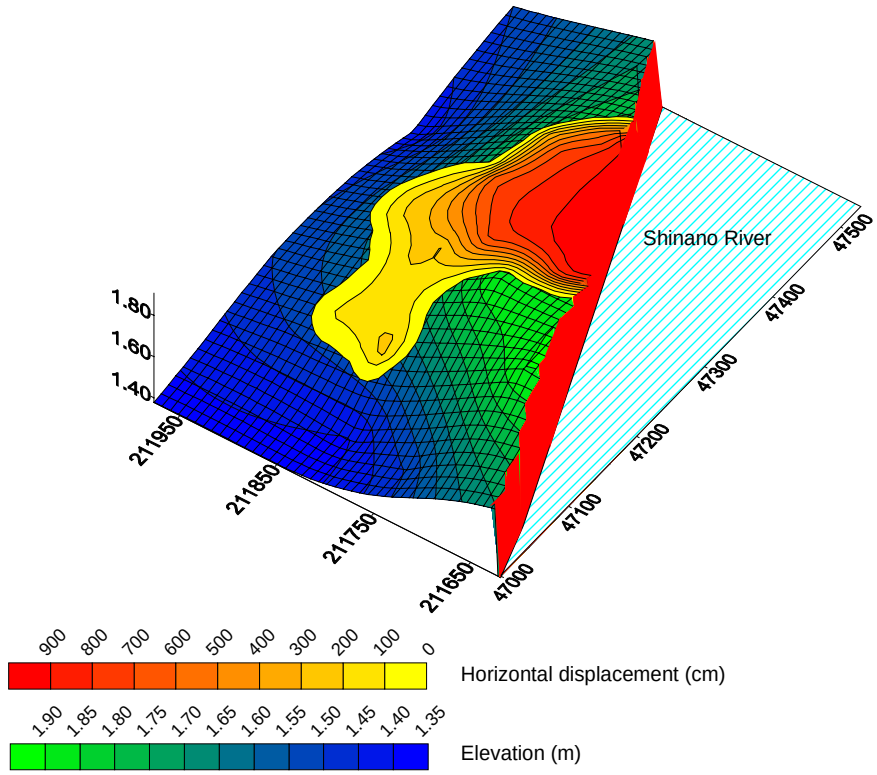

Figure 5-22. Contours of ground surface elevation and measured amplitude of lateral ground displacement for slide G-10 FF' during 1964 Niigata, Japan, earthquake (coordinates are in meters).

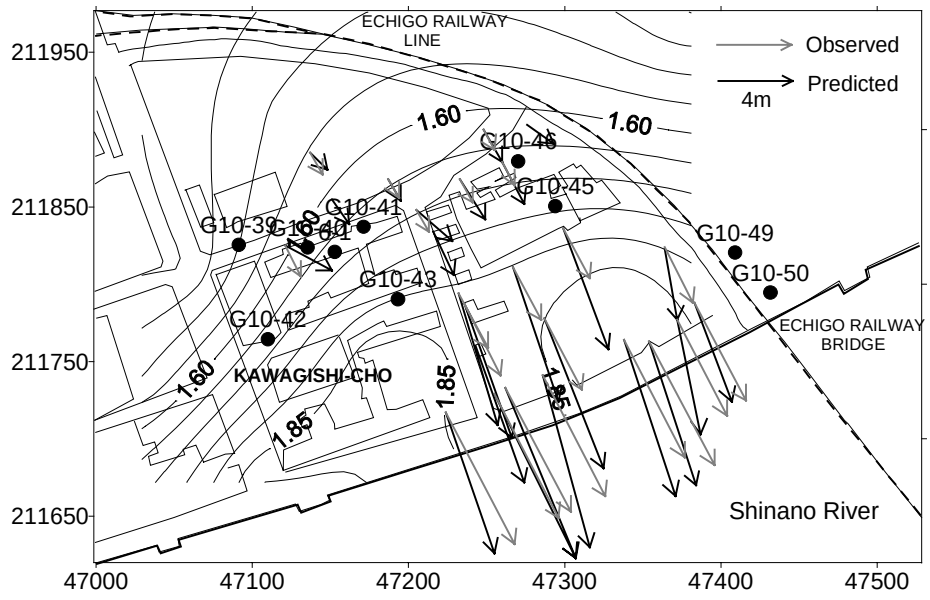

Figure 5-23. Comparison of measured and predicted liquefaction-induced displacements for slide G-10 FF' at Niigata, Japan, during 1964 Niigata earthquake (coordinates are in meters).

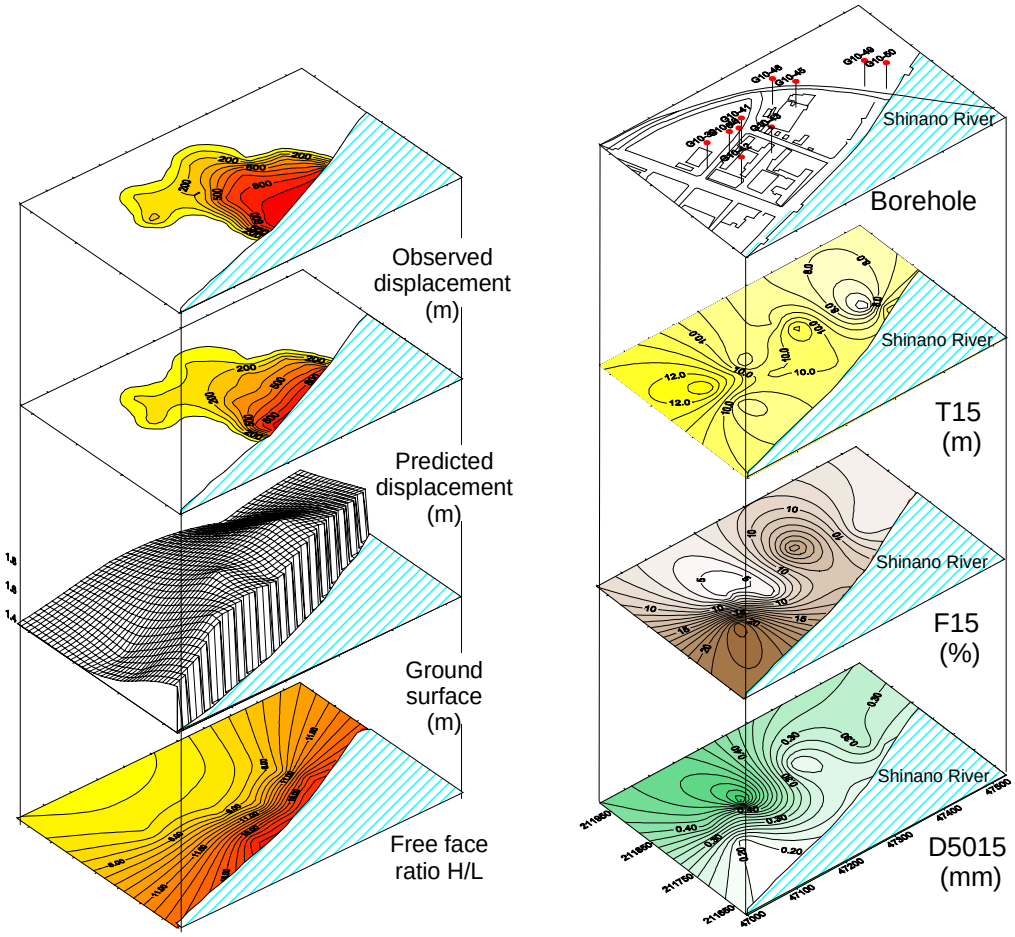

Figure 5-24. Representations of ground surface, spatial distribution of average geotechnical properties, and predicted and measured amplitude of liquefaction-induced lateral ground deformation for slide G10-FF' in Niigata during the 1964 Niigata, Japan, earthquake (coordinates are in meters).

Figure 25 shows the ground surface elevation and the contours of measured displacement amplitudes for the slide H-10 MM' at Niigata, Japan, during the 1964 Niigata earthquake. The magnitudes of the liquefaction-induced displacement vectors are clearly related to the ground slope. This slide, which took place far away from any free-faces, is considered to be a representative example of ground-slope cases. As shown in Fig. 25, the slide boundaries were assumed to be rather abrupt due to the absence of measured displacement vectors. It is likely that there were small deformations around this slide, which were difficult to obtain from aerial photographs. As shown in Fig. 26, the measured displacement vectors have almost the same direction as the average slope direction. Figure 27 shows the continuous spatial distributions of the geotechnical properties, T_{15}, F_{15}, and $D50_{15}$, which were calculated from the discrete boreholes represented as numbered pins. As shown in Figs. 26 and 27, model FFGS6-A predicts reasonably the amplitude and spatial distribution of liquefied displacement within the slide area. There are however uncertainties in extrapolating the results beyond the slide area, and defining the extent of the liquefaction-induced slides, which deserve to be studied in greater detail in the future.

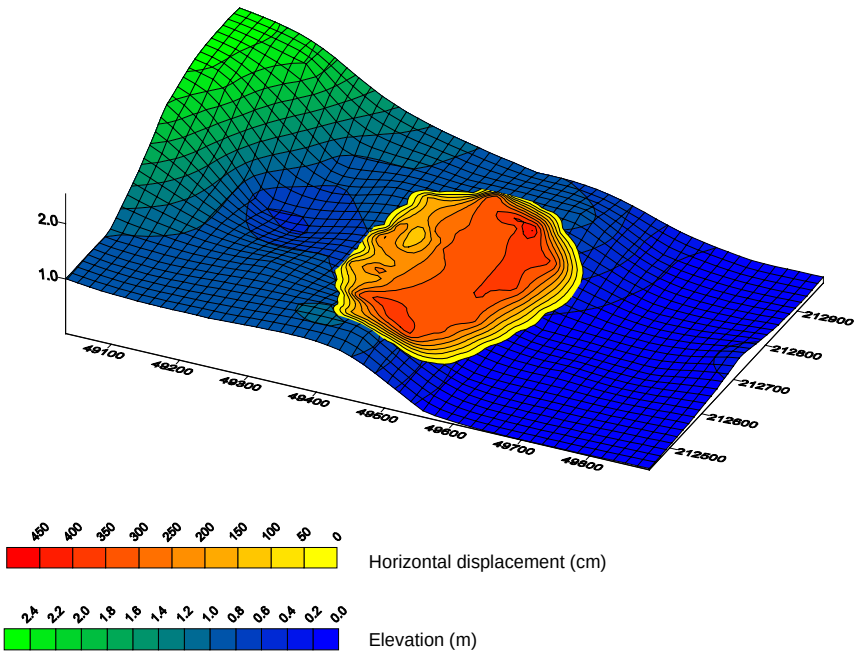

Figure 5-25. Contours of ground surface elevation and measured amplitude of lateral ground displacement measured for slide H10-MM' during 1964 Niigata, Japan, earthquake (coordinates are in meters).

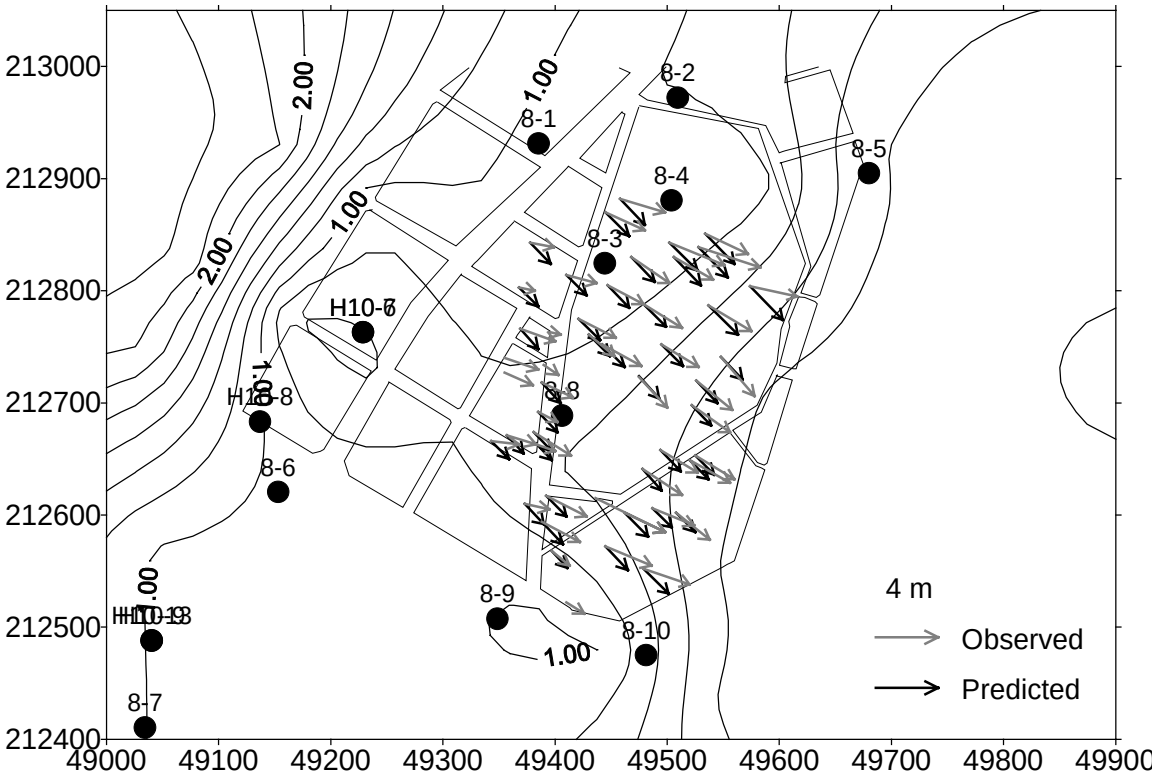

Figure 5-26. Comparison of measured and predicted liquefaction-induced displacements for slide H10-MM' during 1964 Niigata, Japan, earthquake (coordinates are in meters).

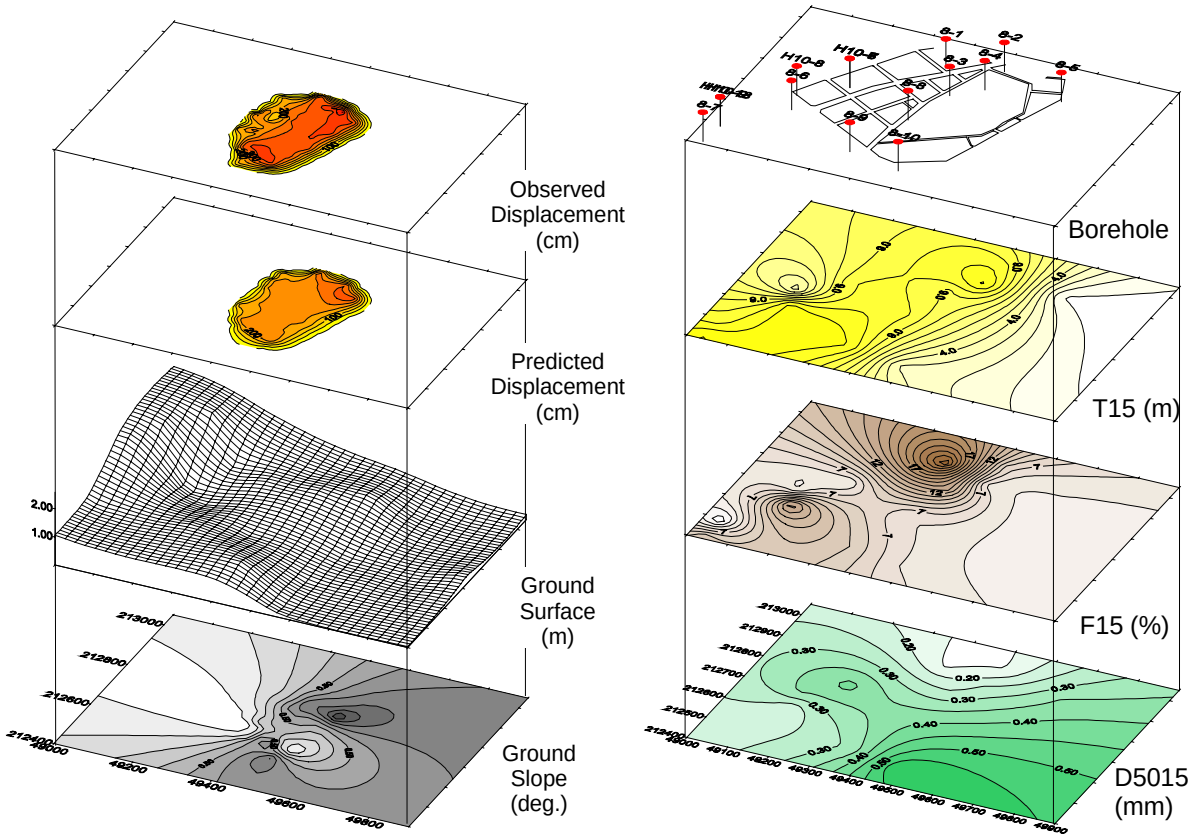

Figure 5-27. Representations of ground surface and gradient, spatial distribution of average geotechnical properties, and predicted and measured amplitude of liquefaction-induced lateral ground deformation for slide H10-MM' in Niigata, Japan, during the 1964 Niigata earthquake (coordinates are in meters).

6. PROBABILISTIC MODEL OF LIQUEFACTION-INDUCED GROUND DEFORMATION

As described previously, twelve MLR models have been calibrated, based on data sets A and B. These MLR models predict the mean values of liquefaction-induced ground deformation. Based on the previously developed MLR models, this section determines (1) the confidence limits for liquefaction-induced ground deformation and (2) the probability of exceeding some level of ground deformation. The reader is referred to Draper and Smith (1981) for details on probability analysis.

6.1 Mean and variance of ground deformation

The MLR models for liquefaction-induced ground deformation predict the mean value of ground deformation $\hat{D}$ as follows:

$$\hat{D} = b_0 + b_1 X_1 + ... + b_p X_p \tag{6.1}$$

where b_0, …, b_p are constant coefficients, X_1 ,…, X_p are the model variables and p the total number of model variables. The variance of $\hat{D}$ is:

$$V(\hat{D}) = V(b_0 + b_1 X_1 + ... + b_p X_p) \tag{6.2}$$

Equation 2 can be expanded as follows:

$$\begin{aligned} V(\hat{D}) = {} & V(b_0) + X_1^2 V(b_1) + ... + X_p^2 V(b_p) \\ & + 2X_1 \text{covar}(b_0, b_1) + ... + 2X_p \text{covar}(b_0, b_p) \\ & + 2X_1 X_2 \text{covar}(b_1, b_2) + ... + 2X_{p-1} X_p \text{covar}(b_{p-1}, b_p) \end{aligned} \tag{6.3}$$

where V(b_i) is the variance of coefficient b_i, and covar(b_i, b_j) is the covariance of coefficient b_i and b_j. Equation 3 can be written in a matrix form as follows:

$$V(\hat{D}) = s^2 \mathbf{X}_0^T \mathbf{C} \mathbf{X}_0 \tag{6.4}$$

s^2 is the residual mean square:

$$s^2 = \frac{1}{n-p-1} \sum_{i=1}^{n} \left(\hat{D}_i - D_i \right)^2 \tag{6.5}$$

where D_i is the ith observed value of D, and $\hat{D}_i$ is ith predicted value corresponding to D_i (i=1 to n).The variance-covariance matrix $s^2\mathbf{C}$ has p+1 columns and p+1 rows:

$$\mathbf{C} = \left(\mathbf{X}^T \mathbf{X}\right)^{-1} = \begin{pmatrix} c_{00} & c_{01} & \cdots & c_{0p} \\ c_{10} & c_{11} & \cdots & c_{1p} \\ \vdots & & \ddots & \vdots \\ c_{p0} & & & c_{pp} \end{pmatrix} \tag{6.6}$$

The matrix **X** with p+1 columns and n rows is defined as:

$$\mathbf{X} = \begin{pmatrix} 1 & X_{1,1} & \cdots & X_{1,p} \\ 1 & X_{2,1} & \cdots & X_{2,p} \\ \vdots & \vdots & \vdots & \vdots \\ 1 & X_{n,1} & \cdots & X_{n,p} \end{pmatrix} \tag{6.7}$$

where $X_{i,j}$ is the value of jth variable of the ith observation. In Eq. 4, the vector $\mathbf{X}_0$ represents the values of the model variables for an individual observation. $\mathbf{X}_0$ has the same type of components as a row of **X**. The vector $\mathbf{X}_0$ and its transpose $\mathbf{X}_0^T$ are:

$$\mathbf{X}_0 = \begin{pmatrix} 1 \\ X_1 \\ X_2 \\ \vdots \\ X_p \end{pmatrix} \quad \text{and } \mathbf{X}_0^T = \begin{pmatrix} 1 & X_1 & X_2 & \cdots & X_p \end{pmatrix} \tag{6.8}$$

In the case of the six-parameter MLR models of liquefaction-induced ground deformation (e.g., FFGS6-A), the components of $\mathbf{X}_0$ are given in Table 1. For the four-parameter MLR models of liquefaction-induced ground deformation (e.g., FFGS4-A), the last two components (i.e., X_8 and X_9) are omitted.

The variance-covariance matrix **C** and residual mean square s^2 for the twelve MLR models were calculated by using the computer program Minitab (1989). Table 2 lists the values of **C** and s^2 for model FFGS6-A. All the coefficient values for other models are given in Appendix B. Based on the values of **C** and s^2, the confidence limits for ground deformation and probability of exceeding some amplitude threshold can be defined.

Table 6-1 Components of observation vector $\mathbf{X}_0$.

Component	Variable	Definition
1		
X_1	1 for free face and 0 for ground slope	
X_2	*M*	Earthquake moment magnitude
X_3	*R*	Closest distance to source (km)
X_4	*Log R*	
X_5	*Log W*	Free face ratio
X_6	*Log S*	Ground slope (%)
X_7	*Log* T_{15}	Thickness of saturated cohesionless soils with $(N1)_{60}$<15 (m)
X_8	*Log(100 -*F_{15}*)*	Average fines (<75 μm) content in T_{15} (%)
X_9	$D50_{15}$	Average mean grain size D_{50} in T_{15} (mm)

Table 6-2. Parameter values for probabilistic model FFGS6-A.

Covariance matrix **C** (symmetric)

0.001	0.000	0.002	0.000	0.000	-0.001	0.000	0.000	-0.007	0.001
	0.047	0.002	0.000	0.000	-0.040	-0.011	-0.005	-0.011	0.001
		0.029	0.000	-0.001	-0.004	0.004	0.000	-0.104	-0.005
			0.026	-0.001	0.005	-0.003	-0.005	-0.007	-0.014
				0.000	0.000	0.000	0.000	0.002	-0.001
					0.047	0.000	0.000	0.011	0.007
						0.045	0.011	-0.011	0.000
							0.022	-0.003	-0.004
								0.386	0.005
									0.196

Number of observations (n) = 467

Number of degrees of freedom (p) = 9

Residual mean square (s^2) = 0.046

6.2 Confidence limits

The 1-α confidence limits for the predicted mean value of D at observation state $\mathbf{X}_0$ are:

$$D_{\pm} = \hat{D} \pm t(n-p-1, 1-\tfrac{1}{2}\alpha)s\sqrt{\frac{1}{q}+\frac{1}{n}+\mathbf{X}_0^T\mathbf{C}\mathbf{X}_0} \tag{6.9}$$

where t is the t-distribution with n-p-1 degrees of freedom (Fig. 1), α is the significance level, s is the residual mean, q is the number of values used for the mean predicted value of D at state $\mathbf{X}_0$, and n is the total number of observations used in the regression. The confidence limit for a single predicted value of D is obtained by setting q equal to 1 in Eq. 9. The size of the confidence interval decreases when one wishes to obtain a mean value of D (i.e., $q > 1$) instead of a single value of D (i.e., $q = 1$). This interval is minimum when one wishes a mean value of D based on many values (i.e., $1/q \rightarrow 0$). When n becomes large (e.g., n > 500), the t-distribution becomes identical to the normal distribution. The probability for the value D at state $\mathbf{X}_0$ to be comprised between D_- and D_+ is equal to 1-α, i.e.:

$$p(D_- \le D \le D_+) = 1-\alpha \tag{6.10}$$

In Microsoft Excel (1994), the *t*-distribution is given by the function *TINV* as follows:

$$t(n-p-1, 1-\tfrac{1}{2}\alpha) = TINV(\alpha, n-p-1) \tag{6.11}$$

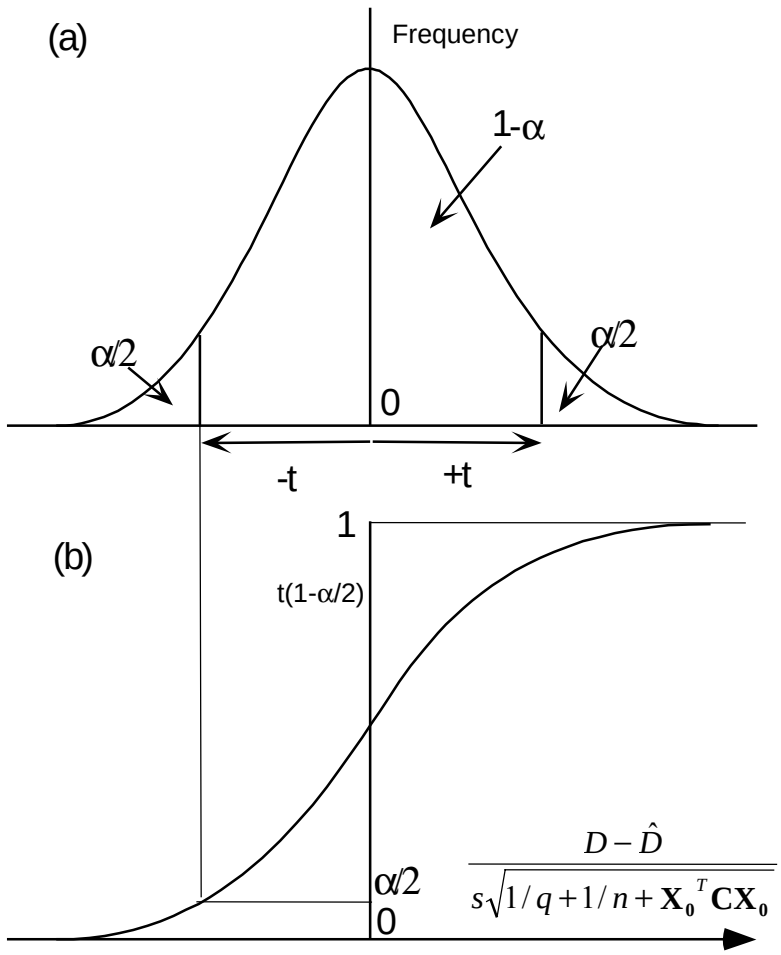

Figure 6-1. Representation of *t*-distribution: (a) probability distribution function of *t*-distribution with two tails, and (b) inverse *t*-distribution.

6.3 Probabilistic model

Based on Eq. 9, the probability $p(D>D^*)$ for the mean deformation D at state $\mathbf{X}_0$ to exceed some value D^* is estimated as follows:

$$p(D > D^*) = \beta \tag{6.13}$$

where β is the area under the *t*-probability distribution curve as shown in Fig. 2a. Using the inverse *t*-distribution t^{-1} (see Fig. 2b), Eq. 13 can be written as follows:

$$p(D > D^*) = \begin{cases} 1 - t^{-1}\left(n - p - 1, \dfrac{\hat{D} - D^*}{s\sqrt{1/q + 1/n + \mathbf{X}_0^T \mathbf{C} \mathbf{X}_0}} \right) & if\ D^* < \hat{D} \\ t^{-1}\left(n - p - 1, \dfrac{D^* - \hat{D}}{s\sqrt{1/q + 1/n + \mathbf{X}_0^T \mathbf{C} \mathbf{X}_0}} \right) & if\ D^* \geq \hat{D} \end{cases} \tag{6.14}$$

Equation 14 gives the probability that the mean value D of liquefaction-induced ground deformation at state $\mathbf{X}_0$ exceeds some value D^*. The parameter n refers to the total number of observations used in the regression analysis. The parameter q is the number of values used for the mean value of D. The probability for a single value of D to exceed D^* at state $\mathbf{X}_0$ is given by setting q equal to 1. The probability for a mean value of D based on many values is given by setting $1/q$ equal to zero.

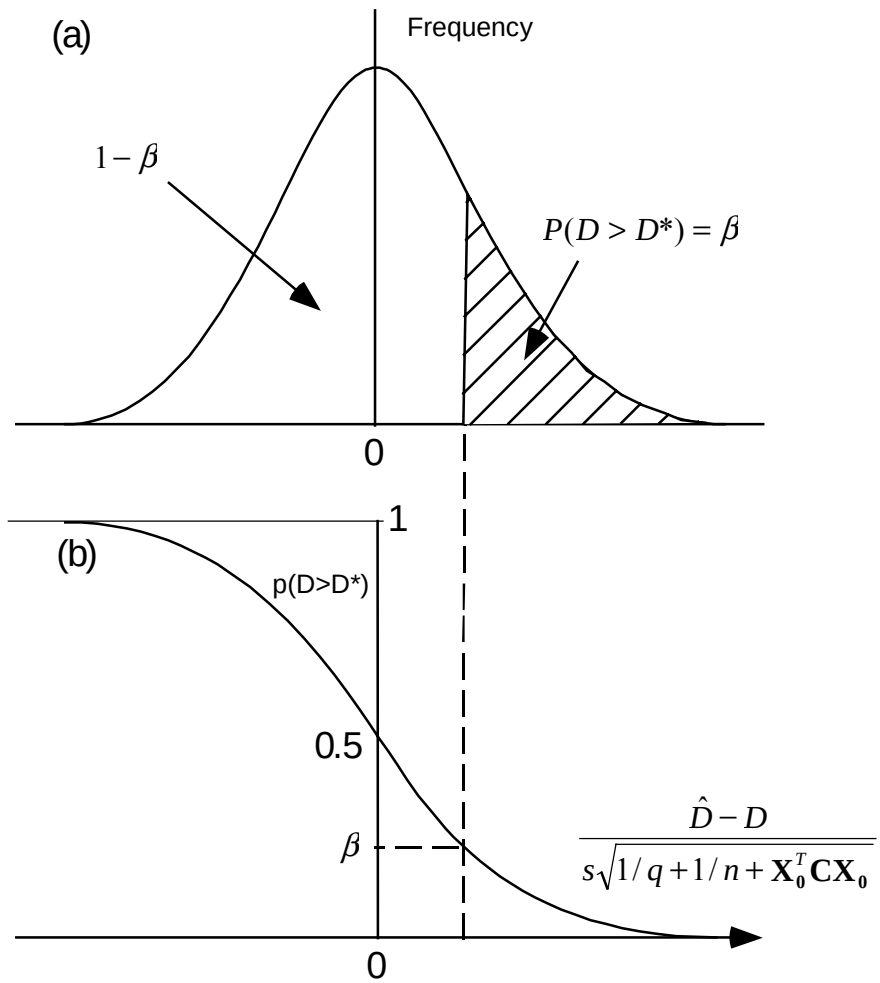

Figure 6-2. Representation of probabilistic model for exceeding a threshold of deformation: (a) probability distribution function of t-distribution with single tail, and (b) inverse t-distribution $D^* < \hat{D}$.

In Microsoft Excel, the inverse *t*-distribution is defined by the function TDIST. Equation 14 can therefore be implemented as follows:

$$p(D > D^*) = \begin{cases} 1 - TDIST\left(\dfrac{\hat{D} - D^*}{s\sqrt{1/q + 1/n + \mathbf{X}_0^T \mathbf{C} \mathbf{X}_0}}, n - p - 1, 1 \right) & if\ D^* < \hat{D} \\ TDIST\left(\dfrac{D^* - \hat{D}}{s\sqrt{1/q + 1/n + \mathbf{X}_0^T \mathbf{C} \mathbf{X}_0}}, n - p - 1, 1 \right) & if\ D^* \geq \hat{D} \end{cases} \tag{6.15}$$

6.4 Confidence intervals for liquefaction-induced ground deformation

Figure 3 shows the confidence limits of liquefaction-induced deformation predicted by model FFGS6-A for $q = 1$. The confidence limits corresponding to 95% confidence are represented by error bars. The numbers along the horizontal axis refer to the numbering system in data set A, which regroups data points by earthquakes. Figure 3 also shows the measured displacement values, and the values of mean displacement predicted by model FFGS6-A as a line centered at the error bars. As shown in Fig. 3, the confidence intervals enclose most of the measured displacement values. In some cases however, these intervals become large and do not encompass the measured displacement.

Figures 4 and 5 show the confidence limits predicted by models FF6-A and GS6-A, respectively. The confidence intervals in the ground-slope model (i.e., GS6-A) are smaller and enclose a little better the measured values than the free-face model (i.e., FF6-A) and the combined model (i.e., FFGS6-A).

Figures 6, 7 and 8 show the confidence limits for the models FFGS6-B, FF6-B, and GS6-B, respectively, which were calibrated from data sets B including only displacements smaller than 2 meters. Overall, the confidence intervals enclose the measured values more accurately than the models based on data set A.

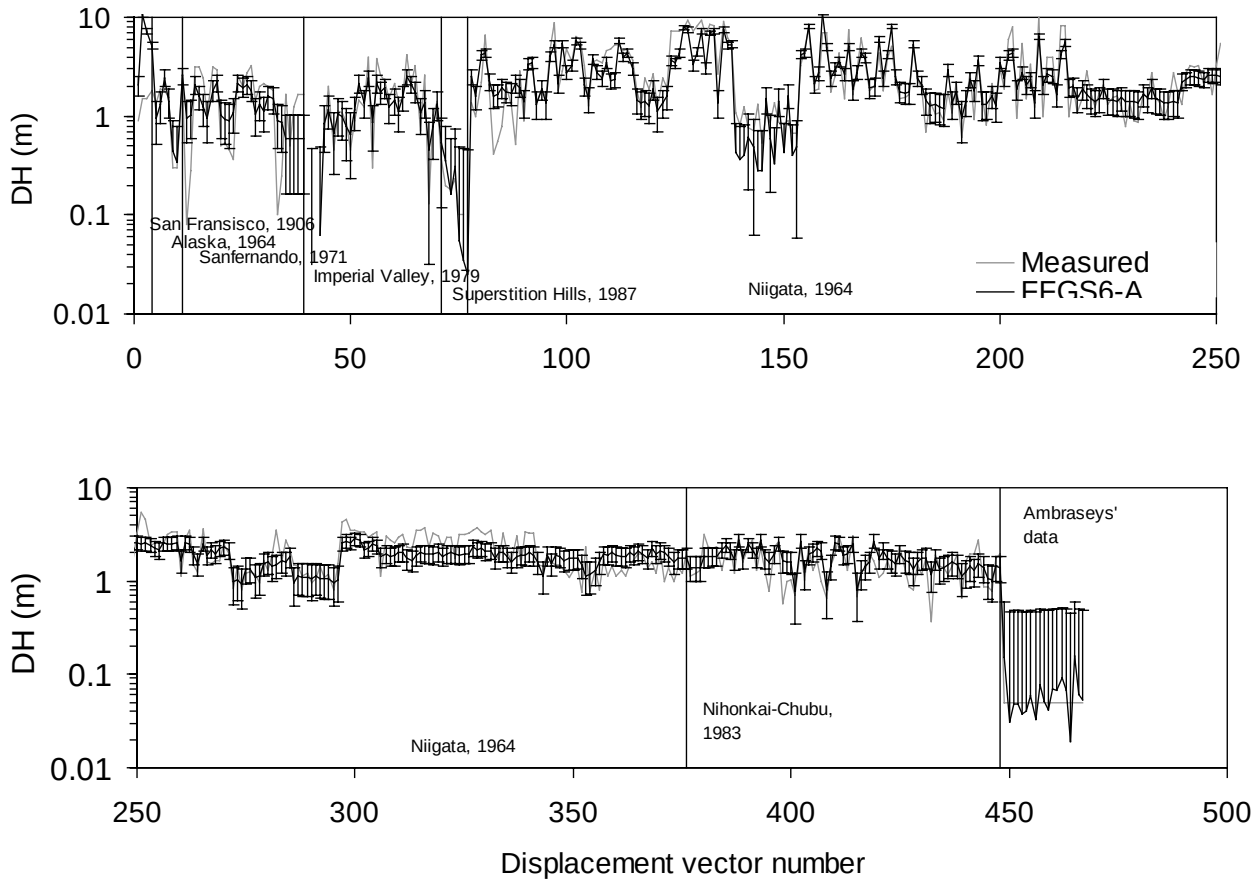

Figure 6-3. Model FFGS6-A for liquefaction-induced lateral displacement: measured displacement, and predicted mean displacement and confidence interval (95% *t*-distribution).

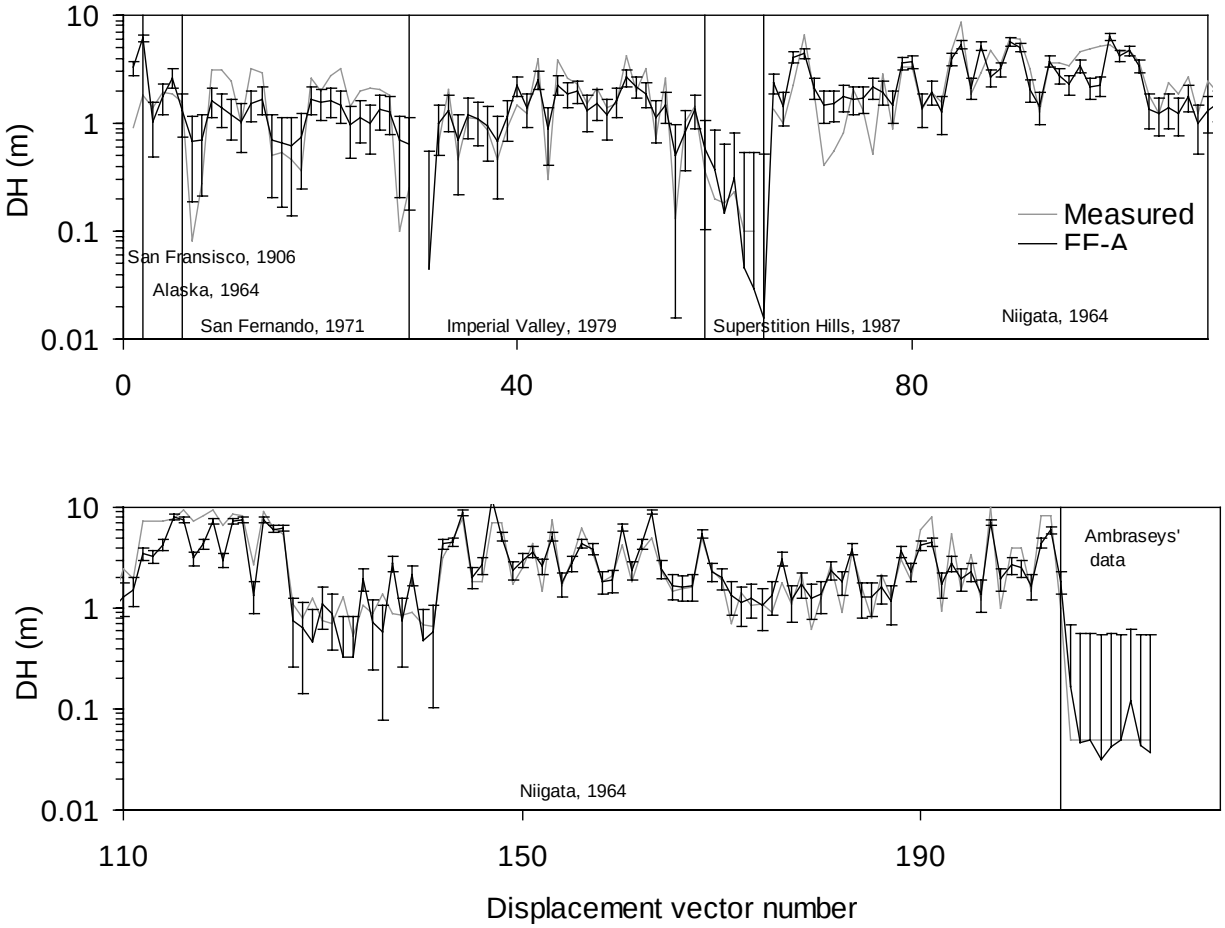

Figure 6-4. Model FF6-A for liquefaction-induced lateral displacement: measured displacement, and predicted mean displacement and confidence interval (95% t-distribution).

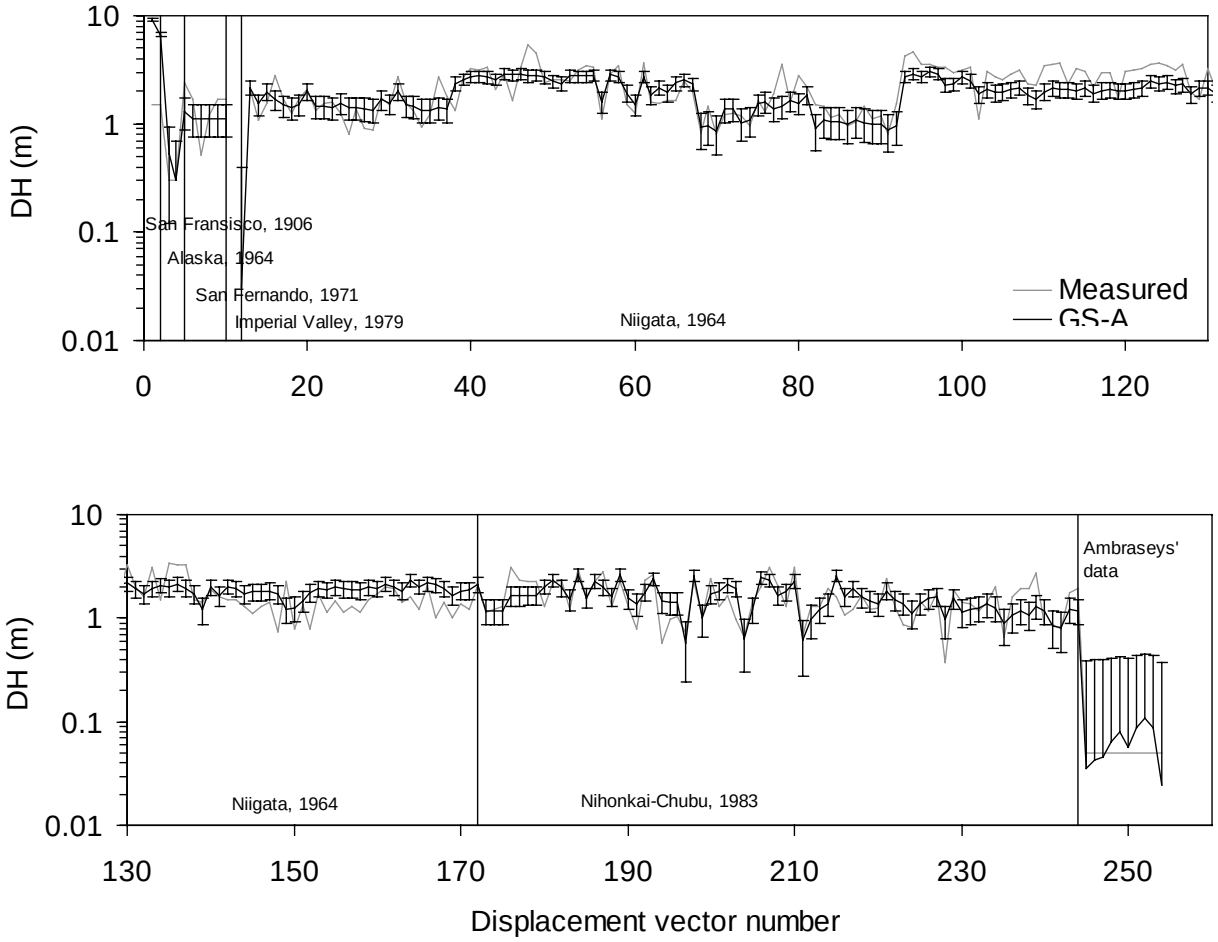

Figure 6-5. Model GS6-A for liquefaction-induced lateral displacement: measured displacement, and predicted mean displacement and confidence interval (95% t-distribution).

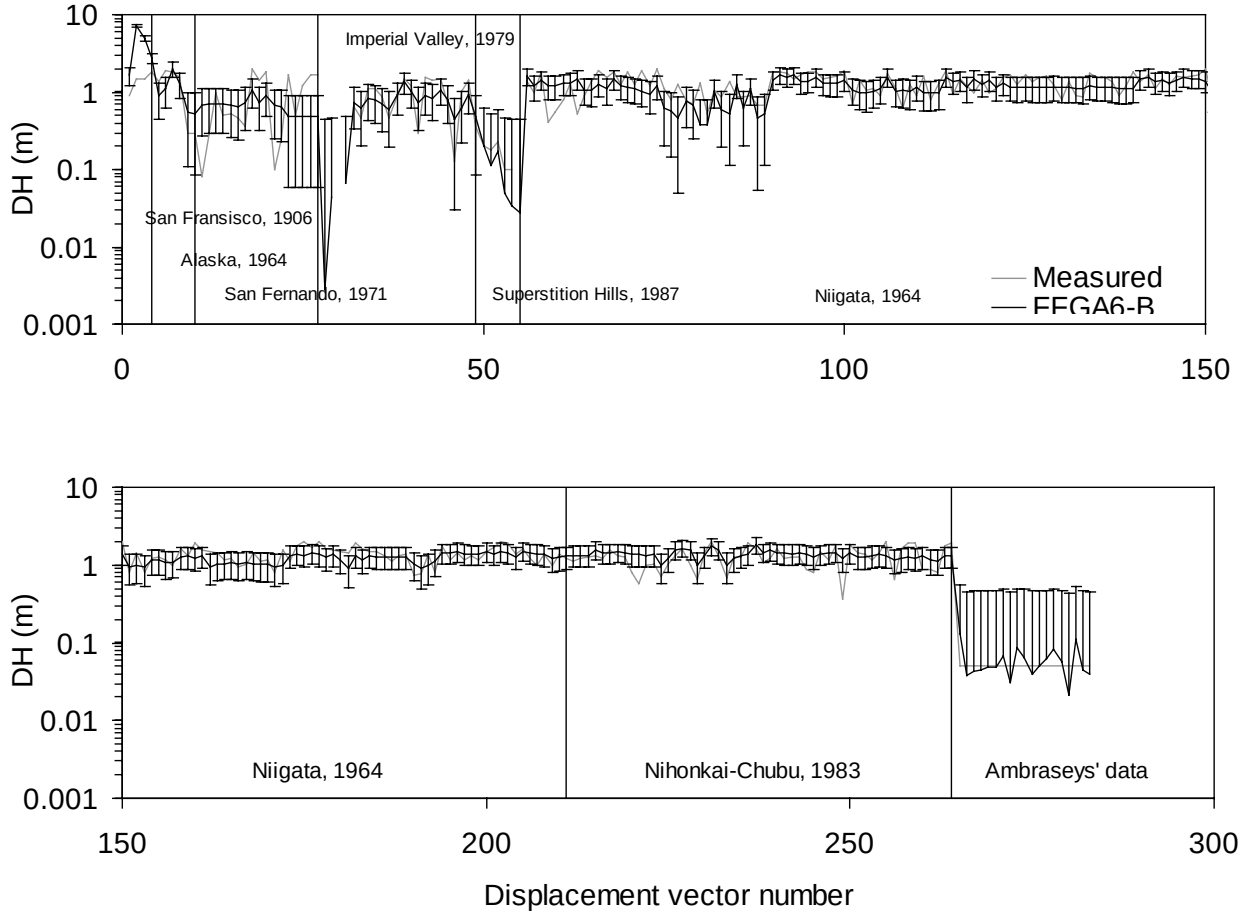

Figure 6-6. Model FFGS6-B for liquefaction-induced lateral displacement: measured displacement, and predicted mean displacement and confidence interval (95% t-distribution).

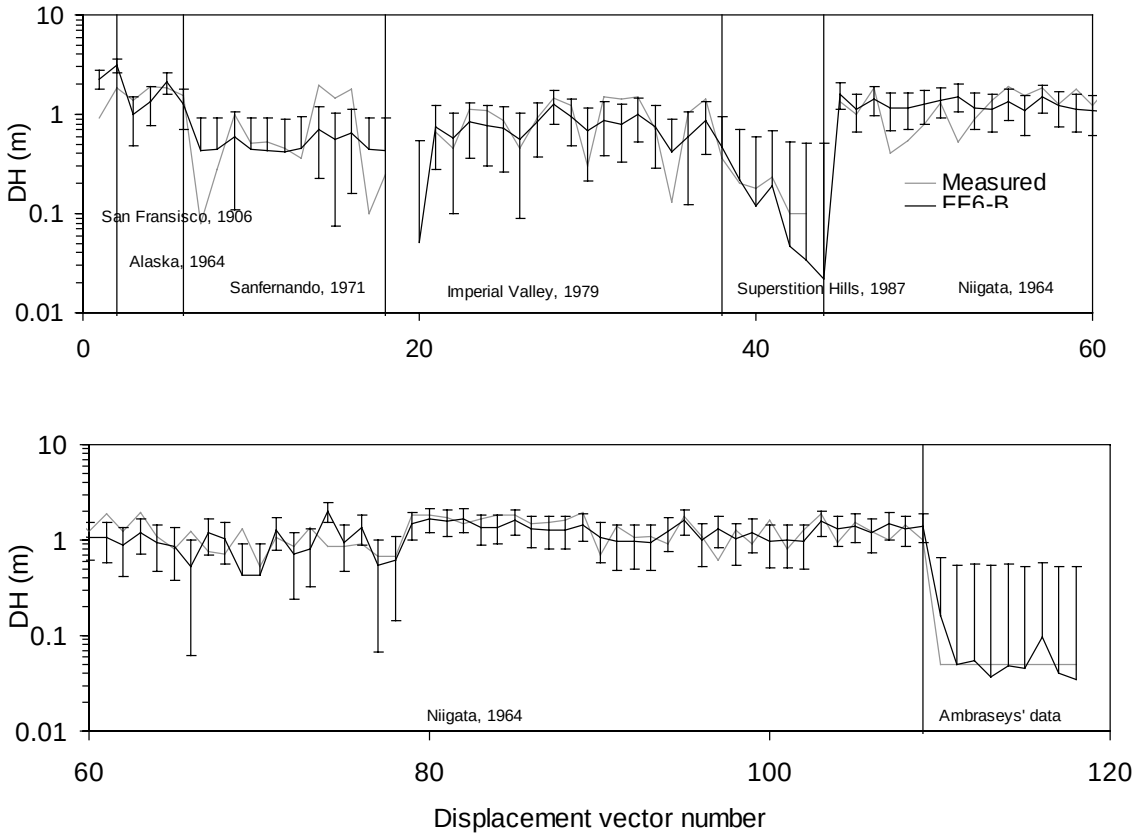

Figure 6-7. Model FF6-B for liquefaction-induced lateral displacement: measured displacement, and predicted mean displacement and confidence interval (95% t-distribution).

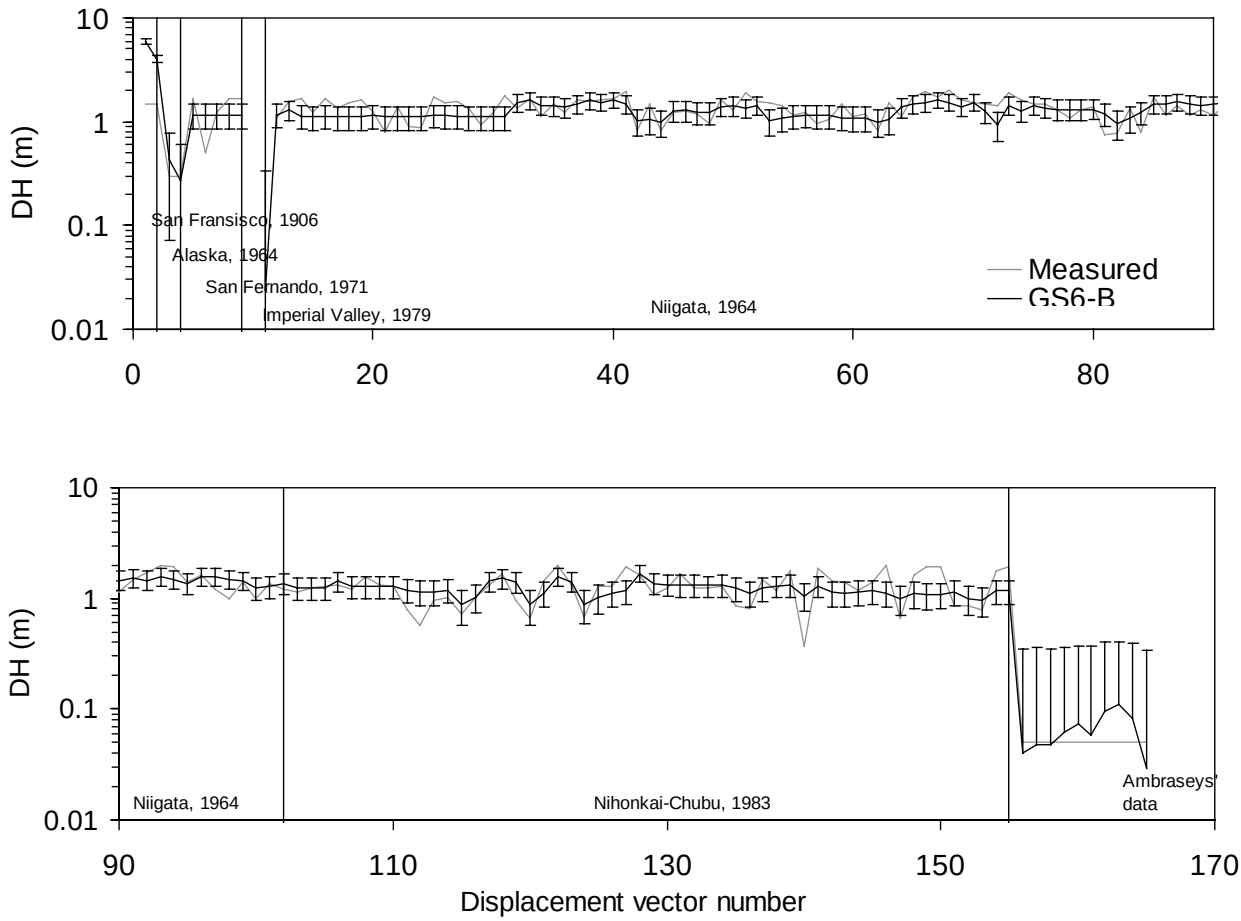

Figure 6-8. Model GS6-B for liquefaction-induced lateral displacement: measured displacement, and predicted mean displacement and confidence interval (95% t-distribution).

6.5 Probability calculation

Equation 14 defines the probabilistic models for assessing the probability of the liquefaction-induced ground deformation to exceed some threshold value D^*, given some local conditions characterized by the parameter values $\mathbf{X}_0$. The value of q should be set equal to 1 for the probability associated to a single event. The calculation of probability at a given site characterized by the parameter values $\mathbf{X}_0$ requires the values of the covariance matrix $\mathbf{C}$, the residual mean square s, the total number n of observations in the regression analysis, the total number p of MLR variables, and the values of the coefficients of the MLR analysis. All the required values are listed in Appendix B. Equation 15 is the Excel implementation of Eq. 14, which permits users to multiply the matrix $\mathbf{C}$ and vector $\mathbf{X}_0$.

Figure 9 shows an example of probability map which was generated by model FFGS6-A for slide G-10 FF' at Niigata, Japan, during 1964 Niigata earthquake. For comparison, Fig. 10 shows the measured displacement vectors in the same area.

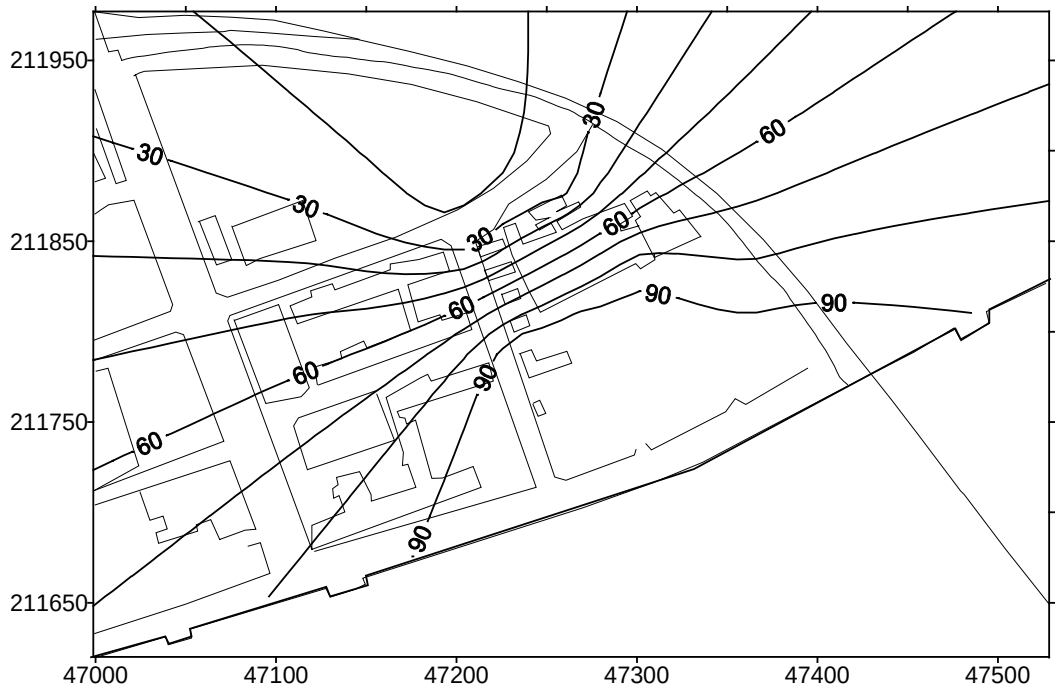

Figure 6-9. Probability of liquefaction-induced lateral spread larger than 2 m for slide G-10 FF' at Niigata, Japan, during 1964 Niigata earthquake (model FFGS6-A).

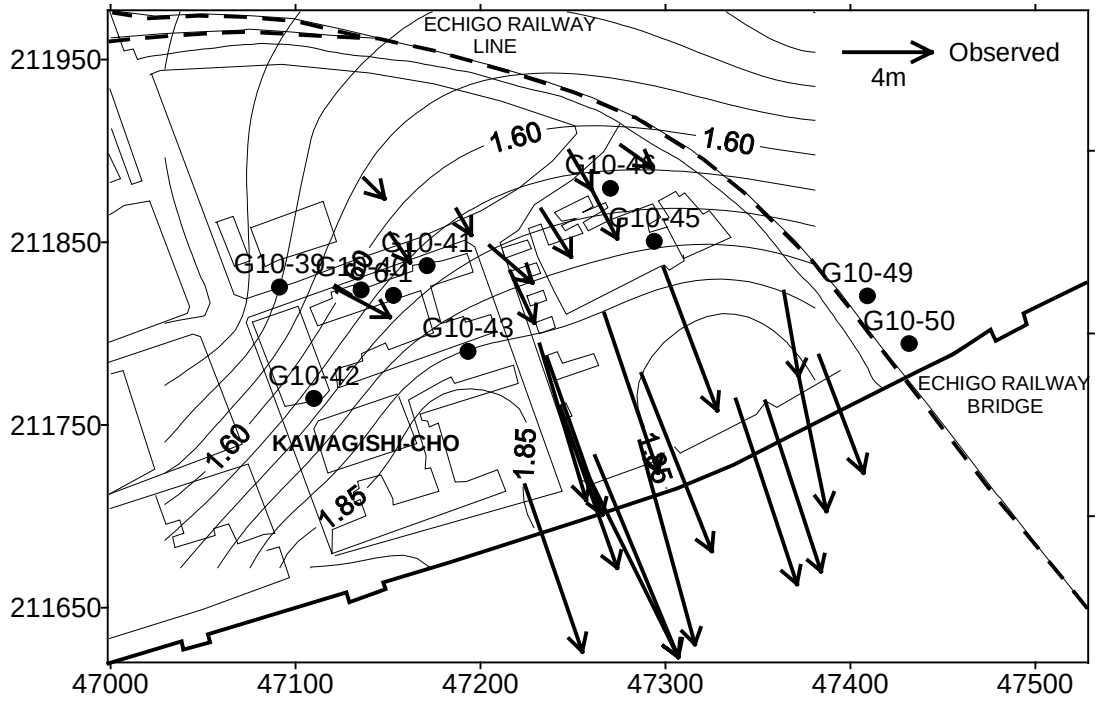

Figure 6-10. Liquefaction-induced displacements measured for slide G-10 FF' during 1964 Niigata, Japan, earthquake.

Mapping the probability of liquefaction-induced displacement amplitudes requires the use of spatial interpolation techniques similar to those used for mapping the predicted mean values of displacement. There are definite uncertainties in extending the probability maps outside the slide areas, which result from the uncertainties of mapping displacement amplitudes, as previously mentioned. Again, there is a need for collecting data outside liquefaction-induced slide area.

6.6 Future work

The MLR and probabilistic models developed in this study are based on a corrected version (Bartlett, 1998) of the database originally collected by Bartlett and Youd (1992). This database was constructed from data collected prior to the 1994 Northridge and 1995 Hyogoken Nanbu earthquakes. The multiple linear regression analyses in this study were based on this database and yielded a MLR model (i.e., FFGS6-A) similar to the original model developed by Bartlett and Youd (1992). There is a need to improve and extend the present database on liquefaction-induced lateral spreads by including the large data sets of high quality which were collected in the vicinity of the Van Norman Complex after the 1994 Northridge earthquake and in Kobe, Japan, after the 1995 Hyogoken Nanbu earthquake. The data should be collected inside and outside the areas where liquefaction-induced displacements were observed to take place. This effort is presently ongoing during the second research phase.

7. CONCLUSION

This report summarizes the findings of the first phase of a long-term research program. It has reviewed the theories and experiments on the mechanisms of liquefaction-induced ground deformation, including past work in the field, laboratory, shaking table tests, centrifuge experiments, and empirical and analytical modeling. Laboratory tests indicate that liquefied soils may deform during and after transient earthquake loadings. The lower amplitude range of liquefaction-induced deformation amplitude correspond mainly to cyclic ratchetting during transient earthquake loading, and is controlled by transient shear stress, number of loading cycles, relative density and stress-dilatancy. The upper amplitude range of liquefaction-induced deformation corresponds to post-liquefaction behavior with a regain of shear strength, which is also induced by a shear strain dependent dilatancy. There are still some disagreements between field observations and experiments in shaking table, centrifuge and laboratory tests about the relative timing of liquefaction-induced ground deformations and earthquake transient ground motions. Analytical models are capable of explaining successfully a few, but not all, aspects of liquefaction-induced deformations. Most of the analytical models require the calibration of numerous parameters for predicting liquefaction-induced deformations, which render them impractical to use over the large areas covered by gas distribution networks. The empirical models calibrated from case histories emerge as the most relevant, immediate and practical approach for predicting liquefaction-induced deformation over large areas.

This report provides some preliminary results and recommendations for estimating (1) the amplitude of liquefaction-induced ground displacement and (2) the probability for liquefaction-induced displacements to exceed some threshold amplitude. The models for assessment of the amplitude and probability of liquefaction-induced ground deformation are based on measured permanent displacements, topographical data, borehole information, and earthquake data prior to the 1994 Northridge and 1995 Hyogoken Nanbu earthquakes. Twelve Multiple Linear Regression (MLR) models have been calibrated from a revised database on liquefaction-induced ground deformations. These MLR models have six and four parameters, respectively, and cover ground-slope and free-face conditions. They have been calibrated from two data sets including all the displacement ranges, and displacements smaller than 2 meters, respectively. As companions to these MLR models, twelve probabilistic models have been proposed for assessing the confidence interval for predicting ground deformation and the probability of exceeding some ground deformation levels. The four-parameter models are recommended for assessing liquefaction-induced ground deformation when only regional geologic data is available. The six-parameter models are to be applied when there is sufficient information from soil boreholes.

Both MLR and probabilistic models are preliminary because they are only based on data collected from earthquakes prior to 1994. The next phase of the research is now focusing on data collection of high-quality case histories of liquefaction-induced ground deformation in the 1994 Northridge and 1995 Hyogoken Nanbu earthquakes. Following the completion of the new database on liquefaction-induced ground deformation, new generations of probabilistic models will be proposed.

8. REFERENCES

1. **Adachi, T., and F. Oka,** 1982, "Constitutive equations for sands and overconsolidated clays and assigned works for sands," *Proceedings of the International Workshop on Constitutive Relations for Soils*, Grenoble, pp. 141-157.

2. **Ambraseys, N. N.,** 1988, "Engineering Seismology," *Earthquake Engineering and Structural Dynamics,* Vol. 17, pp. 1-105.

3. **Arulanandan, K., and R. F. Scott,** 1993-1994, Verification of Numerical procedures for the analysis of soil liquefaction problems," *Proceedings of the International Conference on the Verification of Numerical Procedures for the Analysis of Soil Liquefaction Problems,* Vols. 1 and 2, A. A. Balkema, Rotterdam, the Netherlands.

4. **Arulmoli, K., K. K. Muraleetharan, M. M. Hossain, and L. S. Fruth,** 1992, "VELACS: Verification of Liquefaction Analysis by Centrifuge Studies. Laboratory Testing Program. Soil Data Report," *The Earth Technology Corporation*, Long Beach, CA, report for the National Science Foundation.

5. **Bardet, J. P.,** 1986, "A Bounding Surface Plasticity Model for Sands," *Journal of Engineering Mechanics, ASCE,* Vol. 112, No. 11, pp. 1198 -1217.

6. **Bardet, J. P.,** 1989, "LINOS: a nonlinear finite element program for Geomechanics and Geotechnical Engineering," *University of Southern California, Los Angeles.*

7. **Bardet, J. P.,** 1990, "A Hypoplastic Model for Sand," *Journal of Engineering Mechanics, ASCE,* Vol. 116, No. 9, pp. 1973 -1998.

8. **Bardet, J. P.,** 1995, "A Scaled Memory Model for the Cyclic Behavior of Soils," *Journal of Geotechnical Engineering, ASCE,* Vol. 121, No. 11, pp. 766 - 775.

9. **Bardet, J. P.,** 1995, "A Scaled Memory Model for the Undrained Behavior of Anisotropic Clays," *Journal of Geotechnical Engineering, ASCE,* Vol. 121, No. 1, pp. 755 - 764.

10. **Bardet, J. P., and C. A. Davis,** 1996, " Engineering Observations on Ground Motion At the Van Norman Complex after the 1994 Northridge Earthquake," *Bulletin of the Seismological Society of America,* Vol. 86, No. 1B, pp. S333-S349.

11. **Bardet, J. P., and C. A. Davis,** 1996, . Performance of San Fernando Dams during the 1994 Northridge Earthquake,. *Journal of Geotechnical Engineering,* ASCE, Vol. 122, No. 7, pp. 554-564.

12. **Bardet, J. P., Q. Huang, and S. W. Chi,** 1993, "Numerical Prediction for Model No. 1; Numerical Prediction for Model No. 3; and Numerical Prediction for Model No. 7," *Proceedings of the International Conference on the Verification of Numerical Procedures for the Analysis of Soil Liquefaction Problems,* K. Arulanandan and R. F. Scott eds., A. A. Balkema pub., pp. 67 - 86, 483 - 488, and 829 - 834.

13. **Bartlett, S. F. and T. L. Youd,** 1992, . Empirical analysis of horizontal ground displacement generated by liquefaction-induced lateral spreads,. *Technical report NCEER-92-0021*, National Center for Earthquake Engineering Research, State University of New York, Buffalo, pp. 5-14-15.

14. **Bartlett, S. F.,** 1998, Revised liquefaction-induced database, *Private communication.*

15. **Bartlett, S. F. and T. L. Youd,** 1995, . Empirical prediction of Lateral Spread Displacement,. *Journal of Geotechnical Engineering*, ASCE, Vol. 121, No. 4, pp. 316-329.

16. **Baziar, M. H., R. Dobry, and A. W. M. Elgamal,** 1992, . Engineering evaluation of permanent ground deformation due to seismically-induced liquefaction," Technical report NCEER-92-0007, *National Center for Earthquake Engineering Research*, State University of New York, Buffalo, 2 Vol.

17. **Byrne, P. M.,** 1991, . A model for predicting liquefaction induced displacement," *Proceedings of the second international conference on recent advances in geotechnical earthquake engineering and soil dynamics*, St. Louis, Missouri, Vol. 2, pp. 1027-1035.

18. **Byrne, P. M.,** 1997, . Liquefaction-induced displacements*," NCEER Workshop on Post-liquefaction Ground Deformation*, Presentation Notes, August.

19. **Cao, Y. L., and K. T. Law,** 1992, "Energy dissipation and dynamic behaviour of clay under cyclic loading," *Canadian Geotechnical Journal,* Vol. 29, pp. 103-111.

20. **Dafalias, Y.F., and L. R. Herrmann,** 1982, "Bounding surface formulation of soil plasticity," *Soil Mechanics - Transient and cyclic loads,* G. Pande and O. C. Zienkiewicz, eds., John Wiley and Sons, London, UK., pp. 253-282.

21. **Davis, C., and J. P. Bardet,** 1996, "Performance of two reservoirs during the 1994 Northridge Earthquake," *Journal of Geotechnical Engineering, ASCE,* Vol. 122, No. 8, pp. 613-622.

22. **Dobry, R., Taboada, V., and L. Liu,** 1995, . Centrifuge modeling of liquefaction effects during earthquakes,. *Proceedings of the 1rst International Conference on Earthquake Geotechnical Engineering, IS-Tokyo*, Keynote and Theme lectures, pp. 129-162.

23. **Draper, N. R., and H. Smith**, 1981, *Applied Regression Analysis*, 2nd edition, John Wiley & Sons, New York, p 709.

24. **FLAC,** 1995, "Fast Lagrangian Analysis of Continua," Version 3.3, Itasca Consulting Group Inc, Minneapolis, Minesota.

25. **Hamada, M., H. Sato, T. Kawakami,** 1994, "A consideration for the mechanism for liquefaction-related large ground displacement," *Proceedings of the 5th U.S. Japan Workshop on Earthquake Resistant Design of Lifeline Facilities and Countermeasures for Soil Liquefaction*, NCEER Report 94-0026, T. D. O'Rourke and M. Hamada, Eds., pp. 217-232.

26. **Hamada, M., and K. Wakamatsu,** 1998, “Liquefaction-induced ground displacement triggered by quaywall movement,” *Soils and Foundations, Special Issue Vol. 2, Japanese Geotechnical Society*, pp. 85-96.

27. **Hamada, M., and T. D. O'Rourke**, 1992, "Case histories of liquefaction and lifeline performance during past earthquakes," Technical report NCEER-92-0001, National Center for Earthquake Engineering Research, State University of New York, Buffalo, 2 Vols.

28. **Hamada, M., R. Isoyama. and K. Wakamatsu,** 1996, “Liquefaction-induced ground displacement and its related damage to lifeline facilities," *Soils and Foundations*, Special Issue on Geotechnical Aspects of the January 17 1995 Hyogoken-Nanbu Earthquake, Japanese Geotechnical Society, pp. 81- 97.

29. **Hamada, M., R. Isoyama. and K. Wakamatsu,** 1996, “The 1995 Hyogoken-Nanbu (Kobe) Earthquake, Liquefaction, Ground Displacement and Soil Condition in Hanshin Area,” *Association for Development of Earthquake Prediction*, The School of Science and Engineering, Waseda University, Japan Engineering Consultants.

30. **Hamada, M., S. Yasuda, R. Isoyama, and K. Emoto,** 1986, . Study on Liquefaction induced permanent ground displacement*," Report for the Association for the Development of Earthquake Prediction.*

31. **Harder, L.,** 1991, "Evaluation of Liquefaction Potential Using the SPT," *Seismic Short Course, Evaluation and Mitigation of Earthquake Induced Liquefaction Hazards*, University of Southern California, Los Angeles, February.

32. **Holzer, T. L., J. C. Tinsley, III, M. J. Bennett, and C. S. Mueller,** 1994, . Observed and predicted ground deformation - Miller Farm lateral spread, Watsonville, California, " *Proceedings of the 6th U.S. Japan Workshop on Earthquake Resistant Design of Lifeline Facilities and Countermeasures for Soil Liquefaction*, NCEER, M. Hamada and T. D. O'Rourke, Eds., pp. 79-98.

33. **Holzer, T. L., M. J. Bennett, D. J. Ponti, and J. C. Tinsley, III,** 1998, . Permanent ground deformation in alluvium during the 194 Northridge, California, earthquake," *USGS Open-file report 98-118,* Menlo Park, CA.

34. **Holzer, T. L., M. J. Bennett, J. C. Tinsley, III, D. J. Ponti, and R. V. Sharp,** 1996, "Causes of ground failure in alluvium during the Northridge," California, earthquake of January 17,1994" *Proceedings of the 6th U.S. Japan Workshop on Earthquake Resistant Design of Lifeline Facilities and Countermeasures for Soil Liquefaction*, NCEER, M. Hamada and T. D. O'Rourke, Eds., pp. 345-360.

35. **Ishihara, K.,** 1993, “Liquefaction and flow failure during earthquakes,” The 33rd Rankine lecture, *Geotechnique*, Vol. 43, No. 3, pp. 351 - 415.

36. **Ishihara, K.,** 1996, *Soil Behavior in Earthquake Geotechnics*, Oxford Science Publications, Clarendon Press, Oxford, UK.

37. **Ishihara, K., K. Yoshida, and M. Kato**, 1997, "Characteristics of lateral Spreading in Liquefied Deposits during the 1995 Hanshin-Awaji Earthquake, *Journal of Earthquake Engineerin*g, Vol. 1, No. 1, pp. 23-55.

38. **Ishihara, K., S. Yasuda, and H. Nagase**, 1996, "Soil characteristics and ground damage," Soils and Foundations, *Special Issue on Geotechnical Aspects of the January 17 1995 Hyogoken-Nanbu Earthquake*, Japanese Geotechnical Society, pp. 109-118.

39. **Isoyama , R.,** 1994, "Liquefaction-Induced Ground Failures and Displacements Along the Shiribeshi-toshibetsu River Caused by the 1993 Hokkaido Nansei-oki Earthquake," *Proceedings of the 5th U.S. Japan Workshop on Earthquake Resistant Design of Lifeline Facilities and Countermeasures for Soil Liquefa*ction, NCEER, T. D. O'Rourke and M.. Hamada, Eds., pp. 1-26.

40. **Jibson, R.,** 1994, "Predicting earthquake-induced landslide displacement using Newmark's sliding block analysis," Transportation Research Record 1411, Transportation Research Board, Washington, D.C., pp. 9-17.

41. **Karube, D., and M. Kimura**, 1996, . Damage to Foundation of Railways Structures,. Soils and Foundations, *Special Issue on Geotechnical Aspects of the January 17 1995 Hyogoken Nanbu Earthquake*, Japanese Geotechnical Society, pp. 201-210.

42. **Ko, H.Y.,** 1988, "Summary of the state-of-the-art in centrifuge model testing," *In Centrifuges in Soil Mechanics* (eds Craig, W.H., James, R.G. and Schofield, A.N.), Balkema, Rotterdam, pp. 11-18.

43. **Kokusho, T., K. Watanabe, and T. Sawano,** 1998, "Effect of water film on lateral flow failure of liquefied sand," *Proceedings of the 11th European Conference on Earthquake Engineering*, A. A. Balkema, Rotterdam, The Netherlands, pp. 1-8.

44. **Kramer, S. L.,** 1996, *Geotechnical Earthquake Engineering*, Prentice-Hall, Upper Saddle River, NJ, pp. 451-453.

45. **Law, K. T., and Y. L. Cao,** 1990, "An energy approach for assessing seismic liquefaction potential," *Canadian Geotechnical Journal,* Vol. 27, pp. 320 -329.

46. **Liao, S. S. C.,** 1986, "Statistical modeling of earthquake-induced liquefaction," *Ph.D. Thesis*, Department of Civil Engineering, Massachusetts Institute of Technology, 470 p.

47. **Matsui, T., and K. Oda,** 1996, "Foundation Damage of Structures," *Soils and Foundations, Special Issue on Geotechnical Aspects of the January 17 1995 Hyogoken Nanbu Earthquake*, Japanese Geotechnical Society, pp. 189-200.

48. **Microsoft Excel,** 1994, *Microsoft Excel, Version 5.0*, Microsoft Corporation.

49. **Minitab,** 1989, *Minitab Statistical Software, Release 7*, Minitab Inc., 3081 Enterprise Drive, State College, PA 16801.

50. **Nakase, H., A. Hiro-oka, and T. Yanagihata,** 1997, "Deformation characteristics of liquefied loose sand by triaxial compression tests," *Proceedings of IS-Nagoya 97, Deformation and Progressive Failure in Geomechanics*, A. Asaoka, T. Adachi, and F. Oka, eds., Pergamon, Elsevier Science, pp. 559-564.

51. **Newmark, N. M.,** 1965, "Effects of Earthquakes on Embankments and Dams," *Géotechnique,* 15, No.2, pp.139-160.

52. **O'Rourke, T. D., and P. A. Lane,** 1989, . Liquefaction hazards and their effects on buried pipelines,. Technical report NCEER-89-0007, National Center for Earthquake Engineering Research, State University of New York, Buffalo.

53. **Para-Colmenares, E. J.,** 1996, "Numerical modeling of liquefaction and lateral ground deformation including cyclic mobility and dilation response in soil systems," *Ph.D. Thesis,* Rensselaer Polytechnic Institute, Troy, NY.

54. **Pastor, M., O. C. Zienkiewicz, and K. H. Leung**, 1985, "Simple model for transient soil loading in earthquake analysis," *International Journal of Analytical Numerical Methods in Geomechanics,* Vol. 9, pp. 453-498.

55. **Pease, J. W., and T. D. O'Rourke,** 1993, . Liquefaction Hazards in the Mission District and South of Market Stress Areas, San Francisco, California," *U.S. Geological Survey*, External Contract No. 14-08-001-G2128.

56. **Peiris, T. A. and Yoshida, N.,** 1995, "Dilatancy characteristics of sand under cyclic loading," *Proc. Of First International Conference on Earthquake Geotechnical Engineering*, Tokyo, pp. 265-270.

57. **Peiris, T. A. and Yoshida, N.,** 1996, "Modeling of Volume Change Characteristics of Sand under Cyclic Loading*," Proc. of Eleventh World Conference on Earthquake Engineering*, Acapulco, Mexico, Paper No. 1087.

58. **Robertson, P. K., and R. G. Campanella,** 1985, Liquefaction Potential of Sands Using the Cone Penetration Test*," Journal of Geotechnical Engineering*, ASCE, Vol. 111, No. 3, pp. 298-307.

59. **Rauch, A. F.,** 1997, EPOLLS: An empirical method for predicting surface displacement due to liquefaction-induced lateral spreading in earthquakes, *PhD thesis*, Virginia Polytechnic Institute, Virginia.

60. **Sasaki, Y., I. Towahata, K. Tokida, K. Yamada, H. Matsumoto, Y. Tamari, and S. Saya,** 1992, "Mechanism of permanent displacement of ground caused by seismic liquefaction," *Soils and Foundations*, Vol. 32, No. 3, pp. 76-96.

61. **Scott, R.F., and B. Hushmand, 1995,** . Piezometer performance at Wildlife liquefaction site, California," Journal of Geotechnical Engineering Division, ASCE, Discussion, Vol. 121, No. 12, pp. 912-919.

62. **Seed, H. B., and P. De Alba,** 1986, “Use of SPT and CPT Tests for evaluating the liquefaction resistance of sands," *Use of In-Situ Tests in Geotechnical Engineering*, ASCE, Geotechnical Special Publication No. 6, pp. 281-302.

63. **Seed, H. B., and I. M. Idriss,** 1971, “Simplified procedure for evaluating soil liquefaction potential,” *Journal of the Soil Mechanics and Foundation Division, ASCE,* Vol. 97, No. 9, pp. 1249-1274.

64. **Seed, H. B., Tokimatsu, F. K., Harder, L. F. and R. M. Chung,** 1985, "Influence of SPT Procedures in Soil Liquefaction Resistance Evaluation," *Journal of Geotechnical Engineering Division*, ASCE, No. 12, pp. 1425-1445.

65. **Shamoto, Y. J.-M. Zhang, and S. Goto,** 1997, "Mechanism of large Post-Liquefaction Deformation in Saturated sand," *Soils and Foundations*, *Japanese Geotechnical Society*, Vol. 37, No. 2, pp. 71-80.

66. **Shamoto, Y., J.-M. Zhang, and K. Tokimatsu**, 1997, "New charts for predicting large residual post-liquefaction ground deformation," Extended abstract for *the 8th International Conference on Soil Dynamics and Earthquake Engineering* (SDEE-97), 2 p.

67. **Shamoto, Y., J.-M. Zhang, and K. Tokimatsu**, 1998, "Methods for evaluating residual post-liquefaction ground settlement and horizontal displacement," *Soils and Foundations, Special Issue Vol. 2, Japanese Geotechnical Society*, pp. 69-84.

68. **Smith, I. M.,** 1994, “An overview of numerical procedures used in the VELACS project,” *Proceedings of the international conference on the Verification of Numerical Procedures for the Analysis of Soil Liquefaction Problems*, Vol. 2, K. Arulanandan and R. F. Scott, eds., A. A. Balkema, Rotterdam, pp. 1321 - 1337.

69. **Stokoe, K. H. II, J. M. Roesset, J. G. Biecherwale, and M. Aoouad,** 1988, "Liquefaction potential of sands from shear wave velocity," *Proceedings of the 9th world conference on earthquake engineering,* Tokyo, Japan, Vol. III, pp. 213-218.

70. **Surfer**, 1998, *Surfer for Windows, User’s guide, Version 6*, Golden Software, Inc., Golden, Colorado.

71. **Taguchi, Y., A. Tateishi, F. Oka, and A. Yashima,** 1995, "A cyclic elasto-plastic model for sand based on the generalized flow rule and its application," *Proceedings of the 5th International Symposium on Numerical Methods in Geomechanics*, Davos, pp. 57-62.

72. **Tokimatsu, K., and H. B. Seed,** 1987, "Evaluation of settlements in sand due to earthquake shaking,” *Journal of Geotechnical Engineering, ASCE,* Vol. 113, No. 8, pp. 861-878.

73. **Tokimatsu, K., H. Mizumo, and M. Kakurai**, 1996, "Building Damage Associated with Geotechnical Problems," *Soils and Foundations*, *Special Issue on Geotechnical Aspects of the January 17 1995 Hyogoken-Nanbu Earthquake*, Japanese Geotechnical Society, pp. 219-234.

74. **Towhata, I., H. Toyota, and W. M. Vargas,** 1995**,** "Dynamics in lateral flow of liquefied ground," *Proceedings of the 10th Asian Regional Conference on Soil Mechanics and Foundation Engineering, Beijing,* Vol. 2, pp. 245-247.

75. **Towhata, I., H. Toyota, and W. M. Vargas,** 1996**,** "A transient study on lateral flow on liquefied ground," *Proceedings of the 7th International Symposium on Landslides,* Trondheim, Norway, A. A. Balkema, The Netherlands, Vol. 2, pp. 1047-1054.

76. **Towhata, I., R. P. Orense, and H. Toyota,** 1997**,** . Mathematical principles in prediction of lateral ground displacement induced by seismic liquefaction," *Soils and Foundations,* Accepted for publication.

77. **Orense, R. P., and I. Towhata,** 1996**,** . Three-dimensional analysis on lateral displacement of liquefied subsoil," *Soils and Foundations,* Accepted for publication.

78. **Towhata, I., Y. Kogai, K. Amimoto, and H. G. Putra,** 1996, . Theory and model tests on mitigation measures against lateral flow of liquefied ground," *Proceedings of the 6th U.S. Japan Workshop on Earthquake Resistant Design of Lifeline Facilities and Countermeasures for Soil Liquefaction*, NCEER, M. Hamada and T. D. O'Rourke, Eds., pp. 403-419.

79. **Towhata, I., Y. Kogai, K. Amimoto, and H. G. Putra,** 1996, . Mitigation of lateral flow of liquefied ground," *Proceedings of the 28th Joint Meeting, Panels for Earthquake Engineering and Wind Engineering*, UJNR, Gaithersburg, Maryland, US, pp. 39-51.

80. **Yashima, A., F. Oka, J. M. Konrad, R. Uzuoka, and Y. Taguchi,** 1997, "Analysis of a progressive flow failure in an embankment of compacted fill," *Proceedings of IS-Nagoya, A.* Asaoka, T. Adachi, and F. Oka, eds., *Pergamon,* pp. 599-604.

81. **Yasuda, S., K. Ishihara, and S. Iai,** 1997, "A simple procedure to predict ground flow due to liquefaction behind quaywalls," *Extended abstract for the 8th International Conference on Soil Dynamics and Earthquake Engineering* (SDEE-97), 2 p.

82. **Yasuda, S., Masuda, T., Yoshida, N., Kiku, H., Itafuji, S., Mine, K. and Sato, K.,** 1994, "Torsional shear and triaxial compression tests on deformation characteristics of sands before and after liquefaction," *Proc., 5th U.S.-Japan Workshop on Earthquake Resistant Design of Lifeline Facilities and Countermeasures Against Soil Liquefaction*, Salt Lake City, Technical Report NCEER-94-0026, National Center for Earthquake Engineering Research, U.S.A., pp. 249-266.

83. **Yegian, M. K., E. A. Marciano, and V. G. Gharaman,** 1991, "Earthquake-induced permanent deformation: probabilistic approach," *Journal of Geotechnical Engineering, ASCE,* Vol. 117, No. 1, pp. 35-50.

84. **Yoshida, N.,** 1994, "Applicability of conventional computer code SHAKE to nonlinear problem," *Proceedings of the Symposium on Amplification of Ground Shaking in Soft Ground,* JSSMFE, pp.14-31 (in Japanese).

85. **Yoshida, N.,** 1996, "Initial Stress Effect on Response of Level Ground," *Eleventh World Conference on Earthquake Engineering,* Acapulco, Mexico, Paper No. 102.3.

86. **Yoshida, N., Tsujino, S. and Inadomaru,K.,** 1995, "Preliminary study on the settlement of ground after liquefaction," *Proc., The 29th Japan National Conference of Soil Mechanics and Foundation Engineering*, pp.859-860 (in Japanese).

87. **Youd, T. L., and D. M. Perkins,** 1987, . Mapping of Liquefaction Severity Index,. *Journal of Geotechnical Engineering Division*, ASCE, No. 11, pp. 1374-1392.

88. **Youd, T. L., and I. M. Idriss,** 1998, *Proceedings of NCEER workshop on evaluation of liquefaction resistance of soils*, National Center for Earthquake Engineering Research, State University of New York, Buffalo.

89. **Youd, T. L., and S. J. Kiehl,** 1996, "Ground deformation characteristics caused by lateral spreading during the 1995 Hanshin-Awaji earthquake," *Proceedings of the 6th U.S. Japan Workshop on Earthquake Resistant Design of Lifeline Facilities and Countermeasures for Soil Liquefaction*, NCEER, M. Hamada and T. D. O'Rourke, Eds., pp. 221-242.

90. **Youd, T. L., and T. L. Holzer,** 1994, "Piezometer performance at Wildlife liquefaction site, California," Journal of Geotechnical Engineering Division, ASCE, Vol. 120, No. 6.

91. **Youd, T. L., E. L. Harp, D. K. Keefer, and R. C. Wilson,** 1985, "The Borah peak, Idaho earthquake of October 28, 1983 - liquefaction," Earthquake Spectra, Vol. 2, No. 6.

92. **Zienkiewicz, O. C. and T. Shiomi,** 1984, "Dynamic behavior of saturated porous media: the generalized Biot formulation and its numerical solution," *International Journal of Numerical and Analytical Methods in Geomechanics*, Vol. 8, pp. 71-96.

93. **Zienkiewicz, O. C., A. H. C. Chan, M. Pastor, D. K. Paul, and T. Shiomi,** 1990, "Static and dynamic behavior of soils: a rational approach to quantitative solutions: Part I-fully saturated problems," *Proc. Roy. Soc. A.,* 429, pp. 285-309.

APPENDIX A: LIQUEFACTION DATABASES

The following databases have been used in the course of this research:

- Database of liquefaction occurrence (Harder, 1991).
- Database of liquefaction-induced ground deformation (Bartlett and Youd, 1992).
- Database of liquefaction-induced ground deformation (Bartlett, 1998).

All these databases are available as EXCEL files from http://rccg03.usc.edu/gees/

APPENDIX B: COEFFICIENTS FOR MLR AND PROBALISTIC MODELS

Appendix B provides the values of the coefficients required for calculating (1) MLR mean values of liquefaction-induced ground displacement, (2) confidence intervals on predicted displacement, and (3) probability of exceeding some amplitude of liquefaction-induced ground deformation. There is a total of twelve probabilistic models corresponding to the twelve MLR models FFGS6-A, FF6-A, GS6-A, FFGS6-B, FF6-B, GS6-B, FFGS4-A, FF4-A, GS4-A, FFGS4-B, FF4-B, and GS4-B. The model variables are defined by the vector **X**, as introduced in Chapter 6. Appendix B provides for each model the MLR coefficients, the covariance matrix **C**, the total number *n* of observations, the total number *p* of degrees of freedom, and the residual mean square s^2.

Table B1. Values of coefficients for MLR and probabilistic models FFGS6-A.

Components of **X**									
1.0	*0 or 1*	M_w	*LOG(R)*	*R*	*LOG(W_{ff})*	*LOG(S)*	*LOG(T_{15})*	*LOG(100-F_{15})*	*D50$_{15}$*
MLR coefficients									
b_0	b_{off}	b_1	b_2	b_3	b_4	b_5	b_6	b_7	b_8
-14.551	-0.483	1.096	-0.873	-0.014	0.634	0.275	0.494	4.053	-0.814
Covariance matrix **C** (symmetric)									
0.001	0.000	0.002	0.000	0.000	-0.001	0.000	0.000	-0.007	0.001
	0.047	0.002	0.000	0.000	-0.040	-0.011	-0.005	-0.011	0.001
		0.029	0.000	-0.001	-0.004	0.004	0.000	-0.104	-0.005
			0.026	-0.001	0.005	-0.003	-0.005	-0.007	-0.014
				0.000	0.000	0.000	0.000	0.002	-0.001
					0.047	0.000	0.000	0.011	0.007
						0.045	0.011	-0.011	0.000
Number of observations (n) = 467							0.022	-0.003	-0.004
Number of degrees of freedom (p) = 9								0.386	0.005
Residual mean square (s^2) = 0.046									0.196

Table B2. Values of coefficients for MLR and probabilistic models FF6-A.

Components of **X**							
1.0	M_w	*LOG(R)*	*R*	*LOG(W_{ff})*	*LOG(T_{15})*	*LOG(100-F_{15})*	*D50$_{15}$*
MLR coefficients							
b_0	b_1	b_2	b_3	b_4	b_6	b_7	b_8
-17.372	1.248	-0.923	-0.014	0.685	0.300	4.826	-1.091
Covariance matrix **C** (symmetric)							
11.171	-0.701	0.720	-0.008	-0.204	0.260	-3.712	1.371
	0.084	-0.050	0.000	0.006	-0.015	0.097	-0.113
		0.088	-0.001	0.000	0.005	-0.233	0.078
			0.000	0.000	0.000	0.004	-0.002
				0.052	-0.005	0.068	-0.003
Number of observations (n) = 213					0.049	-0.102	0.017
Number of degrees of freedom (p) = 7						1.727	-0.383
Residual mean square (s^2) = 0.058							0.466

Table B3. Values of coefficients for MLR and probabilistic models GS6-A.

Components of **X**							
1.0	M_w	*LOG(R)*	*R*	*LOG(S)*	*LOG(T_{15})*	*LOG(100-F_{15})*	*D50$_{15}$*
MLR coefficients							
b_0	b_1	b_2	b_3	b_5	b_6	b_7	b_8
-14.152	0.988	-1.049	-0.011	0.318	0.619	4.287	-0.705
Covariance matrix **C** (symmetric)							
12.655	-0.528	1.218	-0.015	0.173	-0.121	-5.293	1.635
	0.097	-0.030	-0.001	0.005	0.006	-0.068	-0.048
		0.209	-0.003	0.022	-0.014	-0.625	0.115
			0.000	0.000	0.000	0.012	-0.004
				0.058	0.025	-0.130	0.045
Number of observations (n) = 254					0.052	0.030	-0.003
Number of degrees of freedom (p) = 7						3.362	-0.819
Residual mean square (s^2) = 0.028							0.841

Table B4. Values of coefficients for MLR and probabilistic models FFGS6-B.

Components of **X**									
1.0	*0 or 1*	M_w	*LOG(R)*	*R*	*LOG(W_{ff})*	*LOG(S)*	*LOG(T_{15})*	*LOG(100-F_{15})*	*D50$_{15}$*
MLR coefficients									
b_0	b_{off}	b_1	b_2	b_3	b_4	b_5	b_6	b_7	b_8
-13.261	-0.261	1.050	-0.778	-0.013	0.370	0.106	0.270	3.481	-0.715
Covariance matrix **C** (symmetric)									
6.232	0.070	-0.359	0.429	-0.004	-0.248	0.082	0.000	-2.169	0.776
	0.081	-0.003	0.004	0.000	-0.076	-0.029	-0.016	-0.034	0.005
		0.053	-0.024	0.000	0.011	-0.003	0.000	0.009	-0.065
			0.064	-0.001	-0.010	0.007	-0.001	-0.165	0.037
				0.000	0.000	0.000	0.000	0.003	-0.001
					0.104	0.004	0.011	0.095	-0.016
						0.085	0.020	-0.032	0.014
Number of observations (n) = 467							0.035	-0.007	-0.004
Number of degrees of freedom (p) = 9								1.183	-0.211
Residual mean square (s^2) = 0.046									0.320

Table B5. Values of coefficients for MLR and probabilistic models FF6-B.

Components of **X**							
1.0	M_w	*LOG(R)*	*R*	*LOG(W_{ff})*	*LOG(T_{15})*	*LOG(100-F_{15})*	*D50*$_{15}$
MLR coefficients							
b_0	b_1	b_2	b_3	b_4	b_6	b_7	b_8
-15.067	1.130	-0.738	-0.012	0.396	0.135	4.032	-0.908
Covariance matrix **C** (symmetric)							
15.080	-0.854	0.795	-0.004	-0.690	0.130	-5.121	1.706
	0.094	-0.054	0.000	0.029	-0.007	0.135	-0.131
		0.106	-0.002	-0.014	0.004	-0.265	0.082
			0.000	-0.001	0.000	0.003	-0.001
				0.132	0.014	0.220	-0.042
Number of observations (n) = 118					0.063	-0.071	0.005
Number of degrees of freedom (p) = 7						2.309	-0.486
Residual mean square (s^2) = 0.054							0.518

Table B6. Values of coefficients for MLR and probabilistic models GS6-B.

Components of **X**							
1.0	M_w	*LOG(R)*	*R*	*LOG(S)*	*LOG(T_{15})*	*LOG(100-F_{15})*	*D50*$_{15}$
MLR coefficients							
b_0	b_1	b_2	b_3	b_5	b_6	b_7	b_8
-14.212	0.800	-1.198	-0.006	0.071	0.373	5.090	-0.704
Covariance matrix **C** (symmetric)							
13.595	-0.359	1.381	-0.019	0.199	-0.121	-6.501	1.778
	0.187	0.031	-0.002	0.022	0.011	-0.513	-0.100
		0.255	-0.004	0.041	-0.006	-0.955	0.103
			0.000	-0.001	0.000	0.021	-0.003
				0.118	0.055	-0.217	0.067
Number of observations (n) = 165					0.089	0.000	0.001
Number of degrees of freedom (p) = 7						5.780	-0.717
Residual mean square (s^2) = 0.021							1.017

Table B7. Values of coefficients for MLR and probabilistic models FFGS4-A.

Components of **X**							
1.0	*0 or 1*	M_w	*LOG(R)*	*R*	*LOG(W_{ff})*	*LOG(S)*	*LOG(T_{15})*
MLR coefficients							
b_0	b_{off}	b_1	b_2	b_3	b_4	b_5	b_6
-6.815	-0.465	1.017	-0.278	-0.026	0.497	0.454	0.558
Covariance matrix **C** (symmetric)							
0.0005	0.0001	0.0000	0.0001	0.0000	-0.0004	0.0000	0.0000
	0.0465	-0.0008	-0.0003	0.0001	-0.0399	-0.0113	-0.0051
		0.0006	-0.0023	0.0000	-0.0004	0.0006	-0.0012
			0.0247	-0.0005	0.0061	-0.0027	-0.0056
				0.0000	-0.0002	0.0001	0.0001
					0.0468	0.0000	-0.0002
						0.0443	0.0106
							0.0223

Number of observations (n) = 467

Number of degrees of freedom (p) = 7

Residual mean square (s^2) = 0.084

Table B8. Values of coefficients for MLR and probabilistic models FF4-A.

Components of **X**					
1.0	M_w	*LOG(R)*	*R*	*LOG(W_{ff})*	*LOG(T_{15})*
MLR coefficients					
b_0	b_1	b_2	b_3	b_4	b_6
-6.968	0.972	-0.271	-0.027	0.497	0.584
Covariance matrix **C** (symmetric)					
2.403	-0.362	0.183	0.003	-0.075	0.050
	0.056	-0.031	0.000	0.005	-0.011
		0.055	-0.001	0.008	-0.008
			0.000	0.000	0.000
				0.049	-0.001
					0.043

Number of observations (n) = 213

Number of degrees of freedom (p) = 5

Residual mean square (s^2) = 0.123

Table B9. Values of coefficients for MLR and probabilistic models GS4-A.

Components of **X**					
1.0	M_w	*LOG(R)*	*R*	*LOG(S)*	*LOG(T_{15})*
MLR coefficients					
b_0	b_1	b_2	b_3	b_5	b_6
-7.586	1.109	-0.233	-0.025	0.477	0.579
Covariance matrix **C** (symmetric)					
4.137	-0.600	0.255	0.004	-0.039	-0.076
	0.089	-0.046	-0.001	0.004	0.007
		0.091	-0.001	-0.001	-0.009
			0.000	0.000	0.000
				0.052	0.026
Number of observations (n) =			254		0.051
Number of degrees of freedom (p) =			5		
Residual mean square (s^2) =			0.051		

Table B10. Values of coefficients for MLR and probabilistic models FFGS4-B.

Components of **X**							
1.0	*0 or 1*	M_w	*LOG(R)*	*R*	*LOG(W_{ff})*	*LOG(S)*	*LOG(T_{15})*
MLR coefficients							
b_0	b_{off}	b_1	b_2	b_3	b_4	b_5	b_6
-6.747	-0.162	1.001	-0.289	-0.021	0.090	0.203	0.289
Covariance matrix **C** (symmetric)							
1.718	0.009	-0.254	0.115	0.002	-0.076	0.012	-0.005
	0.080	-0.003	0.000	0.000	-0.073	-0.030	-0.016
		0.038	-0.021	0.000	0.011	0.000	-0.001
			0.041	0.000	0.003	0.002	-0.002
				0.000	-0.001	0.000	0.000
Number of observations (n) =	283				0.096	0.006	0.011
Number of degrees of freedom (p) =	7					0.084	0.020
Residual mean square (s^2) =	0.079						0.035

Table B11. Values of coefficients for MLR and probabilistic models FF4-B.

Components of **X**					
1.0	M_w	$LOG(R)$	R	$LOG(W_{ff})$	$LOG(T_{15})$
MLR coefficients					
b_0	b_1	b_2	b_3	b_4	b_6
-6.034	0.880	-0.271	-0.018	0.013	0.257
Covariance matrix **C** (symmetric)					
2.770	-0.398	0.167	0.005	-0.209	-0.011
	0.060	-0.031	-0.001	0.017	-0.005
		0.073	-0.001	0.011	-0.003
			0.000	-0.001	0.000
				0.111	0.020
					0.061

Number of observations (n) = 118

Number of degrees of freedom (p) = 5

Residual mean square (s^2) = 0.116

Table B12. Values of coefficients for MLR and probabilistic models GS4-B.

Components of **X**					
1.0	M_w	$LOG(R)$	R	$LOG(S)$	$LOG(T_{15})$
MLR coefficients					
b_0	b_1	b_2	b_3	b_5	b_6
-8.410	1.239	-0.358	-0.024	0.266	0.373
Covariance matrix **C** (symmetric)					
5.264	-0.765	0.324	0.005	-0.088	-0.121
	0.113	-0.057	-0.001	0.010	0.012
		0.097	-0.001	0.005	-0.006
			0.000	0.000	0.000
				0.108	0.055
					0.089

Number of observations (n) = 165

Number of degrees of freedom (p) = 5

Residual mean square (s^2) = 0.049

APPENDIX C: OUTPUTS OF MINITAB REGRESSION ANALYSES

Appendix C contains the outputs of Minitab regression analyses of:

- the Bartlett and Youd (1992) model calibrated from the original database of Bartlett and Youd (1992), and

- the twelve MLR models developed in this study from the corrected database of Bartlett (1998) including data sets A and B.

Minitab regression analysis from the original database by Bartlett and Youd (1992)

```
MTB > Regress 'log(Dh)' 9 'B0ff' 'M' 'log R' 'R' 'log Wff' 'log Sgs'  &
CONT>     'log T15' 'log (100-F15)' 'D5015';
SUBC>   Constant.

Regression Analysis


The regression equation is
log(Dh) = - 15.8 - 0.579 B0ff + 1.18 M - 0.927 log R - 0.0133 R + 0.657 log Wff
           + 0.429 log Sgs + 0.348 log T15 + 4.53 log (100-F15) - 0.922 D5015

Predictor       Coef       Stdev    t-ratio        p
Constant    -15.7869      0.4752     -33.22    0.000
B0off        -0.57883     0.04504     -12.85    0.000
M             1.17817     0.04274      27.57    0.000
log R        -0.92745     0.04819     -19.24    0.000
R           -0.013289    0.001231     -10.79    0.000
log Wff       0.65716     0.04570      14.38    0.000
log Sgs       0.42932     0.04484       9.57    0.000
log T15       0.34834     0.03140      11.09    0.000
log (100-F15) 4.5270      0.2005       22.58    0.000
D5015        -0.9223      0.1092       -8.45    0.000

s = 0.2086      R-sq = 82.6%     R-sq(adj) = 82.3%

Analysis of Variance

SOURCE       DF          SS          MS         F        p
Regression    9      94.633      10.515    241.75    0.000
Error       457      19.877       0.043
Total       466     114.510

SOURCE       DF      SEQ SS
B0off         1       0.477
M             1      11.604
log R         1      13.880
R             1      28.419
log Wff       1       5.538
log Sgs       1       4.681
log T15       1       7.841
log (100      1      19.087
D5015         1       3.105

Unusual Observations
Obs.     B0off    log(Dh)        Fit  Stdev.Fit   Residual    St.Resid
  1      1.00   -0.03621    0.43331    0.04353   -0.46952      -2.30R
```

2	0.00	0.17898	1.16221	0.03632	-0.98323	-4.79R
3	0.00	0.17898	0.99454	0.02609	-0.81556	-3.94R
4	1.00	0.26482	0.74533	0.03425	-0.48051	-2.34R
5	1.00	0.13988	0.05827	0.07990	0.08161	0.42 X
6	1.00	0.28330	0.17724	0.10318	0.10606	0.59 X
7	1.00	0.26951	0.47337	0.10022	-0.20386	-1.11 X
8	1.00	0.19866	0.20391	0.11030	-0.00525	-0.03 X
9	0.00	-0.50864	-0.40477	0.08985	-0.10387	-0.55 X
10	0.00	-0.50864	-0.52308	0.08487	0.01444	0.08 X
11	0.00	0.38917	0.34106	0.09785	0.04811	0.26 X
12	1.00	-1.04576	-0.08656	0.03592	-0.95920	-4.67R
13	1.00	-0.53760	-0.07156	0.03604	-0.46604	-2.27R
33	1.00	-0.95861	-0.08889	0.03378	-0.86972	-4.23R
34	1.00	-0.58503	-0.11530	0.03467	-0.46973	-2.28R
35	0.00	0.22789	-0.17577	0.05433	0.40366	2.00RX
36	0.00	-0.28400	-0.17577	0.05433	-0.10823	-0.54 X
37	0.00	0.08991	-0.17577	0.05433	0.26568	1.32 X
38	0.00	0.22789	-0.17577	0.05433	0.40366	2.00RX
39	0.00	0.22789	-0.17577	0.05433	0.40366	2.00RX
40	0.00	-2.00000	-2.22700	0.08273	0.22700	1.19 X
41	0.00	-2.00000	-1.42365	0.05572	-0.57635	-2.87RX
42	1.00	-2.00000	-2.56716	0.09161	0.56716	3.03RX
43	1.00	-2.00000	-1.20942	0.05097	-0.79058	-3.91R
55	1.00	-0.50864	-0.03466	0.02983	-0.47398	-2.30R
68	1.00	-0.85387	-0.28663	0.02810	-0.56724	-2.74R
76	1.00	-0.95861	-1.37847	0.05107	0.41986	2.08R
77	1.00	-2.00000	-1.54092	0.04939	-0.45908	-2.27R
83	1.00	-0.37675	0.17807	0.02442	-0.55482	-2.68R
84	1.00	-0.25181	0.18622	0.02417	-0.43803	-2.11R
88	1.00	-0.27572	0.32843	0.01904	-0.60415	-2.91R
141	1.00	0.09691	-0.34849	0.03532	0.44540	2.17R
144	1.00	0.12057	-0.49544	0.04114	0.61601	3.01R
148	1.00	0.13988	-0.29365	0.04561	0.43353	2.13R
149	1.00	-0.05552	0.35686	0.04815	-0.41238	-2.03R
432	0.00	-0.14267	0.27199	0.02443	-0.41466	-2.00R
449	1.00	-1.22185	-0.74737	0.05403	-0.47448	-2.36RX
450	0.00	-1.22185	-1.33730	0.05470	0.11545	0.57 X
451	1.00	-1.22185	-1.21864	0.05780	-0.00321	-0.02 X
452	1.00	-1.22185	-1.19877	0.06710	-0.02308	-0.12 X
453	0.00	-1.22185	-1.24779	0.06019	0.02594	0.13 X
456	1.00	-1.22185	-1.34545	0.06456	0.12360	0.62 X
458	0.00	-1.22185	-1.12997	0.05941	-0.09188	-0.46 X
459	1.00	-1.22185	-1.25156	0.07015	0.02971	0.15 X

R denotes an obs. with a large st. resid.
X denotes an obs. whose X value gives it large influence.

Minitab regression analysis for FFGS6-A model

```
The regression equation is
LOG(Dhc+ = - 14.6 - 0.483 B0ff + 1.10 M - 0.873 log R - 0.0140 R
           + 0.635 log Wff + 0.276 log Sgs + 0.494 log T15 + 4.05 Log(100-F15)- 0.814 D5015

Predictor       Coef       Stdev    t-ratio        p
Constant    -14.5511      0.4871     -29.87    0.000
B0ff        -0.48266     0.04618     -10.45    0.000
M            1.09594     0.04382      25.01    0.000
log R       -0.87266     0.04941     -17.66    0.000
R          -0.014013    0.001263     -11.10    0.000
log Wff      0.63455     0.04685      13.54    0.000
log Sgs      0.27569     0.04597       6.00    0.000
log T15      0.49438     0.03219      15.36    0.000
Log(F15       4.0527      0.2056      19.71    0.000
D5015        -0.8141      0.1119      -7.27    0.000

s = 0.2138      R-sq = 81.0%     R-sq(adj) = 80.6%

Analysis of Variance

SOURCE       DF          SS          MS         F        p
Regression    9     88.9562      9.8840    216.21    0.000
Error       457     20.8919      0.0457
Total       466    109.8481

SOURCE       DF      SEQ SS
B0ff          1      0.0239
M             1      9.3503
log R         1     13.0621
R             1     28.5023
log Wff       1      5.4340
log Sgs       1      0.8981
log T15       1     13.8932
Log(F15       1     15.3734
D5015         1      2.4189

Unusual Observations
Obs.     B0ff   LOG(Dhc+        Fit  Stdev.Fit   Residual    St.Resid
  2      0.00    0.17900    1.02157    0.03724   -0.84257      -4.00R
  3      0.00    0.17900    0.86004    0.02675   -0.68104      -3.21R
  4      1.00    0.26500    0.71380    0.03511   -0.44880      -2.13R
  5      1.00    0.14000   -0.01138    0.08191    0.15138       0.77 X
  6      1.00    0.28300    0.12139    0.10578    0.16161       0.87 X
  7      1.00    0.27000    0.39488    0.10275   -0.12488      -0.67 X
  8      1.00    0.19900    0.15536    0.11308    0.04364       0.24 X
  9      0.00   -0.50900   -0.33908    0.09212   -0.16992      -0.88 X
 10      0.00   -0.50900   -0.45469    0.08701   -0.05431      -0.28 X
 11      0.00    0.38900    0.41125    0.10032   -0.02225      -0.12 X
 12      1.00   -1.04600   -0.01035    0.03683   -1.03565      -4.92R
 13      1.00   -0.53800    0.00864    0.03695   -0.54664      -2.60R
 23      1.00   -0.43200    0.04282    0.03738   -0.47482      -2.26R
 33      1.00   -0.95900   -0.04101    0.03463   -0.91799      -4.35R
 34      1.00   -0.58500   -0.05981    0.03555   -0.52519      -2.49R
 35      0.00    0.22800   -0.21593    0.05570    0.44393       2.15RX
 36      0.00   -0.28400   -0.21593    0.05570   -0.06807      -0.33 X
 37      0.00    0.09000   -0.21593    0.05570    0.30593       1.48 X
 38      0.00    0.22800   -0.21593    0.05570    0.44393       2.15RX
 39      0.00    0.22800   -0.21593    0.05570    0.44393       2.15RX
 40      0.00   -2.00000   -2.18570    0.08481    0.18570       0.95 X
 41      0.00   -2.00000   -1.37956    0.05712   -0.62044      -3.01RX
 42      1.00   -2.00000   -2.55267    0.09392    0.55267       2.88RX
 43      1.00   -2.00000   -1.14361    0.05226   -0.85639      -4.13R
 55      1.00   -0.50900   -0.05965    0.03058   -0.44935      -2.12R
 68      1.00   -0.85400   -0.33133    0.02881   -0.52267      -2.47R
 77      1.00   -2.00000   -1.45376    0.05064   -0.54624      -2.63R
 83      1.00   -0.37700    0.21374    0.02503   -0.59074      -2.78R
 84      1.00   -0.25200    0.22206    0.02478   -0.47406      -2.23R
```

88	1.00	-0.27600	0.33513	0.01952	-0.61113	-2.87R
141	1.00	0.09700	-0.39161	0.03621	0.48861	2.32R
144	1.00	0.12100	-0.53217	0.04218	0.65317	3.12R
148	1.00	0.14000	-0.47125	0.04676	0.61125	2.93R
398	0.00	-0.23400	0.21876	0.02345	-0.45276	-2.13R
432	0.00	-0.41600	0.07806	0.02504	-0.49406	-2.33R
449	1.00	-1.22200	-0.79597	0.05540	-0.42603	-2.06RX
450	0.00	-1.22200	-1.39036	0.05608	0.16836	0.82 X
451	1.00	-1.22200	-1.23435	0.05926	0.01235	0.06 X
452	1.00	-1.22200	-1.23629	0.06880	0.01429	0.07 X
453	0.00	-1.22200	-1.32074	0.06171	0.09874	0.48 X
456	1.00	-1.22200	-1.36423	0.06619	0.14223	0.70 X
458	0.00	-1.22200	-1.21115	0.06091	-0.01085	-0.05 X
459	1.00	-1.22200	-1.29048	0.07192	0.06848	0.34 X
465	1.00	-1.22200	-0.77743	0.04372	-0.44457	-2.12R

R denotes an obs. with a large st. resid.
X denotes an obs. whose X value gives it large influence.

Minitab regression analysis for model FF6-A

```
The regression equation is
LOG(Dhc+ = - 17.4 + 1.25 M - 0.923 log R - 0.0140 R + 0.685 log Wff
           + 0.300 log T15 + 4.83 log (100-F15) - 1.09 D5015

Predictor       Coef       Stdev    t-ratio        p
Constant    -17.3724      0.8063     -21.55    0.000
M            1.24779     0.06974      17.89    0.000
log R       -0.92338     0.07176     -12.87    0.000
R          -0.014032    0.001957      -7.17    0.000
log Wff      0.68539     0.05490      12.48    0.000
log T15      0.30041     0.05356       5.61    0.000
log (F15      4.8257      0.3170      15.22    0.000
D5015        -1.0912      0.1647      -6.62    0.000

s = 0.2412      R-sq = 82.7%     R-sq(adj) = 82.1%

Analysis of Variance

SOURCE       DF          SS          MS         F        p
Regression    7     56.9659      8.1380    139.83    0.000
Error       205     11.9305      0.0582
Total       212     68.8964

SOURCE       DF      SEQ SS
M             1      7.0852
log R         1      9.2075
R             1     13.8422
log Wff       1      5.4487
log T15       1      7.8966
log (F15      1     10.9317
D5015         1      2.5539

Unusual Observations
Obs.        M   LOG(Dhc+        Fit  Stdev.Fit   Residual    St.Resid
  1      7.90    -0.0360     0.5157     0.0655    -0.5517      -2.38R
  2      7.90     0.2650     0.7922     0.0452    -0.5272      -2.22R
  3      9.20     0.1400     0.0114     0.1215     0.1286       0.62 X
  4      9.20     0.2830     0.2434     0.1500     0.0396       0.21 X
  5      9.20     0.2700     0.4227     0.1348    -0.1527      -0.76 X
  6      9.20     0.1990     0.1215     0.1493     0.0775       0.41 X
  7      6.40    -1.0460    -0.1648     0.0526    -0.8812      -3.74R
 28      6.40    -0.9590    -0.1559     0.0475    -0.8031      -3.40R
 30      6.60    -2.0000    -2.6293     0.1301     0.6293       3.10RX
 31      6.60    -2.0000    -1.2647     0.0764    -0.7353      -3.21R
 56      6.50    -0.8540    -0.2945     0.0368    -0.5595      -2.35R
 71      7.50    -0.3770     0.1733     0.0301    -0.5503      -2.30R
 76      7.50    -0.2760     0.3334     0.0229    -0.6094      -2.54R
132      7.50     0.1210    -0.4704     0.0539     0.5914       2.51R
137      7.50    -0.0560     0.4448     0.0794    -0.5008      -2.20R
205      7.80    -1.2220    -0.7497     0.0852    -0.4723      -2.09RX
206      7.40    -1.2220    -1.2488     0.0892     0.0268       0.12 X
207      7.60    -1.2220    -1.2237     0.1058     0.0017       0.01 X
208      7.40    -1.2220    -1.3807     0.1004     0.1587       0.72 X
209      7.60    -1.2220    -1.2787     0.1108     0.0567       0.26 X

R denotes an obs. with a large st. resid.
X denotes an obs. whose X value gives it large influence.
```

Minitab regression analysis for model GS6-A

```
The regression equation is
LOG(Dhc+ = - 14.2 + 0.988 M - 1.05 log R - 0.0108 R + 0.319 log Sgs
           + 0.619 log T15 + 4.29 Log(100-F15) - 0.705 D5015

Predictor       Coef       Stdev    t-ratio        p
Constant    -14.1525      0.6001     -23.58    0.000
M            0.98784     0.05253      18.81    0.000
log R       -1.04910     0.07707     -13.61    0.000
R          -0.010841    0.001643      -6.60    0.000
log Sgs      0.31865     0.04046       7.87    0.000
log T15      0.61931     0.03838      16.13    0.000
Log(F15       4.2871      0.3093      13.86    0.000
D5015        -0.7049      0.1547      -4.56    0.000

s = 0.1687      R-sq = 82.9%     R-sq(adj) = 82.4%

Analysis of Variance

SOURCE       DF          SS          MS         F        p
Regression    7     33.9285      4.8469    170.35    0.000
Error       246      6.9993      0.0285
Total       253     40.9279

SOURCE       DF      SEQ SS
M             1      2.2741
log R         1      4.2227
R             1     14.3698
log Sgs       1      0.9079
log T15       1      6.5082
Log(F15       1      5.0553
D5015         1      0.5905

Unusual Observations
Obs.        M   LOG(Dhc+        Fit  Stdev.Fit   Residual    St.Resid
  1      7.90     0.1790     0.9597     0.0418    -0.7807      -4.78R
  2      7.90     0.1790     0.8252     0.0308    -0.6462      -3.90R
  3      9.20    -0.5090    -0.2663     0.1213    -0.2427      -2.07RX
  4      9.20    -0.5090    -0.5007     0.0924    -0.0083      -0.06 X
  5      9.20     0.3890     0.1192     0.1314     0.2698       2.55RX
  6      6.40     0.2280     0.0555     0.0748     0.1725       1.14 X
  7      6.40    -0.2840     0.0555     0.0748    -0.3395      -2.25RX
  8      6.40     0.0900     0.0555     0.0748     0.0345       0.23 X
  9      6.40     0.2280     0.0555     0.0748     0.1725       1.14 X
 10      6.40     0.2280     0.0555     0.0748     0.1725       1.14 X
 11      6.60    -2.0000    -2.2883     0.1169     0.2883       2.37RX
 12      6.60    -2.0000    -1.3915     0.0731    -0.6085      -4.00RX
 78      7.50     0.5450     0.1607     0.0178     0.3843       2.29R
148      7.50    -0.1190     0.2372     0.0405    -0.3562      -2.18R
152      7.50    -0.0920     0.2483     0.0288    -0.3403      -2.05R
194      7.70    -0.2340     0.1662     0.0199    -0.4002      -2.39R
228      7.70    -0.4160    -0.0073     0.0249    -0.4087      -2.45R
245      7.50    -1.2220    -1.3432     0.0651     0.1212       0.78 X
246      7.70    -1.2220    -1.2774     0.0709     0.0554       0.36 X
247      7.50    -1.2220    -1.2584     0.0593     0.0364       0.23 X
250      7.80    -1.2220    -1.1786     0.0694    -0.0434      -0.28 X
251      6.40    -1.2220    -1.0124     0.0553    -0.2096      -1.32 X
253      6.40    -1.2220    -1.0089     0.0580    -0.2131      -1.35 X
254      6.60    -1.2220    -1.4647     0.0616     0.2427       1.55 X

R denotes an obs. with a large st. resid.
X denotes an obs. whose X value gives it large influence.
```

Minitab regression analysis for model FFGS6-B

```
The regression equation is
LOG(Dhc+ = - 13.3 - 0.261 B0ff + 1.05 M - 0.778 log R - 0.0126 R
           + 0.370 log Wff + 0.106 log Sgs + 0.270 log T15 + 3.48 log (100-F15)
           - 0.715 D5015

Predictor        Coef       Stdev    t-ratio        p
Constant     -13.2613      0.5100     -26.00    0.000
B0ff         -0.26103     0.05811      -4.49    0.000
M             1.05006     0.04696      22.36    0.000
log R        -0.77763     0.05176     -15.02    0.000
R           -0.012555    0.001263      -9.94    0.000
log Wff       0.36999     0.06575       5.63    0.000
log Sgs       0.10633     0.05965       1.78    0.076
log T15       0.27042     0.03830       7.06    0.000
log (F15       3.4809      0.2222      15.67    0.000
D5015         -0.7151      0.1156      -6.19    0.000

s = 0.2043      R-sq = 81.7%     R-sq(adj) = 81.1%

Analysis of Variance

SOURCE        DF          SS          MS         F        p
Regression     9     50.7979      5.6442    135.24    0.000
Error        273     11.3933      0.0417
Total        282     62.1912

SOURCE        DF      SEQ SS
B0ff           1      2.1261
M              1      7.0842
log R          1     12.2982
R              1     16.6171
log Wff        1      0.0000
log Sgs        1      0.0171
log T15        1      2.3814
log (F15       1      8.6758
D5015          1      1.5981

Unusual Observations
Obs.     B0ff   LOG(Dhc+        Fit  Stdev.Fit   Residual    St.Resid
  2      0.00     0.1790     0.8582     0.0414    -0.6792      -3.40R
  3      0.00     0.1790     0.6958     0.0317    -0.5168      -2.56R
  5      1.00     0.1400    -0.0480     0.0803     0.1880       1.00 X
  6      1.00     0.2830     0.0413     0.1229     0.2417       1.48 X
  7      1.00     0.2700     0.3021     0.1048    -0.0321      -0.18 X
  8      1.00     0.1990     0.1193     0.1133     0.0797       0.47 X
  9      0.00    -0.5090    -0.2501     0.0923    -0.2589      -1.42 X
 10      0.00    -0.5090    -0.2710     0.0931    -0.2380      -1.31 X
 11      1.00    -1.0460    -0.1586     0.0413    -0.8874      -4.44R
 21      1.00    -0.9590    -0.1732     0.0402    -0.7858      -3.92R
 23      0.00     0.2280    -0.3099     0.0631     0.5379       2.77R
 25      0.00     0.0900    -0.3099     0.0631     0.3999       2.06R
 26      0.00     0.2280    -0.3099     0.0631     0.5379       2.77R
 27      0.00     0.2280    -0.3099     0.0631     0.5379       2.77R
 28      0.00    -2.0000    -1.8922     0.0924    -0.1078      -0.59 X
 29      0.00    -2.0000    -1.2732     0.0611    -0.7268      -3.73R
 30      1.00    -2.0000    -2.1124     0.1025     0.1124       0.64 X
 31      1.00    -2.0000    -1.1203     0.0518    -0.8797      -4.45R
 46      1.00    -0.8540    -0.3495     0.0327    -0.5045      -2.50R
 54      1.00    -0.9590    -1.3566     0.0520     0.3976       2.01R
 55      1.00    -2.0000    -1.4309     0.0493    -0.5691      -2.87R
 59      1.00    -0.3770     0.0811     0.0295    -0.4581      -2.27R
 63      1.00    -0.2760     0.1729     0.0250    -0.4489      -2.21R
 77      1.00     0.0970    -0.3288     0.0395     0.4258       2.12R
 80      1.00     0.1210    -0.4157     0.0480     0.5367       2.70R
 84      1.00     0.1400    -0.2690     0.0531     0.4090       2.07R
249      0.00    -0.4160     0.0860     0.0261    -0.5020      -2.48R
268      1.00    -1.2220    -1.2626     0.0672     0.0406       0.21 X
```

```
275      1.00    -1.2220    -1.3111     0.0701     0.0891       0.46 X
R denotes an obs. with a large st. resid.
X denotes an obs. whose X value gives it large influence.
```

Minitab regression analysis for model FF6-B

```
The regression equation is
LOG(Dhc+ = - 15.1 + 1.13 M - 0.738 log R - 0.0124 R + 0.396 log Wff
           + 0.135 log T15 + 4.03 log (100-F15) - 0.908 D5015

Predictor        Coef       Stdev    t-ratio        p
Constant     -15.0668      0.9054     -16.64    0.000
M             1.13037     0.07130      15.85    0.000
log R        -0.73793     0.07576      -9.74    0.000
R           -0.012366    0.002006      -6.17    0.000
log Wff       0.39563     0.08471       4.67    0.000
log T15       0.13451     0.05865       2.29    0.024
log (F15       4.0315      0.3543      11.38    0.000
D5015         -0.9079      0.1678      -5.41    0.000

s = 0.2332      R-sq = 81.4%     R-sq(adj) = 80.2%

Analysis of Variance

SOURCE        DF          SS          MS         F        p
Regression     7     26.2002      3.7429     68.85    0.000
Error        110      5.9803      0.0544
Total        117     32.1805

SOURCE        DF      SEQ SS
M              1      4.8734
log R          1      6.6454
R              1      6.4996
log Wff        1      0.0515
log T15        1      1.0820
log (F15       1      5.4568
D5015          1      1.5914

Unusual Observations
Obs.         M   LOG(Dhc+        Fit  Stdev.Fit   Residual    St.Resid
  3       9.20     0.1400     0.0032     0.1193     0.1368       0.68 X
  4       9.20     0.2830     0.1238     0.1588     0.1592       0.93 X
  5       9.20     0.2700     0.3267     0.1352    -0.0567      -0.30 X
  6       9.20     0.1990     0.1025     0.1486     0.0965       0.54 X
  7       6.40    -1.0460    -0.3536     0.0623    -0.6924      -3.08R
 17       6.40    -0.9590    -0.3415     0.0583    -0.6175      -2.74R
 19       6.60    -2.0000    -2.1774     0.1524     0.1774       1.01 X
 20       6.60    -2.0000    -1.2185     0.0779    -0.7815      -3.56R
 35       6.50    -0.8540    -0.3671     0.0416    -0.4869      -2.12R
 44       6.60    -2.0000    -1.4913     0.0756    -0.5087      -2.31R
 69       7.50     0.1210    -0.3567     0.0606     0.4777       2.12R
110       7.80    -1.2220    -0.7666     0.0826    -0.4554      -2.09R
114       7.60    -1.2220    -1.2332     0.1078     0.0112       0.05 X

R denotes an obs. with a large st. resid.
X denotes an obs. whose X value gives it large influence.
```

Minitab regression analysis for model GS6-B

```
The regression equation is
LOG(Dhc+ = - 14.2 + 0.800 M - 1.20 log R - 0.00584 R + 0.0713 log Sgs
           + 0.373 log T15 + 5.09 log (100-F15) - 0.704 D5015

Predictor       Coef       Stdev    t-ratio        p
Constant    -14.2122      0.5295     -26.84    0.000
M            0.80003     0.06217      12.87    0.000
log R       -1.19836     0.07252     -16.52    0.000
R          -0.005839    0.001646      -3.55    0.001
log Sgs      0.07132     0.04936       1.44    0.150
log T15      0.37276     0.04292       8.68    0.000
log (F15      5.0903      0.3452      14.74    0.000
D5015        -0.7038      0.1448      -4.86    0.000

s = 0.1436      R-sq = 88.4%     R-sq(adj) = 87.9%

Analysis of Variance

SOURCE       DF          SS          MS         F        p
Regression    7     24.6471      3.5210    170.75    0.000
Error       157      3.2376      0.0206
Total       164     27.8846

SOURCE       DF      SEQ SS
M             1      2.2109
log R         1      5.7259
R             1     10.6486
log Sgs       1      0.0169
log T15       1      1.5560
log (F15      1      4.0015
D5015         1      0.4872

Unusual Observations
Obs.        M   LOG(Dhc+        Fit  Stdev.Fit   Residual    St.Resid
  1      7.90     0.1790     0.7741     0.0447    -0.5951      -4.36R
  2      7.90     0.1790     0.6046     0.0362    -0.4256      -3.06R
  3      9.20    -0.5090    -0.3607     0.1077    -0.1483      -1.56 X
  4      9.20    -0.5090    -0.5475     0.0905     0.0385       0.35 X
  5      6.40     0.2280     0.0701     0.0640     0.1579       1.23 X
  6      6.40    -0.2840     0.0701     0.0640    -0.3541      -2.75RX
  7      6.40     0.0900     0.0701     0.0640     0.0199       0.15 X
  8      6.40     0.2280     0.0701     0.0640     0.1579       1.23 X
  9      6.40     0.2280     0.0701     0.0640     0.1579       1.23 X
 10      6.60    -2.0000    -2.3642     0.1188     0.3642       4.52RX
 11      6.60    -2.0000    -1.4739     0.0707    -0.5261      -4.21RX
112      7.70    -0.2340     0.0654     0.0229    -0.2994      -2.11R
140      7.70    -0.4160     0.0270     0.0235    -0.4430      -3.13R
156      7.50    -1.2220    -1.3053     0.0568     0.0833       0.63 X
157      7.70    -1.2220    -1.2434     0.0615     0.0214       0.17 X
161      7.80    -1.2220    -1.1634     0.0600    -0.0586      -0.45 X
162      6.40    -1.2220    -0.9720     0.0551    -0.2500      -1.89 X
163      6.60    -1.2220    -0.9244     0.0461    -0.2976      -2.19R
164      6.40    -1.2220    -1.0304     0.0575    -0.1916      -1.46 X
165      6.60    -1.2220    -1.4103     0.0584     0.1883       1.44 X

R denotes an obs. with a large st. resid.
X denotes an obs. whose X value gives it large influence.
```

Minitab regression analysis for model FFGS4-A

```
The regression equation is
LOG(Dhc+ = - 6.82 - 0.465 B0ff + 1.02 M - 0.278 log R - 0.0257 R
           + 0.497 log Wff + 0.454 log Sgs + 0.558 log T15

Predictor        Coef       Stdev    t-ratio        p
Constant      -6.8155      0.3511     -19.41    0.000
B0ff         -0.46505     0.06268      -7.42    0.000
M             1.01716     0.05305      19.17    0.000
log R        -0.27811     0.05303      -5.24    0.000
R           -0.025741    0.001493     -17.24    0.000
log Wff       0.49685     0.06282       7.91    0.000
log Sgs       0.45441     0.06117       7.43    0.000
log T15       0.55795     0.04346      12.84    0.000

s = 0.2903      R-sq = 64.8%     R-sq(adj) = 64.2%

Analysis of Variance

SOURCE       DF          SS          MS         F        p
Regression    7      71.164      10.166    120.63    0.000
Error       459      38.684       0.084
Total       466     109.848

SOURCE       DF      SEQ SS
B0ff          1       0.024
M             1       9.350
log R         1      13.062
R             1      28.502
log Wff       1       5.434
log Sgs       1       0.898
log T15       1      13.893

Unusual Observations
Obs.     B0ff   LOG(Dhc+        Fit  Stdev.Fit   Residual    St.Resid
  2      0.00     0.1790     0.8498     0.0369    -0.6708      -2.33R
  3      0.00     0.1790     0.8819     0.0361    -0.7029      -2.44R
  5      1.00     0.1400    -0.0650     0.1048     0.2050       0.76 X
  6      1.00     0.2830     1.1521     0.0979    -0.8691      -3.18RX
  7      1.00     0.2700     1.0258     0.0891    -0.7558      -2.74RX
  8      1.00     0.1990     0.9609     0.0852    -0.7619      -2.75RX
  9      0.00    -0.5090    -0.3202     0.1097    -0.1888      -0.70 X
 10      0.00    -0.5090    -0.5672     0.1168     0.0582       0.22 X
 11      0.00     0.3890     1.2926     0.0921    -0.9036      -3.28RX
 12      1.00    -1.0460     0.0823     0.0496    -1.1283      -3.94R
 13      1.00    -0.5380     0.1020     0.0497    -0.6400      -2.24R
 33      1.00    -0.9590     0.0276     0.0468    -0.9866      -3.44R
 34      1.00    -0.5850     0.0201     0.0479    -0.6051      -2.11R
 35      0.00     0.2280     0.1559     0.0710     0.0721       0.26 X
 36      0.00    -0.2840     0.1559     0.0710    -0.4399      -1.56 X
 37      0.00     0.0900     0.1559     0.0710    -0.0659      -0.23 X
 38      0.00     0.2280     0.1559     0.0710     0.0721       0.26 X
 39      0.00     0.2280     0.1559     0.0710     0.0721       0.26 X
 40      0.00    -2.0000    -0.6740     0.0493    -1.3260      -4.63R
 41      0.00    -2.0000    -0.4078     0.0387    -1.5922      -5.53R
 42      1.00    -2.0000    -1.0153     0.0710    -0.9847      -3.50RX
 43      1.00    -2.0000    -0.2852     0.0391    -1.7148      -5.96R
 54      1.00     0.6020     0.0008     0.0314     0.6012       2.08R
 56      1.00     0.5820    -0.0298     0.0314     0.6118       2.12R
 63      1.00     0.6280     0.0022     0.0312     0.6258       2.17R
 72      1.00    -0.6780    -0.4455     0.0687    -0.2325      -0.82 X
 74      1.00    -0.6200    -0.4383     0.0686    -0.1817      -0.64 X
 77      1.00    -2.0000    -0.7929     0.0512    -1.2071      -4.22R
 83      1.00    -0.3770     0.2991     0.0334    -0.6761      -2.34R
 88      1.00    -0.2760     0.3175     0.0258    -0.5935      -2.05R
148      1.00     0.1400    -0.5494     0.0629     0.6894       2.43R
449      1.00    -1.2220    -0.9709     0.0713    -0.2511      -0.89 X
450      0.00    -1.2220    -1.4208     0.0746     0.1988       0.71 X
```

451	1.00	-1.2220	-1.3777	0.0792	0.1557	0.56	X
452	1.00	-1.2220	-1.5001	0.0898	0.2781	1.01	X
453	0.00	-1.2220	-1.4353	0.0804	0.2133	0.76	X
454	0.00	-1.2220	-1.2840	0.0680	0.0620	0.22	X
456	1.00	-1.2220	-1.5681	0.0880	0.3461	1.25	X
458	0.00	-1.2220	-1.3336	0.0785	0.1116	0.40	X
459	1.00	-1.2220	-1.5812	0.0937	0.3592	1.31	X
462	0.00	-1.2220	-0.6420	0.0492	-0.5800	-2.03	R
465	1.00	-1.2220	-0.5112	0.0515	-0.7108	-2.49	R

R denotes an obs. with a large st. resid.
X denotes an obs. whose X value gives it large influence.

Minitab regression analysis for model FF4-A

```
The regression equation is
LOG(Dhc+ = - 6.97 + 0.972 M - 0.272 log R - 0.0266 R + 0.497 log Wff
           + 0.584 log T15

Predictor        Coef       Stdev    t-ratio        p
Constant      -6.9684      0.5432     -12.83    0.000
M             0.97233     0.08312      11.70    0.000
log R        -0.27154     0.08241      -3.29    0.001
R           -0.026572    0.002541     -10.46    0.000
log Wff       0.49732     0.07741       6.42    0.000
log T15       0.58413     0.07284       8.02    0.000

s = 0.3504      R-sq = 63.1%     R-sq(adj) = 62.2%

Analysis of Variance

SOURCE       DF          SS          MS         F        p
Regression    5     43.4803      8.6961     70.82    0.000
Error       207     25.4160      0.1228
Total       212     68.8963

SOURCE       DF      SEQ SS
M             1      7.0852
log R         1      9.2075
R             1     13.8422
log Wff       1      5.4487
log T15       1      7.8966

Unusual Observations
Obs.         M   LOG(Dhc+        Fit  Stdev.Fit   Residual    St.Resid
  3      9.20     0.1400    -0.2081     0.1713     0.3481       1.14 X
  4      9.20     0.2830     1.0274     0.1462    -0.7444      -2.34RX
  5      9.20     0.2700     0.9020     0.1375    -0.6320      -1.96 X
  6      9.20     0.1990     0.8382     0.1333    -0.6392      -1.97 X
  7      6.40    -1.0460     0.1257     0.0708    -1.1717      -3.41R
 28      6.40    -0.9590     0.0663     0.0655    -1.0253      -2.98R
 30      6.60    -2.0000    -1.0169     0.1094    -0.9831      -2.95RX
 31      6.60    -2.0000    -0.2616     0.0556    -1.7384      -5.02R
 65      6.60    -2.0000    -0.7718     0.0758    -1.2282      -3.59R
136      7.50     0.1400    -0.5899     0.0971     0.7299       2.17R
205      7.80    -1.2220    -1.0435     0.1154    -0.1785      -0.54 X
206      7.40    -1.2220    -1.4324     0.1275     0.2104       0.64 X
207      7.60    -1.2220    -1.5733     0.1471     0.3513       1.10 X
208      7.40    -1.2220    -1.6283     0.1429     0.4063       1.27 X
209      7.60    -1.2220    -1.6568     0.1539     0.4348       1.38 X
211      6.60    -1.2220    -0.4848     0.0754    -0.7372      -2.15R

R denotes an obs. with a large st. resid.
X denotes an obs. whose X value gives it large influence.
```

Minitab regression analysis for model GS4-A

```
The regression equation is
LOG(Dhc+ = - 7.59 + 1.11 M - 0.233 log R - 0.0254 R + 0.477 log Sgs
           + 0.579 log T15

Predictor        Coef       Stdev    t-ratio        p
Constant      -7.5863      0.4593     -16.52    0.000
M             1.10888     0.06738      16.46    0.000
log R        -0.23274     0.06793      -3.43    0.001
R           -0.025354    0.001654     -15.33    0.000
log Sgs       0.47691     0.05162       9.24    0.000
log T15       0.57886     0.05124      11.30    0.000

s = 0.2258      R-sq = 69.1%     R-sq(adj) = 68.5%

Analysis of Variance

SOURCE       DF          SS          MS         F        p
Regression    5     28.2828      5.6566    110.94    0.000
Error       248     12.6451      0.0510
Total       253     40.9279

SOURCE       DF      SEQ SS
M             1      2.2741
log R         1      4.2227
R             1     14.3698
log Sgs       1      0.9079
log T15       1      6.5082

Unusual Observations
Obs.         M   LOG(Dhc+        Fit  Stdev.Fit   Residual    St.Resid
  1      7.90     0.1790     0.8683     0.0416    -0.6893      -3.11R
  2      7.90     0.1790     0.9055     0.0404    -0.7265      -3.27R
  3      9.20    -0.5090    -0.1130     0.1220    -0.3960      -2.08RX
  4      9.20    -0.5090    -0.3709     0.1230    -0.1381      -0.73 X
  5      9.20     0.3890     1.4469     0.1059    -1.0579      -5.30RX
  6      6.40     0.2280    -0.0487     0.0997     0.2767       1.37 X
  7      6.40    -0.2840    -0.0487     0.0997    -0.2353      -1.16 X
  8      6.40     0.0900    -0.0487     0.0997     0.1387       0.68 X
  9      6.40     0.2280    -0.0487     0.0997     0.2767       1.37 X
 10      6.40     0.2280    -0.0487     0.0997     0.2767       1.37 X
 11      6.60    -2.0000    -0.8106     0.0689    -1.1894      -5.53RX
 12      6.60    -2.0000    -0.5344     0.0536    -1.4656      -6.68R
 78      7.50     0.5450     0.0624     0.0217     0.4826       2.15R
148      7.50    -0.1190     0.3488     0.0200    -0.4678      -2.08R
245      7.50    -1.2220    -1.3794     0.0836     0.1574       0.75 X
246      7.70    -1.2220    -1.3704     0.0892     0.1484       0.72 X
247      7.50    -1.2220    -1.2458     0.0762     0.0238       0.11 X
248      7.50    -1.2220    -1.0580     0.0660    -0.1640      -0.76 X
250      7.80    -1.2220    -1.2596     0.0866     0.0376       0.18 X
251      6.40    -1.2220    -0.8619     0.0701    -0.3601      -1.68 X
252      6.60    -1.2220    -0.7346     0.0605    -0.4874      -2.24RX
253      6.40    -1.2220    -0.8022     0.0723    -0.4198      -1.96 X
254      6.60    -1.2220    -1.2892     0.0804     0.0672       0.32 X

R denotes an obs. with a large st. resid.
X denotes an obs. whose X value gives it large influence.
```

Minitab regression analysis for model FFGS4-B

```
The regression equation is
LOG(Dhc+ = - 6.75 - 0.162 B0ff + 1.00 M - 0.289 log R - 0.0215 R
           + 0.0904 log Wff + 0.203 log Sgs + 0.289 log T15

Predictor        Coef       Stdev    t-ratio        p
Constant      -6.7472      0.3679     -18.34    0.000
B0ff         -0.16205     0.07937      -2.04    0.042
M             1.00124     0.05503      18.19    0.000
log R        -0.28932     0.05679      -5.09    0.000
R           -0.021456    0.001546     -13.88    0.000
log Wff       0.09041     0.08693       1.04    0.299
log Sgs       0.20319     0.08141       2.50    0.013
log T15       0.28872     0.05252       5.50    0.000

s = 0.2807      R-sq = 65.2%     R-sq(adj) = 64.3%

Analysis of Variance

SOURCE        DF          SS          MS         F        p
Regression     7     40.5240      5.7891     73.48    0.000
Error        275     21.6672      0.0788
Total        282     62.1912

SOURCE        DF      SEQ SS
B0ff           1      2.1261
M              1      7.0842
log R          1     12.2982
R              1     16.6171
log Wff        1      0.0000
log Sgs        1      0.0171
log T15        1      2.3814

Unusual Observations
Obs.     B0ff   LOG(Dhc+        Fit  Stdev.Fit   Residual    St.Resid
  5      1.00     0.1400    -0.0519     0.1048     0.1919       0.74 X
  6      1.00     0.2830     0.7950     0.1187    -0.5120      -2.01RX
  7      1.00     0.2700     0.7795     0.1028    -0.5095      -1.95 X
  8      1.00     0.1990     0.7768     0.0950    -0.5778      -2.19RX
  9      0.00    -0.5090    -0.0894     0.1127    -0.4196      -1.63 X
 10      0.00    -0.5090    -0.2076     0.1253    -0.3014      -1.20 X
 11      1.00    -1.0460    -0.1383     0.0568    -0.9077      -3.30R
 21      1.00    -0.9590    -0.1819     0.0552    -0.7771      -2.82R
 23      0.00     0.2280    -0.0033     0.0823     0.2313       0.86 X
 24      0.00    -0.2840    -0.0033     0.0823    -0.2807      -1.05 X
 25      0.00     0.0900    -0.0033     0.0823     0.0933       0.35 X
 26      0.00     0.2280    -0.0033     0.0823     0.2313       0.86 X
 27      0.00     0.2280    -0.0033     0.0823     0.2313       0.86 X
 28      0.00    -2.0000    -0.5888     0.0545    -1.4112      -5.13R
 29      0.00    -2.0000    -0.4510     0.0418    -1.5490      -5.58R
 30      1.00    -2.0000    -0.7998     0.0803    -1.2002      -4.46R
 31      1.00    -2.0000    -0.4883     0.0447    -1.5117      -5.45R
 50      1.00    -0.6780    -0.8927     0.0849     0.2147       0.80 X
 52      1.00    -0.6200    -0.8889     0.0849     0.2689       1.01 X
 55      1.00    -2.0000    -0.9488     0.0525    -1.0512      -3.81R
268      1.00    -1.2220    -1.5356     0.0878     0.3136       1.18 X
269      0.00    -1.2220    -1.2702     0.0822     0.0482       0.18 X
272      1.00    -1.2220    -1.6215     0.0862     0.3995       1.50 X
275      1.00    -1.2220    -1.6040     0.0915     0.3820       1.44 X

R denotes an obs. with a large st. resid.
X denotes an obs. whose X value gives it large influence.
```

Minitab regression analysis for model FF4-B

```
The regression equation is
LOG(Dhc+ = - 6.03 + 0.880 M - 0.271 log R - 0.0184 R + 0.013 log Wff
           + 0.257 log T15

Predictor        Coef       Stdev    t-ratio        p
Constant      -6.0349      0.5677     -10.63    0.000
M             0.87989     0.08364      10.52    0.000
log R        -0.27137     0.09243      -2.94    0.004
R           -0.018443    0.002804      -6.58    0.000
log Wff        0.0127      0.1137       0.11    0.911
log T15       0.25658     0.08413       3.05    0.003

s = 0.3411      R-sq = 59.5%     R-sq(adj) = 57.7%

Analysis of Variance

SOURCE       DF          SS          MS         F        p
Regression    5     19.1520      3.8304     32.93    0.000
Error       112     13.0285      0.1163
Total       117     32.1805

SOURCE       DF      SEQ SS
M             1      4.8734
log R         1      6.6454
R             1      6.4996
log Wff       1      0.0515
log T15       1      1.0820

Unusual Observations
Obs.         M   LOG(Dhc+        Fit  Stdev.Fit   Residual    St.Resid
  3      9.20     0.1400    -0.0552     0.1704     0.1952       0.66 X
  4      9.20     0.2830     0.6186     0.1632    -0.3356      -1.12 X
  5      9.20     0.2700     0.6251     0.1454    -0.3551      -1.15 X
  6      9.20     0.1990     0.6351     0.1370    -0.4361      -1.40 X
  7      6.40    -1.0460    -0.1243     0.0859    -0.9217      -2.79R
 17      6.40    -0.9590    -0.1693     0.0823    -0.7897      -2.39R
 19      6.60    -2.0000    -0.7208     0.1205    -1.2792      -4.01R
 20      6.60    -2.0000    -0.4708     0.0609    -1.5292      -4.56R
 44      6.60    -2.0000    -0.8675     0.0760    -1.1325      -3.41R
112      7.60    -1.2220    -1.3833     0.1456     0.1613       0.52 X
113      7.40    -1.2220    -1.4605     0.1411     0.2385       0.77 X
114      7.60    -1.2220    -1.4424     0.1528     0.2204       0.72 X

R denotes an obs. with a large st. resid.
X denotes an obs. whose X value gives it large influence.
```

Minitab regression analysis for model GS4-B

```
The regression equation is
log(Dhc+ = - 8.41 + 1.24 M - 0.358 log R - 0.0243 R + 0.266 log Sgs
           + 0.373 log T15

Predictor        Coef       Stdev    t-ratio        p
Constant      -8.4104      0.5057     -16.63    0.000
M             1.23887     0.07417      16.70    0.000
log R        -0.35833     0.06861      -5.22    0.000
R           -0.024273    0.001641     -14.79    0.000
log Sgs       0.26553     0.07252       3.66    0.000
log T15       0.37286     0.06588       5.66    0.000

s = 0.2204      R-sq = 72.3%     R-sq(adj) = 71.4%

Analysis of Variance

SOURCE       DF          SS          MS         F        p
Regression    5     20.1549      4.0310     82.97    0.000
Error       159      7.7246      0.0486
Total       164     27.8795

SOURCE       DF      SEQ SS
M             1      2.2114
log R         1      5.7243
R             1     10.6462
log Sgs       1      0.0167
log T15       1      1.5562

Unusual Observations
Obs.         M   log(Dhc+        Fit  Stdev.Fit   Residual    St.Resid
  1      7.90     0.1790     0.8537     0.0474    -0.6747      -3.13R
  2      7.90     0.1790     0.8578     0.0485    -0.6788      -3.16R
  3      9.20    -0.5086     0.0604     0.1256    -0.5690      -3.14RX
  4      9.20    -0.5086    -0.0932     0.1290    -0.4154      -2.32RX
  5      6.40     0.2279    -0.0574     0.0973     0.2853       1.44 X
  6      6.40    -0.2840    -0.0574     0.0973    -0.2266      -1.15 X
  7      6.40     0.0899    -0.0574     0.0973     0.1473       0.74 X
  8      6.40     0.2279    -0.0574     0.0973     0.2853       1.44 X
  9      6.40     0.2279    -0.0574     0.0973     0.2853       1.44 X
 10      6.60    -2.0000    -0.7829     0.0760    -1.2171      -5.88RX
 11      6.60    -2.0000    -0.6050     0.0565    -1.3950      -6.55R
156      7.50    -1.2218    -1.4717     0.0836     0.2499       1.23 X
157      7.70    -1.2218    -1.4335     0.0883     0.2117       1.05 X
158      7.50    -1.2218    -1.3399     0.0763     0.1181       0.57 X
161      7.80    -1.2218    -1.3097     0.0854     0.0878       0.43 X
162      6.40    -1.2218    -1.0750     0.0762    -0.1468      -0.71 X
164      6.40    -1.2218    -1.0746     0.0801    -0.1473      -0.72 X
165      6.60    -1.2218    -1.5018     0.0862     0.2799       1.38 X

R denotes an obs. with a large st. resid.
X denotes an obs. whose X value gives it large influence.
```

Seismic Evaluation of 550 kV Porcelain Transformer Bushings

Amir S. Gilani
University of California, Berkeley

Andrew S. Whittaker
University of California, Berkeley

Gregory L. Fenves
University of California, Berkeley

Eric Fujisaki
Pacific Gas & Electric Company

This research was sponsored by the Pacific Gas & Electric Company and the California Energy Commission. Additional support was provided by the Pacific Earthquake Engineering Research Center and the National Science Foundation.

PEER Report 1999/05
Pacific Earthquake Engineering Research Center
College of Engineering
University of California, Berkeley

October 1999

ABSTRACT

Three 550 kV porcelain transformer bushings were evaluated for their response to severe earthquake shaking. The first bushing was similar to bushings currently in service in the United States; the other two bushings were modified versions of the first bushing. The modifications to the second and third bushings were intended to enhance seismic performance and included added tiers of springs, increased preload, and stiffer gaskets. The dynamic properties, vibration frequencies, and damping ratios of the bushings were evaluated from the experimental data. Tri-directional earthquake simulator testing was undertaken to investigate the dynamic response of the bushings, to qualify one of the modified bushings for moderate earthquake shaking (per IEEE 693-1997), and to evaluate the response of the other two bushings to extreme shaking effects. For earthquake testing, the bushings were mounted at 20° to the vertical in a stiff support frame. Two sets of spectrum-compatible ground motion records, derived from motions recorded during the 1978 Tabas earthquake in Iran, were used for testing. None of the bushings met the IEEE criteria for Moderate Level qualification. However, the response of the modified bushings was superior to the response of the unmodified bushing.

ACKNOWLEDGMENTS

The work described in this report was funded by the Pacific Gas and Electric (PG&E) Company. This work was supported in part by the Pacific Earthquake Engineering Research Center through the Earthquake Engineering Research Centers program of the National Science Foundation under Award Number EEC-9701568. This financial support is gratefully acknowledged. The transformer bushings were supplied by ABB Power T&D Company, Inc., Components Division of Alamo, Tennessee.

The significant technical contributions of Messrs. Ed Matsuda of PG&E, Mr. Lonnie Elder of ABB, and Mr. Don Clyde of the University of California, Berkeley, made possible the work described in this report. The authors also thank Ms. Janine Hannel for editing this report.

CONTENTS

ABSTRACT		i
ACKNOWLEDGMENTS		iii
CONTENTS		v
LIST OF TABLES		vii
LIST OF FIGURES		ix
CHAPTER 1:	INTRODUCTION	1
1.1	Overview	1
1.2	Seismic Qualification and Fragility Testing	1
1.3	ABB 550 kV Transformer Bushings	2
1.4	Report Organization	3
CHAPTER 2:	EARTHQUAKE SIMULATOR TESTING	7
2.1	Introduction	7
2.2	Earthquake Simulator	7
2.3	Mounting Frame	7
2.4	Instrumentation	8
CHAPTER 3:	QUALIFICATION AND FRAGILITY TESTING	15
3.1	Introduction	15
3.2	IEEE 693-1997 Requirements for Bushing Qualification	15
	3.2.1 Resonant search tests	15
	3.2.2 Earthquake test response spectrum	15
	3.2.3 Earthquake ground motions	17
CHAPTER 4:	SUMMARY OF EXPERIMENTAL DATA	29
4.1	Overview	29
4.2	Dynamic Properties of 550 kV Bushings	29
4.3	Earthquake Testing of Bushing-1, Bushing-2, and Bushing-3	30
	4.3.1 Introduction	30
	4.3.2 Peak Responses	31
	4.3.3 Response of the Mounting Frame	32
	4.3.4 Response of Bushing-1	34
	4.3.5 Response of Bushing-2	37
	4.3.6 Response of Bushing-3	37
4.4	Seismic Qualification of Bushing-3	38
4.5	Fragility Testing of Bushings	39
	4.5.1 Introduction	39

	4.5.2	Fragility Data for Peak Ground (Input) Acceleration	39
	4.5.3	Fragility Data for Spectral Acceleration	40
	4.5.4	Fragility Data for Average Spectral Acceleration	40
	4.5.5	Fragility Estimates from Principal Acceleration Data	41
	4.5.6	Summary	42
CHAPTER 5:	SUMMARY AND CONCLUSIONS		65
5.1	Summary		65
	5.1.1	Introduction	65
	5.1.2	Earthquake testing program	65
5.2	Conclusions and Recommendations		66
	5.2.1	Seismic Response of 550 kV Transformer Bushings	66
	5.2.2	Recommendations for Future Study	67
	REFERENCES		69
APPENDIX A:	IEEE PRACTICE FOR EARTHQUAKE TESTING OF TRANSFORMER BUSHINGS		71
A.1	Introduction		71
A.2	Performance Level and Performance factor		72
A.3	Performance Level Qualification		72
A.4	Support Frame and Mounting Configuration		72
A.5	Testing procedures for Transformer Bushings		73
	A.5.1	Resonant search tests	73
	A.5.2	Earthquake ground motion tests	73
A.6	Instrumentation of Transformer Bushings		73
A.7	Acceptance Criteria for Transformer Bushings		74

LIST OF TABLES

Table 1-1	Key differences between modified and unmodified bushings	2
Table 2-1	Modal properties of mounting frame by analysis	8
Table 2-2	Instrumentation for 550 kV bushing tests	9
Table 3-1	IEEE earthquake-history testing requirements for Moderate Level qualification	17
Table 3-2	High-pass filter frequencies for earthquake histories	18
Table 4-1	Modal properties of bushings from sine-sweep tests	29
Table 4-2	Summary of earthquake testing of Bushing-1	30
Table 4-3	Summary of earthquake testing of Bushing-2	31
Table 4-4	Summary of earthquake testing for Bushing-3	32
Table 4-5	Peak accelerations of the mounting frame	33
Table 4-6	Peak acceleration responses of the upper tip of the bushings	34
Table 4-7	Peak relative tip displacement of the bushing relative to the mounting frame	35
Table 4-8	Peak local responses of UPPER-1 porcelain units	36
Table 4-9	Fragility data for Bushing-3, Tabas-A, Test Number 4	43
Table 4-10	Summary of fragility data for Bushing-3 from Test Number 4	43

-

LIST OF FIGURES

Figure 1-1	Bushing mounted on an oil-filled transformer	4
Figure 1-2	550 kV bushing installed in mounting frame atop the Berkeley simulator	4
Figure 1-3	Longitudinal section through a modified 550 kV porcelain bushing	5
Figure 2-1	The 550 kV bushing mounting frame	11
Figure 2-2	Instrumentation for 550 kV bushings	12
Figure 2-3	Instrumentation at the base of one of the 550 kV bushings	13
Figure 2-4	Instrumentation of an UPPER-1 porcelain unit	13
Figure 3-1	Spectra for the Moderate Seismic Performance Level (IEEE, 1998)	19
Figure 3-2	Test Response Spectra at bushing flange for Moderate PL	19
Figure 3-3	Normalized acceleration history, power spectrum, and response spectra for the longitudinal (X-) component of the original Tabas record	20
Figure 3-4	Normalized acceleration history, power spectrum, and response spectra for the lateral (Y-) component of the Tabas record	21
Figure 3-5	Normalized acceleration history, power spectrum, and response spectra for the vertical (Z-) component of the original Tabas record	22
Figure 3-6	Acceleration history, power spectrum, and response spectra for the longitudinal (X-) component of the Tabas-A record	23
Figure 3-7	Acceleration history, power spectrum, and response spectra for the lateral (Y-) component of the Tabas-A record	24
Figure 3-8	Acceleration history, power spectrum, and response spectra for the vertical (Z-) component of the Tabas-A record	25
Figure 3-9	Acceleration history, power spectrum, and response spectra for the longitudinal (X-) component of the Tabas-B record	26
Figure 3-10	Acceleration history, power spectrum, and response spectra for the lateral (Y-) component of the Tabas-B record	27
Figure 3-11	Acceleration history, power spectrum, and response spectra for the vertical (Z-) component of the Tabas-B record	28
Figure 4-1	Bushing-1 upper tip to mounting frame transfer functions	44
Figure 4-2	Bushing-2 upper tip to mounting frame transfer functions 45	45
Figure 4-3	Bushing-3 upper tip to mounting frame transfer functions 46	46
Figure 4-4	Bushing-1 following Test Number 12 showing UPPER-1 porcelain unit slip	47
Figure 4-5	Bushing-2 following Test Number 13 showing UPPER-1 porcelain unit slip	47

Figure 4-6	Bushing-3 following Test Number 5 showing UPPER-1 porcelain unit slip	48
Figure 4-7	Bushing-3 following Test Number 5 showing the exposed gasket	48
Figure 4-8	Mounting frame to earthquake simulator transfer functions	49
Figure 4-9	Relative displacement response of upper tip of Bushing-1, Test Number 17, Tabas-A, target PGA = 1.0g	50
Figure 4-10	Acceleration response spectra calculated using measured mounting frame acceleration histories for Bushing-1, Test Number 17, Tabas-A, target peak acceleration = 1.0g	51
Figure 4-11	Average relative vertical displacement versus rocking response of Bushing-1, Test Number 17, Tabas-A, target PGA = 1.0g	52
Figure 4-12	Orbit of relative displacement of UPPER-1 porcelain unit over gasket for Bushing-1, Test Number 17, Tabas-A, target PGA = 1.0g	53
Figure 4-13	Relative displacement response of upper tip of Bushing-2, Test Number 13, Tabas-B, target PGA = 1.2g	54
Figure 4-14	Acceleration response spectra calculated using measured mounting frame acceleration histories for Bushing-2, Test Number 13, Tabas-B, target peak acceleration = 1.2g	55
Figure 4-15	Average relative vertical displacement versus rocking response of Bushing-2, Test Number 13, Tabas-B, target PGA = 1.2g	56
Figure 4-16	Orbit of relative displacement of UPPER-1 porcelain unit over gasket for Bushing-2, Test Number 13, Tabas-B, target PGA = 1.2g	57
Figure 4-17	Relative displacement response of upper tip of Bushing-3, Test Number 5, Tabas-A, target PGA = 1.0g	58
Figure 4-18	Acceleration response spectra calculated using measured mounting frame acceleration histories for Bushing-3, Test Number 5, Tabas-A, target peak acceleration = 1.0g	59
Figure 4-19	Average relative vertical displacement versus rocking response of Bushing-3, Test Number 5, Tabas-A, target PGA = 1.0g	60
Figure 4-20	Orbit of relative displacement of UPPER-1 porcelain unit over gasket for Bushing-3, Test Number 5, Tabas-A, target PGA = 1.0g	61
Figure 4-21	Fragility data for Bushing-3, Tabas-A, Test Number 4	62
Figure 4-22	Acceleration response spectra for rotated components for Bushing-3, Tabas-A, Test Number 4	63
Figure A-1	Spectra for High Seismic Performance Level (IEEE, 1998)	75
Figure A-2	Spectra for Moderate Seismic Performance Level (IEEE, 1998)	75
Figure A-3	Spectra for High Required Response Spectrum (IEEE, 1998)	76

Figure A-4	Spectra for Moderate Required Response Spectrum (IEEE, 1998)	77
Figure A-5	Test Response Spectra for Moderate Level qualification of a transformer-mounted bushing	78

CHAPTER 1
INTRODUCTION

1.1 Overview

Recent major earthquakes in the United States (Northridge, 1994), Japan (Kobe, 1995) and Turkey (Izmit, 1999) have demonstrated that the reliability of a power transmission and distribution (T&D) system in a region exposed to earthquake shaking is dependent upon the seismic response of its individual components. Porcelain transformer bushings, which are insulated conductors providing electrical connection between a high-voltage line and an oil-filled transformer, have been vulnerable to moderate and severe earthquake shaking (EERI, 1995; Shinozuka, 1995). Bushings are typically mounted on the top of a transformer (see Figure 1-1) using a bolted flange connection.

The research described in this report addresses the vulnerability of high-voltage 550 kV porcelain transformer bushings during moderate earthquake shaking. This work was made possible by a partnership between the Pacific Earthquake Engineering Research (PEER) Center and Pacific Gas & Electric (PG&E) that was formed to investigate the seismic reliability of utility lifelines.

This report documents the seismic response of three 550 kV transformer bushings manufactured by Asea Brown Boveri (ABB) of Alamo, Tennessee. The key objectives of the studies described in the following chapters were to

1. Develop earthquake ground motion records suitable for the seismic evaluation, qualification, and fragility testing of 550 kV bushings.

2. Test three 550 kV bushings on the earthquake simulator at the Pacific Earthquake Engineering Research (PEER) Center using levels of earthquake shaking consistent with those adopted for seismic qualification and fragility testing of electrical equipment.

3. Analyze the data acquired from the earthquake simulator tests to serve four purposes: (a) determine the dynamic properties of the bushings, (b) evaluate the seismic response of the bushings during moderate earthquake shaking, (c) determine the failure mode of two of the bushings subjected to earthquake shaking (fragility testing), and (d) qualify the third 550 kV bushing for moderate earthquake shaking.

4. Draw conclusions about (a) the performance of porcelain transformer bushings, (b) the likely failure modes of a bushing during severe earthquake shaking, (c) the efficacy of the improvements incorporated in the design of 550 kV bushings by the manufacturer, and (d) the utility of the seismic qualification and fragility testing procedures set forth in IEEE 693-1997.

1.2 Seismic Qualification and Fragility Testing

Structural and nonstructural components that do not lend themselves to analysis are often *qualified* for use in specific applications by full-scale testing. Qualification has long been used by the Nuclear Regulatory Commission (NRC) for equipment and hardware (e.g., valves and snubbers)

in nuclear power plants, and by the Departments of Defense and Energy for military hardware. Qualification is a binary decision-making process: equipment or hardware either passes or fails.

The objective of fragility testing is to establish a relation between limiting states of response (e.g., electrical connectivity, gasket failure, and cracking of porcelain) and peak ground acceleration for a selected piece of equipment. This information is then used to develop fragility curves that plot the cumulative probability of reaching a limit state as a function of peak ground acceleration.

In California, electrical equipment is seismically qualified using a standard developed by the Institute of Electrical and Electronic Engineers (IEEE 693-1997). The IEEE standard (IEEE, 1998) entitled *IEEE 693-1997 Recommended Practices for Seismic Design of Substations* details procedures for qualification of electrical substation equipment for different seismic performance levels. The key features of the draft standard as they pertain to this report are described in Section 3.2. Additional information is presented in Appendix A.

1.3 ABB 550 kV Transformer Bushings

One Model 550X2000UW (termed the *unmodified* bushing) and two Model 550SEIS2000-1 (termed the *modified* bushings) 550 kV transformer bushings, manufactured by ABB Power T&D Company, Inc., Components Division were tested as part of the research program described in this report. Figure 1-2 is a photograph of one of the 550kV bushings installed in a mounting frame on the PEER simulator at the University of California at Berkeley.

The *unmodified* bushing is similar to those currently in service at many substations operated by a number of utilities. The modified bushings are prototypes of a new line of 550 kV bushings that incorporate three key changes to the unmodified bushing that are intended to improve seismic performance. The key changes are summarized in Table 1-1.

Table 1-1 Key differences between modified and unmodified bushings

Property	*Unmodified bushing*	*Modified bushings*
Bushing prestressing force	'Standard prestress'	1.4 times 'Standard prestress'
Post-tensioning dome springs	single-tier	multi-tier
Gasket at flange plate-to-porcelain joint	Nitrile rubber	Rubber-impregnated fiber and O-ring seal

A longitudinal section through a typical 550 kV bushing is shown in Figure 1-3. The overall length of the transformer bushing is 256.5 in. (6.5 m). The segment of the bushing above the flange plate (which protrudes above the top of the transformer as seen in Figure 1-1) is 191.5 in. (4.8 m) long and includes three porcelain insulator units (hereafter referred to as UPPER-1, UPPER-2, and UPPER-3), and a metallic dome at the top of the bushing (above porcelain unit UPPER-3). The porcelain units, the cast steel flange, and the metallic dome are separated by gaskets. The segment of the bushing below the steel flange plate includes an extension of the flange plate, one porcelain insulator, and an aluminum lower support. Annular gaskets separate these components. The flange, which is used to connect the bushing to the transformer, is a steel weldment with three lifting lugs to facilitate movement and installation of the bushing.

In cross section, the bushing has an aluminum core, a multi-layered kraft paper condenser wrapped around the core; an annular gap between the porcelain and condenser that is filled with an oil to provide electrical insulation; and a porcelain insulator. The bushing is post-tensioned along its longitudinal axis through the aluminum core. Springs in the metallic dome ensure a uniform distribution of compression around the perimeter of the porcelain units and the gaskets. The weight of the bushing is approximately 3,740 lb (16.6 kN).

The unmodified bushing (Bushing-1) and the first of the two modified bushings (Bushing-2) were designated for fragility testing. No electrical tests were planned for these bushings. ABB did not assign serial numbers to these bushings. The second modified bushing (Bushing-3) was built for seismic qualification testing and passed the requisite electrical tests before shipment to Berkeley. ABB assigned serial number *9C01352502* to this bushing.

1.4 Report Organization

This report is divided into five chapters, references, and one appendix. Following the introduction, Chapter 2 provides information on the simulator used for earthquake testing, the mounting frame designed to support the bushings during testing, and a list of the transducers used to monitor the response of the bushings. Chapter 3 describes the earthquake histories developed for qualification and fragility testing. Chapter 4 provides a summary of the key test results. Chapter 5 includes a summary of the key findings and conclusions drawn from the research project. References are listed following Chapter 5. The IEEE Recommended Practice for earthquake testing of transformer bushings is summarized in Appendix A. Raw data and video images from all earthquake tests were supplied to Pacific Gas & Electric under separate cover.

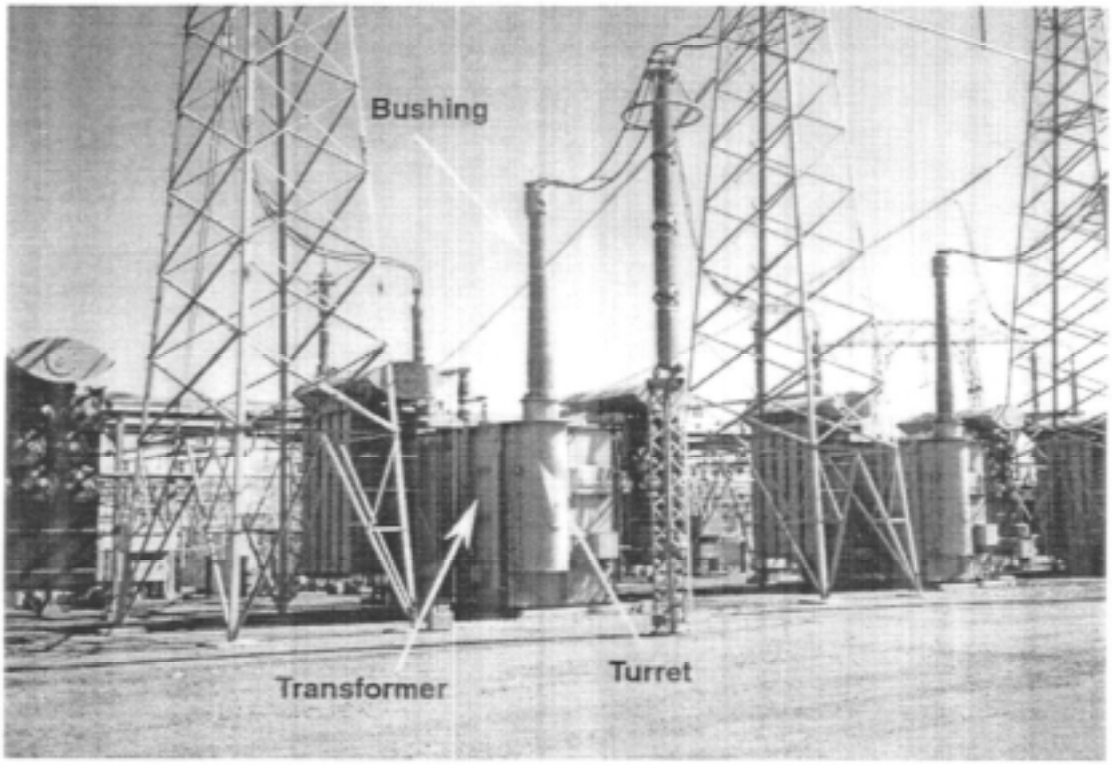

Figure 1-1 Bushing mounted on an oil-filled transformer

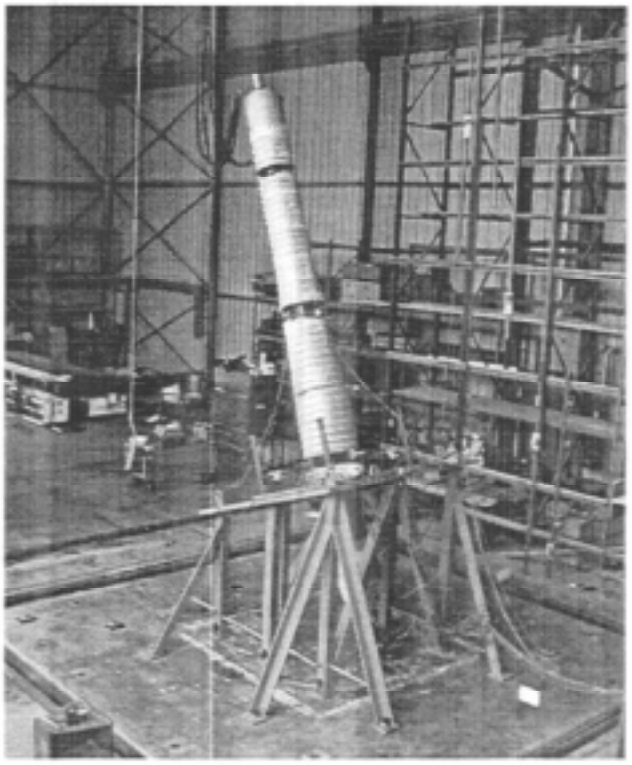

Figure 1-2 550 kV bushing installed in mounting frame atop the Berkeley simulator

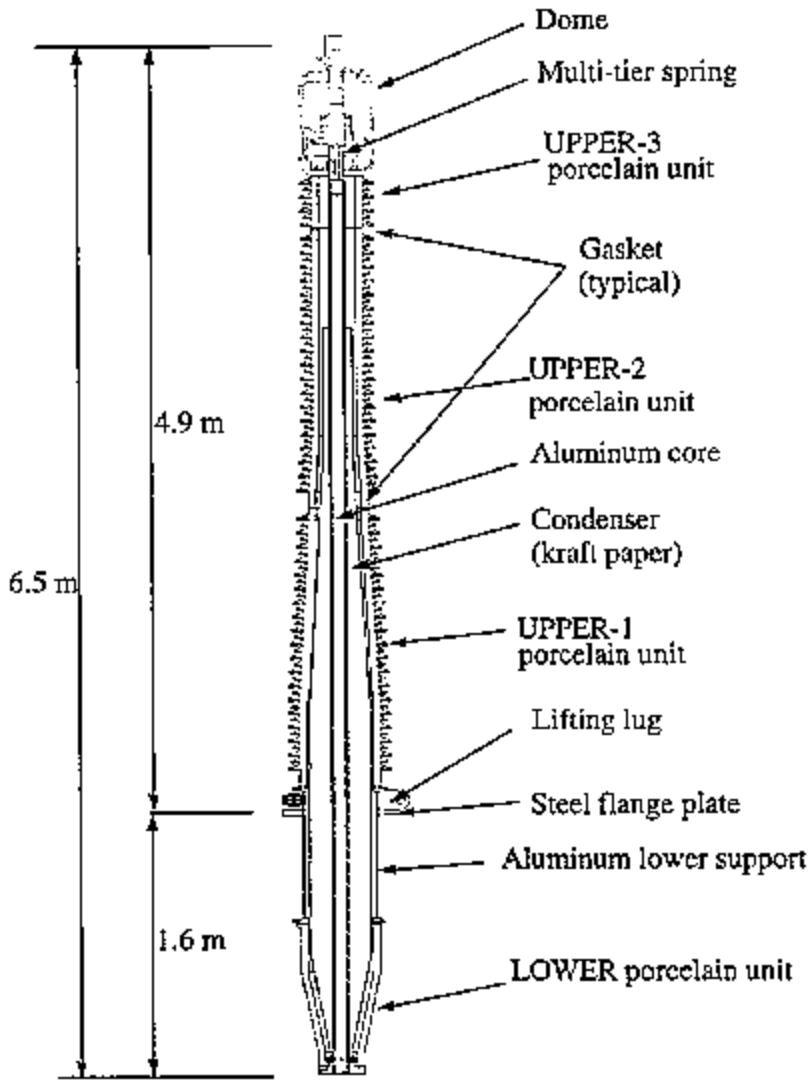

Figure 1-3 Longitudinal section through a modified 550 kV porcelain bushing

CHAPTER 2
EARTHQUAKE SIMULATOR TESTING

2.1 Introduction

Triaxial earthquake simulator testing was used to evaluate the seismic behavior of three 550 kV transformer bushings. The earthquake testing protocol for transformer bushings set forth in IEEE 693-1997 (IEEE, 1998) was adopted for this study. The following sections in this chapter describe the earthquake simulator used for testing the bushings, the *rigid* mounting frame used to support the bushings during testing, and the instrumentation scheme used to monitor the response of the bushings during earthquake testing.

2.2 Earthquake Simulator

The earthquake simulator at the Pacific Earthquake Engineering Research (PEER) Center at the University of California at Berkeley was used for the seismic evaluation and qualification studies described in this report. The simulator, also known as a shaking table, measures 20 ft by 20 ft (6.1 by 6.1 m) in plan; the maximum payload is 140 kips (623 kN). Models up to 40 ft (12.2 m) in height can be tested. The six-degree-of-freedom simulator can be programmed to reproduce any waveform (e.g., sinusoidal, white noise, earthquake history). The maximum stroke and velocity of the simulator are ±5 in. (±127 mm) and 25 in./sec (635 mm/sec), respectively.

2.3 Mounting Frame

IEEE 693-1997 states that bushings rated at 161 kV and above must be qualified using three-component earthquake-simulator testing. Because it is impractical to test bushings mounted on a transformer, IEEE specifies that bushings must be mounted on a rigid stand for earthquake testing and qualification. IEEE also recommends that a transformer bushing be tested at 20 degrees measured from the vertical because a bushing, if so tested and qualified, is assumed to be qualified for use on all transformers with angles from vertical to 20 degrees.

Figure 2-1 is a photograph of the mounting frame used for the earthquake simulator testing. The fully welded mounting frame was specifically designed to support 550 kV bushings, and was constructed of TS-5"x5"x3/8" columns, L-5"x5"x3/4" braces, and a 2-in. (51 mm) thick steel mounting plate (sloping at 20 degrees to the horizontal). The mounting frame was post-tensioned to the earthquake simulator platform using fifteen 1-in. (25 mm) diameter high-strength threaded rods. A special 1.75 in. (44 mm) adaptor plate was designed and fabricated to connect the flange plate of the 550 kV bushings to the support frame. Twelve 1-1/4 in. (32 mm) diameter high-strength bolts were used for the adaptor plate-to-mounting plate connection The flange of the bushing was joined to the adaptor plate with twelve 3/4 in. (19 mm) diameter Grade 2 steel bolts (equivalent to A307 steel) torqued to 100 ft-lb (136 N-m) per the ABB installation specification. The support frame was designed to be extremely stiff to minimize the amplification of the simulator input to the bushing. Table 2-1 reports the computed analytical modal properties of (a) the frame alone and (b) the frame including the mass of the 550 kV bushing.

Table 2-1 Modal properties of mounting frame by analysis

		Frequency (Hz)	
Mode	*Predominant direction*[1]	*Frame only*	*Frame and Bushing*
1	X	78	60
2	Y	72	58
3	Z	88	37
4	θ_z	113	107

1. See Figure 2-2 for coordinate system

2.4 Instrumentation

For seismic testing, IEEE 693-1997 states that porcelain bushings must be instrumented to record (a) maximum vertical and horizontal accelerations at the top of the bushing, at the bushing flange, and at the top of the earthquake simulator platform, (b) maximum displacement of the top of the bushing relative to the flange, and (c) maximum porcelain stresses at the base of the bushing near the flange.

The instrumentation scheme developed for the tests described in this report exceeds the IEEE requirements. Fifty-four channels of data were recorded for each test. Table 2-2 lists the channel number, instrument type, response quantity, coordinate system, and location for each transducer. Figure 2-2 presents information on the instrumentation of the earthquake simulator platform (Figure 2-2a), the bushing and the mounting frame (Figure 2-2b), and the porcelain unit immediately above the flange (UPPER-1) of the bushing (Figure 2-2c). The global (X, Y, Z) and local (x, y, z) coordinate systems adopted for the testing program are shown in the figure. Figure 2-3 shows the instrumentation at the base of one of the 550 kV bushings and Figure 2-4 is a photograph of the instrumentation immediately above the flange plate.

Sixteen channels (channels 3 through 18) recorded the acceleration and displacement of the earthquake simulator platform in the global coordinate system. The accelerations of the mounting frame in the local coordinate system (channels 28, 29, and 30) and the absolute displacements of the mounting frame in the global coordinate system (channels 37 and 38) were recorded. The accelerations of the bushing in the local coordinate system (channels 19 through 27) and the absolute displacements of the bushing in the global coordinate system (channels 31 through 36) were measured at the top, midheight, and bottom of the bushing. Four strain gages (channels 39 through 42) monitored the axial strains in the UPPER-1 porcelain unit. Four displacement transducers (channels 43 through 46), located immediately below the gasket, measured the radial slip of the flange plate relative to the support frame. Another four displacement transducers (channels 47 through 50), located immediately above the gasket, measured radial slip of the UPPER-1 porcelain unit relative to the support frame. The relative slip of the porcelain over the flange plate was computed using these eight transducers. Four displacement transducers (channels 51 through 54) recorded UPPER-1 displacements across the gasket, parallel to the axis of the bushing.

Table 2-2 Instrumentation for 550 kV bushing tests

Channel Number	*Transducer*[1]	*Response Quantity*	*Coordinate System and Orientation*	*Transducer Location*
1	-	date	-	-
2	-	time	-	-
3	LVDT	table displacement	global X	simulator platform
4	LVDT	table displacement	global Y	simulator platform
5	LVDT	table displacement	global X	simulator platform
6	LVDT	table displacement	global Y	simulator platform
7	LVDT	table displacement	global Z	simulator platform
8	LVDT	table displacement	global Z	simulator platform
9	LVDT	table displacement	global Z	simulator platform
10	LVDT	table displacement	global Z	simulator platform
11	A	table acceleration	global X	simulator platform
12	A	table acceleration	global X	simulator platform
13	A	table acceleration	global Y	simulator platform
14	A	table acceleration	global Y	simulator platform
15	A	table acceleration	global Z	simulator platform
16	A	table acceleration	global Z	simulator platform
17	A	table acceleration	global Z	simulator platform
18	A	table acceleration	global Z	simulator platform
19	A	bushing acceleration	local x	bottom of bushing
20	A	bushing acceleration	local y	bottom of bushing
21	A	bushing acceleration	local z	bottom of bushing
22	A	bushing acceleration	local x	midheight of bushing
23	A	bushing acceleration	local y	midheight of bushing
24	A	bushing acceleration	local z	midheight of bushing
25	A	bushing acceleration	local x	top of bushing
26	A	bushing acceleration	local y	top of bushing
27	A	bushing acceleration	local z	top of bushing
28	A	frame acceleration	local x	top of mounting frame

Table 2-2 Instrumentation for 550 kV bushing tests

Channel Number	*Transducer*[1]	*Response Quantity*	*Coordinate System and Orientation*	*Transducer Location*
29	A	frame acceleration	local y	top of mounting frame
30	A	frame acceleration	local z	top of mounting frame
31	LP	bushing displacement	global X	bottom of bushing
32	LP	bushing displacement	global Y	bottom of bushing
33	LP	bushing displacement	global X	midheight of bushing
34	LP	bushing displacement	global Y	midheight of bushing
35	LP	bushing displacement	global X	top of bushing
36	LP	bushing displacement	global Y	top of bushing
37	LP	frame displacement	global X	top of mounting frame
38	LP	frame displacement	global Y	top of mounting frame
39	SG	porcelain strain	-	UPPER-1 porcelain unit
40	SG	porcelain strain	-	UPPER-1 porcelain unit
41	SG	porcelain strain	-	UPPER-1 porcelain unit
42	SG	porcelain strain	-	UPPER-1 porcelain unit
43	DCDT	flange plate slip	relative to frame	UPPER-1 porcelain unit
44	DCDT	flange plate slip	relative to frame	UPPER-1 porcelain unit
45	DCDT	flange plate slip	relative to frame	UPPER-1 porcelain unit
46	DCDT	flange plate slip	relative to frame	UPPER-1 porcelain unit
47	DCDT	UPPER-1 slip	relative to frame	UPPER-1 porcelain unit
48	DCDT	UPPER-1 slip	relative to frame	UPPER-1 porcelain unit
49	DCDT	UPPER-1 slip	relative to frame	UPPER-1 porcelain unit
50	DCDT	UPPER-1 slip	relative to frame	UPPER-1 porcelain unit
51	DCDT	longitudinal uplift	relative to frame	UPPER-1 porcelain unit
52	DCDT	longitudinal uplift	relative to frame	UPPER-1 porcelain unit
53	DCDT	longitudinal uplift	relative to frame	UPPER-1 porcelain unit
54	DCDT	longitudinal uplift	relative to frame	UPPER-1 porcelain unit

1. A = accelerometer; LVDT = displacement transducer; LP = linear potentiometer; SG = strain gage; DCDT = displacement transducer

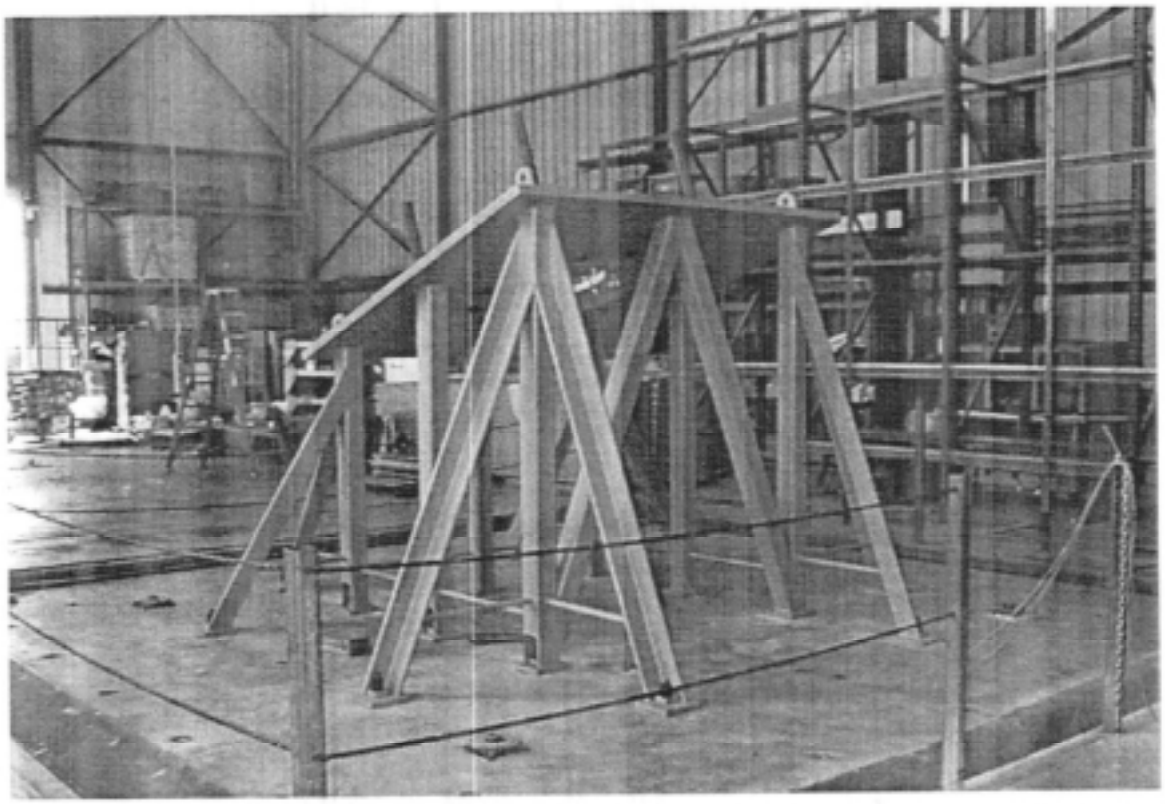

Figure 2-1 550 kV bushing mounting frame

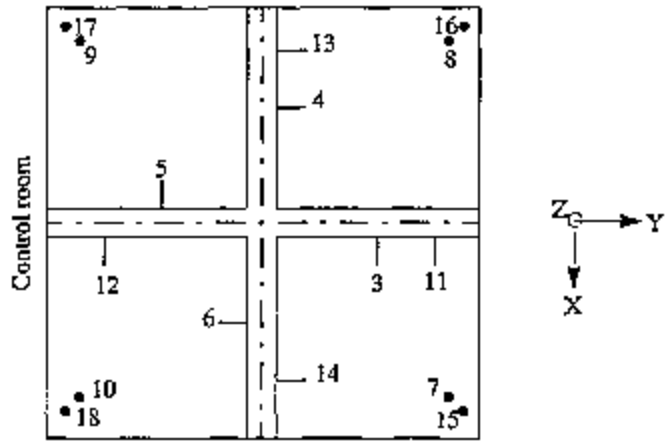

(a) Earthquake simulator (view from beneath)

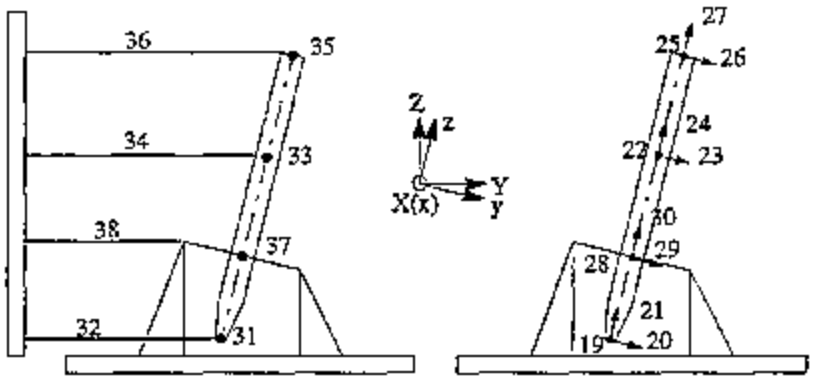

(b) Bushing and mounting frame

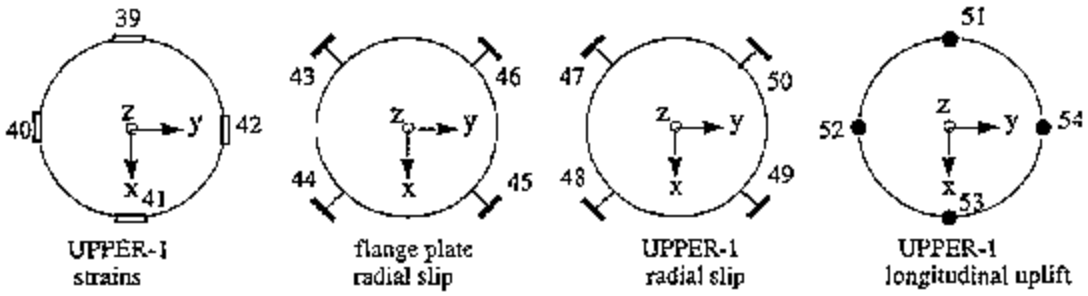

(c) UPPER-1 porcelain unit and flange plate

Figure 2-2 Instrumentation for 550 kV bushings

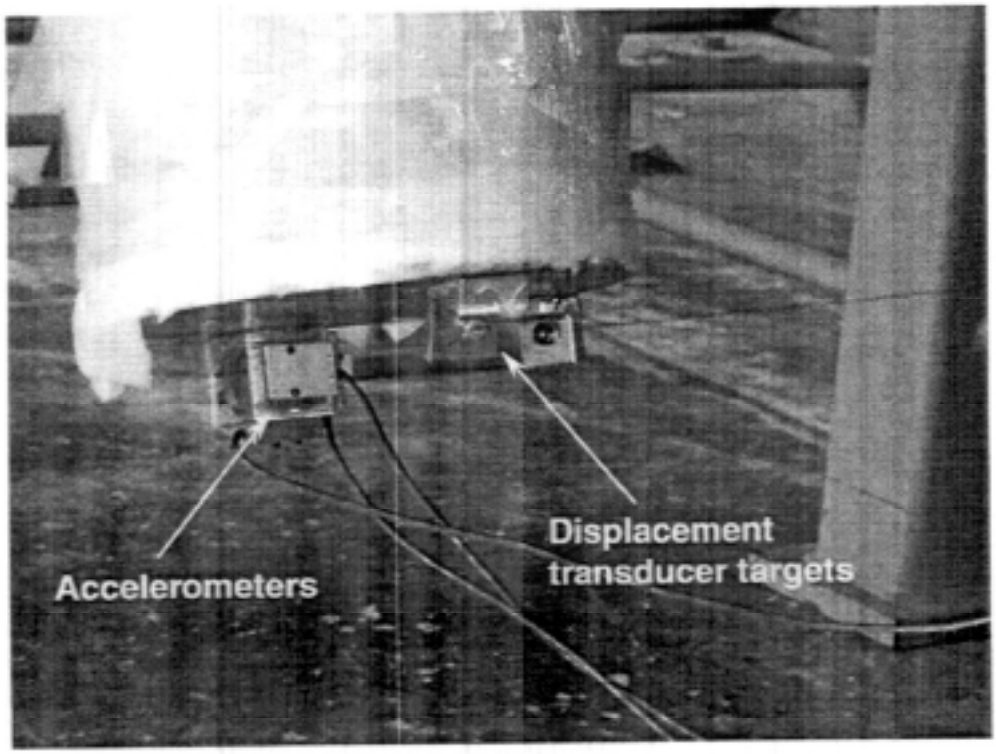

Figure 2-3 Instrumentation at the base of one of the 550 kV bushings

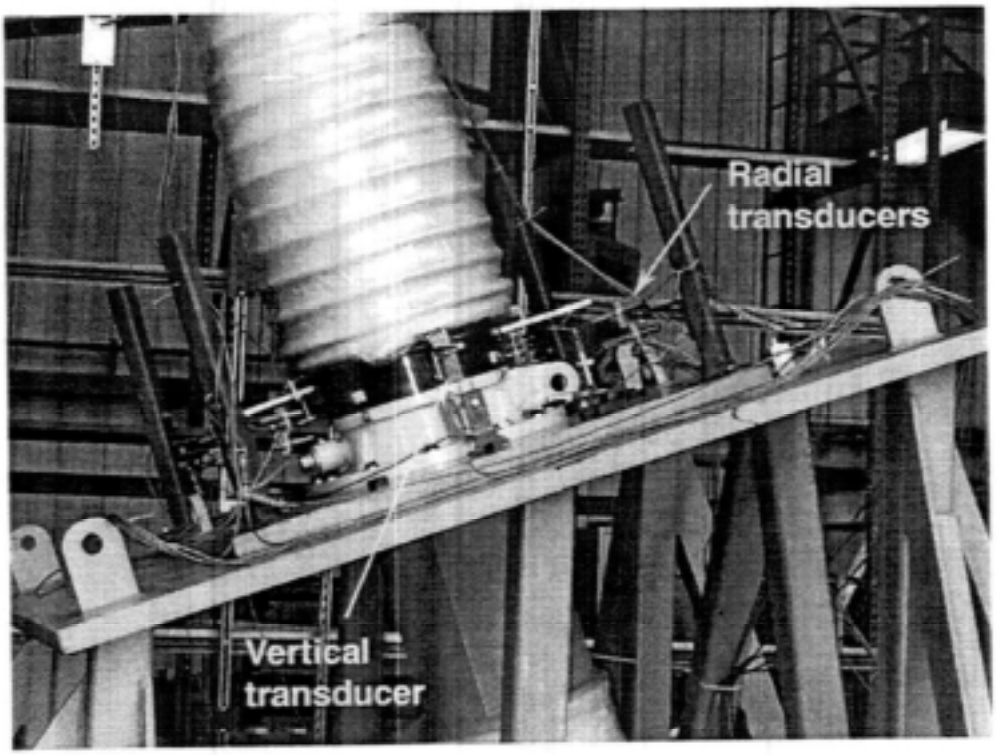

Figure 2-4 Instrumentation of an UPPER-1 porcelain unit

CHAPTER 3
QUALIFICATION AND FRAGILITY TESTING

3.1 Introduction

Recorded earthquake ground motion histories were used to evaluate the seismic response of the three 550 kV transformer bushings (hereafter termed Bushing-1, Bushing-2, and Bushing-3). The following section describes the requirements of IEEE 693-1997 (IEEE, 1998) for the qualification of transformer bushings and the procedures used to develop earthquake histories for testing.

3.2 IEEE 693-1997 Requirements for Bushing Qualification

Three types of earthquake-simulator testing are identified in IEEE 693-1997 for the seismic qualification of transformer bushings: (a) earthquake ground motions, (b) resonant frequency search, and (c) sine-beat testing. Earthquake ground motion tests (termed *time-history shake table tests* in IEEE) and resonant frequency tests are mandatory. Information on these two types of tests follow.

3.2.1 Resonant search tests

Sine-sweep or broadband white noise tests are used to establish the dynamic characteristics (natural frequencies and damping ratios) of a bushing. These so-called *resonant search* tests are undertaken using uni-directional excitation along each global axis of the earthquake simulator platform. If only broadband white noise tests are performed, the amplitude of the white noise must not be less than 0.25g. If only sine-sweep tests are used, IEEE 693-1997 specifies that the resonant search be conducted at a rate not exceeding one octave per minute in the range for which the equipment has resonant frequencies but at least at 1 Hz; frequency searching above 33 Hz is not required. Because both sine-sweep and white-noise tests were used in this testing program to identify the modal properties of the transformer bushings, the recommendations of IEEE 693-1997 were not followed exactly.

The history for the banded white-noise tests was prepared using a random signal generator. The sine sweep history was developed using a rate of two octaves per minute. (At two octaves per minute, the input frequency doubles every 30 seconds.) A continuous frequency function was used to develop the sine-sweep function

$$x(t) = x_0 \sin\left(2\pi\left[\frac{30}{\log 2}\right]2^{t/30}\right) \tag{3-1}$$

where x is the displacement, and x_0 is the maximum displacement. For both sine-sweep and white-noise tests, a simulator input acceleration of 0.1g was used.

3.2.2 Earthquake test response spectrum

IEEE 693-1997 identifies several response spectra of identical shape but different amplitudes for the qualification of transformer bushings. These spectra are described below; a more detailed description is presented in Appendix A.

Test Response Spectrum (TRS). For earthquake simulator testing, IEEE 693-1997 states that the TRS for each horizontal earthquake motion must match or exceed the target spectrum and that the TRS for vertical earthquake motion be no less than 80 percent of target spectrum. IEEE 693-1997 recommends that 2-percent damping be used for spectral matching and requires at least 20 seconds of strong motion shaking be present in each earthquake record. Earthquake motions can be established using either synthetic or recorded histories. Recorded motions formed the basis of the earthquake histories used to test the 550 kV bushings.

Performance Level (PL). IEEE 693-1997 represents a PL for substation equipment by a response spectrum. The PL represents the expected level of performance when a piece of equipment is qualified to the RRS and meets the requirements for allowable stress design. The two PLs relevant to California are *Moderate* and *High*. The Moderate PL was selected by PG&E, ABB, and PEER for the studies reported herein. Equipment that is shown to perform acceptably in ground shaking consistent with the Moderate Seismic Performance Level (see Table 3-1) is said to be seismically qualified to the Moderate Level.

Required Response Spectrum (RRS). It is often neither practical nor cost effective to test components to the Moderate PL. As such, IEEE 693-1997 permits equipment to be tested using a reduced level of shaking called the RRS. The shapes of the RRS and the PL are identical, but the ordinates of the PL are twice (referred to as performance factor in IEEE 693-1997) that of the RRS. Equipment tested or analyzed using the RRS is expected to have acceptable performance at the PL. This assumption is checked by measuring the stresses obtained from testing at the RRS, and (a) comparing the stresses to 50 percent (equal to the inverse of the performance factor) of the ultimate strength of the porcelain (assumed to be brittle) or cast aluminum components and (b) using a factor of safety against yield combined with an allowance for ductility of steel and other ductile materials.

Test Response Spectra for Mounted Equipment (TRSME). To account for the amplification of earthquake motion due to the influence of the transformer body and local flexibility of the transformer near the bushing mount, IEEE 693-1997 states that the input motion *as measured at the bushing flange* shall match a spectrum with ordinates twice that of the RRS, termed herein as the TRSME. For this level of shaking, IEEE 693-1997 states that the stresses in the porcelain components must be less than 50 percent of the ultimate stress, and the factor of safety against oil leakage must be greater than or equal to 2.0.

An alternate approach that is identified in Annex D5.1(d) of IEEE 693-1997 was used for the studies reported herein. Namely, earthquake histories with spectral ordinates twice those of the TRSME were used for testing: the target peak horizontal acceleration at the bushing flange was 1.0g. Porcelain stresses at this level of earthquake shaking were required to be less than or equal to the ultimate value, and there was to be no evidence of oil leakage. The spectrum for this motion is shown in Figure 3-2 and is the same as the Moderate PL spectrum.

The key requirements of IEEE 693-1997 for qualification and fragility testing of bushings are summarized in Table 3-1.

Table 3-1 IEEE earthquake-history testing requirements for Moderate Level qualification

Peak Ground Acceleration	*Comments*
0.5g	Moderate Seismic Performance Level (PL) for substation equipment
0.25g	Required Response Spectrum (RRS) for Moderate Seismic Performance Level for substation equipment
0.5g	Test Response Spectrum for mounted equipment (TRSME) for Moderate Seismic Performance Level.
1.0g	Response spectrum for checking porcelain stresses and oil leakage for bushings mounted on transformers.

3.2.3 Earthquake ground motions

The earthquake histories used for the qualification and fragility testing of the 550 kV bushings were developed using the three-component set of near-fault earthquake motions recorded during the 1978 Tabas earthquake. Figures 3-3 through 3-5 present the acceleration history, power spectrum, and pseudo-acceleration response spectra for the three components of the Tabas record. The amplitude of each history (X-, Y-, and Z-) record was normalized to a peak acceleration of 1.0g. The power spectrum for each history has moderate bandwidth. The 2-percent and 5-percent damped IEEE spectra for Moderate Level qualification, anchored to a peak ground acceleration of 1.0g are also shown in the figures. The response-spectrum ordinates for each normalized earthquake history exceed the target IEEE values for frequencies greater than 2 to 3 Hz and drop below the target values for frequencies less than 2 Hz.

To obtain IEEE 693-1997 spectrum-compatible normalized histories, the original Tabas acceleration records were modified using a non-stationary response-spectrum matching technique developed by Abrahamson (Abrahamson, 1996). In traditional spectrum-matching routines, adjustments are performed in the frequency domain. Specifically, the original acceleration record is transformed into the frequency domain, the amplitude of the Fourier spectrum is adjusted at each frequency to match the target value, and the record is then transformed back into the time domain. Two key disadvantages of the frequency-domain method are that the modified earthquake history rarely resembles the original earthquake history, and that frequency leakage often makes convergence to the target spectrum difficult. Abrahamson's time-domain method is based on the algorithm proposed by Lilhanad and Tseng (1988) wherein short-duration wavelets are added to the original earthquake history at optimal times in the history to match the spectral amplitude at each frequency to the target value. The modified history generally resembles the original earthquake history and frequency leakage is negligible.

The testing of 196 kV ABB bushings (Gilani, et al., 1998) at Berkeley utilized spectrum-compatible earthquake histories developed using the Abrahamson technique. The resulting spectra matched the target spectrum across a broad frequency range (0.1 Hz to 100 Hz). Because the maximum displacement and velocity of the simulator platform are 5 in. (127 mm) and 25 in./

sec (635 mm/sec), respectively, the spectrum-compatible motions were high-pass filtered (removal of low-frequency content) to reduce the peak displacements and velocities of the simulator platform. However, the resulting power spectra of the filtered histories were narrow-banded, and not representative of strong earthquake ground motion.

A different strategy was used to develop earthquake histories for the studies reported herein. This strategy combined the Abrahamson spectrum-matching algorithm and frequency-domain trapezoidal high-pass filters. Input ground motions to the simulator were developed in a three-step process as follows. First, the original earthquake history was high-pass filtered to remove low frequency content (see Table 3-2) such that the maximum displacement and velocity of the filtered history were approximately equal to 5 in. (127 mm) and 25 in./sec (635 mm/sec), respectively. (All content below the cut-off frequency was eliminated; all content above the corner frequency was retained; and content between these frequencies was multiplied by a linearly increasing value that ranged from zero at the cut-off frequency to unity at the corner frequency. The cut-off frequencies were much smaller than the resonant frequency of the 550 kV bushings [known to range between 6 Hz and 9 Hz]. Removal of such low-frequency components from the input signals to the simulator is known to have a negligible impact on the dynamic response of the bushings.) Second, the filtered earthquake history from step one was matched to the target spectrum for frequencies greater than the corner frequency of the trapezoidal filter using the Abrahamson algorithm. Third, the spectrum compatible motions from step two were high-pass filtered to exactly limit the maximum displacement and velocity to 5 in. (127 mm) and 25 in./sec (635 mm/sec), respectively.

Two independent sets of three earthquake histories (Tabas-A and Tabas-B) were generated using the above procedure. Tabas-A was used for all simulations up to and including the Moderate Level qualification for which the target simulator acceleration was 1.0g (see Table 3-2). Tabas-B was used for all other tests up to those corresponding to High Level qualification for which the target acceleration was 2.0g. Table 3-2 summarizes the step-one filter frequencies used to generate the Tabas-A and Tabas-B histories. Figures 3-6 through 3-8 present the acceleration history, power spectrum, and response spectra for the three spectrum-compatible Tabas-A records. Figures 3-9 through 3-11 present the same information for the three spectrum-compatible Tabas-B records.

Table 3-2 High-pass filter frequencies for earthquake histories

		Filter frequencies (Hz)	
Set	*Component*	*Cut-off*	*Corner*
Tabas-A	*X*	1.0	1.5
	Y	1.0	1.5
	Z	1.0	1.5
Tabas-B	*X*	2.0	2.5
	Y	2.2	2.5
	Z	2.2	2.5

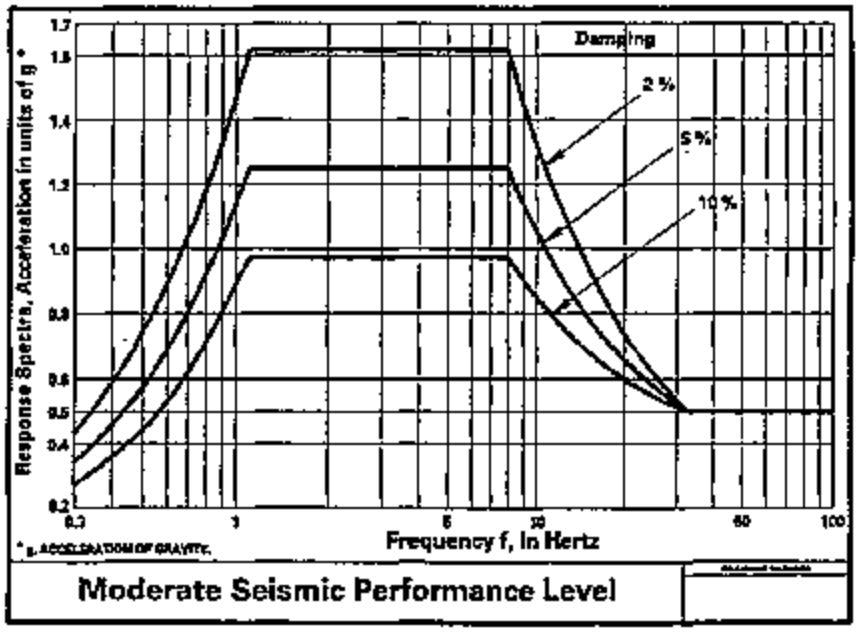

Figure 3-1 Spectra for the Moderate Seismic Performance Level (IEEE, 1998)

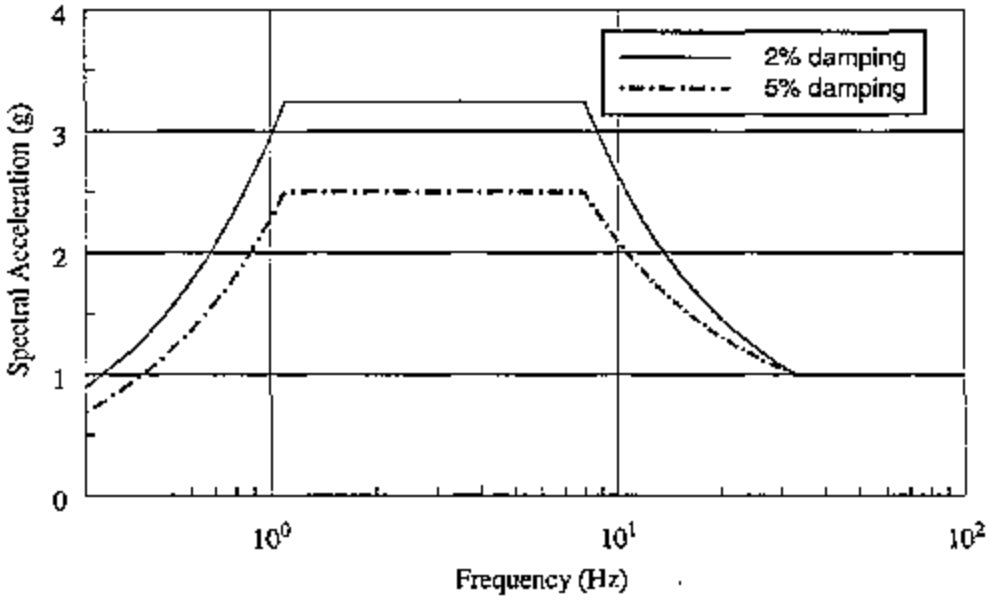

Figure 3-2 Test Response Spectra at bushing flange for Moderate PL

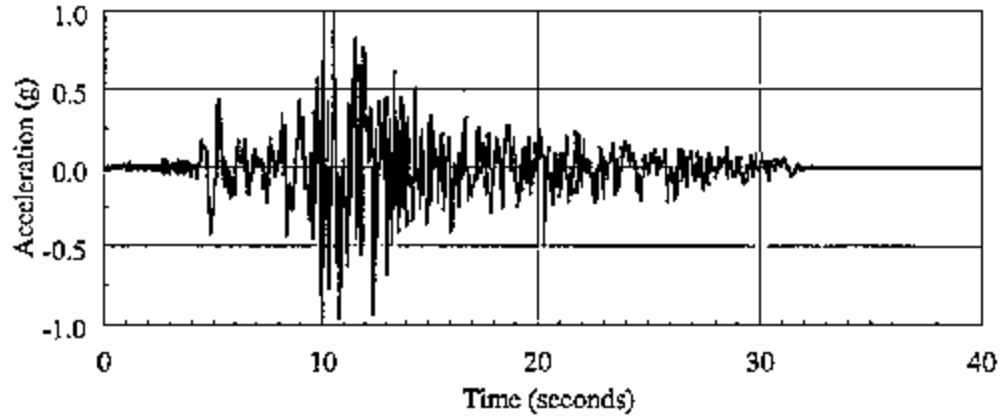

a. Normalized acceleration history

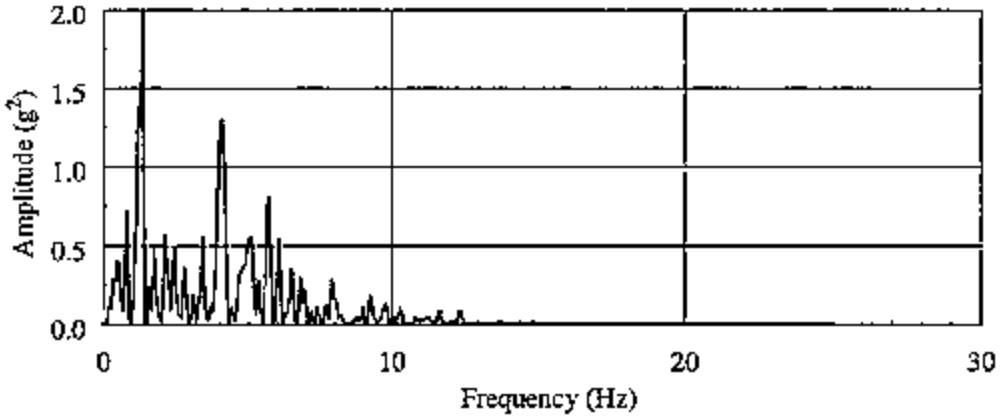

b. Power spectrum

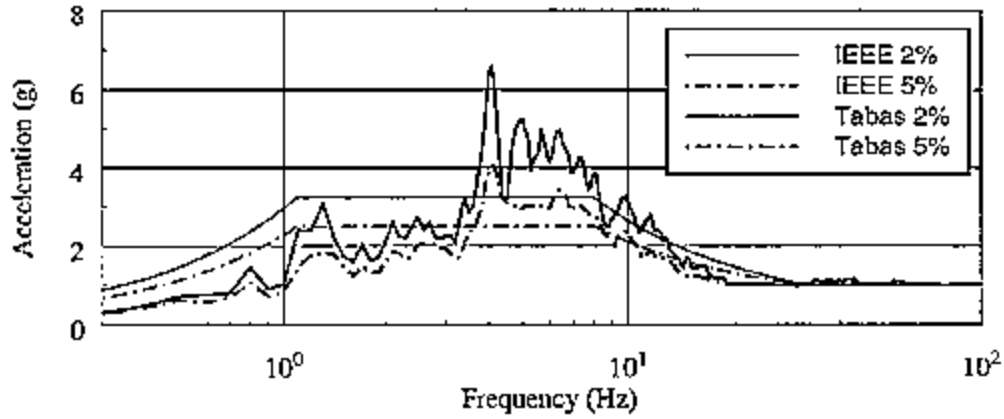

c. Response spectrum

Figure 3-3 Normalized acceleration history, power spectrum, and response spectra for the longitudinal (X-) component of the original Tabas record

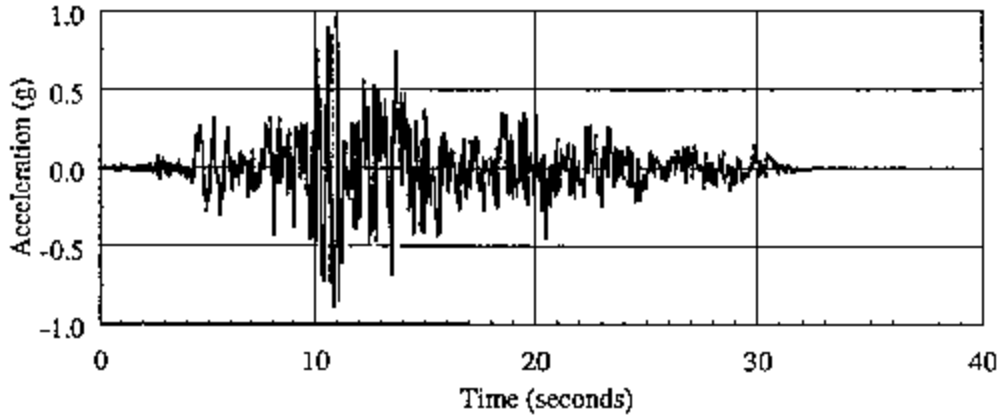

a. Normalized acceleration history

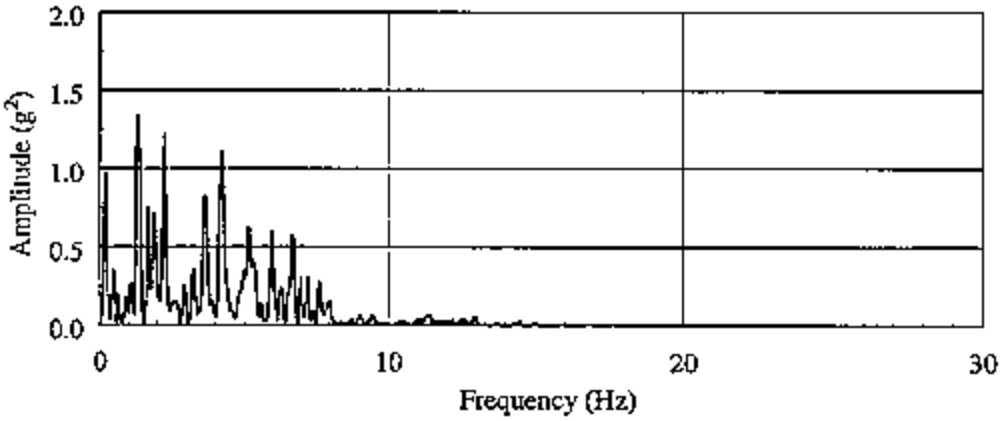

b. Power spectrum

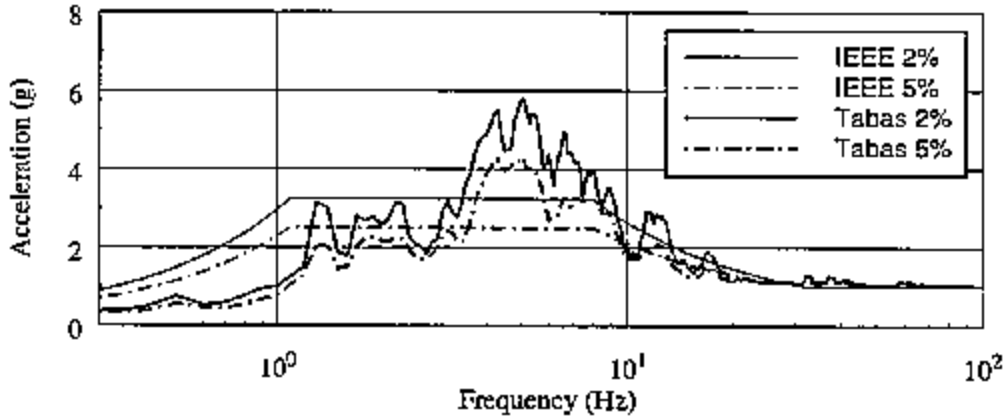

c. Response spectrum

Figure 3-4 Normalized acceleration history, power spectrum, and response spectra for the lateral (Y-) component of the Tabas record

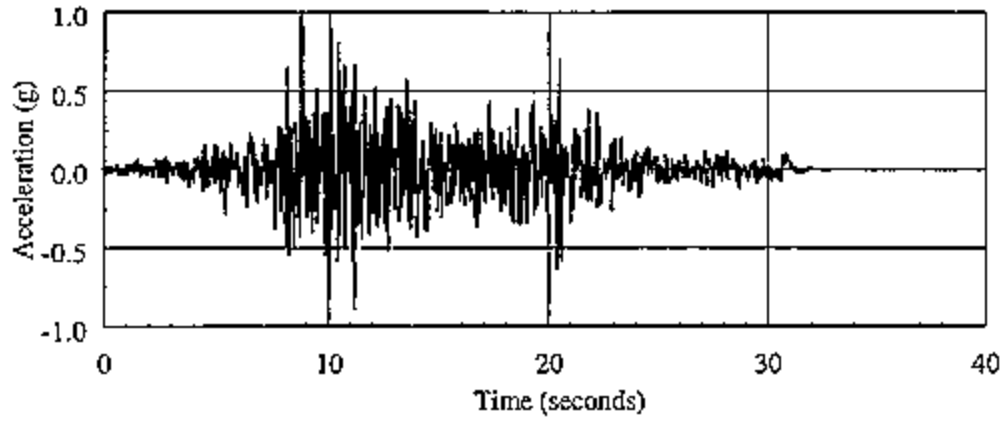

a. Normalized acceleration history

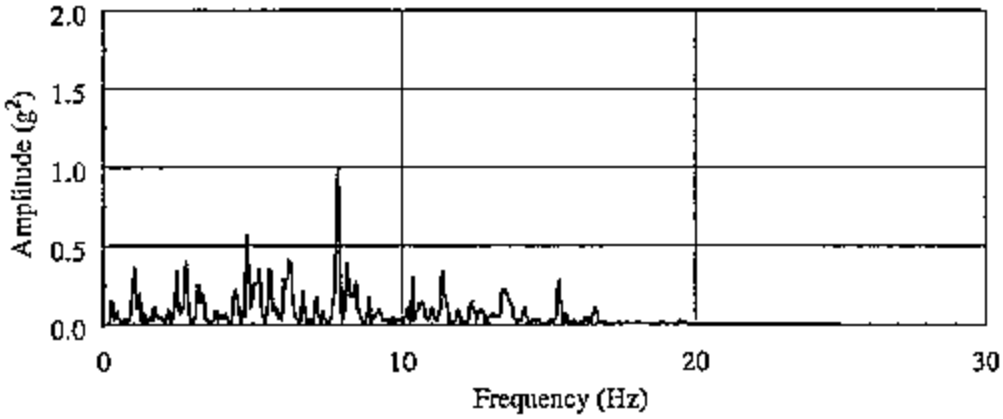

b. Power spectrum

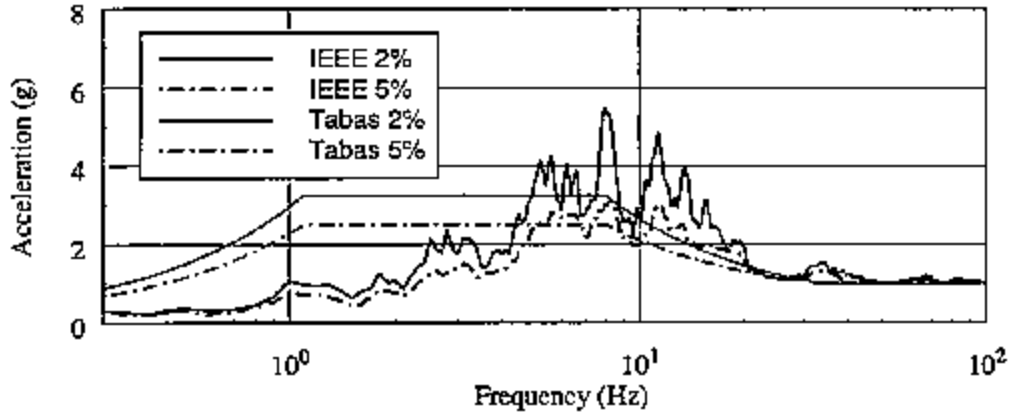

c. Response spectrum

Figure 3-5 Normalized acceleration history, power spectrum, and response spectra for the vertical (Z-) component of the original Tabas record

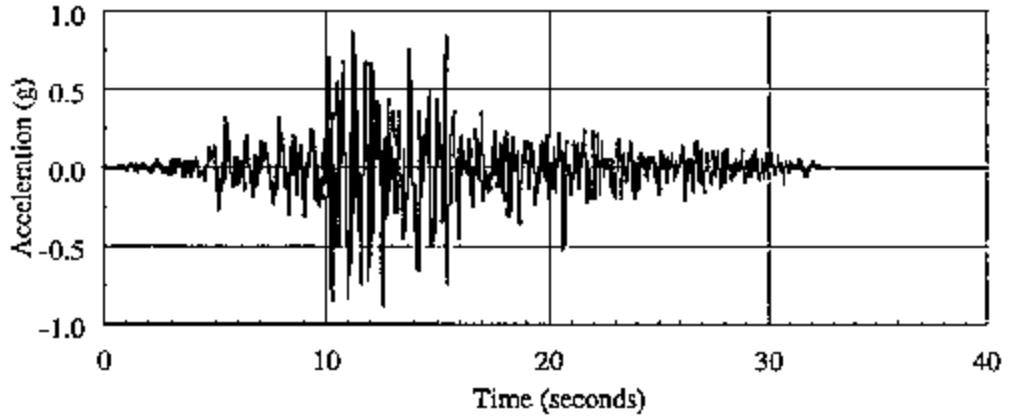

a. Acceleration history

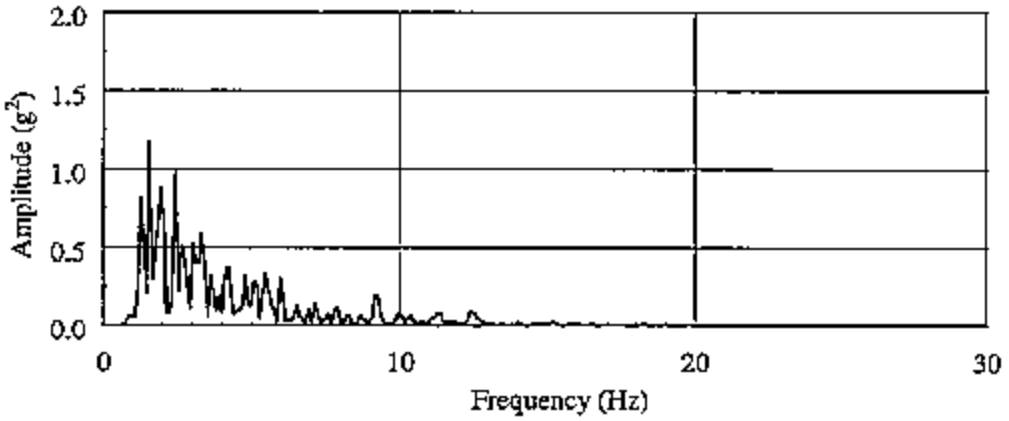

b. Power spectrum

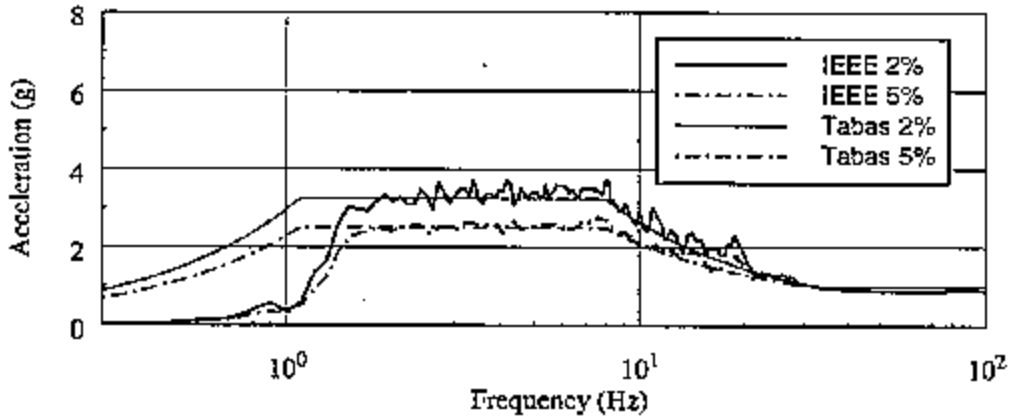

c. Response spectrum

Figure 3-6 Acceleration history, power spectrum, and response spectra for the longitudinal (*X*-) component of the Tabas-A record

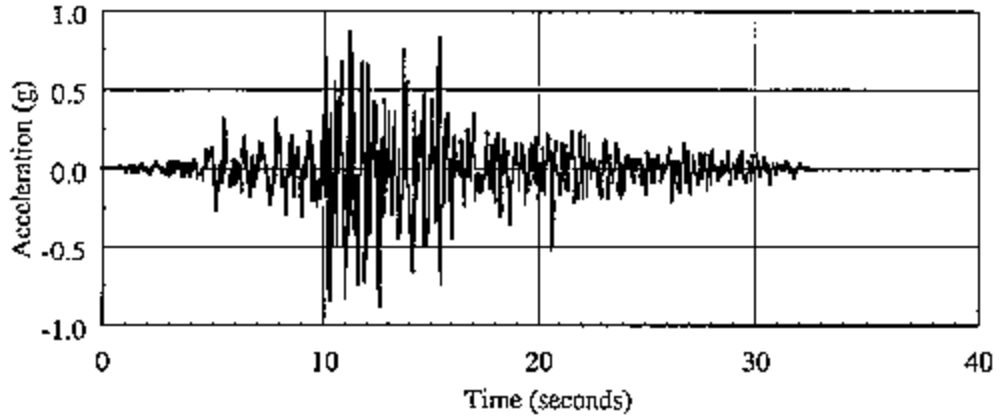

a. Acceleration history

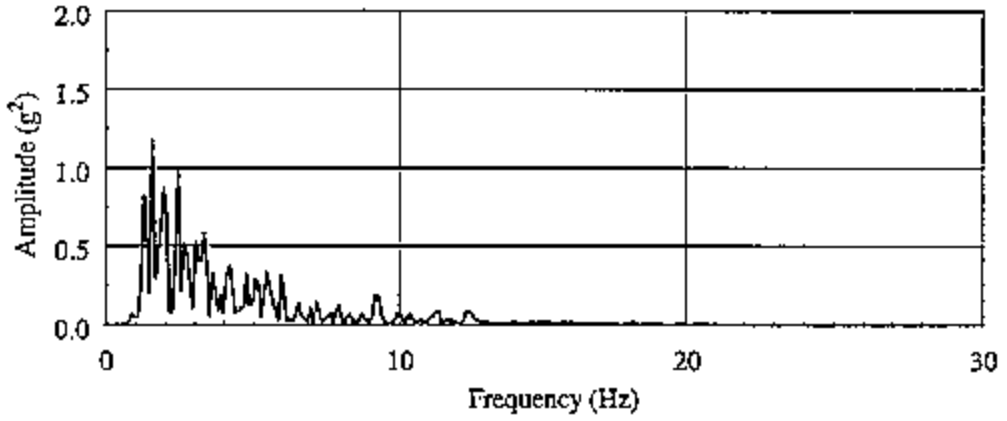

b. Power spectrum

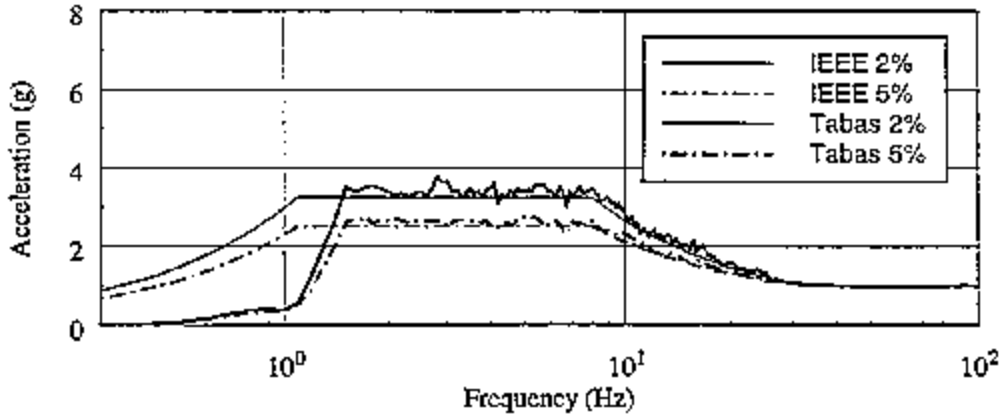

c. Response spectrum

Figure 3-7 Acceleration history, power spectrum, and response spectra for the lateral (*Y*-) component of the Tabas-A record

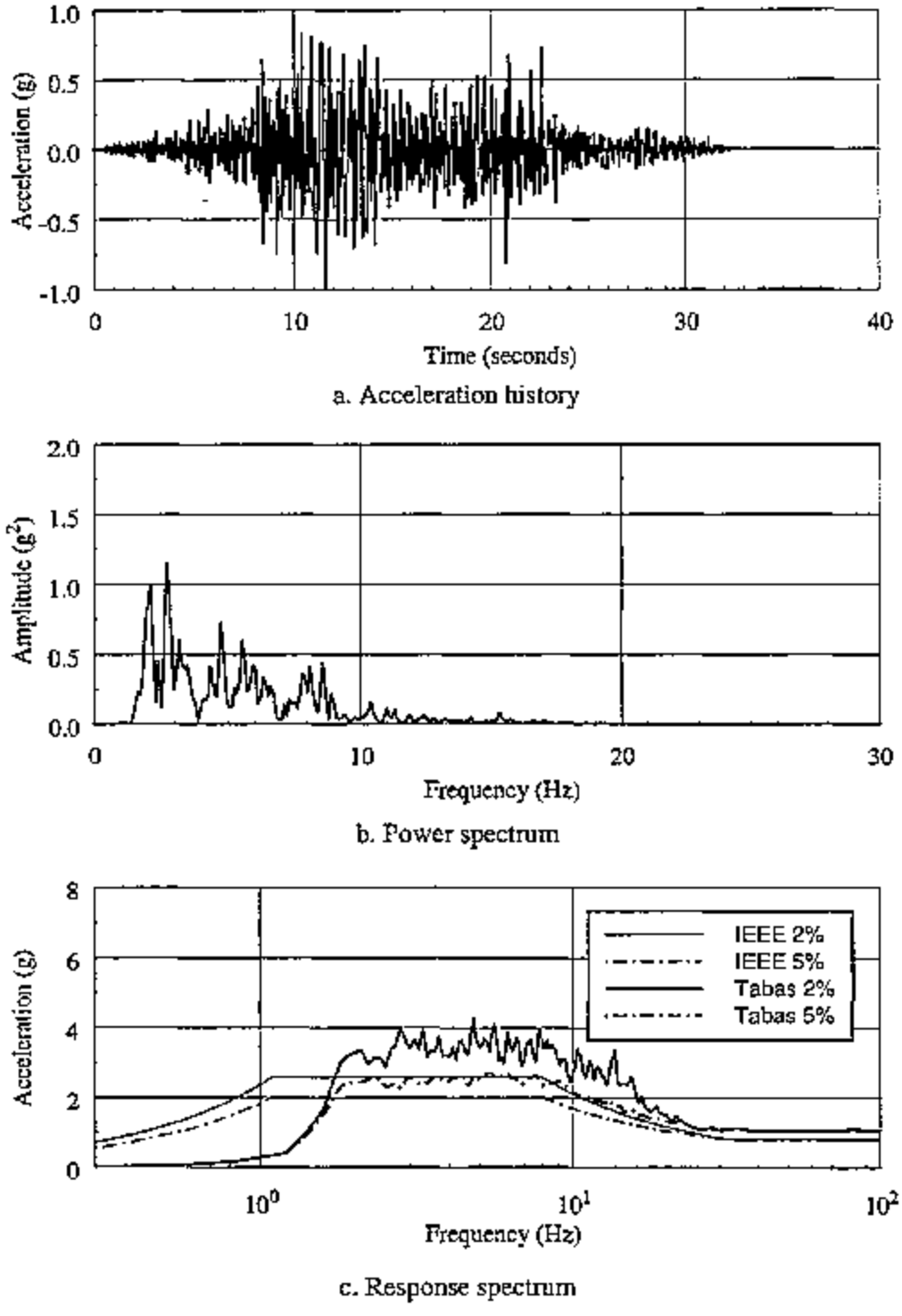

Figure 3-8 Acceleration history, power spectrum, and response spectra for the vertical (Z-) component of the Tabas-A record

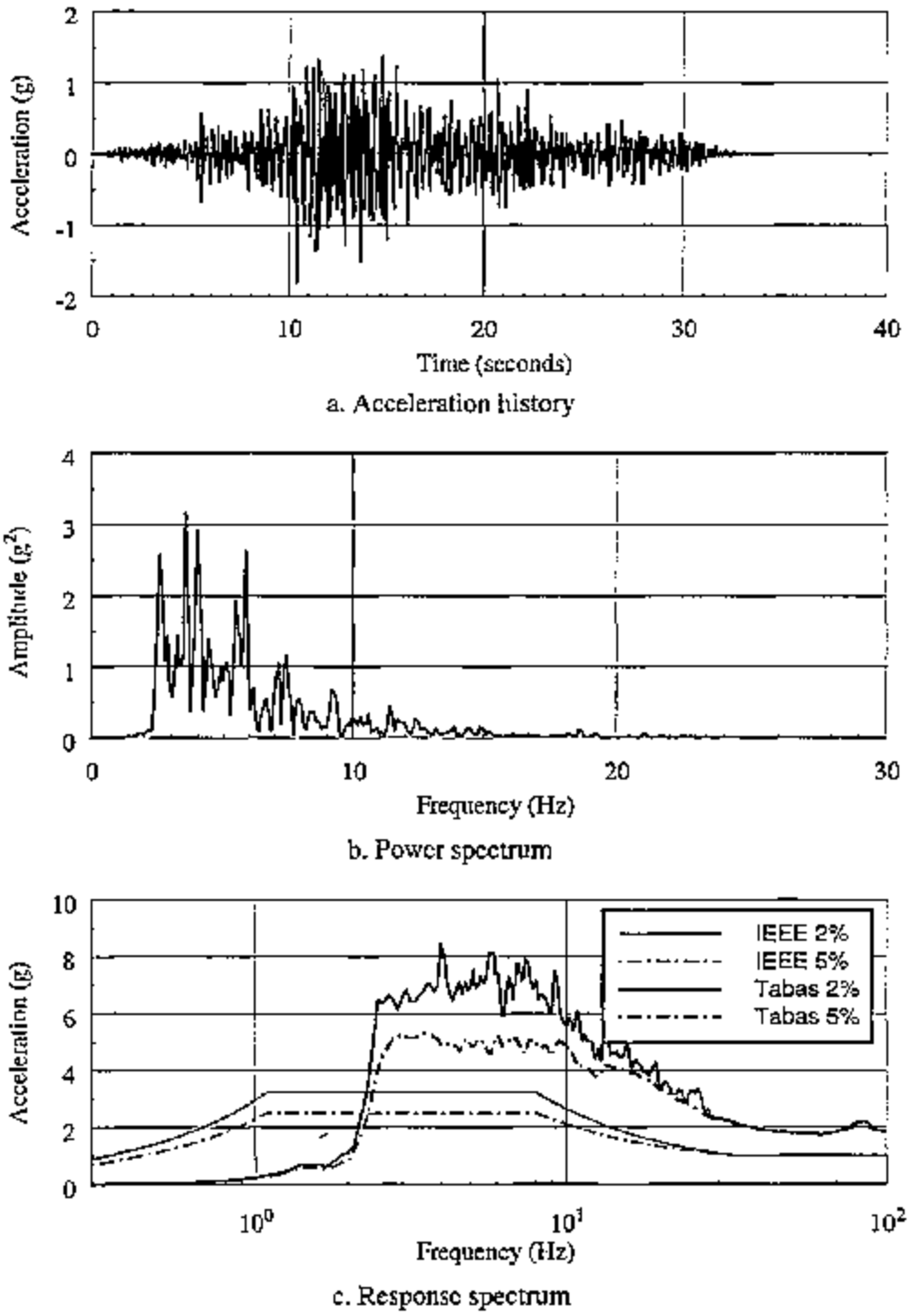

Figure 3-9 Acceleration history, power spectrum, and response spectra for the longitudinal (*X*-) component of the Tabas-B record

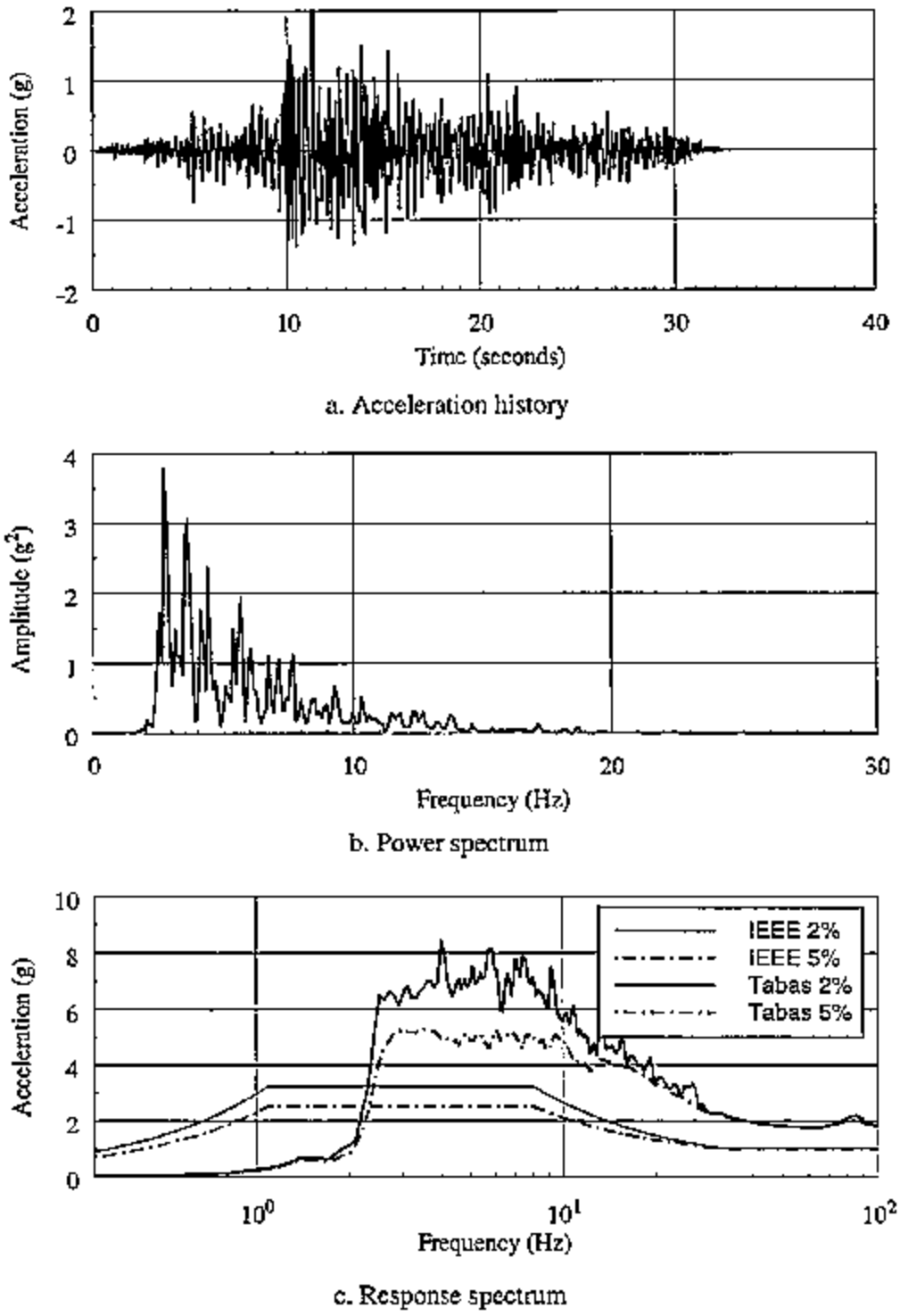

Figure 3-10 Acceleration history, power spectrum, and response spectra for the lateral (*Y*-) component of the Tabas-B record

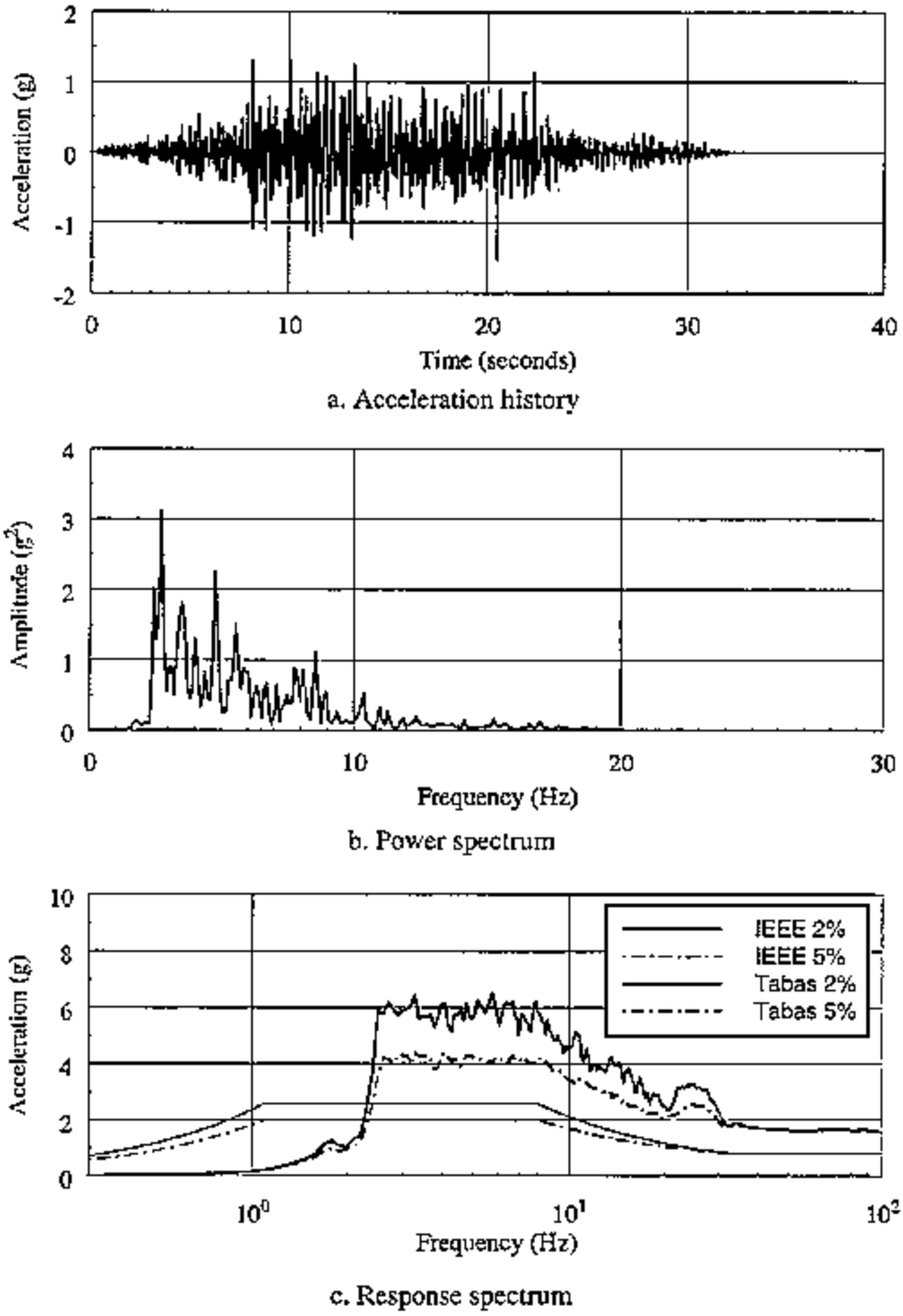

Figure 3-11 Acceleration history, power spectrum, and response spectra for the vertical (Z-) component of the Tabas-B record

CHAPTER 4
SUMMARY OF EXPERIMENTAL DATA

4.1 Overview

The objectives of the testing program were to evaluate the seismic behavior of 550 kV transformer bushings by testing Bushing-1 and Bushing-2 to failure, to qualify Bushing-3 to the Moderate Level, and to evaluate the efficacy of manufacturer-detailed modifications to 550 kV bushings (Bushing-2 and Bushing-3). The key modifications are listed in Table 1-1. For seismic testing, each bushing was installed in the rigid mounting frame described in Section 2.3. A photograph of one of the bushings installed in the mounting frame is presented in Figure 1-2.

The following sections summarize the dynamic properties and the seismic response of the bushings. Section 4.4 discusses the qualification of Bushing-3. Section 4.5 presents fragility data for Bushing-1 and Bushing-2, and critiques the IEEE 693-1997 procedures for fragility testing of substation equipment.

4.2 Dynamic Properties of 550 kV Bushings

Sine-sweep and white-noise tests were used to calculate the modal frequencies and damping ratios for each bushing. Matlab (Mathworks, 1999) was used to process the experimental data. The data was zero-corrected and low-pass filtered with a corner and cut-off frequencies of 30 Hz. Figures 4-1 to 4-3 show the transfer functions between the upper tip of the bushing and the mounting frame in the three local directions (x, y, z) for Bushing-1, Bushing-2, and Bushing-3, respectively. The resonant frequency in the local x- and y-directions is approximately 8 Hz. Damping ratios of approximately 4 percent of critical were obtained using the half-power bandwidth method.

Table 4-1 summarizes the measured dynamic properties of the bushings. Modal data could not be determined for the local z-direction. The modal frequencies differ slightly in x- and y- directions due to the unsymmetric distribution of lifting lugs immediately above the flange plate.

Table 4-1 Modal properties of bushings from sine-sweep tests

	Frequency (Hz)		*Damping Ratio (% critical)*	
Bushing	*x-direction*	*y-direction*	*x-direction*	*y-direction*
1	8.2	7.9	4	4
2	8.0	8.2	4	4
3	8.0	7.8	4	4

4.3 Earthquake Testing of Bushing-1, Bushing-2, and Bushing-3

4.3.1 Introduction

The list of earthquake tests and key observations for Bushing-1, Bushing-2, and Bushing-3 are listed in Tables 4-2 to 4-4, respectively. After each earthquake test, the response data were analyzed, the bushing was inspected for damage and oil seepage, and the bolts joining the bushing flange plate to the adaptor plate, and the adaptor plate to the mounting plate, were checked for tightness. All bolts were found to be tight for all tests.

Table 4-2 Summary of earthquake testing of Bushing-1

Test No.	*Test date*	*Identification*[1]	*PGA*[2]	*Comments*
1	03/29/99	WN-X	0.1g	
2	03/29/99	WN-Y	0.1g	
3	03/29/99	WN-Z	0.1g	
4	03/29/99	SS-X	0.1g	
5	03/29/99	SS-Y	0.1g	
6	03/29/99	SS-Z	0.1g	
7	03/29/99	Tabas-A	0.1g	
8	03/30/99	Tabas-A	0.2g	
9	03/30/99	Tabas-A	0.3g	
10	03/30/99	Tabas-A	0.5g	Oil leak at the gasket connection[3].
11	03/30/99	Tabas-A	0.5g	Repeat test to investigate whether oil will lubricate gasket and facilitate slip of porcelain.
12	03/30/99	Tabas-A	0.7g	Oil leak and slip of porcelain above gasket.
13	03/31/99	SS-X	0.1g	Install manufacturer's shipping ring around gasket connection.
14	03/31/99	SS-Y	0.1g	
15	03/31/99	SS-Z	0.1g	
16	03/31/99	Tabas-A	0.7g	Oil leak at gasket connection
17	03/31/99	Tabas-A	1.0g	Large slip of porcelain over gasket; rotation of shipping ring; see Figure 4-4.

1. WN = white noise, SS = sine sweep; -X, -Y, and -Z denote direction of testing in global coordinate system; Tabas-A = spectrum-compatible Tabas-A earthquake histories; Tabas-B = spectrum-compatible Tabas-B earthquake histories

2. PGA = target peak acceleration of the simulator platform

3. Connection of UPPER-1 porcelain unit to the flange plate

Table 4-3 Summary of earthquake testing of Bushing-2

Test No.	*Test date*	*Identification*[1]	*PGA*[2]	*Comments*
1	04/05/99	WN-X	0.1g	
2	04/05/99	WN-Y	0.1g	
3	04/05/99	WN-Z	0.1g	
4	04/05/99	SS-X	0.1g	
5	04/05/99	SS-Y	0.1g	
6	04/05/99	SS-Z	0.1g	
7	04/05/99	Tabas-A	0.1g	
8	04/05/99	Tabas-A	0.2g	
9	04/05/99	Tabas-A	0.3g	
10	04/05/99	Tabas-A	0.5g	
11	04/05/99	Tabas-A	0.7g	
12	04/05/99	Tabas-A	1.0g	
13	04/05/99	Tabas-B	1.2g	Oil leak at the gasket connection[3]; large slip of UPPER-1 porcelain unit over the flange plate; gasket visible; see Figure 4-5.

1. WN = white noise, SS = sine sweep; -X, -Y, and -Z denote direction of testing in global coordinate system; Tabas-A = spectrum-compatible Tabas-A earthquake histories; Tabas-B = spectrum-compatible Tabas-B earthquake histories

2. PGA = target peak acceleration of the simulator platform

3. Connection of UPPER-1 porcelain unit to the flange plate

The following subsections present peak responses of the mounting frame and the bushings; data related to the qualification and fragility testing of Bushing-1, Bushing-2, and Bushing-3; and local response characteristics of the bushings measured at the junction of the UPPER-1 porcelain unit and the flange plate.

4.3.2 Peak Responses

The transducer response histories were processed using the computer program Matlab (Mathworks, 1999). Experimental histories were low-passed filtered using a rectangular filter with a cut-off frequency of 30 Hz and then zero-corrected if necessary.

The peak acceleration responses of the mounting frame and the bushings are presented in Tables 4-5 and 4-6, respectively. Only the peak responses at the upper tip of each bushing are reported; the maximum accelerations at the base of the bushings were always less than those at the upper tip.

Table 4-4 Summary of earthquake testing for Bushing-3

Test No.	*Test date*	*Identification*[1]	*PGA*[2]	*Comments*
1	04/20/99	SS-X	0.1g	
2	04/20/99	SS-Y	0.1g	
3	04/20/99	SS-Z	0.1g	
4	04/20/99	Tabas-A	1.0g	Slight slip of porcelain; no evidence of oil leak. spectral amplitude lower than target value at bushing frequency of approximately 8 Hz; adjust simulator span setting and retest.
5	04/20/99	Tabas-A	1.0g	Noticeable slip of porcelain over the gasket connection[3]; gasket visible; significant oil leakage; see Figures 4-6 and 4-7.

1. WN = white noise, SS = sine sweep; -X, -Y, and -Z denote direction of testing in global coordinate system; Tabas-A = spectrum-compatible Tabas-A earthquake histories; Tabas-B = spectrum-compatible Tabas-B earthquake histories

2. PGA = target peak acceleration of the simulator platform

3. Connection of UPPER-1 porcelain unit to the flange plate

The peak displacement responses of the bushings relative to the mounting frame are presented in Table 4-7. Only the peak responses in the global X-direction and global Y-direction at the upper tip of each bushing are reported; the maximum displacements at the base of the bushings were always less than those at the upper tip.

A total of sixteen transducers measured porcelain strain (channels 39 through 42), radial motion of the flange plate with respect to mounting frame (channels 43 through 46), radial motion of the UPPER-1 porcelain unit with respect to mounting frame (channels 47 through 50), and local vertical motion of the UPPER-1 porcelain unit with respect to the flange plate (channels 51 through 54). Maximum values, computed as the peak value of the four transducers, for porcelain strain, local UPPER-1 radial motion, and local UPPER-1 vertical motion, are presented in Table 4-8.

4.3.3 Response of the Mounting Frame

The mounting frame was designed to be *rigid* and thus not amplify the motions of the earthquake simulator. Figure 4-8 shows the mounting frame-to-earthquake simulator transfer functions (in the X-, Y-, and Z-directions) calculated from the sine-sweep tests of Bushing-1 (Test Numbers 4 through 6). The mounting-frame accelerations were transformed into the global coordinate system for these calculations. If the mounting frame were truly rigid, the transfer function would be flat with a value equal to 1.0 across the entire frequency range. The transfer functions show little amplification of motion in the frequency range of 0 to 10 Hz, but significant amplification of

Table 4-5 Peak accelerations of the mounting frame

				Peak Acceleration (g)		
Bushing	*Test No.*	*Identification*[1]	*PGA*[2]	*x-direction*[3]	*y-direction*[3]	*z- direction*[3]
1	7	Tabas-A	0.1g	0.21	0.33	0.16
1	8	Tabas-A	0.2g	0.37	0.43	0.24
1	9	Tabas-A	0.3g	0.51	0.47	0.37
1	10	Tabas-A	0.5g	0.65	0.65	0.49
1	11	Tabas-A	0.5g	0.69	0.65	0.47
1	12	Tabas-A	0.7g	0.92	0.79	0.72
1	16	Tabas-A	0.7g	0.84	0.86	0.72
1	17	Tabas-A	1.0g	1.23	1.00	0.96
2	7	Tabas-A	0.1g	0.21	0.30	0.17
2	8	Tabas-A	0.2g	0.38	0.46	0.24
2	9	Tabas-A	0.3g	0.57	0.57	0.29
2	10	Tabas-A	0.5g	0.79	0.65	0.46
2	11	Tabas-A	0.7g	1.00	0.75	0.66
2	12	Tabas-A	1.0g	1.18	1.09	0.99
2	13	Tabas-B	1.2g	1.22	1.26	0.86
3	4	Tabas-A	1.0g	1.32	1.03	0.89
3	5	Tabas-A	1.0g	1.45	1.65	1.33

1. Tabas-A = spectrum-compatible Tabas-A earthquake histories; Tabas-B = spectrum-compatible Tabas-B earthquake histories

2. PGA = target peak acceleration of the simulator platform

3. Local coordinate system

horizontal motion for frequencies between 10 and 20 Hz. For reference, the fundamental frequency of the bushing in the *x*- and *y*- directions was approximately 8 Hz. For such a frequency the amplitude of the transfer functions range in value between 0.8 and 1.2. Accordingly, the mounting frame can be assumed to be *rigid* for the purpose of the experiments described below.

The amplification of horizontal motion above 10 Hz is due to rotational accelerations of the simulator platform which produce translational accelerations in the mounting frame. The rotational accelerations of the simulator platform are related to the oil-column frequencies of the vertical actuators that support the platform: the pitch and roll frequencies of the simulator are in the range of 13 to 18 Hz.

Table 4-6 Peak acceleration responses of the upper tip of the bushings

				Peak Acceleration (g)		
Bushing	*Test No.*	*Identification*[1]	*PGA*[2]	*x-direction*[3]	*y-direction*[3]	*Maximum*[4]
1	7	Tabas-A	0.1g	1.00	1.12	1.12
1	8	Tabas-A	0.2g	1.54	1.64	1.87
1	9	Tabas-A	0.3g	1.48	1.68	2.10
1	10	Tabas-A	0.5g	1.95	1.80	2.12
1	11	Tabas-A	0.5g	1.94	1.93	2.22
1	12	Tabas-A	0.7g	2.43	2.18	2.52
1	16	Tabas-A	0.7g	2.30	2.33	2.36
1	17	Tabas-A	1.0g	2.64	2.93	2.96
2	7	Tabas-A	0.1g	0.99	1.07	1.32
2	8	Tabas-A	0.2g	1.51	1.60	1.98
2	9	Tabas-A	0.3g	1.61	2.08	2.36
2	10	Tabas-A	0.5g	2.24	2.39	2.62
2	11	Tabas-A	0.7g	2.68	2.86	2.96
2	12	Tabas-A	1.0g	3.69	4.04	4.04
2	13	Tabas-B	1.2g	4.09	6.40	6.46
3	4	Tabas-A	1.0g	3.56	3.81	3.91
3	5	Tabas-A	1.0g	3.92	4.13	4.17

1. Tabas-A = spectrum-compatible Tabas-A earthquake histories; Tabas-B = spectrum-compatible Tabas-B earthquake histories

2. PGA = target peak acceleration of the simulator platform

3. Local coordinate system

4. Maximum vector value calculated at each time step in the response history

4.3.4 Response of Bushing-1

The global response of Bushing-1 was assessed by analysis of data from Test Number 17 (Tabas-A, target PGA equal to 1.0g). Figure 4-9 presents the translation histories in the global X- and Y-directions of the upper tip of Bushing-1 relative to the mounting frame. The maximum relative displacement between the bushing tip and the mounting frame was 2.20 in. (56 mm). The maximum total acceleration at the upper tip of the bushing was approximately 3.0g. Acceleration response spectra for Bushing-1 in the local coordinate system, generated using measured

Table 4-7 Peak relative tip displacement of the bushing relative to the mounting frame

				Peak relative displacement (in.)		
Bushing	*Test No.*	*Identification*[1]	*PGA*[2]	*X-direction*[3]	*Y-direction*[3]	*Maximum*[4]
1	7	Tabas-A	0.1g	0.20	0.32	0.32
1	8	Tabas-A	0.2g	0.23	0.31	0.32
1	9	Tabas-A	0.3g	0.26	0.39	0.40
1	10	Tabas-A	0.5g	0.46	0.54	0.57
1	11	Tabas-A	0.5g	0.47	0.67	0.69
1	12	Tabas-A	0.7g	0.93	0.95	1.11
1	16	Tabas-A	0.7g	0.78	0.88	0.94
1	17	Tabas-A	1.0g	1.70	1.51	2.20
2	7	Tabas-A	0.1g	0.17	0.23	0.25
2	8	Tabas-A	0.2g	0.23	0.30	0.35
2	9	Tabas-A	0.3g	0.24	0.38	0.41
2	10	Tabas-A	0.5g	0.37	0.47	0.47
2	11	Tabas-A	0.7g	0.50	0.58	0.64
2	12	Tabas-A	1.0g	0.89	1.14	1.14
2	13	Tabas-B	1.2g	0.97	1.67	1.68
3	4	Tabas-A	1.0g	0.91	1.29	1.35
3	5	Tabas-A	1.0g	1.44	2.15	2.40

1. Tabas-A = spectrum-compatible Tabas-A earthquake histories; Tabas-B = spectrum-compatible Tabas-B earthquake histories

2. PGA = target peak acceleration of the simulator platform

3. Global coordinate system

4. Maximum vector value calculated at each step in the response history

acceleration histories at the flange plate are shown in Figure 4-10. The zero-period accelerations for these spectra are given in Table 4-5. For information, the 2-percent and 5-percent damped IEEE 693-1997 response spectra for Moderate Level qualification (see row 5 of Table 3-1) are also shown in this figure.

Figure 4-11a shows the relation between the average vertical displacement in the local z-direction and rocking about the local y-axis. The average vertical displacement in the z-direction was calculated as one-half of the sum of the channel 51 and channel 53 displacements. Rocking about the local y-axis was calculated as the difference between the channel 51 and 53 displacements divided by the 36-in. (914 mm) distance between these transducers. Figure 4-11b shows the relation between the average vertical displacement in the local z-direction and rocking about the local x-axis. The average vertical displacement in the z-direction was calculated as one-half of the

Table 4-8 Peak local responses of UPPER-1 porcelain units

				Maximum response[3]		
Test Number	*Bushing*	*Identification*[1]	*PGA*[2]	*Porcelain strain (με)*	*Radial displacement (inches)*	*Vertical displacement (inches)*
1	7	Tabas-A	0.1g	14	0.010	0.005
1	8	Tabas-A	0.2g	22	0.014	0.009
1	9	Tabas-A	0.3g	27	0.018	0.013
1	10	Tabas-A	0.5g	36	0.036	0.024
1	11	Tabas-A	0.5g	33	0.051	0.028
1	12	Tabas-A	0.7g	47	0.261	0.053
1	16	Tabas-A	0.7g	67	0.040	0.040
1	17	Tabas-A	1.0g	100	0.410	0.090
2	7	Tabas-A	0.1g	15	0.007	0.004
2	8	Tabas-A	0.2g	19	0.011	0.007
2	9	Tabas-A	0.3g	22	0.012	0.010
2	10	Tabas-A	0.5g	39	0.015	0.014
2	11	Tabas-A	0.7g	31	0.020	0.018
2	12	Tabas-A	1.0g	74	0.041	0.036
2	13	Tabas-B	1.2g	140	0.520	0.100
3	4	Tabas-A	1.0g	76	0.060	0.040
3	5	Tabas-A	1.0g	490	1.100	0.126

1. Tabas-A = spectrum-compatible Tabas-A earthquake histories; Tabas-B = spectrum-compatible Tabas-B earthquake histories

2. PGA = target peak acceleration of the simulator platform

3. Local coordinate system; maximum displacement relative to flange plate for each test after zero-correction

sum of the channel 52 and channel 54 displacements; the rocking about the local x-axis was calculated as the difference between the channel 52 and 54 displacements divided by the 36-in. (914 mm) distance between these transducers. The maximum uplift at the edge of porcelain unit (listed in Table 4-8) can be computed by adding the product of the rocking angle and the radius of the UPPER-1 porcelain unit, at the flange plate, to the average longitudinal displacement.

Figure 4-12 presents the zero-corrected displacement orbit of the center of the bushing, measured at the height of the radial displacement transducers, relative to the flange plate. The coordinates (x,y) of the UPPER-1 porcelain unit at the start of the test (corresponding to prior slip of the unit) were (0.12, 0.20) inch. The predominant relative displacement of the bushing lies along an axis at

45 degrees to the local x-axis and y-axis of the bushing. It is noted that both the shear deformation in the gasket and the slip of UPPER-1 porcelain over the gasket contribute to the displacement orbit. At the conclusion of the test, the coordinates of the unit were (0.12, 0.32) in., corresponding to a 0.35 in. (9 mm) of total slip.

4.3.5 Response of Bushing-2

The global response of Bushing-2 was assessed by analysis of data from Test Number 13 (Tabas-B, target PGA equal to 1.2g). Figure 4-13 presents the translation histories in the global X- and Y-directions of the upper tip of Bushing-2 relative to the mounting frame. The maximum relative displacement between the bushing tip and the mounting frame was 1.68 in. (43 mm). The maximum total acceleration at the upper tip of the bushing exceeded 6.4g. Acceleration response spectra for Bushing-2 in the local coordinate system, generated using measured acceleration histories of the flange plate are shown in Figure 4-14. The zero-period accelerations for these spectra are given in Table 4-5. For information, the 2-percent and 5-percent damped IEEE 693-1997 response spectra for Moderate Level qualification (see row 5 of Table 3-1) are also shown in this figure.

Figure 4-15a shows the relation between the average vertical displacement in the local z-direction and rocking about the local y-axis. Figure 4-15b shows the relation between the average vertical displacement in the local z-direction and rocking about the local x-axis. Rocking of the UPPER-1 porcelain unit was accompanied by translation in the local z-direction. Such translation of 0.03 inch (0.8 mm) likely led to oil leakage.

Figure 4-16 presents the zero-corrected displacement orbit of the center of the bushing, measured at the height of the radial displacement transducers, relative to the flange plate. The coordinates (x,y) of the UPPER-1 porcelain unit at the start of the test (corresponding to prior slip of the unit) were (0.06, 0.06) inch. The predominant relative displacement of the bushing lies along the local y-axis of the bushing. It is noted that both the shear deformation in the gasket and the slip of UPPER-1 porcelain over the gasket contribute to the displacement orbit. At the conclusion of the test, the coordinates of the unit were (0.10, 0.58) in., corresponding to a 0.59 in. (15 mm) of total slip.

4.3.6 Response of Bushing-3

The global response of Bushing-3 was assessed by analysis of data from Test Number 5 (Tabas-A, target PGA equal to 1.0g). Figure 4-17 presents the translation histories in the global X- and Y-directions of the upper tip of Bushing-3 relative to the mounting frame. The maximum relative displacement between the bushing tip and the mounting frame was 2.40 in. (61 mm). The maximum total acceleration at the upper tip of the bushing was approximately equal to 4.2g. Acceleration response spectra for Bushing-3 in the local coordinate system, generated using measured acceleration histories of the flange plate are shown in Figure 4-18. The zero-period accelerations for these spectra are given in Table 4-5. For information, the 2-percent and 5-percent damped IEEE 693-1997 response spectra for Moderate Level qualification (see row 5 of Table 3-1) are also shown in this figure.

Figure 4-19a shows the relation between the average vertical displacement in the local z-direction and rocking about the local y-axis. Figure 4-19b shows the relation between the average vertical displacement in the local z-direction and rocking about the local x-axis. Rocking of the UPPER-1 porcelain unit was accompanied by translation in the local z-direction. Such translation of 0.07 in. (1.8 mm) likely led to oil leakage.

Figure 4-20 presents the displacement orbit of the center of the bushing, measured at the height of the radial displacement transducers, relative to the flange plate. The coordinates (x,y) of the UPPER-1 porcelain unit at the start of the test (corresponding to prior slip of the unit) were (0.01, 0.03) inch. The predominant relative displacement of the bushing lies along an axis at 45 degrees to the local x-axis and y-axis of the bushing. It is noted that both the shear deformation in the gasket and the slip of UPPER-1 porcelain over the gasket contribute to the displacement orbit. At the conclusion of the test, the coordinates of the unit were (0.72, 0.81) in., corresponding to a 1.1 in. (28 mm) of total slip.

4.4 Seismic Qualification of Bushing-3

To satisfy the IEEE 693-1997 requirements for Moderate Level qualification, the measured peak horizontal acceleration at the bushing flange is required to be 0.50g (see Appendix A). For this level of shaking, IEEE 693-1997 states that the stresses in the porcelain components must be less than 50 percent of the ultimate stress, and the factor of safety against oil leakage must be greater than or equal to 2.0. An alternative approach that is identified in Annex D5.1(d) of IEEE 693-1997 was used to evaluate qualification of Bushings. Namely, earthquake histories with spectral ordinates twice those of the Test Response Spectrum were used for testing: the target peak horizontal acceleration at the bushing flange was 1.0g. Porcelain stresses at this level of earthquake shaking were required to be less than or equal to the ultimate value, and there was to be no evidence of oil leakage. Similarly, qualification of transformer bushings at the High Level requires the use of earthquake histories with spectral ordinates twice those of the target spectrum described in the previous paragraph. Using a target peak acceleration for these histories of 2.0g, a bushing would be qualified at the High Level if the porcelain stresses were less than the ultimate value and there was no evidence of oil leakage.

Bushing-3 was built for the purpose of qualification to the Moderate Level. The bushing passed the requisite IEEE electrical tests prior to shipment to Berkeley for testing. Table 4-4 lists the tests of Bushing-3. Bushing-3 leaked oil and its UPPER-1 porcelain unit slipped significantly during Test Number 5 (see Figures 4-6 and 4-7). As such, data from Test Number 4 was used to judge the response of Bushing-3. The peak accelerations of the mounting frame during this test were 1.32g, 1.03g, and 0.89g, in the local x-, y-, and z-directions, respectively (see Table 4-5). Figure 4-21 presents 5-percent damped spectra evaluated using the x- and y-histories of the mounting plate of Test Number 4.

The peak input accelerations of the mounting plate exceed the zero-period accelerations of the IEEE spectrum (1.0g, 1.0g, and 0.8g, in the local x-, y-, and z-directions, respectively). The local x-direction spectral acceleration at the fundamental frequency of the bushing (8 Hz) exceeds the target IEEE spectral value of 2.5g by approximately 15 percent (see Figure 4-21a). The local y-

direction spectral acceleration at a frequency of 8 Hz is less than 80 percent of the target value (see Figure 4-21b). For qualification, the spectral accelerations in both principal directions must exceed the target IEEE values. As such, Bushing-3 did not meet the IEEE 693-1997 standards for qualification at the Moderate Level.

4.5 Fragility Testing of Bushings

4.5.1 Introduction

Fragility curves for electrical equipment are often developed using information from testing programs such as the program described in this report. Such curves typically relate the cumulative probability of exceeding a limit state to a ground motion parameter such as spectral acceleration or peak ground acceleration and serve to partly account for randomness and uncertainty in both seismic demand and component capacity. Seismic demand and component capacity are typically assumed to be random variables that conform to either a normal or log-normal distribution. Component performance can then be described by a log-normal distribution and the component fragility curve is given by a log-normal cumulative probability density function.

Peak ground acceleration is a poor seismic demand parameter because acceleration alone is a poor descriptor of the damage potential of an earthquake history. Spectral acceleration at the fundamental frequency of the bushing is an improved demand parameter but unless the installed configuration exactly replicates the tested configuration, spectral capacities measured in the laboratory are likely unreliable. (For example, the 550-kV bushings tested on the Berkeley simulator had no top-mounted terminal and were attached to a stiff mounting frame. In the field, such bushings are often equipped with terminals of significant weight, the terminals are connected to other substation equipment, and the bushings are mounted on transformers with flexible turrets. Such differences between the tested and installed configurations can substantially modify the dynamic characteristics of the bushings.) An average value of spectral acceleration over a broad range of frequencies would provide a better estimate of bushing capacity (resistance to either porcelain-unit slip or oil leakage) than a single value of spectral acceleration.

4.5.2 Fragility Data for Peak Ground (Input) Acceleration

Each value of peak acceleration listed below was taken as the greater of the maximum accelerations of the mounting frame along the local x- and y-axes for the test immediately prior to that test in which the specified limit state was exceeded. For example, if a bushing was subjected to increasing levels of ground shaking with each test in the fragility sequence, and if the bushing exceeded a limit state in Test 100, fragility data would be collected from Test 99. If during Test 99, the maximum local x- and y- accelerations of the mounting frame were 0.5g and 0.4g, respectively, the fragility data point would be taken as 0.5g. Although the utility of such an approach is questionable unless the reported acceleration is a principal acceleration and the limit state is exceeded due to shaking along the principal acceleration axis, this procedure is conventional and is therefore adopted herein.

If the limiting state of bushing response is oil leakage, Bushing-1 reached this limit state at a peak horizontal acceleration (in the local coordinate system) of 0.51g. (Bushing-1 leaked oil during Test Number 10 and fragility data are calculated using data from Test Number 9.) Bushing-2 and Bushing-3 reached this limit state at peak accelerations of 1.18g and 1.32g, respectively. If the limiting state of response is slip of the porcelain unit above the flange plate, Bushing-1 reached this limit state at a peak horizontal acceleration (in the local coordinate system) of 0.69g. Bushing-2 and Bushing-3 reached this limit state at peak accelerations of 1.18 and 1.32g, respectively.

Figure 4-21 illustrates this process for Test Number 4 of Bushing-3. The 5-percent damped spectra in parts (a) and (b) of this figure were generated using the acceleration histories of the mounting plate in the local x- and y-directions. The maximum accelerations of the mounting frame were 1.32 g and 1.03 g in the local x- and y-directions, respectively (see Table 4-5).

4.5.3 Fragility Data for Spectral Acceleration

Each value of spectral acceleration listed below was taken as the greater of the two spectral accelerations calculated using the acceleration histories of the mounting plate in the local x- and y-directions. If 5-percent damped spectral acceleration at the fundamental frequency of the bushing (=8 Hz) is used as the seismic demand parameter and if the limiting state of response is oil leakage, Bushing-1 reached this limit state at a spectral acceleration (in the local coordinate system) of 1.18g. Bushing-2 and Bushing-3 reached this limit state at spectral accelerations of 2.79g and 2.92g, respectively. If the limiting state of response is slip of the porcelain unit above the flange plate, Bushing-1 reached this limit state at a spectral acceleration (in the local coordinate system) of 1.53g. Bushing-2 and Bushing-3 reached this limit state at spectral accelerations of 2.79g and 2.92g, respectively.

Figure 4-21 illustrates this calculation for Test Number 4 of Bushing-3. At a frequency of 8 Hz (see vertical dash-dot line in the figure), the spectral accelerations in the local x- and y-directions were 2.92g and 1.88g, respectively.

4.5.4 Fragility Data for Average Spectral Acceleration

Average spectral acceleration over a range of frequencies including the fundamental frequency of the bushing will provide fragility data for a range of bushing-support conditions. If the test configuration includes a near-rigid mounting frame, the frequency range should be less than and equal to the fundamental frequency of the bushing. The spectral response should not vary widely over the selected frequency range otherwise the reported value may be substantially unconservative for a number of support conditions. A frequency range of 4 Hz to 8 Hz was selected to calculate the average spectral acceleration for these studies. If the limiting state of response is oil leakage, Bushing-1 reached this limit state at an average spectral acceleration (in the local coordinate system) of 0.99g. Bushing-2 and Bushing-3 reached this limit state at a average spectral accelerations of 2.85g and 2.94g, respectively. If the limiting state of response is slip of the porcelain unit above the flange plate, Bushing-1 reached this limit state at a average spectral acceleration (in the local coordinate system) of 1.48g. Bushing-2 and Bushing-3 reached this limit state at average spectral accelerations of 2.85g and 2.94g, respectively.

Figure 4-21 illustrates the above process for Test Number 4 of Bushing-3. In the frequency range of 4 Hz to 8 Hz, the average spectral accelerations in the local x- and y-directions were 2.94g and 2.39g, respectively (see the horizontal dashed line in each figure). In the local x- and y-directions, the spectral accelerations at a frequency of 8 Hz are equal to or less than the average spectral accelerations by factors of 1.0 and 0.8, respectively.

4.5.5 Fragility Estimates from Principal Acceleration Data

The fragility data presented in the preceding sections listed peak values and made use of measured acceleration histories in the local x- and y-directions of the 550 kV bushings. Although the approach adopted above constitutes conventional practice, it may be inappropriate for several reasons. First, if damage (oil leakage, slippage) is maximized along an axis that is rotated from the coordinate system from which the fragility data (maximum acceleration, spectral acceleration) were calculated, do the reported values correctly characterize the response of the bushing? Second, should principal acceleration data be used instead of acceleration data from the local coordinate system? Third, should maximum or minimum values be reported?

The following paragraphs present fragility data calculated using acceleration histories from coordinate systems (Axis 1, Axis 2) that are rotated from the local x- and y-directions. Such data are presented to foster discussion on the utility of the IEEE 693-1997 procedures for equipment fragility testing and qualification. No recommendations for changing the current IEEE procedures are made at this time.

Accelerations along axes rotated from the local x- and y-directions were calculated using the following transformation:

$$\begin{bmatrix} a_1 \\ a_2 \end{bmatrix} = \begin{bmatrix} \cos\theta & \sin\theta \\ -\sin\theta & \cos\theta \end{bmatrix} \begin{bmatrix} a_x \\ a_y \end{bmatrix} \tag{4-1}$$

where a_1 and a_2 are the accelerations along Axis 1 and Axis 2, respectively; θ is the angle of rotation from the horizontal (x) axis (measured in the x-y plane); and a_x and a_y are the accelerations along the local x- and y-axes. Table 4-9 lists peak and spectral acceleration data for 10-degree increments of axis rotation for Test Number 4 of Bushing-3. Figure 4-22 presents 5-percent damped acceleration response spectra for 10-degree increments of axis rotation for Test Number 4 of Bushing-3. For reference, Bushing-3 slipped in a direction at 45 degrees to the local coordinate system (see Figure 4-20 for Test Number 5).

In the unrotated coordinate system, the *fragility* peak acceleration of Bushing-3 was 1.32g. In the direction of slip, the maximum peak acceleration of 1.50g is greater than the *fragility* peak acceleration by 15 percent. The minimum value of peak acceleration was 0.92g, 70 percent of the *fragility* value in the unrotated coordinate system.

Columns 4 and 5 of Table 4-9 list 5-percent damped spectral accelerations at a frequency of 8 Hz. The *fragility* spectral acceleration of Bushing-3 was 2.92g. The maximum and minimum values of spectral acceleration listed in columns 4 and 5 are 112 percent and 62 percent of the *fragility* spectral acceleration. Figure 4-22 shows the variations in spectral response along Axes 1 and 2 as a function of the rotation angle θ.

Mean values of spectral acceleration in the frequency range of 4 to 8 Hz are listed in columns 6 and 7 of Table 4-9. Such a frequency range would cover a broad range of support conditions for a bushing with a fundamental frequency of 8 Hz. The maximum and minimum values of spectral acceleration listed in these columns are 110 percent and 70 percent of the *fragility* spectral acceleration. In this frequency range, the ordinates of the response spectra (see Figure 4-21) vary widely and the use of mean spectral values might be unconservative.

Variations in spectral response over a frequency range could be addressed through the use of mean-minus-one-standard-deviation values of spectral acceleration. For Test Number 4, these values of spectral acceleration range between 80 and 90 percent of mean values, and the maximum and minimum values are 93 percent and 59 percent of the *fragility* spectral acceleration of 2.92g.

4.5.6 Summary

Conventional procedures for reporting fragility data for substation equipment such as transformer may be neither appropriate nor conservative. The fragility data reported above were based on earthquake simulator testing of a bushing installed in a *rigid* mounting frame. This configuration is likely not representative of a field installation because (a) bushings are often mounted on flexible components, (b) terminals of significant weight are often attached to the upper tip of the bushing, and (c) the terminals are connected to other substation equipment. Such differences could substantially modify both the modal properties of the bushing and the critical loading environment.

Putting aside these shortcomings, the fragility data presented in the previous sections are substantially scattered. Maximum and minimum values for different fragility parameters are summarized in Table 4-10. Use of the minimum values for the fragility parameters will be conservative but will likely be misleading. Improved strategies for characterizing the fragility of substation equipment are obviously needed.

Table 4-9 Fragility data for Bushing-3, Tabas-A, Test Number 4

	PGA *[g]*[1]		*PSa(f=8Hz,ξ=0.05)* *[g]*[2]		*PSa(4<f<8Hz,ξ=0.05)*$_{\mu}$ *[g]*[3]		*PSa(4<f<8Hz,ξ=0.05)*$_{\mu-1\sigma}$ *[g]*[4]	
θ[5]	*Axis 1*	*Axis 2*	*Axis 1*	*Axis 2*	*Axis 1*	*Axis 2*	*Axis 1*	*Axis 2*
0	1.32	1.03	2.92	1.88	2.94	2.39	2.65	2.10
10	1.40	1.00	3.13	1.83	3.11	2.21	2.70	1.89
20	1.45	0.95	3.25	1.89	3.20	2.10	2.71	1.78
30	1.50	0.92	3.27	1.94	3.22	2.06	2.66	1.72
40	1.51	0.98	3.19	1.95	3.17	2.13	2.58	1.82
50	1.48	1.00	3.02	2.15	3.06	2.29	2.46	2.03
60	1.40	1.09	2.75	2.29	2.91	2.46	2.34	2.21
70	1.28	1.16	2.40	2.39	2.73	2.60	2.25	2.37
80	1.15	1.26	2.13	2.65	2.56	2.74	2.21	2.52
90	1.03	1.32	1.88	2.92	2.39	2.94	2.10	2.65

1. Peak acceleration of mounting plate along axes of rotated (*Axis 1, Axis 2*) coordinate system

2. Spectral acceleration at frequency of 8 Hz and damping ratio of 5 percent, along axes of rotated (*Axis 1, Axis 2*) coordinate system

3. Mean spectral acceleration over frequency range of 4 Hz to 8 Hz and damping ratio of 5 percent, along axes of rotated (*Axis 1, Axis 2*) coordinate system

4. Mean minus one standard deviation spectral acceleration over frequency range of 4 Hz to 8 Hz and damping ratio of 5 percent, along axes of rotated (*Axis 1, Axis 2*) coordinate system

5. Counter-clockwise angle of rotation of local (x,y) coordinate system into (*Axis 1, Axis 2*) coordinate system

Table 4-10 Summary of fragility data for Bushing-3 from Test Number 4

	PGA *[g]*[1]	*PSa(f=8Hz,ξ=0.05)* *[g]*[2]
Maximum	1.52	3.27
Minimum	0.92	1.83

1. Peak acceleration of mounting plate along all axes of rotated (*Axis 1, Axis 2*) coordinate system

2. Spectral acceleration at frequency of 8 Hz and damping ratio of 5 percent, along all axes of rotated (*Axis 1, Axis 2*) coordinate system

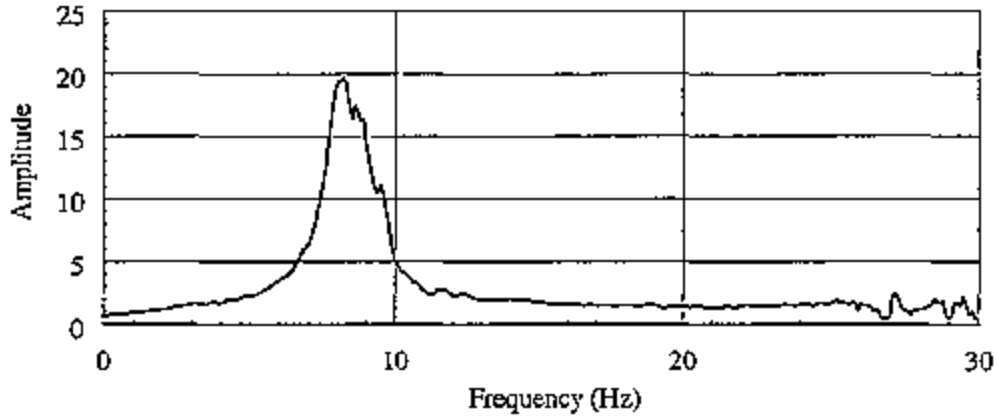

a. x-direction

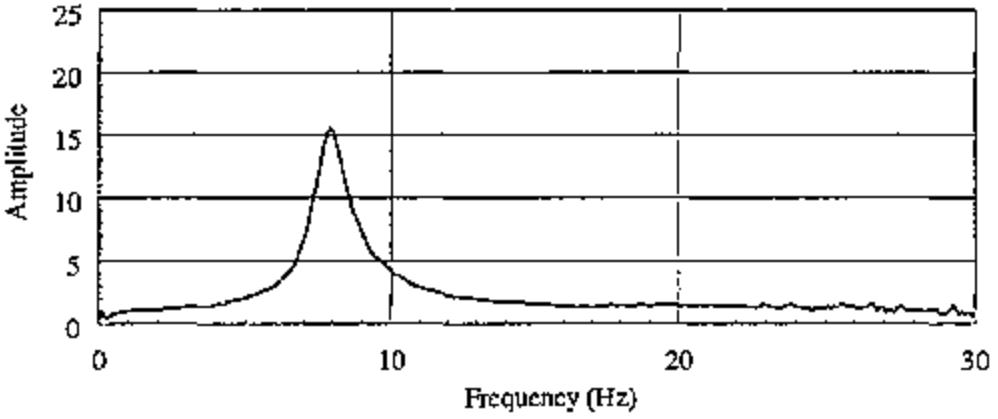

b. y-direction

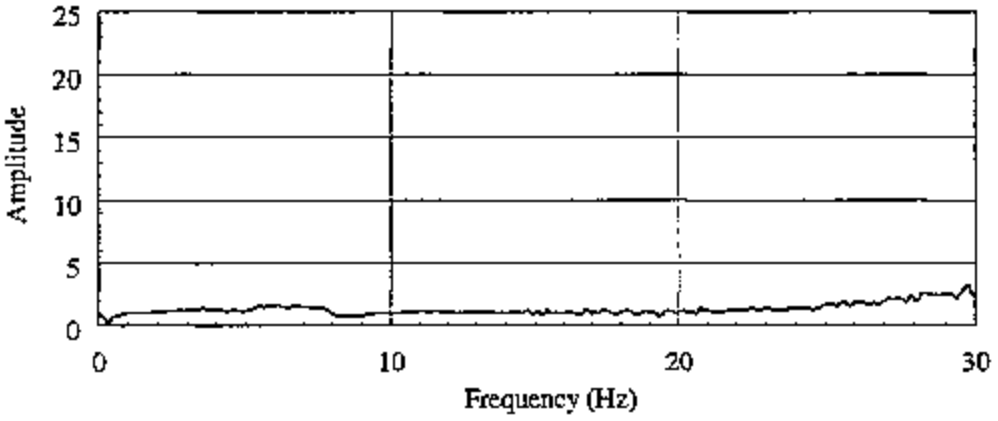

c. z-direction

Figure 4-1 Bushing-1 upper tip to mounting frame transfer functions

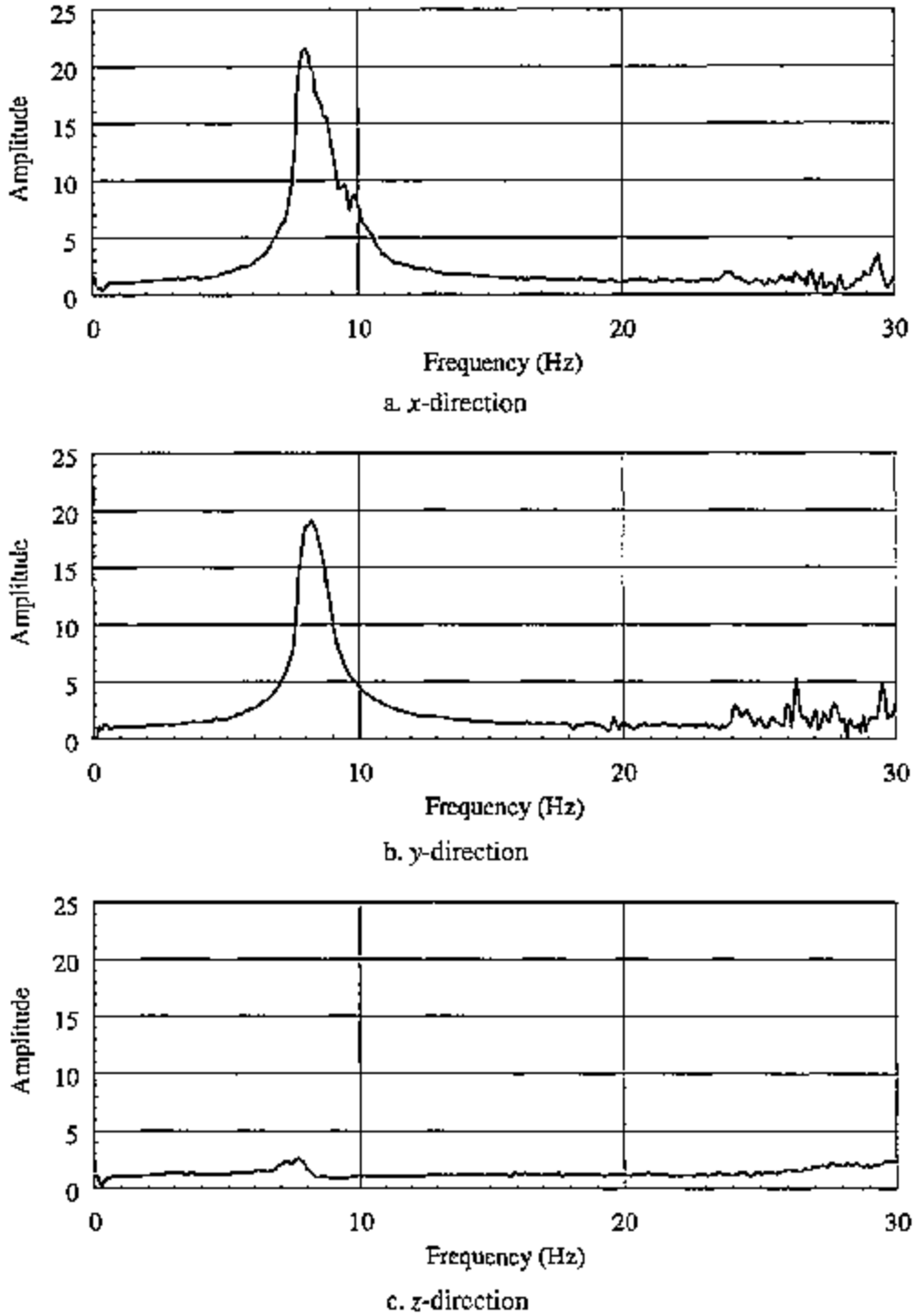

Figure 4-2 Bushing-2 upper tip to mounting frame transfer functions

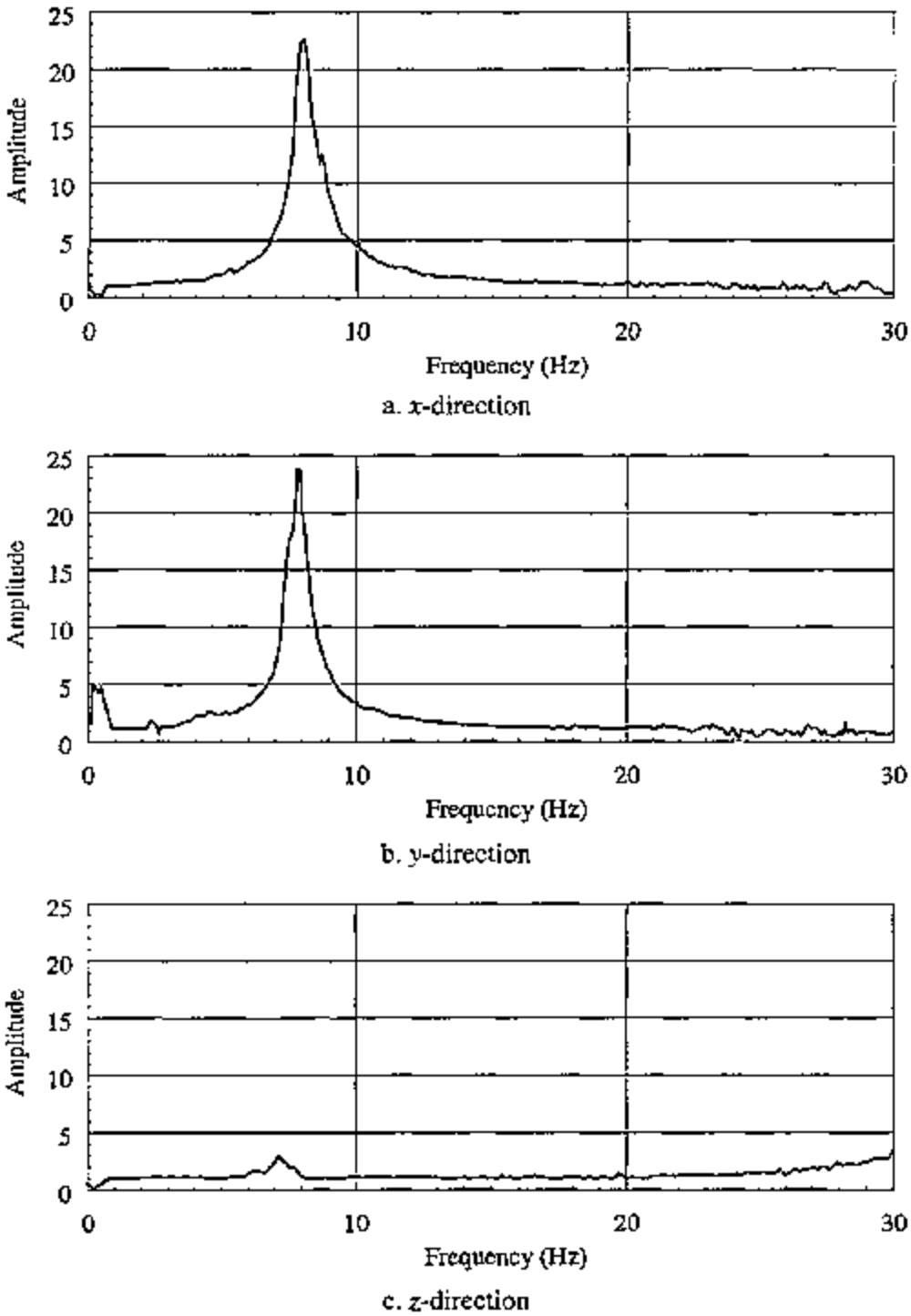

Figure 4-3 Bushing-3 upper tip to mounting frame transfer functions

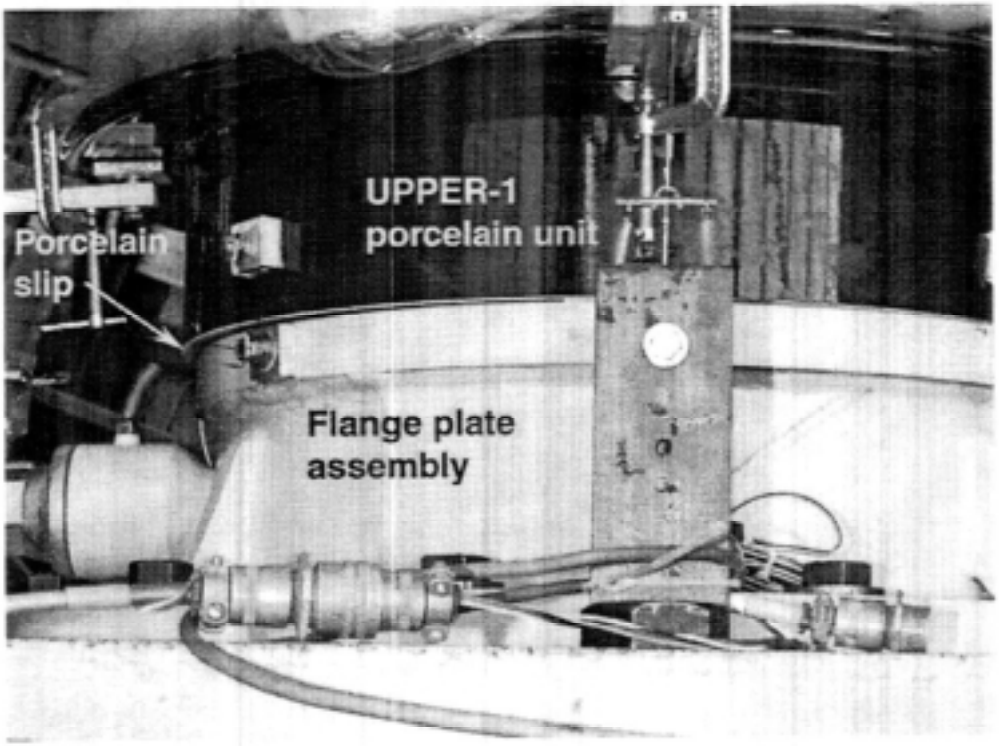

Figure 4-4 Bushing-1 following Test Number 12 showing UPPER-1 porcelain unit slip

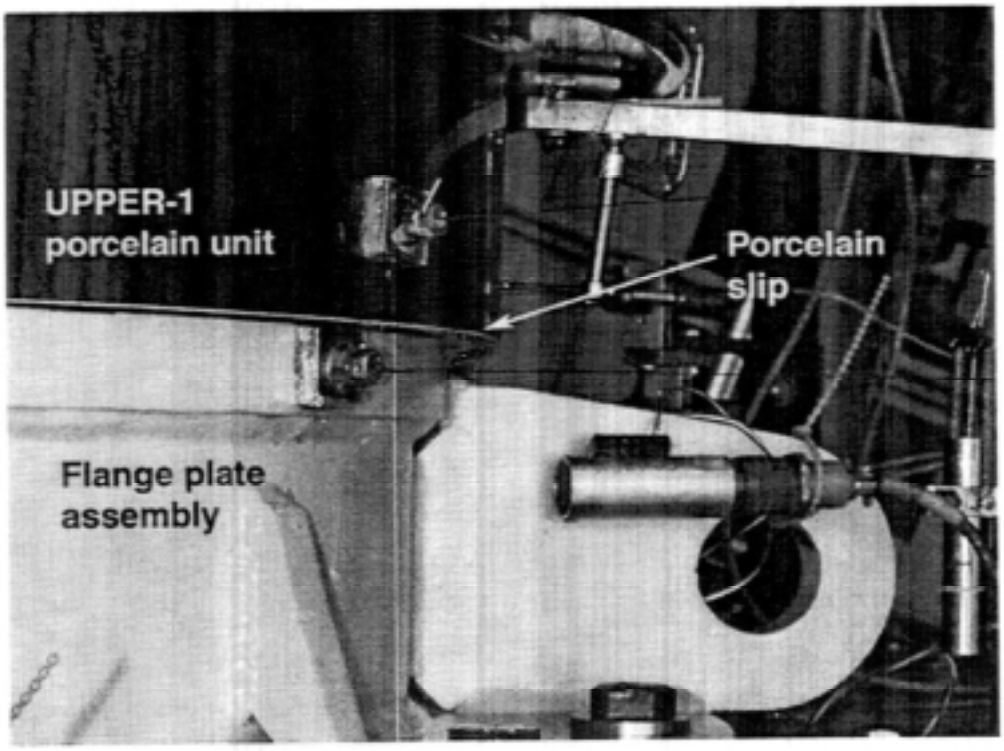

Figure 4-5 Bushing-2 following Test Number 13 showing UPPER-1 porcelain unit slip

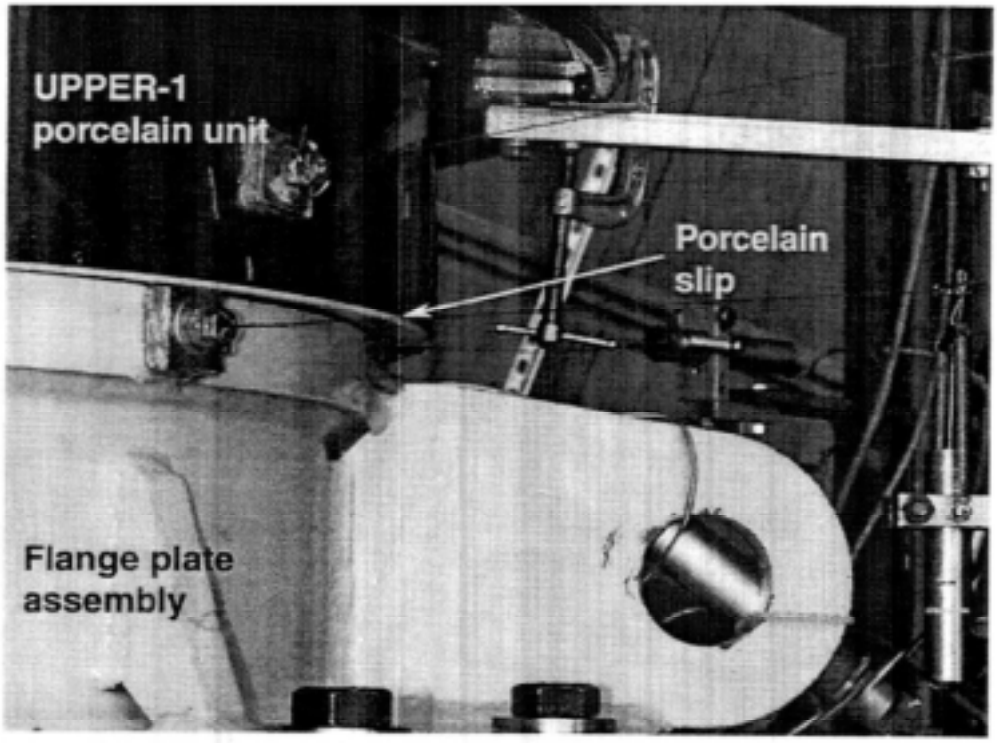

Figure 4-6 Bushing-3 following Test Number 5 showing UPPER-1 porcelain unit slip

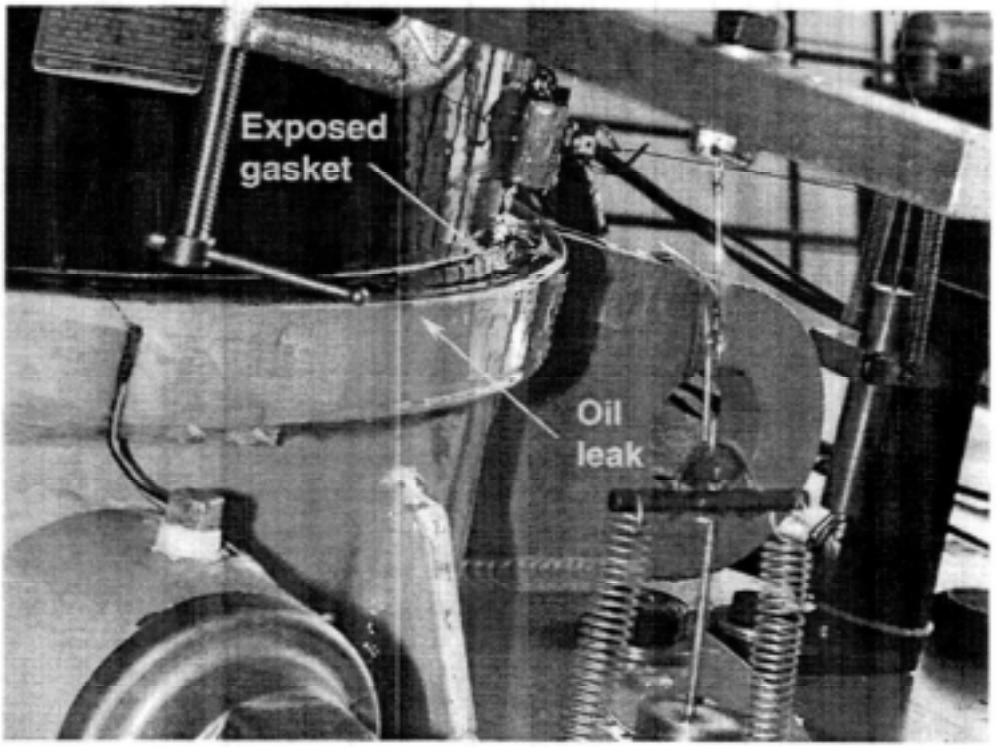

Figure 4-7 Bushing-3 following Test Number 5 showing the exposed gasket

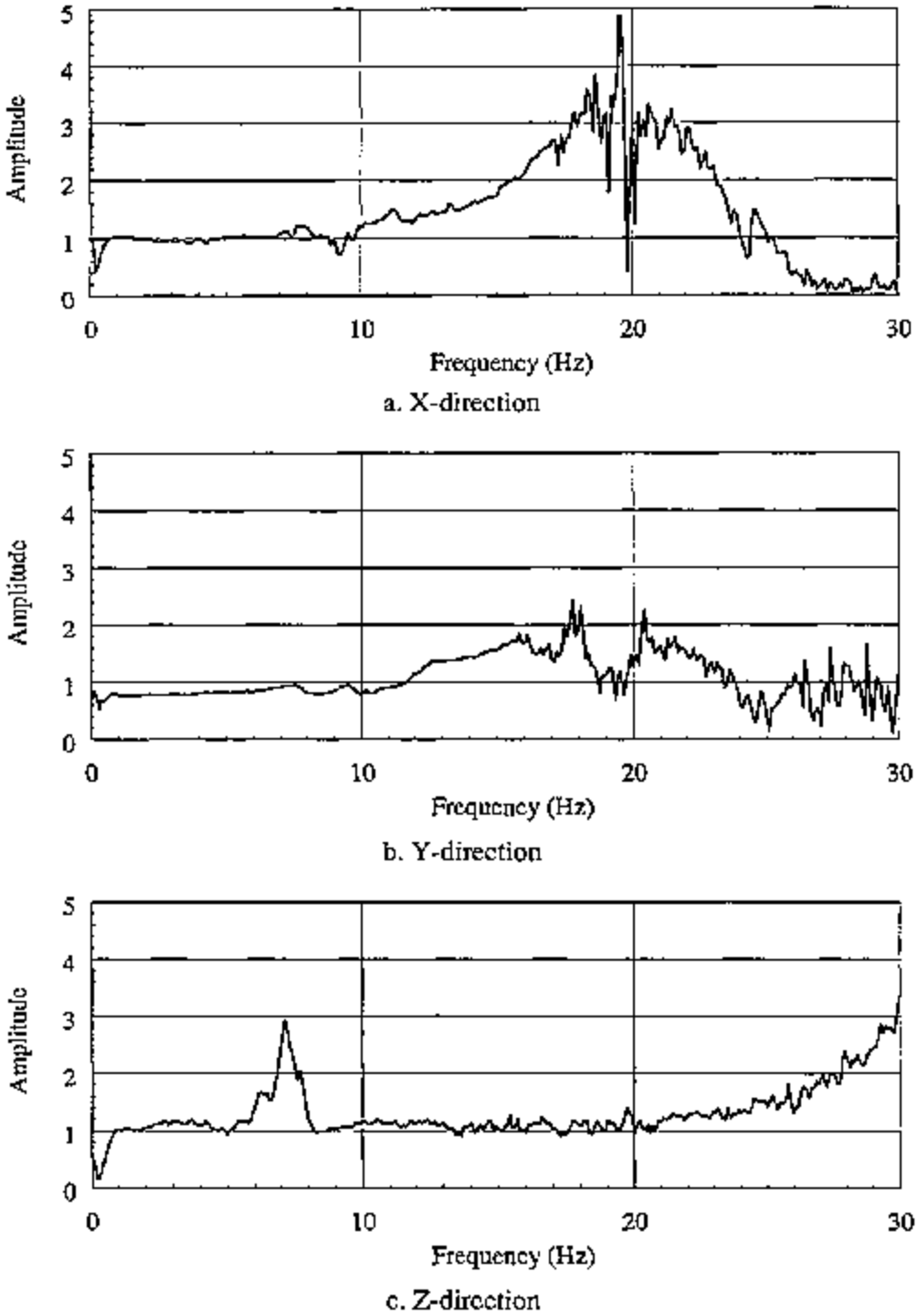

Figure 4-8 Mounting frame to earthquake simulator transfer functions

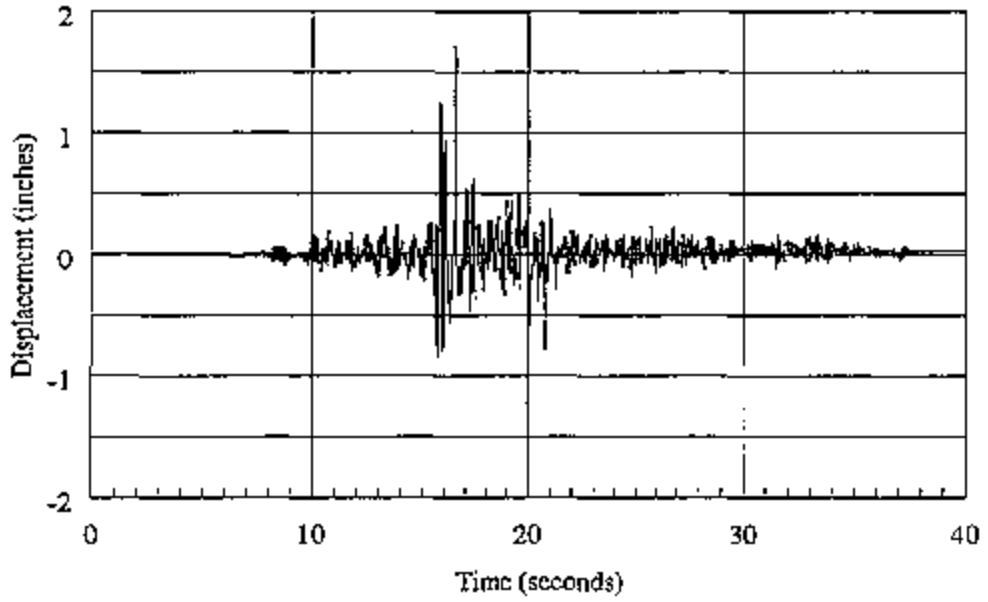

a. X-direction

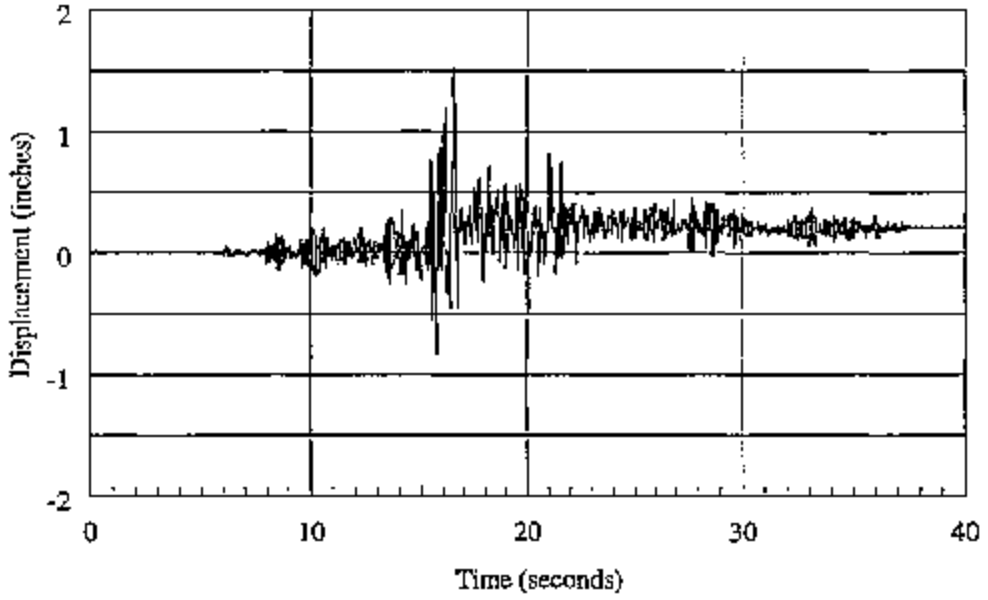

b. Y-direction

Figure 4-9 Relative displacement response of upper tip of Bushing-1, Test Number 17, Tabas-A, target PGA = 1.0g

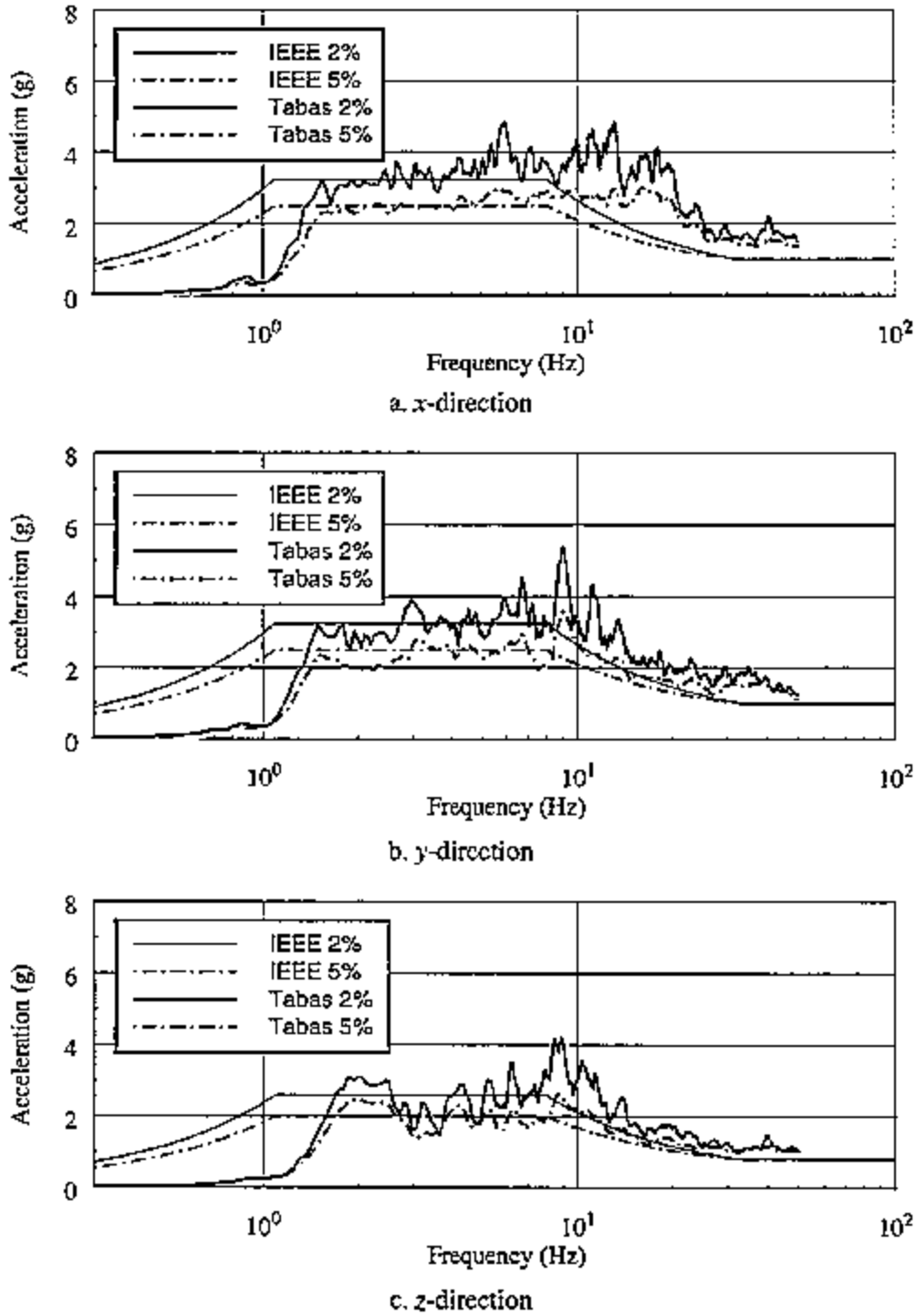

Figure 4–10 Acceleration response spectra calculated using measured mounting frame acceleration histories for Bushing-1, Test Number 17, Tabas-A, target peak acceleration = 1.0g

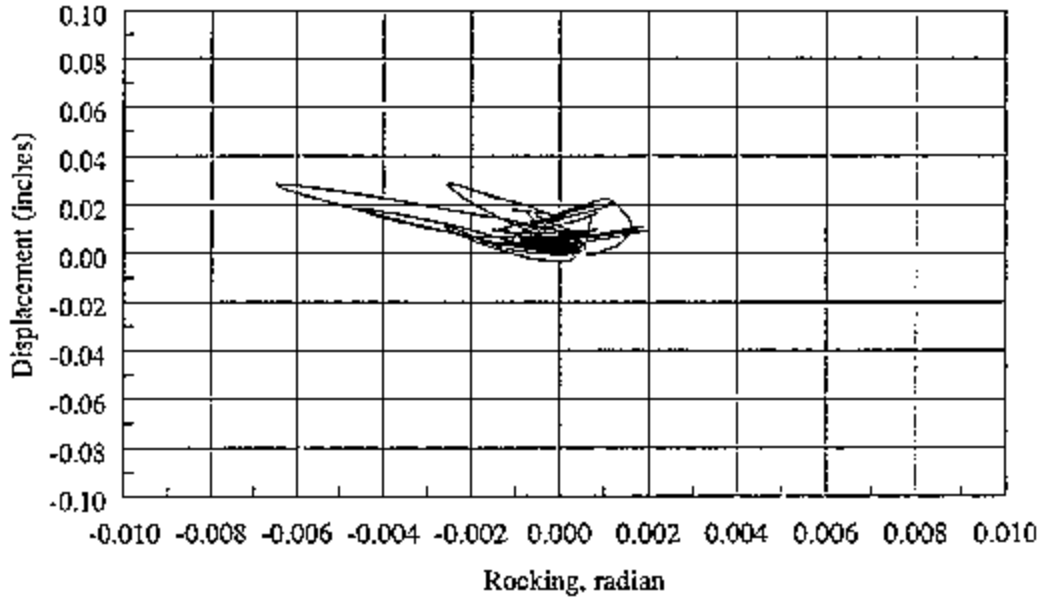

a. rocking about *y*-axis

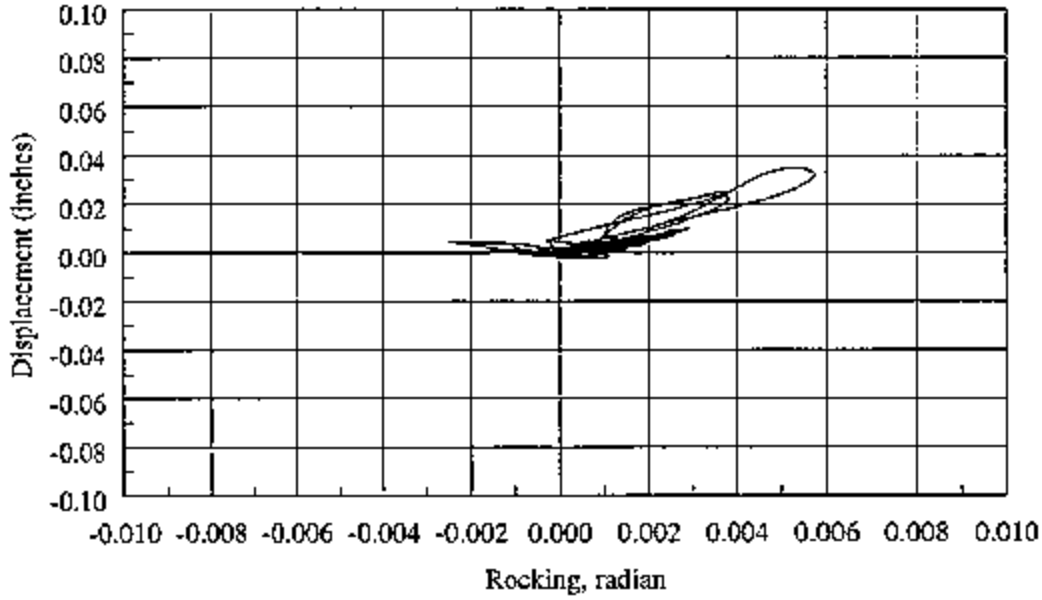

b. rocking about *x*-axis

Figure 4-11 Average relative vertical displacement versus rocking response of Bushing-1, Test Number 17, Tabas-A, target PGA = 1.0g

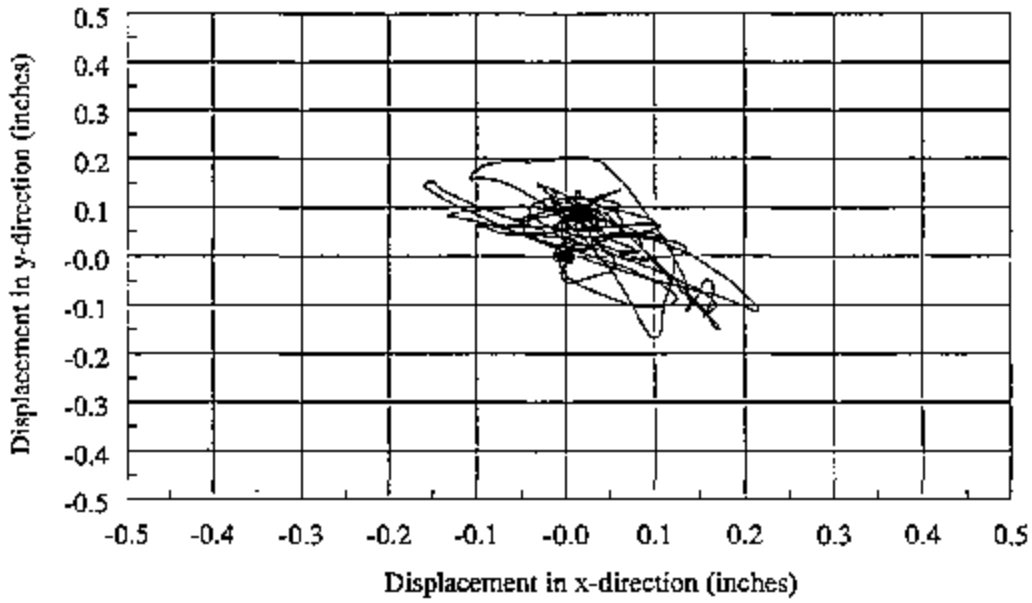

Figure 4-12 Orbit of relative displacement of UPPER-1 porcelain unit over gasket for Bushing-1, Test Number 17, Tabas-A, target PGA = 1.0g

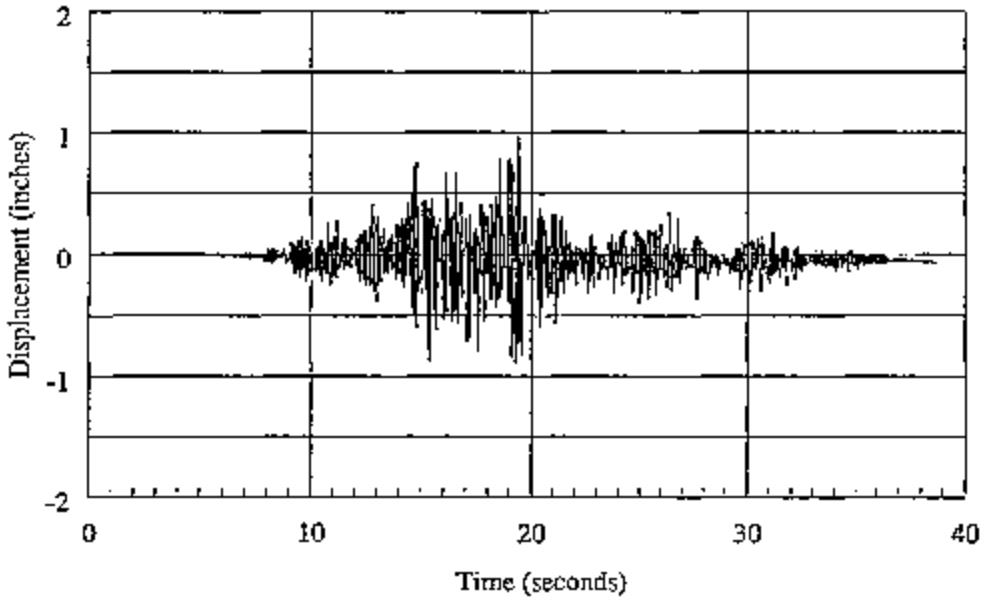

a. X-direction

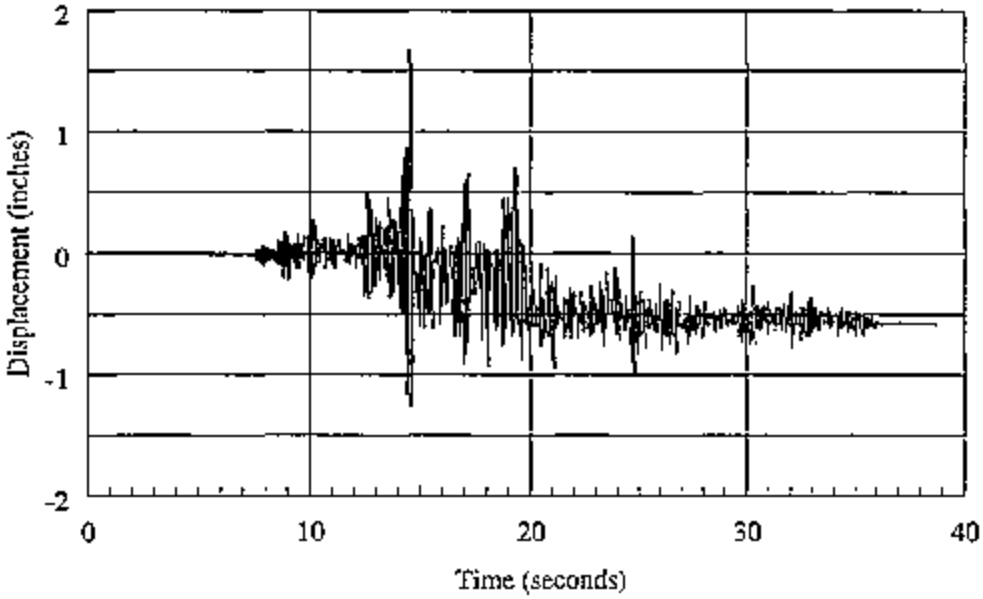

b. Y-direction

Figure 4-13 Relative displacement response of upper tip of Bushing-2, Test Number 13, Tabas-B, target PGA = 1.2g

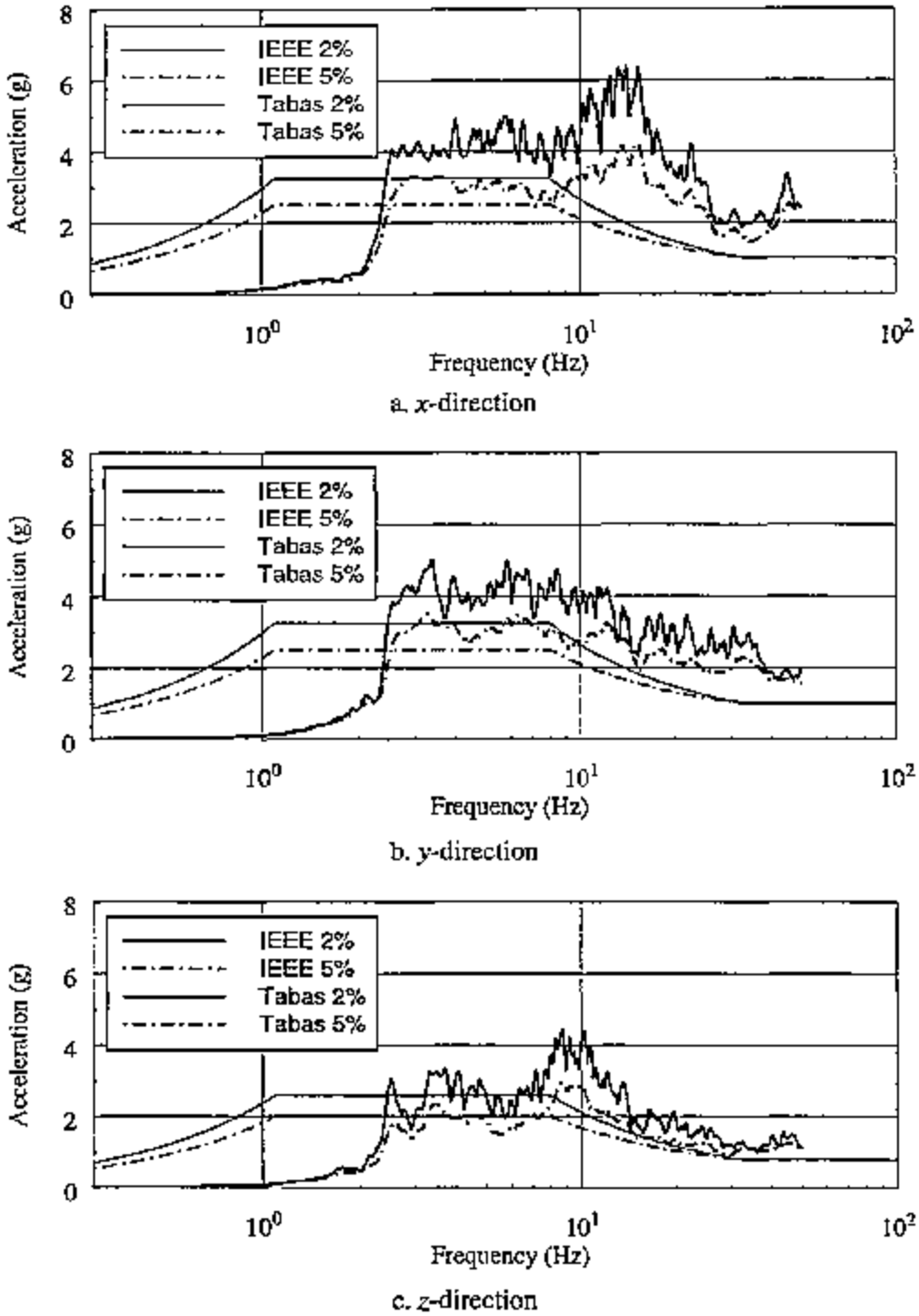

Figure 4-14 Acceleration response spectra calculated using measured mounting frame acceleration histories for Bushing-2, Test Number 13, Tabas-B, target peak acceleration = 1.2g

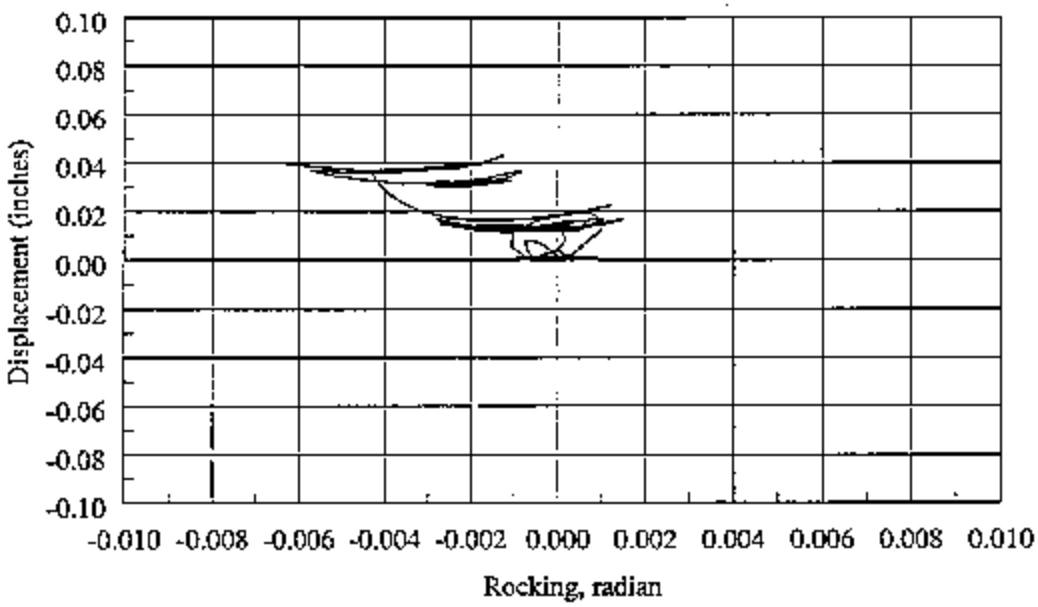

a. rocking about *y*-axis

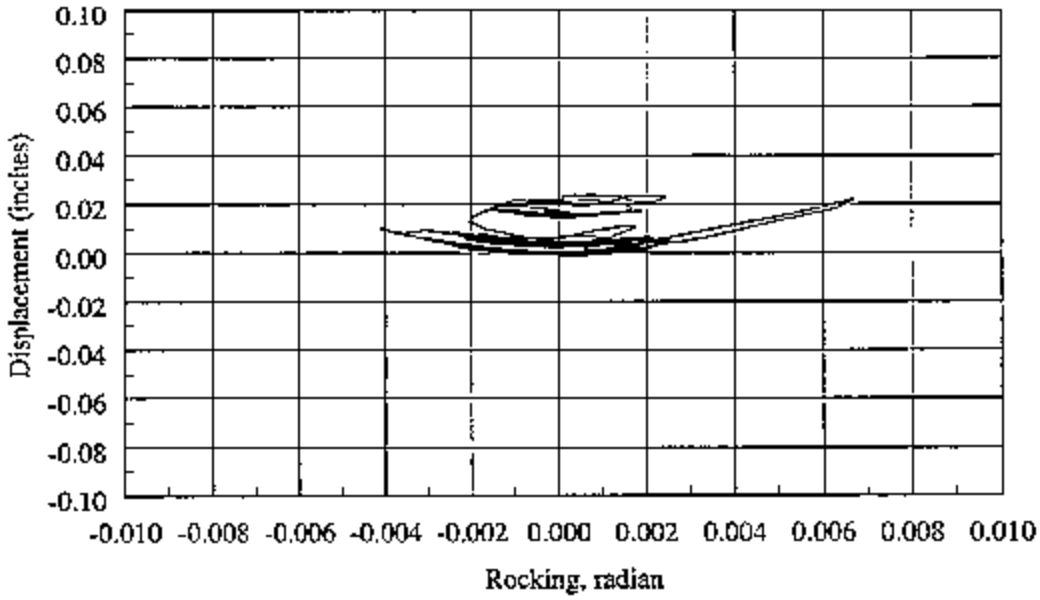

b. rocking about *x*-axis

Figure 4-15 Average relative vertical displacement versus rocking response of Bushing-2, Test Number 13, Tabas-B, target PGA = 1.2g

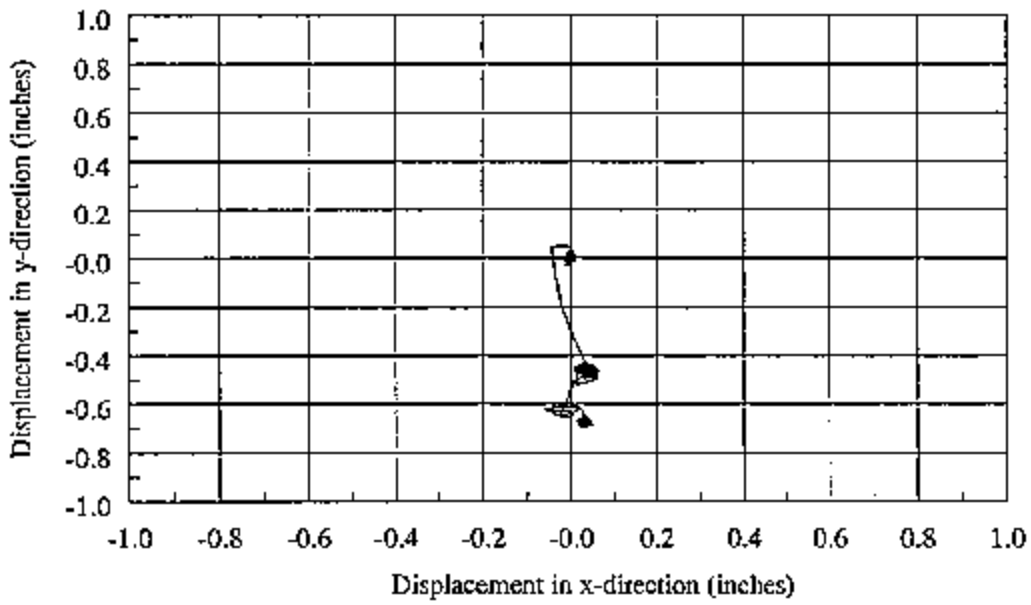

Figure 4-16 Orbit of relative displacement of UPPER-1 porcelain unit over gasket for Bushing-2, Test Number 13, Tabas-B, target PGA = 1.2g

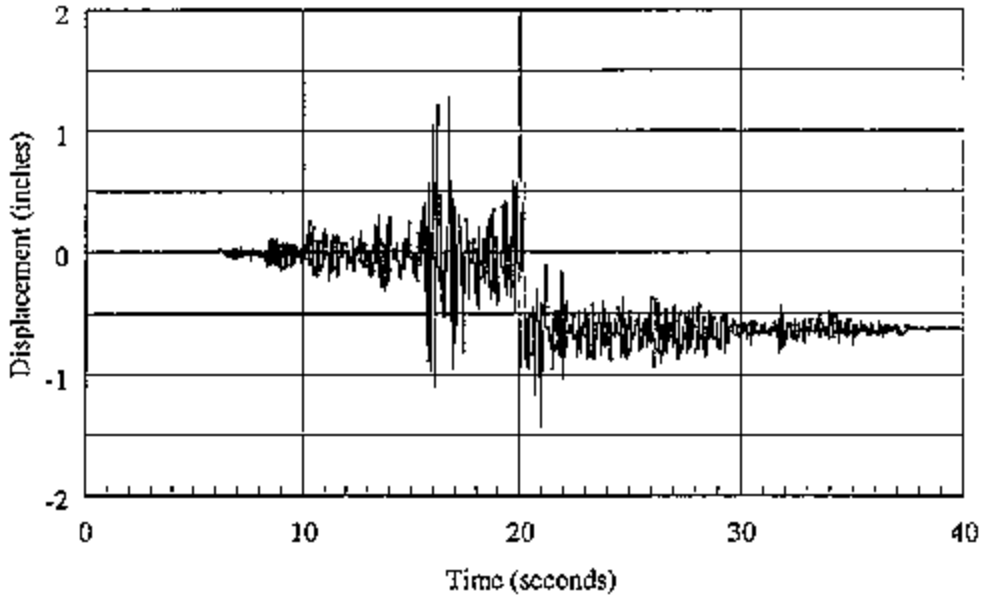

a. X-direction

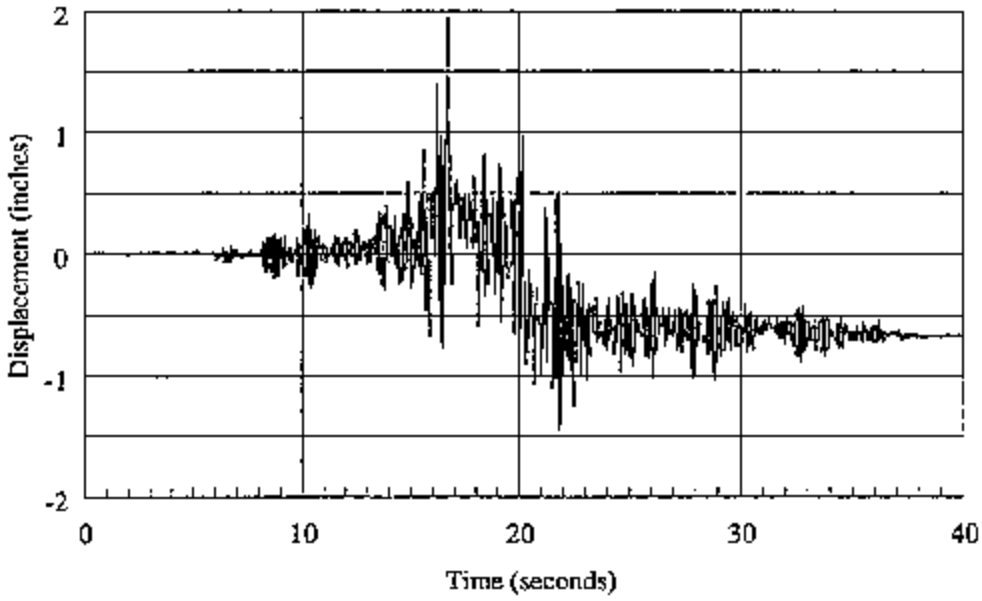

b. Y-direction

Figure 4-17 Relative displacement response of upper tip of Bushing-3, Test Number 5, Tabas-A, target PGA = 1.0g

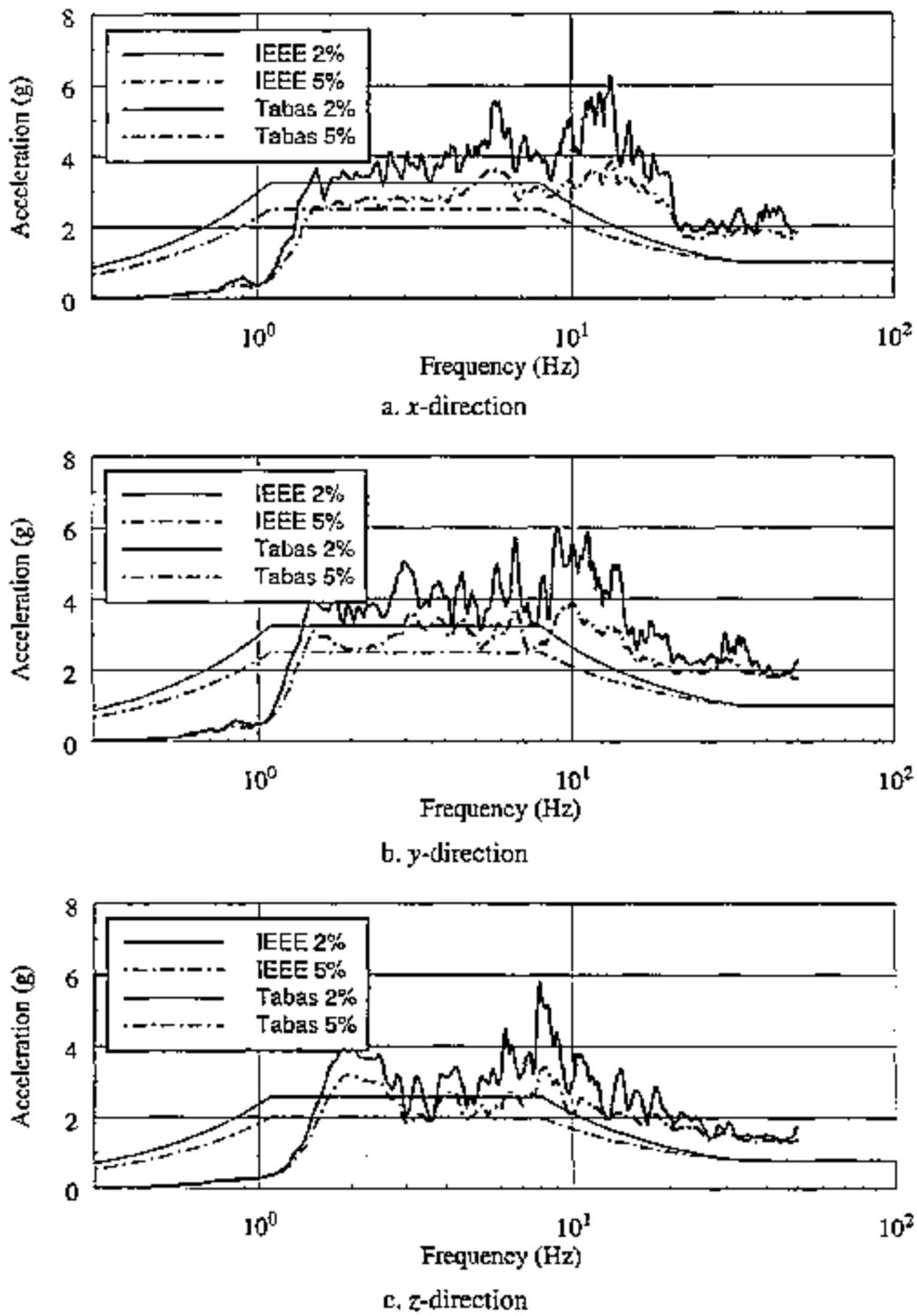

Figure 4-18 Acceleration response spectra calculated using measured mounting frame acceleration histories for Bushing-3, Test Number 5, Tabas-A, target peak acceleration = 1.0g

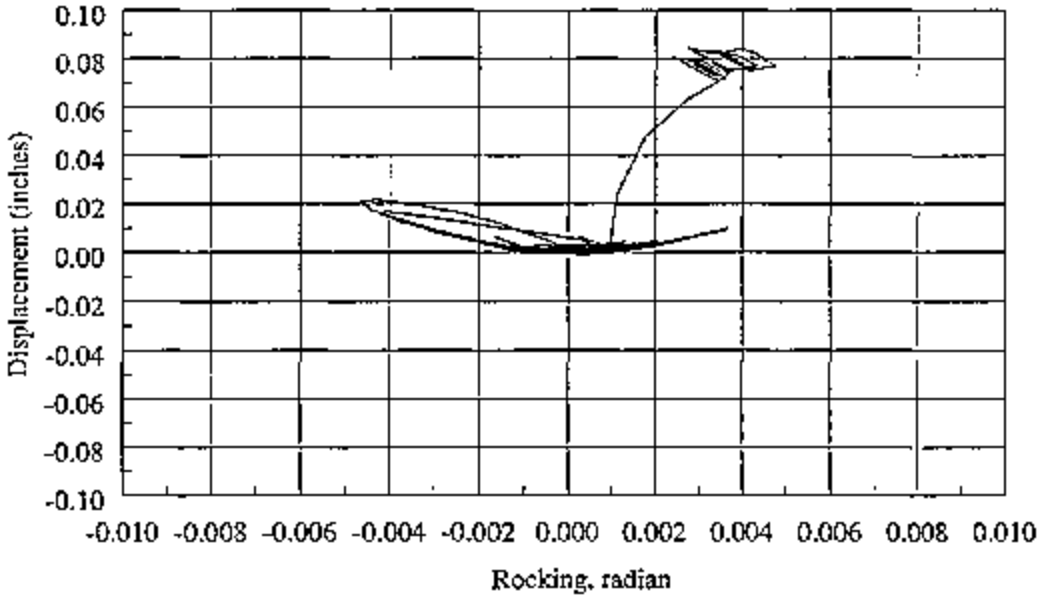

a. rocking about *y*-axis

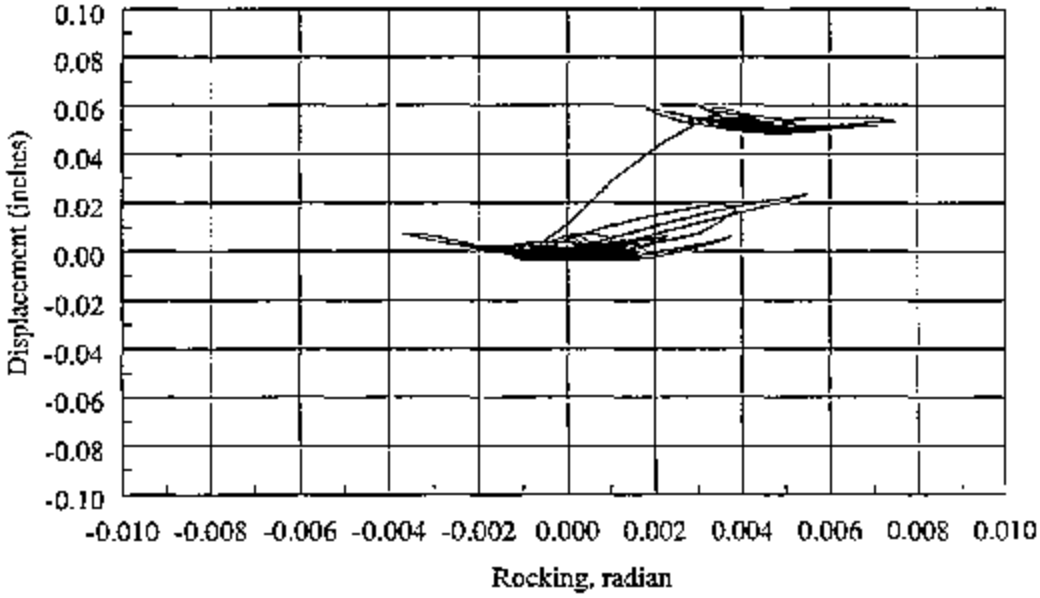

b. rocking about *x*-axis

Figure 4-19 Average relative vertical displacement versus rocking response of Bushing-3, Test Number 5, Tabas-A, target PGA = 1.0g

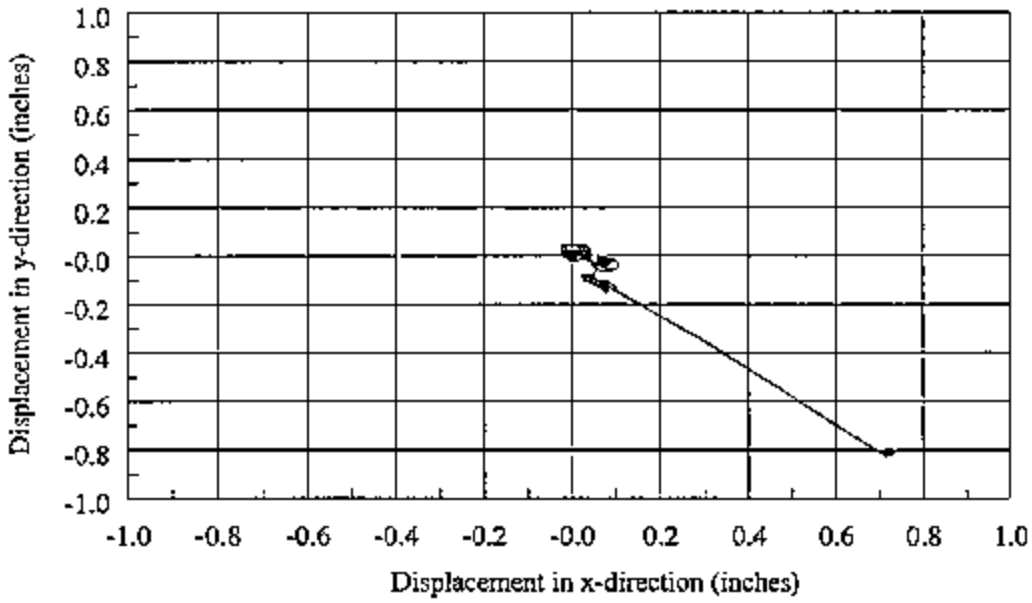

Figure 4-20 Orbit of relative displacement of UPPER-1 porcelain unit over gasket for Bushing-3, Test Number 5, Tabas-A, target PGA = 1.0g

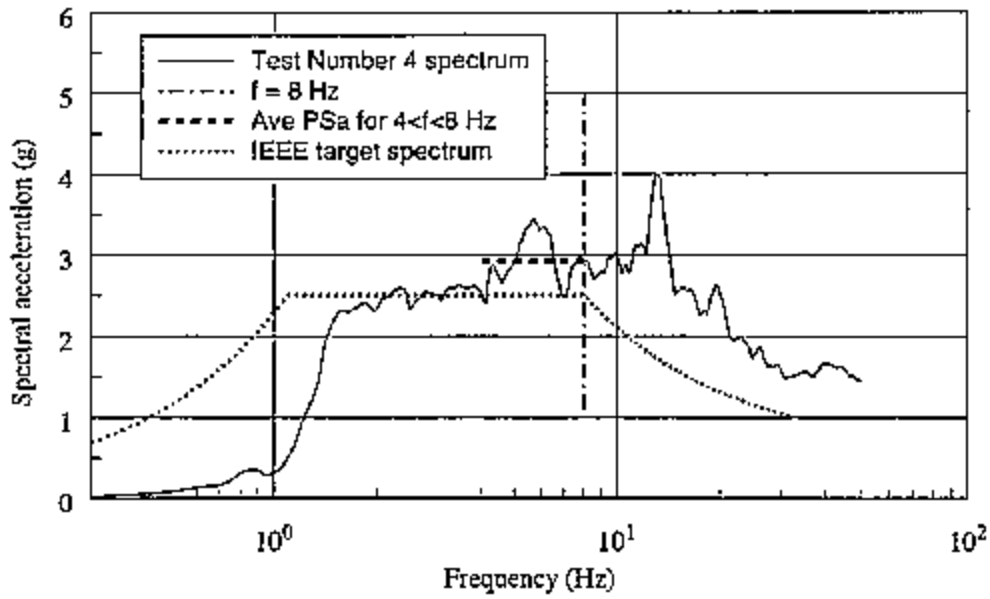

a. local x-direction

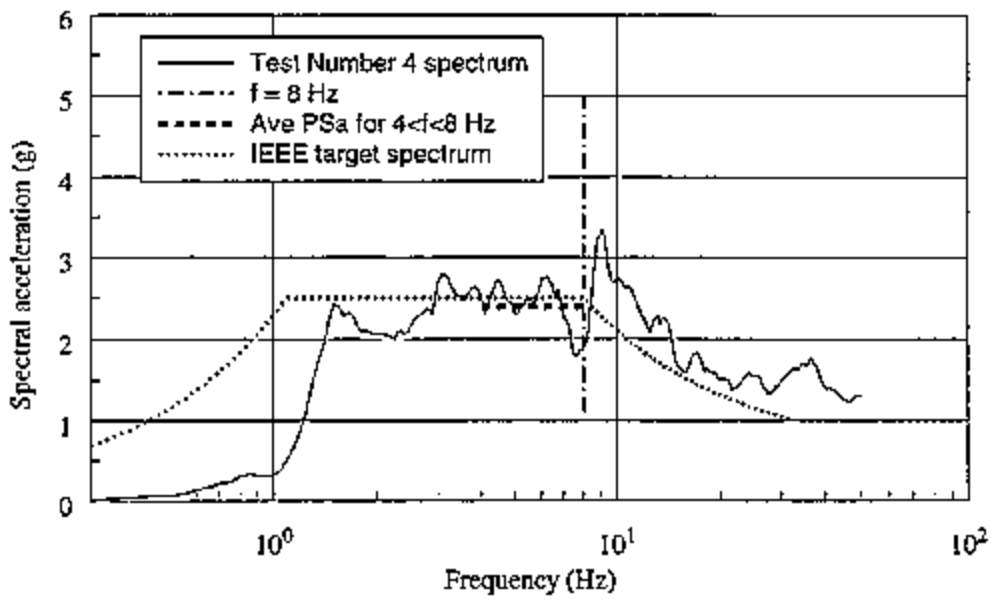

b. local y-direction

Figure 4-21 Fragility data for Bushing-3, Tabas-A, Test Number 4

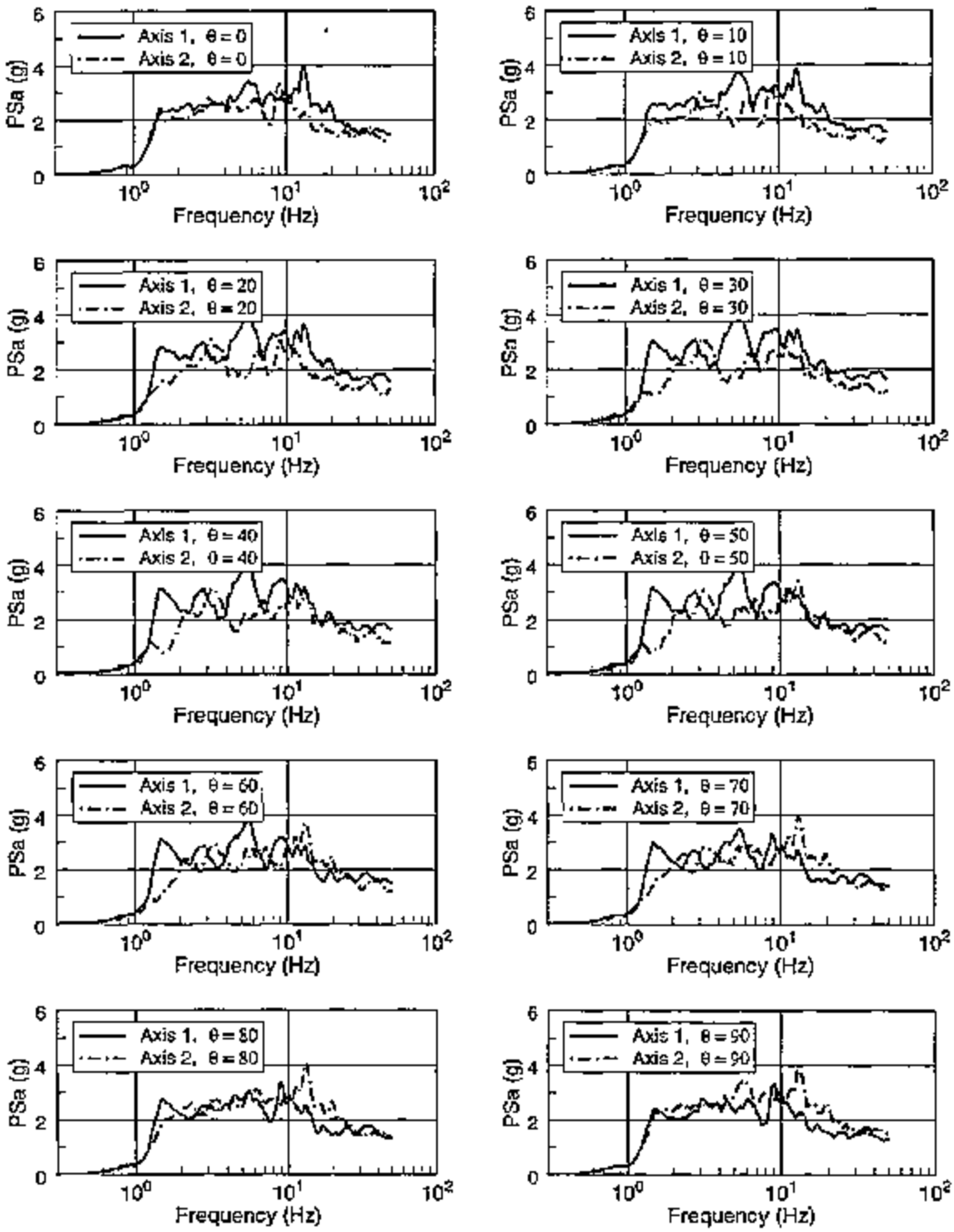

Figure 4-22 Acceleration response spectra for rotated components for Bushing-3, Tabas-A, Test Number 4

CHAPTER 5
SUMMARY AND CONCLUSIONS

5.1 Summary

5.1.1 Introduction

The reliability and safety of electrical transmission and distribution systems after an earthquake depend on the seismic response of individual substation components such as transformer bushings. Post-earthquake reconnaissance of electrical substations has identified porcelain transformer bushings as being particularly vulnerable to severe earthquake shaking.

Pacific Gas & Electric (PG&E) Company sponsored a research project to investigate the seismic response of in-service and proposed-modified 550 kV transformer bushings. The key objectives of the project were to: (1) develop earthquake ground motion records suitable for the seismic evaluation, qualification and fragility testing of bushings, (2) test three 550 kV bushings on the earthquake simulator at the Pacific Earthquake Engineering Research (PEER) Center using levels of earthquake shaking consistent with those adopted for seismic qualification and fragility testing of electrical equipment, (3) reduce and analyze the data acquired from the earthquake simulator tests, and (4) draw conclusions about the seismic performance of porcelain transformer bushings, including the likely failure modes of a bushing during severe earthquake shaking, the efficacy of the improvements in the modified bushings, and the utility of the seismic qualification and fragility testing procedures set forth in IEEE 693-1997.

5.1.2 Earthquake testing program

The earthquake testing was performed on the earthquake simulator at the Pacific Earthquake Engineering Research Center, which is headquartered at the University of California, Berkeley. The 20 ft by 20 ft (6.1 by 6.1 m) simulator can accommodate models up to 140 kips (623 kN) in weight and 40 ft (12.2 m) in height.

The three 550 kV bushings were supplied by ABB Power T&D Company, Inc., Components Division (ABB) for earthquake testing. Bushing-1 was similar to bushings that are currently in service in the United States and was designated for fragility testing. Bushing-2 and Bushing-3 were modified versions of Bushing-1 incorporating design changes intended to improve the seismic performance of 550 kv bushings. The modifications consisted of: (a) increased preload on the bushing, (b) use of a rubber-impregnated fiber gasket and an O-ring seal instead of nitrile rubber gasket at the porcelain-to-flange plate connection, and (c) increased spring travel in the bushing dome by use of multi-tiered springs. Bushing-2 was designated for fragility testing and Bushing-3 was identified for qualification testing.

For earthquake testing, the bushings were mounted on a support frame that was designed to accommodate 550 kV bushings. The mounting plate in the frame was sloped at 20 degrees measured to the vertical because a bushing qualified at this angle is deemed by IEEE 693-1997 to be qualified for all angles between vertical and 20 degrees measured to the vertical. Bushings

were attached to the support frame using 12 3/4" bolts. During the test program, there was no evidence of slip between the bushing flange plate and the mounting plate.

Earthquake simulation testing of the bushings consisted of resonant search tests (sine-sweep and white-noise) and triaxial earthquake-history tests. The resonant search tests were undertaken to establish the dynamic characteristics of the bushings. The first modal frequency of the bushing was approximately 8 Hz; this frequency corresponded to motion in the local *x-y* plane. The first mode damping ratio for Bushing-1 prior to earthquake testing was approximately 4 percent of critical. No values of modal frequency and damping ratio for response along the local z-axis or longitudinal axis of the bushing could be evaluated using the resonant search tests.

The earthquake histories used for triaxial shaking of the bushings were derived from sets of ground motion records recorded during the 1978 Tabas, Iran, earthquake. The time-domain procedures of Abrahamson were used to develop IEEE spectrum-compatible earthquake histories. Two three-component sets of IEEE spectrum-compatible motions were developed: Tabas-A for tests with peak horizontal accelerations up to 1.0g, and Tabas-B for tests with peak horizontal accelerations exceeding 1.0g.

For the Moderate Level qualification of Bushing-3, the earthquake histories were matched to the 2- and 5-percent damped IEEE spectra with peak accelerations of 1.0g (horizontal shaking) and 0.8g (vertical shaking). At this level of shaking, the porcelain stresses are required to be less than or equal to the ultimate value and the bushing must show no evidence of oil leakage. Test Number 5 met the requirements of IEEE 693-1997 for qualification at the Moderate Level. During this test, Bushing-3 leaked oil and its UPPER-1 porcelain unit slipped substantially above the gasket and flange plate. As such, Bushing-3 did not qualify at the Moderate Level.

Bushing-1 and Bushing-2 were fabricated for the purpose of fragility testing. Two limiting states of response were identified for fragility testing: oil leakage and slip of the UPPER-1 porcelain unit. For the limit state of oil leakage, the *fragility* peak accelerations of Bushing-1, Bushing-2, and Bushing-3, were 0.51g, 1.18g, and 1.32g, respectively. For the limit state of slip of the UPPER-1 porcelain unit, the *fragility* peak accelerations of Bushing-1, Bushing-2, and Bushing-3, were 0.69g, 1.18g, and 1.32g, respectively.

5.2 Conclusions and Recommendations

5.2.1 Seismic Response of 550 kV Transformer Bushings

The modified 550 kV bushing (Bushing-3) did not qualify to the Moderate Level per IEEE 693-1997 (IEEE, 1998).

Bushing-1 and Bushing-2 were built for the purpose of fragility testing. Two limiting states of response were identified for fragility testing of these bushings: oil leakage and slip of the UPPER-1 porcelain unit. Bushing-2, a modified version of Bushing-1, sustained peak accelerations approximately twice those of Bushing-1, indicating that the modifications proposed and implemented by ABB were most effective.

5.2.2 Recommendations for Future Study

Procedures for Seismic Qualification

The 550-kV bushings were installed in a *rigid* mounting frame without electrical connections and upper-tip-mounted terminals for earthquake testing. Such a configuration does not likely adequately represent the field installation and loading environment and the results of IEEE qualification must be viewed with caution.

For qualification of equipment attached to a foundation, IEEE 693-1997 specifies a response spectrum for earthquake-simulator testing. The amplitude of the input motion for qualification of bushings is doubled to account for flexibility and ground-motion amplification in the transformer or support equipment. It is not known whether the IEEE 693-1997 assumptions are reasonable, conservative, or non-conservative. Numerical (finite element) studies of transformer bushings and other turret structures should be undertaken to review the current specifications for equipment qualification. At a minimum, such studies should identify (a) the stiffness characteristics of typical bushing support structures, (b) the damping effects of the oil contained in the support structure, if any, (c) the amplification of earthquake shaking effects, if any, through the support structure to the base of a bushing, and d) the importance of rotational input to a bushing resulting from flexibility in the upper plate of the transformer to which bushings are attached. Answers to these questions will provide valuable guidance to those tasked with revising the IEEE 693-1997 *Recommended Practices for Seismic Design of Substations.*

Development of Fragility Curves for Substation Equipment

Currently adopted procedures for reporting fragility data for substation equipment such as transformer bushings are neither appropriate nor conservative. Fragility data presented in the form of peak ground (input) acceleration are of limited value because peak input acceleration is a poor descriptor of damage. Fragility data based on spectral acceleration at the frequency of the bushing provides an improved estimate of damage but cannot account for substructure flexibility and damping, both of which will profoundly affect bushing response. Mean spectral acceleration over a range of frequencies provides a means by which to account for substructure flexibility. Mean-minus-one-standard-deviation spectral acceleration *fragility* data over a range of frequencies could account for variations in spectral acceleration over a frequency range.

The fragility data presented in Chapter 4 were widely scattered. Improved, rational procedures are needed to analyze and interpret fragility test data. Such procedures must both better reflect the field installation of equipment and account for substructure flexibility, installation of terminals (for bushings), and the effects of interconnected equipment.

Interconnected Equipment

Although IEEE 693-1997 acknowledges that physical (electrical) connections between substation equipment may detrimentally affect the seismic response of individual pieces of equipment, the testing procedures described in IEEE 693-1997 do not account for the important effects of such connectivity. These physical connections can vary widely in flexibility and strength. There is substantial evidence from past earthquakes that such electrical connections may have precipitated

bushing failures because of dynamic interaction between the interconnected equipment. Analytical studies are under way to identify the important parameters affecting dynamic interaction between interconnected equipment. An experimental earthquake-simulator-testing program should be developed to investigate both the characteristics of standard interconnections and strategies to mitigate the effects of dynamic interaction.

Mathematical modeling of porcelain transformer bushings

Data on the mechanical characteristics of gaskets are needed if accurate mathematical models of bushings are to be developed. Nonlinear springs should be developed to model gaskets, and the constraint to relative lateral movement of the aluminum core and the perimeter porcelain units offered by the oil inside the bushing must be studied. Models of porcelain bushings that would be suitable for rigorous vulnerability studies could be developed with such information.

REFERENCES

Abrahamson, N. 1996. Nonstationary response-spectrum matching. Unpublished papers.

EERI. 1995. Northridge reconnaissance report. *Earthquake Spectra*, Supplement C. Oakland, Calif.: Earthquake Engineering Research Institute.

IEEE. 1998. *IEEE Std 693-1997, Recommended practices for seismic design of substations.* Piscataway, N.J.: IEEE Standards Department.

Gilani, A. S., Chavez, J. W., Fenves, G. L., and Whittaker, A. S. 1998. *Seismic evaluation of 196 kV porcelain transformer bushings*, PEER 98/02 Berkeley, Calif., Pacific Earthquake Engineering Research Center, University of California.

Lilhanand, K. and Tseng, W.S. 1988. Development and application of realistic earthquake time histories compatible with multiple-damping design spectra. *Proceedings of Ninth World Conference on Earthquake Engineering, Tokyo, Japan.*

Mathworks. 1999. *The language of technical computing*. Natick, Mass.: The Mathworks, Inc.

Shinozuka, M., ed. 1995. *The Hanshin-Awaji earthquake of January 17, 1995: Performance of lifelines*. Technical Report NCEER-95-0015 Buffalo, N.Y.: National Center for Earthquake Engineering Research, State University of New York.

APPENDIX A

IEEE PRACTICE FOR EARTHQUAKE TESTING OF TRANSFORMER BUSHINGS

A.1 Introduction

The document IEEE 693-1997 (IEEE 1998) entitled "Recommended Practices for Seismic Design of Substations" is used in the United States for the seismic qualification and fragility testing of electrical equipment such as transformer bushings. This recommended practice provides qualification requirements for substation equipment and supports manufactured from steel, aluminum, porcelain, and composites. Procedures for equipment qualification using analytical studies (static analysis, static coefficient analysis, and response-spectrum analysis) and experimental methods (response-history testing, sine-beat testing, and static pull testing) are described in the practice. The objective of the document is "... to secure equipment such that it performs acceptably under reasonably anticipated strong ground motion."

IEEE 693-1997 identifies eleven methods for experimental testing. The most rigorous method is earthquake-response analysis using earthquake ground motion records, the spectral ordinates of which equal or exceed those of a Required Response Spectrum (RRS). Categories of earthquake simulator testing include (a) single-axis, (b) biaxial (i.e., horizontal and vertical), (c) multiaxis, and (d) triaxial.

Section 9 of IEEE 693-1997 describes seismic performance criteria for electrical substation equipment. Information on three seismic qualification levels (Low, Moderate, and High), Performance Levels, the Required Response Spectrum (RRS), the relation between PL and RRS, and acceptance criteria are provided.

The studies described in the body of this report employed triaxial earthquake simulator testing for the qualification and fragility testing of the 550 kV bushings. IEEE 693-1997 writes text on six key topics related to the seismic qualification of transformer bushings:

- Performance level and performance factor
- Performance level qualification
- Support frame and mounting configuration
- Testing procedures
- Instrumentation
- Acceptance criteria

Each of these topics are elaborated upon in the following sections. For fragility testing, the amplitude of the seismic excitation is increased in small increments to determine the level of shaking that causes damage to the bushing, thereby establishing a point on a fragility curve.

A.2 Performance Level and Performance Factor

A Performance Level (PL) for substation equipment is represented in IEEE 693-1997 by a response spectrum. The shape of this spectrum represents a broadband response that envelopes earthquake effects in different areas considering site conditions that range from soft soil to rock. Three values of equivalent viscous damping are specified: 2 percent, 5 percent, and 10 percent. IEEE 693-1997 states that very soft sites and hill sites might not be adequately covered by the PL shapes.

Three seismic performance levels are identified in IEEE 693-1997: High, Moderate, and Low. In California, the relevant performance levels are High and Moderate. Equipment that is shown to perform acceptably in ground shaking consistent with the High Seismic Performance Level (see Figure A-1) is said to be seismically qualified to the High Level. Equipment that is shown to perform acceptably in ground shaking consistent with the Moderate Seismic Performance Level (see Figure A-2) is said to be seismically qualified to the Moderate Level.

IEEE 693-1997 states that it is often impractical or not cost effective to test to the High or Moderate PL because (a) laboratory testing equipment might be unable to attain the necessary high accelerations, and/or (b) damage to ductile components at the PL, although acceptable in terms of component qualification, would result in the component being discarded following testing. For these reasons, equipment may be tested using accelerations that are one-half of the PL. The reduced level of shaking is called the Required Response Spectrum (RRS). The ratio of PL to RRS, termed the performance factor in IEEE 693-1997, is equal to 2. The High and Moderate RRSs are shown in Figures A-3 and A-4, respectively. The shapes of the RRS and the PL are identical, but the ordinates of the RRS are one-half of the PL.

Equipment tested or analyzed using the RRS is expected to have acceptable performance at the PL. This assumption is checked by measuring the stresses obtained from testing at the RRS, and a) comparing the stresses to 50 percent (equal to the inverse of the performance factor) of the ultimate strength of the porcelain (assumed to be brittle) or cast aluminum components, and b) using a lower factor of safety against yield combined with an allowance for ductility of steel and other ductile materials.

A.3 Performance Level Qualification

Procedures for selecting the appropriate seismic qualification level for a site are presented in IEEE 693-1997. Qualification levels are directly related to site-specific peak acceleration values calculated using a 2-percent probability of exceedance in 50 years. If the peak ground acceleration is less than 0.1g, the site is classified as Low. If the peak ground acceleration exceeds 0.5g, the site is classified as High. If the peak ground acceleration ranges in value between 0.1g and 0.5g, the site is classified as Moderate. Sites in California are classified as either Moderate or High.

A.4 Support Frame and Mounting Configuration

IEEE 693-1997 writes that bushings 161 kV and larger must be qualified using earthquake-simulator testing. Recognizing that it is impractical to test bushings mounted on a transformer, IEEE requires bushings to be mounted on a rigid stand during testing. To account for the amplification

of earthquake motion due to the influence of the transformer body and local flexibility of the transformer near the bushing mount, the input motion as measured at the bushing flange shall match a spectrum with ordinates twice that of the Required Response Spectrum. The resulting spectra, termed the Test Response Spectra (TRS), for Moderate Level qualification are shown in Figure A-5.

A transformer bushing must be tested at no less than its in-service slope, which is defined as the slope angle measured from the vertical. IEEE 693-1997 recommends that a bushing be tested at 20 degrees measured from the vertical. If so tested, a bushing is assumed to be qualified for use on all transformers with angles from vertical to 20 degrees. (A bushing installed at an angle greater than 20 degrees must be tested at its in-service angle.)

A.5 Testing Procedures for Transformer Bushings

Three types of earthquake-simulator testing are identified in IEEE 693-1997 for the seismic qualification of transformer bushings: (a) earthquake ground motions, (b) resonant frequency search, and (c) sine-beat testing. Earthquake ground motion tests (termed *time-history shake table tests* in IEEE 693-1997) and resonant frequency tests are mandatory; additional information on these two types of tests follow.

A.5.1 Resonant search tests

Sine-sweep or broadband white noise tests are used to establish the dynamic characteristics (natural frequencies and damping ratios) of a bushing. These so-called *resonant search* tests are undertaken using uni-directional excitation along each principal axis of the earthquake simulator platform. If broadband white noise tests are performed, the amplitude of the white noise must not be less than 0.25g.

If sine-sweep tests are used, IEEE 693-1997 specifies that the resonant search be conducted at a rate not exceeding one octave per minute in the range for which the equipment has resonant frequencies, but at least at 1 Hz; frequency searching above 33 Hz is not required. Modal damping is calculated using the half-power bandwidth method.

A.5.2 Earthquake ground motion tests

Triaxial earthquake simulator testing is mandated for the seismic qualification of 161 kV and above bushings. The Test Response Spectrum (TRS) for each horizontal earthquake motion must match or exceed the target spectrum. The TRS for the vertical earthquake motion shall be no less than 80 percent of target spectrum. Earthquake motions can be established using either synthetic or recorded histories. IEEE 693-1997 recommends that 2-percent damping be used for spectral matching and requires at least 20 seconds of strong motion shaking be present in each earthquake record.

A.6 Instrumentation of Transformer Bushings

IEEE 693-1997 states that porcelain bushings must be instrumented to record the following response quantities:

1. maximum vertical and horizontal accelerations at the top of the bushing, at the bushing flange, and at the top of the earthquake-simulator platform

2. maximum displacement of the top of the bushing relative to the flange

3. maximum porcelain stresses at the base of the bushing near the flange

A.7 Acceptance Criteria for Transformer Bushings

IEEE 693-1997 writes that a bushing is considered to have passed the qualification tests if all the criteria tabulated below related to general performance, allowable stresses, and leakage are met. The data obtained from testing using ground motions compatible with the Test Response Spectrum (see Figure A-5) are used to assess general performance and allowable stresses. Oil leakage is checked for a higher level of earthquake shaking.

General Performance	No evidence of damage such as broken, shifted, or dislodged insulators. No visible leakage of oil or broken support flanges.
Allowable Stresses	The stresses in components are below the limiting values. (See Section A.2. For example, the stresses in the porcelain components associated with earthquake shaking characterized by the spectrum presented in Figure A-5 must be less than 50 percent of the ultimate value.)
Leakage	Bushings qualified by earthquake simulator testing shall have a minimum factor of safety of two against gasket leaks for loads imposed during application of the Test Response Spectrum. IEEE 693-1997 states that an acceptable method to demonstrate this factor of safety is to have no leaks after shaking characterized by twice the Test Response Spectrum. (Such shaking corresponds to a Performance Factor equal to 1.0.)

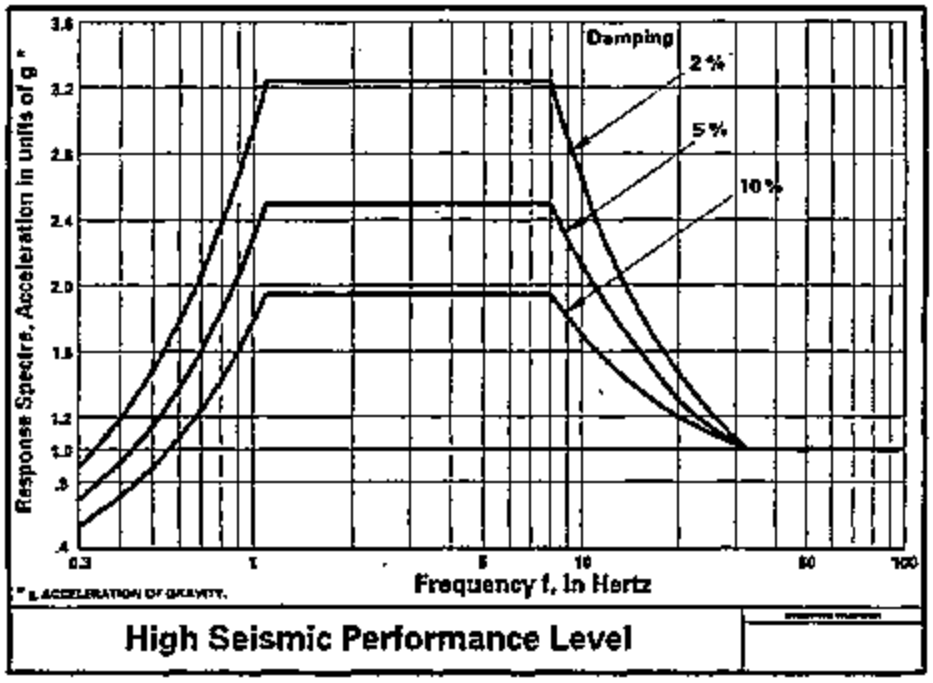

Figure A-1 Spectra for High Seismic Performance Level (IEEE, 1998)

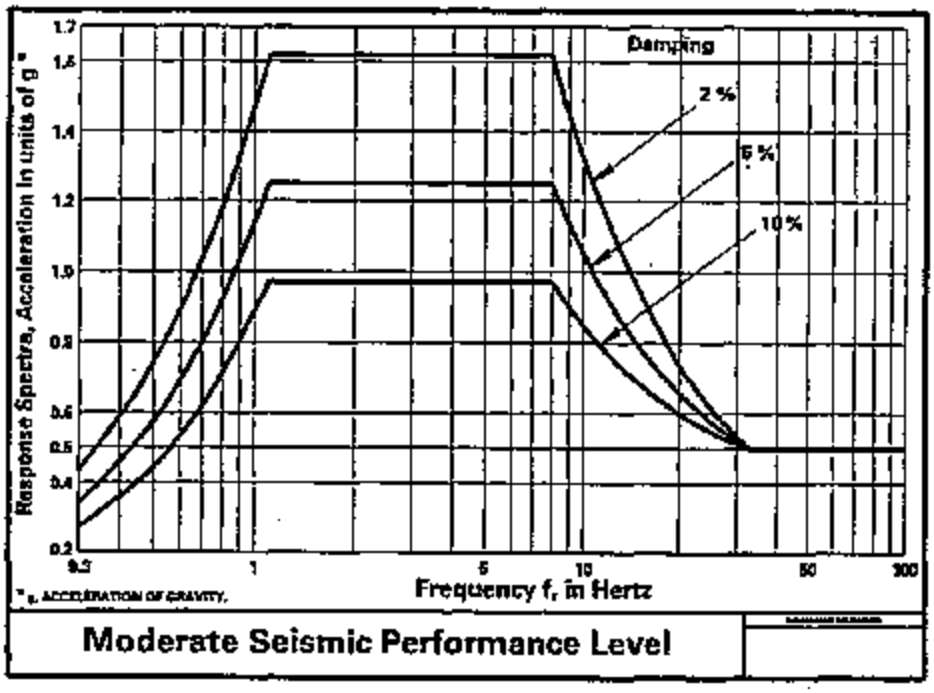

Figure A-2 Spectra for Moderate Seismic Performance Level (IEEE, 1998)

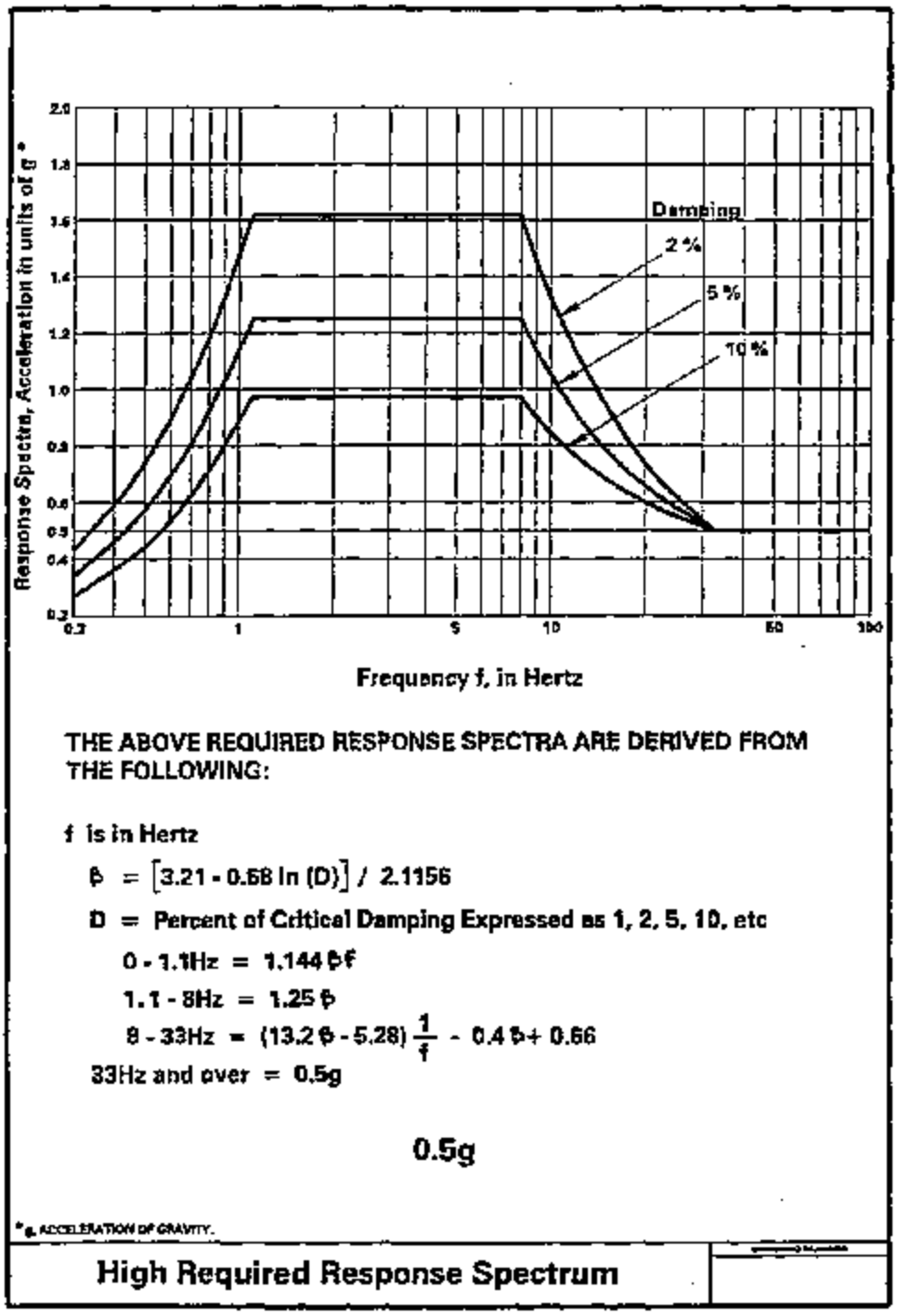

Figure A-3 Spectra for High Required Response Spectrum (IEEE, 1998)

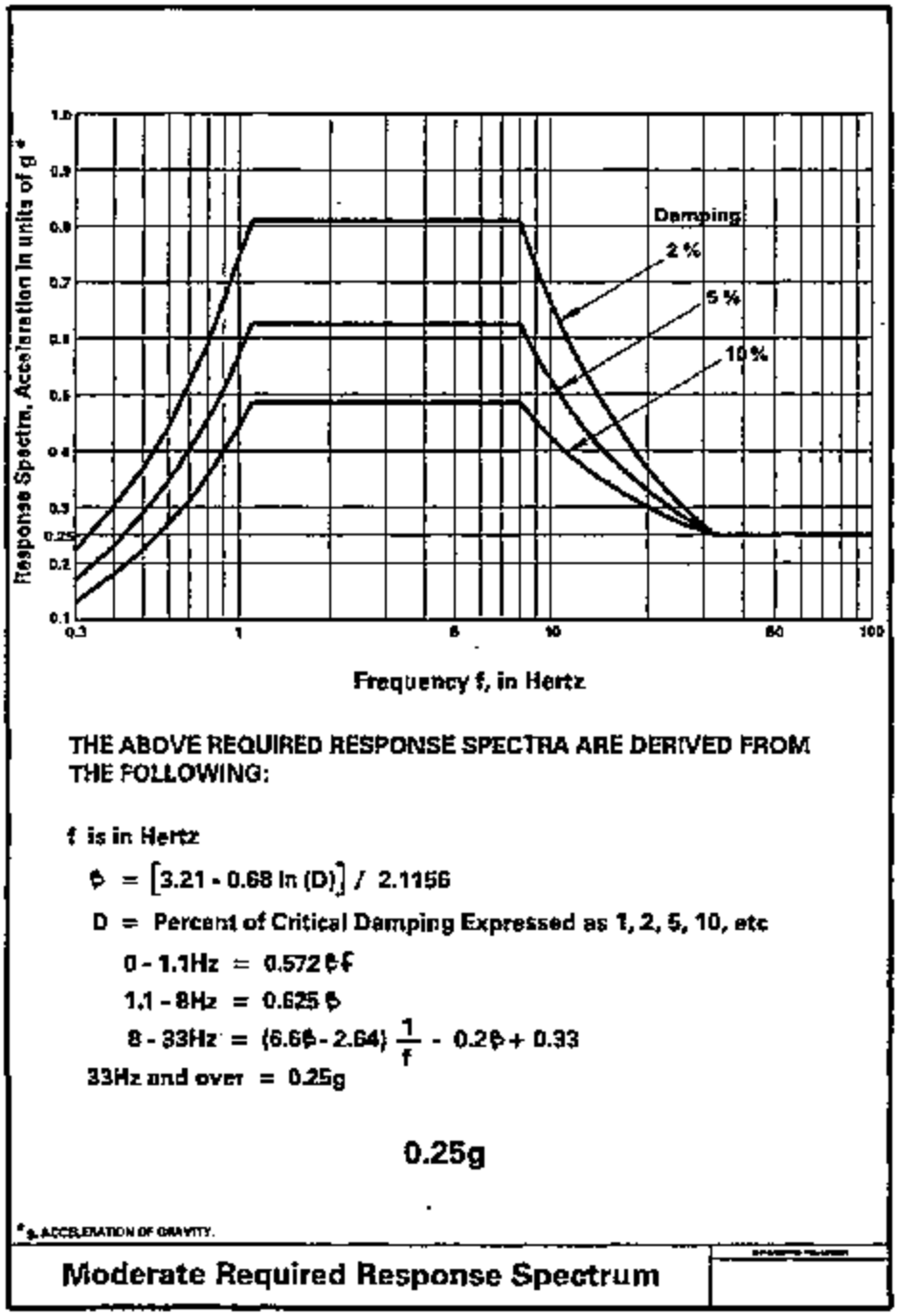

Figure A-4 Spectra for Moderate Required Response Spectrum (IEEE, 1998)

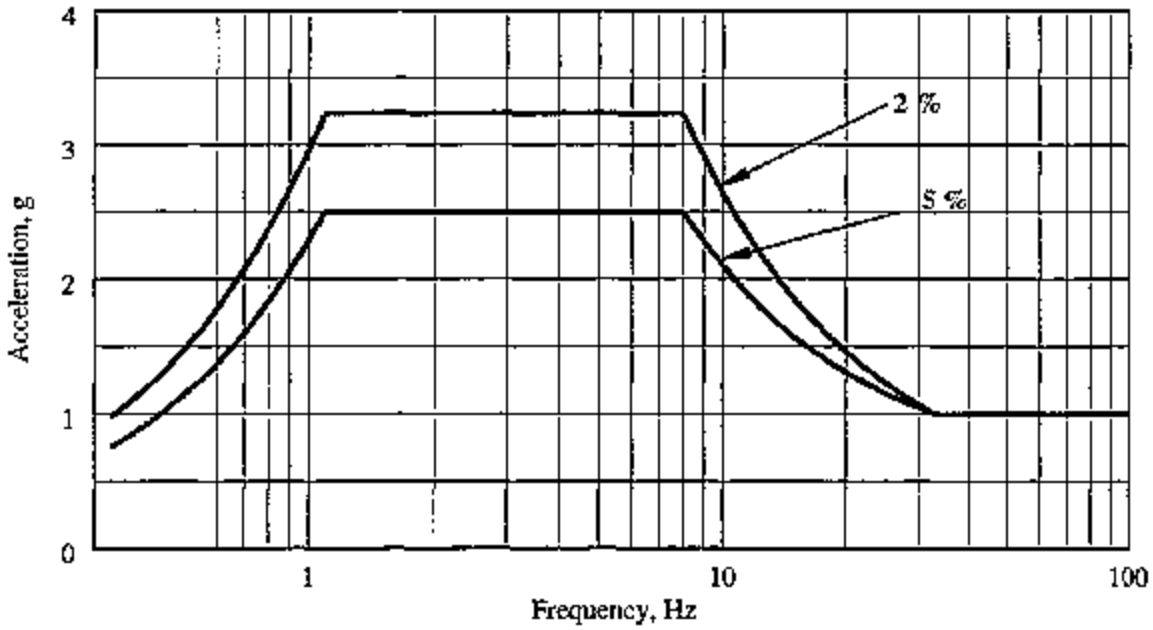

Figure A-5 Test Response Spectra for Moderate Level qualification of a transformer-mounted bushing

PEER REPORTS

PEER reports are available from the National Information Service for Earthquake Engineering (NISEE) and from the National Technical Information Service (NTIS). To order PEER reports, please contact the Pacific Earthquake Engineering Research Center, 1301 South 46th Street, Richmond, California 94804-4698. Tel.: (510) 231-9468; Fax: (510) 231-9461.

PEER 1999/05 *Seismic Evaluation of 550 Kv Porcelain Transformer Bushings.* Amir S. Gilani, Andrew S. Whittaker, Gregory L. Fenves, Eric Fujisaki. October 1999. $15.00.

PEER 1999/04 *Adoption and Enforcement of Earthquake Risk-Reduction Measures.* Peter J. May, Raymond J. Burby, T. Jens Feeley, and Robert Wood. August 1999. $15.00.

PEER 1999/03 *Task 3 Characterization of Site Response General Site Categories.* Adrian Rodriguez-Marek, Jonathan D. Bray, and Norman Abrahamson. February 1999. $20.00

PEER 1999/02 *Capacity-Demand-Diagram Methods for Estimating Seismic Deformation of Inelastic Structures: SDF Systems.* Anil K. Chopra and Rakesh Goel. April 1999. $15.00

PEER 1999/01 *Interaction in Interconnected Electrical Substation Equipment Subjected to Earthquake Ground Motions.* Armen Der Kiureghian, Jerome L. Sackman, and Kee-Jeung Hong. February 1999. $20.00

PEER-1998/08 *Behavior and Failure Analysis of a Multiple-Frame Highway Bridge in the 1994 Northridge Earthquake.* Gregory L. Fenves and Michael Ellery. December 1998. $20.00

PEER-1998/07 *Empirical Evaluation of Inertial Soil-Structure Interaction Effects.* Jonathan P. Stewart, Raymond B. Seed, and Gregory L. Fenves. November 1998. $26.00

PEER-1998/06 Effect of Damping Mechanisms on the Response of Seismic Isolated Structures. Nicos Makris and Shih-Po Chang. November 1998. $$15.00

PEER-1998/05 *Rocking Response and Overturning of Equipment Under Horizontal Pulse-Type Motions.* Nicos Makris and Yiannis Roussos, October 1998. $15.00

PEER-1998/04 *Pacific Earthquake Engineering Research Invitational Workshop Proceedings, May 14-15, 1998: Defining the Links Between Planning, Policy Analysis, Economics and Earthquake Engineering.* Mary Comerio and Peter Gordon. September 1998. $15.00

PEER1998/03 *Repair/Upgrade Procedures for Welded Beam to Column Connections.* James C. Anderson and Xiaojing Duan, May 1998. $33.00

PEER-1998/02 *Seismic Evaluation of 196 kV Porcelain Transformer Bushings.* Amir S. Gilani, Juan W. Chavez, Gregory L. Fenves, and Andrew S. Whittaker, May 1998. $20.00

The Pacific Earthquake Engineering Research Center (PEER) is a consortium of western U.S. universities working in partnership with business, industry, and government to identify and reduce the risks from major earthquakes to life safety and to the economy.

PEER achieves its objectives of earthquake risk reduction through a coordinated program of research, education, and partnerships with users of research results. PEER's research program includes basic and applied components of seismology, engineering, architecture, urban planning, and economics.

PEER is headquartered at UC Berkeley.

PEER reports are available individually or by yearly subscription from the National Information Service for Earthquake Engineering (NISEE) and from the National Technical Information Service (NTIS).

To order PEER Reports, contact the Pacific Earthquake Engineering Research Center, 1301 S. 46th St., Richmond, California 94804-4698, Tel: 510-231-9468, Fax: 510-231-9461.

Seismic Evaluation and Retrofit of 230-kV Porcelain Transformer Bushings

Amir S. Gilani
Andrew S. Whittaker
Gregory L. Fenves
University of California, Berkeley

Eric Fujisaki
Pacific Gas & Electric Co.

PEER Report 1999/14
Pacific Earthquake Engineering Research Center
College of Engineering
University of California, Berkeley
December 1999

ABSTRACT

Two identical 230-kV porcelain transformer bushings and two retrofit details were selected for testing and evaluation. The class of the bushing tested was built in the mid-1980s and was known to be vulnerable to earthquake shaking. Resonance-search tests were conducted to determine the dynamic properties of the bushings. Static testing was undertaken to determine the limit states of the bushing and to assess the effectiveness of a retrofit detail. For static testing, the bushing was vertically mounted on a stiff frame and four target displacement orbits were used: unidirectional, unidirectional with offset, bidirectional, and monotonic. During the static tests, oil leaked from the gasket connection, and the porcelain unit immediately above the flange slipped at a displacement of 10 mm. Reduction of the bushing post-tensioning force reduced the uplift displacement at which the bushing leaked oil. The addition of the first retrofit detail (Ring-1) did not prevent the oil leakage or the slip of the porcelain unit. Triaxial earthquake-simulator testing was conducted to evaluate the seismic performance of the bushings mounted on rigid and flexible frames and to evaluate the efficacy of a second retrofit detail (Ring-2). Two sets of spectrum-compatible ground motion records, derived from motions recorded during the 1978 Tabas earthquake in Iran, were used for testing. The fundamental frequency and damping ratio of the bushing were 18 to 20 Hz, and 2 to 3 percent of critical, respectively when mounted on a rigid frame. When subjected to motions compatible with the IEEE 693-1997 spectrum for High Level qualification, there was no structural damage and no oil leakage. The fundamental frequency of the bushing-support system was reduced to approximately 7 Hz when the bushing was installed on a flexible plate. This reduction in frequency substantially increased the response of the bushing. The bushing leaked oil, the porcelain unit immediately above the flange slipped, and the gasket extruded from the porcelain to flange interface when the bushing was subjected to severe shaking. The addition of Ring-2 reduced the slip of the porcelain unit, prevented the extrusion of the gasket, and delayed oil leakage.

ACKNOWLEDGMENTS

The work described in this report was undertaken by the Pacific Earthquake Engineering Research Center (PEER) with funding from the California Energy Commission (CEC), Pacific Gas and Electric (PG&E) Company, Bonneville Power Administration (BPA), Southern California Edison (SCE), and British Columbia Hydro (BC Hydro). This financial support is gratefully acknowledged. The two 230-kV transformer bushings used in the testing program were supplied by BPA.

The authors wish to thank the following individuals for their significant technical contributions to the project: Mr. Ed Matsuda (PG&E), Dr. Anshel Schiff (Precision Measurement Instruments), Dr. Leon Kempner (BPA), Dr. Alan King (BC Hydro), Mr. Jim Kennedy (SCE), and Mr. Lonnie Elder of ABB Power T&D Company, Inc., Components Division (ABB). Thanks are also due to Mr. Don Clyde (PEER), who made significant contributions to the experimental program and Ms. Janine Hannel (PEER), who edited this report. Dr. Schiff designed and installed the two retrofit details described in this report.

This work made use of the Pacific Earthquake Engineering Research Center shared facilities supported by the Earthquake Engineering Research Centers Program of the National Science Foundation under Award Number EEC-9701568.

CONTENTS

Abstract iii

Acknowledgments v

Table of Contents vii

List of Tables xi

List of Figures xiii

1 Introduction 1
- 1.1 Porcelain Transformer Bushings 1
- 1.2 Laboratory Testing of Bushings 2
  - 1.2.1 Introduction 2
  - 1.2.2 Earthquake simulator tests 2
  - 1.2.3 Cantilever tests 2
  - 1.2.4 Static tests 2
- 1.3 Literature Survey 3
  - 1.3.1 Background 3
  - 1.3.2 Laboratory testing of a 500-kV bushing in CERL, 1997 3
  - 1.3.3 Laboratory testing of bushings and transformers by ENEL, 1997-1998 3
  - 1.3.4 Field testing of bushings and transformers, UC Irvine, 1998-1999 4
  - 1.3.5 Laboratory testing of bushings, UC Berkeley, 1997-1999 4
- 1.4 Objectives of the Current Study 5
- 1.5 Report Organization 5

2 Selection Criteria and Properties of Test Bushings 11
- 2.1 Introduction 11
- 2.2 Selection of Candidate Bushing 11
- 2.3 230-kV Type-U Bushing Manufactured by GE 12
- 2.4 Limit States for 230-kV Bushings 15
  - 2.4.1 Background 15
  - 2.4.2 Oil leakage 15
  - 2.4.3 Porcelain slip 16
  - 2.4.4 Gasket extrusion 16
  - 2.4.5 Porcelain fracture 16
- 2.5 Components of Deformation for 230-kV Bushings 16
  - 2.5.1 Introduction 16

3 Qualification and Fragility Testing 23
- 3.1 Introduction 23
- 3.2 IEEE 693-1997 Requirements for Bushing Qualification 23
  - 3.2.1 Resonant-search tests 23
  - 3.2.2 Earthquake test response spectrum 24
  - 3.2.3 Earthquake ground motions 25

4 Fragility Testing of Rigidly Mounted Bushings 39
- 4.1 Introduction 39
- 4.2 Test Setup 39
  - 4.2.1 Overview 39

4.2.2 Earthquake simulator 39
4.2.3 Rigid mounting frame 40
4.2.4 Earthquake ground motions 40
4.2.4.1 Resonant-search tests 40
4.2.4.2 Earthquake test response spectrum 40
4.2.5 Instrumentation 41
4.3 Summary of Experimental Data 41
4.3.1 Overview 41
4.3.2 Dynamic properties of rigidly mounted 230-kV bushings 46
4.3.3 Earthquake testing of Bushing-1 and Bushing-2 46
4.3.3.1 Introduction 46
4.3.3.2 Peak responses 47
4.3.3.3 Response of Bushing-1 47
4.3.3.4 Response of Bushing-2 49
4.3.3.5 Evaluation of seismic response of bushings 50
4.3.4 Response of Bushing-2 to harmonic excitations 50
4.3.4.1 Overview 50
4.3.4.2 Summary of bushing response 51
4.3.4.3 Peak responses 51
4.3.4.4 Response of the simulator platform 52
4.3.4.5 Response of the bushing 53

5 Bushing Retrofit Details 79
5.1 Introduction 79
5.2 Selection of a Candidate Retrofit Detail 79
5.3 Retrofit Rings 80
5.3.1 Introduction 80
5.3.2 Epoxy filler material 80
5.3.2.1 Geometry of Ring-1 81
5.3.3 Retrofit Ring-2 81

6 Static Cyclic Testing of Rigidly Mounted Bushing-1 85
6.1 Overview 85
6.2 Experimental Setup 85
6.2.1 Mounting frame 85
6.2.2 Post-tensioning mechanism 85
6.2.3 Loading collar and joint collar 86
6.2.4 Loading mechanism and test control 86
6.2.5 Instrumentation 86
6.3 Test Protocol 88
6.3.1 Pull-back, quick-release tests 88
6.3.2 Static tests 88
6.4 Experimental Results from Quick-Release Tests 89
6.5 Experimental Results from Static Tests of Bushing-1 without Ring-1 90
6.5.1 Unidirectional tests 90
6.5.2 Unidirectional tests with offset 92
6.5.3 Bidirectional tests 92
6.6 Experimental Results from Static Tests of Bushing-1 with Ring-1 93
6.6.1 Background 93
6.6.2 Unidirectional tests 93
6.6.3 Bidirectional tests 93
6.6.4 Monotonic test 93

6.7 Evaluation of Response of Bushing-1 94
6.7.1 Introduction 94
6.7.2 Modification of recorded data 94
6.7.3 Displacement response of Bushing-1 95
6.7.4 Slip properties of the gasket at the gasket connection 95
6.7.5 Efficacy of Ring-1 96
6.8 Summary 96

7 Fragility Testing of Flexibly Mounted Bushing-2 117
7.1 Overview 117
7.2 Attachment of 230-kV Bushings to Transformers 117
7.3 Test Setup 118
7.3.1 Mounting setup 118
7.3.2 Simulator input motions 118
7.3.2.1 Resonant-search tests 118
7.3.2.2 Earthquake test response spectrum 119
7.3.3 Instrumentation 119
7.3.4 Preparation of Bushing-2 120
7.4 Summary of Experimental Data from Pull-Back, Quick-Release Tests 120
7.4.1 Introduction 120
7.4.2 Test setup 123
7.4.3 Evaluation of the dynamic properties 123
7.4.4 Summary of experimental results 123
7.5 Experimental Results from Seismic Tests 125
7.5.1 Introduction 125
7.5.2 Summary of experimental data 125
7.5.3 Dynamic properties of Bushing-2 mounted on the flexible plate 125
7.5.4 Response of the rigid mounting frame and the flexible plate 128
7.5.5 Response of Bushing-2 without Ring-2 128
7.5.5.1 Peak response 128
7.5.5.2 Bushing response 129
7.5.5.3 Post-test tear-down of Bushing-2 131
7.5.6 Response of Bushing-2 retrofitted with Ring-2 132
7.5.6.1 Peak response 132
7.5.6.2 Bushing response 132
7.5.6.3 Post-test tear-down of Bushing-2 134
7.6 Effect of Support Flexibility and Ring-2 on the Response of Bushing-2 135
7.6.1 Influence of support flexibility 135
7.6.2 Efficacy of Ring-2 136

8 Summary and Conclusions 163
8.1 Summary 163
8.1.1 Overview 163
8.1.2 Test bushings 164
8.1.3 Experimental program 165
8.1.3.1 Introduction 165
8.1.3.2 Mounting frames 165
8.1.3.3 Test program 166
8.1.3.4 Development of ground motions for triaxial earthquake testing 166
8.1.4 Retrofit details 166
8.1.5 Summary of experimental results 167
8.1.5.1 Introduction 167

8.1.5.2 Experimental results from resonant-search tests 167
8.1.5.3 Experimental results from rigidly mounted bushings 167
8.1.5.4 Experimental results from static tests of Bushing-1 169
8.1.5.5 Experimental results from flexibly mounted Bushing-2 169
8.2 Conclusions 171
8.2.1 Seismic response of 230-kV transformer bushings 171
8.2.2 Effect of support flexibility 171
8.2.3 Effect of post-tensioning force 171
8.2.4 Efficacy of retrofit design 172
8.3 Recommendations for future study 172
8.3.1 Procedures for seismic qualification and fragility testing 172
8.3.2 Development of fragility curves for substation equipment 172
8.3.3 Interconnected equipment 173
8.3.4 Behavioral studies of porcelain transformer bushings 173
8.3.5 Mathematical modeling of porcelain transformer bushings 173

References 175

Appendix A IEEE Practice for Earthquake Testing of Transformer Bushings 177
A.1 Introduction 177
A.2 Performance Level and Performance Factor 178
A.3 Performance Level Qualification 178
A.4 Support Frame and Mounting Configuration 179
A.5 Testing Procedures for Transformer Bushings 179
A.5.1 Resonant search tests 179
A.5.2 Earthquake ground motion tests 179
A.6 Instrumentation of Transformer Bushings 180
A.7 Acceptance Criteria for Transformer Bushings 180

LIST OF TABLES

Chapter 2
Characteristics of the GE type-U test bushings 14
Material properties of the bushing components 15

Chapter 3
IEEE earthquake-history testing requirements for Moderate Level qualification 25
High-pass filter frequencies for earthquake histories 27

Chapter 4
Instrumentation for rigidly mounted 230-kV bushings 42
Summary of earthquake testing of Bushing-1 44
Summary of earthquake testing of Bushing-2 45
Modal properties of bushings from resonance-search tests 46
Peak responses of the bushings 48
Peak responses of Bushing-2 to the high-amplitude 5-Hz harmonic tests 51

Chapter 6
Instrumentation for static tests of Bushing-1 87
Protocol for quick-release testing of Bushing-1 88
Protocol for static testing of Bushing-1 90
Modal properties obtained from frequency tests 91

Chapter 7
Instrumentation of Bushing-2 mounted on the flexible plate 121
Modal properties of Bushing-2 along the x-axis 124
Modal properties of Bushing-2 along the y-axis 124
Modal properties of Bushing-2 along the x- axis 124
Summary of earthquake testing of flexibly mounted Bushing-2 without Ring-2 126
Summary of earthquake testing of flexibly mounted Bushing-2 with Ring-2 127
Modal properties of Bushing-2 from resonance-search tests 128
Peak acceleration response of the simulator platform and the mounting frames 129
Peak responses of the Bushing-2 without Ring-2 130
Peak responses of the Bushing-2 retrofitted with Ring-2 133
Response of the UPPER-1 porcelain unit 136

Chapter 8
Characteristics of the 230-kV type-U bushings manufactured by GE 165
Modal properties of 230 kV bushings1 168
Response of flexibly mounted Bushing-2 at the gasket connection 170

LIST OF FIGURES

Chapter 1
Bushing mounted on an oil-filled transformer 7
Cross section of a typical bushing 7
Fracture of an UPPER-1 porcelain unit from severe earthquake shaking 8
Seismic testing of a 500-kV bushing (Courtesy of CERL, Ill) 8
Laboratory testing of a bushing (Courtesy of ENEL and ISMES, Italy) 9
Field testing of a bushing (Courtesy of University of California, Irvine) 9
Laboratory testing of a 550-kV bushing 10

Chapter 2
Typical porcelain-flange interface details for the gasket connection 18
Slip of porcelain in a transformer-mounted 230-kV bushing 19
Bushing-2 prior to testing on the Berkeley simulator 19
Longitudinal section and cross section through a 230-kV type-U bushing, manufactured by General Electric 20
Exploded view of gasket connection detail for a 230-kV type-U bushing 21
Compression stiffness of 6-mm thick nitrile gaskets (Elder, 1999) 21
Deformation modes for components of a 230-kV bushing 22

Chapter 3
Spectra for the Moderate Seismic Performance Level (IEEE, 1998) 28
Test Response Spectra at bushing flange for Moderate PL 28
Normalized acceleration history, power spectrum, and response spectra for the longitudinal (*X*-) component of the original Tabas record 29
Normalized acceleration history, power spectrum, and response spectra for the lateral (*Y*-) component of the Tabas record 30
Normalized acceleration history, power spectrum, and response spectra for the vertical (*Z*-) component of the original Tabas record 31
Acceleration history, power spectrum, and response spectra for the longitudinal (*X*-) component of the Tabas-A record 32
Acceleration history, power spectrum, and response spectra for the lateral (*Y*-) component of the Tabas-A record 33
Acceleration history, power spectrum, and response spectra for the vertical (*Z*-) component of the Tabas-A record 34
Acceleration history, power spectrum, and response spectra for the longitudinal (*X*-) component of the Tabas-B record 35
Acceleration history, power spectrum, and response spectra for the lateral (*Y*-) component of the Tabas-B record 36
Acceleration history, power spectrum, and response spectra for the vertical (*Z*-) component of the Tabas-B record 37

Chapter 4
A rigidly mounted 230-kV bushing on the earthquake simulator 55
IEEE 693-1997 test response spectrum for High Level Qualification 55
Instrumentation for 230-kV bushings 56
Instrumentation at top of Bushing-1 57
Instrumentation of the UPPER-1 porcelain unit 57
Terminal attached to the top of Bushing-2 58

Bushing-2 after Test No 38 showing oil leakage and slip of porcelain 58
Transfer function amplitudes between the top of Bushing-1 and frame 59
Transfer function amplitudes between the top of Bushing-2 and frame 60
Response spectra for Bushing-1; Test No 12, target PGA=1.0g 61
Response spectra for Bushing-1; Test No 17, target PGA=2.0g 62
Vertical displacement versus rocking for Bushing-1; Test No 17, target PGA=2.0g 63
Orbit of motion for Bushing-1; Test No 17, target PGA=2.0g 64
Response spectra for Bushing-2; Test No 19, target PGA=1.0g 65
Response spectra for Bushing-2; Test No 24, target PGA=2.0g 66
Vertical displacement versus rocking for Bushing-2; Test No 24, target PGA=2.0g 67
Orbit of motion for Bushing-1; Test No 24, target PGA=2.0g 68
Simulator x- direction input for the high-amplitude 5-Hz harmonic tests, Test No 37 69
Response spectrum for high-amplitude harmonic tests 70
Acceleration response of Bushing-2 without terminal, Test No 38 71
Acceleration response of Bushing-2 with terminal, Test No 37 72
Displacement history of Bushing-2 relative to support frame, Test No 38 73
Displacement history of Bushing-2 relative to support frame, Test No 37 74
Vertical displacement of the UPPER-1 porcelain unit, Test No 38 75
Vertical displacement of the UPPER-1 porcelain unit, Test No 37 76
Stress history of the UPPER-1 porcelain unit, Test No 38 77
Stress history of the UPPER-1 porcelain unit, Test No 37 78

Chapter 5

Geometry of Ring-1 82
Geometry of Ring-2 83
Ring-1 placed around the gasket connection of Bushing-1 84
Ring-2 prior to installation around the gasket connection of Bushing-2 84

Chapter 6

Bushing-1 and the mounting frame 98
Post-tensioning setup for Bushing-1 98
Joint collar for Bushing-1 99
Bushing-1 prior to cyclic testing 99
Instrumentation for static tests of Bushing-1 100
Instrumentation at the top of Bushing-1 100
Instrumentation of the UPPER-1 porcelain unit 101
Test setup for pull-back, quick-release test 101
Displacement orbits for static tests 102
Displacement history for static cyclic tests 102
Time and frequency response of displacement sensors 103
Effect of preload on the gasket stiffness 104
Bushing-1 at conclusion of Test Set 1 105
Force-displacement response of Bushing-1 (Test No 8, Test Set 1) 105
Displacement histories of Bushing-1 for Test Sets 1, 5, 6, and 7 106
Force-displacement history for Bushing-1, Test No 4, Test Set 3 107
Actuator orbits during bidirectional tests (Test No 6, Test Set 4) 108
Rotation of Ring-1 following Test Set 12 109
Oil leakage from the gasket connection following Test Set 12 109
Separation of Ring-1 from the epoxy filler material, Test Set 13 110
Twist of the UPPER-1 porcelain unit over the flange, Test Set 13 110

Slip of the UPPER-1 porcelain unit following Test Set 14 111
Fracture of the bottom shed of the UPPER-1 porcelain unit, Test Set 14 111
Torn portion of gasket at the gasket connection, Test Set 14 112
Fracture of cast aluminum flange following Test Set 14 112
Response of Bushing-1 during the monotonic test (Test Set 14) 113
Force-displacement response of Bushing-1 at the gasket connection 114
Response of Bushing 1 at the gasket connection (Test Sets 1 and 12) 115

Chapter 7

Details for flexible plate 137
230 kV-bushing installed atop the flexible plate 138
View of the flange connection showing the mounting gasket and bolts 138
Gasket connection showing Ring-2 retrofit detail 139
IEEE 693-1997 test response spectrum for High Level Qualification 139
Acceleration history, power spectrum, and response spectrum for the longitudinal (*X*- component of the CERL record 140
Acceleration history, power spectrum, and response spectrum for the transverse (*Y*- component of the CERL record 141
Acceleration history, power spectrum, and response spectrum for the vertical (*Z*- component of the CERL record 142
Instrumentation for seismic testing of Bushing-2 mounted on a flexible plate 143
Instrumentation at the top of Bushing-2 144
Instrumentation of the UPPER-1 porcelain unit and the flexible mounting plate 144
Bushing-2 after Test No 15 (target PGA=1.4g) showing oil leakage 145
Bushing-2 after Test No 17 (target PGA=1.8g) showing slip of porcelain 145
Bushing-2 after Test No 18 (target PGA=2.0g) showing extruded gasket 146
Retrofitted Bushing-2 after Test No 23 (target PGA=2.8g) showing oil leakage 146
Transfer function amplitudes between the top of Bushing-2 and the flexible plate 147
Transfer function amplitudes between the flexible plate and the rigid support 148
Response spectrum for Bushing-2 without Ring-2; Test No 13, Tabas-A, target PGA=1.0g 149
Response spectrum for Bushing-2 without Ring-2; Test No 18, Tabas-A, target PGA=2.0g 150
Components of vertical motion for Bushing-2 without Ring-2; Test No 18, Tabas-B, target PGA=2.0g 151
Components of horizontal motion for Bushing-2 without Ring-2; Test No 18, Tabas-B, target PGA=2.0g 152
Bushing-2 after earthquake testing showing the largest tear in the gasket 153
Drawing of the gasket locating tears 153
Response spectrum for Bushing-2 retrofitted with Ring-2; Test No 13, Tabas-A, target PGA=1.0g 154
Response spectrum for Bushing-2 retrofitted with Ring-2; Test No 18, Tabas-B, target PGA=2.0g 155
Response spectrum for Bushing-2 retrofitted with Ring-2; Test No 19, CERL, target PGA=1.0g 156
Response spectrum for Bushing-2 retrofitted with Ring-2; Test No 24, Tabas-B, target PGA=3.0g 157
Components of vertical motion for Bushing-2 retrofitted with Ring-2; Test No 24, Tabas-B, target PGA=3.0g 158
Components of horizontal motion for Bushing-2 retrofitted with Ring-2; Test No 24, Tabas-B, target PGA=3.0g 159
Post-test photograph of gasket locating tears and lacerations 160

Effects of support flexibility on the spectral acceleration response of a bushing 161
Displacement response of flexible plate in *z*- direction; Test No 24,
Tabas-B, target PGA=3.0g 162

Appendix A

Spectra for High Seismic Performance Level (IEEE 1998) 181
Spectra for Moderate Seismic Performance Level (IEEE 1998) 181
Spectra for High Level Required Response Spectrum (IEEE 1998) 182
Spectra for Moderate Level Required Response Spectrum (IEEE 1998) 183
Test Response Spectrum for Moderate Level qualification of a transformer-mounted bushing 184

1 Introduction

1.1 Porcelain Transformer Bushings

Porcelain transformer bushings are a key component of power transmission and distribution (T&D) systems. They are insulated conductors used to provide electrical connectivity between a high-voltage line and an oil-filled transformer, and are typically mounted on the top of a transformer or on a turret attached to the transformer (see Figure 1-1) using a bolted flange connection. A section through a typical bushing at its connection to a transformer is shown in Figure 1-2. The bushing flange, the porcelain stack immediately above the flange (referred to as UPPER-1 porcelain unit herein), and the gasket between the bushing flange and the UPPER-1 porcelain unit are shown in Figure 1-2.

Recent major earthquakes (Northridge, 1994; Kobe, 1995; Izmit, 1999; and Southern California, 1999) have demonstrated that porcelain transformer bushings, especially the high-voltage bushings rated at 196 kV and above, are susceptible to damage during severe ground shaking. For these bushings, it has been postulated that the inertia forces produce large shear forces and bending moments at the connection between the UPPER-1 porcelain unit and the bushing flange (termed the gasket connection herein, see Figure 1-2), and that these forces can cause failure. Four types of failure have been documented (Schiff, 1997): (a) oil leakage at the gasket connection, (b) slip of the UPPER-1 porcelain unit relative to the bushing flange, (c) gasket extrusion from the gasket connection, and (d) cracking of porcelain. Figure 1-3 shows a bushing with cracked porcelain mounted atop a turret (Schiff, 1997).

Since transformer bushings form an integral part of power T&D systems, their structural and electrical integrity are critical to maintaining power transmission. To mitigate the vulnerability of new bushings and other electrical substation equipment, representatives from electrical utilities and equipment manufacturers, together with consulting engineers and members of the academic community jointly developed a new national standard, IEEE 693-1997 (IEEE 1998). These requirements are expected to improve the seismic capability of substation equipment. However, electrical utilities will continue to maintain substantial inventories of the older equipment procured prior to the development of the current standard. The investigation reported herein was motivated by the need to develop retrofit methods to improve the seismic performance of older, vulnerable transformer bushings.

Section 1.2 describes the experimental methods used in this study, Section 1.3 summarizes previous research on bushings, Section 1.4 lists the objectives of the current study, and Section 1.5 describe the organization of this report.

1.2 Laboratory Testing of Bushings

1.2.1 Introduction

In the current study, three types of tests were used to characterize the performance of transformer bushings: earthquake simulator tests, pull-back quick-release tests, and static tests. Summary information on these tests follow.

1.2.2 Earthquake simulator tests

In the United States, the Institute for Electrical and Electronics Engineers, (IEEE) has developed guidelines for seismic testing and qualification of bushings. These guidelines are described in *IEEE Recommended Practice for Seismic Design of Substations*, IEEE 693-1997. According to these standards, transformer bushings rated at 161 kV and above need to be qualified by means of triaxial simulator testing. The key IEEE 693-1997 requirements for seismic qualification tests are identified in Appendix A. Three types of simulator testing are typically undertaken: resonance-search tests, seismic qualification tests, and seismic fragility tests.

Resonant-search tests are conducted at low levels of shaking and are used to determine the dynamic properties (fundamental frequency and damping ratio) of the equipment. Seismic *qualification* tests are intended to demonstrate (through experimentation) that a piece of equipment is able to perform its function during and after an earthquake. Seismic *fragility* tests are experiments that test to failure and are intended to obtain data points correlating a particular limit state (or failure) with a representative ground motion parameter (typically selected as the peak ground acceleration, PGA). This information is then used to develop fragility curves that plot the cumulative probability of reaching a limit state as a function of the chosen ground motion parameter.

1.2.3 Cantilever tests

Cantilever tests are mechanical tests performed by the bushing manufacturers to determine the static lateral load capacity of a bushing. Elastic (stiffness) and dynamic (frequency) properties of the bushing may also be derived from such tests. The bushing is typically mounted vertically on a stiff frame and a static concentrated force is applied at the top of the bushing. The rated cantilever strength of the bushing is a conservative estimate of the maximum load that may be applied before structural or functional failure. Oil leakage is the typical failure mode.

1.2.4 Static tests

Static (cyclic and monotonic) tests have been extensively and successfully used to test many structures and structural components (steel beam-column connections, concrete structures, supplementary dampers, and isolation bearings). Quasi-static cyclic tests are cost efficient and the slow rate of testing allows the investigator to observe and document the response during the

testing. The testing program described in this report is the first to use this method of testing to evaluate the response of transformer bushings and to supplement earthquake simulator tests.

1.3 Literature Survey

1.3.1 Background

In the past five years, a number of seismic tests of transformer bushings have been completed. A summary of selected tests and some of the key findings are presented in this section.

1.3.2 Laboratory testing of a 500-kV bushing in CERL, 1997

Wilcoski and Smith (1997) conducted triaxial seismic qualification and fragility testing of a 500-kV bushing supplied by the Tennessee Valley Authority (TVA), and manufactured by the General Electric Company (GE). The objectives of the tests were to determine the dynamic characteristics of the bushing, to qualify the bushing to the IEEE 693-1997 spectrum anchored at 0.5g, and to investigate the application of the CERL equipment fragility and protection procedure (CEFAPP) to electrical equipment.

The bushing was mounted on a small braced frame (see Figure 1-4) and tested using input motions generated from random signal. The motions consisted of a set of narrow-banded input signals whose amplitudes at the prescribed center frequency were adjusted to equal the IEEE 693-1997 acceleration spectrum ordinates. A fundamental frequency of approximately 6 Hz and a damping ratio of between 2 to 3 percent of critical were reported. During the qualification test (matched to the 2-percent IEEE 693-1997 response spectrum with a PGA of 0.5g), the bushing sustained no damage. During the fragility tests, (matched to the 2-percent IEEE 693-1997 response spectrum with a PGA of 1.0g), the bushing leaked oil.

1.3.3 Laboratory testing of bushings and transformers by ENEL, 1997-1998

Bellorini et al., (1997, 1998) conducted experimental and analytical studies of 230-kV bushings and transformers. The objectives of the tests were to determine the dynamic characteristics of the transformer-bushing system, to develop a finite element model of the transformer, to evaluate the amplification factor between the accelerations at the bushing flange and the transformer base, and to test a bushing to failure.

Forced vibration tests were used to determine the natural frequency of the transformer-bushing system. For the transformer-mounted bushing, a fundamental frequency and a damping ratio of 11 Hz and 2 percent of critical were reported. A linear three-dimensional finite element model of the transformer-bushing system was prepared and was calibrated using the experimental data. Utilizing the calibrated finite element model, the authors conducted response-history analysis of the transformer-bushing system. Two types of input motions were used: (1) a synthetic history derived from IEC-61463 (IEC 1996) matched to a 2-percent response spectrum with a PGA of 0.5g, and (2) two recorded ground motion histories (Friuli 1976 and Irpinia 1980) scaled to a PGA of 0.5g. The results of the dynamic analyses indicated an amplification factor of approximately 1.0 between the top of the transformer and the transformer base, and an amplification factor of approximately 2.2 between the bushing flange (top of turret) and the base of the transformer;

therefore the accelerations at the bushing flange were nearly 2.2 times greater than the transformer-base acceleration due to the flexibility of the transformer-turret support. For the earthquake simulator tests, the 230-kV bushing was attached to a rigid supporting frame (Figure 1-5). The bushing was subjected to (1) a synthetic history compatible with the IEC 61463-1996 (IEC 1996) 2-percent damped response spectrum with a PGA of 0.5g and (2) recorded ground motion histories. Oil leakage, large deformations, or breakage were not observed in any of these tests.

1.3.4 Field testing of bushings and transformers, UC Irvine, 1998-1999

Villaverde et al., (1999) conducted field testing and analytical studies of 230-kV and 500-kV bushings mounted on transformers. The objectives of the studies were to evaluate the dynamic characteristics of the transformer-bushing systems and to compute the amplification between the accelerations at the bushing flange and the ground as a result of the flexibility of the transformer tank and the turrets to which the bushings were attached.

Figure 1-6 shows part of the instrumentation used during the field testing of a 230-kV bushing. The tests were conducted by placing a vibrating shaker on the top of the transformer tank and laterally exciting the transformer. A fundamental frequency of approximately 6 Hz, and a damping ratio of 2 percent of critical for the 230-kV transformer-mounted bushings and a fundamental frequency of between 3 to 4 Hz, and a damping ratio of between 2 and 4 percent of critical for the 500-kV transformer-mounted bushings were reported. Linear three-dimensional finite element models of the transformer-bushing systems were prepared and calibrated using the experimental data. Using the calibrated finite element model, the authors conducted response-history analysis of the transformer-bushing systems. Two types of input motions were used: synthetic histories compatible with the IEEE 693-1997 (IEEE 1998) 2-percent damped response spectrum with a PGA of 0.5g, and recorded ground motion histories from 1989 Loma Prieta, and 1994 Northridge earthquakes.

1.3.5 Laboratory testing of bushings, UC Berkeley, 1997-1999

As part of a cooperative effort between the Pacific Earthquake Engineering Research (PEER) Center, the Pacific Gas and Electric (PG&E) Company, and the California Energy Commission (CEC), seismic testing and evaluation of two 196-kV and three 550-kV bushings was recently completed at the University of California at Berkeley. These bushings were manufactured by ABB Power T&D Company, Inc., Components Division of Alamo, Tennessee (ABB). The objectives of the studies were to compute the dynamic properties of the bushings, to qualify the bushings to either the IEEE 693-1997 moderate- or high-level spectrum, and to characterize the seismic performance of the bushings.

The bushings were mounted on a stiff braced frame and subjected to IEEE 693-1997 spectrum-compatible triaxial earthquake histories. The motions were developed from recorded near-field accelerations, using a time-domain spectrum matching technique. For the 196-kV bushings (Gilani et. al, 1998), fundamental frequencies of between 14 and 16 Hz and damping ratios of between 2 to 4 percent of critical were measured. One 196-kV bushing was qualified to the IEEE 693-1997 moderate-level spectrum (target PGA equal to 1.0g) and the second 196-kV bushing

was qualified to the IEEE 693-1997 high-level spectrum (target PGA equal to 2.0g). For the 550-kV bushings (Gilani et. al, 1999), a fundamental frequency of approximately 8 Hz and damping ratio of between 3 to 4 percent of critical were measured. None of the three 550-kV bushings met the IEEE 693-1997 requirements for the moderate-level qualification (target PGA equal to 1.0g) and when subjected to severe shaking, all three bushings experienced oil leakage at the gasket connection and slip of the UPPER-1 porcelain unit over the flange, (see Figure 1-7).

1.4 Objectives of the Current Study

In this study, PEER researchers, representatives from electrical utilities and transformer-bushing equipment manufacturers collaborated to develop new information on the response of bushings and to improve the seismic performance of *in-service* transformer bushings. This research program addressed three issues not explored in the previous studies, namely: (1) retrofit of (existing) in-service bushings; (2) the influence of support flexibility and bushing preload on bushing response; and (3) the utility of static testing as a complement to triaxial earthquake simulator seismic tests.

The five objectives of the study were to:

1. Identify bushings that were susceptible to severe earthquake shaking and select a vulnerable bushing type for further investigation.

2. Conduct fragility tests of bushings mounted on a rigid base (termed hereafter as a *rigidly* mounted bushing) to identify dynamic properties and limit states of the bushings.

3. Develop a retrofit procedure for a sample bushing that was cost effective, could be implemented simply, and met the electrical requirements specified by the manufacturers.

4. Conduct static tests of a bushing to identify its limit states of response (e.g., oil leakage and slip of porcelain) and to evaluate the efficacy of the retrofit detail.

5. Conduct fragility tests of a bushing mounted on a flexible base (termed hereafter as a *flexibly* mounted bushing) to investigate the influence of support flexibility on bushing response and to assess the efficacy of the retrofit detail.

1.5 Report Organization

This report comprises into eight chapters, references, and one appendix. Chapter 2 provides information on the two bushings used for testing. Chapter 3 discusses the simulator motions developed for the seismic tests. Chapter 4 describes the test setup (including the rigid mounting frame and a list of the transducers used to monitor the response of the bushings) and results from the earthquake testing of *rigidly* mounted bushings. Chapter 5 provides information on the retrofit details. Chapter 6 describes the test setup (including the stiff mounting frame and a list of the transducers used to monitor the response of the bushing) and the results from the static testing of a bushing. Chapter 7 describes the test setup (including the flexible mounting attachment and a list of the transducers used to monitor the response of the bushing) and the results from the earthquake testing of a *flexibly* mounted bushing. Chapter 8 includes a summary of the key

findings and conclusions drawn from the research project. References are listed following Chapter 8. The IEEE 693-1997 Recommended Practice for earthquake testing of transformer bushings is summarized in Appendix A. Raw data and video images from all earthquake tests were supplied to Pacific Gas & Electric under separate cover.

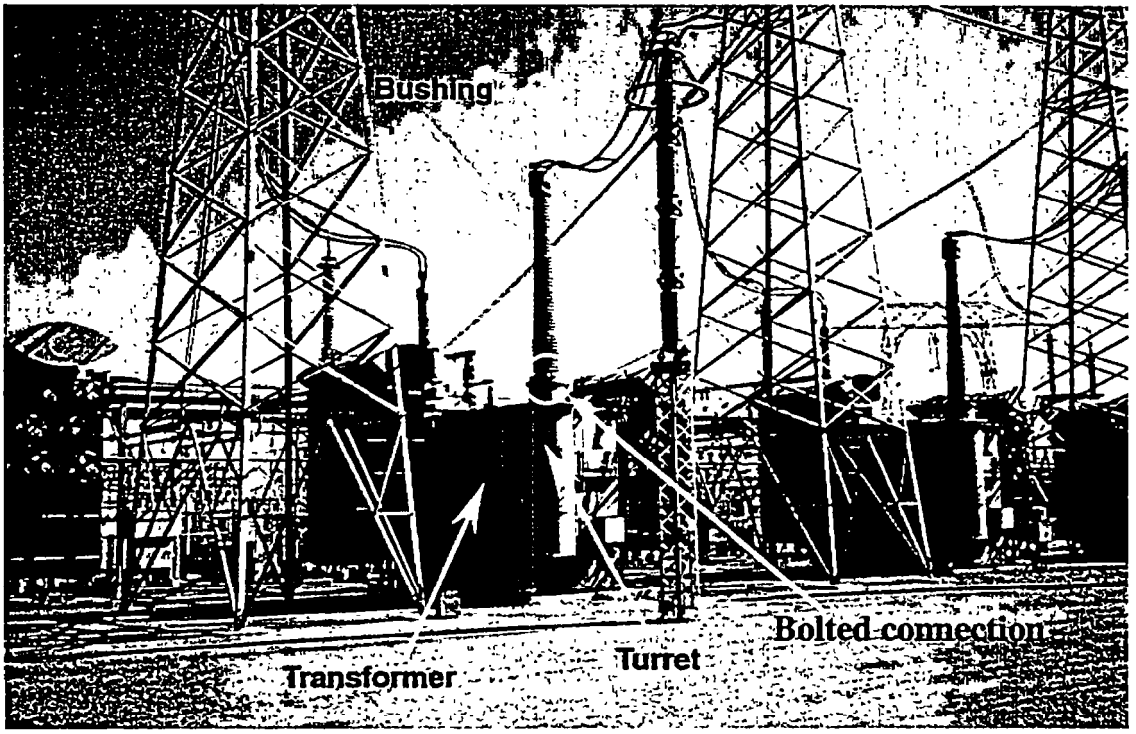

Figure 1-1 Bushing mounted on an oil-filled transformer

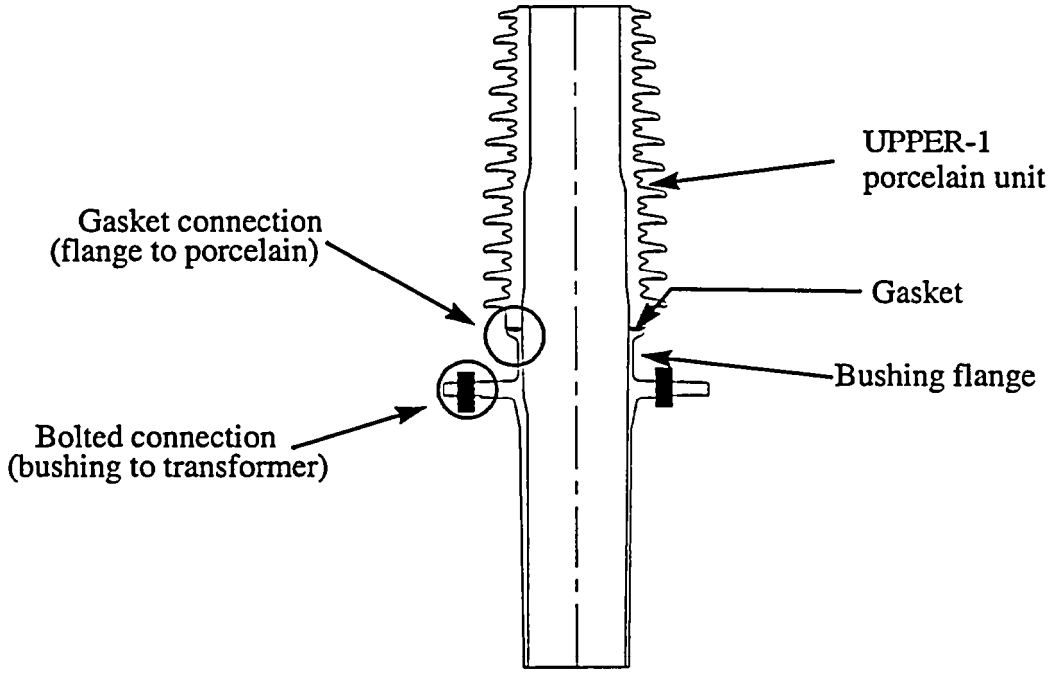

Figure 1-2 Cross section of a typical bushing

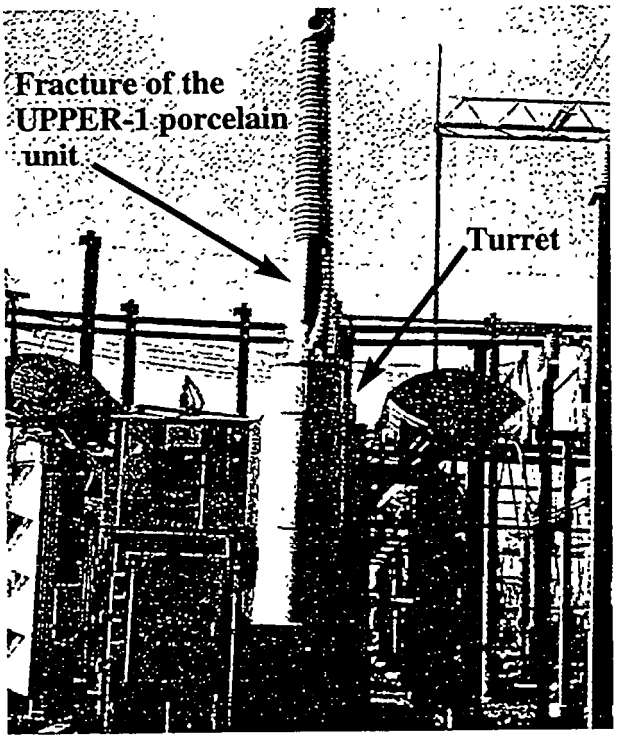

Figure 1-3 Fracture of an UPPER-1 porcelain unit from severe earthquake shaking

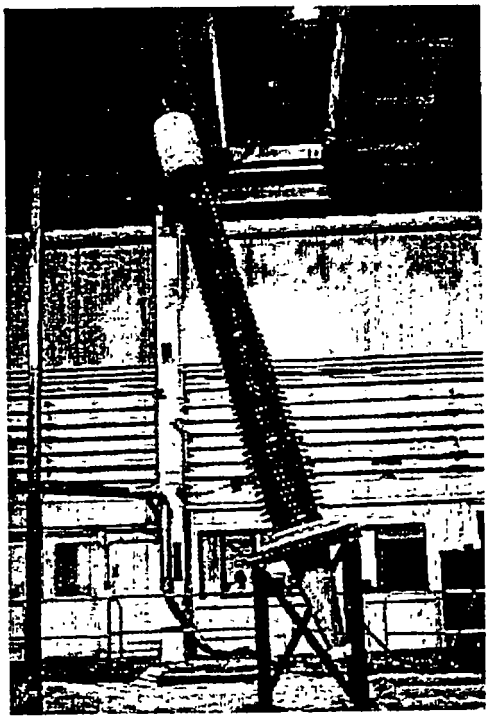

Figure 1-4 Seismic testing of a 500-kV bushing (Courtesy of CERL, Ill)

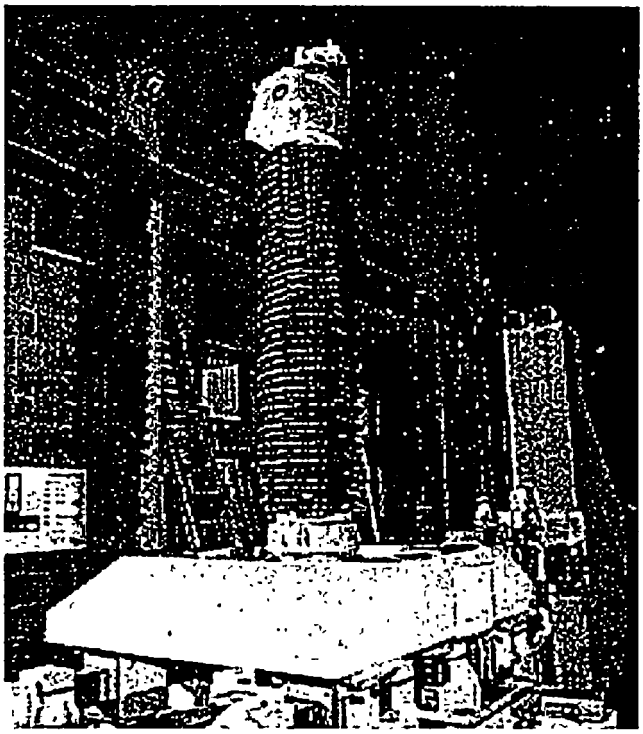

Figure 1-5 Laboratory testing of a bushing (Courtesy of ENEL and ISMES, Italy)

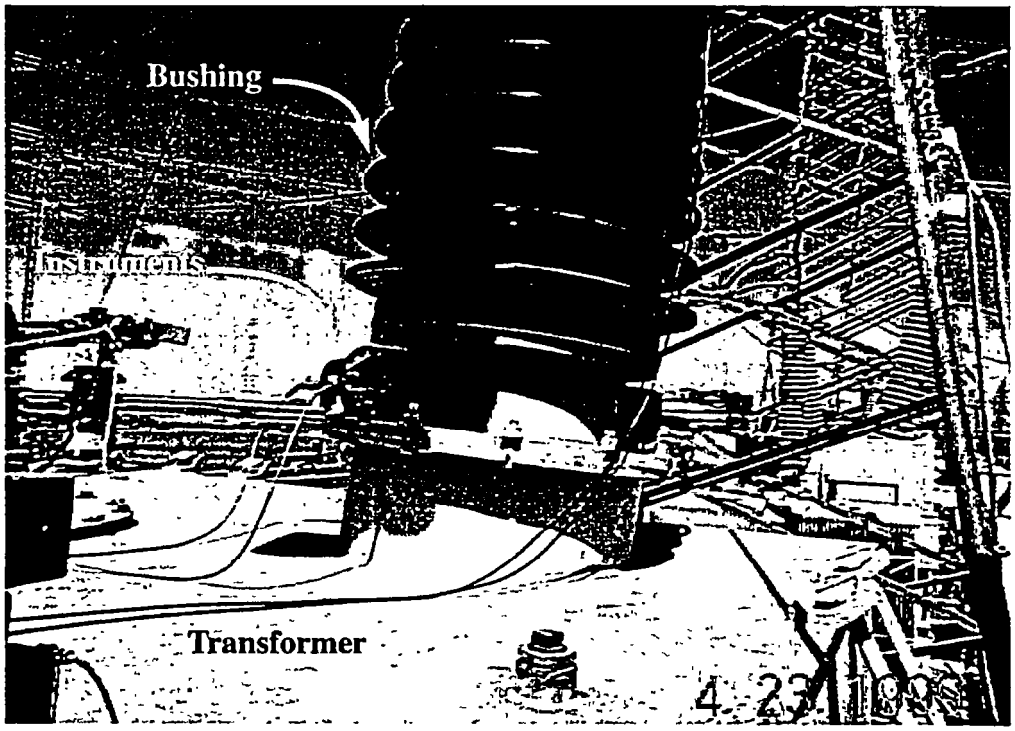

Figure 1-6 Field testing of a bushing (Courtesy of University of California, Irvine)

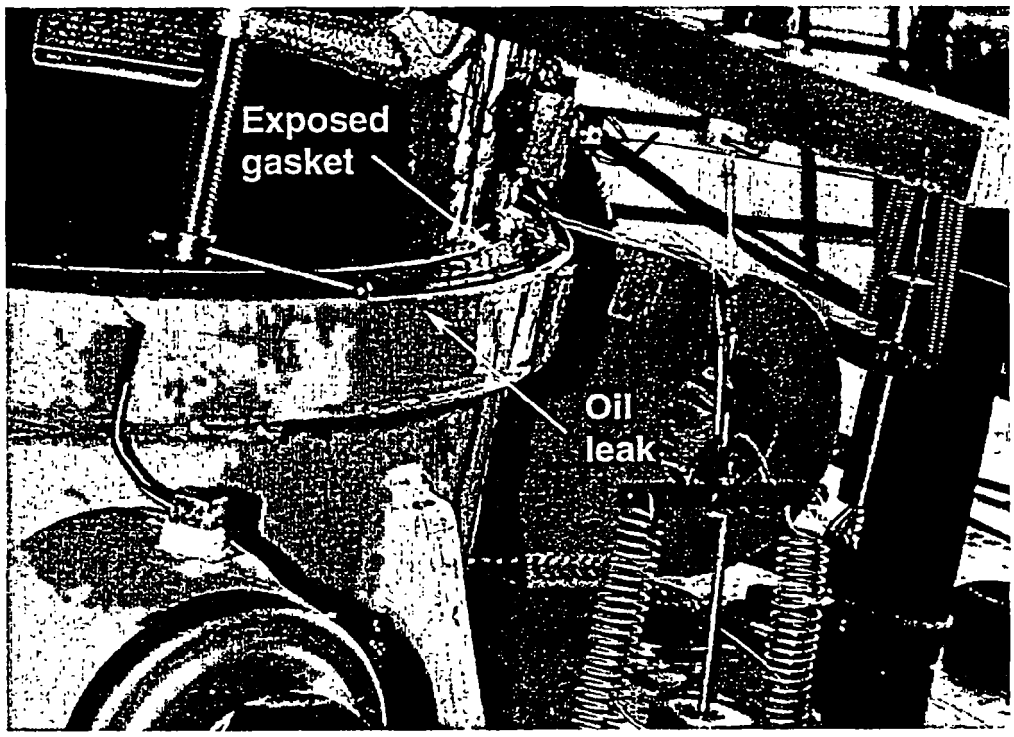

Figure 1-7 Laboratory testing of a 550-kV bushing

2 Selection Criteria and Properties of Test Bushings

2.1 Introduction

Review of reconnaissance reports from past earthquakes provides one source of information on the performance of electrical substation equipment. Electrical substations are often widely distributed and are unmanned. As a result, there are few witnesses to damage sustained during earthquakes, and evidence of failures is often disturbed because utility maintenance crews must quickly repair damaged equipment to restore service. Nonetheless, post-earthquake reconnaissance has shown that higher-voltage porcelain substation equipment, and in particular high-voltage porcelain transformer bushings, tend to be vulnerable to earthquake-induced damage due to their size, mass, and height.

The following sections list the evaluation criteria used to select the high-voltage bushing for testing and evaluation, describe the test bushing, and discuss the limit states and components of deformation of the test bushing.

2.2 Selection of Candidate Bushing

It is impractical to evaluate the seismic performance of all types and designs of higher voltage bushings. In general, documentation of bushing failures due to earthquake shaking by manufacturer, model, and key construction details are not available. Two criteria were used to select the test bushing. First, the bushing was to be widely used in practice and second, there was to be evidence that the candidate bushing had sustained earthquake-induced damage. A survey of electrical substations by the utilities indicated that 230-kV porcelain bushings (or similar bushings de-rated to 196 kV) were widely used, and that this class of bushing had sustained damage in past earthquakes. Two hundred and thirty kV bushings were selected for study and the utilities identified a number of spare 230-kV bushings of an older design for laboratory testing.

Porcelain bushings are composed of an inner core (used for electrical conduction and post-tensioning) and a number of outer stacks of unconnected porcelain (used for insulation). Most porcelain bushings are post-tensioned through the core to hold the stacks (units) of porcelain and the flange assembly together. The critical joint for the 230-kV transformer bushings is the

interface between the bushing flange and the porcelain stack immediately above it (hereafter referred to as the gasket connection), shown in Figure 1.2. Most bushing failure modes (oil leakage, porcelain slip, gasket extrusion, and porcelain fracture) have been linked to this connection.

Bushing manufacturers use a number of design details and geometries for this connection. Four of the more widely used gasket connections are shown in Figure 2-1. In the Type-A connection, the bushing flange is cast with a shallow groove or pocket, the porcelain unit is placed in the groove above a gasket, and the annular gaps between the flange groove and the porcelain are sealed using a flexible grout. In the Type-B connection, the bushing flange has an annular lip that extends above the connection and overlaps the inner face of the porcelain unit, and is cast with a shallow groove to accept the gasket. An O-ring seals the gap between the inside face of the porcelain unit and the outside face of the annular lip: An annular gasket is placed in the shallow groove and the porcelain is placed atop the gasket. In the Type-C connection, the bushing flange is cast with a groove, a gasket is placed in the groove and the porcelain unit is placed on the gasket. In the Type-D connection, the bushing flange has an annular lip that extends above the connection and overlaps the outer face of porcelain. The gap between the flange and porcelain is grouted using Portland cement. An O-ring gasket is placed in a specifically designed groove and the porcelain is placed on the O-ring gasket.

One of the predominant modes of failure of porcelain bushings is slip of the porcelain unit above the flange (see Figure 2-2). Since three of the gasket connections (Type-A, Type-B, and Type-D) are only moderately susceptible to this type of failure, only transformer bushings with Type-C gasket connection were considered for further investigation.

2.3 230-kV Type-U Bushing Manufactured by GE

Two identical 230-kV, 3000-A, type-U transformer bushings, manufactured in the mid-1980s by the General Electric (GE) Company, were supplied by BPA for testing and evaluation. These bushings are widely used in electrical substations and use a Type-C gasket connection, which does not prevent slip of porcelain over the bushing flange. Figure 2-3 shows one of the bushings prior to testing. The two bushings were identified by Serial Numbers 1795450 and 1795451, and were designated Bushing-1 and Bushing-2, respectively.

A longitudinal section and a cross section through one of the test bushings is shown in Figure 2-4. Also shown in the same figure are the coordinate system and designations for selected bushing elevations (top, midheight, and bottom) used in this report. The overall length of the transformer bushing is 144.5 in. (3.7 m). The segment of the bushing above the cast aluminum flange, which protrudes above the top of the transformer as seen in Figure 1.1, is 85 in. (2.2 m) long and this segment includes two porcelain insulator units or stacks (hereafter referred to as UPPER-1 and UPPER-2), and a metallic dome at the top of the bushing above porcelain unit UPPER-2. The porcelain units, the cast aluminum flange, and the metallic dome are separated by gaskets made of nitrile rubber. The gasket between the bushing flange and UPPER-1 porcelain unit is a flat annular strip of rubber; details of the gasket and the flange at the gasket connection are shown in Figure 2-5. The segment of the bushing below the flange, which is immersed in oil in the transformer tank, includes an extension of the cast aluminum flange, one porcelain insulator, and a cast aluminum

lower support. Flat annular gaskets separate these components. The flange plate, which is used to connect the bushing to the transformer, is cast with two lifting lugs (set 180 degrees apart, along the x-axis of the bushing as defined in Figure 2-4) to facilitate movement and installation of the bushing.

In cross section, the bushing has an aluminum core that provides the electrical connection; a multilayered, oil-impregnated, kraft paper condenser wrapped around the core; an annular gap between the porcelain and condenser that is filled with oil to provide electrical insulation; and a porcelain insulator. The weight of the bushing is approximately 920 lbs (4.1 kN), and its center of mass is located approximately 18 in. (0.45 m) above the flange plate. The portion of the bushing extending from the top of flange to the top of the bushing, weighs approximately 560 lbs (2.5 kN), with its center of mass located 44 in. (1.1 m) above the flange plate.

The bushing is post-tensioned along its longitudinal axis through its core. Twenty-seven springs in the metallic dome provide a uniform distribution of compression force around the perimeter of the porcelain units and the gaskets.

Prior to shipment for testing, the bushing post-tensioning (PT) force was set at approximately at 22 kips (98 kN) by PBA. This value was determined by subtracting 5 kips (22 kN) from the manufacturer recommended PT value of 27 kips (120 kN) to account for the PT loss due to elevated operating temperatures.

The key physical and electrical characteristics of the bushings are summarized in Table 2-1.

Table 2-2 lists material properties for the key components of the bushing. The manufacturer (Elder, 1999) provided the material data for the porcelain, bushing flange, transformer oil, condenser, and core tube.

Test data for 1/4-in. (6-mm) thick nitrile rubber gaskets were supplied by Elder (Elder, 1999). Tests were performed by GE on 3/4-in. (19-mm) and 1-in. (25-mm) wide gaskets. Test specimens were 6-in. (152-mm) long samples with a Durometer hardness of 65. The test setup involved compression loading of unconfined rubber strips between plates having F6 finished surfaces. Test data are reproduced in Figure 2-6. The dashed line at 6.2 MPa corresponds to the gasket pressure (stress) for a post-tensioning force of 27 kips (120 kN). A gasket elastic modulus of approximately 7 ksi (48 MPa) is computed from averaging the two tangent moduli shown as dashed lines in the figure. This computed compression modulus value is substantially larger than the value of 6 MPa listed by Roberts (Roberts, 1988) and Lindley (Lindley, 1978) for a 65-Durometer hardness rubber. This discrepancy is likely due to the different rubber types tested and variations in the test setup. The compression modulus of rubber is highly dependent on the confinement of rubber.

The compression modulus of confined rubber (E_c) can be computed from the elastic modulus of rubber (E_0) as:

$$E_c = E_0(1 + 2kS^2) \tag{2-1}$$

Table 2-1 Characteristics of the GE type-U test bushings

Property	*Parameter*	*Value*
Electrical	Voltage rating	230 kV
	Amperage	3,000 A
	BIL[1]	900 kV
	Conductor core	Aluminum
	Electrical connection type (draw lead or bottom connect)	Bottom connect
Physical	Weight	4.1 kN
	Total length	3.7 m
	Length above flange	2.2 m
	Length below flange	1.5 m
	Initial post-tensioning force	98 kN
	No. of porcelain stacks above flange	2
Gasket connection	Porcelain-flange interface	Type-C (see Section 2.2)
	Gasket material	Nitrile rubber
	Gasket geometry	Annular ring (OD = 300 mm, ID = 250 mm)
		Thickness: 6.4-mm nominal and 5.6-mm compressed
	Flange material	Cast aluminum
	Flange groove	Annular, 24-mm wide, 4.8-mm deep
	Separation[2]	13 mm
Identification plate	Model No.	11B802BB G10
	Serial No.: Bushing-1, Bushing-2	1795450, 1795451

1. Basic Impulse level (BIL) designates the impulse voltage the bushing can withstand.
2. Denotes distance between UPPER- inner surface and the voltage tap electrical wire, adjacent to the kraft paper.

In Equation 2.1, k denotes a hardness-dependent numerical factor and S designates the shape factor (defined as the ratio of the one loaded area to the total force-free area). For the annular gasket with a Durometer hardness of 65, an outside diameter of 11.75 in. (298 mm), an inside diameter of 10 in. (254 mm), and a thickness of 0.25 in. (6 mm), the k factor equals 0.54 (Roberts, 1988) and S equals 1.75. As such, the compression modulus of confined rubber (E_c) is nearly four times the elastic modulus (E_0).

In the Type-C gasket connection, the gasket is placed in an annular groove in the bushing flange and can be considered to be confined. If the gasket is so confined, then the value of E_c should be used as its effective compression modulus.

Table 2-2 Material properties of the bushing components

Component	*Material*	*Unit weight (kN / m[1])*	*E (MPa)*[1]
porcelain	porcelain	24	97,000
flange assembly	cast aluminum	27	69,000
transformer oil	mineral oil	9	-
condenser	kraft paper	12	10,000
core tube	aluminum	27	69,000
gasket	nitrile rubber	-	48[2]

1. Material properties for all components except the gasket was provided by the manufacturer (Elder, 1999).
2. Elastic modulus, E_0, was estimated from available test data (Elder, 1999).

2.4 Limit States for 230-kV Bushings

2.4.1 Background

As noted in Chapter 1, inspection of failed bushings following major earthquakes has identified four distinct and related failure modes at the gasket connection. The following subsections give a brief description of these limit states and their likely causes.

Although no previous test data was available for the 230-kV bushings tested at PEER, prior cantilever laboratory tests conducted on a similar bushing, a 196-kV bushing that has replaced the 230-kV type-U bushing provided some insight into the response of the test bushing. Examination of such test data by the manufacturer (Elder, 1999) indicated that the bushing leaked oil when the porcelain uplift at the gasket connection exceeded a threshold value of 0.03 to 0.04 in. (0.8 to 1 mm) and that the bushing withstood the application of a concentrated static force of 1.4 kips (6.3 kN) at the top without failure.

2.4.2 Oil leakage

The gasket, seated in the annular flange groove, provides a barrier against oil leakage. When unprestressed, the gasket protrudes approximately 1/16 in. (1.6 mm) above the upper surface of the pocket or groove. The application of the nominal post-tensioning force of 27 kips (120 kN), compresses the gasket, and reduces the gasket protrusion above the flange groove to approximately 0.04 in. (0.8 mm).

Under the application of lateral forces above the gasket connection, an overturning moment is produced at the gasket connection. This moment is resisted by the stabilizing post-tensioning moment equal to Nr, where N is the applied post-tensioning force, and r is the bushing radius measured the center of the bushing to the centerline of the gasket. When the value of the overturning moment exceeds the value of the stabilizing moment, the porcelain will uplift at a discrete location. When the maximum uplifts exceeds the threshold value of approximately 0.03 in. (0.8 mm), oil will leak from the bushing.

2.4.3 Porcelain slip

In the absence of uplift, the gasket is in contact with the UPPER-1 porcelain unit; the lateral force required to initiate porcelain slip is μN, where N is the applied post-tensioning force and μ is a slip coefficient. The core kraft paper assembly provides resistance to the slip and as such, the slip coefficient is larger than the friction coefficient between porcelain and rubber. The value of the friction coefficient is reduced if the gasket surface is coated with oil (lubricated).

2.4.4 Gasket extrusion

The gasket is seated in the bushing flange groove or pocket and can not extrude from the groove under the application of lateral loading. However, once the UPPER-1 porcelain unit slips or uplifts over the gasket connection, it can bear down unevenly on the gasket and force a portion of the gasket out of the flange groove.

2.4.5 Porcelain fracture

The porcelain is under nearly uniform compressive force from post-tensioning of the inner core and bears uniformly over the gasket. There is little stress concentration and there is no direct contact between the UPPER-1 porcelain unit and bushing flange. However, once the UPPER-1 porcelain unit slips or uplifts over the gasket connection, comes into direct contact with the bushing flange and is subjected to concentrated compressive axial forces and tensile circumferential stresses that can fracture brittle porcelain.

2.5 Components of Deformation for 230-kV Bushings

2.5.1 Introduction

Four modes of deformation contribute to the displaced shape of the segment of the bushing extending from the flange to the top of the bushing under the application of a concentrated horizontal load or horizontal inertial loads. The four modes of deformation are bending of the porcelain, rigid rotation of the UPPER-1 porcelain unit over the flange, translation of UPPER-1 porcelain unit over the gasket in the gasket connection, and slip of the UPPER-1 porcelain unit over the flange. The horizontal motion of a point at elevation z above the gasket connection can be written as:

$$u(z) = u(z)_{porcelain} + u(z)_{uplift} + u(z)_{gasket} + u(z)_{slip} \qquad (2\text{-}2)$$

The first term, $u_{porcelain}$, denotes the cubic (cantilever) deformation of the porcelain above the gasket connection (see Figure 2-7a). Porcelain has high stiffness and this component is assumed to be zero.

The second term, u_{uplift}, designates the rigid rotation of the porcelain above the gasket connection due to the axial (flexural) flexibility of the gasket in the gasket connection (see Figure 2-7b). Under the application of a lateral load, P, at a point z_0 above the gasket connection, the linear deformation of the porcelain can be written as:

$$u(z)_{uplift} = \theta_{base} z = \frac{P z_0}{k_{\theta gasket}} z = \frac{t_g}{E_g I_g} P z_0 z \qquad (2\text{-}3)$$

In this equation, θ_{base} denotes the concentrated rotation at the gasket connection due to the flexibility of the gasket. The stiffness of the gasket ($k_{\theta gasket}$) is approximately equal to the product of the gasket compression modulus (E_g) and gasket moment of inertia (I_g) about the vertical (z-) axis, divided by the gasket thickness (t_g).

The third term, u_{gasket}, corresponds to the height-independent (constant) translation of the porcelain above the gasket connection due to the shear flexibility of the gasket in the gasket connection (see Figure 2-7c). Under the application of a lateral load, P, at a point z_0 above the gasket connection, the constant displacement of the porcelain can be written as:

$$u_{gasket} = \frac{P}{k_{vgasket}} = \frac{\tau_g}{G_g A_g} P \qquad (2\text{-}4)$$

In this equation, ($k_{vgasket}$) denotes the shear stiffness of the gasket and is computed as equal to the gasket effective thickness (τ_g) divided by the product of the gasket shear modulus (G_g) and the gasket plan area (A_g) in the horizontal (x-y) plane. Because the gasket is placed in a groove at the gasket connection, the value of the effective gasket thickness τ_g is smaller than the nominal thickness (t_g), and can be assumed to be approximately equal 0.02 in. (0.8 mm) — amount by which the compressed gasket projects above the flange groove.

The fourth term (u_{slip}) corresponds to the height-independent (constant) motion of the bushing above the gasket connection due to the slip of UPPER-1 porcelain unit over the gasket (see Figure 2-7d). Under the application of a lateral load, P, at a point z_0 above the gasket connection, this displacement is non-zero when the value of the applied load, P, exceeds the slip resistance at the gasket connection. The friction between the nitrile gasket and the porcelain, and the restraint provided by the core kraft paper assembly contribute to the slip resistance at the gasket connection. The friction component depends on the value of normal (post-tensioning) load, N, and the friction coefficient, f, between porcelain and nitrile rubber. This friction coefficient depends on the surface condition of the gasket (dry or coated with oil).

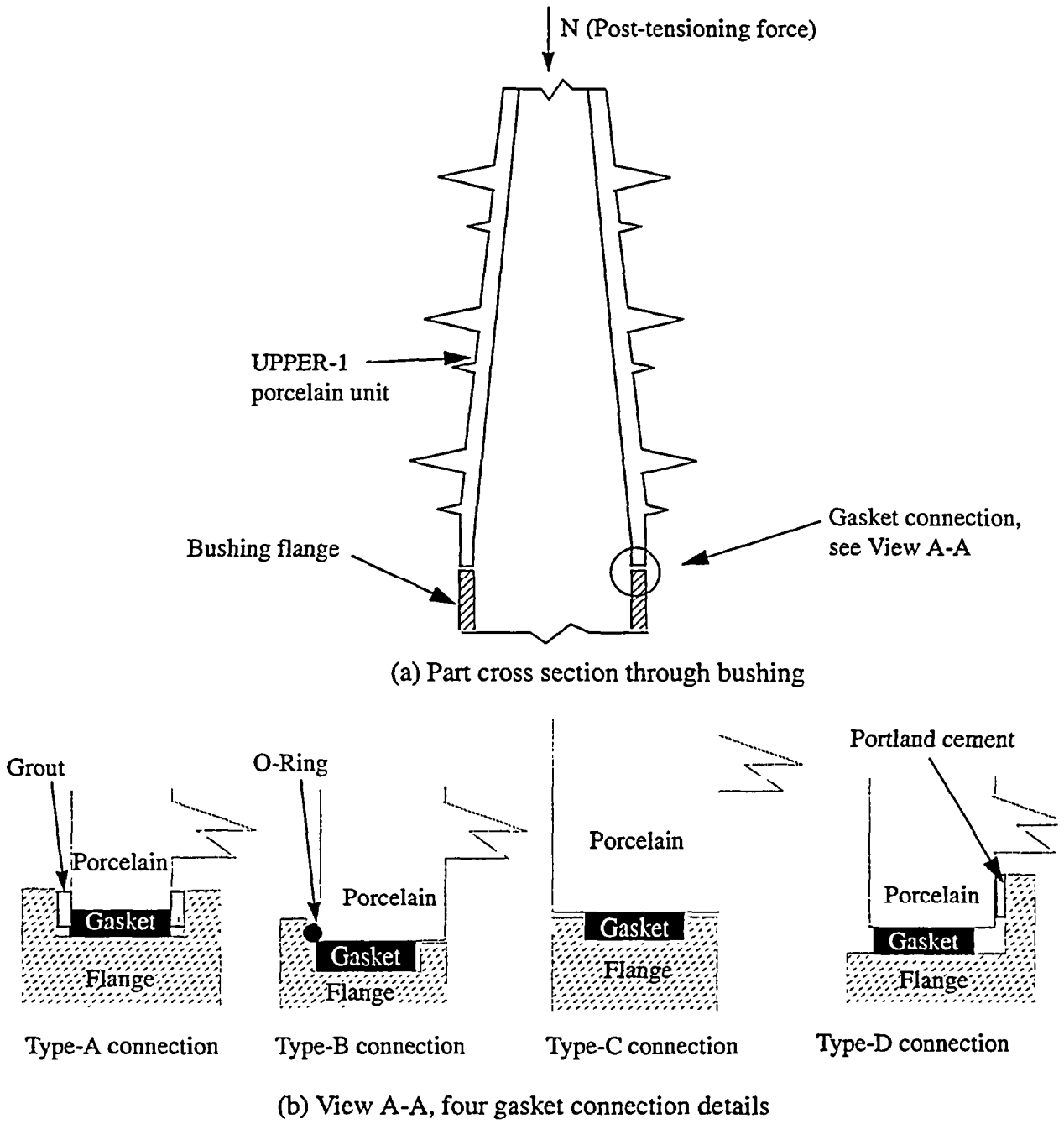

Figure 2-1 Typical porcelain-flange interface details for the gasket connection

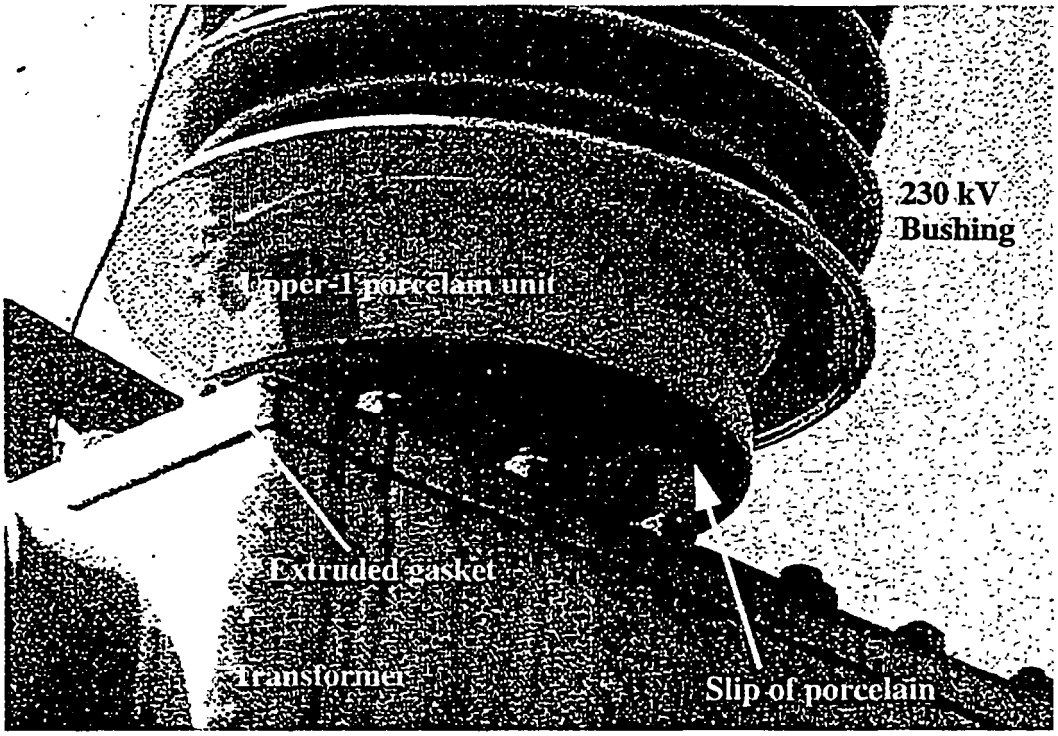

Figure 2-2 Slip of porcelain in a transformer-mounted 230-kV bushing

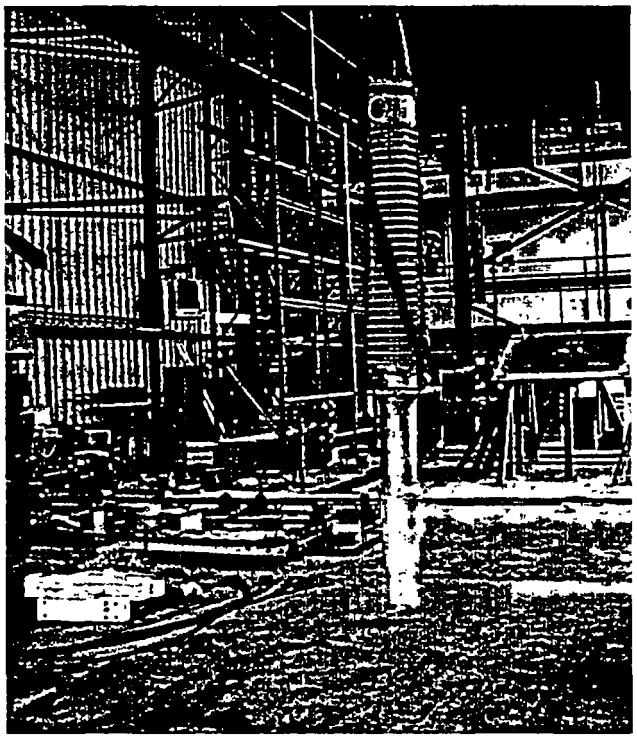

Figure 2-3 Bushing-2 prior to testing on the Berkeley simulator

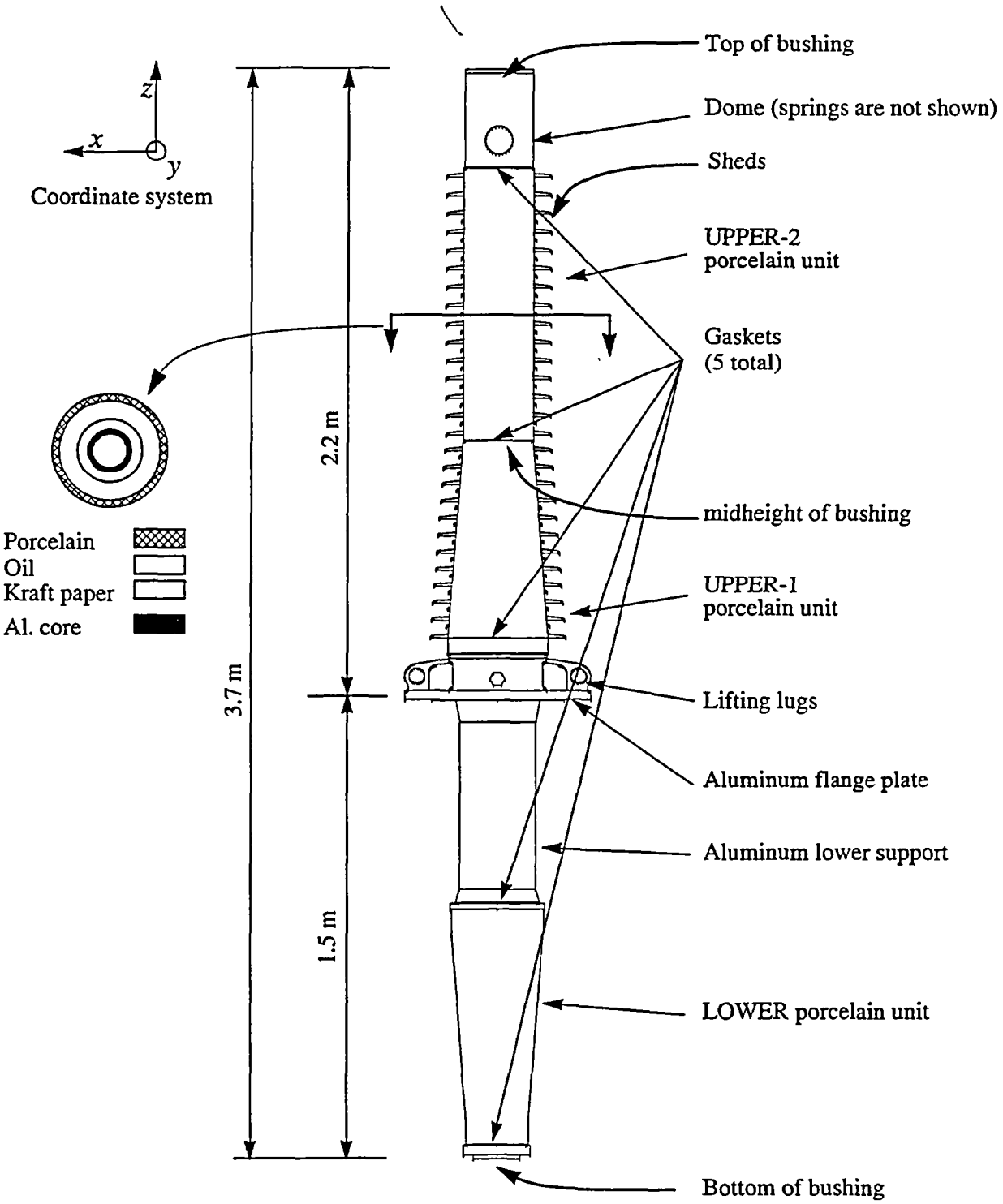

Figure 2-4 Longitudinal section and cross section through a 230-kV type-U bushing, manufactured by General Electric

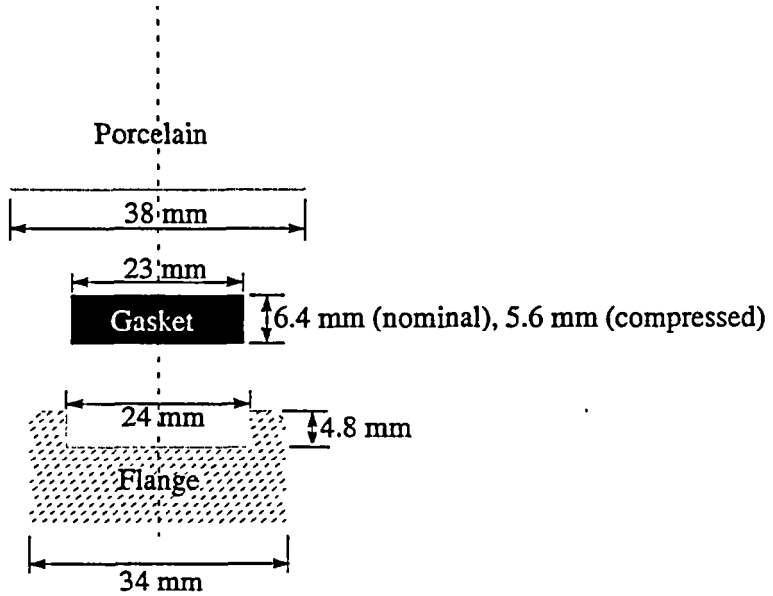

Figure 2-5 Exploded view of gasket connection detail for a 230-kV type-U bushing

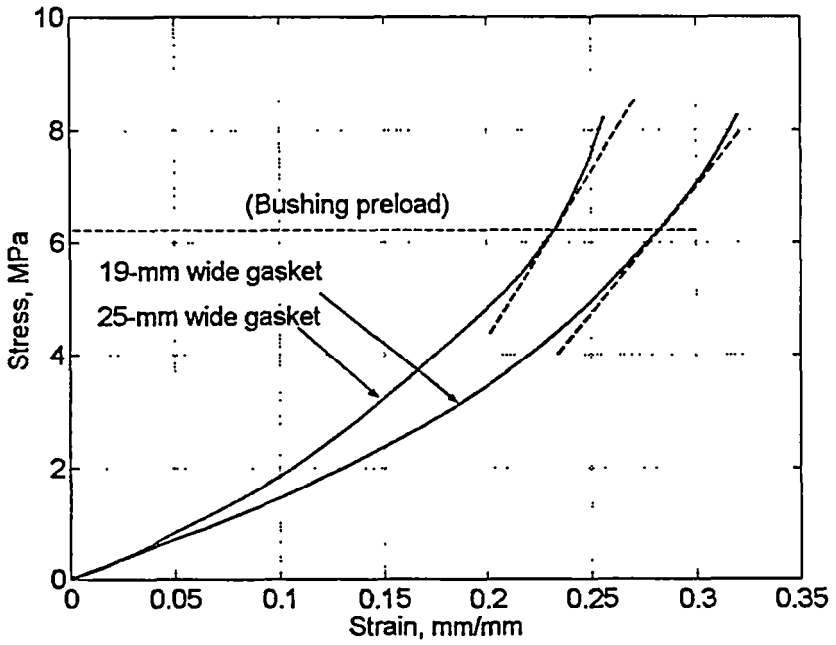

Figure 2-6 Compression stiffness of 6-mm thick nitrile gaskets (Elder, 1999)

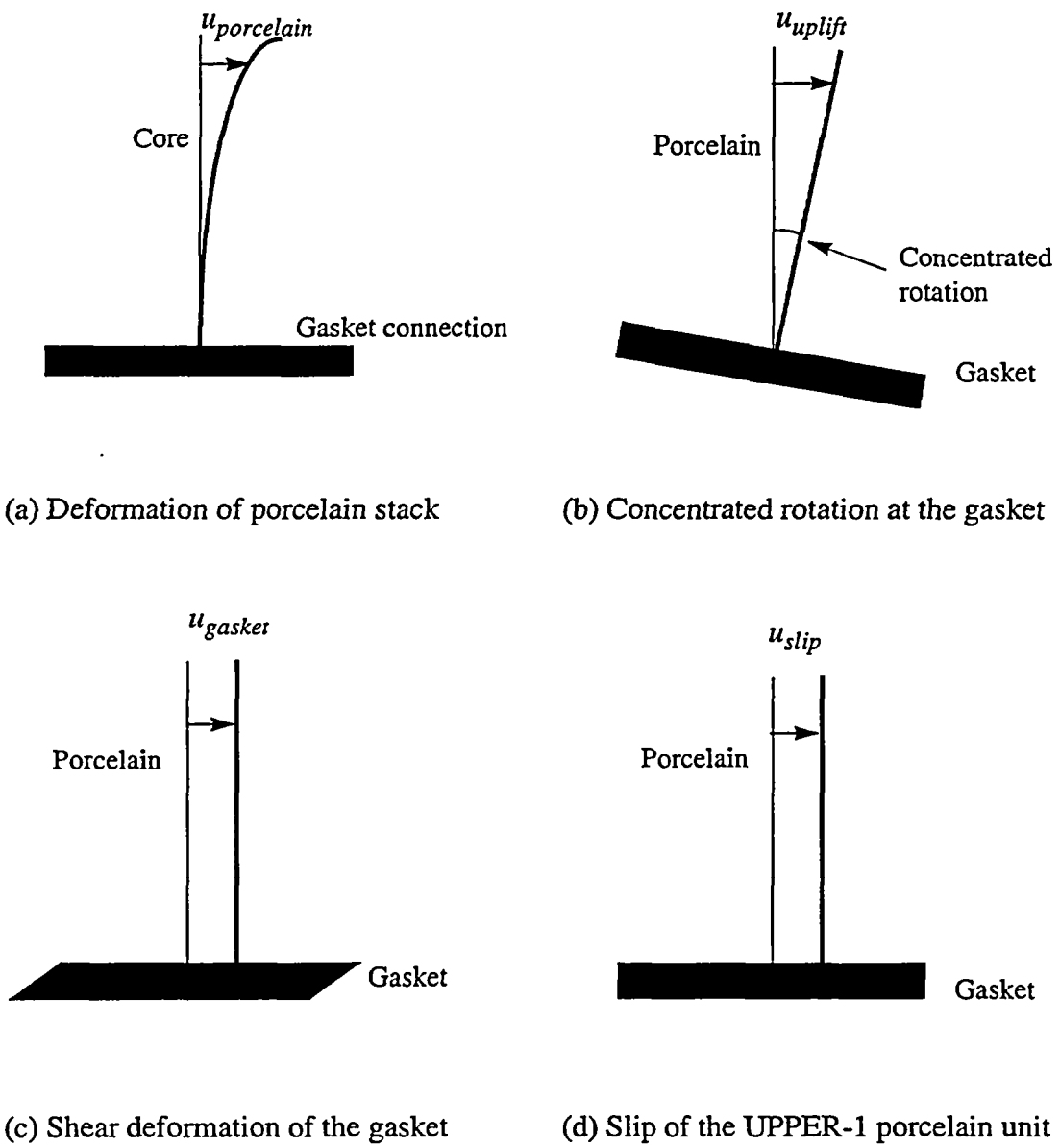

(a) Deformation of porcelain stack

(b) Concentrated rotation at the gasket

(c) Shear deformation of the gasket

(d) Slip of the UPPER-1 porcelain unit

Figure 2-7 Deformation modes for components of a 230-kV bushing

3 Qualification and Fragility Testing

3.1 Introduction

Recorded earthquake ground motion histories were used to evaluate the seismic response of the two 230-kV transformer bushings: Bushing-1 and Bushing-2. The following section describes the requirements of IEEE 693-1997 (IEEE, 1998) for the qualification of transformer bushings and the procedures used to develop earthquake histories for testing.

3.2 IEEE 693-1997 Requirements for Bushing Qualification

Three types of earthquake-simulator testing are identified in IEEE 693-1997 for the seismic qualification of transformer bushings: (a) earthquake ground motions, (b) resonant frequency search, and (c) sine-beat testing. Earthquake ground motion tests (termed *time-history shake table tests* in IEEE) and resonant frequency tests are mandatory. Information on these two types of tests follows.

3.2.1 Resonant-search tests

Sine-sweep or broadband white-noise tests are used to establish the dynamic characteristics (natural frequencies and damping ratios) of a bushing. These so-called *resonant-search* tests are undertaken using unidirectional excitation along each global axis of the earthquake simulator platform. If only broadband white-noise tests are performed, the amplitude of the white-noise must not be less than 0.25g. If only sine-sweep tests are used, IEEE 693-1997 specifies that the resonant-search be conducted at a rate not exceeding one octave per minute in the range for which the equipment has resonant frequencies but at least 1 Hz. Frequency searching above 33 Hz is not required. Because both sine-sweep and white-noise tests were used in this testing program to identify the modal properties of the transformer bushings, the recommendations of IEEE 693-1997 were not followed exactly.

The history for the banded white-noise tests was prepared using a random signal generator. The sine-sweep history was developed using a rate of two octaves per minute. (At two octaves per minute, the input frequency doubles every 30 seconds.) A continuous frequency function was used to develop the sine-sweep function

$$x(t) = x_0 \sin\left(2\pi\left[\frac{30}{\log 2}\right]2^{t/30}\right) \tag{3-1}$$

where x is the displacement, and x_0 is the maximum displacement. For both sine-sweep and white-noise tests, a simulator input acceleration amplitude of 0.1g was used.

3.2.2 Earthquake test response spectrum

IEEE 693-1997 identifies several response spectra of identical shape but different amplitudes for the qualification of transformer bushings. These spectra are described below; a more detailed description is presented in Appendix A.

Test Response Spectrum (TRS). For earthquake simulator testing, IEEE 693-1997 states that the TRS for each horizontal earthquake motion must match or exceed the target spectrum and that the TRS for vertical earthquake motion be no less than 80 percent of target spectrum. IEEE 693-1997 recommends that 2-percent damping be used for spectral matching and requires at least 20 seconds of strong motion shaking be present in each earthquake record. Earthquake motions can be established using either synthetic or recorded histories. Recorded motions formed the basis of the earthquake histories used to test the 230-kV bushings.

Performance Level (PL). IEEE 693-1997 represents a PL for substation equipment by a response spectrum. The PL represents the expected level of performance when a piece of equipment is qualified to the RRS and meets the requirements for allowable stress design. The two PLs relevant to California are *Moderate* and *High*. For reference, the Moderate Level ground motion spectra are shown in Figure 3-1.

Required Response Spectrum (RRS). It is often neither practical nor cost effective to test components to the Moderate PL. As such, IEEE 693-1997 permits equipment to be tested using a reduced level of shaking called the RRS. The shapes of the RRS and the PL are identical, but the ordinates of the PL are twice that (referred to as performance factor in IEEE 693-1997) of the RRS. Equipment tested or analyzed using the RRS is expected to have acceptable performance at the PL. This assumption is checked by measuring the stresses obtained from testing at the RRS, and (a) comparing the stresses to 50 percent (equal to the inverse of the performance factor) of the ultimate strength of the porcelain (assumed to be brittle) or cast aluminum components and (b) using a factor of safety against yield combined with an allowance for ductility of steel and other ductile materials.

Test Response Spectra for Mounted Equipment (TRSME). To account for the possible amplification of earthquake motion due to the influence of the transformer body and local flexibility of the transformer near the bushing mount, IEEE 693-1997 states that the input motion *as measured at the bushing flange* shall match a spectrum with ordinates twice that of the RRS, termed herein as the TRSME. For this level of shaking, IEEE 693-1997 states that the stresses in the porcelain components must be less than 50 percent of the ultimate stress, and the factor of safety against oil leakage must be greater than or equal to 2.0.

An alternate approach that is identified in Annex D5.1(d) of IEEE 693-1997 was used for the studies reported herein. Namely, earthquake histories with spectral ordinates twice those of the TRSME were used for testing: the target peak horizontal acceleration at the bushing flange was 1.0g. Porcelain stresses at this level of earthquake shaking were required to be less than or equal to the ultimate value, and there was to be no evidence of oil leakage. The spectrum for this motion is shown in Figure 3-2 and is the same as the Moderate PL spectrum.

The key requirements of IEEE 693-1997 for qualification and fragility testing of bushings are summarized in Table 3-1.

Table 3-1 IEEE earthquake-history testing requirements for Moderate Level qualification

Peak Ground Acceleration	*Comments*
0.5g	Moderate Seismic Performance Level (PL) for substation equipment
0.25g	Required Response Spectrum (RRS) for Moderate Seismic Performance Level for substation equipment
0.5g	Test Response Spectrum for Mounted Equipment (TRSME) for Moderate Seismic Performance Level.
1.0g	Response spectrum for checking porcelain stresses and oil leakage for bushings mounted on transformers.

3.2.3 Earthquake ground motions

The earthquake histories used for the qualification and fragility testing of the 230-kV bushings were developed using the three-component set of near-fault earthquake motions recorded during the 1978 Tabas earthquake. Figures 3-3 through 3-5 present the acceleration history, power spectrum, and pseudo-acceleration response spectra for the three components of the Tabas record. The amplitude of each history (*X*-, *Y*-, and *Z*-) record was normalized to a peak acceleration of 1.0g. The power spectrum for each history has moderate bandwidth. The 2-percent and 5-percent damped IEEE spectra for Moderate Level qualification, anchored to a peak ground acceleration of 1.0g, are also shown in the figures. The response-spectrum ordinates for each normalized earthquake history exceed the target IEEE values for frequencies greater than 2 to 3 Hz and drop below the target values for frequencies less than 2 Hz.

To obtain IEEE 693-1997 spectrum-compatible normalized histories, the original Tabas acceleration records were modified using a non-stationary response-spectrum matching technique developed by Abrahamson (Abrahamson, 1996). In traditional spectrum-matching routines, adjustments are performed in the frequency domain. Specifically, the original acceleration record is transformed into the frequency domain, the amplitude of the Fourier spectrum is adjusted at each frequency to match the target value, and the record is then transformed back into the time domain. Two key disadvantages of the frequency-domain method are that the modified earthquake history rarely resembles the original earthquake history, and that frequency leakage often makes convergence to the target spectrum difficult. Abrahamson's time-domain method is

based on the algorithm proposed by Lilhanand and Tseng (1988) wherein short-duration wavelets are added to the original earthquake history at optimal times in the history to match the spectral amplitude at each frequency to the target value. The modified history generally resembles the original earthquake history and frequency leakage is negligible.

The testing of 196-kV ABB bushings (Gilani, et al., 1998) at Berkeley utilized spectrum-compatible earthquake histories developed using the Abrahamson technique. The resulting spectra matched the target spectra across a broad frequency range (0.1 Hz to 100 Hz). Because the maximum displacement and velocity of the Berkeley simulator platform are 5 in. (127 mm) and 25 in./sec (635 mm/sec), respectively, the spectrum-compatible motions were high-pass filtered (removal of low-frequency content) to reduce the peak displacements and velocities of the simulator platform. However, the resulting power spectra of the filtered histories were narrow banded, and not particularly representative of strong earthquake ground motion.

A different strategy was used to develop earthquake histories for the studies reported herein. This strategy combined the Abrahamson spectrum-matching algorithm and frequency-domain trapezoidal high-pass filters. Input ground motions to the simulator were developed in a three-step process as follows. First, the original earthquake history was high-pass filtered to remove low-frequency content (see Table 3-2) such that the maximum displacement and velocity of the filtered history were approximately equal to 5 in. (127 mm) and 25 in./sec (635 mm/sec), respectively. (All content below the cut-off frequency was eliminated; all content above the corner frequency was retained; and content between these frequencies was multiplied by a linearly increasing value that ranged from zero at the cut-off frequency to unity at the corner frequency. The cut-off frequencies were much smaller than the resonant frequency of the 230-kV bushings (known to range between 16 to 20 Hz for *rigidly* mounted bushings and estimated to range between 6 to 8 Hz for *flexibly* mounted bushings). Removal of such low-frequency components from the input signals to the simulator is known to have a negligible impact on the dynamic response of the bushings. Second, the filtered earthquake history was matched to the target spectrum for frequencies greater than the corner frequency of the trapezoidal filter using the Abrahamson algorithm. Third, the spectrum-compatible motions from step two were high-pass filtered to exactly limit the maximum displacement and velocity to 5 in. (127 mm) and 25 in./sec (635 mm/sec), respectively.

Two independent sets of three earthquake histories (Tabas-A and Tabas-B) were generated using the above procedure. Tabas-A was used for all simulations up to and including the Moderate Level qualification for which the target simulator acceleration was 1.0g (see Figure 3-2). Tabas-B was used for all other tests up to those corresponding to High Level qualification for which the target acceleration was 2.0g. Table 3-2 summarizes the step-one filter frequencies used to generate the Tabas-A and Tabas-B histories. Figures 3-6 through 3-8 present the acceleration history, power spectrum, and response spectra for the three spectrum-compatible Tabas-A records. Figures 3-9 through 3-11 present the same information for the three spectrum-compatible Tabas-B records.

Table 3-2 High-pass filter frequencies for earthquake histories

		Filter frequencies (Hz)	
Set	*Component*	*Cut-off*	*Corner*
Tabas-A	*X*	1.0	1.5
	Y	1.0	1.5
	Z	1.0	1.5
Tabas-B	*X*	2.0	2.5
	Y	2.2	2.5
	Z	2.2	2.5

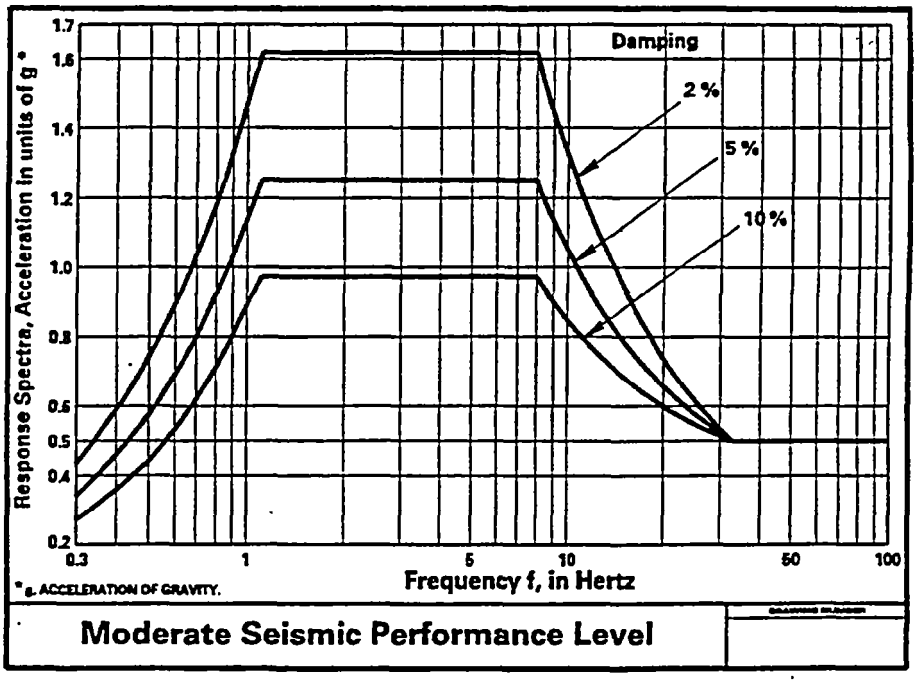

Figure 3-1 Spectra for the Moderate Seismic Performance Level (IEEE, 1998)

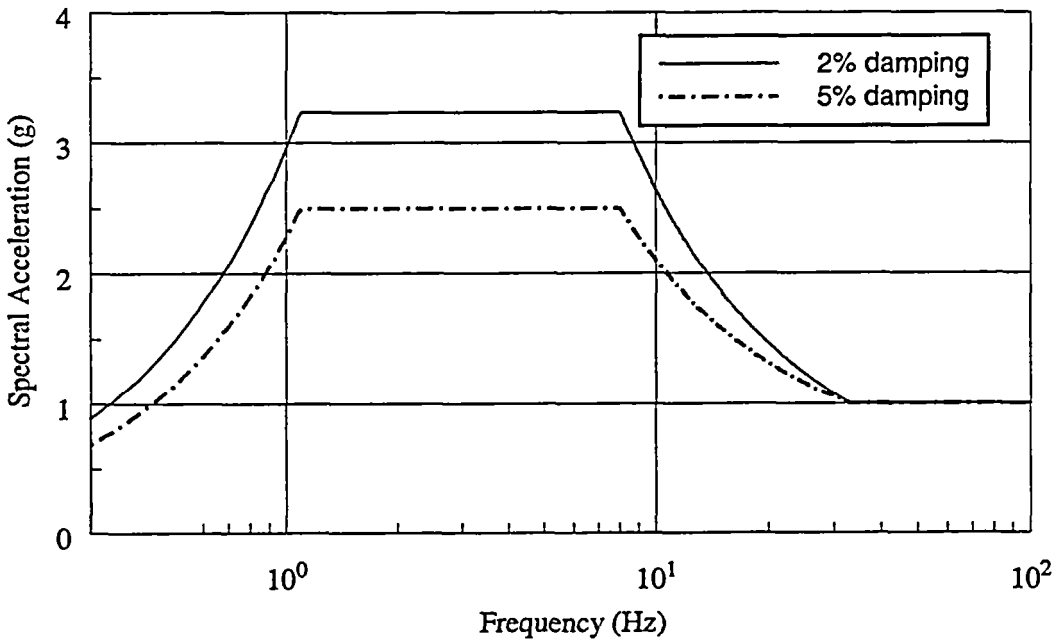

Figure 3-2 Test Response Spectra at bushing flange for Moderate PL

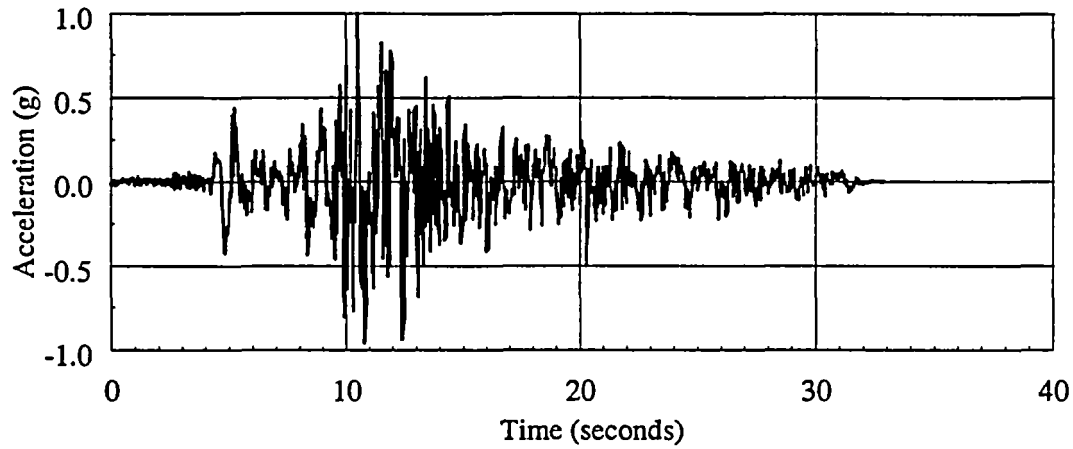

(a) Normalized acceleration history

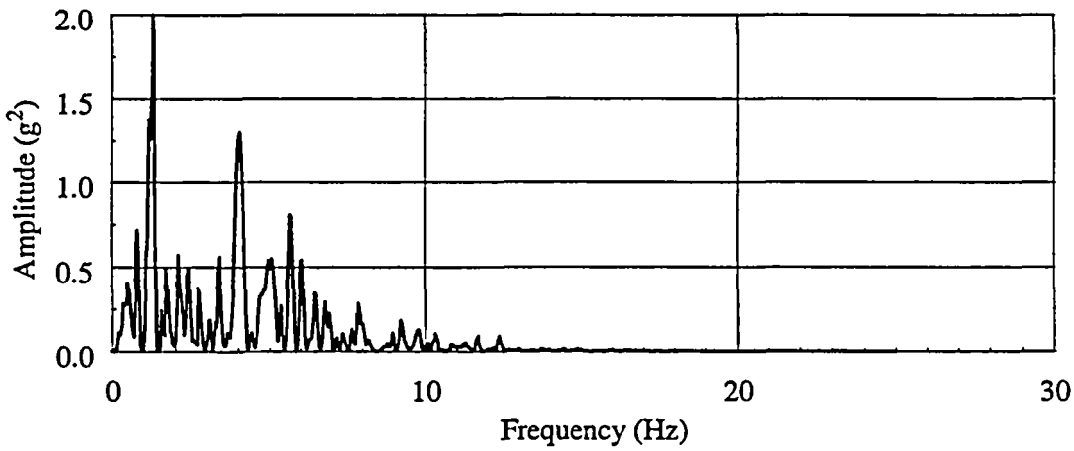

(b) Power spectrum

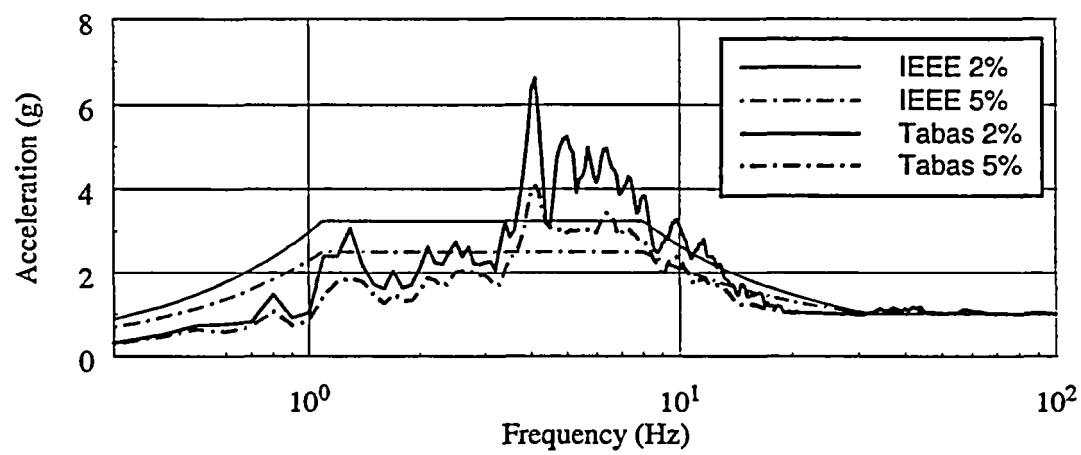

(c) Response spectrum

Figure 3-3 Normalized acceleration history, power spectrum, and response spectra for the longitudinal (*X*-) component of the original Tabas record

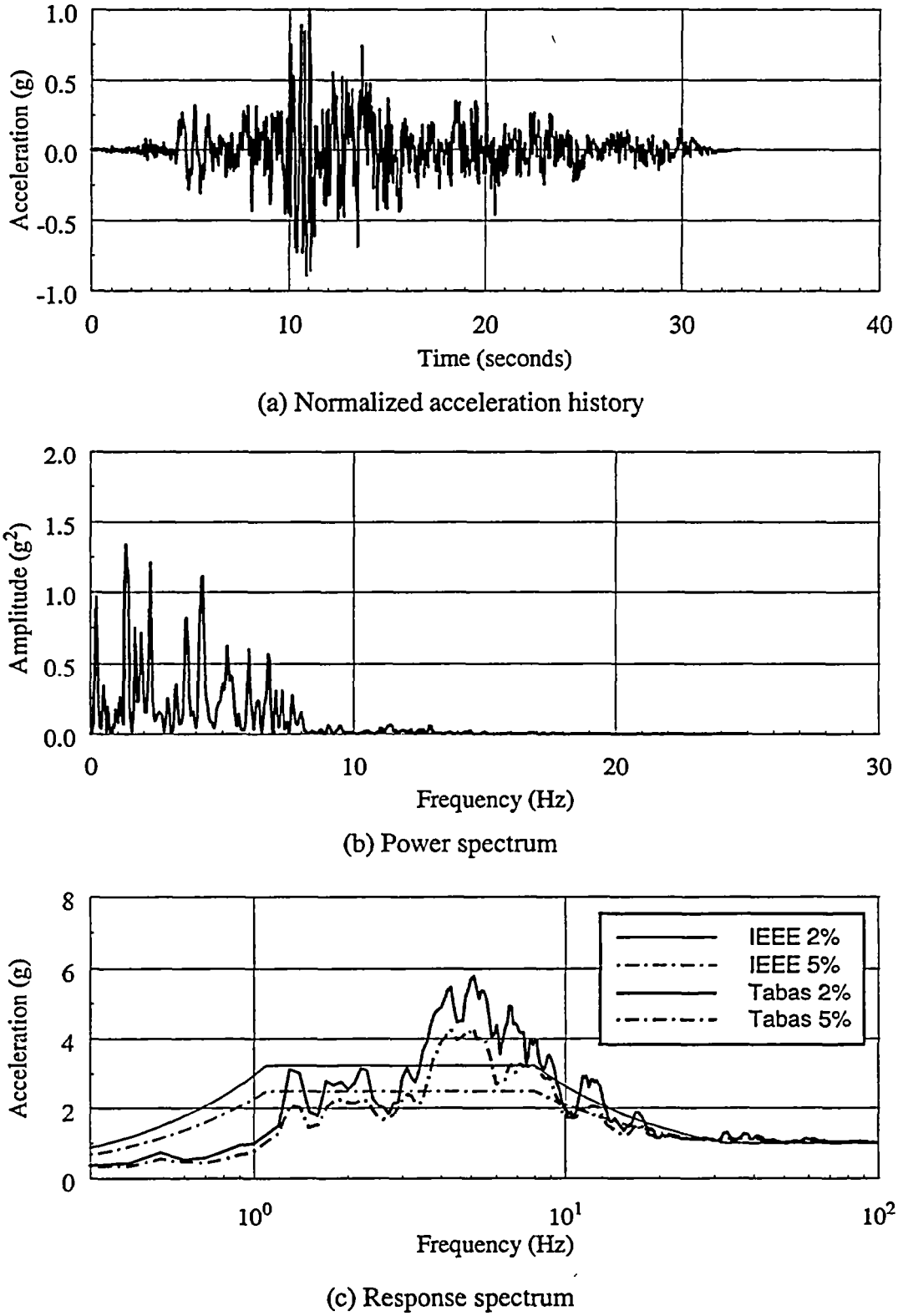

Figure 3-4 Normalized acceleration history, power spectrum, and response spectra for the lateral (*Y*-) component of the Tabas record

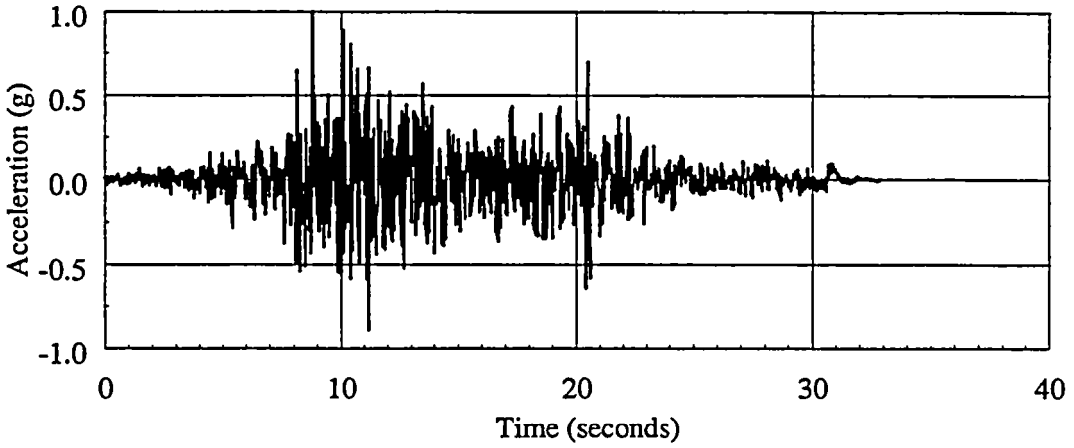

(a) Normalized acceleration history

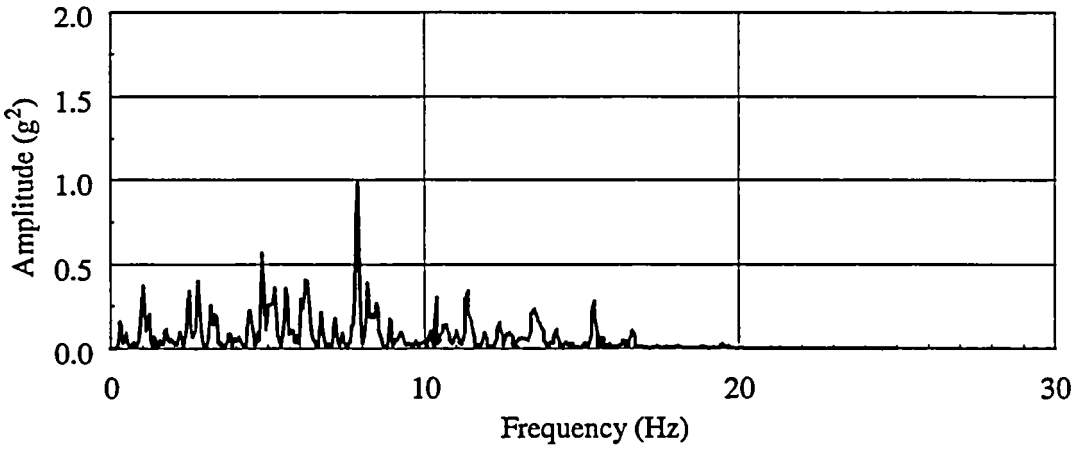

(b) Power spectrum

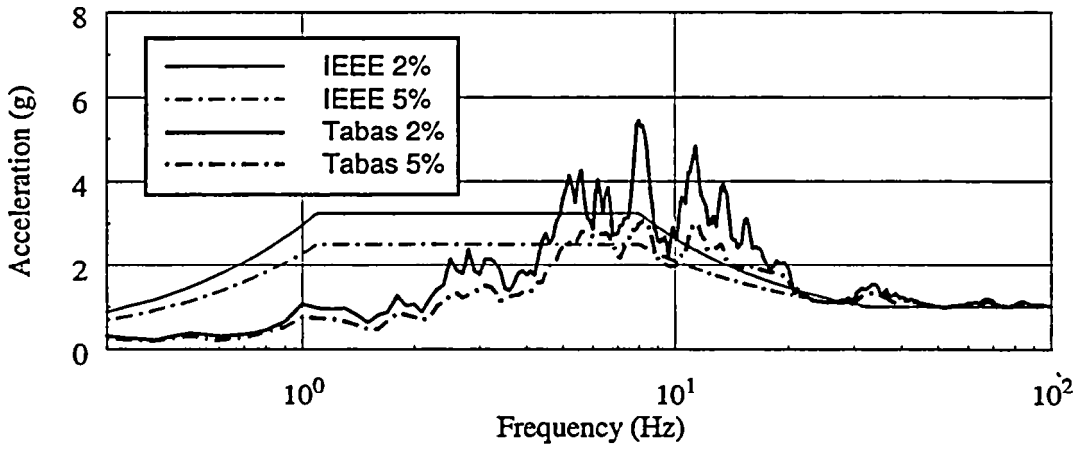

(c) Response spectrum

Figure 3-5 Normalized acceleration history, power spectrum, and response spectra for the vertical (Z-) component of the original Tabas record

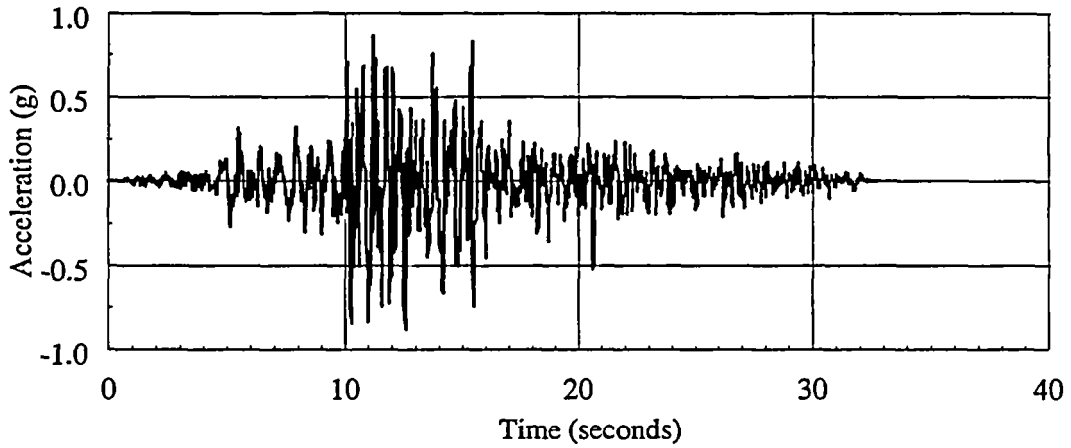

(a) Acceleration history

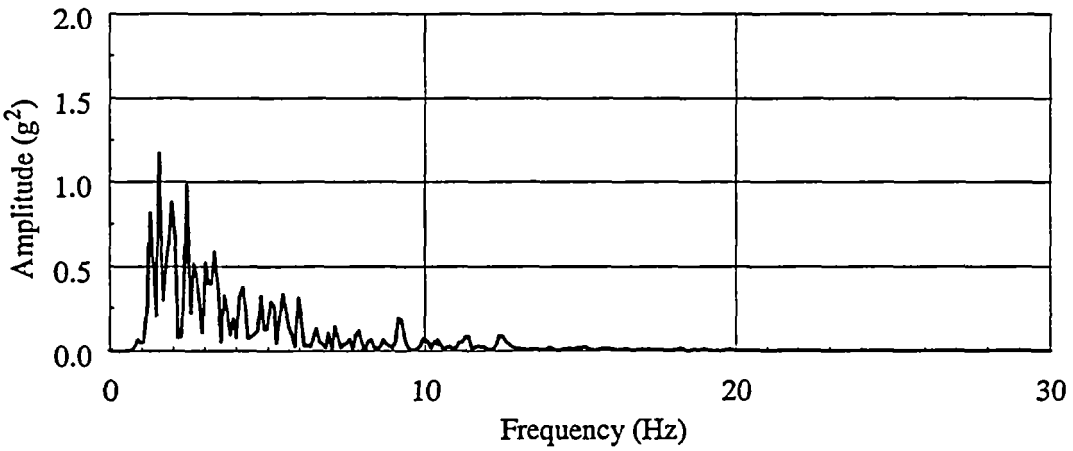

(b) Power spectrum

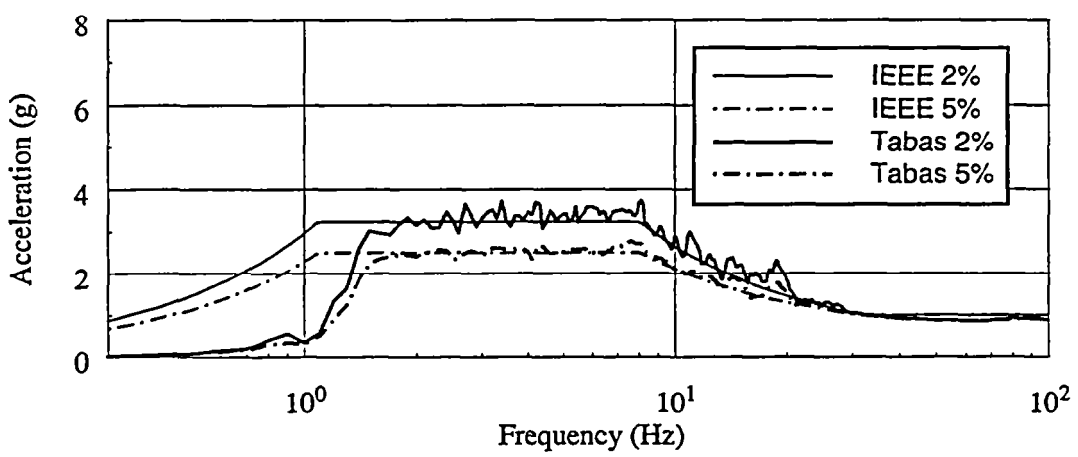

(c) Response spectrum

Figure 3-6 Acceleration history, power spectrum, and response spectra for the longitudinal (*X*-) component of the Tabas-A record

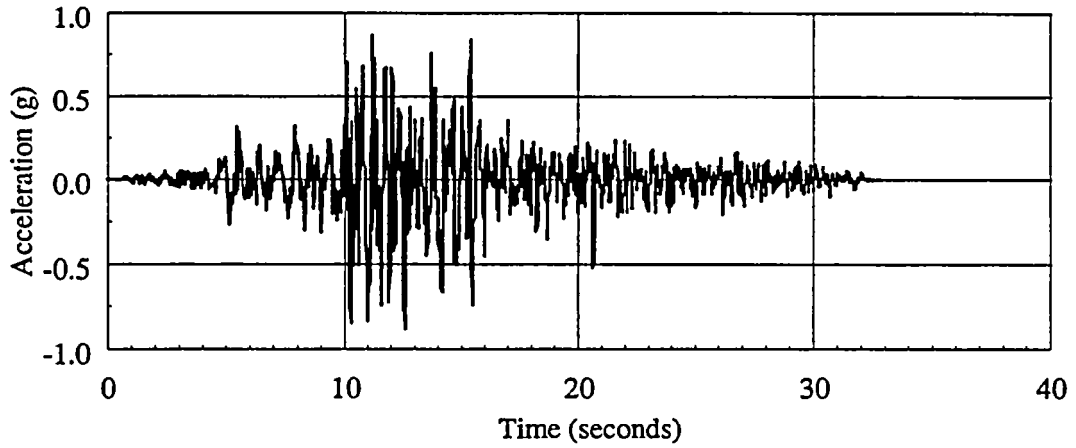

(a) Acceleration history

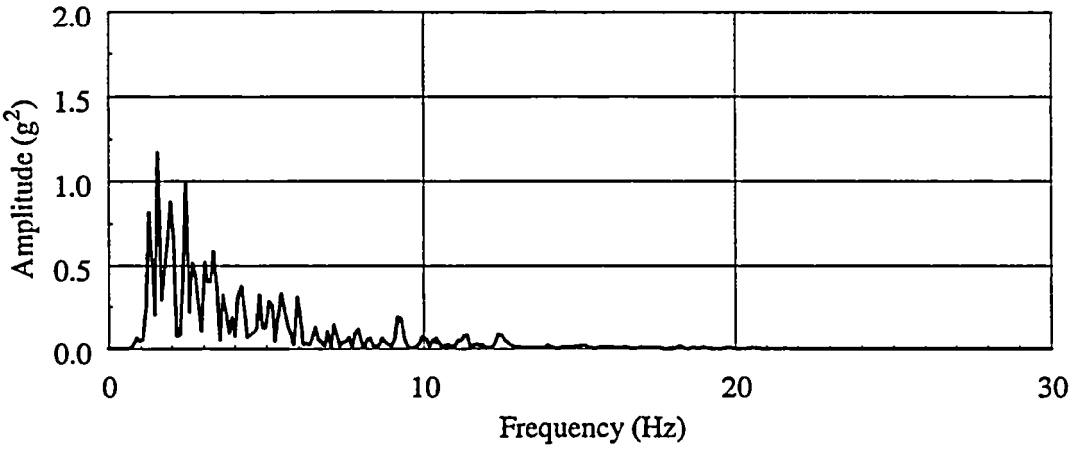

(b) Power spectrum

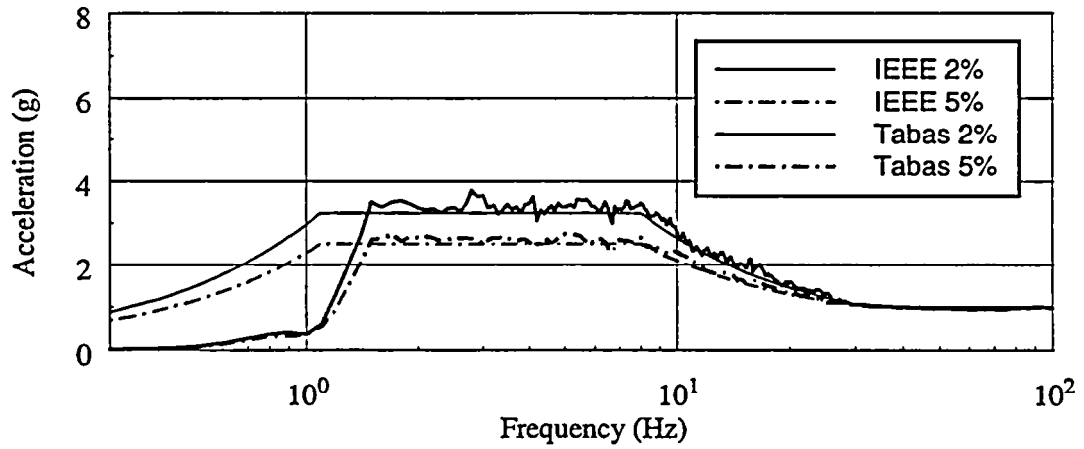

(c) Response spectrum

Figure 3-7 Acceleration history, power spectrum, and response spectra for the lateral (*Y*-) component of the Tabas-A record

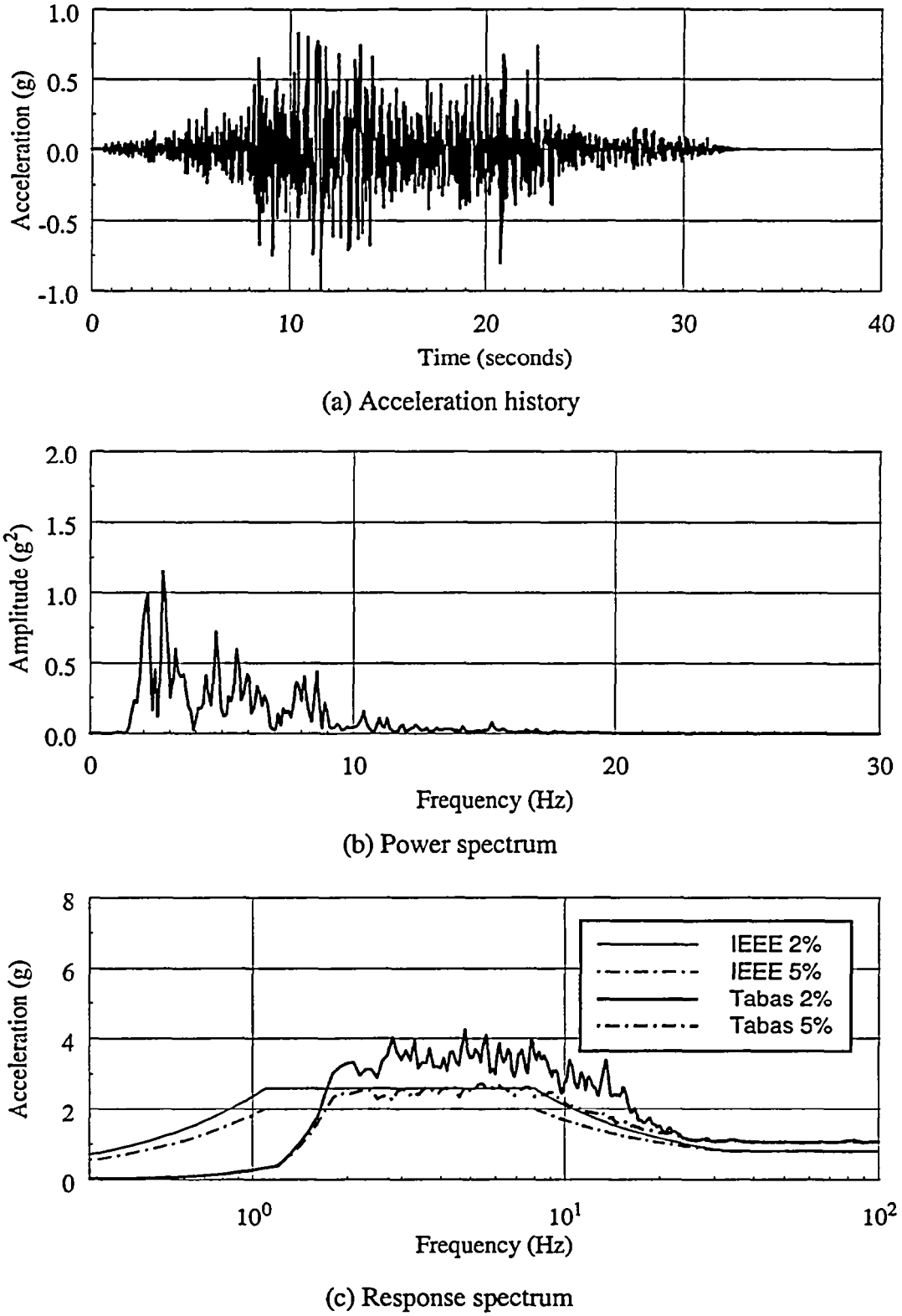

Figure 3-8 Acceleration history, power spectrum, and response spectra for the vertical (Z-) component of the Tabas-A record

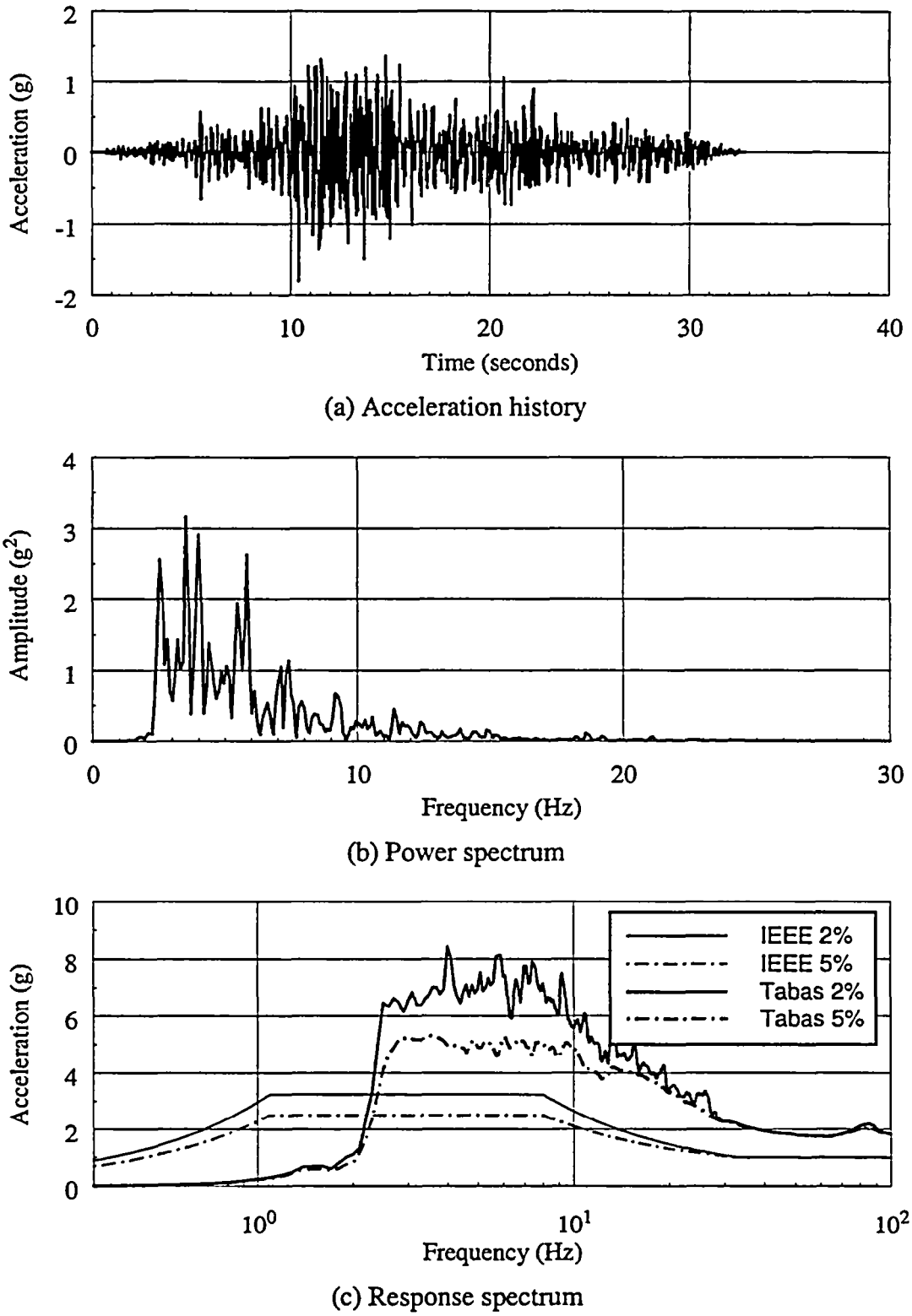

Figure 3-9 Acceleration history, power spectrum, and response spectra for the longitudinal (*X*-) component of the Tabas-B record

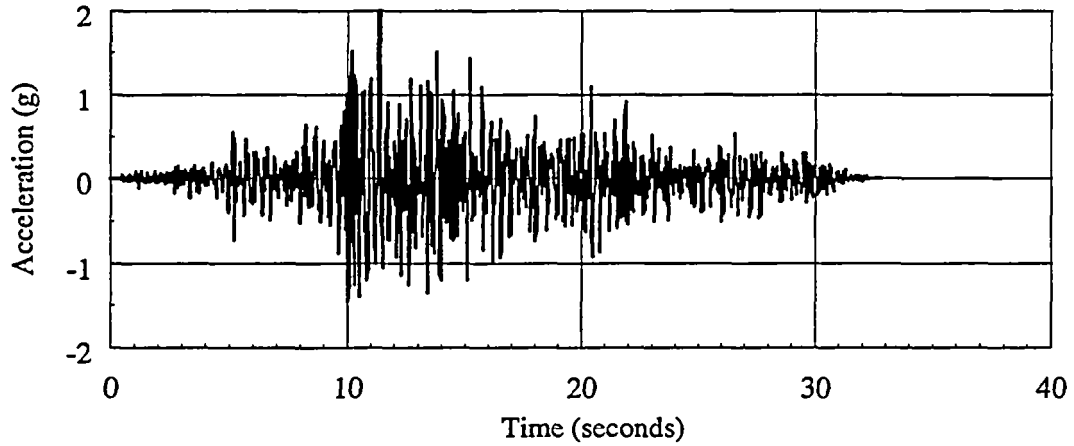

(a) Acceleration history

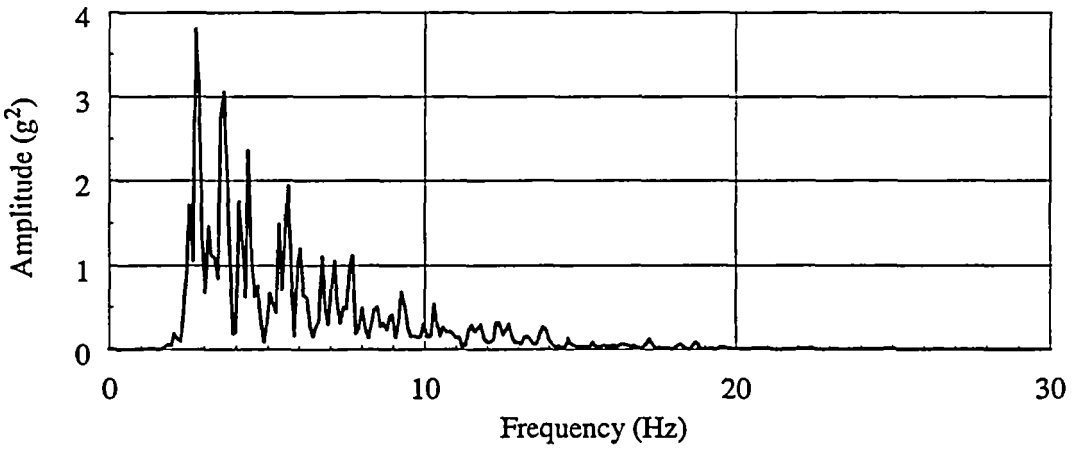

(b) Power spectrum

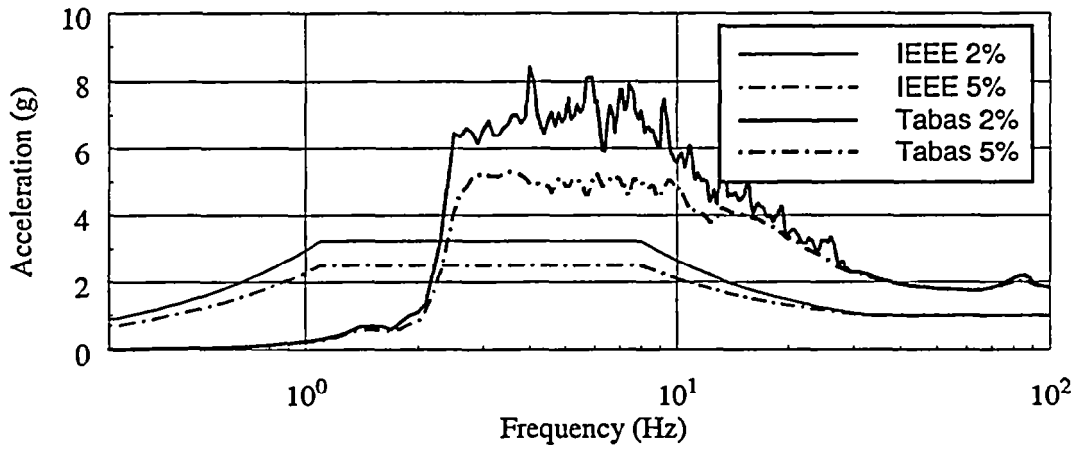

(c) Response spectrum

Figure 3-10 Acceleration history, power spectrum, and response spectra for the lateral (*Y*-) component of the Tabas-B record

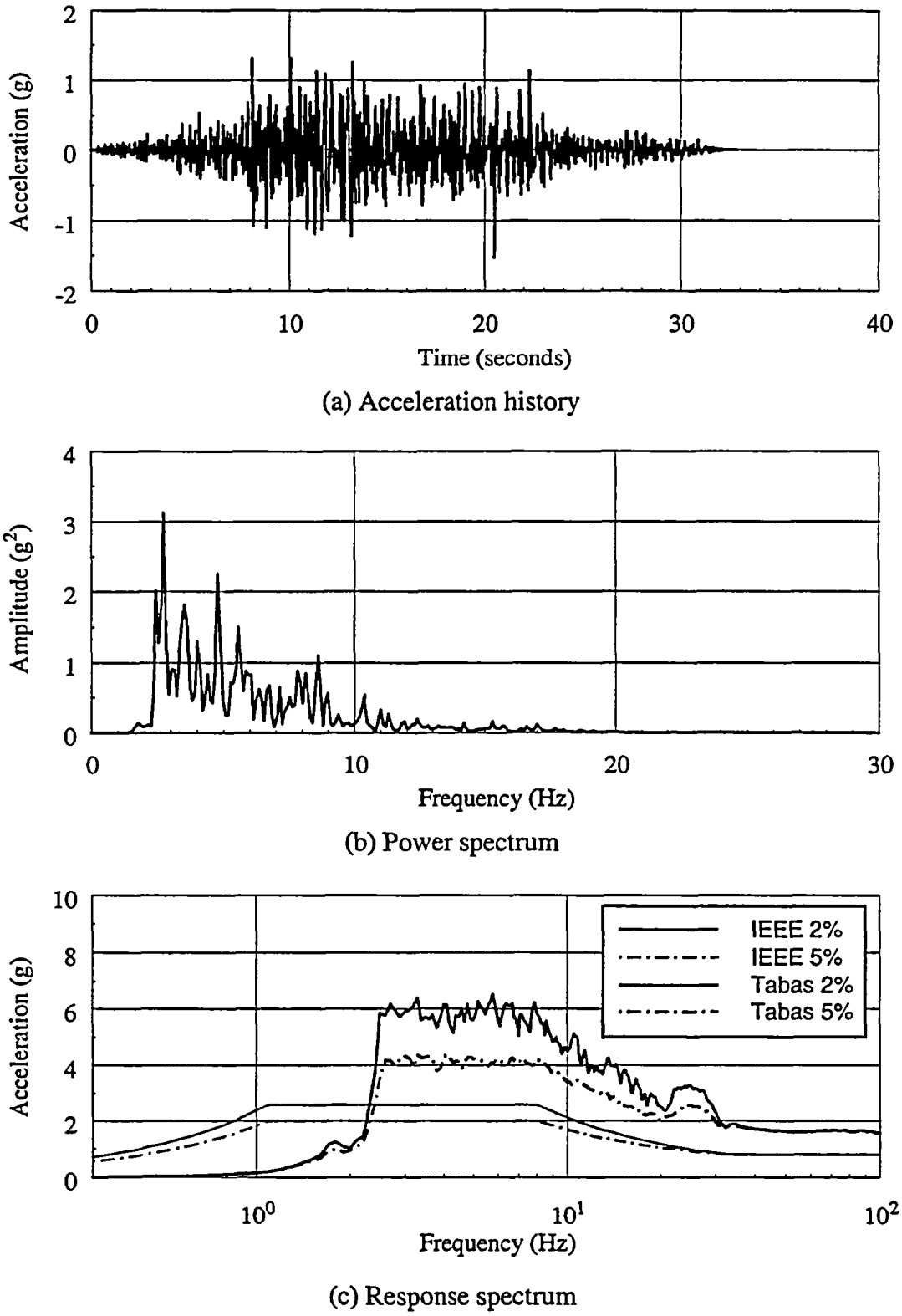

Figure 3-11 Acceleration history, power spectrum, and response spectra for the vertical (Z-) component of the Tabas-B record

4 Fragility Testing of Rigidly Mounted Bushings

4.1 Introduction

Triaxial earthquake simulator testing was used to evaluate the seismic response of the two 230-kV transformer bushings mounted on a *rigid* frame. The following sections describe the test setup, the earthquake motions used for the fragility tests, the instrumentation of the bushings, and selected test results.

4.2 Test Setup

4.2.1 Overview

The fragility tests of the two 230-kV bushings were conducted using the earthquake simulator. For testing, the bushings were placed in a *rigid* mounting frame, designed for the testing of bushings of sizes varying between 196 kV and 550 kV. Two sets of three-component spectrum-compatible input motions were developed for the fragility tests. For seismic testing, IEEE 693-1997 (see Appendix A) states that porcelain bushings must be instrumented to record (a) maximum vertical and horizontal accelerations at the top of the bushing, at the bushing flange, and at the top of the earthquake simulator platform, (b) maximum displacement of the top of the bushing relative to the flange, and (c) maximum porcelain stresses at the base of the bushing near the flange. The instrumentation scheme developed for the tests described in this chapter exceeded the IEEE 693-1997 requirements. The following sections provide a brief review of the test setup.

4.2.2 Earthquake simulator

The earthquake simulator at the Pacific Earthquake Engineering Research (PEER) Center at the University of California at Berkeley was used for the seismic evaluation of the bushings. The 20 ft by 20 ft (6.1 by 6.1 m) simulator has a maximum payload of 140 kips (623 kN) and can accommodate models up to 40 ft (12.2 m) in height. The six-degree-of-freedom simulator (three translations and three rotations) can be programmed to reproduce any waveform (e.g., sinusoidal, white-noise, earthquake history). The maximum horizontal displacement and velocity of the simulator are ±5 in. (±127 mm) and 25 in./sec (635 mm/sec), respectively.

4.2.3 Rigid mounting frame

IEEE 693-1997 (see Appendix A) states that bushings rated at 161 kV and above must be qualified using three-component earthquake-simulator testing. Because it is impractical to test bushings mounted on a transformer, IEEE 693-1997 specifies that bushings must be mounted on a rigid stand for earthquake testing and qualification. IEEE 693-1997 also recommends that a transformer bushing be tested at 20 degrees measured from the vertical because a bushing, if so tested and qualified, is assumed to be qualified for use on all transformers with angles from vertical to 20 degrees.

The mounting frame used for the fragility tests was a fully welded steel frame consisting of TS 5x5x3/8" (127x127x10 mm) columns, L 5x5x3/4" (127x127x19 mm) braces, and a 2.0-in. (51-mm) thick steel mounting plate (sloping at 20 degrees to the horizontal). The mounting frame was post-tensioned to the earthquake simulator platform using fifteen 1-in. (25-mm) diameter high-strength threaded rods. A special 1.5-in. (38-mm) adaptor plate was designed and fabricated to connect the flange plate of the 230-kV bushings to the support frame. Twelve 1-1/4 in. (32 mm) diameter high-strength (Grade 8, equivalent to A490 steel) bolts were used for the adaptor plate-to-mounting plate connection The flange of the bushing was joined to the adaptor plate with twelve 3/4 in. (19 mm) diameter Grade 2 steel bolts (equivalent to A307 steel) torqued to 100 ft-lb (136 N-m) per the field installation specification supplied by Elder (Elder, 1999). The support frame was designed to be extremely stiff to minimize the amplification of the simulator input to the bushing. Figure 4-1 shows one of the 230-kV bushings installed in the mounting frame atop the earthquake simulator.

4.2.4 Earthquake ground motions

IEEE 693-1997 requires that experimental testing of bushings include: (a) resonant-search tests to identify the dynamic properties of the bushings and (b) triaxial earthquake ground motions tests for bushing qualification and fragility testing.

4.2.4.1 Resonant-search tests

Sine-sweep and broad band white-noise tests were used to establish the dynamic characteristics (natural frequencies and damping ratios) of the bushings. These so-called *resonant-search* tests were undertaken using unidirectional excitation along each global axis of the earthquake simulator platform. For both sine-sweep and white-noise tests, a simulator input acceleration amplitude of 0.1g was used.

4.2.4.2 Earthquake test response spectrum

IEEE 693-1997 identifies several response spectra of identical shape but different amplitudes for the qualification of transformer bushings. For a detailed description of these spectra, the reader is referred to Appendix A. Figure 4-2 shows an IEEE 693-1997 High Level qualification response spectrum used for checking porcelain stresses and oil leakage. The spectrum is anchored to a peak ground acceleration (PGA) equal to 2.0g. Spectrum-compatible earthquake histories were generated using the procedures set forth in Section 3.2.3.

Two separate and independent three-component records were utilized for fragility testing. The Tabas-A motion was used for all the tests up to and including motions with target PGAs of 1.0g. The Tabas-B motion was used for all tests with a target PGA exceeding 1.0g but less than 2.0g.

4.2.5 Instrumentation

The instrumentation scheme developed for the tests described in this chapter included 52 transducers and 54 channels of data. Table 4-1 lists the channel number, instrument type, response quantity, coordinate system, and location for each transducer. Figure 4-3 presents information on the instrumentation of the earthquake simulator platform (Figure 4-3a), the bushing and the mounting frame (Figure 4-3b), and the porcelain unit immediately above the flange (UPPER-1) of the bushing (Figure 4-3c). The global *(X, Y, Z)* and local *(x, y, z)* coordinate systems adopted for the testing program are shown in the figure. Figure 4-4 shows the instrumentation at the top of Bushing-1. Figure 4-5 is a photograph of the instrumentation immediately above the flange plate for this bushing.

Sixteen channels (channels 3 through 18) recorded the acceleration and displacement of the earthquake simulator platform in the global coordinate system. The accelerations of the mounting frame in the local coordinate system (channels 28, 29, and 30) and the absolute displacements of the mounting frame in the global coordinate system (channels 37 and 38) were recorded. The accelerations of the bushing in the local coordinate system (channels 19 through 27) and the absolute displacements of the bushing in the global coordinate system (channels 31 through 36) were measured at the top, midheight, and bottom of the bushing. Four strain gages (channels 39 through 42) monitored the axial strains in the UPPER-1 porcelain unit immediately above the gasket. Four displacement transducers (channels 43 through 46), located immediately below the gasket, measured the radial slip of the flange plate relative to the support frame. Another four displacement transducers (channels 47 through 50), located immediately above the gasket, measured radial slip of the UPPER-1 porcelain unit relative to the support frame. The relative slip of the porcelain over the flange plate was computed using these eight transducers. Four displacement transducers (channels 51 through 54) recorded vertical displacements of the UPPER-1 porcelain unit across the gasket, parallel to the local *z*- axis of the bushing.

4.3 Summary of Experimental Data

4.3.1 Overview

The objective of the testing program described in this chapter was to evaluate the seismic behavior of *rigidly* mounted 230-kV transformer bushings by testing Bushing-1 and Bushing-2 to motions with target PGAs of up to 2.0g. The list of earthquake tests and key observations for Bushing-1 and Bushing-2 are presented in Table 4-2 and Table 4-3, respectively. After each earthquake test, the response data were analyzed, the bushing was inspected for damage and oil leakage, and the bolts joining the bushing flange plate to the adaptor plate, and the adaptor plate to the mounting plate, were checked for tightness. All bolts were found to be tight for all tests. The

following sections summarize the dynamic properties and the seismic response of the bushings. Section 4.3.2 discusses the dynamic properties of the two bushings and Section 4.3.3 presents fragility data for Bushing-1 and Bushing-2. Section 4.3.4 describes the response of Bushing-2 to harmonic excitation.

Table 4-1 Instrumentation for rigidly mounted 230-kV bushings

Channel Number	*Transducer*[1]	*Response Quantity*	*Coordinate System and Orientation*[2]	*Transducer Location*[3]
1	-	date	-	-
2	-	time	-	-
3	LVDT	platform displacement	global *X*	simulator platform
4	LVDT	platform displacement	global *Y*	simulator platform
5	LVDT	platform displacement	global *X*	simulator platform
6	LVDT	platform displacement	global *Y*	simulator platform
7	LVDT	platform displacement	global *Z*	simulator platform
8	LVDT	platform displacement	global *Z*	simulator platform
9	LVDT	platform displacement	global *Z*	simulator platform
10	LVDT	platform displacement	global Z	simulator platform
11	A	platform acceleration	global *X*	simulator platform
12	A	platform acceleration	global *X*	simulator platform
13	A	platform acceleration	global *Y*	simulator platform
14	A	platform acceleration	global *Y*	simulator platform
15	A	platform acceleration	global *Z*	simulator platform
16	A	platform acceleration	global *Z*	simulator platform
17	A	platform acceleration	global *Z*	simulator platform
18	A	platform acceleration	global Z	simulator platform
19	A	bushing acceleration	local *x*	bottom of bushing
20	A	bushing acceleration	local *y*	bottom of bushing
21	A	bushing acceleration	local *z*	bottom of bushing
22	A	bushing acceleration	local *x*	midheight of bushing
23	A	bushing acceleration	local *y*	midheight of bushing
24	A	bushing acceleration	local *z*	midheight of bushing
25	A	bushing acceleration	local *x*	top of bushing
26	A	bushing acceleration	local *y*	top of bushing
27	A	bushing acceleration	local *z*	top of bushing

Table 4-1 Instrumentation for rigidly mounted 230-kV bushings

Channel Number	*Transducer*[1]	*Response Quantity*	*Coordinate System and Orientation*[2]	*Transducer Location*[3]
28	A	frame acceleration	local *x*	top of mounting frame
29	A	frame acceleration	local *y*	top of mounting frame
30	A	frame acceleration	local *z*	top of mounting frame
31	LP	bushing displacement	global *X*	bottom of bushing
32	LP	bushing displacement	global *Y*	bottom of bushing
33	LP	bushing displacement	global *X*	midheight of bushing
34	LP	bushing displacement	global *Y*	midheight of bushing
35	LP	bushing displacement	global *X*	top of bushing
36	LP	bushing displacement	global *Y*	top of bushing
37	LP	frame displacement	global *X*	top of mounting frame
38	LP	frame displacement	global *Y*	top of mounting frame
39	SG	porcelain strain	local *z*	gasket connection
40	SG	porcelain strain	local *z*	gasket connection
41	SG	porcelain strain	local *z*	gasket connection
42	SG	porcelain strain	local *z*	gasket connection
43	DCDT	flange plate slip	relative to frame	gasket connection
44	DCDT	flange plate slip	relative to frame	gasket connection
45	DCDT	flange plate slip	relative to frame	gasket connection
46	DCDT	flange plate slip	relative to frame	gasket connection
47	DCDT	UPPER-1 slip	relative to frame	gasket connection
48	DCDT	UPPER-1 slip	relative to frame	gasket connection
49	DCDT	UPPER-1 slip	relative to frame	gasket connection
50	DCDT	UPPER-1 slip	relative to frame	gasket connection
51	DCDT	UPPER-1 uplift	relative to frame	gasket connection
52	DCDT	UPPER-1 uplift	relative to frame	gasket connection
53	DCDT	UPPER-1 uplift	relative to frame	gasket connection
54	DCDT	UPPER-1 uplift	relative to frame	gasket connection

1. A = accelerometer; LVDT = displacement transducer; LP = linear potentiometer; SG = strain gage; DCDT = displacement transducer.
2. For the local (*x*-, *y*-, *z*-) and global (*X*- *Y*- *Z*-) coordinate systems see Figure 4-3.
3. For transducer locations on the bushings see Figure 4-3.

Table 4-2 Summary of earthquake testing of Bushing-1

Test No.	*Test Date*	*Identification*[1]	*PGA*[2]	*Comments*
1	4/6/99	WN-X	0.1g	Data scanned at 100 Hz.
2	4/6/99	WN-Y	0.1g	
3	4/6/99	WN-Z	0.1g	
4	4/6/99	SS-X	0.1g	
5	4/6/99	SS-Y	0.1g	
6	4/6/99	SS-Z	0.1g	
7	4/6/99	Tabas-A	0.1g	
8	4/7/99	Tabas-A	0.2g	Scan rate increased to 200 Hz.
9	4/7/99	Tabas-A	0.3g	
10	4/7/99	Tabas-A	0.5g	
11	4/7/99	Tabas-A	0.7g	
12	4/7/99	Tabas-A	1.0g	Spectrum equivalent to moderate-level qualification.
13	4/7/99	Tabas-B	1.2g	
14	4/7/99	Tabas-B	1.4g	
15	4/7/99	Tabas-B	1.6g	
16	4/7/99	Tabas-B	1.8g	
17	4/7/99	Tabas-B	2.0g	Spectrum equivalent to high-level qualification.
18	4/7/99	SS-X	0.1g	
19	4/7/99	SS-Y	0.1g	
20	4/7/99	SS-Z	0.1g	

1. WN = white-noise, SS = sine-sweep; *-X*, *-Y*, and *-Z* denote direction of testing in global coordinate system; Tabas-A = spectrum-compatible Tabas-A earthquake histories; Tabas-B = spectrum-compatible Tabas-B earthquake histories.

2. PGA = target peak acceleration of the simulator platform.

For all tests, the transducer response histories were processed using the computer program Matlab (Mathworks, 1999). Experimental histories were low-passed filtered using a rectangular filter with a cut-off frequency of 40 Hz and then zero-corrected.

Table 4-3 Summary of earthquake testing of Bushing-2

Test No.	*Test Date*	*Identification*[1]	*PGA*[2]	*Comments*
1	5/10/99	WN-X	0.1g	Data scanned at 200 Hz.
12	5/11/99	WN-Y	0.1g	Data scanned at 100 Hz.
13	5/11/99	WN-Z	0.1g	
14	5/11/99	SS-X	0.1g	
15	5/11/99	SS-Y	0.1g	
16	5/11/99	SS-Z	0.1g	
18	5/11/99	Tabas-A	0.5g	
19	5/11/99	Tabas-A	1.0g	Spectrum equivalent to moderate-level qualification.
20	5/11/99	Tabas-B	1.2g	
21	5/11/99	Tabas-B	1.4g	
22	5/11/99	Tabas-B	1.6g	
23	5/11/99	Tabas-B	1.8g	
24	5/11/99	Tabas-B	2.0g	Spectrum equivalent to high-level qualification.
25	5/11/99	5 Hz-X	2.0g	Bushing leaked oil at the gasket connection.
26	5/11/99	WN-X	0.1g	
27	5/11/99	WN-Y	0.1g	
28	5/11/99	WN-Z	0.1g	
29	5/11/99	Tabas-A	1.0g	Spectrum equivalent to moderate-level qualification, no oil leakage.
30	5/11/99	Tabas-B	2.0g	Spectrum equivalent to high-level qualification, no oil leakage.
31	5/11/99	WN-X	0.1g	Added terminal to top of bushing, see Figure 4-6.
32	5/11/99	WN-Y	0.1g	
33	5/11/99	WN-Z	0.1g	
34	5/11/99	Tabas-A	1.0g	Spectrum equivalent to moderate-level qualification, no oil leakage.
35	5/11/99	Tabas-B	2.0g	Spectrum equivalent to high-level qualification, no oil leakage.
36	5/11/99	5 Hz-X	1.0g	
37	5/11/99	5 Hz-X	2.0g	No oil leakage.
38	5/11/99	5 Hz-X	2.0g	Removed terminal prior to testing; bushing leaked oil and porcelain slipped noticeably, see Figure 4-7.

1. WN = white-noise, SS = sine-sweep; *-X*, *-Y*, and *-Z* denote direction of testing in global coordinate system; Tabas-A = spectrum-compatible Tabas-A earthquake histories; Tabas-B = spectrum- compatible Tabas-B earthquake histories; 5 Hz = 20-cycle constant-amplitude harmonic input.

2. PGA = target peak acceleration of the simulator platform.

4.3.2 Dynamic properties of rigidly mounted 230-kV bushings

Sine-sweep and white-noise tests were used to calculate the modal frequencies and damping ratios for the bushings. Figure 4-8 and Figure 4-9 show the transfer functions between the top of the bushing and the mounting frame in the three local directions (*x, y, z*) for Bushing-1 and Bushing-2, respectively. These tests were conducted prior to the earthquake tests. The resonant frequency in the local *x*- and *y*-directions were approximately 20 Hz and 18 Hz, respectively. Damping ratios of between 2 to 3 percent of critical were obtained using the half-power bandwidth method.

Table 4-4 summarizes the measured dynamic properties of the bushings in the *x*- and *y*-directions. Modal data could not be determined for the local *z*-direction. Three key observations are: (1) the modal frequencies differ slightly in the *x*- and *y*- directions due to the unsymmetrical distribution of lifting lugs immediately above the flange plate; (2) although Bushing-2 leaked oil during Test Number 25, the modal properties of the bushing measured immediately after leakage (Test Set 26-31) do not differ from the properties measured prior to earthquake simulator testing (Test Set 1 and 12-16); and (3) the addition of the 64-lb (280-N) terminal and its 11-lb (50-N) attachment to the top of the bushing introduced a second vibration frequency to the bushing response and reduced the first mode frequencies of the bushing in the *x*- and *y*- directions significantly.

Table 4-4 Modal properties of bushings from resonance-search tests

		Frequency (Hz)		*Damping Ratio (% critical)*	
Bushing	*Test Set*	*x-direction*	*y-direction*	*x-direction*	*y-direction*
1	1-6	20	18	2	2
1	18-20	20	18	3	2
2	1, 12-16	20	18	3	2
2	26-28	20	18	3	2
2	31-33	14[1]	13[1]	3	3

1. During the tests with the terminal attached to the top of bushing, a second mode frequency of 26.5 Hz was evident in the *x*- and *y*- directions.

4.3.3 Earthquake testing of Bushing-1 and Bushing-2

4.3.3.1 Introduction

The following subsections present peak responses of Bushing-1 and Bushing-2 and local response characteristics of the bushings measured at the junction of the UPPER-1 porcelain unit and the flange plate.

4.3.3.2 Peak responses

The peak acceleration, relative displacements, and strain responses of the bushings are presented in Table 4-5. Only the peak responses at the top of bushings are reported; the maximum acceleration responses at the bottom of the bushings were of the same order as than those at the top and the accelerations at midheight were smaller than the values measured at either the top or the bottom of bushings. The values of peak absolute accelerations are defined as the maximum of the vector sum of acceleration components in the local *x*- and local *y*- directions, evaluated from acceleration histories. Similarly, the values of peak relative displacements (relative to the mounting frame) are defined as the maximum of the vector sum of relative displacement components in the global *X*- and local *Y*- directions, evaluated from displacement histories. The values of maximum strain were computed from measured porcelain strains (channels 39 through 42); the largest maximum value is tabulated.

Although, the target PGAs are listed in increasing order in Table 4-5, the tabulated response values do not necessarily increase in a corresponding manner. Among the factors contributing to this variation are the temperature-dependent dynamics of the simulator's hydraulic system, interaction between the simulator platform and bushing-support system, simulator rotational accelerations, and the phase difference between the *x*- (or *X-)* and *y*- (or *Y-*) components of response used to compute the vector sum of the response.

4.3.3.3 Response of Bushing-1

The global response of Bushing-1 was assessed by analysis of data from Test Number 12 (Tabas-A, target PGA equal to 1.0g) and Test Number 17 (Tabas-B, target PGA equal to 2.0g).

During Test Number 12, a maximum acceleration and relative displacement of 3.9g and 0.17 in. (4 mm) were recorded at the top of the bushing, respectively. (see Table 4-5). Acceleration response spectra for Bushing-1 in the local coordinate system, generated using measured acceleration histories at the flange are shown in Figure 4-10. For information, the 2-percent and 5-percent damped IEEE 693-1997 response spectra for Moderate Level qualification are also shown in this figure. In the range of the fundamental frequency of the bushing (18-20 Hz), the computed spectral accelerations exceed the IEEE 693-1997 ordinates for Moderate Level qualification.

During Test Number 17, a maximum acceleration and relative displacement of 6.0g and 0.40 in. (10 mm) were recorded at the top of the bushing, respectively. (see Table 4-5). Acceleration response spectra for Bushing-1 in the local coordinate system, generated using measured acceleration histories at the flange are shown in Figure 4-11. For information, the 2-percent and 5-percent damped IEEE 693-1997 response spectra for High Level qualification are also shown in this figure. In the range of the fundamental frequency of the bushing, the computed spectral accelerations exceed the IEEE 693-1997 ordinates for High Level qualification.

Table 4-5 Peak responses of the bushings

Bushing	*Test No.*	*Identification*[1]	*PGA*[2]	*Peak Acceleration (g)*	*Peak Relative Displacement (mm)*	*Peak Porcelain Strain (με)*
1	7	Tabas-A	0.1g	1.2	1.3	3
1	8	Tabas-A	0.2g	2.0	2.3	4
1	9	Tabas-A	0.3g	3.0	2.6	7
1	10	Tabas-A	0.5g	3.3	3.6	7
1	11	Tabas-A	0.7g	3.2	3.3	8
1	12	Tabas-A	1.0g	3.9	4.3	9
1	13	Tabas-B	1.2g	3.9	5.3	8
1	14	Tabas-B	1.4g	4.5	7.6	9
1	15	Tabas-B	1.6g	4.5	8.9	8
1	16	Tabas-B	1.8g	4.5	9.7	8
1	17	Tabas-B	2.0g	6.0	10.2	11
2	18	Tabas-A	0.5g	3.8	3.0	8
2	19	Tabas-A	1.0g	3.9	4.1	10
2	20	Tabas-B	1.2g	4.3	5.8	12
2	21	Tabas-B	1.4g	3.9	7.1	13
2	22	Tabas-B	1.6g	4.6	8.9	11
2	23	Tabas-B	1.8g	5.1	9.9	10
2	24	Tabas-B	2.0g	5.7	9.8	12
2	29	Tabas-A	1.0g	3.6	4.3	11
2	30	Tabas-B	2.0g	5.4	9.7	19
2	34	Tabas-A	1.0g	2.8	5.8	12
2	35	Tabas-B	2.0g	4.6	14.0	29

1. Tabas-A = spectrum-compatible Tabas-A earthquake histories; Tabas-B = spectrum-compatible Tabas-B earthquake histories

2. PGA = target peak acceleration of the simulator platform

Figure 4-12a shows the relation between the average vertical displacement in the local z-direction and rocking about the local y-axis. The average vertical displacement in the z-direction was calculated as one-half of the corrected, to the face of the bushing, sum of the channel 51 and channel 53 displacements. Rocking about the local y-axis was calculated as the difference between the channel 51 and 53 displacements divided by the 25-in. (635-mm) distance between these transducers. Figure 4-12b shows the relation between the average vertical displacement in the local z-direction and rocking about the local x-axis. The average vertical displacement in the z-direction was calculated as one half of the sum of the channel 52 and channel 54 displacements; the rocking about the local x-axis was calculated as the difference between the channel 52 and 54 displacements divided by the 25-in. (635-mm) distance between these transducers. The maximum uplift at the edge of porcelain unit can be computed by adding the product of the rocking angle and the radius of the UPPER-1 porcelain unit, at the flange plate, to the average longitudinal displacement.

Figure 4-13 presents the zero-corrected displacement orbit of the center of the bushing, measured at the height of the radial displacement transducers, relative to the flange plate. Shear deformation in the gasket and slip of UPPER-1 porcelain over the gasket contribute to the measured displacement. The maximum value of this displacement is approximately 0.02 in. (0.5 mm).

4.3.3.4 Response of Bushing-2

The global response of Bushing-2 was assessed by analysis of data from Test No 19 (Tabas-A, target PGA equal to 1.0g) and Test No 24 (Tabas-B, target PGA equal to 2.0g).

During Test No 19, a maximum acceleration and relative displacement of 3.9g and 0.16 in. (4 mm) were recorded at the top of the bushing, respectively. (see Table 4-5). Acceleration response spectra for Bushing-2 in the local coordinate system, generated using measured acceleration histories at the flange are shown in Figure 4-14. For information, the 2-percent and 5-percent damped IEEE 693-1997 response spectra for Moderate Level qualification are also shown in this figure. In the range of the fundamental frequency of the bushing (18-20 Hz), the computed spectral accelerations exceed the IEEE 693-1997 ordinates for Moderate Level qualification.

During Test No 24, a maximum acceleration and relative displacement of 6.0g and 0.38 in. (10 mm) were recorded at the top of the bushing, respectively. (see Table 4-5). Acceleration response spectra for Bushing-2 in the local coordinate system, generated using measured acceleration histories at the flange are shown in Figure 4-15. For information, the 2-percent and 5-percent damped IEEE 693-1997 response spectra for High Level qualification are also shown in this figure. In the range of the fundamental frequency of the bushing, the computed spectral accelerations exceed the IEEE 693-1997 ordinates for High Level qualification.

Figure 4-16a shows the relation between the average vertical displacement in the local z-direction and rocking about the local y-axis. Values of displacement and rocking were computed per Section 4.3.3.3.

Figure 4-17 presents the zero-corrected displacement orbit of the center of the bushing, measured at the height of the radial displacement transducers, relative to the flange plate. Shear deformation in the gasket and slip of UPPER-1 porcelain over the gasket contribute to the measured displacement. The maximum value of this displacement is less than 0.02 in. (0.4 mm).

4.3.3.5 Evaluation of seismic response of bushings

Neither bushing was designated for seismic qualification as part of this study. However, when mounted on a stiff frame, both bushings withstood severe shaking compatible with IEEE 693-1997 spectrum for High Level qualification. In the range of the fundamental frequency of the bushings (18-20 Hz), the computed spectral accelerations exceeded the recommended IEEE 693-1997 ordinates for High Level qualification (see Figures 4-11 and 4-15). For these tests, there was no structural damage and no oil leakage, and the recorded stresses in the UPPER-1 porcelain unit were substantially smaller than the ultimate values (see Table 4-5). Bushing-1 and Bushing-2 were therefore qualified by test to the High Level.

4.3.4 Response of Bushing-2 to harmonic excitations

4.3.4.1 Overview

At the request of the utilities, Bushing-2 was subjected to four constant-amplitude unidirectional (*X*-direction) harmonic motions. Although such input is neither representative of earthquake shaking nor the type of motion typically used for qualification and fragility testing of bushings, these tests were undertaken to complement the triaxial earthquake tests, because the IEEE-required High Level qualification time history tests for the *rigidly* mounted bushing were not severe enough to reproduce the bushing failures observed in the field during moderate to severe earthquakes.

The input displacement for the harmonic tests took the form:

$$d(t) = d_o \sin(2\pi f t) \tag{4-1}$$

where, $d(t)$ is the time-dependent simulator platform displacement, d_o is the simulator platform displacement amplitude, and f is the frequency (= 5 Hz) of the harmonic signal.

For the three high-amplitude harmonic tests (Test Nos 25, 37, and 38), the maximum target velocity of the harmonic signal was set at 25 in./sec (635 mm/sec) to avoid exceeding the velocity limits of the earthquake simulator. The corresponding target displacement and acceleration amplitudes were 0.8 in. (20 mm) and 2.0g, respectively. Each test was four seconds (20 cycles) long.

For the low-amplitude harmonic test (Test No 36), the amplitude of input signal was one half of the amplitude of the high-level tests.

4.3.4.2 Summary of bushing response

Bushing-2 was subjected to three identical, 5-Hz harmonics with a target peak simulator acceleration of 2.0g (Test Nos 25, 37, and 38). For one of these tests (Test No 37) a terminal was attached to the top of the bushing. For the other two tests (Test Nos 25 and 38), the terminal was not attached. Oil leakage was observed during Test No 25. Oil leakage and significant slip of the UPPER-1 porcelain unit were observed during Test No 38. When the terminal was not attached to the bushing, the fundamental frequency of the bushing in the x- direction (as measured at the top of the bushing) was approximately 20 Hz. When the terminal was attached to the bushing dome, the fundamental frequency of the bushing in the x-direction (as measured at the top of the bushing) dropped to approximately 14 Hz and an additional mode with a frequency of 26.5 Hz was identified (see Table 4-4).

4.3.4.3 Peak responses

The recorded test data were used to compute the peak acceleration and displacement responses of Bushing-2 relative to the mounting frame and peak values of slip, uplift, and stress for the UPPER-1 porcelain unit. These values are presented in Table 4-6. The values of peak absolute accelerations are defined as the maximum of the vector sum of acceleration components in the local x- and local y- directions, evaluated from the acceleration histories. Similarly, the values of peak relative displacements (relative to the mounting frame) are defined as the maximum of the vector sum of the relative displacement components in the global X- and local Y- directions, evaluated from the displacement histories. The peak values for porcelain slip, uplift, and strain were computed as the largest value of porcelain slip (channels 47 through 50), porcelain uplift (channels 51 through 54), and porcelain stress (channels 39 through 42).

Table 4-6 Peak responses of Bushing-2 to the high-amplitude 5-Hz harmonic tests

	Peak Acceleration (g)			*Peak Relative Displacement (mm)*			*Slip (mm)*	*Uplift (mm)*	*Stress*[2] *(MPa)*
Test No.[1]	*Top*	*Midheight*	*Bottom*	*Top*	*Midheight*	*Bottom*			
25	5.9	NA[3]	6.0	22	20	5	0.2	2	7
37	5.4	NA	5.3	11	16	5	0.1	0.5	1
38	6.0	NA	5.9	33	31	4	0.9	2	17

1. Terminal attached to the bushing for Tests 31 to 37 only.
2. Stress is computed by multiplying measured strain by porcelain elastic modulus (assumed 97,000 MPa).
3. NA designates not available.

It is evident from Table 4-6 that when the terminal was not attached to the top of the bushing, the bushing experienced large accelerations at its top and bottom, and that the relative displacement (relative to the mounting frame) at the top and midheight of the bushing were significantly larger than the motion at the bottom of the bushing. At the gasket connection, large values of porcelain

stress, slip, and uplift were recorded. When the terminal was attached to the bushing, large accelerations were measured at the top and bottom of the bushing and the relative displacement at the bushing midheight was larger than the motion at the top. At the gasket connection, porcelain stress, slip, and uplift were all small.

To investigate the response of Bushing-2, data from Test Nos 37 and 38 were selected for further analysis.

4.3.4.4 Response of the simulator platform

Figure 4-18 presents the simulator response for a six-second segment of the harmonic tests from Test No 37. The simulator response from test No 38 was similar. The average simulator displacement history in the *x*- direction (Figure 4-18a) was calculated as one half of the sum of the channel 3 and channel 5 displacements. The average simulator translational acceleration history in the *x*- direction (Figure 4-18c) was calculated as one half of the sum of the channel 11 and channel 12 accelerations. The average frame translational acceleration history in the *x*- direction caused by the simulator rotational accelerations or pitch (about the *y*- axis) was computed by linearly combining the vertical accelerometer measurements (channels 15 through 18), dividing the computed value by the 192-in. (4.9-m) distance between these accelerometers, and multiplying the resulting value by the 73-in. (1.8-m) distance between the top of the platform and the top of the mounting frame (Figure 4-18e).

Although the desired target input motion for the harmonic tests was a constant-amplitude single-harmonic displacement history along the *x*-axis of the simulator (Figures 4-18a and b), the input histories were distorted because of the oil-column resonance in the vertical actuators. The simulator histories included harmonics of the target 5-Hz frequency and rotational accelerations. Examination of the simulator translational acceleration along the *x*-axis (Figure 4-18d) shows that the input acceleration history included harmonics of the 5-Hz input at 15 and 25 Hz. Examination of the simulator rotational acceleration about the *y*-axis (scaled and shown in Figure 4-18e as the *x*-acceleration at top of the mounting frame) shows rotational accelerations and harmonics of the 5-Hz target frequency (Figure 4-18f).

Figure 4-19 shows the 2-percent damped acceleration spectra for the recorded harmonic signal and the target harmonic signal. For reference, the 2-percent damped IEEE 693-1997 response spectrum for high-level qualification is also shown. *Rigidly* mounted Bushing-1 has a fundamental frequency of 20 Hz. At this frequency, the acceleration ordinate for the IEEE 693-1997 spectrum is 3g, and is labeled as point A in the figure. If the bushing had been subjected to target history, the bushing acceleration would have been 2.6g. However, the acceleration ordinate calculated using the measured response of the simulator platform was 9g (point C in the figure) — three times greater than the IEEE 693-1997 ordinate. This large spectral acceleration caused the oil leakage and slip of the UPPER-1 porcelain unit observed during Test Nos 25 and 38.

4.3.4.5 Response of the bushing

The zero-corrected acceleration histories for the bushing along the x-axis were studied by examining a six-second segment of the data from channels 19 and 25. The acceleration data for the test without the terminal is shown in Figure 4-20 and the acceleration data for the test with the terminal is shown in Figure 4-21. The peak acceleration at the top and bottom of the bushing for both tests exceeded 5g. For Test No 38 (test without the terminal), the acceleration histories were out-of-phase as shown by the large amplitude of the difference in the acceleration at the top and bottom of bushing; the power spectrum had a peak at 5 Hz and a larger peak at 15 Hz. For Test No 37 (test with the terminal), acceleration histories were nearly in-phase as shown by the much smaller amplitude of the difference between the acceleration at the top and bottom of bushing; the power spectrum had a peak at 5 Hz and a smaller peak at 15 Hz.

The zero-corrected displacement histories of the bushing relative to the mounting frame in the x-axis were studied by examining a six-second segment of the data from channels 31, 33, and 35. The displacements of the bushing relative to the support frame were computed by subtracting the history of the mounting frame displacement (channel 37) from the recorded bushing displacements (channels 31, 33, and 35). Slip of the UPPER-1 porcelain unit was computed by combining the data from the radial sensors, (channels 47 through 51) and applying geometric transformations to obtain the slip along the x-axis. The computed displacements for the test without the terminal and the test with the terminal are shown in Figure 4-22 and Figure 4-23, respectively. During Test No 38 (test without the terminal), the displacement at the bottom of bushing was small, there was significant slip of the UPPER-1 porcelain unit over the flange, and the displacement at the top of the bushing was larger than the displacement at the midheight. The residual displacement of the top and midheight of the bushing, at the conclusion of the test, were due to the slip of the porcelain. The slip history of the UPPER-1 porcelain unit shows slip initiating at approximately 4 seconds into the response. At the conclusion of the test, Bushing-2 had a permanent slip of 0.8 in. (20 mm). During Test No 37 (test with the terminal), displacement at the bottom of bushing was small, the displacement at the top of the bushing smaller than the displacement at the midheight (possibly due to the interaction between two modes of vibrations of the bushing when the terminal was attached). At the conclusion of the test, Bushing-2 had no significant residual slip.

The zero-corrected porcelain uplift histories along the x-axis for the UPPER-1 porcelain unit were studied by examining data from channels 51 and 53. The average vertical displacement in the z-direction was calculated as one-half of the sum of the channel 51 and channel 53 displacements. Rocking about the local y-axis was calculated as the difference between the channel 51 and 53 displacements divided by the 25-in. (635-mm) distance between these transducers. The data for the test without the terminal are shown in Figure 4-24 and the data for the test with the terminal are shown in Figure 4-25. During Test No 38 (test without the terminal), there was large uplift of the UPPER-1 porcelain unit. The uplift history of the UPPER-1 porcelain unit shows uplift initiating at approximately 4 seconds into the response. Slip and uplift of the UPPER-1 porcelain unit initiated at the same time, and resulted in oil leakage from the bushing. At the conclusion of

the test, the residual uplift of channel 51 was greater than that of channel 53, which indicates residual rotation at the gasket connection. The vertical displacements in the UPPER-1 porcelain unit were smaller, and there was no oil leakage and no residual uplift or rotation of the unit During Test No 37 (test with the terminal).

The zero-corrected stress histories for the UPPER-1 porcelain unit along the x-axis were studied by examining data from channels 39 and 41. The recorded strain data were converted to stress by multiplying the measured values by the porcelain modulus of elasticity (assumed to equal 97,000 MPa, see Chapter 2). The stress data for the test without the terminal are shown in Figure 4-26, and the stress data for the test with the terminal are shown in Figure 4-27. The stress histories shown in these figures are *relative* values and represent the change in porcelain stress during the earthquake simulator testing. In these figures, compressive stresses are designated as positive. To obtain the absolute stress in the UPPER-1 porcelain unit, the initial compressive post-tensioning stress of 0.9 ksi (6.2 MPa) has to be added to the values shown. As a result, data indicate no tensile stress in the UPPER-1 porcelain unit. During Test No 38 (test without the terminal), the relative stress values on the opposite sides of the UPPER-1 porcelain unit had opposite signs. On one side, there was additional compressive stress, whereas on the opposite side, some of the post-tensioning force was relieved. At the conclusion of the test, the residual stress in the UPPER-1 porcelain unit was positive on one side and negative on the other side. This observation is consistent with the differential residual vertical displacements discussed in the last paragraph. The strain gage data of Test No 37 (test with the terminal) show that the stress in the UPPER-1 porcelain unit was small — an observation consistent with the data presented in the last paragraph.

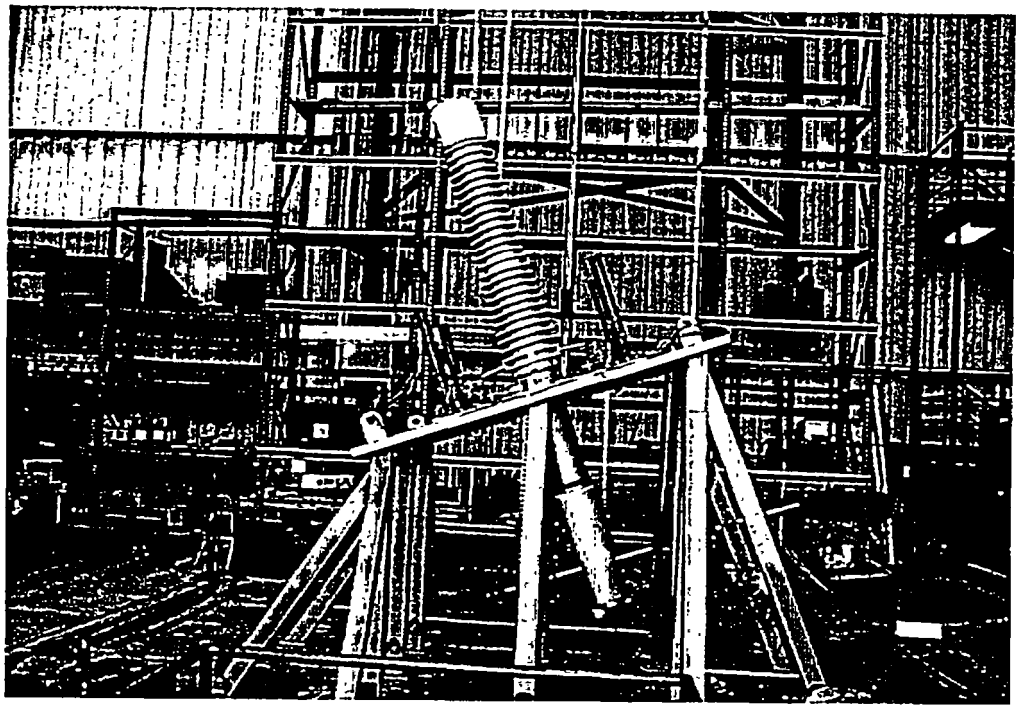

Figure 4-1 A rigidly mounted 230-kV bushing on the earthquake simulator

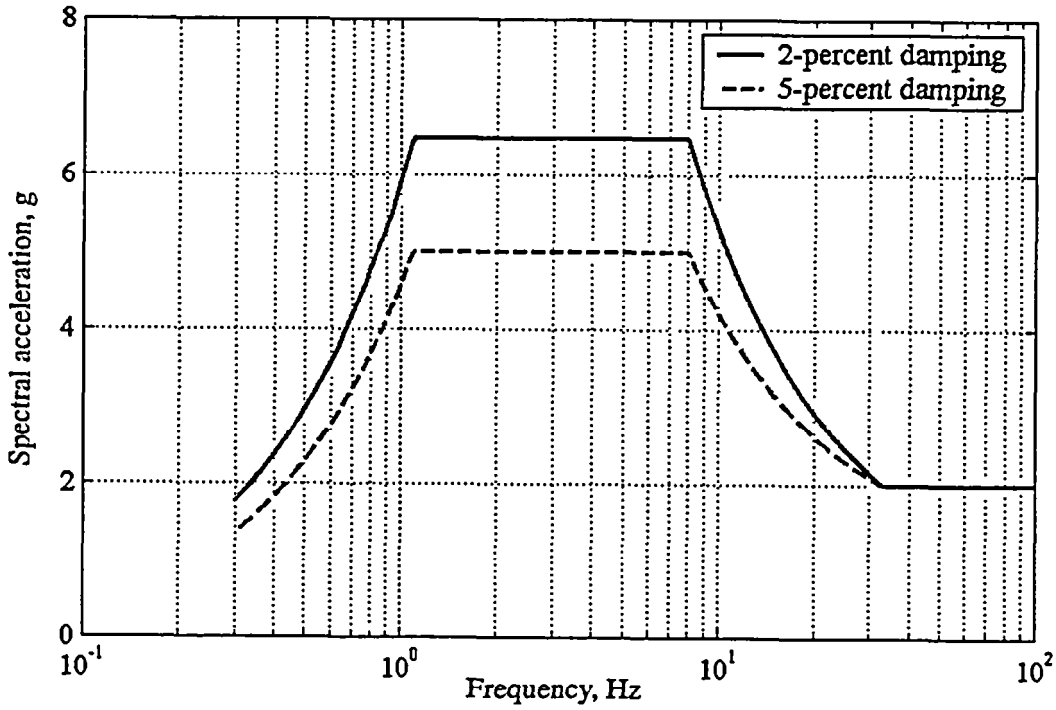

Figure 4-2 IEEE 693-1997 test response spectrum for High Level Qualification

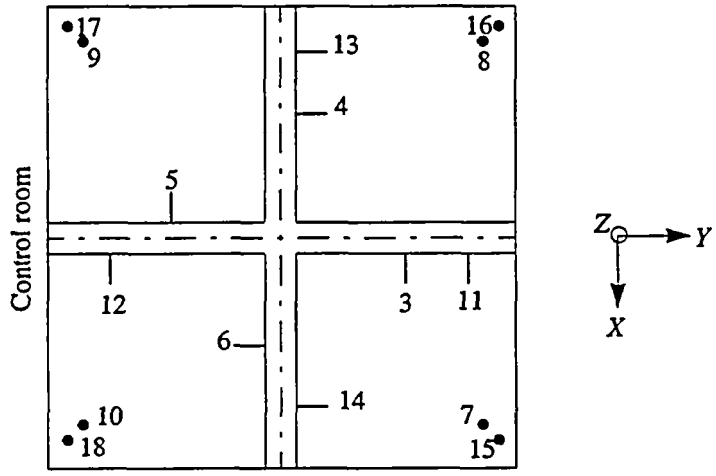

(a) Earthquake simulator (view from beneath)

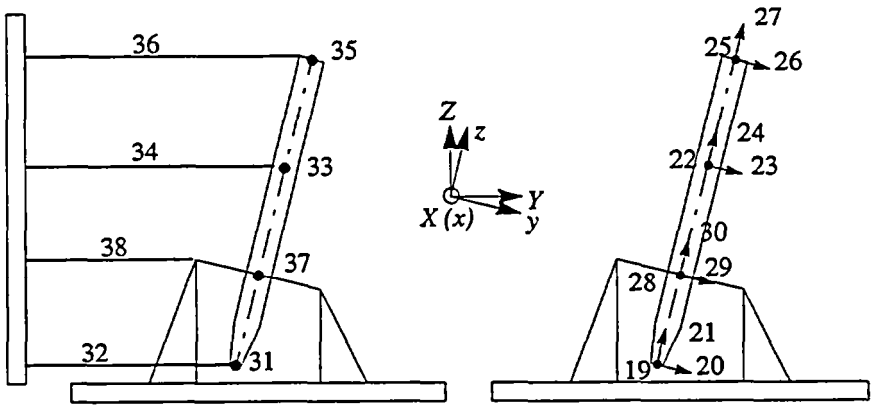

(b) Bushing and mounting frame

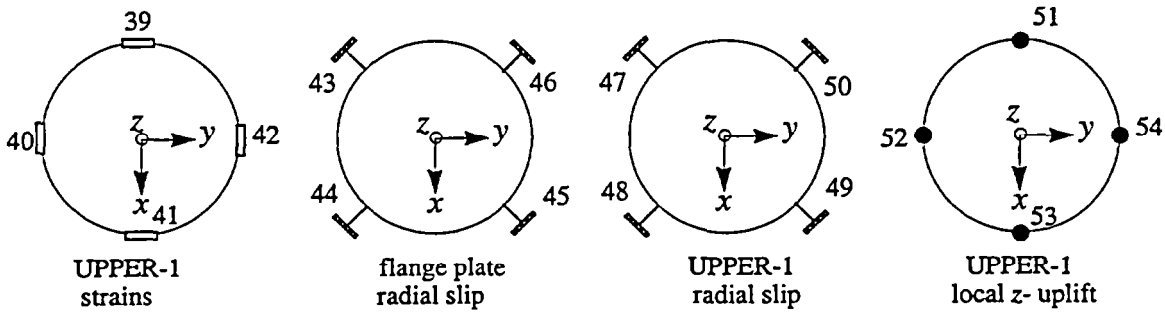

(c) UPPER-1 porcelain unit and flange plate

Figure 4-3 Instrumentation for 230-kV bushings

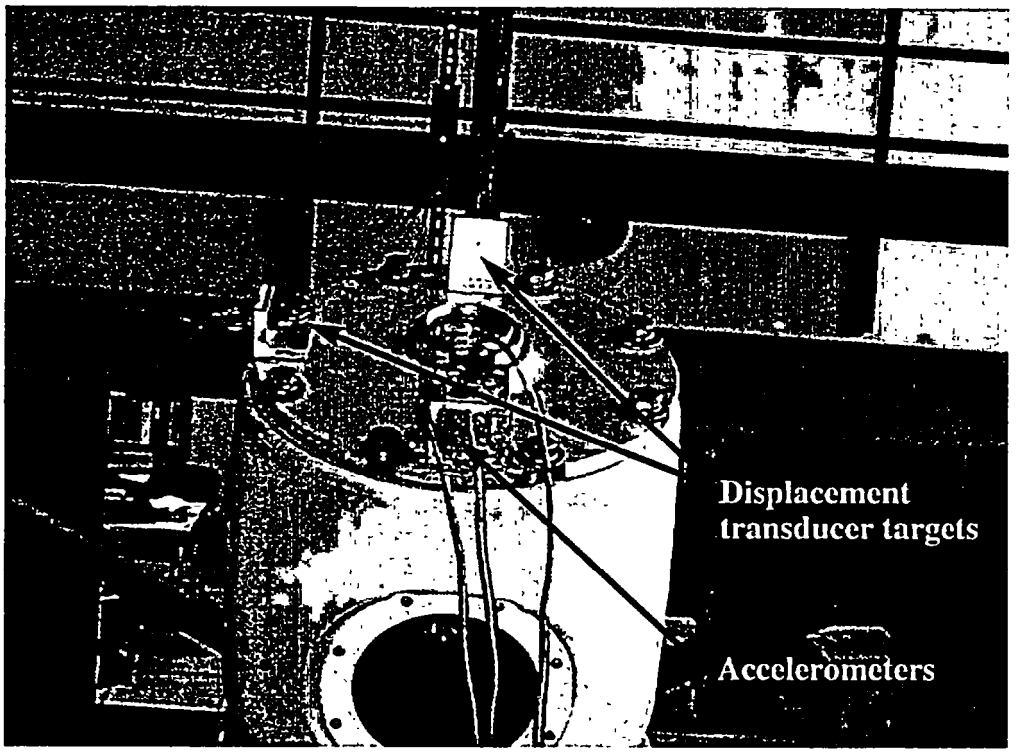

Figure 4-4 Instrumentation at top of Bushing-1

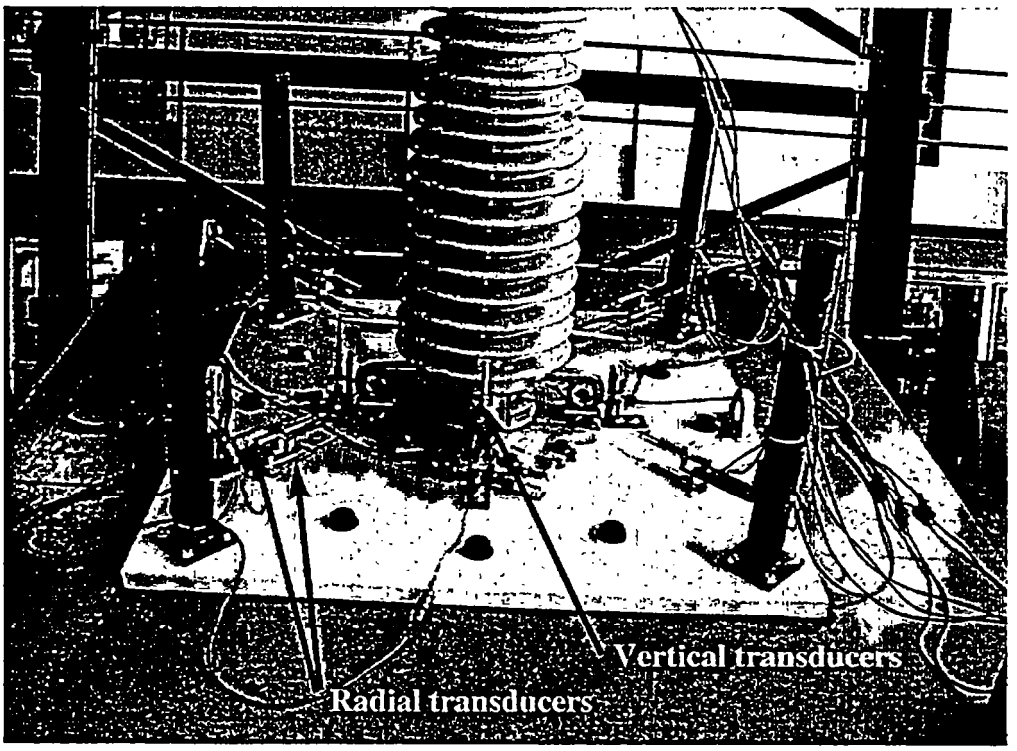

Figure 4-5 Instrumentation of the UPPER-1 porcelain unit

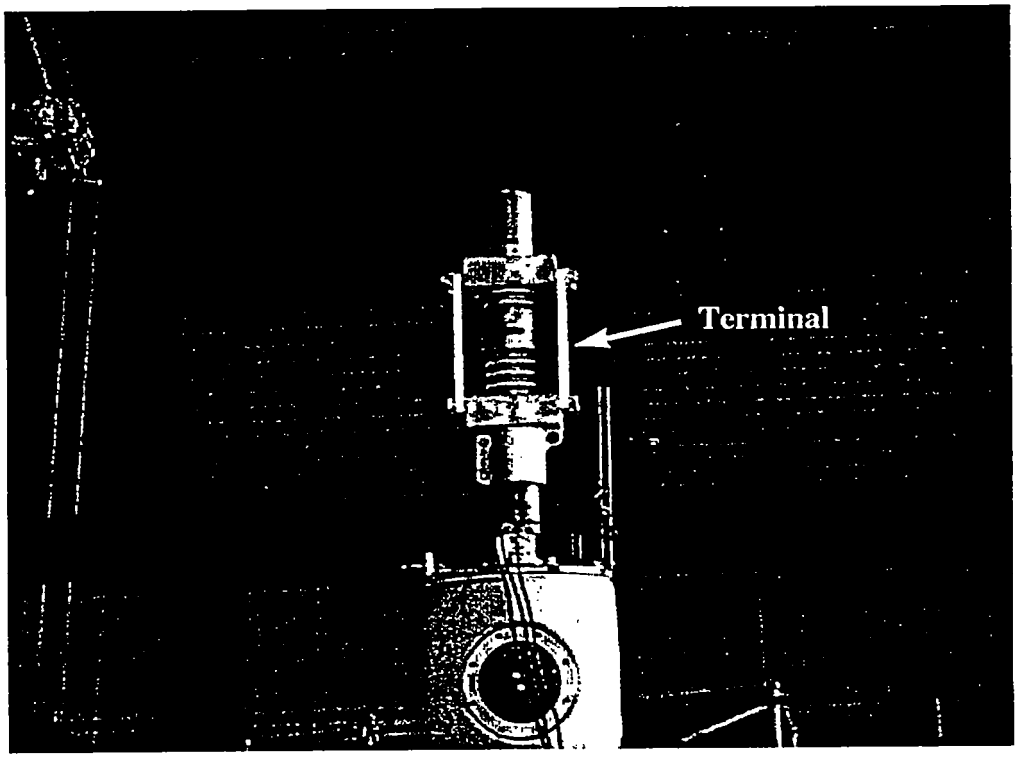

Figure 4-6 Terminal attached to the top of Bushing-2

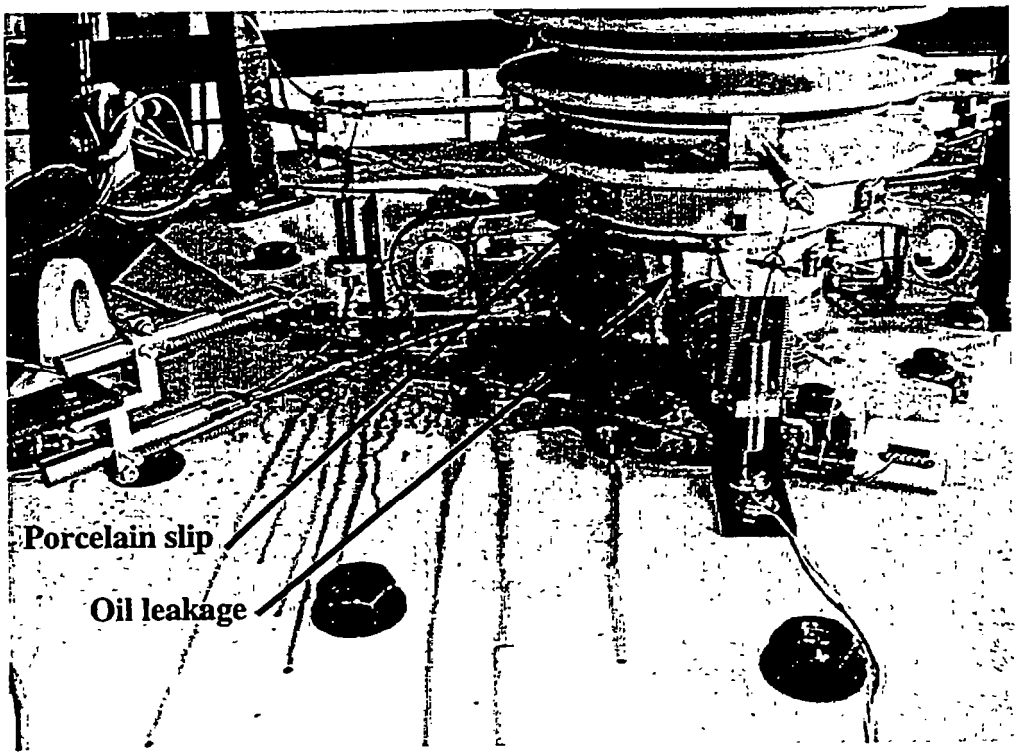

Figure 4-7 Bushing-2 after Test No 38 showing oil leakage and slip of porcelain

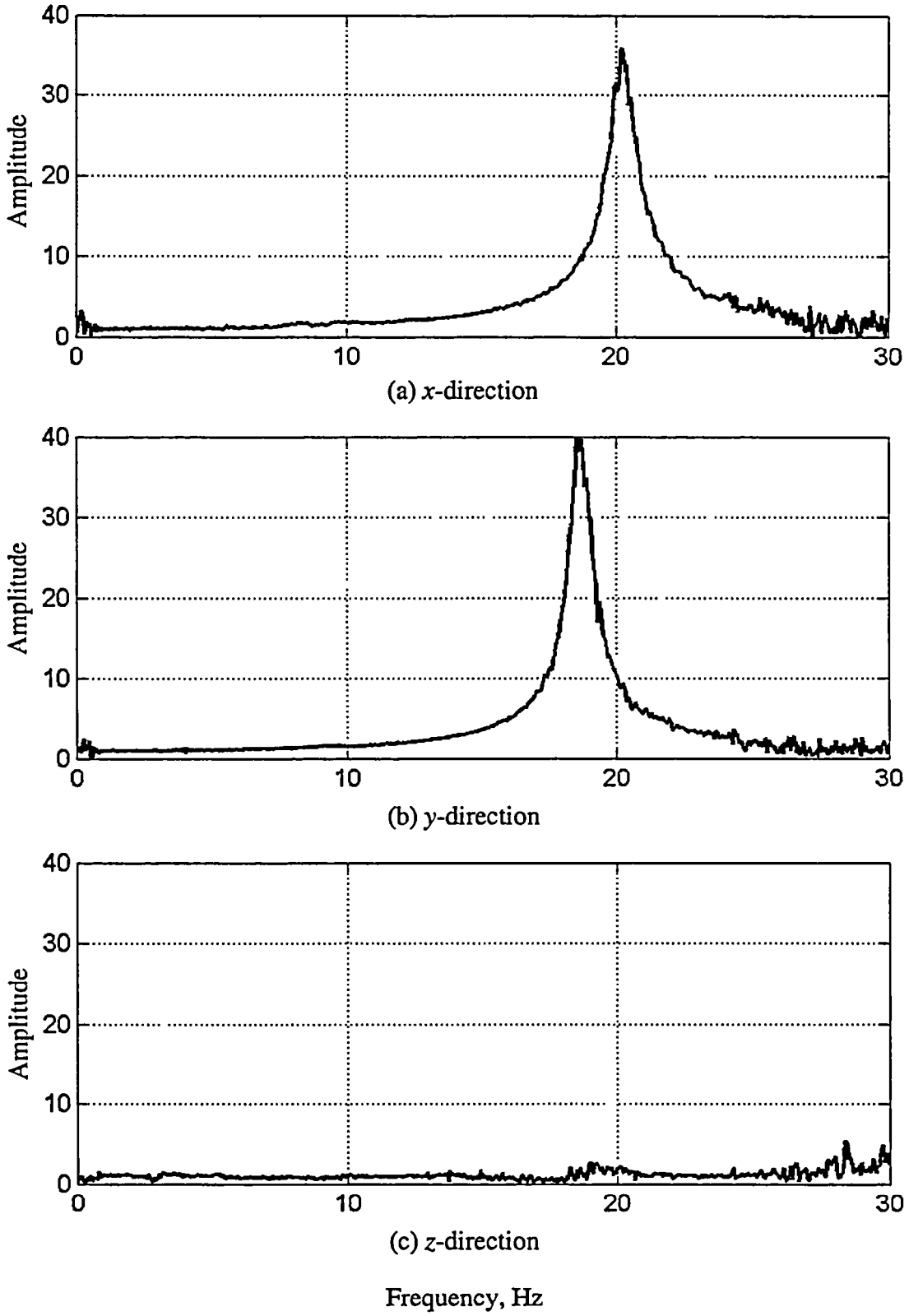

Figure 4-8 Transfer function amplitudes between the top of Bushing-1 and frame

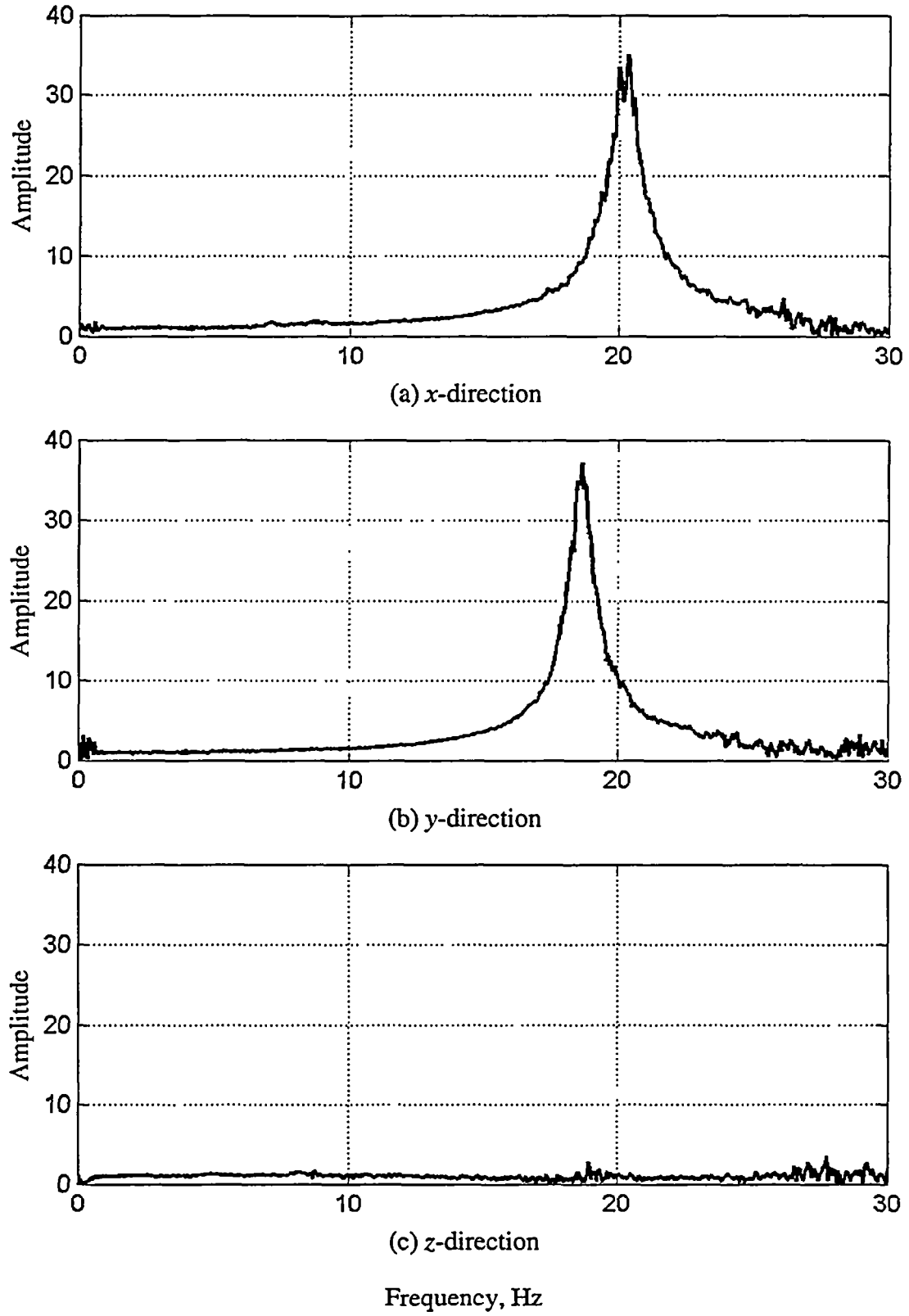

Figure 4-9 Transfer function amplitudes between the top of Bushing-2 and frame

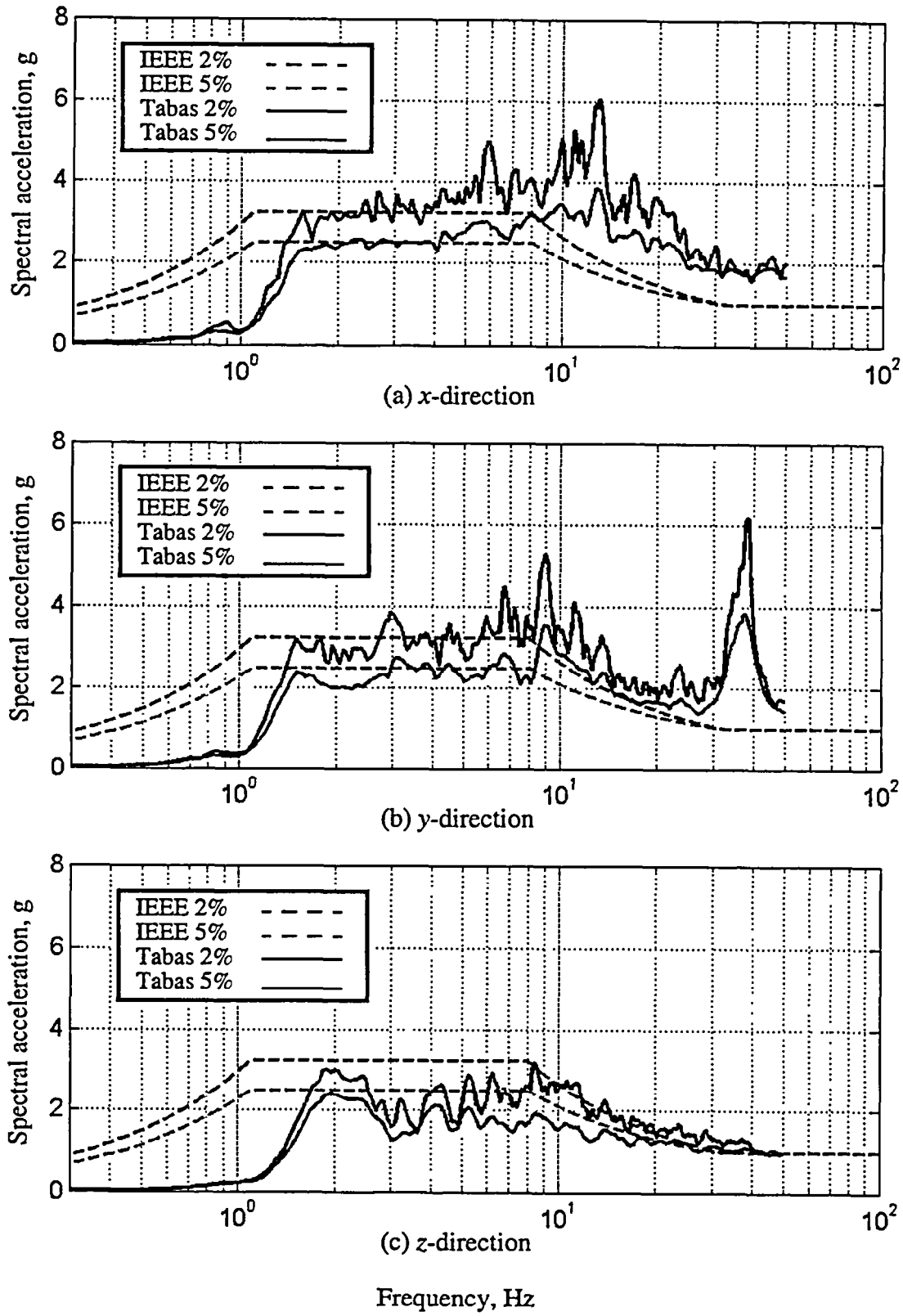

Figure 4-10 Response spectra for Bushing-1; Test No 12, target PGA=1.0g

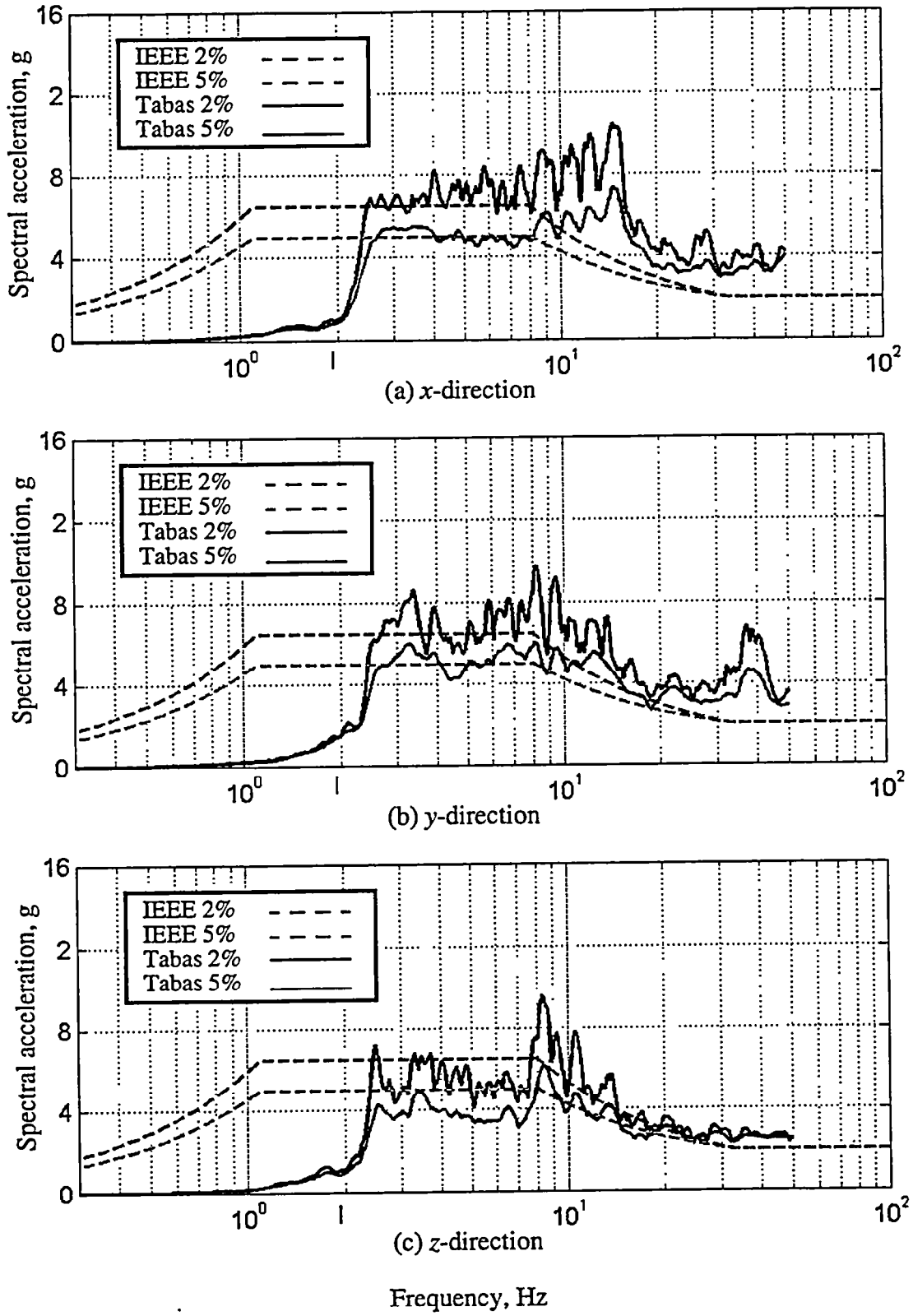

Figure 4-11 Response spectra for Bushing-1; Test No 17, target PGA=2.0g

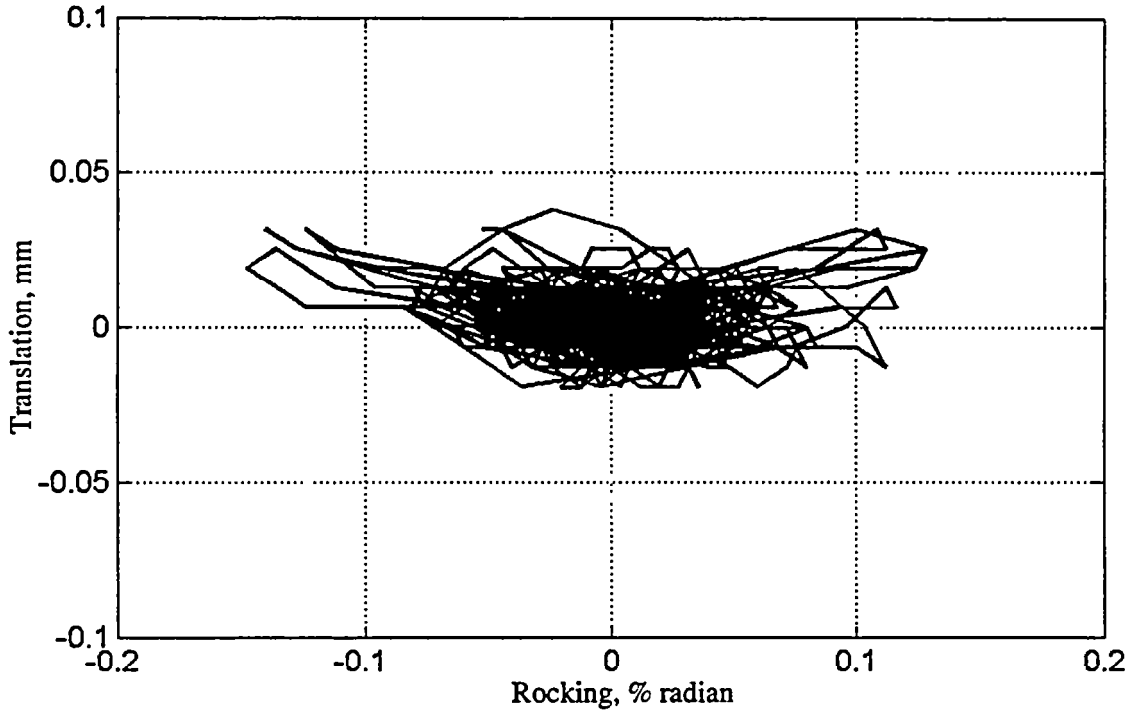

(a) About y- axis

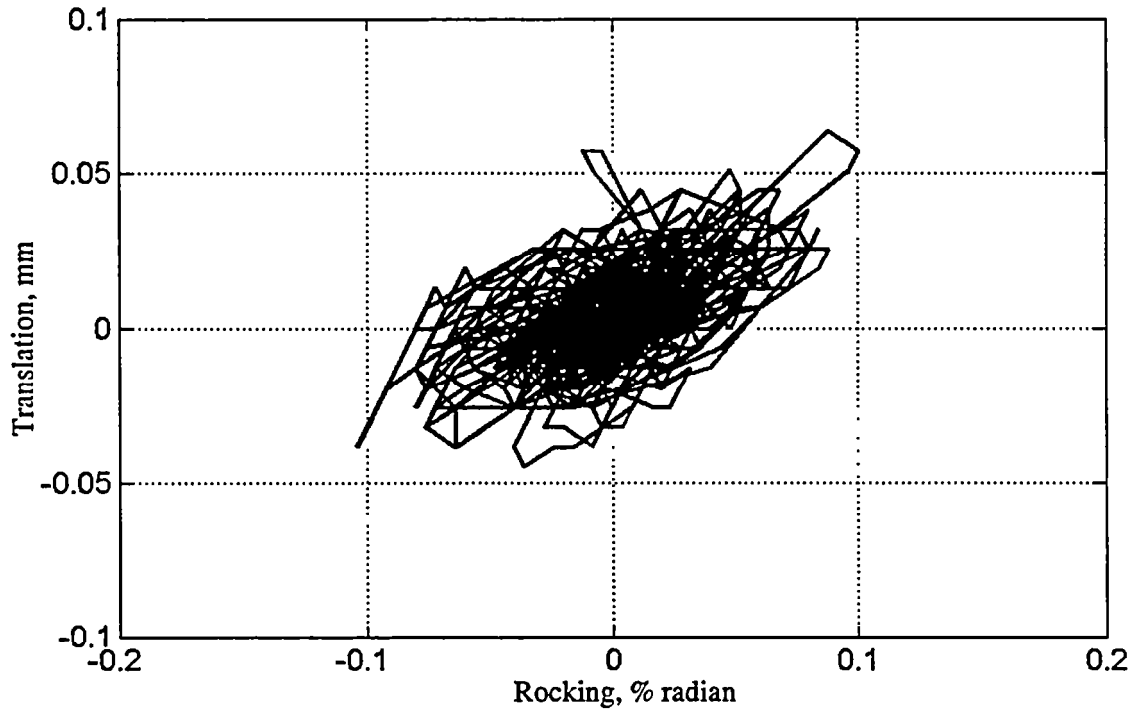

(b) About x- axis

Figure 4-12 Vertical displacement versus rocking for Bushing-1; Test No 17, target PGA=2.0g

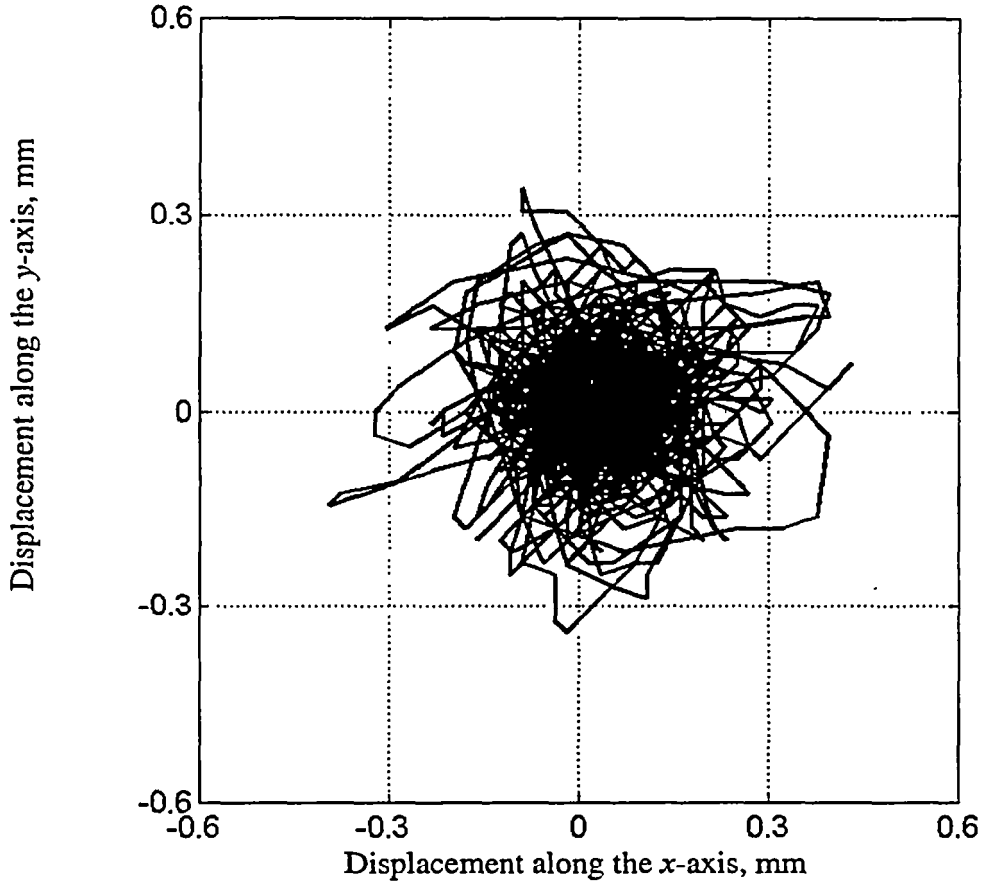

Figure 4-13 Orbit of motion for Bushing-1; Test No 17, target PGA=2.0g

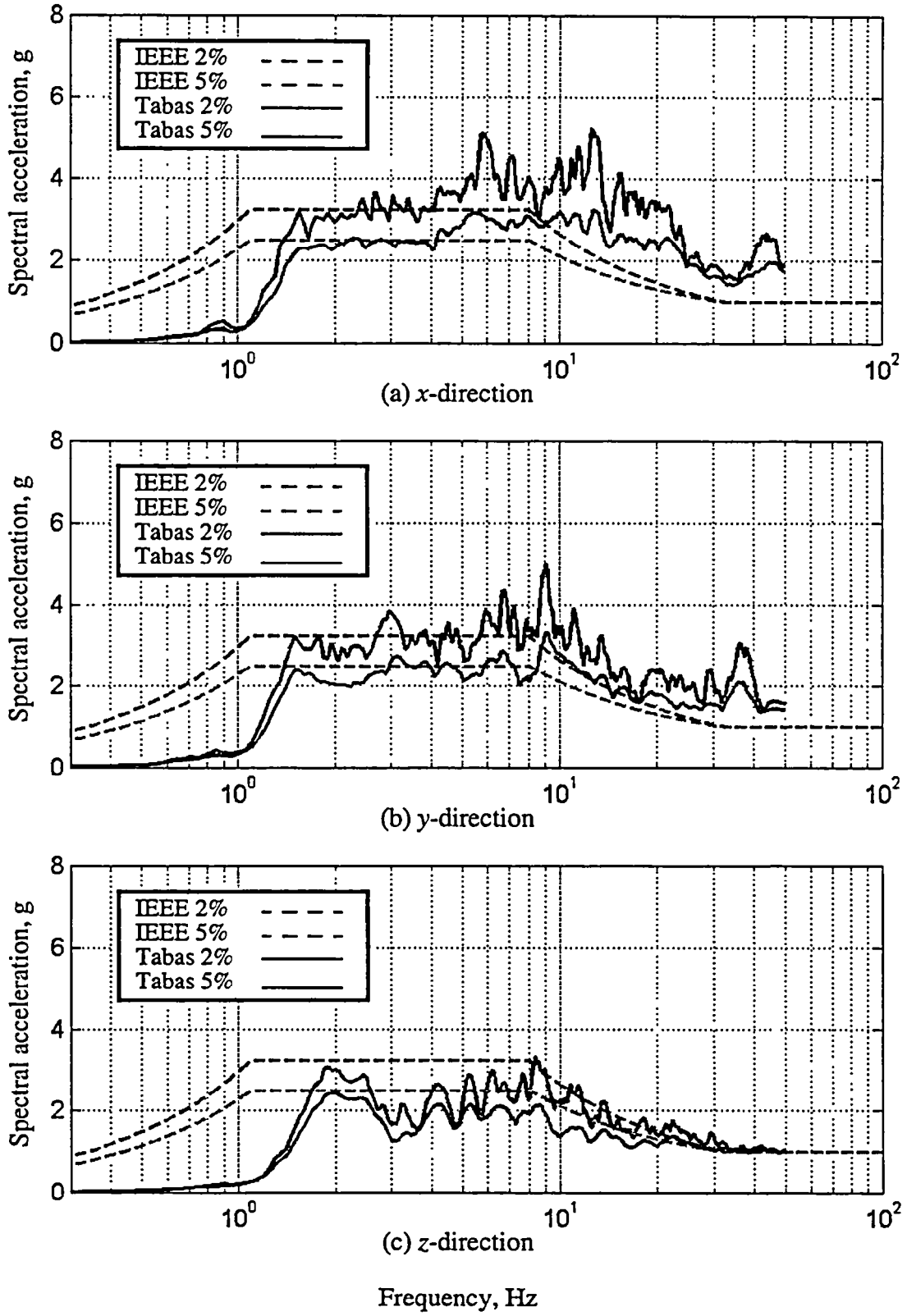

Figure 4-14 Response spectra for Bushing-2; Test No 19, target PGA=1.0g

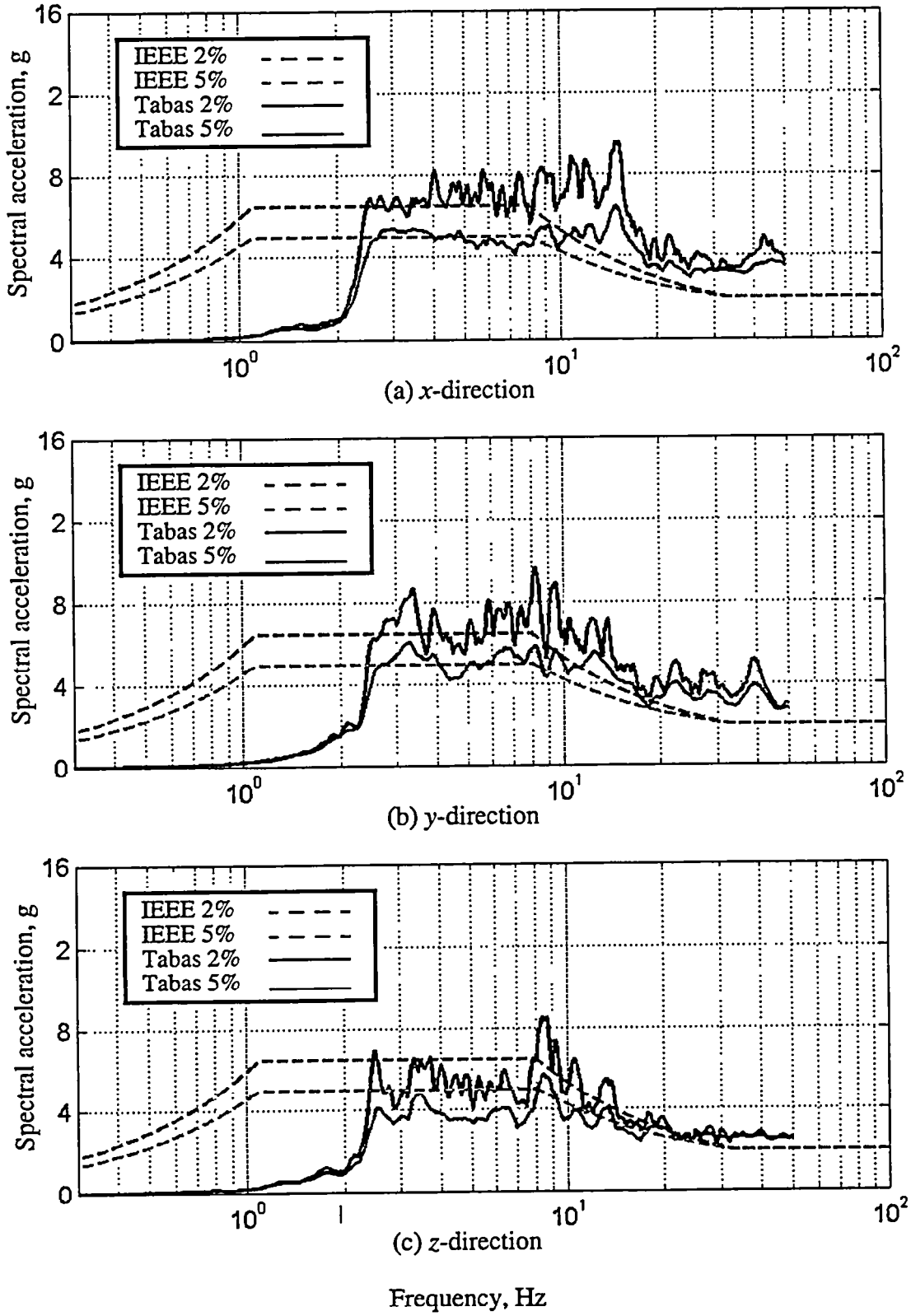

Figure 4-15 Response spectra for Bushing-2; Test No 24, target PGA=2.0g

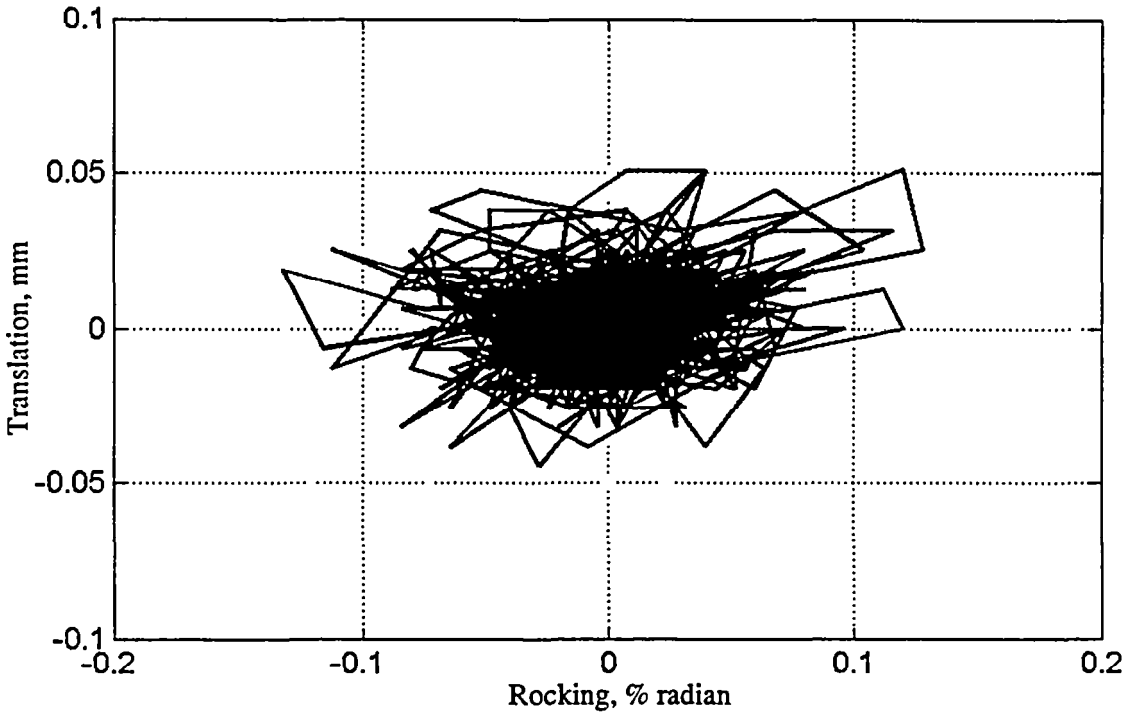

(a) About y- axis

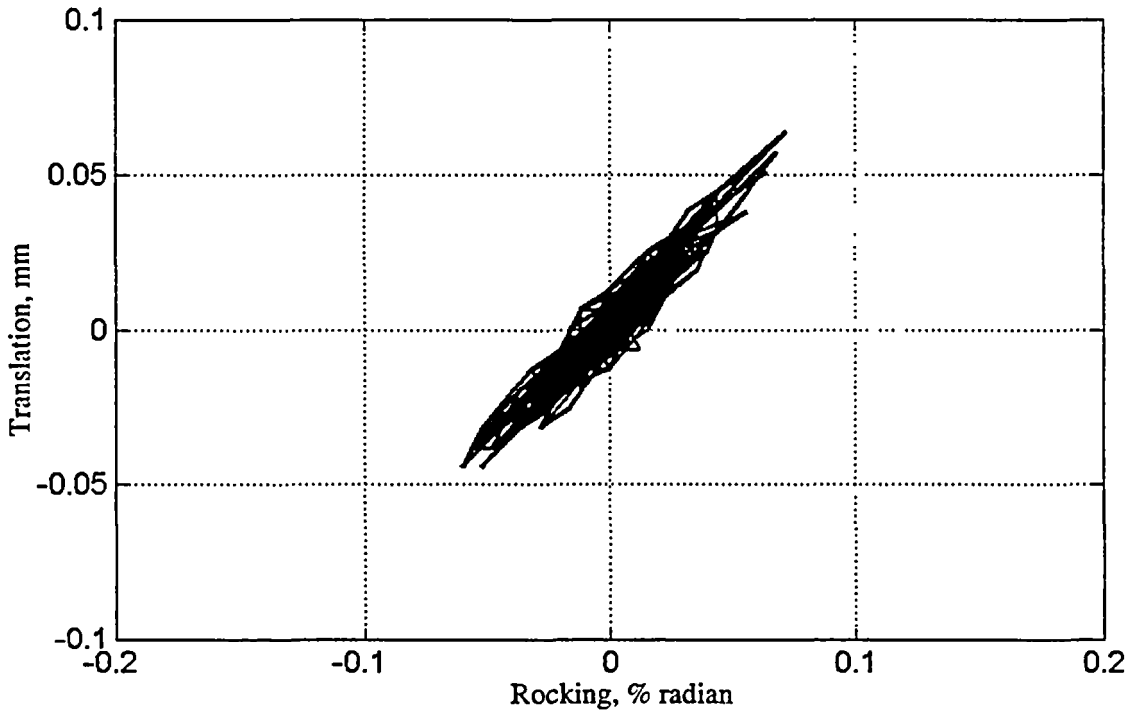

(b) About x- axis

Figure 4-16 Vertical displacement versus rocking for Bushing-2; Test No 24, target PGA=2.0g

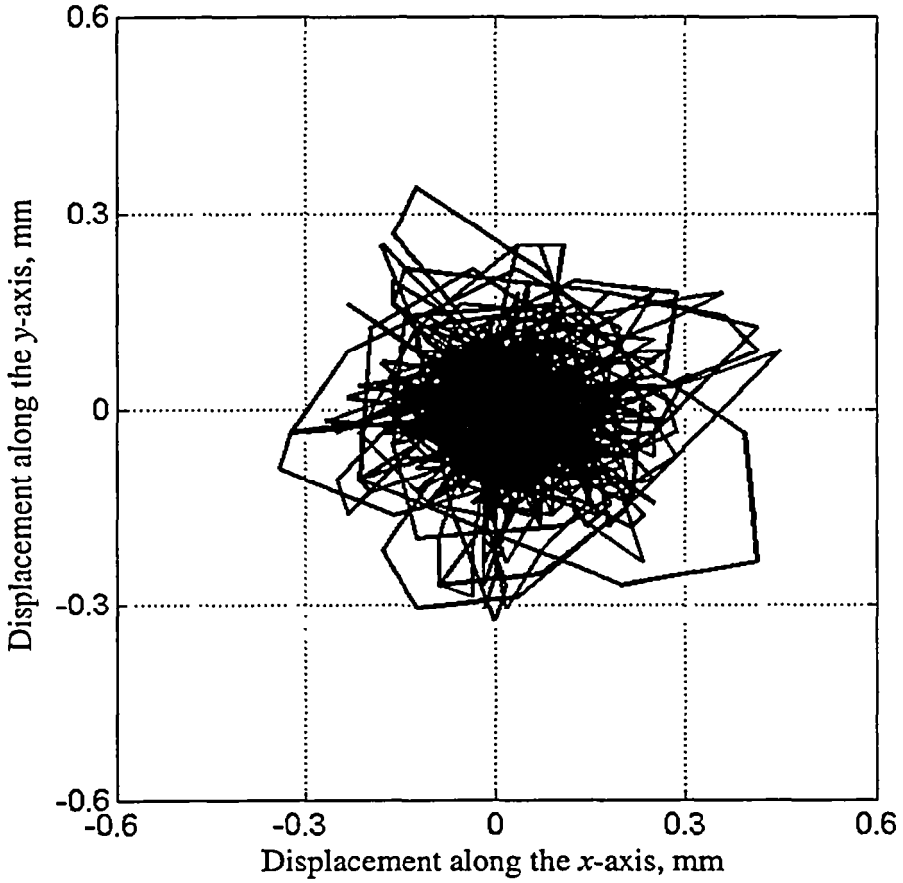

Figure 4-17 Orbit of motion for Bushing-1; Test No 24, target PGA=2.0g

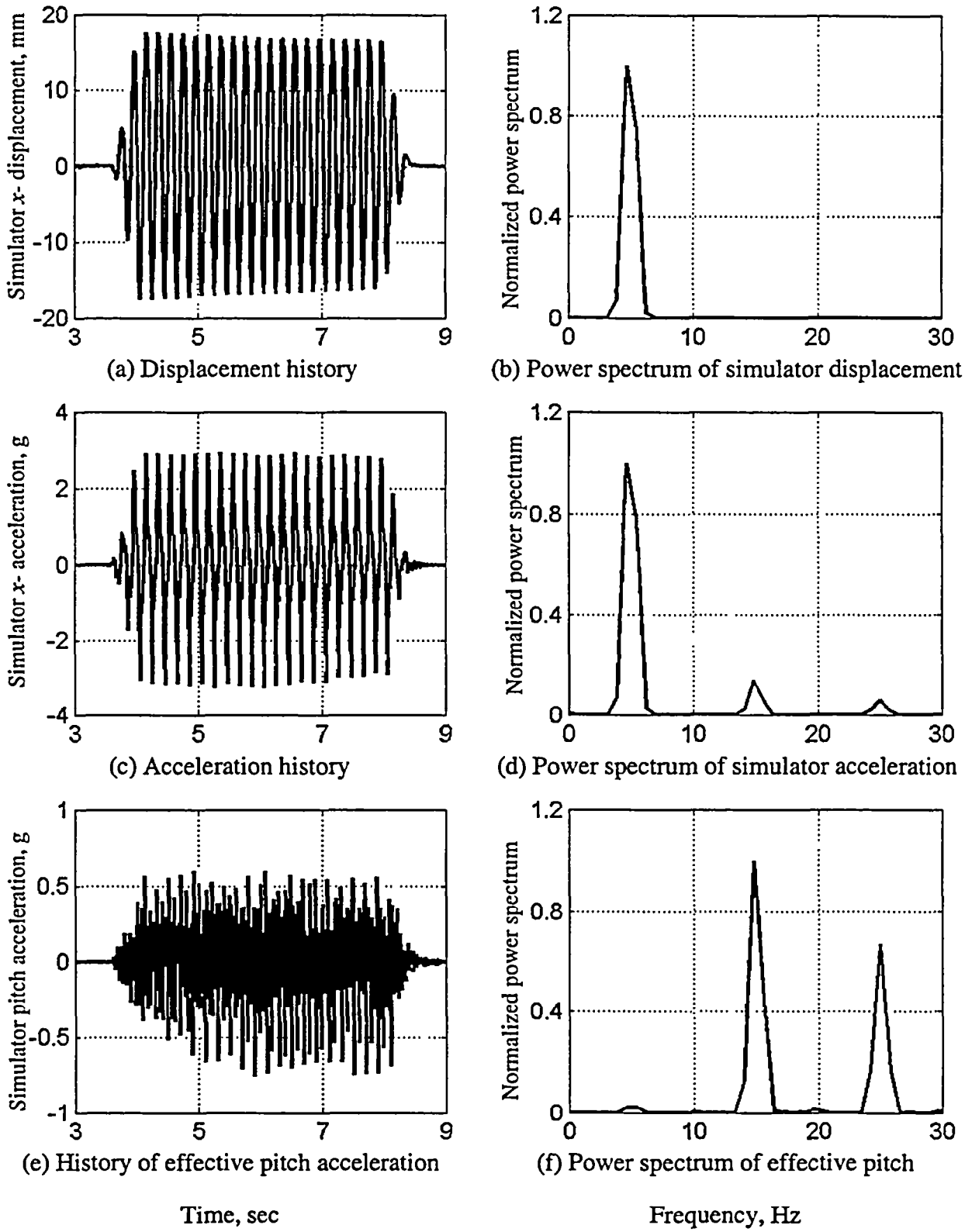

Figure 4-18 Simulator x- direction input for the high-amplitude 5-Hz harmonic tests, Test No 37

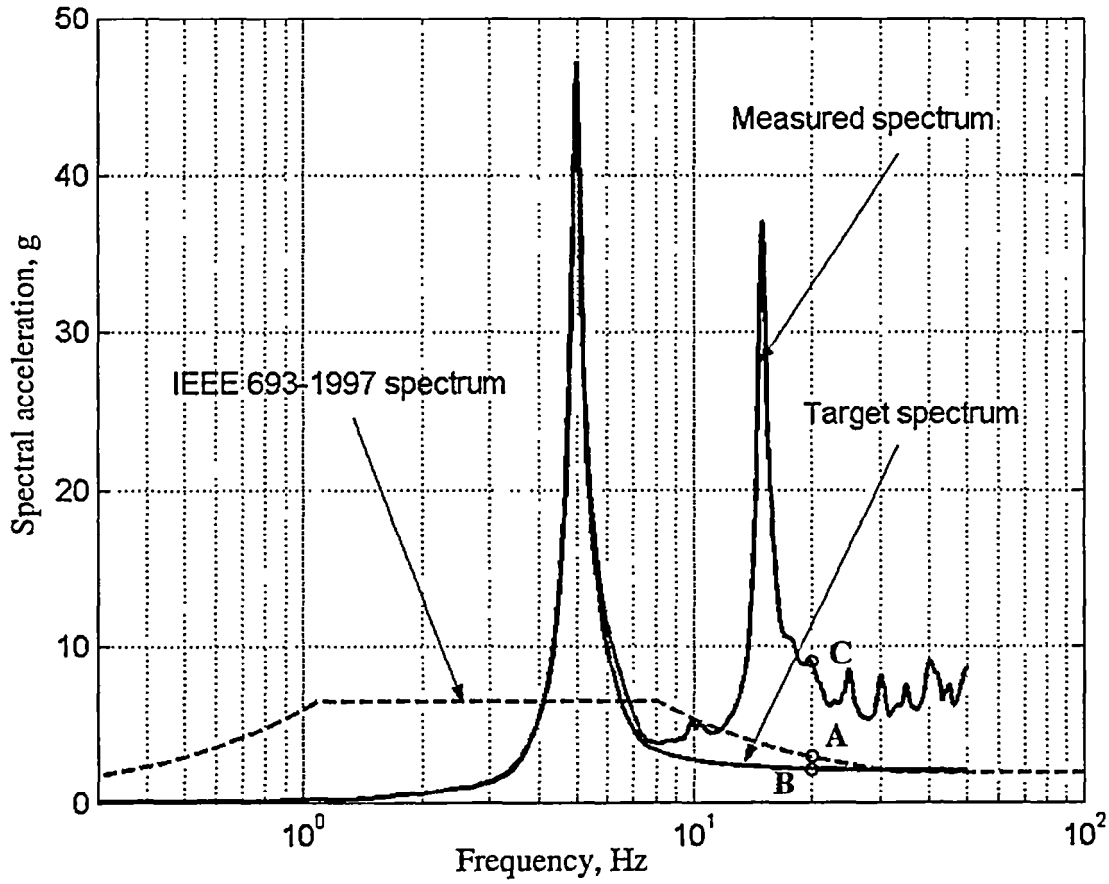

Figure 4-19 Response spectrum for high-amplitude harmonic tests

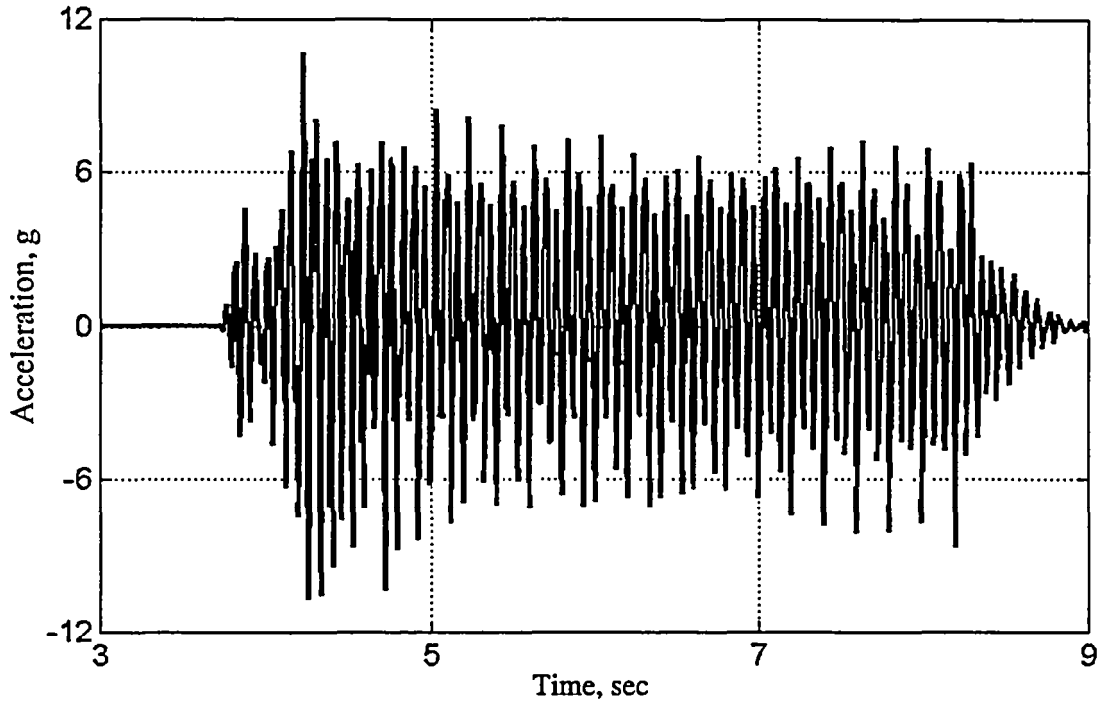

(a) History of the difference in acceleration between the top and bottom of bushing

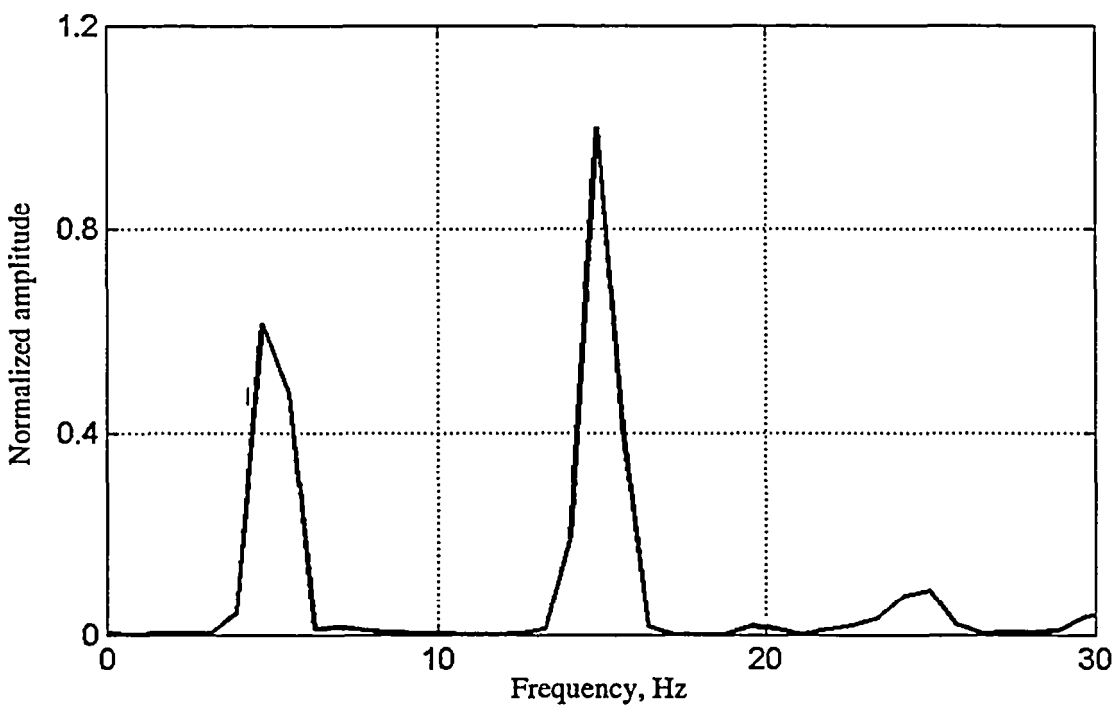

(b) Power spectrum for the acceleration at the top of the bushing

Figure 4-20 Acceleration response of Bushing-2 without terminal, Test No 38

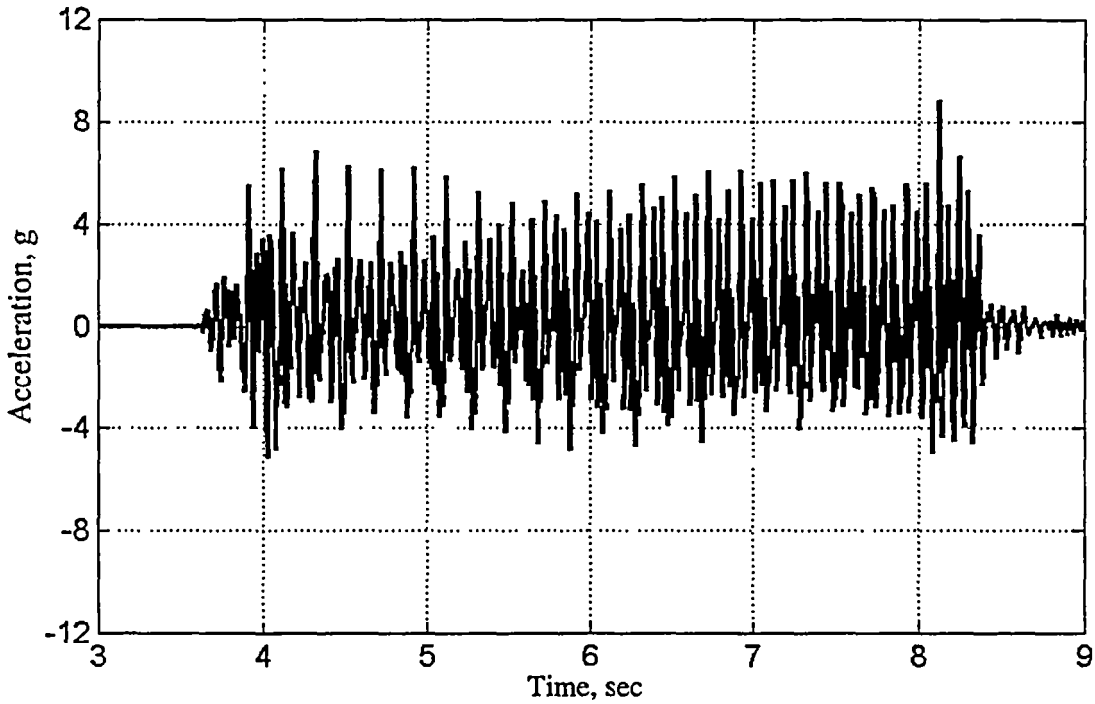

(a) History of the difference in acceleration between the top and bottom of bushing

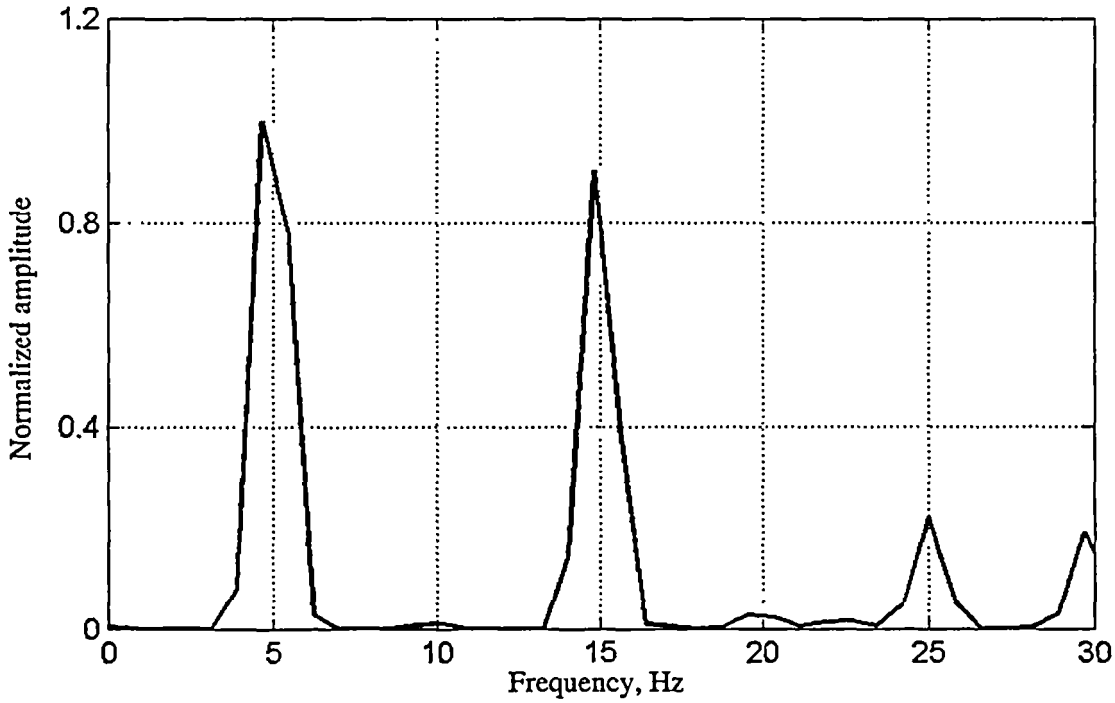

(b) Power spectrum for the acceleration at the top of the bushing

Figure 4-21 Acceleration response of Bushing-2 with terminal, Test No 37

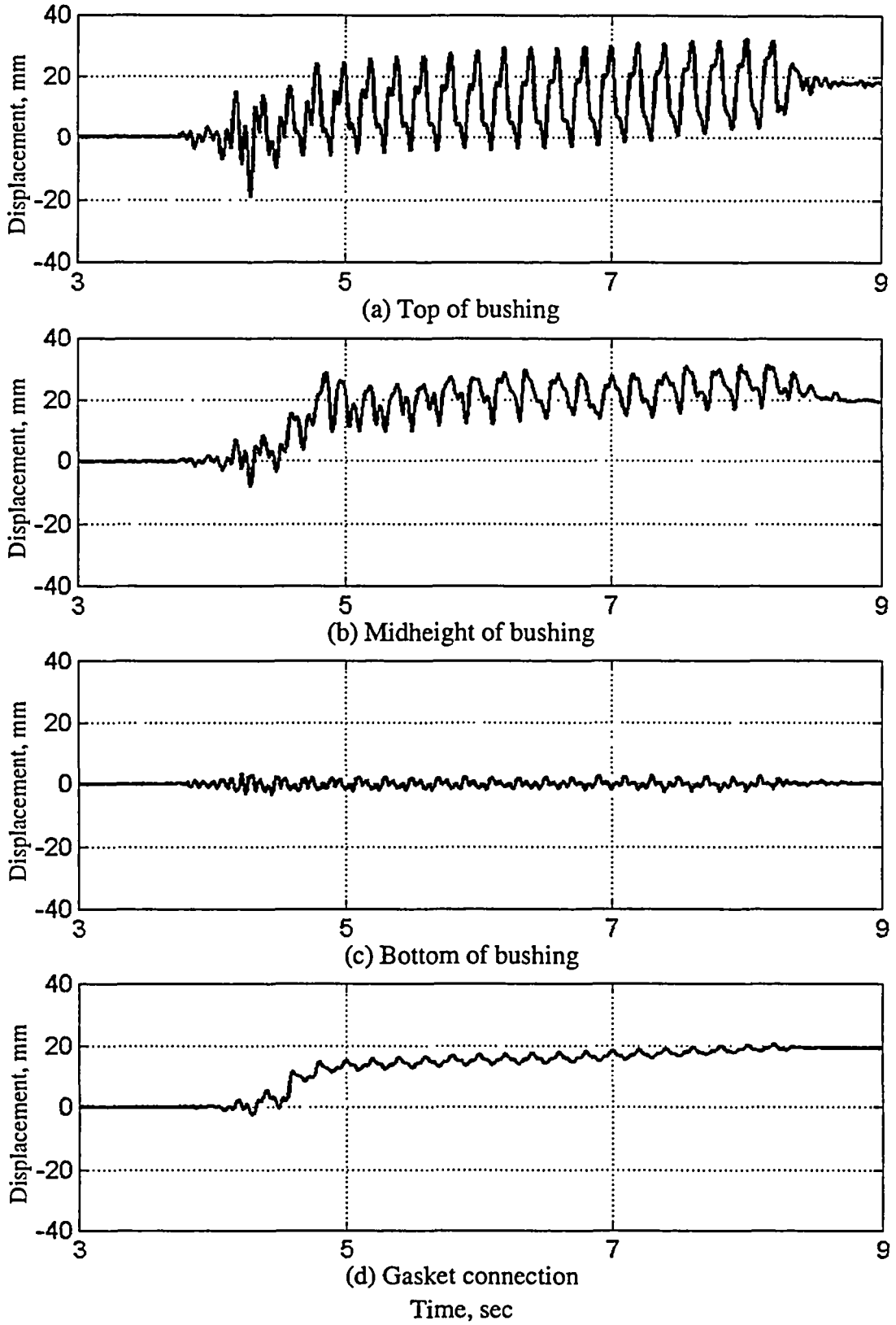

Figure 4-22 Displacement history of Bushing-2 relative to support frame, Test No 38

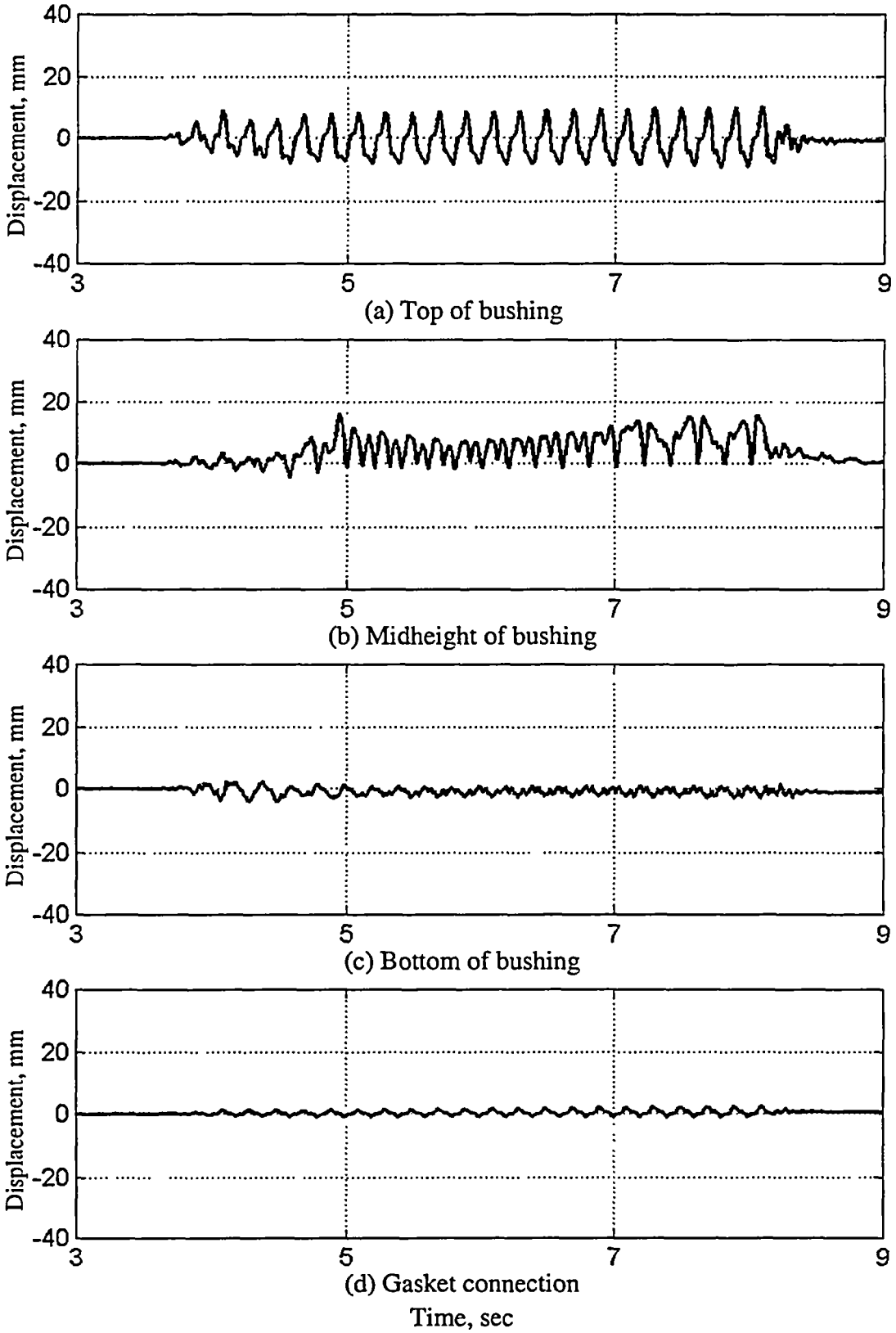

Figure 4-23 Displacement history of Bushing-2 relative to support frame, Test No 37

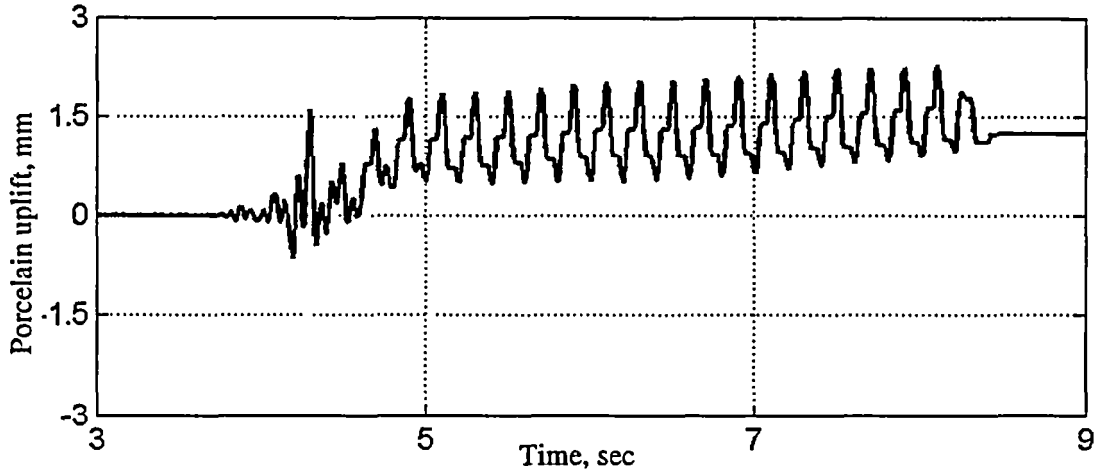

(a) Uplift history in x-direction (channel 51)

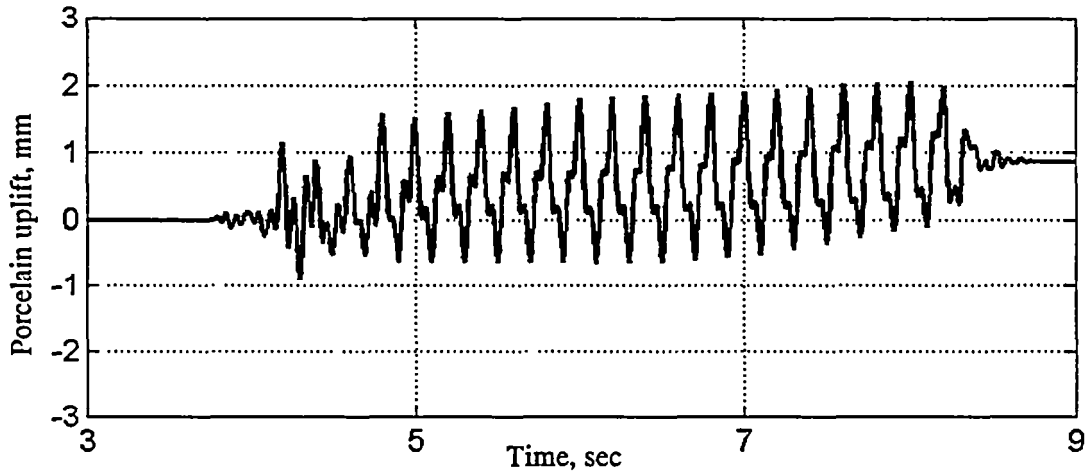

(b) Uplift history in x-direction (channel 53)

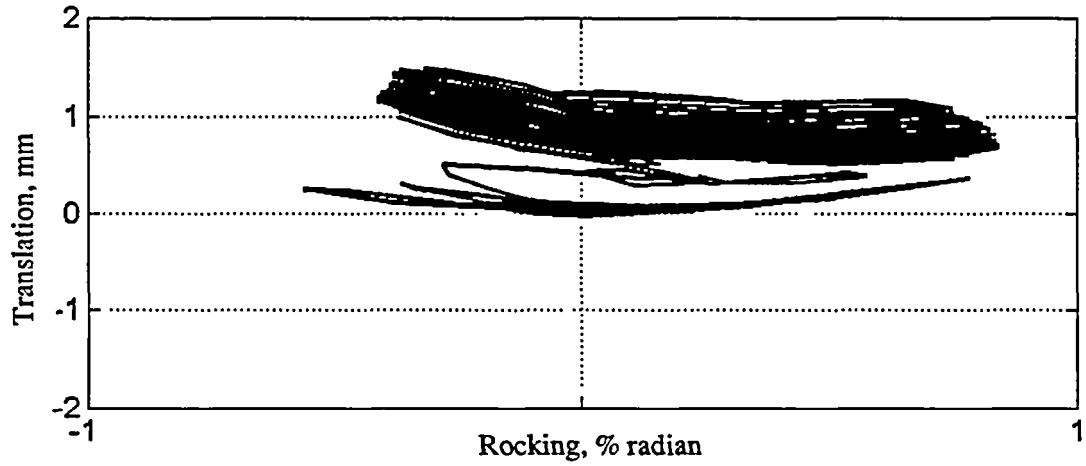

(c) Vertical displacement versus rocking about x-axis

Figure 4-24 Vertical displacement of the UPPER-1 porcelain unit, Test No 38

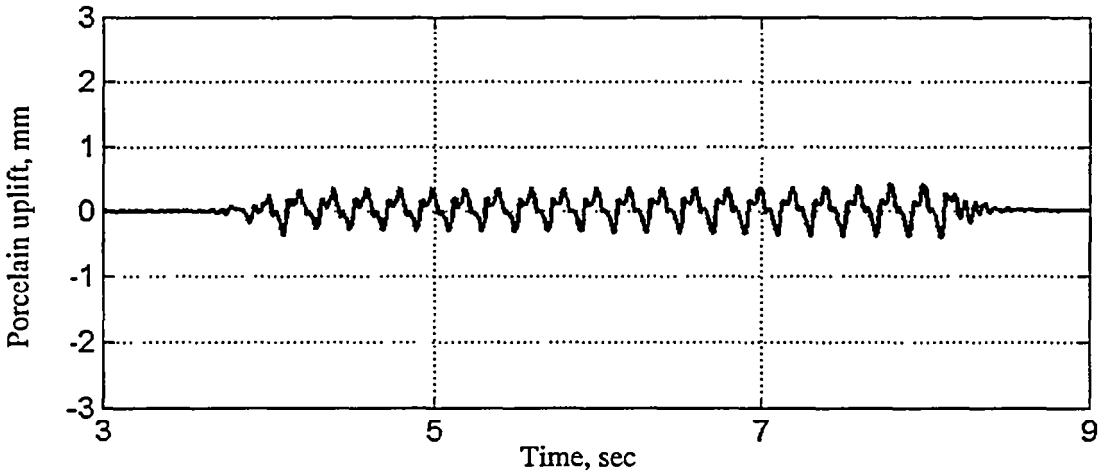

(a) Uplift history in x-direction (channel 51)

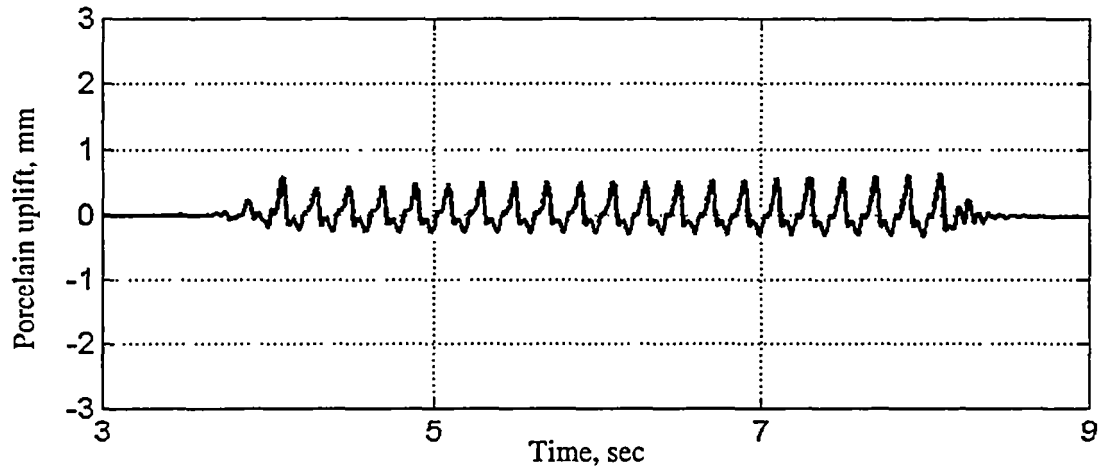

(b) Uplift history in x-direction (channel 53)

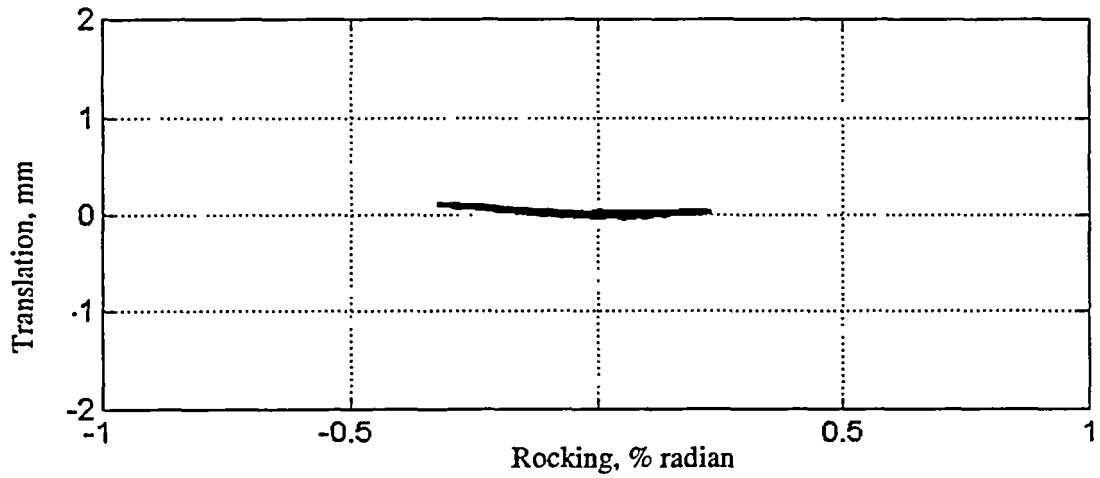

(c) Vertical displacement versus rocking about x-axis

Figure 4-25 Vertical displacement of the UPPER-1 porcelain unit, Test No 37

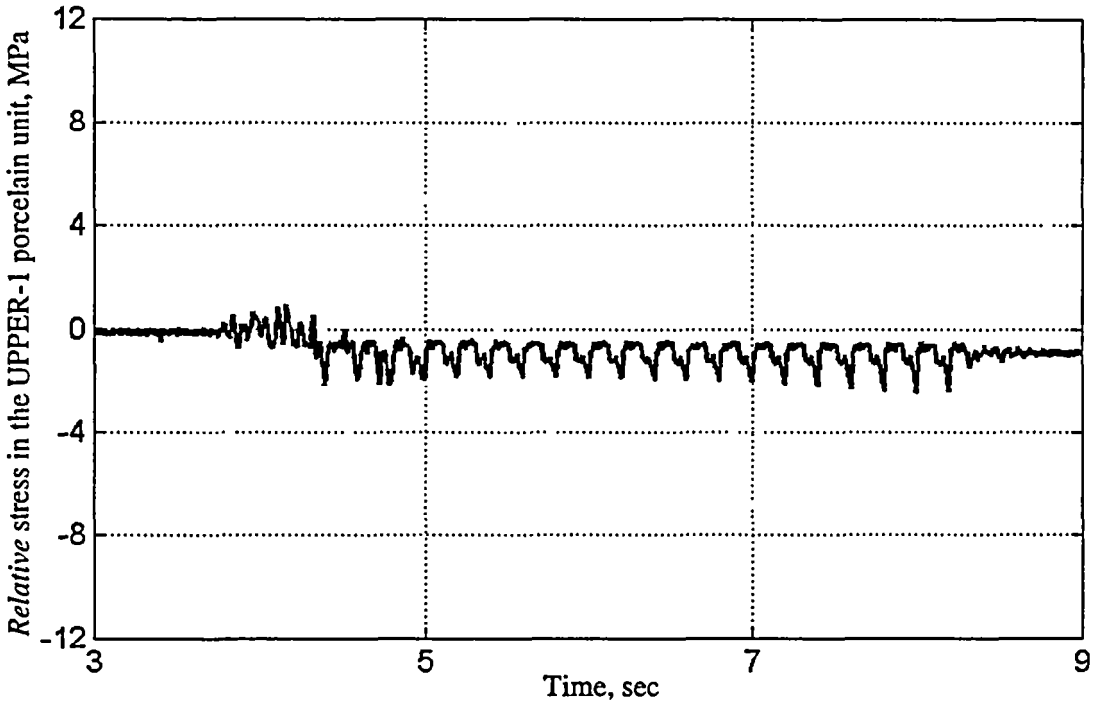

(a) Stress history of channel 39

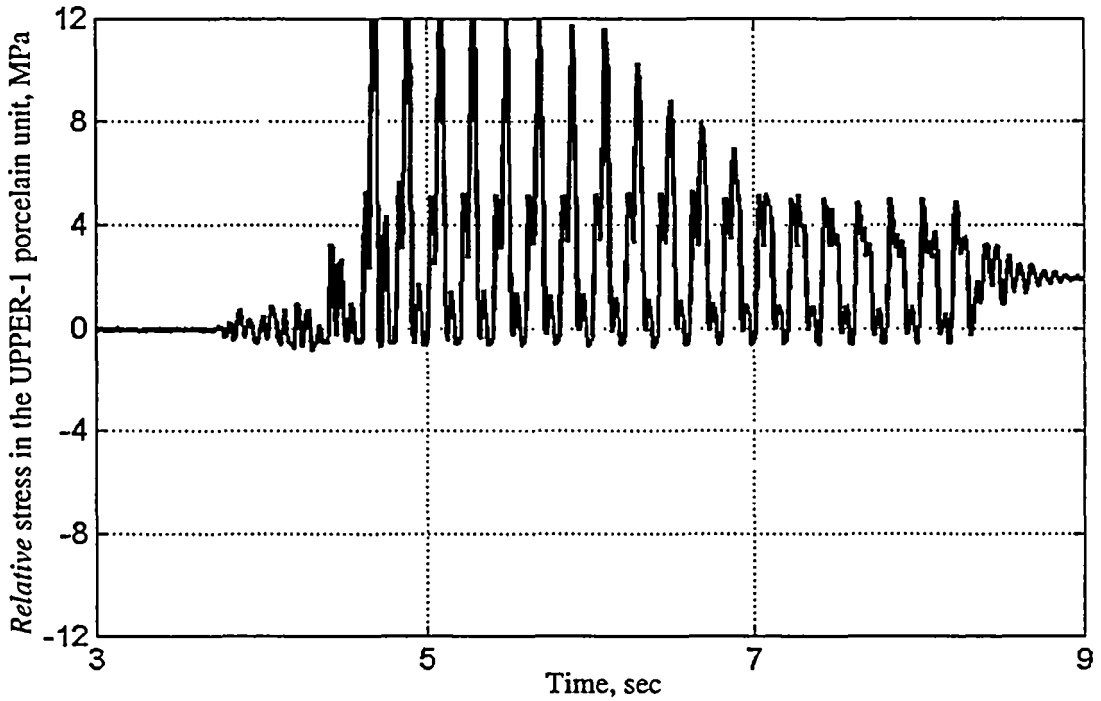

(b) Stress history of channel 41

Figure 4-26 Stress history of the UPPER-1 porcelain unit, Test No 38

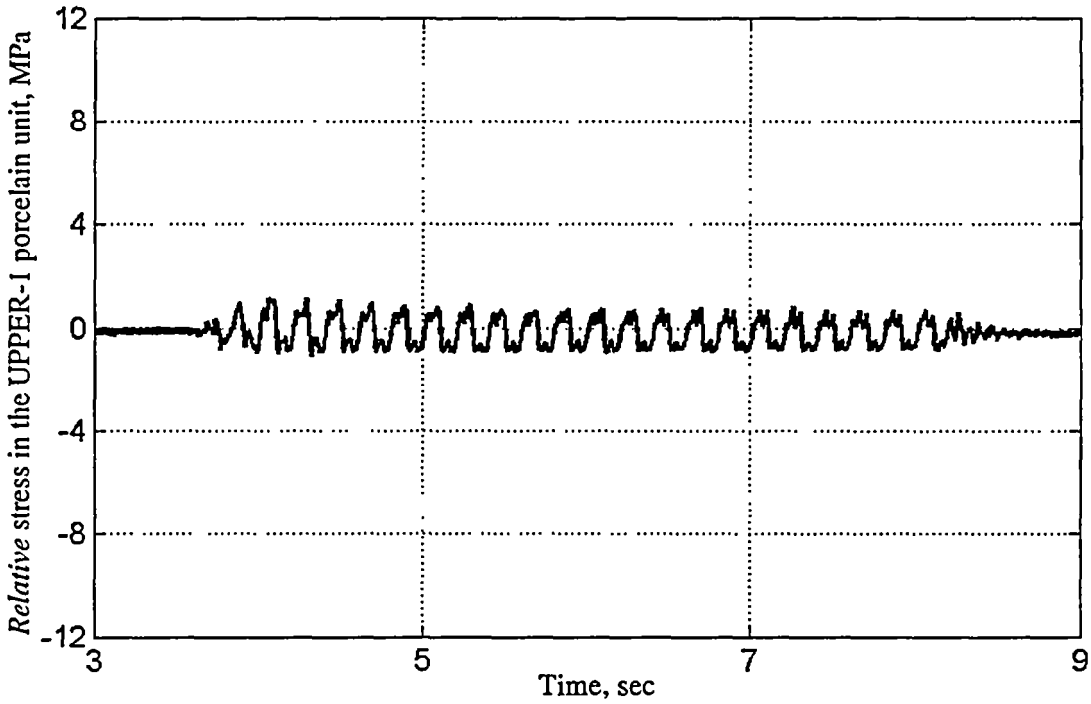

(a) Stress history of channel 39

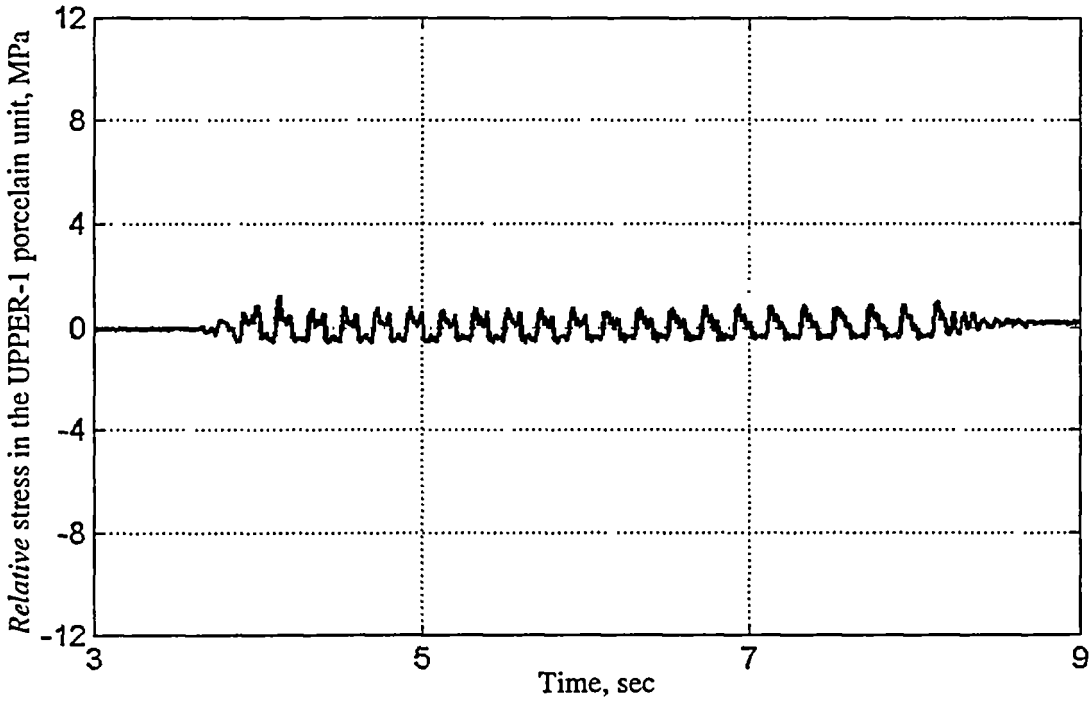

(b) Stress history of channel 41

Figure 4-27 Stress history of the UPPER-1 porcelain unit, Test No 37

5 Bushing Retrofit Details

5.1 Introduction

Oil leakage and excessive slip of the UPPER-1 porcelain unit over the flange have been observed in many porcelain bushings damaged in past earthquakes. Oil leakage is the most common failure mode and is caused by the uplift or rocking of the porcelain relative to the flange (see Chapter 2). Retrofitting in the field to eliminate oil leakage is difficult to achieve, since a more effective sealing or clamping mechanism would be required. Under emergency conditions such as those following a major earthquake, some utilities may choose to temporarily operate a transformer with a bushing that has leaked oil, provided that the gasket connection has re-sealed with only minor loss of oil, and there is high confidence that no internal damage has occurred. In contrast, most utilities will not operate a transformer bushing that has sustained large slip of porcelain relative to the flange. In a number of bushing failures, it has been hypothesized that excessive slip may have resulted in impact between the core tube condenser and the bushing flange. Damage to the condenser at the impact site, or contamination of the insulating oil in the bushing may have caused high electrical stresses that eventually lead to the bushing failures. Such bushing failures can be catastrophic and lead to costly transformer damage. In addition to preventing internal damage to the bushing components, reduction of slip displacement may limit the leakage of oil at the gasket connection by maintaining the porcelain in a central position, and possibly preventing gasket extrusion from the gasket connection, which has been observed in past failures. Reducing the slip displacement may therefore be an effective method of minimizing the damage sustained by porcelain bushings, and was the primary objective of the retrofit details developed by Dr. Schiff and the utilities.

The variation in bushing details poses a significant obstacle to developing a workable retrofit. Differing flange profiles, interferences caused by the lifting lugs and voltage tap fittings, and porcelain tolerances contribute to the need for a detail that can accommodate these variables. Because of difficulties, the detailing for the retrofit devices described in this chapter was not based on rigorous engineering analysis and design, and as such their details and effectiveness may not be readily extrapolated to other bushings.

5.2 Selection of a Candidate Retrofit Detail

Several criteria were used to develop the retrofit details for the bushings, namely, ease of application to different porcelain-to-flange interfaces (gasket connections), cost, and effect of the retrofit detail on the electrical functions of the bushing.

A retrofit detail using a ring, similar to shipping rings routinely used by manufacturers, was selected by the utilities and Dr. Schiff as the candidate detail. This detail is inexpensive and was intended to be placed around the gasket connection. A filler material was used to seal the gap between the inner face of the metal ring and the outer surface of the UPPER-1 porcelain unit. The primary intent of this detail was to restrain the porcelain from sliding over the flange.

For ease of installation, two semicircular rings were used. The two semicircular rings were bolted together as shown in Figure 5-1. To reduce the likelihood of slip of the UPPER-1 porcelain unit, the semicircular rings were extended approximately 1 in. (25 mm) above the gasket connection. Slots were cut in the lower part of the rings to accommodate the lifting lugs. The gap between the porcelain and the semicircular rings was grouted with a filler material. Three types of material were investigated: epoxy (silicone-brand), grout (cementitious), and rubber. The durability, elasticity, ease of placement, and electrical properties of the filler were evaluated.

5.3 Retrofit Rings

5.3.1 Introduction

Two retrofit rings were detailed for the testing program. Ring-1 was used for the static testing of Bushing-1. Ring-2 was used for the seismic testing of Bushing-2. Both rings used the same filler material. Ring-2 was a modified version of Ring-1 and was developed to both increase the bond between the filler and the ring and to prevent uplift and rotation of the ring.

5.3.2 Epoxy filler material

The filler material used for the retrofit rings was *CCS Bonder, Polyurea LWL* (Long Working Life) manufactured by ChemCo Systems Inc. of Redwood City of California. This material is a two-component (Part A or resin and Part B or hardener) elastomeric polyurea bonder designed for both interior and exterior use. The manufacturer recommends that the users remove any standing water from the surface prior to the application of the material. When mixing the two components, the proportions must be kept within 5 percent of the manufacturers recommended mix ratio of one-to-one. Proper mixing of the two components takes approximately two to three minutes and it is recommended that the material be allowed to cure overnight. The recommended minimum substrate temperature is 50° F (11° C). The material safety data sheet for the material indicates that it is of moderate hazard and does not require any special handling. The material can be cleaned with soap and water before it hardens. A safe solvent for the polyurea is DuPont DBE-6 Dimehyl Adipate (Dibasic Ester). A bond-breaker compound was applied to the ring and the bushing surface prior to placement of the ring to prevent the filler from bonding either to the ring or the bushing to facilitate removal and installation during the test program.

5.3.2.1 Geometry of Ring-1

Figure 5-1 shows the geometry of Ring-1. It was composed of two semicircular 1/4-in. (6-mm) thick 1.5-in. (38-mm) tall, plates bent to an inner radius of 14 in. (356 mm); 2 in. (51 mm) by 2.5 in. (64 mm) steel tabs were fillet welded to the semicircular rings. The two semicircular rings were connected by two 0.5 in. (13 mm) bolts at each end; 1-in. (25-mm) square washers were used to fill the gap between the semicircular rings.

Ring-1 was designed and installed to provide a uniform 5/8-in. (16-mm) gap (to be grouted with epoxy) between the inner surface of the ring and the outer surface of the porcelain. Holes were drilled and tapped in the ring around its circumference; 3/8 in. (10 mm) bolts were used to maintain the gap (the bolts were removed once the gap was grouted). To accommodate the lifting lugs, two notches were cut in the ring. The ring was placed such that the lower edge of the UPPER-1 porcelain unit was approximately 3/4 in. (19 mm) above the lower edge of the ring. Figure 5-3 shows Ring-1 placed around Bushing-1 during the static tests of the bushing.

5.3.3 Retrofit Ring-2

During the cyclic tests of Bushing-1, Ring-1 separated from the epoxy, rotated with respect to the bushing, and uplifted. Ring-1 improved the response of the 230-kV bushing only marginally. The detail was modified by Dr. Schiff and the utilities, and designated as Ring-2. The gap between the two semicircular rings was eliminated by reducing the gap between the porcelain and the ring from 5/8 in. (16 mm) to 3/8 in. (10 mm), and 1/2-in. (13-mm) thick steel angles were used to secure the ring to the bushing to prevent uplift of the ring.

Figure 5-2 shows the geometry of Ring-2. Ring-2 was designed and installed to provide a uniform 3/8 in. (10 mm) gap (to be grouted with epoxy) between the inner surface of the ring and the outer surface of the bushing. Ten steel tabs made from 3x3x1/2 in. (76x76x13 mm) steel angle sections were bolted to the ring at the location of the 3/8 in. (10 mm) threaded holes. The tabs were clipped under the bushing flange to prevent the uplift and rotation of the ring. The ring was placed such that its centerline coincided with the centerline of the gasket at the gasket connection. Figure 5-4 shows Ring-2 prior to placement around the gasket connection of Bushing-2.

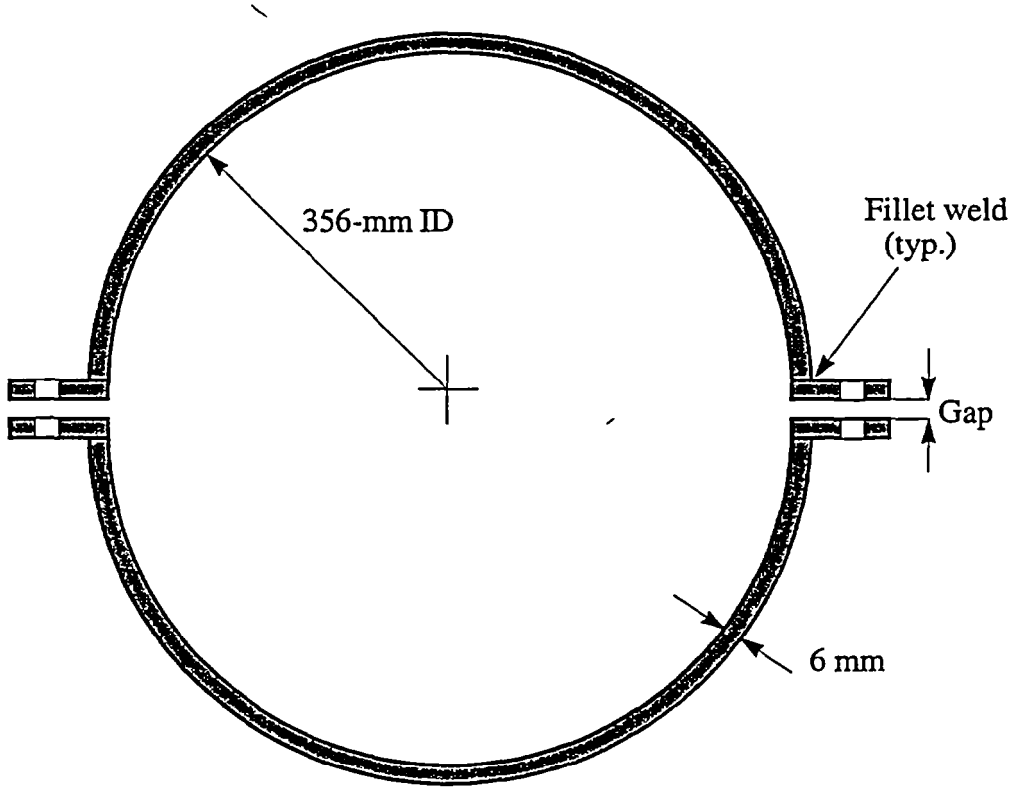

(a) Plan

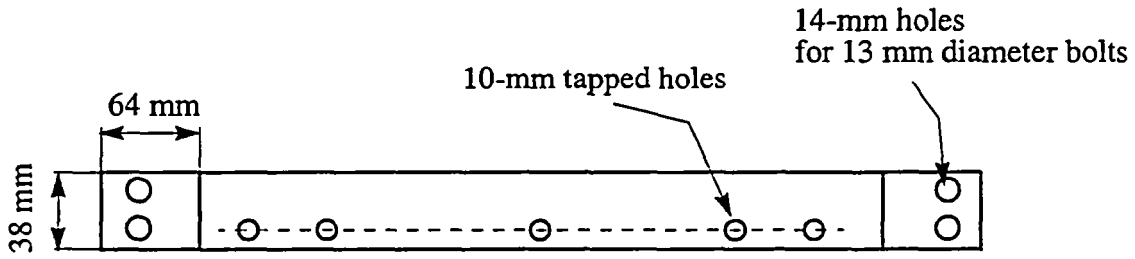

(b) Elevation

Figure 5-1 Geometry of Ring-1

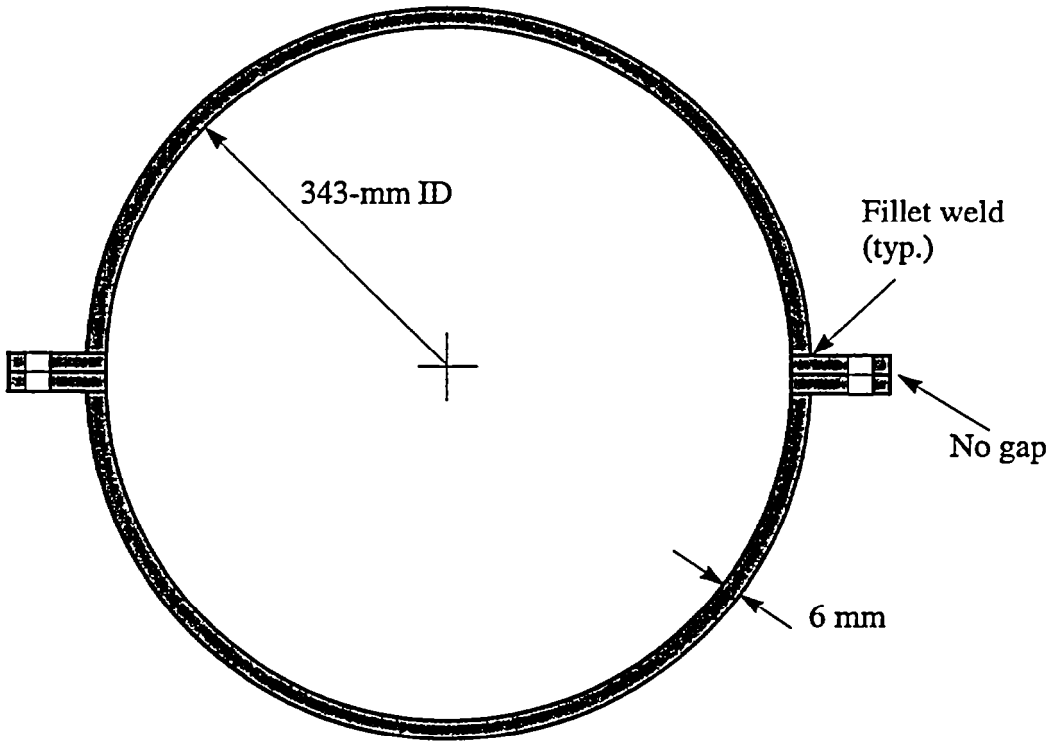

(a) Plan

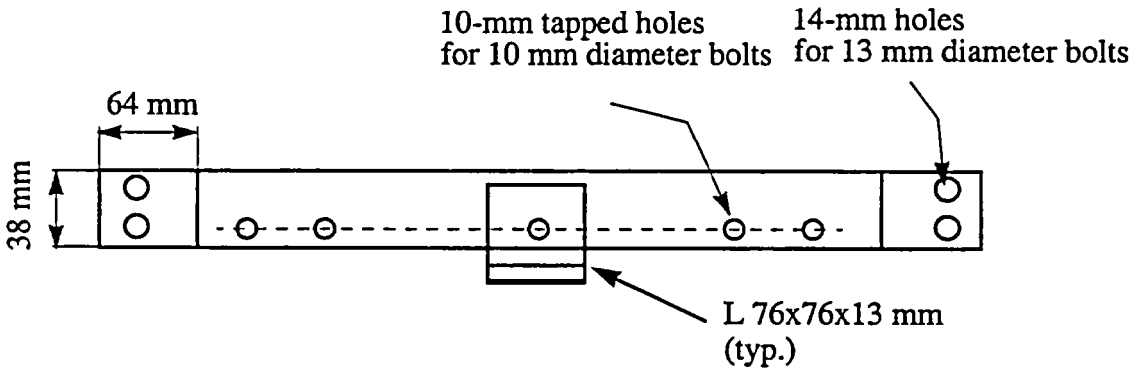

(b) Elevation

Figure 5-2 Geometry of Ring-2

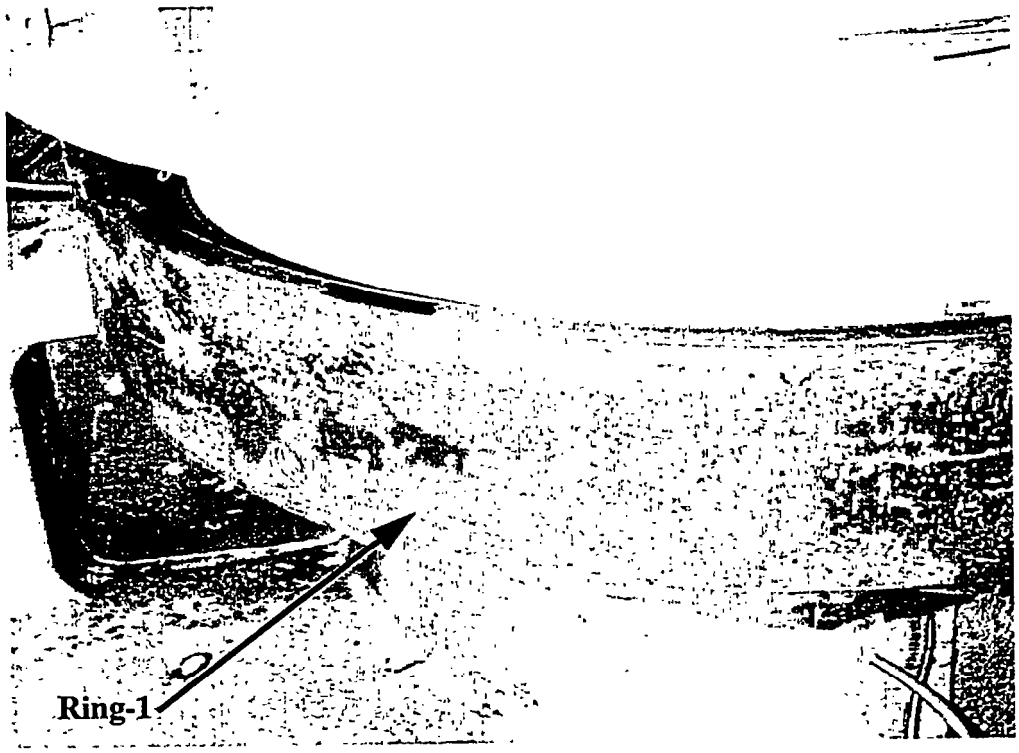

Figure 5-3 Ring-1 placed around the gasket connection of Bushing-1

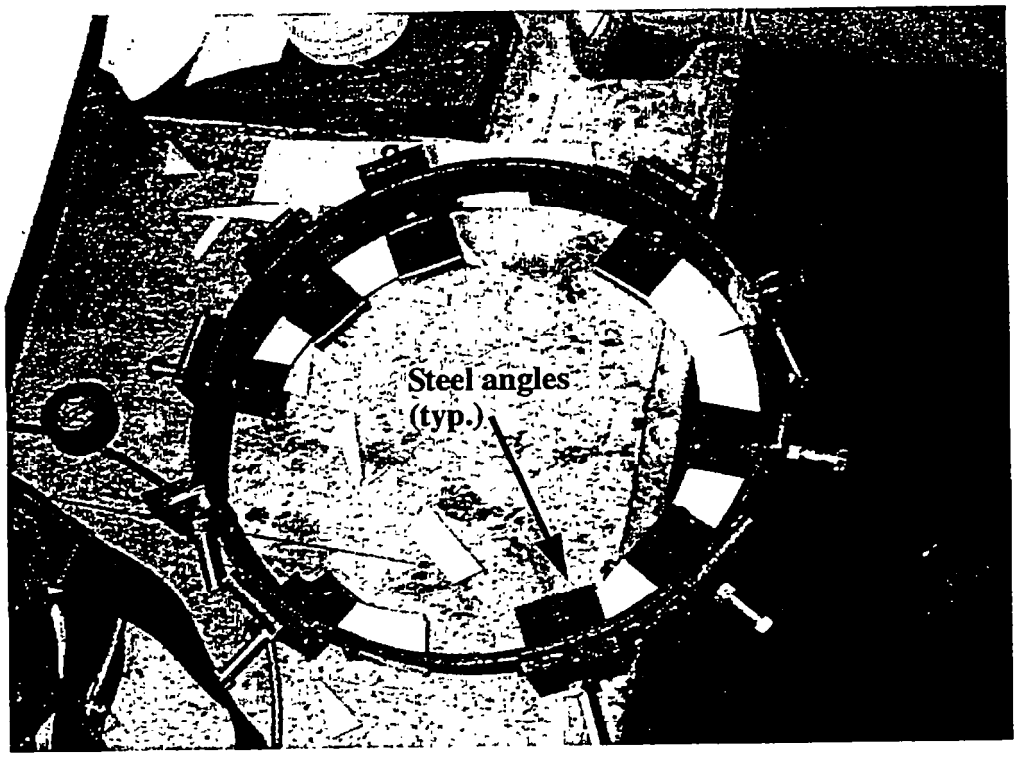

Figure 5-4 Ring-2 prior to installation around the gasket connection of Bushing-2

6 Static Cyclic Testing of Rigidly Mounted Bushing-1

6.1 Overview

Static tests were conducted to characterize the response of Bushing-1. The bushing was placed vertically in a stiff mounting frame and two actuators loaded the bushing horizontally. Bushing-1 was subjected to pull-back, quick-release tests, static cyclic (reversible) tests and static monotonic tests. The static tests were conducted at a low rate of loading and there was no dynamic effect. During the cyclic tests, three loading orbits (unidirectional, unidirectional with offset, and bidirectional) were used. Pull-back, quick-release tests were conducted to measure the dynamic properties of Bushing-1. Static tests were conducted to determine the limit states of response for the Bushing-1 as a function of the bushing post-tensioning force and actuator loading orbits, and to evaluate the efficacy of Ring-1 for retrofitting 230-kV bushings. The following sections present the experimental setup including the stiff mounting frame, instrumentation, and loading protocol and summary of experimental data.

6.2 Experimental Setup

6.2.1 Mounting frame

The *rigid* mounting frame used for static testing of Bushing-1 was a fully welded frame made of a 54 by 54 in. (1.4 x1.4 m) by 1.5-in. (38-mm)-thick top plate supported by four TS 5x5x3/8" (127x127x9.5 mm) columns. The frame was attached to the laboratory floor using four 1 in. (25 mm) high-strength post-tensioning rods, one per column. Four 3x3x3/8" (76x76x9.5 mm) angle braces were bolted to the top plate and attached to the existing reaction frame to provide lateral stiffness. Figure 6-1 shows Bushing-1 mounted on the test frame prior to the static tests. The four 3x3x3/8" (76x76x9.5 mm) angle braces can be seen on the left hand side of the photograph.

6.2.2 Post-tensioning mechanism

A 50-ton (450 kN) flat ram was used to post-tension the bushing. The post-tensioning (PT) setup consisted of: the flat ram located at the bottom of the bushing; a 48-in. (1.2-m) long TS 10x10x1/2" (250x250x13 mm) steel loading beam; a loading attachment bolted to the loading beam and resting on the loading plate in the dome of the bushing; a special bushing wrench that engaged the

loading plate in the dome of Bushing-1; and two 1.25 in. (32 mm) high-strength, fully threaded post-tensioning rods. The rods were anchored to the mounting frame at the bottom and to the loading beam at the top and were used to transfer the tensile force from the loading beam to the mounting frame. Figure 6-2 shows components of the post-tensioning assembly.

The post-tensioning procedure consisted of: loosening the 3/4 in. (19 mm) bolts attaching the bushing flange to the mounting frame, loading the bushing via the flat ram, monitoring the ram force via an in-line pressure sensor, and releasing the post-tensioning load in the bushing by loosening the nut at the top end of the bushing core (located in the dome). The post-tensioning force in the bushing was taken as the ram load at which the nut disengaged from the core.

6.2.3 Loading collar and joint collar

To distribute the horizontal actuator loads to Bushing-1, a loading collar was placed around the bushing. The collar consisted of a welded tubular section built up from four 10 x 3/8 in. (254 x 10 mm) steel plates. High-strength grout, placed between the porcelain and the collar, uniformly distributed the actuator load; 5/8-in. (16-mm)-thick plates were welded to two perpendicular faces of the collar to connect the actuators to the collar. One objective of the static tests was to characterize the response of the bushing at the gasket connection. To eliminate the movement at the joint between the UPPER-1 and UPPER-2 porcelain units (see Figure 6-3), a joint collar (similar to the loading collar) was installed. Figure 6-4 shows the loading and joint collars.

6.2.4 Loading mechanism and test control

The static cyclic tests were carried out using two actuators, each with a capacity of 10 kips (45 kN) and a stroke of 7.5 in. (190 mm). The actuators were attached to the loading collar with bolted clevises. Each actuator load was reacted via a trunnion mount that was attached to 4x4x3/8" (102x102x10 mm) angle steel supports that were welded to a TS 4x4x3/8" (102x102x10 mm) steel beam that was welded to the existing reaction frame. The applied force was measured using load cells in line with the actuators.

The center line of the horizontal actuators (point of application of the concentrated load) was located 47 in. (1.2 m) above the gasket connection. This dimension was selected to reproduce the ratio of the bending moment to the shear force at the gasket connection that would occur if the bushing mode shape was triangular in profile. Figure 6-4 shows the test setup prior to cyclic testing. The initial static cyclic test was conducted under displacement control with the actuator clevises oriented to allow rotation about the vertical axis.

6.2.5 Instrumentation

Sixteen channels of data were recorded for each static test. Table 6-1 lists the channel number, instrument type, response quantity, coordinate system, and location for each transducer. The bushing (x_{00} and y_{00}) and actuator (x_{45} and y_{45}) coordinate systems adopted for the testing program are shown in Figure 6-5. The numbers in this figure correspond to the channel number in Table 6-1.

Four channels (channels 1 through 4) recorded the force and displacement of the actuators. The displacements at top of the Bushing-1 and at the centerline of the actuators were monitored by four displacement transducers (channels 5 through 8). Four displacement transducers (channels 9 through 12), measured the radial displacement of the UPPER-1 porcelain unit relative to the flange plate. Four displacement transducers (channels 13 through 16) recorded the uplift of the UPPER-1 porcelain unit relative to the flange plate. Figure 6-6 shows the instrumentation at the top of Bushing-1. Figure 6-7 shows instrumentation of the UPPER-1 porcelain unit.

Table 6-1 Instrumentation for static tests of Bushing-1

Channel Number	*Transducer*[1]	*Response Quantity*	*Orientation*[2]	*Transducer Location*[3]
1	LC-1	actuator-1 force	x_{45}	actuator centerline
2	LC-2[4]	actuator-2 force	y_{45}	actuator centerline
3	LVDT-1	actuator-1 displacement	x_{45}	actuator centerline
4	LVDT-2	actuator-2 displacement	y_{45}	actuator centerline
5	DCDT-1	bushing displacement	x_{00}	top of bushing
6	DCDT-2	bushing displacement	y_{00}	top of bushing
7	DCDT-3	bushing displacement	x_{00}	actuator centerline
8	DCDT-4	bushing displacement	y_{00}	actuator centerline
9	DCDT-5	UPPER-1 slip	$-x_{45}$	gasket connection
10	DCDT-6	UPPER-1 slip	$-y_{45}$	gasket connection
11	DCDT-7	UPPER-1 slip	x_{45}	gasket connection
12	DCDT-8	UPPER-1 slip	y_{45}	gasket connection
13	DCDT-9	UPPER-1 uplift	z	gasket connection
14	DCDT-10	UPPER-1 uplift	z	gasket connection
15	DCDT-11	UPPER-1 uplift	z	gasket connection
16	DCDT-12	UPPER-1 uplift	z	gasket connection

1. LC = load cell; LVDT = displacement transducer; DCDT = displacement transducer.
2. For sensor orientation refer to Figure 6-5.
3. For location of instruments refer to Figure 6-5.
4. Channel used to measure the force during the pull-back tests.

6.3 Test Protocol

6.3.1 Pull-back, quick-release tests

Pull-back, quick-release tests were conducted to determine the lateral stiffness, vibration frequency, and modal damping of Bushing-1. The sequence of quick-release testing for Bushing-1 is presented in Table 6-2. The pull-back tests were carried out at selected intervals during the test program to evaluate the effects of bushing preload, the addition of Ring-1, and the lubrication of the gasket at the gasket connection on the dynamic properties of Bushing-1. These tests were conducted in both x_{00}- and y_{00}- directions (see Figure 6-5). Each test set was repeated to improve the accuracy of the results.

Table 6-2 Protocol for quick-release testing of Bushing-1

Test Set	*Test Date*	*Preload (kN)*	*Ring-1 Installed*	*Comments*
0	9/08/99	120	No	Initial quick-release test.
8	9/10/99	120	No	Gasket at the gasket connection was lubricated.
9	9/13/99	90	No	Bushing preload was reduced.
11	9/15/99	120	Yes	Bushing-1 was retrofitted with Ring-1.

The setup for the quick-release tests, shown in Figure 6-8, consisted of a nylon cable connecting the top of Bushing-1 to the reaction frame in-line with a turnbuckle, a load cell, and a machined bolt. During the pull-back stage of the tests, the bushing was gradually loaded to approximately 0.5 kips (2 kN). The applied force and the resulting displacement at top of the bushing were monitored and recorded using the in-line load cell and displacement transducers. The applied force was then released by cutting the machined bolt and the free vibration response was recorded.

6.3.2 Static tests

Static tests were conducted to determine the limit states of response for Bushing-1. One objective of the static testing of Bushing-1 was to characterize the bushing response as a function of the post-tensioning force. Another objective was to evaluate the efficacy of Ring-1.

The sequence for static testing of Bushing-1, including the test orbits, is presented in Table 6-3. Bushing-1 was tested using three cyclic (unidirectional, unidirectional with offset, and bidirectional) and one monotonic orbit. The orbits are shown in Figure 6-9. Unidirectional tests were conducted to characterize the response of Bushing-1. In the unidirectional with offset tests, an initial offset in the lateral direction was introduced to see if that offset increased rocking of the UPPER-1 porcelain unit at the gasket connection. In the bidirectional tests, Bushing-1 was displaced around a circular orbit to see if the circular orbit facilitated extrusion of the gasket from the gasket connection. The monotonic test was used to determine the limit state of response for Bushing-1.

The displacement history for each cyclic test, referred to as Test Set in the first column of Table 6-3 and shown in Figure 6-10, consisted of three complete cycles (referred to as Test Nos in the second column of Table 6-3) to a target displacement. The target displacement for Test No. 1 was 0.05 in. (1.25 mm) and the target displacements were increased by 0.05 in. (1.25 mm) for each subsequent test.

Previous analytical studies by the authors (Gilani et al., 1998) have shown that the stiffness of gasket in the gasket connection is the key determinant of the fundamental frequency and mode shape of porcelain transformer bushings. Gasket stiffness is a function of the contact pressure (equal to the preload divided by the plan area of the gasket) and the geometry of the groove into which the gasket is placed. Only the effect of contact pressure could be studied in this research program because the geometry of the groove could not be altered.

The manufacturer of Bushing-1 specifies a post-tensioning force of 27 kips (120 kN) for 230-kV type-U bushings. Test data from the manufacturer have shown that when the post-tensioning force is increased to 31 kips (138 kN), the springs in the bushing dome bottom out (reach the end of their travel). For a majority of the tests listed in Table 6-2, the post-tensioning force in the bushing was set at the manufacturer's specified value. To evaluate the effect of the post-tensioning force on the response of the bushing, static tests were conducted with the post-tensioning force set at 20 kips (90 kN): a 30-percent reduction in the preload. Static tests with a post-tensioning force set at 36 kips (160 kN): a 30-percent increase in the preload were not possible due to the travel limit of the springs in the bushing dome.

6.4 Experimental Results from Quick-Release Tests

Response histories of Bushing-1 for Test Set 0 are shown in Figure 6-11. The computed elastic (stiffness) and dynamic (frequency and damping ratio) properties at the top of Bushing-1 for quick-release tests are listed in Table 6-4. The stiffness of Bushing-1 was computed from the slope of the force-displacement relations (Figures 6-11a and 6-11b); the vibration frequencies of Bushing-1 were computed from peaks in the power spectra of the recorded displacement signals (Figures 6-11c and 6-11d); and the damping ratios of Bushing-1 were obtained using the log-decrement method (Clough and Penzien, 1993) for a segment of the free-vibration response history (Figures 6-11e and 6-11f). The effective weight of the bushing was computed from the stiffness and frequency data and assuming that the bushing is a single-degree-of-freedom system with a lumped mass at its top. The vibration properties of the bushing were approximately constant during the testing program.

Changes in the bushing post-tensioning force did not substantially alter the frequency of the bushing, although previous analytical studies have indicated that the fundamental frequency and mode shape of porcelain transformer bushings are directly dependent on the stiffness of the gasket in the gasket connection (Gilani, et al., 1998). This apparent discrepancy is due to the existing boundary condition of the gasket. For an unconfined gasket (the boundary condition on which the previous analysis was based), the relation between the gasket stiffness (tangent modulus) and the post-tensioning force can be derived using the stress-strain relation for the nitrile rubber (Elder, 1999). Figure 6-12 presents the gasket tangent modulus as a function of the post-tensioning force for the two unconfined gaskets. This figure shows that the gasket tangent stiffness is sensitive to

variations in the post-tensioning force in the range from 20 to 27 kips (90 to 120 kN). However, the gasket in Bushing-1 was confined in the flange groove (pocket). As a result, the tangent stiffness of the gasket was not sensitive to variations in the bushing preload in the 20 to 27 kip (90 to 120 kN) range, and the frequency of the Bushing-1 was not effected by modest changes in the preload.

Table 6-3 Protocol for static testing of Bushing-1

Test Set	*Test Nos*	*Test Date*	*Preload (kN)*	*Test orbit*[1]	*Ring-1 installed*	*Comments*[2]
1	1 to 8	9/08/99	120	a	No	Initial cyclic test.
2	1 to 4	9/09/99	120	b	No	Offset was 2.5 mm.
3	1 to 4	9/09/99	120	b	No	Offset was 5 mm.
4	1 to 6	9/09/99	120	c	No	Maximum orbit radius was 7.5 mm.
5	1 to 6	9/09/99	120	a	No	Gasket at the gasket connection was lubricated by oil.
6	1 to 6	9/09/99	120	a	No	Actuator 1 was disconnected and Bushing-1 was tested under load control.
7	1 to 6	9/10/99	120	a	No	Actuator 1 was disconnected and clevis for actuator 2 was rotated 90 degrees.
10	1 to 6	9/13/99	90	a	No	Bushing preload was reduced.
12	1 to 10	9/15/99	120	a	Yes	Ring-1 added to the gasket connection.
13	1 to 9	9/16/99	120	c	Yes	Maximum orbit radius was 11.25 mm.
14	-	9/16/99	120	d	Yes	Retrofitted Bushing-1 tested to failure.

1. a = unidirectional, b = unidirectional with offset, c = bidirectional, d = monotonic; see Figure 6-9.
2. For definition of offset and orbit radius see Figure 6-9.

The frequencies of Bushing-1 listed in Table 6-4 are approximately 20 percent lower than the values computed from the resonant-search tests listed in Table 4-4. These differences are due to the additional weight of the loading and joint collars, each weighing approximately 100 lbs (450 N).

6.5 Experimental Results from Static Tests of Bushing-1 without Ring-1

6.5.1 Unidirectional tests

The initial unidirectional test set, Test Set 1, was used to characterize Bushing-1 and to evaluate limit states of response for the bushing. There was no oil leakage or slip of the UPPER-1 porcelain unit for cycles with target displacements equal to or less than 0.3 in. (7.6 mm). During the 0.35-in. (8.75-mm) displacement cycles, the bushing leaked oil at the gasket connection and the UPPER-1 porcelain unit slipped a small amount. During the displacement cycles to 0.4 in. (10

mm), the bushing leaked a large amount of oil at the gasket connection and the UPPER-1 porcelain unit slipped significantly. The peak force in actuator 2 during these cycles was approximately 2 kips (9 kN). Figure 6-13 is a photograph of the gasket connection at the conclusion of Test Set 1 showing slip of the porcelain unit over the gasket connection.

Table 6-4 Modal properties obtained from frequency tests

	Lateral Stiffness (kN/mm)		*Frequency (Hz)*		*Damping Ratio (percent)*		*Effective Weight (N)*
Test Set	x^1_{00}	y_{00}	x_{00}	y_{00}	x_{00}	y_{00}	x_{00} or y_{00}
0	11	11	16	15	3	2	1030
8	11	10	16	15	3	3	1080
9	11	11	16	15	3	2	1030
11	11	10	16	15	3	2	1080

1. For definition of coordinate system, see Figure 6-5.

Figure 6-14 shows the relation between zero-corrected actuator-2 force and displacement at the top of the bushing during the 0.4-in. (10-mm) displacement cycles. The hysteretic behavior and lack of symmetry in force-displacement response were due to the slip of porcelain at the gasket connection and the test setup, respectively. Under displacement control testing, the displacements in actuators 1 and 2 (along the x_{45} and y_{45}) were specified as the target displacement and zero, respectively. As a result, the force in actuator 2 was not zero. Due to the force in the x_{45}- direction, the hysteretic response of Bushing-1 was not symmetric. The peak response values reported in this chapter were computed by averaging the maximum values in the forward and reverse half cycles.

At the conclusion of Test Set 1, the post-tensioning force in Bushing-1 was measured at 30.5 kips (137 kN), the bushing was de-stressed, oil was drained from the bushing, the bushing was partially disassembled, and the gasket at the gasket connection was examined. The gasket was neither distorted nor damaged, but was covered with a thin coat of oil (termed lubricated in this report).

Test Sets 5, 6, and 7 were conducted to investigate the effect of variations in the test setup on the response of the bushing. In Test Set 01, the gasket in the gasket connection was not lubricated, the actuator clevises were oriented to rotate in the horizontal plane, and the tests were conducted under displacement control. The maximum target displacement for Test Sets 5, 6, and 7 was set at 0.3 in. (7.5 mm) to avoid large slip of the UPPER-1 porcelain unit. Test Set 05 was conducted to study the effect of gasket lubrication on the response of the bushing. Prior to Test Sets 6 and 7, actuator 1 (along the x_{45} axis) was disengaged. Both Test Sets were conducted under load control. For Test Set 7, the clevis on actuator 2 was rotated 90 degrees to rotate in the vertical plane.

Figure 6-15 shows the zero-corrected displacement response of Bushing-1 at a target actuator displacement of 0.3 in. (7.6 mm) for Test Sets 1, 5, 6, and 7. The displacement histories are shown at three heights: top of bushing, actuator centerline, and gasket connection.

For Test Set 1, the initial cyclic test, the displacement history at the gasket connection is linear (Figure 6-15a) and corresponds primarily to the recoverable shear deformation in the gasket. For Test Set 5, cyclic tests with the lubricated gasket, the displacement history at the gasket connection is nonlinear (Figure 6-15b) due to the non-recoverable slip of the UPPER-1 porcelain unit.

The response of Bushing-1 from Test Set 1 using displacement control testing (Figure 6-15a) and Test Set 6 using load control testing (Figure 6-15c) are similar. A comparison of displacement histories from Test Set 6 (Figure 6-15c) and Test Set 7 (Figure 6-15d) shows that the clevis orientation and the test control had little or no effect on the response.

Test Set 10 was conducted to characterize the bushing response for a smaller post-tensioning force of 20 kips (90 kN). Oil leaked from the gasket connection during the tests to target actuator displacements of 0.2 in. (5 mm) and 0.25 in. (6.25 mm). During the tests to a maximum displacement of 0.3 in. (7.5 mm), oil leaked from the gasket connection and the UPPER-1 porcelain unit slipped over the flange. The post-tensioning force was checked following Test Set 10 and was found to be unchanged. A reduction in the post-tensioning force or preload reduced the uplift displacement at which the bushing will leak oil.

6.5.2 Unidirectional tests with offset

Two unidirectional tests along the y_{45} axis with an initial offset along the x_{45} axis, (see Figure 6-10b) were conducted. During Test Set 2, the bushing was initially displaced 0.1 in. (2.5 mm) in the x_{45} direction and then was cyclically loaded in the y_{45} direction. During Test Set 3, the bushing was initially displaced 0.2 in. (5.0 mm) in the x_{45} direction prior to cyclic loading in the y_{45} direction. For both Test Sets, the maximum target displacement along the y_{45} axis was 0.2 in. (5 mm). No oil leakage or slip of UPPER-1 porcelain unit over the flange was observed for either test. Figure 6-16 shows the actuator force-displacement response at the top of the bushing for the cycles to 0.2 in. (5 mm) of Test Set 3. The hysteresis loops along the y_{45} axis (Figure 6-16b) are not symmetric for the reasons cited in Section 6.5.1.

6.5.3 Bidirectional tests

Cyclic tests using the bidirectional (circular) orbit of Figure 6-10c were conducted to investigate whether circular motion of the bushing could dislodge the gasket from the groove in the flange plate. The cyclic tests were conducted to a maximum actuator displacement of 0.3 in. (7.5 mm). During the tests to a maximum displacement of 0.25 in. (6.25mm) and 0.3 in. (7.5 mm), there was minuscule oil leakage, and small slip of the UPPER-1 porcelain unit. No extrusion of the gasket was observed during the tests. Figure 6-17a shows the actuator 1-actuator 2 displacement orbit, and Figure 6-17b shows the actuator 1-actuator 2 force orbit during the cycles to a peak displacement of 0.3 in. (7.5 mm).

6.6 Experimental Results from Static Tests of Bushing-1 with Ring-1

6.6.1 Background

At the conclusion of Test Set 10, Bushing-1 was de-stressed, drained of oil, and partially disassembled. The gasket at the gasket connection inspected and air dried, the porcelain units were re-centered, and the bushing was post-tensioned to 27 kips (120 kN) and was refilled with oil. After post-tensioning, the retrofit ring (Ring-1) was attached around the gasket connection of the bushing. Pull-back, quick-release, unidirectional and bidirectional cyclic and monotonic tests were carried out to compute the dynamic properties of the retrofitted bushing, to evaluate the effect of the retrofit ring on response of the bushing, and to test the bushing to failure. Test results from quick-release tests are listed in Table 6-4. A summary of test results from the cyclic and monotonic tests is presented below.

6.6.2 Unidirectional tests

The unidirectional tests were conducted to a maximum actuator displacement of 0.5 in. (11.25 mm). During the tests to target displacements of 0.4 in. (10 mm) and 0.45 in. (12.5 mm), oil leaked from the gasket connection. During the 0.5-in. (12.5-mm) displacement cycles, Bushing-1 leaked oil and Ring-1 rotated about a horizontal (x-y plane) axis. Figure 6-18 shows Bushing-1 at the conclusion of the unidirectional tests. The original and final positions of Ring-1 are identified in the figure. Figure 6-19 shows oil leakage following Test Set 13.

6.6.3 Bidirectional tests

The bidirectional tests were conducted to a maximum actuator displacement of 0.45 in. (12.5 mm). During the tests to a maximum displacement of 0.35 in (8.75 mm) and 0.4 in (10 mm), the bushing leaked oil from the gasket connection. During the 0.45-in. (11.25-mm) displacement cycles, oil leaked from the gasket connection, Ring-1 rotated about a horizontal (x-y plane) axis and separated from the epoxy filler material (which was used to grout the gap between Bushing-1 and Ring-1), and the UPPER-1 porcelain unit twisted about the vertical (z-) axis. Figure 6-20 shows the separation of Ring-1 from the epoxy filler material at the conclusion of the bidirectional tests. Figure 6-21 shows the twist of UPPER-1 porcelain unit at the conclusion of the bidirectional tests.

6.6.4 Monotonic test

Actuator 2 (along the y_{45} axis) was disconnected from Bushing-1 and the bushing was monotonically loaded by actuator 1 (along the x_{45} axis). When the displacement in actuator 1 exceeded 0.4 in. (10 mm), Bushing-1 began to leak oil. At actuator displacements larger than approximately 1.5 in. (38 mm), the oil leakage was continuous. As the actuator displacement was increased further, Ring-1 rotated and separated from the epoxy filler material. The side of Ring-1 closest to actuator 1 (see Figure 6-4) lifted with respect to the UPPER-1 porcelain unit. At an actuator displacement of approximately 5.5 in. (140 mm), a loud noise was heard. Testing continued to the actuator stroke limit of approximately 6 in. (152 mm). At this displacement, the

maximum force in actuator 1 exceeded 5 kips (22 kN). To complete the test, actuator 1 was slowly retracted to its original position. During retraction, the uplifted side of Ring-1 pressed against the surface of the bottom shed in the UPPER-1 porcelain unit (see Figure 2-4) and fractured the porcelain in two locations. Testing was stopped at an actuator force equal to zero.

At the conclusion of Test Set 14, Ring-1 was removed. Examination of Bushing-1 revealed that the UPPER-1 porcelain unit had slid as shown in Figure 6-22, and Ring-1 had rotated and separated from the epoxy filler material and had made contact with and fractured the bottom shed of the UPPER-1 porcelain unit (see Figure 6-23). Although the gasket in the gasket connection had severed at one location as shown in Figure 6-24, it had not extruded from the groove in the flange. The cast aluminum flange of Bushing-1 had fractured as shown in Figure 6-25. This fracture was the likely cause of the loud noise heard during the test. Bushing-1 was then de-stressed. The post-tensioning force in the bushing was measured to be 29.3 kips (130 kN).

Figure 6-26a shows the relation between displacement at the top of the bushing and the force in actuator 1, and Figure 6-26b shows the relation between displacement at the gasket connection and force in the actuator 1. Up to an actuator load of approximately 1.4 kips (6 kN), the force-displacement relations are linear. At larger values of actuator force, the stiffness of the bushing is significantly reduced due to the large slip of the UPPER-1 porcelain unit over the bushing flange.

6.7 Evaluation of Response of Bushing-1

6.7.1 Introduction

The data from static tests of Bushing-1 were used to characterize the response of the bushing and to evaluate the efficacy of Ring-1.

6.7.2 Modification of recorded data

Prior to examining the response of Bushing-1, the recorded data were corrected by first transforming the data to the appropriate coordinate system and then by applying the second order geometric corrections. For the pull-back, quick-release tests, the recorded data were transformed to the x_{00}-y_{00} coordinate system (coinciding with the bushing x-y axes) and for the static tests, the recorded data were transferred to the x_{45}-y_{45} coordinate system (coinciding with the axes of the two actuators). The transformation between these two coordinate systems is given by:

$$\begin{bmatrix} x_{45} \\ y_{45} \end{bmatrix} = \frac{1}{\sqrt{2}} \begin{bmatrix} 1 & -1 \\ -1 & 1 \end{bmatrix} \begin{bmatrix} x_{00} \\ y_{00} \end{bmatrix} \tag{6-1}$$

The recorded data from the radial sensors at the gasket connection (channels 9-12 of Table 6-1) were used to compute the horizontal motion of the UPPER-1 porcelain unit at the gasket connection (u_{45} and v_{45}, denote the translation of the UPPER-1 porcelain unit along the x_{45} and y_{45} directions; the twist about the z-axis was small and was ignored).

The data collected from the sensors recording the vertical motion of the UPPER-1 porcelain unit at the gasket connection (channels 13-16, see Table 6-1) were corrected to eliminate the second-order geometric effects due to the horizontal motion of the UPPER-1 porcelain unit at the gasket connection. The corrected data were used to compute the concentrated rotation at the gasket connection (due to the flexibility of the gasket). Rotation about the y_{00}-axis was calculated as the difference between the channel 15 and 13 displacements divided by the 25-in. (635-mm) distance between these transducers. Rotation about the x_{00}-axis was calculated as the difference between the channel 16 and 14 displacements divided by the 25-in. (635-mm) distance between these transducers. Rotation about the x_{45}-axis was computed by computing the vector sum of the rotations about the x_{00} and y_{00} axes.

6.7.3 Displacement response of Bushing-1

Test Set 1 was used to further characterize the response of Bushing-1. During Test No 3 to a target displacement of 0.1 in. (2.5 mm), the slip of the UPPER-1 porcelain unit was negligible and the maximum force in actuator 2 (along y_{45}-axis) was 1.16 kips (5.1 kN). Maximum displacements of 0.11 in. (2.8 mm), 0.07 in. (1.8 mm), and 0.017 in. (0.4 mm), were measured along the y_{45}-axis at the top of the bushing, at the actuator, and at the gasket connection, respectively. At the gasket connection, concentrated rotations were 0.06 percent radian about the y_{00}-axis and 0.04 percent radian about the x_{00}-axis, respectively; the rotation about the x_{45}-axis was estimated by averaging these value. The displacement of 0.05 in. (1.4 mm) at the top of the bushing along the y_{45}-axis due to this rotation at the gasket connection was calculated by multiplying the 74-in. (1.9-m) height of the segment of the bushing between the gasket connection and the top of the bushing by the rotation about the x_{45} axis.

As noted in Chapter 2, the bushing displacement (in the segment between the gasket connection and the top of bushing) comprises contributions from the cantilever deformation of the porcelain stacks, the concentrated rotation at the gasket connection, the shear deformation in the gasket, and the slip of UPPER-1 porcelain unit over the flange. The total displacement at the top of Bushing-1 for Test No 3 of Test Set 1 consisted of 15 percent contribution from the shear deformation of the gasket in the gasket connection and 50 percent from the concentrated rotation at the gasket connection.

6.7.4 Slip properties of the gasket at the gasket connection

As noted in Chapter 2, two factors resist the slip of the porcelain unit over the gasket: (1) the friction between the nitrile gasket and porcelain and (2) the restraint provided by the core kraft paper assembly. Data recorded during Test Sets 1 and 5 were used to estimate the slip coefficient between at the gasket connection. During Test Set 1, the gasket was not covered with oil (herein termed dry), whereas during Test Set 5, the gasket was partially covered with oil (herein termed lubricated). Figure 6-27 shows the relation between the force in actuator 2 and the displacement of the UPPER-1 porcelain unit at the gasket connection along the y_{45}- axis.

Figure 6-27a shows the force-displacement relation for Test No 8 (target actuator displacement of 0.40 in. or 10 mm) for Test Set 1. During this test, the UPPER-1 porcelain unit slipped when the force in actuator 2 was approximately 2.4 kips (11 kN). The slip coefficient at the gasket connection was obtained as the ratio of this force and the post-tensioning of 27 kips (120 kN). Figure 6-27b shows the force-displacement relation for Test No 6 (target actuator displacement of 0.30 in. or 7.5 mm) for Test Set 5. During this test, the UPPER-1 porcelain unit slipped when the force in actuator 2 was approximately 1.9 kips (9 kN). The slip coefficient at the gasket connection was obtained as the ratio of this force and the post-tensioning force of 27 kips (120 kN). A comparison of the actuator force required to initiate slip of the porcelain over the gasket for the dry and lubricated gaskets suggests that the core kraft paper assembly provides a significant portion of the resistance to the slip of the UPPER-1 porcelain unit.

6.7.5 Efficacy of Ring-1

Test data from Test No 8 of Test Set 1 (Bushing-1 without Ring-1) and Test No 8 of Test Set 12 (Bushing-1 with Ring-1) were used to evaluate the efficacy of Ring-1 in improving the response of Bushing-1. Figure 6-28a shows the relation between the force in actuator 2 and the displacement of the UPPER-1 porcelain unit at the gasket connection along the y_{45}- axis for these two tests. The addition of Ring-1 neither prevented nor significantly reduced the slip of the UPPER-1 porcelain unit over the flange. Figure 6-28b shows the relation between the force in actuator 2 and vertical (z-axis) motion at the face of the UPPER-1 porcelain unit at the gasket connection for the two tests. The addition of Ring-1 did not prevent the uplift of the UPPER-1 porcelain unit at the gasket connection.

During the bidirectional tests of Test Set 13, Ring-1 did not prevent slip or rotation of UPPER-1 porcelain unit at the gasket connection. During the monotonic test to failure of Test Set 14, Ring-1 rotated, separated from the epoxy filler material and fractured the bottom shed of the UPPER-1 porcelain unit.

6.8 Summary

Test data from the quick-release and static tests of Bushing-1 were used to evaluate the dynamic properties of the bushing and characterize its response.

Data from the pull-back, quick-release tests were used to measure the frequency and damping ratio of the bushing. The frequency of the bushing in the x- and y-directions were approximately 16 and 15 Hz. The additional mass of the loading and the joint collars reduced the fundamental frequency of the bushing and increased its effective weight. Due to the confinement of the gasket in the groove, the bushing frequency was not effected by the reduction in the preload from 27 kips (120 kN) to 20 kips (90 kN).

Data from the static tests were used to characterize the response of the bushing response and to evaluate limit states of response. During the first unidirectional test, oil leaked from the gasket connection at an actuator displacement of 0.4 in. (10 mm). Reduction in the post-tensioning force from 27 kips (120 kN) to 20 kips (90 kN), reduced the uplift displacement at which the bushing

leaked oil. When the gasket was lubricated with oil, the actuator force required to initiate slip of the UPPER-1 porcelain unit over the flange was reduced. During the tests in which Ring-1 was added to the bushing, oil leaked from the gasket connection, the UPPER-1 porcelain unit twisted above the flange, and Ring-1 rotated and separated from the filler material.

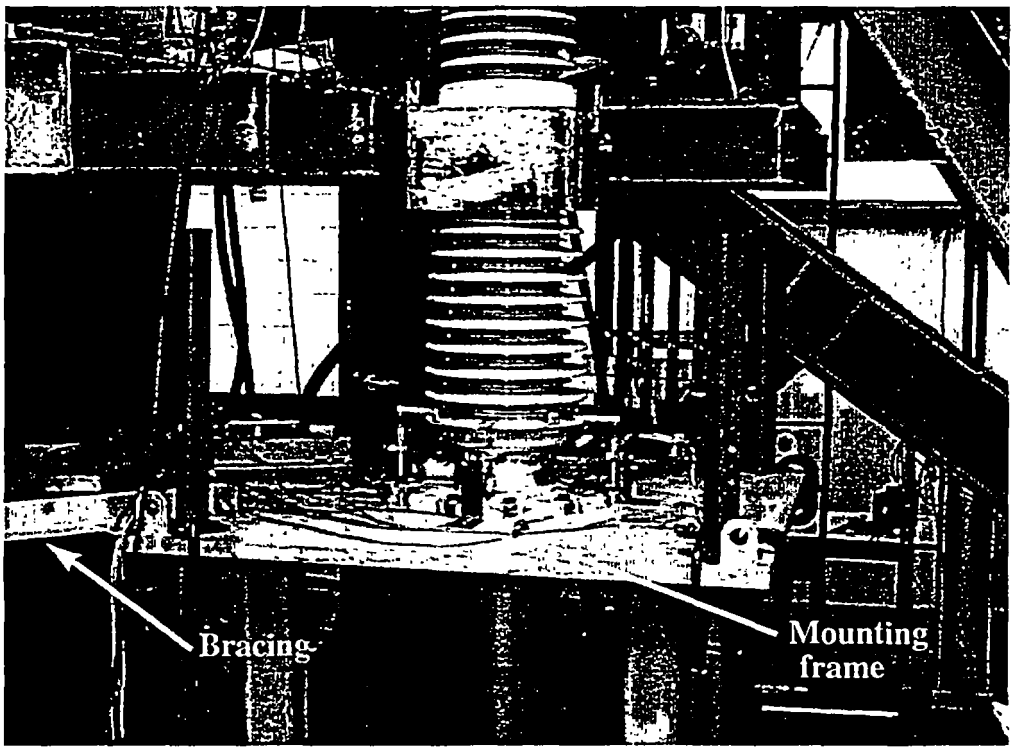

Figure 6-1 Bushing-1 and the mounting frame

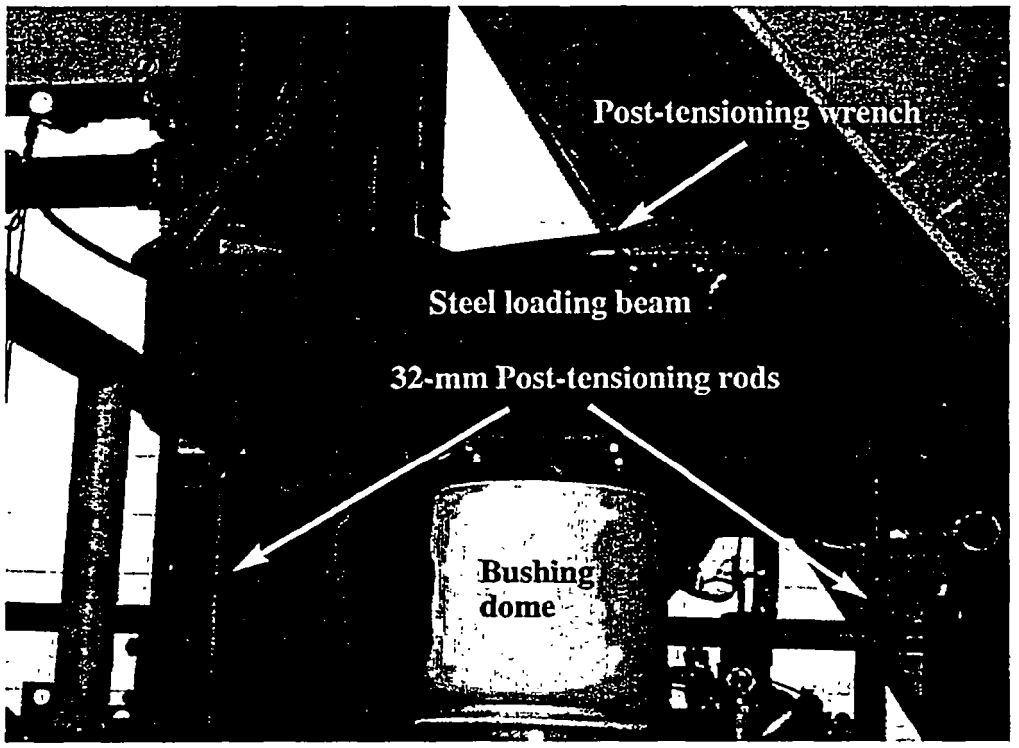

Figure 6-2 Post-tensioning setup for Bushing-1

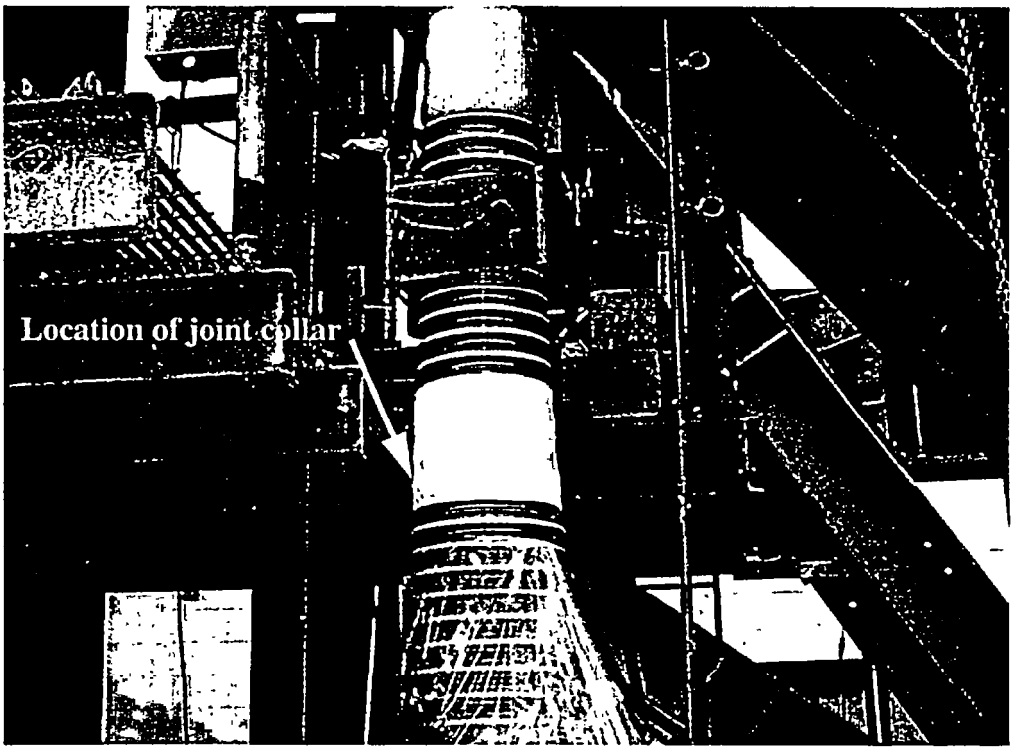

Figure 6-3 Joint collar for Bushing-1

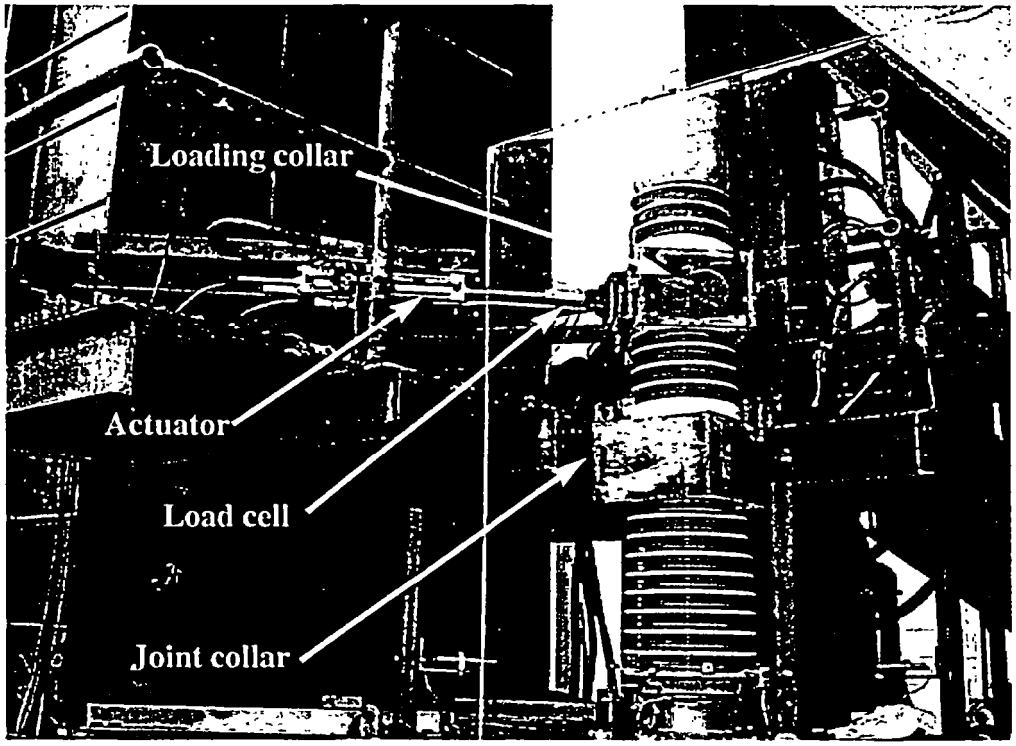

Figure 6-4 Bushing-1 prior to cyclic testing

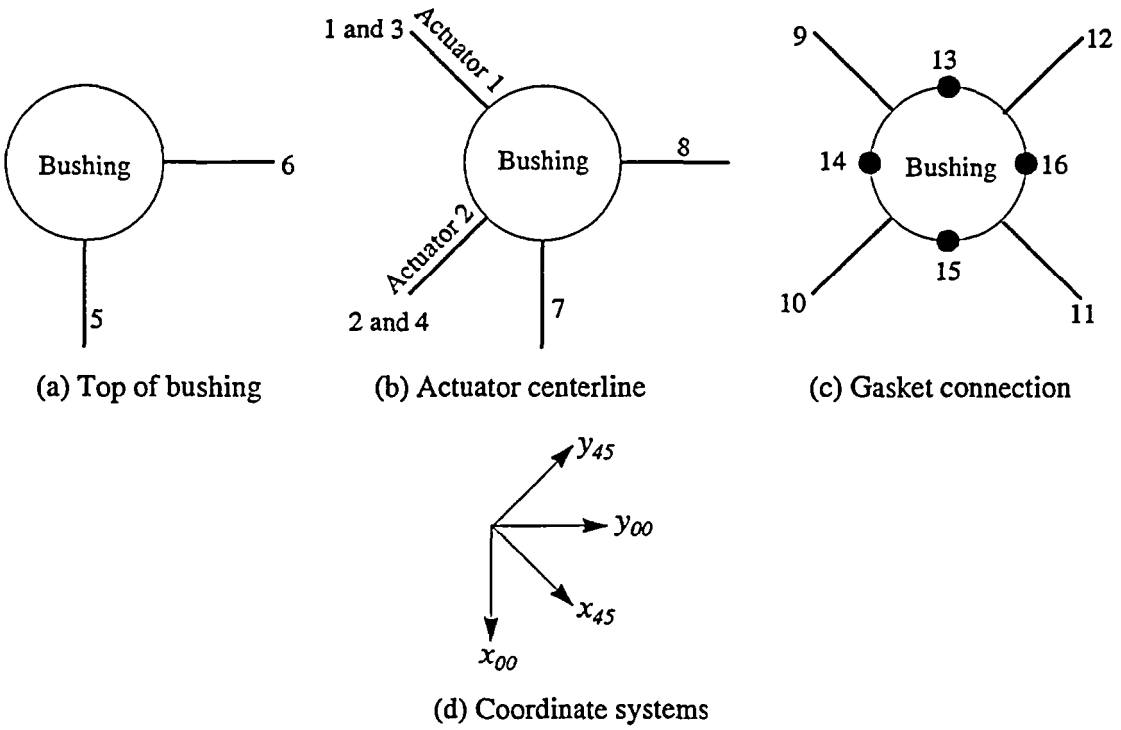

(a) Top of bushing (b) Actuator centerline (c) Gasket connection

(d) Coordinate systems

Figure 6-5 Instrumentation for static tests of Bushing-1

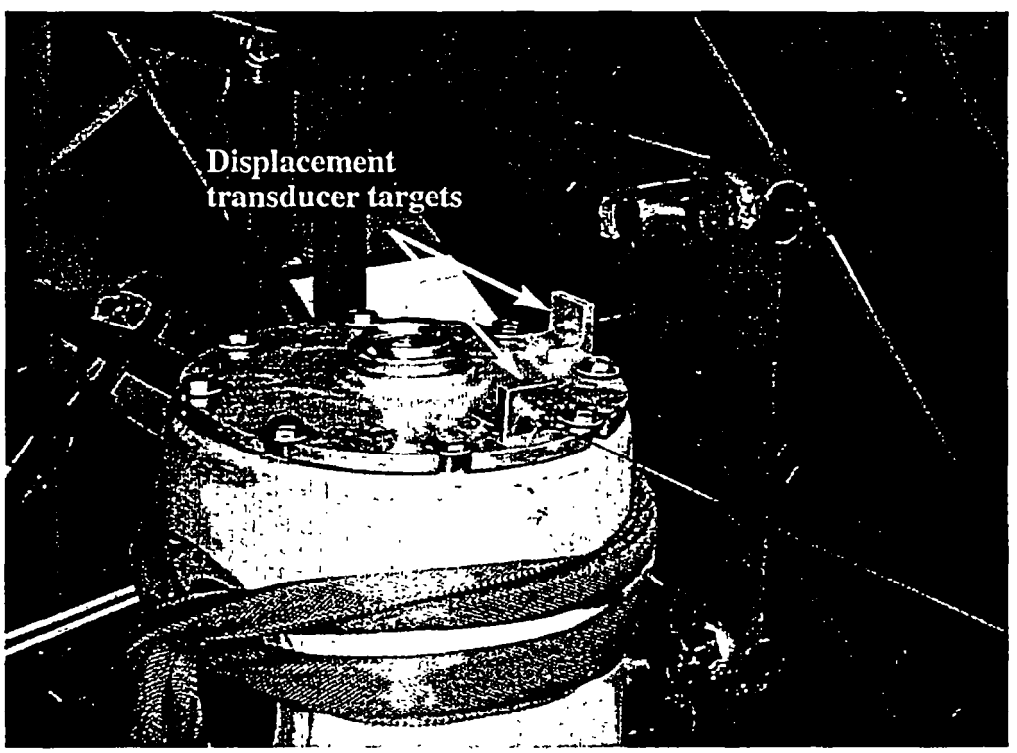

Figure 6-6 Instrumentation at the top of Bushing-1

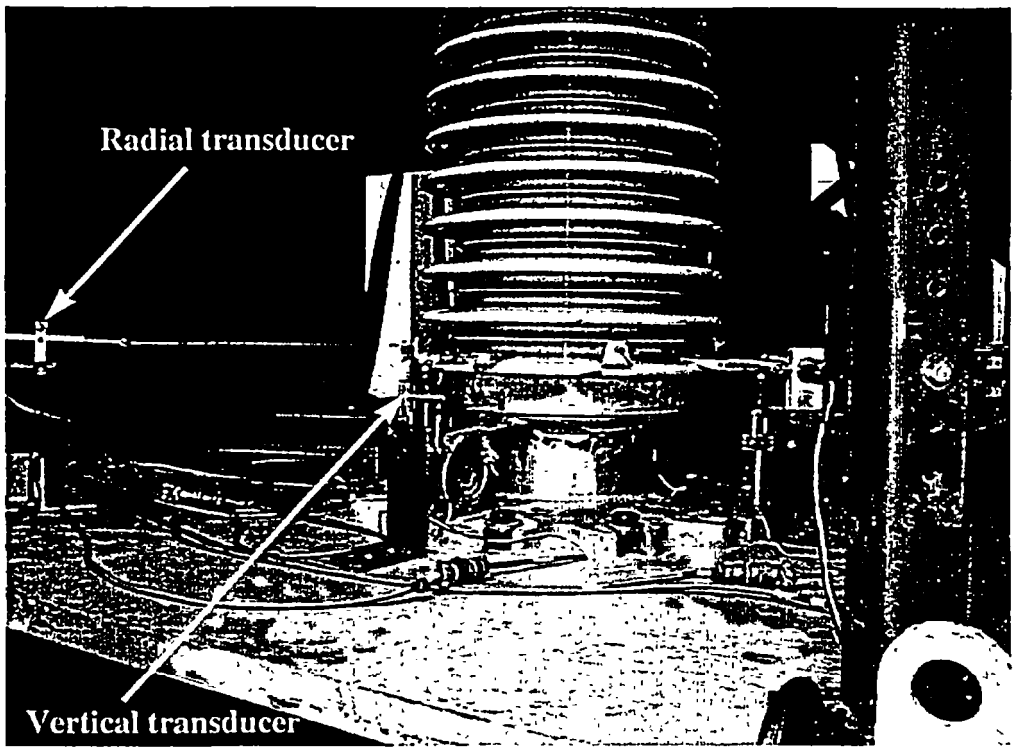

Figure 6-7 Instrumentation of the UPPER-1 porcelain unit

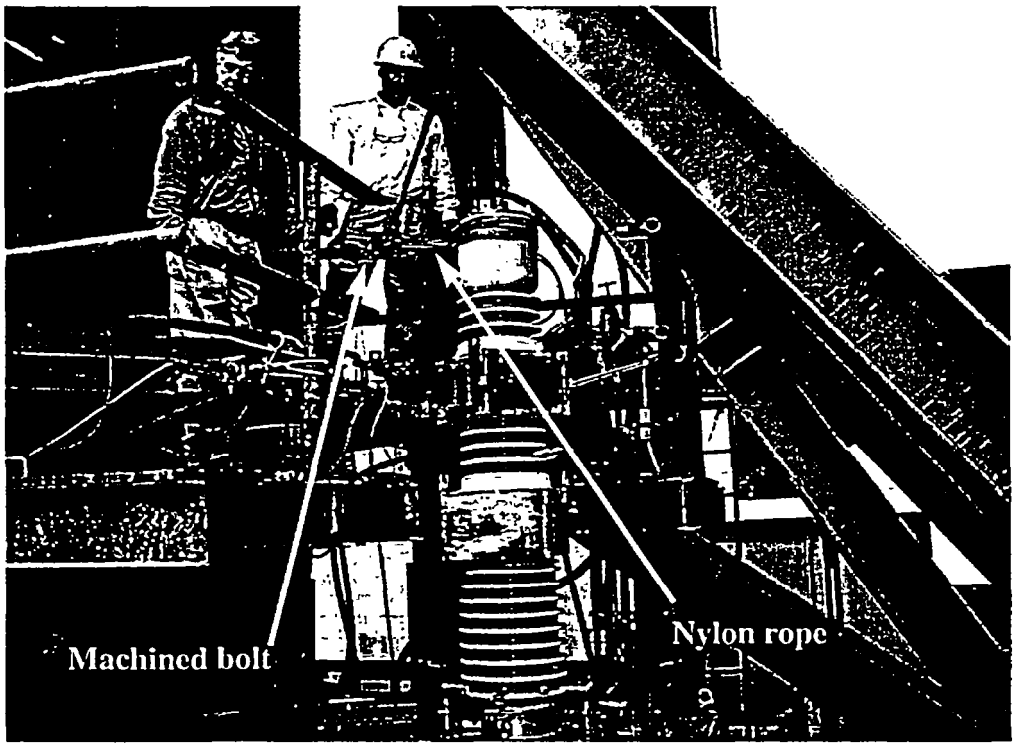

Figure 6-8 Test setup for pull-back, quick-release test

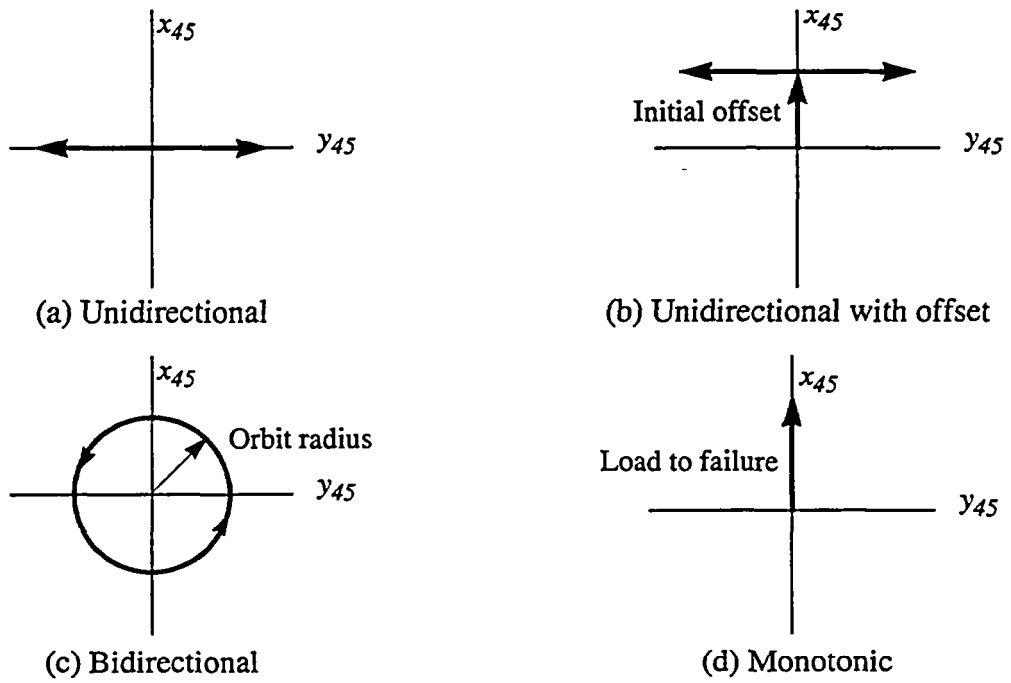

Figure 6-9 Displacement orbits for static tests

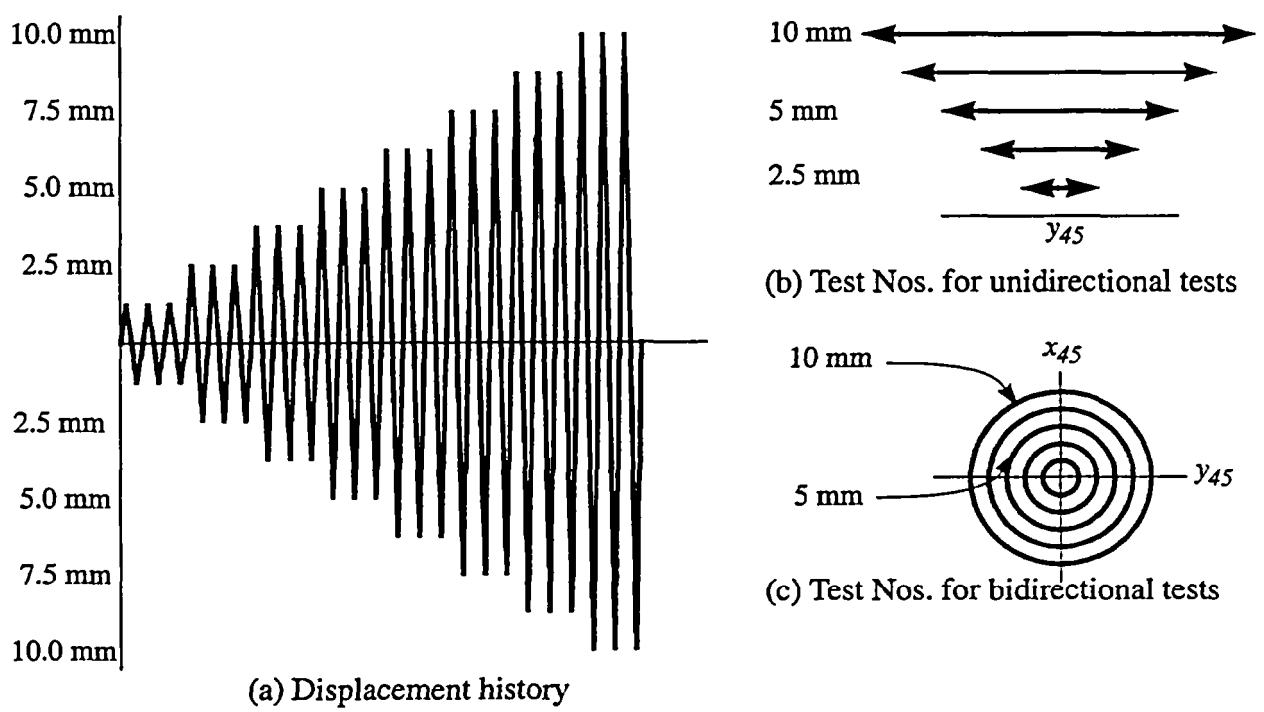

Figure 6-10 Displacement history for static cyclic tests

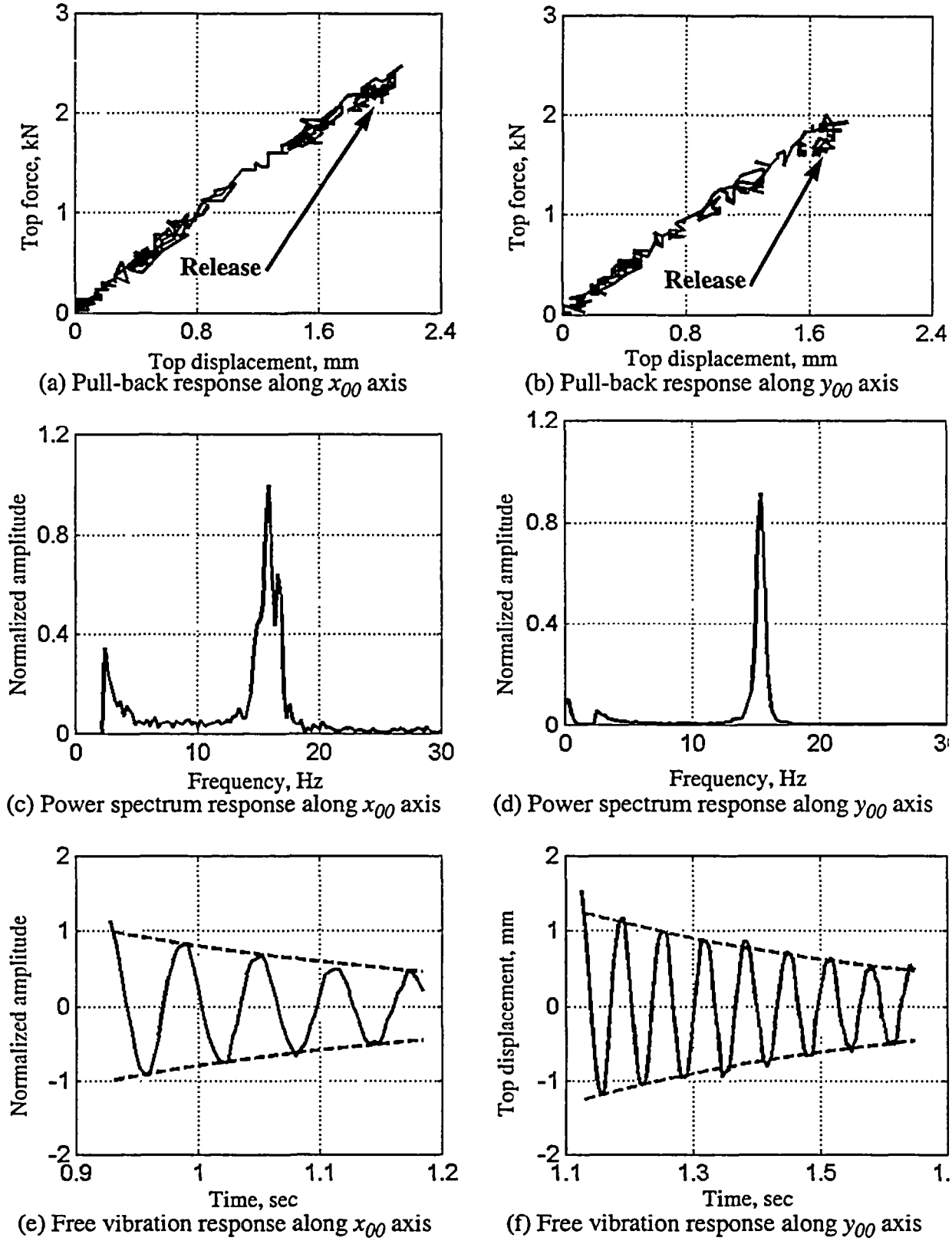

(a) Pull-back response along x_{00} axis

(b) Pull-back response along y_{00} axis

(c) Power spectrum response along x_{00} axis

(d) Power spectrum response along y_{00} axis

(e) Free vibration response along x_{00} axis

(f) Free vibration response along y_{00} axis

Figure 6-11 Time and frequency response of displacement sensors

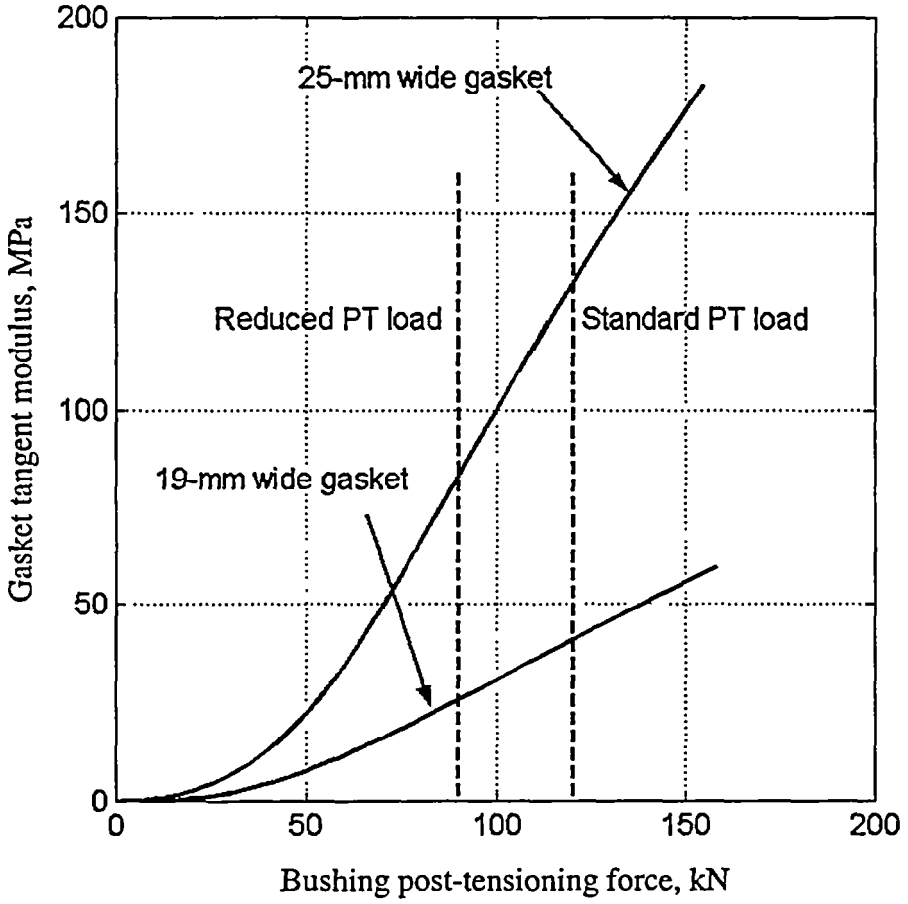

Figure 6-12 Effect of preload on the gasket stiffness

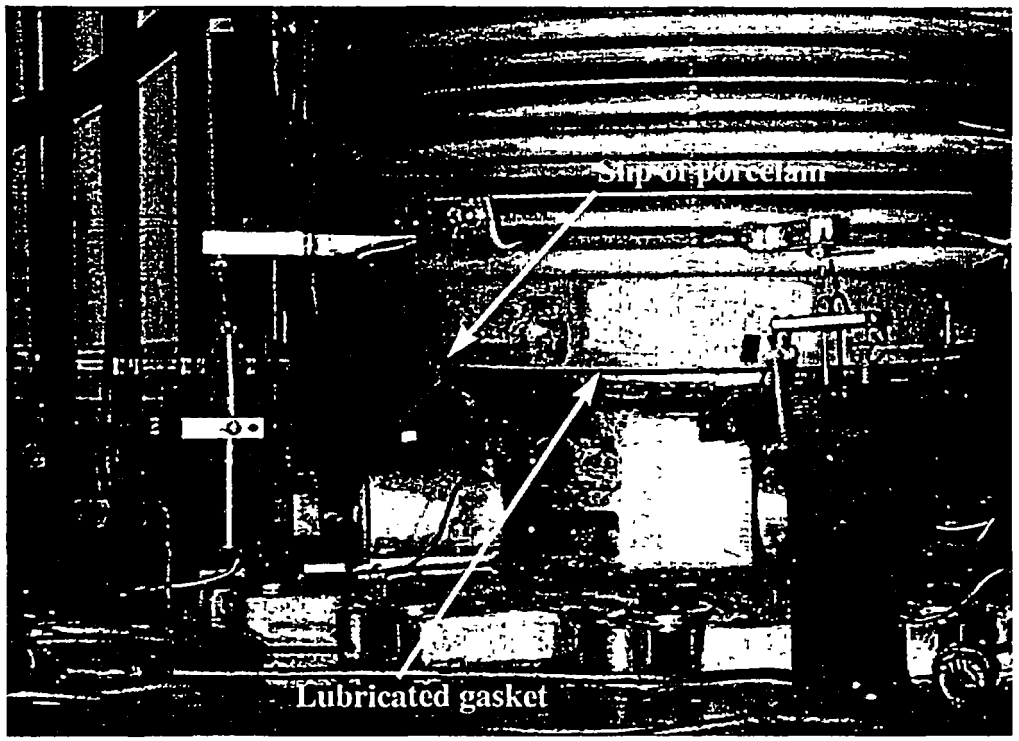

Figure 6-13 Bushing-1 at conclusion of Test Set 1

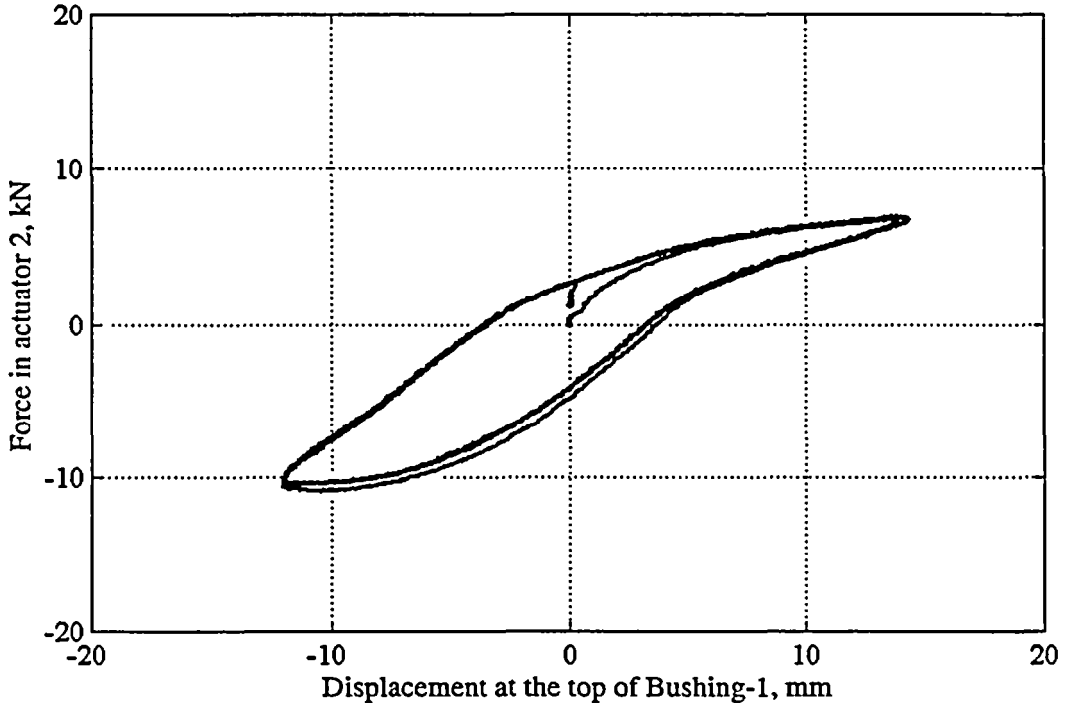

Figure 6-14 Force-displacement response of Bushing-1 (Test No 8, Test Set 1)

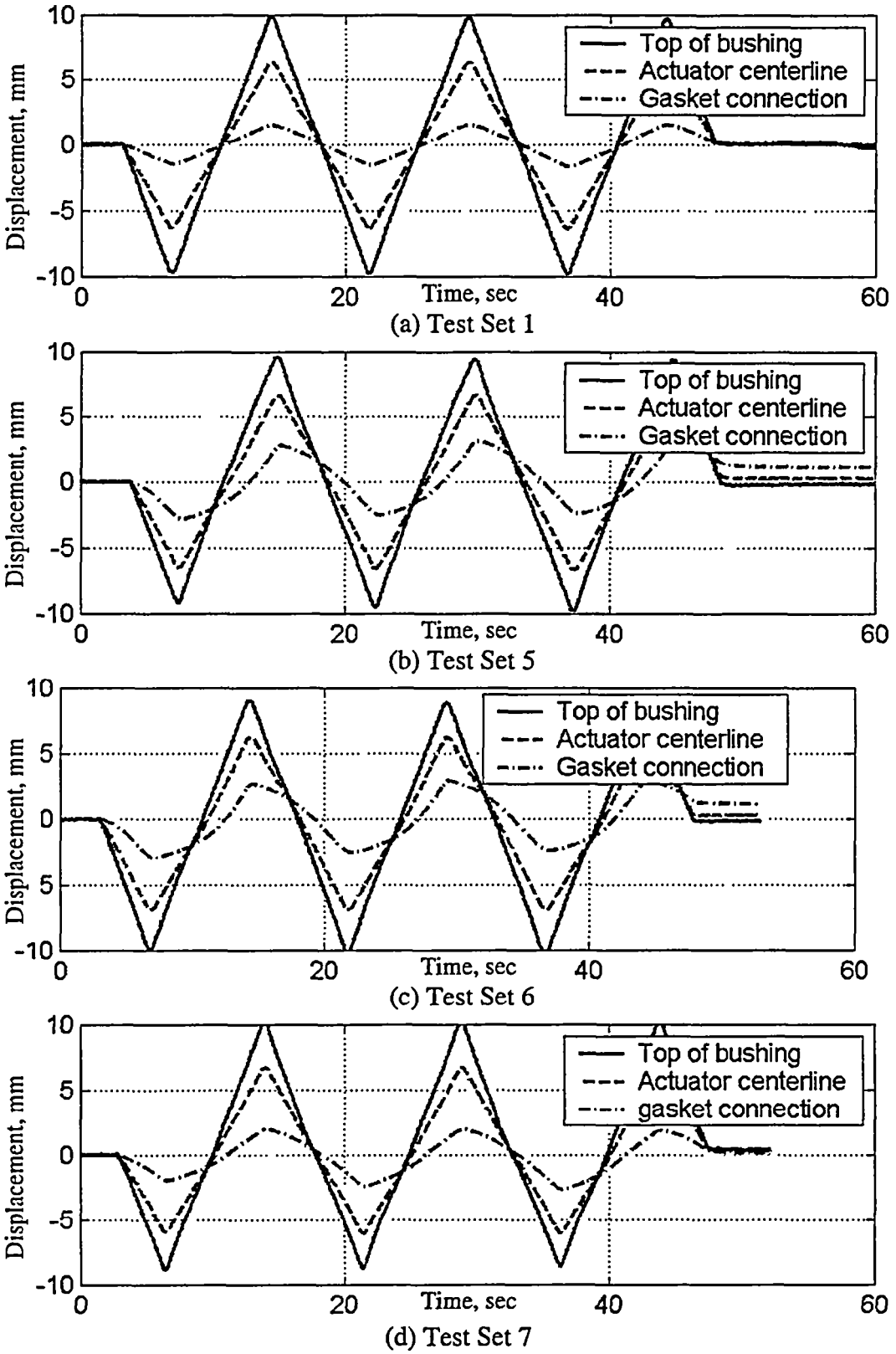

Figure 6-15 Displacement histories of Bushing-1 for Test Sets 1, 5, 6, and 7

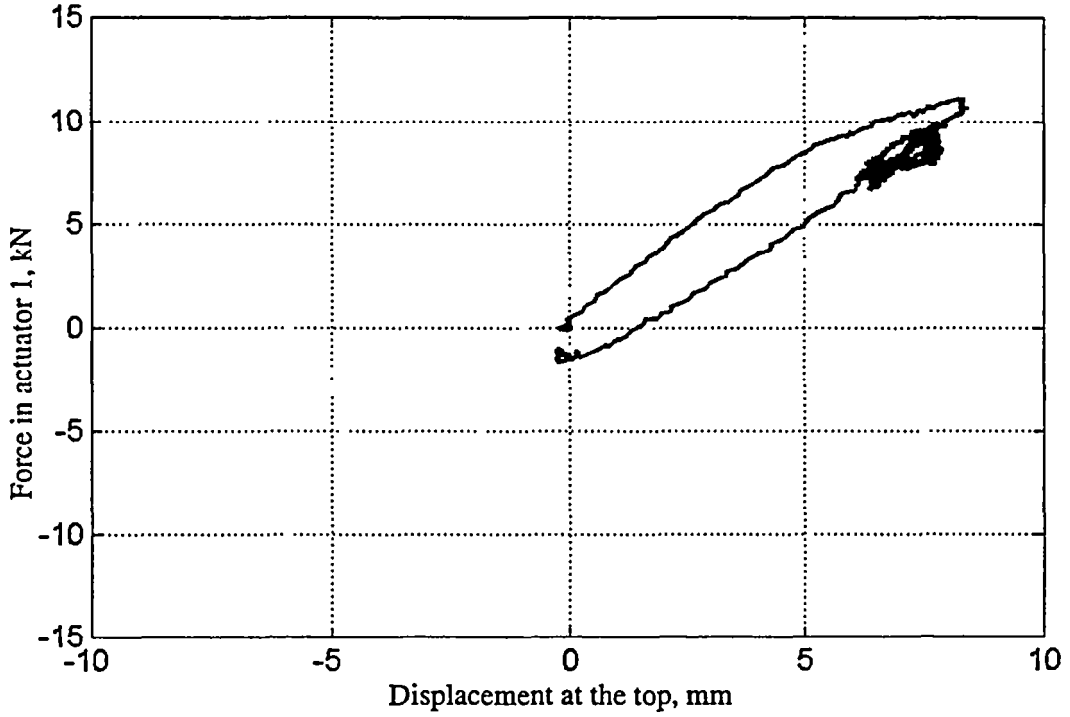

(a) Response along the x_{45} axis

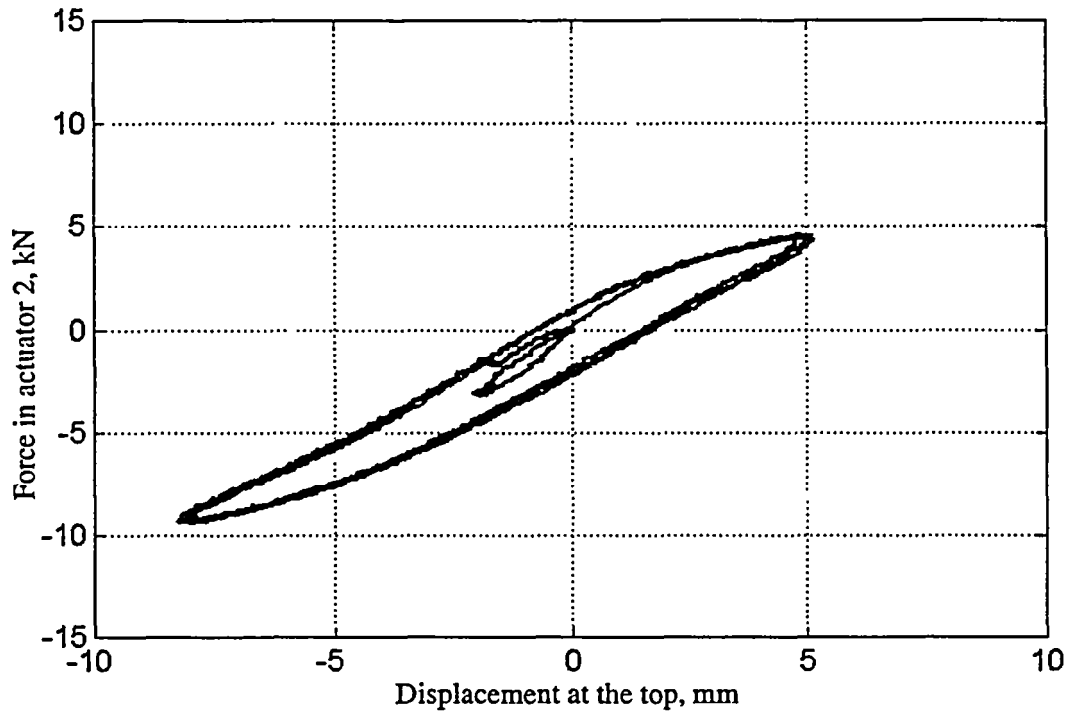

(b) Response along the y_{45} axis

Figure 6-16 Force-displacement history for Bushing-1, Test No 4, Test Set 3

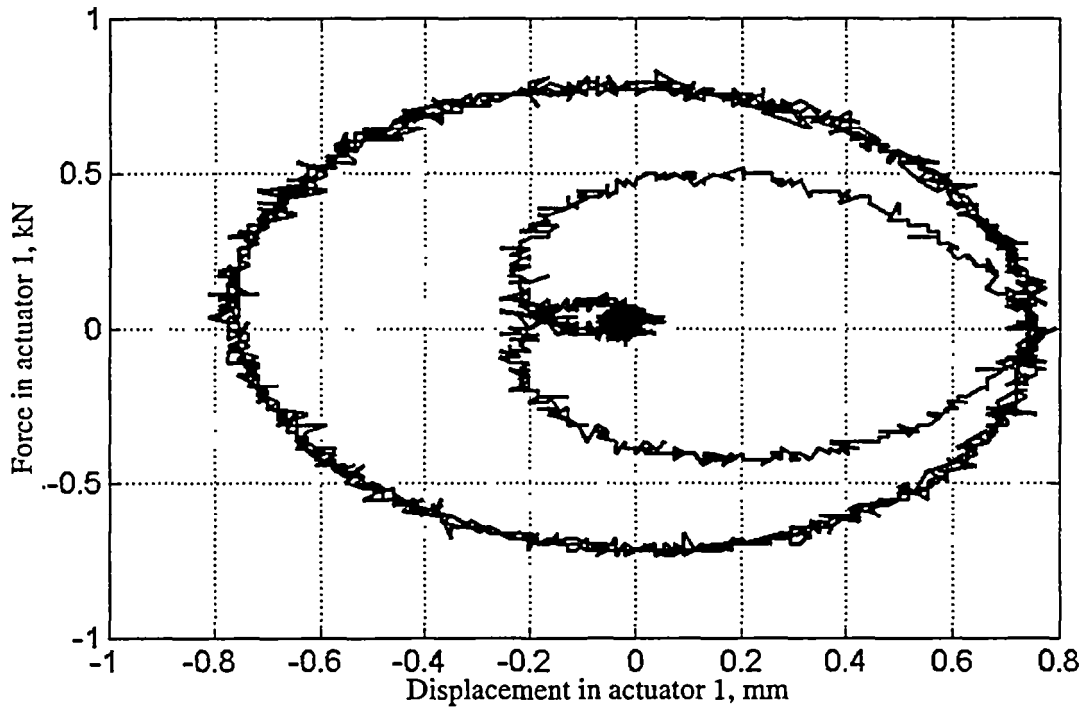

(a) Displacement orbits

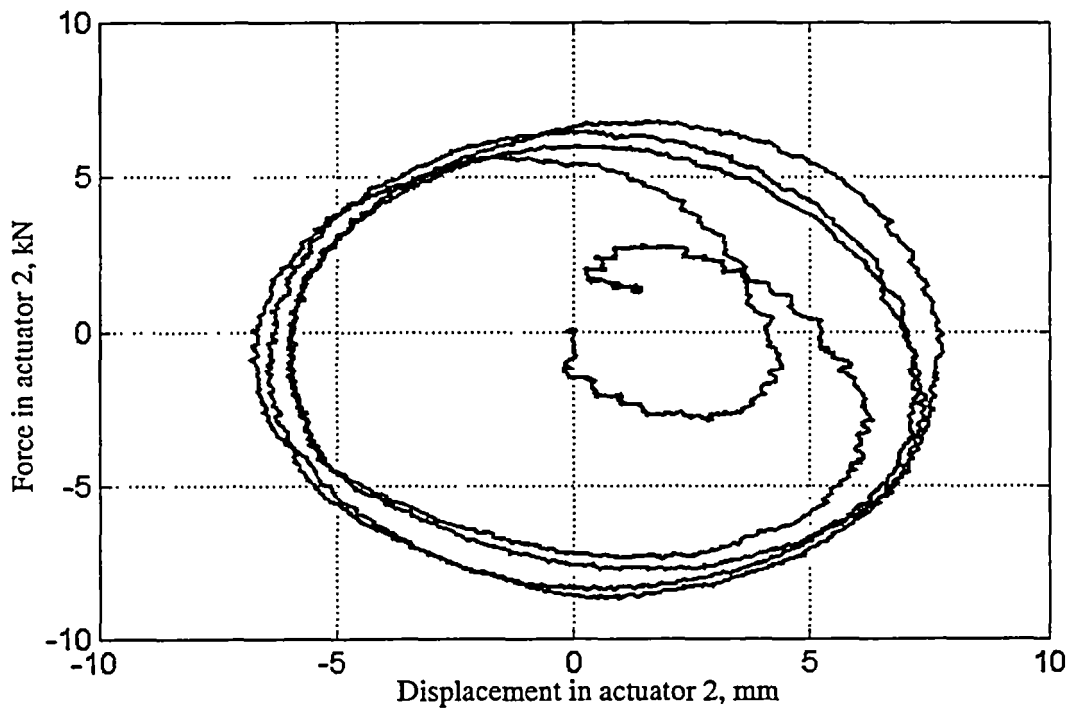

(b) Force orbits

Figure 6-17 Actuator orbits during bidirectional tests (Test No 6, Test Set 4)

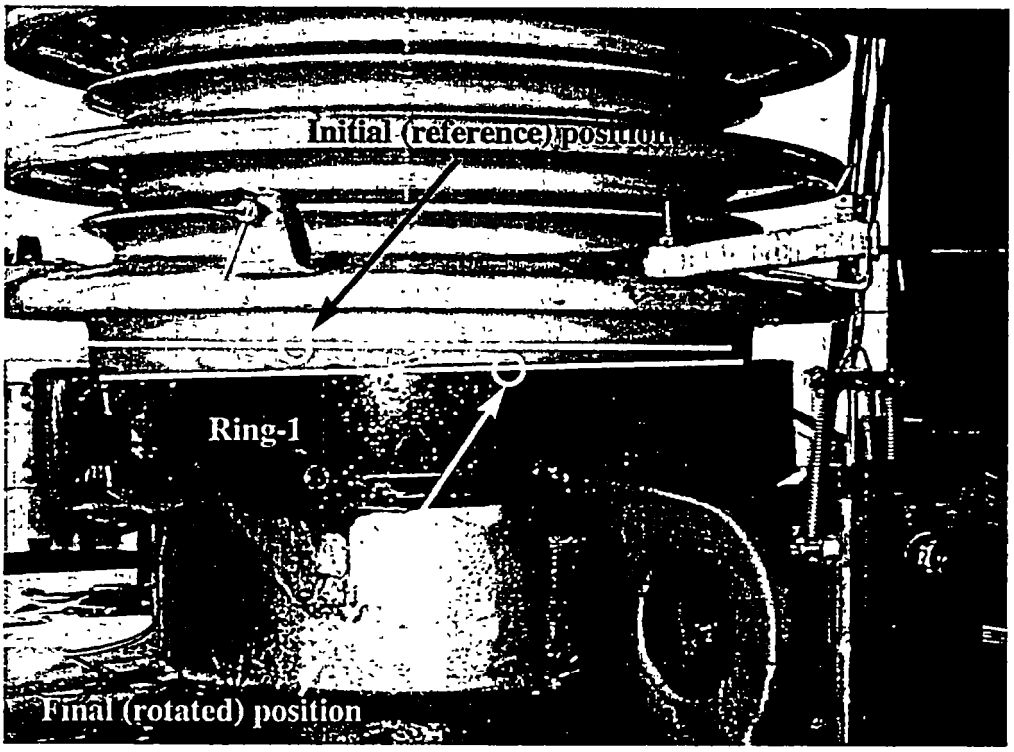

Figure 6-18 Rotation of Ring-1 following Test Set 12

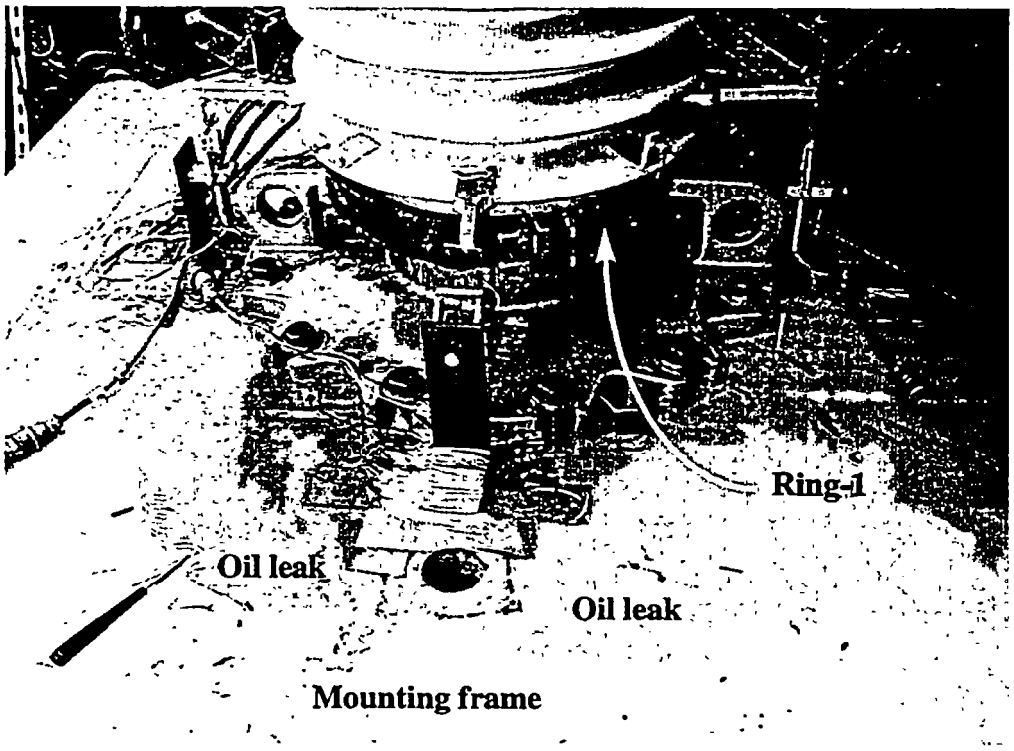

Figure 6-19 Oil leakage from the gasket connection following Test Set 12

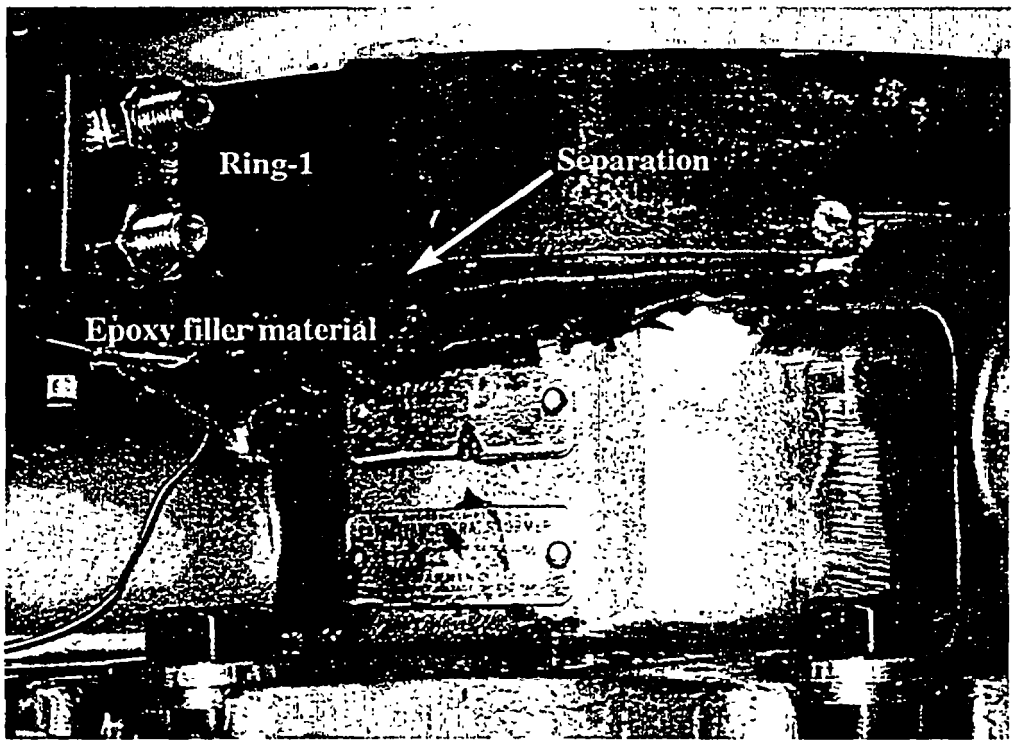

Figure 6-20 Separation of Ring-1 from the epoxy filler material, Test Set 13

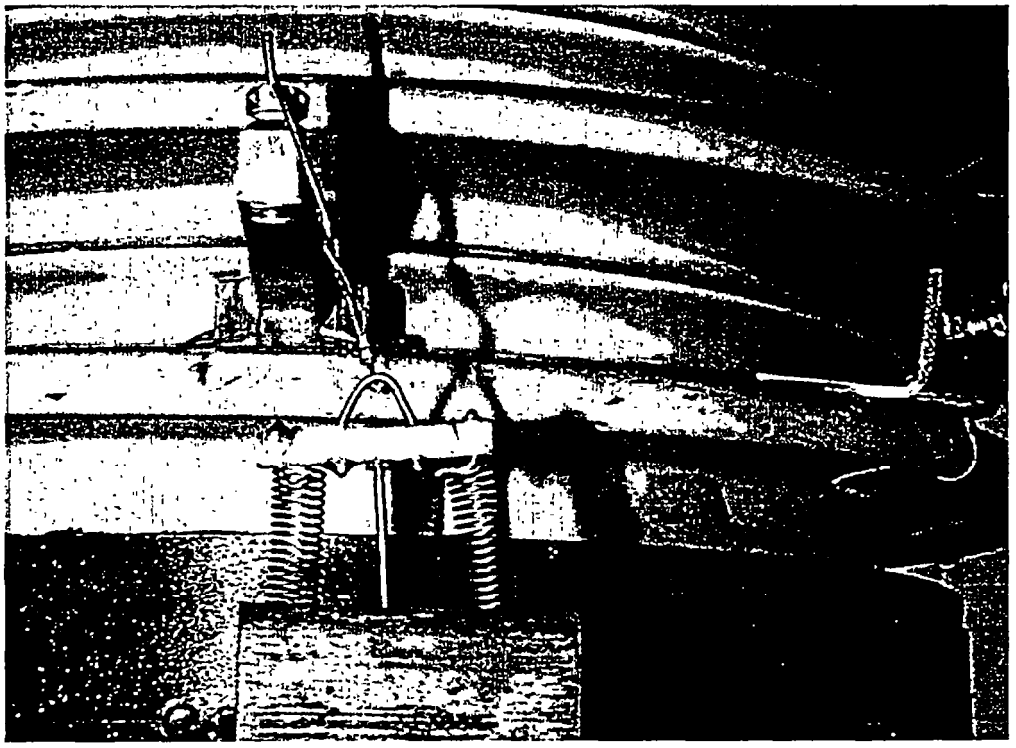

Figure 6-21 Twist of the UPPER-1 porcelain unit over the flange, Test Set 13

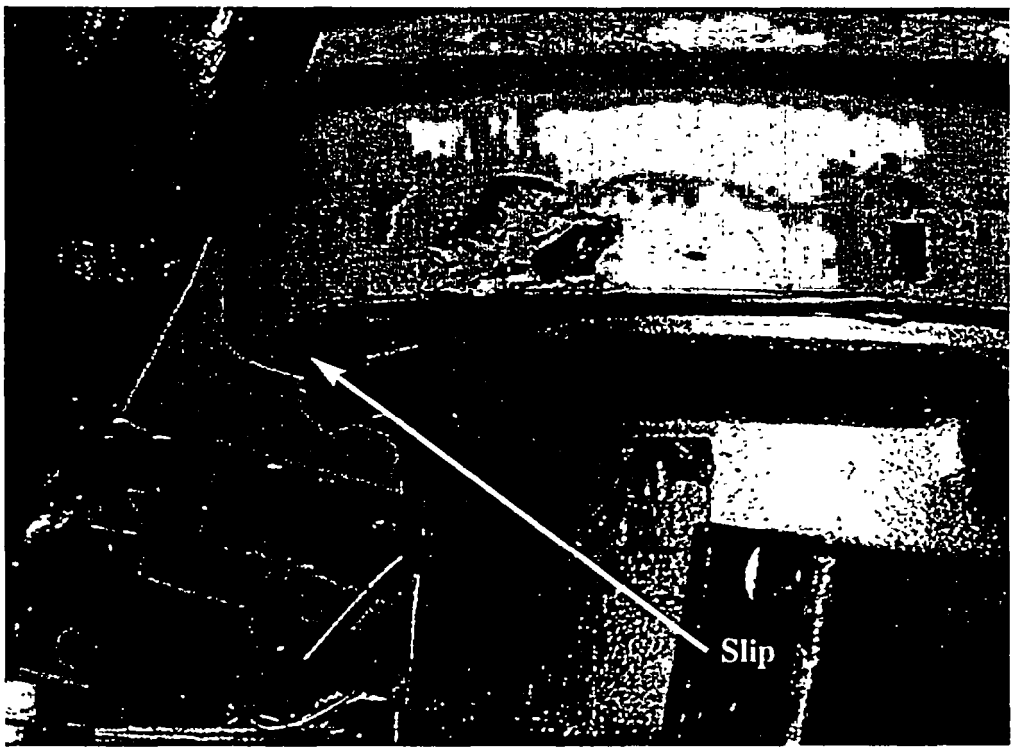

Figure 6-22 Slip of the UPPER-1 porcelain unit following Test Set 14

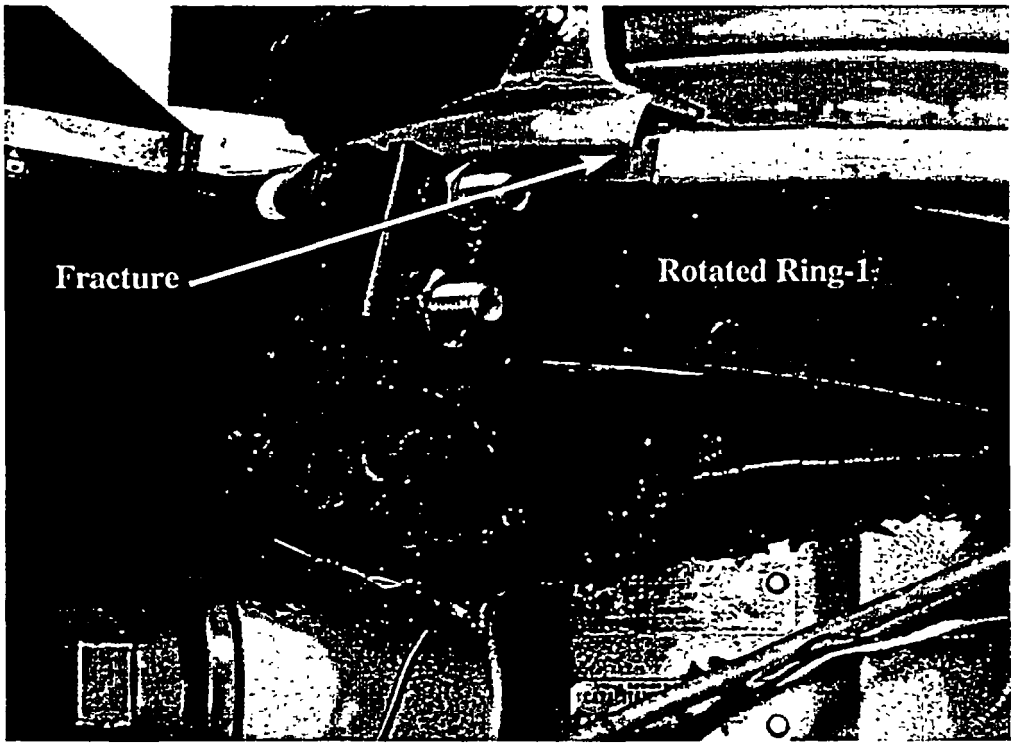

Figure 6-23 Fracture of the bottom shed of the UPPER-1 porcelain unit, Test Set 14

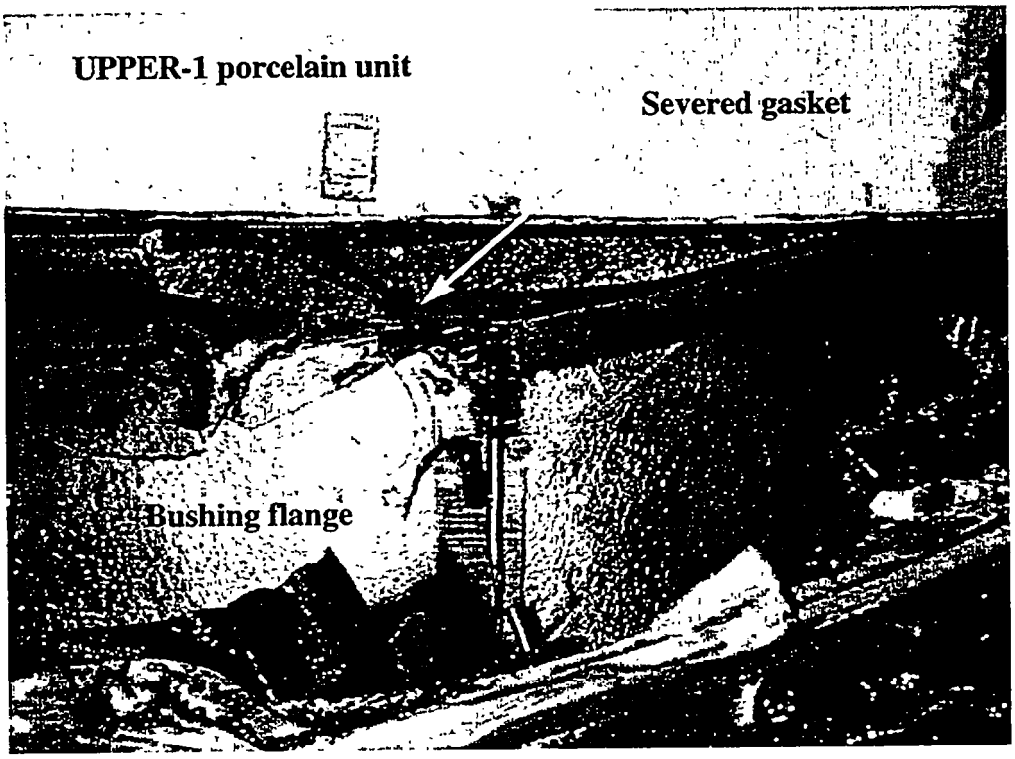

Figure 6-24 Torn portion of gasket at the gasket connection, Test Set 14

Figure 6-25 Fracture of cast aluminum flange following Test Set 14

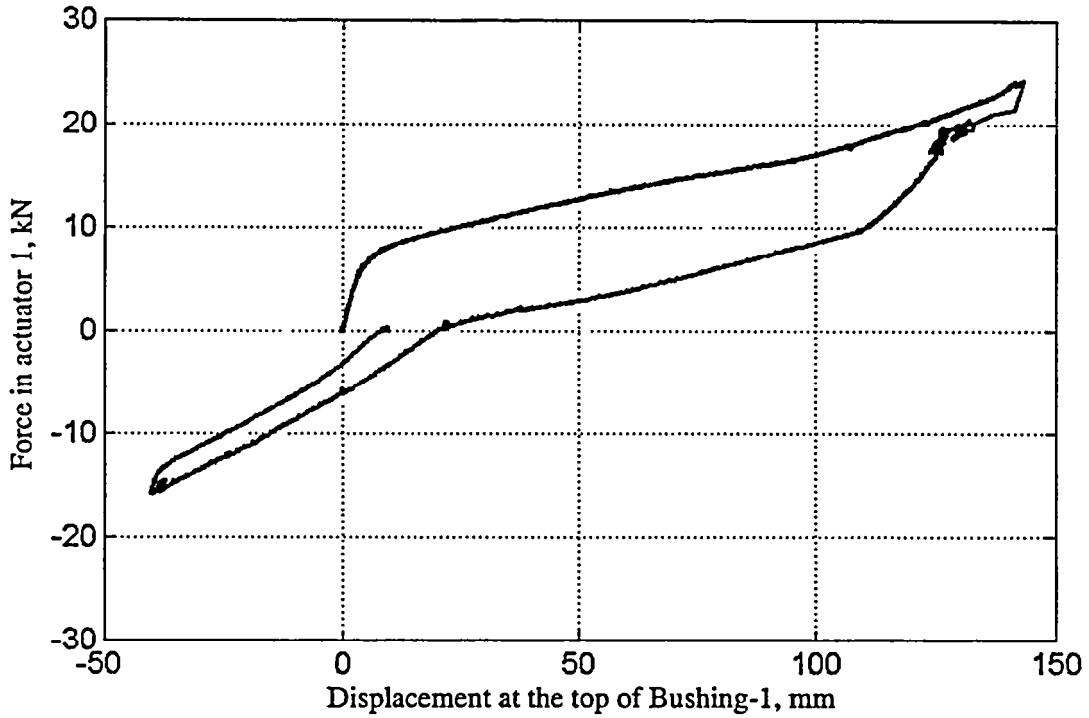

(a) Hysteretic response at the top of Bushing-1

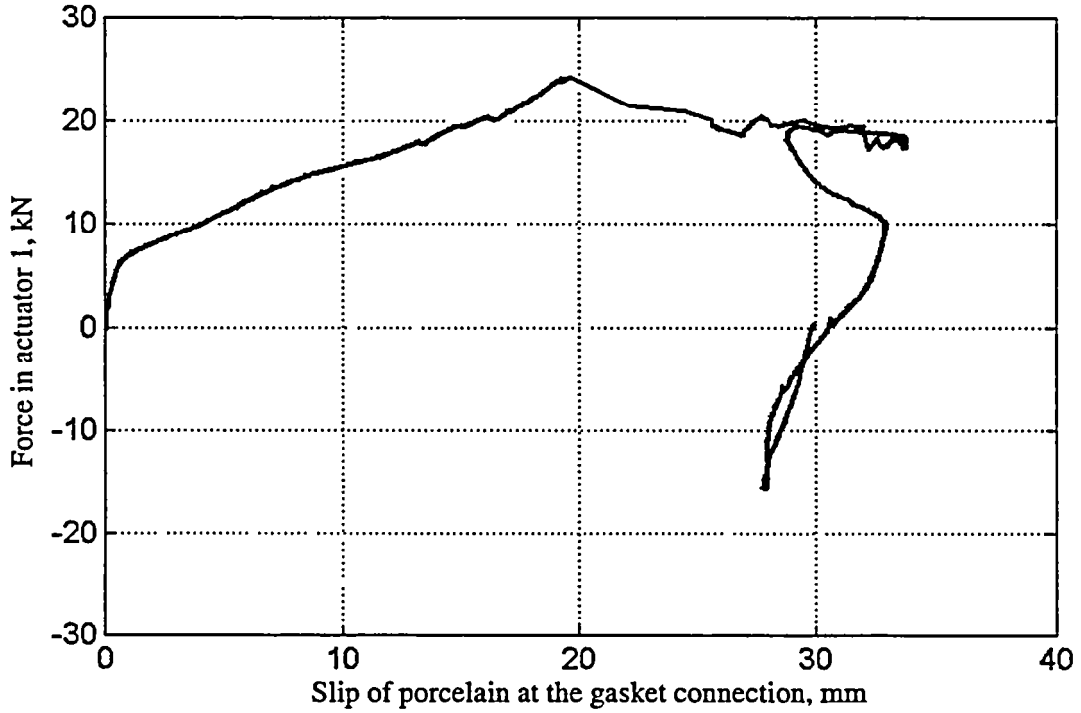

(b) Hysteretic response at the gasket connection of Bushing-1

Figure 6-26 Response of Bushing-1 during the monotonic test (Test Set 14)

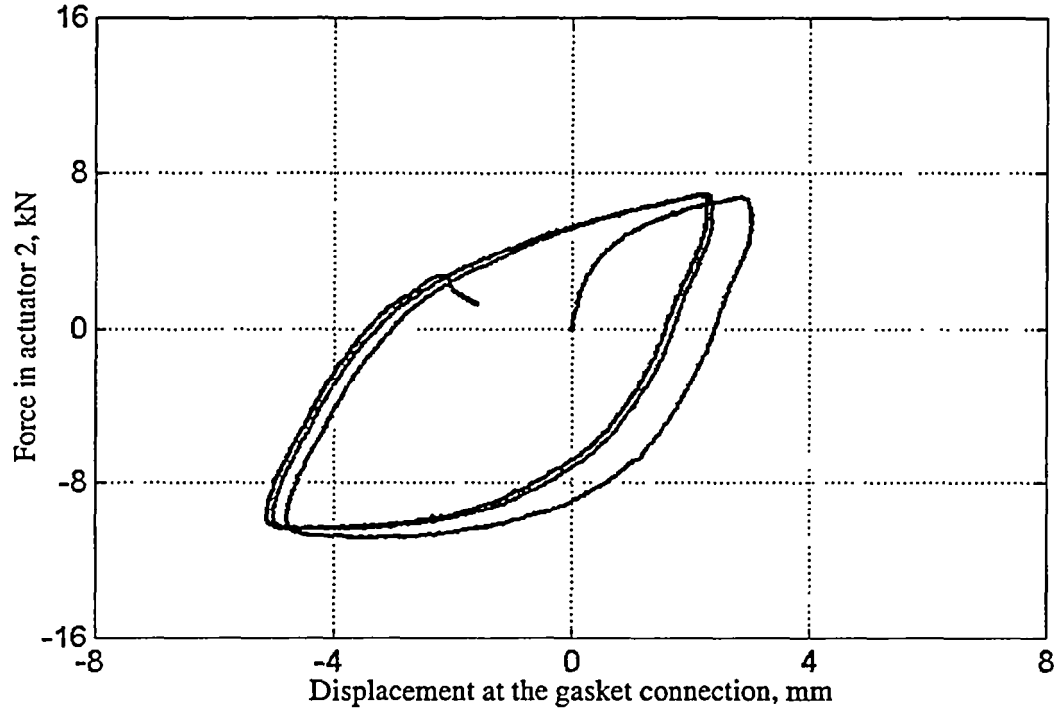

(a) Hysteretic response at the gasket connection, Test No 8, Test Set 01 (dry gasket)

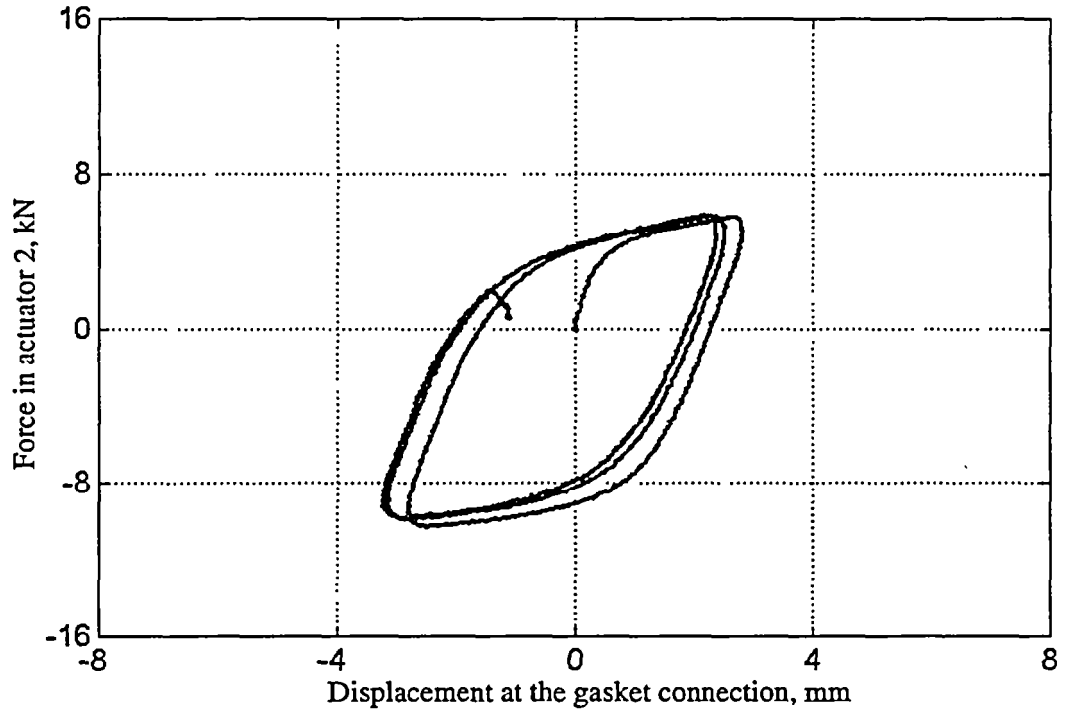

(b) Hysteretic response at the gasket connection, Test No 6, Test Set 05 (lubricated gasket)

Figure 6-27 Force-displacement response of Bushing-1 at the gasket connection

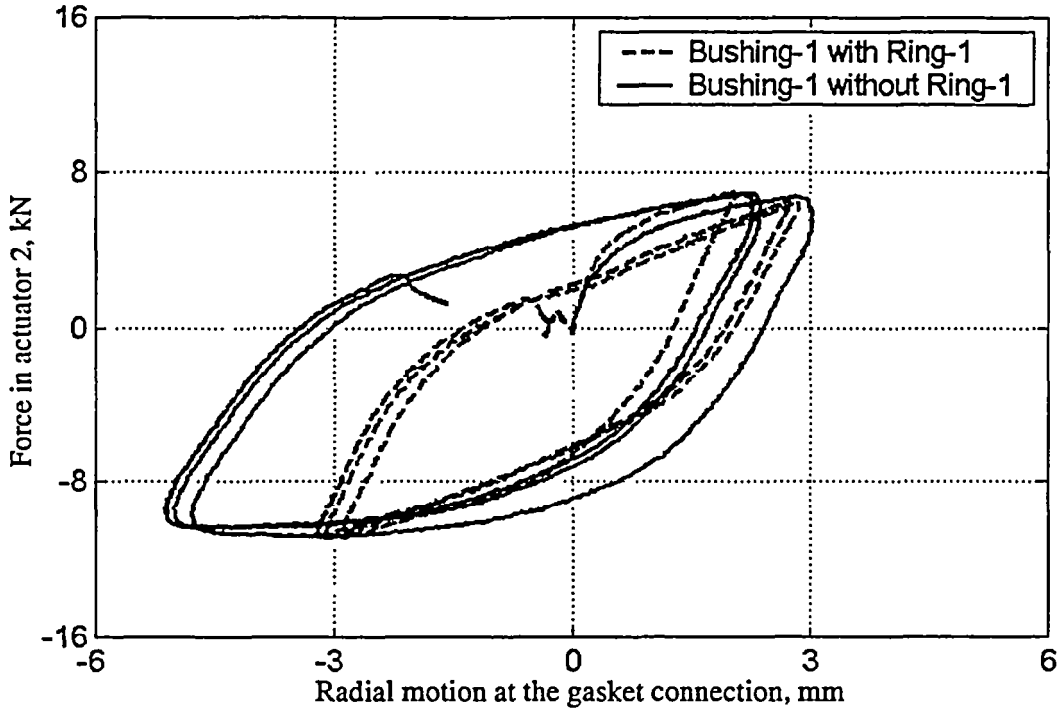

(a) Actuator 2 force-porcelain slip relation at the gasket connection

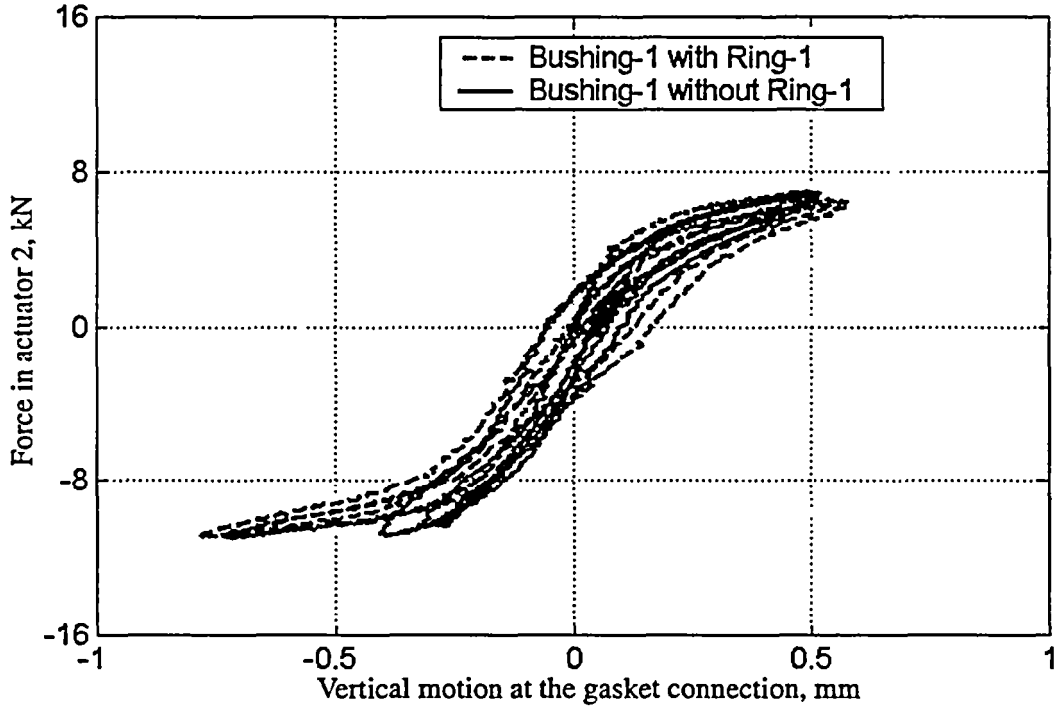

(b) Actuator 2 force-porcelain uplift relation at the gasket connection

Figure 6-28 Response of Bushing 1 at the gasket connection (Test Sets 1 and 12)

7 Fragility Testing of Flexibly Mounted Bushing-2

7.1 Overview

Triaxial earthquake simulator testing was used to evaluate the seismic response of Bushing-2 mounted on a *flexible* support and to evaluate the efficacy of the Ring-2 retrofit detail. The following sections describe the test setup including the *flexible* mounting attachment, the earthquake motions developed for the fragility tests, the instrumentation of the bushing, and selected test results.

7.2 Attachment of 230-kV Bushings to Transformers

Porcelain transformer bushings are typically mounted either to the transformer top plate or to a turret that is attached to the transformer top plate or cantilevered from the side of the transformer. The top plate of the transformers for 230-kV bushings are typically 3/8 in. (10 mm) to 1/2 in. (13 mm) thick; longitudinal and transverse stiffeners are usually welded to the underside of the top plate to provide additional vertical stiffness. In a typical installation, a 1/4-in. (6-mm) thick annular gasket (herein referred to as the mounting gasket) with a Durometer hardness of between 55 to 65 is inserted between the bushing flange and the transformer or turret top plate. The flexibility in both the transformer top plate and the mounting gasket lowers the fundamental frequency of the transformer-bushing system. Field data and analytical studies (Villaverde, et al., 1999) have shown that for the 230-kV bushings mounted on transformers, the frequency of the bushing-transformer system was between 6 and 8 Hz and that the ground accelerations were amplified at the bushing flange.

The *flexible* support described in this chapter was designed to lower the frequency of the bushing-support system (the fundamental frequency of the bushing mounted on the support frame is referred to as the frequency of the bushing-support system hereafter) but did not amplify the horizontal input motions at the bushing flange.

7.3 Test Setup

7.3.1 Mounting setup

In lieu of detailed information regarding transformer design, modeling, and connection details, a flexible mounting plate that reduced the frequency of the installed Bushing-2 from 20 Hz to 7 Hz was designed. Finite element analysis program SAP 2000 (CSI, 1997) was used to select the plan dimensions and the thickness of the mounting plate.

The *flexible* support, shown in Figure 7-1, consisted of a 1/2-in. (13-mm) thick plate supported by 1 in. (25 mm) plates along each edge. Small 1 in. (25 mm) stiffener plates were welded to each support plate to provide additional lateral stiffness. The *flexible* support was fillet welded to the top of the existing rigid mounting frame to facilitate testing of the bushing at 20 degrees to the vertical. A 1/4-in. (6.3-mm) thick Shore-A annular neoprene rubber gasket with a Durometer hardness of between 55 and 65 was inserted between the bushing flange and the *flexible* mounting plate. Figure 7-2 shows Bushing-2 installed in the mounting frame atop the earthquake simulator. Figure 7-3 is a photograph of the flange connection and shows the mounting gasket. Figure 7-4 shows Ring-2 installed on Bushing-2.

The twelve 3/4-in. (19-mm) bolts connecting the bushing flange to the *flexible* plate were tightened, one at a time, to the manufacturer-specified torque of 100 ft-lbs (136 N-m). However, due to the compressibility of the mounting gasket, the specified torque was not sustained completely. After retightening the bolts a second time, all bolts retained a minimum torque of 60 ft-lbs (82 N-m). During the course of testing program, the torque in the bolts was periodically checked to detect slip (if any) of the bushing flange relative to the *flexible* plate.

7.3.2 Simulator input motions

The test protocol for Bushing-2 installed on a *flexible* mounting frame included resonant-search tests: triaxial earthquake ground motion tests: and pull-back, quick-release tests. The quick-release tests were conducted to investigate the effect of support flexibility, terminal mass, and the mounting gasket on the dynamic properties of bushing-frame system. Information on these tests follow.

7.3.2.1 Resonant-search tests

Sine-sweep and broad band white-noise tests were used to establish the dynamic characteristics (natural frequencies and damping ratios) of a bushing. These so-called *resonant-search* tests were undertaken using unidirectional excitation along each global axis of the earthquake simulator platform. For both sine-sweep and white-noise tests, a simulator input acceleration amplitude of 0.1g was used.

Pull-back, quick-release tests were conducted to measure the lateral stiffness and dynamic properties of the bushing. The pull-back tests were conducted using a maximum concentrated force of approximately 0.5 kips (2 kN) applied at the top of the bushing.

7.3.2.2 Earthquake test response spectrum

IEEE 693-1997 identifies several response spectra of identical shapes but different amplitudes for the qualification of transformer bushings. For a detailed description of these spectra, the reader is referred to Appendix A. Figure 7-5 shows an IEEE 693-1997 High Level qualification response spectrum used for checking porcelain stresses and oil leakage. The spectrum is anchored to a peak ground acceleration (PGA) equal to 2.0g. Spectrum-compatible earthquake histories were generated using the procedures set forth in Section 3.2.3.

Two separate and independent three-component records were utilized for fragility testing. Chapter 3 provides details for these records. The Tabas-A motion was used for all the tests up to and including motions with target PGAs of 1.0g. The Tabas-B motion was used for tests with target PGAs exceeding 1.0g but less than 2.0g.

At the request of the utility participants, one additional three-component spectrum-compatible input motion was used for testing Bushing-2. This motion (hereafter referred to as CERL) was the motion used by the Construction Engineering Research Laboratories of the US Army Corps of Engineers to test a 500-kV bushing and was generated using random input motion (Wilcoski, et al., 1997). Figure 7-6 through Figure 7-8 present the acceleration history, power spectrum, and response spectra for the three components of the spectrum-compatible CERL record. The power spectra for these three histories are narrow banded and are not representative of strong motion shaking.

7.3.3 Instrumentation

For seismic testing, IEEE 693-1997 (see Appendix A) states that porcelain bushings must be instrumented to record (a) maximum vertical and horizontal accelerations at the top of the bushing, at the bushing flange, and at the top of the earthquake simulator platform, (b) maximum displacement of the top of the bushing relative to the flange, and (c) maximum porcelain stresses at the base of the bushing near the flange. The instrumentation scheme developed for the tests described in this chapter differed from the IEEE 693-1997 requirements. Specifically, since previous tests of 230-kV bushings at PEER had shown that the porcelain stresses were significantly smaller than the ultimate value, no strain gages were attached to the UPPER-1 porcelain unit.

The instrumentation scheme developed for the tests described in this chapter consisted of 59 transducers and 61 channels of data. Table 7-1 lists the channel number, instrument type, response quantity, coordinate system, and location for each transducer. Figure 7-9 presents information on the instrumentation of the earthquake simulator platform (Figure 7-9a), the flexible mounting plate (Figure 7-9b), the bushing and the mounting frames (Figure 7-9c), and the UPPER-1 porcelain unit (Figure 7-9d). The global (X, Y, Z) and local (x, y, z) coordinate systems adopted for the testing program are shown in the figure. Figure 7-10 is a photograph of the instrumentation at the top of Bushing-2. Figure 7-11 is a photograph of the instrumentation immediately above the flange plate.

Sixteen channels (channels 3 through 18) recorded the acceleration and displacement of the earthquake simulator platform in the global coordinate system. The accelerations of the *rigid* mounting frame in the local coordinate system (channels 28 through 30) and the absolute displacements of the *rigid* mounting frame in the global coordinate system (channels 40 and 41) were recorded. The accelerations of the *flexible* mounting plate in the local coordinate system (channels 31 through 33) and the absolute displacements of the *flexible* mounting plate in the global coordinate system (channels 42 and 43) were recorded. The accelerations of the bushing in the local coordinate system (channels 19 through 27) and the absolute displacements of the bushing in the global coordinate system (channels 34 through 39) were measured at the top, midheight, and bottom of the bushing. Four displacement transducers (channels 44 through 47), located immediately above the gasket, measured radial slip of the UPPER-1 porcelain unit relative to the *rigid* support frame. Four displacement transducers (channels 48 through 51) recorded the UPPER-1 porcelain unit displacements (relative to the *flexible* plate) across the gasket, parallel to the local-z axis of the bushing. Another two displacement transducers (channels 52 and 53), located immediately above the gasket, measured the twist of the UPPER-1 porcelain unit relative to the *rigid* support frame. Eight displacement transducers (channels 54 through 61) measured the out-of-plane deformation of the *flexible* mounting plate along the local z- axis, relative to the *rigid* frame. Channels 55, 57, 59, and 61 were located approximately 11 in. (280 mm) from the centerline of the bushing. Channels 54, 56, 58, and 60 were located approximately 21 in. (533 mm) from the centerline of the bushing.

7.3.4 Preparation of Bushing-2

Previous tests of Bushing-2 mounted on a *rigid* support was described in Chapter 4. Prior to retesting this bushing on the *flexible* support, the bushing was de-stressed, drained of its oil, and partially disassembled. The gasket at the gasket connection was inspected and air dried, the porcelain units were re-centered, the bushing was post-tensioned to 27 kips (120 kN), and then refilled with oil.

7.4 Summary of Experimental Data from Pull-Back, Quick-Release Tests

7.4.1 Introduction

Pull-back, quick-release tests were conducted to evaluate the effect of the plate flexibility, the mounting gasket, and the top terminal on the dynamic properties of Bushing-2. Three sets of tests were conducted. A complete set of data was collected from the pull-back, quick-release tests at the top of the bushing along the x-axis. Additional data was gathered from the pull-back, quick-release tests at the top of the bushing in the y- direction and from the tests at the bottom of the bushing in the x- direction.

Table 7-1 Instrumentation of Bushing-2 mounted on the flexible plate

Channel Number	*Transducer*[1]	*Response Quantity*	*Coordinate System and Orientation*[2]	*Transducer Location*[3]
3	LVDT	platform displacement	global *X*	simulator platform
4	LVDT	platform displacement	global *Y*	simulator platform
5	LVDT	platform displacement	global *X*	simulator platform
6	LVDT	platform displacement	global *Y*	simulator platform
7	LVDT	platform displacement	global *Z*	simulator platform
8	LVDT	platform displacement	global *Z*	simulator platform
9	LVDT	platform displacement	global *Z*	simulator platform
10	LVDT	platform displacement	global Z	simulator platform
11	A	platform acceleration	global *X*	simulator platform
12	A	platform acceleration	global *X*	simulator platform
13	A	platform acceleration	global *Y*	simulator platform
14	A	platform acceleration	global *Y*	simulator platform
15	A	platform acceleration	global *Z*	simulator platform
16	A	platform acceleration	global *Z*	simulator platform
17	A	platform acceleration	global *Z*	simulator platform
18	A	platform acceleration	global Z	simulator platform
19	A	bushing acceleration	local *x*	bottom of bushing
20	A	bushing acceleration	local *y*	bottom of bushing
21	A	bushing acceleration	local *z*	bottom of bushing
22	A	bushing acceleration	local *x*	midheight of bushing
23	A	bushing acceleration	local *y*	midheight of bushing
24	A	bushing acceleration	local *z*	midheight of bushing
25	A	bushing acceleration	local *x*	top of bushing
26	A	bushing acceleration	local *y*	top of bushing
27	A	bushing acceleration	local *z*	top of bushing
28	A	frame acceleration	local *x*	rigid mounting frame
29	A	frame acceleration	local *y*	rigid mounting frame
30	A	frame acceleration	local *z*	rigid mounting frame
31	A	frame acceleration	local *x*	flexible mounting plate
32	A	frame acceleration	local *y*	flexible mounting plate
33	A	frame acceleration	local *z*	flexible mounting plate

Table 7-1 Instrumentation of Bushing-2 mounted on the flexible plate

Channel Number	*Transducer*[1]	*Response Quantity*	*Coordinate System and Orientation*[2]	*Transducer Location*[3]
34	LP	bushing displacement	global *X*	bottom of bushing
35	LP	bushing displacement	global *Y*	bottom of bushing
36	LP	bushing displacement	global *X*	midheight of bushing
37	LP	bushing displacement	global *Y*	midheight of bushing
38	LP	bushing displacement	global *X*	top of bushing
39	LP	bushing displacement	global *Y*	top of bushing
40	LP	frame displacement	global *X*	rigid mounting frame
41	LP	frame displacement	global *Y*	rigid mounting frame
42	LP	frame displacement	global *X*	flexible mounting plate
43	LP	frame displacement	global *Y*	flexible mounting plate
44	DCDT	UPPER-1 slip	local *x*	gasket connection
45	DCDT	UPPER-1 slip	local *y*	gasket connection
46	DCDT	UPPER-1 slip	local *x*	gasket connection
47	DCDT	UPPER-1 slip	local *y*	gasket connection
48	DCDT	UPPER-1 uplift	local *z*	gasket connection
49	DCDT	UPPER-1 uplift	local *z*	gasket connection
50	DCDT	UPPER-1 uplift	local *z*	gasket connection
51	DCDT	UPPER-1 uplift	local *z*	gasket connection
52	DCDT	UPPER-1 twist	local *x*	gasket connection
53	DCDT	UPPER-1 twist	local *x*	gasket connection
54	DCDT	flexible plate uplift	local *z*	flexible mounting plate
55	DCDT	flexible plate uplift	local *z*	flexible mounting plate
56	DCDT	flexible plate uplift	local *z*	flexible mounting plate
57	DCDT	flexible plate uplift	local *z*	flexible mounting plate
58	DCDT	flexible plate uplift	local *z*	flexible mounting plate
59	DCDT	flexible plate uplift	local *z*	flexible mounting plate
60	DCDT	flexible plate uplift	local *z*	flexible mounting plate
61	DCDT	flexible plate uplift	local *z*	flexible mounting plate

1. A = accelerometer; LVDT = displacement transducer; LP = linear potentiometer; SG = strain gage; DCDT = displacement transducer.
2. For the local (*x*-, *y*-, *z*-) and global (*X*- *Y*- *Z*-) coordinate systems see Figure 7-9.
3. For transducer locations on the bushing see Figure 7-9.

7.4.2 Test setup

The test setup for the pull-back, quick-release tests, consisted of a nylon cable connecting the top (or the bottom) of bushing to the reaction frame in-line with a turnbuckle, a load cell, and a machined bolt. During the pull-back stage, the bushing was gradually pulled to approximately 0.5 kips (2 kN). The applied force and the resulting bushing displacement were monitored and recorded using the in-line load cell and displacement transducers. Next, the applied force was suddenly released by cutting the machined bolt. The resulting free vibration response was recorded using accelerometers mounted on the top and bottom of the bushing.

7.4.3 Evaluation of the dynamic properties

The vibration frequencies of Bushing-2 were computed from peaks in the power spectra of the recorded accelerations. The damping ratios were computed from the log-decrement method (Clough and Penzien, 1993). The effective weight of the bushing was computed using the bushing lateral stiffness and frequency and assuming that the bushing is a single-degree-of-freedom system with a lumped mass at the top (or bottom).

7.4.4 Summary of experimental results

The computed dynamic properties of Bushing-2 from the pull-back, quick-release tests along the *x*- direction at the top of the bushing are listed in Table 7-2. The fundamental frequencies of the bushing-support system were 19 and 7.5 Hz for the *rigidly* mounted and *flexibly* mounted bushing, respectively. The computed system frequency for the *rigidly* mounted bushing was consistent with the values previously computed in Chapter 4, and the computed system frequency for *flexibly* mounted bushing was consistent with both the values measured in the field and the value computed from the finite element analysis. The addition of the 1/4-in. (6-mm) thick mounting gasket at the bushing flange-to-support connection reduced the lateral stiffness of the bushing-support system by approximately 25 percent. When the top terminal was not attached to the top of Bushing-2, the effective weight of the bushing was 140 lbs (630 N) for the *rigidly* mounted bushing and 190 lbs (860 N) for the *flexibly* mounted bushing. The tabulated effective weight of 140 lbs (630 N) is approximately 25 percent of the estimated weight of the portion of bushing extending from the bushing flange to the top of bushing (see Chapter 2). When the terminal was attached to the top of the bushing, the fundamental frequency of the bushing-support system was reduced from 19 to 14 Hz for the *rigidly* mounted bushing and from 7.5 to 6.5 Hz for the *flexibly* mounted bushing.

Table 7-2 Modal properties of Bushing-2 along the x-axis[1]

Test ID	*Mounting Frame*[2]	*Top Terminal Installed*[3]	*Mounting Gasket Installed*[4]	*Stiffness (kN/mm)*	*Frequency (Hz)*	*Damping Ratio (% critical)*	*Effective Weight (N)*
1	Rigid	No	No	0.9	19	2	630
2	Rigid	Yes	No	0.9	14	3	1080
3	Rigid	No	Yes	0.8	18	3	630
4	Rigid	Yes	Yes	0.8	13	4	1220
5	Flexible	No	No	0.2	7.5	2	860
6	Flexible	Yes	No	0.2	6.5	3	1170
7	Flexible	No	Yes	0.1	6.5	4	860
8	Flexible	Yes	Yes	0.1	5.5	5	1220

1. Loads imposed at top of bushing.
2. Rigid mounting frame is shown in Figure 4.1; flexible mounting plate is shown in Figure 7-1.
3. Top terminal, shown in Figure 4-6, weighs 280 N; the threaded rod attachment weighs 50 N.
4. Mounting gasket: 6-mm thick annular rubber.

The computed dynamic properties of Bushing-2 from the pull-back, quick-release tests in the y-direction at the top of the bushing are listed in Table 7-3.

Table 7-3 Modal properties of Bushing-2 along the y-axis[1]

Test ID	*Mounting Frame*[2]	*Mounting Gasket Installed*[3]	*Stiffness (kN/mm)*	*Frequency (Hz)*	*Damping Ratio (% critical)*	*Effective Weight (N)*
1	Flexible	No	0.2	7.4	2	880
2	Flexible	Yes	0.1	6.4	4	860

1. Loads imposed at top of bushing.
2. Flexible mounting plate is shown in Figure 7-1.
3. Mounting gasket: 6-mm thick annular rubber.

The computed dynamic properties of Bushing-2 from the pull-back, quick-release tests in the x-direction at the bottom of the bushing are listed in Table 7-4.

Table 7-4 Modal properties of Bushing-2 along the x- axis[1]

Test ID	*Mounting Frame*[2]	*Mounting Gasket Installed*[3]	*Stiffness (kN/mm)*	*Frequency (Hz)*	*Damping Ratio (% critical)*	*Effective Weight (N)*
1	Rigid	No	2.1	52	2	200

1. Loads imposed at bottom of bushing.
2. Rigid mounting frame is shown in Figure 4.1.
3. Mounting gasket: 6-mm thick annular rubber.

7.5 Experimental Results from Seismic Tests

7.5.1 Introduction

The objective of the testing program was to determine the dynamic properties and seismic response of the *flexibly* mounted Bushing-2 and to evaluate the efficacy of retrofit Ring-2 detail in improving the seismic response of the bushing.

7.5.2 Summary of experimental data

The list of earthquake tests and key observations for Bushing-2 with and without retrofit Ring-2 are presented in Table 7-5 and Table 7-6, respectively.

After each earthquake test, the response data were analyzed, the bushing was inspected for damage and oil seepage, and the bolts joining the bushing flange plate to the *flexible* mounting frame were checked for tightness. All bolts were found to be tight after all tests.

For all tests, the transducer response histories were processed using the computer program Matlab (Mathworks, 1999). Experimental histories were low-passed filtered using a rectangular filter with a cut-off frequency of 50 Hz and then zero-corrected.

7.5.3 Dynamic properties of Bushing-2 mounted on the flexible plate

Sine-sweep and white-noise tests were used to calculate the modal frequencies and damping ratios for Bushing-2. Figure 7-16 shows the transfer functions between the top of the bushing and the *flexible* plate in the three local directions (x, y, z) for Bushing-2, as calculated from Test Nos 1 through 3 of Table 7-5. The resonant frequencies in the local x- and y-directions are approximately 6.8 Hz and 6.5 Hz, respectively. Damping ratios of between 3 to 4 percent of critical were obtained using the half-power bandwidth method. The addition of Ring-2 did not significantly alter the dynamic properties of Bushing-2 — similar fundamental frequencies and damping ratios were obtained for the retrofitted bushing.

Table 7-7 summarizes the measured dynamic properties of Bushing-2 in the x- and y-directions; modal data could not be determined for the local z-direction. The modal frequencies differ slightly in x- and y- directions due to the unsymmetrical distribution of lifting lugs immediately above the flange plate of the bushing.

Table 7-5 Summary of earthquake testing of flexibly mounted Bushing-2 without Ring-2

Test No.	*Test Date*	*Identification*[1]	*PGA*[2]	*Comments*
1	12/14/99	WN-X	0.1g	
2	12/14/99	WN-Y	0.1g	
3	12/14/99	WN-Z	0.1g	
4	12/14/99	SS-X	0.1g	
5	12/14/99	SS-Y	0.1g	
6	12/14/99	SS-Z	0.1g	
7	12/14/99	Tabas-A	0.1g	
8	12/14/99	CERL	0.1g	
9	12/14/99	Tabas-A	0.2g	
10	12/14/99	Tabas-A	0.3g	
11	12/14/99	Tabas-A	0.5g	
12	12/14/99	Tabas-A	0.7g	
13	12/14/99	Tabas-A	1.0g	Spectrum equivalent to moderate level qualification.
14	12/14/99	Tabas-B	1.2g	
15	12/14/99	Tabas-B	1.4g	Small oil leakage at the gasket connection[3]; see Figure 7-12.
16	12/14/99	Tabas-B	1.6g	Oil leakage; minor slip of the UPPER-1 porcelain unit.
17	12/14/99	Tabas-B	1.8g	Large slip of the UPPER-1 porcelain unit; gasket visible; see Figure 7-13.
18	12/14/99	Tabas-B	2.0g	Large slip of the UPPER-1 porcelain unit; gasket visible and extruding from the gasket connection; see Figure 7-14.

1. WN = white-noise, SS = sine-sweep; -*X*, -*Y*, and -*Z* denote direction of testing in global coordinate system; Tabas-A = spectrum-compatible Tabas-A earthquake histories; Tabas-B = spectrum-compatible Tabas-B earthquake histories; CERL = spectrum-compatible CERL histories.
2. PGA = target peak acceleration of the simulator platform.
3. Connection of the UPPER-1 porcelain unit to the flange plate.

Table 7-6 Summary of earthquake testing of flexibly mounted Bushing-2 with Ring-2

Test No.	*Test Date*	*Identification*[1]	*PGA*[2]	*Comments*
1	12/17/99	WN-X	0.1g	
2	12/17/99	WN-Y	0.1g	
3	12/17/99	WN-Z	0.1g	
4	12/17/99	SS-X	0.1g	
5	12/17/99	SS-Y	0.1g	
6	12/17/99	SS-Z	0.1g	
7	12/17/99	Tabas-A	0.1g	
8	12/17/99	CERL	0.1g	
9	12/17/99	Tabas-A	0.2g	
10	12/17/99	Tabas-A	0.3g	
11	12/17/99	Tabas-A	0.5g	
12	12/17/99	Tabas-A	0.7g	
13	12/17/99	Tabas-A	1.0g	Spectrum equivalent to moderate level qualification.
14	12/17/99	Tabas-B	1.2g	
15	12/17/99	Tabas-B	1.4g	
16	12/17/99	Tabas-B	1.6g	
17	12/17/99	Tabas-B	1.8g	
18	12/17/99	Tabas-B	2.0g	Spectrum equivalent to high level qualification.
19	12/17/99	CERL	1.0g	
20	12/17/99	Tabas-B	2.2g	
21	12/17/99	Tabas-B	2.4g	
22	12/17/99	Tabas-B	2.6g	Oil leakage at the gasket connection[3].
23	12/17/99	Tabas-B	2.8g	Oil leakage at the gasket connection and twist of the UPPER-1 porcelain unit; see Figure 7-15.
24	12/17/99	Tabas-B	3.0g	Excessive oil leakage and uplift of the UPPER-1 porcelain unit during the test.
25	12/17/99	WN-X	0.1g	
26	12/17/99	WN-Y	0.1g	
27	12/17/99	WN-Z	0.1g	

1. WN = white-noise, SS = sine-sweep; -X, -Y, and -Z denote direction of testing in global coordinate system; Tabas-A = spectrum-compatible Tabas-A earthquake histories; Tabas-B = spectrum-compatible Tabas-B earthquake histories; CERL = spectrum-compatible CERL histories.
2. PGA = target peak acceleration of the simulator platform.
3. Connection of the UPPER-1 porcelain unit to the flange plate.

Table 7-7 Modal properties of Bushing-2 from resonance-search tests

		Frequency (Hz)		*Damping Ratio (% critical)*	
Test No.	*Ring-2 Installed*	*x-direction*	*y-direction*	*x-direction*	*y-direction*
1-6	No	6.8	6.5	4	4
1-6	Yes	6.8	6.5	3	3
25-27	Yes	6.5	6.3	4	4

7.5.4 Response of the rigid mounting frame and the flexible plate

The measured peak accelerations of the simulator platform, the *rigid* frame, and the *flexible* mounting plate for the seismic tests of Bushing-2 are presented in Table 7-8. The data are tabulated for the tests of Bushing-2 without Ring-2; data for the tests of Bushing-2 with Ring-2 were similar. The transfer functions of Figure 7-17, as calculated from Test Nos 1 through 3 of Table 7-5, show that there is almost no amplification of the longitudinal (x-) acceleration, some reduction in the lateral (y-) acceleration, but large amplification of vertical (z-) acceleration due to the flexibility of the 1/2-in. (13-mm) thick plate. The out-of-plane (z- direction) frequency of the flexible plate, with the bushing installed, is approximately 17 Hz.

7.5.5 Response of Bushing-2 without Ring-2

7.5.5.1 Peak response

The peak acceleration and displacement responses of the Bushing-2 (at the top, midheight, and bottom) without the retrofit ring are presented in Table 7-9. The maximum responses at the midheight of the bushing were less than those at the top or bottom. The values of peak absolute accelerations are defined as the maximum of the vector sum of acceleration components in the local x- and local y-directions, evaluated from acceleration histories. Similarly, the values of peak displacements relative to the mounting frame are defined as the maximum of the vector sum of relative displacement components in the global X- and local Y- directions, evaluated from displacement histories.

Although the target PGAs are listed in increasing order in Table 7-9, the tabulated response values do not necessarily increase in a corresponding manner. Among the factors contributing to this variation are the temperature-dependent dynamics of the simulator's hydraulic system, interaction between the simulator platform and bushing-support system, simulator rotational accelerations, and the phase difference between the x- (or X-) and y- (or Y-) components of response used to compute the vector sum of response.

Table 7-8 Peak acceleration response of the simulator platform and the mounting frames

			Simulator Platform (g)			*Rigid Frame (g)*			*Flexible Plate (g)*		
Test No.[1]	*Identification*[2]	*PGA*[3]	*X*[4]	*Y*	*Z*	*x*	*y*	*z*	*x*	*y*	*z*
7	Tabas-A	0.1g	0.1	0.2	0.1	0.2	0.3	0.1	0.2	0.2	0.2
8	CERL	0.1g	0.2	0.2	0.1	0.3	0.3	0.1	0.3	0.2	0.2
9	Tabas-A	0.2g	0.3	0.4	0.1	0.5	0.5	0.2	0.4	0.3	0.3
10	Tabas-A	0.3g	0.5	0.4	0.2	0.6	0.6	0.3	0.6	0.4	0.4
11	Tabas-A	0.5g	0.6	0.5	0.4	0.9	0.8	0.5	0.9	0.5	0.5
12	Tabas-A	0.7g	0.9	0.7	0.5	1.0	0.9	0.7	1.0	0.6	0.9
13	Tabas-A	1.0g	1.2	1.0	0.5	1.7	1.1	0.7	1.6	0.8	0.8
14	Tabas-B	1.2g	1.2	1.1	0.7	1.4	1.1	1.0	1.4	0.9	0.9
15	Tabas-B	1.4g	1.4	1.2	1.0	1.6	1.4	1.3	1.6	1.1	1.1
16	Tabas-B	1.6g	1.6	1.5	0.9	2.0	1.6	1.2	2.0	1.3	1.4
17	Tabas-B	1.8g	1.9	1.6	1.0	2.3	1.8	1.1	2.2	1.0	1.2
18	Tabas-B	2.0g	2.4	1.9	0.9	2.6	2.1	1.2	2.4	1.6	1.2
19	CERL	1.0g	1.4	1.6	0.4	1.5	1.5	0.7	1.4	1.2	0.8
20	Tabas-B	2.2g	2.7	2.2	0.8	3.0	2.3	1.0	2.8	1.7	1.4
21	Tabas-B	2.4g	2.9	2.5	0.9	3.3	2.5	1.3	3.0	1.9	1.6
22	Tabas-B	2.6g	3.2	2.6	0.8	3.6	3.2	1.3	3.4	2.1	1.7
23	Tabas-B	2.8g	3.4	2.8	0.8	4.1	3.4	1.4	3.6	2.2	1.6
24	Tabas-B	3.0g	3.8	3.0	0.8	4.7	3.6	1.4	4.1	2.3	1.8

1. Data are from the retrofitted bushing seismic tests.
2. Tabas-A = spectrum-compatible Tabas-A earthquake histories; Tabas-B = spectrum-compatible Tabas-B earthquake histories; CERL = spectrum-compatible CERL histories.
3. PGA = target peak acceleration of the simulator platform.
4. For orientation of global (*X*- *Y*- *Z*-) and local (*x*- *y*- *z*-) coordinate systems, refer to Figure 7-9.

7.5.5.2 Bushing response

The global response of Bushing-2 was assessed by analysis of data from Test No 13 (Tabas-A, target PGA equal to 1.0g) and Test No 18 (Tabas-B, target PGA equal to 2.0g).

Table 7-9 Peak responses of the Bushing-2 without Ring-2

			Peak Acceleration (g)			*Peak Relative Displacement (mm)*		
Test No.	*Identification*[1]	*PGA*[2]	*Top*	*Midheight*	*Bottom*	*Top*	*Midheight*	*Bottom*
7	Tabas-A	0.1g	0.6	0.4	0.7	4	2	3
8	CERL	0.1g	0.5	0.3	0.7	3	2	3
9	Tabas-A	0.2g	0.9	0.5	1.1	5	2	3
10	Tabas-A	0.3g	1.1	0.6	1.5	6	3	4
11	Tabas-A	0.5g	1.6	1.0	2.1	9	4	6
12	Tabas-A	0.7g	2.2	1.3	3.2	13	6	8
13	Tabas-A	1.0g	2.9	1.9	3.0	17	9	10
14	Tabas-B	1.2g	3.3	1.8	3.5	21	10	13
15	Tabas-B	1.4g	3.8	2.0	4.2	28	13	16
16	Tabas-B	1.6g	3.9	2.4	4.2	33	17	17
17	Tabas-B	1.8g	5.0	2.6	4.2	41	23	18
18	Tabas-B	2.0g	4.8	3.0	4.5	40	19	21

1. Tabas-A = spectrum-compatible Tabas-A earthquake histories; Tabas-B = spectrum-compatible Tabas-B earthquake histories; CERL = spectrum-compatible CERL histories.
2. PGA = target peak acceleration of the simulator platform.

During Test No 13, (Tabas-A, target PGA equal to 1.0g) a maximum acceleration and displacement relative to the mounting frame of 2.9g and 0.7 in. (17 mm) respectively, were recorded at the top of the bushing. Acceleration response spectra for Bushing-2 in the local coordinate system, generated using measured acceleration histories of the *flexible* plate are shown in Figure 7-18. For information, the 2-percent and 5-percent damped IEEE 693-1997 response spectra for Moderate Level qualification are also shown in this figure. The spectrum acceleration ordinates in the *y*- and *z*- directions are smaller than those of the IEEE spectra.

During Test No 18, (Tabas-B, target PGA equal to 2.0g) a maximum acceleration and displacement relative to the mounting frame of 4.8g and 1.6 in. (40 mm) respectively, were recorded at the top of the bushing. Acceleration response spectra for Bushing-2 in the local coordinate system, generated using measured acceleration histories of the *flexible* plate are shown in Figure 7-19. For information, the 2-percent and 5-percent damped IEEE 693-1997 response spectra for High Level qualification are also shown in this figure. The spectrum acceleration ordinates in the *y*- and *z*- directions are smaller than those of the IEEE spectra.

Figure 7-20 presents the zero-corrected vertical displacement history of the UPPER-1 porcelain unit, measured at the height of the radial displacement transducers, relative to the *rigid* mounting frame. The vertical displacement histories were obtained by subtracting the vertical deformation of the *flexible* plate with respect to the *rigid* frame (e.g., channel 55) from the recorded vertical

history of the UPPER-1 porcelain unit relative to the *flexible* plate (e.g., channel 48). To obtain the vertical displacements at the side of the bushing, geometric corrections were applied to the measurements. The uplift of the UPPER-1 porcelain unit over the flange is given by residual positive vertical displacements. The settlement of the UPPER-1 porcelain unit is given by the residual negative vertical displacement. The maximum vertical displacement at the side of the porcelain unit was approximately 0.09 in. (2 mm). At the conclusion of the test, the residual vertical displacement on one side of the bushing was +0.03 in. (+0.8 mm) and -0.04 in. (-1 mm) on the opposite side. The gasket had extruded from the groove (Figure 7-14), resulting in a permanent uplift at one side of the bushing. The UPPER-1 porcelain unit had slipped (Figure 7-13) and rotated downward resulting in a permanent settlement on the opposite side.

Figure 7-21 presents the zero-corrected horizontal displacement and twist histories of the UPPER-1 porcelain unit, measured at the height of the radial displacement transducers, relative to the rigid mounting frame. These displacements and twists can be considered equal to those relative to the flange plate because the lateral stiffness of the flexible mounting plate was large. The shear deformation in the gasket and the slip of the UPPER-1 porcelain over the flange contribute to the measured displacements, although the slip contribution is the larger of the two. The slip in the x- direction was computed as one half of the sum of channels 44 and 46; the slip in the y- direction was computed as one half of the sum of channels 45 and 47. The twist around the z- axis was computed as the difference between channels 52 and 53 divided by 21-in. (533-mm) distance between these transducers. The maximum and residual twist (rotation) about the z-axis were approximately 1.4 and 0.3 percent radian, respectively. The computed maximum and residual slips were approximately 0.35 in. (9 mm) and 0.26 in. (7 mm) along the x- axis, and 0.3 in. (8 mm) and 0.2 in. (5 mm) along the y- axis.

7.5.5.3 Post-test tear-down of Bushing-2

At the conclusion of the seismic tests, the bushing was removed from the test fixture and disassembled. At that time, the gasket in the gasket connection had been extruded from the groove in the flange (see Figure 7-14) and the post-tensioning force in the bushing was measured at 9.5 kips (42 kN), that is approximately one-third the original value of 27 kips (120 kN). The bushing was de-stressed, its oil drained, and the porcelain stack above the flange was separated from the bushing flange, thus exposing the gasket in the gasket connection. There was no structural damage to either the UPPER-1 porcelain unit or the bushing flange. Examination of the gasket revealed a number of small surface cracks. Figure 7-22 indicates the location of the largest tear. Figure 7-23 is a plan view of the gasket indicating all observed cracks. The gasket also developed a small lip on its top surface (likely as a result of contact between the gasket and the edge of the groove into which it was placed) and was coated with oil due to leakage of oil at the gasket connection.

Although there were several small cracks in the gasket, none extended far below the surface. As such, the gasket was used for the remainder of the test program. The gasket was air-dried, the porcelain stacks were re-centered, and the bushing was refilled with oil and post-tensioned to 27 kips (120 kN) prior to the installation of Ring-2.

7.5.6 Response of Bushing-2 retrofitted with Ring-2

7.5.6.1 Peak response

The peak acceleration and displacement responses of the Bushing-2 (at the top, midheight, and bottom) retrofitted with Ring-2 are presented in Table 7-10. The maximum responses at the midheight of the bushing were always less than those at the top or bottom. The values of peak absolute accelerations are defined as the maximum of the vector sum of acceleration components in the local x- and local y-directions, evaluated from acceleration histories. The values of peak displacements relative to the mounting frame are defined as the maximum of the vector sum of relative displacement components in the global *X*- and local *Y*-directions, evaluated from displacement histories. The tabulated peak accelerations in Table 7-8 indicate that the CERL histories (Test No 19) had larger input peak accelerations than the Tabas histories (Test No 13), but the peak bushing accelerations are larger for the Tabas histories as indicated in Table 7-10. The power spectra for the CERL histories presented in Figure 7-6 through Figure 7-8 show that the CERL record has significant energy concentrated between 1 to 2 Hz. However, such energy did not significantly excite the *flexibly* mounted Bushing-2 because its fundamental frequency ranged between 5 and 6 Hz (see Table 7-2). As such, the Tabas histories provided a more severe test for this bushing than the CERL histories and tests using the CERL histories with target PGAs greater that 1.0g were not conducted.

7.5.6.2 Bushing response

The global response of Bushing-2 retrofitted with Ring-2 was assessed by analysis of data from Test No 13 (Tabas-A, target PGA equal to 1.0g), Test No 18 (Tabas-B, target PGA equal to 2.0g), Test No 19 (CERL, target PGA equal to 1.0g), and Test No 24 (Tabas-B, target PGA equal to 3.0g).

During Test No 13, (Tabas-A, target PGA equal to 1.0g) a maximum acceleration and displacement relative to the mounting frame of 3.4g and 0.8 in. (21 mm) respectively, were recorded at the top of the bushing. Acceleration response spectra for Bushing-2 in the local coordinate system, generated using measured acceleration histories of the *flexible* plate are shown in Figure 7-24. For information, the 2-percent and 5-percent damped IEEE 693-1997 response spectra for Moderate Level qualification are also shown in this figure. The spectrum acceleration ordinates in the *y*- and *z*- directions are smaller than those of the IEEE spectra.

During Test No 18, (Tabas-B, target PGA equal to 2.0g) a maximum acceleration and displacement relative to the mounting frame of 6.4g and 1.8 in. (45 mm) respectively, were recorded at the top of the bushing. Acceleration response spectra for Bushing-2 in the local coordinate system, generated using measured acceleration histories of the *flexible* plate are shown in Figure 7-25. For information, the 2-percent and 5-percent damped IEEE 693-1997 response spectra for High Level qualification are also shown in this figure. The spectrum acceleration ordinates in the *y*- and *z*- directions are smaller than those of the IEEE spectra.

Table 7-10 Peak responses of the Bushing-2 retrofitted with Ring-2

			Peak Acceleration (g)			*Peak Relative Displacement (mm)*		
Test No.	*Identification*[1]	*PGA*[2]	*Top*	*Midheight*	*Bottom*	*Top*	*Midheight*	*Bottom*
7	Tabas-A	0.1g	0.6	0.3	0.8	4	2	3
8	CERL	0.1g	0.5	0.4	0.8	4	2	3
9	Tabas-A	0.2g	1.1	0.6	1.2	8	4	6
10	Tabas-A	0.3g	1.6	0.8	1.5	12	4	8
11	Tabas-A	0.5g	3.3	1.8	2.5	22	9	14
12	Tabas-A	0.7g	2.9	1.7	3.1	19	8	13
13	Tabas-A	1.0g	3.4	2.2	3.8	21	9	16
14	Tabas-B	1.2g	3.4	1.8	3.5	20	9	15
15	Tabas-B	1.4g	4.5	2.3	4.2	27	12	20
16	Tabas-B	1.6g	5.5	2.6	4.6	33	15	24
17	Tabas-B	1.8g	6.3	2.8	4.5	40	18	29
18	Tabas-B	2.0g	6.4	3.0	5.5	45	20	31
19	CERL	1.0g	3.1	1.7	3.3	20	8	14
20	Tabas-B	2.2g	6.8	3.3	5.8	52	22	33
21	Tabas-B	2.4g	7.7	4.2	6.6	60	25	36
22	Tabas-B	2.6g	7.3	4.3	7.0	64	27	34
23	Tabas-B	2.8g	7.3	4.0	5.8	58	25	32
24	Tabas-B	3.0g	7.7	4.0	6.6	61	26	33

1. Tabas-A = spectrum-compatible Tabas-A earthquake histories; Tabas-B = spectrum-compatible Tabas-B earthquake histories; CERL = spectrum-compatible CERL histories.
2. PGA = target peak acceleration of the simulator platform.

During Test No 19, (CERL, target PGA equal to 1.0g) a maximum acceleration and displacement relative to the mounting frame of 3.1g and 0.8 in. (20 mm) respectively, were recorded at the top of the bushing. Acceleration response spectra for Bushing-2 in the local coordinate system, generated using measured acceleration histories of the *flexible* plate are shown in Figure 7-26. For information, the 2-percent and 5-percent damped IEEE 693-1997 response spectra for Moderate Level qualification are also shown in this figure. The spectrum acceleration ordinates in the *y*- and *z*- directions are smaller than those of the IEEE spectra.

During Test No 24, (Tabas-B, target PGA equal to 3.0g) a maximum acceleration and displacement relative to the mounting frame of 7.6g and 2.4 in. (61 mm) respectively, were recorded at the top of the bushing. Acceleration response spectra for Bushing-2 in the local coordinate system, generated using measured acceleration histories of the *flexible* plate are shown in Figure 7-27. For information, the 2-percent and 5-percent damped IEEE 693-1997 response spectra anchored at a PGA of 3.0g are also shown in this figure. The spectrum acceleration ordinates in the *y*- and *z*- directions are smaller than those of the IEEE spectra.

Figure 7-28 presents the zero-corrected vertical displacement history of the UPPER-1 porcelain unit, measured at the height of the radial displacement transducers, relative to the *rigid* mounting frame. The vertical displacement histories were calculated per Section 7.5.6.2. The maximum uplift at the edge of the porcelain unit was approximately 0.13 in. (3 mm). At the test conclusion, the residual uplift of the UPPER-1 porcelain unit was approximately 0.004 in. (0.1 mm), and for approximately 2 seconds in the history (14 to 16 seconds), there was a gap between the UPPER-1 porcelain unit and the flange in the *y*- direction.

Figure 7-29 presents the zero-corrected horizontal displacement and twist histories of the UPPER-1 porcelain unit, measured at the height of the radial displacement transducers, relative to the rigid mounting frame. These displacements and twists can be considered equal to those relative to the flange plate because the lateral stiffness of the flexible mounting plate was large. The shear deformation in the gasket and the slip of the UPPER-1 porcelain over the flange contribute to the measured displacements, although the slip contribution is the larger of the two. The slip in the *x*- direction was computed as one half of the sum of channels 44 and 46; the slip in the *y*- direction was computed as one half of the sum of channels 45 and 47. The twist around the *z*- axis was computed as the difference between channels 52 and 53 divided by the 21-in. (533-mm) distance between these transducers. The maximum twist (rotation) about the *z*-axis were approximately 0.22 percent radian. The computed maximum slips were approximately 0.16 in. (4 mm) and 0.21 in. (5 mm) along the *x*- and *y*- axes, respectively. There was negligible permanent slip in the bushing.

7.5.6.3 Post-test tear-down of Bushing-2

At the conclusion of the seismic tests, Ring-2 was removed, the bushing was removed from the test fixture and disassembled. A small portion of the gasket had extruded from the groove. The PT force in the bushing was measured at 22 kips (98 kN): approximately 80 percent the original value of 27 kips (120 kN). The bushing was de-stressed, its oil drained, and the porcelain stack above the flange was separated from the bushing flange, exposing the gasket in the gasket connection. There was no structural damage to either the UPPER-1 porcelain unit or the bushing flange. Examination of the gasket revealed a number of cracks in addition to those reported in Section 7.5.5.3. Figure 7-30 is a plan view of the gasket showing all cracks. A small portion of the gasket was torn and the gasket was coated with oil due to leakage at the gasket connection.

7.6 Effect of Support Flexibility and Ring-2 on the Response of Bushing-2

The main objectives of the testing program described in this chapter were to evaluate the seismic response of the bushing mounted on a *flexible* support and to evaluate the efficacy of Ring-2 in improving the seismic response of the bushing. The following sections describe the effect of the *flexible* plate and Ring-2 on the seismic response of Bushing-2.

7.6.1 Influence of support flexibility

For bushings mounted on transformers, the rotational flexibilities of the turret and top plate of the transformer amplify the *vertical* component of the ground acceleration. The flexibilities of the turret and top plate of the transformer have two effects on the *horizontal* response of the bushing-transformer system. A typical IEEE 693-1997 acceleration spectrum is reproduced in Figure 7-31 and is used to illustrate these two effects. The spectral acceleration for a *rigidly* mounted bushing is identified by point A in the figure. Installation of the bushing on a turret or transformer tank top plate with rotational flexibility reduces the frequency of the bushing-transformer system and results in larger spectral accelerations (point B in the figure). Installation of the bushing on a turret or transformer tank top plate with horizontal flexibility will amplify the motions at the flange of the bushing and result in larger spectral accelerations (point C in the figure). For bushings mounted directly on transformer top plates, the amplification factor will nearly equal unity (Bellorini, 1997) due to the large lateral stiffness of the transformer. For bushings attached to turrets, this amplification factor could be greater than unity.

The second factor is explicitly accounted for in IEEE 693-1997 through the use of an amplification factor equal to 2.0. The *flexible* support used in the studies reported herein replicated the first but not the second effect. As such, the histories used for the tests reported in this chapter incorporated the IEEE amplification factor of 2. For example the spectrum for High Level qualification was anchored at 2g as shown in Figure 7-5.

The reduction in the frequency of the bushing-support system from 20 Hz to 7 Hz substantially increased the response of the 230-kV bushing. Figure 7-5 provides insight into the likely increase in the response for IEEE 693-1997 spectrum compatible ground motions. For a *rigidly* mounted 230-kV bushing with a frequency of 20 Hz, the 2-percent damped spectral acceleration is approximately 3g. A change in the frequency of this bushing to 7 Hz increases the spectral accelerations by a factor of 2.1 to 6.4g.

The vertical displacement data from channels 54 through 61 from Test No 24 was used to examine the response of the *flexible* plate. Displacement histories of two typical records (channels 60 and 61) are shown in Figure 7-32. The displacements near the bushing flange had a maximum value of 0.17 in. (4 mm) and were two to three times larger than the displacements at the plate mid-circle (see Figure 7-9). The displacement histories for the sensors on a side of the bushing (e.g., channels 56 and 57) were in-phase. These displacements were out-of-phase with the displacement histories on the opposite side of the bushing (e.g. channels 57 and 61). This is caused by the rocking motion of the bushing on the *flexible* plate.

7.6.2 *Efficacy of Ring-2*

To evaluate the efficacy of Ring-2, data collected from identical tests for Bushing-2 both without and with Ring-2 were examined. For the retrofitted bushing, visual inspection of the gasket connection was not possible prior to the end of the test program and the subsequent removal of the ring. As such, it was not possible to determine the first test during which oil leaked from the bushing. However, a comparison of zero-corrected data collected from Test Nos 14 (Tabas-B, target PGA equal to 1.2g), 15 (Tabas-B, target PGA equal to 1.4g), and 18 (Tabas-B, target PGA equal to 2.0g) for Bushing-2 with and without Ring-2 provides information regarding the response of Bushing-2 at the gasket connection. Table 7-11 presents selected slip, uplift, and twist data for the UPPER-1 porcelain unit.

Table 7-11 Response of the UPPER-1 porcelain unit

Ring-2 Installed	*Test No*[1]	*Radial Slip (mm)*		*Vertical Uplift (mm)*		*Twist (% radian)*	
		Peak	*Residual*	*Peak*	*Residual*	*Peak*	*Residual*
No	14	2	-	0.8	-	0.08	-
	15	4	-	1	-	0.6	0.4
	18	9	7	2	0.8	1.4	0.3
Yes	14	2	-	0.8	-	0.02	-
	15	3	-	1	-	0.03	-
	18	4	-	2	-	0.05	0.02

1. Test No 14: last test without oil leakage for Bushing-2 without Ring-2; Test No 15: first test with oil leakage for Bushing-2 without Ring-2; Test No 18: test with acceleration spectrum equivalent to the IEEE 693-1997 spectrum for high-level qualification.

From Table 7-11, it is clear that the addition of Ring-2 reduced the maximum and residual slip and maximum and residual twist of the UPPER-1 porcelain unit. Ring-2 reduced the residual uplift of the porcelain but had negligible influence on the maximum porcelain uplift.

For earthquake tests with target PGAs exceeding 2.4g, oil leaked from the ring-to-bushing connection. Although the ring retrofit detail delayed oil leakage, it was unable to prevent oil leakage for extreme shaking.

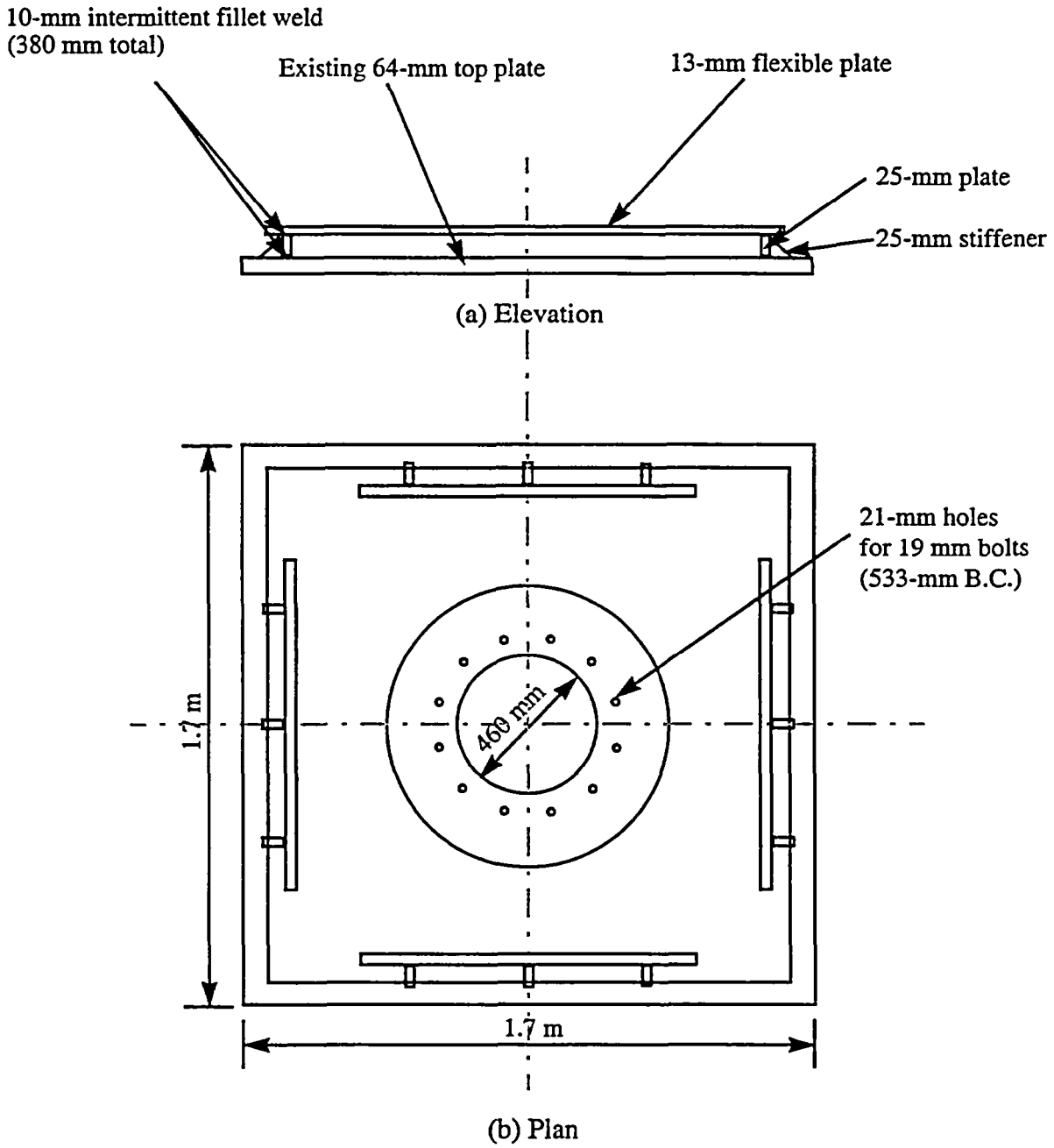

Figure 7-1 Details for flexible plate

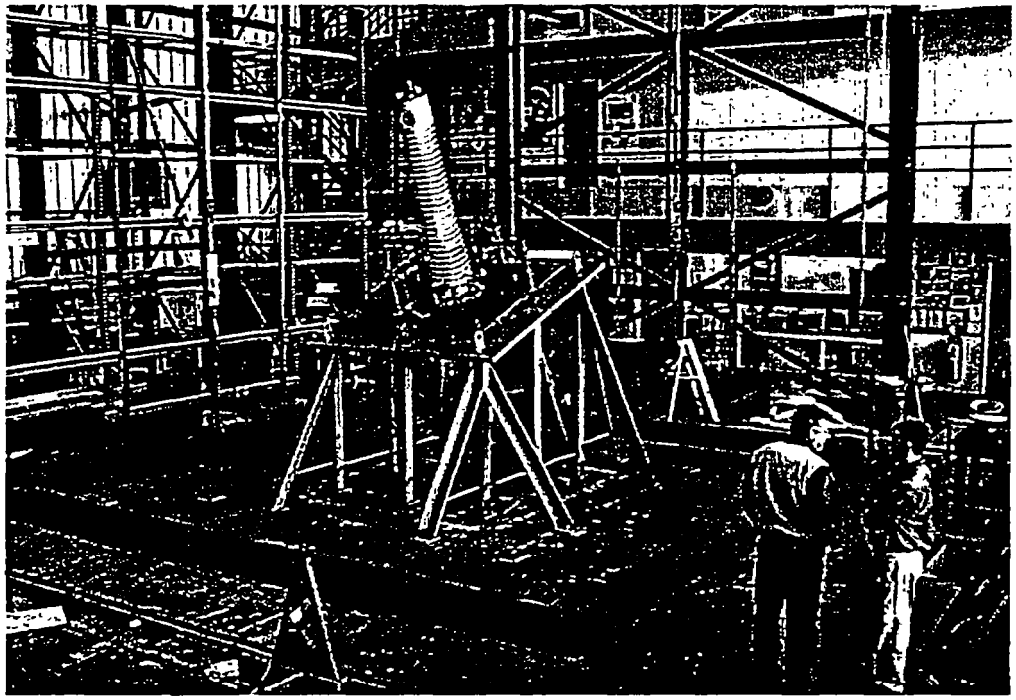

Figure 7-2 230 kV-bushing installed atop the flexible plate

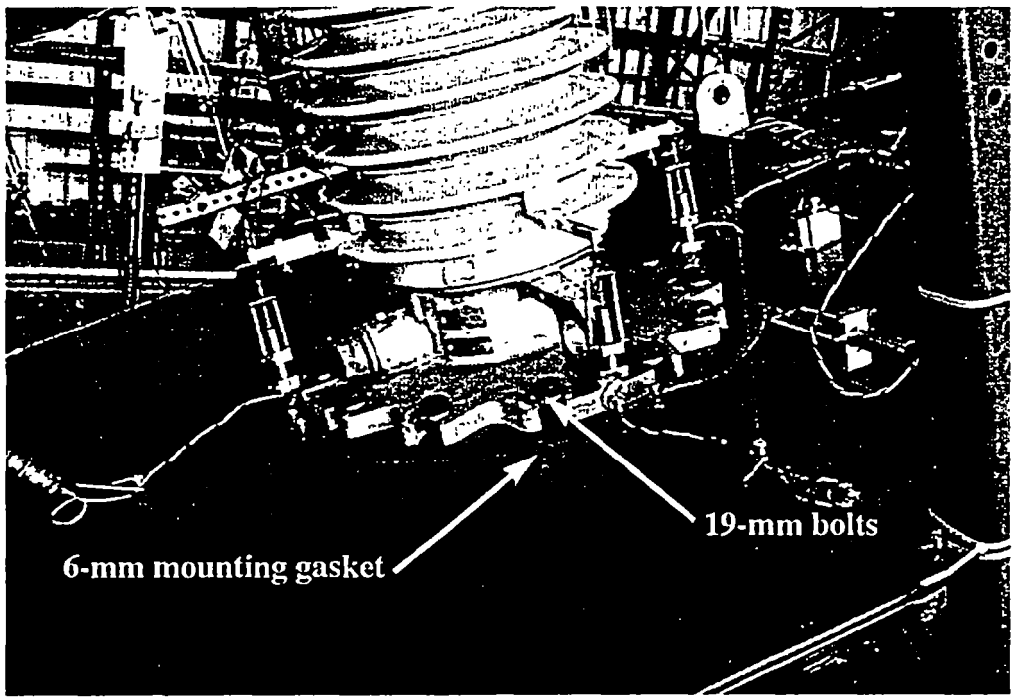

Figure 7-3 View of the flange connection showing the mounting gasket and bolts

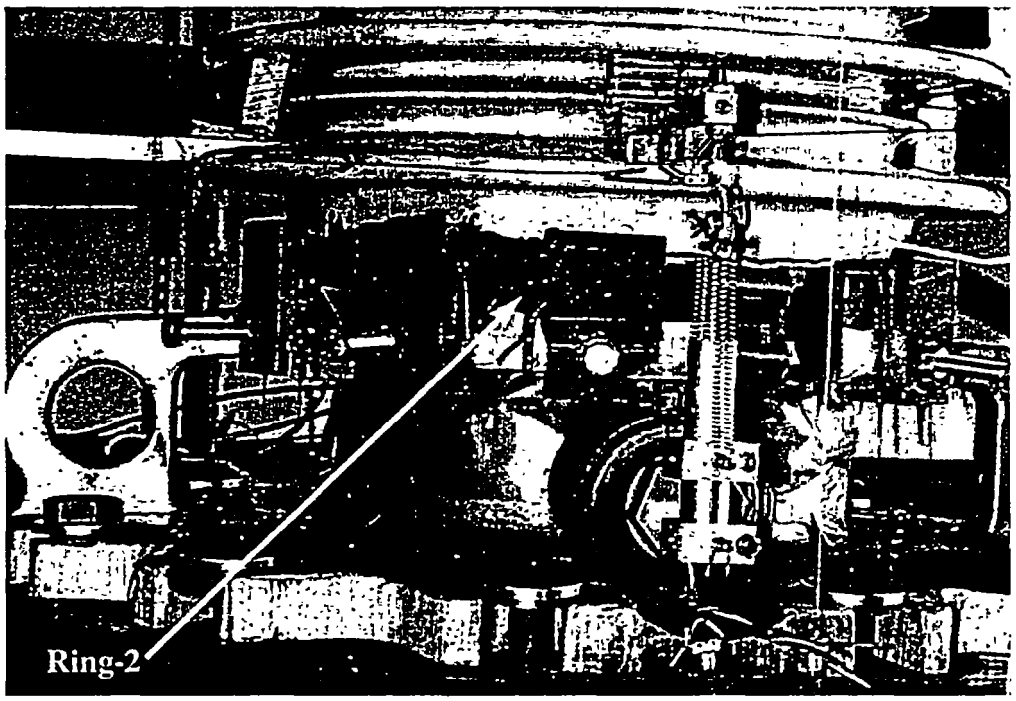

Figure 7-4 Gasket connection showing Ring-2 retrofit detail

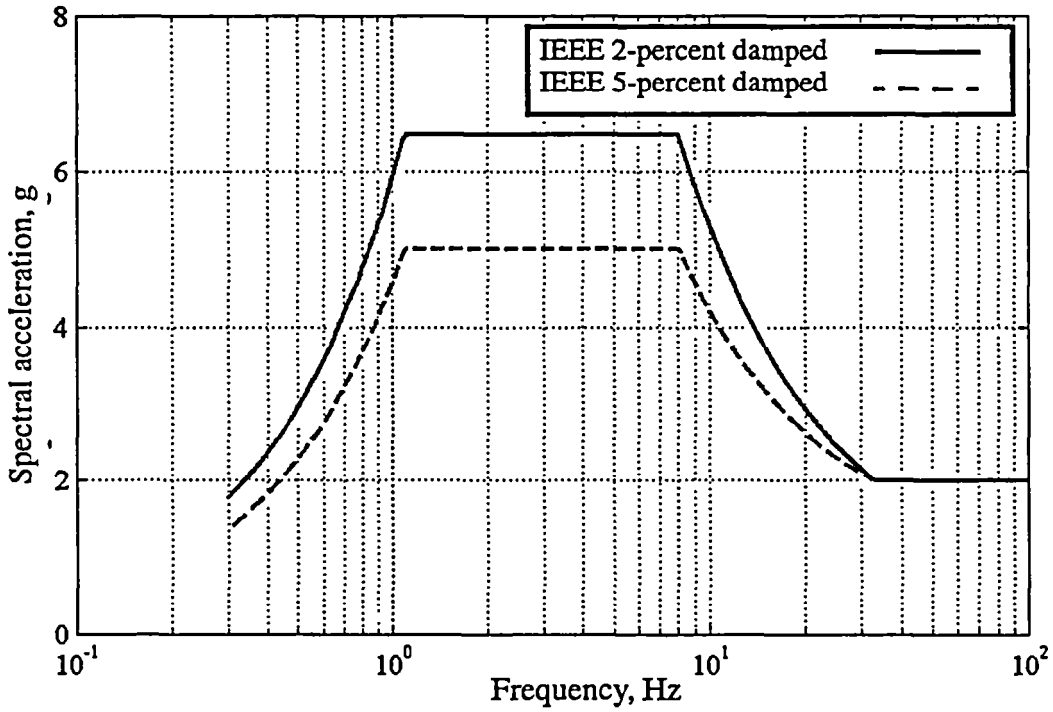

Figure 7-5 IEEE 693-1997 test response spectrum for High Level Qualification

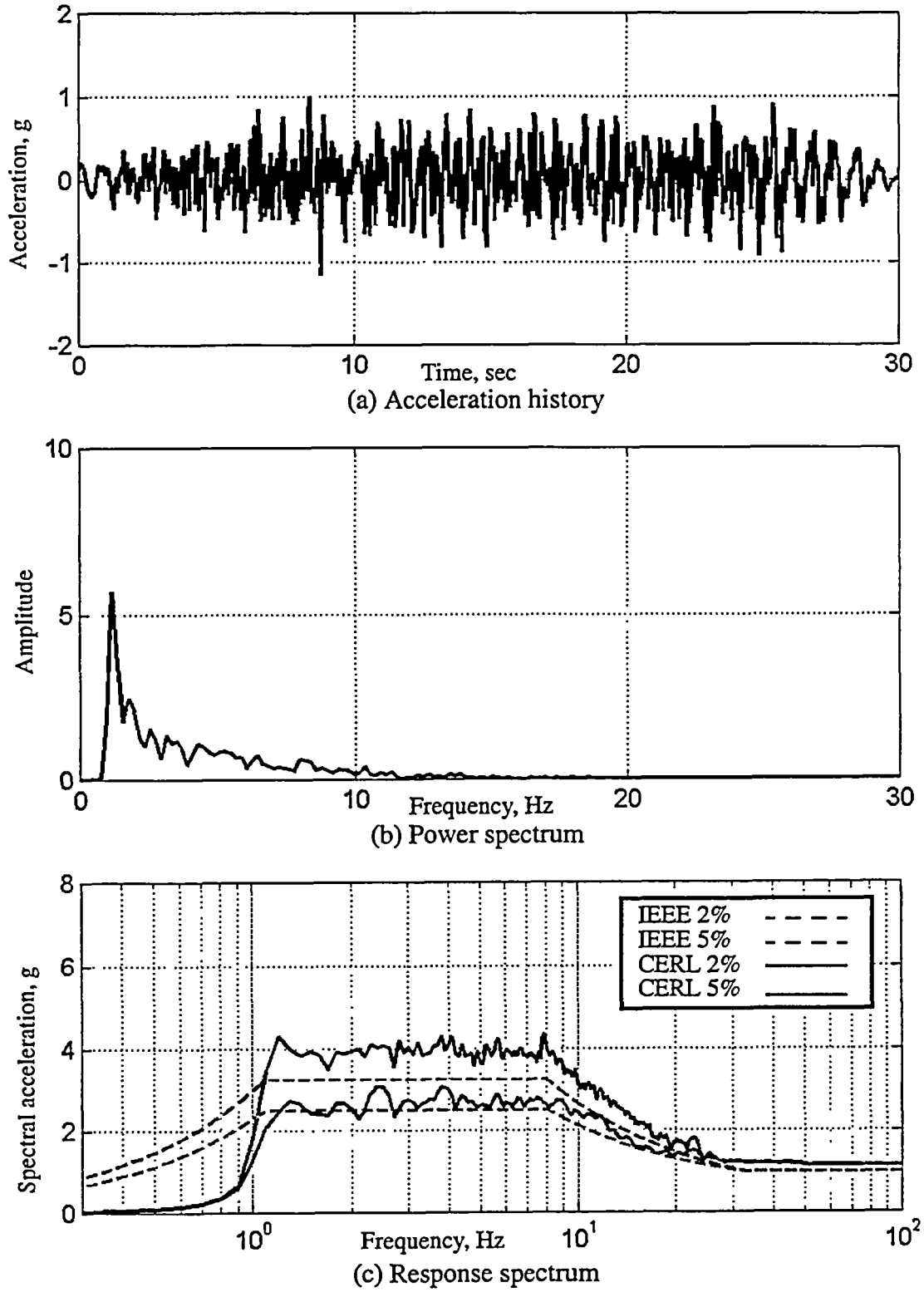

Figure 7-6 Acceleration history, power spectrum, and response spectrum for the longitudinal (*X*-component of the CERL record

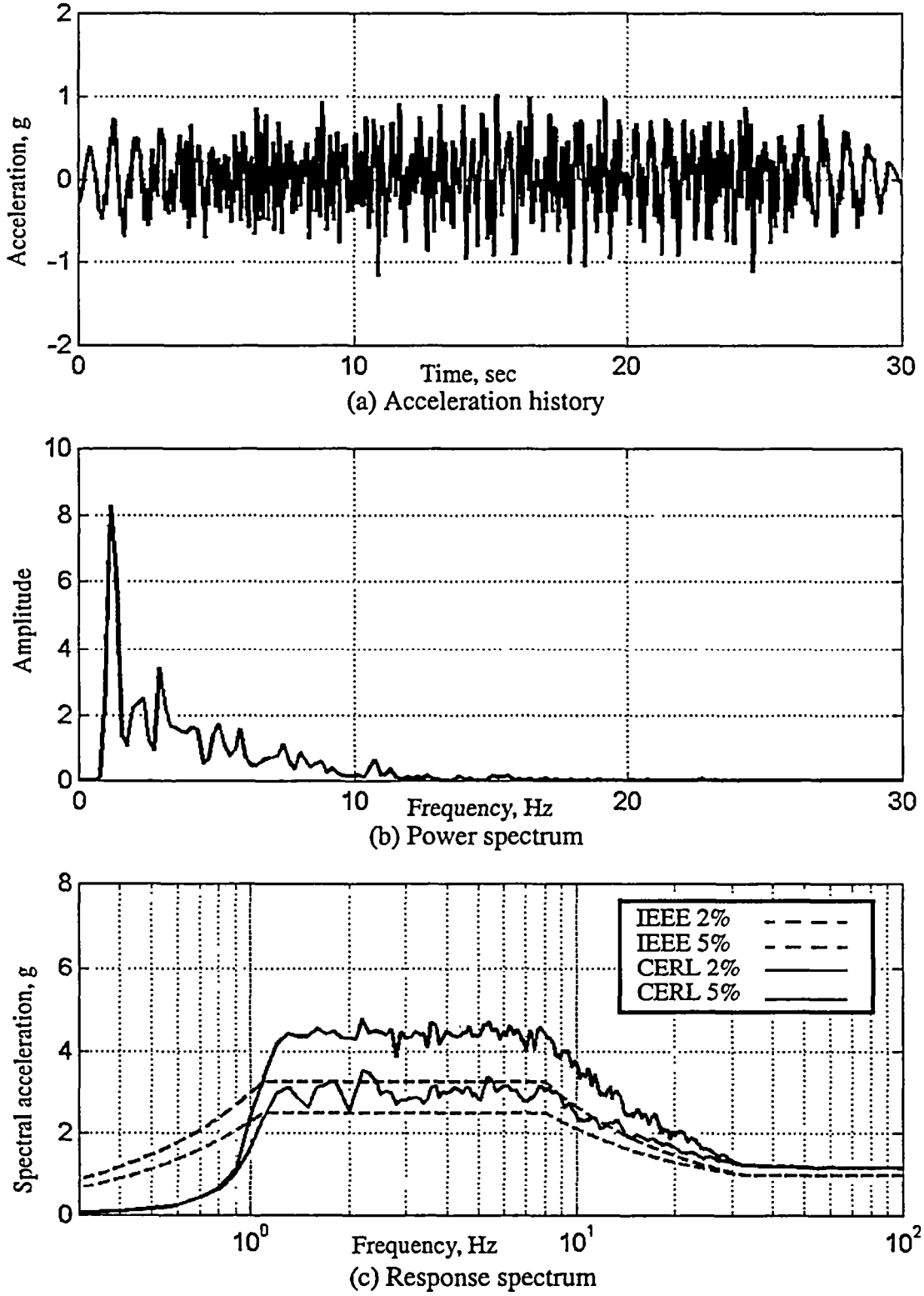

Figure 7-7 Acceleration history, power spectrum, and response spectrum for the transverse (*Y*-component of the CERL record

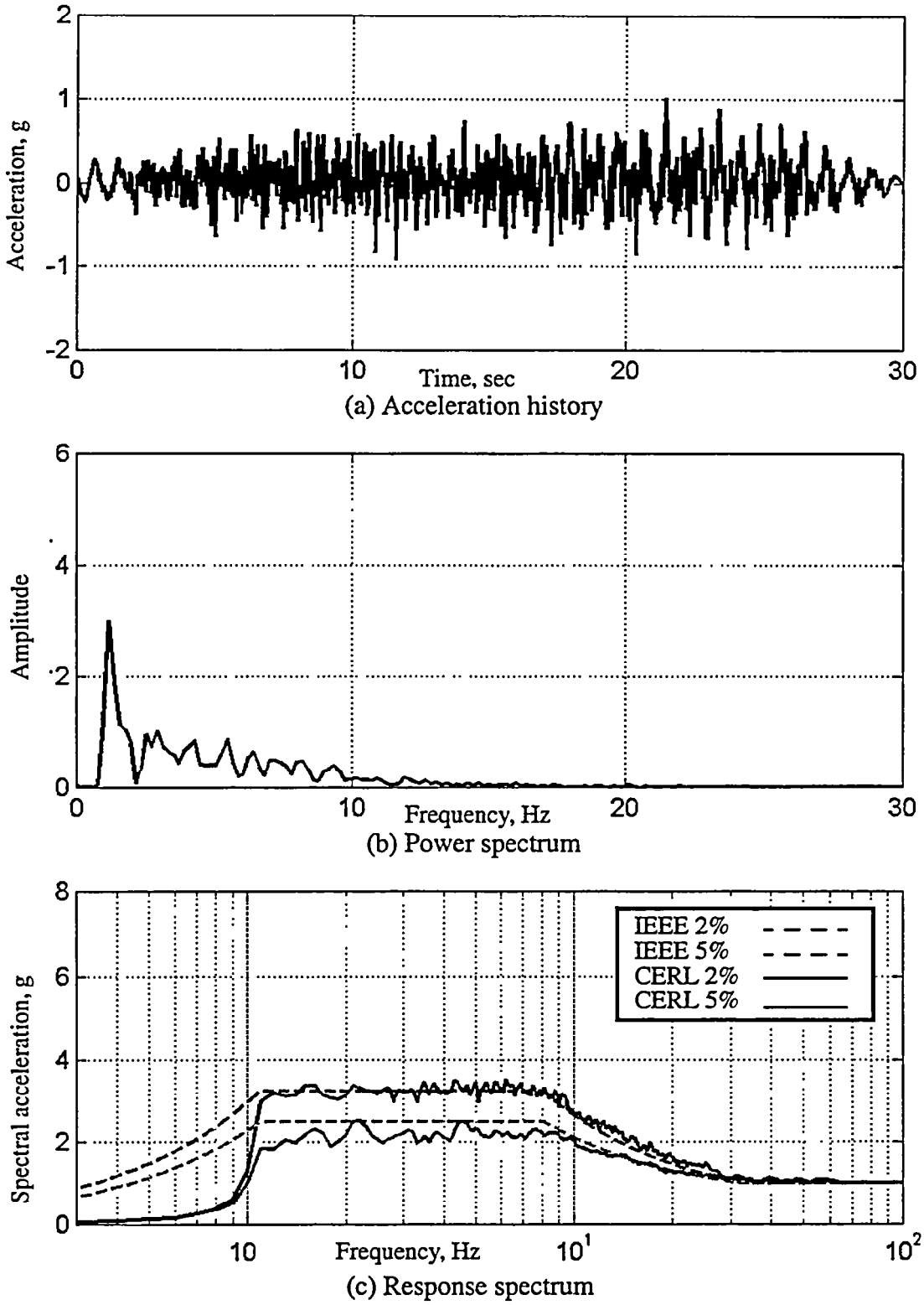

Figure 7-8 Acceleration history, power spectrum, and response spectrum for the vertical (Z-component of the CERL record

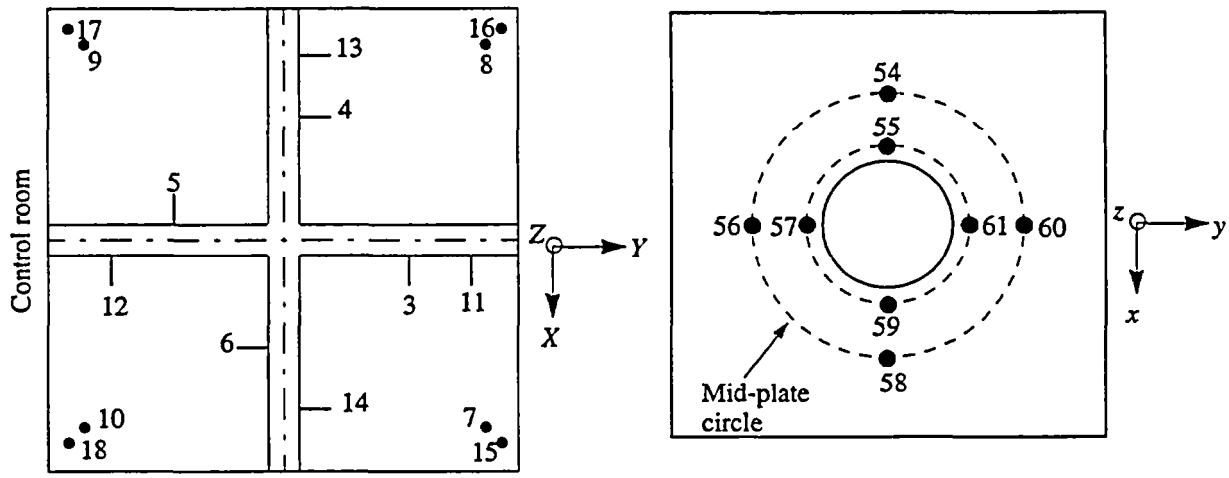

(a) Earthquake simulator

(b) *Flexible* mounting plate

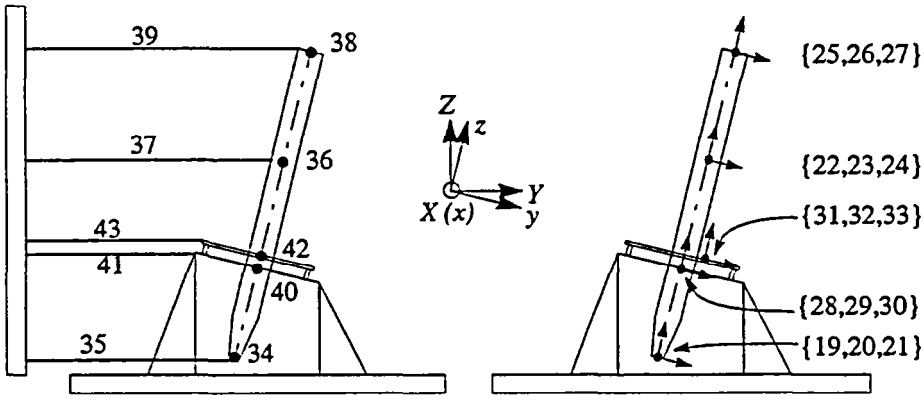

(c) Bushing and mounting frames

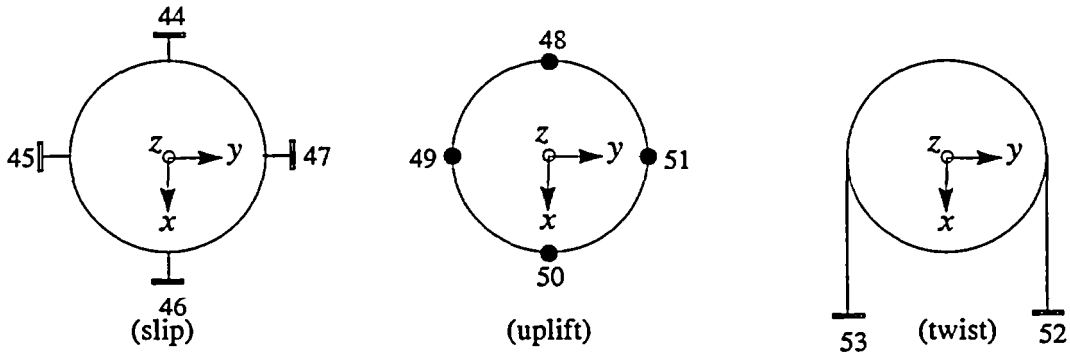

(d) UPPER-1 porcelain unit

Figure 7-9 Instrumentation for seismic testing of Bushing-2 mounted on a flexible plate

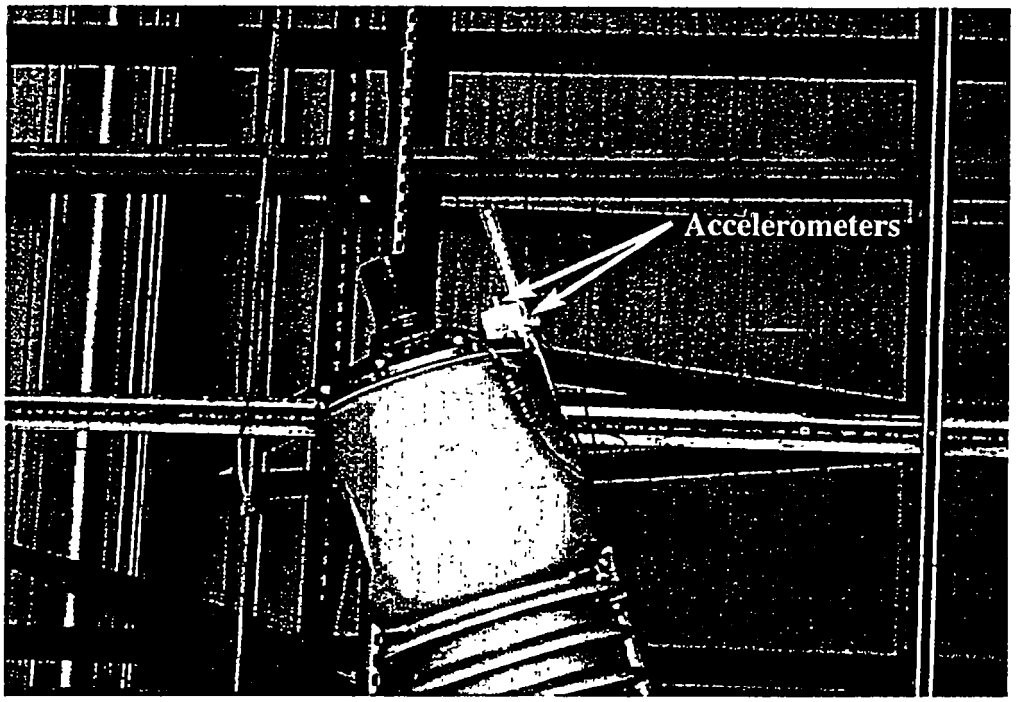

Figure 7-10 Instrumentation at the top of Bushing-2

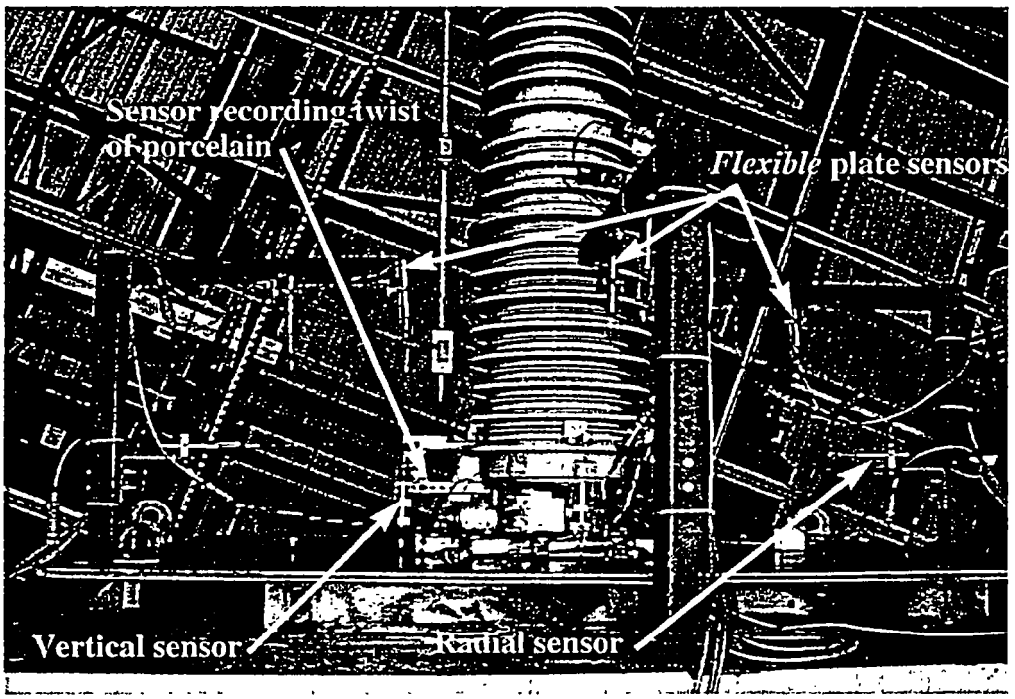

Figure 7-11 Instrumentation of the UPPER-1 porcelain unit and the flexible mounting plate

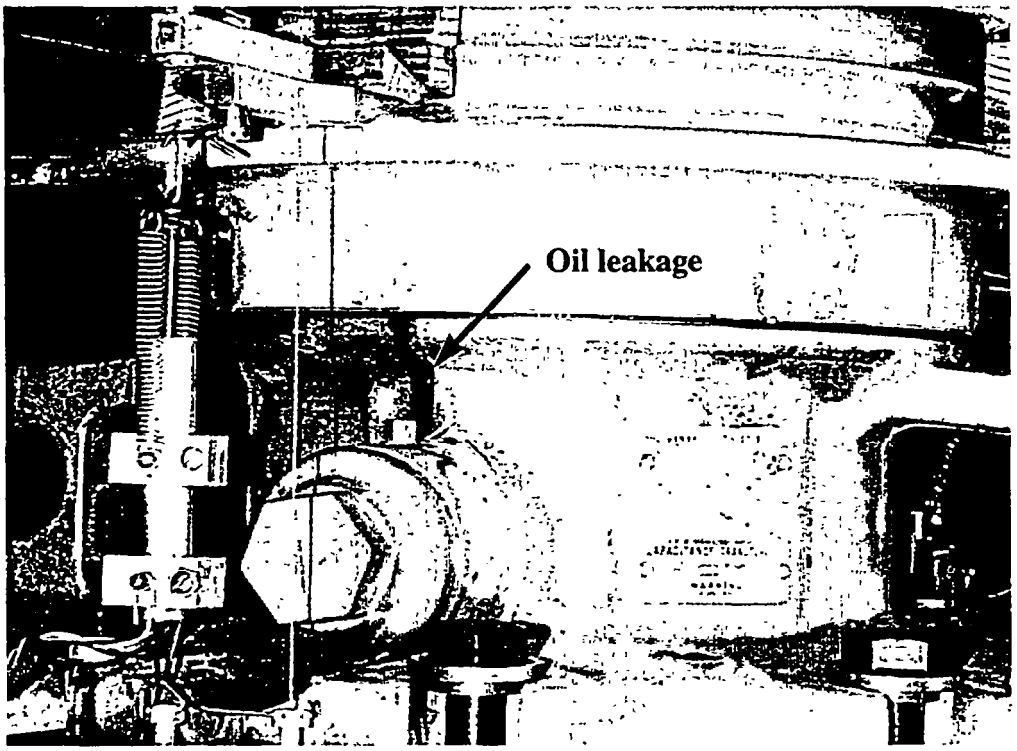

Figure 7-12 Bushing-2 after Test No 15 (target PGA=1.4g) showing oil leakage

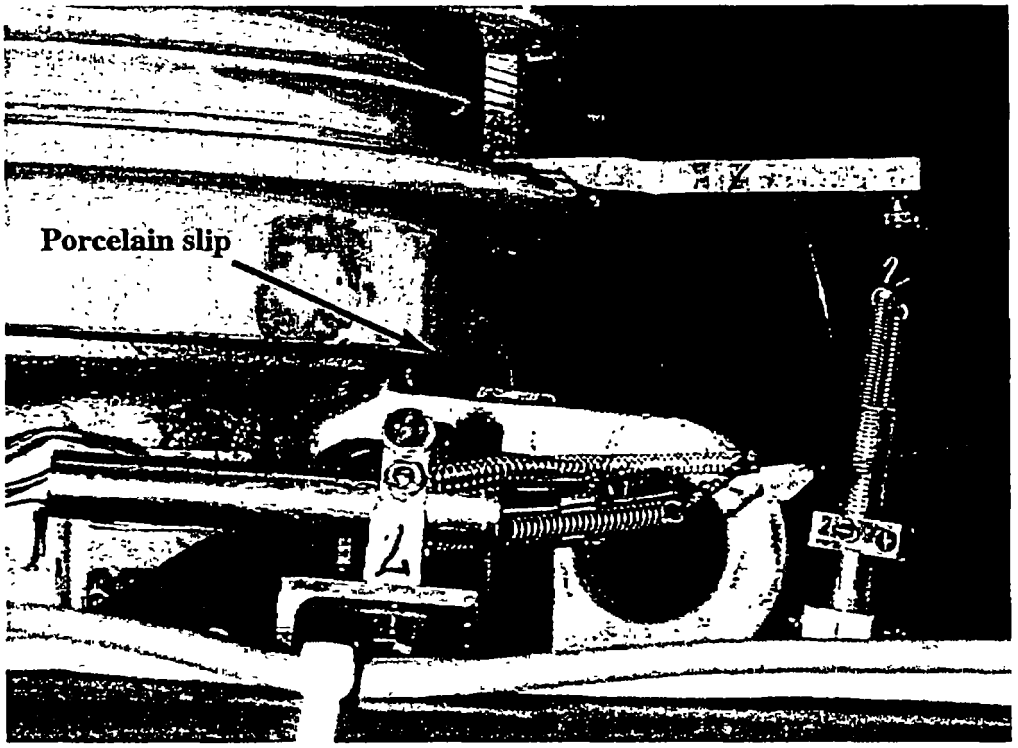

Figure 7-13 Bushing-2 after Test No 17 (target PGA=1.8g) showing slip of porcelain

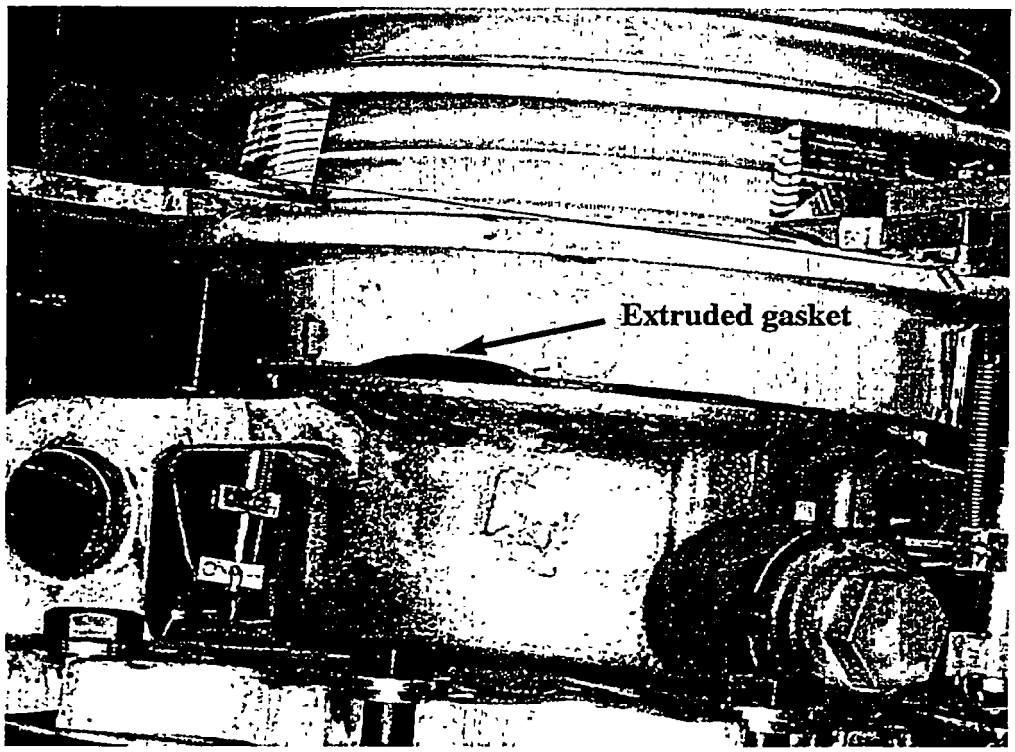

Figure 7-14 Bushing-2 after Test No 18 (target PGA=2.0g) showing extruded gasket

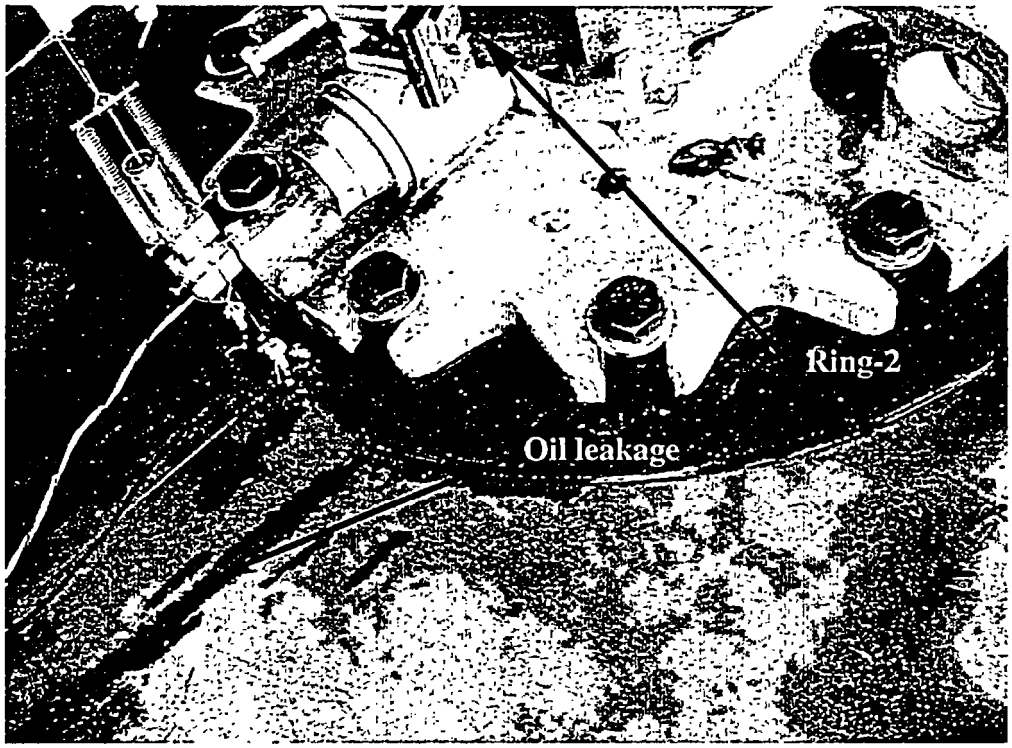

Figure 7-15 Retrofitted Bushing-2 after Test No 23 (target PGA=2.8g) showing oil leakage

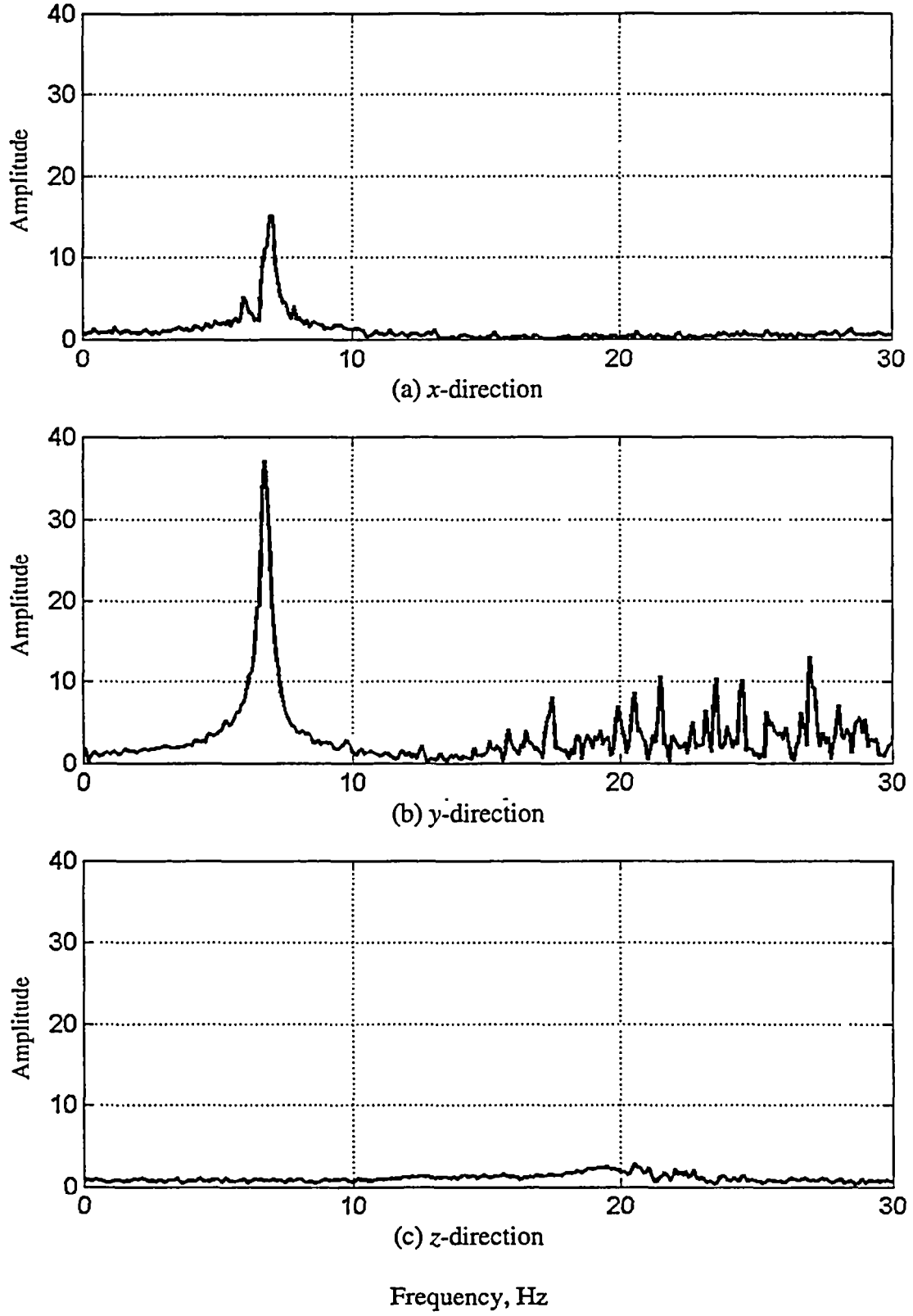

Figure 7-16 Transfer function amplitudes between the top of Bushing-2 and the flexible plate

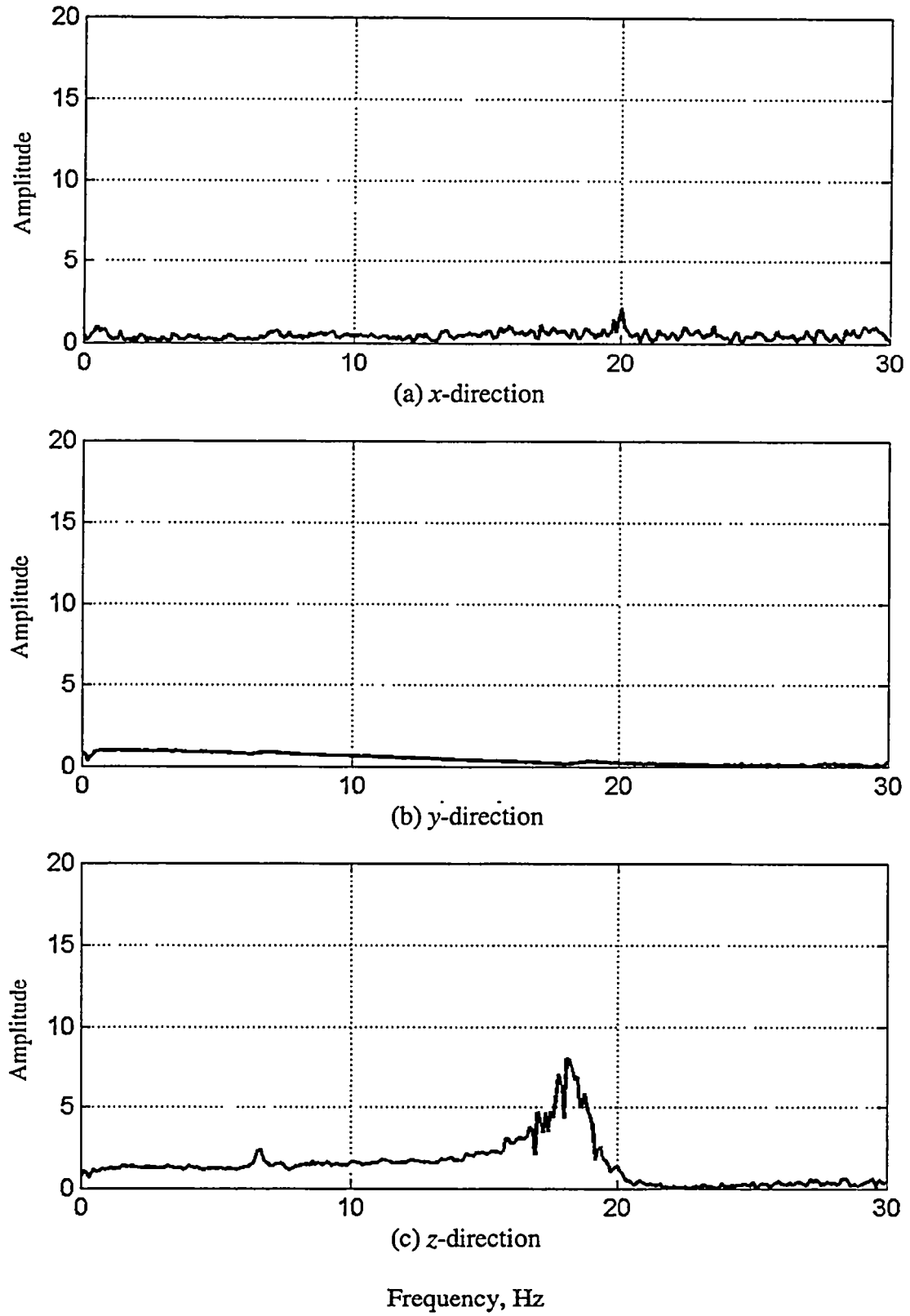

Figure 7-17 Transfer function amplitudes between the flexible plate and the rigid support

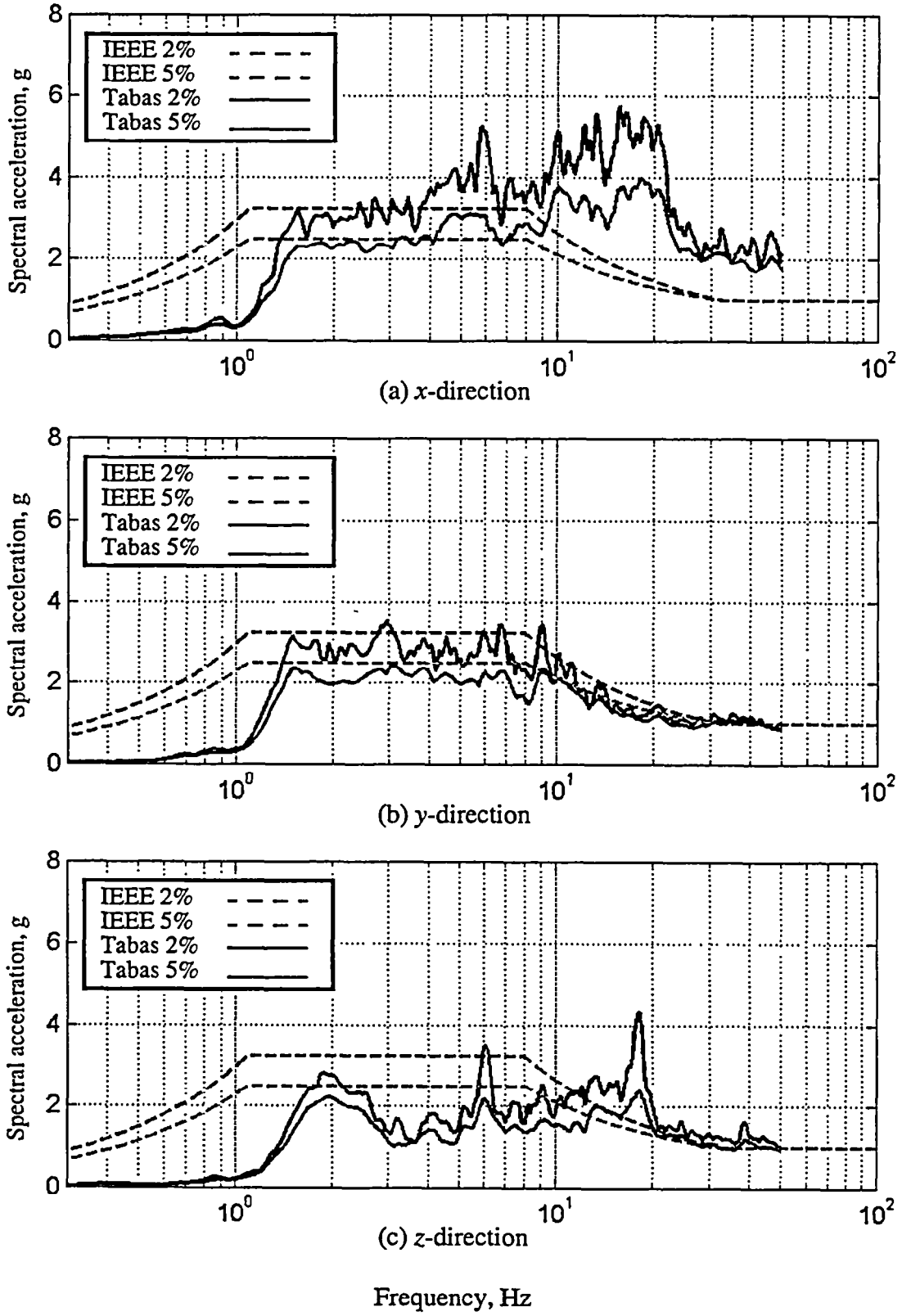

Figure 7-18 Response spectrum for Bushing-2 without Ring-2; Test No 13, Tabas-A, target PGA=1.0g

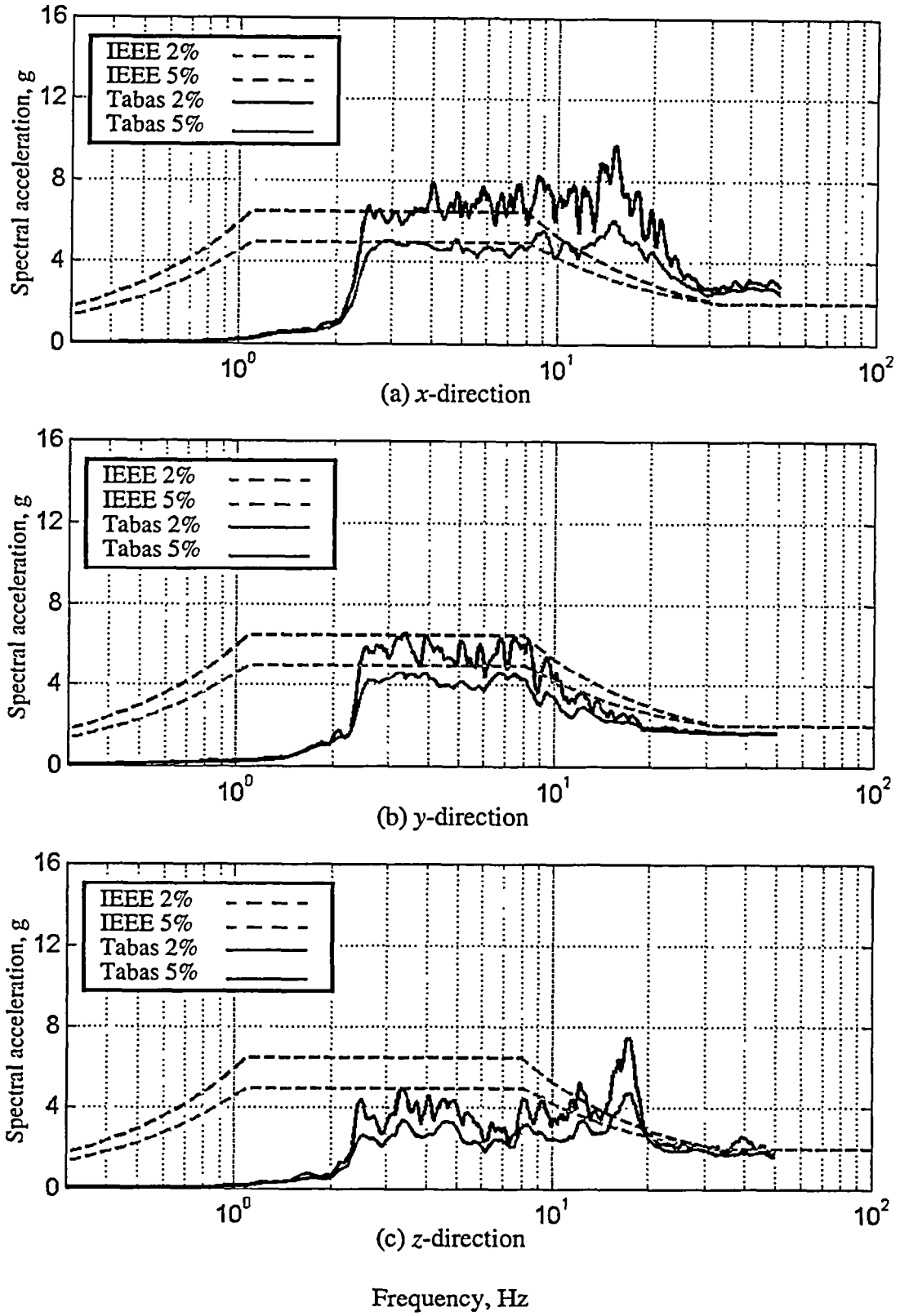

Figure 7-19 Response spectrum for Bushing-2 without Ring-2; Test No 18, Tabas-A, target PGA=2.0g

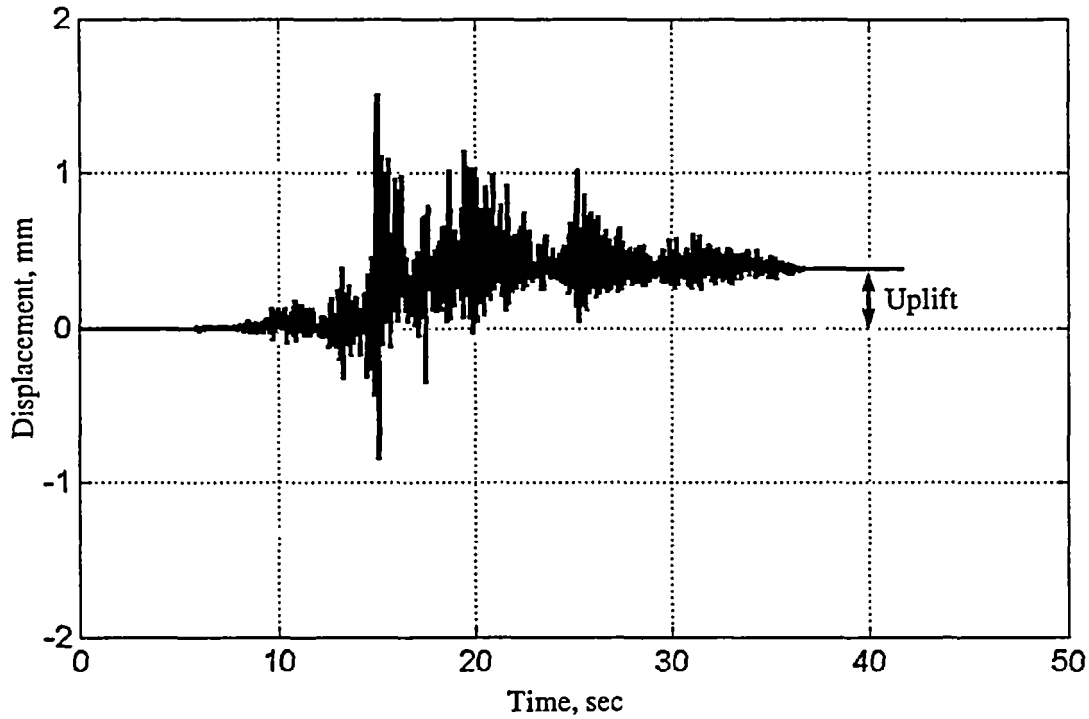

(a) Along y-axis (Channel 49)

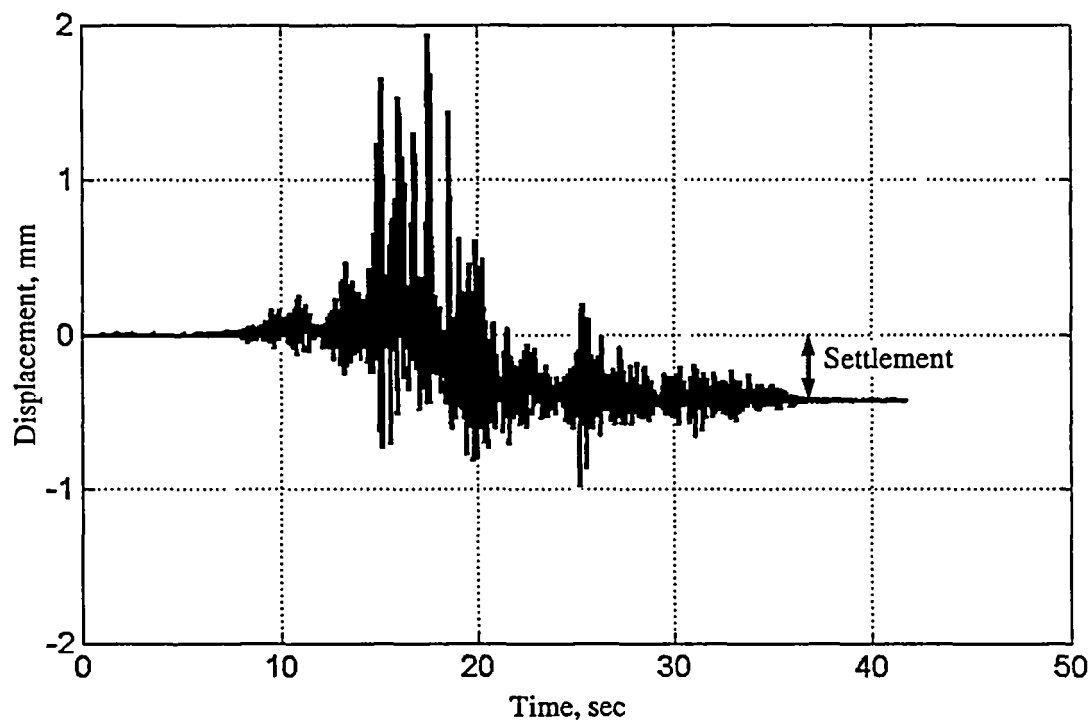

(b) Along y-axis (channel 51)

Figure 7-20 Components of vertical motion for Bushing-2 without Ring-2; Test No 18, Tabas-B, target PGA=2.0g

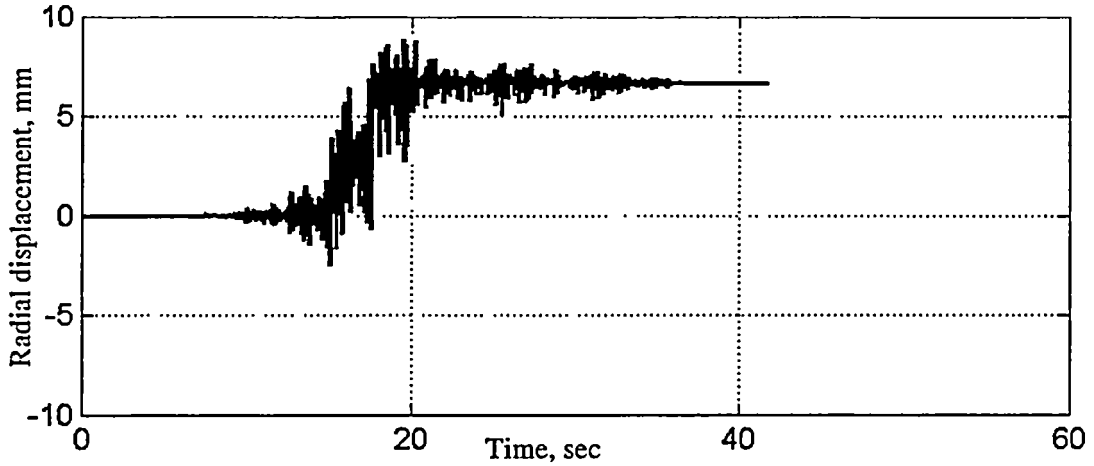

(a) Slip of the UPPER-1 porcelain in the *x*- direction

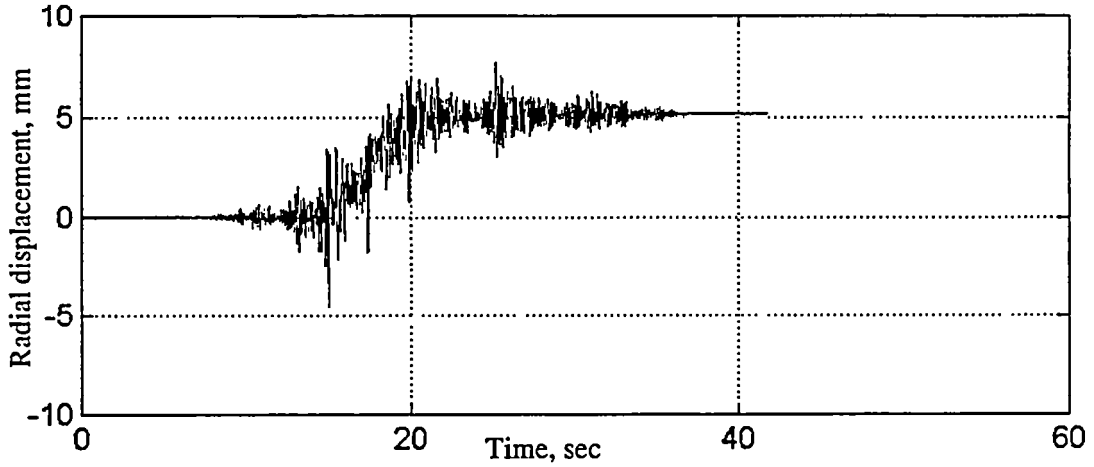

(b) Slip of the UPPER-1 porcelain in the *y*- direction

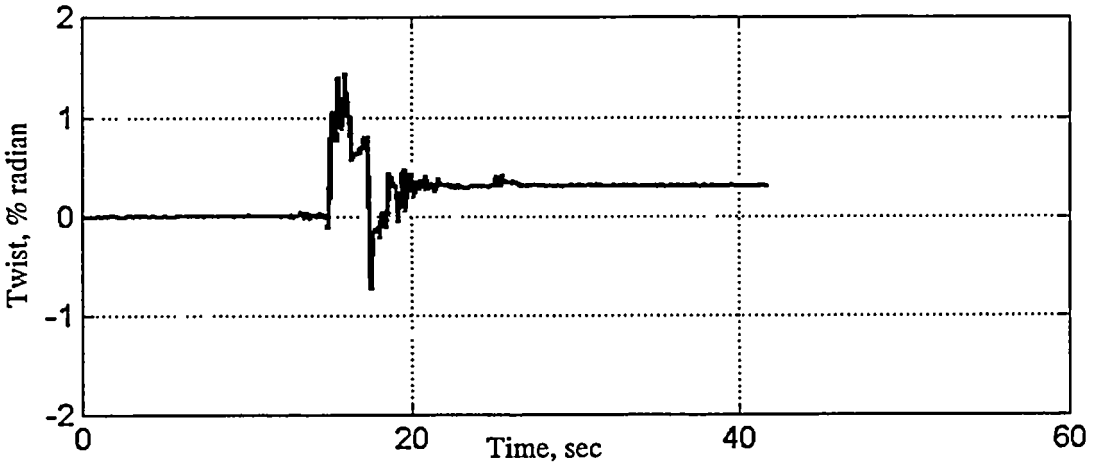

(c) Twist of the UPPER-1 porcelain unit about the *z*- axis

Figure 7-21 Components of horizontal motion for Bushing-2 without Ring-2; Test No 18, Tabas-B, target PGA=2.0g

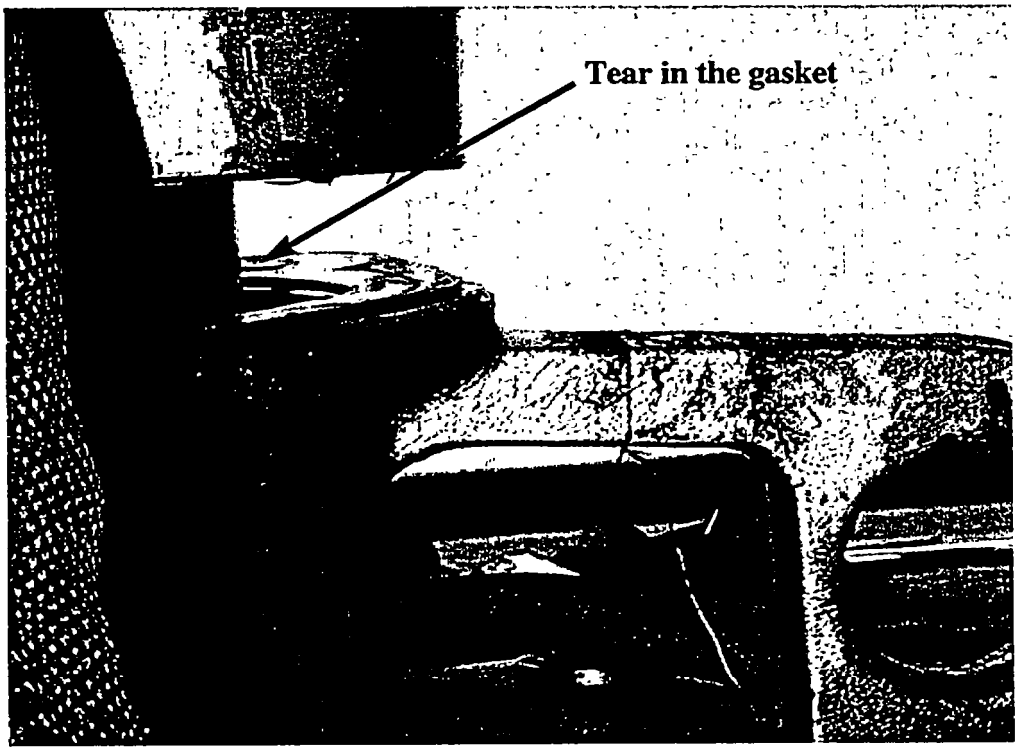

Figure 7-22 Bushing-2 after earthquake testing showing the largest tear in the gasket

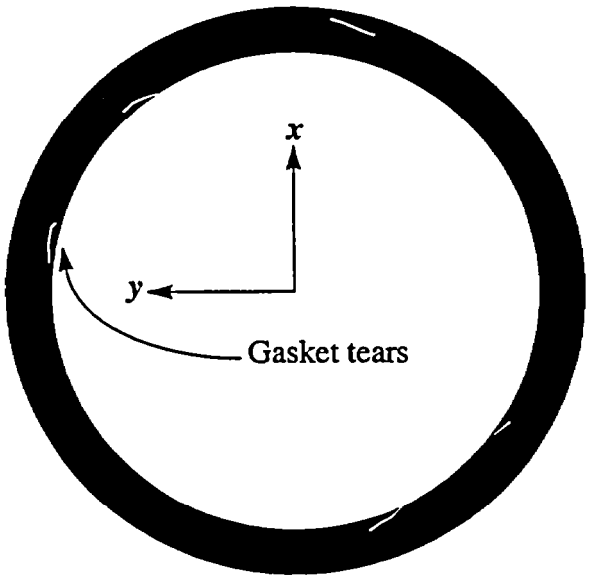

Figure 7-23 Drawing of the gasket locating tears

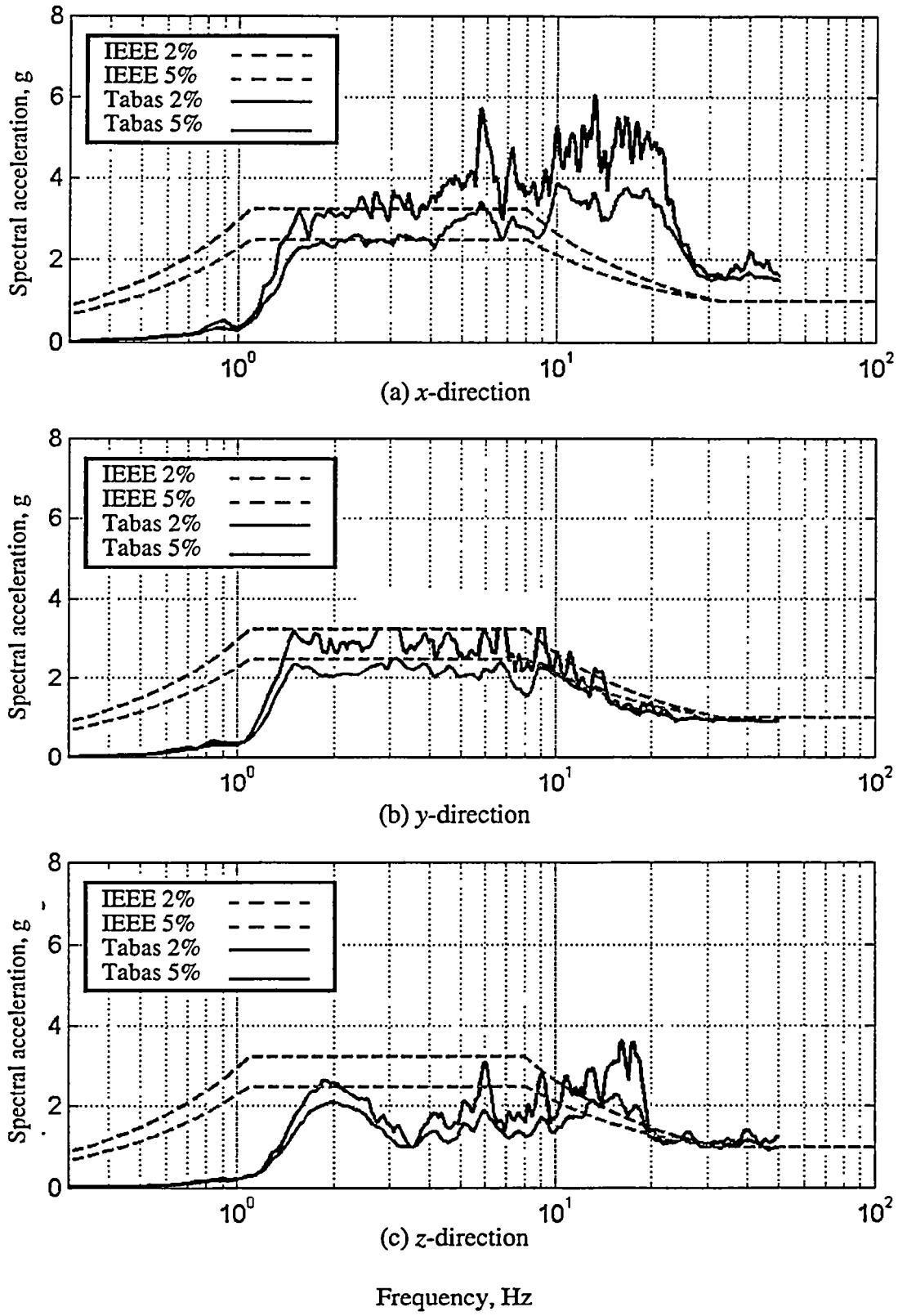

Figure 7-24 Response spectrum for Bushing-2 retrofitted with Ring-2; Test No 13, Tabas-A, target PGA=1.0g

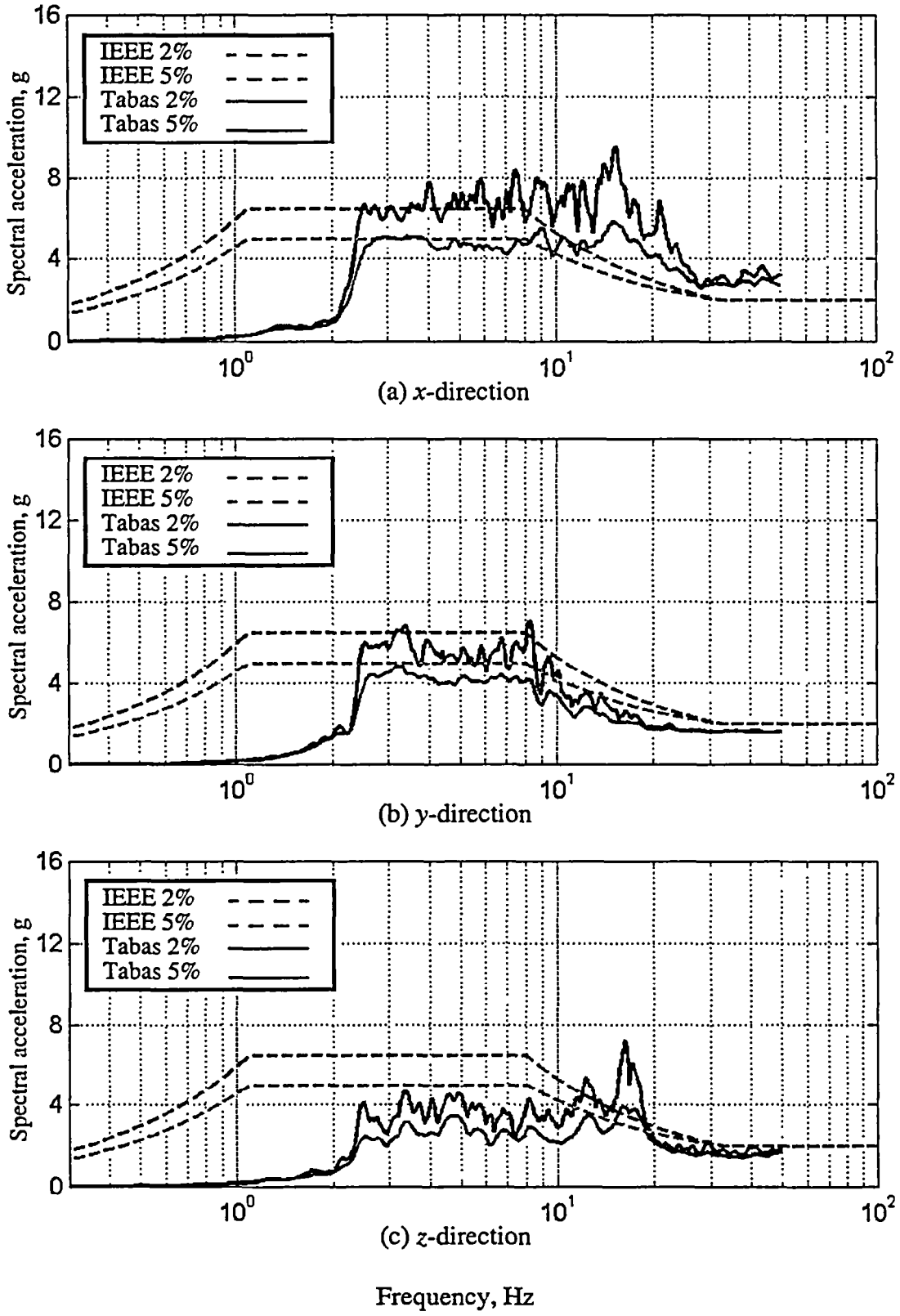

Figure 7-25 Response spectrum for Bushing-2 retrofitted with Ring-2; Test No 18, Tabas-B, target PGA=2.0g

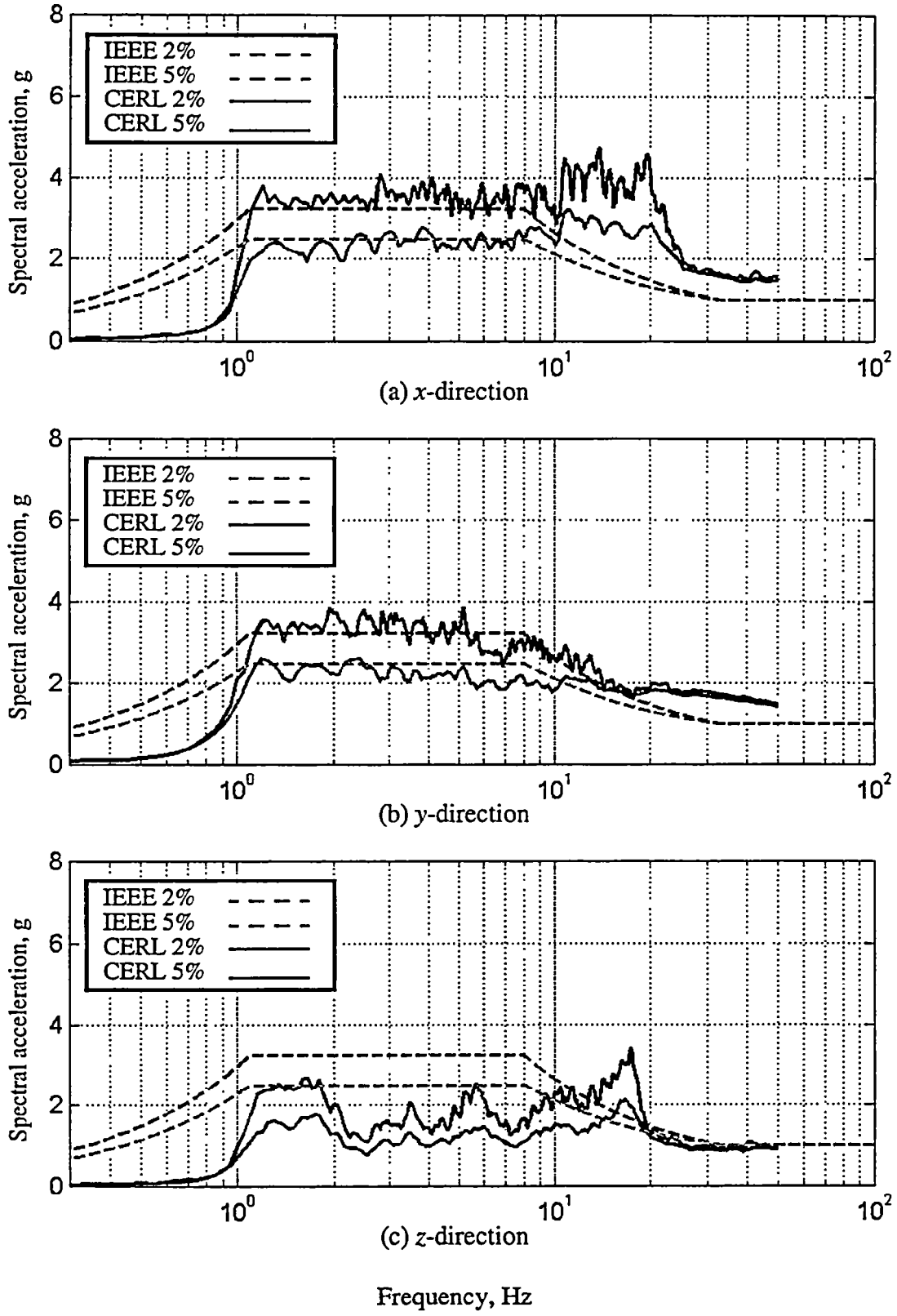

Figure 7-26 Response spectrum for Bushing-2 retrofitted with Ring-2; Test No 19, CERL, target PGA=1.0g

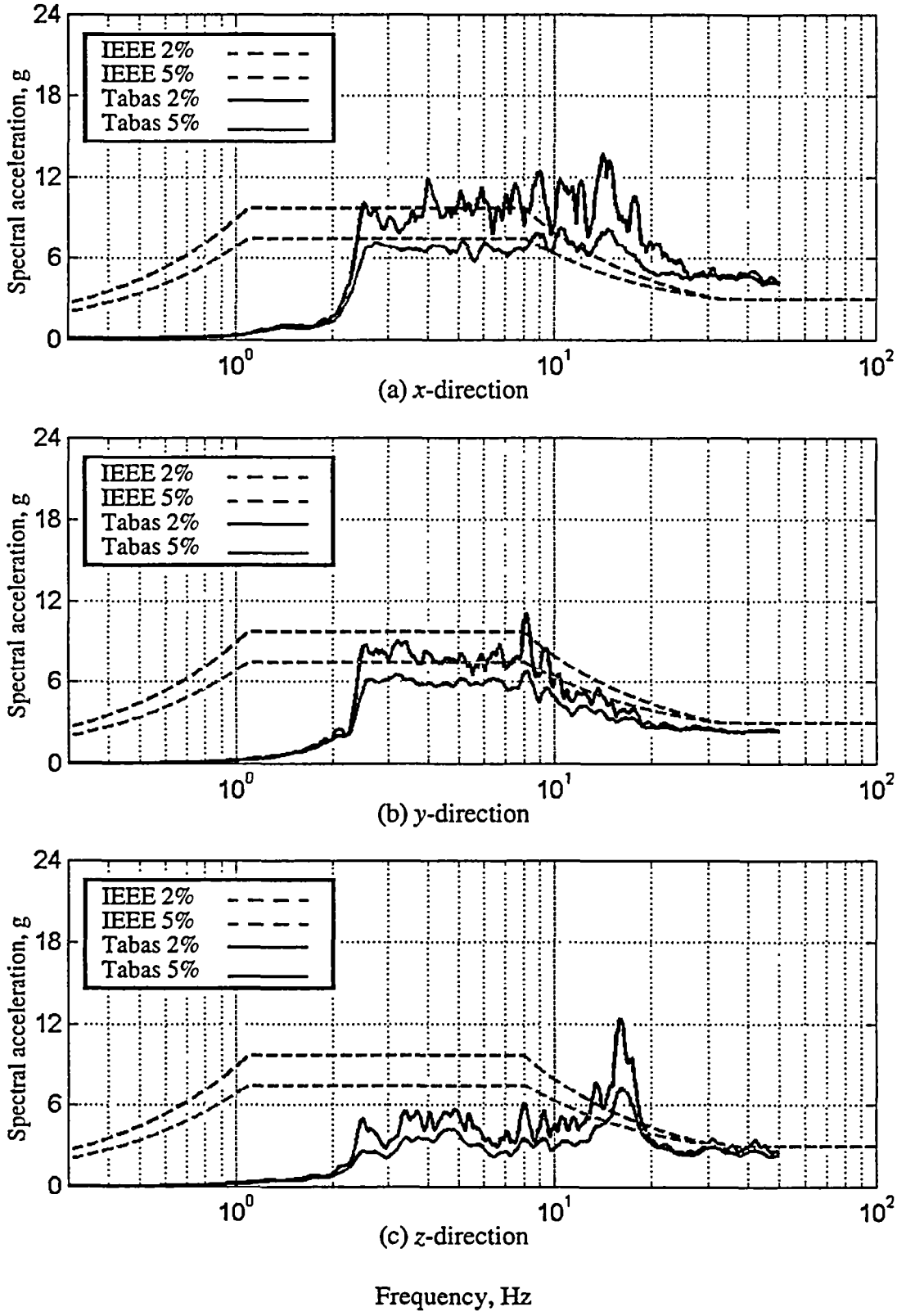

Figure 7-27 Response spectrum for Bushing-2 retrofitted with Ring-2; Test No 24, Tabas-B, target PGA=3.0g

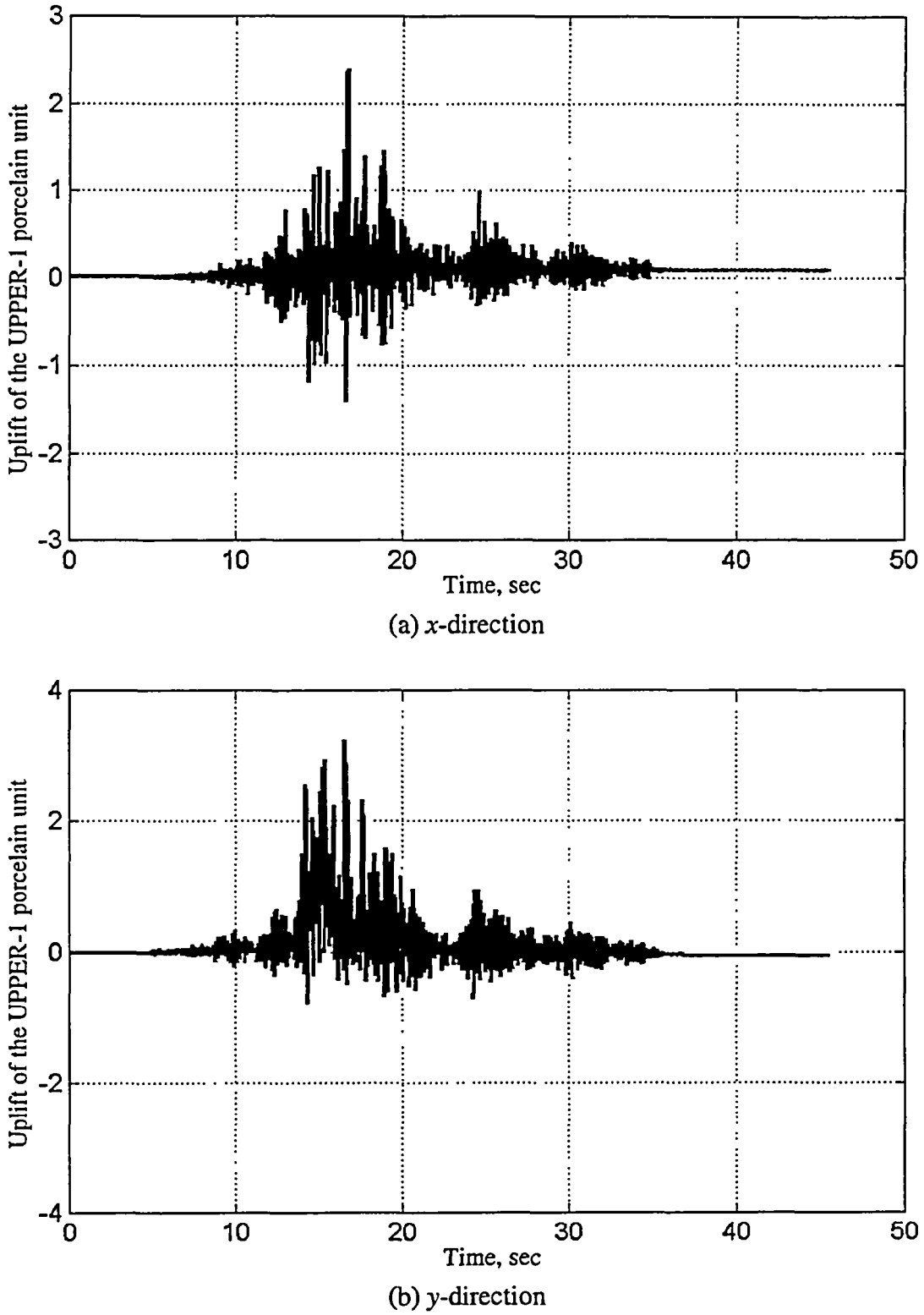

Figure 7-28 Components of vertical motion for Bushing-2 retrofitted with Ring-2; Test No 24, Tabas-B, target PGA=3.0g

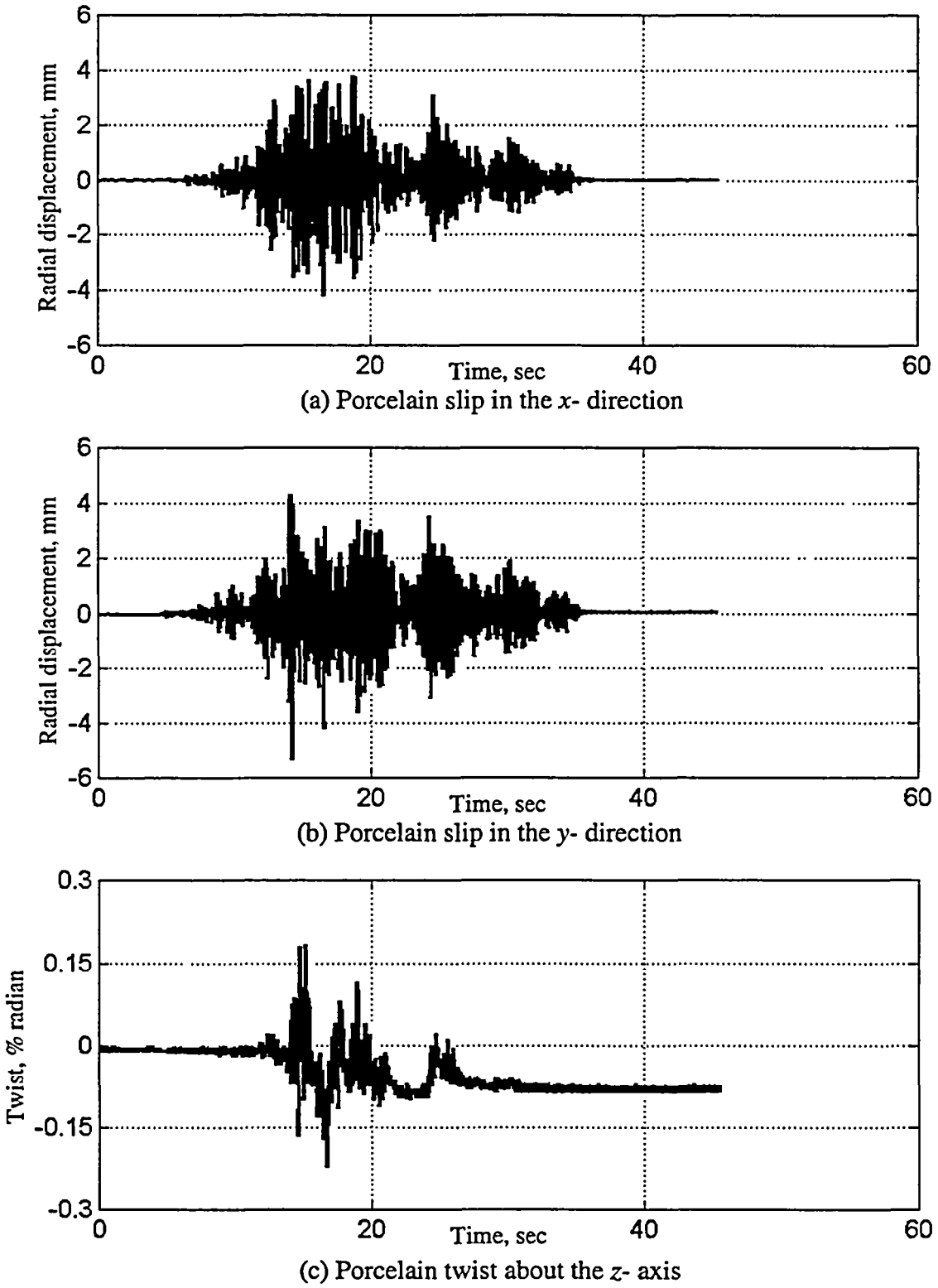

Figure 7-29 Components of horizontal motion for Bushing-2 retrofitted with Ring-2; Test No 24, Tabas-B, target PGA=3.0g

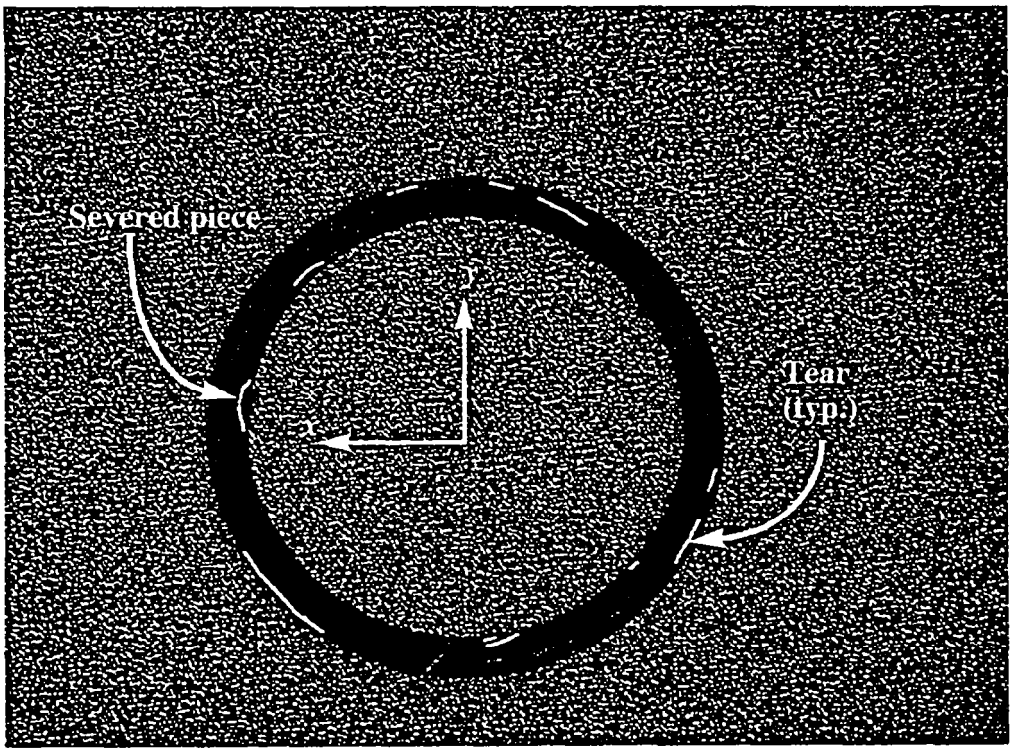

Figure 7-30 Post-test photograph of gasket locating tears and lacerations

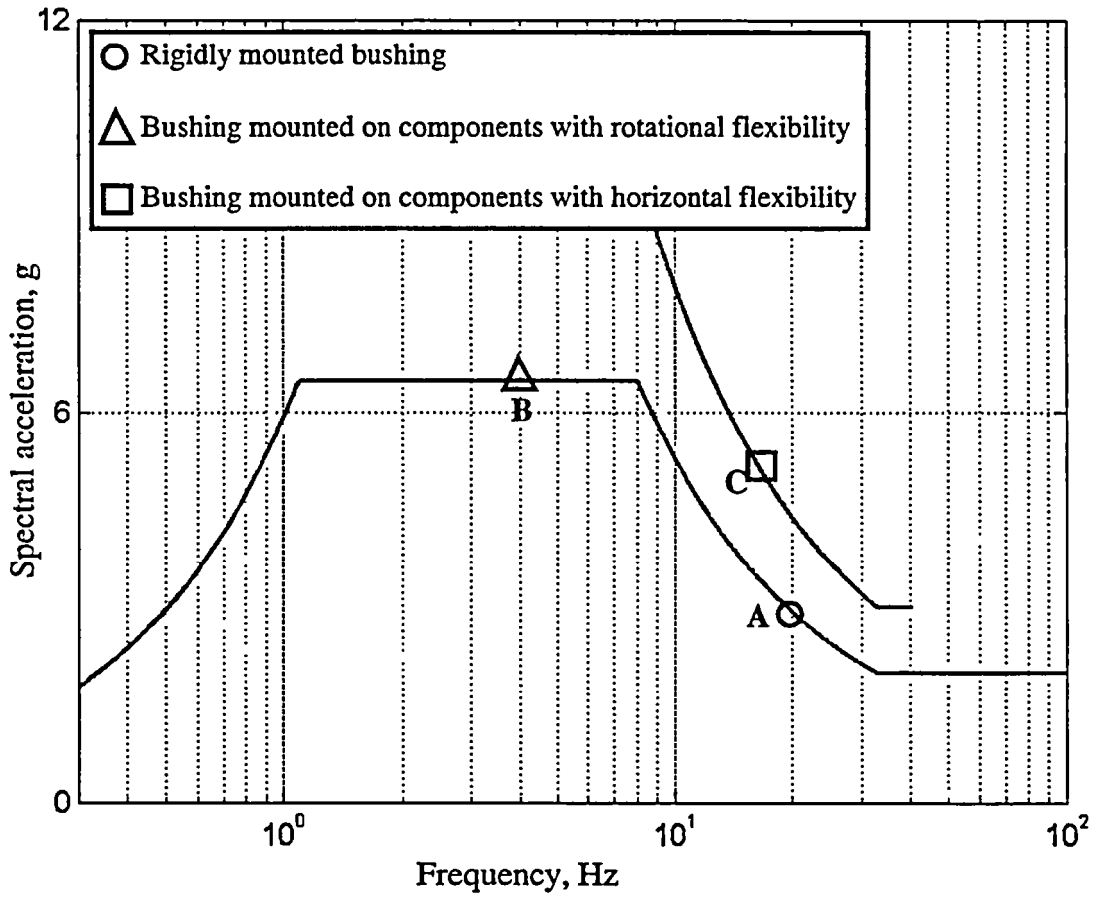

Figure 7-31 Effects of support flexibility on the spectral acceleration response of a bushing

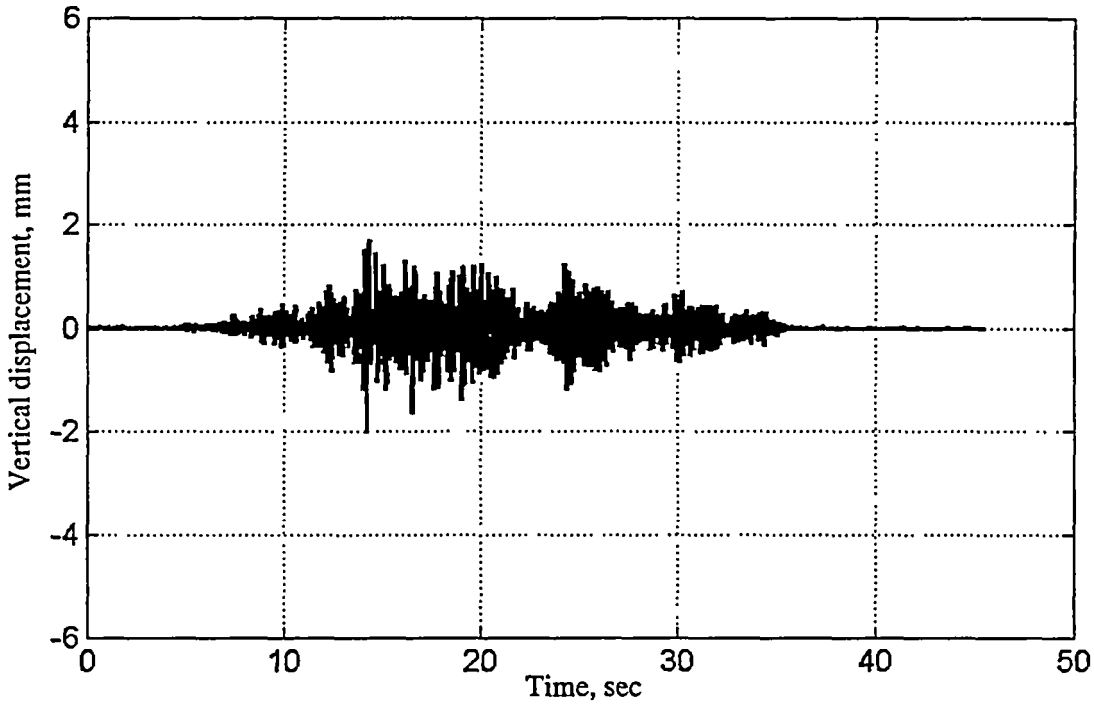

(a) At mid-circle of *flexible* plate (channel 60)

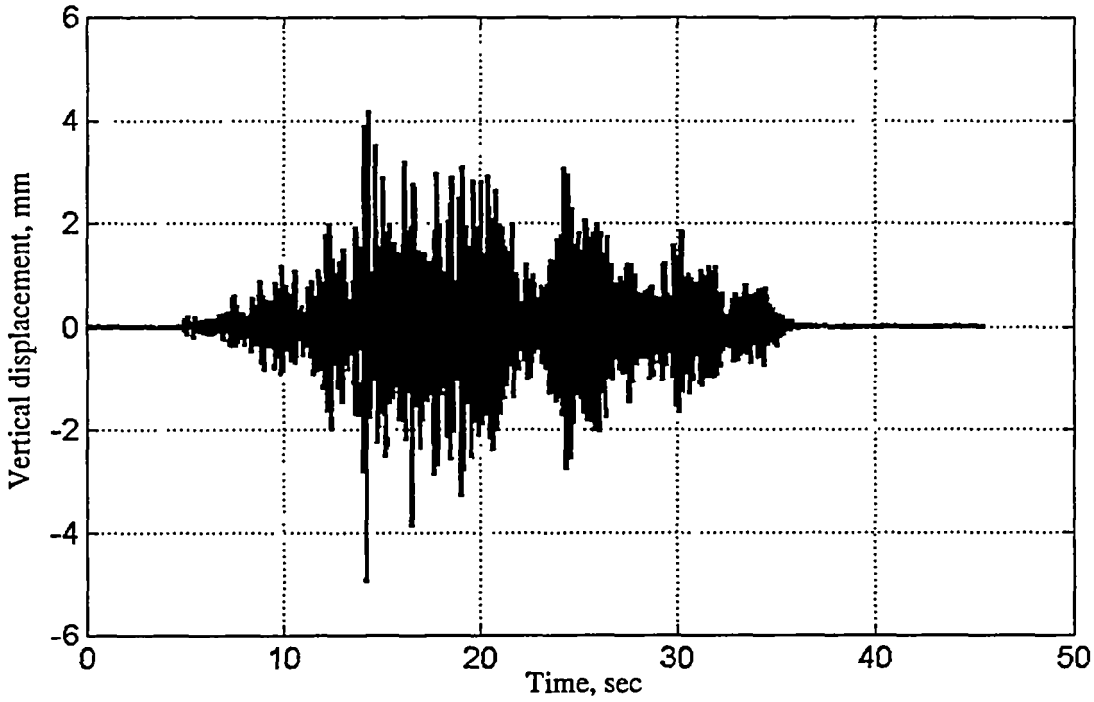

(b) At the bushing flange (channel 61)

Figure 7-32 Displacement response of flexible plate in *z*- direction; Test No 24, Tabas-B, target PGA=3.0g

8 Summary and Conclusions

8.1 Summary

8.1.1 Overview

The reliability and functionality of electrical transmission and distribution (T&D) systems after an earthquake depend on the seismic response of individual substation components. Porcelain transformer bushings (insulated conductors used to provide electrical connection between a high-voltage line) are a key component of power transmission and distribution (T&D) systems. Bushings are typically mounted on the top of an oil-filled transformer or on a turret attached to the transformer. High-voltage bushings (bushings rated at 196 kV and higher) have sustained major damage during recent severe ground shaking. For these bushings, because of their size and mass, earthquake motions can generate large shear forces and bending moments at the gasket connection (interface between the flange and porcelain), which can lead to failure. Four major failure modes have been documented: oil leakage, porcelain slip, gasket extrusion, and porcelain fracture.

Since transformer bushings form an integral part of power T&D systems, their structural and electrical integrity are critical to maintaining power transmission. To mitigate the vulnerability of new bushings and other electrical substation equipment, representatives from electrical utilities and equipment manufacturers in North America, consulting engineers, and members of the academic community jointly developed a new national standard, IEEE 693-1997. Both IEEE 693-1997 and IEC 61463 (a code similar to IEEE 693-1997 that is used in Europe) state that new equipment rated for high voltage (typically 161 kV and higher) must be qualified by triaxial earthquake simulator testing. These requirements are expected to improve the seismic capability of new equipment. However, electrical utilities will continue to maintain substantial inventories of the older equipment that were procured to specifications less stringent than current seismic standards.

The investigation reported in this document was sponsored by the California Electric Commission and a consortium of utilities (Pacific Gas & Electric Company, Bonneville Power Administration, Southern California Edison, and British Columbia Hydro) for the purpose of characterizing the response of older bushings and developing retrofit details to improve the seismic performance of such equipment. The key objectives of the project were: (a) identify vulnerable bushings, (b) develop a testing program that incorporated both dynamic and static testing, and both flexible and rigid support frames, (c) develop the appropriate earthquake ground motion records suitable for

the seismic evaluation and fragility testing, (d) develop a practical and cost-effective retrofit detail, and (e) draw conclusions regarding the seismic performance of the vulnerable porcelain transformer bushings, the influence of support condition on the bushing response, and the efficacy of the retrofit detail.

8.1.2 Test bushings

Two criteria were used to select the candidate bushing. First, the bushing had to be widely used in practice, and second, there had to be tangible evidence that the candidate bushing had sustained earthquake-induced damage. A survey of electrical substations by the utilities indicated that 230-kV type-U bushings manufactured by General Electric (GE) Company are widely used in electrical substations and have been damaged in past earthquakes.

Two identical 230-kV, 3,000-A, type-U transformer bushings manufactured in the mid-1980s by GE were used for testing and evaluation. The two bushings were identified by serial numbers 1795450 and 1795451 and were designated Bushing-1 and Bushing-2, respectively. The overall length of the transformer bushing was 144.5 in. (3.7 m). The segment of the bushing above the cast aluminum flange was 85 in. (2.2 m) long and included two porcelain insulator units or stacks (UPPER-1 and UPPER-2), and a metallic dome at the top of the bushing (above porcelain unit UPPER-2). The porcelain units, the cast aluminum flange, and the metallic dome were separated by nitrile-rubber gaskets. The gasket between the flange and porcelain unit UPPER-1 was a flat annular strip of rubber. The segment of the bushing below the flange included an extension of the cast aluminum flange, one porcelain insulator, and a cast aluminum lower support. Flat annular gaskets separate these components. The flange plate, which was used to connect the bushing to the transformer, was cast with two lifting lugs to facilitate movement and installation of the bushing.

In cross section, the bushing had an aluminum core that provided the electrical connection; a multilayered oil-impregnated kraft paper condenser wrapped around the core; an annular gap between the porcelain and condenser that was filled with oil to provide electrical insulation; and a porcelain insulator. The weight of the bushing was approximately 920 lbs (4.1 kN), and its center of mass was located approximately 18 in. (0.45 m) above the flange plate. The portion of the bushing extending from the top of flange to the top of the bushing, weighed approximately 560 lbs (2.5 kN), with its center of mass located 44 in. (1.1 m) above the flange plate. The bushing was post-tensioned along its longitudinal axis through its core. The main physical and electrical characteristics of the bushings are summarize in Table 8-1.

8.1.3 Experimental program

8.1.3.1 Introduction

The seismic characterization and fragility testing of the test bushings consisted of three parts: (1) fragility testing of two *rigidly* mounted bushings; (2) static testing of Bushing-1 (with and without retrofit detail); and (3) fragility testing of *flexibly* mounted Bushing-2, (with and without retrofit detail). The earthquake testing was performed on the earthquake simulator at the PEER Center, which is headquartered at the University of California at Berkeley. The 20 ft by 20 ft (6.1 by 6.1 m) simulator can accommodate models up to 140 kips (623 kN) in weight and 40 ft (12.2 m) in height.

Table 8-1 Characteristics of the 230-kV type-U bushings manufactured by GE

Property	*Parameter*	*Value*
Electrical properties	Voltage rating	230 kV
	Amperage	3,000 A
	BIL[1]	900 kV
Physical properties	Weight	4.1 kN
	Total length	3.7 m
	Initial PT force	98 kN
Component material	insulator	porcelain
	bushing oil	mineral oil
	condenser	kraft paper
	core	aluminum
	gasket	nitrile rubber
Identification plate	Model No.	11B802BB G10
	Serial No.: Bushing-1; Bushing-2	1795450; 1795451

1. Basic Impulse level (BIL) designates the impulse voltage the bushing can withstand.

8.1.3.2 Mounting frames

A stiff frame previously used for the qualification and fragility testing of 196-kV and 550-kV bushings was re-used for the earthquake testing of the *rigidly* mounted bushings. For earthquake testing of the *flexibly* mounted bushings, a *flexible* plate was attached to the top of the stiff frame. The mounting plates for both setups were sloped at 20 degrees measured to the vertical; since a bushing qualified at this angle is deemed by IEEE 693-1997 to be qualified for all angles between vertical and 20 degrees measured to the vertical.

8.1.3.3 Test program

The testing program consisted of three components: (1) resonant-search tests, (2) static tests, and (3) triaxial earthquake tests. The resonant-search (white-noise, sine-sweep, pull-back and free-vibration) tests were conducted to determine the dynamic properties of the bushings. Static tests (unidirectional, unidirectional with offset, and bidirectional) were conducted to characterize the response of Bushing-1 and to evaluate the effectiveness of the first retrofit detail (Ring-1). Triaxial earthquake tests were used to evaluate the response of the bushings, to examine the effect of support flexibility, and to evaluate the efficacy of the second retrofit detail (Ring-2).

8.1.3.4 Development of ground motions for triaxial earthquake testing

Recorded earthquake ground motion histories were used to evaluate the seismic response of the two 230-kV transformer bushings. The earthquake histories used for the fragility testing of the 230-kV bushings were developed using the three-component set of near-fault earthquake motions recorded during the 1978 Tabas earthquake. The power spectrum for each history has moderate bandwidth. To obtain IEEE 693-1997 spectrum-compatible normalized histories, a three-step process was utilized combining time-domain spectrum-matching algorithm and frequency-domain high-pass filtering. First, the original earthquake history was high-pass filtered to remove low-frequency content such that the maximum displacement and velocity of the filtered history were approximately equal to 5 in. (127 mm) and 25 in./sec (635 mm/sec), respectively. The cut-off frequencies (1 to 2.2 Hz) were much smaller than the resonant frequency of the 230-kV bushings (known to range between 16 to 20 Hz for *rigidly* mounted bushings and between 6 to 8 Hz for *flexibly* mounted bushings). Removal of such low-frequency components from the input signals to the simulator was known to have a negligible impact on the dynamic response of the bushings. Second, the filtered earthquake histories from step one were matched to the target spectrum for frequencies greater than the corner frequency of the trapezoidal filter using the Abrahamson (Abrahamson, 1996) algorithm. Third, the spectrum-compatible motions from step two were high-pass filtered to exactly limit the maximum displacement and velocity to 5 in. (127 mm) and 25 in./sec (635 mm/sec), respectively.

8.1.4 Retrofit details

A cost-effective external retrofit detail for the gasket connection of 230-kV bushings was developed by Dr. Schiff and utility representatives. The retrofit detail consisted of two semicircular rings clamped around the gasket connection. A two-compound filler material was used to grout the space between the detail and the bushing. Two retrofit rings were developed for the purpose of testing and evaluation. Ring-1 was placed around the gasket connection of Bushing-1. During the static tests, Ring-1 was not effective in improving the response of Bushing-1. A modified version of Ring-1 was developed for further evaluation. Ring-2 was similar to Ring-1 with the addition of steel tabs; these tabs were bolted to the ring and clipped under the bushing flange to delay uplift and rotation of the ring.

8.1.5 Summary of experimental results

8.1.5.1 Introduction

The following sections present a summary of experimental results and findings from the resonant-search tests, seismic testing of two *rigidly* mounted bushings, static tests of Bushing-1 (without and with Ring-1), and seismic tests of *flexibly* mounted Bushing-2 (without and with Ring-2).

8.1.5.2 Experimental results from resonant-search tests

Experimental data from resonant-search tests were used to calculate the dynamic properties of the bushings and to evaluate the effects of the bushing post-tensioning force, the flexibility of the mounting frame, and the addition of terminal mass at the top of the bushing on the dynamic properties of the bushings.

The vibration frequency of the *rigidly* mounted bushings in the x- and y-directions (measured at the top of bushings) were 20 Hz and 18 Hz, respectively. The lateral stiffness and damping ratios of bushing were approximately 6 kips/in. (0.9 kN/mm) and between 2 to 3 percent of critical, respectively. The fundamental frequency and the lateral stiffness of the bushing were slightly larger in the x- direction due to the presence of the lifting lugs on the bushing flange. The effective weight of the bushing (at the top) of 140 lbs (0.6 kN) was computed assuming that the bushing was a single-degree-of-freedom system with a lumped mass at its top. This weight was only 25 percent of the weight of the segment of the bushing between the flange and the top. The frequency and damping ratio in the x-direction of the bushing (measured at the bottom) were 52 Hz and 3 percent of critical, respectively.

The modal properties of the bushing where unchanged when the bushing preload was reduced from 27 kips (120 kN) to 20 kips (89 kN), when the gasket at the gasket connection was lubricated (coated with oil), or when the retrofit ring was added to the gasket connection. The attachment of the terminal (to simulate equipment interconnection jumper weight) at the top of the bushing reduced the frequency of the bushing significantly, (from 20 Hz to 14 Hz) and introduced a second vibration mode to the response. When the bushing was mounted on a *flexible* plate, the frequency of the bushing-support system was approximately 7.5 Hz. When a 1/4-in. (6-mm) thick gasket was placed between the bushing flange and the mounting plate, the frequency of the bushing-support system dropped to 6.5 Hz. The measured dynamic properties of the 230-kV bushings in the different test configurations are presented in Table 8-2.

8.1.5.3 Experimental results from rigidly mounted bushings

Seismic testing of *rigidly* mounted Bushing-1 and Bushing-2 included fragility testing of the bushings up to a test with the spectrum equal to the IEEE 693-1997 spectrum for High Level qualification (Tabas-B, target PGA equal to 2.0g). At the request of the utilities, Bushing-2 was also subjected to a 5-Hz constant amplitude unidirectional motion along the x-axis.

At the level of shaking consistent with Moderate Level qualification (target PGA equal to 1.0g), the maximum acceleration and displacement relative to the mounting frame (recorded at the top of the bushing) were approximately 4g and 0.17 in. (4 mm), respectively.

Table 8-2 Modal properties of 230 kV bushings[1]

			Stiffness (kN/mm)		*Frequency (Hz)*		*Damping Ratio (% critical)*	
Mounting Frame[2]	*Top Terminal Attached*[3]	*Mounting Gasket Attached*[4]	*x-dir*	*y-dir*	*x-dir*	*y-dir*	*x-dir*	*y-dir*
Rigid	No	No	0.9	0.9	20	18	3	2
Rigid	Yes	No	0.9	-	14	13	3	3
Rigid	No	Yes	0.8	-	18	-	3	-
Rigid	Yes	Yes	0.8	-	13	-	4	-
Flexible	No	No	0.2	0.2	7.5	7.5	2	2
Flexible	Yes	No	0.2	-	6.5	-	3	-
Flexible	No	Yes	0.1	0.1	6.5	6.5	4	4
Flexible	Yes	Yes	0.1	-	5.5	-	5	-

1. Data reported only for the top of the bushing.
2. Rigid mounting frame is shown in Figure 4.1; flexible mounting plate is shown in Figure 7.1.
3. Terminal, shown in Figure 4.6, weighs 280 N; the threaded attachment weighs 50 N.
4. Mounting gasket: 6-mm thick annular rubber.

At the level of shaking consistent with High Level qualification (target PGA equal to 2.0g), the maximum acceleration and displacement relative to the mounting frame (recorded at the top of the bushing) were approximately 6g and 0.4 in. (10 mm), respectively. In the range of the bushing frequency (18 to 20 Hz), the 2-percent and 5-percent damped acceleration response spectra for the bushings generated using measured acceleration histories at the flange plate exceeded the IEEE 693-1997 acceleration ordinates for High Level qualification: There was no oil leakage or evidence of structural damage, and porcelain stresses were well below the ultimate value.

Although neither Bushing-1 nor Bushing-2 were originally designated for qualification, given that the measured spectral amplitudes in the range of the measured bushing frequency exceeded the IEEE 693 1997 high-level spectrum, there was no oil leakage, and the measured porcelain stresses were less than the ultimate stress, Bushing-1 and Bushing-2 *were qualified by test to the high-level.*

Bushing-2 was subjected to a constant-amplitude, single-frequency harmonic motion with an input frequency equal to 5 Hz. During this tests, oil leaked from the gasket connection and the UPPER-1 porcelain unit slipped over the flange. Examination of the simulator input data showed that due to the dynamics of the earthquake simulator, harmonics of the input motion at 15, 20, and

25 Hz were present in the translational and rotational simulator accelerations. Examination of the response spectrum for the input signal showed that because of these higher harmonics, the bushing was subjected to spectral accelerations which significantly exceeded those of the IEEE 693-1997 spectrum for High Level qualification.

8.1.5.4 Experimental results from static tests of Bushing-1

Static testing of Bushing-1 mounted on a stiff frame included cyclic testing of Bushing-1 without Ring-1 and cyclic and monotonic testing of Bushing-1 with Ring-1.

During the unidirectional tests (Test Set 1) of Bushing-1 without Ring-1, during the cycles to a target displacement of 0.35 in. (8.75 mm) and 0.4 in. (10 mm), the bushing leaked oil and the UPPER-1 porcelain unit slipped over the gasket connection. When the gasket at the gasket connection was lubricated (Test Set 5), the bushing leaked oil at the gasket connection during displacement cycles to 0.3 in. (7.5 mm). When the post-tensioning force was reduced from 27 kips (120 kN) to 20 kips (90 kN), the bushing leaked oil during the cycles to a target displacement of 0.3 in. (7.5 mm). During the bidirectional tests (Test Set 4), the bushing leaked oil during displacement cycles to 0.3 in. (7.5 mm).

During the unidirectional tests (Test Set 12) of Bushing-1 with Ring-1, the bushing leaked oil and the UPPER-1 porcelain unit slipped over the gasket connection during the cycles to a target displacement of 0.4 in. (10 mm) and 0.45 in. (11.25 mm). During the cycles to a target displacement of 0.5 (12.5 mm), Ring-1 rotated with respect to the longitudinal axis of the bushing. During the bidirectional tests (Test Set 13), the bushing leaked oil, Ring-1 rotated, and the UPPER-1 porcelain unit twisted above the flange during the cycles to a target displacement of 0.45 in. (11.25 mm).

During the monotonic test (Test Set 14), the bushing leaked oil at the gasket connection at a displacement of approximately 0.4 in. (10 mm). When the actuator displacement exceeded approximately 1.5 in. (38 mm), the oil leak became continuous. At a displacement of approximately 5.5 in. (140 mm), the cast aluminum flange fractured. At a displacement of approximately 6 in. (152 mm), the displacement limit of the actuator was reached. As the actuator was retracted, the rotated Ring-1 made contact with and fractured the bottom shed of the UPPER-1 porcelain unit.

8.1.5.5 Experimental results from flexibly mounted Bushing-2

Seismic fragility testing of the *flexibly* mounted Bushing-2 included fragility testing of Bushing-2 without Ring-2 up to a test with the spectrum equivalent to the IEEE 693-1997 spectrum for the High Level qualification (Tabas-B, target PGA equal to 2.0g), and fragility testing of Bushing-2 with Ring-2 up to a test with the spectrum equivalent to the 150 percent of IEEE 693-1997 spectrum for High Level qualification (Tabas-B, target PGA equal to 3.0g). At the request of the utilities, Bushing-2 was also subjected to a single test using a three-component input motion developed at CERL with spectrum equivalent to the IEEE 693-1997 spectrum for Moderate Level qualification (CERL, target PGA equal to 1.0g).

At a level of shaking consistent with the moderate-level qualification test per IEEE 693-1997 (target PGA equal to 1.0g), the maximum acceleration and displacement relative to the mounting frame (recorded at the top of the bushing) of Bushing-2 without Ring-2 were approximately 3g and 0.7 in. (17 mm), respectively. During the tests with target PGAs equal to 1.4g and 1.6g, the bushing leaked oil. During the tests with target PGAs equal to 1.8g and 2.0g, the bushing leaked oil from the gasket connection, the UPPER-1 porcelain unit slipped over the gasket connection, and the gasket extruded from the gasket connection. At the conclusion of the testing, the bushing was de-stressed and partially disassembled. The value of post-tensioning load was measured at 9 kips (40 kN) — approximately one third of the original value. Examination of the gasket at the gasket connection revealed that the gasket had several shallow tears.

At a level of shaking consistent with the IEEE 693-1997 Moderate Level qualification spectrum (target PGA equal to 1.0g), the maximum acceleration and displacement relative to the mounting frame (recorded at the top of the bushing) of Bushing-2 with Ring-2 were approximately 3.4g and 0.8 in. (21 mm), respectively. At a level of shaking consistent with the IEEE 693-1997 High Level qualification spectrum (target PGA equal to 1.0g), the maximum acceleration and displacement relative to the mounting frame (recorded at the top of the bushing) of Bushing-2 with Ring-2 were 6.4g and 1.8 in. (45 mm), respectively. During the tests with target PGAs equal to 2.6g and 2.8g, oil leaked from around Ring-2. During the test with a target PGA of 3.0g, the bushing leaked oil and the UPPER-1 porcelain unit uplifted over the gasket connection. At the conclusion of the testing, Ring-2 was removed. A small segment of the gasket had extruded from the gasket connection. The bushing was de-stressed and disassembled. The value of the post-tensioning load was measured at 22 kips (98 kN). Examination of the gasket at the gasket connection revealed that the gasket had additional tears and a small portion of the gasket had severed.

Table 8-3 presents selected peak response values gasket connection for Bushing-2 with and without Ring-2.

Table 8-3 Response of flexibly mounted Bushing-2 at the gasket connection

Ring-2 Installed	*Target PGA (g)*	*Maximum Slip (mm)*	*Maximum Uplift (mm)*	*Comments*
No	1.2	2	0.8	
	1.4	4	1	First test with oil leakage.
	2.0	9	2	Spectrum equivalent to high-level qualification.
Yes	1.2	2	0.8	No *visible* oil leakage or porcelain slip[1].
	1.4	3	1	
	2.0	4	2	

1. Presence of Ring-2 made visual identification of small slip and uplift impossible.

8.2 Conclusions

8.2.1 Seismic response of 230-kV transformer bushings

Two 230-kV transformer bushings were undamaged by severe earthquake shaking when mounted on a *rigid* frame. Bushing-1 and Bushing-2 passed the IEEE 693-1997 requirements for High Level qualification. Both bushings were subjected to six earthquake simulations with input accelerations exceeding 1.0g and suffered no visible damage. When mounted on a *flexible* support, Bushing-2 passed the IEEE 693-197 requirements for Moderate Level qualification.

Bushing-1 was subjected to a series of static tests using four displacement orbits. Oil leakage and slip of the UPPER-1 porcelain unit was only observed when the imposed actuator loads exceeded 1.5 kips (6.7 kN)—approximately three times the weight of the portion of the bushing above the flange.

Field reconnaissance and observations from past earthquakes suggest that failures (oil leakage and slip of porcelain units) of similar bushings occurred at levels of ground shaking significantly lower than those to which the two bushings were subjected. The reason for this discrepancy in performance is somewhat unclear. However, it is likely that the IEEE procedures do not adequately capture the critical loading environment for bushings because the electrical equipment attached at the top of the bushing in the field (termed interconnected equipment elsewhere in this report) are not included in the qualification and fragility testing.

8.2.2 Effect of support flexibility

For bushings mounted on transformers, the flexibilities of the turret and top plate of the transformer have two effects on the *horizontal* response of the bushing-transformer system. First, the *rotational* flexibility of turrets or transformer-tank tops will reduce the frequency of the bushing-transformer system and generally result in larger spectral accelerations. Second, the *horizontal* flexibility of turrets or transformer-tank tops can amplify the shaking effects at the bushing flange plate with respect to the ground. Only the first effect was simulated in the studies reported herein. A two-fold increase in maximum bushing acceleration was observed for similar ground-motion inputs when the bushing was installed on a mounting plate with rotational flexibility.

8.2.3 Effect of post-tensioning force

Previous analytical studies (Gilani et al., 1998) have indicated that the dynamic properties of a bushing are highly dependent upon the axial stiffness of the rubber gasket that is routinely placed immediately above the bushing flange plate. The gasket in the bushings tested in this study was placed in an annular groove or pocket that rendered it substantially incompressible. Changes in the bushing post-tensioning force therefore had little effect on the dynamic properties of the bushing. However, reductions in the post-tensioning force from the value typically used by the manufacturer did reduce the uplift displacement at which the oil leaked from the gasket connection.

8.2.4 Efficacy of retrofit design

The two retrofit details (Ring-1 and Ring-2) described in this report were detailed primarily to limit the slip of the UPPER-1 porcelain unit over the bushing flange. Both details utilized semicircular rings and epoxy filler material. Neither ring was engineered and the test results cannot be extrapolated to other bushings. Ring-1 was not effective. Ring-2, similar in design to Ring-1 but with steel tabs to attach the ring to the bushing flange, was effective in reducing the slip of the UPPER-1 porcelain unit and preventing oil leakage for earthquake inputs with PGAs less than 2.6g.

8.3 Recommendations for future study

8.3.1 Procedures for seismic qualification and fragility testing

The 230-kV bushings were installed in a *rigid* and a *flexible* mounting frame without electrical connections for earthquake testing. It was noted that when the bushing was mounted on the *flexible* plate, the fundamental frequency of the bushing-support system was reduced, however, the horizontal accelerations were not amplified. For qualification of equipment attached to a foundation, IEEE 693-1997 specifies a response spectrum for earthquake-simulator testing. The amplitude of the input motion for qualification of bushings is doubled to account for flexibility and ground-motion amplification in the transformer or support equipment. It is not known whether the IEEE 693 assumptions are reasonable, conservative, or non-conservative. Numerical (finite element) studies of transformer bushings and other turret structures should be undertaken to review the current specifications for equipment qualification. At a minimum, such studies should identify: (a) the stiffness characteristics of typical bushing support structures, (b) stiffness and damping properties of the mounting gasket(s) used to connect the bushing to the turret and to the transformer top plate, (c) the damping effects of the oil contained in the support structure, if any, (d) the amplification of earthquake shaking effects, if any, through the support structure to the base of a bushing, and (d) the importance of rotational input to a bushing resulting from flexibility in the upper plate of the transformer to which bushings are attached. Answers to these questions will provide valuable guidance to those tasked with revising the IEEE 693-1997 *Recommended Practices for Seismic Design of Substations.*

8.3.2 Development of fragility curves for substation equipment

Currently adopted procedures for reporting fragility data for substation equipment such as transformer bushings are neither appropriate nor conservative. Fragility data presented in the form of peak ground (input) acceleration are of limited value because peak input acceleration is a poor descriptor of damage. Fragility data based on spectral acceleration at the frequency of the bushing provides an improved estimate of damage but cannot account for substructure flexibility and damping, both of which will profoundly affect bushing response. Mean spectral acceleration over a range of frequencies provides a means by which to account for substructure flexibility. Mean-minus-one-standard-deviation spectral acceleration *fragility* data over a range of frequencies

could account for variations in spectral acceleration over a frequency range. Improved, rational procedures are needed to analyze and interpret fragility test data. Such procedures must both better reflect the field installation of equipment and account for substructure flexibility, installation of terminals (for bushings), and the effects of interconnected equipment.

8.3.3 Interconnected equipment

Although IEEE 693-1997 acknowledges that physical (electrical) connections between substation equipment may detrimentally affect the seismic response of individual pieces of equipment, the testing procedures described in IEEE 693-1997 do not adequately account for the effects of such connectivity. These physical connections can vary widely in flexibility and strength. There is substantial evidence from past earthquakes that such electrical connections may have precipitated bushing failures because of dynamic interaction between the interconnected equipment. The analytical and experimental studies completed so far have identified several important parameters affecting dynamic interaction between interconnected equipment. An experimental program should be pursued to investigate both the characteristics of standard interconnections and strategies to mitigate the effects of dynamic interaction.

8.3.4 Behavioral studies of porcelain transformer bushings

Future experimental work will be useful to attain a better understanding of the properties of the components of the bushings. In particular, tests of the nitrile rubber gaskets will provide valuable information regarding the stiffness properties of the gasket and the relation between the post-tensioning force, gasket stiffness, and the dynamic properties of bushings.

8.3.5 Mathematical modeling of porcelain transformer bushings

A three-dimensional finite element model of the bushing incorporating all the critical components is needed to gain a better understanding into the bushing response. The model need to incorporate nonlinear springs developed to simulate the nitrile rubber gaskets (detailed mechanical characteristics of the gaskets will be needed); variation in the post-tensioning force during the analysis; fluid elements to model the bushing oil and the constraint to relative lateral movement of the aluminum core and the perimeter porcelain units offered by the this oil; boundary conditions (support flexibility and mounting gaskets) of the bushing flange; and attachments at the bushing tip (terminals, cables, connections to other equipment). Accurate models of porcelain bushings that would be suitable for rigorous vulnerability (fragility and parametric) studies could be developed with such information.

References

Abrahamson, N. 1996. "Nonstationary response-spectrum matching." Unpublished paper.

Elder, L. 1999. *Personal communications*, ABB Power T&D Company, Inc., Components Division of Alamo, Tennessee.

Schiff, A. J., ed. 1997. *Guide to post-earthquake investigation of lifelines.* Technical Council on Lifeline Earthquake Engineering, Monograph No. 11. Reston, Va.: ASCE.

Bellorini, S., Bettinali, F., Salvetti, M., and Zafferani, G. 1997. *Seismic qualification of transformer high voltage bushings*, IEEE Transactions on Power Delivery.

Bellorini, S., Bettinali, F., Salvetti, M., Gatti, F., Zafferani, G., and Monzari, O. 1998. *Mechanical seismic behavior of power transformers.* IEEE Transactions on Power Delivery.

Villaverde, R., Pardoen, G., and Carnella, S. 1999. *Ground motion amplification at the base of bushings mounted on electronic substation transformers.* A technical report of research supported by PEER/PG&E. Irvine: Dept. of Civil Engineering, University of California.

Wilcoski, J., and Smith S. J. 1997. *Fragility testing of a power transformer bushing.* USACERL Technical Report 97/57. Champaign, Ill.: US Army Corps of Engineers Construction Engineering Research Laboratories.

IEEE. 1998. *IEEE Standard 693-1997, Recommended practices for seismic design of substations.* Piscataway, N.J.: IEEE Standards Department. [New York].

IEC. 1996. *Bushings, seismic qualification.* IEC technical report 61463-1996. Luglio, Italy: IEC.

Gilani, A. S., Whittaker, A. S., Fenves, G. L., and Fujisaki, E. 1999. *Seismic evaluation of 550 kV porcelain transformer bushings.* PEER 1999/05. Berkeley, Calif.: Pacific Earthquake Engineering Research Center, University of California.

Gilani, A. S., Chavez, J. W., Fenves, G. L., and Whittaker, A. S. 1998. *Seismic evaluation of 196 kV porcelain transformer bushings.* PEER 1998/02. Berkeley, Calif.: Pacific Earthquake Engineering Research Center, University of California.

Mathworks. 1999. *The language of technical computing.* Natick, Mass.: The Mathworks, Inc.

Computers and Structures, Inc., *SAP 2000 Integrated finite element analysis and design of structures*, Version 6.1. Berkeley, California, 1997.

Roberts, A. D., 1988. *Natural rubber science and technology.* Oxford science publications. New York: Oxford University Press.

Lindley, P. B. 1978. *Engineering design with natural rubber.* The Malaysian Rubber Producers' Research Association, Hertford Offset Ltd., U.K.

Lilhanand, K., and Tseng, W. S. 1988. "Development and application of realistic earthquake time histories compatible with multiple-damping design spectra." *Proceedings of Ninth World Conference on Earthquake Engineering, Tokyo, Japan.* [Tokyo]: 9WCEE Organizing Committee, Japan Association for Earthquake Disaster Prevention.

Clough R. W., and Penzien J. 1993. *Dynamics of structures.* New York: McGraw-Hill, Inc.

Appendix A IEEE Practice for Earthquake Testing of Transformer Bushings

A.1 Introduction

The document IEEE 693-1997 (IEEE 1998) entitled "Recommended Practices for Seismic Design of Substations" is used in the United States for the seismic qualification and fragility testing of electrical equipment such as transformer bushings. This document provides qualification requirements for substation equipment and supports manufactured from steel, aluminum, porcelain, and composites. Procedures for equipment qualification using analytical studies (static analysis, static coefficient analysis, and response-spectrum analysis) and experimental methods (response-history testing, sine-beat testing, and static pull testing) are described. The objective of the document is "... to secure equipment such that it performs acceptably under reasonably anticipated strong ground motion."

IEEE 693-1997 identifies eleven methods for experimental testing. The most rigorous method is earthquake-response analysis using earthquake ground motion records, the spectral ordinates of which equal or exceed those of a Required Response Spectrum (RRS). Categories of earthquake simulator testing include (a) single-axis, (b) biaxial (i.e., horizontal and vertical), (c) multiaxis, and (d) triaxial.

Section 9 of IEEE 693-1997 describes seismic performance criteria for electrical substation equipment. Information on three seismic qualification levels (Low, Moderate, and High), Performance Levels, the Required Response Spectrum (RRS), the relation between PL and RRS, and acceptance criteria are provided.

The studies described in the body of this report employed triaxial earthquake simulator testing for the qualification and fragility testing of 230-kV bushings. IEEE 693-1997 writes text on six key topics related to the seismic qualification of transformer bushings:

- Performance level and performance factor
- Performance level qualification
- Support frame and mounting configuration

- Testing procedures
- Instrumentation
- Acceptance criteria

Each of these topics are elaborated upon in the following sections. For fragility testing, the amplitude of the seismic excitation is increased in small increments to determine the level of shaking that causes damage to the bushing, thereby establishing a point on a fragility curve.

A.2 Performance Level and Performance Factor

A Performance Level (PL) for substation equipment is represented in IEEE 693-1997 by a response spectrum. The shape of this spectrum represents a broadband response that envelopes earthquake effects in different areas considering site conditions that range from soft soil to rock. Three values of equivalent viscous damping are specified: 2 percent, 5 percent, and 10 percent. IEEE 693-1997 states that very soft sites and hill sites might not be adequately covered by the PL shapes.

Three seismic performance levels are identified in IEEE 693-1997: High, Moderate, and Low. In California, the relevant performance levels are High and Moderate. Equipment that is shown to perform acceptably in ground shaking consistent with the High Seismic Performance Level (see Figure A-1) is said to be seismically qualified to the High Level. Equipment that is shown to perform acceptably in ground shaking consistent with the Moderate Seismic Performance Level (see Figure A-2) is said to be seismically qualified to the Moderate Level.

IEEE 693-1997 states that it is often impractical or not cost effective to test to the High or Moderate PL because (a) laboratory testing equipment might be unable to attain the necessary high accelerations, and/or (b) damage to ductile components at the PL, although acceptable in terms of component qualification, would result in the component being discarded following testing. For these reasons, equipment may be tested using accelerations that are one-half of the PL. The reduced level of shaking is called the Required Response Spectrum (RRS). The ratio of PL to RRS, termed the performance factor in IEEE 693-1997, is equal to 2. The High and Moderate RRSs are shown in Figures A-3 and A-4, respectively. The shapes of the RRS and the PL are identical, but the ordinates of the RRS are one-half of the PL.

Equipment tested or analyzed using the RRS is expected to have acceptable performance at the PL. This assumption is checked by measuring the stresses obtained from testing at the RRS, and a) comparing the stresses to 50 percent (equal to the inverse of the performance factor) of the ultimate strength of the porcelain (assumed to be brittle) or cast aluminum components, and b) using a lower factor of safety against yield combined with an allowance for ductility of steel and other ductile materials.

A.3 Performance Level Qualification

Procedures for selecting the appropriate seismic qualification level for a site are presented in IEEE 693-1997. Qualification levels are directly related to site-specific peak acceleration values

calculated using a 2-percent probability of exceedance in 50 years. If the peak ground acceleration is less than 0.1g, the site is classified as Low. If the peak ground acceleration exceeds 0.5g, the site is classified as High. If the peak ground acceleration ranges in value between 0.1g and 0.5g, the site is classified as Moderate. Sites in California are classified as either Moderate or High.

A.4 Support Frame and Mounting Configuration

IEEE 693-1997 writes that bushings 161 kV and larger must be qualified using earthquake-simulator testing. Recognizing that it is impractical to test bushings mounted on a transformer, IEEE requires bushings to be mounted on a rigid stand during testing. To account for the amplification of earthquake motion due to the influence of the transformer body and local flexibility of the transformer near the bushing mount, the input motion measured at the bushing flange shall match a spectrum with ordinates twice that of the Required Response Spectrum. The resulting spectra, termed the Test Response Spectra (TRS), for Moderate Level qualification are shown in Figure A-5.

A transformer bushing must be tested at no less than its in-service slope, which is defined as the slope angle measured from the vertical. IEEE 693-1997 recommends that a bushing be tested at 20 degrees measured from the vertical. If so tested, a bushing is assumed to be qualified for use on all transformers with angles from vertical to 20 degrees. (A bushing installed at an angle greater than 20 degrees must be tested at its in-service angle.)

A.5 Testing Procedures for Transformer Bushings

Three types of earthquake-simulator testing are identified in IEEE 693-1997 for the seismic qualification of transformer bushings: (a) earthquake ground motions, (b) resonant frequency search, and (c) sine-beat testing. Earthquake ground motion tests (termed *time-history shake table tests* in IEEE 693-1997) and resonant frequency tests are mandatory; additional information on these two types of tests follow.

A.5.1 Resonant search tests

Sine-sweep or broadband white noise tests are used to establish the dynamic characteristics (natural frequencies and damping ratios) of a bushing. These so-called *resonant search* tests are undertaken using uni-directional excitation along each principal axis of the earthquake simulator platform. If broadband white noise tests are performed, the amplitude of the white noise must not be less than 0.25g.

If sine-sweep tests are used, IEEE 693-1997 specifies that the resonant search be conducted at a rate not exceeding one octave per minute in the range for which the equipment has resonant frequencies, but at least at 1 Hz. Frequency searching above 33 Hz is not required. Modal damping is calculated using the half-power bandwidth method.

A.5.2 Earthquake ground motion tests

Triaxial earthquake simulator testing is mandated for the seismic qualification of bushings rated at or above 161 kV. The Test Response Spectrum (TRS) for each horizontal earthquake motion must

match or exceed the target spectrum. The TRS for the vertical earthquake motion shall be no less than 80 percent of target spectrum. Earthquake motions can be established using either synthetic or recorded histories. IEEE 693-1997 recommends that 2-percent damping be used for spectral matching and requires at least 20 seconds of strong motion shaking be present in each earthquake record.

A.6 Instrumentation of Transformer Bushings

IEEE 693-1997 states that porcelain bushings must be instrumented to record the following response quantities:

1. maximum vertical and horizontal accelerations at the top of the bushing, at the bushing flange, and at the top of the earthquake-simulator platform

2. maximum displacement of the top of the bushing relative to the flange

3. maximum porcelain stresses at the base of the bushing near the flange

A.7 Acceptance Criteria for Transformer Bushings

IEEE 693-1997 writes that a bushing is considered to have passed the qualification tests if all the criteria tabulated below related to general performance, allowable stresses, and leakage are met. The data obtained from testing using ground motions compatible with the Test Response Spectrum (see Figure A-5) are used to assess general performance and allowable stresses. Oil leakage is checked for a higher level of earthquake shaking.

General Performance:	No evidence of damage such as broken, shifted, or dislodged insulators. No visible leakage of oil or broken support flanges.
Allowable Stresses:	The stresses in components are below the limiting values. (See Section A.2. For example, the stresses in the porcelain components associated with earthquake shaking characterized by the spectrum presented in Figure A-5 must be less than 50 percent of the ultimate value.)
Leakage:	Bushings qualified by earthquake simulator testing shall have a minimum factor of safety of two against gasket leaks for loads imposed during application of the Test Response Spectrum. IEEE 693-1997 states that an acceptable method to demonstrate this factor of safety is to have no leaks after shaking characterized by twice the Test Response Spectrum. (Such shaking corresponds to a Performance Factor equal to 1.0.)

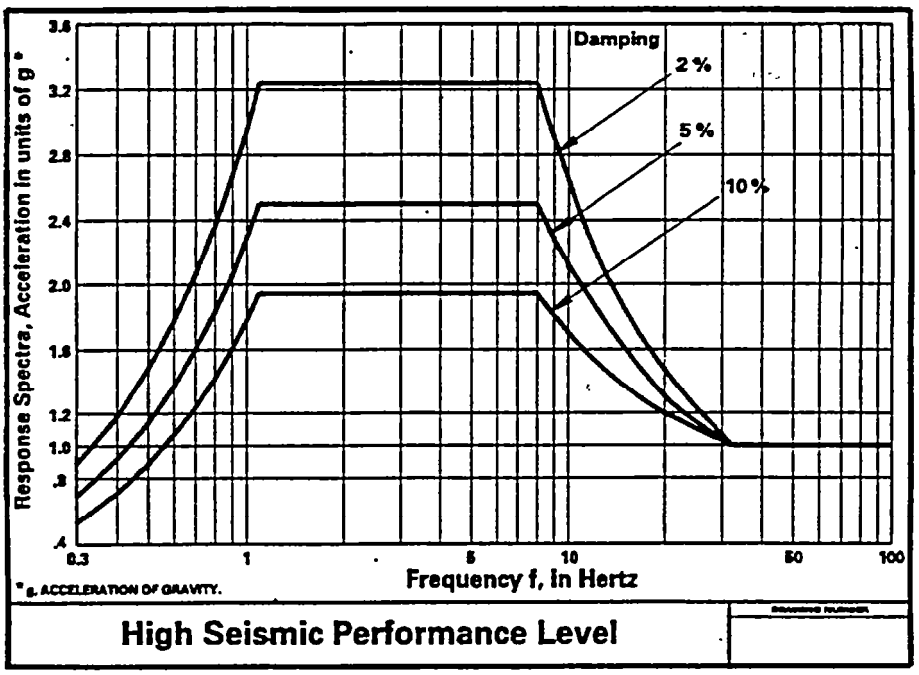

Figure A-1 Spectra for High Seismic Performance Level (IEEE, 1998)

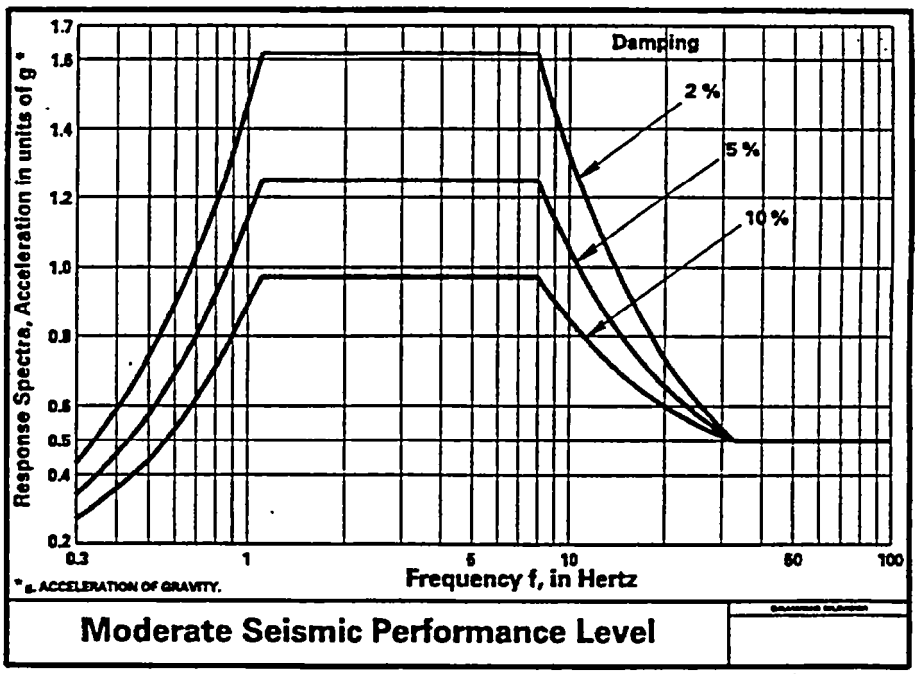

Figure A-2 Spectra for Moderate Seismic Performance Level (IEEE, 1998)

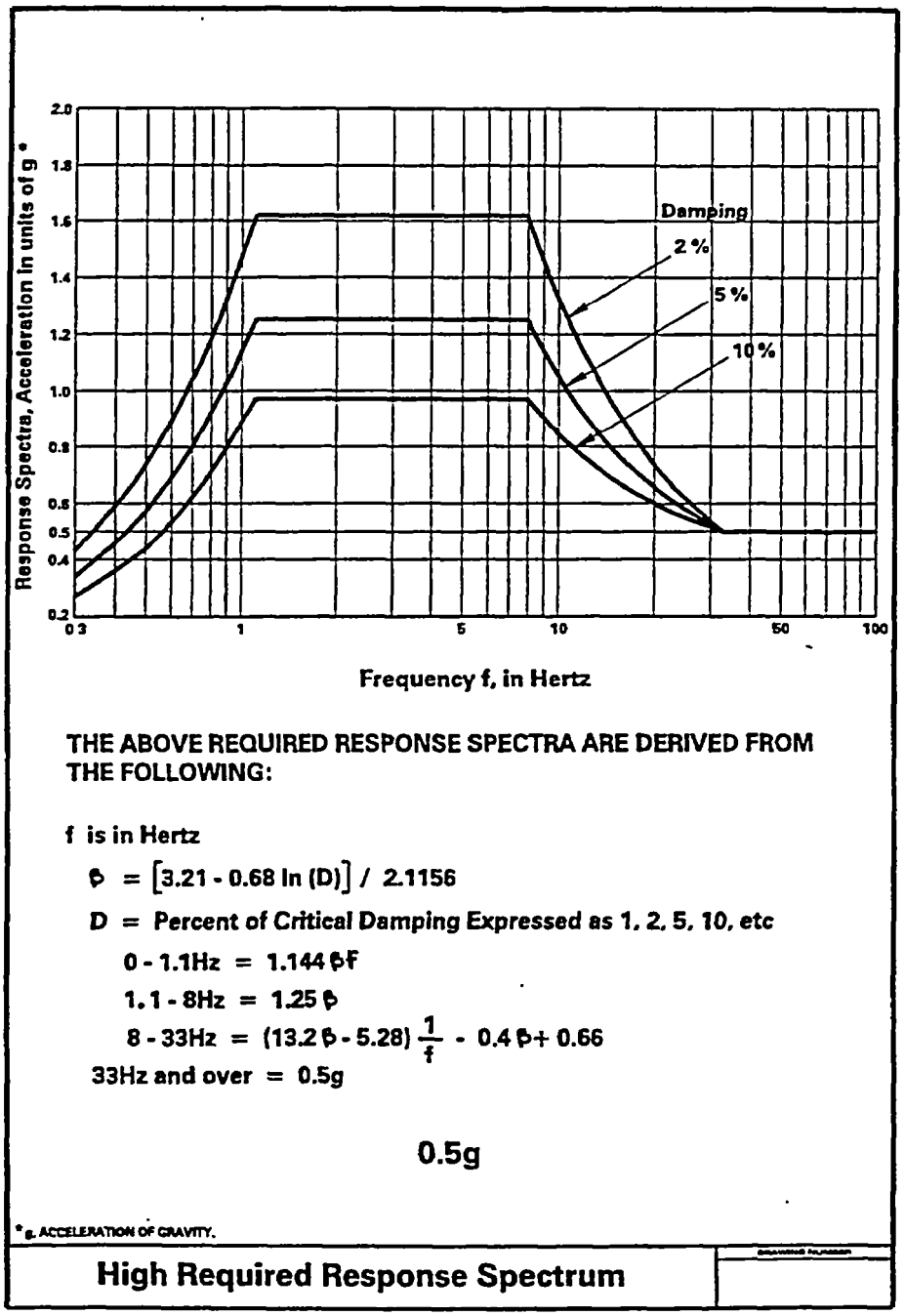

Figure A-3 Spectra for High Level Required Response Spectrum (IEEE, 1998)

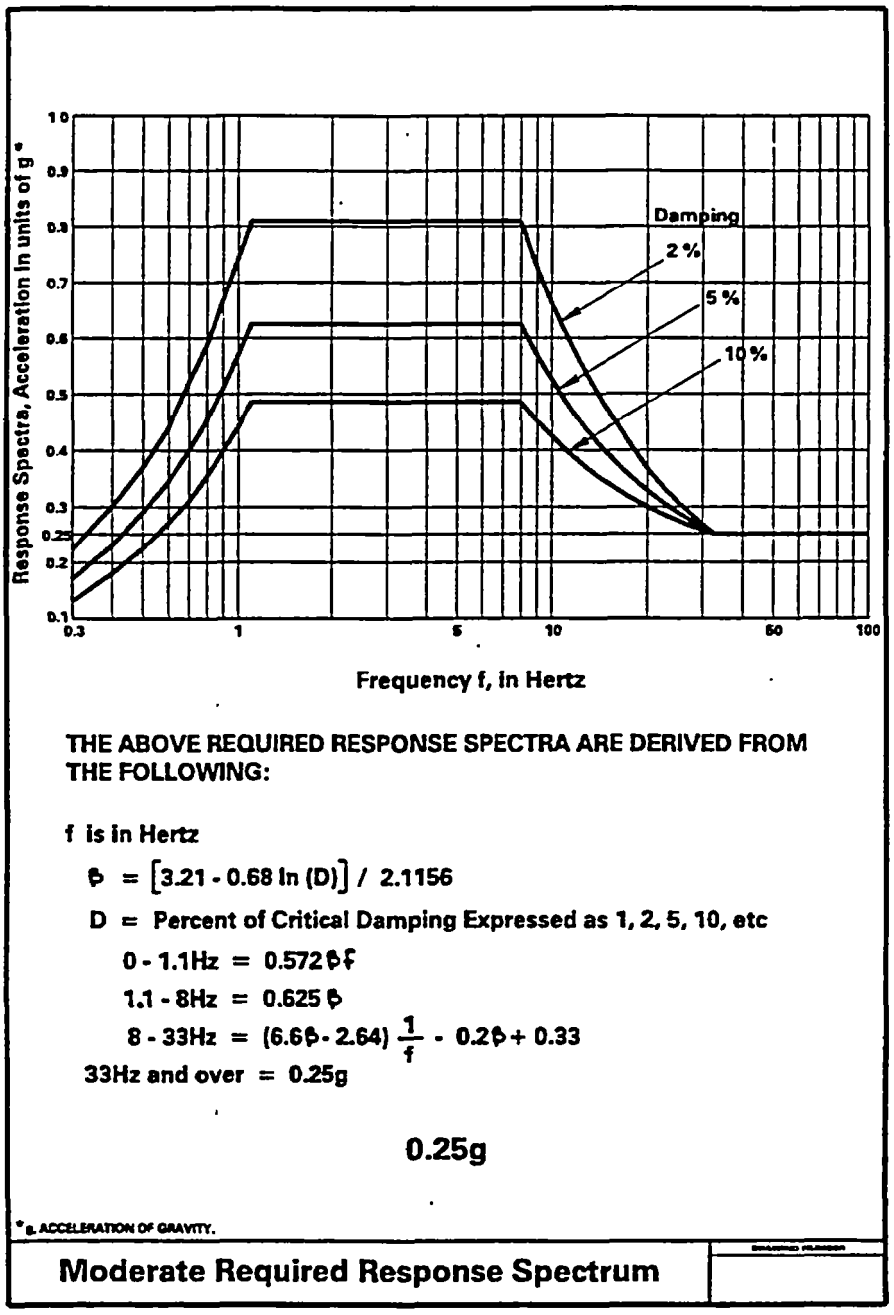

Figure A-4 Spectra for Moderate Level Required Response Spectrum (IEEE, 1998)

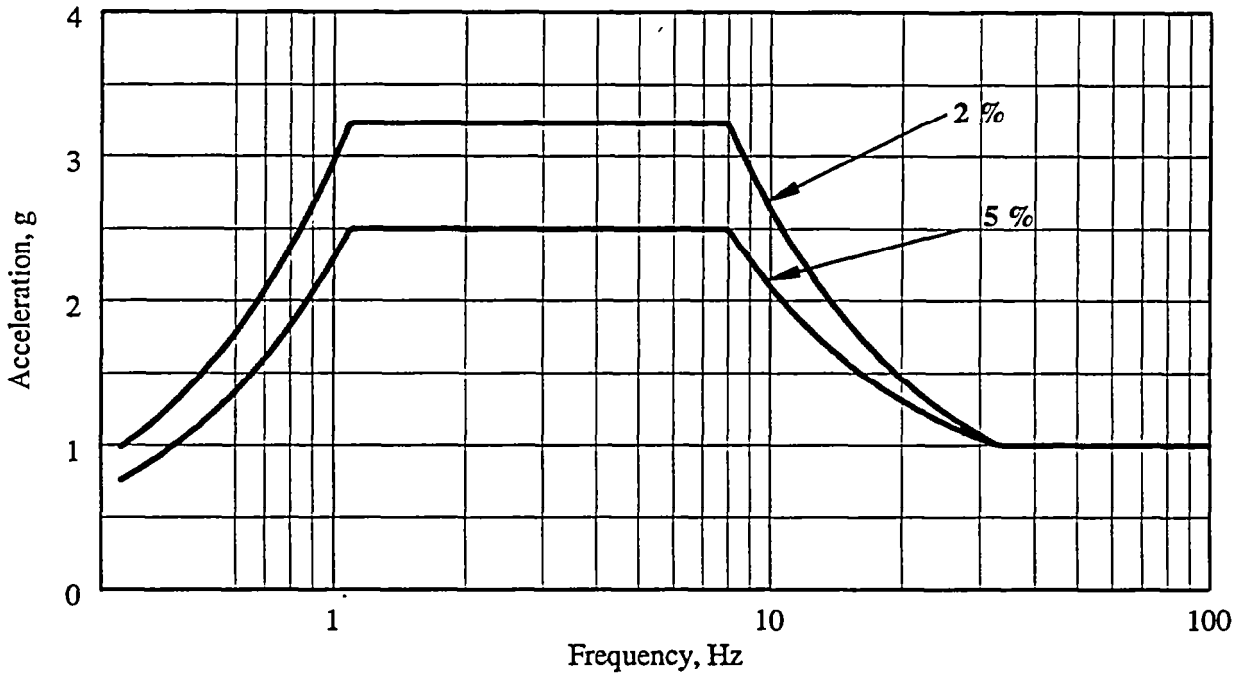

Figure A-5 Test Response Spectra for Moderate Level qualification of a transformer-mounted Bushing

PEER REPORTS

PEER reports are available from the National Information Service for Earthquake Engineering (NISEE). To order PEER reports, please contact the Pacific Earthquake Engineering Research Center, 1301 South 46th Street, Richmond, California 94804-4698. Tel.: (510) 231-9468; Fax: (510) 231-9461.

PEER 2000/01 *Further Studies on Seismic Interaction in Interconnected Electrical Substation Equipment.* Armen Der Kiureghian, Kee-Jeung Hong, and Jerome L. Sackman. November 1999. $20.00

PEER 1999/14 *Seismic Evaluation and Retrofit of 230-kV Porcelain Transformer Bushings.* Amir S. Gilani, Andrew S. Whittaker, Gregory L. Fenves, and Eric Fujisaki. December 1999. $26.00

PEER 1999/11 *Performance Evaluation Database for Concrete Bridge Components and Systems under Simulated Seismic Loads.* Yael D. Hose and Frieder Seible. November 1999. $20.00

PEER 1999/08 *Envelopes for Seismic Response Vectors.* Charles Menun and Armen Der Kiureghian. July 1999. $26.00

PEER 1999/07 *Documentation of Strengths and Weaknesses of Current Computer Analysis Methods for Seismic Performance of Reinforced Concrete Members.* William F. Cofer. November 1999. $15.00

PEER 1999/06 *Rocking Response and Overturning of Anchored Equipment under Seismic Excitations.* Nicos Makris and Jian Zhang. November 1999. $15.00

PEER 1999/05 *Seismic Evaluation of 550 kV Porcelain Transformer Bushings.* Amir S. Gilani, Andrew S. Whittaker, Gregory L. Fenves, and Eric Fujisaki. October 1999. $15.00

PEER 1999/04 *Adoption and Enforcement of Earthquake Risk-Reduction Measures.* Peter J. May, Raymond J. Burby, T. Jens Feeley, and Robert Wood. $15.00

PEER 1999/03 *Task 3 Characterization of Site Response General Site Categories.* Adrian Rodriguez-Marek, Jonathan D. Bray, and Norman Abrahamson. February 1999. $20.00

PEER 1999/02 *Capacity-Demand-Diagram Methods for Estimating Seismic Deformation of Inelastic Structures: SDF Systems.* Anil K. Chopra and Rakesh Goel. April 1999. $15.00

PEER 1999/01 *Interaction in Interconnected Electrical Substation Equipment Subjected to Earthquake Ground Motions.* Armen Der Kiureghian, Jerome L. Sackman, and Kee-Jeung Hong. February 1999. $20.00

PEER 1998/08 *Behavior and Failure Analysis of a Multiple-Frame Highway Bridge in the 1994 Northridge Earthquake.* Gregory L. Fenves and Michael Ellery. December 1998. $20.00

PEER 1998/07 *Empirical Evaluation of Inertial Soil-Structure Interaction Effects.* Jonathan P. Stewart, Raymond B. Seed, and Gregory L. Fenves. November 1998. $26.00

PEER 1998/06 *Effect of Damping Mechanisms on the Response of Seismic Isolated Structures.* Nicos Makris and Shih-Po Chang. November 1998. $15.00

PEER 1998/05 *Rocking Response and Overturning of Equipment under Horizontal Pulse-Type Motions.* Nicos Makris and Yiannis Roussos. October 1998. $15.00

PEER 1998/04 *Pacific Earthquake Engineering Research Invitational Workshop Proceedings, May 14–15, 1998: Defining the Links between Planning, Policy Analysis, Economics and Earthquake Engineering.* Mary Comerio and Peter Gordon. September 1998. $15.00

PEER 1998/03 *Repair/Upgrade Procedures for Welded Beam to Column Connections.* James C. Anderson and Xiaojing Duan. May 1998. $33.00

PEER 1998/02 *Seismic Evaluation of 196 kV Porcelain Transformer Bushings.* Amir S. Gilani, Juan W. Chavez, Gregory L. Fenves, and Andrew S. Whittaker. May 1998. $20.00

PEER 1998/01 Unassigned.

The Pacific Earthquake Engineering Research Center (PEER) is a consortium of western U.S. universities working in partnership with business, industry, and government to identify and reduce the risks from major earthquakes to life safety and to the economy.

PEER achieves its objectives of earthquake risk reduction through a coordinated program of research, education, and partnerships with users of research results. PEER's research program includes basic and applied components of seismology, engineering, architecture, urban planning, and economics.

PEER is headquartered at UC Berkeley.

PEER reports are available individually or by yearly subscription from the National Information Service for Earthquake Engineering (NISEE).

To order PEER Reports, contact the Pacific Earthquake Engineering Research Center, 1301 S. 46th St., Richmond, California 94804-4698, Tel: 510-231-9468, Fax: 510-231-9461.

Further Studies on Seismic Interaction in Interconnected Electrical Substation Equipment

Armen Der Kiureghian
Kee-Jeung Hong
Jerome L. Sackman

Structural Engineering, Mechanics & Materials
Department of Civil & Environmental Engineering
University of California, Berkeley

A report on research sponsored by Pacific Gas & Electric Company (PG&E)
under Contract No. Z19-5-274-86 and the California Energy Commission
under Contract No. 500-97-101

PEER Report 2000/01
Pacific Earthquake Engineering Research Center
College of Engineering
University of California, Berkeley

November 1999

EXECUTIVE SUMMARY

In a previous study, we investigated the effect of interaction between interconnected electrical substation equipment subjected to ground motions. Each equipment item was modeled as a system with distributed mass and stiffness properties and, through the use of a displacement shape function, was characterized by a single degree of freedom. Two kinds of connecting elements were considered: One was a linear spring-dashpot-mass element, representing a rigid bus conductor, and another was an extensible cable, representing a flexible conductor, in which the flexural rigidity and inertia effects were neglected. It was shown that the interaction effect resulting from the interconnection could have a significant influence on the equipment responses. Amplification factors as high as 6 to 8 in the response of the higher frequency equipment item, relative to its stand-alone response, were estimated. In the cable-connected system, the response of the lower frequency equipment item may also be amplified but to a lesser extent.

The present study extends the results of the previous investigation in two important directions. First, it extends the investigation of the rigid bus conductor by accounting for the nonlinear behavior of the flexible strap connector (FSC), which is usually installed at one end of the bus conductor to allow for thermal expansion. Second, it extends the investigation of the flexible (cable) conductor by accounting for its flexural rigidity, inertia and damping characteristics. Both problems are highly nonlinear and advanced finite element models are used to perform the analyses.

To idealize the FSC, an elasto-plastic, large deformation finite element model is used with more than 500 elements. The material properties are determined from the results of monotonic uniaxial tests of the material coupons performed at the University of California at San Diego (UCSD). More accurate characterization of the material properties is possible if cyclic test data of the material coupons are available. The finite element model of the FSC is used to compute force-elongation hysteresis loops under a prescribed cyclic loading. These predictions show reasonable agreement with the experimental results obtained at UCSD. Closer agreement can be achieved by using a refined finite element model that accounts for contact and friction between the bars and straps of the FSC.

With such refinement, the finite element model can be used to predict the behavior of other FSC configurations, thus avoiding costly tests.

For dynamic analysis of the combined system, we develop a mathematical model of the hysteretic behavior of the FSC. For this purpose, we use a modified version of the well-known Bouc-Wen model. Using this model, time history analysis of a combined system, consisting of two equipment items connected by a rigid bus with a FSC, is carried out for two recorded ground motions. The effect of interaction on each equipment item is measured by computing the ratio of its response in the connected system to its stand-alone response. Separate analyses are performed to show the influences of the flexibility and energy dissipation of the FSC on the interaction effect. The results show that the flexibility and energy dissipation characteristics of the FSC significantly reduce the adverse effect of interaction on the higher frequency equipment item. These results appear to be in agreement with test results obtained at UCSD. The analytical approach developed can be used with confidence in the future to investigate the effect of interaction on equipment items connected by conductors that have grossly nonlinear behavior.

For the flexible (cable) conductor, a finite element model using frame elements and a Lagrangian formulation is used that accounts for large displacements. First, comparisons are made with previous experimental results for cables subjected to out-of-phase support motions. Good qualitative agreement with experimental results are obtained, which show very large amplification of the cable force due to the flexural rigidity and inertia effects. Parametric studies showing the influences of the flexural rigidity and damping of the cable are carried out. Next, the finite element model is used to carry out time history analyses of a combined system, consisting of two equipment items and a connecting cable, for five different recorded ground motions. Separate analyses are performed to show the influences of the cable flexural rigidity, inertia and damping. The effect of interaction on each equipment item is measured in terms of the ratio of the equipment response in the connected system to its stand-alone response. These response ratios are plotted as functions of an interaction parameter introduced in our previous study. The results show that, for certain ground motions and equipment/cable configurations, the cable flexural rigidity and inertia may further amplify the adverse effect of interaction. Based on these results, a

recommendation for the minimum cable length to avoid the adverse interaction effect is developed.

Conductor cables used in the power industry are usually made of braided aluminum strands of wire. Under dynamic excitation, the strands may slip against each other under friction forces. The present study accounts for this effect in an approximate manner by using an equivalent moment of inertia and a judgmentally assigned damping value. For a more accurate prediction of the cable response, it is necessary to develop a refined model that explicitly accounts for the slippage and friction between the cable strands. Until verified by such refined analyses, the results and recommendations presented in this study should be regarded as preliminary in nature.

CONTENTS

EXECUTIVE SUMMARY iii

ACKNOWLEDGMENTS vi

TABLE OF CONTENTS vii

LIST OF TABLES ix

LIST OF FIGURES xi

CHAPTER 1 — INTRODUCTION 1

1.1 Introduction 1

1.2 Organization of the Report 3

CHAPTER 2 — MODELING AND ANALYSIS OF SYSTEMS CONNECTED BY A RIGID BUS WITH A FLEXIBLE STRAP CONNECTOR ..5

2.1 Introduction 5

2.2 Model of the Rigid Bus with Flexible Strap Connector 6

2.3 Analytical Model of the RB-FSC 10

2.4 The Combined Equipment RB-FSC System 14

2.5 Investigation of the Interaction Effect in Example Systems 15

CHAPTER 3 — INFLUENCE OF THE BENDING STIFFNESS AND INERTIA OF THE CONNECTING CABLE ON THE INTERACTION EFFECT 49

3.1 Introduction 49

3.2 Section Properties of the Flexible Conductor 51

3.3 Finite Element Model of the Cable 53

3.4 Comparison of the Finite Element Model with the Catenary Cable 55

3.5 Comparison with Experimental Results of Dastous and Pierre 56

3.5.1 Experiment 1: Sine-Start Test 57

3.5.2 Experiment 2: Sine-Sweep Test 60

3.6 Cable-Connected Equipment Items 61

3.6.1 Effect of Flexural Rigidity, Inertia and Damping of the Cable on the Equipment Response 62

3.6.2 Effect of Interaction in the Cable-Connected System 64

CHAPTER 4 — SUMMARY AND RECOMMENDATIONS FOR FURTHER STUDY 87

4.1 Summary 87

4.2 Recommendations for Further Study 89

REFERENCES 91

LIST OF TABLES

CHAPTER 2

Table 2.1 Influence of the flexibility and energy dissipation of the RB-FSC on the effect of interaction on equipment items 20

Table 2.2 Influence of the flexibility and energy dissipation of the RB-FSC on the effect of interaction on the equipment combination 2 in the UCSD test 21

Table 2.3 Influence of the flexibility and energy dissipation of the RB-FSC on the effect of interaction on equipment the equipment combination 5 in the UCSD test 22

CHAPTER 3

Table 3.1 Properties of conductor cables used in the experiments by Dastous and Pierre 66

LIST OF FIGURES

CHAPTER 2

Figure 2.1 Rigid bus with a symmetric flexible strap connector 23

Figure 2.2 Dimensions of FSC No. 30-2022 23

Figure 2.3 Rigid bus with an asymmetric flexible strap connector 24

Figure 2.4 Dimensions of FSC No. 30-2021 24

Figure 2.5 Comparison of uniaxial tensile stress-strain relationship of FSC coupons generated in the UCSD tests with fitted model 25

Figure 2.6 Schematics of the finite element layout of the RB with symmetric FSC: (a) frame elements for the RB-FSC, (b) frame elements for the FSC, (c) extreme deformed shape under compression, and (d) extreme deformed shape under tension 26

Figure 2.7 Schematics of the finite element layout of the RB with asymmetric FSC: (a) frame elements for the RB-FSC, (b) frame elements for the FSC, (c) extreme deformed shape under compression, and (d) extreme deformed shape under tension 27

Figure 2.8 History of imposed support displacement used in the UCSD test 28

Figure 2.9 Comparison of FE predicted force-elongation relationship of the RB with the symmetric FSC with UCSD test results: (a) $H_{kin} = E/100$, (b) $H_{kin} = E/20$ 29

Figure 2.10 Comparison of FE predicted force-elongation relationship of the RB with the asymmetric FSC with UCSD test results for $H_{kin} = E/20$ 30

Figure 2.11 Force-elongation relationship of the first RB with symmetric FSC obtained from the UCSD test and from the modified Bouc-Wen model 31

Figure 2.12 Model of equipment items connected by a RB-FSC 32
Figure 2.13 Displacement time histories of the lower-frequency equipment item for the Newhall-Northridge record: (a) response in the stand-alone configuration and (b) response in the connected system 33
Figure 2.14 Displacement time histories of the higher-frequency equipment item for the Newhall-Northridge record: (a) response in the stand-alone configuration and (b) response in the connected system 34
Figure 2.15 Displacement time histories of the lower-frequency equipment item for the TabasLN record: (a) response in the stand-alone configuration and (b) response in the connected system 35
Figure 2.16 Displacement time histories of the higher-frequency equipment item for the TabasLN record: (a) response in the stand-alone configuration and (b) response in the connected system 36
Figure 2.17 Force-elongation hysteresis loops of the RB-FSC in the connected system subjected to the Newhall-Northridge record 37
Figure 2.18 Force-elongation hysteresis loops of the RB-FSC in the connected system subjected to the TabasLN record 37
Figure 2.19 Displacement time histories of the lower-frequency equipment item in the stand-alone configuration for the table motion TRB127 (Newhall 100%): (a) experiment and (b) analysis 38
Figure 2.20 Displacement time histories of the higher-frequency equipment item in the stand-alone configuration for the table motion TRB127 (Newhall 100%): (a) experiment and (b) analysis 39
Figure 2.21 Displacement time histories of the lower-frequency equipment item in the connected system for the table motion TRB101 (Newhall 100%): (a) experiment and (b) analysis 40
Figure 2.22 Displacement time histories of the higher-frequency equipment item in the connected system for the table motion TRB101 (Newhall 100%): (a) experiment and (b) analysis 41

Figure 2.23 Force-elongation hysteresis loops of the RB-FSC in the connected system subjected to the table motion TRB101 (Newhall 100%): (a) experiment and (b) analysis 42

Figure 2.24 Displacement time histories of the lower-frequency equipment item in the stand-alone configuration for the table motion TRB126 (Tabas 50%): (a) experiment and (b) analysis 43

Figure 2.25 Displacement time histories of the higher-frequency equipment item in the stand-alone configuration for the table motion TRB126 (Tabas 50%): (a) experiment and (b) analysis 44

Figure 2.26 Displacement time histories of the lower-frequency equipment item in the connected system for the table motion TRB100 (Tabas 50%): (a) experiment and (b) analysis 45

Figure 2.27 Displacement time histories of the higher-frequency equipment item in the connected system for the table motion TRB100 (Tabas 50%): (a) experiment and (b) analysis 46

Figure 2.28 Force-elongation hysteresis loops of the RB-FSC in the connected system subjected to the table motion TRB100 (Tabas 50%): (a) experiment and (b) analysis 47

CHAPTER 3

Figure 3.1 Cross section of a conductor cable made of braided wire strands 67

Figure 3.2 Comparison of exact and computed normalized responses of an oscillator to step loading : (a) oscillator with 5Hz frequency and 2% damping ratio, (b) oscillator with 50Hz frequency and 2% damping ratio 68

Figure 3.3 Horizontal force versus slackness for a cable with no flexural rigidity under its own weight 69

Figure 3.4 Shapes of cables of length $s_0 = 6\,\mathrm{m}$: (a) without flexural rigidity, (b) with flexural rigidity 70

Figure 3.5 Comparison of horizontal force-slackness relationship for a catenary cable and a cable with flexural rigidity 71
Figure 3.6 Time history of horizontal force at the cable support (after Dastous and Pierre, 1996) 72
Figure 3.7 Time history of horizontal force at the cable support as predicted by the finite element model 72
Figure 3.8 Sensitivity of the horizontal force at the support to cable moment of inertia 73
Figure 3.9 Finite element model of distributed viscous damping 74
Figure 3.10 Sensitivity of the horizontal force at the support to cable damping 74
Figure 3.11 Horizontal support force spectrum obtained from the experiment (after Dastous and Pierre, 1996) 75
Figure 3.12 Horizontal support force spectrum predicted by the finite element model 75
Figure 3.13 Cable-connected equipment items 76
Figure 3.14 N-S component of Newhall record, 1994 Northridge Earthquake 77
Figure 3.15 Displacement time histories of the stand-alone equipment items calculated by the damped energy-conserving algorithm 78
Figure 3.16 Displacement time histories of equipment items in the connected system, using catenary cable formulation and neglecting flexural rigidity, inertia and damping of the cable 79
Figure 3.17 Displacement time histories of equipment items in the connected system, including the inertia effect but neglecting the flexural rigidity and damping of the cable 80
Figure 3.18 Displacement time histories of equipment items in the connected system, including the flexural rigidity but neglecting the inertia and damping of the cable 81
Figure 3.19 Displacement time histories of equipment items in the connected system, including flexural rigidity and inertia, but neglecting the damping of the cable 82

Figure 3.20 Displacement time histories of equipment items in the connected system, including the flexural rigidity, inertia and damping of the cable 83

Figure 3.21 Response ratios for five earthquakes as functions of the interaction parameter neglecting the flexural rigidity, inertia and damping of the cable 84

Figure 3.22 Response ratios for five earthquakes as functions of the interaction parameter, including the flexural rigidity and inertia of the cable with zero damping 85

Chapter 1 Introduction

1.1 Introduction

In a previous report (Der Kiureghian et al., 1999), we studied the effects of interaction between interconnected electrical substation equipment subjected to ground motions. Investigated were equipment items connected by a linear spring-dashpot-mass element, representing a rigid bus conductor, and by an extensible cable representing a flexible conductor, in which the flexural rigidity and inertia effects of the cable were neglected. It was shown that the interaction effect resulting from the interconnection could have a significant influence on the equipment response. Amplification factors as high as 6 to 8 in the response of the higher-frequency equipment item, relative to its stand-alone response, were estimated. In cable-connected systems, the response of the lower-frequency equipment may also be amplified but normally by a much lesser extent.

The purpose of the present study is to further investigate the effects of seismic interaction between interconnected equipment items considering two specific problems: (a) the nonlinear behavior of the spring used for thermal expansion with rigid bus connectors and comparison with experimental results conducted at the University of California, San Diego, and (b) the influence of the flexural rigidity and inertia effect of the flexible (cable) conductor on the interaction effect.

The response of the rigid bus with the spring connector under severe earthquake loading is strongly inelastic with large deformations. Hence, it requires careful modeling and analysis to accurately reflect the real behavior. We have used an elasto-plastic, large deformation finite element model to predict the hysteretic behavior of the conductor consisting of a rigid bus and a flexible strap connector, which was tested at UCSD. The fi-

nite element code FEAP, developed by R. L. Taylor (1998), is used for this purpose. This study shows that the behavior of such systems can be predicted by finite element analysis with reasonable accuracy. For the dynamic analysis of the combined equipment conductor system, a modified version of the Bouc-Wen hysteretic model, which is fitted to the experimentally obtained hysteretic loops, is utilized. The results show that the flexibility and energy dissipation characteristics of the flexible strap conductor significantly reduce the adverse effect of interaction on the high-frequency equipment item, which is present when a rigid bus without the flexible strap connector is used. Quantitative estimates of the interaction effect are found to be in agreement with experimental results obtained at UCSD.

The cable dynamics problem is highly nonlinear and because of the special construction of the conductor cable as braided strands of wire involves significant uncertainties as to the effective cable properties, such as the flexural rigidity, damping and initial configuration. For this analysis, a finite element model with a Lagrangian strain formulation is utilized. Comparisons are made with previous experimental results for cables subjected to harmonic support excitations. While good qualitative agreement between the experimental and analytical results are achieved, questions regarding the effective cable stiffness and damping remain unanswered. Time history analyses of the cable-connected equipment items for five different recorded motions are carried out, separately accounting for the contributions of cable flexural rigidity, inertia and damping. The results show that, for certain ground motions and equipment/cable configurations, the cable flexural rigidity and inertia tend to further amplify the adverse interaction effect on the equipment items in comparison to what we had estimated without accounting for these effects. Based on this limited study, a preliminary recommendation for the minimum cable length to avoid the adverse interaction effect is formulated. Because of the importance of this problem, the scope of this part of the study was substantially broadened to include comparisons with experimental results that were discovered during the course of the study.

1.2 Organization of the Report

Following this introductory chapter, in Chapter 2 we present the analysis of the rigid bus with the flexible strap connector and the effect of interaction between two equipment items connected by such a conductor. Chapter 3 deals with the modeling and response analysis of cables and cable-connected equipment items. Chapter 4 summarizes the main results of the study and describes areas needing further investigation.

Chapter 2 Modeling and Analysis of Systems Connected by a Rigid Bus with a Flexible Strap Connector

2.1 Introduction

A rigid bus typically consists of an aluminum pipe connected between two electrical equipment items for conduction. To accommodate thermal expansion, a U-shaped spring element made of copper bars is normally inserted at one end of the rigid bus between the pipe and the attachment point on one of the equipment items. In the case of a severe earthquake, the relative displacement demand between the two equipment items in general will cause large inelastic deformation of the spring connector. In the first section of this chapter, we use an elasto-plastic model of the spring material together with a large deformation finite element analysis to predict the hysteretic response of the spring element under cyclic loading. Data from monotonic uni-axial testing of the material coupons is used to determine the material property constants. The predicted hysteresis loop is compared with experimental results obtained at the University of California, San Diego (UCSD, Filiatrault et al., 1999). A fairly good agreement between the two sets of results is obtained. However, in order to achieve more accuracy in the prediction, it is necessary to include in the finite element model the effects of contact and friction between bars, which give additional effective stiffness to the spring. Furthermore, it is necessary to have unloading data of the material coupons in order to more accurately determine the constitutive properties.

For dynamic analysis of the equipment items connected by the rigid bus and spring element, it is more convenient to employ an analytical model of the hysteretic behavior

for computational simplicity. To this end, we employ the well-known Bouc-Wen model (Wang and Wen, 1998), which we modify to fit the experimental results obtained at UCSD. This model, thereby, includes the effects of both material and geometric nonlinearities and the effects of both contact and friction between bars. The fitted model is subsequently used in a step-by-step dynamic analysis of the connected equipment system to determine the effect of interaction.

2.2 Model of the Rigid Bus with Flexible Strap Connector

Figure 2.1 shows a sketch of a typical rigid bus (RB) with a flexible strap connector (FSC). The RB consists of an aluminum pipe segment. At one end, it is rigidly attached to one of the equipment items. At the other end, the RB is attached to the FSC, which in turn is rigidly attached to the other equipment item. The FSC shown in Figure 2.2 is constructed from three straps, where each strap consists of two copper bars in the form of an inverted U. The dimensions shown in Figure 2.2 are consistent with the PG&E specification for FSC No. 30-2022 (Pacific Gas & Electric Company). Figures 2.3 and 2.4 show sketches of another typical RB-FSC and FSC, respectively. The dimensions shown in Figure 2.4 are consistent with the PG&E specification for FSC No. 30-2021.

Three coupons from a sample FSC were tested at UCSD under monotonic uniaxial tension to determine the material properties. Figure 2.5 shows the test results as dotted lines. Two of the curves exhibit small amplitude oscillations, which are presumed to be due to measurement noise. For the finite element analysis of the RB-FSC using the finite element analysis program FEAP (Taylor 1998), we employ an 1-dimensional elasto-plastic material model with hardening. In this model an additive split of the strain in the form

$$\varepsilon = \varepsilon^{el} + \varepsilon^{pl} \tag{2.1}$$

is assumed, where ε is the total strain, ε^{el} is the elastic strain and ε^{pl} is the plastic strain. The uniaxial constitutive relation is given by the following set of equations: The elastic stress-strain relation of the material is

$$\sigma = E(\varepsilon - \varepsilon^{pl}) \tag{2.2}$$

where σ is the applied stress and E is the Young's modulus. The yield condition is defined as

$$f(\sigma,\hat{q},\alpha)=|\sigma-\hat{q}|-\sigma_Y(\alpha)\leq 0 \tag{2.3}$$

where $\hat{q}$ is the back stress, α is the internal isotropic-hardening variable, and $\sigma_Y(\alpha)$ is the flow stress defined by the linear and saturated form of isotropic hardening, given by

$$\sigma_Y(\alpha)=\sigma_\infty+(\sigma_0-\sigma_\infty)\exp(-\beta\alpha)+H_{iso}\alpha \tag{2.4}$$

where $\alpha=|\varepsilon^{pl}|$ is assumed, σ_∞ is the stress at large strain, σ_0 is the initial yield stress, β is a delay constant, and H_{iso} is the modulus of linear isotropic hardening. The evolution of the back stress is defined by a linear kinematic hardening rule

$$\dot{\hat{q}}=H_{kin}\dot{\varepsilon}^{pl} \tag{2.5}$$

The associative flow rule gives the plastic strain rate in terms of the derivative of the yield function f, as

$$\dot{\varepsilon}^{pl}=\gamma\frac{\partial f}{\partial\sigma}=\gamma\,\mathrm{sgn}(\sigma-\hat{q}) \tag{2.6}$$

where γ is the absolute value of the flow rate. Since σ must satisfy the yield condition given by (2.3) and γ must be non-negative, we have the conditions

$$\gamma\geq 0 \quad\text{and}\quad f\leq 0 \tag{2.7}$$

If the absolute value of the applied stress, $|\sigma|$, is less than the flow stress σ_Y, no change in ε^{pl} takes place, i.e., $\gamma=0$ if $f<0$. On the other hand, a change in ε^{pl} can take place only if $f=0$, i.e., $\gamma>0$ only if $f=0$. Therefore, the condition

$$\gamma f=0 \tag{2.8}$$

always holds. The conditions given by (2.7) and (2.8) are known as the Kuhn-Tucker conditions. The additional condition

$$\gamma\dot{f}=0 \quad\text{when}\quad f=0 \tag{2.9}$$

is necessary because, when $f=0$, we specify $\gamma>0$ only if $\dot{f}=0$, and set $\gamma=0$ if $\dot{f}<0$. This condition is referred to as the consistency condition and is used, together

with the Kuhn-Tucker conditions, to determine the actual value of $\gamma \geq 0$ at any given time. A more detailed description of this plastic model can be found in Simo and Hughes (1998).

The uniaxial tensile test results of the FSC coupons supplied by UCSD did not contain any unloading data. Therefore, it is difficult to determine both isotropic and kinematic hardening moduli from this data. If we simulate the tensile test by a finite element analysis using one frame element with a judgmentally chosen elasto-plastic hardening model having parameters $E = 14{,}000\,\text{ksi}$, $\sigma_0 = 18\,\text{ksi}$, $\sigma_\infty = 27.5\,\text{ksi}$, $\beta = 1000$, $H_{iso} = 0$ and $H_{kin} = E/100$, we obtain the solid line shown in Figure 2.5, which closely matches the actual data. We apply this model below to analyze the RB-FSC by the finite element method.

Figures 2.6a and 2.6b show schematics of the finite element layout of an RB-FSC, which was tested at UCSD. The RB is a 4in-diameter SPS aluminum pipe of 10ft length, having an inner radius of 2.013in. and an outer radius of 2.250in. The main body of the RB is modeled with 10 elastic frame elements, whereas connections A and B shown in Figure 2.2 are modeled with 1 and 6 elastic frame elements, respectively. The Young's modulus of the RB is assumed to be $E = 10{,}000\,\text{ksi}$. The selected FSC is consistent with the PG&E specification No. 30-2022. It is made of three parallel straps, each consisting of a pair of copper bars, and has the material properties mentioned earlier. Each bar of the FSC is modeled by 80 elasto-plastic frame elements, each element consisting of 10 layers to properly account for the plastic behavior through the thickness of the bar. In addition, 20 elastic frame elements are used to model the spacers between the bars at the ends and 2 elastic frame elements are used to model the spacers between the RB and the FSC. Thus, in total, the RB-FSC is modeled by 519 frame elements of which 480 are elasto-plastic.

Figures 2.7a and 2.7b show schematics of the finite element layout of a second RB-FSC, which was also tested at UCSD. The RB is the same as described above, whereas the FSC is consistent with the PG&E specification No. 30-2021. A finite element mesh similar to that described in the previous paragraph was used to model this RB-FSC.

For the finite element analysis, one end of the RB-FSC is assumed to be fixed, while the other end is subjected to the horizontal displacement time history utilized in the UCSD tests, which is shown in Figure 2.8. The finite element program FEAP by R. L. Taylor (1998), which employs a Lagrangian strain formulation to account for large deformations, is used to predict the cyclic response of the RB with the 30-2022 FSC. The computed force-elongation relationship is plotted in Figure 2.9a. The agreement between the two hysteresis loops is fairly good. However, the experimental curves show apparent hardening for large elongation or contraction values, which are not well predicted by the finite element model. This might be due to the wrong choice of the hardening moduli and/or due to the effect of contact and friction between bars and straps, which are not accounted for in the finite element model. In the test, significant friction could occur between bars in a strap, and contact between straps would occur for extreme states of deformation. The contact and friction between the bars and straps would provide additional effective stiffness to the RB-FSC. To account for this effect in an approximate manner, we can use a larger value of the kinematic hardening modulus, even though we lose accuracy in matching the uniaxial test results. After a number of trials, we found the value $H_{\text{kin}} = E/20$ of the kinematic hardening coefficient produce results that best fit the test hysteresis loops. The result, shown in Figure 2.9b, demonstrates much closer agreement with the test results. The extreme deformed shapes of the RB-FSC obtained from this analysis are shown in Figures 2.6c and 2.6d.

If the deviations between the computed and test results in Figure 2.9a were truly due to material effects, then this revised value of the hardening parameter should produce good results for other FSC models as well. However, as we will shortly see, this is not the case. That is, the deviations seen in Figure 2.9a are more due to contact and friction between the bars and straps than due to material characterization.

Next, we use the chosen material parameter values to conduct finite element analysis of the RB with the 30-2021 FSC, which has an asymmetric shape as shown in Figure 2.7. The computed hysteresis loops are compared with the UCSD test results in Figure 2.10 and the extreme deformed shapes are shown in Figures 2.7c and 2.7d. It is seen that there is a more significant difference between the computed and test results. This difference is

due to a more significant effect of contact and friction between bars and straps for this asymmetric configuration of the FSC. It is clear that the material characterization alone cannot account for this effective added hardening across different RB-FSC systems.

The above comparisons show that, while the finite element predictions of the cyclic behavior of the RB-FSC are in reasonable agreement with test results, for enhanced accuracy it is necessary to develop a finite element model that accounts for the effect of contact and friction between the bars and straps of the FSC. Furthermore, it is necessary to perform cyclic tests of the FSC coupons so that the hardening moduli can be estimated properly. By achieving these, the behavior of the RB-FSC under large deformations can be well predicted by a finite element model that accounts for the elasto-plastic material behavior, the effect of contact and friction between bars, and large deformations. Such an analysis can be performed in the future in lieu of costly testing to determine the behavior of other RB-FSC configurations.

2.3 Analytical Model of the RB-FSC

For the analysis of the RB-FSC-connected equipment system, the above finite element model is not convenient, as it would involve a very large nonlinear dynamic model. In this section, we use an analytical model to fit the hysteresis loops of the RB-FSC, which is then used in the subsequent section to carry out dynamic analysis of the combined system. This approach has the advantage of computational simplicity. Furthermore, it allows for a random vibration analysis of the combined system, which we intend to carry out as a follow-up to this study. Such an approach would properly account for the variability that is present in the earthquake excitation.

To analytically describe the behavior of the RB-FSC, we employ the well-known hysteresis model originally proposed by Bouc (1967) and later modified by Wen (1976). This model has been generalized by Baber and Wen (1979) for degrading systems and by Wang and Wen (1998) to account for asymmetric yielding behavior. Since the hysteresis loops of the RB-FSC element exhibit asymmetric behavior due to geometric nonlinearity, we employ the form of the model suggested by Wang and Wen (1998). According to this model, the nonlinear force-elongation relationship for the RB-FSC element is defined by

$$q(\Delta u, z) = \alpha k \Delta u + (1-\alpha) k z \tag{2.10}$$

where $q(\Delta u, z)$ is the force acting on the element, Δu is the resulting elongation, k is the initial elastic stiffness, α is the post-to-pre-yielding stiffness ratio, and z is the hysteretic part of the elongation satisfying the differential equation

$$\dot{z} = \frac{\Delta \dot{u}}{\eta}\left[A - \nu |z|^n \{\beta \operatorname{sgn}(\Delta \dot{u} z) + \gamma + \phi(\operatorname{sgn}(z) + \operatorname{sgn}(\Delta \dot{u}))\}\right] \tag{2.11}$$

In the preceding equation, A, β, γ, and n are parameters that control the shape of hysteresis loop, η is a parameter that controls the pre-yielding stiffness, ν is a parameter that controls the ultimate strength, and ϕ is a parameter that accounts for the asymmetric yielding behavior. Also, $\operatorname{sgn}(x) = 1$ for $x > 0$, $\operatorname{sgn}(x) = -1$ for $x < 0$, and $\operatorname{sgn}(x) = 0$ for $x = 0$.

Baber and Wen defined A, η and ν as functions of the total dissipated energy, ε_T,

$$A(\varepsilon_T) = A_0 - \delta_A \varepsilon_T, \quad \eta(\varepsilon_T) = \eta_0 - \delta_\eta \varepsilon_T, \quad \nu(\varepsilon_T) = \nu_0 - \delta_\nu \varepsilon_T \tag{2.12}$$

$$\varepsilon_T = (1-\alpha) k \int_0^t z \Delta \dot{u} \, dt \tag{2.13}$$

In the preceding equations, A_0, η_0 and ν_0 are initial values of A, η and ν, respectively, and δ_A, δ_η and δ_ν are parameters that control the rate of degradation. This model of deterioration is capable of accounting for the duration and severity of the response. The quasi-static tests conducted at UCSD incorporate geometric and material nonlinearities and contact and friction between bars. It is difficult to derive equations that simulate the behavior of the RB-FSC and account for these effects. Motivated by the Baber-Wen approach, we fit the test behavior of the RB-FSC by letting the parameters A, η and ν be functions of the response. Specifically, these parameters are considered to be functions of the elongation/contraction Δu and its rate $\Delta \dot{u}$ to account for the dependency of the nonlinearity on the response and the state of loading. For this purpose, we introduce the following limiting response values:

Δu_t^E marker for the limit of the nearly elastic elongation zone

Δu_c^E marker for the limit of the nearly elastic contraction zone

Δu_t^m maximum elongation experienced during the test

Δu_c^m maximum contraction experienced during the test

Associated with the nearly elastic zone, we define the parameter values A^E, η^E and ν^E. Associated with Δu_t^u (Δu_c^u), we define the parameter values A_t^+, η_t^+, ν_t^+ A_t^-, η_t^- and ν_t^- (A_c^+, η_c^+, ν_c^+, A_c^-, η_c^- and ν_c^-), where a superposed + denotes a "loading" state, i.e., $\Delta\dot{u} \geq 0$, and a superposed – denotes an "unloading" state, i.e., $\Delta\dot{u} < 0$. Furthermore, we define the set of parameters A_0^+, η_0^+, ν_0^+, A_0^-, η_0^- and ν_0^- associated with the state $\Delta u = 0$.

Initially, the parameters A, η and ν are set to the values A^E, η^E and ν^E. These values are kept fixed until a reversal of loading occurs outside the nearly elastic zone. From that point on, the parameters A, η and ν are made functions of Δu. For a given Δu, their values are obtained by interpolating between the extreme values associated with the states $\Delta u = 0$ and either Δu_t^m or Δu_c^m, depending on whether the RB-FSC is elongated or compressed. The extreme parameter values selected are those with superscript + if $\Delta\dot{u} \geq 0$ and those with superscript – if $\Delta\dot{u} < 0$. A simple parabolic interpolation between the two extreme parameter values is used to determine the current value of each parameter. For example, subsequent to a point of load reversal outside the nearly elastic zone when the element is in contraction and $\Delta\dot{u} < 0$, we obtain the value of parameter A for a given Δu from

$$A(\Delta u) = (A_c^- - A_0^-)\left(\frac{\Delta u}{\Delta u_c^m}\right)^2 + A_0^- \tag{2.14}$$

If a reversal of loading occurs inside the nearly elastic zone, the parameter values are again set to the constant values A^E, η^E and ν^E.

Based on the extreme displacements imposed on the test RB-FSC, we selected $\Delta u_t^m = 8$ in. and $\Delta u_c^m = -6$ in. Furthermore, observing the range of nearly elastic behavior, the limiting values $\Delta u_t^E = 2$ in. and $\Delta u_c^E = -2$ in. were chosen. Of the parameters of

the Bouc-Wen model, $k = 200$ lbs/in., $n = 2$, $\alpha = 0.1$, $\beta = 0.507$, $\gamma = 0.485$, $A^E = 0.42$, $\eta^E = 0.34$ and $\nu^E = 0.08\,\text{in.}^{-2}$ were selected by trial-and-error fitting of the overall features of the hysteresis loops obtained in the test. For the parameter ϕ, which controls the asymmetric yielding behavior, the initial value $\phi = 0.1$ is selected. This value is used until a reversal of loading outside the nearly elastic zone is encountered, in which case the parameter is set to $\phi = -0.1$. This value remains in effect until a reversal of loading within the nearly elastic zone occurs, in which case the parameter is reset to $\phi = 0.1$. This modification is necessary to avoid vertical shifting of the narrow hysteresis loop in the nearly elastic zone. This leaves us 18 parameters associated with the three extreme values of the parameter set A, η and ν. These are obtained by minimizing the cumulative squared error between the experimental values and the predictions by the Bouc-Wen model together with trial-and-error to search for a better local minimum. The resulting optimal parameter values were:

$$A_0^+ = 0.27,\ A_0^- = 0.42,\ A_t^+ = 0.47,\ A_t^- = 0.42,\ A_c^+ = 0.42,\ A_c^- = 0.42$$

$$\eta_0^+ = 0.27,\ \eta_0^- = 0.34,\ \eta_t^+ = 0.30,\ \eta_t^- = 0.14,\ \eta_c^+ = 0.34,\ \eta_c^- = 0.34$$

$$\nu_0^+ = 0.06\,\text{in.}^{-2},\ \nu_0^- = 0.08\,\text{in.}^{-2},\ \nu_t^+ = 0.04\,\text{in.}^{-2},\ \nu_t^- = 0.04\,\text{in.}^{-2},\ \nu_c^+ = 0.04\,\text{in.}^{-2},\ \nu_c^- = 0.08\,\text{in.}^{-2}$$

where A and η are dimensionless and ν has the unit of in.$^{-2}$ (for $n = 2$).

Figure 2.11 shows a comparison of the hysteresis loops obtained in the UCSD experiments together with the hysteresis loops obtained from the modified Bouc-Wen model described above. It is evident that the model predictions are in close agreement with the test results. It is particularly noteworthy that the model closely follows the asymmetric features of the actual hysteresis loops. This model is used in the following section to investigate the interaction between two equipment items attached by a RB-FSC.

2.4 The Combined Equipment RB-FSC System

In this section, we develop the equations for the system shown in Figure 2.12, which consists of two equipment items connected by a RB-FSC represented by the modified Bouc-Wen model described above. In the subsequent section, we carry out time history analyses to compute the responses of the stand-alone and connected systems to selected earthquake ground motions in order to determine the effect of the interaction on the equipment items.

As in our previous study (Der Kiureghian et al., 1999), we employ a single-degree-of-freedom model for each equipment item that is characterized by distributed mass and stiffness properties and a single displacement shape function. The displacement of equipment i is written in the form $u_i(y,t) = \psi_i(y) z_i(t)$, where y is the spatial coordinate, $\psi_i(y)$ is the displacement shape function, and $z_i(t)$ is the generalized coordinate that defines the variations of the displacement shape in time. For an equipment item modeled as a beam of length L_i, the equivalent mass and stiffness are respectively given by

$$m_i = \int_0^{L_i} \rho_i(y) [\psi_i(y)]^2 dy, \tag{2.15}$$

$$k_i = \int_0^{L_i} EI_i(y) [\psi_i''(y)]^2 dy \tag{2.16}$$

and the effective mass producing the external inertia force is given by

$$l_i(y_i) = \psi_i(y_i) \int_0^{L_i} \rho_i(y) \psi_i(y) dy \tag{2.17}$$

In the above expressions, $\rho_i(y)$ is the mass per unit length of the equipment, $EI_i(y)$ is the flexural stiffness, and y_i is the coordinate at the point where the connecting element is attached to the equipment. For reasons described in the previous study, it is advantageous to scale the shape functions such that $\psi_i(y_i) = 1$. Furthermore, it is convenient to introduce the abbreviated notation $u_i(t) = u_i(y_i, t)$ and $l_i = l_i(y_i)$. The equations of motion of the connected system expressed in terms of the displacements at the attachment points when it is subjected to base acceleration $\ddot{x}_g$ can now be written as

$$\mathbf{M}\,\ddot{\mathbf{u}} + \mathbf{C}\,\dot{\mathbf{u}} + \mathbf{R}(\mathbf{u}, z) = -\mathbf{L}\,\ddot{x}_g \tag{2.18}$$

where

$$\mathbf{u} = \begin{Bmatrix} u_1(t) \\ u_2(t) \end{Bmatrix},\ \mathbf{M} = \begin{bmatrix} m_1 & 0 \\ 0 & m_2 \end{bmatrix},\ \mathbf{C} = \begin{bmatrix} c_1 + c_0 & -c_0 \\ -c_0 & c_2 + c_0 \end{bmatrix}, \tag{2.19a}$$

$$\mathbf{R}(\mathbf{u}, z) = \begin{Bmatrix} k_1\, u_1(t) - q(\Delta u, z) \\ k_2\, u_2(t) + q(\Delta u, z) \end{Bmatrix},\ \mathbf{L} = \begin{Bmatrix} l_1 \\ l_2 \end{Bmatrix} \tag{2.19b}$$

and the modified Bouc-Wen model is defined by

$$q(\Delta u, z) = \alpha k\, \Delta u + (1 - \alpha) k z \tag{2.20a}$$

$$\dot{z} = \frac{\Delta \dot{u}}{\eta}\left[A - \nu |z|^n \{\beta \operatorname{sgn}(\Delta \dot{u}\, z) + \gamma + \phi(\operatorname{sgn}(z) + \operatorname{sgn}(\Delta \dot{u}))\}\right] \tag{2.20b}$$

where $\Delta u = u_2(t) - u_1(t)$ is the relative displacement between the two equipment items, which is equivalent to the elongation/contraction of the RB-FSC. In (2.18), we have added a viscous damping matrix similar to that described in our previous study (see Equation (2.10) in Chapter 2 of Der Kiureghian et al., 1999). Elements c_1 and c_2 of the damping matrix in (2.19a) represent the damping coefficients of the two equipment items, whereas c_0 represents the viscous damping of the RB-FSC. In the following analysis, we have used $c_0 = 0$, since the amount of energy dissipated by viscous damping would be negligible in comparison to that dissipated by the inelastic action in the FSC.

For the numerical results reported in the following section, the above system of equations were solved by a 4th order Runge-Kutta algorithm using automatically varying time steps with a relative tolerance of 10^{-6}.

2.5 Investigation of the Interaction Effect in Example Systems

In this section, we examine the effect of interaction between two equipment items connected by a RB-FSC and subjected to selected earthquake ground motions. As in our previous study, we examine the effect of interaction by computing the response ratios

$$R_i = \frac{\max|u_i(t)|}{\max|u_{i0}(t)|}, \quad i = 1,2 \tag{2.21}$$

where $u_i(t)$ and $u_{i0}(t)$ denote the responses of equipment i in the connected and stand-alone systems, respectively. As should be clear, a value greater than unity for a response ratio implies amplification of the corresponding equipment response in the connected system in comparison to its stand-alone response. To the contrary, a value smaller than unity for a response ratio implies de-amplification of the corresponding equipment response. As discussed in the earlier study, although these response ratios are computed for the displacement responses, they are equally valid for internal forces in each equipment item.

In the following, we investigate three example systems. The first system has properties that are similar to that of a system investigated in our previous study (described in page 55 of Der Kiureghian et al., 1999). The other two examples have properties similar to two of the systems tested at UCSD.

The first example system has the properties: $m_1 = 5.71\,\text{lb.s}^2/\text{in}$, $\omega_1 = \sqrt{k_1/m_1} = 4\pi\,\text{rad/s}$ and $\zeta_1 = c_1/(2\omega_1 m_1) = 0.02$ for equipment 1, and $m_2 = 2.85\,\text{lb.s}^2/\text{in.}$, $\omega_2 = \sqrt{k_2/m_2} = 10\pi\,\text{rad/s}$, and $\zeta_2 = c_2/(2\omega_2 m_2) = 0.02$ for equipment 2. The RB has the properties described earlier in this chapter. The FSC is selected in accordance to the PG&E specification No. 30-2022. Figures 2.13 and 2.14 show the response pairs $(u_{10}(t), u_1(t))$ and $(u_{20}(t), u_2(t))$, respectively, of the two equipment items in the stand-alone and connected configurations, when the system is subjected to the N-S component of the Newhall record of the Northridge (1994) earthquake. Figures 2.15 and 2.16 show the same for the system subjected to the longitudinal record of Tabas (1978) earthquake (TabasLN). The ratios of the peak responses in the connected and stand-alone systems are $R_1 = 0.757$ and $R_2 = 0.931$ for the Northridge earthquake and $R_1 = 0.845$ and $R_2 = 0.776$ for the TabasLN. It is apparent that the responses of both equipment items in the connected system are de-amplified relative to their stand-alone responses. Figures 2.17 and 2.18 show the force-elongation hysteresis loops of the RB-FSC for the two

earthquakes. These plots show significant nonlinearity and energy dissipation in the FSC.

To quantify the influences of the flexibility and energy dissipation characteristics of the FSC, we repeat the above analysis while entirely removing the FSC. In this case, the connection has the full elastic axial rigidity of the RB, which is equal to $k_0 = 264{,}504$ lbs/in. According to the definition in our previous study, this corresponds to a stiffness ratio of $\kappa = k_0/(k_1 + k_2) = 71.2$. To quantify the influence of the energy dissipation capacity of the FSC, we repeat the analysis while using an ideally elastic model of the FSC with its initial stiffness $k_0 = 225$ lbs/in., which corresponds to the stiffness ratio $\kappa = k_0/(k_1 + k_2) = 0.0606$. The response ratios from these analyses are summarized in Table 2.1.

Our interest is in cases where $R_2 > 1$ in Table 2.1, since a response ratio larger than 1 indicates an adverse interaction effect on an equipment item. By attaching the FSC to RB, we increase the flexibility of the conductor and thereby reduce the response ratio R_2 of the higher-frequency equipment from 3.526 to 1.053 (70% reduction) for the Northridge earthquake and from 1.272 to 0.884 (31% reduction) for the TabasLN earthquake. Furthermore, when we consider the energy dissipation provided by the FSC, R_2 is further reduced from 1.053 to 0.931 (12% reduction) for the Northridge earthquake and from 0.884 to 0.776 (12% reduction) for the TabasLN earthquake. This comparison clearly shows that, for this example system, the flexibility of the FSC is much more significant in reducing the adverse effect of the interaction than the energy dissipation of the RB-FSC. However, it is expected that if the RB-FSC is subjected to a larger relative displacement, then energy dissipation will be larger so that it will have more influence on reducing responses. Clearly, the considered flexible strap connector (the PG&E 30-2022 FSC) provides a significant advantage in reducing the adverse effects of interaction between the connected equipment items.

The second example considered is the equipment combination (pair) 2 used in the UCSD experiments (Filiatrault et al. 1999). Adjusted frequency and damping values for this system were determined through discussions with A. Filiatrault of UCSD. The as-

sumed displacement shape function corresponds to the static displacement of a cantilever with an end load. The property values used in the analysis are: $m_1 = 2.057$ lb.s^2/in., $\omega_1 / 2\pi = 1.945$ Hz and $\zeta_1 = 0.013$ for equipment 1, and $m_2 = 0.422$ lb.s^2/in., $\omega_2 / 2\pi = 5.47$ Hz and $\zeta_2 = 0.013$ for equipment 2. Figures 2.19-2.22 compare the responses of the two equipment items in their stand-alone (Figures 2.19 and 2.20) and connected (Figures 2.21 and 2.22) configurations, as obtained in the experiments (top figures) and as predicted by analysis, for the table motion simulating the Newhall 1994 record at 100% span. While the two sets of response time histories are not in close agreement, general features are alike. For example, both experimental and analytical results show that the response of the lower-frequency equipment item is de-amplified as a result of the interaction, whereas that of the higher-frequency equipment item is amplified. This is consistent with the results established in our previous study for linearly connected equipment systems. Figure 2.23 shows the force-displacement hysteresis loop for the FSC under this excitation. Whereas the overall shapes of the experimental and analytical hysteresis loops are similar, the effective stiffness of the FSC deduced from the test is found to be much larger than that predicted analytically. The analytical value actually matches the effective stiffness of the FSC directly measured under quasi-static cyclic loads at UCSD. Based on our discussions with A. Filiatrault, we believe the higher stiffness measured for the FSC in this dynamic test has to do with the manner of attachment of the RB-FSC to the equipment items. It is noteworthy that for the present example the FSC does not experience a large degree of nonlinearity or energy dissipation.

Figures 2.24-2.28 show similar comparisons between experimental and analytical predictions of the equipment responses to a table motion simulating the Tabas 1978 ground motion at 50% span. The trends here are similar to those observed in Figures 2.19-2.23 for the Newhall motion.

Table 2.2 lists the response ratios for the example system for the two table motions. In addition to the cases described above, we have included the response ratios for systems without the FSC and for systems with linear FSC in the same manner as in Table 2.1. The experimental values are listed in parenthesis in the last row of the table. It is observed that the flexibility of the FSC significantly contributes to reducing the interaction

effect, whereas the energy dissipation within the FSC reduces the interaction effect by a small amount. Furthermore, the response predictions by the analytical method are in reasonably close agreement with those measured in the experiments.

Analyses similar to the above were carried out for the system with equipment combination 5 in the UCSD tests. This system has the properties: $m_1 = 2.057\,\text{lb.s}^2/\text{in.}$, $\omega_1/2\pi = 1.945\,\text{Hz}$ and $\zeta_1 = 0.013$ for equipment 1, and $m_2 = 0.422\,\text{lb.s}^2/\text{in.}$, $\omega_2/2\pi = 12.23\,\text{Hz}$ and $\zeta_2 = 0.009$ for equipment 2. In this case, equipment 2 had displacements smaller than the measurement error, and reliable experimental estimates of its response consequently could not be obtained. For the sake of brevity, here we list only the predicted response ratios in Table 2.3, where the test values only for equipment 1 are shown in parenthesis in the last row. The very large amplification of the higher-frequency equipment item for this system, even when the flexibility and energy dissipation of the FSC are accounted for, is due to the large separation between the frequencies of the two equipment items. This example serves to once again demonstrate the adverse effect of interaction when equipment items with widely separated frequencies are connected.

Table 2.1 Influence of the flexibility and energy dissipation of the RB-FSC on the effect of interaction on equipment items

Connector	R_1		R_2	
	Northridge	TabasLN	Northridge	TabasLN
RB ($\kappa = 71.2$)	0.4172	0.513	**3.5256**	**1.272**
Linear Spring with Initial Stiffness ($\kappa = 0.0606$)	0.844	0.901	**1.053**	0.884
RB-FSC	0.757	0.845	0.931	0.776

Table 2.2 Influence of the flexibility and energy dissipation of the RB-FSC on the effect of interaction on the equipment combination 2 in the UCSD test

Connector	R_1		R_2	
	Newhall 100% span	Tabas 50% span	Newhall 100% span	Tabas 50% span
RB (κ=328)	0.4461	0.7012	**2.8767**	**3.2682**
Linear Spring with Initial Stiffness (κ=0.2793)	0.5804	0.8001	**1.5953**	**1.4083**
RB-FSC (UCSD experiment)	0.5277 (0.5689)	0.6879 (0.6255)	**1.5509 (1.2150)**	**1.2707 (1.2959)**

Table 2.3 Influence of the flexibility and energy dissipation of the RB-FSC on the effect of interaction on equipment the equipment combination 5 in the UCSD test

Connector	R_1		R_2	
	Newhall 100% span	Tabas 50% span	Newhall 100% span	Tabas 50% span
RB (κ=94.5)	0.1068	0.1431	**7.9218**	**7.8270**
Linear Spring with Initial Stiffness (κ=0.08)	0.5595	0.7677	**3.6879**	**3.6610**
RB-FSC (UCSD experiment)	0.4107 (0.3854)	0.6790 (0.4367)	**3.0058**	**2.5939**

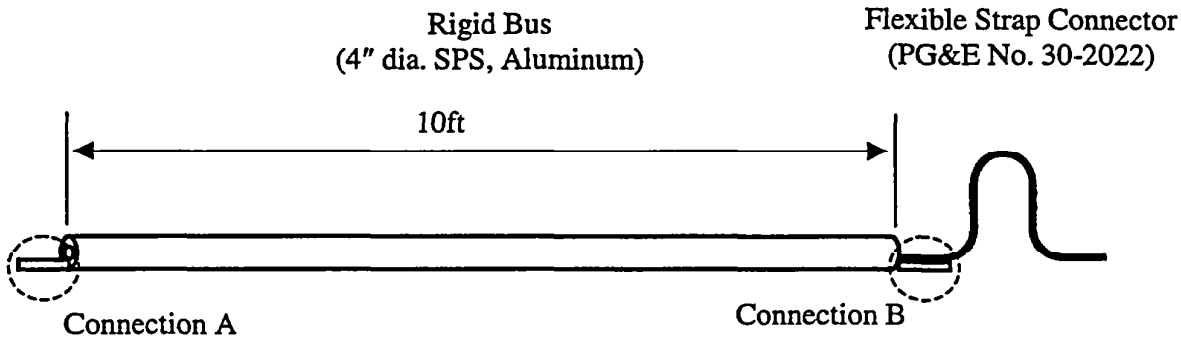

Figure 2.1 Rigid bus with a symmetric flexible strap connector

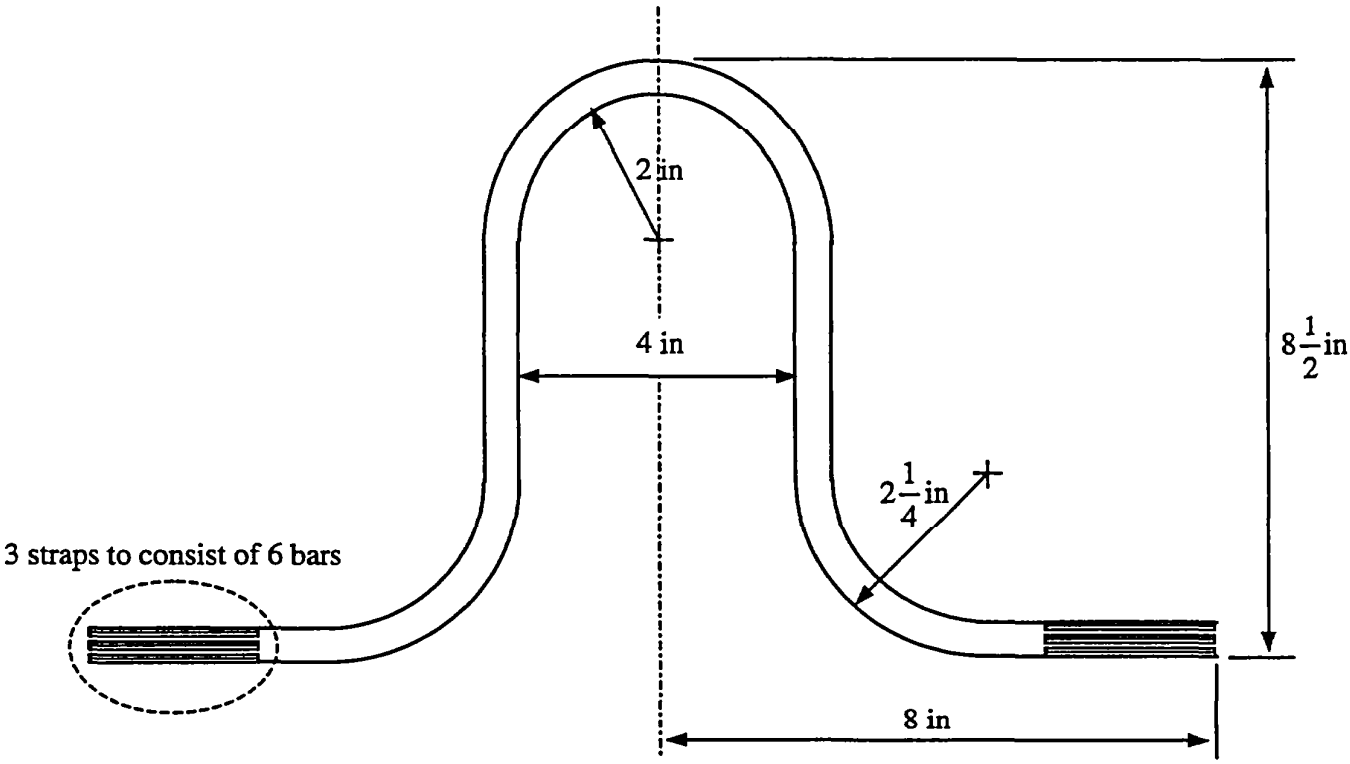

Figure 2.2 Dimensions of FSC No. 30-2022

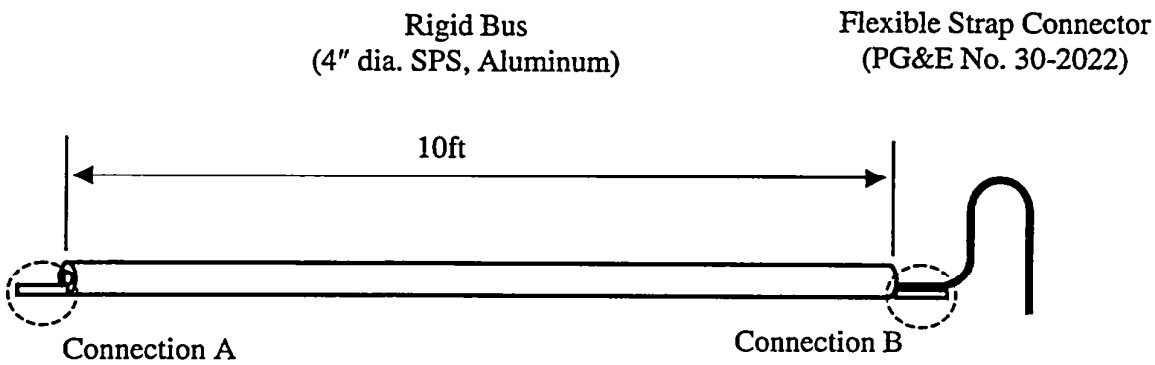

Figure 2.3 Rigid bus with an asymmetric flexible strap connector

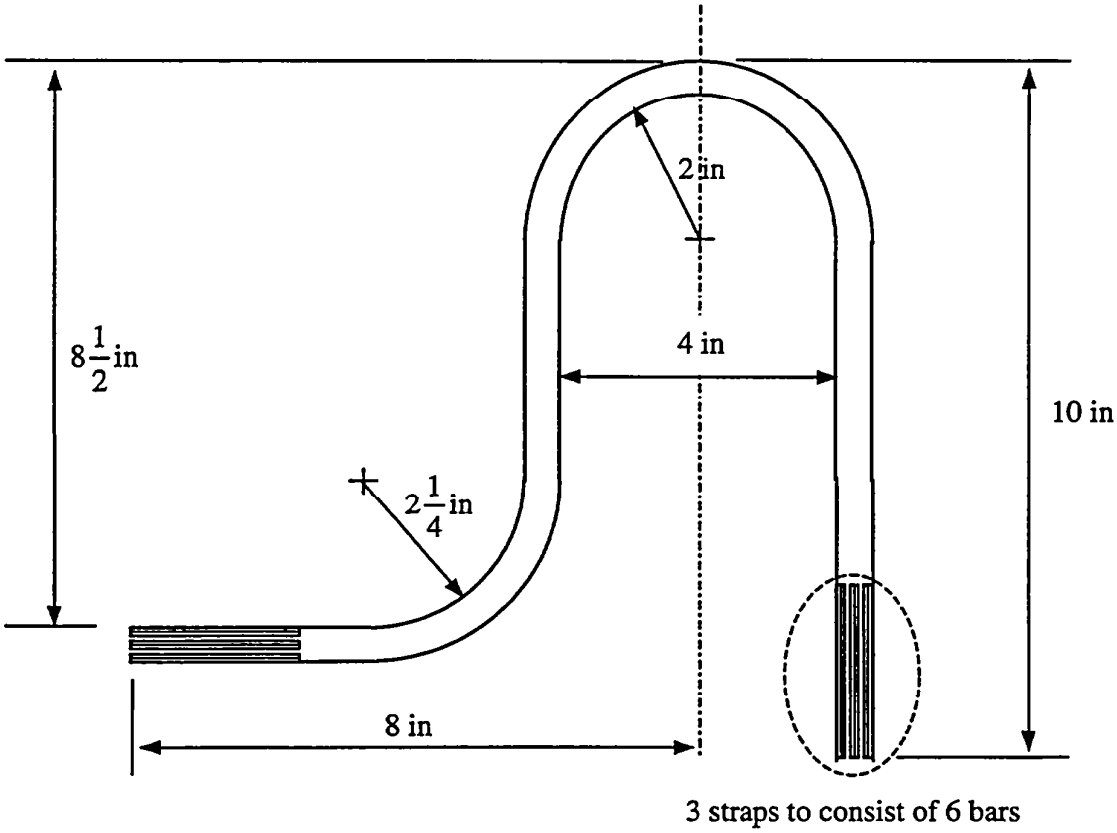

Figure 2.4 Dimensions of FSC No. 30-2021

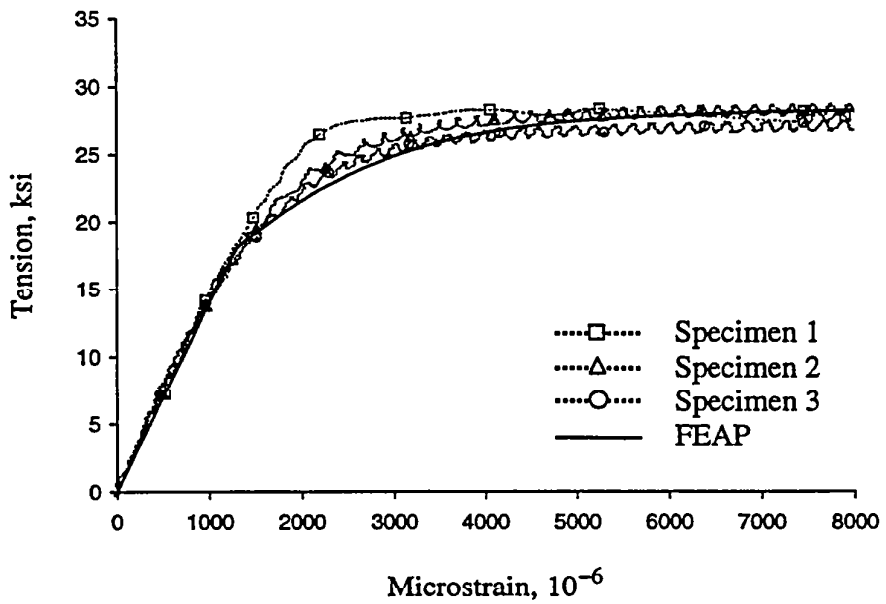

Figure 2.5 Comparison of uniaxial tensile stress-strain relationship of FSC coupons generated in the UCSD tests with fitted model

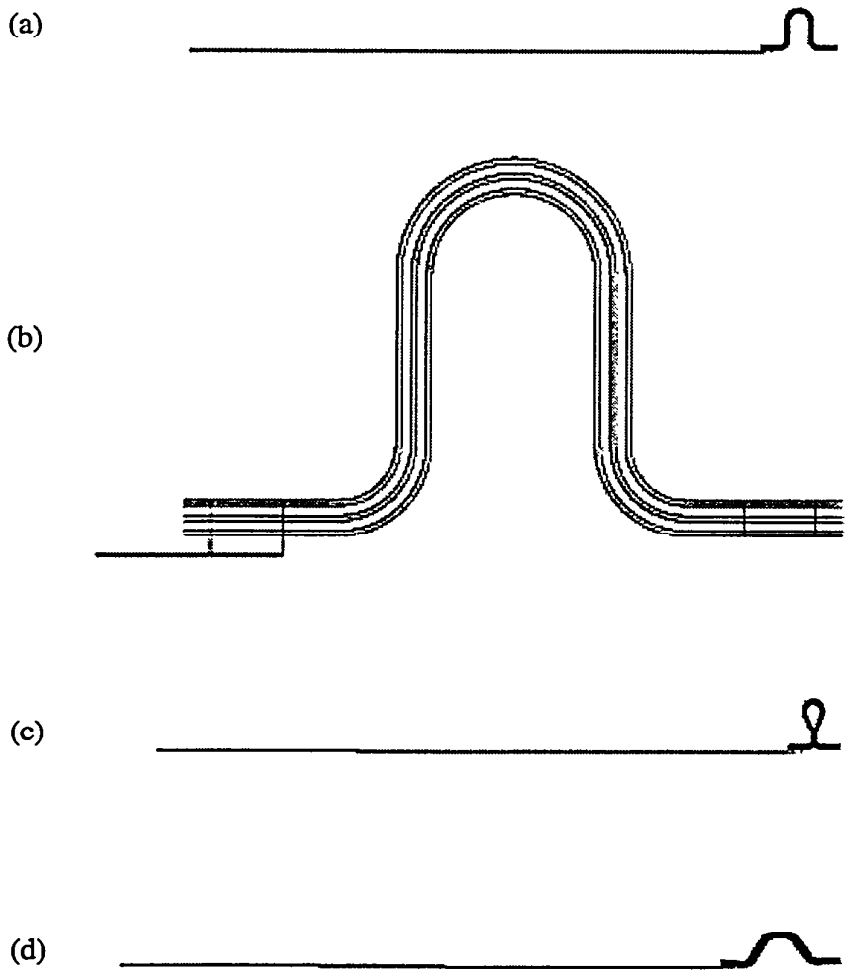

Figure 2.6 Schematics of the finite element layout of the RB with symmetric FSC: (a) frame elements for the RB-FSC, (b) frame elements for the FSC, (c) extreme deformed shape under compression, and (d) extreme deformed shape under tension

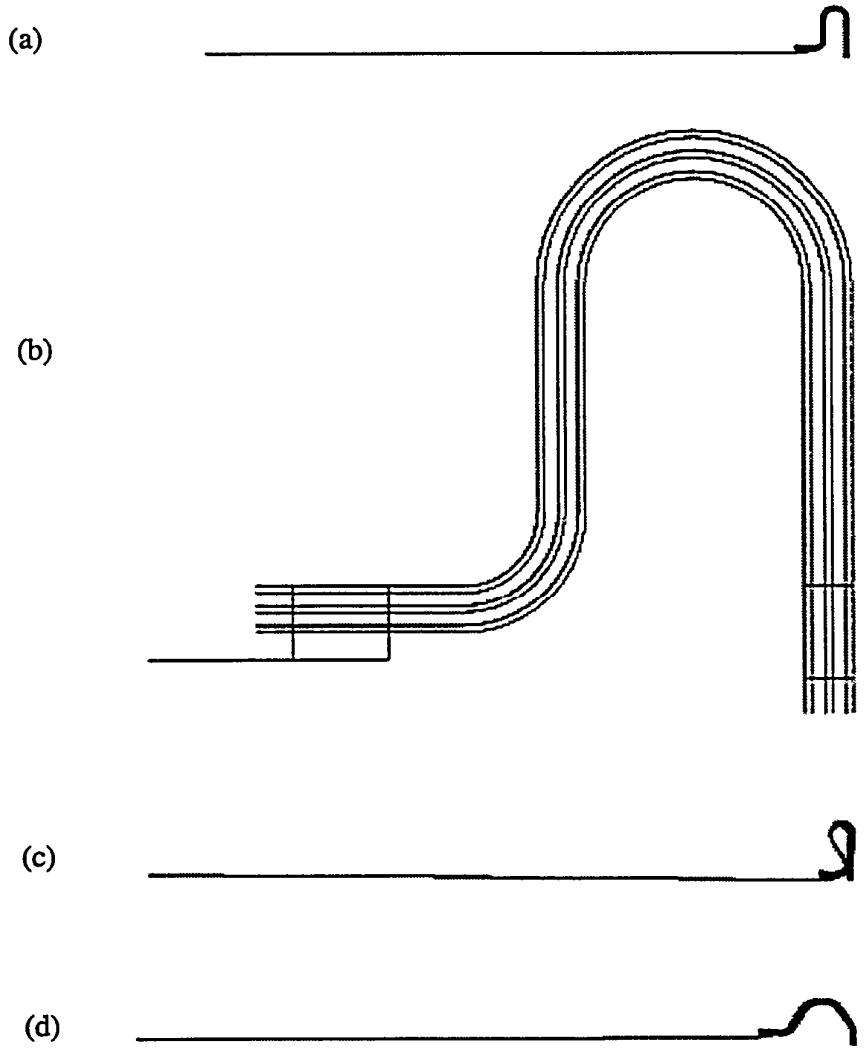

Figure 2.7 Schematics of the finite element layout of the RB with asymmetric FSC: (a) frame elements for the RB-FSC, (b) frame elements for the FSC, (c) extreme deformed shape under compression, and (d) extreme deformed shape under tension

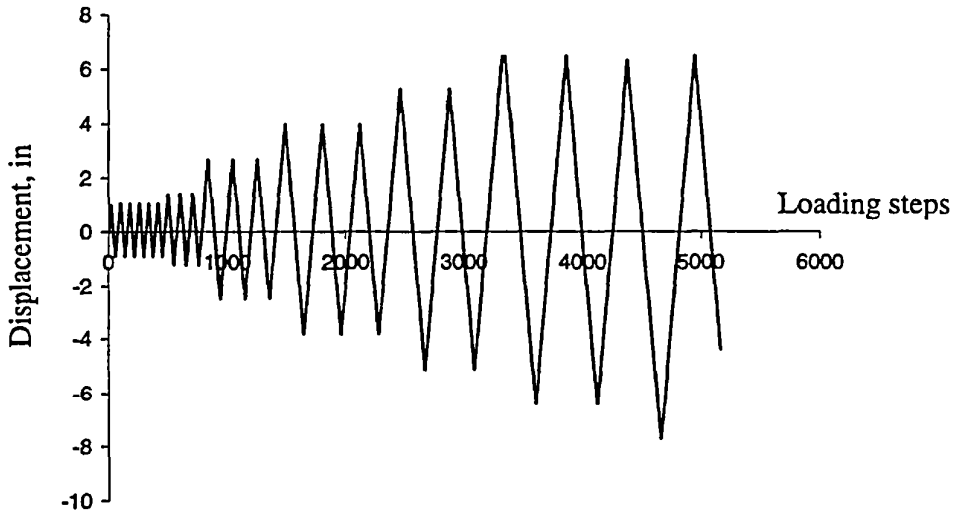

Figure 2.8 History of imposed support displacement used in the UCSD test

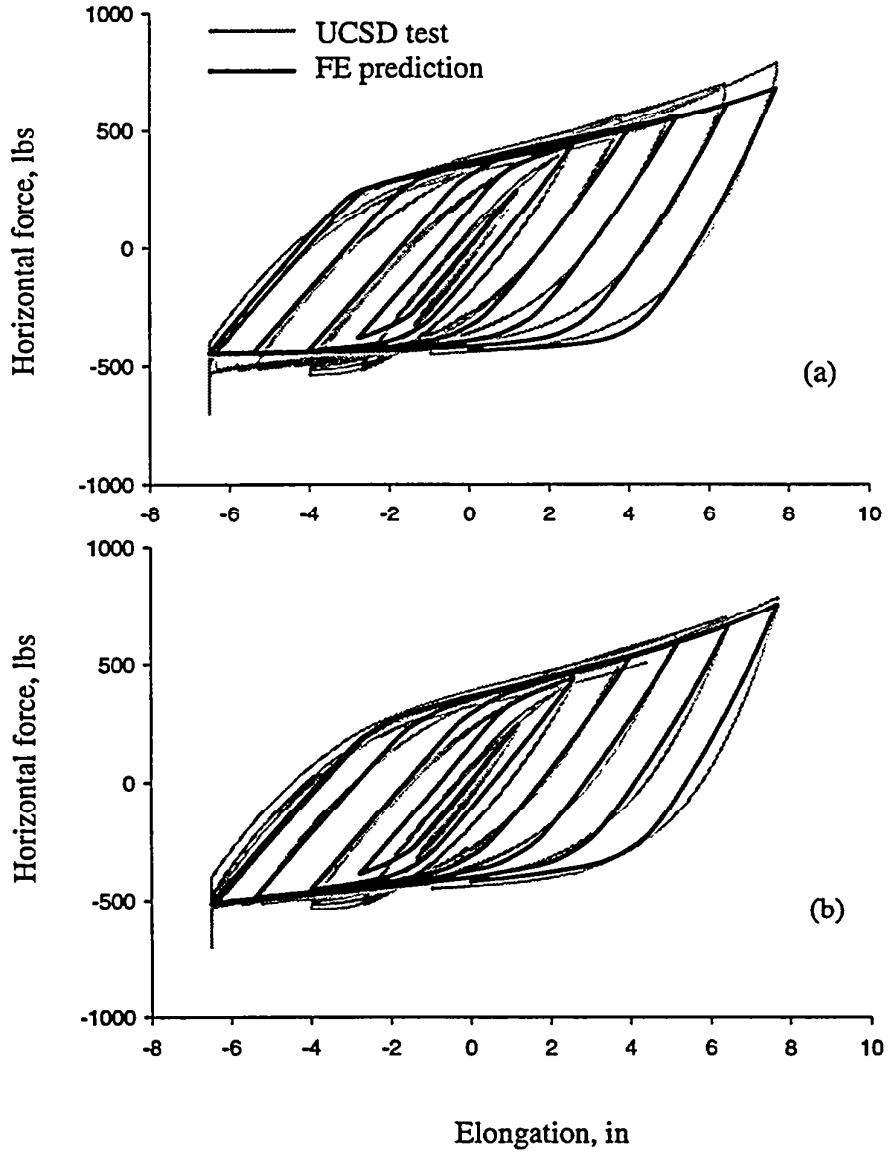

Figure 2.9 Comparison of FE predicted force-elongation relationship of the RB with the symmetric FSC with UCSD test results: (a) $H_{kin} = E/100$, (b) $H_{kin} = E/20$

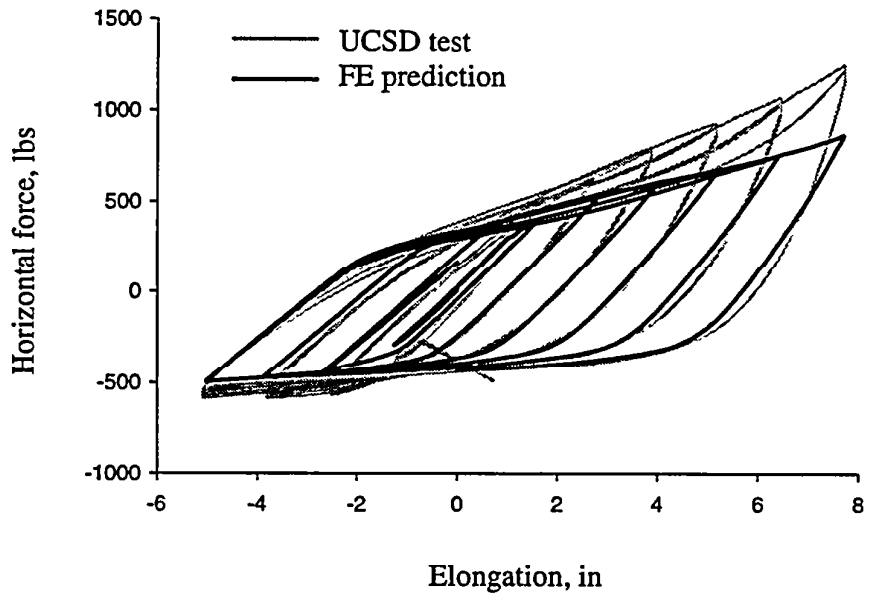

Figure 2.10 Comparison of FE predicted force-elongation relationship of the RB with the asymmetric FSC with UCSD test results for $H_{kin} = E/20$

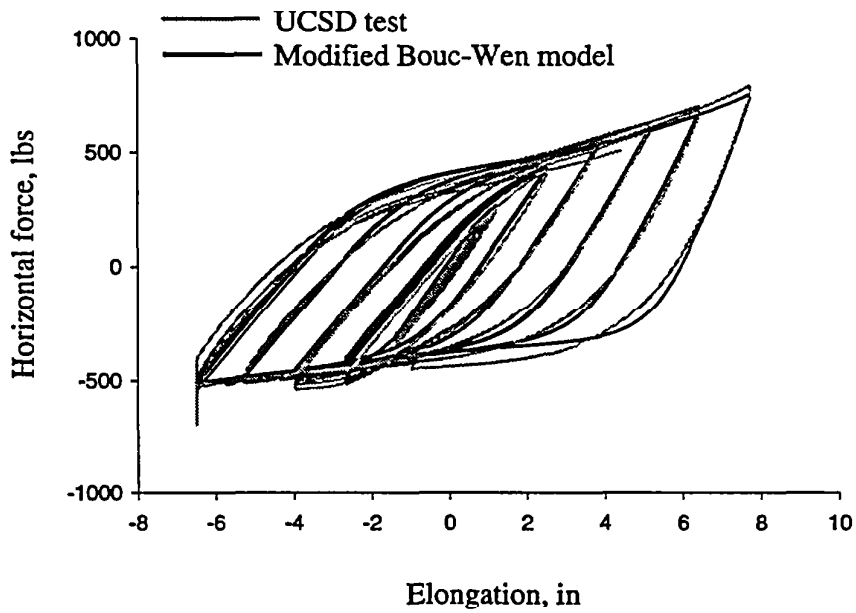

Figure 2.11 Force-elongation relationship of the first RB with symmetric FSC obtained from the UCSD test and from the modified Bouc-Wen model

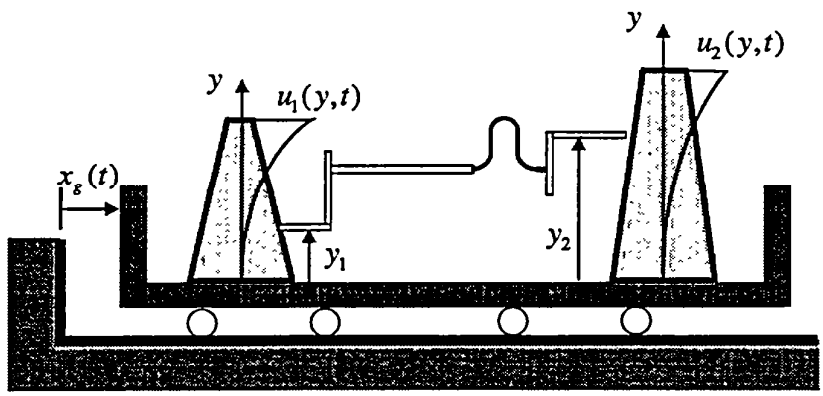

Figure 2.12 Model of equipment items connected by a RB-FSC

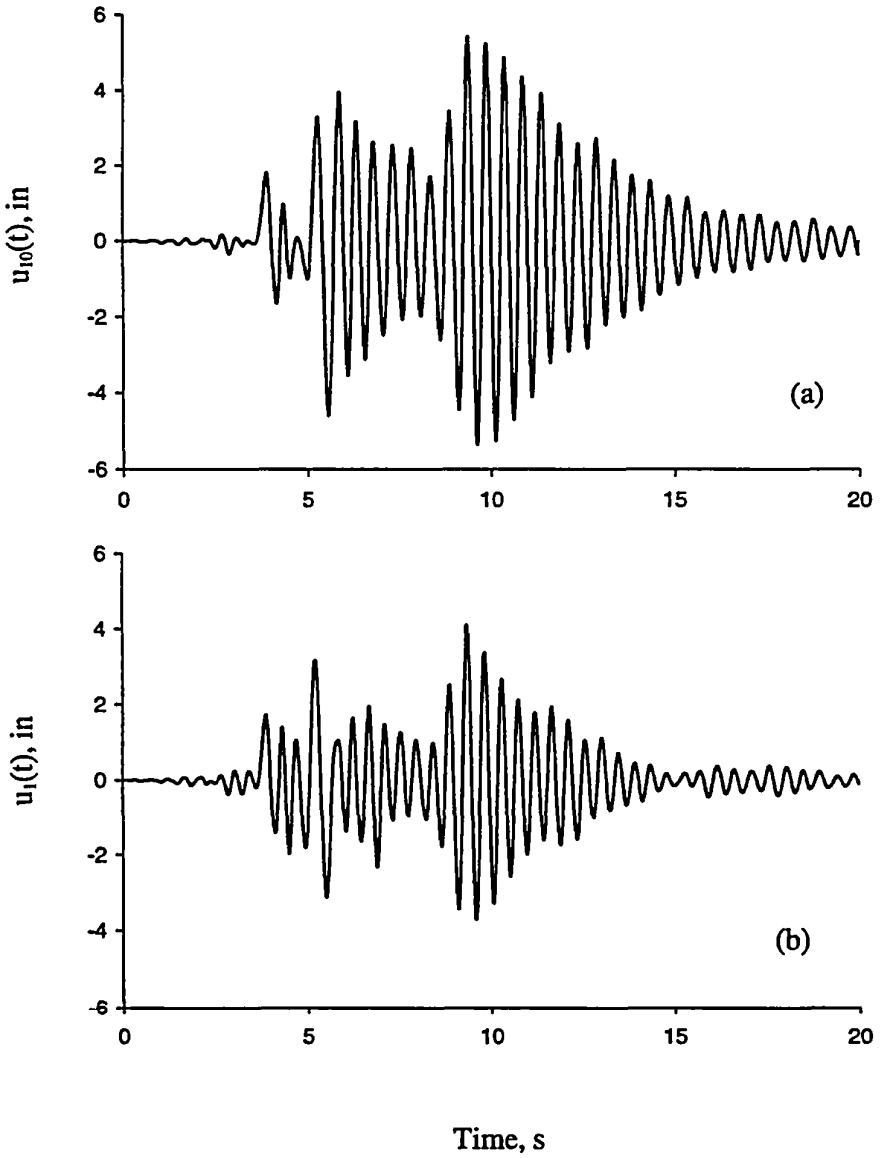

Figure 2.13 Displacement time histories of the lower-frequency equipment item for the Newhall-Northridge record: (a) response in the stand-alone configuration and (b) response in the connected system

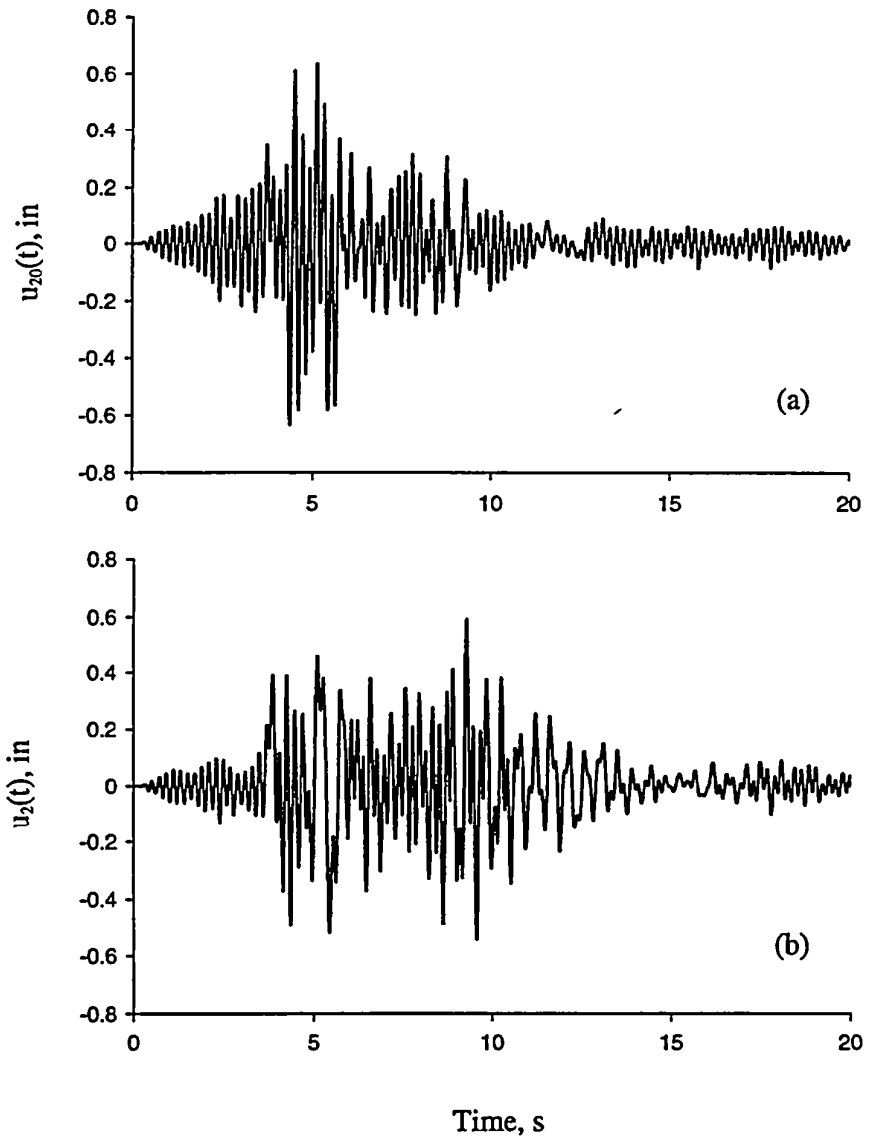

Figure 2.14 Displacement time histories of the higher-frequency equipment item for the Newhall-Northridge record: (a) response in the stand-alone configuration and (b) response in the connected system

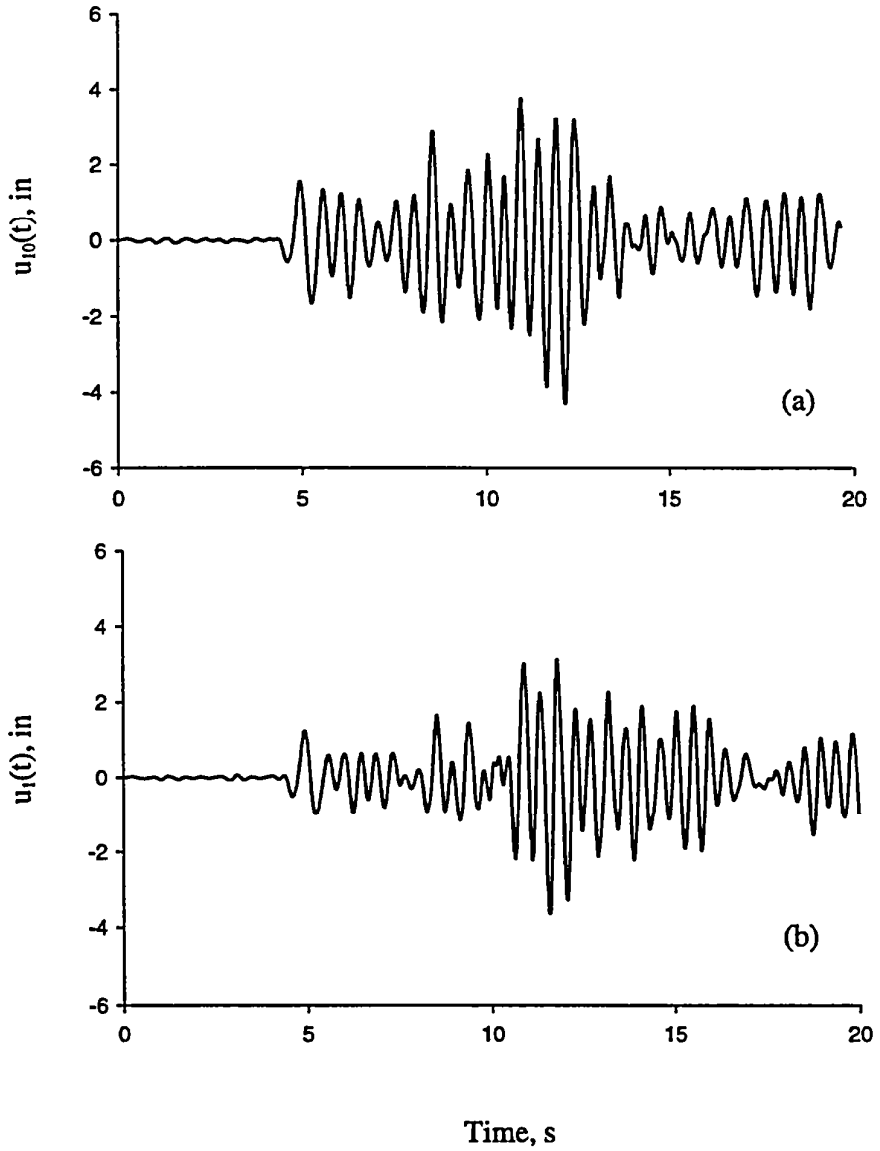

Figure 2.15 Displacement time histories of the lower-frequency equipment item for the TabasLN record: (a) response in the stand-alone configuration and (b) response in the connected system

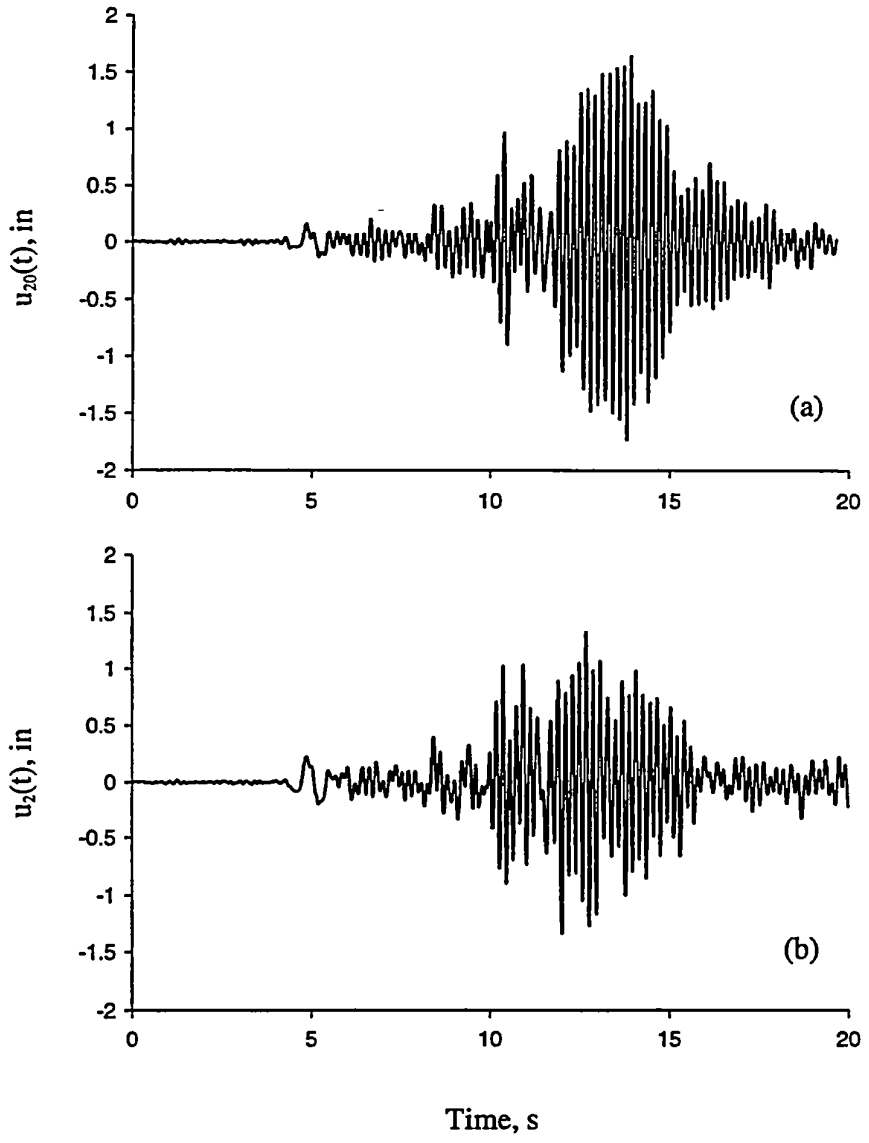

Figure 2.16 Displacement time histories of the higher-frequency equipment item for the TabasLN record: (a) response in the stand-alone configuration and (b) response in the connected system

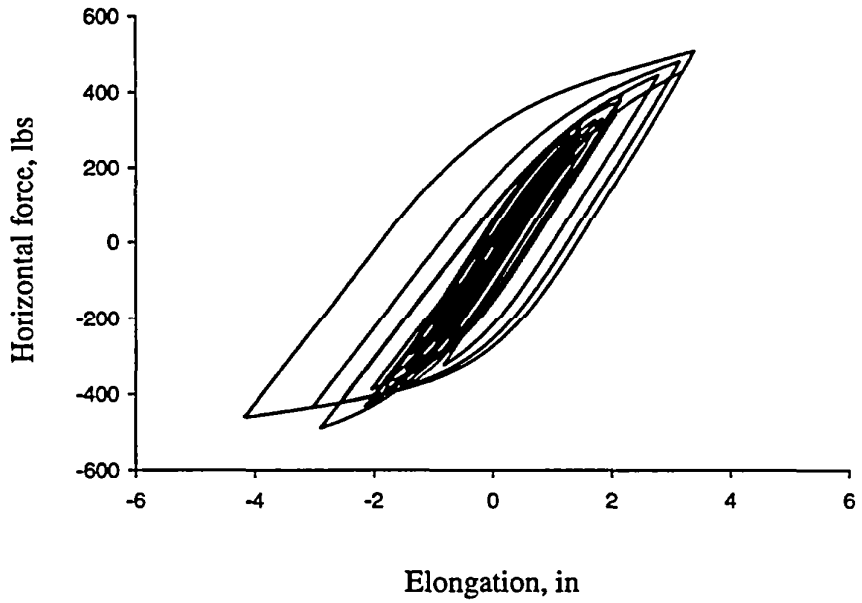

Figure 2.17 Force-elongation hysteresis loops of the RB-FSC in the connected system subjected to the Newhall-Northridge record

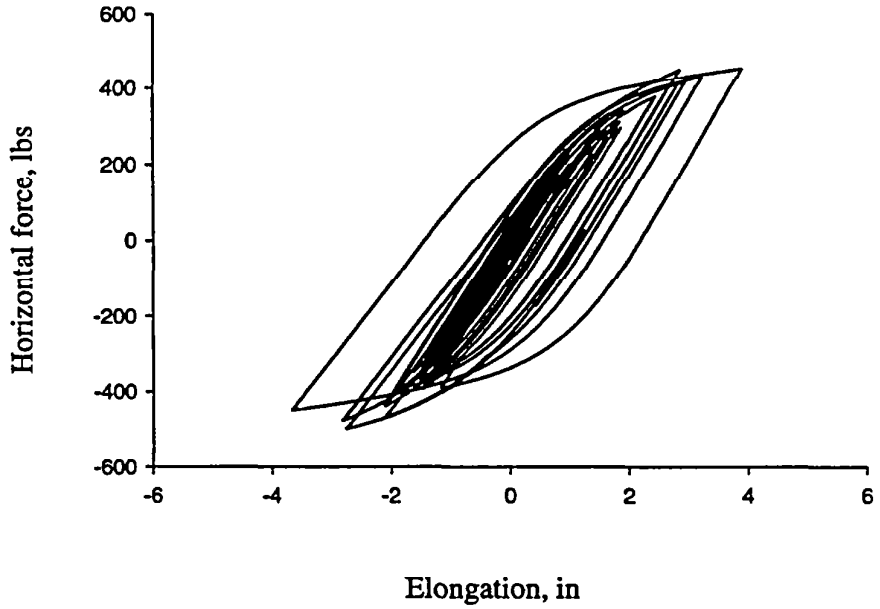

Figure 2.18 Force-elongation hysteresis loops of the RB-FSC in the connected system subjected to the TabasLN record

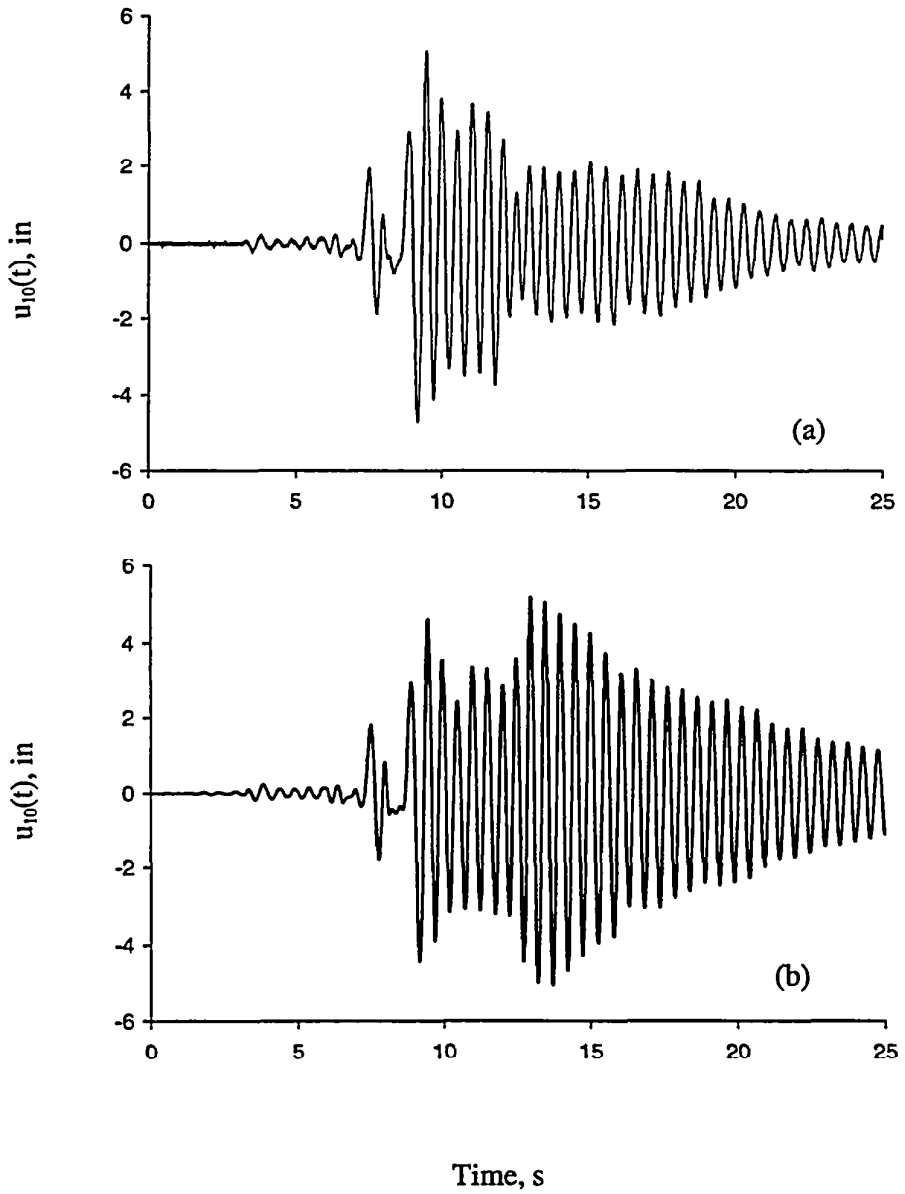

Figure 2.19 Displacement time histories of the lower-frequency equipment item in the stand-alone configuration for the table motion TRB127 (Newhall 100%): (a) experiment and (b) analysis

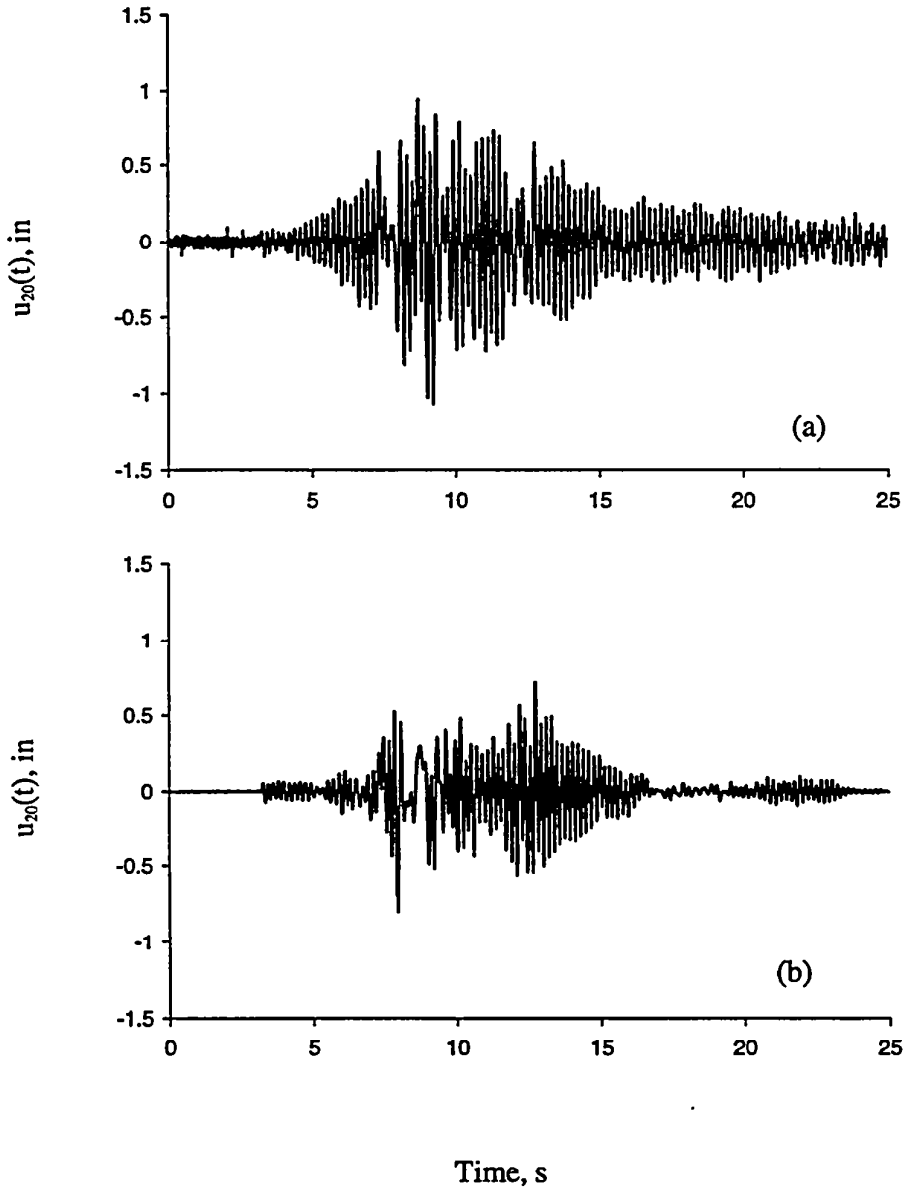

Figure 2.20 Displacement time histories of the higher-frequency equipment item in the stand-alone configuration for the table motion TRB127 (Newhall 100%): (a) experiment and (b) analysis

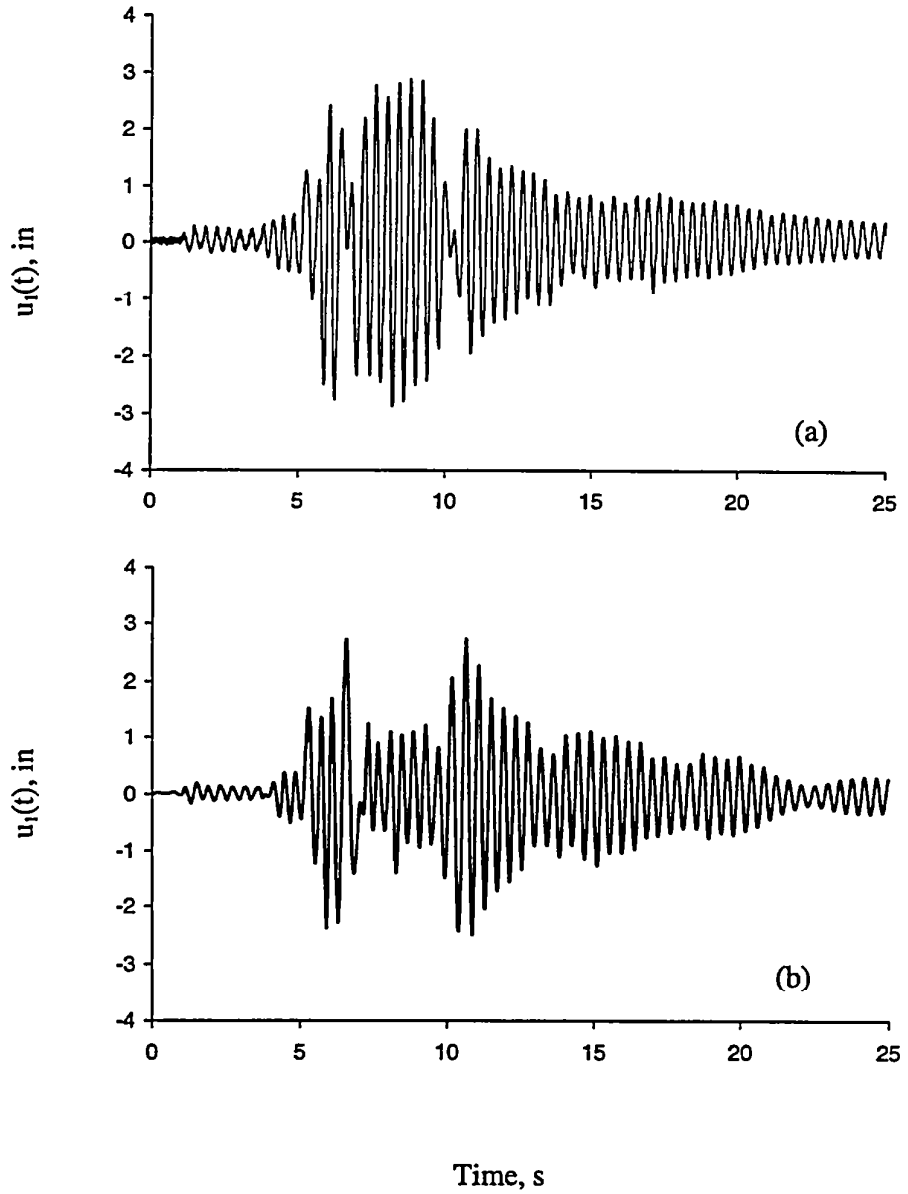

Figure 2.21 Displacement time histories of the lower-frequency equipment item in the connected system for the table motion TRB101 (Newhall 100%): (a) experiment and (b) analysis

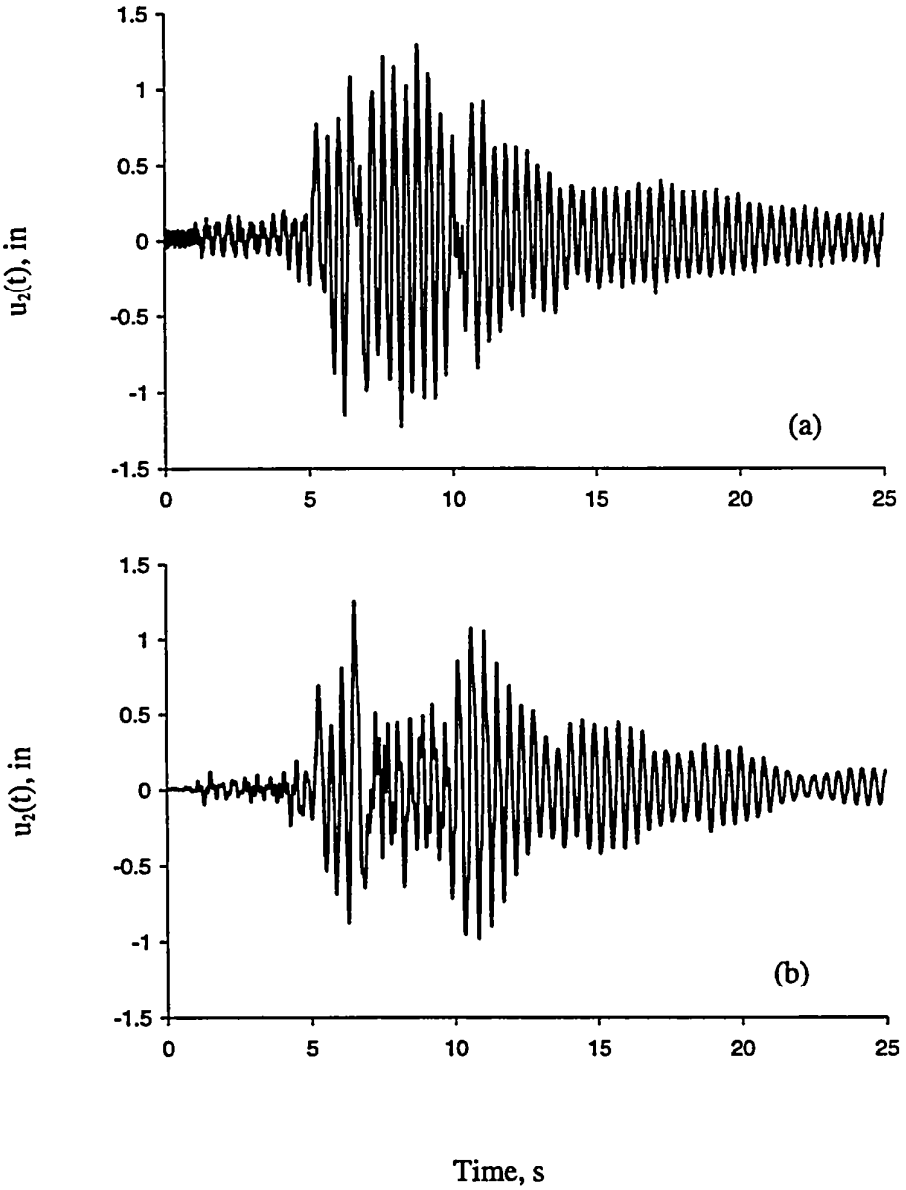

Figure 2.22 Displacement time histories of the higher-frequency equipment item in the connected system for the table motion TRB101 (Newhall 100%): (a) experiment and (b) analysis

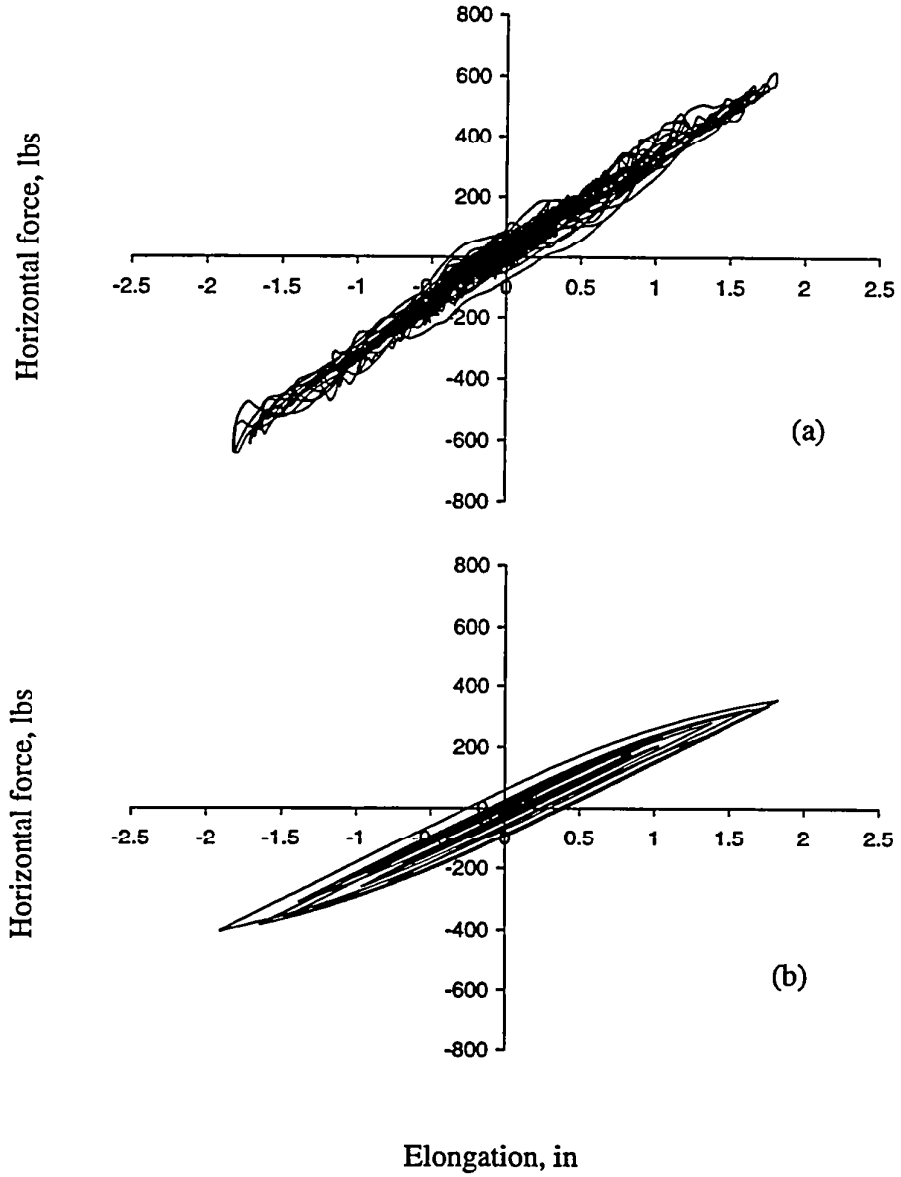

Figure 2.23 Force-elongation hysteresis loops of the RB-FSC in the connected system subjected to the table motion TRB101 (Newhall 100%): (a) experiment and (b) analysis

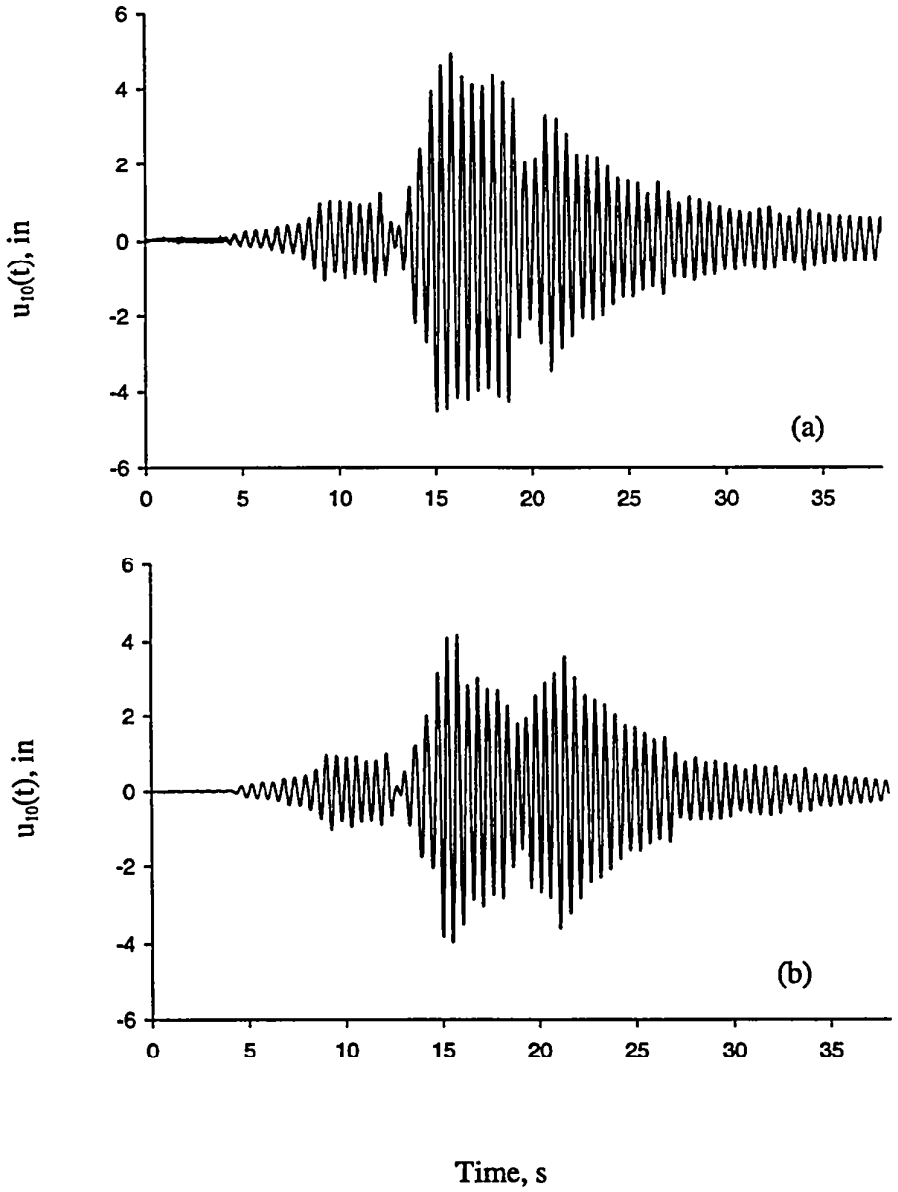

Figure 2.24 Displacement time histories of the lower-frequency equipment item in the stand-alone configuration for the table motion TRB126 (Tabas 50%): (a) experiment and (b) analysis

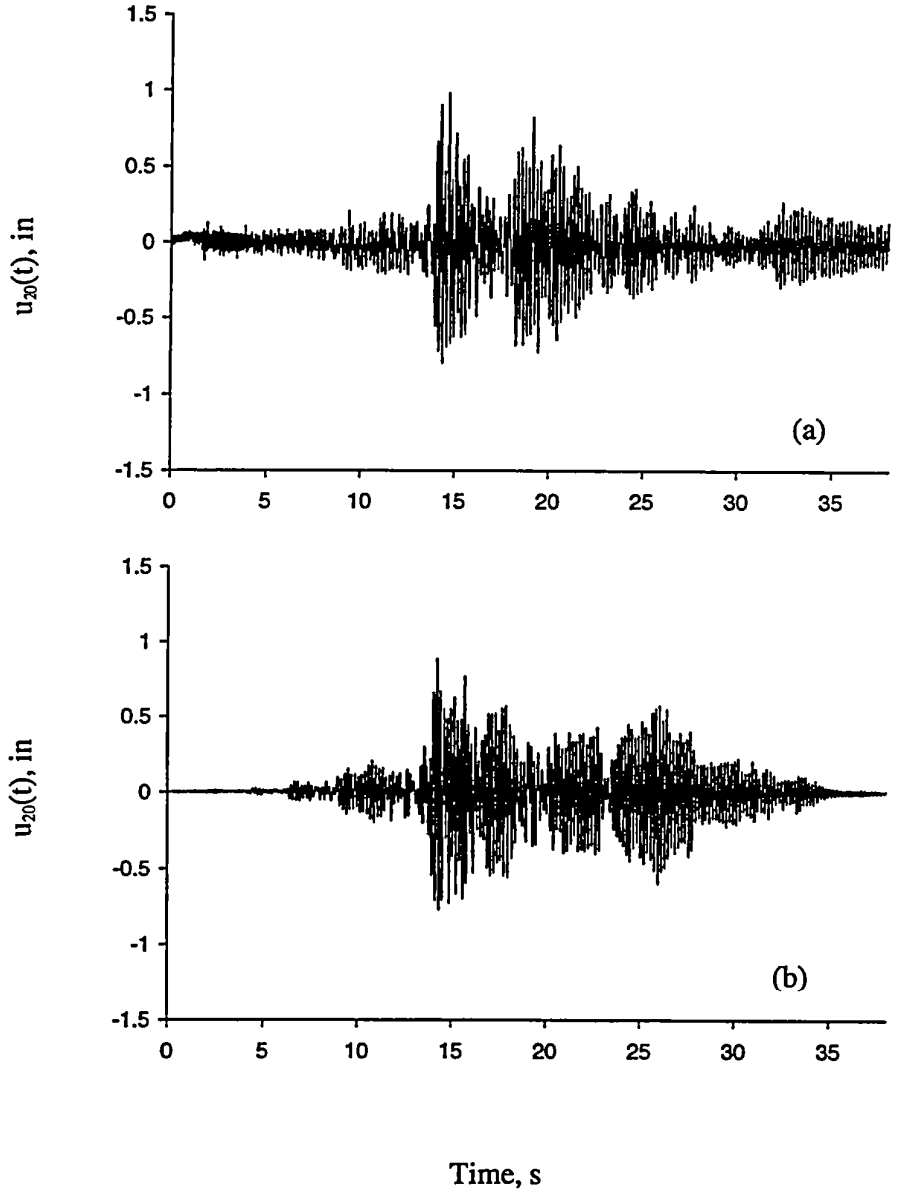

Figure 2.25 Displacement time histories of the higher-frequency equipment item in the stand-alone configuration for the table motion TRB126 (Tabas 50%): (a) experiment and (b) analysis

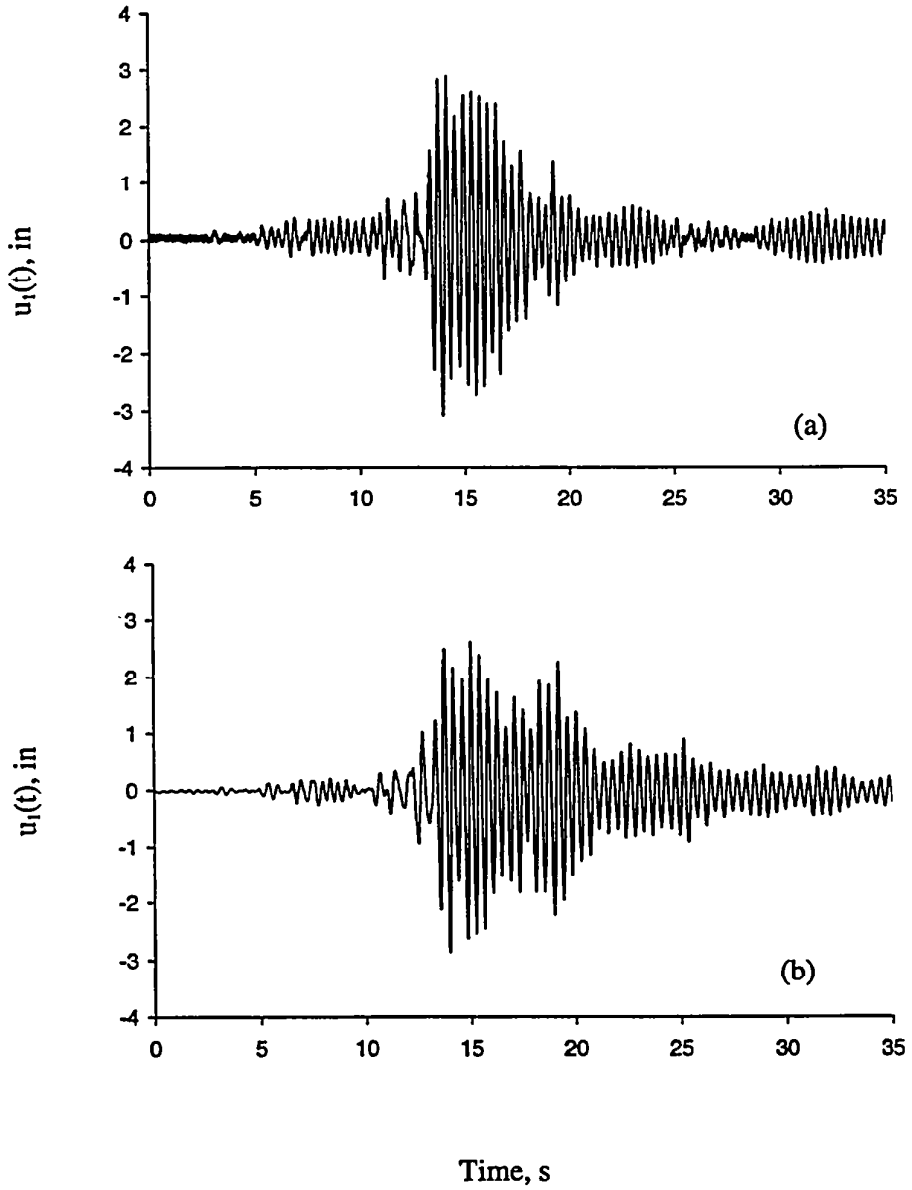

Figure 2.26 Displacement time histories of the lower-frequency equipment item in the connected system for the table motion TRB100 (Tabas 50%): (a) experiment and (b) analysis

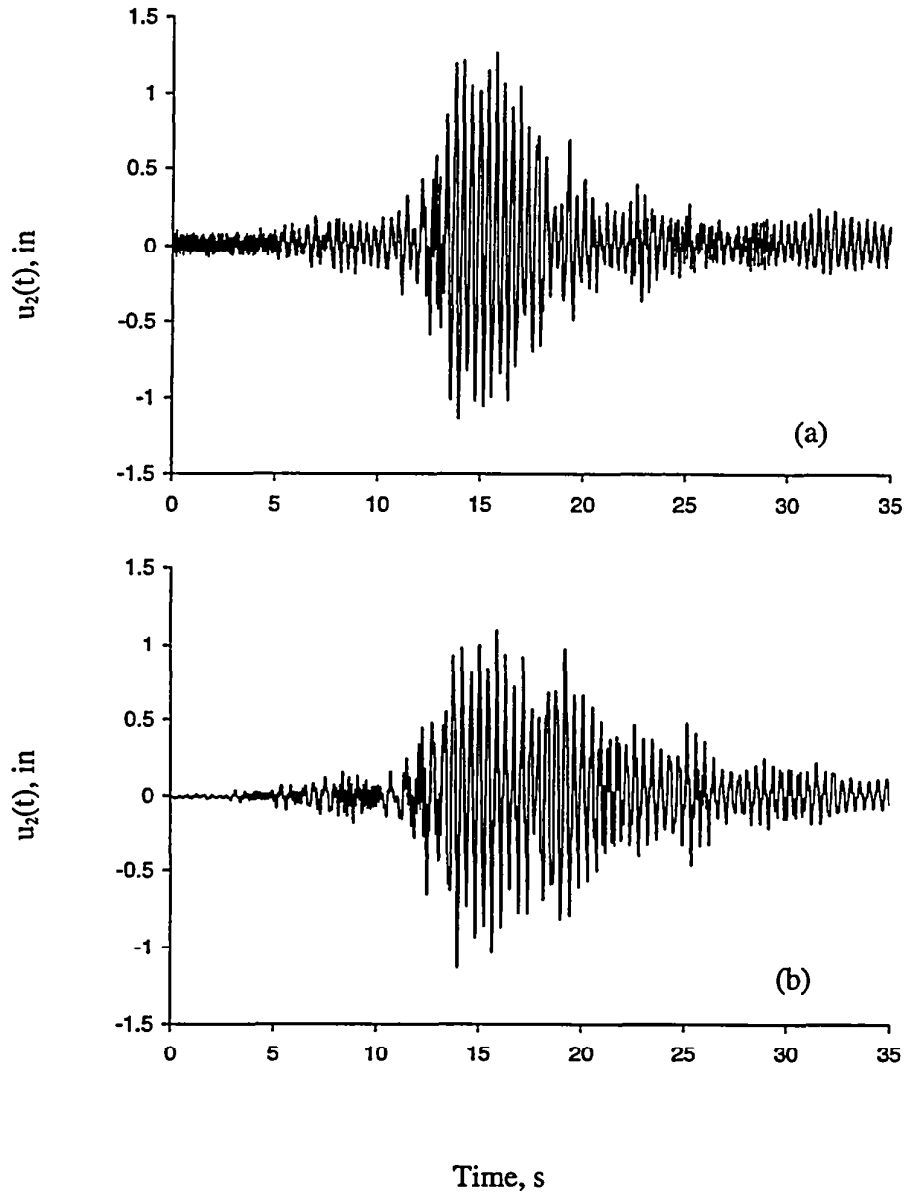

Figure 2.27 Displacement time histories of the higher-frequency equipment item in the connected system for the table motion TRB100 (Tabas 50%): (a) experiment and (b) analysis

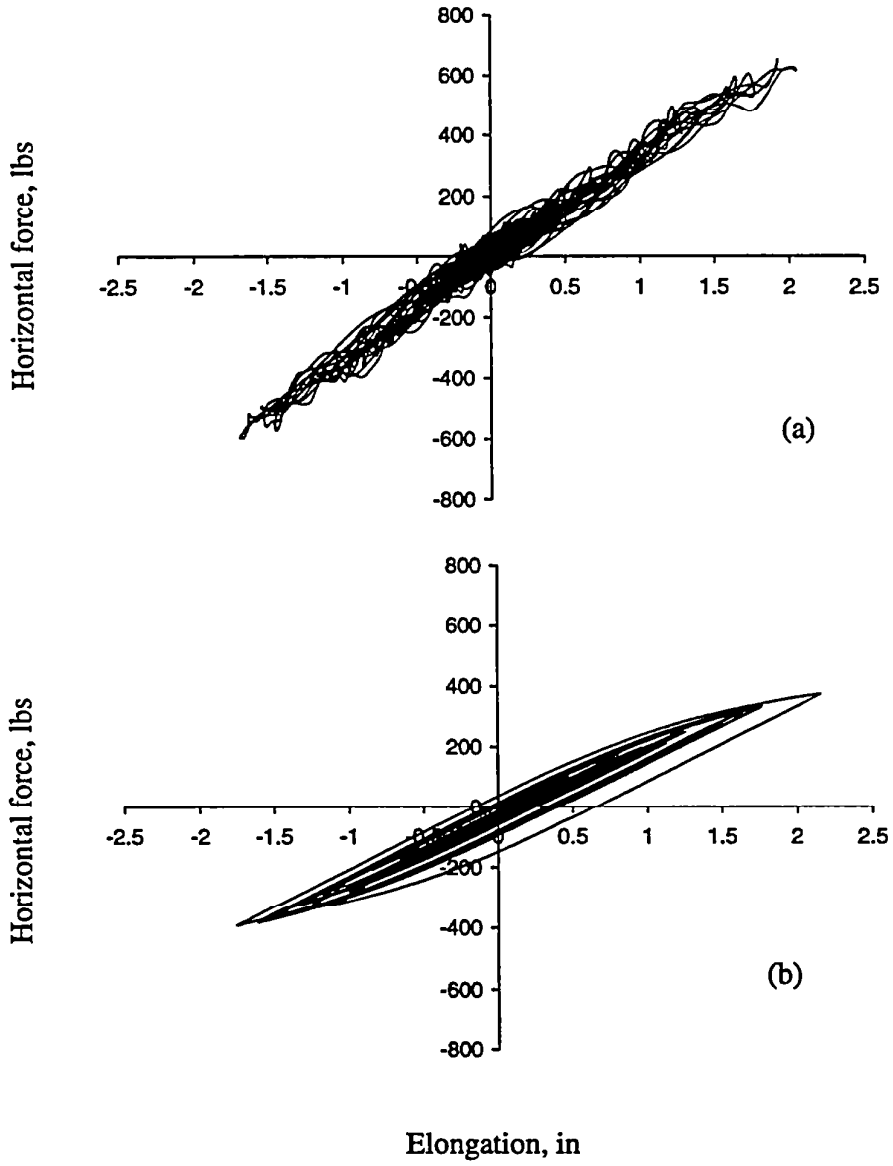

Figure 2.28 Force-elongation hysteresis loops of the RB-FSC in the connected system subjected to the table motion TRB100 (Tabas 50%): (a) experiment; and (b) analysis

Chapter 3 Influence of the Bending Stiffness and Inertia of the Connecting Cable on the Interaction Effect

3.1 Introduction

Many equipment items in electrical substations are connected to each other by flexible conductors, typically cables made of braided aluminum wire strands. In our previous study (Der Kiureghian et al., 1999), we investigated the effect of interaction in such systems when the flexible conductor was considered to be an extensible cable with negligible flexural rigidity and inertia effects. Under these approximations, the flexible conductor was modeled as an extensible catenary cable and closed form expressions were derived for its effective stiffness as a function of its geometry, i.e., span length, vertical separation of the supports, cable length, its weight per unit length w, and its axial rigidity EA, where E denotes the Young's modulus and A is the cross-sectional area of the cable. Extensive parametric studies using time history analyses with recorded ground motions were carried out to determine the effect of interaction on two equipment items connected by such a cable. It was found that, depending on the equipment characteristics and the selected ground motion, the response of both equipment items could be strongly amplified (in relation to their stand-alone responses) when the cable has a small sag. To quantify the needed sag in order to avoid a large response amplification, the response ratios R_1 and R_2 (see their definitions in (2.21)) were computed as functions of the "interaction" parameter β defined as

$$\beta = \frac{\Delta \cdot L_0 / c_0^2}{s_0 / c_0 - 1} \tag{3.1}$$

In this formula, L_0 denotes the initial span of the cable, $c_0 = \sqrt{L_0^2 + H^2}$ is the initial chord length of the cable, in which H denotes the vertical separation between the supports, s_0 denotes the cable length under the initial static equilibrium conditions, and Δ denotes the maximum relative displacement between the stand-alone equipment items for the specified ground motion. Investigations with five different ground motions and several equipment configurations revealed that there is virtually no interaction between the equipment items when β is less than about 1. Based on this finding, the minimum required cable length to avoid the adverse interaction effect was determined to be

$$s_0 = c_0 + \frac{L_0}{c_0}\Delta \tag{3.2}$$

A procedure for estimating the maximum relative displacement Δ for a specified ground motion in terms of a specified response spectrum was described in our previous study.

After completion of our previous study, we came across a paper by Dastous and Pierre (1996) that described experimental results on flexible conductors subjected to imposed horizontal harmonic excitation either at one end or out-of-phase motions at both ends. The paper argued that these experiments were relevant to the equipment interaction problem, since the response of each equipment item in the connected system would tend to be essentially in first mode and, thus, well represented by an harmonic motion. This experimental study revealed a significant effect on the cable forces arising from the inertia of the cable mass in the vertical direction. Compared to the results based on quasi-static analysis, the horizontal force in the cable could be amplified by several orders of magnitude when end motions were applied at certain frequencies. Furthermore, significant compression forces developed in the cable, thus indicating the potential importance of the flexural rigidity. These results suggest that the effect of interaction in cable-connected equipment items can be greater than that indicated in our previous study, which ignored the inertia and flexural rigidity of the cable. Furthermore, the minimum required cable length given in (3.2) may not be sufficient to avoid the adverse effect of interaction, when inertia and flexural stiffness effects are present.

The aim of the present study is to re-examine the effect of interaction in cable-connected equipment items while accounting for the cable inertia and flexural rigidity. A finite element approach using truss and frame elements with a Lagrangian strain formulation is used to properly account for the geometric nonlinearity in the response. In order to validate the finite element model, first comparisons are made with our previous results for the catenary cable under static loads without including the flexural rigidity effect. Next, comparisons are made with the experimental results of Dastous and Pierre (1996) for a cable subjected to out-of-phase end motions. Reasonable qualitative agreement between the finite element and experimental results is obtained. In the final section of the chapter, the cable-connected equipment system is modeled and numerical time history analyses for the set of five earthquake ground motions from our previous study are carried out to determine the interaction effect. The results indicate that cable inertia and flexural rigidity have small influences for relatively taut cables. For cables with larger sag, the cable inertia and flexural rigidity tend to amply the interaction effect for certain ground motions. However, these amplifications are not as dramatic as anticipated from the discussion in the paper by Dastous and Pierre (1996). Evidently, the interaction between the equipment items and the cable in the case of an imposed ground motion significantly alters the dynamic response of the cable from that of a cable subjected to imposed end motions. While a definitive criterion for minimum slackness cannot be given at this time due to the limited number of ground motions studied, a preliminary recommendation is provided.

3.2 Section Properties of the Flexible Conductor

In order to develop a finite element model of the flexible conductor, it is necessary to describe the axial and flexural rigidity of the conductor at each section. As mentioned earlier, the flexible conductor is typically a cable made of braided strands of aluminum wire. The two ends of the cable usually are attached to the equipment items through welded aluminum connectors so that no unwrapping of the strands is possible. For the following discussion, we let n denote the number of strands and d denote the diameter of each strand.

When the cable is subjected to a tension force, it is conceivable that some tightening of the braids will occur before the full axial stiffness of the strands is developed. Likewise, when a segment of the cable is subjected to compression, opening of the braids or even buckling of the outer strands may occur. These imply that the axial stiffness of the cable for a small tension force or a large compression force could be smaller than the sum of the axial stiffnesses of the individual strands. We are not aware of any experiments that have investigated these effects. For the sake of simplicity, in the following analysis we ignore these effects and assume that the effective cross-sectional area of the cable throughout its length is a constant and is equal to the sum of cross-sectional areas of the strands, i.e.,

$$A = \frac{n\pi d^2}{4} \tag{3.3}$$

The flexural rigidity of the cable at a cross section is given by the product EI, where I denotes the section moment of inertia. The value of I depends on whether the strands at the cross section remain attached or slide with respect to one another as the cable is bent. The minimum value of the moment of inertia, denoted $I_{\min}$, is obtained by assuming that the strands freely slide against one another. In that case the moment of inertia is simply the sum of the moments of inertia of the individual strands and is given by

$$I_{\min} = \frac{n\pi d^4}{64} \tag{3.4}$$

In the actual system, significant friction forces may develop between the strands, particularly at locations where the cable has a strong curvature and is under tension. These friction forces may prevent sliding of some of the strands and, hence, a larger effective moment of inertia may develop. The maximum value of I is obtained when all strands remain attached and is given by

$$I_{\max} = \sum_{i=1}^{n} \frac{\pi d^2}{4}\left(\frac{d^2}{16} + y_i^2\right) \tag{3.5}$$

where y_i is the distance of the i-th strand from the neutral axis, as shown in Figure 3.1. The actual moment of inertia of the cable is somewhere between the above two extremes.

Furthermore, the moment of inertia would tend to vary along the cable depending on the cable curvature and the force magnitude. Unfortunately the two bounding values in (3.4) and (3.5) are widely apart for typical cables used in the power industry. For example, for a 1796-MCM cable consisting of 61 strands in 5 layers, the upper bound in (3.5) is about 80 times the lower bound in (3.4). Based on experiments conducted by BC Hydro in the 1990's, a recent IEEE guideline (IEEE 1999) recommends the use of the approximation

$$I \cong (1+N)I_{\min} \tag{3.6}$$

for short length aluminum conductors, where N denotes the number of layers of strand. In the following analyses, unless stated otherwise, this approximation is employed. Furthermore, it is assumed that the moment of inertia remains constant throughout the length of the cable at all times. A parametric study is performed to investigate the sensitivity to the assumed value of the moment of inertia. Unfortunately, the large uncertainty associated with this characteristic of the cable will prevent us from making predictions of the cable response that are in close quantitative agreement with the experimental results of Dastous and Pierre.

For the subsequent analysis, it is also necessary to assign a value to the Young's modulus. IEEE guidelines (IEEE 1999) recommend $E = 5.72\times10^6\,\mathrm{N/cm^2}$ ($=8.30\times10^6$ psi) for all-aluminum conductors. Unless stated otherwise, this value is used in the subsequent analyses.

3.3 Finite Element Model of the Cable

The dynamic analysis of a taut cable with large displacements and rotations is a highly nonlinear elastodynamic problem that has no known analytical solution. Even a numerical solution of this problem is challenging. During the dynamic response, whenever the cable is fully stretched the axial stiffness dominates the cable behavior and significant high-frequency effects are generated. With finite element spatial discretization, these high frequencies may give rise to errors and instability in the numerical computations (Armero and Romero, 1999). Under these conditions, the Newmark time-integration algorithm, which we had successfully used in our previous study with the catenary cable (using an exact expression of the cable stiffness, but neglecting inertia and flexural rigid-

ity effects), does not lead to stable, accurate results. Furthermore, the classical Newmark family of algorithms and its variants generally fail to conserve total angular momentum for nonlinear elastodynamics. This is a significant shortcoming, since the angular momentum can have an important influence on the cable dynamics. An algorithm that preserves the conservation laws is presented by Simo et al. (1992). A modified version of this algorithm, by controlling parameters, introduces numerical damping to stabilize the computations while slightly compromising on the conservation of energy. Our experience showed that this algorithm with parameter values $\alpha = 0.55$, $\beta = 0.5$ and $\gamma = 1$ (see Simo et al., 1995, for the definitions of these parameters) and time step $\Delta t = 0.0005$s works successfully for the cable dynamics problem. Hereafter we call this the damped energy-conserving (DEC) algorithm. We note that parameter values $\alpha = 0.5$, $\beta = 0.5$ and $\gamma = 1$ correspond to the energy-conserving algorithm with no numerical damping.

As a test of this algorithm, Figure 3.2 shows plots of the computed and exact responses of two single-degree-of-freedom oscillators subjected to a step loading, as normalized by the corresponding static responses. The top plot is for an oscillator with 5Hz frequency and 2% damping ratio. For this oscillator, the solution based on the DEC algorithm coincides with the exact solution. The bottom plot is for an oscillator with 50Hz frequency and 2% damping ratio. Due to the numerical damping, the solution based on the DEC algorithm in this case shows a slightly faster decay than the exact solution. Since such high frequencies have no significant contribution to the response of the cable-connected systems of interest, we conclude that the DEC algorithm with the parameters described above produces accurate results for the purpose of the present study.

Two finite element models of the cable are considered in this study. The first model idealizes the cable with 100 truss elements having the same cross section as the cable. This model is intended to idealize the catenary cable under static conditions. The second model idealizes the cable with 100 frame elements having the same cross section properties as the cable. This model is intended to account for both the cable inertia and flexural rigidity. Full account of the geometric nonlinearity arising from large displacements and large rotations of the cable is made in the analyses by using a Lagrangian strain formula-

tion. The finite element program FEAP, developed by Taylor (1998), and the DEC algorithm, described above, are used for the analyses.

3.4 Comparison of the Finite Element Model with the Catenary Cable

Before proceeding with dynamic analysis, we investigate the responses of a cable under static loading and compare them with the theoretical results obtained for the catenary cable in our previous study. The cable consists of 271 strands in 10 layers, each strand having a diameter of 0.3038cm so that the total cross-sectional area of the cable is $A = 19.6\,\text{cm}^2$. The moment of inertia, computed using (3.6), is $I = 1.246\,\text{cm}^4$. The weight per unit length of the cable is $w = 52.2\,\text{N/m}$. The cable is assumed to have an initial length of 6m, when it is held over two supports 5m apart horizontally with zero vertical separation between the supports. To be consistent with our previous results for the catenary cable, $E = 7.0\times10^6\,\text{N/cm}^2$ is used for the present analysis. Using each finite element model, the horizontal force T in the left support is computed as the right support is moved quasi-statically in the horizontal direction. The normalized force $T/(wL)$, in which L denotes the current span length, is plotted as a function of the slackness $s/L-1$. Note that s denotes the actual length of the cable at each configuration, accounting for the extensibility of the cable.

Figure 3.3 shows a comparison of the horizontal force versus slackness curve for the catenary cable and the finite element model with truss elements. Recall that this model does not account for the flexural rigidity of the cable and, hence, it closely idealizes the catenary cable conditions. The results from the two analyses are virtually identical over a broad range of slackness values, thus demonstrating the accuracy of the finite element model.

It is important to note that a cable having flexural rigidity and held between two fixed supports is a statically indeterminate system. This is because the horizontal support force for such a system cannot be determined from equilibrium considerations alone. For the present analysis with the finite element model with frame elements, we have assumed that the cable is initially straight. After fixing both ends, the gravity load is applied and then the right support is moved horizontally towards the left support. Due to the flexural

rigidity, the shape of the cable is considerably different from the catenary shape. This can be seen in Figure 3.4, which shows the two shapes when the span is 5m. Figure 3.5 compares the normalized horizontal support force $T/(wL)$ as a function of the slackness $s/L-1$ for the catenary cable and the finite element model with frame elements. Due to the flexural rigidity, the support force is in compression for slackness values greater than 0.00275. It is seen that the horizontal force-slackness relationship for the cable with flexural rigidity is similar to that of the catenary cable but shifted downward in the vertical direction. It is of course possible to consider an initially curved cable. In that case, the horizontal force-slackness curve would tend to shift vertically upward so that the zero force point would occur at a slackness value at which no horizontal support force is necessary to hold the cable in its position. This indeterminacy of the initial shape of the cable with flexural rigidity is one more reason why it will not be possible to quantitatively match the experimental results of Dastous and Pierre, as described in the following section.

3.5 Comparison with Experimental Results of Dastous and Pierre

In this section, we compare finite element predictions of the cable response with the experimental results of Dastous and Pierre (1996). Two different cables used by Dastous and Pierre are considered for this analysis. These are code named 1796-MCM and 4000-MCM cable conductors. Their properties are listed in Table 3.1.

As mentioned earlier, our finite element model assumes constant cross-sectional area and moment of inertia along the cable. This is an approximation, since during the experiments the actual effective cross-sectional properties vary along the cable and in time, depending on whether the strands slide against each other or remain attached. It is practically impossible to predict the damping in the cable, which can be significant when the cable strands slide against one another under friction forces. An additional uncertainty has to do with the initial shape of the cable in the experiments. As mentioned earlier, the cable with flexural rigidity and fixed ends is a statically indeterminate system. Unfortunately the paper by Dastous and Pierre did not describe how the cables were shaped and put in their positions before starting the tests. In the analysis in this section, we have used

the following steps to set the initial shape of the cable: A straight cable of the specified length is modeled with both its ends fixed. The weight of the cable is applied as dead load and the cable is allowed to deform. One end of the cable is then moved toward the other end until the specified initial span length used in the experiment is achieved. The deformed shape of the cable in this position is computed. This shape is considered to be the initial shape of the cable without any internal forces. The cable with this shape is now placed on the supports with fixed ends and the reaction forces under the dead load are computed. Note that this will generate an initial horizontal tension force at each support. As described below, because of the uncertainty in the initial conditions of the cable in the experiments, this horizontal force as well as the cable sag will be somewhat different from the initial conditions reported in the experiments by Dastous and Pierre.

Because of the unavoidable differences between the finite element model and the experimental setup used by Dastous and Pierre, it is not possible to expect that the finite element predictions will closely match the experimental results. Hence, instead of a quantitative agreement, we seek to make a qualitative comparison between the theoretical predictions and the experimental results. In particular, we aim at verifying the large amplifications in the horizontal cable force under harmonic excitations, which were observed by Dastous and Pierre. We also carry out parameter variations in order to determine the importance of the flexural rigidity of the cable and the effect of energy dissipation due to friction forces in the cable.

3.5.1 Experiment 1: Sine-Start Test

In this experiment, a 1796-MCM conductor cable of length 5.52m and span length 5.19m was subjected to out-of-phase harmonic support motions having an amplitude of 0.02m and a frequency of 3.5Hz. Figure 3.6, taken from the paper by Dastous and Pierre (1996), shows the time history of the horizontal support force measured during the experiment. We note that the initial horizontal force is around 40N in tension. During the dynamic excitation, the horizontal cable force at each support fluctuates, taking on both positive (tension) and negative (compression) values. The maximum tension force achieved is approximately 400N, whereas the maximum compression force achieved is approxi-

mately 260N. It is important to note that under quasi-static conditions, the horizontal cable force would have varied only a small amount from its initial value of 40N. It is clear, therefore, that the cable inertia and flexural rigidity significantly amplify the cable force.

In the finite element analysis, we apply out-of-phase, harmonic horizontal support displacements of the form

$$u(t) = [1 - \exp(-2\pi\alpha f t)]A\sin(2\pi f t) \tag{3.7}$$

where $A = 0.02\,\text{m}$ is the amplitude and $f = 3.5\,\text{Hz}$ is the frequency. The term inside the square brackets is a loading ramp that is included to avoid numerical instability caused by non-zero initial conditions. For the present analysis, $\alpha = 0.1$ is used. Note that the term inside the square brackets approaches unity in a few cycles and the motion becomes purely harmonic. The Young's modulus of the cable is assumed to be the IEEE-recommended value of $E = 5.72\times10^6\,\text{N/cm}^2$ and the moment of inertia is computed from (3.6). No damping in the cable is assumed for this analysis.

Figure 3.7 shows a plot of the time history of the horizontal cable force as predicted by the finite element model. The overall features of the response are similar to those observed for the experimental result shown in Figure 3.6. In particular, the response shows large amplification of the horizontal cable force due to the inertia and flexural rigidity effects. We also note that the cable experiences significant compression forces. Whereas the initial cable force is 83N, the maximum tension force achieved is 265N and the maximum compression force achieved is 97N. These values are significantly different from the values observed in the experiment. As mentioned earlier, the reasons for this discrepancy may include the assumed values of the cable moment of inertia and damping, as well as the assumed initial shape of the cable. More detailed information about the conditions of the experiment as well as a more refined model of the cable that accounts for the variability of stiffness and damping properties along the length and in time are necessary if a close agreement between the theoretical and experimental results is to be achieved. Nevertheless, the above comparison shows that the large amplification of the cable force, including compression forces, observed by Dastous and Pierre for cables

subjected to harmonic support motions is realistic and is predicted by the finite element model.

The differences observed between the experimental and theoretical results suggests that the cable response might be sensitive to the assumed values of the moment of inertia and damping. To explore the sensitivity with respect to the moment of inertia, we repeat the above analysis while varying the moment of inertia in the range $I = I_{min}$ to $I = 12I_{min}$, where I_{min} is as given in (3.4). It is assumed that the cable has zero damping. The maximum horizontal tension and compression forces, after 3 seconds of motion, are plotted in Figure 3.8 as a function of the ratio I / I_{min}. The maximum responses are found to have mild dependence on the moment of inertia, except in the region of $I < 3I_{min}$. For this value of the moment of inertia, the maximum forces in both tension and compression side are sharply amplified. Evidently, for this value of the moment of inertia the cable is in some sort of resonance with the harmonic excitation. A similar but much smaller resonance effect is noticeable around the value $I = 9I_{min}$. Unfortunately we have no means of knowing what value of I best reflects the conditions of the cable tested by Dastous and Pierre.

In the above analysis, the cable was assumed to have no damping. However, as mentioned earlier, there can be significant dissipation of energy due to sliding of the cable strands against one another under the action of friction forces. Such damping would of course depend on the cable force and curvature at each location and, hence, would vary along the cable and in time. Noiseux (1992) has proposed a hysteretic damping model for cables, which is reported to agree well with experimental results. Unfortunately, implementation of this class of models in FEAP was not possible within the time scope of this project. Instead, we attempted to investigate the sensitivity to damping by using a uniformly distributed viscous damping model, which is already available in FEAP. In this model, the distributed viscous damping is achieved by placing a dashpot at each node of the finite element model, as shown in Figure 3.9. While this model may not be realistic in describing energy dissipation by internal friction forces, it provides a preliminary estimate of the importance of the damping effect on the dynamic response of cables.

For the numerical study, $I = 6I_{min}$ is assumed and the damping coefficient is varied over the range of zero to 100Ns/m^2 per unit length of the cable. To provide a scale for this damping value, it is noted that when the damping value of 100Ns/m^2 is used, the maximum damping force achieved in the cable under the harmonic motion with frequency 3.5Hz is approximately 111N/m. This can be compared with the maximum inertia force, which is approximately 58N/m, and the weight per unit length of the cable, which is 24.6N/m. Thus, while 100Ns/m^2 might be an unrealistically high value for the distributed damping, values around 10-50Ns/m^2 might be quite realistic. Figure 3.10 shows a plot of the maximum horizontal tension and compression forces, after 3 seconds of motion, as a function of the distributed damping coefficient. It is seen that the maximum horizontal forces in the cable increase with increasing damping. This is because the excitation is an imposed support displacement and, naturally, larger forces are necessary to counter the damping effect. Unfortunately we have no means of knowing what value of the damping coefficient best represents the conditions present during the tests by Dastous and Pierre. Nevertheless, this study shows that some of the discrepancy between our theoretical predictions and the experimental results could be attributed to the effect of damping in the cable. We believe further study on the effect of damping in conductor cables is highly desirable.

3.5.2 Experiment 2: Sine-Sweep Test

In this experiment by Dastous and Pierre (1996), a 4000-MCM conductor cable was subjected to out-of-phase harmonic support motions of amplitude 0.02m and frequencies in the range 0.5-5Hz. The cable has a length of 5.64m and an initial span length of 5.35m. Figure 3.11, taken from the paper by Dastous and Pierre, shows plots of the peak horizontal tension and compression forces at the support as functions of the excitation frequency. It is seen that the maximum tension and compression forces vary by several orders of magnitude, depending on the excitation frequency. A peak appears to occur in the maximum tension force at around 4.3Hz, which could be due to some sort of resonance.

For the finite element analysis, the cable is assumed to have constant cross-sectional area and moment of inertia as given by (3.3) and (3.6), respectively. Zero damping is as-

sumed. The support motions are taken to be out of phase and described by (3.7) with the frequency f varying from 0.5 to 5Hz. The resulting maximum tension and compression forces, after 3 seconds of response at each frequency, are plotted in Figure 3.12 as functions of the excitation frequency. The overall features of these plots are similar to the experimental results shown in Figure 3.11. The maximum tension and compression forces show variations by several orders of magnitude, depending on the excitation frequency. Peaks on both tension and compression sides appear at around 2.7Hz frequency, possibly indicating some sort of resonance effect. A similar effect may be present at around 4.6Hz frequency, where the peak responses appear to grow unboundedly. The differences between the experimental and analytical results can be attributed to our assumed values of the cross-sectional area, moment of inertia and damping, and the assumed initial shape of the cable. Unfortunately we have no means of knowing which values of these parameters better represent the experimental conditions. In spite of the quantitative discrepancy between the experimental and analytical results, this study shows that indeed extremely large forces can develop in the cable when it is subjected to harmonic support motions.

3.6 Cable-Connected Equipment Items

In this section we study the effect of flexural rigidity and inertia of the cable conductor on the interaction between two connected equipment items. Figure 3.13 shows a schematic description of the connected system. For the conductor, we consider the aluminum cable investigated in our previous study, which consists of 271 strands in 10 layers, each strand having a diameter of 0.3038cm. The cross-sectional area is $A = 19.6\,\text{cm}^2$, the moment of inertia computed from (3.6) is $I = 1.246\,\text{cm}^4$, the Young's modulus is $E = 7.0\times10^6\,\text{N/cm}^2$, and the weight per unit length of the cable is $w = 52.2$ N/m. First, we consider the case when the cable has an initial length $s_0 = 5.0332\,\text{m}$ and an initial span of $L_0 = 5\,\text{m}$. For the catenary cable, this corresponds to a sag to span ratio of 0.05. This is a rather taut cable and represents perhaps an extreme case. We select it to highlight the effect of interaction and the highly nonlinear nature of the response. Subsequently, we vary the length of the cable in order to investigate the interaction effect for varying cable slackness values. The cable is assumed to connect two equipment items having masses

$m_1 = 1000\,\text{kg}$ and $m_2 = 500\,\text{kg}$, an attachment configuration such that $l_1/m_1 = l_2/m_2 = 1$, stand-alone frequencies $\omega_1 = 2\pi$ rad/s and $\omega_2 = 10\pi$ rad/s, and damping ratios $\zeta_1 = \zeta_2 = 0.02$.

3.6.1 Effect of Flexural Rigidity, Inertia and Damping of the Cable on the Equipment Response

We examine the responses of the above system to the N-S component of the Newhall record of the 1994 Northridge earthquake. The accelerogram of this ground motion is shown in Figure 3.14. Figure 3.15 shows the stand-alone responses of the two equipment items calculated by finite element analysis using the DEC algorithm. The calculated maximum stand-alone displacements are $\max|u_{10}(t)| = 0.3358$m and $\max|u_{20}(t)| = 0.0159$m, respectively, and the maximum relative separation between the two stand-alone equipment items is $\Delta = \max[u_{20}(t) - u_{10}(t)] = 0.3163\,\text{m}$. These estimates are slightly different from the values computed in our previous study (0.3375m, 0.0162m and 0.3163m, respectively), which were based on the Newmark algorithm.

Figure 3.16 shows displacement responses of the two equipment items when both the flexural rigidity and inertia of the cable are neglected. These results are from our previous study and were computed using the Newmark algorithm together with an analytical expression of the catenary cable stiffness. Note that the scales used in Figure 3.16 (and the subsequent five figures) are different from the scales used in Figure 3.15. The maximum responses in Figure 3.16 are $\max|u_1(t)| = 0.500$m and $\max|u_2(t)| = 0.124\,\text{m}$, respectively, which are much larger than the peak stand-alone responses given in the preceding paragraph. It is also noticeable that the response is asymmetric with larger peaks in the equipment responses occurring in the direction of the cable. Unfortunately, using time steps of reasonable size, it was not possible to generate similar results with the finite element model because the numerical integration did not converge when the flexural rigidity and inertia of each frame element were set to zero or small values.

To see the effect of the cable inertia alone, we use the finite element model with the frame elements but set the section moment of inertia of each element to a negligibly small value. The displacement responses for the two equipment items in this system are shown in Figure 3.17. The peak absolute responses now are $\max|u_1(t)| = 0.444\text{m}$ and $\max|u_2(t)| = 0.105\text{m}$, respectively. These values are smaller than the peak values for the case without the inertia effect in Figure 3.16. However, the response curves show stronger asymmetry. Evidently, for this cable, the inertia effect tends to reduce the peaks in the equipment responses, but accentuates the asymmetry of the response. Slightly longer periods in the equipment responses in Figure 3.17 are detectable, when compared with the responses in Figure 3.16 for the cable without mass. These are due to the added mass of the cable.

To see the effect of the cable flexural rigidity alone, we use the finite element model with the frame elements but set the mass of each element to zero, while representing the weight as a dead load. The displacement responses for the two equipment items in this case are shown in Figure 3.18. The peak absolute responses now are $\max|u_1(t)| = 0.422\text{m}$ and $\max|u_2(t)| = 0.130\text{m}$, respectively. In comparison to the case without cable inertia and flexural rigidity shown in Figure 3.16, the peak absolute response of the lower-frequency equipment item is smaller, while that of the higher-frequency equipment item is larger. This agrees with the finding in our previous study that a larger stiffness of the connecting element tends to increase the response of the higher-frequency equipment item and decrease that of the lower-frequency equipment item. Furthermore, with the cable flexural rigidity included, the response of the system is less asymmetric. This is due to increased "beam effect" in the cable. Finally, in the tail region, the response time histories show shorter periods than in Figure 3.16 because of the added flexural stiffness of the cable. In the region of strong response, the cable stiffness is dominated by its axial stiffness, which is the same for both cases, and as a result the predominant period of the response does not change.

Now we consider the system with both the flexural rigidity and inertia of the cable included. Figure 3.19 shows the displacement responses of the two equipment items for

this case. The peak absolute responses now are $\max|u_1(t)| = 0.393\text{m}$ and $\max|u_2(t)| = 0.121\text{m}$, respectively. These peak values are slightly smaller than the values for the previous case, which included only the flexural rigidity of the cable. Evidently, for this cable, cable inertia tends to reduce the peak responses with or without the effect of flexural rigidity. This result, however, may not apply to other cable/equipment configurations or ground motions. As we will see, it is possible that resonance-type effects arise in the cable response leading to larger responses of the equipment items.

In the above analysis, the cable was assumed to have zero damping. As discussed earlier, slippage of the cable strands under friction forces could dissipate significant amounts of energy. To explore this effect, finite element analysis with the frame element was carried out, while including the flexural rigidity and inertia of the cable as well as a uniformly distributed viscous damping with a coefficient of 10Ns/m^2. Figure 3.20 shows the displacement responses of the two equipment items for this case. The peak absolute responses now are $\max|u_1(t)| = 0.355\text{m}$ and $\max|u_2(t)| = 0.112\text{m}$, respectively. As expected, these peak values are smaller than those without cable damping shown in Figure 3.19.

3.6.2 Effect of Interaction in the Cable-Connected System

To determine the effect of interaction on equipment items in a cable-connected system, we compute and plot the response ratios R_1 and R_2 for the system described in the previous section for five different ground motions, which were described in our previous study (Der Kiureghian et al. 1999). All system parameters are kept constant, with the exception of the initial cable length s_0, which is varied to cover a range of the interaction parameter β defined in (3.1). Since the vertical separation between the support points is zero, we have $c_0 = L_0$ and the interaction parameter simplifies to

$$\beta = \frac{\Delta}{s_0 - L_0} \tag{3.8}$$

where $L_0 = 5\,\text{m}$ is the initial span and $\Delta = \max[u_{20}(t) - u_{10}(t)]$ is the maximum relative separation between the two stand-alone equipment items for the selected ground motion.

Figure 3.21 shows plots of the response ratios R_1 and R_2 as functions of the interaction parameter β for the five selected ground motions, where the effects of flexural rigidity and inertia of the cable are neglected. These results are copied from our previous study. As we had discussed, there is virtually no amplification of the equipment responses for values of β less than 1. Based on this finding, in our previous report we recommended a cable length based on $\beta = 1$.

Figure 3.22 shows plots of the response ratios R_1 and R_2 as functions of the interaction parameter β for the five selected ground motions, where we have included the effects of flexural rigidity and inertia of the cable. For $\beta > 1$, significant amplification of the equipment responses occurs similar to that in Figure 3.21. The response ratios for a specific ground motion and β value in the two figures are not identical, but the overall features are the same. For $\beta < 1$, Figure 3.22 shows small amplifications of the equipment responses, which are absent in Figure 3.21. In particular, for the TabasLN record, a local peak of 1.36 appears in the response ratio R_1 around $\beta = 0.9$, which may be due to some sort of resonance for this particular cable configuration and input ground motion. This is similar to the resonance-like behavior observed in the experiments by Dastous and Pierre (1996) and our own analytical results in Section 3.5.

Based on the results shown in Figure 3.22, it appears that the recommendation of selecting a cable length for which $\beta \leq 1$ is still valid. This corresponds to a length of $s_0 > L_0 + \Delta$ for a cable with no vertical offset between its supports. However, in light of possible resonance-type amplification of the cable, it is advisable to design the equipment items for forces slightly (about 50%) higher than the forces obtained for the stand-alone configuration. It should be emphasized that this recommendation is based on a rather limited study. Further investigations are advisable to ascertain the range of applicability of this rule for different types of ground motions and cable/equipment configurations.

Table 3.1. Properties of conductor cables used in the experiments by Dastous and Pierre

Property	1796-MCM	4000-MCM
material	all aluminum	all aluminum
Young's modulus	5.72×10^6 N/cm^2	5.72×10^6 N/cm^2
number of layers	5	10
number of strands	61	271
strand diameter	0.436 cm	0.309 cm
overall conductor diameter	3.92 cm	5.86 cm
cross section area	910 mm^2	2027 mm^2
mass per unit length	2.509 kg/m	5.698 kg/m

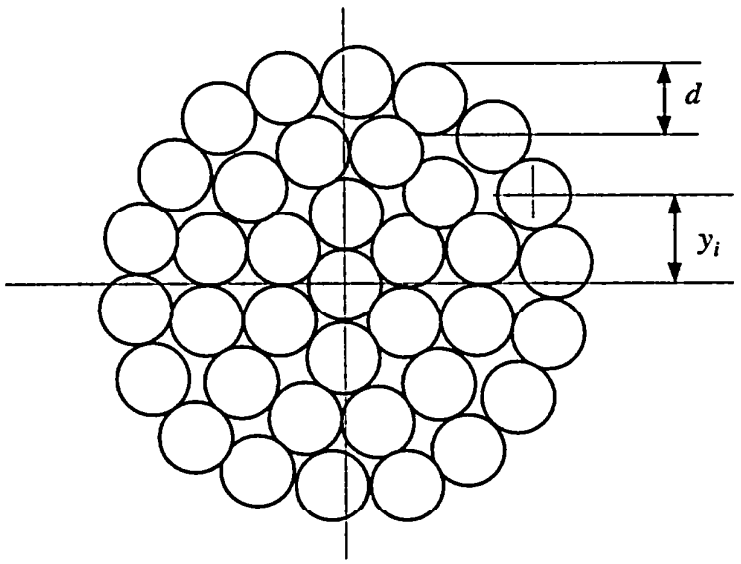

Figure 3.1 Cross section of a conductor cable made of braided wire strands

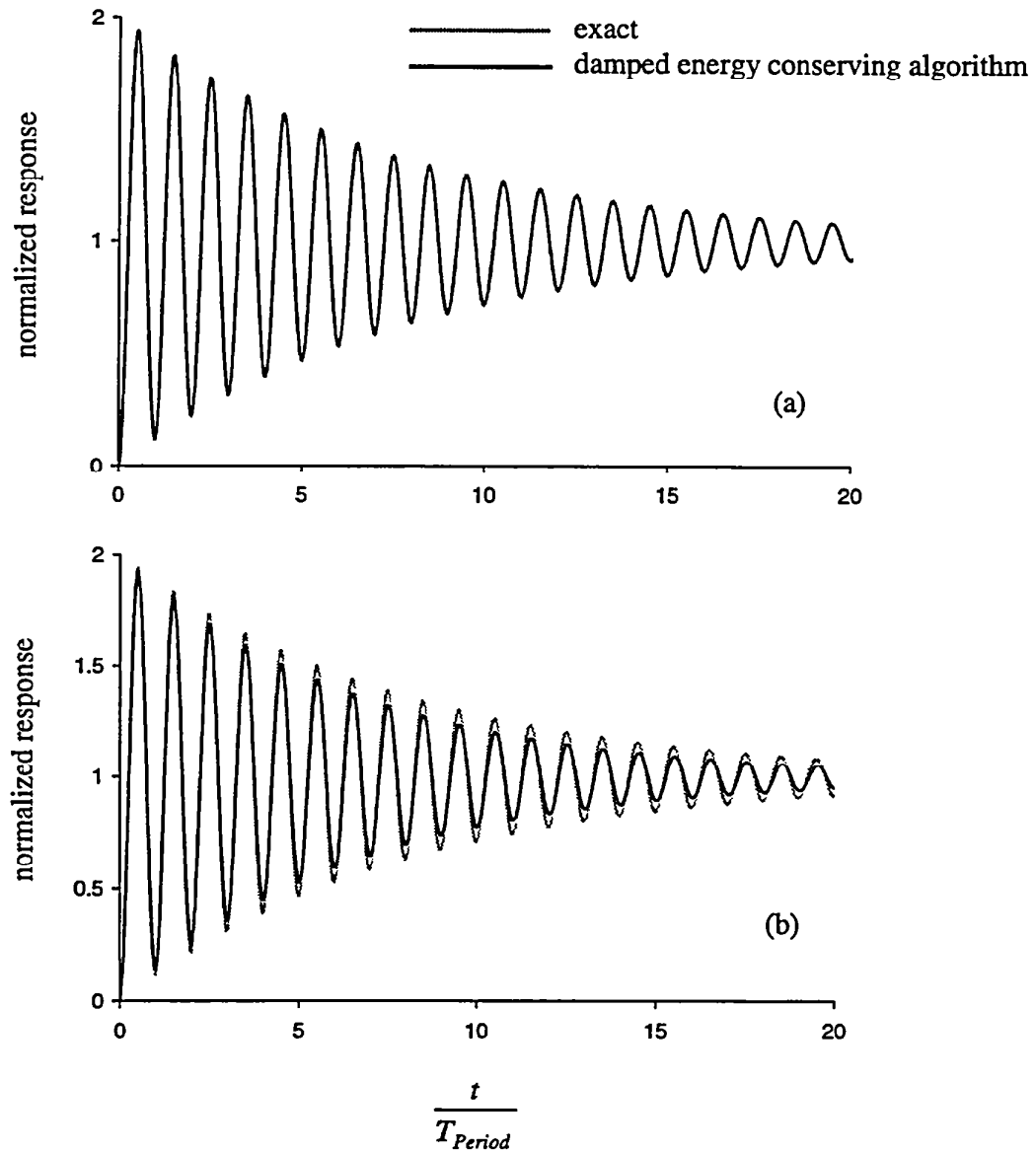

Figure 3.2 Comparison of exact and computed normalized responses of an oscillator to step loading: (a) oscillator with 5Hz frequency and 2% damping ratio, (b) oscillator with 50Hz frequency and 2% damping ratio

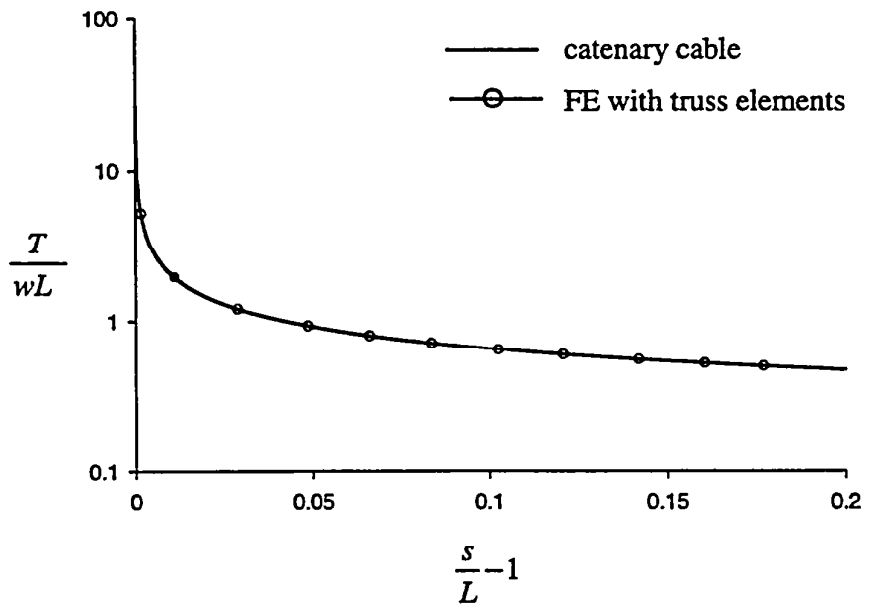

Figure 3.3 Horizontal force versus slackness for a cable with no flexural rigidity under its own weight

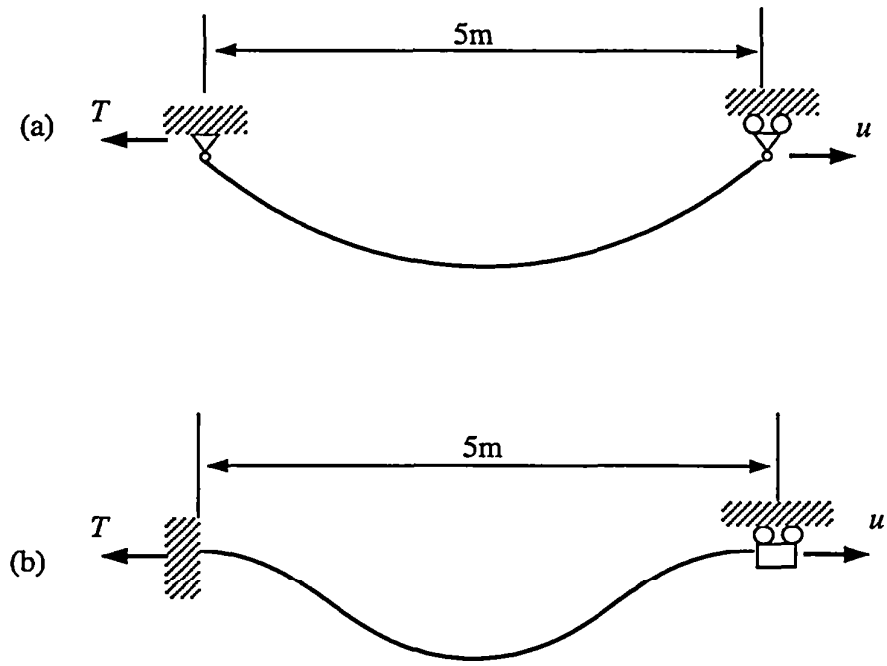

Figure 3.4 Shapes of cables of length $s_0 = 6\,\mathrm{m}$: (a) without flexural rigidity, (b) with flexural rigidity

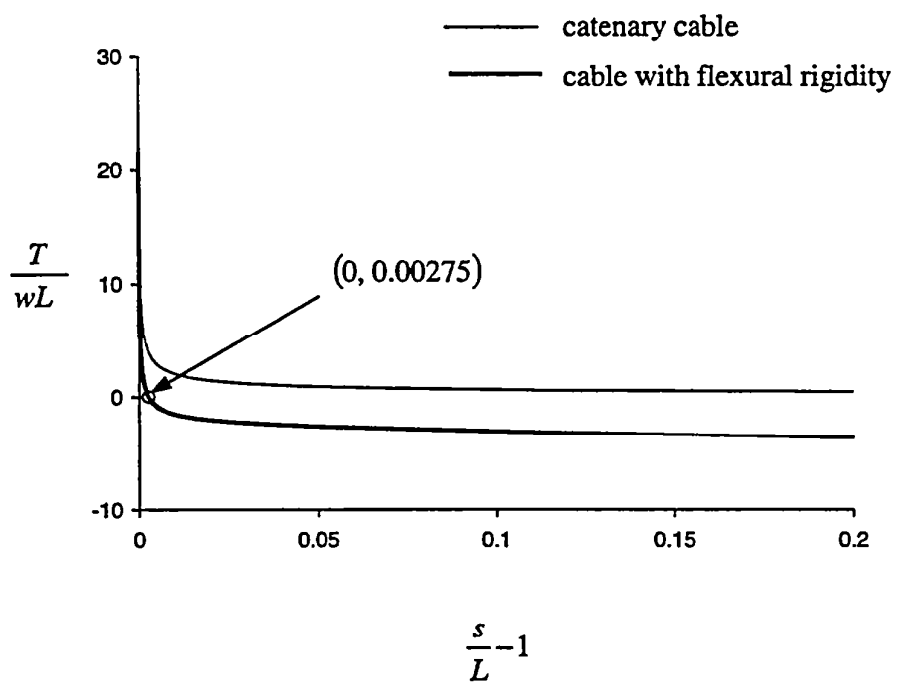

Figure 3.5 Comparison of horizontal force-slackness relationship for a catenary cable and a cable with flexural rigidity

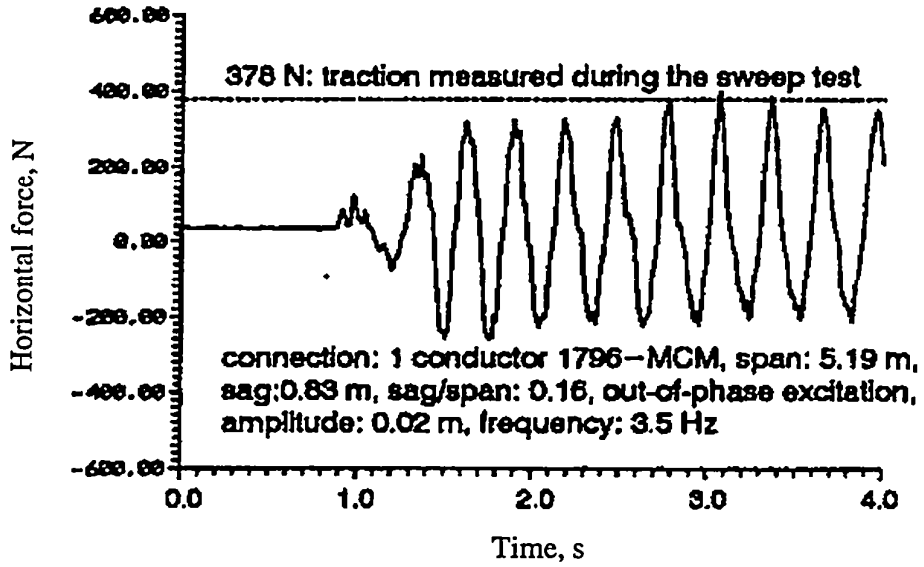

Figure 3.6 Time history of horizontal force at the cable support (after Dastous and Pierre, 1996)

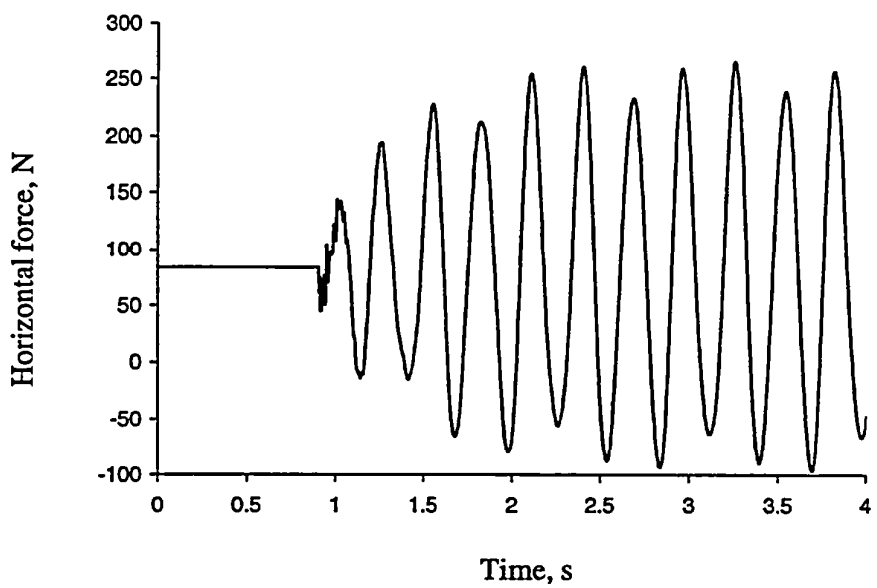

Figure 3.7 Time history of horizontal force at the cable support as predicted by the finite element model

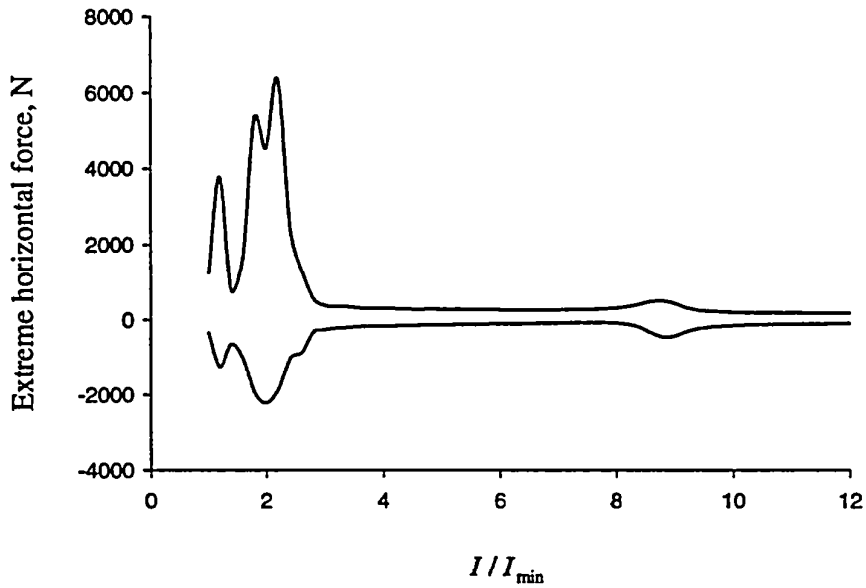

Figure 3.8 Sensitivity of the horizontal force at the support to cable moment of inertia

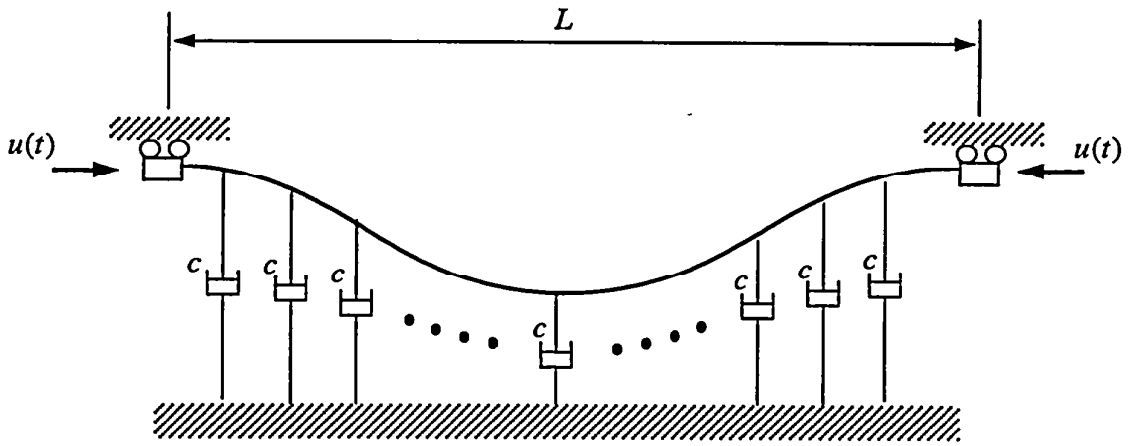

Figure 3.9 Finite element model of distributed viscous damping

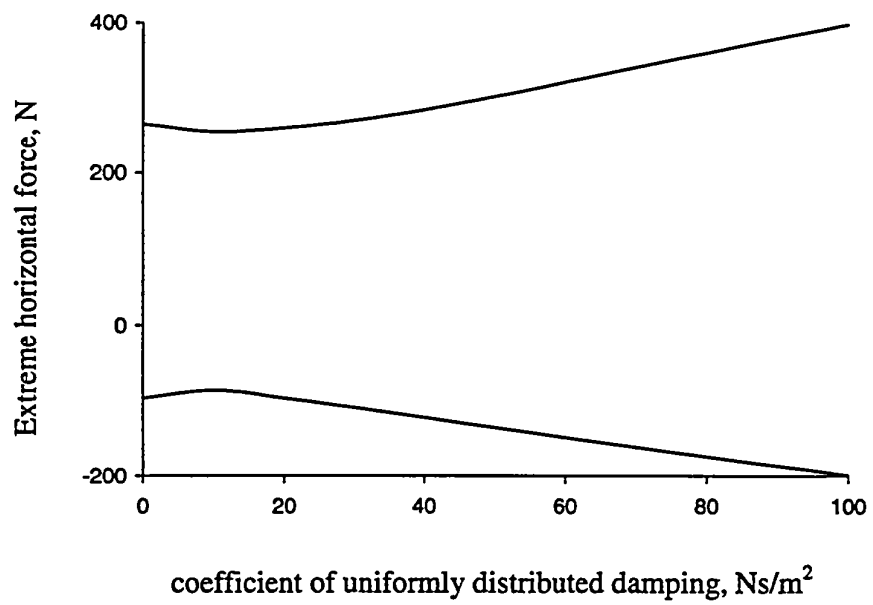

Figure 3.10 Sensitivity of the horizontal force at the support to cable damping

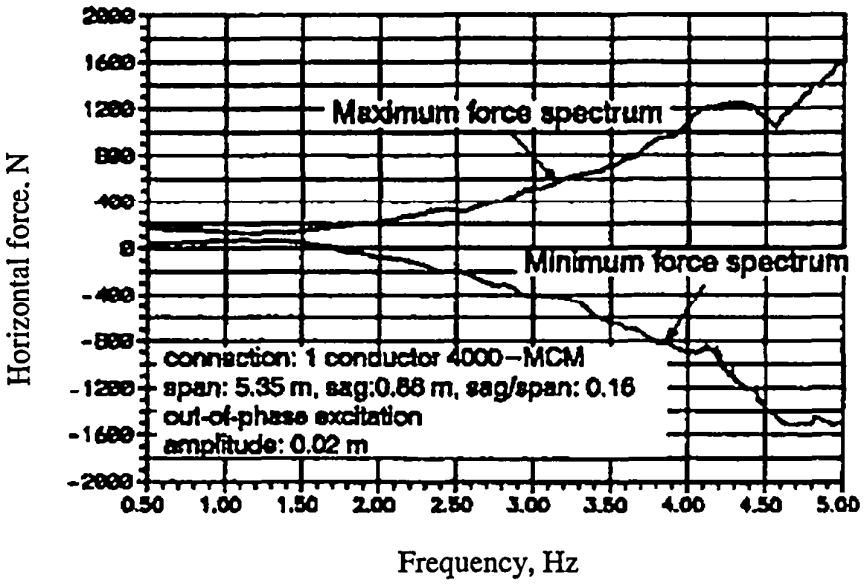

Figure 3.11 Horizontal support force spectrum obtained from the experiment (after Dastous and Pierre, 1996)

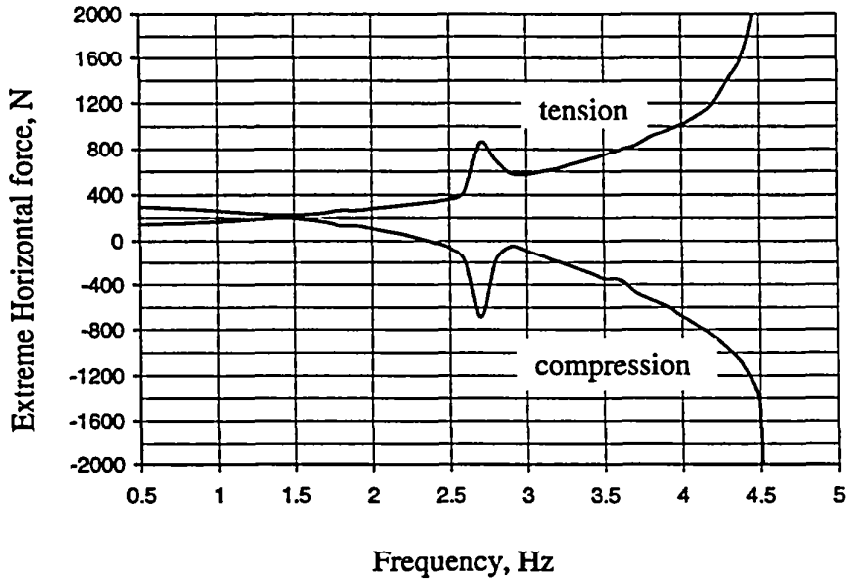

Figure 3.12 Horizontal support force spectrum predicted by the finite element model

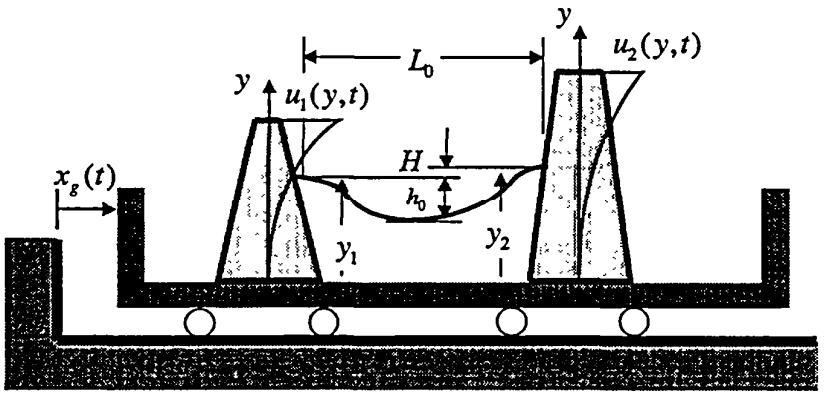

Figure 3.13 Cable-connected equipment items

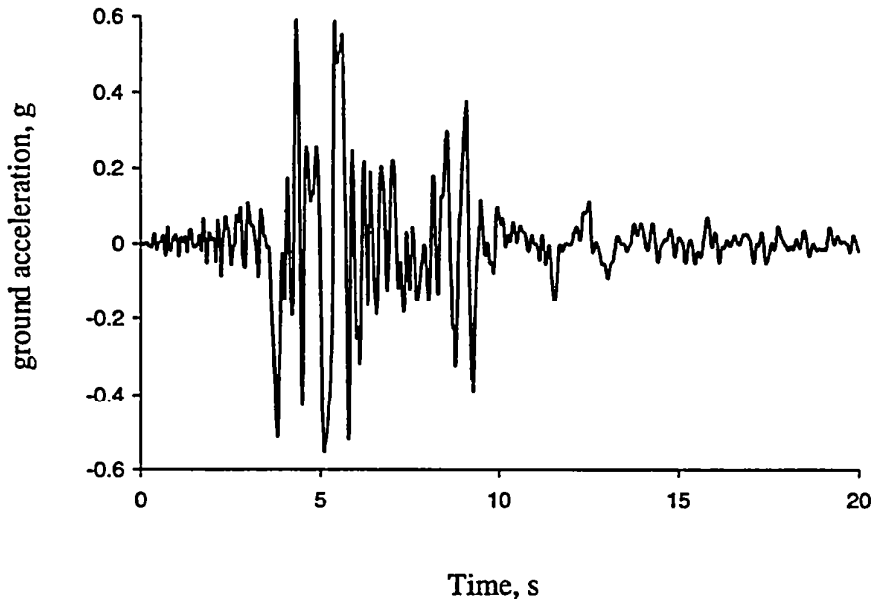

Figure 3.14 N-S component of Newhall record, 1994 Northridge Earthquake

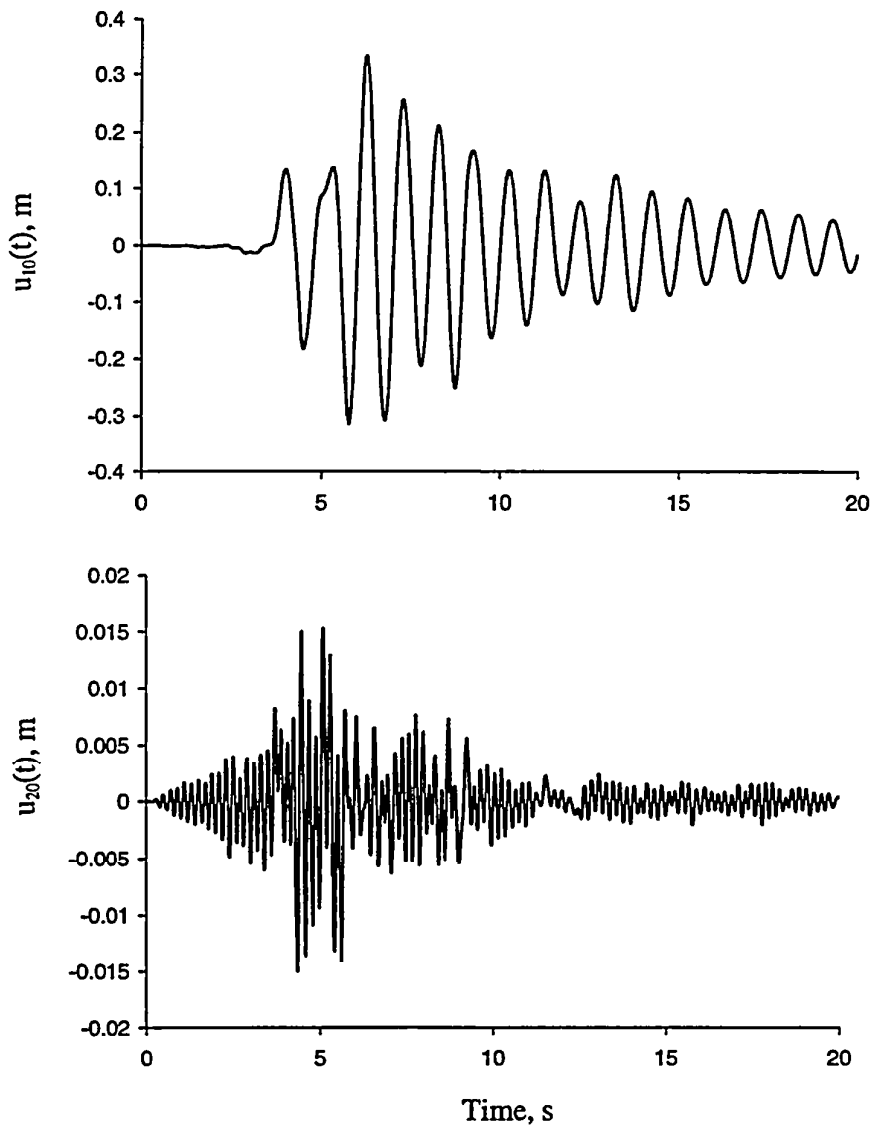

Figure 3.15 Displacement time histories of the stand-alone equipment items calculated by the damped energy-conserving algorithm

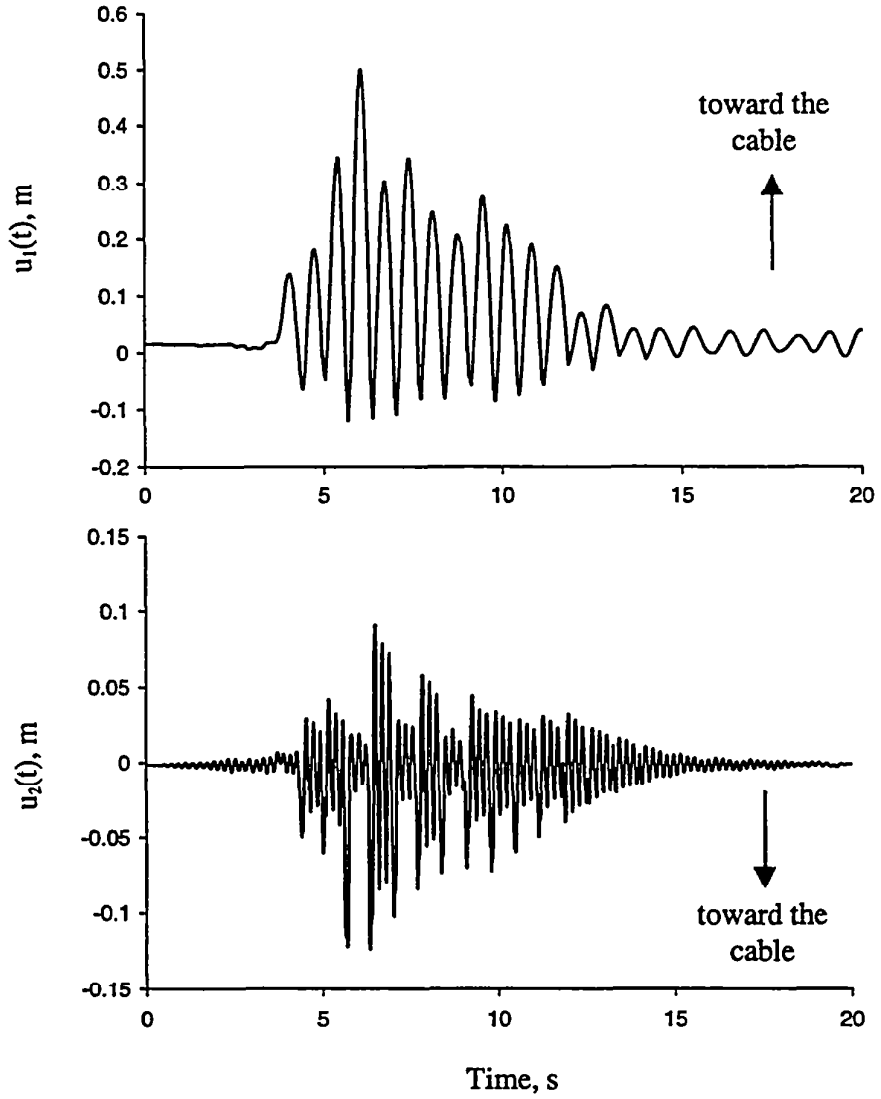

Figure 3.16 Displacement time histories of equipment items in the connected system, using catenary cable formulation and neglecting flexural rigidity, inertia and damping of the cable

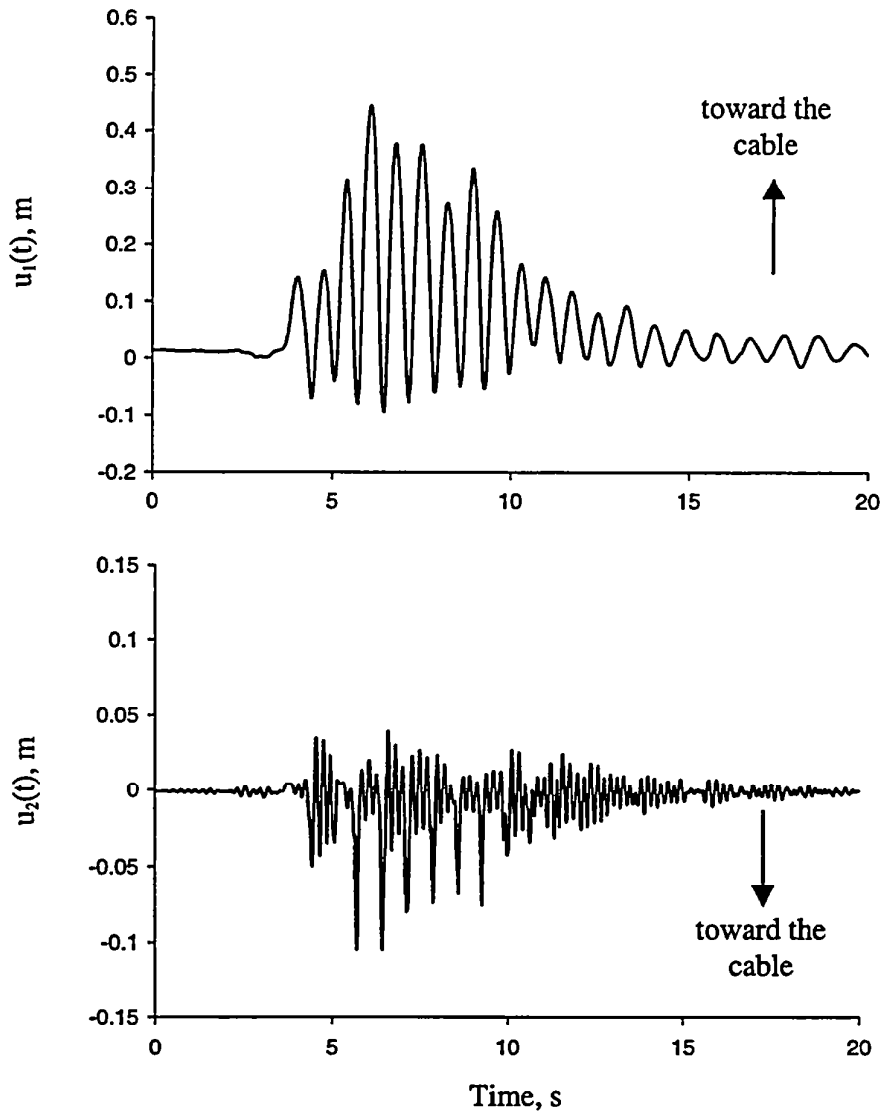

Figure 3.17 Displacement time histories of equipment items in the connected system, including the inertia effect but neglecting the flexural rigidity and damping of the cable

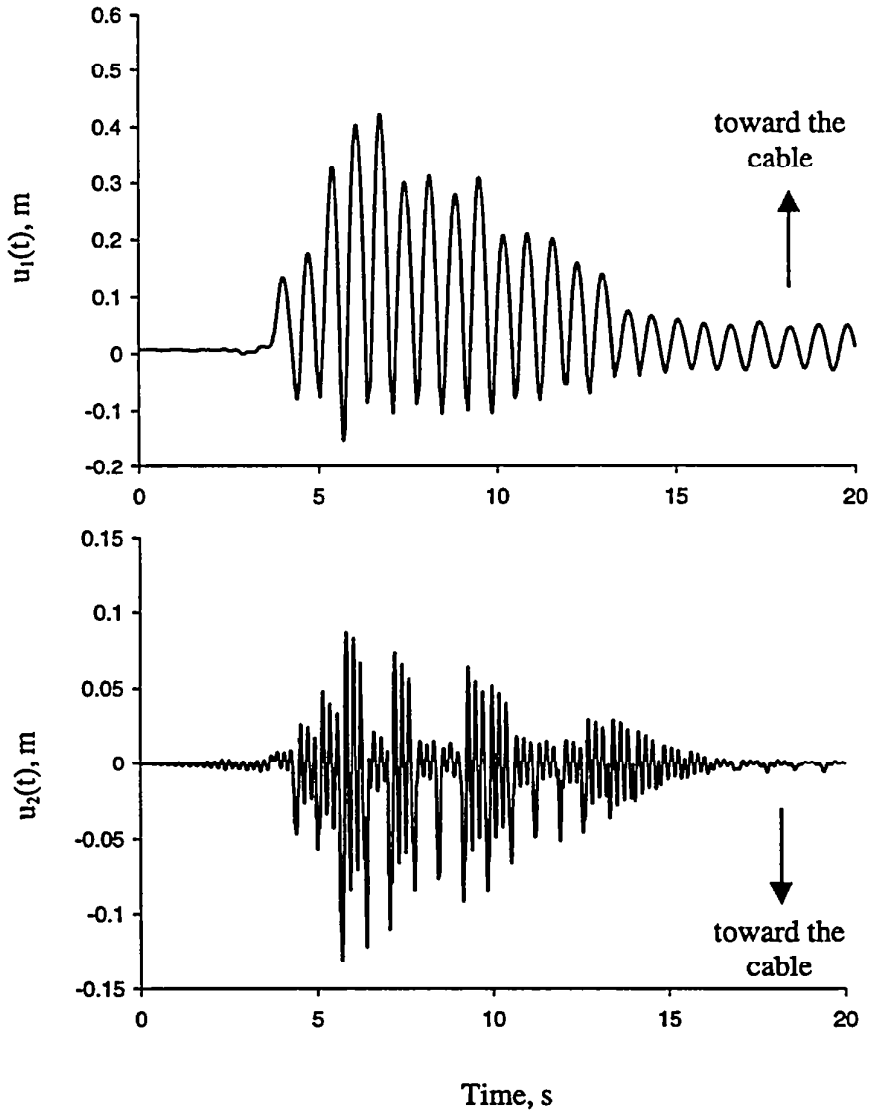

Figure 3.18 Displacement time histories of equipment items in the connected system, including the flexural rigidity but neglecting the inertia and damping of the cable

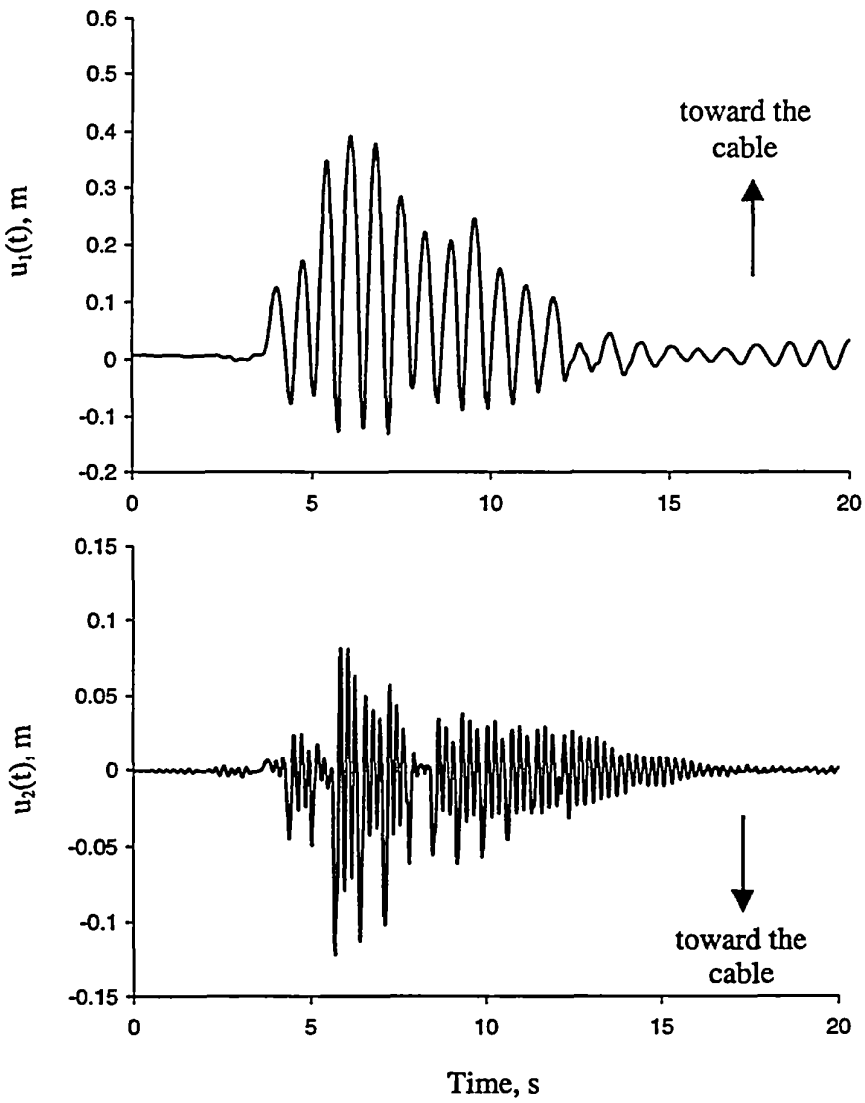

Figure 3.19 Displacement time histories of equipment items in the connected system, including flexural rigidity and inertia, but neglecting the damping of the cable

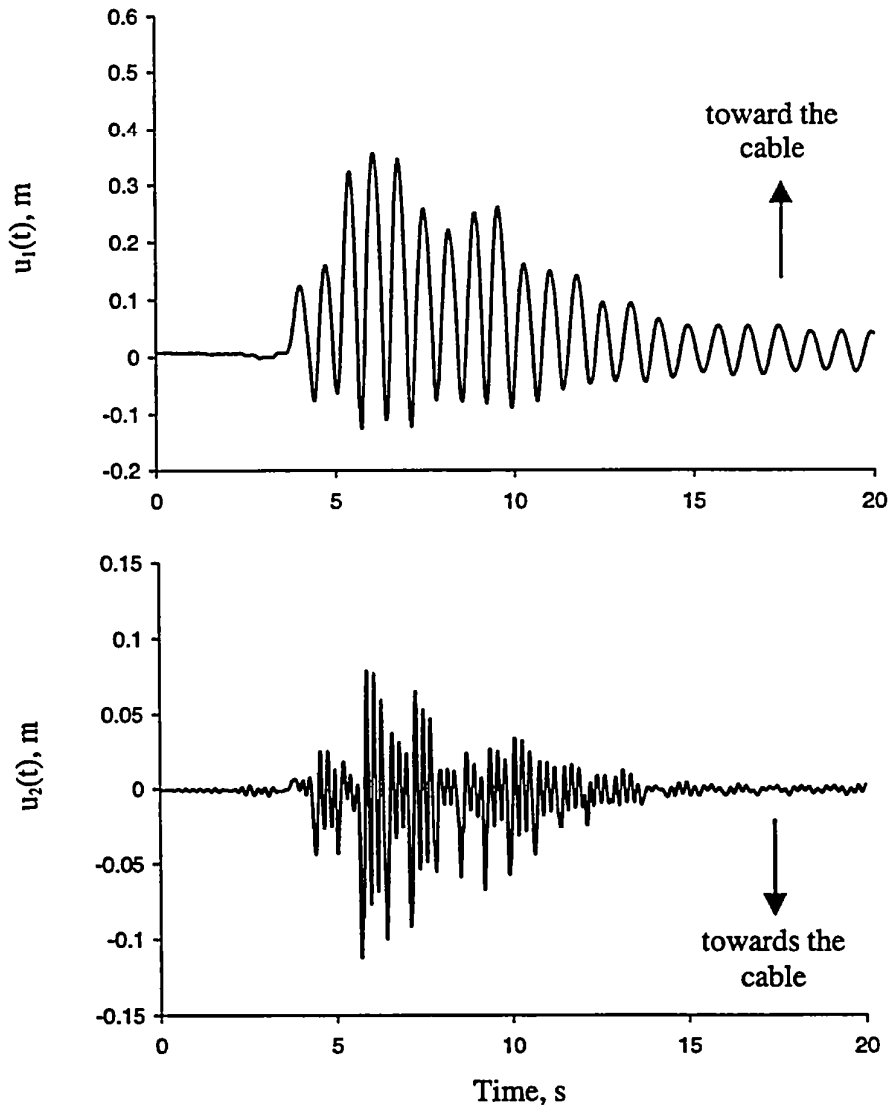

Figure 3.20 Displacement time histories of equipment items in the connected system, including the flexural rigidity, inertia and damping of the cable

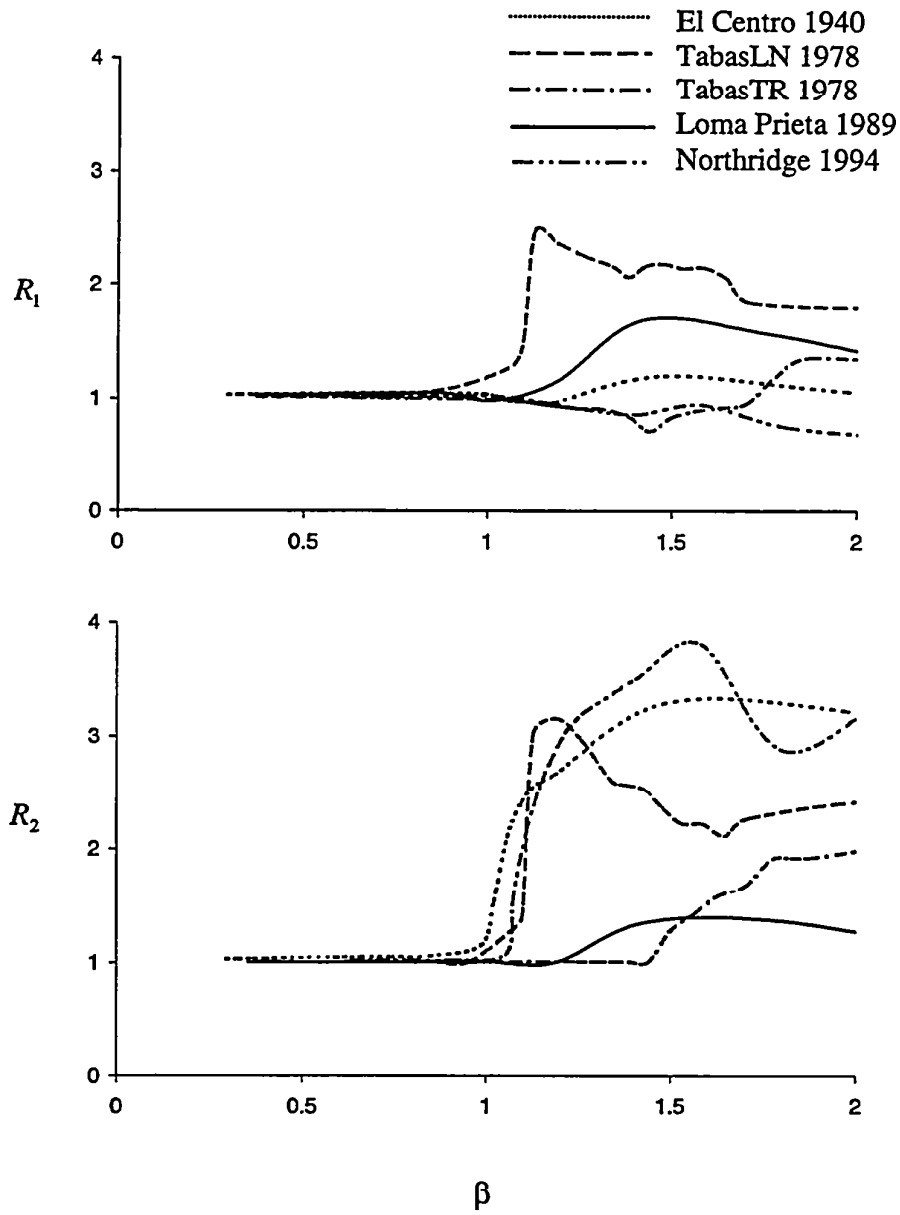

Figure 3.21 Response ratios for five earthquakes as functions of the interaction parameter neglecting the flexural rigidity, inertia and damping of the cable

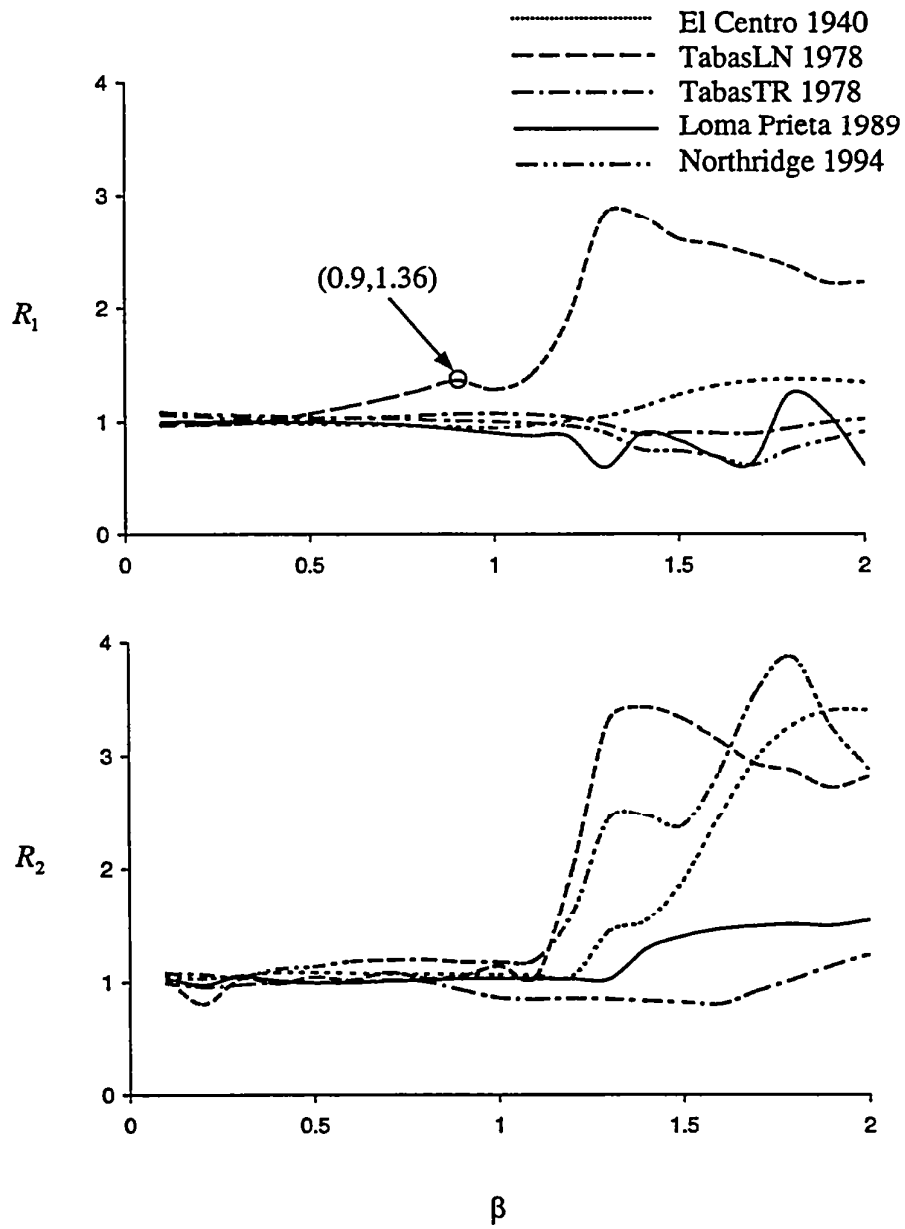

Figure 3.22 Response ratios for five earthquakes as functions of the interaction parameter, including the flexural rigidity and inertia of the cable with zero damping

Chapter 4 Summary and Recommendations for Further Study

4.1 Summary

The main results of the study can be summarized as follows:

(a) An elasto-plastic, large deformation finite element model of the flexible strap connector (FSC) was developed and used to predict the cyclic behavior of the a rigid bus (RB) -FSC system under imposed quasi-static cyclic displacement. The predictions are in reasonably close agreement with the results of tests conducted at the University of California at San Diego (UCSD). More accuracy in the characterization of the material can be achieved if cyclic test results of the material coupon are available. Under large deformations, the bars and straps of the FSC develop contacts and slippage under friction forces. These effects are not included in the current finite element model. A refined model including these effects is expected to provide more accurate predictions. Such a refined model can be used in the future to predict the behavior of other FSC configurations to large cyclic deformations, thus avoiding costly experiments.

(b) An analytical model of the hysteretic behavior of the RB-FSC is developed by use of a modified version of the well known Bouc-Wen differential representation. This model is subsequently used for dynamic analysis of two equipment items connected by an RB-FSC conductor. Time history analysis for two recorded earthquake ground motions are carried out to determine the effects of interaction on each equipment item. Separate analyses are performed to investigate the influences of the flexibility and energy dissipation characteristics of the FSC on the interaction effect. The results show that the flexibility and energy dissipation characteristics of the FSC sig-

nificantly reduce the adverse interaction effect, particularly on the higher-frequency equipment item. Reasonably good agreement with experimental results is achieved.

(c) For the flexible cable conductor, which is made of braided aluminum wire strands, a finite element model using elastic frame elements and a Lagrangian formulation is developed that accounts for large displacements and rotations. Comparisons with existing experimental results for conductor cables subjected to imposed harmonic support displacements are made. Qualitative agreement between the analytical and experimental results is obtained, but large differences in the force magnitudes occur. These differences are attributed to prevailing uncertainties associated with determining the rigidity and damping characteristics of the cable and its initial shape. Nevertheless, the analytical predictions verify the important experimental finding that cable forces can be magnified by several orders of magnitude when the cable is subjected to imposed harmonic end displacement of certain amplitude and frequency.

(d) The finite element model of the cable is used to investigate the effect of interaction in a combined system consisting of two equipment items connected by a conductor cable. Detailed time history results are presented for the Newhall record of the Northridge earthquake, where separate analyses are performed to demonstrate the influences of the cable flexural rigidity, inertia and damping on the interaction effect. These influences are found to be rather mild, certainly not nearly as large as had been anticipated by previous investigators based on the experiments mentioned above.

(e) Extensive time history analyses are carried out for five different recorded ground motions and for varying cable slackness to determine the effect of interaction on each connected equipment item as a function of an interaction parameter. Based on this study, a recommendation for the minimum cable length to avoid the adverse effect of interaction is formulated. This formulation now accounts for the effects of cable flexural rigidity and inertia, but not damping. Since no accurate information regarding the cable damping is currently available, for the sake of conservatism the above recommendation was formulated assuming zero damping in the cable.

4.2 Recommendations for Further Study

In light of the results obtained in the present study, we recommend consideration of the following topics for further study:

(a) Develop a more refined finite element model of the flexible strap connector that accounts for the contact and friction between the bars and straps. Similar models can be developed for the slider connector, as well as for other connectors of different geometry. With such refinement, accurate prediction of the behavior of flexible connectors under large cyclic deformations can be made by finite element analysis, accounting for both material and geometric nonlinearities and for the contact and friction effects, thus avoiding costly experiments that so far have been necessary. This approach can also be used to explore new designs of the connecting element that are aimed at improving its seismic performance or electrical function.

(b) Conduct experiments and develop analytical models to better characterize the flexural rigidity and energy dissipation of conductor cables that are made of braided wire strands. Finite element models should be developed that account for the slippage of the strands against each other under friction forces. These effects should be related to the deformation and force in the cable, so that variation of properties along the cable can be determined. With such refined models, it should be possible to accurately predict the dynamic behavior of conductor cables under imposed end displacements, for which experimental results are available. It is believed that results from such analysis will be of interest in determining the response of transmission cables subjected to earthquake and wind loading.

(c) The recommendation for the minimum cable length to avoid the adverse effect of interaction formulated in this study is preliminary in nature. This is because we are uncertain about the effective values of cable rigidity and damping. For the sake of conservatism, we have used zero cable damping to develop the present recommendation. Furthermore, the investigation so far has considered only five recorded ground motions. Since the response is highly nonlinear and strongly sensitive to the details of the ground motion, a broader set of records should be investigated before a final rec-

ommendation can be made. Study item (b) listed above will also allow us to re-examine this recommendation with a more refined characterization of the cable properties.

(d) Throughout this study we have used a deterministic method of analysis with specifically selected ground motions. Ideally, a random vibration approach should be used to properly account for the variability present in the ground motion. Such a study can be conducted with relative ease by use of the analytical hysteresis model developed for the RB-FSC in this study. For the cable-connected system, the nonlinear random vibration problem can be considerably more difficult.

REFERENCES

Armero, F., and I. Romero. 1999. *On the formulation of high-frequency dissipative time-stepping algorithms for nonlinear dynamics. Part I: Low order methods for two model problems and nonlinear elastodynamics.* Report UCB/SEMM-1999/05. Berkeley, Calif.: Department of Civil & Environmental Engineering, University of California.

Baber, T. T., and Y. K. Wen. 1979. *Stochastic equivalent linearization for hysteretic, degrading, multistory structures.* Report UILU-ENG-80-2001. Urbana, Ill: University of Illinois at Urbana-Champaign.

Bouc, R. 1967. Forced vibration of a mechanical system with hysteresis. Abstract in *Proceedings of the Fourth Conference on Nonlinear Oscillations.* p315. Prague, Czechoslovakia: Academia Publishing.

Dastous, J.-B., and J.-R. Pierre. 1996. Experimental investigation on the dynamic behavior of flexible conductors between substation equipment during an earthquake. *IEEE Transaction on Power Delivery* 11(2): 801–7.

Der Kiureghian, A., J. L. Sackman, and K.-J. Hong. 1999. *Interaction in interconnected electrical substation equipment subjected to earthquake ground motions.* PEER report 1999/01. Berkeley, Calif.: University of California.

Pacific Gas & Electrical Company. Electrical Design Standards. *Flexible strap connectors 700 to 3200 amps.* San Francisco: Department of Engineering.

Filiatrault, A., S. Kremmaidas, A. Elgamal, and F. Seible. 1999. *Substation equipment interaction: Rigid and flexible conductor studies.* Report SSRP-99/09. La Jolla, California: Division of Structural Engineering, University of California, San Diego.

IEEE. 1999. *Draft recommended practice for the design of flexible buswork located in seismically active area.* IEEE P1527/D5. Piscataway, N.J.: IEEE Standards Department.

Noiseux, D. U. 1992. Similarity laws of the internal damping of stranded cables in transverse vibrations. *IEEE Transactions on Power Delivery* 7(3): 1574–81.

Simo, J. C., and T. J. R. Hughes. 1998. *Computational Inelasticity.* Berlin: Springer Verlag.

Simo, J. C., N. Tarnow, and K. K. Wong. 1992. Exact energy-momentum conserving algorithms and symplectic schemes for nonlinear Dynamics. *Computer Methods in Applied Mechanics and Engineering* 100(1): 63–116.

Simo, J. C., N. Tarnow, and M. Doblare. 1995. Non-linear dynamics of three-dimensional rods: Exact energy and momentum conserving algorithms. *International Journal for Numerical Methods in Engineering*, 38(9): 1431–73.

Taylor, R. L. 1998. *FEAP Version 7.1 User Manual.* Berkeley, Calif.: Department of Civil and Environmental Engineering, University of California.

Transmission Line Reference Book: Wind-induced conductor motion. 1979. Palo Alto, Calif.: Electrical Power Research Institute.

Wang, C.-H., and Y. K. Wen. 1998. *Reliability and redundancy of pre-Northridge low-rise steel building under seismic excitation.* UILU-ENG-99-2002. Urbana, Ill.: University of Illinois at Urbana-Champaign.

Wen, Y. K. 1976. Method for random vibration of hysteretic systems. *Journal of the Engineering Mechanics Division*, ASCE 102(EM2): 249–63.

PEER REPORTS

PEER reports are available from the National Information Service for Earthquake Engineering (NISEE). To order PEER reports, please contact the Pacific Earthquake Engineering Research Center, 1301 South 46th Street, Richmond, California 94804-4698. Tel.: (510) 231-9468; Fax: (510) 231-9461.

PEER 2000/01 *Further Studies on Seismic Interaction in Interconnected Electrical Substation Equipment.* Armen Der Kiureghian, Kee-Jeung Hong, and Jerome L. Sackman. November 1999. $20.00

PEER 1999/11 *Performance Evaluation Database for Concrete Bridge Components and Systems under Simulated Seismic Loads.* Yael D. Hose and Frieder Seible. November 1999. $20.00

PEER 1999/08 *Envelopes for Seismic Response Vectors.* Charles Menun and Armen Der Kiureghian. July 1999. $26.00

PEER 1999/07 *Documentation of Strengths and Weaknesses of Current Computer Analysis Methods for Seismic Performance of Reinforced Concrete Members.* William F. Cofer. November 1999. $15.00

PEER 1999/06 *Rocking Response and Overturning of Anchored Equipment under Seismic Excitations.* Nicos Makris and Jian Zhang. November 1999. $15.00

PEER 1999/05 *Seismic Evaluation of 550 kV Porcelain Transformer Bushings.* Amir S. Gilani, Andrew S. Whittaker, Gregory L. Fenves, and Eric Fujisaki. October 1999. $15.00.

PEER 1999/04 *Adoption and Enforcement of Earthquake Risk-Reduction Measures.* Peter J. May, Raymond J. Burby, T. Jens Feeley, and Robert Wood. $15.00.

PEER 1999/03 *Task 3 Characterization of Site Response General Site Categories.* Adrian Rodriguez-Marek, Jonathan D. Bray, and Norman Abrahamson. February 1999. $20.00

PEER 1999/02 *Capacity-Demand-Diagram Methods for Estimating Seismic Deformation of Inelastic Structures: SDF Systems.* Anil K. Chopra and Rakesh Goel. April 1999. $15.00

PEER 1999/01 *Interaction in Interconnected Electrical Substation Equipment Subjected to Earthquake Ground Motions.* Armen Der Kiureghian, Jerome L. Sackman, and Kee-Jeung Hong. February 1999. $20.00

PEER 1998/08 *Behavior and Failure Analysis of a Multiple-Frame Highway Bridge in the 1994 Northridge Earthquake.* Gregory L. Fenves and Michael Ellery. December 1998. $20.00

PEER 1998/07 *Empirical Evaluation of Inertial Soil-Structure Interaction Effects.* Jonathan P. Stewart, Raymond B. Seed, and Gregory L. Fenves. November 1998. $26.00

PEER-1998/06 *Effect of Damping Mechanisms on the Response of Seismic Isolated Structures.* Nicos Makris and Shih-Po Chang. November 1998. $15.00

PEER 1998/05 *Rocking Response and Overturning of Equipment Under Horizontal Pulse-Type Motions.* Nicos Makris and Yiannis Roussos. October 1998. $15.00

PEER 1998/04 *Pacific Earthquake Engineering Research Invitational Workshop Proceedings, May 14–15, 1998: Defining the Links between Planning, Policy Analysis, Economics and Earthquake Engineering.* Mary Comerio and Peter Gordon. September 1998. $15.00

PEER 1998/03 *Repair/Upgrade Procedures for Welded Beam to Column Connections.* James C. Anderson and Xiaojing Duan. May 1998. $33.00

PEER 1998/02 *Seismic Evaluation of 196 kV Porcelain Transformer Bushings.* Amir S. Gilani, Juan W. Chavez, Gregory L. Fenves, and Andrew S. Whittaker. May 1998. $20.00

PEER 1998/01 Unassigned.

The Pacific Earthquake Engineering Research Center (PEER) is a consortium of western U.S. universities working in partnership with business, industry, and government to identify and reduce the risks from major earthquakes to life safety and to the economy.

PEER achieves its objectives of earthquake risk reduction through a coordinated program of research, education, and partnerships with users of research results. PEER's research program includes basic and applied components of seismology, engineering, architecture, urban planning, and economics.

PEER is headquartered at UC Berkeley.

PEER reports are available individually or by yearly subscription from the National Information Service for Earthquake Engineering (NISEE).

To order PEER Reports, contact the Pacific Earthquake Engineering Research Center, 1301 S. 46th St., Richmond, California 94804-4698, Tel: 510-231-9468, Fax: 510-231-9461.

University of California, San Diego
Division of Structural Engineering
Structural Systems Research Project

Report No. SSRP- 99/09

SUBSTATION EQUIPMENT INTERACTION – RIGID AND FLEXIBLE CONDUCTOR STUDIES

by

André Filiatrault
Professor of Structural Engineering

Spyridon Kremmidas
Assistant Development Engineer

Ahmed Elgamal
Professor of Structural Engineering

Frieder Seible
Professor of Structural Engineering

Division of Structural Engineering
University of California, San Diego
La Jolla, California 92093-0085

September 24, 1999

DISCLAIMER

Opinions, findings, conclusions and recommendations expressed in this report are those of the authors and do not necessarily reflect views of the Pacific Gas and Electric Company (PG&E) and the Pacific Earthquake Engineering Research Center (PEER).

ACKNOWLEDGEMENTS

The research project described in this report was funded by the PEER/PG&E Directed Studies under the PG&E Agreement No. 09566 (Prime Agreement CEC 500-97-010) "Electric System Seismic Safety and Reliability" – SA2115-59652.

We greatly appreciated the input and coordination provided by Professor Gregory Fenves from the University of California at Berkeley and Mr. Eric Fujisaki and Dr. William Savage from PG&E during the development of this research project. The support of Dr. Leon Kempner from Bonneville Power Administration is also gratefully acknowledged.

The authors extend their sincere appreciation to Mr. Constantin Christopoulos, Doctorate student at UC-San Diego, for his assistance in conducting the shake table tests.

LIST OF SYMBOLS

A1	First double amplitude for damping evaluation
A2	Second double amplitude for damping evaluation
c_A	Viscous damping coefficient of generic equipment A
$E_{D\delta}$	Energy dissipated per cycle at displacement amplitude δ
F_δ	Force at the displacement amplitude δ
F_s	Slip force of bus slider
F_y	Yield force
k_A	Lateral stiffness of generic equipment A
K_e	Elastic restoring stiffness of bus slider
K_o	Elastic stiffness
m_A	Mass of generic equipment A
n_j	Number of cycles to be performed in load step j
p	Number of intermediate cycles between double amplitudes
Q_y	Yield force
$x_{rA}(t)$	Relative displacement at the top of generic equipment A
$\dot{x}_{rA}(t)$	Relative velocity at the top of generic equipment A
$\ddot{x}_{aA}(t)$	Absolute acceleration at the top of generic equipment A
β	Strain-hardening ratio
βK_o	Post-yield stiffness
δ	Displacement
δ^*	Displacement at 75% of yield force
δ_y	Yield displacement
δ_j	Peak displacement in load step j
Δ	Increment in peak displacement between two consecutive steps
μ	Displacement ductility factor
ζ	Equivalent viscous damping ratio

TABLE OF CONTENTS

1 INTRODUCTION 1

1.1 Scope of Research 1
1.2 Report Layout 2

2 QUASI-STATIC TESTS OF RIGID BUS WITH SPRING CONNECTORS 3

2.1 Description of Test Specimens 3
2.2 Preliminary Tensile Tests 4
2.3 Experimental Set-Up for Quasi-Static Cyclic Tests 5
2.4 Instrumentation 6
2.5 Test Protocol 7
2.6 Static Linear Elastic Analysis of Spring Connectors 9
2.7 Experimental Results 10
2.8 Bilinear Modeling 13
2.9 Equivalent Viscous Damping Ratios 17

3 QUASI-STATIC TEST OF RIGID BUS SLIDER 19

3.1 Description of Test Specimen 19
3.2 Experimental Set-Up for Quasi-Static Test 19
3.3 Instrumentation 20
3.4 Test Protocol 21
3.5 Experimental Results 21
3.6 Equivalent Viscous Damping Ratios 23

4 QUASI-STATIC TESTS OF FLEXIBLE BUS ASSEMBLIES 25

4.1 Description of Test Specimens 25
4.2 Experimental Set-Up for Quasi-Static Tests 26
4.3 Instrumentation 27
4.4 Test Protocol 27
4.5 Experimental Results 28

5 SHAKE TABLE TESTS ON PAIRS OF GENERIC SUBSTATION EQUIPMENT CONNECTED WITH RIGID BUS ASSEMBLIES 30

5.1 Description of UC-San Diego Uniaxial Earthquake Simulation Facility 30
5.2 Descriptions of Generic Substation Equipment 31
5.3 Instrumentation 34
5.4 Earthquake Ground Motions and Shake Table Fidelity 34
5.5 Shake Table Test Program 36
5.5.1 Frequency Evaluation Tests 38
5.5.2 Damping Evaluation Tests 38

5.5.3 Seismic Tests 39
5.6 Rigid Bus Specimens 39
5.7 Test Sequence 41
5.8 Results of Frequency and Damping Evaluation Tests 44
5.9 Results of Seismic Tests 47

6 CONCLUSIONS 63

7 REFERENCES 66

APPENDIX A
Drawings of Rigid and Flexible Bus Specimens A1

APPENDIX B
Shop Drawings of Generic Equipment Specimens B1

APPENDIX C
Results of Frequency Evaluation Tests C1

APPENDIX D
Results of Damping Evaluation Tests D1

APPENDIX E
Results of Seismic Tests E1

1. INTRODUCTION

Both rigid and flexible conductors interconnect electrical substation equipment. During earthquakes, significant interaction and equipment damage due to forces transferred through the connectors have been observed. Flexible bus ("cables") exert relatively little force, provided that they remain slack. Rigid bus (typically aluminum tubular sections) may utilize connectors with small gaps for thermal displacement, thus accommodating some seismic displacement before transferring forces between the connected equipment. Some utilities have implemented slack or loops in flexible and rigid bus to provide flexibility between interconnected pieces of equipment.

1.1 Scope of Research

The primary objective of this research project was to investigate experimentally, through quasi-static and shake table testing, the interactions between components of substation equipment connected by both flexible and rigid bus. The intention was to generate experimental data that would provide guidance in the seismic design of conductor assemblies. Another objective was to provide experimental validation data for a current PEER-PG&E project in which analytical methods are being used to study substation equipment connected by flexible and rigid bus. Specific tests conducted in this project were:

(i) Full-scale quasi-static cyclic tests of three different types of rigid bus with spring connectors.

(ii) Full-scale quasi-static cyclic tests of one rigid bus-slider.

(iii) Full-scale quasi-static tests of two different types of flexible bus.

(iv) Full-scale shake table tests of five different pairs of generic substation equipment connected with three different rigid bus assemblies.

1.2 Report Layout

Following an introduction to the project, and scope of the current study in this chapter, **Chapter 2** describes the quasi-static tests performed on rigid bus assemblies with spring connectors. **Chapter 3** presents the quasi-static tests performed on a rigid bus slider. **Chapter 4** describes the quasi-static tests performed on flexible bus specimens. **Chapter 5** presents the shake table tests performed on five pairs of generic substation equipment connected with three different rigid bus assemblies. Finally, the report concludes with specific recommendations for the seismic design of interconnected equipment.

2. QUASI-STATIC TESTS OF RIGID BUS WITH SPRING CONNECTORS

This chapter describes the full-scale quasi-static tests performed on three different types of rigid bus with spring connectors. These tests were performed in the longitudinal directions of the bus assemblies under prescribed displacement history.

2.1 Description of Test Specimens

Three different rigid bus-spring connector assemblies were supplied by PG&E and were tested under quasi-static loading. Two specimens of each spring type were provided; one specimen was tested under quasi-static loading and the other was used for the shake table tests. Figure 2.1 presents a general view of the three specimens. Drawings of the specimens are included in Appendix A.

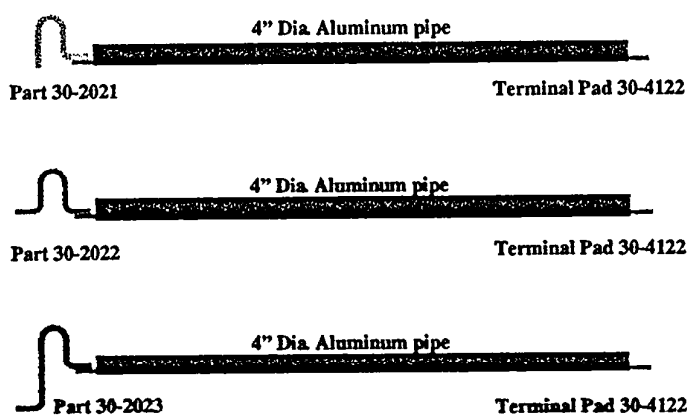

Figure 2.1 Rigid Bus Assemblies with Spring Connectors.

Each rigid bus was made of a 10-ft long SPS aluminum pipe (4.5 in outside diameter and 4.026 in inside diameter) with offset terminal pads welded at each end. Each bus incorporated a different spring connector. The first spring connector (Part 30-2021) is non-symmetrical with one horizontal and one vertical terminal pad. The second spring connector (Part 30-2022) is symmetrical with two horizontal terminal pads. Finally, the third spring connector is non-symmetrical with two horizontal terminal pads at different elevations. Figure 2.2 presents the dimensions of the three spring connectors tested.

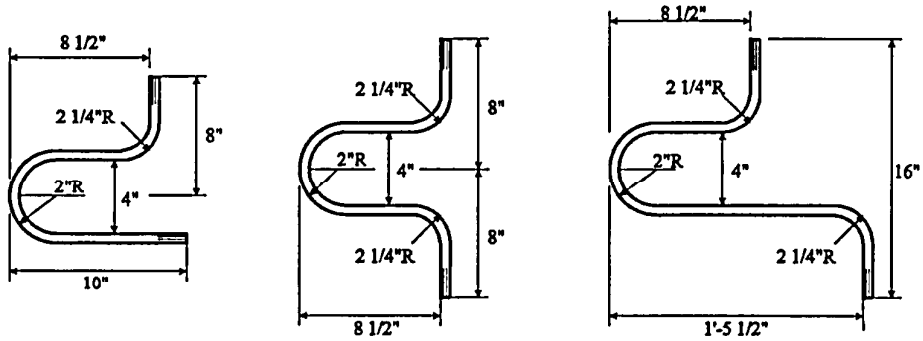

PG&E Code No 30-2021 PG&E Code No 30-2022 PG&E Code No 30-2023

Figure 2.2 Dimensions of Spring Connectors.

Each spring was made up of three pairs of copper alloy straps (1/8" thick by 3" wide) separated by two ¼" gaps. Shim plates were inserted in the gaps only at the ends of the springs to provide continuous connections to the terminal pads.

2.2 Preliminary Tensile Tests

Preliminary monotonic tensile tests were performed on three different coupons taken from one of the spring connector (Part 30-2023) in order to evaluate the properties of the copper alloy. Three different coupons were tested according to the ASTM E8-98 standard (American Society for Testing Materials, 1999). Figure 2.3 presents the tensile stress-strain curve obtained from one of the test. It can be seen that the copper alloy exhibits almost a perfect elastic-plastic behavior that can be characterized by Young's modulus and yield strength. Table 3.1 presents these material properties based on the mean values of the three tests performed. The yield strain of the material is also indicated in this table.

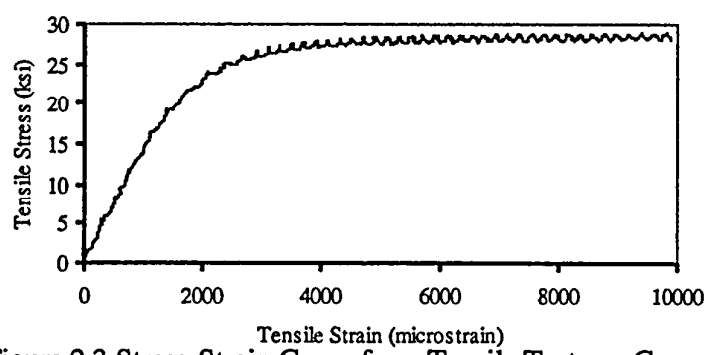

Figure 2.3 Stress-Strain Curve from Tensile Tests on Copper Alloy.

Table 2.1 Material Properties for Copper Alloy.

Young's Modulus	14 100 ksi
Yield Strength	27 ksi
Yield Strain	1915 $\mu\varepsilon$

2.3 Experimental Set-Up for Quasi-Static Cyclic Tests

Figure 2.4 illustrates the experimental set-up used to perform the quasi-static cyclic tests on the three rigid bus-spring connector assemblies. A 220-kip actuator with a 24-in stroke was attached to the strong wall of the laboratory and applied horizontal loading in the longitudinal direction of the bus assembly. The head of the actuator was prevented from moving in perpendicular directions of the loading by a supporting chain system. Also, locking the swivel near the bus assembly prevented rotation of the head of the actuator. The bus assembly was inserted between the head of the actuator and a vertical steel column anchored to the strong floor of the laboratory. The terminal pad of the spring connector was attached to the column by a transfer plate and the other end of the bus was connected to the head of the actuator by a similar transfer plate. A 10-kip capacity axial load-cell was inserted between the head of the actuator and the terminal pad of the pipe to measure accurately the applied load during the test. Figure 2.5 presents photographs of the connection details at each end of the rigid bus assembly.

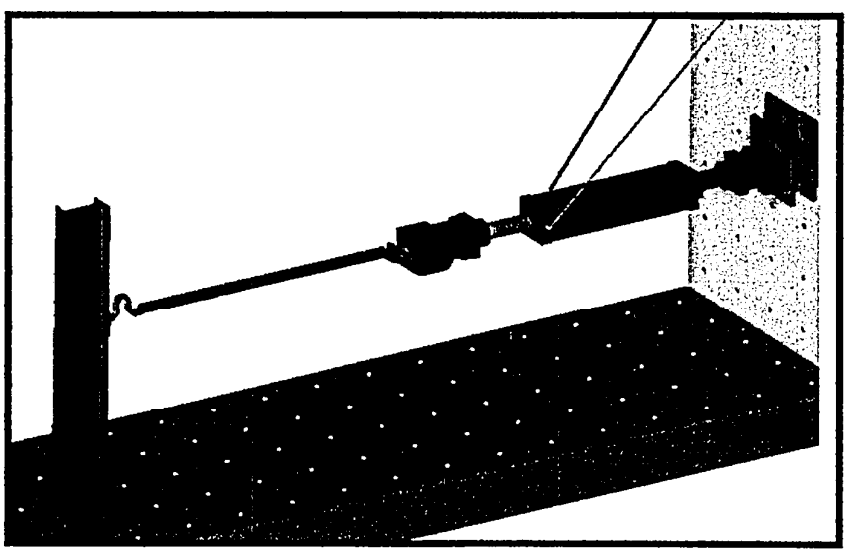

Figure 2.4 Experimental Set-Up for Quasi-Static Tests on Rigid Bus Assemblies.

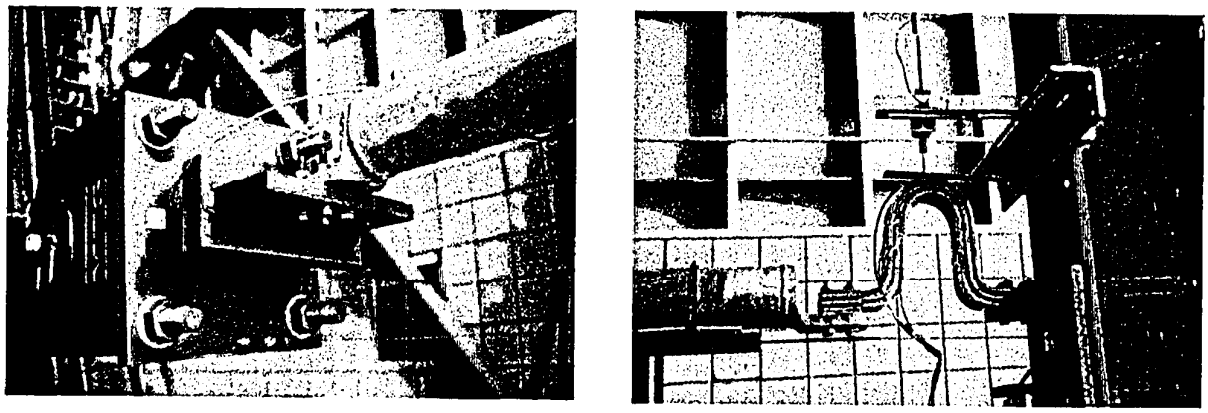

Figure 2.5 Details of Connections at Ends of Rigid Bus Assemblies.

2.4 Instrumentation

Figure 2.6 illustrates the instrumentation used for the quasi-static tests on the rigid bus assemblies. The force-displacement hysteresis loops were obtained by measuring the load across the 10-kip load cell and the displacement across the spring connector. Also, six strain gauges were installed on the top and bottom surface of each pair of straps at the position of maximum bending moment. The strain gauge readings were used at the beginning of each test to define the yield displacement of the specimen, as described in the next section.

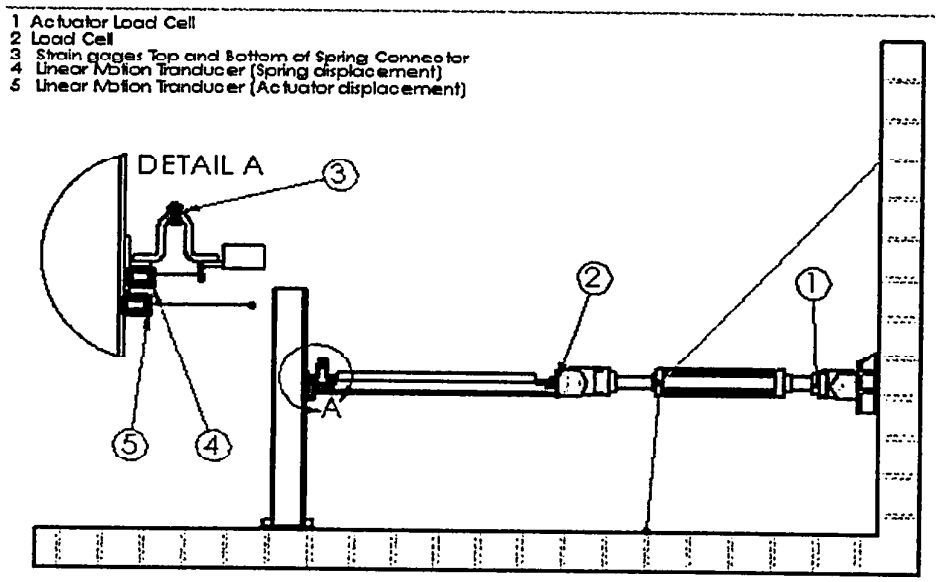

Figure 2.6 Instrumentation for Quasi-Static Tests on Rigid Bus Assemblies.

2.5 Test Protocol

The ATC-24 loading protocol (Applied Technology Council, 1992) was used to perform the quasi-static tests on the rigid bus assemblies. This protocol has been developed for the cyclic seismic testing of components of steel structures. The protocol consists of stepwise increasing displacement cycles as illustrated in Fig.2.7.

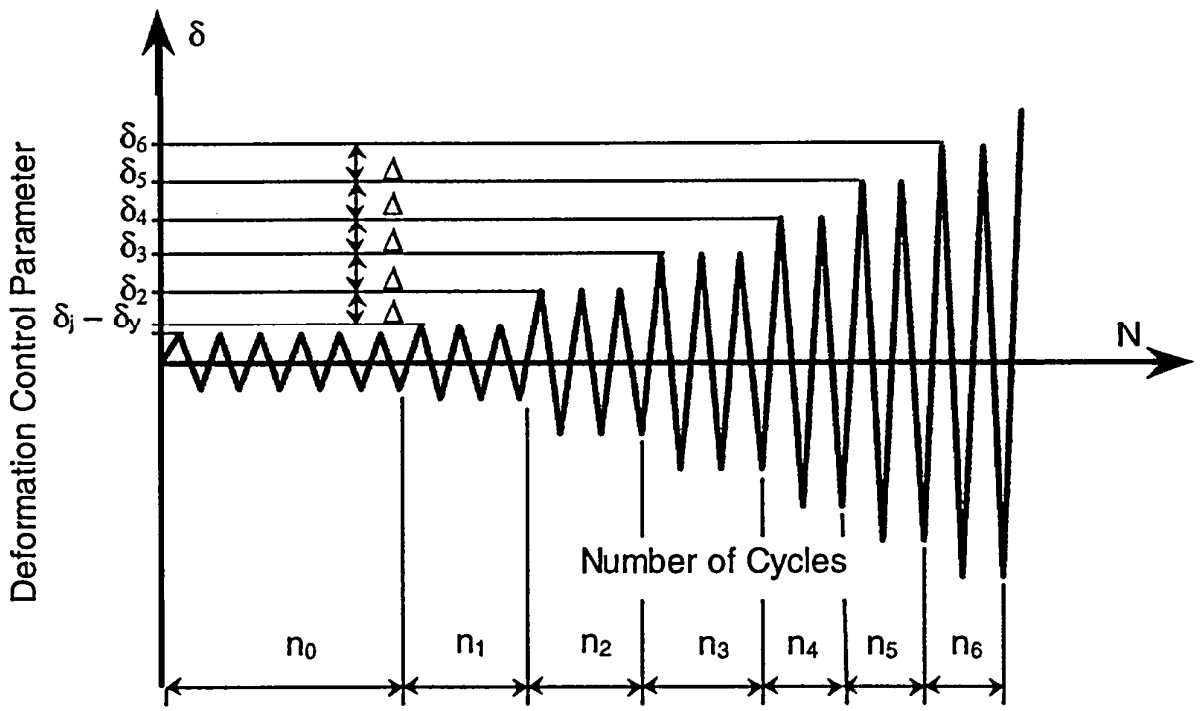

Figure 2.7 ATC-24 Test Protocol Used for Quasi-Static Tests of Rigid Bus Assemblies.

The loading history is defined by the following parameters:

δ_y	the yield displacement across the spring connector;
$\delta_j = \delta_y + (j-1)\Delta$	the peak displacement across the spring connector in load step j;
n_j	the number of cycles to be performed in load step j;
Δ	the increment in peak displacement between two consecutive steps.

The displacement is expressed in terms of the displacement ductility factor, μ, defined as:

$$\mu = \frac{\delta}{\delta_y} \tag{1.1}$$

The following parameters were used during the tests:

$$\begin{aligned} &\Delta = \delta_y \\ &n_0 = 6; \quad n_1 = n_2 = n_3 = 3; \quad n_j = 2 \; for \; j > 3 \end{aligned} \tag{1.2}$$

The yield displacement, δ_y, was obtained from the strain gauge readings during the first cycle in each loading direction. The specimen was displaced until a strain-gauge reading of $1500\,\mu\varepsilon$ was obtained at the location of maximum bending moment on the spring connector. It was then assumed that this displacement, δ^*, corresponded to 75% of the yield force of the specimen, $0.75Q_y$. The yield force, Q_y, and the yield displacement, δ_y, were obtained by linear extrapolation from these 75% yield values, as illustrated in Fig. 2.8. The procedure was then repeated in the other loading direction and the mean values were taken as the final yield displacement and yield force.

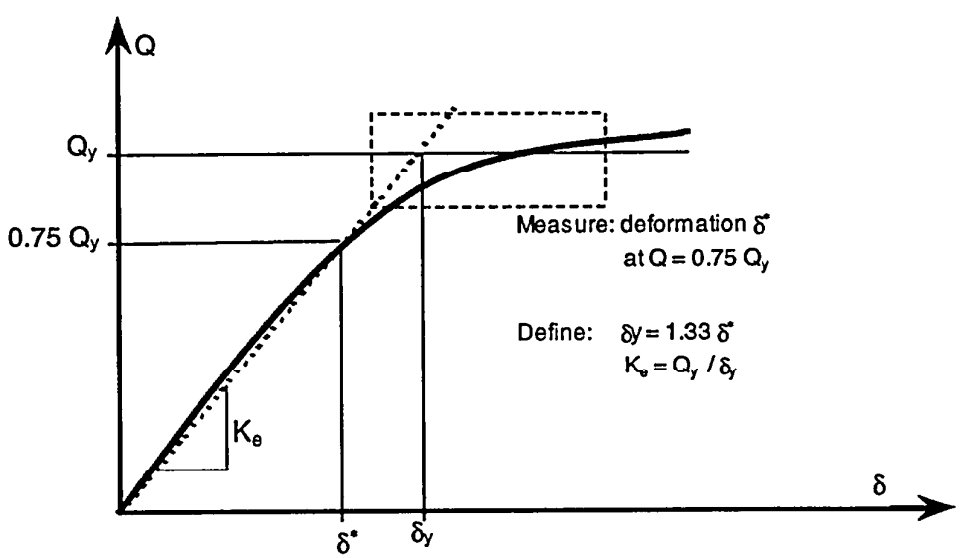

Figure 2.8 Determination of Yield Displacement and Yield Force of Rigid-Bus Assemblies.

Table 2.2 presents the experimental values of yield displacements and yield forces obtained for the three rigid bus assemblies tested. The 30-2021 and 30-2022 spring connectors have similar yield displacements and yield forces. The 30-2023 spring connector, being significantly more flexible, exhibits higher yield displacement and lower yield force than the other two springs.

Table 2.2 Experimental Yield Displacements and Yield Forces for Rigid Bus Assemblies

Spring Part No.	Yield Displacement, δ_y (in)	Yield Force, F_y (lbs)
30-2021	1.3	401
30-2022	1.3	347
30-2023	3.0	188

2.6 Static Linear Elastic Analysis of Spring Connectors

In order to predict the yield force, yield displacement, and location of maximum stress of each spring connector before the quasi-static tests, static linear analyses were performed. The commercial computer program SAP2000 (Computers and Structures, 1998) was used for this purpose. Each spring connector was modeled by straight linear-elastic frame elements capable of flexural and axial deformations. Each pair of straps was modeled as superimposed frame elements. The gaps between pairs of strap were also incorporated in the model. It was assumed that the terminal pads acted as fixed supports by constraining the rotation of the three end nodes at each end of the spring. Note that because of symmetry, only half of the 30-2022 spring was modeled. The elastic modulus shown in Table 2.1 was used in the models.

Figure 2.9 illustrates the displaced shape of the spring 30-2022 model under a horizontal concentrated force applied at one end of the spring and causing a maximum axial strain of 1915 $\mu\varepsilon$, corresponding to the yield strain of the material (see Table 2.1). From these analyses, the initial stiffness, the yield force and the yield displacement of each spring connector could be estimated and are indicated on each deformed shape.

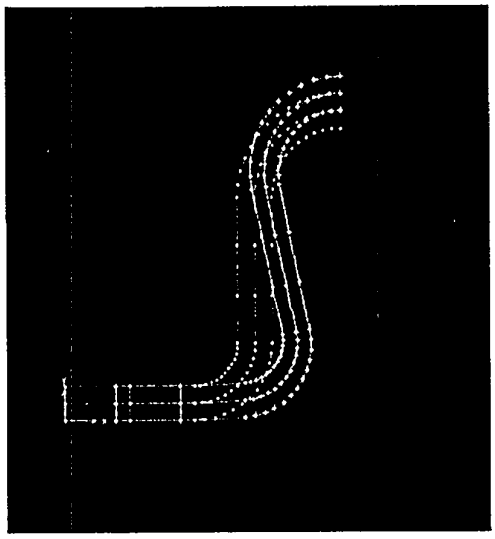

Figure 2.9 Static Linear Elastic Analysis of 30-2022 Spring Connectors.

2.7 Experimental Results

Figure 2.10 to 2.12 presents photographs of each specimen at the maximum displacement ductility factors achieved during each test. In the positive direction, the ductility factor was increased until the gap of the connector closed and contact occurred. The photographs clearly indicate the ductile characters of the spring connectors. Note also the significant vertical motion at the end of the rigid bus caused by the bending flexibility of the aluminum pipe.

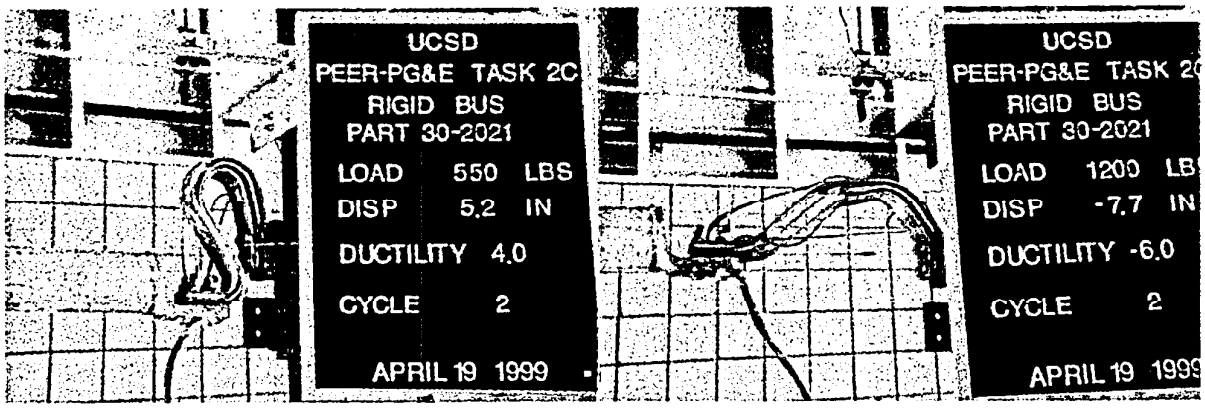

Figure 2.10 Rigid Bus with 30-2021 Spring Connector at Maximum Ductility.

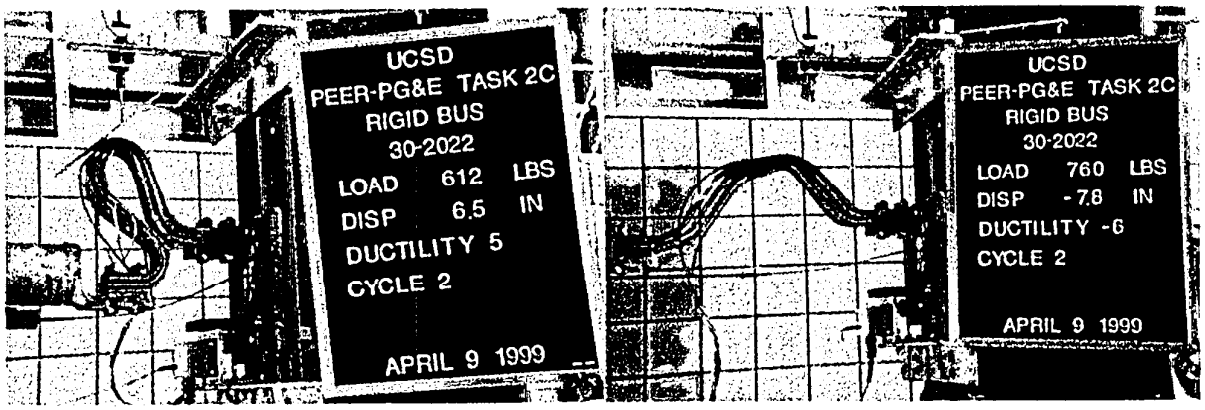

Figure 2.11 Rigid Bus with 30-2022 Spring Connector at Maximum Ductility.

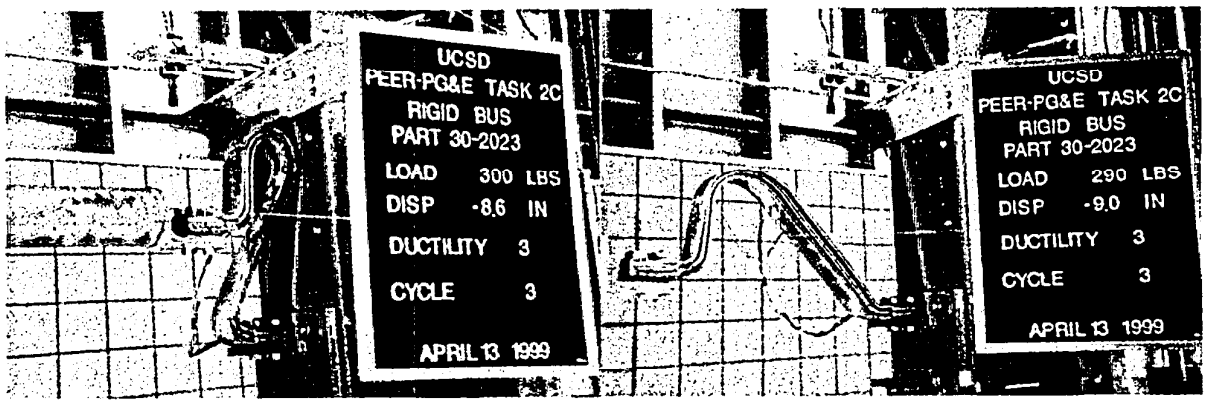

Figure 2.12 Rigid Bus with 30-2023 Spring Connector at Maximum Ductility.

Figure 2.13 presents the load-displacement response of each spring connector obtained at ductility levels less than unity. Also shown on the figures are the load-displacement responses predicted by the SAP-2000 analyses described in the previous section. For the 30-2021 spring, the numerical model slightly underestimates the elastic stiffness of the unit. This can be explained by the fact that the vertical terminal pad induces a rotation constraint on a longer length than assumed in the model. For the 30-2022 spring, the situation is reversed; the numerical model overestimates the elastic stiffness of the unit. This can be attributed to the vertical motion of the end of the pipe (see Fig. 2.11) that introduces a rotational flexibility at one end of the spring. Finally, for the 30-2023 spring, the predictions of the numerical model agree well with the test results.

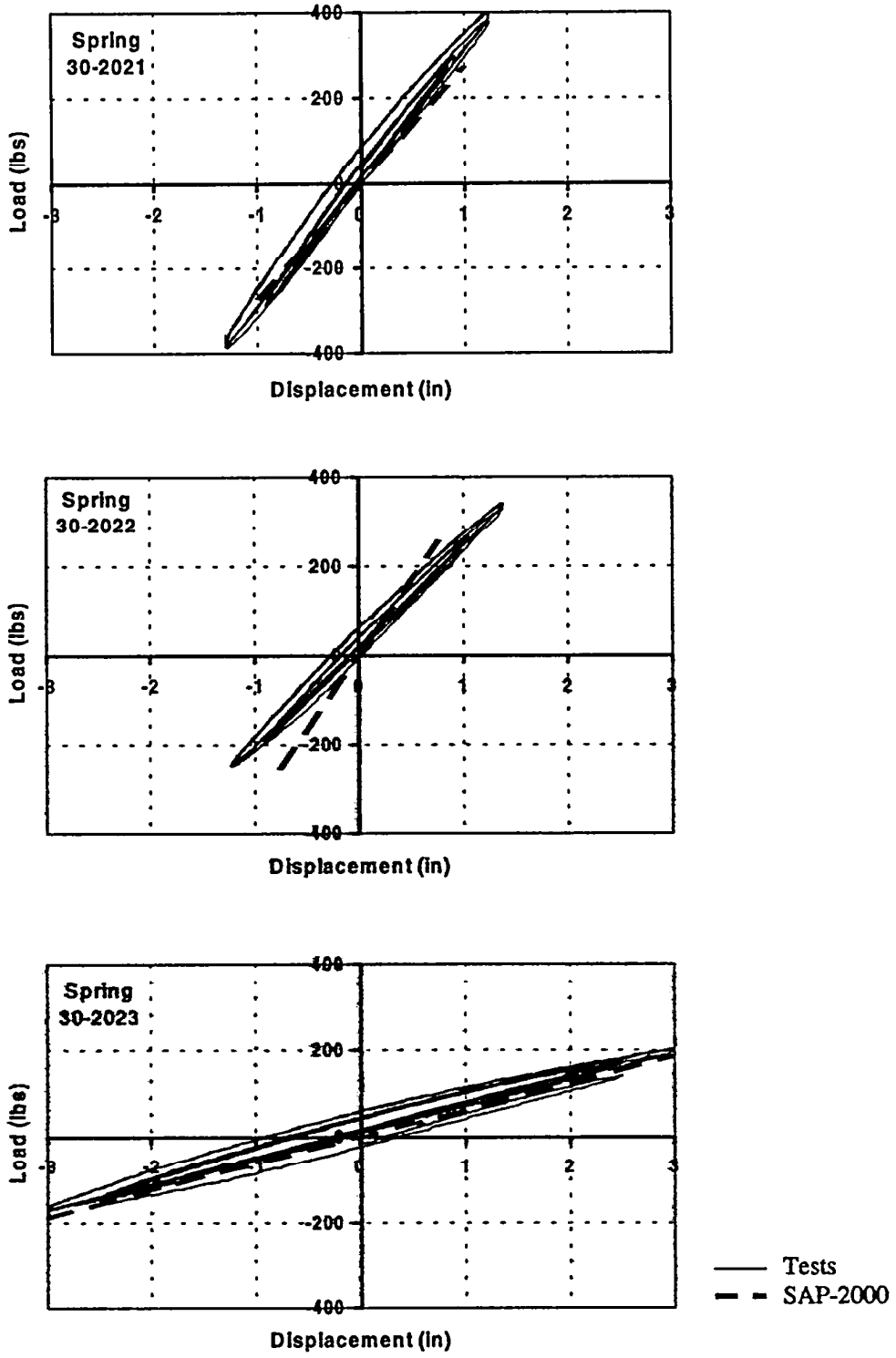

Figure 2.13 Load-Displacement Responses of Spring Connectors for Ductility Less than Unity.

Figure 2.14 presents the load-displacement response of each spring connector obtained for the complete range of ductility levels considered in the tests. The three spring connectors tested exhibit large and stable hysteresis loops with good energy dissipation capabilities. For ductility levels less than four, the hysteresis loops are nearly symmetric about the load axis. For larger ductility levels, the stiffness of springs 30-2021 and 30-2022 increases for negative loading and deformation (opening of the spring conductor) because of the tension stiffening effect. This effect is more predominant for spring 30-2021 than for spring 30-2022. Because of its lower stiffness, this tension stiffening effect is not observable for spring 30-2023. Also the load level developed by

Spring 30-2023 is significantly lower than the loads induced in the other two springs.

Two of the spring connectors (30-2022 and 30-2023) were tested to failure. During the last cycle of each test, the specimen was pulled monotonically until failure occurred. Figure 2.15 presents photographs of the failure region of each of the spring connectors. For both specimens, failure occurred across the net area of the cast-aluminum terminal pad connection that is welded to the aluminum tubing. Although failures occurred for large ductility levels in the spring connector of about 10, they were extremely brittle. The recorded failure loads were 8.3 kips and 9.0 kips for springs 30-2022 and 30-2023, respectively. These correspond to a very low failure tensile stress of less than 4 ksi across the net area.

2.8 Bilinear Modeling

The load-displacement hysteretic behavior of the three spring connectors can be simply modeled by a bi-linear solid with elastic stiffness K_o, post-yield stiffness βK_o, and yield force F_y, as illustrated in Fig. 2.16. Table 2.3 presents numerical values K_o, βK_o, and F_y, based on linear-regressions of the envelope curves of each of the loops (backbone curves). Figure 2.17 compares the predictions of the bi-linear models to the experimental data for the same displacement histories used in the quasi-static tests.

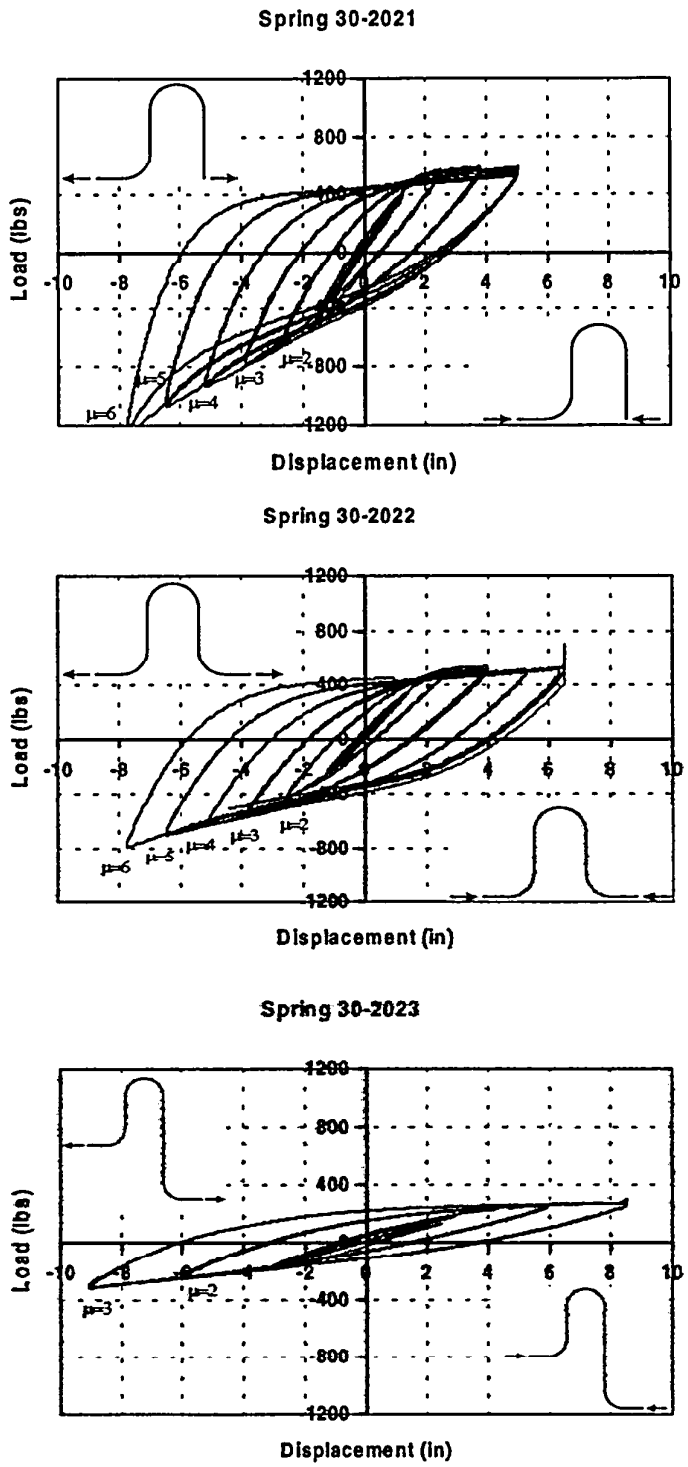

Figure 2.14 Load-Displacement Responses of Spring Connectors for all Ductility Levels.

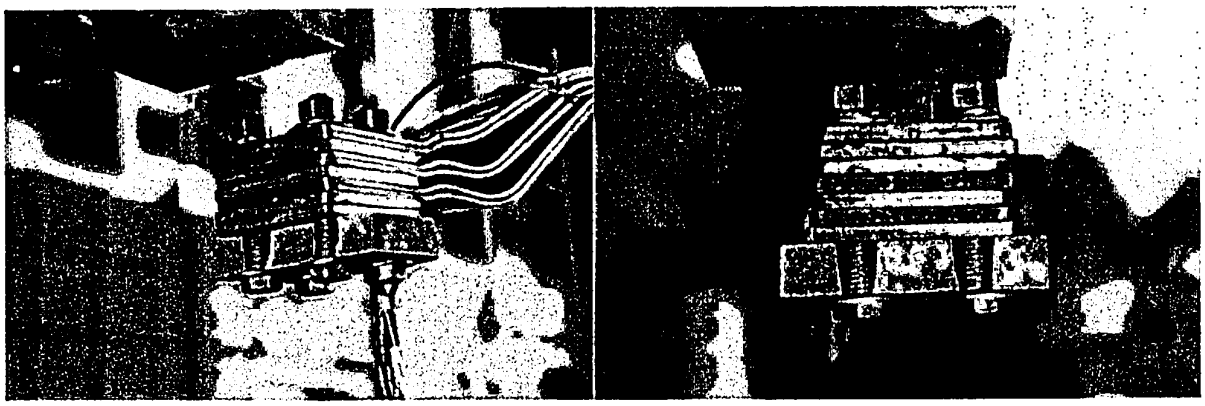

Spring 30-2022 **Spring 30-2023**

Figure 2.15 Failure Surfaces for Springs 30-2022 and 30-2023.

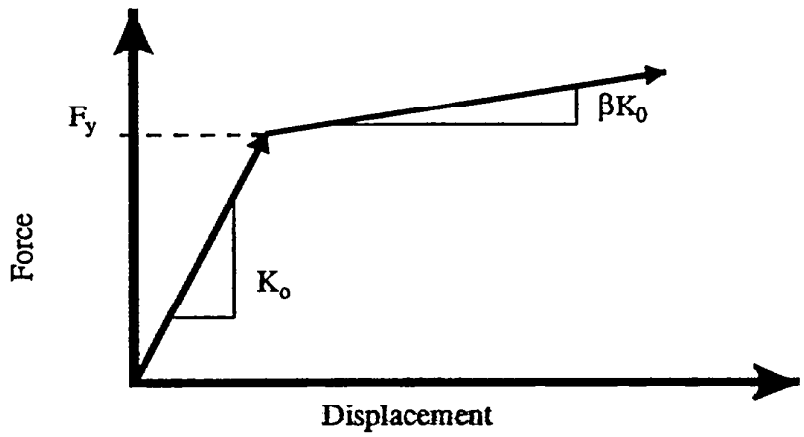

Figure 2.16 Bi-Linear Modeling of Spring Connectors.

Table 2.3 Numerical Values of Parameters for Bi-Linear Modeling of Spring Connectors.

Spring	Initial Stiffness K_o (lbs/in)	Post-Yield Stiffness βK_o (lbs/in)	Strain-Hardening Ratio, β	Yield Force F_y (lbs)
30-2021	308	79	0.26	401
30-2022	233	61	0.26	347
30-2023	63	21	0.33	188

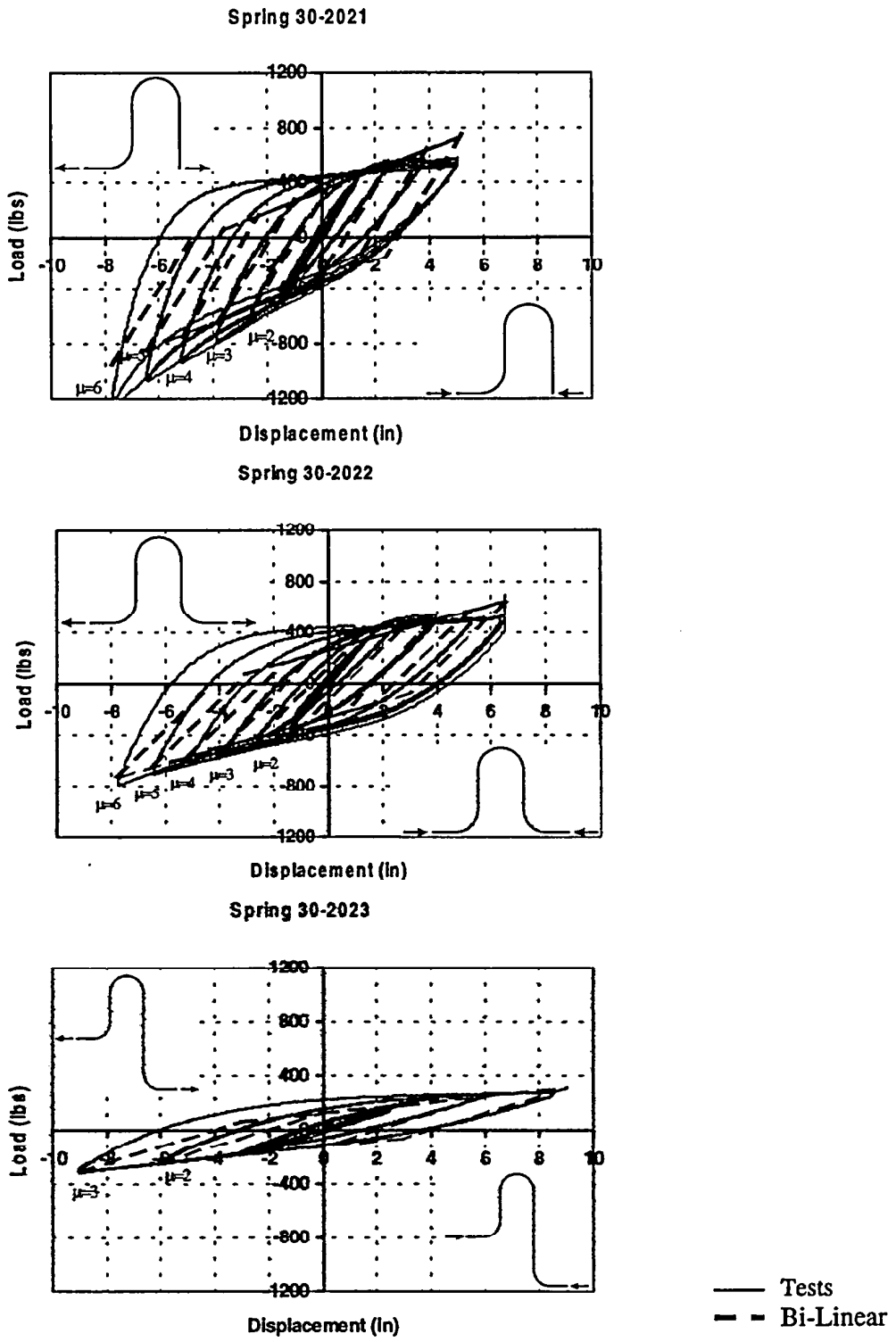

Figure 2.16 Bi-Linear Modeling of Spring Connectors.

2.9 Equivalent Viscous Damping Ratios

The energy dissipation capacity of each spring connector, for different displacement amplitudes, can be characterized by an equivalent viscous damping ratio, ζ. This equivalent damping ratio corresponds, for a given displacement amplitude, to a purely viscous dashpot that will dissipate the same amount of energy per cycle as the real spring connector. Based on the hysteresis loops shown in Fig. 2.14, the equivalent viscous damping ratio of a spring connector, ζ, at a given displacement amplitude, δ, is given by (Clough and Penzien, 1993):

$$\zeta = \frac{E_{D\delta}}{2\pi F_{\delta}\, \delta} \tag{1.3}$$

where $E_{D\delta}$ is the energy dissipated per cycle at a displacement amplitude δ and F_{δ} is the force at the displacement amplitude δ.

Table 2.4 presents the equivalent damping ratios for the three spring connectors tested at different displacement amplitudes corresponding to ductility levels greater or equal than one. The values presented correspond to the mean values of the different cycles for a given displacement amplitude. Only the symmetric cycles, before contact occurred, are presented. Figure 2.18 compares graphically these same results.

For the three specimens tested, the equivalent damping ratios increase with displacement amplitude, indicating higher energy dissipation capacity of the spring connectors at large inelastic displacements. Spring 30-2021 and spring 30-2022 exhibit damping ratios significantly higher than the more flexible spring 30-2023 for the complete range of displacement amplitudes.

Table 2.4 Equivalent Viscous Damping Ratios for Spring Connectors.

Spring 30-2021		Spring 30-2022		Spring 30-2023	
Displacement Amplitude (in)	Equivalent Damping Ratio (%)	Displacement Amplitude (in)	Equivalent Damping Ratio (%)	Displacement Amplitude (in)	Equivalent Damping Ratio (%)
1.0	2.84	1.0	2.00	2.3	4.52
1.3	4.75	1.3	3.00	3.0	5.56
2.6	13.1	2.6	10.1	6.0	17.6
3.9	18.0	3.9	20.8	6.0	23.0
5.2	20.1	5.2	29.9		
6.5	---	6.5	31.3		

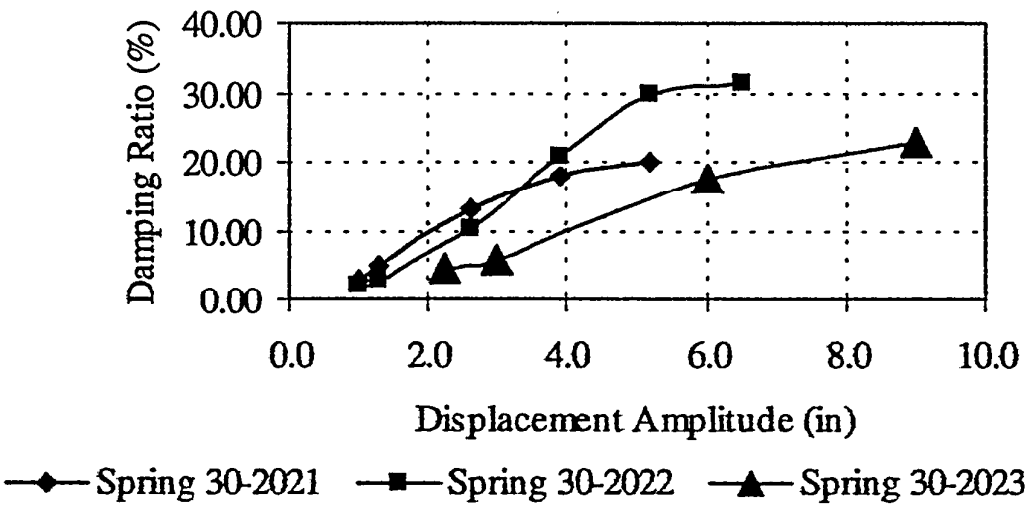

Figure 2.18 Comparison of Equivalent Viscous Damping Ratios for Spring Connectors.

3. QUASI-STATIC TEST OF RIGID BUS SLIDER

This chapter describes the quasi-static test performed on the rigid bus slider specimen provided by PG&E. This test was performed in the longitudinal direction of the bus assembly under prescribed displacement history.

3.1 Description of Test Specimen

Two identical rigid bus slider assemblies were supplied by PG&E. One was used for the quasi-static test and the other for the shake table tests. Figure 3.1 presents a general view of the specimen. Drawings of the specimen are also included in Appendix A.

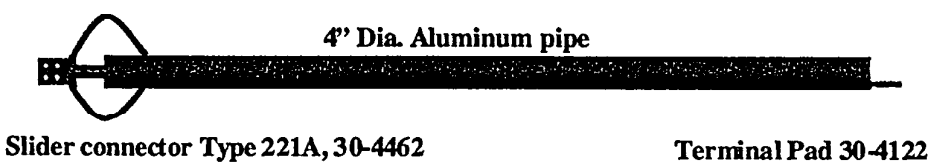

Figure 3.1 Rigid Bus Slider.

The specimen was made of a 10-ft long SPS aluminum pipe (4.5 in outside diameter and 4.026 in inside diameter) with a slider connection at one end, and an offset terminal pad at the other end.

The details of the slider connector are shown in Fig. 3.2. A shaft sliding against the inside surface of the pipe generates the friction force. A restoring force is also provided by two looped aluminum cables, welded on the pipe and on a terminal pad that is attached to the end of the shaft.

3.2 Experimental Set-Up for Quasi-Static Test

The experimental set-up used for the quasi-static test on the rigid bus slider assembly was similar as the one used for the quasi-static tests on the rigid bus-spring connector assemblies described in Chapter 2 (see section 2.3). Figure 3.3 presents a photograph of the connection detail at the end of the slider connector.

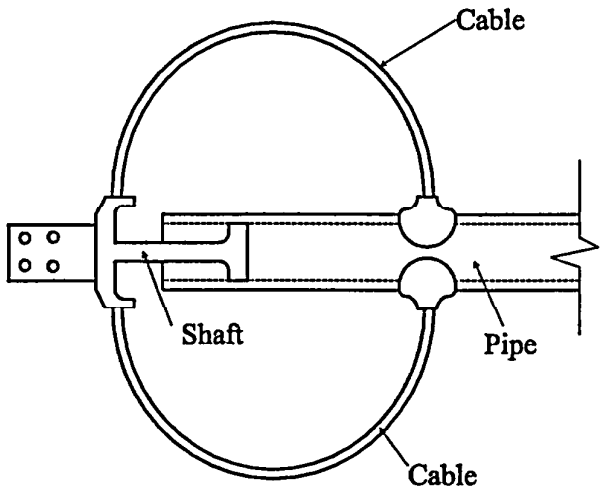

Figure 3.2 Slider Connector.

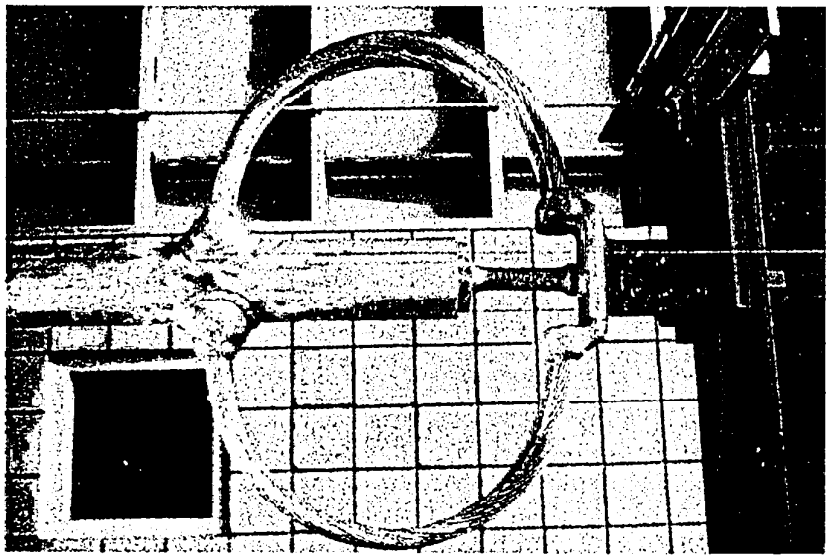

Figure 3.3 Connection at End of Slider Connector.

3.3 Instrumentation

Only the instrumentation required to measure the force displacement hysteresis loops in the longitudinal direction of the rigid bus slider assembly was installed. The force was measured across the 10-kip load cell that was inserted between the head of the actuator and the aluminum pipe (see section 2.3), and the displacement was measured across the full length of the specimen.

3.4 Test Protocol

The ATC-24 loading protocol (Applied Technology Council, 1992), used for the quasi-static tests of the rigid bus assemblies (see section 2.5), was used once again to perform the quasi-static test on the rigid bus slider assembly. In the case of the slider, however, the yield displacement must be defined differently since Coulomb-type friction is responsible for the nonlinear behavior of the specimen. An arbitrary value of 1 in was taken as the yield displacement, δ_y, across the slider connector.

3.5 Experimental Results

Figure 3.4 presents photographs of the specimen at the maximum displacements achieved during the test. In the positive direction, the displacement was increased until contact occurred between the aluminum pipe and the terminal pad. In the negative direction, the displacement was increased until the shaft slid out of the aluminum pipe.

$\delta = +3.5$ in $\delta = -3.5$ in

Figure 3.4 Rigid Bus Slider at Maximum Displacements.

Figure 3.5 presents the load-displacement response of the rigid bus slider obtained for the complete range of displacements considered in the test. The specimen exhibits a behavior that is typical of a Coulomb-type friction system coupled with an elastic restoring force mechanism. Before the slider can move, the static friction between the shaft and the interior surface of the pipe must be overcome. For the specimen tested, this slip force can be estimated at 53 lbs. After slipping has started, the force increment is obtained by the elastic flexural deformation of the two cable loops. For the specimen tested, this elastic post-slip stiffness can be estimated at 83 lbs/in.

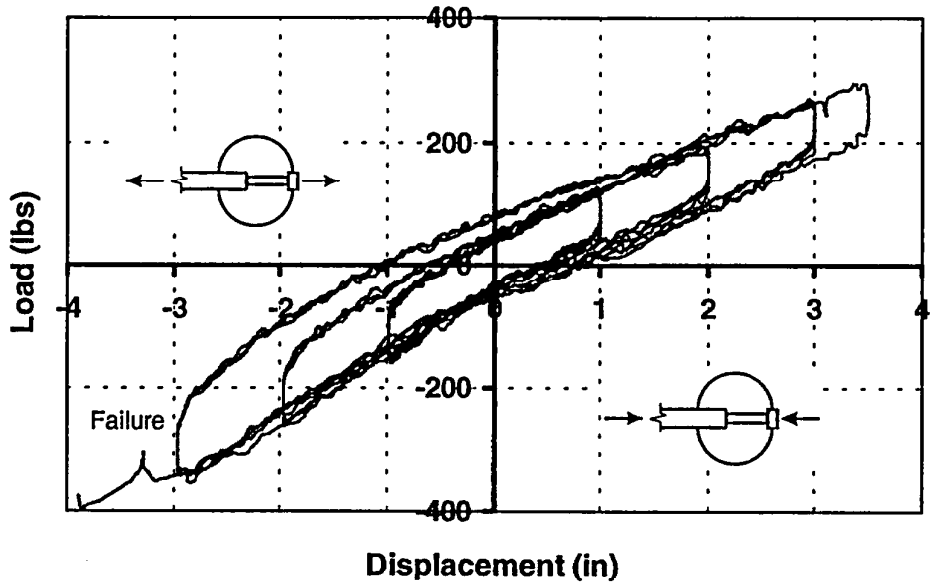

Figure 3.5 Load-Displacement Response of Rigid-Bus Slider.

Therefore, the overall behavior of the rigid bus slider tested can be simply modeled as a rigid-plastic behavior with a slip force of 53 lbs, and a post-slip stiffness of 83 lbs/in. Figure 3.6 compares the predictions of this simple model to the experimental data for the same displacement history used in the quasi-static-test.

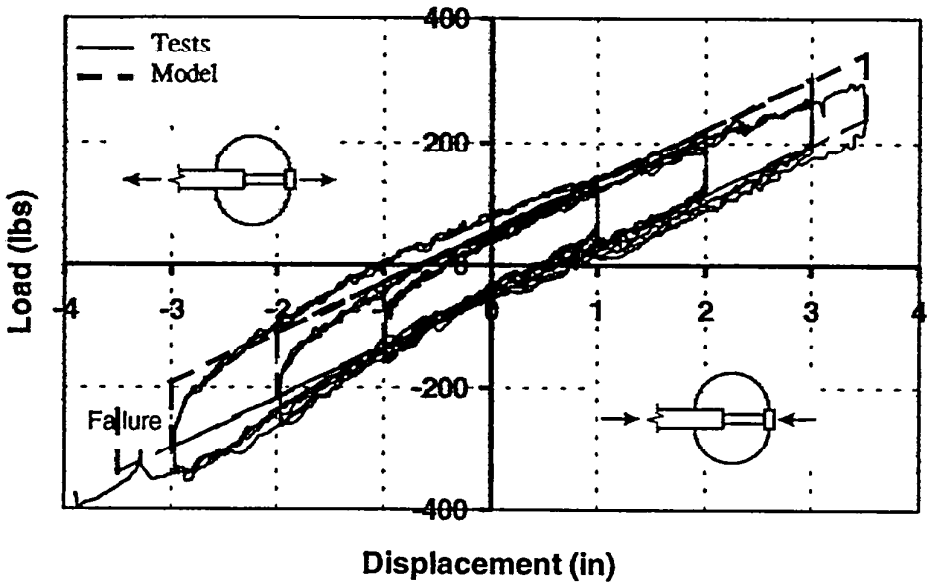

Figure 3.6 Rigid-Plastic Modeling of Rigid Bus Slider.

3.6 Equivalent Viscous Damping Ratios

The procedure described in section 2.9 was applied again on the hysteresis loops of Fig. 3.5 to evaluate the equivalent viscous damping ratio, ζ, of the bus slider for various displacement amplitudes. The resulting damping ratios are presented in Table 3.4 and are graphically shown in Fig. 3.7. For comparison purposes, the damping ratios computed for the three spring connectors tested and discussed in Chapter 2 are also shown in this figure.

Contrary to the spring connectors, the equivalent damping ratio of the bus slider decreases slightly with increasing displacement amplitude. The energy dissipated per cycle, $E_{D\delta}$, at a displacement amplitude δ can be written as:

$$E_{D\delta} = 4F_s\delta \tag{3.1}$$

where F_s is the slip force of the bus slider. The force, F_δ, at a displacement δ is given by:

$$F_\delta = F_s + K_e\delta \tag{3.2}$$

where K_e is the elastic restoring stiffness. Substituting equations (3.1) and (3.2) into equation (1.3) leads to a theoretical expression for the damping ratio, ζ, for the bus slider:

$$\zeta = \frac{2F_s}{\pi(F_s + K_e\delta)} \tag{3.3}$$

Equation (3.3) shows that the damping ratio of the bus slider decreases with increasing displacement amplitudes. For a slip force $F_s = 53\,lbs$, and a restoring stiffness $K_e = 83\,lbs/in$, equation (3.3) yields damping ratios of 0.25, 0.15, and 0.11 for displacement amplitudes $\delta = 1, 2, and\ 3\,in$, respectively. These predicted values agree reasonably well with the experimental values shown in Fig. 3.7.

For the range of displacements allowed by the slider, however, the equivalent viscous damping ratios provided by the bus slider are higher that the ones exhibited by the three

spring connectors. This result indicates the superior energy dissipation capacity of the bus slider at small displacement amplitudes.

Table 3.4 Equivalent Viscous Damping Ratios for Bus Slider.

Displacement Amplitude (in)	Equivalent Damping Ratio (%)
1.0	19.1
2.0	17.5
3.0	15.6

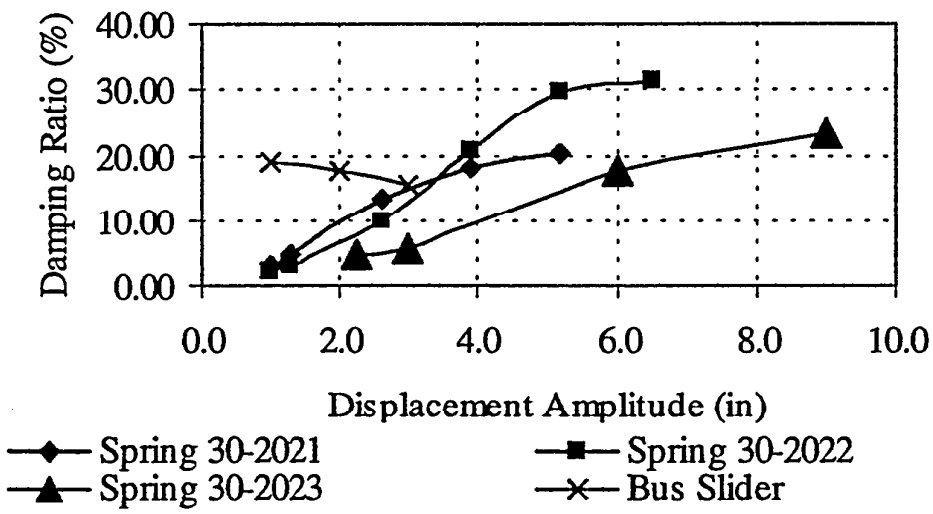

Figure 3.7 Comparison of Equivalent Viscous Damping Ratios for Bus Slider and Spring Connectors.

4. QUASI-STATIC TESTS OF FLEXIBLE BUS ASSEMBLIES

This chapter describes the full-scale quasi-static tests performed on two different types of flexible bus assemblies (cables). These tests were performed in the longitudinal direction of the assemblies under prescribed initial slackness and displacement history.

4.1 Description of Test Specimens

Three different flexible bus assemblies were supplied by PG&E for the quasi-static and shake table tests. Figure 4.1 presents a general view of the three specimens. Drawings of the specimens are included in Appendix A.

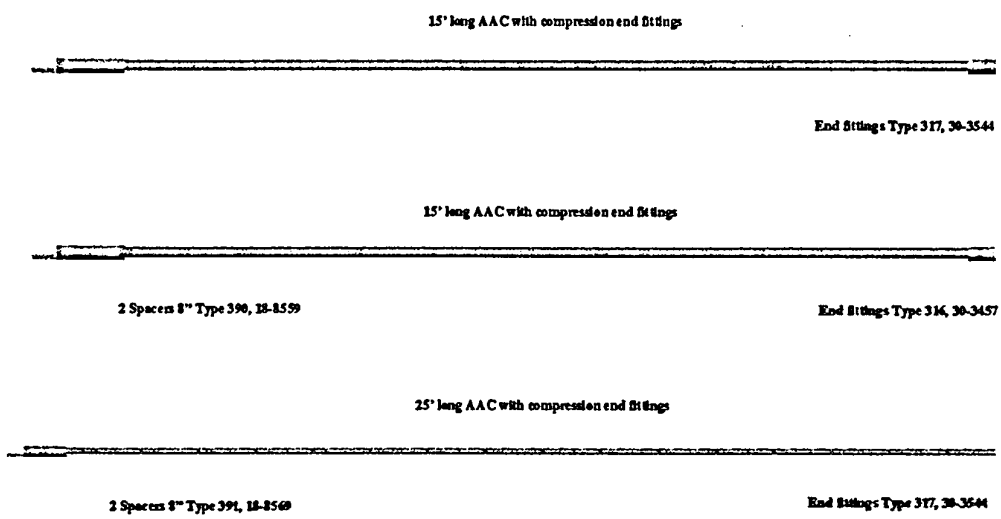

Figure 4.1 Flexible Bus Assemblies.

The first specimen consisted of a 2300 MCM single conductor, 15 ft long, with two compression end fittings. The 2300-type all aluminum cable (AAC) has a nominal diameter of 3.000 in and is composed of 49 wires. Its rated tensile strength is 34 300 lbs. The second specimen consisted of 1113 MCM bundled conductors, 15 ft long, with two spacers and two compression end fittings. The 1133-type all aluminum cable (AAC) has a nominal diameter of 1.095 in and is composed of 31 wires. Its rated tensile strength is 18 500 lbs. Finally, the third specimen consisted of a 2300 MCM bundled conductors, 25 ft long, with two spacers and two compression end fittings.

During unpacking of the specimens, it was observed that the cables were damaged at several locations. As shown in Fig. 4.2, individual strands were pulled apart permanently presumably because of the very tight loops used for shipping the cables. This local damage induced zones of unequal flexural flexibility in the cables, and caused problems in setting the initial geometry of the test specimens.

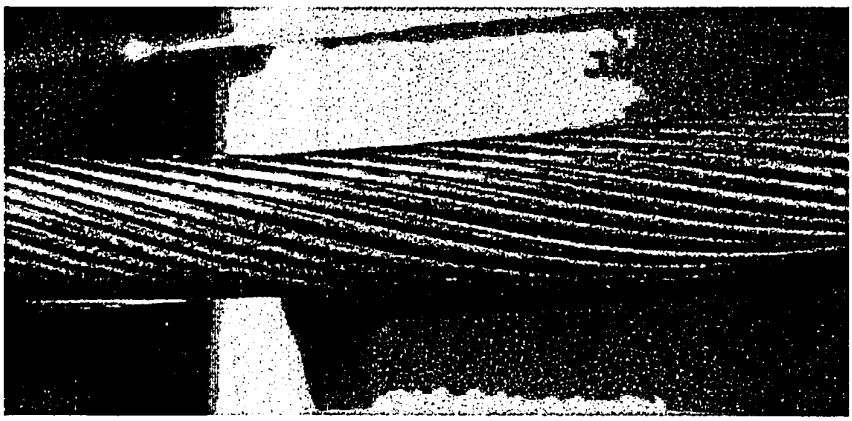

Figure 4.2 Local Damage to Flexible Conductor.

4.2 Experimental Set-Up for Quasi-Static Tests

The experimental set-up for the quasi-static tests on the flexible bus assemblies was similar as the one used for the quasi-static tests on the rigid bus-spring connector assemblies in Chapter 2 (see section 2.3).

The amount of initial slackness introduced in the cables was based on a single vertical loop having a maximum vertical displacement approximately equal to 10% of the length of each specimen. Because of the very low flexural rigidity of the specimens and the local damage experienced by the cables, it became very difficult to shape the specimens in this initial geometry. Figure 4.3 shows photograph of the first specimen (a 2300 MCM single conductor) supported in its initial geometry by a crane. When the crane support was removed just before the start of the test, the cable sagged laterally. For the 1113 MCM bundled conductors, it was easier to maintain the initial geometry of the specimen, as shown in Fig. 4.4.

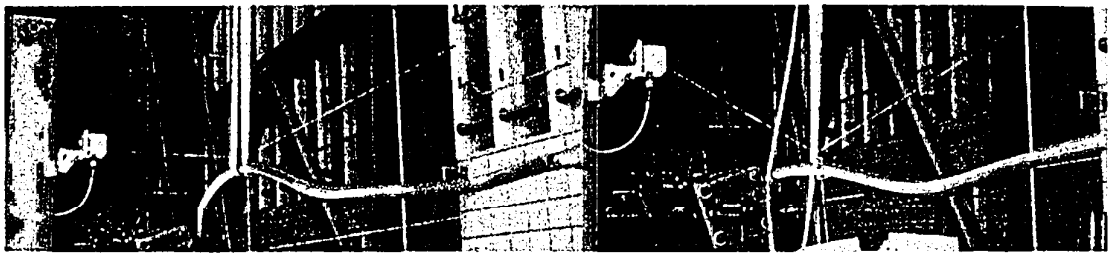

With Crane Support **Without Crane Support**

Figure 4.3 Initial Geometry of 2300 MCM Single Conductor.

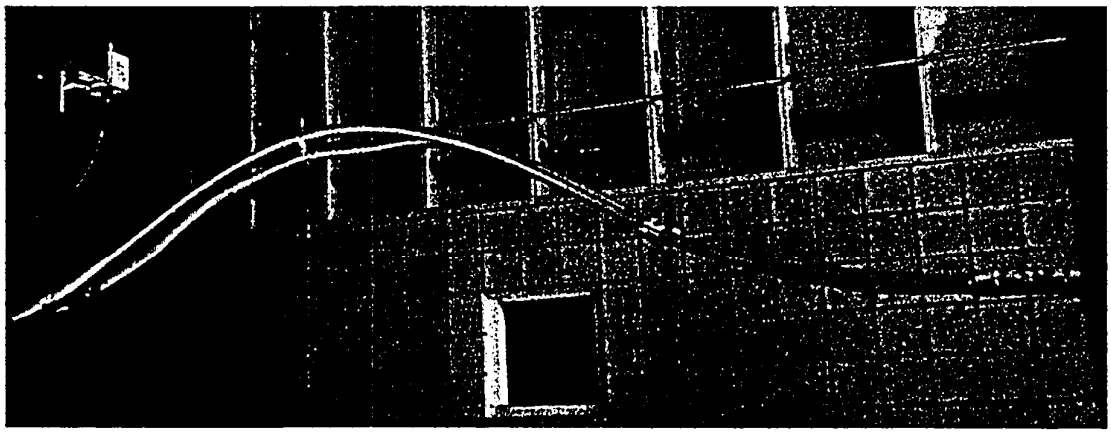

Figure 4.4 Initial Geometry of 1113 MCM Bundled Conductors.

4.3 Instrumentation

Only the instrumentation required to measure the force displacement hysteresis loops in the longitudinal direction of the flexible bus assemblies was installed. The force was measured across the 10-kip load cell that was inserted between the head of the actuator and the aluminum pipe (see section 2.3), and the displacement was measured across the full length of the specimens.

4.4 Test Protocol

The ATC-24 loading protocol (Applied Technology Council, 1992), used for the quasi-static tests of the rigid bus assemblies (see section 2.5), was used once again to perform the quasi-static tests on the flexible bus assemblies. As for the case of the rigid bus slider, an arbitrary value of 1 in was taken as the yield displacement, δ_y, across each of the specimen.

4.5 Experimental Results

Figures 4.5 and 4.6 present the load-displacement responses of the 2300 MCM single conductor and of the 1113 MCM bundled conductors, respectively. The behavior is similar for both specimens with virtually zero stiffness in compression and elastic tensile stiffness when the initial slack is overcome. The maximum compressive load measured during the two tests was less than 50 lbs. For the specimen incorporating 1113 MCM bundled conductors, the cable dropped from its initial geometry at a tensile displacement of 2.5 in. This reduced the compressive resistance of the cables to approximately 20 lbs for the subsequent cycles. Also for the 1113 MCM bundled conductors, the two cables were manufactured with different lengths, as seen in Fig. 4.7. This caused one cable to be taut much more than the other one.

Based on these results, it became clear that for the length of conductors tested the flexural stiffness of the cables played an insignificant role in the load-displacement responses. Therefore, it was decided not to test the third specimen that incorporated even longer cables (25 ft).

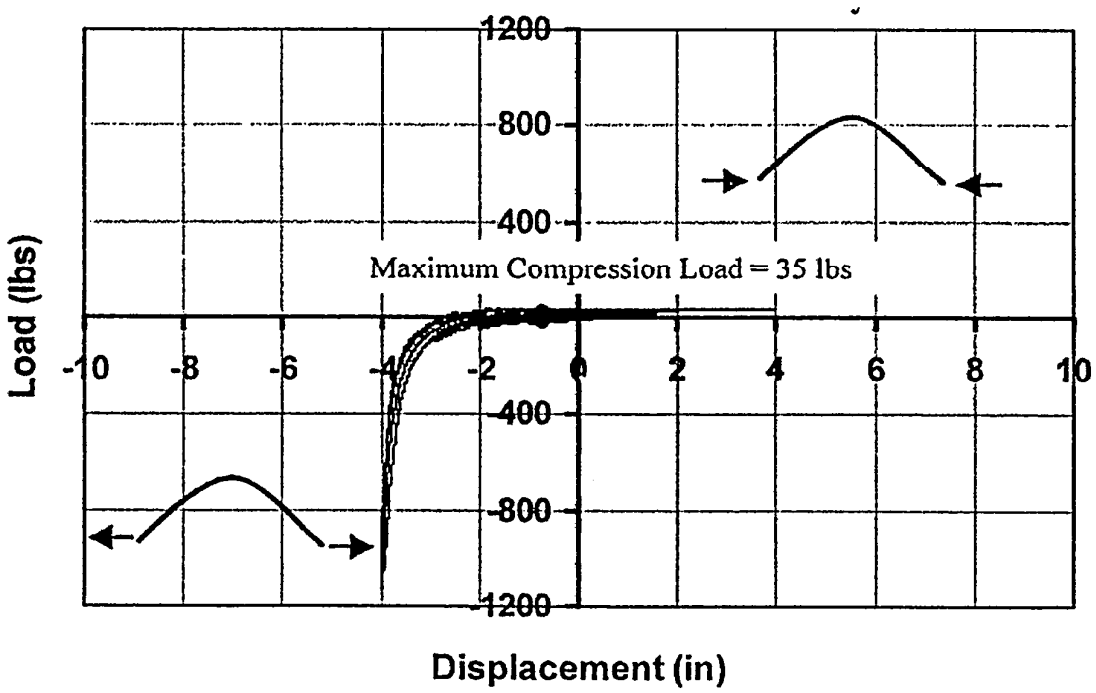

Figure 4.5 Load-Displacement Response of 2300 MCM Single Conductor.

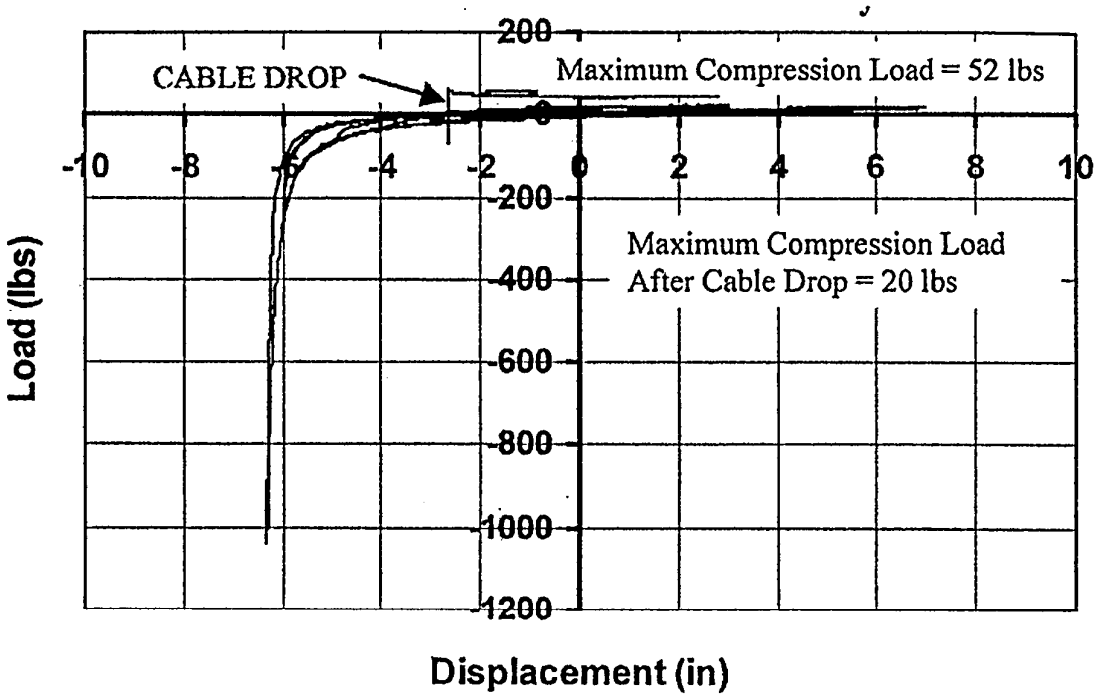

Figure 4.6 Load-Displacement Response of 1113 MCM Bundled Conductors.

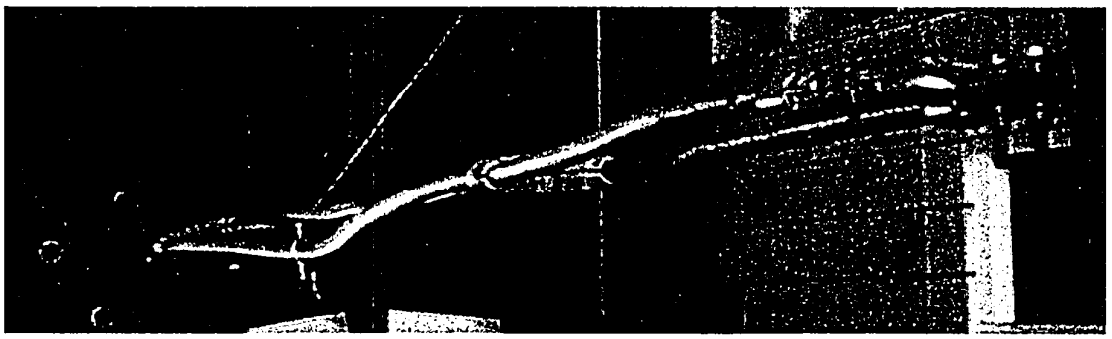

Figure 4.7 Unequal Cable Lengths for 1113 MCM Bundled Conductors.

5 SHAKE TABLE TESTS OF PAIRS OF GENERIC SUBSTATION EQUIPMENT CONNECTED WITH RIGID BUS ASSEMBLIES

This chapter describes the shake table tests performed on five pairs of generic substation equipment connected with three different rigid bus assemblies. Simulated horizontal ground motions were applied in the longitudinal direction of the bus assemblies by the uniaxial earthquake simulation facility at UC-San Diego. The variables considered in the tests were:

- the dynamic characteristics of the generic equipment
- the types of rigid bus assemblies
- the simulated ground motions
- the intensities of the simulated ground motions

5.1 Description of UC-San Diego Uniaxial Earthquake Simulation Facility

The uniaxial earthquake simulation system at UC-San Diego features a 4.8 tons shake table made of an all-welded steel construction, as shown in Figure 5.1. The shake table has plan dimensions of 10 ft x 16 ft with a specimen payload capacity of 40 tons. A 90-kips fatigue-rated actuator drives the system. The bearing system consists of eight 5-in Garlock DU cylinders sliding on two stationary shafts. The usable peak-to-peak stroke is 12 in. The flow rate of the hydraulic system allows a peak sinusoidal velocity of 40 in/s. The actuator can induce peak accelerations of 9.0 g for the bare table and 1.0 g for the fully loaded table. The workable frequency range of the simulator spans from 0 to 50 Hz.

The control system of the shake table includes an advanced, second generation, digital controller incorporating a Three-Variable-Control (TVC), together with Adaptive Inverse Control (AIC), On-Line Iteration (OLI) techniques and Resonance Canceling Notch Filters. This advanced control system allows the reproduction of earthquake ground motions with high fidelity (Filiatrault et al., 1996, 2000).

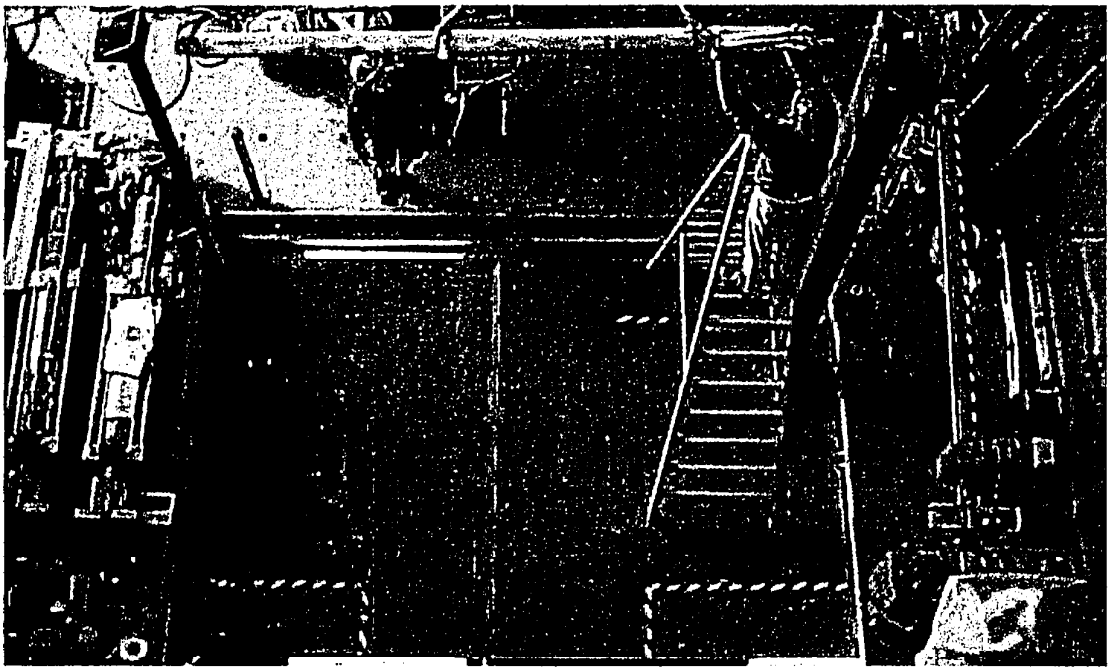

Figure 5.1 Shake Table of the UC-San Diego Uniaxial Earthquake Simulation System.

5.2 Description of Generic Substation Equipment

Initially, four different pairs of generic substation equipment were considered for the shake table tests. Each pair of generic equipment was designed to be representative of the dynamic properties of actual interconnected substation electrical equipment. Table 5.1 presents the target dynamic characteristics of the four pairs of generic equipment.

Table 5.1 Target Dynamic Characteristics of Pairs of Generic Equipment.

Pair	Equipment A			Equipment B		
	Equipment No.	Seismic Weight (lbs)	Natural Frequency (Hz)	Equipment No.	Seismic Weight (lbs)	Natural Frequency (Hz)
1	1	800	2	3	150	6
2	1	800	2	4	150	12
3	2	90	2	3	150	6
4	2	90	2	4	150	12

From table 5.1, four different generic equipment specimens are required to satisfy the test schedule. For each specimen, the seismic weight and the natural frequency are fixed.

Therefore, the design variables are the lateral stiffness of each specimen and the appropriate strength to assure an elastic dynamic response. For simplicity, it was decided to anchor steel cantilevered columns of appropriate stiffness and strength to the shake table. Figure 5.2 illustrates the test set-up for the shake table tests. In order to mobilize sufficient strength for a given lateral stiffness, the height of all cantilevers was fixed at 14 ft. Table 5.2 presents the tubular steel sections used to fabricate each column. Appendix B presents the shop drawings used to fabricate the specimens.

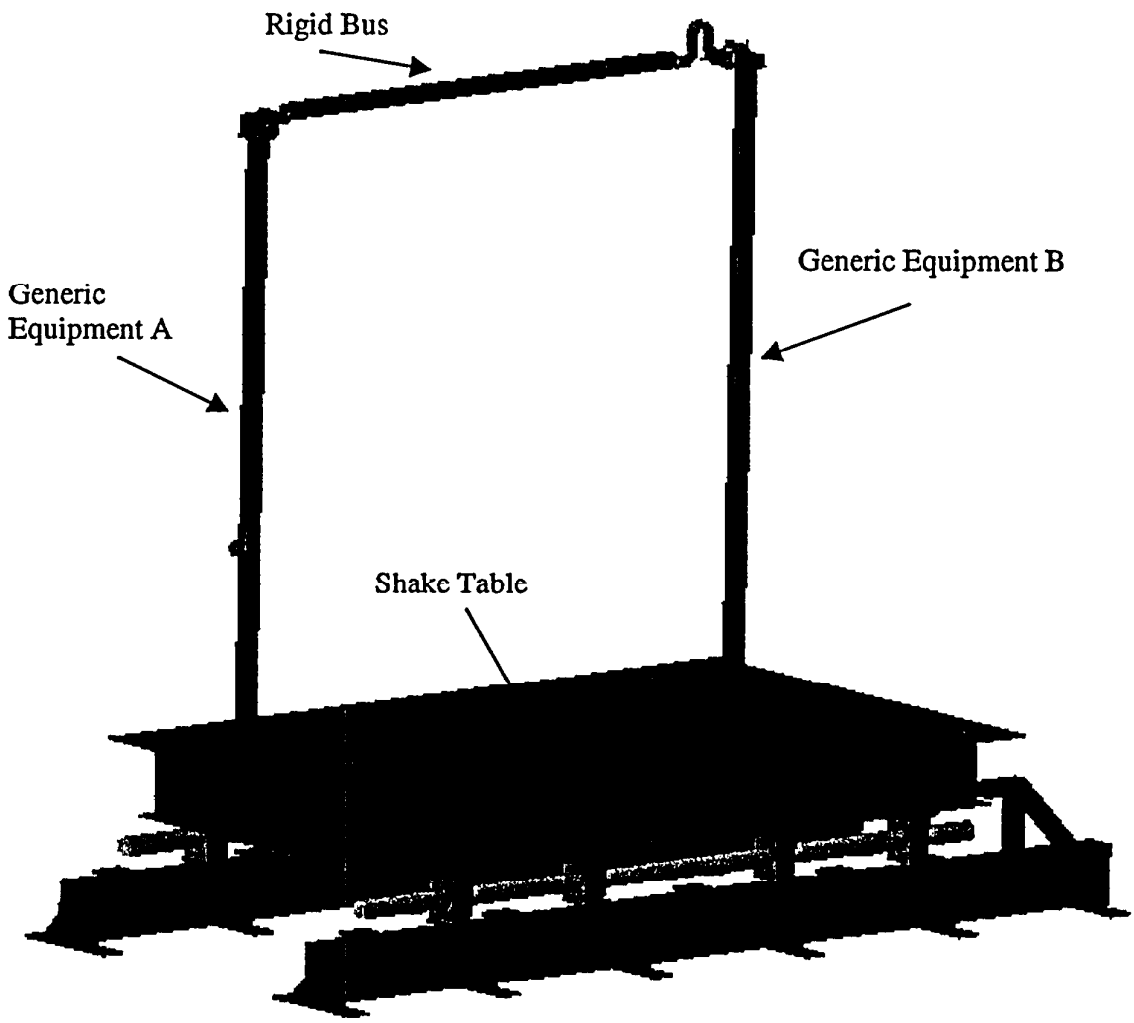

Figure 5.2 Test Set-Up for Shake Table Tests.

Table 5.2 Tubular Steel Sections Used for Generic Equipment Specimens.

Equipment	Seismic Weight (lbs)	Natural Frequency (Hz)	Tubular Section
1	800	2	7x5x3/16 in
2	90	2	3-1/2x2-1/2x1/4 in
3	150	6	8x6x3/16 in
4	150	12	12x8x5/16 in

In order to adjust the natural frequency of each equipment specimen, supplemental steel weights were added at the top of the columns, as illustrated in Fig. 5.3. Table 5.3 indicates the final lumped weight added at the top of each equipment specimen along with the total weight of each specimen.

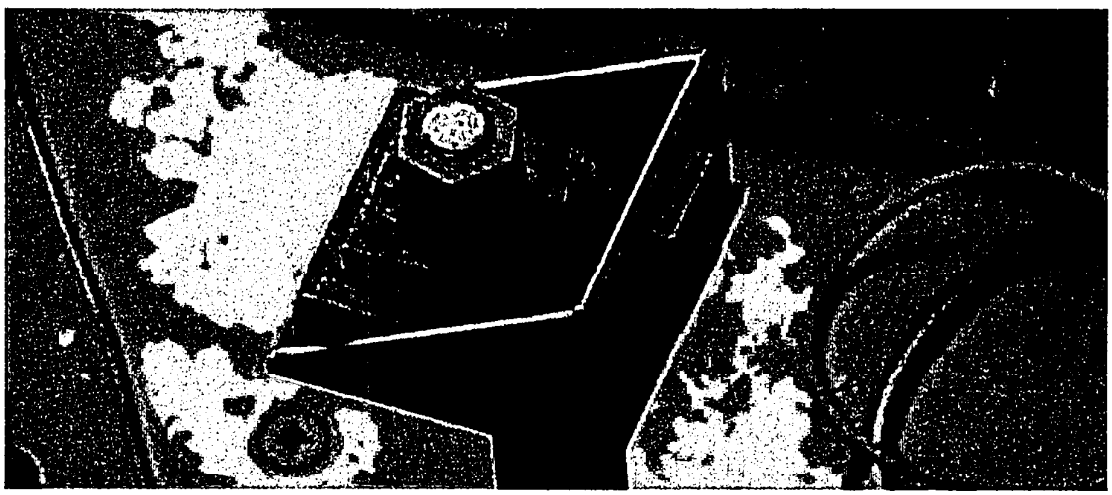

Figure 5.3 Supplemental Steel Weights at Top of Generic Equipment Specimen.

Table 5.3 Values of Steel Weights at Lumped Top of Generic Equipment Specimen.

Equipment	Target Seismic Weight (lbs)	Target Natural Frequency (Hz)	Lumped Top Weight (lbs)	Total Weight (lbs)
1	800	2	747	951
2	90	2	76	200
3	150	6	94	334
4	150	12	30	595

5.3 Instrumentation

The instrumentation used during the shake table tests of the generic interconnected equipment included the following measurements:

- Absolute displacement, velocity and acceleration of the shake table;
- Absolute displacement, velocity and acceleration at the top of each equipment
- Relative displacement between equipment
- Axial strain at the location of maximum moment in the spring connector

The velocity measurements were obtained directly with special string potentiometers calibrated with velocity.

5.4 Earthquake Ground Motions and Shake Table Fidelity

Two recorded components of near-field earthquake ground motions were used for the seismic tests on the shake table: Tabas (1978 Iran earthquake) and Newhall (1994 Northridge, California, earthquake). These two records are representative of earthquakes known to have a high potential for damaging structures and equipment. Figure 5.4 presents the acceleration time-histories for both full-scale records (100% span).

The Tabas record was modified using a nonstationary response-spectrum matching technique developed by Abrahamson (1997) to match the IEEE 693 (1997) target response spectrum for testing, and it was further high-pass filtered using a cut-off frequency of 1.5 Hz so as not to exceed the displacement limit of 6 in of the shake table.

Preliminary nonlinear dynamic time-history analyses were performed to estimate the response of the interconnected equipment. Based on the results of these preliminary analyses, different intensities were retained for each ground motion record. Table 5.4 presents these intensities for the two ground motions considered. Significant inelastic response of the rigid bus conductors was anticipated at the largest intensities. Note also that certain tests were conducted at intermediate intensity levels.

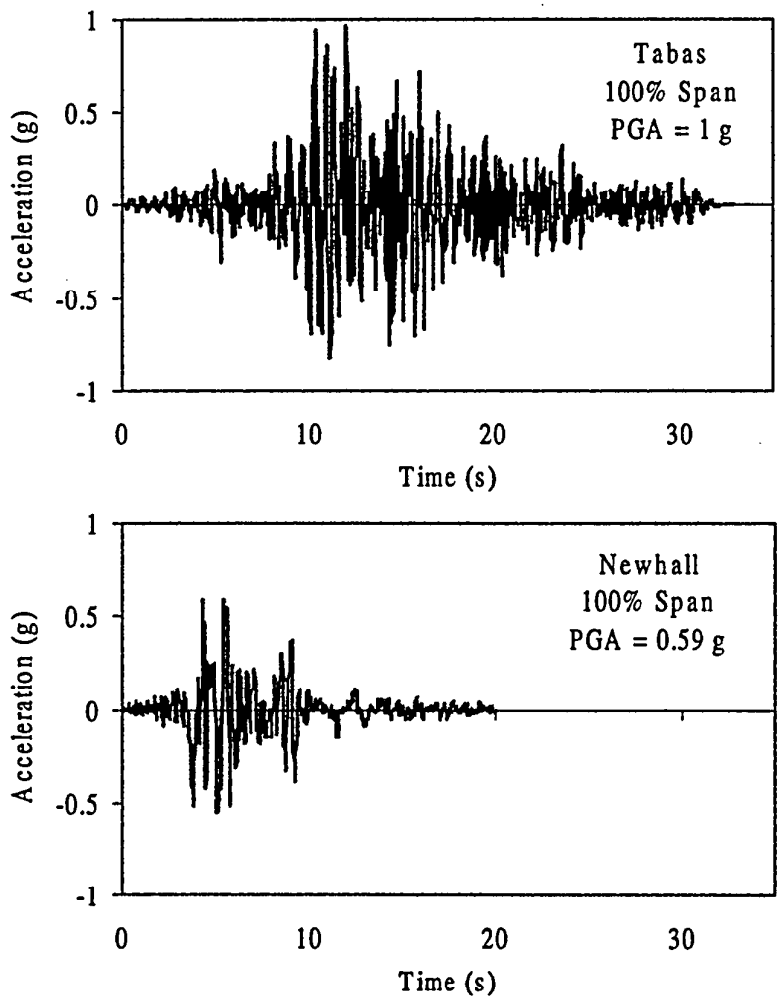

Figure 5.4 Acceleration Time-Histories of Earthquake Ground Motions.

Table 5.4 Intensities of Earthquake Ground Motions Retained for the Shake Table Tests

Record	Intensity 1 (% Span)	Intensity 2 (% Span)	Intensity 3 (% Span)
Tabas	25	50	200
Newhall	30	100	---

The performance of the shake table was optimized for each record and intensity using the On-Line Iteration (OLI) technique of the electronic controller. Figure 5.5 compares the absolute acceleration response spectra, at 5% damping, of the accelerograms of Fig. 5.4 scaled at the different intensities listed in Table 5.4 (desired signals) with the response spectra of the acceleration time-histories recorded on the shake table (feedback signals). The feedback signals shown represent the mean values of three different tests on the shake table.

As discussed earlier, the target natural frequencies of the generic equipment varied between 2 and 12 Hz. The mean differences (in %) between the desired and the feedback spectral values in the 2-12 Hz frequency range are also indicated in Fig. 5.5. The maximum difference for all records is less than 6%. Based on this result, the performance of the shake table was considered adequate. For comparison purposes, each graph in Fig. 5.6 shows also the IEEE 693 (IEEE, 1997) required response spectrum for 2% damping and for high performance level amplified by a factor of two to account for the amplification of earthquake motion at the base of the generic equipment.

5.5 Shake Table Test Program

Three different types of shake table tests were conducted on the rigid bus conductors:

1) Frequency Evaluation Tests
2) Damping Evaluation Tests
3) Seismic Tests

These tests are briefly described below.

Tabas Record

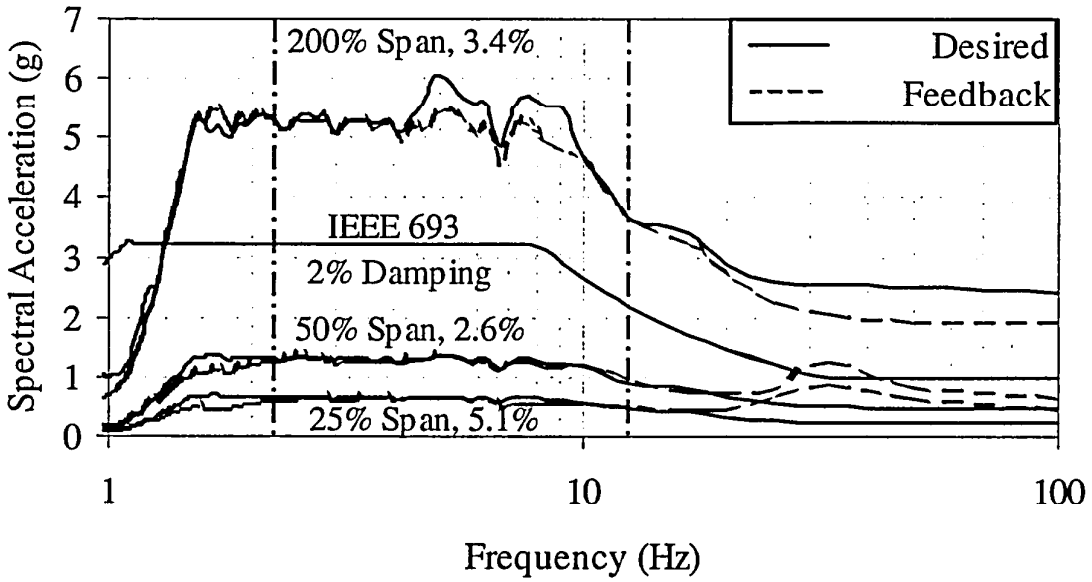

Newhall Record

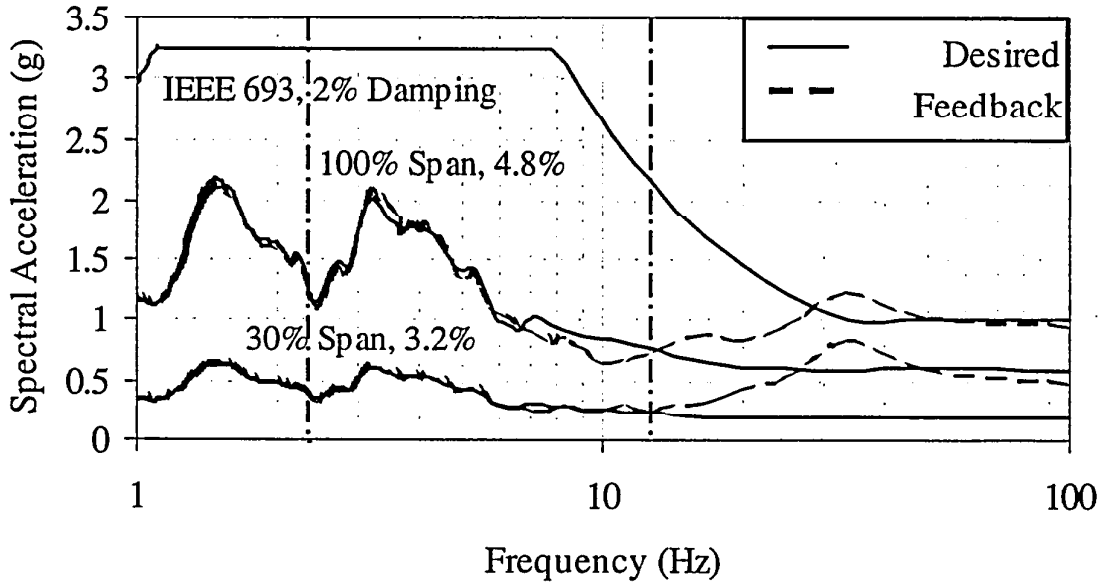

Figure 5.5 Absolute Acceleration Response Spectra, 5% Damping, Bare Shake Table.

5.5.1 Frequency Evaluation Tests

The purpose of the frequency evaluation tests was to identify the natural frequencies and mode shapes of the various pairs of interconnected generic substation equipment. For this purpose, a low-amplitude 0-40 Hz, clipped-band, and flat white noise excited each configuration. A dedicated ambient vibration analysis software (Experimental Dynamic Investigations, 1993) was used to determine the natural frequencies from power spectral density plots of the absolute acceleration records at the top of each equipment. The structural mode shapes were obtained from the amplitudes of the spectral peaks and by the phase and coherence between the measured acceleration time-histories. For all frequency evaluation tests, the following test protocol was followed:

- Nyquist frequency = 40 Hz
- Sampling rate = 80 Hz
- Number of points per sampling windows = 2048
- Duration of each sampling window = 25.6 s
- Frequency resolution = 0.0391 Hz
- Number of sampling windows = 8
- Total duration = 204.8 s

5.5.2 Damping Evaluation Tests

The purpose of the damping evaluation tests was to estimate the first modal equivalent viscous damping of each equipment configuration. In these tests, each pair of generic equipment was excited by a low-amplitude base sinusoidal input at its previously identified fundamental frequency. When a steady-state response was obtained, the input was suddenly stopped and the absolute accelerations at the top of the equipment were recorded. The first modal damping ratio of the structural configuration was then established by the logarithmic decrement method (Clough and Penzien, 1993).

5.5.3 Seismic Tests

In the seismic tests, the ground motions defined in section 5.4 excited the pairs of interconnected equipment. All seismic test data were acquired at a sampling rate of 200 Hz to capture potential impacts between the rigid bus and the top of the Equipment.

5.6 Rigid Bus Specimens

Three different rigid bus connector assemblies were tested with each of the four pairs of interconnected equipment defined in Table 5.1. These rigid bus assemblies were:

1) The bus assembly with the spring connector 30-2022 described in Section 2.2.
2) The rigid bus slider described in Section 3.1.
3) A seismic connector with a 4 in diameter rigid bus developed by Bonneville Power Administration (BPA).

The first two rigid bus specimens were tested previously under quasi-static loading, as described in Chapters 2 and 3. The third rigid bus specimen was provided by PG&E only for the shake table tests and was not tested under quasi-static loading.

Figure 5.6 presents photographs of the BPA seismic connector tested on the shake table. The connector includes three vertically parallel 6061-T6 aluminum alloy, 1.3 in diameter, cables (Hood conductor, AAC/TW). These cables are welded to 6061-T6-aluminum alloy T-shape plates that are mounted to the rigid conductor. This seismic connector was similar to the specimen tested in a previous investigation at Portland State University (Starkel et al., 1998). Drawings of the BPA seismic connector are included in Appendix A of this report.

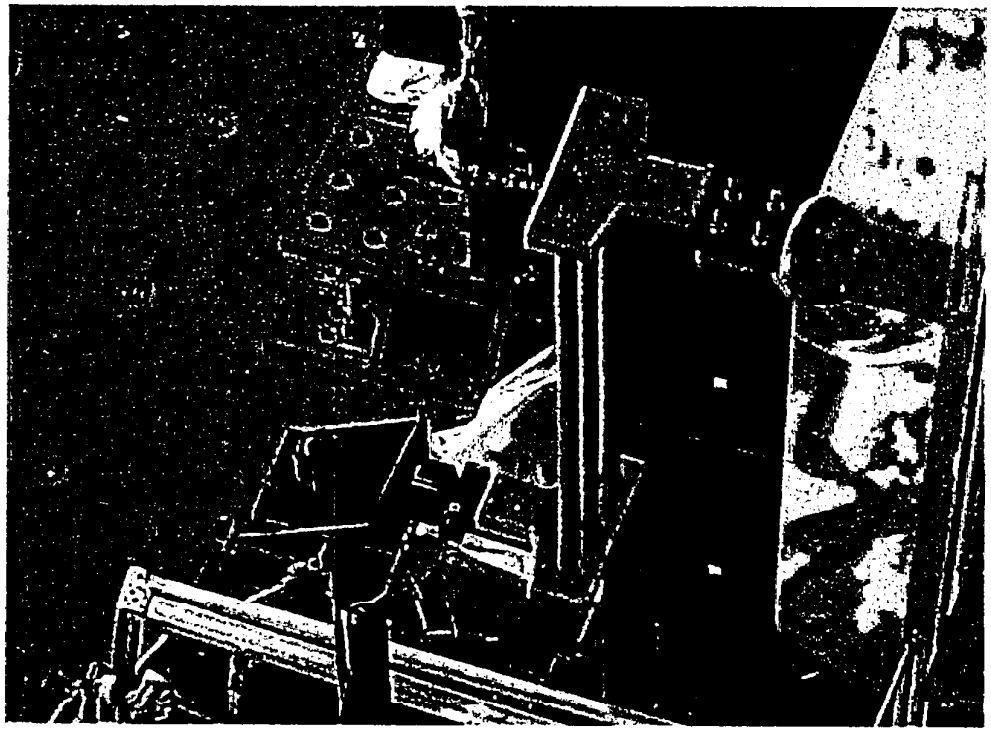

Detail of Seismic Connector

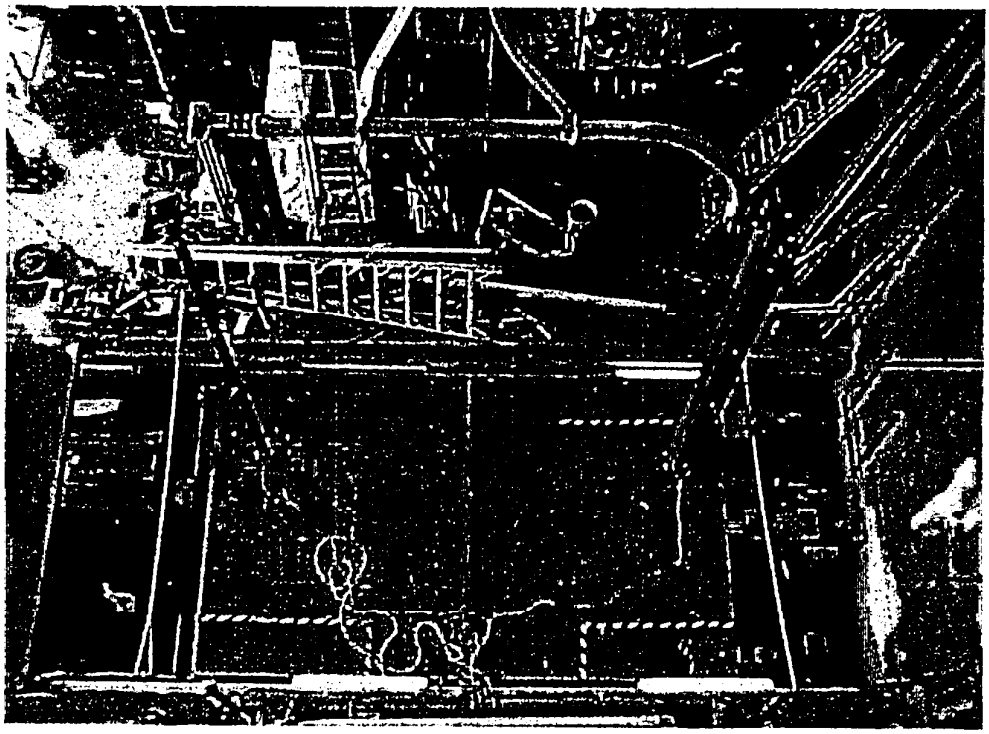

General Arrangement on Shake Table

Figure 5.6 BPA Seismic Connector.

5.7 Test Sequence

Table 5.4 presents the test sequence that was adopted for the shake table tests. Included are the frequency and damping evaluation tests, as well as the seismic tests under the various earthquake ground motion records. This sequence was developed in order to optimize the use of the rigid bus conductor specimens provided by PG&E. Note that some test numbers are missing from Table 5.4. These are tests that were originally scheduled but later cancelled in order to maintain the integrity of the equipment configurations until the end of the test sequence. Finally, tests listed with Pair No. 5 in Table 5.4 refers to Pair No. 2 with Equipment 4 modified with a lateral bracing member, as described in section 5.6.3.

Table 5.4 Shake Table Test Sequence

Test RB-#	Pair No.	Conductor	Test Description	Input Signal	Span (%)
1	4	None	Frequencies of Uncoupled Equipment	White Noise	---
2	4	None	Damping - A	Sinusoidal	---
3	4	None	Damping - B	Sinusoidal	---
4	4	Spring 30-2022	Frequencies of Coupled Equipment	White Noise	---
5	4	Spring 30-2022	Damping - A & B	Sinusoidal	---
6	4	Spring 30-2022	Seismic	Newhall	30
7	4	Spring 30-2022	Seismic	Newhall	100
8	4	Spring 30-2022	Seismic	Tabas	25
9	4	Spring 30-2022	Seismic	Tabas	50
10	4	None	Frequencies of Uncoupled Equipment	White Noise	---
11	4	None	Damping - A	Sinusoidal	---
12	4	None	Damping - B	Sinusoidal	---
13	4	Bus Slider	Frequencies of Coupled Equipment	White Noise	---
14	4	Bus Slider	Damping - A & B	Sinusoidal	---
15	4	Bus Slider	Seismic	Newhall	100
17	4	Bus Slider	Seismic	Tabas	50
18	4	Bus Slider	Seismic	Tabas	200
22	4	BPA Isolator	Frequencies of Coupled Equipment	White Noise	---
23	4	BPA Isolator	Damping – A & B	Sinusoidal	---
24	4	BPA Isolator	Seismic	Newhall	30
26	4	BPA Isolator	Seismic	Tabas	25
28	4	None	Seismic	Newhall	30
29	4	None	Seismic,	Newhall	100
30	4	None	Seismic	Tabas	25
31	4	None	Seismic	Tabas	50
33	3	None	Frequencies of Uncoupled Equipment	White Noise	100
35	3	None	Damping - B	Sinusoidal	100

Test RB-#	Pair No.	Conductor	Test Description	Input Signal	Span (%)
36	3	Spring 30-2022	Frequencies of Coupled Equipment	White Noise	---
37	3	Spring 30-2022	Damping – A & B	Sinusoidal	---
38	3	Spring 30-2022	Seismic	Newhall	30
39	3	Spring 30-2022	Seismic	Newhall	100
40	3	Spring 30-2022	Seismic	Tabas	25
41	3	Spring 30-2022	Seismic	Tabas	50
45	3	Bus Slider	Frequencies of Coupled Equipment	White Noise	---
46	3	Bus Slider	Damping – A & B	Sinusoidal	---
47	3	Bus Slider	Seismic	Newhall	100
49	3	Bus Slider	Seismic	Tabas	50
54	3	BPA Isolator	Frequencies of Coupled Equipment	White Noise	---
55	3	BPA Isolator	Damping – A & B	Sinusoidal	---
56	3	BPA Isolator	Seismic	Newhall	30
58	3	BPA Isolator	Seismic	Tabas	25
60	3	None	Seismic	Newhall	30
61	3	None	Seismic	Newhall	100
62	3	None	Seismic	Tabas	25
63	3	None	Seismic	Tabas	50
66	1	None	Frequencies	White Noise	---
67	1	None	Damping - A	Sinusoidal	---
68	1	None	Damping - B	Sinusoidal	100
69	1	Spring 30-2022	Frequencies of Coupled Equipment	White Noise	---
70	1	Spring 30-2022	Damping – A & B	Sinusoidal	---
71	1	Spring 30-2022	Seismic	Newhall	30
72	1	Spring 30-2022	Seismic	Tabas	25
76	1	Bus Slider	Frequencies of Coupled Equipment	White Noise	---
77	1	Bus Slider	Damping – A & B	Sinusoidal	---
78	1	Bus Slider	Seismic	Newhall	100
79	1	Bus Slider	Seismic	Tabas	50
83	1	BPA Isolator	Frequencies of Coupled Equipment	White Noise	---
84	1	BPA Isolator	Damping – A & B	Sinusoidal	---
85	1	BPA Isolator	Seismic	Newhall	30
87	1	BPA Isolator	Seismic	Tabas	25
96	2	Spring 30-2022	Frequencies of Coupled Equipment	White Noise	---
97	2	Spring 30-2022	Damping – A & B	Sinusoidal	---
98	2	Spring 30-2022	Seismic	Newhall	30
99	2	Spring 30-2022	Seismic	Tabas	25
100	2	Spring 30-2022	Seismic	Tabas	50
101	2	Spring 30-2022	Seismic	Newhall	100
102	2	Spring 30-2022	Seismic	Tabas	100
103	2	Spring 30-2022	Seismic	Tabas	150
107	2	Bus Slider	Frequencies of Coupled Equipment	White Noise	---
108	2	Bus Slider	Damping – A & B	Sinusoidal	---
109	2	Bus Slider	Seismic	Newhall	30
110	2	Bus Slider	Seismic	Tabas	25
111	2	Bus Slider	Seismic	Tabas	50
112	2	Bus Slider	Seismic	Newhall	100
116	2	BPA Isolator	Frequencies of Coupled Equipment	White Noise	---
117	2	BPA Isolator	Damping - A & B	Sinusoidal	---
118	2	BPA Isolator	Seismic	Newhall	30

Test RB-#	Pair No.	Conductor	Test Description	Input Signal	Span (%)
119	2	BPA Isolator	Seismic	Tabas	25
120	2	BPA Isolator	Seismic	Tabas	50
121	2	BPA Isolator	Seismic	Newhall	100
122	2	BPA Isolator	Seismic	Tabas	75
123	2	BPA Isolator	Seismic	Tabas	100
124	2	None	Seismic	Newhall	30
125	2	None	Seismic	Tabas	25
126	2	None	Seismic	Tabas	50
127	2	None	Seismic	Newhall	100
130	5	None	Frequencies	White Noise	---
131	5	None	Damping - A	Sinusoidal	---
132	5	None	Damping - B	Sinusoidal	---
133	5	Spring 30-2022	Frequencies	White Noise	---
134	5	Spring 30-2022	Damping A-B, First Mode	Sinusoidal	---
135	5	Spring 30-2022	Damping A-B, Second Mode	Sinusoidal	---
136	5	Spring 30-2022	Seismic	Newhall	30
137	5	Spring 30-2022	Seismic	Tabas	25
138	5	Spring 30-2022	Seismic	Tabas	50
139	5	Spring 30-2022	Seismic	Newhall	100
140	5	Spring 30-2022	Seismic	Tabas	100
141	5	Spring 30-2022	Seismic	Tabas	150
142	5	Bus Slider	Frequencies	White Noise	---
143	5	Bus Slider	Damping A-B	Sinusoidal	---
144	5	Bus Slider	Seismic	Newhall	30
145	5	Bus Slider	Seismic	Tabas	25
146	5	Bus Slider	Seismic	Tabas	50
147	5	Bus Slider	Seismic	Newhall	100
148	5	Bus Slider	Seismic	Tabas	100
149	5	BPA Isolator	Frequencies	White Noise	---
150	5	BPA Isolator	Damping – First Mode	Sinusoidal	---
151	5	BPA Isolator	Damping – Second Mode	Sinusoidal	
152	5	BPA Isolator	Seismic	Newhall	30
153	5	BPA Isolator	Seismic	Tabas	25
154	5	BPA Isolator	Seismic	Tabas	50
155	5	BPA Isolator	Seismic	Newhall	100
156	5	BPA Isolator	Seismic	Tabas	100
157	5	None	Seismic	Newhall	30
158	5	None	Seismic	Tabas	25
159	5	None	Seismic	Tabas	50
160	5	None	Seismic	Newhall	100

5.8 Results of Frequency and Damping Evaluation Tests

The detailed results of all frequency evaluation tests conducted on all generic equipment combinations are presented in Appendix C. Included are power spectral density, phase, and coherence plots obtained from the absolute acceleration records at the top of each equipment. The results of the damping evaluation tests are presented in Appendix D. For each damping evaluation test, the detailed calculations of the first modal damping ratios by the logarithmic decrement method are included.

Table 5.5 summarizes the results of the frequency and damping evaluation tests on the stand alone (unconnected) generic equipment specimens. The fundamental frequencies of equipment 3 and 4 are substantially lower than the target frequencies shown in Table 5.3. For these stiffer equipment specimens, it was not possible to completely prevent rotation at the base. Rocking of the base caused the fundamental frequencies to be lower than anticipated. Therefore, it was decided to repeat the tests on Pair No. 2 with Equipment 4 equipped with a lateral bracing member (2 angles 3x3x3/8 back-to-back) to increase its natural frequency to 12 Hz. This new pair of equipment is referred to as Pair No. 5. Figure 5.7 presents a photograph of the modified Equipment 4. The shop drawings of the brace assembly are included in Appendix B.

Table 5.5 Measured Natural Frequencies and Damping of Generic Equipment Specimens.

Equipment	Natural Frequency (± 0.04 Hz)			First Modal Damping Ratio (%)
	Mode 1	Mode 2	Mode 3	
1	1.99	19.84	23.75	0.42
2	1.88	16.88	29.22	0.52
3	4.10	Not Measured	Not Measured	0.41
4	5.47	28.30	Not Measured	0.39
4 with Brace	12.23	Not Measured	Not Measured	0.29

Figure 5.7 Equipment 4 Retrofitted with Bracing Element.

Tables 5.6 to 5.8 summarize the results of the frequency and damping evaluation tests on the five pairs of generic equipment specimens interconnected by the three different rigid bus assemblies. The mode shapes are represented by the relative motions at the top of the equipment specimens. For the tests involving the bus slider, a mechanical locking device was introduced at the sliding interface to prevent slippage. This locking device was removed for the seismic tests.

The natural frequencies measured on the generic equipment specimens interconnected by the bus assemblies fall between the natural frequencies obtained for the stand alone generic equipment specimens (see Table 5.5). The lowest natural frequencies were

obtained with the flexible BPA seismic connector, while the highest natural frequencies correspond to the pairs of equipment interconnected with the rigid bus slider. With the bus slider, the vibrations of at the top the equipment specimens are in phase for all frequencies since the bus slider is rigid.

Table 5.6 Results of Frequency and Damping Evaluation tests on Equipment Interconnected by Bus Assembly with Spring Connector.

Pair	Mode 1				Mode 2			Mode 3		
	Natural Frequency (± 0.04 Hz)	Mode Shape		Damping Ratio (%)	Natural Frequency (± 0.04 Hz)	Mode Shape		Natural Frequency (± 0.04 Hz)	Mode Shape	
		A	B			A	B		A	B
1	2.38	1	0.64	1.10	5.15	1	-3.71	20.08	1	0.70
2	2.58	1	0.49	0.63	5.82	1	-4.52	20.08	1	0.60
3	3.01	1	0.83	1.00	6.60	1	-0.78	17.31	1	-0.16
4	3.79	1	0.54	0.90	6.72	1	-0.98	17.31	1	-0.05
5	2.96	1	0.14	1.85	11.37	1	-15.3	Not Measured	-	---

Table 5.7 Results of Frequency and Damping Evaluation Tests on Equipment Interconnected by Bus Slider.

Pair	Mode 1				Mode 2			Mode 3		
	Natural Frequency (± 0.04 Hz)	Mode Shape		Damping Ratio (%)	Natural Frequency (± 0.04 Hz)	Mode Shape		Natural Frequency (± 0.04 Hz)	Mode Shapc	
		A	B			A	B		A	B
1	2.54	1	0.99	1.08	19.81	1	0.66	28.20	1	0.40
2	3.05	1	1.00	1.16	19.81	1	0.47	26.02	1	1.11
3	3.16	1	1.06	1.86	15.43	1	0.88	20.04	1	0.72
4	4.30	1	1.00	1.57	14.92	1	0.66	20.08	1	0.56
5	5.78	1	0.96	0.47	Not Measured	-	---	Not Measured	-	---
Note: These tests were performed with the slider mechanically locked to prevent slippage										

Table 5.8 Results of Frequency and Damping Evaluation Tests on Equipment Interconnected by Rigid Bus with BPA Seismic Connector.

Pair	Mode 1				Mode 2			Mode 3		
	Natural Frequency (± 0.04 Hz)	Mode Shape		Damping Ratio (%)	Natural Frequency (± 0.04 Hz)	Mode Shape		Natural Frequency (± 0.04 Hz)	Mode Shape	
		A	B			A	B		A	B
1	2.07	1	0.16	1.84	3.39	1	---	20.08	1	0.86
2	2.07	1	0.10	1.60	4.22	1	-17.8	20.08	1	0.63
3	2.34	1	0.24	1.65	3.40	1	-1.75	15.66	1	-0.63
4	2.38	1	0.10	1.85	4.34	1	-4.47	15.39	1	-0.62
5	2.11	1	0.01	0.36	8.42	-	---	15.43	-	---

5.9 Results of Seismic Tests

The results of all seismic tests conducted on the five pairs of generic equipment specimens interconnected by the three different rigid bus assemblies are presented in Appendix E. Included for each seismic test are time-history plots of:

- Absolute acceleration of the shake table
- Relative horizontal displacement at the top of Equipment A
- Relative horizontal displacement at the top of Equipment B
- Absolute horizontal acceleration at the top of Equipment A
- Absolute horizontal acceleration at the top of Equipment B
- Relative displacement between Equipment A and Equipment B
- Longitudinal force in the connector
- Force-displacement hysteresis loops across the connector
- Axial strain at the apex of the spring connector

The longitudinal force in the connector, $F_c(t)$, was obtained by considering the dynamic equilibrium at the top of equipment specimen A, adjacent to the connector:

$$F_c(t) = m_A \ddot{x}_{aA}(t) + c_A \dot{x}_{rA}(t) + k_A x_{rA}(t) \tag{5.1}$$

where $m_A, c_A, and\ k_A$ are the mass, viscous damping coefficient and lateral stiffness of equipment specimen A, respectively, and $x_{rA}(t), \dot{x}_{rA}(t), and\ \ddot{x}_{aA}(t)$ are the relative displacement, relative velocity, and absolute acceleration at the top of equipment specimen A, respectively.

The test series with Equipment Pairs No. 4, 3, and 1 were performed for low intensity ground motions so that no damage occurred in the connectors. For the tests with Equipment Pairs No. 2 and No. 5, higher intensity ground motions were used to evaluate the behavior of the various connectors for their full range of performance.

The spring connector 30-2022 exhibited slight inelastic behavior in Tests RB-7, RB-100, RB-101, RB-138, and RB-139 (pages E3, E35, E36, E55, and E56) and severe yielding in Tests RB-102, RB-103, RB-140, and RB141 (pages E37, E38, E57, and E58). In these latter tests, maximum axial strains in excess of 10 000 $\mu\varepsilon$ were recorded in the spring connector.

Figure 5.8 shows photographs of the spring connector at the completion of Test RB-103. The yielding regions are clearly visible along with the significant permanent vertical deformation between the two ends of the connector.

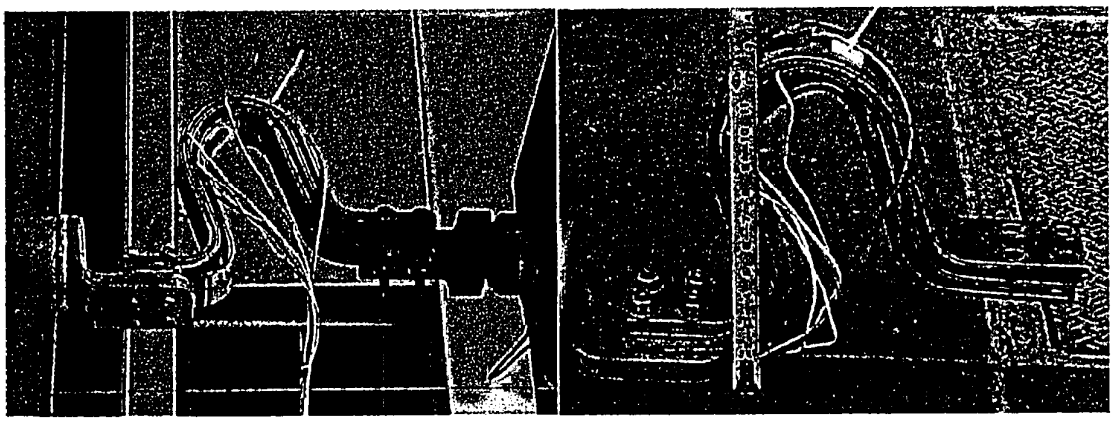

Figure 5.8 Spring 30-2022 After Shake Table Test No. RB-103.

The bus slider performed well except for Tests RB-18 and RB-148 where the shaft came out of the aluminum pipe during the shaking. This induced sever impact loading between the shaft and the pipe as shown by the very large forces and accelerations recorded at the top of the generic equipment specimens. After Test RB-18, the looped cables had yielded permanently and it was not possible to re-insert the shaft inside the pipe. The unit had to be replaced for the following tests. Figure 5.9 presents a photograph of the bus slider at the end of Test RB-18. This damage could be avoided by increasing the available travel distance of the shaft inside the aluminum pipe.

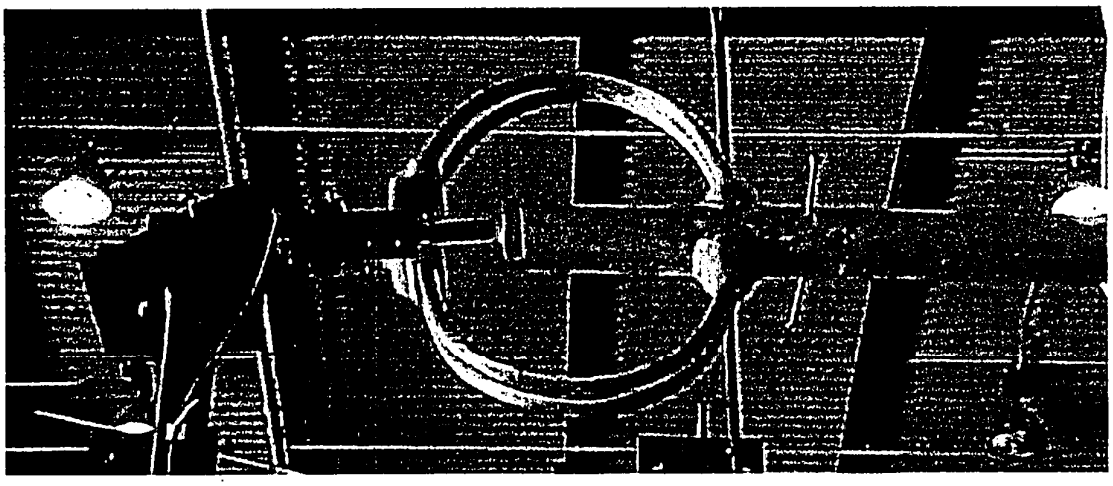

Figure 5.9 Bus Slider After Shake Table Test RB-18.

The BPA isolator did not suffer any visible damage during the shake table testing. For the largest intensity tests (Tests RB-121, RB-122, RB-123, and RB-156), significant second-order vertical deflections were observed between the top and bottom ends of the isolator. These deflections introduced significant bending strains in the two load cells.

The physical arrangement of the rigid bus along with its significant mass caused a rigid-body rotation of the whole specimen during some of the tests, since no torsional stiffness was provided by the load-cell connections. This observation suggests that a rigid bus equipped with a BPA isolator could induce significant torsional couples at the top of the equipment under transverse seismic loading.

The maximum experimental values recorded for all seismic tests are summarized presented in Table 5.9. Included in this table for each seismic test are: the maximum relative displacement and maximum absolute acceleration at the top of both equipment specimens, and the maximum force induced in the connector. Note that, although no yielding occurred in the equipment specimens, the behavior of the stand alone equipment specimens is not perfectly linear (e.g. the maximum displacement and acceleration values more than double when the ground motion intensity is increased by a factor of two). This non-linearity is particularly important for equipment specimens A (1 and 2 in Table 5.5), and is believed to be the results of the rocking of the base.

The maximum forces induced in the various connectors during the seismic shake table tests are presented in Figs. 5.10 and 5.11. The results are presented for each ground motion, equipment pair, and intensity level. The BPA connector, being more flexible than the other two connectors, consistently induces the smaller forces. The spring connector consistently induces the largest forces.

Table 5.9. Maximum Experimental Values from Seismic Tests.

Pair	Ground Motion-Span (%)	Peak Relative Displacement Equipment A (in)				Peak Relative Displacement Equipment B (in)				Peak Absolute Acceleration Equipment A (g)				Peak Absolute Acceleration Equipment B (g)				Peak Connector Force (lbs)		
		Spring	Slider	BPA	Stand Alone	Spring	Slider	BPA	Stand Alone	Spring	Slider	BPA	Stand Alone	Spring	Slider	BPA	Stand Alone	Spring	Slider	BPA
1	Newhall-30	0.98	---	2.07	1.50	0.70	---	0.71	0.63	0.55	---	0.91	0.59	0.76	---	0.78	1.14	218	---	71
	Newhall-100	---	3.65	---	5.08	---	1.51	---	2.06	---	1.84	---	1.92	---	1.56	---	3.59	---	334	---
	Tabas-25	1.69	---	2.22	2.06	1.17	---	0.85	1.13	1.01	---	1.00	0.81	1.13	---	0.84	1.97	293	---	99
	Tabas-50	---	3.04	---	4.94	---	1.15	---	2.00	---	1.51	---	1.90	---	1.45	---	3.54	---	301	---
2	Newhall-30	1.40	0.63	1.88	1.50	0.67	0.29	0.45	0.40	0.96	0.40	0.81	0.59	0.61	0.47	0.73	0.80	313	120	77
	Newhall-100	2.89	3.16	6.25	5.08	1.30	0.93	1.55	1.07	1.97	1.75	2.55	1.92	1.23	1.51	2.79	2.56	642	380	195
	Tabas-25	1.56	1.00	1.94	2.06	0.71	0.29	0.74	0.46	1.07	0.56	0.87	0.81	0.85	0.53	1.24	1.19	373	137	96
	Tabas-50	3.09	2.91	4.59	4.94	1.27	0.61	1.39	0.98	2.08	1.49	1.95	1.90	1.69	1.28	2.34	2.32	652	284	150
3	Newhall-30	1.03	---	1.53	1.73	0.79	---	0.87	0.63	0.96	---	0.88	0.87	0.78	---	0.84	1.14	47	---	30
	Newhall-100	3.15	2.95	---	5.67	2.51	1.29	---	2.06	3.15	2.55	---	2.24	2.36	1.53	---	3.59	153	118	---
	Tabas-25	1.68	---	2.41	3.04	1.33	---	0.83	1.13	2.00	---	1.55	1.17	1.28	---	0.79	1.97	110	---	52
	Tabas-50	3.61	2.04	---	7.82	2.72	1.09	---	2.00	3.92	2.19	---	3.04	2.76	1.44	---	3.54	205	123	---
4	Newhall-30	1.05	---	1.10	1.77	0.55	---	0.43	0.36	1.60	---	0.71	0.70	0.80	---	0.74	0.93	94	---	28
	Newhall-100	2.80	2.36	---	5.71	1.49	0.78	---	1.11	3.88	2.82	---	2.43	2.07	1.48	---	2.73	224	164	---
	Tabas-25	0.92	---	1.94	2.94	0.47	---	0.71	0.49	1.54	---	1.21	1.11	0.75	---	1.22	1.20	93	---	41
	Tabas-50	1.97	1.25	---	7.75	0.95	0.45	---	0.96	3.52	1.73	---	2.84	1.73	1.08	---	2.36	217	97	---
	Tabas-200	---	8.17	---	---	---	4.49	---	---	---	31.8	---	---	---	9.4	---	---	---	2433	---
5	Newhall-30	0.71	0.66	1.50	1.91	0.20	0.18	0.17	0.18	0.65	0.41	0.67	0.79	0.61	0.44	0.51	0.49	273	207	106
	Newhall-100	2.00	2.56	5.91	5.19	0.33	0.31	0.25	0.20	1.66	1.65	2.40	1.90	1.35	2.25	1.01	1.22	698	511	121
	Tabas-25	1.05	0.81	1.88	3.23	0.25	0.17	0.28	0.20	1.02	0.47	0.84	0.73	0.98	0.60	0.91	1.71	478	168	93
	Tabas-50	1.93	2.42	3.91	4.42	0.36	0.34	0.31	0.34	1.75	1.34	1.63	1.73	1.75	1.38	1.59	3.13	748	323	137

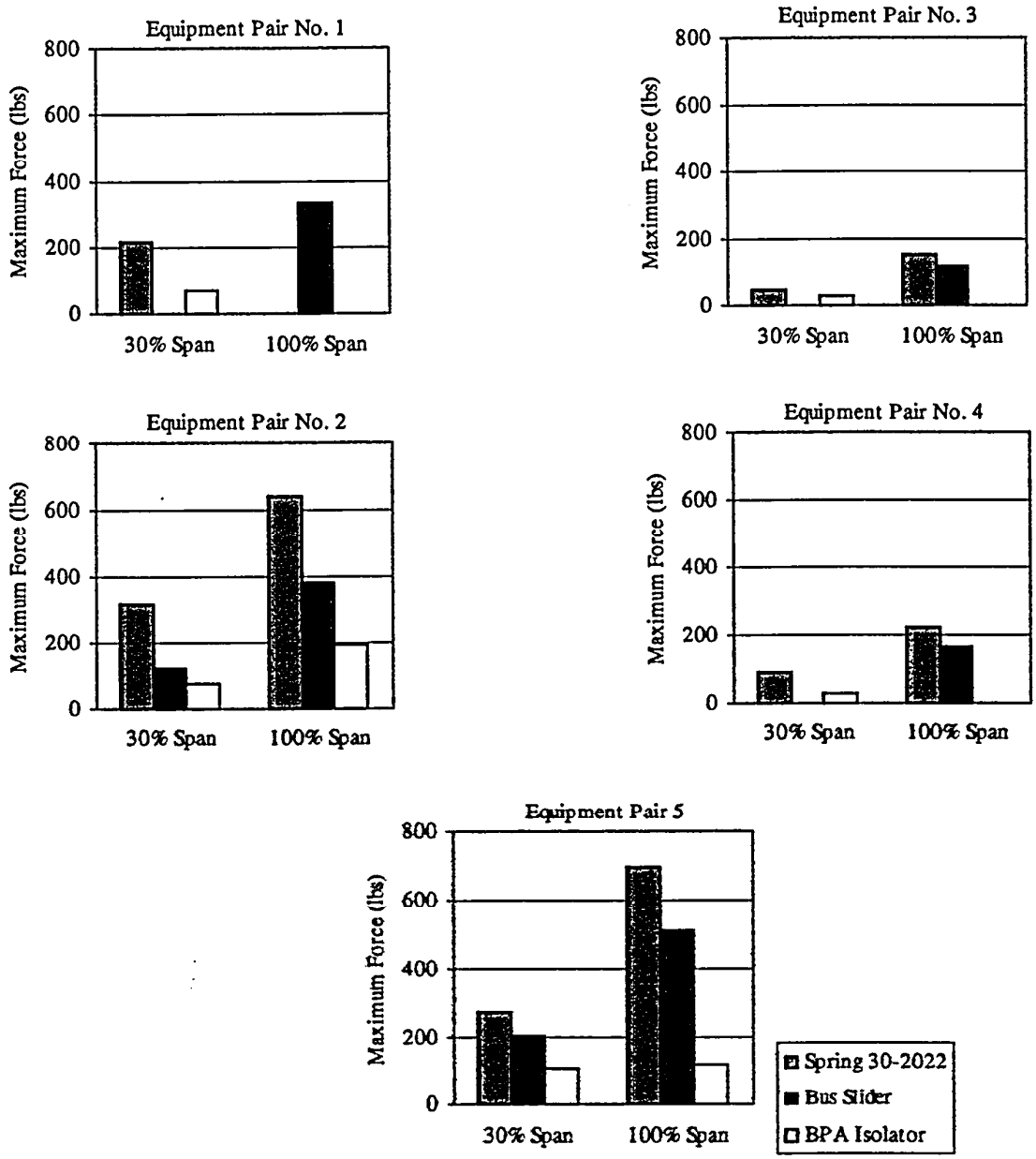

Figure 5.10 Maximum Forces in Connectors, Newhall Ground Motion.

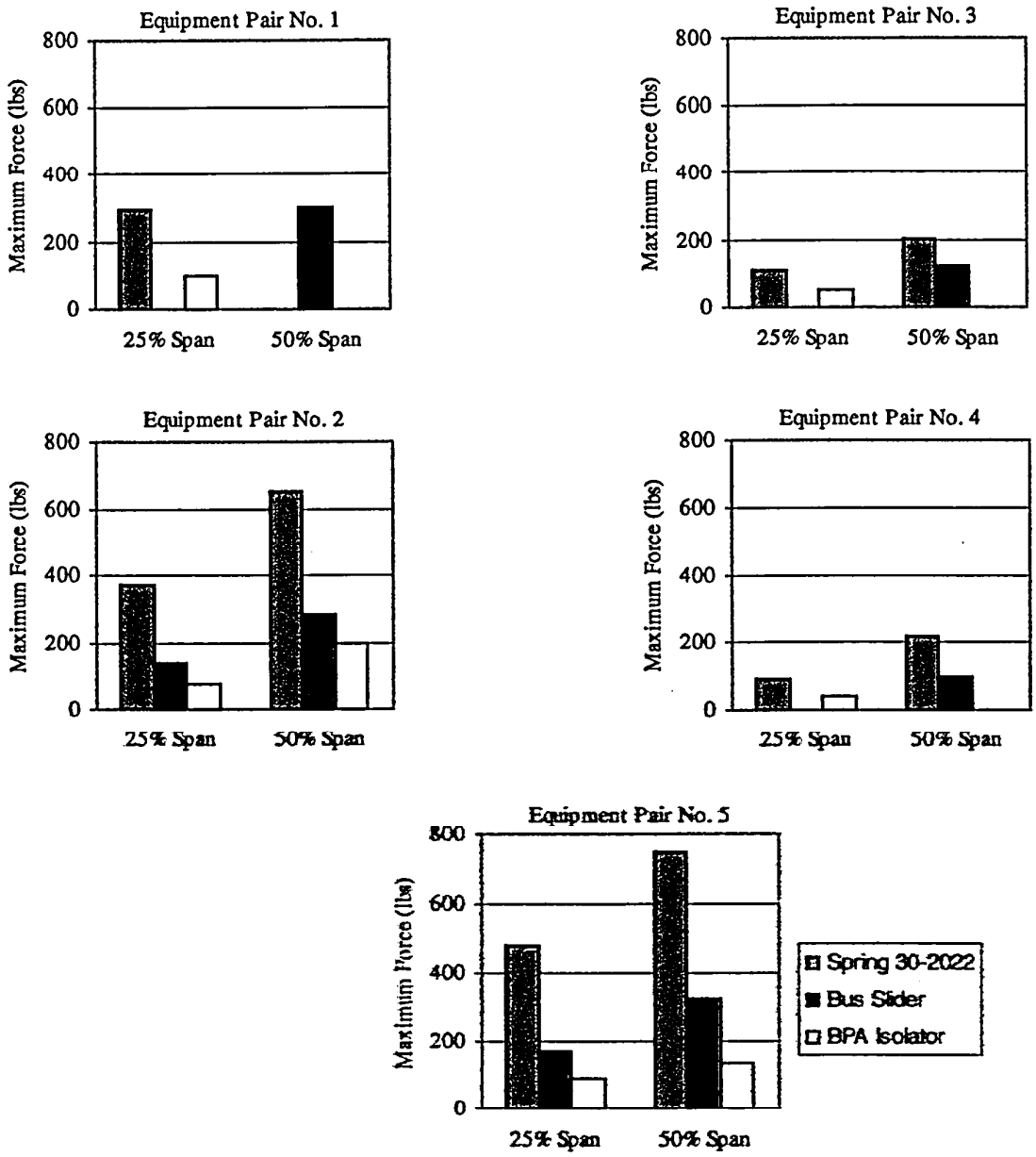

Figure 5.11 Maximum Forces in Connectors, Tabas Ground Motion.

The effect of the various connectors on the dynamic response of the generic equipment specimens can be evaluated by defining a Displacement Amplification Factor (DAF) and an Acceleration Amplification Factor (AAF) as:

$$\text{DAF} = \frac{\text{Maximum Relative Displacement of Interconnected Equipment}}{\text{Maximum Relative Displacement of Stand Alone Equipment}} \tag{5.2}$$

$$\text{AAF} = \frac{\text{Maximum Absolute Acceleration of Interconnected Equipment}}{\text{Maximum Absolute Acceleration of Stand Alone Equipment}} \tag{5.3}$$

The DAF and AAF values computed at the top of Equipment A and Equipment B during the seismic tests are presented in Figs.5.12 to 5.19. The results are presented for each ground motion, equipment pair, and intensity level.

The presence of rigid bus connectors can amplify or reduce the dynamic response of equipment components depending on their dynamic characteristics and the frequency content and intensity of the earthquake ground motion input. In general, the displacement at the top of the lighter and stiffer equipment B is more amplified than the displacement at the top of the heavier and more flexible equipment A.

Among the three connectors investigated, the bus slider consistently reduces the response at the top of both equipment specimens. The only case where the bus slider amplifies the response is for equipment B of Pair No. 5 under the 100% Newhall ground motion.

This response reduction occurs despite that the bus slider induces larger forces than the BPA connector does (see Figs. 5.110 and 5.11). The energy dissipation capacity of the bus slider is larger than of the BPA connector and causes an increase of the equivalent damping of the coupled system.

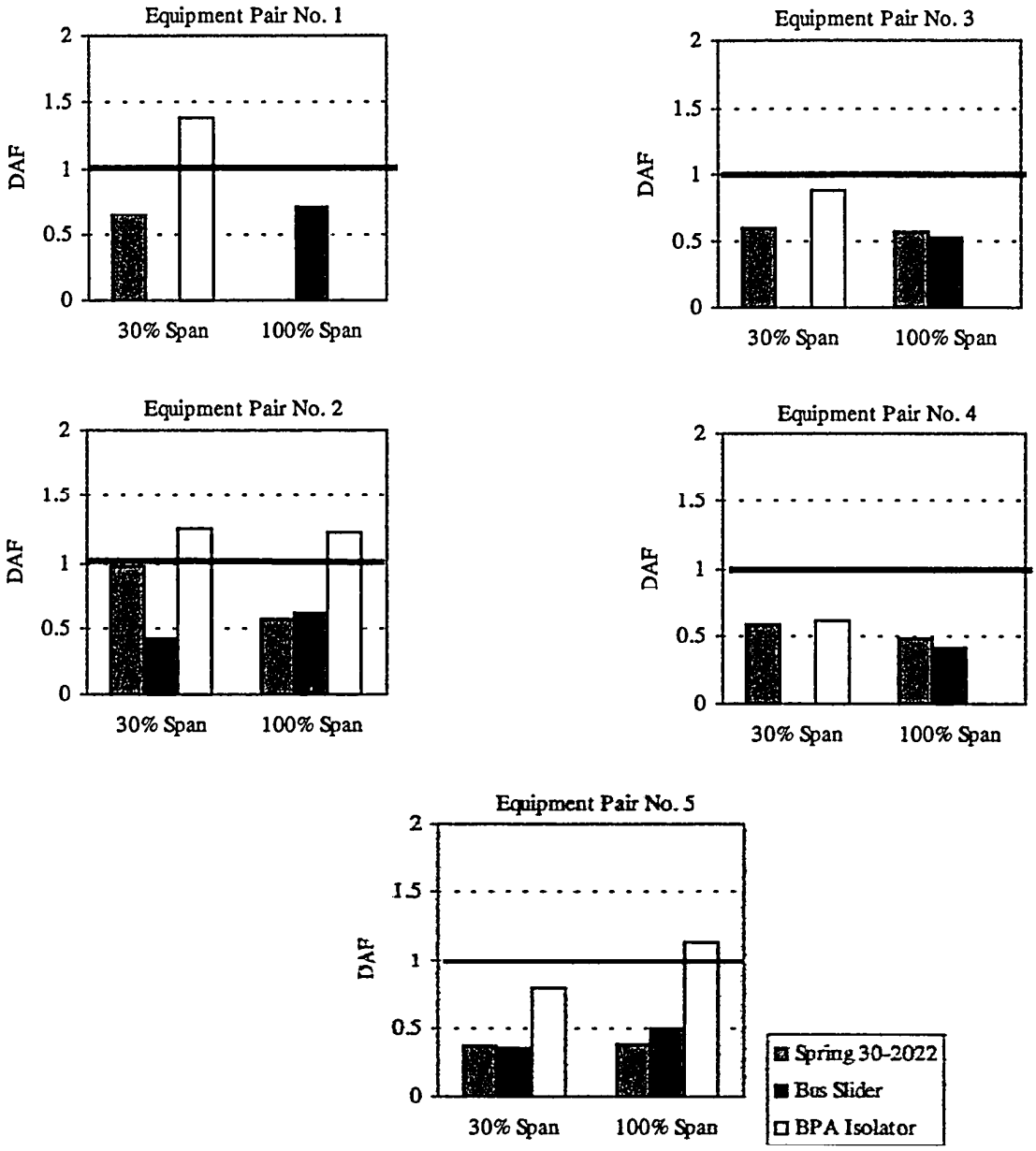

Figure 5.12 Displacement Amplification Factor (DAF), Equipment A, Newhall Ground Motion.

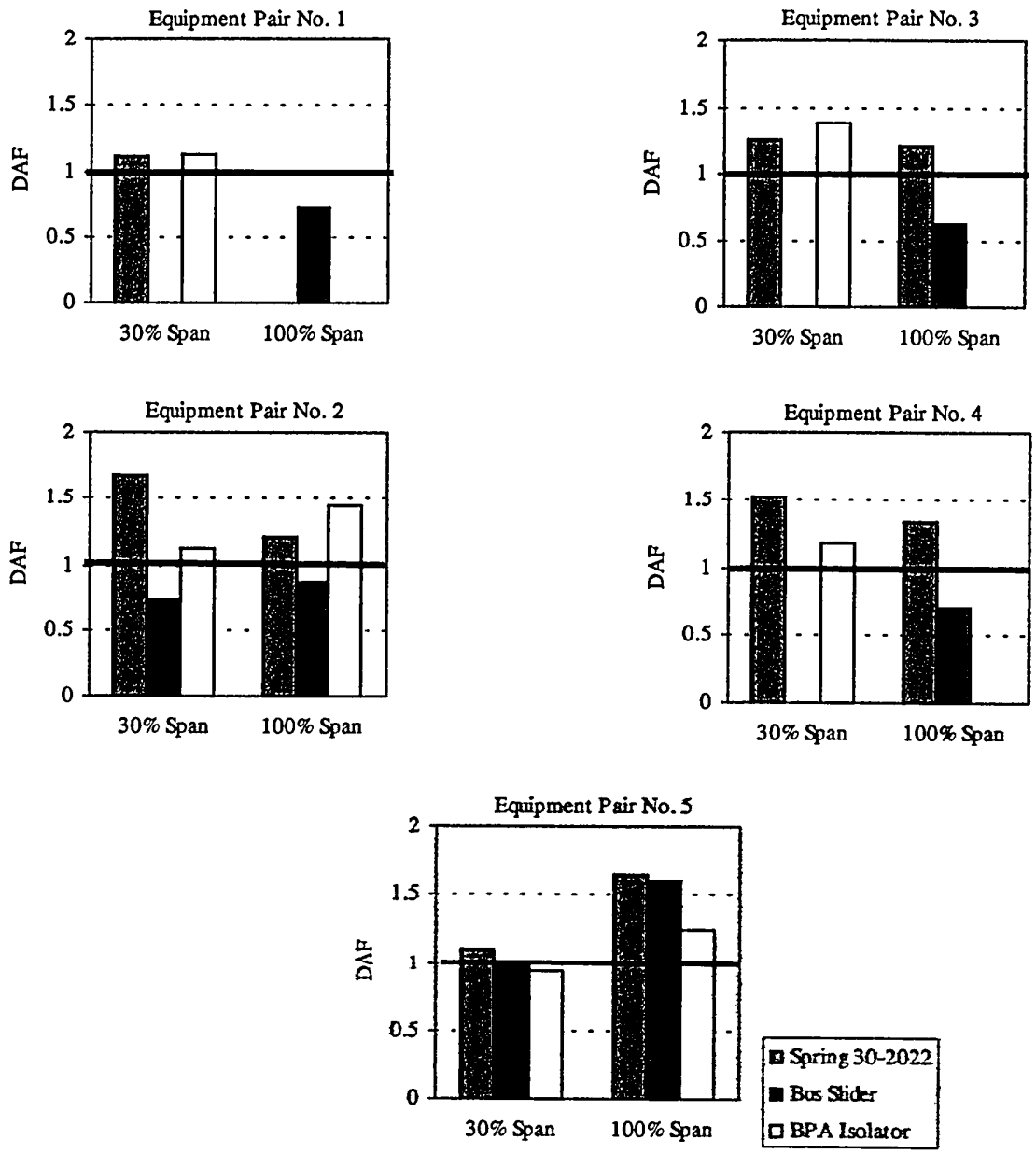

Figure 5.13 Displacement Amplification Factor (DAF), Equipment B, Newhall Ground Motion.

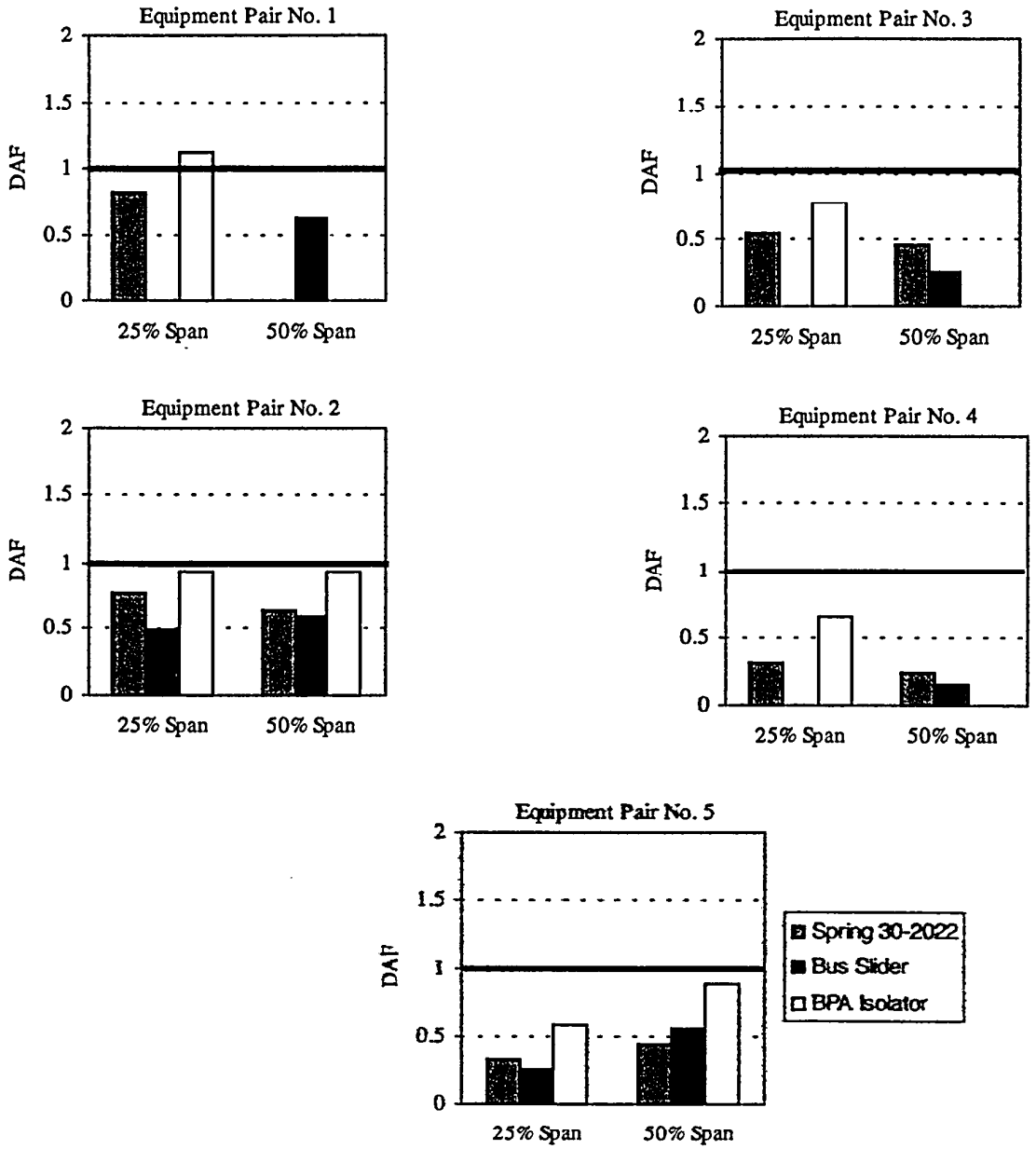

Figure 5.14 Displacement Amplification Factor (DAF), Equipment A, Tabas Ground Motion.

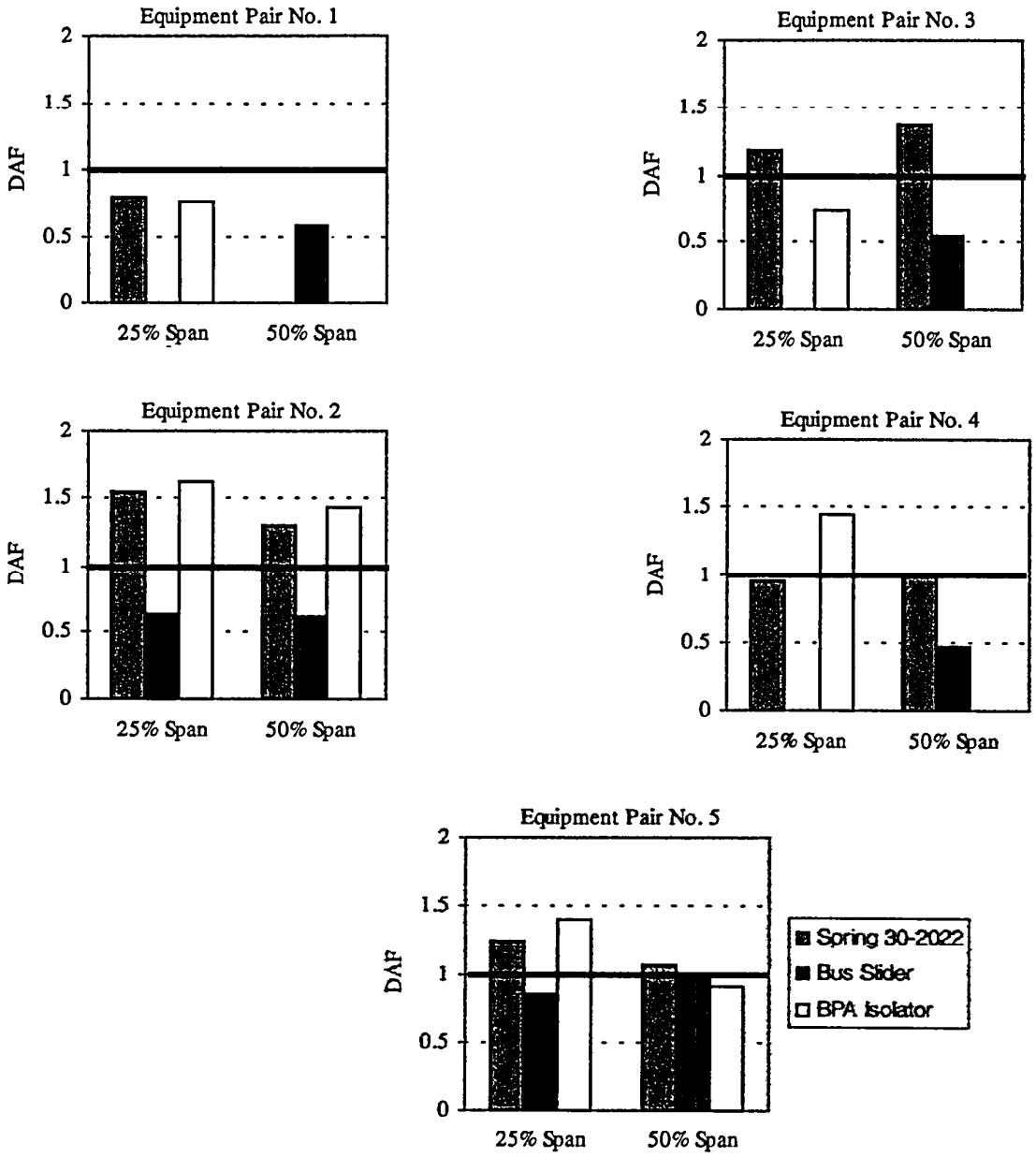

Figure 5.15 Displacement Amplification Factor (DAF), Equipment B, Tabas Ground Motion.

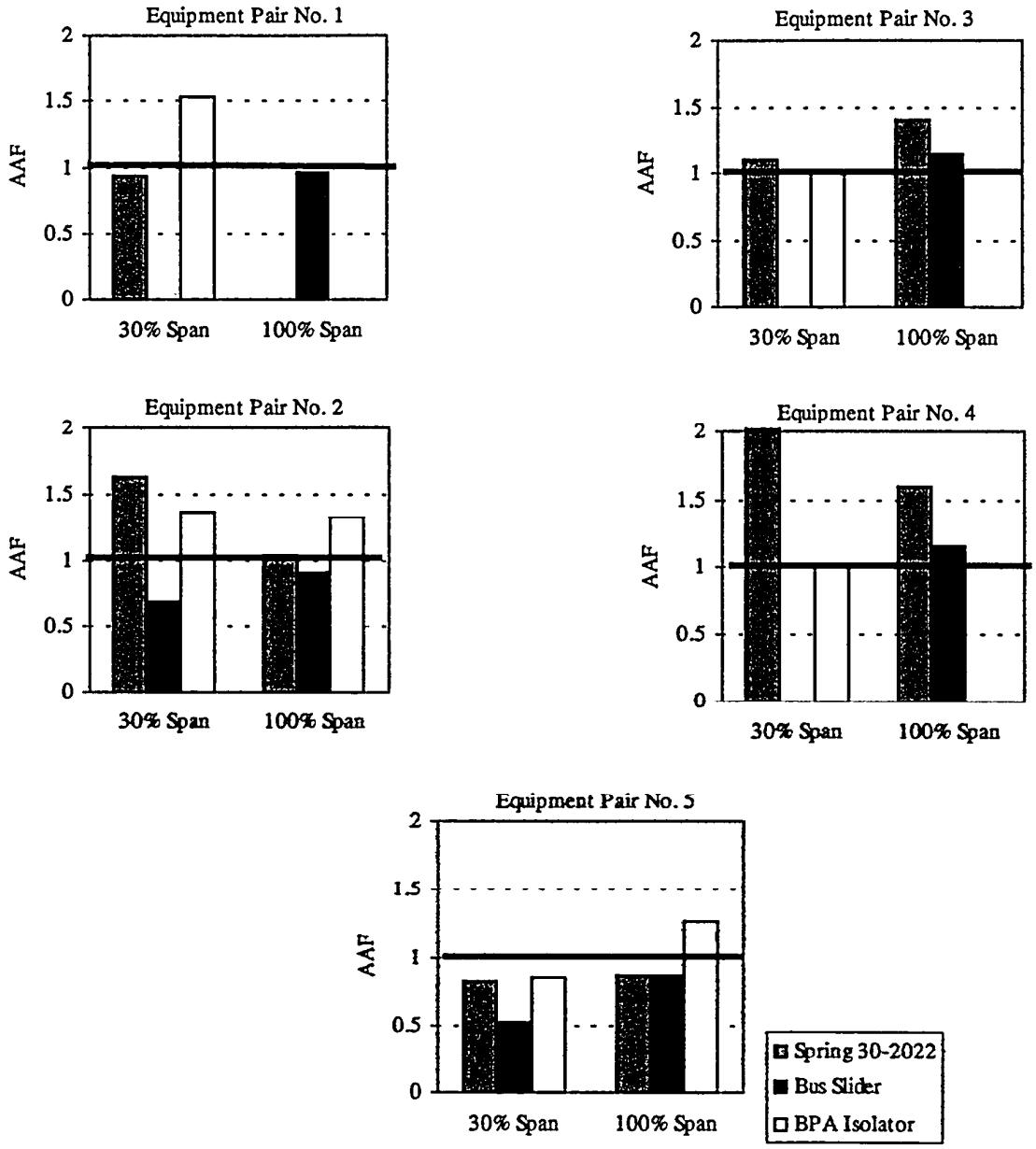

Figure 5.16 Acceleration Amplification Factor (AAF), Equipment A, Newhall Ground Motion.

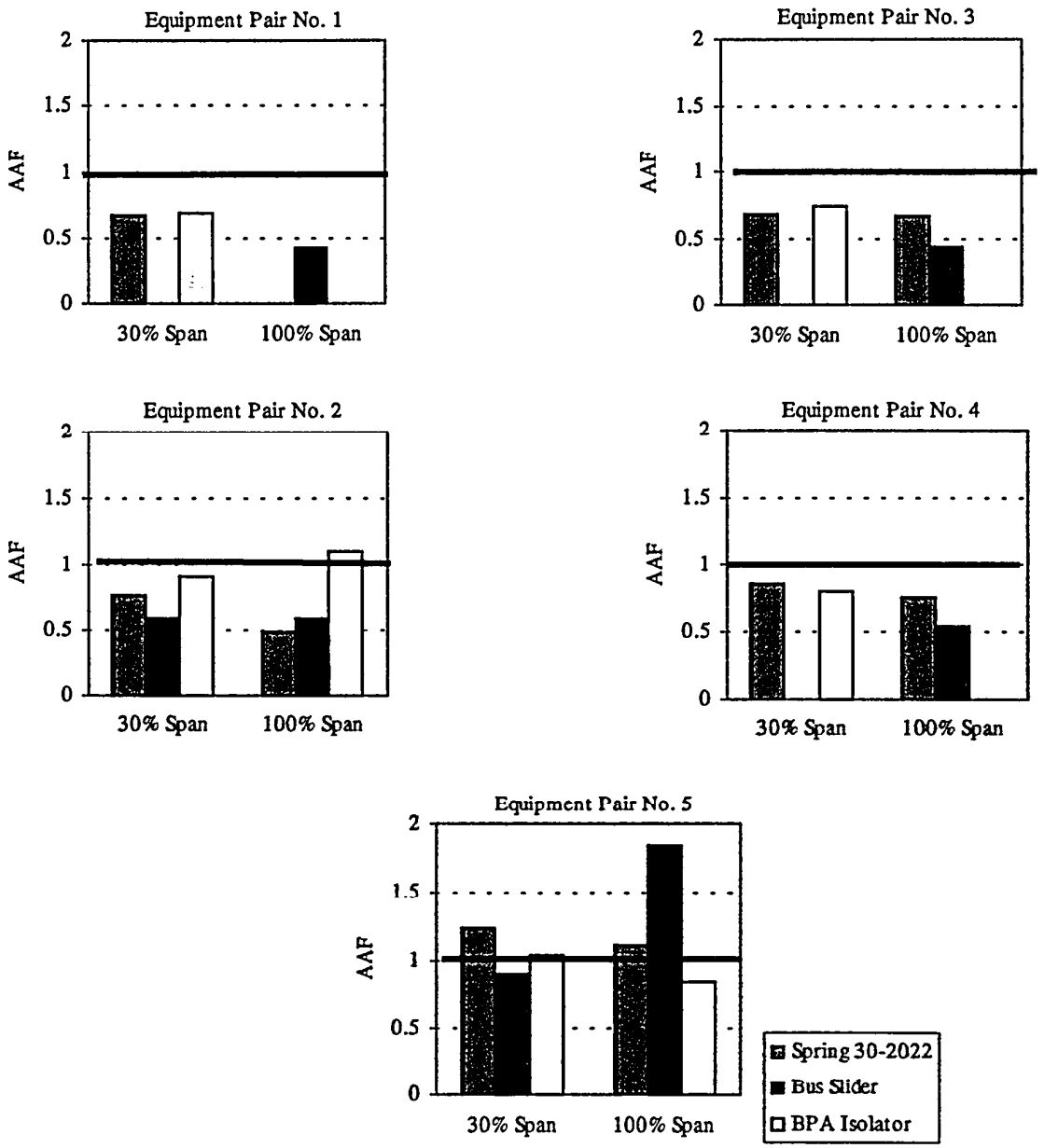

Figure 5.17 Acceleration Amplification Factor (AAF), Equipment B, Newhall Ground Motion.

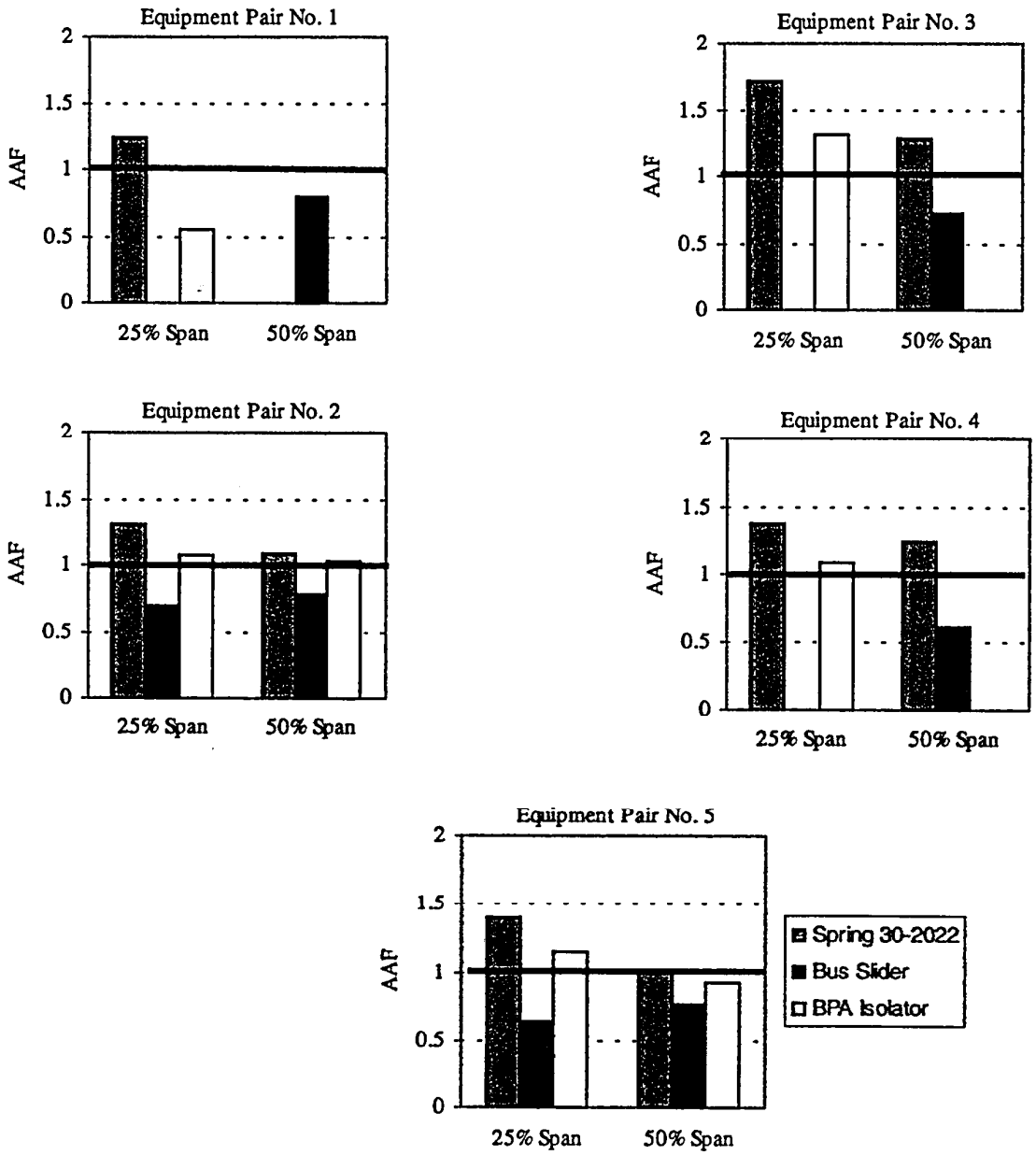

Figure 5.18 Acceleration Amplification Factor (AAF), Equipment A, Tabas Ground Motion.

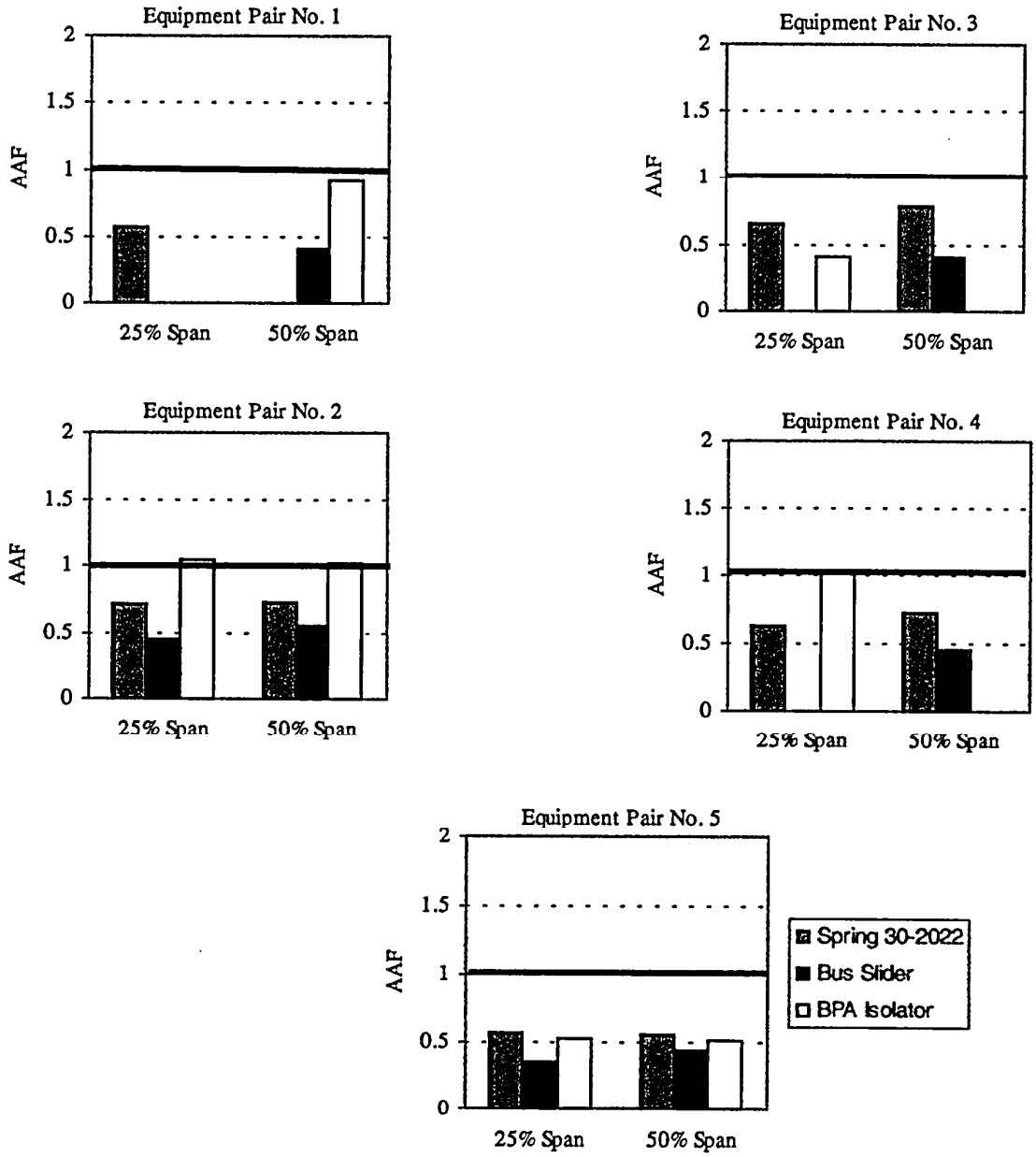

Figure 5.15 Displacement Amplification Factor (DAF), Equipment B, Tabas Ground Motion.

6 CONCLUSIONS

The quasi-static and shake table tests performed in this project has provided an opportunity to evaluate the interactions between components of substation equipment connected by both flexible and rigid bus. The tests have provided also validation data for a current PEER-PG&E analytical project.

Based on the results of the quasi-static tests performed on flexible and rigid bus connectors, the following conclusions can be drawn:

- The copper alloy used to manufacture the three spring connectors tested (Parts 30-2021, 30-2022, and 30-2023) exhibits almost a perfect elastic-plastic behavior that can be characterized by an elastic modulus of 14 100 ksi and yield strength of 27 ksi.
- The modeling of spring connectors by straight linear-elastic frame elements with a commercial structural analysis package is reasonably accurate to estimate the elastic stiffness, yield force and yield displacement of the connectors.
- The three spring connectors tested exhibited large and stable hysteresis loops with good energy dissipation capabilities. For ductility levels less than four, the hysteresis loops were nearly symmetric in tension and compression. For larger deformations, tension-stiffening effects were observed. These effects were more predominant for spring 30-2021. Finally, the load level developed by spring 30-2023 was significantly lower than the loads induced in the other two spring connectors.
- For the two spring connectors tested to failure (30-2022 and 30-2023), a brittle fracture occurred across the net area of the cast-aluminum terminal pad connection that is welded to the aluminum tubing. Failure stresses less than 4 ksi were recorded.
- The load-displacement hysteretic behavior of the three spring connectors tested can be simply modeled by a bi-linear solid.
- The equivalent damping ratios of the three spring connectors increase with displacement amplitude, indicating higher energy dissipation capacity at large inelastic displacements. Spring 30-2021 and spring 30-2022 exhibit damping ratios

significantly higher than the more flexible spring 30-2023 for the complete range of displacement amplitudes considered in the tests.

- The rigid bus slider tested exhibited a behavior that is typical of a Coulomb-type friction system coupled with an elastic restoring force mechanism. The hysteretic behavior of the bus slider tested can be simply modeled by a rigid-plastic solid with a slip force of 53 lbs and a post-slip stiffness of 83 lbs/in.
- Contrary to the spring connectors, the equivalent damping ratio of the bus slider decreases slightly with displacement amplitude. For the range of displacements allowed by the slider, however, the equivalent viscous damping ratios provided by the bus slider were higher than the ones exhibited by the three spring connectors. This result indicates the superior energy dissipation capacity of the bus slider at small displacement amplitudes.
- For the lengths of the two flexible bus specimens tested (15 ft), the flexural stiffness of the cables played an insignificant role in the load-displacement responses. The specimens can be simply modeled by an elastic gap element.
- For the 1113 MSM bundled conductors tested, the two cables were manufactured with different lengths causing one cable to be taut much more than the other one.

Based on the results of the shake table tests performed on four different pairs of generic equipment connected by three different types of rigid bus connectors, the following conclusions can be drawn:

- The natural frequencies measured on the generic equipment specimens interconnected by the bus assemblies were always between the natural frequencies obtained for the uncoupled equipment specimens. The lowest natural frequencies were obtained with the BPA isolator, while the highest natural frequencies corresponded to the pairs of equipment connected by the rigid bus slider.
- The spring connector (30-2022) tested performed similarly as the quasi-static tests. Yielding occurred under the highest intensity ground motions along with significant vertical deformation at the end of the aluminum pipe.

- The bus slider performed well except for two high intensity tests where the shaft came out of the aluminum pipe during shaking. This induced sever impact loading between the shaft and the pipe as shown by the very large accelerations recorded at the top of the generic equipment. This damage could be avoided by increasing the available travel distance of the shaft inside the aluminum pipe and by increasing the length of the looped cables to avoid an undesirable increase of the elastic restoring stiffness.
- The BPA isolator did not suffer any visible damage during the shake table testing
- The physical arrangement of the rigid bus and BPA assembly along with its significant mass caused a rigid-body rotation of the whole specimen during some of the tests. This observation suggests that a rigid bus equipped with a BPA isolator could induce significant torsional couples at the top of the equipments under transverse seismic loading.
- The BPA connector, being more flexible than the other two connectors, consistently induces the smaller forces. The spring connector consistently induces the largest forces.
- Among the three connectors investigated, the bus slider consistently reduces the response at the top of both equipment specimens. This response reduction occurs despite that the bus slider induces larger forces than the BPA connector does. The energy dissipation capacity of the bus slider is larger than of the BPA connector and causes an increase of the effective damping of the coupled system.

7 REFERENCES

Abrahamson, M. 1997. Private Communication

American Society for Testing Materials, 1999. "E8-99 Standard Test Methods for Tension Testing of Metallic Materials", ASTM E8-99 Standard, West Conshohocken, PA.

Applied Technology Council, 1992. "Guidelines for Cyclic Seismic Testing of Components of Steel Structures", ATC-24, Redwood City, CA .

Clough, R.W., and Penzien, J., 1993. "Dynamics of Structures", Second Edition, McGraw-Hill, New York.

Computers and Structures, 1998. "SAP 2000 Three Dimensional Static and Dynamic Finite Element Analysis of Structures", Computers and Structures Inc., Berkeley, CA.

Experimental Dynamic Investigations, 1993. "U2 & V2 Manual", Vancouver, Canada

Filiatrault, A., Tremblay, R., Thoen, B.K. and Rood, J., **1996**."A Second Generation Earthquake Simulation System in Canada: Description and Performance Evaluation", 11th World Conference on Earthquake Engineering, Acapulco, Mexico, Paper # 1204 on CD-ROM.

Filiatrault, A., Kremmidas, S., Seible, F., Clark, A.J., Nowak, R., and Thoen, B.K. **2000**. "Upgrade of First Generation Uniaxial Seismic Simulation System with Second Generation Real-Time Three-Variable Digital Control System", 12th World Conference on Earthquake Engineering, Auckland, New Zealand (in press).

IEEE. 1997. "Recommended practices for Seismic Design of Substations, Draft No. 6", Piscataway, NJ.: IEEE Standards department.

Starkel, D.L., Mueller III, W., and Kempner, L., 1998." Seismic Evaluation Seismic Connection with Rigid Bus Conductor", Portland State University, Bonneville Power Administration.

APPENDIX A

DRAWINGS OF RIGID AND FLEXIBLE BUS SPECIMENS

To: Andre Filiatrault/Ahmed Elgamal, UCSD, Fax 619/822-2260
From: Eric Fujisaki, PG&E 415/973-9857, Fax 415 973-9209

PEER-PG&E Task 2C
Substation Equipment Interaction

The attached figures outline the hardware associated with the suggested experiments for Task 2C. These are described as follows:

1. Rigid bus with spring connectors (dwg. 417440 Figures 1, 2, and 3). A 3" dia. aluminum pipe with welded end fittings, rigidly connected at one end, and having spring connector at other end. 3" standard NEMA terminal pads to be used. Three different springs proposed (Figures 1, 2, and 3).

2. Rigid bus with slider connector (dwg. 0462267 Type 221A). A 3" dia. aluminum pipe with welded end fitting on one end, slider connector on other end. 4" standard NEMA pad on slider end, 3" pad on other. Bolt hole pattern for 3" and 4" pads are the same; bolt hole edge distances different (see figures).

3. Various cable connectors with either 3" or 4" standard NEMA terminal pads at their ends. The exact cables to be used are not yet determined.

4. "BPA" type connector with 4" dia. rigid bus. This experiment will be similar to the tests done by BPA at Portland State University, except that the boundary conditions used will be different. A BPA flexible connector will be attached at one end of a 4" dia. rigid bus (aluminum tube) at one end. The other end of the 4" rigid bus will have two 45 degree bends, ending in a vertically oriented terminal pad. All terminal pads will be 5" non-standard (needs further discussion with BPA).

Adaptability of Support Hardware: The support hardware in the experiment that represents the two pieces of substation equipment should be designed to accommodate the different types of terminal pads described above. These differences include terminal pad size, bolt hole size and spacing, and orientation of the pad (horizontal and vertical). It would be beneficial to design the bus support points to be able to accept a bolt-on adapter such that the appropriate type of terminal pad could be installed and changed easily. Since terminal pad strength is not the focus of this project, the pads on the equipment ends could be made as stiff and strong as needed.

Support Spacing on the Shake Table: This needs further discussion. The spacing is probably not critical for rigid bus, but some provisions for testing different lengths for flexible bus is desirable.

Instrumentation for Shake Table Tests: In addition to displacements and accelerations at the terminal pads, there should be some way to measure forces applied to the terminals, since this is an important parameter for the equipment that is actually attached to the terminals in the field. The axial force in the bus is probably the most important, but maybe there are other components of force that should also be measured (e.g., for eccentrically loaded connectors); needs some thought.

PG&E-PEER Project Task 2C

The following summarizes the required parts and assemblies to be provided by PG&E.

Item	Description	PG&E Ident./Code	Number Req'd	Sketch
Spring connector	Flexible connector, 2000A, 3" NEMA pad	Dwg. 417440, Grp. 3, Figure 1, code 30-2021	2	1
Spring connector	Flexible connector, 2000A, 3" NEMA pad	Dwg. 417440, Grp. 3, Figure 2, code 30-2022	2	1
Spring connector	Flexible connector, 2000A, 3" NEMA pad	Dwg. 417440, Grp. 3, Figure 3, code 30-2023	2	1
Rigid bus assy., straight	4" dia. SPS, aluminum rigid bus, make from 10'-0" long pipe, with offset terminal pads attached.	Terminal pads: Dwg 046267 Type 174, code 30-4122 at each end. Alternate: Dwg. 046267 Type 608, code 30-0233.	1 assy.	1
Rigid bus-slider assy	4" dia. SPS, aluminum rigid bus, make from 10'-0" long pipe, with slider connection on one end, offset terminal pad on other end, attached.	Slider connector: Dwg 046267 Type 221A, code 30-4462. Alternate: Dwg. 046267, Type 685, code 30-0381. Terminal pad: Dwg. 046267 Type 174, code 30-4462. Alternate: Dwg. 046267 Type 608, code 30-0233.	2 assy.	2
Rigid bus with (2)-45 deg. bends.	4" dia. SPS, aluminum rigid bus, make from 10'-0" long pipe, 2'-0" drop, offset terminal pads attached at each end.	Terminal pads: Dwg. 064116 Figure 14, code 30-4404 at each end. Alternate: Dwg. 046267 Type 608, code 30-0233 at each end.	1 assy.	4
Flexible jumper, 2300 MCM single conductor	15'-0" long, AAC, with compression end fittings.	End fittings: Dwg 046267 Type 317, code 30-3544.	1	3
Flexible jumper, (2)-1113 MCM bundled conductors	15'-0" long, AAC, with compression end fittings, 2 spacers.	End fittings: Dwg 046267 Type 316, code 30-3457. Spacers: Dwg 046267 Type 390, code 18-8559.	1	3
Flexible jumper, (2)-2300 MCM bundled conductors	25'-0" long, AAC, with compression end fittings, 2 spacers.	End fittings: Dwg 046267 Type 317, code 30-3544. Spacers: Dwg 046267 Type 391, code 18-8569.	1	3
Spare rigid bus	4" dia. SPS aluminum rigid bus	Spares for expanding length of specimens if needed	4	NA
Welded splice connectors	Splice connectors for 4" SPS aluminum rigid bus	Dwg 046267 type 203, code 30-7139.	8	NA

Design Drafting
62-3690

PACIFIC GAS AND ELECTRIC COMPANY

GENERAL COMPUTATION SHEET

SHEET NO. ____ OF ____ SHEETS
JOB FILE NO. ____
LOCATION ____

SUBJECT PEER TASK 2C

MADE BY ____ DATE ____ CHECKED BY ____ APPROVED BY ____

LENGTHS, SCOPE OF WORK

(1)

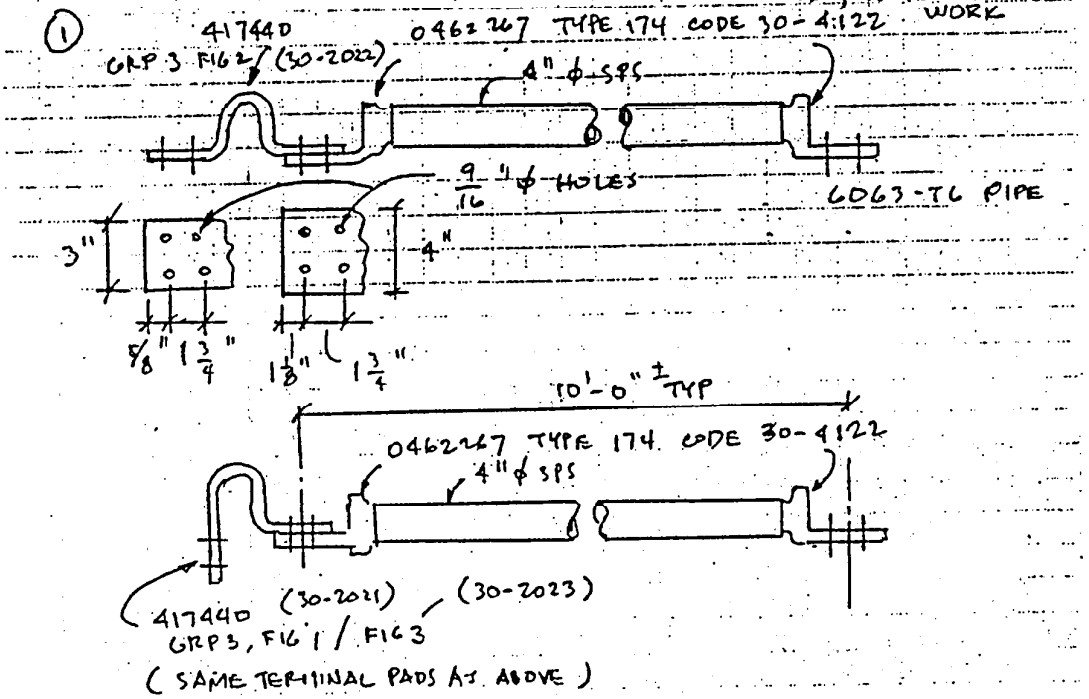

(2)

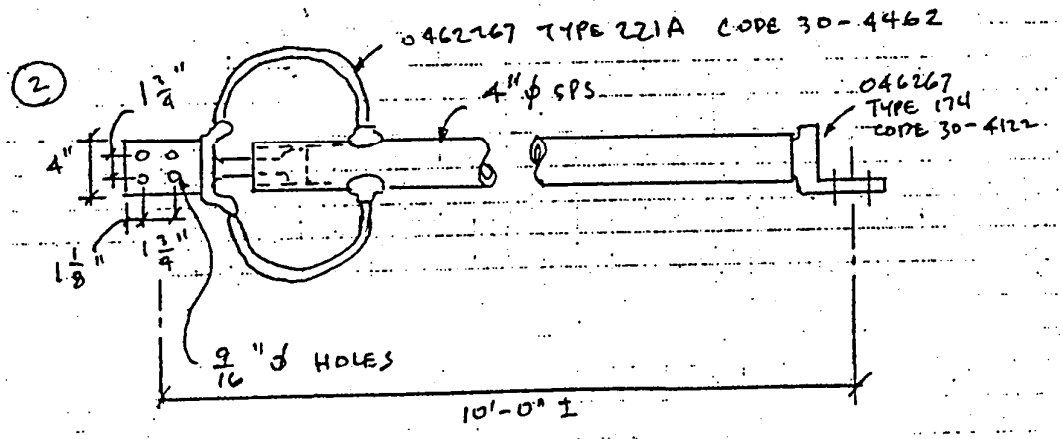

Design Drafting
62-3690

PACIFIC GAS AND ELECTRIC COMPANY

GENERAL COMPUTATION SHEET

SHEET NO. ____ OF ____ SHEETS
JOB FILE NO. ____
LOCATION ____

SUBJECT TASK 2C

MADE BY ____ DATE ____ CHECKED BY ____ APPROVED BY ____

(3) VARIOUS CABLE CONFIGURATIONS

TYP. TERMINAL PAD FOR CABLE CONNECTOR
(MAY BE WELDED, BOLTED OR CRIMPED TO CABLE

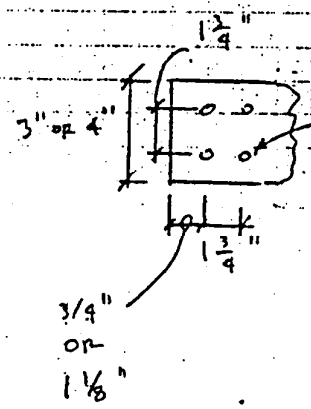

2300 MCM - 1 & 2 BUNDLED
1113 MCM - 2 BUNDLED

x 25' SPAN MAX
x 15' SPAN FOR 1113 & SINGLE 2300

SPACERS - 2 REQD IN EACH BUNDLED ASSY, 6" SP.

(4) "BPA" TYPE CONNECTOR (CODE 30-4404) TYP. BOTH ENDS

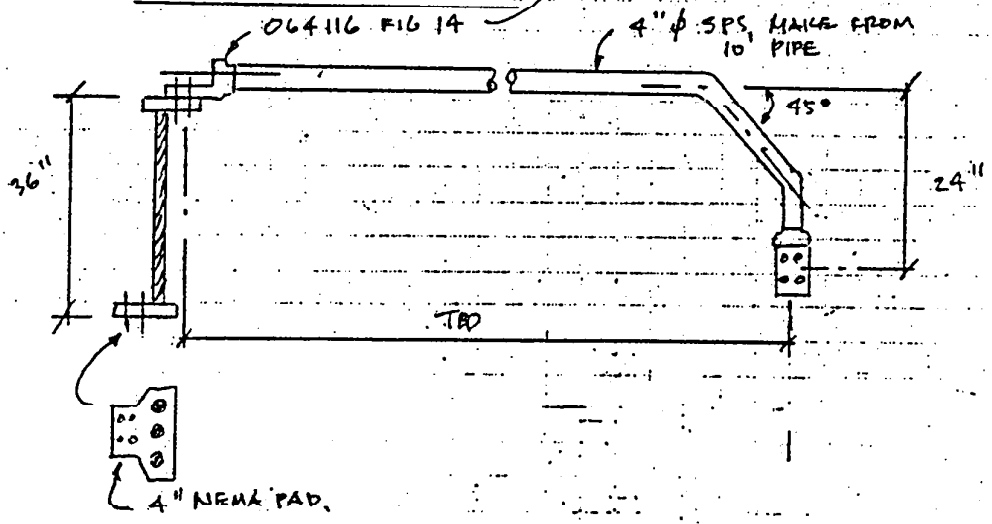

Design Drafting
62-3690

PACIFIC GAS AND ELECTRIC COMPANY

GENERAL COMPUTATION SHEET

SHEET NO. ____ OF ____ SHEETS
JOB FILE NO. ____
LOCATION ____

SUBJECT ____

MADE BY ____ DATE ____ CHECKED BY ____ APPROVED BY ____

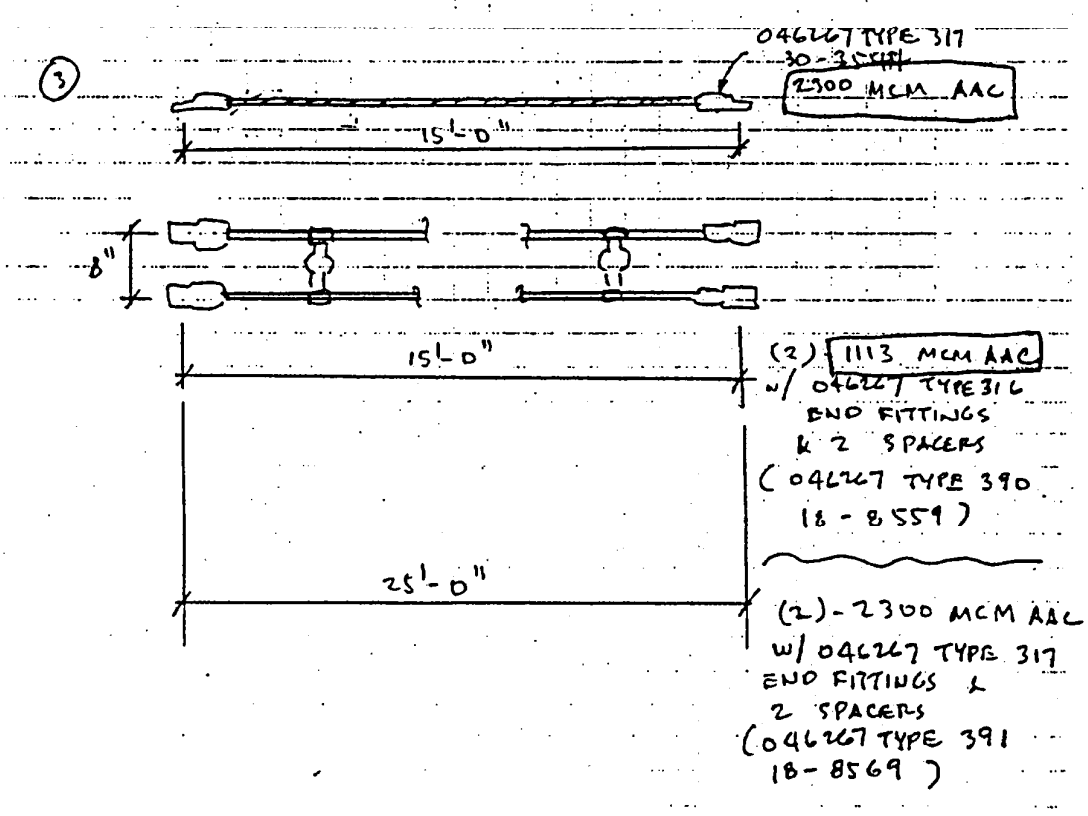

APPENDIX B

SHOP DRAWINGS OF GENERIC EQUIPMENT SPECIMENS

EQUIPMENT 1 : 2 Hz 800lbs

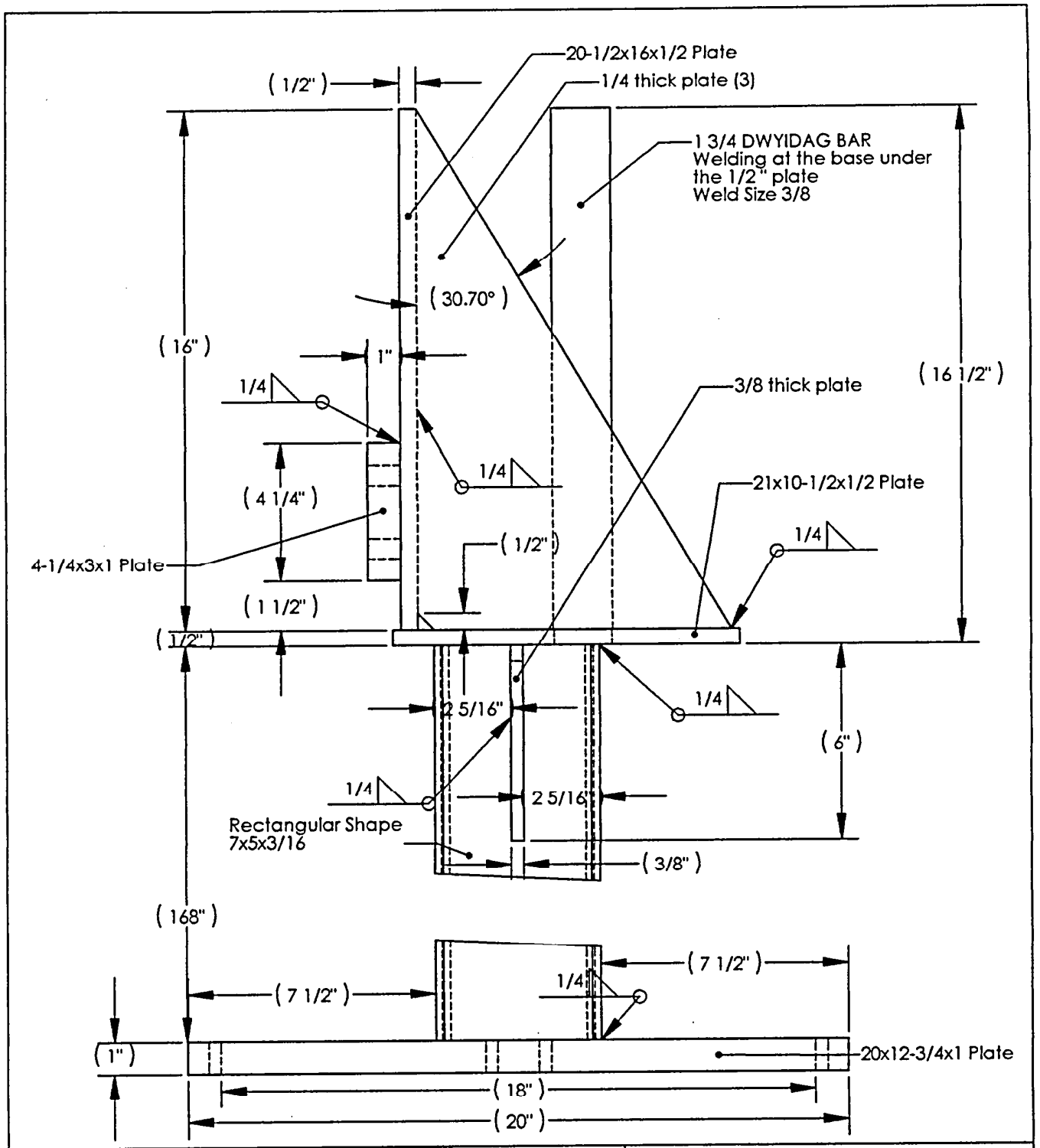

UNLESS OTHERWISE SPECIFIED DIMENSIONS ARE IN INCHES. TOLERANCES ARE: FRACTIONS ±X/X DECIMALS .XX ±.XX .XXX ±.XXX ANGLES ±X°	CONTRACT NO.		UCSD University of California, San Diego
	APPROVALS	DATE	HSS 7x5x3/16 BEAM Side View
	DRAWN Spiro Kremmidas	5/20/1999	
	CHECKED Andre Filiatrault	5/20/1999	
MATERIAL	ENGR.		SIZE A / DWG. NO. / REV. 1
FINISH	ISSUED		
DO NOT SCALE DRAWING			SCALE 1:4 / CAD FILE: / SHEET 1 OF 4

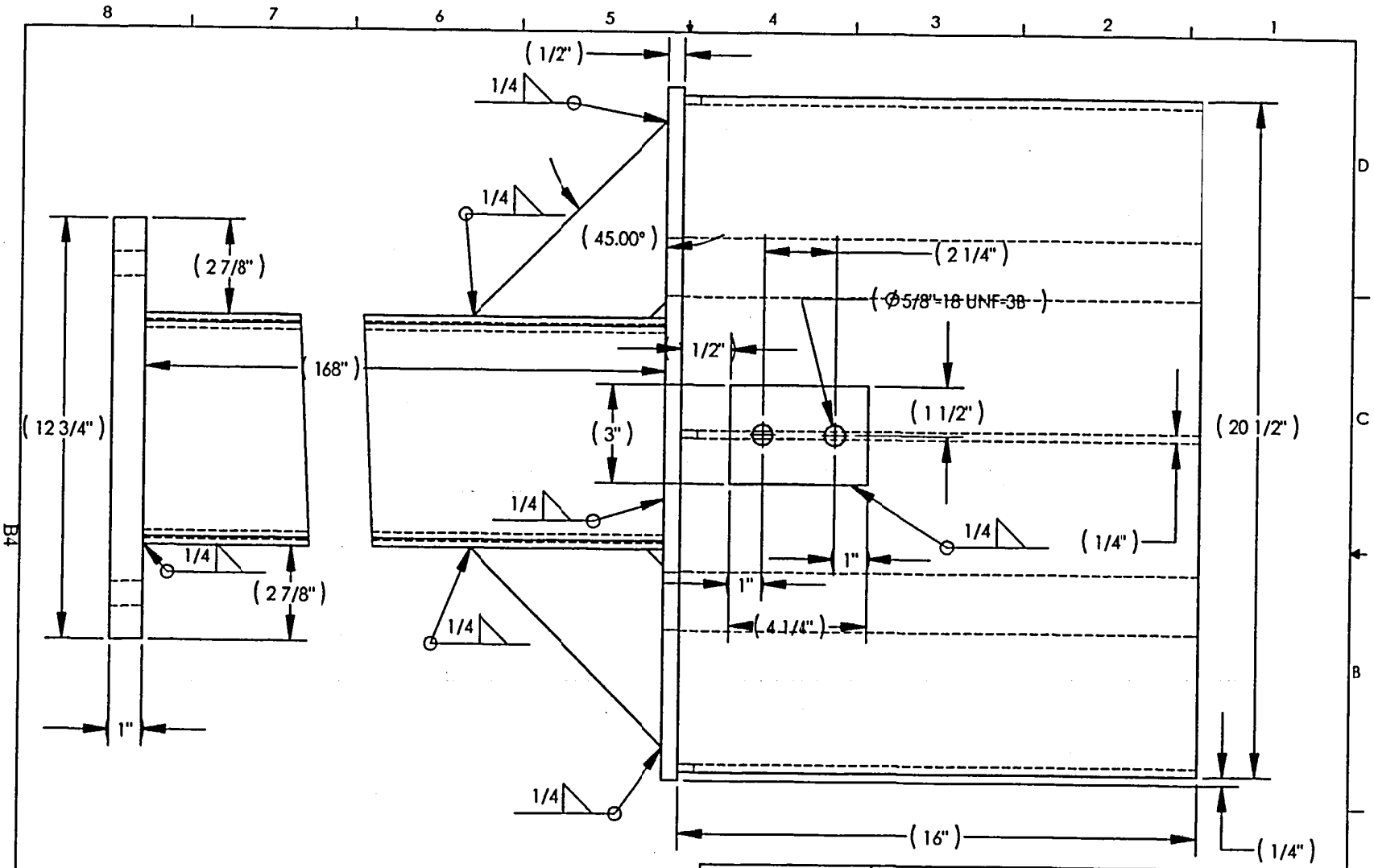

Plates A-36	Quantity
20x12-3/4x1	1
21x10-1/2x1/2	1
20-1/2x16x1/2	1
4-1/4x3x1	1
1/4 thick plate	3
3/8 thick plate	2

UNLESS OTHERWISE SPECIFIED DIMENSIONS ARE IN INCHES
TOLERANCES ARE:
FRACTIONS ± DECIMALS .XX± .XX ± 1 .XXX±.XXX ANGLES ± 1

MATERIAL --

FINISH --

DO NOT SCALE DRAWING

CAD GENERATED DRAWING, DO NOT MANUALLY UPDATE

APPROVALS	DATE
DRAWN Spiro Kremmidas	5/20/1999
CHECKED Andre Filiatrault	5/20/1999
RESP ENG	
MFG ENG	
QUAL ENG	

UCSD
University of California, San Diego

HSS 7x5x3/16 BEAM
Front View

SIZE A | DWG. NO. | REV. 1

SCALE 1:4 | CAD FILE: | SHEET 2 OF 4

NOTE:
Same Base Plate as
the one in HSS 3-1/2x2-1/2x1/4 BEAM

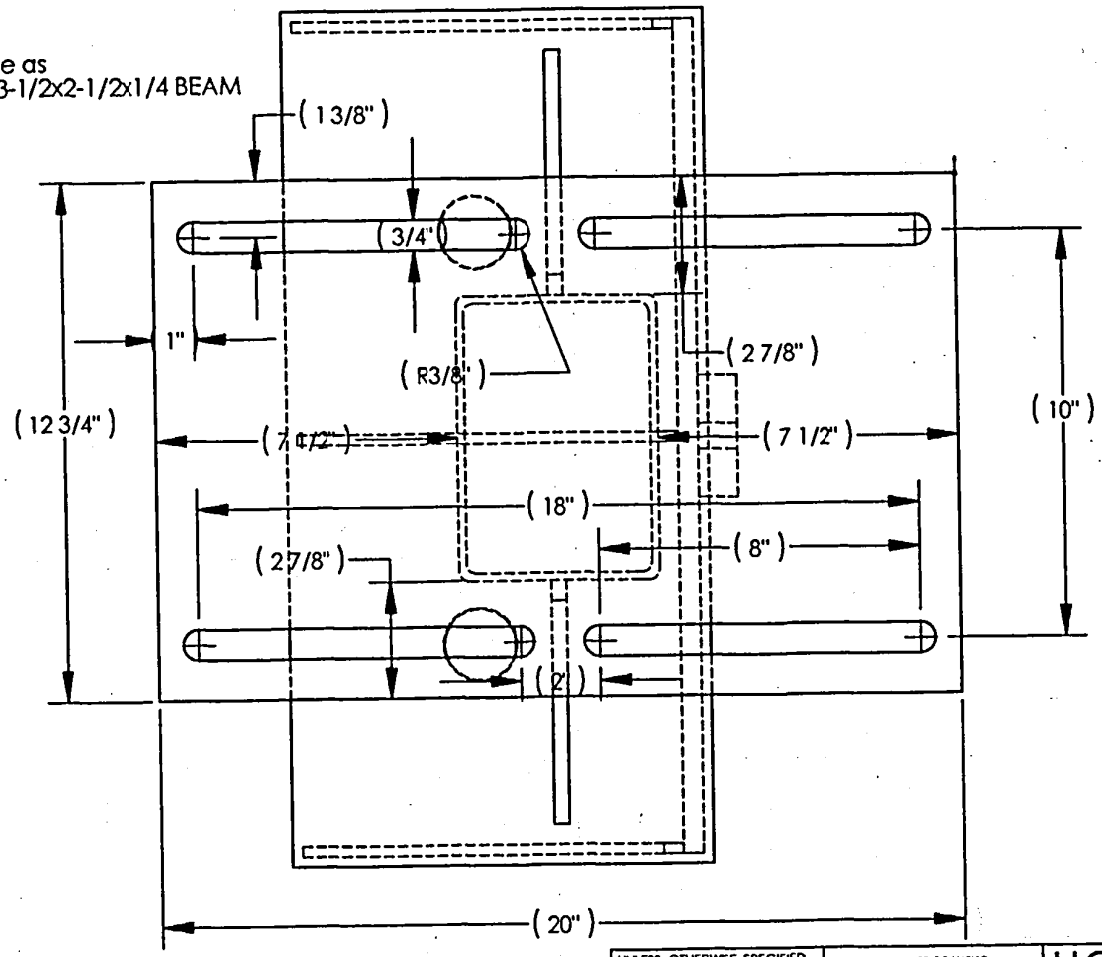

UNLESS OTHERWISE SPECIFIED DIMENSIONS ARE IN INCHES TOLERANCES ARE: FRACTIONS ± DECIMALS .XX± .XX ± 1 .XXX±.XXX ANGLES	CAD GENERATED DRAWING, DO NOT MANUALLY UPDATE		UCSD University of California, San Diego
	APPROVALS	DATE	HSS 7x5x3/16 BEAM Bottom View
	DRAWN Spiro Kremmidas	5/20/1999	
	CHECKED Andre Filiatrault	5/20/1999	
MATERIAL --	RESP ENG		
FINISH --	MFG ENG		SIZE A · DWG. NO. · REV. 1
DO NOT SCALE DRAWING	QUAL ENG		SCALE 1:4 · CAD FILE: · SHEET 3 OF 4

B5

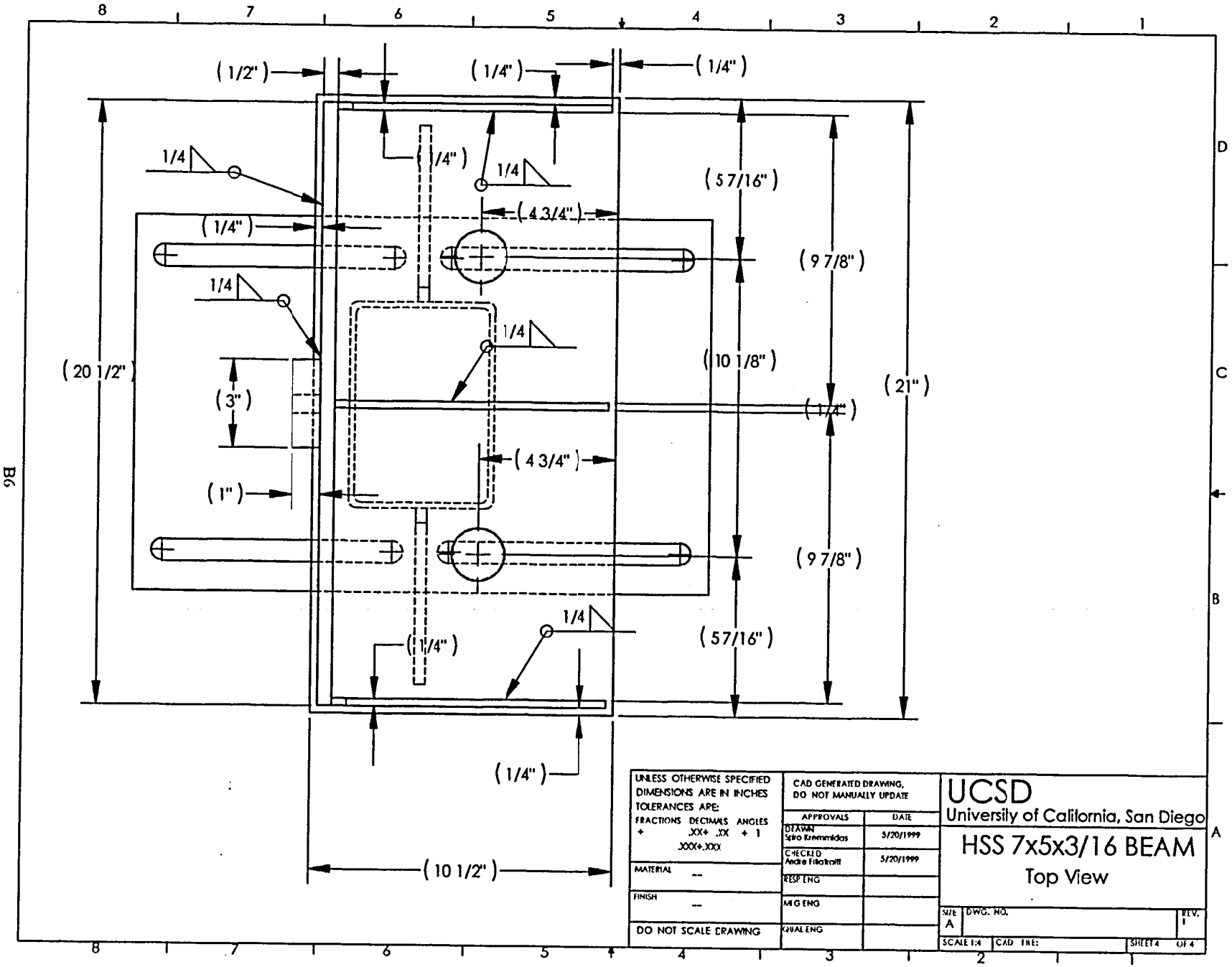
(1/2")
(1/4")
(1/4")
(1/4")
1/4
1/4
(4 3/4")
(1/4")
(5 7/16")
(9 7/8")
1/4
1/4
(20 1/2")
(3")
(10 1/8")
(21")
(1/4")
(4 3/4")
(1")
(9 7/8")
1/4
(1/4")
(5 7/16")
(1/4")
(10 1/2")
UNLESS OTHERWISE SPECIFIED DIMENSIONS ARE IN INCHES
TOLERANCES ARE:
FRACTIONS ± DECIMALS .XX± .XX ± .XXX± .XXX ANGLES ± 1
MATERIAL --
FINISH --
DO NOT SCALE DRAWING
CAD GENERATED DRAWING, DO NOT MANUALLY UPDATE
APPROVALS DATE
DRAWN Spiro Kremmidas 5/20/1999
CHECKED Andre Filiatrault 5/20/1999
RESP ENG
MFG ENG
QUAL ENG
UCSD
University of California, San Diego
HSS 7x5x3/16 BEAM
Top View
SIZE A
DWG. NO.
REV. 1
SCALE 1:4
CAD FILE:
SHEET 4 OF 4

EQUIPMENT 2: 2 Hz 90lbs

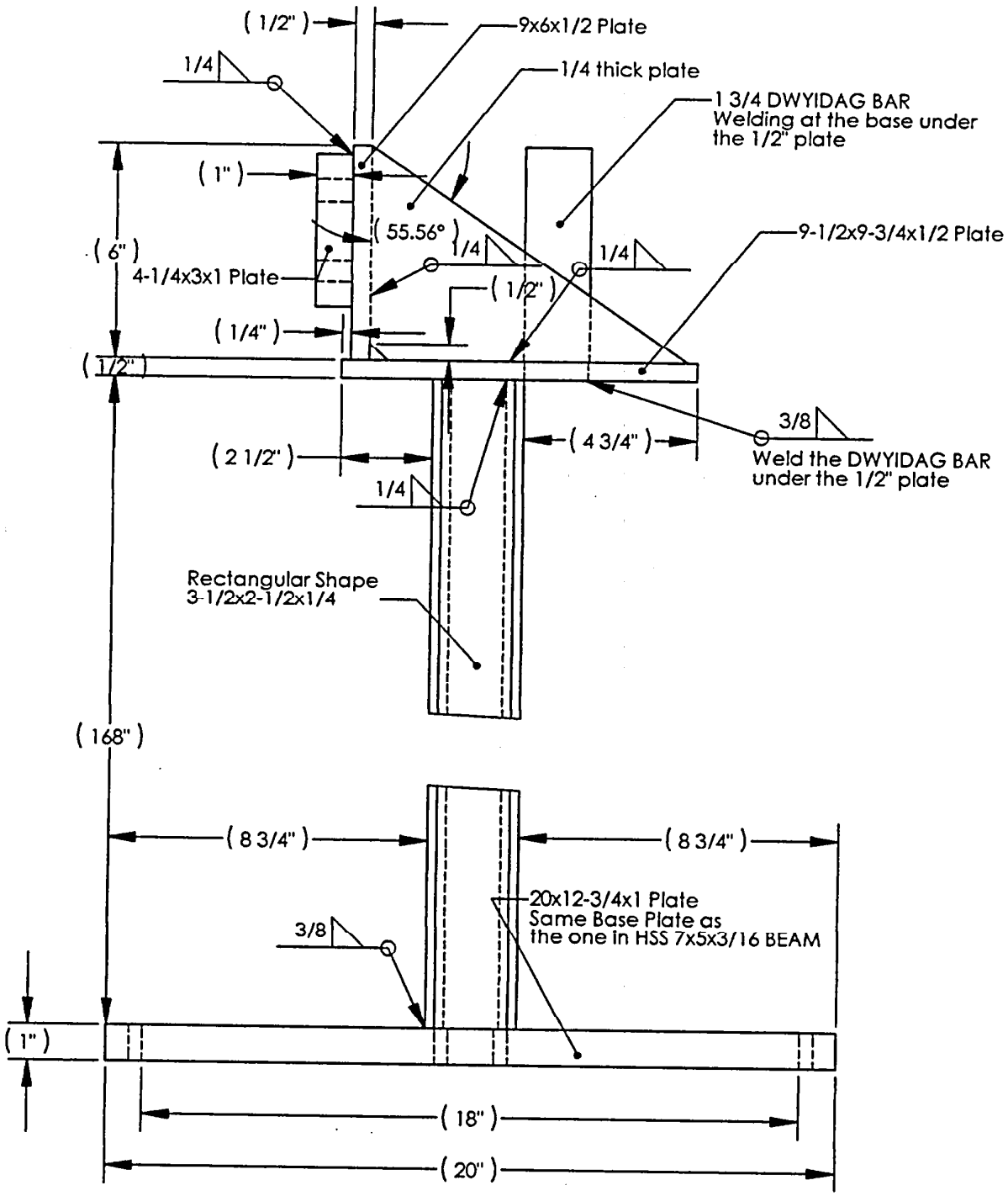

UNLESS OTHERWISE SPECIFIED DIMENSIONS ARE IN INCHES. TOLERANCES ARE:	CONTRACT NO.		UCSD University of California, San Diego
FRACTIONS ±X/X DECIMALS .XX ±.XX .XXX ±.XXX ANGLES ±X°	APPROVALS	DATE	HSS 3-1/2x2-1/2x1/4 BEAM Side View
	DRAWN Spiro Kremmidas	5/20/1999	
	CHECKED Andre Filiatrault	5/20/1999	
MATERIAL	ENGR.		SIZE A / DWG. NO. / REV. 1
FINISH	ISSUED		
DO NOT SCALE DRAWING			SCALE 1:4 / CAD FILE: / SHEET 1 OF 4

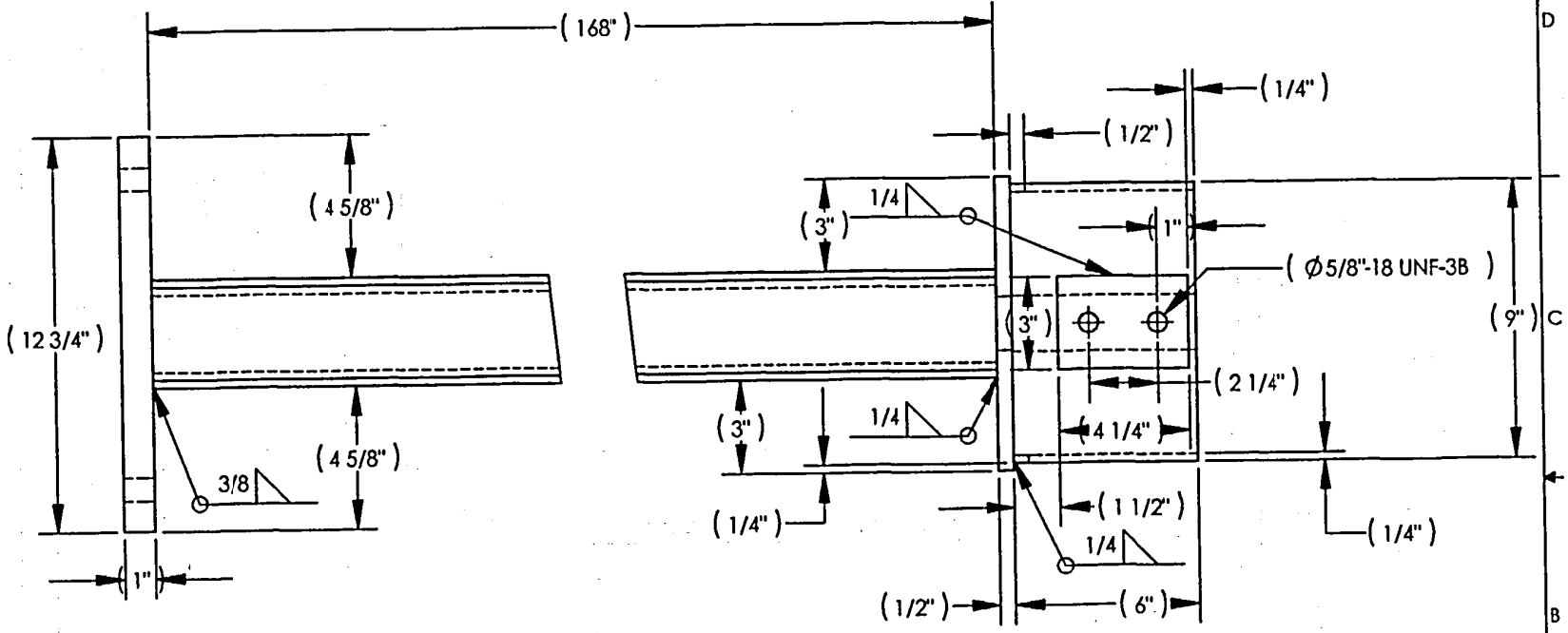

	Quantity
Plates A-36	
20x12-3/4x1	1
9-1/2x9-3/4x1/2	1
9x6x1/2	1
4-1/4x3x1	1
1/4 thick plates	2

UNLESS OTHERWISE SPECIFIED DIMENSIONS ARE IN INCHES
TOLERANCES ARE:
FRACTIONS + DECIMALS .XX+ .XX + 1 .XXX+.XXX ANGLES +

MATERIAL --

FINISH --

DO NOT SCALE DRAWING

CAD GENERATED DRAWING, DO NOT MANUALLY UPDATE

APPROVALS	DATE
DRAWN Spiro Kremmidas	5/20/1999
CHECKED Andre Filiatrault	5/20/1999
RESP ENG	
MFG ENG	
QUAL ENG	

UCSD
University of California, San Diego

HSS 3-1/2x2-1/2x1/4 BEAM
Front View

SIZE A | DWG. NO. | REV. 1
SCALE 1:4 | CAD FILE: | SHEET 2 OF 4

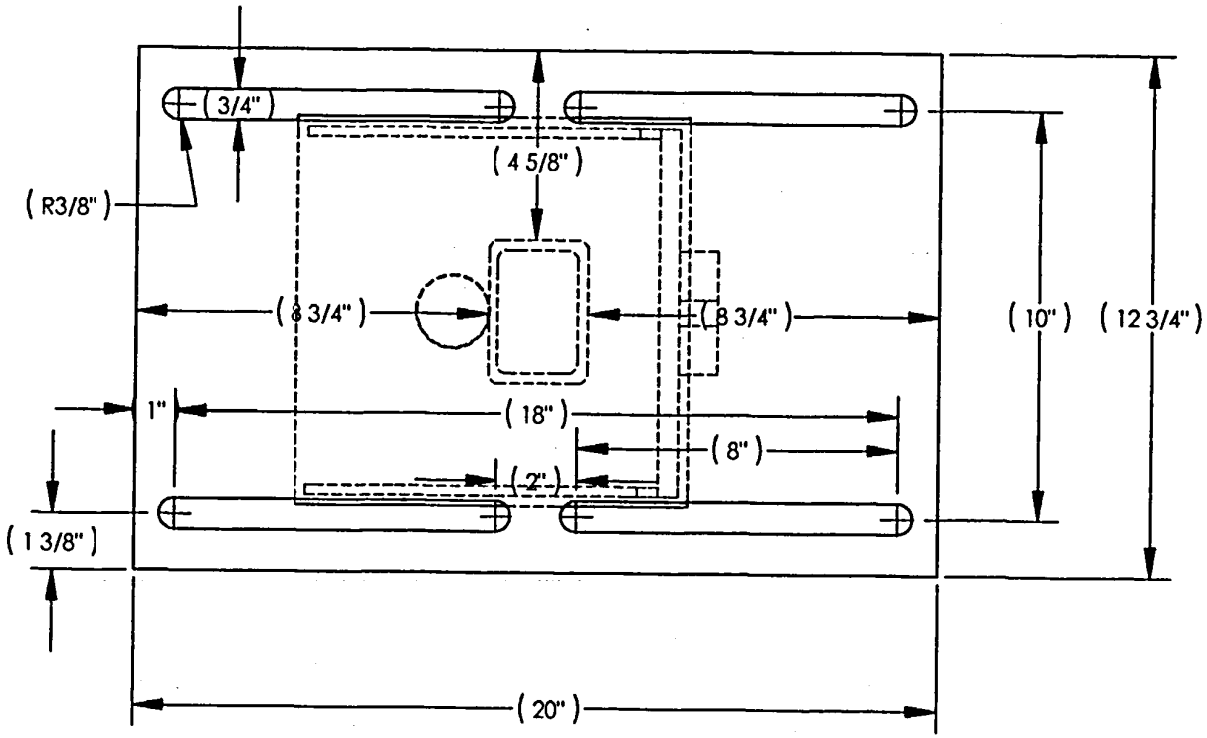

UNLESS OTHERWISE SPECIFIED DIMENSIONS ARE IN INCHES TOLERANCES ARE: FRACTIONS ± DECIMALS .XX± .XX ± 1 .XXX±.XXX ANGLES	CAD GENERATED DRAWING, DO NOT MANUALLY UPDATE		UCSD University of California, San Diego
	APPROVALS	DATE	
	DRAWN Spiro Kremmidas	5/20/1999	HSS 3-1/2x2-1/2-1/4 BEAM
	CHECKED Andre Filiatrault	5/20/1999	Bottom View
MATERIAL —	RESP ENG		
FINISH —	MFG ENG		SIZE A · DWG. NO. · REV. 1
DO NOT SCALE DRAWING	QUAL ENG		SCALE 1:4 · CAD FILE: · SHEET 3 OF 4

B10

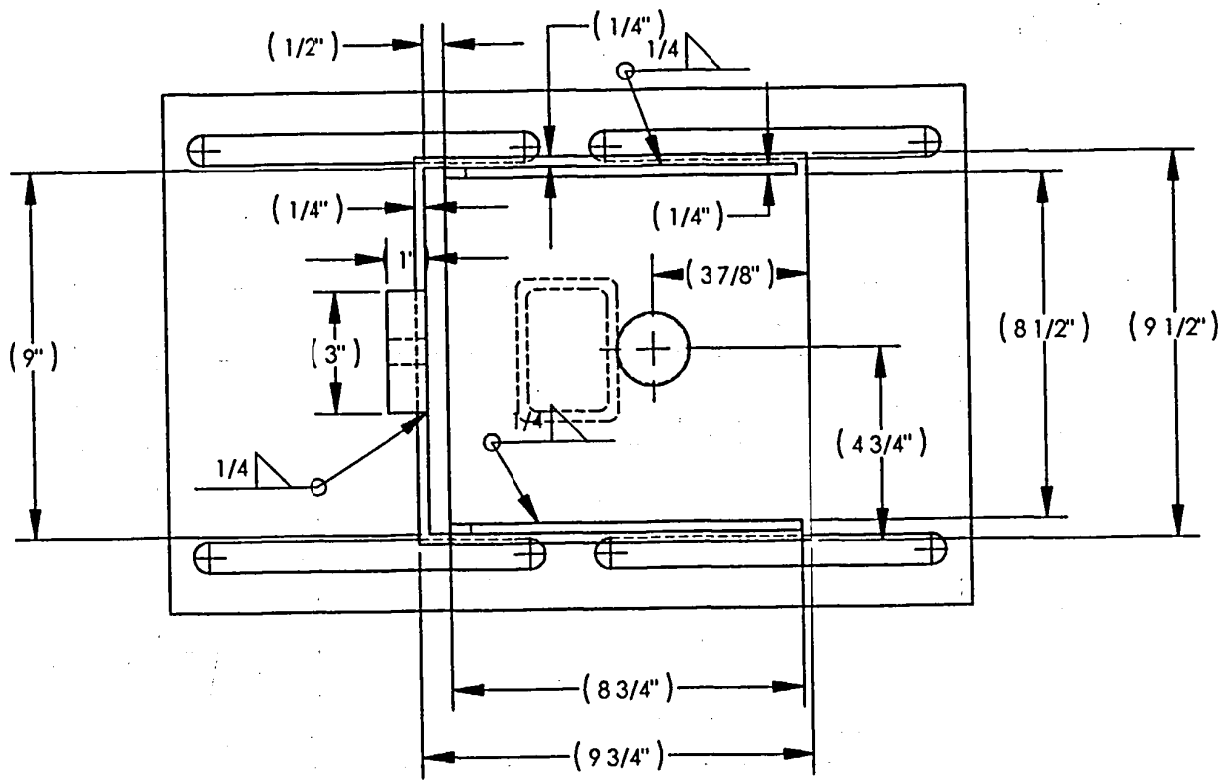

UNLESS OTHERWISE SPECIFIED DIMENSIONS ARE IN INCHES TOLERANCES ARE: FRACTIONS + DECIMALS .XX+ .XX .XXX+.XXX ANGLES + 1	CAD GENERATED DRAWING, DO NOT MANUALLY UPDATE	UCSD University of California, San Diego
	APPROVALS / DATE	HSS 3-1/2x2-1/2x1/4 BEAM
	DRAWN Spiro Kremmidas 5/20/1999	Top View
	CHECKED Andre Filiatrault 5/20/1999	
MATERIAL --	RESP ENG	
FINISH --	MFG ENG	SIZE A / DWG. NO. / REV. 1
DO NOT SCALE DRAWING	QUAL ENG	SCALE 1:4 / CAD FILE: / SHEET 4 OF 4

EQUIPMENT 3 : 6 Hz 150lbs

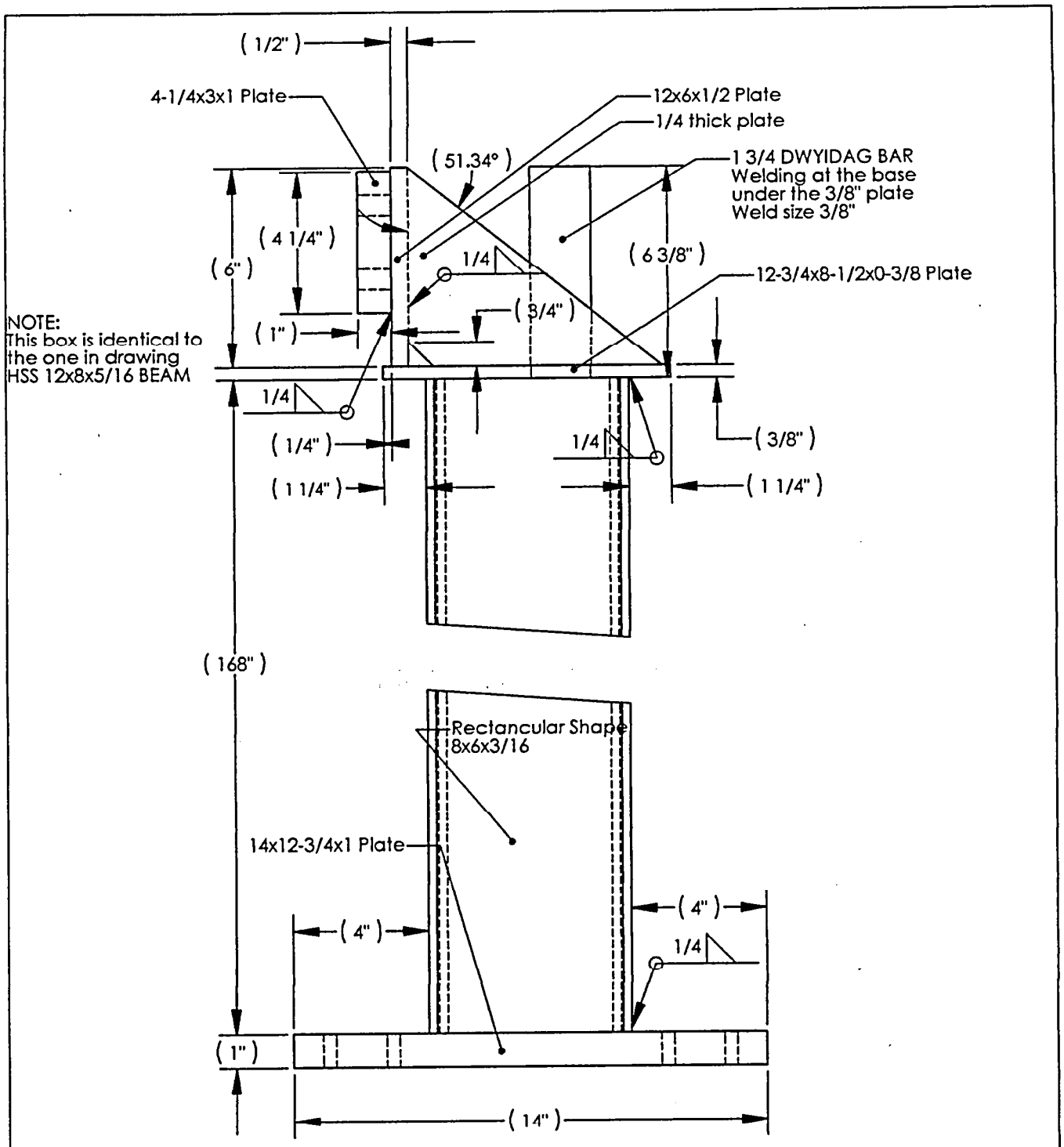

UNLESS OTHERWISE SPECIFIED DIMENSIONS ARE IN INCHES. TOLERANCES ARE: FRACTIONS ±X/X DECIMALS .XX ±.XX .XXX ±.XXX ANGLES ±X°	CONTRACT NO.		UCSD University of California, San Diego
	APPROVALS	DATE	HSS 8x6x3/16 BEAM Side View
	DRAWN Spiro Kremmidas	5/20/1999	
	CHECKED Andre Filiatrault	5/20/1999	
MATERIAL	ENGR.		SIZE A / DWG. NO. / REV. 1
FINISH	ISSUED		
DO NOT SCALE DRAWING			SCALE 1:4 / CAD FILE: / SHEET 1 OF 3

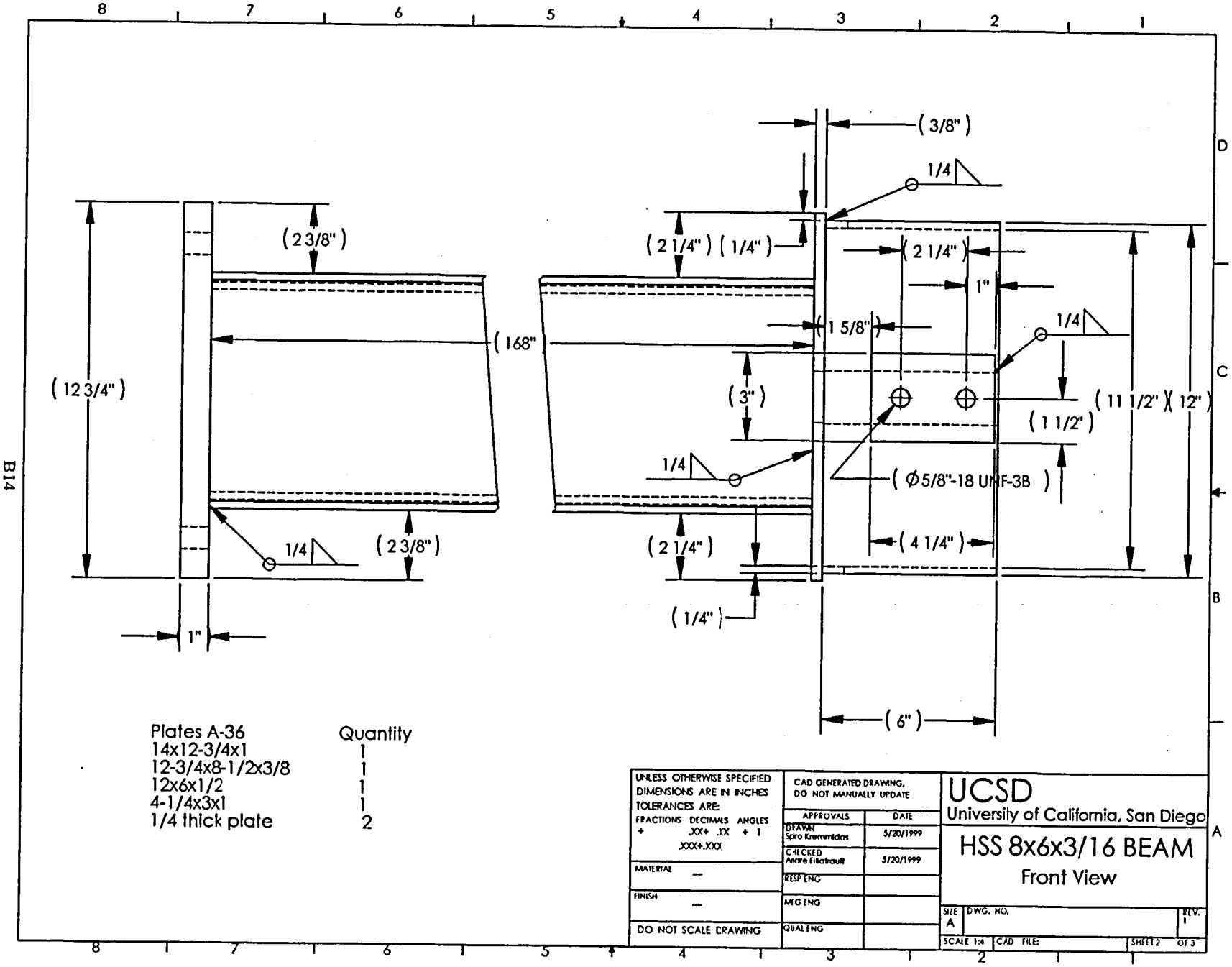

Plates A-36	Quantity
14x12-3/4x1	1
12-3/4x8-1/2x3/8	1
12x6x1/2	1
4-1/4x3x1	1
1/4 thick plate	2

UNLESS OTHERWISE SPECIFIED DIMENSIONS ARE IN INCHES
TOLERANCES ARE:
FRACTIONS ± DECIMALS .XX± .XX ± .XXX±.XXX ANGLES ± 1

MATERIAL --

FINISH --

DO NOT SCALE DRAWING

CAD GENERATED DRAWING, DO NOT MANUALLY UPDATE

APPROVALS	DATE
DRAWN Spiro Kremmidas	5/20/1999
CHECKED Andre Filiatrault	5/20/1999
RESP ENG	
MFG ENG	
QUAL ENG	

UCSD
University of California, San Diego

HSS 8x6x3/16 BEAM
Front View

SIZE A | DWG. NO. | REV. 1
SCALE 1:4 | CAD FILE: | SHEET 2 OF 3

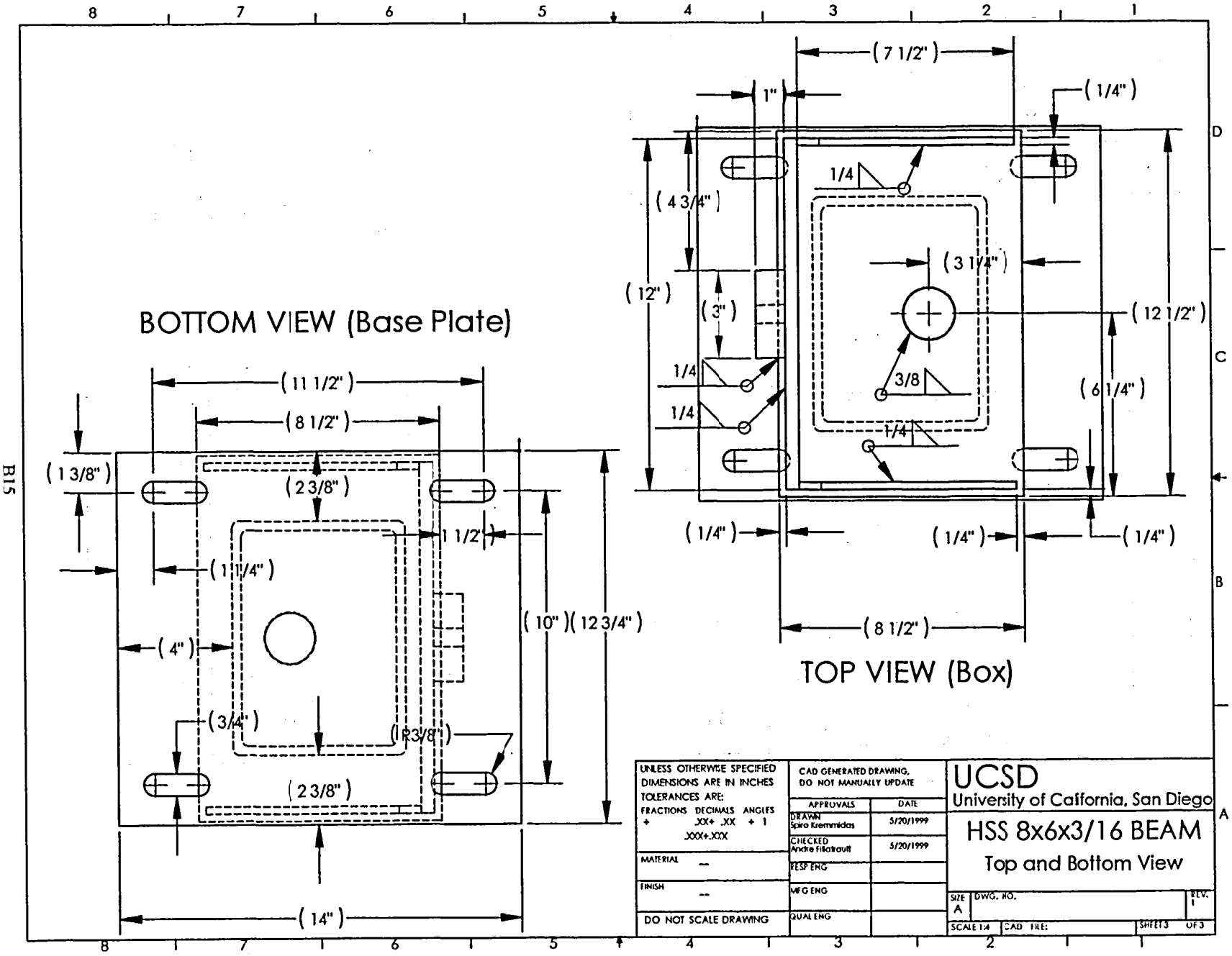
BOTTOM VIEW (Base Plate)
(11 1/2")
(8 1/2")
(1 3/8")
(2 3/8")
(1 1/2")
(1 1/4")
(4")
(10")
(12 3/4")
(3/4")
(1 3/8")
(2 3/8")
(14")
TOP VIEW (Box)
(7 1/2")
1"
(1/4")
(4 3/4")
(3 1/4")
(12")
(3")
(12 1/2")
1/4
3/8
(6 1/4")
(1/4")
(8 1/2")
UNLESS OTHERWISE SPECIFIED
DIMENSIONS ARE IN INCHES
TOLERANCES ARE:
FRACTIONS DECIMALS ANGLES
± .XX± .XX ± 1
.XXX±.XXX
MATERIAL --
FINISH --
DO NOT SCALE DRAWING
CAD GENERATED DRAWING,
DO NOT MANUALLY UPDATE
APPROVALS DATE
DRAWN Spiro Kremmidas 5/20/1999
CHECKED Andre Filiatrault 5/20/1999
RESP ENG
MFG ENG
QUAL ENG
UCSD
University of California, San Diego
HSS 8x6x3/16 BEAM
Top and Bottom View
SIZE A
DWG. NO.
REV. 1
SCALE 1:4
CAD FILE:
SHEET 3 OF 3

EQUIPMENT 4 : 12 Hz 150lbs

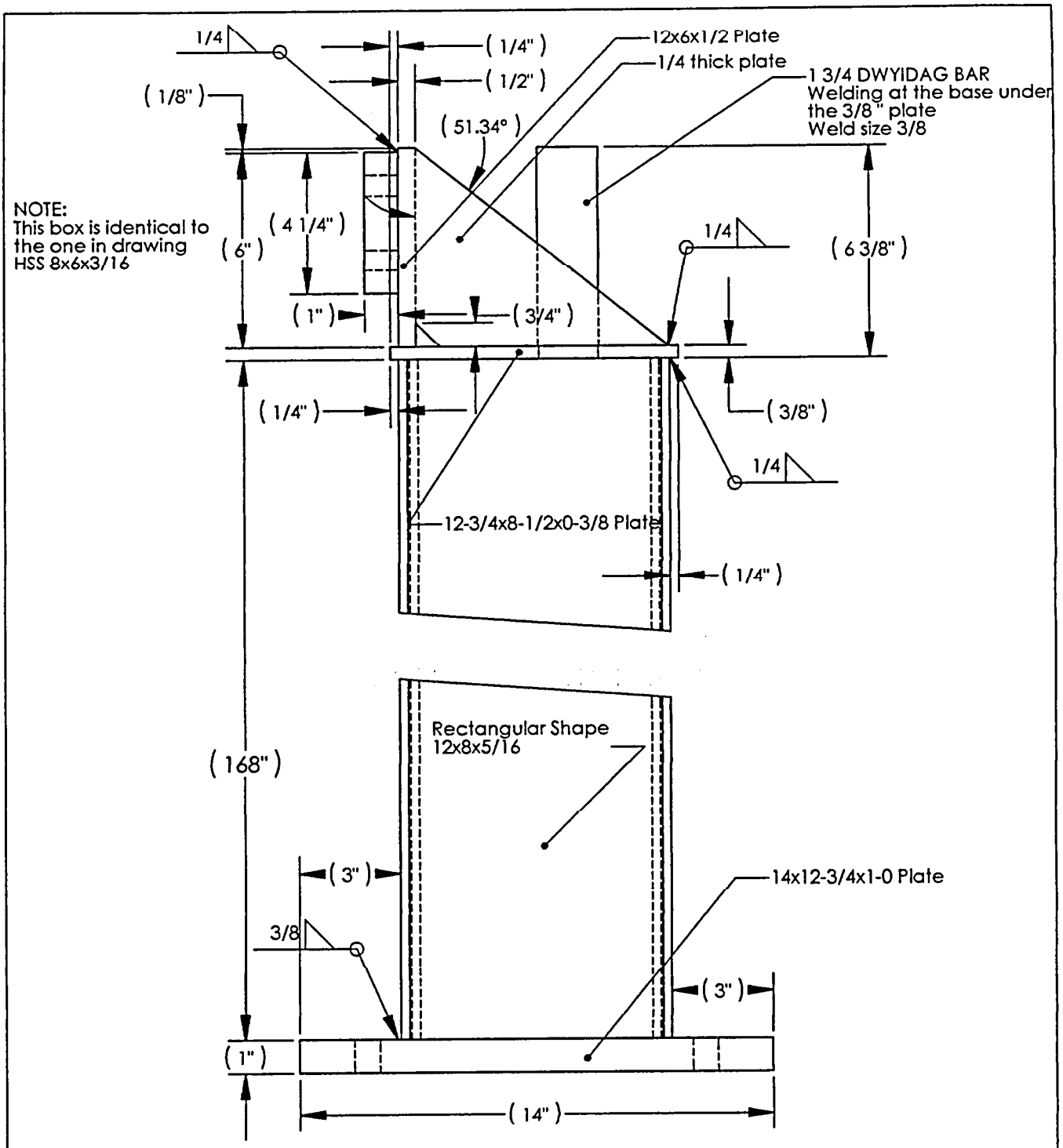

UNLESS OTHERWISE SPECIFIED DIMENSIONS ARE IN INCHES. TOLERANCES ARE:	CONTRACT NO.		UCSD University of California, San Diego
FRACTIONS ±X/X DECIMALS .XX ±.XX .XXX ±.XXX ANGLES ±X°	APPROVALS	DATE	HSS 12x8x5/16 BEAM Side View
	DRAWN Spiro Kremmidas	5/19/1999	
	CHECKED Andre Filiatrault	5/19/1999	
MATERIAL	ENGR.		SIZE A / DWG. NO. / REV. 1
FINISH	ISSUED		
DO NOT SCALE DRAWING			SCALE 1:4 / CAD FILE: / SHEET 1 OF 3

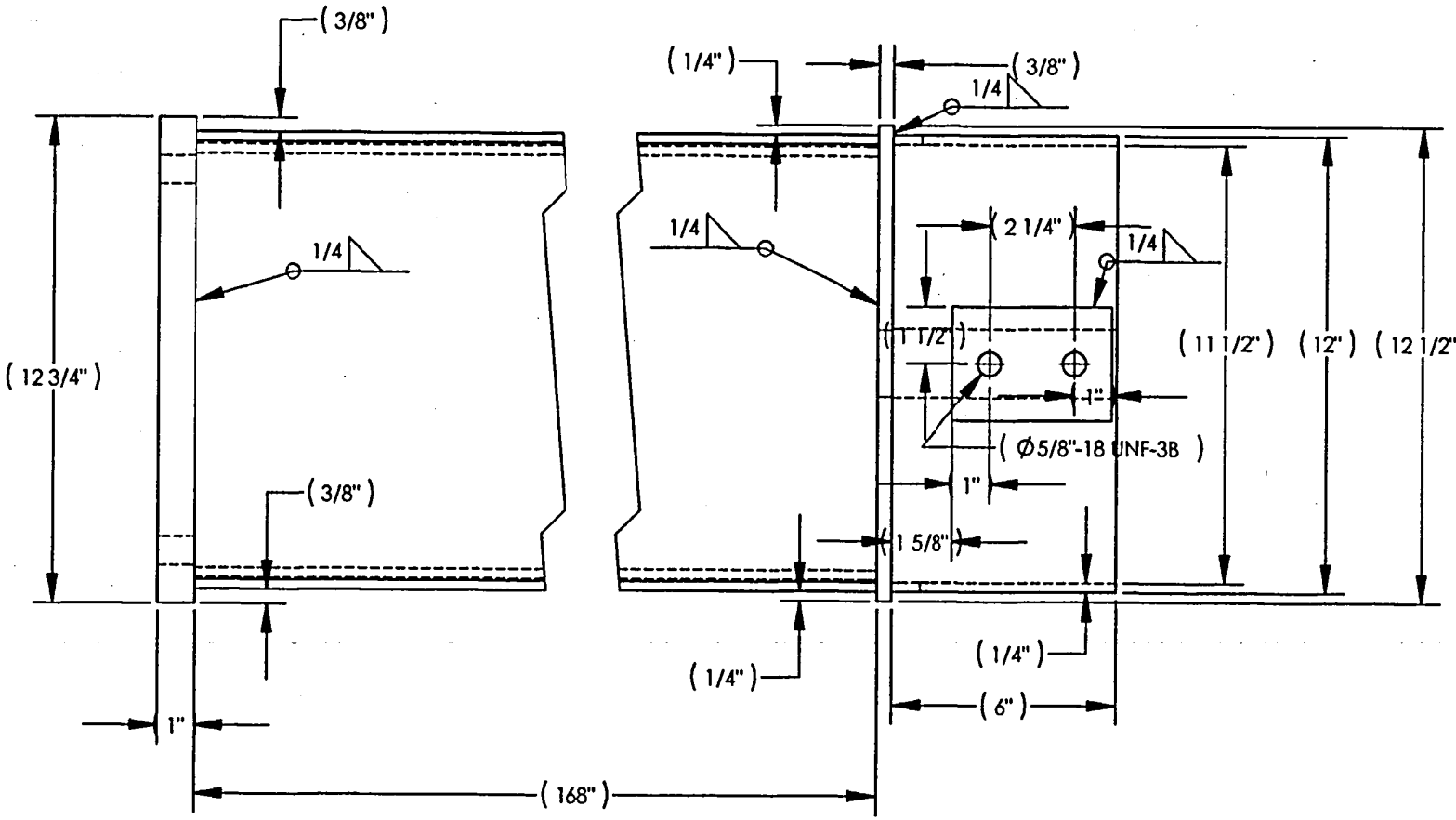

Plates A-36	Quantity
14x12-3/4x1	1
12-3/4x8-1/2x3/8	1
12x6x1/2	1
4-1/4x3x1	1
1/4 thick plates	2

UNLESS OTHERWISE SPECIFIED DIMENSIONS ARE IN INCHES
TOLERANCES ARE:
FRACTIONS + DECIMALS .XX+ .XX + 1 .XXX+.XXX ANGLES +

MATERIAL --

FINISH --

DO NOT SCALE DRAWING

CAD GENERATED DRAWING. DO NOT MANUALLY UPDATE

APPROVALS	DATE
DRAWN Sakis Kremmidas	5/20/1999
CHECKED Andre Filiatrault	5/20/1999
RESP ENG	
MFG ENG	
QUAL ENG	

UCSD
University of California, San Diego

HSS 12x8x5/16 BEAM
Front View

SIZE A | DWG. NO. | REV. 1

SCALE 1:4 | CAD FILE: | SHEET 2 OF 3

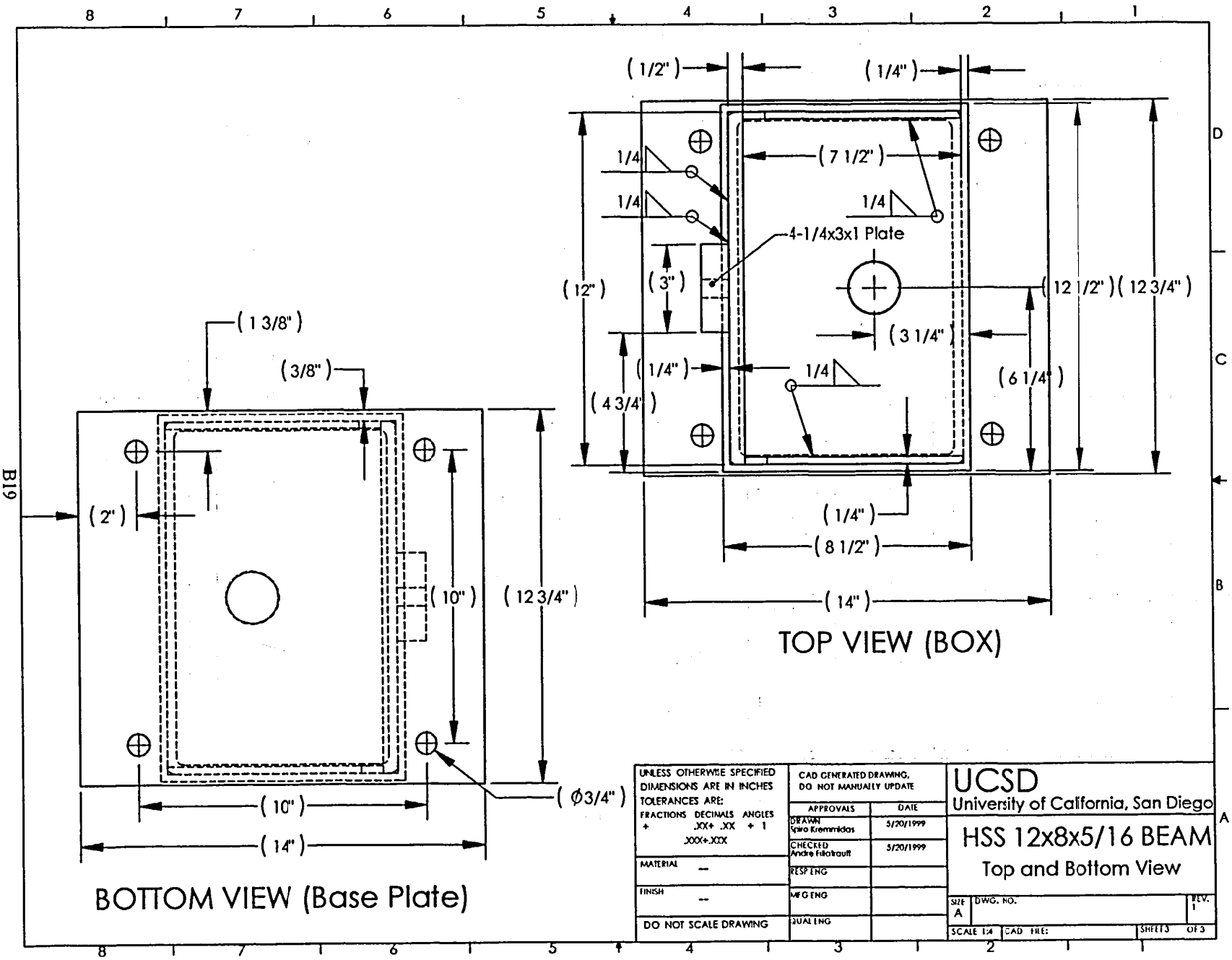
(1/2")
(1/4")
(7 1/2")
1/4
1/4
1/4
4-1/4x3x1 Plate
(12")
(3")
(12 1/2")
(12 3/4")
(3 1/4")
(1/4")
1/4
(6 1/4")
(4 3/4")
(1/4")
(8 1/2")
(14")
TOP VIEW (BOX)
(1 3/8")
(3/8")
(2")
(10")
(12 3/4")
(Ø3/4")
(10")
(14")
BOTTOM VIEW (Base Plate)
UNLESS OTHERWISE SPECIFIED
DIMENSIONS ARE IN INCHES
TOLERANCES ARE:
FRACTIONS DECIMALS ANGLES
+ .XX+ .XX + 1
.XXX+.XXX
MATERIAL --
FINISH --
DO NOT SCALE DRAWING
CAD GENERATED DRAWING,
DO NOT MANUALLY UPDATE
APPROVALS DATE
DRAWN Spiro Kremmidas 5/20/1999
CHECKED Andre Filiatrault 5/20/1999
RESP ENG
MFG ENG
QUAL ENG
UCSD
University of California, San Diego
HSS 12x8x5/16 BEAM
Top and Bottom View
SIZE A
DWG. NO.
REV. 1
SCALE 1:4
CAD FILE:
SHEET 3 OF 3

BRACING ELEMENT FOR EQUIPMENT 4

L3x3x3/8
STEEL GRADE A36
Quantity = 2

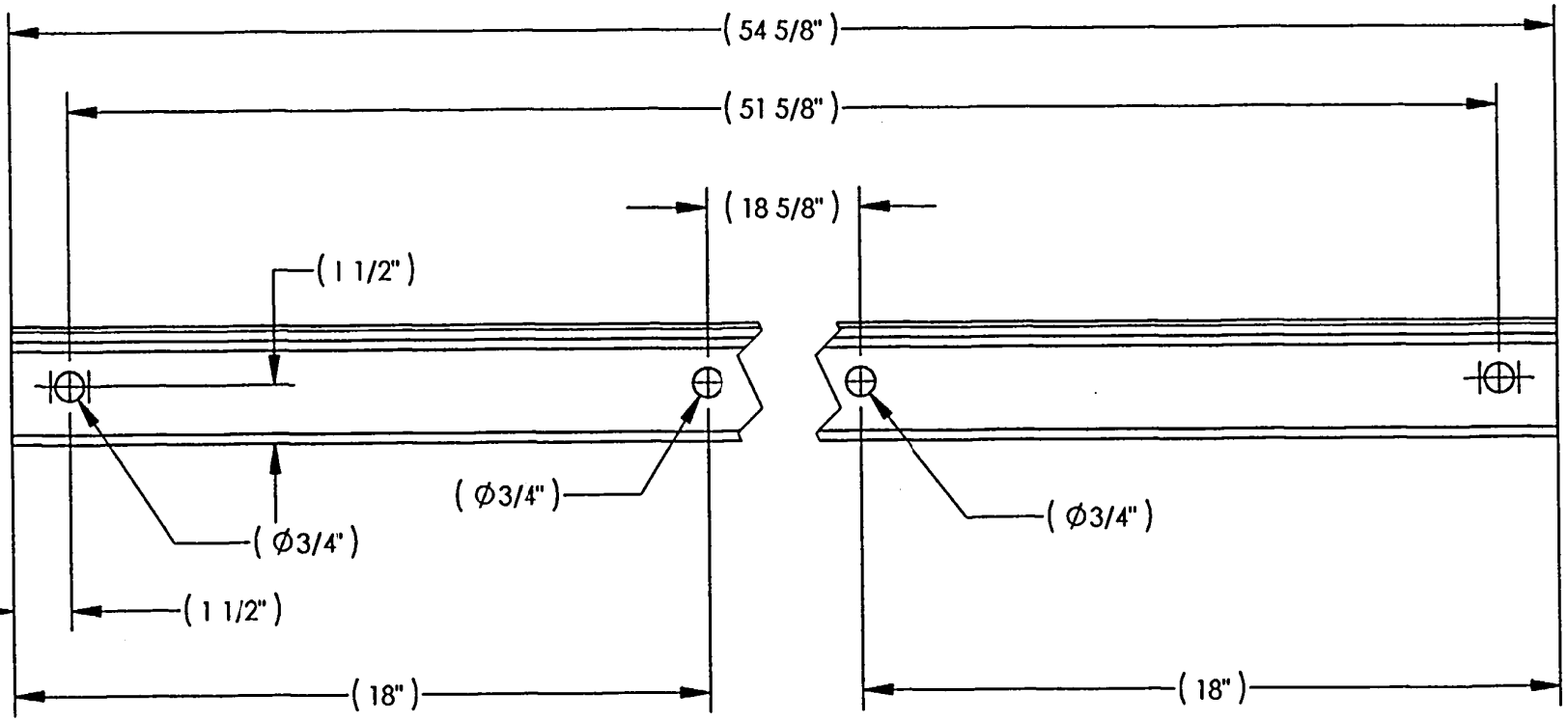

UNLESS OTHERWISE SPECIFIED DIMENSIONS ARE IN INCHES TOLERANCES ARE: FRACTIONS ± DECIMALS .XX± .XX ± .XXX±.XXX ANGLES ± 1	CAD GENERATED DRAWING, DO NOT MANUALLY UPDATE		UCSD University of California, San Diego
	APPROVALS	DATE	
	DRAWN Spiro Kremmidas	7-27-1999	Brace PEER/PG&E
MATERIAL --	CHECKED		
	RESP ENG		
FINISH --	MFG ENG		SIZE A / DWG. NO. / REV. 1
DO NOT SCALE DRAWING	QUAL ENG		SCALE 1:4 / CAD FILE: / SHEET 1 OF 1

B21

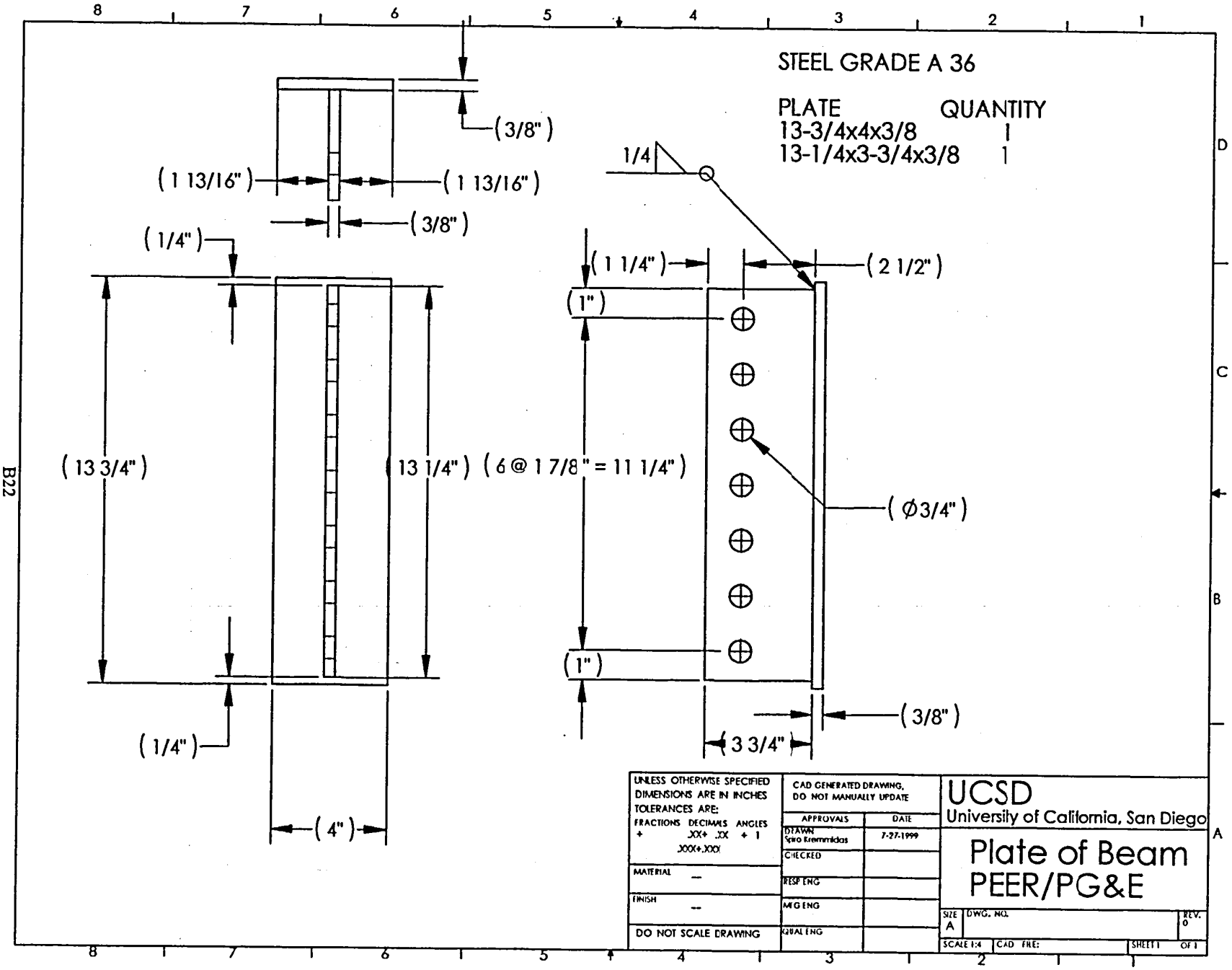
STEEL GRADE A 36
PLATE QUANTITY
13-3/4x4x3/8 1
13-1/4x3-3/4x3/8 1
(3/8")
(1 13/16")
(1 13/16")
(3/8")
(1/4")
(13 3/4")
(13 1/4")
(1/4")
(4")
1/4
(1 1/4")
(2 1/2")
(1")
(6 @ 1 7/8" = 11 1/4")
(Ø3/4")
(1")
(3/8")
(3 3/4")
UNLESS OTHERWISE SPECIFIED
DIMENSIONS ARE IN INCHES
TOLERANCES ARE:
FRACTIONS DECIMALS ANGLES
+ .XX+ .XX + 1
.XXX+.XXX
MATERIAL --
FINISH --
DO NOT SCALE DRAWING
CAD GENERATED DRAWING,
DO NOT MANUALLY UPDATE
APPROVALS DATE
DRAWN Spiro Kremmidas 7-27-1999
CHECKED
RESP ENG
MFG ENG
QUAL ENG
UCSD
University of California, San Diego
Plate of Beam
PEER/PG&E
SIZE A
DWG. NO.
REV. 0
SCALE 1:4
CAD FILE:
SHEET 1 OF 1

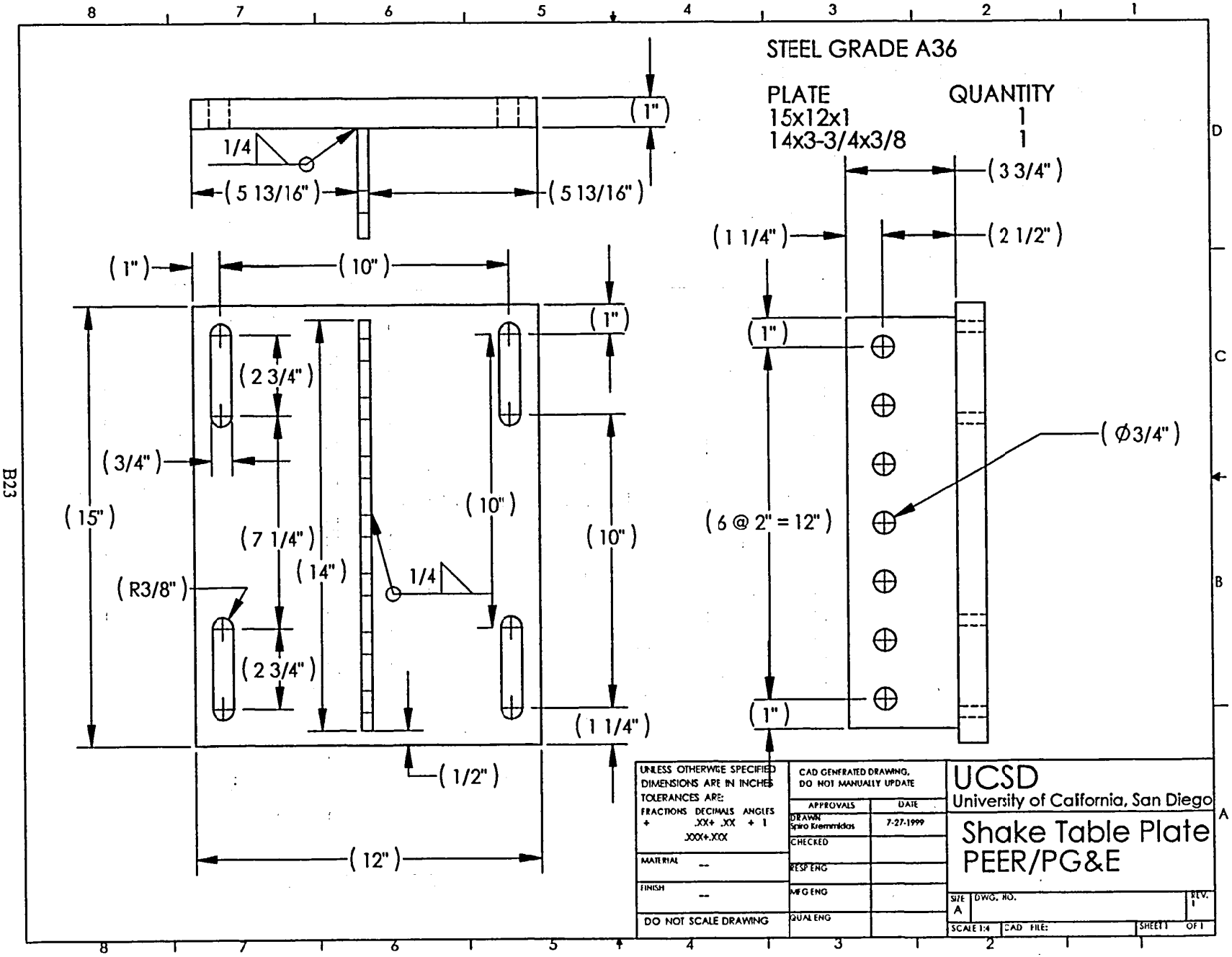
STEEL GRADE A36
PLATE
15x12x1
14x3-3/4x3/8
QUANTITY
1
1
(1")
1/4
(5 13/16")
(5 13/16")
(1")
(10")
(1")
(2 3/4")
(3/4")
(15")
(7 1/4")
(14")
(10")
(10")
(R3/8")
1/4
(2 3/4")
(1 1/4")
(1/2")
(12")
(3 3/4")
(1 1/4")
(2 1/2")
(1")
(Ø3/4")
(6 @ 2" = 12")
(1")
UNLESS OTHERWISE SPECIFIED
DIMENSIONS ARE IN INCHES
TOLERANCES ARE:
FRACTIONS DECIMALS ANGLES
+ .XX+ .XX + 1
.XXX+.XXX
MATERIAL --
FINISH --
DO NOT SCALE DRAWING
CAD GENERATED DRAWING,
DO NOT MANUALLY UPDATE
APPROVALS DATE
DRAWN Spiro Kremmidas 7-27-1999
CHECKED
RESP ENG
MFG ENG
QUAL ENG
UCSD
University of California, San Diego
Shake Table Plate
PEER/PG&E
SIZE A
DWG. NO.
REV. 1
SCALE 1:4
CAD FILE:
SHEET 1 OF 1

APPENDIX C

RESULTS OF FREQUENCY EVALUATION TESTS

TEST RB-1
EQUIPMENT COMBINATION 4
INDIVIDUAL EQUIPMENT

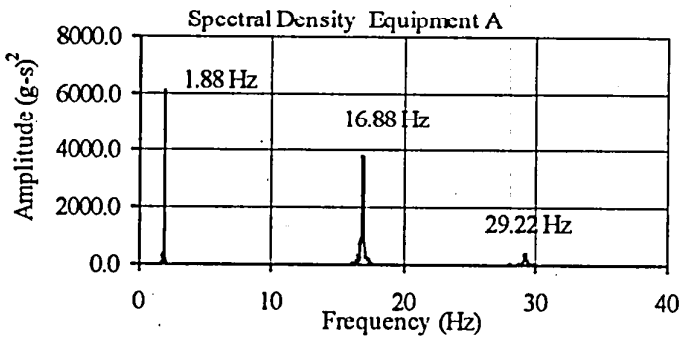

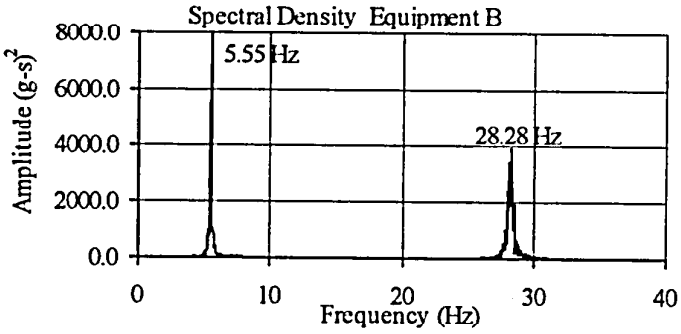

TEST RB-4
EQUIPMENT COMBINATION 4
SPRING 30-2022 CONNECTOR

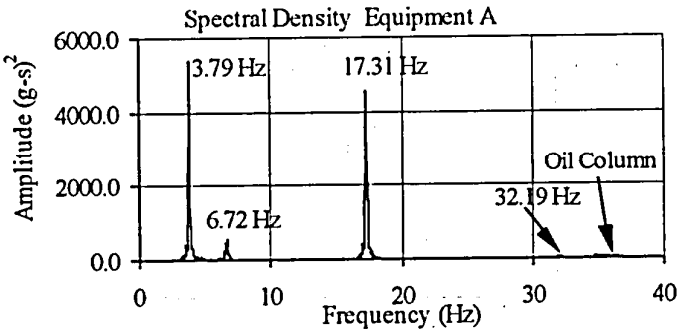

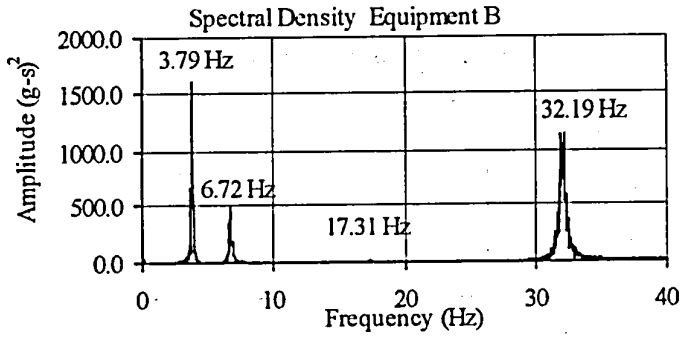

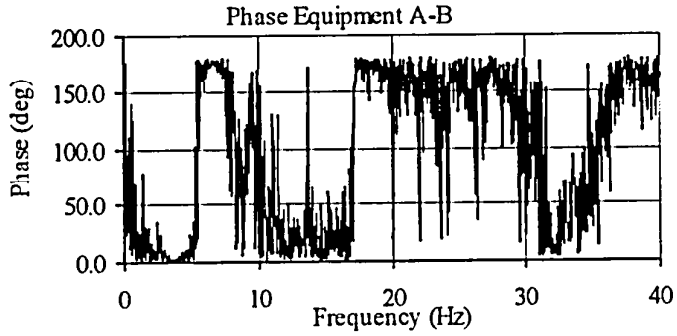

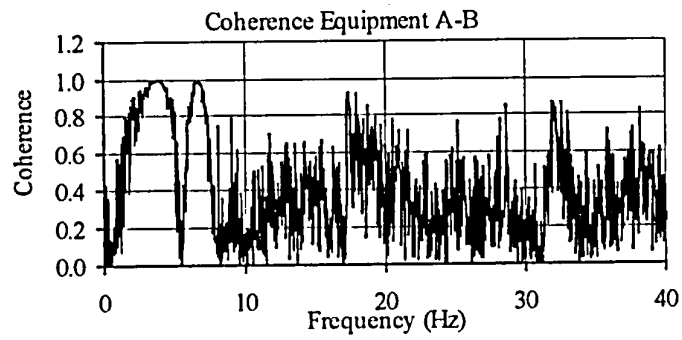

TEST RB-10
EQUIPMENT COMBINATION 4
INDIVIDUAL EQUIPMENT

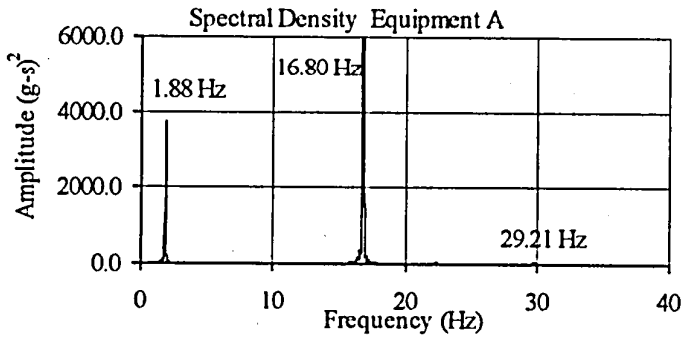

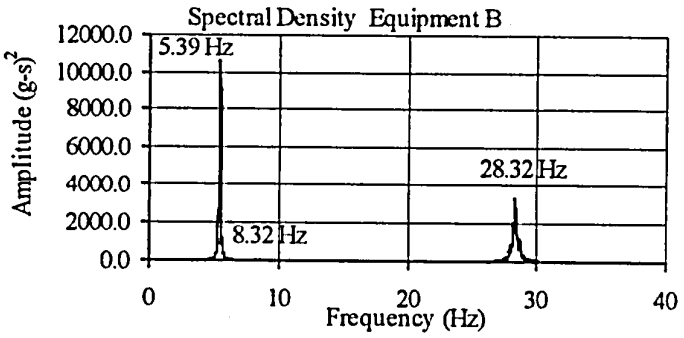

TEST RB-13
EQUIPMENT COMBINATION 4
BUS SLIDER CONNECTOR

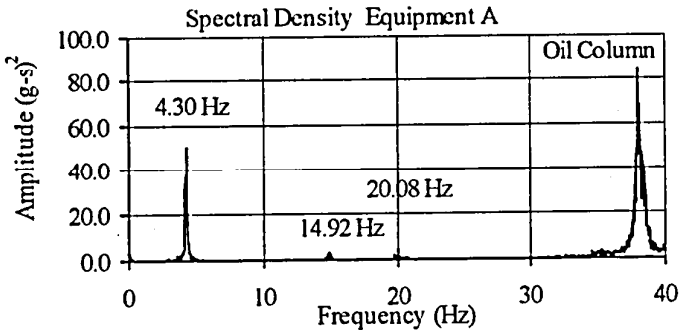

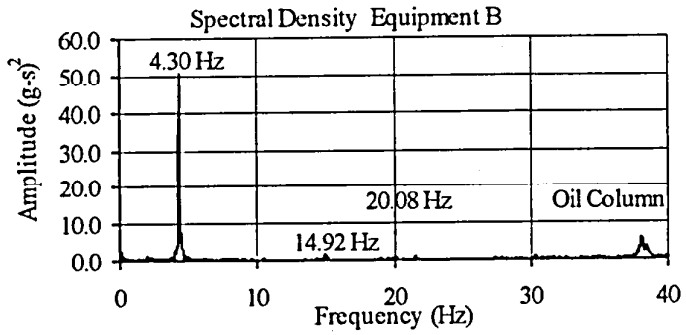

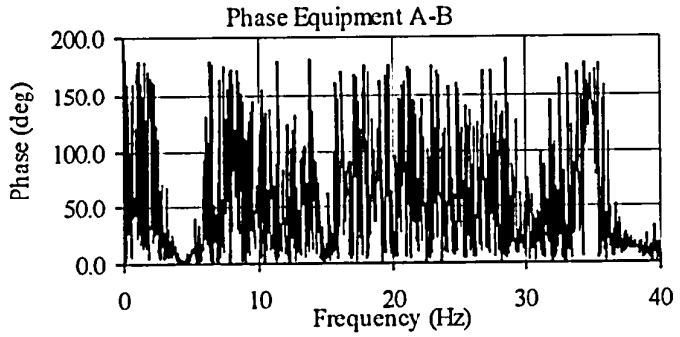

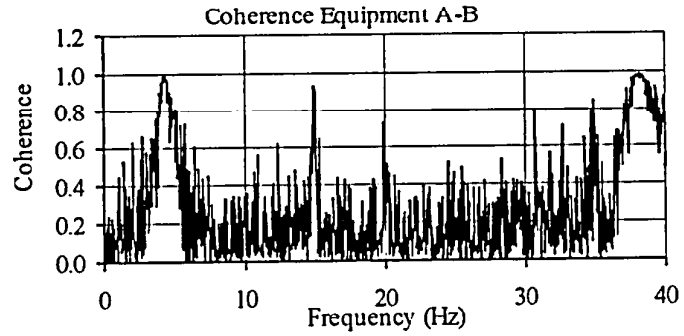

TEST RB-22
EQUIPMENT COMBINATION 4
BPA ISOLATOR CONNECTOR

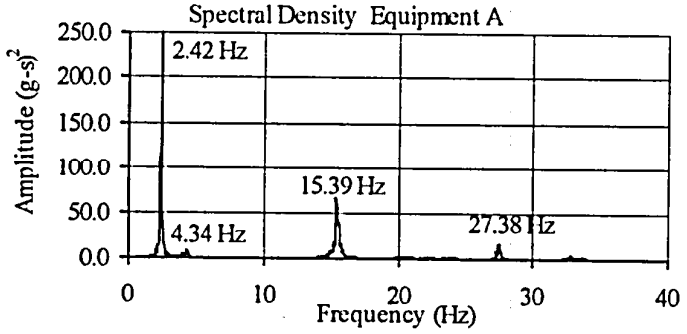

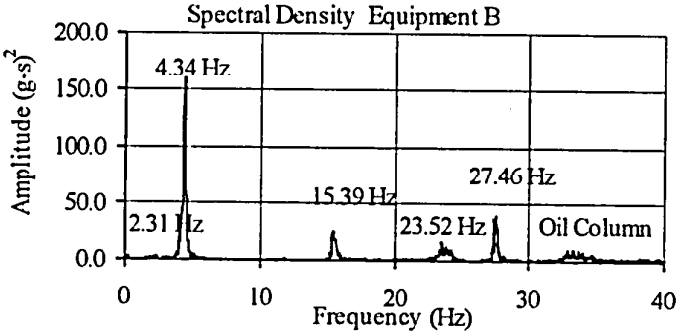

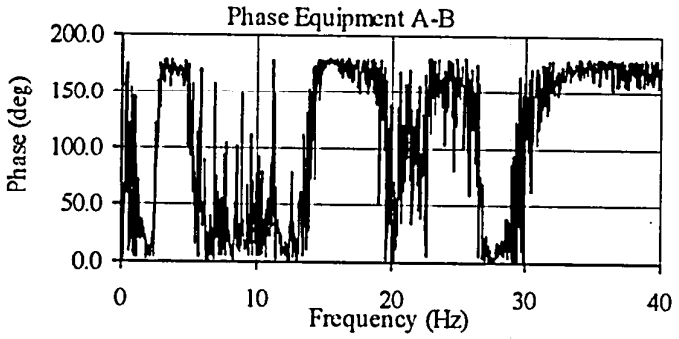

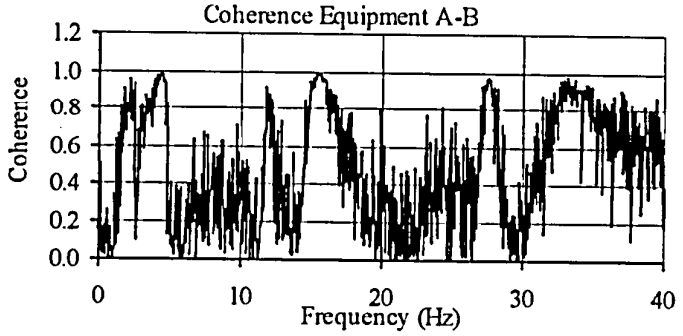

TEST RB-33
EQUIPMENT COMBINATION 3
INDIVIDUAL EQUIPMENT

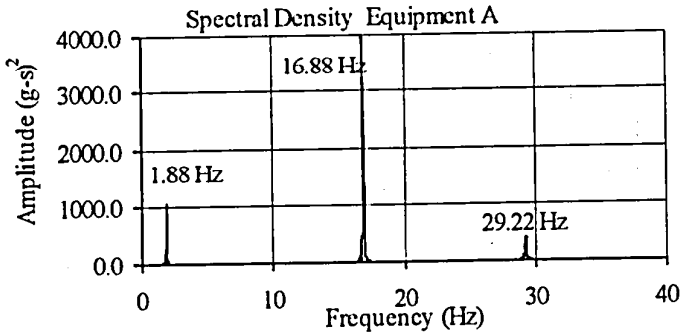

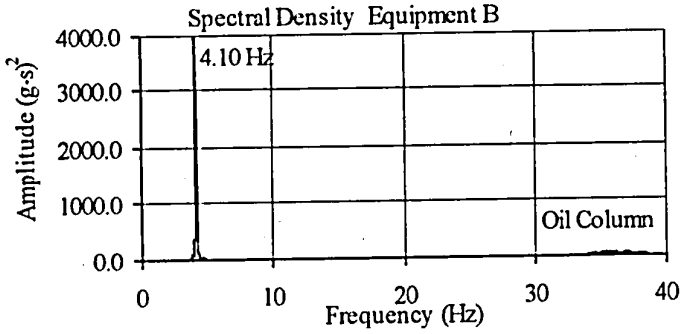

TEST RB-36
EQUIPMENT COMBINATION 3
SPRING 30-2022 CONNECTOR

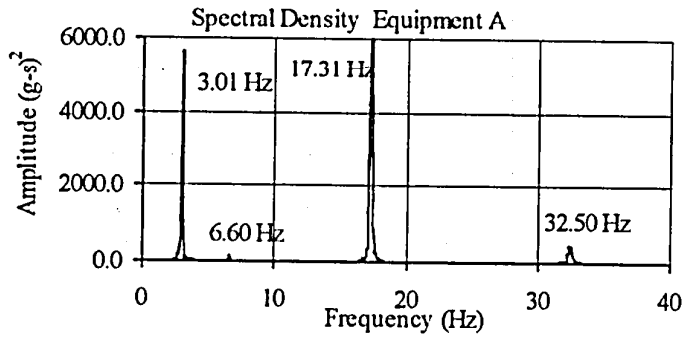

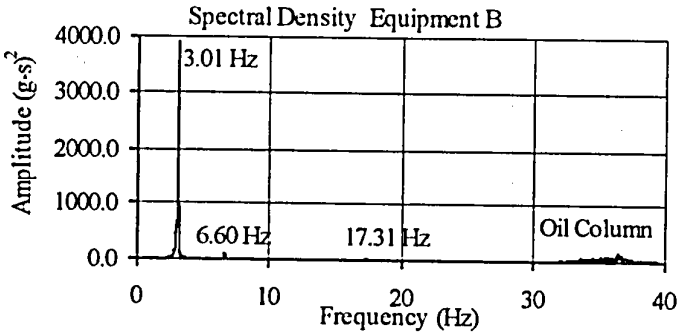

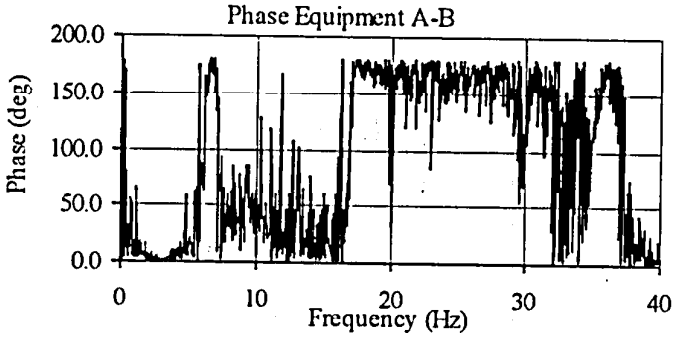

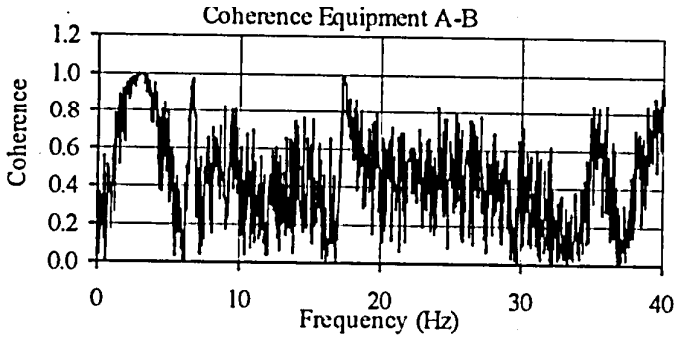

TEST RB-45
EQUIPMENT COMBINATION 3
BUS SLIDER CONNECTOR

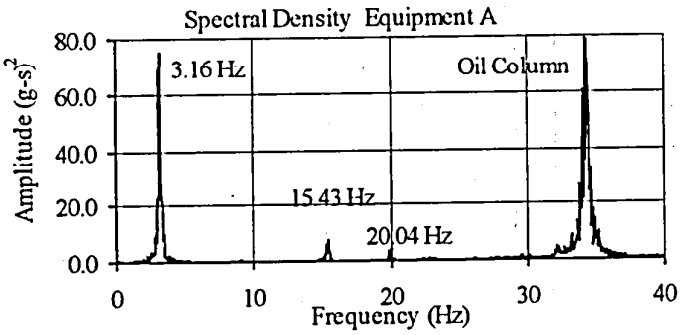

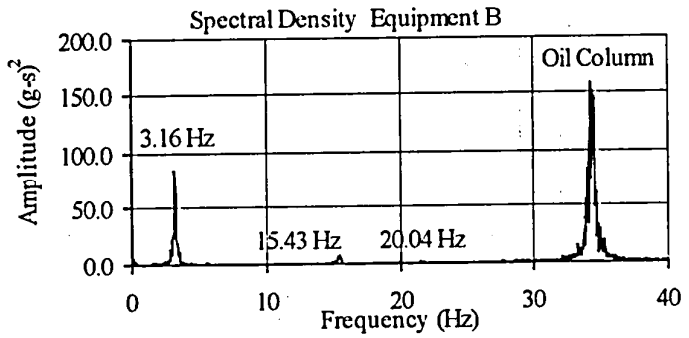

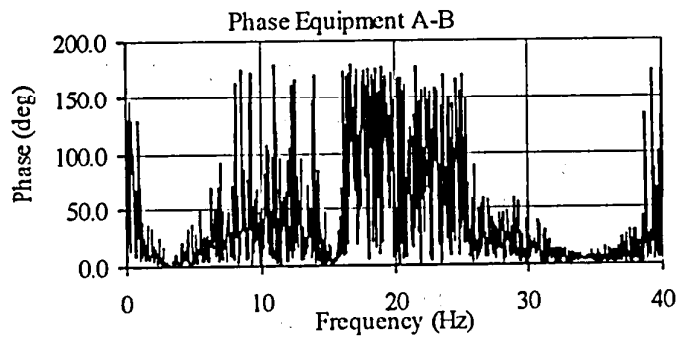

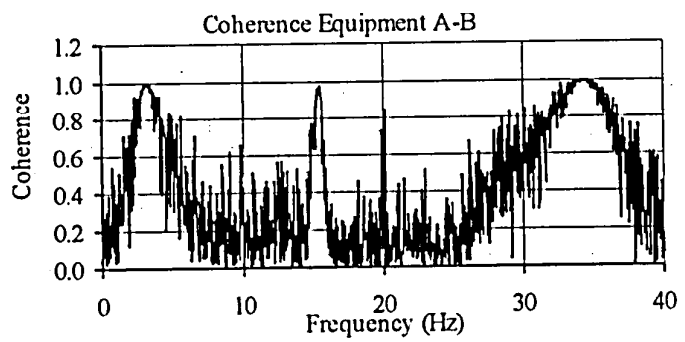

TEST RB-54
EQUIPMENT COMBINATION 3
BPA ISOLATOR CONNECTOR

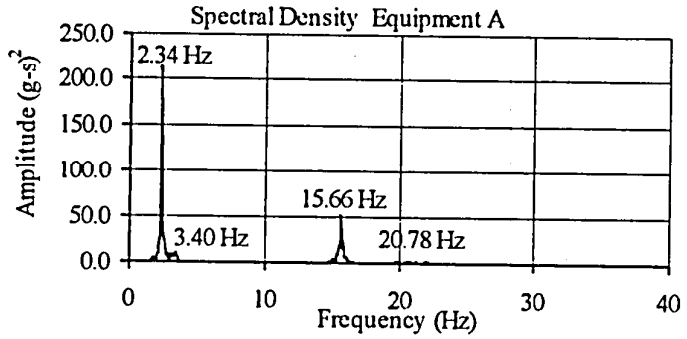

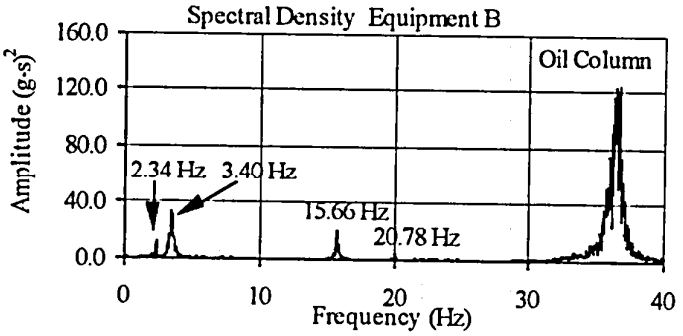

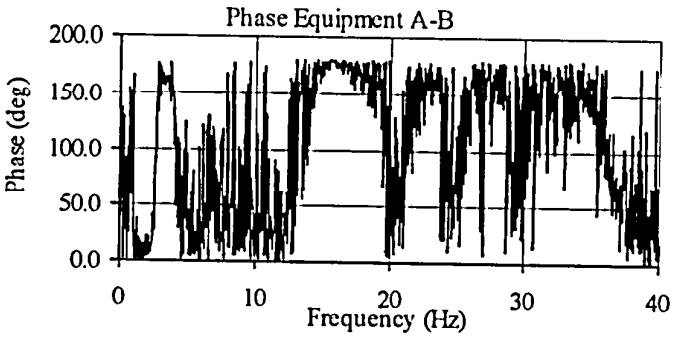

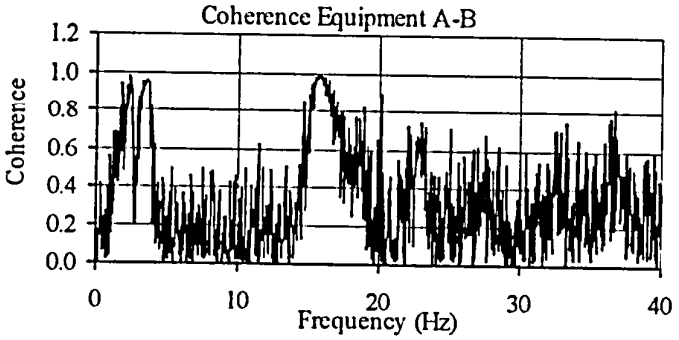

TEST RB-66
EQUIPMENT COMBINATION 1
INDIVIDUAL EQUIPMENT

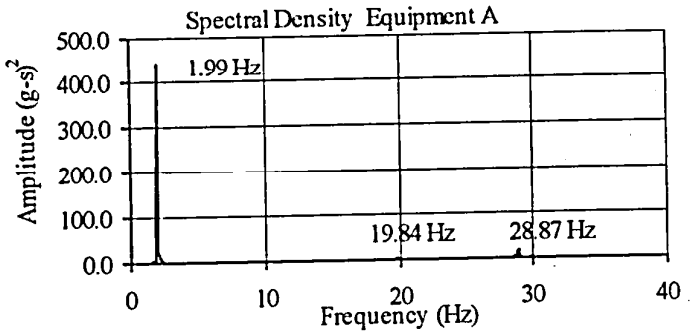

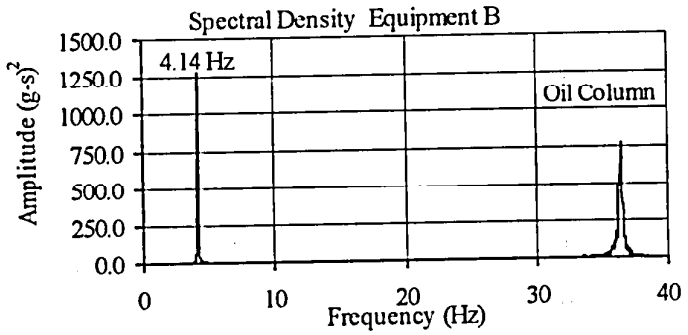

TEST RB-69
EQUIPMENT COMBINATION 1
SPRING 30-2022 CONNECTOR

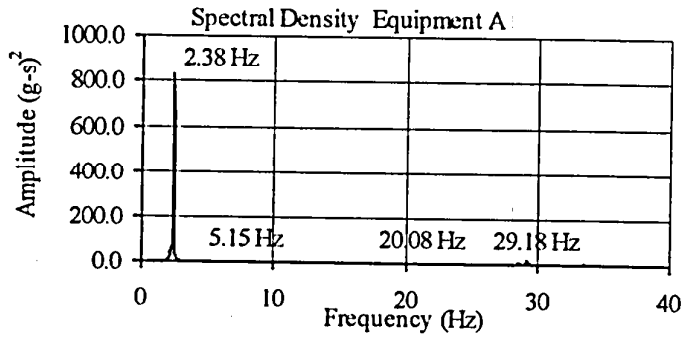

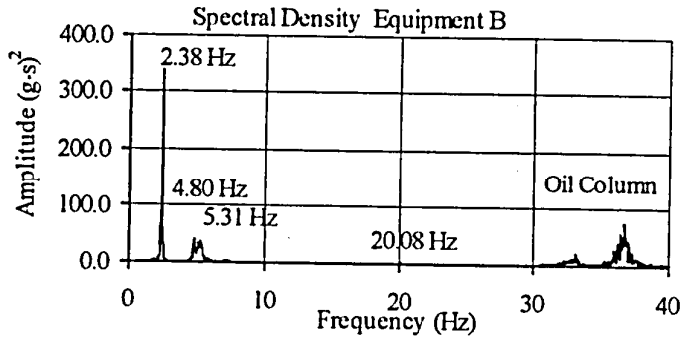

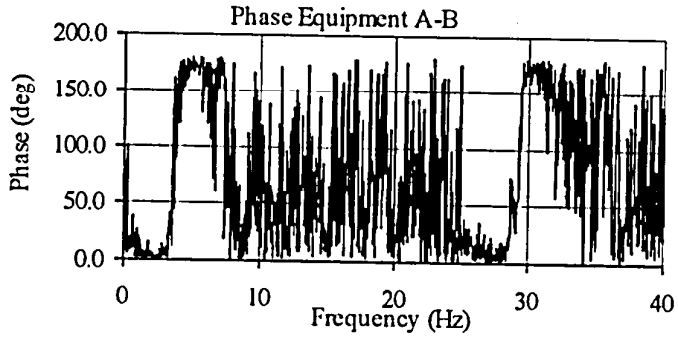

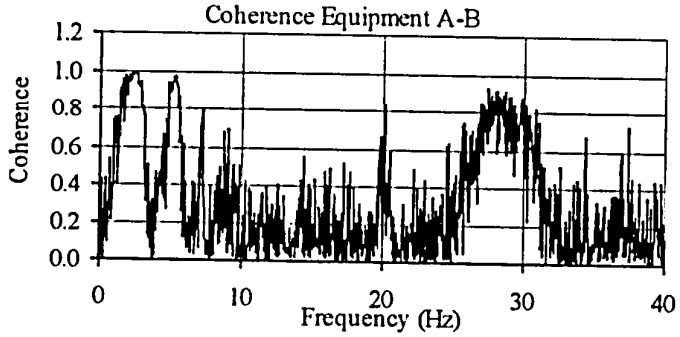

TEST RB-76
EQUIPMENT COMBINATION 1
BUS SLIDER CONNECTOR

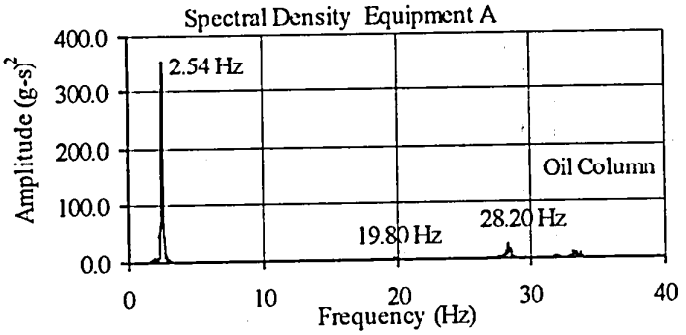

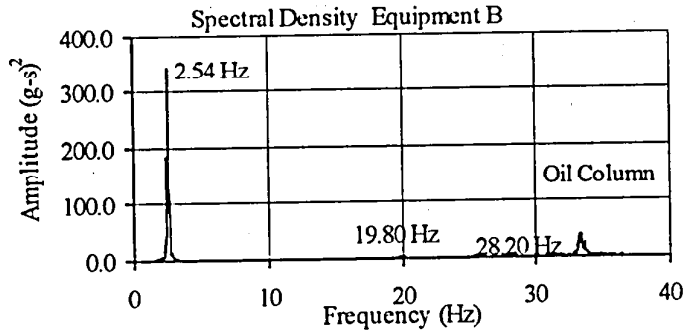

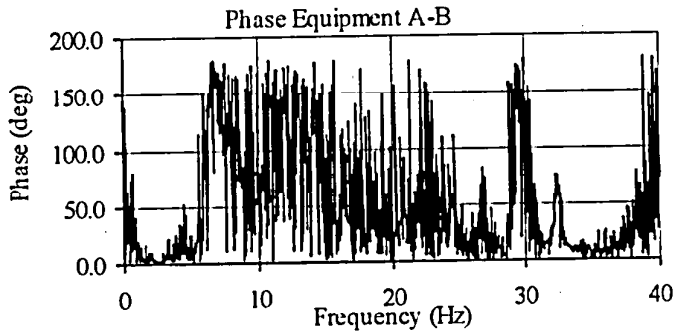

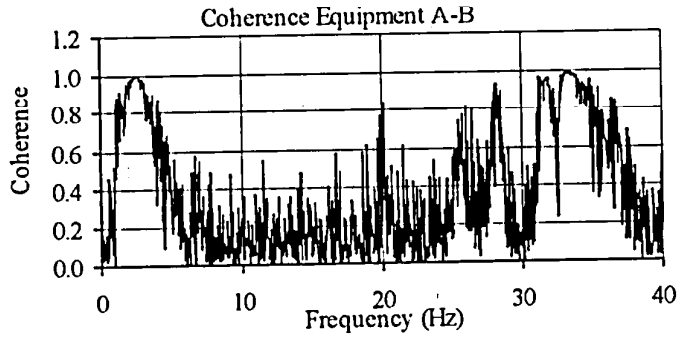

TEST RB-83
EQUIPMENT COMBINATION 1
BPA ISOLATOR CONNECTOR

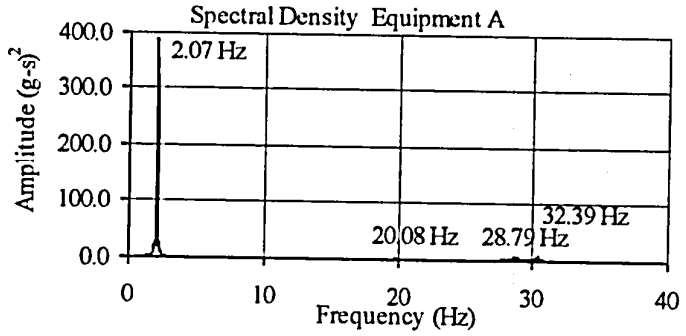

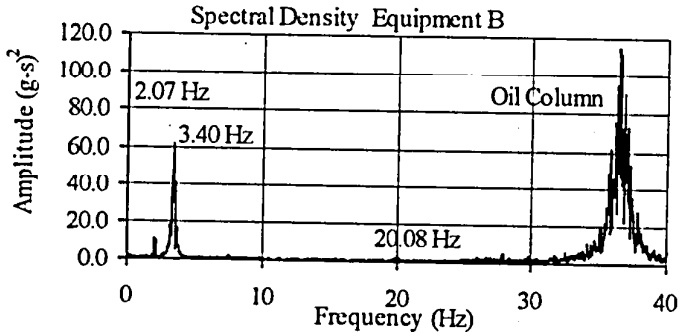

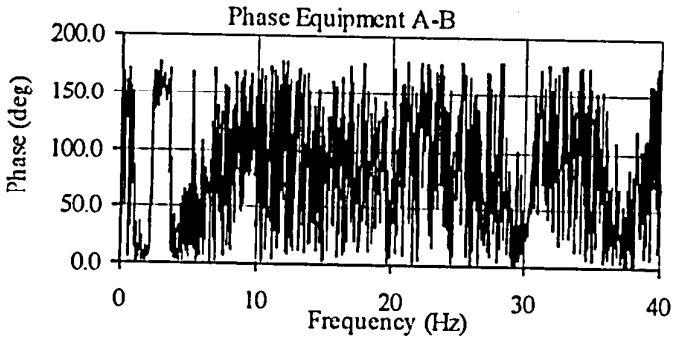

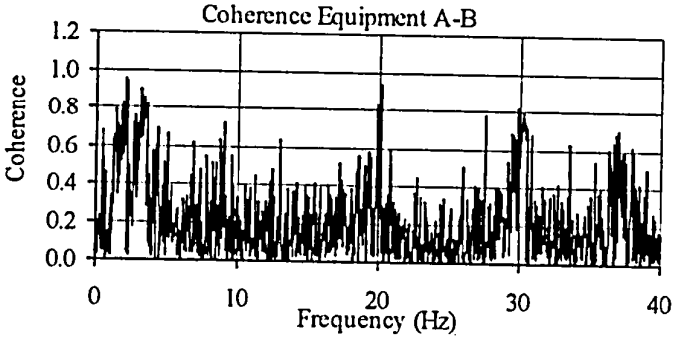

TEST RB-93
EQUIPMENT COMBINATION 2
INDIVIDUAL EQUIPMENT

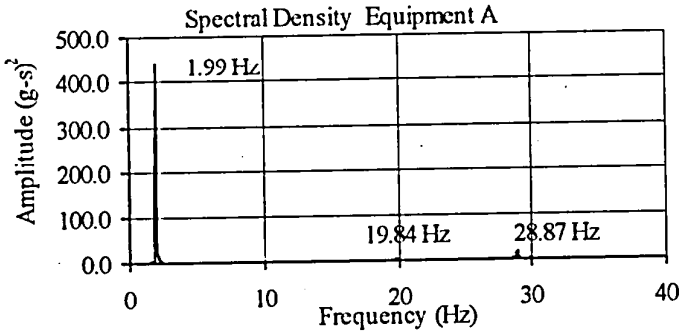

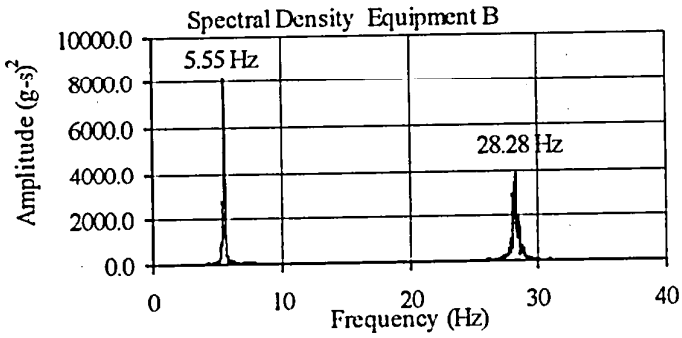

TEST RB-96
EQUIPMENT COMBINATION 2
SPRING 30-2022 CONNECTOR

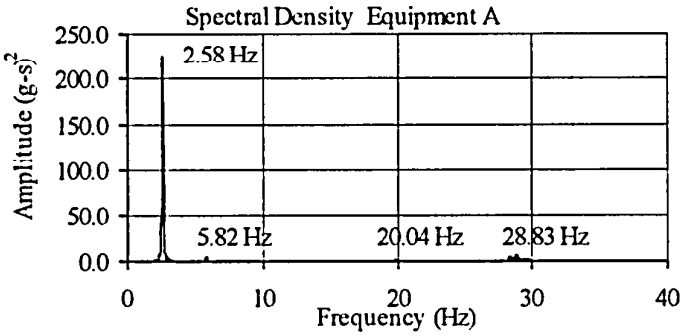

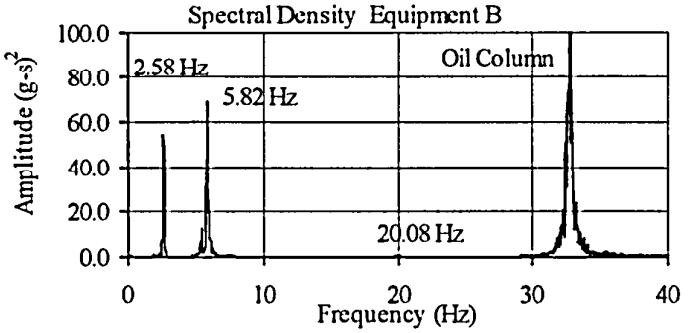

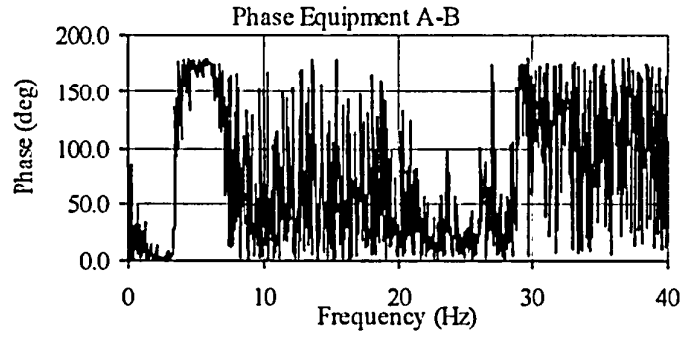

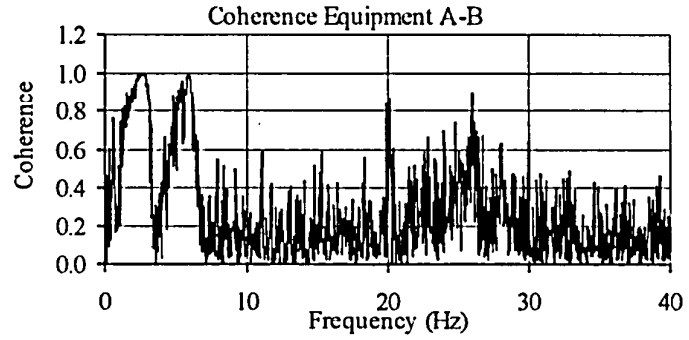

TEST RB-107
EQUIPMENT COMBINATION 2
BUS SLIDER CONNECTOR

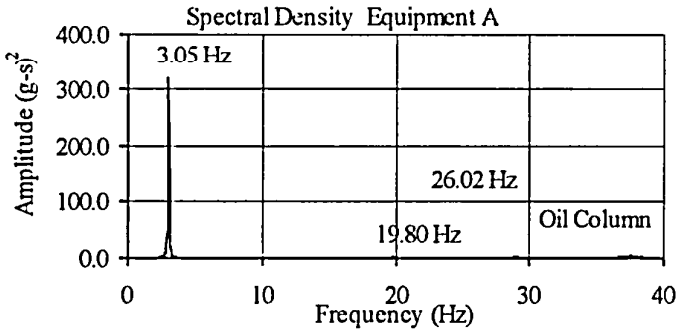

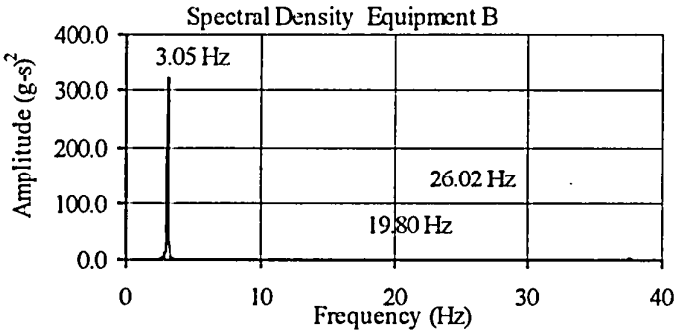

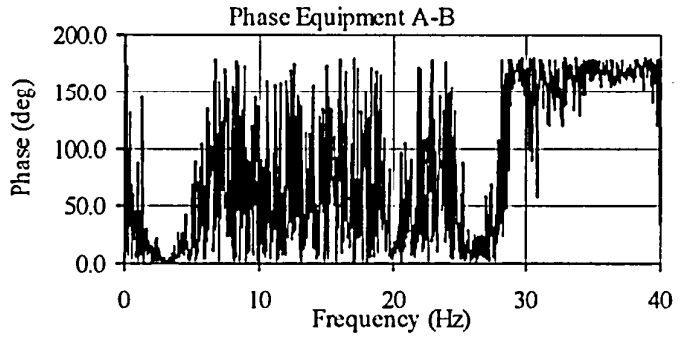

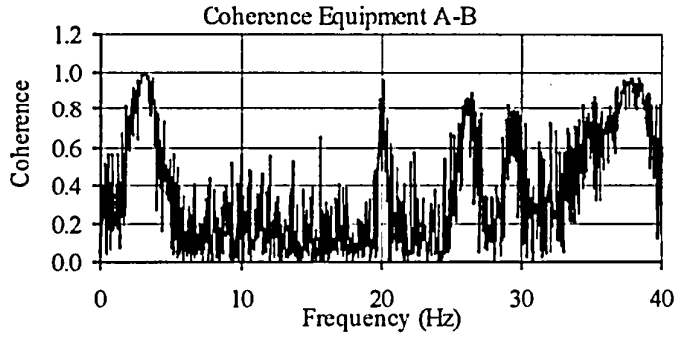

TEST RB-116
EQUIPMENT COMBINATION 2
BPA ISOLATOR CONNECTOR

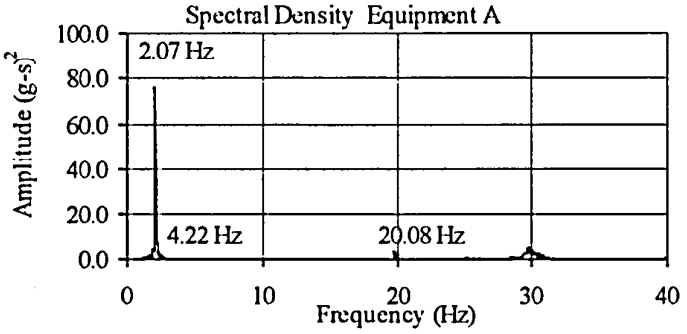

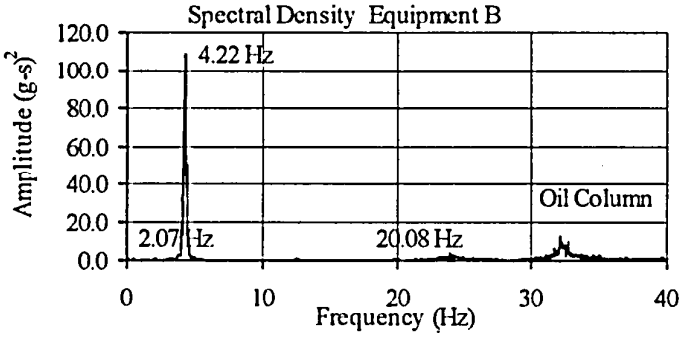

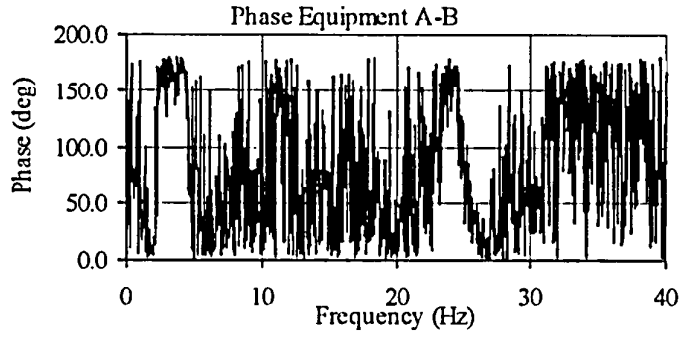

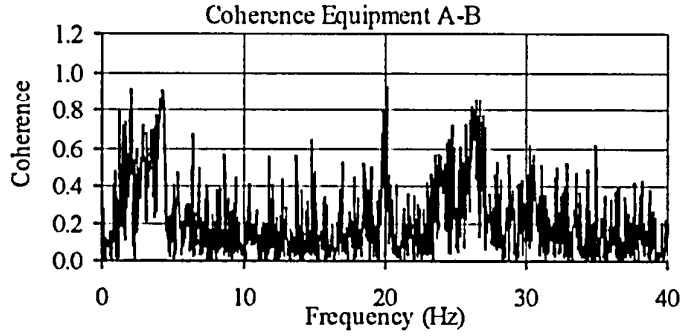

TEST RB-130
ADDITIONAL TESTS EQUIPMENT COMBINATION 5
INDIVIDUAL EQUIPMENT

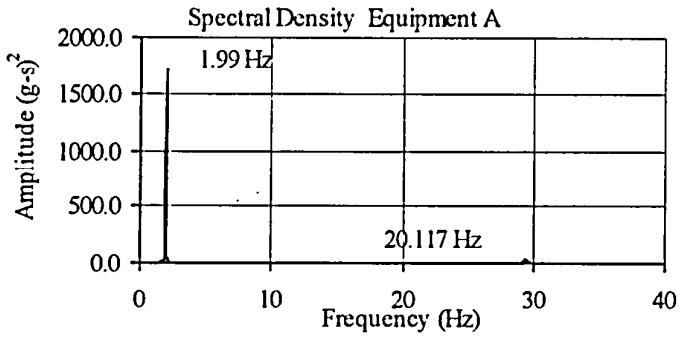

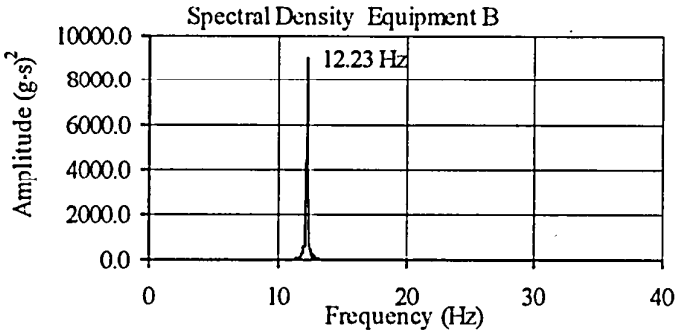

TEST RB-133
ADDITIONAL TESTS EQUIPMENT COMBINATION 5
SPRING 30-2022 CONNECTOR

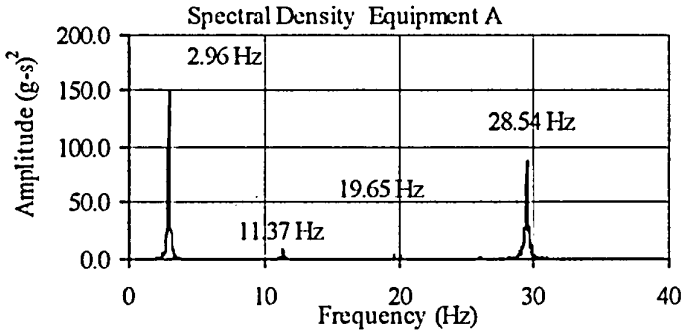

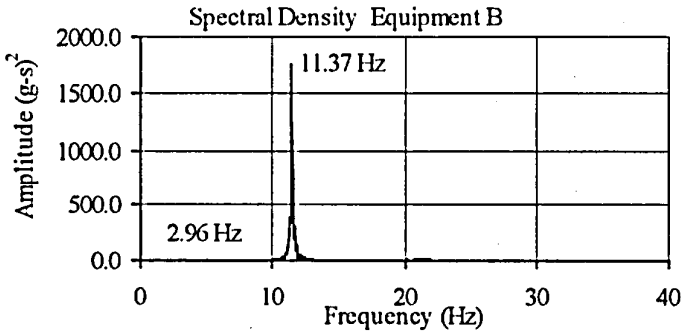

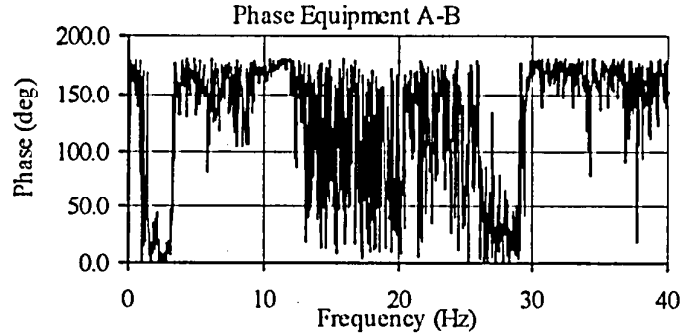

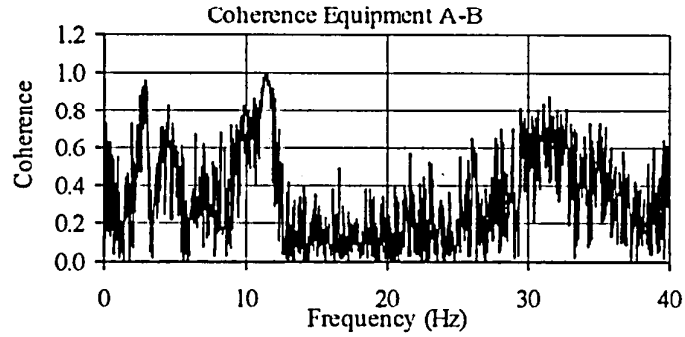

TEST RB-142
ADDITIONAL TESTS EQUIPMENT COMBINATION 5
BUS SLIDER CONNECTOR

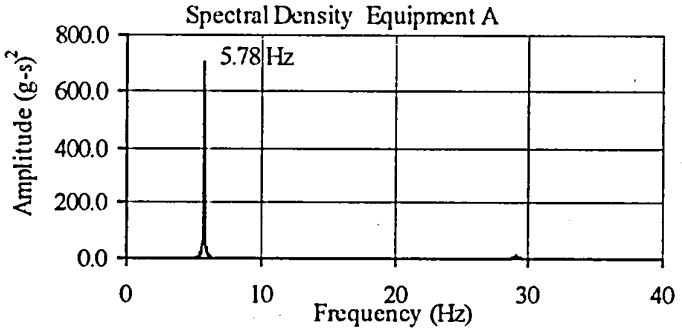

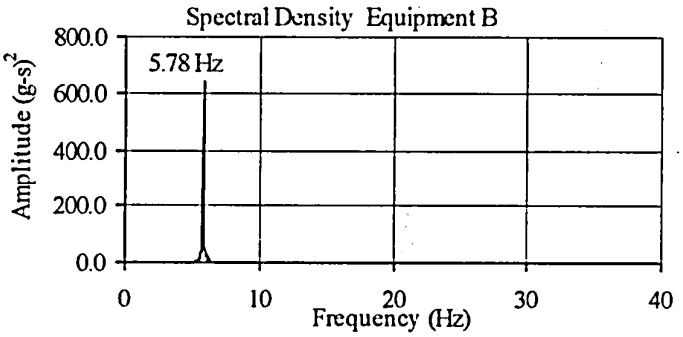

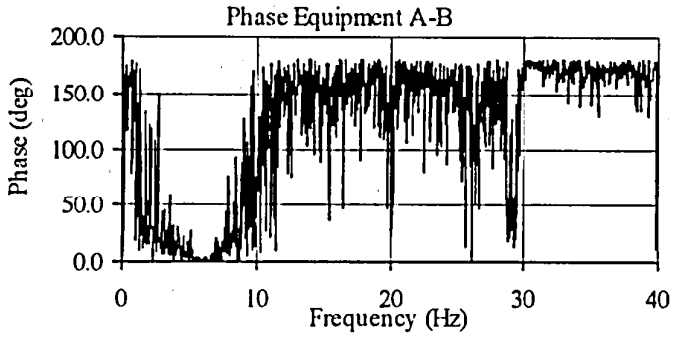

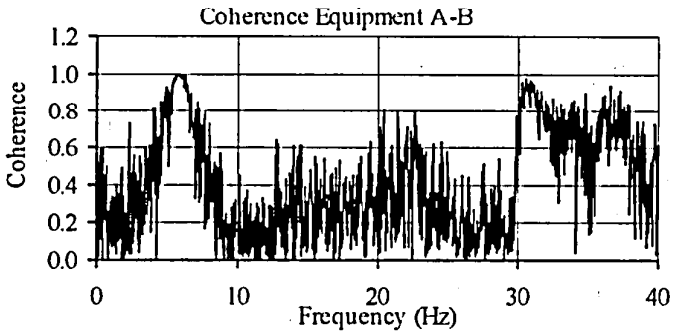

TEST RB-149
ADDITIONAL TESTS EQUIPMENT COMBINATION 5
BPA ISOLATOR CONNECTOR

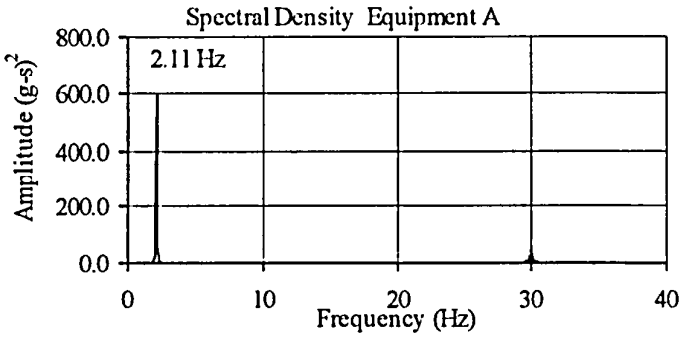

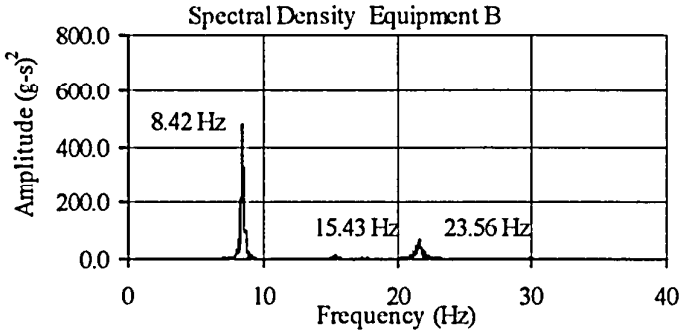

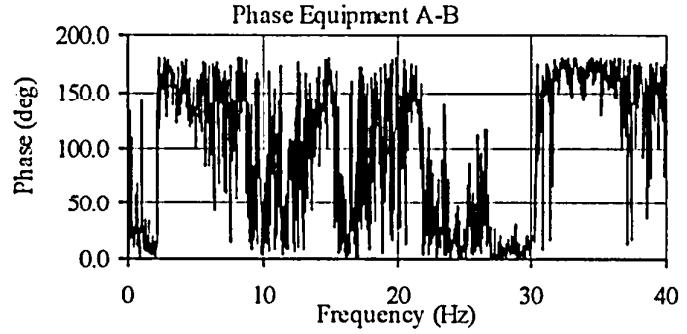

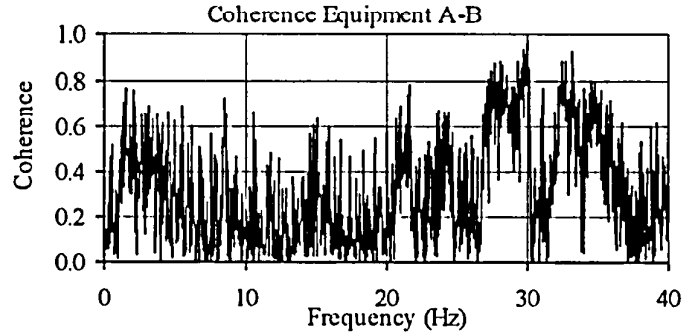

APPENDIX D

RESULTS OF DAMPING EVALUATION TESTS

TEST RB-2 AND TEST RB-3
EQUIPMENT COMBINATION 4
INDIVIDUAL EQUIPMENT

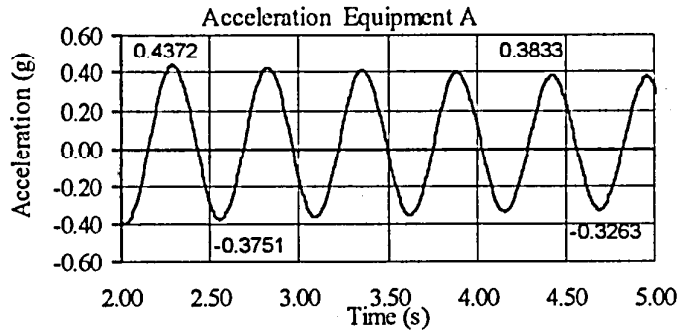

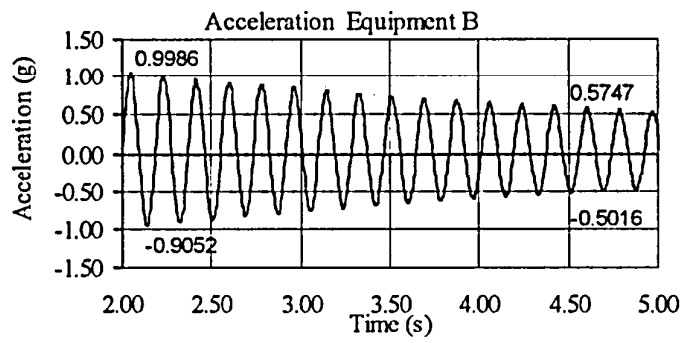

Equipment	First Double Amplitude A1 (g)	Second Double Amplitude A2 (g)	Number of intermediate cycles, p	Damping Ratio $\zeta = \frac{1}{2\pi p}\ln\left(\frac{A1}{A2}\right)$
A	0.8123	0.7096	4	0.0053
B	1.9038	1.0763	13	0.0070
Mean Damping Ratio				----

TEST RB-5 (FIRST MODE)
EQUIPMENT COMBINATION 4
SPRING 30-2022

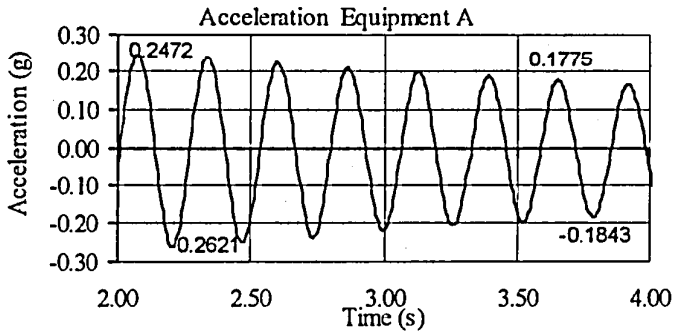

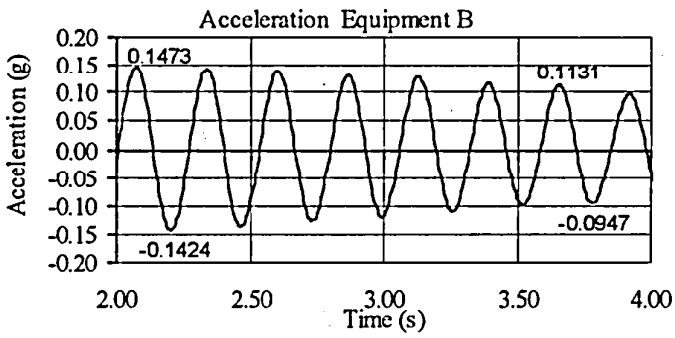

Equipment	First Double Amplitude A1 (g)	Second Double Amplitude A2 (g)	Number of intermediate cycles, p	Damping Ratio $\zeta = \frac{1}{2\pi p}\ln\left(\frac{A1}{A2}\right)$
A	0.5093	0.3618	6	0.0091
B	0.2897	0.2078	6	0.0088
Mean Damping Ratio				0.0090

TEST RB-5B (SECOND MODE)
EQUIPMENT COMBINATION 4
SPRING 30-2022

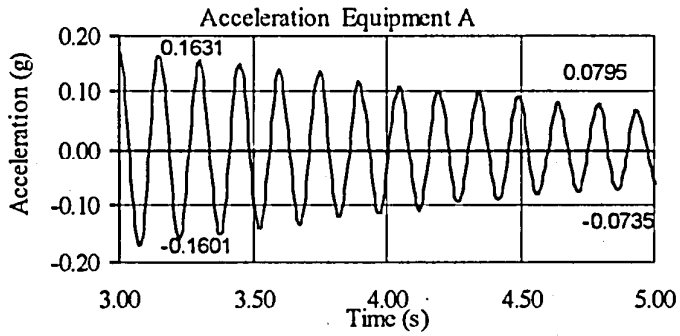

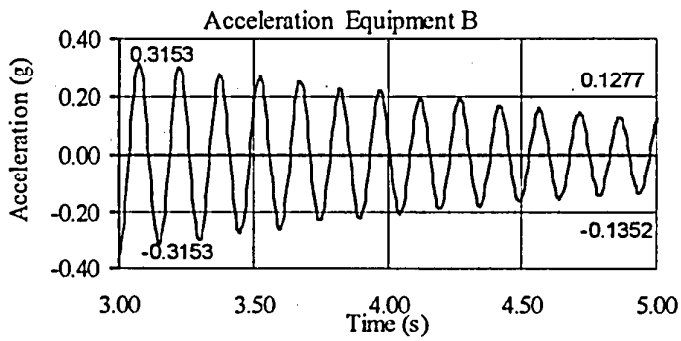

Equipment	First Double Amplitude A1 (g)	Second Double Amplitude A2 (g)	Number of intermediate cycles, p	Damping Ratio $\zeta = \frac{1}{2\pi p}\ln\left(\frac{A1}{A2}\right)$
A	0.3232	0.1530	11	0.0108
B	0.6306	0.2629	12	0.0116
Mean Damping Ratio				0.0112

TEST RB-11 AND TEST RB-12
EQUIPMENT COMBINATION 4
INDIVIDUAL EQUIPMENT

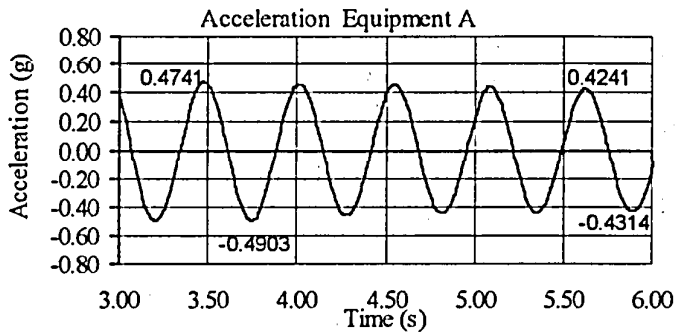

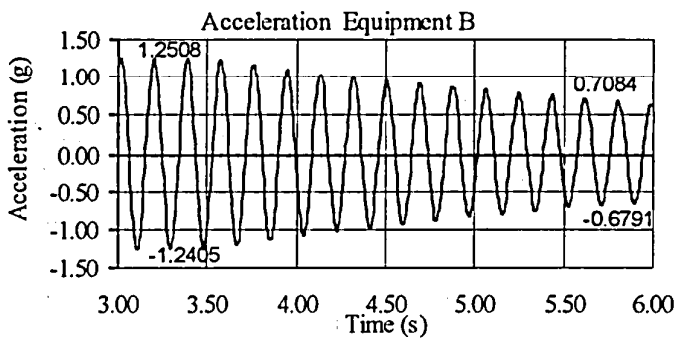

Equipment	First Double Amplitude A1 (g)	Second Double Amplitude A2 (g)	Number of intermediate cycles, p	Damping Ratio $\zeta = \frac{1}{2\pi p}\ln\left(\frac{A1}{A2}\right)$
A	0.9644	0.8555	4	0.0048
B	1.4913	1.3875	14	0.0008
Mean Damping Ratio				----

TEST RB-14
EQUIPMENT COMBINATION 4
BUS SLIDER

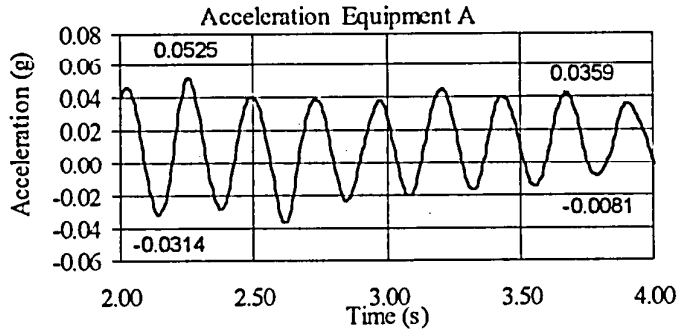

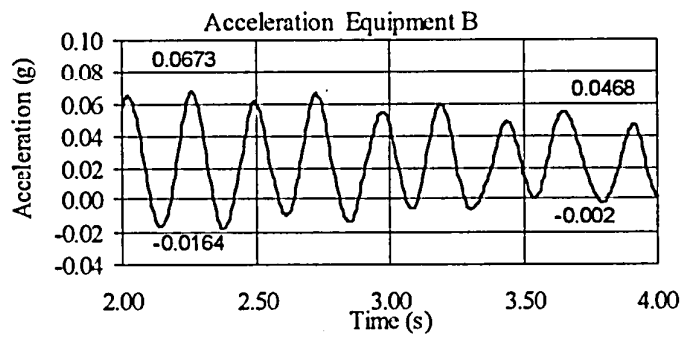

Equipment	First Double Amplitude A1 (g)	Second Double Amplitude A2 (g)	Number of intermediate cycles, p	Damping Ratio $\zeta = \frac{1}{2\pi p}\ln\left(\frac{A1}{A2}\right)$
A	0.0839	0.0440	6	0.0171
B	0.0837	0.0488	6	0.0143
Mean Damping Ratio				0.0157

TEST RB-23 (FIRST MODE)
EQUIPMENT COMBINATION 4
BPA ISOLATOR

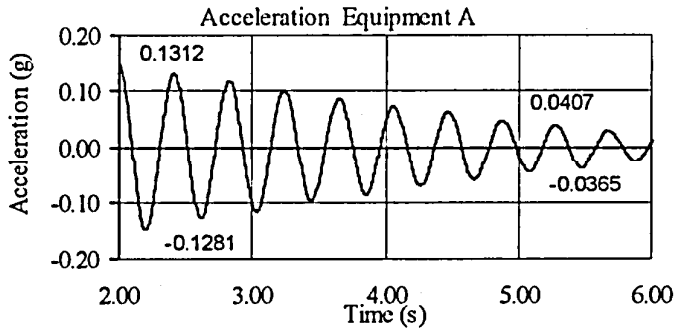

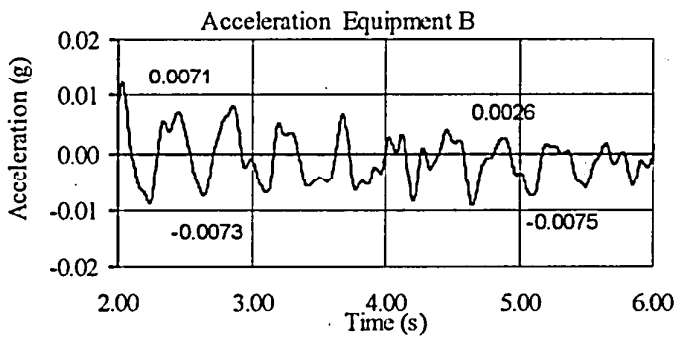

Equipment	First Double Amplitude A1 (g)	Second Double Amplitude A2 (g)	Number of intermediate cycles, p	Damping Ratio $\zeta = \frac{1}{2\pi p}\ln\left(\frac{A1}{A2}\right)$
A	0.2593	0.0772	7	0.0275
B	0.0144	0.0101	6	0.0094
Mean Damping Ratio				0.0185

TEST RB-23B (SECOND MODE)
EQUIPMENT COMBINATION 4
BPA ISOLATOR

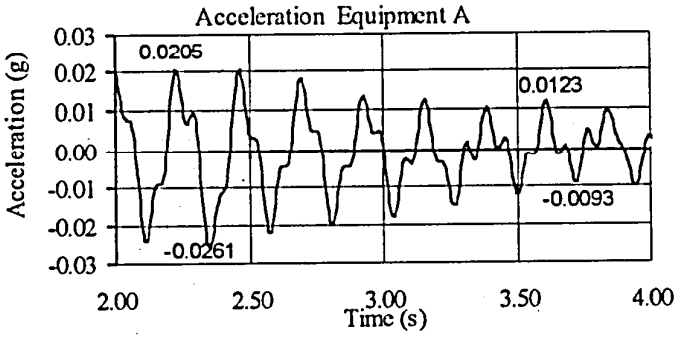

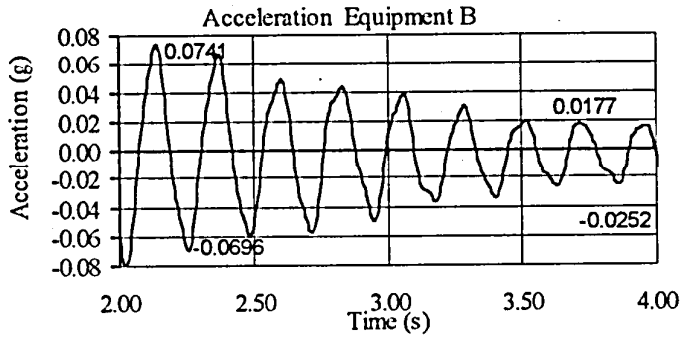

Equipment	First Double Amplitude A1 (g)	Second Double Amplitude A2 (g)	Number of intermediate cycles, p	Damping Ratio $\zeta = \frac{1}{2\pi p}\ln\left(\frac{A1}{A2}\right)$
A	0.0466	0.0216	6	0.0204
B	0.1437	0.0429	7	0.0275
Mean Damping Ratio				0.0240

TEST RB-34 AND TEST RB-35
EQUIPMENT COMBINATION 3
INDIVIDUAL EQUIPMENT

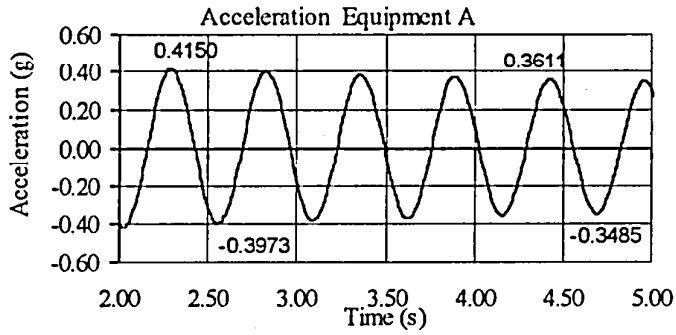

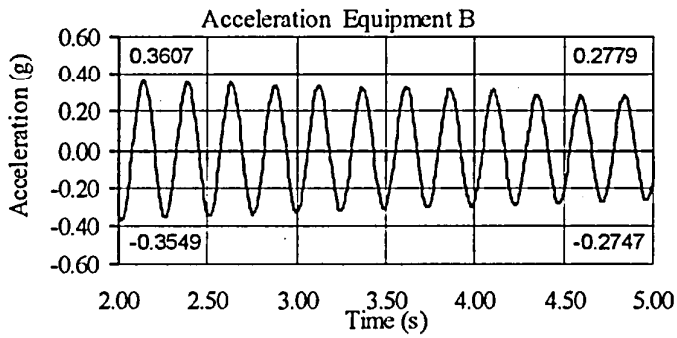

Equipment	First Double Amplitude A1 (g)	Second Double Amplitude A2 (g)	Number of intermediate cycles, p	Damping Ratio $\zeta = \frac{1}{2\pi p}\ln\left(\frac{A1}{A2}\right)$
A	0.8123	0.7096	4	0.0054
B	0.7156	0.5526	10	0.0041
Mean Damping Ratio				----

TEST RB-37 (FIRST MODE)
EQUIPMENT COMBINATION 3
SPRING 30-2022

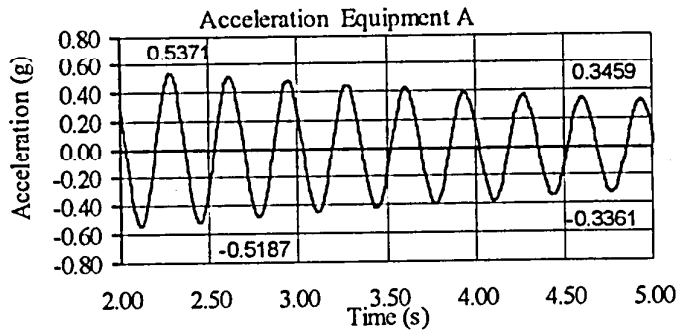

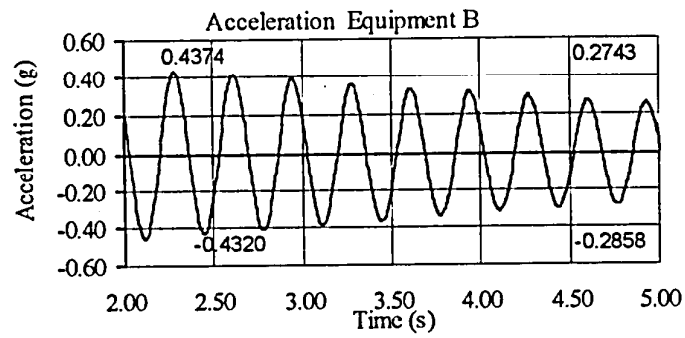

Equipment	First Double Amplitude A1 (g)	Second Double Amplitude A2 (g)	Number of intermediate cycles, p	Damping Ratio $\zeta = \frac{1}{2\pi p}\ln\left(\frac{A1}{A2}\right)$
A	1.0558	0.6820	7	0.0099
B	0.8694	0.5601	7	0.0100
Mean Damping Ratio				0.0100

TEST RB-37B (SECOND MODE)
EQUIPMENT COMBINATION 3
SPRING 30-2022

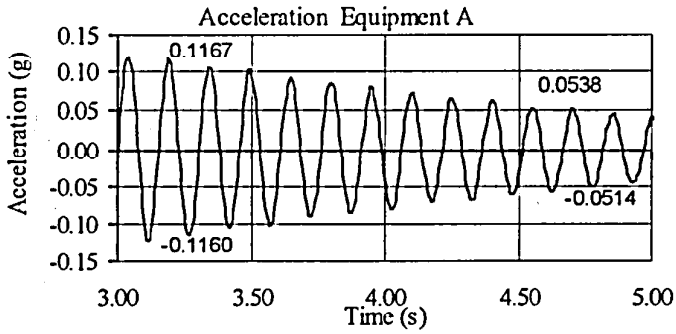

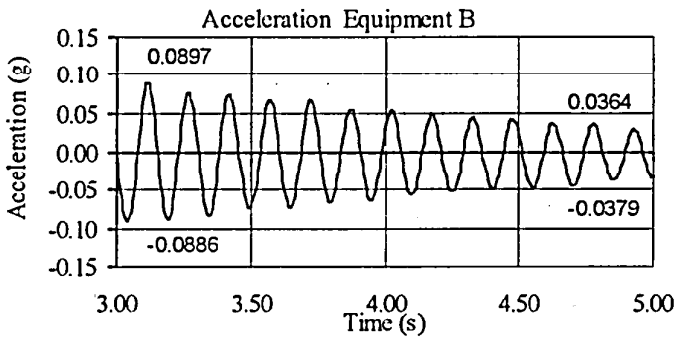

Equipment	First Double Amplitude A1 (g)	Second Double Amplitude A2 (g)	Number of intermediate cycles, p	Damping Ratio $\zeta = \frac{1}{2\pi p}\ln\left(\frac{A1}{A2}\right)$
A	0.2327	0.1052	10	0.0126
B	0.1783	0.0743	11	0.0127
Mean Damping Ratio				0.0127

TEST RB-46
EQUIPMENT COMBINATION 3
BUS SLIDER

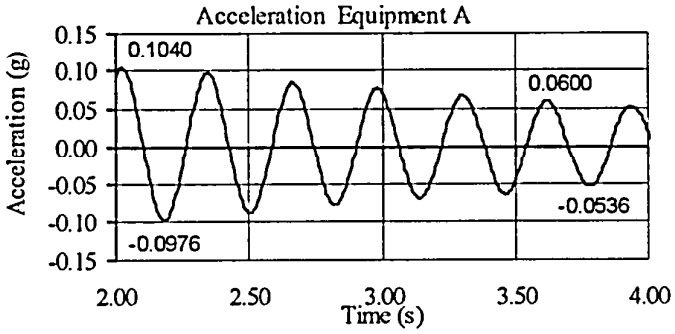

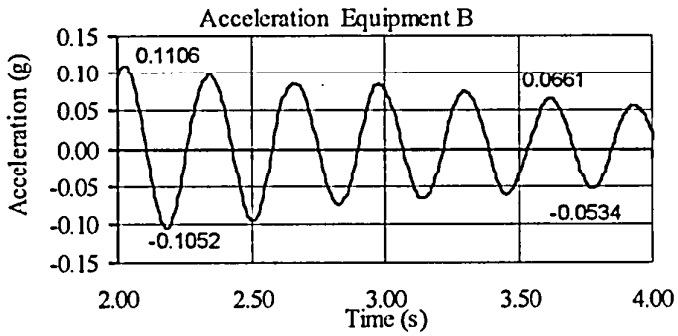

Equipment	First Double Amplitude A1 (g)	Second Double Amplitude A2 (g)	Number of intermediate cycles, p	Damping Ratio $\zeta = \frac{1}{2\pi p}\ln\left(\frac{A1}{A2}\right)$
A	0.2016	0.1136	5	0.0183
B	0.2158	0.1195	5	0.0188
Mean Damping Ratio				0.0186

TEST RB-55 (FIRST MODE)
EQUIPMENT COMBINATION 3
BPA ISOLATOR

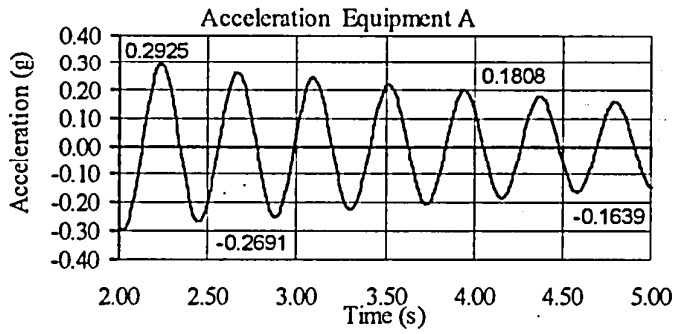

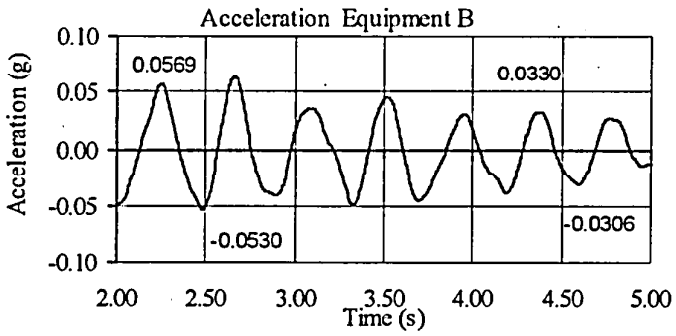

Equipment	First Double Amplitude A1 (g)	Second Double Amplitude A2 (g)	Number of intermediate cycles, p	Damping Ratio $\zeta = \frac{1}{2\pi p}\ln\left(\frac{A1}{A2}\right)$
A	0.5616	0.3447	5	0.0155
B	0.1099	0.0636	5	0.0174
Mean Damping Ratio				0.0165

TEST RB-55B (SECOND MODE)
EQUIPMENT COMBINATION 3
BPA ISOLATOR

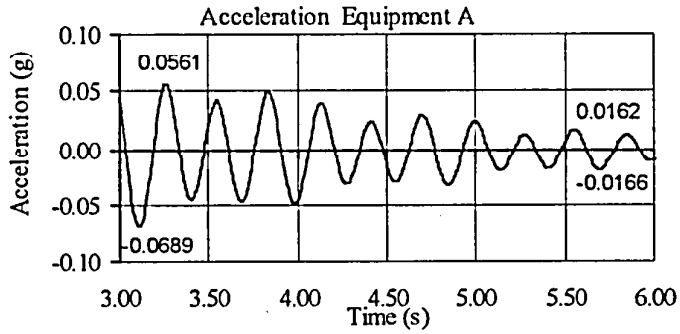

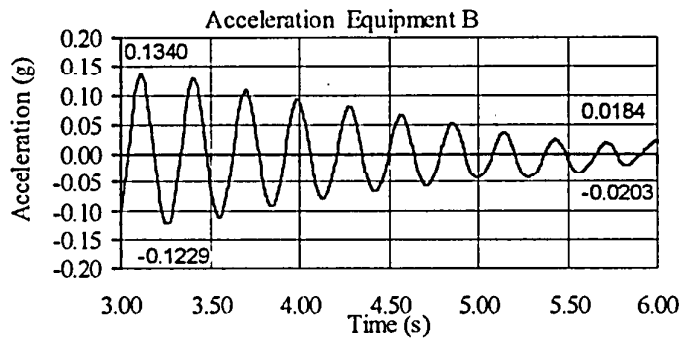

Equipment	First Double Amplitude A1 (g)	Second Double Amplitude A2 (g)	Number of intermediate cycles, p	Damping Ratio $\zeta = \frac{1}{2\pi p}\ln\left(\frac{A1}{A2}\right)$
A	0.125	0.0328	8	0.0266
B	0.2569	0.0387	9	0.0335
Mean Damping Ratio				0.0301

TEST RB-67 AND TEST RB-68
EQUIPMENT COMBINATION 1
INDIVIDUAL EQUIPMENT

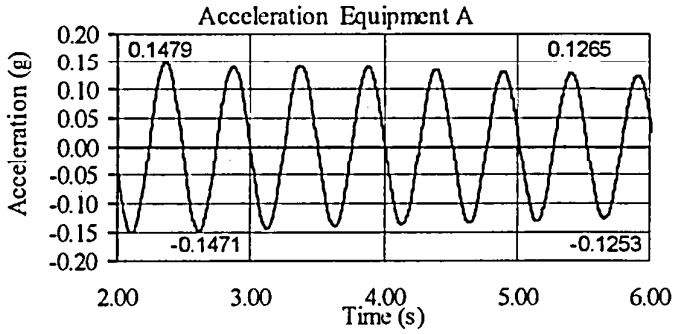

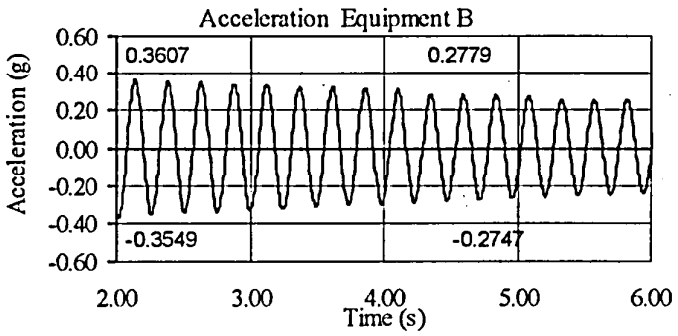

Equipment	First Double Amplitude A1 (g)	Second Double Amplitude A2 (g)	Number of intermediate cycles, p	Damping Ratio $\zeta = \frac{1}{2\pi p}\ln\left(\frac{A1}{A2}\right)$
A	0.2950	0.2518	6	0.0042
B	0.7156	0.5526	10	0.0041
Mean Damping Ratio				----

TEST RB-70 (FIRST MODE)
EQUIPMENT COMBINATION 1
SPRING 30-2022

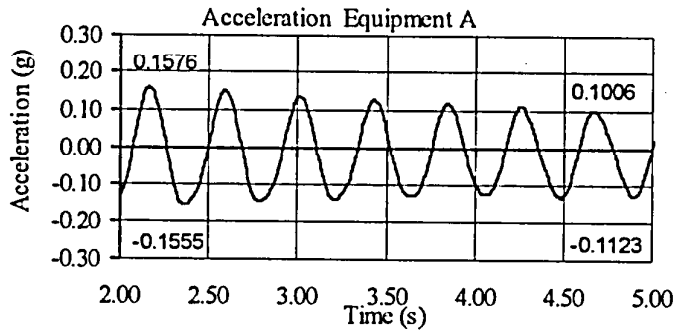

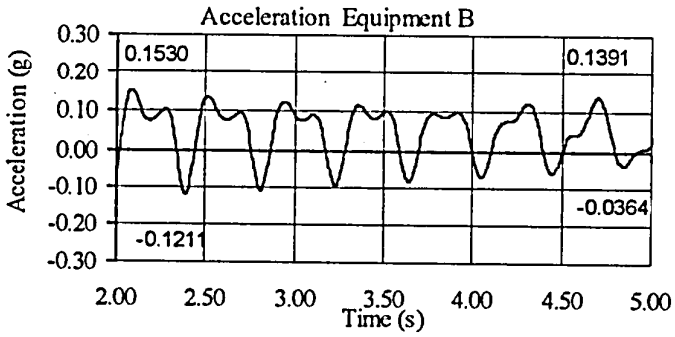

Equipment	First Double Amplitude A1 (g)	Second Double Amplitude A2 (g)	Number of intermediate cycles, p	Damping Ratio $\zeta = \frac{1}{2\pi p}\ln\left(\frac{A1}{A2}\right)$
A	0.3131	0.2129	6	0.0102
B	0.2741	0.1755	6.	0.0118
Mean Damping Ratio				0.0110

TEST RB-70B (SECOND MODE)
EQUIPMENT COMBINATION 1
SPRING 30-2022

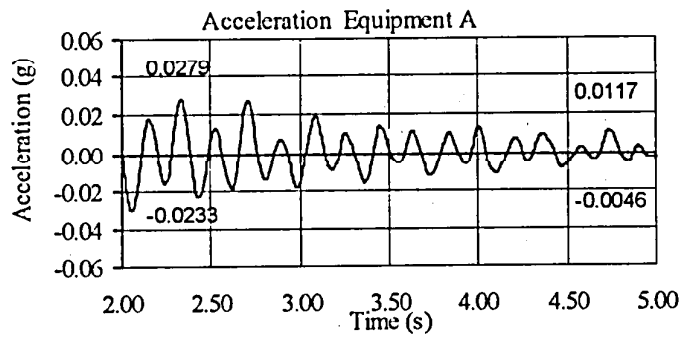

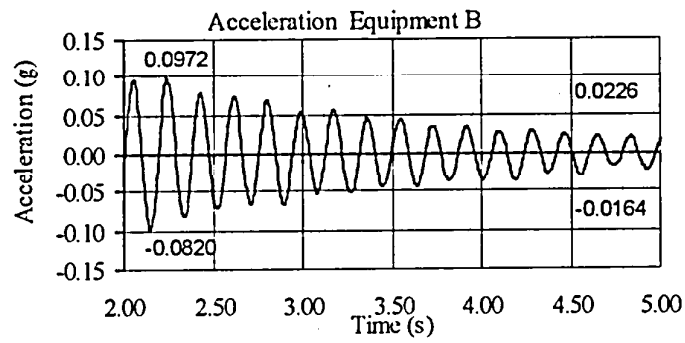

Equipment	First Double Amplitude A1 (g)	Second Double Amplitude A2 (g)	Number of intermediate cycles, p	Damping Ratio $\zeta = \frac{1}{2\pi p}\ln\left(\frac{A1}{A2}\right)$
A	0.0512	0.0163	13	0.0140
B	0.1792	0.0390	13	0.0187
Mean Damping Ratio				0.0164

TEST RB-77
EQUIPMENT COMBINATION 1
BUS SLIDER

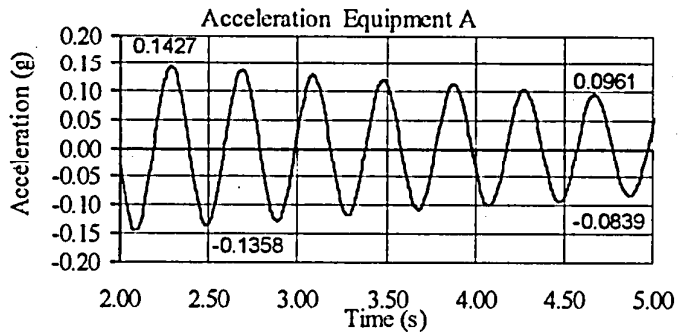

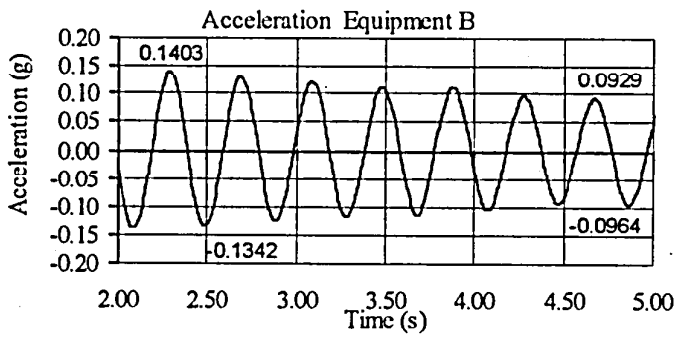

Equipment	First Double Amplitude A1 (g)	Second Double Amplitude A2 (g)	Number of intermediate cycles, p	Damping Ratio $\zeta = \frac{1}{2\pi p}\ln\left(\frac{A1}{A2}\right)$
A	0.2785	0.1800	6	0.0116
B	0.2745	0.1893	6	0.0099
Mean Damping Ratio				0.0108

TEST RB-84 (FIRST MODE)
EQUIPMENT COMBINATION 1
BPA ISOLATOR

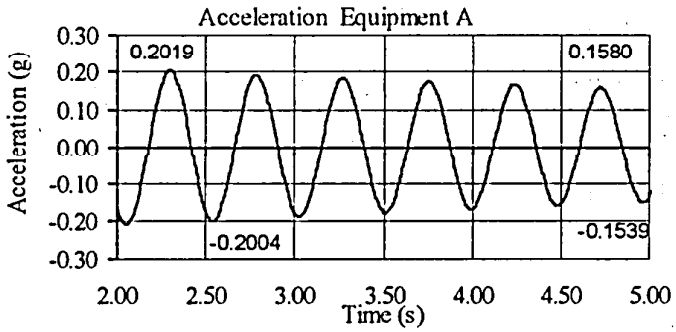

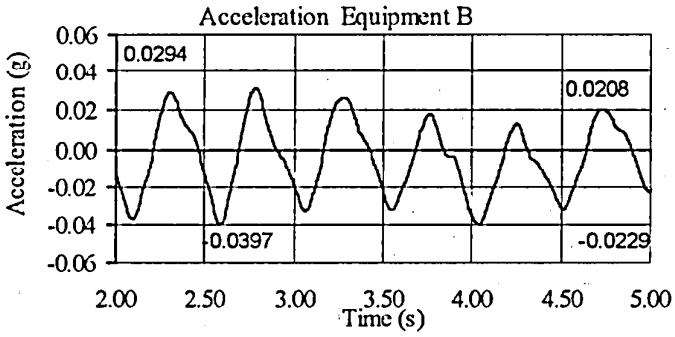

Equipment	First Double Amplitude A1 (g)	Second Double Amplitude A2 (g)	Number of intermediate cycles, p	Damping Ratio $\zeta = \frac{1}{2\pi p}\ln\left(\frac{A1}{A2}\right)$
A	0.4023	0.3119	5	0.0081
B	0.0691	0.0437	5	0.0146
Mean Damping Ratio				0.0114

TEST RB-84B (SECOND MODE)
EQUIPMENT COMBINATION 1
BPA ISOLATOR

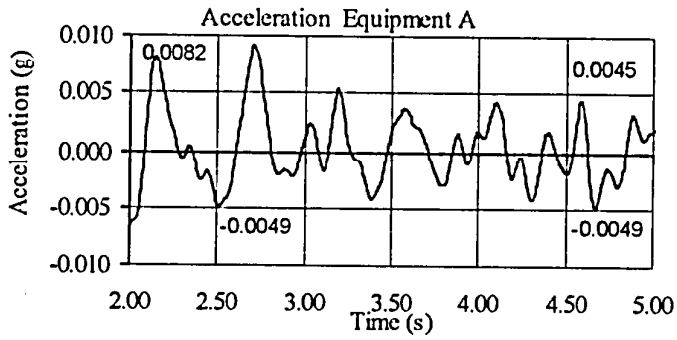

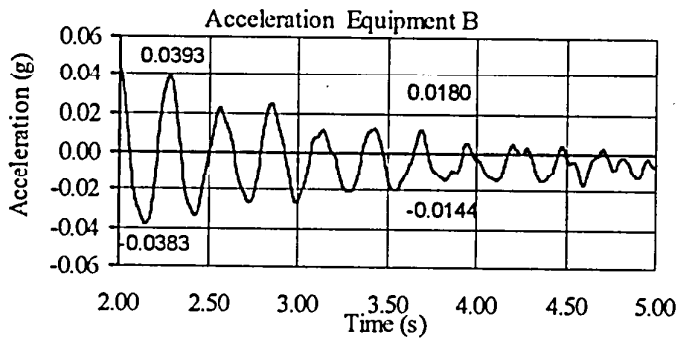

Equipment	First Double Amplitude A1 (g)	Second Double Amplitude A2 (g)	Number of intermediate cycles, p	Damping Ratio $\zeta = \frac{1}{2\pi p}\ln\left(\frac{A1}{A2}\right)$
A	0.0131	0.0094	5	0.0106
B	0.0776	0.0324	5	0.0278
Mean Damping Ratio				0.0192

TEST RB-97
EQUIPMENT COMBINATION 2
SPRING 30-2022

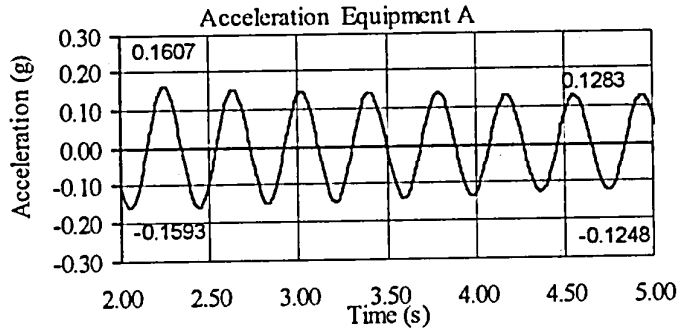

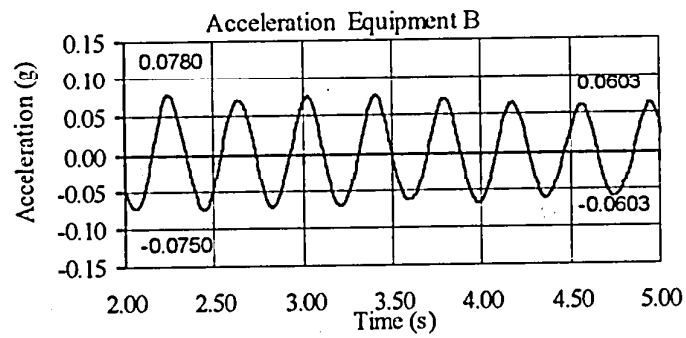

Equipment	First Double Amplitude A1 (g)	Second Double Amplitude A2 (g)	Number of intermediate cycles, p	Damping Ratio $\zeta = \frac{1}{2\pi p}\ln\left(\frac{A1}{A2}\right)$
A	0.3200	0.2531	6	0.0062
B	0.1530	0.1206	6	0.0063
Mean Damping Ratio				0.0063

TEST RB-108
EQUIPMENT COMBINATION 2
BUS SLIDER

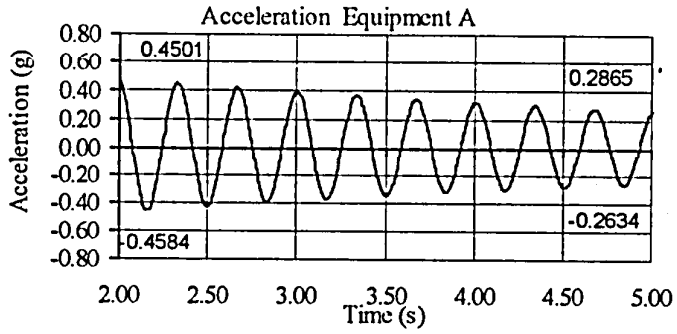

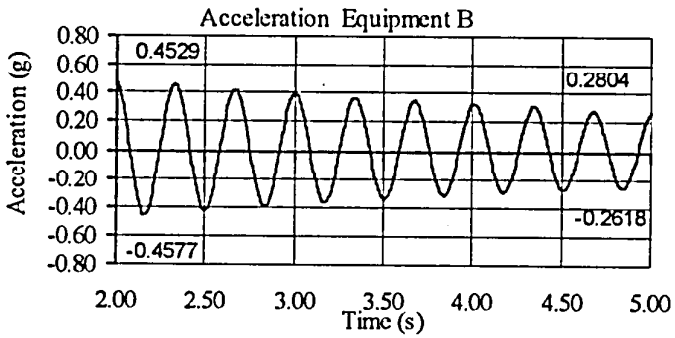

Equipment	First Double Amplitude A1 (g)	Second Double Amplitude A2 (g)	Number of intermediate cycles, p	Damping Ratio $\zeta = \frac{1}{2\pi p}\ln\left(\frac{A1}{A2}\right)$
A	0.9085	0.5499	7	0.0114
B	0.9106	0.5422	7	0.0118
Mean Damping Ratio				0.0116

TEST RB-117
EQUIPMENT COMBINATION 5
BPA ISOLATOR

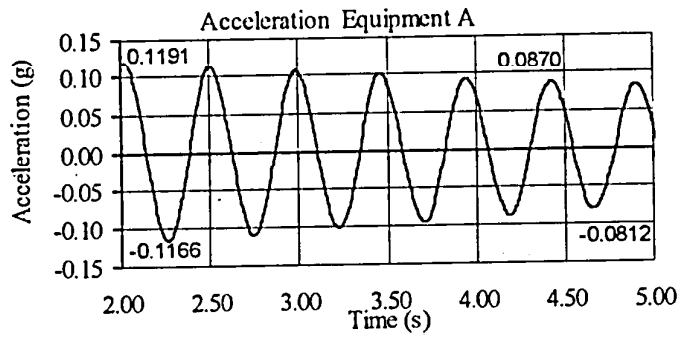

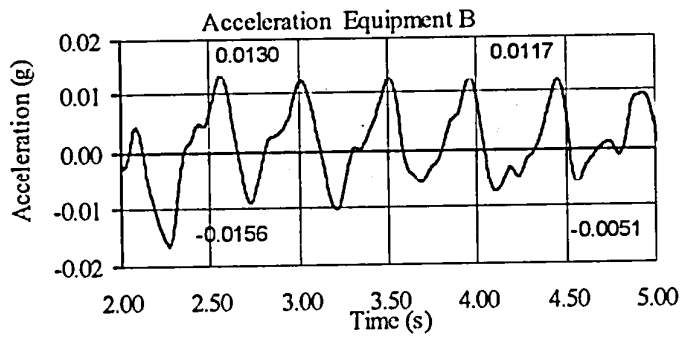

Equipment	First Double Amplitude A1 (g)	Second Double Amplitude A2 (g)	Number of intermediate cycles, p	Damping Ratio $\zeta = \frac{1}{2\pi p}\ln\left(\frac{A1}{A2}\right)$
A	0.2357	0.1682	5	0.0107
B	0.0286	0.0168	4	0.0212
Mean Damping Ratio				0.0160

TEST RB-131 AND TEST RB 132
ADDITIONAL TESTS EQUIPMENT COMBINATION 5
INDIVIDUAL EQUIPMENT

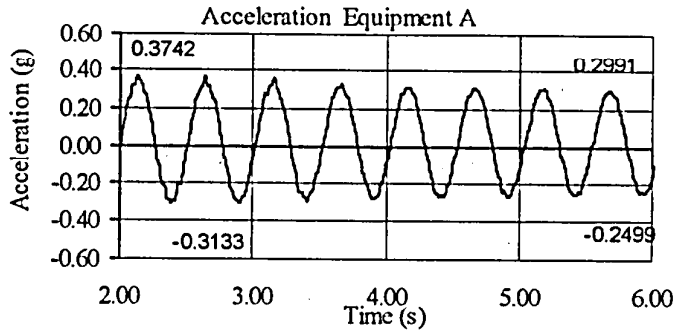

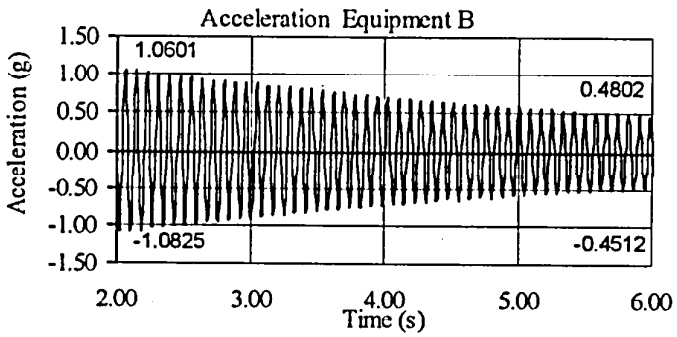

Equipment	First Double Amplitude A1 (g)	Second Double Amplitude A2 (g)	Number of intermediate cycles, p	Damping Ratio $\zeta = \frac{1}{2\pi p}\ln\left(\frac{A1}{A2}\right)$
A	0.6875	0.5490	7	0.0051
B	2.1426	0.9314	45	0.0029
Mean Damping Ratio				----

TEST RB-134 (FIRST MODE)
ADDITIONAL TESTS EQUIPMENT COMBINATION 5
SPRING 30-2022

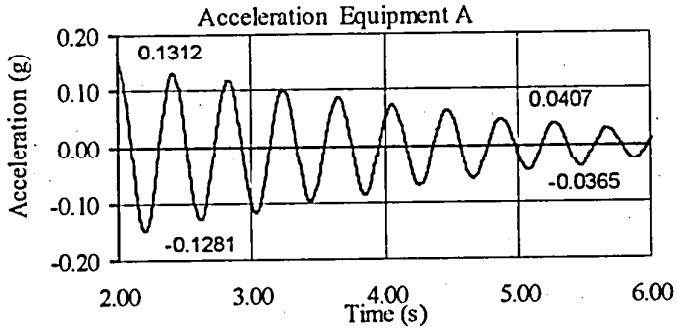

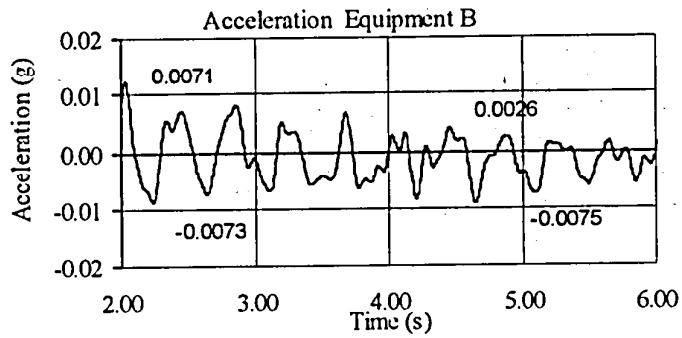

Equipment	First Double Amplitude A1 (g)	Second Double Amplitude A2 (g)	Number of intermediate cycles, p	Damping Ratio $\zeta = \frac{1}{2\pi p}\ln\left(\frac{A1}{A2}\right)$
A	0.2593	0.0772	7	0.0275
B	0.0144	0.0101	6	0.0094
Mean Damping Ratio				0.0185

TEST RB-135 (SECOND MODE)
ADDITIONAL TESTS EQUIPMENT COMBINATION 5
SPRING 30-2022

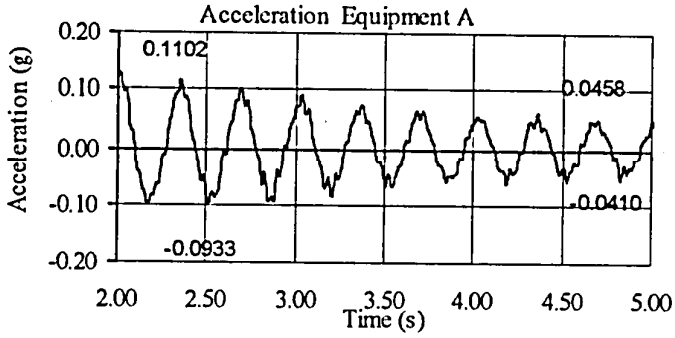

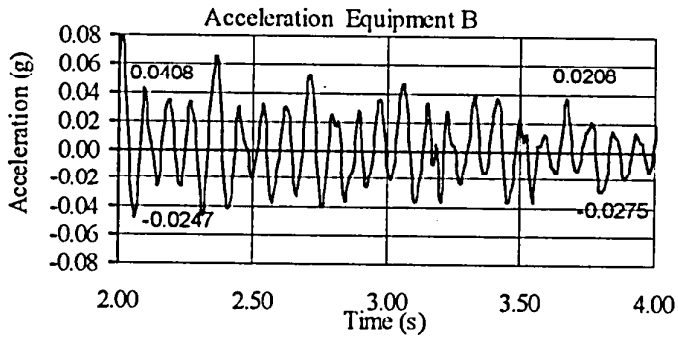

Equipment	First Double Amplitude A1 (g)	Second Double Amplitude A2 (g)	Number of intermediate cycles, p	Damping Ratio $\zeta = \frac{1}{2\pi p}\ln\left(\frac{A1}{A2}\right)$
A	0.2035	0.0868	7	0.0193
B	0.0655	0.0483	17	0.0285
Mean Damping Ratio				0.0239

TEST RB-143
ADDITIONAL TESTS EQUIPMENT COMBINATION 5
BUS SLIDER

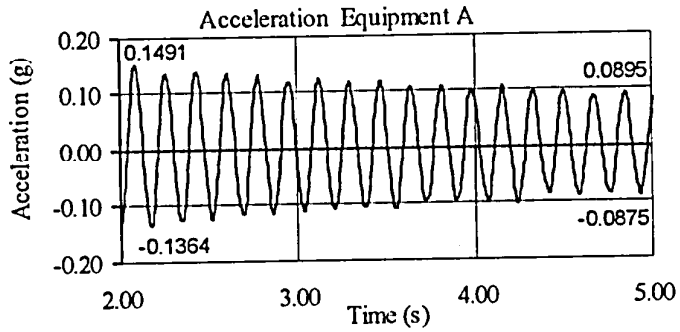

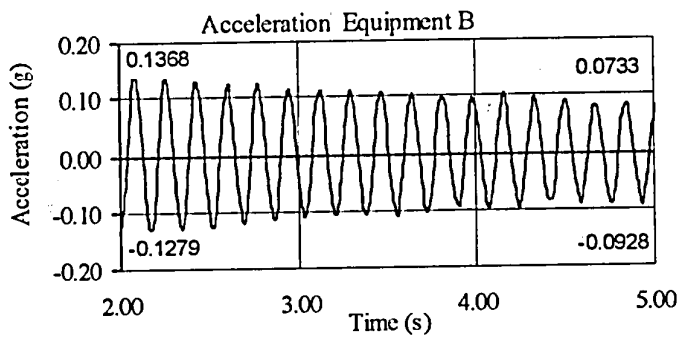

Equipment	First Double Amplitude A1 (g)	Second Double Amplitude A2 (g)	Number of intermediate cycles, p	Damping Ratio $\zeta = \frac{1}{2\pi p}\ln\left(\frac{A1}{A2}\right)$
A	0.2855	0.1770	16	0.0048
B	0.2647	0.1661	16	0.0046
Mean Damping Ratio				0.0047

TEST RB-150
ADDITIONAL TESTS EQUIPMENT COMBINATION 5
BPA ISOLATOR

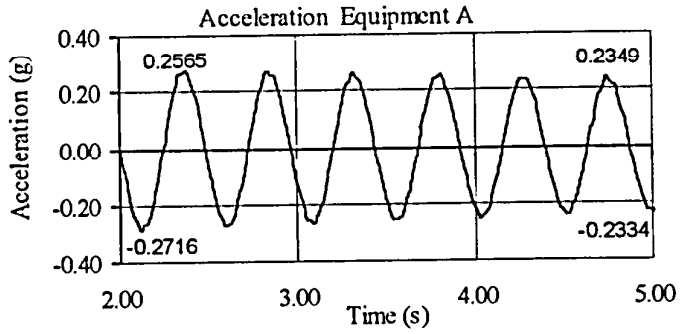

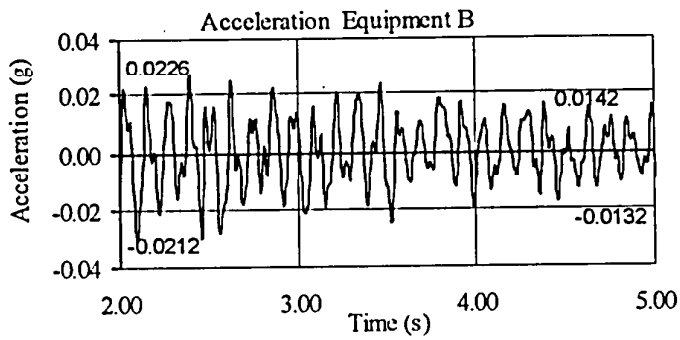

Equipment	First Double Amplitude A1 (g)	Second Double Amplitude A2 (g)	Number of intermediate cycles, p	Damping Ratio $\zeta = \frac{1}{2\pi p}\ln\left(\frac{A1}{A2}\right)$
A	0.5281	0.4683	5	0.0038
B	0.0438	0.0274	22	0.0034
Mean Damping Ratio				0.0036

APPENDIX E

RESULTS OF SEISMIC TESTS

TEST RB-6
EQUIPMENT COMBINATION 4, SPRING 30-2022
NEWHALL GROUND MOTION, 30% SPAN

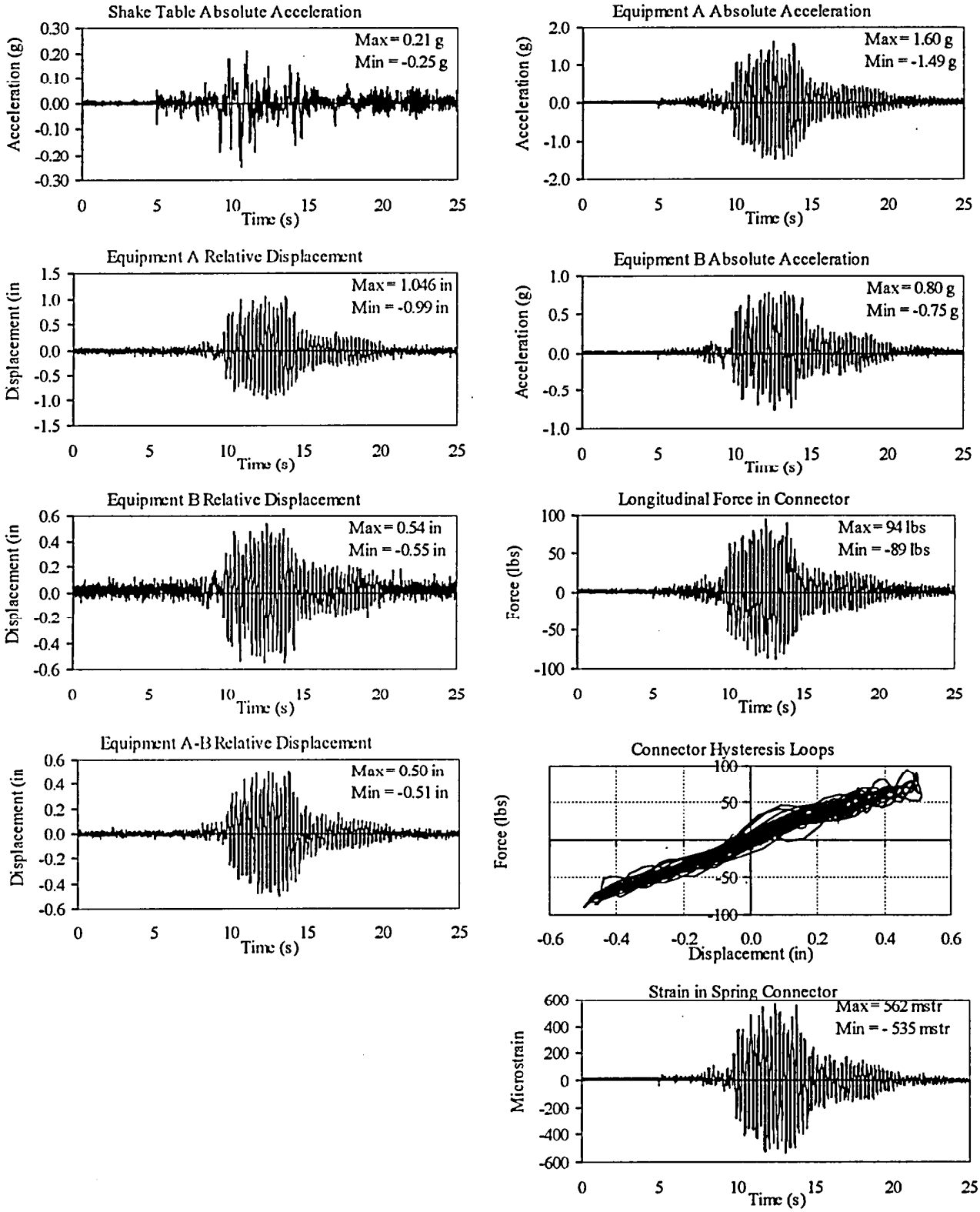

TEST RB-7
EQUIPMENT COMBINATION 4, SPRING 30-2022
NEWHALL GROUND MOTION, 100% SPAN

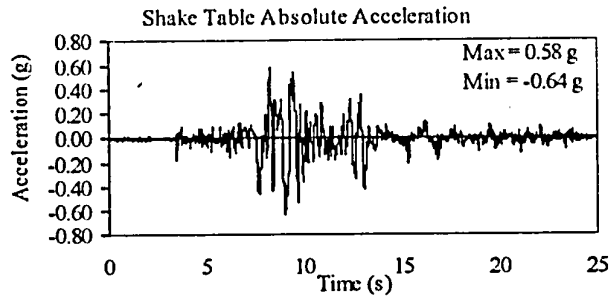

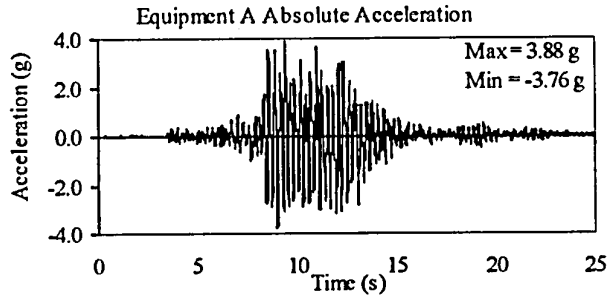

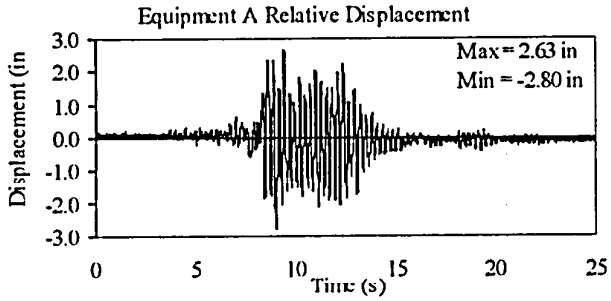

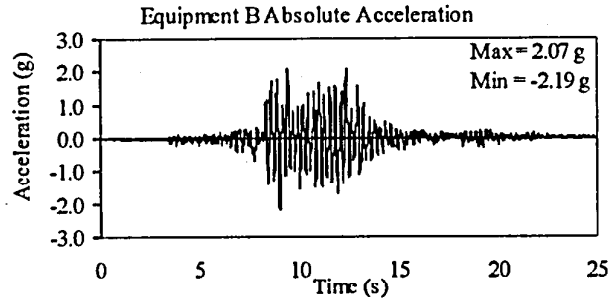

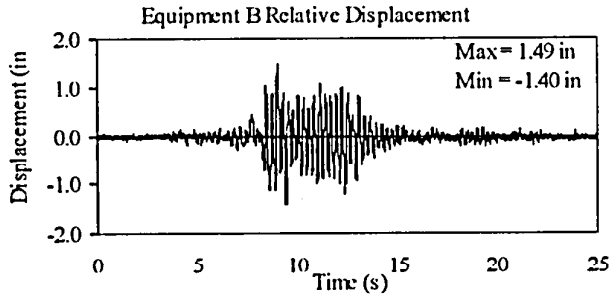

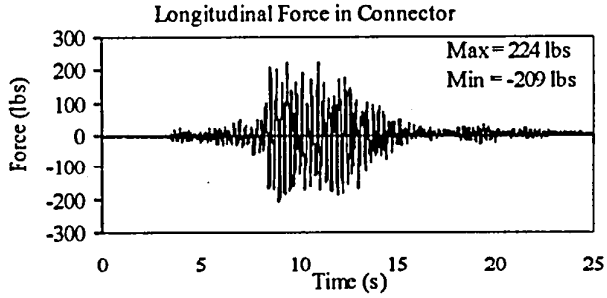

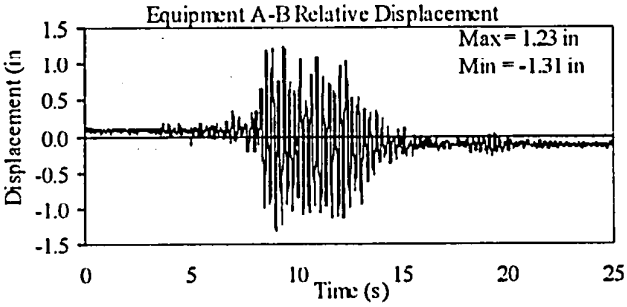

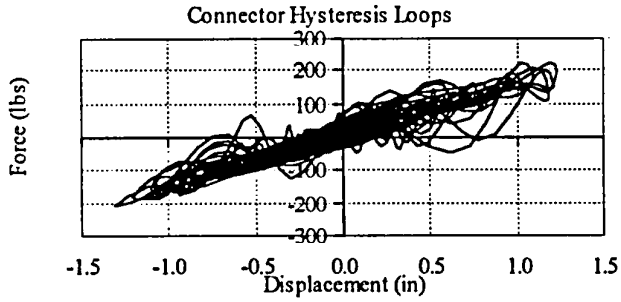

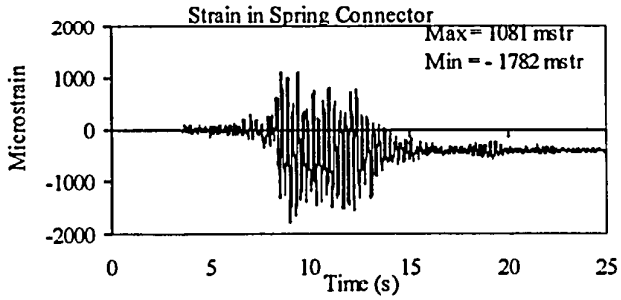

TEST RB-8
EQUIPMENT COMBINATION 4, SPRING 30-2022
TABAS GROUND MOTION, 25% SPAN

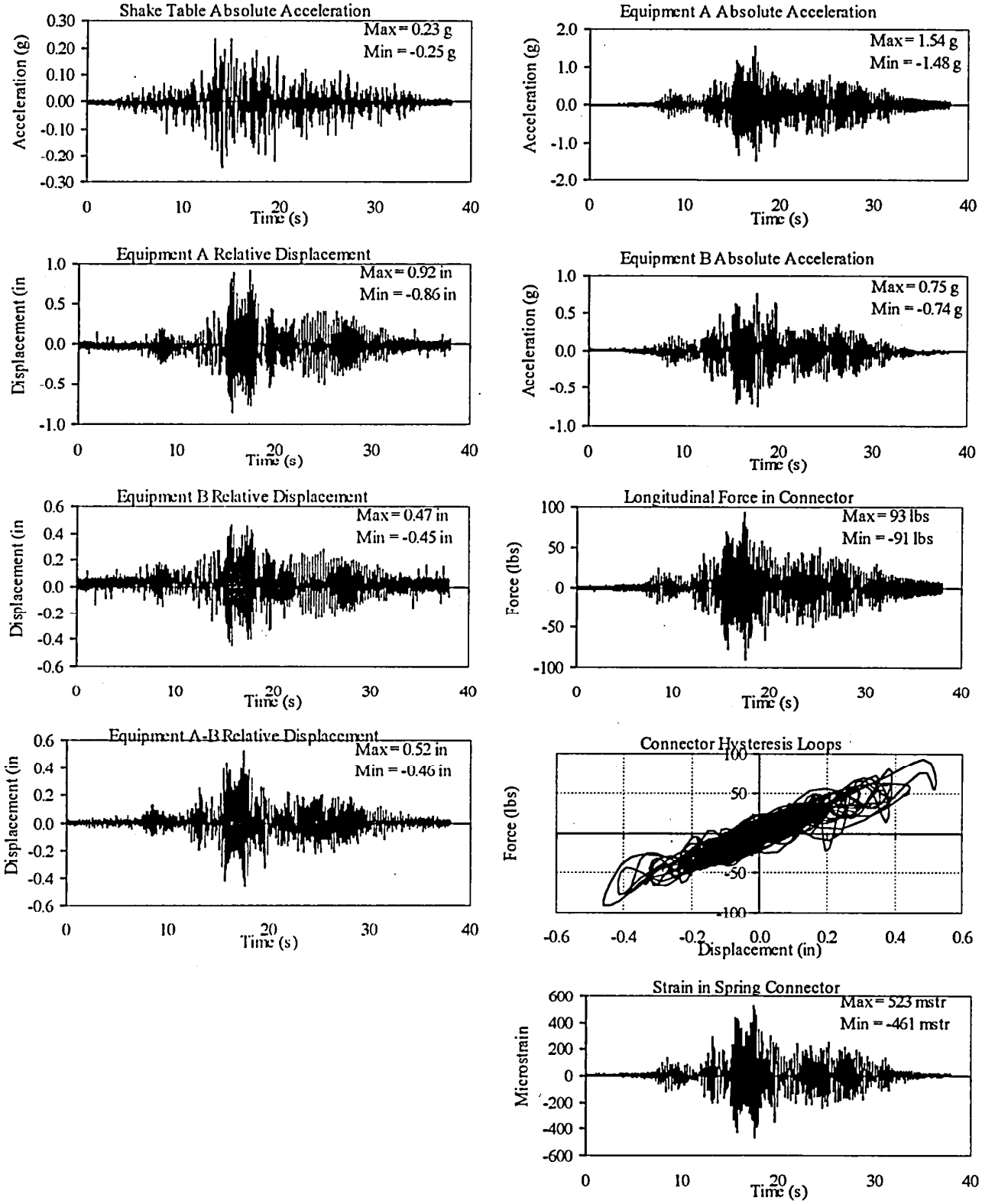

TEST RB-9
EQUIPMENT COMBINATION 4, SPRING 30-2022
TABAS GROUND MOTION, 50% SPAN

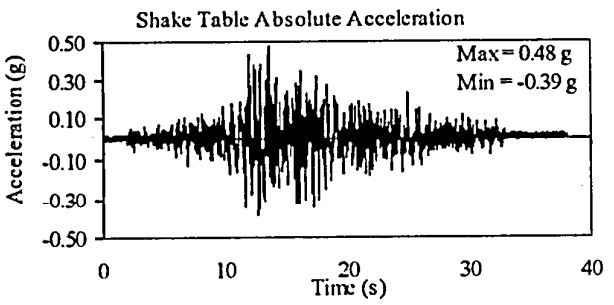

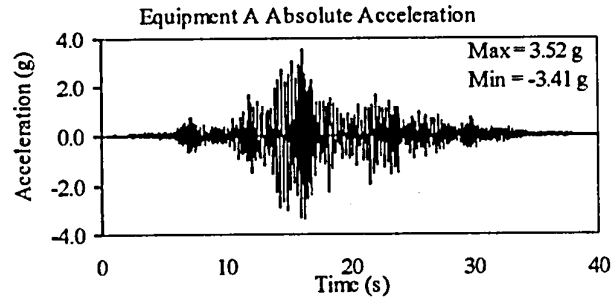

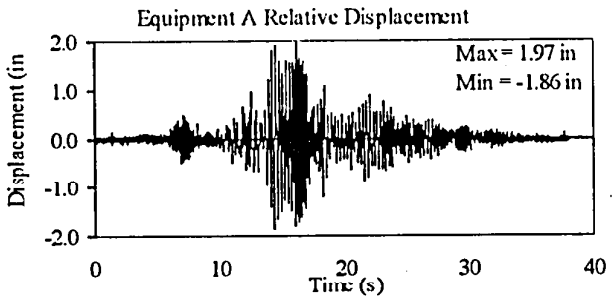

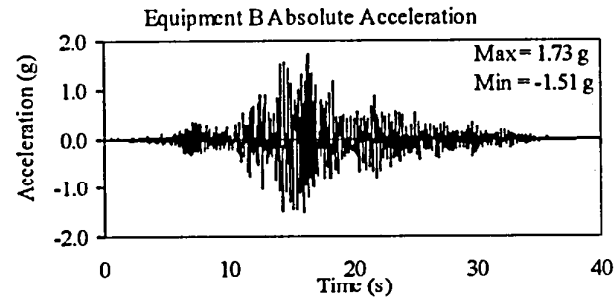

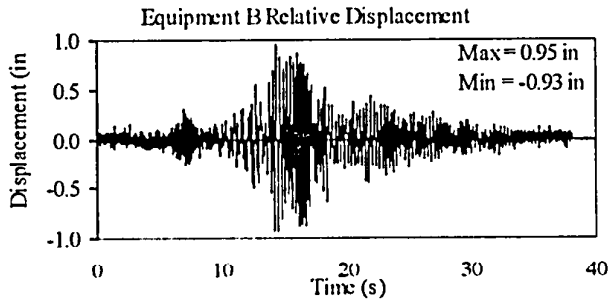

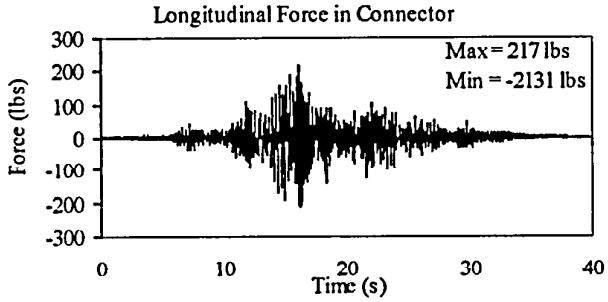

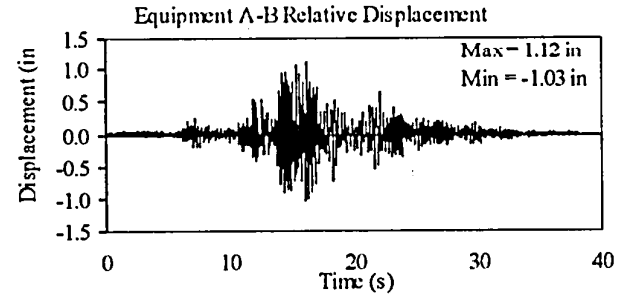

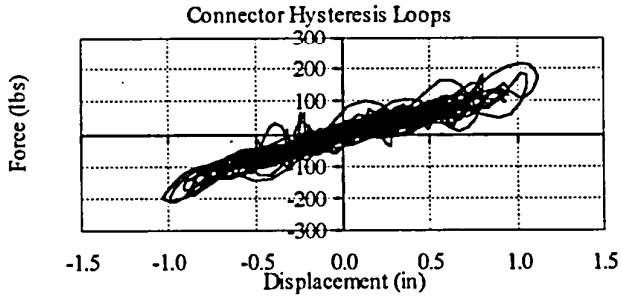

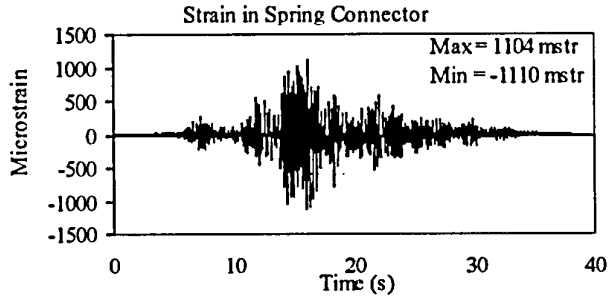

TEST RB-15
EQUIPMENT COMBINATION 4, BUS SLIDER
NEWHALL GROUND MOTION, 100% SPAN

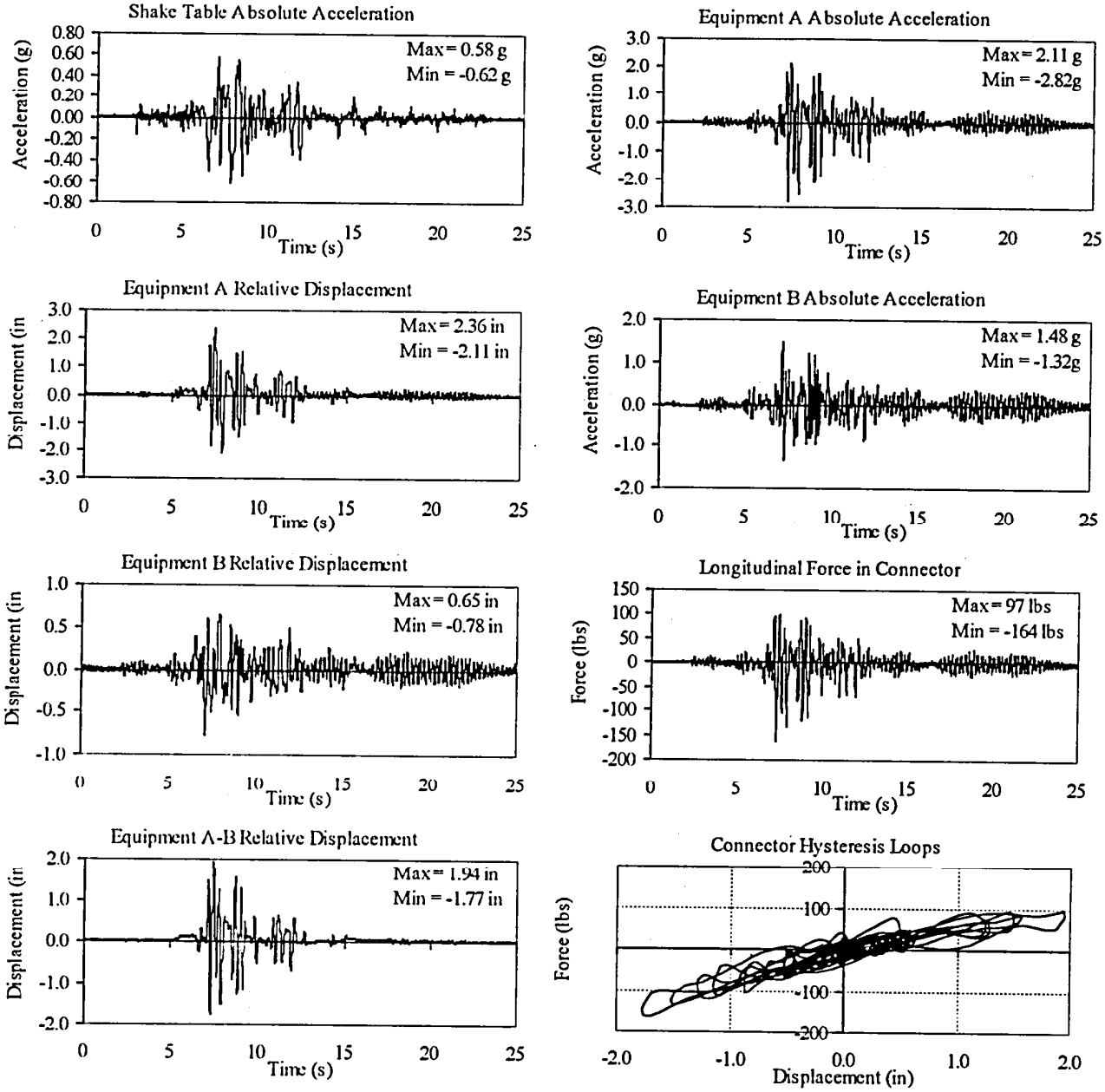

TEST RB-17
EQUIPMENT COMBINATION 4, BUS SLIDER
TABAS GROUND MOTION, 50% SPAN

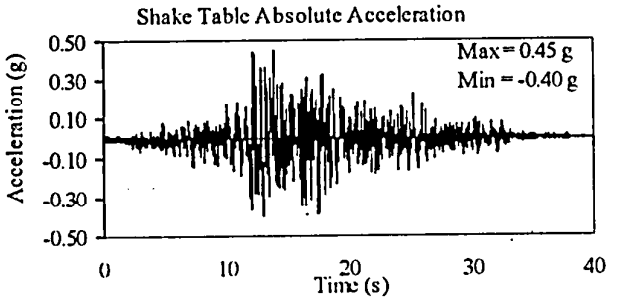

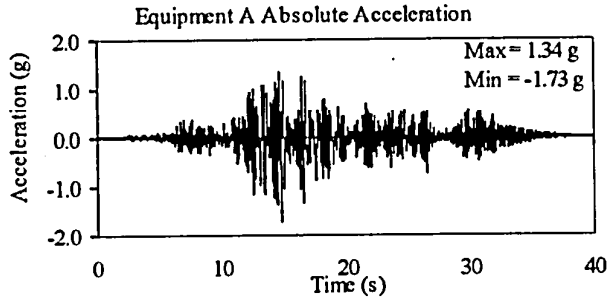

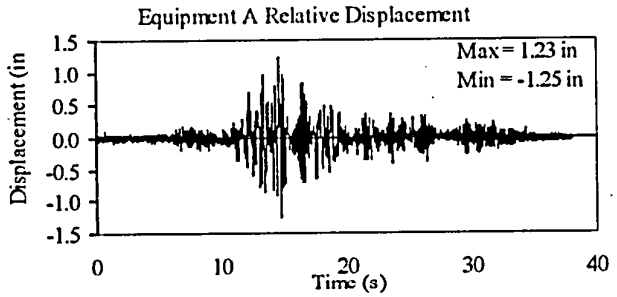

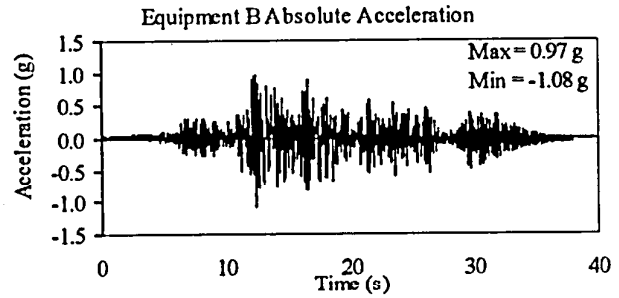

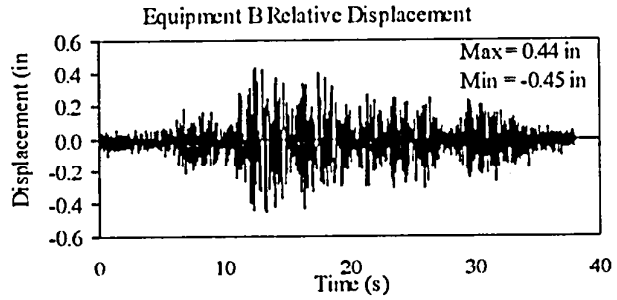

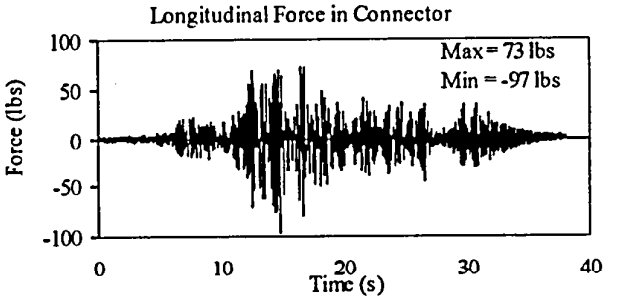

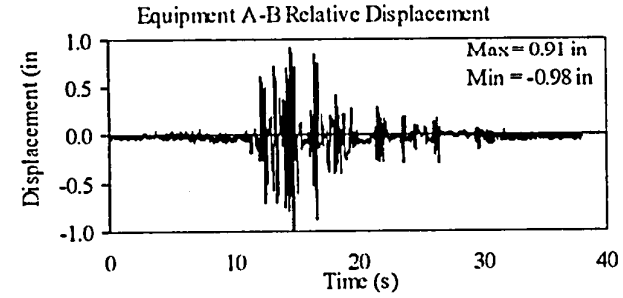

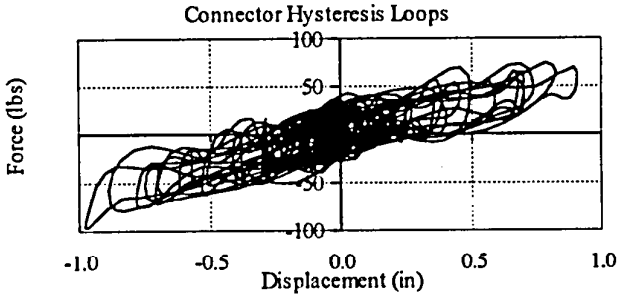

TEST RB-18
EQUIPMENT COMBINATION 4, BUS SLIDER
TABAS GROUND MOTION, 200% SPAN

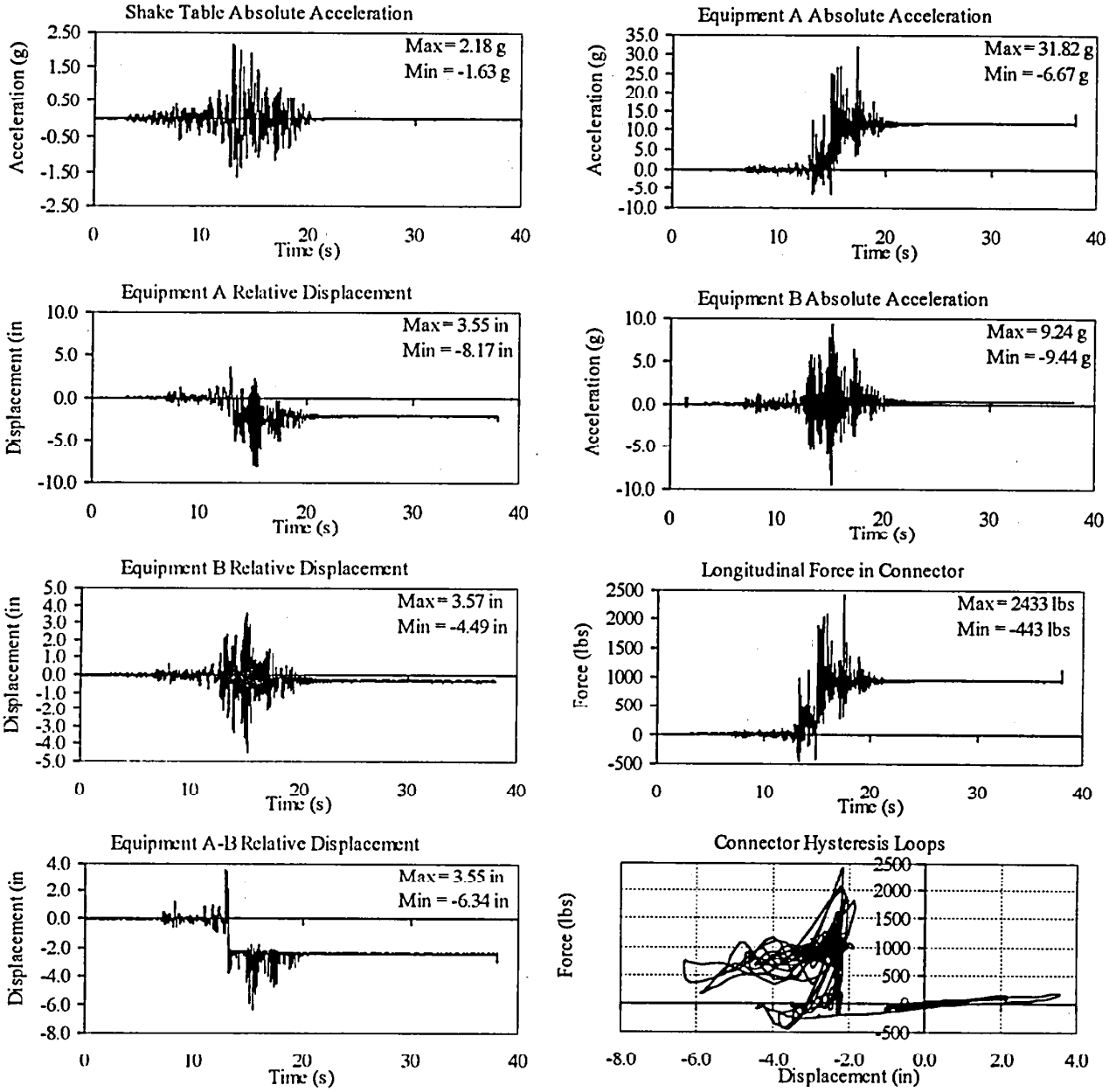

TEST RB-24
EQUIPMENT COMBINATION 4, BPA ISOLATOR
NEWHALL GROUND MOTION, 30% SPAN

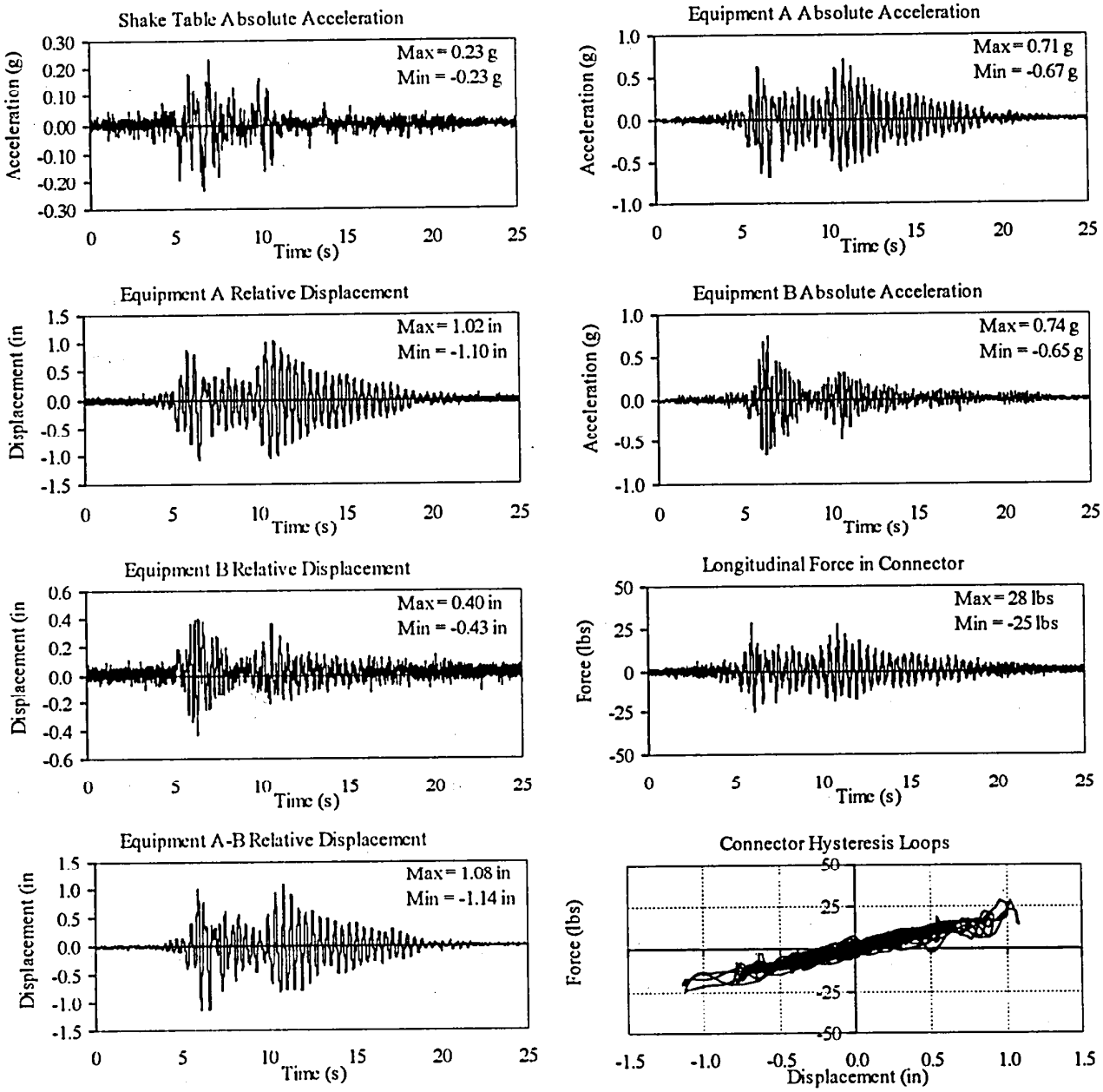

TEST RB-26
EQUIPMENT COMBINATION 4, BPA ISOLATOR
TABAS GROUND MOTION, 25% SPAN

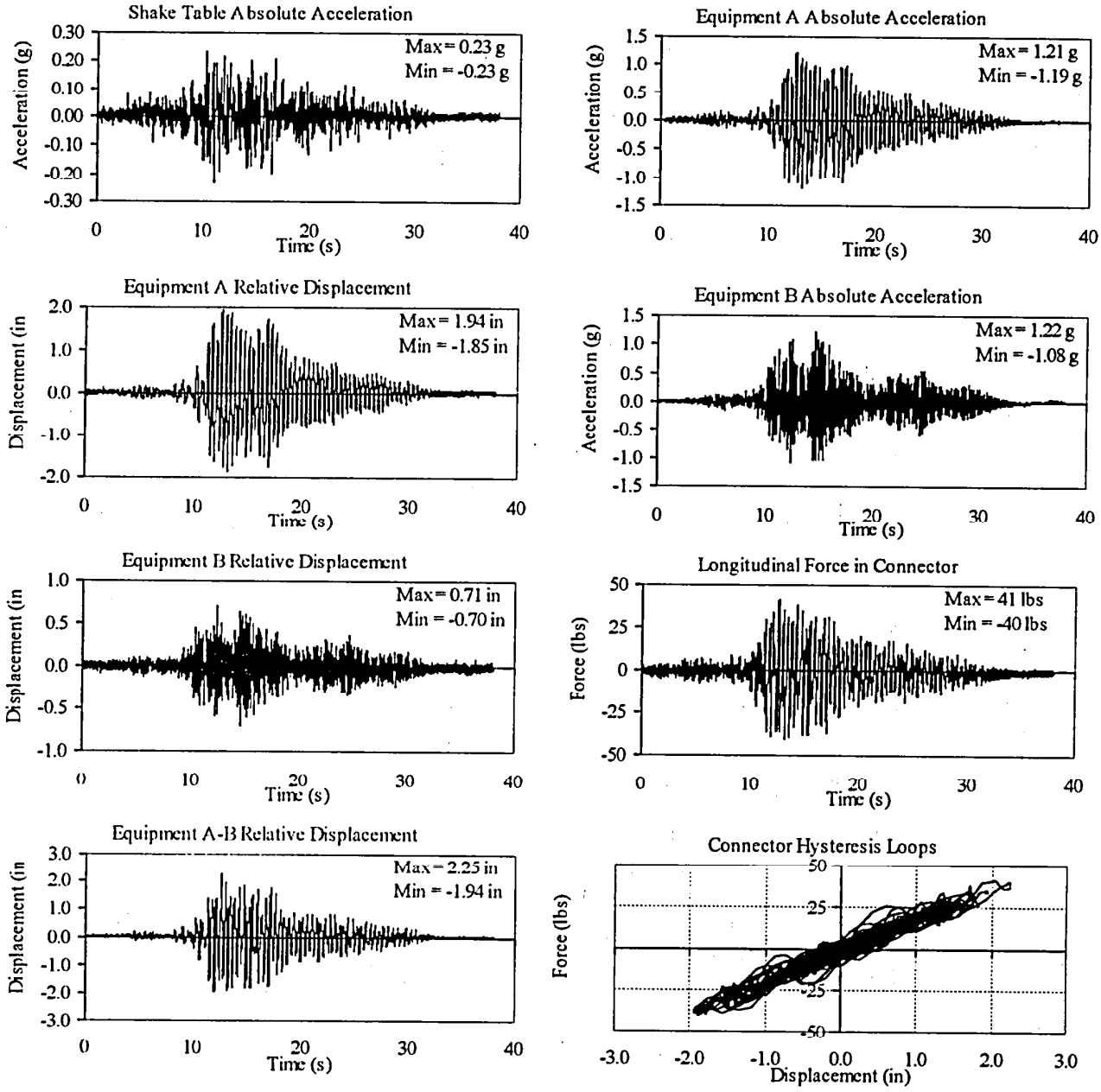

TEST RB-28
EQUIPMENT COMBINATION 4, INDIVIDUAL EQUIPMENT
NEWHALL GROUND MOTION, 30% SPAN

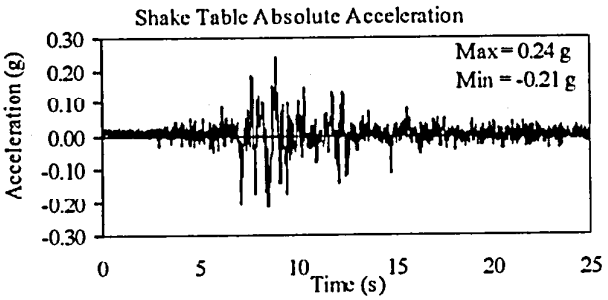

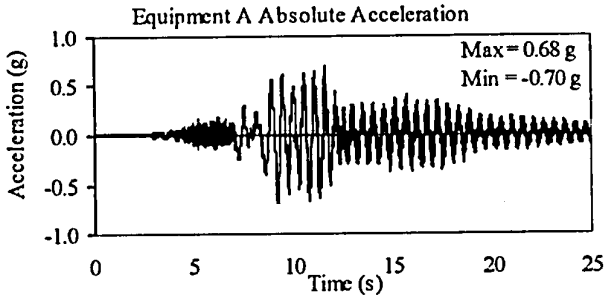

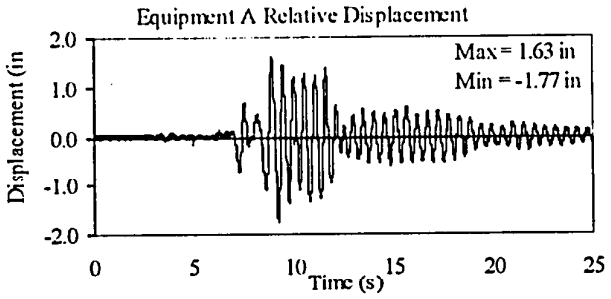

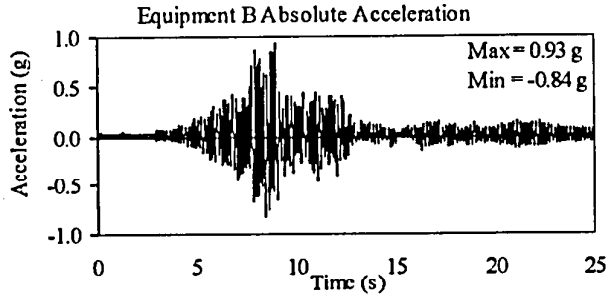

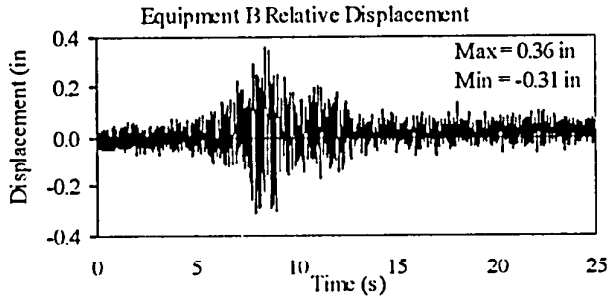

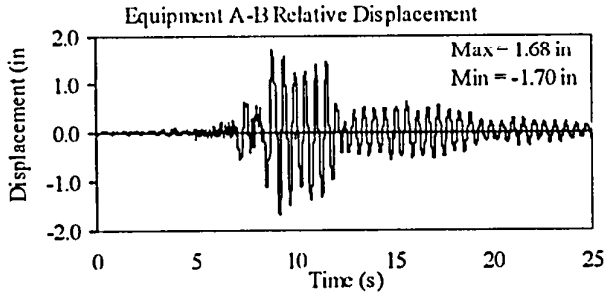

TEST RB-29
EQUIPMENT COMBINATION 4, INDIVIDUAL EQUIPMENT
NEWHALL GROUND MOTION, 100% SPAN

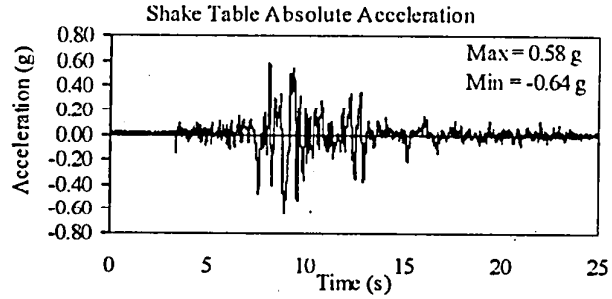

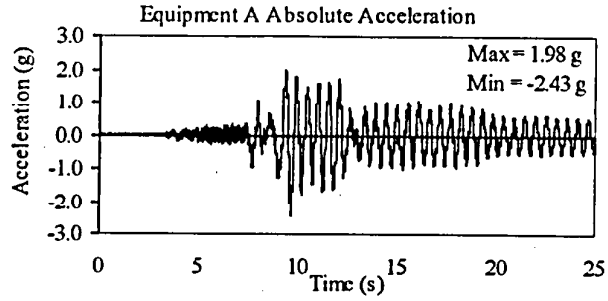

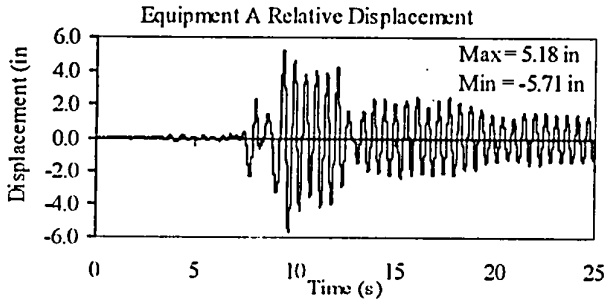

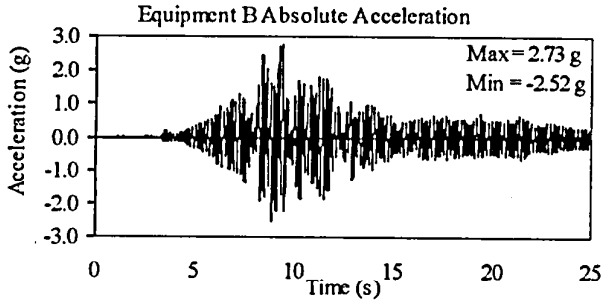

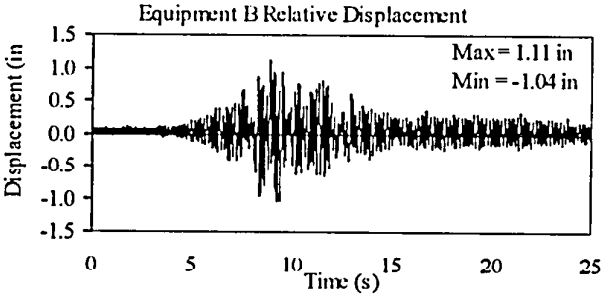

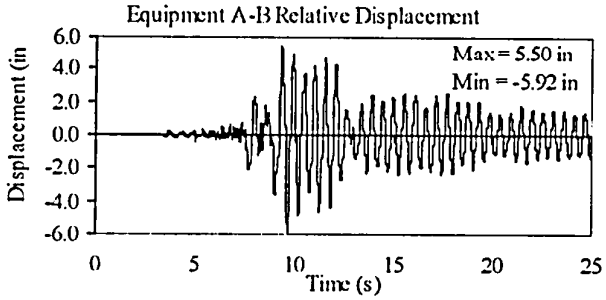

TEST RB-30
EQUIPMENT COMBINATION 4, INDIVIDUAL EQUIPMENT
TABAS GROUND MOTION, 25% SPAN

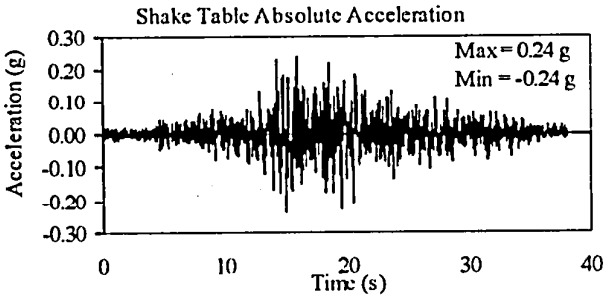

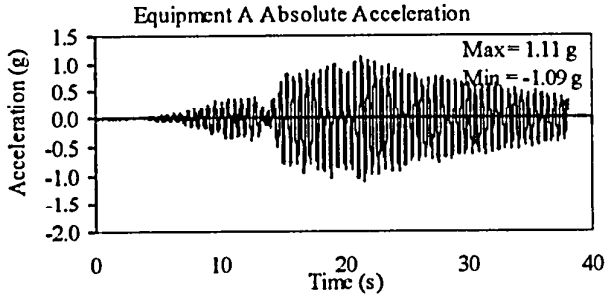

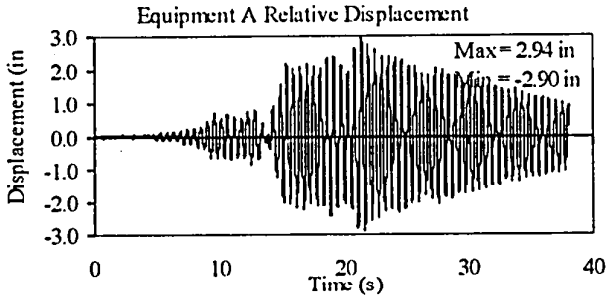

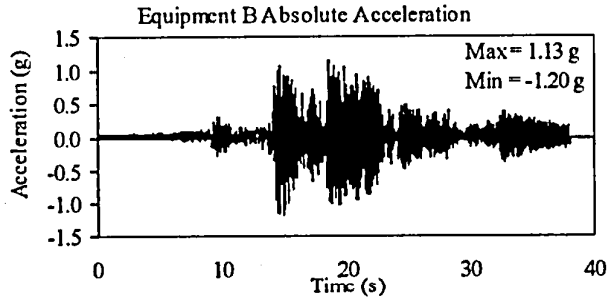

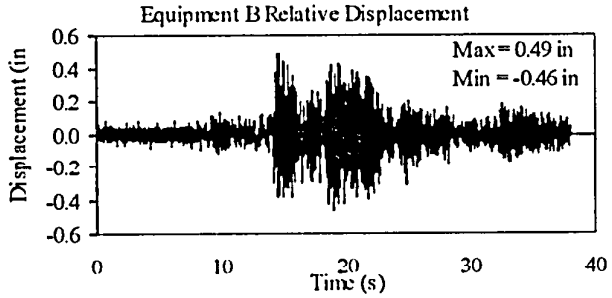

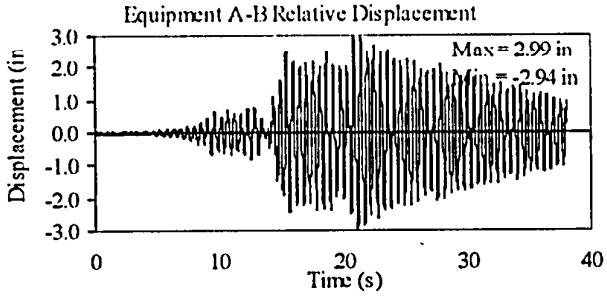

TEST RB-31
EQUIPMENT COMBINATION 4, INDIVIDUAL EQUIPMENT
TABAS GROUND MOTION, 50% SPAN

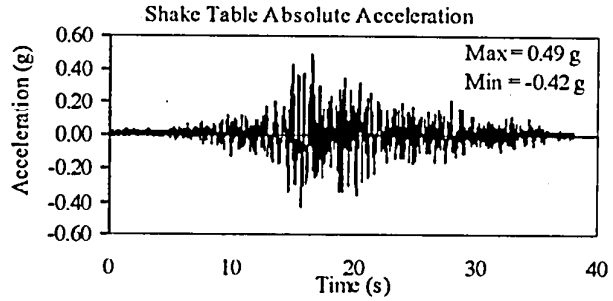

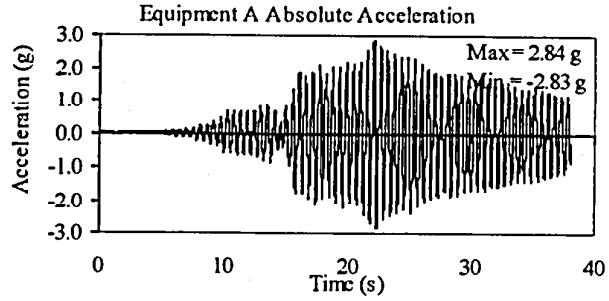

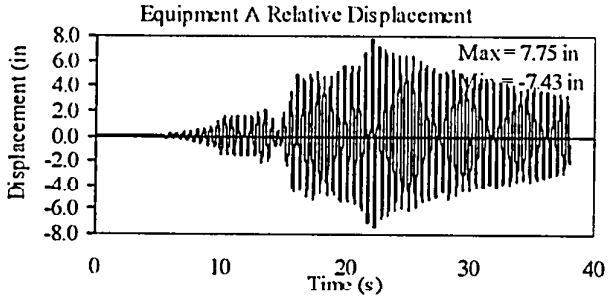

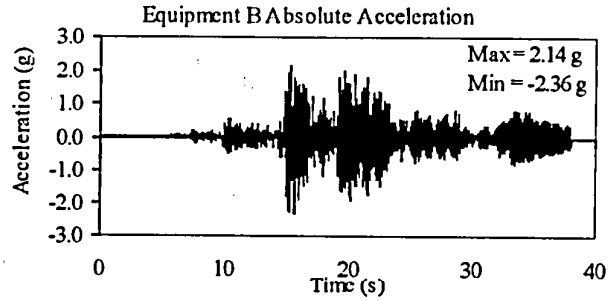

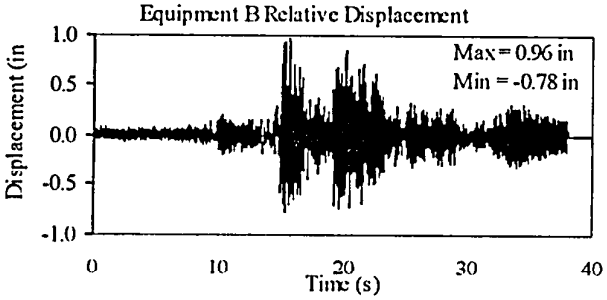

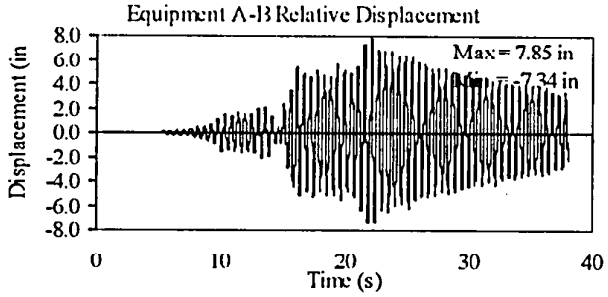

TEST RB-38
EQUIPMENT COMBINATION 3, SPRING 30-2022
NEWHALL GROUND MOTION, 30% SPAN

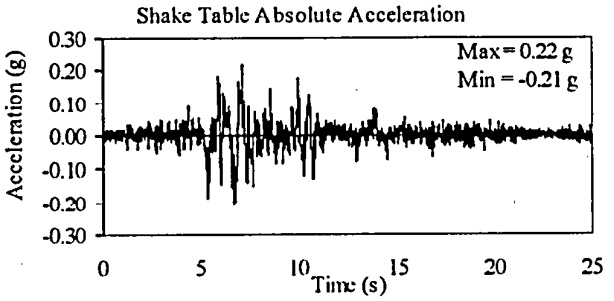

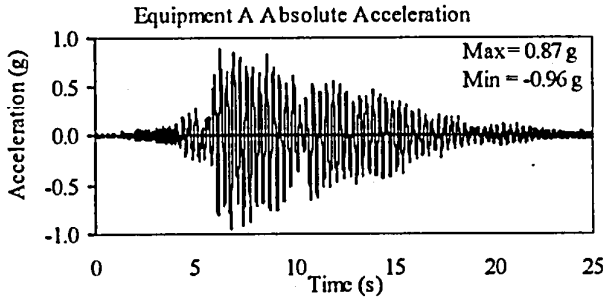

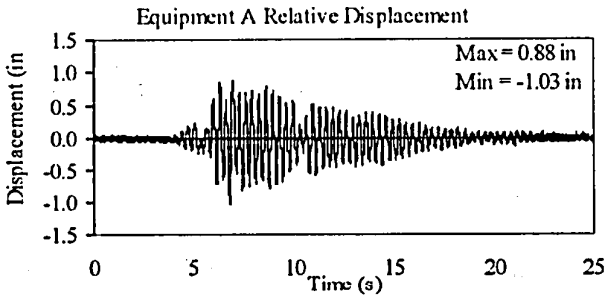

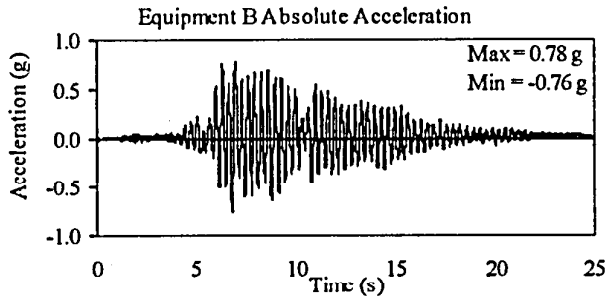

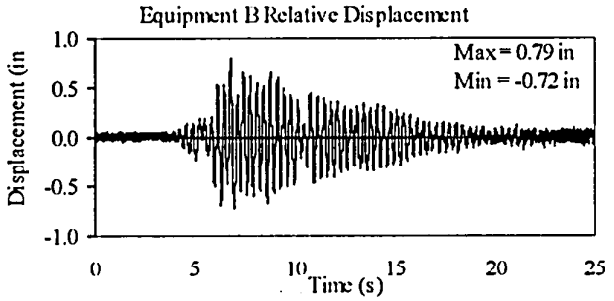

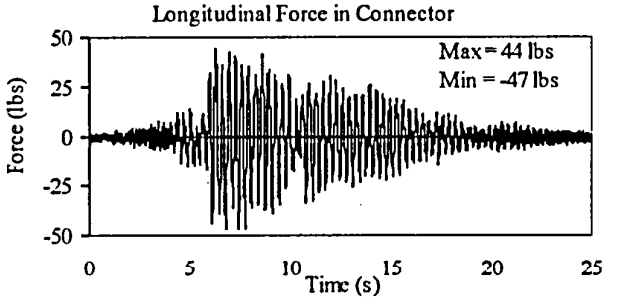

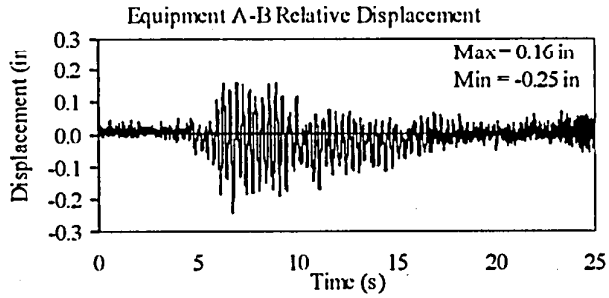

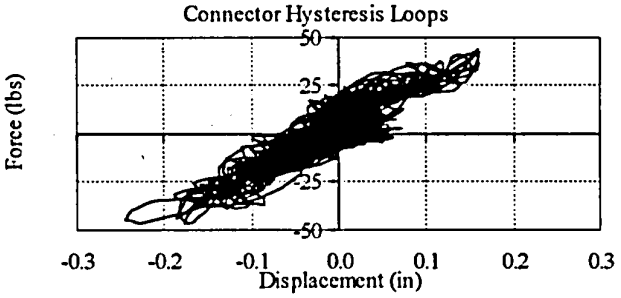

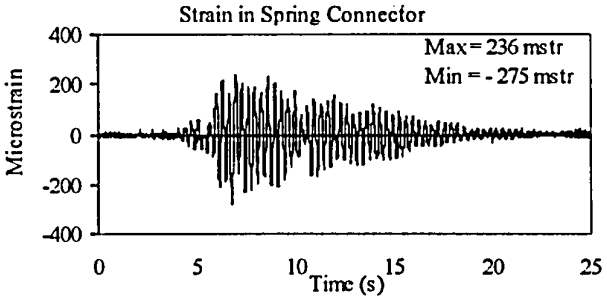

TEST RB-39
EQUIPMENT COMBINATION 3, SPRING 30-2022
NEWHALL GROUND MOTION, 100% SPAN

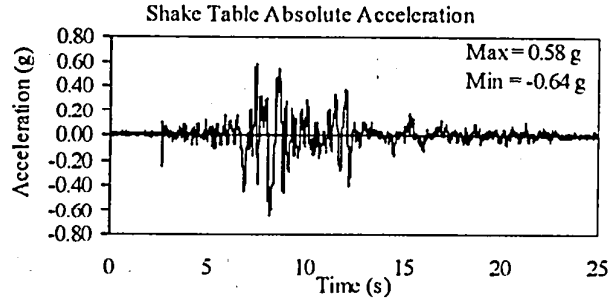

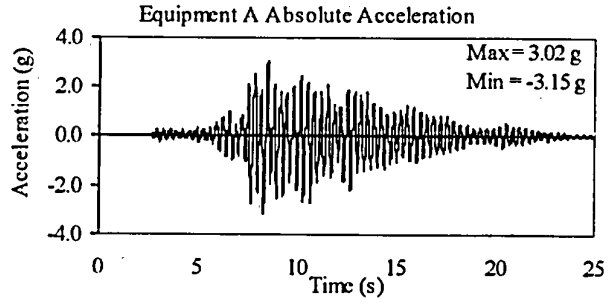

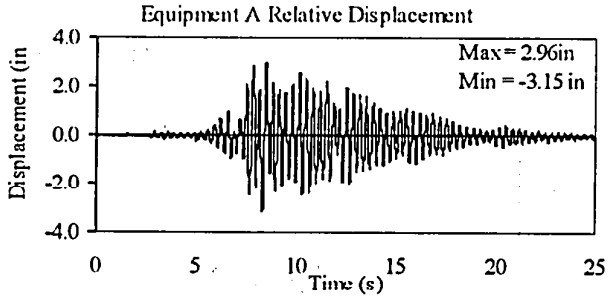

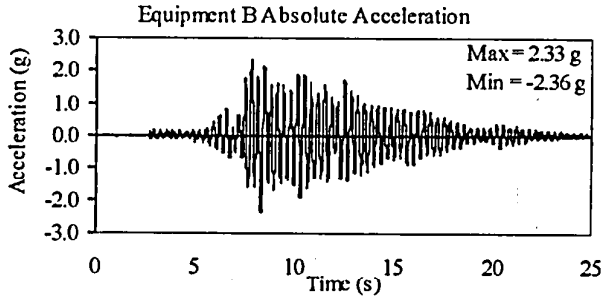

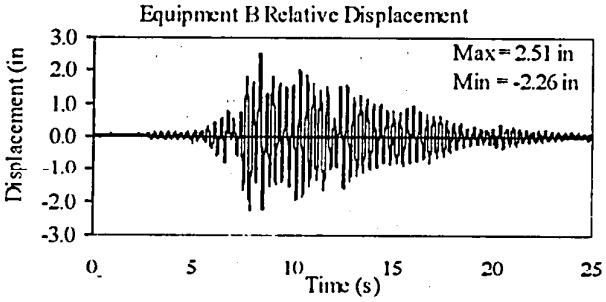

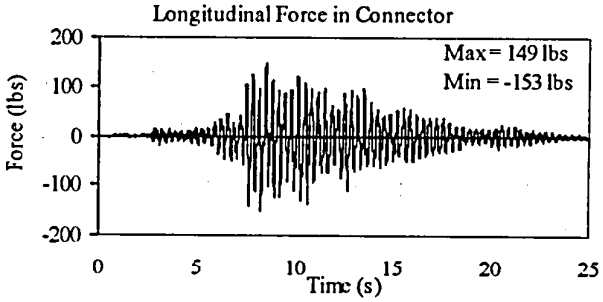

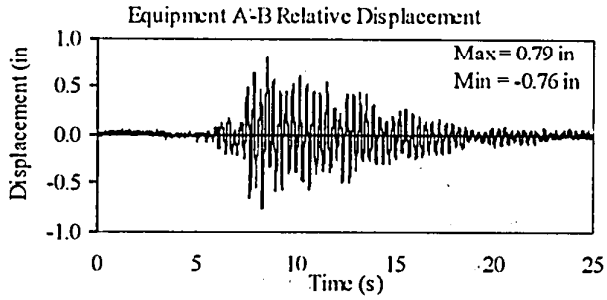

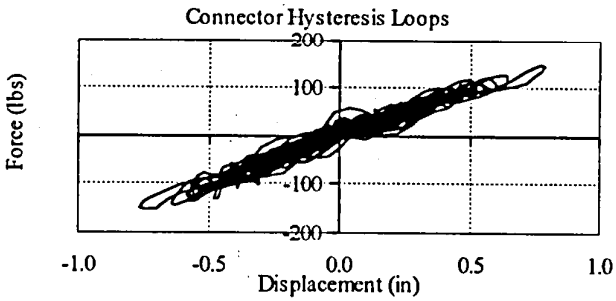

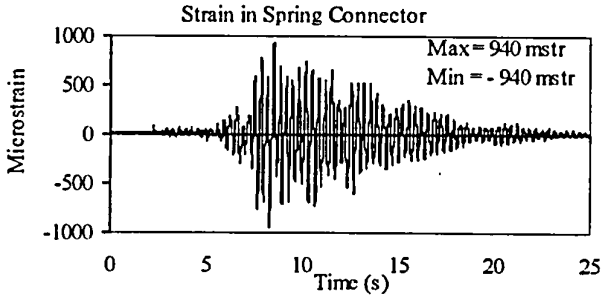

TEST RB-40
EQUIPMENT COMBINATION 3, SPRING 30-2022
TABAS GROUND MOTION, 25% SPAN

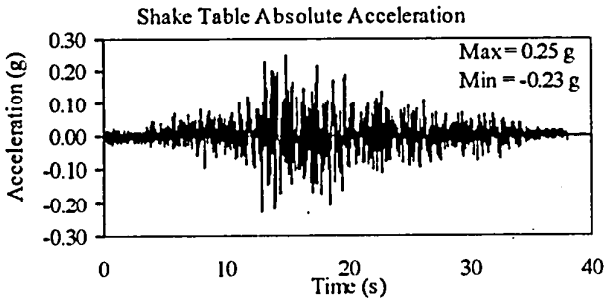

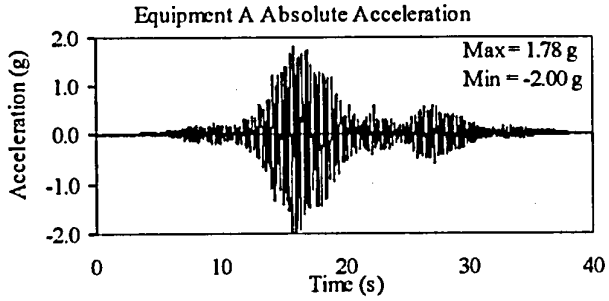

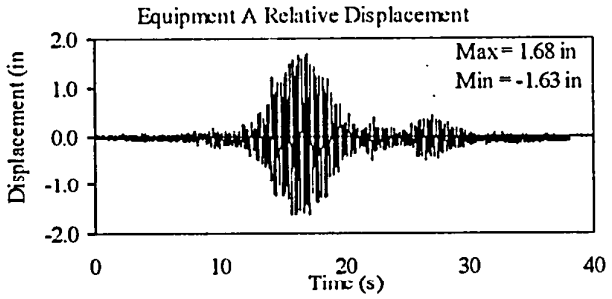

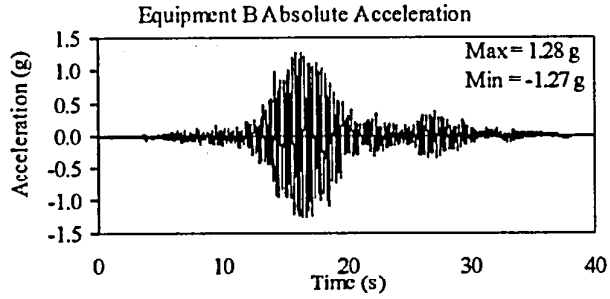

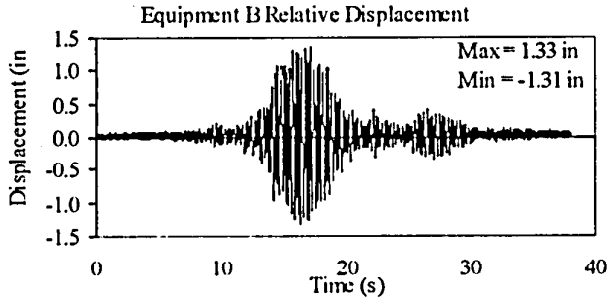

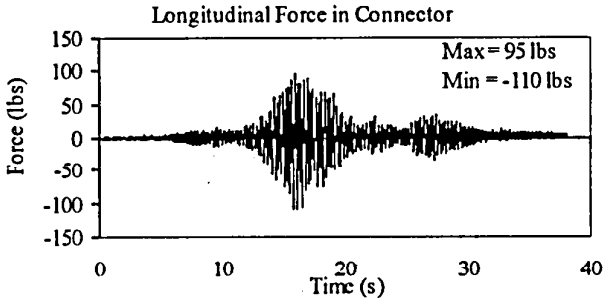

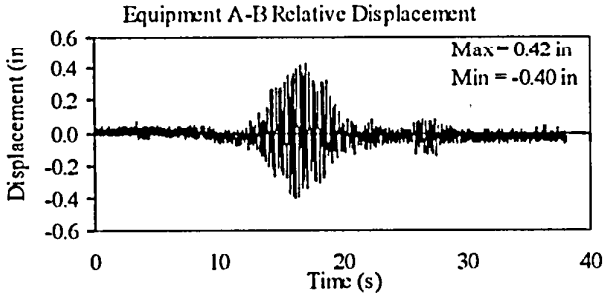

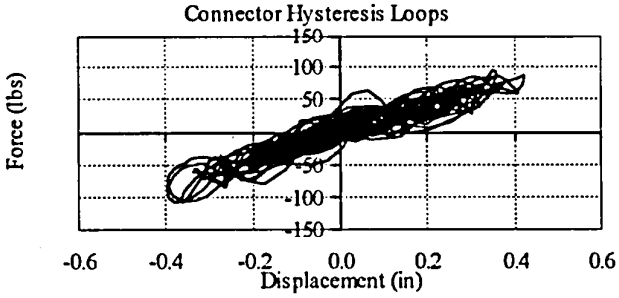

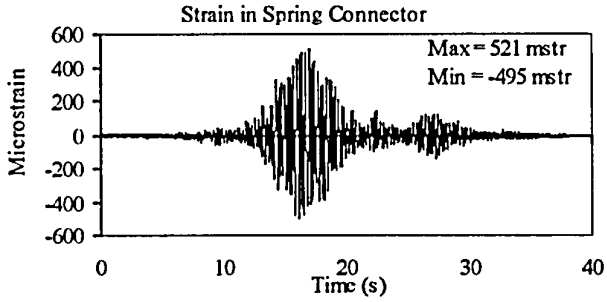

TEST RB-41
EQUIPMENT COMBINATION 3, SPRING 30-2022
TABAS GROUND MOTION, 50% SPAN

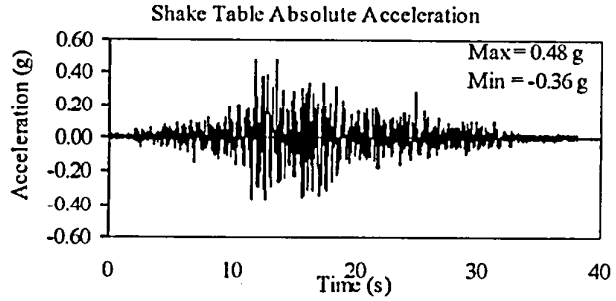

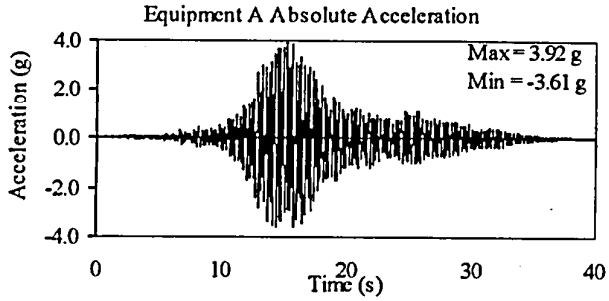

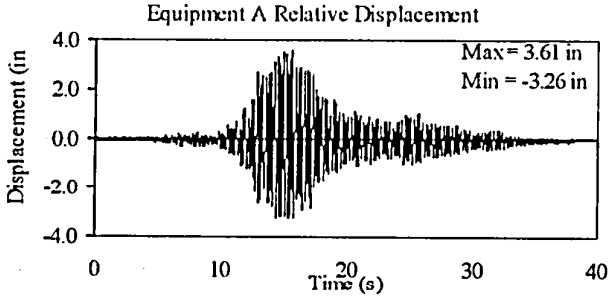

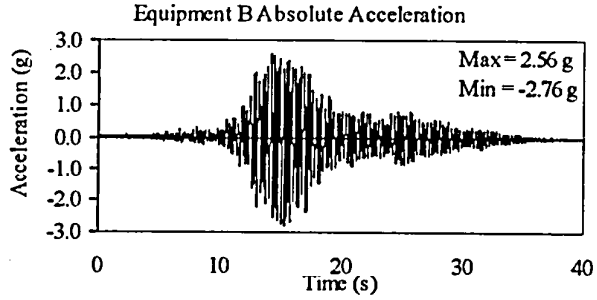

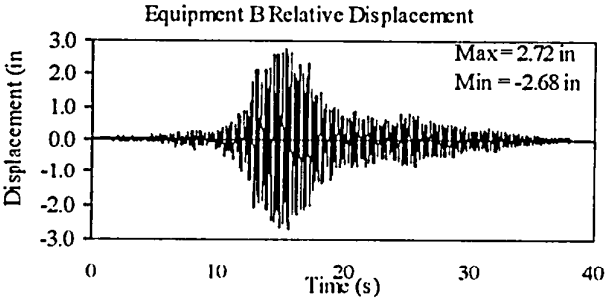

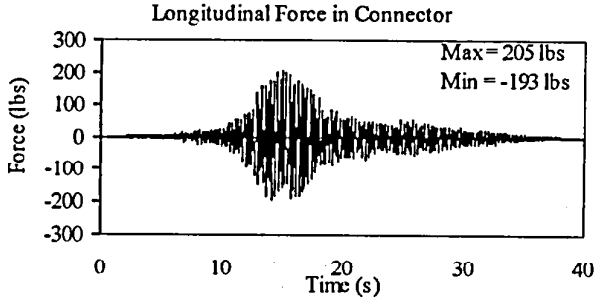

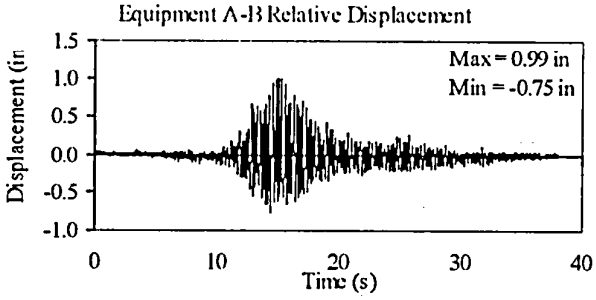

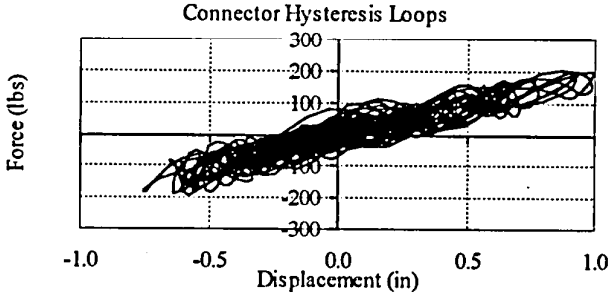

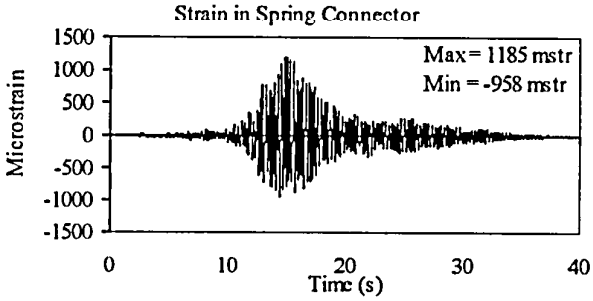

TEST RB-47
EQUIPMENT COMBINATION 3, BUS SLIDER
NEWHALL GROUND MOTION, 100% SPAN

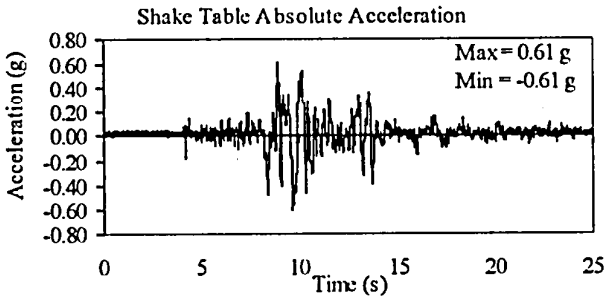

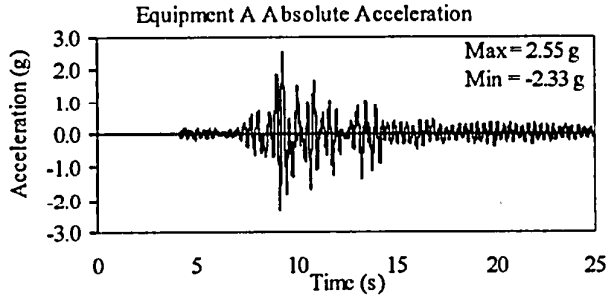

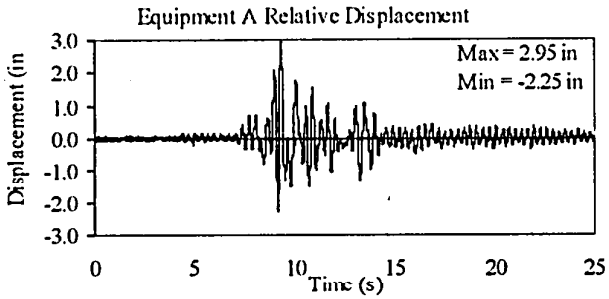

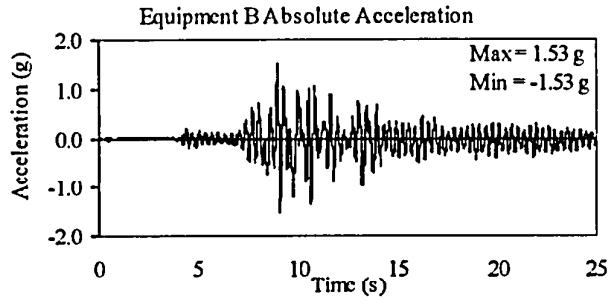

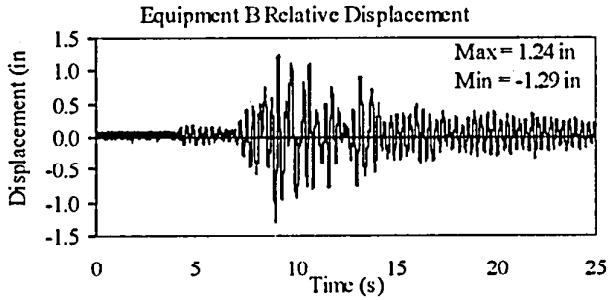

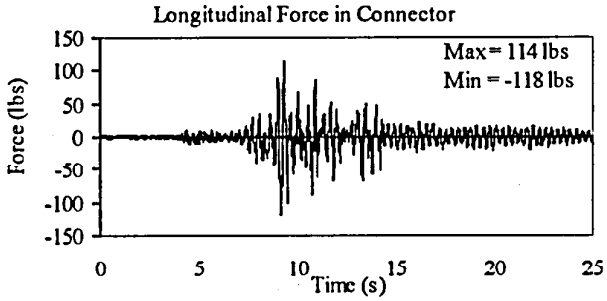

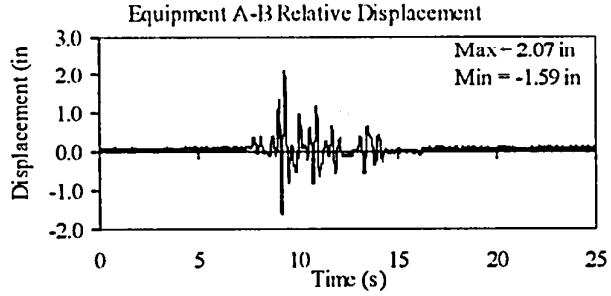

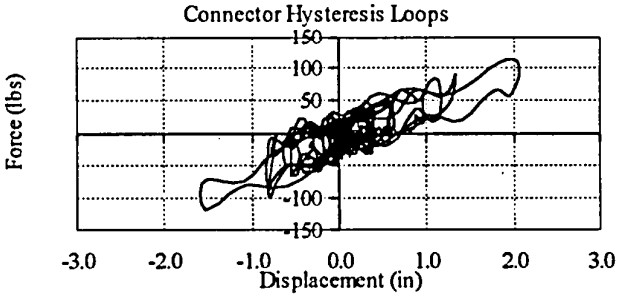

TEST RB-100
EQUIPMENT COMBINATION 2, SPRING 30-2022
TABAS GROUND MOTION, 50% SPAN

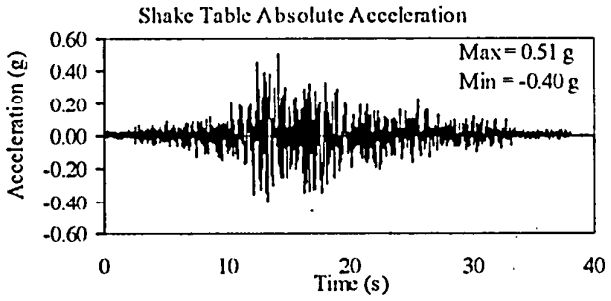

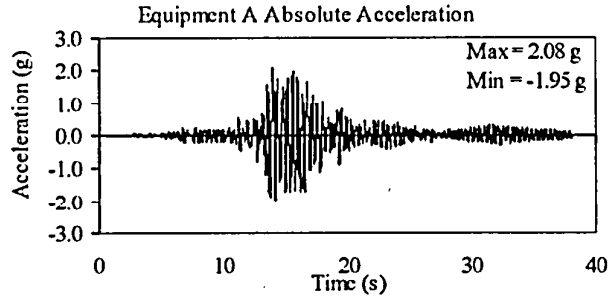

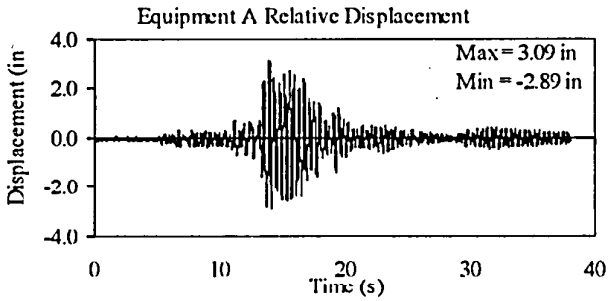

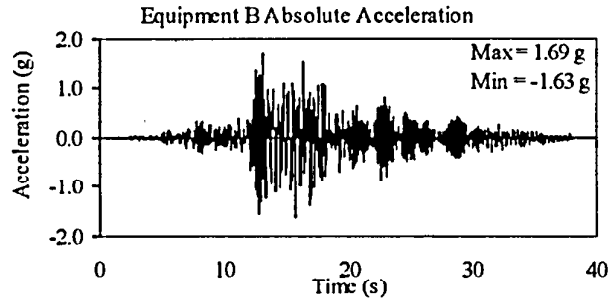

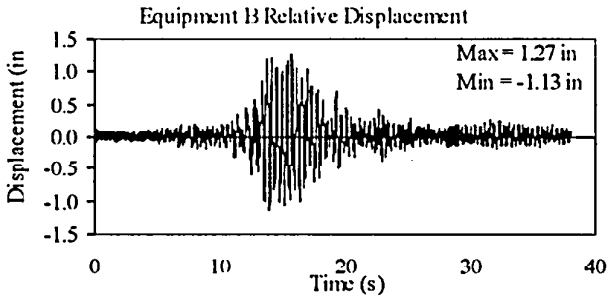

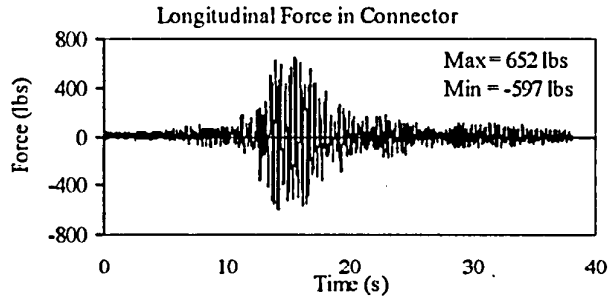

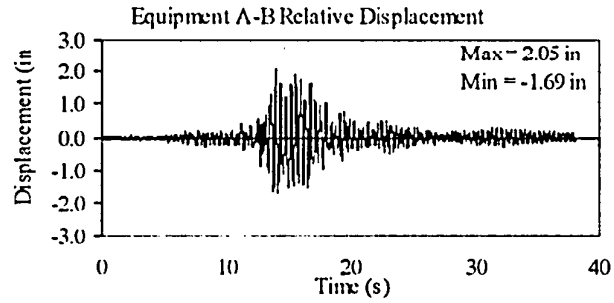

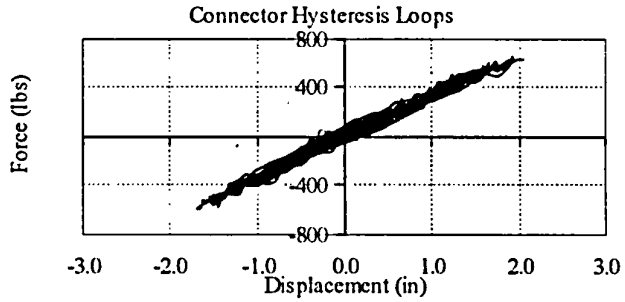

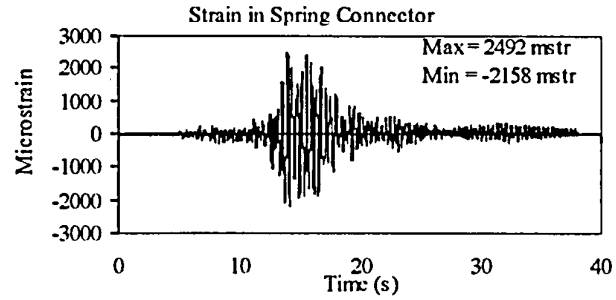

TEST RB-101
EQUIPMENT COMBINATION 2, SPRING 30-2022
NEWHALL GROUND MOTION, 100% SPAN

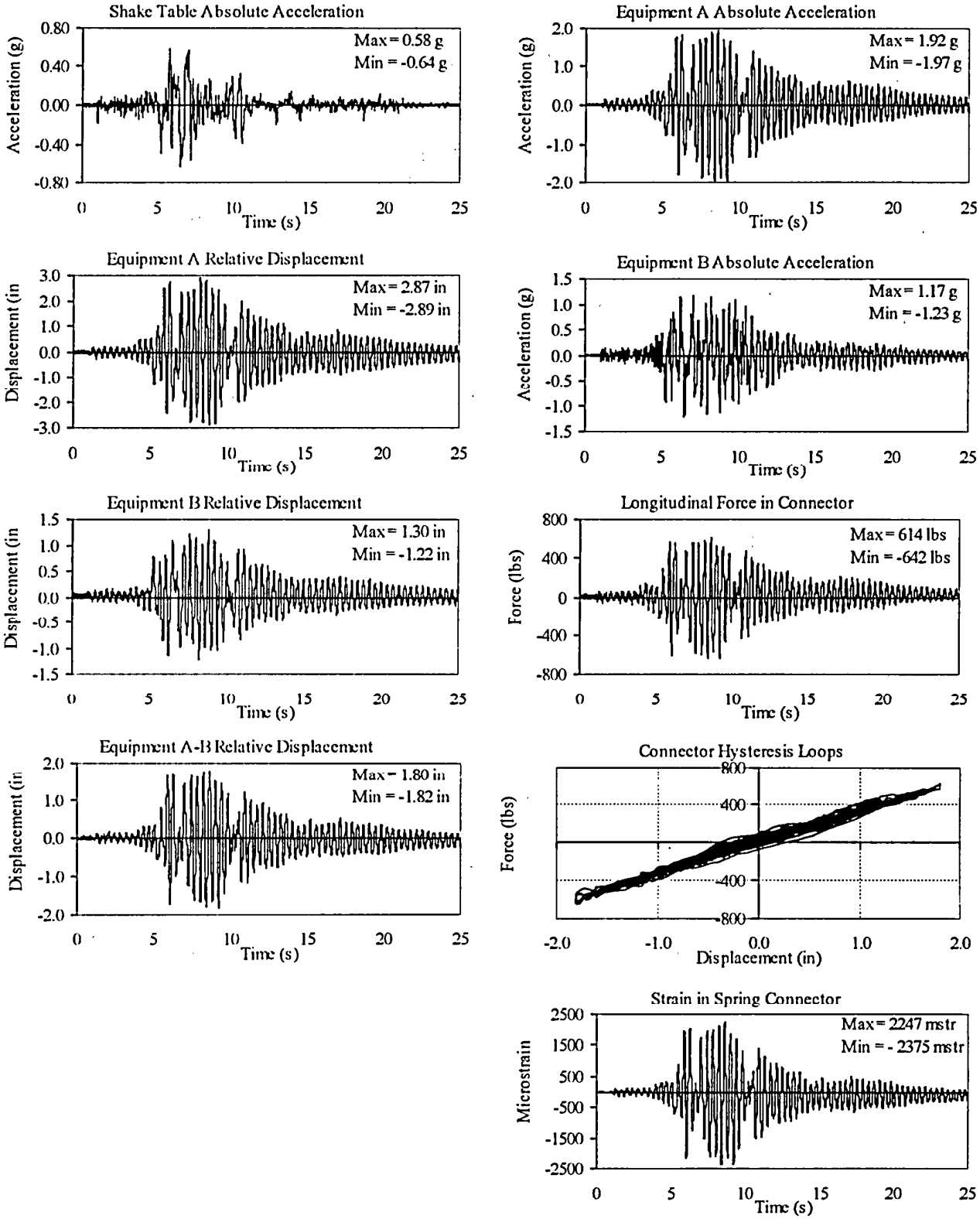

TEST RB-102
EQUIPMENT COMBINATION 2, SPRING 30-2022
TABAS GROUND MOTION, 100% SPAN

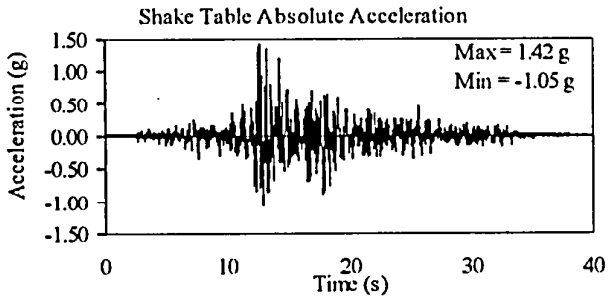

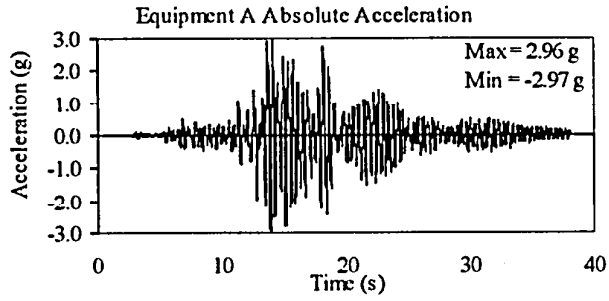

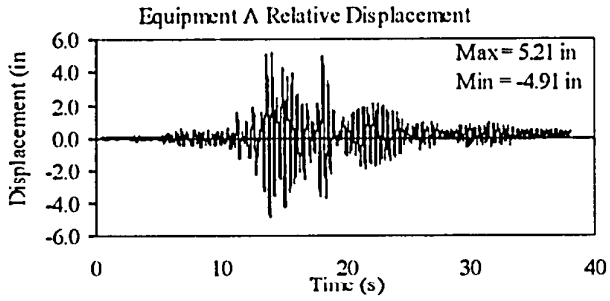

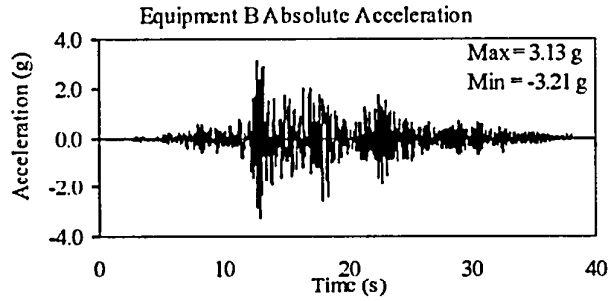

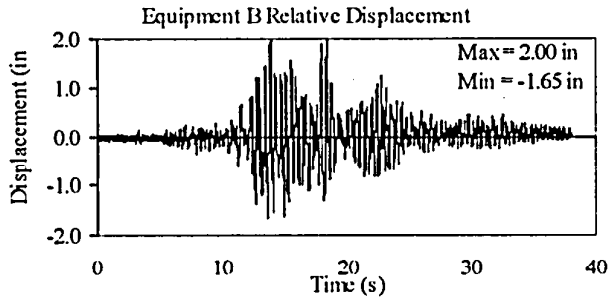

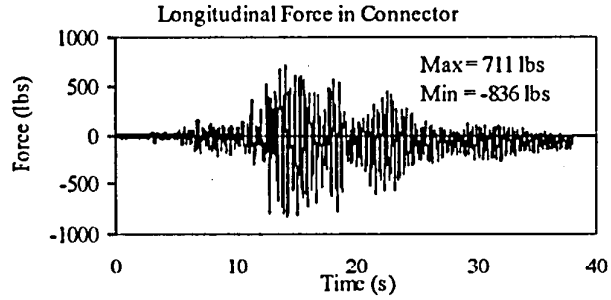

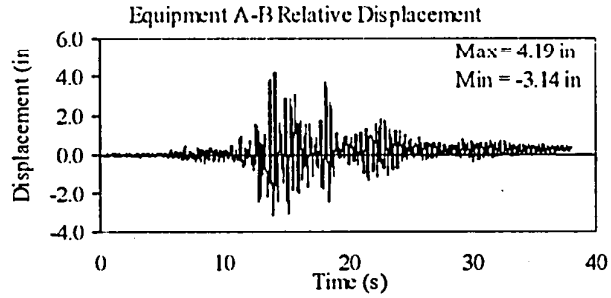

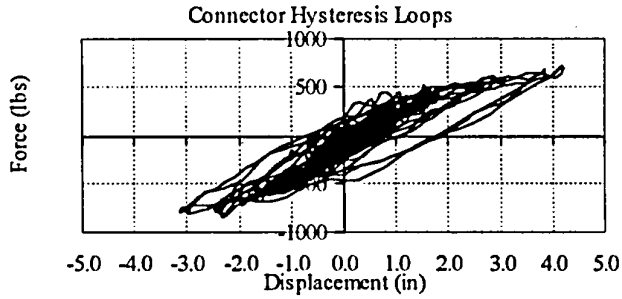

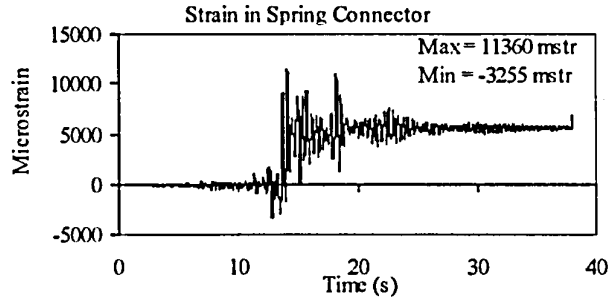

TEST RB-103
EQUIPMENT COMBINATION 2, SPRING 30-2022
TABAS GROUND MOTION, 150% SPAN

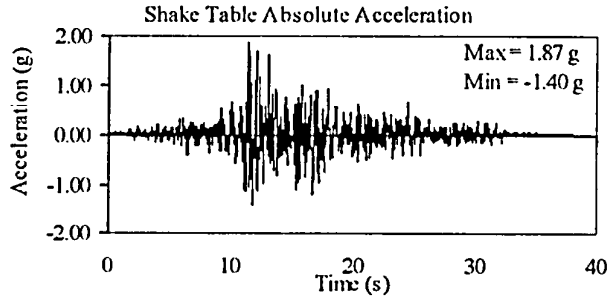

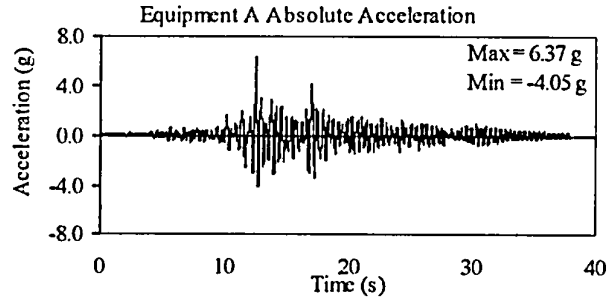

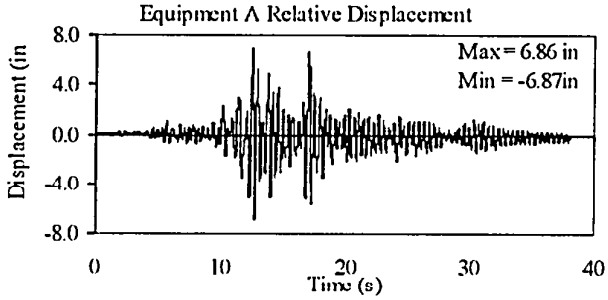

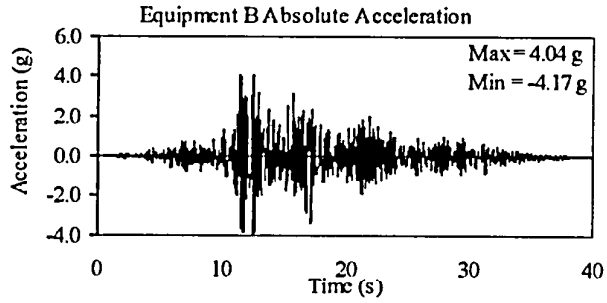

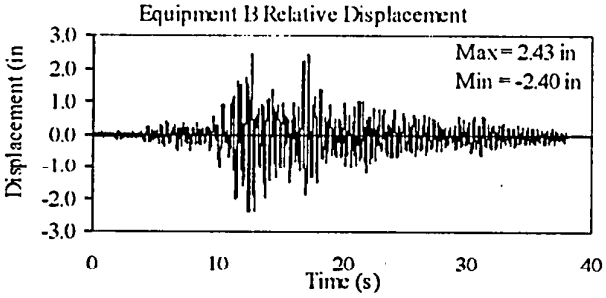

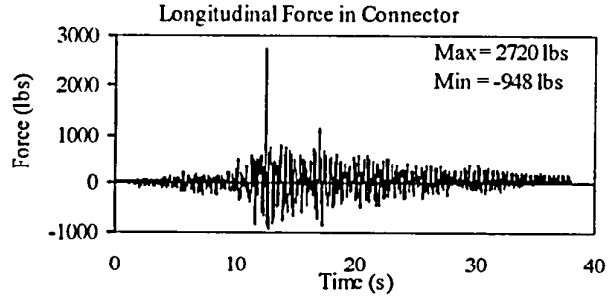

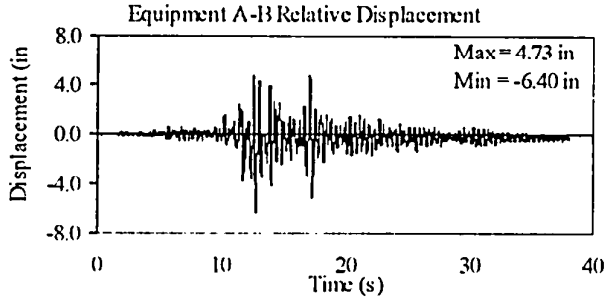

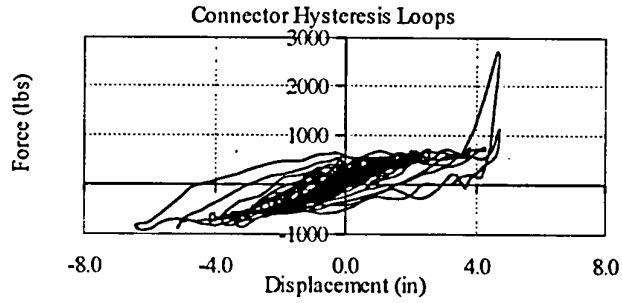

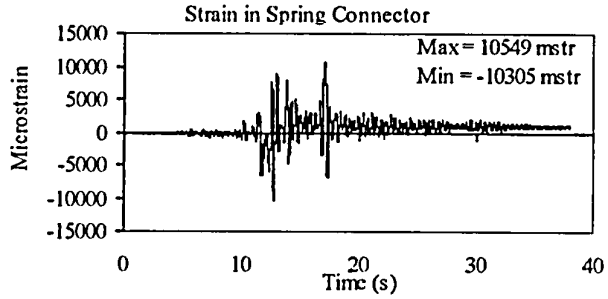

TEST RB-109
EQUIPMENT COMBINATION 2, BUS SLIDER
NEWHALL GROUND MOTION, 30% SPAN

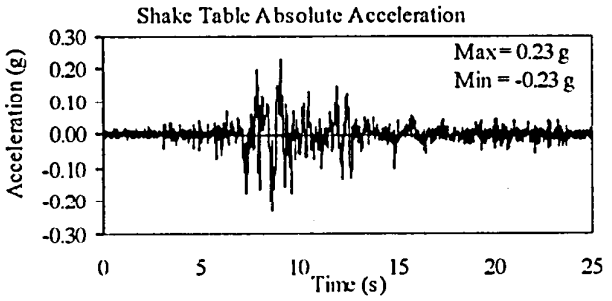

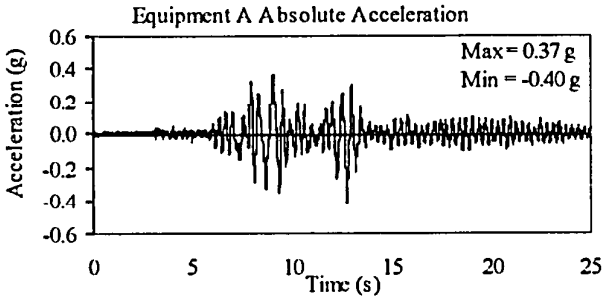

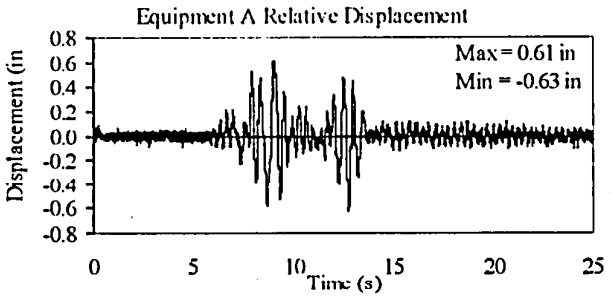

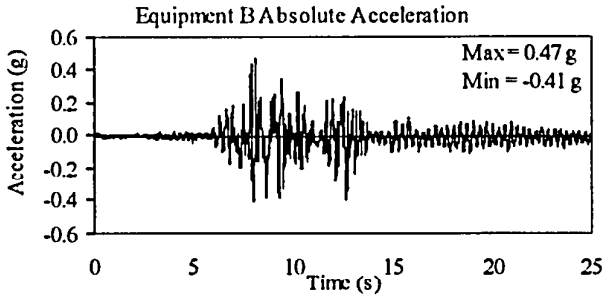

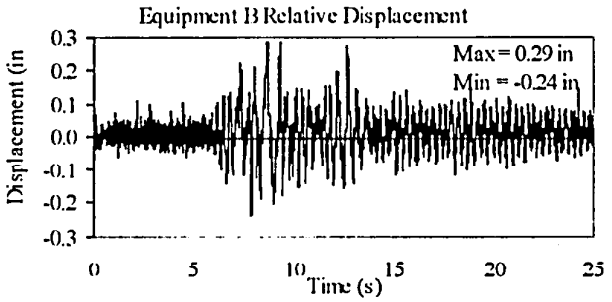

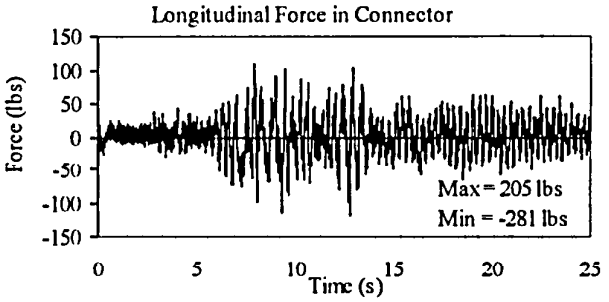

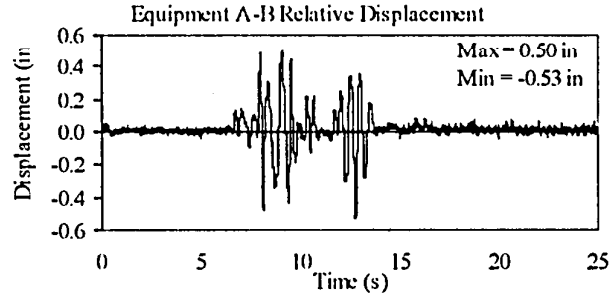

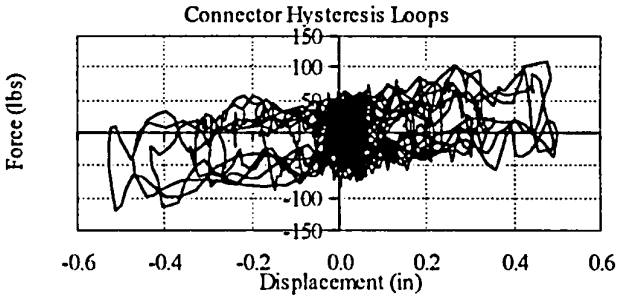

TEST RB-110
EQUIPMENT COMBINATION 2, BUS SLIDER
TABAS GROUND MOTION, 25% SPAN

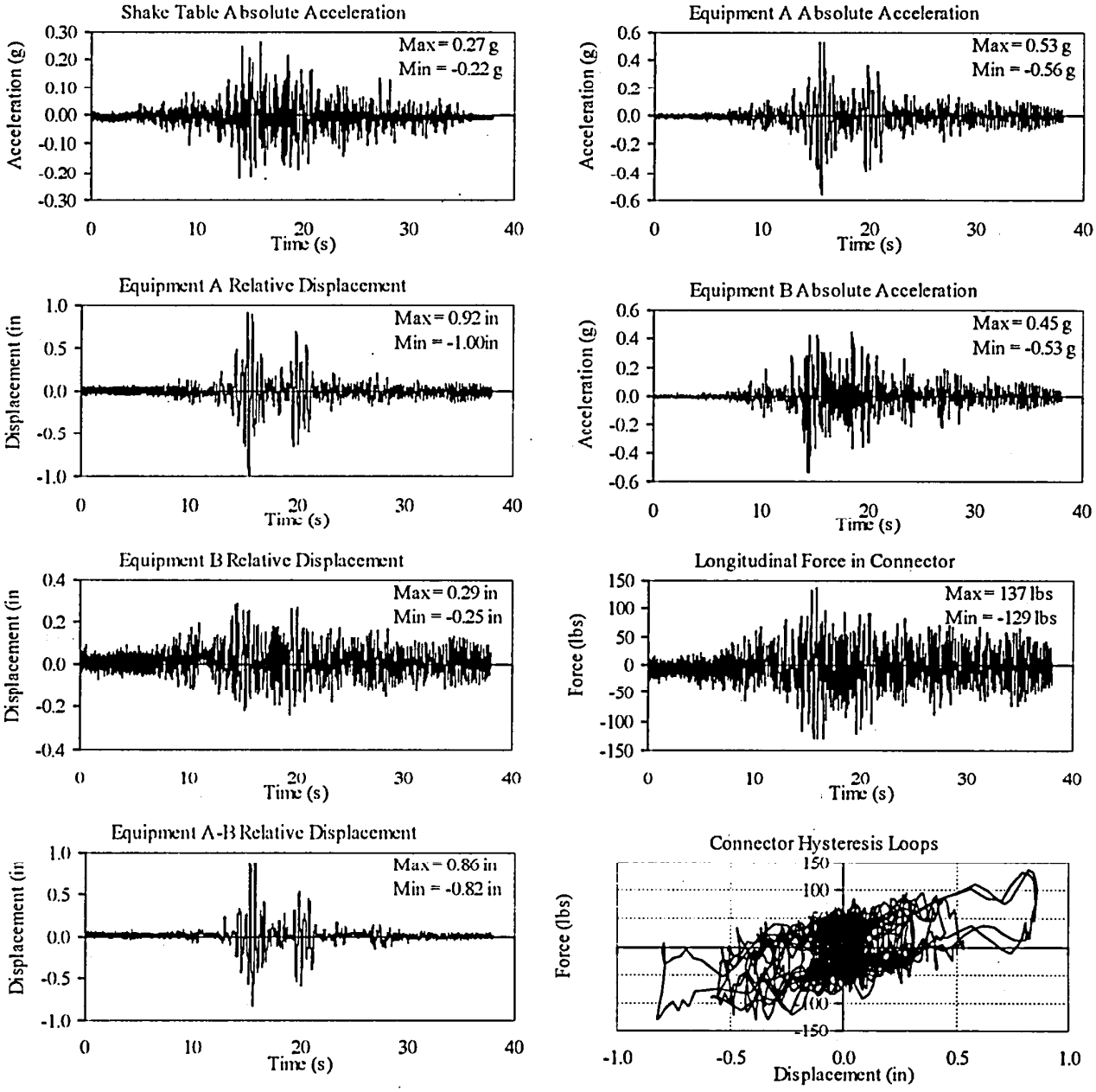

TEST RB-111
EQUIPMENT COMBINATION 2, BUS SLIDER
TABAS GROUND MOTION, 50% SPAN

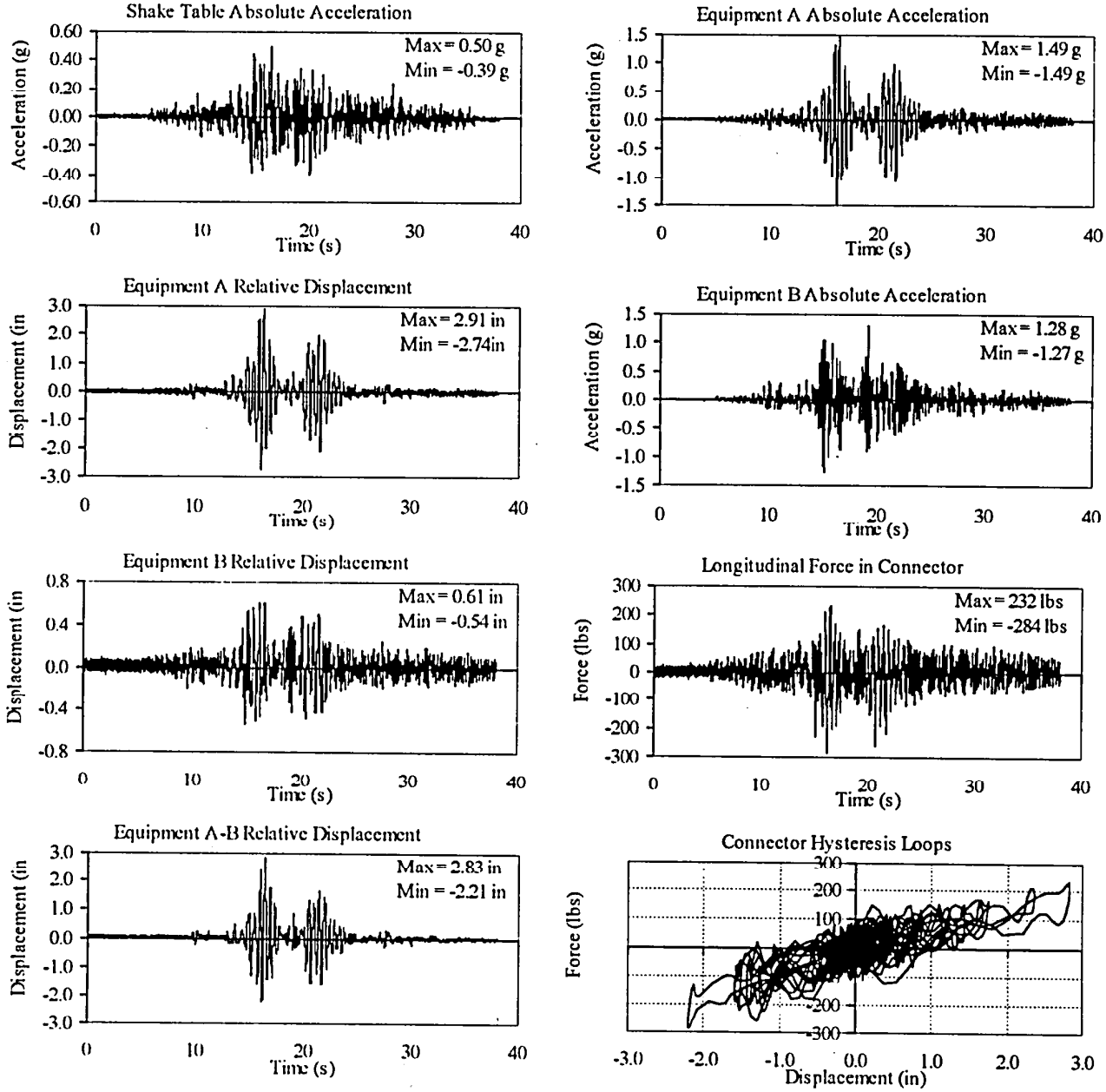

TEST RB-112
EQUIPMENT COMBINATION 2, BUS SLIDER
NEWHALL GROUND MOTION, 100% SPAN

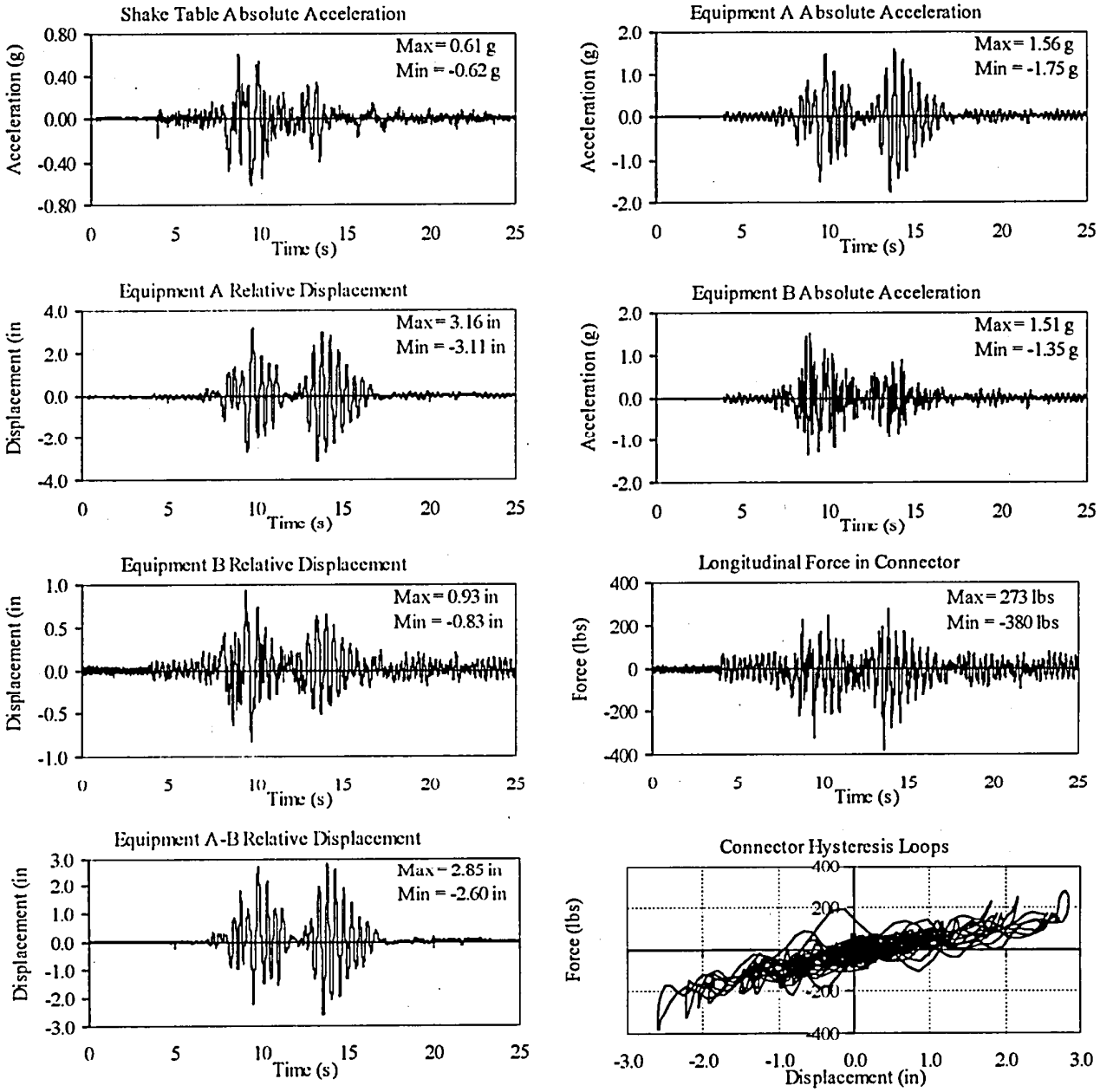

TEST RB-118
EQUIPMENT COMBINATION 2, BPA ISOLATOR
NEWHALL GROUND MOTION, 30% SPAN

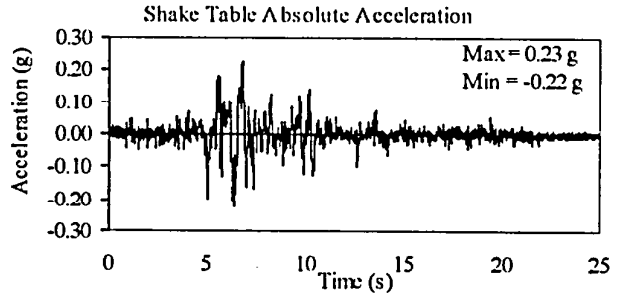

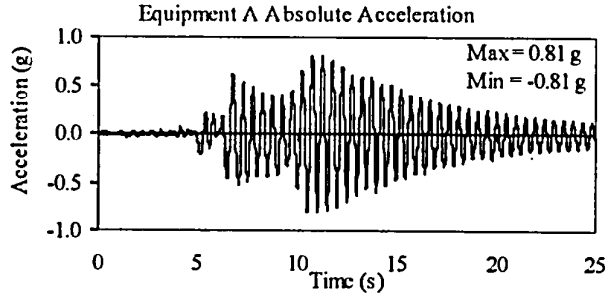

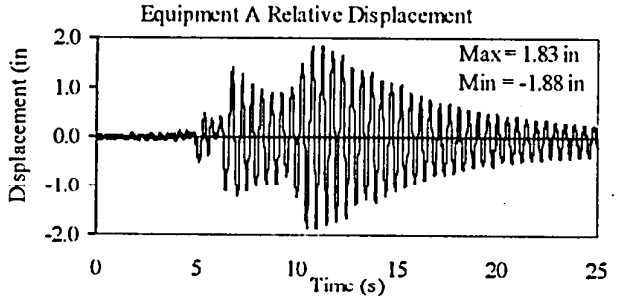

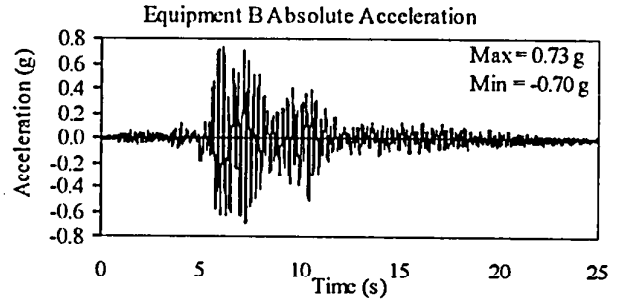

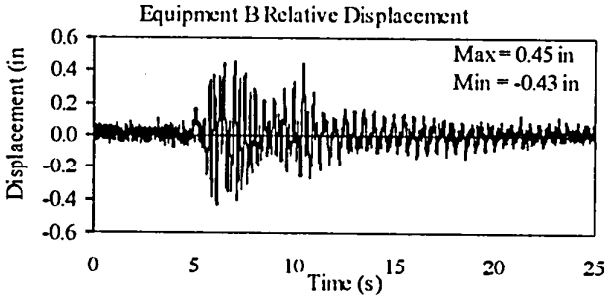

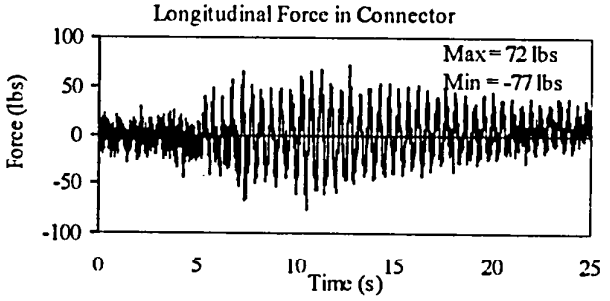

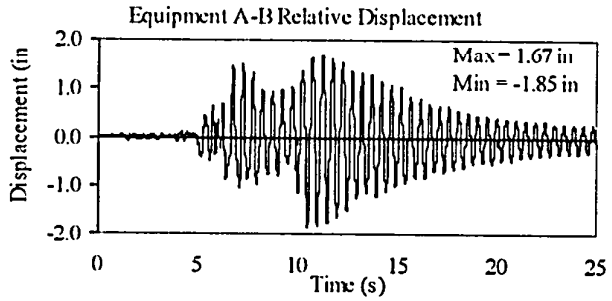

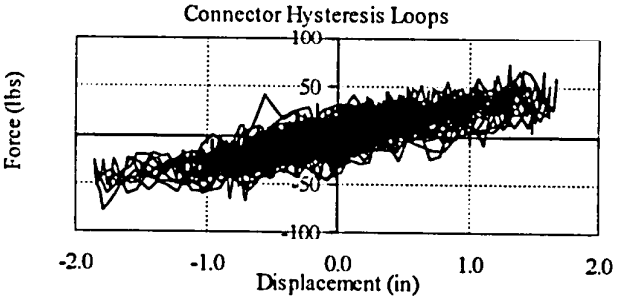

TEST RB-119
EQUIPMENT COMBINATION 2, BPA ISOLATOR
TABAS GROUND MOTION, 25% SPAN

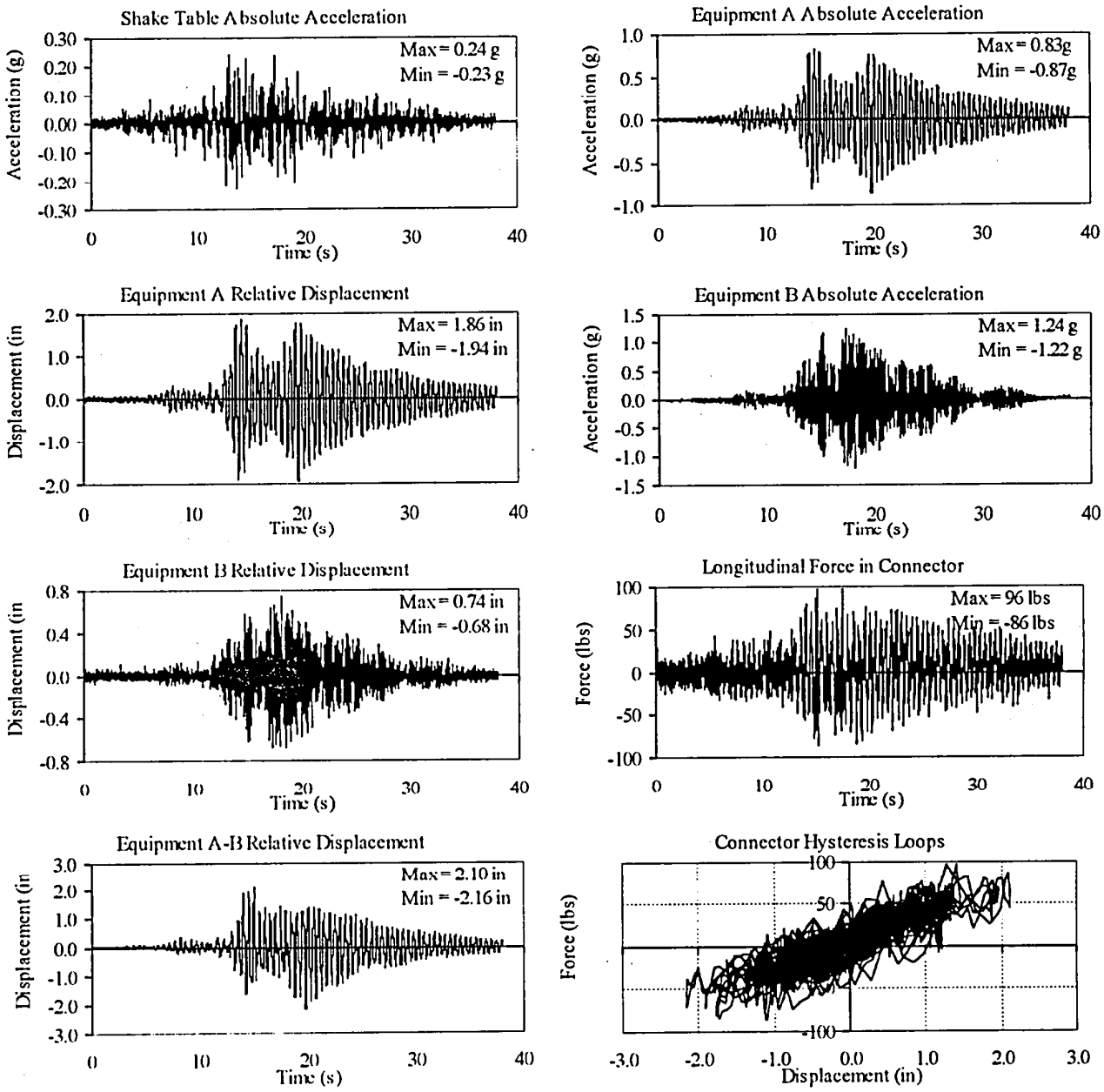

TEST RB-120
EQUIPMENT COMBINATION 2, BPA ISOLATOR
TABAS GROUND MOTION, 50% SPAN

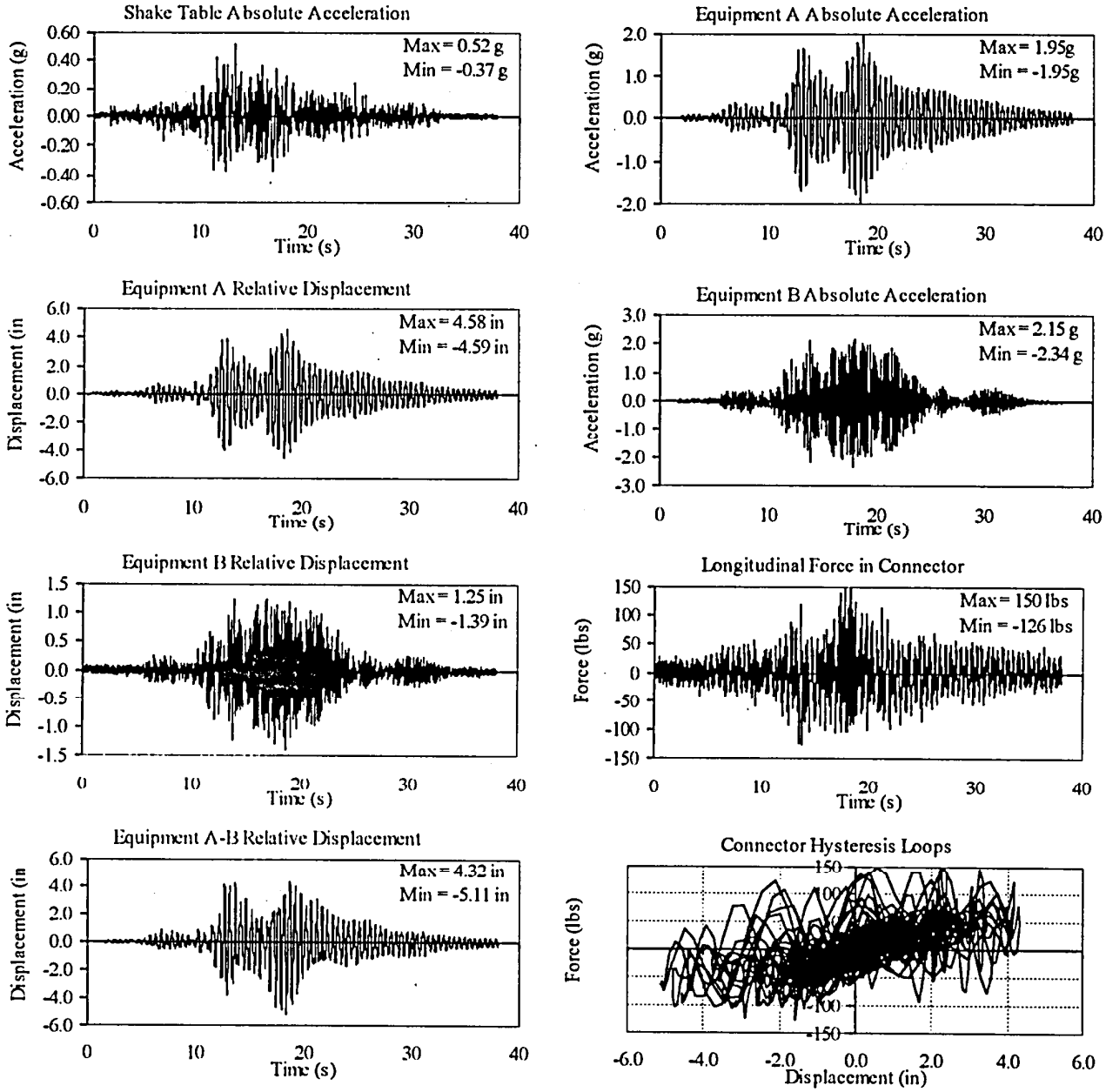

TEST RB-121
EQUIPMENT COMBINATION 2, BPA ISOLATOR
NEWHALL GROUND MOTION, 100% SPAN

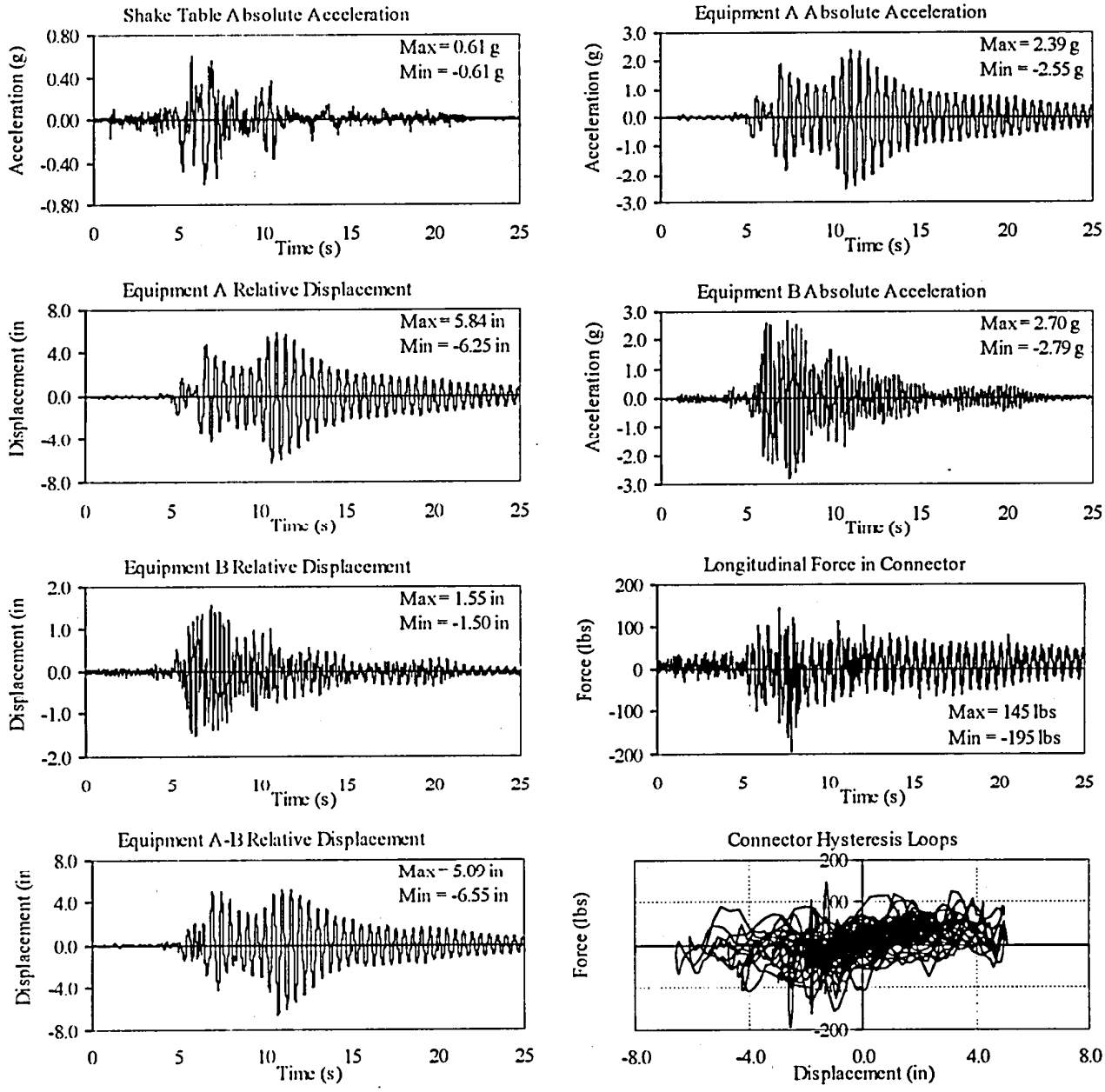

TEST RB-122
EQUIPMENT COMBINATION 2, BPA ISOLATOR
TABAS GROUND MOTION, 75% SPAN

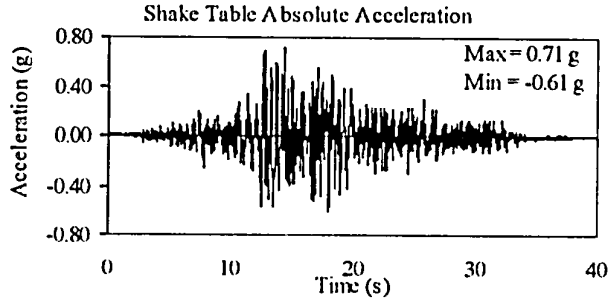

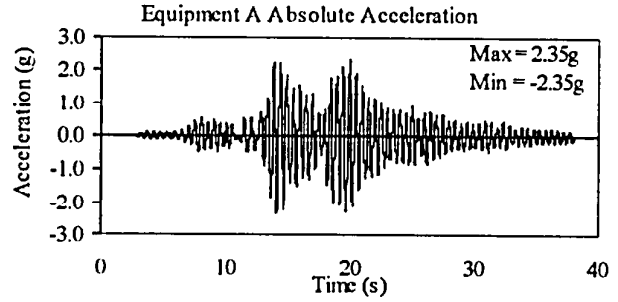

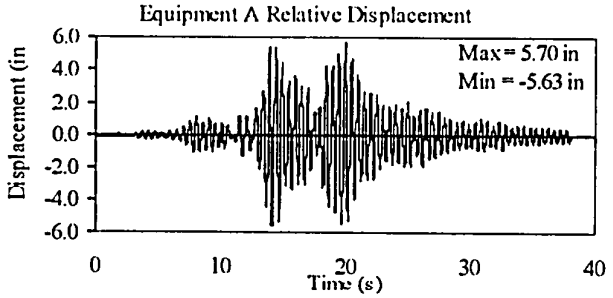

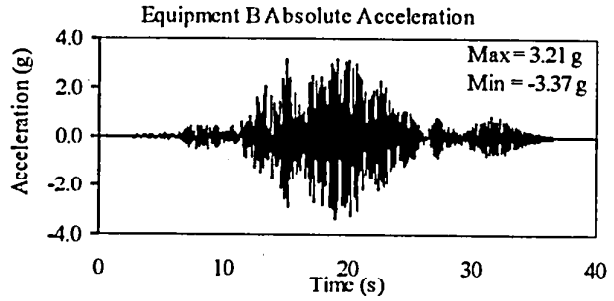

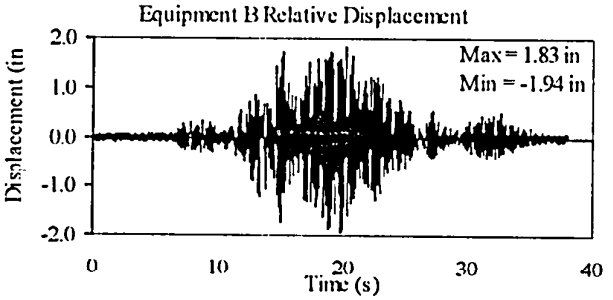

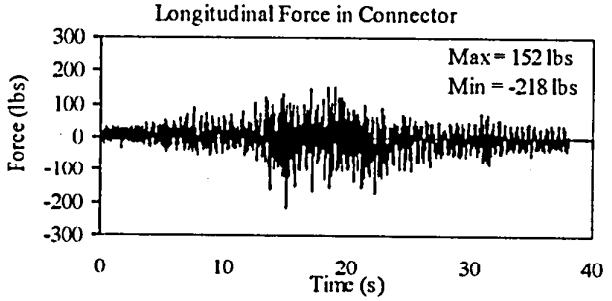

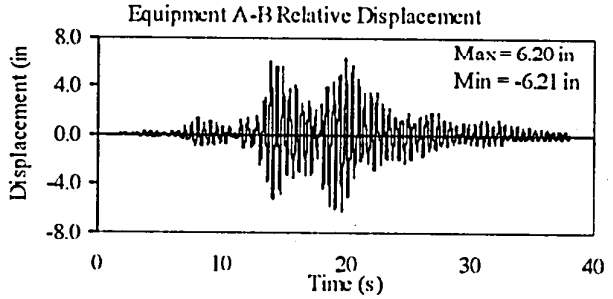

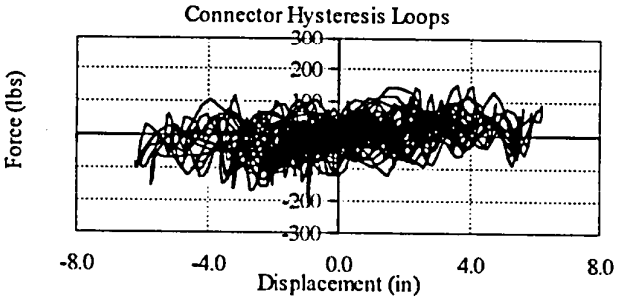

TEST RB-123
EQUIPMENT COMBINATION 2, BPA ISOLATOR
TABAS GROUND MOTION, 100% SPAN

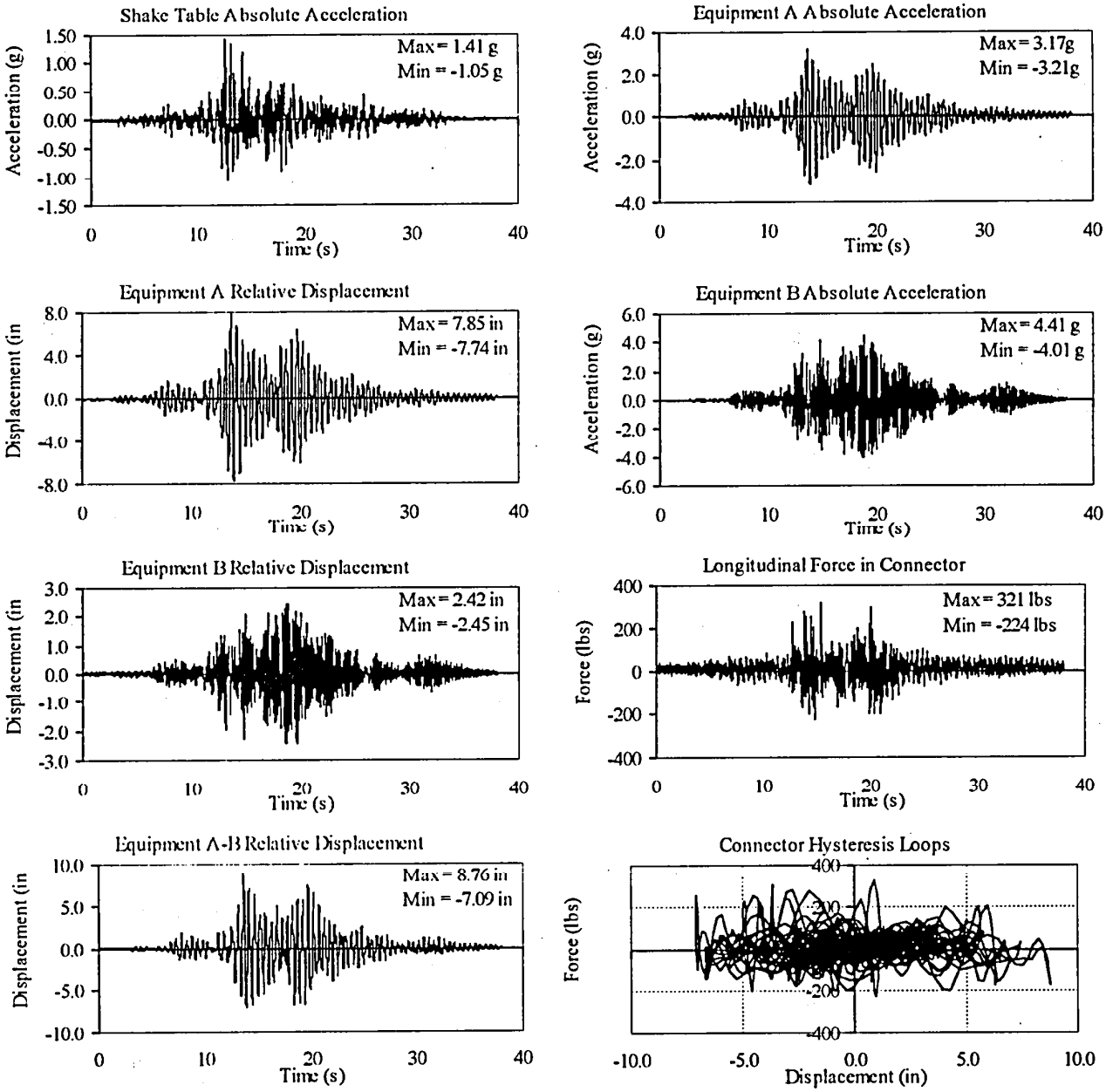

TEST RB-124
EQUIPMENT COMBINATION 2, INDIVIDUAL EQUIPMENT
NEWHALL GROUND MOTION, 30% SPAN

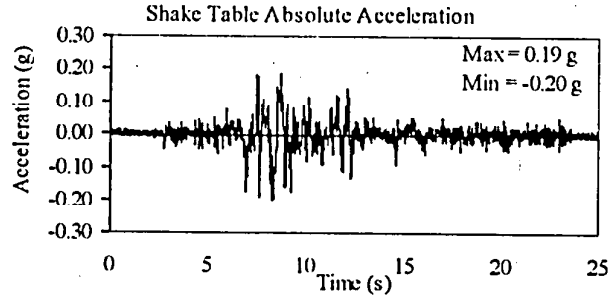

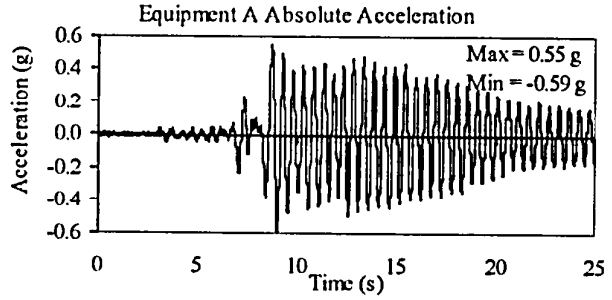

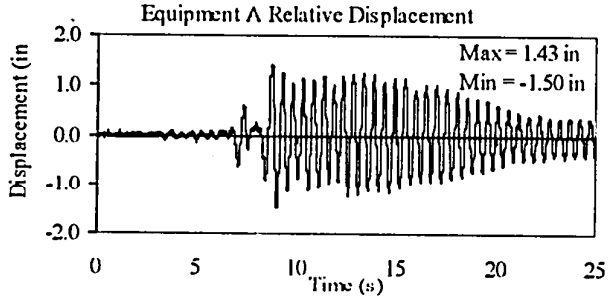

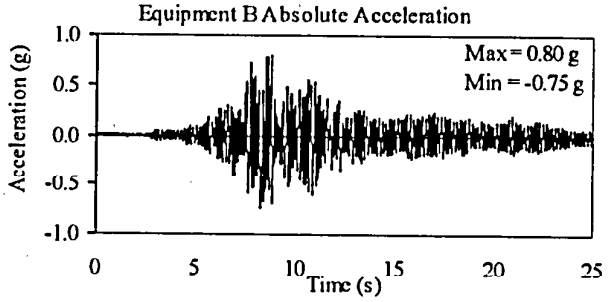

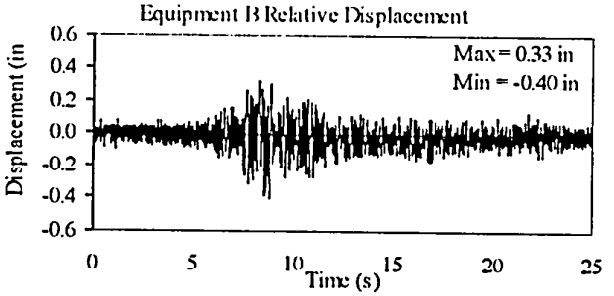

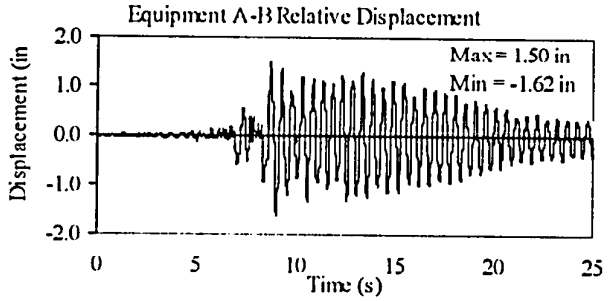

TEST RB-125
EQUIPMENT COMBINATION 2, INDIVIDUAL EQUIPMENT
TABAS GROUND MOTION, 25% SPAN

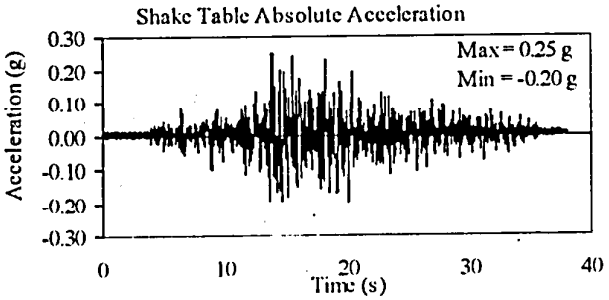

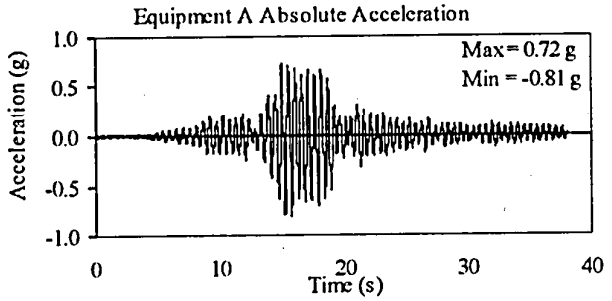

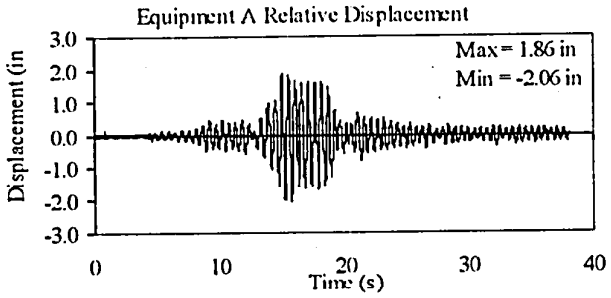

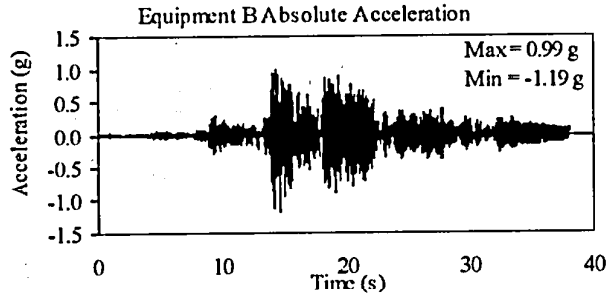

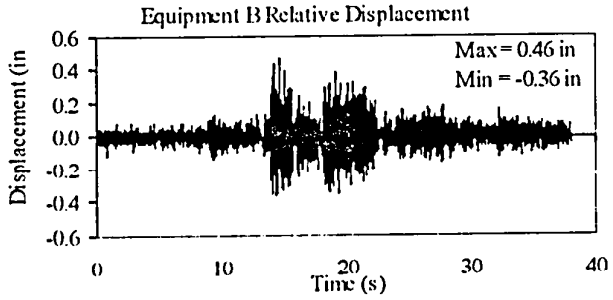

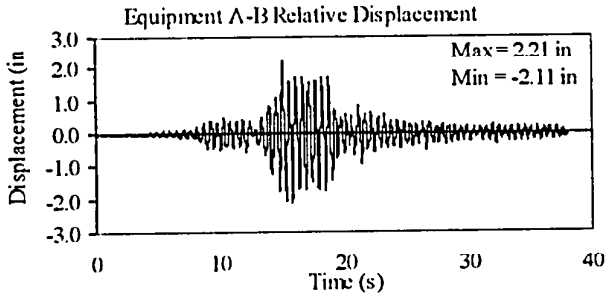

TEST RB-126
EQUIPMENT COMBINATION 2, INDIVIDUAL EQUIPMENT
TABAS GROUND MOTION, 50% SPAN

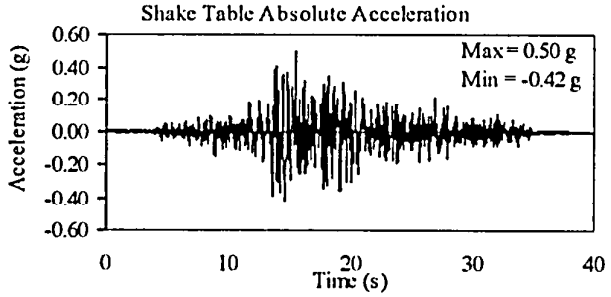

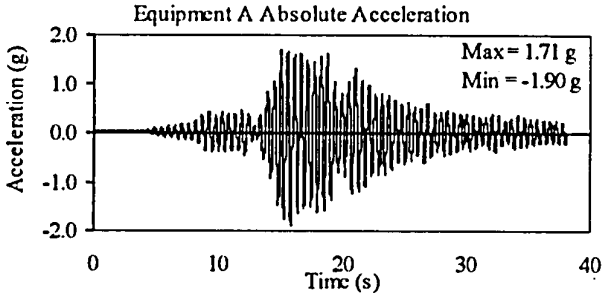

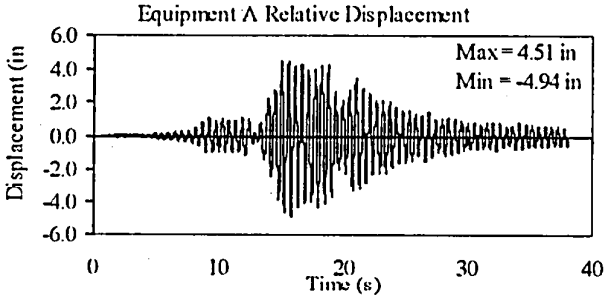

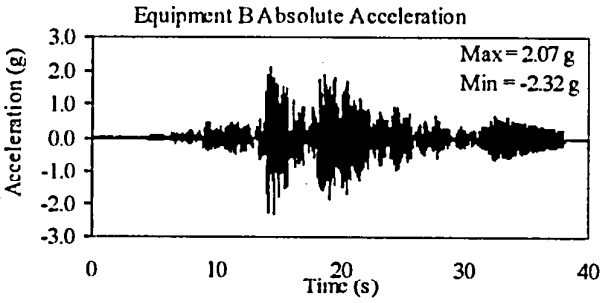

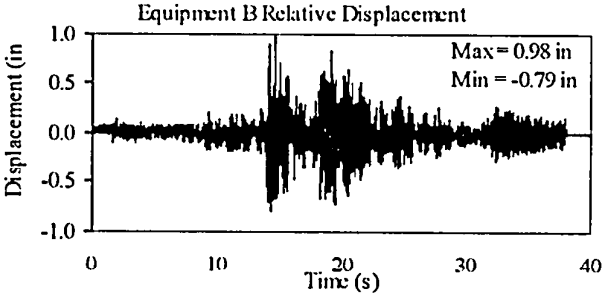

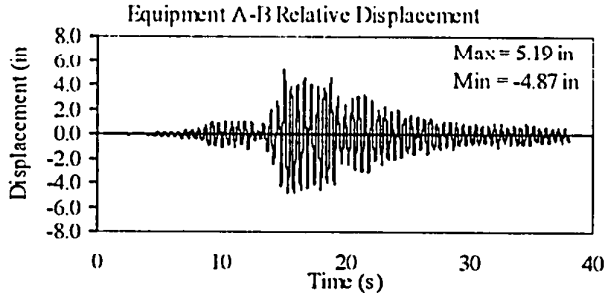

TEST RB-127
EQUIPMENT COMBINATION 2, INDIVIDUAL EQUIPMENT
NEWHALL GROUND MOTION, 100% SPAN

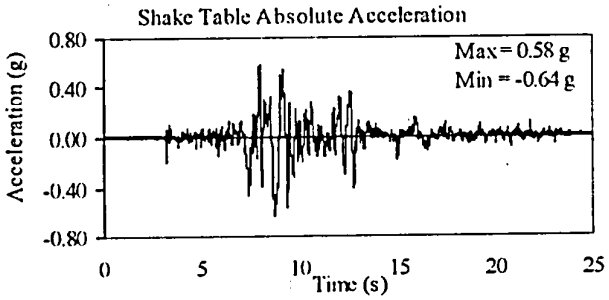

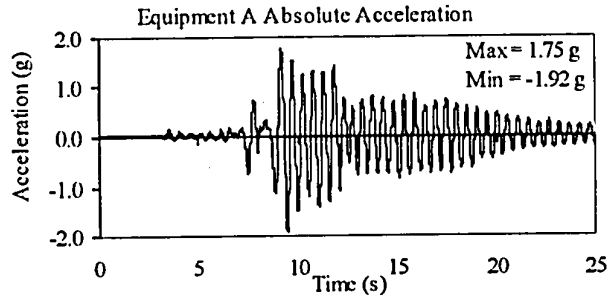

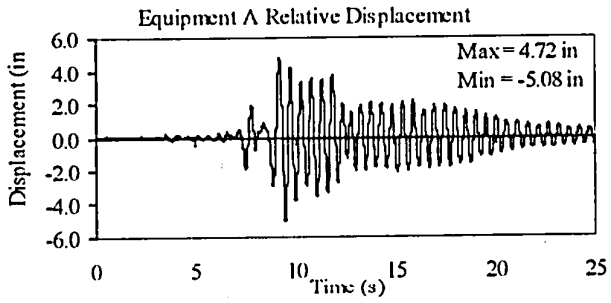

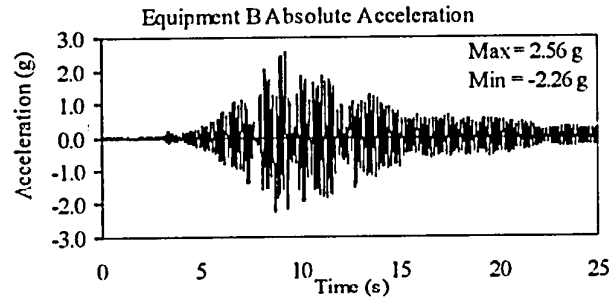

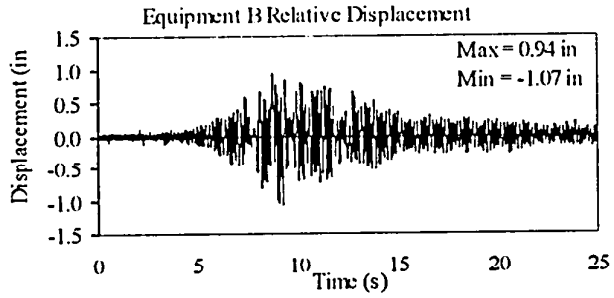

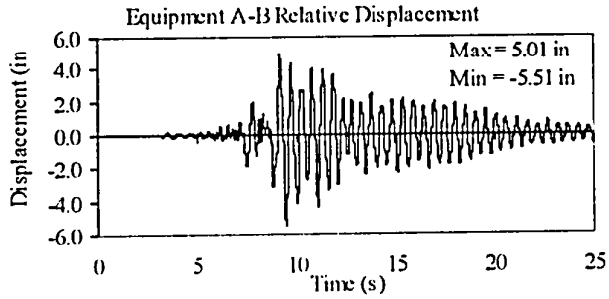

TEST RB-136
EQUIPMENT COMBINATION 5, SPRING 30-2022
NEWHALL GROUND MOTION, 30% SPAN

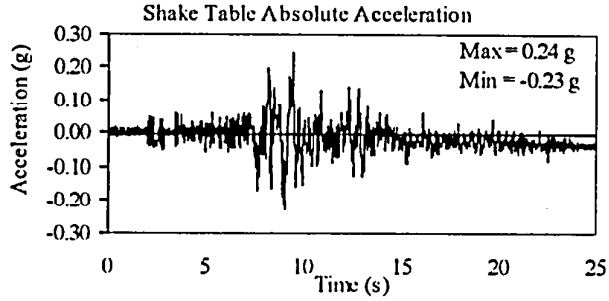

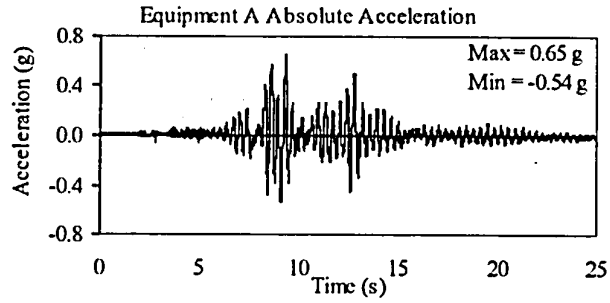

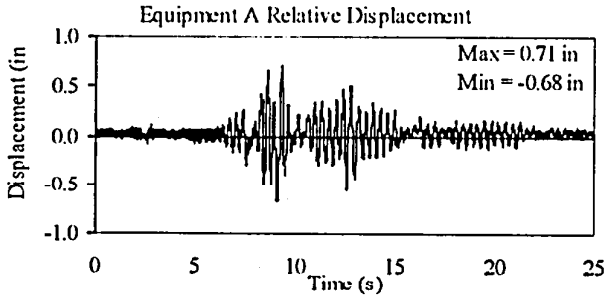

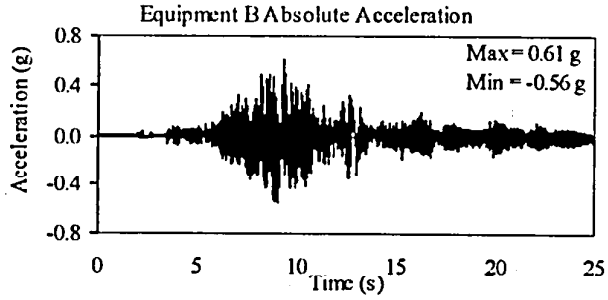

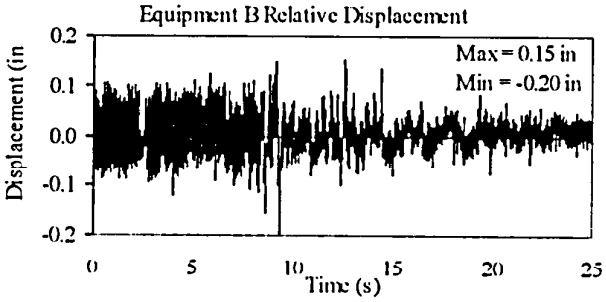

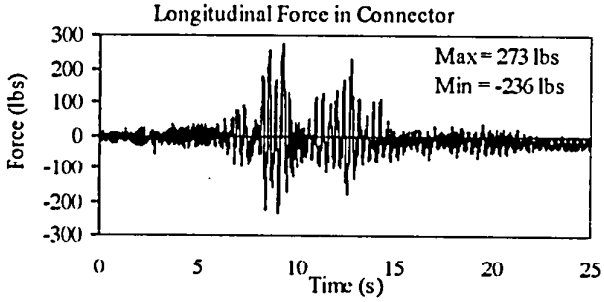

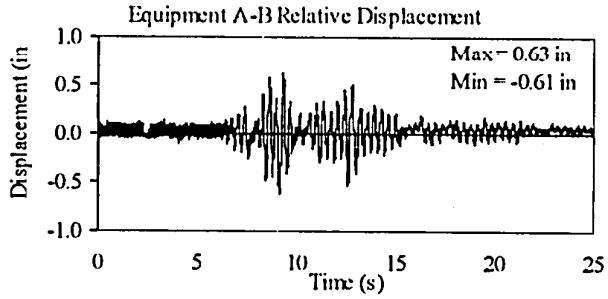

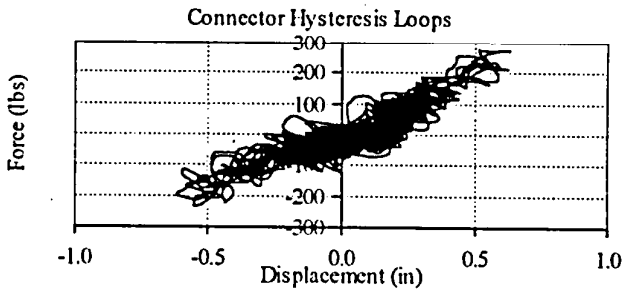

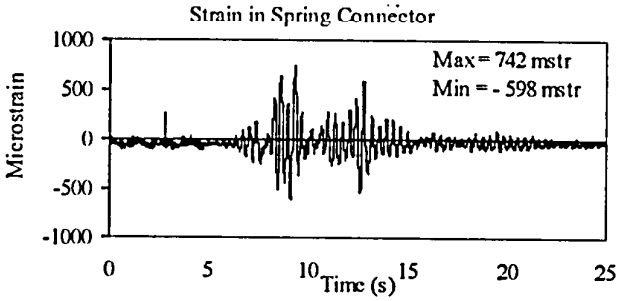

TEST RB-137
EQUIPMENT COMBINATION 5, SPRING 30-2022
TABAS GROUND MOTION, 25% SPAN

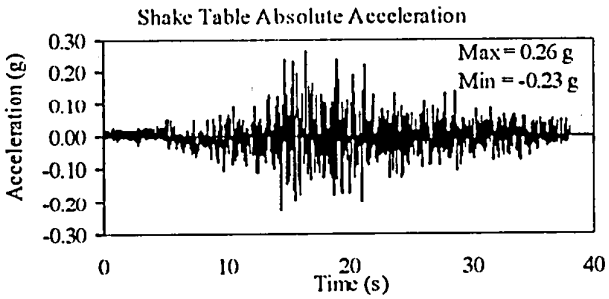

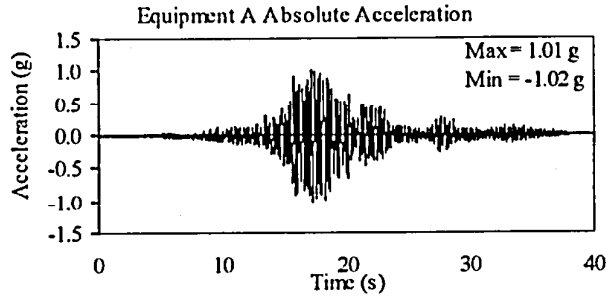

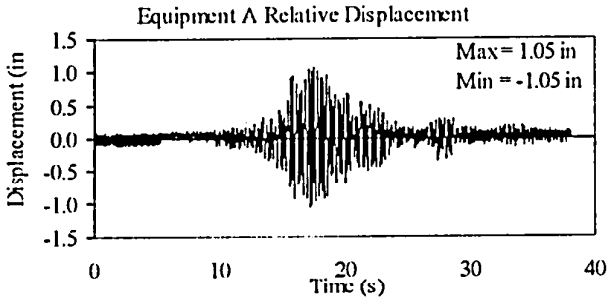

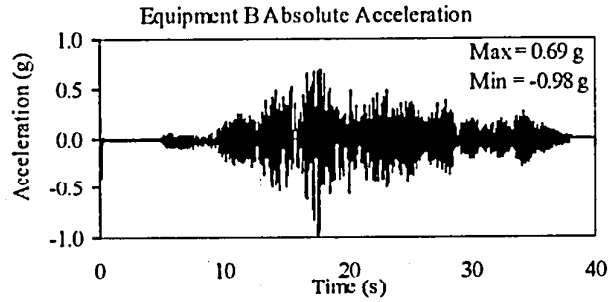

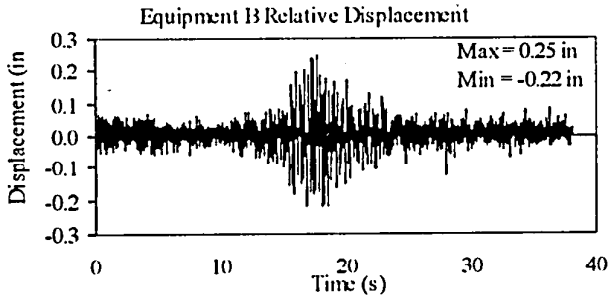

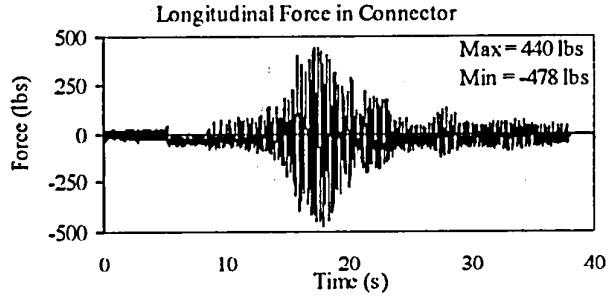

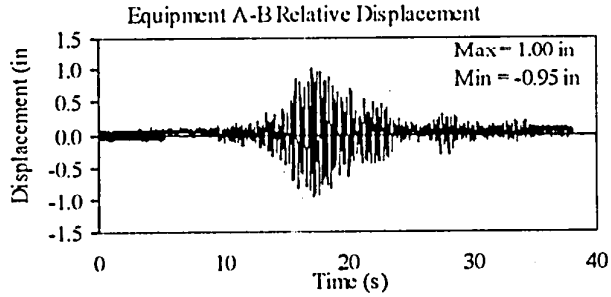

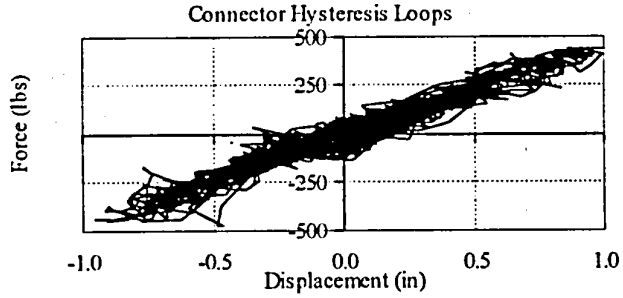

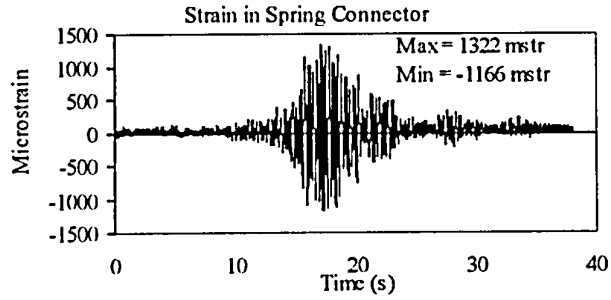

TEST RB-138
EQUIPMENT COMBINATION 5, SPRING 30-2022
TABAS GROUND MOTION, 50% SPAN

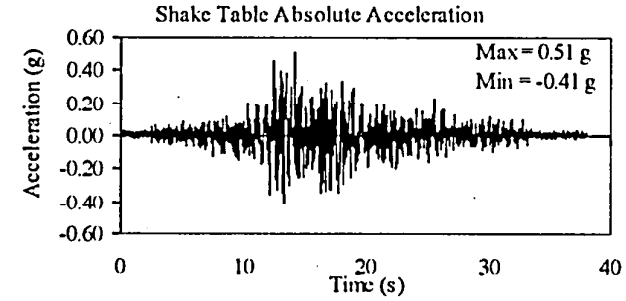

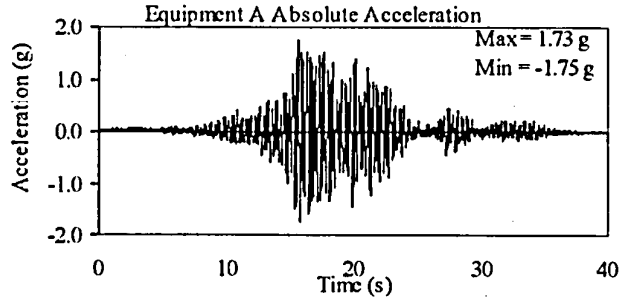

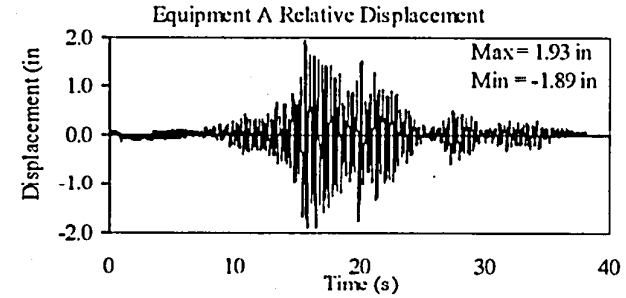

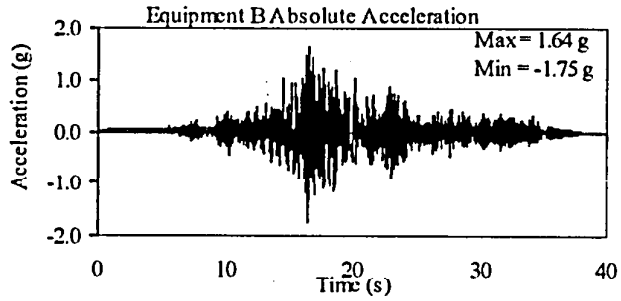

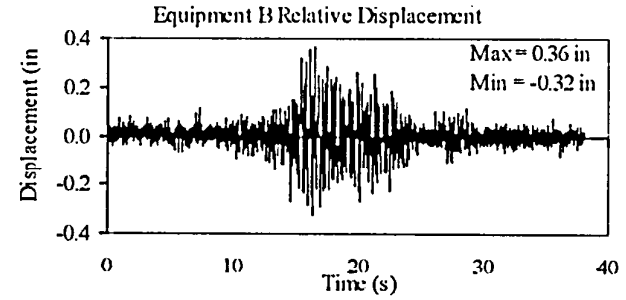

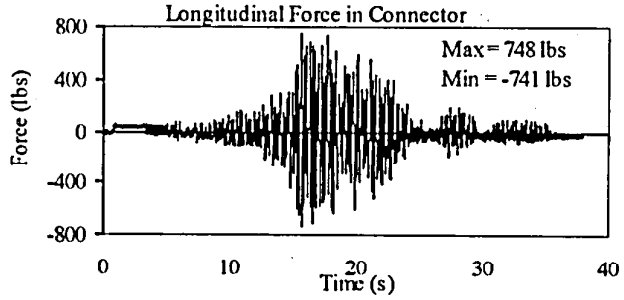

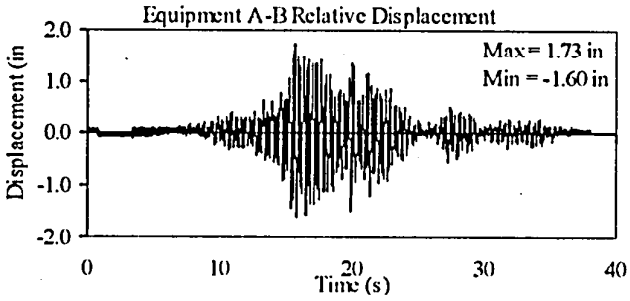

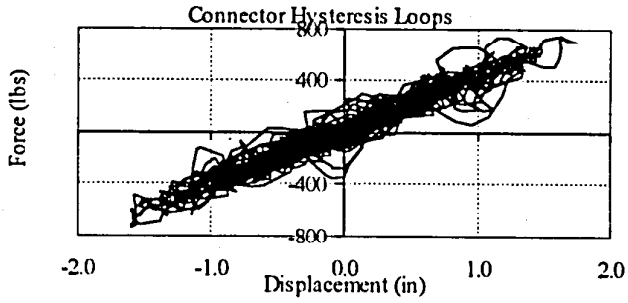

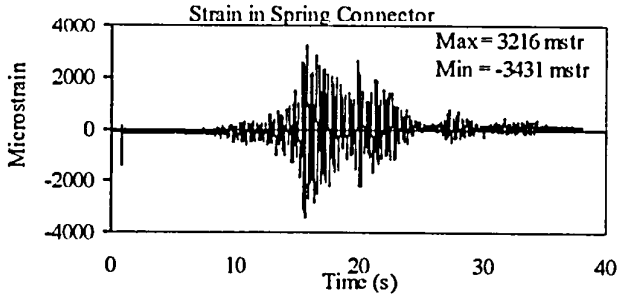

TEST RB-139
EQUIPMENT COMBINATION 5, SPRING 30-2022
NEWHALL GROUND MOTION, 100% SPAN

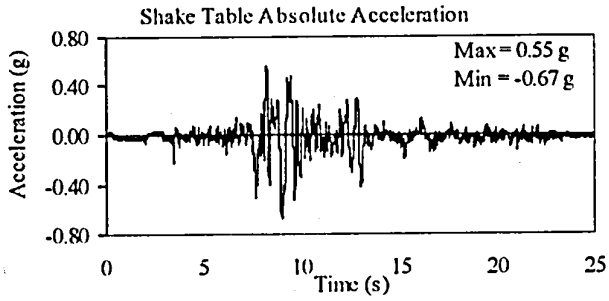

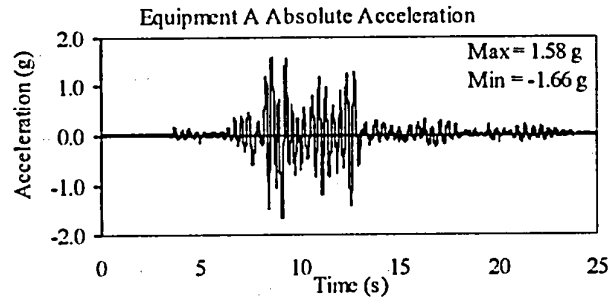

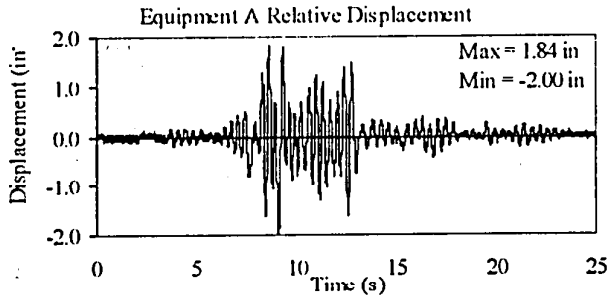

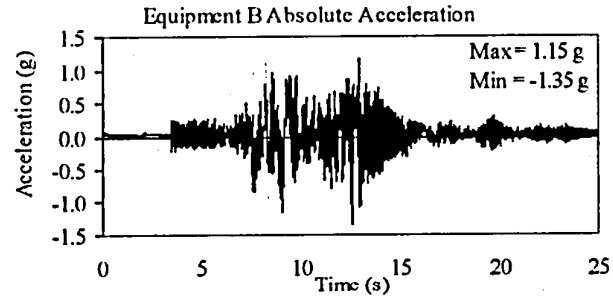

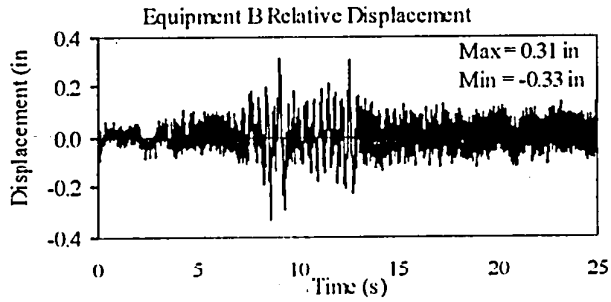

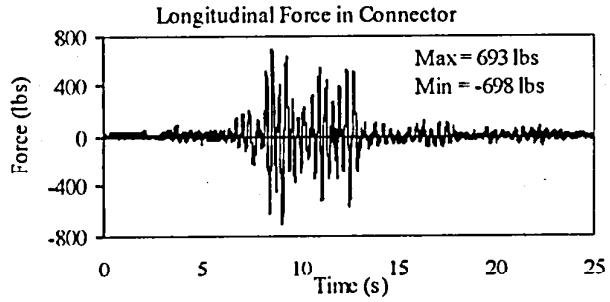

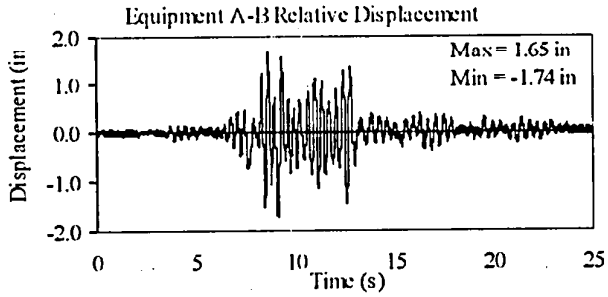

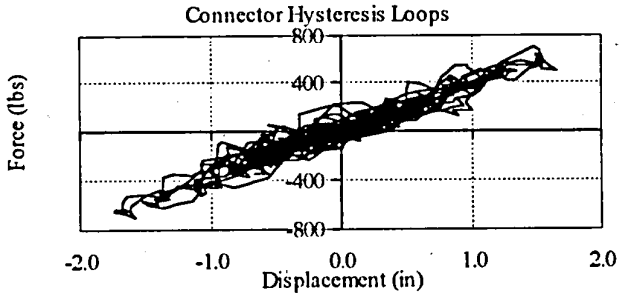

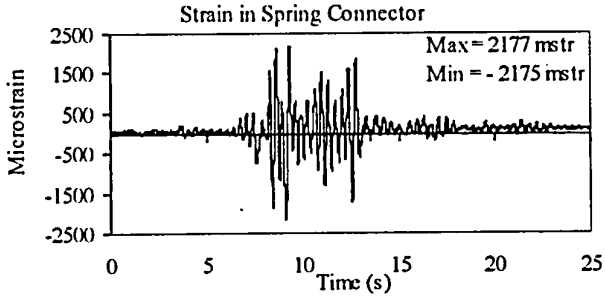

TEST RB-140
EQUIPMENT COMBINATION 5, SPRING 30-2022
TABAS GROUND MOTION, 100% SPAN

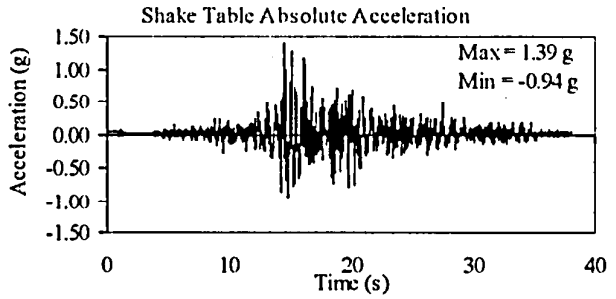

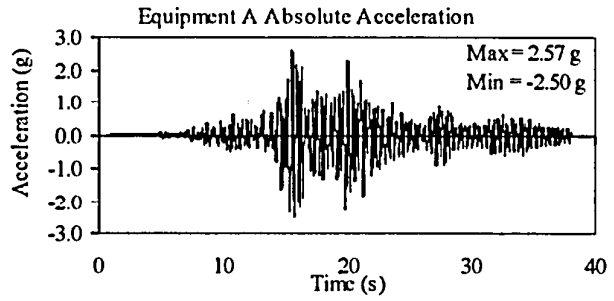

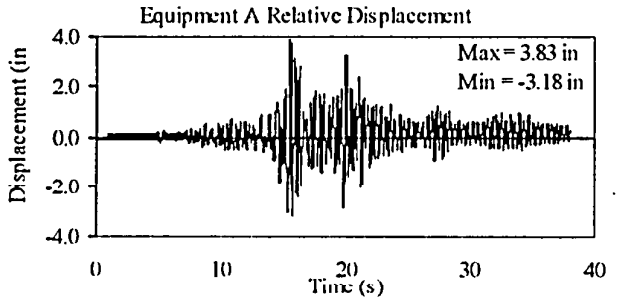

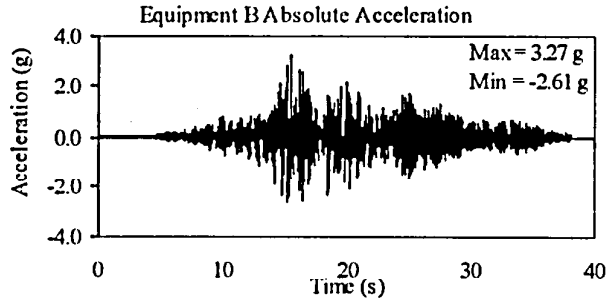

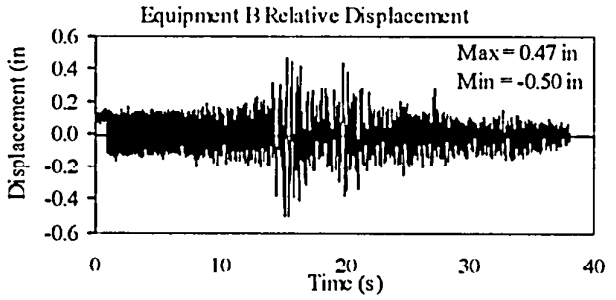

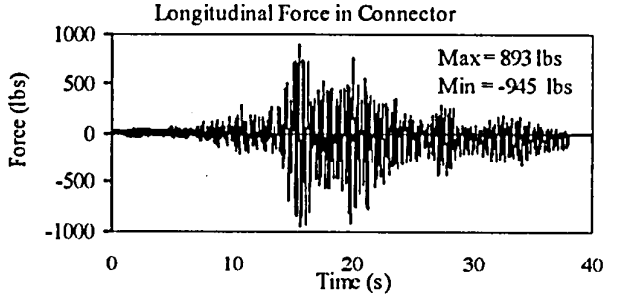

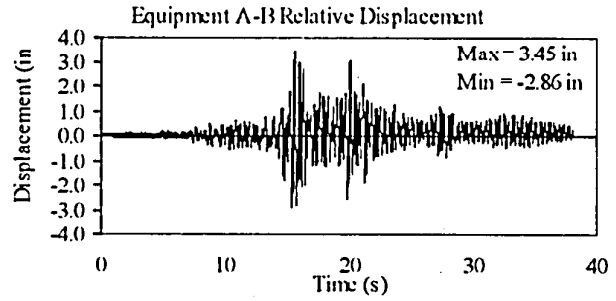

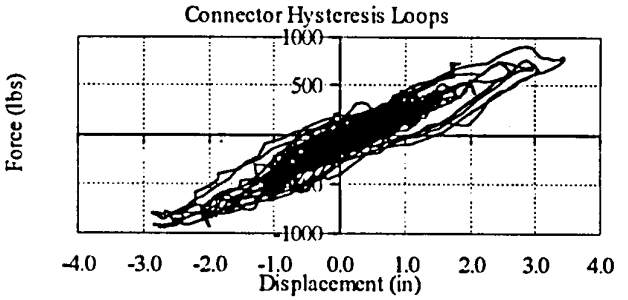

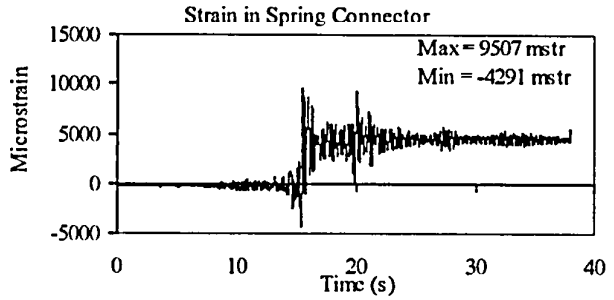

TEST RB-141
EQUIPMENT COMBINATION 5, SPRING 30-2022
TABAS GROUND MOTION, 150% SPAN

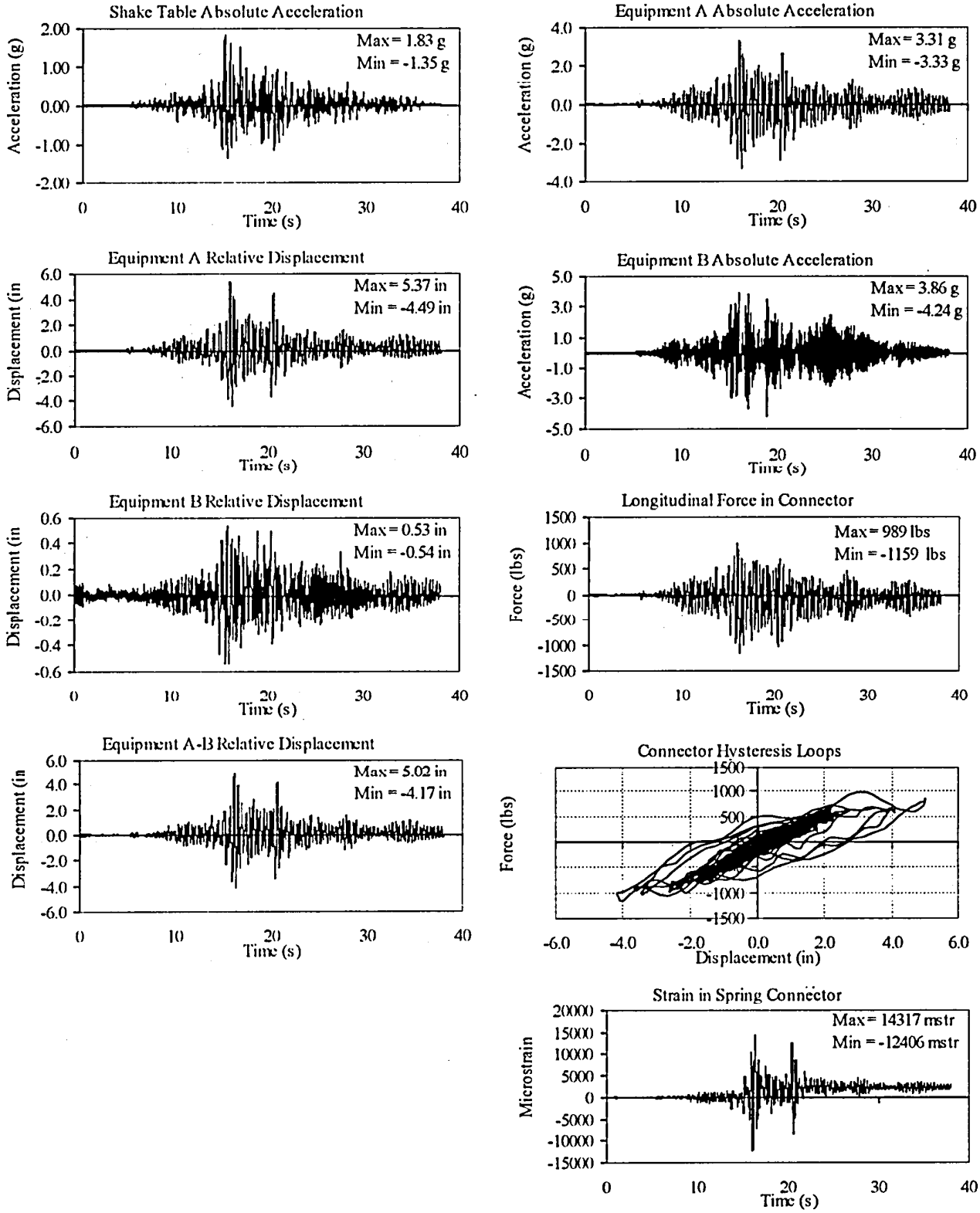

TEST RB-144
EQUIPMENT COMBINATION 5, BUS SLIDER
NEWHALL GROUND MOTION, 30% SPAN

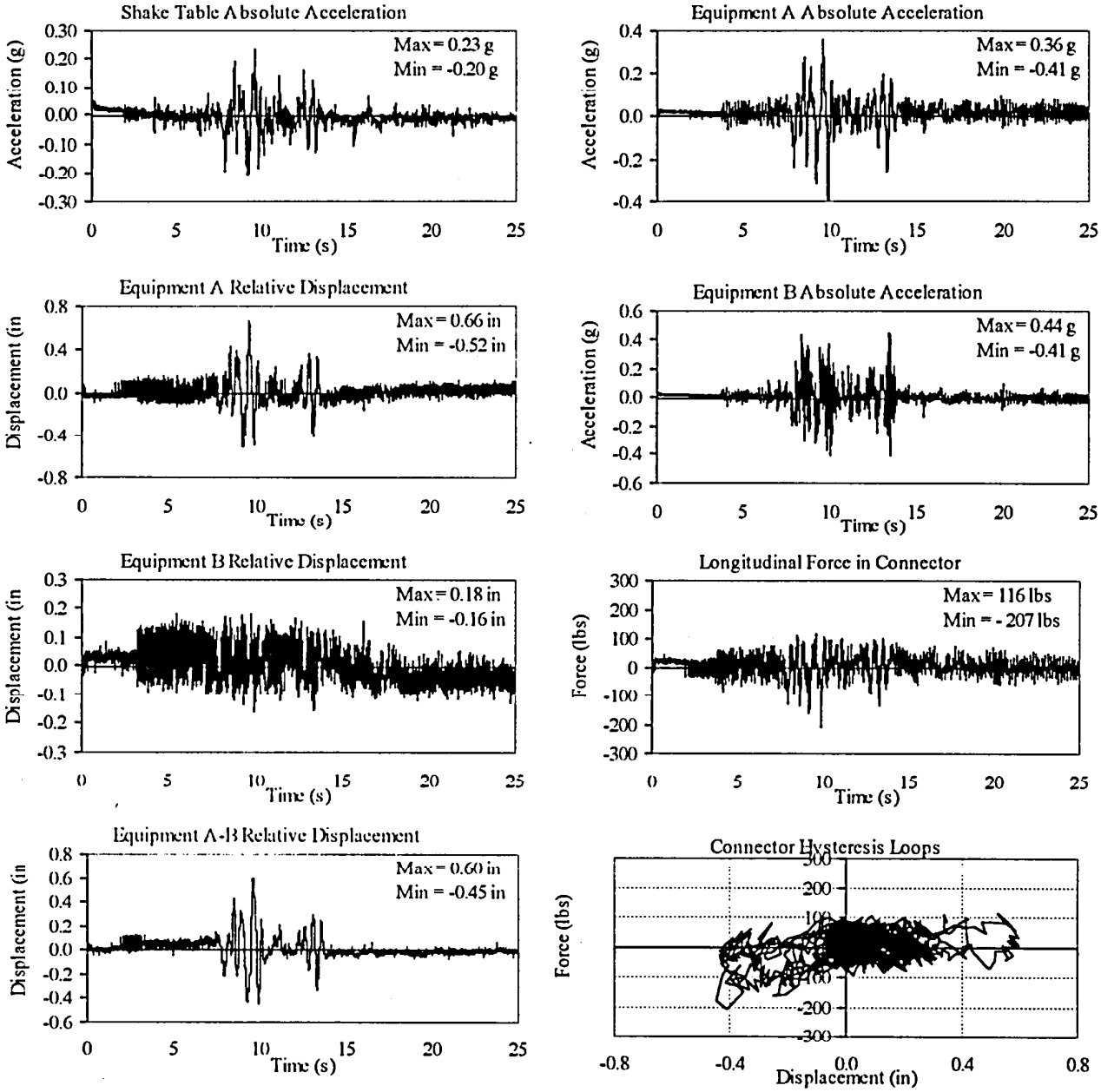

TEST RB-145
EQUIPMENT COMBINATION 5, BUS SLIDER
TABAS GROUND MOTION, 25% SPAN

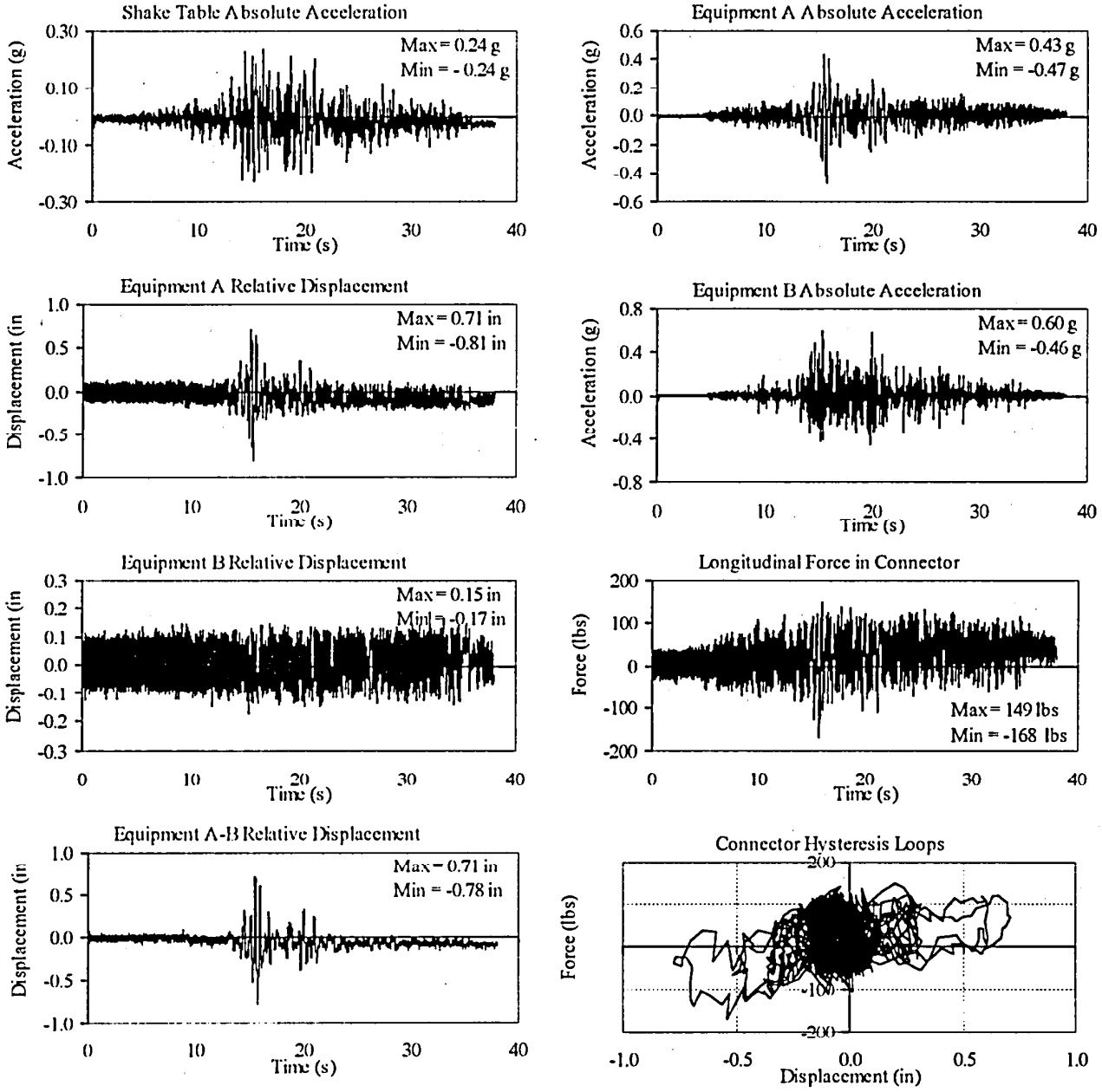

TEST RB-146
EQUIPMENT COMBINATION 5, BUS SLIDER
TABAS GROUND MOTION, 50% SPAN

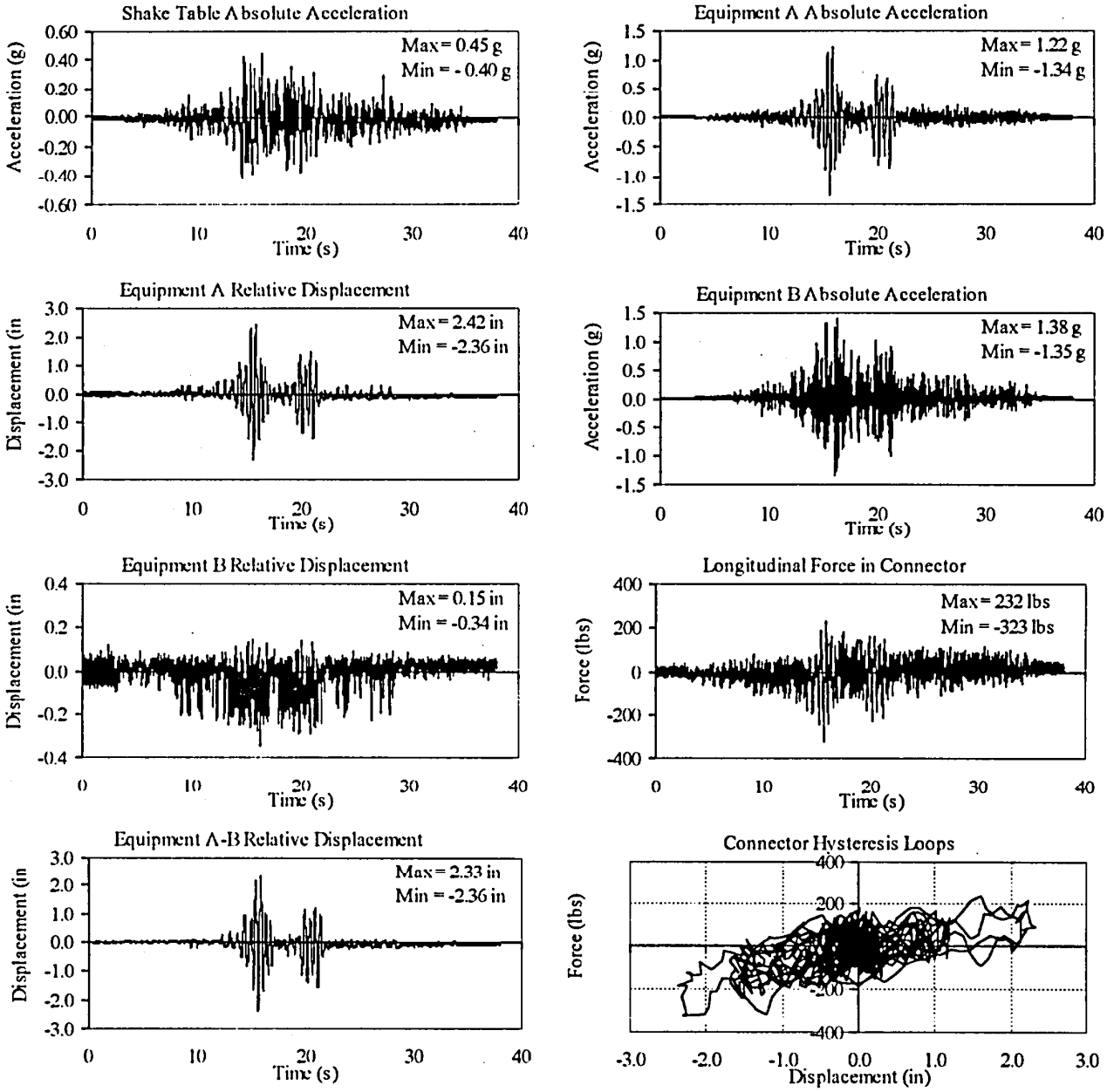

TEST RB-147
EQUIPMENT COMBINATION 5, BUS SLIDER
NEWHALL GROUND MOTION, 100% SPAN

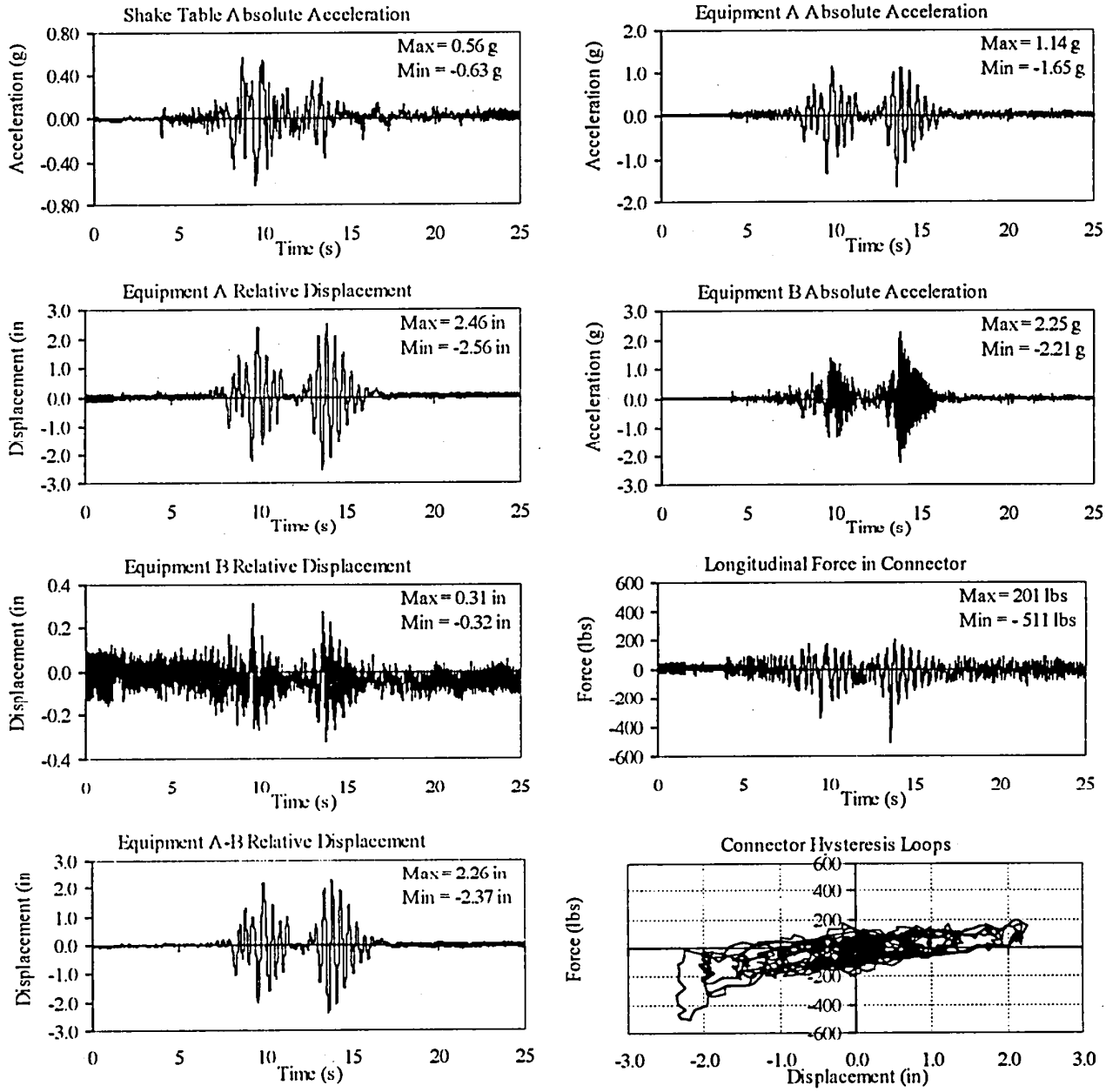

TEST RB-148
EQUIPMENT COMBINATION 5, BUS SLIDER
TABAS GROUND MOTION, 100% SPAN

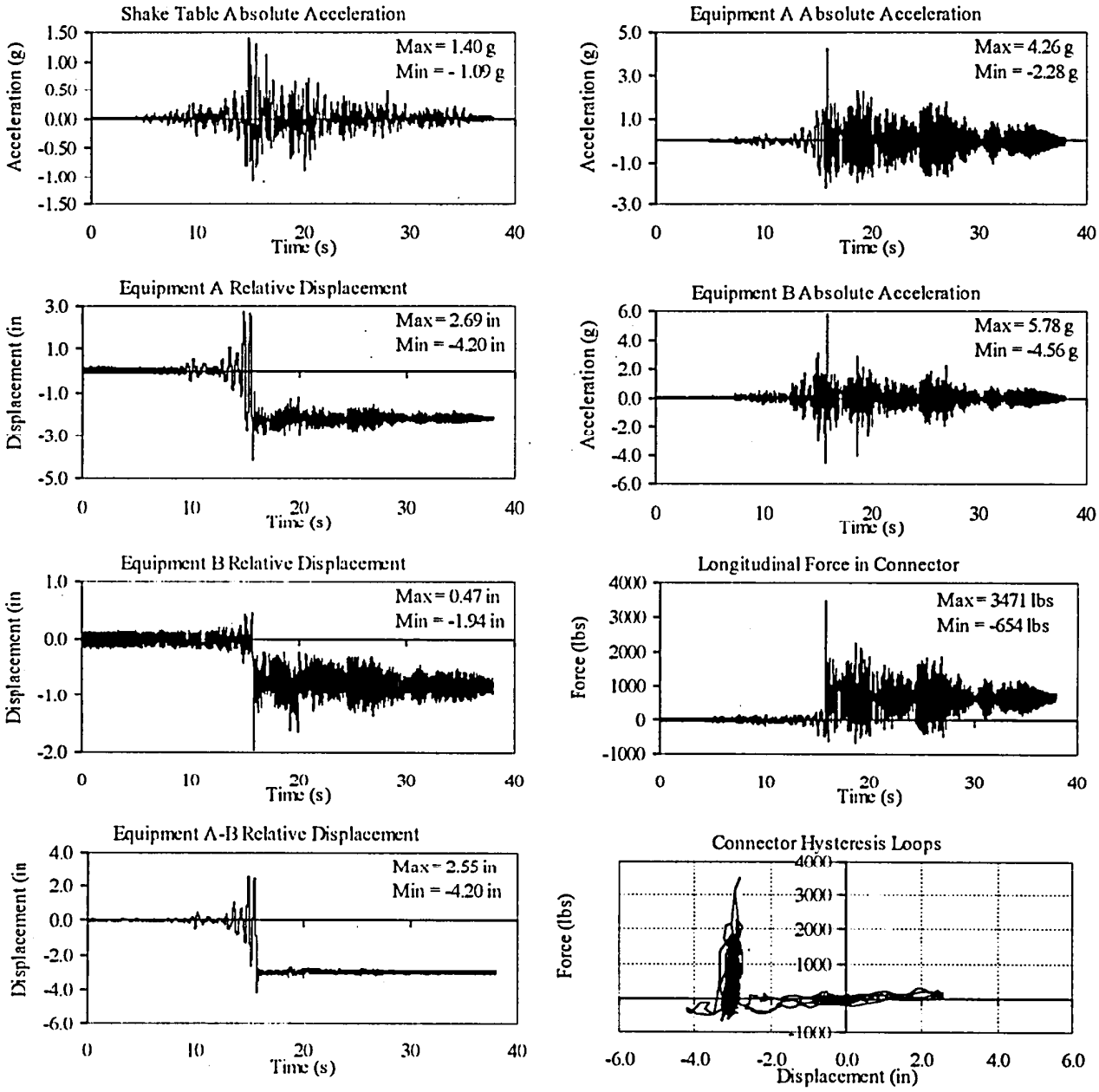

TEST RB-152
EQUIPMENT COMBINATION 5, BPA ISOLATOR
NEWHALL GROUND MOTION, 30% SPAN

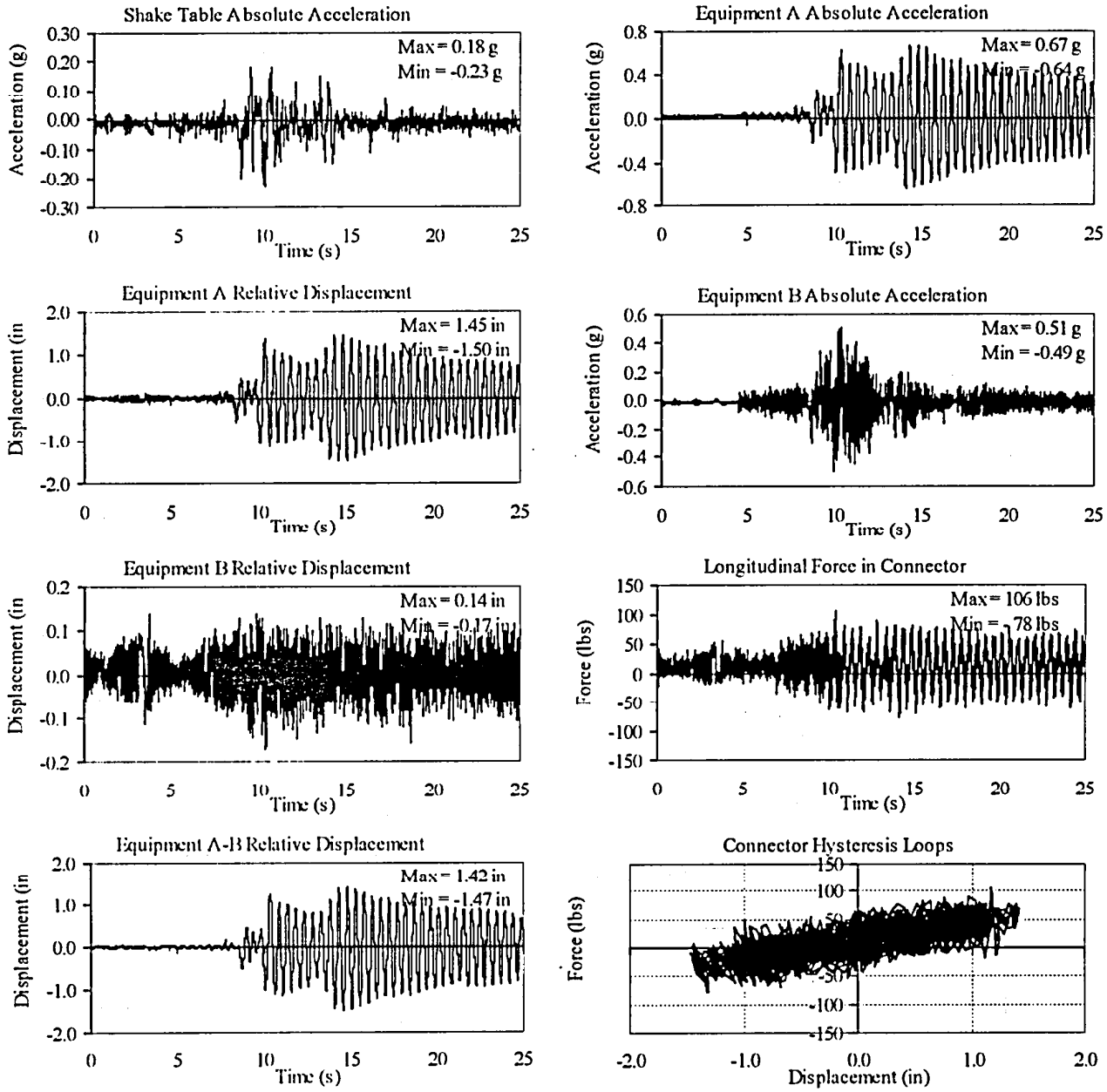

TEST RB-153
EQUIPMENT COMBINATION 5, BPA ISOLATOR
TABAS GROUND MOTION, 25% SPAN

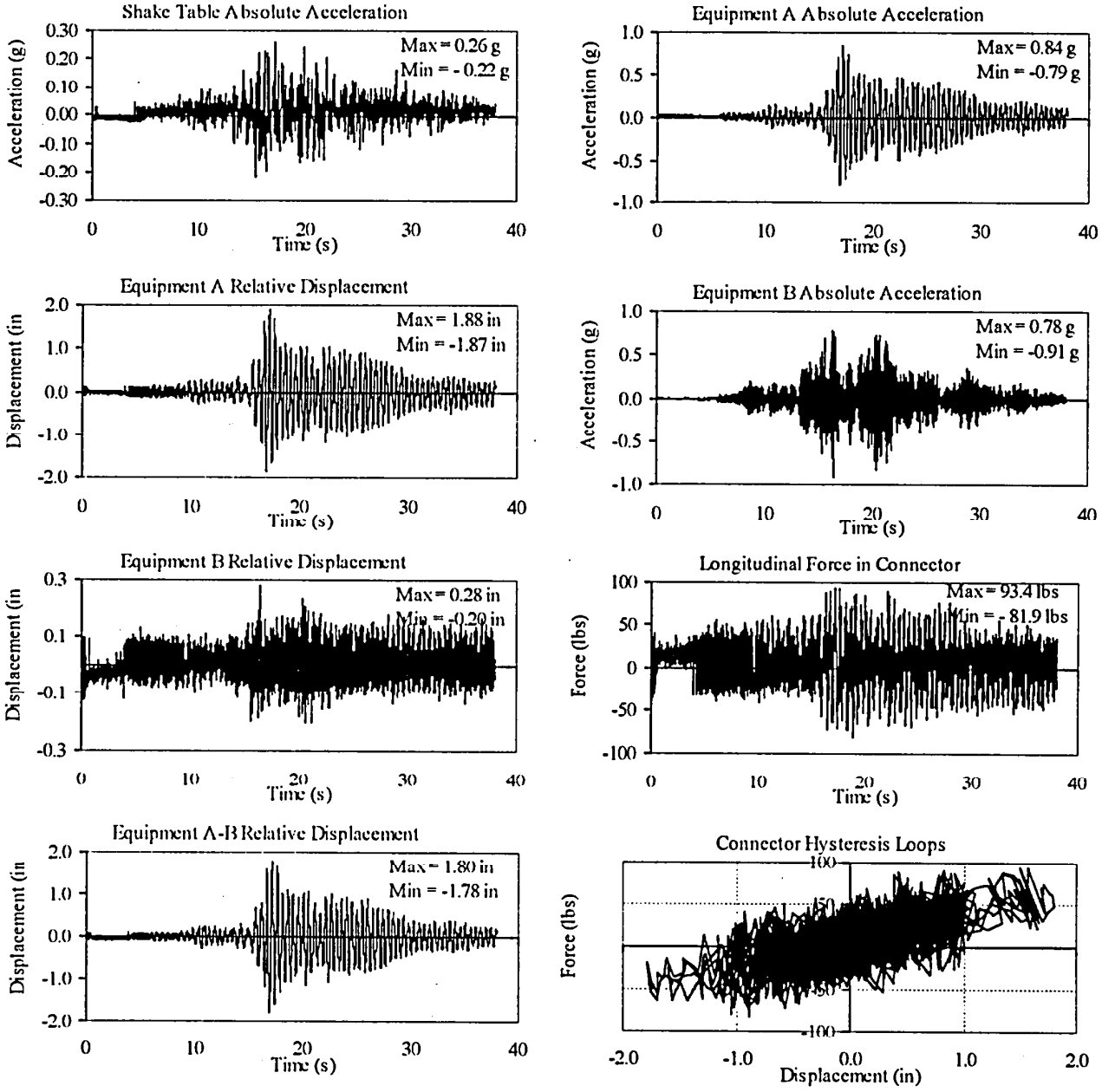

TEST RB-154
EQUIPMENT COMBINATION 5, BPA ISOLATOR
TABAS GROUND MOTION, 50% SPAN

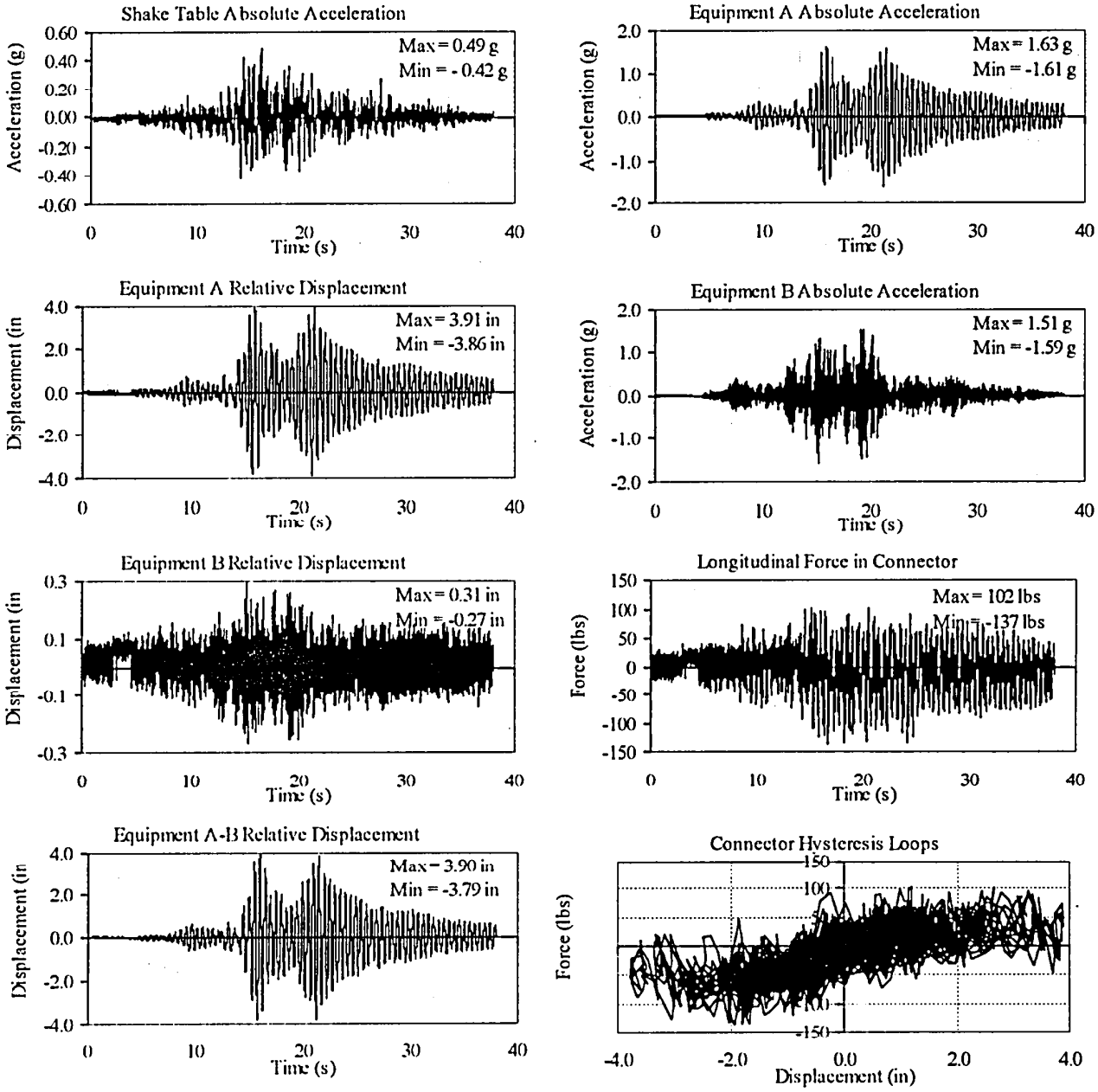

TEST RB-155
EQUIPMENT COMBINATION 5, BPA ISOLATOR
NEWHALL GROUND MOTION, 100% SPAN

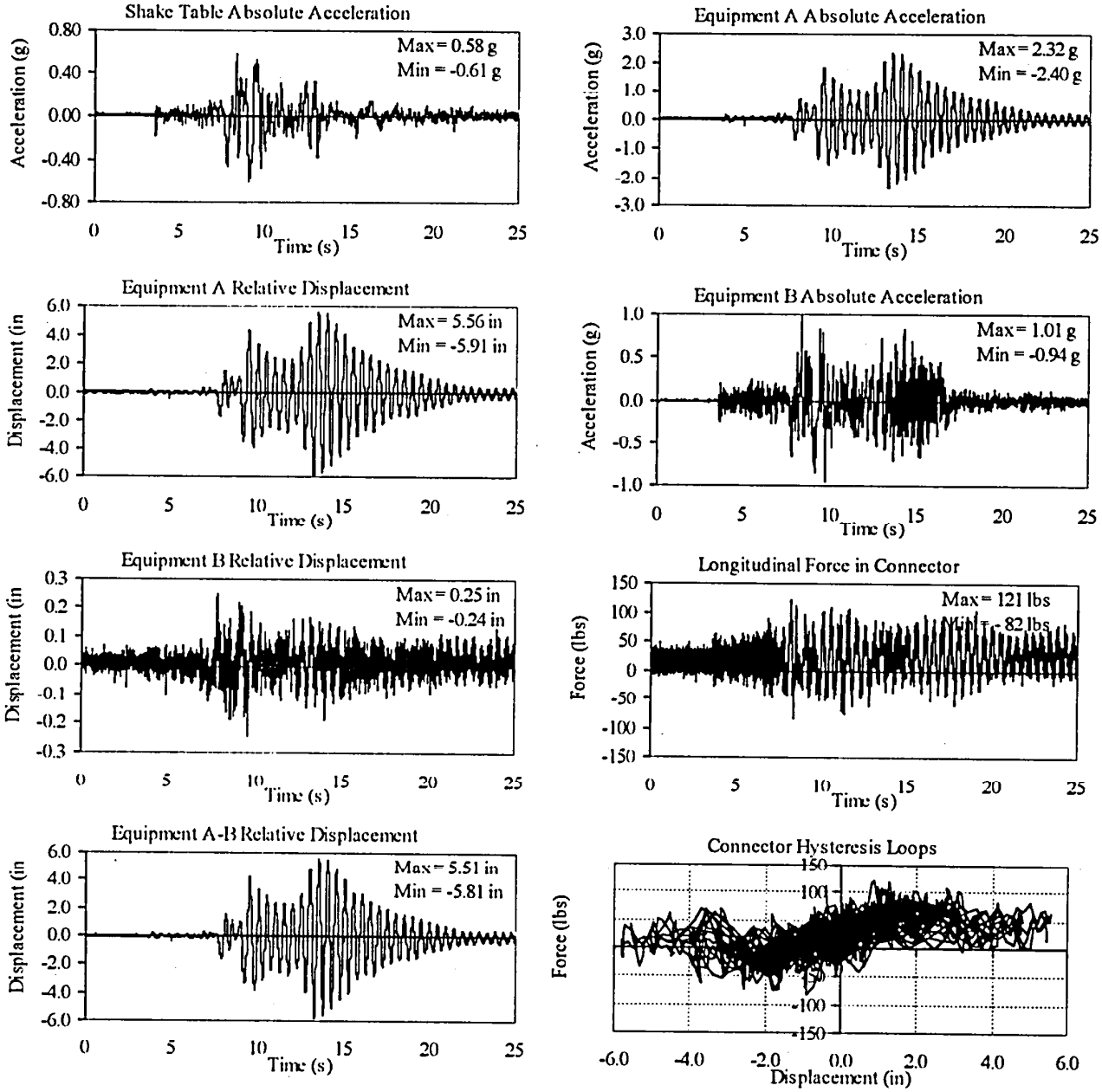

TEST RB-156
EQUIPMENT COMBINATION 5, BPA ISOLATOR
TABAS GROUND MOTION, 100% SPAN

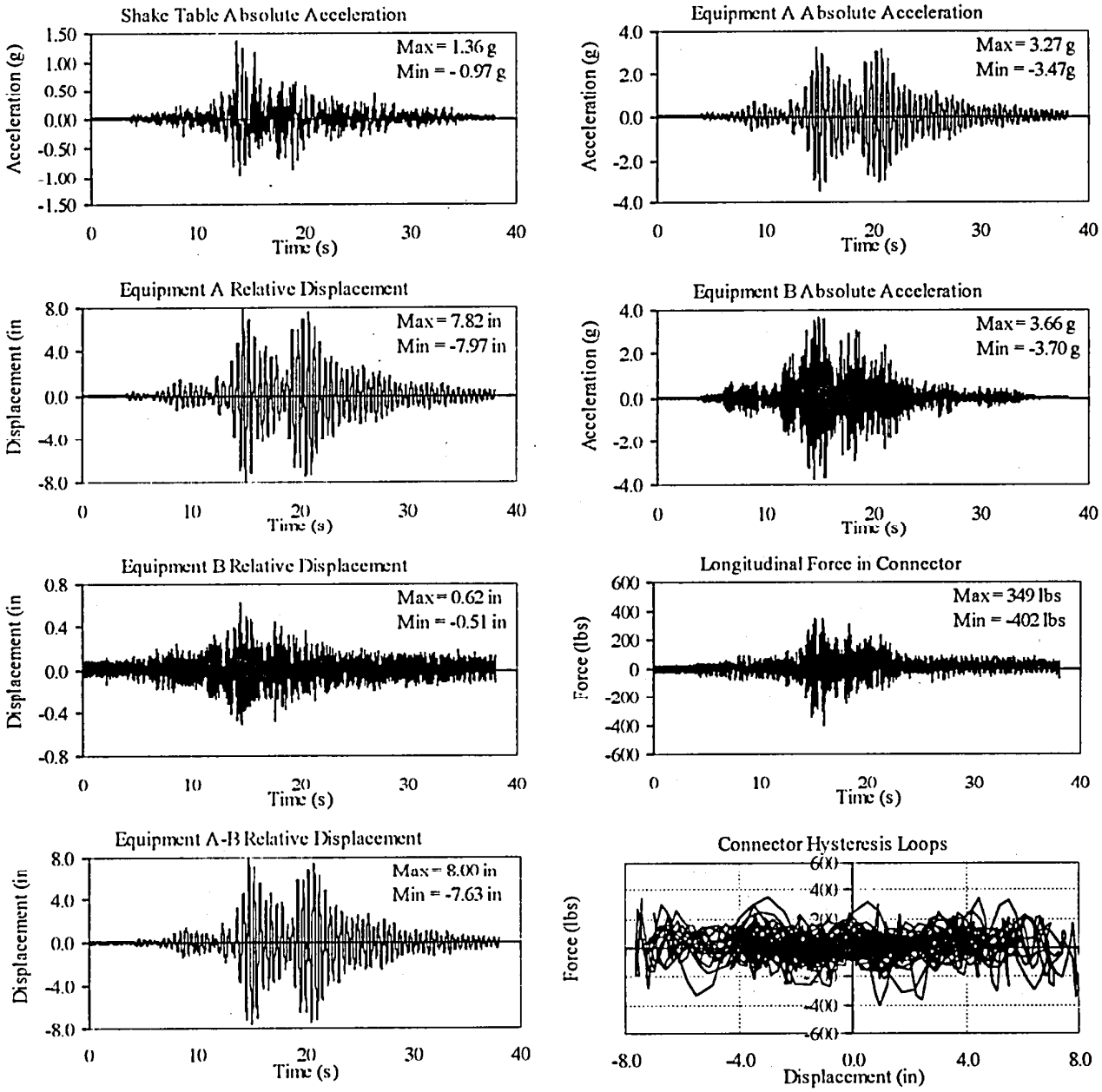

TEST RB-158
EQUIPMENT COMBINATION 5, INDIVIDUAL EQUIPMENT
NEWHALL GROUND MOTION, 30% SPAN

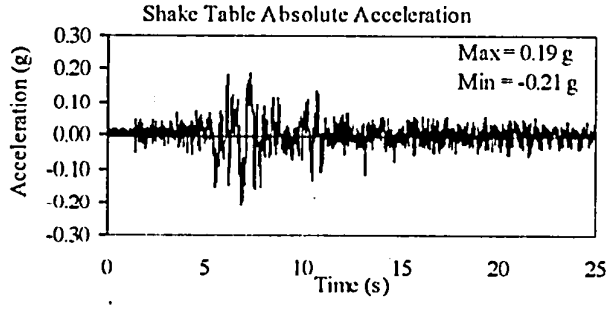

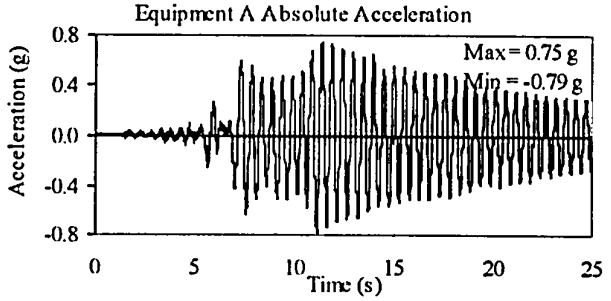

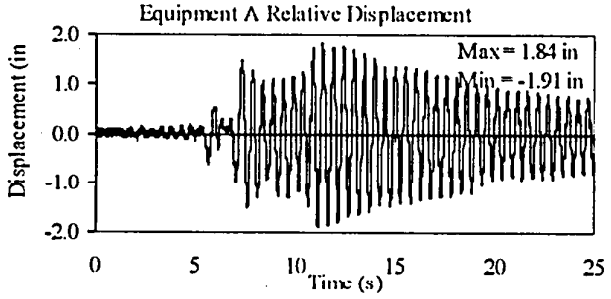

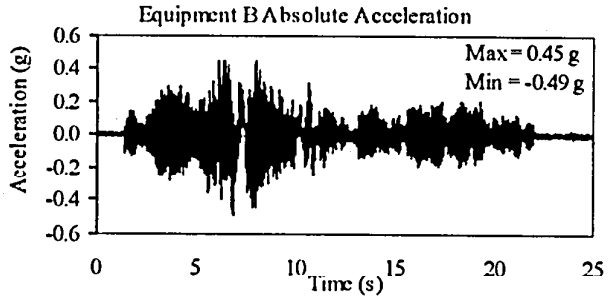

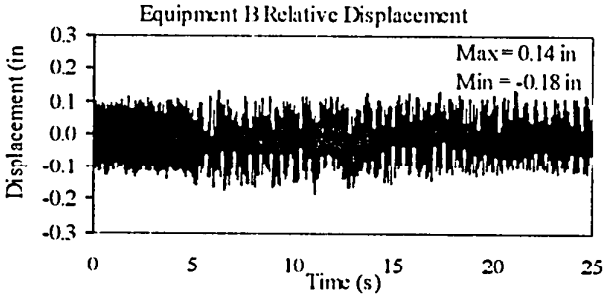

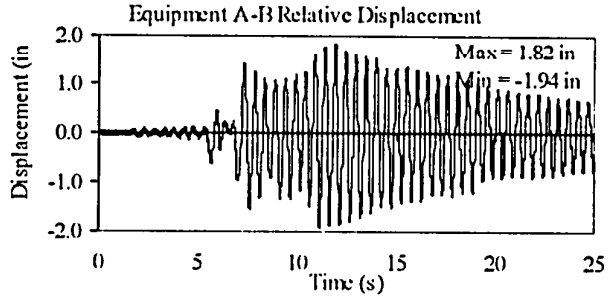

TEST RB-159
EQUIPMENT COMBINATION 5, INDIVIDUAL EQUIPMENT
TABAS GROUND MOTION, 25% SPAN

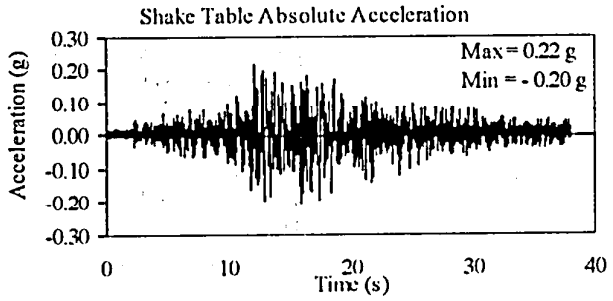

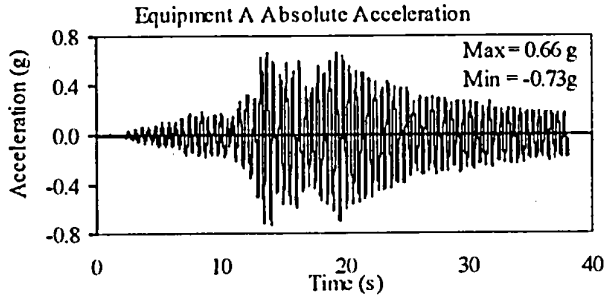

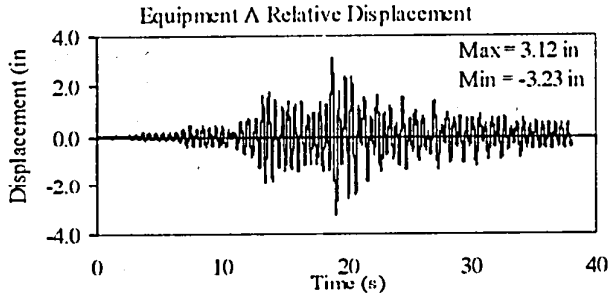

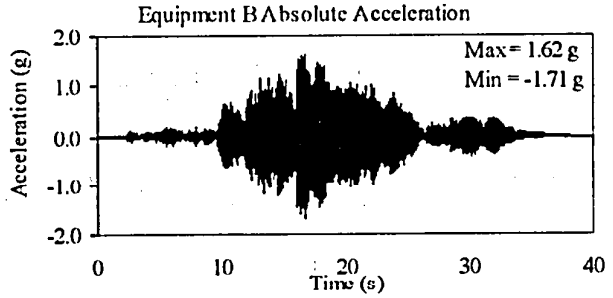

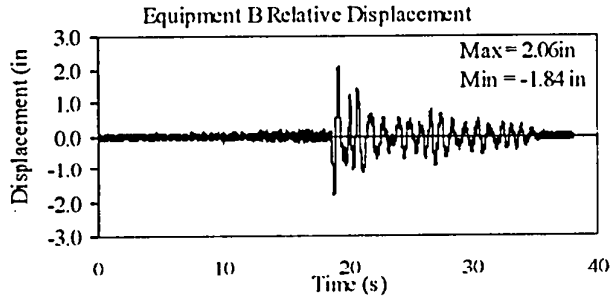

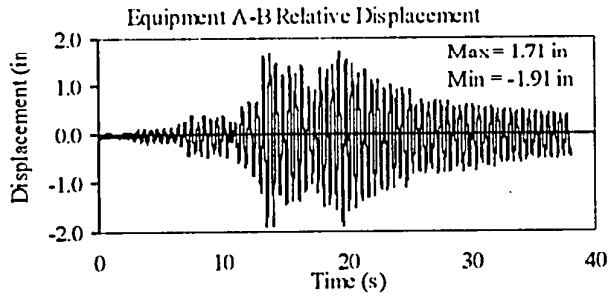

TEST RB-160
EQUIPMENT COMBINATION 5, INDIVIDUAL EQUIPMENT
TABAS GROUND MOTION, 50% SPAN

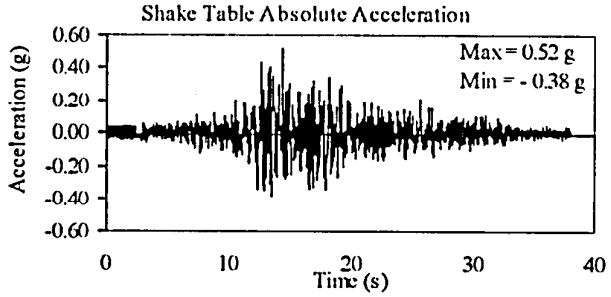

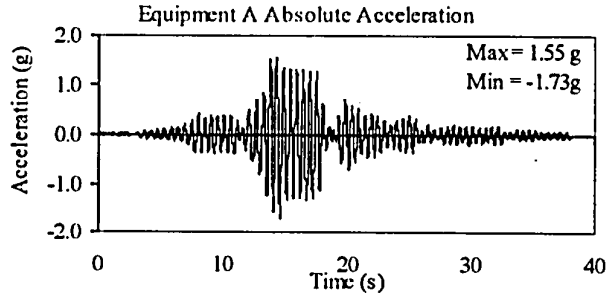

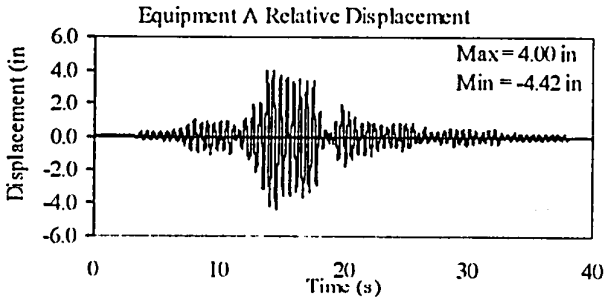

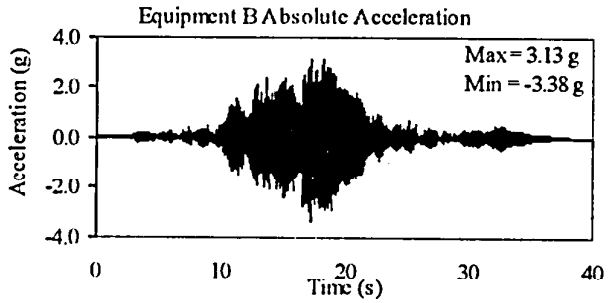

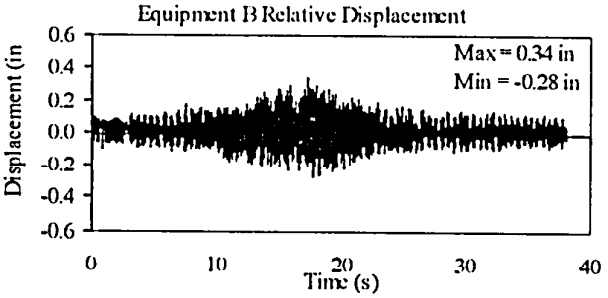

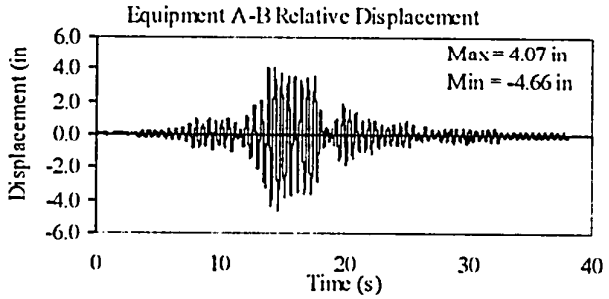

TEST RB-161
EQUIPMENT COMBINATION 5, INDIVIDUAL EQUIPMENT
NEWHALL GROUND MOTION, 100% SPAN

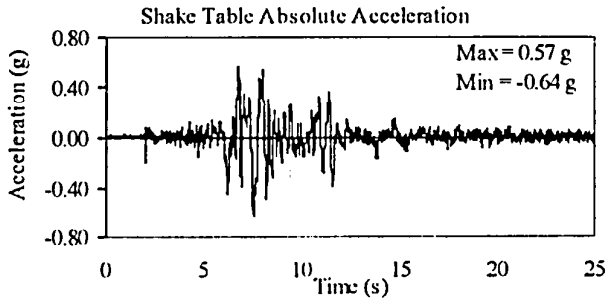

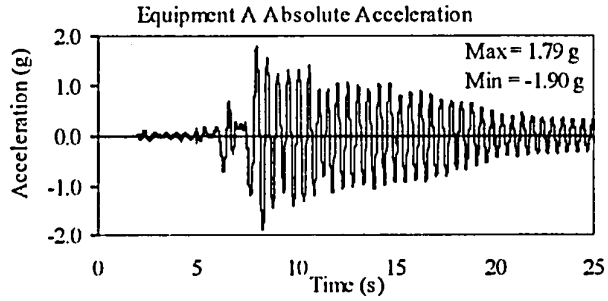

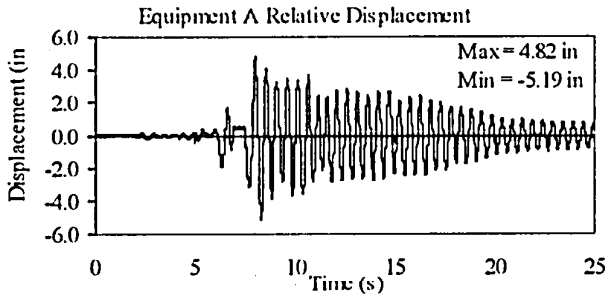

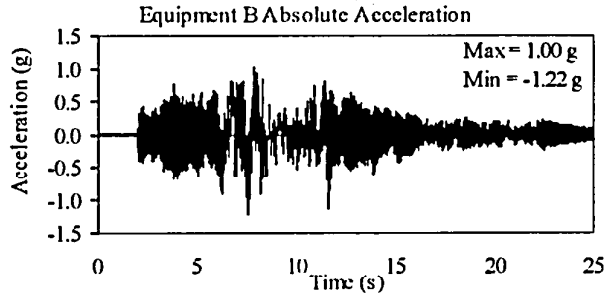

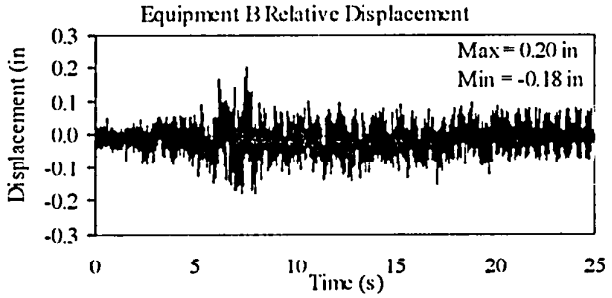

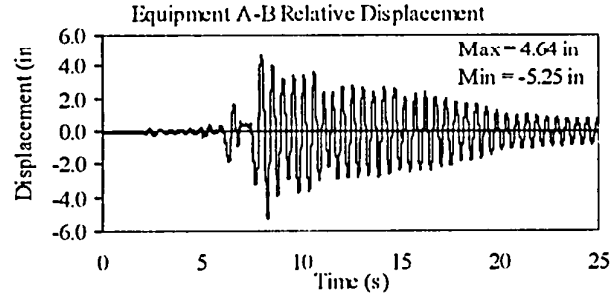

DEPARTMENT OF CIVIL ENGINEERING

SCHOOL OF ENGINEERING

GROUND MOTION AMPLIFICATION AT BASE OF BUSHINGS MOUNTED ON ELECTRIC SUBSTAION TRANSFORMERS

By

Roberto Villaverde

Gerald C. Pardoen

And

Sergio Carnalla

A Technical Report of Research Supported by PEER/PG&E
Under Award No. PGE-09566

September 1999

UNIVERSITY
OF CALIFORNIA
IRVINE

GROUND MOTION AMPLIFICATION AT BASE OF BUSHINGS MOUNTED ON ELECTRIC SUBSTATION TRANSFORMERS

By

Roberto Villaverde, Gerald C. Pardoen, and Sergio Carnalla

A Technical Report of Research Supported by PEER/PG&E
Under Award No. PGE-09566

Department of Civil Engineering

University of California, Irvine

September 1999

Executive Summary

A study was conducted to quantify the ground motion amplification that takes place at the base of bushings mounted on electric substation transformers as a result of the flexibility of the transformer tank and turrets to which they are connected. This study was part of a comprehensive project sponsored by the Pacific Gas and Electric Company to reduce the seismic vulnerability of gas and electrical distribution and transmission systems, and was undertaken to assess the adequacy of the amplification factor of 2.0 specified by the Institute of Electrical and Electronic Engineers in Standard IEEE 693-1997 for the seismic qualification of transformer bushings. The study included field tests of typical transformers to obtain experimentally their natural frequencies and damping ratios, the development of simple analytical models that closely matched the experimental data, and the calculation of the transformers' dynamic response under different earthquake excitations using these analytical models.

The field tests were conducted on four different units at four different Pacific Gas & Electric substations: (a) a Pauwels, single phase, 500 kV transformer at the Moss Landing substation in Moss Landing, Calif.; (b) a Westinghouse, single-phase, 500 kV transformer at the Midway substation in Buttonwillow, Calif.; (c) a Smit, three-phase 230 kV transformer at the Gold Hill substation in Folsom, Calif.; and (d) a Westinghouse, single-phase, 230 kV transformer at the Ignacio substation in Novato, Calif. The tests were conducted by placing a 160-lb shaker on top of the transformers' tank, laterally exciting the transformers with a random force of up to 100 pounds, and measuring the transformers' acceleration or velocity response at several points along their height. The fundamental frequencies obtained from such field tests were 3.4, 2.4, 4.1, and 3.8 Hz, respectively for each of the transformers listed above. The modal damping ratios were all centered around the average of 2 per cent of critical.

Three-dimensional analytical models were developed for the two 500 kV transformers and their seismic response calculated using either a response spectrum or a time-history analysis. The models were developed using linear elastic beam elements with lumped masses to represent the behavior of the 500-kV and 230-kV bushings, turrets, and transformer case. All other components were considered as rigid elements connected to the transformer's centers of gravity with a single lumped mass located at the components' centers of gravity. The exception were the conservator tank for the Pauwels 500 kV transformer and the lightning arrester for the 500 kV Westinghouse transformer, both flexible components with low natural frequencies, which were also modeled with beam elements and lumped masses. The transformers' base was assumed fully fixed so soil-structure interaction effects were neglected. Similarly, no oil sloshing effects were considered since the transformers' tanks are supposed to be always completely full under operating conditions. In both cases, adjustments were made to the dimensions and properties of the transformers' components to match as closely as possible the values of the transformers' lower natural frequencies obtained from the field tests. The excitations considered in the analysis were (a) the 2 %-damping response spectrum specified in Standard IEEE 693-1997 for the seismic design of substations (IEEE 693 response spectrum); (b) acceleration time histories that envelope the low frequency range of the 2 %-damping IEEE 693 response spectrum; (c) acceleration time histories that envelope the high frequency range of the 2 %-damping IEEE 693 response spectrum; (d) acceleration time histories recorded at Los Gatos near-fault station during the 1989 Loma Prieta earthquake; and (e) acceleration time histories recorded at the Olive View Hospital near-fault station during the 1994 Northridge earthquake. In each case, the analysis was carried out considering simultaneously the three components of ground motion. In the case of the IEEE 693 response spectrum, the excitation along each of the three orthogonal directions was defined by this spectrum, except that in the vertical direction the spectrum was scaled by a factor of 2/3.

For each of the excitations considered, the transformers' peak response and the corresponding ground motion amplification factors were calculated at the base of the 500-kV and 230-kV bushings. These amplification factors were obtained by dividing the computed peak shear force at the base of the bushings by the corresponding shear force when the bushings are assumed mounted directly on the ground. Respectively for the 500-kV and 230-kV bushings, amplification factors as large as 1.89 and 3.39 were obtained for the Pauwels transformer and 1.74 and 3.95 for the Westinghouse transformer.

It is found, thus, that the amplification factors for the 500-kV bushings are within the amplification factor of 2.0 specified by Standard IEEE 693 but not those for the 230-kV bushings, which exceed the IEEE 693 amplification factor by almost a factor of two. Another conclusion that can be drawn from the study is that the use of simple analytical models calibrated with experimental data constitutes an adequate but inexpensive way to define the earthquake input to equipment in electric substations. It is recommended, however, the use of impact tests as opposed to the use of the shaker employed in this study, as it was found that the input energy imparted by the shaker was in many instances inadequate to define the transformers' dynamic properties with sufficient clarity.

ACKNOWLEDGMENTS

This study was part of a project entitled "Directed Study Program for Increasing The Seismic Reliability and Safety of Gas And Electric Transmission Systems, Phase II," awarded to the Pacific Earthquake Engineering (PEER) Center by the Pacific Gas and Electric Company (PG&E), and was sponsored through a sub-award from the PEER Center. This support is herein gratefully acknowledged. The authors also wish to express their appreciation to Henry Ho, their PG&E technical contact, who worked very closely with them in the development of the project and was instrumental in having access to the PG&E substations and the transformers' technical drawings. Thanks are also due to Tom Olson, senior construction specialist at PG&E, who assisted the authors in numerous ways during the field tests and answered their never-ending questions. Finally, the authors extend their sincere thanks to graduate students Charles Hamilton, Matt Steiner, and Rick Tavares, who help at one time or another to conduct the field tests entirely on a voluntary basis. Without the contribution of all these individuals, it would have been virtually impossible to carry the study to a successful completion.

TABLE OF CONTENTS

EXECUTIVE SUMMARY II

ACKNOWLEDGMENTS IV

LIST OF TABLES VI

LIST OF FIGURES VII

CHAPTER 1: INTRODUCTION 1

1.1 BACKGROUND 1
1.2 OBJECTIVE 1
1.3 APPROACH 2
1.4 PREVIOUS RELATED WORK 2
1.5 ORGANIZATION 3

CHAPTER 2: EXPERIMENTAL STUDY 4

2.1 .INTRODUCTION 4
2.2 .TRANSFORMERS TESTED 4
2.3. EQUIPMENT 4
2.4 .TEST PROCEDURE 5
2.6 MEASURED NATURAL FREQUENCIES AND DAMPING RATIOS 6

CHAPTER 3: ANALYTICAL STUDY 7

3.1 INTRODUCTION 7
3.2 ANALYTICAL MODELS 7
3.3 ANALYTICAL NATURAL FREQUENCIES AND MODE SHAPES 8
3.4 RESPONSE SPECTRUM AND TIME HISTORY ANALYSES 9
3.5 GROUND MOTION AMPLIFICATION FACTORS 10

CHAPTER 4: CONCLUSIONS 11

4.1 SUMMARY 11
4.2 CONCLUSIONS 11
4.3 RECOMMENDATIONS FOR FUTURE STUDIES 12

REFERENCES 13

APPENDIX A 63

APPENDIX B 82

APPENDIX C 94

APPENDIX D 107

LIST OF TABLES

Table 2.1. Natural frequencies and damping ratios of Pauwels 500-kV transformer from experimental data 14

Table 2.2. Natural frequencies and damping ratios of Westinghouse 500-kV transformer from experimental data 14

Table 2.3. Natural frequencies and damping ratios of Smit 230-kV transformer from experimental data 15

Table 2.4. Natural frequencies and damping ratios of Westinghouse 230-kV transformer from experimental data 15

Table 3.1. Natural frequencies of Pauwels 500-kV transformer according to analytical model and comparison with values obtained experimentally 16

Table 3.2. Natural frequencies of Westinghouse 500-kV transformer according to analytical model and comparison with values obtained experimentally 16

Table 3.3. Peak shear force under different excitations at base of transformers' high-voltage (HV) and low-voltage (LV) bushings and corresponding ground motion amplification factors when the bushings are mounted on top of turrets and directly on the ground 17

LIST OF FIGURES

Figure 2.1. Panoramic view of Pauwels 500-kV transformer showing oil conservator tank in foreground 18

Figure 2.2. Close-up view of high-voltage turret and bushing in Pauwels 500-kV transformer 19

Figure 2.3. Close-up view of turret-bushing connection in Pauwels 500-kV transformer, showing also a seismometer resting on turret cover plate 20

Figure 2.4. Panoramic view of Westinghouse 500-kV transformer 21

Figure 2.5. Close-up view of high-voltage bushing in Westinghouse 500-kV transformer 22

Figure 2.6. Close-up view of turret-bushing connection in Westinghouse 500-kV transformer, showing also a pair of seismometers resting on turret cover plate 23

Figure 2.7. Panoramic view of Smit 230-kV transformer showing oil conservator tank in foreground 24

Figure 2.8. Top view of Smit 230-kV transformer showing high- and low-voltage bushings and turrets 25

Figure 2.9. Panoramic view of Westinghouse 230-kV transformer showing bushings and lightning arrester 26

Figure 2.10. Schematic view of experimental set up during field tests 27

Figure 3.1. Plan view of Pauwels 500-kV transformer 28

Figure 3.2. Transverse elevation of Pauwels 500-kV transformer 29

Figure 3.3. Longitudinal elevation of Pauwels 500-kV transformer 30

Figure 3.4. Plan view of Westinghouse 500-kV transformer 31

Figure 3.5. Transverse elevation of Westinghouse 500-kV transformer 32

Figure 3.6. Longitudinal elevation of Westinghouse 500-kV transformer 33

Figure 3.7. Dimensions and configuration of studied 500-kV bushings 34

Figure 3.8. Dimensions and configuration of studied 230-kV bushings 35

Figure 3.9. Analytical model for Pauwels 500-kV transformer (note: dots represent nodal masses) 36

Figure 3.10. Analytical model for Westinghouse 500-kV transformer (note: dots represent nodal masses) 37

Figure 3.11. First mode of vibration, Pauwels 500-kV transformer 38

Figure 3.12. Second mode of vibration, Pauwels 500-kV transformer 39

Figure 3.13. Third mode of vibration, Pauwels 500-kV transformer 40

Figure 3.14. Fourth mode of vibration, Pauwels 500-kV transformer 41

Figure 3.15. Fifth mode of vibration, Pauwels 500-kV transformer 42

Figure 3.16. Sixth mode of vibration, Pauwels 500-kV transformer 43

Figure 3.17. Seventh mode of vibration, Pauwels 500-kV transformer 44

Figure 3.18. Eighth mode of vibration, Pauwels 500-kV transformer 45

Figure 3.19. First mode of vibration, Westinghouse 500-kV transformer 46

Figure 3.20. Second mode of vibration, Westinghouse 500-kV transformer 47

Figure 3.21. Third mode of vibration, Westinghouse 500-kV transformer 48

Figure 3.22. Fourth mode of vibration, Westinghouse 500-kV transformer 49

Figure 3.23. Fifth mode of vibration, Westinghouse 500-kV transformer 50

Figure 3.24. Sixth mode of vibration, Westinghouse 500-kV transformer 51

Figure 3.25. Seventh mode of vibration, Westinghouse 500-kV transformer 52

Figure 3.26. Eighth mode of vibration, Westinghouse 500-kV transformer 53

Figure 3.27. IEEE 693 acceleration response spectrum for 2 per cent damping 54

Figure 3.28. Synthetic acceleration time histories generated to match the low frequency range of the 2 %-damping IEEE 693 response spectrum 55

Figure 3.29. Synthetic acceleration time histories generated to match the high frequency range of the 2 %-damping IEEE 693 response spectrum 56

Figure 3.30. Acceleration time histories recorded at Los Gatos near-fault station during the 1989 Loma Prieta earthquake 57

Figure 3.31. Acceleration time histories recorded at Olive View Hospital near-fault station during the 1994 Northridge earthquake 58

Figure 3.32. 2 %-damping acceleration response spectra of synthetic acceleration time histories generated to match low frequency range of 2 %-damping IEEE 693 response spectrum 59

Figure 3.33. 2 %-damping acceleration response spectra of synthetic acceleration time histories generated to match high frequency range of 2 %-damping IEEE 693 response spectrum 60

Figure 3.34. 2 %-damping acceleration response spectra of acceleration time histories recorded at Los Gatos near-fault station during the 1989 Loma Prieta earthquake..... 61

Figure 3.35. 2 %-damping acceleration response spectra of acceleration time histories recorded at Olive View Hospital near-fault station during the 1994 Northridge earthquake..... 62

Chapter 1

INTRODUCTION

1.1 Background

When the distance between the generating station and the load is significant in electric power transmission systems, it is advantageous to transmit electricity at a high voltage. For the same power, a high voltage line carries less current and thus has fewer losses for the same conductor size. In such cases, voltage transformers are installed at the generating station end to step up the voltage and at the load end to step it down. Ordinarily, voltage transformers are also installed between the generating station end and the load end. Transformers and related auxiliary equipment are generally placed in a dedicated plant known as a substation.

An integral part of a voltage transformer is its bushings, which serve to isolate the metal rod that connects the external power line to the coils inside the transformer and prevent a flashover. Normally, bushings are filled with oil, which surrounds the connecting metal rod and insulates it. The external part of a bushing is usually constructed with porcelain, which further insulates the connecting metal rod. To prevent a flashover, the porcelain is designed to have a relatively large distance along the external surface between the power line and the transformer coils. This large distance is achieved with "petticoats," the accordion-like rings along the external surface of the bushing.

Transformer bushings have a limited capacity to withstand strong earthquakes. The porcelain used in their construction has little strength, is inherently brittle, and its non-homogeneous nature causes a wide variation in strength in otherwise identical members. Furthermore, their long slender design compounds the problem by creating a large bending moment at the base of the bushing.

Transformers in electric power substations have been the subject of severe damage during past earthquakes. For example, transformers in substations owned by the Pacific Gas and Electric Company in northern California were damaged during the 1989 Loma Prieta earthquake. Most of the damage was to 500- and 230-kV transformers and consisted of cracked porcelain bushings, anchorage failures, and development of oil leaks (Benuska, 1990). Damage was also observed in transformers at substations owned by Southern California Edison during the 1994 Northridge earthquake in southern California. During this earthquake, transformers experienced problems with their bushings, anchorage, radiators, lightning arresters, and conservator tanks (Schiff, 1995). The most common form of failure was a shift in the porcelain bushings in relation to the flange at their base, resulting in oil leaks. However, two 500-kV transformer bushings experienced extensive porcelain cracking. Similarly, in an isolated case, the bolts attaching the bushing-supporting turret to the transformer tank broke, causing the bushing to fall and shatter.

1.2 Objective

In view of the damage experienced by electric power transmission and distribution systems during past earthquakes and a recognition of their susceptibility to earthquake damage during future events, Pacific Gas and Electric (PG&E), the California Energy Commission, and the Pacific Earthquake Engineering Research Center (PEER) initiated a comprehensive research project with the purpose of reducing the seismic vulnerability of these systems and improving their safety and

reliability. An important component of this project were studies directed to reduce the vulnerability of existing equipment in electric power substations known to be critical for the post-earthquake operability of the entire transmission system. A task within this component aimed at estimating the level of ground motion amplification that takes place at the base of the bushings mounted on electric substation transformers as a result of the flexibility of the transformer tanks and turrets to which they are connected. Quantification of this factor has important implications in the design and retrofit of transformer bushings, as only limited information in this regard is currently available. The research herein reported was dedicated to this task. Hence, the objective of this study was to shed some light as to what is the magnitude of such an amplification factor and assess, in addition, the adequacy of the amplification factor specified by Standard IEEE 693-1997 for the seismic qualification of transformer bushings.

1.3 Approach

The objectives of the study were accomplished by means of experimental and analytical investigations. In the experimental investigation, field tests were conducted on four different types of transformers with the purpose of determining their natural frequencies and damping ratios. In the analytical investigation, mathematical models that closely matched the natural frequencies obtained from the filed tests were developed and used to determine the transformers' dynamic response to a variety of earthquake excitations. Only 500- and 230-kV were considered in the study as experience from past earthquakes has shown that earthquakes affect these types of transformers the most. Also, only two different types of transformers were considered in the analytical investigation despite the fact that transformer bushings are mounted in a large variety of ways that differ between different models and different manufacturers. The reason for this limitation was simply the enormous task that would represents to consider a number that is more representative of the existing large variety of models. The desired amplification factors were computed in terms of the maximum shear force observed at the level of the bushings' mounting flange when the bushings are mounted on the transformers and the corresponding force when the bushings are assumed mounted directly on the ground.

1.4 Previous Related Work

Not much work has been reported in the literature to define the dynamic properties of power transformers or the seismic input to transformer bushings. The only few studies that deal with this subject are those of Ibáñez et al. (1973), Palk et al. (1975) Suzuki et al. (1987), and Bellorini et al. (1996). Bellorini et al. performed experimental field tests and finite element analyses of a three-phase, ATR, 230-kV transformer to determine the dynamic properties of the transformer and evaluate the ground motion amplification at the level of the bushing flange and the bushing's center of gravity. From the experimental tests, they found that the fundamental natural frequency of the transformer was 3.5 Hz and the corresponding damping ratio was around two percent of critical. From the finite element analyses, they found that the average ground motion amplification factor at the level of the bushing flange and bushing's center of gravity when the transformer was subjected to a series of different ground motions was 2.16 and 2.8, respectively. Suzuki et al. studied the effectiveness of a base-isolated scheme to reduce the response of porcelain bushings in electric power transformers. For this purpose, they conducted a shake table test with a scaled model of a 275-kV transformer mounted on sliding isolators. The prototype weighed 617 kips and its high-voltage

bushings exhibited a natural frequency of 7.5 Hz. They also base isolated, instrumented, and measured the response under several earthquakes of a three-phase, 154 kV spare transformer weighing 476 kips. In both cases, they found that the isolators were effective to reduce the response of the bushings for excitations that exceeded the frictional resistance of the isolators. Finally, Ibáñez et al. (1973) and Palk et al. (1975) reported the results of forced vibration tests of, among several pieces of equipment, a 386-kip, 500-kV transformer at a Los Angeles Department of Water and Power's substation. In these tests, they found that the first three natural frequencies of the transformer were 2.70, 3.35, and 3.38 Hz, which approximately correspond to the natural frequencies of the oil conservator tank and the high-voltage bushing in the north-south and east-west directions, respectively. They also found that the damping ratios of the transformer varied between 2 and 10 per cent of critical.

1.5 Organization

This report is organized into this introductory chapter, three additional chapters, and four appendices. The details of the experimental study are presented in Chapter 3. The natural frequencies and damping ratios obtained from this experimental study are also presented in Chapter 3. Chapter 4 is devoted to the analytical investigation. This chapter describes the way this analytical investigation was carried out and the results from the simulation studies that were conducted to quantify the desired ground motion amplification factors. The conclusions of the study and recommendations for future work are stated in Chapter 4. The power spectra obtained from the experimental data are shown in Appendices A through D.

Chapter 2

EXPERIMENTAL STUDY

2.1 Introduction

As mentioned above, field tests were conducted with the purpose of determining the natural frequencies and damping ratios of representative 500- and 230-kv power transformers. This chapter will describe the transformers tested, the procedure used to carry out the tests, and the equipment used in these tests. It will also summarize the main results obtained from the tests.

2.2 Transformers Tested

The field tests were conducted on four different transformers at four different Pacific Gas & Electric substations. These transformers were: (a) a Pauwels 500-kV, single-phase transformer at the Moss Landing substation in Moss Landing, Calif.; (b) a Westinghouse 500-kV, single-phase transformer at the Midway substation in Buttonwillow, Calif.; (c) a Smit 230-kV, three-phase transformer at the Gold Hill substation in Folsom, Calif.; and (d) a Westinghouse 230-kV, single-phase transformer at the Ignacio substation in Novato, Calif. Figure 2.1 through 2.9 show panoramic views of these transformers, close ups of their high-voltage bushings and turrets, and details of the bushing-turret connections. The weights and dimensions of the 500-kV transformers will be described in detail in Chapter 3. It should be noted here that the tested transformers were all disconnected from the external power line to which they are connected when they are in service. Hence, the results from these tests do not account for the interaction that might exist between a transformer and such an external power line.

2.3 Equipment

The primary equipment utilized in the field tests was a shaker, a signal analyzer, and an assortment of accelerometers and seismometers. The following subsections briefly describe the main characteristics of these pieces of equipment.

Accelerometers

The accelerometers used were PCB Piezotronics Structcel motion sensors, Models 333A12 and 308B. These accelerometers contain a moving mass, a piezoelectric element, and a built-in signal conditioner that together convert the acceleration of the moving mass to a voltage. The 308B model has an operational range of 50g with a resolution of 0.001g and a nominal sensitivity of 100mV/g. The 333A12 model has an operational range of 5g, a sensitivity of 1V/g and a resolution of 0.0005 g. The frequency range of both models is between 1 and 3,000 Hz. These accelerometers work with an external DC power unit. Those employed in the tests were Models 480, also from Piezotronics.

Seismometers

The seismometers used were Model SS-1 Ranger Seismometers linked to a Model SC-1 Signal Conditioner, both produced by Kinemetrics. The SS-1 Ranger Seismometer is a high-sensitivity portable spring-mass instrument with electromagnetic transduction, specifically designed for a variety of seismic field applications. It has a permanent magnet assembly, which constitutes its seismic mass, and a coil that is attached to its frame. Its spring-mass system produces a voltage proportional to the velocity imparted to its mass. The SC-1 signal conditioner is a low-noise wideband amplifier with up to a 142-dB gain. When the SS-1 Ranger seismometer is used as a sensor, the system's sensitivity outputs ± 6 volts if the vibratory motion produces a displacement of 1.5×10^{-8} meters, a velocity of 4×10^{-7} meters/second, or an acceleration of 2×10^{-6} meters/sec^2. Its frequency range is between 0.03 and 100 Hz.

Shaker

The shaker used was a Model 400 electromagnetic shaker produced by APS Dynamics, Inc. This shaker weighs 160 pounds, can exert a lateral force of up to 100 pounds, and has a stroke of 6.25 inches. It has a frequency range between 0 and 200 Hz. It is powered by a Model 144 amplifier, also produced by APS Dynamics, Inc. The shaker is controlled by a signal generated by the signal analyzer and fed into the shaker's amplifier.

Signal Analyzer

The signal analyzer used was a Hewlett Packard 3567A, a PC-based system with up to 14 channels, a dynamic range of 72 dB, and a maximum frequency span of 12.8 kHz. Its basic function is to capture time signals and characterize these signals in either the time or the frequency domain via the fast Fourier transform. It can also generate continuous random, continuous sine, and other signals that can be used as a source for an external excitation. It consists of a personal computer, application software, and measurement hardware, which together form a complete multichannel signal analyzing system with the capabilities to store vast amounts of data on conventional IBM formatted media. The measurement hardware includes a HP 35654B interface/signal processor, a HP 35652A input card, and a HP 25653A source (signal generating) card.

2.4 Test Procedure

The tests were conducted by placing the 160-lb shaker on top (off-center) of the transformers' tanks, laterally exciting the transformers with a random force of up to 100 pounds, and measuring the transformers' acceleration or velocity response with the accelerometers and seismometers at several points along their height. The general arrangement of the accelerometers and seismometers is shown schematically in Figure 2.10. In particular, two seismometers, one along the north-south and the other along the east-west direction, were placed on the concrete foundation and another two on top of the tank. The accelerometers were placed on top of the bushings, also along the north-south and east-west directions. An accelerometer was also installed on the shaker to record the input signal. In the case of the Moss Landing Station transformer, the first unit tested, sensors were also placed at some other points along the height of the transformer's tank, turrets and bushings with the purpose of examining in detail the variation with height of the transformer's dynamic response. Each transformer was tested several times, varying from test to test the direction of the shaker, the location of the accelerometers, or the range of the sensors. In each case, the duration of the excitation was determined automatically by the signal analyzer after specifying the desired number of frequency lines, frequency span, and number of averages. In all tests, the number of

frequency lines was set to 400. Similarly, the frequency span was set to either from 0 to 25 Hz or from 0 to 50 Hz. The number of averages was set to 30. The output signals from the seismometers and accelerometers were digitized and recorded by the signal analyzer for processing at a later time.

Limited impact tests were also conducted at the Ignacio substation. In these tests, the structure or structural component is excited by hitting it with an instrumented sledgehammer. This sledgehammer is implemented with a force transducer that is connected to the signal analyzer. Thus, when the structure or structural component is impacted during an experiment, the force transducer measures the applied force and sends the information to the signal analyzer. Once it receives this information, the signal analyzer computes the corresponding transfer function by dividing the Fourier transform of the recorded output signal by the Fourier transform of the input signal. Impact tests offer the advantage that through a series of them one can excite all the desired components of a structure.

2.6 Measured Natural Frequencies and Damping Ratios

The output signals from the accelerometers and seismometers were all transformed to the frequency domain by the signal analyzer via the fast Fourier transform. These signals were further processed to generate average power spectra. These average power spectra were obtained by averaging the power spectra of the collected output time histories (samples). As described above, the number of time histories considered corresponds to the number of averages set in each test. Power spectrum averaging is an effective technique to remove extraneous noise from measurements. The spectra obtained are presented in Appendices A through C, respectively for the Moss Landing, Midway, Gold Hill, and Ignacio transformers.

The transformer's natural frequencies and damping ratios were obtained from these average power spectra. The natural frequencies were determined from the most prominent peaks in the spectra and those that consistently appeared in several of the spectra. The damping ratios were estimated by means of the half-power method applied to peaks in the spectra that defined the obtained natural frequencies. In this regard, it is important to note that the half-power method is, strictly speaking, only valid for single-degree of freedom systems. It may, nevertheless, provide good estimates of the modal damping ratios of multi-degree-of-freedom system when there is not a significant coupling between modes. That is, when the resonance curves from other modes are not close to the resonance peak of the mode in question (Richardson, 1978).

The frequencies and damping ratios obtained are listed in Tables 2.1 through 2.4. In particular, it was found that the fundamental frequencies of the Moss Landing, Midway, Gold Hill, and Ignacio transformers were 3.4, 2.4, 4.1, and 3.8 Hz, respectively. The modal damping ratios varied between 0.4 and 5.4 per cent of critical, with an average around 2 per cent.

Chapter 3

ANALYTICAL STUDY

3.1 Introduction

As indicated in Chapter 1, the quantification of the amplification factors under investigation was determined by developing simple analytical models that closely match the natural frequencies obtained from the filed tests, and by analyzing these analytical models under a series of earthquake excitations. This chapter describes these analytical models, the excitations used to analyze them, and the method employed to obtain the desired amplification factors. It also describes the obtained results.

3.2 Analytical Models

Three-dimensional analytical models were developed for the two 500-kV transformers. That is, the Pauwels transformer at the Moss Landing substation and the Westinghouse transformer at the Midway substation. The models were developed using linear elastic beam elements with lumped masses to represent the behavior of the 500-kV and 230-kV bushings, the two supporting turrets, and the transformer's tank. All other components were considered as rigid elements connected to the transformer's centers of gravity with a single lumped mass located at the components' centers of gravity. The exception were the conservator tank for the Pauwels transformer and the lightning arrester for the Westinghouse transformer, both flexible components with low natural frequencies, which were also modeled with beam elements and lumped masses. Box sections were considered for the transformer tank and annular sections for the bushings, turrets, and lightning arresters. The transformers' base was assumed fully fixed so soil-structure interaction effects were neglected. Similarly, no oil sloshing effects were considered since the transformers' tanks are supposed to be completely full under operating conditions. In both cases, adjustments were made to the dimensions and properties of the transformers' components to match as closely as possible the values of the transformers' lower natural frequencies obtained from the field tests.

The main dimensions and the nodes used in the analytical models are shown in Figures 3.1 through 3.3 for the Pauwels transformer and Figures 3.4 through 3.6 for the Westinghouse transformer. The configuration and dimensions (in inches) of the considered 500-kV and 230-kV bushings are depicted in Figures 3.7 and 3.8. These dimensions and configuration correspond to the bushings manufactured by ABB Power T&D Company, Inc., of Alamo, Tennessee. Exactly the same bushings were considered for the two transformers. The weights considered for the Pauwels transformer were the following:

Tank and fittings:	16,915 lb.
Core and coil:	252,270 lb.
Tank oil:	91,675 lb.
Oil conservator with oil and support:	16,068 lb.
Lightning arrester and support:	1,036 lb.
Headers and coolers with oil:	24,018 lb.

Similarly, the weights considered for the Westinghouse transformer were:

Case and fittings:	48,800 lb.
Core and coils:	254,000 lb.
Radiators:	72,000 lb.
Main unit oil:	67,350 lb.
Radiator oil:	20,750 lb.
Lightning arrester:	1,036 lb.

The weight of the turrets was estimated in terms of the weight of the steel section with which they are made and the oil contained by them in the case of the Pauwels transformer. The weights considered for the bushings were 4,190 pounds for the 500-kV bushings and 1100 pounds for the 230-kV bushings. These weights and the dimensions shown in Figures 3.1 through 3.8 were obtained from copies of the manufacturers' drawings as well as the identification plates attached to the transformers' tanks. It should be noted, however, that some of the weights and dimensions used in the study were estimated since they were not given explicitly in the drawings and the drawings were not to scale.

The nodal masses in the analytical models were calculated according to the weights listed above and the corresponding tributary volumes. In regard to the masses considered for the transformers' tanks, it was assumed that the core and coils mass were an integral part of them. This assumption was based on the fact that, according to the notes in the drawings for the Westinghouse transformer, the core and coils inside a transformer's tank are permanently braced to withstand handling, shipping, and operating forces.

It should be noted at this point that the analytical models described above do not account for many local flexibilities. An example is the flexibility of the cover plate on top of the turrets, which serves as the mounting surface for a bushing's flange. It has been shown that as result of this flexibility, the natural frequency of a bushing may change appreciably from the natural frequency that would be obtained under the assumption of a fixed base. Another example is the flexibility of the rubber gaskets that separate the different porcelain units in a bushing. It should be realized, thus, that the intention of the developed analytical models was to capture the main vibrational characteristics of the transformers. It should be realized too that these main vibrational characteristics may be captured accurately if the models have the same natural frequencies and damping ratios than the prototypes they are supposed to represent. Furthermore, it should be realized that an attempt to model these local flexibilities without a detailed knowledge of the dimensions, properties, and boundary conditions of all the transformers' components would be just an exercise in futility.

The developed analytical models are shown in their undeformed configuration in Figures 3.9 and 3.10.

3.3 Analytical Natural Frequencies and Mode Shapes

The natural frequencies and mode shapes of the three-dimensional models described in the foregoing section were computed using the computer program SAP 2000 (Computers and Structures, 1997). The natural frequencies obtained and a comparison with the values attained experimentally are listed in Tables 3.1 and 3.2, respectively for the Pauwels and Westinghouse transformers. The mode shapes for the first eight modes are depicted in Figures 3.11 through 3.18 for the Pauwels transformer and Figures 3.19 through 3.26 for the Westinghouse transformer. From

the analysis of these figures and the animation of the mode shapes using SAP 2000, it was found that the first six modes of the Pauwels transformer respectively corresponded to the predominant vibration of the (1) HV bushing in the X direction; (2) HV bushing in the Y direction; (3) conservator tank in the Y direction; (4) LV bushing in the X direction; (5) LV bushing in the Y direction; and (6) conservator tank in the X direction; where the X and Y directions respectively correspond to the transformer's longitudinal and transverse directions. Similarly, it was found that the first six modes of the Westinghouse transformer corresponded to the predominant vibration of the (1) lightning arrester along a line between the positive X and Y directions; (2) lightning arrester along a line between the positive X and negative Y directions; (3) HV bushing in the Y direction; (4) HV bushing in the X direction; (5) LV bushing in the Y direction; and (6) LV bushing in the X direction; where the X and Y directions respectively correspond to the transformer's transverse and longitudinal directions.

3.4 Response Spectrum and Time History Analyses

The analytical models described above were also analyzed under a variety of earthquake excitations to study the transformers' dynamic response and quantify the desired amplification factors. The excitations considered in this analysis were: (a) the 2 %-damping response spectrum specified by the Institute of Electrical and Electronic Engineers for the seismic design of substations (IEEE 693 response spectrum); (b) acceleration time histories that envelope the low frequency range of the 2 %-damping IEEE 693 response spectrum (scaled to a peak ground acceleration of 0.5 g in the two horizontal directions and g/3 in the vertical direction); (c) acceleration time histories that envelope the high frequency range of the 2 %-damping IEEE 693 response spectrum (scaled as in the previous case); and (d) acceleration time histories recorded at Los Gatos near-fault station during the 1989 Loma Prieta earthquake [obtained from the suit of near-fault time histories developed for the SAC steel project (Somerville, 1997)]; and (e) acceleration time histories recorded at Olive View Hospital near-fault station during the 1994 Northridge earthquake (also obtained from the aforementioned suite). The IEEE 693 acceleration response spectrum for 2 per cent damping is shown in Figure 3.27. Figures 3.28 through 3.35 depict the aforementioned acceleration time histories and their corresponding acceleration response spectra. Note that together these excitations represent a broad variety of ground motions, ranging from excitations with a wide frequency content, such as the IEEE 693 spectrum, to excitations with a strong pulse that is characteristic of the ground motions recorded at near-fault sites.

As with the calculation of the models' natural frequencies and mode shapes, the computation of their dynamic response was also performed with the computer program SAP 2000, which has the capability of representing an earthquake input either in the form of a response spectrum or an acceleration time history. In each case, this computation was carried out considering simultaneously three components of ground motion, two horizontal and one vertical. In the case of the IEEE 693 response spectrum, the excitation along each of the three orthogonal directions was defined by this spectrum, except that in the vertical direction the spectrum was scaled by a factor of 2/3. It was considered, also, that every mode was damped with a damping ratio of 2 per cent, which is the average value obtained from the field tests. The response of interest was in all cases the shear force at the base of the bushings as the objective of the analysis was to quantify the amplification factors under investigation and, as indicated in Section 1.3, these amplification factors were defined in terms of such forces.

3.5 Ground Motion Amplification Factors

The results of the response analysis are summarized in Table 3.3. For each of the excitations considered, this table shows the peak shear force at the base of the transformers' bushings for two different cases. In the first case, the bushings are considered mounted on the top of the turrets, i.e., the actual turret and transformer tank flexibility is taken into account. In the second case, the bushings are assumed mounted directly on the ground. That is, it is considered that the turrets and transformer tanks are infinitely rigid. Table 3.3 also shows the corresponding ground motion amplification factors, which are computed by dividing the peak shear force obtained in the first case by the peak shear force obtained in the second case.

It may be observed from the results in Table 3.3 that, respectively for the 500-kV and 230-kV bushings, the obtained ground motion amplification factors were as large as 1.89 and 3.39 for the Pauwels transformer and 1.74 and 3.95 for the Westinghouse transformer. In other words, the largest ground motion amplification factors turned out to be close to 2.0 for the 500-kV bushings and close to 4.0 for the 230-kV bushings.

Chapter 4

CONCLUSIONS

4.1 Summary

A study was conducted to quantify the ground motion amplification that takes place at the base of the bushings mounted on electric substation transformers as a result of the flexibility of the transformer tank and turrets to which they are connected. The study included field tests of typical transformers to obtain experimentally their natural frequencies and damping ratios, the development of simple, three-dimensional, analytical models that closely matched the experimental data, and the calculation of the transformers' dynamic response under a series of different earthquake excitations using these analytical models. The field tests were conducted by placing a 160-lb shaker on top of the transformers' tanks, laterally exciting the transformers with a random force of up to 100 pounds, and measuring the transformers' acceleration or velocity response at several points along their height. The calculation of the transformers' dynamic response involved response spectrum and time history analyses under three components of ground motion. It also entailed the calculation of the transformers' ground motion amplification factors at the base of the 500-kV and 230-kV bushings for each of the excitations considered. These amplification factors were obtained by dividing the computed peak shear force at the base of the bushings by the corresponding shear force when the bushings are assumed mounted directly on the ground.

4.2 Conclusions

From the results of the analytical study, it is found that the ground motion amplification factors may be as large as 1.89 for the 500-kV bushings, and as large as 3.95 for the 230-kV bushings. Hence, it is found that the amplification factors for the 500-kV bushings are within the amplification factor of 2.0 specified by Standard IEEE 693 but not those for the 230-kV bushings, which exceed the Standard IEEE 693 amplification factor by a factor of almost two.

In the interpretation of these findings, it is important to keep in mind that only two out of an existing large variety of transformers were studied. It is possible, therefore, that other types of transformers could exhibit larger amplification factors, particularly older models with no seismic design. It is also important to keep in mind that the experimental and analytical studies on which these findings are based were both conducted with some limitations. The experimental studies were limited by the small level of the force used to excite the transformers. Although useful information was extracted with such a small exciting force, it is possible that some parts or components were not sufficiently excited during the tests and, hence, it is possible that the contribution of these parts or components towards the overall vibrational characteristics of the transformers was not accounted for. Along the same lines, the small exciting force prevented the activation of nonlinear effects such as the interaction between internal components and the slippage of the bushings' porcelain units. These nonlinear effects are likely to affect the vibrational characteristics of the transformers and likely to be present during a strong earthquake, although it is not know at this time how significant this influence might be. Low excitation levels may also result in unrealistic damping values since, as is well known, these damping values may increase significantly with the level of excitation. The limitations of the analytical study lie on the simplicity of the models used and the assumptions made in regard to some of the dimensions and properties of the transformers'

components. As indicated in Section 3.2, the models neglect soil-structure interaction effects and important local flexibilities such as the flexibility of the turret cover plates on which the bushings are mounted and the flexibility of the rubber gaskets that separate the different porcelain units in a bushing. They also neglect the aforementioned interaction between internal components and non-linear effects.

Despite its limitations, it is believed that the study herein reported gives an overall idea of the dynamic properties of the investigated transformers and their response to earthquake ground motions. Therefore, another conclusion that can be drawn from this study is that the use of simple analytical models calibrated with experimental data constitutes an adequate but inexpensive way to define the earthquake input to equipment in electric substations.

4.3 Recommendations for Future Studies

Power transformers are large, complicated, asymmetric structures with a large number of parts and components, materials that defy characterization, and a large number of closely coupled modes of vibration. Further field tests are therefore recommended to investigate fully their dynamic characteristics and generate the experimental data that is needed to be able to develop and calibrate advanced analytical models. To this end, it is recommended to conduct tests under levels of excitations higher than the levels used in this study. In particular, it is suggested the use of impact tests as opposed to the use of the shaker employed in this investigation, as it was found that the input energy imparted by the shaker was in many instances inadequate to define the transformers' dynamic properties with sufficient clarity. An exhaustive test using an impact hammer at a large number of locations may provide the data that is needed to thoroughly define the dynamic characteristics of power transformers.

Another recommendation is the instrumentation of a number of transformers with strong motion accelerographs. Field instrumentation is the only viable alternative to investigate the actual behavior of transformers under earthquake ground motions and may provide, in the event of a strong earthquake, with invaluable data to validate findings from this and other studies.

REFERENCES

1. Bellorini, S., Bettinali, F., Salvetti, M., and Zafferani, G., "Seismic qualification of transformer high voltage bushings," *IEEE Transactions on Power Delivery*, Vol. 13, No.4, Institute of Electrical and Electronic Engineers, Oct. 1998, pp. 1208-1213.

2. Benuska, L., Technical Editor, "Loma Prieta Earthquake Reconnaissance Report," *Earthquake Spectra,* supplement to Volume 6, May 1990.

3. Computers and Structures, Inc., *SAP 2000: Integrated Finite Element Analysis and Design of Structures,* Version 6.1, Berkeley, Calif., Sept. 1997.

4. Ibáñez, P., Vasudevan, R., and E. J. Vineberg, "A comparison of experimental methods for seismic testing of equipment," *Nuclear Engineering and Design*, Vol. 25, 1973, pp. 150-162.

5. Palk, B. V., Hawley, J. W., P. Ibáñez, and C. B. Smith, "A comparative study of seismic testing methods," *IEEE Transactions on Power Apparatus and Systems*, Vol. PAS-94, No. 3, May/ June 1975, pp. 1003-1012.

6. Richardson, M. H., "Measurement and analysis of the dynamics of mechanical structures," *Proc. Hewlett-Packard Conference for Automotive and Related Industries*, Detroit, Mich., Oct. 1978.

7. Schiff, A. J., Editor, *Northridge Earthquake: Lifeline Performance and Post-Earthquake Response,* Technical Council on Lifeline Earthquake Engineering, Monograph No. 8, ASCE, Aug. 1995.

8. Somerville, P., *Suites of Earthquake Ground Motions for Analysis of Steel Moment Frame Structures*, Draft Report, SAC Joint Venture Steel Project, Phase 2, March 21, 1997.

9. Suzuki, H., Sugi, T., Kuwahara, H., and Kaizu, N., "Studies on aseismic isolation device for electric substation equipment," in *Soil-Structure Interaction*, A. S. Cakmak, Editor, Developments in Geotechnical Engineering, Vol. 43, Elsevier, 1987.

Table 2.1. Natural frequencies and damping ratios of Pauwels 500-kV transformer from experimental data

Mode	Natural frequency (Hz)	Damping ratio (%)
1	3.4	1.5
2	3.4	2.1
3	5.1	2.6
4	5.6	1.6
5	5.8	1.8
6	6.4	1.7
7	13.1	1.7
8	18.4	0.8
9	19.8	0.3
10	22.1	0.7

Table 2.2. Natural frequencies and damping ratios of Westinghouse 500-kV transformer from experimental data

Mode	Natural Frequency (Hz)	Damping ratio (%)
1	2.4	3.6
2	2.4	3.6
3	3.1	3.8
4	3.6	3.7
5	4.6	2.3
6	6.2	2.0
7	8.2	1.4
8	9.2	1.6
9	10.1	1.8
10	12.0	0.7
11	19.1	0.4
12	20.2	0.4

Table 2.3. Natural frequencies and damping ratios of Smit 230-kV transformer from experimental data

Mode	Natural frequency (Hz)	Damping ratio (%)
1	4.1	4.5
2	4.6	4.2
3	5.9	1.9
4	6.0	2.1
5	7.4	1.8
6	8.1	2.5
7	8.8	1.3
8	10.4	1.0
9	10.5	1.2
10	11.0	0.9
11	11.6	1.3
12	12.9	2.1

Table 2.4. Natural frequencies and damping ratios of Westinghouse 230-kV transformer from experimental data

Mode	Natural frequency (Hz)	Damping ratio (%)
1	3.8	1.4
2	3.9	2.0
3	5.1	3.0
4	5.9	5.4
5	6.1	5.2
6	6.2	3.0
7	6.7	2.3
8	7.1	1.3
9	7.9	2.7
10	8.1	3.6
11	8.7	1.8
12	13.4	3.7

Table 3.1. Natural frequencies of Pauwels 500-kV transformer according to analytical model and comparison with values obtained experimentally

Mode	Direction	Analytical natural frequency (Hz)	Experimental natural frequency (Hz)
1	Longitudinal	3.5	3.4
2	Transverse	3.5	3.4
3	Transverse	5.1	5.1
4	Longitudinal	5.5	5.6
5	Transverse	5.5	5.8
6	Longitudinal	6.4	6.4
7	Longitudinal	18.6	13.1
8	Transverse	18.8	18.4
9	Transverse	21.2	19.8
10	Longitudinal	23.1	22.1
11	Transverse	24.9	-
12	Longitudinal	30.5	-

Table 3.2. Natural frequencies of Westinghouse 500-kV transformer according to analytical model and comparison with values obtained experimentally

Mode	Direction	Analytical natural frequency (Hz)	Experimental natural frequency (Hz)
1	Both	2.4	2.4
2	Both	2.5	2.4
3	Longitudinal	3.6	3.1
4	Transverse	3.6	3.6
5	Longitudinal	6.0	4.6
6	Transverse	6.0	6.2
7	Longitudinal	7.5	8.2
8	Transverse	9.3	9.2
9	Both	11.1	10.1
10	Both	11.5	12.0
11	Both	15.3	19.1
12	Both	20.3	20.2

Table 3.3. Peak shear force under different excitations at base of transformers' high-voltage (HV) and low-voltage (LV) bushings and corresponding ground motion amplification factors when the bushings are mounted on top of turrets and directly on the ground

Transformer	Excitation	Bushing	Direction					
			Transverse			Longitudinal		
			Shear force (Lb)		Amplification factor	Shear force (Lb)		Amplification factor
			On ground	On turret		On ground	On turret	
Pauwels 500 kV	IEEE 693 spectrum	HV	2139.3	2520.1	1.18	3208.9	6055.3	1.89
		LV	512.0	845.5	1.65	767.9	1769.0	2.30
	IEEE 693 time history, set 1	HV	2009.6	2303.4	1.15	3261.1	5042.1	1.55
		LV	609.5	704.7	1.16	842.8	1300.8	1.54
	IEEE 693 time history, set 2	HV	2019.5	2220.3	1.10	4108.8	4522.5	1.10
		LV	561.5	675.7	1.20	912.6	996.4	1.09
	1989 Los Gatos near-fault record	HV	3369.0	3014.9	0.89	2582.7	4313.1	1.67
		LV	716.4	2427.3	3.39	589.6	1049.0	1.78
	1994 Olive View near-fault record	HV	1107.0	1633.4	1.48	3587.1	4604.5	1.28
		LV	586.8	744.1	1.27	837.1	1023.6	1.22
Westinghouse 500 kV	IEEE 693 spectrum	HV	2630.4	4092.7	1.56	2626.6	4081.4	1.55
		LV	502.3	1641.3	3.27	586.1	2276.1	3.88
	IEEE 693 time history, set 1	HV	3127.6	4474.9	1.43	2313.9	4025.1	1.74
		LV	510.3	1511.1	2.96	579.2	2289.9	3.95
	IEEE 693 time history, set 2	HV	3250.0	4749.2	1.46	3001.9	4791.2	1.60
		LV	383.2	1035.0	2.70	515.4	1826.8	3.54
	1989 Los Gatos near-fault record	HV	3451.6	3958.2	1.15	3970.3	5226.6	1.32
		LV	462.8	665.6	1.44	501.1	1211.6	2.42
	1994 Olive View near-fault record	HV	2828.4	4115.6	1.46	2402.8	3020.8	1.26
		LV	286.5	698.0	2.44	462.1	1260.6	2.73

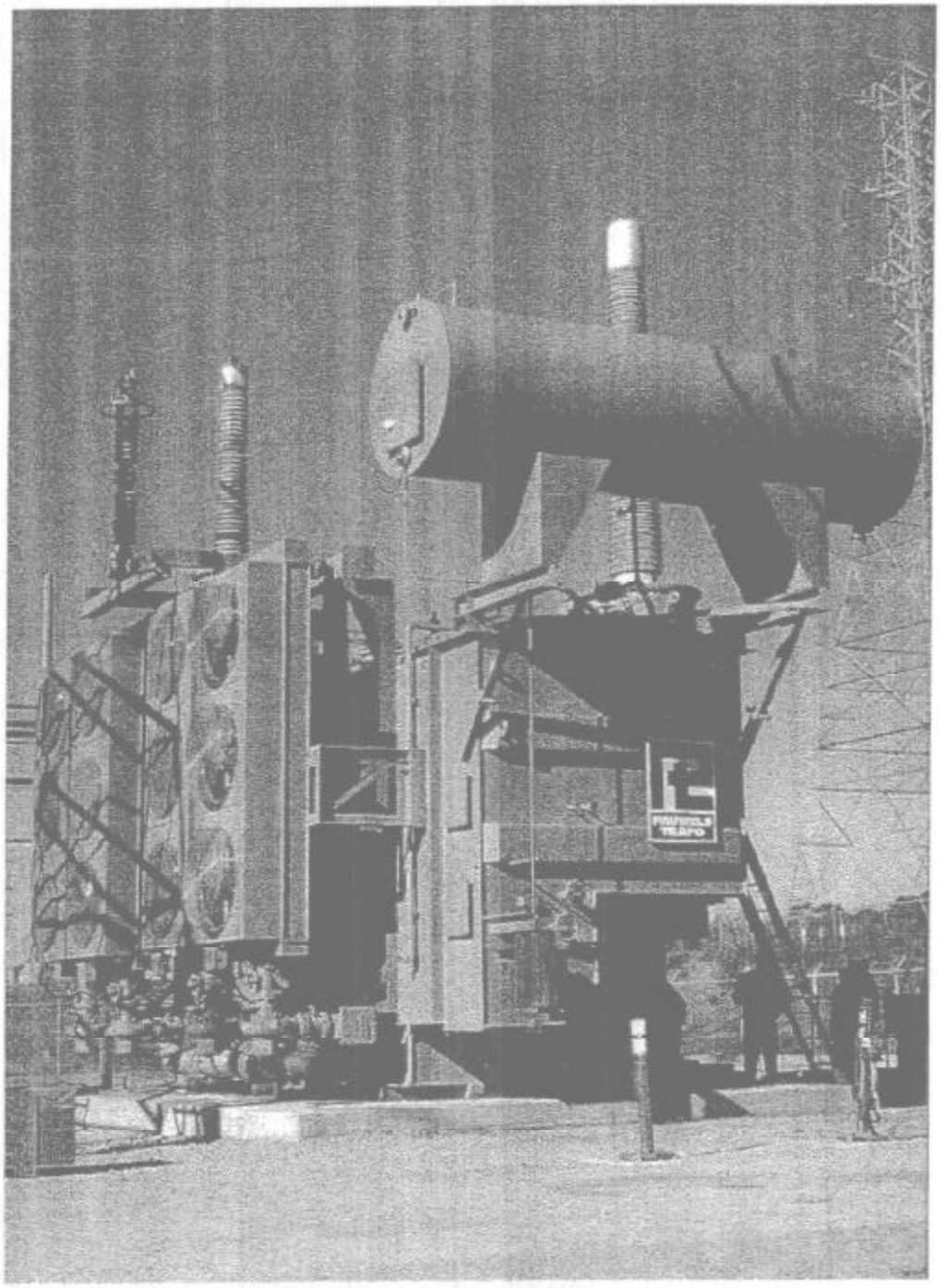

Figure 2.1. Panoramic view of Pauwels 500-kV transformer showing oil conservator tank in foreground

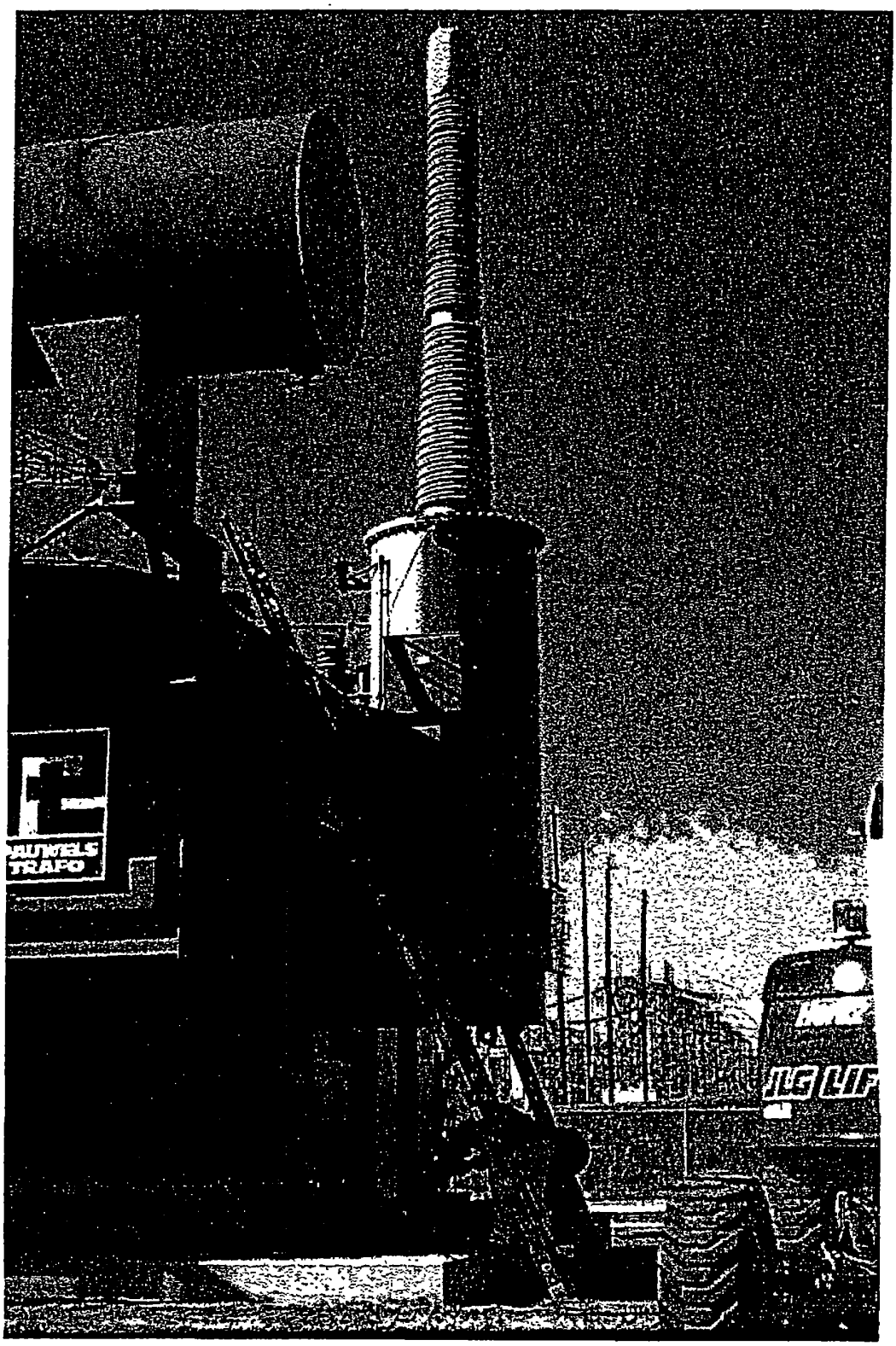

Figure 2.2. Close-up view of high-voltage turret and bushing in Pauwels 500-kV transformer

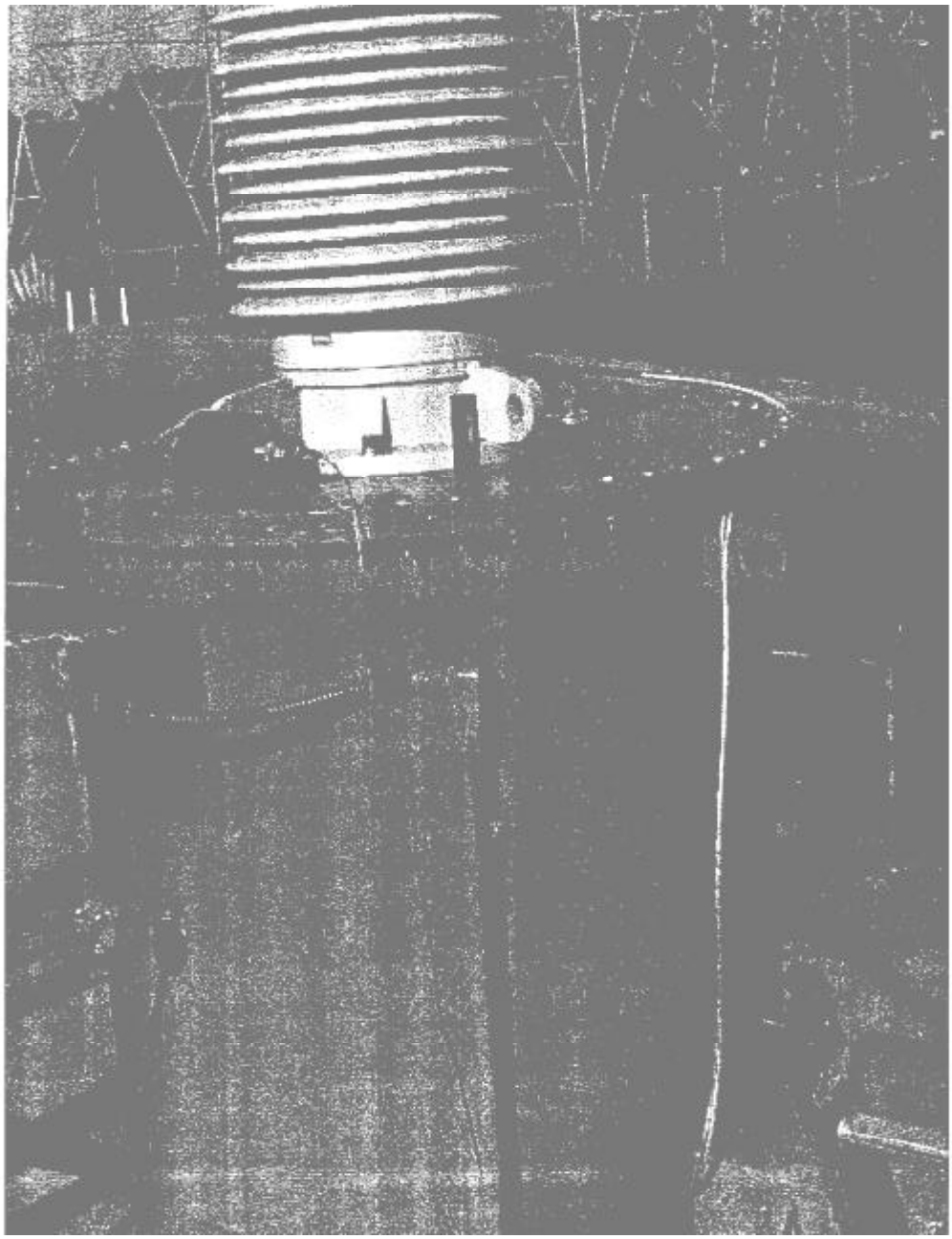

Figure 2.3. Close-up view of turret-bushing connection in Pauwels 500-kV transformer showing also a seisometer resting on turret cover plate

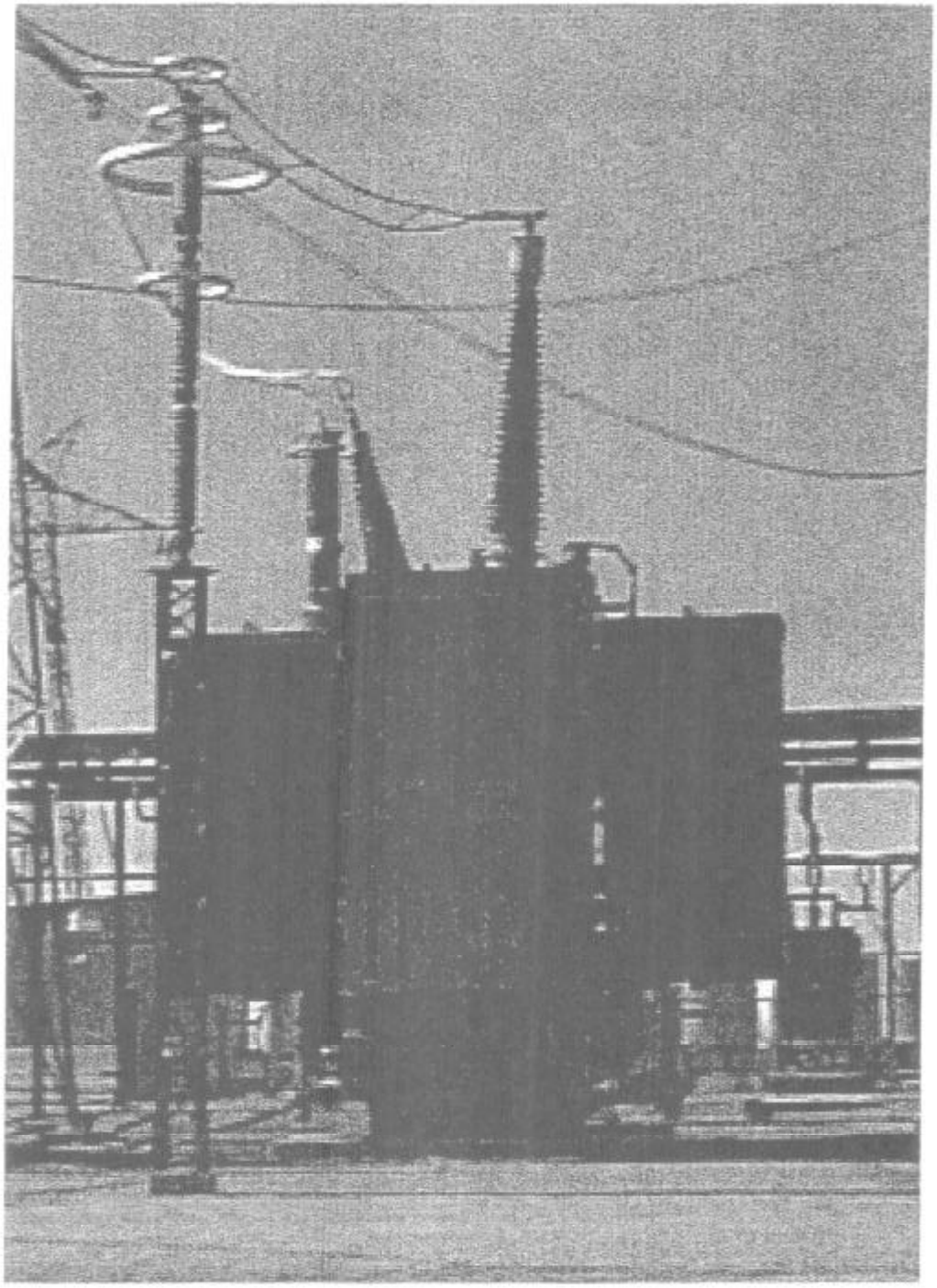

Figure 2.4. Panaramic view of Westinghouse 500-kV transformer

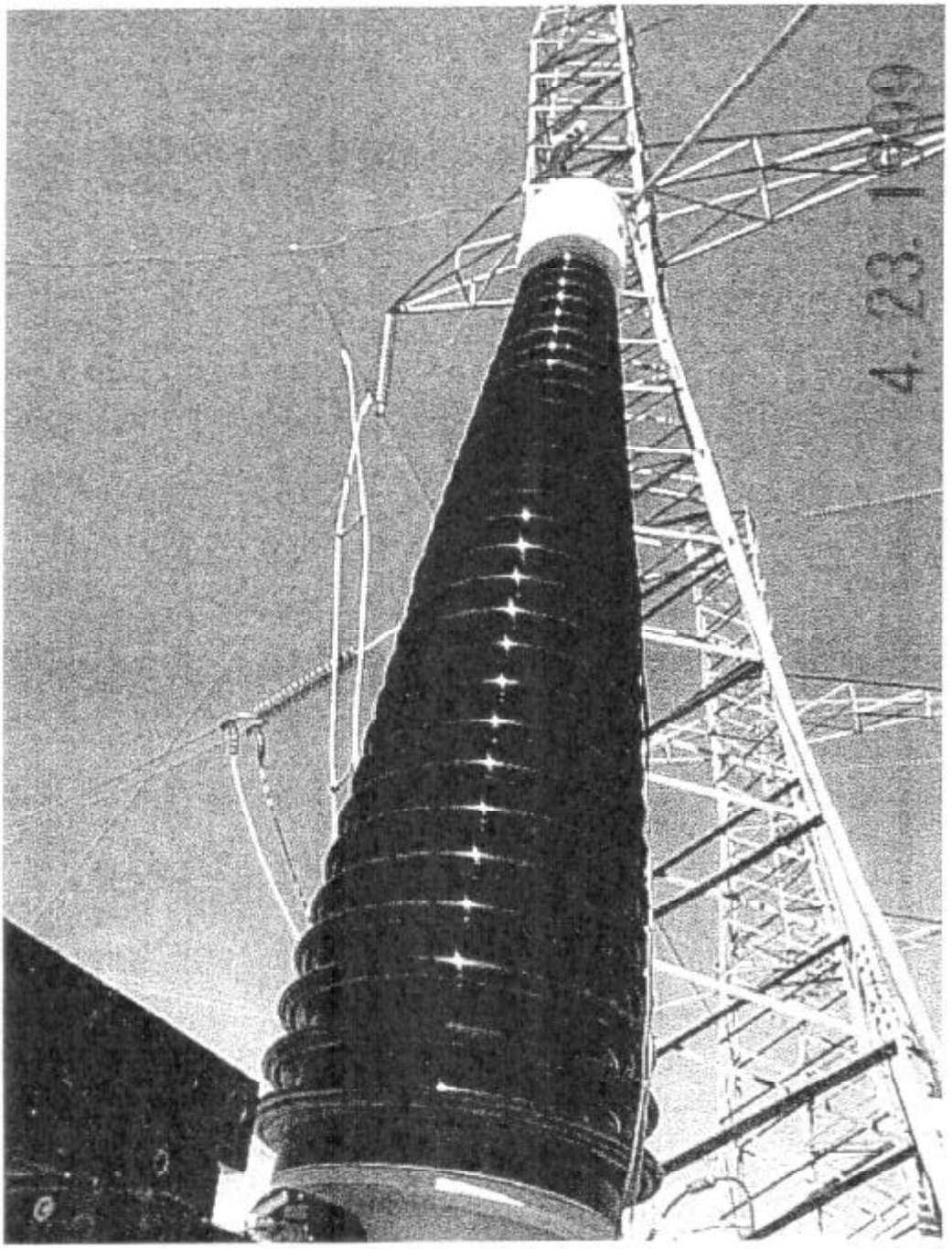

Figure 2.5. Close-up view of high-voltage bushing in Westinghouse 500-kV transformer

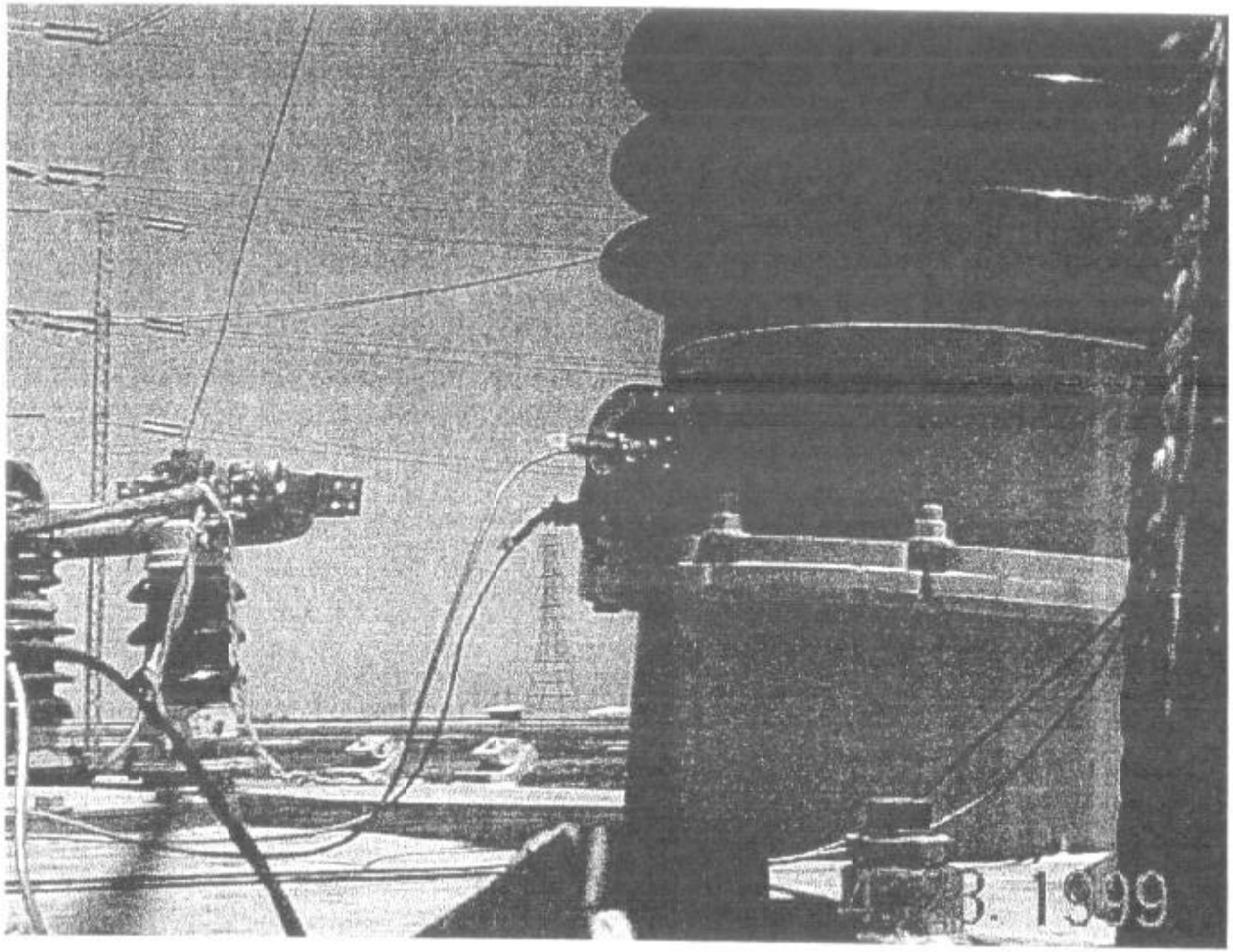

Figure 2.6. Close-up view of turret bushing connection in Westinghouse 500kV transformer, showing also a pair of seismometers resting on turret cover plate

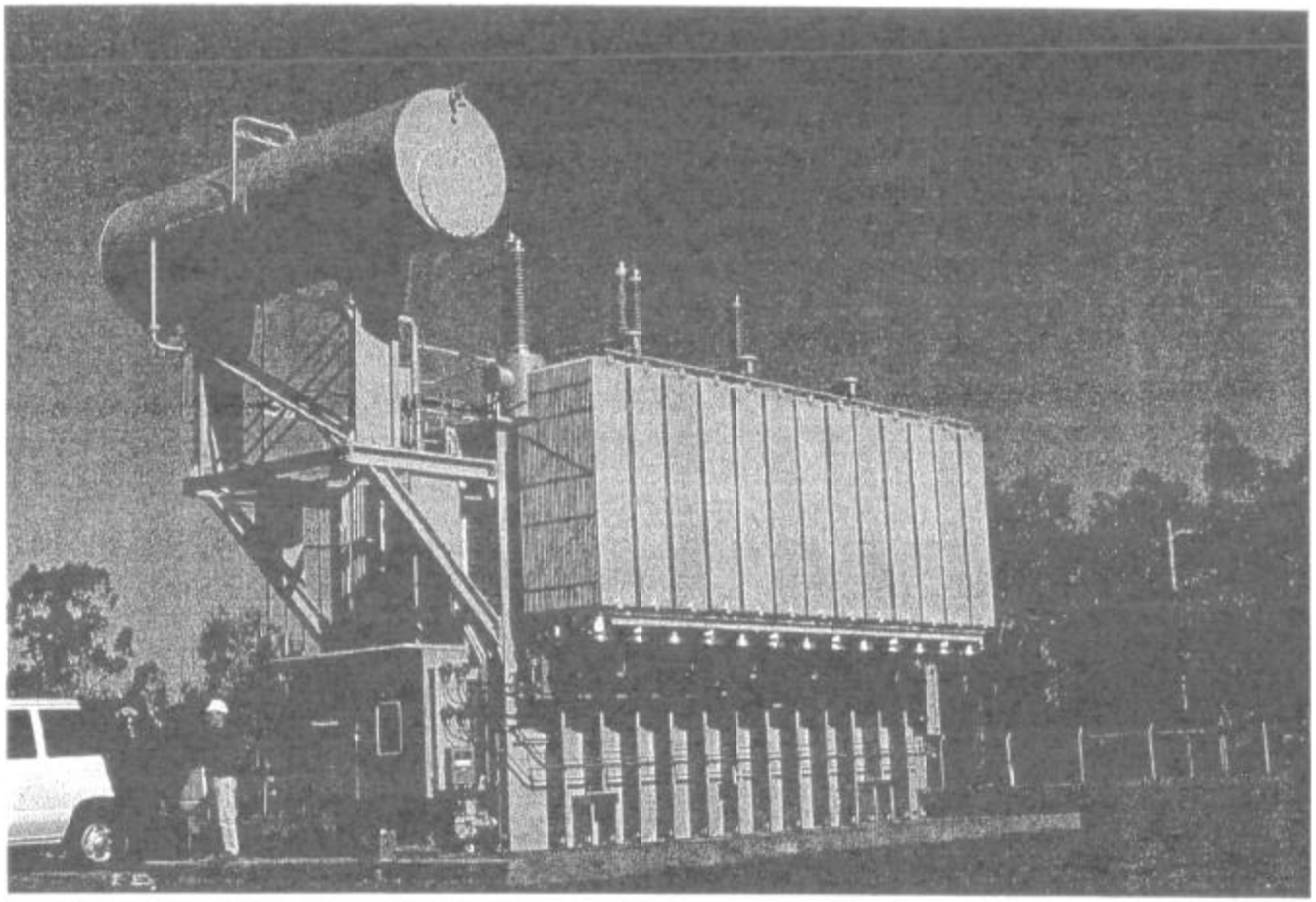

Figure 2.7. Panoramic view of Smit 230-kV transformer showing oil conservator tank in foreground

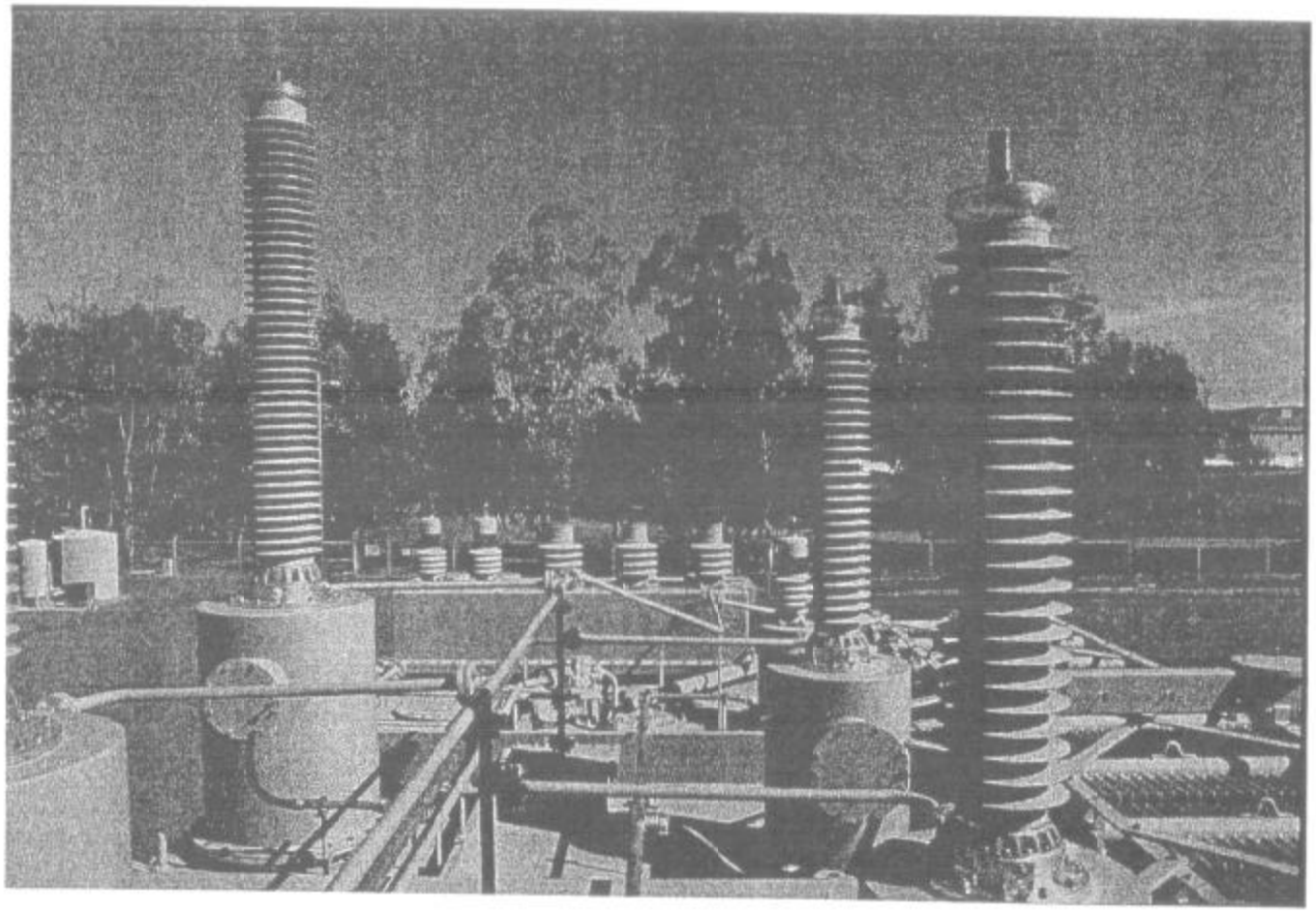

Figure 2.8. Top view of Smit 230-kV transformer showing high- and low-voltage bushings and turrets

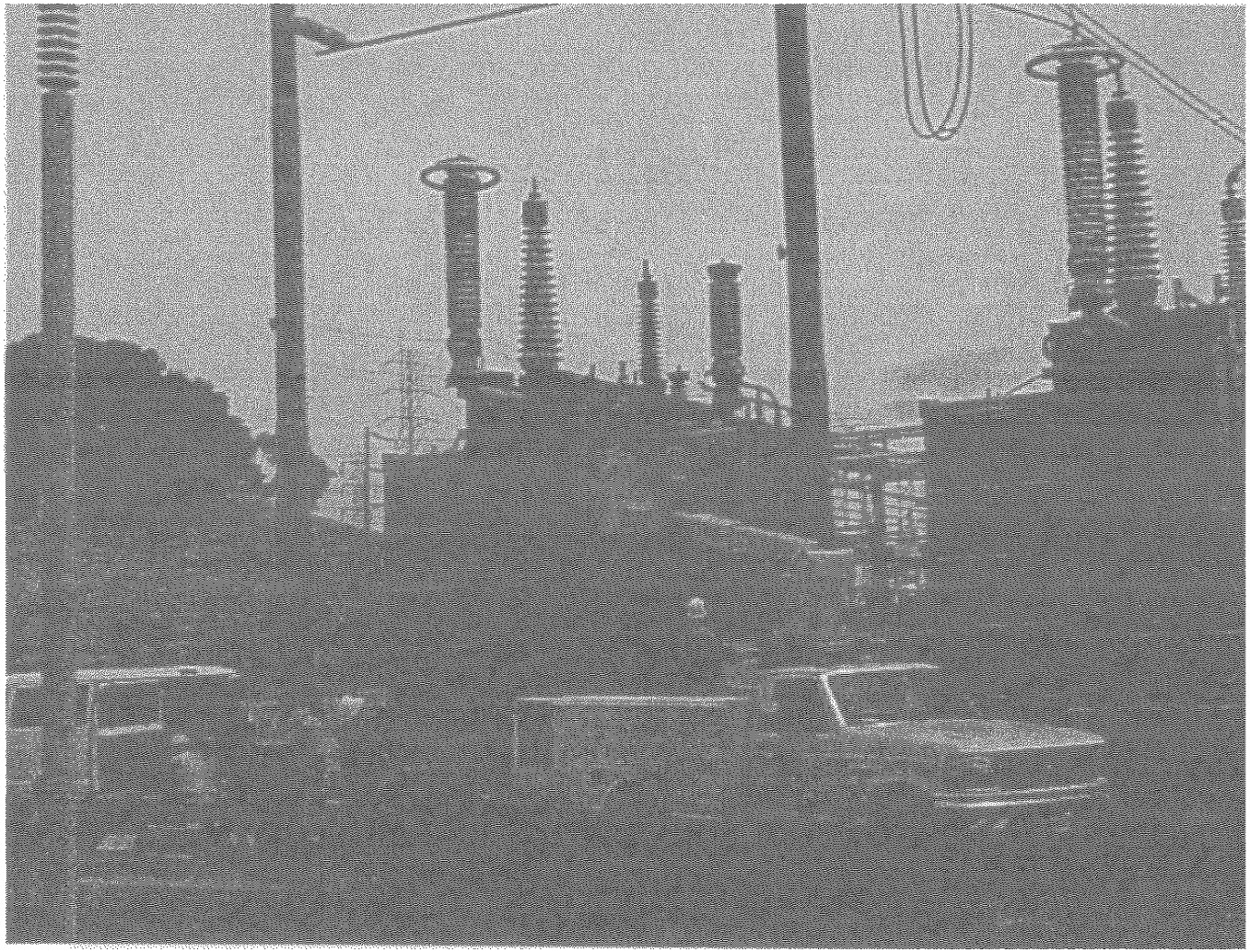

Figure 2.9. Panoramic view of Westinghouse 230-kV transformer showing bushings and lightning arrester

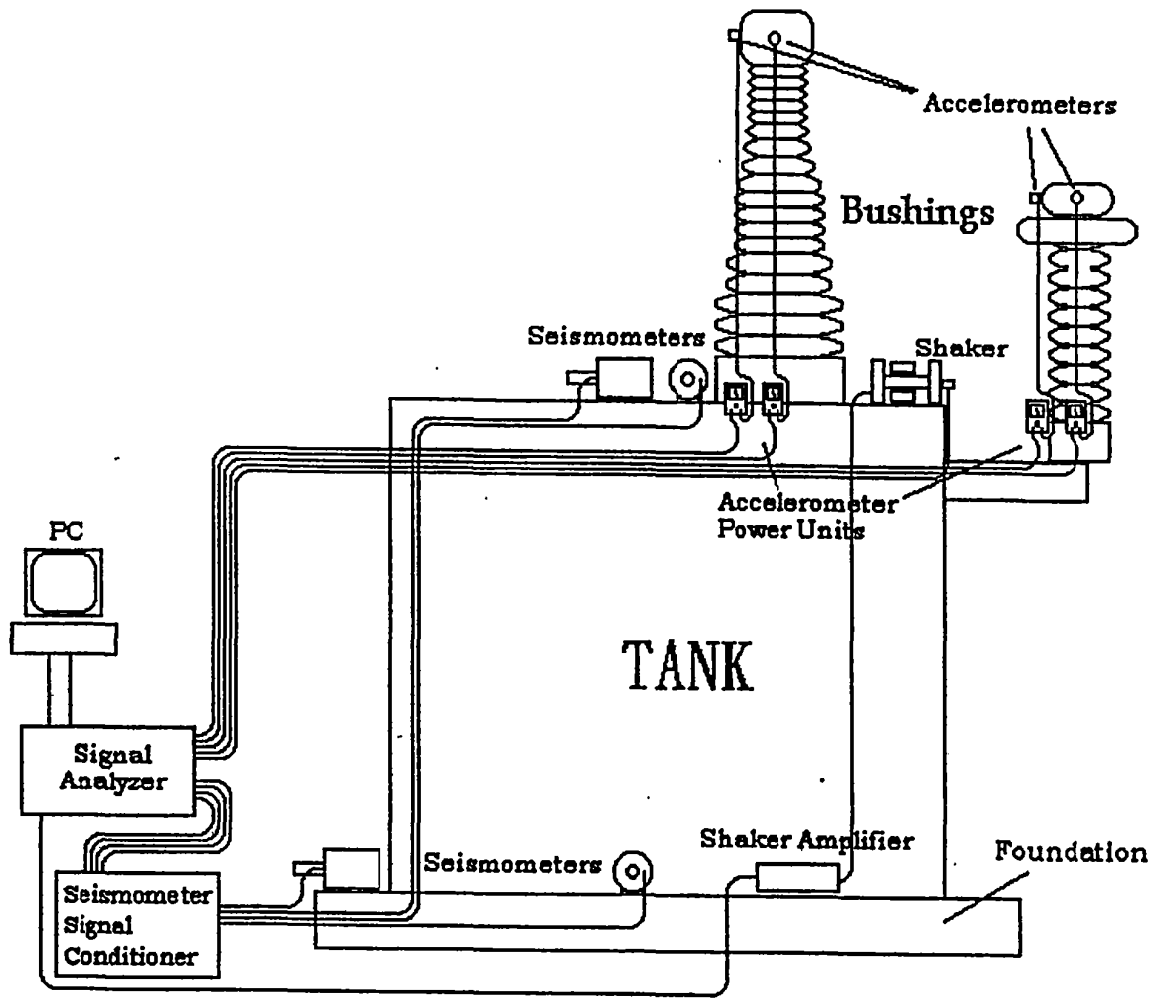

Figure 2.10. Schematic view of experimental set up during field tests

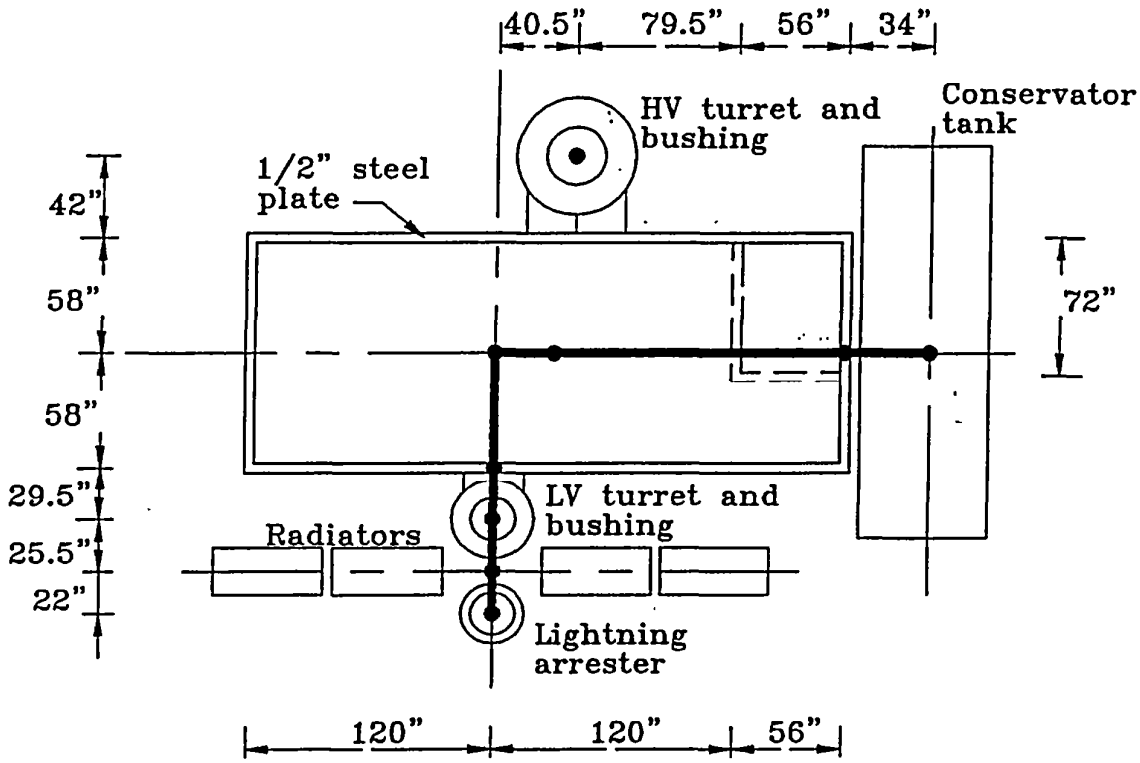

Figure 3.1. Plan view of Pauwels 500-kV transformer

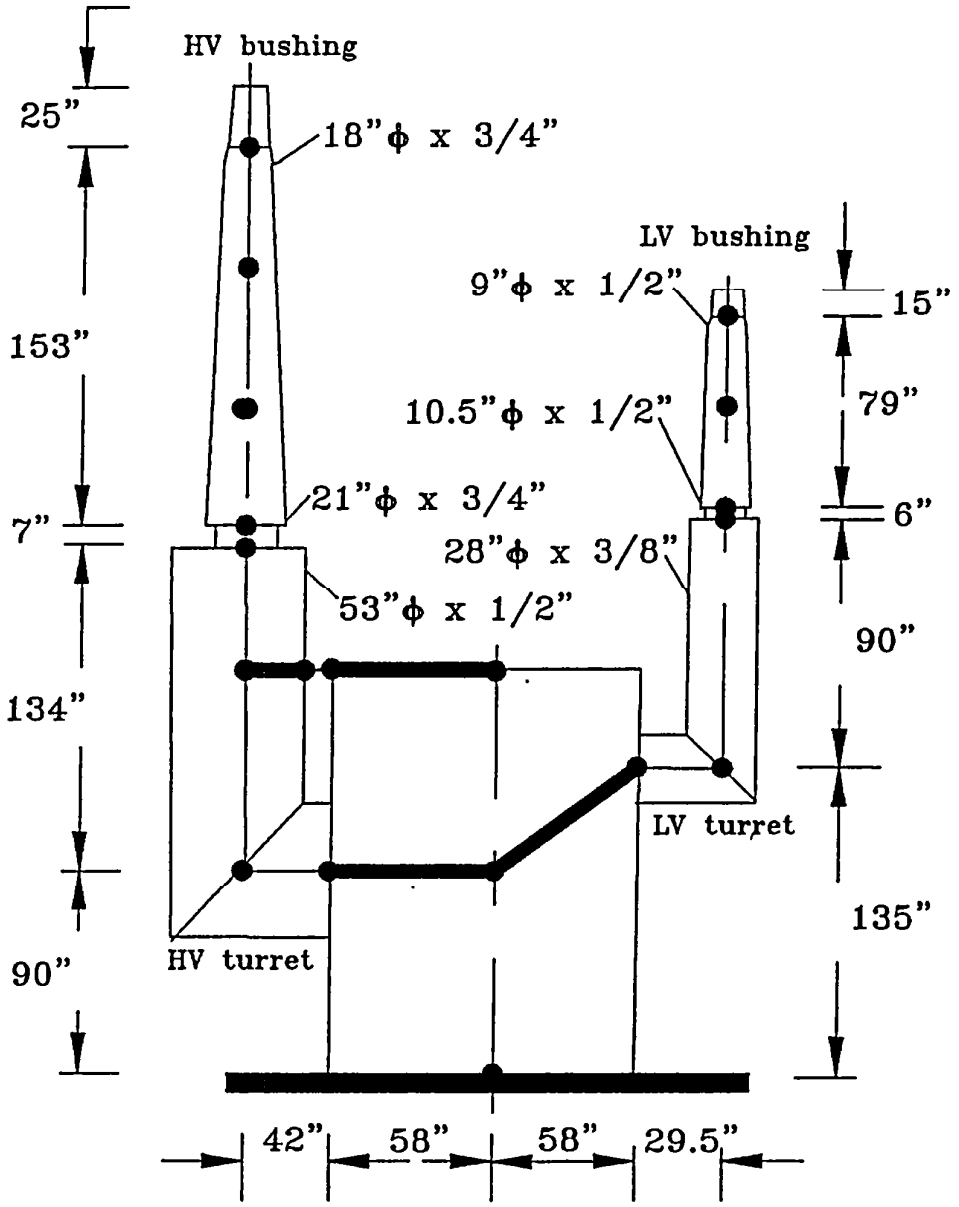

Figure 3.2. Transverse elevation of Pauwels 500-kV transformer

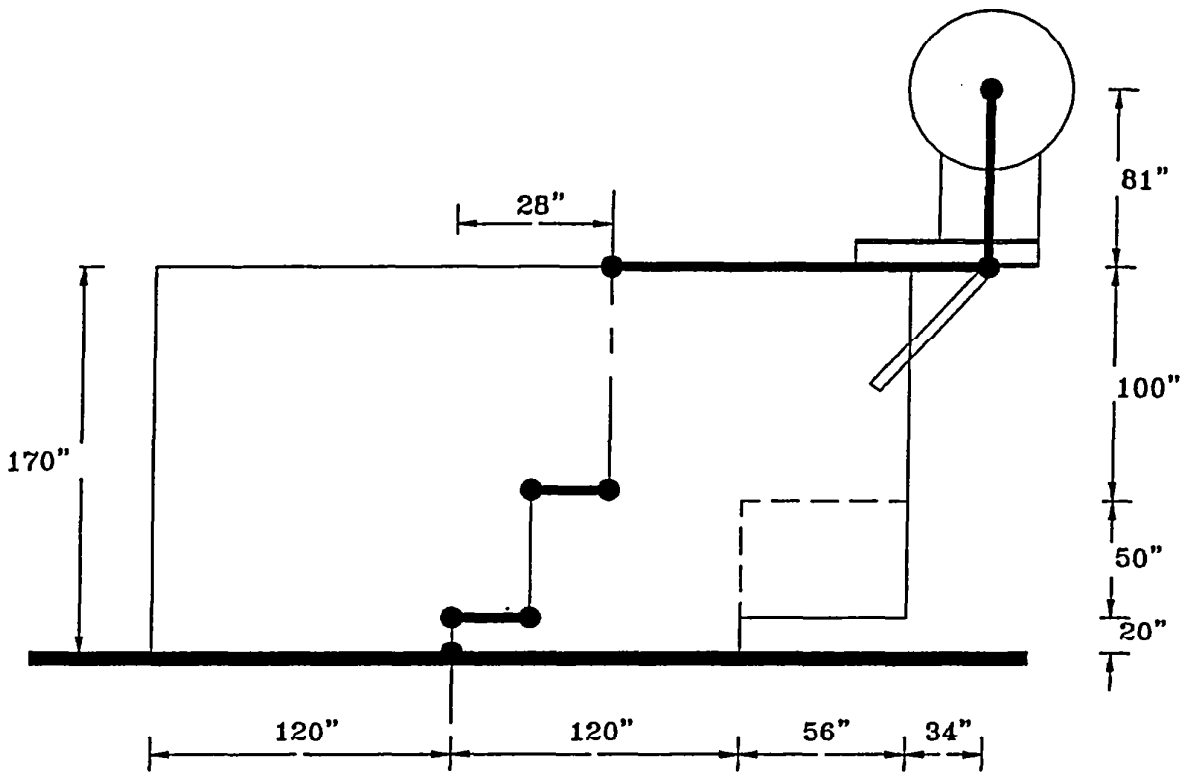

Figure 3.3. Longitudinal elevation of Pauwels 500-kV transformer

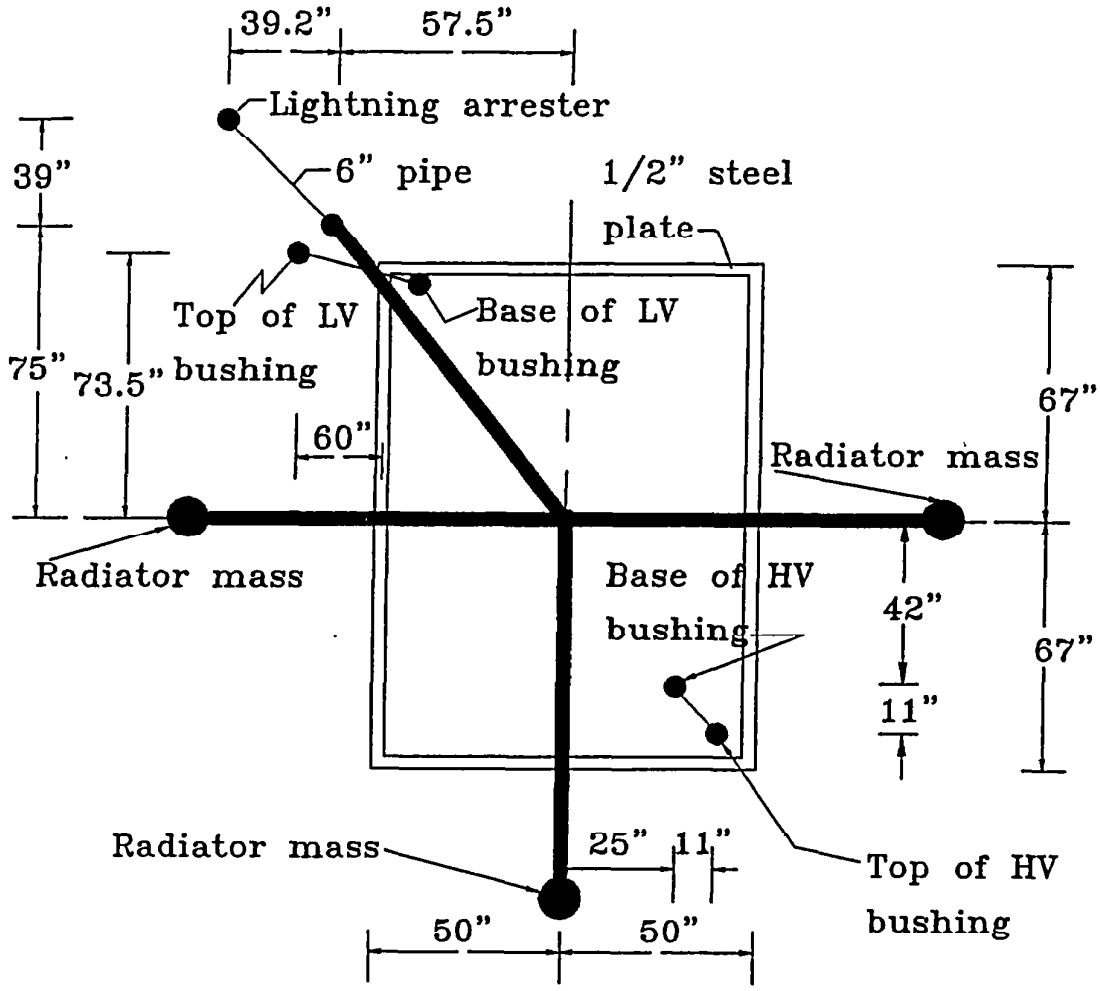

Figure 3.4. Plan view of Westinghouse 500-kV transformer

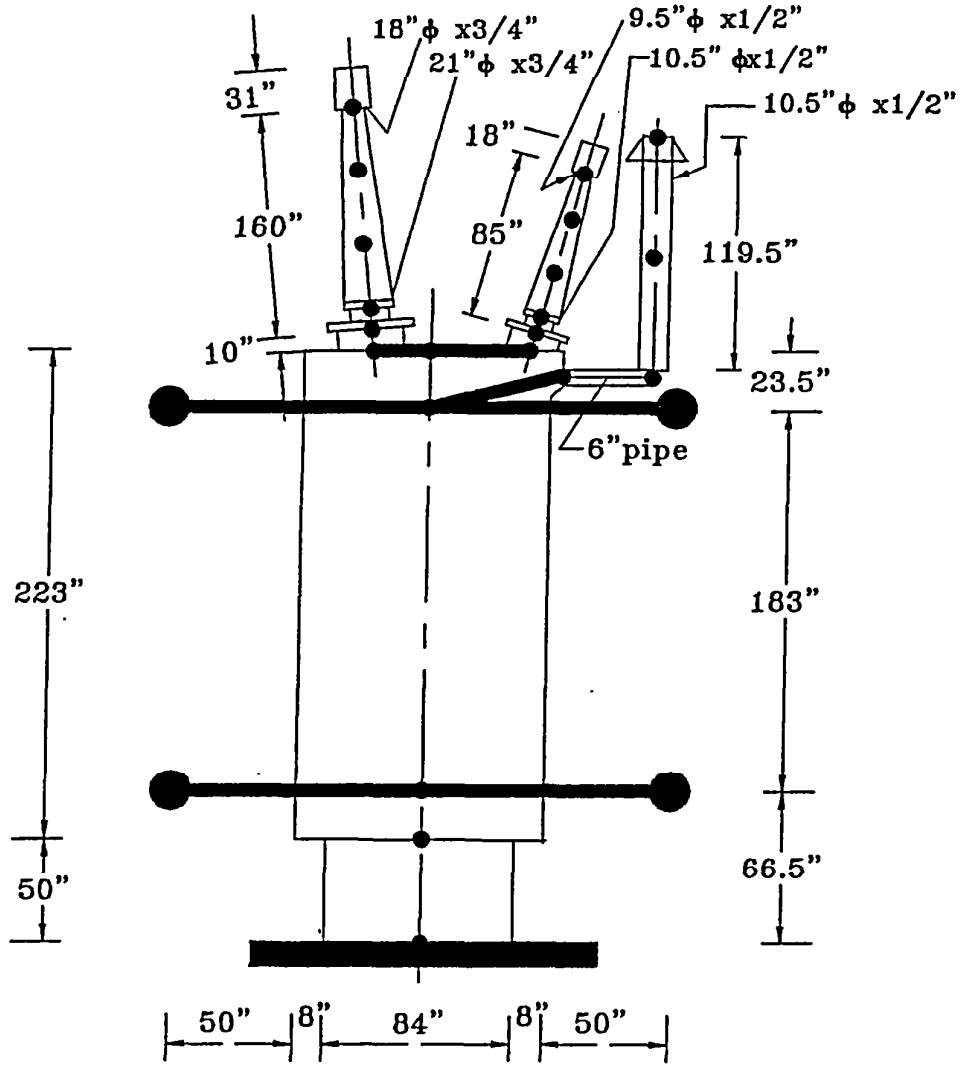

Figure 3.5. Transverse elevation of Westinghouse 500-kV transformer

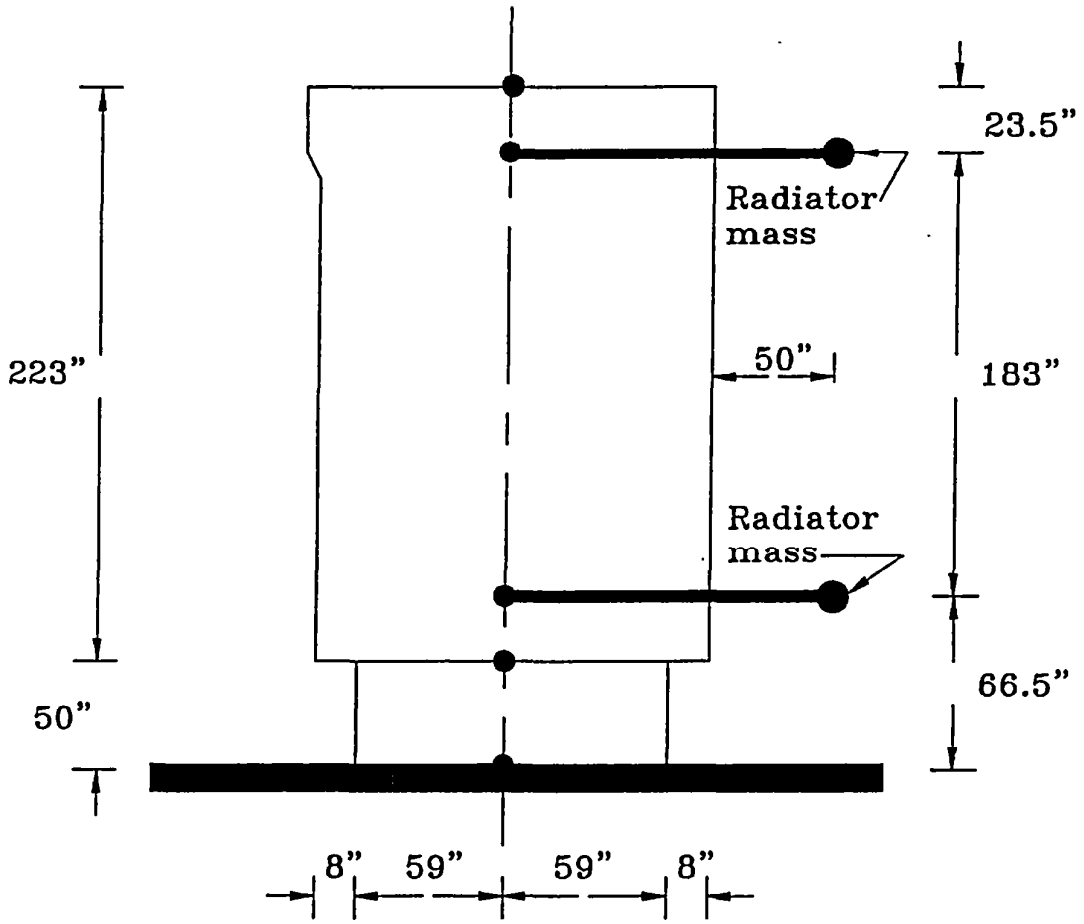

Figure 3.6. Longitudinal elevation of Westinghouse 500-kV transformer

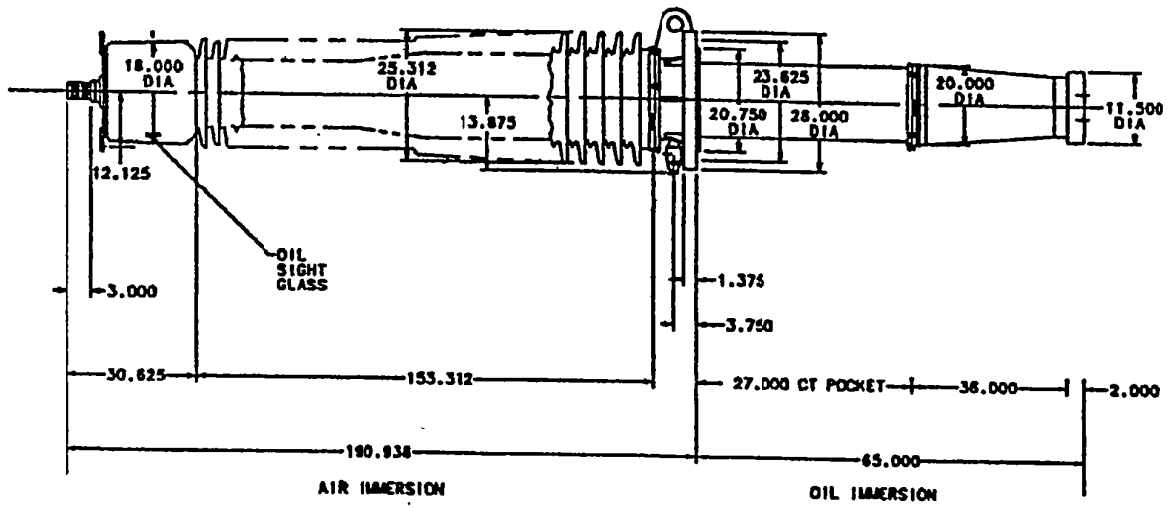

Figure 3.7. Dimensions and configuration of studied 500-kV bushings

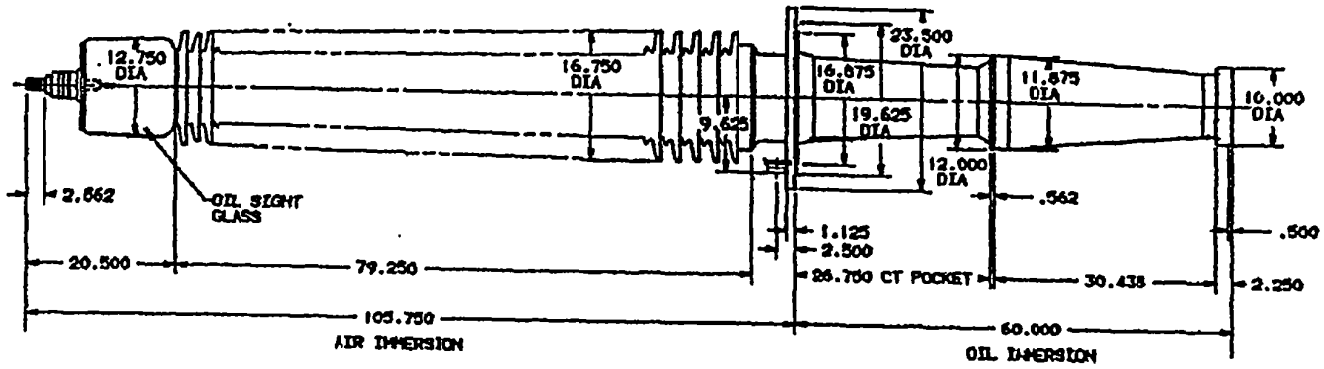

Figure 3.8. Dimensions and configuration of studied 230-kV bushings

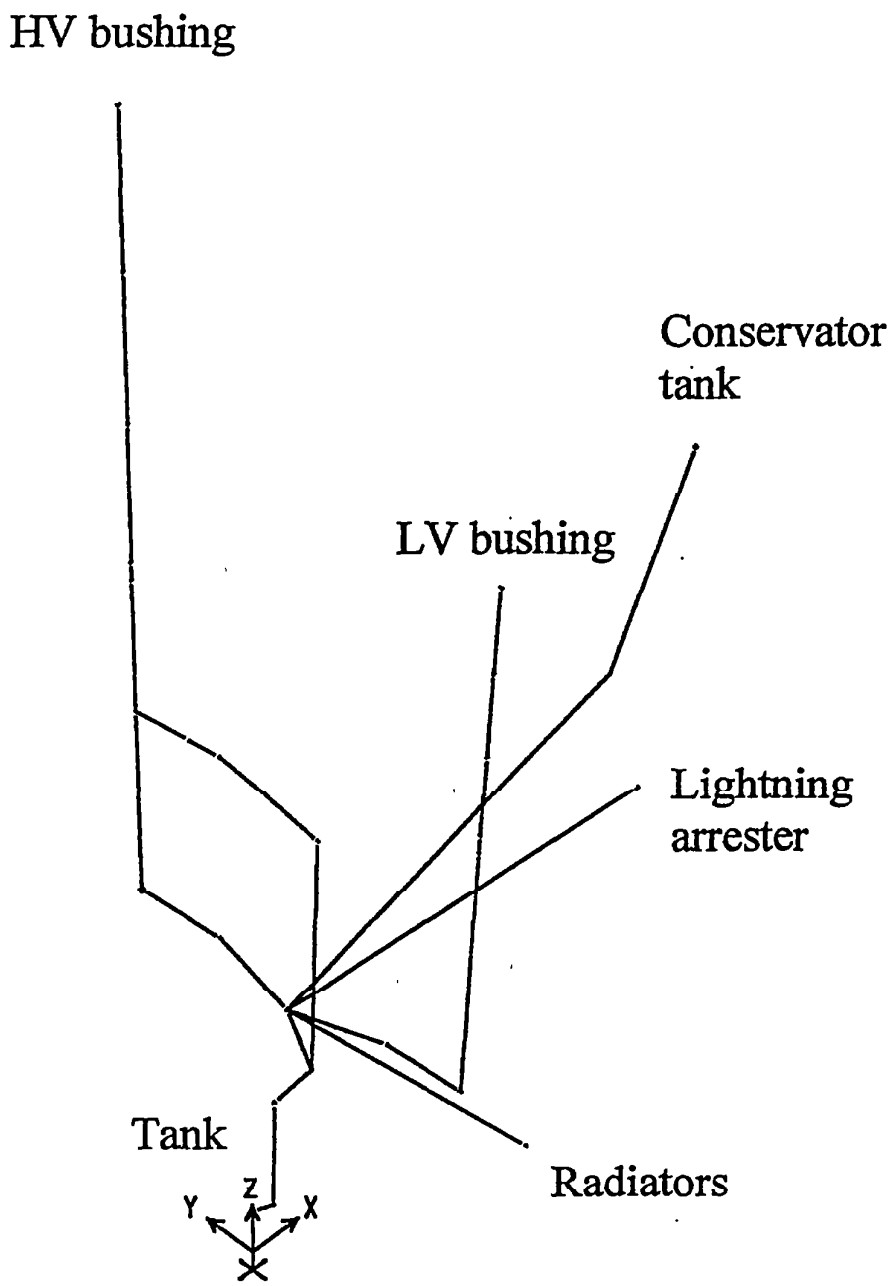

Figure 3.9. Analytical model for Pauwels 500-kV transformer (note: dots represent nodal masses)

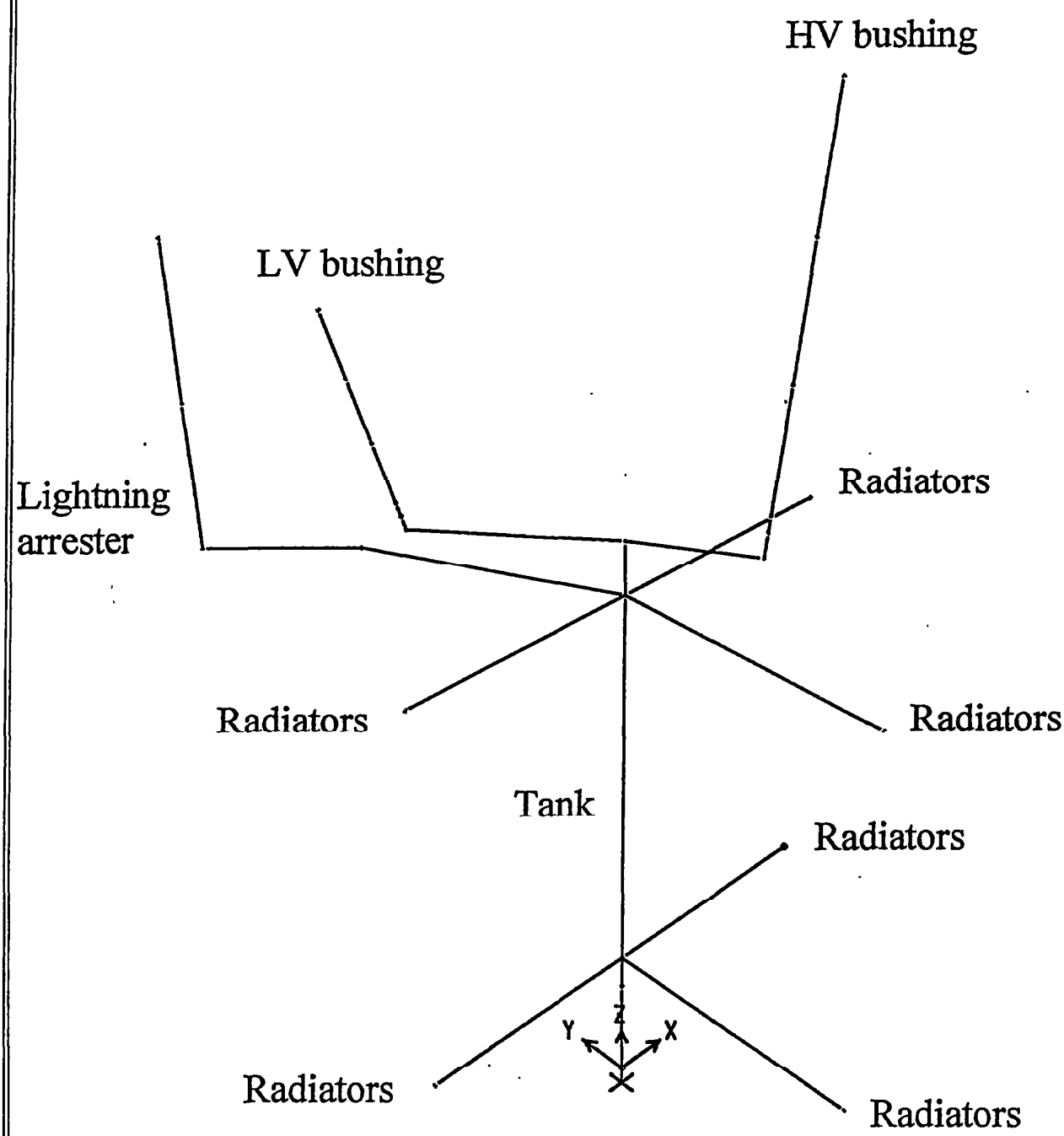

Figure 3.10. Analytical model for Westinghouse 500-kV transformer (note: dots represent nodal masses)

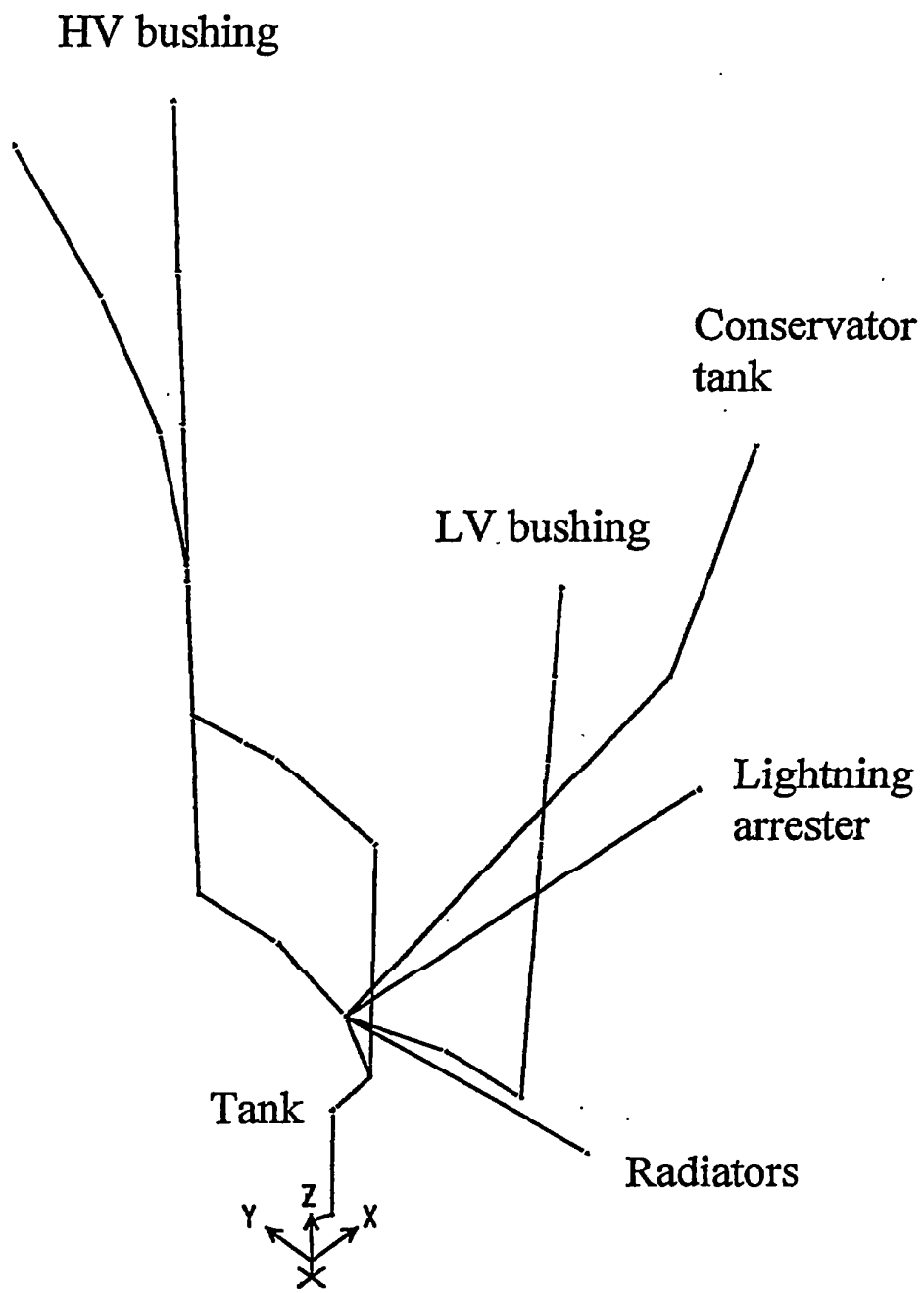

Figure 3.11. First mode of vibration, Pauwels 500-kV transformer

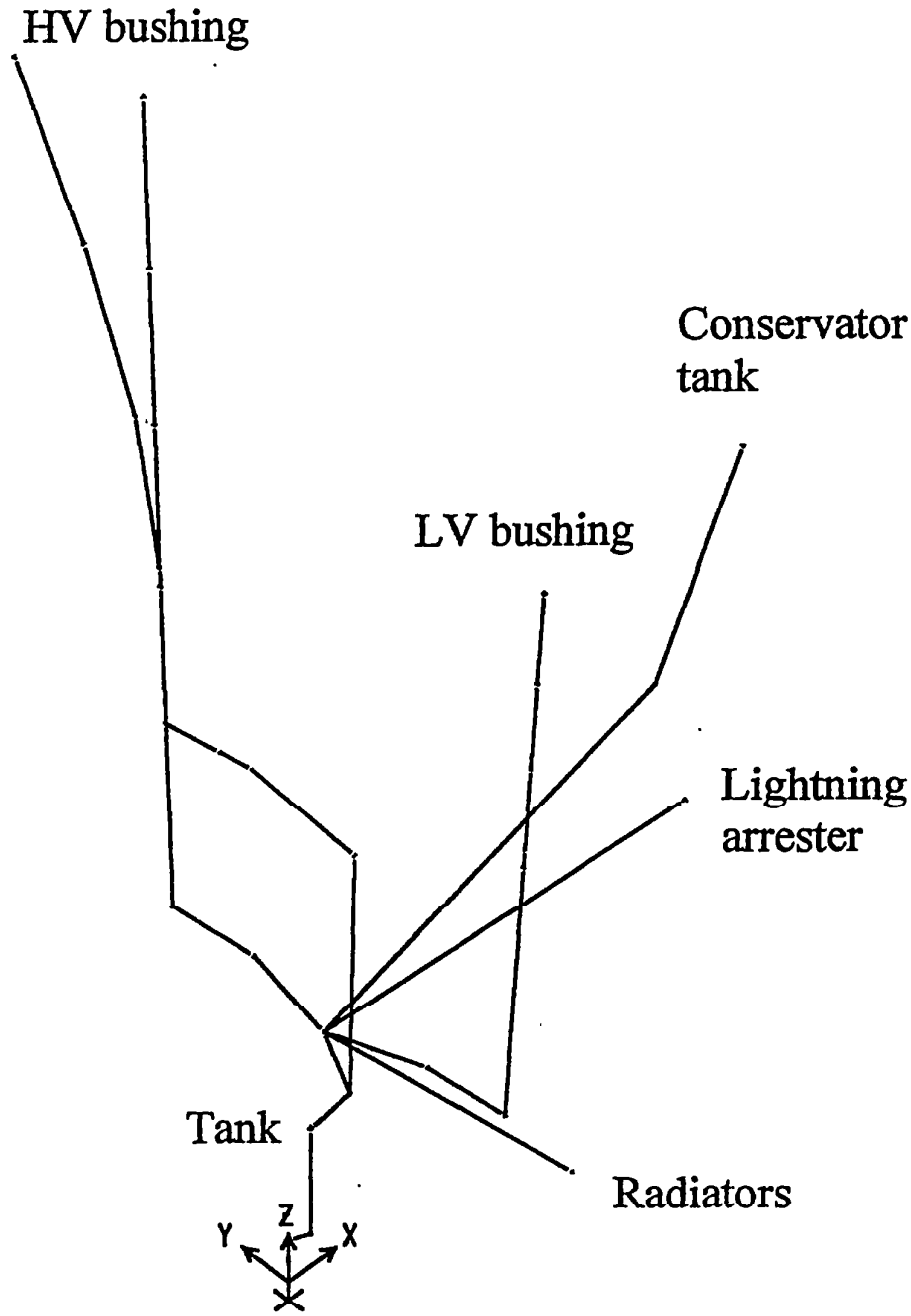

Figure 3.12. Second mode of vibration, Pauwels 500-kV transformer

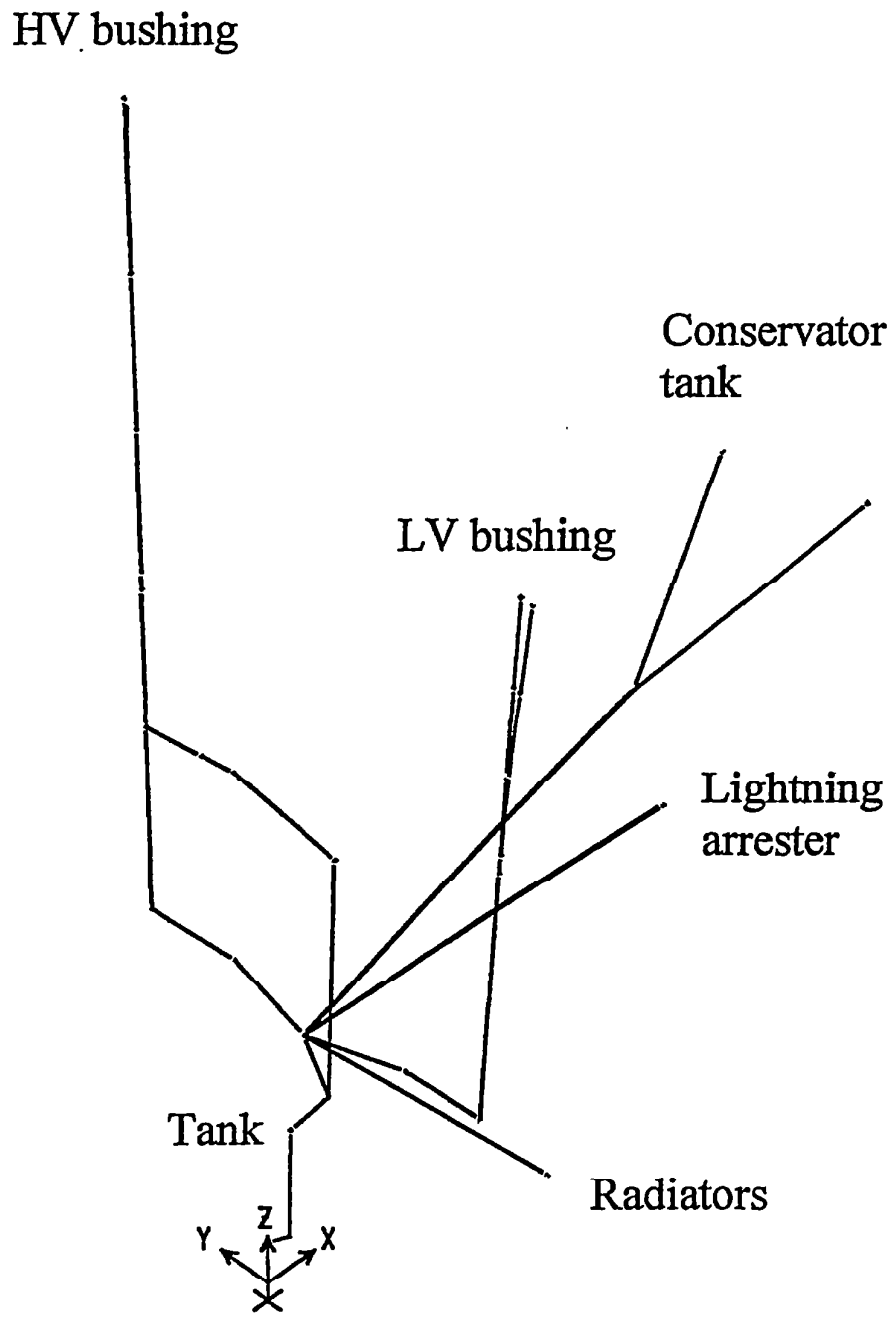

Figure 3.13. Third mode of vibration, Pauwels 500-kV transformer

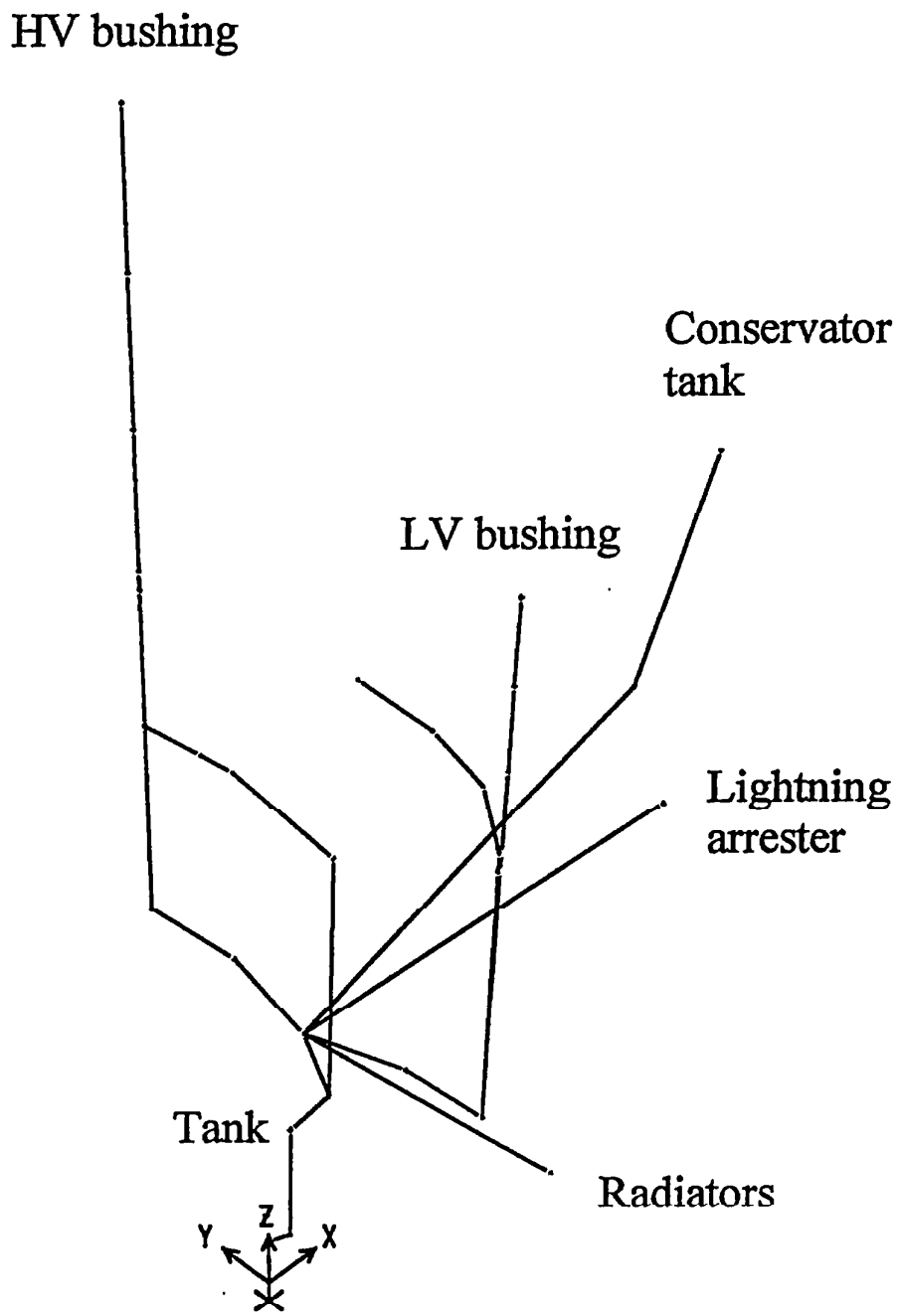

Figure 3.14. Fourth mode of vibration, Pauwels 500-kV transformer

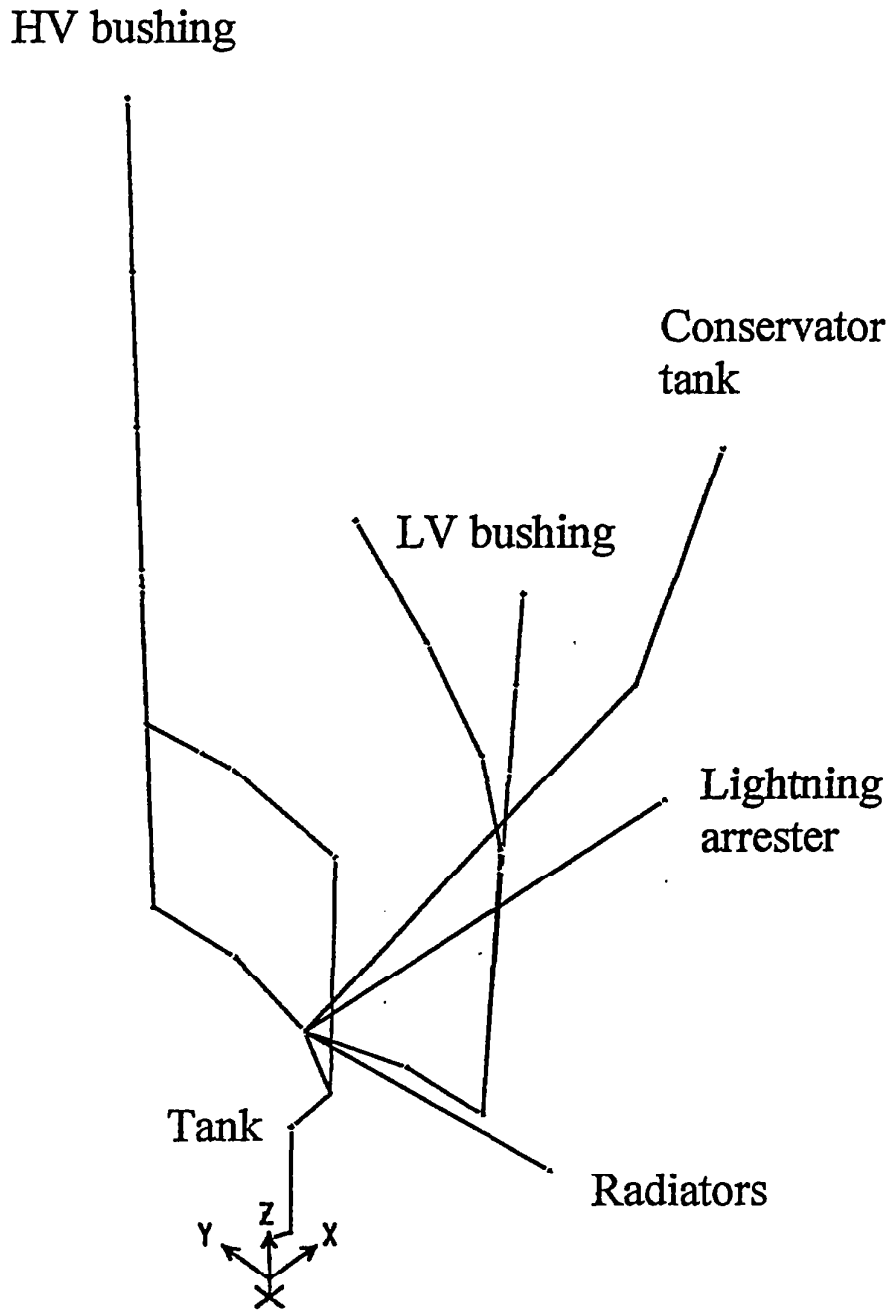

Figure 3.15. Fifth mode of vibration, Pauwels 500-kV transformer

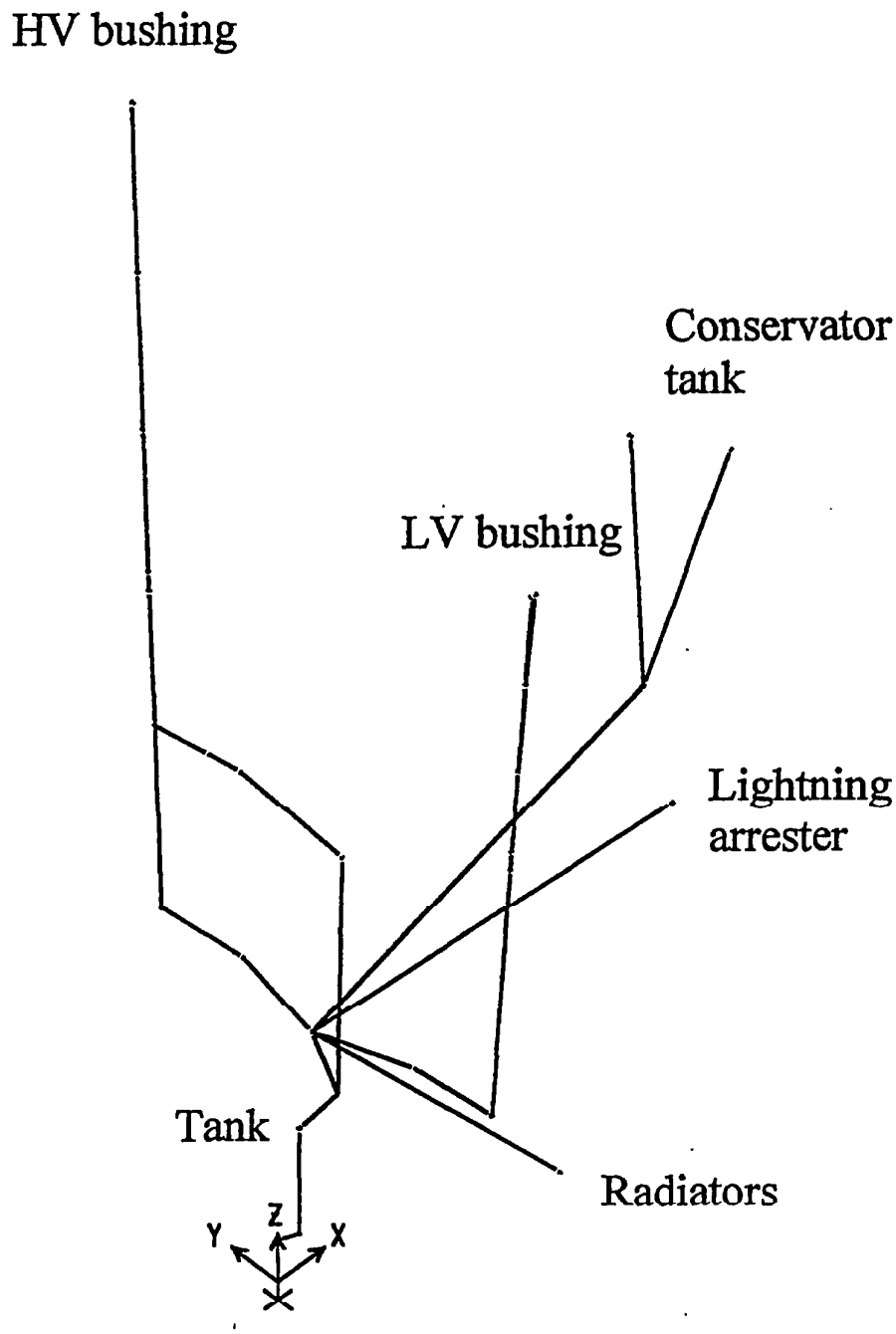

Figure 3.16. Sixth mode of vibration, Pauwels 500-kV transformer

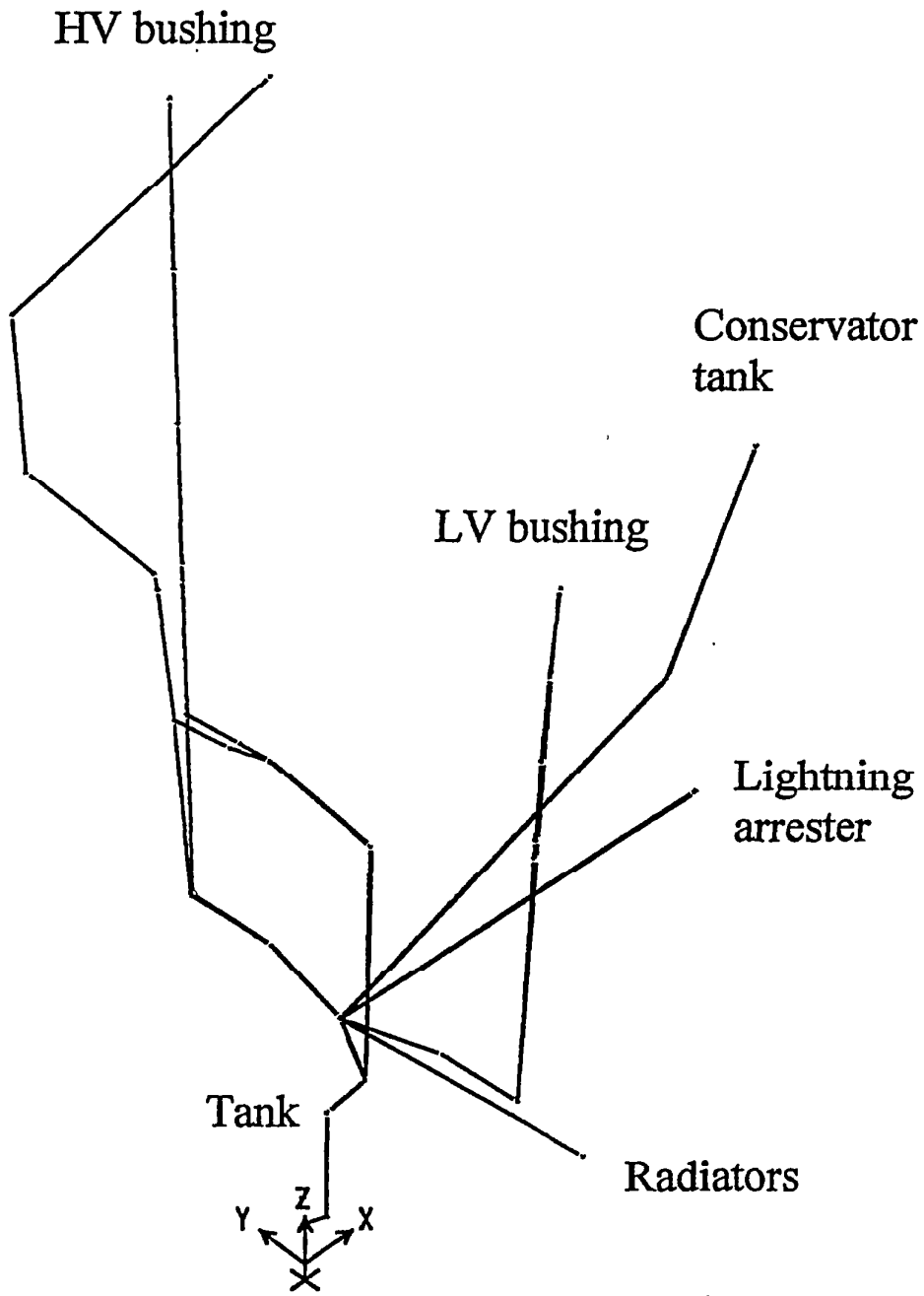

Figure 3.17. Seventh mode of vibration, Pauwels 500-kV transformer

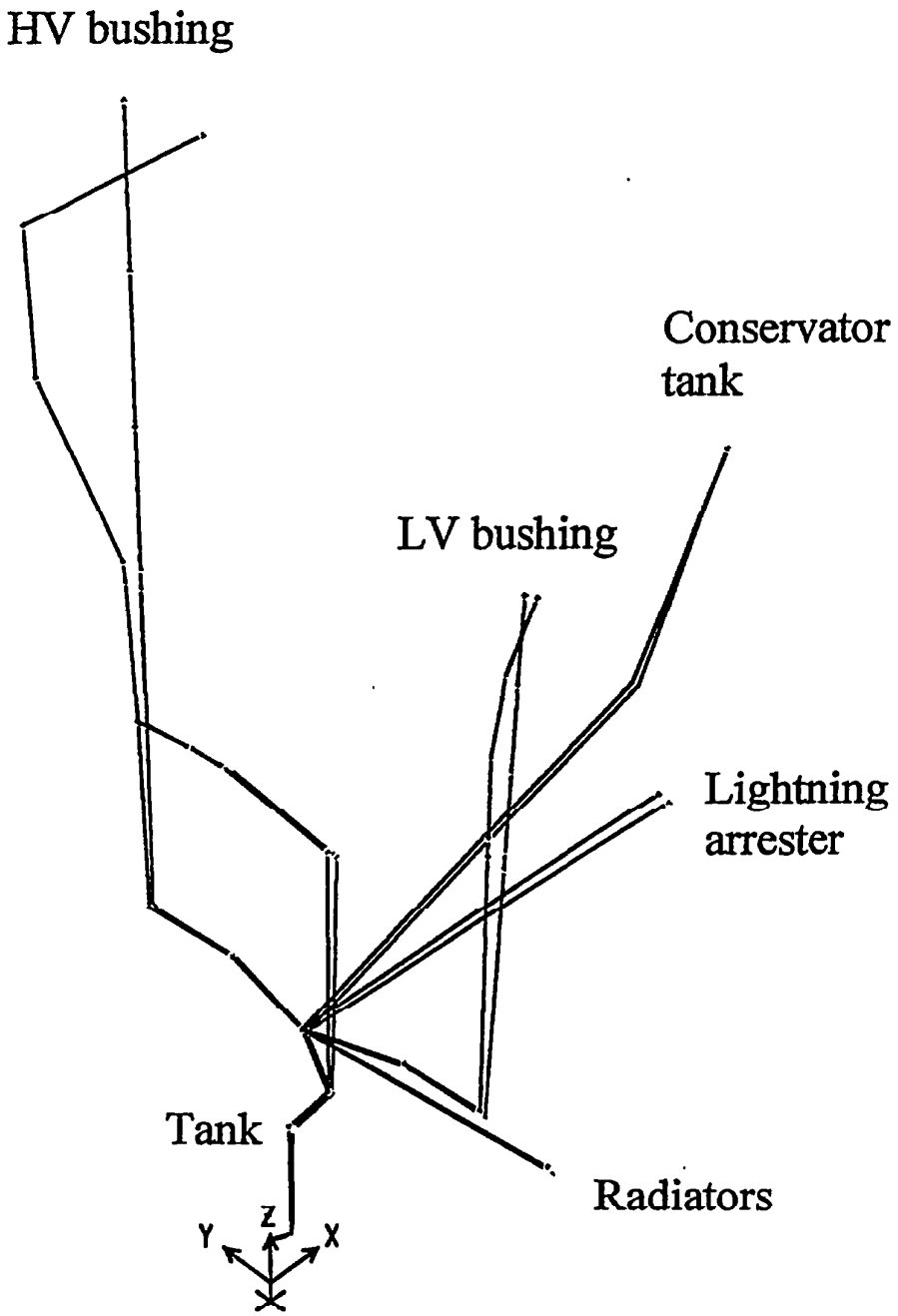

Figure 3.18. Eighth mode of vibration, Pauwels 500-kV transformer

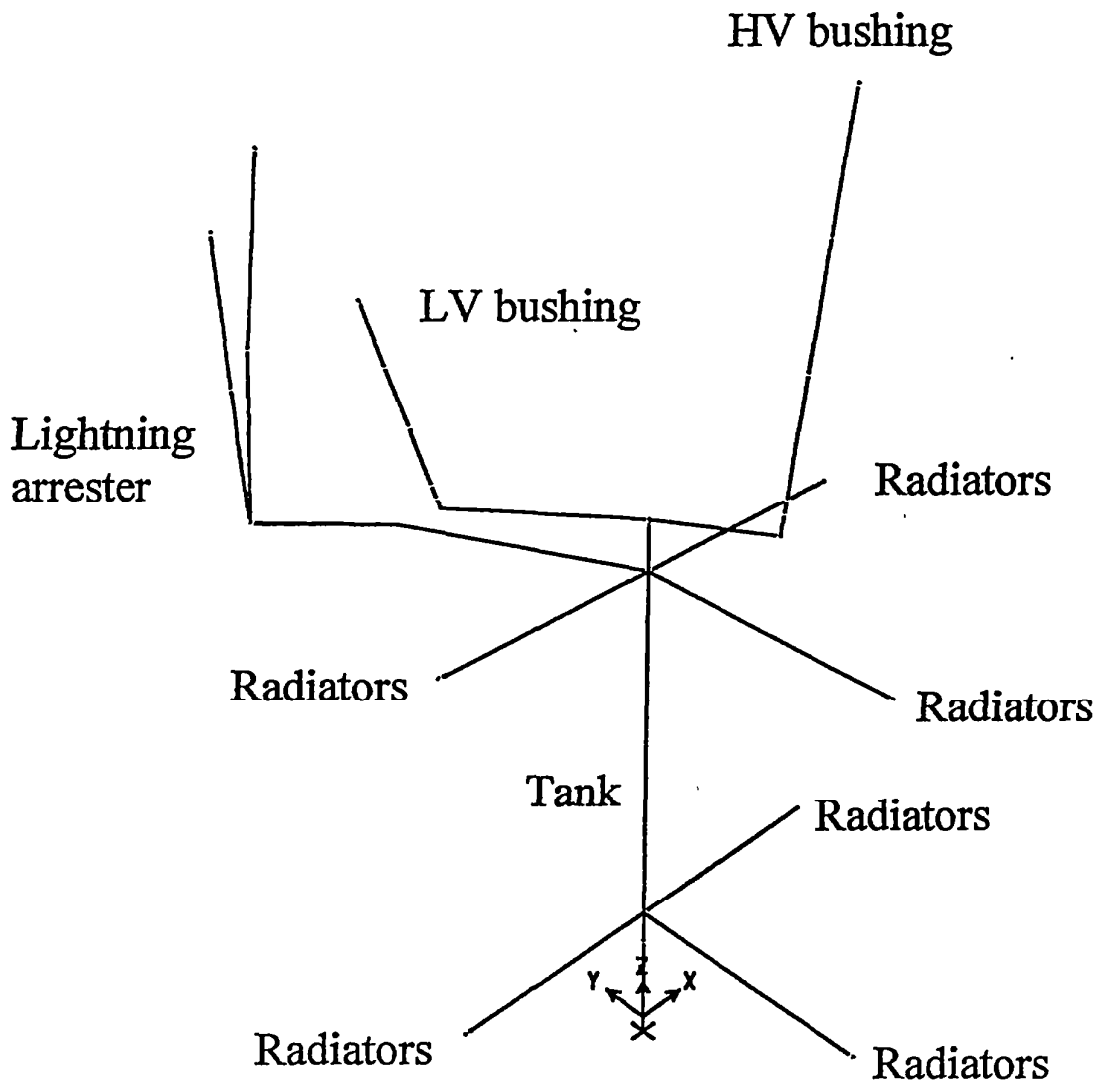

Figure 3.19. First mode of vibration, Westinghouse 500-kV transformer

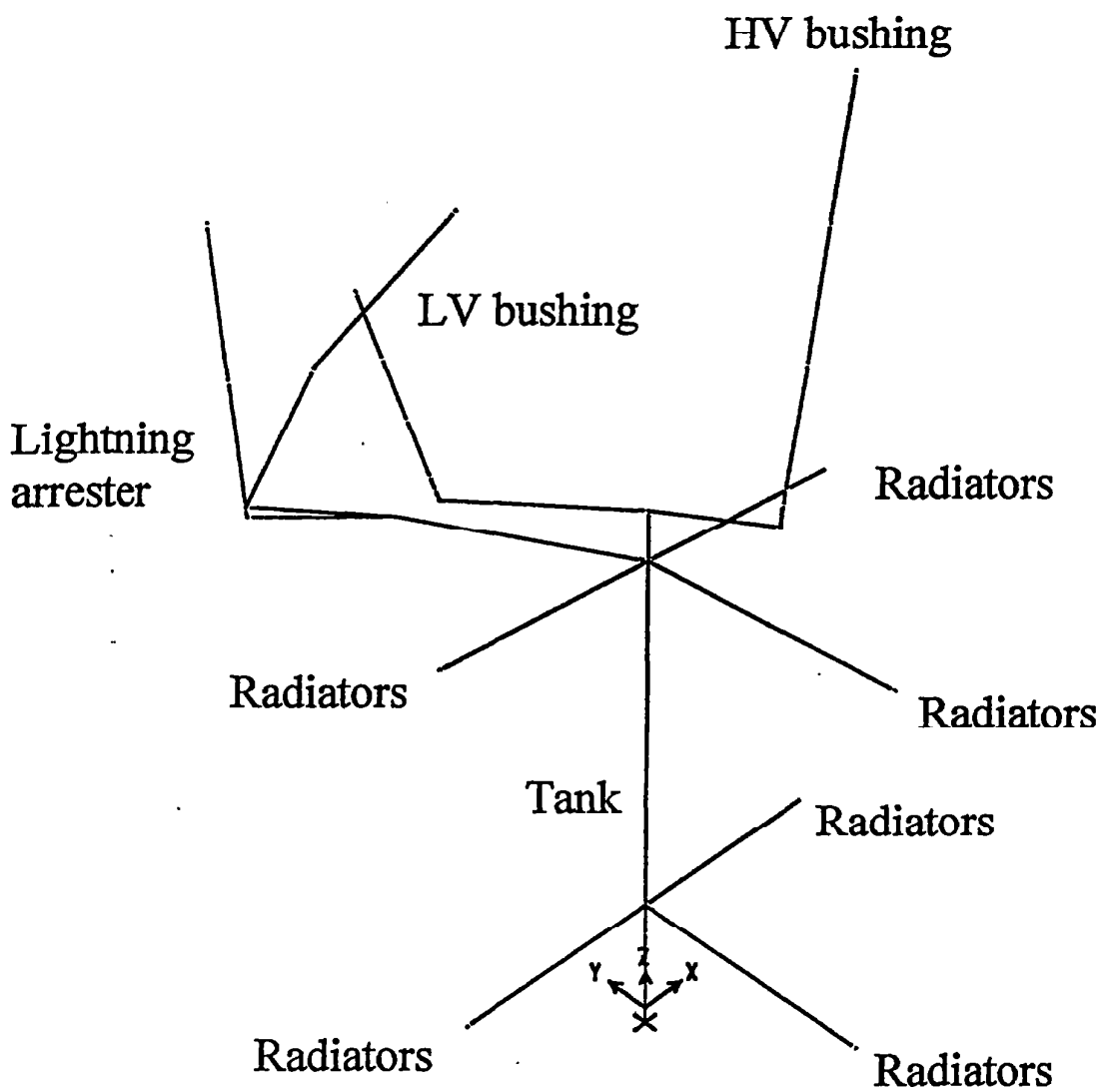

Figure 3.20. Second mode of vibration, Westinghouse 500-kV transformer

SAP2000 v6.10 - File:WestinRSA - Mode 2 Period 0.4001 seconds - lb-in Units

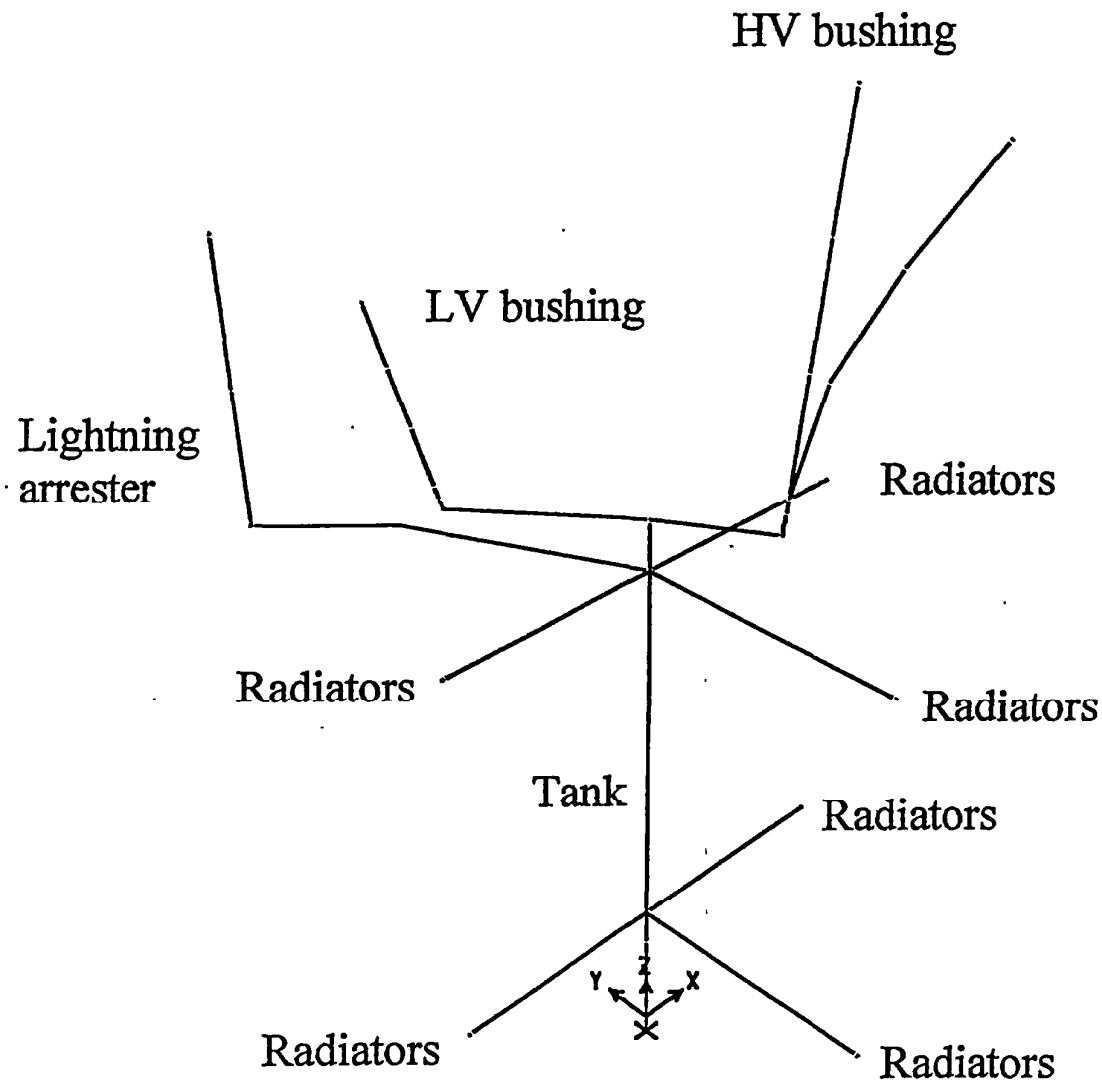

Figure 3.21. Third mode of vibration, Westinghouse 500-kV transformer

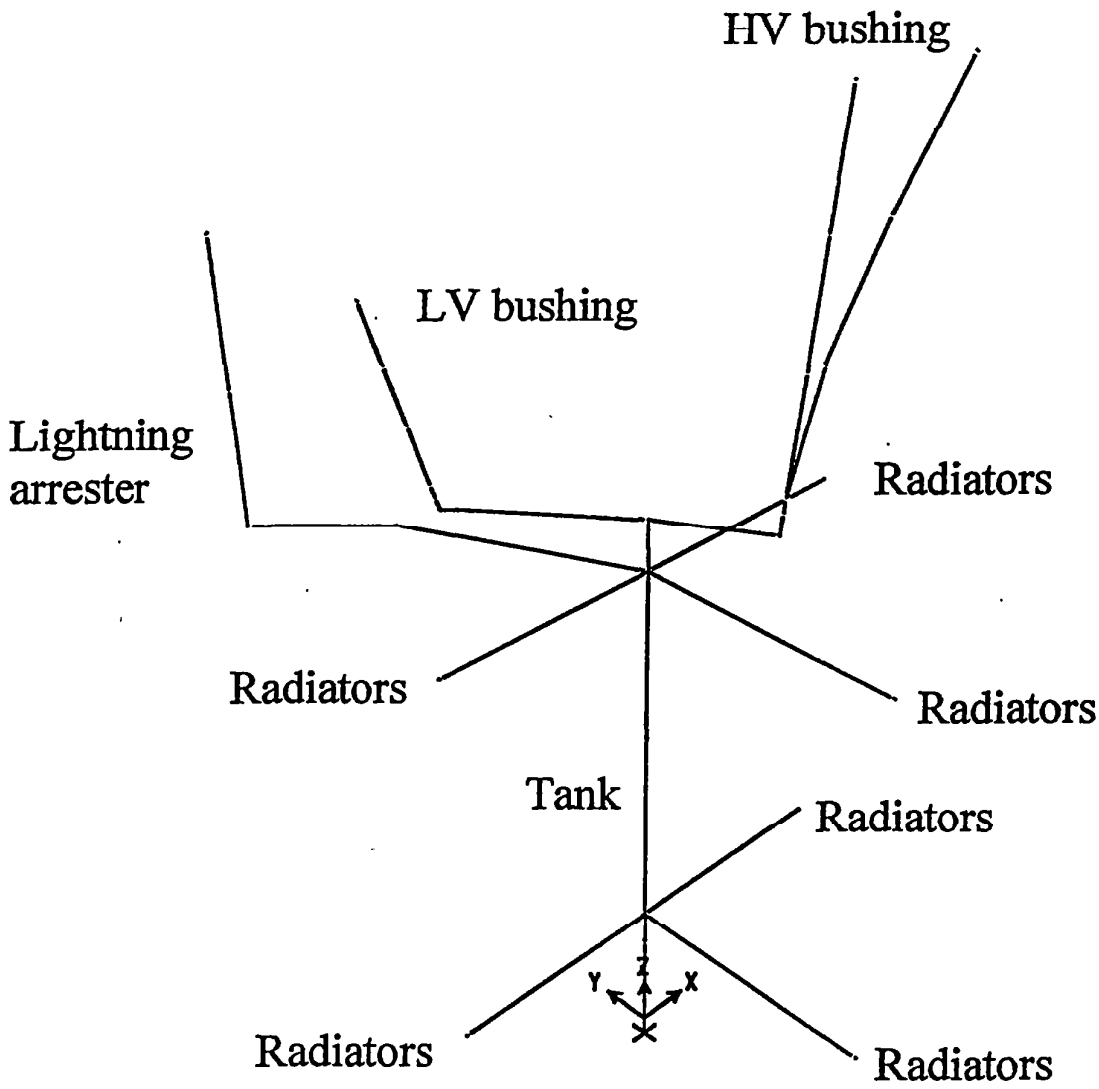

Figure 3.22. Fourth mode of vibration, Westinghouse 500-kV transformer

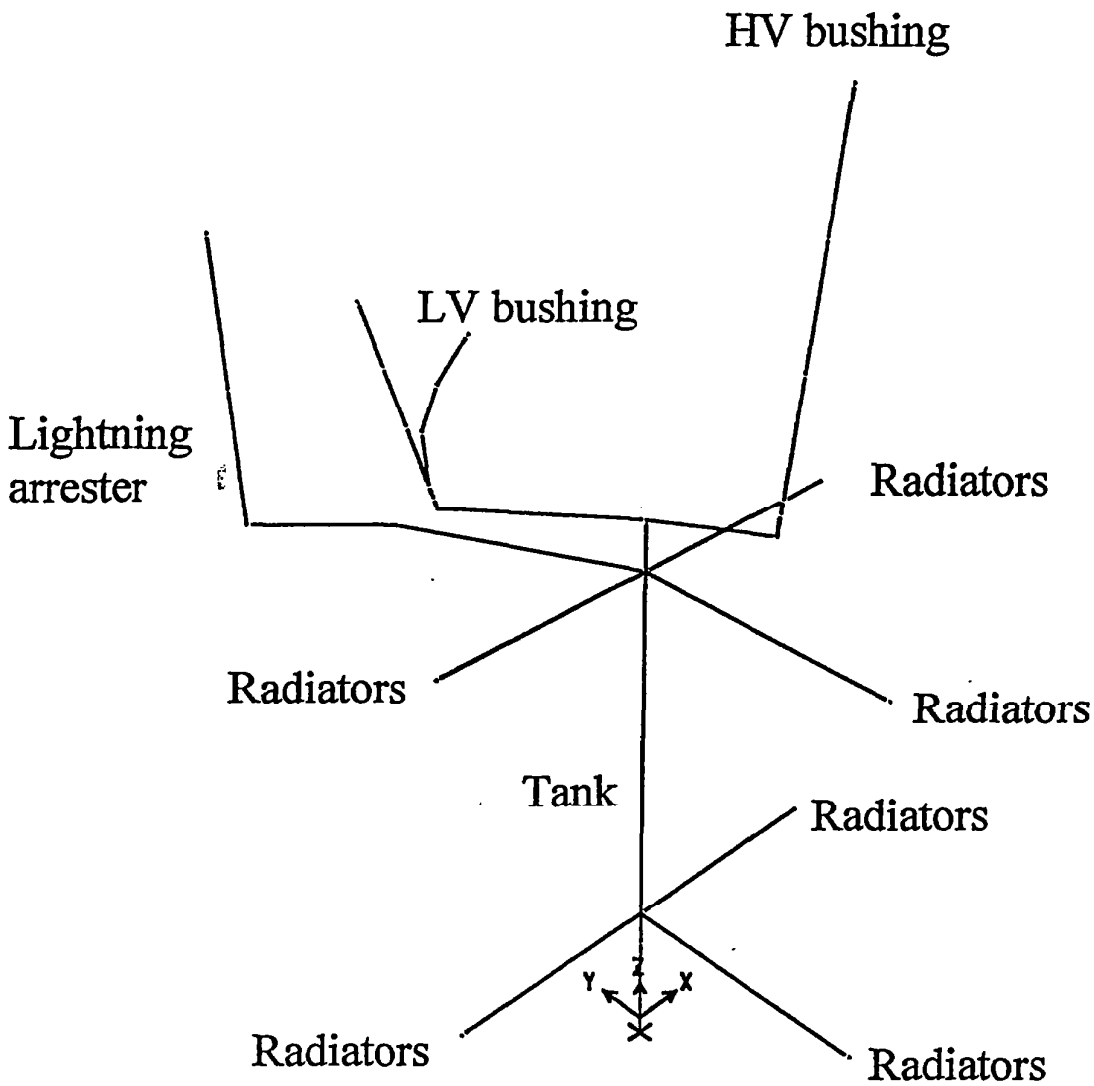

Figure 3.23. Fifth mode of vibration, Westinghouse 500-kV transformer

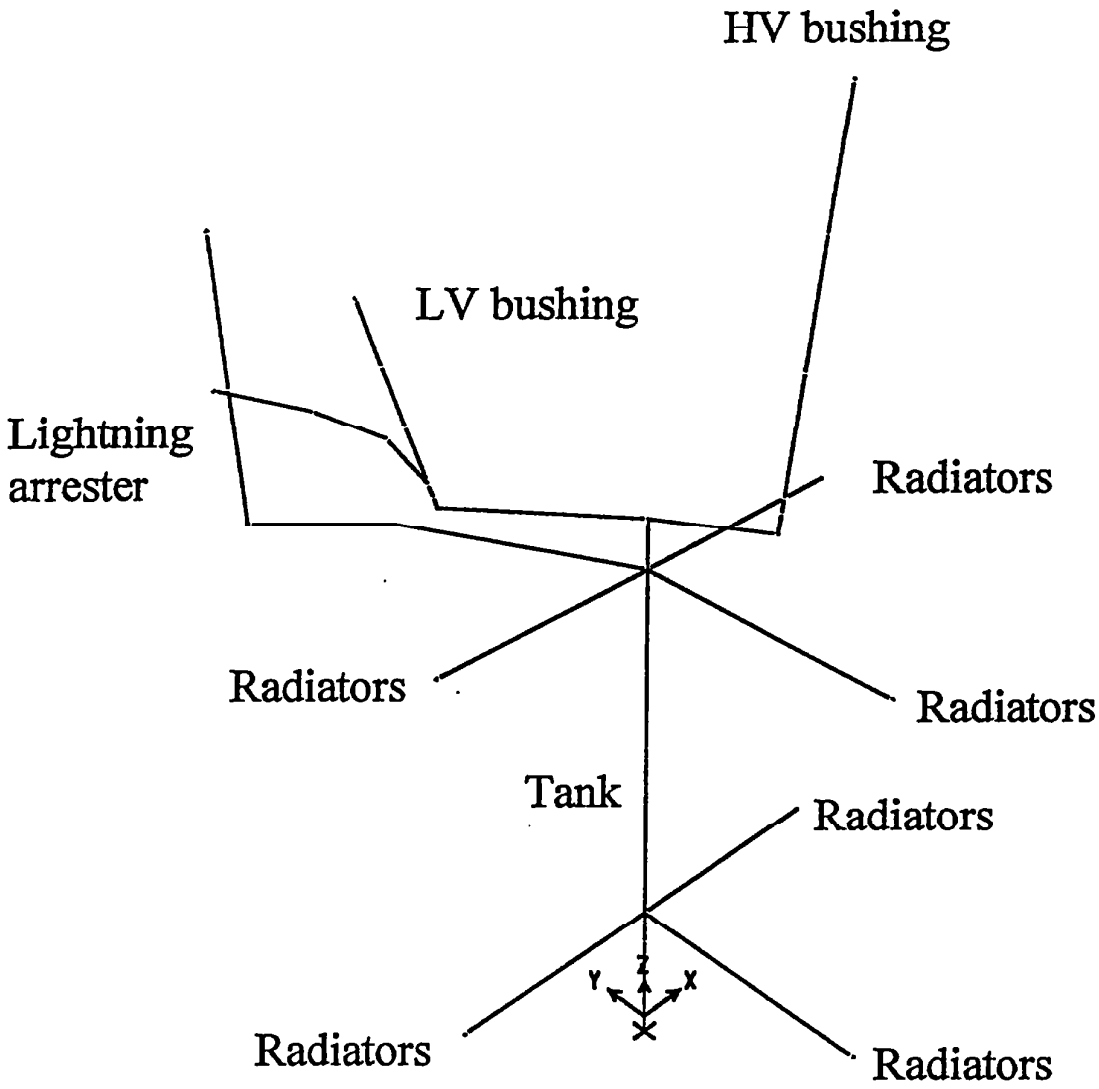

Figure 3.24. Sixth mode of vibration, Westinghouse 500-kV transformer

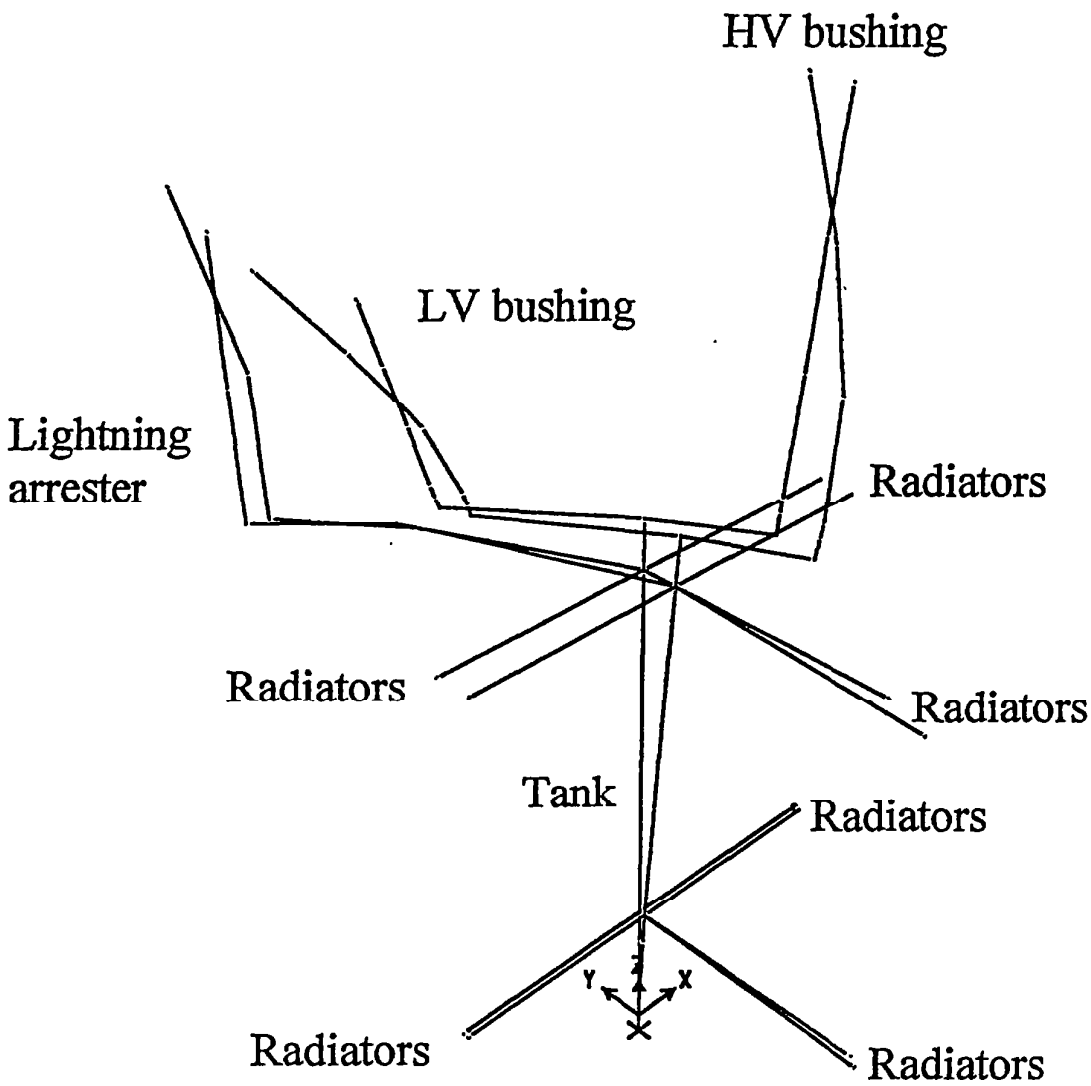

Figure 3.25. Seventh mode of vibration, Westinghouse 500-kV transformer

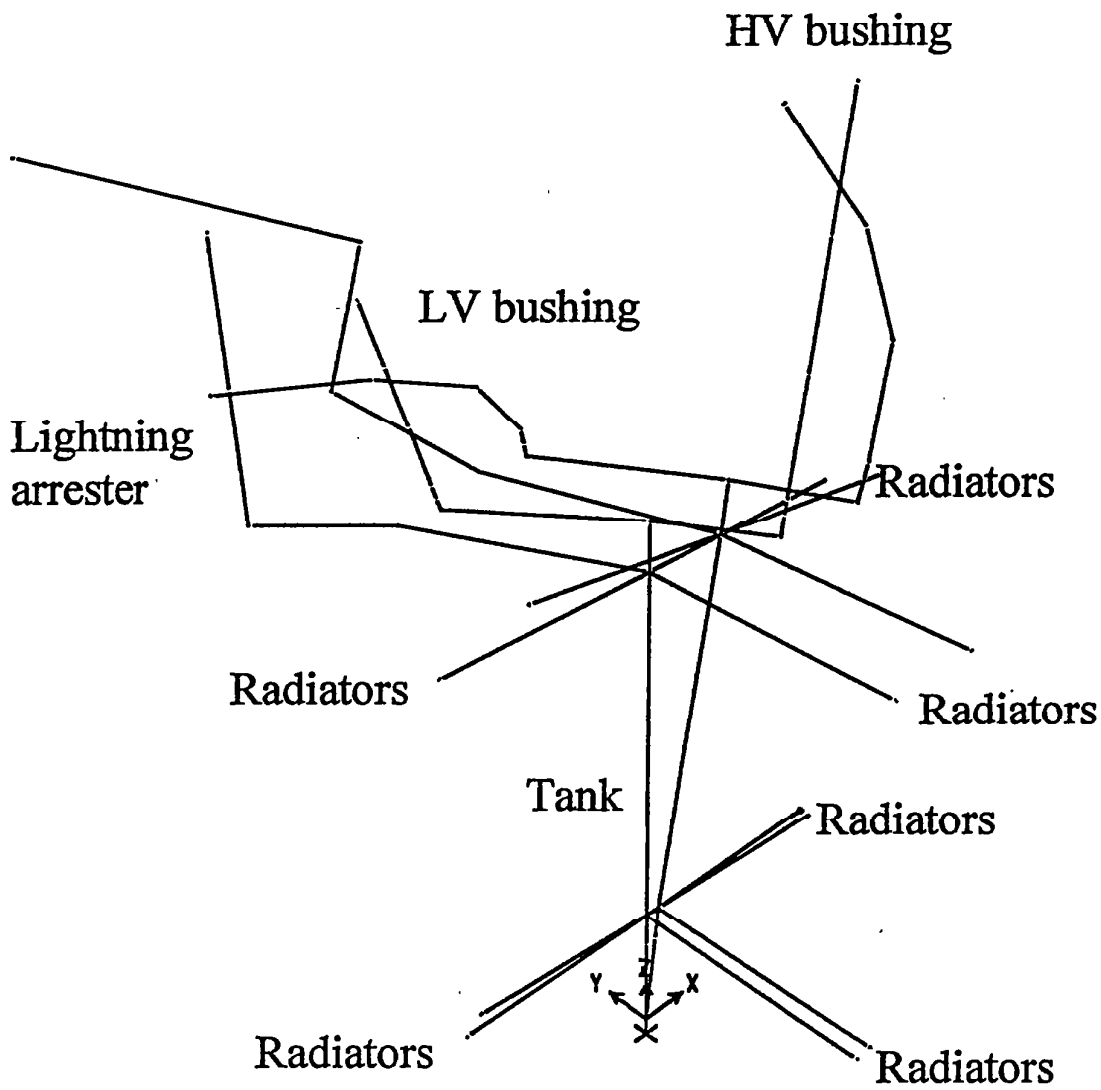

Figure 3.26. Eighth mode of vibration, Westinghouse 500-kV transformer

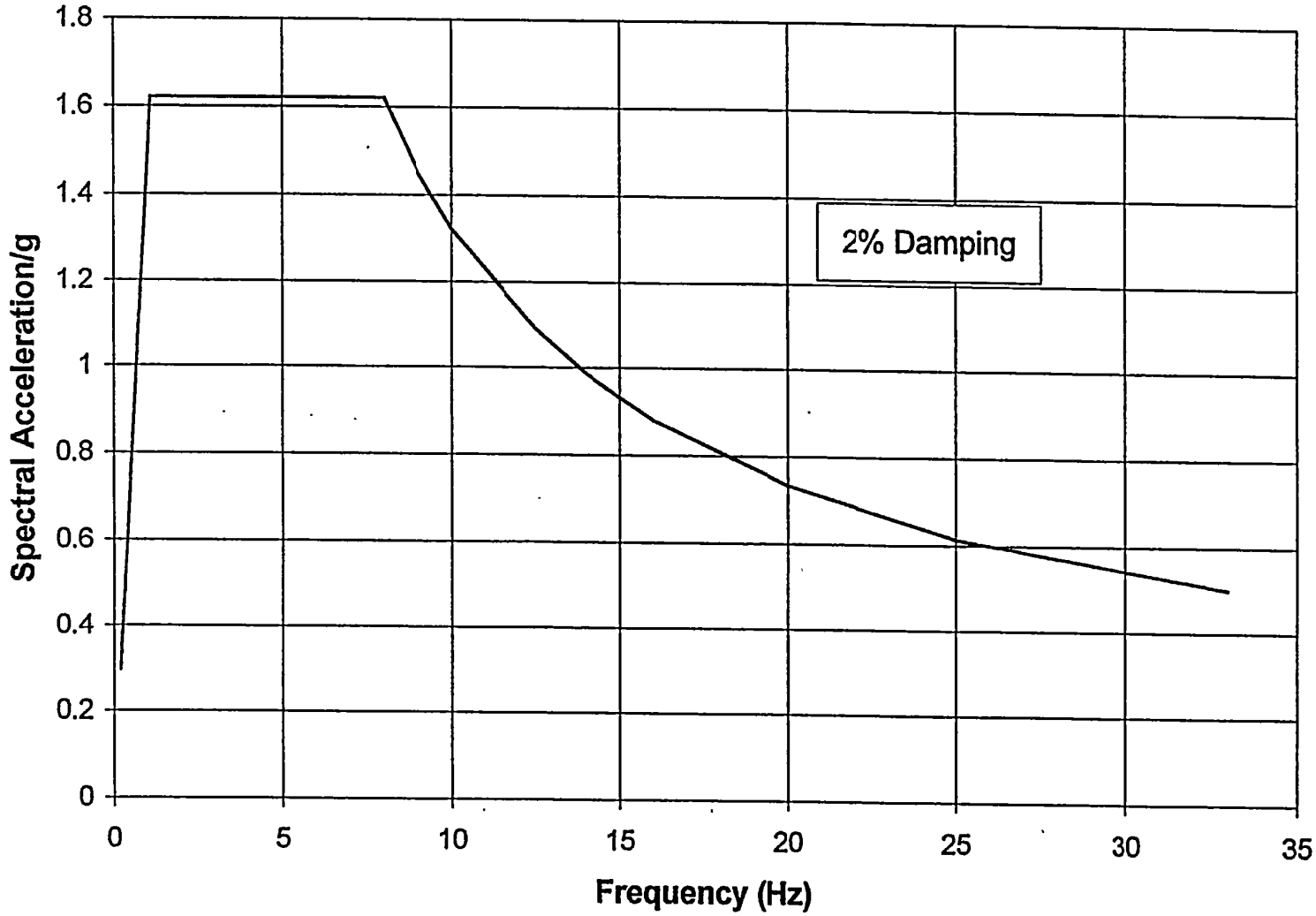

Figure 3.27. IEEE 693 acceleration response spectrum for 2 per cent damping

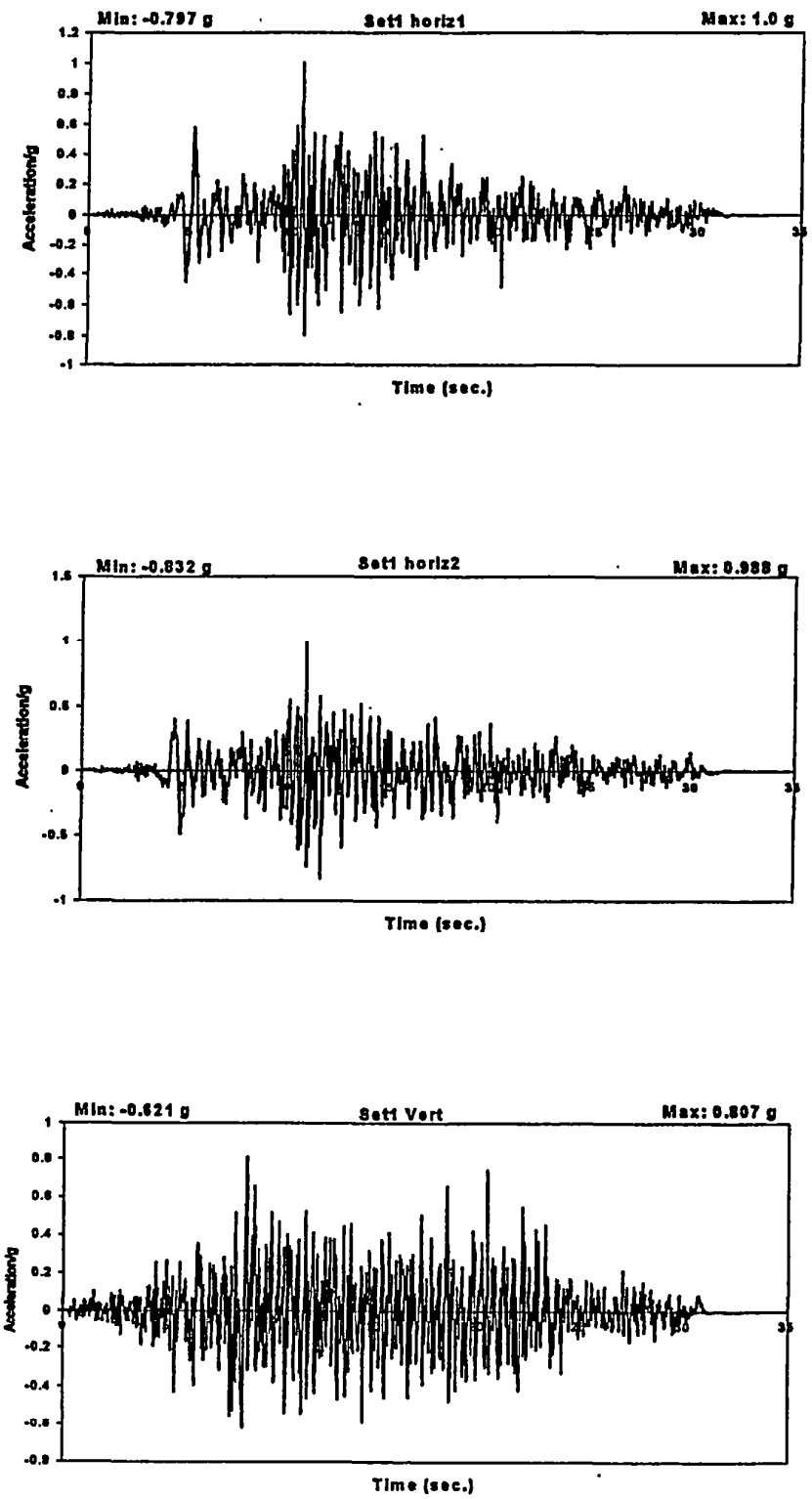

Figure 3.28. Synthetic acceleration time histories generated to match low frequency range of 2 %-damping IEEE 693 response spectrum

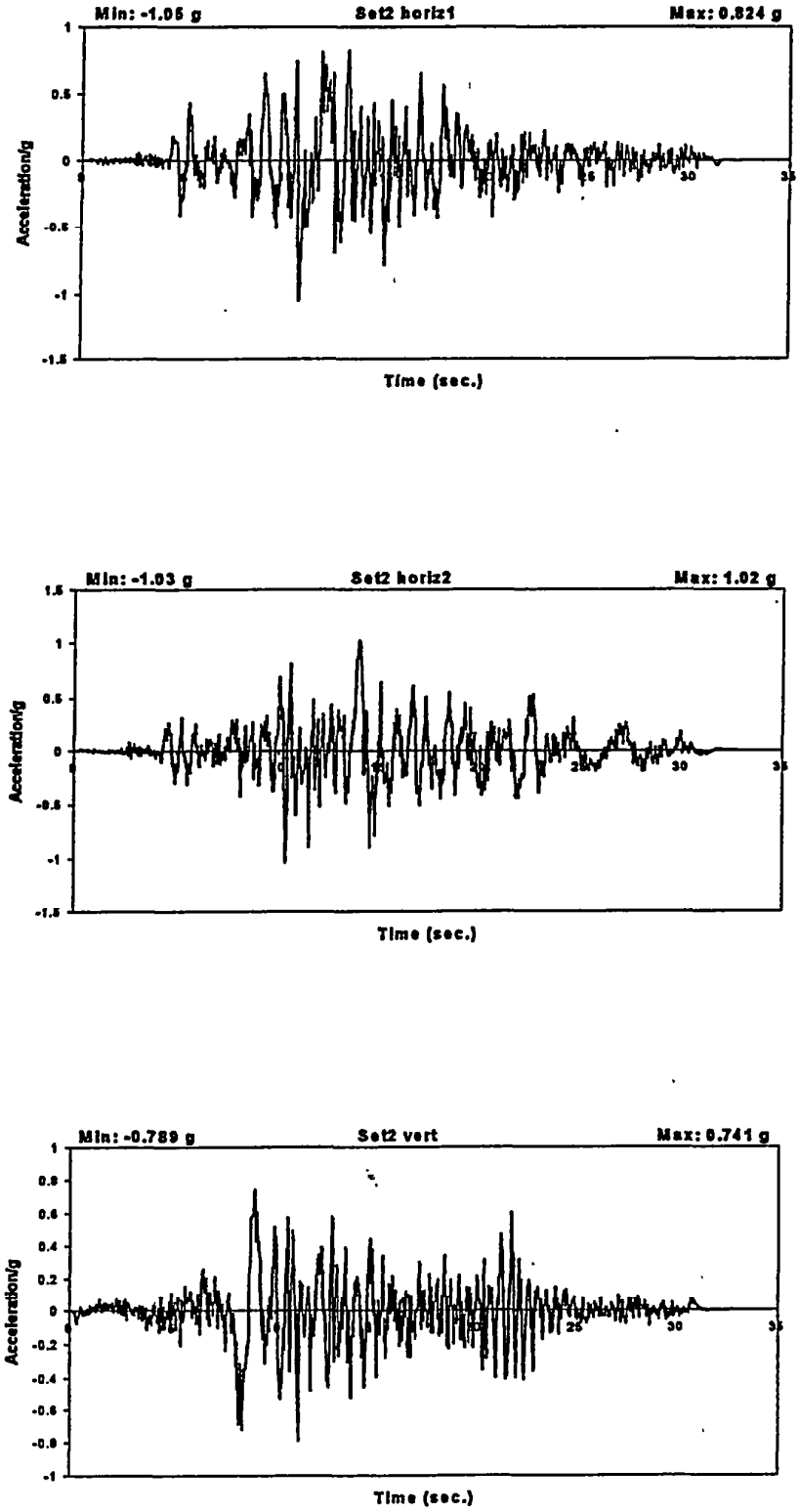

Figure 3.29. Synthetic acceleration time histories generated to match high frequency range of 2 %-damping IEEE 693 response spectrum

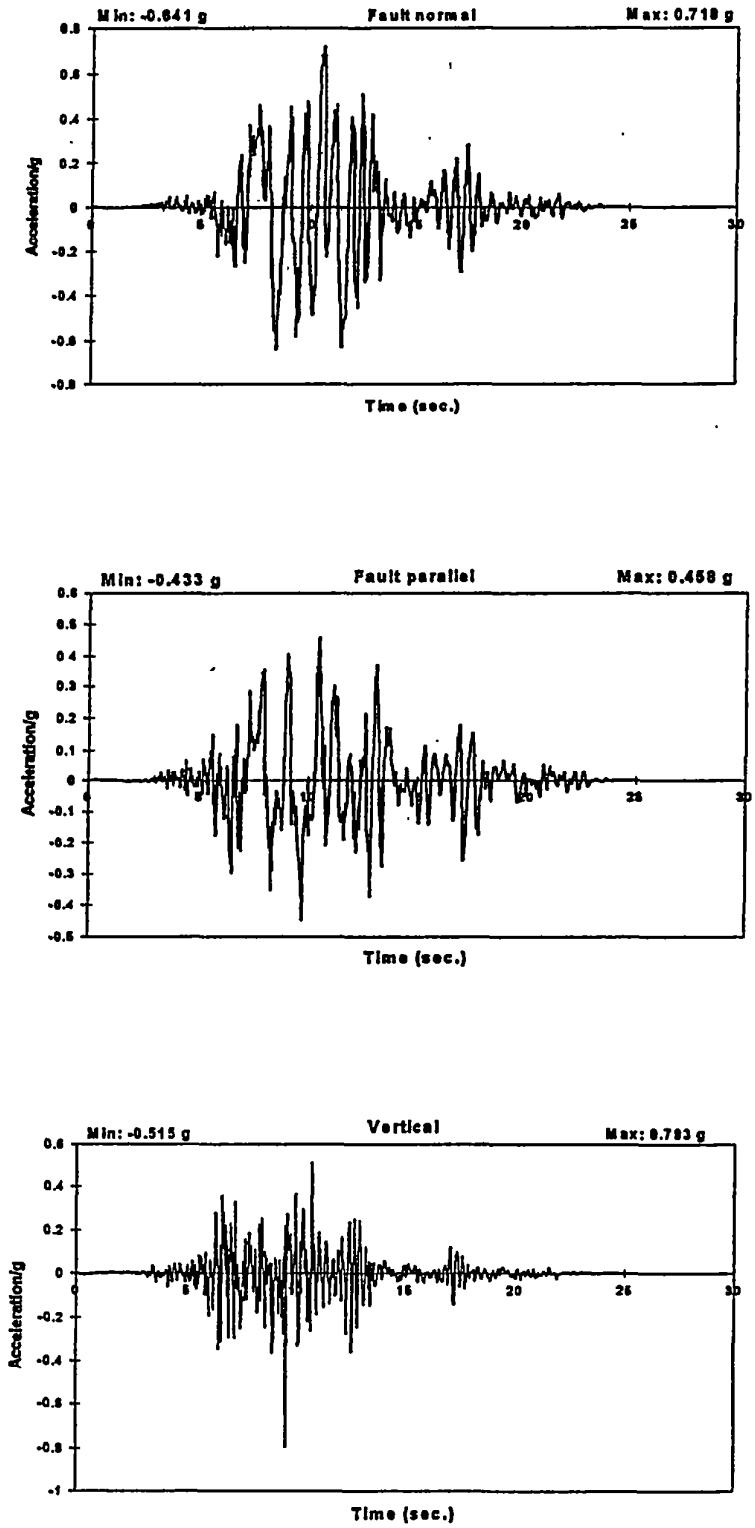

Figure 3.30. Acceleration time histories recorded at Los Gatos near-fault station during the 1989 Loma Prieta earthquake

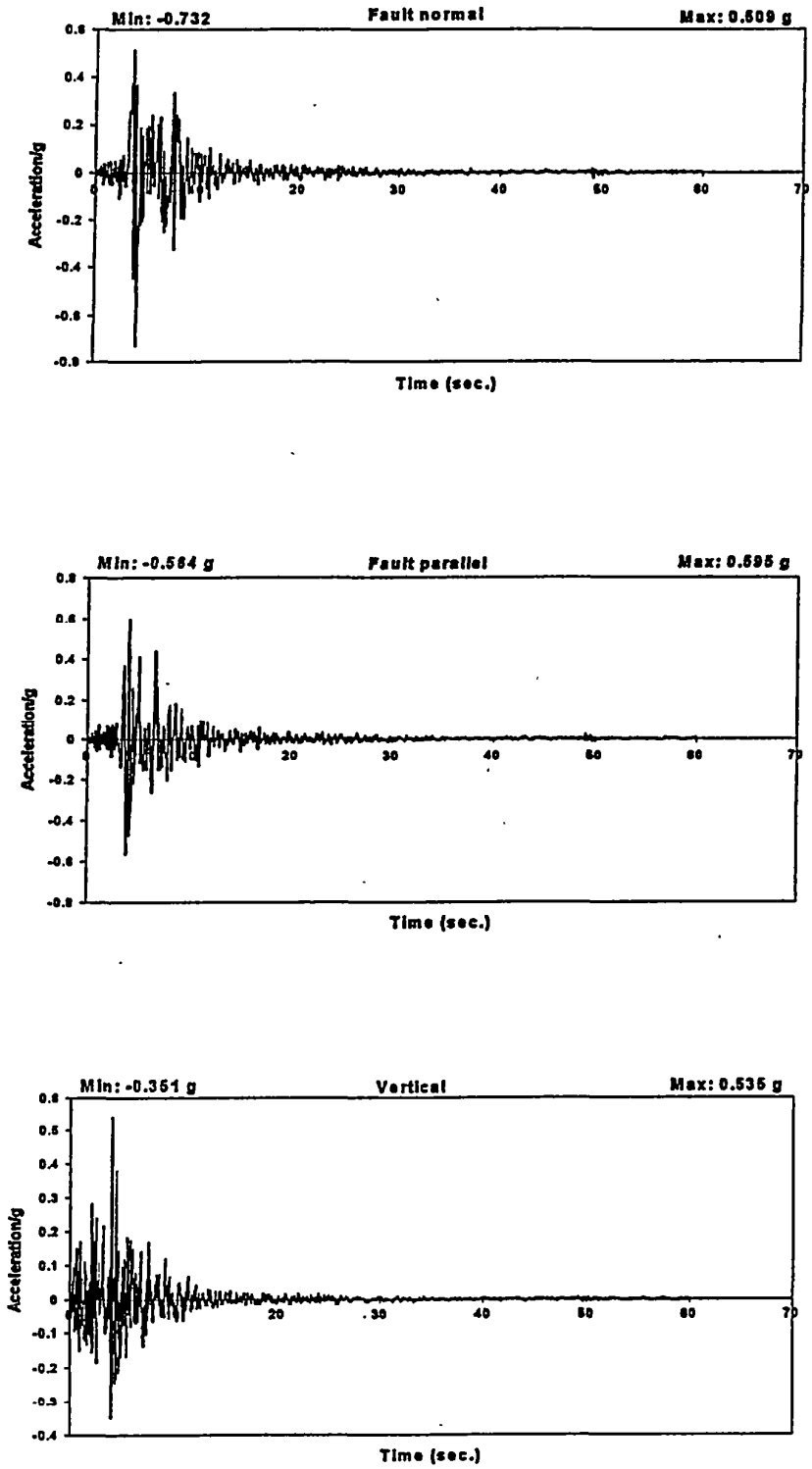

Figure 3.31. Acceleration time histories recorded at Olive View Hospital near-fault station during the 1994 Northridge earthquake

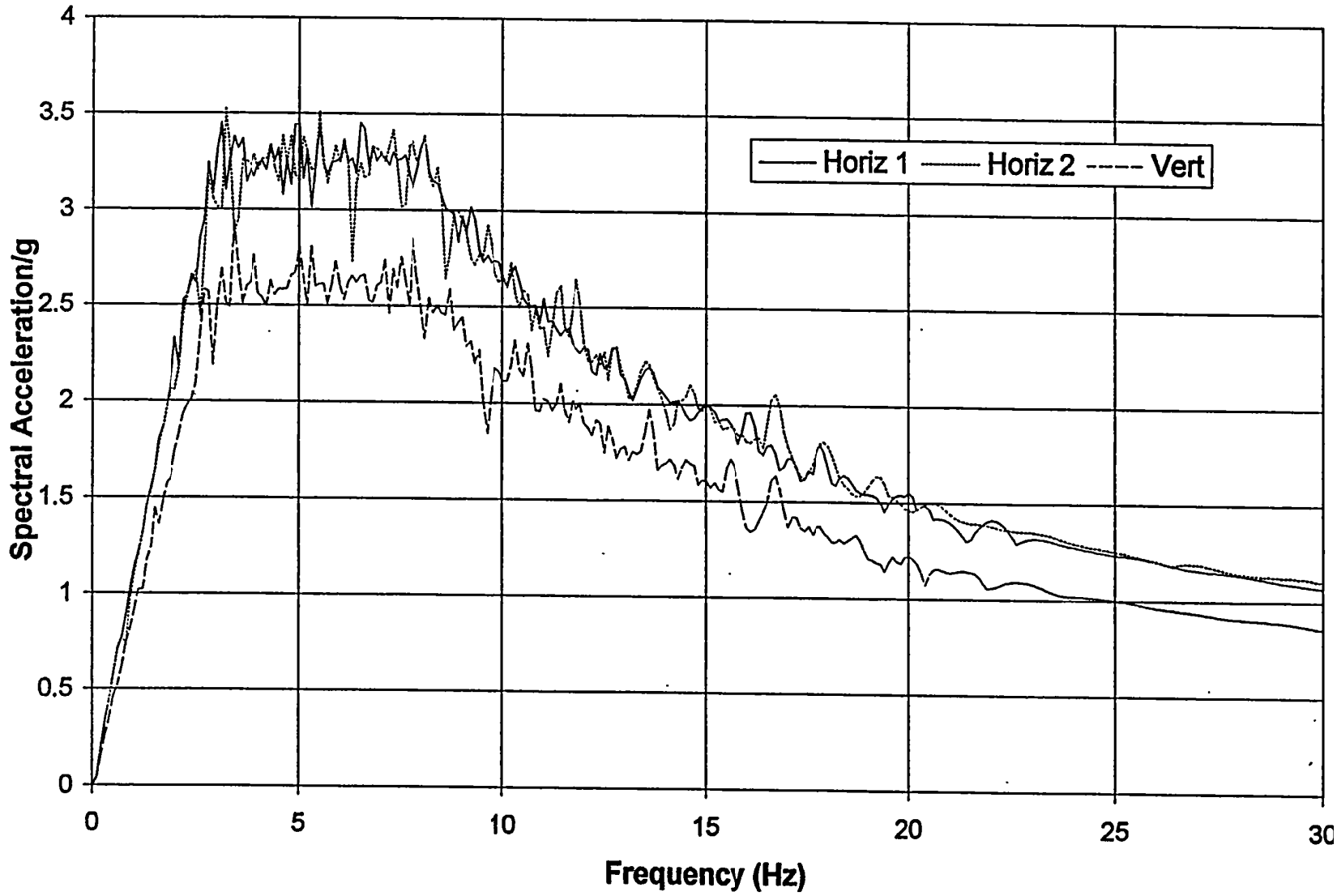

Figure 3.32. 2 %-damping acceleration response spectra of synthetic acceleration time histories generated to match low frequency range of 2 %-damping IEEE 693 response spectrum

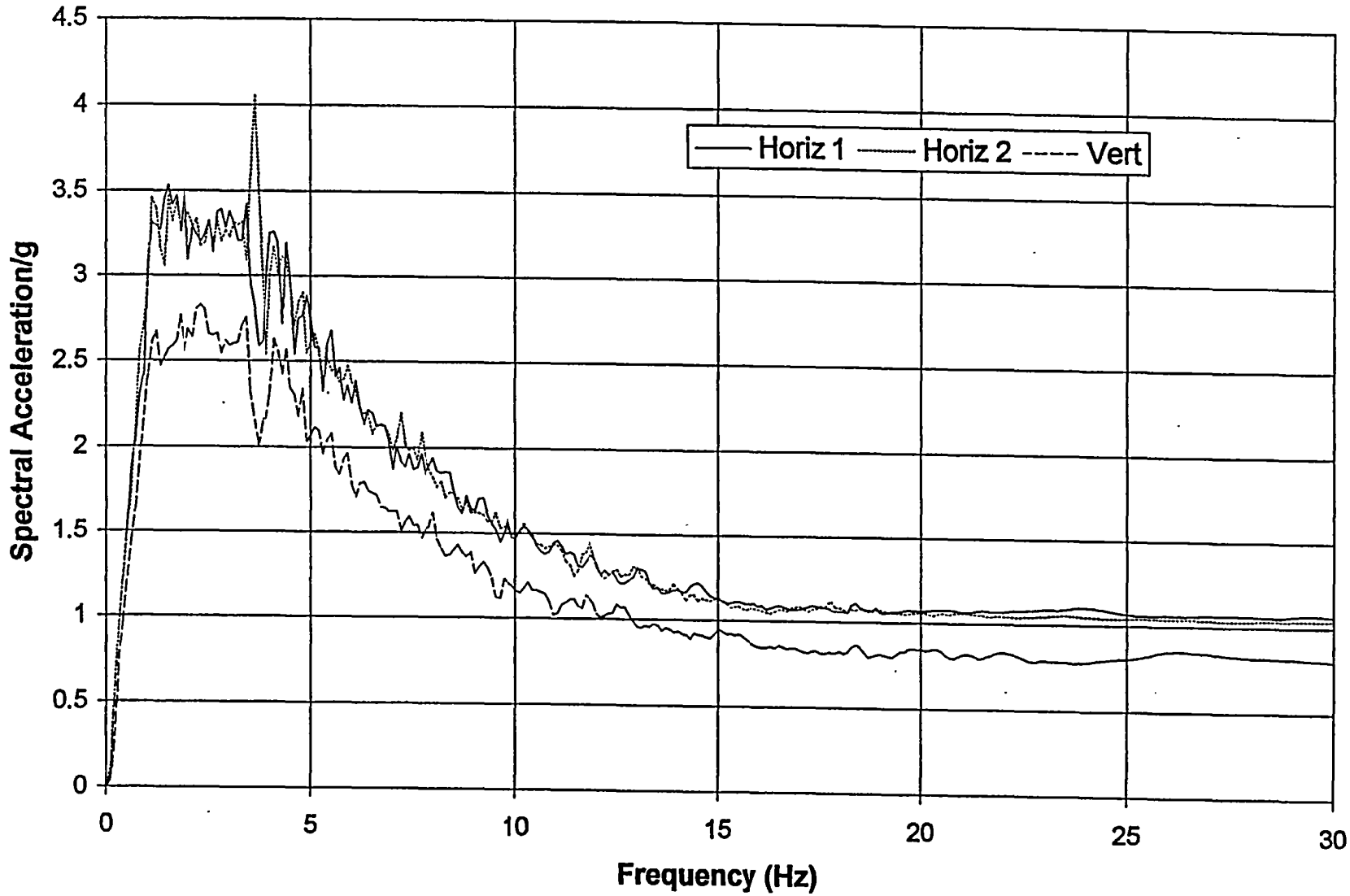

Figure 3.33. 2 %-damping acceleration response spectra of synthetic acceleration time histories generated to match high frequency range of 2 %-damping IEEE 693 response spectrum

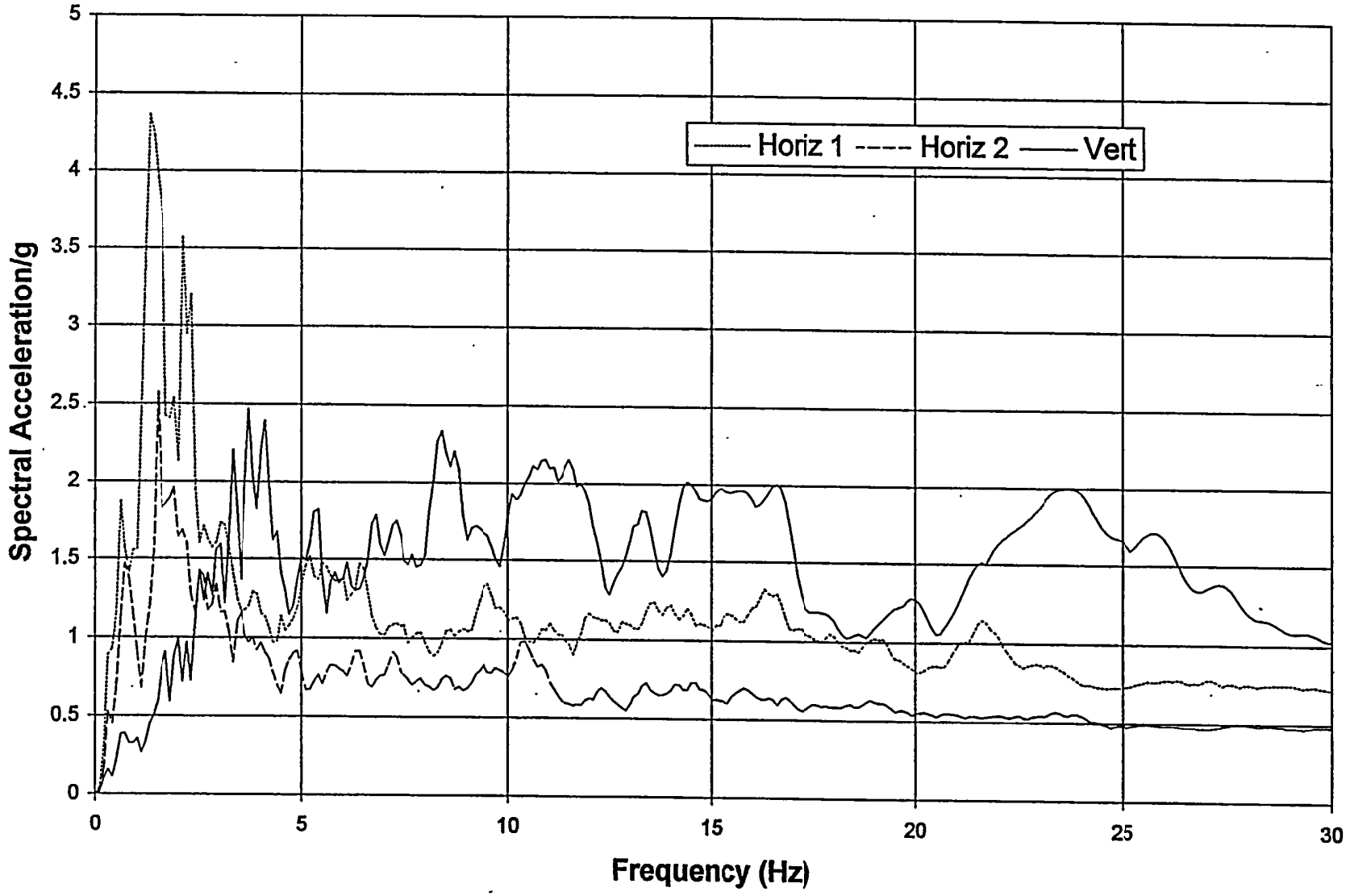

Figure 3.34. 2 %-damping acceleration response spectra of acceleration time histories recorded at Los Gatos near-fault station during the 1989 Loma Prieta earthquake

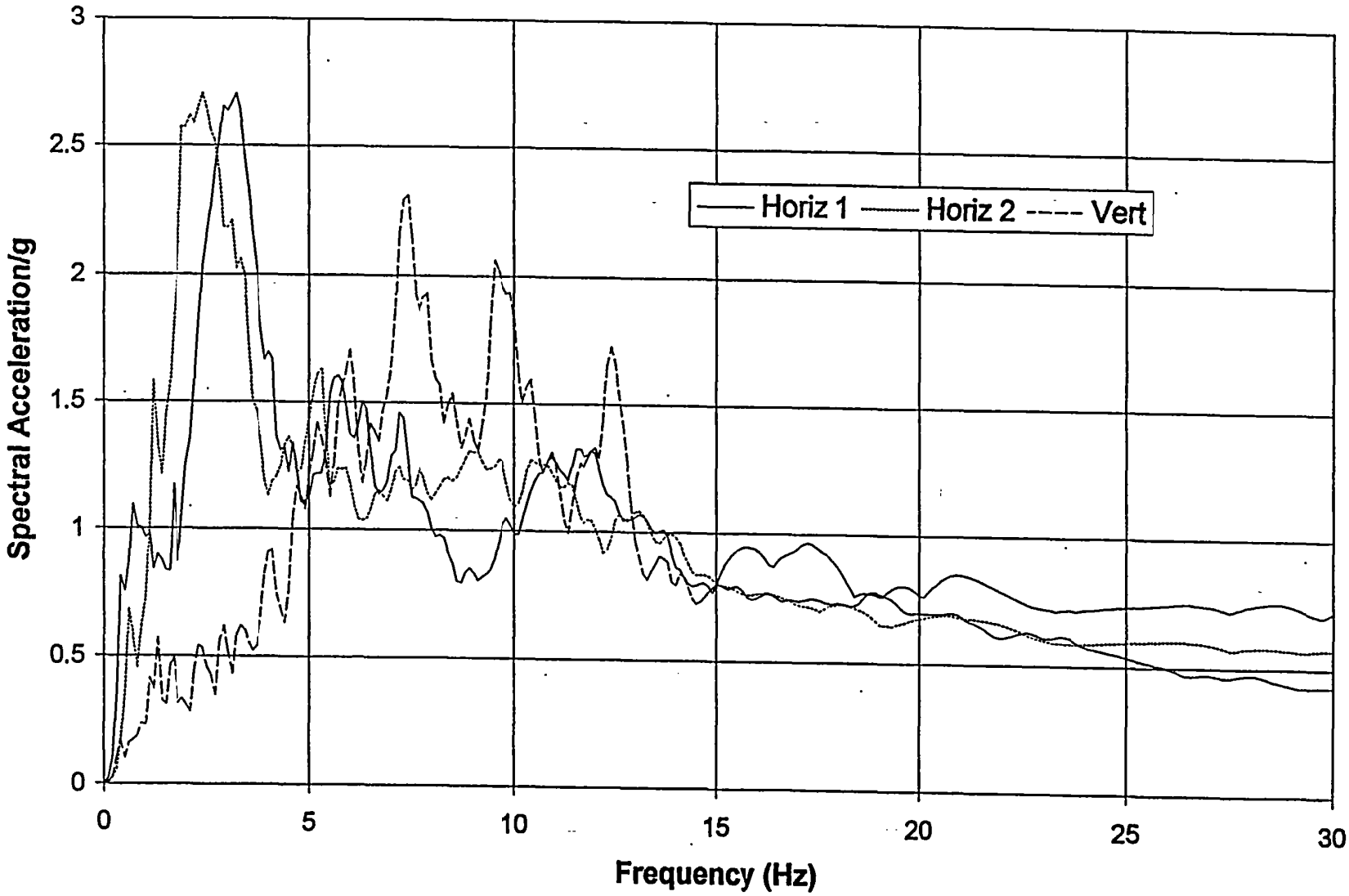

Figure 3.35. 2 %-damping acceleration response spectra of acceleration time histories recorded at Olive View Hospital near-fault station during the 1994 Northridge earthquake

Appendix A

POWER SPECTRA FROM FIELD TESTS OF PAUWELS 500-KV TRANSFORMER AT MOSS LANDING SUBSTATION

Five separate tests were conducted on the Pauwels 500-kV transformer using up to seven sensors in each test. The sensor orientation, sensor type, and correspondence between channel number and sensor location are shown in the table below. The average power spectra corresponding to the signals recorded by each of the listed channels are given in Figures A1 through A18.

Test No.	Direction	Channel	Sensor location	Sensor type
1	Transverse	1	Shaker	Accelerometer
		2	Tank top	Accelerometer
		3	Tank mid-height	Accelerometer
		4	Tank bottom	Accelerometer
		5	Foundation	Accelerometer
		6	Foundation	Seismometer
2	Transverse	1	Shaker	Accelerometer
		2	HV turret cover plate	Accelerometer
		3	HV turret 2/3 height	Accelerometer
		4	HV turret bottom	Accelerometer
		5	HV turret flange	Accelerometer
		6	Foundation	Seismometer
3	Transverse	1	Shaker	Accelerometer
		2	HV turret cover plate	Accelerometer
		3	HV bushing bottom	Accelerometer
		4	HV bushing mid-height	Accelerometer
		5	HV bushing top	Accelerometer
		6	HV turret cover plate	Seismometer
		7	Foundation	Seismometer
4	Longitudinal	1	Shaker	Accelerometer
		2	HV turret cover plate	Accelerometer
		3	HV bushing bottom	Accelerometer
		4	HV bushing mid-height	Accelerometer
		5	HV bushing top	Accelerometer
		6	HV turret cover plate	Seismometer
		7	Foundation	Seismometer
5	Longitudinal	1	Shaker	Accelerometer
		2	HV turret cover plate	Accelerometer
		3	HV turret mid-height	Accelerometer
		4	HV turret bottom	Accelerometer
		5	HV turret flange	Accelerometer
		6	HV turret cover plate	Seismometer
		7	Foundation	Seismometer

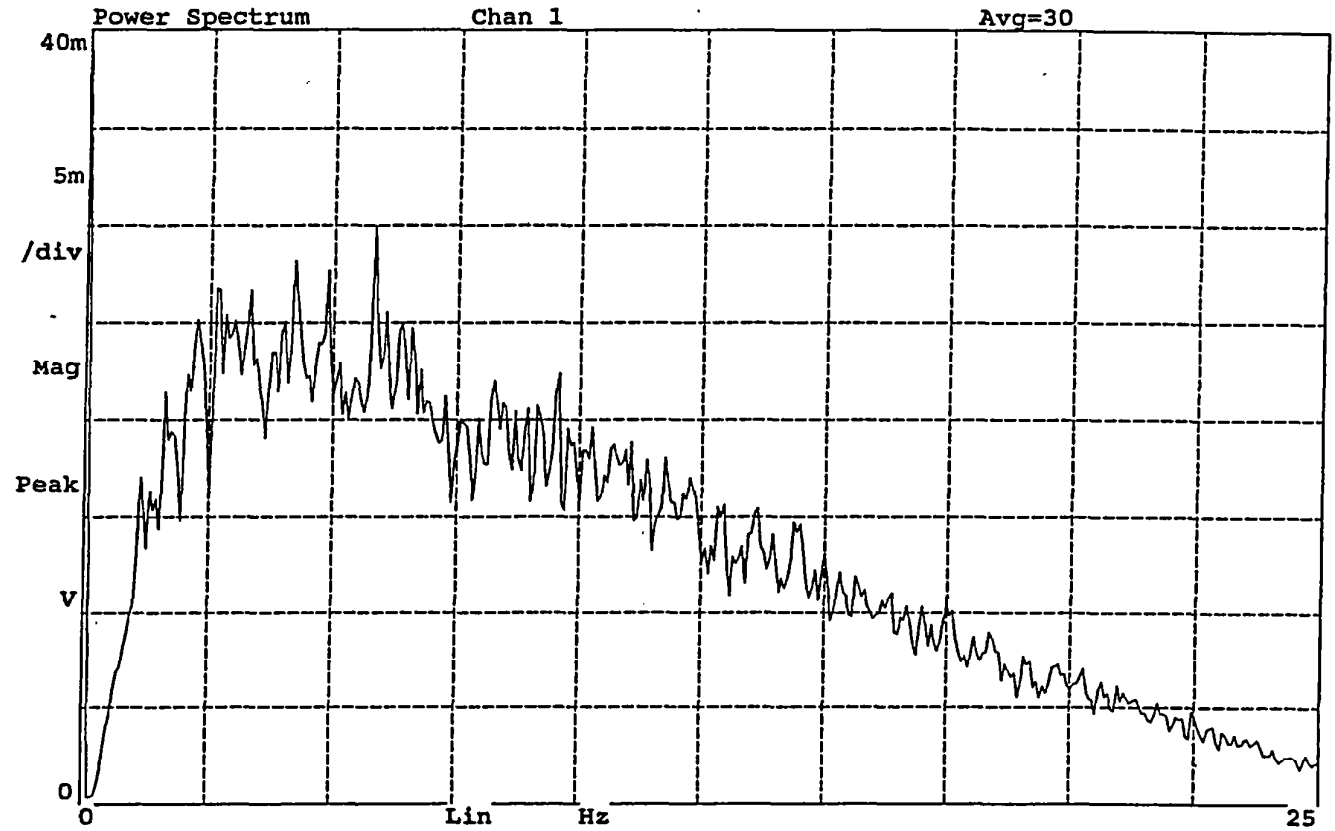

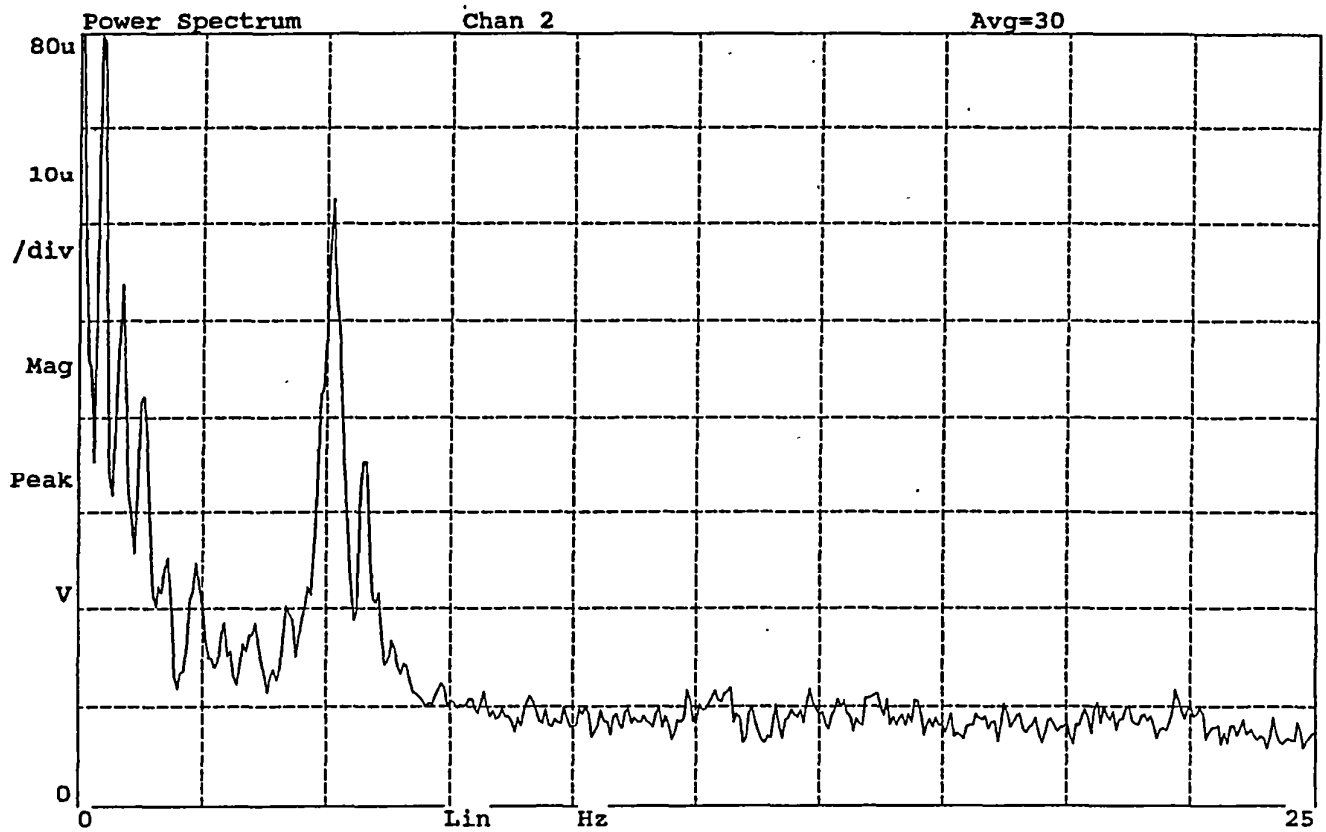

Figure A1. Average power spectra of signals from Channels 1 and 2, Test No. 1

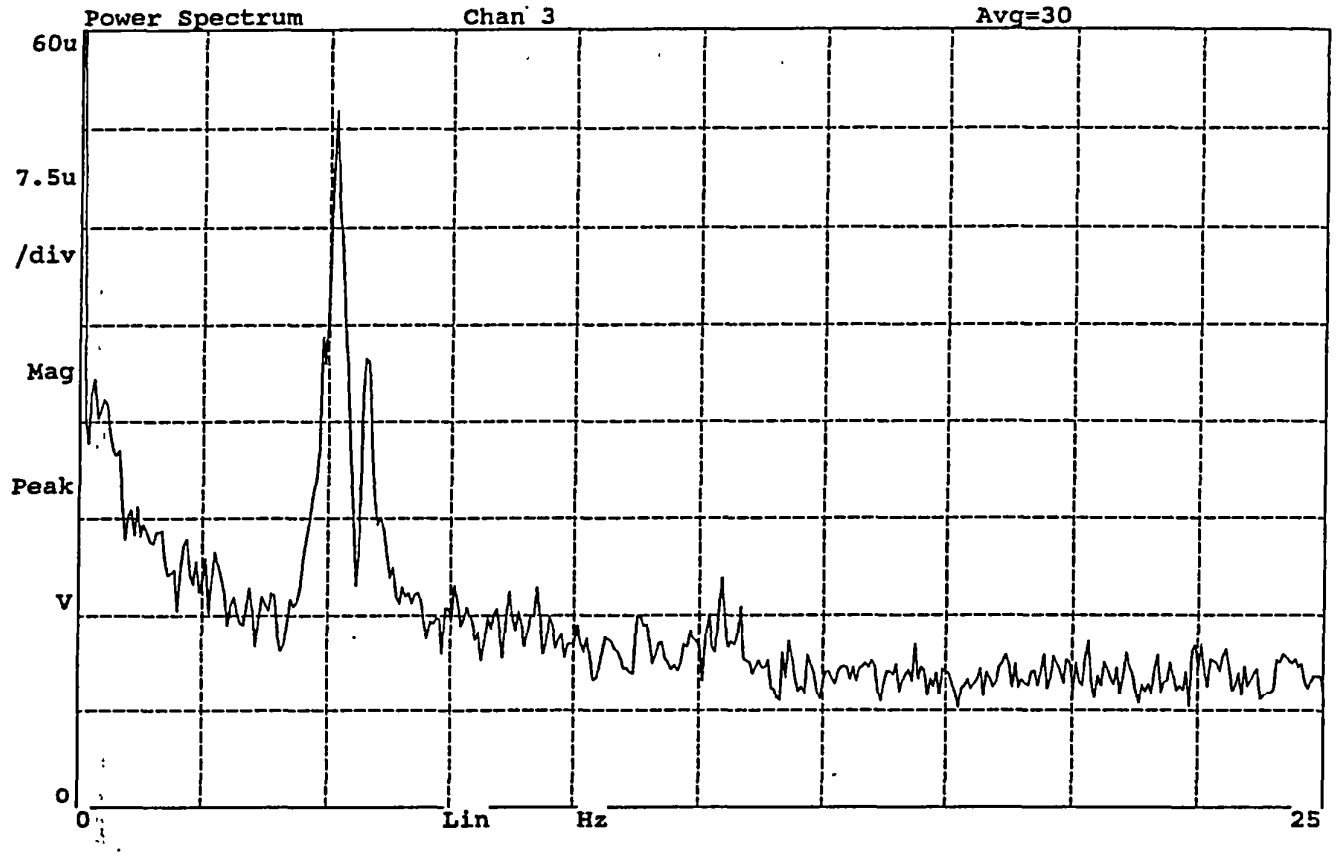

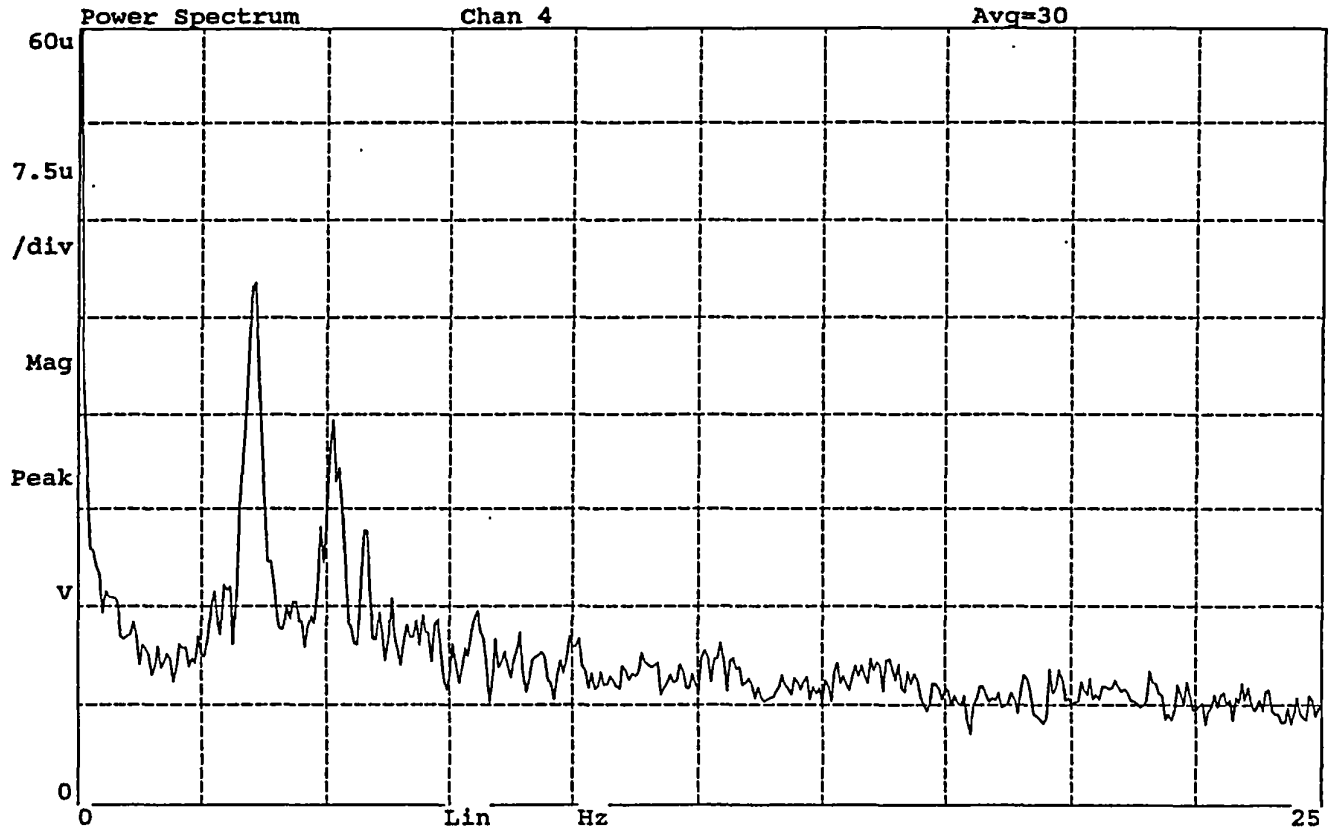

Figure A2. Average power spectra of signals from Channels 3 and 4, Test No. 1

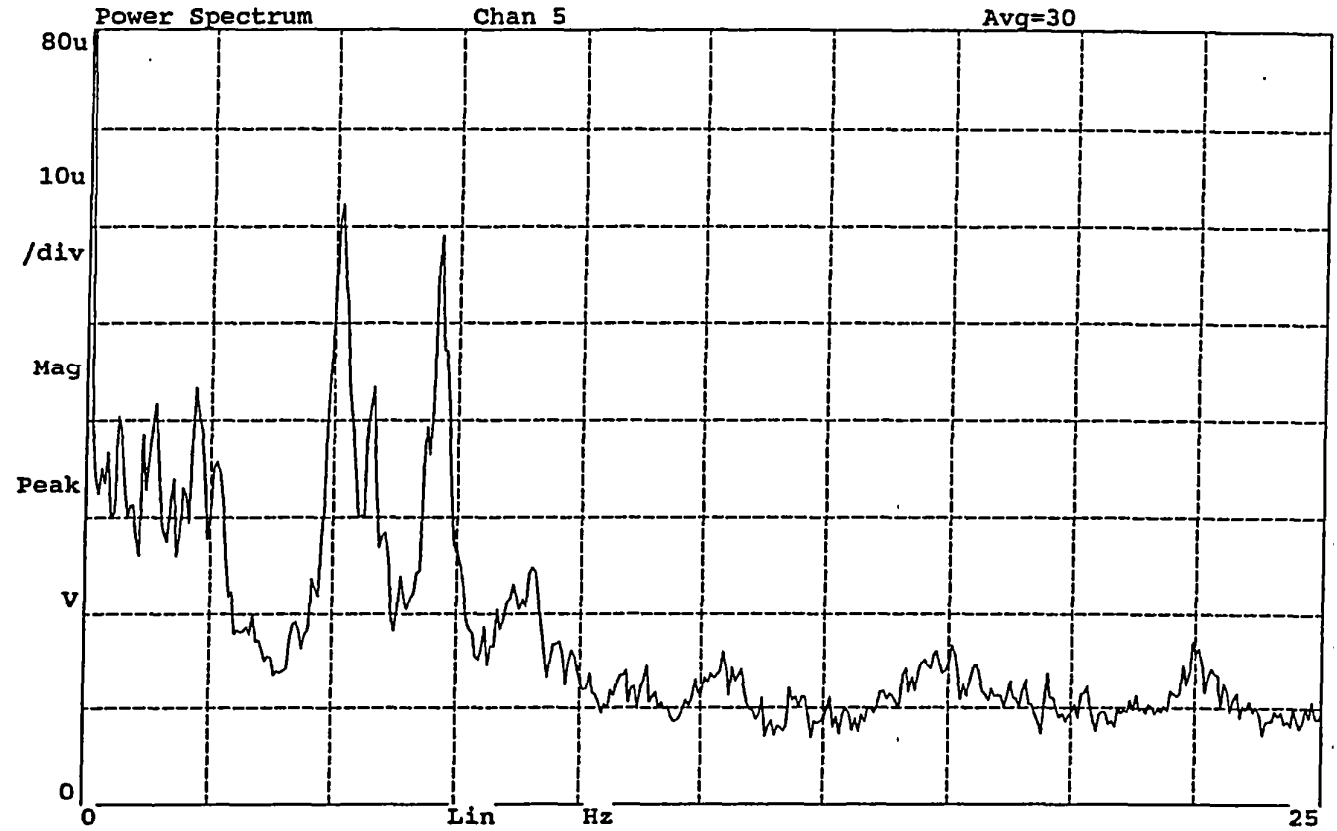

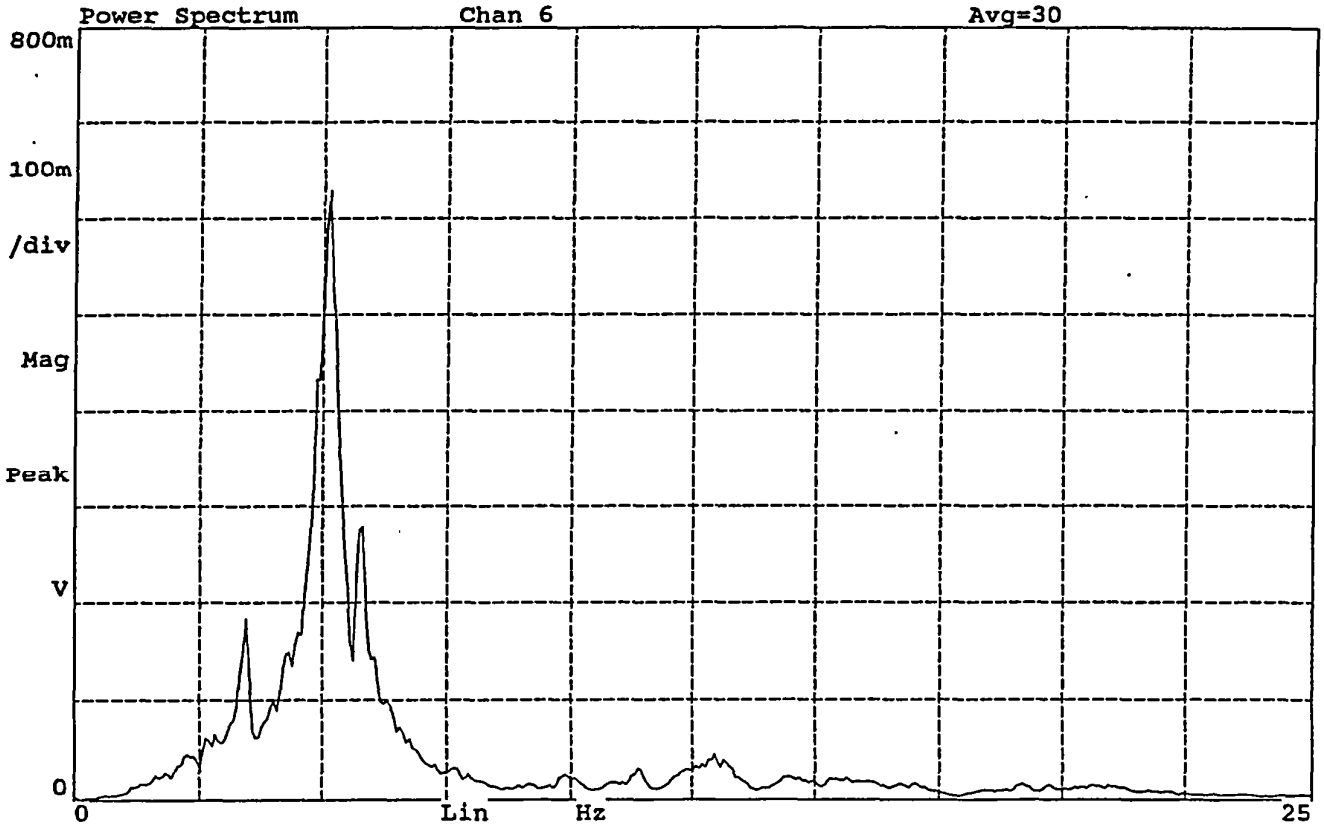

Figure A3. Average power spectra of signals from Channels 5 and 6, Test No. 1

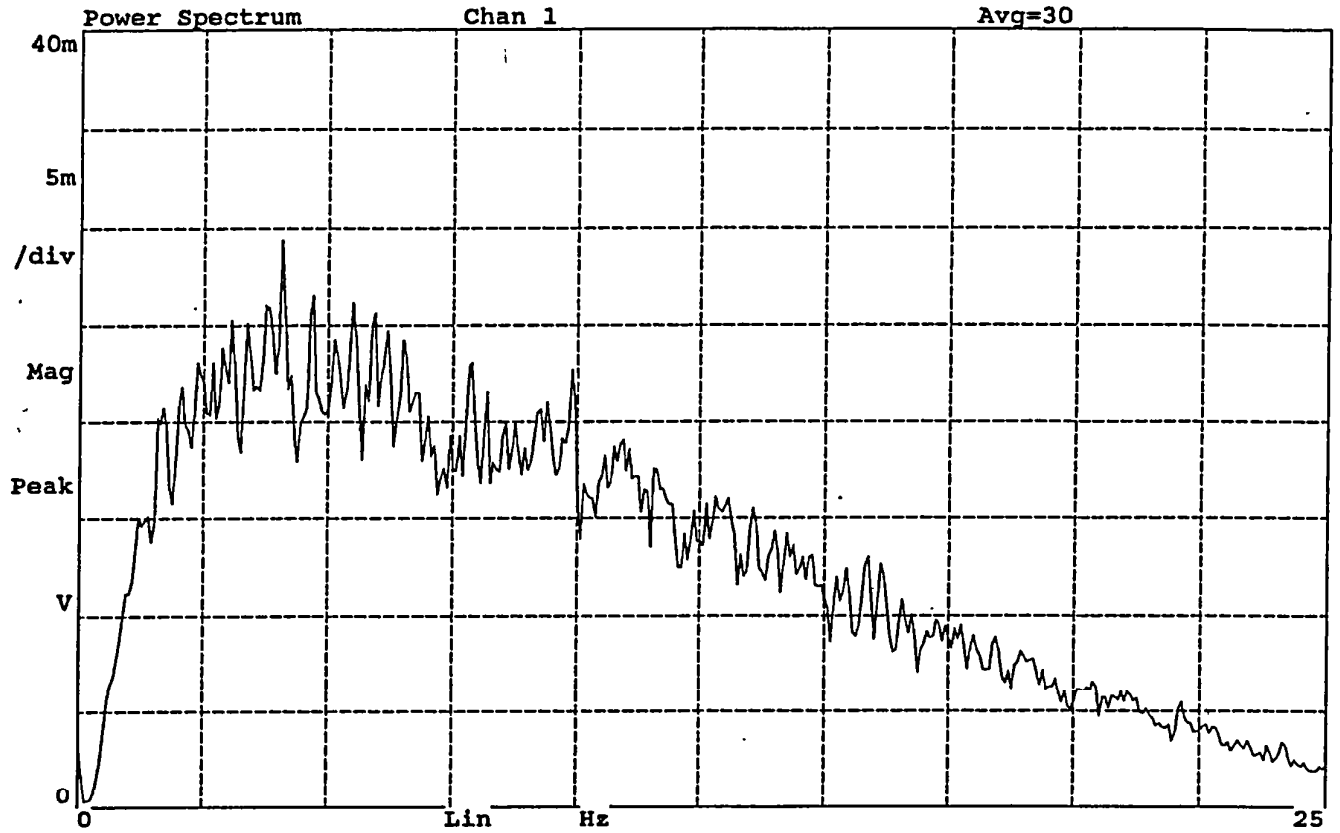

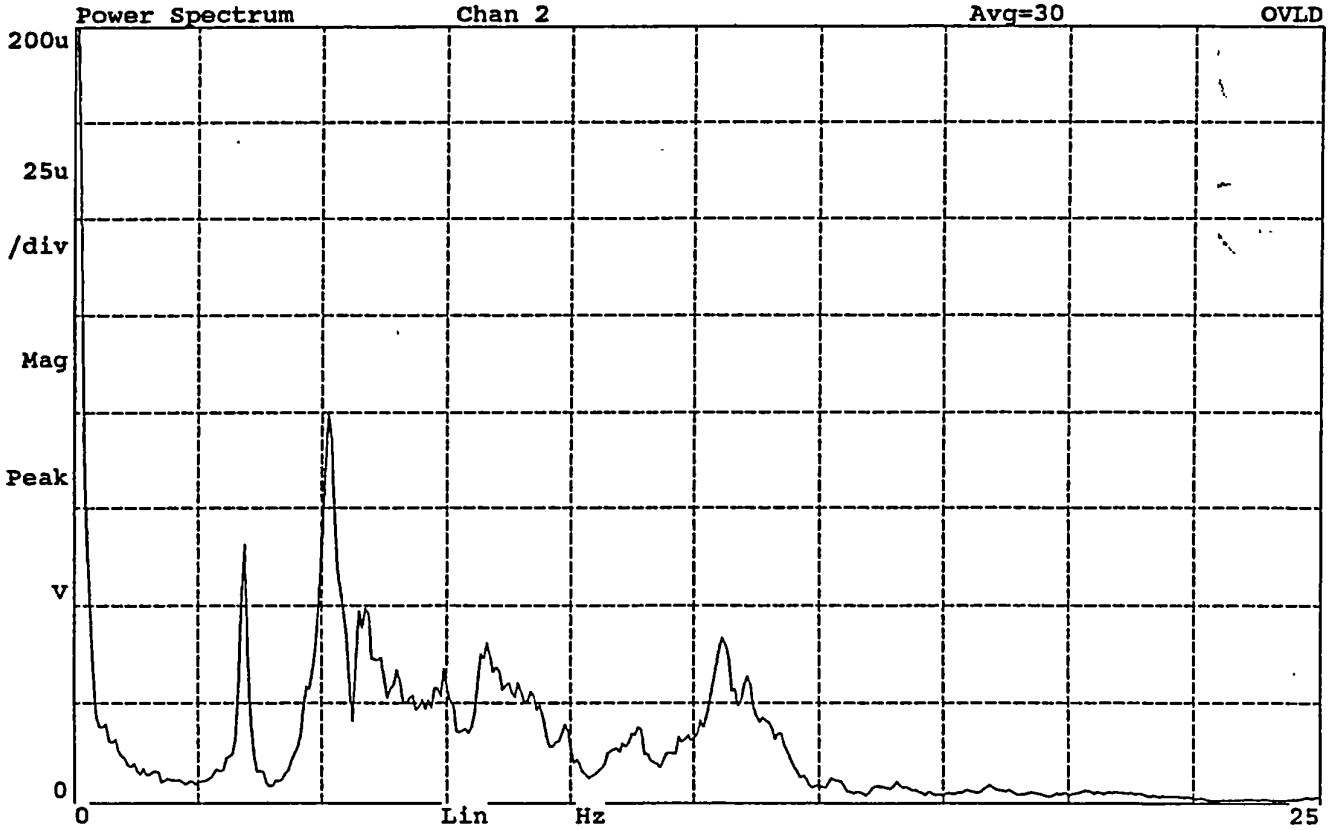

Figure A4. Average power spectra of signals from Channels 1 and 2, Test No. 2

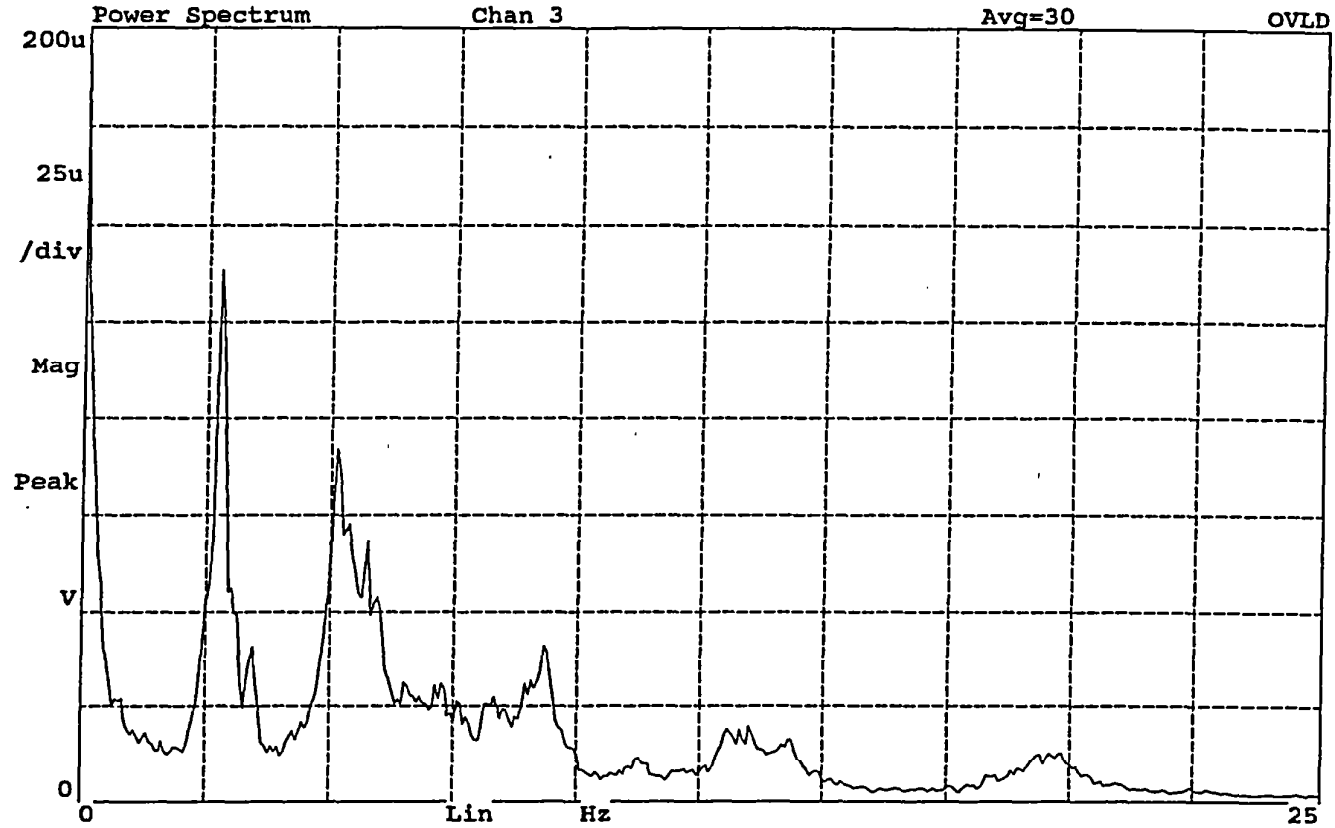

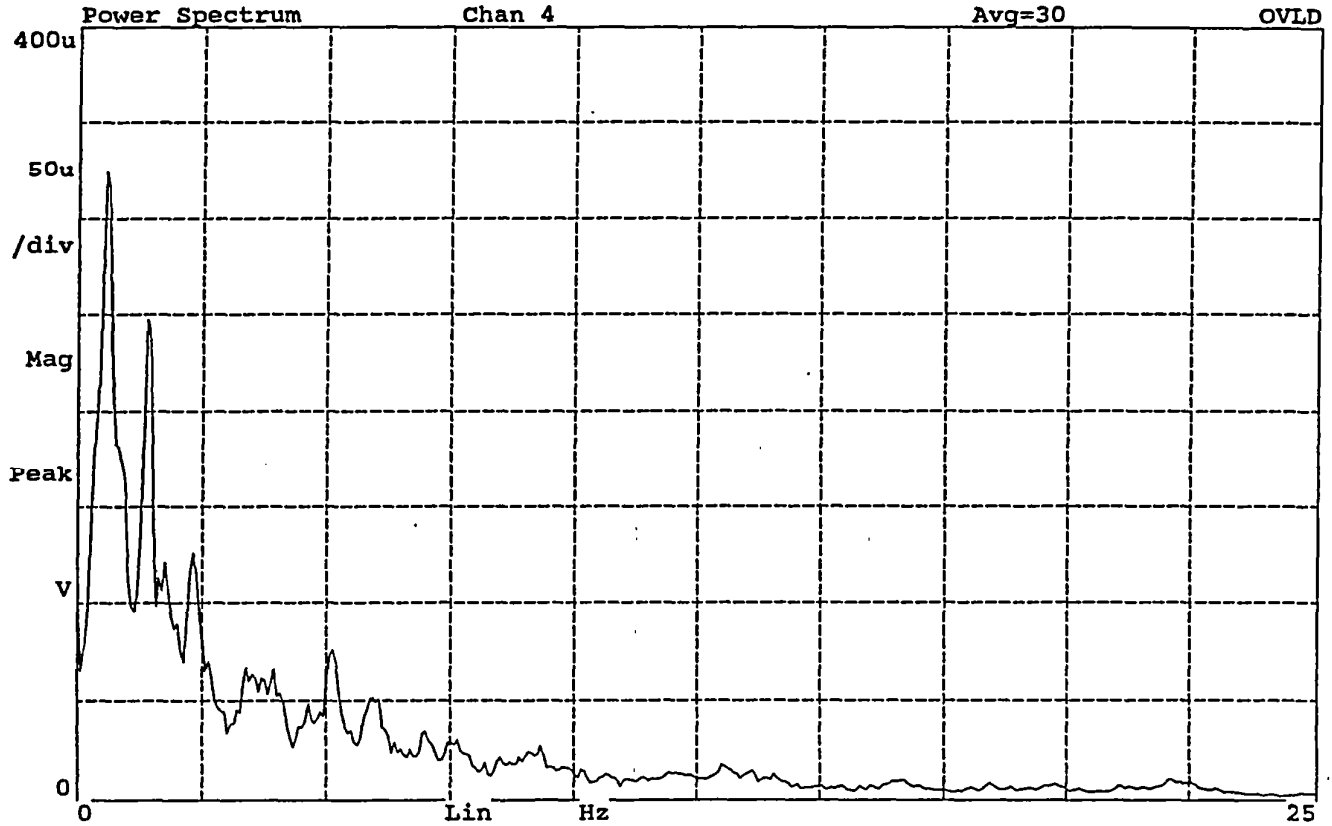

Figure A5. Average power spectra of signals from Channels 3 and 4, Test No. 2

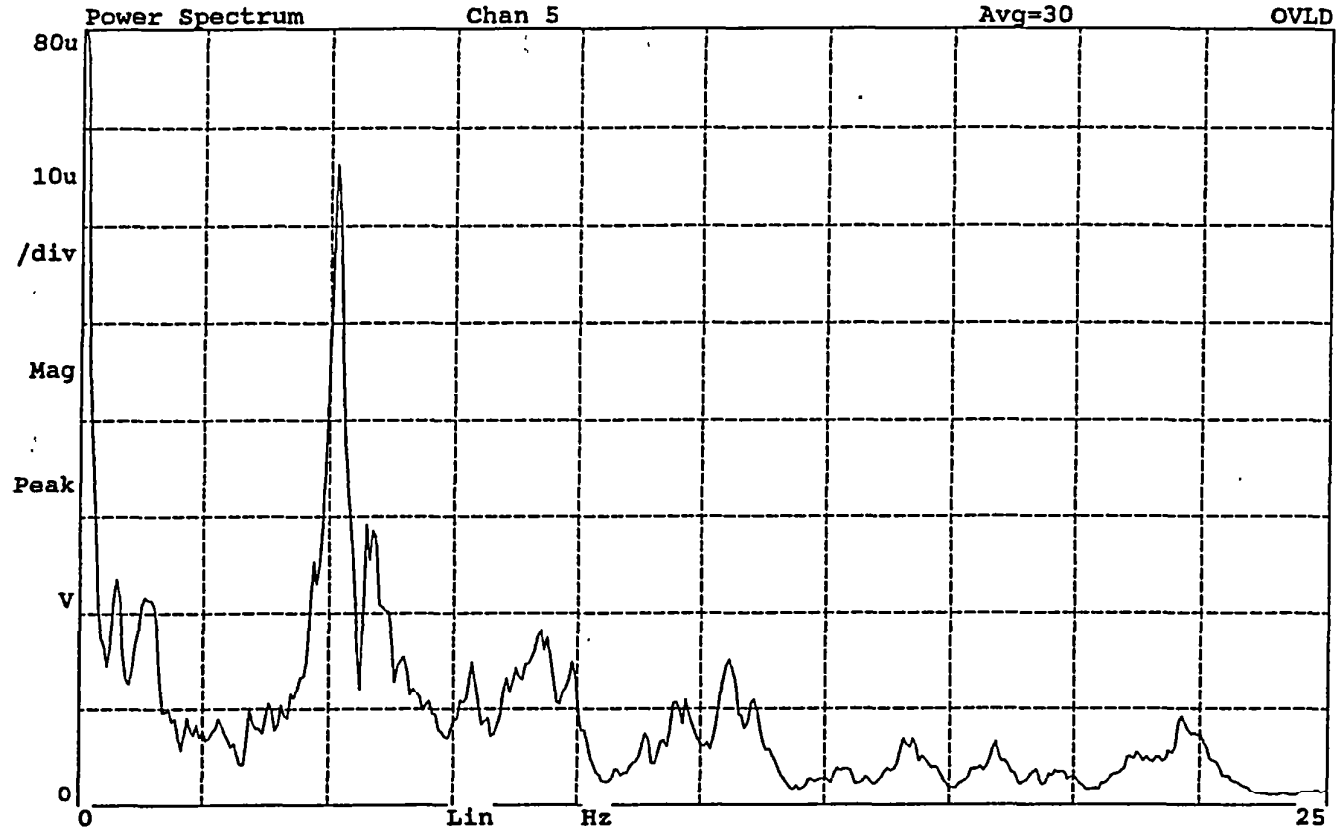

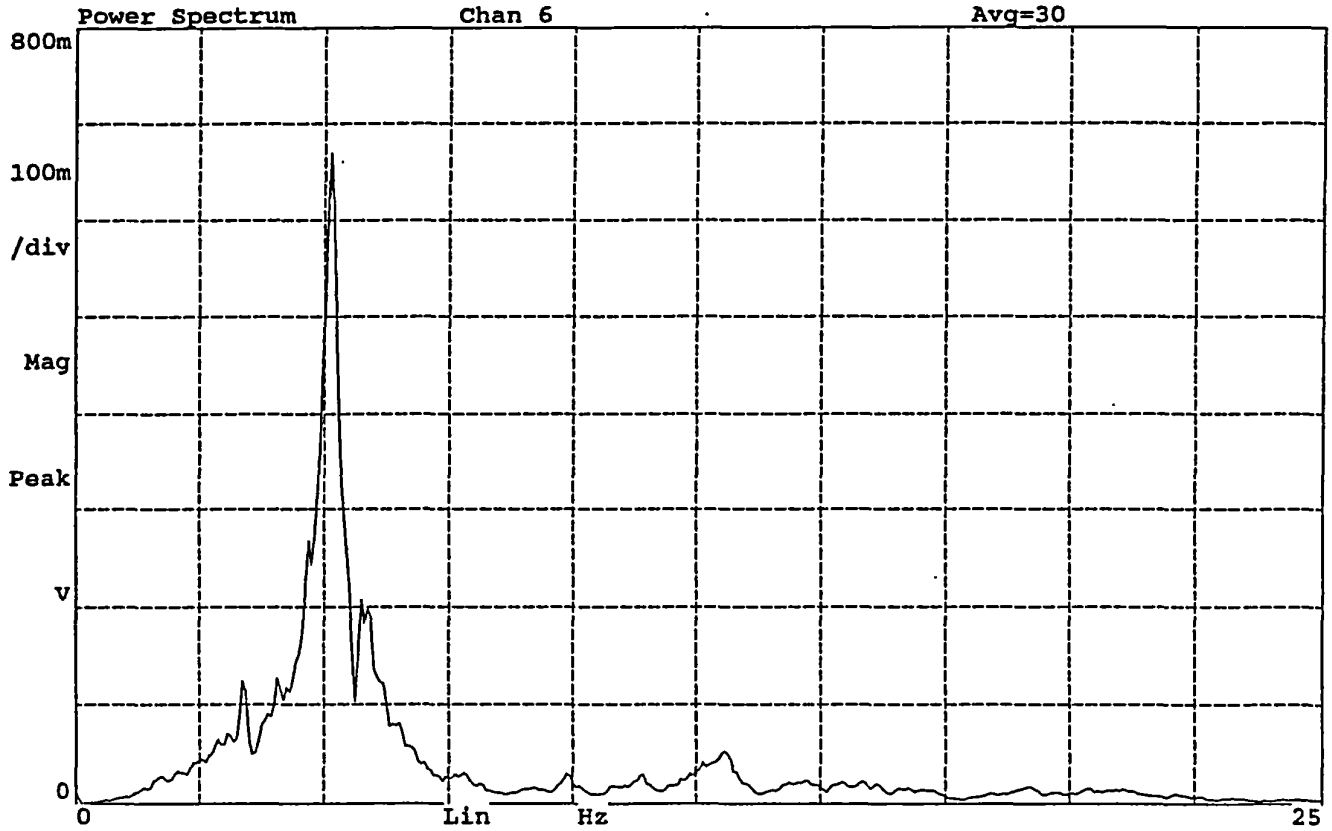

Figure A6. Average power spectra of signals from Channels 5 and 6, Test No. 2

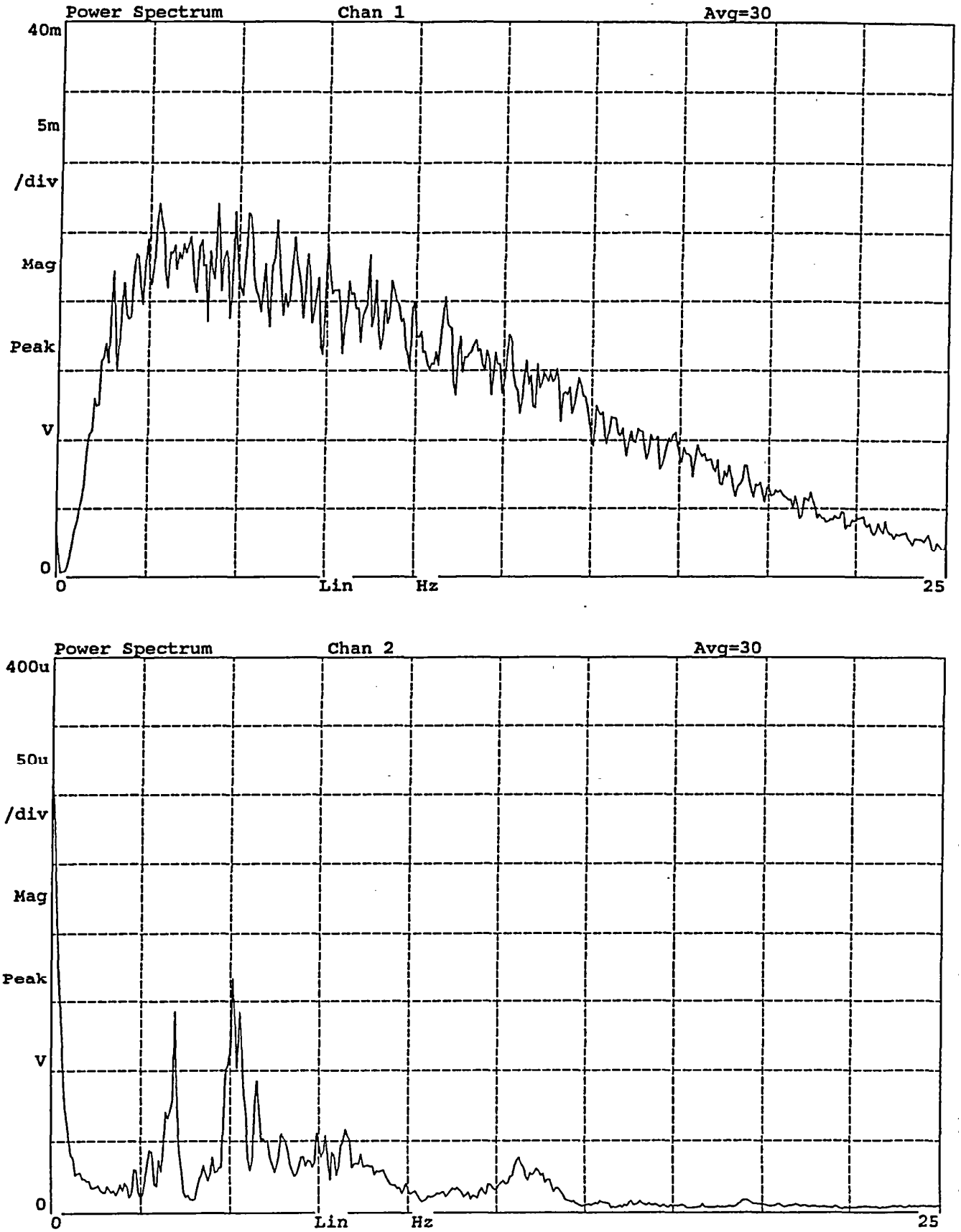

Figure A7. Average power spectra of signals from Channels 1 and 2, Test No. 3

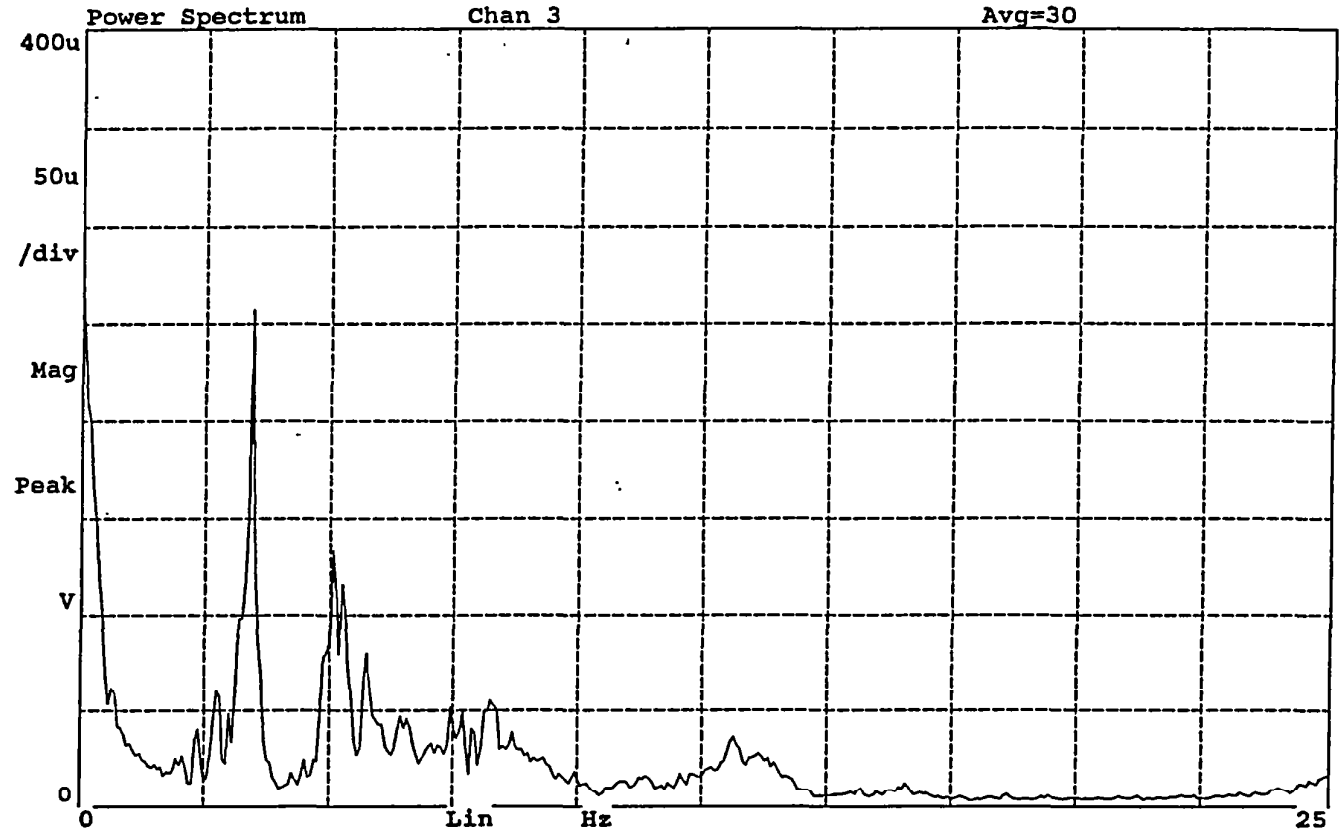

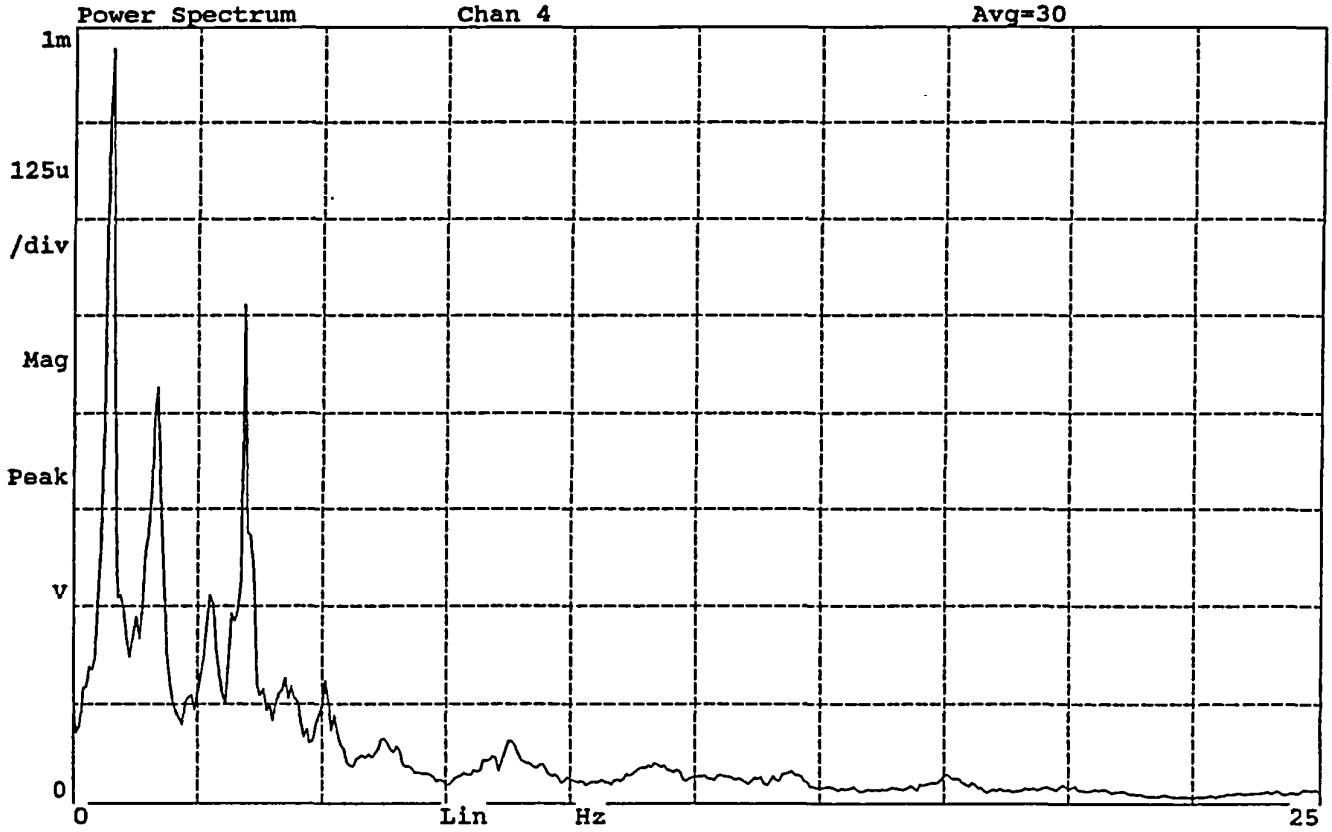

Figure A8. Average power spectra of signals from Channels 3 and 4, Test No. 3

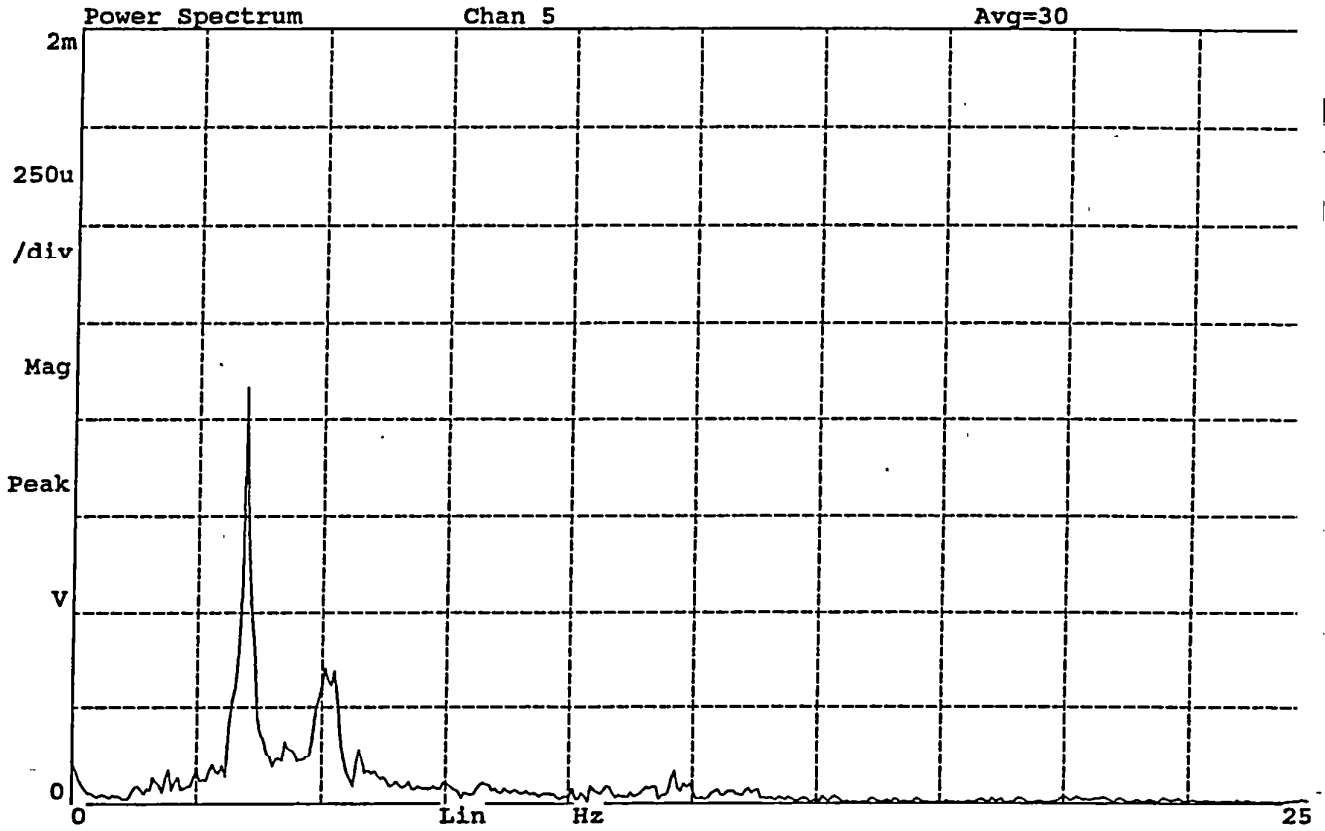

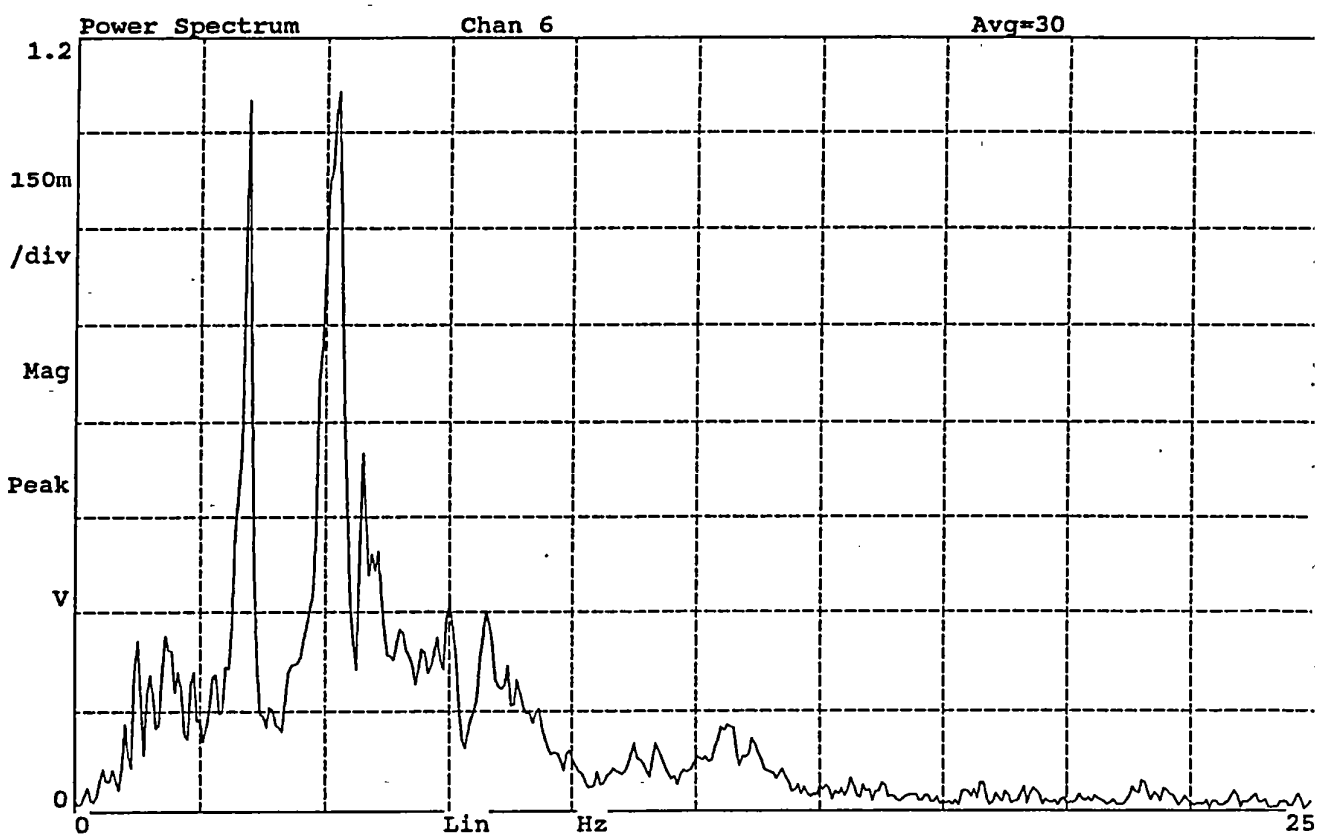

Figure A9. Average power spectra of signals from Channels 5 and 6, Test No. 3

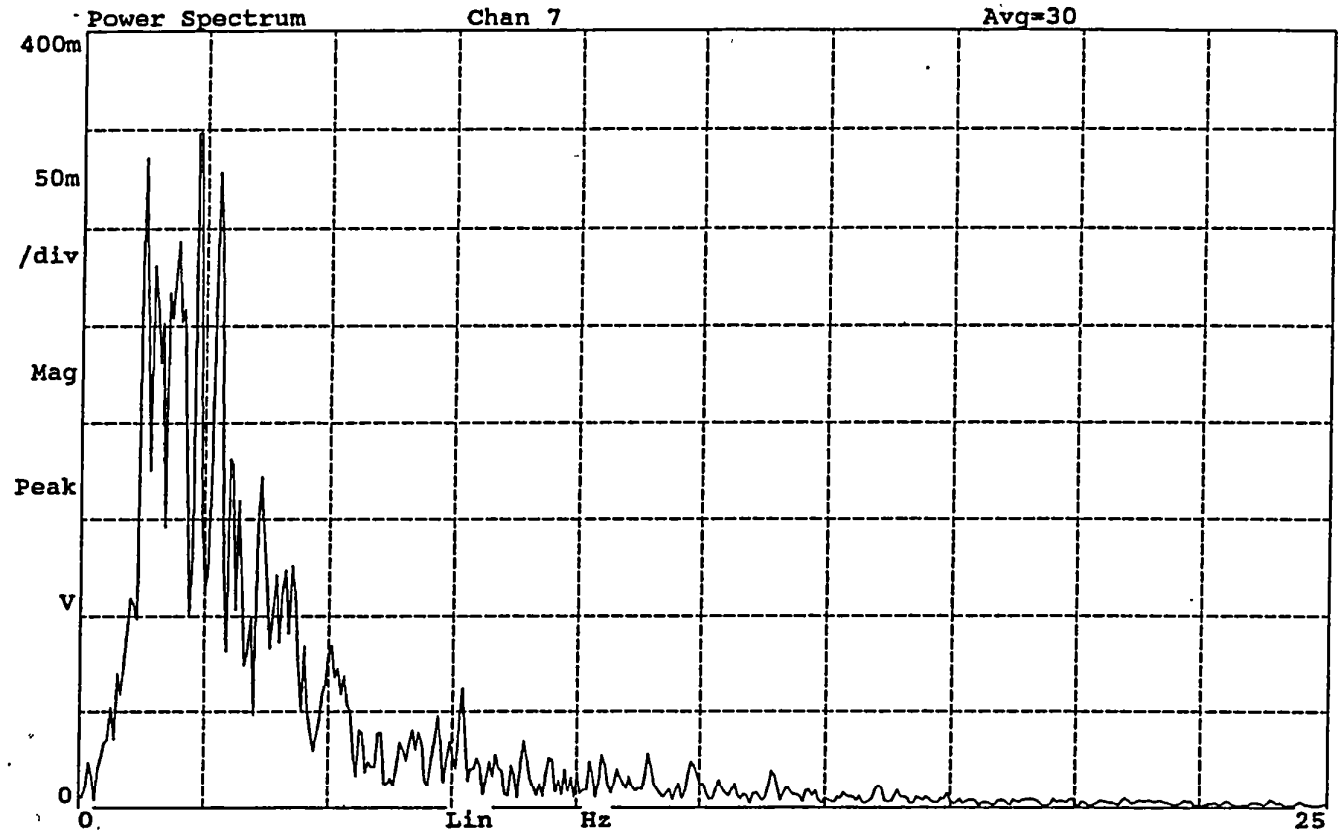

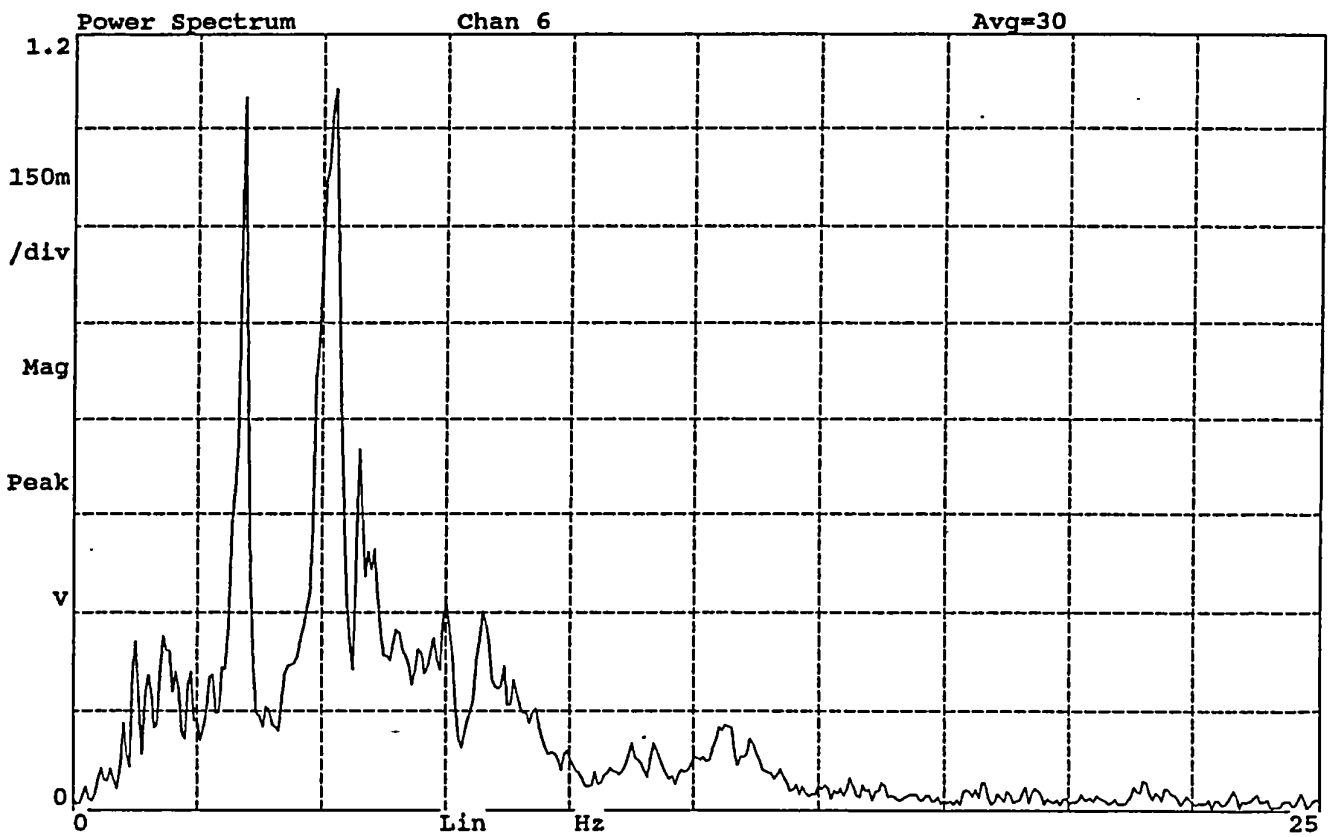

Figure A10. Average power spectra of signals from Channels 7 and 6, Test No. 3

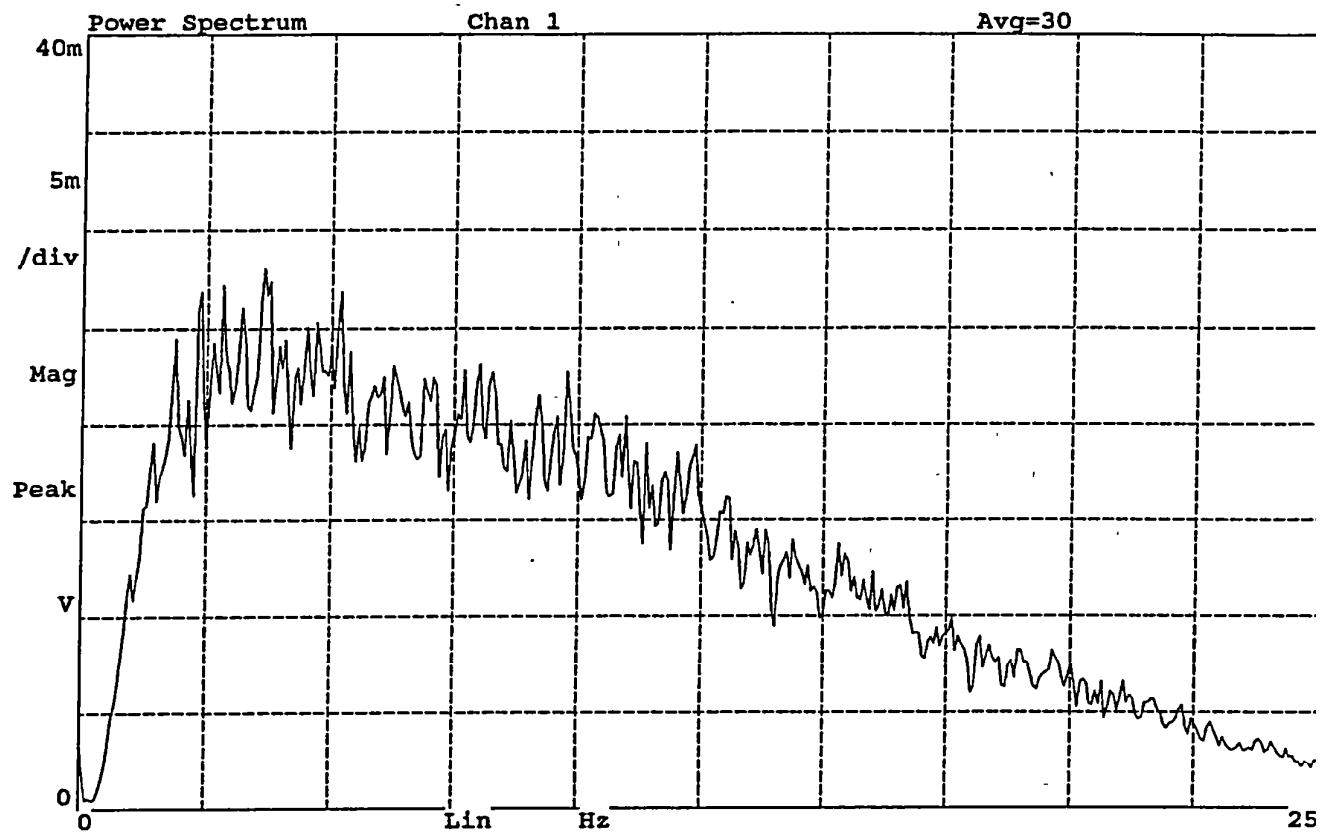

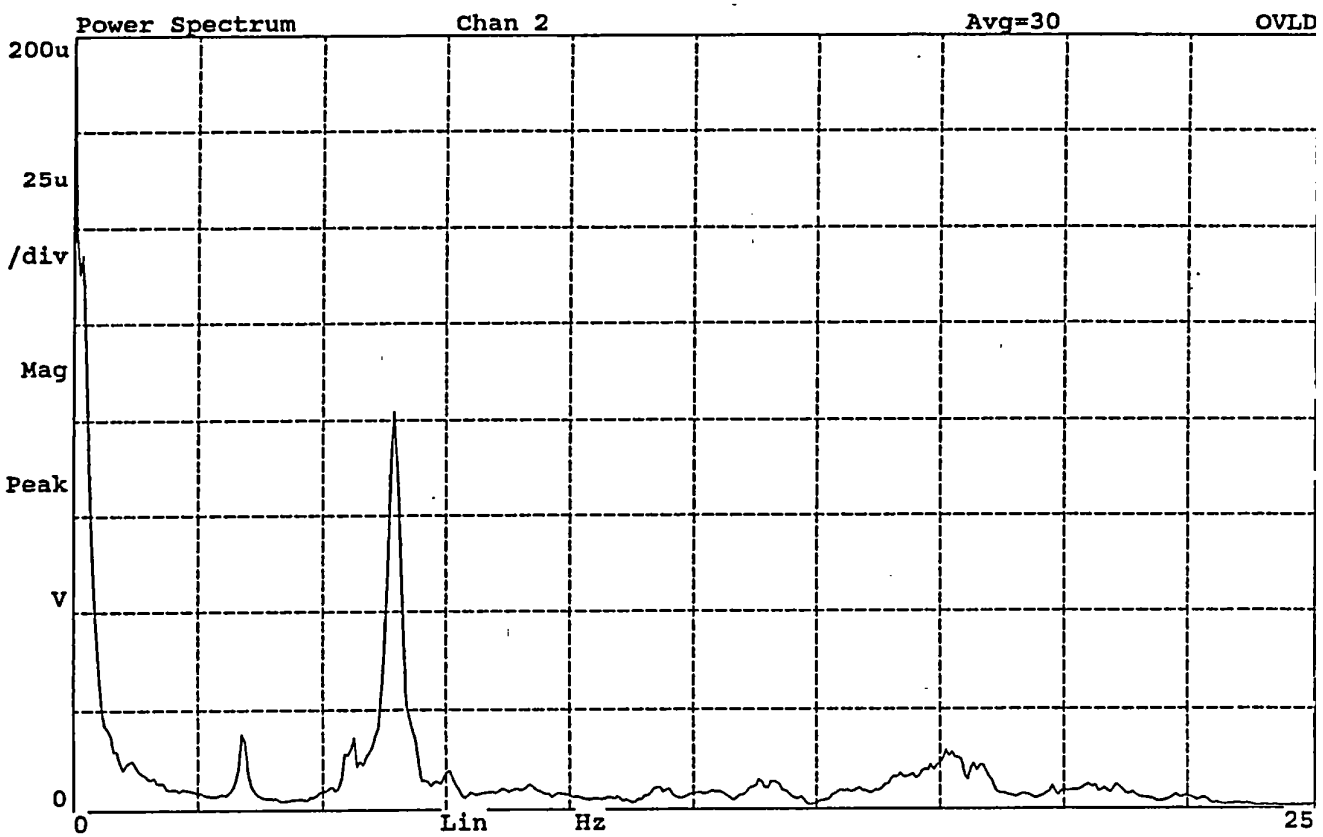

Figure A11. Average power spectra of signals from Channels 1 and 2, Test No. 4

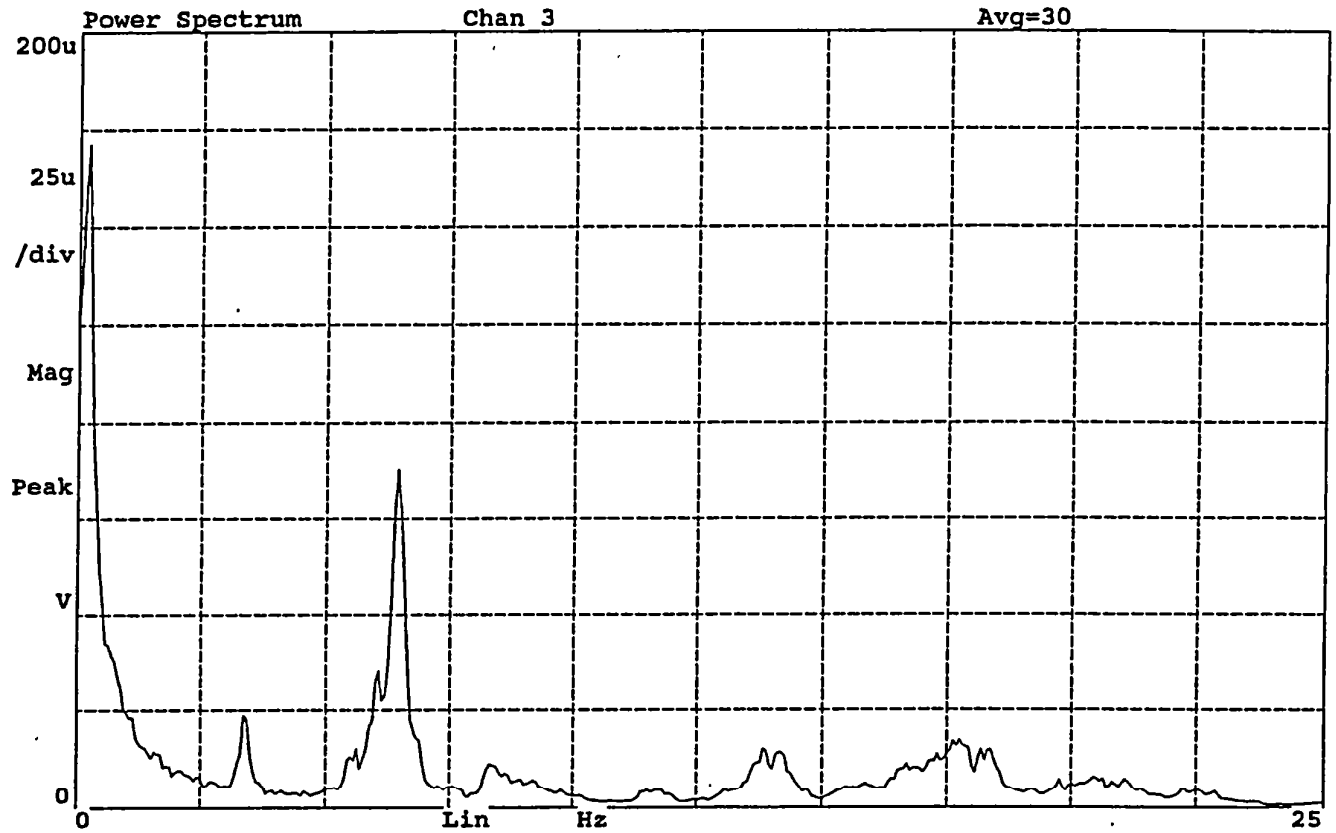

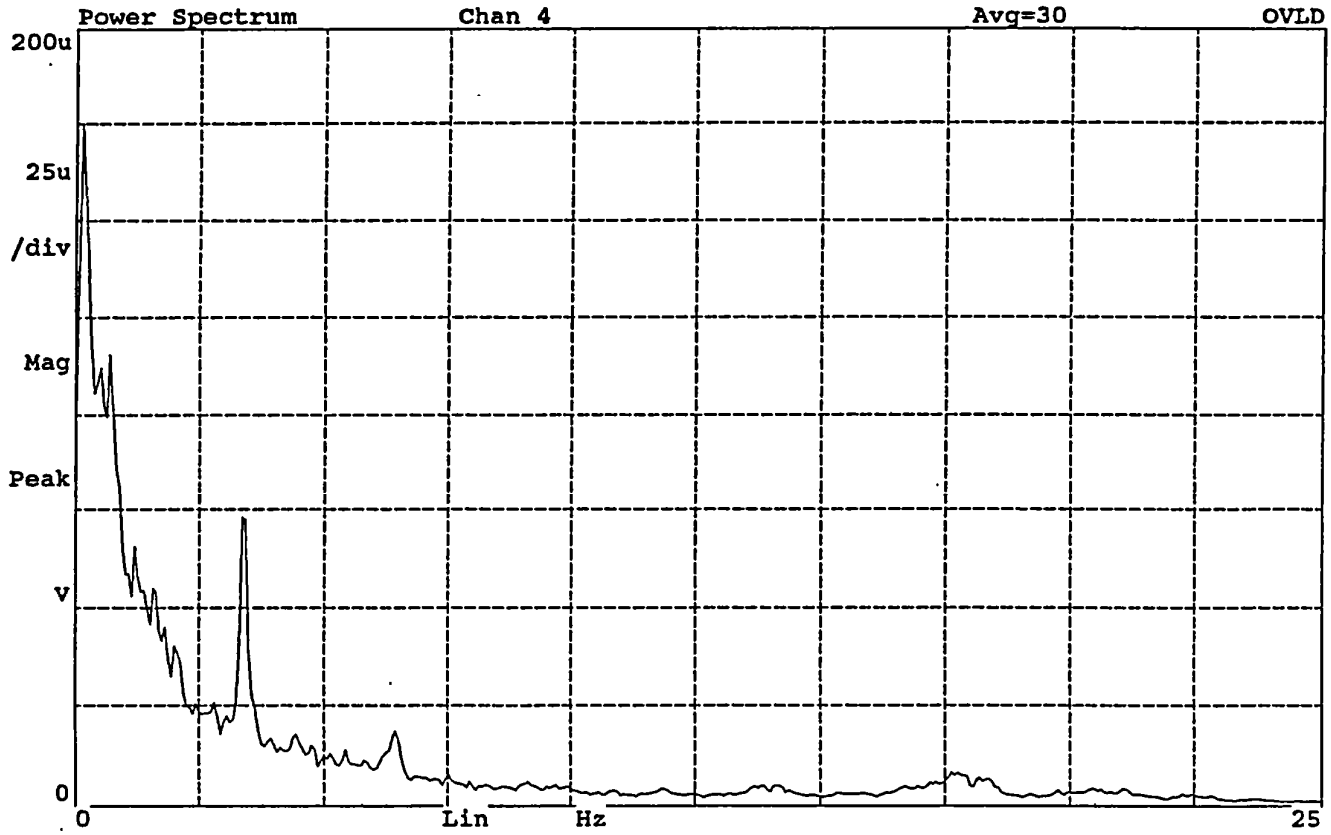

Figure A12. Average power spectra of signals from Channels 3 and Channel 4, Test No. 4

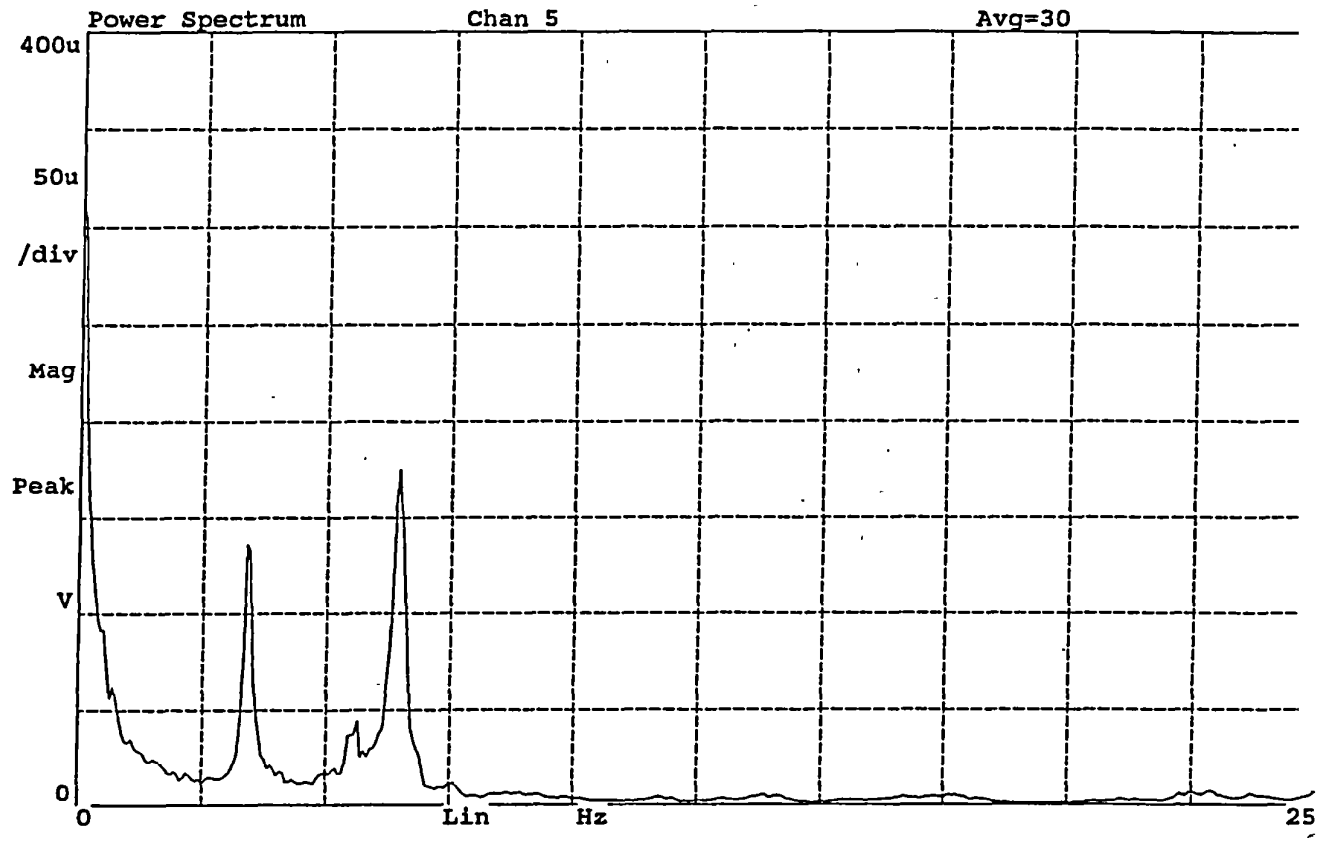

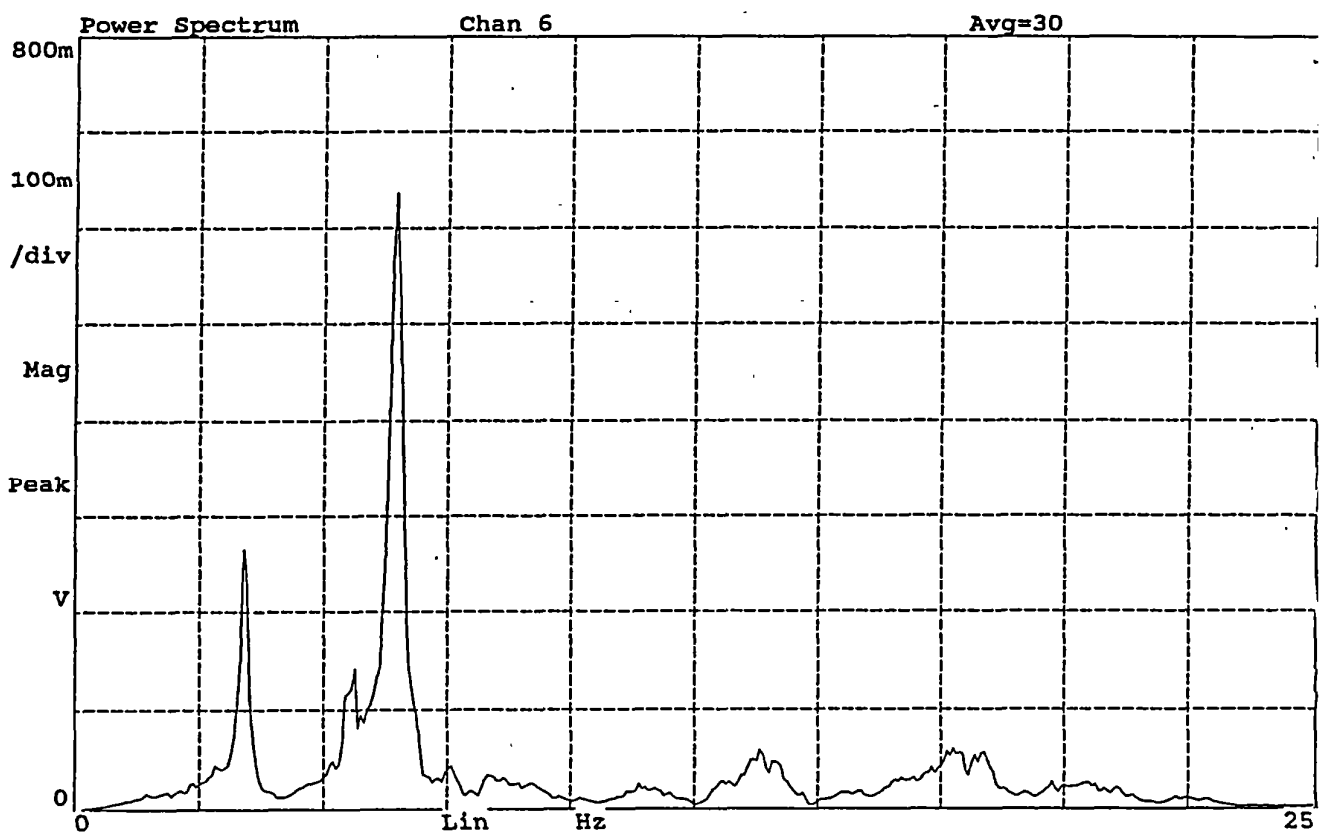

Figure A13. Average power spectra of signals from Channels 5 and 6, Test No. 4

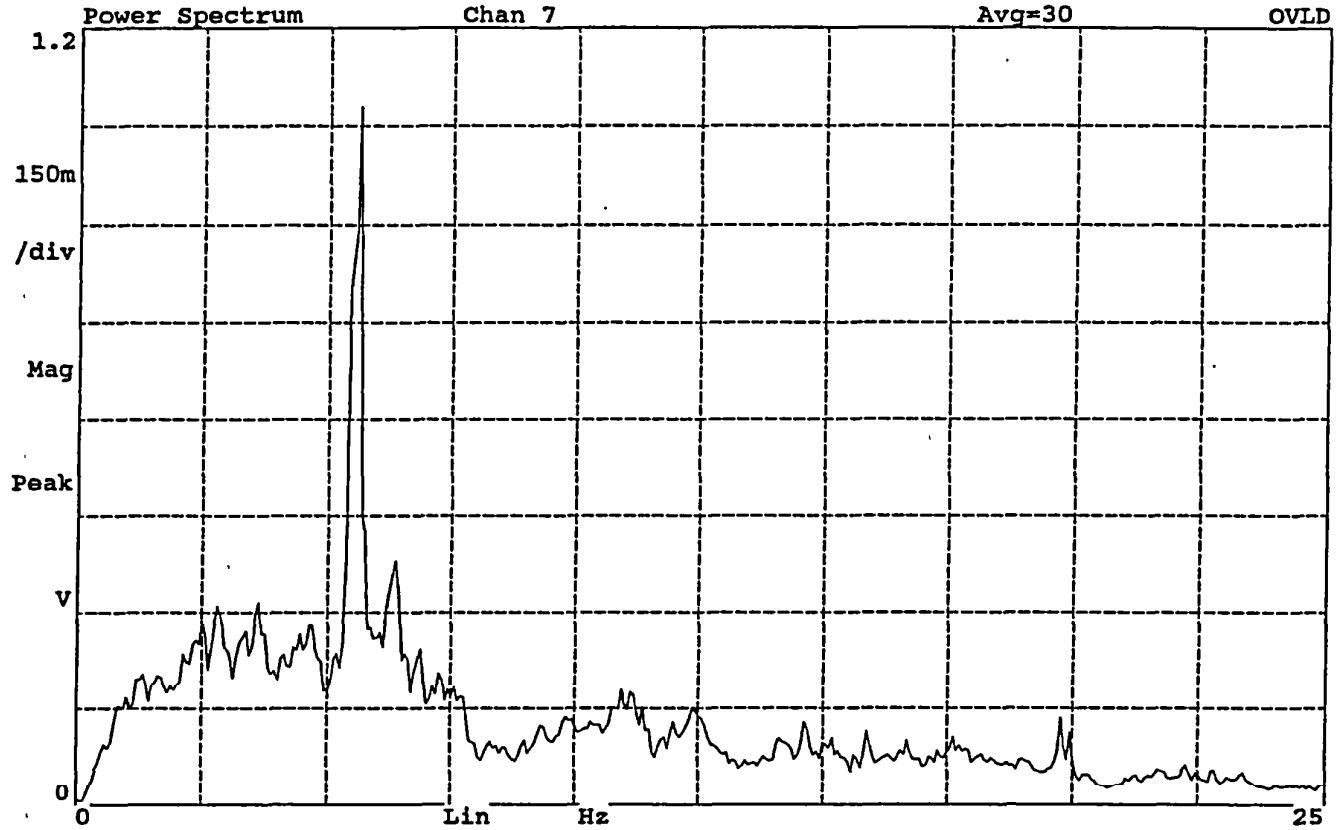

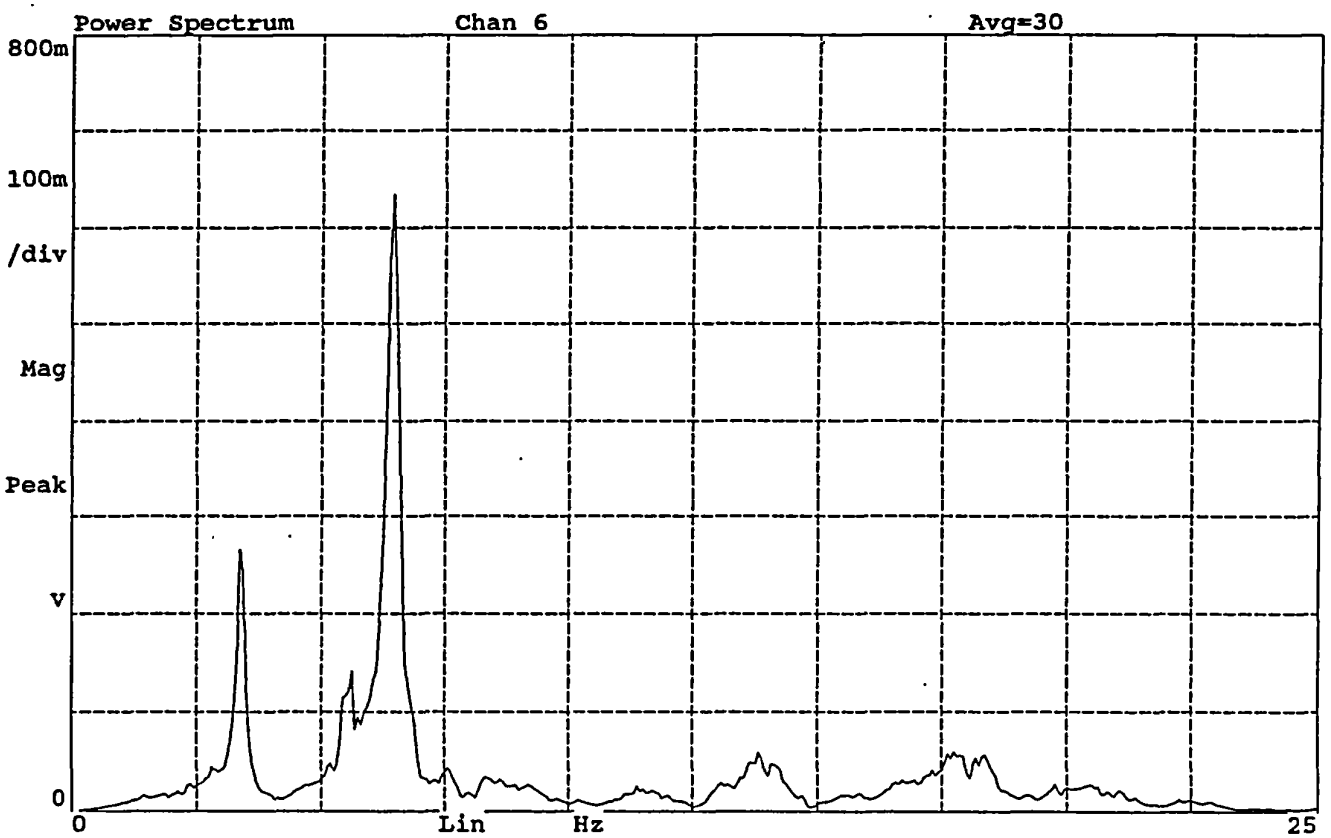

Figure A14. Average power spectra of signals from Channels 7 and 6, Test No. 4

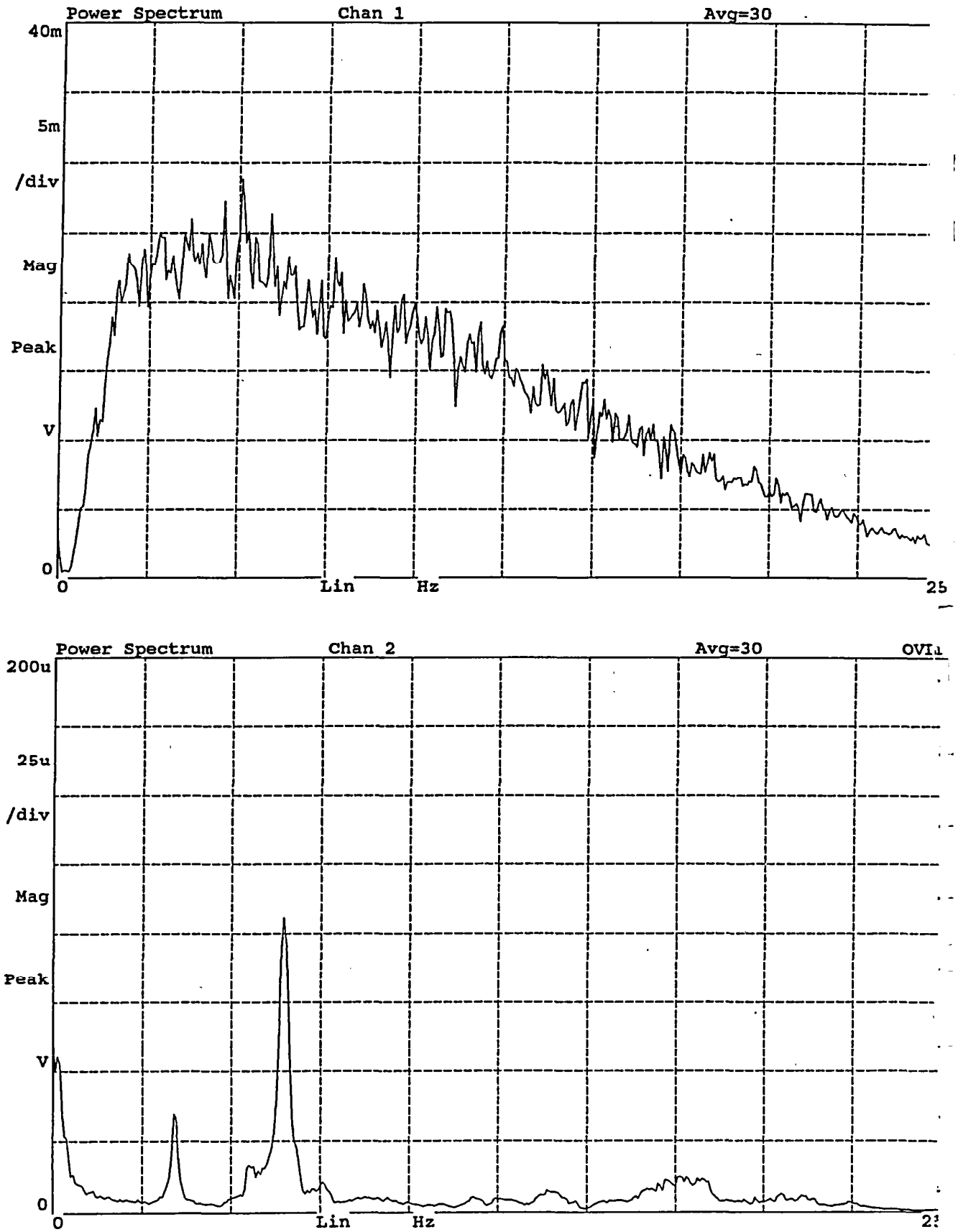

Figure A15. Average power spectra of signals from Channels 1 and 2, Test No. 5

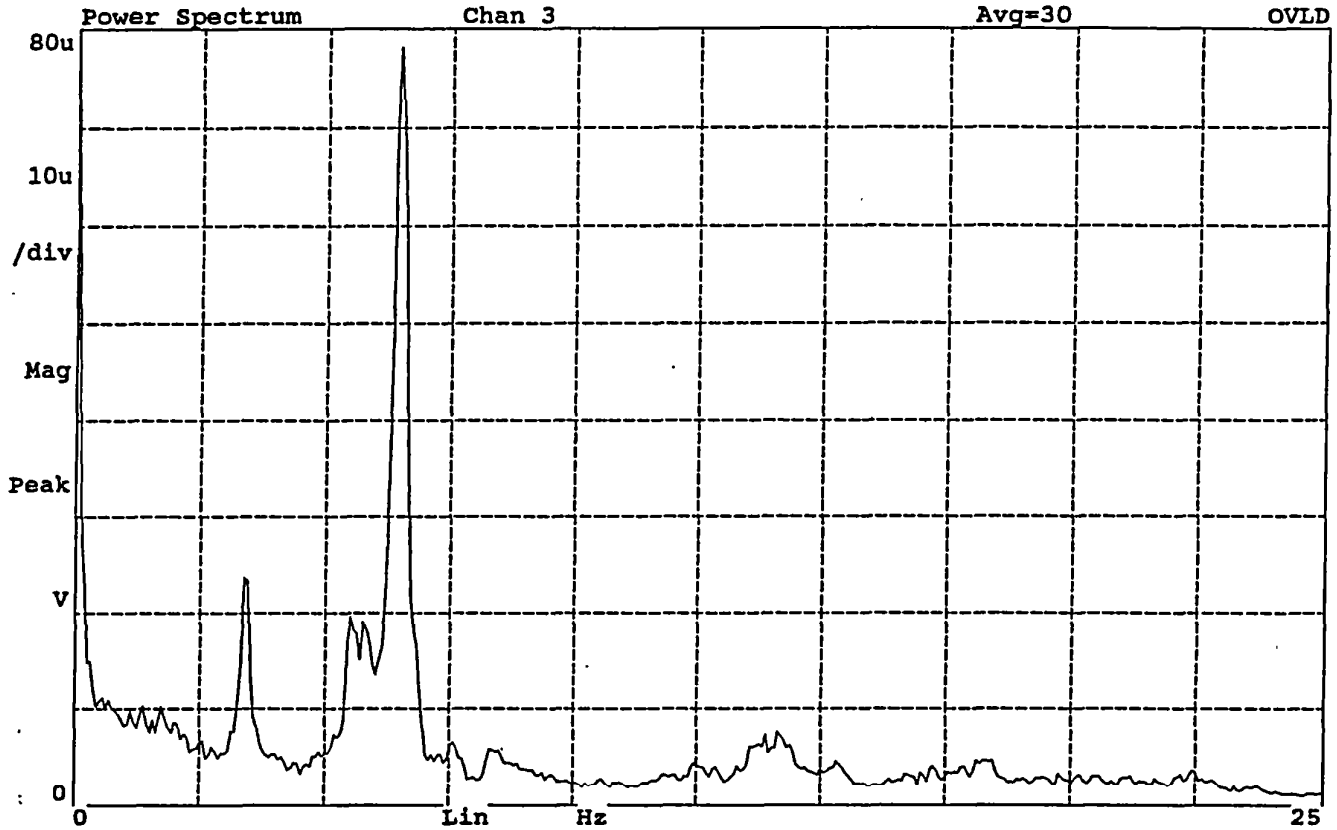

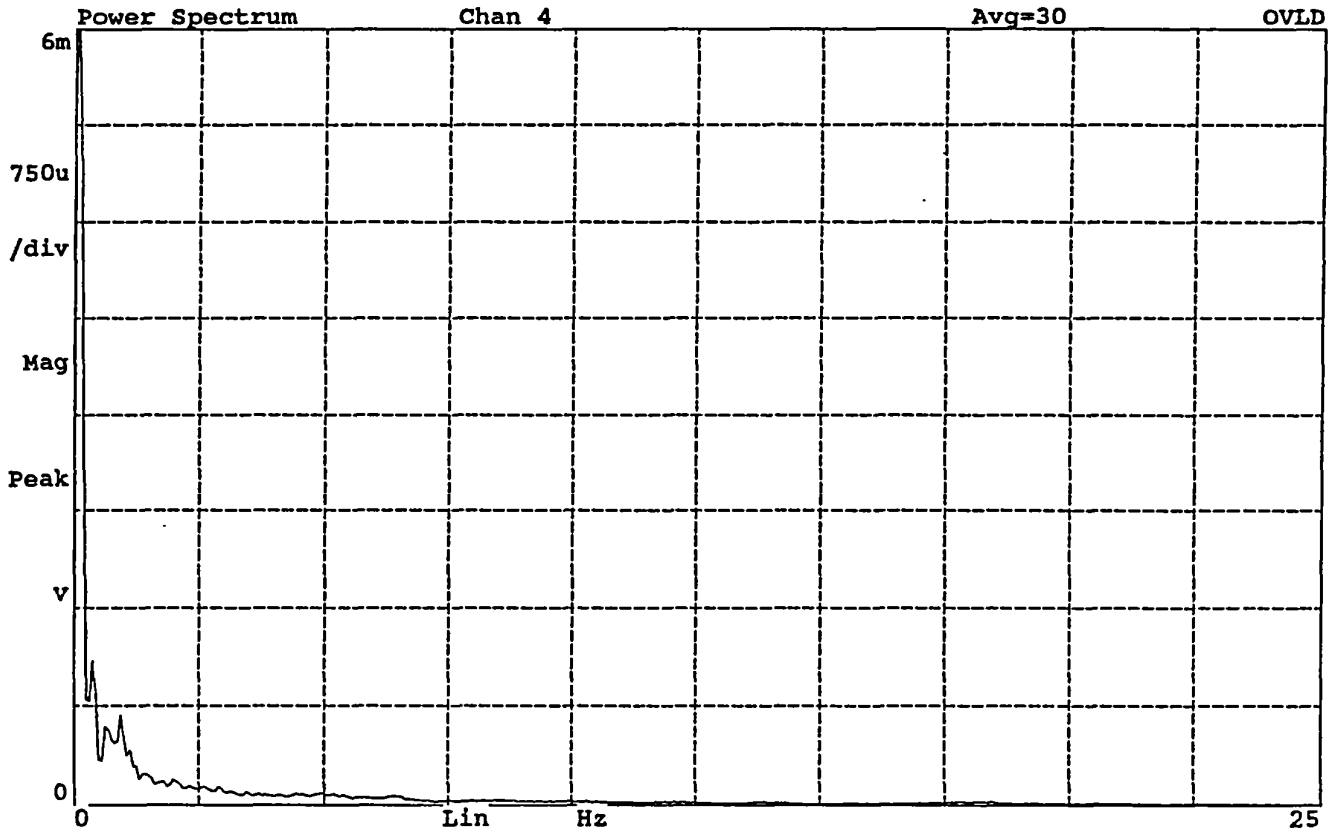

Figure A16. Average power spectra of signals from Channels 3 and 4, Test No. 5

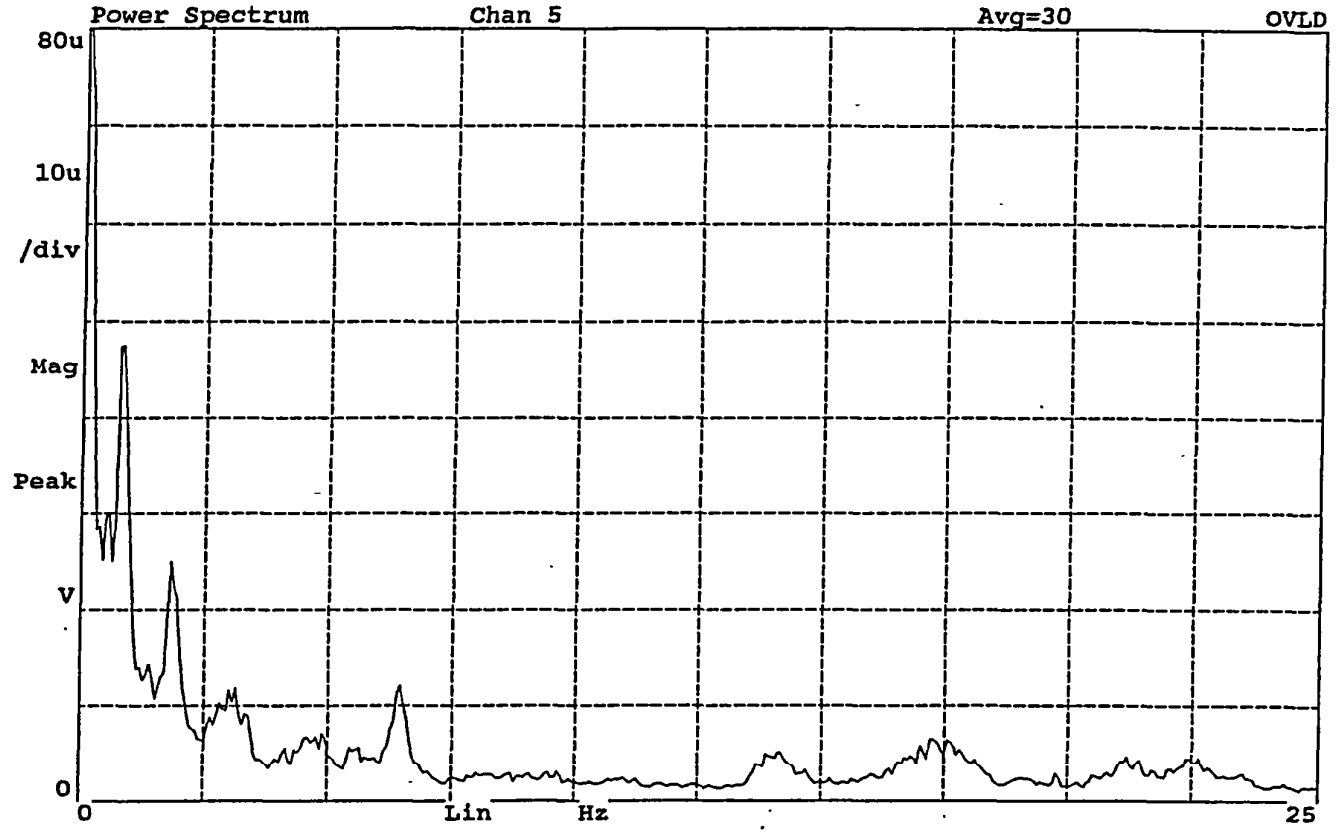

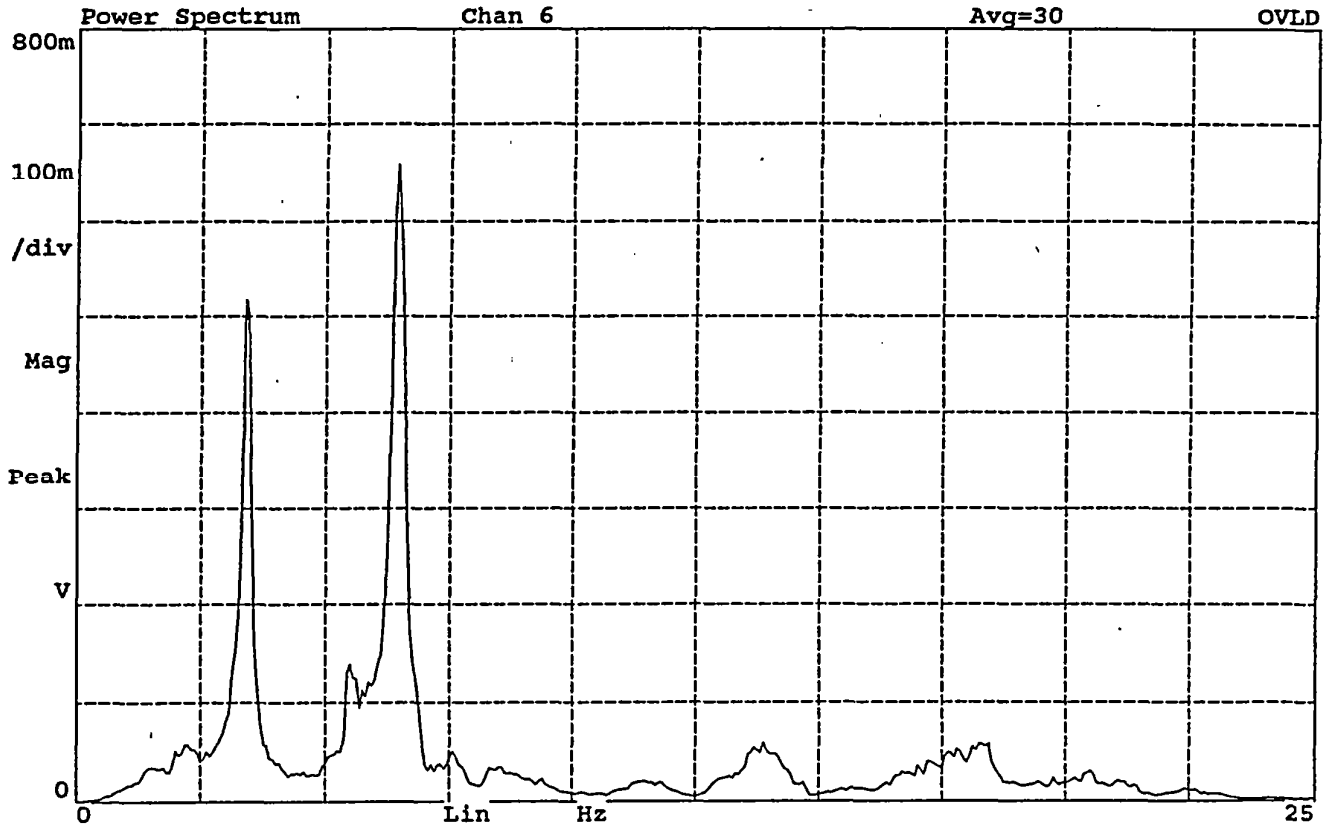

Figure A17. Average power spectra of signals from Channels 5 and 6, Test No. 5

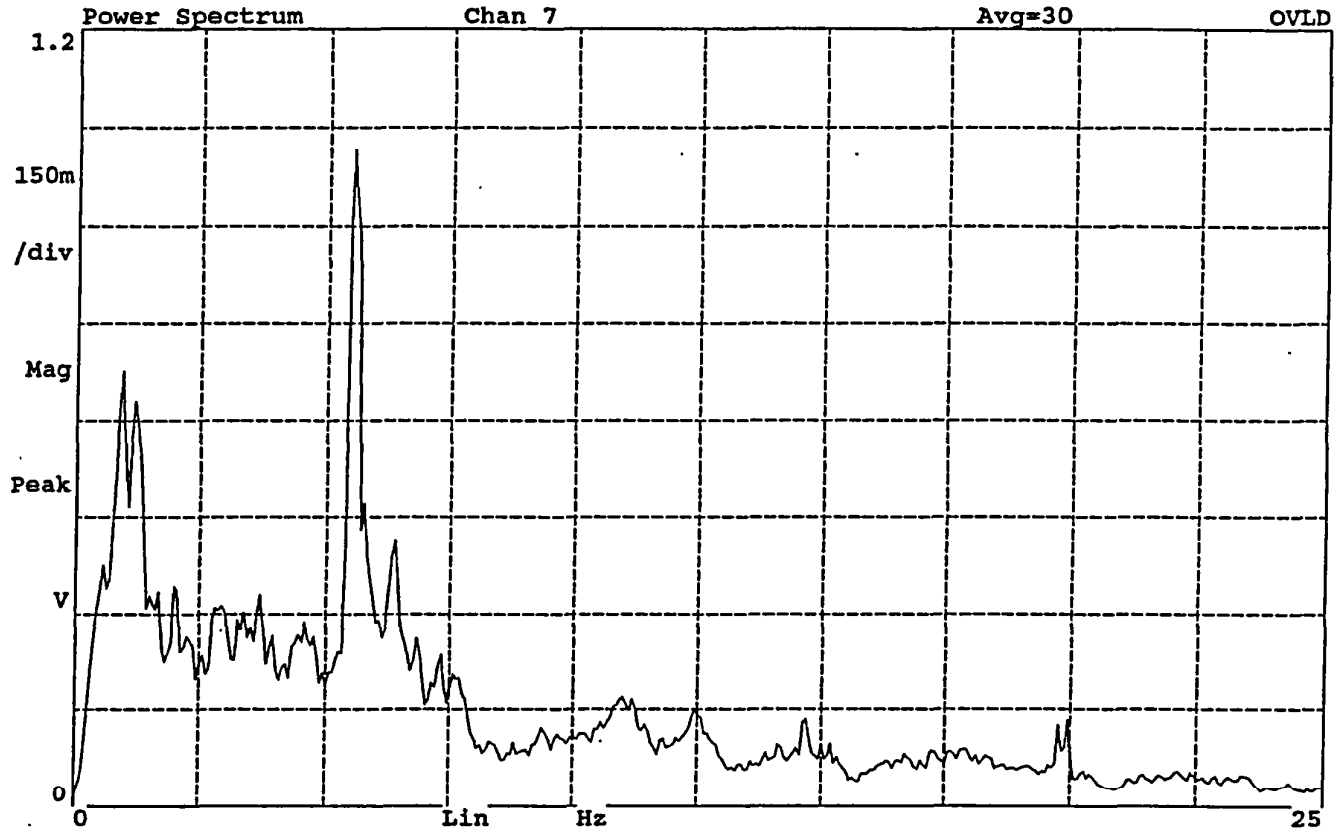

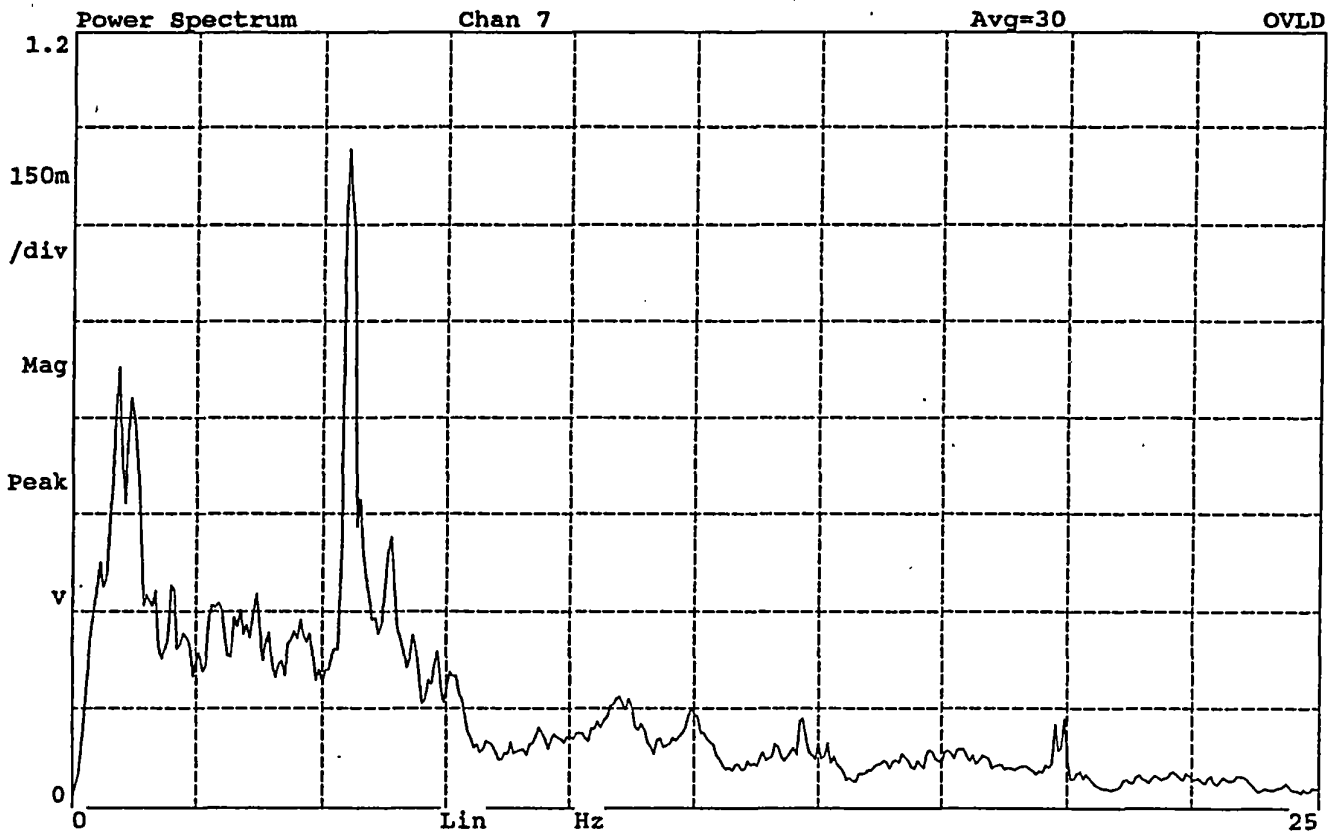

Figure A18. Average power spectra of signal from Channel 7, Test No. 5

Appendix B

POWER SPECTRA FROM FIELD TESTS OF WESTINGHOUSE 500-KV TRANSFORMER AT MIDWAY SUBSTATION

Seven separate tests were conducted on the Westinghouse 500-kV transformer using up to six sensors in each test. The sensor orientation, sensor type, and correspondence between channel number and sensor location are shown in the table below. The average power spectra corresponding to the signals recorded by each of the listed channels are given in Figures B1 through B11.

Test No.	Direction	Channel	Sensor location	Sensor type
1	Longitudinal	1	Foundation	Seismometer
	Transverse	2	Foundation	Seismometer
	Longitudinal	3	HV turret top	Seismometer
	Transverse	4	HV turret top	Seismometer
	Longitudinal	5	HV bushing top	Accelerometer
	Transverse	6	HV bushing top	Accelerometer
2	Longitudinal	1	Foundation	Seismometer
	Transverse	2	Foundation	Seismometer
	Longitudinal	3	HV turret top	Seismometer
	Transverse	4	HV turret top	Seismometer
	Longitudinal	5	HV bushing top	Accelerometer
	Transverse	6	HV bushing top	Accelerometer
3	Longitudinal	1	Foundation	Seismometer
	Transverse	2	Foundation	Seismometer
	Longitudinal	3	HV turret top	Seismometer
	Transverse	4	HV turret top	Seismometer
	Longitudinal	5	HV bushing top	Accelerometer
	Transverse	6	HV bushing top	Accelerometer
4	Longitudinal	1	Shaker	Seismometer
	Longitudinal	3	HV turret top	Seismometer
	Transverse	4	HV turret top	Seismometer
	Longitudinal	5	HV bushing top	Accelerometer
	Transverse	6	HV bushing top	Accelerometer
5	Transverse	1	Shaker	Accelerometer
	Longitudinal	5	HV bushing top	Accelerometer
	Transverse	6	HV bushing top	Accelerometer
6	Transverse	1	Shaker	Accelerometer
	Longitudinal	5	HV bushing top	Accelerometer
	Transverse	6	HV bushing top	Accelerometer
7	Longitudinal	1	Shaker	Accelerometer
	Longitudinal	5	HV bushing top	Accelerometer
	Transverse	6	HV bushing top	Accelerometer

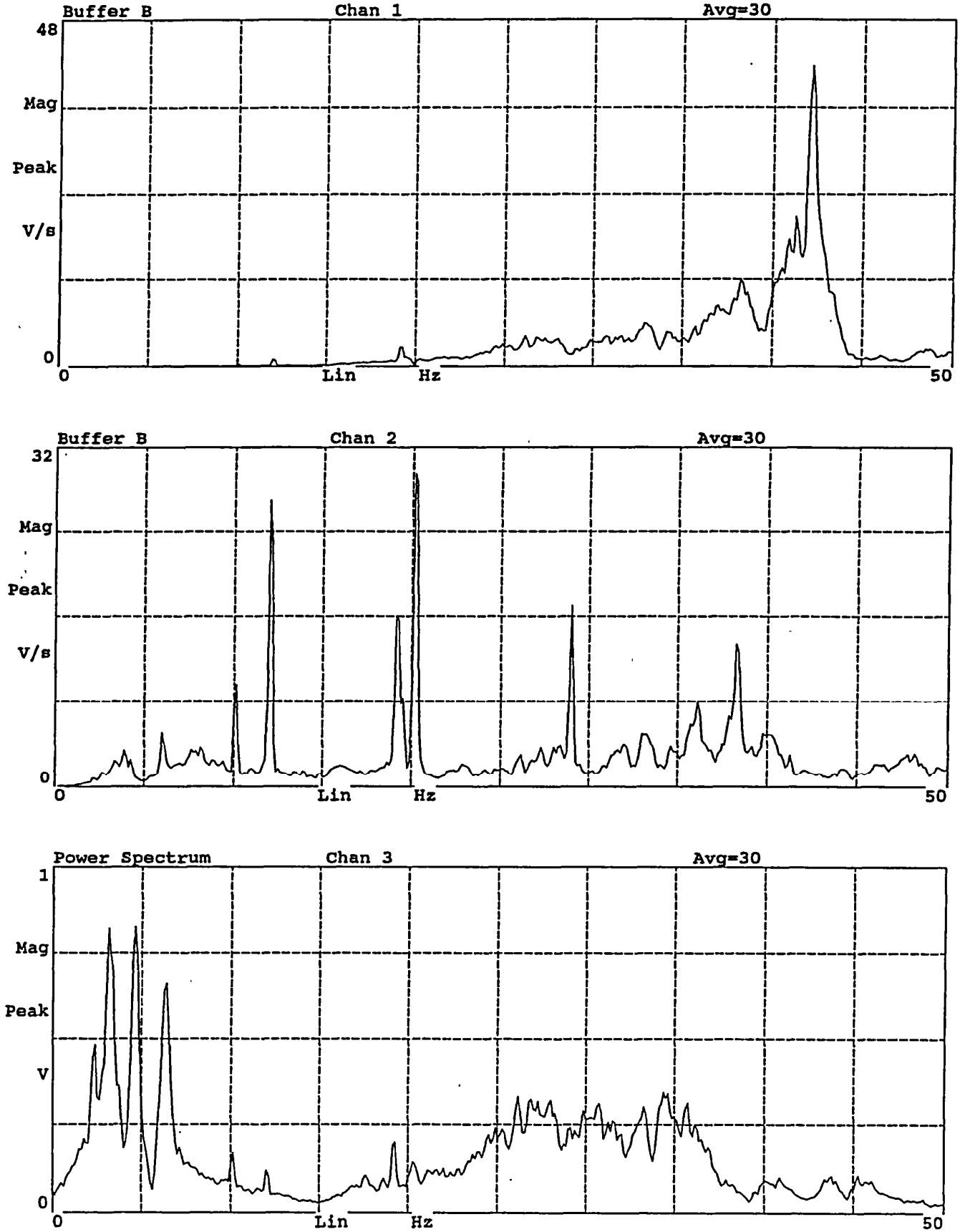

Figure B1. Average power spectra of signals from Channels 1 through 3, Test No. 1

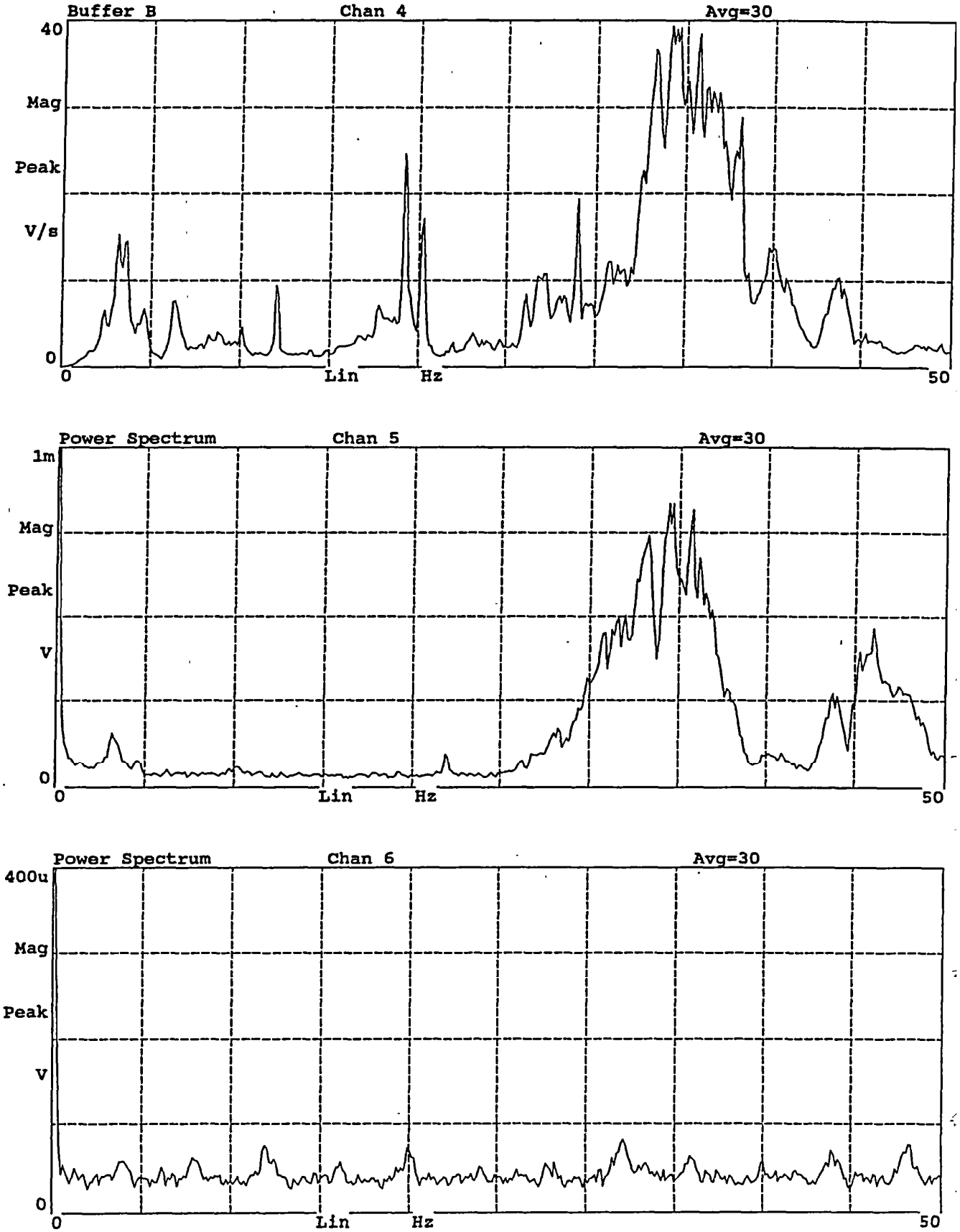

Figure B2. Average power spectra of signals from Channels 4 through 6, Test No. 1

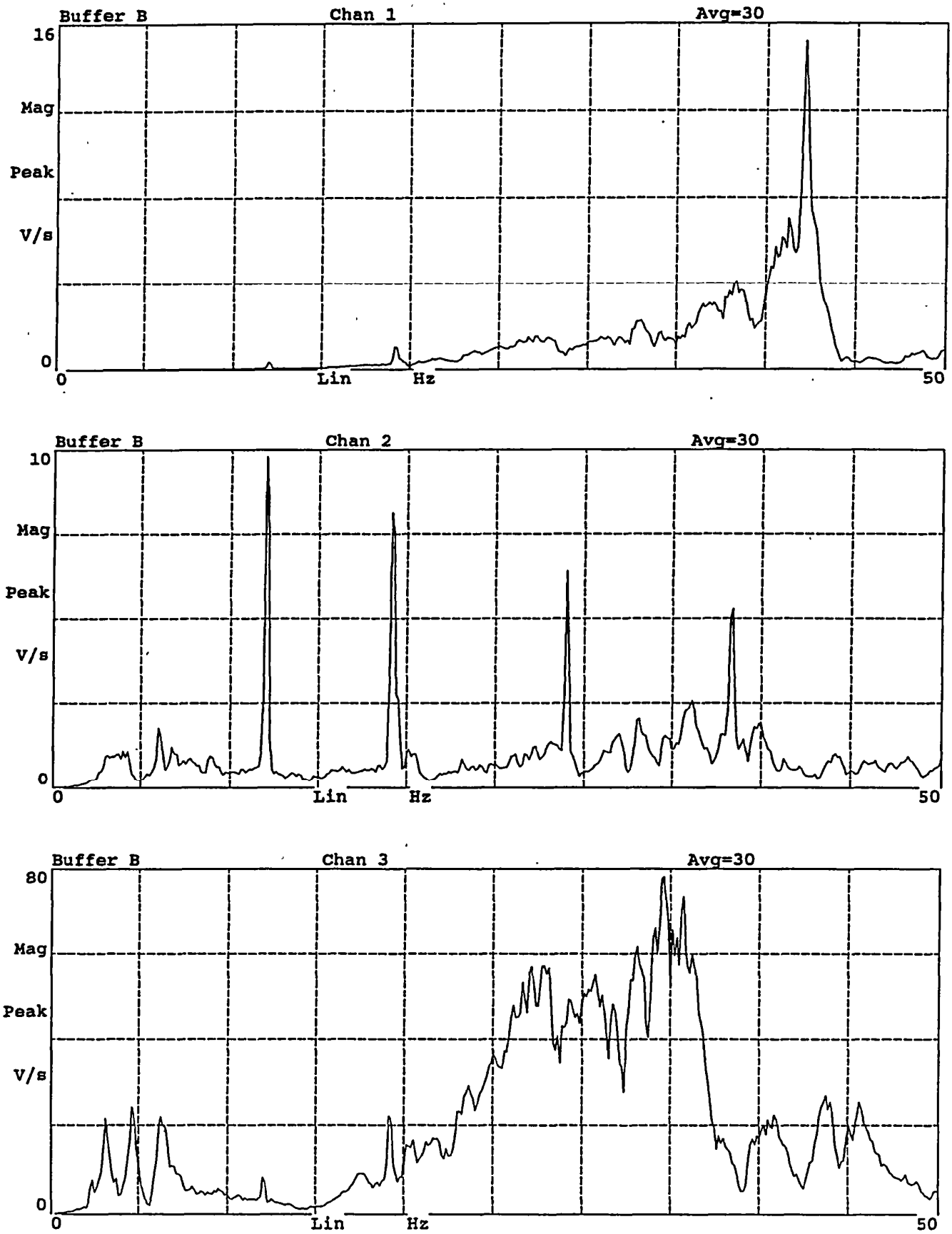

Figure B3. Average power spectra of signals from Channels 1 through 3, Test No. 2

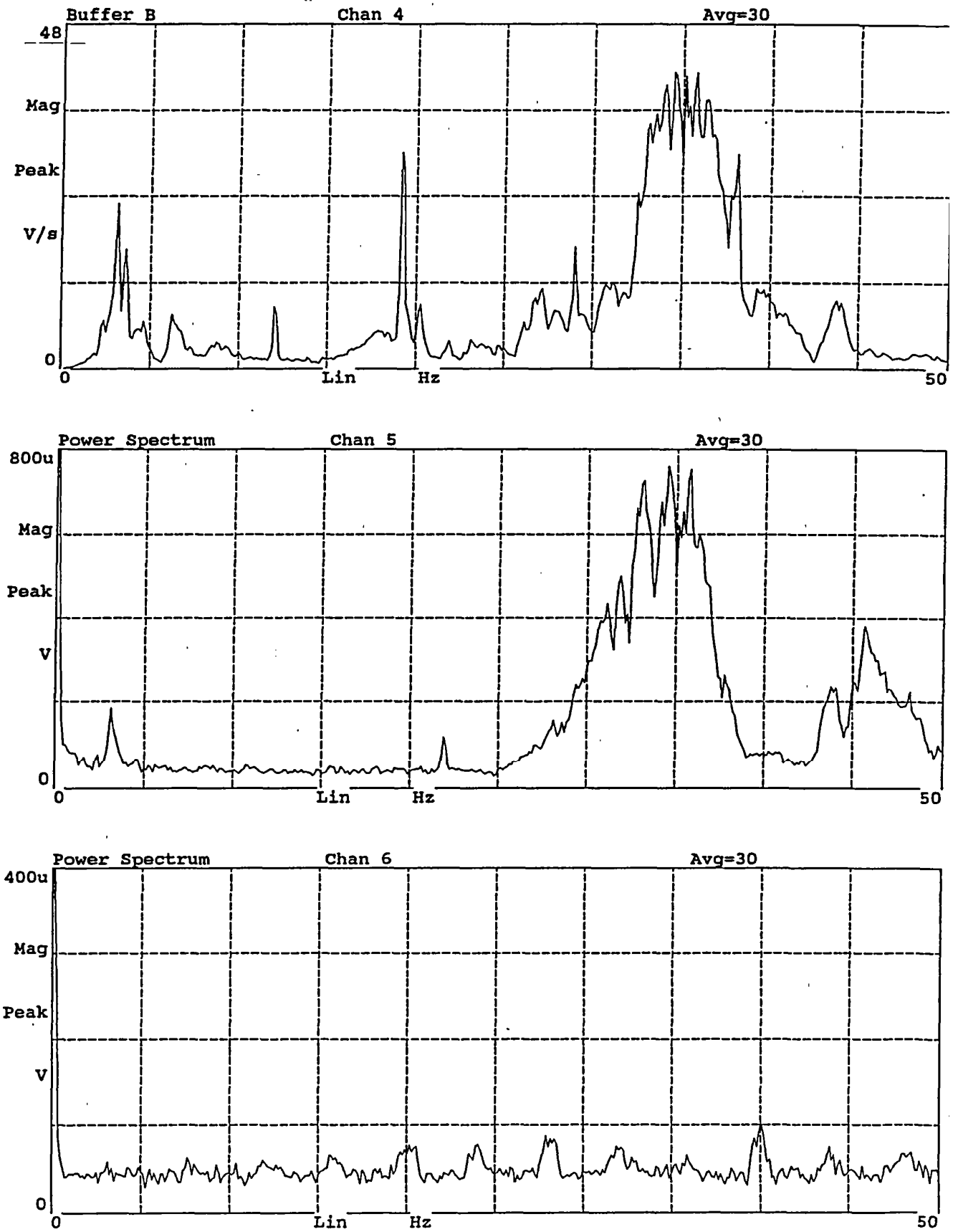

Figure B4. Average power spectra of signals from Channels 4 through 6, Test No. 2

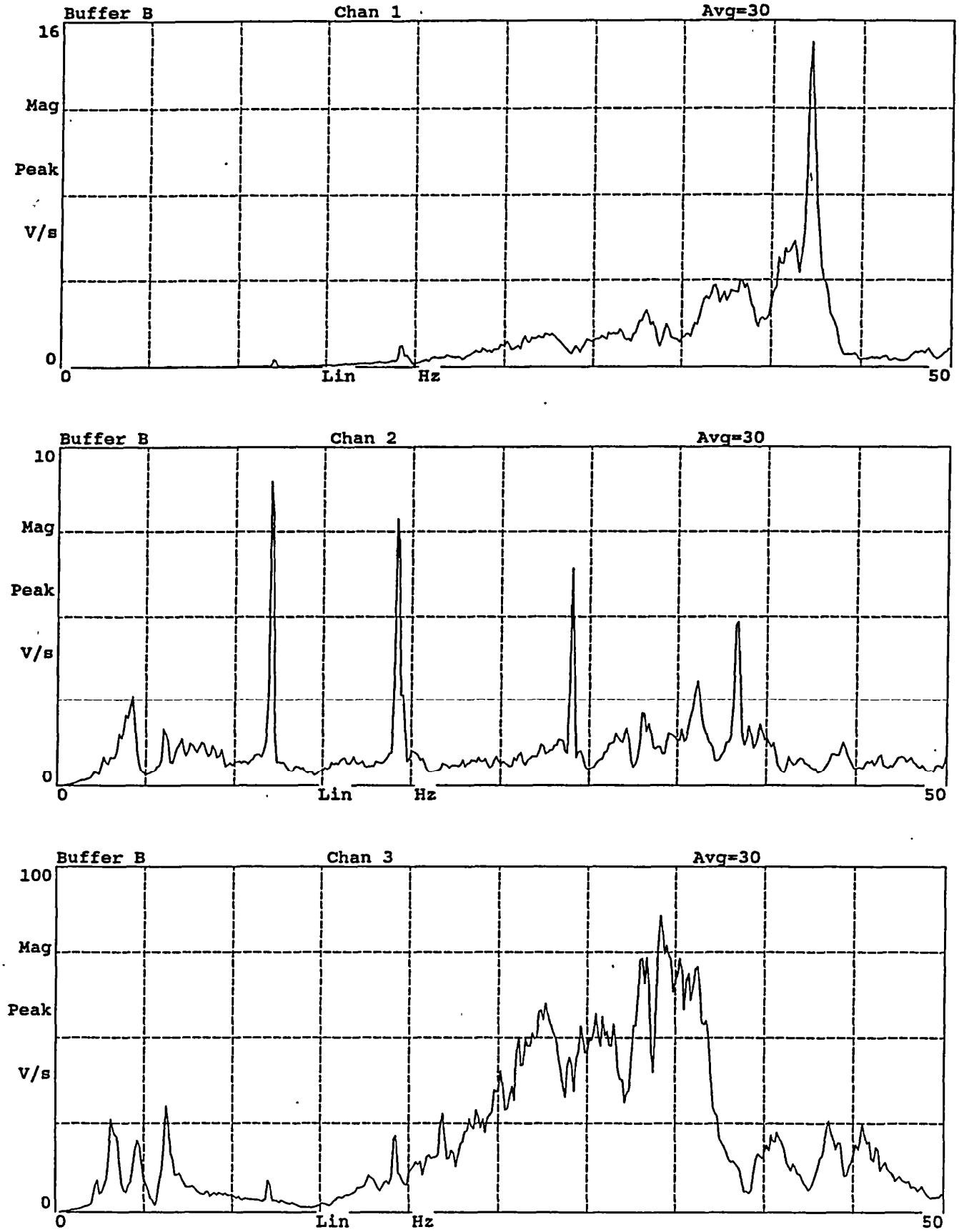

Figure B5. Average power spectra of signals from Channels 1 through 3, Test No. 3

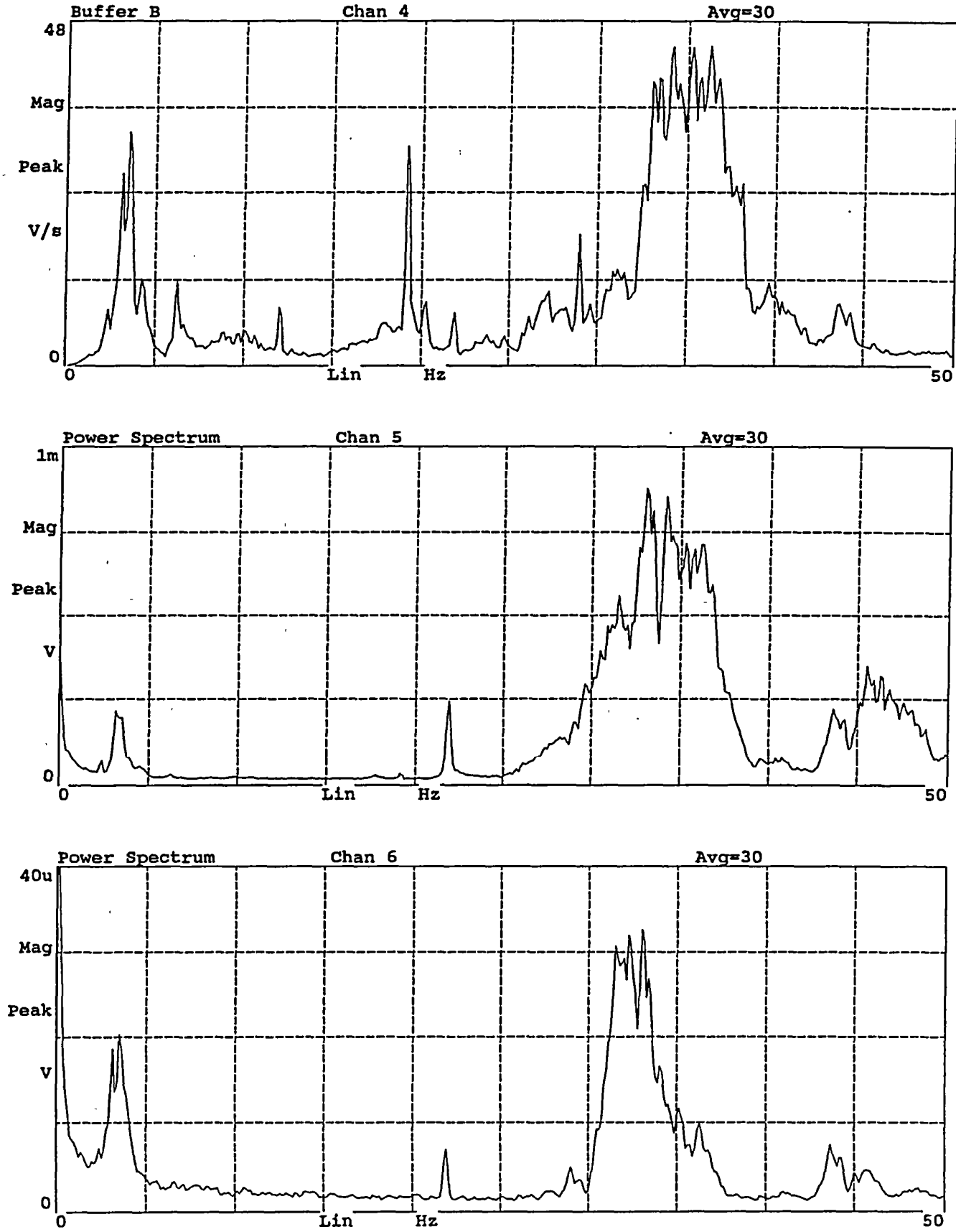

Figure B6. Average power spectra of signals from Channels 4 through 6, Test No. 3

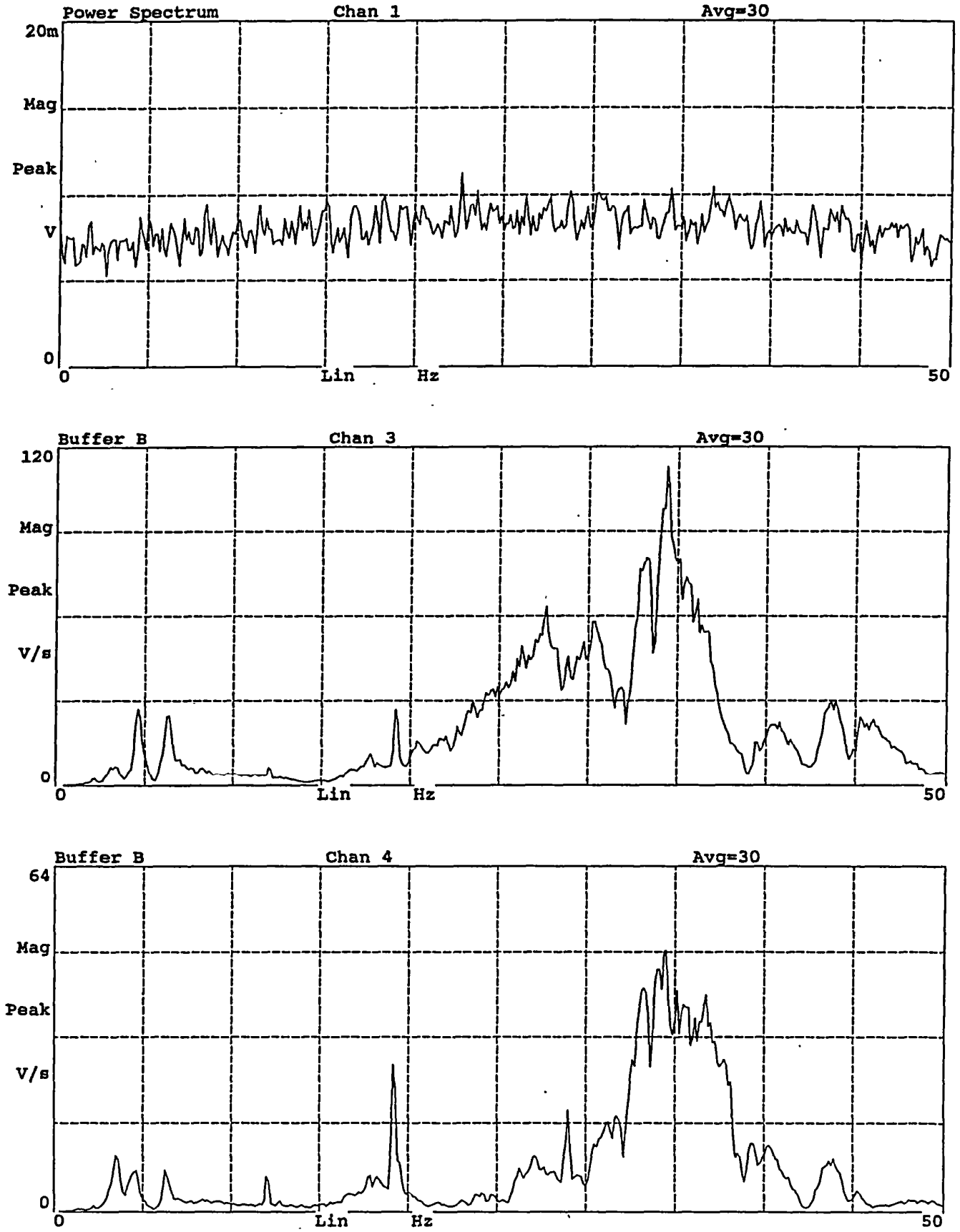

Figure B7. Average power spectra of signals from Channels 1, 3, and 4, Test No. 4

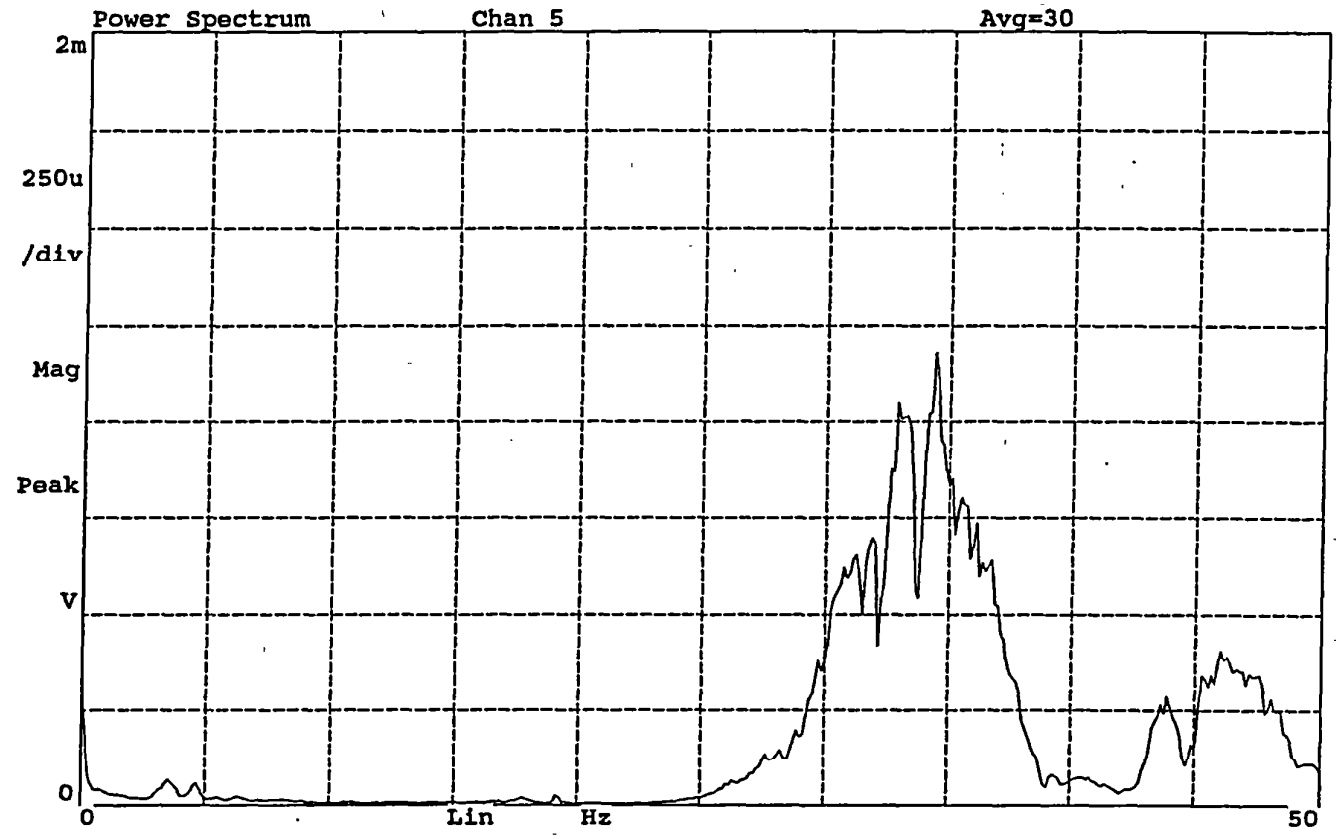

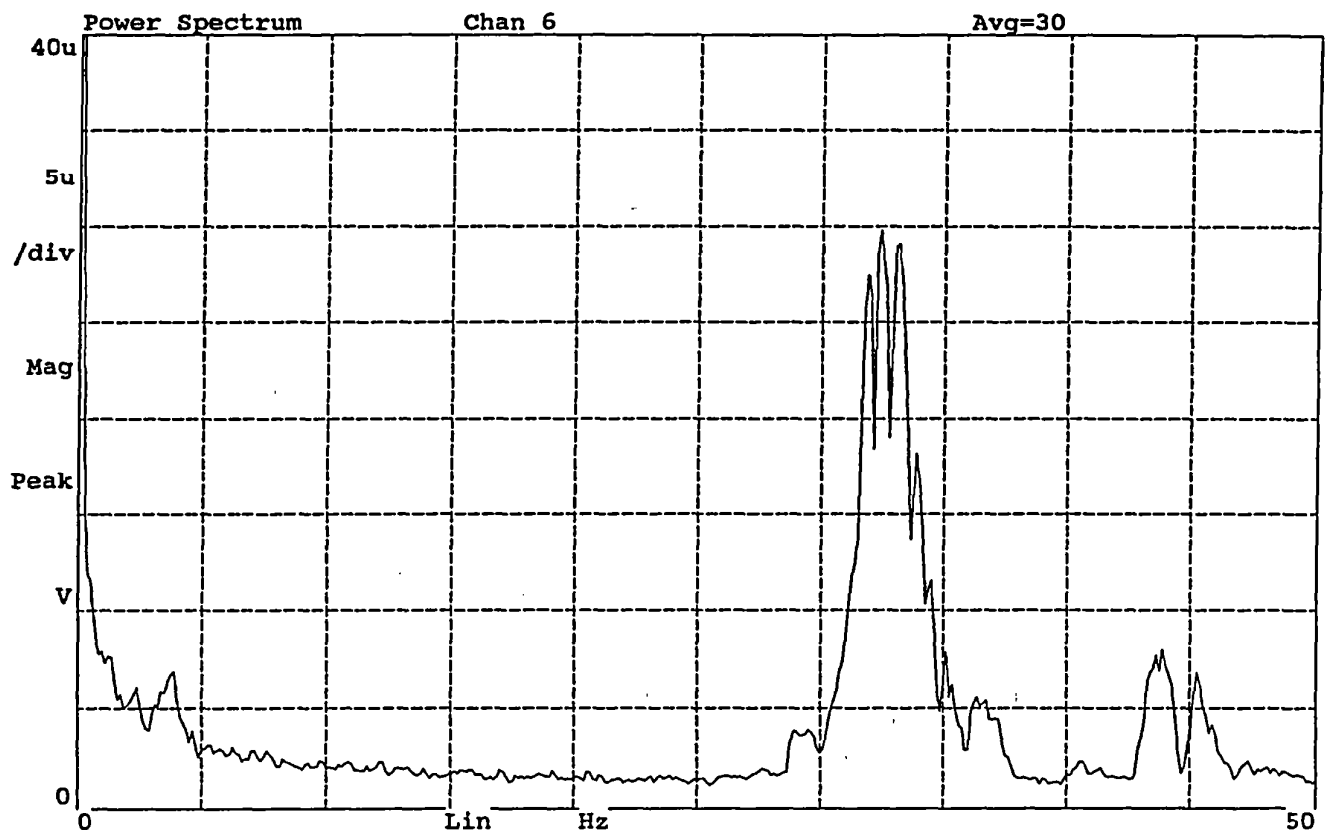

Figure B8. Average power spectra of signals from Channels 5 and 6, Test No. 4

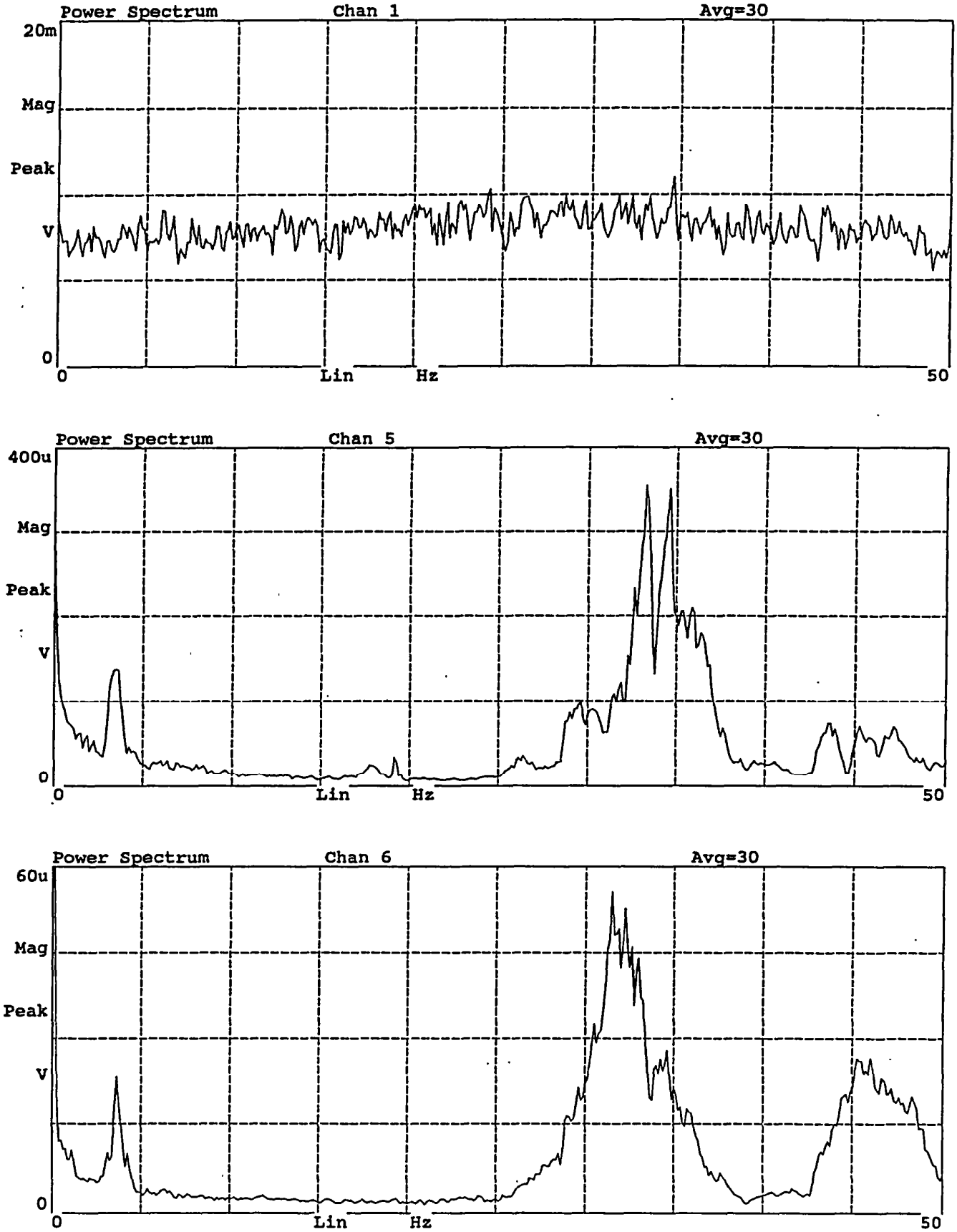

Figure B9. Average power spectra of signals from Channels 1, 5, and 6, Test No. 5

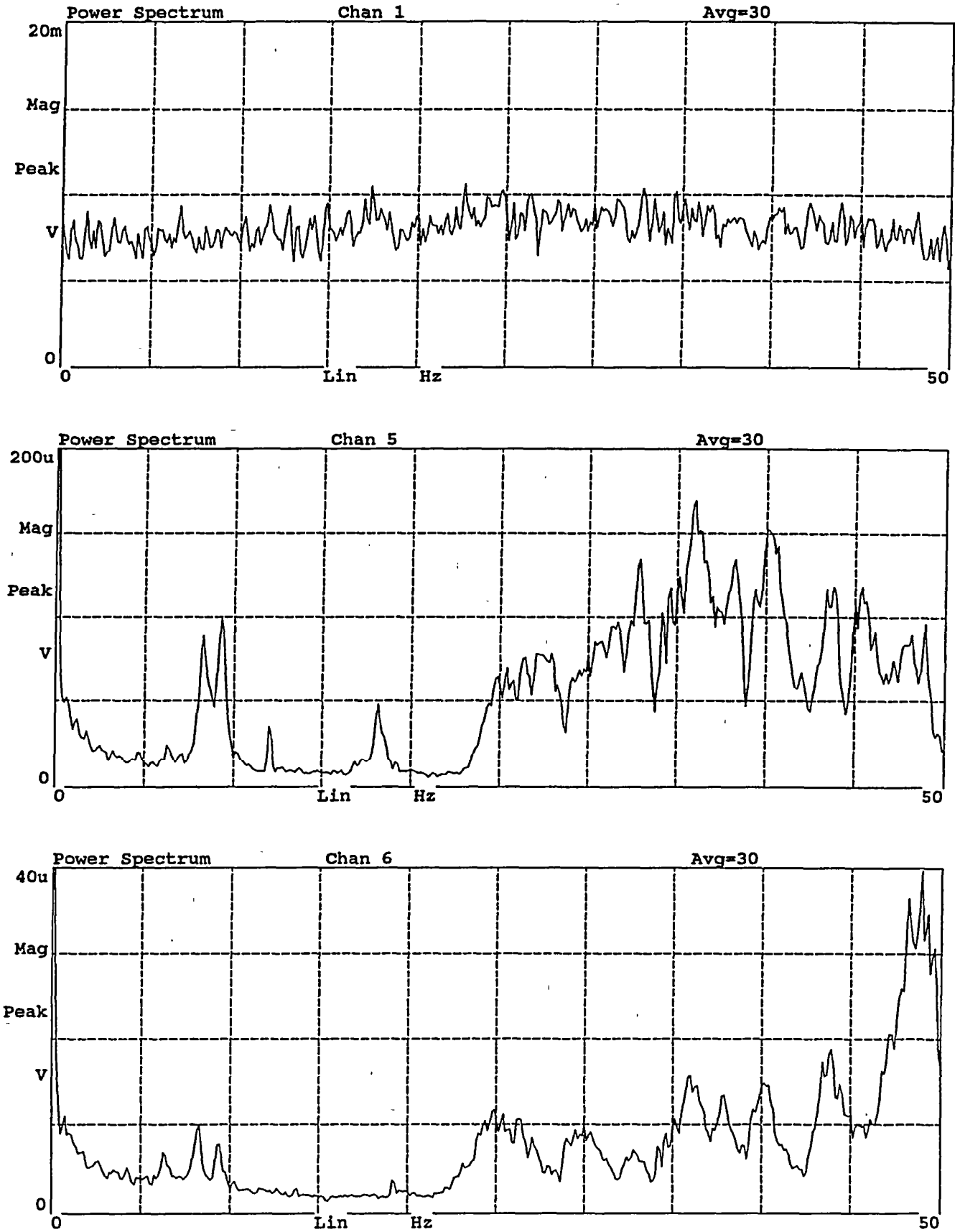

Figure B10. Average power spectra of signals from Channels 1, 5, and 6, Test No. 6

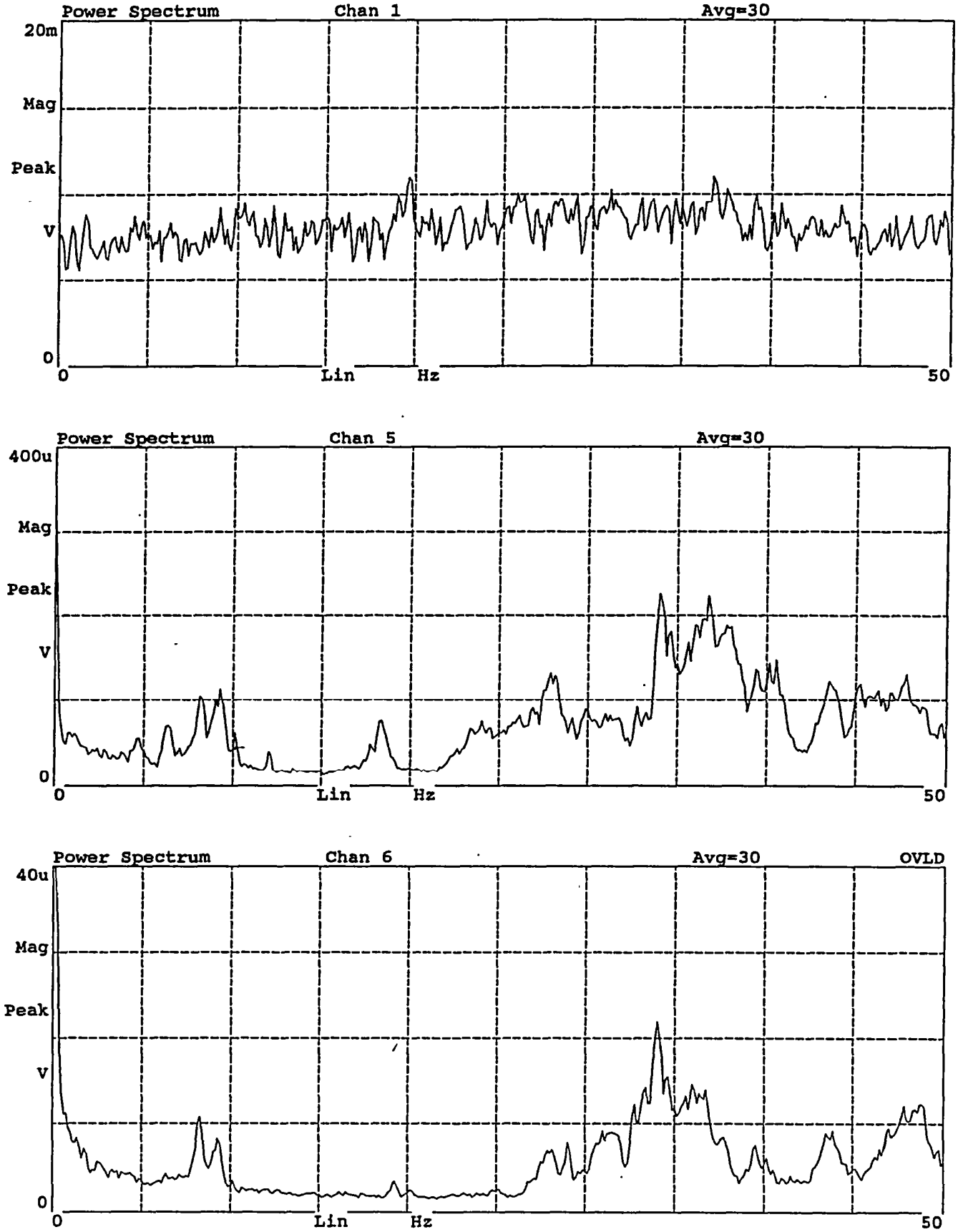

Figure B11. Average power spectra of signals from Channels 1, 5, and 6, Test No. 7

Appendix C

POWER SPECTRA FROM FIELD TESTS OF SMIT 230-KV TRANSFORMER AT GOLD HILL SUBSTATION

Four separate tests were conducted on the Smit 230-kV transformer using up to nine sensors in each test. The sensor orientation, sensor type, and correspondence between channel number and sensor location are shown in the table below. The average power spectra corresponding to the signals recorded by each of the listed channels are given in Figures C1 through C12.

Test No.	Direction	Channel	Sensor location	Sensor type
1	Longitudinal	1	Foundation	Seismometer
	Transverse	2	Foundation	Seismometer
	Longitudinal	3	Tank top	Seismometer
	Transverse	4	Tank top	Seismometer
	Transverse	5	HV bushing top	Accelerometer
	Longitudinal	6	HV bushing top	Accelerometer
	Longitudinal	7	Tank 1/3 height	Accelerometer
	Longitudinal	8	Tank 2/3 height	Accelerometer
	Transverse	9	Shaker	Accelerometer
2	Longitudinal	1	Foundation	Seismometer
	Transverse	2	Foundation	Seismometer
	Longitudinal	3	Tank top	Seismometer
	Transverse	4	Tank top	Seismometer
	Transverse	5	HV bushing top	Accelerometer
	Longitudinal	6	HV bushing top	Accelerometer
	Longitudinal	7	Tank 1/3 height	Accelerometer
	Longitudinal	8	Tank 2/3 height	Accelerometer
	Transverse	9	Shaker	Accelerometer
3	Longitudinal	1	Foundation	Seismometer
	Transverse	2	Foundation	Seismometer
	Longitudinal	3	Tank top	Seismometer
	Transverse	4	Tank top	Seismometer
	Transverse	5	HV bushing top	Accelerometer
	Longitudinal	6	HV bushing top	Accelerometer
	Longitudinal	7	Tank 1/3 height	Accelerometer
	Longitudinal	8	Tank 2/3 height	Accelerometer
	Longitudinal	9	Shaker	Accelerometer
4	Longitudinal	1	Foundation	Seismometer
	Transverse	2	Foundation	Seismometer
	Longitudinal	3	Tank top	Seismometer
	Transverse	4	Tank top	Seismometer
	Transverse	5	HV bushing top	Accelerometer
	Longitudinal	6	HV bushing top	Accelerometer
	Longitudinal	7	Tank 1/3 height	Accelerometer
	Longitudinal	8	Tank 2/3 height	Accelerometer
	Longitudinal	9	Shaker	Accelerometer

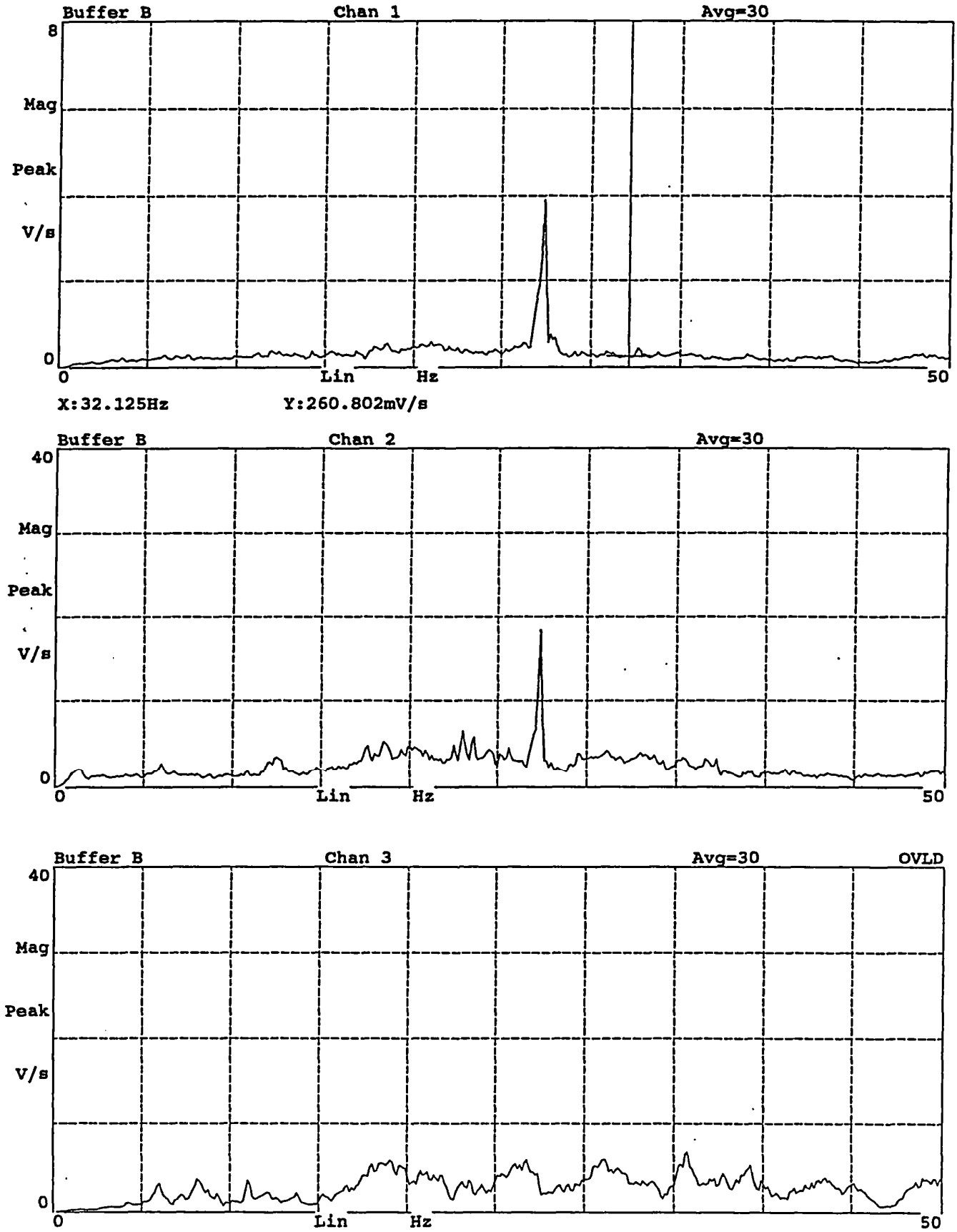

Figure C1. Average power spectra of signals from Channels 1 through 3, Test No. 1

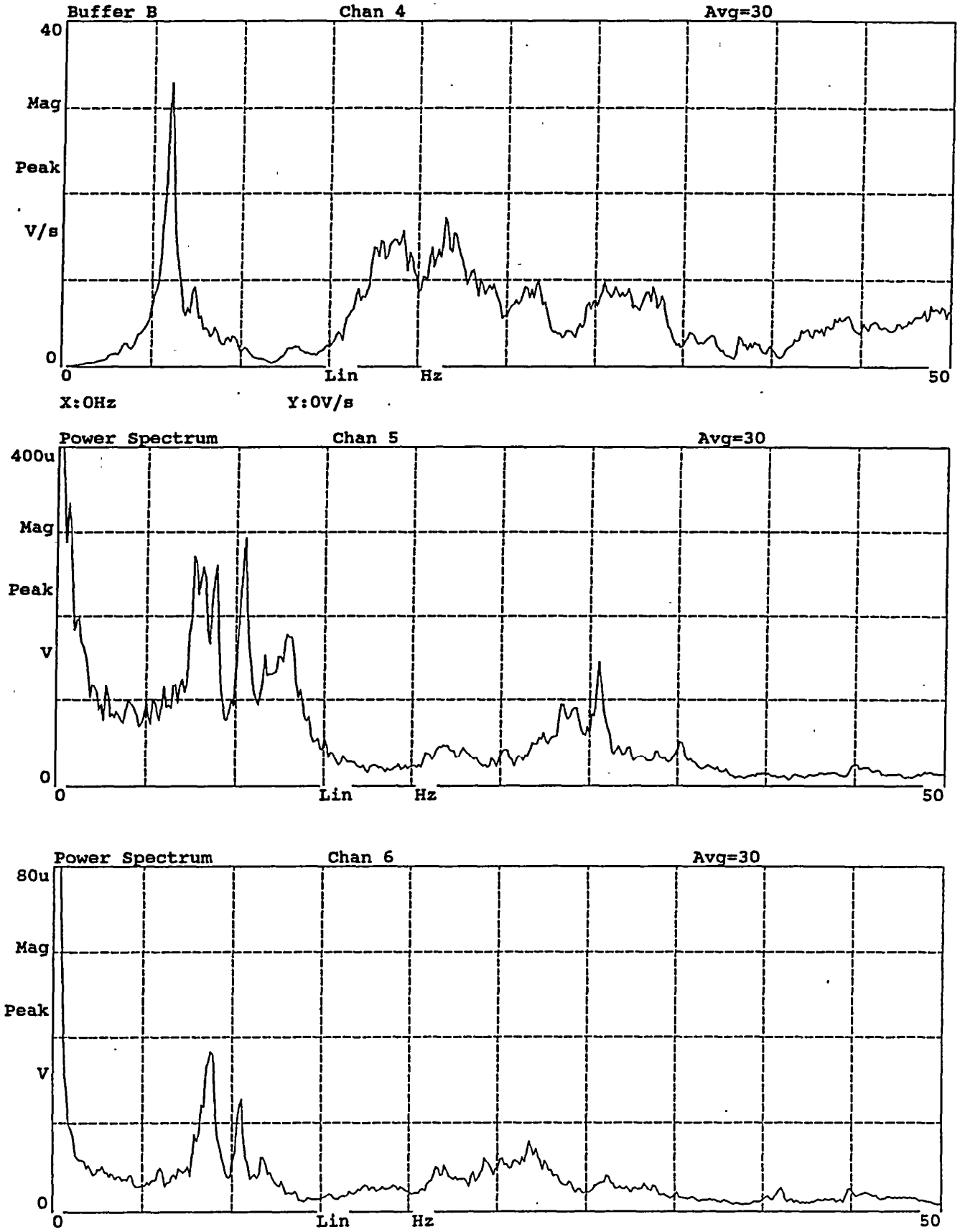

Figure C2. Average power spectra of signals from Channels 4 through 6, Test No. 1

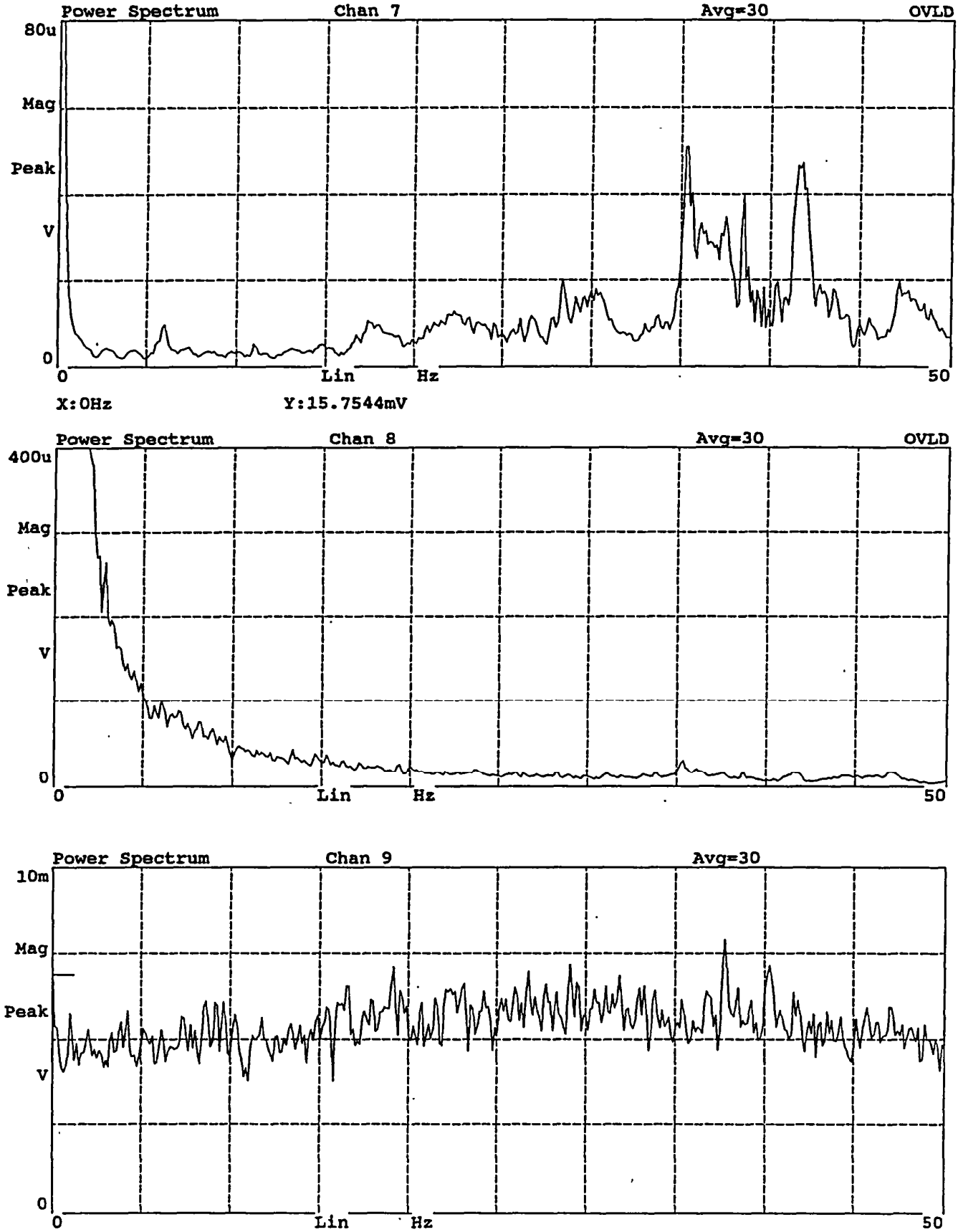

Figure C3. Average power spectra of signals from Channels 7 through 9, Test No. 1

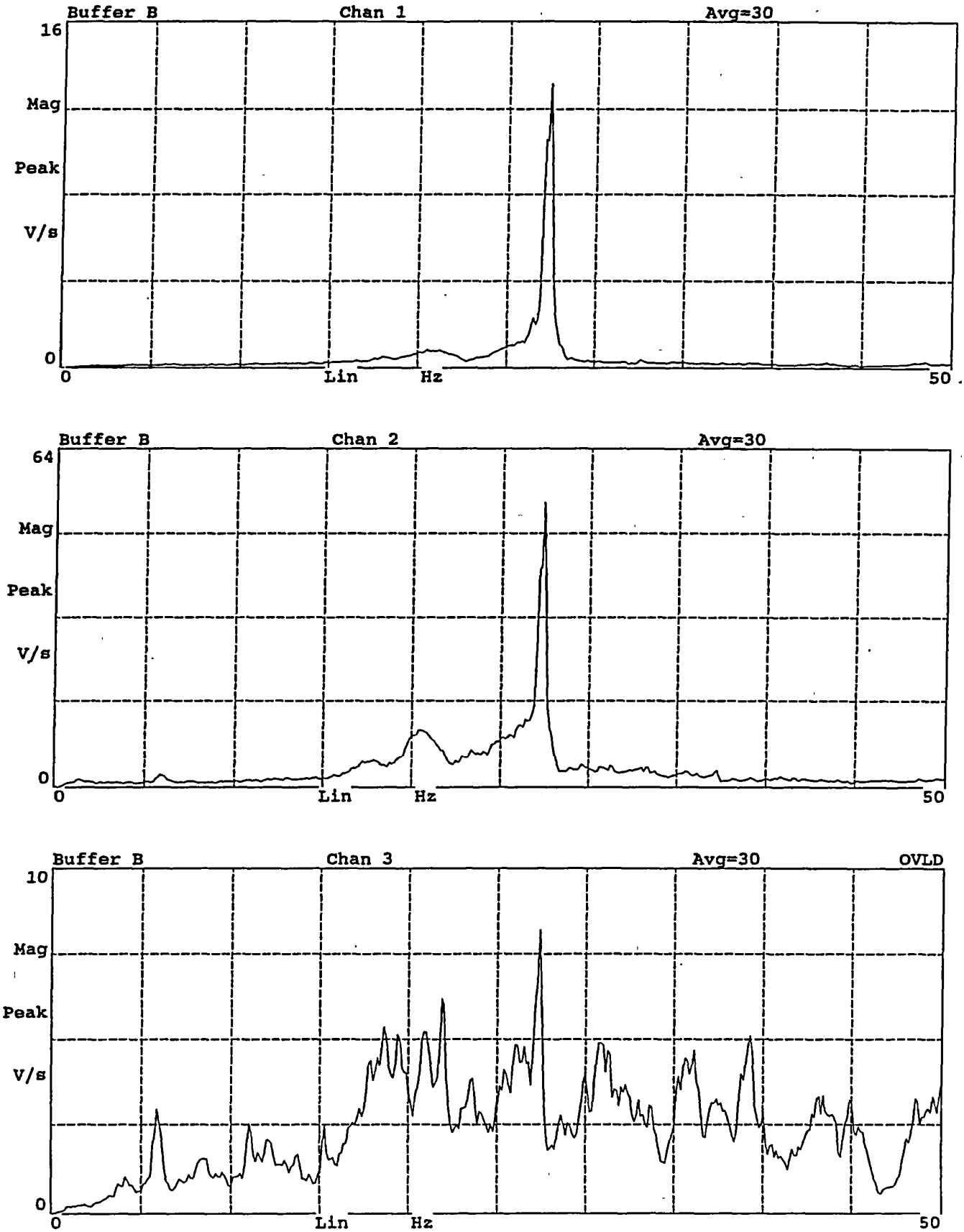

Figure C4. Average power spectra of signals from Channels 1 through 3, Test No. 2

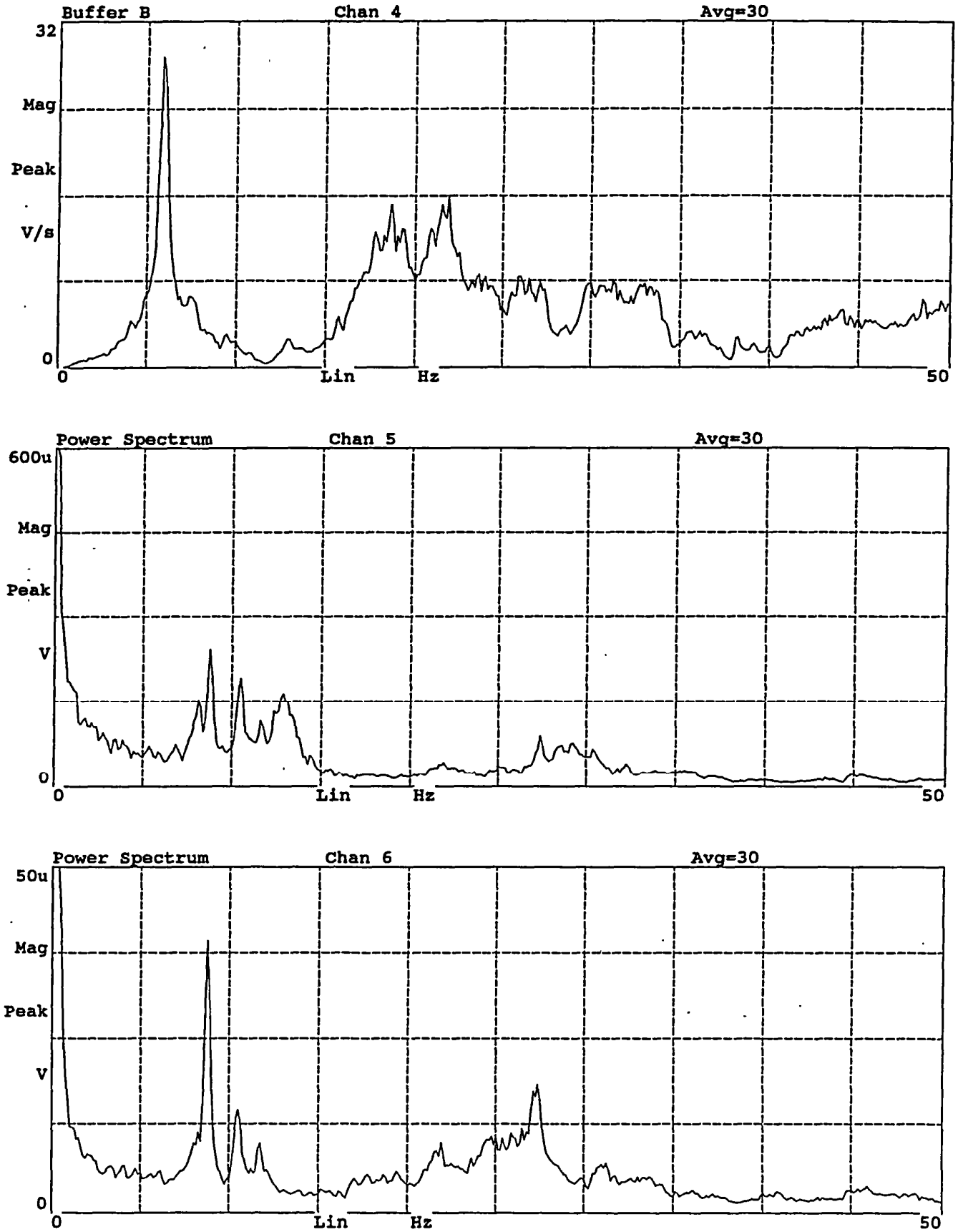

Figure C5. Average power spectra of signals from Channels 4 through 6, Test No. 2

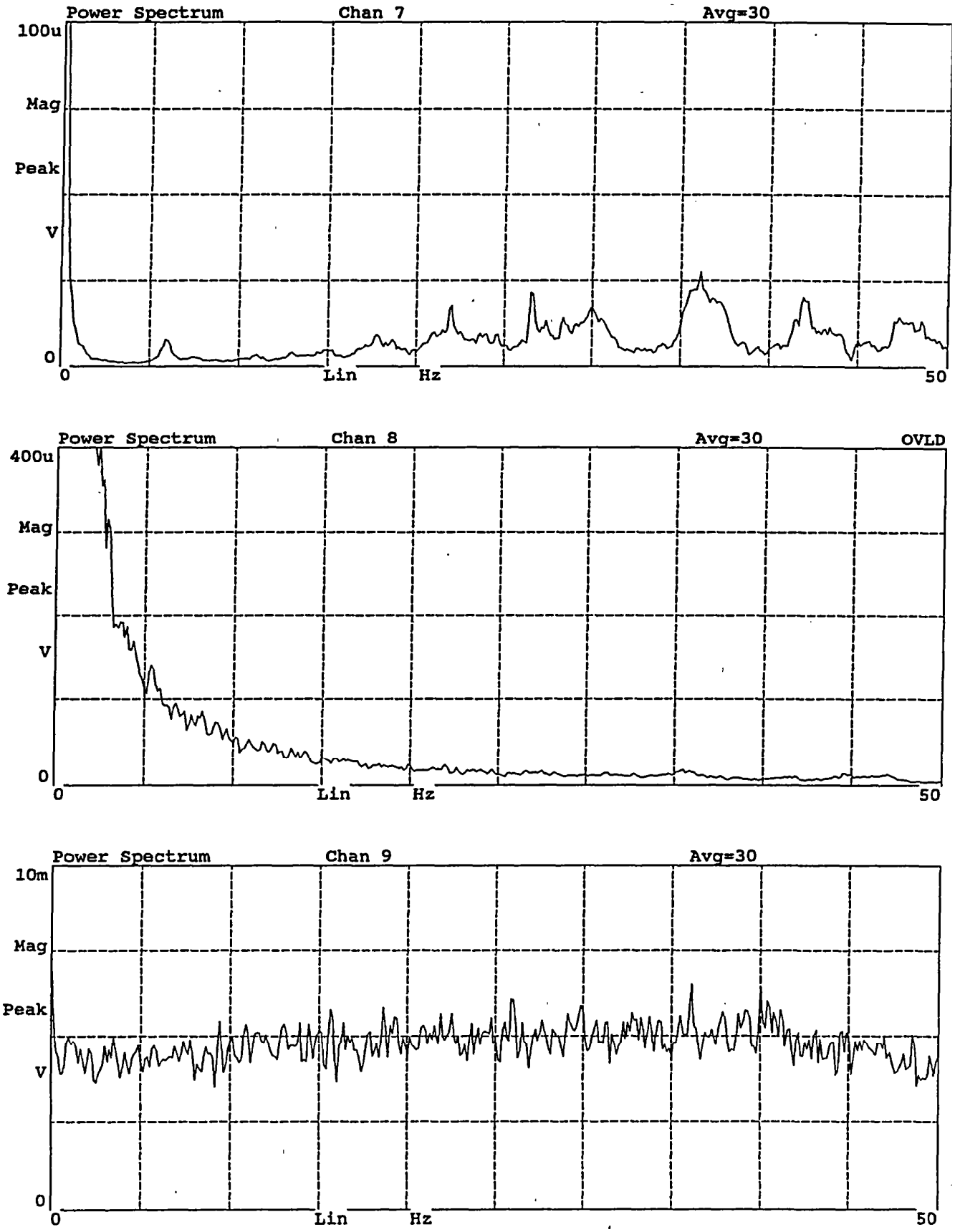

Figure C6. Average power spectra of signals from Channels 7 through 9, Test No. 2

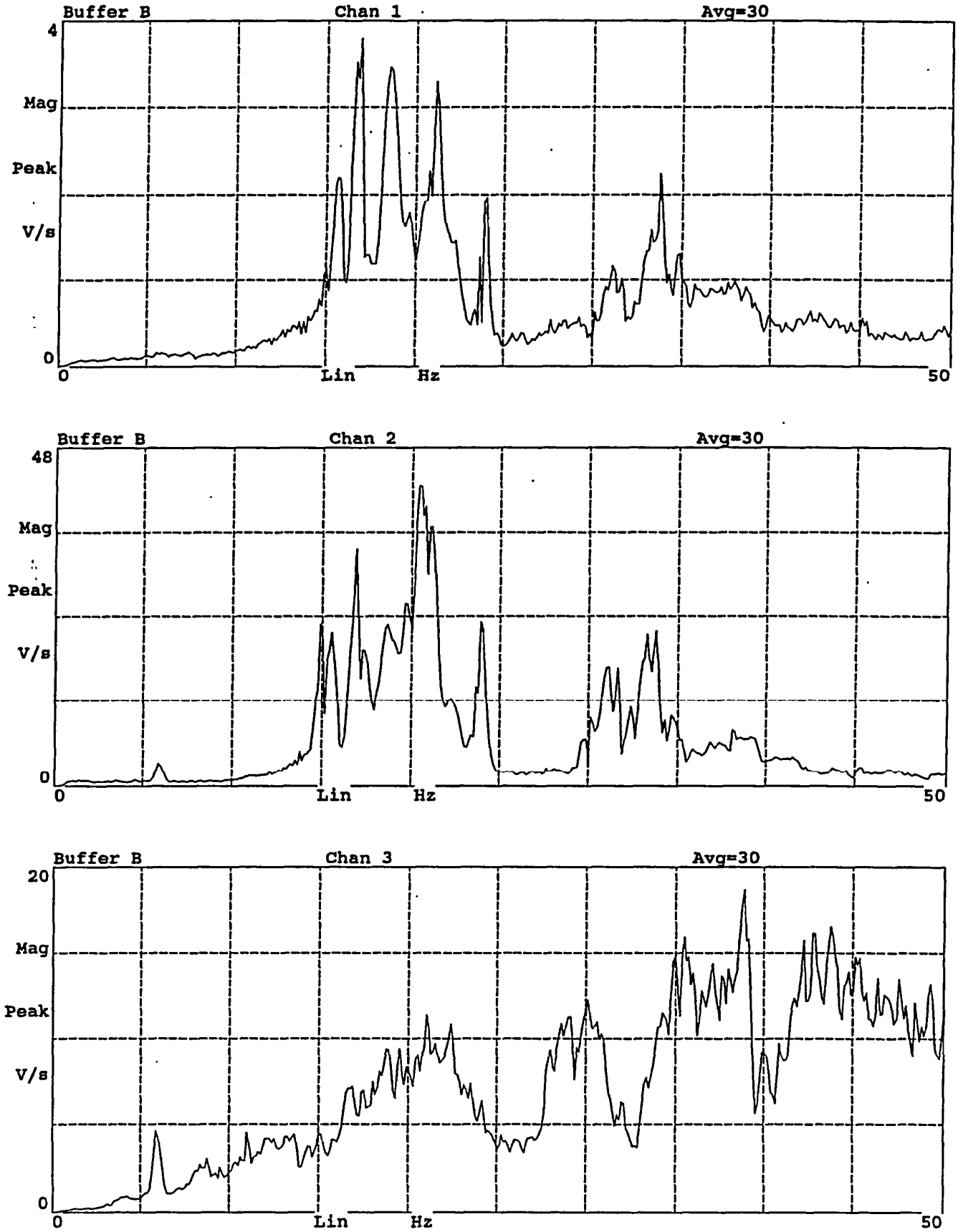

Figure C7. Average power spectra of signals from Channels 1 through 3, Test No. 3

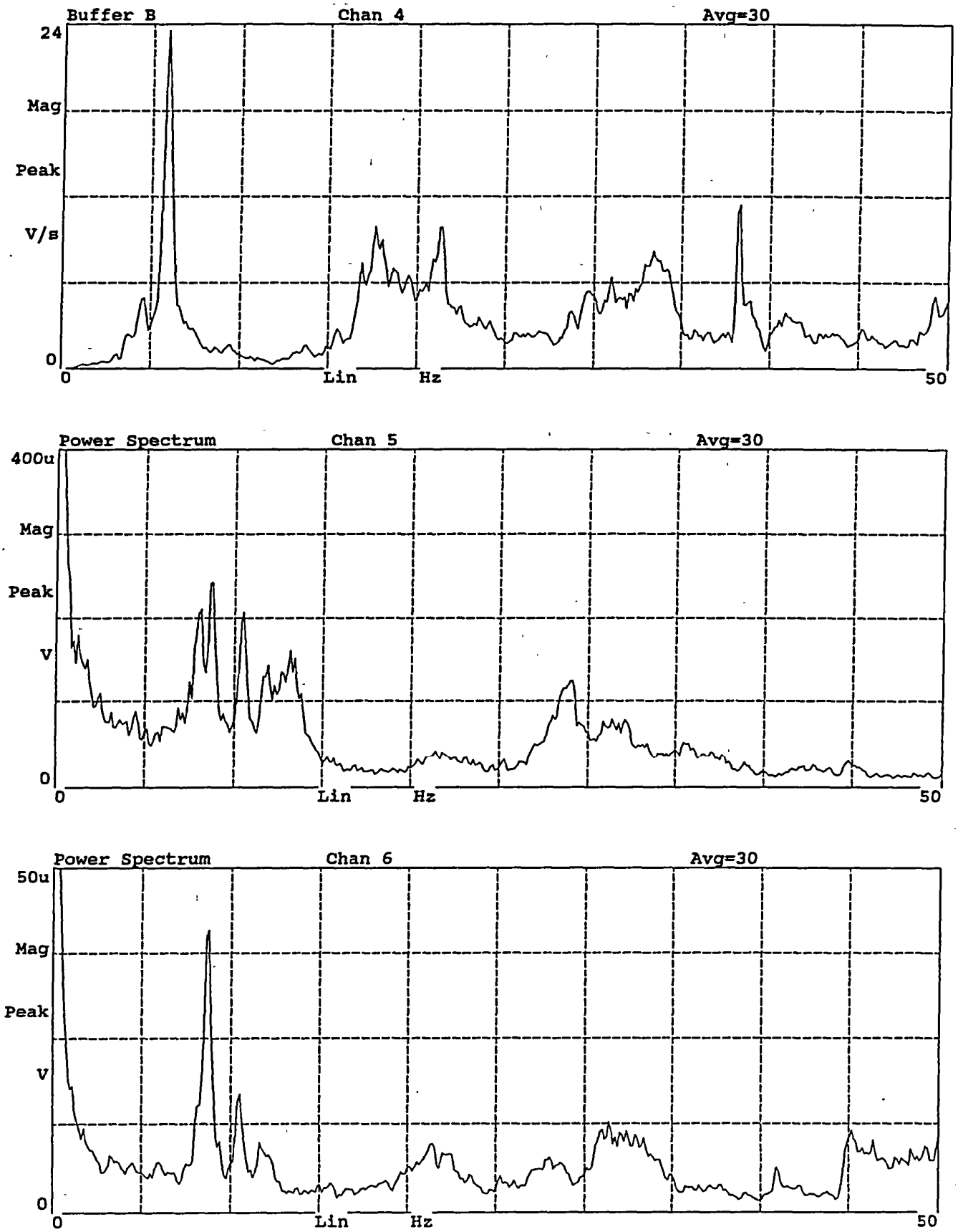

Figure C8. Average power spectra of signals from Channels 4 through 6, Test No. 3

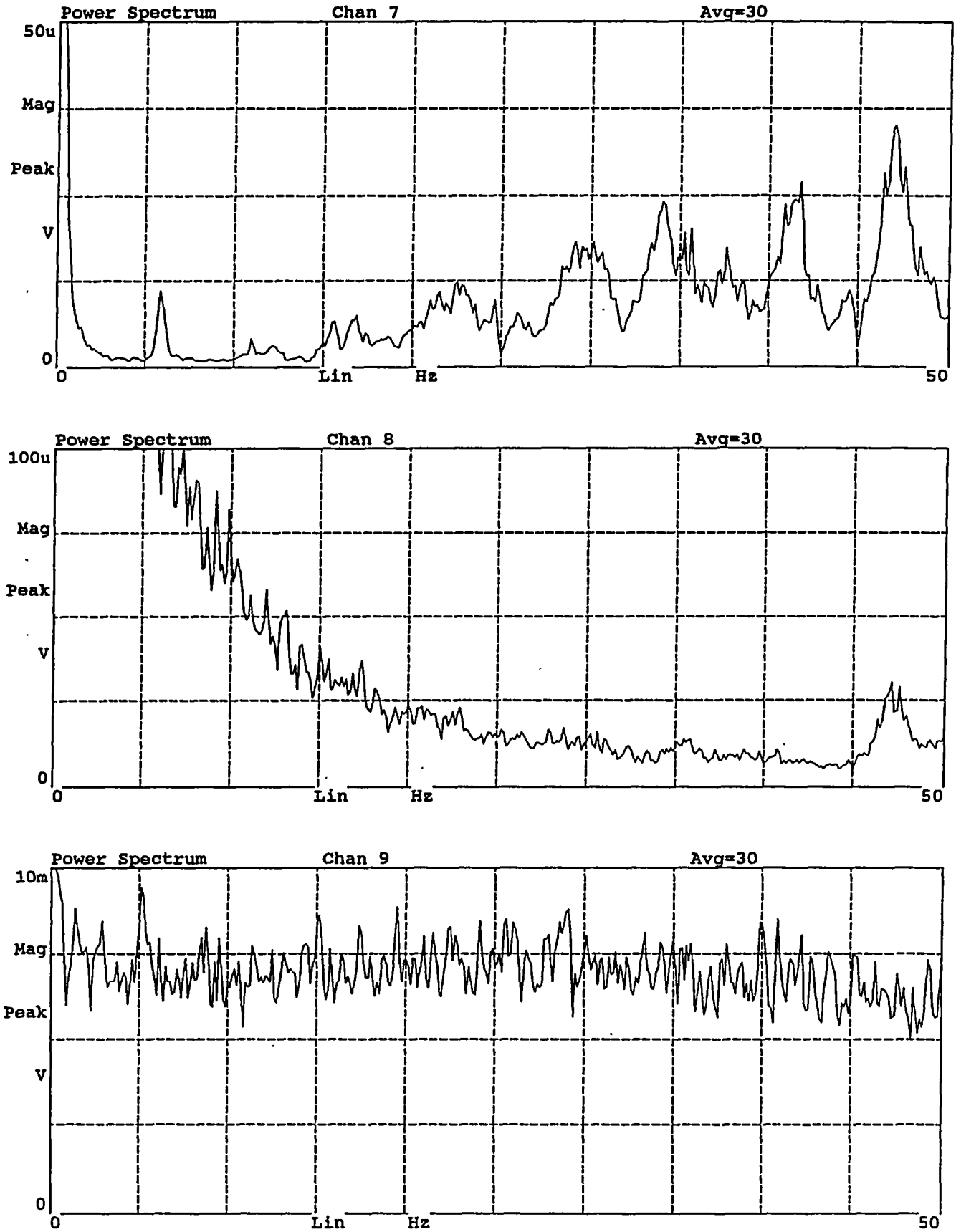

Figure C9. Average power spectra of signals from Channels 7 through 9, Test No. 3

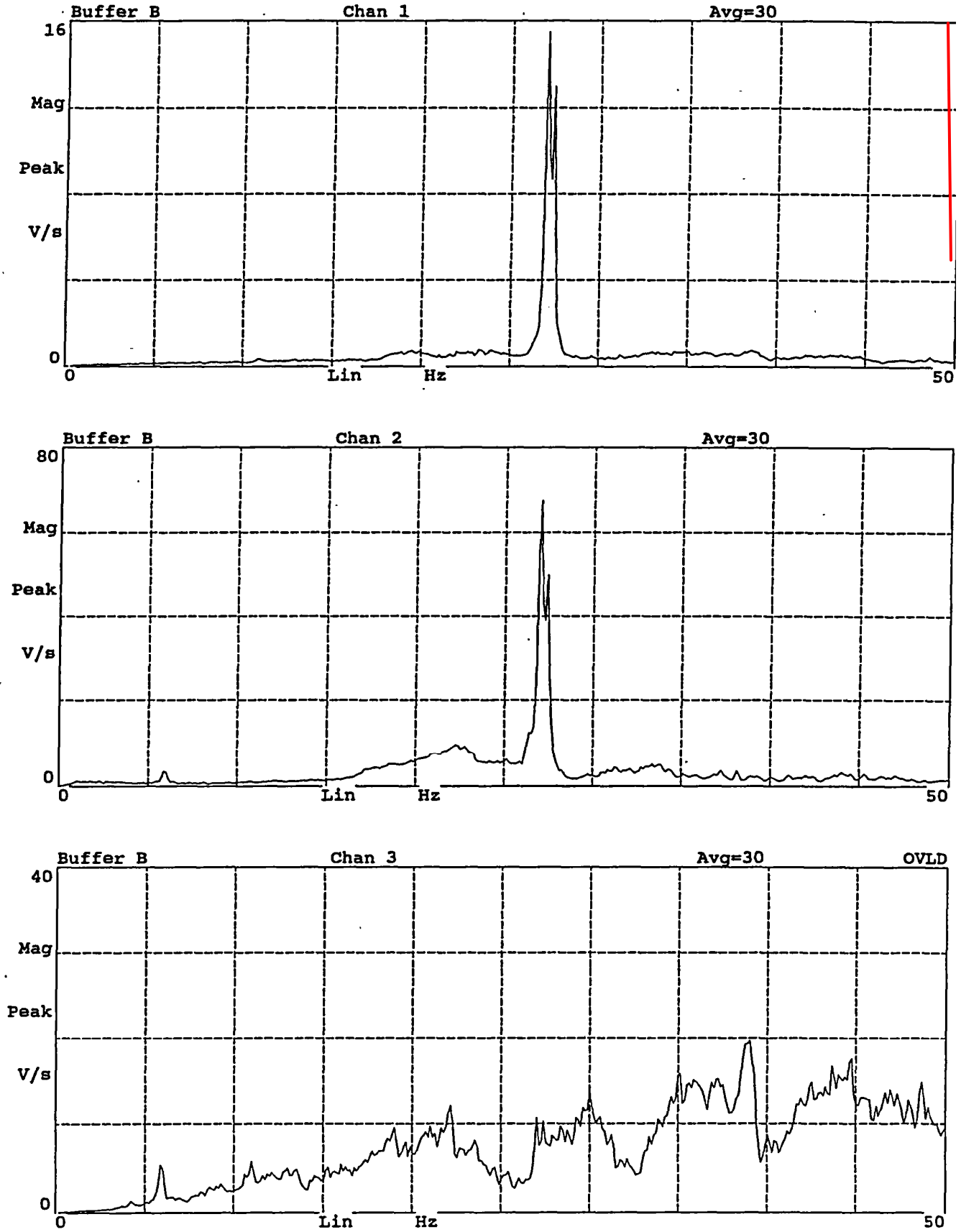

Figure C10. Average power spectra of signals from Channels 1 through 3, Test No. 4

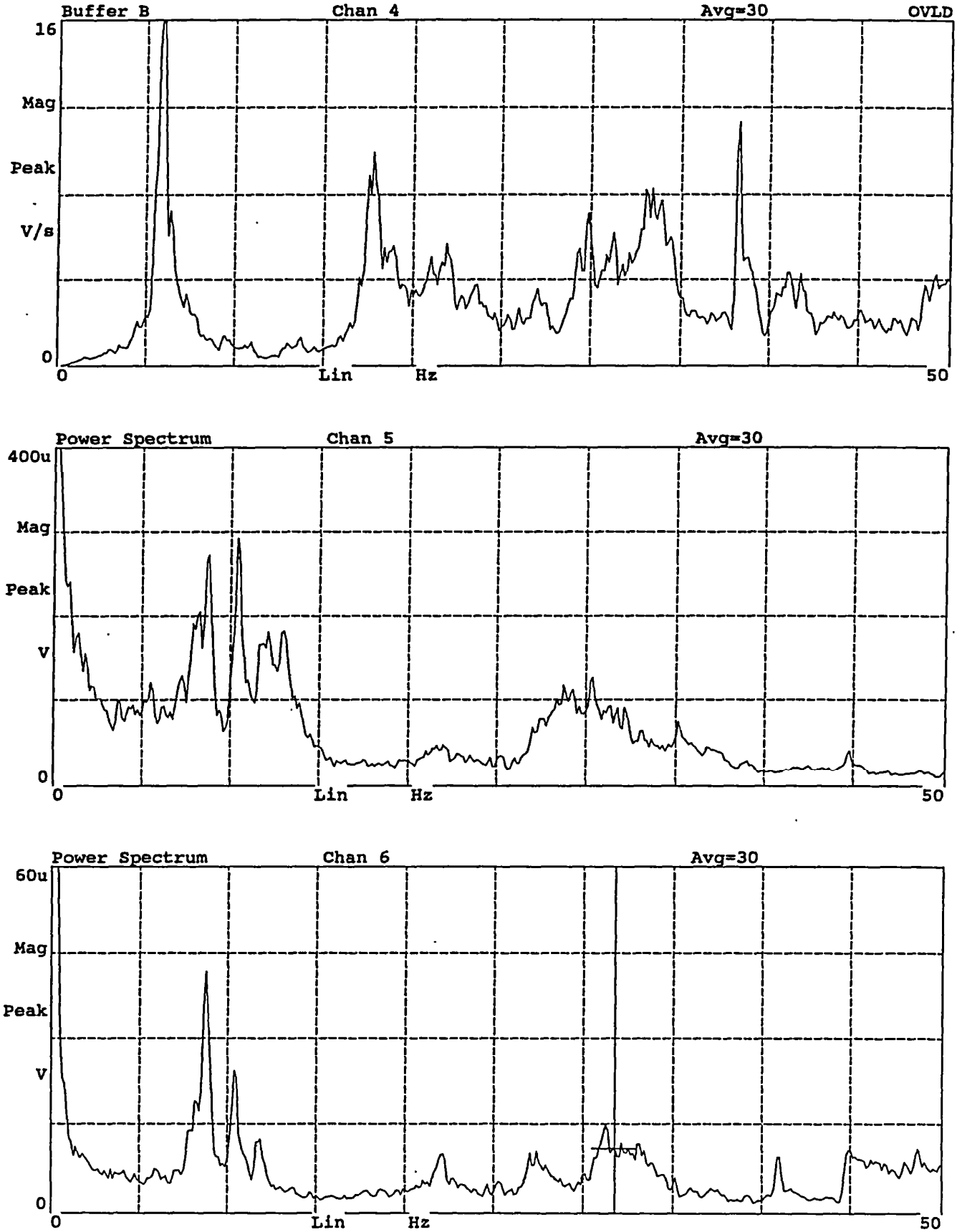

Figure C11. Average power spectra of signals from Channels 4 through 6, Test No. 4

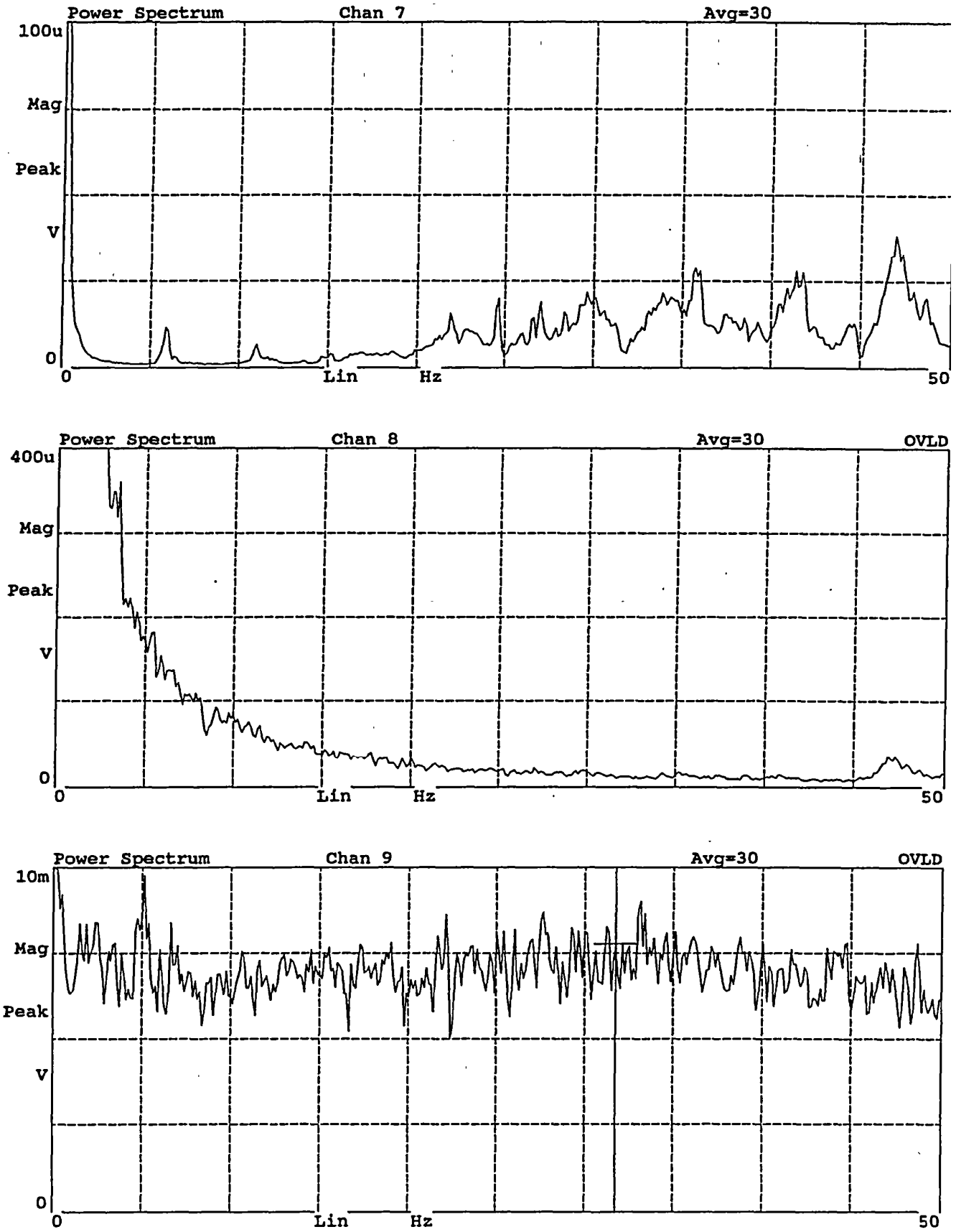

Figure C12. Average power spectra of signals from Channels 7 through 9, Test No. 4

Appendix D

POWER SPECTRA FROM FIELD TESTS OF WESTINGHOUSE 230-KV TRANSFORMER AT IGNACIO SUBSTATION

Five separate tests were conducted on the Westinghouse 230-kV transformer using up to nine sensors in each test. The sensor orientation, sensor type, and correspondence between channel number and sensor location are shown in the table below. The average power spectra or frequency response functions corresponding to the signals recorded by each of the listed channels are given in Figures D1 through D13. Note that tests 3, 4 and 5 were conducted with a sledgehammer instead of the shaker used in the other tests. In these special tests, the transformer was excited by hitting the HV bushing or the lightning arrester with the sledgehammer.

Test No.	Direction	Channel	Sensor location	Sensor type
1	Longitudinal	1	Shaker	Accelerometer
	Transverse	2	HV bushing top	Accelerometer
	Longitudinal	3	HV bushing top	Accelerometer
	Transverse	4	Foundation	Seismometer
	Longitudinal	5	Foundation	Seismometer
	Transverse	6	Tank top	Seismometer
	Longitudinal	7	Tank top	Seismometer
	Transverse	8	Lightning arrester	Accelerometer
	Longitudinal	9	Lightning arrester	Accelerometer
2	Transverse	1	Shaker	Accelerometer
	Transverse	2	HV bushing top	Accelerometer
	Longitudinal	3	HV bushing top	Accelerometer
	Transverse	4	Foundation	Seismometer
	Longitudinal	5	Foundation	Seismometer
	Transverse	6	Tank top	Seismometer
	Longitudinal	7	Tank top	Seismometer
	Transverse	8	Lightning arrester	Accelerometer
	Longitudinal	9	Lightning arrester	Accelerometer
3*	Transverse	1	Sledgehammer	Transducer
	Transverse	2	HV bushing	Accelerometer
	Longitudinal	3	HV bushing	Accelerometer
	Transverse	4	Foundation	Seismometer
4*	Longitudinal	1	Sledgehammer	Transducer
	Transverse	2	HV bushing	Accelerometer
	Longitudinal	3	HV bushing	Accelerometer
	Longitudinal	4	Foundation	Seismometer
5*	Transverse	1	Sledgehammer	Transducer
	Transverse	2	Lightning arrester	Accelerometer
	Longitudinal	3	Lightning arrester	Accelerometer
	Transverse	4	Foundation	Seismometer

* Test conducted with sledgehammer

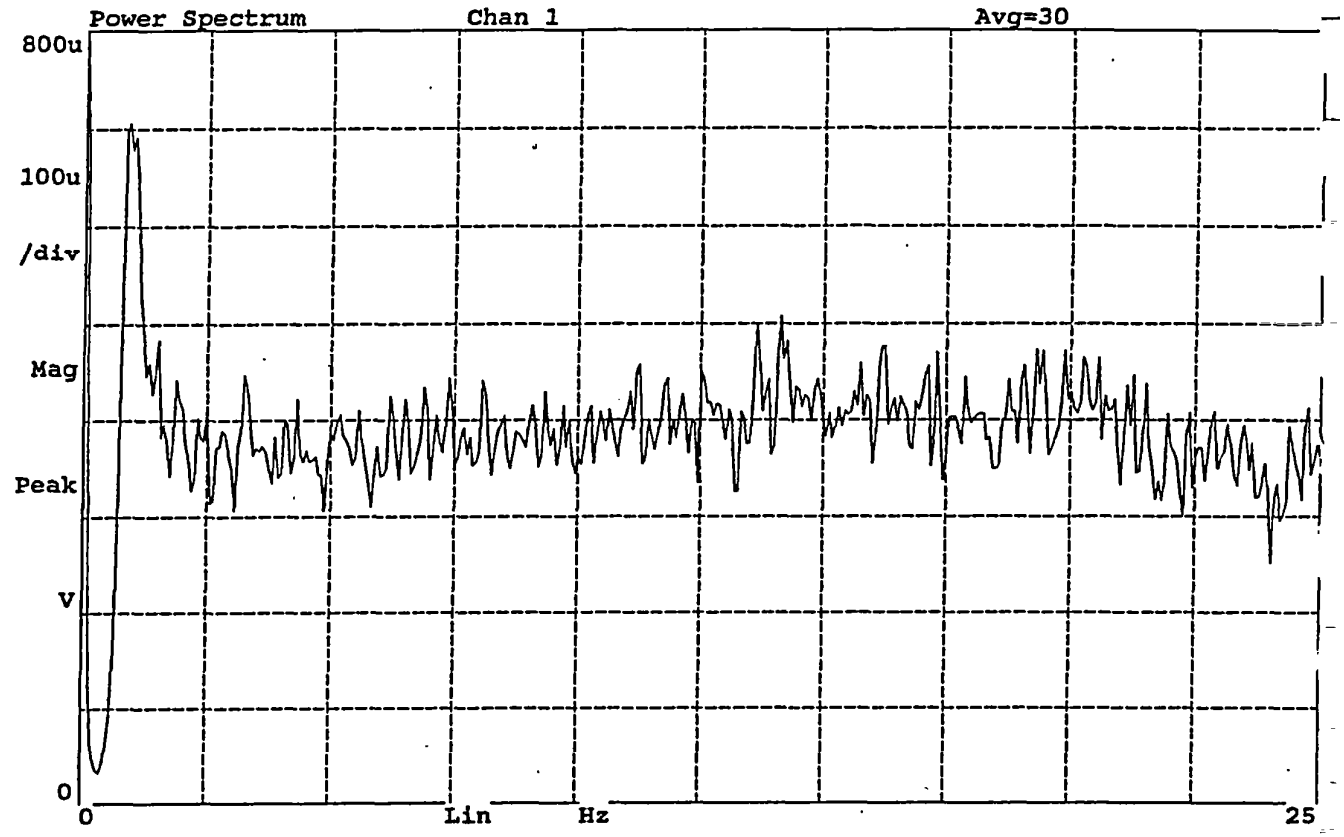

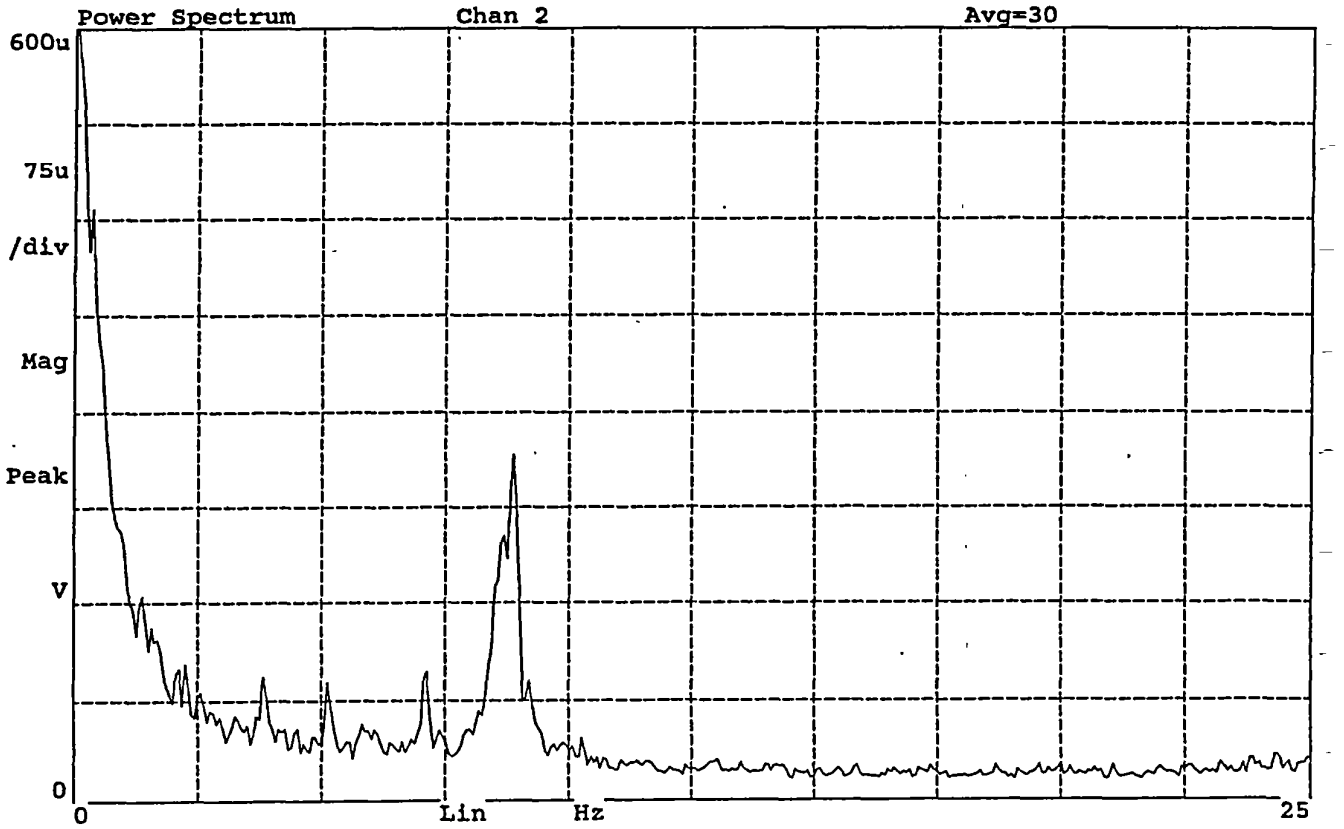

Figure D1. Average power spectra of signals from Channels 1 and 2, Test No. 1

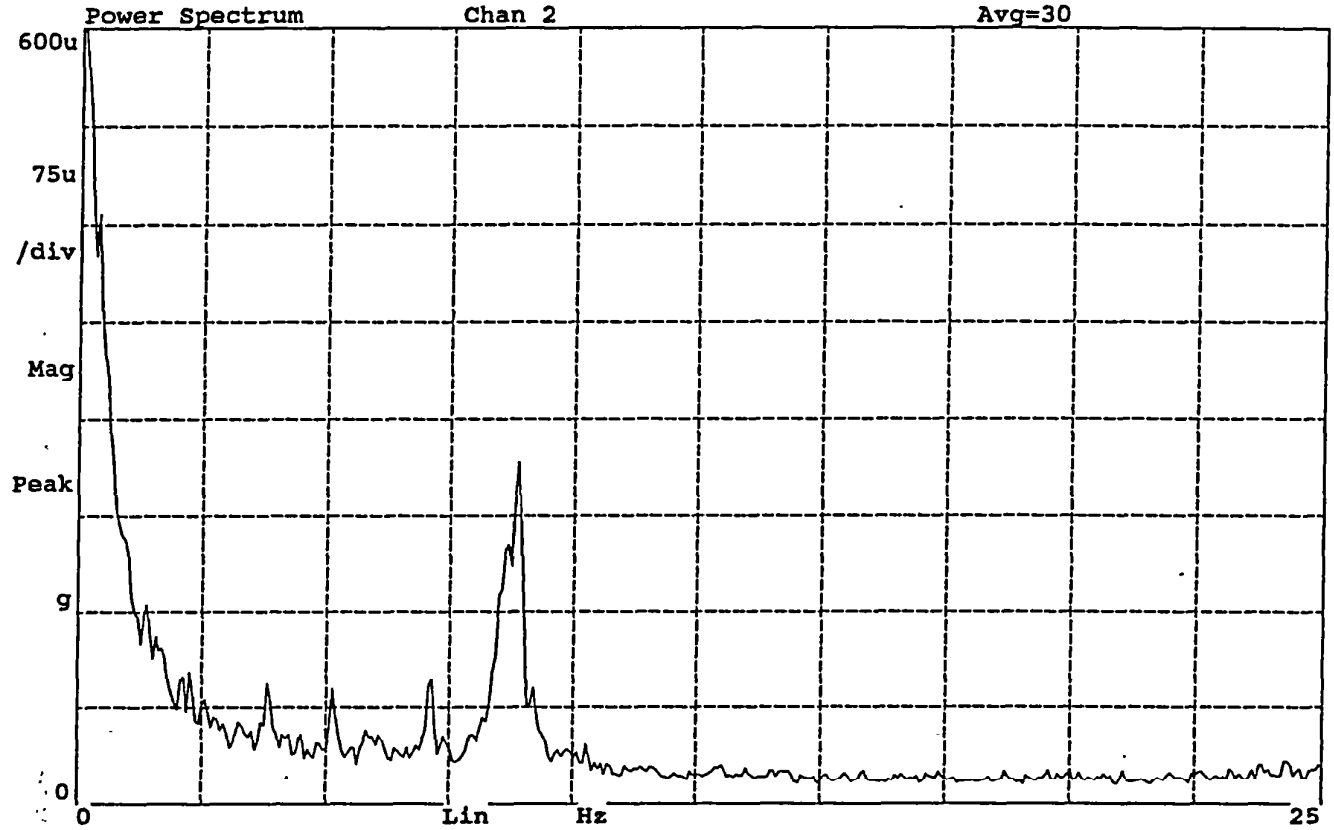

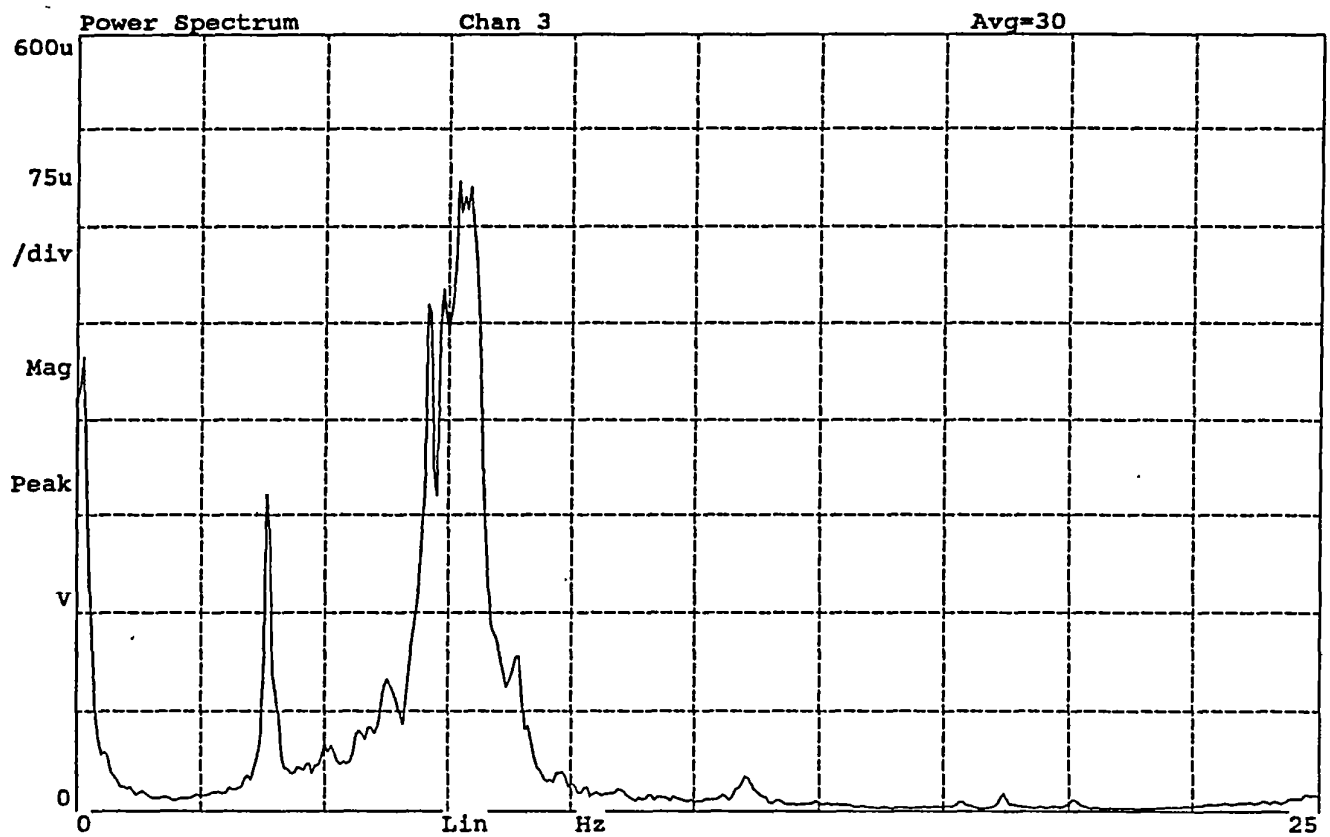

Figure D2. Average power spectra of signals from Channels 2 and 3, Test No. 1

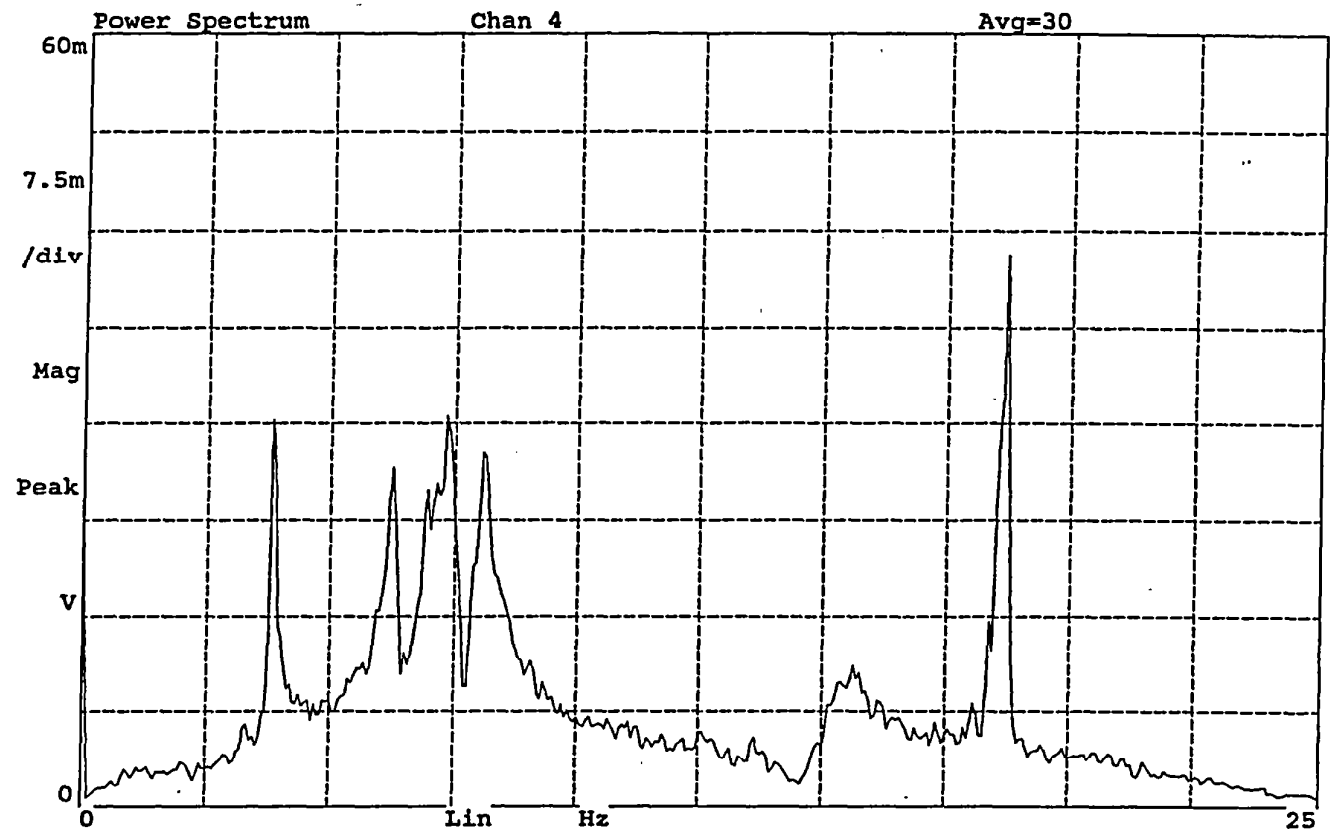

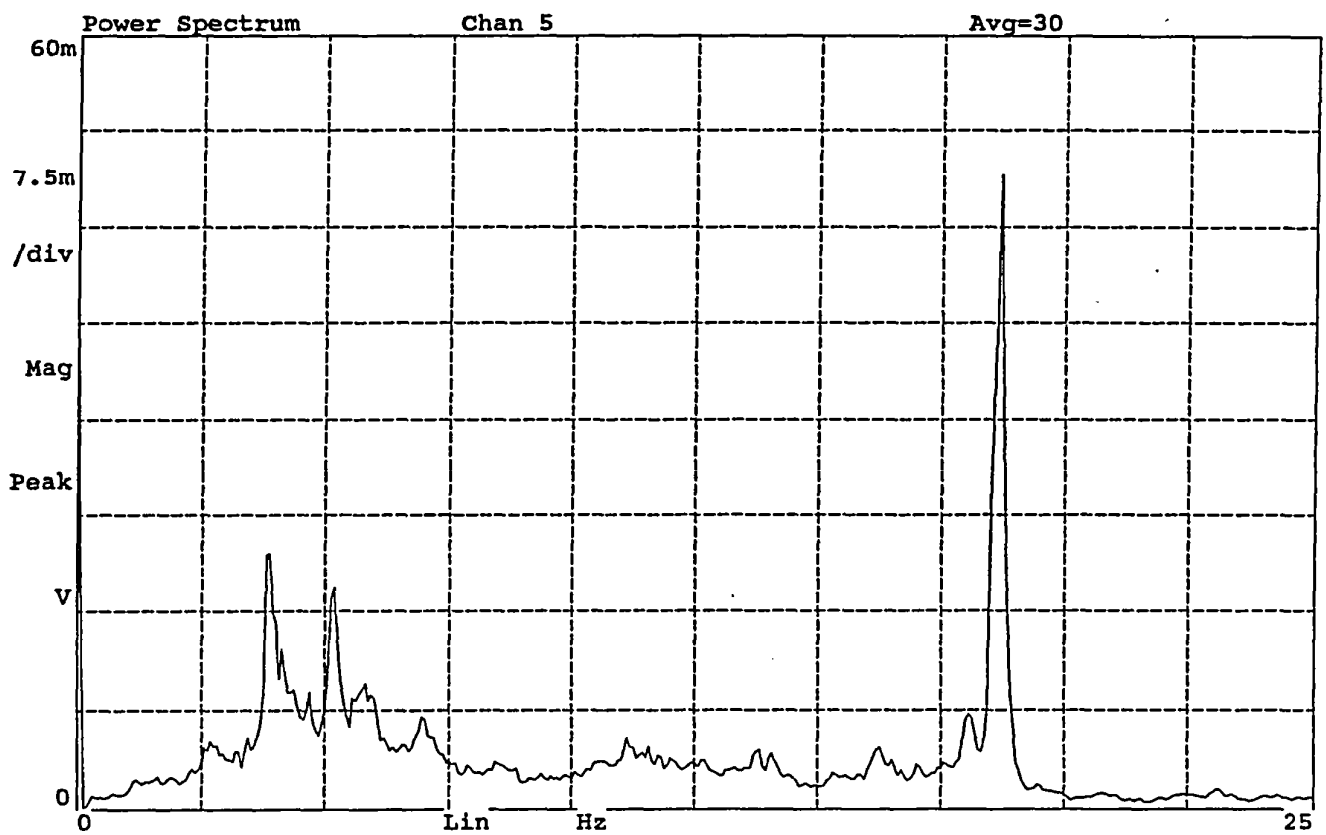

Figure D3. Average power spectra of signals from Channels 4 and 5, Test No. 1

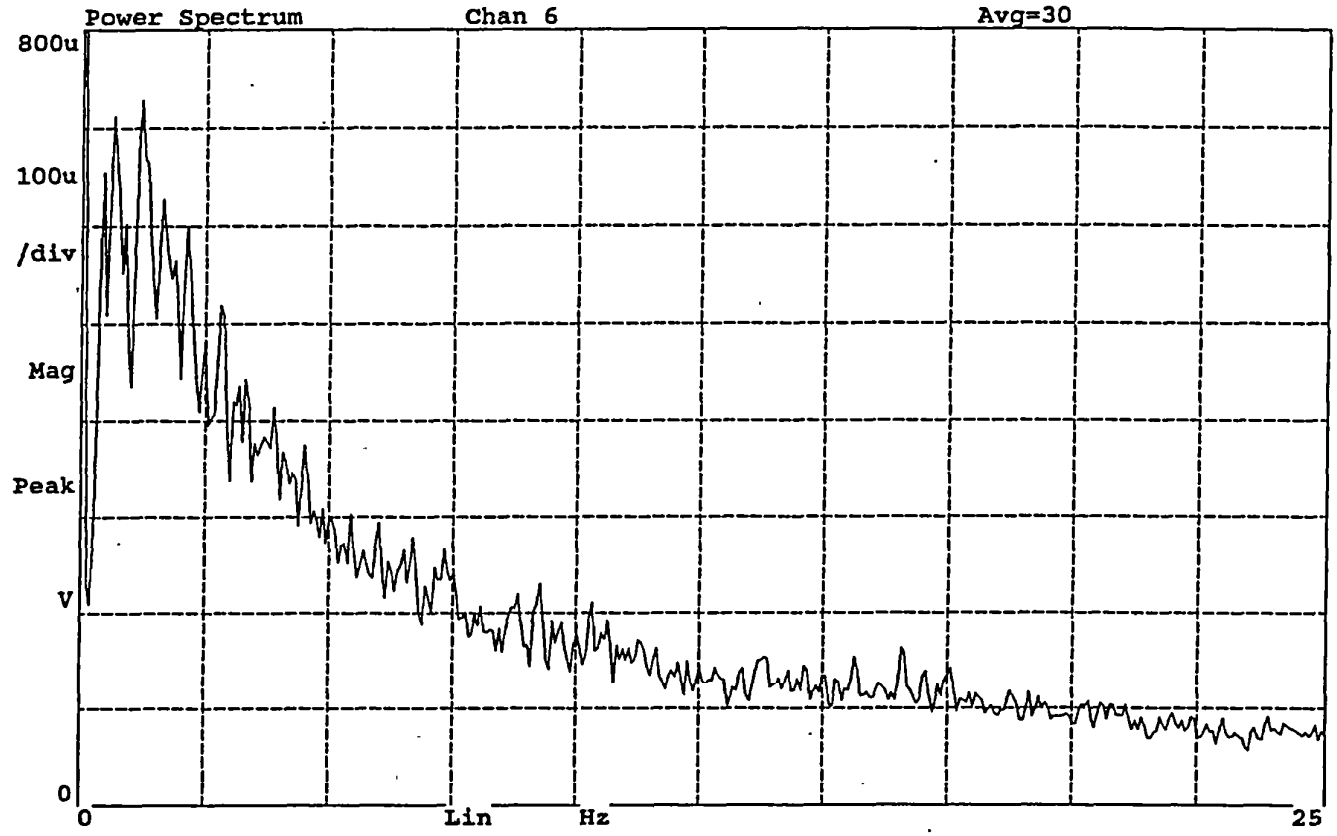

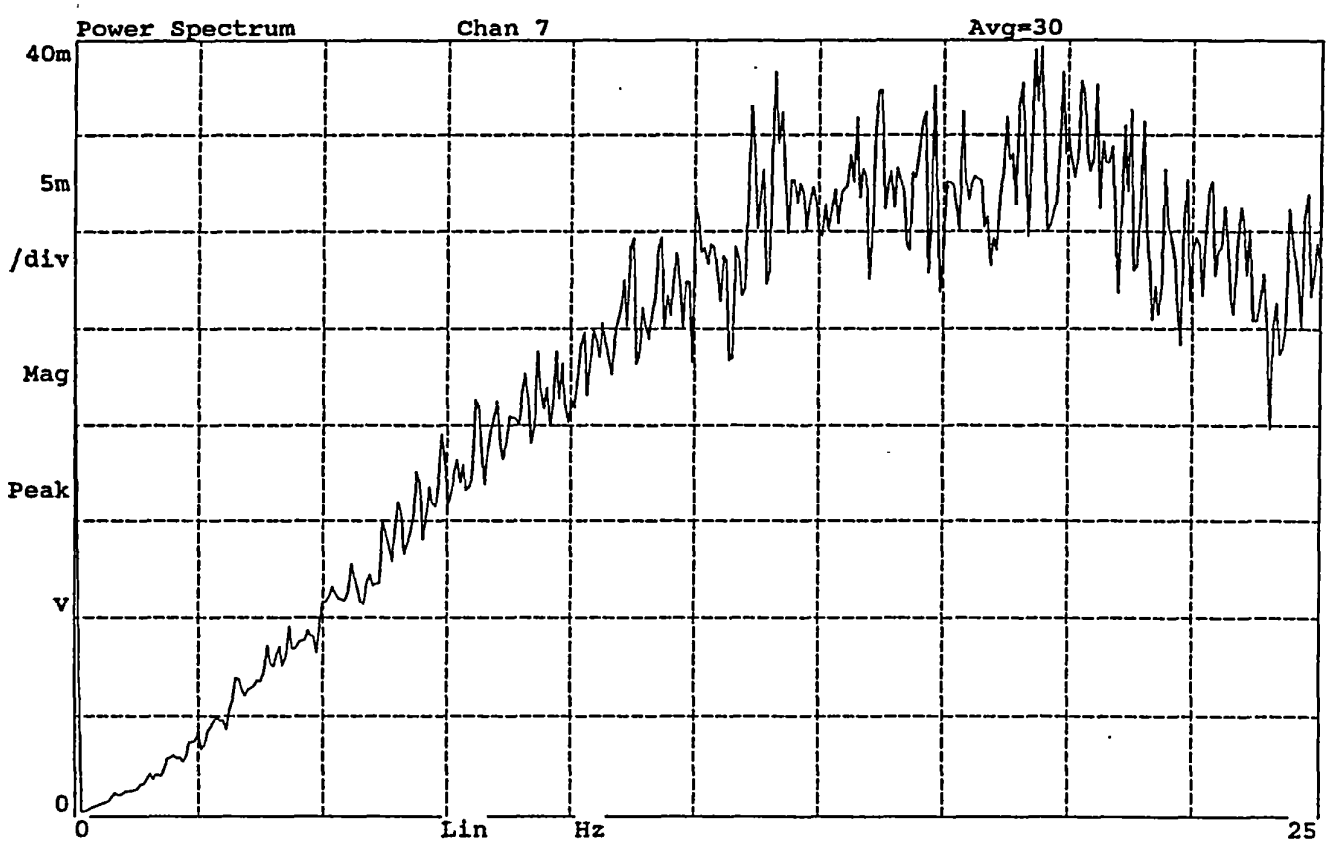

Figure D4. Average power spectra of signals from Channels 6 and 7, Test No. 1

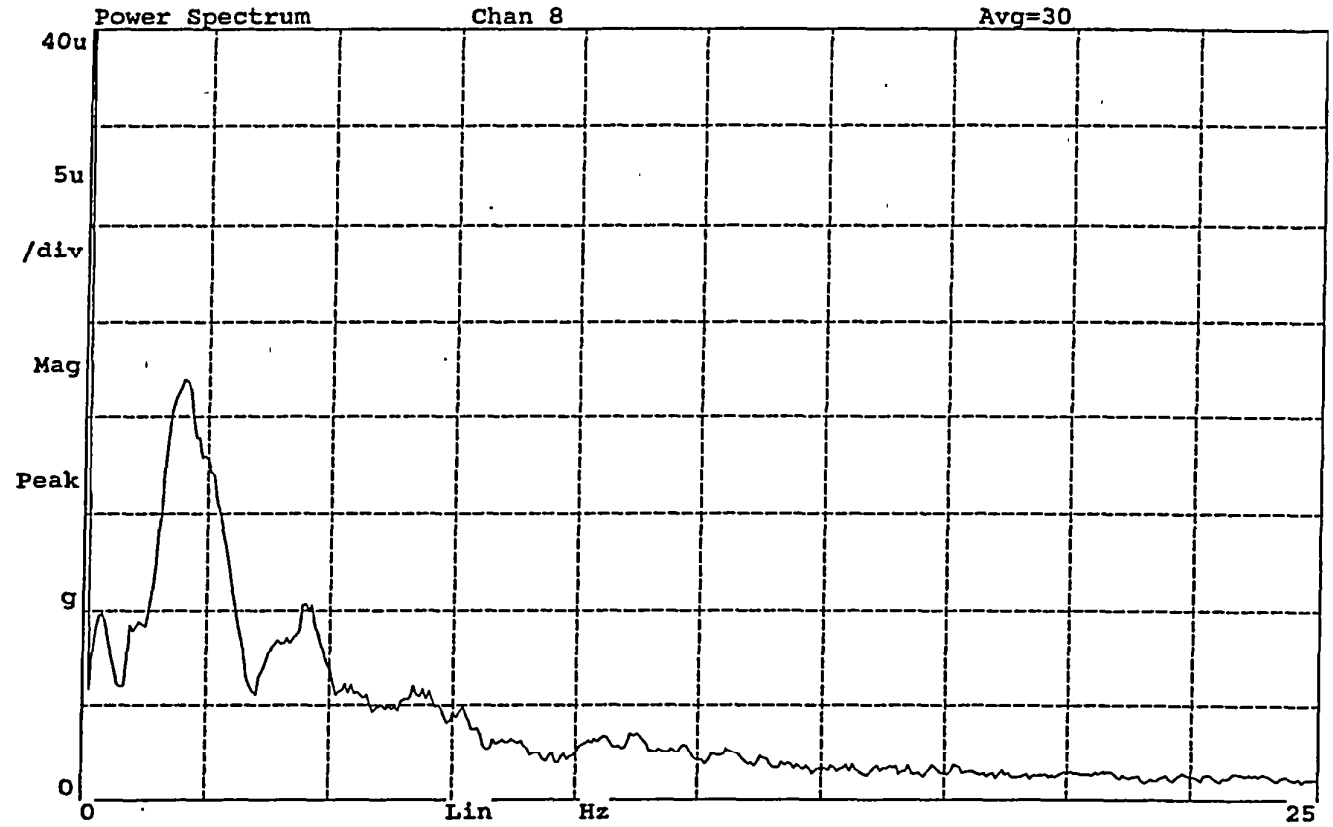

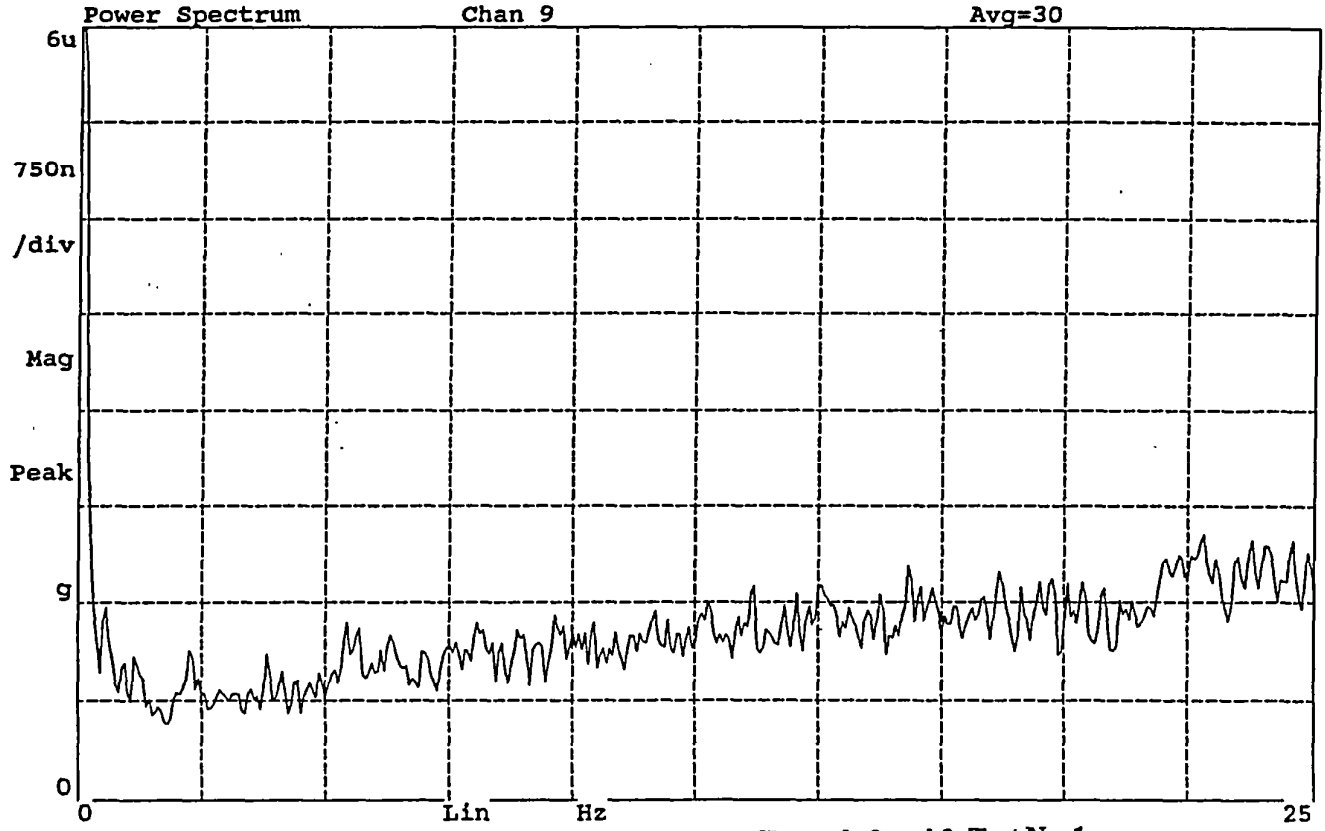

Figure D5. Average power spectra of signals from Channels 8 and 9, Test No. 1

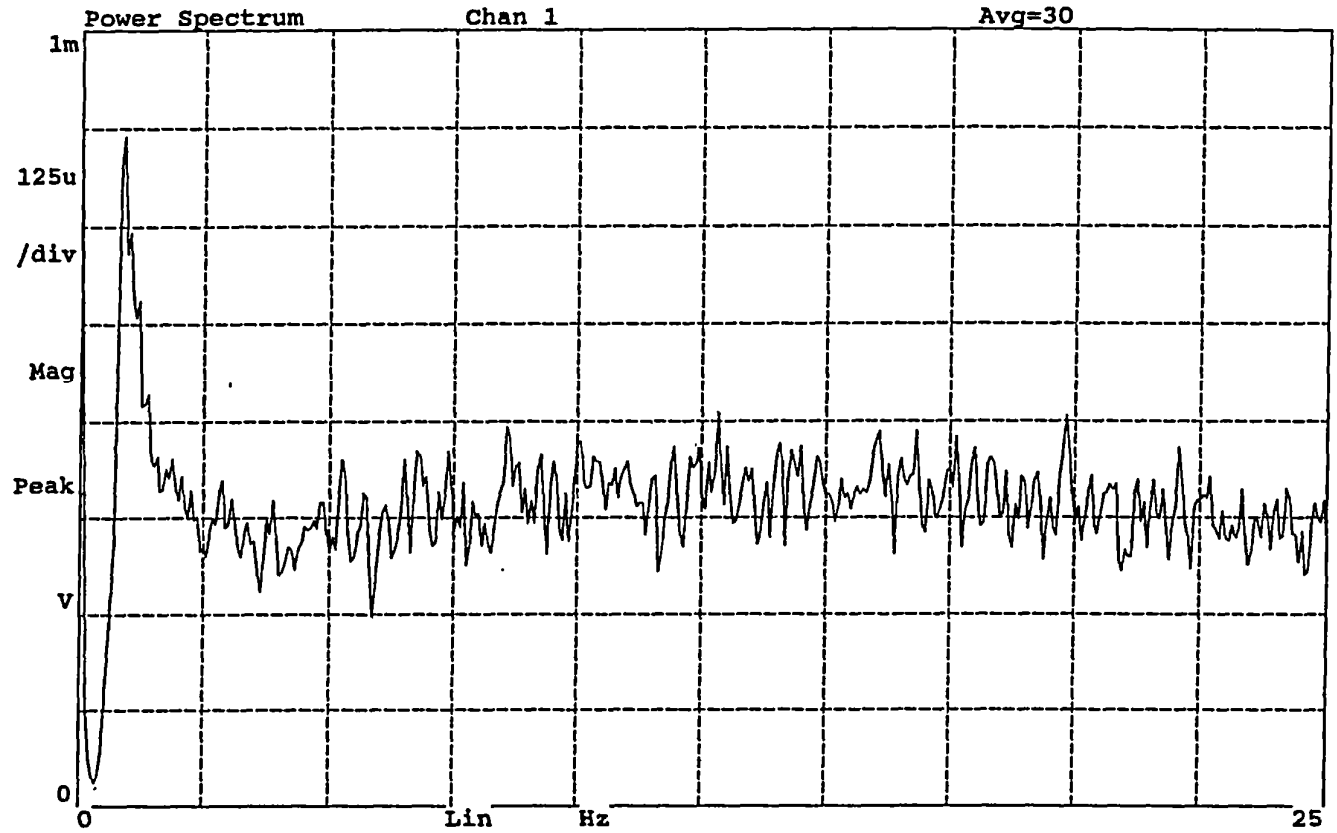

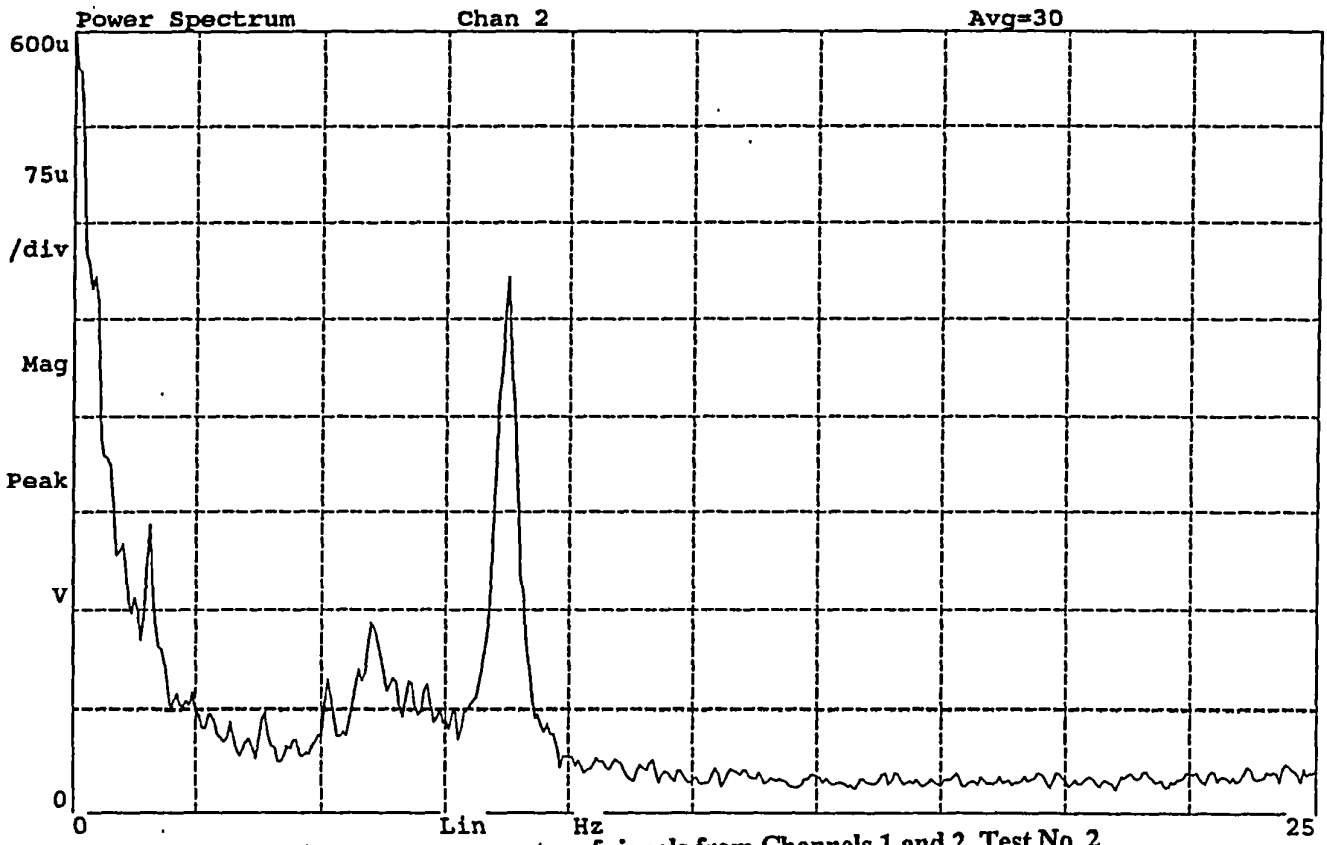

Figure D6. Average power spectra of signals from Channels 1 and 2, Test No. 2

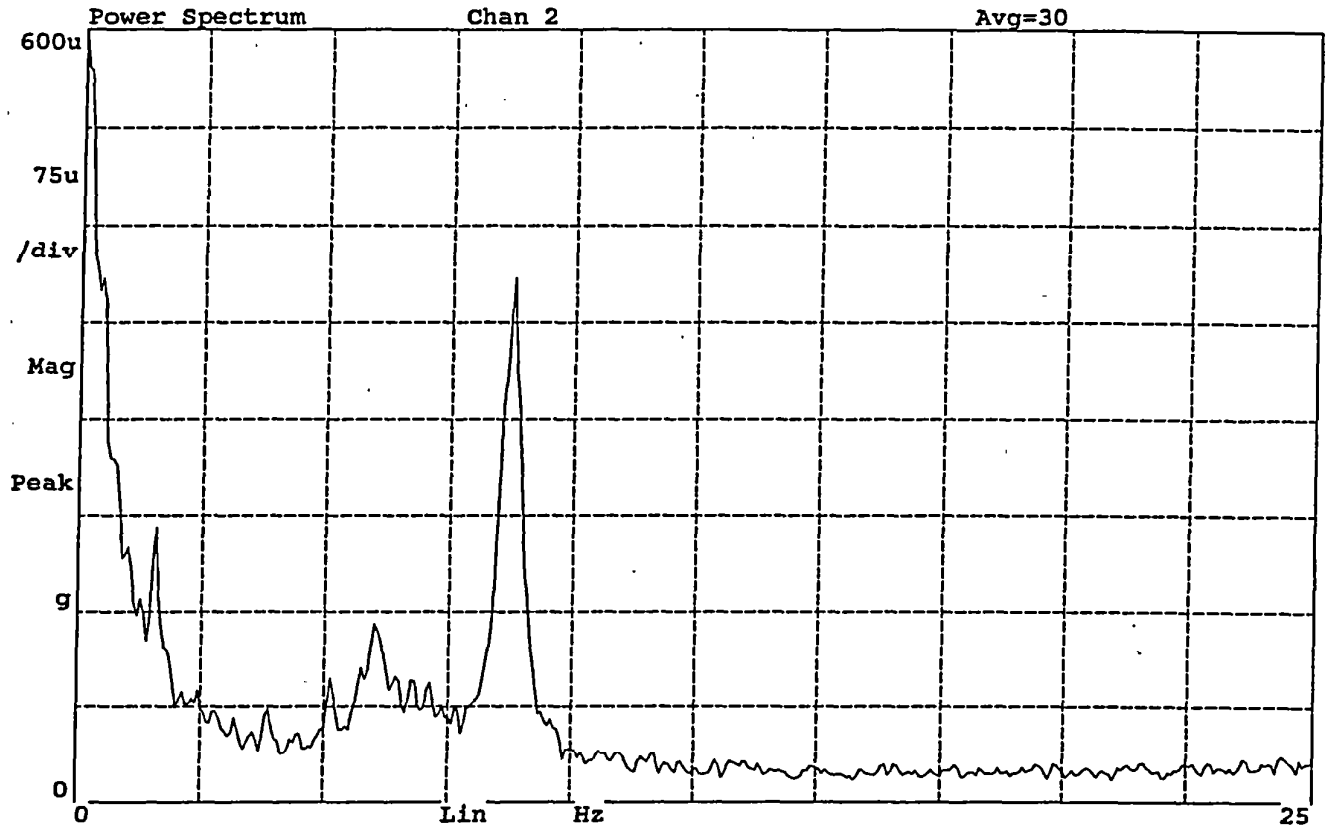

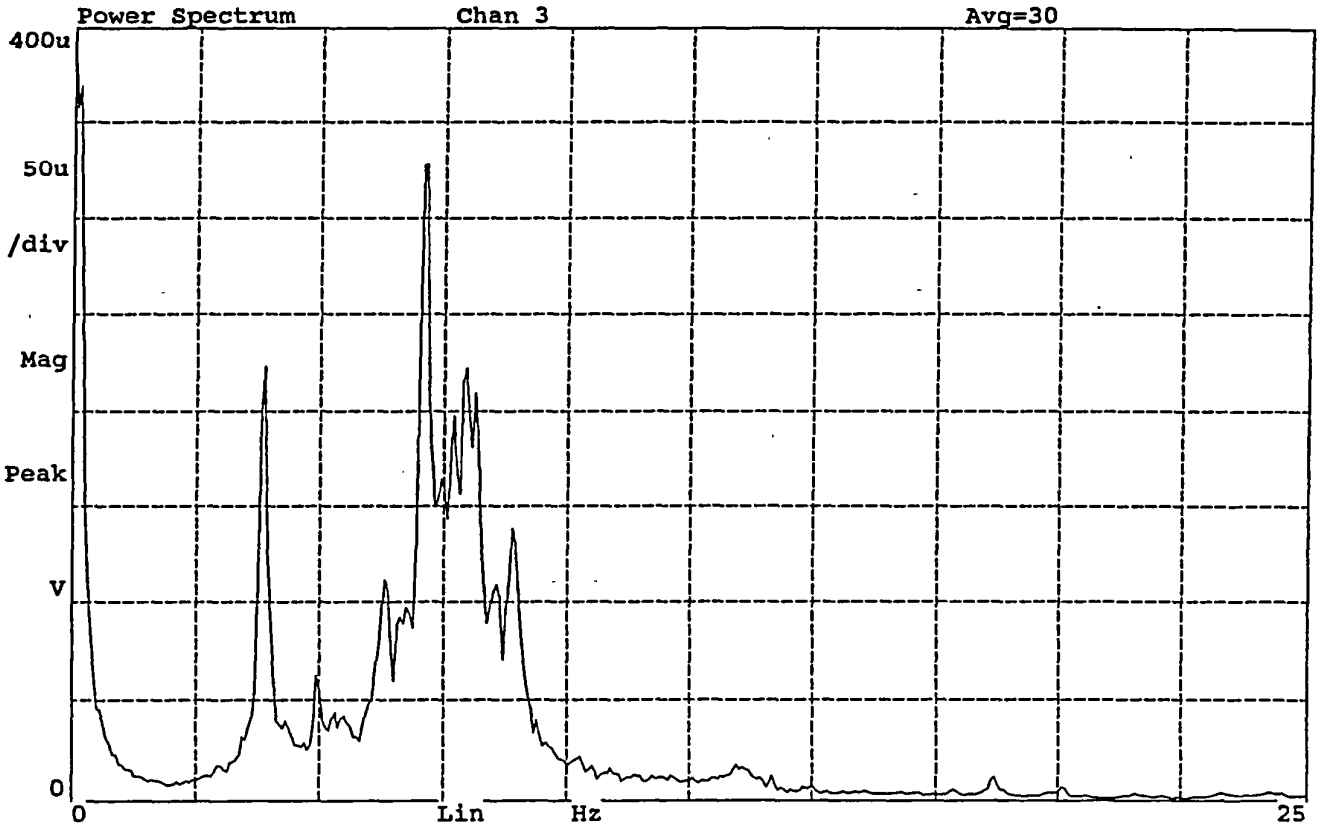

Figure D7. Average power spectra of signals from Channels 2 and 3, Test No. 2

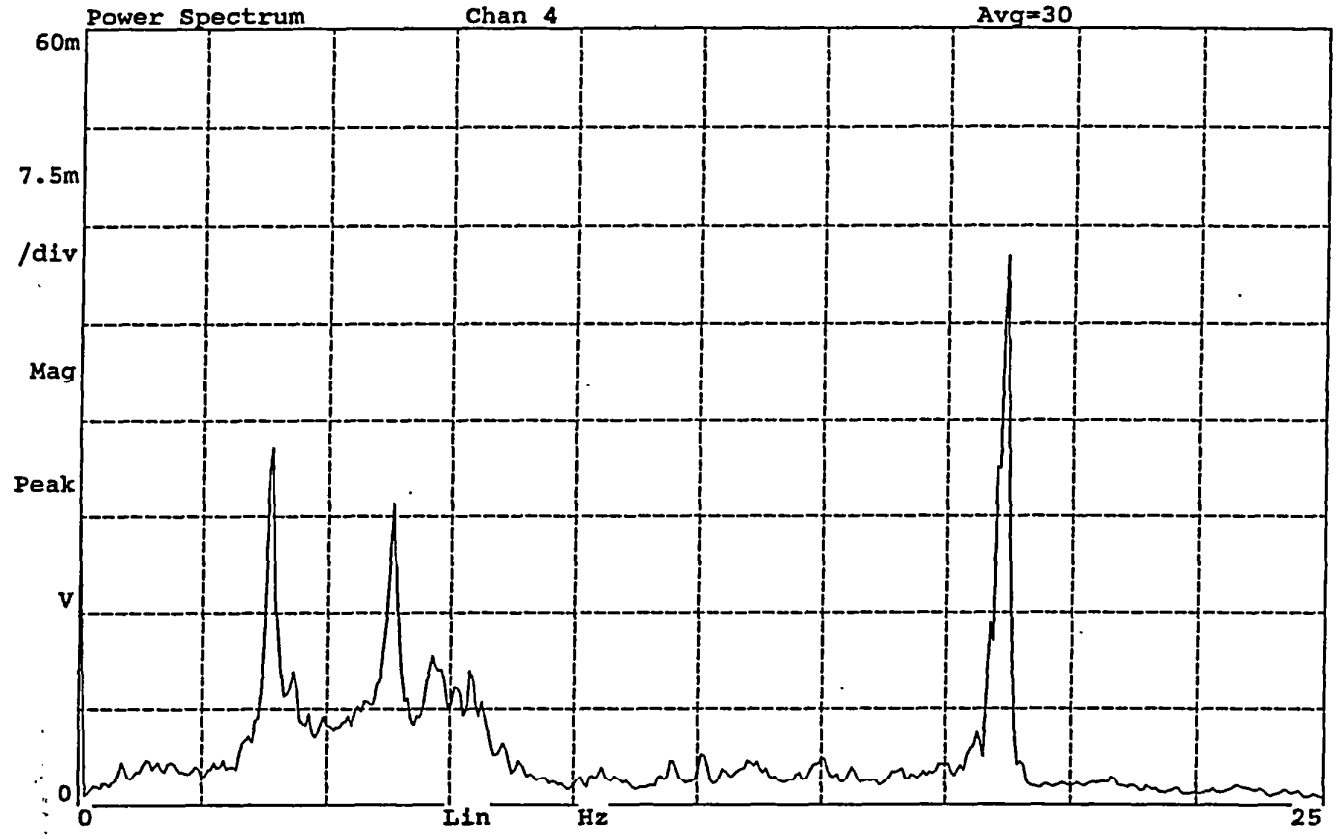

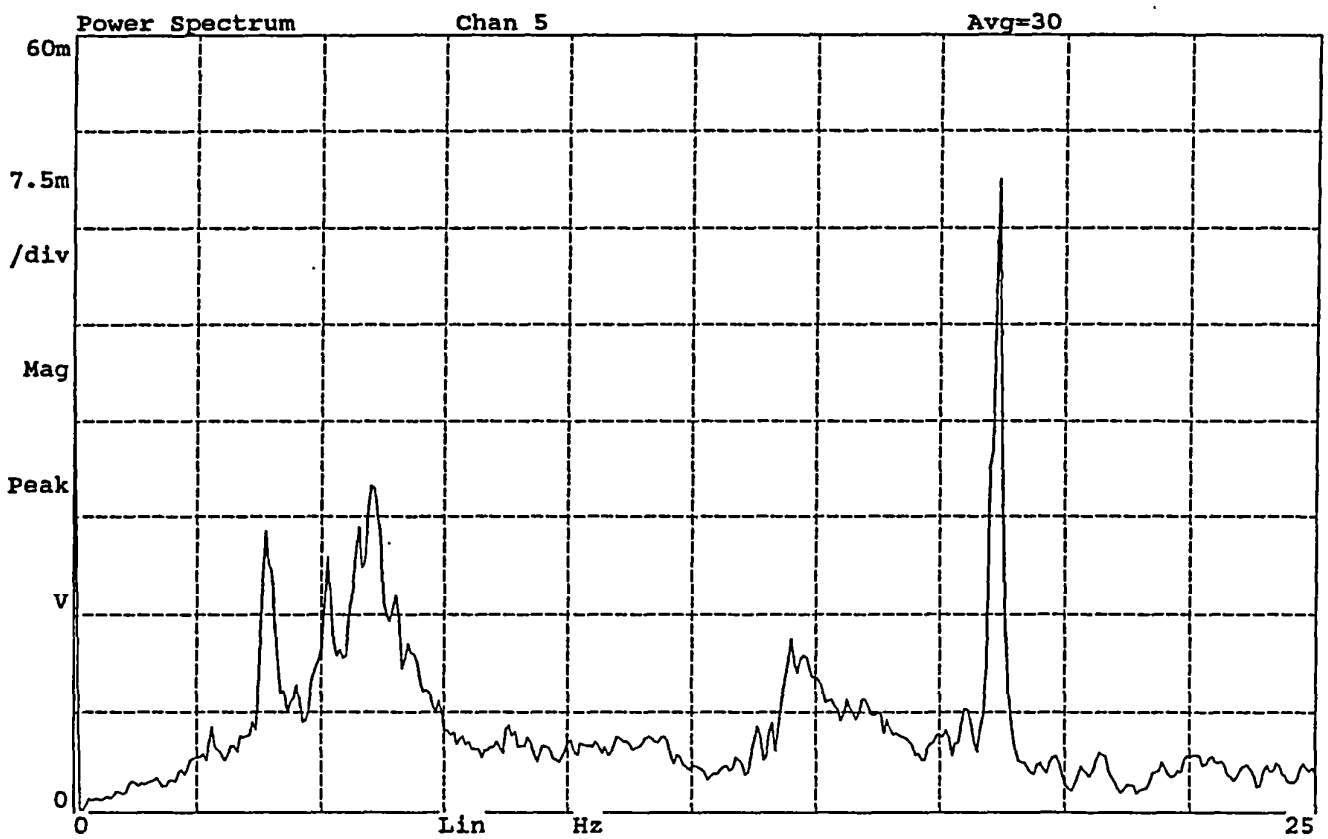

Figure D8. Average power spectra of signals from Channels 4 and 5, Test No. 2

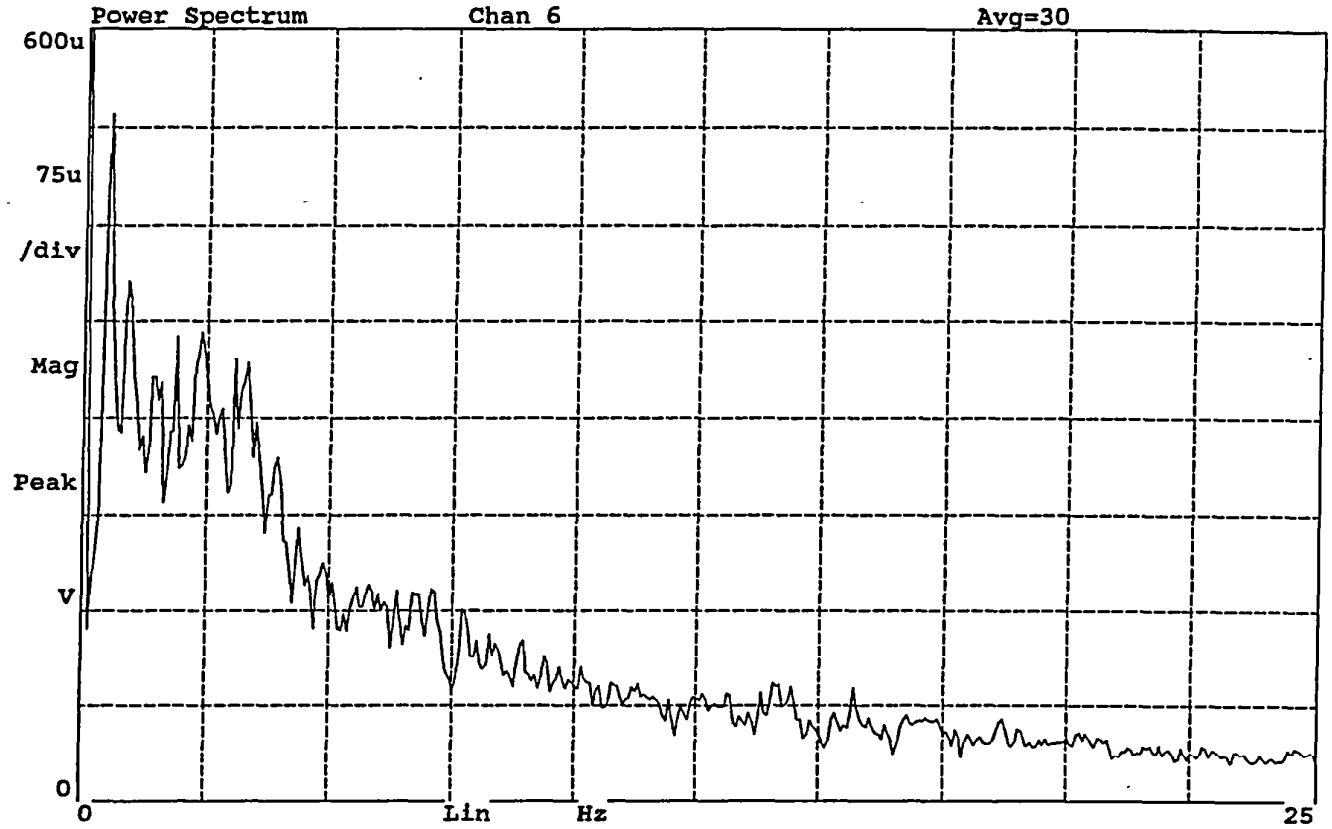

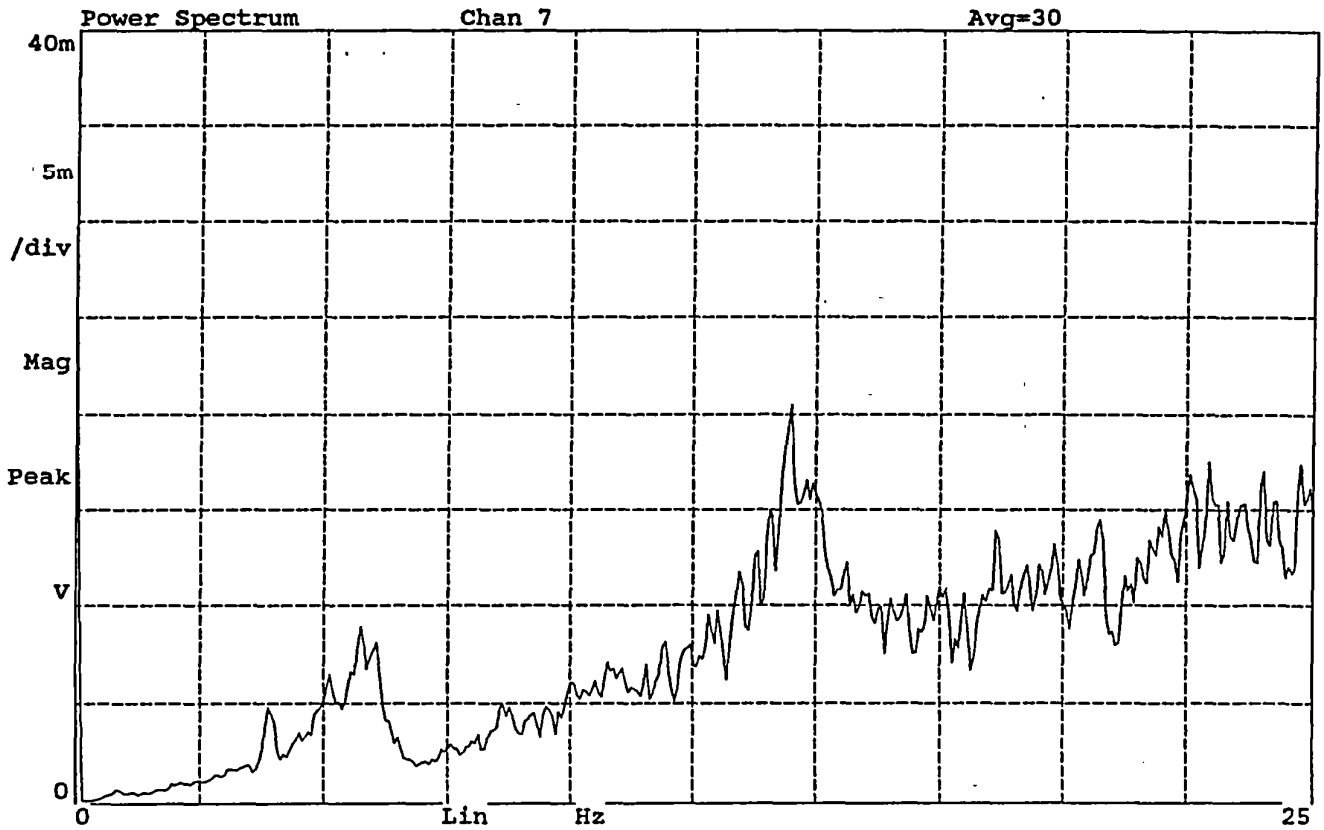

Figure D9. Average power spectra of signals from Channels 6 and 7, Test No. 2

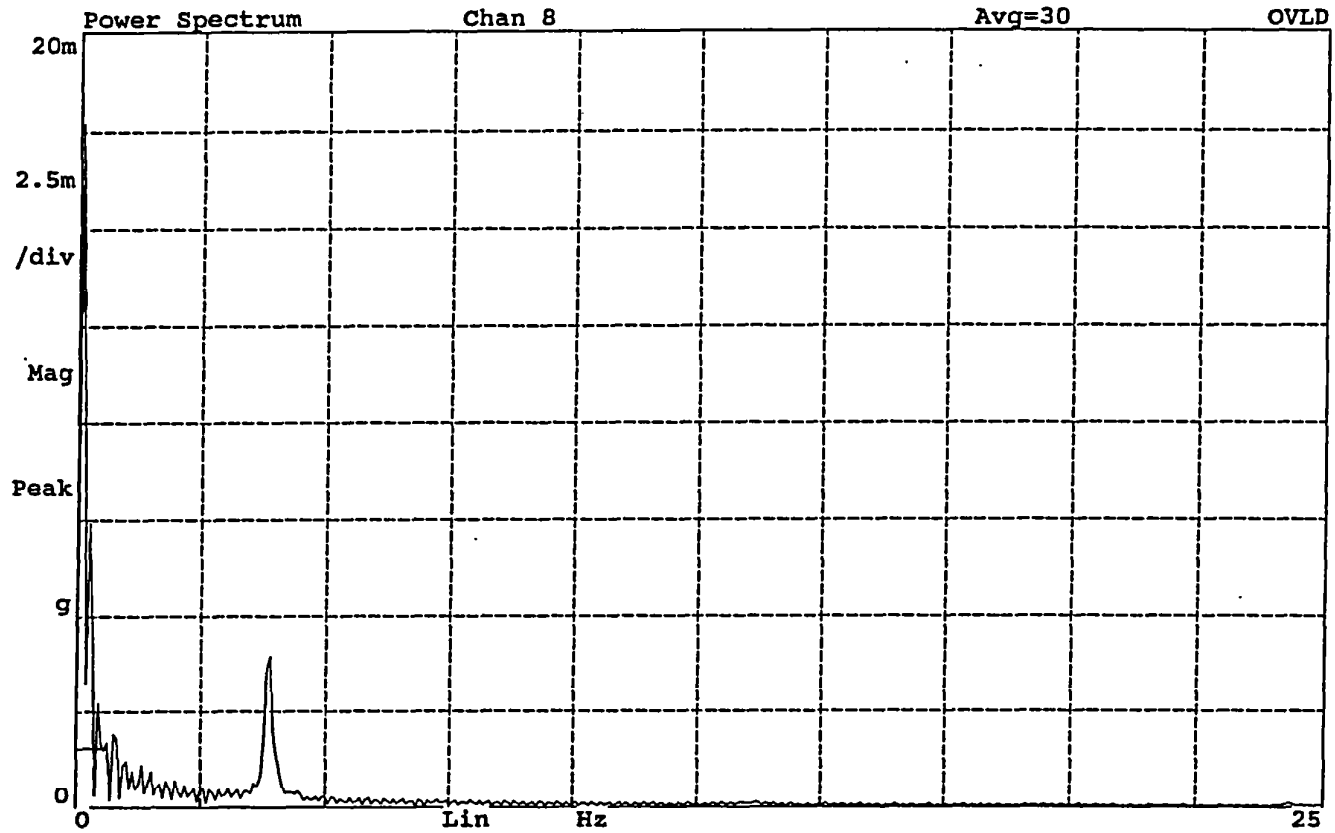

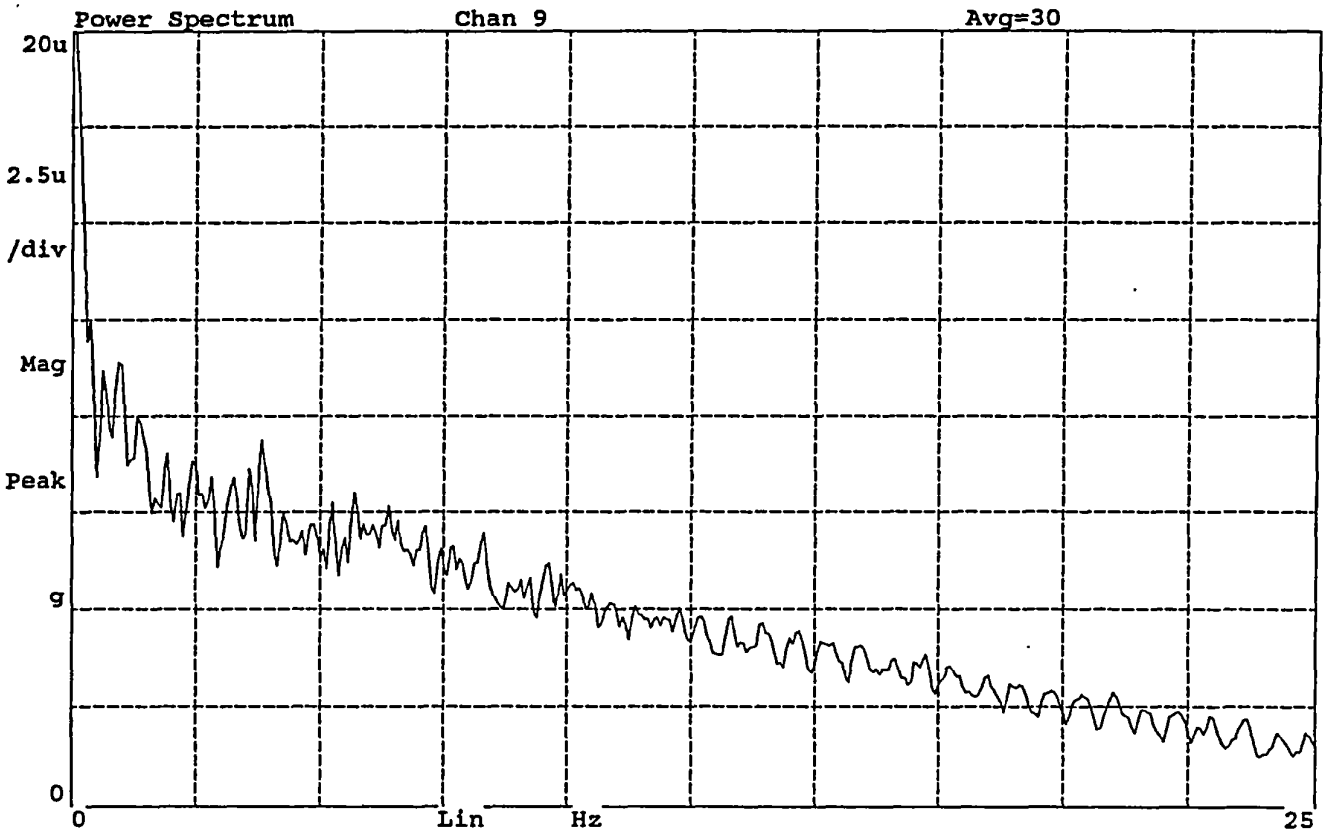

Figure D10. Average power spectra of signals from Channels 8 and 9, Test No. 2

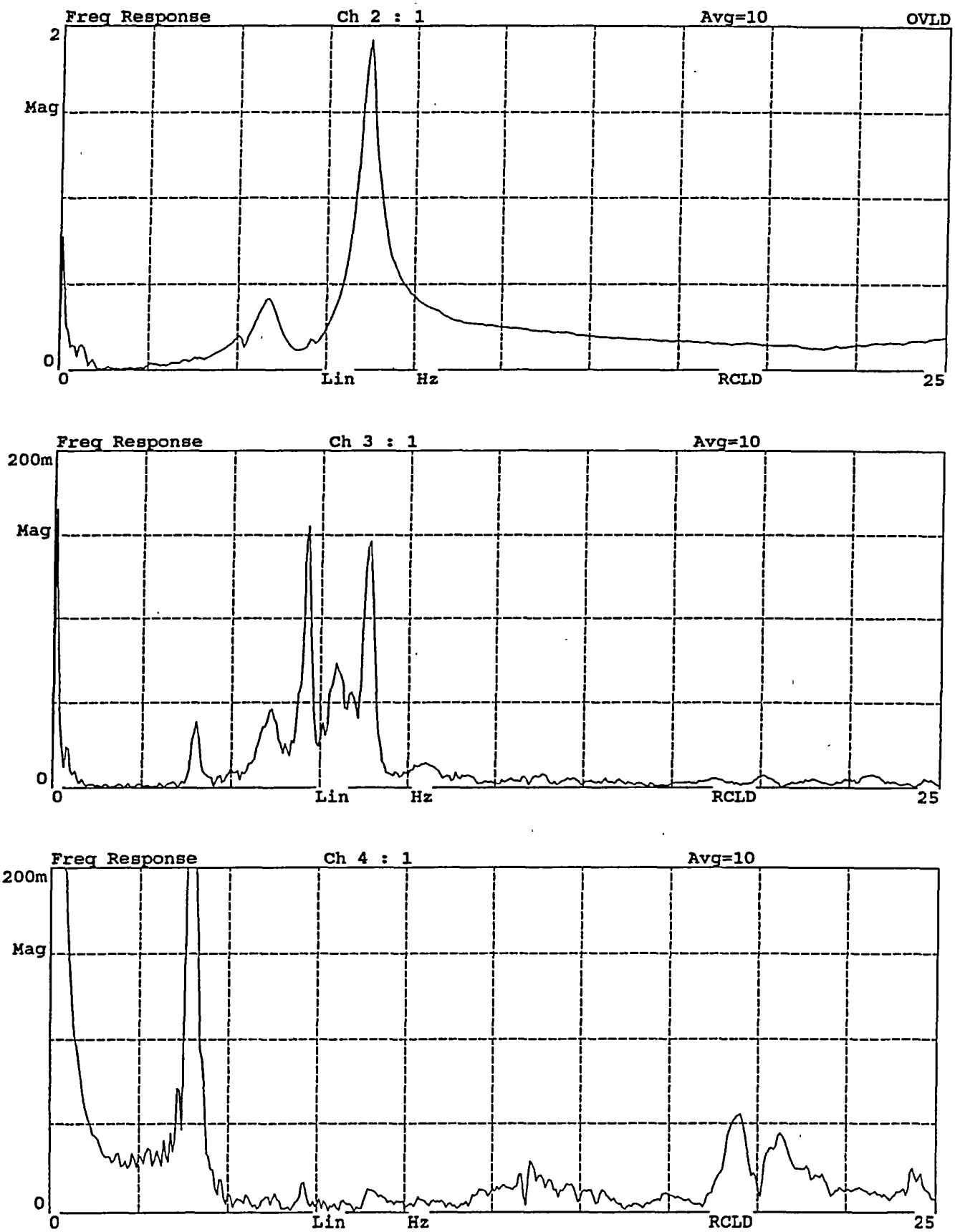

Figure D11. Average frequency response function of signals from Channels 2, 3 and 4, Test No. 3

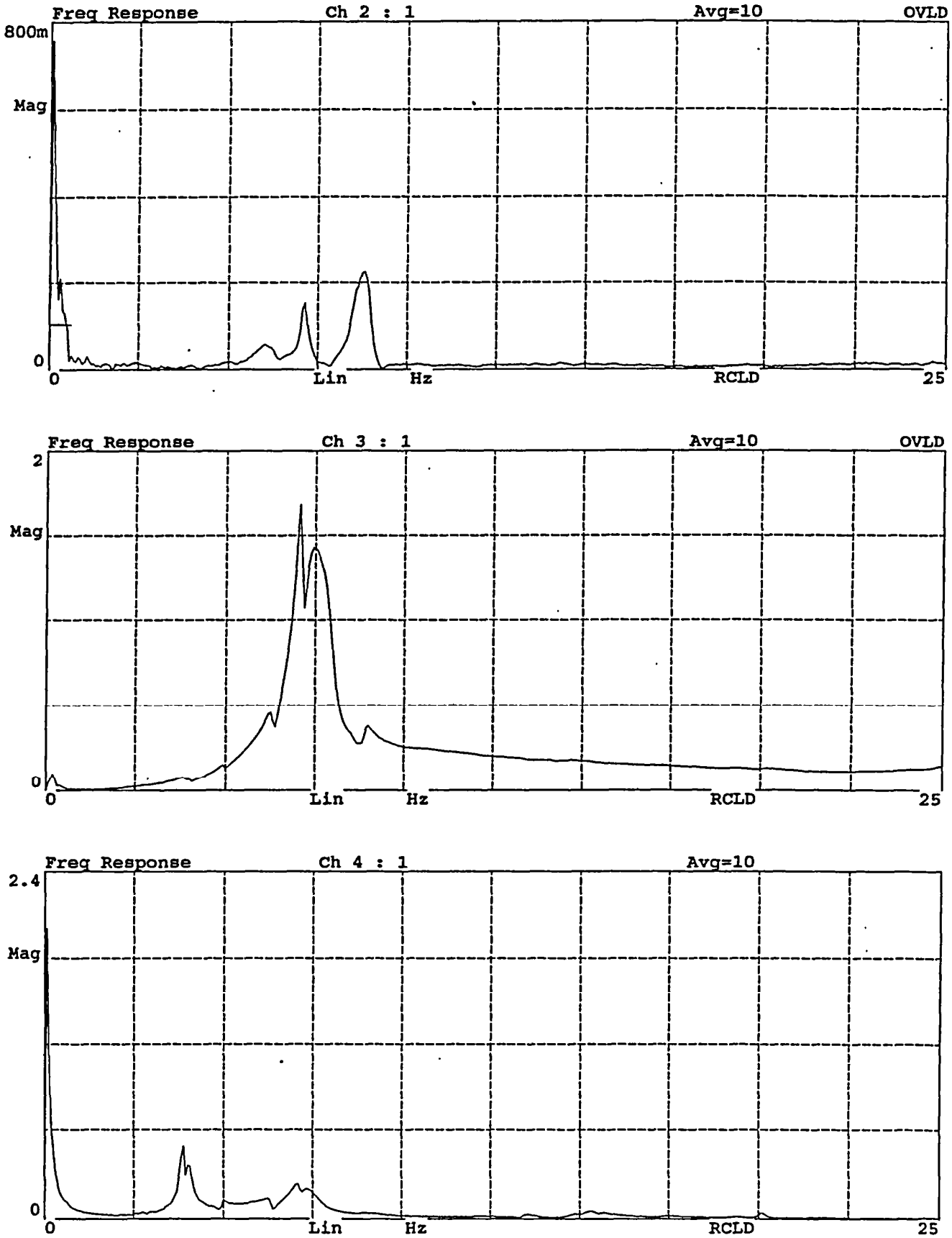

Figure D12. Average frequency response function of signals from Channels 2, 3 and 4, Test No. 4

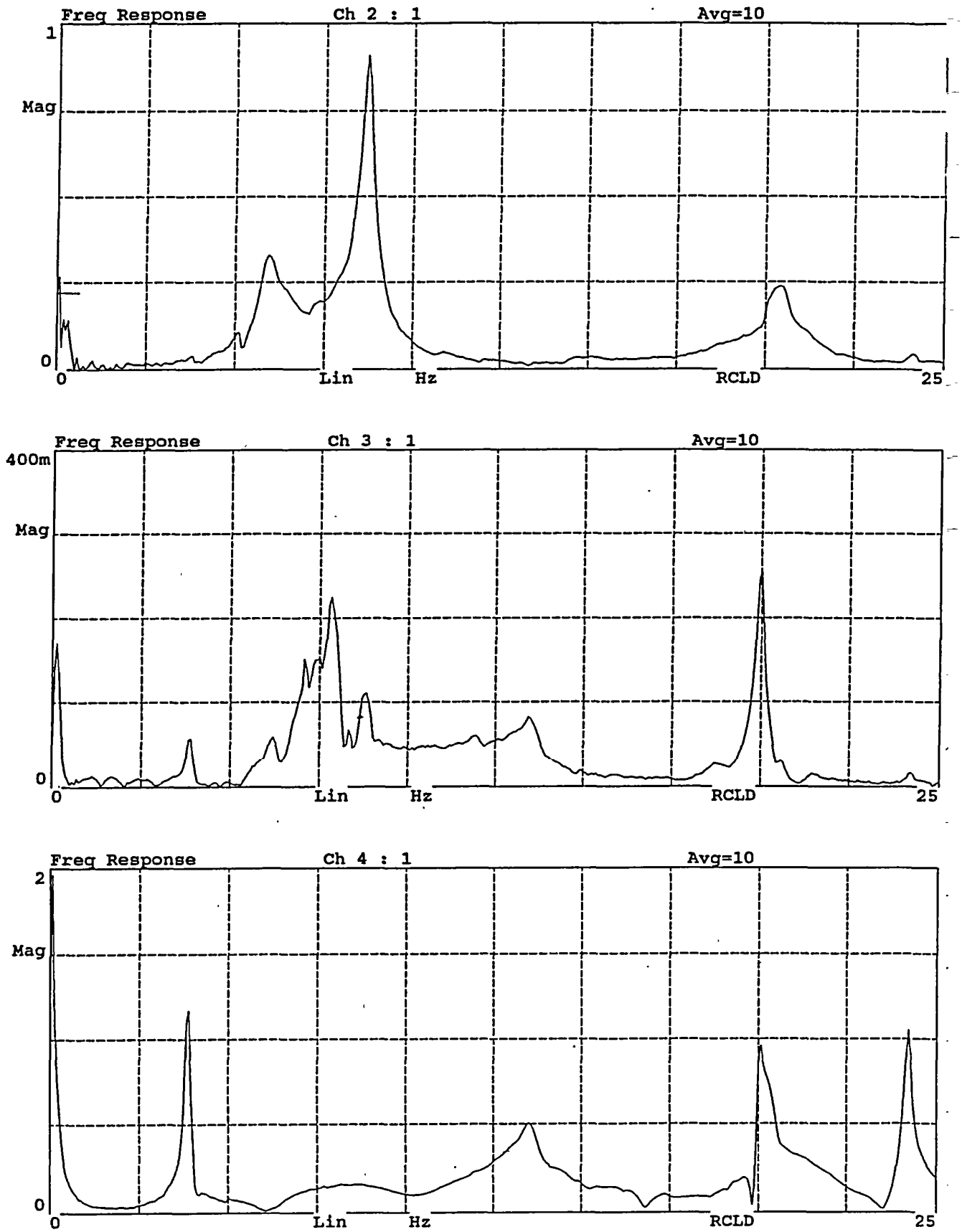

Figure D13. Average frequency response function of signals from Channels 2, 3 and 4, Test No. 5

PACIFIC EARTHQUAKE ENGINEERING RESEARCH CENTER

Rocking Response and Overturning of Equipment

Nicos Makris

Jian Zhang
University of California, Berkeley

A report to the PEER Program of Applied Earthquake Engineering Research on Lifeline Systems

The financial support of the sponsor organizations including the Pacific Gas & Electric Company (PG&E) and the California Energy Commission (CEC) is acknowledged.

PEER UTILITIES PROGRAM
REPORT NO. 2000/13

Rocking Response and Overturning of Anchored Equipment under Seismic Excitations

Final Report to PG&E

by

NICOS MAKRIS, PI
Associate Professor

JIAN ZHANG
Graduate Student Researcher

Department of Civil and Environmental Engineering,
University of California, Berkeley

September 1999

ABSTRACT

This report investigates the transient rocking response of anchored electrical equipment and other anchored structures that can be approximated as rigid blocks. Practical issues that control overturning, such as the effect of the vertical component of ground accelerations and the effect of the coefficient of restitution during impact, are also addressed.

The anchorages of equipment are assumed to have a pre-yielding linear behavior, a finite post-yielding strength, and some ductility. The nonlinear behavior of the restrainers in conjunction with the nonlinear dynamics of a rocking block yield a set of highly nonlinear equations which are solved numerically using a state-space formulation. The study uncovers that while for most of the frequency range, anchored blocks survive higher accelerations than free-standing blocks, there is a short frequency range where the opposite happens. This counterintuitive behavior is the result of the many ways that a block might overturn. It is shown that under a one-sine (Type-A) pulse or one-cosine (Type-B) pulse with frequency ω_p, a free-standing block with frequency parameter p has two modes of overturning; one with impact (mode 1), and one without impact (mode 2). The transition from mode 1 to mode 2 is sudden, and once ω_p/p is sufficiently large, then a substantial increase in the acceleration amplitude of the one-sine pulse is needed to achieve overturning. When a block is anchored the transition from mode 1 to mode 2 happens at slightly larger values of ω_p/p, and this results in a finite frequency range where a free-standing block survives acceleration levels that are capable of overturning the same block when it is anchored. The presence of restrainers is effective in preventing toppling of small, slender blocks. Prior to the transition from mode 1 to mode 2, the presence of restrainers has a destructive effect. When blocks overturn without impact (mode 2) the presence of restrainers has a marginal effect.

Furthermore, the investigation concludes that the effect of the vertical component of recorded ground motions is marginal and virtually does not affect the level of the horizontal acceleration needed to overturn an electrical equipment. An increasingly inelastic impact (smaller coefficient of restitution) results in smaller angles of rotation; however, the values of the impact velocities might be occasionally larger.

PROLOGUE

This report summarizes the work conducted during Phase II of the PEER-PG&E Program. The work is the continuation of a Phase I study during which the PI and a former graduate student examined the rocking response and overturning of free-standing equipment under pulse-type motions[1]. In that study it was indicated that the minimum overturning acceleration amplitude, a_{p0}, of a half-sine pulse as was computed by Housner[2] was incorrect. This result was corrected by showing that under the weaker half-sine pulse that accomplishes overturning, the block topples during its free-vibration regime — after a theoretically infinite long time — not at the instant that the pulse expires, as was assumed by Housner. Within the limits of the linear approximation the correct expression was derived, which yields the minimum overturning acceleration, a_{p0} (equation 3.8 of Reference 1):

$$\begin{aligned}&\cos\psi\cosh\left[\frac{p}{\omega_p}(\pi-\psi)\right]-\frac{\omega_p}{p}\sin\psi\sinh\left[\frac{p}{\omega_p}(\pi-\psi)\right]+1\\&+\cos\psi\sinh\left[\frac{p}{\omega_p}(\pi-\psi)\right]-\frac{\omega_p}{p}\sin\psi\cosh\left[\frac{p}{\omega_p}(\pi-\psi)\right]=0\end{aligned} \tag{1}$$

The solution of this transcendental equation gives the value of ψ for which the acceleration, $a_{p0} = \alpha g/\sin\psi$, is the minimum acceleration amplitude of the half-sine pulse with duration $T_p = 2\pi/\omega_p$ able to overturn a block with slenderness α and frequency parameter p.

Equation (1) can be further simplified by using the definition of the hyperbolic function, $\cosh x = (e^x + e^{-x})/2$ and $\sinh x = (e^x - e^{-x})/2$, and then factoring the terms $\cos\psi$ and $\sin\psi$. This gives

$$\frac{\omega_p}{p}\sin\psi-\cos\psi = e^{-\frac{p}{\omega_p}(\pi-\psi)} \tag{2}$$

Equation (2) was derived independently by Shi et al.[3] who stated correctly that under a half-sine pulse with the minimum acceleration that is needed to overturn a block, the kinetic energy of the block at the verge of overturning should be zero.

We take this opportunity to thank Professor James N. Brune (University of Nevada-Reno) for his interest to our work and for communicating to us reference 3. We are pleased to report that the energy approach followed by Shi et al.[3] and the kinematic approach followed by Makris and Roussos[1] are in agreement.

---

1. Makris, N., and Y. Roussos. 1998. *Rocking Response and Overturning of Equipment Under Horizontal Pulse-Type Motions*. PEER-98/05. Pacific Earthquake Engineering Research Center, University of California, Berkeley.
2. Housner, G. W. 1963. The behaviour of inverted pendulum structures during Earthquakes. *Bull. Seismological Soc.of America,* **53**: 404-17.
3. Shi, B., A. Anooshehpoor, Y. Zeng, and J. N. Brune. 1996. Rocking and overturning of precariously balanced rocks by earthquake. *Bull. Seismological Soc. of America* **86**(5): 1364-71.

CONTENTS

ABSTRACT iii
PROLOGUE v
TABLE OF CONTENTS vii
LIST OF FIGURES ix
LIST OF TABLES xv
ACKNOWLEDGMENTS xvii
CHAPTER 1: INTRODUCTION 1
CHAPTER 2: REVIEW OF THE ROCKING RESPONSE OF A FREE-STANDING BLOCK 5
2.1 Condition for Initiation of Rocking Motion 5
2.2 Governing Equations under Rocking Motion 10
2.3 Rocking Response to a One-Sine (Type-A) Pulse 12
2.3.1 Linear Formulation 12
2.3.2 Nonlinear Formulation 21
2.4 Rocking Response to a One-Cosine (Type-B) Pulse 24
CHAPTER 3: ROCKING RESPONSE OF A FREE-STANDING BLOCK UNDER HORIZONTAL AND VERTICAL EXCITATION 31
3.1 Numerical Formulation and Solution 31
3.2 Response Spectra and Effect of the Coefficient of Restitution 41
CHAPTER 4 ROCKING RESPONSE OF ANCHORED EQUIPMENT TO ONE-SINE (TYPE-A) PULSE 45
4.1 Elastic-Brittle Behavior 45
4.1.1 Nonlinear Formulation 45
4.1.2 Linear Formulation 54
4.2 Ductile Behavior 57
4.2.1 Elasto-Plastic Behavior 60
CHAPTER 5: ROCKING RESPONSE OF ANCHORED EQUIPMENT TO EARTHQUAKE EXCITATIONS 69
CHAPTER 6: CONCLUSIONS 79
REFERENCES 81

LIST OF FIGURES

Figure 1: Overturned electrical equipment at Sylmar Converter Station damaged after the 1971 San Fernando earthquake. Top: Front view. Bottom: Side view. — Steinbrugge Collection, PEER, University of California, Berkeley 2

Figure 2: Schematic of a free-standing block in rocking motion (top); and its moment rotation diagram (bottom) 6

Figure 3: Acceleration, velocity, and displacement histories of a one-sine pulse (left) and a one-cosine pulse (right) 7

Figure 4: Free-body diagram of a rigid block at the instant that it enters rocking 9

Figure 5: Overturning acceleration spectrum of a free-standing block with $\eta = 0.9$ subjected to a one-sine acceleration pulse with frequency ω_p. The analytical and numerical solutions shown are computed with the linear formulation. When ω_p/p is sufficiently large, a free-standing block overturns only without impact (mode 2) 17

Figure 6: Rotation and angular velocity time histories of a rigid block ($p = 2.14\ rad/sec$, $\alpha = 0.25\ rad$ and $\eta = 0.9$) subjected to a one-sine pulse with $\omega_p/p = 5$. Left: $a_p = 3.00\alpha g$, no overturning. Center: $a_p = 3.01\alpha g$, overturning with one impact (mode 1). Right: $a_p = 6.32\alpha g$, overturning with one impact (mode 1).....18

Figure 7: Rotation and angular velocity time histories of the same rigid block as in Figure 4 ($p = 2.14\ rad/sec$, $\alpha = 0.25\ rad$ and $\eta = 0.9$) subjected to a one-sine pulse with $\omega_p/p = 5$. Left: No overturning with $a_p = 6.33\alpha g$, that is slightly larger than the acceleration level, $a_p = 6.32\alpha g$, that created overturning. Center: The block does not overturn even for the acceleration amplitude $a_p = 7.17\alpha g$. Right: The block eventually overturns with $a_p = 7.18\alpha g$, without impact (mode 2) 19

Figure 8: Comparison of overturning acceleration spectra of a slender block ($p = 2.14\ rad/sec$, $\alpha = 0.25\ rad = 14.32°$, $\eta = 0.9$) under a one-sine pulse, computed with the linear and nonlinear formulations. When the frequency of the one-sine pulse is relatively low, both formulations yield comparable results. As the excitation frequency increases, the linear formulation yields minimum overturning acceleration amplitudes drastically larger than those obtained with the nonlinear formulation. This is because under the nonlinear formulation the overturning "bay" generated by mode 1 penetrates further into the safe area under the overturning spectrum due to mode 2. As the excitation frequency further increases the linear and nonlinear formulations again yield comparable results since under both formulations and a high-frequency pulse the block overturns with mode 2..... 22

Figure 9: Comparison of overturning acceleration spectra of a free-standing equipment with $\alpha = 0.349\ rad = 20°$, $p = 2\ rad/sec$ and $\eta = \sqrt{r_{max}} = 0.825$, under a one-sine pulse, computed with the linear and the nonlinear formulation 23

Figure 10: Normalized minimum coefficient of friction over the slenderness of a block that is needed to sustain pure rocking motion 25

Figure 11: Comparison of overturning acceleration spectra of a slender block ($p = 2.14\ rad/sec$, $\alpha = 0.25\ rad = 14.32°$, $\eta = 0.9$) under a one-cosine pulse, computed with the linear and the nonlinear formulation. In this case the difference between the results of the two formulations are less drastic than those observed under a one-sine pulse 26

Figure 12: Rotation and angular velocity time histories of a rigid block ($p = 2.14\ rad/sec$, $\alpha = 0.25\ rad$ and $\eta = 0.9$) subjected to a one-cosine pulse with $\omega_p/p = 3$. Left: $a_p = 1.91\alpha g$, no overturning. Center: $a_p = 1.92\alpha g$, overturning with one impact (mode 1). Right: $a_p = 6.54\alpha g$, overturning with one impact (mode 1).....28

Figure 13: Rotation and angular velocity time histories of the same rigid block as in Figure 9 ($p = 2.14\ rad/sec$, $\alpha = 0.25\ rad$ and $\eta = 0.9$) subjected to a one-cosine pulse with $\omega_p/p = 3$. Left: No overturning with $a_p = 6.55\alpha g$, that is slightly larger than the acceleration level, $a_p = 6.54\alpha g$, that created overturning. Center: The block does not overturn even for the acceleration amplitude $a_p = 11.18\alpha g$. Right: The block eventually overturns with $a_p = 11.19\alpha g$, without impact (mode 2).....29

Figure 14: Comparison of overturning acceleration spectra of a slender block ($\alpha = 0.349\ rad = 20°$, $p = 2.0\ rad/sec$, $\eta = 0.825$) under a one-cosine pulse, computed with the linear and the nonlinear formulation. In this case the difference between the results of the two formulations are less drastic than those observed under a one-sine pulse.....30

Figure 15: Rotation and angular velocity time histories of a rigid block ($b = 0.5\ m$, $h = 1.5\ m$) subjected to the fault-normal and vertical Rinaldi station records. Left: overturning under horizontal component alone (78% acceleration level). Center: overturning under horizontal and vertical components (74% acceleration level). Right: overturning under horizontal and vertical components with reversed polarity (83% acceleration level) 32

Figure 16: Rotation and angular velocity time histories of a rigid block ($b = 0.5\ m$, $h = 1.5\ m$) subjected to the fault-normal and vertical Sylmar station records. Left: overturning under horizontal component alone (118% acceleration level). Center: overturning under horizontal and vertical components (116% acceleration level). Right: overturning under horizontal and vertical components with reversed polarity (120% acceleration level).....33

Figure 17: Rotation and angular velocity time histories of a rigid block ($b = 0.5\ m$, $h = 1.5\ m$) subjected to the N-S and vertical Newhall station records. Left: overturning under horizontal component alone (183% acceleration level). Center: overturning under horizontal and vertical components (186% acceleration level). Right: overturning under horizontal and vertical components with reversed polarity (180% acceleration level).....35

Figure 18: Rotation and angular velocity time histories of a rigid block (*b = 0.5 m, h = 1.5 m*) subjected to the fault-normal and vertical El Centro Array #5 records. Left: overturning under horizontal component alone (129% acceleration level). Center: overturning under horizontal and vertical components (126% acceleration level). Right: overturning under horizontal and vertical components with reversed polarity (130% acceleration level) 36

Figure 19: Rotation and angular velocity time histories of a rigid block (*b = 0.5 m, h = 1.5 m*) subjected to the fault-normal and vertical El Centro Array #6 records. Left: overturning under horizontal component alone (149% acceleration level). Center: overturning under horizontal and vertical components (149% acceleration level). Right: overturning under horizontal and vertical components with reversed polarity (161% acceleration level) 37

Figure 20: Rotation and angular velocity time histories of a rigid block (*b = 0.5 m, h = 1.5 m*) subjected to the fault-normal and vertical El Centro Array #7 records. Left: overturning under horizontal component alone (152% acceleration level). Center: overturning under horizontal and vertical components (152% acceleration level). Right: overturning under horizontal and vertical components with reversed polarity (152% acceleration level) 38

Figure 21: Rotation and angular velocity time histories of a rigid block (*b = 0.5 m, h = 1.5 m*) subjected to the fault-parallel and vertical Los Gatos station records. Left: overturning under horizontal component alone (146% acceleration level). Center: overturning under horizontal and vertical components (145% acceleration level). Right: overturning under horizontal and vertical components with reversed polarity (151% acceleration level)....39

Figure 22: Rotation and angular velocity time histories of a rigid block (*b = 0.5 m, h = 1.5 m*) subjected to the fault-parallel and vertical Lucerne Valley records. Left: overturning under horizontal component alone (275% acceleration level). Center: overturning under horizontal and vertical components (285% acceleration level). Right: overturning under horizontal and vertical components with reversed polarity (295% acceleration level)....40

Figure 23: Rotation and angular velocity spectra due to the fault-normal motion recorded at the Rinaldi station for different values of the coefficient of restitution and various values of block slenderness....42

Figure 24: Rotation and angular velocity spectra due to the fault-normal motion recorded at the Sylmar station for different values of the coefficient of restitution and various values of block slenderness....43

Figure 25: Schematic of an anchored block in rocking motion 46

Figure 26: Moment-rotation curves of: (Top) Free-standing block; (Center) Elastic-brittle anchorage; (Bottom) Anchored block with elastic-brittle restrainers....47

Figure 27: Comparison of overturning acceleration spectra due to a one-sine pulse of an anchored equipment ($\alpha = 0.349\ rad = 20°$, $p = 2\ rad/sec$, $\eta = 0.825$, $q = 5.2\times10^{-4}$ and $\mu = 1$) computed with the nonlinear formulation for $F_u/W = 0$, 0.4 and 1.0 51

Figure 28: Normalized minimum overturning acceleration levels needed to overturn an anchored block (elastic-brittle behavior, $\mu = 1$) to the acceleration levels needed to overturn the same block when it is free standing 52

Figure 29: Comparison of overturning acceleration spectra due to a one-sine pulse of an anchored equipment ($\alpha = 0.349\ rad = 20°$, $p = 2\ rad/sec$, $\eta = 0.825$, $q = 5.2\times10^{-4}$ and $\mu = 1$) computed with the linear formulation for $F_u/W = 0$ and 0.6. Lines: analytical solution. Points: numerical solution 56

Figure 30: Comparison of the overturning acceleration spectra due to a one-sine pulse of an anchored equipment ($\alpha = 0.349\ rad = 20°$, $p = 2\ rad/sec$, $\eta = 0.825$, $q = 5.2\times10^{-4}$ and $\mu = 1$) computed with the linear and nonlinear formulations for $F_u/W = 0.4$ (top) and $F_u/W = 0.6$ (bottom) 58

Figure 31: Force-displacement curve of an element with bilinear behavior 59

Figure 32: Moment-rotation curves of: (Top) Free-standing block; (Center) Elastic-plastic anchorage; (Bottom) Anchored block with elastic-plastic restrainers 61

Figure 33: Overturning acceleration spectra due to a one-sine pulse of an anchored block ($\alpha = 0.349\ rad = 20°$, $p = 2\ rad/sec$, $\eta = 0.825$, $q = 5.2\times10^{-4}$ and $\mu = 5$) with restrainer strength $F_u/W = 0$, 0.4 and 1.0. The solution is computed with the nonlinear formulation 64

Figure 34: Normalized minimum overturning acceleration levels needed to overturn an anchored block (elastic-plastic behavior, $\mu = 5$) to the acceleration level needed to overturn the same block when it is free standing. When $\omega_p/p > 4$ blocks should not be anchored since the effect of the restrainers is destructive or virtually insignificant 66

Figure 35: Comparison of overturning acceleration spectra computed with the nonlinear formulation for an anchored block ($\alpha = 0.349\ rad = 20°$, $p = 2\ rad/sec$, $\eta = 0.825$ and $q = 5.2\times10^{-4}$) with two levels of ductility: $\mu = 1$ and $\mu = 5$. Top: $F_u/W = 0.4$; Bottom: $F_u/W = 1.0$ 67

Figure 36: Fault-normal components of the acceleration, velocity and displacement time histories recorded at the Rinaldi station during the January 17, 1994, Northridge, California earthquake (left), a cycloidal type-A pulse (center), and a cycloidal type-B pulse (right) 70

Figure 37: Rotation and angular velocity time histories of an anchored block ($b = 0.5\ m$, $h = 1.5\ m$, $F_u/W = 0.4$) subjected to the fault-normal Rinaldi station motion. An 88% acceleration level is capable of overturning the block with restrainers exhibiting ductility $\mu = 1$ 72

Figure 38: Rotation and angular velocity time histories of an anchored block ($b = 0.5\ m$, $h = 1.5\ m$, $F_u/W = 0.4$) subjected to the fault-normal Rinaldi station motion. A 93% acceleration level is capable of overturning the block with restrainers exhibiting ductility $\mu = 5$; whereas when $\mu = 10$ the block survives 73

Figure 39: Rotation and angular velocity time histories of an anchored block ($b = 0.5\ m$, $h = 1.5\ m$, $F_u/W = 0.4$, $\mu = 10$) subjected to the fault-normal Rinaldi station motion. Left: no overturning (98% acceleration level). Right: overturning (99% acceleration level) 74

Figure 40: Rotation and angular velocity time histories of the free-standing block ($b = 1.0\ m$, $h = 3.0\ m$) subjected to the fault-normal Rinaldi station motion. Left: no overturning (126% acceleration level). Right: overturning (127% acceleration level).....76

Figure 41: Rotation and angular velocity time histories of a larger anchored block ($b = 1.0\ m$, $h = 3.0\ m$, $F_u/W = 0.4$ and $\mu = 5$) subjected to the fault-normal Rinaldi station motion. Left: no overturning (118% acceleration level). Right: overturning (119% acceleration level). The free-standing block can survive a stronger acceleration level than the anchored block (see Figure 40) 77

LIST OF TABLES

Table 1: Minimum level of acceleration records needed to overturn a $0.5\ m \times 1.5\ m$ free-standing block ($\alpha = 18.43°$, $p = 2.157\ rad/sec$) 34

Table 2: Geometrical, physical and structural parameters of electrical equipment. 50

ACKNOWLEDGMENTS

The work described in this report was funded by the Pacific Earthquake Engineering Research (PEER) Center under the Pacific Gas & Electric Company Contract No. 09566. This financial support is gratefully acknowledged.

The valuable input and comments of Dr. Norman Abrahamson, Mr. Eric Fujisaki, and Mr. Henry Ho are greatly appreciated. Professor Gregory Fenves's efforts to coordinate this task are also acknowledged.

This work made use of Pacific Earthquake Engineering Research Center Shared Facilities supported by the Earthquake Engineering Research Center Program of the National Science Foundation under Award Number EEC-9701568.

CHAPTER 1
INTRODUCTION

The study of the rocking response and overturning of electrical equipment to near-source ground motions was motivated by the proximity of electric power substations in major urban areas to active faults. In the Bay Area the San Andreas fault runs 10 km west of San Francisco; the Hayward fault runs less than 10 km from most of Oakland; additionally, other smaller nearby faults such as the Rodgers Creek, Gregorio, Calaveras, Concord, and Green Valley faults have the potential to subject urban areas to strong ground motions. Similarly, a large part of metropolitan Los Angeles lies over buried thrust faults capable of generating strong motions like those recorded during the January 17, 1994, Northridge earthquake. The city of Kobe, Japan, was devastated by the January 17, 1995, Hyogoken-Nanbu earthquake, which generated unusually strong motions. Figure 1 shows electrical equipment at the Sylmar Converter Station that overturned during the 1971 San Fernando, California, earthquake.

In a recent study the transient response of a free-standing equipment subjected to horizontal pulse-type and near-source ground motions was investigated in depth (Makris and Roussos 1998). What makes these motions particularly destructive to a variety of structures is not only their occasionally high peak-ground acceleration, but also the area under the relatively long-duration acceleration pulse. This area represents the “incremental” ground velocity (Anderson and Bertero 1986), which is the net increment of the ground velocity along a monotonic segment of its time history. Such velocity increments are of the order of 0.5 m/sec or even higher. Although they do not happen very fast to generate an excessive ground acceleration, they happen at just the right pace to generate devastating shears at the base of flexible structures (Bertero et al. 1978; Anderson and Bertero 1986; Hall et al. 1995). The Makris and Roussos study showed that near-source ground motions do not bear any exceptional overturning potential for electrical equipment. This finding is because typical electrical equipments have dynamic properties that are too stiff to be resonated by the two- or three-second long coherent pulse of the near-source ground motion. In that study it was found that the toppling of smaller blocks is more sensitive to the peak ground acceleration; whereas, the toppling of larger blocks depends mostly on the incremental ground velocity. Accordingly, a smaller block will overturn due to the high-frequency fluctuations that override the long-duration pulse; whereas a larger block will overturn due to the long-duration pulse. In this light the overturning response of free-standing equipment was shown to be quite

Figure 1. Overturned electrical equipment at Sylmar Converter Station damaged after the 1971 San Fernando earthquake. Top: Front view. Bottom: Side view --- Steinbrugge collection, PEER, University of California, Berkeley

ordered and predictable despite the presence of the high-frequency content that overrides the coherent component of near-source ground motions.

After having established that peak ground acceleration controls the overturning of electrical equipment, in this study the rocking stability of electrical equipment is further investigated by looking into several practical issues such as (1) the effect of the vertical component of the ground motion; (2) the effect of an increasingly inelastic coefficient of restitution; and (3) the efficiency of typical anchorages used to prevent toppling.

In Chapter 2, the rocking response of a free-standing block subjected to a one-sine (Type-A) pulse and one-cosine (Type-B) pulses is revisited. The study reveals that blocks can overturn with two distinct modes: (a) by exhibiting one impact (mode 1) and (b) without impact (mode 2). The second mode (no impact) is responsible for the existence of a safe region that is located over the minimum overturning acceleration spectrum. The shape of this safe region depends on the coefficient of restitution and is sensitive to the nonlinear nature of the problem. The transition from mode 1 to mode 2 is sudden and results in a finite jump in the minimum overturning acceleration spectrum. In a recent study, Anooshehpoor et al. (1999) attempted to construct the minimum overturning acceleration spectra due to one-sine pulse. Their study failed to identify the second mode of overturning (without impact) and to indicate the presence of the aforementioned safe region. These conceptual oversights in the paper by Anooshehpoor et al. have been addressed in detail in the discussion by Zhang and Makris (1999). Chapter 3 concentrates on the effect of the vertical component of the ground motion, which is found to be negligible.

In Chapter 4 the rocking response and overturning of anchored blocks is investigated in depth. Restrainers with elastic-brittle and elastic-plastic behavior are considered. The elastic-plastic behavior is approximated with the Bouc-Wen hysteretic model. It is found that the restrainers are more efficient in preventing overturning of small slender blocks. Larger blocks overturn only without experiencing any impact, and in this case the effect of restrainers is marginal even when their strength equals the weight of the equipment. Easy-to-use graphs are offered to evaluate the effect of anchorages with various strength and ductility. Chapter 5 concentrates on the rocking response of anchored equipment subjected to selected recorded ground motions. Similar trends to those identified under a cycloidal pulse excitation are observed. Chapter 6 is devoted to a summary of the findings and conclusions.

CHAPTER 2
REVIEW OF THE ROCKING RESPONSE OF A FREE-STANDING BLOCK

2.1 Condition for Initiation of Rocking Motion

We consider the rigid block shown on Figure 2 (top) which can oscillate about the centers of rotation O and O' when it is set to rocking. Depending on the level and form of the ground acceleration, the block may translate with the ground, slide, rock or slide-rock. Prior to 1996, the mode of rigid-body motion that prevailed has been determined by comparing the available static friction to the width-to-height ratio of the block, irrespective of the magnitude of the horizontal ground acceleration. Shenton (1996) indicated that in addition to pure sliding and pure rocking, there is a slide-rock mode and its manifestation depends not only on the width-to-height ratio and the static friction coefficient, but also on the magnitude of the base acceleration.

Physically realizable cycloidal pulses have displacement histories which are continuous and differentiable signals that build up gradually from zero. Their corresponding acceleration histories might be zero at the time origin or exhibiting a finite value that can be as large as their maximum amplitude. Figure 3 plots the acceleration, velocity and displacement histories of a one-sine pulse (left) and one-cosine pulse (right). In the case of the one-sine pulse the ground acceleration is zero at the initiation of motion and builds up gradually. In contrast, in the case of a one-cosine pulse, the ground acceleration assumes its maximum value at the initiation of motion. Under other cycloidal pulses such as Type-C_n pulses (Makris and Chang 1998) the ground acceleration is finite at the initiation of motion but assumes a value that is smaller than its maximum amplitude a_p. With reference to Figure 2 and assuming that the coefficient of friction $\mu > \frac{b}{h} = \tan\alpha$, static equilibrium yields that the minimum horizontal acceleration that is needed to initiate rocking is $a_{p,\,min} = g\tan\alpha$. Consequently, pulses with amplitude $a_p > g\tan\alpha$ will induce rocking to a rectangular block with slenderness α.

Consider a cycloidal pulse with acceleration amplitude $a_p > g\tan\alpha$ and let, λa_p, to be the value of the ground acceleration when a block with slenderness α is about to enter rocking motion. Depending on the type of pulse, λ assumes different values; however it is bounded by

$$\frac{g\tan\alpha}{a_p} < \lambda \le 1 \tag{2-1}$$

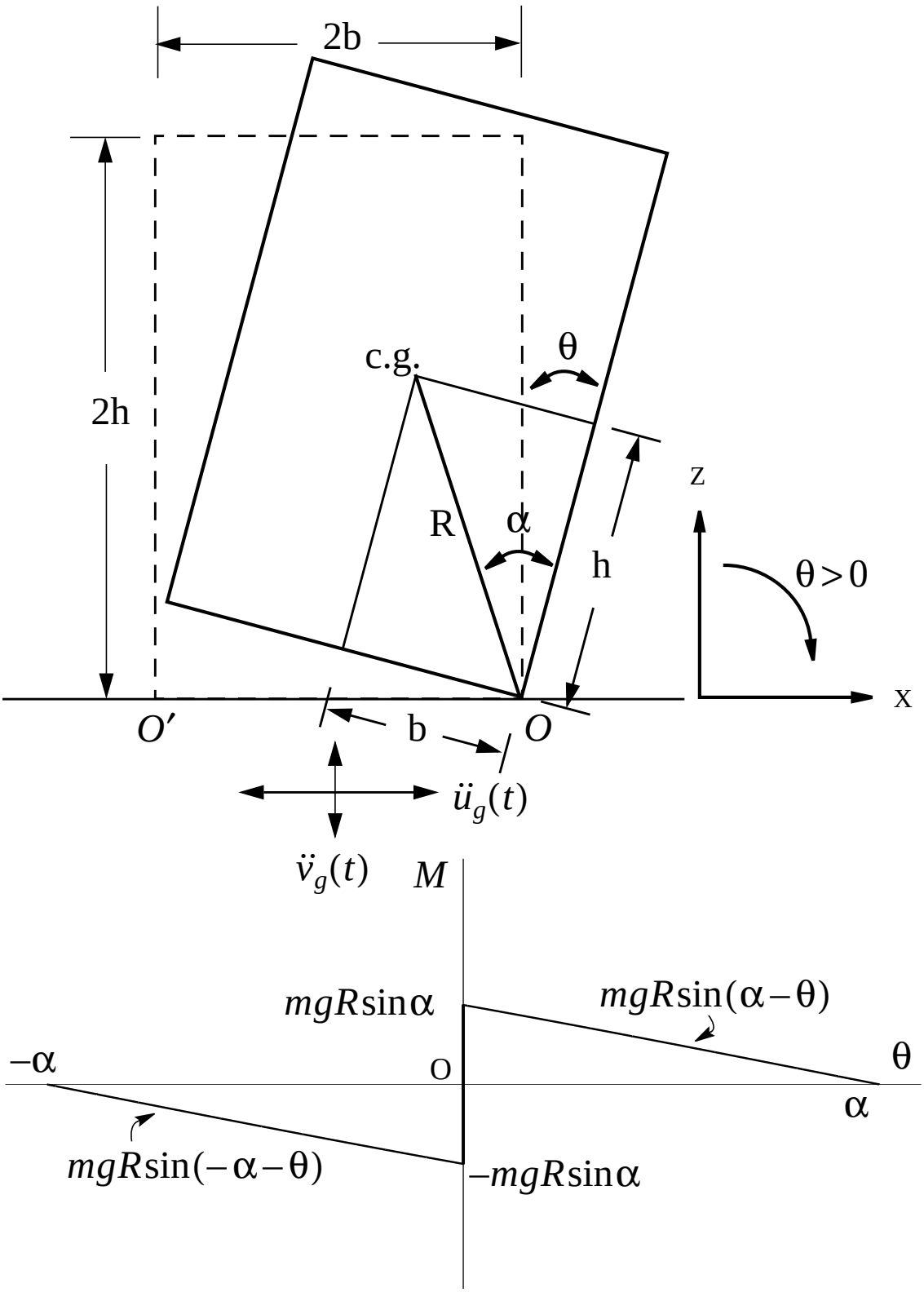

Figure 2. Schematic of a free-standing block in rocking motion (top); and its moment rotation diagram (bottom)

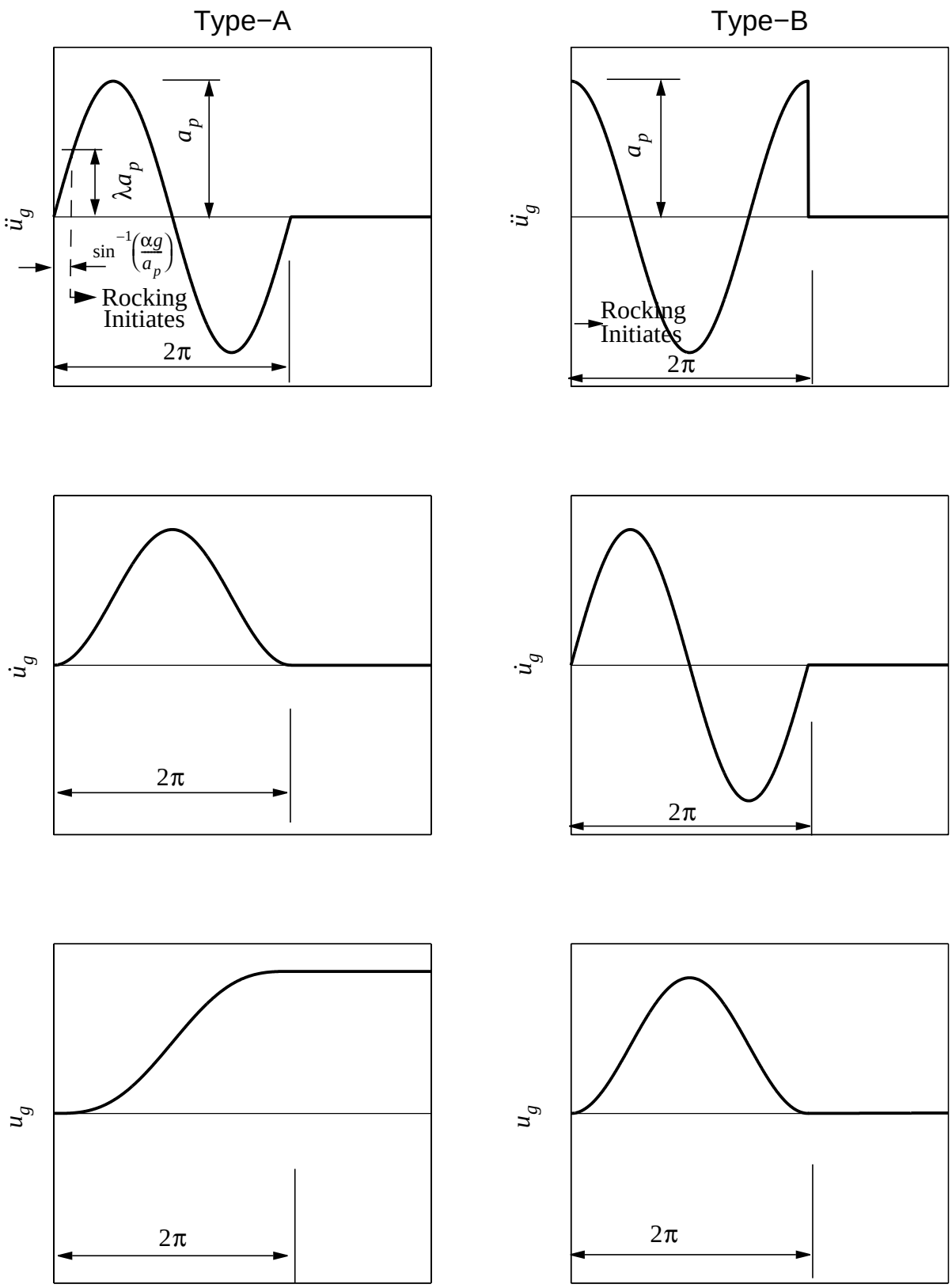

Figure 3. Acceleration, velocity, and displacement histories of a one-sine pulse (left) and a one-cosine pulse (right)

Figure 4 shows the free-body diagram of a free-standing block that is about to enter rocking motion due to a positive ground acceleration. With the system of axis shown, a positive acceleration will induce an initial negative rotation ($\theta < 0$). Adopting the notation introduced by Shenton (1996), let f_x and f_z be the horizontal and vertical reactions at the tip O' of the block. Dynamic equilibrium at this instant gives

$$f_x = m(\lambda a_p + h\ddot{\theta}) \tag{2-2}$$

$$f_z = m(g - b\ddot{\theta}) \tag{2-3}$$

$$I_{cg}\ddot{\theta} = -f_x h + f_z b \tag{2-4}$$

where I_{cg} is the moment of inertia of the block about its center of gravity (for rectangular blocks $I_{cg} = mR^2/3$). Substitution of (2-2) and (2-3) into (2-4) gives the value of the angular acceleration, $\ddot{\theta}_0$, at the instant when rocking initiates

$$\ddot{\theta}_0 = -p^2 \frac{h}{R} \tan\alpha \left(\frac{\lambda a_p}{g \tan\alpha} - 1 \right) \tag{2-5}$$

in which $p = \sqrt{3g/(4R)}$ is the frequency parameter of the block and is a quantity in rad/sec, whereas $R = \sqrt{b^2 + h^2}$ is the half diameter of the block — a measure of its size. In order to avoid sliding at this instant

$$\frac{f_x}{f_z} \le \mu \tag{2-6}$$

and substitution of the value computed by (2-5) into (2-2) and (2-3) gives the condition for a block to rock without sliding

$$\frac{\lambda a_p - \frac{3}{4} g \cos\alpha \sin\alpha \left(\lambda \frac{a_p}{g \tan\alpha} - 1 \right)}{g + \frac{3}{4} g \sin^2\alpha \left(\lambda \frac{a_p}{g \tan\alpha} - 1 \right)} \le \mu \tag{2-7}$$

Equation (2-7), initially presented by Shenton (1996), indicates that under some excitation pulses with amplitude a_p, the condition for a block to enter rocking motion without sliding depends on the value of a_p. However, this is true only for pulses that have a finite acceleration at the initiation of motion. For pulses that their acceleration history build up gradually (such as a one-sine pulse), the value of λa_p at the initiation of rocking is equal to $g \tan\alpha$ and equation (2-7) reduces to

$$\tan\alpha = \frac{b}{h} \le \mu \tag{2-8}$$

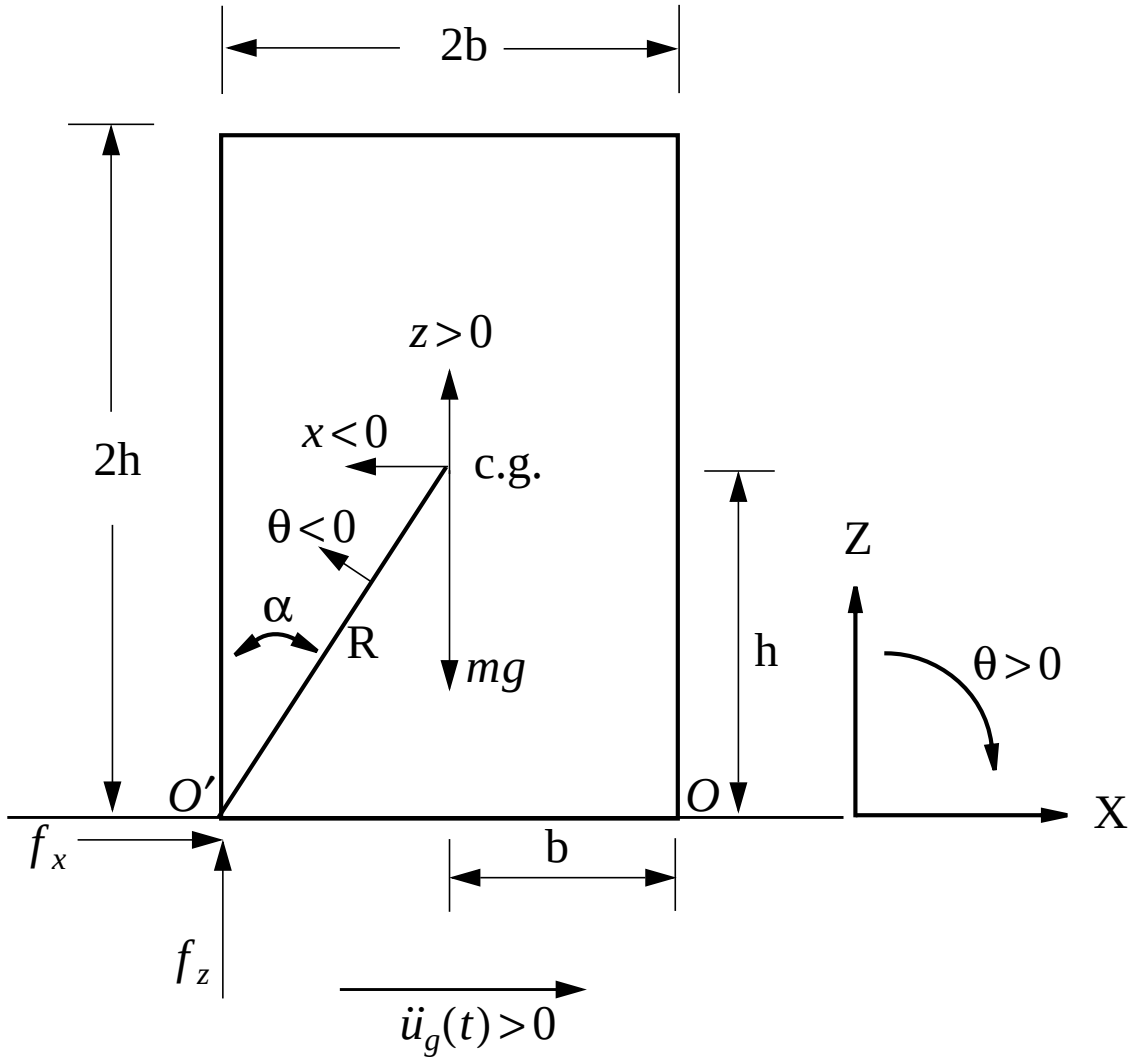

Figure 4. Free-body diagram of a rigid block at the instant that enters rocking

which is the traditional condition imposed in order for rocking to prevail. Consequently, the slide-rock mode introduced by Shenton (1996) will develop only under excitations with non-zero acceleration at the initiation of the motion.

2.2 Governing Equations Under Rocking Motion

Under a positive horizontal ground acceleration and assuming that the coefficient of friction is large enough so that there is no sliding, the block will initially rotate with a negative rotation, $\theta < 0$, and if it does not overturn, it will eventually assume a positive rotation, and so forth. The equations that govern the rocking motion under the simultaneous presence of horizontal, $\ddot{u}_g(t)$, and vertical, $\ddot{v}_g(t)$ ground acceleration are

$$I_0\ddot{\theta}(t) + mg\left(1 + \frac{\ddot{v}_g(t)}{g}\right)R\sin(-\alpha-\theta) = -m\ddot{u}_g(t)R\cos(-\alpha-\theta) \ , \ \theta < 0 \tag{2-9}$$

and

$$I_0\ddot{\theta}(t) + mg\left(1 + \frac{\ddot{v}_g(t)}{g}\right)R\sin(\alpha-\theta) = -m\ddot{u}_g(t)R\cos(\alpha-\theta) \ , \ \theta > 0 \tag{2-10}$$

Equation (2-9) and (2-10) are well known in the literature (Yim et al. 1980) and are valid for arbitrary values of the angle $\alpha = \operatorname{atan}(b/h)$. For rectangular blocks, $I_0 = \frac{4}{3}mR^2$, equation (2-9) and (2-10) can be expressed in the compact form

$$\ddot{\theta}(t) = -p^2\left\{\sin[\alpha\operatorname{sgn}[\theta(t)] - \theta(t)]\left(1 + \frac{\ddot{v}_g(t)}{g}\right) + \frac{\ddot{u}_g}{g}\cos[\alpha\operatorname{sgn}[\theta(t)] - \theta(t)]\right\} \tag{2-11}$$

where $p = \sqrt{\frac{3g}{4R}}$ is the frequency parameter of the block. The larger the block (larger *R*), the smaller *p*. The oscillation frequency of a rigid block under free vibration is not constant since it strongly depends on the vibration amplitude (Housner 1963). Nevertheless, the quantity *p* is a measure of the dynamic characteristics of the block. For an electrical transformer, $p \approx 2 \ rad/sec$, and for a household brick, $p \approx 8 \ rad/sec$.

Figure 2 (bottom) shows the moment-rotation relation during the rocking motion of a free-standing block. The system has infinite stiffness until the magnitude of the applied moment reaches $mgR\sin\alpha$, and once the block is rocking its stiffness decreases monotonically, reaching zero when $\theta = \alpha$. During the oscillatory rocking motion, the moment-rotation curve follows this curve without enclosing any area. Energy is lost only during impact when the angle of rotation reverses.

When the angle of rotation reverses, it is assumed that the rotation continues smoothly from point O to O'. Conservation of momentum about point O' just before the impact and right after the impact gives

$$I_0\dot{\theta}_1 - m\dot{\theta}_1 2bR\sin(\alpha) = I_0\dot{\theta}_2 \ , \tag{2-12}$$

where $\dot{\theta}_1$ is the angular velocity just prior to the impact, and $\dot{\theta}_2$ is the angular velocity right after the impact. The ratio of kinetic energy after and before the impact is

$$r = \frac{\dot{\theta}_2^2}{\dot{\theta}_1^2}, \tag{2-13}$$

which means that the angular velocity after the impact is only $\sqrt{r}$ times the velocity before the impact. Substitution of (2-13) into (2-12) gives

$$r = \left[1 - \frac{3}{2}sin^2\alpha\right]^2 . \tag{2-14}$$

The value of the coefficient of restitution given by (2-14) is the maximum value of *r* under which a block with slenderness, α, will undergo rocking motion. Consequently, in order to observe rocking motion the impact has to be inelastic. The less slender a block (larger α) the more plastic the impact, and for the value of $\alpha = \sin^{-1}\sqrt{2/3} = 54.73°$, the impact is perfectly plastic. During the rocking motion of slender blocks, if additional energy is lost due to interface mechanisms, the value of the true coefficient of restitution, *r*, will be less than the one computed from (2-14). The effect of the coefficient of restitution on the rocking response of free-standing blocks is shown later in this study.

In this chapter the rocking response of a free-standing block subjected to simple trigonometric pulses is revisited since new findings further elucidate the complex dynamic nature of the rocking problem.

The response of a free-standing block subjected to various horizontal cycloidal pulses, with frequency ω_p, such as one-sine pulse (Type-A pulse), a one-cosine pulse (Type-B pulse) and pulses with n-cycles in their displacement histories (Type-C_n pulses) was investigated in a recent study by Makris and Roussos (1998). That study was motivated by an increasing number of ground motions, recorded near the source of strong earthquakes, that contain one or more relatively long-duration coherent pulses. In view of the relatively long duration of the coherent pulses, the range of interest of the frequency ratio, ω_p/p, for electrical equipment with $p \approx 2\ rad/sec$ is $0 \le \omega_p/p \le 3$. Within this range of excitation frequencies ($0 \le \omega_p/p \le 3$), the minimum over-

turning acceleration spectrum of cycloidal pulses is nearly linear; Makris and Roussos (1998) proposed the approximate expression

$$\frac{a_{p0}}{\alpha g} \approx 1 + \beta \frac{\omega_p}{p} \tag{2-15}$$

where a_{p0} is the minimum overturning acceleration of the pulse and α is the angle of the block slenderness. The coefficient $\beta = 1/6$ for Type-A or -C_n pulses, and $\beta = 1/4$ for a Type-B pulse.

For values of $\omega_p/p \geq 3$ the minimum overturning acceleration spectra become increasingly nonlinear. Although the range of $\omega_p/p \geq 3$ is not of central interest in evaluating the overturning potential of near-source ground motions, it is of prime interest when the overturning of a block is the result of a high-frequency spike of short duration.

2.3 Rocking Response to a One-sine (Type-A) Pulse

The analysis presented in this section concentrates on the overturning potential of a one-sine pulse with ground acceleration

$$\ddot{u}_g(t) = \begin{cases} a_p \sin(\omega_p t + \psi) & -\psi/\omega_p \leq t \leq (2\pi - \psi)/\omega_p \\ 0 & otherwise \end{cases} \tag{2-16}$$

where $\psi = \sin^{-1}(\alpha g/a_p)$ is the phase angle when rocking initiates. At this instant $\ddot{u}_g(0) = \alpha g = \lambda a_p$ and according to equation (2-8) the condition for the block to enter pure rocking is $\tan\alpha = \frac{b}{h} < \mu$.

2.3.1 Linear Formulation

For tall, slender blocks, the angle $\alpha = \operatorname{atan}(b/h)$ is relatively small, and equations (2-9) and (2-10) can be linearized. Within the limits of the linear approximation and for a horizontal ground acceleration given by (2-16), equations (2-9) and (2-10) become

$$\ddot{\theta}(t) - p^2\theta(t) = -\frac{a_p}{g} p^2 \sin(\omega t + \psi) + p^2\alpha, \ \theta < 0 \tag{2-17}$$

and

$$\ddot{\theta}(t) - p^2\theta(t) = -\frac{a_p}{g} p^2 \sin(\omega t + \psi) - p^2\alpha, \ \theta > 0 \tag{2-18}$$

where $p = \sqrt{3g/(4R)}$ is the frequency parameter of a rectangular block with a half diagonal = R. The integration of (2-17) and (2-18) gives

$$\theta(t) = A_1 \sinh(pt) + A_2 \cosh(pt) - \alpha + \frac{1}{1+\frac{\omega_p^2}{p^2}} \frac{a_p}{g} \sin(\omega_p t + \psi)\,,\ \theta < 0 \tag{2-19}$$

and

$$\theta(t) = A_3 \sinh(pt) + A_4 \cosh(pt) + \alpha + \frac{1}{1+\frac{\omega_p^2}{p^2}} \frac{a_p}{g} \sin(\omega_p t + \psi)\,,\ \theta > 0 \tag{2-20}$$

where

$$A_1 = A_3 = \frac{\dot{\theta}_0}{p} - \frac{\omega_p/p}{1+\omega_p^2/p^2} \frac{a_p}{g} \cos(\psi) = \frac{\dot{\theta}_0}{p} - \alpha \frac{\omega_p/p}{1+\omega_p^2/p^2} \frac{\cos(\psi)}{\sin(\psi)}\,, \tag{2-21}$$

$$A_2 = \theta_0 + \alpha - \frac{1}{1+\omega_p^2/p^2} \frac{a_p}{g} \sin(\psi) = \theta_0 + \alpha - \frac{\alpha}{1+\omega_p^2/p^2}\,, \tag{2-22}$$

$$A_4 = \theta_0 - \alpha - \frac{1}{1+\omega_p^2/p^2} \frac{a_p}{g} \sin(\psi) = \theta_0 - \alpha - \frac{\alpha}{1+\omega_p^2/p^2}\,. \tag{2-23}$$

The time histories for the angular velocities are directly obtained from the time derivatives of (2-19) and (2-20)

$$\dot{\theta}(t) = pA_1 \cosh(pt) + pA_2 \sinh(pt) + \frac{\omega_p}{1+\frac{\omega_p^2}{p^2}} \frac{a_p}{g} \cos(\omega_p t + \psi)\,,\ \theta < 0 \tag{2-24}$$

and

$$\dot{\theta}(t) = pA_3 \cosh(pt) + pA_4 \sinh(pt) + \frac{\omega_p}{1+\frac{\omega_p^2}{p^2}} \frac{a_p}{g} \cos(\omega_p t + \psi)\,,\ \theta > 0 \tag{2-25}$$

The solutions given by equations (2-19) and (2-20) can be pieced together to construct the time history of the rocking response under a given acceleration amplitude, a_p. Furthermore, this solution can provide the minimum overturning acceleration amplitude, provided that a condition of overturning is available.

Under the minimum acceleration amplitude blocks overturn during their free-vibration regime at a theoretically infinite large time when the velocity tends to reach a local minimum (Makris and Roussos 1998). Accordingly the condition for overturning is that

$$\ddot{\theta}(t_\infty) = 0 \tag{2-26}$$

where t_∞ is a sufficiently large time where $\tanh(pt_\infty) = 1$.

Under a one-sine pulse, a free-standing block has two modes of overturning: (a) overturning with one impact (mode 1) and (b) overturning with no impact (mode 2). This result is true as long as ω_p/p is sufficiently small. As ω_p/p increases the first mode of impact vanishes, and the block overturns only without impact (mode 2). Accordingly, in order to back-figure the minimum overturning acceleration amplitude by imposing the condition of overturning given by (2-26) it is necessary to distinguish between mode 1 and mode 2.

Mode 1

Denoting by t_{fv}, the time when the block enters its free vibration regime, the condition for overturning after the block has experienced one impact (mode 1) is

$$\dot{\theta}(t_{fv}) + p[\theta(t_{fv}) - \alpha] = 0 \tag{2-27}$$

In the case where the impact happens before the excitation expires ($t_i < T_{ex}$), then $t_{fv} = T_{ex} = (2\pi - \psi)/\omega_p$ (CASE 1). In the case where the impact happens after the excitation expires ($t_i > T_{ex}$), then $t_{fv} = t_i$ (CASE 2).

CASE 1 ($t_i < T_{ex}$).

In this case the condition of overturning given by (2-26) yields:

$$\dot{\theta}(T_{ex}) + p[\theta(T_{ex}) - \alpha] = 0 \tag{2-28}$$

where

$$\theta(T_{ex}) = A_3 \sinh[p(T_{ex} - t_i)] + A_4 \cosh[p(T_{ex} - t_i)] + \alpha + \frac{a_p/g}{1 + \left(\frac{\omega_p}{p}\right)^2} \sin(\omega_p T_{ex} + \psi) \tag{2-29}$$

$$\dot{\theta}(T_{ex}) = pA_3 \cosh[p(T_{ex} - t_i)] + pA_4 \sinh[p(T_{ex} - t_i)] + \frac{\omega_p (a_p/g)}{1 + \left(\frac{\omega_p}{p}\right)^2} \cos(\omega_p T_{ex} + \psi) \tag{2-30}$$

where

$$A_3 = \frac{\eta \dot{\theta}^{before}(t_i)}{p} - \frac{\omega_p/p}{1 + \left(\frac{\omega_p}{p}\right)^2} \frac{a_p}{g} \cos(\omega_p t_i + \psi)\,, \tag{2-31}$$

$$A_4 = -\alpha - \frac{1}{1 + \left(\frac{\omega_p}{p}\right)^2} \frac{a_p}{g} \sin(\omega_p t_i + \psi)\,, \tag{2-32}$$

and η is the coefficient of restitution. The time of impact t_i is related to the acceleration amplitude, $a_p = \alpha g/\sin\psi$, with the expression

$$\tan\psi = \frac{\sin(\omega_p t_i) - \frac{\omega_p}{p}\sinh(p t_i)}{1 + \left(\frac{\omega_p}{p}\right)^2 - \left(\frac{\omega_p}{p}\right)^2 \cosh(p t_i) - \cos(\omega_p t_i)} \tag{2-33}$$

The condition of overturning given by (2-28) takes the form

$$(A_3 + A_4) e^{p(T_{ex} - t_i)} + \frac{\omega_p / p}{1 + \left(\frac{\omega_p}{p}\right)^2} \frac{a_p}{g} = 0 \tag{2-34}$$

where A_3 and A_4 are given by (2-31) and (2-32) and t_i is the solution of (2-33). The value of $a_p/(\alpha g)$ that satisfies (2-34) is the minimum overturning acceleration. Equation (2-34) is valid when $t_i \le T_{ex}$. Within the limits of the linear approximation (slender block) and assuming a value of $\eta = 0.9$, this happens when $0 \le \omega_p / p \le 4.8$.

CASE 2 ($t_i > T_{ex}$)

In this case the condition of overturning yields:

$$\dot{\theta}^{after}(t_i) - p\alpha = 0 \tag{2-35}$$

where $\dot{\theta}^{after}(t_i) = \eta \dot{\theta}^{before}(t_i)$, and

$$\begin{aligned} \dot{\theta}^{before}(t_i) = & \frac{\alpha\omega_p}{1 + \frac{\omega_p^2}{p^2}} \left[\frac{1}{\sin\psi} - \frac{\cosh(pT_{ex})}{\tan\psi} + \frac{\omega_p}{p}\sinh(pT_{ex}) \right] \cosh[p(t_i - T_{ex})] \\ & + \frac{\alpha\omega_p}{1 + \frac{\omega_p^2}{p^2}} \left[-\frac{\sinh(pT_{ex})}{\tan\psi} + \frac{\omega_p}{p}\cosh(pT_{ex}) \right] \sinh[p(t_i - T_{ex})] \end{aligned} . \tag{2-36}$$

In the above equations the impact time t_i is the solution of the transcendental equation

$$\begin{aligned} g(t_i, \psi) = & \frac{\alpha(\omega_p/p)}{1 + (\omega_p/p)^2} \Bigg(\left[\frac{1}{\sin\psi} - \frac{\cosh(pT_{ex})}{\tan\psi} + \frac{\omega_p}{p}\sinh(pT_{ex}) \right] \sinh[p(t_i - T_{ex})] + \\ & \left[-\frac{\sinh(pT_{ex})}{\tan\psi} + \frac{\omega_p}{p}\cosh(pT_{ex}) \right] \cosh[p(t_i - T_{ex})] - \alpha \Bigg) = 0 \end{aligned} \tag{2-37}$$

The solution of equations (2-35) and (2-37) gives the minimum overturning acceleration for the case $t_i > T_{ex}$.

Mode 2

Under this mode, the block does not experience any impact. The condition of overturning becomes

$$\frac{\dot{\theta}(T_{ex})}{p} + [\theta(T_{ex}) + \alpha] = 0 \tag{2-38}$$

where

$$\theta(T_{ex}) = \frac{\alpha(\omega_p/p)}{1+(\omega_p/p)^2}\left[-\frac{\sinh(pT_{ex})}{\tan\psi} + \frac{\omega_p}{p}\cosh(pT_{ex})\right] - \alpha \tag{2-39}$$

$$\dot{\theta}(T_{ex}) = \frac{\alpha\omega_p}{1+(\omega_p/p)^2}\left[-\frac{\cosh(pT_{ex})}{\tan\psi} + \frac{\omega_p}{p}\sinh(pT_{ex}) + \frac{1}{\sin\psi}\right] \tag{2-40}$$

The substitution of (2-39) and (2-40) into (2-38) leads to

$$\frac{\omega_p}{p}\sin\psi - \cos\psi = -e^{\frac{p}{\omega_p}(2\pi-\psi)} \tag{2-41}$$

The solution of (2-41) gives the minimum acceleration amplitude that is capable of overturning the block without any impact. Equation (2-41) is similar to equation (2) of the prologue; however, the duration of the forced vibration due to a one-sine pulse is $T_{ex} = (2\pi - \psi)/\omega_p$, rather than $T_{ex} = (\pi - \psi)/\omega_p$, which is the duration of the forced vibration under a half-sine pulse; and the sign in front of the exponential term in the right-hand side is negative rather than positive.

Figure 5 plots the solutions of the condition of overturning (for $\eta = 0.9$) after distinguishing carefully between mode 1 and mode 2 of overturning. Although the roots are computed numerically, this solution is referred to as an *analytical solution* since it is based on the analytical expressions of the response given by (2-19) and (2-20).

The distinction between mode 1 and mode 2 of overturning is of particular interest since the transition from overturning with one impact to overturning without impact is not immediate; and there is a finite margin of acceleration amplitudes with magnitudes larger than the minimum overturning acceleration (that corresponds to mode 1) that are unable to overturn the block. This interesting behavior is illustrated in Figures 6 and 7, where response time histories of a free-standing block with $p = 2.14$, $\alpha = 0.25$, $\eta = 0.9$ and $\omega/p = 5$ are shown for various levels of the amplitude, a_p, of the acceleration pulse.

The left and center plots in Figure 6 show normalized rotations and angular velocity histories at the verge of overturning due to the first (minimum) level of the acceleration amplitude. With $a_p = 3\alpha g$ the block does not overturn; whereas when $a_p = 3.01\alpha g$ the block overturns after experiencing one impact (mode 1). In this case the impact happens after the expiration of the pulse. A similar pattern of overturning prevails until the acceleration amplitude reaches,

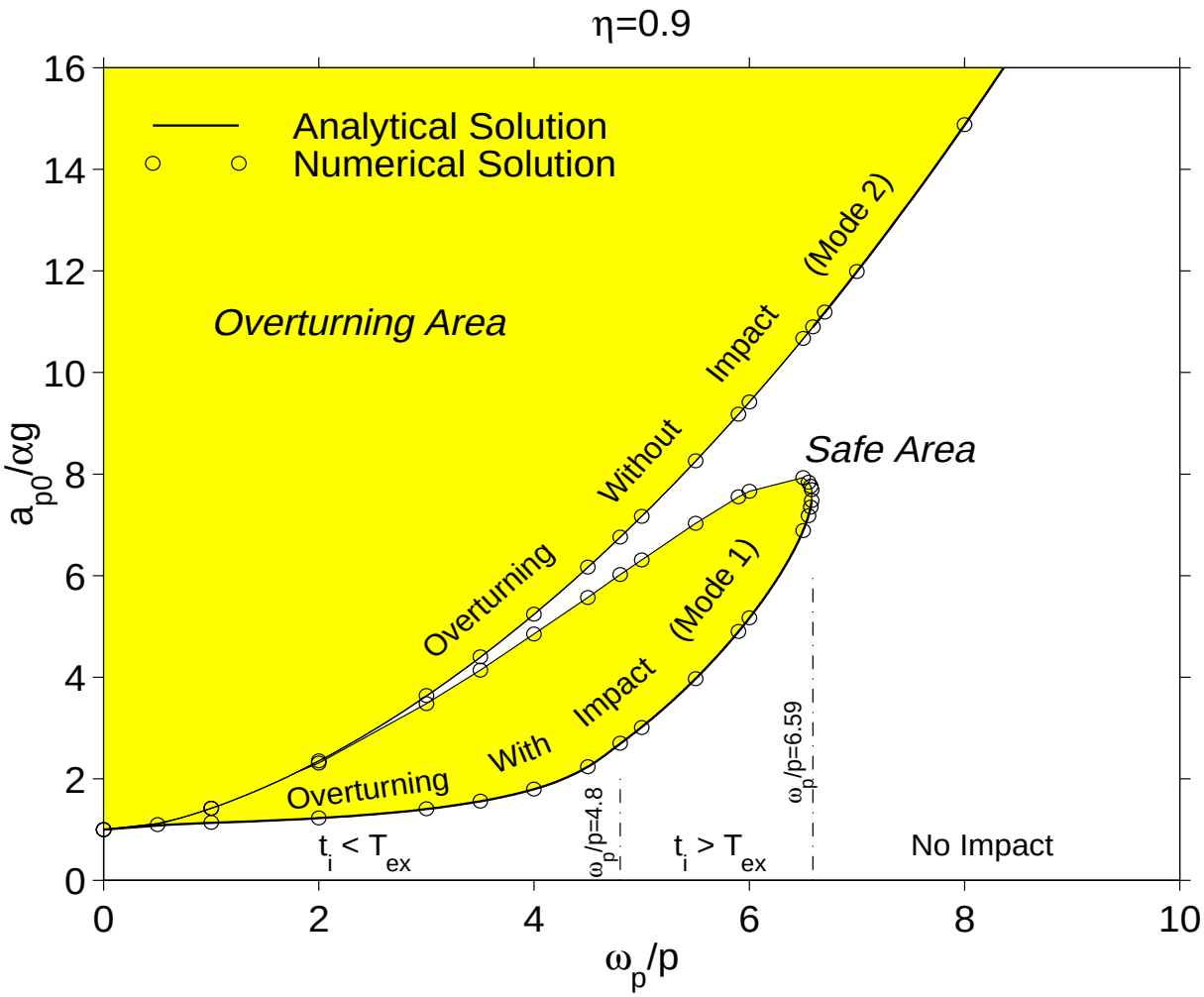

Figure 5. Overturning acceleration spectrum of a free-standing block with $\eta = 0.9$ subjected to a one-sine acceleration pulse with frequency ω_p. The analytical and numerical solutions shown are computed with the linear formulation. When ω_p / p is sufficiently large, a free-standing block overturns only without impact (mode 2).

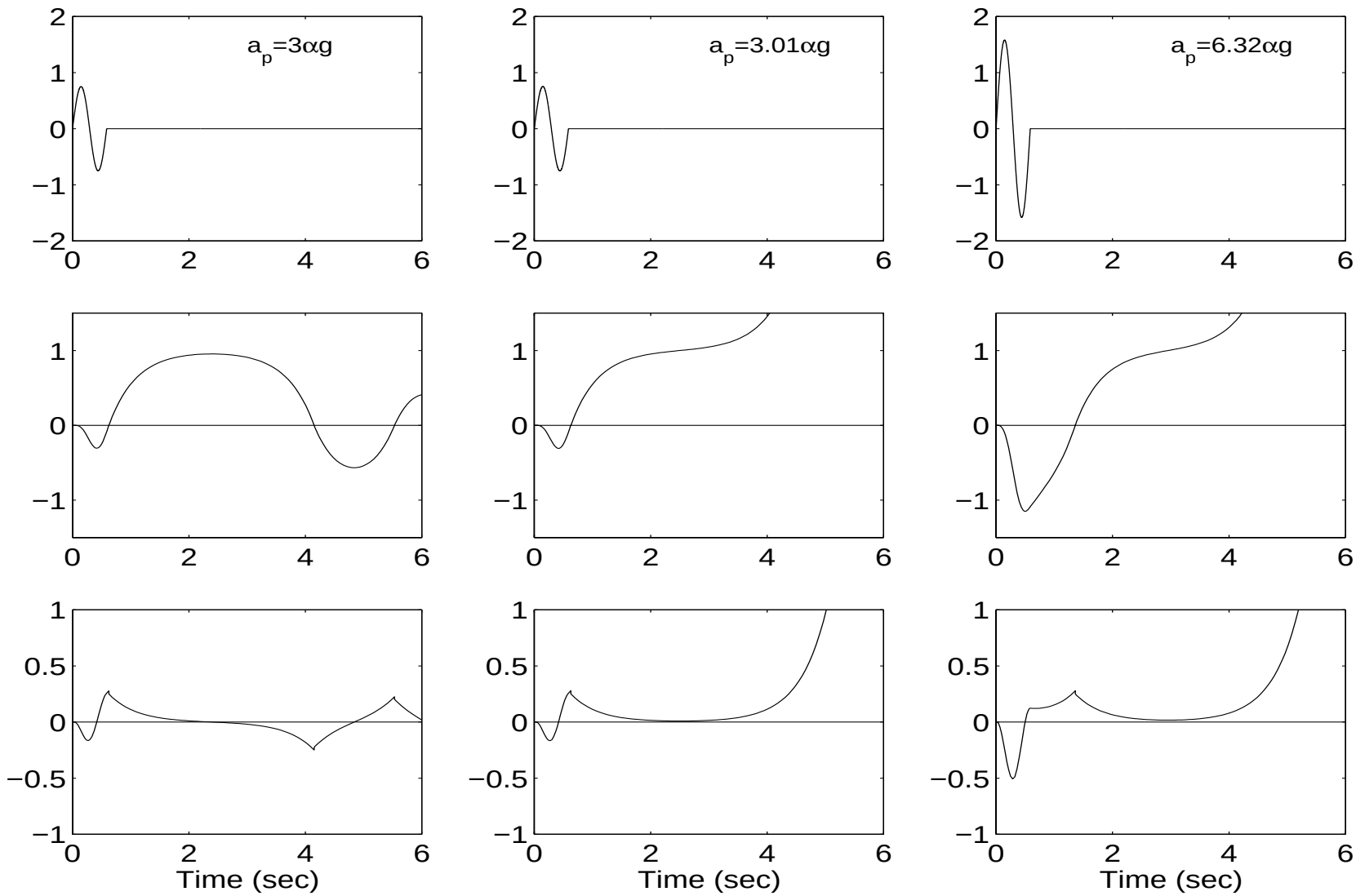

Figure 6. Rotation and angular velocity time histories of a rigid block ($p = 2.14\ rad/sec$, $\alpha = 0.25\ rad$ and $\eta = 0.9$) subjected to a one-sine pulse with $\omega_p/p = 5$. Left: $a_p = 3.00\alpha g$, no overturning. Center: $a_p = 3.01\alpha g$, overturning with one impact (mode 1). Right: $a_p = 6.32\alpha g$, overturning with one impact (mode 1).

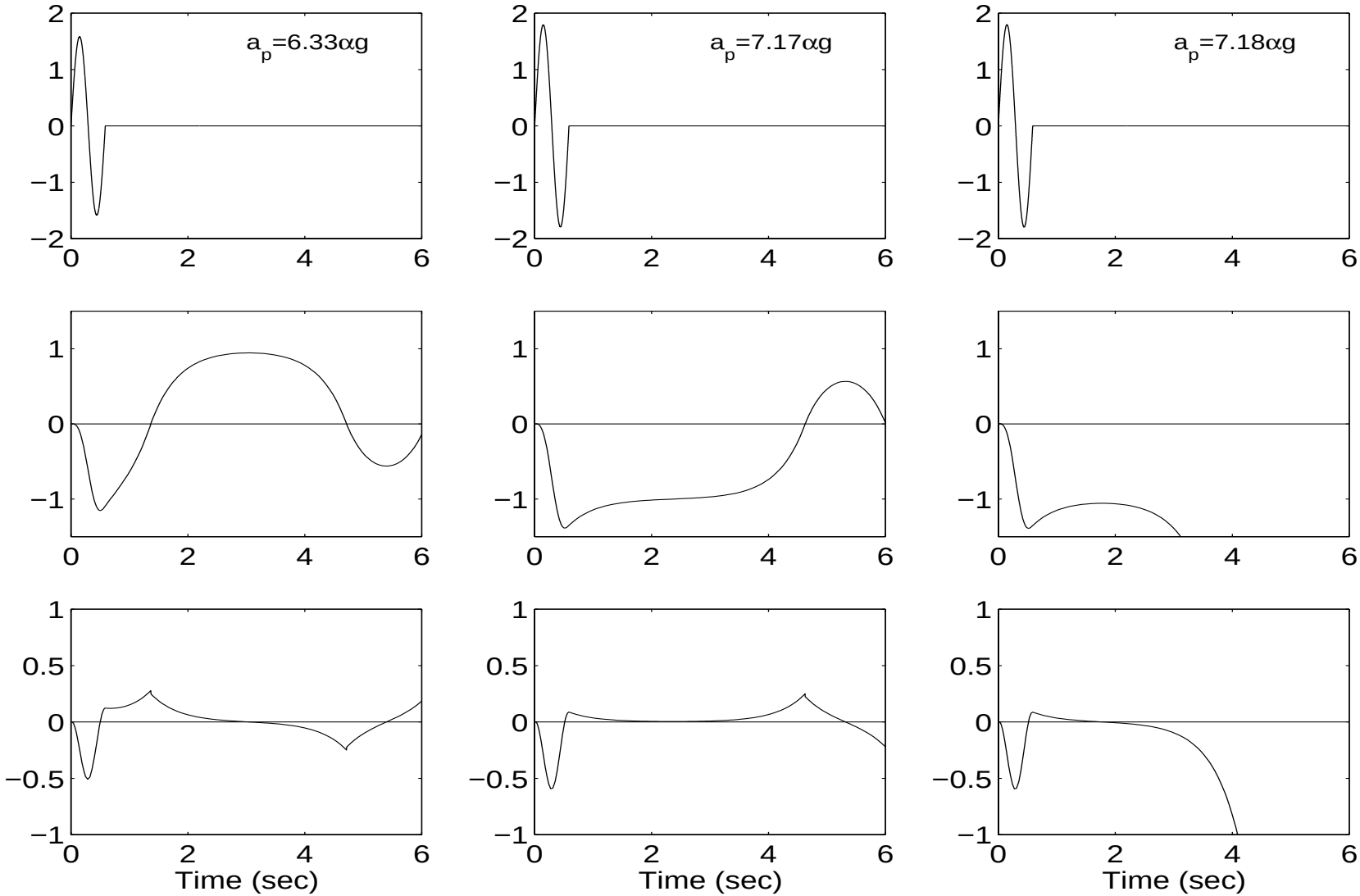

Figure 7. Rotation and angular velocity time histories of the same rigid block as in Figure 4 ($p = 2.14\ rad/sec$, $\alpha = 0.25\ rad$ and $\eta = 0.9$) subjected to a one-sine pulse with $\omega_p/p = 5$. Left: No overturning with $a_p = 6.33\alpha g$, that is slightly larger than the acceleration level, $a_p = 6.32\alpha g$, that created overturning. Center: The block does not overturn even for the acceleration amplitude $a_p = 7.17\alpha g$. Right: The block eventually overturns with $a_p = 7.18\alpha g$, without impact (mode 2).

$a_p = 6.32\alpha g$. A notable difference, shown in the right plots, is that although the first maximum positive rotation, θ, exceeds α, the deaccelerating motion of the ground is capable of recentering the block, which will experience an impact at a considerable later time and eventually overturn.

Figure 7 (left) shows the response of the same free-standing block when the acceleration amplitude of the one-sine pulse has been slightly increased, $a_p = 6.33\alpha g$. Interestingly, the block does not overturn. This is because the acceleration pulse is intense enough to induce such a large rotation that the block escapes most of the overturning effect of the deaccelerating portion of the excitation pulse. This beneficial arrangement of inertia and gravity forces holds until $a_p = 7.17\alpha g$, as shown in the center of Figure 7. Eventually, if the acceleration amplitude, a_p, is further increased the block will overturn without experiencing any impact (mode 2), as shown in Figure 7 (right). It should be noted that Yim et al. (1980) have reported the situation where a free-standing block topples under a certain level of a given ground motion, yet does not topple when the acceleration of the same ground motion is further increased. Figures 6 and 7 in association with the foregoing discussion elucidate this counterintuitive result.

Accordingly, in the frequency-acceleration plane there is a safe area that extends above the minimum overturning acceleration boundary due to mode 1 of overturning. When $0 < \omega_p / p \leq 6.59$, ($\eta = 0.9$), the minimum overturning acceleration is the result of mode 1 (one impact). With reference to Figure 5, when $\omega_p / p > 6.59$, blocks overturn only with mode 2 (no impact) and a substantial increase in the acceleration amplitude is needed to create overturning.

To further validate these results the various overturning boundaries were computed numerically via a state-space formulation that was developed to account for the nonlinear nature of the problem. With reference to equations (2-17) and (2-18), the state vector of the system is merely

$$\{y(t)\} = \begin{Bmatrix} \theta(t) \\ \dot{\theta}(t) \end{Bmatrix} \tag{2-42}$$

and the time-derivative vector $f(t)$ is

$$f(t) = \{\dot{y}(t)\} = \begin{Bmatrix} \dot{\theta}(t) \\ -p^2\left[\sin[\alpha \operatorname{sgn}[\theta(t)] - \theta(t)] + \dfrac{\ddot{u}_g}{g}\cos[\alpha \operatorname{sgn}[\theta(t)] - \theta(t)]\right] \end{Bmatrix} \tag{2-43}$$

For slender blocks, the linear approximation becomes dependable, and equation (2-43) reduces to

$$f(t) = \{\dot{y}(t)\} = \left\{ \begin{array}{c} \dot{\theta}(t) \\ p^2\left[-\alpha \mathrm{sgn}[\theta(t)] + \theta(t) - \dfrac{\ddot{u}_g(t)}{g}\right] \end{array} \right\} \tag{2-44}$$

The numerical integration of (2-43) or (2-44) is performed with standard ODE solvers available in MATLAB (1992). The results of the numerical solution of equation (2-44), shown on Figure 5 with circles, are in excellent agreement with the analytical solution.

2.3.2 Nonlinear Formulation

Figure 8 plots with crosses the overturning acceleration spectra of a rigid block with $\alpha = 0.25$ *rad*, $p = 2.14$ *rad/sec*, and $\eta = 0.9$, where the various overturning boundaries are computed numerically with the nonlinear formulation expressed with equation (2-43). The circles shown on Figure 8 are the results computed with the linear formulation expressed by equation (2-44). It is interesting to note that while for values of ω_p / p up to 6, the linear approximation gives equally good results as the nonlinear formulation, for $6 \le \omega_p / p \le 7.58$, the two formulations give drastically different results. As an example under a one-sine pulse with $\omega_p = 15.7$ rad/sec ($f = 2.5$ Hz), the linear formulation yields that the block with $\alpha = 0.25$ rad, $p = 2.14$ rad/sec, and $\eta = 0.9$ will overturn under a minimum acceleration amplitude, $a_{p0} = 3.24\ g$; whereas the nonlinear formulation yields $a_{p0} = 2.22\ g$. This drastic difference is because under the nonlinear formulation, the overturning "bay" penetrates further into the safe area. These drastic differences disappear for pulse frequencies beyond 2.58 Hz since, according to both formulations, the free-standing block overturns with mode 2 (no impact).

A recent study by Anooshehpoor et al. (1999) attempted to produce the minimum overturning acceleration spectra under one-sine pulses within the frequency range $0 \le \omega_p / p \le 10$. Unfortunately, the study by Anooshehpoor et al. failed to identify the existence of the second mode of overturning, the existence of the safe "cape" that embraces the overturning "bay", and the sensitivity of the response to the nonlinear nature of the problem even for blocks as slender as a train locomotive with $\alpha = 0.25\ rad = 14.32°$.

Figure 9 plots overturning acceleration spectra of a rigid equipment with $\alpha = 0.349\ rad = 20°$, $p = 2.0\ rad/sec$ and $\eta = \sqrt{r_{max}} \approx 0.825$. The crosses are the result of the nonlinear formulation, whereas the circles are the results computed with a linear formulation. Again within the low range of ω_p / p, the linear formulation gives equally good results as the non-

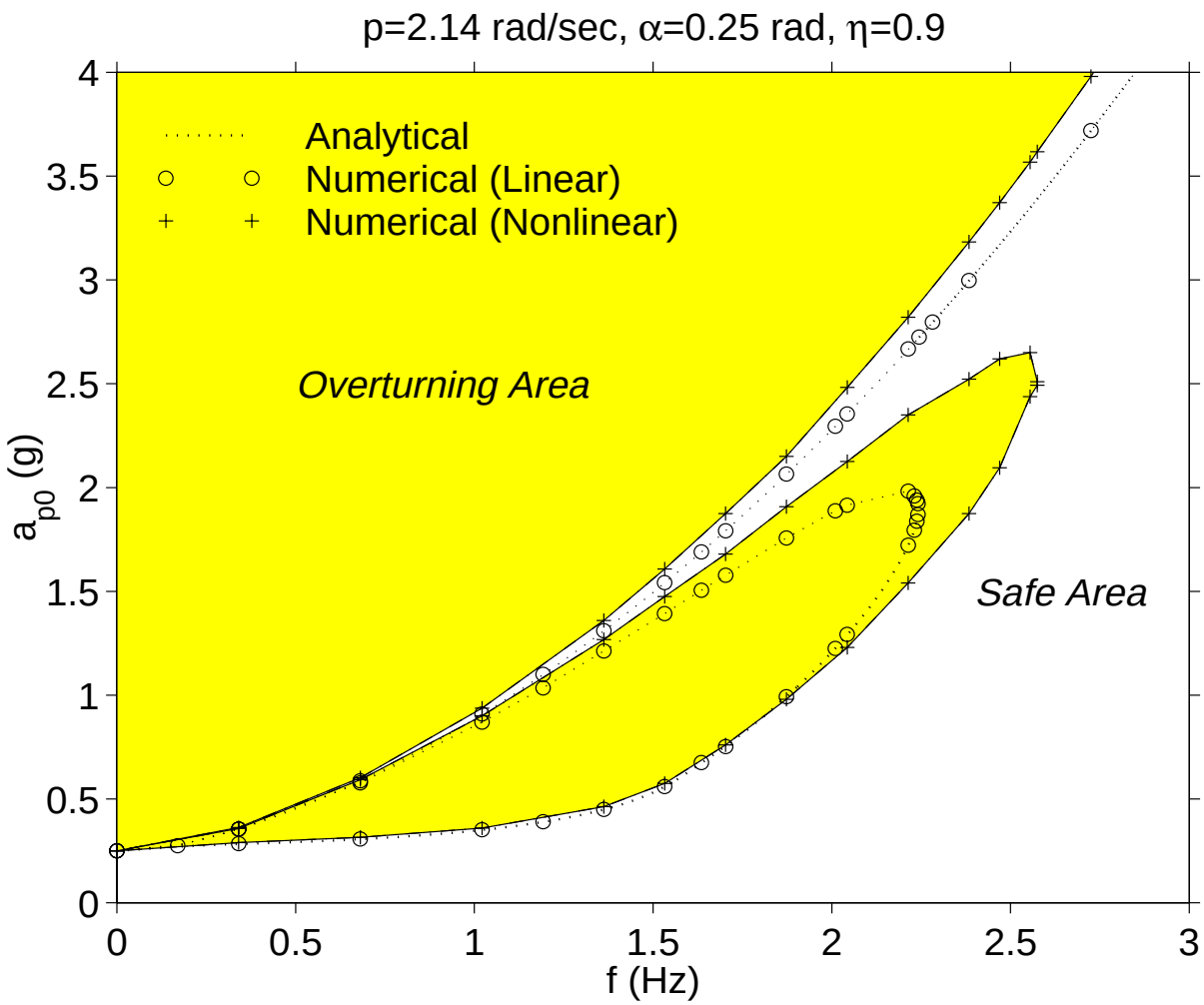

Figure 8. Comparison of overturning acceleration spectra of a slender block ($\alpha = 0.25\ rad = 14.32°$, $p = 2.14\ rad/sec$, $\eta = 0.9$) under a one-sine pulse, computed with linear and nonlinear formulations respectively. When the frequency of the one-sine pulse is relatively low, both formulations yield comparable results. As the excitation frequency increases, the linear formulation yields minimum overturning acceleration amplitudes drastically larger than those obtained with the nonlinear formulation. This is because under the nonlinear formulation the overturning "bay" generated by mode 1 penetrates further into the safe area under the overturning spectrum due to mode 2. As the excitation frequency further increases the linear and nonlinear formulations again yield comparable results since under both formulations and a high-frequency pulse the block overturns with mode 2.

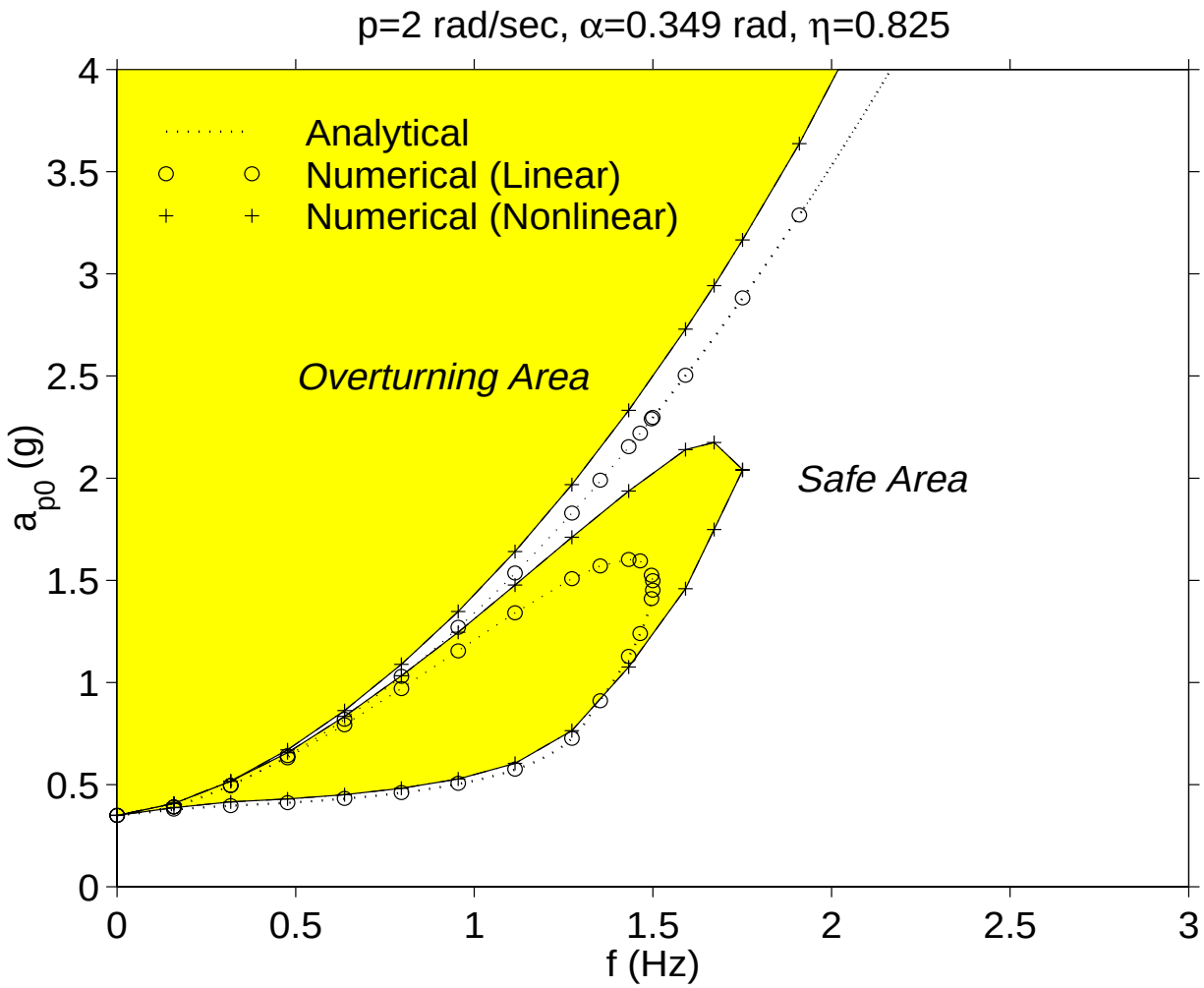

Figure 9. Comparison of overturning acceleration spectra of a free-standing equipment with $\alpha = 0.349\ rad = 20°$, $p = 2\ rad/sec$ and $\eta = \sqrt{r_{max}} = 0.825$, under a one-sine pulse, computed with the linear and the nonlinear formulation

linear formulation. However, within the range $5.8 \le \omega_p / p \le 7.35$, the two formulations gives drastically different results.

2.4 Rocking Response to a One-cosine (Type-B) Pulse

Whereas a one-sine acceleration pulse results to a forward ground displacement, a one-cosine acceleration pulse results to a forward-and-back ground displacement. With reference to Figure 3, under a one-cosine acceleration pulse the maximum ground acceleration is induced at the instant when rocking initiates ($\lambda = 1$) and the condition for pure rocking given by (2-7) becomes

$$\tan\alpha \cdot \frac{\dfrac{a_p}{g\sin\alpha} - \dfrac{3}{4}\cos\alpha\left(\dfrac{a_p}{g\tan\alpha} - 1\right)}{\dfrac{\tan\alpha}{\sin\alpha} + \dfrac{3}{4}\tan\alpha\sin\alpha\left(\dfrac{a_p}{g\tan\alpha} - 1\right)} < \mu \tag{2-45}$$

which for slender blocks ($\sin\alpha \approx \tan\alpha \approx \alpha$ and $\cos\alpha \approx 1$) simplifies to

$$\alpha \cdot \frac{\dfrac{3}{4} + \dfrac{1}{4}\dfrac{a_p}{\alpha g}}{1 + \dfrac{3}{4}\alpha^2\left(\dfrac{a_p}{\alpha g} - 1\right)} < \mu \tag{2-46}$$

Equation (2-45) or its slender block approximation given by (2-46) indicates that the stronger the acceleration pulse is, the larger needs to be the static coefficient of friction to sustain pure rocking. Figure 10 plots the magnification factor of the slenderness $\tan\alpha$, or α in equation (2-45) and (2-46) respectively as a function of $a_p/(\alpha g)$ for different values of the slenderness α. As an example, Figure 10 indicates that when a free-standing block with $\alpha = 0.25$ is subjected to a Type-B pulse with $a_p/(\alpha g) \approx 6$, the minimum coefficient of friction needed to sustain pure rocking is approximately two times the value of the block slenderness.

Figure 11 plots the overturning acceleration spectra due to a one-cosine acceleration pulse with time history

$$\ddot{u}_g(t) = \begin{cases} a_p \cos(\omega_p t) & 0 < t < 2\pi/\omega_p \\ 0 & otherwise \end{cases} \tag{2-47}$$

In this case the phase angle, ψ, when rocking initiates is zero since a one-cosine pulse yields its maximum acceleration at the instant when the pulse initiates. The same rigid block ($\alpha = 0.25$ *rad*, $p = 2.14$ *rad/sec*, and $\eta = 0.9$) is considered. The circles, shown on Figure 11, are the results computed with the linear formulation, whereas the crosses are the results obtained with the nonlinear formulation. In this case, the differences observed between the linear and the nonlinear

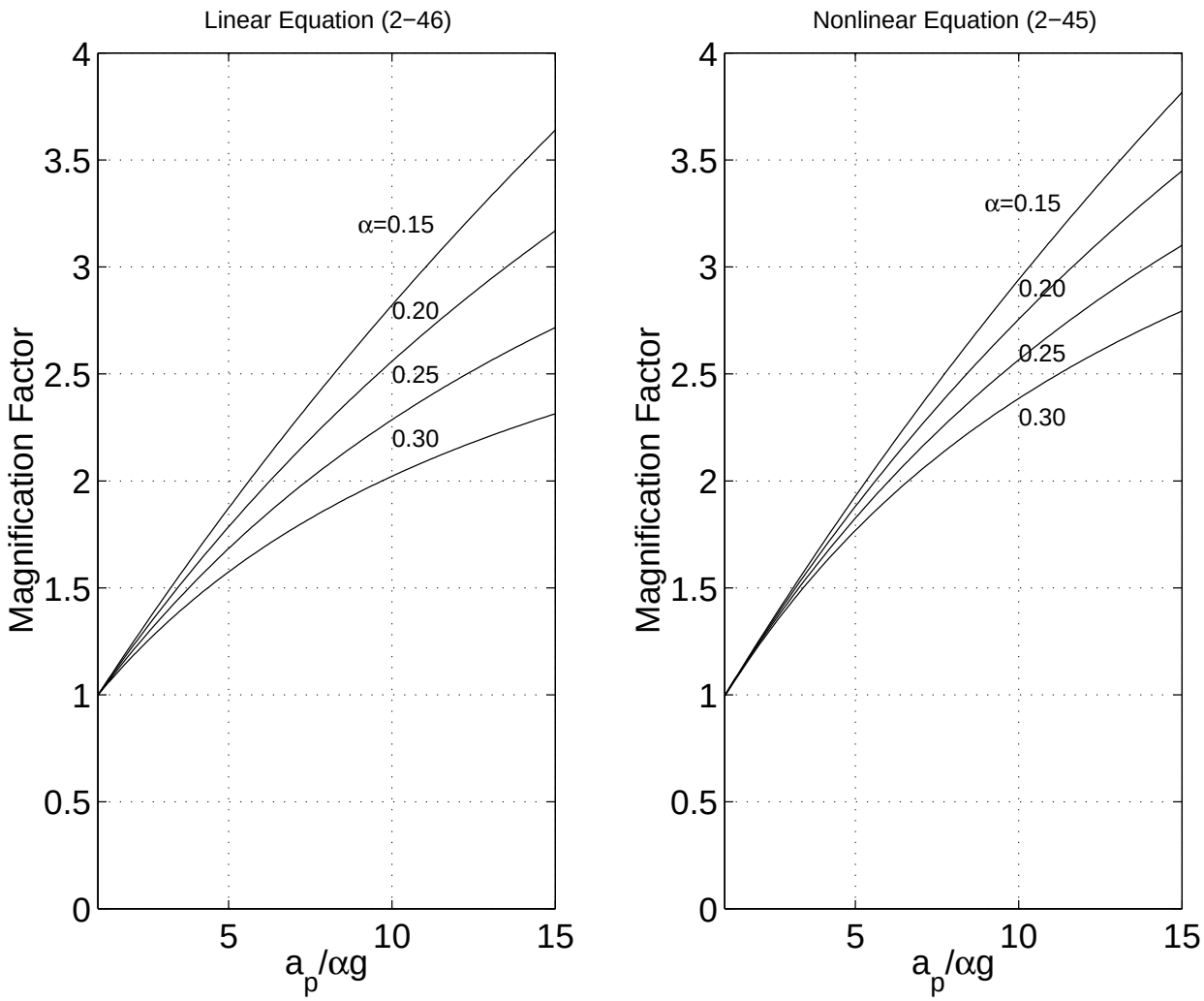

Figure 10. Normalized minimum coefficient of friction over the slenderness of a block that is needed to sustain pure rocking motion

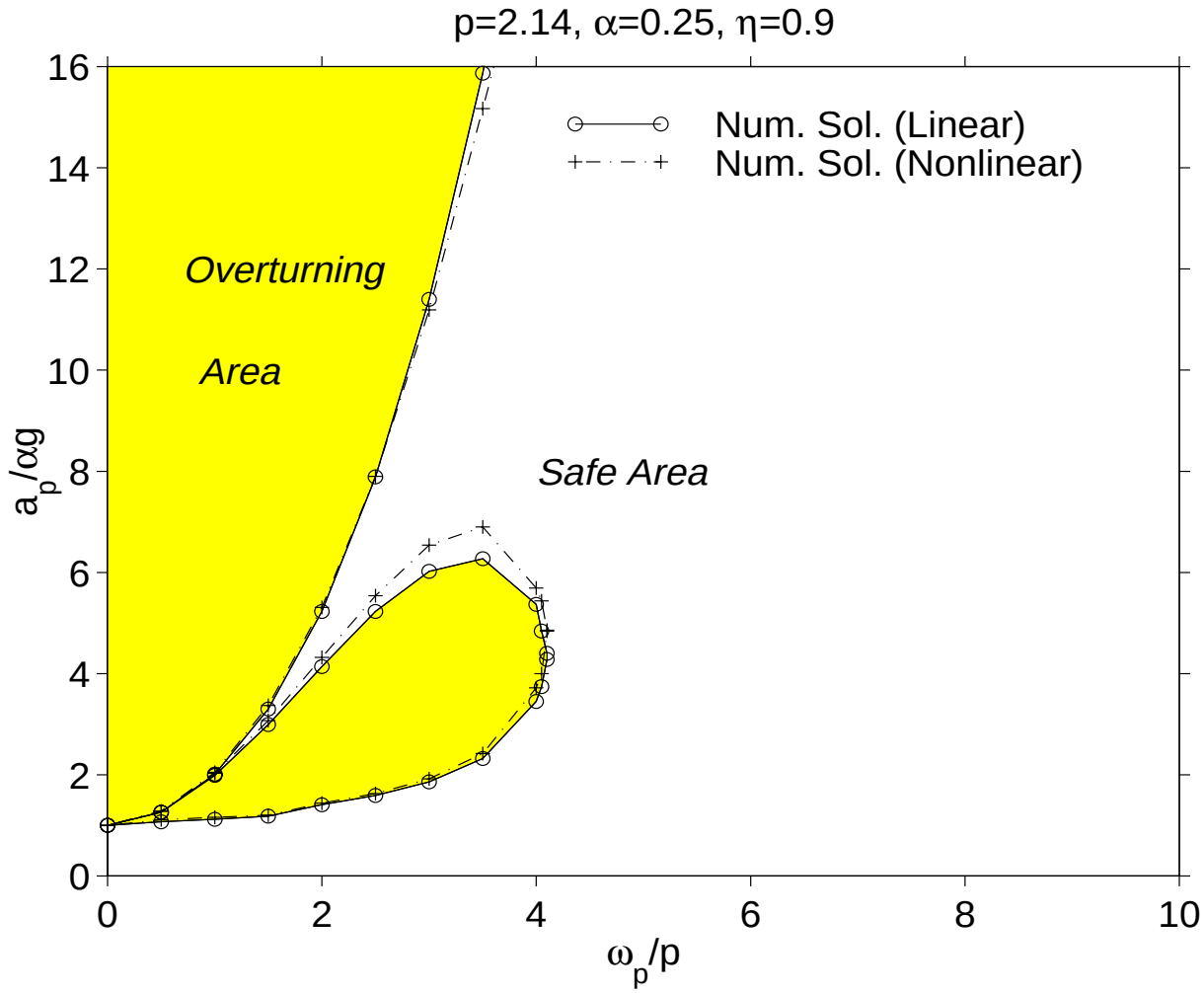

Figure 11. Comparison of overturning acceleration spectra of a slender block ($\alpha = 0.25\ rad = 14.32°$, $p = 2.14\ rad/sec$, $\eta = 0.9$) under a one-cosine pulse, computed with the linear and the nonlinear formulation. In this case the difference between the results of the two formulations are less drastic than those observed under a one-sine pulse.

formulation are less drastic. Figure 11 indicates that under a one-cosine pulse with frequency ω_p, blocks that are small enough so that $\omega_p / p \leq 4$, can experience two distinct modes of overturning. Again, the existence of these two modes are responsible for the generation of a safe region that embraces the minimum overturning acceleration spectrum. Consequently, similar to the case of a one-sine pulse, there is a finite margin of acceleration amplitudes with magnitudes larger than the minimum overturning acceleration (that corresponds to mode 1) that are unable to overturn the block. This interesting behavior is illustrated in Figures 12 and 13 where the response time histories of a free-standing block with α = 0.25 rad, p = 2.14 rad/sec η = 0.9 and ω_p / p = 3 are shown for various levels of the amplitude, a_p. Figure 14 plots overturning acceleration spectra under a one-cosine pulse of a rigid equipment with α = 0.349 rad = 20°, p = 2.0 rad$/sec$, and η = $\sqrt{r_{max}}$ = 0.825. The crosses are the result of the nonlinear formulation, whereas the circles are the results computed with the linear formulation. In comparing Figure 14 with 11 one concludes that the normalized overturning acceleration spectra have a mild dependence on the slenderness of the block, α.

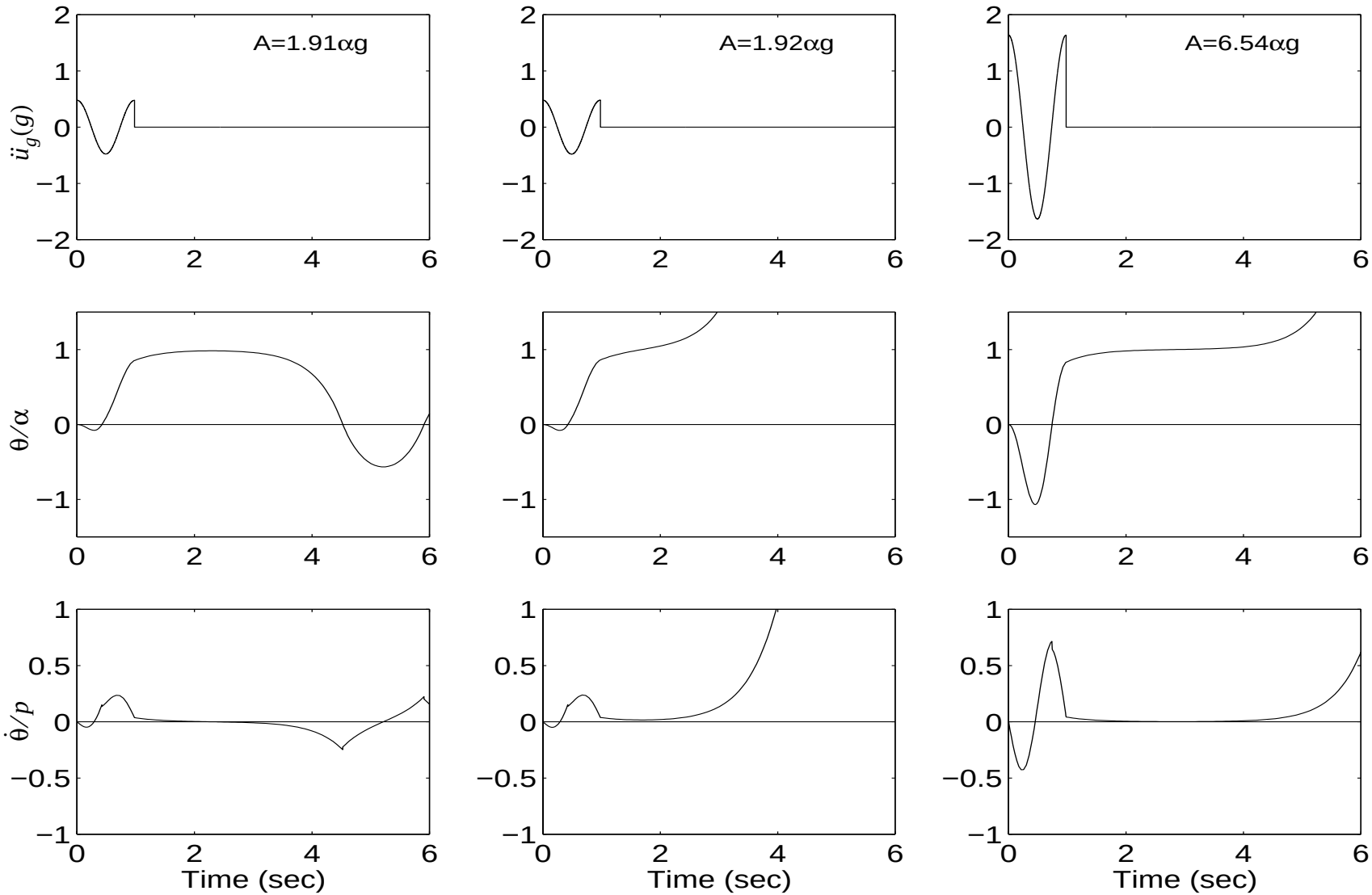

Figure 12. Rotation and angular velocity time histories of a rigid block ($p = 2.14\ rad/sec$, $\alpha = 0.25\ rad$ and $\eta = 0.9$) subjected to a one-cosine pulse with $\omega_p/p = 3$. Left: $a_p = 1.91\alpha g$, no overturning. Center: $a_p = 1.92\alpha g$, overturning with one impact (mode 1). Right: $a_p = 6.54\alpha g$, overturning with one impact (mode 1).

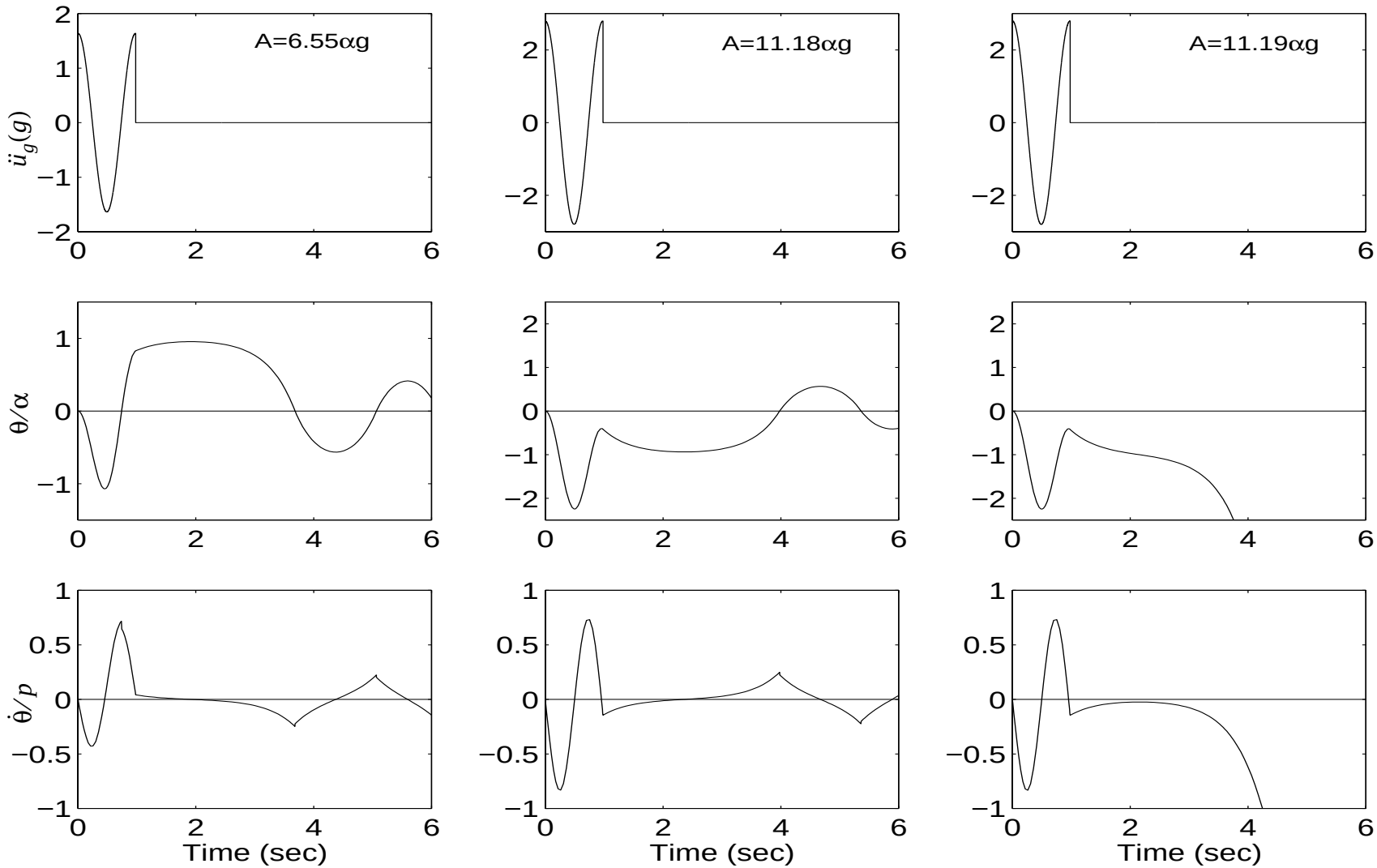

Figure 13. Rotation and angular velocity time histories of the same rigid block as in Figure 9 ($p = 2.14\ rad/sec$, $\alpha = 0.25\ rad$ and $\eta = 0.9$) subjected to a one-cosine pulse with $\omega_p/p = 3$. Left: No overturning with $a_p = 6.55\alpha g$, that is slightly larger than the acceleration level, $a_p = 6.54\alpha g$, that created overturning. Center: The block does not overturn even for the acceleration amplitude $a_p = 11.18\alpha g$. Right: The block eventually overturns with $a_p = 11.19\alpha g$, without impact (mode 2).

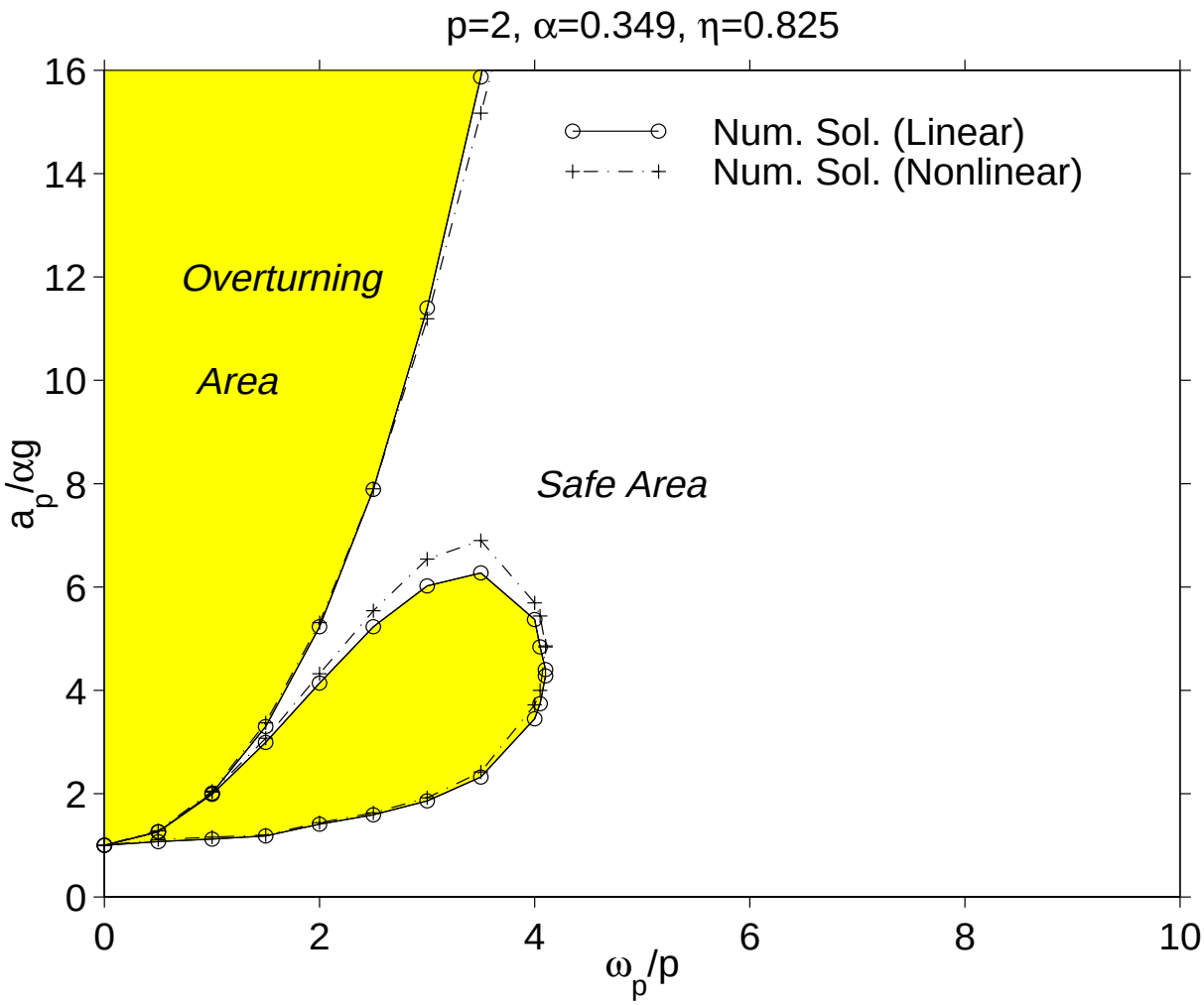

Figure 14. Comparison of overturning acceleration spectra of a slender block ($\alpha = 0.349\ rad = 20°$, $p = 2.0\ rad/sec$, $\eta = 0.825$) under a one-cosine pulse, computed with the linear and the nonlinear formulation. In this case the difference between the results of the two formulations are less drastic than those observed under a one-sine pulse.

CHAPTER 3
ROCKING RESPONSE OF A FREE-STANDING BLOCK UNDER HORIZONTAL AND VERTICAL EXCITATION

3.1 Numerical Formulation and Solution

The rocking response of a rigid block subjected to concurrent horizontal and vertical earthquake excitation is computed numerically via a state-space formulation that can accommodate the non-linear nature of the problem. Similar integration of the equation of motion has been carried out by Yim et al. (1980), Spanos and Koh (1984), Hogan (1989), and Shi et al. (1996) among others. The state vector of the system is merely

$$\{y(t)\} = \begin{Bmatrix} \theta(t) \\ \dot{\theta}(t) \end{Bmatrix} \tag{3-1}$$

and the time-derivative vector $f(t)$ is

$$f(t) = \{\dot{y}(t)\} = \begin{Bmatrix} \dot{\theta}(t) \\ -p^2\left[\sin[\alpha\,\mathrm{sgn}[\theta(t)] - \theta(t)]\left(1 + \frac{\ddot{v}_g}{g}\right) + \frac{\ddot{u}_g}{g}\cos[\alpha\,\mathrm{sgn}[\theta(t)] - \theta(t)]\right] \end{Bmatrix} \tag{3-2}$$

The numerical integration of (3-2) is performed with standard ODE solvers available in MATLAB (1992). Figure 15 plots the rotation and angular velocity of a $0.5\ m \times 1.5\ m$ free-standing block subjected to the minimum acceleration level of the Rinaldi station records (January 17, 1994, Northridge earthquake) that are needed to overturn it. In the first column of Figure 15 the vertical component of the acceleration is assumed to be zero and the horizontal component is 78% of the recorded motion. In the second column of Figure 15 the vertical component is considered and it is found that only 74% of the recorded time histories is needed to overturn the block. In this case the vertical acceleration contributes constructively to the overturning. However, as shown in the third column of Figure 15, when the polarity of the vertical motion is reversed, the vertical component contributes destructively, since 83% of the recorded time histories is now needed to overturn the block. Figure 15 also indicates that the rocking response of the block when the vertical acceleration is absent does not differ significantly from the case where the vertical excitation is included.

Similar trends are observed in Figure 16 that plots the rotation and angular velocity of the same $0.5\ m \times 1.5\ m$ block subjected to the minimum acceleration level of the Sylmar station records from the 1994 Northridge earthquake that are needed to overturn it. The second column of

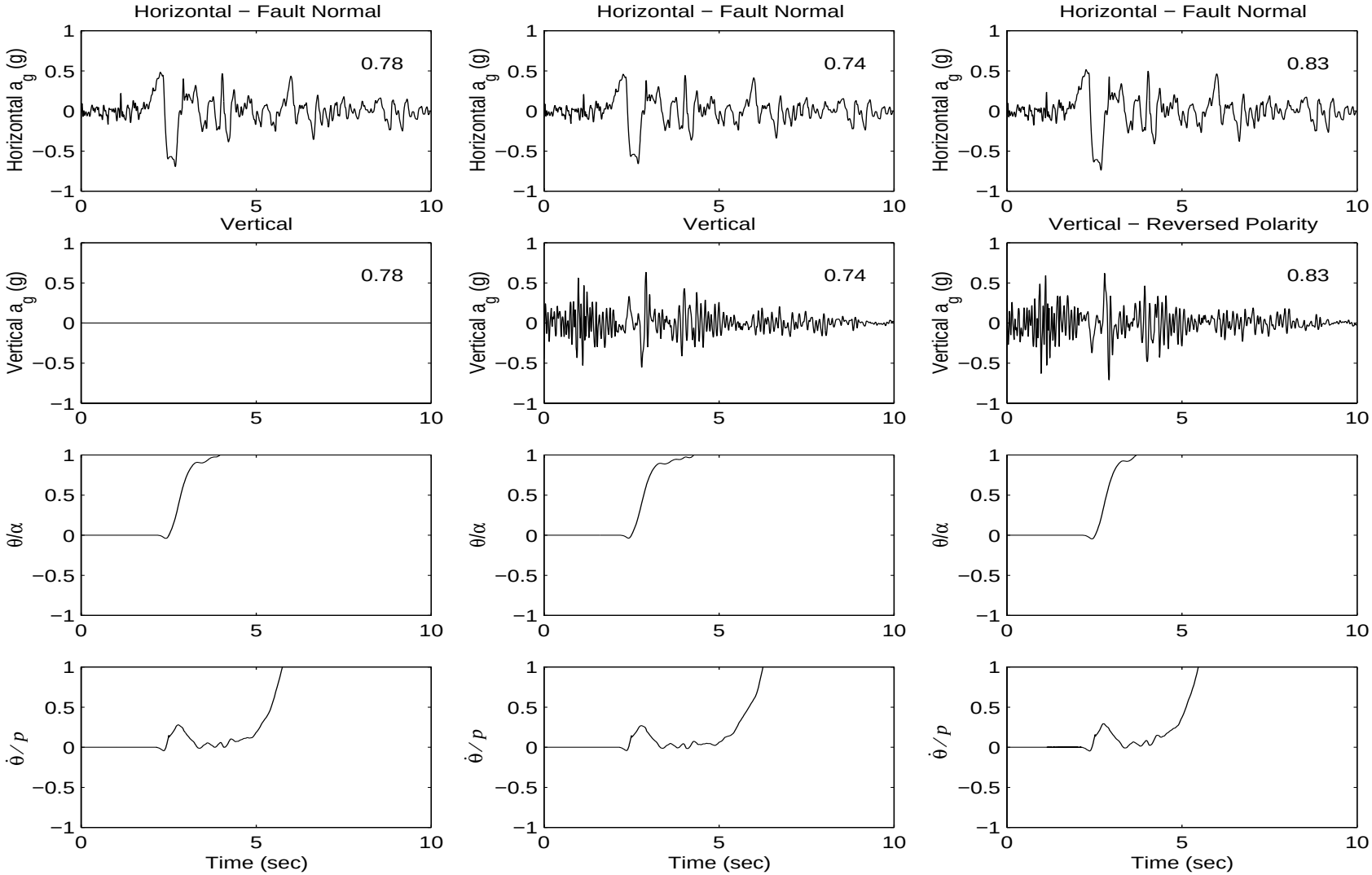

Figure 15. Rotation and angular velocity time histories of a rigid block (*b = 0.5 m*, *h = 1.5 m*) subjected to the fault-normal and vertical Rinaldi station records. Left: overturning under horizontal component alone (78% acceleration level). Center: overturning under horizontal and vertical components (74% acceleration level). Right: overturning under horizontal and vertical components with reversed polarity (83% acceleration level).

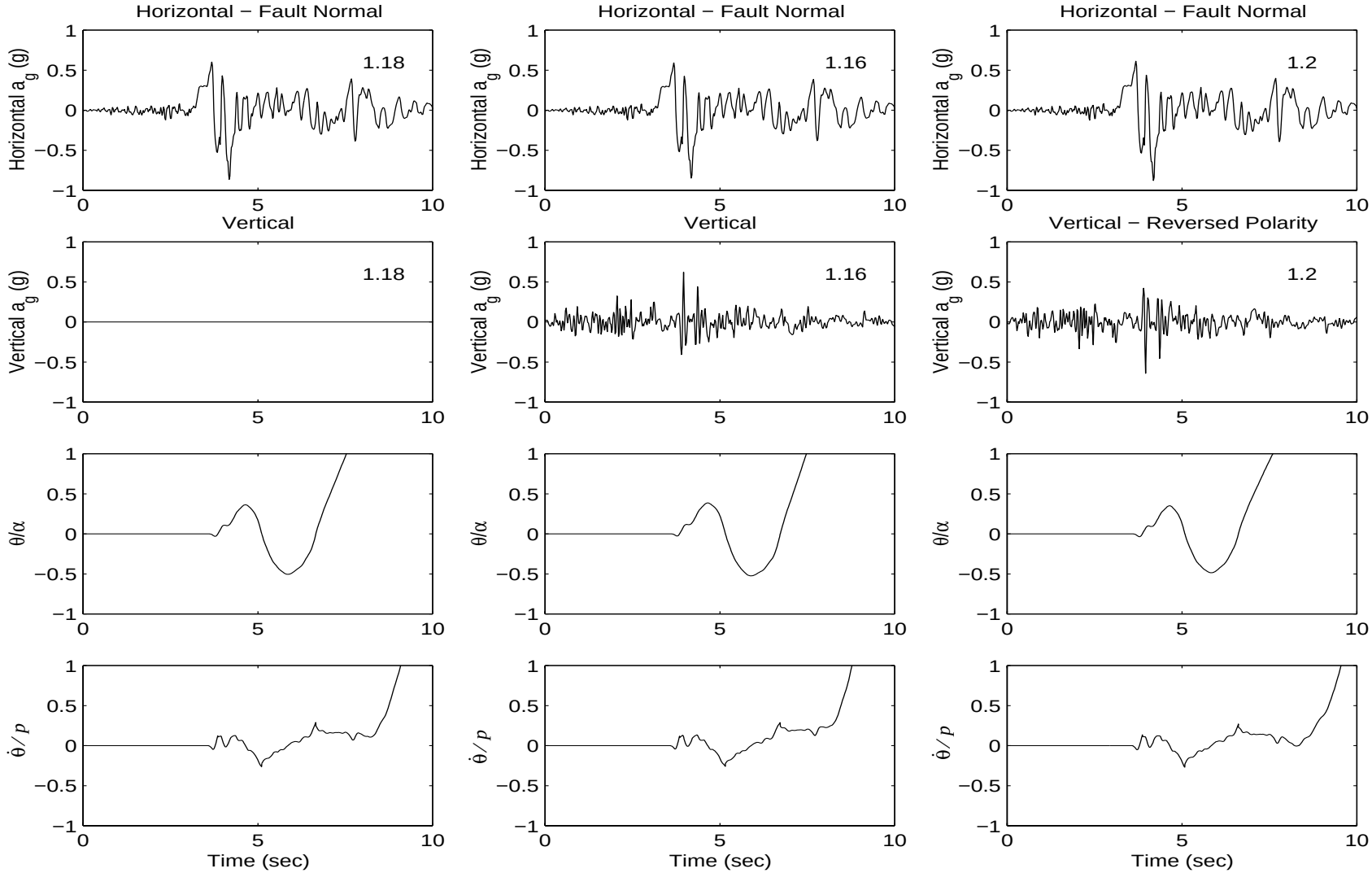

Figure 16. Rotation and angular velocity time histories of a rigid block (*b = 0.5 m, h = 1.5 m*) subjected to the fault-normal and vertical Sylmar station records. Left: overturning under horizontal component alone (118% acceleration level). Center: overturning under horizontal and vertical components (116% acceleration level). Right: overturning under horizontal and vertical components with reversed polarity (120% acceleration level).

Figure 16 shows that when the vertical component of the motion is considered, 116% of the recorded time histories is capable of overturning the block. This level of excitation is marginally lower than the 118% of the horizontal component alone that can overturn the block. Again, when the polarity of the vertical motion is reversed, the vertical component contributes destructively since now 120% of the recorded time histories is needed to overturn the block. It should be noted that the reversal of the polarity does not yield a destructive effect with all the records. Figure 17 plots the rotation and angular velocity of the $0.5\ m \times 1.5\ m$ block subjected to the minimum acceleration level of another Northridge record --- the Newhall record. In this case the right polarity of the vertical component has a destructive effect, whereas the reverse polarity has a constructive effect. Whatever the polarity, Figures 16 and 17 indicate that the simultaneous consideration of the vertical motion has a marginal effect on the acceleration level of the horizontal motion that is needed to overturn a given block. This finding is also shown in Figures 18 to 22 where the minimum overturning accelerations of other historic ground motions are shown. Table 1 summarizes the minimum levels of acceleration records, without and with the vertical component, that are needed to overturn a $0.5\ m \times 1.5\ m$ free-standing block.

TABLE 1. Minimum Level of Acceleration Records Needed to Overturn a $0.5\ m \times 1.5\ m$ Free-standing Block ($\alpha = 18.43°$, $p = 2.157\ rad/sec$).

Records	Levels of Acceleration Records		
	Horizontal	**Horizontal & Vertical**	**Horizontal & Vertical (reversed polarity)**
Rinaldi (FN), 1994 Northridge	0.78	0.74	0.83
Sylmar (FN), 1994 Northridge	1.18	1.16	1.20
Newhall (N-S), 1994 Northridge	1.83	1.86	1.80
El Centro #5 (FN), 1979 Imperial	1.29	1.26	1.30
El Centro #6 (FN), 1979 Imperial	1.49	1.49	1.61
El Centro #7 (FN), 1979 Imperial	1.52	1.52	1.52
Los Gatos (0), 1989 Loma Prieta	1.46	1.45	1.51
Lucerne Valley (FP), 1992 Landers	2.75	2.85	2.95

The marginal effect that the vertical acceleration has on the level of the horizontal acceleration that is needed to overturn a rigid block was also reported by Shi et al (1996).

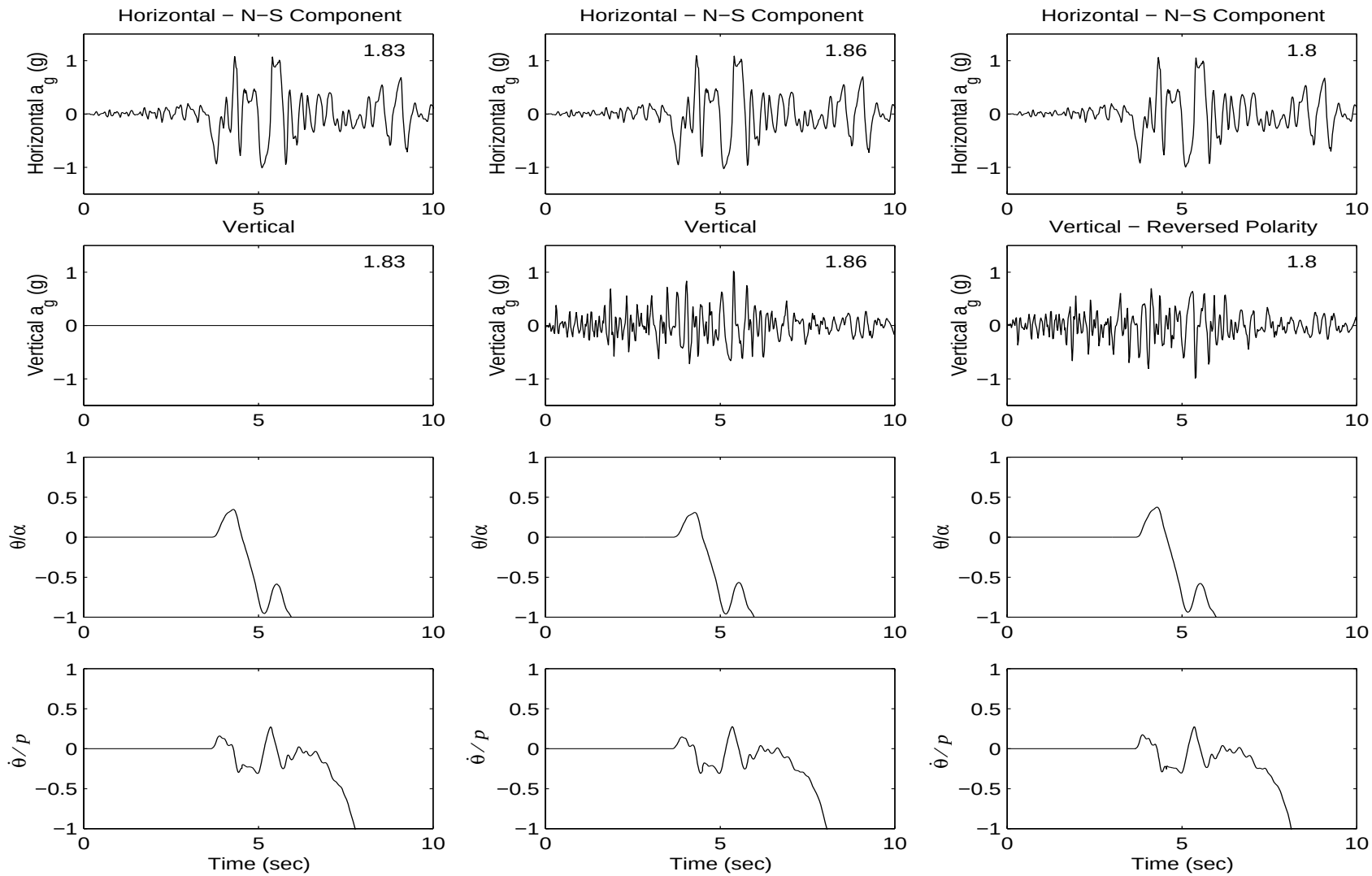

Figure 17. Rotation and angular velocity time histories of a rigid block (*b = 0.5 m, h = 1.5 m*) subjected to the N-S and vertical Newhall station records. Left: overturning under horizontal component alone (183% acceleration level). Center: overturning under horizontal and vertical components (186% acceleration level). Right: overturning under horizontal and vertical components with reversed polarity (180% acceleration level).

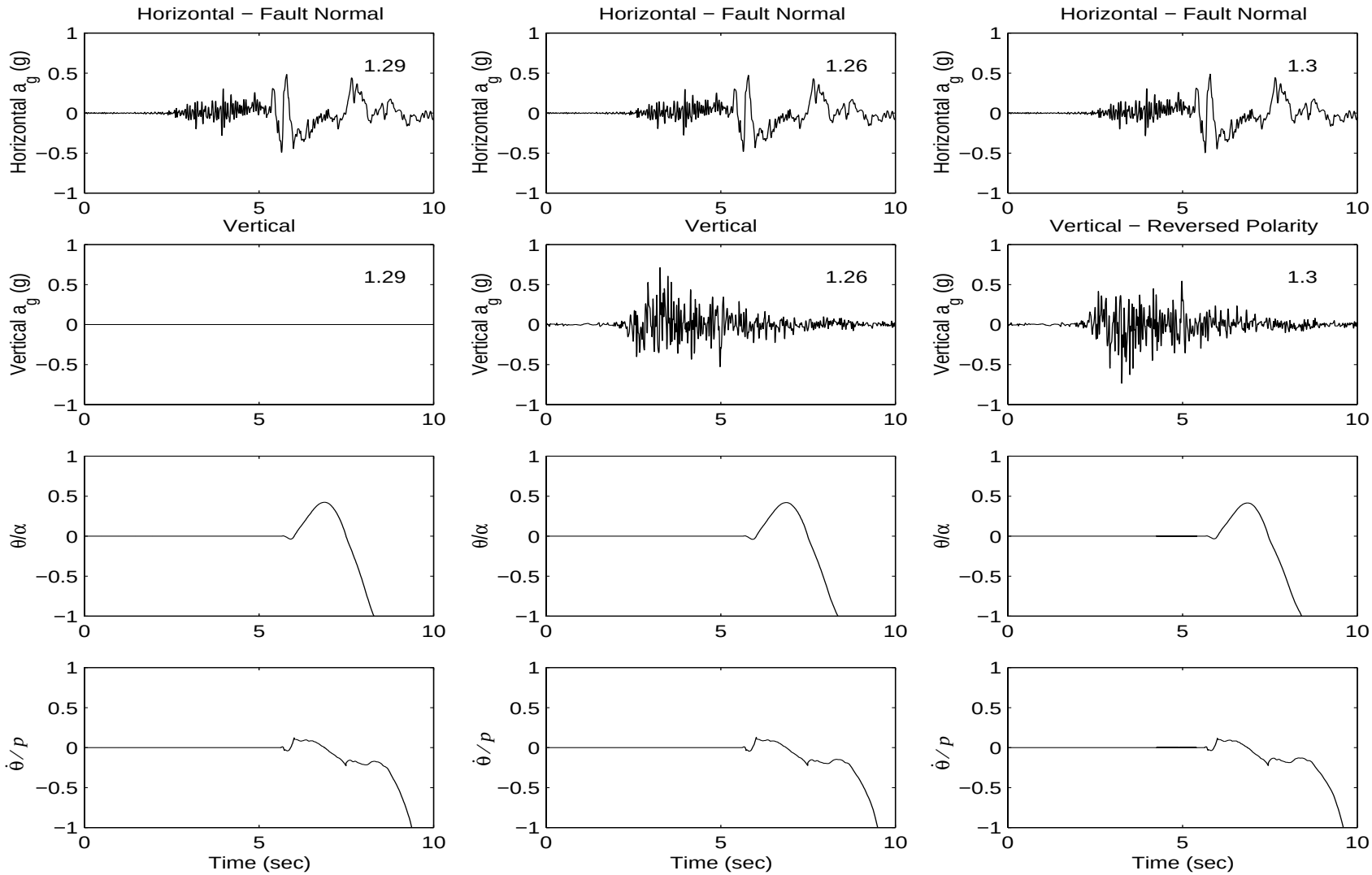

Figure 18. Rotation and angular velocity time histories of a rigid block (*b = 0.5 m*, *h = 1.5 m*) subjected to the fault-normal and vertical El Centro Array #5 records. Left: overturning under horizontal component alone (129% acceleration level). Center: overturning under horizontal and vertical components (126% acceleration level). Right: overturning under horizontal and vertical components with reversed polarity (130% acceleration level).

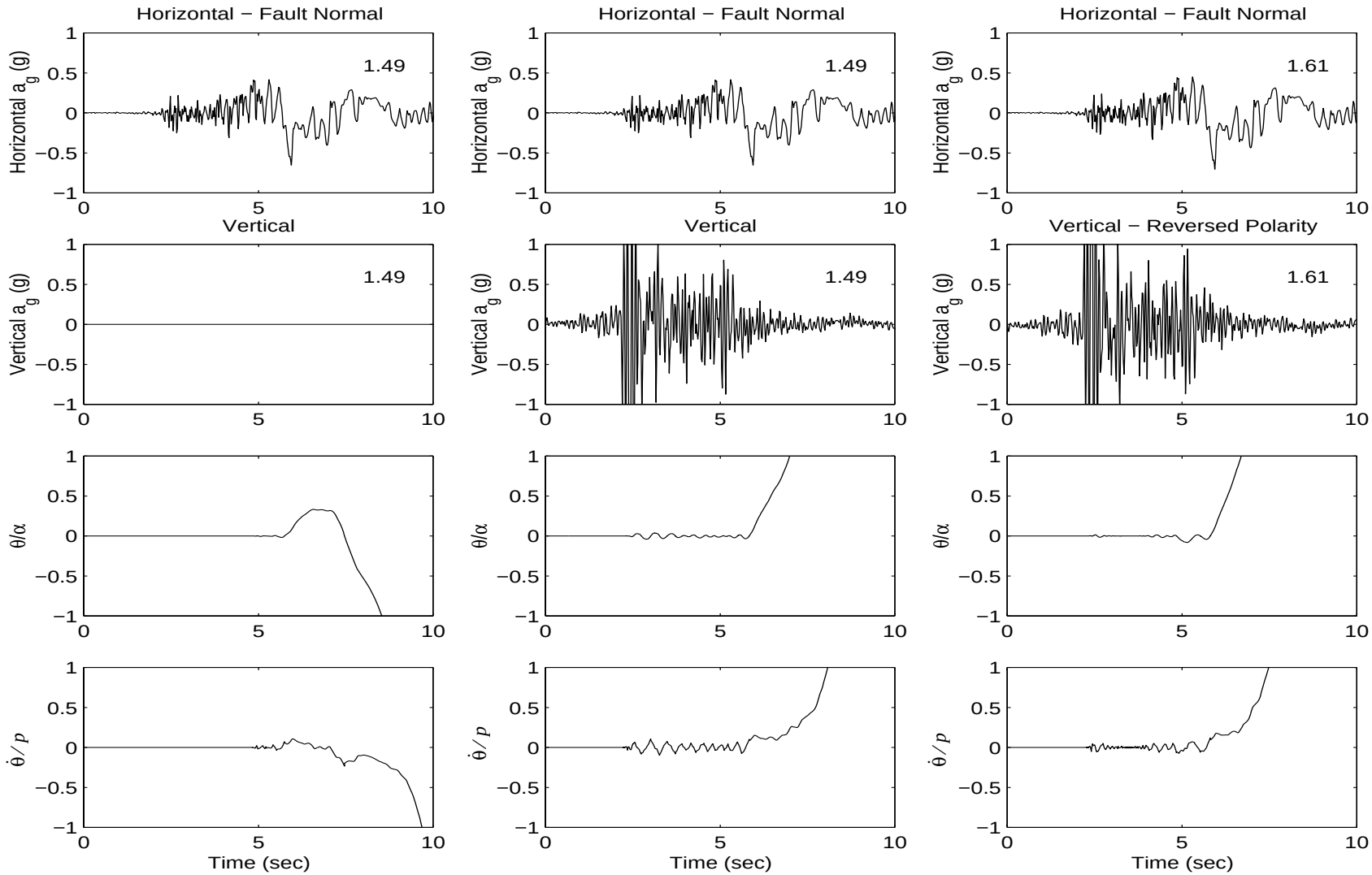

Figure 19. Rotation and angular velocity time histories of a rigid block (*b = 0.5 m, h = 1.5 m*) subjected to the fault-normal and vertical El Centro Array #6 records. Left: overturning under horizontal component alone (149% acceleration level). Center: overturning under horizontal and vertical components (149% acceleration level). Right: overturning under horizontal and vertical components with reversed polarity (161% acceleration level).

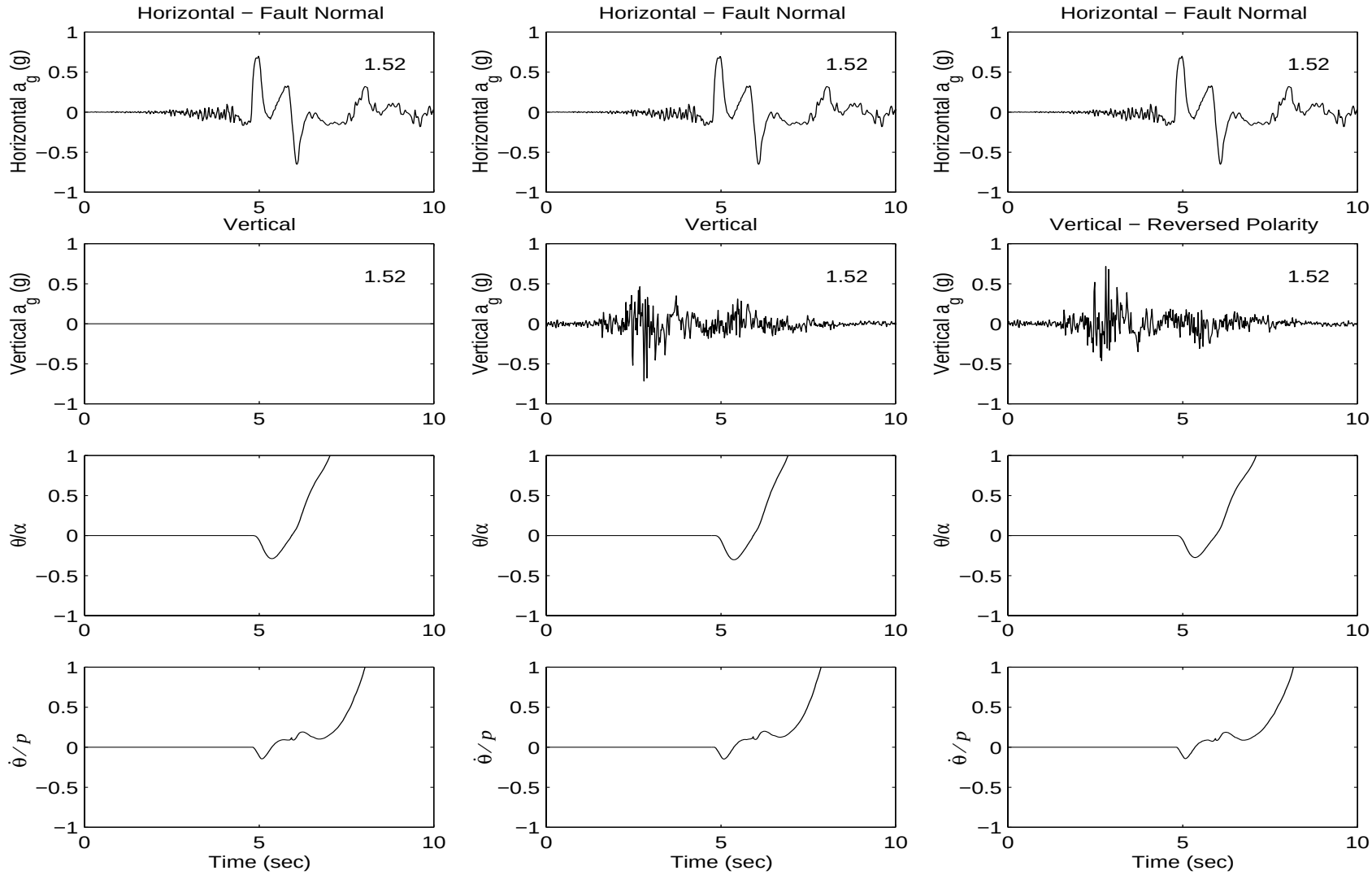

Figure 20. Rotation and angular velocity time histories of a rigid block (*b = 0.5 m, h = 1.5 m*) subjected to the fault-normal and vertical El Centro Array #7 records. Left: overturning under horizontal component alone (152% acceleration level). Center: overturning under horizontal and vertical components (152% acceleration level). Right: overturning under horizontal and vertical components with reversed polarity (152% acceleration level).

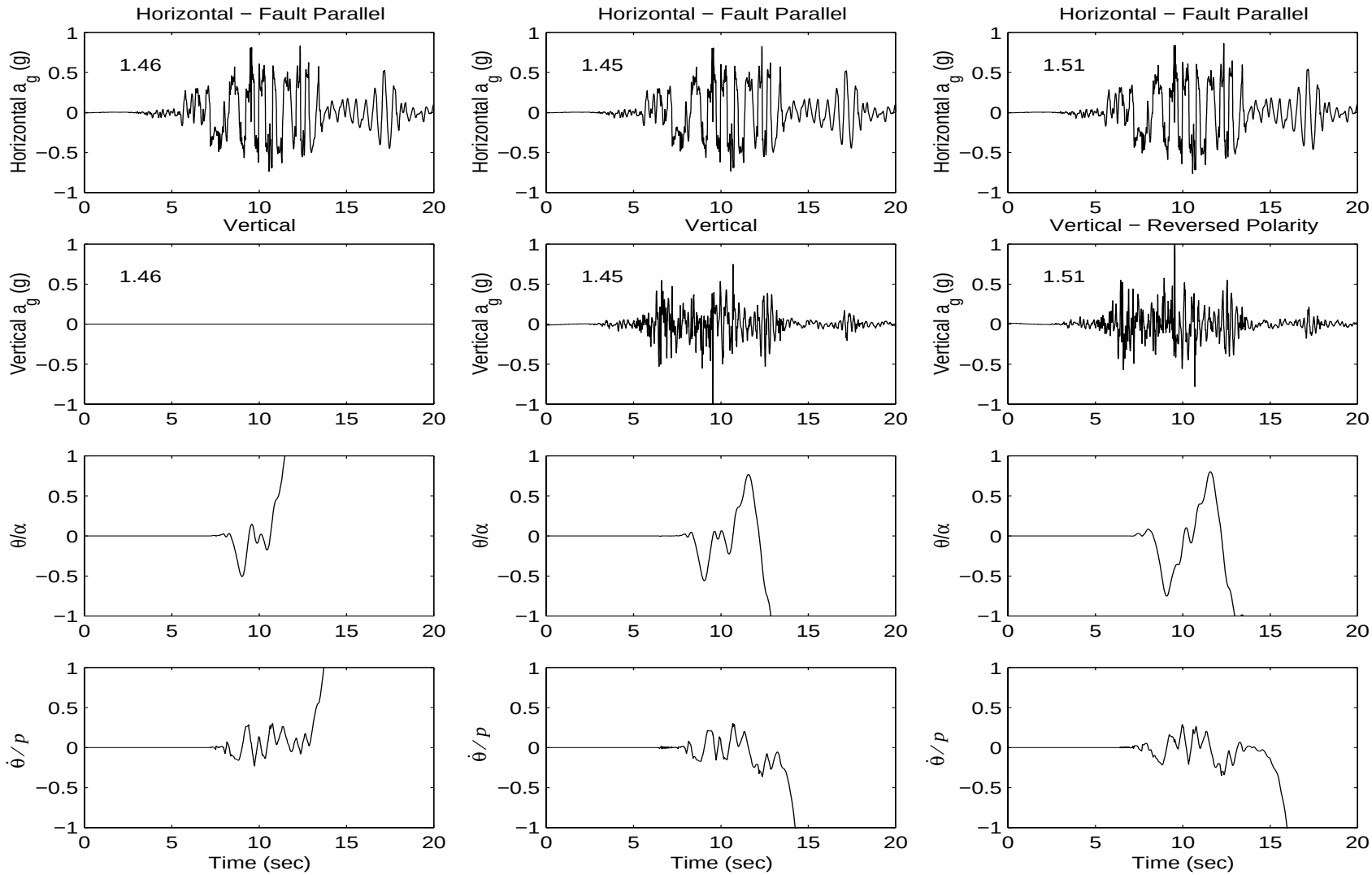

Figure 21. Rotation and angular velocity time histories of a rigid block (*b = 0.5 m, h = 1.5 m*) subjected to the fault-parallel and vertical Los Gatos station records. Left: overturning under horizontal component alone (146% acceleration level). Center: overturning under horizontal and vertical components (145% acceleration level). Right: overturning under horizontal and vertical components with reversed polarity (151% acceleration level).

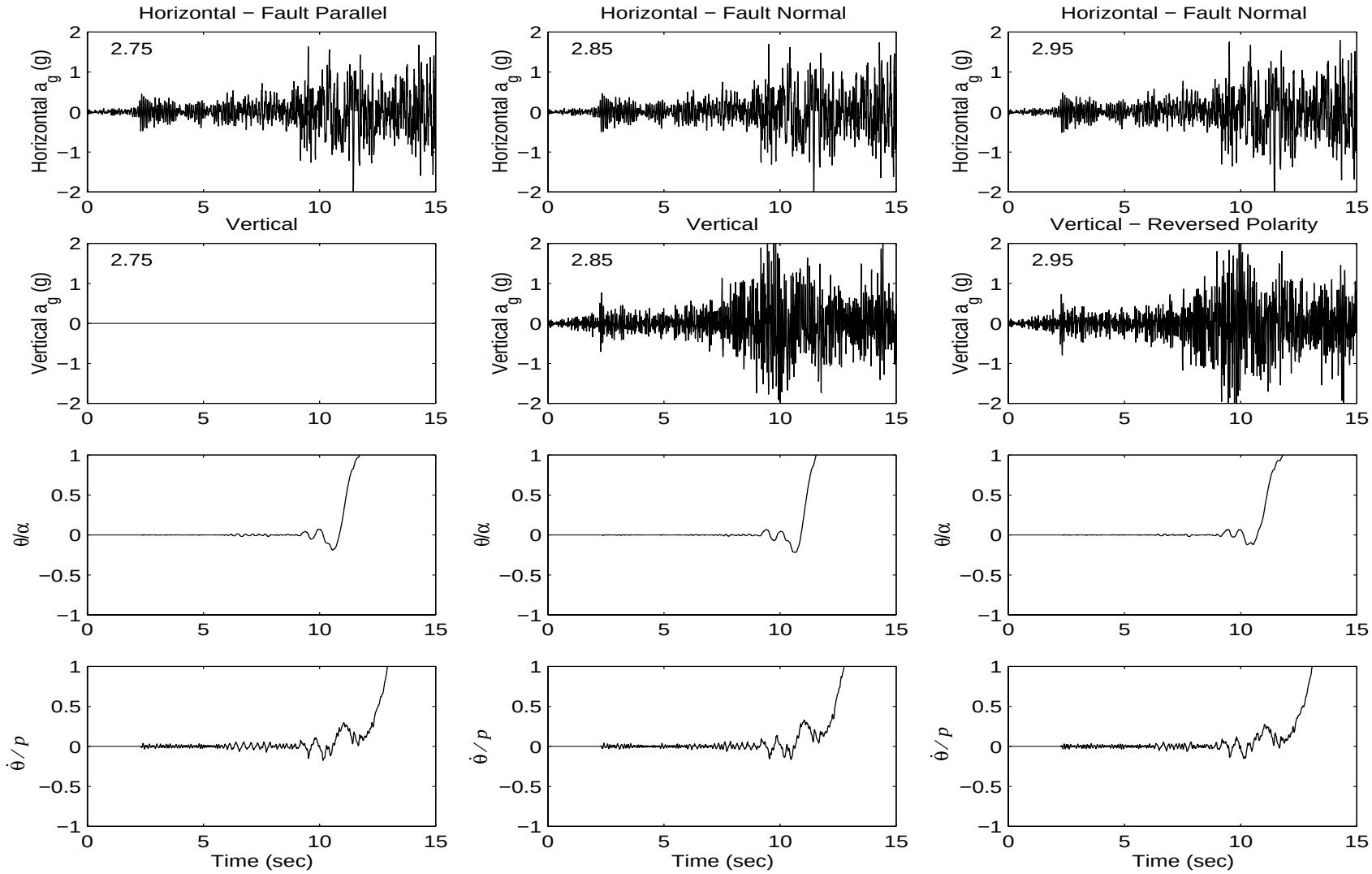

Figure 22. Rotation and angular velocity time histories of a rigid block (*b = 0.5 m*, *h = 1.5 m*) subjected to the fault-parallel and vertical Lucerne Valley records. Left: overturning under horizontal component alone (275% acceleration level). Center: overturning under horizontal and vertical components (285% acceleration level). Right: overturning under horizontal and vertical components with reversed polarity (295% acceleration level).

3.2 Response Spectra and Effect of the Coefficient of Restitution

In the foregoing analysis, Figures 15 to 22 show time histories of the response of a given block to the minimum acceleration level of a given ground motion that is needed to overturn it. In this section response maxima are computed of various blocks subjected to a given ground motion at its 100% level. Three different values of the block slenderness, $\alpha = 15°$, $20°$ and $25°$ have been selected while the frequency parameter, *p*, ranges from 1 rad/sec to 3 rad/sec. These values of slenderness and frequency parameter represent the geometric and dynamic characteristics of most electrical equipment of interest. Figure 23 plots response spectra for the maximum angle of rotation, θ_{max}/α, and the maximum angular velocity, $\dot{\theta}_{max}/p$, under the excitation recorded along the fault normal component at the Rinaldi station during the 1994 Northridge earthquake. The spectra shown in the left column of Figure 23 are computed by using the maximum value of the coefficient of restitution, $r = r_{max} = [1 - 1.5\sin^2\alpha]^2$, that allows for a rocking motion. For $\alpha = 15°$, $\sqrt{r_{max}} = 0.90$; whereas for $\alpha = 20°$ and $25°$, $\sqrt{r_{max}} = 0.825$ and 0.732 respectively. Figure 23 (center) shows the rotation and angular velocity spectra for $\sqrt{r} = 0.75$. In this case only the response of blocks with $\alpha = 15°$ and $\alpha = 20°$ are shown since for the case $\alpha = 25°$, $\sqrt{r_{max}} = 0.732 < 0.75$. Figure 23 (right) shows the rotation and angular velocity spectra for $\sqrt{r} = 0.5$.

The response spectra in Figure 23 show that a reduced coefficient of restitution (more energy lost during impact) results in smaller angles of rotation; however the values of the impact velocities might be larger. Similar trends are observed in Figure 24, where rocking response spectra are shown for the fault-normal motion recorded at the Sylmar station during the 1994 Northridge earthquake.

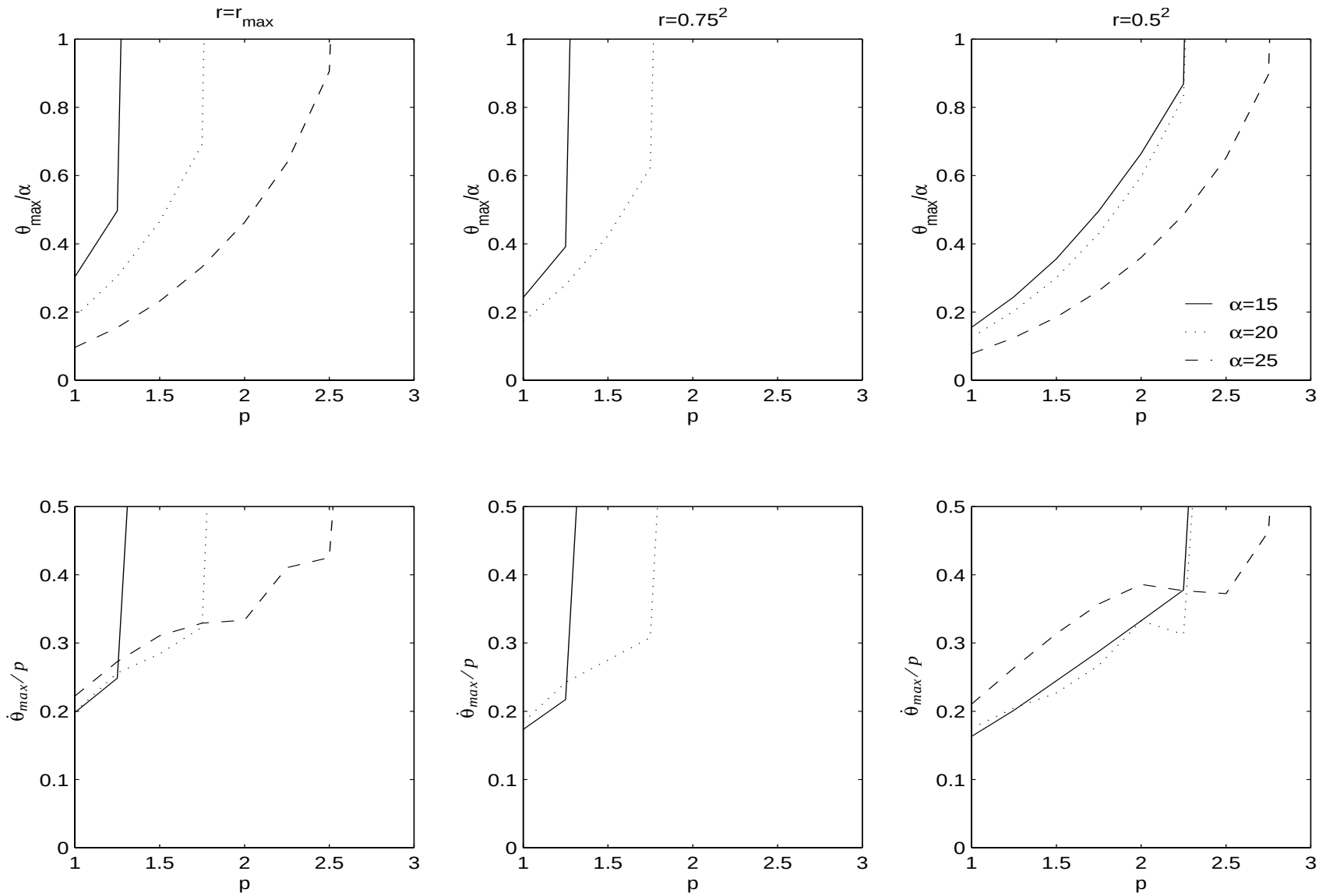

Figure 23. Rotation and angular velocity spectra due to the fault normal motion recorded at the Rinaldi station for different values of the coefficient of restitution and various values of block slenderness

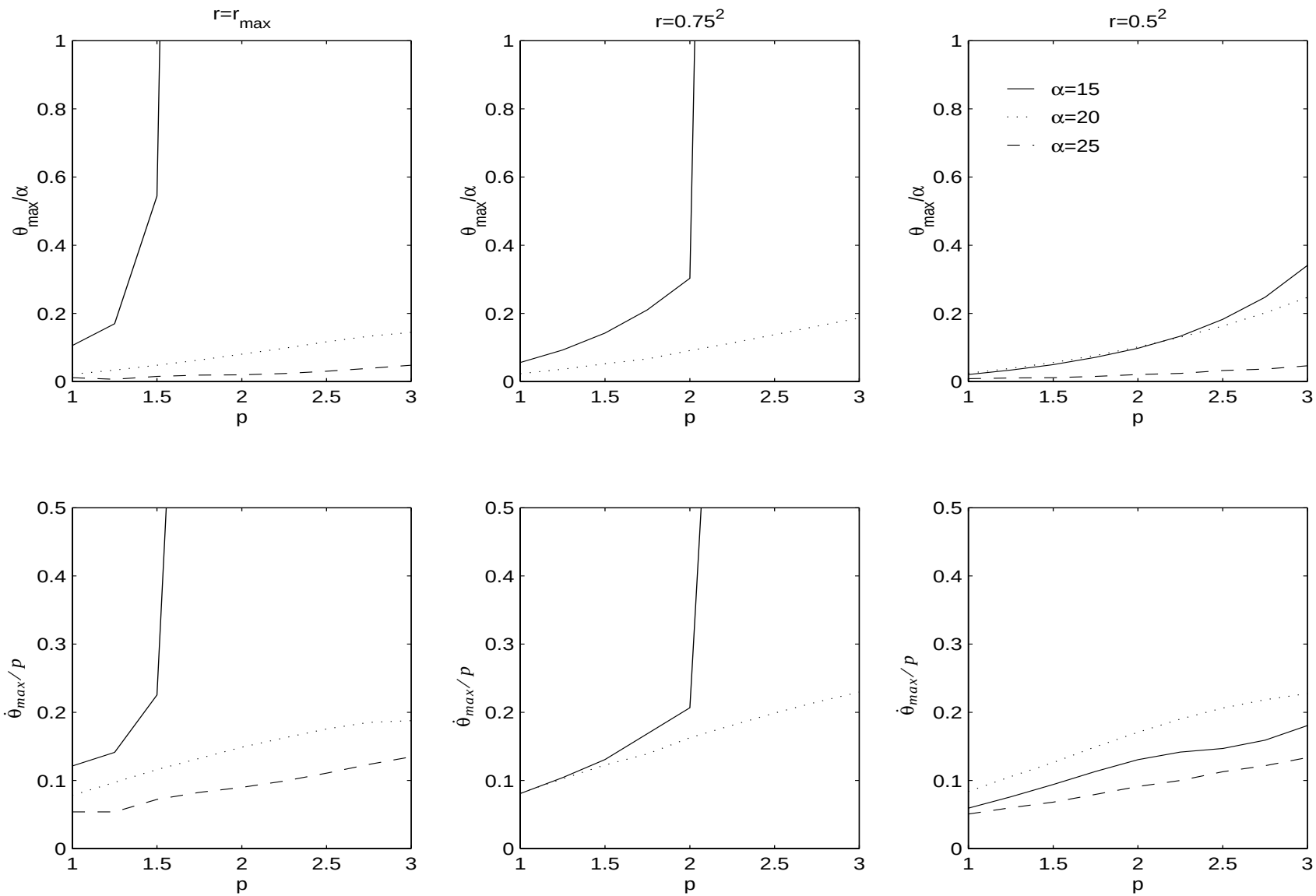

Figure 24. Rotation and angular velocity spectra due to the fault normal motion recorded at the Sylmar station for different values of the coefficient of restitution and various values of block slenderness

CHAPTER 4
ROCKING RESPONSE OF ANCHORED EQUIPMENT SUBJECTED TO A ONE-SINE (TYPE-A) PULSE

In order to prevent violent rocking of electrical equipment, restrainers (hold-downs) are placed at the base to anchor the equipment to its foundation. These restrainers have finite strength, F_u, that can be as low as 1 kip per anchorage up to 50 kips or even higher. Their stiffness also varies from a low value of $K = 10\ kips/in$ up to 500 $kips/in$. Considering that the weight, $W = mg$, of the electrical equipment of interest ranges from 40 kips up to 500 kips, the ratio between the restraining strength on each side of the equipment to the weight of the equipment is within $0.1 < F_u/W \leq 1.0$.

In this study two idealizations for the mechanical behavior of the restrainers are considered. The first simpler idealization is an elastic-brittle behavior. It assumes linear elastic behavior until the ultimate strength, F_u, is reached; and once the strength of the restrainer is exceeded it fractures and the block continues to rock without enjoining any restoring force. It is assumed that the stiffness of the restrainer maintains a constant value, K, until the restrainer fractures and subsequently its stiffness and strength are zero. The second more realistic idealization assumes an elastic-plastic behavior. The restrainer behaves linearly until the ultimate strength, F_u, is reached and subsequently deforms plastically until the fracture displacement, u_f, is reached. Beyond that point the restrainers fractures and the block continues to rock without enjoying any restoring or dissipative force.

In the entire analysis that follows, the base excitation is assumed to be along the horizontal direction only, since the findings of chapter 3 indicate that the vertical acceleration has a marginal constructive or destructive effect. Figure 25 shows a schematic of the problem at hand where the restoring elements on each side of the block represent the combined stiffnesses of all the restrainers that are present at the edge of the block that uplifts.

4.1 Elastic-Brittle Behavior

4.1.1 Nonlinear Formulation

Figure 26 (center) illustrates the moment-rotation relation that results from the presence of restrainers with elastic-brittle behavior; while Figure 26 (top) illustrates the moment-rotation relation of a free-standing block. Under these two restoring mechanisms and assuming horizontal

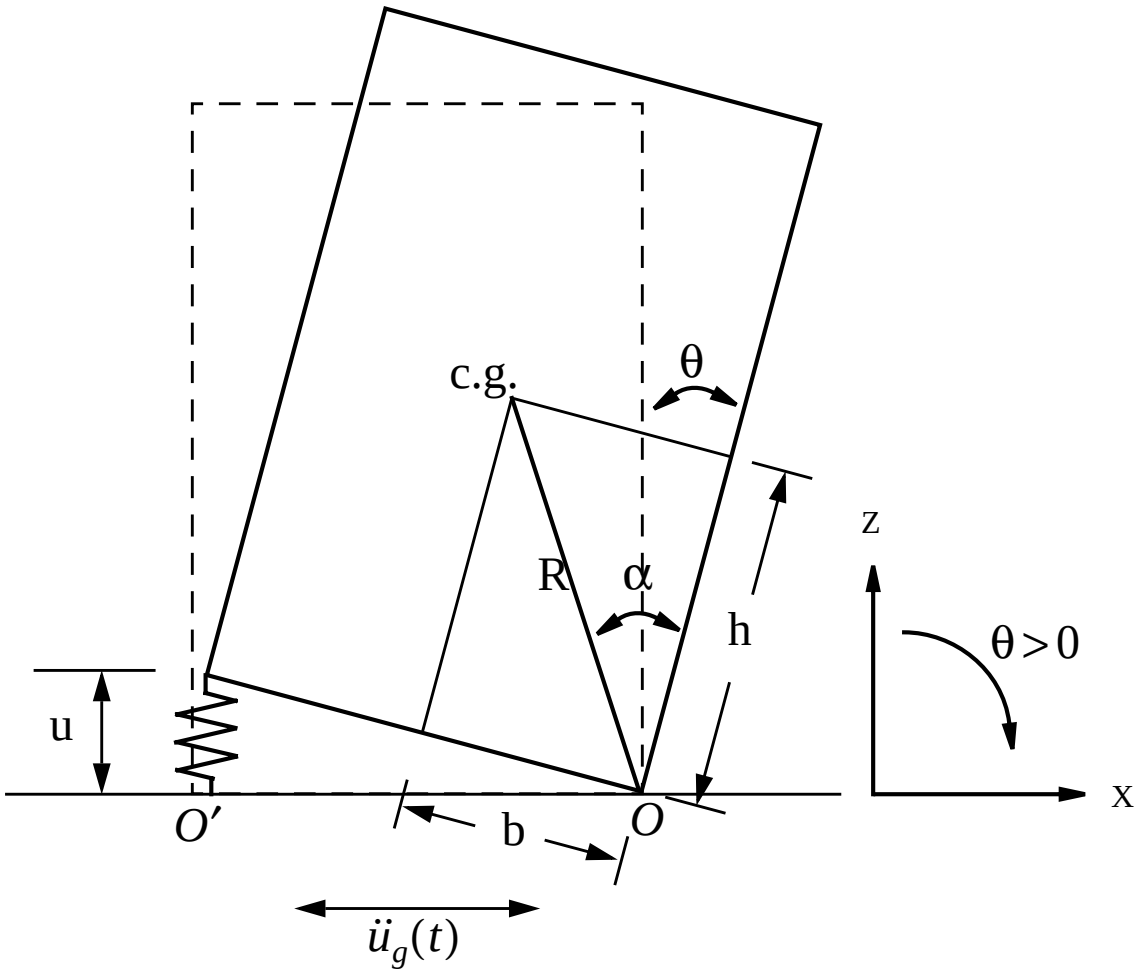

Figure 25. Schematic of an anchored block in rocking motion

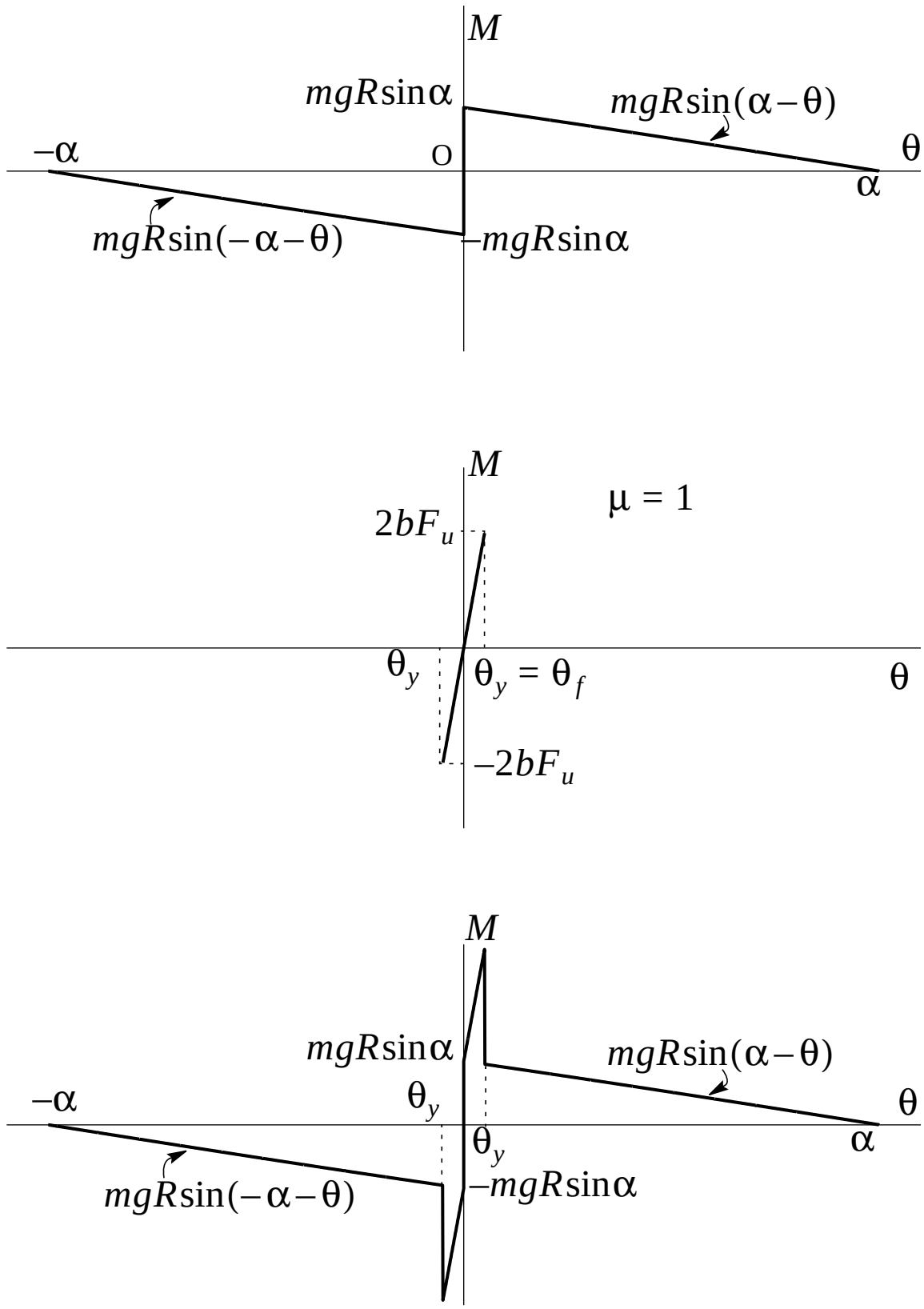

Figure 26. Moment-rotation curves of: (Top) Free-standing block; (Center) Elastic-brittle anchorage; (Bottom) Anchored block with elastic-brittle restrainers

excitation only, the equations that govern the rocking motion of an anchored block with mass m are

$$I_0\ddot{\theta}(t) + mgR\sin[-\alpha-\theta(t)] + 4Kb^2\sin\theta(t) = -m\ddot{u}_g(t)R\cos[-\alpha-\theta(t)]\,,\ \theta<0 \tag{4-1}$$

$$I_0\ddot{\theta}(t) + mgR\sin[\alpha-\theta(t)] + 4Kb^2\sin\theta(t) = -m\ddot{u}_g(t)R\cos[\alpha-\theta(t)]\,,\ \theta>0 \tag{4-2}$$

For a rectangular block, $I_0 = \frac{4}{3}mR^2$, equations (4-1) and (4-2) can be expressed in the compact form:

$$\ddot{\theta}(t) = -p^2\left\{\sin(\alpha\,\mathrm{sgn}[\theta(t)]-\theta(t)) + \frac{3K\sin^2\alpha}{mp^2}\sin\theta(t) + \frac{\ddot{u}_g}{g}\cos[\alpha\,\mathrm{sgn}\theta(t)-\theta(t)]\right\} \tag{4-3}$$

in which $p = \sqrt{3g/(4R)}$.

Equation (4-3) is valid as long as the restrainers hold. Once they fail it reduces to

$$\ddot{\theta}(t) = -p^2\left\{\sin(\alpha\,\mathrm{sgn}[\theta(t)]-\theta(t)) + \frac{\ddot{u}_g}{g}\cos(\alpha\,\mathrm{sgn}\theta(t)-\theta(t))\right\} \tag{4-4}$$

which is the equation of motion of the free-standing block under horizontal excitation only.

Figure 26 (bottom) shows the moment-rotation relation during the rocking motion of an anchored block. For rotation angles, $|\theta(t)| \le \theta_y$, energy is lost only during impact. Once θ_y is exceeded, the restrainer from the uplifted side fractures and additional energy is dissipated equal to the area of the small triangle that is superimposed to the moment-rotation graph of the free-standing block. This energy is dissipated once, since in subsequent post-fracture oscillations the moment-rotation relation reduces to that of the free-standing block.

The transition from equation (4-3) to (4-4) is conducted by following a fracture function $f(\theta)$. The finite ultimate strength of the restrainer, F_u, in conjunction with the linear pre-fracture behavior defines the angle of rotation θ_y that the restrainers yield and also, in this case, fracture

$$F_u = Ku_y = 2Kb\theta_y\,; \tag{4-5}$$

from which

$$\theta_y = \frac{F_u}{2Kb}\,. \tag{4-6}$$

The fracture function $f(\theta)$ is defined as

$$f(\theta) = 1 \text{ when } |\theta(t)| \le \theta_y \tag{4-7}$$

and

$$f(\theta) = 0 \text{ when } |\theta(t)| \ge \theta_y \tag{4-8}$$

With the help of the fracture function, after replacing K/m with $(F_u/u_y)(g/W)$, the pre-fracture and post-fracture equation of motion of the rigid block can be expressed in a compact form

$$\ddot{\theta}(t) = -p^2\left\{\sin[\alpha\,\mathrm{sgn}\theta - \theta(t)] + \frac{3F_u g\sin^2\alpha}{Wu_y p^2}\sin\theta(t)\,f(\theta) + \frac{\ddot{u}_g}{g}\cos[\alpha\,\mathrm{sgn}\theta - \theta(t)]\right\}. \qquad (4\text{-}9)$$

With this formulation the rocking response of anchored blocks is described by four parameters: the slenderness, α, the frequency parameter, p (that includes the size effect), the strength parameter, $\sigma = F_u/W$, and the influence factor, $q = u_y p^2/g$. Table 2 summarizes the physical and mechanical parameters of selected electrical equipment utilized by PG&E (Fujisaki 1999).

The solution of (4-9) is computed numerically via the same state-space formulation introduced in chapter 3. The state vector of the system is the one given by (3-1). The time-derivative vector, $f(t)$, is the one given by (3-2) in which its second component is replaced with the right-hand side of (4-9).

Figure 27 plots overturning acceleration spectra of a rigid equipment with $\alpha = 0.349\ rad\ (20°)$, $p = 2.0\ rad/sec$ and $\eta = \sqrt{r_{max}} = 0.825$. The results are computed with the nonlinear formulation given by (4-9) for the case where $F_u/W = 0$ (free-standing), $F_u/W = 0.4$ and $F_u/W = 1.0$. For small values ω_p/p (approximately $\omega_p/p < 4$) anchored equipment survive higher accelerations; however for values of $4 < \omega_p/p < 6$, anchored equipment topple under a lower acceleration than the acceleration needed to overturn the same equipment when it is free standing. This counterintuitive behavior happens in the neighborhood of the transition from mode 1 to mode 2. Anchored equipment enter this transition at a slightly larger value of ω_p/p. Furthermore, when a free-standing equipment has just entered mode 2 of overturning, the anchored equipment still overturns due to mode 1 (overturning with impact) under a smaller acceleration amplitude. As ω_p/p increases, the anchored equipment will also overturn due to mode 2, and now a higher acceleration is needed to topple it in comparison to the acceleration needed to topple the free-standing block. However, the additional acceleration amplitude that an anchored block can withstand, even with $F_u/W = 1.0$, is negligible compared to the acceleration amplitude needed to overturn the free-standing block. Figure 27 indicates that anchorages are effective at the low range of ω_p/p (low frequency pulses and/or small blocks).

Figure 28 plots the ratio of the minimum acceleration needed to overturn an anchored block, a_{p0}^{AN}, to the minimum acceleration needed to overturn a free-standing block, a_{p0}^{FS}, for vari-

Table 2: Geometrical, Physical and Structural Parameters of Electrical Equipment

Equip Weight (kips)	b (in)	h (in)	K (kips/in)	F_u (kips)	$\sigma = \frac{F_u}{W}$	α (degree)	p (rad/sec)	$q = \frac{u_y p^2}{g}$	θ_y	b/B
40	36	84	175	4	0.100	23.20	1.7803	1.8×10^{-4}	5.56×10^{-4}	N/A
40	20	59	300	16	0.400	18.43	2.157	6.4×10^{-4}	1.33×10^{-3}	N/A
550	69	100	1500	79	0.144	34.61	1.5441	3.2×10^{-4}	3.82×10^{-4}	0.7188
193	38	89	1000	53	0.275	23.12	1.7301	4.1×10^{-4}	6.97×10^{-4}	0.6667
150	44	68	1000	53	0.353	32.91	1.8911	4.9×10^{-4}	6.02×10^{-4}	0.5641
230	38	90	1500	79	0.343	22.89	1.7219	4.0×10^{-4}	6.93×10^{-4}	0.5067
175	38	74	1500	79	0.451	27.18	1.8660	4.7×10^{-4}	6.93×10^{-4}	0.5758
60	35	90	500	26	0.433	21.25	1.7320	4.0×10^{-4}	7.43×10^{-4}	0.6140
44	34	68	500	26	0.591	26.57	1.9519	5.7×10^{-4}	7.65×10^{-4}	0.5965

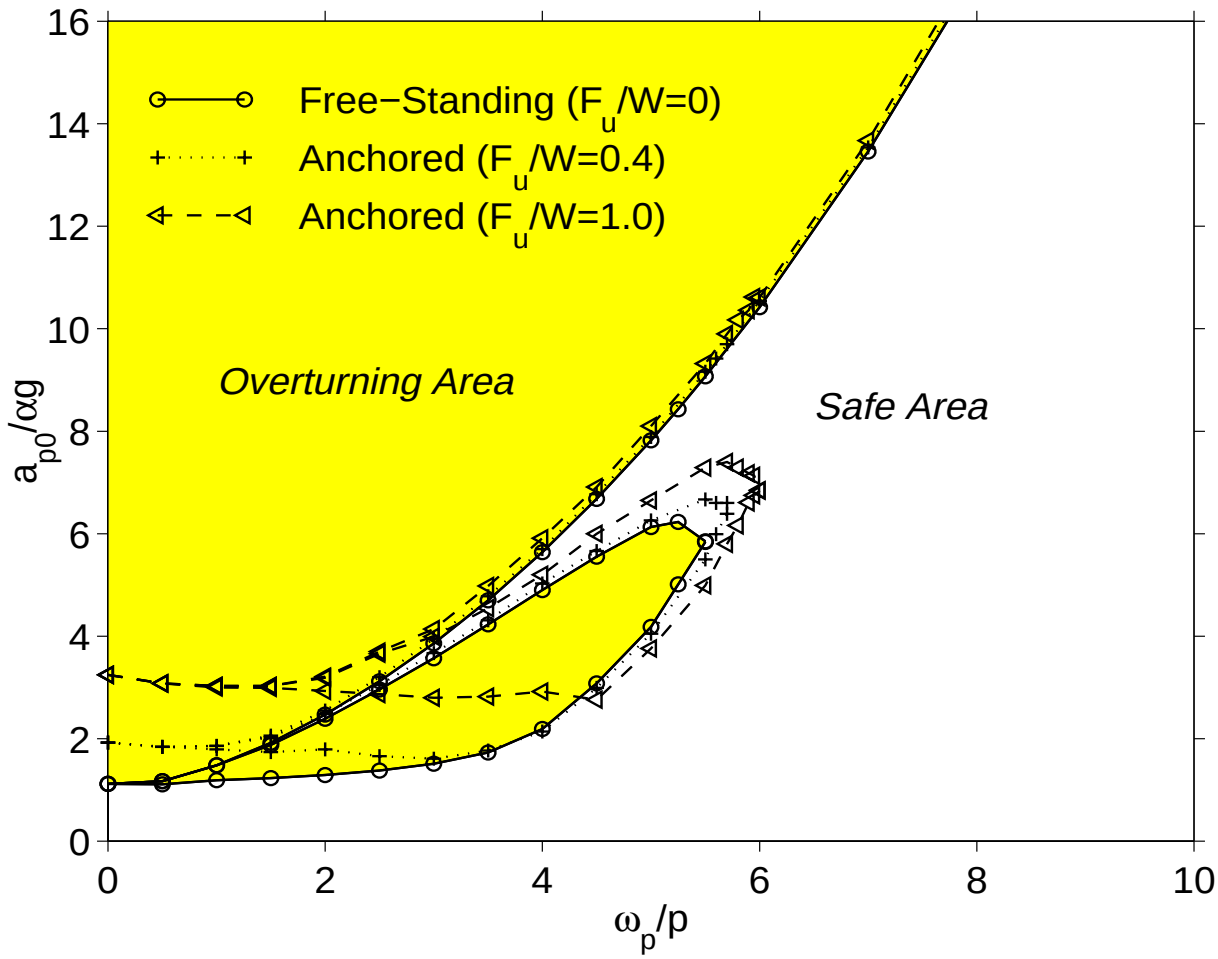

Figure 27. Comparison of overturning acceleration spectra due to a one-sine pulse of an anchored equipment ($\alpha = 0.349\ rad = 20°$, $p = 2\ rad/sec$, $\eta = 0.825$, $q = 5.2\times10^{-4}$ and $\mu = 1$) computed with the nonlinear formulation for $F_u/W = 0$, *0.4* and *1.0*

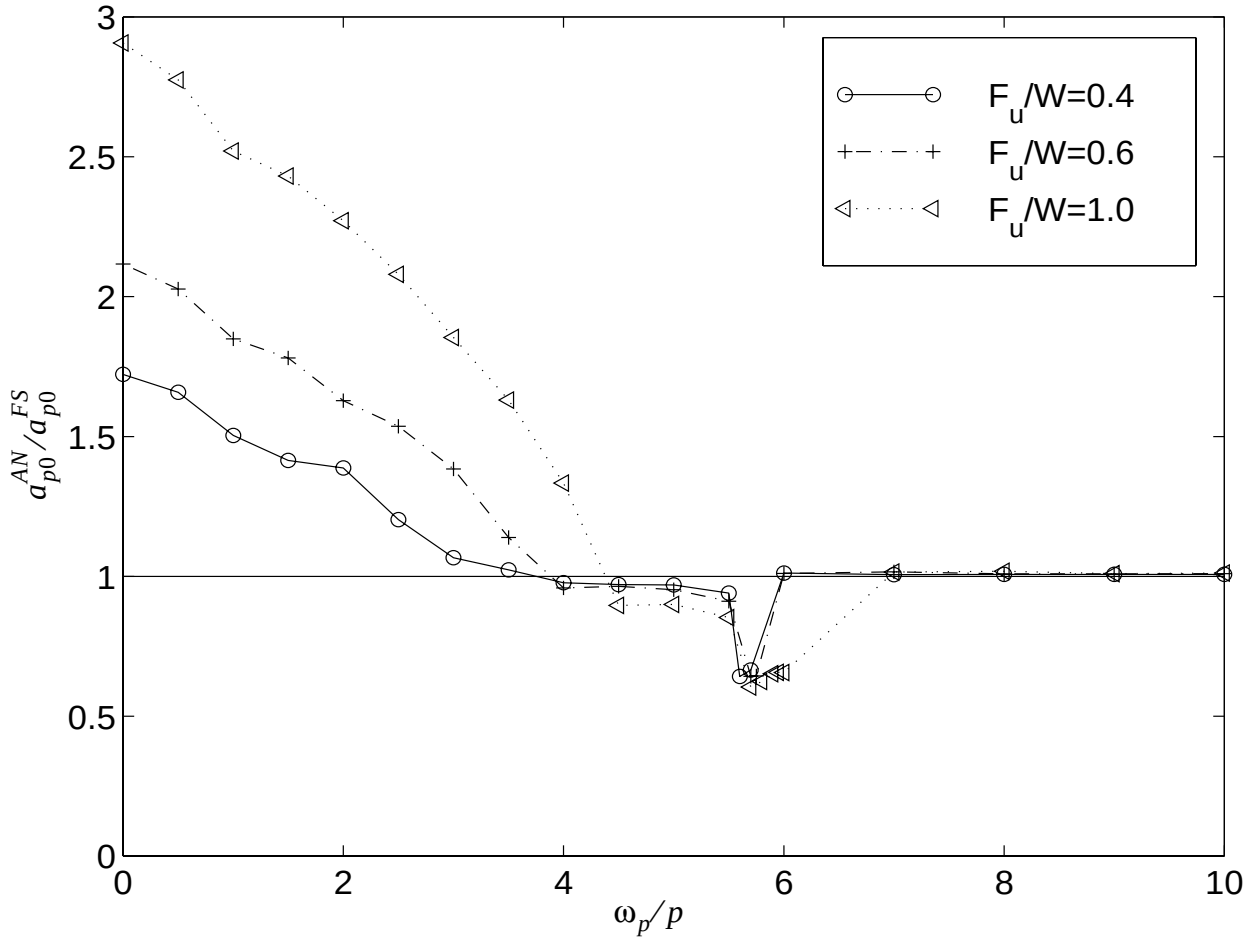

Figure 28. Normalized minimum overturning acceleration levels needed to overturn an anchored block (elastic-brittle behavior, $\mu = 1$) to the acceleration levels needed to overturn the same block when it is free-standing

ous values of the strength parameter $\sigma = F_u/W$. The results shown on Figure 28 indicate that for pulses with $\omega_p/p > 4$, blocks should not be anchored since the effect of restrainers is either destructive or virtually insignificant.

The limit capacity of the restrainers to prevent the toppling of a larger block is illustrated by comparing the potential energy of the block at the verge of overturning with the strain energy dissipated by the restrainers.

Assuming an elastic-brittle behavior, Figure 26 (center) indicates that the strain energy dissipated by the restrainers before they fracture is

$$SE = \frac{1}{2}F_u u_y \tag{4-10}$$

At the verge of overturning ($\theta = \alpha$), the kinetic energy of the block is zero since the one-sine pulse has expired and its potential energy is

$$PE = mgR(1-\cos\alpha) \tag{4-11}$$

The substitution of $\cos\alpha$ in (4-11) with its series expansion $1-\frac{\alpha^2}{2}+\ldots$ gives

$$PE \approx mgR\frac{\alpha^2}{2} \tag{4-12}$$

and the ratio of the dissipated strain energy to the total energy of the block at the verge of overturning is

$$\frac{SE}{PE} \approx \frac{F_u u_f}{mgR\alpha^2} = \frac{1}{\alpha^2}\frac{F_u}{W}\frac{u_y}{R} \tag{4-13}$$

where, $u_y = F_u/K$, is the yield displacement.

For a block with $\alpha = 0.349\ rad\ (20°)$, $p = 2.0\ rad/sec$, $R = 1.839\ m$, $u_y = 1.25\times10^{-3}\ m$ and $F_u = W$, the strain energy lost from the failure of each restrainer is approximately 0.6% of the energy that is needed to topple the free-standing block.

Equation (4-13) reveals some interesting geometrical and scale effects:

(i) The $1/\alpha^2$ term indicates that restrainers are much more effective in preventing toppling the slender of two blocks of the same size (same *R*).

(ii) The $1/R$ term indicates that restrainers are more effective in preventing toppling the smaller of two geometrically similar blocks that have the same F_u/W.

4.1.2 Linear Formulation

Equations (4-1) and (4-2) and their compact form given by (4-9) are valid for arbitrary values of the block angle, α. For slender blocks, the angle $\alpha = \tan^{-1}(b/h)$ is relatively small and equations (4-1) and (4-2) can be linearized. This linearization allows for the derivation of closed-form solutions when the excitation is expressed in a functional form. Herein, the solution of the linearized equations is derived for a sinusoidal ground motion for both positive and negative rotations in order to validate the fidelity of the numerical solution presented in the foregoing subsection. Within the limits of the linear approximation and for a ground acceleration

$$\ddot{u}_g(t) = a_p \sin(\omega_p t + \psi) \tag{4-14}$$

equations (4-1) and (4-2) become

$$\ddot{\theta}(t) + \lambda^2 p^2 \theta(t) = -p^2 \frac{a_p}{g} \sin(\omega_p t + \psi) + \alpha p^2 \,,\ \theta < 0 \tag{4-15}$$

and

$$\ddot{\theta}(t) + \lambda^2 p^2 \theta(t) = -p^2 \frac{a_p}{g} \sin(\omega_p t + \psi) - \alpha p^2 \,,\ \theta > 0 \tag{4-16}$$

where $\psi = \sin^{-1}(\alpha g / a_p)$ is the phase when rocking initiates and $\lambda^2 = 3(F_u/W)(g/u_y p^2)\sin^2\alpha - 1 = 3(\sigma/q)\sin^2\alpha - 1$. For typical anchorages of electrical equipment $\lambda^2 > 0$. Once the restrainers fail, $\lambda^2 = -1$. Accordingly, the solution of (4-15) and (4-16) is presented for the four segment $-\theta_y \le \theta(t) \le 0$, $\theta(t) < -\theta_y \le 0$, $0 < \theta(t) < \theta_y$ and $0 < \theta_y < \theta(t)$:

$$\theta(t) = A_1 \sin(\lambda p t) + A_2 \cos(\lambda p t) + \frac{\alpha}{\lambda^2} - \frac{1}{\lambda^2 - \frac{\omega_p^2}{p^2}} \frac{a_p}{g} \sin(\omega_p t + \psi_1) \,,\ -\theta_y \le \theta(t) \le 0 \tag{4-17}$$

$$\theta(t) = A_3 \sinh(pt) + A_4 \cosh(pt) - \alpha + \frac{1}{1 + \frac{\omega_p^2}{p^2}} \frac{a_p}{g} \sin(\omega_p t + \psi_2) \,,\ \theta(t) < -\theta_y \le 0 \tag{4-18}$$

$$\theta(t) = A_5 \sin(\lambda p t) + A_6 \cos(\lambda p t) - \frac{\alpha}{\lambda^2} - \frac{1}{\lambda^2 - \frac{\omega_p^2}{p^2}} \frac{a_p}{g} \sin(\omega_p t + \psi_3) \,,\ 0 < \theta(t) < \theta_y \tag{4-19}$$

$$\theta(t) = A_7 \sinh(pt) + A_8 \cosh(pt) + \alpha + \frac{1}{1+\frac{\omega_p^2}{p^2}} \frac{a_p}{g} \sin(\omega_p t + \psi_4),\ 0 < \theta_y < \theta(t) \tag{4-20}$$

where

$$A_1 = \frac{\dot{\theta}_0}{\lambda p} + \frac{1}{\lambda} \frac{\omega_p / p}{\lambda^2 - \omega_p^2 / p^2} \frac{a_p}{g} \cos\psi_1 \tag{4-21}$$

$$A_2 = -\frac{\alpha}{\lambda^2} + \frac{1}{\lambda^2 - \omega_p^2 / p^2} \frac{a_p}{g} \sin\psi_1 \tag{4-22}$$

$$A_3 = \frac{\dot{\theta}_y^-}{p} - \frac{\omega_p / p}{1 + \omega_p^2 / p^2} \frac{a_p}{g} \cos\psi_2 \tag{4-23}$$

$$A_4 = -\theta_y + \alpha - \frac{1}{1 + \omega_p^2 / p^2} \frac{a_p}{g} \sin\psi_2 \tag{4-24}$$

$$A_5 = \frac{\dot{\theta}_0}{\lambda p} + \frac{1}{\lambda} \frac{\omega_p / p}{\lambda^2 - \omega_p^2 / p^2} \frac{a_p}{g} \cos\psi_3 \tag{4-25}$$

$$A_6 = \frac{\alpha}{\lambda^2} + \frac{1}{\lambda^2 - \omega_p^2 / p^2} \frac{a_p}{g} \sin\psi_3 \tag{4-26}$$

$$A_7 = \frac{\dot{\theta}_y^+}{p} - \frac{\omega_p / p}{1 + \omega_p^2 / p^2} \frac{a_p}{g} \cos\psi_4 \tag{4-27}$$

$$A_8 = \theta_y - \alpha - \frac{1}{1 + \omega_p^2 / p^2} \frac{a_p}{g} \sin\psi_4 \tag{4-28}$$

In (4-21) and (4-22) $\psi_1 = \psi = \sin^{-1}(\alpha g / a_p)$ is the phase when rocking initiates. In (4-23) and (4-24) $\psi_2 = \omega_p t_y^- + \psi$, where t_y^- is the time that $-\theta_y$ is reached. In (4-25) and (4-26), $\psi_3 = \omega_p t_i + \psi$, where t_i is the time that $\theta = 0$ and the block experiences its first impact. In (4-27) and (4-28), $\psi_4 = \omega_p t_y^+ + \psi$, where t_y^+ is the time that θ_y is reached. Stepping through time the values of t_y^-, t_i and t_y^+ are detected by monitoring the value of the rotation angle θ. The solution obtained with the linear formulation is used to validate the fidelity of the numerical solution of (4-9) that is achieved with a state-space formulation.

Figure 29 plots the minimum overturning acceleration spectra computed with the linear formulation. A behavior similar to that computed with the nonlinear formulation is observed. For small values ω_p / p (approximately $\omega_p / p < 4$) anchored equipment survive higher accelerations;

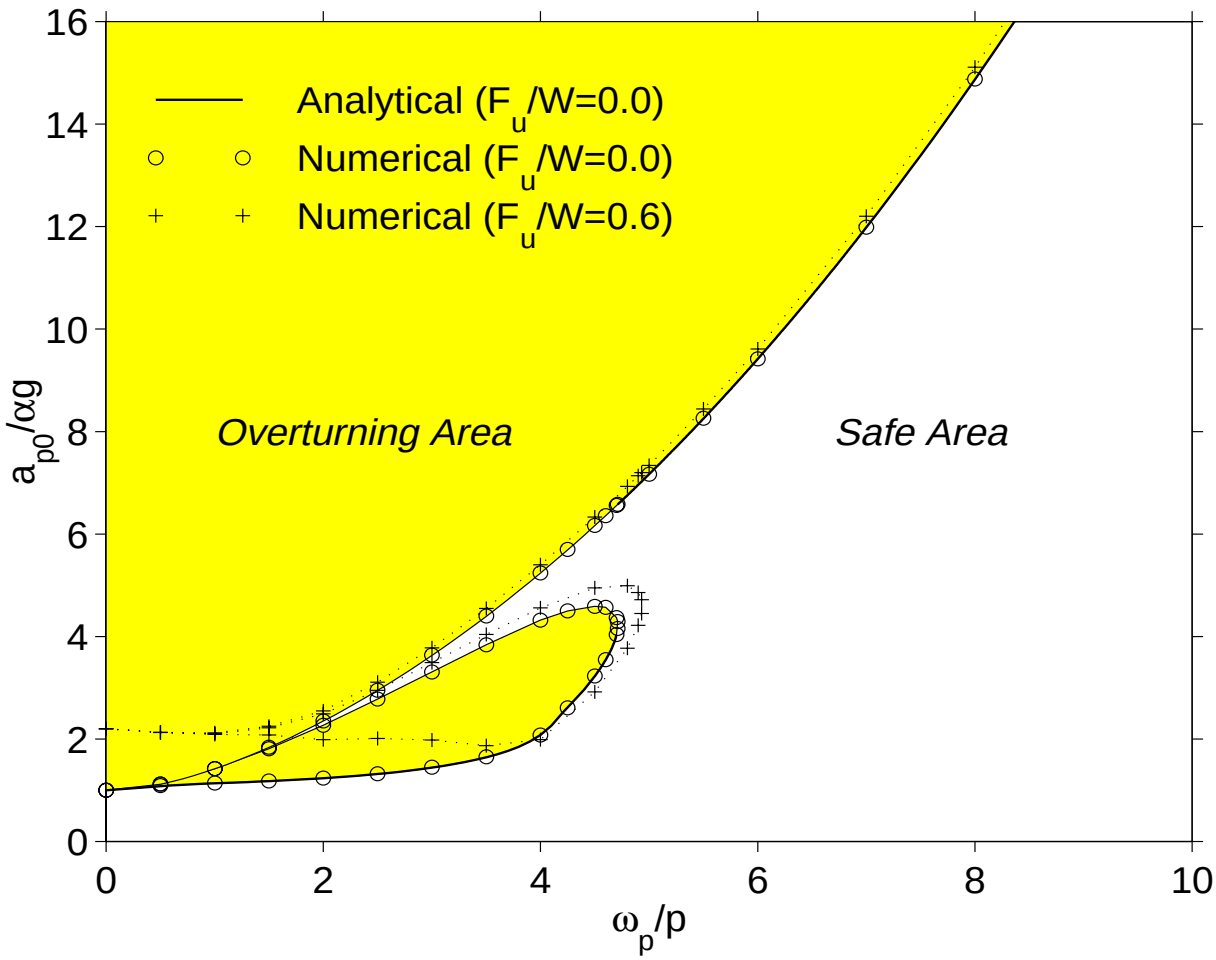

Figure 29. Comparison of overturning acceleration spectra due to a one-sine pulse of an anchored equipment ($\alpha = 0.349\ rad = 20°$, $p = 2\ rad/sec$, $\eta = 0.825$, $q = 5.2\times10^{-4}$, and $\mu = 1$) computed with the linear formulation for $F_u/W = 0$ and *0.6*. Lines: analytical solution. Points: numerical solution.

however for values of $\omega_p/p > 4$, anchored equipment topple under a lower acceleration than that needed to overturn the same equipment that is free standing. The results are computed with the analytical solution presented herein and the numerical integration that is achieved with a state-space formulation. The agreement of the two solutions is excellent.

The elastic-brittle behavior in conjunction with the linear formulation allows for an analytical solution that was used to validate the fidelity of the numerical integration. It was found that even at the limit of the linear approximation, there is a neighborhood of ω_p/p values where a free-standing block can survive a stronger acceleration than anchored blocks. Figure 30 compares the overturning spectra of an anchored block with $F_u/W = 0.4$ (top) and $F_u/W = 0.6$ (bottom) computed with the linear and nonlinear formulation. When the frequency of the one-sine pulse is relatively low, both formulations yield comparable results. As the excitation frequency increases, the linear formulation yields minimum overturning acceleration amplitudes drastically larger than those obtained with the nonlinear formulation. This result is because under the nonlinear formulation, the overturning "bay" generated by mode 1 of overturning penetrates further into the safe area under the overturning spectrum due to mode 2. As the excitation frequency further increases, the linear and nonlinear formulations again yield comparable results. This finding indicates that when $4 < \omega_p/p < 6$, the linear formulation should be avoided since it gives erroneous results even for slender blocks.

4.2 Ductile Behavior

Figure 31 illustrates the force-displacement relation of restrainers with ductile behavior. In general the restrainers can exhibit a post-yielding stiffness and maintain their strength until they reach a fracture displacement, u_f. A measure of their ductile behavior is the ductility coefficient, $\mu = u_f/u_y$. A suitable model to approximate such nonlinear hysteretic behavior is given by

$$P(t) = \varepsilon K u(t) + (1-\varepsilon) K u_y Z(t) \tag{4-29}$$

where $u(t)$ is the extension of the restrainer, K is the pre-yielding stiffness, ε is the ratio of the post- to pre-yielding stiffness, u_y is the yield displacement, and $Z(t)$ is a hysteretic dimensionless quantity that is governed by

$$u_y \dot{Z}(t) + \gamma |\dot{u}(t)| Z(t) |Z(t)|^{n-1} + \beta \dot{Z}(t) |Z(t)|^n - \dot{u}(t) = 0 \tag{4-30}$$

In the above equation β, γ and n are dimensionless quantities that control the shape of the hysteretic loop. The hysteretic model, expressed by (4-29) and (4-30), was originally proposed by

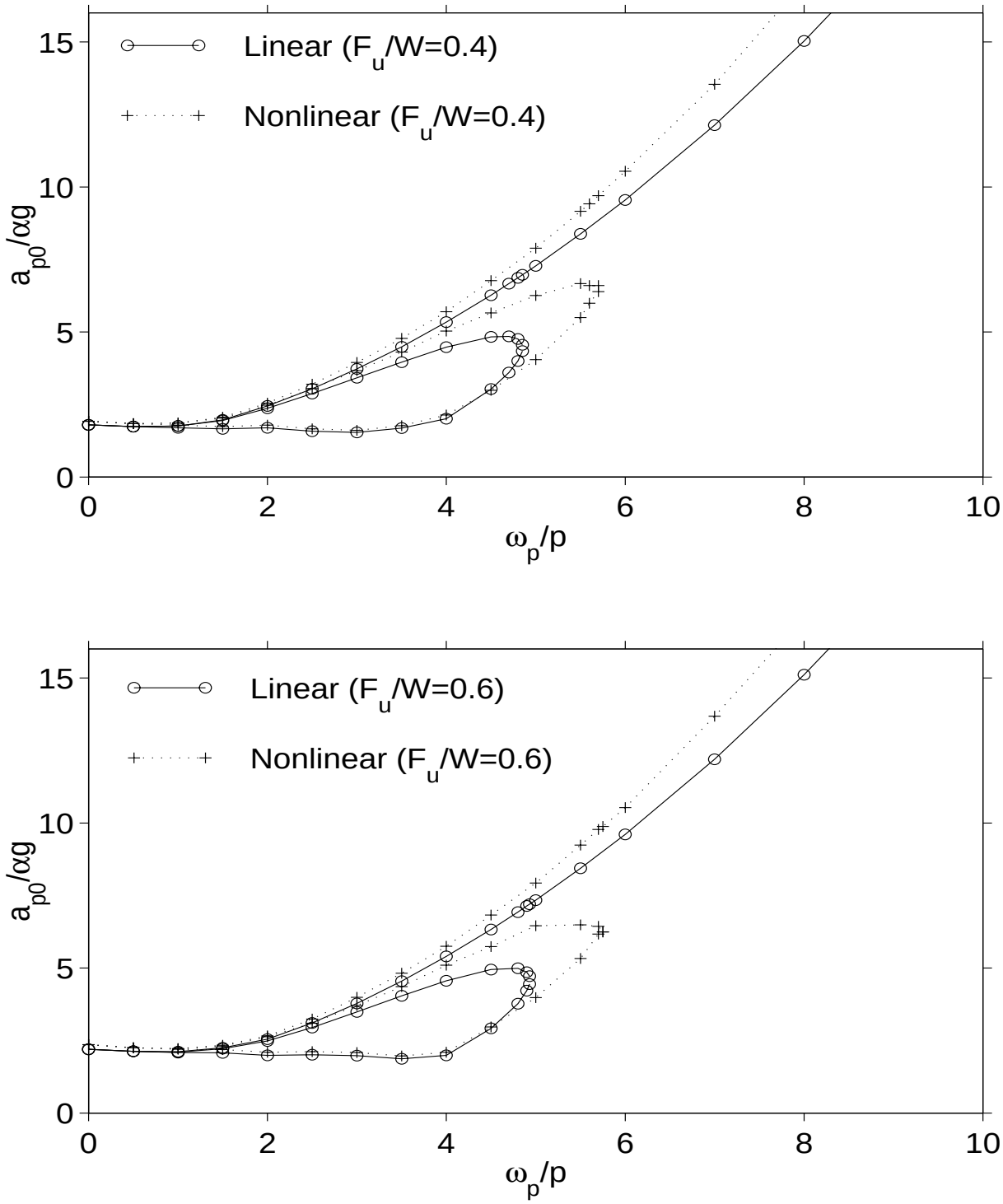

Figure 30. Comparison of the overturning acceleration spectra due to a one-sine pulse of an anchored equipment ($\alpha = 0.349\ rad = 20°$, $p = 2\ rad/sec$, $\eta = 0.825$, $q = 5.2\times10^{-4}$ and $\mu = 1$) computed with the linear and nonlinear formulation for $F_u/W = 0.4$ (top) and $F_u/W = 0.6$ (bottom)

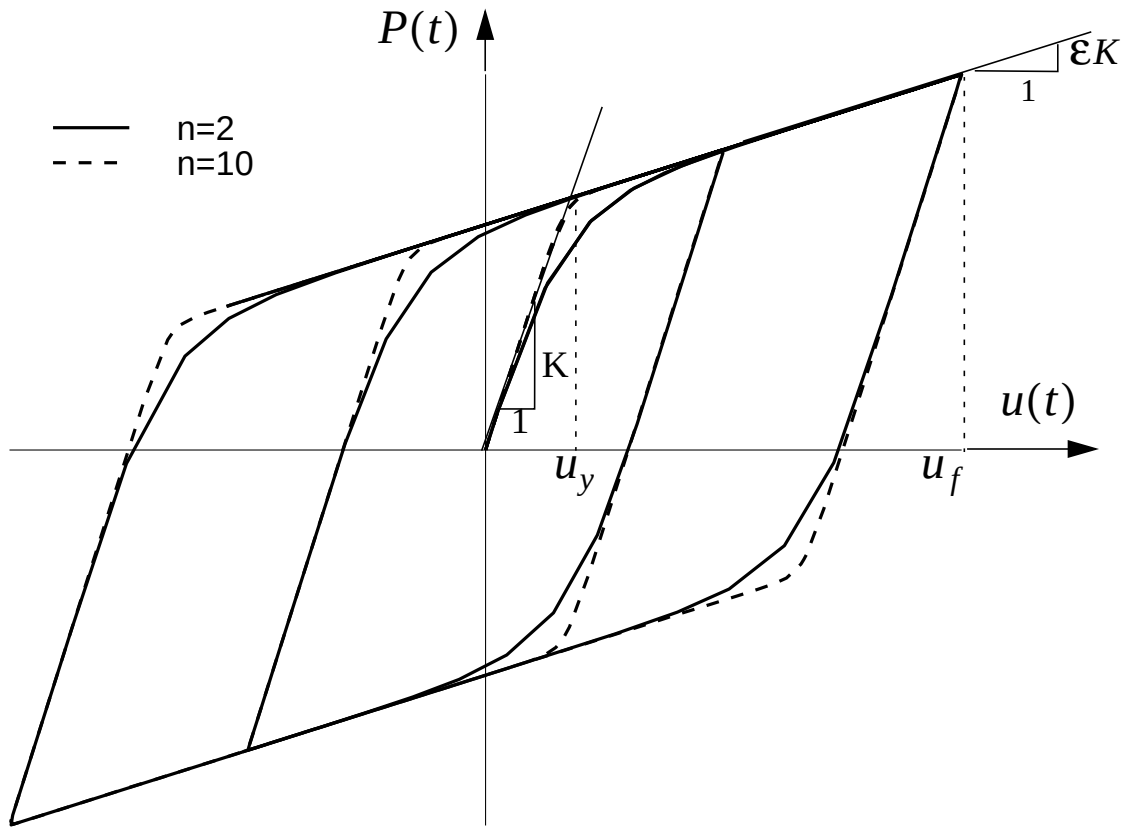

Figure 31. Force-displacement curve of an element with bilinear behavior

Bouc (1971) for n = 1, subsequently extended by Wen (1975, 1976), and used in random vibration studies of inelastic systems.

In this study the special case of elasto-plastic behavior is considered by setting the post-yielding stiffness equal to zero ($\varepsilon = 0$). However, the developed formulation can easily be extended to account for situations with $\varepsilon \neq 0$.

4.2.1 Elasto-Plastic Behavior

Figure 32 (center) illustrates the moment-rotation relation that results from the presence of restrainers with elasto-plastic behavior; while Figure 32 (top) illustrates again the moment-rotation relation of a free-standing block. Under these two restoring mechanisms, the equations that govern the rocking motion of an anchored block with mass m and moment of inertia I_0 (about pivot point O or O') is

$$I_0\ddot{\theta}(t) + m\ddot{u}_g R\cos(-\alpha-\theta) = -mgR\sin(-\alpha-\theta) - P(t)2b\cos\left(\frac{\theta}{2}\right),\ \theta<0 \tag{4-31}$$

and

$$I_0\ddot{\theta}(t) + m\ddot{u}_g R\cos(\alpha-\theta) = -mgR\sin(\alpha-\theta) - P(t)2b\cos\left(\frac{\theta}{2}\right),\ \theta>0 \tag{4-32}$$

where $P(t)$ is the force originating from the restrainers that for the general case is give by (4-29) and the special elasto-plastic case ($\varepsilon = 0$) reduces to

$$P(t) = Ku_yZ(t) \tag{4-33}$$

With reference to Figure 32, $u_y = 2b\theta_y$, and equation (4-33) gives

$$P(t) = 2Kb\theta_yZ(t) \tag{4-34}$$

Substitution of (4-34) into (4-31) and (4-32)gives

$$I_0\ddot{\theta}(t) + mgR\sin(-\alpha-\theta) + 4Kb^2\theta_yZ(t)\cos\left(\frac{\theta}{2}\right) = -m\ddot{u}_g(t)R\cos(-\alpha-\theta),\ \theta<0 \tag{4-35}$$

and

$$I_0\ddot{\theta}(t) + mgR\sin(\alpha-\theta) + 4Kb^2\theta_yZ(t)\cos\left(\frac{\theta}{2}\right) = -m\ddot{u}_g(t)R\cos(\alpha-\theta),\ \theta>0 \tag{4-36}$$

Using that for a rectangular block, $I_0 = \frac{4}{3}mR^2$, equation (4-35) and (4-36) can be expressed in the compact form:

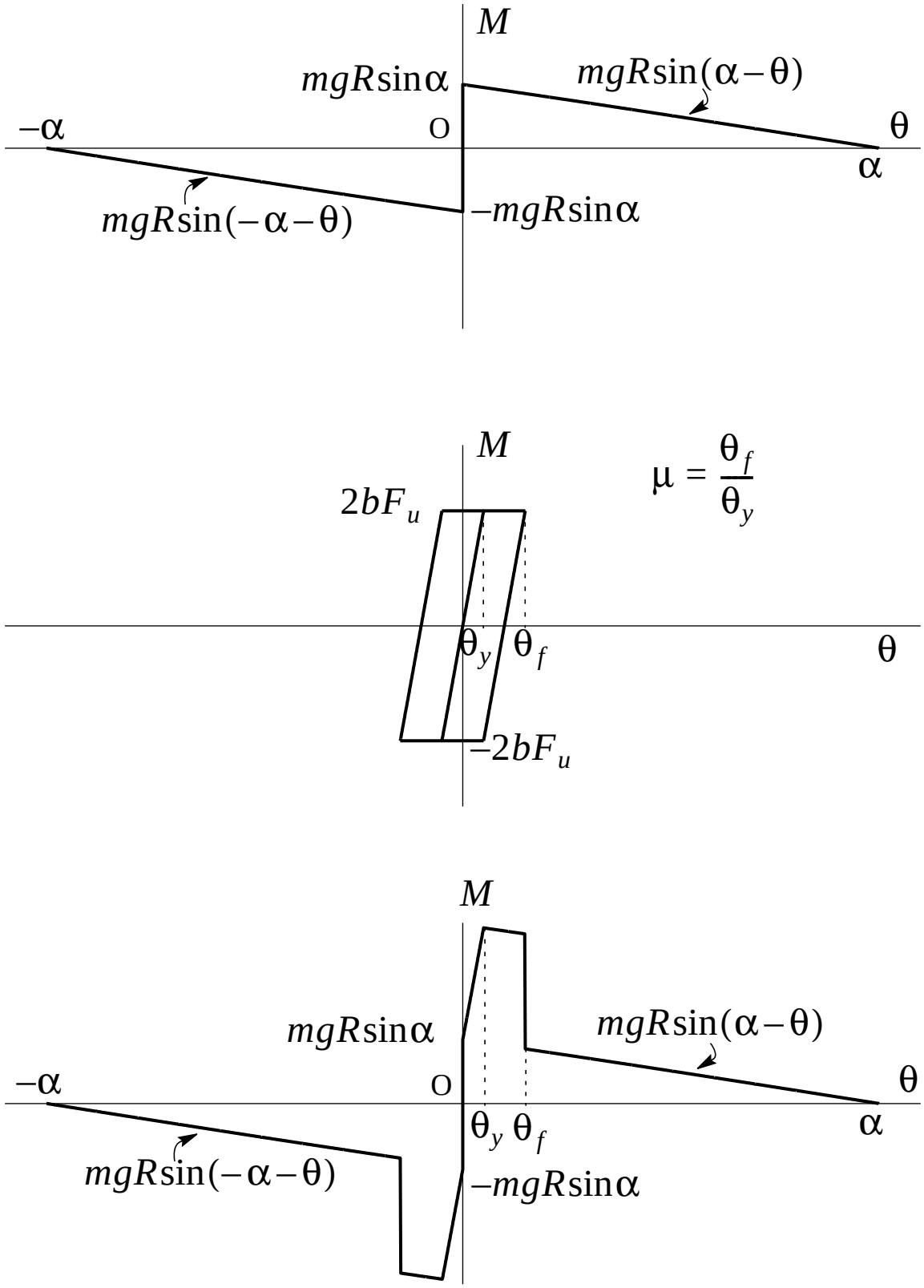

Figure 32. Moment-rotation curves of (Top) Free-standing block; (Center) Elastic-plastic anchorage; (Bottom) Anchored block with elastic-plastic restrainers

$$\ddot{\theta}(t) = -p^2\left\{\sin[\alpha\,\mathrm{sgn}\,\theta(t)-\theta(t)] + \frac{\ddot{u}_g(t)}{g}\cos[\alpha\,\mathrm{sgn}\,\theta(t)-\theta(t)] + \frac{3\sigma\sin^2\alpha}{q}\theta_y Z(t)\cos\left(\frac{\theta}{2}\right)\right\} \tag{4-37}$$

where $p = \sqrt{3g/(4R)}$, $\sigma = F_u/W$, $q = u_y p^2/g$, and $Z(t)$ is the solution of (4-30) which in terms of rotations takes the form

$$\theta_y\dot{Z}(t) + \gamma|\dot{\theta}(t)|Z(t)|Z(t)|^{n-1} + \beta\dot{\theta}(t)|Z(t)|^n - \dot{\theta}(t) = 0 \tag{4-38}$$

Equation (4-37) is valid as long as the restrainers hold. Once their fracture displacement, $u_f = 2b\sin\theta_f$, is reached they do not provide any resistance, and equation (4-37) reduces to the equation of motion of the free-standing block given by (4-4).

Figure 32 (bottom) shows the moment-rotation relation during the rocking motion of an anchored block that its restrainers exhibit elasto-plastic behavior. For rotation angles $|\theta(t)| \le \theta_y$, energy is lost only during the reversal of motion due to impact. Once θ_y is exceeded, the restrainers along the uplifted side yield. In the case that the motion reverses before the rotation reaches θ_f, additional energy is dissipated equal to the area of the flag-shape shaded regions. This dissipation mechanism will be repeated as long as the maximum rotation does not reach the fracture rotation, θ_f. If θ_f is exceeded, the restrainers fracture and the moment curvature curve reduces to that of the free-standing block.

The transition from equation (4-37) to (4-4) is conducted with the fracture function $f(\theta)$ defined as

$$f(\theta) = 1 \text{ when } |\theta(t)| \le \theta_f \tag{4-39}$$

and

$$f(\theta) = 0 \text{ when } |\theta(t)| \ge \theta_f \tag{4-40}$$

where $\theta_f = \mu\theta_y$ and θ_y is given by (4-6). With the help of the fracture function, the pre-fracture and post-fracture equation of rocking motion can be expressed as

$$\ddot{\theta}(t) = -p^2\left\{\sin[\alpha\,\mathrm{sgn}\,\theta-\theta(t)] + \frac{\ddot{u}_g(t)}{g}\cos[\alpha\,\mathrm{sgn}\,\theta-\theta(t)] + \frac{3\sigma\sin^2\alpha}{q}\theta_y Z(t)\cos\left(\frac{\theta(t)}{2}\right)f(\theta)\right\} \tag{4-41}$$

The integration of (4-41) requires the simultaneous integration of (4-38). In this case the state vector of the system is

$$\{y(t)\} = \begin{Bmatrix} \theta(t) \\ \dot{\theta}(t) \\ Z(t) \end{Bmatrix} \tag{4-42}$$

and the time derivative vector $f(t)$ is

$$f(t) = \begin{Bmatrix} \dot{\theta}(t) \\ -p^2\Big(\sin[\alpha \operatorname{sgn}\theta(t) - \theta(t)] + \dfrac{\ddot{u}_g}{g}\cos[\alpha \operatorname{sgn}\theta(t) - \theta(t)] \\ + \dfrac{3\sigma \sin^2\alpha}{q}\theta_y Z(t)\cos\Big(\dfrac{\theta(t)}{2}\Big) f(\theta)\Big) \\ \dfrac{1}{\theta_y}[\dot{\theta}(t) - \gamma|\dot{\theta}(t)|Z(t)|Z(t)|^{n-1} - \beta\dot{\theta}(t)|Z(t)|^n] \end{Bmatrix} \tag{4-43}$$

Figure 33 plots the normalized minimum acceleration amplitude, $a_{p0}/\alpha g$, of a one-sine pulse needed to overturn an anchored block. The results are computed with the nonlinear formulation for an influence factor $q = 5.2\times10^{-4}$, ductility $\mu = 5$, and various values of the restrainer strength F_u/W.

At the zero-limit of ω_p/p a block with finite size is subjected to a very long duration pulse. When this pulse is near its peak, the block is subjected to a nearly constant acceleration a_{p0}. When the restrainers yield elastic-plastic behavior (see Figure 32) the balance of moment when the restrainers reach their ultimate strength is

$$ma_{p0}R\cos(\alpha-\theta_y) = mg\sin(\alpha-\theta_y) + F_u 2b\cos\Big(\frac{\theta_y}{2}\Big) \tag{4-44}$$

in which θ_y is given by (4-6). After dividing both sides of (4-44) with $mR\cos(\alpha-\theta_y)$ one obtains

$$a_{p0} = g\frac{\sin(\alpha-\theta_y)}{\cos(\alpha-\theta_y)} + 2\frac{F_u}{W}g\tan\alpha\frac{\cos(\theta_y/2)}{\cos(\alpha-\theta_y)} \tag{4-45}$$

Equation (4-45) is the equivalent West's formula (Milne 1885) for an anchored block with elasto-plastic restrainers that exhibit ultimate strength F_u. The parameters F_u, K, and b, related to electrical equipment, yield a value of θ_y much smaller than α, while $\cos\frac{\theta_y}{2} \approx 1$. Under these conditions equation (4-45) simplifies to

$$a_{p0} = g\tan\alpha + 2\frac{F_u}{W}g\tan\alpha\frac{1}{\cos\alpha}, \tag{4-46}$$

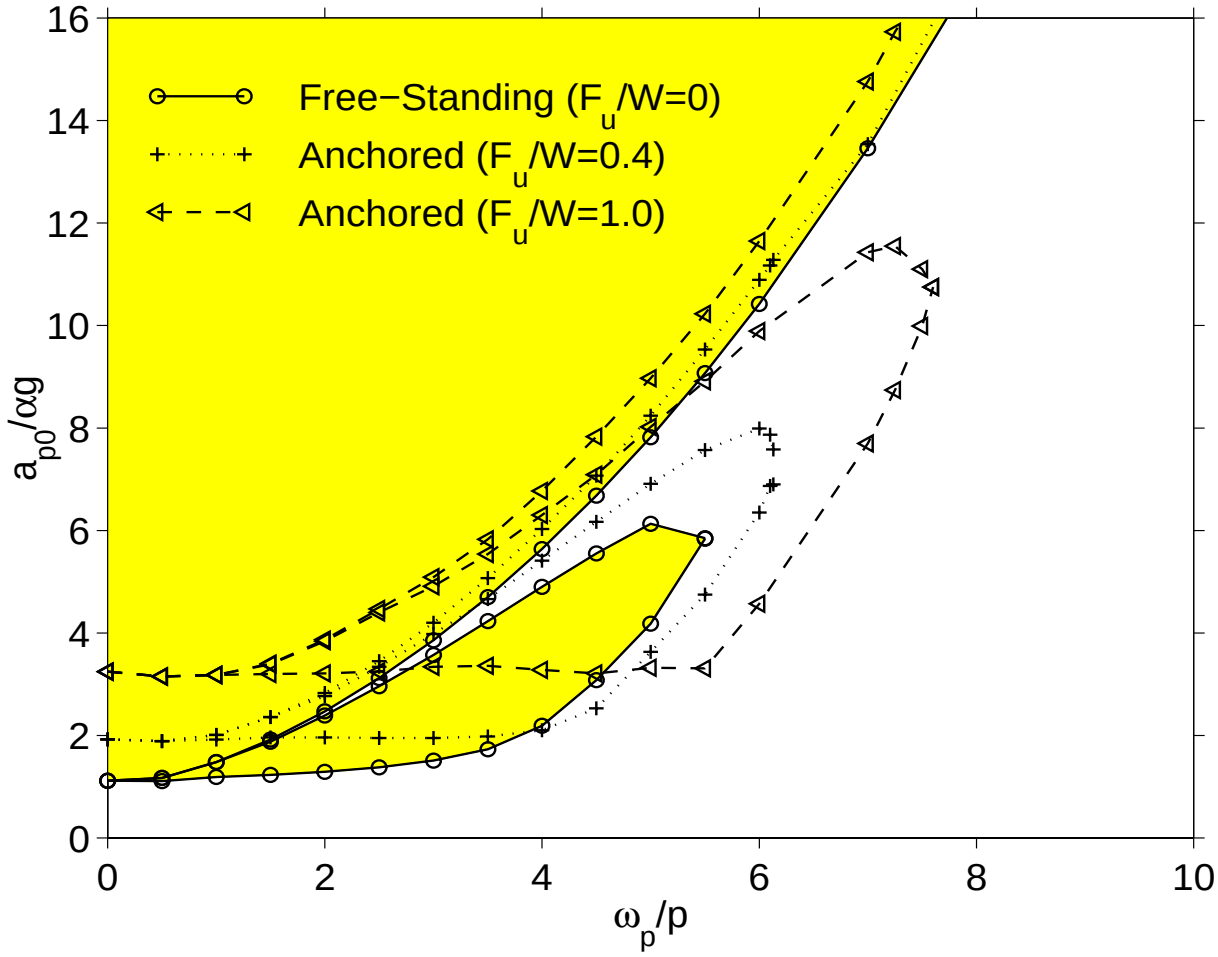

Figure 33. Overturning acceleration spectra due to a one-sine pulse of an anchored block ($\alpha = 0.349\ rad = 20°$, $p = 2\ rad/sec$, $\eta = 0.825$, $q = 5.2\times10^{-4}$ and $\mu = 5$) with restrainer strength $F_u/W = 0$, *0.4*, and *1.0*. The solution is computed with the nonlinear formulation.

and for slender blocks, $\tan\alpha \approx \alpha + \alpha^3/3$, $\cos\alpha \approx 1 - \alpha^2/2$; therefore, equation (4-46) further simplifies to

$$\frac{a_{p0}}{\alpha g} \approx \left[1 + 2\frac{F_u}{W} + \alpha^2\left(\frac{1}{3} + \frac{5}{3}\frac{F_u}{W}\right)\right] \tag{4-47}$$

when terms are retained up to α^2.

At the zero-frequency limit the numerical solution for a_{p0} approaches the static limit computed with (4-46) or with its slender-block approximation given by (4-47). As the ratio ω_p/p increases, the acceleration needed to overturn an anchored block with ductility $\mu = 5$ maintains a nearly constant value and then increases drastically. The larger the strength ratio, $\sigma = F_u/W$, the larger is the frequency range that the minimum overturning acceleration is constant. This finding leads to the counterintuitive situation where within the range $4 < \omega_p/p < 7.5$, the stronger the restrainers, the smaller the acceleration needed to overturn the block; whereas, free-standing blocks are the most stable. When ω_p/p is sufficiently large so that an anchored block overturns with mode 2, then an anchored block can sustain a slightly larger acceleration than free-standing blocks.

Figure 34 plots the ratio between the minimum overturning acceleration of an anchored block, a_{p0}^{AN}, to the minimum overturning acceleration, a_{p0}^{FS}, of a free-standing block. In the frequency range, $4 < \omega_p/p < 7.5$, the ratio a_{p0}^{AN}/a_{p0}^{FS} is less than one; therefore, the effect of anchorage is destructive. For an electrical equipment with frequency parameter $p \approx 2\ rad/sec$, this range corresponds to frequencies $1.27\ Hz < f_p < 2.28\ Hz$; or in terms of predominant pulse periods $0.4\ sec < T_p < 0.8\ sec$. For this period range that is of central interest to earthquake engineering, a free-standing block can withstand a larger acceleration amplitude than an anchored block.

Figure 35 compares the overturning acceleration spectra of anchored blocks that have restrainers with the same strength but different ductility. Again there is a frequency range where the block equipped with the less ductile restrainers will survive stronger accelerations than the block with more ductile restrainers.

The limited capacity of the restrainers with finite ductility to prevent the toppling of large blocks can be illustrated again by comparing the potential energy of the block at the verge of overturning with the strain energy dissipated by the ductile restrainers. Assuming an elasto-plastic behavior ($\varepsilon = 0$), Figure 32 (center) indicates that the strain energy dissipated by the restrainers before they fracture is

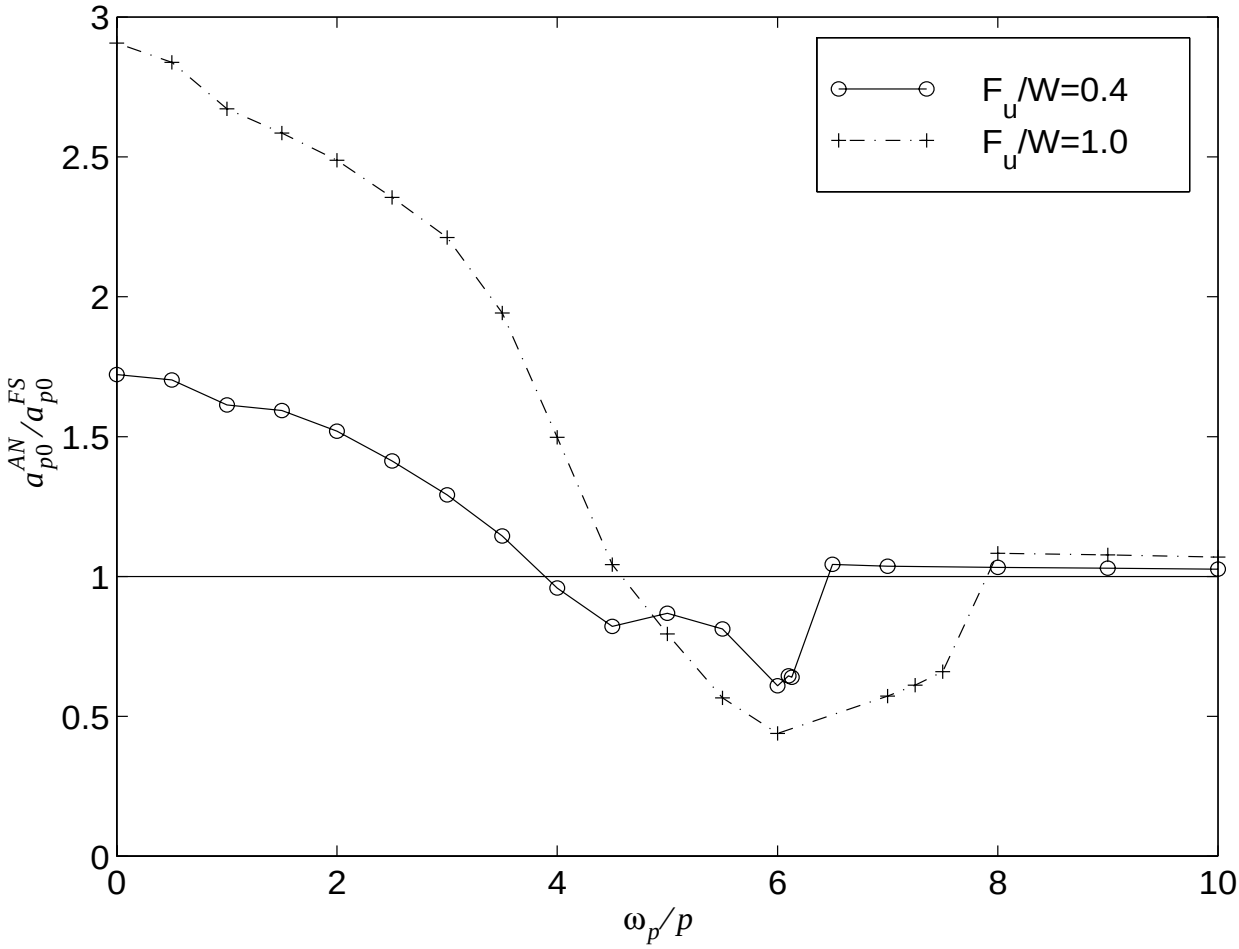

Figure 34. Normalized minimum overturning acceleration levels needed to overturn an anchored block (elastic-plastic behavior, $\mu = 5$) to the acceleration level needed to overturn the same block when it is free standing. When $\omega_p/p > 4$, blocks should not be anchored since the effect of the restrainers is destructive or virtually insignificant.

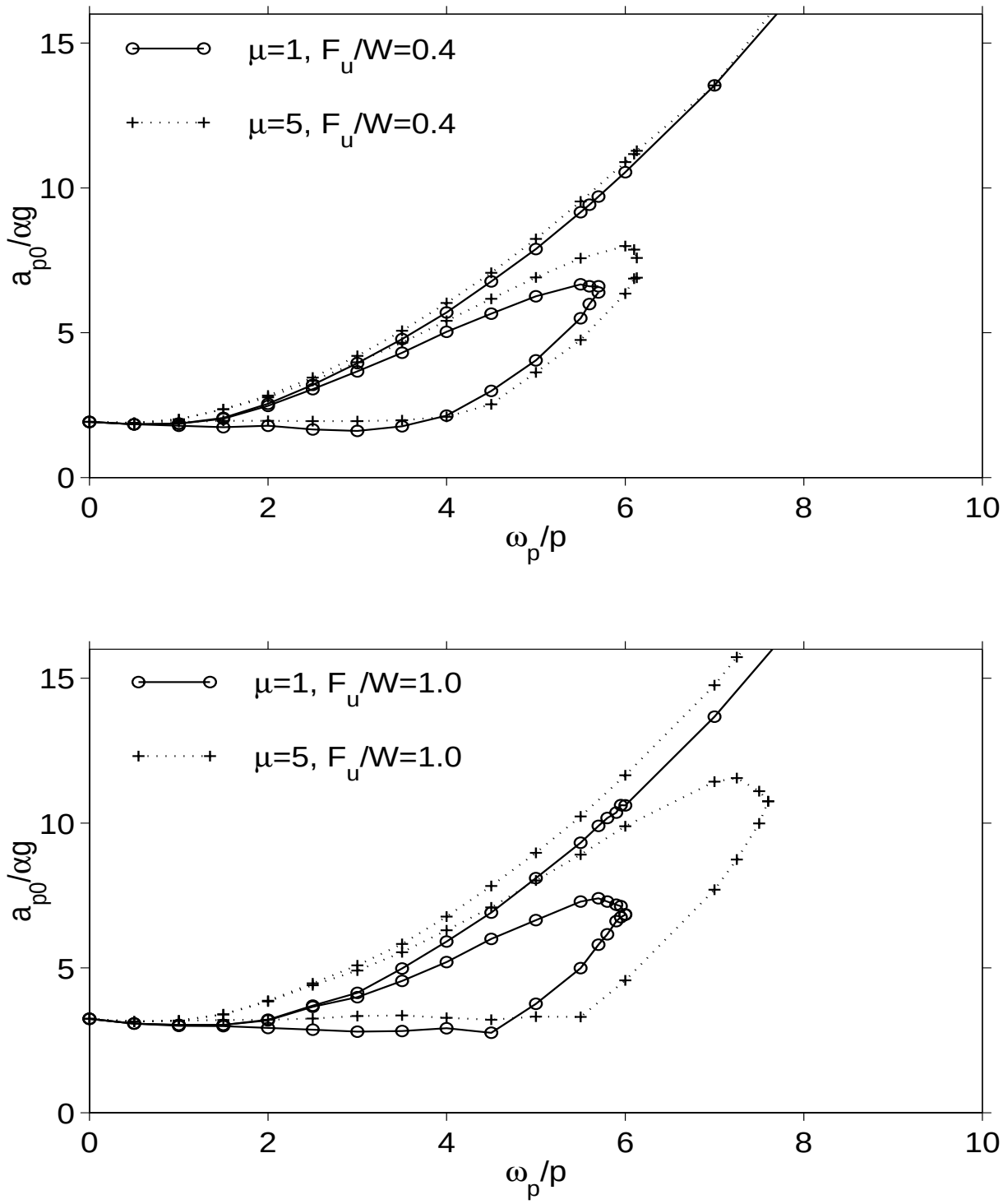

Figure 35. Comparison of overturning acceleration spectra computed with the nonlinear formulation for an anchored block ($\alpha = 0.349\ rad = 20°$, $p = 2\ rad/sec$, $\eta = 0.825$ and $q = 5.2\times10^{-4}$) with two levels of ductility: $\mu = 1$ and $\mu = 5$. Top: $F_u/W = 0.4$; Bottom: $F_u/W = 1.0$.

$$SE \approx F_u u_f \tag{4-48}$$

At the verge of overturning ($\theta = \alpha$) the kinetic energy of the block is zero since the one-sine pulse has expired and its potential energy is given by (4-12). Therefore, the ratio of the dissipated strain energy to the total energy of the block at the verge of overturning is

$$\frac{SE}{PE} \approx \frac{2F_u u_f}{mgR\alpha^2} = \frac{2}{\alpha^2}\frac{F_u}{W}\mu\frac{u_y}{R} \tag{4-49}$$

where, $u_y = F_u/K$, is the yield displacement.

For a value of $F_u/W = 0.1$ and ductility $\mu = 5$, the ratio SE/PE for the $0.5\ m \times 1.5\ m$ block ($\alpha = 0.3217$, $u_y = 1.30\times10^{-3}\ m$ and $R = 1.581\ m$) is equal to 0.83%, which is a very small fraction. Even if the restrainers had strength $F_u = W$, the strain energy lost due to ductile behavior is 8.3% of the energy needed to topple the free-standing block.

Equation (4-49) reveals the same geometrical and scale effects:

(i) The $1/\alpha^2$ term indicates that restrainers are much more effective in preventing toppling the slender of two blocks of the same size (same *R*).

(ii) The $1/R$ term indicates that restrainers are more effective in preventing toppling the smaller of two geometrically similar blocks that have the same F_u/W.

Equation (4-49) can be expressed alternatively in terms of the length, L_B, of the bolts used to anchored the equipment. Using that the yield strain of the bolt $\varepsilon_y = u_y/L_B$, equation (4-49) gives

$$\frac{SE}{PE} \approx \frac{2}{\alpha^2}\frac{F_u}{W}\mu\varepsilon_y\frac{L_B}{R} \tag{4-50}$$

in which $10^{-3} \le \varepsilon_y \le 5\times10^{-3}$ depending on the bolt steel.

Equation (4-49) or (4-50) is the result of an ultimate strength approach that is independent of the dynamic effect. Consequently the ratio $(PE + SE)/PE$, which is the ratio of the total energy that the anchored block has adopted at the verge of overturning, to the corresponding energy that the free-standing block has adopted does not relate directly to the ratio between the minimum overturning acceleration of the anchored block, a_{p0}^{AN}, and the minimum overturning acceleration, a_{p0}^{FS}, of the free-standing block.

CHAPTER 5
ROCKING RESPONSE OF ANCHORED EQUIPMENT TO EARTHQUAKE EXCITATIONS

In chapter 4 an in-depth analysis of the rocking response of anchored equipment subjected to a Type-A trigonometric pulse was presented. The analysis revealed that under a one-sine (Type-A) pulse there are two modes of overturning. The presence of restrainers is more effective for low-frequency pulses or small blocks. As the size of the block or the frequency of the pulse increases, the presence of restrainers is destructive, since anchored blocks overturn under acceleration amplitudes smaller than those needed to overturn free-standing blocks. For large values of ω_p / p, blocks overturn only along mode 2 (no impact) and the effect of the restrainers is marginal.

In this chapter the seismic response of anchored blocks subjected to selected strong ground motions is presented. Figure 36 (left) portrays the fault-normal component of the acceleration, velocity, and displacement histories of the January 17, 1994, Northridge California, earthquake recorded at the Rinaldi station. This motion resulted in a forward ground displacement that recovered partially. The velocity history has a large positive pulse and a smaller negative pulse that is responsible for the partial recovery of the ground displacement. Had the negative velocity pulse generated the same area as the positive velocity pulse, the ground displacement would have fully recovered. Accordingly, the fault-normal component of the Rinaldi station record is in between a forward and a forward-and-back pulse. Figure 36 (center) plots the acceleration, velocity and displacement histories of a Type-A cycloidal pulse given by (Jacobsen and Ayre 1958; Makris 1997)

$$\ddot{u}_g(\tau) = \omega_p \frac{v_p}{2} \sin(\omega_p \tau) \ , \ 0 \le \tau \le T_p \ , \tag{5-1}$$

$$\dot{u}_g(\tau) = \frac{v_p}{2} - \frac{v_p}{2} \cos(\omega_p \tau) \ , \ 0 \le \tau \le T_p \ , \tag{5-2}$$

$$u_g(\tau) = \frac{v_p}{2} \tau - \frac{v_p}{2\omega_p} \sin(\omega_p \tau) \ , \ 0 \le \tau \le T_p \ . \tag{5-3}$$

by assuming a pulse duration $T_p = 0.8 \ sec$ and a velocity amplitude $v_p = 1.75 \ m/sec$ which are approximations of the duration and velocity amplitude of the first main pulse shown in the record. This comparison indicates that the simple one-sine pulse that was used in this study to uncover the many complexities of the rocking response of a rigid block can approximate the kine-

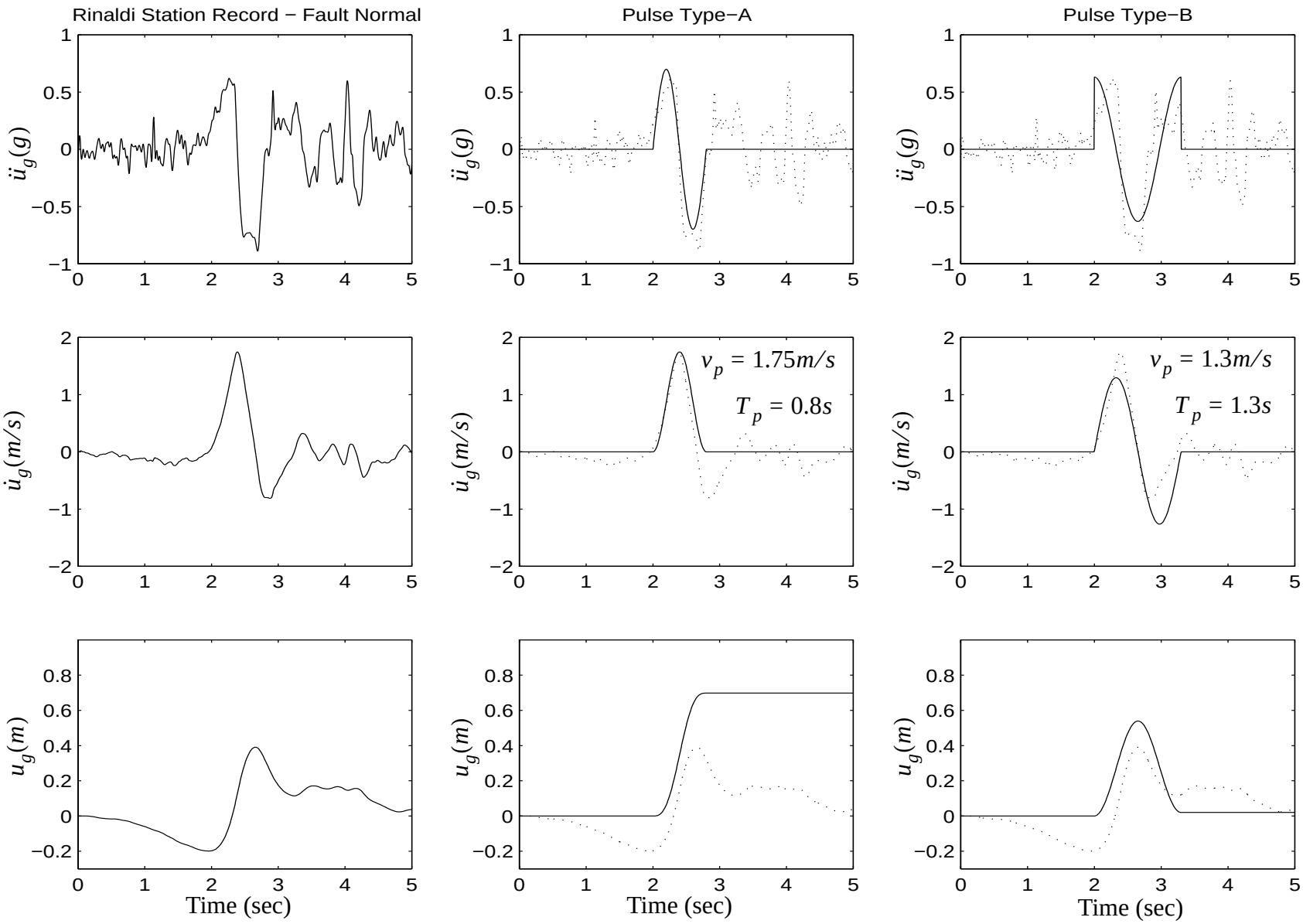

Figure 36. Fault normal components of the acceleration, velocity, and displacement time histories recorded at the Rinaldi station during the January 17, 1994, Northridge, California, earthquake (left); a cycloidal type-A pulse (center); and a cycloidal type-B pulse (right)

matic characteristics of some recorded ground motions. Figure 36 (right) plots the acceleration, velocity and displacement histories of a Type-B cycloidal pulse given by (Makris 1997)

$$\ddot{u}_g(\tau) = \omega_p v_p \cos(\omega_p \tau) \ , \ 0 \le \tau \le T_p \ , \tag{5-4}$$

$$\dot{u}_g(\tau) = v_p \sin(\omega_p \tau) \ , \ 0 \le \tau \le T_p \ , \tag{5-5}$$

$$u_g(\tau) = \frac{v_p}{\omega_p} - \frac{v_p}{\omega_p} \cos(\omega_p \tau) \ , \ 0 \le \tau \le T_p \ . \tag{5-6}$$

by considering a pulse duration $T_p = 1.3\ sec$ and a velocity amplitude $v_p = 1.3\ m/sec$.

We commence our analysis by computing rocking time histories of a $0.5\ m \times 1.5\ m$ $(19.7\ in \times 59.0\ in)$ block with frequency parameter, $p = 2.157$, and slenderness, $\alpha = 18.43°$. Consider that this block is the idealization of an electrical equipment with weight, $W = mg = 40\ kips$ that is anchored with restrainers that exhibit an ultimate strength from each side of $F_u = 0.4W = 16\ kips$ and a yield displacement $u_y = 0.05\ in$. Consider further that the stiffness of these restrainers is $K = 300\ kips/in$. These parameters yield an influence factor $q = u_y p^2/g = 6.0 \times 10^{-4}$ and $\sigma = F_u/W = 0.4$. Under a horizontal excitation only, Figure 15 indicates that a level of 78% of the Rinaldi station record is capable of overturning the block.

Figure 37 plots the response of the block with restrainer ductility, $\mu = 1$, at the verge of overturning. A 88% level of the Rinaldi station record is capable of overturning the block. Assuming that the Rinaldi station record can be approximated with a one-sine pulse with $T_p = 0.8\ sec$, the corresponding frequency ratio is $\omega_p/p = 3.64$. For this value of the frequency ratio, Figure 27 (that has been generated by considering a slightly different block) indicates an approximate acceleration amplitude, $a_{p0} = 1.87\alpha g = 0.65\ g$, which is close to the acceleration level $0.88 \times (PGA \approx 0.8g) \approx 0.7\ g$.

Figure 35 indicates that when the ductility of the restrainers is increased from $\mu = 1$ to $\mu = 5$, a slight increase is expected in the acceleration needed to overturn the same $0.5\ m \times 1.5\ m$ block. Indeed Figure 38 shows that when the restrainers have ductility, $\mu = 5$, a 93% level of the Rinaldi station record is capable of overturning the block. For this level restrainers with ductility, $\mu = 10$, are capable of preventing overturning. Figure 39 shows that a 99% level of the Rinaldi station record is capable of overturning the block that is anchored with restrainers that have $F_u = 16\ kips$, $K = 300\ kips/in$ and $\mu = 10$. Comparing this level with the 78% one that was needed to overturn the free-standing block, one concludes that restrainers have a limited effect in preventing toppling.

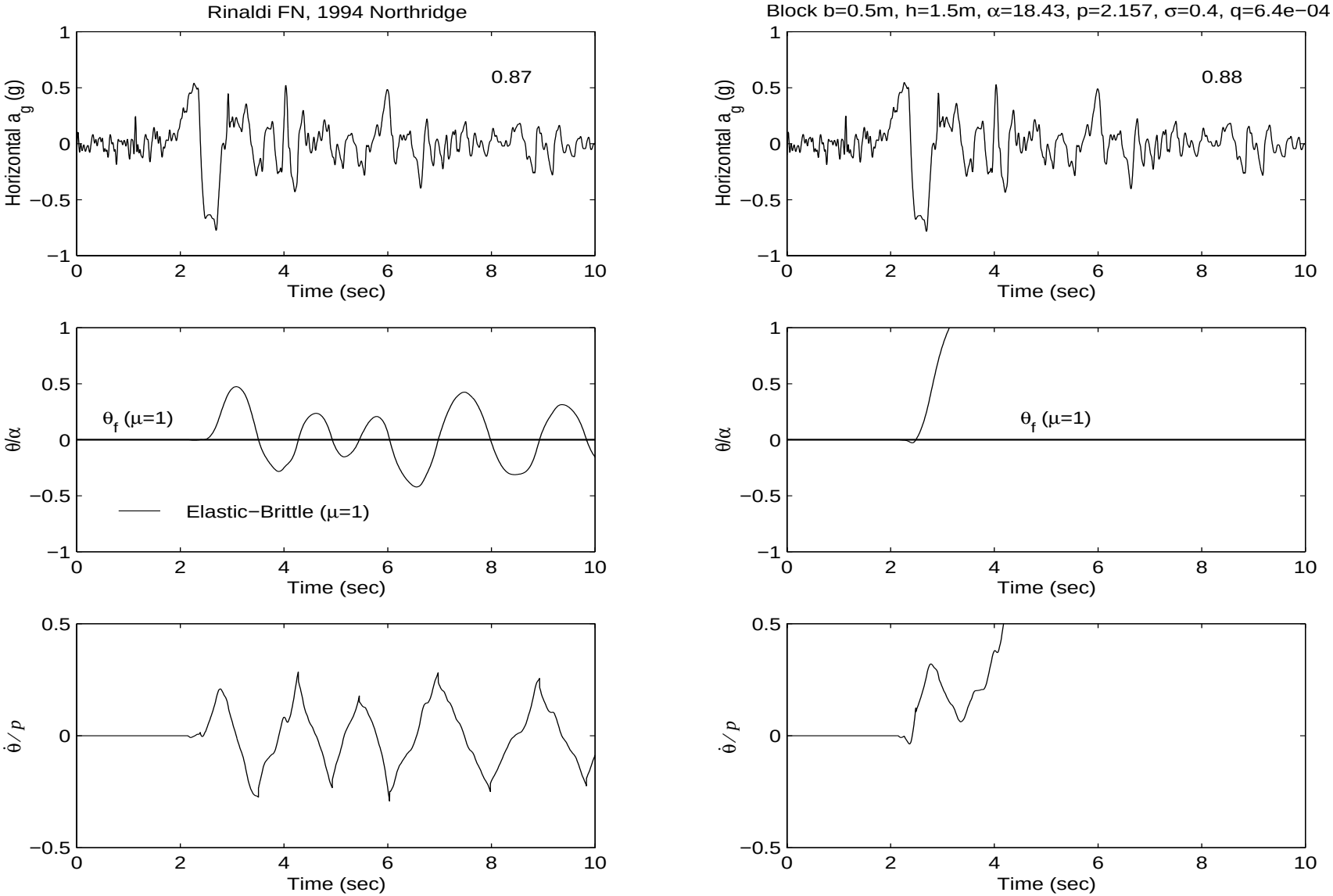

Figure 37. Rotation and angular velocity time histories of an anchored block ($b = 0.5\ m$, $h = 1.5\ m$, $F_u/W = 0.4$) subjected to the fault-normal Rinaldi station motion. An 88% acceleration level is capable of overturning the block with restrainers exhibiting ductility $\mu = 1$.

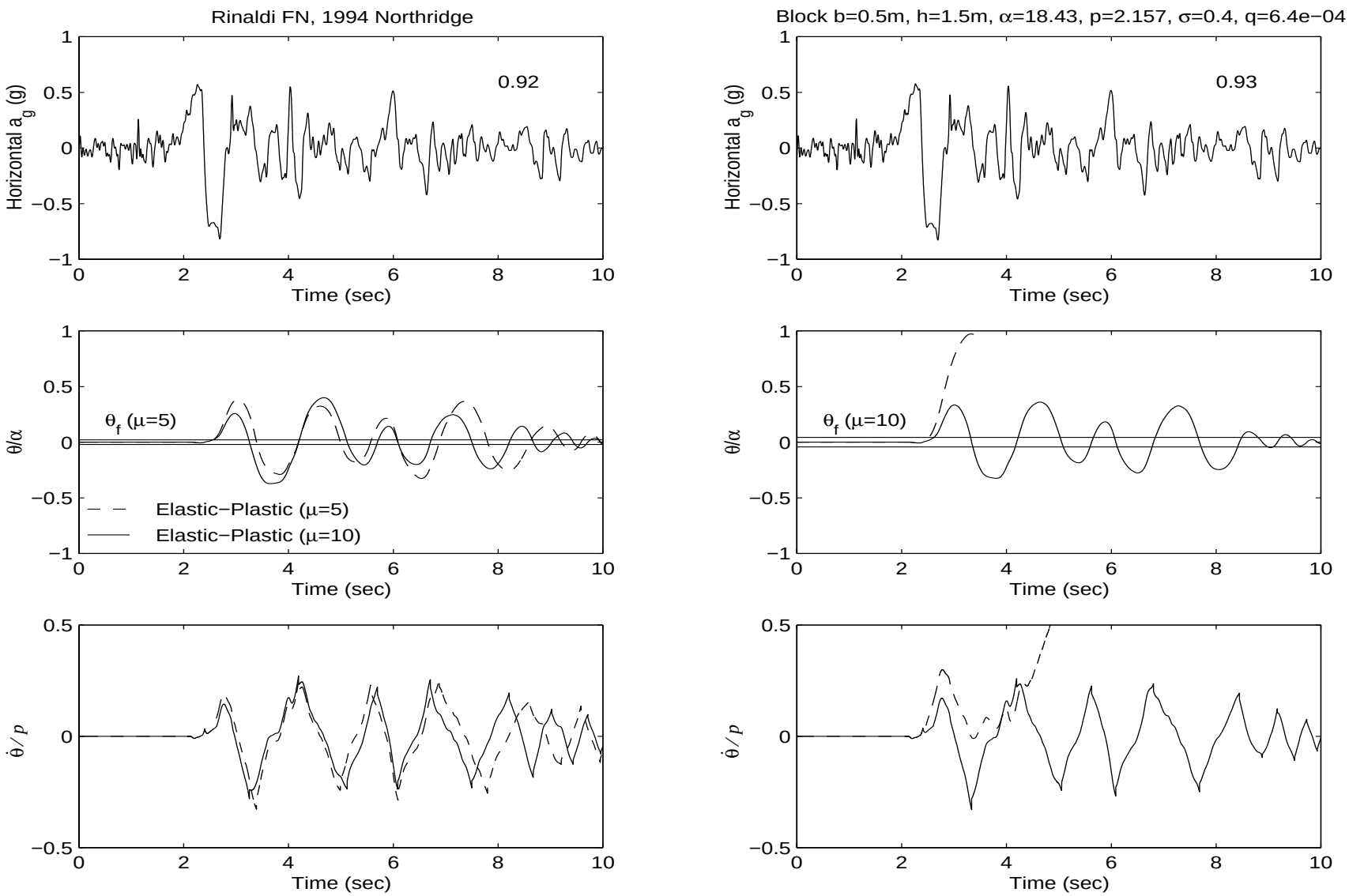

Figure 38. Rotation and angular velocity time histories of an anchored block ($b = 0.5\ m$, $h = 1.5\ m$, $F_u/W = 0.4$) subjected to the fault-normal Rinaldi station motion. A 93% acceleration level is capable of overturning the block with restrainers exhibiting ductility $\mu = 5$; whereas when $\mu = 10$ the block survives.

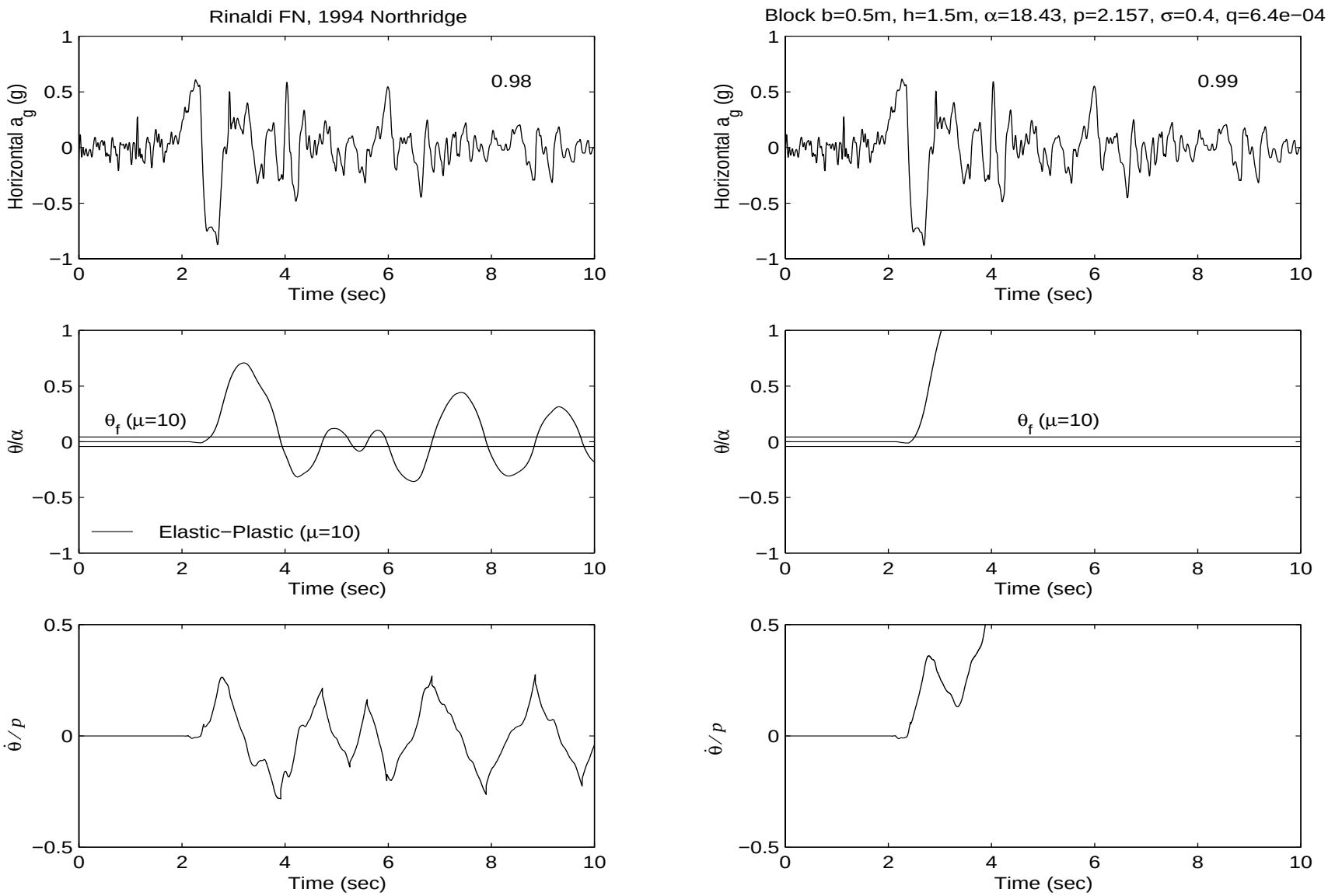

Figure 39. Rotation and angular velocity time histories of an anchored block ($b = 0.5\ m$, $h = 1.5\ m$, $F_u/W = 0.4$, $\mu = 10$) subjected to the fault-normal Rinaldi station motion. Left: no overturning (98% acceleration level). Right: overturning (99% acceleration level).

To proceed with the analysis the rocking response is computed for a larger block ($1.0\ m \times 3.0\ m$) that has a frequency parameter, $p = 1.525\ rad/sec$, and the same slenderness, $\alpha = 18.43°$. Under the same assumption that the Rinaldi station record can be approximated with a one-sine pulse with $T_p = 0.8\ sec$, the corresponding frequency ratio is $\omega_p/p = 5.15$. For this value of the frequency ratio, Figure 33 (that has been generated for a smaller, less slender block, $\alpha = 20°$, $p = 2\ rad/sec$ and $\eta = 0.825$) indicates that a free-standing block might survive a stronger acceleration level than an anchored block. Indeed Figure 40 indicates that the $1.0\ m \times 3.0\ m$ free-standing block overturns at a 127% level of the Rinaldi record, whereas the same block anchored with restrainers having strength $F_u = 0.4W = 16\ kips$ and ductility $\mu = 5$ overturns under only a 119% level of the Rinaldi acceleration record, as shown in Figure 41. This study was partly motivated by this puzzling result, and sought to address the problem in a systematic and lucid manner.

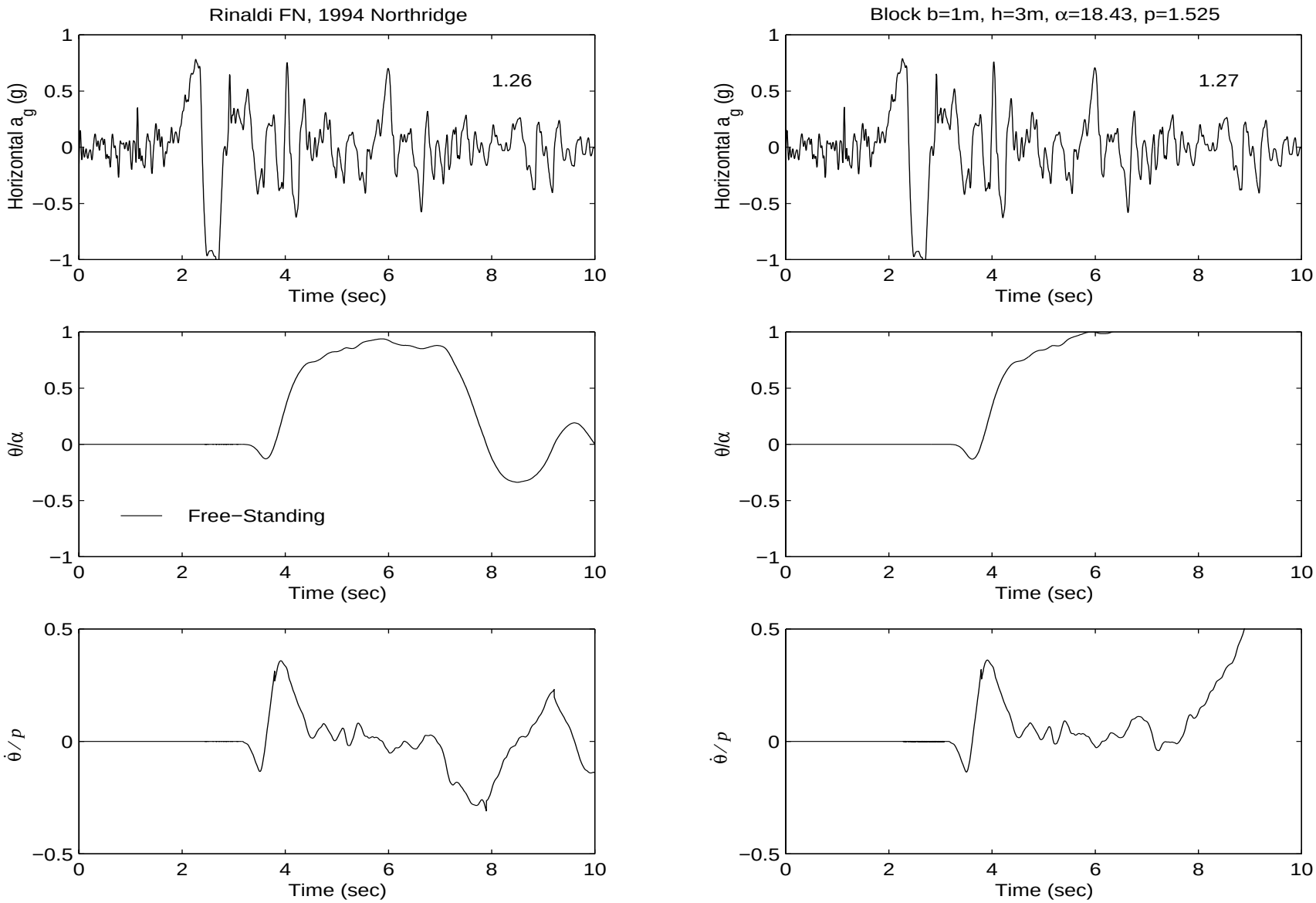

Figure 40. Rotation and angular velocity time histories of the free-standing block (*b = 1.0 m, h = 3.0 m*) subjected to the fault-normal Rinaldi station motion. Left: no overturning (126% acceleration level). Right: overturning (127% acceleration level).

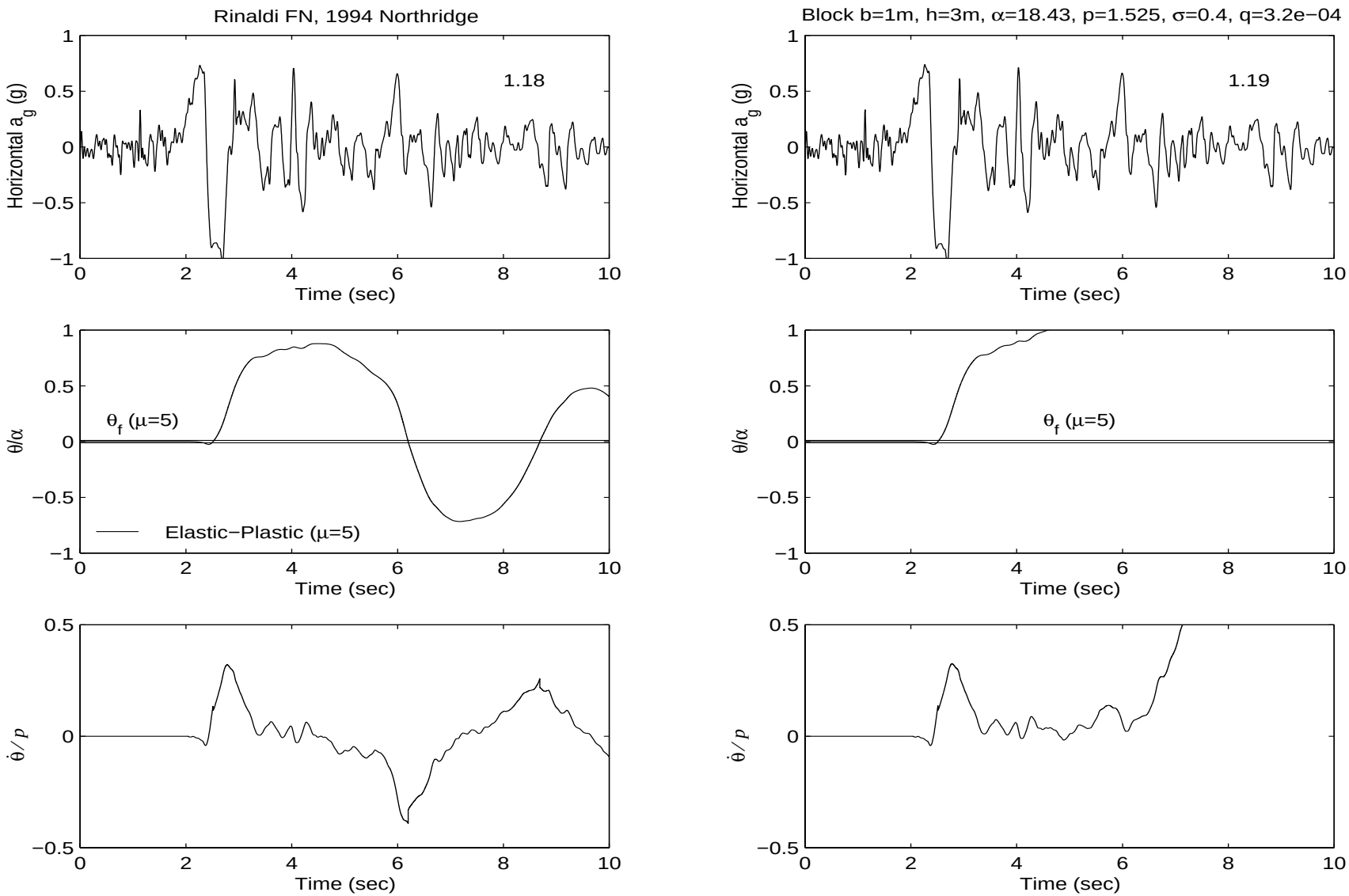

Figure 41. Rotation and angular velocity time histories of a larger anchored block ($b = 1.0\ m$, $h = 3.0\ m$, $F_u/W = 0.4$ and $\mu = 5$) subjected to the fault-normal Rinaldi station motion. Left: no overturning (118% acceleration level). Right: overturning (119% acceleration level). The free-standing block can survive a stronger acceleration level than the anchored block (see Figure 40).

CHAPTER 6
CONCLUSIONS

This report investigates the transient rocking response of anchored electrical equipment and other tall structures that can be approximated as rigid blocks. In addition, various practical issues that control overturning, such as the effect of the vertical component of ground acceleration and the effect of the coefficient of restitution during impact, are also addressed.

An in-depth study of the rocking response of a free-standing equipment subjected to a one-sine (Type-A) pulse is first presented. It is shown that under a one-sine pulse (forward displacement) rigid blocks can overturn with two distinct modes: (a) with one impact; (b) without impact. The second mode (no impact) is responsible for the existence of a safe region that is located over the minimum overturning acceleration spectrum. It is found that the shape of this region depends on the coefficient of restitution and is very sensitive to the nonlinear nature of the problem. The study uncovers a frequency range where the linear formulation can give erroneous results even for slender blocks. Under a one-cosine (Type-B) pulse, a similar safe region located over the minimum overturning acceleration spectrum exists. In this case the differences in the response obtained with the linear and nonlinear formulations are less drastic to those observed under a one-sine pulse.

Restrainers with elastic-brittle and elastic-plastic behavior are considered. It is found that restrainers are more efficient in preventing overturning of small slender blocks subjected to a low-frequency ground excitation. Again, under one-sine pulse anchored blocks can overturn with the two aforementioned modes of overturning. Before the transition from mode 1 to mode 2, the presence of restrainers has a destructive effect. The stronger the restrainer, the smaller is the acceleration amplitude needed to overturn a rigid block; whereas a free-standing block can withstand the higher acceleration amplitude. This counterintuitive response extends when the restrainers exhibit finite ductility, since the study shows that there is a frequency range where blocks with the most ductile restrainers will withstand the smaller acceleration level. Larger blocks can overturn only without experiencing any impact, and in this case the effect of restrainers is marginal even when their strength equals the weight of the equipment. The limited effect of restrainers in preventing toppling is also found under earthquake excitations. The study shows that under the Rinaldi station record restrainers with strength $F_u/W = 0.4$ and ductility $\mu = 5$ have a mild constructive effect in preventing toppling of a $0.5\ m \times 1.5\ m$ block; they have a destructive effect in prevent-

ing toppling of a $1.0\ m \times 3.0\ m$ block. The $1.0\ m \times 3.0\ m$ free-standing block survives the motion that overturns it when it is anchored.

Furthermore, the report concludes that the effect of the vertical component of recorded ground motions is marginal and virtually does not affect the level of the horizontal acceleration needed to overturn an electrical equipment. An increasingly inelastic impact (smaller coefficient of restitution) results in smaller angles of rotation; however the values of the impact velocities might occasionally be larger.

REFERENCES

Anderson, J. C., and V. V. Bertero. 1986. Uncertainties in establishing design earthquakes. *J. of Struct. Engrg.* **113**: 1709-24. ASCE.

Anooshehpoor, A., T. H. Heaton, B. Shi and J. N. Brune. 1999. Estimates of the ground acceleration at Point Reyes station during the 1906 San Francisco earthquake. *Bull. Seismological Soc. of America* 89(4): 843-53.

Aslam, M., W. G. Godden, and D. T. Scalise. 1980. Earthquake rocking response of rigid bodies. *J. of Engrg. Mech. Div.* **106**: 377-92. ASCE.

Bertero, V. V., S. A. Mahin, and R. A. Herrera. 1978. Aseismic design implications of near-fault San Fernando earthquake records. *Earthquake Engrg. and Struc. Dynamics* 6: 31-42.

Bouc, R. 1971. Modele mathematique d'hysteresis. *Acustica* **24**: 16-25.

Fujisaki, E. 1999. Personal communication.

Hall, J. F., T. H. Heaton, M. W. Halling, and D. J. Wald. 1995. Near-source ground motions and its effects on flexible buildings. *Earthquake Spectra* **11**: 569-605.

Hogan S. J. 1989. On the dynamics of rigid-block motion under harmonic forcing. *Proc. R. Soc. London* **A425**: 441-76.

Housner, G. W. 1963. The behaviour of inverted pendulum structures during earthquakes. *Bull. Seismological Soc. of America* **53**: 404-17.

Jacobsen, L. S., and R. S. Ayre. 1958. *Engineering Vibrations*. New York: McGraw-Hill.

Makris, N., and S. P. Chang. 1998. *Effect of damping mechanisms on the response of seismically isolated structures.* PEER-98/06. Pacific Earthquake Engineering Research Center, University of California, Berkeley.

Makris, N., and Y. Roussos. 1998. *Rocking response and overturning of equipment under horizontal pulse-type motions*. PEER-98/05. Pacific Earthquake Engineering Research Center, University of California, Berkeley.

Makris, N. 1997. Rigidity-plasticity-viscosity: Can electrorheological dampers protect base-isolated structures from near-source ground motions? *Earthq. Engrg. and Struc. Dynamics* **26**: 571-91.

MATLAB. 1992. *High-Performance numeric computation and visualization software*. Natick, Mass: The MathWorks.

Milne, J. 1885. Seismic experiments. *Trans. Seism. Soc. Japan* **8**: 1-82.

Scalia, A., and M. A. Sumbatyan. 1996. Slide rotation of rigid bodies subjected to a horizontal ground motion. *Earthq. Engrg. and Struc. Dynamics* **25**: 1139-49.

Shenton, H. W. III. 1996. Criteria for initiation of slide, rock, and slide-rock rigid-body modes. *J. of Engrg. Mech. Div.* **122**: 690-93. ASCE.

Shi, B., A. Anooshehpoor, Y. Zeng, and J. N. Brune. 1996. Rocking and overturning of precariously balanced rocks by earthquake. *Bull. Seismological Soc. of America* **86**(5): 1364-71.

Spanos, P. D., and A. S. Koh. 1984. Rocking of rigid blocks due to harmonic shaking. *J. of Engrg. Mech. Div.* **110**: 1627-42. ASCE.

Yim, C. K., A. K. Chopra, and J. Penzien. 1980. Rocking response of rigid blocks to earthquakes. *Earthq. Engrg. and Struc. Dynamics* **8**: 565-87.

Wen, Y-K. 1975. Approximate method for nonlinear random vibration. *J. of Engrg. Mech.* **101**(EM4): 389-401. ASCE.

Wen, Y-K. 1976. Method for random vibration of hysteretic systems. *J. of Engrg. Mech.* **102**(EM2): 249-63. ASCE.

Zhang, J., and N. Makris. 1999. Discussion on “Estimates of the ground acceleration at Point Reyes station during the 1906 San Francisco earthquake” by A. Anooshehpoor et al. *Bull. Seismological Soc. of America* (forthcoming).

PACIFIC EARTHQUAKE ENGINEERING RESEARCH CENTER

August 17, 1999, Kocaeli, Turkey Earthquake Field Investigation Report

Robert L. Anderson
California Energy Commission

William U. Savage
Pacific Gas and Electric Company

Fakir H. Erdogan
Turkish Electric Generation and Transmission Company

A report to the PEER Program of Applied Earthquake Engineering Research on Lifeline Systems

The financial support of the sponsor organizations including the Pacific Gas & Electric Company (PG&E) and the California Energy Commission (CEC) is acknowledged.

PEER UTILITIES PROGRAM
REPORT NO. 2000/17

ACKNOWLEDGMENTS

The work described in this report was funded by the Pacific Earthquake Engineering Research (PEER) Center under the Pacific Gas & Electric Company Contract No. 09566 and Contract No. 500-97-101 from the California Energy Commission through the Pacific Earthquake Engineering Research Center. This financial support is gratefully acknowledged.

This field investigation benefited enormously from the support and assistance of the following individuals and organizations: Mr Fakir Erdogan and Mr. Muzaffer Genc from the Turkish Electric Generating and Transmission (TEAS) Nuclear Engineering Department, Mr Lufti Serici, General Manager of TEAS, Dr. Aykut Barka, from the Geology Department of the Istanbul Technical University, Mr. Lloyd Cluff the manager of the PG&E Geosciences Division, Dr. David Rohy, CEC Commissioner (retired), and Mr. Kent Smith, Deputy Executive Director of the CEC, TEAS and TEDAS managers and staff provided detailed information on electric system damage, and provided visits to substations and other facilities. General Managers of Enerji SA, IZGAS, and BOTAS provided detailed information about their facilities.

This work was supported in part by the Pacific Earthquake Engineering Research Center through the Earthquake Engineering Research Centers Program of the National Science Foundation under Award number EEC-9701568.

August 17, 1999, Kocaeli, Turkey Earthquake Field Investigation Report

Robert L. Anderson, William U. Savage, and Fakir H. Erdogan

Summary

On August 17, 1999, at 3:01 AM, the industrial heart of the country of Turkey, the Izmit Bay area, was hard hit by a magnitude 7.4 earthquake, accompanied by severe ground shaking, extensive surface fault rupture of several meters, and shaking-induced ground failure in urbanized areas. In the days following the earthquake, as televised reports and information on the Internet flowed out of the densely urbanized Kocaeli Province and adjacent provinces in western Turkey, it became clear that there was significant information regarding the performance of the Turkish electric power system to be gained by studying this earthquake. This information would bring timely and relevant data to the earthquake research program funded by the California Energy Commission (CEC).

The Turkish Electric Generation and Transmission Company (TEAS) invited the Pacific Gas and Electric Company (PG&E) to send a team to Turkey to examine the damage and performance of the TEAS electric generation and transmission system after the earthquake. PG&E formed a joint CEC/PG&E reconnaissance team to gather critical, time-sensitive data and information regarding the earthquake and its effects on electric power reliability, electric utility customers, and the accuracy of earthquake loss prediction models.

Detailed briefings were held with TEAS in Ankara regarding the performance of the utility systems in the earthquake. Several field tours enabled the team to inspect many features of the surface fault rupture and its effect on structures and utility and transportation systems. Inspection of the surface fault features at selected locations illustrated many examples of poor and good performance of buildings, pipelines, and transportation corridors. It was noted by the field team that the site soil conditions and/or poor construction practices had played an important part in the amount of damaged or destroyed buildings in the area affected by the earthquake. The natural gas transmission and distribution systems performed quite well. The systems in the vicinity of the earthquake were well made and did not cross the fault rupture zone. The well-built trans-European motorway way also performed quite well. The only significant damage to the motorway was to an overcrossing that was built over the fault rupture zone, and to the toll collection stations in the vicinity of the earthquake.

The physical damage to electric generation, transmission, and distribution equipment was consistent with the experiences in past earthquakes in California, Japan, and elsewhere. In spite

of the severe earthquake conditions, the electric power transmission system was quickly restored on the day of the earthquake, thus promoting the timely restoration of customer service in all but the most severely damaged urban areas.

This investigation has had a large impact on the importance of the joint CEC-PG&E-PEER research program, and has reinforced the necessity of continuing to analyze the critical issues that affect safety and reliability of electric power in California. The detailed observations and data collected during and following the field investigation are being utilized in the planning of ongoing and future research activities covering all the topics of the program.

Introduction

West Coast electric utilities, such as PG&E, Southern California Edison, Los Angeles Department of Water and Power, Bonneville Power Authority, and British Columbia Hydro, have been assessing electric system performance after earthquakes for many years. In 1999, the CEC and PG&E were in the final stages of a research project regarding electric system seismic safety and reliability. Research on this topic was originally started by PG&E in 1996.

On August 17, 1999, a moment magnitude 7.4 earthquake struck near the cities of Izmit and Golcuk Turkey, in the Marmara Sea. The earthquake occurred on the North Anatolian fault, a fault that had been intensely studied by earthquake specialists from around the world for some time. The North Anatolian fault was recognized as sharing some highly significant similarities to the San Andreas fault in California (see figure 1). The similarity to the San Andreas fault and the similarities between TEAS and PG&E, combined with earthquake related effects in an urban setting, made Western Turkey an important case study area for assessing and refining the CEC/PG&E electric system seismic safety and reliability project.

In response to the Kocaeli earthquake, Lloyd Cluff, Manager of the PG&E Geosciences Department, contacted his associates in the Turkish geological community and established contact with TEAS to arrange for a field investigation. The purposes of the field investigation were:

1) to make observations and collect data that were time sensitive and would not be available after significant recovery efforts had taken place;
2) to interview TEAS representatives regarding their observations and actions taken to recover from the effects of the mainshock and aftershocks.
3) to make observations regarding the performance of the natural gas system in the area affected by the earthquake; and
4) to collect strong ground motion data related to the earthquake and aftershocks.

Funding for the field investigation came from three sources: 1) PG&E; 2) the CEC/PG&E contract; and 3) the Office of the Executive Director of the CEC. On September 2, 1999, the

CEC/PG&E team departed from San Francisco, California and flew to Istanbul, Turkey to conduct the field investigation..

The field team consisted of the following personnel:

Name	Primary Topics of Investigation	Organization
Lloyd Cluff, Team Leader	Seismic Geology, Damage Assessment and Structural Performance	PG&E Geosciences Dept.
Norman Abrahamson	Engineering Seismology	PG&E Geosciences Dept.
Robert Panero	Utility Risk Management	PG&E Insurance Dept.
William Savage	Seismology, Damage Assessment, and Electric and Natural Gas Utility Performance	PG&E Geosciences Dept.
Robert Anderson	Engineering Geology, Power Systems Performance	CEC Engineering Office
Aykut Barka	Geology, Seismology	Istanbul Technical University, Geology Dept.
Fakir Erdogan	Electric Power Systems	TEAS, Nuclear Engineering Dept.
Muzaffer Genc	Geology	TEAS, Nuclear Engineering Dept.

The field investigation performed by this team has provided input to the EERI reconnaissance report on the Kocaeli earthquake (Bardet and Bray, 2000).

Background

The country of Turkey is about 30% larger than the state of California. The population of Turkey is approximately 65 million. Istanbul, the largest city, is located on the east and west shores of the Bosphorus, approximately 40 kilometers northwest of Izmit. The industrial center of Turkey lies between Istanbul in the west and the valley east of the Bay of Izmit, where the August 17, 1999, Kocaeli earthquake took place.

The Turkish Electric Generation and Transmission Company (TEAS) owns and operates a modern electric power generation and transmission system. The total generation capacity in the country (1998 figures) is about 23,000 megawatts (MW), composed of hydroelectric plants (44%), and thermal plants fueled by coal (28%), natural gas (19%), liquid fuels (7%), and other (3%). TEAS produces 70% of the energy generated in Turkey, with the rest produced primarily by private thermal plants. TEAS operates almost 13,000 km of transmission lines at 380,000 volts (380 kV), and more than 27,000 km lines at 154 kV. The first 154 kV line was built in 1952, and the first 380 kV line in 1979. The Turkish electrical network is connected to Bulgaria, Georgia, Iran, Armenia, Azerbaijan, Iraq, and Syria; energy is currently imported from the first three.

In 1993, the Turkish Electricity Authority was separated into two state-owned entities, TEAS and the Turkish Electricity Distribution Company (TEDAS). TEDAS divided the distribution system into provincial or regional units, which operate either as affiliated partnerships or as

subunits of TEDAS. The distribution substations primarily operate at 34.5 kV (including 30 kV and 31.5 kV), 15 kV, and 0.4 kV. Power is distributed with overhead lines installed on metal towers or concrete poles, and with underground direct-burial cables.

There are several independent power producers in this area as well as several small dams. The Turkish electric system is about the size of the PG&E system in California. At the time of the Kocaeli earthquake the electric system in Turkey was undergoing a major expansion, so new equipment and materials were readily available in country which greatly facilitated the restoration effort. The National Transmission Grid Project is financed by the World Bank and is intended to be completed in 2004. This project will establish among other elements the independent operation of the transmission grid system.

The total lengths of the North Anatolian and the San Andreas fault zones are approximately 1,500 kilometers and 1,200 kilometers respectively. The North Anatolian fault zone, like the San Andreas fault zone, is segmented and has numerous related faults. The western end of the North Anatolian fault extends off shore from Yalova and goes west under the Marmara Sea towards Europe and the Aegean Sea. Prior to the Kocaeli earthquake, the North Anatolian fault system had experienced ten major earthquakes since 1939. The total of the aggregate rupture length for the ten earthquakes is approximately 1,000 kilometers (Stein and others, 1997). They had estimated that the North Anatolian fault zone segment south of Izmit had a 12% chance of having a magnitude 6.7 or greater earthquake by 2026.

Findings

The surface rupture associated with the Kocaeli earthquake occurred in four segments. The total length was approximately 120 kilometers along the North Anatolian fault. The rupture propagated in a bi-directional (east and west) manner with the epicenter of the earthquake occurring approximately 11 kilometers southeast of Izmit, Turkey. The type of faulting was primarily right lateral strike slip, the same style of faulting that occurs on the San Andreas fault. The maximum total horizontal displacement at any one site was 5 meters. The total vertical displacement did not exceed 3 meters at any one site. The amount of horizontal displacement was less than that observed at some locations after the 1992 Landers, California earthquake (6 meters) or the 1999 Hector Mine earthquake (5.2 meters). The duration of strong ground shaking from the earthquake wasr 45 seconds. The recorded peak horizontal ground acceleration was 0.42g. However, none of the power plants, substations, or switchyards in the area affected by the earthquake had strong motion recorders. There have not been any aftershocks over magnitude 6, out of more than 2,400 aftershocks.

Site-specific conditions and the quality of construction had significant impacts on the performance of buildings and infrastructure elements such as transmission and distribution of electricity, natural gas, and water. Facilities located on semiconsolidated to unconsolidated alluvium or fluvial or lacustrine deposits generally performed relatively poorly. In general,

facilities located on limestone, sandstone, and other well-indurated materials performed better than their counterparts built on softer geologic materials.

The August 17, 1999, Kocaeli earthquake caused an immediate, countrywide blackout of the transmission system due to high-voltage substation damage and power plants tripping off. Major distribution system damage occurred in five provinces: Sakarya (Adapazari), Kocaeli (Izmit), Yalova, Istanbul, and Bolu. Additional affected provinces were Bursa and Eskisehir. These seven provinces consume more that 40 per cent of all the power used in the country. In the following sections, the generation and transmission system damage is summarized, and the process of transmission system restoration is described. Then the electric distribution system damage is summarized, the performance of the natural gas system is discussed, and conclusions from the earthquake are drawn.

ELECTRIC POWER SYSTEM PERFORMANCE

Damage to Power Generation

None of the TEAS generating stations were damaged by the earthquake. The closest thermal power plants to the earthquake are the fuel-oil and natural gas plants at Ambarli, on the west side of Istanbul. Two small hydroelectric plants located north and south of the eastern segment of the fault rupture had no damage reported. No geothermal, solar, or wind farm power generating facilities were located in the area affected by the earthquake. Currently there are no nuclear power plants operating or under construction in Turkey.

Enerji SA Autoproducer (Cogeneration) Plant, Kosekoy, Kocaeli Province. A 40 MW natural gas fired cogeneration plant, the Enerji SA plant (see figure 2), is part of an industrial park several kilometers west of the Kosekoy substation southeast of Izmit and within about three kilometers of the fault rupture. The estimated peak horizontal ground acceleration at the site was 0.4 g. The plant consists of a frame 6 combustion turbine generator (CTG) and Heat Recovery Steam Generation (HRSG) unit and was put into service in March 1998. Two additional units were under construction at the time of the earthquake. The CTG was built on piles due to the soft soil conditions, but the HRSG was not, even though both units were built on semiconsolidated alluvium.

At the time of the earthquake, the CTG's lubrication oil high/low alarm signaled, and the plant tripped. The emergency diesel generator started in two minutes. The turbine was cooled down, turning slowly for two days. The immediate post-earthquake inspection revealed only minor damage: the CTG foundation settled differentially by 0.5 cm; nuts on the foundation connection bolts partially loosened; nuts on the anchorage for the water treatment plant also loosened; the HRSG displaced sufficiently to pull a base plate off its threaded anchors; there was some concrete spalling on the west side of the HRSG foundation; and unanchored parts storage shelves and other inadequately restrained objects were damaged. This amount of differential settlement is within the preliminary design tolerance for some modern US built natural gas-fired

plants. The facility manager said that were no procedures and experience to base what to do for a frame 6 CTG power plant that had just had experienced a magnitude 7.4 earthquake. The fact that a frame 6 CTG withstood this amount of settlement and was able to resume operation after minor repairs and an inspection lends credence that 0.5 cm of settlement was not overly excessive for the Enerji SA plant. There was no damage to the plant's natural gas supply connections.

There was some damage to the two units under construction, including twisted I-beams, the input flue colliding with other parts in the HRSG, and an 80-tonne package boiler jumping off its foundation because it was not yet attached. The plant manager said that the inlet flue of the partially built HRSG had been damaged by colliding with other parts of the HRSG.

The plant office building had cracks and one broken column. The building was not built on piles, but had a continuous perimeter footing and a concrete slab on grade. The stairway dilated and there were large cracks in the shear walls. In addition bookcases overturned in the offices..

Although the transformers at the generator were mounted on wheels that rolled in steel channels, they did not move enough to cause damage. In the 154 kV switchyard adjacent to the power plant, a bus bar was damaged and high-voltage bushings on the two 154/34.5 kV transformers were broken at their bases. Connections to the bushings were by flexible conductors, so the plant personnel concluded that the bushings failed due to strong shaking. The transformers were rail mounted with brakes on the wheels, but it is not known if they moved significantly during the earthquake.

The insurance carrier for Enerji SA asked for a detailed inspection before the plant could be restarted, which took about 3 1/2 weeks following the earthquake to reach the final testing stage. All the pressure switches had to be re-calibrated. This was an unforeseen delay and if there had been a customer available to receive power this could have been a significant financial loss to Enerji SA. During that period, the substation was repaired using spares on hand for the new construction, and was reconnected to the TEAS grid at 34.5 kV in 40 hours and at 154 kV in 60 hours. As the Enerji SA customers recovered their operations, they could be supplied by the grid until the plant restarted.

Damage to Electric Power Transmission

Turkey has interconnections with Azerbaijan, Georgia, Armenia, Bulgaria, Iran, Iraq, and Syria. After the earthquake Turkey was importing power from Bulgaria. There are two main electric transmission systems in Turkey, one at 380kV and the other at 154kV. The 380 kV lines were out of service after the mainshock. The 154kV electric transmission system remained operational after the mainshock and aftershock of the morning of August 17, 1999.

There were no transmission towers that were taken out of service due to earthquake damage. The most severely threatened tower was a 154 kV electric transmission tower on a short

connection to a substation that is part of a large Ford automotive manufacturing facility under construction near the city of Golcuk (see figure 3). Surface strike-slip faulting with a large normal component crossed the foundation of the tower, and twisted and elevated one leg and its concrete footing about two meters out of the ground. The tower did not tilt. It was supported by the remaining three legs, and remained in service.

Nine transmission substations suffered damage or disruption to transformers, switching equipment, and buildings. All of the damage was associated with strong ground shaking. Tang (2000) provides additional descriptions of substation damage. Figure 4 shows the locations of the substations. Estimates of the peak ground acceleration at each substation have been provided by Dr. Ellen Rathje (personal communication, August 2000)

1. Adapazari 380 kV Substation

The Adapazari substation is located in the southern part of the city of Adapazari, at a cut-and-fill site on the south flank of a low hill. The 380 kV facilities were installed in 1983. The site is about 3 km from the nearest fault rupture segment. The peak horizontal ground acceleration estimated for the site is 0.4 g.

Six Asea minimum-oil-type circuit breaker sets failed (three individual breakers in each set) due to oil leakage and porcelain breakage. The connecting equipment was also broken and fell, including six horizontal and seven vertical disconnecting switches, their rigid aluminum connectors, and two post insulators. A marshaling kiosk that housed signaling cables and equipment for one circuit breaker was also damaged. The damaged Asea circuit breakers were located on what appeared to be the fill part of the site, with undamaged Asea breakers still standing on the cut side. Three 1986-vintage Hitachi minimum-oil-type breakers also were located on the fill, but were not damaged.

The rigid pipe connections between the reserve oil tanks and main tanks for two 380/154 kV power transformers were damaged due to displacement of the transformers on their rails. The transformer displacements also appeared to cause breakage (with oil leaks) of two tertiary bushings due to insufficient slack in the flexible connectors.

Two other 380/154 kV rail-mounted power transformers also were displaced about 30 cm, and two neutral bushings, two tertiary bushings, and six 154 kV arresters were broken. One 380 kV bushing with a rigid connector was also broken.

One post insulator of a 154 kV circuit breaker feeder was broken.

The three-story, concrete-frame and masonry-infill building housing the Regional Load Dispatching Center for northwest Turkey was damaged to the point that staff did not enter the building for several days, and some critical control equipment was moved into an adjacent portable building. Unanchored battery racks for an emergency power supply toppled, and

some SCADA computer equipment was damaged internally (circuit cards and a hard disk drive) due to strong shaking.

The operation management facility at the substation, also a three-story, concrete-frame and masonry-infill building, was moderately damaged. Activities were relocated to four temporary buildings and tents erected nearby.

As a result of the circuit-breaker damage at the Adapazari substation, four 380 kV transmission lines were out of operation after the earthquake. However, two 380 kV transmission lines bypassed this substation, linking undamaged substations to the northwest and southeast. These two lines were critical to power restoration, as will be discussed later. TEAS planned these two lines to afford reliability protection in the event of fire affecting the Adapazari facility.

A small substation located next to the north side of the Adapazari Substation and been out of service for several years when the earthquake hit. No damage was apparent to the substation; however it did not have its components hooked up to the local power grid. The small substation had been in operation during the 1957 Turkish earthquake and was partially damaged. The Adapazari substation personnel told us that shortly after the substation had been repaired in 1957, an aftershock knocked it right back down and out of service.

2. Osmanca 380 kV Substation

The Osmancha substation is located near the Black Sea coast just south of Akcakoca, about 40 km north of the eastern end of the earthquake fault rupture. Similar circuit-breaker damage to that at the Adapazari Substation occurred, taking the two 380 kV lines passing through the station out of service. Six sets of Asea 380 kV minimum-oil-type current breakers fell over, along with four post insulators and 10 vertical and seven horizontal disconnect switches. Also, one marshaling kiosk was damaged due to broken anchor bolts. The peak horizontal ground acceleration estimated for the site is 0.2g.

3. Eregli 380 kV Substation

The Eregli substation is located on the Black Sea coast about 65 km from the eastern end of the earthquake rupture. A small oil leakage occurred on a 380 kV bushing of a 380/154/15.8 kV transformer. The cause of the leakage is unknown, and may have been due to cracked porcelain or gasket slippage. The peak horizontal ground acceleration estimated for the site is 0.1g.

4. Bursa Sanayi 380 kV Substation

This substation, located 80 km southwest of the fault rupture, contains nine transformers. The two largest ones, 250 MVA 380/154 kV units, moved 16 cm and 11 cm respectively on their

rails with clamps, but no damage occurred. The peak horizontal ground acceleration estimated for the site is 0.1g.

5. Kosekoy 154 kV Substation

This substation is located southeast of Izmit close to the fault rupture. Of two 154/33 kV transformers, the unit in service had no damage, but the spare fell off the end of its rail mount. The peak horizontal ground acceleration estimated for the site is 0.4g.

6. Yalova 154 kV Substation

The Yalova substation is located at the city of Yalova. The 154/33 kV transformer in service went off its rails and fell over. The spare transformer slid off its platform and nearly fell over; an oil leak on one of the 154 kV bushings was noted. Electrical contacts of the 154 kV disconnect switches were damaged due to pounding, but were either repaired or used as is. Post insulators on the 154 kV wave trap were broken. The 34.5 kV switchyard building had some concrete damage but continued to be used, and a residential building on the site had cracked walls and a collapsed roof. The peak horizontal ground acceleration estimated for the site is 0.3g.

7. Yarimca-1 154 kV Substation

This substation is located on the north side of the Bay of Izmit, northwest of Golcuk near the refinery and petrochemical plant, and about 4 km from the fault rupture. Three 154/34/5 kV transformers went off their rails, but were still operable. The peak horizontal ground acceleration estimated for the site is 0.3g.

8. Sultanmurat 154 kV Substation

This substation on the west side of Istanbul is a gas insulated (GIS) facility. At the time of the earthquake, a Buscholz warning and disconnect signals were received from two transformers, causing the fire protection systems to engage and take the transformers out of service. No damage occurred. The peak horizontal ground acceleration estimated for the site is 0.1g.

9. Ikitelli 380 kV Substation

This substation is also located on the west side of Istanbul. Cracks were observed in residential buildings at the substation, but the damage did not interfere with operation of the substation. The peak horizontal ground acceleration estimated for the site is 0.1g.

A small substation was under construction at the Ford Motor Company car manufacturing plant in Golcuk. The substation had not yet been connected to the 154 kV electric transmission system located just to the south of the facility. Surface rupture was observed in the substation, but the substation was otherwise undamaged. The amount of surface rupture was not measured

but appeared to be less than a vertical offset of 4 cm. This amount of vertical offset may not have adversely affected the substation had it been on-line at the time of the earthquake.

Recovery of the National Electric Transmission System

The following time line summarizes the process of power transmission restoration and other recovery actions taken by TEAS personnel in response to the Kocaeli earthquake.

3:02 AM, August 17

The TEAS national electric system was de-energized during the earthquake shaking, principally due to substation damage. Only isolated regions that were fed from Bulgaria, Georgia, and Iran, and areas in the far western part of the country that could be maintained by local power plants were able to stay in service. All the hydroelectric plants and the thermal plants outside of the Aegean region tripped off. All staff responsible for load dispatching were called in to begin working.

3:30 AM

The appropriate staff under the chairmanship of the General Manager assembled in the National Load Dispatching Center near Ankara to supervise the recovery actions and to organize necessary activities using all the resources of the company. Buses began to be energized.

4:00 AM

The Hamitabat thermal plant 140 km west of Istanbul was energized from the Bulgarian connection and put back in service so that Istanbul could be energized. Similarly, plants to the east and south of the earthquake-affected area were brought back in service, and lines in the 380 kV and 154 kV grids began to be energized.

6:30 AM

The connection between the Istanbul region and the Central Anatolian region was established using the two 380 kV lines that crossed the Izmit-Adapazari area but bypassed the damaged Adapazari and Osmanca substations (Figure 4). The step-by-step restoration of generation plants and transmission lines proceeded outside of the strongly damaged area. Inspection of substation damage continued.

7:30 AM

The determination of damage to the 380 kV portions of the Adapazari and Osmanca substations prevented their being energized. The 154 kV sides of these substations were being checked.

8:00 AM

Although it was determined that the 154 kV buses could be energized in the damaged substations in the strongly shaken areas, the local governors requested that the local distribution system not be energized because of the serious risks associated with introducing power into damaged areas and potentially damaged customer equipment.

8:30 AM

With the exception of the specific damaged substations and areas mentioned above, the 380 kV and 154 kV system returned to normal operation. An expert commission composed of technical staff and assistance teams was established by TEAS headquarters, and was assigned the responsibility for determining the earthquake-related damages for recovery planning purposes. They departed shortly to the earthquake affected areas.

8:54 AM

A strong aftershock in the Duzce area caused the 380 kV connection between Ankara and Istanbul to relay off, thus causing the entire grid to de-energize again. The line-by-line and plant-by-plant restoration process began again.

11:30 AM

The grid was restored once again, except for the 380 kV sides of the Adapazari, Osmanca, and Eregli substations.

1:30 PM

The 154 kV side of the Adapazari substation was checked and verified as safe, so the local grid was energized and electricity was made available at 34.5 kV whenever it would be needed.

2:00 PM

The 154/34.5 kV transformers at the other damaged substations in the strongly shaken area were energized so that distribution circuits could be energized as needed. At this time, the transmission system was brought back to normal operation except for the damaged parts. Distribution system components were subsequently brought back online as soon as circuits could be tested and damaged areas disconnected. Most distribution service was restored by the evening of August 17, except for areas with damaged circuits.

August 30

By this date after the main shock, all substation equipment damages were repaired. These repairs were made possible in part by the fortunate availability of new circuit breakers and other equipment that had been received by TEAS in preparation for extensive new construction. Efficient and effective TEAS teams were formed to carry out repairs with assistance from personnel from equipment manufacturers. In particular, a team of 130 engineers and maintenance specialists rebuilt the 380 kV side of the Adapazari substation, and a similar team of 100 repaired the 380 kV side of the Osmanca substation. As noted previously, the redundant configuration of the 380 kV system enabled these substations to be bypassed while repairs were made, without delaying grid restoration and distribution circuit restoration.

The cost for damaged equipment that TEAS replaced immediately following the earthquake was US$1,483,000. This included 9 circuit breaker sets, 11 disconnect switches, three transformer bushings, and six lighting arresters. TEAS estimates that they will spend an additional US$10.5 million to replace weak or damaged but operational equipment.

Damage and Restoration of Electric Distribution

In the affected provinces, the distribution systems experienced heavy damage that was closely associated with the intense building damage and the associated strong shaking and ground failure. The distribution systems include KORFEZ (Izmit), SEDAS (Sakarya and Bolu), TEDAS (Yalova), and BEDAS and AKTAS (Istanbul).

A common type of damage to tower mounted electric transformers in Adapazari and Golcuk was falling out of their box frame attachments to the towers due to a lack of adequate restraints on the transformers. There were two main types of damage to the underground portion of the electric distribution system in Turkey. First the connections to the buildings and other lines were broken, and second, emergency crews would dig up portions of underground power lines. The need for power distribution service was reduced by several hundred thousand customers due to the large number of buildings that were either destroyed or so heavily damaged that they may not be saved.

The distribution systems generally contain the following elements, with the typical damage indicated:

Medium voltage (MV) lines operating typically at 34.5 kV or 15.8 kV; damaged by failure of towers, building collapse knocking down lines, line burndown.

Low voltage (LV) lines operating at below 15.8 kV down to 400 volts; damaged by failure of towers, building collapse knocking down or pulling down lines.

MV-MV transformers typically housed in small substations: damaged by bushing breakage or oil leaks caused by strong shaking, building debris falling on transformers, cables

pulling on insulators, large displacement or toppling of transformers due to inadequate anchorage.

MV-LV transformers typically pole-mounted; damaged by falling of transformer due to inadequate anchorage, pole failure causing transformer to fall, building collapse pulling on overhead lines breaking insulators.

MV and LV direct burial cables used primarily in urban areas; damaged by ground failure, foundation failure of buildings, and cables being pulled during post-earthquake building rescue and demolition activities.

Damage statistics for the five primary provinces are shown in Table 1.

Table 1. Distribution System Damage in the Kocaeli Earthquake. The upper number refers to the pre-earthquake totals within the province, and the lower number refers to the amount damaged due to the earthquake. Note that the length of cables and overhead lines represents the entire length of the circuits that were damaged or destroyed.

Province	MV-MV Transfmr	MV-LV Transfmr	MV Lines (km)	MV Towers	MV Cables (km)	LV lines (km)	LV Towers	LV cables (km)	Service Trucks
Kocaeli	39 13	2,267 233	2,620 130	28,833 1,210	95 19	6,597 270	80,718 3,449	225 61	53 23
Sakarya	9 4	2,299 248	1,805 165	29,913 750	120 65	5,159 215	114,301 550	580 135	127 11
Istanbul	157 4	8,372 750	6,826 72	38,802 2175	2,613 900	124,662 2,665	208,000 20,700	4,998 2,400	108 32
Yalova	3 0	369 101	289 100	5,798 200	45 0	787 125	14,828 850	75 35	11 5
Bolu	4 0	2,477 101	3,239 200	34,297 0	28 5	4,482 25	106,885 500	125 35	65 0
Total Damage Cost USD	$960K	$9,609K	$19,029K	(incl. w/ Lines)	$6,238K	$11,790K	(incl. w/ Lines)	$15,934K	$648K

Restoration of distribution service was closely controlled by local officials and distribution company personnel to assure that power was restored only when circuits had been disconnected from damaged structures and properly tested. The TEDAS maintenance personnel had the transformers operational by noon on the 17th; however, the crisis control center delayed authorizing the engerizing of the transformers until the threat of electrically ignited fires was past. Electric power was restored locally by two p.m. Electric power was first restored to hospitals and municipal water wells. Most distribution areas in the affected provinces were restored in a matter of days. Emergency response and recovery facilities, such as hospitals and water pumps, received high priority for restoration. A shortage of emergency power generators and rescue equipment was a problem.

Because of the extensive damage to underground cables, it is planned to collocate replacement cables with other utilities. The existing damaged cables are being abandoned in place.

The total cost of distribution system damage is estimated to be US$69.6 million. This includes the damage cost of $64.2 million shown in Table 1, plus an additional $5.4 million that includes new equipment used to replace damaged equipment and new construction of poles and lines to serve the tent encampments and other temporary housing established for people who lost their housing. The actual total cost will not be determined until all the repairs have been completed.

Lessons Learned

The electric power system in Turkey was hit by extreme earthquake effects due to the Kocaeli earthquake: severe ground shaking, more than 100 km of surface fault rupture of several meters, and shaking-induced ground failure in urbanized areas. The earthquake-affection region contained the heart of Turkey's industrial facilities, and was densely urbanized. In spite of these conditions, the transmission system was restored quickly, thus promoting the timely restoration of customer service in all but the most severely damaged urban areas. There are several important observations:

The extensive damage to several 380 kV substations was not a major factor in transmission power restoration due to the existence of 380 kV transmission lines that bypassed the damaged stations (see Figure 4). Power could then be rerouted to the distribution system via the 154 kV transmission system, whose substations were much less damaged. The redundant system design used by TEAS performed successfully in this earthquake, even though explicit planning for such earthquakes had not been done. Also, the electric power feed from Bulgaria to Istanbul provided important redundancy from the west.

The power generation and transmission personnel were responsive and organized in their efforts to stabilize the post-earthquake situation, rapidly assess critical damage, and restore system operations. In general, the crisis management actions taken by TEAS were effective. The distribution company actions were also responsive and effective. Of particular importance was the coordination between local government representatives and the local distribution companies to safely restore power. Thus the dangers of restoring power into damaged or collapsed buildings could be avoided.

The physical damage to generation, transmission, and distribution equipment was consistent with the experiences in past earthquakes in California, Japan, and elsewhere, and included the following typical observations:

Generating plants may not have experienced high ground accelerations (0.4+ g) and did not suffer significant damage.

Transmission towers and lines are highly resistant to earthquake damage, even when displaced by surface fault rupture.

Porcelain insulators used in high-voltage substation equipment are generally vulnerable to strong earthquake shaking and loading caused by interconnection with other equipment, unless high-strength insulators and appropriate seismic designs are used.
Unanchored equipment is seismically vulnerable, particularly transformers sitting on rails or inadequately attached pole-mounted transformers. Transformer damage can significantly delay customer service restoration.
Distribution power poles and towers are vulnerable to damage due to liquefaction and other ground failures, particularly in urban areas where buildings are likely to be damaged as well and can fail into the poles and towers.
Pole-mounted transformers fail if shaking causes the poles to break, or if they are not adequately anchored to the poles.
Underground cables are prone to damage where they connect to surface electrical supplies or buildings, and due to subsequent degradation in cable insulation due to physical or electrical effects. Such damage can lead to long delays in power restoration because of the relative difficulty in repairing underground cables compared to overhead lines.

It is interesting to note that the TEAS and TEDAS staff did not report any distribution transformer explosions or fires. Some pole mounted transformers in both the Northridge and Hector Mine, California earthquake areas exploded. It is thought that the electric transmission and distribution lines did not arc and transformers did not blow up in the Kocaeli earthquake since the loss of the high-voltage power supply was initiated by the earthquake damage to the Adapazari substation so that the distribution lines were not energized. This prevented the arcing of power lines or the exploding of transformers. One important element of the effect of the loss of power was the loss of power to the water distribution and treatment systems. The loss of power caused pumps to shut down until emergency generators could be located and brought into service. The water systems had to be carefully checked before water service could be restored to those customers able to receive water through the restored elements of the water supply system.

NATURAL GAS SYSTEM PERFORMANCE

Background

Turkey does not produce any significant quantities of natural gas. Most of the gas used in Turkey is bottled propane. Natural gas distribution lines are being developed but are not nearly as prevalent as in California. The natural gas transmission system in the vicinity of the earthquake was limited to the BOTAS main natural gas transmission lines, and the IZGAS natural gas distribution system in the vicinity of Izmit.

The natural gas transmission system serving Turkey is operated by BOTAS, and is comprised of modern high-pressure steel pipelines. In the region of the earthquake, the BOTAS pipeline crosses the Bay of Izmit between Muallim on the north and the western side of the Hersek

Peninsula on the south. The pipeline thus crosses the North Anatolian fault essentially at the western end of the observed surface fault rupture. Following the earthquake, BOTAS personnel inspected the system, and found no damage. A single gas leak was found near the north side of the Bay of Izmit crossing, west of Izmit, at a flange connection that was repaired by tightening the bolts.

The field team visited the local natural gas distribution company in Izmit called IZGAS. IZGAS was the fifth largest natural distribution company in Turkey when the earthquake struck. At the time of the earthquake IZGAS had 26,000 customers and 380 kilometers of newly built (1995) steel and polyethylene pipes. Natural gas is supplied to the IZGAS system by two connections with the BOTAS natural gas transmission lines. The IZGAS system was located to the north of the North Anatolian fault. IZGAS reported that their system did not cross any fault ruptures associated with the Kocaeli earthquake. The IZGAS system was built in the mid-to late 1990s and was made of steel and polyethylene pipe. The main loss to the IZGAS company due to the earthquake was the loss of customers, damage to the gas meters, and the loss of revenue due to the loss of demand for natural gas. IZGAS reported that 860 gas meters were damaged due to collapsed buildings, and that they had lost 8,000 customers during the earthquake. What was clear is that the IZGAS system performed well but buildings that the gas was fed into were destroyed or heavily damaged. None of the gas pipelines were seriously damaged by the earthquake. Fortunately, there were no fires associated with gas leaks. The SCADA system survived the earthquake, but the SCADA operator fled from his station. Locally, the electric system was not re-energized until the potential for electrically ignited gas fires was mitigated.

Dr. Aykut Barka mentioned that a Turkish television crew had video taped some lights over the area of the epicenter and the shorelines near Izmit and Golcuk. He referred to the lights as possibly being earthquake lights. The engineer for the Minister of State had mentioned that some lights were observed close to a major chemical plant near Izmit, and was concerned about the possibility of gas being released during an earthquake and setting the plant on fire. He also mentioned that a methane pocket was released and had exploded along the Marmara Sea coast during the earthquake. Earthquake lights may be a potential fire or explosive hazard, especially in areas that may have methane, hydrogen sulfide, or natural gas deposits near ground surface.

Lessons Learned

The IZGAS distribution pipelines did not cross the surface fault rupture segments of the North Anatolian fault. The BOTAS natural gas transmission line crossed the North Anatolian fault near Yalova, in the Marmara Sea. Nevertheless, the gas lines were exposed to ground accelerations estimated to be in the range of approximately 0.2 to 0.35 g. The gas system performed similarly to the newer gas systems installed (polyethylene and steel) in the Northridge and Loma Prieta earthquakes. Standard practice for natural gas system siting, design and construction appears to be effective in coping with moderate to strong levels of earthquake shaking (0.2 to 0.35+g) in the Kocaeli earthquake, or much higher levels up to about 1.0 g as experienced in the Northridge earthquake. For pipelines sited crossing active faults or other locations of large

permanent ground displacement, detailed seismic analysis and associated design adjustments should be carried out.

CONCLUDING REMARKS

Californians have benefited from the observations made and interviews conducted after the Kocaeli earthquake, since the Turkish electric generation, transmission, and distribution systems are similar to those in California. Major benefits from this earthquake were the collection of strong ground motion records, the first-hand field observations of substation equipment design and damage, and the interviews with engineers, managers and technicians of both TEAS and TEDAS, all without actually having suffered a major urban earthquake in California. It is important to note that the Kocaeli earthquake was similar in size to the moment magnitude 7.4 Landers, California earthquake of June 1992. A major difference between the Kocaeli and the Landers earthquakes is that the Kocaeli earthquake occurred in an area that was locally highly urbanized, while the Landers earthquake occurred in a sparsely populated (desert rural) region of California. Personnel from PG&E and the CEC, working with TEAS, TEDAS, and the Istanbul Technical University Geology Department, reaffirmed the importance and applicability of the electric system seismic safety and reliability research carried out under the Public Interest Energy Research program by PG&E and the Pacific Earthquake Engineering Research Center (PG&E's subcontractor). It is noted that PG&E has continued to investigate the earthquake and the North Anatolian fault on their own.

Turkey has been experiencing rapid industrial and population growth, which has led to a significant expansion in the number of water supply, natural gas distribution, and electric power facilities. As this development continues, and as the full recovery from the Kocaeli earthquake occurs, more attention is needed to address the threats from future earthquakes, particularly those occurring to the west along the North Anatolian fault, and thus closer to Istanbul. To improve future performance of lifeline systems in Turkey, an assessment of equipment and system performance vulnerabilities to earthquake activity would serve to identify potential damage conditions that the current level of system resiliency could not adequately handle. Then appropriate mitigation plans could be developed and implemented. These actions would enable the gas delivery and electric power systems in Turkey to continue to provide responsive service restoration after future earthquakes.

California is also experiencing significant population and industrial growth which has led to a need to expand our infrastructure base of electric power generation, transmission distribution, natural gas transmission and distribution and water collection, transmission and distribution systems. By applying lessons learned from the Kocaeli and other large earthquakes, we are able to help prudently develop our infrastructure so that it is more resistant to significant damage from earthquakes. This is a major goal for electric system safety and reliability improvement within California.

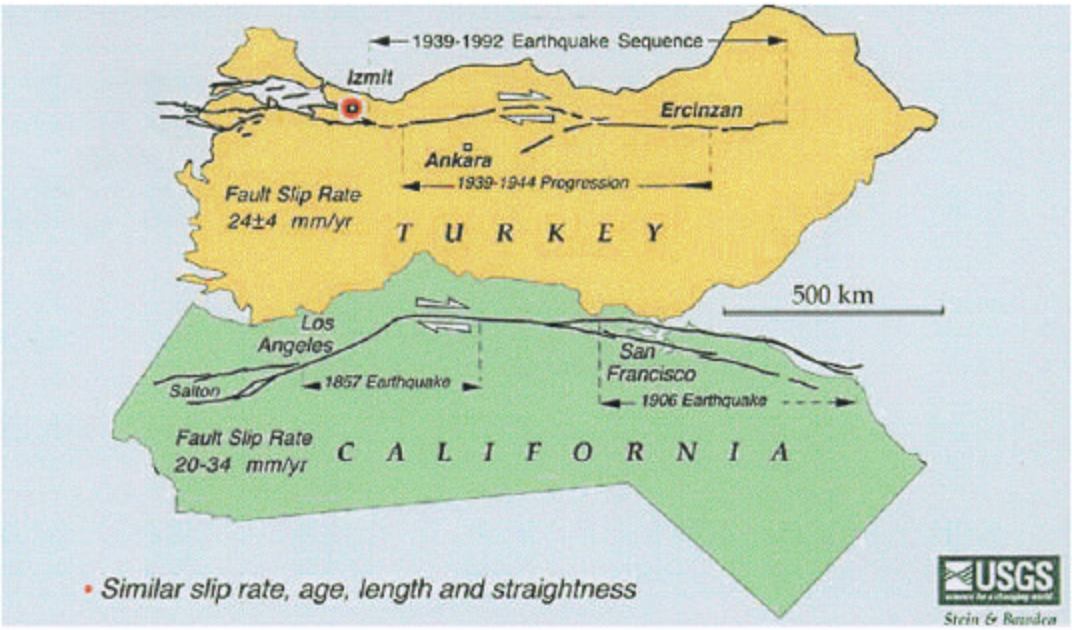

Figure 1. Map of Turkey and California showing the traces of the North Anatolian and San Andreas faults.

Figure 2. Oblique aerial photo of the Enerji SA cogeneration plant showing the housing for the frame 6 CTG and the HRSG.

Figure 3. Photograph of the footing of a 154 kV electric transmission line tower displaced by surface rutpure along the North Anatolian fault near Golcuck, Turkey.

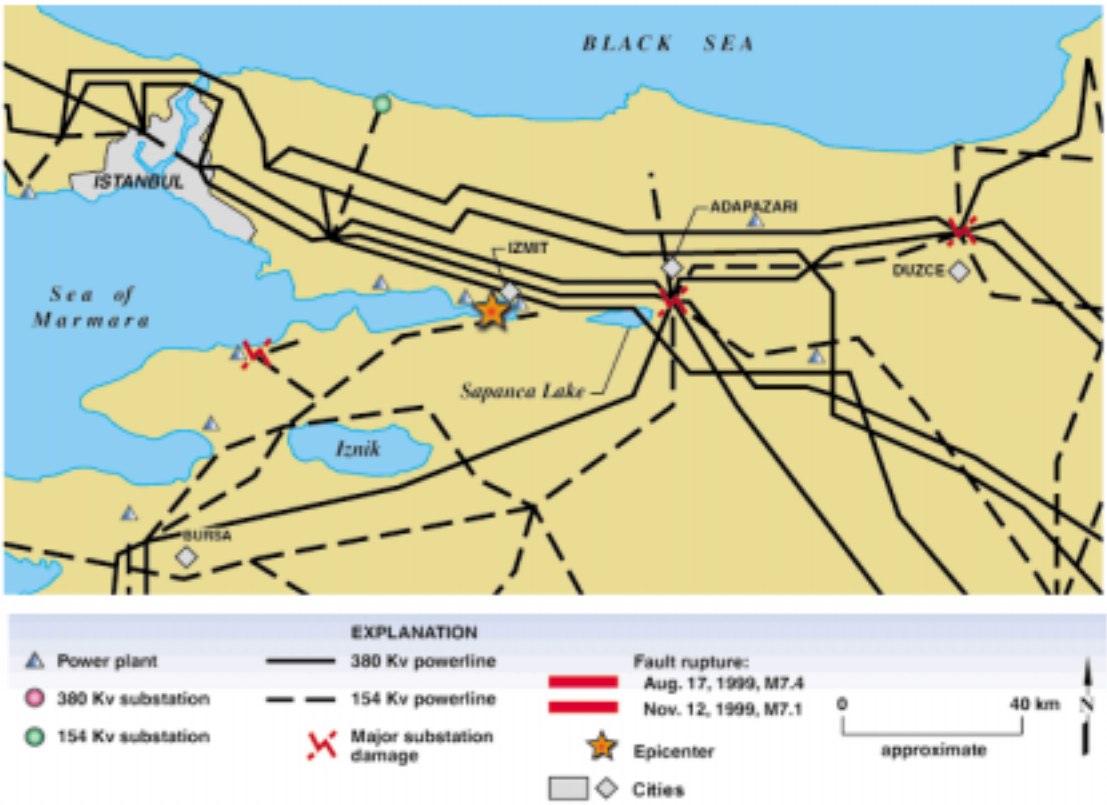

Figure 4. Map of 380 kV electric power transmission system in the earthquake affected region. Also shown are selected portions of the 154 kV transmission system and selected power generation plants.

PACIFIC EARTHQUAKE ENGINEERING RESEARCH CENTER

PEER DIRECTED STUDIES PROGRAM FOR REDUCING SEISMIC VULNERABILITY OF GAS AND ELECTRICAL DISTRIBUTION AND TRANSMISSION SYSTEMS

IGNITION OF FIRES FOLLOWING EARTHQUAKES ASSOCIATED WITH NATURAL GAS AND ELECTRIC DISTRIBUTION SYSTEMS

Robert Brady Williamson
and
Norman Groner
Department of Civil and Environmental Engineering

University of California
Berkeley, CA

2000

TABLE OF CONTENTS

EXECUTIVE SUMMARY 1

INTRODUCTION 3

BACKGROUND 3

Causes of Post-Earthquake Fires Related to Gas and Electric Utility Service 5

San Francisco, California, Earthquake of 1906 6

The Kanto, Japan, Earthquake of 1923 7

Hawkes Bay, New Zealand, Earthquake of 1931 8

Long Beach, California, Earthquake of 1933 9

Managua, Nicaragua, Earthquakes of 1972 9

Morgan Hill, California, Earthquake of 1984 10

Mexico City, Mexico, Earthquake of 1985 10

Whittier Narrows, Los Angeles, California, Earthquake of 1987 11

Loma Prieta, California, Earthquake of 1989 11

Northridge, California, Earthquake of 1994 12

The Hyogo-ken Nanbu (Kobe), Japan, Earthquake of 1995 15

Inventory of Post-Earthquake Fire Scenarios 15

Ignition Scenarios 16

Post-Ignition Residential Fire Scenarios 17

SYSTEMS APPROACH TO POST-EARTHQUAKE FIRE SAFETY 18

Goal Decompositions 21

Gas line Fault Ignition in One and Two Family Dwellings 26

Influence Diagrams 27

Alternate Means to Reduce Fire Risks Following Earthquakes 32

Relationship between Earthquake Shaking Intensity and Fire Occurrence 32

Reducing Gas Faults Inside Buildings 33

Alternative Means to Stop Delivery of Gas 36

Automatic Seismic Shutoff Valves versus Excess Flow Valves 37

Advantages & Disadvantages of Automatic Seismic Shutoff Valves 40

Advantages & Disadvantages of Excess Flow Shutoff Valves 41

Conflagration Issues 42

Electrical Ignition Following Earthquakes 43

CONCLUSIONS 45

RECOMMENDATIONS FOR FURTHER RESEARCH 47

REFERENCES 48

EXECUTIVE SUMMARY

The Pacific Earthquake Engineering Research Center (PEER) is conducting a research program on gas and electric utility lifeline systems. The key tasks of this research are the development and rapid application of advanced methods and technologies for reducing earthquake vulnerability and improving the system reliability and safety of natural gas and electrical distribution systems. This report describes the research project that was carried out to investigate the causes and impacts of fires following earthquakes. This effort takes a broad view of all possible causes of fires following earthquakes by using reported information from past earthquakes and sound reasoning to assess what caused the fires, including both ignition and fuel source. The gas and electric utility infrastructure and customer systems are investigated to determine to what degree they play a factor either as a source of ignition or as a fuel source. These results could help responsible parties to take appropriate action to reduce earthquake vulnerability and improve overall reliability and safety.

The first part of the report contains a survey of the literature describing fire ignitions during past earthquakes. Eleven 20th century earthquakes are reviewed. They are:

San Francisco, California	1906
Kanto (Tokyo) , Japan	1923
Hawkes Bay, New Zealand	1931
Long Beach, California	1933
Managua, Nicaragua	1972
Morgan Hill, California	1984
Mexico City, Mexico	1985
Whittier Narrows, Los Angeles, California	1987
Loma Prieta, California	1989
Northridge, California	1994
Hyogo-ken Nanbu (Kobe), Japan	1995

Based on these events, a list of ignition scenarios is developed in which the natural gas and/or the electric service play a role in the ignition of the first fuel in the fire, or as a fuel source. This report focuses on ignition scenarios associated with two types of residential structures. The first is one and two family housing (R-3 occupancies), and the second is multi-family residential buildings (R-1 occupancies). The scenarios identify the role that natural gas or electricity plays as a contributor to the original ignition and/or fueling of fires following earthquakes.

A systems approach for the analysis of post-earthquake fire safety is presented. The "Fire Safety Concepts Tree" or "Decision Tree" that was developed by the National Fire Protection Association (NFPA) on systems concepts for fire protection in structures is described. It is useful as a checklist for the analysis. It is essentially generalized goal decomposition intended to be applicable to any structural fire safety problem. It uses ends means logic to associate more abstract goals with more specific strategies for achieving those goals. The authors introduced two original systems, the Scenario-based Goal Decomposition (SGD) and the Influence Diagram. The SGD is described as an

intentional systems model to design and evaluate fire safety systems. It represents fire scenarios as a series of desirable system states that are driven by goals. The SGD approach defines fire safety goals as desirable states for a fire safety system. A schematic goal-decomposition model for utility-related earthquake fires is presented. This model is presented as an example of how goal decomposition can be used to link high-level objectives to the very specific strategies that can be used to accomplish them. The model is constructed to allow the calculation of probabilities associated with the prevention of ignition in a specific type of building. Influence diagrams show the dynamic relationships between events and/or systems states over time. A general model of fire ignition related to gas and electrical service during earthquakes is presented. The model can be modified and changed in many different ways as more details are added.

After a careful analysis, we concluded that the current stock of R-3 buildings in California does not pose a significant life-safety risk for post-earthquake fires. However, we also determined that there is some exposure for property loss. To address this exposure, we recommend that the proper reinforcement of hot water heaters and the awareness of earthquake preparedness in general should be fostered by utilities and other agencies. We believe it is the older multi-family residential buildings (R-1 occupancies) that are susceptible to structural damage and potential collapse, that represent the most likely places for people to be trapped during the initial hours of a major earthquake. Then before these people can be rescued, they become potential victims in the event of a fire. The improvement of structural integrity, appliance integrity, and the installation of seismically actuated shutoff valves or excess flow valves could ameliorate fire safety in these buildings. This includes appliance anchorage, flexible gas connection for appliances, gas and electric shutoff devices for homes and businesses, gas and electric distribution system shutdowns, improving the structural integrity of buildings, and finally public education and safety awareness in the earthquake aftermath. A discussion is given on the relative advantages and disadvantages of automatic earthquake actuated shutoff valves and excess flow shutoff valves.

Past earthquakes have shown that electrical power service will most likely be interrupted in the area affected by a very intense earthquake. Thus, except during a very short time after the initial shock of the earthquake, there are few ignitions caused by electrical shorts and arcs. The potential problems with electrical fire ignitions occur during the restoration of power. Before power is restored to an area, the electric utility needs to ensure that conditions are safe there. There should be an exchange of information between the emergency responders at the scene and the utility command center. Power should not be restored until services with damage have been isolated from the electrical supply.

A general review of a systems approach led to the important conclusion that in the post-earthquake environment, where fire fighting is likely to be severely restricted, attention must be paid to ignition prevention rather than fire management.

INTRODUCTION

The Pacific Earthquake Engineering Research Center (PEER) is conducting a research program on utility lifeline systems. Key research projects were identified that support development and rapid application of advanced methods and technologies for reducing earthquake vulnerability and improving the system reliability and safety of gas and electrical distribution systems. This report presents the research carried out to investigate the causes and impacts of fires following earthquakes. The objective was to take an interdisciplinary approach that will lead to methods to reduce the dangers of fires in the post-earthquake environment. The first phase of this project concentrated on ignition of fires following earthquakes with a primary emphasis on natural gas systems, while the second phase concentrated on the role of electric power systems with fire ignition. The research began with the identification of the causes of post-earthquake fires related to gas and electric distribution systems and customer facilities. Then various alternative means to reduce the safety threats posed by fires were evaluated. They included appliance anchorage, flexible gas connection for appliances, gas and electric shutoff devices for homes and businesses, gas and electric distribution system shutdowns, coordination of gas and electric service restorations, improving the structural integrity of buildings, and finally public education and safety awareness in the earthquake aftermath. Two systems approaches were used to describe the post-earthquake systems relationships, Scenario-based Goal Decomposition (SGD) and Influence Diagrams (ID). Both were found to be effective in evaluating the safety associated with these alternatives.

BACKGROUND

This report, reflecting the logical progression of our analysis, is organized as follows:

1. The literature describing fire ignitions during past earthquake events is described.
2. Based on that literature, a list of fire ignition scenarios is provided.
3. Systems analyses are described, based in part on the scenarios that would be expected to cause fires and resulting casualties. However, our analysis is not exclusively based on past earthquake events for three reasons:
    - Earthquakes are relatively rare, and their impacts are highly dependent on local factors. Therefore, generalizing from prior to anticipated events is difficult and highly speculative.
    - Earthquake events* inherently involve very high levels of variability; apart from the magnitude of the causative earthquake, many factors (e.g., the time of day and geographical location) will strongly affect outcomes.

---

* By earthquake "event" we mean the earthquake itself, the damage caused by the earthquake, and the human response to the earthquake.

- The effects of an earthquake event are influenced by the characteristics of utility systems, by the current utility operational practices, and by building types and occupancy characteristics, which differ from other areas that have experienced or will experience earthquakes.

Certain aspects of fire scenarios are not included in the detailed analysis because they do not involve gas and electric ignition or fueling aspects. Most notable among them is the risk of conflagration, which is largely a function of building construction and proximity as well as wind and humidity, regardless of the source of ignition.

The project started with a review of the causes of ignition of fires in recent earthquakes, and has focused on the injuries and damage caused by these fires. Fires after earthquakes occur in many different ways. Perhaps one of the most important challenges of this area of research is to take the lessons from past post-earthquake fires and apply them to reduce injuries and property damage in future earthquakes. An inventory of fire ignition scenarios was created that was quantified with the earthquake severity by either Peak Ground Acceleration (PGA) or Modified Mercalli Intensity (MMI) and with the source of energy such as natural gas, electricity, heating oil, coal, or cooking oil. The experiences of the Northridge and Kobe earthquakes were incorporated into this study. Of particular interest was A. Sekizawa's[48] discussion of the causes of fire ignition in the Kobe earthquake. He found that when one excludes unknown fire causes, most fires were derived from "gas leakage or gas apparatuses" and "other fire apparatuses or chemicals" rather than "electrical causes" for fires occurring shortly after the main shock. With elapsed time, the proportion of these fire causes decreased and the proportion of electrical causes increased and became the main source of ignition as the electrical service was restored.

It is important to take a broad view of each potential fire scenario and to include as many aspects of the system as possible. In addition, there are important human behavioral as well as organizational factors in both the home and commercial settings that can further complicate the situation.

It is also important to take a broad systems approach to identify post-earthquake fire scenarios, since future earthquakes may or may not experience some of the same elements that occurred in previous earthquakes. This is particularly important when the fire scenarios are the basis for investigating alternative means to reduce the threats posed by these scenarios.

System states are often used in the fire sciences to describe the growth and development of fires. Fire development progresses through a series of fairly discrete stages, or system states. Some models are based on an explicit description of how and when systems states change from one stage to another, and they are generally labeled as state-transition models. Stochastic models can be used to represent uncertainty in the transitions between system states[1,2]. Examples of models specific to fire growth include those developed by Beck[3] and by Ling and Williamson[4]. In general, the feasibility and value of such models have been well demonstrated when applied to the physical development of fire scenarios. Groner and Williamson[5] have demonstrated that system states can also be used to describe the manner in which human behavior affects the way that a fire incident develops.

We decided to base our analyses around the use of Desirable Systems States (DSS). A DSS is simply a way of describing a systems state that emergency planners or engineers hope to either preserve or establish. For example, a desirable system state might have the goal to prevent a fire from reaching flashover, or to limit the amount of natural gas available to fuel an unintentional post-earthquake fire. It is important to note that a desirable system state can be achieved or maintained through the actions of both hardware systems and/or people. For example, a sprinkler system activation might achieve the DSS of preventing flashover, or a person closing a door might achieve the same end. Groner and Williamson[6] have demonstrated that a fire incident, including both physical changes in the fire itself and the actions of active fire protection hardware and human behavior, can be modeled using DSS.

One can ask the question: "Why did you decide to base your analyses around the use of DSS?" The answer is that we wanted to make a positive goal as the objective of our analysis. It is feasible to also structure an analysis to prevent a given result or "undesirable" system state, but here the focus is on an unwanted results rather than on "success". It is far more acceptable to achieve a positive result than to prevent a bad result. It all boils down to the "glass is half full" is more positive than the "glass is half empty".

In this study, post-earthquake system states are described using two diagrammatic approaches: (1) "*Goal Decompositions*" and (2) "*Influence Diagrams*." In both cases, system states are the nodes in the diagrams. Either approach can be quantified if and when it appears that it is worthwhile. The relationships among nodes (DSS) can be associated by probabilities that one system state will lead to another and by benefits and costs. For example, the costs associated with a desirable system state can be defined as the amount of resources that would be needed to change from an undesirable system state that will result without intervention to a desirable system state.

Causes of Post-Earthquake Fires Related to Gas and Electric Utility Service

As stated in the Background section, this project started with a review of the causes of ignition of fires in recent earthquakes, with a focus on the injuries and damage caused by these fires. In this section we will present comments from the literature on selected earthquakes, which will create an inventory of fire ignition scenarios. This section is patterned after Botting[7], who recently wrote a very interesting analysis of the impact of post-earthquake fires from the perspective of a fire safety engineer in New Zealand.

The goal of this section is to review the reports of past earthquakes, and summarize the fire scenarios that were directly related to the earthquake events. Fire safety analysis usually begins with the identification of fire scenarios[8], and once they are identified, the solution to the fire problem can be tailored to block one or more of the critical the "fire events"[#] that make up the fire scenario. This has been discussed above,

[#] Every fire can be considered a "chain of fire events," and if the chain is broken the fire will stop or be limited in size

but it is being restated here to bring attention to these aspects of the records of past earthquakes. A fire scenario is a generalized description of a possible fire incident that includes a description of the pre-fire conditions, the fire itself, and the subsequent behavior of people and the performance of fire protection devices. The use of fire scenarios can play an important part in improving building and fire codes.

At the end of this section, an "*Inventory of Post-earthquake Fire Scenarios*" is provided to identify the causes of post-earthquake fires related to gas and electric distribution systems and customer facilities. In addition, there is a discussion of the life safety and property damage impact of various post-earthquake fire scenarios.

San Francisco, California, Earthquake of 1906

The earthquake occurred at 5:12 am on April 18, 1906. The main shock had a reported "moment magnitude[§]" of 7.8 (Richter magnitude 8.3) and a maximum intensity of MMI IX in San Francisco. Scawthorn[9] estimated that the associated fires razed more than 12.2 sq km of the city, and destroyed at least 20,000 buildings. Scawthorn[10] also estimated that 50 outbreaks of fire were reported within the hour following the earthquake.

According to a 1985 EERI report[11], these 50 fires grew quickly to conflagration proportions because of lack of water. Steinbrugge[12] reported that the conflagration lasted 3 days, and caused substantially more damage than the earthquake. He noted that the original outbreaks of fire were in an area characterized by soft ground, which coincided with the predominance of building damage and of breaks in water, gas, and sewer pipes. Scawthorn et al.[13] described the post-earthquake fire problem as typically complex, involving many diverse elements as follows:

1. The earthquake caused structural and non-structural damage to buildings. The structural damage resulted in loss of integrity of many of the "passive"[**] fire-safety elements of buildings. In a similar fashion, there was a loss of serviceability of "active" fire protection systems such as automatic fire alarm systems, and sprinkler systems.
2. The earthquake caused damage to the infrastructure and to urban lifelines including water supplies, gas and electrical supplies, transportation systems, and communications networks (delays in reporting fires to the fire service allowed them to grow rapidly, escalating the demands on fire response).

[§] The seismic moment of an earthquake is a measure of the size of the earthquake that is related to the leverages of forces (couples) across the area of the fault slip. It is equal to the rigidity of the rock times the area of faulting times the amount of slip. Dimensions are in dyne-cm (or Newton-meters). The "moment magnitude" of an earthquake is estimated by using the seismic moment. (from Bolt, B., ***Earthquakes***, 4th ed., W. H. Freeman, New York, 1999, 340 p.

[**] Examples of "passive" fire protection components are fire resistant walls, floor/ceiling assemblies, and doors as well as the fire resistant coating, (often called "fire-proofing"), which are covering the structural components of a building. The word passive is used to distinguish these building elements from "active" fire protection elements such as sprinklers or heat and smoke vents.

3. Fires broke out initially and then spread before fire fighting teams had arrived. The severity of these fires depended on building density, the nature of the fire load*, and climatic conditions (wind and humidity).
4. Fire-fighting teams had to respond to multi-skill demands (fight fires, attend to other emergencies such as chemical spills and building collapses), and had impairment of water supplies, communications, and road access. This resulted in not all fires being responded to, and some fires spreading. The final result was that there were many small fires and a few that led to the conflagration.

One of the fire causes reported by Steinbrugge[14] was the breaking of internal electrical wiring as the result of structural damage to buildings, and since the electrical service current was not shut off for some minutes after the initial shock, this started fires. Other sources of fire were attributed to: the arcing of 550 volt tram wires with other wires, the consequent sparking and arcing of working electrical appliances and circuits in buildings, the collapse of buildings with fires in open fire places, lit kerosene lamps and gas lights in dwellings and businesses, and boiler fires in factories.

Steinbrugge[15] analyzed the mechanisms for fire spread, and identified three major elements for why the conflagration occurred:

1. Fire load per unit area was high,
2. Many fire houses and other fire-fighting facilities were damaged, and
3. Adversity of climatic conditions (there was a persistent wind and absence of rain).

In early 1906, San Francisco contained more than 90% wood frame buildings, also true today in many of its neighborhoods. Many of these wood frame buildings were four or five stories high, and they collapsed across streets. This was particularly common in residential neighborhoods.

During the early hours of the day of the earthquake, the wind was generally light, and from the west. It carried the fire into an area of low, spread-out blocks bounded by the Bay. Some water could be obtained, and some fires were brought under control. But as wind changes were occurring, the conflagration changed its direction of travel and systematically maximized the devastation. A major firebreak along Van Ness Avenue was regarded as one of the principal approaches to preventing spread to the west. If one goes to the neighborhoods west of Van Ness Avenue today, there are many wood-frame apartment houses and commercial buildings that are quite large and up to five stories in height. Many of these survived the 1906 earthquake as well as the fire.

The Kanto, Japan, Earthquake of 1923

This earthquake occurred at 11:58 am on September 1, 1923, and the main shock had a moment magnitude of 7.8 (Richter magnitude 8.3). Steinbrugge[16] reported that over 100,000 lives were lost in Tokyo and its environs. There were 277 outbreaks of fire in Tokyo, and 133 of these spread. He also reported that fire damage was far in excess of direct earthquake damage, and that post-earthquake fires were uncontrolled and burnt large areas for days. Fires that burned for nearly 40 hours destroyed about 40% of

---

* Fire load is the combustible content per unit floor area

Tokyo's structures. The earthquake and subsequent fires also destroyed 90% of Yokohama.

Botting[17] references a New Zealand study by Kenna who recounted that 53 initial outbreaks of fire were reported within a few minutes of the earthquake. He also reported that there were a total of 134 initial outbreaks, of which over 100 were of miscellaneous nature, and 30 were chemical fires. In Tokyo, fires burned 38 km^2 and destroyed 450,000 houses.

Kenna classified primary outbreaks as follows:

1. Direct contact between combustibles and open fire or hot materials as result of
   a. dislodgment of heat source
   b. dislodgment of materials falling onto heat source
   c. fracturing of heat source container
2. Overturning of heat sources (stoves, kerosene lamps, heaters, cookers
3. Electrical short-circuits as a result of movement of defective wiring and dislodgment of supports between circuits normally separated
4. Burst fuel tanks
5 Rupture of gas and oil supply lines (Botting's summary does not say what proportion of the gas lines were inside buildings as compared with the distribution system outside of buildings).
6 Chemical fires started by liquids and vapors from broken containers
7 Fires intentionally started
8 Freak fires (presumably unexplained or of unknown origin).

Expert reviewers of this earthquake have generally concluded that the Japanese construction and contents of buildings seriously affected the ignition and spread of fire following this earthquake. In addition, the wind speeds were in excess of 25 mph for more than two days. Some of these winds may have been induced by the size of the conflagration.

Hawkes Bay, New Zealand, Earthquake of 1931

This earthquake took place on February 3, 1931 at 10:48 am. According to Kenna[18], the main shock lasted at least one minute and had a moment magnitude of 7.75(Richter magnitude 7.8). It was followed by many severe aftershocks during the weeks following the main event.

There were three primary outbreaks of fire that occurred almost immediately after the earthquake and they were in chemists' shops. Fire spread to a fourth building, a hotel, and it was fully expected that these fires would be contained. But just before noon a brisk easterly wind blew up, and before many minutes, the fire was raging throughout the whole of the central business district. The change of wind direction drove the fire from the chemists' shops to adjoining buildings, and from there the fire spread through the central business section. Moreover, the conditions were favorable for fire spread since the day of the earthquake was hot and dry and followed a dry spell of weather.

After an inquest, it was determined that fires that had originated in the chemists' shops were caused by conditions following the earthquake including the following:

1. damaged buildings
2. scattered wares. Bottles containing inflammable and highly volatile liquids were broken and released fluids and vapors that were readily ignitable by the Bunsen lamps used in the chemists' shops.
3. broken light, heat, and power distribution systems inside and outside buildings.

Long Beach, California, Earthquake of 1933

This earthquake happened at 5:54 p.m. on March 10, 1933. The main shock had a moment magnitude of 6.3 (Richter magnitude 6.3) and a maximum intensity of MMI IX.

Kenna[19] reported that this earthquake occurred while many evening meals were being prepared, and estimated 35,000 gas flames were burning, but the gas supply utility lessened the chance of conflagration through quick cutoffs at gas supply points. According to Kenna[20], the primary fire hazard can be reduced by rapid shutting off of gas and electricity supplies either by a pre-arranged disaster procedure or by automatic cut-off valves actuated by seismic shock.

Managua, Nicaragua, Earthquakes of 1972

Three earthquakes occurred between 12:30 am and 1:20 am on December 23, 1972 of magnitude M_s.5 5 to 6.5. Duration of the main shock was 5-10 seconds. The greatest damage occurred in the downtown area, which exhibited intensities of up to MMI IX

According to the EERI proceedings[21], fires broke out in four or five places within a very short time of the earthquake. Fire department resources were overwhelmed, as much of their equipment was buried in fallen buildings. Fires developed into a conflagration and raged virtually uncontrolled for three days. The fire was finally stopped on December 27 by a firebreak and continued firefighting. Steinbrugge reported from personal observations that fires were still burning ten days after shock

According to Kenna[22], the hazard of fire spread in two modern high-rise buildings, where several hundred occupants might have been trapped by fire in the higher floors, could have been a possibility had it not been for the time of day that the earthquake struck. Had fire occurred immediately after the earthquake, and had the shock taken place during working hours, life loss would have been substantial because of the debris-littered stairwells, jammed doors, and inoperative elevators. Fires on any floor would have spread rapidly from floor to floor through shattered fire-resistive enclosures, and around stairs and elevator shafts. Fire suppression and rescue efforts would have been very difficult.

The EERI Proceedings[23] stressed the importance of the impact of building damage on fire safety in multi-story buildings. After this earthquake, many stairways were partially or wholly blocked due to jammed doors and debris. When debris and smoke block stairways, and elevators are out of operation, critical emergency egress and fire-fighting response problems arise. These problems are compounded at night due to electrical power failure and lack of emergency lighting.

Morgan Hill, California, Earthquake of 1984

The moment magnitude of this earthquake was 6.2 with 5 to 10 seconds of strong shaking. The maximum intensity was MMI VII at Morgan Hill. According to Schiff[24], post-earthquake fire was the primary cause of damage in Morgan Hill and San Jose

Scawthorn et al.[25]reported that the causes of two major structural fires were broken natural gas pipes to heating elements in gas appliances, a water heater and a gas heater. Scawthorn[26] also reported that several residential fires were due to chimney and gas heater flue damage. One of the fires occurred when the gas service had been restored one hour prior to the fire.

According to Scawthorn[27], several fires were ignited by electricity.

1. There was an attic fire in a commercial laundry where electrical shorting in steel conduit caused a hot spot and the ignition of cotton lint in contact with it.
2. A snapped power line fell onto a dwelling roof, arced through the metallic roof covering, and ignited wooden structural members and house contents.
3. A floodlight fell onto the roof of a residence at the time of earthquake. It was turned on automatically by a timer device and the light overheated and ignited the roof covering.
4. There were three grass fires caused by arcing of fallen wires

Scawthorn[28] reported residents of the Jackson Oaks area were effective in preventing ignition when they turned off about 30% of their gas service, and the Fire Department completed the cut-off of all gas and electricity.

Mexico City, Mexico, Earthquake of 1985

The epicenter of this earthquake was in Michoacán, Mexico, and the event had a moment magnitude of 7.9[+] (Richter Scale 8.1), and 60 seconds of severe shaking. Although Mexico City was at a large distance from the epicenter, some of the worst damage occurred there. In the worst hit area, the intensity was MMI IX. According to Earthquake Spectra[29], this earthquake was exceptional in that it led to the largest toll of collapsed buildings produced by a single event in the country, and it was one of the largest experienced by a modern city built in accordance with advanced seismic design provisions. Bolt[30] reports that there were 9,500 deaths and 30,000 injuries

Botting[31] references a New Zealand Reconnaissance Team report identified in his paper as NZNSEE (1988). This report noted that Mexico City did not have a network gas supply system. Instead, tankers supplied LPG to storage tanks, commonly seen on building roofs. The NZNSEE (1988) study noted the following items about the post-earthquake fires:

1. Within 24 hours following the earthquake, about 200 fires were reported.
2. There was no major conflagration, presumably due to the type of construction, i.e. the absence of wooden buildings, and the absence of buried gas pipelines.
3. The fires played no part in the structural damage, but they probably killed trapped people who otherwise might have been saved.

[+] Bolt, Bruce, Earthquakes, 4th Ed., W. H. Freeman, NY. 1999, p. 295.

4. The only serious fire was due to a leak in the gas storage tank of the St. Regis Hotel, and the fire spread to an adjacent department store and office building.

The New Zealand team noted that although the earthquake occurred at about breakfast time for many people, there were no reports of cooking fires.

Bertero[32] reported that he had arrived in Mexico City early enough to see a fire in the St. Regis Hotel, and he believes that the fire had prevented the rescue of some people trapped in the building. As far as we could determine, the toll of persons lost in that fire has not been documented.

Whittier Narrows, Los Angeles, California, Earthquake of 1987

This earthquake occurred at 7:42 am on October 1, 1987, with a moment magnitude of 6.0 (Richter magnitude 5.7) with a major aftershock of 5.5 at 3.59 am on October 4.

It was reported in Earthquake Spectra[33] that the overall performance of the electrical distribution system, as measured by customer service disruptions, was good, although power was lost to about 37,000 customers that was due to a transformer fire fueled by an oil leak. In Los Angeles County there were numerous disruptions due mostly to burned-down systems, and entanglement of electric lines.

The same article in Earthquake Spectra reported about 1,400 gas leaks of which 75% were due to leaks from water heater appliance connections. Public service announcements right after the earthquake advised people to shut gas off to their homes; however the number of responses was not reported.

Smoke[34] reported that during first 5 hours after the earthquake, the LA Fire Department responded to 75 gas fires and 38 other structure fires, but no large-scale fires occurred. Approximately 5 hours after the earthquake, there were no new outbreaks of fires, and most of the fires that had occurred were extinguished.

The article in Earthquake Spectra[35] reported that there were only 20 earthquake-related structure fires within the LA County Fire Department area, with 10 of these in the Whittier area. The causes of the fires were reported as follows:

1. Arcing and shorting when power was restored to damaged electrical appliances or fallen light fixtures,
2. Combustible material moved towards a heater by earthquake motion,
3. Mixing of spilled chemicals, and
4. Burned down power lines

The same article further reported that a significant number of gas leaks were associated with the motion of water heaters, but it did not identify them as a cause of fire.

Loma Prieta, California, Earthquake of 1989

This earthquake occurred on October 17, 1989, at 5:04 p.m. as a result of a slippage of some 40 km of the San Andreas fault producing an estimated average surface wave moment magnitude of 7.0 (Richter magnitude 7.1)[36]. Its epicenter was located in the Santa Cruz Mountains, 16 km north-east of Santa Cruz, and 30 km south of San Jose. The toll was reported as 62 deaths, nearly 3,800 injured, in excess of 7,500 homeless, and

property damages of 5.6 billion dollars. The MMI for San Francisco was typically VI, but in San Francisco's hardest hit area, the Marina district, the MMI was reported as IX and with ground motion amplification with intensity estimations of as much as 0.35 g's. There were heavy structural damages in this area, and, in addition, a fire destroyed one block of buildings. According to Coleman[37], there were 27 structural fires in San Francisco during the first seven hours after the earthquake. In all there were 41 fires reported in San Francisco[38]. The most serious fire started in a 4-story wood frame building containing 21 apartments, and a parking garage on the ground floor in the Marina district. The two lower floors of the building collapsed during the earthquake, but the cause of ignition of this fire is uncertain, though it was not believed to be from natural gas since the gas distribution pipes in the streets were extensively damaged. Fire fighters arrived at approximately 5:45 p.m., and found that there was no water pressure in the hydrant in front of the building. Shortly thereafter, an explosion shook the building and several other buildings were ignited. Water was found and relayed from a more distant hydrant but more explosions occurred destroying a number of hose sections. At 6:00 p.m. a fireboat and 3 hose tenders arrived. The water from the boat had positive effects and the fire was controlled by 8:00 p.m., Most of the 41 fires reported (33 out of 41) were at sites on unconsolidated soil, 5 on mud and fill, and the rest on stable bedrock. According to Alyasin and Bak [39], the low number of fires for an earthquake of this magnitude was due to the following factors: nearly zero wind speed, the relatively short duration of the earthquake, about 40 seconds, and well managed fire fighting efforts. In addition, according to Lew[40] the shutdown of electric power eliminated this as an ignition source, and caused electricity-powered safety valves to close, shutting off the pilot and interrupting the flow of gas at that point. Also the caution exercised by citizens was effective in preventing ignition of leaking gas.

Fires in other areas were also reported. In Berkeley an auto-body shop building was completely destroyed by fire, but the fire was contained to the building of origin. It was believed to have started when flammable liquids were spilled during the earthquake. Santa Cruz County had 20 fires. In the city of Santa Cruz, only one residential structure was destroyed by fire. The cause of this fire was reported as a main gas leak. A wildland fire erupted at Niesene Marks State Park, and in Watsonville, one single-family dwelling and two mobile homes were destroyed by fire. In Santa Clara County, a residential fire was due to a ruptured propane tank.

Northridge, California, Earthquake of 1994

This earthquake occurred at 4:31 am, Monday January 17, 1994, with a moment magnitude of 6.9 (Richter magnitude 6.7), and shaking intensity ranging up to MMI VII to MMI IX. Chung[41] reported that for first time in LA history electrical power was out in the entire city. It was restored to 90% of LA Dept of Water and Power customers within one day of earthquake.

No type of building came through unscathed. At least 200 three-story wood-framed and stucco-clad apartment buildings collapsed, and a further 650 suffered serious damage. A number of multi-story car parks collapsed due to column failure. Many reinforced concrete office building older than 20 years performed badly due to

insufficient reinforcing. Many moment-resisting steel framed building experienced welding failures. Six freeway bridges collapsed.

There are a number of reports and articles written about the fire ignitions associated with this earthquake, and there are some conflicting statements regarding the numbers of events that occurred. In general, these discrepancies are probably due to the many different sources of information that have been used to amass this data. In the following paragraphs a variety of information will be presented without an attempt to compare the validity of the data. There will be a discussion at the end of the section.

Scawthorn, Cowell, and Borden[42] estimate in the period of 4:31 a.m. (time of main shock) to midnight, there were approximately 110 earthquake-related fires. They emphasized the collection, documentation, and preservation of data, with some limited analysis. Fire incident data are compiled in a database termed FFNRE (available on the Internet: www. eqe.com) and details are given for fire departments at 5 selected fire incidents. Limited analysis led to the following most important conclusions:

1. More than 70% (66) of the earthquake-related fires occurred in single-or multiple-family residences.
2. The major cause of ignition was electric arcing as a result of a short circuit, although gas flame from an appliance was also a recurring source of ignition.
3. Escaping natural gas, presumably from a broken gas line, was the single most common ignition material
4. Ignition rates are comparable with prior US earthquakes, and when compared with the San Fernando and Kobe earthquakes, all three events share winter early morning occurrence times.

Scawthorn, et al.[43] also included a discussion on damage to fire stations, water systems and gas systems. They estimated that about 151,000 gas customer outages had occurred, (81% customer initiated) and three months after the earthquake, repairs had been made to about 800 gas systems at separate locations. Of the 8,000 seismic gas shut-off valves in the region, about 10% (841) had tripped off and among those 19% (162) had leaks. One can summarize some of their conclusions as follows:

1. While there were a significant number of fires, they were all brought under control within hours of the earthquake.
2. The LA resources were sufficient to deal with all fire ignitions
3. Water supply failed in heavily affected areas, and firefighters resorted to alternative sources, which, however, would likely not have sufficed had conflagrations developed.
4. Arson fires were not a significant factor

One can infer a list of "*Lessons learned*" within the report of Scawthorn, et al[44]:

1. Alternatives to water need to be developed and water systems need to seismically upgraded
2. Gas and electric seismic shut-off devices offer a potential for mitigation.

3. Multiple fires can be expected as a result of earthquakes in urban areas. The experiences of the Northridge earthquake show that in a larger earthquake more ignitions might result, which may overwhelm the resources of the emergency responders.

4. The weather was not a major factor in the Northridge earthquake, but in future earthquakes it may make the deciding difference. Coupled with inadequacies in the water supply, this may lead to large conflagrations that could rival the 1906 San Francisco earthquake.

Finally, Scawthorn, et al[45] show three photographs of the collapse of the Northridge Meadows apartment at 9565 Reseda Blvd. where 16 persons were killed and "hundreds rescued". One can well imagine how the ratio of "killed-to-rescued" would have been changed had there been a fire in the debris like they report at 11611 Blucher Ave, Granada Hills[46]. The latter structure contained 2-story condominiums that did not trap as many people as the Meadows apartment building.

Todd, Carino, and Chung[47] listed the natural gas leaks as the principal cause of fires with other causes such as hazardous chemical interactions causing a small number of fires. Todd also reported that some fires occurred in the days following the earthquake that were attributable to the restoration of electricity and gas service.

Strand[48] reports that there were 14,062 natural-gas leaks on consumers' lines and cites an unpublished Southern California Gas Company (SoCalGas) report. More significantly, Strand personally performed a survey of the performance of 424 seismic gas shutoff valves and concluded that most of them within a 29 km radius of the epicenter tripped. The closest one that did not trip was 14 km away. Strand also quoted the number 841 tripped seismic gas shutoff valve referenced by Scawthorn, et al[49], but Strand attributes that number to the unpublished SoCalGas report mentioned above[50].

Strand further states that in Los Angeles, leaking gas caused fires in at least 24 single-family dwellings, 5 apartment buildings, 3 businesses, and 6 mobile home parks with a loss of 144 trailers. Causes include broken gas lines to 21 water heaters, 5 trailers, 2 floor heaters, and 2 dryers; leaks in an attic, in a kitchen, at 2 meters, and between a meter and a building. Two more fires occurred due to damaged gas mains, one where a block-wall fell, and another where a large gas main under Balboa Boulevard in Granada Hills ruptured resulting in the loss of 5 homes. Strand also notes that local fire departments and SoCalGas recorded about 60 gas-related structure fires, not including the mobile home fires. One hundred and seventy-six mobile homes were reported to have burned.

The US-Japan Workshop[51] notes that the major ignition sources were electric arcing as the result of a short circuit, and gas flames from an appliance. Southern Cal Gas reported about 2,500 damaged water heaters. Approximately 20 fires were due to inadequately secured water heaters tipping over.

According to Chung[52], the water heater was the most vulnerable appliance. He quoted that approximately 2,500 water heaters were damaged during this earthquake, and approximately 20 fires were due to inadequately secured water heaters tipping over. After the earthquake, Chung noted that the technical feasibility of seismically operated

shut-offs and control mechanisms should be assessed along with a cost/benefit analysis for the use of these systems. Guidelines for the installation and use of these devices should be developed. He also suggested that earthquake-activated electric shutoff switches should be assessed. He noted that these should have some value for the following two scenarios:

1. When damage to electric service has occurred, particularly in buildings sustaining serious structural damage. This may include faults to ground and short circuits that could act as potential ignition sources.
2. When electric service is restored, before the removal of combustibles that have toppled over and fallen on electrical appliances.

The Hyogo-ken Nanbu (Kobe), Japan, Earthquake of 1995

The Hyogo-ken Nanbu earthquake occurred at 5:46 am on 17 January 1995 with a with a moment magnitude of 6.9 (Richter magnitude 7.2), resulting in shaking intensity exceeding MMI VIII. Nearly 6,000 people were killed, and over 33,000 injured. Many were trapped alive in collapsed buildings and killed by the firestorms that followed. Over 500 deaths were caused by fire.

According to Sekizawa[53], for cities other than Kobe, about 73% of fires that started by 6:00 am on the day of earthquake were single fires confined to structure of origin. About 3% of these fires spread to be large fires having burned an area greater than 1,000m^2. This indicates that the fire brigades functioned fairly well in regions other than Kobe.

Sekizawa[54] discusses the causes of fire ignition and noted that when one excludes unknown fire causes, most fires were derived from "gas leakage or gas apparatuses" and "other fire apparatuses or chemicals" rather than "electrical causes" for fires occurring by 6:00 a.m., i.e. shortly after the main shock. With the elapse of time, the proportion of these fires decreased and the proportion of electrical causes increased and became the main source of ignition after 7:00 a.m., when the electrical service was being restored.

Chung[55] reports the following combinations of fuels and ignition sources that most likely caused the fires: broken natural gas pipes that were evident at many of the fire sites of homes and factories; kerosene heaters that were present in the ruins of many of the buildings; power lines knocked down by the earthquake or torn from collapsed buildings; activities associated with the recovery activities such as use of candles and fires for warming displaced survivors getting out of control; and arson. Chung also partially supports the theory that when electric power was restored, damaged appliances, wiring, and light fixtures ignited combustibles.

According to NZNSEE[56], there does not appear to have been a close liaison with gas and electricity suppliers before power was restored. The rapid reinstatement of power was a significant cause of fire ignitions.

Inventory of Post-Earthquake Fire Scenarios

The fire aspects of eleven different damaging twentieth century earthquakes have been presented in this section. They started with the 1906 San Francisco event and ended with the 1995 Kobe event. The eleven events were chosen to illustrate the range of fire scenarios that can follow an earthquake. The eleven events appear to follow Sekizawa's

observation[57] that "the incidence of fires following an earthquake is in proportion to the ratio of damaged-to-undamaged structures". Structural damage relates directly to disruption of gas pipes and gas appliances and the damage of electrical wires or electric appliances, a fraction of which in turn lead to fire ignitions fed by gas leakage or electric arcing.

IGNITION SCENARIOS

An analysis of the eleven large twentieth century earthquake occurrences yields a list of ignition scenarios in which the gas and/or electric service played a role in the ignition of the first fuel in the fire:

1. A gas pipe in a building is broken, **and** an electric arc from damaged electrical wiring is present near the released gas to ignite it promptly.
2. Bottles and/or open cans of flammable liquids are thrown to the floor by the earthquake, **and** an open gas flame or an electric arc is present to ignite the vapors from the spilled liquid.
3. A hot water heater is overturned by the earthquake motions resulting in a rupture of the gas supply piping, **and** the released gas is ignited by the pilot light of the heater.
4. A gas pipe in a building is broken because the structure deformed so much that pipe could not remain undamaged **and** the delayed ignition of the released gas occurs when an ignitable mixture of gas and air has been created. This scenario can lead to an explosion[&]. The ignition can vary for this scenario. Certainly, rescue efforts can potentially be a significant source of ignition.
5. Cooking oils and other kitchen fuels are spilled during the earthquake, **and** either electrical- or gas-based cooking equipment ignites these fuels
6. While the electrical service to a structure is interrupted by the initial earthquake event, an electric-powered device is displaced and/or damaged by the earthquake motions and put into contact with a quantity of fuel. Then when the electric power is restored to the building, this displaced device causes the ignition of the exposed fuel. An example of such a scenario might be a high intensity light falling onto a polyurethane mattress or couch.
7. A person ignites a fire by such means as arson or turning on light switches with natural gas present.

[&] The term "explosion" can be used to describe a range of phenomena. If the gas and air are well mixed the ignition of the pre-mixed gas cloud can result in a "detonation" with the release of a great deal of energy and supersonic shock waves. If the gas cloud has not mixed with air to a large extent, and if the ignition occurs at a boundary of the gas cloud where air is present, the burning of the gas can cause local turbulence which in turn causes more air to mix with the gas cloud that accelerates the burning. This accelerated burning leads to a "deflagration" which sounds like and looks like an explosion, but it lacks the energy release and the destructive power of a detonation.

Our analyses do not focus equally on all of the above scenarios for the following reasons. These scenarios are for ignition of the first fuel, but the life-safety and property-damage impact of various post-earthquake fire scenarios depends much more on other factors than the initial first fuel ignition. The time of day, which affects the various activities of people, can have a large impact on the consequences of post-earthquake fires. In the same fashion, the type of occupancy of a building can change the life-safety impact more than any other feature of the structure. We are focusing on residential occupancies in this report, because the potential life- safety implications are much greater in this sector. Other occupancies such as elementary schools and hospitals, have received special treatment in the building codes for seismic safety resulting in less potential for harm in those structures than in residential structures.

POST-IGNITION RESIDENTIAL FIRE SCENARIOS

Residential occupancies differ according to the number of residential units that are located within a building. The number of units within a building is important to fire safety for many reasons. For example, building layouts differ as to whether occupants must use shared paths of emergency egress or they can leave the building by a direct unshared route. In multiunit occupancies (R-1 occupancies**), common paths of egress and limited means of escape make it more likely that persons can become trapped after an earthquake. The greater the number of occupants in a building, the greater is the likelihood of their being trapped. The possibility of structural damage that prevents the operation of doors leading out of apartment and condominium units often cause this inability to exit safely. In buildings of more than two or three stories, the escape paths usually include enclosed stairways whose doors can be jammed by the racking deflections of the doorframes caused by the earthquake. Frequently, the elevators in these buildings are also unusable. Some older buildings may have exterior fire escapes, but they may not be well attached after the earthquake. Single-family residential units (R-3 occupancies), on the other hand, cannot, by code, be more than 3 stories in height, and their windows are usually constructed in such a way that they can serve as secondary exits[58]. Thus there are more and easier pathways for escape in R-3 occupancies than is generally true in R-1 occupancies. In addition, if the R-3 structure is properly tied to its foundation, such a building is less likely to lose its means of escape than the larger and more complex R-1 structures.

Mallick and Saud[59] wrote about post-earthquake scenarios in the context of a "developing country like India" in which the "earthquake aftermath presents a scenario of collapsed and damaged buildings and bridges, fires raging out of control, people trapped inside the burning houses and/or under the debris of collapsed buildings". In many ways, their scenarios could also be appropriate for the more developed countries under conditions of damaged R-1 structures in dense urban areas.

A great deal of the attention in the US has been on conflagrations following earthquakes as being the most damaging fire impact of earthquakes. This scenario has been well developed by Scawthorn[60] who notes that fires following earthquakes have caused the largest single losses due to earthquakes in the United States and Japan. He

** Occupancies are defined in the model building codes; R-1 and R-3 are the designations for residential occupancies, see Table 1.

considers the following factors in scenarios for post-earthquake fires: structural and non-structural damage, initial and spreading fires, wind, building density, water supply functionality and emergency response. He has written an analytical model that has been the basis of several computer models that have been applied to predict the conflagration potential of various possible earthquakes

SYSTEMS APPROACH TO POST-EARTHQUAKE FIRE SAFETY

A fire must go through many stages before it becomes a conflagration. Once an ignition occurs within a space in a building, the fire will have to grow in size that is a process that can be described by an "Event Tree". In most interior spaces, fire spread will not occur unless there is "flashover" in the room-of-origin, which depends on many factors including other sources of fuel, damage to surrounding structural elements, and housekeeping. Many different fire scenarios may occur, and small changes in the conditions can make a large difference in the outcome of the fire ignition. For instance, whether a door is open or closed can make a very significant difference. If the occupants can escape from a building, the principle impact of the fire is one of property damage rather than of life-safety if the people cannot escape. One of the best ways to describe these differences is through the use of the "Systems Approach" for fire safety.

A good starting point for analyzing the fire safety associated with a given operation or structure is the "Fire Safety Concepts Tree [61] or "Decision Tree" as developed by the National Fire Protection Association (NFPA) on Systems Concepts for Fire Protection in Structures. It can be used as a checklist for the analysis. The Fire Safety Concepts Tree is essentially a generalized goal decomposition intended to be applicable to any structural fire safety problem. Like the focused goal decomposition presented later in this report, it uses an ends-means logic to associate more abstract goals to more specific strategies for achieving those goals. Thus, it provides a good introduction to the special problems associated with fire safety during earthquakes.

Starting at the top with the **Fire Safety Objective(s)**, the tree proposes alternative ways, not necessarily mutually exclusive, of meeting those objectives. The first choice in the tree is to **Prevent Fire Ignition** or **Manage the Fire Impact**, as shown in Figure 1. The objectives can be listed as

(1) Prevention of loss of life or personal injury,

(2) Prevention of the loss of property,

(3) Prevention of the interruption of business,

(4) Prevention of environmental damage,

(5) Prevention of loss of historical artifacts and buildings, and

(6) Preservation of emergency response, hospitals, water response, etc., in the post-earthquake environment.

The small box with the "+" is an "or gate" which signifies that the objectives can be achieved by either of the two choices. In practice, it is usually not possible to just follow one approach, but the "or gate" represents the logical relationship between the two sides of the tree. Thus in principle, if you prevent the ignition, you will reach the objectives.

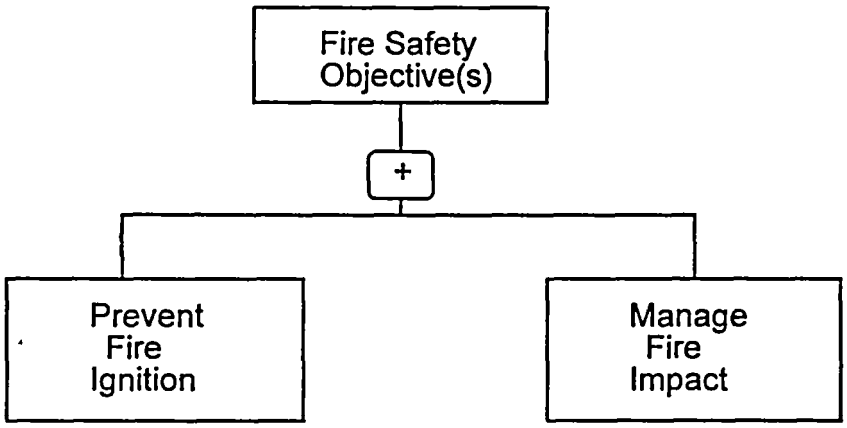

Figure 1. The principal branches of the "Fire Safety Concepts Tree" or "Decision Tree," as developed by the NFPA on Systems Concepts for Fire Protection in Structures.

The branch of the Decision Tree headed by **Prevent Fire Ignition** is followed by an "or gate" and three choices that are relatively independent of each other. This branch is shown in Figure 2. The prevention of ignition is divided into **Control of Heat-Energy Source(s), Control of Source-Fuel Interaction,** and **Control of Fuel,** and the goal of preventing the ignition can be achieved, in principle, by controlling any one of those entries in the tree. In the post-earthquake scenarios, if there is a gas leak then the control of the fuel has been lost and thus the ignition event can only be prevented if the potential ignition sources and their interaction with the gas leak are controlled.

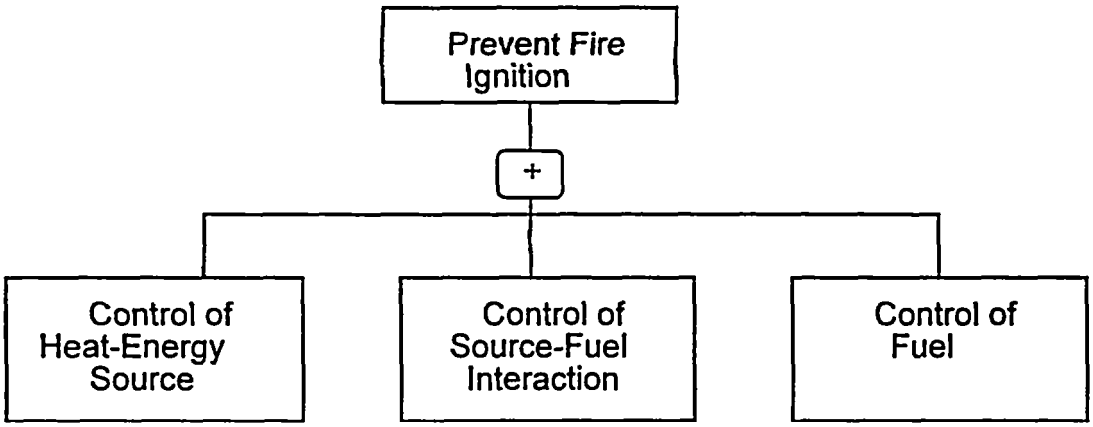

Figure 2. The branch of the Decision Tree headed by **Prevent Fire Ignition** has three choices that are relatively independent of each other.

If one is not successful in preventing the fire ignition, then the decision tree gives an alternate solution that is given on the right-hand side of the tree, under **Manage (the) Fire Impact.** There the choices are either to **Manage the Fire** or **Manage the Exposed,** as shown in Figure 3.

Thus if one option does not prevent the ignition, the tree indicates that one has the alternate option of managing the impact of the fire by either managing the fire itself or managing the exposed people, property or operations to prevent the loss.

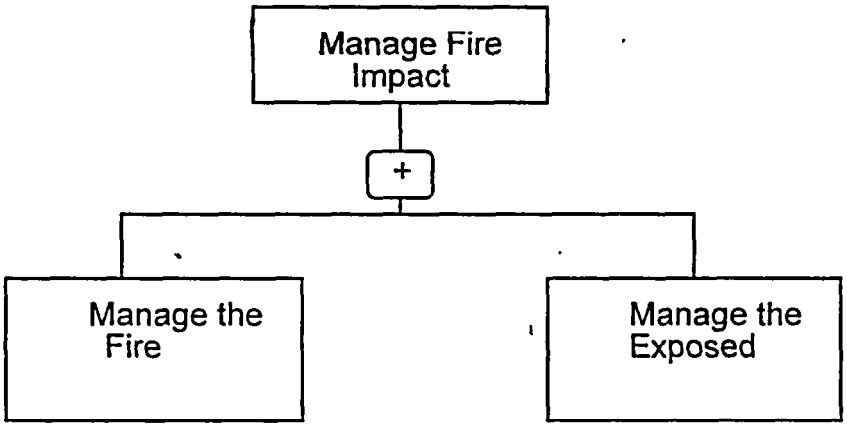

Figure 3. The choice of reducing fire impacts is divided into Managing the Fire or Managing the Exposed people, property or operations.

The top three levels of the NFPA Decision tree are shown in Figs. 1, 2, and 3. For the post-earthquake environment it is important to point out that this Fire Safety Concepts Tree or Decision Tree is a "success tree" because the top items represent a successful application of fire safety logic. This tree can be converted to a "fault tree" by changing all the "and gates" to "or gates" and all the "or gates" to "and gates"[@]. Thus one can have a large loss of life in a fire in which the ignition had occurred and the fire impact was not controlled. The Fire Safety Concepts Tree has three or four additional levels of detail below those shown in Figs. 1, 2, and 3, but for our purposes the levels shown here are sufficient.

In the post-earthquake environment, the probability of managing the fire impact is reduced. To Manage the Fire Impact, one either has to manage the fire by applying fire suppression or containing it in compartments bounded by fire-resistant construction, for example, or one has to Manage the Exposed people, property or operations. If we consider life safety, there are two ways to Manage the Exposed people: (1) cause them to move to safety, or (2) defend them in place. Both these approaches are inconsistent with damaged or partially collapsed buildings where people are trapped inside, which is one of the most life-threatening fire scenarios.

[@] This is true with regards to the fire safety concepts tree, and in general, it is accurate to say that a success tree can be changed to a failure tree by reversing the gates. However, fault trees use a causal logic to link event nodes, while a success or goal tree uses ends-means logic to link nodes that vary in their level of abstraction.

GOAL DECOMPOSITIONS

Goal decompositions have the advantage of solving problems by breaking down general desirable systems states into continually more specific and measurable goals. Eventually, goals can be decomposed into all the specific actions that various parties should consider in their effort to realize general goals such as preventing casualties and property damage and minimizing expenses. The word "scenario-based" has been added to goal decompositions to distinguish the context in which it will be applied. Thus it will be called "scenario-based goal decomposition" (SGD). Groner and Williamson [62] describe this approach as an "intentional systems" model to design and evaluate fire safety systems. Scenario-based goal decomposition differs from traditional engineering methodologies that rely on physical (causal) models where events are driven by laws of causation. Instead, SGD represents fire scenarios as a series of desirable system states that are driven by goals. These goals originate with the people who design for a fire emergency (e.g., fire protection engineers and emergency planners) as well as those who participate during an emergency (e.g., building occupants, utility staff, fire fighters, and others). The SGD approach defines fire safety goals as desirable states for a "fire safety system." A fire safety system is viewed as being comprised of all relevant components, including people, which play significant roles in the defense against a fire threat. In a goal decomposition analysis, desirable system states are "decomposed" to increasingly specific and measurable levels. Various fire scenarios often present many different elements where trade-offs can substitute hardware for action or visa-versa. If we paraphrase Groner[63]: "When evaluating and designing fire safety plans, it is important to understand that weakness in the system can be offset by improving capabilities in another part of the system. Hardware is used to compensate for limitations in procedures, and procedures are used to compensate for limitations of hardware." This principle cuts across types and categories of components.

A schematic goal decomposition model for utility-related earthquake fires is shown in Figure 4. Separate symbols are shown for "Intentional Systems States" and "Lowest Level System States". Figure 4 is divided into four parts that show how the goal decomposition model can detail some of the more specific means for preventing fire ignitions in individual buildings. The reader, however, is cautioned that the means provided are not exhaustive. The model is presented as an example of how a goal decomposition can be used to link high level objectives to the very specific strategies that can be used to accomplish them.

The model can be extended to allow the calculation of probabilities associated with the prevention of ignition in a specific type of building. When the number of such buildings is known for a selected geographical area, the probability of preventing ignitions in that area can be calculated. The probability of preventing an ignition in a particular building can be calculated when the probabilities for the specific low level enabling states is known. Various means for obtaining such probabilities might include historical data and expert judgment.

Scenario-Based Goal Decomposition for Gas-related Fire Ignitions inside Residential Dwelling Units during Earthquakes

Goals are defined as desirable system states. Desirable systems states are "decomposed" into increasingly specific levels of definition. System states are divided into two types. "Scenario" system states are those states which are not under consideration for manipulation (rounded corners). "Intentional" system states are being considered for manipulation (sharp corners).

Logic gates and calculations of probabilities are the same as for event trees (e.g., fault trees). Probabilities are assigned to system states are for a single type of residential dwelling (e.g., detached one- and two- family residences. Regional risk assessment requires the multiplication of the top probability of preventing ignition by the number of dwellings of a specific type.

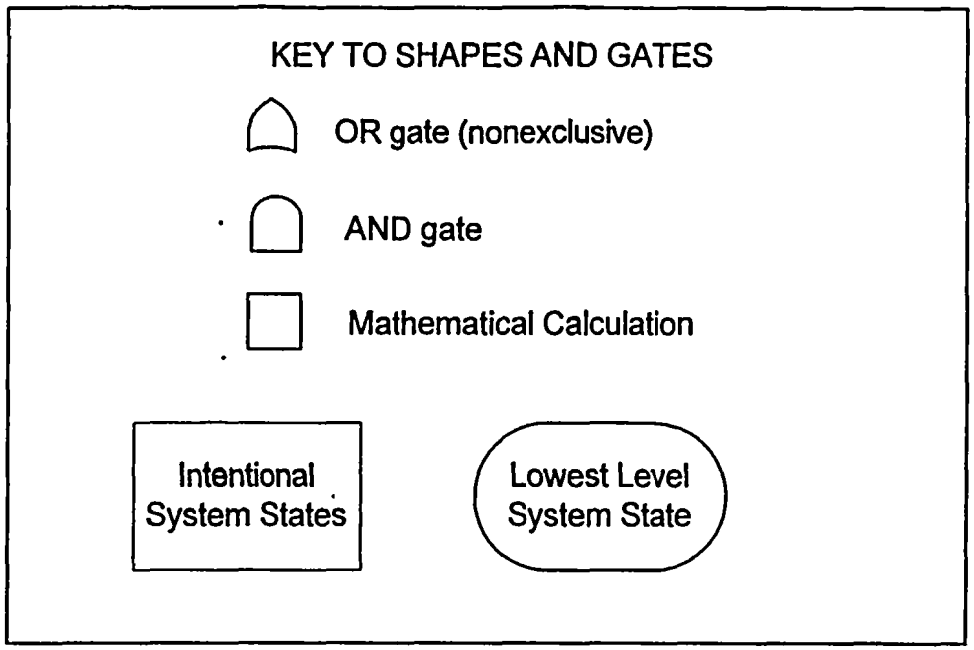

Fig. 4 (a)

SCENARIO: Fire ignitions related to gas line faults inside 1 & 2 Family residential dwelling buildings, (i.e., R-3 Occupancies by '97 UBC). This model calculates the probabilities of desirable system states associated with preventing earthquake related fires where natural gas is the first ignited fuel. It does not include ignitions unrelated to gas as a fuel or associated with the restoration of gas service.

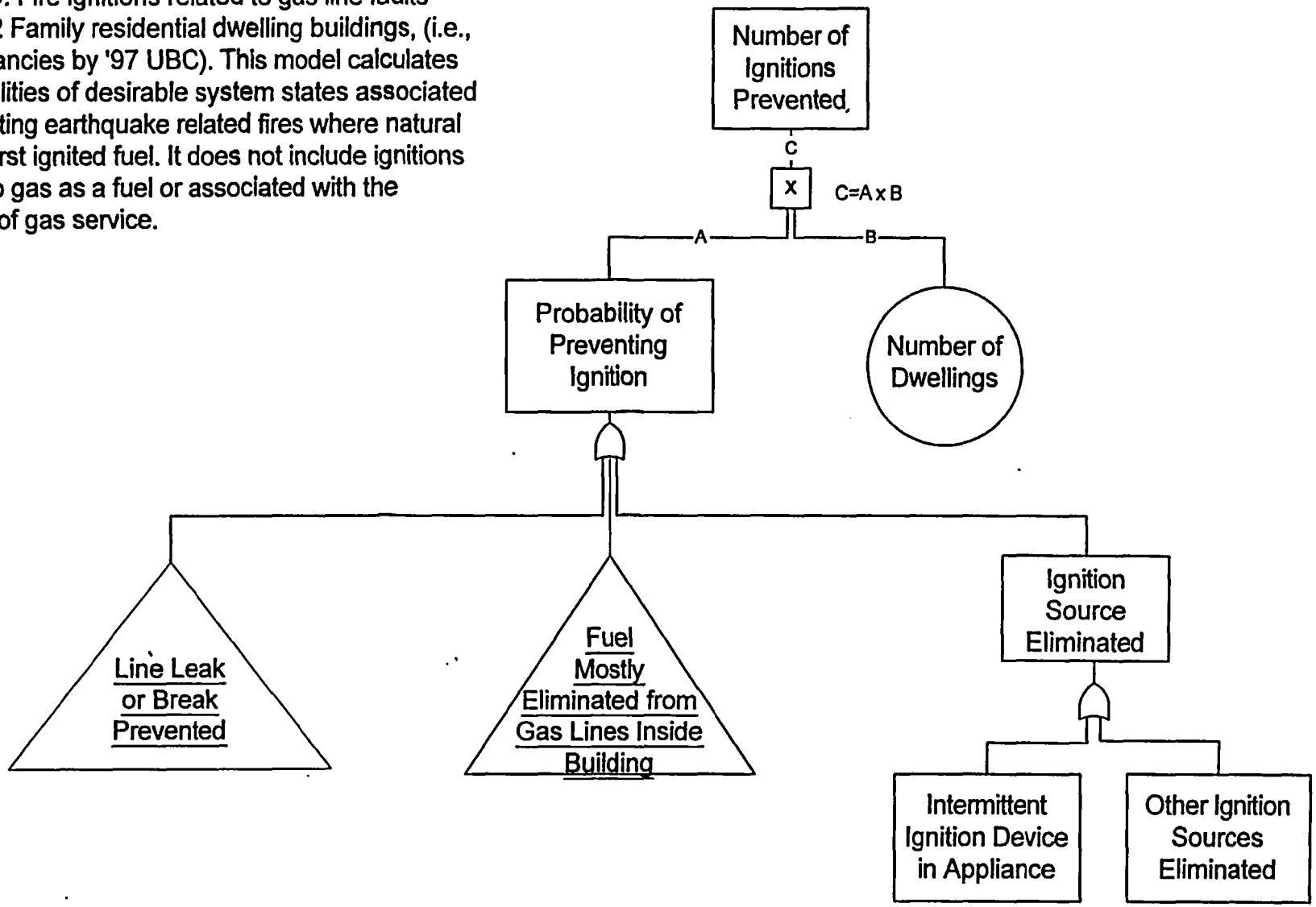

Fig. 4(b)

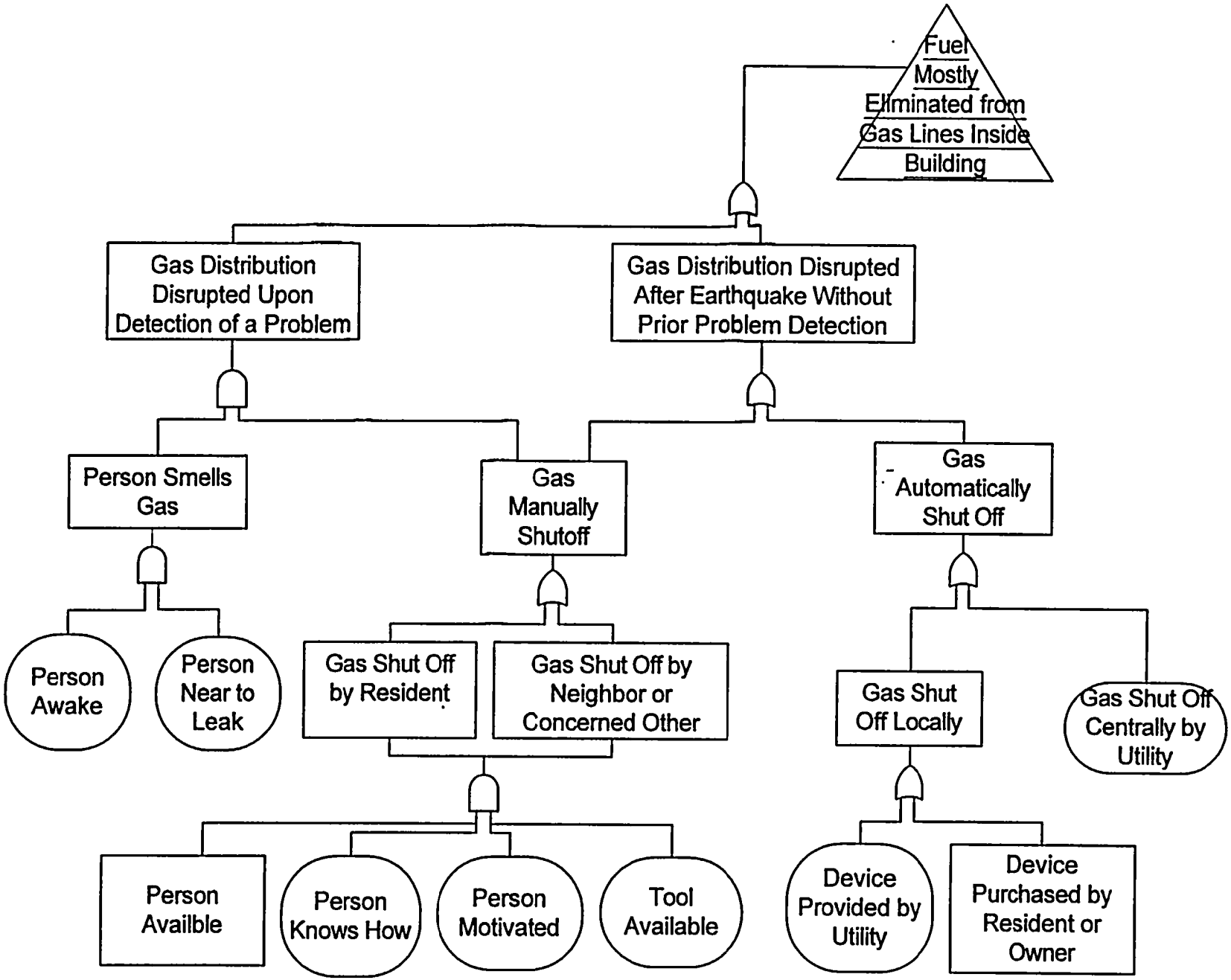
Fuel Mostly Eliminated from Gas Lines Inside Building
Gas Distribution Disrupted Upon Detection of a Problem
Gas Distribution Disrupted After Earthquake Without Prior Problem Detection
Person Smells Gas
Gas Manually Shutoff
Gas Automatically Shut Off
Person Awake
Person Near to Leak
Gas Shut Off by Resident
Gas Shut Off by Neighbor or Concerned Other
Gas Shut Off Locally
Gas Shut Off Centrally by Utility
Person Availble
Person Knows How
Person Motivated
Tool Available
Device Provided by Utility
Device Purchased by Resident or Owner

Fig. 4(c)

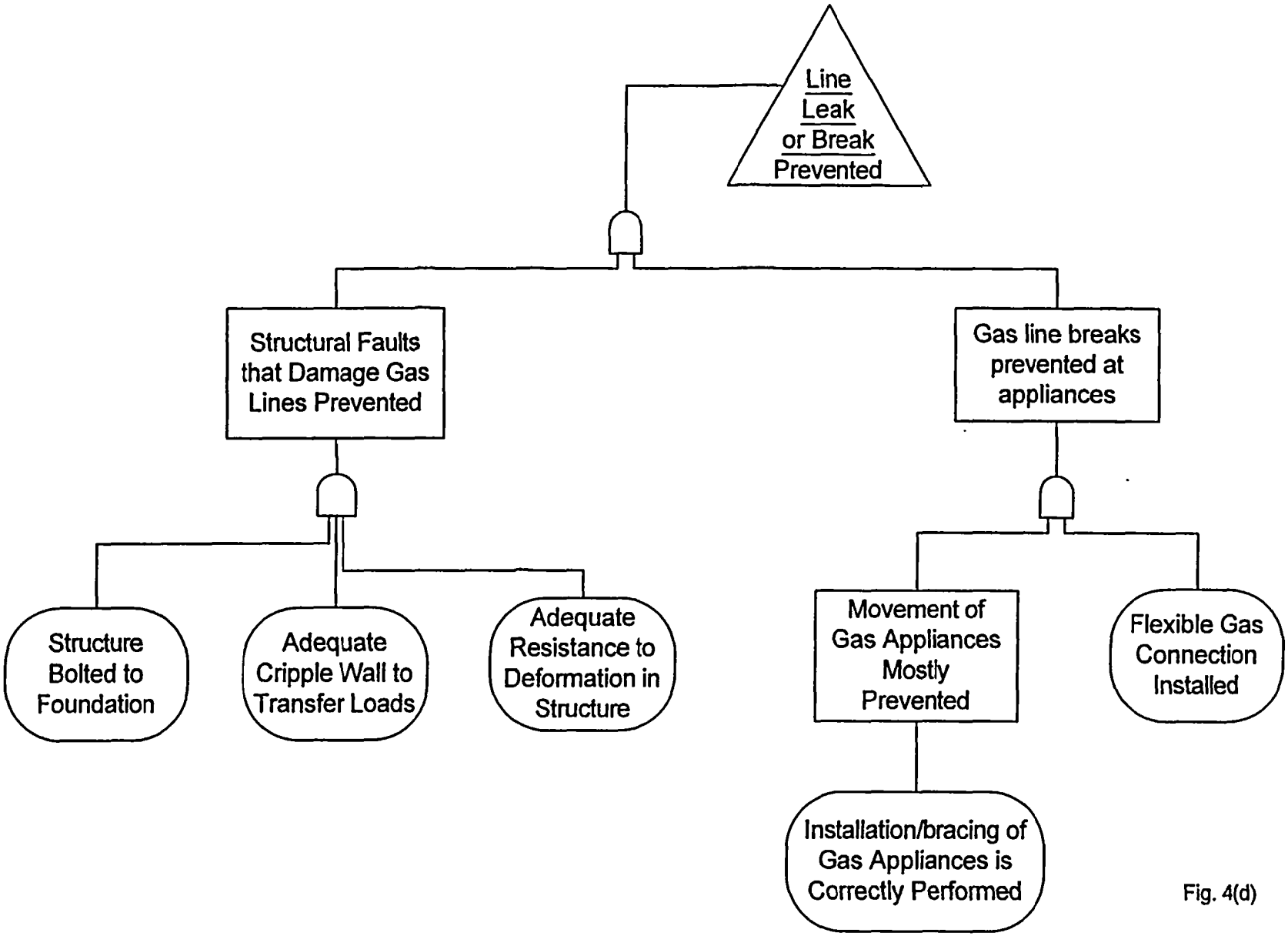
Line Leak or Break Prevented
Structural Faults that Damage Gas Lines Prevented
Gas line breaks prevented at appliances
Structure Bolted to Foundation
Adequate Cripple Wall to Transfer Loads
Adequate Resistance to Deformation in Structure
Movement of Gas Appliances Mostly Prevented
Flexible Gas Connection Installed
Installation/bracing of Gas Appliances is Correctly Performed

Fig. 4(d)

GAS LINE FAULT IGNITION IN ONE AND TWO FAMILY DWELLINGS

Table 1 gives short descriptions of the *"Residential"* Occupancies, as defined by the 1997 Uniform Building Code[64] where one and two family dwellings are defined. Note they are called "Group R-Division 3", (or R-3, for short) occupancies. The "top state" in Figure 4(b) is the "Number of Ignitions Prevented" which is dependent on two elements: (1) the Probability of Preventing Ignition, and (2) the Number of Dwellings. The number of dwellings is given by the scenario and is therefore "intractable[+]", but the Probability of Preventing Ignition can be influenced by three different activities. The first is "Line Leak or Break Prevented" which is the "top state" in the diagram shown on Figure 4(d) where the two principle ways of achieving this goal are connected with an "and" gate since they both must be accomplished to prevent the gas line from breaking.

TABLE I. RESIDENTIAL OCCUPANCIES AS DEFINED BY THE 1997 UNIFORM BUILDING CODE

GROUP R. "Residential" Occupancies are defined in Section 310 of the UBC as follows:

Division 1. Hotels and apartment houses. Congregate residences (each accommodating more than 10 persons)

Division 2. Not used.

Division 3. Dwellings and lodging houses. Congregate residences (each accommodating 10 persons or less)

Definitions as defined in Chapter 2 of UBC:

Dwelling Unit is any building or portion thereof which contains living facilities, including provisions for sleeping, eating, cooking and sanitation as required by this code, for not more than one family or a congregate residence for 10 or less persons.

Dwelling is any building or portion thereof which contains not more than two dwelling units.

Apartment House is any building or portion thereof which contains three or more dwelling units and, for the purpose of this code, includes residential condominiums.

Congregate Residence is any building or portion thereof which contains facilities for living, sleeping and sanitation, as required by this code, and may include facilities for eating and cooking, for occupancy by other than a family. A congregate residence may be a shelter, convent, monastery, dormitory, and fraternity or sorority house but does not include jails, hospitals, nursing homes, hotels or lodging houses.

The second approach to Preventing Ignition is "Fuel Mostly Eliminated from Distribution" which is the "top state" in the diagram shown in Figure 4(c). Here the two principle ways of achieving this goal are connected with an "or gate," since they are alternative means of achieving the same results. Up to this point we have been applying simple logic and known methods of strengthening buildings for earthquake damage, but in Figure 4(c) the underlying assumption is based on fire science. The element of fire science is that it requires more than 30 seconds of continuous gas flame impingement to ignite most wooden building components. The ignition times for two exposures are shown below in Table 2.

[+] The number of dwellings subjected to a given level of earthquake exposure depends on the details of the earthquake source, the soil/rock conditions at each building, and the distribution of the buildings around the earthquake source.

TABLE 2. IGNITION TIMES FOR WOODEN BUILDING MATERIALS*

MATERIAL	IGNITION TIME, T_i, SEC	
	25 FT. TUNNEL	20 LB CRIB/CORNER
Untreated♦ Wood Fiberboard, ½ in. (12.7mm)	32	25
Untreated♦ Plywood, ¼ in. (6.35)	32	50
Untreated♦ Wood Particle Board, ½ in. (12.7mm)	60	90
Untreated♦ Plywood, 11/64 in. (4.4 mm)	60	93
Treated♣ Plywood, ½ in. (12.7mm)	90	80
Treated♣ Wood Particle Board, ½ in. (12.7mm)	100	265

♦"Untreated" means it is not "fire-retarded", and ♣ "Treated" means it is "fire-retarded"

The "25-ft. tunnel" data were obtained in the *ASTM E-84 Standard Test Method for Surface Burning Characteristics of Building Materials*[65] in which the sample is exposed to an 88 kW natural gas diffusion flame that impinges on an area approximately 1.5 ft (0.46 m) wide by approximately 4.5 ft (1.37 m) long. The "20 lb (9.07 kg) wood crib" exposure is a burning stack of small sticks with a heat release rate of approximately 120 to 180 kW. Both ignition sources give approximately the same ignition times. It is assumed that in the post-earthquake environment of an ignited gas source, it would require more than a minute of continuous flaming to ignite materials around the diffusion flame. The diagram on Fig. 4 (c) shows either a manual or an automatic shutoff of the gas supply to the dwelling. Another illustrated approach is to eliminate the ignition source and thereby preventing ignition of the leaking gas[#,&] The overall assumption in this approach is that the gas supply to the dwelling is not interrupted, thus allowing natural gas to continue to leak into the building with the potential of a fire or explosion if an ignition is exposed to the gas/air mixture.

INFLUENCE DIAGRAMS

Influence diagrams have the advantage of showing the dynamic relationships between events and/or systems states over time. A general model of fire ignition related to gas and electrical service during earthquakes is shown in Figure 5(a). As more details are added, the model can be modified and changed in many different ways.

---

* Excerpt from Flammability Studies of Cellular Plastics and Other Building Material Used for Interior Finishes, Underwriters Laboratories, Inc., Northbrook, IL, 1975

Fire Protection Engineers do not rely solely on the prevention of ignition as a reliable fire safety measure. Note discussion for Fig. 2.

& The notes shown in Fig. 5 are not necessarily complete. For instance, an additional system state during disruption and restoration that is missing is the utility's ability to shut off the sections of the gas distribution system to isolate an area that is damaged. This can be done in several ways including zone valves, squeezing the main if a valve is not available, and in a catastrophic situation shutting off the supply of gas from its supply source, typically pressure regulating stations off the transmission line.

GENERAL MODEL OF FIRE IGNITION

RELATED TO GAS AND ELECTRICAL SERVICE

DURING EARTHQUAKES

Influence Diagrams 5a – 5d

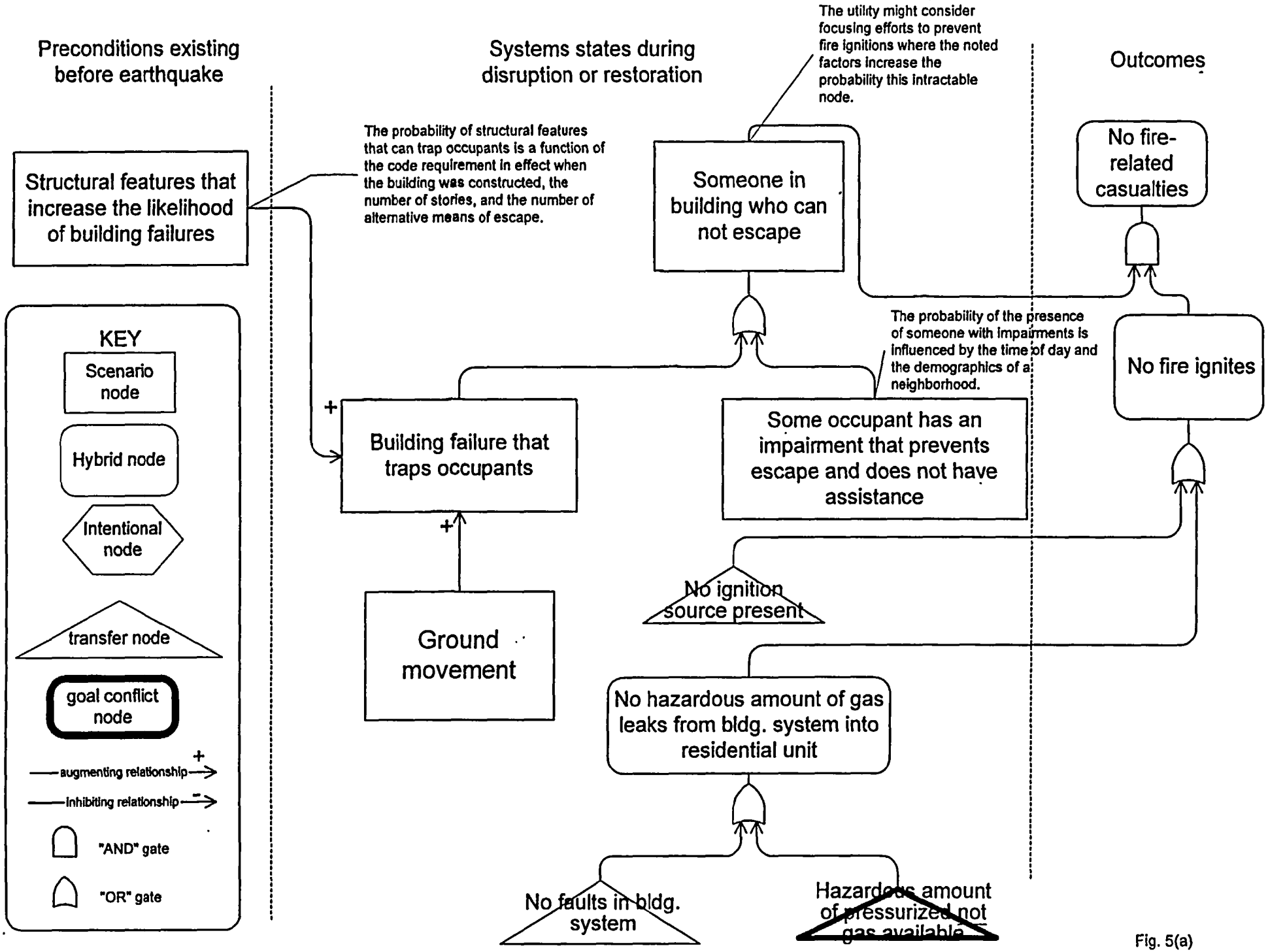
Preconditions existing before earthquake
Systems states during disruption or restoration
Outcomes
The utility might consider focusing efforts to prevent fire ignitions where the noted factors increase the probability this intractable node.
The probability of structural features that can trap occupants is a function of the code requirement in effect when the building was constructed, the number of stories, and the number of alternative means of escape.
Structural features that increase the likelihood of building failures
Someone in building who can not escape
No fire-related casualties
The probability of the presence of someone with impairments is influenced by the time of day and the demographics of a neighborhood.
No fire ignites
Building failure that traps occupants
Some occupant has an impairment that prevents escape and does not have assistance
Ground movement
No ignition source present
No hazardous amount of gas leaks from bldg. system into residential unit
No faults in bldg. system
Hazardous amount of pressurized gas available
not
KEY
Scenario node
Hybrid node
Intentional node
transfer node
goal conflict node
augmenting relationship
inhibiting relationship
"AND" gate
"OR" gate

Fig. 5(a)

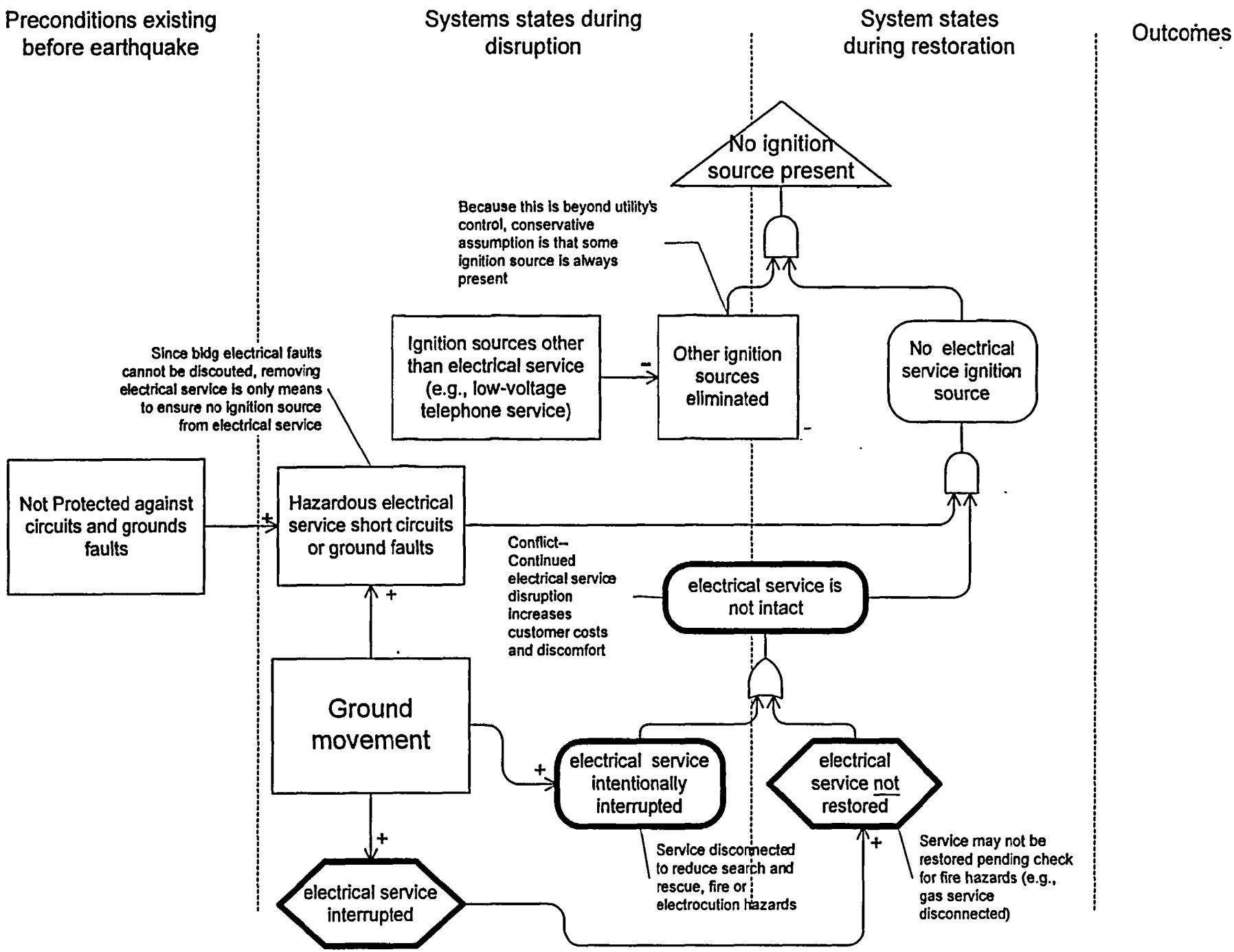
Preconditions existing before earthquake
Systems states during disruption
System states during restoration
Outcomes
No ignition source present
Because this is beyond utility's control, conservative assumption is that some ignition source is always present
Ignition sources other than electrical service (e.g., low-voltage telephone service)
Other ignition sources eliminated
No electrical service ignition source
Since bldg electrical faults cannot be discouted, removing electrical service is only means to ensure no ignition source from electrical service
Not Protected against circuits and grounds faults
Hazardous electrical service short circuits or ground faults
Conflict-- Continued electrical service disruption increases customer costs and discomfort
electrical service is not intact
Ground movement
electrical service intentionally interrupted
electrical service not restored
Service disconnected to reduce search and rescue, fire or electrocution hazards
Service may not be restored pending check for fire hazards (e.g., gas service disconnected)
electrical service interrupted

Fig. 5(b)

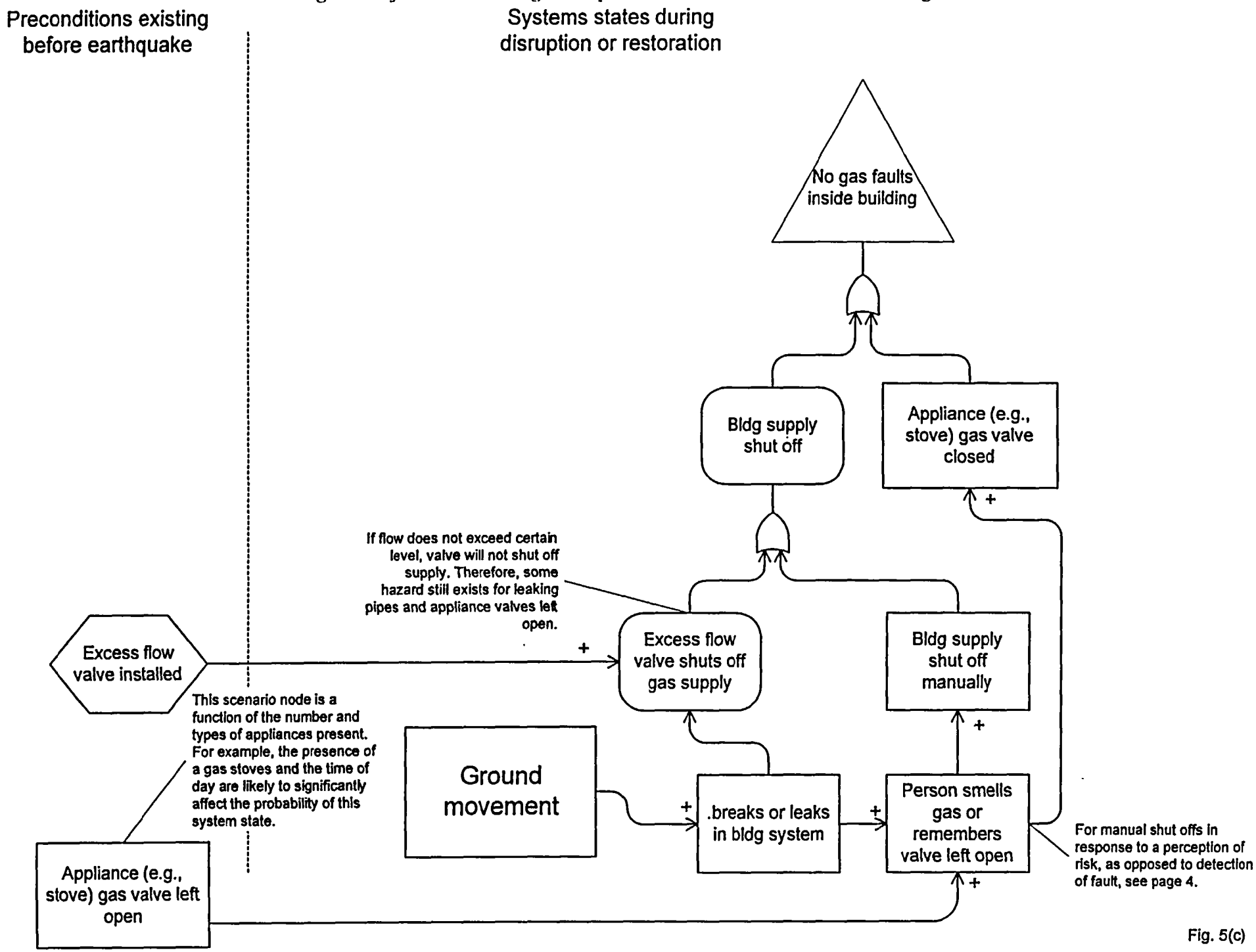
Preconditions existing before earthquake
Systems states during disruption or restoration
No gas faults inside building
Bldg supply shut off
Appliance (e.g., stove) gas valve closed
If flow does not exceed certain level, valve will not shut off supply. Therefore, some hazard still exists for leaking pipes and appliance valves left open.
Excess flow valve installed
Excess flow valve shuts off gas supply
Bldg supply shut off manually
This scenario node is a function of the number and types of appliances present. For example, the presence of a gas stoves and the time of day are likely to significantly affect the probability of this system state.
Ground movement
.breaks or leaks in bldg system
Person smells gas or remembers valve left open
For manual shut offs in response to a perception of risk, as opposed to detection of fault, see page 4.
Appliance (e.g., stove) gas valve left open
+

Fig. 5(c)

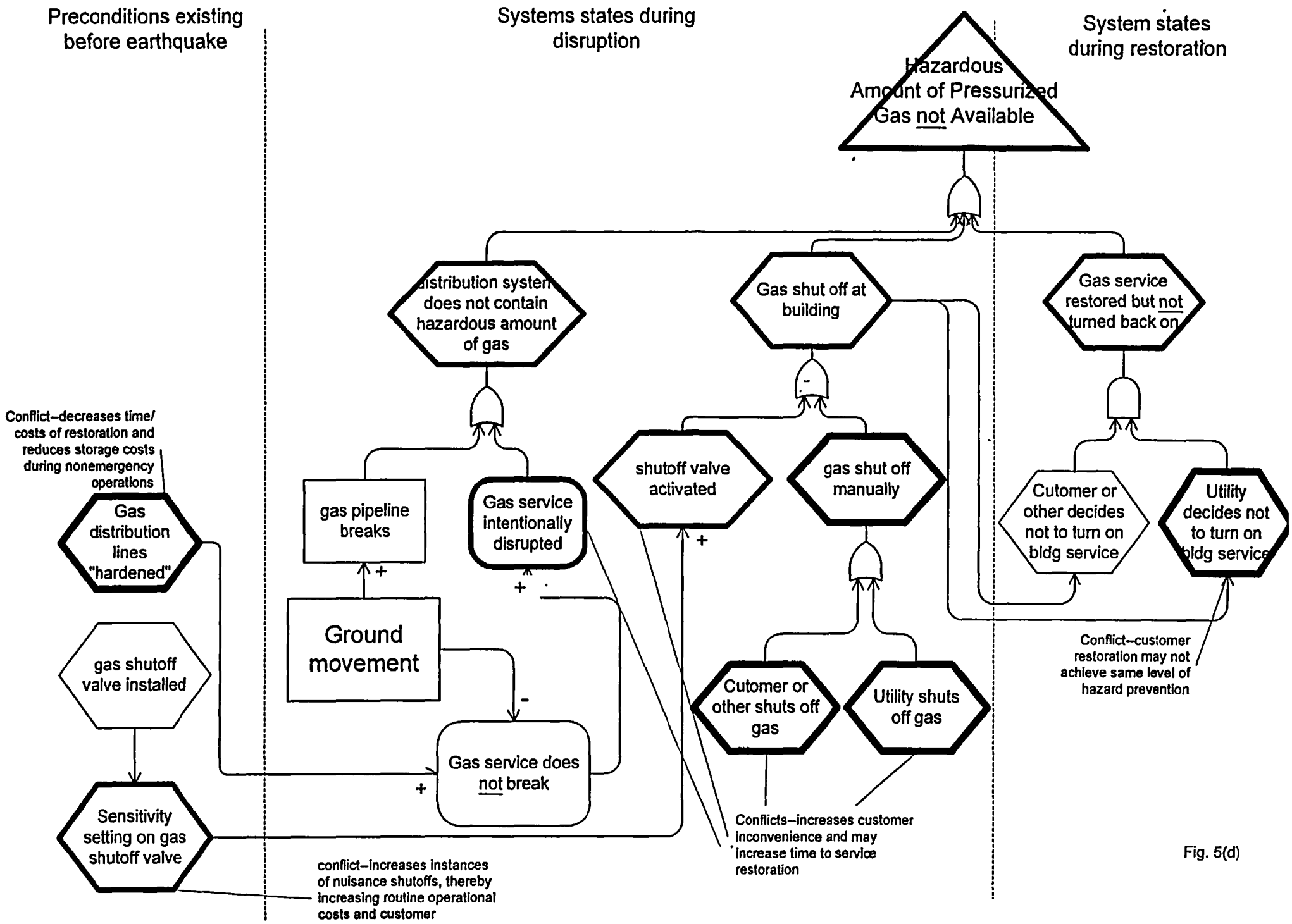
Preconditions existing before earthquake
Systems states during disruption
System states during restoration
Hazardous Amount of Pressurized Gas not Available
distribution system does not contain hazardous amount of gas
Gas shut off at building
Gas service restored but not turned back on
Conflict–decreases time/ costs of restoration and reduces storage costs during nonemergency operations
Gas distribution lines "hardened"
gas pipeline breaks
Gas service intentionally disrupted
shutoff valve activated
gas shut off manually
Cutomer or other decides not to turn on bldg service
Utility decides not to turn on bldg service
Ground movement
gas shutoff valve installed
Cutomer or other shuts off gas
Utility shuts off gas
Conflict–customer restoration may not achieve same level of hazard prevention
Gas service does not break
Sensitivity setting on gas shutoff valve
Conflicts–increases customer inconvenience and may increase time to service restoration
conflict–increases instances of nuisance shutoffs, thereby increasing routine operational costs and customer

Fig. 5(d)

In Figure 5, nodes (events or system states) are related to time by assigning them to four groups: 1. Preconditions that exist before the earthquake; 2. States that occur during system disruption; 3. System states that occur during restoration efforts; and 4. Outcomes (i.e., criteria for measuring the success of systems behavior). Nodes are of three types: 1.Scenario (uncontrolled events or systems states); 2. Intentional (events or system states that the gas and electricity provider(s) can directly affect); and 3. Process/outcome (events or states that the gas and electricity provider(s) can indirectly affect via one or more intentional nodes). These diagrams will be further discussed later in this report. They are shown here to introduce some of the important ideas and to illustrate a way to depict them for subsequent analysis. Further systems states that involve goal conflicts are identical. Certain system states are desirable from a fire safety standpoint, but are undesirable from the standpoint of delays in service restoration causing customer inconvenience, unsafe service restoration performed by inadequately trained personnel, financial costs to customers and utilities, etc.

Alternate Means to Reduce Fire Risks Following Earthquakes

Relationship between Earthquake Shaking Intensity and Fire Occurrence

The likelihood of the occurrence of a fire scenario is dependent on the damage caused by the earthquake. If the intensity of shaking is moderate, certain situations make it more likely for fire ignitions to occur. For instance, if hot water heaters are not equipped with flexible gas supply lines and are not reinforced to prevent rocking or overturning, they may topple and lead to a number of ignitions that could occur even with a moderate earthquake intensity. On the other hand, for properly anchored water heater with a flexible connection, even very severe shaking intensity levels will likely cause only isolated water heater failures, and only a fraction of those will result in ignition. A correlation between ground movement and damage is usually expected, as indicated in the review of past earthquakes and revealed in the abridged table of "observed effects" for various MMI values (Table 3).

Our analyses of scenarios reveal the possibility of a paradoxical and unintuitive nonlinear relationship between the intensity of ground movement and the likelihood of gas-fueled fires. For example, at a lower earthquake intensity of an MMI of VI or VII, a hot water heater that is not equipped with a flexible gas supply line and is not reinforced to prevent rocking or overturning will probably fail, releasing gas. Yet, the distribution system will probably remain intact, ensuring a large supply of escaping gas. At a higher MMI of perhaps XI, the water heater will more likely fail. However, the gas distribution could also fail particularly older more fragile distribution systems constructed of brittle pipe and with poor support conditions, preventing the release of large amounts of gas inside the building, thereby reducing the probability of gas-fueled ignitions. In this case, the relationship between earthquake intensity and gas-fueled fires is apt to be nonlinear.

In unusual land conditions in California, there is the potential for a non-linear relationship between the intensity of ground shaking and the likelihood of gas-fueled fires. In these situations, buildings are constructed on soil conditions that are vulnerable to large ground failures and significant displacements due to landslides or liquefaction and lateral spreading. As a consequence, gas distribution mains or service connections

can be severed, quickly stopping the supply of gas to connected buildings. Damage in these buildings would not lead to fire because of the lack of available gas leaking into the structures. In limited areas in Northern California, high levels of earthquake-caused damage to cast iron gas distribution pipe could also interrupt the supply of gas. This type of pipe is being replaced by modern ductile pipe, which is highly resistant to earthquake effects. Aside from these special situations, greater shaking severity will generally lead to higher levels of building damage in seismically vulnerable structures, and to more fire ignitions. This is particularly true where the gas distribution system has been upgraded to give better seismic performance.

TABLE 3 MODIFIED MERCALLI INTENSITY SCALE (ABRIDGED)[66] This table contains changes which have been introduced by the authors of this report that are written in *italics (with underlining).* Some other entries from the reference are highlighted with **bold type** because they are significant for the subject of this report.

EARTHQUAKE INTENSITY (MMI)	OBSERVED EFFECTS
VI	Felt by all, many frightened and run outdoors. ***Some heavy furniture moved***; a few instances of fallen plaster or damaged chimneys. Damage slight.
VII	Everyone runs outdoors. Damage negligible in buildings of good design and construction; slight to moderate in well-built ordinary structures; considerable in poorly or badly designed structures; some chimneys broken. Noticed **by persons driving** motor vehicles. *Most hot water heaters that are not tied down will probably fall over and potentially start fires.*
VIII	Damage slight in specially designed structures; considerable in ordinary substantial buildings with partial collapse; great in poorly built structures. *Modern 1 and 2 family structures (R-3 occupancies) are generally not damaged.* Panel walls thrown out of frame structures. Fall of chimneys, factory stacks, columns, monuments, walls. Heavy furniture overturned. Sand and mud ejected in small amounts. Changes in well water. Disturbs persons driving motor vehicles.
IX	Damage considerable even in specially designed structures; well designed frame structures thrown out of plumb; great in substantial buildings, with partial collapse. Buildings shifted off foundations. Ground cracked conspicuously. *Underground pipes broken that have not been designed to take this level of seismic shaking.*
X	Some well-built bridges **and wooden structures seriously damaged**; most masonry and frame structures with foundations **destroyed; ground badly cracked**. Rails bent. Landslides considerable from river banks and steep slopes. Shifted sand and mud. Water splashed (slopped) over banks.
XI	Few (if any) masonry structures remain standing. Bridges destroyed. Broad fissures in ground. *Brittle, and non-seismically designed* underground pipe lines completely out of service. Earth slumps and land slips in soft ground. Rails bent greatly.
XII	Damage total to non-seismically designed structures. Waves seen on ground surfaces. Line of sight and level distorted. Objects thrown upwards into the air.

Reducing Gas Faults Inside Buildings

The portion of the general influence diagram model shown in Figure 5(c) focuses on realizing the desirable system state of having "no gas faults inside the building." Scenarios relevant to this concern are as follows:

1. A gas pipe in a building is broken, **and** an electric arc from damaged electrical wiring is present near the released gas to ignite it promptly.

2. A hot water heater is overturned by the earthquake motions resulting in a rupture of the gas supply piping, **and** the released gas is ignited by the pilot light of the heater.
3. A gas pipe in a building is broken because the structure deformed so much that pipe could not remain undamaged **and** the ignition of the released gas is delayed until a mixture of gas and air has been created. This scenario can lead to an explosion.
4. Cooking oils and other kitchen fuels are released during the earthquake, **and** in the presence of either electrical- or gas-based cooking equipment these fuels are ignited.

While not identified as part of the literature review, the following scenario was also identified through the analysis.

5. A gas valve that had been open prior to the earthquake (e.g., on a range top) and then was not shut off at the time of restoration of gas service **and** an ignition source, such as a light switch, ignites a fire or an explosion.

The first three scenarios all require the existence of some type of fault involving the distribution of gas **inside** the building. This problem is addressed in the general model, Figure 5(c), where the top desirable systems state is "no gas faults inside the building." On this diagram, increased ground shaking is shown as increasing the likelihood of the scenario state "breaks or leaks in building system." Should such faults exist, then the only viable approach is to shut the supply of gas to the building, which can be accomplished in two ways, either manually or with an automatic shutoff valve that responds to an abnormal release of natural gas. (The role of seismic shutoff valves is discussed below because their activation is not instigated by a fault *per se*) (See Fig. 5(c).

While the general model shows the dynamic relationships between system states, it does not clearly describe the means by which desirable system states are achieved. Goal decompositions are better suited to this purpose. Two such goal decompositions are provided: one covers "the prevention of breaks or leads inside the building," the other covers "building supply shutoff manually."

The shutoff of the gas supply is examined in the goal decomposition model in Figure 4(c). The gas supply can be shut off by the utility, the customer, a neighbor or concerned other person. Regardless of who shuts off the gas supply, all of the following conditions must apply: someone must be available and that person must know how and where to shutoff the gas supply and he/she must have an appropriate tool, typically a wrench. Importantly, the person must be motivated, a condition that could result from the smell of gas or from a perception of risk resulting from the earthquake. The first motivating condition is always desirable; people should always shut off the supply if they detect any smell of gas or identify a risk such as structural damage to the building. Utilities generally recommend that customers not shut off gas supplies if no risk is present because it can delay restoration of gas service. The basis for this recommendation is that safety risks are created by extensive customer outages. These include increased fire risks due to improper use of open fires for cooking and heating, unsafe procedures used to re-light appliance pilot lights by untrained personnel, and lack

of checking for gas leaks or damage to gas appliance vents prior to re-lighting pilot lights. The issue is whether customers or other concerned people can reliably detect leaks and shut off gas supplies before hazardous conditions develop.

The problem of preventing a line break at a building is covered in the goal decomposition model shown in Figure 4(d). This desirable system state can be accomplished by either preventing the structural failures that sever gas lines or by preventing breaks at appliances. The first issue is limited to older structures that either have poor shear strength on lower floors or are not secured to a proper foundation. Due to code requirements enforced in recent years, these problems are likely to be limited to older buildings even in the most severe earthquakes, except when earthquake-caused ground failure causes damage to the gas distribution system in the street. The structural vulnerability of a building and the selection of possible structural retrofits of older buildings are within the control of the building owner, but there is little progress in that area in most of California.

The problem of gas line breaks at appliances has received a great deal of attention in recent years. Two strategies are advocated: preventing movement of the appliance (e.g. strapping water heaters) and using flexible connectors. When used together, they largely ensure the realization of this desirable system state. Even when either system is used by itself, especially preventing the movement of appliances, there is a significant reduction in risk.

Returning to the influence diagram model, of Figure 5(c), the desirable system state "an opened gas appliance valve has been closed" addresses scenario 5 above. This is one of two system states, along with "building supply shutoff," either of which can prevent gas faults inside a building. The related sequence of system states is most likely encountered in connection with a stove. A building occupant would be cooking on the stovetop when the earthquake occurs and service is interrupted. Later, when service is restored the open valve leaks gas into the building.

Figure 5(a) of the general influence diagram model illustrates the service restoration problem. In order to realize the desirable system state "no hazardous amount of gas leaks into building," either of two system states must be realized: (1) there must be "no faults in the building system;" or (2) "a hazardous amount of pressurized gas must not be available." A utility's restoration program is based on eliminating faults from the system before restoring building service. Before service is restored to an area, all shutoff valves to buildings are closed. Then, trained technicians or plumbers are recommended to restore service and re-ignite pilots lights after checking for leaks. The process becomes problematic when building occupants or other persons restore service. Customers, building managers, owners, or whoever else are increasingly likely to restore service after having waited for days or weeks without being visited by a qualified technician, a situation that is likely to occur following a large earthquake. The hazard involved in customer restoration depends on the likelihood of easy detection of faults, as discussed earlier.

Alternative Means to Stop Delivery of Gas

As noted previously, many of the older **R-1** occupancies are not expected to respond well to a high-intensity earthquake. If the MMI reaches VIII or IX in such older urban areas, there is a high probability that people will be trapped in one or more older buildings due to partial collapse of structural elements as well as damage to non-structural elements such as doors and stairways. After the earthquake, it is most probable that the gas distribution system* will continue to supply gas to these buildings, but the buildings' internal gas pipe systems will likely have been damaged as these old structures respond to the earthquake. The gas pipe systems in any building, but particularly in the older buildings, are not generally designed to be earthquake-resistant. Architects roughly plan the gas pipe systems in most buildings, and then they are installed by plumbers or pipe-fitters who have little or no training in earthquake resistant features. In general, the pipe material is of a low-grade steel with threaded connectors that do not behave in a ductile fashion. It is possible to improve the design of a pipe system within a building that will respond properly in an earthquake by using corrugated stainless steel tubing (CSST).

Figure 5(d) of the general model shows, in part, the relationship between earthquake performance of gas distribution lines and earthquake-related fires. The top-level system state is "hazardous amount of pressurized gas not available." The system state will exist if any of the following three system states are found:

1. The distribution system does not contain a hazardous amount of gas; or
2. The gas supply to the building has been shut off; or
3. The gas supply has been restored, but the service to the building has not been turned back on.

A distribution system will not contain a hazardous quantity of gas if either of the following system states is found: (1) the gas pipeline breaks and vents the gas; (2) intentionally disrupting gas supply to a small area that has suffered extensive damage, which can be accomplished by using distribution pipeline shut-off valves, or by shutting off the flow of gas by squeezing the main where a valve may not exist **. There are other means to reduce the amount of gas leakage into a building, as discussed below in the section on "Automatic Seismic Shutoff Valves versus Excess Flow Valves." The second means for preventing a hazardous amount of gas, i.e., shutting off the supply to the building, can be achieved by either of two approaches: (1) a shutoff valve can activate; or (2) the service can be shut off manually. Both approaches can cost the customers considerable inconvenience while they wait for an authorized person to restore their service. The third means for preventing a hazardous amount of gas is accomplished during the restoration phase. In this instance, the gas distribution system has been restored, but the service to the building has not been turned back on, delaying restoration of the natural gas service++ until the building has been fully checked out.

---

* This is particularly true where the gas distribution system has been upgraded to give better seismic performance.

** There are pre-defined shut off areas in a utility's system, (e.g, the Marina District in San Francisco.

++ The gas service to a given unit in a multifamily building means that there is natural gas available beyond the meter for that unit.

Another characteristic that is relevant to this analysis is whether single or multiple gas meters are used to measure the use of natural gas in the building. This characteristic is important for the following reasons: the seismic shutoff valve is often required to be on the customer's side of the meter. In an apartment house or condominium building with 40 units there would have to be 40 shutoff valves. Thus the cost and organizational complexities of installing automatic seismic shut-off valves would be greater in multi-metered buildings. For example, owners, managers, and residents may have different interests in whether shutoff valves should be installed. Moreover, in multi-metered buildings there is a greater likelihood of false trips due to the location and the number of required shutoff valves. This is also true for older valve designs where there is the possibility of false trips. Another approach would be to install excess-flow valves on the gas line to each apartment or condominium so that if a gas line breaks the gas to that particular customer is shutoff. It should be recognized that the excess-flow valve would not be sensitive enough to shutoff the gas flow if it is below the individual valve's designed trip characteristics (e.g. partial break). It would then simply function as normal usage. A third alternative would be to install an excess-flow valve on the service line coming to the building from the street main. These valves are typically installed to prevent gas leakage due to pipe damage during street excavations, but they can also protect against major high-pressure gas leakage inside a building due to severe structural damage.

Automatic Seismic Shutoff Valves versus Excess Flow Valves

There are two common ways to automatically stop the flow of gas to a leaking or broken gas pipe following an earthquake. One is to install an automatic seismic actuated shutoff valve that is designed to close under specific dynamic conditions, and the second is to install an excess flow valve that is designed to close under abnormally high flow conditions*. The use of each of these devices has certain advantages as well as certain disadvantages that will be reviewed here.

Earthquake-actuated automatic seismic shutoff valves used in California currently comply with ANSI Standard Z21.70-1981. At the time of this report, an updated standard prepared by the American Society of Civil Engineers (ASCE), Standard ASCE 25-97 *Earthquake-Actuated Automatic Gas Shutoff Devices*[67] updates the ANSI standard, and is being considered for use in the State of California. The abstract on the inside cover of the ASCE standard summarizes its purpose and limitations.

> This standard provides *minimum functionality* requirements for earthquake-actuated automatic gas shutoff devices and systems meant to include mechanical devices consisting of a sensing means and a means to shut off the flow of gaseous fuels. It basically applies to single-family or multi-family structures of three stories or less. The seismic performance established by this Standard are based upon data from recent earthquakes, primarily in Southern California.

The range of motions defining the response of devices tested to this standard are shown in Figure 6. For actuation the standard specifies that: "the sensing means of the device shall

---

* Other ways also exist such as methane sensors that trigger valves when methane is detected. The methods can be accomplished any time a break in the gas line is detected, not just after an earthquake.

actuate the shutoff means within 5 seconds when subjected to horizontal sinusoidal oscillation having

1. a peak acceleration of 0.70 g (6.87 m/s^2) with a period of 0.13 seconds,
2. a peak acceleration of 0 40 g (3.92 m/s^2) with a period of 0.20 seconds
3. a peak acceleration of 0.30 g (2.94 m/s^2) with a period of 0.40 seconds and
4. a peak acceleration of 0.25 g.(2.45m/s^2) with a period of 1.00 seconds

These conditions shall be met for horizontal axes of the sensing means."

Of perhaps more importance, the standard specifies the requirements for non-actuation to be that: "the sensing means of the device shall not actuate the shutoff means within when subjected for 5 seconds to sinusoidal oscillation having

1. a peak acceleration of 0.40 g (3.92 m/s^2) with a period of 0.10 seconds,
2. a peak açceleration of 0.20 g (1.96 m/s^2) with a period of 0.20 seconds,
3. a peak acceleration of 015 g (1.47 m/s^2) with a period of 0.40 seconds, and
4. a peak acceleration of 0.10 g (0.98 m/s^2) with a period of 1.00 seconds

These conditions shall be met for both horizontal and vertical axes of the sensing means."

A short history of the development of the standard is given in the preamble of the standard. Draft standards were developed in the 1970s, and an ANSI Standard was approved in 1981. This standard was not considered adequate, and in 1991 the ASCE Technical Council on Lifeline Earthquake Engineering formed a Pre-standards Committee to revise the shutoff valve standard. A full Standards Committee was formed in 1992, but their work did not really begin in earnest until after the Northridge earthquake of January 17, 1994. The result of the committee's initial study was a recommendation for the initiation of a research project that should focus on two key areas:

1. The dynamic testing of current devices in order to quantify performance characteristics, and
2. An in-depth examination of the Northridge earthquake data on ground motions, structural damage, fire initiation, and actuation of existing shutoff devices.

A research project was initiated in March 1995, and completed in November 1995[68]. The performance response characteristics of the devices on the market at that time were evaluated for both discrete dynamic loads as well as complex motions such as simulated earthquakes. The committee set the levels of actuation in the standard using these research findings. In the "commentary" section of the standard the committee writes:

> "Based on the Northridge earthquake, the Standard requirements are judged to be conservative by 30% to 50% in the critical frequency range of 2.5 Hz to 5 Hz."

The reliance on the Northridge earthquake may be one of the most important aspects of this standard. There is a list of seven assumptions given in the commentary section of the standard:

1. "The identified limits are based on encompassing more than 95% of all gas-related fires (in the Northridge earthquake).
2. The typical structural configuration is considered to be a wood-frame, single-family or multi-family structure of three stories or less.
3. The atypical structural or gas installation configuration may require an engineered system, suitable for the type of facility and end-user's risk tolerance.
4. The dynamic loads on gas appliances caused by the earthquake can be related to free-field ground motions. Global response of gas-fired equipment located at ground level (sliding or overturning) was considered in establishing actuation limits.
5. The structure and the gas appliance configurations are consistent with an assumed damping ratio of 5% or greater.
6. Within the actuation limits, it is assumed that leaks in gas-fired equipment or the houselines do not occur. Houseline damage is generally associated with significant structural damage, which is not expected within the actuation ranges.
7. The post-Northridge earthquake research activity did not investigate the complex relationship among observed structural damage, peak spectral acceleration levels, underlying soil and geologic conditions, or ages of the structures.

The "Appendix" of the standard contains several sections devoted to various topics:

Issues and Considerations for Public Officials Formulating Regulations for Mandated Installation of Earthquake-Actuated Automatic Gas Shutoff Devices

Reducing Risk of Post-Earthquake Conflagration

Structural Performance Issues

Interruption of Gas Service

Cost Versus Benefit Considerations

Monitoring Performance

Although the appendices of a U. S. Standard are not considered a part of the required language of a standard, they can be of considerable use for a critical review of the document. For instance, in the Section on *Cost versus Benefit Considerations* there is a statement "Consideration should be given to mandating installation of appliance restraints. This action alone is estimated to accomplish 80% of the risk reduction provided by earthquake-actuated gas shutoff devices based upon historical fire data and analytical investigations." This viewpoint is largely a product of using the Northridge Earthquake as a principle source of information. A statement is made in a preceding paragraph that: "An overwhelming majority of post-earthquake, gas-related fire incidents are related to shifting or overturning of gas appliances, especially water heaters." The ASCE Standard thus provides a wide range of information about the use and operation of seismic shutoff valves.

At the time of this report, the State of California is considering adoption of American Gas Association (AGA) Requirements for Excess Flow Valves No. 3-92, dated January 30, 1996, as the applicable standard to be used for certification of excess flow valves. This standard applies to devices not in excess of 2-inch size and operating pressure not in excess of 5 psi.

There are several manufacturers of low-pressure excess flow valve for both natural gas and propane. The excess flow valves operate at pressures as low as 0.25 psi and even lower. They close when the flow of gas exceeds a specific design limit, usually at a point above the maximum flow calculated from the rated capacities of all of the connected appliances. The valve is installed on the customers' houseline. Then, when an earthquake occurs, the valve would close if a gas leak resulted that was greater than the factory-set shutoff flow value. There is the possibility that a partial break in the gas line would result in a gas flow lower than the excess limit set and the valve will not trigger closed.

Utilities install excess gas flow valves in accordance with DOT guidelines 192.381 and 192.383. They are installed on single-family residences (1 meter) only. They are not installed on branch services, commercial buildings, or multi-family buildings. Utilities have the option to voluntarily install the excess gas flow valves or take the customer notification approach discussed in 192.383. There are two industry standards that specify the manufacturing requirements for excess gas flow valves that operate at 10 psi and above. One was developed by the Manufacturers Standardization Society (MSS) for the Valve and Fittings Industry and is called Standard Practice for Excess Flow Valves for Natural Gas Service (#SP-115). The other is ASTM F-1802 and is called the Standard Test Method for Performance Testing of Excess Flow Valves. These standards are for the manufacture and performance of the excess gas flow valves, not for their installation. [Reference for entire paragraph][69]

DOT 192.381 states that excess gas flow valves do not need to be installed if the main pressure is less than 10 psi. Thus in practice excess gas flow valves are not designed to operate at pressures less than 10 psi. Different flow models are designed to activate at different capacities. As the flow in the main pressure increases, the flow required to activate the excess gas flow valve also increases. At the same main pressure, the flow to activate the excess gas flow valve is higher when the service is 6' in length than when it is 100' in length. These high pressure excess gas flow valves are not designed to activate at low flows and will not shutoff if there is a small leak less than the designed activation flow of the excess gas flow valve. Activation will occur if the service tubing is severed. [Reference for entire paragraph][70]

The advantages and disadvantages of each of these types of control valves depend on many factors. A partial listing is as follows:

ADVANTAGES & DISADVANTAGES OF AUTOMATIC SEISMIC SHUTOFF VALVES

Advantages:

1. The valves operate automatically when they detect motions above their designed threshold. Their performance is governed by standards as they are adopted by regulatory agencies.
2. Previously installed valves have a proven record in protection of **R-3** occupancies.
3. Activation completely eliminates leakage of gas beyond the valve.
4. Their installation is site specific, which permits only those structures that are vulnerable to damage during an earthquake to be protected, without incurring the cost of installation on structures that are otherwise protected.

Disadvantages:

1. Standard ASCE 25-97 *Earthquake-Actuated Automatic Gas Shutoff Devices* is in place and gives performance standards for the devices as well as guidance in their installation, but it is not being used by the State of California. Valves currently approved by the State of California only have to meet the requirements of ANSI Standard Z21.70-1981. This could change soon pending adoption by the State of California.
2. The standard ASCE 25-97 applies to single-family or multi-family structures of three stories or less, and does not explicitly address all R-1 occupancies.
3. Some valves are prone to being tripped by accidental impacts or vibrations from normal (non-seismic) activities.
4. Many valve models currently installed or available, activate closed solely on motion alone, and do not have the ability to determine if a hazardous condition actually exists, thus causing unnecessary interruption of customer gas service.
5. Widespread valve installations can result in the shutting off of gas service at a time (i.e., post-earthquake) when utility and community resources are in high demand for leak repairs, safety checks, and service restorations, and thus can create delays in the restoration of service.
6. Aftershocks could cause devices to activate after has service has been restored.
7. The major problem in R-3 occupancies is the overturned hot water heater, which can be effectively addressed by less expensive means than the seismic valve.
8. Many models of valves that are available can be manually reset by unqualified personnel, without requiring that checking be done to assure that a hazardous condition does not exist.
9. Extensive structural damage may render a device ineffective due to damage to the gas piping system or the device itself. The device will not provide any protection from damage upstream of the device.

ADVANTAGES & DISADVANTAGES OF EXCESS FLOW SHUTOFF VALVES

Advantages:

1. The valve responds to the presence of a hazard when it operates automatically after detecting a gas flow rate above its designed threshold.
2. This valve only shuts off the gas if there is a large leak on the piping system. Because the probability of activation is far less than with the seismic valves, much of the potential delay in restoration of service is eliminated.
3. There is a by-pass feature that causes the valve to automatically reset itself when the gas leak is repaired.
4. Their installation is site specific, which permits only those structures that are vulnerable to damage during an earthquake to be protected, without incurring the cost of installation on structures that are otherwise protected.

Disadvantages:

1. The valve activates only when a catastrophic break in the gas line occurs, there can still be leak(s) in the system that are below the set-point of the valve, resulting in gas flow not being stopped.
2. Available valves have limits in their designed operating conditions, and may not be available for some installations.
3. The major problem in R-3 occupancies is the overturned hot water heater, which can be solved by less expensive means than the excess flow valve.
4. Extensive structural damage may render a device ineffective due to damage to the gas piping system or the device itself. The device will not provide any protection from damage upstream of the device.

It appears that the automatic seismic shutoff valves that conform to the ASCE 25-97 standard are designed to activate prior to the overturning of an un-reinforced hot water heater, which we estimate to occur at about MMI VII. However, automatic seismic shutoff valves that conform to the ASCE 25-97 standard are tested at no more than 0.5 psi pressure, and thus they are not designed to be attached to high-pressure gas distribution systems. Additionally, these valves are not designed to protect R-1 occupancies. High-pressure automatic seismic shutoff valves exist, but there is no general standard, such as ASCE No. 25-97, to provide a basis for their performance. Such seismic shutoff valves that were qualified for R-1 occupancies could be an effective solution to the scenario with people trapped in a partially collapsed building, as discussed above. The dynamic setting of the device would have to be chosen for activation before the MMI or PGA that would substantially damage the specific existing R-1 building. This may correspond to MMI VIII or even IX. If the seismic shutoff valves were installed on the customers' side of the meter, effective performance would depend on the response of the devices installed at the building. Seismic valves installed on a manifold system with 20 or more meters may have a different seismic response than the simple valve tested and described in ASCE 25-97. The use of seismic valves intended for R-3 occupancies might not be at all appropriate for R-1 occupancies where multiple meters dictate the installation of multiple seismic shutoff valves.

The choice of low-pressure excess flow-valves could be an appropriate alternative in those situations where the shutoff valve is on the customers' side of the gas meters. The major disadvantage of this device is its inability to detect a partial loss of integrity in the gas line that would cause a leak below the shutoff setting of the valve. A very small leak could probably be tolerated without substantial risk of fire or explosion, but a leak comparable to the full BTU/hr rating of a cooking range is probably dangerous.

Conflagration Issues

In the Northridge earthquake there were a number of fires in one and two family buildings (R-3 occupancies), and particularly in trailer homes, but there were no reported deaths in these fires. There was, of course, significant property damage in these fires, but compared with the huge financial loss in that earthquake as a whole, the fire losses were insignificant. The real danger for significant property loss lies in the possibility of a conflagration like the one that occurred in the 1906 earthquake in San Francisco. The usual construction of R-3 buildings in the United States, and particularly in California,

has a spacing of 6 ft (1.83 m) or more between buildings[71], and this spacing slows down the fire spread between structures unless there are significant winds and the humidity is low. In his discussion of the Northridge earthquake, Scawthorn[72] mentioned the 1991 East Bay Hills Fire as the prototype of a future post-earthquake fire, but from a practical stochastic viewpoint, the combination of a major earthquake and dry windy conditions is a very rare event. There are approximately 5 "fire danger days" per year in the San Francisco Bay Area when the hot dry wind blows from the east[73]. The more normal winds are cool westerly winds that carry the moisture from the Pacific Ocean. These winds do not spread fires as easily as the easterly winds. This is based on fire science that maintains that fire spread depends on "flying brands" to cause "spot fires" to start ahead of the main fire front, and the moist cool maritime air quenches these small air borne brands. The occurrence of hot dry winds in Southern California (Santa Ana conditions) is more frequent than in Northern California. Other steps are being taken in California to prevent the spread of fire between houses. Roofing materials now have to be fire retardant, and older wooden shake roofs cannot be replaced without being upgraded to a fire retardant system. Highly combustible plants are being eliminated between buildings, and the fire service has taken many steps to prevent the kind of fire that occurred in the East Bay Hills in 1991. All of this leads us to conclude that the current stock of R-3 buildings in California does not pose a significant life safety risk for post earthquake fires. The utilities and other governmental agencies could reduce the existent exposure for R-3 property loss by fostering a proper reinforcement of gas hot water heaters and an awareness of earthquake preparations in general.

As discussed previously, it is the older multi-family residential buildings (R-1 occupancies) that are the most likely places for people to be trapped in during the initial hours of a major earthquake and then become the potential victims of a fire before they can be rescued.

The widespread use of wooden construction is another important factor that makes the R-1 fire scenario more dangerous in California. In today's building codes wooden construction (Type V) is restricted to low rise, small area buildings, but in many urban areas much of the R-1 building stock predate these height and area rules. Thus one finds 6 to 10 story apartment houses of a mixed construction of wood, masonry, and concrete. Many of these structures are not designed to withstand the level of seismic shaking that a modern gas system can handle with ease. In addition, many of these buildings have internal gas piping that will fracture as the structure deforms, increasing the likelihood of fire. The wooden buildings will be extremely vulnerable to rapid fire spread since much of the passive fire protection will have been compromised by the earthquake damage.

Either seismic shutoff valves or a system of excess flow valves could be installed in these buildings to reduce the risk of the R-1 fire scenario. In time this risk will go away as these older buildings are replaced by modern construction, but today the potential exists for major post-earthquake life loss.

Electrical Ignition Following Earthquakes

As mentioned in the description of the Kobe earthquake, Sekizawa[74] found that a number of fires started one or two hours after the Kobe earthquake when the electric

power was restored to damaged structures. As discussed in conjunction with gas fires, the most dangerous post-earthquake scenarios are in buildings that are heavily damaged and in which people are trapped.

The electrical system of a building already has a circuit breaker or fuses installed to prevent excess current flow, but there are certain damage conditions that can lead to a fire without activating these protection devices. There are also electrically powered appliances such as portable space heaters or high-intensity lights that can cause a fire if they come into contact with potential fuel sources.

Figure 5(b) of the general influence diagram model explores the relationships associated with the top desirable system state "no ignition source present." To realize this state, two system states must be true: (1) "other ignition sources (have been) eliminated;" and, (2) there is "no electrical service ignition source."

The elimination of other ignition sources is a scenario (negative) system state over which the electric utility service has no control. An important example is the increased use of telephone systems that are powered independently of the electrical system and that may remain operational even when the electrical power distribution system has been interrupted. Other possible sources of ignition can include battery-powered devices, static electrical charges, and the use of tools during rescue operations. The conclusion is that it is impossible to eliminate all potential sources of ignition by electricity. Nonetheless, the energized electrical distribution lines are the most likely electrical ignition sources following an earthquake.

Two system states are associated with the desirable system state of "no electrical service ignition source." One of these is the scenario (negative) state of "hazardous electrical service short circuits or ground faults," the elimination of which is beyond the control of electric utilities. Adequate protection against short circuits and ground faults is a function of having a properly designed and maintained building electrical system. Since this scenario state cannot be eliminated, the removal of electrical service to the building is the only fully reliable means to ensure that there are no sources of electrical service ignition.

Electrical service may not be intact for either of two reasons: (1) the earthquake disrupted electrical distribution and it has not been restored (whether intentionally or not); or (2) electrical service is cut off at the service switch or breaker/fuse box to the building. Removal of electrical service is a goal conflict state since it will increase customer discomfort and losses. Therefore, the intentional disruption of electrical service needs to be applied in accordance with the associated hazard. Nonetheless, the delaying of electrical service restoration is an important strategy for reducing ignitions where widespread building damage is evident.

The second approach, when electrical service is intentionally cut off from a building, is an important strategy where: (1) particular buildings with significant damage can be identified, especially those buildings that might contain trapped occupants; and, (2) either electrical service was not disrupted in the first place, or there is not enough damage to justify further delays in restoration of electrical service. In these instances, it is advisable to cut off electrical service to individual buildings to ensure that there will be

no possibility of electrical service-related fire ignitions in the cut-off buildings after service has been restored to a geographical area.

There are strong parallels between the discussion of natural gas systems and electrical systems. We do not believe that the one and two family buildings (R-3 occupancies) pose a significant post-earthquake fire problem for essentially the same reasons given for natural gas systems. It is the older multi-family residential buildings (R-1 occupancies), we believe, that are the most likely places for people to be trapped in during the initial hours of a major earthquake and become the potential victims of a fire before they can be rescued. The current electrical system is not capable of continued operation with a very intense earthquake, so except for the short time of the initial shocks of the earthquake, there are few ignitions caused by electrical shorts and arcs. Routing the natural gas and electric service in separate spaces in the building could prevent some of these ignitions. This practice is used in commercial aircraft because it was found that in accidents the close spacing of fuel and electrical lines ignited fires. In subsequent accidents that were essentially of a similar nature, there was no fire because the fuel and electrical lines had been separated[75].

The potential problems with electrical ignitions occur during the restoration of power. Before power is restored to an area, the electric utility needs to have a positive way to know about collapsed or damaged buildings that still have people trapped inside them. Plans are in place to coordinate this kind of effort, but the training of fire fighters and other emergency responders need to be included in this planning. The information chain starts with the people in the field who identify the buildings with trapped people. The emergency responders need to be made aware that the power utility might try to restore power as soon as possible after the earthquake, and that it is their responsibility to send communication about the current situation. It might also be effective if the emergency responders could be made to be responsible for disconnecting the electrical service to the building. If that is not practical, then they should contact the utility to have their service personnel come out to disconnect the service. This could be part of the information exchange between the emergency responders at the scene and the utility command center.

CONCLUSIONS

A survey of the literature on the fire aspects of eleven large twentieth century earthquake events has been conducted. They are as follows:

San Francisco, California	1906
Kanto (Tokyo) , Japan	1923
Hawkes Bay, New Zealand	1931
Long Beach, California	1933
Managua, Nicaragua	1972
Morgan Hill, California	1984
Mexico City, Mexico	1985
Whittier Narrows, Los Angeles, California	1987
Loma Prieta, California	1989
Northridge, California	1994

Hyogo-ken Nanbu (Kobe), Japan 1995

A review of the literature on the fire aspects of these earthquakes yields a list of ignition scenarios in which either the gas or electric service played a role in the ignition of the first fuel in the fire:

1. A gas pipe in a building is broken, **and** an electric arc from damaged electrical wiring was present near the released gas to ignite it promptly.
2. Bottles and/or open cans of flammable liquids are thrown to the floor by the earthquake, **and** an open gas flame or an electric arc is present to ignite the vapors from the spilled liquid
3. A hot water heater is overturned resulting in a rupture of the gas supply piping, **and** the released gas is ignited by the pilot light of the heater
4. A gas pipe in a building is broken because the structure deformed so much that pipe could not remain undamaged **and** the ignition of the released gas is delayed until a mixture of gas and air has been created. This scenario can lead to an explosion
5. Cooking oils and other kitchen fuels are spilled or released during the earthquake, **and** either electrical- or gas-based cooking equipment ignites these fuels
6. While the electrical service to a structure is interrupted by the initial earthquake event, the earthquake motions displace or damage an electric-powered device and put it into contact with some quantity of fuel. Then when the electric power is restored to the building, this displaced device causes the ignition of the exposed fuel.
7. A person ignites a fire by such means as arson or turning on a light switch with natural gas present.

This report focuses on two scenarios that can occur in residential structures. The first is in one and two family housing (R-3 occupancies), and the second scenario is in older multi-family residential buildings (R-1 occupancies). Here are our conclusions:

1. An analysis of many factors has lead us to conclude that the current stock of R-3 buildings in California do not pose a significant life safety risk for post earthquake fires. There is some exposure for R-3 property loss that utilities and other governmental agencies could reduce by fostering the proper reinforcement of gas hot water heaters and an awareness of earthquake preparations in general.
2. The most dangerous post-earthquake fire threat appears to be the R-1 fire scenario where people are trapped in multifamily buildings which have partially collapsed and in which gas pipes are broken with gas leaking into the structure. The rescue of these people will be very difficult, and the potential for fire is very great. Either seismic shutoff valves or a system of excess flow valves could be installed in these buildings to reduce the risk of the R-1 fire scenario. In time this risk will go away as these older buildings are replaced by modern construction, but today the potential exists for major post-earthquake life loss.

A review of a systems approach to the problem leads to the important conclusion that in the post-earthquake environment attention must be paid to **Ignition Prevention** rather than **Fire Management**. Reducing the potential dangers of the R-1 fire scenario should be one of the top priorities in earthquake preparations in California. It will take a concerted effort of government, private property owners, and the utilities to find solutions to this problem. The rational and central emphasis of this effort will be to prevent **Ignition of Fire** by eliminating the leaking of natural gas in the expected partial collapse of older R-1 buildings.

RECOMMENDATIONS FOR FURTHER RESEARCH

The post-earthquake R-1 fire scenario appears to be the most important topic for future research. Here are a few ideas:

1. The models shown in Figures 4 and 5 should be quantified. Expert opinion and some surveys of existing conditions could be used to develop these models. The results of this quantification should lead to an estimate of likelihood and the consequences of this scenario occurring under various potential earthquakes. The emphasis in this quantification should be in the area of the R-1 fire scenario discussed above.

2. Once the models shown in Figures 4 and 5 have been quantified they can be updated by Baysian methods following any earthquake that might occur in areas that are prone to the R-1 fire scenario. Part of this phase of the research should be directed at creating techniques and strategies for the post-earthquake investigation of potential R-1 fire scenarios. This would be important for the Baysian updating of models.

3. It is apparent from the discussion of seismic shut-off valves as well as excess flow valves that there are many problems connected with their application, design and testing. It would be important to have a long-range research program to investigate the whole scope of issues in this area. We recommend a University program since it can serve as a "third-party" testing agency to evaluate and certify performance under a Service-to-Industry program at the same time that it is developing the test methods and performance criteria. In addition, the University has a broad staff of professors in many important areas of expertise, and technicians and students with the necessary backgrounds. For instance, within the PEER family of institutions there is an impressive array of people to carry out the proposed program.

The three research topics presented here could be divided into many subparts, but it would be important to involve the potential governmental and private sector individuals who would be the users of the research findings. The next phase of the research should involve the California Office of Emergency Service (OES) and the California State Fire Marshall's (CFM) office. In the private sector there should be liaison with utilities as well as R-1 building owners and managers. It will be important at some point to involve the city building and fire departments, although initially the OES and CFM represent their interests.

REFERENCES

[1] Williamson, R. B., *Coupling Deterministic and Stochastic Modeling to Unwanted Fire*, **Fire Safety Journal, 3**, 4, 243-259, (1981).

[2] Ramachandran, G. *Stochastic Models of Fire Growth.* In the **SFPE Handbook of Fire Protection Engineering**, 2nd Edition, Quincy, MA: National Fire Protection Association (1995).

[3] Beck, V. R., *A Cost-Effective Decision-Making Model for Building Fire Safety and Protection*, **Fire Safety Journal, 12**, 121-138 (1987).

[4] Ling, T. L., and Williamson, R. B., *Modeling of Fire Spread through Probabilistic Networks*, **Fire Safety Journal, 9**, 287-300 (1985).

[5] Groner, N. E., and Williamson, R. B., *Scenario-Based Goal Decomposition: A Method for Implementing Performance-Based Fire Safety Analysis*, presented at the 2nd International Conference on Fire Research and Engineering, National Institute of Standards and Technology, Gaithersburg, MD, August 10-15, 1997.

[6] Ibid

[7] Botting , R., *The Impact of Post-earthquake Fire on the Urban Environment*, Fire Engineering Research Report 98/1, Christchurch, New Zealand, University of Canterbury, School of Engineering, p 173, (1998).

[8] Williamson, R. B., and Dembsey, N. A., *Advances in Assessment Methods for Fire Safety*, **Fire Safety Journal, 20**, 15-38, (1993).

[9] Scawthorn, C., *Simulation Modeling of Fire Following Earthquake, Proceedings of the Third U. S. National Conference on Earthquake Engineering, Charleston, SC, 1986*, volume III, El Cerrito, CA, Earthquake Engineering Research Institute, (1986).

[10] Ibid. p. 5

[11] *U.S.-Japan Workshop on Urban Earthquake Hazards Reduction, Stanford University, July 29-August 1, 1984, Proceedings*, Berkeley, CA, Earthquake Engineering Research Institute, EERI Publication No. 85-03, p. 5, (1985).

[12] Steinbrugge, K. V., *Earthquakes, Volcanos, and Tsunamis – an Anatomy of Hazards*, SKANDIA America Group, (1982).

[13] Scawthorn, C., Blackburn, F.T. , and Seagraves, D.. W., *Earthquakes, Fires & Urban Areas – All the Ingredients for a Disaster*, **Fire Safety Journal, 82**, 4, 20-30, (1988).

[14] Steinbrugge, K. V., *Earthquakes, Volcanos, and Tsunamis – an Anatomy of Hazards*, SKANDIA America Group, (1982).

[15] Ibid., p. 94.

[16] Ibid., p. 95.

[17] Botting , R., *The Impact of Post-earthquake Fire on the Urban Environment*, Fire Engineering Research Report 98/1, Christchurch, New Zealand, University of Canterbury, School of Engineering, p. 173, (1998)

[18] Ibid., p. 177.

[19] Ibid., p. 181.

[20] Ibid., p. 181-182.

[21] Earthquake Engineering Research Institute, *Managua, Nicaragua Earthquake of December 23, 1972, Conference Proceedings*, vol. II, Berkeley, CA, (1973).

[22] Botting , R., *The Impact of Post-earthquake Fire on the Urban Environment*, Fire Engineering Research Report 98/1, Christchurch, New Zealand, University of Canterbury, School of Engineering, p. 193, (1998).

[23] Earthquake Engineering Research Institute, *Managua, Nicaragua Earthquake of December 23, 1972, Conference Proceedings*, vol. II, Berkeley, CA, (1973).

[24] Schiff, A. J., *Investigation of Lifelines*, **Earthquake Spectra, 1**, 3, p. 623, (1985)

[25] Scawthorn, C., Bureau, G., Jessup, C., and Delgado, R., *The Morgan Hill Earthquake of April 24, 1984 – Fire Related Aspects*, **Earthquake Spectra, 1**, 3, , p. 678, (1985).

[26] Scawthorn, C., *Fire Following Earthquake*, **Fire Engineering**, p.138 (1985).

[27] Scawthorn, C., Bureau, G., Jessup, C., and Delgado, R., *The Morgan Hill Earthquake of April 24, 1984 – Fire Related Aspects*, **Earthquake Spectra, 1**, 3, pp. 675-681, (1985).

[28] Ibid., p. 682.

[29] *The Mexico Earthquake of September 19, 1985*, **Earthquake Spectra, 4**, 3, 1988.

[30] Bolt, B. A. *Earthquakes*, 4th ed., W.H. Freeman, New York, 1999, p. 295.

[31] Botting, R ., *The Impact of Post-earthquake Fire on the Urban Environment*, Fire Engineering Research Report 98/1, Christchurch, New Zealand, University of Canterbury, School of Engineering, p. 201 (1998)

[32] Bertero, V., personal communication, (1998).

[33] *Whittier Narrow Earthquake of October 1, 1987*, **Earthquake Spectra, 9**, 1, (1993).

[34] Smoke, C. H., *A Real Life Practice Run*, **Fire Journal, 82**, 4, p. 29, (1988).

[35] *Whittier Narrow Earthquake of October 1, 1987*, **Earthquake Spectra, 9**, 1, (1993).

[36] Alyasin, M. S., and Bak, D. N. *Investigation of Cause and Effects of Fires Following The Loma Prieta Earthquake*, IIT, Department of Civil Engineering, IIT-CE-92-01, Chicago, Illinois Institute of Technology, 1992, 181 p.

[37] Coleman, R. J., *Fire Department Response During Earthquake Emergency Operations, Firesafety Frontier '94, Proceedings of the Tokyo International Fire Conference*, Tokyo Fire Department, (1994).

[38] Alyasin, M. S., and Bak, D. N. *Investigation of Cause and Effects of Fires Following The Loma Prieta Earthquake*, IIT, Department of Civil Engineering, IIT-CE-92-01, Chicago, Illinois Institute of Technology, 1992, 181 p.

[39] Ibid, pp115-117.

[40] Lew, H. S., ed. *Performance of Structures During the Loma Prieta Earthquake of October 17, 1989*, NIST Special Publication 778, Gaithersburg, MD, National Institute of Standards and Technology, pp. 6-10, (1990).

[41] Chung, R. M., Jason, N. H., Mohraz, B., et al., eds., *Post-earthquake Fire and Lifelines Workshop, Long Beach, California, January 30-31, 1995, Proceedings*, NIST Special

Publication 889, Gaithersburg, MD, National Institute of Standards and Technology, pp. 27-28, (1995).

[42] Scawthorn, C., Cowell, A. D., and Borden, F., *Fire-related Aspects of the Northridge Earthquake*, NIST GCR 98-743, Gaithersburg, MD, National Institute of Standards and Technology, 164 p. (1998).

[43] Ibid., pp. 3-56 to 3-57

[44] Ibid

[45] Ibid, pp. 3-56 to 3-57

[46] Ibid, pp. 3-51 to 3-52

[47] Todd, D., Carino, N., and Chung, R. M, *1994 Northridge Earthquake; Performance of Structures, Lifelines and Fire Protection Systems,* NIST Special Publication, 862, Gaithersburg, MD, National Institute of Standards and Technology, (1994).

[48] Strand, C. L., *Gas Leaks, Gas-related Fires, and Performance of Seismic Gas Shutoff Valves During the Northridge Earthquake*, in **Proceedings of the 4th U.S. Conference, San Francisco, August 10-12, 1995**, (O'Rourke, M. J., ed.), Technical Council on Lifeline Earthquake Engineering, Monograph, No. 6., New York, N.Y., American Society of Civil Engineers, pp. 692-699 (1996).

[49] Scawthorn, C., Cowell, A. D., and Borden, F., *Fire-related Aspects of the Northridge Earthquake*, NIST GCR 98-743, Gaithersburg, MD, National Institute of Standards and Technology, 164 p. (1998).

[50] Strand, C. L., *Gas Leaks, Gas-related Fires, and Performance of Seismic Gas Shutoff Valves During the Northridge Earthquake*, in **Proceedings of the 4th U.S. Conference, San Francisco, August 10-12, 1995**, (O'Rourke, M. J., ed.), Technical Council on Lifeline Earthquake Engineering, Monograph, No. 6., New York, N.Y., American Society of Civil Engineers, p. 698, (1996).

[51] *Proceedings of the Sixth US-Japan Workshop on Earthquake Disaster Prevention of Lifeline Systems, July 1995, Osaka, Japan,* Berkeley, CA, Earthquake Engineering Research Institute (1996).

[52] Chung, R. M., Jason, N. H., Mohraz, B., et al., eds., *Post-earthquake Fire and Lifelines Workshop, Long Beach, California, January 30-31, 1995, Proceedings*, NIST Special Publication 889, Gaithersburg, MD, National Institute of Standards and Technology, pp. 29-33, (1995).

[53] Sekizawa, A., *Post-Earthquake Fires and Performance of Firefighting Activity in the Early Stages in the 1995 Great Hanshin Earthquake* in **Fire Safety Science - Proceedings of the Fifth International Symposium**, (Hasemi, Y, ed.), International Association for Fire Safety Science, p. 972, (1997).

[54] Ibid., p. 973

[55] Chung, R., ed., *The January 7, 1995 Hyogoken-Nanbu (Kobe) Earthquake; Performance of Structures, Lifelines, and Fire Protection Systems,* NIST Special Publication, 901, Gaithersburg, MD, National Institute of Standards and Technology, pp. 497-502, (1996).

[56] Botting , R., The Impact of Post-earthquake Fire on the Urban Environment, Fire Engineering Research Report 98/1, Christchurch, New Zealand, University of

Canterbury, School of Engineering, p. 233, (1998).

[57] Sekizawa, A., *Post-Earthquake Fires and Performance of Firefighting Activity in the Early Stages in the 1995 Great Hanshin Earthquake* in **Fire Safety Science - Proceedings of the Fifth International Symposium**, (Hasemi, Y, ed.), International Association for Fire Safety Science, p. 981, (1997).

[58] International Conference of Building Officials, *1997 Uniform Building* Code, Sec. 310.4 Whittier CA, pp. 1-26 to 1-27, (1997).

[59] Mallick, D. V., and Saud, A. F. B., *Post Earthquake Scenario, Proceedings of the 4th U.S. Conference, San Francisco, August 10-12, 1995,* in Technical Council on Lifeline Earthquake Engineering, Monograph, No. 6., (O'Rourke, M. J., ed.), New York, N. Y., American Society of Civil Engineers, pp. 779-786 (1996).

[60] Scawthorn, C., *Fire Following Earthquake,* in **Fire Safety Science, Proceedings of the First International Symposium** (eds. C. E. Grant, and P. J. Pagni), pp. 971-979, Washington, D.C., Hemisphere Publishing Corporation, (1986).

[61] National Fire Protection Association, *Fire Concepts Tree,* NFPA Standards 550, Quincy, MA, (1983).

[62] Groner, N. E., and Williamson, R. B., *Scenario-Based Goal Decomposition: A Method for Implementing Performance-Based Fire Safety Analysis*, presented at the 2nd International Conference on Fire Research and Engineering, National Institute of Standards and Technology, Gaithersburg, MD, August 10-15, 1997.

[63] Groner, N. E., *A Fire Department Guide to Evaluate Fire Emergency Plans,* presented at a Seminar for the California State Fire Chiefs Association, Oct. 18, 1989, San Luis Obispo, California, Sacramento, CA, Favro, McLaughlin & Associates, (1989).

[64] International Conference of Building Officials, *1997Uniform Building* Code, Sec. 310.4 , Whittier CA, p. 1-26, (1997).

[65] American Society for Testing and Materials, *Annual Book of ASTM Standards*, Vol. 04.07, West Conshohocken, PA, revisions issued annually.

[66] Botting , R., *The Impact of Post-earthquake Fire on the Urban Environment*, Fire Engineering Research Report 98/1, Christchurch, New Zealand, University of Canterbury, School of Engineering, p. 153, (1998). [Source: Cousins et al., *Fire Following Earthquake*, DSIR Physical Sciences, Lower Hutt, New Zealand, (1990)].

[67] American Society of Civil Engineers *Earthquake-actuated Automatic Gas Shutoff Devices,* ASCE Standard 25-97, Reston, VA (1998).

[68] Honegger, D. G., *Automatic Gas Shutoff Device Actuation Requirements Based on Damage in the Jan. 17, 1994 Northridge Earthquake*, a report for ASCE by EQE International, Inc., project 52316.01, San Francisco, CA (1995).

[69] Sullivan, Gene, P. G. & E., private communication, August 1999.

[70] Sullivan, Gene, P. G. & E., private communication, August 1999

[71] International Conference of Building Officials, *1997Uniform Building Code,* Table 5A, and Section 503, Whittier CA, pp. 1-51 & 1-57, (1997).

[72] Scawthorn, C., Cowell, et al. , *Fire-related Aspects of the January 17, 1994 Northridge Earthquake*, in **Proceedings of the 4th U.S. Conference, San Francisco, August 10-12,**

1995, (O'Rourke, M. J., ed.), Technical Council on Lifeline Earthquake Engineering, Monograph, No. 6. New York, N.Y., American Society of Civil Engineers, p. 688, (1996).

[73] Pagni, P. J., private communication.

[74] Sekizawa, A., *Post-Earthquake Fires and Performance of Firefighting Activity in the Early Stages in the 1995 Great Hanshin Earthquake* in **Fire Safety Science - Proceedings of the Fifth International Symposium,** (Hasemi, Y, ed.), International Association for Fire Safety Science, p. 972, (1997).

[75] Brenneman, J., private communication about the Boeing 727 accidents in Salt Lake City and New York in the late 1960's.